CODEN: JASMAN

ISSN: 0001-4966

The Journal of the Acoustical Society of America

Vol. 118, No. 4 October 2005

(Continued)

THE JOURNAL OF THE ACOUSTICAL SOCIETY OF AMERICA VOL. 118, NO. 4, OCTOBER 2005

CONTENTS—*Continued from preceding page*

(Continued)

THE JOURNAL OF THE ACOUSTICAL SOCIETY OF AMERICA VOL. 118, NO. 4, OCTOBER 2005

CONTENTS—*Continued from preceding page*

(Continued)

THE JOURNAL OF THE ACOUSTICAL SOCIETY OF AMERICA VOL. 118, NO. 4, OCTOBER 2005

CONTENTS—*Continued from preceding page*

ACOUSTICAL NEWS—USA

Elaine Moran
Acoustical Society of America, Suite 1NO1, 2 Huntington Quadrangle, Melville, NY 11747–4502

Editor's Note: *Readers of this journal are encouraged to submit news items on awards, appointments, and other activities about themselves or their colleagues. Deadline dates for news items and notices are 2 months prior to publication.*

New Fellows of the Acoustical Society of America

Kim C. Benjamin—For the development of underwater piezocomposite transducers.

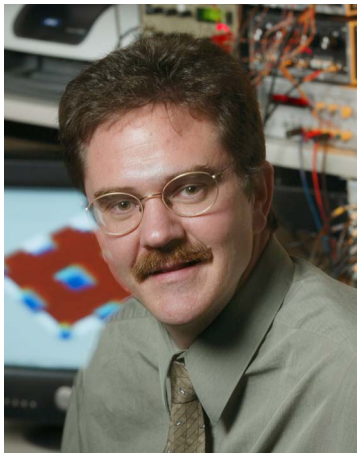

Robert L. Clark—For contributions to adaptive control of structural acoustic systems.

James P. Cottingham—For his work on free-reed musical instruments.

C. Craig Formby—For contributions to temporal processing in both normal and impaired human audition.

 0001-4966/2005/118(4)/2091/5/$22.50

Minority Fellowship Awarded to Bobby E. Gibbs

Bobby E. Gibbs, has been selected the recipient of the Acoustical Society of America's 2005 Graduate Fellowship for Minorities. Mr. Gibbs is a student at Rensselaer Polytechnic Institute School of Architecture in Troy, New York. He received his B.S. at Howard University and an M.M. degree from Bowling Green State University. He is working toward a M.S. degree at Rensselaer, where he will return in the fall to pursue his Ph.D.

The Acoustical Society of America established the Minority Fellowship in 1992 with the goal of supporting minority students in their pursuit of graduate-level degrees in acoustics. The scholarship is awarded for one year in odd numbered years and may be renewed. Recipients have been: Brian Scott, 1993; J. Sean Allan, 1997; Guillermo E. Aldana, 1999, Vernecia S. McKay 2001, David T. Bradley, 2002; and Gaylon C. Hollis, 2003.

For further information about the fellowship contact the Acoustical Society of America, Suite 1NO1, 2 Huntington Quadrangle, Melville, NY 11747-4502; Telephone: 516-576-2360; fax: 516-576-2377; e-mail: asa@aip.org; web:http://asa.aip.org

Jelena Krivokapic Selected Recipient of the 2005 Stetson Award

ASA member Jelena Krivokapic was selected the recipient of the 2005–06 Raymond H. Stetson Scholarship in Phonetics and Speech Production. Ms. Krivokapic is a graduate student in the Linguistics Department at the University of Southern California where she received an M.A. in Linguistics in 2003. Her current work is in examining the nature of prosodic boundaries with the main objective being to illuminate how prosodic structure is phonetically implemented.

The Stetson Scholarship, which was established in 1998, honors the memory of Professor Raymond H. Stetson, a pioneer investigator in phonetics and speech science. Its purpose is to facilitate the research efforts of promising graduate students and postgraduates. The Scholarship includes a $3000 stipend for one academic year. Past recipients have been Roger Steeve (1999), Elizabeth K. Johnson (2000), Jeffery Jones (2001), Meena Agarwal (2002), and Cynthia Clopper (2003).

Applications for the award are due in March each year. For further information about the award, please contact the Acoustical Society of America, Suite 1NO1, 2 Huntington Quadrangle, Melville, NY 11747-4502; Telephone: 516-576-2360; fax: 516-576-2377; e-mail: asa@aip.org; Web: http://asa.aip.org.

USA Meetings Calendar

Listed below is a summary of meetings related to acoustics to be held in the U.S. in the near future. The month/year notation refers to the issue in which a complete meeting announcement appeared.

	2006
9–12 February	46th Annual Convention, Illinois Speech-Language-Hearing Association, Rosemont, IL [ISHA, 230 E. Ohio St., Suite 400, Chicago, IL 60611-3265; Tel.: 312-644-0828; Fax: 315-644-8557; Web: www.aishil.org].
16–18 February	31st Annual Conference, National Hearing Conservation Association, Tampa, FL [NHCA, 7995 E. Prentice Ave., Suite 100 East, Greenwood Village, CO 80111-2710; Tel: 303-224-9022; Fax: 303-770-1614; E-mail: nhca@gwami.com; Web: www.hearingconservation.org].
6–9 June	151st Meeting of the Acoustical Society of America, Providence, Rhode Island [Acoustical Society of America, Suite 1NO1, 2 Huntington Quadrangle, Melville, NY 11747-4502; Tel.: 516-576-2360; Fax: 516-576-2377; E-mail: asa@aip.org; Web: http://asa.aip.org]. Deadline for receipt of abstracts: 24 January 2006.
17–21 September	INTERSPEECH 2006 (ICSLP 2006), Pittsburgh, PA [www.interspeech2006.org ⟨http://www.interspeech2006.org/⟩]
28 November–2 December	152nd Meeting of the Acoustical Society of America joint with the Acoustical Society of Japan, Honolulu, Hawaii [Acoustical Society of America, Suite 1NO1, 2 Huntington Quadrangle, Melville, NY 11747-4502; Tel.: 516-576-2360; Fax: 516-576-2377; E-mail: asa@aip.org; WWW: http://asa.aip.org]. Deadline for receipt of abstracts: 30 June 2006.
	2007
4–8 June	153rd Meeting of the Acoustical Society of America, Salt Lake City, Utah [Acoustical Society of America, Suite 1NO1, 2 Huntington Quadrangle, Melville, NY 11747-4502; Tel.: 516-576-2360; Fax: 516-576-2377; E-mail: asa@aip.org; WWW: http://asa.aip.org].
27 November–2 December	154th Meeting of the Acoustical Society of America, New Orleans, Louisiana (note Tuesday through Saturday) [Acoustical Society of America, Suite 1NO1, 2 Huntington Quadrangle, Melville, NY 11747-4502; Tel.: 516-576-2360; Fax: 516-576-2377; E-mail: asa@aip.org; WWW: http://asa.aip.org].
	2008
28 July–1 August	9th International Congress on Noise as a Public Health Problem (Quintennial meeting of ICBEN, the International Commission on Biological Effects of Noise). Foxwoods Resort, Mashantucket, CT [Jerry V. Tobias, ICBEN 9, Post Office Box 1609; Groton, CT 06340-1609, Tel: 860-572-0680; Web: www.icben.org; E-mail icben2008@att.net].

Cumulative Indexes to the Journal of the Acoustical Society of America

Ordering information: Orders must be paid by check or money order in U.S. funds drawn on a U.S. bank or by Mastercard, Visa, or American Express credit cards. Send orders to Circulation and Fulfillment Division, American Institute of Physics, Suite 1NO1, 2 Huntington Quadrangle, Melville, NY 11747-4502; Tel.: 516-576-2270. Non-U.S. orders add $11 per index.

Some indexes are out of print, as noted below.

Volumes 1–10, 1929–1938: JASA, and Contemporary Literature, 1937–1939. Classified by subject and indexed by author. Pp. 131. Price: ASA members $5; nonmembers $10.epepep.

Volumes 11–20, 1939–1948: JASA, Contemporary Literature and Patents. Classified by subject and indexed by author and inventor. Pp. 395. Out of print.

Volumes 21–30, 1949–1958: JASA, Contemporary Literature and Patents. Classified by subject and indexed by author and inventor. Pp. 952. Price: ASA members $20; nonmembers $75.

Volumes 31–35, 1959–1963: JASA, Contemporary Literature and Patents.

Classified by subject and indexed by author and inventor. Pp. 1140. Price: ASA members $20; nonmembers $90.

Volumes 36–44, 1964–1968: JASA and Patents. Classified by subject and indexed by author and inventor. Pp. 485. Out of print.

Volumes 36–44, 1964–1968: Contemporary Literature. Classified by subject and indexed by author. Pp. 1060. Out of Print.

Volumes 45–54, 1969–1973: JASA and Patents. Classified by subject and indexed by author and inventor. Pp. 540. Price: $20 (paperbound); ASA members $25 (clothbound); nonmembers $60 (clothbound).

Volumes 55–64, 1974–1978: JASA and Patents. Classified by subject and indexed by author and inventor. Pp. 816. Price: $20 (paperbound); ASA members $25 (clothbound); nonmembers $60 (cloth bound).

Volumes 65–74, 1979–1983: JASA and Patents. Classified by subject and indexed by author and inventor. Pp. 624. Price: ASA members $25 (paperbound); nonmembers $75 (clothbound).

Volumes 75–84, 1984–1988: JASA and Patents. Classified by subject and indexed by author and inventor. Pp. 625. Price: ASA members $30 (paperbound); nonmembers $80 (clothbound).

Volumes 85–94, 1989–1993: JASA and Patents. Classified by subject and indexed by author and inventor. Pp. 736. Price: ASA members $30 (paperbound); nonmembers $80 (clothbound).

Volumes 95–104, 1994–1998: JASA and Patents. Classified by subject and indexed by author and inventor. Pp. 632, Price: ASA members $40 (paperbound); nonmembers $90 (clothbound).

Volumes 105–114, 1999–2003: JASA and Patents. Classified by subject and indexed by author and inventor. Pp. 616, Price: ASA members $50; nonmembers $90 (paperbound).

REVISION LIST

New Associates

Bird, Michael T., 2636 Worden St., Unit 128, San Diego, CA 92110

Bogomolov, Elizabeth, The Greenbusch Group, 1900 West Nickerson St., Seattle, WA 98119

Buma, Corjan, ACI Acoustical Consultants Inc., 107, 9920 63rd Ave., Edmonton AB T6E 0G9 Canada

Carey, Anne L., Faculty of Engineering, Sci. and Built Eng., London South Bank Univ., 103 Borough Rd., Soothwark, London SE1 0AA, U.K.

Cavuto, Silvio, via San Geminiano, 5, Albinea, RE I-42020 Italy

Cipolla, Jeffrey L., Applications Development, Abaqus, Inc., 166 Valley St., Providence, RI 02909

Clukey, Jeffrey W., Charles M. Salter Associates, Inc., 325 South First St., Ste. 160, San Jose, CA 95113

Davis, Steven A., Lewis Goodfriend & Associates, 760 Route 10 West, Whippany, NJ 07981-1159

DeStephen, Anthony, 27716 Mt. Pleasant Rd., Columbus, NJ 08022

Dolman, Sarah J., WDCS, 28 St. Paul St., Chippenham, Wiltshire, SN15 1LJ, U.K.

Faber, Benjamin, 3047 East Canyon Crest Dr., Spanish Fork, UT 84660

Figueroa, Juan M., Advanced Scientific Applications, Privada 31 Oriente #2015, Puebla 72540, Mexico

Flood, Jane D., Physics Dept., Muhlenberg College, 2400 Chew St., Allentown, PA 18104

Gaddis, David J., SenSound, LLC, 221 Lewiston, Grosse Pointe Farms, MI 48236-3519

Galloway, Michael A., Northrop Grumman, Loads & Dynamics, 2000 West NASA Blvd., MS 8454/H08-223, Melbourne, FL 32904

Ghering, Marcia J., Naval and Maritime Systems, Northrop Grumman Corporation, P.O. Box 1488, MS 9910, Annapolis, MD 21404

Gough, Colin E., Physics and Astronomy, Univ. of Birmingham, P.O. Box 363, Birmingham B15 2TT, U.K.

Guldberg, Peter H., Tech. Environmental, Inc., 1601 Trapelo Rd., Waltham, MA 02451

Ito, Mika, UCLA, Head and Neck Surgery, 31-24 Rehab Ctr., 1000 Veteran Ave., Rm. 31-24, Los Angeles, CA 90095-1794

Jessop, Andrew M., Wilson, Ihrig Associates, Inc., 5776 Broadway, Oakland, CA 94618

Jiang, Yongmin, Ctr. for Earth and Ocean Research, Univ. of Victoria, E-Hutt 122, P.O. Box 3055, Victoria BC V8W 3P6, Canada

Jinhoi, Gu, Mechanical Engineering, Inha Univ., Yong Hyun 3-Dong, Incheon 402-751, South Korea

John, Christoph A., BiJohnic, Erasmusstr. 2-8, Rottenburg D-72076, Germany

Johnston, Peter J., AJAAC, HMAS Albatross, Nowra NSW 2540, Australia

Jones, David M., HFP Acoustical Consultants, Inc., 6001 Savoy Dr., Ste. 115, Houston, TX 77036

Juliusson, Halldor K., VST Ltd., Armuli 4, Reykjavik IS 108, Iceland

Koeppel, Robert J., Koeppel Communications, 767 West Omaha Ave., Clovis, CA 93619

Leigh, Charlotte V., Applied Physics Lab., Univ. of Washington, Box 355640, Seattle, WA 98139

Leisses, Mary E., Envoy Medical, Audiology, 5301 East River Rd., Ste. 113, Minneapolis, MN 55421

Madsen, Peter T., Caryn House #44, Woods Hole House 266, Woods Hole, MA 02543

Martinez, Charles D., VA Greater LA Healthcare System, 11301 Wilshire Blvd., Los Angeles, CA 90073

McBride, Ingrid K., Arizona State Univ., Dept. of Speech & Hearing Science, P.O. Box 870102, Tempe, AZ 85287-0102

Mohan, William L., 336 Old Sutton Rd., Barrington, IL 60010

Moore, Elliot, Electrical and Computer Engineering, Georgia Inst. of Technology, 210 Technology Cir., Savannah, GA 31407-3039

Oh, Sunyoung, 2495 Van Horne, #4, Montreal QC H3S 1P4, Canada

Ohkawa, Keiichi, The Research Ctr., TRDI, JDA, 3-13-1 Nagase, Yokosuka, Japan

Orlowski, Michael P., Alpine Vista Home Theaters, P.O. Box 8599, Breckenridge, CO 80424

Park, Seok Tae, Dept. of Acoustical Engineering, Juseong College, SATIC, 201-31, Choengju, Korea

Parthasarathi, Anand A., Bose Corporation, MS 15C, R&D Bldg., The Mountain, Framingham, MA 01701

Picaut, Judicael, Section Acoustique Routiere dt Urbaine, Lab. Central des Ponts et Chaussees, Route de Bouaye, BP 4129, 44341 Bouguenais, Cedex, France

Rafaelof, Menachem, Seagate Technology, 389 Disc Dr., Longmont, CO 80503

Reaves, David P., Speckhorner Str. 215, Recklinghausen NRW 45659, Germany

Reid, Ceri S., 31 Bruntsfield Ave., Edinburgh EH10 4EN, U.K.

Roads, Curtis B., Media Arts and Technology, Univ. of California, 3431 South Hall, Santa Barbara, CA 93106-6065

Robert, Jean-Luc F.M., Philips Research, Healthcare & It, 345 Scarborough Rd., Briarcliff Manor, NY 10510

Roh, Heui-Seol, 805 College Hill Rd., Apt. 6, Oxford, MS 38655

Rowan, Daniel, ISVR, Univ. of Southampton, University Rd., Southampton SO17 1BJ, U.K.

Schulley, Robert D., 3469 Oyster Bay Ave., Davis, CA 95616-5605

Scofano, Antonio, Aermacchi SPA, via Forosio 1, Venegono Sup., Varese 21040, Italy

Scott, David E., Devasco International, Inc., 9618 West Tidwell Rd., Houston, TX 77041

Shearer, John C., Wilson, Ihrig and Associates, Inc., 5776 Broadway, Oakland, CA 94618

Shouichi, Takane, Electronics and Information Systems, Akita Prefectural Univ., 84-4 Ebinokuchi, Tsuchiya, Yurihonjo, Akita, Japan

Sutanto, Ron J., Pacific American Company, 3172 North Rainbow Blvd., Ste. 119, Las Vegas, NV 89108-5354

Sykes, David M., The Remington Group LP, 23 Buckingham St., Cambridge, MA 02138

Symko, Orest G., Dept. of Physics, Univ. of Utah, 115 South 1400 East, Rm. 201, Salt Lake City, UT 84112-0830

Takaso, Hideki, Dept. of Communication Sciences and Disorders, Northwestern Univ., 2249 Campus Dr., Evanston, IL 60208

Tomlinson, Gary E., 34 Cambria Dr., Bella Vista, AR 72715

Tougaard, Jakob, National Environmental Research Inst., Arctic Environment, 399 Frederikborgvej, P.O. Box 359, Roskilde, DK-4000, Denmark

Troyan, Joseph V., Electrical Engineering, Eckles Architecture, New Castle, PA 16101

Wadsworth, Glenn J., National Security Technology Dept., The Johns Hopkins Univ., Applied Physics Lab., 11100 Johns Hopkins Rd., Laurel, MD 20723-6099

Walls, Chris P., 39 New Rd., Clanfield, Hampshire, PO8 0NR, U.K.

Weber, Michael, MSW Consulting, 2023 'N' St., Ste. 205, Sacramento, CA 95814
Wellington, James T., Systems Engineering, Sonic Innovations, 2795 East Cottonwood Parkway, Ste. 660, Salt Lake City, UT 84121-7036
Wilkie, Zach B., SPL Control, Inc., 1400 Bishop St., Oakville ON N1R 6W8, Canada
Wolfe, Eric, 1521 NE 95th St., Seattle, WA 98115
Yasutaka, Ueda, Hazama Corp., 515-1 Nishimukai Karima, Tsukuba City, Ibaraki 305-0822, Japan
Yeung, Maurice K.L., Flat F, 16/F, Block 2, Ronsdale Garden, 25, TA, Hang Dr., Hong Kong
Yoshinobu, Kajikawa, Kansai Univ., Dept. of Electronics, Faculty of Engineering, 3-3-35,Yamate-cho, Japan

New Students

Acikgoz, Serhan, Mechanical Engineering, Univ. of Illinois at Chicago, 847 West Taylor, ERF 2039, Chicago, IL 60607
Amiri, Hadi, No. 164, Shahran St., Tehran, 14788-53545, Iran
Atkins, Joshua D., Electrical Engineering, Johns Hopkins Univ., 3400 North Charles St., Baltimore, MD 21218
Bader, Kenneth B., Physics, Grand Valley State Univ., 125 Padnos, One Campus Dr., Allendale, MI 49401
Barroso, Celia, 3556 Maplewood Ave., Los Angeles, CA 90066
Belanger, Andrea J., Biological Sciences, Univ. of Windsor, 401 Sunset Ave., Windsor, ON N9B 3P4, Canada
Bohm, Tamas M., 7 Fulkerson St., Apt. 3, Cambridge, MA 02141
Bollinger, Benjamin R., Thayer School of Engineering, Dartmouth College, 8000 Cummings Hall, Hanover, NH 03755
Boone, Andrew J., Brigham Young Univ., Mechanical Engineering, 435 CTB, Provo, UT 84602
Brown, Jason C., 79 West 17th Ave., Vancouver, BC V5Y 1Z5, Canada
Canney, Michael, Univ. of Washington, Bioengineering, 1013 NE 40th St., Seattle, WA 98105
Cardillo, Gina C., Speech and Hearing Sciences, 1417 NE 42nd St., Box 354875, Seattle, WA 98105
Carmignani, Dario, Via Quintino Sella 26, Busto Arsizio 21052, Italy
Carr, Suzanne P., Biomedical Engineering, Boston Univ., 44 Cummington St., Boston, MA 02215
Chen, Hsuan-fang S., Graduate Inst. of Linguistics, National Taiwan Univ., 1, Sec. 4, Roosevelt Rd., Taipei 106, Taiwan
Clark, Linde J., Graduate Program in Acoustics, Pennsylvania State Univ., P.O. Box 30, State College, PA 16804
Cornish, Jennifer L., 144 Ayrault Dr. (Upper), Amherst, NY 14228
Cosharek, Elizabeth, Graduate Program in Acoustics, Pennsylvania State Univ., P.O. Box 30, State College, PA 16804
Costantino, Tony, Univ. of Notre Dame, Hessert Lab. for Aerospace Research, Aerospace Engineering, Notre Dame, IN 46556
Crosby, Justin D., 1068 Westshire Place, NW, Atlanta, GA 30318
Escolano, Jose, Avenida Consititucion 49 2G, Novelda, Alicante E-03660, Spain
Grandhi, Gangadhar, NCA & TSU, 1601 East Market St., Greensboro, NC 27411
Graybill, Justin, Univ. of Salford, Greater Manchester M5 4WT, UK
Greg, Okopal N., 146 Mayer Dr., Oakdale, PA 15071
Gregory, James W., 106 Sylvia St., West Lafayette, IN 47906-2925
Gridley, Teresa, Univ. of Aberdeen, Zoology, Lighthouse Field Station, George St., Cromarty, Ross-shire IV11 8YJ, Great Britain
Hattori, Kota, 2615 Varsity Place, #1D, Honolulu, HI 96826
Ingle, Jennifer K., Linguistics, Univ. of Washington, Box 354340, Seattle, WA 98195-4340
Israr, Ali, Mechanical Engineering, Purdue Univ., 465 Northwestern Ave., West Lafayette, IN 47907
Jensen, Carl R., NCPA, Univ. of Mississippi, 1 Coliseum Dr., University, MS 38677
Jung, Ki Won, Graduate Program in Acoustics, Pennsylvania State Univ., P.O. Box 30, University Park, PA 16802
Kang, Kyoung-Ho, 2040 West 17th Ave., #2040, Eugene, OR 97402
Kim, Sungyoung, McGill Univ., Strathcona Music Building, Rm. E203, 555 Sherbrooke West, Montreal QC H3A 1E3, Canada
Kluk, Karolina, 134B Cherry Hinton Rd., Cambridge, CB1 7AJ, UK
Konopka, Kenneth, Linguistics, Northwestern Univ., 2016 Sheridan Rd., Evanston, IL 60208
Kwon, Bo-Young, Linguistics, Michigan State Univ., A-614 Wells Hall, East Lansing, MI 48824-1027
Lee, YoungHan, DIC 216, Gwangju Inst. of Sci. and Tech., 1 Oryong-dong, Buk-gu, Jeollanam-do, Gwangju, 500 712, Korea
Link, Andreas, Lehrstuhl Fuer Technische Elektronik, Univ. of Erlangen, Cauerstrasse 9, Erlangen 91058, Germany
Luangvilai, Kritsakorn, Civil Engineering, Georgia Inst. of Technology, 790 Atlantic Dr., Atlanta, GA 30332
Mao, Xiaoan, School of Engineering, Univ. of Manchester, Goldstein Research Lab., Liverpool Rd., Manchester, M30 7RU, Great Britain
Martin, Bryn A., Mechanical Engineering, Univ. of Illinois at Chicago, Rm. 2037 ERF , 842 West Taylor St., Chicago, IL 60607
Mathias, Delphine, 12 bis rue guichen, Brest 29200, France
Maxwell, Adam D., Ctr. for Industrial and Medical Ultrasound, Applied Physics Lab., 1013 NE 40th St., Seattle, WA 98105
Mehta, Daryush, 70 Pacific St., Apt. 516, Cambridge, MA 02139
Meigh, Kimberly M., 1866 Jancey St., Pittsburgh, PA 15206
Melendez, Karla, Neuroscience, Univ. of Illinois Urbana-Champaign, 405 North Mathews Ave., Urbana, IL 61801
Michaud, Alexander P., 3831 Fenway Crossing, Marietta, GA 30062
Mirante, Nicole, 5-1208 Salsbury Dr., Vancouver, BC V5L 4B2, Canada
Monten, Fabian, Lyckans vag 52, Kristianstad 291-43, Sweden
Morrison, Geoffrey S., Dept. of Linguistics, Univ. of Alberta, 4-32 Assiniboia Hall, Edmonton, AB T6G 2E7, Canada
Nadjm, Mahmood, 36 Brunel Close, Micheldever, Winchester, Hampshire, SO21 3BX, U.K.
Namdaran, Nahal, 2070 Rufus Dr., North Vancouver, BC V7J 3P9, Canada
Nordstrom, Karl L., 4036 Cumberland Rd., Victoria BC, V8X 2E6, Canada
Olsen, Stephanie A., 2060 Frederick Norris Rd., Victoria, BC V8P 2B2, Canada
Owns, Thomas, 5052 Cassia Dr., Pensacola, FL 32506
Philips, Scott M., Electrical Engineering, Univ. of Washington, Campus Box 352500, Seattle, WA 98195-2500
Prieto, Alvaro F., Aerospace Eng., Georgia Inst. of Technology, 270 Ferst Dr., Atlanta, GA 30332-0150
Rife, David J., 114 South Elson, Apt. 2, Kirksville, MO 63501
Roxworthy, John S., Mechanical and Industrial Eng., Univ. of Illinois at Chicago, 842 West Taylor St., Rm. 2039, Chicago, IL 60607
Ruvalcaba, Mario D., Garcia-BBM, cC/Madrid 2 Oficina 11, Colmenar Viejo, Madrid 28770, Spain
Sandrich, Eric, Music Synthesis, Berklee College of Music, 150 Massachusetts Ave., Boston, MA 02215
Segnini, Rodrigo, Stanford Univ., CCRMA Music Dept., 660 Lomita Dr., Stanford, CA 94305
Sodagar, Sina, Mechanical Engineering, K.N. Toosi Univ. of Technology, P.O. Box 16765-3381, Tehran, Iran
Terry, Sean D., 5506 West 128th Place, Crestwood, IL 60445
Thompson, James J., 1126 Salsbury Dr., Vancouver, BC V5L 4A8, Canada
Thomson, Ronald I., #222, 2327 119 St., Edmonton, AB T6J 4E2, Canada
Tsai, Kuen-Shian, Inst. of Biomedical Engineering, National Yang-Ming Univ., No. 155 Li-Nong St., Sec. 2, Taipei, 112 Taiwan
Uglova, Nataliya, Usachova St. 62-515, Moscow 119048, Russia
Urban, Matthew W., Dept. of Physiology and Biomedical Eng., Mayo Clinic and Foundation, 200 First St., SW, Rochester, MN 55905
Van Heukelem, Kristin J., Linguistics, Northwestern Univ., 2016 Sheridan Rd., Evanston, IL 60208
Vogt, Florian, Electrical and Computer Engineering, Univ. of British Columbia, 2356 Main Mall, Vancouver, BC V6T 1Z4, Canada
Wall, Bob, 222 Westridge Dr., Bozeman, MT 59715
Williams, Erica J., Speech and Hearing Science, Arizona State Univ., P.O. Box 870102, Tempe, AZ 85281
Woolston, Scott R., Acoustics Research Group — BYU, Mechanical Engineering, N283 ESC, Provo, UT 84604
Zhang, Yan, Georgia Inst. of Technology, 247 4th St., Atlanta, GA 30332
Zhang, Yuxuan, Northwestern Univ., Commun. Sciences & Disorders, 2240 North Campus Dr., Evanston, IL 60208

New Electronic Associates

Abramson, Marianne, California State Univ., Bakersfield, Psychology, 9001 Stockdale Highway, Bakersfield, CA 93311-1022
Anraku, Kazuhiko, Faculty of Fisheries, Kagoshima Univ., 4-50-20 Shimoarata, Kagoshima 890-0056, Japan
Bernasconi, Giancarlo, Dip. Elettronica e Informazione, Politecnico di Milano, Piazza L. da Vinci 32, Milano 20133, Italy
Ceranna, Lars, Stillewect 2, Hannover 30655, Germany
Faller, Christof, EPFL/LCAV, BC 366, Station 14, Laussane VD 1015, Switzerland
Fuka, Mary Z., Colorado Physics Consultants, 1035 Pearl St., Boulder, CO 80302
Gamba, Jonah M., Denso IT Lab., Inc., Shibuya Prestige, 6th Floor, 3-12-22 Shibuya-Ku, Tokyo 150-0002, Japan
Gent, Robert J., Paediatric Ultrasound, Women's and Children's Hospital, 72 King William Rd., North Adelaide, Adelaide SA 5006 Australia
Grobaski, Thomas C., 1519 North Rolfe St., Arlington, VA 22209
Igarashi, Yosuke, RIKEN Brain Science Inst., Lab. for Language Development, 2-1 Hirosawa, Wako, Saitama, 351-0198, Japan
Jacobs, Arnaud, Luchtvaartsquare 19, Brussels 1070, Belgium
Jeong, Jeong Ho, School of Architectural Eng., Hanyang Univ., 17 Haedangdong, Seongdonggu, Seoul 133-791, Korea
Khan, Tahseen A., B-17, Block 11, F. B. Area, Karachi 75950, Pakistan
Kloss, Claudia, 41 Sunset Ave., #204, Venice, CA 90291
Kong, Ying-Yee, MRC Cognition & Brain Sciences Unit, 15 Chaucer Rd., Cambridge, CB2 2EF, U.K.
Kuhn, Frank R., Air and Noise Compliance, 26 Chandler Ave., Ste. 14, Plaistow, NH 03865
Latimer, Mark A., 2753 Lakeview Dr., Santa Rosa, CA 95405
Owen, Megan A., Office of Giant Panda Conservation, Zoological Society of San Diego, 2920 Zoo Dr., San Diego, CA 92101-1649
Pierce, Carol D., Sound Pharmaceuticals, 4010 Stone Way, North, Seattle, WA 98028,
Riddle, Alfred N., Macallan Consulting, 1583 Pinewood Way, Milpitas, CA 95035
Sandrin, Laurent, Echosens, R&D, 32 Rue Des Jeuneurs, Paris 75002, France
Shakespeare, Simon A., 1 Weavers Field, Giton, Cambridge, Cambridgeshire CB3 0XB, U.K.
Sperber, Ray, SES Astra, Chateau de Betzdorf, Betzdorf L-6815, Luxembourg
Totten, Donald J., 3414 Heather Brook, Macedon, NY 14502
Ucar, Umit, Old Dominion Univ., Norfolk, VA 23507
Wong, Kainan T., 1517 South Palm Ave., #G, San Gabriel, CA 91776

New Corresponding Electronic Associates

Giner, Jose C., Rue Bartira 1430, Ste. 63, Sao Paulo 05009-000, Brazil
Kim, Youngshin, Dept. of Environmental Marine Science, Ocean Acoustics Lab., 1271 Sa-1-dong, Sangrok-gu, Ansan, Gyunggi-do, Korea
Upegui Fernandez, Juan F., Copacabana Antioquia, Antioquia 4, Colombia
Umat, Cila, Univ. Kebangsaan Malaysia, Dept. of Audiology & Speech Sciences, Jalan Raja Muda Abdul Aziz, Kuala Lampur, WP 50300

Reinstated

E. M. Benjamin, S. A. Kostarev, H. Sakai—*Members*
D. Lord, B. G. L. Vaupel—*Associates*

Members Elected Fellows

W. Ahnert, K. C. Benjamin, C. C. Church, R. L. Clark, Jr., J. P. Cottingham, C. C. Formby, S. N. Y. Gerges, S. M. Gracewski, K. W. Grant, P. A. Johnson, J. M. Kates, Q. H. Liu, P. B. Nelson, J-X. Zhou

Associates Elected Members

R. Berger, S. Clements, I. Lucifredi, D. F. Macomber, P. P. Mitra, S. S. Narayanan, Y. Qin, C. R. Kastak, T. J. Royston, R. E. Thomas, P. J. Wolfe

Students to Associates

O. S. Blacklock, M. G. Colburn, W. F. Conklin, M. J. Daley, Y-S. Lai, I. N. Pieleanu, R. M. Sa Ribeiro, S. Shirai, J. K. Spiewla

Associates to Electronic Associate

L. Lachs, P. Marvit, G. D. Meegan

Associate to Corresponding Electronic Associate

D-G. Paeng

Student to Electronic Associate

S. V. Levi, A. Sarampalis, L. S. J. Tsaih

Associate to Student

J. C. Vick

Resigned

L. B. Felsen—*Fellow*
Y. T. Didenko, M. R. Jones, H. Suzuki—*Members*
R. A. Griffin, N. S. Hockley—*Associates*
M. Aida—*Student*

Deceased

S. J. Bolanowski, Jr., F. H. Fisher, E. M. Kerwin, Jr., G. Krishnappa, F. L. Lizzi, H. S. Ribner, Fellows
J. S. Lukas, D. R. Milsom, L. P. Mulcahy, H. A. Newby, C. M. Sroka, M. Szponka—*Members*

Fellows	888
Members	2299
Associates	2656
Students	969
Electronic Associates	454
	7266

ACOUSTICAL NEWS—INTERNATIONAL

Walter G. Mayer
Physics Department, Georgetown University, Washington, DC 20057

International Meetings Calendar

Below are announcements of meetings and conferences to be held abroad. Entries preceded by an * are new or updated listings.

October 2005

12–14 **Acoustics Weeks in Canada** (London, Ontario, Canada; Web: caa-aca.ca).

17–18 **Wind Turbine Noise: Perspectives for Control**, Berlin, Germany (G. Leventhall, 150 Craddocks Avenue, Ashtead Surry KT21 1NL, UK; Fax: +44 1372 273 406; Web: www.windturbinenoise2005.org).

19–21 **36th Spanish Congress on Acoustics Joint with 2005 Iberian Meeting on Acoustics**, Terrassa (Barcelona), Spain (Sociedad Española de Acústica, Serrano 114, 28006 Madrid, Spain: Fax: +34 914 117 651; Web: www.ia.csic.es/sea/index.html).

25–26 **Autumn Conference 2005 of the UK Institute of Acoustics**, Oxford, UK (Web: www.ioa.org.uk).

27–28 **Autumn Meeting of the Acoustical Society of Switzerland**, Aarau, Switzerland (Web: www.sga-ssa.ch).

November 2005

4–5 **Reproduced Sound 21**, Oxford, UK (Web: www.ioa.org.uk).

9–11 **Australian Acoustical Society Conference on "Acoustics in a Changing Environment,"** Busselton, WA, Australia (Web: www.acoustics.asn.au/divisions/2005-conference.shtml).

14–18 **XVI Session of the Russian Acoustical Society**, Moscow, Russia (Web: www.akin.ru).

16–18 *__26th Symposium on Ultrasonic Electronics__, Yokohama, Japan (Web: www.use-jp.org/index.html).

December 2005

7–9 **Symposium on the Acoustics of Poro-Elastic Materials**, Lyon, France (Fax: +33 4 72 04 70 41; Web: v0.intellagence.eu.com/sapem2005).

January 2006

5–7 **First International Conference on Marine Hydrodynamics**, Visakhapatnam, India (V. B. Rao, Naval Science & Technological Laboratory, Vigyan Nagar, Visakhapatnam-530 027, India; Web: www.mahy2006.com).

17–19 *__Anglo-French Physical Acoustics Conference__, Wye College, Kent, UK (www.ioa.org.uk/viewupcoming.asp).

March 2006

14–16 *__Spring Meeting of the Acoustical Society of Japan__, Tokyo, Japan (Acoustical Society of Japan, Nakaura 5th-Bldg., 2-18-20 Sotokanda, Chiyoda-ku, Tokyo 101-0021, Japan; Fax: +81 3 5256 1022; Web: www.asj.gr.jp/index-en.html).

20–23 **Meeting of the German Acoustical Society (DAGA 2006)**, Braunschweig, Germany (Web: www.daga2006.de).

April 2006

24–27 *__French Congress on Acoustics__, Tours, France (Web: www.lussi.univ-tours.fr).

May 2006

2–5 *__International Conference on Speech Prosody 2006__, Dresden, Germany (Web: www.ias.et.tu-dresden.de/sp2006).

15–19 **IEEE International Conference on Acoustics, Speech, and Signal Processing**, Toulouse, France (Web: icassp2006.org)

23–26 *__17th Session of the Russian Acoustical Society__, Moscow, Russia (Web: www.akin.ru).

30–1 **6th European Conference on Noise Control (EURONOISE2006)**, Tampere, Finland (Fax: +358 9 7206 4711; Web: www.euronoise2006.org).

June 2006

12–15 *__8th European Conference on Underwater Acoustics__, Carvoeiro, Portugal (Web: www.euca2006.org).

26–28 **9th Western Pacific Acoustics Conference (WESPAC 9)**, Seoul, Korea (Web: wespac9.org).

July 2006

3–7 **13th International Congress on Sound and Vibration (ICSV13)**, Vienna, Austria (Web: info.tuwienac.at/icsv13)

17–20 **International Symposium for the Advancement of Boundary Layer Remote Sensing (ISARS13)**, Garmisch-Partenkirchen, Germany (Fax: +49 8821 73 573; Web: imk-ifu.fzk.de/isars)

17–19 **9th International Conference on Recent Advances in Structural Dynamics**, Southampton, UK (Web: www.isvr.soton.ac.uk/sd2006/index.htm).

September 2006

13–15 **Autumn Meeting of the Acoustical Society of Japan**, Kanazawa, Japan (Acoustical Society of Japan, Nakaura 5th-Bldg., 2-18-20 Sotokanda, Chiyoda-ku, Tokyo 101-0021, Japan; Fax: +81 3 5256 1022; Web: www.asj.gr.jp/index-en.html).

18–20 **International Conference on Noise and Vibration Engineering (ISMA2006)**, Leuven, Belgium (Fax: 32 16 32 29 87; Web: www.isma-isaac.be).

November 2006

20–22 **1st Joint Australian and New Zealand Acoustical Societies Conference**, Christchurch, New Zealand (Web: www.acoustics.org.nz).

July 2007

9–12 **14th International Congress on Sound and Vibration (ICSV14)**, Cairns, Australia (E-mail: n.kessissoglou@unsw.edu.au).

August 2007

27–31 **Interspeech 2007**, Antwerp, Belgium (E-mail: conf@isca-speech.org).

 0001-4966/2005/118(4)/2097/2/$22.50

September 2007

2–7 **19th International Congress on Acoustics (ICA2007)**, Madrid, Spain (SEA, Serrano 144, 28006 Madrid, Spain; Web: www.ica2007madrid.org).

9–12 **ICA Satellite Symposium on Musical Acoustics (ISMA2007)**, Barcelona, Spain (SEA, Serano 144, 28006 Madrid, Spain: Web: www.ica2007madrid.org).

June 2008

30–4 **Joint Meeting of European Acoustical Association (EAA), Acoustical Society of America (ASA), and Acoustical Society of France (SFA)**, Paris, France (E-mail: phillipe.blanc-benon@ec-lyon.fr; Web: www.sfa.asso.fr).

July 2008

28–1 **9th International Congress on Noise as a Public Health Problem**, Mashantucket, Pequot Tribal Nation (ICBEN 9, P.O. Box 1609, Groton, CT 06340-1609, USA: Web: www.icben.org).

Preliminary Announcements

October 2006

3–6 **IEEE Ultrasonics Symposium**, Vancouver, BC, Canada (TBA).

August 2010

TBA **20th International Congress on Acoustics (ICA2010)**, Sydney, Australia (Web: www.acoustics.asn.au).

A special honor for Academician Brekhovskikh

The next meeting of the Russian Acoustical Society (May 2006) will include in its program a special Seminar in memory of Academician Leonid Maksimovich Brekhovskikh (1917–2005) honoring him for his many theoretical studies of sound wave propagation in layered and inhomogeneous media.

BOOK REVIEWS

P. L. Marston
Physics Department, Washington State University, Pullman, Washington 99164

These reviews of books and other forms of information express the opinions of the individual reviewers and are not necessarily endorsed by the Editorial Board of this Journal.

*Editorial Policy: If there is a negative review, the author of the book will be given a chance to respond to the review in this section of the Journal and the reviewer will be allowed to respond to the author's comments. [See "Book Reviews Editor's Note," J. Acoust. Soc. Am. **81**, 1651 (May 1987).]*

Mathematical Theory of Diffraction

Arnold Sommerfeld

Translated by Raymond Nagem, Mario Zampolli, and Guido Sandri

Series on Progress in Mathematical Physics, Birkhauser, Boston, 2003 157 pp., Price $54.95 (hardcover). ISBN: 0817636048.

This book begins with a brief description of the history of the theory of diffraction prior to Sommerfeld's article and the historic importance of this article. Divided into two portions, the first part of the book is the translation of Sommerfeld's article. The second part is a collection of notes by the translators on various sections of the article. The only complaint I have is that the separation of the translation and translators' notes requires the reader to constantly page back and forth between the translation and the notes. A more appealing organization would be to merge the two sections into a coherent text, where the notes are italicized or placed in side bars. However, the translators' notes are well written and offer fruitful insights into Sommerfeld's work.

Sommerfeld's article presents a generalization of conformal mapping used in the construction of solutions of the Laplace equation to one that constructs solutions of the Helmholtz equation from analytic functions; that is, Sommerfeld describes a process by which a solution of the Laplace equation is transformed into an equivalent solution of the Helmholtz equation. Let $\varsigma = x + iy$ be the complex coordinates of a point in the xy plane. The Cauchy-Riemann conditions are of the following form:

$$\frac{\partial^2}{\partial \varsigma\, \partial \bar{\varsigma}} f = \frac{\partial^2}{\partial x^2} f + \frac{\partial^2}{\partial y^2} f = 0, \quad \frac{\partial^2}{\partial \varsigma\, \partial \bar{\varsigma}} f - \frac{\partial^2}{\partial \bar{\varsigma}\, \partial \varsigma} f = 0,$$

which is equivalent to requiring the function $f(x,y)$ be a solution of the two-dimensional Laplace equation. The above equation is satisified by any holomorphic or antiholomorphic function in the complex plane. Sommerfeld's article creates a solution of the Laplace equation on a sphere by performing a stereographic projection of the sphere onto the complex plane for an arbitrary analytic function. In particular, Sommerfeld uses the following stereographic projection:

$$\varsigma = \frac{(x + iy)}{(z \pm a)},$$

where (x,y,z) are the coordinates of a point on the sphere of radius $a = \sqrt{x^2+y^2+z^2}$. Sommerfeld uses differentiation and integration to raise and lower the order of analytic functions. Here, Sommerfeld uses Cauchy's theorem to represent a function of order m−1 by the following integra

$$\frac{1}{2\pi i} \int d\varsigma \frac{1}{(\varsigma - z)^{m+1}} f\left(\frac{x + iy}{z \pm a}\right) \frac{dz}{a}, \quad a = \sqrt{x^2 + y^2 + z^2}.$$

In this manner Sommerfeld is able to represent the spherical harmonics in terms of a contour integral. He attributes this method to Klein. Sommmerfeld then performs a particular limit as the order of the spherical harmonics approach infinity to obtain a solution of the two-dimensional Helmholtz equation. The following limit:

$$\frac{(x + iy)}{a} = \frac{k(\tilde{x} + i\tilde{y})}{l} = \frac{kr \exp(+ i\varphi)}{l}, \quad l \gg kr,$$

$$\cos(\vartheta) = \frac{z}{a} = \pm \sqrt{1 - \frac{k^2 r^2}{l^2}},$$

$$\lim_{l \to \infty} P_l\left(\sqrt{1 - \frac{k^2 r^2}{l^2}}\right) = J_0(kr),$$

is the asymptotic limit of the Legendre polynomial in terms of the regular Bessel function of order zero. The remainder of the text describes applications of this technique to two-dimensional diffraction, where the modal solution of propagation in a rigid (soft) wedge is obtained as a particular solution of the above technique, and Keller's geometric theory of diffraction appears as a stationary phase approximation of the diffraction integral.

Overall, this book is well written and illustrates how the theory of diffraction was developed before the age of computers and numerical solutions were developed. It is worth reading to gain insights into the methods employed by Sommerfeld and others to obtain analytic solutions of the theory of diffraction.

GARY STEVEN SAMMELMANN
Naval Surface Warfare Center Panama City
110 Vernon Avenue
Panama City, Florida 32407-7001

 0001-4966/2005/118(4)/2099/1/$22.50

OBITUARIES

Clayton Hamilton Allen • 1918–2004

Clayton (Clay) Hamilton Allen, a Fellow of the Society, died on August 25, 2004 at Chebeague Island, Maine. He was born in Whitinsville, Massachusetts, on June 2, 1918 and received a B. S. in Physics in 1940 from the Worcester Polytechnic Institute.

He subsequently did graduate work at Pennsylvania State College (now University) and received an M. S. in Physics in 1942; his Maters's thesis was on luminescence due to cavitation.

The next three years were spent at the Wright-Patterson Air Force Base (Dayton, Ohio), where he worked on modification and quality control of military communication gear. He then resumed graduate work at Penn State, and received a Ph.D. in Physics in 1950. After directing sonic and ultrasonic research at Corning Glass Works, Corning, NY, from 1950 to 1954, Dr. Allen joined Bolt Beranek and Newman (BBN) in Cambridge, Massachusetts, and was associated with that firm for twenty years. He left BBN in 1974 and established his acoustical consulting business as the Clayton H. Allen Corporation in January 1975. He was a member of the Acoustical Society of America (ASA) for 60 years, and he became a Fellow in 1956.

Allen's doctoral work at Penn State, under the supervision of H. K. Schilling and (until he left for UCLA in 1948) Isadore Rudnick, is significant in the history of high-intensity sound. During this time there was an oral presentation by Allen and Rudnick at the May 1947 Acoustical Society meeting, and this was followed by an article, "A Powerful High Frequency Siren," in the September 1947 issue of the *Journal of the Acoustical Society of America* (JASA). The popular media found this work interesting, and there were consequently articles in *Life Magazine* and *Popular Science*, and there was a "new short" shown in movie theaters. In the published paper, two sirens were described, the first having acoustic power output of about 150 watts, the second an improved design that generated 2 kW. Novel demonstrations included suspension of marbles in a standing wave field, acoustical heating of a cup of coffee, and lighting a pipe. Later, studies with the Zoology Department using the 2-kW siren led to the paper by Allen, Frings, and Rudick, "Some Biological Effects of Intense High Frequency Airborne Sound" [J. Acoust. Soc. Am. **20**, 62–65 (1948)].

Allen's doctoral research included a study of finite-amplitude propagation from a piston source (a St. Clair generator). In the course of the study, he discovered what is now termed nonlinear acoustical saturation (he called it "limiting sound pressure level"). Saturation refers to the maximum sound pressure level that can be achieved at a given distance at a given source frequency. Allen correctly attributed saturation to the effects of nonlinear distortion on the propagating wave. Distortion causes energy to be transferred to higher harmonics where it is more efficiently absorbed. Finally, at saturation any further increase in source level is accompanied only by an equal increase in absorption. Allen also discovered the blunting effect that increased absorption has on the directivity pattern of the radiation. Allen reported his work in his thesis, in part of the Penn State Signal Corps Report, "Atmospheric Physics and Sound Propagation, Final Report for Period July 1, 1945 to May 20, 1950," and in two abstracts in the program of the June 1950 ASA Meeting. The work was not reported in a journal paper, and consequently, authors of much of the subsequent literature in nonlinear acoustics were not aware of the priority of Clay's discovery of saturation.

During his year with BBN, Dr. Allen pursued a variety of activities, some of which were concerned with the creation and use of high amplitude sound. In 1958, he designed a high power siren to be used in a high intensity sound facility to measure the potential for failure of electronic and metal structures. The development, testing, and analytical basis of the siren are described in two papers by Allen and Watters: "Siren Design for Producing Controlled Wave Form at High Intensities" and "Siren Design for Producing Controlled Wave Form with Amplitude Modulation," both of which appeared in JASA in 1959. A larger siren was subsequently developed and 25 of these were used in a full-scale facility by the U.S. Air Force at Wright Patterson AFB.

Other work involving the facilities that Dr. Allen helped to develop includes a study of the effect of high flow and high intensity on attenuation in a lined duct, which had applications to noise control in jet aircraft nacelles. A paper, "Influence of Flow and High Sound Level on the Attenuation in a Lined Duct, " by Kurze and Allen describing part of this work was published in JASA in 1971.

At BBN, Dr. Allen also was involved in many projects related to acoustic consulting. One in 1954 was aimed at developing a method for estimating the sound power level (PWL) and octave band spectrum for fans used in the fast developing field of air conditioning. A direct relationship between fan PWL and motor horsepower was found and reported in a paper, "Noise of Centrifugal Fans," by Beranek, Kamperman, and Allen, which appeared in JASA in 1955. An extensive article on fan noise was subsequently published in *Noise Control* in 1957.

Dr. Allen's expertise is fan noise led to the writing of a chapter on sound and vibration for a Guide Book published by the American Society of Heating and Air Conditioning Engineers (ASHAE). This was the first authoritative treatise on sound related to air conditioning systems. This chapter, considerably expanded since 1957, currently appears in the American Society of Heating, Refrigerating, and Air Conditioning (ASHRAE HVAC) Applications Handbook (updated every four years).

Consulting work with BBN on textile noise involved a coner machine used to wind a textile filament on to a rotating cone via a cam driven transverse guide. The principle source of a repetitive impulsive sound in the guide mechanism was a cam follower impacting the side walls of the follower channel. Dr. Allen showed that the sound should be reduced by applying a few elastic bands to the mechanism to reduce the momentum of the cam follower when it was thrown into impact with the channel walls, and he then devised a spring mechanism for installation in new or existing machines to solve the noise problem by eliminating the follower impact, while also increasing the efficiency of the operation. This design resulted in a patent issued in 1976.

A number of the patents, some coauthored with others, resulted from Dr. Allen's work. There were four for ear muffs, two being for a design providing a level dependent attenuation for high level impulses. There was a patent for a phonograph design that gave an eight message voice for the GI Joe toy of the late 60's, another for a sound damping method for circular saw blades, and there were many others. His expertise and interest in patents led to service, from 1980 to 1994, as a contributor to the Patent Reviews section of the *Journal of the Acoustical Society of America*.

Dr. Allen continued with acoustic consulting after leaving BBN and worked out of Chebeague Island off the coast of Maine for the last 27 years of his life.

IRA DYER
DAVID T. BLACKSTOCK
ROBERT M. HOOVER

 0001-4966/2005/118(4)/2100/1/$22.50

REVIEWS OF ACOUSTICAL PATENTS

Lloyd Rice
11222 Flatiron Drive, Lafayette, Colorado 80026

The purpose of these acoustical patent reviews is to provide enough information for a Journal reader to decide whether to seek more information from the patent itself. Any opinions expressed here are those of reviewers as individuals and are not legal opinions. Printed copies of United States Patents may be ordered at $3.00 each from the Commissioner of Patents and Trademarks, Washington, DC 20231. Patents are available via the Internet at http://www.uspto.gov.

Reviewers for this issue:

GEORGE L. AUGSPURGER, *Perception, Incorporated, Box 39536, Los Angeles, California 90039*
JOHN M. EARGLE, *JME Consulting Corporation, 7034 Macapa Drive, Los Angeles, California 90068*
JEROME A. HELFFRICH, *Southwest Research Institute, San Antonio, Texas 78228*
MARK KAHRS, *Department of Electrical Engineering, University of Pittsburgh, Pittsburgh, Pennsylvania 15261*
DAVID PREVES, *Starkey Laboratories, 6600 Washington Ave. S., Eden Prarie, Minnesota 55344*
DANIEL R. RAICHEL, *2727 Moore Lane, Fort Collins, Colorado 80526*
NEIL A. SHAW, *Menlo Scientific Acoustics, Inc., Post Office Box 1610, Topanga, California 90290*
WILLIAM THOMPSON, JR., *Pennsylvania State University, University Park, Pennsylvania 16802*
ERIC E. UNGAR, *Acentech, Incorporated, 33 Moulton Street, Cambridge, Massachusetts 02138*
ROBERT C. WAAG, *University of Rochester, Department of Electrical and Computer Engineering, Rochester, New York 14627*

6,885,615

43.10.Pr PIEZOELECTRIC ACTUATOR, TIME PIECE, AND PORTABLE DEVICE

Osamu Miyazawa *et al.*, assignors to Seiko Epson Corporation
26 April 2005 (Class 368/255); filed in Japan 15 March 1998

This patent discloses the use of scratch drive and some other ingenious methods for driving clockwork. There are several applications diagrammed and lots of construction details.—JAH

6,882,462

43.20.Ks RESONANT SCANNER WITH ASYMMETRIC MASS DISTRIBUTION

Mark P. Helsel *et al.*, assignors to Microvision, Incorporated
19 April 2005 (Class 359/292); filed 22 August 2003

This patent describes the use of torsional plate resonators to create a scanning device for images. The description focuses on the application to retinal displays, but could be applicable to projectors and the like—any sensor that uses a raster scanned input or output. The patent is complete with drive circuits and some analysis of fabrication methods, but does not divulge much about the vibration analysis of such a device.—JAH

6,885,612

43.30.Wi PANORAMIC AUDIO DEVICE FOR PASSIVE SONAR

Pierre Alinat, assignor to Thales
26 April 2005 (Class 367/124); filed 4 March 2003

An audio device to process the impulsive signals received by a passive sonar array is described. The impulsive signals received by each of several beams, which are oriented azimuthally and tilted vertically, are processed in both the frequency and time domains into ''left'' and ''right'' signals and then filtered according to characteristics of the human ear. The sums of all the left and all the right signals are listened to with earphones so that an operator on the vessel develops an impression of the direction of the source of the signals with respect to the axes of the vessel.—WT

6,883,375

43.35.Yb DETECTION OF MOVEMENT OF TERMITES IN WOOD BY ACOUSTIC EMISSION TECHNIQUES

Harold L. Dunegan, Laguna Niguel, California
26 April 2005 (Class 73/587); filed 18 November 2003

Acoustic emission is applied in the usual manner to detect the ultrasonic signals generated by wood-boring or wood-feeding insects as they feed or move within wooden media. The probe consists of a piezoelectric transducer that is adapted to be inserted into a borehole in the wood under-

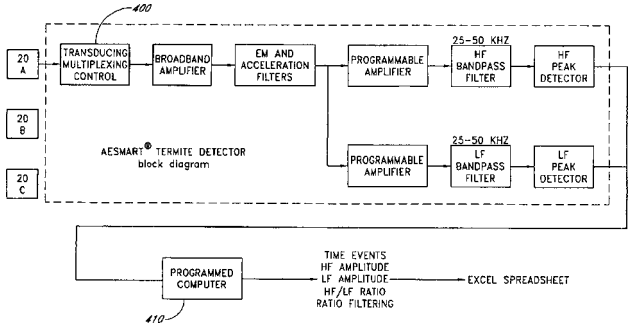

going evaluation. It is argued that the waveguide will intersect the high-frequency longitudinal and shear waves produced by the activities of termites, and which propagate along the grain of the wood, to yield an indication of termite infestation.—DRR

6,889,552

43.35.Zc ACOUSTIC WAVEGUIDE SYSTEM

Toan H. Nguyen and Lawrence C. Lynnworth, assignors to Panametrics, Incorporated
10 May 2005 (Class 73/632); filed 27 September 2002

Ultrasonic waveguide systems using rod-like elongated waveguides are widely used to measure the density, level, and/or temperature of fluids surrounding the waveguide. The fluid property that is measured depends on the type of wave (torsional, extensional, flexural) supported by the waveguide. This patent describes how two shear transducers can be mounted on

opposite sides at the end of a tubular or rod-shaped waveguide so as to produce any of the aforementioned types of wave or combinations of these.—EEU

6,867,374

43.38.Dv CERAMIC INSULATION COATED ELECTRIC WIRE SELF-FUSING CERAMIC INSULATION COATED ELECTRIC WIRE COATING COMPOSITION AND COIL AND VOICES COIL FOR SPEAKER

Toshihiro Ishigaki *et al.*, assignors to Totoku Electric Company, Ltd.
15 March 2005 (Class 174/110 A); filed in Japan 24 January 2001

A voice coil wire is described with a ceramic insulation **2** consisting of a zirconium oxide/silicon polymer which is directly applied on a conductor **1** and thermally cured. This, in turn, is then coated with a polyamide or a polyimide (or a combination thereof) resin **3** which is dissolved in an organic solvent. The patent is relatively straightforward (for patentese). This

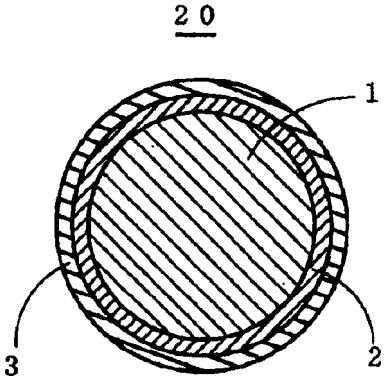

construction and these materials are described as being able to withstand temperatures of 500 °C. If so, the product can find utility in high-power electrodynamic transducers. The patent, written in a tortured dialect of patentese, presents the specific materials used, design charts, and the results of several power tests.—NAS

6,885,262

43.38.Fx BAND-PASS FILTER USING FILM BULK ACOUSTIC RESONATOR

Kosuke Nishimura *et al.*, assignors to Ube Industries, Ltd.
26 April 2005 (Class 333/189); filed in Japan 5 November 2002

This patent describes the fabrication of a bulk SAW resonator made of AlN piezoelectric material and Mo electrodes. There are several design examples given but the methodology for the design is lacking. The majority of the claims are related to electrical impedance matching.—JAH

6,885,753

43.38.Fx COMMUNICATION DEVICE USING BONE CONDUCTION

Graham Bank, assignor to New Transducers Limited
26 April 2005 (Class 381/326); filed in the United Kingdom 10 July 2001

The patent clearly describes and analyzes the problems of achieving relatively wide-band audio for bone conduction, making use of the same principles employed in modern distributed mode loudspeakers (DMLs). Here, a vibrating assembly is "coaxed" into broadband operation through

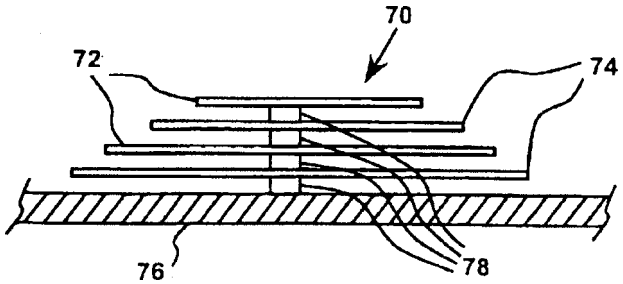

appropriately designed modal distribution. The figure shows "a multiple disc transducer **70** comprising two active piezoelectric elements **72** stacked with two passive resonant elements **74**, so that the modes of the active and passive elements are interleaved."—JME

6,863,152

43.38.Ja LOW PROFILE AUDIO SPEAKER

Joseph Yaacoub Sahyoun, Redwood City, California
8 March 2005 (Class 181/157); filed 30 September 2003

This is a "division of application No. 10/058,868, filed on Jan. 28, 2002, now Pat. No. 6,675,931, which is a continuation-in-part of application" all the way back to 1998. A low-profile electrodynamic loudspeaker based on a low-profile drone is described. The patent contains 46 figures

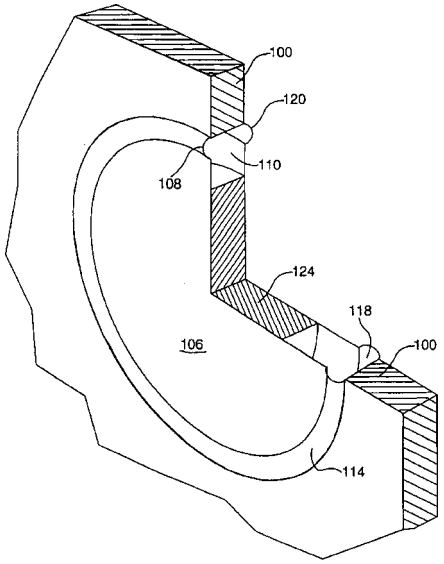

(many of which have several parts) and describes in detail the use of drone radiators in low-frequency (specifically consumer sub-bass) enclosures, and an active version that retains the low profile of the drone, in 10 claims. Readers who follow this market will recall the Carver patent(s) on this theme.—NAS

6,886,658

43.38.Ja LOUDSPEAKER ENCLOSURE SYSTEM

Prince John Charles Rolph, Cathcart, New South Wales, Australia
3 May 2005 (Class 181/199); filed in Australia 23 May 2000

Although their number seems to be diminishing, one still finds an occasional loudspeaker design based on similarity to a musical instrument or the human ear. In the case at hand, the larger rear chamber functions as a normal vented box, whereas the smaller chamber "adopts in reverse function the principle of biological transmission and reception of sound by and

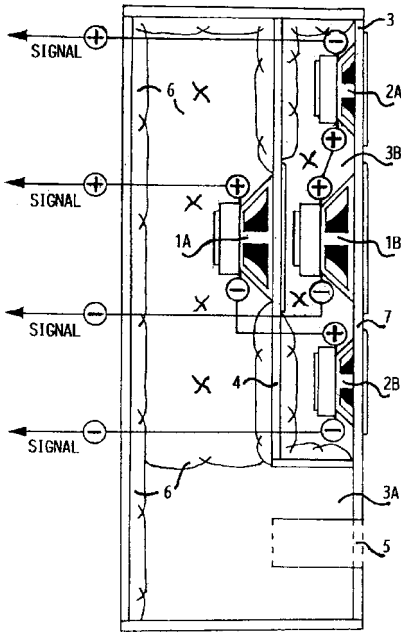

with a tympanic cavity or middle ear.'' Two large loudspeakers and two smaller loudspeakers are required. It will be noted that the two smaller speakers are connected in opposing polarity.—GLA

6,889,796

43.38.Ja LOUDSPEAKER SUSPENSION

Nicholas Pocock and Simon Yorick Pettman, assignors to Goodmans Loudspeakers Limited
10 May 2005 (Class 181/172); filed in the United Kingdom 29 January 2001

Any conventional loudspeaker cone suspension, whether corrugated or U-shaped, develops hoop stresses at long excursions. That is, at least one portion of the suspension is forced to move inward or outward, and in doing

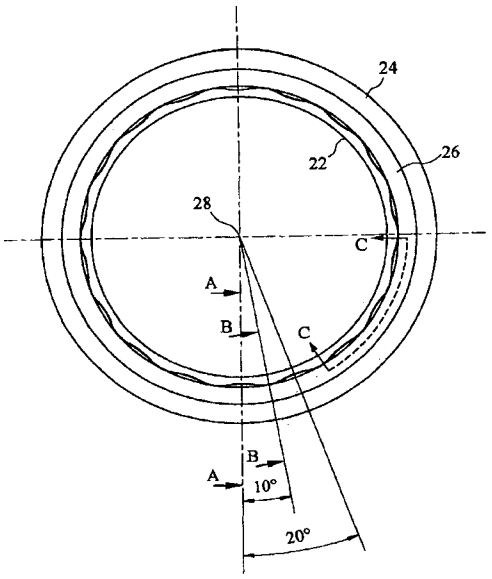

so, its effective circumference changes. In this design, the wiggly line indicates multiple transitions from a semicircular contour to a more elliptical contour, thus accommodating peripheral expansion and contraction.—GLA

6,882,734

43.38.Kb VEHICLE ACCESSORY MICROPHONE

Alan R. Watson *et al.*, assignors to Gentex Corporation
19 April 2005 (Class 381/92); filed 14 February 2002

This hefty patent (52 figures and 46-plus columns of text) deals with hands-free communication in an automobile. A pair of microphones positioned in the rear-view mirror, for example, can be processed to null out

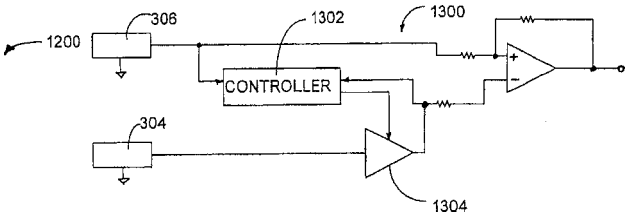

dominant noise components, as shown. Copious mechanical details and measurements are given.—JME

6,885,751

43.38.Kb PRESSURE-GRADIENT MICROPHONE CAPSULE

Richard Pribyl, assignor to AKG Acoustics GmbH
26 April 2005 (Class 381/174); filed in Austria 26 February 2002

Gradient microphones normally have front and rear openings to generate a pressure difference for actuating the diaphragm. When such a microphone has to be mounted flush to a rigid surface, both openings will be more or less side-by-side. This will produce a polar pattern that is essentially

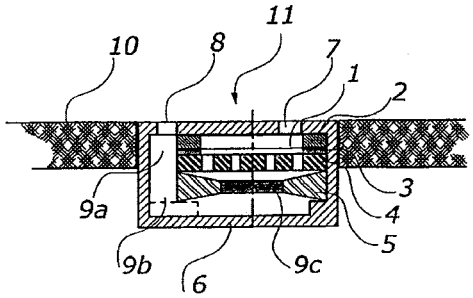

(a)

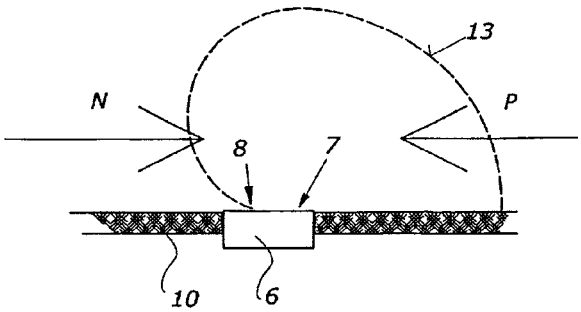

(b)

''half a cardioid'' aimed to one side, as seen in the figure. With a little care, this pattern can be aimed for pickup in a desired direction. Similar arrangements have been used in some commercial directional flush-mount boundary layer microphones.—JME

6,868,296

43.38.Lc AUDIO COMPONENT SYSTEM

Shoji Arikuma and Hideharu Toda, assignors to Sanyo Electric Company, Ltd.
15 March 2005 (Class 700/94); filed in Japan 28 May 1999

The patent describes a digital control bus which interconnects components of an audio system. The intention is that each audio output channel would be able to signal back to the selector logic to convey the status of that

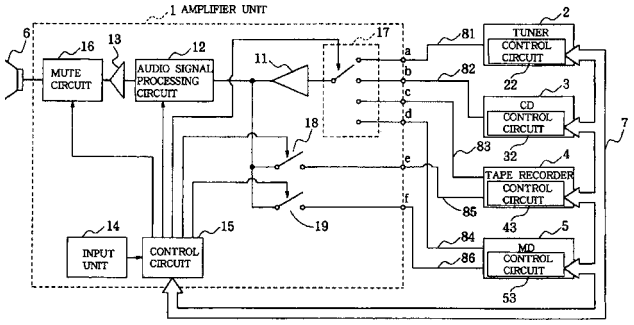

channel. In this way, thumps can be avoided by preventing the audio signal from being fed to an inoperable channel.—DLR

6,888,403

43.38.Lc PULSE WIDTH MODULATION TYPE AUDIO AMPLIFIER HAVING VARIABLE AVERAGE SWITCHING FREQUENCY

Yong Hun Cho and Bong Joo Kim, assignors to Pulsus Technologies
3 May 2005 (Class 330/10); filed in the Republic of Korea 17 August 2001

If a PWM power amplifier is used to reproduce a full-range audio signal, its nominal switching frequency must be higher than if it is used to drive a subwoofer. Rather than providing a selectable switching rate, this design detects the bandwidth of the input signal and then adjusts the switch-

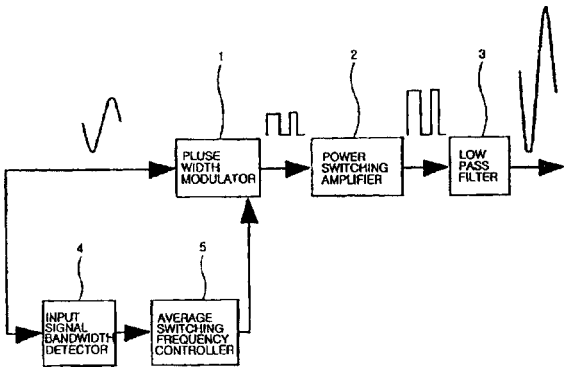

ing frequency and output filter accordingly. "By using the average switching frequency as lower (sic) as possible in accordance with the bandwidth of the input audio signal, the power efficiency is enhanced and the electromagnetic interference affecting peripheral devices can be minimized."—GLA

6,862,356

43.38.Md AUDIO DEVICE

Atsushi Makino, assignor to Pioneer Corporation
1 March 2005 (Class 381/1); filed in Japan 11 June 1999

Providing a "realistic" stereo image in a car, as well as other listening spaces, when the listener is not ideally located between the playback loudspeakers, is the goal of this patent. A head-related transfer circuit **10a** ac

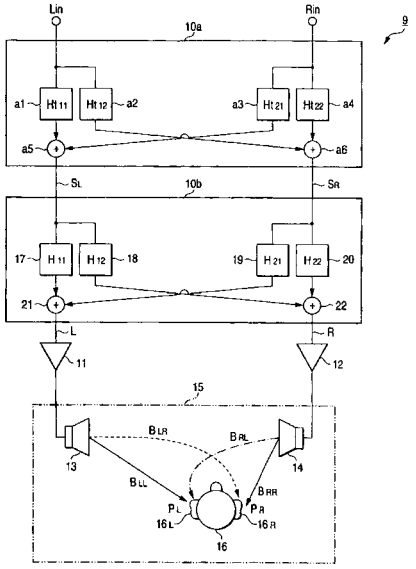

cepts left and right channel inputs and is followed by a correction circuit **10b**. A remote controller is used to adjust the circuits based on the listener's position.—NAS

6,885,876

43.38.Si MOBILE PHONE FEATURING AUDIO-MODULATED VIBROTACTILE MODULE

Olli Aaltonen *et al.*, assignors to Nokia Mobile Phones Ltd.
26 April 2005 (Class 455/550.1); filed 12 March 2001

The basis for this patent is interesting. According to the references cited, speech intelligibility for the hearing impaired, or in the presence of high background noise, can be improved by simultaneously providing an audio-modulated tactile sensation to the listener. The patent describes possible ways of providing such a tactile signal in a cellular phone.—GLA

6,882,335

43.38.Vk STEREOPHONIC REPRODUCTION MAINTAINING MEANS AND METHODS FOR OPERATION IN HORIZONTAL AND VERTICAL A/V APPLIANCE POSITIONS

Pertti Saarinen, assignor to Nokia Corporation
19 April 2005 (Class 345/156); filed in the United Kingdom 8 February 2000

Video displays can be operated in either "landscape" or "portrait" orientation, and each mode requires a different loudspeaker layout for correct stereophonic performance. This can be done with only three loudspeak-

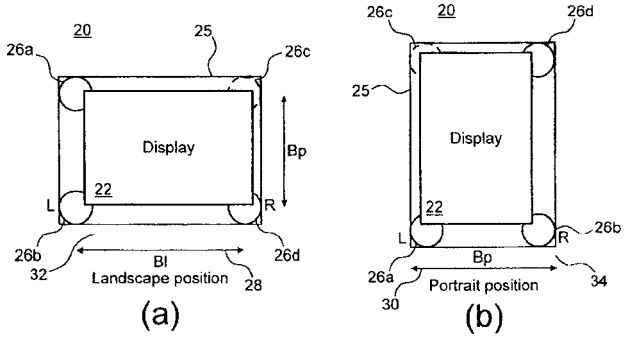

ers if they are positioned as shown in the figure. Both automatic and manual switching between modes are described.—JME

6,882,733

43.38.Vk SURROUND HEADPHONE OUTPUT SIGNAL GENERATOR

Koichi Sato, assignor to Pioneer Corporation
19 April 2005 (Class 381/74); filed in Japan 10 May 2002

In analog audio circuitry, if two uncorrelated, zero-level signals are combined, the peak level of the resulting sum signal may be twice as high (+6 dB). The same thing happens with digital audio, and can be accommodated by rescaling both of the input signals. If one is designing a low-cost circuit with limited word length, the trick is to pick a scaling factor that maintains a good signal-to-noise ratio while avoiding overload. That is the

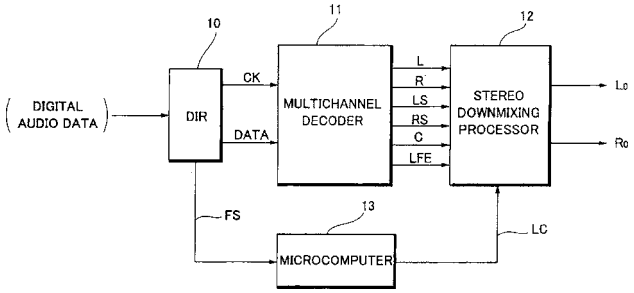

situation depicted here, where six input channels are combined into a two-channel headphone feed. The device first detects whether the program source is a motion picture or a music recording. It then rescales the relative surround sound levels on the basis that surround sound should be louder for film than for music. Any consideration of calibrated levels or the original program balance seems to be ignored.—GLA

6,883,693

43.38.Vk KNAPSACK WITH STEREOPHONIC REPRODUCING KIT

Angela W. Han, Taipei, Taiwan
26 April 2005 (Class 224/576); filed 10 April 2003

This short patent suggests the use of built-in stereo loudspeakers on both sides of a typical knapsack for playback of stereo for travelers on foot.—JME

6,885,899

43.38.Vk METHOD AND APPARATUS FOR CONTROLLING A SOUND FUNCTION OF A COMPUTER SYSTEM

An-Sung Yoon, assignor to Samsung Electronics, Company, LTD
26 April 2005 (Class 700/94); filed in the Republic of Korea 25 August 1998

Most laptop computers and similar products have a stereo pair of loudspeakers as well as a receptacle for accommodating additional stereo headphones. The patent describes circuitry that will mute the loudspeakers when a headphone jack is inserted into the receptacle.—JME

6,888,424

43.40.Dx PIEZOELECTRIC RESONATOR, FILTER, AND ELECTRONIC COMMUNICATION DEVICE

Masaki Takeuchi *et al.*, assignors to Murata Manufacturing Company, Ltd.
3 May 2005 (Class 333/187); filed in Japan 3 July 2001

This patent discloses the use of a flexible plate as a resonant structure. There is nothing new about this as far as this reviewer can tell, and the details of the design method are not given.—JAH

6,870,791

43.40.Le ACOUSTIC PORTAL DETECTION SYSTEM

David D. Caulfield, Spruce Grove, Alberta, Canada *et al.*
22 March 2005 (Class 367/11); filed 26 December 2002

This device would transmit one or more acoustic signals toward a person entering a secured area such as the boarding area at an airline terminal. An array of detectors would pick up acoustic energy reflected and/or refracted from the person, to be analyzed for the presence of materials, such as plastic explosives, drugs, or weapons. The patent text mainly presents the

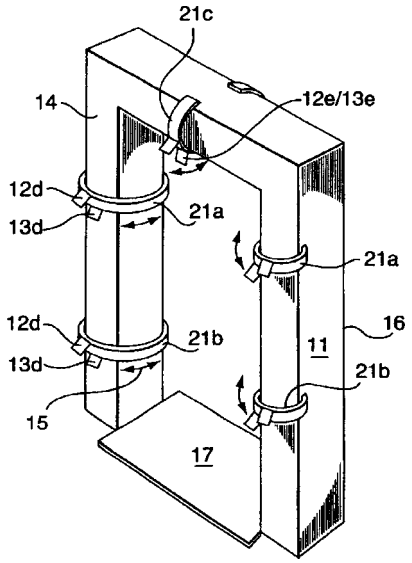

results of a series of experiments that were done to determine coefficients of reflectivity for human bodies, clothing, and various items to be detected by such a system. The 45 claims deal primarily with various arrangements of transmitters and receivers on the portal.—DLR

6,873,918

43.40.Le CONTROL EMBEDDED MACHINE CONDITION MONITOR

Richard A. Curless and Paul E. McCalmont, assignors to Unova IP Corporation
29 March 2005 (Class 702/36); filed 30 November 2001

Vibration from a machine **100** is monitored by a transducer **102**, the signals from which are fed to **106**, which can contain electronic amplification **108**, rms detector **109**, and are periodically sampled and fed to analog-to-digital converter **110**. The sampled signals are stored in predefined rms

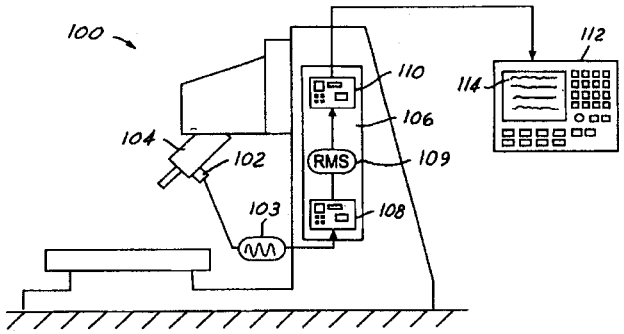

value bands in controller **112**. Each sample increments a counter which keeps track of the number of signal samples in a particular band. The number of accumulated samples can be used to provide the condition of the machine.—NAS

6,874,364

43.40.Le SYSTEM FOR MONITORING MECHANICAL WAVES FROM A MOVING MACHINE

Jonathan Joseph Campbell *et al.*, assignors to Commonwealth Scientific and Industrial Research Organization
5 April 2005 (Class 73/593); filed in Australia 9 July 1999

Accelerometer(s) with radio transmitter(s) **11** is (are) powered by solar panel(s) **12**. These are attached to semi-autonomous grinding (SAG) mill **10**. The location of **11** is detected by a proximity switch, which is wired via terminal block **14** to computer **15**. The signals from **11** are received by **13**, and conveyed to **15** via **14**. The behavior of the grinding media is characterized by tumbling, shearing, cataracting, and abrasion. The SAG mill has a liner that wears as a function of the media behavior. These behaviors can cause the mill liner to wear in different ways, some quicker than others. The analysis of the vibrations of the shell can lead to a reliable way of monitoring and controlling the SAG mill liner wear.—NAS

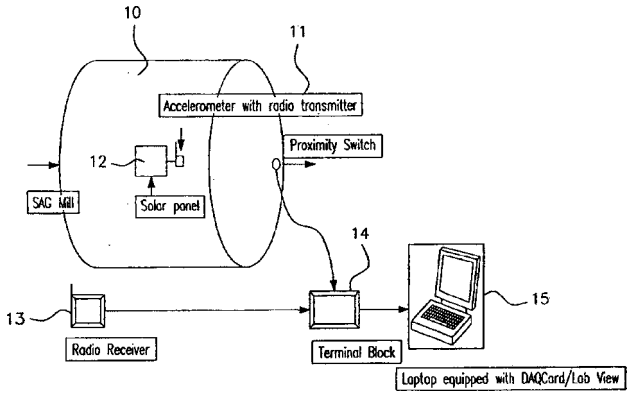

6,872,057

43.50.Gf HERMETIC COMPRESSOR CASING

Saeng-ho Kim, assignor to Samsung Gwangju Electronics Company, Ltd.
29 March 2005 (Class 417/312); filed in the Republic of Korea 17 September 2002

The vibration and noise from a hermetic compressor **10** is decreased by using a multilayer structure for the casing **100**, in which the middle layer is a damping layer.—NAS

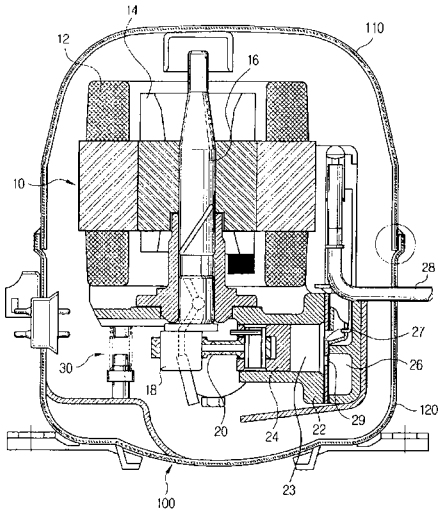

6,872,158

43.50.Gf SILENT CHAIN TRANSMISSION DEVICE

Toyonaga Saitoh, assignor to Tsubakimoto Chain Company
29 March 2005 (Class 474/212); filed in Japan 28 December 2001

Links **11** and the teeth of sprocket **20** have profiles that engage in a way that reduces the up and down motion of the chain relative to the chain traveling line. ''After sufficient engagement time between the inside surface and a sprocket tooth, the engagement of a link plate with the sprocket is gradually shifted to engagement of the outside engaging surface with the sprocket teeth.'' The patent also states that chain pitch **Pc** of the silent chain **10** is set to be the same as the hob pitch **Ph** of the hob cutter **HC** that produces the sprocket teeth.—NAS

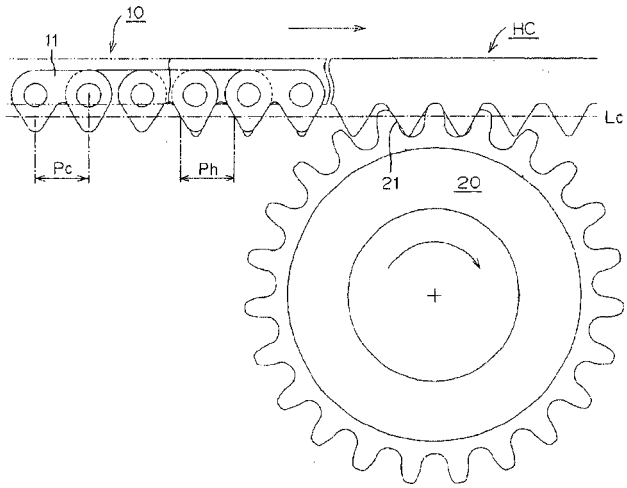

6,882,086

43.40.Tm VARIABLE STIFFNESS ELECTROACTIVE POLYMER SYSTEMS

Roy D. Kornbluh and Ronald E. Pelrine, assignors to SRI International
19 April 2005 (Class 310/328); filed 16 January 2002

Sheets of electroactive polymers are located between flexible electrodes. Depending on the polymer type and the circuits externally connected to the electrodes, which circuits may be passive or active, the assemblies can provide stiffness and/or damping that varies with the deflection amplitude. Assemblies of this type can also be made to serve as actuators.—EEU

6,883,532

43.40.Vn LARGE-SCALE MANIPULATOR COMPRISING A VIBRATION DAMPER

Kurt Rau, assignor to Putzmeister Aktiengesellschaft
26 April 2005 (Class 137/1); filed in Germany 19 September 2000

The boom arms of a large-scale manipulator, such as a concrete pump, are positioned by means of hydraulic cylinders. In order to suppress bending vibrations of these booms, the pressure fluctuations in these double-acting cylinders are sensed, low-pass filtered, and fed to a controller that sends correcting signals to these cylinders.—EEU

6,882,945

43.50.Jh METHOD, APPARATUS, AND PROGRAM FOR ESTIMATING NOISE GENERATION FOR A SYNCHRONOUS BELT

Kiyoshi Okura *et al.*, assignors to Mitsuboshi Belting Ltd.
19 April 2005 (Class 702/69); filed in Japan 27 February 2002

A method is described for estimating the noise generated by the interaction of a belt with the driving and driven sprockets. The noise is said to be primarily due to the transverse belt displacement at or near the first location at which the teeth **34** of the belt and the teeth of sprocket **14** mesh and is generated when the crests of the belt teeth impact the sprocket and when the

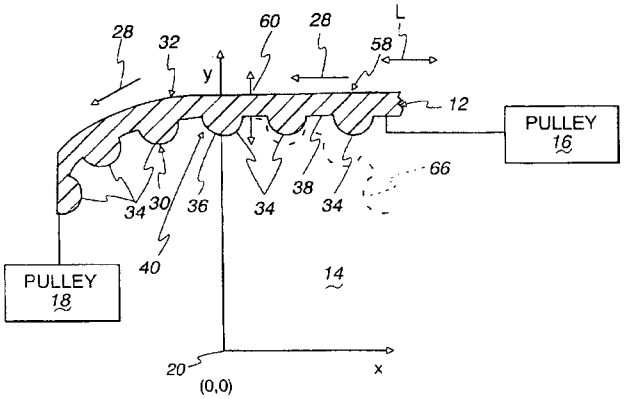

sprocket teeth impact the land region of the belt. The program calculates the transverse belt displacement, then calculates a belt displacement velocity from which the sound pressure level is calculated. The patent has several small typographical errors, starting with the assignee's name.—NAS

6,880,287

43.58.Wc FISHING LURE

Calvin W. Eubanks, Jennings, Oklahoma
19 April 2005 (Class 43/42.13); filed 5 May 2003

As shown, this spinning lure uses the collisions of spinner blades **50**

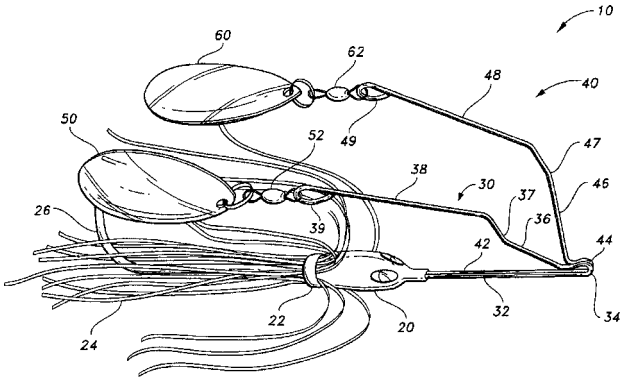

and **60** to create a clicking noise, which, together with the spinning action, will hopefully interest the notoriously inattentive fish.—MK

6,889,466

43.58.Wc DEER STOMP SIMULATOR

Bruce Randall Hamlet, assignor to Hamlett Environmental Technologies Company
10 May 2005 (Class 43/2); filed 7 October 2003

Some hunters evidently believe that artificial deer hoof stomps will attract a susceptible target (and hopefully not other hunters). Sitting in a tree,

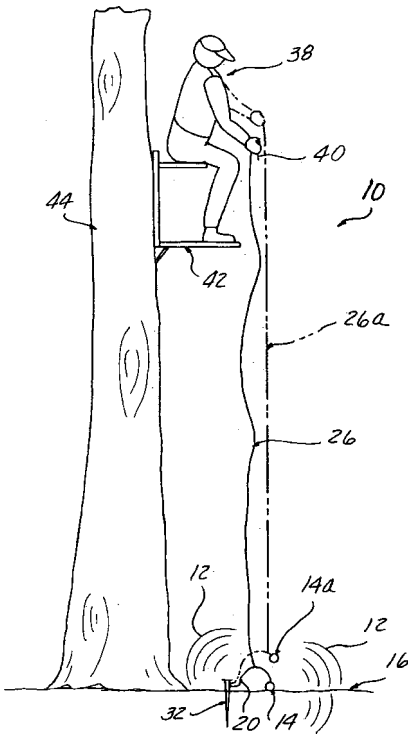

the hunter can pull a cord attached to a spring which hits the ground in a resounding stomp.—MK

6,882,337

43.60.Bf VIRTUAL KEYBOARD FOR TOUCH-TYPING USING AUDIO FEEDBACK

Martin Shetter, assignor to Microsoft Corporation
19 April 2005 (Class 345/173); filed 18 April 2002

This is a system for displaying an image of a keyboard on a computer screen that enables a user to do touch typing in order to enter textual data. Audio feedback is provided that indicates whether the user's fingers are properly striking the keys on the virtual keyboard. By listening to the sounds generated while typing, the user should be able to tell whether his/her hands are drifting to one side and adjust the finger position accordingly. If a finger misses a target area on the virtual keyboard, it will generate a sound different from the one that occurs when the finger strikes the desired key squarely. Presumably a vertical display would either be used sparingly or positioned horizontally for sustained use.—DRR

6,868,372

43.60.Dh IMAGE AND AUDIO DEGRADATION SIMULATOR

Craig D. Cuttner and Robert M. Zitter, assignors to Home Box Office, Incorporated
15 March 2005 (Class 703/2); filed 11 April 2001

In the old days, which for this reviewer is the early 1970s, a producer of an album would many times prepare a cassette tape of a song or songs and listen to it in a car to see how the recording sounded in the end user environment. Today, many producers of video and audio productions can do this by viewing and listening to program material "off the air," even though the signal may never actually be promulgated through the air. This requires

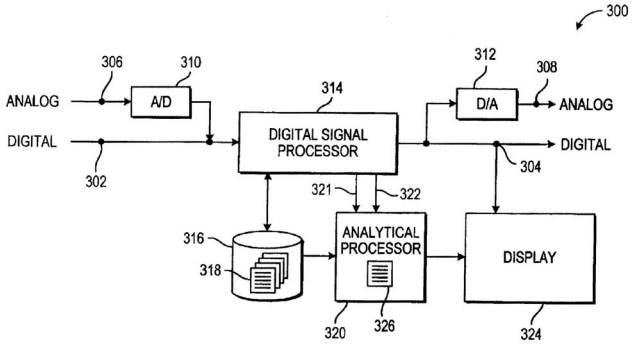

that the whole signal transmission chain be present and used. The patent describes a method that uses real time digital signal processing to simulate the signal path degradation of the signal.—NAS

6,879,864

43.60.Dh DUAL-BAR AUDIO LEVEL METER FOR DIGITAL AUDIO WITH DYNAMIC RANGE CONTROL

Edward J. Cleary, Jr., assignor to Tektronix, Incorporated
12 April 2005 (Class 700/94); filed 3 March 2000

Digital television transmits a full bandwidth signal as well as control signals (DIALNORM, DYNRNG, COMPR) that can automatically control the audio signal. Display **10** simultaneously presents the digital audio signal,

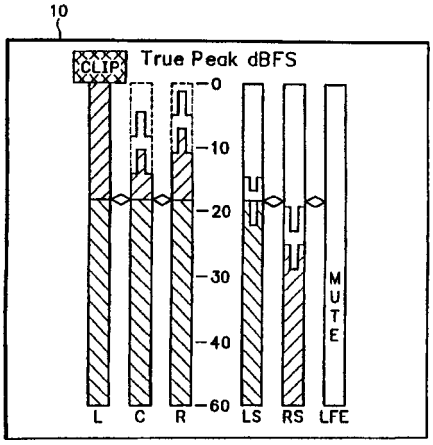

both compressed and uncompressed, by decoding the digital signal and presenting it using an inner bar and an outer bar on each audio channel display.—NAS

6,889,085

43.64.Qh METHOD AND SYSTEM FOR FORMING AN ACOUSTIC SIGNAL FROM NEURAL TIMING DIFFERENCE DATA

Thomas P. Dawson, assignor to Sony Corporation
3 May 2005 (Class 607/54); filed 20 May 2003

A conventional technique for synthetically generating neural activity in the human nervous system necessitates surgical implants. These implants usually interact with and cause neural activity in some portion of the nervous system, such as the neural cortex. Researchers have successfully mapped audio sensory data to the cochlear channel and visual data to the visual cortex. A new system is described in this patent that provides a non-invasive means of generating visual, audio, taste, smell, or touch, within or onto the neural cortex. This system forms acoustic signals from neural timing difference data. One embodiment of the system consists of a primary and a secondary transducer array. The primary array serves as a coherent or

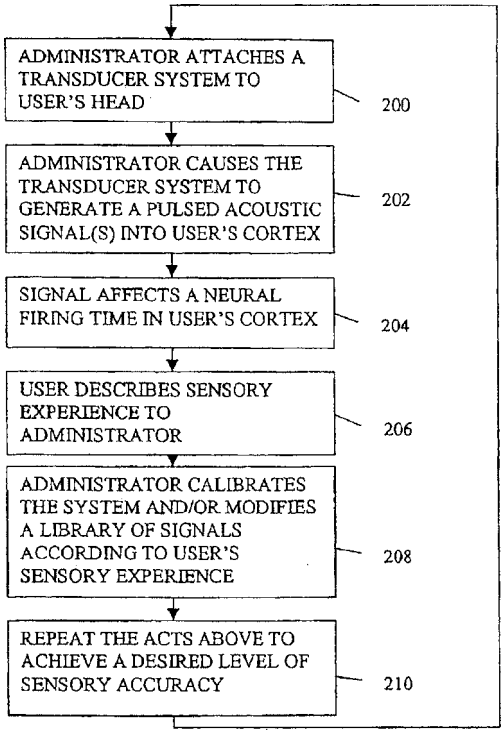

nearly coherent signal source. The secondary array acts as a controllable acoustic diffraction pattern that shapes, focuses, and modulates energy from the primary transducer into the neural cortex in a desired pattern. The secondary transducer emits acoustic energy that may be shifted in phase and amplitude relative to the primary array emissions. Stimulation of the auditory cortex leads to the sensation of sound.—DRR

6,868,345

43.64.Ri MONITORING AUDITORY EVOKED POTENTIALS

Erik Weber Jensen, assignor to Danmeter A/S
15 March 2005 (Class 702/32); filed in Denmark 31 March 2000

This patented technique would measure the intensity of auditory evoked potentials as a way to determine the level of consciousness of a subject, specifically, whether the person is sufficiently anaesthetized as to undergo surgical or other procedures. In use, the patient listens to a series of clicks presented via headphones. In the suggested arrangement, three EEG electrodes are attached to the patient's head, in the middle forehead, the left forehead, and behind the ear. The EEG signal is analyzed using a singular value decomposition method, which is presented in detail in the patent. The resulting index is said to respond within as little as six seconds to changes in the depth of anaesthesia.—DLR

The following review was previously published in J. Acoust. Soc. Am. **117**(5), 2694 (2005), with the wrong figure. The correct figure is included here.

6,829,359

43.66.Qp MULTISPEAKER SOUND IMAGING SYSTEM

Juan Serrano, assignor to Arilg Electronics Company, LLC
7 December 2004 (Class 381/17); filed 8 October 2002

Some years ago while attending a consumer high-fidelity show, this reviewer saw a setup, referred to as a "polyphonic isolator," that fed a two-channel stereo program to a frontal array of four loudspeakers. The signal processing was linear time invariant, and the effect was a pleasant

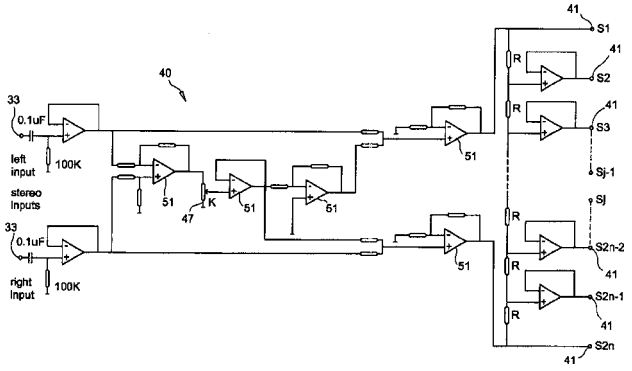

spread of sound from left to right. This patent proposes much the same through a combination of simple stereo stage widening (through the use of careful antiphase crosstalk) and gradual signal panning from left to right over a number of adjacent loudspeakers. The details of this are clearly apparent from the figure.—JME

6,882,736

43.66.Ts METHOD FOR OPERATING A HEARING AID OR HEARING AID SYSTEM, AND A HEARING AID AND HEARING AID SYSTEM

Thomas Dickel and Benno Knapp, assignors to Siemens Audiologische Technik GmbH
19 April 2005 (Class 381/317); filed in Germany 13 September 2000

A methodology is proposed for determining automatically whether wind noise is present in a listening situation and for reducing the wind noise. Wind noise is judged to be present when the difference in the outputs of the two hearing aid microphones due to uncorrelated inputs created by wind

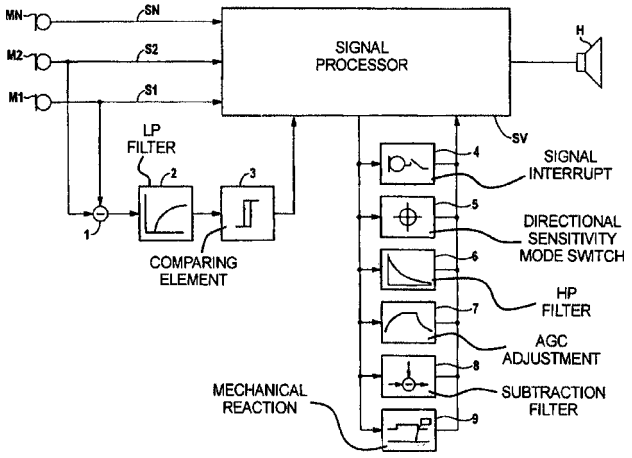

noise is less than a preset threshold. In such cases, wind noise is reduced by switching from directional to omnidirectional mode, by filtering out low frequency energy from the microphone signals, and/or increasing AGC time constants.—DAP

6,885,731

43.66.Ts CAPTIONED TELEPHONE WITH EMERGENCY ACCESS FEATURE

Robert M. Engelke, Madison, Wisconsin *et al.*
26 April 2005 (Class 379/52); filed 28 July 2003

Captioned telephones provide text by using the services of a relay interposed between the assisted user and a hearing user. Under normal operations, the assisted user dials a number and the captioned telephone connects with a relay that, in turn, dials the other party. In this system, the captioned telephone monitors the number being called by the assisted user. If the user is dialing an emergency number such as 911, the call to the relay is terminated and a direct connection to the emergency services is initiated in order to provide the quickest connection. The question, however, is: How would the user, presumably in need of captioned assistance, be able to conduct a two-way conversation?—DRR

6,888,948

43.66.Ts PORTABLE SYSTEM PROGRAMMING HEARING AIDS

Lawrence T. Hagen and David A. Preves, assignors to Micro Ear Technology, Incorporated
3 May 2005 (Class 381/314); filed 11 March 2002

A host computer connects to a programming interface constructed on a PCMCIA (PC) card. Programs are downloaded to hearing aids via the PC card. To accommodate changing acoustical environments, multiple pro-

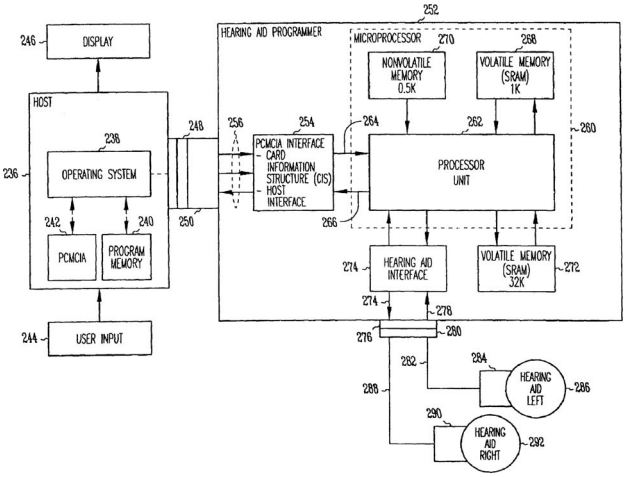

grams may be downloaded to a portable controller, which, under patient control, loads one of several programs into the hearing aids via wireless means.—DAP

6,888,949

43.66.Ts HEARING AID WITH ADAPTIVE NOISE CANCELLER

Jeff Vanden Berghe and Jan Wouters, assignors to GN ReSound A/S
3 May 2005 (Class 381/317); filed 22 December 1999

To increase robustness in adverse signal-to-noise ratio environments, a modified version of the traditional two-microphone adaptive noise canceller

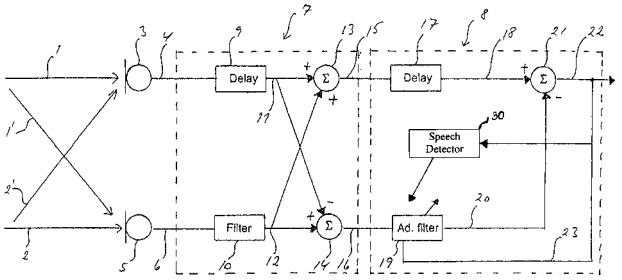

utilizes a fixed rather than adaptive filter in a first section and an adaptive filter in a second section.—DAP

6,889,094

43.66.Ts ELECTRODE ARRAY FOR HYBRID COCHLEAR STIMULATOR

Janusz A. Kuzma *et al.*, assignors to Advanced Bionics Corporation
3 May 2005 (Class 607/137); filed 12 May 2000

A cochlear implant is proposed in which electrical stimulation for high-frequency sounds in the basal end of the cochlea is combined with

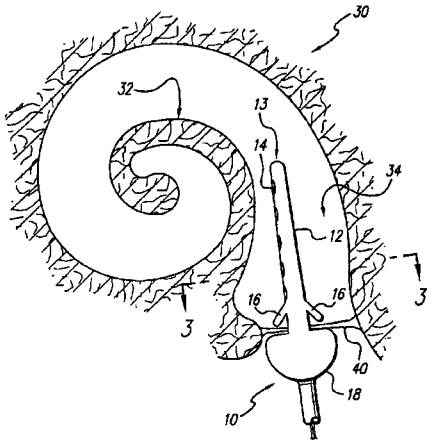

acoustic stimulation with or without a hearing aid for lower-frequency sounds.—DAP

6,891,956

43.66.Ts CERUMEN PROTECTION SYSTEM FOR HEARING AID DEVICES

Markus Heerlein and Christian Schmitt, assignors to Siemens Audiologische Technik GmbH
10 May 2005 (Class 381/325); filed in Germany 28 March 2002

The sound outlet of the hearing aid receiver is directed toward the side

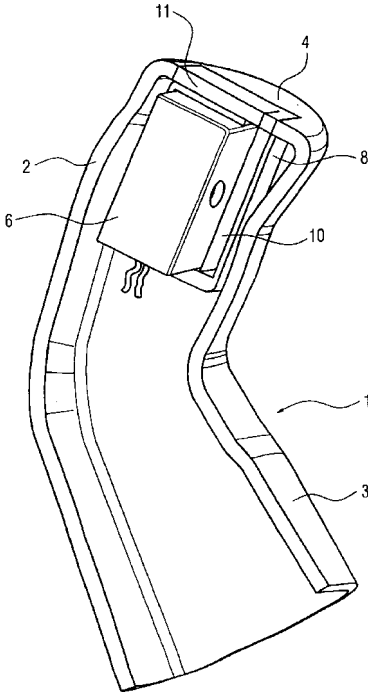

wall of the ear canal and is covered with a large, acoustically transparent membrane that is placed in a plane parallel to the ear canal.—DAP

6,882,732

43.66.Yw INTERNET-BASED AUDIOMETRIC TESTING SYSTEM

Chris M. Pavlakos, Dayton, Ohio
19 April 2005 (Class 381/60); filed 14 December 2000

Owing to the lack of personal contact, this system for conducting audiometric tests via the Internet is perhaps ill-advised. The system includes a client CPU with Internet access at the test site equipped with hearing-test equipment that produces audiometric tones. A person being tested responds in some fashion that determines the course of the testing procedure. A remote Internet-based server contains the software that gathers the data and produces an audiological test report for review by a certified audiologist.—DRR

6,889,189

43.72.Bs SPEECH RECOGNIZER PERFORMANCE IN CAR AND HOME APPLICATIONS UTILIZING NOVEL MULTIPLE MICROPHONE CONFIGURATIONS

Robert Boman *et al.*, assignors to Matsushita Electric Industrial Company, Ltd.
3 May 2005 (Class 704/270); filed 26 September 2003

This system allows automotive loudspeakers to be used as microphone inputs for a speech recognition function. ''Using loudspeakers as microphones improves speech recognition in noisy environments, thus attaining better recognition performance with little added system cost. The loudspeak-

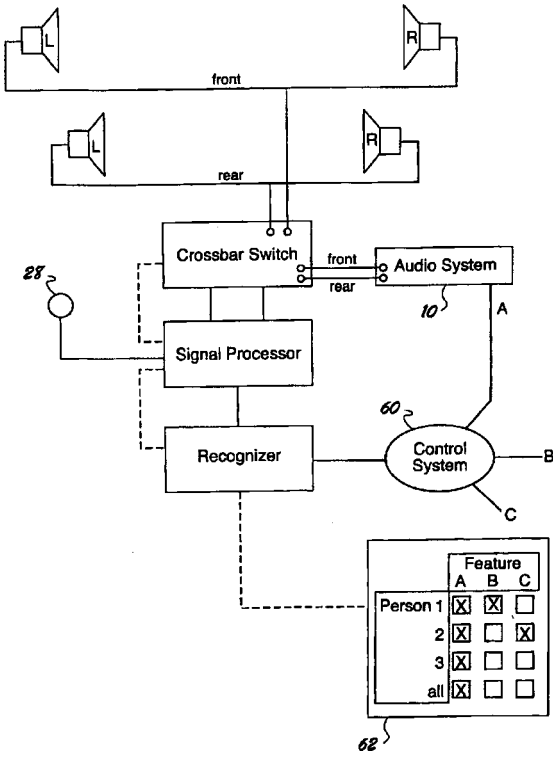

ers, positioned in physically separate locations, also provide spatial information that can be used to determine the location of the person speaking and thereby offer different functionality for different persons.''—JME

6,885,992

43.72.Gy EFFICIENT PCM BUFFER

Vladimir Z. Mesarovic and Miroslav V. Dokic, assignors to Cirrus Logic, Incorporated
26 April 2005 (Class 704/500); filed 26 January 2001

A methodology is proposed to minimize the memory used for buffering while decoding audio PCM data. Speed changing without pitch alteration with Advanced Audio Coding (AAC) permits use of a nonuniform size PCM buffer, as required by available processing capacity and loading/emptying the output FIFO.—DAP

6,885,993

43.72.Gy METHOD AND SYSTEM FOR REDUCTION OF QUANTIZATION-INDUCED BLOCK-DISCONTINUITIES AND GENERAL PURPOSE AUDIO CODEC

Shuwu Wu *et al.*, assignors to America Online, Incorporated
26 April 2005 (Class 704/500); filed 4 February 2002

Quantization-induced block discontinuities are reduced without large latency and computation complexity using a boundary analysis and synthesis technique. Data compression is achieved with an adaptive cosine packet

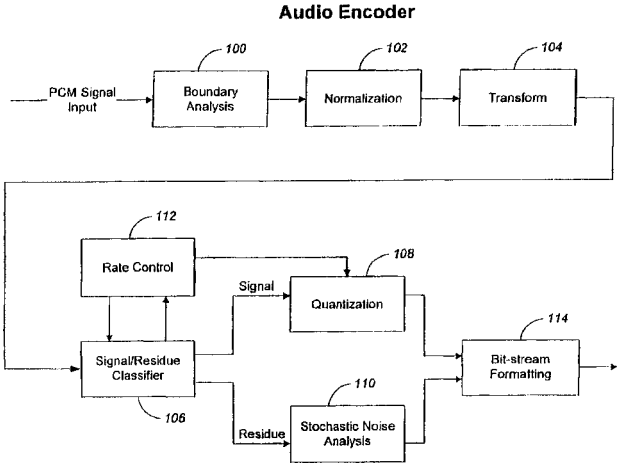

transform. A signal-residue classifier separates strong signal clusters from noise and weak signals.—DAP

6,891,958

43.72.Gy ASYMMETRIC SPREAD-SPECTRUM WATERMARKING SYSTEMS AND METHODS OF USE

Darko Kirovski and Yacov Yacobi, assignors to Microsoft Corporation
10 May 2005 (Class 382/100); filed 27 February 2001

Audio watermarking is used to identify the content producer to prevent pirates from using the content without copyright authorization. Proposed is incorporation and detection of an inaudible watermark in an audio content sequence. A public key watermark is created by incorporating the private key watermark provided by the copyright owner into a watermark carrier

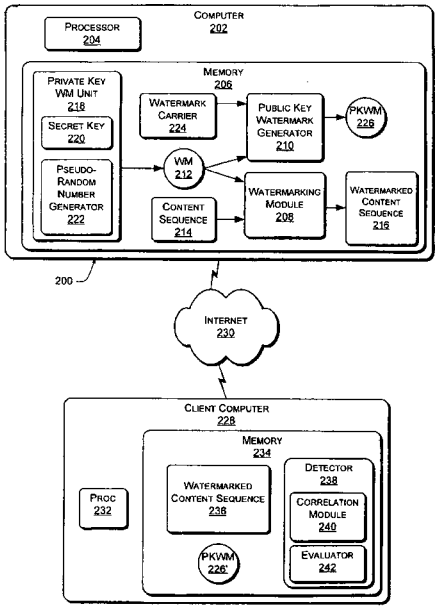

signal. The public key watermark is provided to the client to use in a correlation test to determine if the private watermark is present in the watermarked content sequence.—DAP

6,853,972

43.72.Ne SYSTEM AND METHOD FOR EYE TRACKING CONTROLLED SPEECH PROCESSING

Wolfgang Friedrich *et al.*, assignors to Siemens Aktiengesellschaft
8 February 2005 (Class 704/275); filed in Germany 27 July 2000

This short patent describes a speech recognition application in which an eye movement tracker is used together with the speech input to provide more reliable control over a computer-controlled process or operation. No specific hardware is mentioned, nor is a specific implementation described.

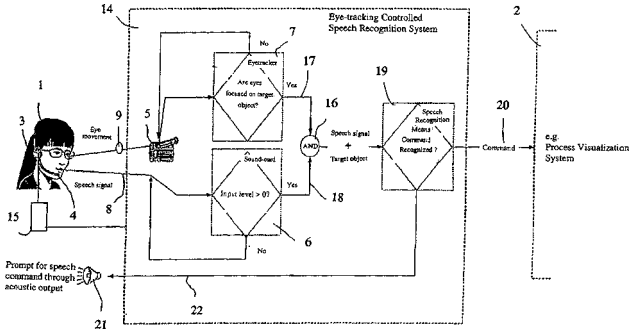

What is described in text and claims are ways to use the operator's attention to details on a visual display, including color, to enhance the performance of the speech input processing.—DLR

6,862,566

43.72.Ne METHOD AND APPARATUS FOR CONVERTING AN EXPRESSION USING KEY WORDS

Yumi Wakita and Kenji Matsui, assignors to Matushita Electric Industrial Company, Ltd.
1 March 2005 (Class 704/2); filed in Japan 10 March 2000

This elaborate recognition system, described with examples in Japanese, selects key words from the input speech and compares them to selected keywords which are associated with the target concepts to be recognized.—DLR

6,856,952

43.72.Ne DETECTING A CHARACTERISTIC OF A RESONATING CAVITY RESPONSIBLE FOR SPEECH

Edward O. Clapper, assignor to Intel Corporation
15 February 2005 (Class 704/200); filed 28 February 2001

This is a speech recognizer—of a sort—which collects vocal tract shape information, rather than audible speech data, from the user. A sensor, such as an ultrasound transmitter/receiver, is located on a small tube which projects through the mouth into the oral cavity. This sensor continually tracks the tract shape, whether the person is actually speaking aloud or just ''mouthing'' the sounds, and transmits that information to the computer for spectral or other analysis. No further information is included on the recognition system.—DLR

6,859,777

43.72.Ne HYPERTEXT NAVIGATION SYSTEM CONTROLLED BY SPOKEN WORDS

Darin Edward Krasle, assignor to Siemens Aktiengesellschaft
22 February 2005 (Class 704/270.1); filed in Germany 14 November 1994

This patent covers an idea which has been bandied about for many years, practically since the introduction of the Internet, and which is immediately obvious to anyone with any past experiences with voice control—the idea of operating a browser by voice. In addition to the broad, general claim, the narrower idea also claimed is that a specific vocabulary and probablility structure for use by a recognizer would be attached to each hypertext document and would be set up to be activated when the document is viewed.—DLR

6,859,778

43.72.Ne METHOD AND APPARATUS FOR TRANSLATING NATURAL-LANGUAGE SPEECH USING MULTIPLE OUTPUT PHRASES

Raimo Bakis *et al.*, assignors to International Business Machines Corporation
22 February 2005 (Class 704/277); filed 16 March 2000

This elaborate speech recognition and translation system would include a variety of related capabilities, including word or phrase spotting, and language understanding and translation. But the capability most strongly emphasized is the ability to speak a given phrase with various moods, intonations, emotions, dialects, accents, loudness, or rates of speech. There is but the briefest discussion of just how this is all to be done, mainly by relying on a variety of tables of various sorts. No further details are given.—DLR

6,868,383

43.72.Ne SYSTEMS AND METHODS FOR EXTRACTING MEANING FROM MULTIMODAL INPUTS USING FINITE-STATE DEVICES

Srinivas Bangalore and Michael J. Johnston, assignors to AT&T Corporation
15 March 2005 (Class 704/254); filed 12 July 2001

This speech recognition system would receive inputs from one or more nonspeech channels, such as a gesture indicator, in addition to the usual audio speech channel. The only examples discussed of gesture inputs seem to involve the speaker pointing at various items displayed on a computer screen. Several pages of patent text describe a finite state parser used to analyze such gestural inputs.—DLR

6,871,179

43.72.Ne METHOD AND APPARATUS FOR EXECUTING VOICE COMMANDS HAVING DICTATION AS A PARAMETER

Thomas A. Kist *et al.*, assignors to International Business Machines Corporation
22 March 2005 (Class 704/275); filed 7 July 1999

This patent addresses the problem of separating control commands from dictated content in a speech recognizer used for dictation. According to the relatively brief discussion presented here as to how this task is to be accomplished, a fairly simple finite state grammar would be able to distinguish the ''patterns of speech'' which would be spoken when a control command is issued. In one short example, a company meeting announcement is parsed to separate the meeting time, place, and subject matter. In a second example, a set of files pertaining to ''first quarter results'' is to be loaded. This hardly seems to be the stuff of novel invention.—DLR

6,885,735

43.72.Ne SYSTEM AND METHOD FOR TRANSMITTING VOICE INPUT FROM A REMOTE LOCATION OVER A WIRELESS DATA CHANNEL

Gilad Odinak *et al.*, Bellevue, Washington
26 April 2005 (Class 379/88.1); filed 29 January 2002

To facilitate reliable recognition of voice commands without a large amount of computing power, for example, by a mobile phone in a vehicle, front-end voice recognition processing, including noise and echo cancellation, is performed in the remotely located user system. The preprocessed output is sent wirelessly to a server which completes the speech recognition activity.—DAP

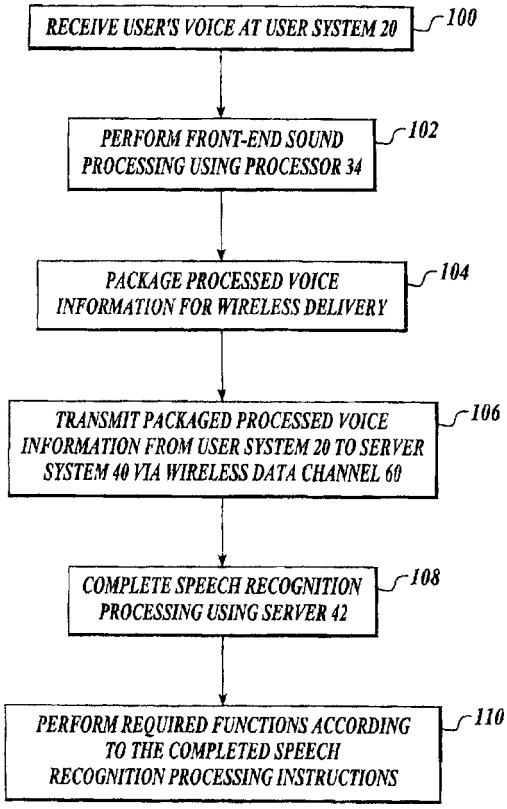

6,885,989

43.72.Ne METHOD AND SYSTEM FOR COLLABORATIVE SPEECH RECOGNITION FOR SMALL-AREA NETWORK

James Gordon McLean *et al.*, assignors to International Business Machines Corporation
26 April 2005 (Class 704/235); filed 2 April 2001

Multiple computing devices, such as several mobile devices communicating on a network via Bluetooth, share audio data and speech recognition results. Audio streams are first captured by at least one capturing device

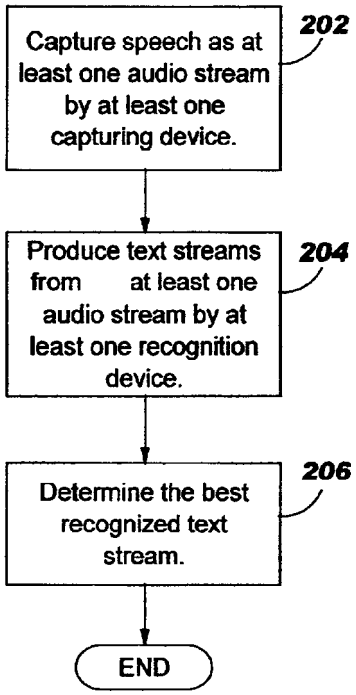

such as a PDA equipped with a microphone. Then, at least one text stream is produced after audio capture by each recognition device. The text stream recognized best is ultimately selected.—DAP

6,889,191

43.72.Ne SYSTEMS AND METHODS FOR TV NAVIGATION WITH COMPRESSED VOICE-ACTIVATED COMMANDS

Arturo A. Rodriguez *et al.*, assignors to Scientific-Atlanta, Incorporated
3 May 2005 (Class 704/275); filed 3 December 2001

To increase reliability and the number of commands possible from voice-activated remote controls of consumer appliances such as televisions, stereo equipment, and cable and satellite receivers, speech recognition is performed in a digital home communication terminal (set-top box) rather than in the remote control. A microphone in the remote picks up the voice signal and digitally transmits it to the set-top box.—DAP

6,881,889

43.75.St GENERATING A MUSIC SNIPPET

Lie Lu *et al.*, assignors to Microsoft Corporation
19 April 2005 (Class 84/616); filed 3 June 2004

A snippet in this case includes the "most salient" segment of a song. After generically describing computer hardware in the beginning of the 21st century, the algorithmic details are exposed. After segmenting the song into frames, the next step is to select the "most salient" frame. Each frame can be given a salience value, which is the product of the relative position of the frame in the song, the frequency of appearance, and the energy, or amplitude, of the frame. The frame frequency is the most complex measure. It uses a clustering measure across all frames and is computed from the clustering. Next, the song is segmented across "musical sentences" using amplitude as a guide for beginning and ending of the sentence. The snippet must include the most salient frame.—MK

6,881,890

43.75.Wx MUSICAL TONE GENERATING APPARATUS AND METHOD FOR GENERATING MUSICAL TONE ON THE BASIS OF DETECTION OF PITCH OF INPUT VIBRATION SIGNAL

Shinya Sakurada, assignor to Yamaha Corporation
19 April 2005 (Class 84/654); filed in Japan 27 December 2002

At issue is an electronic trumpet. There are two tone generators, one for the breathy attack (i.e., noise) and one for the steady state and decaying

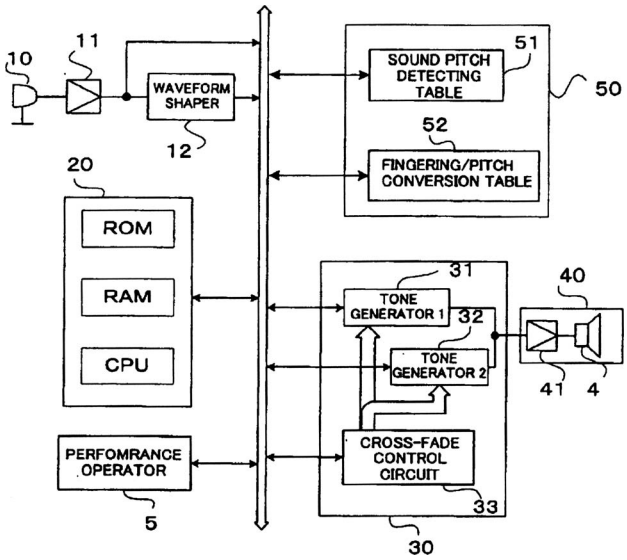

brass tone. An additional wrinkle is the use of a pitch detector at the quasi-mouthpiece and a fingering-to-pitch conversion table.—MK

6,881,892

43.75.Wx METHOD OF CONFIGURATING ACOUSTIC CORRECTION FILTER FOR STRINGED INSTRUMENT

Hideo Miyazaki *et al.*, assignors to Yamaha Corporation
19 April 2005 (Class 84/736); filed in Japan 19 February 2002

Like adding a body response to a solid body guitar, these inventors want to add a body response to a stringed instrument like a violin. So, the idea is to use a mute and measure one frequency response (how is not detailed). Then, measure without the mute and compute the difference (in the frequency domain). Additionally, they note that the phase is adjusted to make it minimum phase. Then a FIR filter is designed. The references notably omit previous work on adding body resonance to solid body instruments well before this patent was filed.—MK

6,888,058

43.75.Wx ELECTRONIC MUSICAL INSTRUMENT

Tomomitsu Urai *et al.*, assignors to Yamaha Corporation
3 May 2005 (Class 84/737); filed in Japan 10 January 2002

This patent proposes a mix of equalization and artificial reverberation applied to electric pianos and synthesizers. As shown, the output of the loudspeakers **16** is received by the microphones **20**. An "Automatic Adjustment Unit" controls the attenuators **32**, equalizers **34**, FIR filters **36**, and

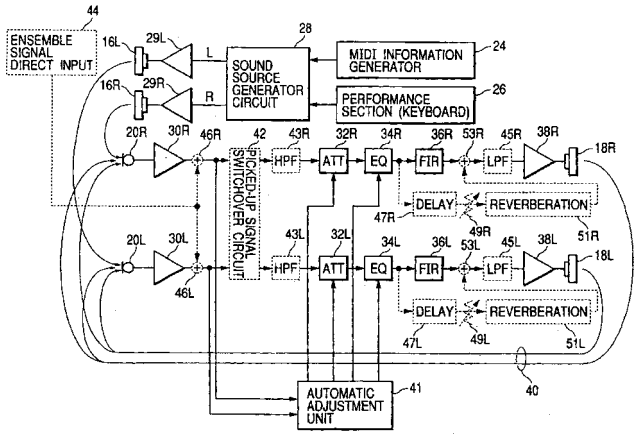

finally reverb **51**. The final result is output on the speakers **18**. Being a feedback system, the output of the speakers could result in howling feedback. The solution is the use of pink noise by the controller, which adjusts the attenuators and the equalizers. The FIR filters supply artificial reflections from the sound board or enclosure.—MK

6,883,639

43.80.Qf STETHOSCOPE

Jack Lam and Yung Hsiang Chen, assignors to Health & Life Company, Ltd.
26 April 2005 (Class 181/131); filed 19 November 2003

This version of a stethoscope is designed either for multitasking or for a one-armed physician, in that only one hand is needed to remove the stethoscope from the ears. This is achieved by squeezing together the semirigid separated tubes which connect to the earpieces and which come together

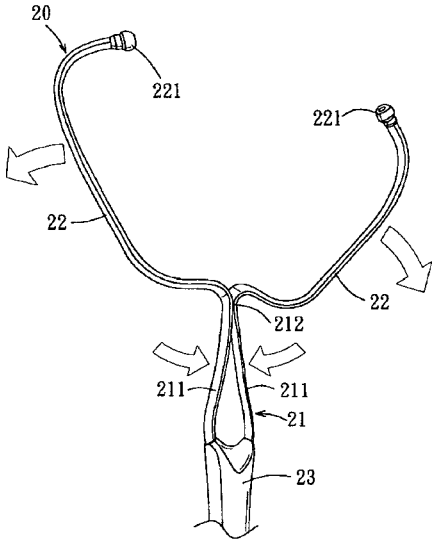

near the distal end (i.e., the chestpiece). As shown in the figure, this has the effect of increasing the distance between the earpieces sufficiently for them to drop away from the ears.—DRR

6,887,199

43.80.Qf BRAIN ASSESSMENT MONITOR

Keith Bridger *et al.*, assignors to Active Signal Technologies, Incorporated
3 May 2005 (Class 600/300); filed 12 March 2002

This noninvasive brain assessment monitor is designed to detect brain trauma, strokes, tumors, and changes in brain blood flow patterns resulting from injury or disease. The device includes a head-mounted brain sensor that passively detects acoustic signals generated by pulsing blood flow

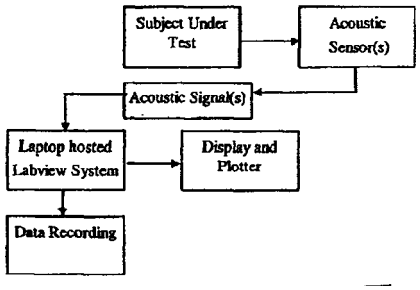

through a patient's brain. A reference sensor may be positioned at another location to sense an arterial pulse, so that the signals from the brain sensor and the reference sensor may be compared.—DRR

6,887,208

43.80.Qf METHOD AND SYSTEM FOR ANALYZING RESPIRATORY TRACT SOUNDS

Igal Kushnir and Meir Botbol, assignors to Deepbreeze Ltd.
3 May 2005 (Class 600/529); filed 9 January 2003

This body sound analyzer consists of several transducers strategically placed over the thorax. Each transducer at a specific location generates a signal indicative of pressure waves at its respective location. A processor

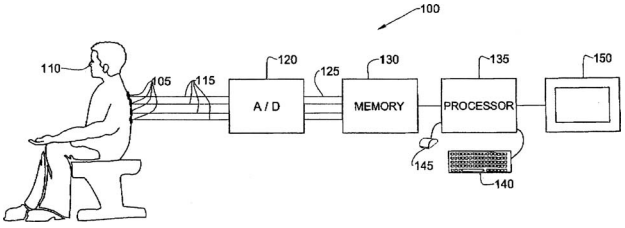

receives signals from the group of transducers and determines an average acoustic energy for a least one position over a time interval.—DRR

6,887,203

43.80.Qf OPHTHALMOLOGICAL ULTRASONOGRAPHY SCANNING APPARATUS

Scott Howard Phillips and Christopher Grant Denny, assignors to Ultralink Ophthalmics Incorporated
3 May 2005 (Class 600/445); filed in Canada 6 January 2000

This apparatus provides optical scanning of the eye through the use of a virtual center translocation mechanism that is said to facilitate precise arcuate motion of an ultrasonic transducer to sustain the focal distance from the eye and to maintain the ultrasound beam normal to the contour of the eye. A radius adjustment mechanism is provided to vary the radius of ultrasonic scanning to enable positioning of the transducer focal point on selected surfaces of the eye. Centrarion optics are applied to align the ultrasonic transducer with the Purkinje (or other optical or geometric) axis of the eye. A hygiene barrier eyeseal protects the patient from the possibility of infection.—DRR

6,884,216

43.80.Vj ULTRASOUND DIAGNOSIS APPARATUS AND ULTRASOUND IMAGE DISPLAY METHOD AND APPARATUS

Yasuhiko Abe and Takuya Sasaki, assignors to Kabushiki Kaisha Toshiba
26 April 2005 (Class 600/440); filed 1 December 2003

A physiological parameter is imaged and an arbitrary line in the image is selected. Along the line, an ultrasound m-mode record is produced. At a position selected by a curser in the m-mode image, a temporal and a spatial profile are produced. The m-mode image, the temporal profile, and the spatial profile are simultaneously displayed.—RCW

6,890,302

43.80.Vj FREQUENCY DOMAIN PROCESSING OF SCANNING ACOUSTIC IMAGING SIGNALS

Michael G. Oravecz *et al.*, assignors to Sonoscan, Incorporated
10 May 2005 (Class 600/443); filed 13 November 2001

A target is scanned with a pulsed acoustic beam and a time-domain signal that results from interaction of the beam with the target is obtained. The time-domain signal is processed to produce a frequency-domain representation of the signal as modified by the interaction. The frequency-domain representation is displayed, altered, and then reconverted to a time-domain signal that is also displayed.—RCW

LETTERS TO THE EDITOR

This Letters section is for publishing (a) brief acoustical research or applied acoustical reports, (b) comments on articles or letters previously published in this Journal, and (c) a reply by the article author to criticism by the Letter author in (b). Extensive reports should be submitted as articles, not in a letter series. Letters are peer-reviewed on the same basis as articles, but usually require less review time before acceptance. Letters cannot exceed four printed pages (approximately 3000–4000 words) including figures, tables, references, and a required abstract of about 100 words.

Measurement of absorption with a *p-u* sound intensity probe in an impedance tube (L)

Yang Liu[a] and Finn Jacobsen[b]
Acoustic Technology, Ørsted•DTU, Technical University of Denmark, Building 352, Ørsteds Plads, DK-2800 Kgs. Lyngby, Denmark

(Received 28 January 2005; revised 4 July 2005; accepted 5 July 2005)

An alternative method of measuring the normal-incidence sound absorption of a sample of material in an impedance tube is examined. The method is based on measurement of the sound pressure and the normal component of the particle velocity using a "*p-u*" sound intensity probe. This technique is compared with the traditional, well-established "transfer function method" based on two pressure microphones. The results suggest that the new method can be as accurate as the established method, but whereas the influence of transducer mismatch on the transfer function method can be eliminated using a simple "sensor-switching technique," the method based on a *p-u* intensity probe relies on accurate calibration of the probe. © *2005 Acoustical Society of America.* [DOI: 10.1121/1.2010387]

PACS number(s): 43.20.Ye, 43.58.Bh, 43.58.Fm [AJZ] Pages: 2117–2120

I. INTRODUCTION

There are two well-established methods of measuring normal-incidence absorption coefficients and other properties in an impedance tube terminated by a sample of the material under test: the traditional method based on measuring the standing wave ratio frequency by frequency, and the method based on two pressure microphones and excitation with a broadband signal. An early version of the latter method involving measurement of the cross spectrum and the auto spectra of the two microphone signals was proposed by Seybert and Ross in 1977.[1] However, the "two-microphone" method in prevailing use was developed by Chung and Blaser a few years later.[2] This method is known as the "transfer function method" since it involves measuring the transfer function between the two microphone signals.[2] Both the traditional standing wave method and the transfer function method are standardized,[3,4] but the transfer function method is much faster and more convenient than the standing wave method. Its errors and limitations have been analyzed by several authors.[5,6]

A particle velocity transducer called the "Microflown" has recently become available,[7] and various "*p-u*" sound intensity probes based on combining this transducer with a small pressure microphone are now in production.[8] Our purpose with this note is to examine an alternative to the transfer function method, based on measuring the sound pressure and the particle velocity at a point in the impedance tube using a Microflown sound intensity probe.

II. OUTLINE OF THEORY

The sound field in the tube consists of an incident plane wave and a reflected plane wave. The transfer function method is based on[2]

$$R = \frac{H_{12} - e^{-jks}}{e^{jks} - H_{12}} e^{j2kl}, \tag{1}$$

where R is the ratio of the sound pressure of the reflected wave to the sound pressure of the incident wave at the termination (at $x=0$), H_{12} is the transfer function between the two microphone signals, k is the wave number, s is the distance between the microphones, and l is the distance between the material under test and microphone No. 1. The absorption coefficient of the termination is

$$\alpha = 1 - |R|^2. \tag{2}$$

The method based on measuring the pressure and the particle velocity is even simpler. Since the sound pressure is

$$p = p_i(e^{jkl} + Re^{-jkl}), \tag{3}$$

and the particle velocity is

[a]Electronic mail: gordan69@163.com
[b]Author to whom correspondence should be addressed; electronic mail: fja@oersted.dtu.dk

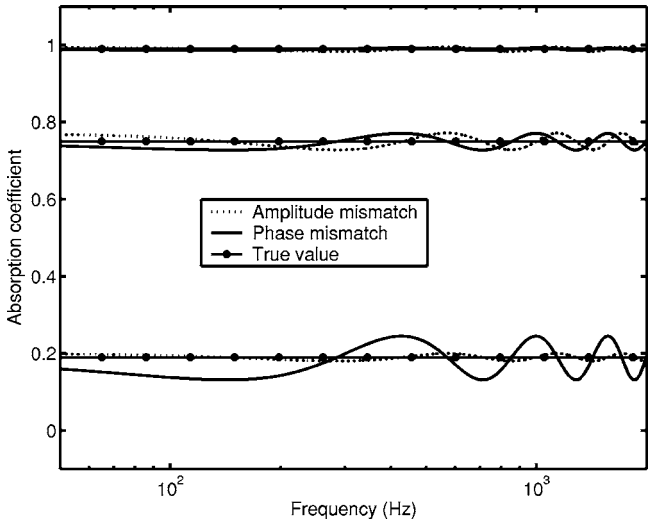

FIG. 1. Estimated absorption coefficient with an amplitude error of 0.5 dB and with a phase error of 2°, calculated assuming a "true" reflection factor of 0.1, 0.5, and 0.9, with $l=30$ cm.

$$u_x = \frac{p_i}{\rho c}(e^{jkl} - Re^{-jkl}), \tag{4}$$

where ρc is the characteristic impedance of air, it follows that the reflection factor is

$$R = \frac{1 - \rho c H_{pu}}{1 + \rho c H_{pu}} e^{j2kl}, \tag{5}$$

where H_{pu} is the transfer function from the sound pressure to the particle velocity.

In principle both methods require well-matched transducers. However, in practice amplitude and phase mismatch between the two pressure microphones used in the transfer function method are eliminated by the "sensor-switching technique" suggested by Chung and Blaser.[2] This technique involves measuring the transfer function twice, the second time with the microphones interchanged. Unfortunately, there is no similar simple technique for removing mismatch between the pressure and the velocity transducer; it is necessary to calibrate the device very carefully.

III. ERRORS AND LIMITATIONS

In practice one must allow for small residual calibration errors of the *p-u* intensity probe. Uncompensated residual amplitude and phase mismatch means that H_{pu} becomes $H_{pu}(1+\varepsilon)e^{j\varphi_e}$, where ε is the fractional amplitude error and φ_e is the phase error. The estimated reflection factor now becomes

$$\hat{R} = \frac{1 - \rho c H_{pu}(1+\varepsilon)e^{j\varphi_e}}{1 + \rho c H_{pu}(1+\varepsilon)e^{j\varphi_e}} e^{j2kl}, \tag{6}$$

where

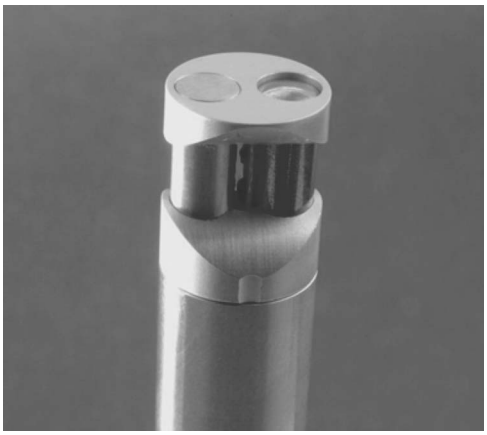

FIG. 2. The Microflown $\frac{1}{2}$-in. sound intensity probe.

$$H_{pu} = \frac{e^{jkl} - Re^{-jkl}}{e^{jkl} + Re^{-jkl}}. \tag{7}$$

Figure 1 shows estimated absorption coefficients calculated with an amplitude error of 0.5 dB and a phase error of 2° for three different values of the "true" reflection factor R, 0.1, 0.5, and 0.9. Obviously the error depends on kl. A more interesting observation is that phase mismatch is more serious than amplitude mismatch, and that both errors are much more critical if the sample under test is strongly reflecting. (The various sources of error in the transfer function method also have a more serious influence when the sample under test is strongly reflecting.[6]) It is not easy to calibrate the velocity channel of the *p-u* probe with smaller errors than 0.5 dB and 2°.[9]

IV. EXPERIMENTAL RESULTS

In order to compare the new method with the established transfer function method some experiments have been carried out in an aluminum tube of quadratic cross section with dimensions 7×7 cm excited by a loudspeaker driven with random noise and terminated by various samples of materials at the other end. Since the mounting of the sample under test is of critical importance for the accuracy of any tube method of measuring absorption[10] the two measurements took place immediately after each other without remounting the sample. The two pressure signals needed for the transfer function method were measured with two Brüel & Kjær (BK) microphones of type 4192, and the pressure and particle velocity signals needed for the alternative method were measured using a Microflown $\frac{1}{2}$-in. *p-u* sound intensity probe. This device measures the sound pressure and the particle velocity component in a direction perpendicular to the axis of the transducer; see Fig. 2. A BK "Pulse" analyzer of type 3560 in the FFT mode was used for all the measurements; postprocessing of the measured frequency responses was done using MATLAB. The first mode of higher order can propagate in tube above 2.4 kHz; therefore the frequency range was limited to 2 kHz. Before the measurements took place the Microflown velocity channel was calibrated relative to the pres-

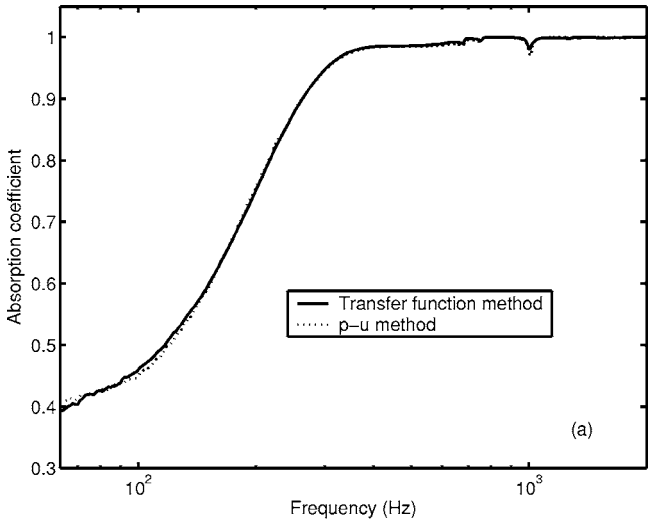

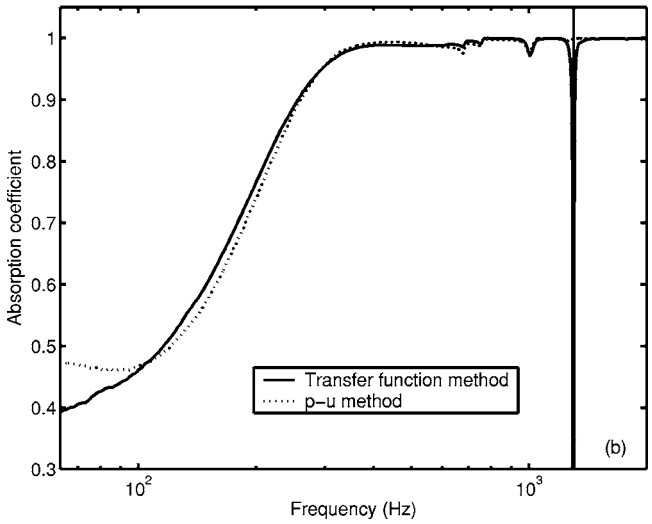

FIG. 3. Absorption coefficient of a wedge of mineral wool. Transducer positions (a) near the material, and (b) far from the material.

sure channel by exposing the devise to the sound field generated by a small loudspeaker at a distance of 4 m in DTU's large anechoic room. The calibration procedure has been described in Refs. 9 and 11.

Figures 3(a) and 3(b) show the results of the two methods with a highly absorbing termination of the tube, a 30-cm-long wedge of mineral wool terminated by a rigid cap, measured using different positions in the tube. It is apparent that the wedge absorbs sound very well from 200 Hz and upwards. The results shown in Fig. 3(a) have been determined with the Microflown probe in the hole nearest the absorbing material and with the two pressure microphones in the two holes nearest the material; the results shown in Fig. 3(b) have been determined with the Microflown probe 21 cm further from the material and with the two pressure microphones in the two holes furthest from the material. The two methods are in excellent agreement when the transducer positions closest to the material are used. The agreement is fair, but less perfect with the other positions. The sharp dip in the results of the transfer function method at 1.3 kHz is due

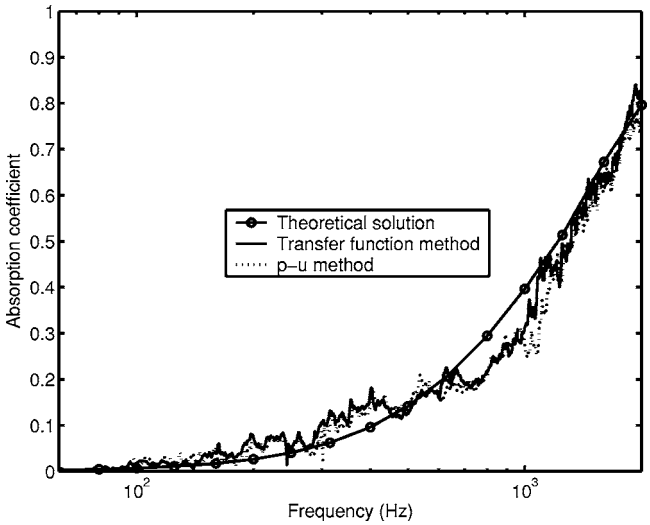

FIG. 4. Apparent absorption coefficient of the open tube.

to the distance between the microphones (13 cm) being half a wavelength—at this frequency Eq. (1) becomes indeterminate—but otherwise the transfer function method is not affected by the transducer positions. There is no obvious explanation for the small irregularities observed in all curves between 680 Hz and 1 kHz, but since all the measurements are in agreement the explanation may well be related with mechanical resonances.

Figure 4 shows the apparent absorption coefficient of the open tube, using the transducer positions closest to the opening. An open tube has the advantage that its reflection factor can be predicted theoretically, if only for an unflanged tube of circular cross section.[12] At low frequencies the opening of the tube reflects sound strongly (in antiphase), but above 1 kHz a significant fraction of the incident sound energy is "absorbed," that is, radiated. The two methods are in good agreement. The fluctuations of the two curves are mainly caused by background noise from outside of the tube. However, both curves differ somewhat from the theoretical solution, in all probability because the expression derived in Ref. 12 is for a tube of circular cross section.

The (small) deviations that have been observed between the absorption coefficient measured with the transfer function method and the absorption coefficient determined with the method based on measurement of sound pressure and particle velocity may well be due to imperfect calibration of the velocity transducer.

V. CONCLUSION

A method of measuring normal-incidence absorption coefficients with a sound intensity probe that provides the sound pressure and the particle velocity at the same position has been examined by comparing with the well-established transfer function method based on two pressure microphones in an impedance tube. The results, which also have implications for *in situ* measurements of the acoustic impedance of materials with *p-u* probes, show that this method can be as accurate as the transfer function method. However, whereas

the influence of transducer mismatch on the transfer function method can be eliminated with a simple sensor-switching technique there is no similar way of removing phase and amplitude mismatch between the two transducers of the *p-u* probe; they must be calibrated within a tolerance of 0.5 dB and 2°.

ACKNOWLEDGMENT

The authors are indebted to Microflown Technologies BV for lending us a *p-u* sound intensity probe.

[1]A. F. Seybert and D. F. Ross, "Experimental determination of acoustic properties using a two-microphone random-excitation technique," J. Acoust. Soc. Am. **61**, 1362–1370 (1977).
[2]J. Y. Chung and D. A. Blaser, "Transfer function method of measuring in-duct acoustic properties. I. Theory," J. Acoust. Soc. Am. **68**, 907–913 (1980).
[3]ISO 10534-1:1996, "Acoustics—Determination of sound absorption coefficient and impedance in impedance tubes—Part 1: Method using standing wave ratio."
[4]ISO 10534-2:1998, "Acoustics—Determination of sound absorption coefficient and impedance in impedance tubes—Part 2: Transfer-function method."
[5]A. F. Seybert and B. Soenarko, "Error analysis of spectral estimates with application to the measurement of acoustic parameters using random sound fields in ducts," J. Acoust. Soc. Am. **69**, 1190–1199 (1981).
[6]H. Bodén and M. Åbom, "Influence of errors on the two-microphone method for measuring acoustic properties in ducts," J. Acoust. Soc. Am. **79**, 541–549 (1986).
[7]H.-E. de Bree, "The Microflown: An acoustic particle velocity sensor," Acoust. Aust. **31**, 91–94 (2003).
[8]R. Raangs, W. F. Druyvesteyn, and H.-E. de Bree, "A low-cost intensity probe," J. Audio Eng. Soc. **51**, 344–357 (2003).
[9]F. Jacobsen and H.-E. de Bree, "Measurement of sound intensity: *p-u* probes versus *p-p* probes," Proceedings of Noise and Vibration Emerging Methods 2005, Saint Raphaël, France, 2005.
[10]A. Cummings, "Impedance tube measurements on porous media: The effect of air-gaps around the sample," J. Sound Vib. **151**, 63–75 (1991).
[11]F. Jacobsen and H.-E. de Bree, "A comparison of two different sound intensity measurement systems," J. Acoust. Soc. Am. **118**, 1510–1517 (2005).
[12]H. Levine and J. Schwinger, "On the radiation of sound from an unflanged circular pipe," Phys. Rev. **73**, 383–406 (1948).

Correcting echo-integration data for transducer motion (L)

Adam J. Dunford
National Institute of Water and Atmospheric Research, P.O. Box 14-901, Wellington, New Zealand

(Received 14 January 2005; revised 28 June 2005; accepted 29 June 2005)

When calculating biomass estimates using acoustic echo-integration it is necessary to account for the change in pointing direction of the transducer between transmission and reception. It is shown that a single correction function can be obtained for a wide range of circular transducers, thus removing the need for the correction to be recalculated for each individual transducer. This correction function is also applicable to those transducers whose beam pattern approximates that of a circular transducer. © *2005 Acoustical Society of America.* [DOI: 10.1121/1.2005927]

PACS number(s): 43.30.Ft, 43.30.Yj, 43.30.Vh, 43.60.−C [DRD] Pages: 2121–2123

I. INTRODUCTION

An important aspect of any quantitative assessment of fish stocks is the correction of errors associated with the measurement technique. One source of error in acoustic biomass estimates obtained using echo-integration is the change in transducer pointing direction between transmission and reception. The acoustic biomass will be biased low if this is not accounted for. This problem has been discussed by Stanton (1982) using a circular transducer and by Furusawa and Sawada (1991) for sinusoidal transducer motion. In general, however, while the effect of transducer motion is well known, corrections for it are not widely applied.

One reason for this may be that in some situations the corrections required are acceptably small, for example when the targets of interest are close to the transducer or when the motion of the transducer is minimal. This is certainly not always the case; Kloser *et al.* (2001) reported correction factors on the order of 1.10–1.5 for a survey of orange roughly and Stanton (1982) obtained corrections of up to 1.64 for a collection of targets at 400 m. Data from acoustic surveys around New Zealand frequently require significant corrections, either because the species of interest occur in deep water [e.g., orange roughy (750–1200 m) and oreos (600–1200 m) (Paul, 2000)] or because the survey area is prone to poor weather (e.g., the Campbell plateau to the south of New Zealand where average wind speeds can exceed 25 knots). In addition, if the transducer is in a towed body, for example to reduce weather-induced surface losses and shadowing effects, it will tend to move more quickly than one mounted on a large vessel; Doonan *et al.* (2003), for example, obtained corrections from 1.13 to 1.84 for a survey of orange roughly using a deep-towed system.

Another possible reason why this correction is not more widely applied is the need to perform a nontrivial numerical integration to determine the motion correction factor for each different transducer beam pattern. While performing these calculations for a number of circular transducers it was noted that there was a high degree of similarity in the shape of the correction function. This suggested that a single relationship could be obtained which would represent the correction for a wide range of transducers. A relationship of this nature is presented, which allows the error due to transducer motion to be determined without the need to recalculate the correction for each transducer. Many transducers have a main lobe which approximates that of a circular transducer and this work is also applicable to these.

II. METHODS

The motion correction factor, κ, is given by

$$\kappa = \frac{\max(\Psi)}{\Psi}, \tag{1}$$

where max indicates the maximum value and Ψ is the directivity of the transmit and receive transducers. The directivity, Ψ, is given by

$$\Psi = \int_0^{\pi} \int_0^{2\pi} B_t^2(\theta,\phi) B_r^2(\theta,\phi) \sin\phi \, d\theta \, d\phi, \tag{2}$$

where $B_t(\theta,\phi)$ and $B_r(\theta,\phi)$ are the beam patterns of the transmitting and receiving transducers and are assumed to be identical apart from being pointed in different directions. θ and ϕ are the azimuthal and zenith angles (Anton, 1988) (see Fig. 1); note that these are defined opposite to Stanton (1982).

For a circular transducer where the transmit and receive directions are equal,

$$B_t = B_r = 2\frac{J_1(ka\sin\phi)}{ka\sin\phi}, \tag{3}$$

where J_1 is the first-order Bessel function of the first kind, $k=2\pi/\lambda$, λ being the acoustic wavelength, and a is the transducer radius. The transducer radius is related to the full-width half-power beamwidth of the transducer, α, by

$$\left(2\frac{J_1(ka\sin(\alpha/2))}{ka\sin\alpha/2}\right)^2 = \frac{1}{2}. \tag{4}$$

By making the variable substitution $z=ka\sin\alpha/2$, Eq. (4) becomes

$$\left(2\frac{J_1(z)}{z}\right)^2 = \frac{1}{2}. \tag{5}$$

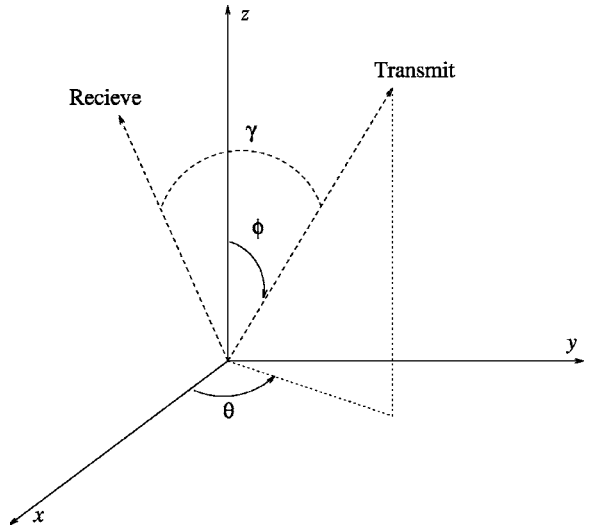

FIG. 1. Coordinate system used for calculating motion correction factors, θ and ϕ are the azimuthal and zenith angles, respectively. The angle between the transducer pointing direction on transmission (transmit) and reception (receive) is the separation angle γ from which the motion correction factor is calculated.

Let χ be the unique solution to Eq. (5), then $\chi = ka \sin \alpha/2 = 1.616\,399\ldots$ Defining

$$\epsilon = \chi \frac{\sin \phi}{\sin(\alpha/2)} = ka \sin \phi \tag{6}$$

then allows Eq. (3) to be written as

$$B_t = B_r = 2\frac{J_1(\epsilon)}{\epsilon}. \tag{7}$$

In the case where the transmit and receive directions are separated by some angle γ, the directivity Ψ, and hence the motion correction factor κ, becomes a function of γ. The separation angle γ is the angle between the transmit and receive transducer normals (see Fig. 1) and, for a real system, would be calculated from measured pitch and roll values using simple trigonometry.

Motion correction factors were calculated for circular transducers with beamwidths from 1° to 20°. For each transducer, κ was calculated at separation angles from 0° to the transducer beamwidth. Although κ exists for separation angles greater than this, differences between the theoretical and real beam patterns mean that the error in the correction increases substantially. Thus, a separation angle equal to the transducer beamwidth is a practical upper limit.

It was observed that the graphs of κ for transducers of different beamwidths showed a high degree of similarity which suggested that a single relationship could be obtained which would represent the correction for a wide range of transducers. While there are an infinite number of functional forms which could be used for κ, only three are considered here. The first, $\kappa(\sin(\gamma)/\sin(\alpha/2))$, was suggested by observing that Eq. (7) expresses the integrand of Eq. (2) in a "nondimensional" form and furthermore that χ in Eq. (6) is a constant. While it should be stressed that there is no direct connection between them, the form of Eq. (6) suggested that the functional form $\kappa(\sin(\gamma)/\sin(\alpha/2))$ could be a suitable candidate. In addition, two other possibilities $\kappa(\sin(\gamma/2)/\sin(\alpha/2))$ and $\kappa(\gamma/\alpha)$ were also investigated.

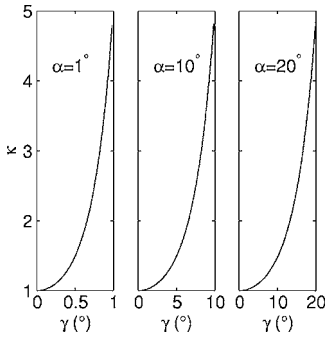

FIG. 2. Motion correction factors, κ, versus beam separation angle, γ, for circular transducers with beamwidths, α, of 1°, 10°, and 20°.

III. RESULTS

Motion correction factors for circular transducers with beamwidths of 1°, 10°, and 20° are shown in Fig. 2. Ignoring the different x axis limits on the plots, it can be seen that κ has a similar functional form over a wide range of beamwidths.

Figure 3 plots κ for circular transducers with beamwidths from 1° to 20° against $\sin(\gamma)/\sin(\alpha/2)$. The variation over this range of beamwidths is less than 1% which supports the hypothesis that κ could be expressed as a function of $\sin(\gamma)/\sin(\alpha/2)$. Plotting κ against other combinations of variables, for example $\sin(\gamma/2)/\sin(\alpha/2)$ and γ/α, produces similar results but with greater variation.

These results show that a single relationship can be obtained which represents the motion correction for a wide range of circular transducers. While there are potentially other functional forms with even lower variation across the range of beamwidths, searching for these would be highly computationally intensive and beyond the scope of this work.

An analytic approximation to κ can be obtained by fitting a constrained polynomial to the mean of the data in Fig. 3. The fit constraints are $\kappa(0)=1$ and $\kappa \geqslant 1$. The fifth-order polynomial fit is

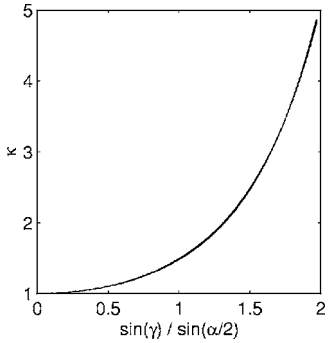

FIG. 3. Motion correction factors, κ, for circular transducers with beamwidths, α, from 1° to 20°. For each beamwidth, κ was calculated for separation angles, γ, from 0° to α°.

$$\kappa = 0.170\,83x^5 - 0.396\,60x^4 + 0.538\,51x^3 + 0.137\,64x^2 + 0.039\,645x + 1, \quad (8)$$

where $x = \sin(\gamma)/\sin(\alpha/2)$. This polynomial approximation to κ has fit residuals of less than 0.2%.

IV. CONCLUSION

Despite the wide knowledge of the errors due to transducer motion it is rare to see explicit corrections in the literature. Correction factors on the order of 1.0–1.3 can be expected for most acoustic systems (MacLennan and Simmonds, 1992), with larger corrections being necessary as the angular motion between transmission and reception becomes comparable to the transducer beamwidth.

It has been shown that the theory of Stanton (1982) can be generalized to derive a single correction function which is applicable to a wide range of circular transducers. The same correction is also applicable to those transducers whose main lobe approximates that of a circular transducer. This removes the need for the computationally intensive and complex calculations required to generate a correction function for each transducer. To perform this correction only knowledge of the motion and beam pattern of the transducer are required.

ACKNOWLEDGMENTS

I would like to thank my colleagues, in particular Richard Barr and Gavin Macaulay, for useful comments on earlier drafts. This research was funded in part by the New Zealand Ministry of Fisheries under Project Nos. ORH1999/01A, OEO2001/01A, and OEO2001/01B.

Anton, H. (**1988**). *Calculus, with analytic geometry*, 3rd ed. (Wiley, New York).

Doonan, I. J., Hicks, A. C., Coombs, R. F., Hart, A. C., and Tracey, D. M. (**2003**). "Acoustic estimates of the abundance of orange roughly in the mid-east coast fishery, June-July 2001," *New Zealand Fisheries Assessment Report 2003/4*, New Zealand Ministry of Fisheries.

Furusawa, M., and Sawada, K. (**1991**). "Effects of transducer motion on quantifying single fish echoes," Nippon Suisan Gakkaishi **57**(5), 857–864.

Kloser, R. J., Ryan, T. E., Williams, A., and Lewis, M. (**2001**). "Development and application of a combined industry/scientific acoustic survey of orange roughly in the eastern zone," *Technical Report* 99/111, Australian Fisheries Research and Development Corporation.

MacLennan, D., and Simmonds, E. (**1992**). *Fisheries Acoustics* (Chapman and Hall, London).

Paul, L. J. (**2000**). *New Zealand Fishes*, 2nd ed. (Reed, Auckland, New Zealand).

Stanton, T. (**1982**). "Effects of transducer motion on echo-integration techniques," J. Acoust. Soc. Am. **72**, 947–949.

Stimulus-frequency otoacoustic emissions measured with amplitude-modulated suppressor tones (L)

Stephen T. Neely, Tiffany A. Johnson, Cassie A. Garner, and Michael P. Gorga
Boys Town National Research Hospital, 555 North 30th Street, Omaha, Nebraska 68131

(Received 7 April 2005; revised 8 July 2005; accepted 13 July 2005)

Stimulus-frequency otoacoustic emissions (SFOAEs) are typically derived as the difference in sound pressure in the ear canal with and without a suppressor tone added to the probe tone. A novel variation of this method applies a sinusoidal amplitude modulation (AM) to the suppressor tone, which causes the SFOAE to also be modulated. The AM-SFOAE can be separated from the probe frequency using spectral methods. AM-SFOAE measurements are described for four normal-hearing subjects using 6-Hz AM. Because the suppressor modulation is at a higher rate, the AM-SFOAE technique avoids the confounding influence of heartbeat, which also modulates the probe tone. [DOI: 10.1121/1.2031969]

PACS number(s): 43.64.Jb [BLM] Pages: 2124–2127

I. INTRODUCTION

Stimulus-frequency otoacoustic emissions (SFOAEs) are signals that originate within the cochlea at the same frequency as the evoking tonal stimulus, which we call the *probe* tone. The separation of the emission from the stimulus is a challenge for SFOAE measurements because they occur at the same frequency. To separate these responses, a common method for SFOAE measurement is to use two intervals, one with and one without a *suppressor* tone (e.g., Driesbach *et al.*, 1998; Schairer *et al.*, 2002; Shera and Guinan, 2003). The suppressor frequency (f_s) is chosen to be close enough to the probe frequency (f_p) to interact with it within the cochlea, but far enough away that spectral techniques can be used to distinguish it from the probe within the ear canal. The suppressor inhibits the cochlear generation of the SFOAE and causes the SFOAE measured in the ear canal to be reduced or eliminated. The SFOAE is then extracted from the response interval without the suppressor by subtracting the response in the interval with the suppressor. This subtraction is sometimes called *vector subtraction* because it includes both real and imaginary parts of the complex spectral components at the probe frequency.

A variation on the vector subtraction technique is described here, in which the suppressor amplitude is modulated sinusoidally instead of being presented at a constant level. When this method is used, the influence of the suppressor on SFOAE generation varies continuously. As a result, the SFOAE measured in the ear canal is modulated in its amplitude at the same rate that the suppressor amplitude is modulated. This amplitude modulation allows the SFOAE to be separated from the probe using spectral techniques instead of vector subtraction.

II. METHODS

The theory behind the amplitude-modulated (AM) SFOAE technique is described first for the simpler case of constant probe level. Our implementation of the AM-SFOAE technique included an additional variation in probe level which occurred at a much slower rate than the amplitude modulation. This probe level variation allowed input/output (I/O) functions to be measured efficiently, but is not an essential part of the AM-SFOAE technique.

A. Theory

The total ear-canal pressure can be modeled as the sum of four components

$$p(t) = p_{\text{stim}}(t) + p_{\text{oae}}(t) + p_{\text{ignor}}(t) + p_{\text{noise}}(t),$$

where $p_{\text{ignor}}(t)$ contains pressure components that are the result of higher-order distortion sidebands (e.g., due to nonlinearities in the earphone) that are synchronized to the stimulus and $p_{\text{noise}}(t)$ contains random pressure components (e.g., cable rub, swallowing, and heartbeat) that are not synchronized to the stimulus. The stimulus pressure waveform includes the probe and suppressor

$$p_{\text{stim}}(t) = p_{\text{probe}}(t) + p_{\text{suppr}}(t).$$

The probe component is a tone with constant amplitude A_p and frequency $\omega_p = 2\pi f_p$

$$p_{\text{probe}}(t) = A_p \cos(\omega_p t).$$

The suppressor component is a tone with constant frequency $\omega_s = 2\pi f_s$ and sinusoidally modulated amplitude

$$p_{\text{suppr}}(t) = A_s[1 + \alpha_s \cos(\omega_m t)]\cos(\omega_s t),$$

where α_s is the modulation depth ($0 \leqslant \alpha_s \leqslant 1$), $\omega_m = 2\pi f_m$ is the modulation frequency, and A_s is the unmodulated amplitude of the suppressor. The suppressor component can also be represented as the sum of three spectral components,

$$p_{\text{suppr}}(t) = A_s\left[\cos(\omega_s t) + \tfrac{1}{2}\alpha_s \cos(\omega_{sl} t) + \tfrac{1}{2}\alpha_s \cos(\omega_{su} t)\right],$$

where $\omega_{sl} = \omega_s - \omega_m$ and $\omega_{su} = \omega_s + \omega_m$ are lower and upper sideband frequencies, respectively, relative to the suppressor frequency. For simplicity, the tones and modulation are specified here as having zero phases.

When the probe and suppressor components combine within the cochlea, they will interact and produce additional distortion components due to the vibration of nonlinear ele-

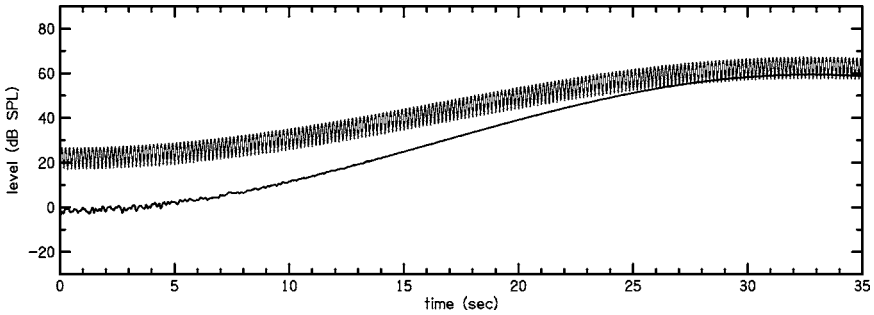

FIG. 1. AM-SFOAE stimulus as a function of time. The thick line shows the slowly varying probe level. The thin line shows the slow variation of the suppressor level, combined with a 6-Hz amplitude modulation. Only a portion of the stimulus is shown here. The entire stimulus was 131 s long with two complete cycles of slow variation.

ments. In addition, we assume that the probe will generate a reflected component at its tonotopic place. The reflected component $p_{\text{refl}}(t)$ will be modulated in amplitude by the presence of the suppressor at the tonotopic place where the probe is represented. We assume that $p_{\text{refl}}(t)$ will be at its maximum amplitude when the suppressor is at its minimum amplitude and vice versa,

$$p_{\text{refl}}(t) = A_r\{1 - \alpha_r \cos[\omega_m(t - t_{\text{in}})]\}\cos[\omega_p(t - t_{\text{in}})],$$

where t_{in} represents the travel time (of both the probe and suppressor) to the tonotopic place of the probe and α_r is the modulation depth of the reflected component at the probe frequency. The reflected component can also be represented as the sum of three spectral components,

$$p_{\text{refl}}(t) = A_r\Big\{\cos[\omega_p(t - t_{\text{in}})] - \tfrac{1}{2}\alpha_r \cos[\omega_{pl}(t - t_{\text{in}})] - \tfrac{1}{2}\alpha_r \cos[\omega_{pu}(t - t_{\text{in}})]\Big\},$$

where $\omega_{pl}=\omega_p-\omega_m$ and $\omega_{pu}=\omega_p+\omega_m$ are lower and upper sideband frequencies, respectively, relative to the probe frequency and A_r is the unmodulated amplitude of the reflected component. The reflected component will travel back to the ear canal, where we observe it as $p_{\text{oae}}(t)$. For simplicity, we choose to ignore the reflected component at the probe frequency and consider $p_{\text{oae}}(t)$ to be the sum of the upper and lower sidebands

$$p_{\text{oae}}(t) = A_{ol}\cos(\omega_{pl}t + \varphi_{ol}) + A_{ou}\cos(\omega_{pu}t + \varphi_{ou}).$$

If we assume that $p_{\text{oae}}(t)$ is related to $p_{\text{refl}}(t)$ by an outward travel time t_{out} and attenuation α_{out}, then $A_{ol}=A_{ou}=-\frac{1}{2}\alpha_{\text{out}}\alpha_r A_r$, $\varphi_{ol}=-\omega_{pl}\cdot(t_{\text{in}}+t_{\text{out}})$, and $\varphi_{ou}=-\omega_{pu}\cdot(t_{\text{in}}+t_{\text{out}})$. Note that when $\alpha_r=1$, the sidebands contain half the total power of the reflected component. Note also that the difference in phase between the two sidebands provides an estimate of the round-trip travel time

$$\varphi_{ol} - \varphi_{ou} = 2\omega_m \cdot (t_{\text{in}} + t_{\text{out}}),$$

$$t_{\text{in}} + t_{\text{out}} = \frac{\varphi_{ol} - \varphi_{ou}}{2\omega_m}.$$

B. Application

To explore the effectiveness of AM suppressors, we rapidly (6 Hz) modulated the *amplitude* of the suppressor while slowly (0.015 Hz) varying the *level* of both probe and suppressor. Our stimulus was 131 s in duration and contained two complete cycles of probe-level variation, ranging between 0 and 60 dB SPL. The suppressor, which was always present, varied in level between 30 and 70 dB SPL coincident with probe-level variation, while simultaneously being sinusoidally amplitude-modulated (99%) at a much higher rate of 6 Hz.

Our measurements were made using an ER-10C probe system (Etymotic Research) and locally developed software (SYSRES, Neely and Stevenson, 2002). Frequency-domain heterodyne analysis (Kim *et al.*, 2001; Guinan *et al.*, 2003) was used to extract the slow variation of both stimulus and response component levels from the recorded waveforms.

The level variation of the probe (thick line) and suppressor (thin line) are illustrated in Fig. 1. These responses were recorded with our measurement system in a 2-cm^3 acoustic cavity and show signs of being influenced by environmental noise at the lowest probe level. The bandwidth that was used to analyze the stimulus-component levels for this figure was wide enough to also reveal the 6-Hz modulation of the suppressor, shown by the rapid excursions of the upper line in the figure. Figure 2 shows the spectrum of the same cavity response. The (unmodulated) probe is situated at $f_p=2$ kHz. The suppressor is centered at $f_s=1920$ Hz with several sidebands at 6-Hz intervals from 1920 Hz. The spectrum of the digital stimulus had only one pair of sidebands. The other sidebands are presumably due to intermodulation distortion

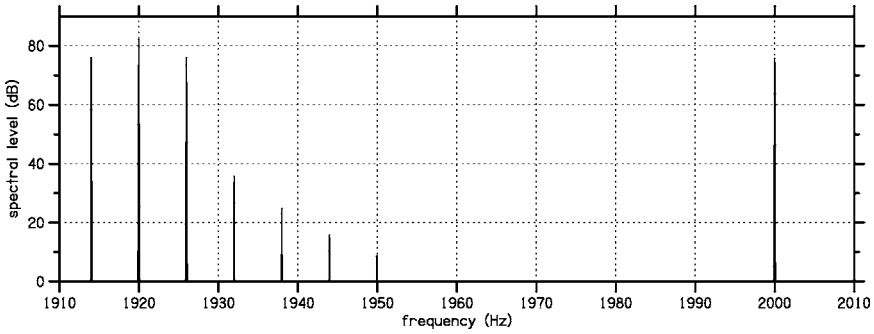

FIG. 2. Spectrum of the AM-SFOAE stimulus in an acoustic cavity. The probe was at 2000 Hz and the suppressor was centered at 1920 Hz. The sidebands at 6-Hz intervals around the suppressor frequency are due to amplitude modulation of the suppressor.

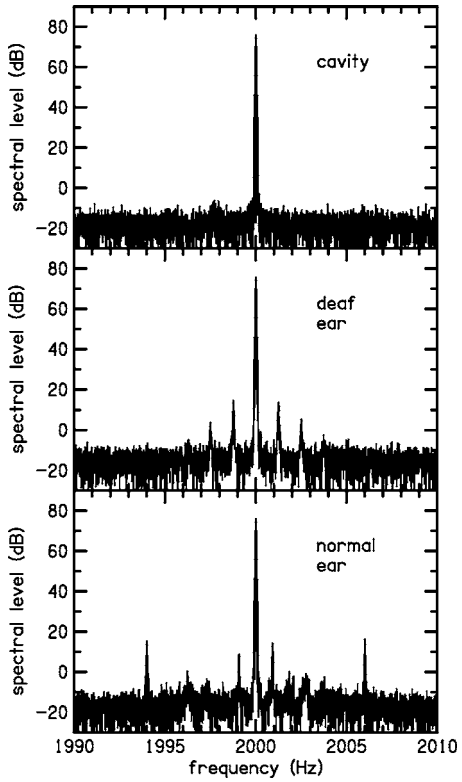

FIG. 3. Spectra of AM-SFOAE measurements. The top panel, measured in a cavity, shows only the 2000-Hz probe frequency. The middle panel, measured in a deaf ear, show sidebands at 1.25-Hz intervals due to heartbeat modulation, but no evidence of any modulation due to the suppressor. The bottom panel, measured in a normal ear, shows evidence of suppressor modulation at ±6 Hz from the probe frequency, in addition to heartbeat modulation.

imposed by the ER-10C. However, this distortion does not contaminate the SFOAE measurement, because the cavity response demonstrates that there is no significant interaction between probe and suppressor in our measurement system. This conclusion is based on the observation that there are no sidebands within 40 Hz of the probe frequency f_p.

In addition to cavity measurements, we also made measurements in four normal-hearing ears and one deaf ear. The deaf ear contained a cochlear implant, which was not activated at the time of the measurement. The deaf ear represents a biological system in which an SFOAE should not be present and provides a test of the linearity of our measurement system.

III. RESULTS

Spectral measurements from a cavity, deaf ear, and normal ear are compared in Fig. 3. The spectra are centered at f_p=2 kHz and include a 10-Hz range on either side of f_p. The top panel (cavity) demonstrates the absence of interaction between the probe and suppressor in our measurement system as evidenced by the lack of any measurable response at $f_p \pm 6$ Hz. Likewise, the middle panel (deaf ear) shows no evidence of the influence of the suppressor, based on the absence of components at $f_p \pm 6$ Hz. However, the deaf ear shows clear evidence of modulation at 1.25 Hz, including harmonics of this frequency. The 1.25-Hz modulation is presumably due to a heartbeat pulse rate of 75 per minute. Heartbeat modulation was frequently, but not always, observed in other ears. It was identified by the appearance of sidebands located 1 to 1.5 Hz relative to the probe frequency. In the lower panel, we see clear evidence of modulation at $f_p \pm 6$ Hz in addition to what is presumed to be heartbeat modulation. The modulation at $f_p \pm 6$ Hz is due to interaction between the probe and suppressor within the cochlea because it is not evident either in an acoustic cavity or in the deaf ear (i.e., a nonfunctioning cochlea). We used the level of the combined energy from both sidebands (L_{oae}) to represent the AM-SFOAE level. For the results shown in Fig. 3, the spectra were computed over the entire 131 s stimulus interval. As a result, the spectral levels are dominated by the maximum levels attained within that interval. In the case of a normal cochlea (bottom panel), the maximum SFOAE exceeded the noise floor by about 25 dB.

The probe and suppressor levels varied slowly in our stimuli to allow I/O functions to be determined for the range of levels over which the probe varied. These I/O functions were constructed by plotting the time course of the SFOAE level as a function of the time course of the probe level. Figure 4 shows SFOAE I/O functions in four normal ears (superimposed) at each of four probe frequencies. The solid lines represent the combined energy of the upper and lower 6-Hz sidebands of the probe. Our stimulus actually produced two I/O functions: one for increasing probe level and one for decreasing probe level. Upward and downward excursions of the I/O function were averaged together to produce a single I/O function. The dashed lines represent the combined noise energy at both 6-Hz sideband frequencies, obtained by subtracting the first and second halves of the response waveform. Although there is variation in the I/O functions across subjects, some general trends were noted. The SFOAEs were largest at 4 kHz, but also were systematically present at 1 and 2 kHz. However, at 8 kHz, the SFOAEs were reduced in two subjects and did not exceed the noise floor at any probe level in the other two subjects.

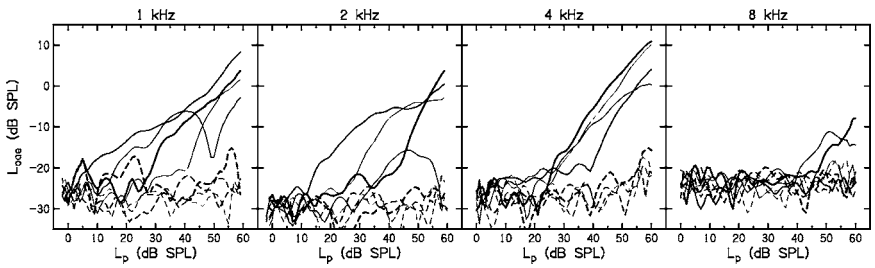

FIG. 4. AM-SFOAE level as a function of probe level at four frequencies. The solid lines show the SFOAE levels from four normal ears superimposed. The dashed lines indicate the noise level at the same frequency as the SFOAE. The line weight varies for each subject.

IV. DISCUSSION

The AM-SFOAE technique described above may be attractive because it eliminates the confounding influence of probe-frequency modulation due to physiological influences, such as heartbeat. It also eliminates the need for vector subtraction, which may be an advantage when maintaining stationarity across two separate measurements is difficult. When combined with slow variation of probe and suppressor levels, the AM-SFOAE method can be used to obtain complete SFOAE I/O functions in a relatively small amount of time. However, the AM-SFOAE technique may also be attractive when used with constant-level probes because vector subtraction is not needed.

The AM-SFOAE technique could be used to estimate the round-trip travel time from the ear canal to the SFOAE generation site and back to the ear canal. As described above, this travel time estimate is based on the phase difference between the sidebands and should be similar to other SFOAE round-trip travel time estimates (e.g., Shera and Guinan, 2003). Travel-time resolution might be improved by increasing the modulation rate above 6 Hz; however, the extent to which travel-time resolution can be improved is limited because the spectrum of the suppressor with higher modulation rates will spread to higher frequencies and eventually overlap the probe frequency. The possible contamination of the response due to overlapping spectra makes it unclear whether a higher modulation rate would be beneficial to the AM-SFOAE technique.

The suppressor level was selected in this study to keep it above the probe level without becoming excessively loud at the highest probe levels. Some attempts were made to determine suppressor levels that would produce the largest AM-SFOAE levels in our four subjects; however, the results were not consistent across subjects or frequencies. Hence, it is still undetermined what suppressor levels provide the best results with this technique.

SFOAE I/O functions recently described by Schairer *et al.* (2003) were about 10 dB higher in level than those shown in Fig. 4. This difference might be attributed to two factors. (1) The sidebands contain only half the power of the total reflected component, so the AM-SFOAE level would be expected to be 3 dB lower than the SFOAE level obtained by vector subtraction. (2) Our suppressor levels were lower than those used by Schairer *et al.* and probably did not achieve 100% amplitude modulation of the reflected component level. Despite the lower I/O function levels, the AM-SFOAE may still have the advantage of greater signal-to-noise ratio. The I/O functions in Fig. 4 are sometimes 25 dB above our measured noise, whereas the Schairer *et al.* I/O functions were rarely more than 15 dB above their measured noise. They attributed the elevated noise at the highest probe levels to an unknown biological source. In light of the present results, the increased noise that they observed may have been due to heartbeat modulation, which was not separated from the SFOAE by their measurement technique.

A different SFOAE technique that involved amplitude modulation was recently described by Goodman *et al.* (2004). In that case, the probe (not the suppressor) was modulated and the purpose of the modulation was to investigate OAE latency, not SFOAE level. Their latency estimates were based on temporal features of the SFOAE measurement, instead of the spectral methods typically employed to measure SFOAE latency. Although the use of AM-SFOAE measurements to estimate travel time was described above as a spectral method, an alternative approach based on temporal features should work equally well.

V. CONCLUSIONS

Measurement of SFOAEs using an amplitude-modulated suppressor appears to be a viable technique which may have some advantages over other methods. In particular, the spectral separation of the SFOAE allows the contaminating influence of heartbeat modulation to be eliminated and does not require vector subtraction to identify the SFOAE.

It is not necessary to vary the probe level to use this method (although doing so provides a means of obtaining the entire SFOAE I/O function quickly). Amplitude-modulated suppressors may also provide an effective means of measuring SFOAEs with constant probe levels and stimuli less than 1 s in duration.

ACKNOWLEDGMENTS

This work was supported by Grant Nos. R01 DC2251, T32 DC0013, and P30 DC4662 from NIH-NIDCD. We thank Christopher Shera, Kim Shairer, and an anonymous reviewer for many helpful suggestions.

Dreisbach, L. E., Siegel, J. H., and Chen, W. (**1998**). "Stimulus-frequency otoacoustic emissions measured at low and high frequencies in untrained human," Assoc. Res. Otolaryngol. Abs. 349.

Goodman, S. S., Withnell, R. H., de Boer, E., Lilly, D. J., and Nuttall, A. L. (**2004**). "Cochlear delays measured with amplitude-modulated tone-burst-evoked OAEs," Hear. Res. **188**, 57–69.

Guinan, J. J., Backus, B. C., Lilaonitkul, W., and Aharonson, V. (**2003**). "Medial olivocochlear efferent reflex in humans: Otoacoustic emission (OAE) measurement issues and the advantages of stimulus frequency OAEs." J. Assoc. Res. Otolaryngol. **4**, 521–540.

Kim, D. O., Dorn, P. A., Neely, S. T., and Gorga, M. P. (**2001**). "Adaptation of distortion-product otoacoustic emission in humans," J. Assoc. Res. Otolaryngol. **2**, 31–40.

Neely, S. T., and Stevenson, R. (**2002**). "SysRes," Tech. Memo. 19, Boys Town, National Research Hospital, Omaha, NE.

Schairer, K. S., Fitzpatrick, D., and Keefe, D. H. (**2003**). "Input–output functions for stimulus-frequency otoacoustic emissions in normal-hearing adult ears," J. Acoust. Soc. Am. **114**, 944–966.

Shera, C. A., and Guinan, J. J. (**2003**). "Stimulus-frequency-emission group delay: A test of coherent reflection filtering and a window on cochlear tuning," J. Acoust. Soc. Am. **113**, 2762–2772.

The tongue stops here: Ultrasound imaging of the palate (L)

Melissa A. Epstein
Department of Biomedical Sciences, Room 5A12, University of Maryland Dental School, 666 West Baltimore Street, Baltimore, Maryland 21201

Maureen Stone
Department of Biomedical Sciences, Room 5A12, and Department of Orthodontics, Room 3E08, University of Maryland Dental School, 666 West Baltimore Street, Baltimore, Maryland 21201

(Received 25 January 2005; revised 7 July 2005; accepted 15 July 2005)

This letter presents a method for imaging the palate and extracting the palate contour from ultrasound images. Ultrasound does not usually capture the palate because the air at the tongue surface reflects the ultrasound beam back to the transducer. However, when the tongue touches the palate during a swallow, the ultrasound beam is transmitted through the soft tissue until it reaches and is reflected by the palate. In combination with tongue contours, the palate contour has the potential for disambiguation of the tongue surface, registration of images within and across subjects, and calculation of phonetically important measures. © *2005 Acoustical Society of America.*
[DOI: 10.1121/1.2031977]

PACS number(s): 43.70.Jt [AL] Pages: 2128–2131

I. INTRODUCTION

Ultrasound has been used to image the surface of the tongue during speech and swallowing for more than 20 years, beginning with Sonies *et al.* (1981). Ultrasound provides real-time images of the tongue surface as a video sequence. Data are easy to collect and the procedure is non-invasive, making the methodology suitable for use with any subject, including patients and children. One of ultrasound's limitations is that only the upper tongue surface appears in the image. Information on other vocal tract structures, such as the palate, would enhance interpretation of the tongue data by providing a vocal tract reference. This paper presents a method for using ultrasound to collect palate contours for use as a reference for tongue movements during speech and swallowing.

Once palatal contour information is available, it allows important applications of ultrasound imaging which are not otherwise possible. For example, Wrench and Scobbie (2003) and Mielke *et al.* (2005) use a palate tracing to better describe subjects' articulations. The present letter addresses three applications. First, the palate contour can be overlaid on raw tongue images to disambiguate the location of the tongue surface. Second, by providing a reference within headspace, the palate contour may be used for within and across subject registration of ultrasound images. Finally, in combination with tongue contours, the palate contour allows the computation of phonetically important measures, such as the location and degree of constrictions in the oral cavity.

II. BACKGROUND

When imaging the tongue the ultrasound transducer is placed beneath the chin. The ultrasound beam travels upward through the tongue body and reflects back from the upper surface because the air has a different acoustic impedance than the tissue. This reflection produces a white line on the ultrasound image. Weaker echoes occur between boundaries of similar densities such as tissue-to-tissue or tissue-to-water. Tissue-to-tissue interfaces occur between muscles, fat, and connective tissue within the tongue. A tissue-to-water interface occurs between the tongue surface and the bolus during a swallow. When either the tongue or a bolus of liquid makes contact with the hard palate or velum the ultrasound beam reflects off the palate (see Fig. 1). The beam reflects off the near side of the bone or, in the case of the velum, the air on the nasal side of the soft tissue. Ultrasound images of the tongue surface and palate are limited anteriorly and posteriorly by "acoustic shadows" (black regions) created by refraction of the ultrasound beam off the mandible and hyoid bones (see Fig. 1).

The palate is normally not seen on an ultrasound image because the ultrasound beam reflects off the air in the vocal tract and never reaches the palate. However, during a swallow the tongue makes full contact with the palate as the bolus is propelled backward. The palate contour may be observed during either dry (saliva) or wet (liquid bolus) swallows. Wet swallows allow the sound to pass through the water and reflect from the palatine bone. However, wet swallows may introduce an artifact because the ultrasound beam can reflect off air ingested with the bolus of water. Since the air stays above the water in the mouth, a bright reflection occurs and can be mistaken for the palate. Figure 2 shows an ultrasound video frame with a reflection off a bolus of water that could be mistaken for the palate.

Data from two subjects executing three to five different kinds of command swallows (e.g., dry, wet, soda, different size boluses) demonstrate that palatal images can be collected from all types of swallows (Epstein *et al.*, 2004). Variability among measured palates is fairly small. There is a 4 mm maximum difference between palate traces for subject 1 across ten swallows; there is a 2 mm maximum difference for subject 2 across three swallows. Measurement and instrumental error account for up to 1 mm. The rest of the variability may be due to air trapped in the bolus.

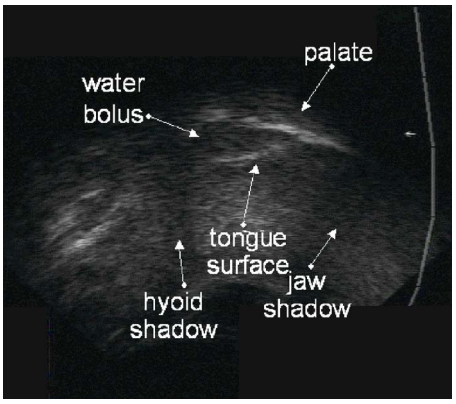

FIG. 1. Ultrasound image of the palate and tongue surface during a 3-cc water swallow. Both the palate and the tongue are visible because of the partial transmission/reflection of the ultrasound beam by the bolus of water. The shadow of the jaw bone obscures the most anterior portion of the tongue.

Anecdotally, palate images are sometimes clearer with wet rather than dry swallows. Consequently, it is useful to collect several types of command swallows and measure the clearest one. In addition, continuous swallowing is especially good because after several swallows the initial air has been swallowed and only water boluses remain. There is also anecdotal evidence that drinking a glass of water before the experiment brightens the ultrasound image of the tongue, possibly because of greater hydration of the tissue (Archangeli, private communication). Encouraging subjects to drink water *during* the experiment may also brighten the image. Although it is possible for sound to pass through to the palate by having the subject "press" his/her tongue against the entire palate at once, subjects often have difficulty doing this well, and full contact cannot be guaranteed, especially for the velum.

Features of the palate image may vary during the swallow and the palate contour may need to be extracted from multiple frames over time as the bolus passes through the vocal tract. The data points for the contour are collected from the front to the back, corresponding to the passage of the bolus through the tract. Initial frames show good alveolar edges and later frames good vault and velar edges. To increase accuracy of intra- and intersubject registration, particular attention should be paid to tracing of palatal landmarks. Subjects tend to have a bend between the rugae and the vault (this is also seen on the dental cast). If no bend is seen on the palatal contour, the tongue—not the palate—may have been measured and careful inspection of the images may show a frame in which the bottom of the white line is curved and the top bent (see Fig. 3). This line contains both tongue and palate data. The lower edge of the palate (between the two lines) should be extracted if at all possible. The bend at the velar/palatal junction can also be used as a landmark by observing frames with velar lowering.

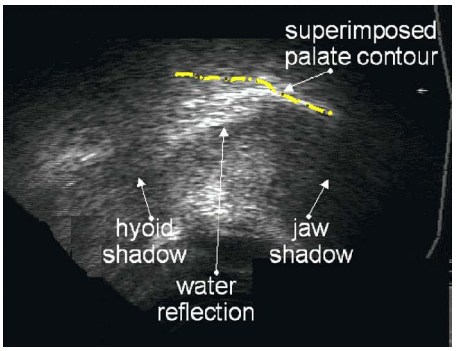

FIG. 2. Reflection of a bolus of water. A palate contour from a dry swallow is superimposed on the ultrasound image (small black and white dots). Note how the water bolus reflection is below the palate contour along the posterior edge.

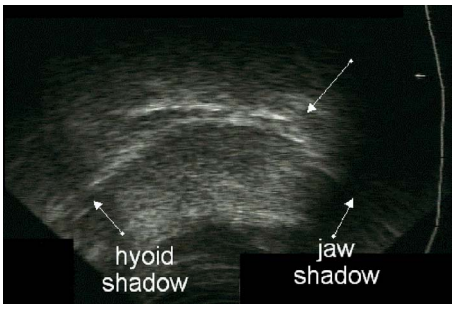

FIG. 3. Ultrasound image illustrating bend between rugae and vault of the palate for subject 2 during a dry swallow. In this frame the tongue contour is curved and the palate contour has an angular bend (marked by white arrow). The lower edge of the palate contour should be extracted.

Ultrasound images of the hard palate and velum may not be directly comparable by visual inspection to a digital midsagittal dental cast representation of the palate for some subjects for several reasons. First, the amount of mucosa covering the palatine bone is thicker posteriorly than anteriorly (see Fig. 4). Ultrasound represents the palatine bone, whereas the dental cast represents the mucosa. Anteriorly, the mucosa is quite thin, 1 mm or less. Posteriorly, the mucosa is thicker and there is a larger distance between the bone and soft tissue surface. Second, the velum is minimally captured, if at all, on a dental cast to prevent a gag reflex; however, the velum is visible on the ultrasound image. Thus the ultra-

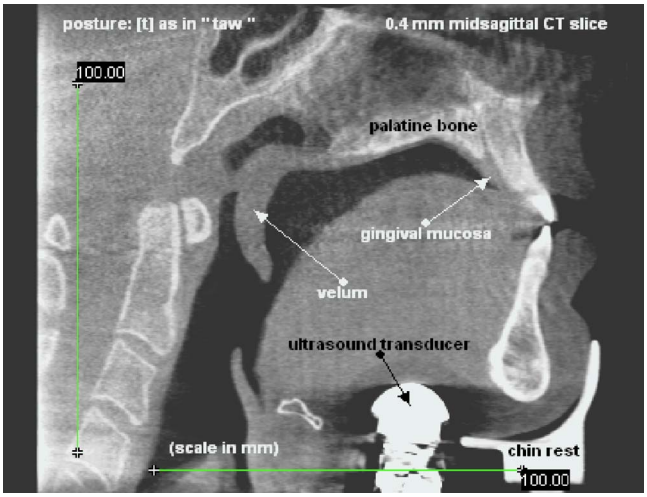

FIG. 4. A 0.4-mm midsagittal CT slice (iCAT, Imaging Sciences International) of subject sustaining /t/. Note how the palatal mucosa thickens from anterior to posterior and the thickness of the velum. Figure courtesy of Ian Wilson, University of British Columbia.

sound palate extends farther back than the dental cast. In addition, the velum may be more than 10 mm in thickness (Kuehn and Kahane, 1990; Kuehn, private communication). On the dental cast the oral side of the velum is captured, and the velum will be in an open position to accomodate the subject's breathing. On the ultrasound image the velar reflection is usually the nasal side since the sound passes through the tissue and reflects off the air in the nasal cavity. Moreover, the velum is closed at certain times during the swallow. Thus, the cast reflects the more rounded surface of the unevenly thick mucosa and, if captured, a lowered velum. The ultrasound image reflects the more level palatine bone and the nasal side of the (possibly raised) velum. A final difference occurs because the anterior portion of the hard palate, including the alveolar ridge, is often not visible in the ultrasound palate, due to a posterior transducer angle or to obscuration by the acoustic shadow cast by the jaw or by air underneath the tongue. Therefore the ultrasound palate will likely be shorter anteriorly due to the jaw shadow, and longer posteriorly due to velar imaging, when compared to the dental cast. However, not all subjects show all the above described differences.

Three types of tongue-palate relationships can occur when comparing a palate contour with tongue contours of certain speech sounds, such as high front stops (e.g., /t,d/) and high back stops (e.g., /k,g/). First, the tongue contour may appear to merge with the palate contour. This is because when the tongue touches the palate the ultrasound beam travels through the tongue and reflects off the palate and not the surface of the tongue. Second, the tongue contour may lie above the palate contour. Then it is possible that at least part of the palate contour is an artifact (e.g., air in the bolus of water). Finally, the elevated tongue may not appear to touch the palate. For the back consonants this may be due to variations in the thickness of the palatal mucosa and velum. For front consonants the palatine bone may be several millimeters higher than the mucosal palate or the point of contact for front consonants may be obscured by the shadow of the jaw and the air beneath the tongue. An additional confound exists for rapid motions, like stop consonants; they tend to be undersampled at the ultrasound frame rate of 30 Hz. Therefore, it is possible that the maximal frame imaged is not actually the maximal tongue position for the stop.

III. APPLICATIONS

To demonstrate the use of palates in ultrasound-based speech research, three applications are described based on palates and speech articulations collected from 12 archived data sets (five females and seven males; ages range from 16 to 34 years). Due to the archival nature of the data, only dry swallows are available for analysis. The same ultrasound machine (Acoustic Imaging, Inc., Phoenix, AZ, Model AI5200S) is used for all 12 subjects. The transducer for all subjects is a 2.0–4.0 MHz multifrequency convex-curved linear array transducer that produces 30 90° wedge-shaped scans per second. Focal depth is 10 cm. Ultrasound and audio data are collected while subjects are seated in a dental chair positioned supine, then upright. Subjects wear a cervical collar with ultrasound transducer attached to restrain head motion and stabilize the transducer. Unless otherwise specified, the data discussed here are from the upright position. Palates are collected from either the frame with the most anterior hyoid bone shadow or reconstructed based on palatal landmarks (e.g., the palatal bend posterior to the rugae) over several frames of the swallow. For validation of the extracted palate contours for subjects 1–5, word-initial /d/ and /g/ are collected from the words "dash" ("dack" for subject 2) and "golly" to locate the palates relative to the tongue contours. Tongue contours for /d/ and /g/ are extracted from the frame where the tongue reaches the maximum constriction height before the release burst seen in the simultaneously collected acoustic signal. Tongue and palate contours are measured using the Maryland Tongue Analysis Package (MTAP), consisting of EdgeTrak, a semi-automatic system for the extraction and tracking of tongue contours (Li *et al.*, 2005), and Surfaces, a contour-sequence display and analysis program (Parthasarathy *et al.*, 2005). Palate and tongue contours for subjects 1–5 are displayed in Fig. 5.

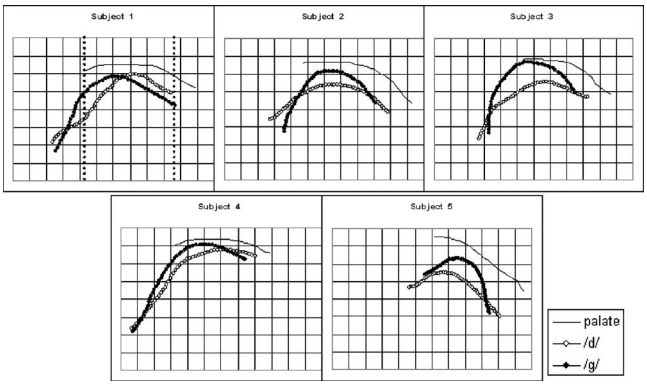

FIG. 5. Tongue and palate contours for five subjects (centimeter scale). Tongue tips are to the right.

The first application is the use of the palate as a reference for tongue contours. Figure 5 displays tongue and palate contours for subjects 1–5. Note how the palate contour disambiguates the location for the constriction for the /g/ tongue contour. Furthermore, the posterior edge of the palate contour provides a landmark for the division between the oral and pharyngeal regions of the tongue contour.

The second application is using the palate for registration across subjects or sessions. Data collected from two subjects or sessions may differ in transducer angle. Imposing the palate contour on the tongue data makes this rotation clear. For example, in Fig. 5, the palate for subject 5 appears rotated further forward compared to the other subjects. This indicates that for subject 5 the ultrasound transducer is rotated backward more than the other subjects when the data was collected. This is because the ultrasound video display always positions the transducer as if it were pointed upward; a backward transducer rotation when transformed in this way rotates all the imaged data anteriorly. To determine what registration is needed to overlay two data sets, landmarks on palatal contours may be aligned. For a single subject's data, two landmarks can be used: the intersection of the velum with the hard palate (in a frame where the velum is lowered)

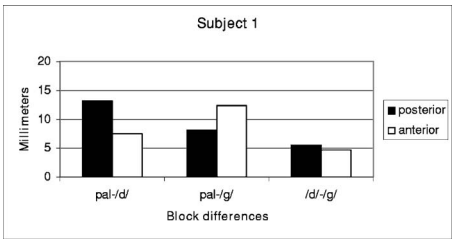

FIG. 6. Block differences between the palate and the tongue contours or between the two tongue contours for subject 1. The contours from Fig. 5 are segmented between the vertical lines. The contours are divided into two equal length segments (anterior and posterior) and average nearest-neighbor differences are calculated between the contours for each segment.

and the angle between the rugae and the vault. Across subjects, caution should be exercised due to different sizes of the palate and differences in vault angle.

Once these landmarks are identified, they can be used to spatially align two palates by rotating and translating the subject's palate at time 2 to overlay the palate with time 1. The alignment parameters are then applied to the tongue data at time 2 to align the two tongue data sets. The following describes the results of a study aligning palate traces from subjects 1–12 in upright and supine positions. The rugae landmark is identified in both palate traces. Palate 2 (supine) is then rotated and translated to overlay palate 1 (upright). The alignment parameters are then applied to the tongue data at time 2 to align the two tongue data sets. Results of the alignment indicate that of the 12 palate pairs, eight differed in anterior-posterior length. Four of these eight have virtually identical palatal traces (maximal difference of less than 1 mm) and four differ only in velar angle. Three additional subjects have a maximal difference between 2–5 mm, and one has two entirely different shapes. There is only one collected swallow per subject, therefore, the nature of the error for this last subject could not be determined or rectified.

The final application discussed here is to use the palate contour for the computation of phonetically important measures, such as the constriction degree and location. For example, Fig. 6 shows local differences between the palate and the tongue contours for subject 1. The local differences are calculated by first cutting the contour and the palate to the same length in the x direction. The contours are then resampled to have 50 points and a nearest-neighbor difference is calculated for each point. Finally, the contours are divided into equal length segments (in this example two segments—anterior and posterior—are used) and average nearest-neighbor differences are calculated between the palate and the tongue contour for each segment. As can be seen in the figure, these differences indicate that for /d/ the palate-tongue distance decreases from back to front and for /g/ the distance increases from back to front. Without a palate contour, it would only be possible to make comparisons in location directly between /d/ and /g/ and none in absolute vocal tract constrictions. The advantages of comparing tongue contours to a single reference palate increase when analyzing a large data set (e.g., several phonemes or an entire sentence), the alternative being comparing each phoneme to all the others or to an arbitrary reference phoneme or rest position.

IV. CONCLUSIONS

The inclusion of a representation of the hard and soft palate in an ultrasound image has the potential to increase our ability to interpret and assess tongue contours. Although there are some limitations in the collection and interpretation of ultrasound images of the palate, palate contours are useful for disambiguation of the tongue surface, across and within subject registration, and for the calculation of phonetically interesting measurements in the oral cavity. The addition of palate information facilitates the reduction and enhances interpretation of the data by providing an oral cavity reference, subject and session registration, and a second vocal tract structure for quantitative analyses. With the inclusion of the palate, ultrasound imaging can present the tongue in its proper position in the vocal tract.

ACKNOWLEDGMENTS

This research was supported in part by NIDCD/NIH Grant No. RO1-DC01758 and by NIH Grant No. T32-DE07309. The authors would like to thank Greg Stock, Marianne Pouplier, Kevin Bunin, and Andy Browne for their assistance in data collection and analysis.

Epstein, M. A., Stone, M., Pouplier, M., and Parthasarathy, V. (**2004**). "Obtaining a palatal trace for ultrasound images," J. Acoust. Soc. Am. **115**, 2631 (Abstract).

Kuehn, D. P., and Kahane, J. C. (**1990**). "Histologic study of the normal human adult soft palate," Cleft Palate J. **27**, 26–34.

Li, M., Kambhamettu, C., and Stone, M. (**2005**). "Tongue motion averaging from contour sequences," Clin. Linguist. Phon. **19**, 515–528.

Mielke, J., Baker, A., Archangeli, D., Richtsmeier, P., and Racy, S. (**2005**). "Aligning tongues and palates with Palatron," Ultrafest III, Tucson, Az, 14–16 April 2005. Available at http://dingo.sbs.arizona.edu/~apilab/ultrafest/Palatron.pdf

Parthasarathy, V., Stone, M., and Prince, J. L. (**2005**). "Spatiotemporal visualization of the tongue surface using ultrasound and kriging (SURFACES)," Clin. Linguist. Phon. **19**, 529–544.

Sonies, B., Shawker, T., Hall, T., Gerber, L., and Leighton, S. (**1981**). "Ultrasonic visualization of tongue motion during speech," J. Acoust. Soc. Am. **70**, 683–686.

Wrench, A. A., and Scobbie, J. M. (**2003**). "Categorising vocalisation of English /l/ using EPG, EMA and ultrasound," in Proceedings of the 6th International Seminar on Speech Production, Sydney, Australia, 7–10 July 2003, pp. 314–319. Available online at http://sls.qmuc.ac.uk/RESEARCH/Ultrasound/child_home_pages/wrench_scobbie.pdf

Dispersion-reducing finite elements for transient acoustics

Bin Yue and Murthy N. Guddati[a)]
Department of Civil, Construction, and Environmental Engineering, North Carolina State University, Raleigh, North Carolina 27695

(Received 15 October 2004; revised 1 July 2005; accepted 9 July 2005)

This paper focuses on increasing the accuracy of low-order (four-node quadrilateral) finite elements for the transient analysis of wave propagation. Modified integration rules, originally proposed for time-harmonic problems, provide the basis for the proposed technique. The modified integration rules shift the integration points to locations away from the conventional Gauss or Gauss-Lobatto integration points with the goal of reducing the discretization errors, specifically the dispersion error. Presented here is an extension of the idea to time-dependent analysis using implicit as well as explicit time-stepping schemes. The locations of the stiffness integration points remain unchanged from those in time-harmonic case. On the other hand, the locations of the integration points for the mass matrix depend on the time-stepping scheme and the step size. Furthermore, the central difference method needs to be modified from its conventional form to facilitate fully explicit computation. The superior performance of the proposed algorithms is illustrated with the help of several numerical examples. © *2005 Acoustical Society of America.* [DOI: 10.1121/1.2011149]

PACS number(s): 43.20.Bi, 43.20.Px, 43.20.Fn [LLT] Pages: 2132–2141

I. INTRODUCTION

Finite element analysis with direct time-stepping methods has been widely applied to simulate transient acoustics (see, e.g., Refs. 1–3). These procedures incur errors due to discretization, which can be classified into amplitude error and dispersion error. The dispersion error is caused by the approximation of wave velocities and results in unwanted oscillations around the wave front, thus polluting the results. This phenomenon is especially problematic for large-scale wave propagation problems; when the wave travels for long distances, the dispersion error accumulates, and the numerical artifacts grow, making the solution cluttered. A side effect of the dispersion error is that the amplitude error also increases as the wave disperses. It is important, therefore, to minimize the dispersion error to obtain accurate solutions for long-range propagation problems.

A straightforward way of reducing the dispersion error is to use a finer mesh and smaller time-step size. However, such a refinement comes with significant computational overhead. Other dispersion reduction techniques involve higher-order finite elements, e.g., Taylor-Galerkin schemes combined with higher-order spatial discretization[4] and an explicit six-stage time-march with a seven-point spatial operator.[5] These methods also demand a significantly high computational cost, making some of the large-scale simulations expensive. Space-time discretizations[6] fall in the same category as they require high computational cost. If possible, it is desirable to reduce the dispersion error for low-order schemes such as those using low-order finite elements with standard Newmark or central difference time-stepping techniques. The development of such methods for bilinear quadrilateral elements is the subject of this paper.

The fundamental feature of the simulation of transient waves is the coupling of spatial and temporal discretization errors. The error in the wave velocity, which is a measure of the dispersion error, depends on the wavelength error resulting from spatial discretization and the frequency error resulting from temporal discretization. Numerous dispersion reduction methods have been employed to reduce the dispersion error. The time-stepping algorithms and their influence on temporal dispersion and dissipation have been analyzed in the literature (see, e.g., Hughes[7]). The dispersion properties of bilinear quadrilateral elements and linear triangular elements have been analyzed with diagonal and nondiagonal mass matrices in uniform meshes.[8] Analyses of combinations of spatial and temporal discretizations for wave propagation can also be found in the literature.[9,10] Krieg and Key[11] studied temporal dispersion control, realized the opposing effect of lumped and consistent mass matrices and suggested matching the mass computation with the time-stepping algorithm. However, their method is robust only for one-dimensional problems and loses accuracy when applied to higher dimensions. Similar difficulties are also faced by the semi-empirical method, developed by Wang *et al.*,[12] as well as the technique of local spatial averaging of the velocity, introduced by Krenk.[13]

The inability of the above-mentioned methods to increase the accuracy in a multidimensional simulation is closely related to the numerical anisotropy; that is, the dispersion error is dependent on the direction of the wave propagation. Since most of the methods are developed for one-dimensional meshes, they are effective for one or only a few propagation direction(s). A desirable dispersion reduction method needs to eliminate or reduce the velocity error in all directions simultaneously.

One of the successful approaches for the reducing dispersion error in time-harmonic analysis is the modified integration rules[14] (recently, it has been brought to our attention

a)Electronic mail: mnguddat@ncsu.edu

that this idea has been developed earlier,[15] but was not published in the open literature). By simply changing the location of the integration points for the system matrix evaluation, the wave-number error and the anisotropy were decreased significantly. In this paper, the modified integration rules are extended for transient analysis to reduce the error in the wave velocity resulting from coupled spatial and temporal discretization. We found that, provided that the integration points are chosen carefully, the numerical wave velocity can be made fourth-order accurate, as opposed to the second-order accuracy obtained from conventional finite element methods.

The outline of the paper is as follows. Section II contains a discussion of the Galerkin finite element method for solving acoustic wave problems and the concept of modified integration rules. Section III presents the dispersion relationships resulting from numerical discretizations in space and time. Dispersion-reducing schemes are developed for implicit time-stepping in Sec. IV. In Sec. V, modified integration rules are developed for the half-step central difference method (hereafter referred to as CDM), resulting in explicit computation with fourth-order accuracy. Section VI focuses on evaluating the performance of the proposed methods with the help of numerical examples. The paper is concluded in Sec. VII with some closing remarks.

II. PRELIMINARIES

A. Finite element formulation for scalar wave propagation

The scalar wave equation governing the propagation of acoustic and antiplane shear waves is given by

$$\frac{\partial^2 u}{\partial t^2} - c_0^2 \nabla^2 u = 0, \tag{1}$$

where u is the field variable and c_0 is the wave velocity. Since the primary concern of the paper is dispersion associated with the propagation of disturbances, we do not consider body forces and assume homogeneous boundary conditions. The initial conditions are given as

$$u(\mathbf{x},0) = u_0(\mathbf{x}), \quad \frac{\partial u}{\partial t}(\mathbf{x},0) = v_0(\mathbf{x}), \tag{2}$$

where, u_0, v_0 are the initial displacement and velocity, respectively.

Using classical variational calculus, the above differential (strong) form of the boundary value problem can be converted to the following variational (weak) form:

$$\left(v, \frac{\partial^2 u}{\partial t^2}\right)_\Omega + c_0^2 (\nabla v, \nabla u)_\Omega = 0. \tag{3}$$

The notation, $(\cdot,\cdot)_\Omega$, is used for the inner product over the domain, Ω, defined as follows:

$$(f,g)_\Omega = \int_\Omega fg \, d\Omega. \tag{4}$$

For a numerical solution of the above variational boundary value problem, the (Bubnov) Galerkin finite element method can be used. Thus, u and v are approximated as u^h and v^h that take the form,

$$\begin{aligned} u^h(\mathbf{x},t) &= \mathbf{N}(\mathbf{x})\mathbf{U}(t), \\ v^h(\mathbf{x},t) &= \mathbf{N}(\mathbf{x})\mathbf{V}(t), \end{aligned} \tag{5}$$

where $\mathbf{N}$ is the shape function matrix, $\mathbf{U}$ is the discretized field variable (degree of freedom vector), and $\mathbf{V}$ is the discretized form of v. By substituting Eq. (5) into Eq. (3) we obtain the semidiscrete system,

$$\mathbf{M}\ddot{\mathbf{U}} + c_0^2 \mathbf{K}\mathbf{U} = \mathbf{0}. \tag{6}$$

In the above, $\mathbf{K}$ and $\mathbf{M}$ are stiffness and mass matrices, respectively. They are obtained by assembling the element matrices that are given by

$$\begin{aligned} \mathbf{K}_e &= \int_{\Omega_e} (\nabla \mathbf{N})^T \nabla \mathbf{N} \, d\Omega_e, \\ \mathbf{M}_e &= \int_{\Omega_e} \mathbf{N}^T \mathbf{N} \, d\Omega_e, \end{aligned} \tag{7}$$

where Ω_e is the domain of the element.

The semidiscretized system (6) is commonly solved using the Newmark method,[16] which consists of the following:[7]

$$\begin{aligned} &\mathbf{M}\ddot{\mathbf{U}}^{(n+1)} + c_0^2 \mathbf{K}\mathbf{U}^{(n+1)} = 0, \\ &\mathbf{U}^{(n+1)} = \mathbf{U}^{(n)} + \Delta t \dot{\mathbf{U}}^{(n)} + \frac{\Delta t^2}{2}[(1-2\beta)\ddot{\mathbf{U}}^{(n)} + 2\beta \ddot{\mathbf{U}}^{(n+1)}], \\ &\dot{\mathbf{U}}^{(n+1)} = \dot{\mathbf{U}}^{(n)} + \Delta t[(1-\gamma)\ddot{\mathbf{U}}^{(n)} + \gamma \ddot{\mathbf{U}}^{(n+1)}]. \end{aligned} \tag{8}$$

The first equation in Eq. (8) is Eq. (6) written at $t=t_{n+1}$, and the other two are finite difference formulas describing the evolution of the approximate solution. The parameters β and γ are the parameters of the method and determine the stability and accuracy characteristics of the algorithm. The time-stepping schemes derived from the Newmark method are normally implicit, involving the solution of a linear system, which could be expensive. The explicit CDM can also be retrieved by choosing $\gamma=1/2$ and $\beta=0$, resulting in a significant reduction in computational cost. This paper analyzes the performance of the explicit CDM method, as well as three implicit schemes.

For the Newmark methods to be stable, $\gamma \geqslant 1/2$ is a necessary condition. However, for the methods using $\gamma > 1/2$, the dissipation error is introduced. For structural dynamics problems, this numerical dissipation is generally viewed as desirable and often considered necessary to damp out erroneous higher modes of semidiscrete structural equation.[7] On the other hand, in wave propagation problems, this error should be avoided in order to minimize the distortion of the wave fronts. For this reason, we choose $\gamma=1/2$ for the remainder of the paper. With $\gamma=1/2$, Eq. (8) can be rewritten as

$$(\boldsymbol{M}+\beta\Delta t^2 c_0^2\boldsymbol{K})\boldsymbol{U}^{(n+1)}+[-2\boldsymbol{M}+(1-2\beta)\Delta t^2 c_0^2\boldsymbol{K}]\boldsymbol{U}^{(n)}+(\boldsymbol{M}+\beta\Delta t^2 c_0^2\boldsymbol{K})\boldsymbol{U}^{(n-1)}=0. \tag{9}$$

The above linear multistep form is chosen to facilitate the analysis of the methods developed here.

B. Modified integration rules

Modified integration rules[14,15] are successfully used to reduce the dispersion error in time-harmonics wave propagation problems and form the basis for the techniques developed in this paper. The fundamental idea behind the techniques is simple; the integration points are shifted from the conventional Gauss/Gauss-Lobatto integration points in order to minimize the dispersion error. Specifically, the integrals in Eq.(7) are first transformed into the master-coordinate system with the help of isoparametric formulation, and the resulting integrals are evaluated using the modified integration rules. For a four-node quadrilateral element, the stiffness and mass matrices in Eq.(7) are each evaluated using modified 2×2 integration rules. The expression for the element stiffness and mass matrices are given by

$$\mathbf{K}_e=\sum \nabla\mathbf{N}^T(\pm\alpha_K,\pm\alpha_K)\,\nabla\mathbf{N}(\pm\alpha_K,\pm\alpha_K)\det(\mathbf{J}),$$
$$\mathbf{M}_e=\sum \mathbf{N}^T(\pm\alpha_M,\pm\alpha_M)\mathbf{N}(\pm\alpha_M,\pm\alpha_M)\det(\mathbf{J}). \tag{10}$$

In the above, α_K and α_M are the locations of the integration points and serve as the parameters of the modified integration rules. The modified integration rules are justified by the fact that the integration errors remain second order in spite of the modifications and do not alter the convergence rate of the finite element solution. In the case of time-harmonic wave propagation problems, it turns out that the dispersion error is reduced by a simple choice of these parameters ($\alpha_K=\alpha_M=\sqrt{2/3}$). The choice of these parameters is more involved for transient problems, and is addressed in the remainder of the paper.

III. DISPERSION ERROR ANALYSIS

In this section, the dispersion error resulting from spatial discretization (i.e., FEM with modified integration rules), coupled with temporal discretization (i.e., the Newmark method), is analyzed. For the differential equation (1), the general solutions are plane waves of the form $e^{i(k_0x\cos\theta+k_0y\sin\theta-\omega_0t)}$, where θ is the direction of wave propagation with respect to the x axis, ω_0 is the circular frequency, and $k_0=\omega_0/c_0$ is the associated wave number. The wave modes, $\mathbf{U}_{x,y}^{(n)}$, for the approximate problem [the solution of Eqs.(6) and (9)] take a similar form,

$$\mathbf{U}_{x,y}^{(n)}=e^{i(kx\cos\theta+ky\sin\theta-\omega n\Delta t)}, \tag{11}$$

at time $n\Delta t$ and location (x,y), where k and ω are the approximate wave number and frequency, respectively. It is important to note that the propagation velocity for the approximate solution, $c=\omega/k$, is different from the exact wave velocity, c_0. The error in the wave velocity depends on the wavelength of the mode, leading to an artificial dispersion of the wave front.

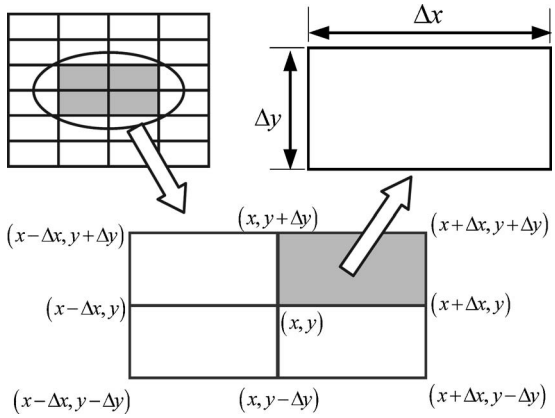

FIG. 1. Four-element nine-node finite element patch used for dispersion error analysis.

The error in the wave velocity can be evaluated in the following way. First, Eq. (9) is written in a form reminiscent of the finite difference discretization of the governing equation (1). This is achieved by multiplying the system matrices with the displacement vectors and writing the equation associated with node (x,y), e.g., the multiplication of $\boldsymbol{MU}^{(n+1)}$ in Eq. (9) results in an expression of

$$4M_0U_{x,y}^{(n+1)}+2M_x(U_{x-\Delta x,y}^{(n+1)}+U_{x+\Delta x,y}^{(n+1)})+2M_y(U_{x,y-\Delta y}^{(n+1)}+U_{x,y+\Delta y}^{(n+1)})+M_{xy}(U_{x-\Delta x,y-\Delta y}^{(n+1)}+U_{x+\Delta x,y-\Delta y}^{(n+1)}+U_{x+\Delta x,y+\Delta y}^{(n+1)}+U_{x-\Delta x,y+\Delta y}^{(n+1)}). \tag{12}$$

In the above, the connectivity given in Fig. 1 is utilized, and M_0,M_x,M_y,M_{xy} are elements in the mass matrix and are given in Eq. (37). Other matrix-vector multiplications are similar. We then substitute Eq. (11) into the resulting finite difference equation and obtain an implicit relationship between c and c_0. Both the finite difference form and the relationship between c and c_0 are lengthy and are not presented here for the sake of brevity. Instead of writing an explicit expression for c, we take the Taylor expansion with respect to k and obtain a simplified, albeit approximate, polynomial expression of the relative error in the wave velocity:

$$\left|\frac{c_0-c}{c_0}\right|=\frac{k^2}{24}|\chi_x\Delta x^2+\chi_y\Delta y^2-(1-12\beta)c_0^2\Delta t^2|+O[(k\Delta x)^4+(k\Delta y)^4+(c_0\Delta t)^4], \tag{13}$$

where

$$\chi_x=3\cos^2\theta\alpha_M^2-2\cos^4\theta-3\sin^2\theta\cos^2\theta\alpha_K^2,$$
$$\chi_y=-2+4\cos^2\theta-2\cos^4\theta+3\sin^2\theta\alpha_M^2-3\sin^2\theta\cos^2\theta\alpha_K^2. \tag{14}$$

Since our goal is to minimize the above-noted error, we attempt to annihilate the leading term by appropriately choosing the integration parameters, α_M and α_K. While such a strategy was successful for the time-harmonic analysis[14] even on rectangular grids, it turns out that it does not work for transient analysis. Specifically, for nonsquare grids ($\Delta x\neq\Delta y$), α_M and α_K that are required for dispersion reduction turn out to be dependent on the direction of the propa-

gation. On the other hand, for square meshes ($\Delta x=\Delta y=h$), the dispersion-reducing values of α_M and α_K turn out to be direction-independent. For this reason, and more importantly because square meshes are the natural choice for transient wave propagation analysis, the rest of the paper focuses on square meshes. The leading-order error in wave velocities for square meshes is obtained from Eq. (13) and is given by

$$\frac{(kh)^2}{24}\left|(3\alpha_M^2-2)-(1-12\beta)\frac{c_0^2\Delta t^2}{h^2}+(4-6\alpha_K^2)\cos^2\theta\sin^2\theta\right|. \tag{15}$$

It is instructive to note that only stiffness integration causes anisotropy in the leading-order term, which is immediately eliminated by choosing

$$\alpha_K=\sqrt{2/3}, \tag{16}$$

thus reducing the expression further to

$$\frac{(kh)^2}{24}\left|(3\alpha_M^2-2)-(1-12\beta)\frac{c_0^2\Delta t^2}{h^2}\right|. \tag{17}$$

In order to make the above expression zero, we need to choose

$$\alpha_M=\sqrt{\frac{2}{3}+\left(\frac{1}{3}-4\beta\right)\frac{c_0^2\Delta t^2}{h^2}}. \tag{18}$$

The main difference between time-harmonic analysis[14] and transient analysis is that α_M is dependent on the time-step size. It should also be noted that the above-noted expression is consistent with the observations for time-harmonic analysis in that when Δt approaches zero, the time-harmonic value of $\sqrt{2/3}$ is recovered.

At first glance, Eq. (18) indicates that dispersion reduction can be achieved in a simple manner, similar to the one used for time-harmonic analysis. Unfortunately, this is not the case, as the stability of the time-stepping scheme is altered by the location of the integration points. For $\gamma=1/2$, the Newmark method is only conditionally stable if $\beta<1/4$ and the stability condition is given by[7]

$$\Delta t\leqslant\frac{1}{\omega_{\max}\sqrt{1/4-\beta}}, \tag{19}$$

where $\omega_{\max}$ is the maximum natural frequency of the system. $\omega_{\max}$ can be taken as the square-root of the largest eigenvalue of $\boldsymbol{K}$ with respect to $\boldsymbol{M}$ for a single finite element in the system. For a uniform square mesh with element size, h, we obtain $\omega_{\max}$ by solving the eigenvalue problem, $c_0^2\boldsymbol{K}_e-\omega^2\boldsymbol{M}_e=0$, resulting in

$$\omega_{\max}=\max\left(\frac{2c_0}{h\alpha_M},\frac{4c_0}{\sqrt{3}h\alpha_M^2}\right). \tag{20}$$

Thus the stability condition, in the form of critical time-step size, is given by

$$\Delta t\leqslant\frac{h\alpha_M}{2c_0}\frac{\min(1,\sqrt{3}\alpha_M/2)}{\sqrt{1/4-\beta}}. \tag{21}$$

Alternatively, written in terms of the dimensionless time-step size ($\tau\equiv c_0\Delta t/h$), the stability condition becomes

$$\tau\leqslant\frac{\alpha_M}{2}\frac{\min(1,\sqrt{3}\alpha_M/2)}{\sqrt{1/4-\beta}}. \tag{22}$$

Therefore, it is important to obtain the appropriate value of α_M satisfying the above condition as well as the dispersion reduction condition (18), which is rewritten as

$$\alpha_M=\sqrt{\frac{2}{3}+\left(\frac{1}{3}-4\beta\right)\tau^2}. \tag{23}$$

It turns out that satisfying conditions (22) and (23) is not always possible and some compromise may be necessary. In the next two sections, we attempt to balance accuracy and stability for both implicit and explicit methods.

IV. DISPERSION-REDUCING TECHNIQUES FOR IMPLICIT METHODS

In this section, we consider three special cases of the Newmark method: constant average acceleration (CAA) with $\beta=1/4$, linear acceleration (LA) with $\beta=1/6$, and Fox-Goodwin (FOX) with $\beta=1/12$. As mentioned earlier, we choose $\gamma=1/2$ to eliminate numerical dissipation.

A. Constant average acceleration method

The constant average acceleration method is unconditionally stable since $\beta=1/4$, and it appears that the dispersion error can be manipulated without any constraints. It is easily observed from Eq. (15) that with the conventional integration points, ($\alpha_K=\alpha_M=\sqrt{1/3}$), the dispersion error is second order and dependent on the propagation direction. Whereas a simple choice of

$$\alpha_K=\sqrt{\frac{2}{3}},\quad \alpha_M=\sqrt{\frac{2}{3}(1-\tau^2)} \tag{24}$$

removes the leading second-order error completely, and the remaining fourth-order error is

$$\frac{(kh)^4}{1440}\left|3-3\tau^4-(9-20\tau^4)\cos^2\theta\sin^2\theta\right|. \tag{25}$$

Although this improvement is impressive, the time-step size is limited by $\tau<1$. Otherwise, $\alpha_M^2\leqslant 0$, which is not realistic. It may be possible to use the negative values of α_M^2 to evaluate $\mathbf{M}$, but the resulting matrix is not positive definite, thus making it susceptible to numerical difficulties in solving the linear system. This is of significant concern as the current modification strips away the ability to choose an arbitrarily high time-step size, if desired.

B. Linear acceleration method

Using $\beta=1/6$, the linear acceleration method has a leading-order error of

$$\frac{(kh)^2}{24}\left|(3\alpha_M^2-2)+(4-6\alpha_K^2)\cos^2\theta\sin^2\theta+\tau^2\right|. \tag{26}$$

To eliminate it, the only choice is

$$\alpha_K=\sqrt{\frac{2}{3}},\quad \alpha_M=\sqrt{\frac{1}{3}(2-\tau^2)}. \tag{27}$$

To analyze the stability condition, we first substitute the values of β and α_K^2 into the stability condition (22), resulting in

$$\tau^2\leqslant 3\alpha_M^2\min\left(1,\frac{3\alpha_M^2}{4}\right). \tag{28}$$

It is observed from Eq. (27) that $\alpha_M^2<2/3$ and thus, $\min(1,3\alpha_M^2/4)=3\alpha_M^2/4$. After substituting the value of α_M^2 in Eq. (27) into Eq. (28) and simplifying the equation, we obtain the stability condition of $\tau\leqslant 0.732$. It is clear that the choice of Eq. (27) reduces the dispersion error while increasing the critical time-step size; the conventional method has a critical time-step size of $\tau\leqslant 0.707$. The leading error becomes fourth order,

$$\frac{(kh)^4}{1440}\left|(3-3\tau^4)-(9-5\tau^4)\cos^2\theta\sin^2\theta\right|, \tag{29}$$

indicating that the proposed procedure is an improvement over the classical linear acceleration method.

C. Fox-Goodwin method

From Eq.(15), it is observed that when $\beta=1/12$, the choice of

$$\alpha_K=\alpha_M=\sqrt{\frac{2}{3}} \tag{30}$$

removes the second-order error for the Fox-Goodwin method, leaving a fourth-order error of

$$\frac{(kh)^4}{480}\left|(1-\tau^4)-3\cos^2\theta\sin^2\theta\right|. \tag{31}$$

It can be shown from Eq. (21) that the critical time-step size becomes $\tau\leqslant 1/\sqrt{2}$ instead of $\tau\leqslant 1/2$ for the standard Fox-Goodwin method. Again, the proposed procedure is an improvement over the Fox-Goodwin method with classical integration rules.

V. DISPERSION-REDUCING TECHNIQUES FOR EXPLICIT METHODS

All the implicit methods discussed in the previous section, when combined with the proposed modified integration rules, are only conditionally stable. Even if they were unconditionally stable, they are not very desirable for wave propagation problems. The accurate simulation of wave propagation often requires the dimensionless time-step size to be around unity, indicating that the expense associated with implicit computation may not be necessary. In this section, we attempt to develop an explicit scheme based on the CDM.

For the CDM, we cannot simply set $\beta=0$ and follow the procedures used in developing the implicit methods, because any choice of $\alpha_M\neq 1$ will result in a nondiagonal mass matrix, and the scheme is no longer explicit. From Eq. (15) we observe that the requirements of $\alpha_M=1$ and $\beta=0$ in the CDM demands that $\alpha_K=\sqrt{2/3}$ and $\tau=1$ for the second-order error to be eliminated. But Eq. (22) indicates the critical time-step size of $\tau\leqslant\sqrt{3}/2$; i.e., $\tau=1$ is not stable. If $\tau=\sqrt{3}/2$, the dispersion error becomes $k^2h^2/96$, which is not fourth order. Another choice is to let $\alpha_K=\sqrt{1/2}$, and we have the critical time-step size, $\tau\leqslant 1$, and the dispersion error, $\frac{1}{96}k^2h^2\sin^2 2\theta$. Although they are both better than using the conventional integration rule ($\alpha_K=\sqrt{1/3}$ and $\tau=1$) with the leading-order error of $\frac{1}{48}k^2h^2\sin^2 2\theta$, the second-order error is not eliminated.

A. Modified (half-step) central difference method (CDM)

In the following, we utilize a modified version of the central difference scheme (used, e.g., by Krenk[13] and Belytschko *et al.*[17]). In Krenk,[13] the diagonal mass matrix is used when an inversion is needed, and a linear combination of diagonal and consistent mass matrices is used otherwise, thus retaining an explicit computation. In this paper, we replace the linear combination of mass matrices by modified integration rules. The ideas are similar, but not equivalent. As illustrated later, the proposed method performs better, especially because the modified integration rules are employed even for the stiffness matrix.

In the modified CDM, the semi-discrete equation of Eq. (6) is written as

$$\begin{aligned}\mathbf{D}\dot{\mathbf{U}}&=\mathbf{M}\mathbf{V},\\ \mathbf{D}\dot{\mathbf{V}}&=-c_0^2\mathbf{K}\mathbf{U},\end{aligned} \tag{32}$$

where $\mathbf{D}$ is the diagonal mass matrix and $\mathbf{M}$ and $\mathbf{K}$ are evaluated using modified integration rules. Based on Eq. (32), Krenk[13] obtained the following time-stepping procedure:

$$\begin{aligned}\mathbf{U}^{(n)}&=\mathbf{U}^{(n-1)}+\Delta t\mathbf{D}^{-1}\mathbf{M}\mathbf{V}^{(n-1/2)},\\ \mathbf{V}^{(n+1/2)}&=\mathbf{V}^{(n-1/2)}-c_0^2\Delta t\mathbf{D}^{-1}\mathbf{K}\mathbf{U}^{(n)}.\end{aligned} \tag{33}$$

For the convenience of dispersion analysis, we rewrite Eq. (33) as an equivalent linear multistep equation,

$$(\mathbf{U}^{(n+1)}-2\mathbf{U}^{(n)}+\mathbf{U}^{(n-1)})+\Delta t^2c_0^2\mathbf{D}^{-1}\mathbf{M}\mathbf{D}^{-1}\mathbf{K}\mathbf{U}^{(n)}=0. \tag{34}$$

Since the procedure is different from the one considered in Sec. III, a dispersion analysis needs to be performed again to obtain the associated dispersion-reducing integration rule. Such analysis is performed in the following.

B. Dispersion-reducing integration rule

We substitute the approximate solutions in Eq. (11) into Eq. (34) to analyze the dispersion relationship. The first term of Eq. (34) is simply

$$2(\cos \omega \Delta t - 1)\mathbf{U}_{x,y}^{(n)}. \tag{35}$$

The matrix multiplications of the second term can be evaluated in the following way, where only the interior is considered. The element matrices are

$$\mathbf{D}_e = \frac{h^2}{4}\begin{bmatrix} 1 & & & \\ & 1 & & \\ & & 1 & \\ & & & 1 \end{bmatrix},$$

$$\mathbf{M}_e = \begin{bmatrix} M_0 & M_x & M_{xy} & M_y \\ M_x & M_0 & M_y & M_{xy} \\ M_{xy} & M_y & M_0 & M_x \\ M_y & M_{xy} & M_x & M_0 \end{bmatrix}, \tag{36}$$

$$\mathbf{K}_e = \begin{bmatrix} K_0 & K_x & K_{xy} & K_y \\ K_x & K_0 & K_y & K_{xy} \\ K_{xy} & K_y & K_0 & K_x \\ K_y & K_{xy} & K_x & K_0 \end{bmatrix},$$

where

$$M_0 = h^2(1+\alpha_M^2)^2/16, \quad K_0 = (\alpha_K^2+1)/2,$$

$$M_x = M_y = h^2(1-\alpha_M^4)/16, \quad K_x = K_y = -\alpha_K^2/2, \tag{37}$$

$$M_{xy} = h^2(1-\alpha_M^2)^2/16, \quad K_{xy} = (\alpha_K^2-1)/2.$$

The global matrices are assembled based on the nodal connectivity. By using a nine-node stencil, shown in Fig. 1 (with $\Delta x = \Delta y = h$), the row associated with the center node (x,y) in the global stiffness matrix, $\mathbf{K}$, is

$$[\cdots\ K_{xy}\ 2K_y\ K_{xy}\ 2K_x\ 4K_0\ 2K_x\ K_{xy}\ 2K_y\ K_{xy}\ \cdots]. \tag{38}$$

Note that all the omitted components are zero, since they are not connected to the center node. In vector $\mathbf{KU}^{(n)}$, the component corresponding to the center node (x,y) is then

$$4K_0\mathbf{U}_{x,y}^{(n)} + 2K_x(\mathbf{U}_{x-h,y}^{(n)} + \mathbf{U}_{x+h,y}^{(n)}) + 2K_y(\mathbf{U}_{x,y-h}^{(n)} + \mathbf{U}_{x,y+h}^{(n)}) + K_{xy}(\mathbf{U}_{x-h,y-h}^{(n)} + \mathbf{U}_{x+h,y-h}^{(n)} + \mathbf{U}_{x+h,y+h}^{(n)} + \mathbf{U}_{x-h,y+h}^{(n)}). \tag{39}$$

Substituting Eq. (11) and other approximate solutions, the above expression simplifies to

$$4(K_0 + K_xC_x + K_yC_y + K_{xy}C_xC_y)\mathbf{U}_{x,y}^{(n)}, \tag{40}$$

where

$$C_x = \cos(kh\cos\theta), \quad C_y = \cos(kh\sin\theta). \tag{41}$$

Other components can be obtained similarly.

The multiplication with $\mathbf{D}^{-1}$ is trivial. The evaluation of $\mathbf{M}(\mathbf{KU}^{(n)})$ is similar to the procedure of evaluating $\mathbf{KU}^{(n)}$. Thus, the second term of Eq.(34) associated with the center node turns out to be

$$\frac{16c_0^2\Delta t^2}{h^4}\begin{bmatrix} (M_0 + M_xC_x + M_yC_y + M_{xy}C_xC_y) \\ \times(K_0 + K_xC_x + K_yC_y + K_{xy}C_xC_y) \end{bmatrix}\mathbf{U}_{x,y}^{(n)}. \tag{42}$$

After substituting Eqs. (42) and (35) into Eq. (34), we solve for the wave velocity c_0:

$$c_0 = \sqrt{\frac{h^4(1-\cos ck\Delta t)}{8\Delta t^2\begin{bmatrix} (M_0 + M_xC_x + M_yC_y + M_{xy}C_xC_y) \\ \times(K_0 + K_xC_x + K_yC_y + K_{xy}C_xC_y) \end{bmatrix}}}. \tag{43}$$

By substituting Eq. (37) into the above equation and taking the Taylor expansion with respect to k, we have

$$\left|\frac{c_0 - c}{c_0}\right| = \frac{(kh)^2}{24}\left|(4-3\alpha_M^2) - \tau^2 + (4-6\alpha_K^2)\sin^2\theta\cos^2\theta\right| + O((kh)^4). \tag{44}$$

The choice of integration points to remove the second-order error is then

$$\alpha_K = \sqrt{\frac{2}{3}}, \quad \alpha_M = \sqrt{\frac{1}{3}(4-\tau^2)}, \tag{45}$$

which leaves a fourth-order error of

$$\frac{(kh)^4}{1440}\left|(8-10\tau^2+2\tau^4) - (19-10\tau^2+5\tau^4)\cos^2\theta\sin^2\theta\right|. \tag{46}$$

C. Stability analysis

We follow the von Neumann's method[18,19] of stability analysis, i.e., we let $\mathbf{U}^{(n+1)} = A\mathbf{U}^{(n)}$, where A is the amplification factor. Considering the equation associated with node (x,y), the first term of Eq. (34) is given by

$$\left(A - 2 + \frac{1}{A}\right)\mathbf{U}_{x,y}^{(n)}. \tag{47}$$

The second term is given by Eq. (42), which we denote by $B\mathbf{U}_{x,y}^{(n)}$. Eliminating $\mathbf{U}_{x,y}^{(n)}$ from Eq. (34), one can obtain A by solving the quadratic equation,

$$A^2 + (B-2)A + 1 = 0. \tag{48}$$

From Eq. (48) it is observed that the product of the two solutions, $\frac{1}{2}[-(B-2) \pm \sqrt{(B-2)^2-4}]$, is always one. This observation indicates that A cannot have two distinct real solutions; otherwise one of the solutions must be larger than one, and the scheme would be unstable. Thus, we need $(B-2)^2-4 \leq 0$, or $0 \leq B \leq 4$. Substituting Eqs. (45) and (37) into the expression for B in Eq. (42), we find that B is a function of C_x, C_y and τ. By the definition in Eq. (41), the two trigonometric functions satisfy $|C_x| \leq 1$ and $|C_y| \leq 1$. Within this range we find that B increases monotonically when C_x, C_y decrease from 1 to -1 and τ increases from 0 to 1. When $C_x = C_y = 1$, B is always zero. The maximum possible value of B, which is 4, is reached at $C_x = C_y = -1$ and $\tau = 0.7587$. Thus, the stability condition is

$$\tau \leq 0.7587. \tag{49}$$

It is worth mentioning that one can also evaluate the mass matrix as a weighted average of lumped and consistent mass matrices, $\mathbf{M} = \delta\mathbf{M}_c + (1-\delta)\mathbf{D}$. Using a similar procedure, it is found that the optimal combination factor is δ

$=(\tau^2-1)/2$ and the critical time-step size is $\tau=0.805$. Since the stability conditions are fairly close and considering the additional computational cost associated with the weighted averaging, we propose the use of modified integration over weighted averaging.

It is also interesting to note that Eqs. (45) and (49) imply that the integration points of the mass matrix are located outside the element, which is unconventional. This choice, however, works well and is similar to the unconventional nonconvex combination ($\mathbf{M}=1.5\mathbf{D}-0.5\mathbf{M}_c$), proposed by Krenk.[13]

D. Procedure of the modified central difference method (CDM)

The procedure of the modified CDM is summarized as:

(1) Obtain system matrices, $\mathbf{K}$ and $\mathbf{M}$.
(2) Impose initial conditions, $\mathbf{U}^{(0)}, \dot{\mathbf{U}}^{(0)}$, and $\mathbf{V}^{(1/2)}=\dot{\mathbf{U}}^{(0)}+c_0^2\Delta t\mathbf{D}^{-1}(\mathbf{F}^{(0)}-\mathbf{K}\mathbf{U}^{(0)})/2$.
(3) Perform time-stepping, for n=1,2,…,

$$\mathbf{U}^{(n)}=\mathbf{U}^{(n-1)}+\Delta t\mathbf{D}^{-1}\mathbf{M}\mathbf{V}^{(n-1/2)},$$

$$\mathbf{V}^{(n+1/2)}=\mathbf{V}^{(n-1/2)}+c_0^2\Delta t\mathbf{D}^{-1}\left(\mathbf{F}^{(n)}-\mathbf{K}\mathbf{U}^{(n)}\right).$$

In the above, $F^{(n)}$ is the discretized force vector at $t=t_n$. Note that an effective finite difference implementation could be easily derived from the above finite element implementation and would have identical accuracy and stability properties.

VI. NUMERICAL EXAMPLES

The effectiveness of the proposed techniques is illustrated using four numerical experiments. The effectiveness of the proposed implicit methods is tested first with the help of a single numerical example. On the other hand, due to its computational efficiency, the proposed explicit method is tested more extensively using three different examples. For all the examples the wave velocity is chosen as $c_0=0.1$.

A. Implicit methods

Consider a concentrated load exerted at the center of a two-dimensional infinite domain. The load pulse is given by

$$f(t)=\begin{cases}4[1-(2t-1)]^2, & 0<t<1\\ 0, & t\geqslant 1.\end{cases} \tag{50}$$

The analytical solution can be obtained using the convolution integral,

$$u(x,y,t)=\int_0^t f(\bar{t})G(x,y,t-\bar{t})d\bar{t}, \tag{51}$$

where G is the Green's function,[20]

$$G(x,y,t)=\frac{H(c_0t-\sqrt{x^2+y^2})}{2\pi c_0\sqrt{c_0^2t^2-x^2-y^2}}, \tag{52}$$

and H is the Heaviside step function.

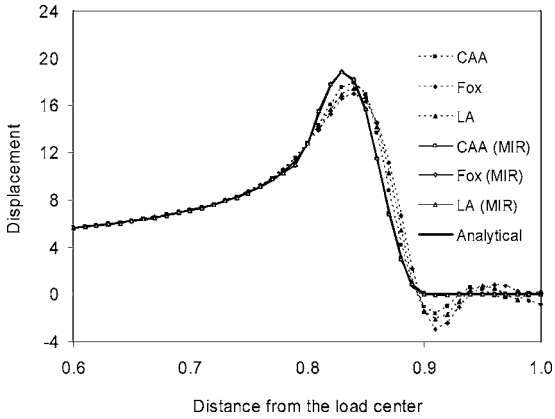

FIG. 2. Displacement variation along $\theta=0°$ at $t=9$ s under concentrated load. The results are obtained using different implicit methods. The dashed lines represent results from existing methods, while solid lines represent the results from the proposed modified integration rules. The results from the modified integration rules almost overlap with the exact solution.

Due to symmetry, we consider the upper right quadrant of the domain with a computational domain of size 1×1. No absorbing boundary conditions are necessary if we let the wave propagate for only 9 s and it does not hit the computational boundaries. A 100×100 mesh is used, implying square elements of size $h=0.01$. The time-step size is chosen such that $\tau=0.5$. The differences between the proposed methods and traditional ones lie only in the locations of the integration points. Instead of using $\alpha_K=\sqrt{1/3}$ and $\alpha_M=\sqrt{1/3}$ for the standard Galerkin FEM and Newmark methods, the proposed methods use $\alpha_K=\sqrt{2/3}$ and $\alpha_M=\sqrt{1/2}$, $\sqrt{7/12}$ and $\sqrt{2/3}$ for CAA, LA, and FOX, respectively (see Sec. IV).

The results obtained from the proposed methods and traditional methods are compared with the analytical solution. The dispersion error expressions in Eqs. (25), (29), and (31) indicate that the error is the highest along the mesh lines, i.e., $\theta=0$ and $\theta=90°$. Based on this observation, we examine the displacements along $\theta=0$. Figure 2 shows the snapshot at $t=9$ with the radius ranging from 0.6 to 1. It is observed that the proposed methods perform much better than traditional ones; they significantly reduce not only the dispersion error, but also the amplitude error.

B. Explicit method

1. Concentrated load

We reanalyze the model used in the previous example. The only differences are the use of explicit methods and the time-step size is now chosen such that $\tau=0.75$. The conventional CDM uses $\alpha_K=\sqrt{1/3}$ and $\alpha_M=\sqrt{1/3}$, whereas the proposed method uses $\alpha_K=\sqrt{2/3}$ and $\alpha_M=\sqrt{55/48}$, according to Eq. (45). In addition, we consider the dispersion-correction explicit scheme developed by Krenk,[13] which uses a traditional stiffness matrix ($\alpha_K=\sqrt{1/3}$) and a linear combination of diagonal and consistent mass matrices, $\mathbf{M}=1.5\mathbf{D}-0.5\mathbf{M}_c$.

Similar to the implicit case, the displacements (obtained at $t=9$ on $\theta=0$) from the analytical solution and the different explicit methods are plotted in Fig. 3. It is clear that the proposed method performs the best with respect to capturing both the phase and the amplitude.

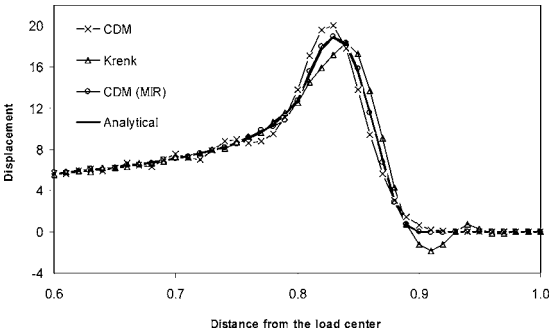

FIG. 3. Displacement variation along $\theta=0°$ at $t=9$ s under concentrated load. The results are obtained using different explicit methods.

2. Gaussian explosion

In order to simulate more realistic loading, we placed a Gaussian-type explosive source (borrowed from Collino and Tsogka[21]) at the center of a two-dimensional infinite domain:

$$f(x,y,t)=\begin{cases} f_1(t)f_2(x,y) & \begin{cases} 0<t<2t_0, \\ x^2+y^2<R^2, \end{cases} \\ 0 \quad \text{otherwise}. \end{cases} \tag{53}$$

where

$$f_1(t)=-8\pi^2 f_0^2(t-t_0)e^{-\pi^2 f_0^2(t-t_0)^2},$$
$$f_2(x,y)=[1-(x^2+y^2)/R^2]^3. \tag{54}$$

In the above, R is the radius of the load, $t_0=1/f_0$, $f_0=c_0/(hN_L)$ is the central frequency and N_L is the number of points per wavelength. In this example, the parameters used are $N_L=4$ and $R=0.1$. We consider the upper right quadrant of the domain with a limited size of 2×2. No absorbing boundary is necessary if we let the wave propagate only for 18 s, before it hits the boundaries. A 100×100 mesh is used, implying square elements of the size, $h=0.02$. We choose the time-step such that $\tau=0.75$.

Since the evaluation of the analytical solution is cumbersome, we used a converged solution as the reference. The converged solution uses a 400×400 mesh with $h=0.005$. The standard Galerkin FEM and the CDM are used with the time-step size corresponding to $\tau=0.75$.

The performances of the CDM, dispersion-correction explicit scheme (Krenk's method), and the proposed modified integration rules (referred to as MIR in the figures) are evaluated by comparing them with the converged solution. Figure 4 shows the contours of the displacements resulting from the different methods, at time $t=18$. The conventional CDM and Krenk's method result in a noncircular wave front clearly illustrating the anisotropy in the error, while the modified integration results in very low anisotropy. We also take a closer look at the displacement variations along the line of $\theta=0$ and radius ranging from 1.2 to 2 (Fig. 5). The results from the modified integration rules and the converged solution almost overlap, indicating that both dispersion and amplitude error are significantly reduced. On the other hand, the results from the other two methods have significant errors. It is clear that the proposed explicit method has superior accuracy properties compared to the traditional CDM as well as the dispersion-correction explicit scheme.

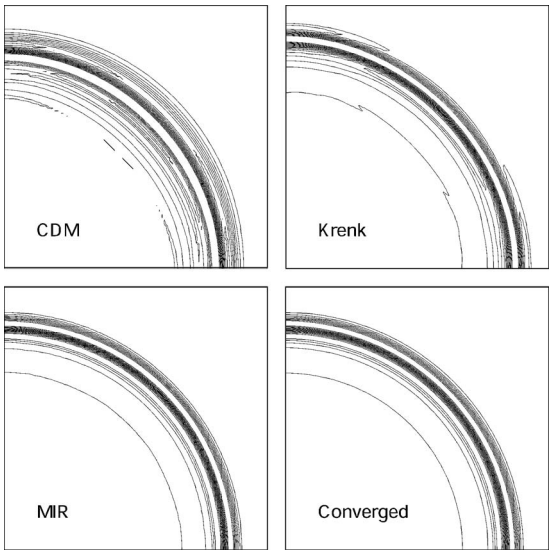

FIG. 4. Displacement contours at $t=18$ s due to a Gaussian explosion.

3. Performance on a distorted (quasiuniform) mesh

The proposed modified integration rule is developed based on uniform square mesh, and is fourth-order accurate under such conditions. In this example, we test its performance on distorted but quasiuniform mesh, again in comparison with the traditional CDM and dispersion-correction explicit scheme.

A point load is applied at the centroid of a trapezoidal domain. The time history of the load is given by Eq. (53), but there is no spatial distribution. The number of points per wavelength for the central frequency is $N_L=6$. The domain has a base width of 1.2, the topside width of 0.8, and the height of 1. The domain is meshed with a 50×50 mapped mesh consisting of distorted elements, with an average element size of $h=0.02$. The converged solution is obtained by using 200×200 mesh with an average element size of $h=0.005$. The shapes of the elements vary from square to nearly parallelograms.

Using $\tau=0.5$, we let the wave propagate for 5 s. The contours obtained using the CDM, Krenk and modified integration methods, as well as the converged one, are plotted in

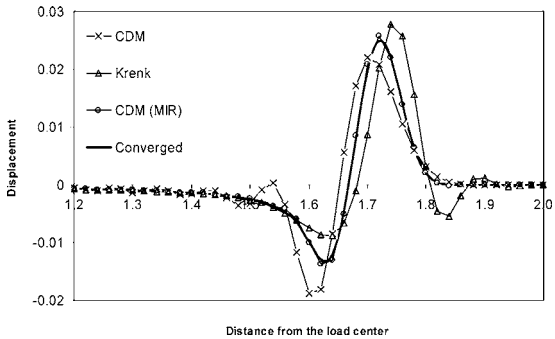

FIG. 5. Displacement variations along $\theta=0°$ at $t=18$ s due to Gaussian explosion.

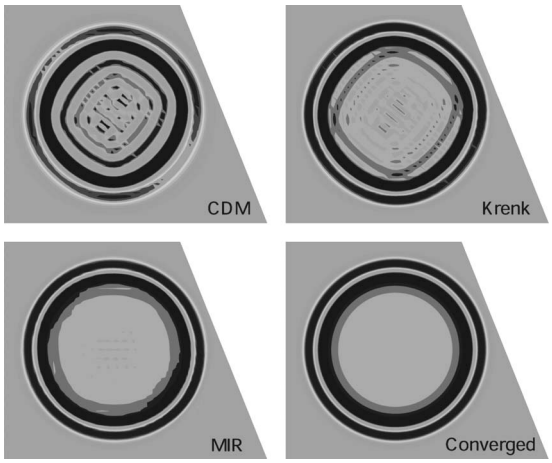

FIG. 6. Displacement contours at $t=5$ s under concentrated load. The results are obtained using different explicit methods with the distorted quasiuniform mesh.

Fig. 6. It is easily observed that the modified integration method outperforms the other two methods, with the anisotropy also significantly reduced.

VII. CONCLUDING REMARKS

The modified integration rules shift the integration points to locations away from conventional Gauss or Gauss-Lobatto integration points with the aim of reducing the discretization error. It was already shown that such a shift effectively reduces the dispersion error in simulating acoustic wave propagation in the frequency domain for square, rectangular as well as distorted meshes.[14] In this paper, we extend this idea to time domain analysis. The fundamental difficulties in simulating transient waves in multidimensions are anisotropy and the coupling of spatial and temporal discretization errors. Unfortunately, it turns out that the dispersion error cannot be significantly reduced for rectangular meshes. On the other hand, for uniform square meshes it was found that using the integration points of $(\pm\sqrt{2/3}, \pm\sqrt{2/3})$ for the stiffness matrix evaluation removes the second-order anisotropy. The location of integration points for the evaluation of the mass matrix depends on the time-step size as well as the time-stepping algorithm. The integration points are obtained for various implicit time-stepping schemes (constant average acceleration, linear acceleration, and Fox-Goodwin), as well as for the explicit CDM. The resulting modified integration rules have fourth-order accuracy with respect to dispersion, as opposed to conventional second-order accuracy.

While the modifications for the linear acceleration and Fox-Goodwin methods can be considered beneficial, the modification for the CAA method imposes an undesirable limit on the time-step size, and is not advocated. On the other hand, the modification for the explicit (half-step) CDM imposes no additional restrictions, except for the slight reduction in the stability limit. Since this method attains fourth-order accuracy while retaining its efficiency and stability, it is advocated as the method of choice. Numerical experiments indicate that the proposed methods significantly reduce the dispersion error not only on uniform square meshes, but also on distorted (quasiuniform) meshes.

The implementation of the proposed methods in existing finite element software is straightforward. While the modified integration rules are developed for two-dimensional problems, they can be directly extended to three-dimensional problems. Other possible extensions include the application to elastic wave modeling and higher-order finite elements. These possibilities are the subjects of future research.

ACKNOWLEDGMENT

This material is based upon work supported by the National Science Foundation under Grant No. 0100188. Any opinions, findings, and conclusions or recommendations expressed in this material are those of the authors and do not necessarily reflect the views of the National Science Foundation.

[1] K. G. Manoj and S. K. Bhattacharya, "Transient acoustic radiation from impulsively accelerated bodies by the finite element method," J. Acoust. Soc. Am. **107**, 1179–1188 (2000).
[2] A. C. Hladky-Hennion, R. Bossut, and M. de Billy, "Time analysis of immersed waveguides using the finite element method," J. Acoust. Soc. Am. **104**, 64–71 (1998).
[3] A. C. Hladky-Hennion and J. N. Decaprigny, "Finite-element modeling of active periodic structures—application to 1–3 piezoxomposites," J. Acoust. Soc. Am. **94**, 621–635 (1993).
[4] A. Safjan and J. T. Oden, "High-order Taylor-Galerkin and adaptive hp-methods for linear hyperbolic systems," J. Comput. Phys. **120**, 206–230 (1995).
[5] D. W. Zingg, H. Lomax, and H. Jurgens, "High-accuracy finite-difference schemes for linear wave propagation," SIAM J. Sci. Comput. (USA) **17**, 328–346 (1996).
[6] T. J. R. Hughes and G. M. Hulber, "Space-time finite element methods for elastodynamics: Formulation and error estimates," Comput. Methods Appl. Mech. Eng. **66**, 339–363 (1988).
[7] T. J. R. Hughes, *The Finite Element Method: Linear Static and Dynamic Finite Element Analysis* (Dover, Mineola, 2000).
[8] R. Mullen and T. Belytschko, "Dispersion analysis of finite element semi-discretizations of the two-dimensional wave equation," Int. J. Numer. Methods Eng. **18**, 11–29 (1982).
[9] K. J. Marfurt, "Accuracy of finite difference and finite element modeling of the scalar and elastic wave equation," Geophysics **49**, 533–549 (1984).
[10] V. Murti, Y. C. Wang, and S. Valliappan, "Discrete dissipation and dispersion in the transient dynamic finite element analysis," in *Proceedings of the sixth international conference in Australia on FEM*, 1991, 41–47.
[11] R. D. Krieg and S. W. Key, "Transient shell response by numerical time integration," Int. J. Numer. Methods Eng. **7**, 273–286 (1973).
[12] Y. C. Wang, V. Murti, and S. Valliappan, "Assessment of the accuracy of the Newmark method in transient analysis of wave propagation problems," Earthquake Eng. Struct. Dyn. **21**, 987–1004 (1992).
[13] S. Krenk, "Dispersion-corrected explicit integration of the wave equation," Comput. Methods Appl. Mech. Eng. **191**, 975–987 (2001).
[14] M. N. Guddati and B. Yue, "Modified integration rules for reducing dispersion error in finite element method," Comput. Methods Appl. Mech. Eng. **193**, 275–287 (2004).
[15] L. L. Thompson and S. Challa, "High-order accurate spectral elements for wave problems," Advanced Computational Engineering and Mechanics Laboratory, Clemson University, Manuscript CMCU-98-03, August 1998 (Master's thesis by S. Challa, Clemson University, Dept. of Mechanical Engineering, August 1998).
[16] N. M. Newmark, "A method of computation for structural dynamics," J. Eng. Mech. Div. **85**, 67–94 (1959).
[17] T. Belytschko, W. K. Liu, and B. Moran, *Nonlinear Finite Elements for Continua and Structures* (Wiley, Chichester, 2000).
[18] G. G. Obrien, M. A. Hyman, and S. Kaplan, "A study of the numerical solution of partial differential equations," J. Math. Phys. (Cambridge, Mass.) **29**, 223–240 (1951).
[19] G. D. Smith, *Numerical Solution of Partial Differential Equations*, 2nd

ed.Oxford Applied Mathematics and Computing Science Series, edited by J. Crank, H. G. Martin, and D. M. Melluish (Oxford University Press, Oxford, 1978).
[20]J. D. Achenbach, *Wave Propagation in Elastic Solids* (North-Holland, Amsterdam, 1973).
[21]F. Collino and C. Tsogka, "Application of the perfectly matched absorbing layer model to the linear elastodynamic problem in anisotropic heterogeneous media," Geophysics **66**, 294–307 (2001).

Acoustic scattering from a finite cylindrical shell with evenly spaced stiffeners: Experimental investigation

R. Liétard,[a] D. Décultot, and G. Maze
Laboratoire d'Acoustique Ultrasonore et d'Electronique, UMR CNRS 6068, Université du Havre, Place Robert Schuman, 76610 Le Havre, France

M. Tran-Van-Nhieu
Thales Underwater Systems, 7-9 rue des Mathurins, 92221 Bagneux, France

(Received 13 May 2005; revised 27 June 2005; accepted 8 July 2005)

The influence of evenly spaced ribs (internal rings) on the acoustic scattering from a finite cylindrical shell is examined over the dimensionless frequency range $1<ka<42$ (where k is the wave number in water and a the outer radius of the cylinder). Experimental results, obtained with a monostatic setup, are discussed in the incidence angle/time and incidence angle/frequency domains. The physical phenomena that give rise to highlights in the experimental spectra (Bragg scattering and scattering from Bloch-Floquet waves) are investigated. Fast Fourier Transform (FFT) processing on different segments of time signals allows us to distinguish influences of these phenomena. Further, comparison is made between frequency based results and numerical results provided by, respectively, a theoretical model using the thin shell theory [Tran-Van-Nhieu, J. Acoust. Soc. Am. **110**, 2858–2866 (2001)] and a simple scattering/interference calculation. [DOI: 10.1121/1.2011148]

PACS number(s): 43.20.Fn, 43.40.Fz, 43.40.Rj [EGW] Pages: 2142–2146

I. INTRODUCTION

The acoustic scattering of an infinite cylindrical shell excited by an incident plane wave has been investigated by a number of authors.[1–4] These studies have demonstrated that resonances of an elastic cylinder are closely linked to surface waves which could propagate on the circumference of the cylinder (in normal incidence) or adopt a helical path on the shell (in oblique incidence). In the case of finite cylindrical shells, identification of temporal echoes and resonance modes in frequency spectra linked to axial and radial dimensions of shells and to the propagation of S_0 and T_0 waves have been achieved.[5–8] Resonances due to the propagation of the S_0 wave in strictly axial incidence have been identified in Ref. 9. More recently, the propagation of the meridional A_0 leaky wave on truncated cylindrical shell has been studied.[10]

The influence of an internal discontinuity on the acoustic response of a cylindrical shell has also been investigated.[11–13] Thus, in the case of an internal lengthwise rib (plate), it has been shown that each type of resonance could be associated with a particular type of interaction between the shell and the rib in terms of the components of the coupling forces, whereas, when considering a lengthwise solder, the key phenomena were the generation of waves by the incident plane wave on the solder and wave type conversions at the discontinuity.

At the same time, other works have been devoted to the study of the effects of radial reinforcing ribs on the acoustic scattering from elastic structures.[14–16] These experimental results, backed up by a theoretical calculation using the thin shell theory and valid for long ribbed cylindrical shells,[17] have shown that subsonic surface waves could play a more dominant role than that played by supersonic helical waves through a new scattering mechanism due to the periodicity of the ribs (Bragg scattering and scattering from Bloch-Floquet waves).

This paper is devoted to the study of a finite cylindrical shell, stiffened by a set of periodically spaced internal rings, which represents the central part of more complex structures such as those of submarines. Experiments are carried out in monostatic configuration.[18] Results are discussed in the incidence angle/time and incidence angle/frequency domains. Two types of data processing Fast Fourier Transform (FFT) and a scattering/interference calculation are performed to distinguish phenomena at the origin of Bragg scattering and scattering from Bloch-Floquet waves.

II. EXPERIMENTAL SETUP

The studied target is an evenly ribbed finite cylindrical shell made of stainless steel (density $\rho=7900$ kg m^{-3}) where longitudinal and transversal velocities are $C_L=5790$ m s^{-1} and $C_T=3100$ m s^{-1}, respectively. It is characterized by a length $L=75$ cm, an outer radius $a=5$ cm, and a radius ratio $b/a=0.98$ (b inner radius). The set of 49 evenly spaced internal ribs (rings) resulting from the machining of a solid cylinder present the following characteristics (Fig. 1): thickness $l_r=1$ mm, height $h_r=0.5$ cm, spacing $d=1.5$ cm. Extremities are closed by disks of the same thickness as that of the shell. The air-filled target is horizontally immersed in water (tank dimensions $30\times10\times3$ m) where sound velocity is $C_{\text{water}}=1470$ m s^{-1}.

Monostatic configuration is used to carry out experiments (Fig. 2).[18] Two acoustic transducers (emitter and receiver) positioned at 4.5 m from the center of the shell are

[a]Electronic mail: romain.lietard@univ-lehavre.fr

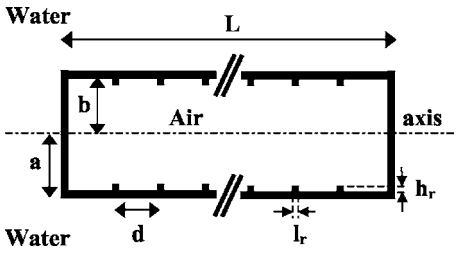

FIG. 1. Ribbed shell longitudinal section. The 49 ribs result from the machining of a full cylinder ($L=75$ cm, $a=5$ cm, $b/a=0.98$, $l_r=1$ mm, $h_r=0.5$ cm, $d=1.5$ cm).

hung from the same support and are oriented in the direction of this center. The target conducts a rotation movement with respect to the normal of its main axis (incidence angle α). The emission signal delivered to the broadband emitter transducer (Van Buren antenna[19]) is one sinusoïd period of frequency 100 kHz ($ka=21$, k wave number in water). The receiver is a broadband Panametrics transducer (model V3052) with a central frequency of 100 kHz. The frequency bandwidth of the coupled emission/reception signal is given in Fig. 3. Temporal echoes are acquired at one degree intervals from normal incidence ($\alpha=0°$) to an incidence angle somewhere near axial incidence ($\alpha=80°$). Before retrieving amplified time signals on a micro-computer, an average of 500 sweeps is performed using a numerical oscilloscope in order to improve the signal/noise ratio.

III. EXPERIMENTAL AND THEORETICAL RESULTS

A. Time analysis

Hilbert transform of time signals obtained from the ribbed shell is given in Fig. 4. Results are presented in the incidence angle/time space. Logarithmic amplitude, presented in grey levels, increases from white to black and the two symbols on the left side of the figure represent normal incidence ($\alpha=0°$) and oblique incidence ($\alpha=80°$), bottom and top, respectively.

At normal incidence we can observe specular reflection on the shell and also, despite the dimensions of the water tank ($30\times10\times3$ m), some parasite reflections (on the water surface). For oblique incidence angles, reflections on target extremities (A and B) are observable. We also notice several geometrical reflections on ribs, and echoes from the T_0 helical wave[20] (with an angular limit of nearly 27°) which result from the first reflection of this wave on the tube extremity. The continuous black line, corresponding to the reflections of the incident wave on extremities C and D, represents the limit between the geometrical reflections and the free reemission signal. A reinforcement of the amplitude of signals is also observable for incidence angles varying from 30° to 37° and time varying from 0.3 to 0.7 ms (asterisked $*$ in the figure). Explanation of this reinforcement will be made thereafter.

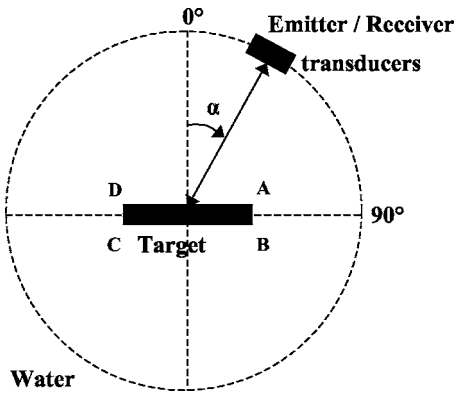

FIG. 2. Monostatic configuration.

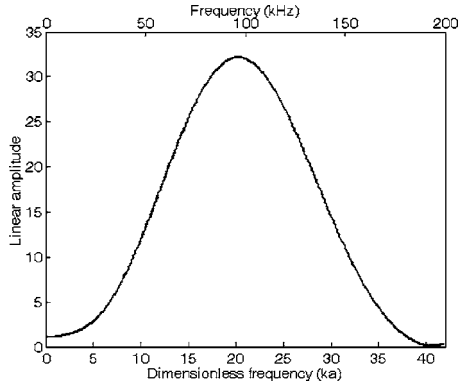

FIG. 3. Coupled emission/reception signal bandwidth.

B. Frequency analysis

To obtain the first type of experimental spectra presented in the incidence angle/frequency space (Fig. 5), we performed a FFT on time signals for each incidence angle after having removed the specular reflection and reflections on extremities A and B. The result (scattered pressure) from the theoretical calculation using the thin shell theory[17] is given in Fig. 6. Although this formalism is derived under several assumptions (slender and simply supported cylindrical shell, only the normal component of the force applied by the rings onto the shell is considered, effects of the extremities are neglected), a good agreement between theoretical and experimental spectra can be noticed. Indeed, in addition to scattering from helical waves ($0°<\alpha<27°$), we can also observe Bragg scattering and scattering from Bloch-Floquet

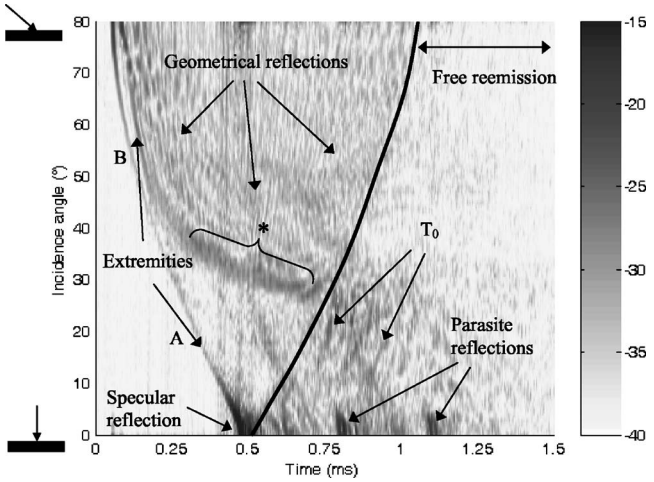

FIG. 4. Hilbert transform of time signals.

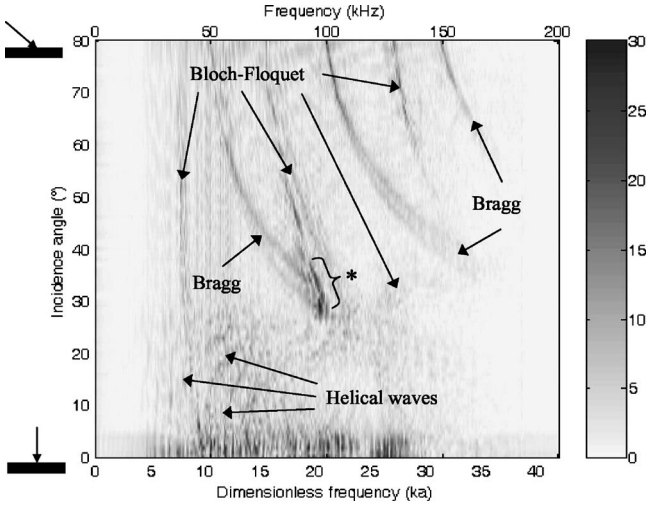

FIG. 5. Experimental spectra.

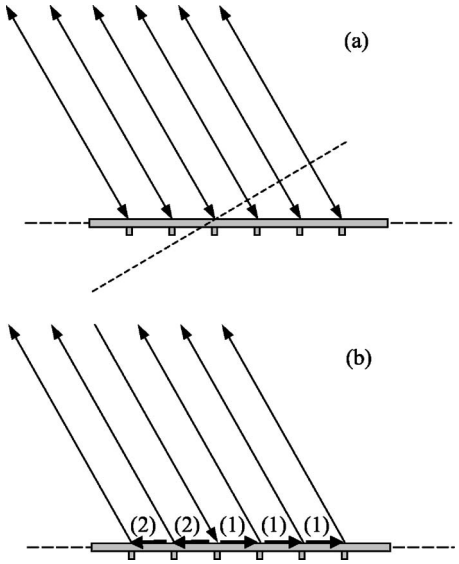

FIG. 7. (a) Bragg scattering; (b) scattering from Bloch-Floquet waves [(1) forward BF, (2) backward BF].

waves.[14–16] We also observe, on the experimental spectra (but not on the theoretical ones), a phenomenon of constructive interference between Bragg, Bloch-Floquet and T_0 waves (asterisked $*$ in the figure) for incidence angles varying from 30° to 37°. This phenomenon is at the origin of the reinforcement on the time signals (Fig. 4).

C. Discussion

In fact these two scattering phenomena, although they are both linked to interferences, do not have the same origin. Bragg scattering is due to the interference of the geometrical reflections of the incident plane wave on the rings: it strongly depends on the spacings between ribs [Fig. 7(a)]. Scattering from Bloch-Floquet waves results from the propagation of the A_0 flexural wave, generated on the ribs by the incident wave, which scatter each time it meets a rib [Fig. 7(b)]. We distinguish forward Bloch-Floquet waves from backward ones (direction of propagation opposite to that given by the projection of the incident wave vector on the shell axis). This scattering mechanism allows us to observe this surface wave which, normally, cannot be generated in this frequency range on a nonribbed shell (subsonic wave).

Results from three different calculations are superposed in Fig. 8. (i) Scattering from helical waves for a nonribbed finite cylindrical shell is first calculated thanks to a model using the theory of elasticity.[6] (ii) Bragg trajectories are obtained by a simple scattering/interference calculation using Eq. (1) where n is the index of the insonified and scatterer rib. (iii) In the case of Bloch-Floquet waves, phase velocity C_{A0} of the A_0 flexural wave is calculated beforehand by considering a plate in air (Fig. 9).[21] Bloch-Floquet trajectories are evaluated using Eq. (2) where n and m are, respectively, the indices of the insonified rib and that of the scatterer. In both cases, the x-origin is at the center of the shell (25th rib).

$$P^{\mathrm{BG}} = P_0 \sum_{n=1}^{49} e^{j2k(n-25)d\,\sin(\alpha)}, \tag{1}$$

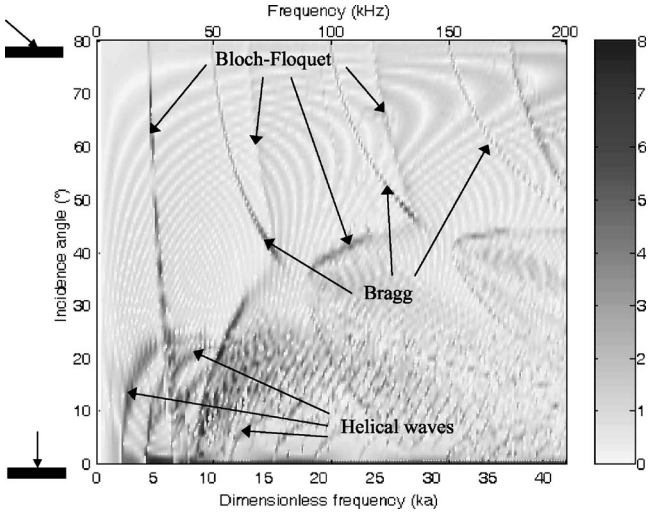

FIG. 6. Theoretical spectra.

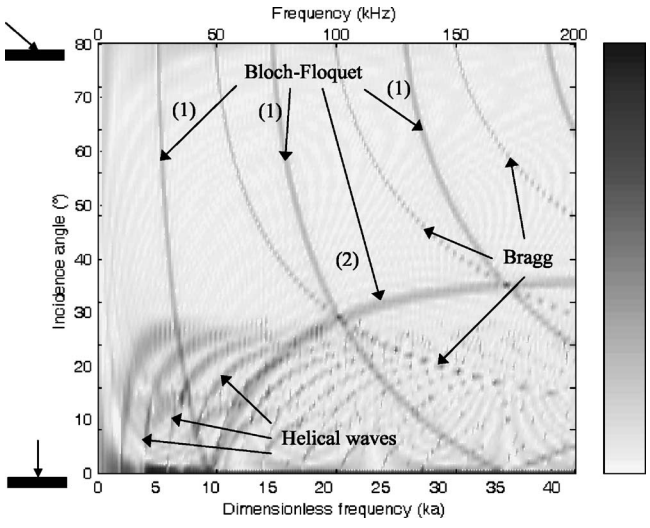

FIG. 8. Helical waves, Bragg and Bloch-Floquet trajectories [(1) forward BF, (2) backward BF].

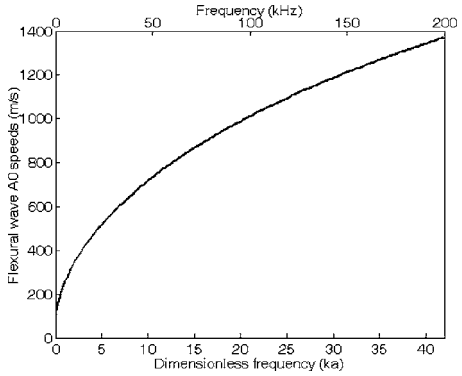

FIG. 9. A_0 flexural wave phase speeds.

$$P^{\mathrm{BF}} = P_0' \sum_{n=1}^{49} e^{j2k(n-25)d\,\sin(\alpha)} \left(\sum_{m=1}^{49} e^{j\varphi_{m-n}} \right), \tag{2}$$

with

$$\varphi_{m-n} = 2\pi f d(m-n)\left(\frac{1}{C_{A0}} + \frac{\sin(\alpha)}{C_{water}}\right) \quad \text{if } m \geqslant n,$$

$$\varphi_{m-n} = 2\pi f d(n-m)\left(\frac{1}{C_{A0}} - \frac{\sin(\alpha)}{C_{water}}\right) \quad \text{if } m < n.$$

In all the three calculations, the amplitudes are normalized by their maximum values. A good agreement with experimental spectra (Fig. 5) is obtained and we can clearly observe the crossing point between Bragg and Bloch-Floquet waves.

The second type of experimental spectra, or resonance spectra (Fig. 10), allows us to differentiate these two scattering phenomena. Indeed, to obtain these resonance spectra, we conducted a FFT on the free reemission signal: all geometrical reflections have been removed. Thus, Bragg scattering has disappeared whereas scattering from Bloch-Floquet waves and helical waves is still detectable. Hence, we have experimentally shown that scattering from Bloch-Floquet waves is linked to the propagation of surface waves (elastic phenomenon) whereas Bragg scattering is only due to rigid contributions from the set of evenly spaced ribs (rigid phenomenon).

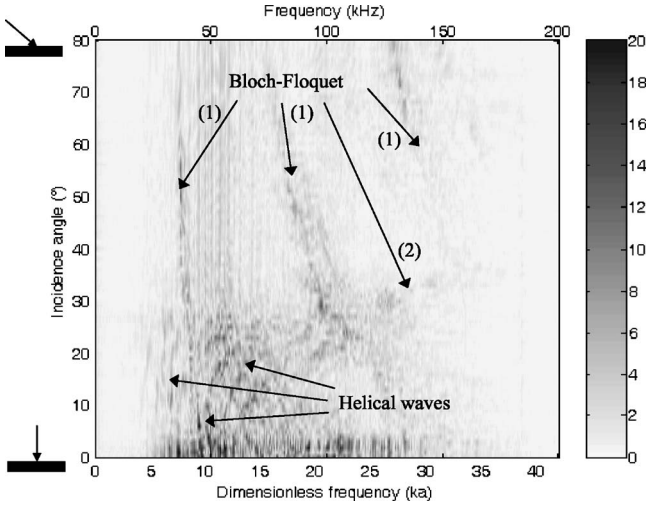

FIG. 10. Resonance spectra [(1) forward BF, (2) backward BF].

IV. CONCLUSION

Measurements of the acoustic scattering from a finite ribbed cylinder have been reported. They provide further information about the influence of a set of periodically spaced rings on the acoustic response from a finite cylindrical shell. Experimental results show that Bragg scattering and scattering from Bloch-Floquet waves can be significant phenomena compared with scattering from helical waves. The two types of data processing allow us to distinguish the origins of these two scattering mechanisms. We have also shown that Bragg and Bloch-Floquet trajectories can be predicted by using, respectively, a simple scattering/interference calculation and a coupled flexural propagation wave computation.

A phenomenon of constructive interference between Bragg and Bloch-Floquet waves has been observed on the experimental spectra (but not on the theoretical ones). Explanation for this difference is under investigation.

ACKNOWLEDGMENTS

The authors are grateful to the Conseil Régional de Haute-Normandie which partly financed this study. They are also grateful to the Director and personnel of the Bassin d'Essais des Carènes de Val de Reuil (France) for allowing them to carry out their experiments under good conditions. The authors are also grateful to Dr. J. G. Chiumia for his careful reading of this manuscript and useful suggestions.

[1] D. D. Doolittle and H. Überall, "Sound scattering by elastic cylinders," J. Acoust. Soc. Am. **39**, 272–275 (1966).
[2] A. Derem, J. L. Rousselot, G. Maze, J. Ripoche, and A. Faure, "Diffusion d'une onde plane par des cylindres solides immergés: Étude expérimentale et théorie des résonances," (Scattering of a plane wave by immersed solid cylinders: experimental study and resonances theory), Acustica **50**, 39–50 (1982).
[3] G. Maze, "Diffusion d'une onde acoustique plane par des cylindres et des tubes immergés dans l'eau. Isolement et identification des résonances," (Scattering of an acoustic plane wave by cylinders and tubes immersed in water. Isolation and identification of resonances), Ph. D. dissertation, Rouen, 1984.
[4] F. Léon, F. Lecroq, D. Décultot, and G. Maze, "Scattering of an obliquely incident acoustic wave by an infinite hollow cylindrical shell," J. Acoust. Soc. Am. **91**, 1388–1397 (1992).
[5] S. F. Morse and P. L. Marston, "Meridional ray contributions to scattering by tilted cylindrical shells above the coincidence frequency: Ray theory and computations," J. Acoust. Soc. Am. **106**, 2595–2600 (1999).
[6] S. F. Morse, "High-frequency acoustic backscattering enhancements for finite cylindrical shells in water at oblique incidence," Ph. D. dissertation, Washington State University, Department of Physics, 1998; S. F. Morse, P. L. Marston, and G. Kaduchak, "High-frequency backscattering enhancements by thick finite cylindrical shells in water at oblique incidence: Experiments, interpretation and calculations," J. Acoust. Soc. Am. **103**, 785–794 (1998).
[7] L. Haumesser, D. Décultot, F. Léon, and G. Maze, "Experimental identification of finite cylindrical shell vibration modes," J. Acoust. Soc. Am. **111**, 2034–2039 (2002).
[8] X. L. Bao, "Echoes and helical surface waves on finite elastic cylinder excited by sound pulses in water," J. Acoust. Soc. Am. **94**, 1461–1466 (1993).
[9] D. Décultot, F. Lecroq, G. Maze, and J. Ripoche, "Acoustic scattering from a cylindrical shell bounded by hemispherical endcaps. Resonance interpretation with surface waves propagating in cylindrical and spherical

shells," J. Acoust. Soc. Am. **94**, 2916–2923 (1993).
[10]S. F. Morse and P. L. Marston, "Backscattering of transients by tilted truncated cylindrical shells: Time-frequency identification of ray contributions from measurements," J. Acoust. Soc. Am. **111**, 1289–1294 (2002).
[11]A. Klauson, J. Metsaveer, D. Décultot, G. Maze, and J. Ripoche, "Identification of the resonances of a cylindrical shell stiffened by an internal lengthwise rib," J. Acoust. Soc. Am. **100**, 3135–3143 (1996).
[12]J. Chiumia, N. Touraine, D. Décultot, G. Maze, A. Klauson, and J. Metsaveer, "Experimental analysis of acoustic scattering from lengthwise soldered cylindrical shells," J. Acoust. Soc. Am. **105**, 183–193 (1999).
[13]A. Baillard, J-M. Conoir, D. Décultot, G. Maze, A. Klauson, and J. Metsaveer, "Acoustic scattering from fluid-loaded stiffened cylindrical shell: Analysis using elasticity theory," J. Acoust. Soc. Am. **107**, 3208–3216 (2000).
[14]D. M. Photiadis, J. A. Bucaro, and B. H. Houston, "Scattering from flexural waves on a ribbed cylindrical shell," J. Acoust. Soc. Am. **96**, 2785–2790 (1994).
[15]B. H. Houston, J. A. Bucaro, and D. M. Photiadis, "Broadband acoustic scattering from a ribbed shell," J. Acoust. Soc. Am. **98**, 2851–2853 (1995).
[16]D. M. Photiadis, B. H. Houston, E. G. Williams, and J. A. Bucaro, "Resonant response of complex shell structures," J. Acoust. Soc. Am. **108**, 1027–1035 (2000).
[17]M. Tran-Van-Nhieu, "Scattering from a ribbed finite cylindrical shell," J. Acoust. Soc. Am. **110**, 2858–2866 (2001).
[18]N. Touraine, L. Haumesser, D. Décultot, G. Maze, A. Klauson, and J. Metsaveer, "Analysis of the acoustic scattering at variable incidences from an extra thin cylindrical shell bounded by hemispherical endcaps," J. Acoust. Soc. Am. **108**, 2187–2196 (2000).
[19]P. H. Rogers and A. L. Van Buren, "New approach to a constant beamwidth transducer," J. Acoust. Soc. Am. **64**, 38–43 (1978).
[20]L. Haumesser, A. Baillard, D. Décultot, and G. Maze, "Behavior of first guided wave on finite cylindrical shells of various lengths: Experimental investigation," J. Acoust. Soc. Am. **109**, 583–590 (2001).
[21]I. A. Viktorov, *Rayleigh and Lamb Waves* (Plenum, New York, 1967).

Estimation of radius and thickness of a thin spherical shell in water using the midfrequency enhancement of a short tone burst response

Wei Li[a)]
Department of Naval and Ocean Engineering, School of Traffic Science & Engineering, Huazhong University of Science and Technology, People's Republic of China 430074

G. R. Liu[b),c)]
Centre for Advanced Computations in Engineering Science (ACES), Department of Mechanical Engineering, National University of Singapore, 10 Kent Ridge Crescent, Singapore 119260, Singapore

V. K. Varadan
Department of Engineering Science and Mechanics, The Pennsylvania State University, University Park, Pennsylvania 16802

(Received 27 May 2004; revised 26 June 2005; accepted 27 July 2005)

The midfrequency enhancement phenomenon for tone burst backscattering by thin spherical shells in water has been discussed by several investigators. In their works, it is found that the earliest elastic tone burst echo is enhanced relative to the specular reflection, and this enhancement is mainly due to the lowest subsonic antisymmetric Lamb wave. In this paper, the tone burst backscattering obtained from the convolution integral of the incident tone burst and the impulse response by a submerged spherical shell is investigated to display the midfrequency enhancement. The modified ray approximations are used to calculate the echo contributions from different Lamb waves. The numerical results show that the ratio of a/h and the dimensionless echo delay have nearly linear relationship with the frequency of greatest enhancement. Based on this property, two linear approximate equations are formulated to evaluate the radius and thickness of a thin spherical shell. A simple method is developed to estimate the frequency of greatest enhancement and the corresponding echo delay from a short tone burst echo with a higher carrier frequency. The evaluated results show that the present method is effective on determination of the radius and thickness of a thin spherical shell in water. © *2005 Acoustical Society of America.* [DOI: 10.1121/1.2040027]

PACS number(s): 43.20.Fn, 43.30.Gv, 43.30.Pc [RAS] Pages: 2147–2153

I. INTRODUCTION

The study of the acoustic scattering from submerged elastic objects has become increasingly fashionable in the last three decades. Much of the more recent research work has an impact upon the general understanding of fluid-elastic structure interactions and its implications for the inverse scattering problem. In this context, we note that the fluid-loaded, elastic spherical shell is the simplest, nontrivial, three-dimensional example of such a dynamical system. A thorough and systematic work of the scattering from the submerged elastic spherical shell will surely benefit the physical understanding of the scattering from the more complicated elastic structures.

The earliest investigation of the acoustic scattering from an elastic spherical shell was apparently done by Junger,[1] who first introduced the concept of the separation of the scattering solution for shells into two terms, a "rigid body scattering" (background) contribution and a "radiation scattering" (resonant) contribution. The conceptual separation may still be regarded as central to resonance scattering theory. Target resonances and the concept of an elastically reradiated wave were a recurrent theme in many of the subsequent articles concerned with the scattering by elastic objects.[2–4] However, in 1978, Flax and co-workers[5] formally extended the quantum-mechanical theory of resonance scattering to acoustics in the wake of several related studies on the subject.[6,7] A number of articles[8–11] on the scattering from spherical shells have been devoted to refining the background concept that is inherent in most applications of resonance scattering theory. The fundamental idea here is to isolate the reradiation associated with the elastic degrees of freedom of the object by subtracting a suitably defined background contribution from the full scattering solution. Although many resonances are quite clearly discernible in steady-state acoustic backscattering spectra,[5] they nevertheless interfere with the smooth geometrical background. It thus appears highly desirable to isolate the individual resonances so that their amplitude heights and widths can be measured directly and with greater precision. This was achieved by Maze and Ripoche,[12] who utilized the ringing of resonances caused by the scattering of wave trains of long duration. Their approach, which led to their and others' very

[a)]Electronic mail: hustliw@yahoo.com.cn
[b)]SMA Fellow, Singapore-MIT Alliance.
[c)]Electronic mail: http://www.nus.edu.sg/ACES/

extensive investigations of many examples of resonance scattering,[13] was termed method of isolation and identification of resonances. By measuring the angular distribution of the scattering amplitude, this method also determines the mode number of each resonance, which constitutes information that is indispensable for the determination of surface-wave phase and group velocities.

Sammelmann *et al.*[14] gave the first reasonable comprehensive study of the pole structure of the acoustic scattering amplitude for a submerged, elastic spherical thin shell in the low- to midfrequency region. In their paper, they demonstrated that the dispersion curve for the equivalent of the lowest order, antisymmetric, flat-plate Lamb wave on a fluid-loaded, spherical shell bifurcates into two distinct curves near the transition frequency. The supersonic portion of the spherical antisymmetric Lamb wave is denoted a_{0+}, while the subsonic portion is denoted a_{0-}. By way of contrast, the first symmetric wave s_0 is essentially unaffected. They also found that the form functions for backscattering from thin spherical shells trended to be enhanced over a rather broad midfrequency range ka, and the frequency-thickness product of this enhancement kh is roughly constant. This midfrequency enhancement phenomenon was also discussed by other authors.[15,16] Zhang *et al.*[17] used the modified ray approximations to investigate the amplitude of the backscattering of tone bursts by thin spherical shells. It was found that the a_{0-} wave could be enhanced relative to the specular echo in the midfrequency range, and the echo amplitude of the a_{0-} wave obtained by the modified ray approximations could be used to predict the frequency of greatest enhancement. However, it is not easy to determine at what carrier frequency the distinct a_{0-} wave echo is maximized for a tone burst in practice. An approximate ray synthesis for the amplitude of the guided wave echo near the midfrequency enhancement was proposed by Marston and Sun.[18] In the form of the ray synthesis, the ray contributions near the midfrequency enhancement consist of the specular echo and the first Lamb waves echoes included the a_{0-}, s_0, and a_0 waves. This ray model and the ray approximations[17,19,20] were supported by the experiments on the backscattering of the tone bursts,[21] the chirp bursts,[22] and the pressure impulse.[23]

In this paper, we first present a method that is used to calculate the tone burst response from a spherical elastic shell in water. In this method, the backscattering response from a shell is the convolution integral of the impulse response and the incident tone burst. The modified ray approximations[17] are used to calculate the echo contributions of different Lamb waves by a submerged spherical shell. The calculations of the backscattering echoes of tone bursts and the echo contributions of Lamb waves both show that the elastic echo associated with the a_{0-} wave becomes stronger than the specular reflection in the midfrequency range, and that is so-called midfrequency enhancement. The calculations also indicate that both the ratio of a/h and the dimensionless echo delay ΔT_{0l} have approximately linear relation with the frequency of greatest enhancement for a thin spherical shell. This property may be utilized to inverse scattering problem, and two approximate equations used to calculate the radius and thickness of a spherical thin shell are formulized based on this property. A novel method is developed to estimate the frequency of greatest enhancement and the time delay from a short tone burst echo by a thin spherical shell. The evaluated results of the radius and thickness are nearly the same with exact values. It suggests that the present method is effective to the inverse scattering problem of estimating the radius and thickness of a submerged spherical shell.

II. BACKSCATTERING OF TONE BURSTS BY A THIN SPHERICAL SHELL

When a plane wave is incident on an elastic sphere shell in water, the scattered pressure in the far field at a distance $r \gg ka^2$ from the center is given by the real part of

$$p_{\text{scat}} = \frac{a}{2r} p_{\text{inc}} e^{ik(r-ct)} f(x), \tag{1}$$

where p_{inc} is the amplitude of the incident plane wave, a is the outer radius of the shell, and $x=ka$ is the dimensionless frequency. The form function f for backscattering[24] is

$$f(x) = \frac{2}{ix} \sum_{n=0}^{\infty} (-1)^n (2n+1) \frac{B_n(x)}{D_n(x)}, \tag{2}$$

where the functions $B_n(x)$ and $D_n(x)$ are 5×5 determinants given in Ref. 24.

In this paper, a sinusoidal tone burst is used to investigate the backscattering by thin spherical shell. Suppose the amplitude of the incident tone burst is unit, and then the sinusoidal tone burst with an integer number of cycles q is expressed in terms of the dimensionless time as follows:

$$s(T) = \begin{cases} \sin(x_0 T), & 0 \leqslant T \leqslant 2\pi q / x_0 \\ 0 & \text{otherwise} \end{cases} \tag{3}$$

where x_0 is the dimensionless carrier frequency of the tone burst, and $T=(ct-r)/a$ is the dimensionless time. It is apparent that an increment in T of one unit corresponds to the amount of time that it takes for sound to propagate a distance equal to the outer radius of the sphere a in the surrounding water. Consequently the spectrum of the incident wave is given in terms of the dimensionless frequency

$$S(x) = \int_{-\infty}^{+\infty} s(T) e^{ixT} dT. \tag{4}$$

It is well known that the impulse response $h_I(T)$ of a spherical shell is given by the Fourier transforms of its form function $f(x)$. Thus, the backscattering response of the tone bursts by a spherical shell can be obtained by calculating the convolution integral of the impulse response $h_I(T)$ and the incident tone bursts $s(T)$. According to the convolution integral theorem, the amplitude of the backscattering response is given by

$$P(T) = h_I(T)^* s(T) = \frac{1}{2\pi} \int_{-\infty}^{+\infty} f(x) S(x) e^{-ixT} dx. \tag{5}$$

TABLE I. Material parameters.

Material	Density (kg/m^3)	Longitudinal velocity (m/s)	Shear velocity (m/s)
440 C stainless steel	7.84×10^3	5.854×10^3	3.150×10^3
Water	1.00×10^3	1.500×10^3	⋯

III. AN INVERSE SCATTERING PROCESS BASED ON THE MIDFREQUENCY ENHANCEMENT

The material properties of the 440C stainless steel shell considered are listed in Table I together with the sound velocity and density of the surrounding water. Figures 1(a) and 1(b) show the backscattered far-field form functions for the spherical 440C stainless steel shells with thickness $h=0.02a$, $0.04a$ in the frequency range $0\leqslant ka\leqslant 150$. It was found that the backscattered responses from the thin shells in a rather broad midfrequency range had been clearly enhanced, i.e., at $ka=59$ for $h=0.02a$, and at $ka=27$ for $h=0.04a$. This midfrequency enhancement phenomenon had also been discussed in Refs. 14 and 17. Here, we characterize the midfrequency range by the requirement that the acoustic wavelength is small compared to the shell radius, but large compared to the shell thickness. It was found that the frequency-thickness product of this enhancement kh was roughly constant. This is precisely the type of scaling behavior that would be expected, as the phenomenon was associated with the excitation of a flat-plate Lamb wave. This property could be used for inverse scattering problem, and the detailed method will be introduced in the Sec. IV.

In order to display the midfrequency enhancement phenomenon, the scattering for a 16-cycle sine wave burst is computed for several carrier frequencies x_0 in the range from 50 to 75. The scatterer is a submerged spherical shell with $h=0.02a$, and the impulse response used in the computation is calculated from $x=0$ to 150. Figures 2(a)–2(c) show the representative results of a significant elastic contribution to the scattering that arrives after the specular reflection, which commences at $T=-2$. Except for structure near the beginning and the end of the computed specular reflection, the reflection had the general appearance of a time-shifted replica of the incident burst. When the carrier frequency x_0 was equal to 59, Fig. 2(b) showed that the relative elastic amplitude exceeded 3.0, and the burst response grew steadily and achieved a constant magnitude. The plots shown in Fig. 2 (and others not reproduced here) suggest that the earliest elastic response becomes greatest near $x_0=59$, which is the demonstration of the midfrequency enhancement of the burst response.

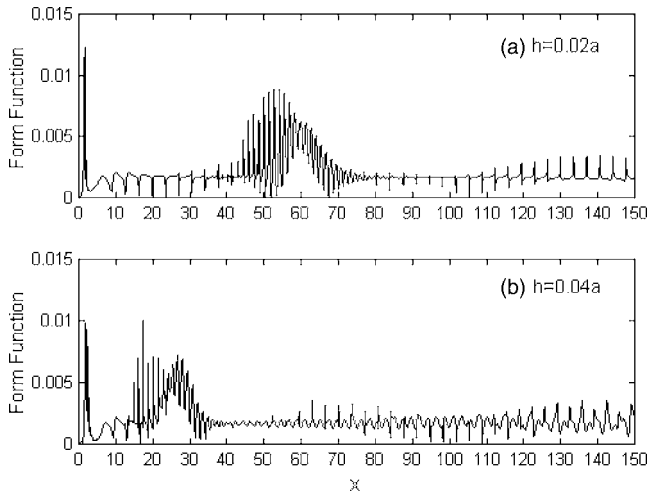

FIG. 1. Backscattered far-field form function for a thin spherical shell with a thickness of (a) $h=0.02a$, (b) $h=0.04a$ in water.

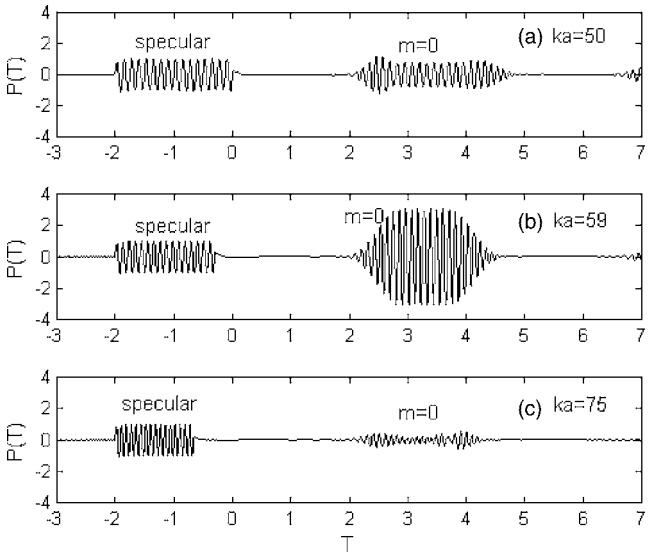

FIG. 2. Backscattering far-field response $P(T)$ from a submerged spherical shell with $h=0.02a$ by the 16-cycle tone burst having a carrier frequency x indicated.

As mentioned in Ref. 17, the echo contribution from the earliest subsonic Lamb wave a_{0-} is absolutely dominant compared with those from the other two types of echoes in the midfrequency range. Therefore, this midfrequency enhancement is mainly due to the echo contribution from the a_{0-} wave. Calculations of the subsonic wave a_{0-} properties are carried out for the 440C stainless steel spherical shells with thickness ranging from $h=0.02a$ to $h=0.10a$. The modified ray approximations[17] are used to calculate the echo amplitude $|f_{0l}|$ and the corresponding dimensionless echo delay ΔT_{0l} associated with the subsonic wave a_{0-}. The principal parameters needed in the modified ray approximations are the phase velocity ratio c_l/c, the radiation damping parameter β_l, and the group velocity c_{gl}, where l is an index that classifies the Lamb waves. The numerical procedure that makes use of the winding-number integral method to compute these parameters c_l, β_l, and c_{gl} was discussed previously[17,24,25] and will not be replicated in this paper. The frequency of greatest enhancement denoted x_P for each shell is estimated from the calculation of the echo amplitude $|f_{0l}|$ associated with the subsonic wave a_{0-}. Also the corresponding dimensionless echo delay ΔT_{0l} at x_P is evaluated for each shell. The calculation results are plotted in Figs. 3(a) and 4(a), respectively, as a function of x_P. It was clear that both the ratio of a/h and the dimensionless echo delay ΔT_{0l} had nearly linear relations with x_P. It suggests that we may use a line to fit the curves plotted in Figs. 3(a) and 4(a), respec-

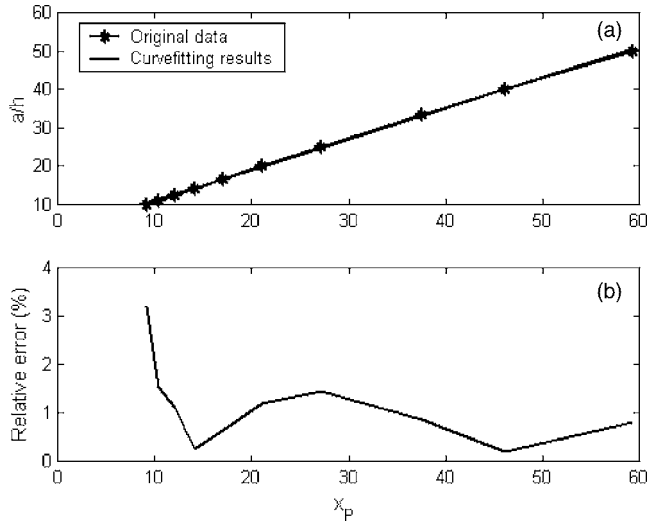

FIG. 3. (a) Comparison between the original data of the ratio of a/h and the curve fitting results as a function of the frequency of greatest enhancement x_P, which is calculated by the modified ray approximations. (b) Relative error of the curve fitting results of the ratio of a/h.

tively. Here, we use the least-squares method to perform the curve fitting of a/h and ΔT_{0l}, and the approximately linear equations are given as follows:

$$a/h = 0.8001x_P + 2.9587, \tag{6a}$$

$$\Delta T_{0l} = 4.6514 \times 10^{-3} x_P + 4.2544. \tag{6b}$$

It should be noted that these linear relations had already been mentioned in Refs. 17 and 21. In Ref. 17, Zhang *et al.* obtained the simple relations for a SS304 shell in water, which are $a/h \approx 0.8850x_p$ and $\Delta T_{0l} \approx 4.4$. Compared with the approximate relations obtained by Zhang *et al.*, Eqs. (6a) and (6b) improve the accuracy of an approximation of this general type for thicker shells by including the constant offset, as the thicker shells have smaller values of a/h.

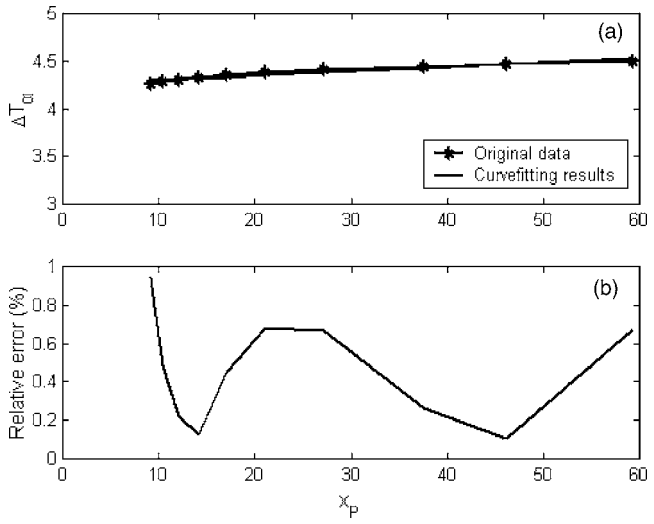

FIG. 4. (a) Comparison between the original data of the dimensionless echo delay ΔT_{0l} and the curve fitting results as a function of the frequency of greatest enhancement x_P, which is calculated by the modified ray approximations. (b) Relative error of the curve fitting results of the dimensionless echo delay ΔT_{0l}.

The curve fitting results are plotted with solid lines in Figs. 3(a) and 4(a), respectively. To demonstrate the quality of the curve fitting results, the relative errors between the original data and the curve fitting results are calculated and displayed in Figs. 3(b) and 4(b). It was apparent that the relative errors were very small. Therefore Eqs. (6a) and (6b) are good approximate expressions to describe the ratio of a/h and the dimensionless echo delay ΔT_{0l} as a function of x_P. Meanwhile, these two equations suggest an inverse scattering procedure for estimating the thickness and outer radius of the spherical shell, as we may measure the frequency of greatest enhancement ω_P and the echo delay Δt_{0l} in practice, which are corresponding to the dimensionless variable x_P and ΔT_{0l}, respectively. The detailed measurement method for ω_P and Δt_{0l} will be introduced in Sec. IV. Once the values of ω_P and Δt_{0l} are known, we can rewrite Eqs. (6a) and (6b) by using the following relations:

$$x_P = \frac{\omega_P a}{c}, \tag{7a}$$

$$\Delta T_{0l} = \frac{c\Delta t_{0l}}{a}, \tag{7b}$$

where c is the sound velocity in water.

Substituting Eqs. (7a) and (7b) into Eq. (6b), then it yields a quadratic equation with unknown variable a. As a should be positive, the following expressions for a and h can be obtained:

$$a = \frac{\sqrt{F_2^2 + 4F_1\omega_P\Delta t_{0l}} - F_2}{2F_1\omega_P}c, \tag{8a}$$

$$h = \frac{ac}{E_1\omega_P a + E_2 c}, \tag{8b}$$

where $E_1 = 0.8001$, $E_2 = 2.9587$, $F_1 = 4.6514 \times 10^{-3}$, and $F_2 = 4.2544$ are all given in Eqs. (6a) and (6b). It should be noted that the values of E_1, E_2, F_1, and F_2 in Eq. (8) would depend on the material properties of the shell considered and of the surrounding fluid.

Equations (8a) and (8b) clearly show that once the values of ω_P and Δt_{0l} are obtained, then the outer radius a and thickness h of the thin spherical shell could be estimated easily. The delay time Δt_{0l} can be given by measuring the temporal displacement between the central portion of the elastic echo associated with a_{0-} wave and the center of the specular reflection from the tone burst response plot. For the frequency of greatest enhancement ω_P, however, it is nearly impossible to determine the position of greatest enhancement through measuring the amplitude of $|f_{0l}|$ for the subsonic wave a_{0-} at all frequencies in practice. Although we could measure the response from tone bursts with different carrier frequencies to determine at what carrier frequency ω_P the distinct a_{0-} wave echo is maximized, this method is also impractical, as too many tests should be done for searching the frequency ω_P. Therefore, it is necessary to develop a practical and effective method to find the frequency ω_P.

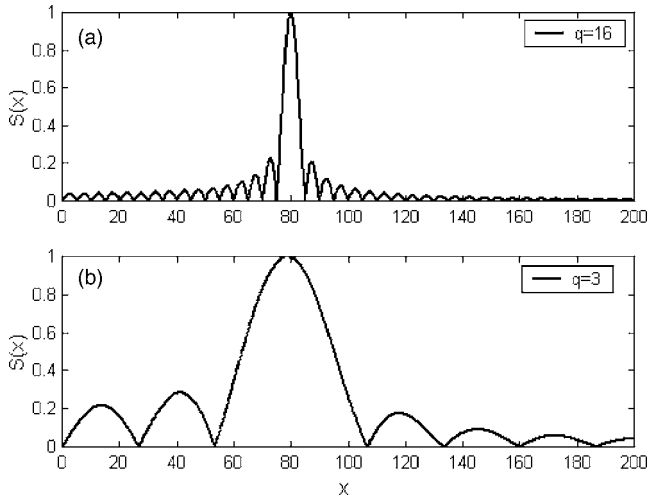

FIG. 5. Normalized spectrums of the (a) 16-cycle and (b) 3-cycle incident tone bursts with the same carrier frequency $x=80$.

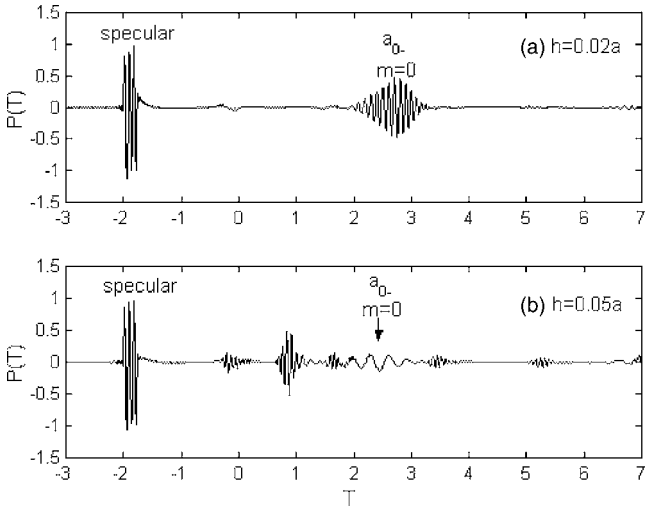

FIG. 6. Backscattering echo $P(T)$ for a 3-cycle tone burst with a carrier frequency $x_0=80$ for a submerged spherical shell with (a) $h=0.02a$ and (b) $h=0.05a$.

IV. ESTIMATION OF RADIUS AND THICKNESS OF A THIN SPHERICAL SHELL

In Sec. III, we make use of a long tone burst with 16 cycles to investigate the echoes from spherical shells. The advantages of using long tone burst are that the most energy carried by long tone burst is concentrated on a very narrow frequency band centered on the corresponding carrier frequency, and the other frequencies' components of long tone burst will be very few and can be neglected. Therefore, we may only excite the elastic response from the spherical shell in the very narrow frequency band of interest. The normalized spectrum of a 16-cycle tone burst with carrier frequency $x_0=80$ is shown in Fig. 5(a) to demonstrate this point. Meanwhile, Fig. 5(b) shows the normalized spectrum of a 3 -cycle tone burst with the same carrier frequency. It was found that the bandwidth of the main lobe shown in Fig. 5(b) was much broader than that shown in Fig. 5(a). Also the sidelobe of the normalized spectrum of a 3-cycle tone burst had a significant magnitude. Suppose that the carrier frequency x_0 of a short tone burst is higher than the frequency of greatest enhancement x_P. It could be expected that the elastic response associated with the a_{0-} wave at x_P would be excited by the sidelobe of the short tone burst, and may have an appreciable magnitude as a consequence of midfrequency enhancement.

Figures 6(a) and 6(b) show the echoes of a 3-cycle tone burst from the spherical shell with $h=0.02a$ and $0.05a$, respectively. In the calculations of Figs. 6(a) and 6(b), the short tone burst has the same carrier frequency $x_0=80$. It was found that the specular reflection had the same carrier frequency with the incident burst. However, it was apparent that the a_{0-} wave packets as marked in Figs. 6(a) and 6(b) had a frequency shifting that was also discussed by Zhang *et al.*[17] for a shell with $h=0.05a$, and the corresponding carrier frequencies of these two a_{0-} wave packets could be estimated from the plot easily. The estimated results are listed in Table II. Table II also lists the estimated results of dimensionless echo delay ΔT_{0l} and the corresponding exact results calculated by the modified ray approximations. The estimation procedure of the carrier frequency for the a_{0-} wave packets is to estimate the average period of the a_{0-} wave packets first, and then calculate the frequency by the inverse of the average period. The estimated echo delay is obtained by estimating the temporal displacement between the center of the specular reflection and the central portion of the a_{0-} wave. Table II clearly showed that the estimated results were nearly the same with the exact values. It suggests that when the carrier frequency of a short tone burst is higher than the frequency of greatest enhancement for a spherical shell, the a_{0-} wave packet excited by the sidelobe could be used to exactly predict x_P and ΔT_{0l}. It is always possible to perform the estimation as the a_{0-} wave packet normally has an appreciable magnitude as a consequence of midfrequency enhancement. The magnitude was, of course, much lower than that of the wave packet shown in Fig. 2(b), where x_0 lay at the frequency of greatest enhancement. There is another advantage of using a short tone burst to investigate the spherical shell, which is to maximally avoid the overlapping among the different types echoes in time. This property makes the a_{0-} wave easier to be discerned in the echoes. It should be noted that the estimated results listed in Table II are all dimensionless as the dimensionless results are convenient to be compared with the exact results obtained by the ray approximations. In practice, the echo from a spherical shell is a function of time and has temporal dimension. But there is no practical difficulty to estimate ω_P^m and Δt_{0l}^m in temporal dimension using the aforementioned method.

TABLE II. Comparison of the frequency of greatest enhancement x_P and the dimensionless time delay ΔT_{0l} obtained by the estimation method and the modified ray approximations for thin spherical elastic shells.

	Estimated results		Exact results	
h	x_P^m	ΔT_{0l}^m	x_P	ΔT_{0l}
$0.02a$	59.5	4.456	59.3	4.500
$0.05a$	21.3	4.381	21.0	4.382

TABLE III. Evaluated results of the radius and thickness of the submerged spherical shells using the estimated ω_P^m and Δt_{0l}^m from the short tone burst echoes.

	Estimated results		Evaluated results	
h (m)	ω_P^m (Hz)	Δt_{0l}^m (s)	$\bar{a}$ (m)	$\bar{h}$ (m)
0.020	8.9251E+004	2.9707E−003	9.8435E−001	1.9758E−002
0.025	6.9604E+004	2.9560E−003	9.9227E−001	2.4934E−002
0.030	5.6398E+004	2.9507E−003	9.9928E−001	3.0262E−002
0.040	4.0952E+004	2.9307E−003	1.0032E+000	4.0336E−002
0.050	3.1953E+004	2.9207E−003	1.0062E+000	5.0043E−002
0.060	2.5050E+004	2.8740E−003	9.9522E−001	6.1220E−002
0.070	2.0549E+004	2.8540E−003	9.9153E−001	7.1708E−002
0.080	1.7848E+004	2.8713E−003	9.9937E−001	8.0117E−002
0.090	1.5006E+004	2.8447E−003	9.9220E−001	9.1050E−002
0.100	1.3795E+004	2.8427E−003	9.9235E−001	9.6689E−002

The backscattering echoes from the spherical shells with different thickness are computed for a 3-cycle tone burst. The carrier frequency of the 3-cycle tone burst for all the shells is $x_0=80$, except for the shell with $h=0.04a$. Because the frequency of greatest enhancement x_P of this shell is 27.1 as shown in Fig. 3(a), and the amplitude of the spectrum of the tone burst is very low in the vicinity of $x=27.1$ [see Fig. 6(b)], this tone burst cannot excite an appreciable a_{0-} wave from the spherical shell with $h=0.04a$. Therefore, we changed the carrier frequency of the tone burst to $x_0=50$ for this shell. In practice, a short tone burst with higher carrier frequency is used to investigate the spherical shell. If the a_{0-} wave packet is too weak to be discerned, then we may need to change the carrier frequency until the a_{0-} wave packet has appreciable amplitude.

The radius of the spherical shell in the computations is 1 m, and the thickness of the spherical shell is from 0.020 to 0.100 m, which are listed in Table III. Table III also lists the estimated results of ω_P^m and Δt_{0l}^m, which are all estimated from the plots of the backscattering echoes from these shells. Substituting these estimated results into Eqs. (8a) and (8b), then it is easy to calculate the evaluated results of the radius and thickness of these shells, which are also shown in Table III. It was apparent that both the evaluated radius $\bar{a}$ and the evaluated thickness $\bar{h}$ were very close to the exact values, and the maximum relative errors were only 1.56% for $\bar{a}$ and 3.31% for $\bar{h}$. It shows that this method is very effective for estimating the radius and thickness of spherical shell in water.

V. CONCLUSIONS

This paper presents a simple method to estimate the radius and thickness of a thin spherical shell in water making use of the midfrequency enhancement phenomenon. The calculations of the backscattering echoes from submerged spherical shells show that the ratio of a/h and the dimensionless time delay associated with the a_{0-} wave have nearly linear relation to the frequency of greatest enhancement. This property is used to inverse scattering problem, and two approximate equations are formulated for this purpose. We also develop a simple method to obtain the frequency of greatest enhancement and the corresponding echo delay from the backscattering echo using a short tone burst. In this method, the a_{0-} wave packet from a thin spherical shell is excited by the sidelobe of the spectrum of the incident short tone burst, and may have an appreciable magnitude. The estimated results obtained by this method have very high precision and could be used to exactly predict the frequency of greatest enhancement and the corresponding echo delay. These two estimated values are used to substitute into two approximate equations obtained earlier [Eqs. (8a) and (8b)] to calculate the radius and thickness of the spherical shell, and the evaluated results are very close to the exact values. It indicates that this method is greatly valid to estimate the radius and thickness of a thin spherical shell in water.

The emphasis of the discussion so far has been on the backscattering from a thin spherical shell. In addition to spherical shell, there are other structures, such as prolate spheroidal shells, where the a_{0-} wave should also radiate a toroidal wave front and produce a stronger than specular contribution to the backscattering. But the curvature of the shell would affect the magnitude of the a_{0-} wave and the frequency of greatest enhancement. Therefore, further research is necessary.

ACKNOWLEDGMENTS

The work received support from the National University of Singapore, Singapore and the Institute of High Performance Computing, Singapore.

[1] M. C. Junger, "Sound scattering by thin elastic shells," J. Acoust. Soc. Am. **24**, 366–373 (1952).
[2] R. R. Goodman and R. Stern, "Reflection and transmission of sound by elastic spherical shells," J. Acoust. Soc. Am. **34**, 338–344 (1962).
[3] R. Hickling, "Analysis of echoes from a hollow metallic sphere in water," J. Acoust. Soc. Am. **36**, 1124–1137 (1964).
[4] K. J. Diercks and R. Hickling, "Echoes from hollow aluminum spheres in water," J. Acoust. Soc. Am. **41**, 380–393 (1967).
[5] L. Flax, L. R. Dragonette, and H. Überall, "Theory of elastic resonance excitation by sound scattering," J. Acoust. Soc. Am. **63**, 723–731 (1978).
[6] H. Überall, L. R. Dragonette, and L. Flax, "Relation between creeping waves and normal modes of vibration of a curved body," J. Acoust. Soc. Am. **61**, 711–715 (1977).
[7] J. W. Dickey and H. Überall, "Surface wave resonances in sound scattering from elastic cylinders," J. Acoust. Soc. Am. **63**, 319–320 (1978).
[8] J. D. Murphy, J. George, A. Nagl, and H. Überall, "Isolation of the resonant component in acoustic scattering from fluid-loaded elastic spherical shells," J. Acoust. Soc. Am. **65**, 368–373 (1979).
[9] M. F. Werby and G. C. Gaunaurd, "Proper background choice in resonance scattering by elastic shells," Int. J. Solids Struct. **22**, 1149–1159 (1986).
[10] M. F. Werby and G. C. Gaunaurd, "Transition from soft to rigid behavior in scattering from submerged elastic shells," Acoust. Lett. **9**, 89–93 (1986).
[11] G. C. Gaunaurd and M. F. Werby, "Lamb and creeping waves around submerged spherical shells resonantly excited by sound scattering," J. Acoust. Soc. Am. **82**, 2021–2033 (1987).
[12] G. Maze and J. Ripoche, "Methode d'isolement et d'identification des résonances (MIIR) de cylindres et de tubes soumis á une onde acoustique plane dans l'eau," Rev. Phys. Appl. **18**, 319–326 (1983).
[13] *Acoustic Resonance Scattering*, edited by H. Überall (Gordon and Beach, Philadelphia, 1992).
[14] G. S. Sammelmann, D. H. Trivett, and R. H. Hackman, "The acoustic scattering by a submerged, spherical shell. I. The bifurcation of the dispersion curve for the spherical antisymmetric Lamb wave," J. Acoust. Soc. Am. **85**, 114–124 (1989).
[15] M. Talmant, H. Überall, R. D. Miller, M. F. Werby, and J. W. Dickey,

"Lamb waves and fluid-borne waves on water-loaded, air-filled thin spherical shells," J. Acoust. Soc. Am. **86**, 278–289 (1989).
[16]G. C. Gaunaurd and M. F. Werby, "Acoustic resonance scattering by submerged elastic shells," Appl. Mech. Rev. **43**, 171–208 (1990).
[17]L. G. Zhang, N. H. Sun, and P. L. Marston, "Midfrequency enhancement of the backscattering of tone bursts by thin spherical shells," J. Acoust. Soc. Am. **91**, 1862–1874 (1992).
[18]P. L. Marston and N. H. Sun, "Resonance and interference scattering near the coincidence frequency of a thin spherical shell: An approximate ray synthesis," J. Acoust. Soc. Am. **92**, 3315–3319 (1992).
[19]P. L. Marston, "GTD for backscattering from elastic spheres and cylinders in water and coupling of surface elastic waves with the acoustic field," J. Acoust. Soc. Am. **83**, 25–37 (1988).
[20]S. G. Kargl and P. L. Marston, "Ray synthesis of the form function for backscattering from an elastic spherical shell: Leaky Lamb waves and longitudinal resonances," J. Acoust. Soc. Am. **89**, 2545–2558 (1991).
[21]G. Kaduchak and P. L. Marston, "Observation of the midfrequency enhancement of tone bursts backscattered by a thin spherical shell in water near the coincidence frequency," J. Acoust. Soc. Am. **93**, 224–230 (1993).
[22]G. Kaduchak and P. L. Marston, "Backscattering of chirped bursts by a thin spherical shell near the coincidence frequency," J. Acoust. Soc. Am. **93**, 2700–2706 (1993).
[23]G. Kaduchak C. S. Kwiatkowski, and P. L. Marston, "Measurement and interpretation of the impulse response for backscattering by a thin spherical shell using a broad-bandwidth source that is nearly acoustically transparent," J. Acoust. Soc. Am. **97**, 2699–2708 (1995).
[24]S. G. Kargl and P. L. Marston, "Observations and modeling of the backscattering of short tone bursts from a spherical shell: Lamb wave echoes, glory, and axial reverberations," J. Acoust. Soc. Am. **85**, 1014–1028 (1989).
[25]S. Ivansson and I. Karasalo, "Computation of modal wave numbers using an adaptive winding-number integral method with error control," J. Sound Vib. **161**, 173–180 (1993).

Scattering of ultrasonic waves by defective adhesion interfaces in submerged laminated plates

Ricardo Leiderman[a] and Arthur M. B. Braga[b]
Department of Mechanical Engineering, Pontificia Universidade Catolica do Rio de Janeiro, Rua Marques de Sao Vicente, 225, Gavea, Rio de Janeiro, RJ—Brazil—22453-900

Paul E. Barbone[c]
Department of Aerospace and Mechanical Engineering, Boston University, 110 Cummington Street, Boston, Massachusetts 02215

(Received 4 May 2004; revised 21 July 2005; accepted 22 July 2005)

We present an analytical-numerical method to simulate time-harmonic ultrasonic scattering from nonhomogeneous adhesive defects in anisotropic elastic laminates. To that end, we combine the quasistatic approximation (QSA) with a very high-order (tens or hundreds of terms) regular perturbation series to allow modeling of nonuniform interfacial flaws. To evaluate each term in the perturbation series, we use a recursive algorithm based on the invariant imbedding method. It is applicable to solve wave propagation problems in arbitrarily anisotropic layered plates and it is stable for high frequencies. We demonstrate examples of convergence and divergence of the perturbation series, and validate the method against the exact solution of plane wave reflection from a layered plate immersed in water. We present a further example of scattering of a Gaussian beam by an inhomogeneous interfacial flaw in the layered plate. We discuss how results of our simulations can be used to indicate the frequencies and angles of incidence where scattering from potential defects is strongest. These parameters, presumably, offer the best potential for flaw characterization. © *2005 Acoustical Society of America.* [DOI: 10.1121/1.2036147]

PACS number(s): 43.20.Gp, 43.40.Le, 43.40.Fz [ANN] Pages: 2154–2166

I. INTRODUCTION

In this paper we address the problem of ultrasonic scattering in adhesively bonded anisotropic laminated materials (i.e., composites). Specifically, the goal here is the development of a systematic modeling procedure that can be used to design ultrasonic inspection methods to detect nonuniform adhesive flaws. The precise problem we solve is that of time-harmonic scattering from nonuniform adhesive flaws at the interfaces of an anisotropic elastic multi-layered medium.

The problem under consideration presents several modeling challenges: treating the disparate length scales in the problem, utilyzing a technique that is both numerically stable and efficient at high frequencies, and modeling the adhesive layer itself. Any successful treatment of the problem considered here must take account of all these potential pitfalls. While standard solutions exist to overcome some of these potential difficulties, there is no solution yet published that treats them all.

In any adhesive bond, there are two adherends: the adhesive layer itself and the two interfaces between the adhesive layer and the adherends. In aerospace applications, adherend thickness is typically measured in milimeters, an adhesive layer has a typical thickness measuring hundreds of microns, while the surface layer associated with the interface of adhesion is just a few microns thick. In most cases degradation of this thin interfacial layer, rather than of the bulk of adhesive, leads to catastrophic failure.[1] Furthermore, wavelengths of interest can range from about 0.1––10 mm, with propagation distances stretching tens of centimeters. This broad range of physical dimensions makes the problem ill suited to standard domain discretization computational modeling procedures. On the other hand, the relatively simple geometry (plane parallel layered plates) makes the problem seemingly well suited to an analytical approach. This is because exploiting the translational symmetry in the problem allows it to be transformed into a one-dimensional problem.

Several analytical approaches exist to model wave propagation in plane layered media. In choosing a method, consideration must be given to its numerical stability at high frequency, and, if a large number of layers is to be treated, to its efficiency in scaling with the number of layers. For example, the most straightforward approach may be the "direct approach," in which a big matrix relating unknown quantities at each interface to each other interface is constructed and inverted.[2] Clearly the size of this matrix grows with N, the number of layers being considered. In composite materials, N can be quite large, and so techniques that scale efficiently with N are advantageous. The Thompson-Haskell transfer matrix technique yields an algorithm that is $O(N)$, but is known to be numerically unstable at high frequencies.[3,4] The major difficulty occurs when one or more wave type is evanescent. The source of instability lies essentially in evaluating the exponential of a matrix operator, a task that leads to difficulties in many areas.[5] Nevertheless, ways to improve

[a]Electronic mail: leider@bu.edu
[b]Electronic mail: abraga@mec.puc-rio.br
[c]Electronic mail: barbone@bu.edu

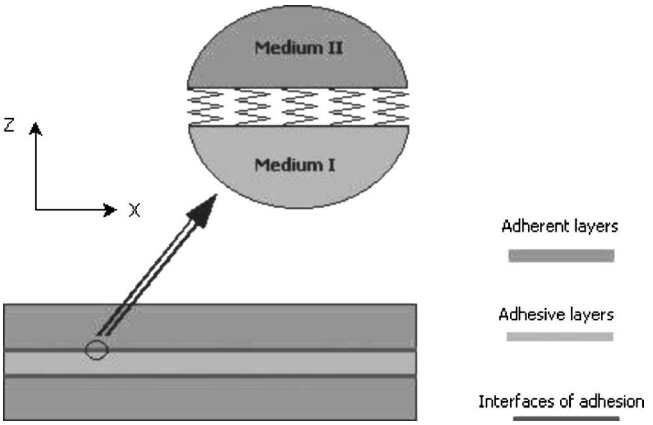

FIG. 1. Quasistatic approximation (QSA). When the ratio of the incident wavelength to the interface-thickness is large, the interfaces of adhesion can be modeled as a distribution of transverse and normal springs.

the numerical stability of transfer matrix approaches have been proposed; see, e.g., Ref. 6 and references therein. Alternatively, several efficient $O(N)$, stable recursive reformulations of the problem have been discovered and generalized over the past half-century.[7–10] In the recursive algorithms, one solves first for an operator characterizing the domain, (e.g., global impedance or global reflection tensor) and different methods differ essentially in the choice of that operator, and the associated operands. The latest, called "the stiffness matrix method" was presented recently in Refs. 11–13.

In the present work we choose a recursive method that is an adaptation of the *invariant imbedding method*[7] to the present application. Like the other recursive methods, this technique is both stable[8] and efficient. We have used it successfully before to model wave propagation in solids with arbitrarily anisotropic plane layers,[14] plane layered piezoelectric solids,[15] and cylindrically layered elastic solids.[16]

The interface between the adhesive and the adherend is modeled here by treating it as a separate layer with its own constitutive properties. By considering the layer to be infinitesimally thick, we can replace the layer by a set of equivalent tangential and normal springs. The springs connect the adhesive to the adherend, and enforce continuity of the traction and (approximately) displacement vectors. This approach to model an imperfect interface was apparently first proposed by Baik and Thompson,[17] who called it the quasistatic approximation (QSA). Since its introduction, many authors have worked to validate the approximation, both theoretically and experimentally, and it is now commonly used to represent imperfect interfaces between adherends.[18–22]

Our chosen model for the adhesive interface deserves some comment. We represent the interface as a continuous distribution of springs, as seen in Fig. 1, with a given stiffness. Thus "flaws" in the interface are modeled by making the springs more compliant than their normal values. That is, an adhesive flaw is modeled as a region with lower than normal stiffness. *Stiffness*, however, is a fundamentally different material property than is *strength*. Our working hypothesis in developing the method presented here is that bond stiffness and bond strength are correlated. One microscopic mechanism that might explain such a correlation is the accumulation of small voids or microcracks at the interface. The voids serve both to diminish the interface stiffness and as nucleation sites for fracture.[23]

In this paper, we consider *localized* adhesive flaws. Within the QSA approximation, local imperfections in the adhesive interface are modeled by local changes in the spring stiffness representing the interface. This spatial inhomogeneity breaks the translational invariance upon which depend the analytical methods described above. The same transform methods therefore lead to a convolution integral equation. We circumvent this difficulty through a high-order regular perturbation expansion, expanding about the undegraded bond stiffness, $\mathbf{K}_0$. Nakagawa *et al.*[24] recently considered a similar problem of an inhomogeneous fracture between two identical half-spaces. Those authors solved directly a discretization of the integral equation, and also considered iterative series solutions corresponding to the two special cases $\mathbf{K}_0=0,\infty$. The perturbation method presented below can be thought of as an iterative solution of the convolution integral equation.

The perturbation method we present below results in a series representation of the scattered pressure as a function of the perturbation parameter, ϵ. In any given example, this series will converge for some values of ϵ and diverge for others. Within the radius of convergence, the perturbation series defines the scattered field as a function of ϵ. Outside the radius of convergence, the series diverges. The perturbation method is not necessarily useless outside the radius of convergence, however. Analytic continuation can, in principal, be used to extend the definition of the scattered pressure field throughout the complex ϵ plane, beyond the radius of convergence of the original series. Though this idea is not explored in this paper, it is worthwhile recognizing the possibility of applying such "summation techniques" to the series obtained by the method presented here.[25]

Ultrasonic inspection of adhesive interfaces is frequently based on the frequency dependence of the reflected field. This technique takes advantage of a relation between spectral minima of the reflection coefficient and the quality of the bond.[21,22,26,27] This technique has been proven to be very sensitive to local material flaws. Its primary disadvantage is that it requires each point of the plate to be investigated separately. Other authors have investigated the use of Lamb waves and other guided waves[20,28–30,32] to probe bond strength, and leaky Lamb waves[31,33,34] have been employed in related inspection contexts. In these cases, one measures the attenuation and phase or group velocity of propagating modes, and relates the measured quantities to interface properties or other properties of interest. Lamb and guided wave techniques can be used to inspect a large area rapidly, but they lack the sensitivity of the reflection coefficient methods.

In what follows, we present a semianalytical method to predict the sound scattered from a layered plate with adhesive flaws. The method is suitable for modeling both of the common ultrasonic inspection approaches described above. In the next section we begin our presentation with the problem formulation, and discuss the role of the quasistatic approximation for the adhesive interface. We then formally solve the problem by constructing a high-order perturbation

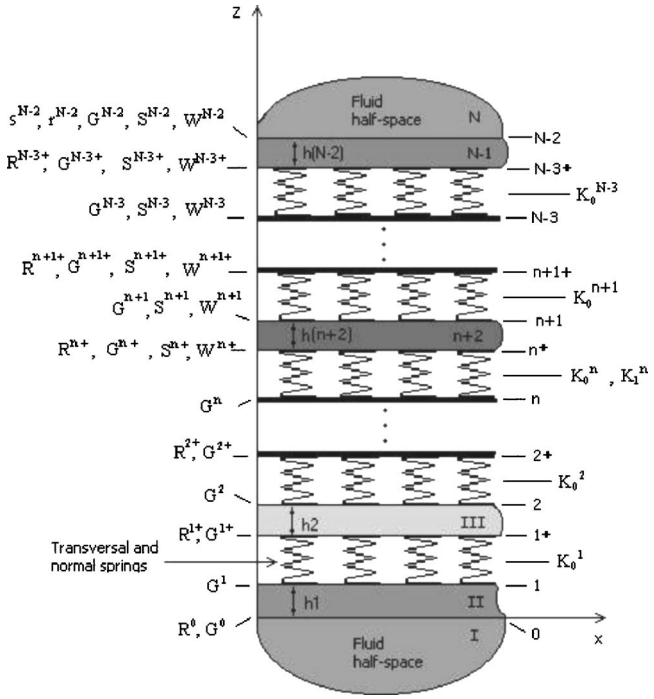

FIG. 2. General problem consisting of a layered plate immersed in an acoustic fluid, in the context of the QSA. The layered plate is infinite in the x and y directions and has its constituent layers joined by adhesive layers. There is an interface of adhesion between each adherent and adhesive layer. Interfaces of adhesion are represented by springs. Roman numerals are used to address each medium while arabic numerals are used to address each interface. N is the total number of layers plus two half-spaces and n stands for the nth layer or interface. The symbols h_1, h_2, etc. represent the thicknesses of the layers. In the figure, only one of the interfaces of adhesion, the nth one is considered to be defective.

expansion of the exact solution. The perturbation parameter is the strength of the inhomogeneity in the adhesive layer. We then present the recursive-invariant imbedding algorithm to solve for each term in the perturbation expansion. We validate the method and explore the issue of convergence in the context of plane wave reflection from a uniform layered plate, for which an exact solution exists. We show how to use our results to indicate the frequencies and angles of incidence at which the scattered field is most sensitive to localized interface defects. We end with an example of scattering from an inhomogeneous adhesive defect in the immersed plate, and highlight the phenomenon of spectral spreading of the incident field.

II. PROBLEM FORMULATION

We consider a layered elastic structure submerged in an acoustic fluid. The solid consists of N layers, bonded together by adhesive bonds. We assume that the z *axis* is normal to the layering, and designate the plane $z=0$ to be the "bottom" of the plate, and $z>0$ "upward," as indicated in Figs. 1 and 2. In the fluid regions, $z<z_0=0$ and $z>z_N>0$, the fluid pressure satisfies

$$\nabla^2 p + k^2 p = 0, \tag{1}$$

$$p = p_{\text{up}} + p_{\text{down}}, \tag{2}$$

$$p_{\text{up}} = 0, \quad z < 0 \tag{3}$$

$$p_{\text{down}} = p_{\text{inc}} = \text{known}, \quad z > z_N. \tag{4}$$

In (2) we have decomposed the pressure field into up- and downgoing components, respectively. The conditions (3) and (4) thus represent radiation conditions. In the equations above and in what follows, we assume and suppress a time dependence of $e^{-i\omega t}$.

The nth layer of the solid is supposed to occupy $z_{n-1} < z < z_n$, and have elasticity tensor $\mathbf{C}^n$ and density ρ^n. Therefore, the stress $\boldsymbol{\sigma}$ and displacement $\mathbf{u}$ in the nth layer satisfy

$$\nabla \cdot \boldsymbol{\sigma} + \rho^n \omega^2 \mathbf{u} = 0, \quad z_{n-1} < z < z_n, \tag{5}$$

$$\boldsymbol{\sigma} = \mathbf{C}^m : \nabla \mathbf{u}, \quad z_{n-1} < z < z_n. \tag{6}$$

We note that the nth layer may be either a structural layer or an adhesive layer.

Making use of the quasistatic approximation for the interface condition gives us the following boundary condition at the interface between the nth and $(n+1)$th layers:

$$\mathbf{K}[\mathbf{u}(z_n^+) - \mathbf{u}(z_n^-)] = \mathbf{t}(z_n^+), \tag{7}$$

$$\mathbf{t}(z_n^+) = \mathbf{t}(z_n^-). \tag{8}$$

Here, $\mathbf{K}$ is a diagonal spring matrix of both normal and tangential spring constants, $\mathbf{u}(z_n)$ is the displacement vector, and $\mathbf{t}$ is the traction vector acting on the xy plane.

Depending on the application, and, in particular, on the frequency range of interest, Eqs. (7) and (8) may be given different interpretations. At high frequencies, where the wavelength is comparable to or shorter than the adhesive layer thickness, then Eqs. (7) and (8) are used to model the interface between the adhesive layer and the adherend. The matrix $\mathbf{K}$ is then interpreted as the interface stiffness. In this case, the adhesive layer itself is modeled as a separate elastic layer of finite thickness. At lower frequencies, where the wavelength is much longer than the thickness of the adhesive layer, Eqs. (7) and (8) may then be used to model the entire adhesive layer. In this case, the matrix $\mathbf{K}$ represents the stiffness of the adhesive layer. In either case, the precise values of $\mathbf{K}$ can be written in terms of the elastic and geometrical properties of the layer, as described in Ref. 18.

Imperfections in the adhesive bond between layers may be modeled by a reduction in spring constants in $\mathbf{K}$. Since imperfections tend to be localized in space, this implies that $\mathbf{K}(x,y)$ must be allowed to depend upon the position in the layer. Therefore, we write

$$\mathbf{K} = \mathbf{K}_0 + \epsilon \mathbf{K}_1(x,y). \tag{9}$$

Here, $\mathbf{K}_0$ is constant and $\mathbf{K}_1(x,y)$ is a function of the in-plane position coordinates (x,y) and is normalized to the same magnitude as $\mathbf{K}_0$. With the magnitude of $\mathbf{K}_1$ fixed, the dimensionless parameter ϵ represents the magnitude of the defect. In the following, we determine the asymptotic expansion of the solution about the point $\epsilon=0$. In many cases of interest, the resulting series expansion converges. The issue of convergence is discussed in more detail in Sec. IV.

We shall seek a solution of the scattering problem in a power series in ϵ. To that end, we expand the displacement and traction fields in the standard way:

$$\mathbf{u} = \mathbf{u}_0 + \epsilon\mathbf{u}_1 + \epsilon^2\mathbf{u}_2 + \epsilon^3\mathbf{u}_3 + \ \dots\ , \tag{10}$$

$$\mathbf{t} = \mathbf{t}_0 + \epsilon\mathbf{t}_1 + \epsilon^2\mathbf{t}_2 + \epsilon^3\mathbf{t}_3 + \ \dots\ . \tag{11}$$

Substituting (9)–(11) into the boundary conditions (7) and (8) leads to the following sequence of boundary conditions for each power of ϵ. For $O(1)$ through $O(\epsilon^2)$, we obtain

$$\mathbf{K}_0[\mathbf{u}_0(z_n^+) - \mathbf{u}_0(z_n^-)] = \mathbf{t}_0(z_n^+), \tag{12}$$

$$\mathbf{t}_0(z_n^+) = \mathbf{t}_0(z_n^-), \tag{13}$$

$$\mathbf{K}_0[\mathbf{u}_1(z_n^+) - \mathbf{u}_1(z_n^-)] + \mathbf{K}_1[\mathbf{u}_0(z_n^+) - \mathbf{u}_0(z_n^-)] = \mathbf{t}_1(z_n^+), \tag{14}$$

$$\mathbf{t}_1(z_n^+) = \mathbf{t}_1(z_n^-), \tag{15}$$

$$\mathbf{K}_0[\mathbf{u}_2(z_n^+) - \mathbf{u}_2(z_n^-)] + \mathbf{K}_1[\mathbf{u}_1(z_n^+) - \mathbf{u}_1(z_n^-)] = \mathbf{t}_2(z_n^+), \tag{16}$$

$$\mathbf{t}_2(z_n^+) = \mathbf{t}_2(z_n^-), \tag{17}$$

etc. The field equations in each layer (5) and (6) remain unchanged in form and are satisfied by each term in the series (10) and (11).

As seen in expressions (14) and (16), the terms $\mathbf{K}_1[\mathbf{u}_m(z_n^+) - \mathbf{u}_m(z_n^-)]$ can be understood as traction sources, or surface forces acting along the interface of adhesion. To simplify the notation we will define $\boldsymbol{\varphi}_m$ for use in later sections of this paper:

$$\boldsymbol{\varphi}_m^n = \mathbf{K}_1[\mathbf{u}_{m-1}(z_n^+) - \mathbf{u}_{m-1}(z_n^-)]. \tag{18}$$

The equations above show that the $O(1)$ terms satisfy the equations in a medium with no adhesion defects. This term will be called the specular field. Further, the terms of $O(\epsilon^n)$ are determined from the terms of $O(\epsilon^{n-1})$. More precisely, the $O(\epsilon^n)$ terms satisfy the equations for a layer without defects, but with an acoustic source term determined from the defect and the $O(\epsilon^{n-1})$ field. Thus, in order to solve for each term in the series, we need to consider the field-radiated by sources embedded in a plate without defects. The terms can be calculated in succession until the sum converges. We refer to the sum $\mathbf{u}_s^n = \epsilon\mathbf{u}_1^n + \epsilon^2\mathbf{u}_2^n + \epsilon^3\mathbf{u}_3^n + \cdots$ as the scattered field.

When ϵ is very small, the series may be accurately truncated after a single term. The resulting approximation is the well-known *Born Approximation*. In other cases, several terms are required to produce an accurate representation of the scattered field. In cases where the series diverges, the sum of a finite number of terms may no longer accurately represent the scattered field. Even in these cases, however, the first term or two often gives at least a qualitatively correct depiction of the scattered field in our experience. See the example in Sec. IV C.

III. RECURSIVE SOLUTION ALGORITHM

For each perturbation order, we need to solve only for the field-radiated (or reflected) from a perfectly bonded layered plate with known forcing. More precisely, each perturbation order $\mathbf{u}_m$ and $\mathbf{t}_m$ in Eqs. (10) and (11) satisfies (5) and (6):

$$\boldsymbol{\nabla}\cdot\boldsymbol{\sigma}_m + \rho^n\omega^2\mathbf{u}_m = 0, \quad z_{n-1} < z < z_n, \tag{19}$$

$$\boldsymbol{\sigma}_m = \mathbf{C}^m{:}\boldsymbol{\nabla}\mathbf{u}_m, \quad z_{n-1} < z < z_n. \tag{20}$$

In addition, at $z=z_n$, the following interface condition must be satisfied:

$$\mathbf{K}_0[\mathbf{u}_m(z_n^+) - \mathbf{u}_m(z_n^-)] + \boldsymbol{\varphi}_m^n = \mathbf{t}_m(z_n^+) = \mathbf{t}_1(z_n^-). \tag{21}$$

Here, $\boldsymbol{\varphi}_m^n$ is known in terms of $\mathbf{K}_1$ and $\mathbf{u}_{m-1}$ via Eq. (18).

In this section we present a variant of the invariant imbedding method well suited to solve precisely this problem at each perturbation order. Our formulation accommodates forcings at any interface in any spatial direction. We follow the methodology described by Braga and Herrmann.[10] Sources embedded within the layered structure are included, as described in the context of piezoelectric media by Honein *et al.*, Ref. 15. The technique is adapted here to accommodate spring boundary conditions, and the backward sweep is described in detail. Below we present a brief sketch of the method. For details, the reader may refer to Refs. 10 or 15.

We work with the *impedance tensor* at the surface of the solid. The impedance is really a nonlocal linear operator, giving the traction in terms of velocity. Due the x translation invariance in our problem, however, the image of the impedance operator under Fourier transformation is a simple rank-two tensor.

The invariant imbedding procedure is as follows. Begin at the "bottom" of the plate ($z=0$), where the plate is in contact with a known substrate. The next step is to consider a single elastic layer overlying the substrate with known surface impedance and traction sources. The goal is to compute the surface impedance and traction sources acting on the top surface of the layer, in terms of the corresponding values on the bottom of the layer and the properties of the layer itself. After this, we perform a similar calculation with the elastic layer replaced by a "spring" interface that models the adhesion interface.

This gives us all the ingredients we need to solve the problem. We build these into a loop, in which the impedance and traction sources at each interface in the structure are successively computed, starting at the bottom of the plate and ending at the top. Once the surface impedance and traction sources at the top are known, we impose the conditions of continuity of pressure and normal velocity at the top fluid interface. This formally completes the solution as both the incident and radiated pressures in the fluid above the plate are known.

To evaluate the fields inside the plate, we must propagate the whole solution back down into the plate. We call this part of the solution the "backward sweep."

A. Elastic layer

We will work with the Fourier transform of the field variables. Therefore, we introduce the transformed displacement, stress, and traction, respectively, $\bar{\mathbf{u}}(z;\alpha)$, $\bar{\boldsymbol{\sigma}}(z;\alpha)$, and $\mathbf{t}(z;\alpha)$, so that

$$\mathbf{u}(x,z) = \int_{-\infty}^{+\infty} \bar{\mathbf{u}}(z;\alpha)\exp(i\alpha x)d\alpha, \tag{22}$$

$$\boldsymbol{\sigma}(x,z) = \int_{-\infty}^{+\infty} \bar{\boldsymbol{\sigma}}(z;\alpha)\exp(i\alpha x)d\alpha, \tag{23}$$

$$\mathbf{t} = \bar{\boldsymbol{\sigma}}(z;\alpha)\cdot\mathbf{n}. \tag{24}$$

Equations (22)–(24) apply to each perturbation order m, which has been suppressed. The unit vector $\mathbf{n}$ is normal to each interface and points in the *positive* z direction, regardless of the orientation of the surface.

Here we consider an elastic layer with thickness h resting on a substrate. The bottom of the layer is located at $z=z_0$. The top of the layer is $z=z_1=z_0+h$. The substrate upon which the layer rests has a known surface impedance $\mathbf{G}_0$ and traction source field $\mathbf{F}$. Thus, at $z=z_0$, the interface between the elastic layer and the substrate,[35]

$$\bar{\mathbf{t}} = -i\omega\mathbf{G}_o\bar{\mathbf{u}} + \mathbf{F}_o. \tag{25}$$

Our goal in this section is to evaluate the equivalent surface impedance and source field at the top surface of the elastic layer, while taking account of the substrate impedance and the elastic properties of the layer itself.

We decompose the total displacement and traction fields into upgoing and downgoing fields, viz.,

$$\bar{\mathbf{u}}(z) = \bar{\mathbf{u}}_1(z) + \bar{\mathbf{u}}_2(z), \tag{26}$$

$$\bar{\mathbf{t}}(z) = \bar{\mathbf{t}}_1(z) + \bar{\mathbf{t}}_2(z). \tag{27}$$

Here, $\bar{\mathbf{u}}_1(\bar{\mathbf{t}}_1)$ and $\bar{\mathbf{u}}_2(\bar{\mathbf{t}}_2)$ denote the sum of all upgoing displacement (traction) and down-going displacement (traction) waves in the solid, respectively.

From the exact solution of the elastodynamic equations of motion (19), we may define the matrix operators $\mathbf{M}_1$, $\mathbf{M}_2$ and $\mathbf{Z}_1$, $\mathbf{Z}_2$. $\mathbf{M}_1$ and $\mathbf{M}_2$ propagate the up- and downgoing displacement fields in the solid:

$$\bar{\mathbf{u}}_j(z) = \mathbf{M}_j(z-z_1)\bar{\mathbf{u}}_j(z_1). \tag{28}$$

The propagator matrices $\mathbf{M}_j$ contain only propagating or decaying exponentials, which helps to keep the method numerically stable. They depend only on the local material properties, the x wave number, and the frequency, as shown in Eq. (A18). Similarly, the local impedance tensors $\mathbf{Z}_j$ defined in (A19) relate up- and downgoing tractions to the corresponding displacement fields:

$$\bar{\mathbf{t}}_j(z) = -i\omega\mathbf{Z}_j\bar{\mathbf{u}}_j(z). \tag{29}$$

Explicit expressions for these quantities can be found in Refs. 10 and 15.

We now compute the reflection tensor at the bottom of the layer using the boundary condition (25) and the elastodynamic solution in the layer. Substituting (27) and (26) in (25), and eliminating $\bar{\mathbf{t}}_j$ using (29), gives a relation between $\bar{\mathbf{u}}_1$ and $\bar{\mathbf{u}}_2$. Solving for the upgoing (reflected) field in terms of the downgoing (incident) field gives

$$\bar{\mathbf{u}}_1(z_0) = \mathbf{R}(z_0)\bar{\mathbf{u}}_2(z_0) + i[\omega\mathbf{Z}_1 - \omega\mathbf{G}_o]^{-1}\mathbf{F}_o, \tag{30}$$

$$\mathbf{R}(z_0) = -[\mathbf{Z}_1 - \mathbf{G}_o]^{-1}[\mathbf{Z}_2 - \mathbf{G}_o]. \tag{31}$$

The tensor $\mathbf{R}(z_0)$ introduced above is called the *reflection tensor* of the interface at $z=z_0$.

By forward and back propagating the up- and downgoing waves up to $z=z_1$, we can write a relation analogous to (30) valid at the top of the layer:

$$\bar{\mathbf{u}}_1(z_1) = \mathbf{R}(z_1)\bar{\mathbf{u}}_2(z_1) + \mathbf{S}\mathbf{F}_o, \tag{32}$$

$$\mathbf{R}(z_1) = \mathbf{M}_1(h)\mathbf{R}(z_0)\mathbf{M}_2(-h), \tag{33}$$

$$\mathbf{S} = i\mathbf{M}_1(h)[\omega\mathbf{Z}_1 - \omega\mathbf{G}_o]^{-1}. \tag{34}$$

Here we introduced $\mathbf{S}$, which transports traction sources at $z=z_0$ into displacement sources at $z=z_1$.

Finally, the total displacement and traction fields at $z=z_1$ are resummed to give the total impedance looking into the layer on the substrate:

$$\bar{\mathbf{t}}(z_1) = -i\omega\mathbf{G}_1\bar{\mathbf{u}}(z_1) + \mathbf{F}_1, \tag{35}$$

$$\mathbf{G}_1 = [\mathbf{Z}_2 + \mathbf{Z}_1\mathbf{R}(z_1)][\mathbf{I} + \mathbf{R}(z_1)]^{-1}, \tag{36}$$

$$\mathbf{W} = [\mathbf{Z}_1 - \mathbf{G}_1]\mathbf{S}, \tag{37}$$

$$\mathbf{F}_1 = -i\omega\mathbf{W}\mathbf{F}_o. \tag{38}$$

Equation (35) is of the same form as the given boundary condition at the bottom of the layer, Eq. (25). These results show how the impedance of a layered elastic structure can be computed, layer by layer. The matrix $\mathbf{W}$ transports the effects of sources below a given elastic layer to the boundary condition at the top of the layer. The adhesion interfaces are modeled next.

B. Adhesion interfaces

Here we consider an adhesion interface in contact with an elastic layer. The layer may be an adherend, or may be a layer of the adhesive itself, depending on the frequency range of interest. The adhesion interface is modeled as a layer of springs, as described earlier. The interface condition is

$$\mathbf{K}_0[\bar{\mathbf{u}}(z_n^+) - \bar{\mathbf{u}}(z_n^-)] + \bar{\boldsymbol{\varphi}}^n = \bar{\mathbf{t}}(z_n^+) = \bar{\mathbf{t}}(z_n^-). \tag{39}$$

Here, as earlier, the superscript + indicates the values of the field variables above the interface, while the superscript − indicates those below. At the bottom of the interface, the adhesion interface is assumed to be in contact with an elastic layer, at the surface of which the following impedance boundary condition holds:

$$\mathbf{t}(z_n^-) = -i\omega\mathbf{G}^-\bar{\mathbf{u}}(z_n^-) + \mathbf{F}^-. \tag{40}$$

To find the equivalent boundary condition at the top of the adhesive interface, we solve (39) for $\bar{\mathbf{u}}(z_n^-)$ and substitute into (40) to find

$$\bar{\mathbf{t}}(z_n^+) = \bar{\mathbf{t}}(z_n^-) = -i\omega\mathbf{G}^+\bar{\mathbf{u}}(z_n^+) + \mathbf{F}^+, \tag{41}$$

$$\mathbf{G}^+ = [\mathbf{I} + i\omega\mathbf{G}^-\mathbf{K}_0^{-1}]^{-1}\mathbf{G}^-, \tag{42}$$

$$\mathbf{F}^+ = \mathbf{G}^-\mathbf{K}_0^{-1}\bar{\boldsymbol{\varphi}}^n + [\mathbf{I} + i\omega\mathbf{G}^-\mathbf{K}_0^{-1}]^{-1}\mathbf{F}^-. \tag{43}$$

C. Forward sweep

By using the results of this and the previous subsections, we can now determine the impedance of a layered plate with the lamina joined by adhesion interfaces modeled according to the QSA. The procedure is roughly as follows. We begin by considering a single elastic layer overlaying a half-space. The half-space occupies the region $z<0$ and has known impedance. We may now use (36) to determine $\mathbf{G}^1$ (see Fig. 2;) the total impedance at $z=h_1$, of the elastic layer/half-space system.

Next, we add a spring layer to the top of the elastic layer. We then compute $\mathbf{G}^{1+}$ the total impedance of the adhesion interface/elastic layer/half-space system, by using (42). We continue to find the impedance of the system for each additional layer added to the system by alternately using Eqs. (36) and (42). Eventually we compute $\mathbf{G}^N$, the total impedance of the entire laminated plate in contact with the upper half-space, and the corresponding transported source vector.

1. Getting started

To begin the forward sweep, we need the initial impedance values for a half-space. For an elastic half-space in which the radiation condition is satisfied at infinity, $\mathbf{G}^0=\mathbf{Z}_2$. For a traction-free surface at the bottom of the plate, we take $\mathbf{G}^0=\mathbf{0}$. For a fluid half-space, a straightforward calculation gives the impedance as follows:

$$\mathbf{G}^0 = Z_f\mathbf{n}\otimes\mathbf{n}, \quad Z_f = \frac{\rho_f\omega}{\beta}. \tag{44}$$

The function $\beta=\beta(\omega,\alpha)=\sqrt{\omega^2/c_f^2-\alpha^2}$ is the wave number in the z direction. The sign is chosen in accord with the radiation condition; c_f denotes the sound speed in the fluid.

2. Scattering and radiation from top surface

Once we can compute $\mathbf{G}^N$ and $\mathbf{F}^N$, the impedance and transported acoustic sources at the top surface of the plate, we can formulate the reflection and radiation problem there. The boundary conditions in terms of the fluid pressure $\bar{p}$ and fluid normal displacement w_f at the top interface are

$$\bar{\mathbf{t}}^N = -\bar{p}\mathbf{n}, \quad \text{and } \mathbf{n}\cdot\bar{\mathbf{u}}^N = w_f. \tag{45}$$

These conditions enforce the continuity of traction and normal displacement at the fluid/solid interface. Of course, we also have our impedance condition on the top surface of the solid:

$$\bar{\mathbf{t}}^N = -i\omega\mathbf{G}^N\bar{\mathbf{u}} + \mathbf{F}^N. \tag{46}$$

Substituting (45) into (46) and solving for $\bar{\mathbf{u}}$ gives

$$\bar{\mathbf{u}} = [i\omega\mathbf{G}^N]^{-1}(\bar{p}\mathbf{n} + \mathbf{F}^N). \tag{47}$$

Equation (47) can be used later to give the total displacement field at the top of the plate, once the total pressure is known.

As in every other layer, we decompose the pressure into downgoing (incident) and upgoing (radiated) fields,

$$\bar{p} = \bar{p}^{\text{inc}} + \bar{p}^{\text{rad}}. \tag{48}$$

Following steps analogous to those that lead to Eqs. (30) and (31) leads us to

$$\bar{p}^{\text{rad}} = r\bar{p}^{\text{inc}} - \frac{Z_sZ_f}{Z_s+Z_f}\mathbf{n}\cdot[\mathbf{G}^N]^{-1}\mathbf{F}^N, \tag{49}$$

$$r = \frac{Z_s - Z_f}{Z_s + Z_f}, \tag{50}$$

$$Z_s = [\mathbf{n}\cdot[\mathbf{G}^N]^{-1}\cdot\mathbf{n}]^{-1}, \tag{51}$$

where r is the scalar representing the reflection coefficient at the plate's upper surface related to the z displacement component.

The right-hand sides of (49)–(51) are all known. At this point, the solution at a given perturbation order is formally known. Thus, in terms of $\bar{p}^{\text{rad}}\equiv\bar{p}_m^{\text{rad}}$ given in (49), the radiated pressure field is given by

$$p_m^{\text{rad}}(x,z) = \int_{-\infty}^{+\infty}\bar{p}_m^{\text{rad}}(\alpha)\exp(i\alpha x + i\beta z)d\alpha. \tag{52}$$

In (52), we reintroduced the perturbation order m in p_m^{rad} to re-emphasize that the calculation just described must be repeated at each order. In order to compute the solution at order $m+1$, however, we must know the interior displacement field at order m in order to evaluate the forcing terms in (18). We call that procedure the "backward sweep," and describe it in the following.

D. The displacement vector at each interface

The backward sweep starts with the evaluation of the displacement vector at the fluid/solid interface shown at the top of Fig. 2. We recall that this was computed in Eq. (47).

We then have the following problem. Given $\bar{\mathbf{u}}(z_n)$, the total displacement field at interface n, determine $\bar{\mathbf{u}}(z_{n-1})$, the total displacement field at the interface below, $z=z_{n-1}$. To do that, we use (25), evaluated at $z=z_n$, to get

$$-i\omega[\mathbf{Z}_1 - \mathbf{G}_o]\bar{\mathbf{u}}_1(z_n) - i\omega[\mathbf{Z}_2 - \mathbf{G}_o]\bar{\mathbf{u}}_2(z_n) = \mathbf{F}_n. \tag{53}$$

We combine (53) with $\bar{\mathbf{u}}_1+\bar{\mathbf{u}}_2=\bar{\mathbf{u}}$ to solve for $\bar{\mathbf{u}}_2$:

$$\bar{\mathbf{u}}_2(z_n) = [\mathbf{Z}_1 - \mathbf{Z}_2]^{-1}\left[[\mathbf{Z}_1 - \mathbf{G}_o]\bar{\mathbf{u}}(z_n) + \frac{1}{i\omega}\mathbf{F}_n\right]. \tag{54}$$

We can now use (28) and (32) to propagate the solutions to the interface below. This yields

$$\bar{\mathbf{u}}_2(z_{n-1}) = \mathbf{M}_2(z_{n-1} - z_n)\bar{\mathbf{u}}_2(z_n), \tag{55}$$

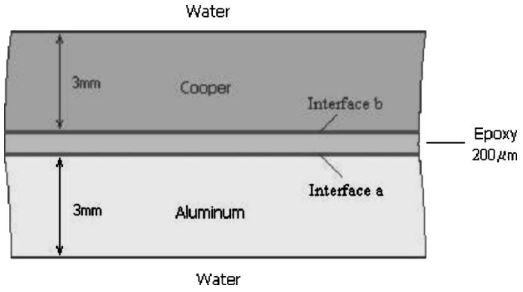

FIG. 3. The modeled plate. It is composed of three layers, a copper layer with 3 mm thickness, an epoxy layer with 200 μm thickness acting as the adhesive layer, and an aluminum layer with 3 mm of thickness. It has consequently two adhesion interfaces, labeled *a* and *b*.

$$\bar{\mathbf{u}}_1(z_{n-1}) = \mathbf{R}(z_{n-1})\bar{\mathbf{u}}_2(z_{n-1}) + \mathbf{S}_{n-1}\mathbf{F}_{n-1}. \tag{56}$$

Once we have the solution at $\bar{\mathbf{u}}(z_{n-1}^+)$, as given in (55) and (56), we need to propagate the solution across the spring interface to evaluate $\bar{\mathbf{u}}(z_{n-1}^-)$. This is most easily accomplished using the continuity of traction, and the previously evaluated impedance tensors. In particular, (41) directly gives $\mathbf{t}(z_{n-1}^-) = \mathbf{t}(z_{n-1}^+)$. Then $\mathbf{t}(z_{n-1}^+)$ can be used in (40) to find

$$\bar{\mathbf{u}}(z_{n-1}^-) = \frac{1}{i\omega}(\mathbf{G}_{n-1}^-)^{-1}[\mathbf{F}_{n-1}^- - \mathbf{t}(z_{n-1}^+)]. \tag{57}$$

This completes one full stage of the backward sweep. The total displacement field is advanced through each layer and each interface, in turn, starting with the total solution at the top of the plate. Once the backward sweep is completed for perturbation order *m*, the forcing $\boldsymbol{\varphi}_{m+1}$ can be calculated by Eq. (18). Thus, the next term in the series for $\mathbf{u}$ can then be computed.

IV. EXAMPLES

We present some simulation results in this section. All the examples chosen correspond to ultrasound inspection of a layered plate immersed in water. The plate is supposed to be composed of three layers: a copper layer with 3 mm thickness, an epoxy layer with 200 μm thickness acting as the adhesive layer, and an aluminum layer with 3 mm thickness. The plate is shown schematically in Fig. 3. It has, consequently, two internal adhesion interfaces: one between the copper and epoxy layers, interface *b*, and another between the epoxy and aluminum layers, interface *a*. The mechanical properties of its constituent materials are shown in Table I. We have applied our method to many different layered structures, including plates with several adhesive layers and plates with anisotropic layers. While the details of the response changes from case to case, many of the qualitative features are the same as in the simple case that we present here.

TABLE I. Mechanical properties of material constituents.

Material	Density (Kg/m^3)	P-wave speed (m/s)	S-wave speed (m/s)
Aluminum	2700	6320	3130
Copper	8930	4660	2660
Epoxy	1200	2150	1030
Water	1000	1480	0

The adhesion interface layers are assumed to have nominal thicknesses of 3 μm each. When intact, they have the same mechanical properties as the epoxy. Accordingly, by the QSA model (Rokhlin and Huang),[18] these interfaces can then be represented by the following spring stiffness matrix:

$$\mathbf{K_0} = \begin{bmatrix} 0.4259 & 0 & 0 \\ 0 & 0.4259 & 0 \\ 0 & 0 & 1.8457 \end{bmatrix} 1 \times 10^{15}\ \text{Pa/m}. \tag{58}$$

We emphasize again that both normal and tangential springs are included in the model.

Here, each assumed bond defect models a "kissing bond." This is a region at the interface in which there is a strong contact between the two media, but poor adhesion. The contact allows the bond to transmit normal traction and displacement, without the ability to transmit shear traction or in-plane displacement. We modeled this defect by changing only the *xx* component (i.e., the in-plane component) of the original adhesion interfacial stiffness.

A. Selecting the angle of incidence

The sensitivity of the scattered field to the presence of the defect depends strongly on the angle of incidence. Trial and error combined with some intuition has revealed a useful rule of thumb to predict an angle of incidence that is sensitive to a given flaw. Angles of maximum sensitivity to a given flaw seem to coincide with minima of the plate reflection coefficient. This is, of course, consistent with the notion that the incident field excites *leaky Lamb modes* in the plate. Not all modes, however, are sensitive to the flaw. We determine which modes are sensitive to a given type of adhesive flaw by computing the reflection coefficient from a plate with a uniformly diminished adhesion interface. By comparing the two reflection coefficients, that for the ideal plate and that for the uniformly degraded plate, we can identify those minima in the reflection coefficient that are most shifted. In this way we effectively identify which incident angles will most strongly couple to leaky-Lamb waves that interact with the interfacial flaw.

The magnitude of the reflection coefficient at 4.9 MHz for our example plate as a function of angle of incidence is shown in Fig. 4. Again, two reflection coefficients are plotted: the solid line represents the reflection coefficient for the plate with the original adhesion stiffness; the dashed line represents the same for the plate with the *xx* component of the adhesion stiffness at interface *a* reduced by half. Several minima in the reflection coefficient exist at this relatively high frequency, but most of these are the same for both plates. The minima near the angles of 3.82° and near 13.34° both shift, however, and so these are selected as interesting angles of incidence. These regions are magnified in Figs. 5 and 6 to show the shift more clearly. The larger shift near 3.82° indicates a stronger interaction with the incident wave, and thus stronger scattering than at 13.34°. Since stronger scattering gives slower convergence in the Born expansion, we have reason to expect *a priori* that convergence for the 3.82° case will be slower and limited to a smaller amplitude defect than that for the 13.34° case.

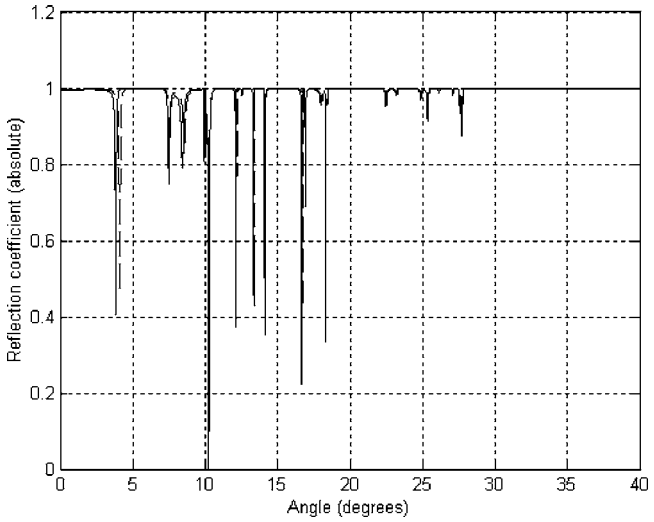

FIG. 4. Plane wave reflection coefficient at 4.9 MHz versus the angle of incidence. The solid line represents the reflection coefficient for the plate with original adhesion stiffness, while the dashed line represents the same for the plate with the stiffness of adhesion-interface a (the in-plane or xx component) reduced by one-half.

B. Series convergence and validation: Reflection from uniform plate

As a test of our code and to explore the limits of convergence of our technique, we consider plane wave reflection from a plate with a "uniform defect." That is, we consider $\epsilon\mathbf{K}_1$=const. In this case the exact solution is simply a reflected plane wave, and the reflection coefficient can be evaluated exactly. The accuracy of the perturbation solution is easily assessed, therefore, by simply comparing the amplitude of the reflected field for the exact and perturbation solution.

The angle of 3.82° was selected as the incident angle for the first example. The defect magnitude ($\epsilon\mathbf{K}_{1xx}$) is 17% of the original interfacial stiffness xx component. To be precise, $\epsilon\mathbf{K}_{1xx}=-0.17\mathbf{K}_{0xx}$. The negative sign indicates that the strength of the interface is diminished. The defect is located at interface a.

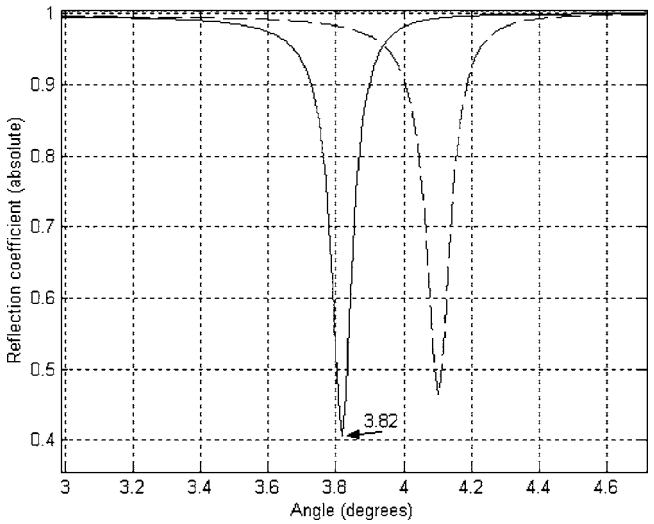

FIG. 5. Detail of Fig. 4 near 3.8°.

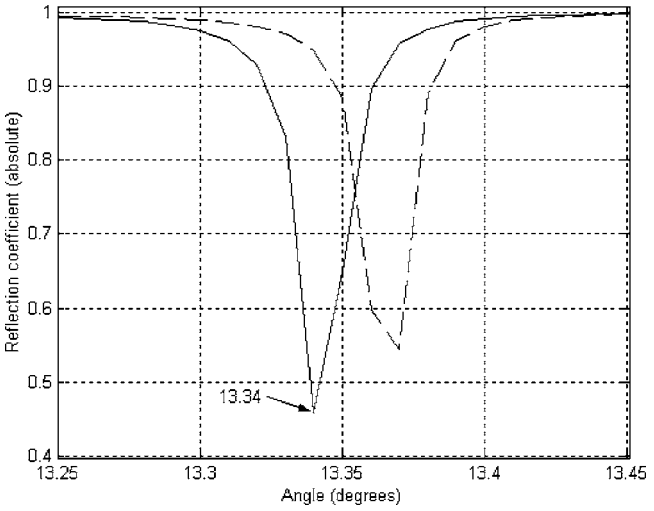

FIG. 6. Detail of Fig. 4 near 13.3°.

The reflected field magnitude as a function of N, the number of terms in the perturbation series, is plotted with o's in Fig. 7; the solid line in that figure shows the exact reflection coefficient. We see that the series has practically converged after about 40 terms, and that a single term is highly inaccurate. Furthermore, the oscillatory nature of the plot indicates that the convergence is highly nonmonotonic. This means that it is not always the case that adding another term improves the accuracy. For example, going from five to six terms makes things worse, not better. For smaller magnitude defects ($0>\epsilon\mathbf{K}_{1xx}>-0.17\mathbf{K}_{0xx}$) that we tried, the series seems to converge. The closer $\epsilon\mathbf{K}_{1xx}$ is to zero, the fewer the number of terms required before the partial sums stabilize.

The slow convergence of the perturbation series in the last example implies that we are near the convergence boundary of the series. Indeed, as we increase the magnitude

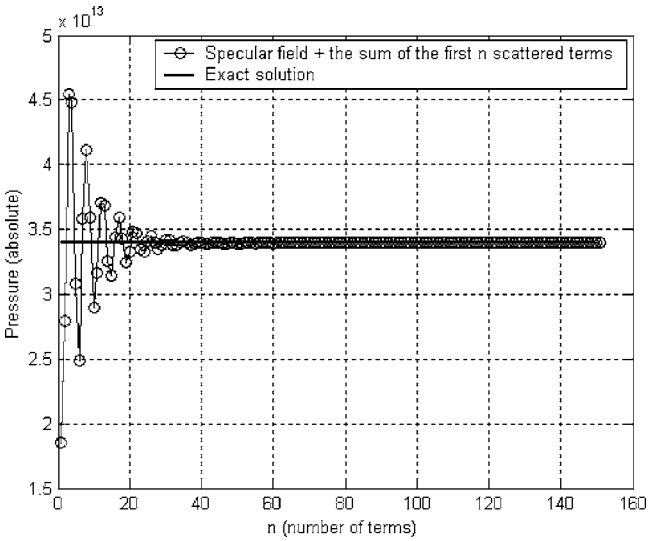

FIG. 7. A comparison between the exact and perturbation method solution. The partial sums for the perturbation series truncated at different terms, representing the amplitude of the total (specular+scattered) reflected pressure field, is represented by the open circles "○." The exact solution is represented by the solid line. The homogeneous defect's magnitude is 17% of the original interfacial stiffness xx component and the angle of incidence is 3.82°.

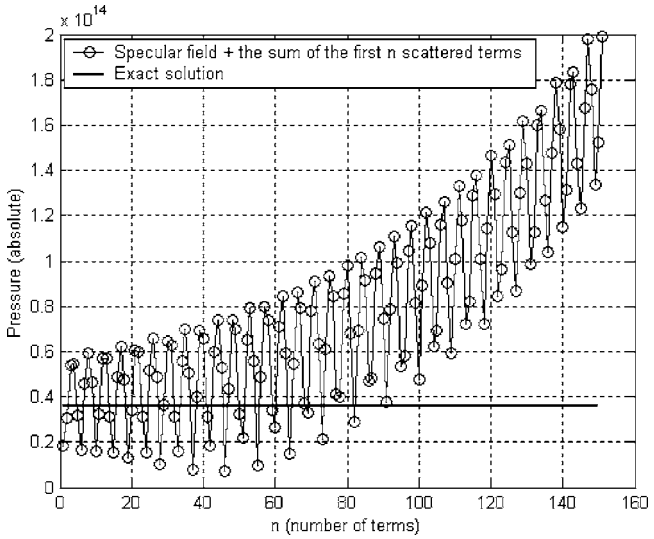

FIG. 8. The same as in the last figure, except the defect magnitude has increased from 17% to 17.5% of the original interfacial stiffness (*xx* component).

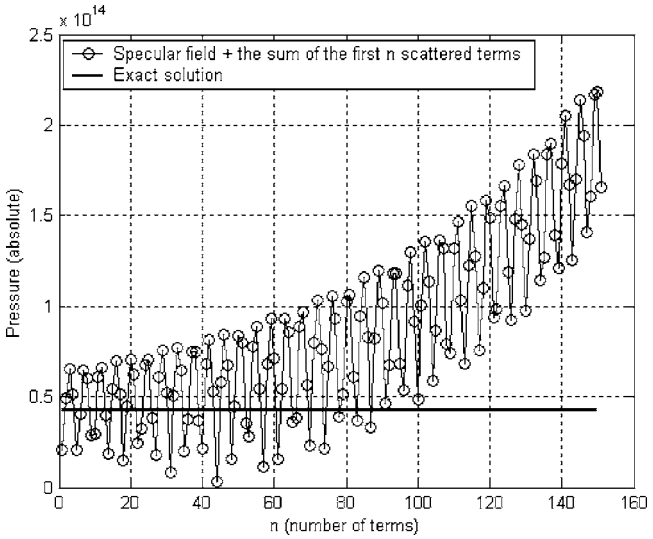

FIG. 10. The same as in the last figure, except the defect magnitude has increased from 40% to 44% of the original interfacial stiffness (*xx* component).

of the defect from 17% to 17.5%, we see that the series no longer converges; Fig. 8. (To be mathematically precise, the partial sums have not stabilized, even after 150 terms, and the terms appear to be growing in magnitude. We have verified (not shown) that they continue to grow up to 1500 terms.) This divergent behavior persists for all homogeneous defect magnitudes that we investigated above $0.175\mathbf{K}_{0xx}$, at this angle of incidence and frequency. That the convergence behavior changes with the angle of incidence (and other parameters) is shown in the next example.

We now change the angle of incidence to 13.34°, and *increase* the defect magnitude from 17.5% to 40% of the original interfacial stiffness *xx* component. Figure 9 shows the partial sums converging toward the exact reflection coefficient. The series has sensibly converged after about 60 terms. As before, we see the convergence is strongly nonmonotonic. It is interesting to note that this convergence occurs for a defect magnitude *larger* than that where divergence occurred in the previous example. We explain this by the fact that the scattering from this defect at this angle of incidence appears to be weaker than at the previously considered angle of incidence. This is consistent with our observation made in connection with the plot of reflection coefficients shown earlier. To understand this physically, consider the limiting case in which an incident wave was totally reflected before reaching a defect. In that case, the reflection coefficient would be completely independent of the defect amplitude and the series would converge after exactly one term. Therefore, what seems to govern convergence is not really the defect magnitude but the magnitude of the scattered field, or the degree of interaction between the incident field and the defect.

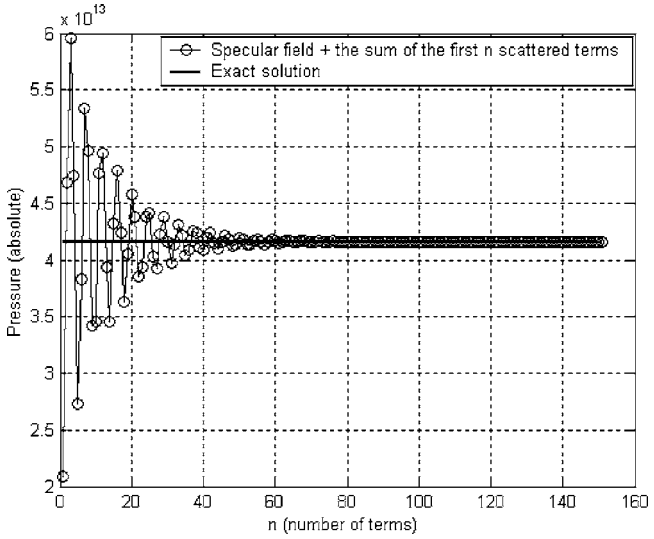

FIG. 9. A comparison between the exact and perturbation method solution. Here the angle of incidence has changed to 13.34°, and the homogeneous defect's magnitude is 40% of the original interfacial stiffness *xx* component.

As in the previous example, the relatively slow convergence of this last case implies we are near the convergence boundary. Increasing the defect magnitude from 40% to 44% causes the series to diverge, as shown in Fig. 10.

In other applications, we accommodate inhomogeneous defects and nonplane waves incident via Fourier transformation. In this context, the examples shown above represent a single incident Fourier mode and a single defect mode (wave number zero). To a certain extent, therefore, these examples (plane wave/homogeneous defect) are also representative for cases where either the incident field is not a plane wave or the defect is not homogeneous, or both. In such cases the interaction between the incident wave and defect can be understood as a superposition of interactions between incident plane waves and homogeneous (in k space; periodic in physical space) defects. Thus, for such cases, the perturbation series behavior illustrated previously (and confirmed in many other cases not shown here), indicating divergence or convergence to the exact solution, persists. If the series diverges, it does so due to the growth of some wave numbers, presumably the most strongly scattering. Beyond simple superposition of wave number effects, there is one additional important effect that ought to be considered. That is the tendency

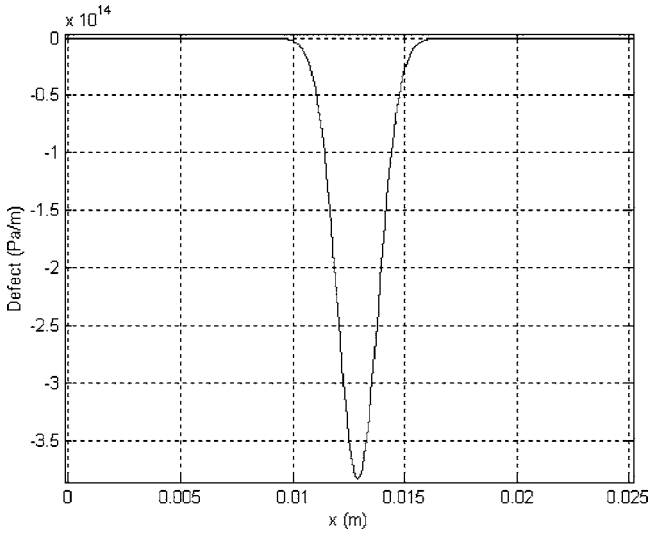

FIG. 11. A defect representing a local "kissing bond," where only the *xx* component of the original stiffness of adhesion is affected. It is located in interface *a*, its maximum value is 90% of the original stiffness of adhesion and its length is about 5 mm.

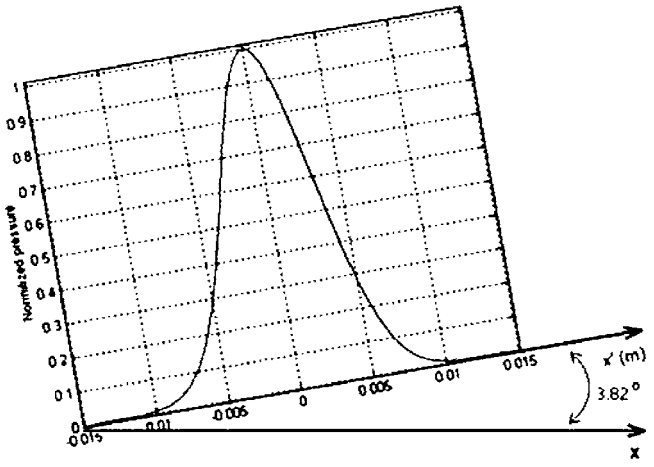

FIG. 12. The acoustic incident field. It is a time-harmonic Gaussian beam with about 20 mm of length and incident at the plate's top surface at an angle of 3.82°.

for "spectral spread" due to scattering of incident waves from one wave number to another. Thus the series might diverge due to the growth of wave numbers that are not present in the incident field, but are present in the scattered field. The spectral spreading phenomenon is demonstrated in a later example.

As shown and discussed above, the convergence behavior of the series depends essentially on the "degree of interaction" between the defect and the incident field. The "degree of interaction" itself depends basically on three factors: the *x* wave number, the defect's magnitude, and the defect's length. The dependence on the *x* wave number and defect magnitude are demonstrated in the examples above. The dependence on the defect's size can be understood in the context of scattering strength: for a given defect magnitude, the strength of the scattered field increases with the defect size. Thus, the series for larger defects tend to diverge at a lower magnitude than smaller defects. Indeed, below we show a converging example for a defect of smaller geometric size but a larger magnitude than one of our diverging cases just discussed.

We conclude our discussion of convergence by noting that while it is possible to identify the factors that affect convergence, it is difficult to predict *a priori* whether our perturbation series will converge or not. For each problem, therefore, it is necessary to check the sequence of partial sums to ensure that convergence is reached.

C. Simulation with a Gaussian defect and a Gaussian incident wave beam

In this simulation, for interface *a* we assumed that the *xx* component of $\epsilon\mathbf{K_1}$ is a Gaussian curve with maximum value equal to 90% of the original interfacial stiffness; i.e., only 10% of the original stiffness remains at the peak of the defect. The length of the defect is approximately 5 mm, as shown in Fig. 11. We chose the incident field to be an obliquely incident 4.9 MHz time harmonic Gaussian beam, with a beam waist about 20 mm wide. The angle of incidence is 3.82° and the incident field is represented schematically in Fig. 12.

The spectra of the specular reflected and the scattered pressure fields in the upper fluid half-space are plotted in Figs. 13 and 14, respectively. In this example the perturbation series is convergent and we show the sums of the first 2, 30, and 50 terms of the perturbation expansion in ϵ, (10) and (11). While the first two terms give a quantitatively inaccurate representation of the scattered field spectrum, the spectrum is qualitatively correct: it shows peaks in many of the right places, and the peaks themselves have approximately the right relative amplitudes. The fact that the sums after 30 and 50 terms are identical shows that the partial sums have stabilized and that this series is apparently convergent. Comparing Figs. 13 and 14 shows that the spectrum of the scattered field is much broader than the spectrum of the specular field, the latter having roughly the same spectral width as the incident field. This broadening effect is associated with scattering of the incident signal by the defective interface, as

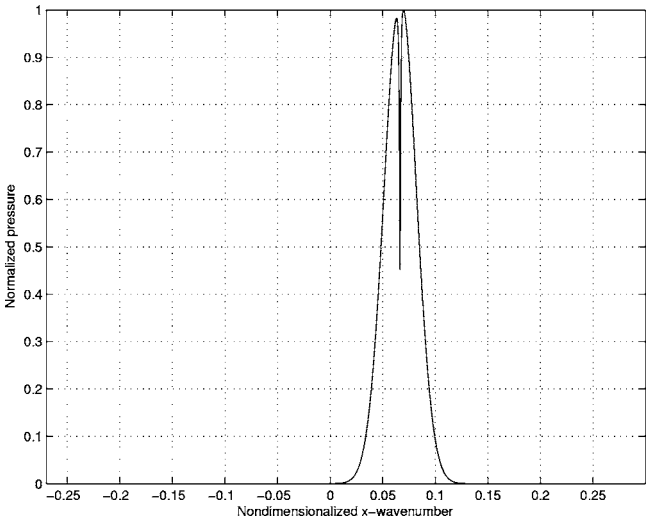

FIG. 13. Spectrum of the reflected pressure field. The wave number is nondimensionalized with respect to the wave number in the fluid.

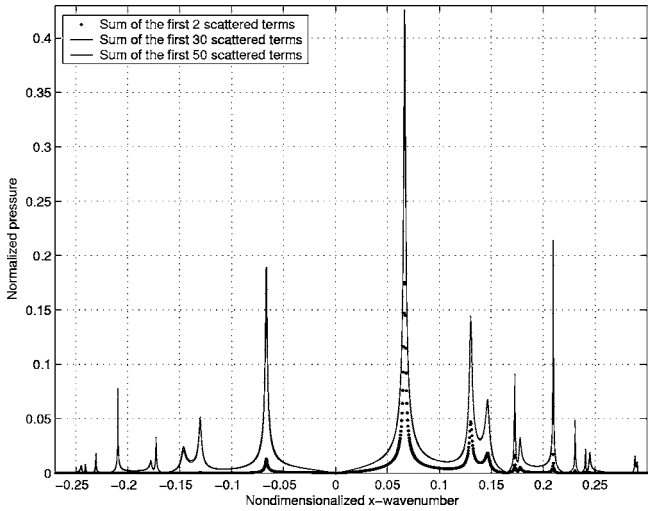

FIG. 14. Spectrum of the scattered pressure field. Note (a) the breadth. The spectrum is significant over a broader wave number range than that depicted in Fig. 13; (b) the peaks. These are coincident with the modes identified in the plot of the reflection coefficient, Fig. 4; (c) the "backscatter." The amplitudes of waves traveling in the negative x direction are significant. These radiate strongly at the leaky angles; and (d) the convergence. The partial sums after 30 and 50 terms are practically identical.

mentioned earlier. The strong peaks in the scattered field are due to excited leaky waves, and correspond to the minima in the reflection coefficient identified in Fig. 4. The scattered field spectrum also shows significant amplitudes for negative propagation directions. These are associated with negative components of an x wave number, indicating pronounced backscattering in the incident direction.

V. SUMMARY AND CONCLUSIONS

We presented an analytic-numerical method to simulate the interaction of ultrasonic waves with imperfectly bonded plates. The primary ingredients in our solution are the QSA approximation for the adhesion interfaces, the perturbation method to account for nonuniform flaws, and the invariant imbedding method to give us numerical stability, even for evanescent wave components at high frequencies. These combine to give us a recursive algorithm to evaluate displacements and generalized stress (pressure) fields in general problems consisting of composite layered plates. The algorithm is equally well suited to treating anisotropic as well as isotropic layers.

We illustrated our perturbation method in Sec. IV by simulating ultrasonic scattering from an imperfectly bonded plate. This example showed that ultrasound can reveal the presence of kissing bonds. Such simulations can be used more generally in the design of ultrasound inspecting systems by exploring the design parameter space, such as transducer placement, frequency, angle of incidence, beam width, pulse length, etc. For the pulse length, an additional Fourier transform is required.

As an example of the above idea, we have identified an empirical rule of thumb for identifying the optimal incident angle. Our experience indicates that this works quite well, though we have yet to confirm our current explanation as to why it works. As inspection success depends strongly on the choice of such parameters, any systematic way to select these is highly desired.

ACKNOWLEDGMENTS

This work has been partially supported by the Brazilian Government through CAPES.

APPENDIX A: HOMOGENEOUS ANISOTROPIC MEDIA

Here we derive the operators $\mathbf{M}_j$ and $\mathbf{Z}_j$ for plane waves propagating in a homogeneous anisotropic layer. The waves are assumed to propagate in the $x-z$ plane, which need not be aligned with crystallographic axes of the anisotropic solid. We first rewrite the transformed (22)–(24) momentum (19) and constitutive (20) equations in the Stroh formalism:

$$\frac{\partial}{\partial z}\bar{\boldsymbol{\xi}}(z,\alpha) = i\mathbf{N}(\alpha)\bar{\boldsymbol{\xi}}(z,\alpha). \tag{A1}$$

Recall that α is the x wave number. The state vector $\boldsymbol{\xi}$ is defined as:

$$\bar{\boldsymbol{\xi}}(z,\alpha) = \begin{Bmatrix} \bar{\mathbf{u}}(z,\alpha) \\ i\bar{\mathbf{t}}(z,\alpha) \end{Bmatrix}, \tag{A2}$$

and $\mathbf{N}$ is the linear operator, given by

$$\mathbf{N} = \begin{bmatrix} -\alpha\mathbf{X}_2^{-1}\mathbf{X}_1 & -\mathbf{X}_2^{-1} \\ -\omega^2\rho\mathbf{I} + \alpha^2\mathbf{Y}_1 - \alpha^2\mathbf{Y}_2\mathbf{X}_2^{-1}\mathbf{X}_1 & -\alpha\mathbf{Y}_2\mathbf{X}_2^{-1} \end{bmatrix}. \tag{A3}$$

Here, $\mathbf{X_1}$, $\mathbf{X_2}$, $\mathbf{Y_1}$, and $\mathbf{Y_2}$ are defined in terms of the elasticity tensor elements as

$$\mathbf{X_1} = \begin{bmatrix} c_{51} & c_{56} & c_{55} \\ c_{41} & c_{46} & c_{45} \\ c_{31} & c_{36} & c_{35} \end{bmatrix}, \tag{A4}$$

$$\mathbf{X_2} = \begin{bmatrix} c_{55} & c_{54} & c_{53} \\ c_{45} & c_{44} & c_{43} \\ c_{35} & c_{34} & c_{33} \end{bmatrix}, \tag{A5}$$

$$\mathbf{Y_1} = \begin{bmatrix} c_{11} & c_{16} & c_{15} \\ c_{11} & c_{16} & c_{15} \\ c_{51} & c_{56} & c_{55} \end{bmatrix}, \tag{A6}$$

$$\mathbf{Y_2} = \begin{bmatrix} c_{15} & c_{14} & c_{13} \\ c_{65} & c_{64} & c_{63} \\ c_{55} & c_{54} & c_{53} \end{bmatrix}. \tag{A7}$$

The propagator matrix for a homogeneous anisotropic medium is given by

$$\mathbf{M}(z) = e^{i\mathbf{N}z}. \tag{A8}$$

If we denote by $k_{z_l}(I=1,2,\ldots,6)$ the eigenvalues, and by $\boldsymbol{\Theta}$ the sextic matrix whose columns are the eigenvectors of $\mathbf{N}$, then the 6-tensors $\mathbf{N}$ and $\mathbf{M}$ may be written as

$$\mathbf{N} = \boldsymbol{\Theta}\{\mathrm{diag}(k_{z_1}, k_{z_2}, \ldots, k_{z_6})\}\boldsymbol{\Theta}^{-1}, \tag{A9}$$

$$\mathbf{M} = \boldsymbol{\Theta}\{\mathrm{diag}(e^{ik_{z_1}z}, e^{ik_{z_2}z}, \ldots, e^{ik_{z_6}z})\}\boldsymbol{\Theta}^{-1}. \tag{A10}$$

Clearly, then, the eigenvalues of $\mathbf{N}$ are the wave numbers in the direction of z, while its eigenvectors, denoted here by $\bar{\boldsymbol{\xi}}_l$, are the polarization vectors. The eigenvalues of $\mathbf{N}$, or the wave numbers in the direction of z, can be decomposed into two subgroups. We order the eigenpairs $(k_{z_l}, \bar{\boldsymbol{\xi}}_l)$ in such a way that the first three are associated with the waves that propagate or are attenuated in the z-positive direction, i.e., for $I=1,2,3, k_{z_I}$ is such that $\mathrm{Re}(k_{z_I})>0$ or $\mathrm{Im}(k_{z_I})>0$. On the other hand, for $I=4,5,6, k_{z_I}$ is such that $\mathrm{Re}(k_{z_I})<0$ or $\mathrm{Im}(k_{z_I})<0$. We use the term "upgoing" wave to refer a partial wave with a wave number in the first subgroup, whereas waves with wave numbers in the second subgroup are referred to as "downgoing" waves.

We decompose the matrix $\boldsymbol{\Theta}$ into four (3×3) submatrices as follows:

$$\boldsymbol{\Theta} = \begin{bmatrix} \mathbf{A}_1 & \mathbf{A}_2 \\ \mathbf{L}_1 & \mathbf{L}_2 \end{bmatrix}. \tag{A11}$$

The state vector at $z=0, \bar{\boldsymbol{\xi}}(0)$, may be expressed as a linear combination of the six linearly independent eigenvectors of the fundamental elasticity tensor, i.e.,

$$\bar{\boldsymbol{\xi}}(0) = \boldsymbol{\Theta}\mathbf{c}, \quad \text{where } \mathbf{c} = \begin{Bmatrix} \mathbf{c}_1 \\ \mathbf{c}_2 \end{Bmatrix}. \tag{A12}$$

In the expression (A12), $\mathbf{c}_1$ and $\mathbf{c}_2$ are three-dimensional constant vectors. Thus it follows that the solution at any z may be written as

$$\bar{\boldsymbol{\xi}}(z) = \begin{bmatrix} \mathbf{A}_1 & \mathbf{A}_2 \\ \mathbf{L}_1 & \mathbf{L}_2 \end{bmatrix} \begin{bmatrix} \boldsymbol{\Phi}_1(z) & \mathbf{0} \\ \mathbf{0} & \boldsymbol{\Phi}_2(z) \end{bmatrix} \begin{Bmatrix} \mathbf{c}_1 \\ \mathbf{c}_2 \end{Bmatrix}, \tag{A13}$$

where

$$\boldsymbol{\Phi}_1(z) = \{\mathrm{diag}(e^{ik_{z_1}z}, e^{ik_{z_2}z}, e^{ik_{z_3}z})\}, \tag{A14}$$

$$\boldsymbol{\Phi}_2(z) = \{\mathrm{diag}(e^{ik_{z_4}z}, e^{ik_{z_5}z}, e^{ik_{z_6}z})\}. \tag{A15}$$

The decomposition of the total displacement and traction fields into upgoing $(\bar{\mathbf{u}}_1, \bar{\mathbf{t}}_1)$ and downgoing $(\bar{\mathbf{u}}_2, \bar{\mathbf{t}}_2)$ components, Eqs. (26) and (27), thus follows with were

$$\bar{\mathbf{u}}_j(z) = \mathbf{A}_j \boldsymbol{\Phi}_j(z)\mathbf{c}_j, \tag{A16}$$

$$\bar{\mathbf{t}}_j(z) = -i\mathbf{L}_j \boldsymbol{\Phi}_j(z)\mathbf{c}_j. \tag{A17}$$

Evaluating (A16) at $z=0$ and eliminating $\mathbf{c}_j$ gives (28) with

$$\mathbf{M}_j(z) = \mathbf{A}_j \boldsymbol{\Phi}_j(z)\mathbf{A}_j^{-1}. \tag{A18}$$

Likewise, eliminating the constants $\mathbf{c}_1$ and $\mathbf{c}_2$ from expression (A17), and using (A18) gives (29), with the local impedance tensors defined by

$$\mathbf{Z}_j = \frac{1}{\omega}\mathbf{L}_j\mathbf{A}_j^{-1}. \tag{A19}$$

The formulation described above is unsuitable for isotropic media. It has to do with the fact that for an isotropic medium, two or more of matrix $\mathbf{N}$'s eigenvalues are equal. For such cases, by taking advantage of the fact that the two wave speeds in the medium (longitudinal and transverse) can be directly determined, the determination of matrices $\mathbf{A}_j$, $\mathbf{L}_j$, $\boldsymbol{\Phi}_j(z)$ is straightforward. Expressions for the propagator matrices, $\mathbf{M}_1(z)$ and $\mathbf{M}_2(z)$, and impedance matrices, $\mathbf{Z}_1$ and $\mathbf{Z}_2$, can then be obtained through (A18) and (A19).

[1] A. I. Lavrentyev and S. I. Rokhlin, "Ultrasonic evaluation of environmental degradation of adhesive joints," Rev. Prog. Quant. Nondestr. Eval. **13**, 1539–1546 (1994).
[2] H. Schmidt and F. B. Jensen, "A full wave solution for propagation in stratified viscoelastic media with application to Gaussian beam reflection at a fluid/solid interface," J. Acoust. Soc. Am. **77**, 813–825 (1985).
[3] T. Kundu and A. K. Mal, "Acoustic material signature of a layered plate," Int. J. Eng. Sci. **24**, 1819–1829 (1986).
[4] R. C. Y. Chin, G. W. Hedstrom, and L. Thigpen, "Matrix methods in synthetic seismograms," Geophys. J. R. Astron. Soc. **77**, 483–502 (1984).
[5] C. Moler and C. VanLoan, "Nineteen dubious ways to compute the exponential of a matrix, Twenty-five years later," SIAM Rev. **45**, 3–49 (2003).
[6] K. Balabasubramian, "On a numerical truncation approximation algorithm for transfer matrix method," J. Acoust. Soc. Am. **107**, 1053–1056 (2000).
[7] R. Bellman and R. Kalaba, "Functional equations, wave propagation, and invariant imbedding," J. Math. Mech. **8**, 683 (1959).
[8] B. L. N. Kennett, *Seismic Wave Propagation in Stratified Media* (Cambridge University Press, London, 1983).
[9] W. W. Hager and R. Rostamian, "Reflection and refraction of elastic waves for stratified materials," Wave Motion **10**, 333–348 (1988).
[10] A. M. B. Braga and G. Herrmann, "Plane waves in anisotropic layered composites," in *Wave Propgation in Structural Composities*, edited by A. K. Mal and T. C. T. Ting (ASME-AMD, New York, 1988), Vol. **90**, pp. 81–98.
[11] L. Wang and S. I. Rokhlin, "Stable reformulation of transfer matrix method for wave propagation in layered anisotropic media," Ultrasonics **39**, 413–424 (2001).
[12] S. I. Rokhlin and L. Wang, "Stable recursive algorithm for elastic wave propagation in layered anisotropic media: Stiffness matrix method," J. Acoust. Soc. Am. **112**, 822–834 (2002).
[13] L. Wang and S. I. Rokhlin, "A recursive stiffness matrix method for wave propagation in stratified media," Bull. Seismol. Soc. Am. **92**, 1129–1135 (2002).
[14] A. M. B. Braga, "Wave propagation in anisotropic layered composites," Ph.D. thesis, Stanford University, Stanford, California, 1990.
[15] B. Honein, A. M. B. Braga, P. E. Barbone, and G. Herrmann, "Active suppression of sound reflected from a piezoelectric plate," J. Intell. Mater. Syst. Struct. **3**, 209–223 (1992).
[16] A. M. B. Braga, P. E. Barbone, and G. Herrmann, "Wave propagation in fluid-loaded laminated cylindrical shells," Appl. Mech. Rev. **43**, 359–365 (1990).
[17] J. M. Baik and R. B. Thompson, "Ultrasonic scattering from imperfect interfaces: A quasi-static model," J. Nondestruct. Eval. **14**, 177–196 (1984).
[18] S. I. Rokhlin and W. Huang, "Ultrasonic wave interaction with a thin layer between two anisotropic solids," J. Acoust. Soc. Am. **92**, 1729–1742 (1992).
[19] B. W. Drinkwater, R. S. Dwyer-Joice, and A. M. Robinson, "The use of ultrasound to investigate rough surface contact phenomena," *Review of Progress in Quantitative Nondestructive Evaluation*, 1999, Vol. **18**, pp. 1455–1462.
[20] P. Karpur, T. Kundu, and J. J. Ditri, "Adhesive joint evaluation using Lamb wave modes with appropriate displacement, stress and energy distribution profiles," Rev. Prog. Quant. Nondestr. Eval. **18**, 1533–1542 (1999).
[21] B. Li, M. Hefetz, and S. I. Rokhlin, "Ultrasonic evaluation of environmentally degraded adhesive joints," Rev. Prog. Quant. Nondestr. Eval. **11**, 1221–1228 (1992).
[22] T. Pialucha and P. Cawley, "The detection of a weak adhesive/adherend interface in bonded joints by ultrasonic reflection measurements," Rev. Prog. Quant. Nondestr. Eval. **11**, 1261–1266 (1992).
[23] Y. C. Angel and J. D. Achenbach, "Reflection and transmission of elastic waves by a periodic array of cracks," J. Appl. Mech. **52**, 33–41 (1985).
[24] S. Nakagawa, K. T. Nihei, and L. R. Myer, "Plane wave solution for elastic wave scattering by a heterogeneous fracture," J. Acoust. Soc. Am. **115**, 2761–2772 (2004).
[25] M. Van Dyke, "Computer-extended series," Annu. Rev. Fluid Mech. **16**, 287–309 (1984).

[26]A. Pilarski, J. L. Rose, and K. Balasubramaniam, "The angular and frequency characteristics of reflectivity from a solid layer embedded between two solids with imperfect boundary conditions," J. Acoust. Soc. Am. **87**, 532–542 (1990).
[27]A. Baltazar, S. I. Rokhlin, and C. Pecorari, "On the relationship between ultrasonic and micro-structural properties of imperfect interfaces in layered solids," Rev. Prog. Quant. Nondestr. Eval. **18**, 1463–1470 (1999).
[28]N. Guo and P. Cawley, "The interaction of Lamb waves with delaminations in composite laminates," J. Acoust. Soc. Am. **94**, 2240–2246 (1993).
[29]T. Kundu and M. Blodgett, "Detection of material defects in layered solids using Lamb waves," Rev. Prog. Quant. Nondestr. Eval. **13**, 1343–1350 (1994).
[30]A. Pilarski, J. L. Rose, J. Ditri, D. Jiao, and K. Rajana, "Lamb wave mode selection for increased sensitivity to interfacial weaknesses of adhesive bonds," Rev. Prog. Quant. Nondestr. Eval. **12**, 1579–1585 (1993).
[31]H. L. Bertoni and T. Tamir, "Unified theory of Rayleigh-angle phenomena for acoustic beams at liquid-solid interfaces," Appl. Phys. **2**, 157–172 (1973).
[32]L. Singher, Y. Segal, and E. Segal, "Considerations in bond strength evaluation by ultrasonic guided waves," J. Acoust. Soc. Am. **96**, 2497–2505 (1994).
[33]J. M. Claeys and O. Leroy, "Reflection and transmission of bounded sound beams on half-spaces and through plates," J. Acoust. Soc. Am. **72**, 585–590 (1982).
[34]D. E. Chimenti and A. H. Nayfeh, "Ultrasonic leaky waves in a solid plate separating a fluid and vacuum," J. Acoust. Soc. Am. **85**(2), 555–560 (1989).
[35]Again, the perturbation order in Eq. (25) is suppressed, and will be throughout this section, since the treatment of each order is formally identical.

Energy pass bands in a ribbed cylindrical shell with periodic asymmetries

Martin H. Marcus and Brian H. Houston
Naval Research Laboratory, Washington DC, 20375-5320

(Received 21 January 2005; accepted 12 July 2005)

The addition of periodically spaced structures to a cylindrical shell causes energy to propagate at additional wave numbers via a phenomenon known as Brillouin folding. As a result, a load representing one axial mode on a cylindrical shell with circumferentially spaced discontinuities, for example stringers, has distinct energy pass bands and stop bands. Similarly, an excitation representing one circumferential mode on a cylindrical shell with axially spaced discontinuities, for example ribs, also has distinct energy pass bands and stop bands. Discontinuities in both directions lead to energy pass bands when a point force is applied. In this paper, periodically spaced point masses in the axial and circumferential directions are added to a submerged, ribbed, finite cylindrical shell and analyzed via the finite element method. It is seen that Brillouin folding occurs and, in certain circumstances, the energy is split into pass bands and stop bands. For the frequency and circumferential modes where the subsonic energy is most narrowly focused in the axisymmetric shell, a distinct peak in radiated power occurs for the shell with point masses. The energy in this peak is about the same for several examples of different amounts of nonaxisymmetric mass. © *2005 Acoustical Society of America.* [DOI: 10.1121/1.2011807]

PACS number(s): 43.20.Ks, 43.40.At, 43.40.Ey, 43.30.Jx [ANN] Pages: 2167–2172

I. INTRODUCTION

Structures with periodicity and the acoustic noise they generate have received much interest in the last several years. Maidanik and Dickey[1] compute the response of infinite fluid-loaded plates with ribs that are regularly spaced. In so doing, they observe replication of the flexural dispersion relations, which is commonly called Brillouin folding.[2] Mead[3] makes a similar calculation and observes that the replication of the normally subsonic flexural dispersion relations leads to flexural energy that is supersonic and is strongly coupled to the fluid in radiation problems. Photiadis also shows strong coupling of the flexural energy to the fluid for scattering off of ribbed plates[4] and ribbed, infinite cylindrical shells.[5] Houston *et al.*[6] later showed this experimentally for ribbed, finite cylindrical shells.

As the work graduates into cylindrical shells, the structural response is often decomposed into circumferential Fourier modes. This is tantamount to determining the response to a load that is a single circumferential mode. For such a load, the flexural dispersion relations tend to break into distinct pass bands and stop bands, as demonstrated by Maidanik and Becker[7] with their calculations on ribbed, infinite cylindrical shells and by Photiadis *et al.*[8] experimentally and Marcus *et al.*[9] computationally on finite, ribbed cylindrical shells. For an excitation comprising many circumferential modes, distinct stop bands do not occur. Energy gets onto the shell at every frequency.

In this paper, the addition of circumferential periodicity (equally spaced point masses) to a cylindrical shell that already has axial periodicity (equally spaced ribs) causes Brillouin folding and the formation of pass bands in both directions. This leads to significantly more acoustic radiation than occurs with periodicity in just one direction. The total radiated power is about 10 dB higher over a broad frequency range in this paper and in previous work.[10] In Sec. II, the response of a load on an infinite cylindrical shell with line masses along the length shows pass bands. In Sec. III, a load on a submerged, finite, ribbed cylindrical shell is shown to admit energy to the structure for all of the frequencies in this study. In Sec. IV, the addition of periodically spaced point masses to the finite shell of Sec. III leads to pass bands and stop bands as well as increased acoustic radiation in the pass bands. Finally, Sec. V summarizes these findings.

II. INFINITE SHELL WITH LINE MASSES

Just as a Dirac delta function applied in the time domain causes a response at all times,[11] a line discontinuity on a cylindrical shell causes a response at all angles, and consequently at all circumferential modes. With the circumferential modes coupled, resonances that occur at high-order modes will be evident at low-order modes. This is demonstrated with an analytical model of an *in vacuo,* infinite cylindrical shell with 11 line masses that are equally spaced circumferentially. The equations of motion use Donnell's formulation and are readily available[12,13] for the axisymmetric shell. For the inclusion of line masses, the kinetic energy becomes

$$T = \int_0^{2\pi}\int_0^1 \frac{\rho h}{2}\left[\left(\frac{\partial u}{\partial t}\right)^2 + \left(\frac{\partial v}{\partial t}\right)^2 + \left(\frac{\partial w}{\partial t}\right)^2\right] R^2\, ds\, d\theta + \int_0^{2\pi}\int_0^1 \frac{M}{2L}\sum_{i=1}^{n_m}\left[\left(\frac{\partial u}{\partial t}\right)^2 + \left(\frac{\partial v}{\partial t}\right)^2 + \left(\frac{\partial w}{\partial t}\right)^2\right] \times \delta\left(\theta - \frac{2\pi i}{n_m}\right) R\, ds\, d\theta. \quad (1)$$

The first term, representing the shell, can be found in Ref. 13 on p. 36, while the second term represents the line masses. ρ is the density, h is the shell thickness, and u, v, and w are the axial, circumferential, and radial displacements, respectively. t is time, R is the shell radius, s is the radius normalized length dimension, θ is the circumferential angle, M/L is the mass per unit length for one line mass, and n_m is the number of line masses. The potential energy, V, is the same as for the axisymmetric shell, so equilibrium is satisfied with

$$\delta \int_{t_0}^{t_1} (T - V)\, dt = 0. \tag{2}$$

Applying the Euler-Lagrange equations to the integrand of Eq. (2) yields three equations of motion. The Euler-Lagrange term for the kinetic energy of the u equation is

$$-\frac{\partial}{\partial t}\left(\frac{\partial T}{\partial(\partial u/\partial t)}\right) = -\rho h R^2 \frac{\partial^2 u}{\partial t^2} \times \left[1 + \sum_{i=1}^{n_m} \frac{M}{L\rho h R}\delta\left(\theta - \frac{2\pi i}{n_m}\right)\right]. \tag{3}$$

The derivation follows the same pattern for the v and w equations, so the result is the same as in Ref. [12] except with the term in brackets in Eq. (3) appearing as a coefficient to the acceleration terms. Since our problem has no axial displacement, the u equation disappears and the others simplify to

$$\frac{\partial^2 v}{\partial \theta^2} + \frac{\partial^2 w}{\partial \theta^2} = \frac{\rho R^2(1-\nu^2)}{E}\frac{\partial^2 v}{\partial t^2}\left[1 + \sum_{i=1}^{n_m} \frac{M}{L\rho h R}\delta\left(\theta - \frac{2\pi i}{n_m}\right)\right], \tag{4}$$

$$\frac{\partial v}{\partial \theta} + w + \frac{R^2 h^2}{12}\nabla^4 w = -\frac{\rho R^2(1-\nu^2)}{E}\frac{\partial^2 w}{\partial t^2} \times \left[1 + \sum_{i=1}^{n_m} \frac{M}{L\rho h R}\delta\left(\theta - \frac{2\pi i}{n_m}\right)\right] + \delta(\theta), \tag{5}$$

where ν is Poisson's ratio, E is Young's modulus, and $\delta(\theta)$ is the applied radial force. v and w are Fourier expanded in angle and time, and a Fourier integral over the equations gives two equations and two unknowns for each Fourier angular mode number. The line mass terms in Eqs. (4) and (5) give rise to terms that couple the modes to each other. Most of the terms integrate to zero, but the terms that couple modes that add or subtract to a multiple of n_m are nonzero. In this study, n_m is 11 and the highest mode is 30.

The shell to be analyzed has a radius of 0.0692 m, a thickness of 0.635 mm, and the shell is made of nickel. Its line masses have a mass per unit length of 3.14 kg/m. Figure 1 shows the normal velocities from a radial line load versus frequency and circumferential mode. The curved white line shows the response when the shell has no line masses. The response for the line mass calculation is seen as having moved down from the curved white line, because the shell now has more mass, and broken into individual pass bands. Also, the response is folded (flipped horizontally) as well as

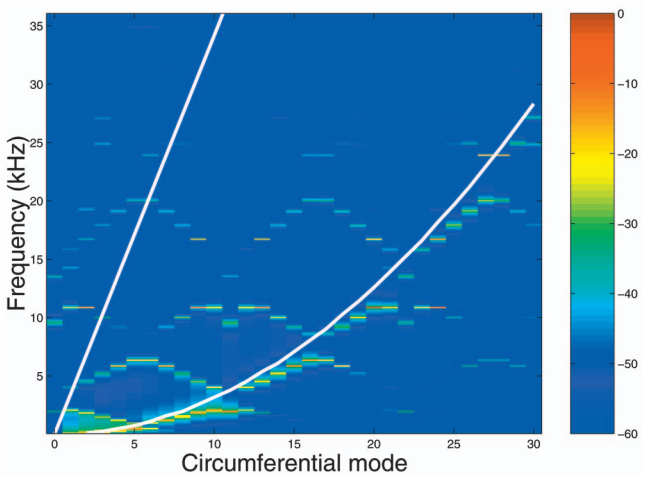

FIG. 1. Normal velocities from a radial line load on an *in vacuo*, infinite cylindrical shell with 11 periodically spaced line masses. Colors refer to the dB level normalized so that the maximum value is 0.

replicated every 11 modes, as one would expect from Brillouin folding.[2] This creates several zigzag patterns. These patterns do not overlap (they have stop bands); otherwise they would have discontinuous group velocities (the slopes of the curves), which is not physically possible.[14] Because the patterns do not cross, the curves flatten at what would have been crossings. This is most obvious at the low-frequency end of Fig. 1.

The straight white line in Fig. 1 is an overlay corresponding to the sonic line for water. If the shell were submerged, the energy to the left of this line would radiate to the far field. Since most of this energy comes from replicating the high circumferential modes, the energy that would radiate is much greater than if there were no line masses.

The most important observation of this section is that the addition of line masses causes pass bands, the lowest of which are the most narrow in frequency. Since part of the pass bands would be supersonic if the shell were submerged, the pass bands represent a potential acoustic radiation path.

III. AXISYMMETRIC SHELL

The axisymmetric shell of this section is shown in Fig. 2. It is a cylindrical shell with 80 straight frames and a cone-sphere endcap. The radius, thickness, and material are the same as for the infinite shell of Sec. II. The load is a point load at halfway between frames 38 and 39. The load is applied at 295 frequencies from 122 Hz to 36 kHz. The finite

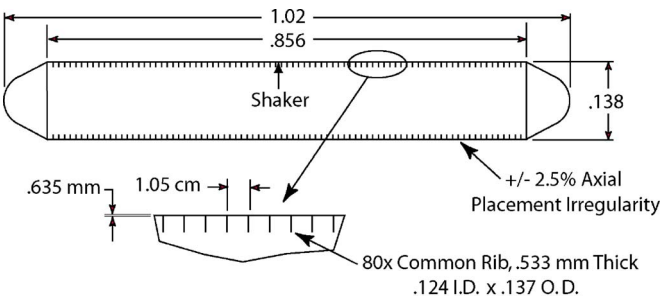

FIG. 2. Axisymmetric shell cross section.

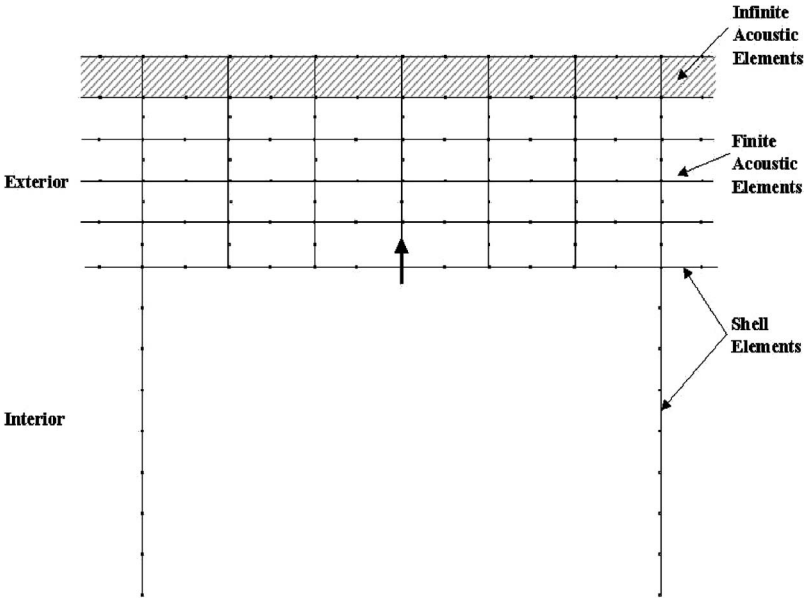

FIG. 3. Finite element mesh for one bay of the axisymmetric shell. The arrow depicts the radial point force.

element mesh for the bay with the load is displayed in Fig. 3. It uses four quadratic elements per frame and six quadratic elements per bay. It has five layers of external, quadratic acoustic elements which vary in thickness depending on the frequency. The first four layers are one-fourth of a wavelength thick and the last layer is infinite. The response to the load is already documented.[9,10] Only the results relevant to the current paper are discussed here. For the above parameters, surface velocities are obtained along the cylindrical section of the shell, but broken down by circumferential mode. For each of these modes, Brillouin folding is evident. Figure 4 presents the rms average along the length of the shell of the surface normal velocities plotted against frequency and circumferential mode number. The straight line indicates the sonic line for axial mode zero. The sonic lines for higher axial modes are to the left of this line. This means that the velocities to the right of this line are subsonic and, for the most part, do not radiate to the far field of the external fluid. (We note that for a finite shell, a small fraction of the subsonic energy leaks to the far field.[15])

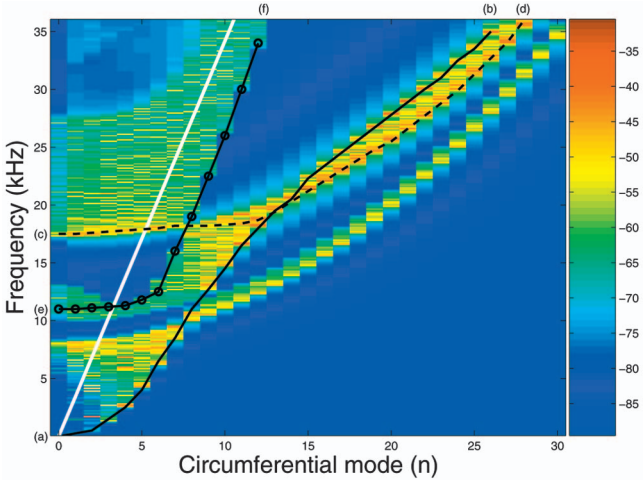

FIG. 4. The rms average of the surface normal velocity of a submerged, axisymmetric, framed cylindrical shell from a point load. Colors refer to the dB level *re*:1 m/s for a 1-N load. Velocities to the right of the white line do not radiate.

Figure 4 also has black curves superimposed to denote certain types of vibration. A close look at the deformations reveals that the frames bend without any axial bending of the shell when at curve ab. In contrast, along curve ef, the frames bend while the shell bends with one half wavelength between frames. Finally, curve cd denotes when the shell bends as it does along curve ef, but with the frames twisting. Hodges, Power, and Woodhouse[16] report the same behavior in the analysis of a t-framed cylindrical shell in air. Of interest here is the narrow band between curves ab and cd above where they cross. In Hodges *et al.*,[16] as well as the current paper, many discrete resonances occur in this band. According to Ashcroft and Mermin,[17] there will be as many resonances as there are frames. Due to symmetry, the shell in this paper will have only half as many resonances, 40 per circumferential mode. These resonances can be thought of as energy states as discussed in references on statistical energy analysis, such as that by Lyon.[18] Each state has an equal amount of energy, so, for each mode, the pass band between curves ab and cd represents 40 frequencies at which the structure has an equal amount of energy, all of which is subsonic. The pass band just below this band also has 40 frequencies per mode, but these are frame resonances and couple weakly to the fluid. Although interesting, they play only a small role in acoustic radiation. Hodges *et al.*[16] do not get such a pass band at this frequency, because they use t frames, which are much stiffer in bending than are straight frames.

The most relevant aspect of Fig. 4 is that energy gets onto the shell at every frequency, with most of the energy at subsonic modes. In the next section, a non-axisymmetric feature is added to this shell to generate frame energy pass bands and stop bands and to couple this frame energy to supersonic modes.

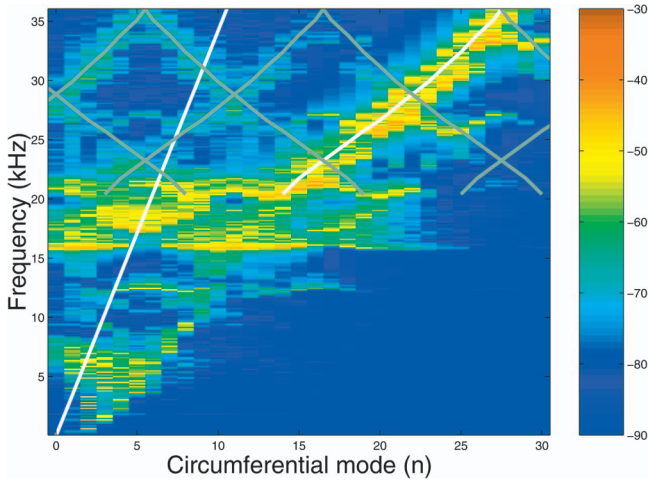

FIG. 5. The rms average of the surface normal velocity of a submerged, framed cylindrical shell with 11 periodically spaced point masses per frame from a point load. Colors refer to the dB level *re*:1 m/s for a 1-N load. Velocities to the right of the white line do not radiate. The white and gray curves are derived from the axisymmetric shell results in Fig. 4.

IV. NON-AXISYMMETRIC SHELL

In Sec. II, line masses were added to an infinite cylindrical shell to generate circumferential pass bands and stop bands. In this section, point masses are added to the finite shell of Sec. III. Eleven point masses are placed equidistantly on the inner edge of each frame, for a total of 880 point masses. Each point mass weighs 3.08 g, so the mass per unit length is the same as for the line mass in the infinite shell of Sec. II.

Figure 5 presents the rms average along the length of the non-axisymmetric shell of the surface normal velocities plotted against frequency and circumferential mode number. These values are shown as colors from blue to red. To help determine a pattern in this plot, the pass band between curves ab and cd in Fig. 4 is shown in Fig. 5 as a curved white line. When point masses break the symmetry of this structure, we should expect to see Brillouin folding of this curve, but not the lower one in Fig. 4, since it represents frame resonances, which do not couple efficiently to shell motion. The expected Brillouin folding is shown as several gray curves in Fig. 5. For the upper third of the spectrum, the gray curves appear to trace the velocity patterns for the non-axisymmetric shell. At about 21 kHz, the pass band is quite flat. This is also the frequency where the pass band in Fig. 4 is the narrowest. At 21 kHz in Fig. 5, a significant amount of energy is to the left of the straight white line, the sonic line for axial mode 0. This means that we should expect an increased amount of radiation to the far field.

Figure 6 shows the radiated power spectral density for the axisymmetric shell (solid curve) and the non-axisymmetric shell (dashed curve). The dashed curve is higher than is the solid curve at the upper half of the spectrum, as expected, since a great deal of energy is Brillouin folded into the supersonic region for the non-axisymmetric shell. The highest part of the dashed curve is at 21 kHz and is about 2 kHz wide. This frequency range is also where modes 13–16 have the highest velocity in Fig. 5. These are also the modes in Fig. 4, for the axisymmetric shell, with the most narrow pass bands. It appears that these four narrow bands are giving rise to the radiated power peak at 21 kHz.

To demonstrate that the largest peak in the radiated power of the non-axisymmetric shell is due to energy states from the axisymmetric shell, the non-axisymmetric analysis is performed for point masses that are two, five, ten, and twenty times the mass of the above analysis. Figure 7 shows the radiated power for these and the original non-axisymmetric cases. In every plot, the highest peak is at 21 kHz and it becomes higher and narrower as the size of the point masses increases. The area under the peak is computed and plotted in Fig. 8. The resulting power spectral density shows very little variation with the amount of non-axisymmetric mass. This implies that the energy must be from an axisymmetric part of the motion. The point masses merely couple the motion to the radiating modes and the amount of mass is relatively unimportant, but cannot be zero.

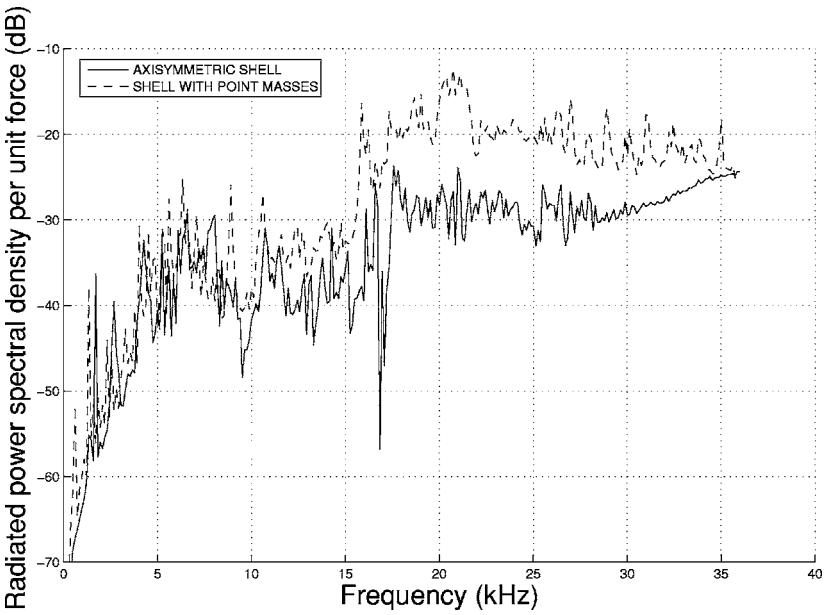

FIG. 6. Radiated power spectral density from a point load on a submerged, framed, axisymmetric, cylindrical shell with and without 11 periodically spaced point masses per frame. Magnitude refers to the dB level *re*:1 W/Hz for a 1-N load.

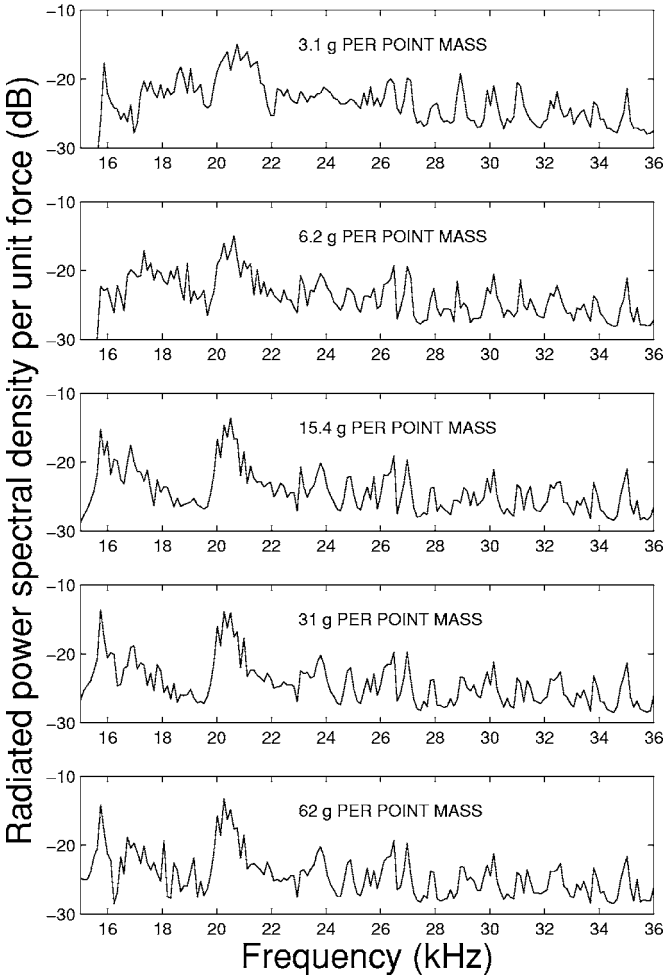

FIG. 7. Radiated power spectral density from a point load on a submerged, framed, axisymmetric, cylindrical shell with 11 periodically spaced point masses per frame. Each plot represents point masses of different amounts. Magnitude refers to the dB level *re*: 1 W/Hz for a 1-N load.

The dashed curve in Fig. 8 shows the power spectral density when there are 12 point masses per ring. The behavior is still roughly constant as non-axisymmetric mass varies.

One can get a rough idea of how the energy states in the narrow pass bands contribute to the radiated power by noting that each band has 40 states. One may assume that the states in each band from modes 13–26 in Fig. 4 are equally distributed in frequency across the band. This is not in general true, but the bands are so narrow that the inaccuracies from this assumption are small. This yields a list of 560 resonant frequencies. According to Lyon,[18] each frequency has an equal amount of energy. Figure 9 shows a histogram of these frequencies. The first two peaks come from modes 13 and 14. Subsequent modes give rise to much lower peaks. Figure 6, representing the non-axisymmetric analysis, shows a single peak near the frequencies corresponding to modes 13 and 14 in Fig. 4. Based on Fig. 5, this peak is apparently from modes 13–16. The fact that there is only one peak in Fig. 6 may be due, in part, to frequency spreading of modes 13 and 14, which are coupled to the fluid in the non-axisymmetric analysis. In addition, modes 15 and 16 may have moved downward in frequency due to the tendency for dispersion curves to flatten when Brillouin folded, as discussed in Sec. II. Figure 9 is only qualitative, but gives a general idea of how the power spectral density can increase when circumferential modes are coupled.

This section shows that when periodically spaced point masses break the axisymmetric geometry of the structure, subsonic energy that is narrowly focused in frequency in the axisymmetric case is coupled to radiating modes. This energy reaches the acoustic far field in an amount that is almost completely independent of the amount of non-axisymmetric mass.

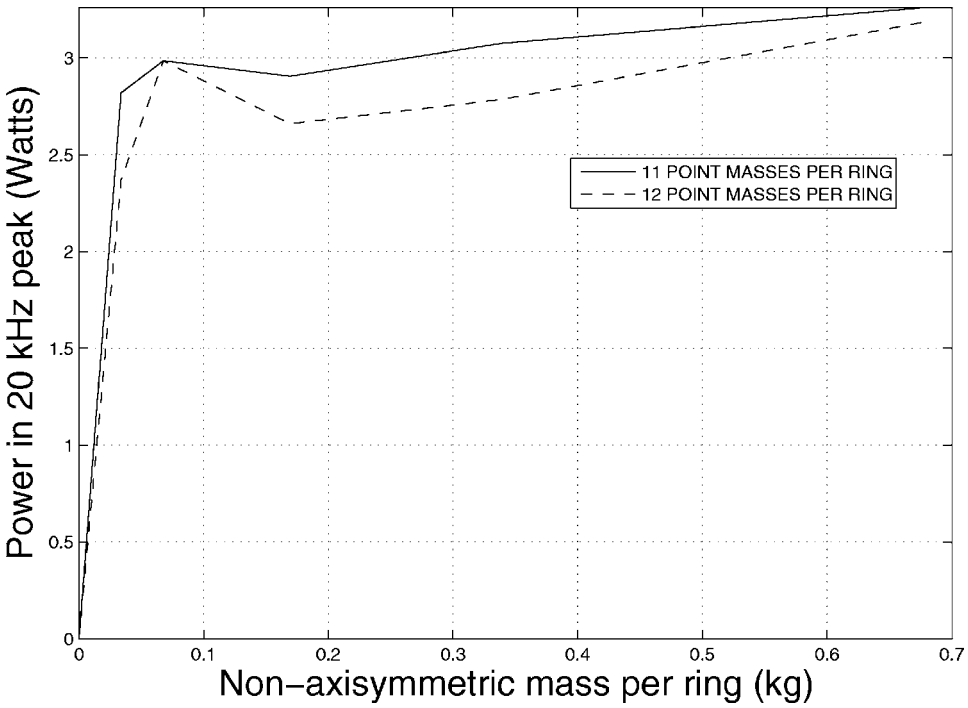

FIG. 8. Power in 20-kHz peak from a point load on a submerged, framed, axisymmetric, cylindrical shell with several (11 or 12) periodically spaced point masses per frame.

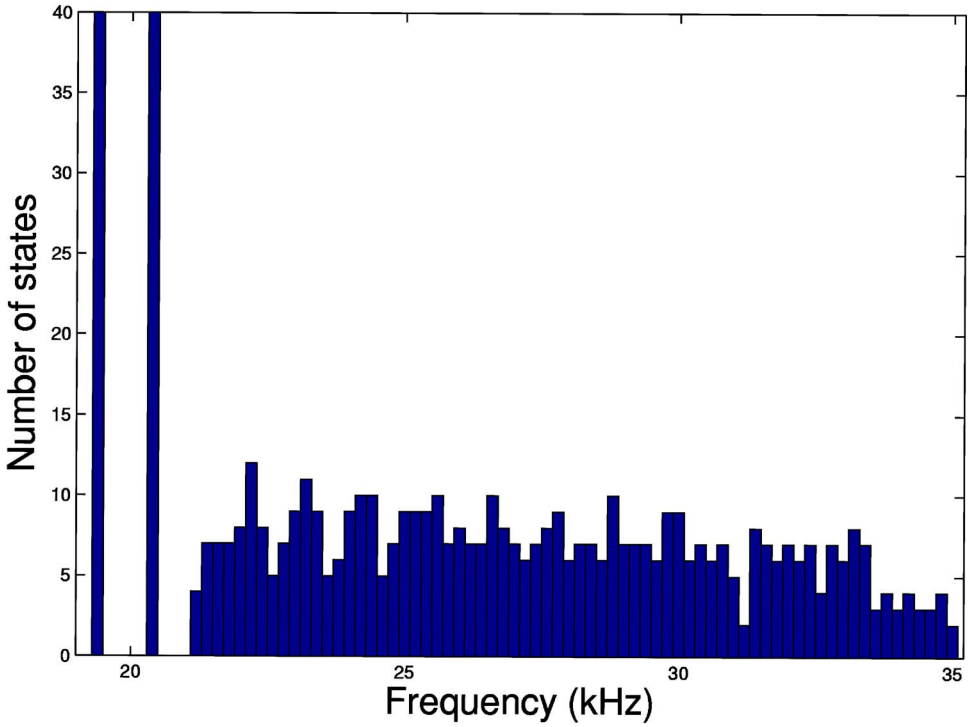

FIG. 9. Histogram of frame energy states that are coupled to the fluid only when the framed shell is not axisymmetric. The frequencies of the energy states are computed from the pass band between curves ab and cd in Fig. 4, which represents the axisymmetric shell.

V. SUMMARY

An infinite cylindrical shell and a finite, framed cylindrical shell have their circumferential symmetries broken with line masses and point masses, respectively. Computations on these structures reveal circumferential Brillouin folding in both cases. Since the finite shell already has axial Brillouin folding from the frames, a point load applied to it produces energy pass bands. At the frequencies where the subsonic energy is narrowly focused in the axisymmetric case, this energy is coupled to the far field for the nonaxisymmetric case. At the frequency where the subsonic energy is most narrowly focused, the radiated power has a distinct peak. The amount of energy comprising this peak is roughly constant with respect to the amount of nonaxisymmetric mass.

ACKNOWLEDGMENTS

The authors gratefully acknowledge the Office of Naval Research for support of this work.

[1]G. Maidanik and J. Dickey. "Response of regularly ribbed fluid loaded panels." J. Sound Vib. **155**, 481–495 (1992).
[2]L. Brillouin. *Wave Propagation in Periodic Structures* (Dover, New York, 1946).
[3]D. J. Mead, "Plates with regular stiffening in acoustic media: Vibration and radiation," J. Acoust. Soc. Am. **88**, 391–401 (1990).
[4]D. M. Photiadis, "The effect of irregularity on the scattering of acoustic waves from a ribbed plate," J. Acoust. Soc. Am. **91** (Pt. 1), 1897–1903 (1992).
[5]D. M. Photiadis, Localization of helical flexural waves by irregularity," J. Acoust. Soc. Am. **96** 2291–2301 (1994).
[6]B. H. Houston, J. A. Bucaro, and D. M. Photiadis, "Broadband acoustic scattering from a ribbed cylinder," J. Acoust. Soc. Am. **98** (Pt. 1), 2851–2853 (1995).
[7]G. Maidanik and K. J. Becker, "Computation of the modal response of regularly ribbed cylinders," J. Acoust. Soc. Am. **101** (Pt. 1), 2452–2472, (1997).
[8]D. M. Photiadis, E. G. Williams, and B. H. Houston, "Wavenumber response of a near periodically ribbed shell," J. Acoust. Soc. Am. **101**, 877–886 (1997).
[9]M. H. Marcus, B. H. Houston, and D. M. Photiadis, "Wave localization on a submerged cylindrical shell with rib aperiodicity," J. Acoust. Soc. Am. **109**, 865–869 (2001).
[10]M. H. Marcus and B. H. Houston, "The effect of internal point masses on the radiation of a ribbed cylindrical shell," J. Acoust. Soc. Am. **112** (Pt. 1), 961–965 (2002).
[11]W. Thomson, *Theory of Vibration with Applications* (Prentice-Hall, Englewood Cliffs, NJ, 1972), p. 80.
[12]H. Kraus, *Thin Elastic Shells* (Wiley, New York, 1967), p. 297.
[13]A. W. Leissa. *Vibration of shells*, NASA SP-288, Washington, DC, 1973. p. 37.
[14]K. F. Graff. *Wave Motion in Elastic Solids* (Dover, New York, 1975), p. 61.
[15]F. Fahy, *Sound and Structural Vibration* (Academic, New York, 1985), pp. 84–87.
[16]C. H. Hodges, J. Power, and J. Woodhouse, "The low frequency vibration of a ribbed cylinder, part 2: Observations and interpretation," J. Sound Vib. **101**(2), 237–256 (1985).
[17]N. W. Ashcroft and N. D. Mermin, *Solid State Physics* (Holt, Rinehart, and Winston, New York, 1976), p. 136.
[18]R. H. Lyon, *Statistical Energy Analysis of Dynamic Systems: Theory and Applications* (MIT, Cambridge, MA, 1975).

Modifications of the equation for gas bubble dynamics in a soft elastic medium

Evgenia A. Zabolotskaya,[a] Yurii A. Ilinskii, G. Douglas Meegan, and Mark F. Hamilton
Applied Research Laboratories, The University of Texas at Austin, Austin, Texas 78713-8029

(Received 23 March 2005; revised 23 June 2005; accepted 4 July 2005)

A model equation for the oscillation of a pressurized gas bubble in a nonlinear incompressible elastic medium [Emelianov *et al.*, J. Acoust. Soc. Am. **115**, 581 (2004)] is extended to include effects of surface tension, viscosity, weak compressibility, and confinement by an elastic shell. The significance of this work is that starting from first principles, the full nonlinearity of the incompressible elastic medium surrounding the bubble and forming its shell is taken into account. Measurements of equilibrium radius as a function of external pressure for a gas bubble in a tissue-like gel are also presented. A general approach to including hysteresis is also discussed.
 [DOI: 10.1121/1.2010348]

PACS number(s): 43.25.Yw, 43.25.Dc [AJS] Pages: 2173–2181

I. INTRODUCTION

In a previous paper,[1] a model equation was derived in Rayleigh-Plesset form for the oscillation of a pressurized gas bubble in a nonlinear incompressible elastic medium. In the present paper, the model is augmented to include effects of surface tension, viscosity, weak compressibility, and confinement by an elastic shell. Augmented forms of the Rayleigh-Plesset equation have been derived previously that include such effects for a gas bubble in a liquid. See, for example, Leighton[2] for discussion of viscosity and surface tension, Prosperetti[3] for weak compressibility, and Church,[4] Khismatullin and Nadim[5] for shells. What distinguishes the present contribution from earlier work is that the theoretical framework accounts for the full nonlinearity of the elastic medium surrounding the bubble and forming its shell.

The model equation for nonlinear bubble dynamics in a soft elastic medium presented in Ref. 1 was derived using Lagrangian mechanics. A simple situation was considered in that paper, namely, a gas bubble oscillating in a nonlinear incompressible elastic medium. Effects such as surface tension, viscosity, and compressibility were not taken into consideration. Lagrangian formalism allows inclusion of additional effects, for example, surface tension that changes the potential energy in the system, and viscous losses that can be taken into account by introducing a dissipative function. Moreover, the energy approach provides a relatively easy and natural way to derive a dynamic equation for an encapsulated bubble with a nonlinear shell of arbitrary thickness in nonlinear elastic media. The present formulation will form a basis for subsequent modeling of complex interactions of bubbles with one another in elastic media, in constrained media, and with particles, e.g., to address phenomena connected with cavitation in lithotripsy,[6] and with the possibility of sonar-induced bubble growth in humans and marine mammals.[7]

We thus use the theoretical model based on Lagrangian mechanics to include surface tension, viscosity, and the effect of an encapsulating elastic shell. A general method for including effects of hysteresis is presented. A different approach is applied to take into account weak compressibility of the elastic medium. In this case, a dynamical method proves to be more useful for identifying the leading order contribution due to compressibility. The mathematical model also accounts for equilibrium gas pressure in the bubble that differs from the equilibrium pressure in the elastic medium far away from the bubble. Measurements are presented showing the dependence of equilibrium radius on external pressure for a gas bubble in a tissue-like gel.

II. BASIC RELATIONS

The starting point is a model equation derived previously for a gas bubble surrounded by an incompressible nonlinear elastic medium.[1] When in equilibrium, the gas pressure in the bubble is denoted P_g, and the pressure infinitely far away is P_∞. For $P_g = P_\infty$ the medium is unstrained and the equilibrium radius is R_0; for $P_g \neq P_\infty$ it is R_1. The model for the bubble dynamics was obtained from Lagrange's equation

$$\frac{d}{dt}\left(\frac{\partial L}{\partial \dot{R}}\right) - \frac{\partial L}{\partial R} = 0, \tag{1}$$

in which

$$L = T - U \tag{2}$$

is the Lagrangian, and the bubble radius $R(t)$ is taken to be the generalized coordinate. The kinetic energy T accounts for motion in the elastic medium, with the kinetic energy of the gas assumed to be negligible. The potential energy U contains contributions due to gas pressure in the bubble (U_g), the pressure infinitely far away from the bubble (U_∞), and the strain energy in the elastic medium (U_e). The resulting dynamical equation for the bubble was expressed in Rayleigh-Plesset form as[1]

[a]Electronic mail: zhenia@arlut.utexas.edu

$$R\ddot{R} + \frac{3}{2}\dot{R}^2 = \frac{1}{\rho}\left[P_g\left(\frac{R_1}{R}\right)^{3\gamma} - P_\infty - P_e(R) \right], \tag{3}$$

where γ is the ratio of specific heats for the gas inside the bubble, and P_e is an effective pressure resulting from elasticity, defined by

$$P_e(R) = \frac{1}{4\pi R^2}\frac{\partial U_e}{\partial R}. \tag{4}$$

Explicit expressions for P_e are provided in Ref. 1. The equilibrium radius R_1 is determined by solving

$$P_e(R_1) = P_g - P_\infty. \tag{5}$$

By definition, $R_1 = R_0$ for $P_g = P_\infty$.

III. SURFACE TENSION

The contribution due to surface tension on a gas bubble confined in an elastic shell immersed in liquid was considered by Church[4] and subsequently in an elastic medium in the linear approximation by Alekseev and Rybak.[8] For completeness and consistency with the Lagrangian approach employed in the present paper, the effect of surface tension is considered here. It is assumed that changes in the density of the medium are sufficiently small that the surface tension σ is constant. The potential energy stored in surface tension is $U_\sigma = 4\pi R^2\sigma$, resulting in an effective pressure

$$P_\sigma(R) = \frac{1}{4\pi R^2}\frac{\partial U_\sigma}{\partial R} = \frac{2\sigma}{R}. \tag{6}$$

Equation (1) thus becomes

$$R\ddot{R} + \frac{3}{2}\dot{R}^2 = \frac{1}{\rho}\left[P_g\left(\frac{R_1}{R}\right)^{3\gamma} - P_\infty - P_e(R) - \frac{2\sigma}{R} \right]. \tag{7}$$

Surface tension reduces the natural frequency of the bubble.[4,8]

IV. VISCOSITY

Lagrange's equation for a dissipative system is

$$\frac{d}{dt}\left(\frac{\partial L}{\partial \dot{R}}\right) - \frac{\partial L}{\partial R} = -\frac{\partial \Psi}{\partial \dot{R}}, \tag{8}$$

where Ψ is a dissipative function. For an isotropic solid, the dissipative function density (per unit volume) is given by[9]

$$\psi = \eta\left(v_{ik} - \tfrac{1}{3}\delta_{ik}v_{ll}\right)^2 + \tfrac{1}{2}\zeta v_{ll}^2, \tag{9}$$

where η and ζ are shear and bulk viscosity coefficients, respectively, δ_{ik} is a Kronecker delta, and

$$v_{ik} = \frac{1}{2}\left(\frac{\partial v_i}{\partial x_k} + \frac{\partial v_k}{\partial x_i}\right), \tag{10}$$

where x_i and v_i are position and velocity components in Eulerian coordinates. Equation (9) is of the same form as for liquids, and for incompressible media it reduces to

$$\psi = \eta v_{ik}^2. \tag{11}$$

As the bubble motion is purely radial, the corresponding radial coordinate r and particle velocity v are introduced, such that $v_i/v = x_i/r$ and thus

$$\frac{\partial v_i}{\partial x_k} = \frac{v}{r}\delta_{ik} + \frac{x_i x_k}{r}\frac{\partial}{\partial r}\left(\frac{v}{r}\right), \tag{12}$$

whereby

$$v_{ik}^2 = 3\frac{v^2}{r^2} + 2v\frac{\partial}{\partial r}\left(\frac{v}{r}\right) + r^2\left[\frac{\partial}{\partial r}\left(\frac{v}{r}\right)\right]^2. \tag{13}$$

For incompressible media $v = \dot{R}R^2/r^2$ and therefore

$$\psi = \frac{6\eta\dot{R}^2R^4}{r^6}. \tag{14}$$

The dissipative function is the integral of ψ over the elastic medium surrounding the bubble,

$$\Psi = 4\pi\int_R^\infty \psi r^2 dr = 8\pi\eta R\dot{R}^2, \tag{15}$$

so that from Eq. (8),

$$\frac{d}{dt}\left(\frac{\partial L}{\partial \dot{R}}\right) - \frac{\partial L}{\partial R} = -16\pi\eta R\dot{R}. \tag{16}$$

Equation (7) thus becomes

$$R\ddot{R} + \frac{3}{2}\dot{R}^2 = \frac{1}{\rho}\left[P_g\left(\frac{R_1}{R}\right)^{3\gamma} - P_\infty - P_e(R) - \frac{2\sigma}{R} - 4\eta\frac{\dot{R}}{R} \right]. \tag{17}$$

The term associated with viscosity is the same as that in the Rayleigh-Plesset equation for bubble oscillations in an incompressible viscous liquid.[2]

V. HYSTERESIS

Experiments were performed to verify the model presented in Sec. II for a gas bubble in a tissue-like gel under equilibrium conditions. The equilibrium radius R_1 was measured as a function of the external pressure P_∞ and compared with Eq. (5). Surface tension may be neglected because of the relatively large size of the bubble, and viscosity may be neglected because the motion is quasistatic. Hysteresis was observed in these experiments. An equation for estimation of energy loss associated with hysteresis is derived on the basis of the equation for bubble dynamics.

A. Measurements of R_1 versus P_∞

The experiments were performed using tissue-like phantoms having low shear moduli. The phantoms were prepared using 7.5% and 15% gelatin (300 bloom, from swine skin), resulting in samples for which the shear moduli are $\mu = 18$ kPa and $\mu = 39$ kPa (± 2 kPa), respectively, as measured by standard methods. As the gelatin cooled, the samples were stirred very slightly until several small air bubbles about 1 mm in diameter were formed, after which the sample was allowed to continue to cool with no stirring. Following several attempts and visual inspection of the samples, individual

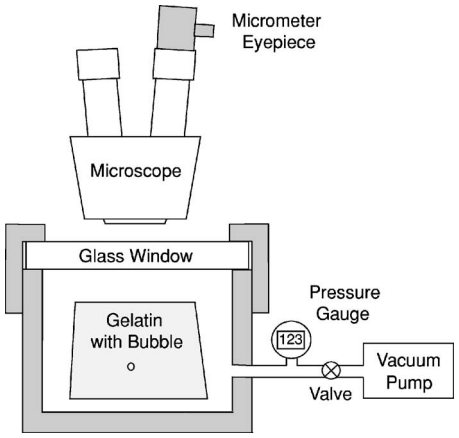

FIG. 1. Experimental setup for measuring the dependence of equilibrium bubble radius on external atmospheric pressure.

bubbles separated by at least 10 diameters from their nearest neighbor or surface were identified, and a surrounding cube of gelatin was excised. The resulting samples were about 3 cm×3 cm×3 cm, each containing a single bubble in its center.

The cubic samples were placed in a small cylindrical pressure vessel with a circular Pyrex window, as shown in Fig. 1. The static pressure in the vessel was controlled by a vacuum pump and pressure gauge. The bubble was observed through the window and its cross section was measured with a microscope. In some cases and at some static pressures, the bubbles were slightly elliptical in cross section. The diameter was determined by taking the average of the major and minor dimensions, which were typically within 10% of each other.

Data from two experiments (one with $\mu=18$ kPa and the other with $\mu=39$ kPa) are shown in Fig. 2(a) as dashed lines. The data were collected after the bubbles were exposed to several pressure cycles over the range of 0.45–1 atm in an attempt to minimize effects of hysteresis. Despite this effort, hysteresis is nevertheless observed, which is typical of stress-strain relationships for tissues and tissue-like materials.[10]

The results are compared with predictions based on Eq. (5) with $P_g=1$ atm, shown in Fig. 2(a) as solid lines. Mooney's constitutive relation for incompressible media was used to evaluate $P_e(R_1)$, given by Eq. (36) in Ref. 1, in which we let the adjustable parameter $\beta=0$, with μ as indicated in Fig. 2(a). The general trend of the measurements follows the predictions. For comparison, the limiting case of a bubble in a liquid is indicated by the prediction for $\mu=0$. The data and model show that larger shear moduli lead to reduced bubble deformation, as expected.

Hysteresis was investigated in greater detail by extending the range of P_∞ down to 0.05 atm. The resulting measurements are presented as dashed lines in Fig. 2(b) for the sample with $\mu=39$ kPa. For these measurements, the sample was not put through pressure cycles prior to data collection. The history of the pressure variations follows the arrows in the plot. Not only is hysteresis observed, but also permanent deformation, i.e., the bubble becomes larger with each pressure cycle. This indicates that the gelatin is undergoing permanent deformation, or that gas is diffusing into the bubble, or both. For comparison, predictions are shown for $\mu=39$ kPa and $\beta=\pm1$ (the most extreme values of β allowed in the Mooney relation). Hysteresis results in divergence from the theory at large negative pressures.

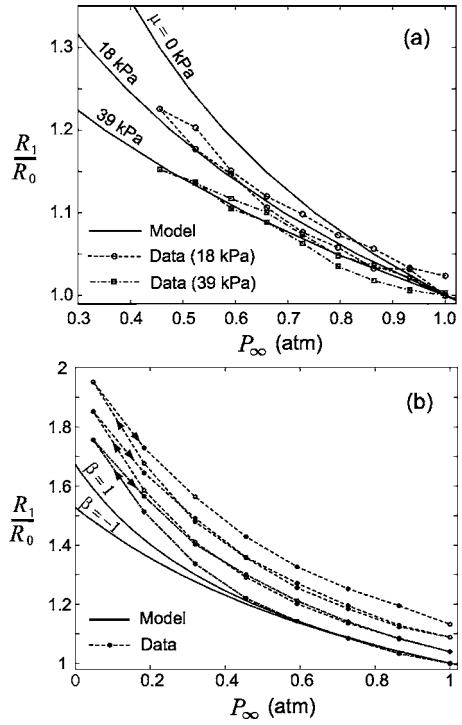

FIG. 2. Measurements of equilibrium bubble radius R_1 as a function of atmospheric pressure P_∞ (dashed lines), compared with predictions based on Eq. (5) calculated using the Mooney potential function for incompressible elastic media to evaluate the function P_e (solid lines): (a) for different values of shear modulus, with $\beta=0$ in the Mooney potential; (b) demonstrating hysteresis associated with three consecutive pressure cycles, with $\beta=\pm1$ in the Mooney potential.

B. Hysteretic losses

For periodic motion in a medium that exhibits hysteresis, P_e in Eq. (17) becomes a two-value function of radius and must be replaced by the functional $P_e=P_e(R,\dot{R}/|\dot{R}|)$. The functional accounts for the fact that the path in the (P_e,R) plane depends on whether the bubble volume is increasing or decreasing, i.e., it is history dependent. For example, the model presented by Ostrovsky[11] for resonant oscillations in hysteretic material can be used to define $P_e(R,\dot{R}/|\dot{R}|)$.

From Eq. (17), where P_e is now a functional, the equation for energy conservation can be derived by multiplying all terms by $4\pi\rho R^2\dot{R}$:

$$\frac{d}{dt}(T+U_g)=-2\Psi-(P_\infty+P_e+P_\sigma)\dot{V}, \tag{18}$$

where T and U_g are the kinetic and potential energies introduced in Sec. II, Ψ is the dissipative function given by Eq. (15), and $V=\frac{4}{3}\pi R^3$ is bubble volume. Equation (18) describes energy changes due to viscous losses (2Ψ), the work done by the external pressure per unit time ($P_\infty\dot{V}$), by surface tension ($P_\sigma\dot{V}$), and by elasticity ($P_e\dot{V}$). When the elastic ma-

terial exhibits no hysteresis and P_e depends only on the instantaneous value of the bubble radius, then the term

$$P_e\dot{V} = 4\pi R^2 \dot{R} P_e = \frac{dU_e}{dt} \tag{19}$$

characterizes the changes in the elastic energy.

For a periodic process, integration of Eq. (18) with respect to time gives

$$-\oint (P_\infty + P_\sigma) dV = 2\oint \Psi\, dt + \oint P_e dV. \tag{20}$$

The left-hand side of Eq. (20) is the work done, averaged over one period, by the external pressure P_∞ and surface tension. The right-hand side describes energy losses due to viscosity and hysteresis. For a material without hysteresis the last term in Eq. (20) accounts for the elastic energy variation, which is zero when averaged over one period.

The integral $\oint P_e dV$ is the area of the hysteresis loop in the (P_e, V) coordinates, and it corresponds to energy losses per period due to hysteresis. If the hysteresis loop at low frequencies is assumed to be the same as, or close to, the loop at zero frequency, as in static experiments, then the energy losses per unit time are

$$E_{\text{hys}} = \frac{\omega}{2\pi}\oint P_e dV, \tag{21}$$

where ω is angular frequency. Equation (21) is used to estimate energy losses associated with hysteresis. We present it to demonstrate that Eq. (17) does not violate conservation of energy. Losses due to hysteresis are thus proportional to ω, as distinguished from losses due to viscosity, which are proportional to ω^2. Hysteretic losses thus dominate viscous losses at low frequencies.

VI. COMPRESSIBILITY

The most comprehensive theoretical study of how weak compressibility affects bubble dynamics in liquid was conducted by Prosperetti and Lezzi.[12,13] Effects of weak compressibility on bubble dynamics in elastic media were considered by Alekseev and Rybak[8] and by Ostrovsky.[14] The analysis by Alekseev and Rybak was in the linear approximation. Ostrovsky allowed for nonlinearity in the bubble dynamics, but the elastic response of the medium was described in the linear approximation. In the analysis to follow, nonlinearity is taken into account in both the bubble dynamics and the elasticity.

A. Momentum equation

In contrast with previous sections, where Lagrange's equations and Lagrangian coordinates have been used, the analysis here will be performed using a dynamical approach rather than an energy approach, and Eulerian coordinates will be used. There are two reasons for this change in approach. First, soft elastic media with shear moduli $\mu \ll \lambda$ (where λ is a Lamé constant) are dynamically similar to liquids. Second, the method developed by Prosperetti[3] for including the effect of compressibility in the equation of motion for a bubble in liquid can be applied here.

The momentum equation in Eulerian coordinates is

$$\rho \dot{v}_l = \frac{\partial \sigma_{kl}}{\partial x_k}, \tag{22}$$

where σ_{kl} is a stress tensor in Eulerian coordinates, ρ is the instantaneous (not initial) density of the solid, x_k are Eulerian coordinates, and v_l are velocity components at the point with coordinates x_l. The dot indicates the total time derivative:

$$\dot{v}_i = \frac{\partial v_i}{\partial t} + \frac{\partial v_i}{\partial x_k} v_k. \tag{23}$$

Equation (22) is referred to as the Cauchy equation. The Cauchy equation is supplemented by the continuity equation:

$$\frac{\partial \rho}{\partial t} + \frac{\partial (\rho v_k)}{\partial x_k} = 0. \tag{24}$$

The next step is calculation of the stress tensor σ_{kl}.

B. Cauchy stress tensor

For finite deformations it is convenient to work with Green's deformation tensor

$$G_{k'l'} = \frac{\partial x_k}{\partial \tilde{x}_{k'}} \frac{\partial x_k}{\partial \tilde{x}_{l'}}, \tag{25}$$

which can be expressed through the strain tensor, e.g., $G_{k'l'} = 2\tilde{u}_{k'l'} + \delta_{k'l'}$, here $\tilde{u}_{k'l'}$ is the strain tensor in Lagrangian coordinates and $\delta_{k'l'}$ is the Kronecker delta.[15] Tildes and primes are used to distinguish Lagrangian coordinates and indices, respectively, from their Eulerian counterparts. The relation between an Eulerian stress tensor and a Green deformation tensor is

$$\sigma_{kl} = 2\rho \frac{\partial \varepsilon}{\partial G_{k'l'}} \frac{\partial x_k}{\partial \tilde{x}_{k'}} \frac{\partial x_l}{\partial \tilde{x}_{l'}}, \tag{26}$$

where ε is an internal energy per unit mass.

For an isotropic solid, the internal energy density can be expressed as

$$\varepsilon = \varepsilon(I_1, I_2, I_3), \tag{27}$$

where I_1, I_2, I_3 are the principal invariants of $G_{k'l'}$.[15]

Equation (26) now takes the forms

$$\begin{aligned}\sigma_{kl} &= 2\rho\left(\frac{\partial \varepsilon}{\partial I_1}\frac{\partial I_1}{\partial G_{k'l'}} + \frac{\partial \varepsilon}{\partial I_2}\frac{\partial I_2}{\partial G_{k'l'}} + \frac{\partial \varepsilon}{\partial I_3}\frac{\partial I_3}{\partial G_{k'l'}}\right)\frac{\partial x_k}{\partial \tilde{x}_{k'}}\frac{\partial x_l}{\partial \tilde{x}_{l'}} \\ &= h_0\delta_{kl} + h_1 g_{kl}^{-1} + h_2 g_{km}^{-1} g_{ml}^{-1} \\ &= (h_1 + h_2 I_1) g_{kl}^{-1} + (h_0 - h_2 I_2)\delta_{kl} + h_2 I_3 g_{kl},\end{aligned} \tag{28}$$

where

$$h_0 = 2\rho_0 I_3^{1/2}\frac{\partial \varepsilon}{\partial I_3}, \quad h_1 = 2\rho_0 I_3^{-1/2}\left(\frac{\partial \varepsilon}{\partial I_1} + I_1\frac{\partial \varepsilon}{\partial I_2}\right),$$

$$h_2 = -2\rho_0 I_3^{-1/2}\frac{\partial \varepsilon}{\partial I_2}, \tag{29}$$

and

$$g_{kl} = \frac{\partial \tilde{x}_{k'}}{\partial x_k}\frac{\partial \tilde{x}_{k'}}{\partial x_l}. \tag{30}$$

For incompressible media $I_3 = J^2 = 1$ and thus $\rho = \rho_0$, such that

$$\sigma_{kl} = -P\delta_{kl} + 2\rho_0\left(\frac{\partial \varepsilon}{\partial I_1} + I_1\frac{\partial \varepsilon}{\partial I_2}\right)g_{kl}^{-1} - 2\rho_0\frac{\partial \varepsilon}{\partial I_2}g_{km}^{-1}g_{ml}^{-1}, \tag{31}$$

or

$$\sigma_{kl} = -P\delta_{kl} + 2\frac{\partial \mathcal{E}}{\partial I_1}g_{kl}^{-1} - 2\frac{\partial \mathcal{E}}{\partial I_2}g_{kl}, \tag{32}$$

where $\mathcal{E} = \rho_0\varepsilon$ is the energy density per unit volume, and the pressure P is the isotropic, scalar part of the stress tensor $P\delta_{kl}$ and depends only on coordinates.

We now assume spherical symmetry and express Eq. (32) as a function of radial coordinates. Given that

$$x_k = \frac{r}{\tilde{r}}\tilde{x}_{k'}\delta_{kk'} = \frac{r}{\tilde{r}}\tilde{x}_k \tag{33}$$

one obtains

$$\frac{\partial x_k}{\partial \tilde{x}_{k'}} = \frac{r}{\tilde{r}}\delta_{kk'} + \frac{x_k x_{k'}}{r^2}\left(\frac{\partial r}{\partial \tilde{r}} - \frac{r}{\tilde{r}}\right), \tag{34}$$

such that

$$g_{kl}^{-1} = \frac{\partial x_k}{\partial \tilde{x}_{k'}}\frac{\partial x_l}{\partial \tilde{x}_{k'}} = \frac{r^2}{\tilde{r}^2}\delta_{kl} + \frac{x_k x_l}{r^2}\left[\left(\frac{\partial r}{\partial \tilde{r}}\right)^2 - \frac{r^2}{\tilde{r}^2}\right]. \tag{35}$$

Setting $(x_1, x_2, x_3) = (0, 0, r)$ in Eq. (30) yields

$$g_{kl}^{-1}(0,0,r) = \begin{bmatrix} r^2/\tilde{r}^2 & 0 & 0 \\ 0 & r^2/\tilde{r}^2 & 0 \\ 0 & 0 & (\partial r/\partial \tilde{r})^2 \end{bmatrix}, \tag{36}$$

and thus

$$g_{rr}^{-1} = \left(\frac{\partial r}{\partial \tilde{r}}\right)^2, \quad g_{\theta\theta}^{-1} = g_{\phi\phi}^{-1} = \frac{r^2}{\tilde{r}^2}, \quad g_{r\theta}^{-1} = g_{r\phi}^{-1} = g_{\theta\phi}^{-1} = 0. \tag{37}$$

Components of the stress tensor can now be calculated using Eq. (32) and taking into account that

$$\frac{\partial r}{\partial \tilde{r}} = \frac{\tilde{r}^2}{r^2} \tag{38}$$

for incompressible media:

$$\sigma_{rr} = -P + 2\frac{\partial \mathcal{E}}{\partial I_1}\frac{\tilde{r}^4}{r^4} - 2\frac{\partial \mathcal{E}}{\partial I_2}\frac{r^4}{\tilde{r}^4}, \tag{39}$$

$$\sigma_{\theta\theta} = \sigma_{\phi\phi} = -P + 2\frac{\partial \mathcal{E}}{\partial I_1}\frac{r^2}{\tilde{r}^2} - 2\frac{\partial \mathcal{E}}{\partial I_2}\frac{\tilde{r}^2}{r^2}, \tag{40}$$

and $\sigma_{r\theta} = \sigma_{r\phi} = \sigma_{\theta\phi} = 0$.

C. Equation of motion

Equation (22) becomes, in spherical coordinates (see Ref. 15, p. 163),

$$\frac{\partial \sigma_{rr}}{\partial r} + \frac{2}{r}(\sigma_{rr} - \sigma_{\theta\theta}) = \rho\ddot{r}. \tag{41}$$

Using the relations $\dot{r} = R^2\dot{R}/r^2$ and $dR/dr = r^2/R^2$ for incompressible media one obtains

$$\ddot{r} = \frac{2R\dot{R}^2 + R^2\ddot{R}}{r^2} - \frac{2R^4\dot{R}^2}{r^5}. \tag{42}$$

The normalized bubble volume

$$w = \tfrac{1}{3}R^3, \tag{43}$$

which is actual bubble volume divided by 4π, permits Eq. (42) to be written more compactly as

$$\ddot{r} = \frac{\ddot{w}}{r^2} - 2\frac{\dot{w}^2}{r^5}. \tag{44}$$

Substitution of Eqs. (39), (40), and (44) in Eq. (41) and integration from r to ∞ yields

$$\sigma_{rr}|_\infty - \sigma_{rr}|_r = \rho\left(\frac{\ddot{w}}{r} - \frac{\dot{w}^2}{2r^4}\right) - 4\int_r^\infty \left(\frac{\partial \mathcal{E}}{\partial I_1} + \frac{r^2}{\tilde{r}^2}\frac{\partial \mathcal{E}}{\partial I_2}\right) \times \left(\frac{r^2}{\tilde{r}^2} - \frac{\tilde{r}^4}{r^4}\right)\frac{dr}{r}. \tag{45}$$

Equation (45) couples a stress in a elastic medium with motion of a bubble wall.

For application of Eq. (45) to bubble dynamics, individual terms are specified as follows. At $r = \infty$ the pressure is designated P_∞, such that

$$\sigma_{rr}|_\infty = -P_\infty. \tag{46}$$

The remaining terms in Eq. (45) are evaluated at $r = R$. For a gas bubble we have

$$\sigma_{rr}|_R = -P_g\left(\frac{w_1}{w}\right)^\gamma, \tag{47}$$

where $w_1 = R_1^3/3$. The integral may be rewritten with $r = R$ and $dr = \tilde{r}^2 d\tilde{r}/r^2$ as

$$4\int_R^\infty \left(\frac{\partial \mathcal{E}}{\partial I_1} + \frac{r^2}{\tilde{r}^2}\frac{\partial \mathcal{E}}{\partial I_2}\right)\left(\frac{r^2}{\tilde{r}^2} - \frac{\tilde{r}^4}{r^4}\right)\frac{dr}{r} = 4\int_{R_0}^\infty \left(\frac{\partial \mathcal{E}}{\partial I_1} + \frac{r^2}{\tilde{r}^2}\frac{\partial \mathcal{E}}{\partial I_2}\right)\left(\frac{\tilde{r}}{r} - \frac{\tilde{r}^7}{r^7}\right)\frac{d\tilde{r}}{\tilde{r}} = P_e, \tag{48}$$

where P_e is defined by Eq. (4). Substitution of Eqs. (46)–(48) in Eq. (45) yields

$$\frac{\ddot{w}}{R} - \frac{\dot{w}^2}{2R^4} = \frac{1}{\rho}\left[P_g\left(\frac{w_1}{w}\right)^\gamma - P_\infty - P_e(w)\right]. \tag{49}$$

Equation (49), obtained following a dynamical approach in Eulerian coordinates, coincides with Eq. (3), derived using Lagrangian mechanics and Lagrangian coordinates. The advantage of a dynamical approach is that it allows one to

include weak compressibility. Indeed, according to Eq. (45) the term $\rho\ddot{w}/r$ contributes mostly to stress in the medium. The other terms on the right-hand side decay more rapidly than $1/r$ and are significant only near the bubble. For weakly compressible media, the term $\rho\ddot{w}/r$ is associated with radiation; see the discussion in Ref. 16. This technique is similar to the one introduced by Lorentz to estimate the force on a charged particle due to its own radiation.[17]

The stress field produced by acoustic radiation is taken to be the diverging spherical wave

$$\sigma_{rr}^{\mathrm{rad}}(r,t) = -\rho\frac{\ddot{w}(t-r/c_l)}{r}, \tag{50}$$

where c_l is the longitudinal wave speed, and it is assumed that the bubble radius is small in comparison with the characteristic radiated wavelength. The radiated stress field is evaluated at the bubble wall and expanded as a power series in R/c_l to obtain[16]

$$\sigma_{rr}^{\mathrm{rad}}(R,t) \simeq -\frac{\rho}{R}\ddot{w}(t) + \frac{\rho}{c_l}\dddot{w}(t). \tag{51}$$

Modification of Eq. (49) to account for weak compressibility thus amounts to replacing $\ddot{w}/R$ by $\ddot{w}/R - \dddot{w}/c_l$, such that

$$\frac{\ddot{w}}{R} - \frac{\dddot{w}}{c_l} - \frac{\dot{w}^2}{2R^4} = \frac{1}{\rho}\left[P_g\left(\frac{w_1}{w}\right)^{\gamma} - P_\infty - P_e(w)\right]. \tag{52}$$

The new term $\dddot{w}/c_l$ accounts for radiation damping.

Substituting $w = \frac{1}{3}R^3$ everywhere except in the compressibility term yields

$$R\ddot{R} + \frac{3}{2}\dot{R}^2 - \frac{\dddot{w}}{c_l} = \frac{1}{\rho}\left[P_g\left(\frac{R_1}{R}\right)^{3\gamma} - P_\infty - P_e(R)\right] \tag{53}$$

in place of Eq. (3). Since differentiation of the bubble volume yields

$$\dddot{w} = 2\dot{R}^3 + 6R\dot{R}\ddot{R}^3 + R^2\dddot{R}, \tag{54}$$

the term $\dddot{w}/c_l$ equals the expression derived by Prosperetti[3] to account for weak compressibility in a liquid. Effects of surface tension and viscosity can be taken into account in Eq. (53) precisely as they appear in Eq. (17).

The appearance of a third-order time derivative of the radius in Eq. (53) creates problems in numerical integration of this equation. The third-order time derivative can be eliminated and the order of Eq. (53) can be reduced by using approximations based on expansions in powers of $1/c_l$. Thus noting that

$$R\ddot{R} + \frac{3}{2}\dot{R}^2 = \frac{1}{\rho}\left[P_g\left(\frac{R_1}{R}\right)^{3\gamma} - P_\infty - P_e(R)\right] + O(1/c_l) \tag{55}$$

and

$$\frac{\dddot{w}}{c_l} = \frac{1}{2c_l}\dot{R}^3 + \frac{1}{c_l}R\dot{R}\ddot{R} + \frac{1}{\rho c_l}\frac{d}{dt}\left\{R\left[P_g\left(\frac{R_1}{R}\right)^{3\gamma} - P_\infty - P_e(R)\right]\right\}, \tag{56}$$

one obtains instead of Eq. (53)

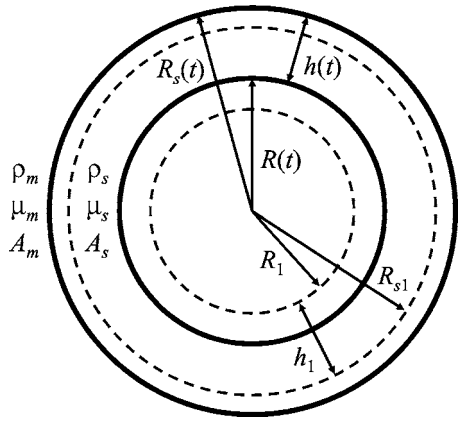

FIG. 3. Equilibrium and time varying dimensions for a gas bubble surrounded by an elastic shell.

$$\left(1 - \frac{\dot{R}}{c_l}\right)R\ddot{R} + \frac{3}{2}\left(1 - \frac{\dot{R}}{3c_l}\right)\dot{R}^2 = \frac{1}{\rho}\left(1 + \frac{\dot{R}}{c_l}\right)\left[P_g\left(\frac{R_1}{R}\right)^{3\gamma} - P_\infty - P_e(R)\right] + \frac{R}{\rho c_l}\frac{d}{dt}\left[P_g\left(\frac{R_1}{R}\right)^{3\gamma} - P_\infty - P_e(R)\right]. \tag{57}$$

Equation (57) is similar to Keller's equation for bubble oscillations in a slightly compressible liquid.[13] In Ref. 3 the third-order equation was derived from Keller's equation.

Both Eqs. (53) and (57) describe bubble dynamics in slightly compressible elastic media. The terms for surface tension and viscosity are included as in previous sections.

VII. ELASTIC SHELL

An equation of motion for an encapsulated bubble in an incompressible liquid was derived by Church[4] and presented in Rayleigh-Plesset form. In his analysis, the elastic response of the shell was described by a linear constitutive relation. Subsequent investigations of an encapsulated bubble surrounded by liquid were conducted by Alekseev and Rybak[8] entirely in the linear approximation, and by Khismatullin and Nadim[5] using a linear constitutive relation for the shell. Here we assume both the shell and surrounding elastic medium to be nonlinear.

A. General equation

The geometry of an encapsulated bubble is shown in Fig. 3, where the instantaneous values of the inner radius, outer radius, and thickness of the shell are $R(t)$, $R_s(t)$, and $h(t)$, respectively, with $R_s = R + h$. The corresponding equilibrium values are R_1, R_{s1}, and h_1 for $P_g \neq P_\infty$, and R_0, R_{s0}, and h_0 for $P_g = P_\infty$. Both the shell and the surrounding medium are assumed to be incompressible. Therefore the volume of the shell is constant, and $R_s(t)$ is related to $R(t)$ by

$$R_s^3(t) = R^3(t) + R_{s1}^3 - R_1^3. \tag{58}$$

The kinetic energy in the system (in the shell and surrounding medium, but ignoring the kinetic energy in the gas) is

$$T = \frac{\rho_s}{2}\int_{r=R}^{r=R_s} v^2 dV + \frac{\rho_m}{2}\int_{r=R_s}^{\infty} v^2 dV, \tag{59}$$

where $v=\dot{r}$. Here and in the following, subscript s shall be used to identify material properties of the shell, and subscript m for those of the outer medium, as indicated in Fig. 3. With $v=\dot{R}R^2/r^2$ in incompressible media and $dV=4\pi r^2 dr$ one obtains

$$T = 2\pi\rho_s \dot{R}^2 R^3 + 2\pi(\rho_m - \rho_s)\dot{R}^2 \frac{R^4}{R_s}. \tag{60}$$

Since $\dot{R}_s=\dot{R}R^2/R_s^2$ and $dR_s/dR=R^2/R_s^2$, the equation of motion for an encapsulated bubble can be presented as

$$F(R)R\ddot{R} + \frac{3}{2}G(R)\dot{R}^2 = \frac{1}{\rho_m}\left[P_g\left(\frac{R_1}{R}\right)^{3\gamma} - P_\infty - P_e(R)\right], \tag{61}$$

where

$$F(R) = \frac{\rho_s}{\rho_m} + \left(1 - \frac{\rho_s}{\rho_m}\right)\frac{R}{R_s}, \tag{62}$$

$$G(R) = \frac{\rho_s}{\rho_m} + \left(1 - \frac{\rho_s}{\rho_m}\right)\left(\frac{4}{3} - \frac{1}{3}\frac{R^3}{R_s^3}\right)\frac{R}{R_s}. \tag{63}$$

Following multiplication by ρ_m/ρ_s, the left-hand side of Eq. (61) becomes equivalent to the left-hand side Eq. (5) derived by Church.[4]

For thick shells, $h_1 \gg R_1$, the resulting inequality $R/R_s \ll 1$ reduces Eqs. (62) and (63) to $F=G=\rho_s/\rho_m$, and the density of the surrounding medium ρ_m cancels out of Eq. (61). For thin shells, $h_1 \ll R_1$, Eqs. (62) and (63) are

$$F(R) = 1 + \left(\frac{\rho_s}{\rho_m} - 1\right)\frac{h}{R}, \quad G(R) = 1 + \left(\frac{\rho_s}{\rho_m} - 1\right)\frac{h^2}{R^2}, \tag{64}$$

through leading order in the small parameter h/R.

We now include the effects of surface tension and viscosity. From Eq. (6) it follows that the effective pressure due to surface tension is

$$P_\sigma = \frac{2\sigma_g}{R} + \frac{2\sigma_m}{R_s}, \tag{65}$$

where σ_g is the surface tension at the inner, gas-shell interface, and σ_m is the surface tension at the outer, medium-shell interface. From Eq. (15), with shell viscosity η_s in the region $R<r<R_s$ and medium viscosity η_m for $r>R_s$, the dissipative function is found to be

$$\Psi = 8\pi R\dot{R}^2\left[\eta_s\left(1 - \frac{R^3}{R_s^3}\right) + \eta_m\frac{R^3}{R_s^3}\right]. \tag{66}$$

Following Secs. III and IV and combining the results in Eq. (61) yields

$$F(R)R\ddot{R} + \frac{3}{2}G(R)\dot{R}^2 = \frac{1}{\rho_m}\left\{P_g\left(\frac{R_1}{R}\right)^{3\gamma} - P_\infty - P_e(R) - \frac{2\sigma_g}{R} - \frac{2\sigma_m}{R_s} - 4\frac{\dot{R}}{R}\left[\eta_s\left(1 - \frac{R^3}{R_s^3}\right) + \eta_m\frac{R^3}{R_s^3}\right]\right\}. \tag{67}$$

It remains to evaluate the effective pressure $P_e(R)$, defined by Eq. (4), due to strain energy stored in shear deformation of both the shell and medium.

B. Elastic effects

The total strain energy U_e is the volume integral over the strain energy densities $\mathcal{E}_s$ for the shell and $\mathcal{E}_m$ for the surrounding medium. Elastic energy densities are normally expressed in Lagrangian coordinates, again distinguished from Eulerian coordinates by tildes, and related to one another as follows:

$$r^3 = \tilde{r}^3 + R^3 - R_0^3. \tag{68}$$

The strain energy in the two elastic media is thus

$$U_e(R) = 4\pi\int_{\tilde{r}=R_0}^{\tilde{r}=R_{s0}} \mathcal{E}_s \tilde{r}^2 d\tilde{r} + 4\pi\int_{\tilde{r}=R_{s0}}^{\infty} \mathcal{E}_m \tilde{r}^2 d\tilde{r}, \tag{69}$$

which reduces to the single integral in Eq. (10) of Ref. 1 in absence of the shell. Following precisely the same steps that lead to Eq. (33) of Ref. 1, but for the two integrals here instead of the single integral there, one obtains

$$P_e(R) = 4\int_{R_0}^{R_{s0}}\left(\frac{\partial\mathcal{E}_s}{\partial I_1} + \frac{r^2}{\tilde{r}^2}\frac{\partial\mathcal{E}_s}{\partial I_2}\right)\left(\frac{\tilde{r}}{r} - \frac{\tilde{r}^7}{r^7}\right)\frac{d\tilde{r}}{\tilde{r}} + 4\int_{R_{s0}}^{\infty}\left(\frac{\partial\mathcal{E}_m}{\partial I_1} + \frac{r^2}{\tilde{r}^2}\frac{\partial\mathcal{E}_m}{\partial I_2}\right)\left(\frac{\tilde{r}}{r} - \frac{\tilde{r}^7}{r^7}\right)\frac{d\tilde{r}}{\tilde{r}}, \tag{70}$$

where $I_1=2(r/\tilde{r})^2+(\tilde{r}/r)^4$ and $I_2=2(\tilde{r}/r)^2+(r/\tilde{r})^4$ are the first and second invariants of Green's deformation tensor.

Equation (70) is a general relation for incompressible media. In particular, it is valid for arbitrarily large deformation. Previously, Mooney's constitutive relation for $\mathcal{E}_m$ was used to calculate Eq. (70) and its derivatives for radial displacements up to ten times their equilibrium value.[1]

We proceed here using the expansion of the elastic energy density introduced by Landau and Lifshitz,[9] which includes terms through cubic order in the Lagrangian strain tensor. For an incompressible medium their expansion reduces to[18]

$$\mathcal{E} = \mu L_2 + \tfrac{1}{3}AL_3, \tag{71}$$

where μ is the shear modulus and A is one of the third-order elastic constants. Measurements of A for soft tissue-like media are provided by Catheline *et al.*[19] The invariants L_2 and L_3 become[1]

$$L_2 = \tfrac{1}{2}[(r/\tilde{r})^2 - 1]^2 + \tfrac{1}{4}[(\tilde{r}/r)^4 - 1]^2,$$

$$L_3 = \tfrac{1}{4}[(r/\tilde{r})^2 - 1]^3 + \tfrac{1}{8}[(\tilde{r}/r)^4 - 1]^3. \quad (72)$$

Equation (71) is an expansion about the unstrained equilibrium state corresponding to $R=R_0$, i.e., for which $P_g=P_\infty$, and the coefficients μ and A are defined accordingly. An unstrained initial state is therefore presumed in what follows, for which the appropriate dimensionless radial perturbation is

$$\xi_0(t) = \frac{R(t) - R_0}{R_0}. \quad (73)$$

Combining Eqs. (68) and (71)–(73) yields[1]

$$\mathcal{E} = 6\mu\left(\frac{R_0^6}{\tilde{r}^6}\xi_0^2 + 2\frac{R_0^6}{\tilde{r}^6}\xi_0^3 - 5\frac{R_0^9}{\tilde{r}^9}\xi_0^3\right) - 2A\frac{R_0^9}{\tilde{r}^9}\xi_0^3 \quad (74)$$

through third order in ξ_0. Equation (69) may now be integrated to obtain

$$U_e = 8\pi R_0^3\left[\mu_s + (\mu_m - \mu_s)\frac{R_0^3}{R_{s0}^3}\right]\xi_0^2 - 4\pi R_0^3\left\{\mu_s + \frac{1}{3}A_s - 4(\mu_m - \mu_s)\frac{R_0^3}{R_{s0}^3} + \left[5(\mu_m - \mu_s) + \frac{1}{3}(A_m - A_s)\right]\frac{R_0^6}{R_{s0}^6}\right\}\xi_0^3, \quad (75)$$

substitution of which in Eq. (4) yields, with $R_0^2/R^2 \simeq 1-2\xi_0$,

$$P_e = 4\left[\mu_s + (\mu_m - \mu_s)\frac{R_0^3}{R_{s0}^3}\right]\xi_0 - \left\{11\mu_s + A_s - 4(\mu_m - \mu_s)\frac{R_0^3}{R_{s0}^3} + [15(\mu_m - \mu_s) + (A_m - A_s)]\frac{R_0^6}{R_{s0}^6}\right\}\xi_0^2. \quad (76)$$

Although restricted to small values of ξ_0, the expressions for U_e and P_e are valid for a shell of arbitrary thickness.

For a thick shell, terms multiplied by powers of $R_0/R_{s0} \ll 1$ may be ignored, and Eq. (76) reduces to

$$P_e \simeq 4\mu_s\xi_0 - (11\mu_s + A_s)\xi_0^2, \quad h_0 \gg R_0. \quad (77)$$

This result is equivalent to Eq. (63) of Ref. 1, except with elastic constants of the shell replacing those of the medium. Properties of the medium surrounding the shell have no influence on the bubble dynamics in this case. For a thin shell, with $(R_0/R_{s0})^n \simeq 1 - n(h_0/R_0)$, Eq. (76) reduces to

$$P_e \simeq \left[4\mu_m + 12(\mu_s - \mu_m)\frac{h_0}{R_0}\right]\xi_0 - \left\{11\mu_m + A_m + 6[13(\mu_s - \mu_m) + (A_s - A_m)]\frac{h_0}{R_0}\right\}\xi_0^2, \quad h_0 \ll R_0, \quad (78)$$

to first order in h_0/R_0.

C. Quadratic approximation

Equation (61) is evaluated here in the quadratic approximation with respect to displacement from equilibrium. The dimensionless displacement

$$\xi_1(t) = \frac{R(t) - R_1}{R_1} \quad (79)$$

is used to account for perturbations about the equilibrium bubble radius R_1 in the general case where the encapsulated bubble may be pressurized, such that $P_g \neq P_\infty$ in equilibrium. The outer equilibrium radius R_{s1} is related to other equilibrium radii by

$$R_{s1}^3 = R_1^3 + R_{s0}^3 - R_0^3. \quad (80)$$

We set $P_\infty = P_0 + p_{ac}(t)$ in Eq. (67) to account for an applied acoustic pressure $p_{ac}(t)$, where P_0 is now the pressure at infinity in the absence of sound. Expansion of Eq. (67) to quadratic order in ξ_1 then yields

$$\ddot{\xi}_1 + \delta_{\eta 1}\dot{\xi} + (\omega_g^2 + \omega_e^2 - \omega_\sigma^2)^{1/2}\xi_1 = b\xi_1^2 - \frac{3G_1}{2F_1}\dot{\xi}_1^2 - \left(1 + \frac{H_1}{F_1}\right)\xi_1\ddot{\xi}_1 + \delta_{\eta 2}\xi\dot{\xi} - \frac{\omega_g^2 p_{ac}(t)}{3\gamma P_g}, \quad (81)$$

where

$$\omega_g^2 = \frac{3\gamma P_g}{\rho_m F_1 R_1^2}, \quad \omega_e^2 = \frac{P_e'(R_1)}{\rho_m F_1 R_1},$$

$$\omega_\sigma^2 = \frac{2}{\rho_m F_1 R_1^3}\left(\sigma_g + \sigma_m\frac{R_1^4}{R_{s1}^4}\right), \quad (82)$$

are components of the natural frequency,

$$\delta_{\eta 1} = \frac{4}{\rho_m F_1 R_1^2}\left[\eta_s\left(1 - \frac{R_1^3}{R_{s1}^3}\right) + \eta_m\frac{R_1^3}{R_{s1}^3}\right], \quad (83)$$

$$\delta_{\eta 2} = \frac{4}{\rho_m F_1 R_1^2}\left[\eta_s\left(1 - \frac{R_1^3}{R_{s1}^3}\right)\left(1 + 3\frac{R_1^3}{R_{s1}^3}\right) - \eta_m\left(2 - 3\frac{R_1^3}{R_{s1}^3}\right)\frac{R_1^3}{R_{s1}^3}\right] \quad (84)$$

are the viscous damping coefficients at linear and quadratic order, respectively,

$$b = \frac{1}{2}(3\gamma + 1)\omega_g^2 - \frac{R_1 P_e''(R_1)}{2P_e'(R_1)}\omega_e^2 - \omega_\sigma^2 + \frac{4\sigma_m R_1}{\rho_m F_1 R_{s1}^4}\left(1 - \frac{R_1^3}{R_{s1}^3}\right) \quad (85)$$

is the nonlinearity coefficient associated with gas compressibility, elasticity, and surface tension, and

$$F_1 = \frac{\rho_s}{\rho_m} + \left(1 - \frac{\rho_s}{\rho_m}\right)\frac{R_1}{R_{s1}}, \quad (86)$$

$$G_1 = \frac{\rho_s}{\rho_m} + \left(1 - \frac{\rho_s}{\rho_m}\right)\left(\frac{4}{3} - \frac{1}{3}\frac{R_1^3}{R_{s1}^3}\right)\frac{R_1}{R_{s1}}, \quad (87)$$

$$H_1 = \left(1 - \frac{\rho_s}{\rho_m}\right)\left(1 - \frac{R_1^3}{R_{s1}^3}\right)\frac{R_1}{R_{s1}} \tag{88}$$

are coefficients connected with inertia. Primes on P_e denote derivatives with respect to R. The natural frequency of the bubble is seen to be $(\omega_g^2+\omega_e^2-\omega_\sigma^2)^{1/2}$, from which $\rho_m F_1$ may be identified as an effective density of the material surrounding the bubble. Although the results are limited to small displacements, $|\xi_1| \ll 1$, they are valid for arbitrary equilibrium gas pressure P_g and shell thickness h_0.

For $P_g = P_\infty$, the initial states of the elastic media are unstrained, and the equilibrium bubble radius is $R_1 = R_0$. In this case, replace subscript 1 by 0 everywhere in Eqs. (81)–(88). Equation (76) may then be used to obtain explicit expressions for the derivatives of P_e that are needed to evaluate ω_e and b:

$$P_e'(R_0) = \frac{4}{R_0}\left[\mu_s + (\mu_m - \mu_s)\frac{R_0^3}{R_{s0}^3}\right], \tag{89}$$

$$P_e''(R_0) = -\frac{2}{R_0^2}\left\{11\mu_s + A_s - 4(\mu_m - \mu_s)\frac{R_0^3}{R_{s0}^3} + [15(\mu_m - \mu_s) + (A_m - A_s)]\frac{R_0^6}{R_{s0}^6}\right\}. \tag{90}$$

Church[4] derived an equation similar to Eq. (81) for the case in which the host medium is a liquid ($\mu_m = 0$), the shell is unstrained in equilibrium ($P_g = P_\infty$), and the elastic response of the shell follows linear stress-strain theory. The linearity in stress is with respect to strain, corresponding to the absence of third-order elastic constants in his result. Since strain is a quadratic function of displacement, however, Church's results do not correspond to setting $P_e'' = 0$ in our results. While our results agree with his for the linear terms, i.e., for the natural frequency and viscous losses, there is some inevitable disagreement in the quadratic terms.

VIII. SUMMARY

A model equation derived previously to describe gas bubble dynamics in a nonlinear incompressible elastic medium[1] was modified to include surface tension, viscosity, weak compressibility, and the presence of an elastic shell. Measurements are reported that show the dependence of equilibrium radius on external pressure for a gas bubble in a tissue phantom. The measurements demonstrate the effect of hysteresis. An approached is discussed for taking hysteresis into account in the equation of motion for the bubble.

ACKNOWLEDGMENTS

This work was supported by the IR&D Program at ARL:UT, the National Institutes of Health Grant No. EB004047, and the Office of Naval Research.

[1] S. Y. Emelianov, M. F. Hamilton, Yu. A. Ilinskii, and E. A. Zabolotskaya, "Nonlinear dynamics of a gas bubble in an incompressible elastic medium," J. Acoust. Soc. Am. **115**, 581–588 (2004).
[2] T. G. Leighton, *The Acoustic Bubble* (Academic, New York, 1994).
[3] A. Prosperetti, "The equation of bubble dynamics in a compressible liquid," Phys. Fluids **30**, 3626–3628 (1987).
[4] C. C. Church, "The effects of an elastic solid surface layer on the radial pulsation of gas bubbles," J. Acoust. Soc. Am. **97**, 1510–1521 (1995).
[5] D. B. Khismatullin and A. Nadim, "Radial oscillation of encapsulated microbubbles in viscoelastic liquids," Phys. Fluids **14**, 3534–3557 (2002).
[6] E. A. Zabolotskaya, Yu. A. Ilinskii, G. D. Meegan, and M. F. Hamilton, "Bubble interactions in clouds produced during shock wave lithotripsy," *Proceedings of the 2004 IEEE International UFFC Joint 50th Anniversary Conference*, pp. 890–893.
[7] L. Crum, S. Kargl, and T. Matula, "A potential explanation for marine mammal strandings," J. Acoust. Soc. Am. **116**, 2533(A) (2004).
[8] V. N. Alekseev and S. A. Rybak, "Gas bubble oscillations in elastic media," Acoust. Phys. **45**, 535-540 (1999).
[9] L. D. Landau and E. M. Lifshitz, *Theory of Elasticity*, 3rd ed. (Pergamon, New York, 1986), pp. 135–137.
[10] Y. C. Fung, *Biomechanics: Mechanical Properties of Living Tissues*, 2nd ed. (Springer, New York, 1993).
[11] L. A. Ostrovsky, "Wave interaction in acoustic resonators with and without hysteresis," J. Acoust. Soc. Am. **116**, 3348–3353 (2004).
[12] A. Prosperetti and A. Lezzi, "Bubble dynamics in a compressible liquid. 1. First-order theory," J. Fluid Mech. **168**, 457–478 (1986).
[13] A. Lezzi and A. Prosperetti, "Bubble dynamics in a compressible liquid. 2. Second-order theory," J. Fluid Mech. **185**, 289–321 (1987).
[14] L. A. Ostrovskii, "Nonlinear acoustics of slightly compressible porous media," Sov. Phys. Acoust. **34**, 523–526 (1988).
[15] A. C. Eringen and E. S. Suhubi, *Elastodynamics* (Academic, New York, 1974).
[16] Yu. A. Ilinskii and E. A. Zabolotskaya, "Cooperative radiation and scattering of acoustic waves by bubbles in liquid," J. Acoust. Soc. Am. **92**, 2837–2841 (1992).
[17] J. D. Jackson, *Electromagnetics*, 2nd ed. (Wiley, New York, 1975), Sec. 17.3.
[18] M. F. Hamilton, Yu. A. Ilinskii, and E. A. Zabolotskaya, "Separation of compressibility and shear deformation in the elastic energy density (L)," J. Acoust. Soc. Am. **116**, 41–44 (2004).
[19] S. Catheline, J.-L. Gennisson, and M. Fink, "Measurement of elastic nonlinearity of soft solid with transient elastography," J. Acoust. Soc. Am. **114**, 3087–3091 (2003).

Acoustic radiation by vortex induced flexible wall vibration

S. K. Tang[a)]
Department of Building Services Engineering, The Hong Kong Polytechnic University, Hung Hom, Hong Kong, Hong Kong nil Hong Kong

R. C. K. Leung and R. M. C. So
Department of Mechanical Engineering, The Hong Kong Polytechnic University, Hong Kong, People's Republic of China

K. M. Lam
Department of Civil Engineering, The University of Hong Kong, Hong Kong, People's Republic of China

(Received 18 February 2005; revised 15 May 2005; accepted 7 July 2005)

Sound radiation due to unsteady interaction between an inviscid vortex (which models a turbulent eddy) and a finite length flexible boundary in a two-dimensional space is studied using potential theory and the matched asymptotic expansion technique. The Mach number of the vortex propagation is kept below 0.15. Results suggest that the monopole field created by the volumetric flow induced by the vibrating flexible boundary dominates the overall acoustic power radiation. The longitudinal dipole directly due to the transverse vortex acceleration is only important when the vortex is moving over the flexible boundary. The longitudinal dipole resulting from the boundary vibration gains slightly in importance in the strong vortex case, but the corresponding transverse dipole remains negligible for the cases considered in the present study. The two longitudinal dipoles give rise to biased radiation directivities on both sides of the flexible boundary. © *2005 Acoustical Society of America.* [DOI: 10.1121/1.2011127]

PACS number(s): 43.28.Ra, 43.40.Rj, 43.50.Nm [GL] Pages: 2182–2189

I. INTRODUCTION

Air conditioning and ventilation system is a major noise source in any commercial building. The associated air ductwork conveys turbulent flows from the fans to the interior workplaces. The ducted elements will affect the turbulence thus generated and the propagation of noise. Understanding the flow-structure-acoustics interactions is therefore of prime importance in modern building noise control.

The study of the interaction between structural vibration and acoustics has attracted the attention of many researchers in the past few decades. For instance, Frendi and Robinson,[1] Cummings,[2] and Huang[3] studied the duct wall vibration induced by a downstream traveling plane acoustic wave in the absence of a mean flow. Blake[4] and Leppington *et al.*[5] examined the acoustic radiation by vibrating panels, while Wu and Maestrello,[6] Dowell,[7] and Howe[8] investigated the acoustic responses of a plate subject to a distributed surface pressure loading (which is used to simulate the effects of a turbulent boundary layer). The scattering of sound by a panel in the absence of a flow was also studied by many researchers, for instance, Abrahams[9] and Leppington.[10] In addition, Graham[11] showed theoretically that the curvature of a panel has significant influence on its sound radiation. Ffowcs Williams and Lovely[12] proved that the presence of a steady low Mach number mean flow tends to amplify the sound generated by surface vibration. Davies[13] studied the overall sound power radiated from panels excited by a turbulent boundary layer and compared his predictions with experimental results. However, details of the flow-structure-acoustics interactions were not presented.

The turbulent air flow inside air conditioning ductwork induces pressure fluctuations on the duct walls, resulting in the vibration of the latter which in turn radiates sound to both the duct interior and the external environment (breakout noise).[14] However, corresponding studies on the effect of flow turbulence on noise generated by flow-induced structural vibrations is rarely found. The effect of turbulent flow on the effectiveness of the duct noise control using flexible membranes proposed by Huang[3] is also not clear.

The air flow inside any ductwork in a building is of very low Mach number ($\leqslant 0.1$). The acoustic analogy[15,16] works well in the estimation of the aerodynamic sound production at such low Mach number condition provided that the flow field and the associated solid surface vibration are precisely known. However, the exact coupling between the turbulent flow with the duct wall cannot be analytically handled such that one has to turn to computational technique whose accuracy might still be subject to query. The computations are also very resource demanding. Vortices, though, are drastic simplifications of the real flows, and have been adapted extensively in the study of sound generation by turbulent flows in the presence of a solid object because of their simplicity such that analytical solutions can be obtained in some cases. Typical examples of these studies include Howe,[17] Obermeier[18] and the more recent work of Leung and So[19] and Tang and Lau.[20]

In the present investigation, a vortex is chosen to represent a turbulent eddy, and the motion of a flexible boundary

[a)]Electronic mail: besktang@polyu.edu.hk

 0001-4966/2005/118(4)/2182/8/$22.50

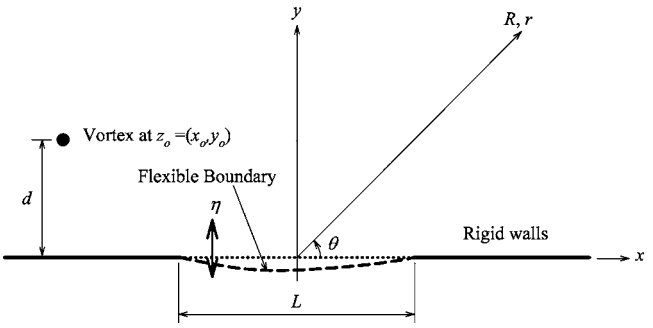

FIG. 1. Schematic of the theoretical model.

in an otherwise rigid plane under the actions of this vortex is calculated. The sound so radiated into the far field on both sides of this boundary will be analyzed in detail. The effects of the mechanical properties of the boundary will also be examined. It is hoped that the present results can provide information for improved duct noise control design and contribute to the fundamental understanding of the flow-structure-acoustic interaction.

II. THEORETICAL MODEL

A. Motions of the vortex and the flexible boundary

Since air viscosity and compressibility are of secondary importance for low Mach number flow noise generation,[21] an incompressible inviscid vortex model is adopted in the present study. Figure 1 illustrates the schematic of the present study model. A vortex of strength (circulation) Γ is initially located far upstream of the flexible boundary of length L at a distance d above the rigid plane. The initial speed of the vortex, U_i, therefore equals $\Gamma/(4\pi d)$[22] and is in a direction parallel to the rigid plane. The flexible boundary is at rest initially. The movement of the vortex creates a time varying fluid pressure on this boundary, causing it to vibrate and this vibration eventually gives rise to a fluctuating velocity field, which affects the motion of the vortex.

It is assumed that the vibration amplitude of the flexible boundary, $\eta(x,\tau)$, is small compared to d (and y_0) and this boundary is modeled as a rigid surface with distributed fluctuating velocity $v(x,\tau)$ $(=\partial\eta/\partial\tau)$, where τ denotes the near field time. The edges of this flexible boundary are kept fixed and thus $\eta(-L/2,\tau)/d=\eta(L/2,\tau)/d=0$. The induced velocity at the vortex position (x_0,y_0) due to the boundary vibration, V_i, can be determined using potential theory[22] as

$$V_i=\frac{\hat{x}}{\pi}\int_{-L/2}^{L/2}\frac{v(x_0-x)}{(x_0-x)^2+y_0^2}dx+\frac{\hat{y}}{\pi}\int_{-L/2}^{L/2}\frac{vy_0}{(x_0-x)^2+y_0^2}dx, \tag{1}$$

where the caret denotes unit vector in the direction indicated. The vortex velocity, V, is thus

$$V=\frac{\Gamma}{4\pi y_0}\hat{x}+V_i. \tag{2}$$

Owing to the very thin flexible duct wall compared to its length in practice, the effect of the bending stiffness is usually insignificant when compared to that of the tension within the wall. For a wall thickness of 0.5 mm, which is the usual value for a flow duct, and a duct length of say 10 mm, the error of neglecting the bending term is less than 0.3%. The longer the duct length, the smaller this error will be. Therefore, for simplicity, the time variations of $v(x,\tau)$ are obtained by solving the dynamic equation governing the forced vibration of a membrane,[3] or

$$M\frac{\partial^2\eta}{\partial\tau^2}=T\frac{\partial^2\eta}{\partial x^2}-D\frac{\partial\eta}{\partial\tau}-\Delta p, \tag{3}$$

where M, T, and D denote the surface density, the tension per unit spanwise length, and the damping coefficient of the membrane, respectively, and Δp represents the differential air pressure between the upper and lower side of the membrane, which is

$$\Delta p=-\rho\frac{\partial\phi}{\partial\tau}=\frac{\rho\Gamma}{2\pi}\frac{\partial}{\partial\tau}\tan^{-1}\left[\frac{2y_0(x-x_0)}{(x-x_0)^2+(\eta^2-y_0^2)}\right]-\frac{2\rho}{\pi}\frac{\partial}{\partial\tau}\int_{-L/2}^{L/2}\frac{\partial\eta'}{\partial\tau}\log\sqrt{(x-x')^2+(\eta-\eta')^2}dx', \tag{4}$$

where the prime denotes a quantity along the flexible boundary. For small magnitude low frequency boundary vibration, contribution from the second term on the right-hand side of Eq. (4), which represents a kind of fluid loading,[23] is weak as long as the vortex is in the proximity of the boundary. This is the case of the present study.

The motion of the vortex and the distributed velocity $v(x,\tau)$ can be updated by solving Eqs. (2)–(4) together with the instantaneous profile $\eta(x,\tau)$ using a fourth order Runge-Kutta time integration scheme. The initial conditions are $V=U_i$, $\eta(x,0)/d=0$ and $v(x,0)/U_i=0$. One can observe that the present approach is very different from that adopted by Walker *et al.*[24] in which the vortex is always moving parallel to the wall.

B. Acoustic far field

The vibration of the flexible boundary and the unsteady motion of the vortex results in acoustic radiation on both sides of the boundary. At distance far away from the vortex and the flexible boundary, the fluid is at rest and the corresponding acoustic potential in frequency domain, ϕ_0, is given by the solution of the Helmholtz equation,

$$\nabla^2\phi_0+(\omega/c)^2\phi_0=0, \tag{5}$$

where ω denotes the angular velocity and c the ambient speed of sound. In two-dimensional space, the outgoing wave solution of Eq. (5) at the radial distance r is[25]

$$\phi_0(r,\theta,\omega)=\sum_\alpha A_\alpha H_\alpha^{(1)}(\omega r/c)e^{i\alpha\theta}, \tag{6}$$

where $H_\alpha^{(1)}$ is the αth order Hankel function of the first kind and A_α is a term to be determined. One way to find α and A_α is by the method of matched asymptotic expansion as in Obermeier[18] and Tang and Lau.[20] The inner solution of the outer wave potential [Eq. (6)] at low frequency is

matched with the outer solution of the inner incompressible near field potential.

1. $y/d \to \infty$

This is the region in which the sound is created by the vibrating flexible boundary alone. The fluid potential at a large distance R in an angular direction θ from the center of the flexible boundary is

$$\phi = -\frac{1}{\pi}\int_{-L/2}^{L/2} v \log\sqrt{(R\cos\theta - x)^2 + (R\sin\theta - \eta)^2}\,dx$$
$$\approx -\frac{1}{\pi}\log R\int_{-L/2}^{L/2} v\,dx + \frac{1}{\pi R}\int_{-L/2}^{L/2} v(x\cos\theta + \eta\sin\theta)\,dx. \quad (7)$$

The properties of the Hankel functions[25] and Eq. (7) suggests that the far field potential is

$$\phi_0(r,\theta,\omega) = A_0 H_0^{(1)}(\omega r/c) + H_1^{(1)}(\omega r/c)(A_1\cos\theta + B_1\sin\theta), \quad (8)$$

where

$$A_0 = \frac{i}{2}\left[\int_{-L/2}^{L/2} v\,dx\right]^F, \quad A_1 = \frac{i\omega}{2c}\left\{\left[\int_{-L/2}^{L/2} v x\,dx\right]^F\right\},$$
$$B_1 = \frac{i\omega}{2c}\left[\int_{-L/2}^{L/2} v\,\eta\,dx\right]^F$$

and $[\ ]^F$ denote the Fourier transform with respect to time. When $r \to \infty$,

$$\phi_0(r,\theta,\omega) \approx \sqrt{\frac{2c}{\pi\omega r}}e^{i\omega r/c}[A_0 e^{-i\pi/4} + (A_1\cos\theta + B_1\sin\theta)e^{-i3\pi/4}], \quad (9)$$

and the time variation of the far field potential can be obtained by taking the inverse Fourier transform of Eq. (9) with respect to time, bearing in mind that ω is kept positive in $\phi_0(\omega)$. It can then be shown[26] that for the observer time $t > r/c$,

$$\left[\frac{1}{\sqrt{t - r/c}}\right]^F = e^{i(\omega r/c + \pi/4)}\sqrt{\frac{\pi}{\omega}}, \quad (10)$$

and the inverse transform of Eq. (9) takes the form of a convolution integral, which is

$$\phi_0(r,\theta,t) = \frac{1}{\pi}\sqrt{\frac{c}{2r}}\int_{-\infty}^{t-r/c}\left(\int_{-L/2}^{L/2} v\,dx + \frac{\cos\theta}{c}\frac{\partial}{\partial\tau}\int_{-L/2}^{L/2} v x\,dx + \frac{\sin\theta}{c}\frac{\partial}{\partial\tau}\int_{-L/2}^{L/2} v\,\eta\,dx\right)\frac{d\tau}{\sqrt{t - \tau - r/c}}, \quad (11)$$

where τ represents the near field time and $\tau < t - r/c$. The far field acoustic pressure, p^-, is

$$p^- = -\rho\frac{\partial\phi_0}{\partial t} = -\frac{\rho}{\pi}\sqrt{\frac{c}{2r}}\frac{\partial}{\partial t}\int_{-\infty}^{t-r/c}\left(\int_{-L/2}^{L/2} v\,dx + \frac{\cos\theta}{c}\frac{\partial}{\partial\tau}\int_{-L/2}^{L/2} v x\,dx + \frac{\sin\theta}{c}\frac{\partial}{\partial\tau}\int_{-L/2}^{L/2} v\,\eta\,dx\right)\frac{d\tau}{\sqrt{t - \tau - r/c}}. \quad (12)$$

Equation (12) shows that the sound radiated consists of a monopole and two dipoles. The monopole is originated from the total fluctuating fluid mass flow due to the boundary vibration. One can notice that for small v/c, the dipoles are very weak when compared to the monopole and can be neglected as in Filippi *et al.*[23]

2. $y/d \to +\infty$

The potential at very large distance in this case is a combination of the vortex potential and the flexible boundary vibration potential [the reverse of Eq. (7)], which is,

$$\phi = \frac{\Gamma}{2\pi}\left[\tan^{-1}\left(\frac{R\sin\theta - y_o}{R\cos\theta - x_o}\right) - \tan^{-1}\left(\frac{R\sin\theta + y_o}{R\cos\theta - x_o}\right)\right] + \frac{1}{\pi}\int_{-L/2}^{L/2} v\log\sqrt{(R\cos\theta - x)^2 + (R\sin\theta - \eta)^2}\,dx$$
$$\approx -\frac{\Gamma y_o}{\pi R}\cos\theta + \frac{1}{\pi}\log R\int_{-L/2}^{L/2} v\,dx - \frac{1}{\pi R}\int_{-L/2}^{L/2} v(x\cos\theta + \eta\sin\theta)\,dx. \quad (13)$$

Following the procedure in the previous section, the far field pressure, p^+, is

$$p^+ = \frac{\rho}{\pi}\sqrt{\frac{c}{2r}}\frac{\partial}{\partial t}\int_{-\infty}^{t-r/c}\left[\int_{-L/2}^{L/2} v\,dx + \frac{\cos\theta}{c}\frac{\partial}{\partial\tau}\left(\int_{-L/2}^{L/2} v x\,dx + \Gamma y_o\right) + \frac{\sin\theta}{c}\frac{\partial}{\partial\tau}\int_{-L/2}^{L/2} v\,\eta\,dx\right]\frac{d\tau}{\sqrt{t - \tau - r/c}}. \quad (14)$$

An additional dipole due to the unsteady axial vortex force is created. Its strength may be comparable to that of the monopole as the vortex velocity can be large compared to v. This will be discussed later.

III. RESULTS AND DISCUSSION

In the foregoing discussion, all length scales are normalized by d. The time is normalized by d/U_i. The tension T, damping D, and the surface density M are normalized by $\rho U_i^2 d$, ρU_i, and ρd, respectively. The *in vacuo* wave speed along the flexible boundary is $c_T = \sqrt{T/M}$ such that this wave speed is also normalized by U_i. In the real scenario, $c_T = 0.1c$ is essentially true.[27] The present analysis is always under the low Mach number condition as in a practical flow duct and L/d is set to 2 in the present investigation. The structural damping effect is insignificant in practice. According to the setup of Frendi *et al.*[28] and the low Mach number

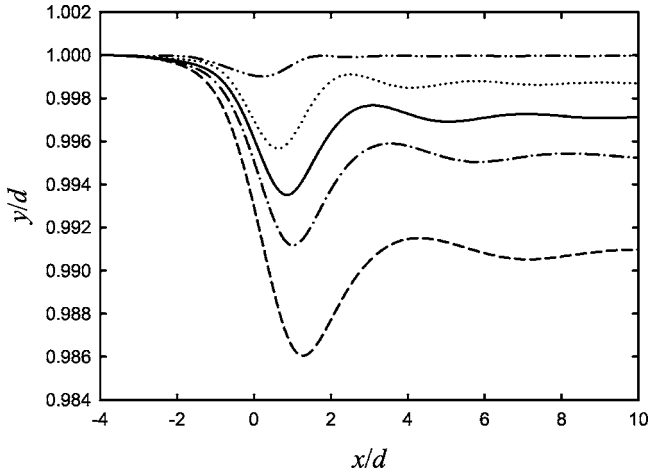

FIG. 2. Vortex flight path at $M=100$: (-·-) $c_T=2$; (···) $c_T=\sqrt{3/2}$; (—) $c_T=1$; (-·-) $c_T=\sqrt{3/4}$; (– – –) $c_T=\sqrt{1/2}$.

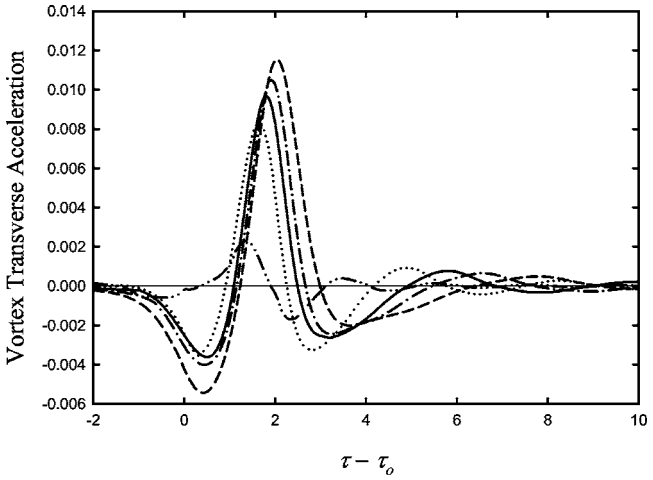

FIG. 3. Time variations of transverse velocity of vortex at $M=100$. Legends: same as those in Fig. 2.

condition invoked in the present study, D ranges from 0.5 to 1. Therefore, D is set to unity in the present study.

The flexible boundary is discretized into 100 equal elements and it has been confirmed that further increase in this number does not produce any significant change to the computed results. Without loss of generality, the vortex is introduced initially at $x/d=-5$ and the corresponding vortex speed is closed to unity. An increase in this initial vortex distance from the flexible boundary does not have any significant effect on the results.

A. Vortex and flexible boundary motion

Figure 2 shows that effects of c_T on the vortex trajectory at $M=100$. The vortex moves toward the flexible boundary for the range of c_T tested. This agrees with the results of Tang[29] for a vortex moving over a surface with flow impedance. The transverse fluctuating vortex motion is due to the vibration of the flexible boundary which is absent in Tang.[29] The vortex gets closer to the wall as it continues its path downstream of the flexible boundary. This appears to be inline with the results of Walker *et al.*[24] though the vortex is kept moving with a constant speed in their study.

It is observed that the deviation of the vortex path from $y/d=1$ is small at large c_T. For $c_T \geqslant 2$, the vortex returns to its initial height above the rigid wall after flying over the flexible wall. For $c_T>1$, the vortex path varies slowly with increasing wave speed. The movement of the vortex path toward the flexible boundary increases rapidly for a relatively strong vortex ($c_T<1$). The amplitude of the boundary vibration also increases with decreasing c_T, but it is observed to be below 5% of d throughout the present investigation. This will be discussed further later. The corresponding trends for other values of M are very similar to that shown in Fig. 2 provided that the maximum boundary vibration amplitude, $|\eta|_{\max}$, is small compared to d and thus are not presented. However, one can expect that a higher c_T is required to keep $|\eta|_{\max}$ small enough for the present model to apply when the surface density M is reduced. For instance, when M is close to 2, which is the value adopted by Huang *et al.*,[27] T must be larger than 30, indicating $c_T>3.87$ and a relatively weak vortex is required. However, such condition guarantees a very low Mach number flow and thus is still valid for air conditioning noise control application.

The transverse accelerations of the vortex with $M=100$ and different c_T are shown in Fig. 3, where τ_0 denotes the instant at which the vortex moves above the leading edge of the flexible boundary ($x=-L/2$). The amplitude of the corresponding axial components of the vortex accelerations are comparable to those shown in Fig. 3 and are more prevailing than the transverse accelerations. However, they are not presented because they do not have any direct contributions to the radiated sound field [Eq. (14)].

At lower T (and thus lower c_T), the transverse acceleration of the vortex is more pulse-like. This is expected from the characteristics of the vortex paths shown in Fig. 2. A weaker T results in a larger deflection of the flexible boundary and a relatively more pronounced effect of the edge at $x=-L/2$, resulting in a faster downward movement of the vortex. Stronger sound scattering is expected but the very directional backward sound radiation by a semi-infinite rigid edge (for instance in Crighton[21]) does not exist in the present study. This is due to the very small vertical vibration of the flexible boundary at its edges so that the sharp edge effect is much attenuated as shown in one of the examples in Tang and Lau.[20]

Figure 4(a) shows the time variation of the flexible boundary displacement η at $c_T=2$, $M=100$. The vortex is at $x/d=1$ (at the downstream edge of the boundary) at $\tau-\tau_0 \sim 2$. A relatively larger displacement ($|\eta|_{\max} \sim 0.5\%$ of d) is found when the vortex is moving over this boundary and a more periodical boundary motion is observed as the vortex propagates away from it. The corresponding vibration velocity of the flexible boundary is given in Fig. 4(b). While its magnitude is comparable or slightly higher than the transverse velocity of the vortex, its maximum is still $\sim 0.5\%$ of the instantaneous vortex speed.

Another example of the flexible boundary vibration at $c_T=0.7071$ and $M=100$ is given in Fig. 5. The weaker tension within the boundary and thus a relatively stronger vortex results in a larger η, where the maximum amplitude is

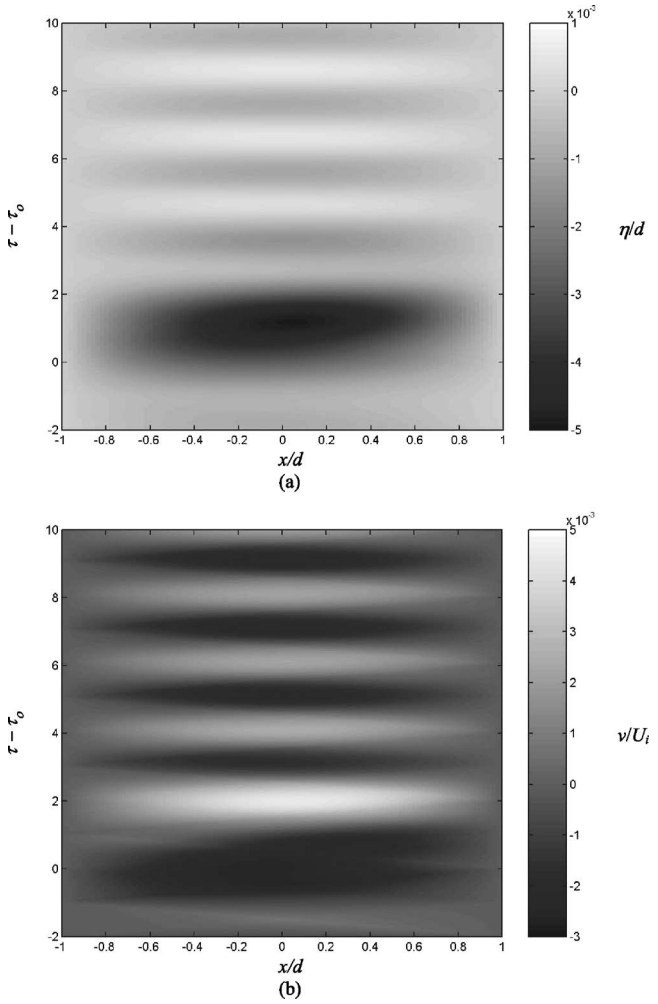

FIG. 4. Vibration pattern of the flexible boundary at $M=100$ and $c_T=2$. (a) Displacement; (b) velocity.

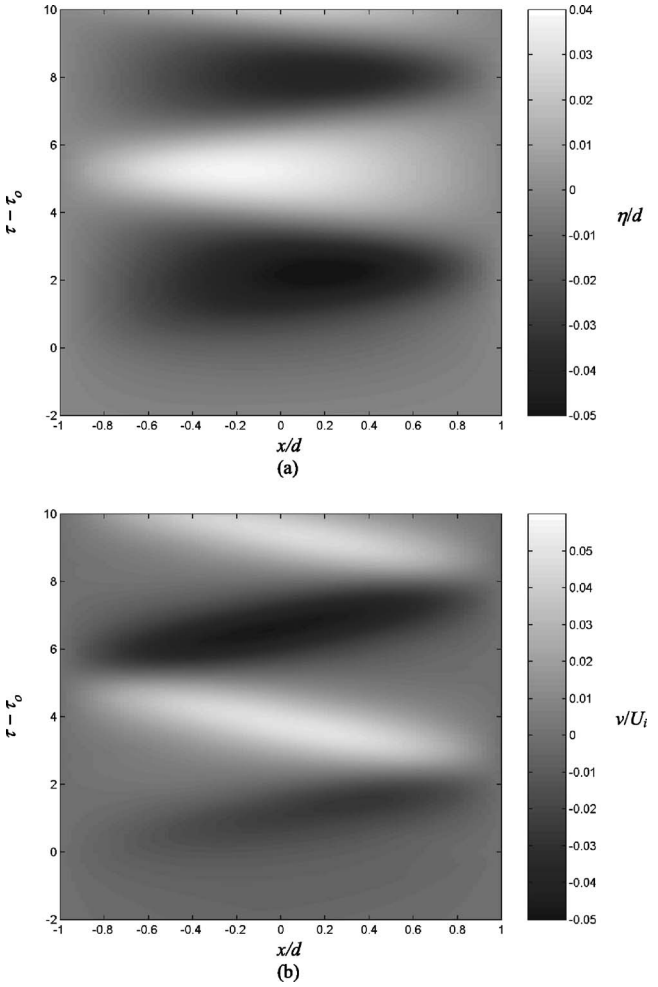

FIG. 5. Vibration pattern of the flexible boundary at $M=100$ and $c_T=\sqrt{1/2}$. (a) Displacement; (b) velocity.

close to 5% of d. Again, the vortex is at $x/d=1$ at $\tau-\tau_0 \sim 2$ as the axial velocity of the vortex is not much affected by the flexible boundary. The vibration of the boundary is periodic. The pattern of boundary vibration velocity is not symmetrical about the central plane of this boundary [Fig. 5(b)]. The maximum boundary vibration velocity reaches ~6% of the vortex speed as shown in Fig. 5(b).

B. Far field acoustic radiation

Since c_T can be chosen to be $\sim 0.1c$ as discussed in Huang *et al.*,[27] $c_T=0.1c$ is set throughout this section. However, it will be discussed later that the foregoing conclusions will not be affected by this assumption as far as the Mach number of the vortex motion remains low. The time integral of Eqs. (12) and (14) can be carried out numerically by a proper argument substitution as in Tang and Ko.[30]

At $y \to \infty$, the monopole radiation due to the boundary vibration dominates the radiated sound field as shown in Fig. 6(a) for a relatively weak vortex at $c_T=2$ ($T=400$, $M=100$) and thus $c=20$. The strength of the longitudinal vibration dipole is weak compared to that of the monopole, while that of the transverse vibration dipole is even much weaker and is not presented. The contribution from the dipole directly created by the transverse acceleration of the vortex (vortex dipole), which is pulse-like, is also weak in this case. However, it is stronger than the dipoles created directly by the boundary vibration when the vortex is in the proximity of the boundary.

The monopole is in-phase with the vortex dipole at $\theta < 90°$ but the opposite is true at $\theta > 90°$. This gives rise to a slightly downstream-biased radiation, especially when the vortex is close to the downstream edge of the flexible boundary ($\tau-\tau_0 \sim 2$). This appears to be in-line with existing results of a low Mach number flow over a cavity where similar downstream-biased overall sound radiation is observed.[31] Uncoupled model, such as that of Walker *et al.*,[24] which assumes no transverse vortex acceleration, appears to be insufficient for the study of flow-induced acoustic radiation. The increase in c_T (and thus c) implies a lower flow Mach number and results in a reduction of the magnitude of the vortex dipole relative to that of the monopole. One should note that the radiation due to boundary vibration at $y \to -\infty$ is the reverse of that at $y \to \infty$ with the vortex dipole excluded.

Figure 6(b) shows the strengths of the monopole and the various dipoles at $c_T=1/\sqrt{2}(c \sim 7.1)$, $T=50$, and $M=100$. A reduction in c_T increases the overall contribution of the vortex dipole and thus the extent of the downstream biased sound radiation. The strength of the vortex dipole is compa-

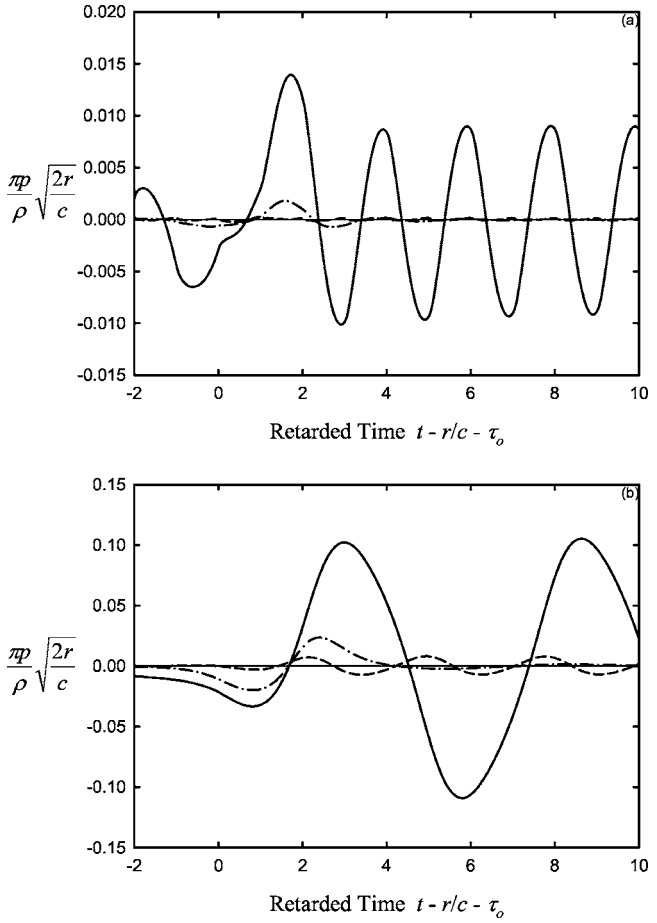

FIG. 6. Time fluctuations of sound fields' magnitudes at $M=100$. (a) $T=400$; (b) $T=50$. (—) Monople; (-·-) vortex dipole; (---) longitudinal vibration dipole.

rable to that of the monopole when the vortex is flying over the flexible boundary, leading to weak upstream radiation. The longitudinal vibration dipole becomes more important, but is still weak when compared to the monopole and the vortex dipole. It can also be noticed that the period of the vibration dipole is shorter than that of the monopole. The transverse vibration dipole remains negligible. A stronger vortex leads to stronger acoustic radiation.

The evolution of the radiation directivity of the stronger vortex case [Fig. 6(b)] when the vortex is in close proximity of the flexible boundary is summarized in Fig. 7. The data at $\theta > 180°$ are those from the side of the boundary without the vortex. The weak longitudinal vibration dipole is capable of producing a slightly biased radiation at $\theta > 180°$, but the bias direction is continuously swapping between downstream and upstream depending on the signs of the dipole and the monopole (whose frequencies are not the same) until the strength of the dipole becomes negligible. For $\theta < 180°$, the stronger vortex dipole dominates the dipole field and creates a downstream biased sound radiation. Similar trends are observed for other values of M (these results are not presented here).

The acoustic powers radiated on the two sides of the boundary are nearly the same at high c_T due to the very weak contributions from the dipoles. At lower c_T, the contribution from the vortex dipole is restricted at the instant of intensive interaction between the vortex and the flexible boundary, but

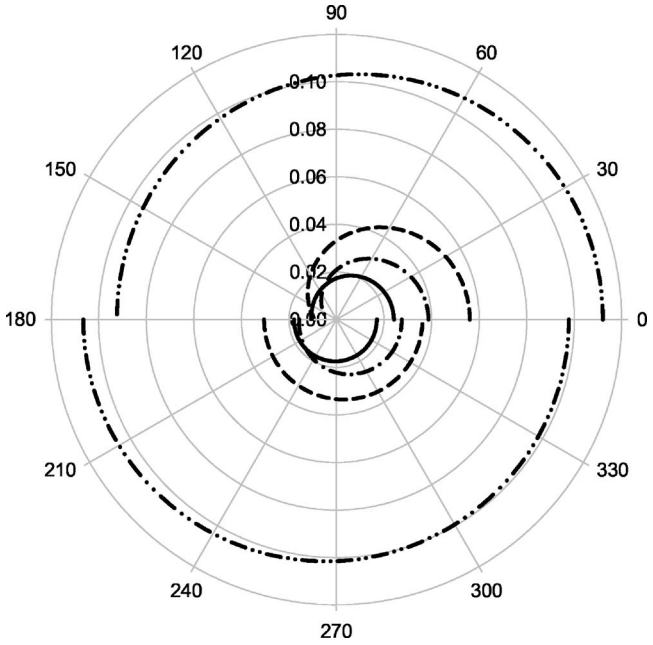

FIG. 7. Evolution of radiation directivity at $M=100$ and $T=50$. (—) $\tau-\tau_0=-0.28$; (- - -) $\tau-\tau_0=0.81$; (-·-) $\tau-\tau_0=1.90$; (-··-) $\tau-\tau_0=2.99$.

is still not very significant. Figure 8 illustrates the time variation of the "per unit spanwise length" acoustic power radiated at $y>0$, denoted by W hereinafter, at various c_T with $M=100$. In general, the acoustic power increases rapidly when the vortex is moving over the downstream edge of the flexible boundary and then reaches a maximum during the next cycle of boundary vibration before it is being damped down gradually due to structural damping and fluid loading. It is only at very high c_T that the acoustic power is reduced quickly after the vortex moves away from the flexible boundary. However, the acoustic power in this case is very weak compared to those of the others presented in Fig. 8.

The maximum W depends also on M as shown in Fig. 9. A lighter boundary produces stronger acoustic radiation mainly in the form of monopole even the wave speed relative to the initial vortex speed is kept fixed (a weaker T). It

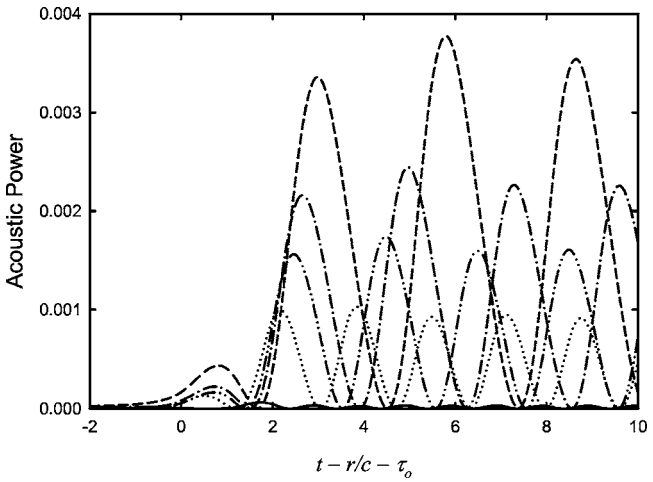

FIG. 8. Time variation of acoustic power radiated to upper side of flexible boundary at $M=100$. (—) $c_T=2$; (···) $c_T=\sqrt{3/2}$; (-··-) $c_T=1$; (-·-) $c_T=\sqrt{3/4}$; (---) $c_T=\sqrt{1/2}$.

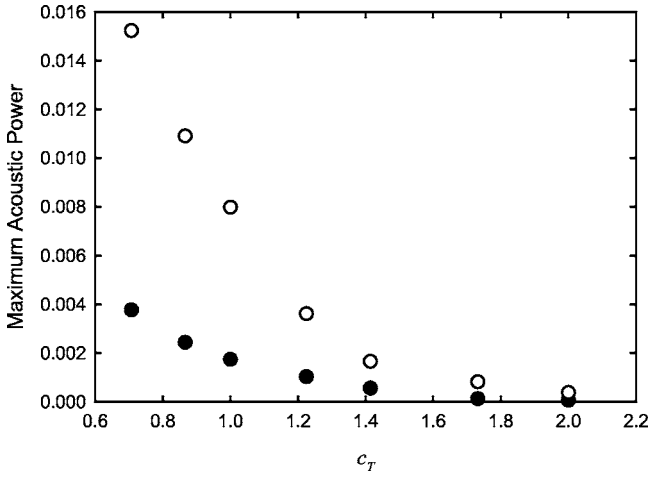

FIG. 9. Variation of maximum acoustic power radiated with c_T. (●) $M=100$; (○) $M=50$.

should be noted that $|\eta|_{\max}$ for the case of $M=50$ and $c_T=0.7071$ reaches 10% of d, which exceeds the prescribed limit of the present study of 5%. Nevertheless, the reduction of M from 100 to 50 at fixed c_T and c in general results in 1.8 to 2.2 times increase in both $|\eta|_{\max}$, $|v|_{\max}$ and the acceleration (not presented here). The radiated acoustic power tends to vary with $|v|_{\max}$ to a power of ~ 2 when c_T is fixed. However, this power law index shows a tendency to increase when $c_T > 1$, suggesting a faster reduction of the acoustical radiation efficiency as the vortex speed Mach number approaches the vanishing value.

For the two values of M studied, the variation of maximum W with $|v|_{\max}$ appears to follow a power law as shown in Fig. 10. The approximated relationship is

$$W_{\max} \sim |v|_{\max}^{1.66}/\sqrt{M}, \tag{15}$$

with the result at $M=50$ and $c_T=0.7071$ falls slightly off-trend probably due to the relatively large boundary deflection. The power index is less than that for the compact harmonic monopole radiation, which is 2 (e.g., Kinsler *et al.*[32]). This is common for two-dimensional radiation where the sound source is noncompact in its spanwise direction. It is expected that W will scale on the overall volume flow induced by the boundary vibration through a similar power law relationship.

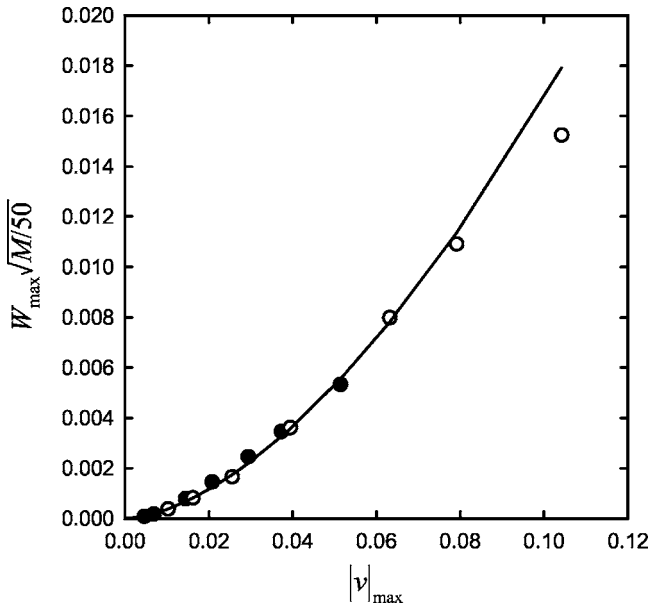

FIG. 10. Power law relations between vibration velocity and acoustic power radiation. (●) $M=100$; (○) $M=50$; (—) power law curve [Eq. (15)].

In the present study, the vortex moves under the influence of solid boundaries in the absence of a mean flow. However, it is believed that the presence of a low Mach number mean flow will tend to increase the acoustic power radiation as shown in Ffowcs Williams and Lovely,[12] though their study is for a compact vibrating source. Such increase is expected to be more significant in the two-dimensional case as the corresponding amplification of acoustic radiation will then depend on the Mach number to a lower order.[33]

IV. CONCLUSIONS

An inviscid model was developed to investigate the sound radiated due to the unsteady interactions between a vortex and a finite length flexible boundary in an otherwise rigid wall at low Mach numbers. The vibration displacement of the latter was kept small. The motion of the vortex was obtained basically through the potential theory and the sound radiated on the two sides of the flexible boundary was estimated using the matched asymptotic expansion technique.

The vortex path is deflected toward the flexible boundary and the deflection is larger as the tension in the boundary decreases. This results in larger boundary vibration magnitude and higher vortex transverse acceleration. The vortex continues its motion parallel to the rigid wall as time goes on, but at a lower height above the wall unless the wave speed along the flexible boundary is considerably higher than the initial vortex speed, which is the case for a relatively weak vortex.

The results of the matched asymptotic expansion show clearly that the rate of change of volumetric flow induced by the flexible boundary vibration and the transverse vortex acceleration are two major sources of sound. The former creates a monopole field and dominates the overall acoustic power radiation. The transverse vortex acceleration gives rise to a longitudinal dipole which is only significant to the acoustic radiation above the flexible boundary when the vortex is flying over this boundary. The interaction between these two sound fields results in a downstream-biased acoustic radiation.

The boundary vibration also creates one longitudinal and one transverse dipole. The latter is too weak to be important. The longitudinal dipole becomes a bit more important when the wave speed of the flexible boundary is reduced. This results in a slight bias in the acoustic radiation direction on the side of the boundary without the vortex. The radiation directivity swaps between downstream and upstream as the period of the longitudinal dipole strength variation is about double that of the monopole. It is also found that the strength of the per unit spanwise length acoustic power radiation scales approximately with the vibration-induced volumetric

flow to a power of ~1.66 and the inverse of the square root of the surface density of the flexible boundary.

ACKNOWLEDGMENT

Funding support under Grant Number PolyU1/02C from the Research Grants Council of the Government of the HKSAR is gratefully acknowledged.

[1]A. Frendi and J. Robinson, "Effect of acoustic coupling on random and harmonic plate vibrations," AIAA J. **31**, 1992–1997 (1993).
[2]A. Cummings, "Low frequency acoustic transmission through the walls of rectangular ducts," J. Sound Vib. **61**, 327–345 (1978).
[3]L. Huang, "A theoretical study of duct noise control by flexible panels," J. Acoust. Soc. Am. **106**, 1801–1809 (1999).
[4]W. K. Blake, "The acoustic radiation from unbaffled strips with application to a class of radiating panels," J. Sound Vib. **39**, 77–103 (1975).
[5]F. G. Leppington, E. G. Broadbent, and K. H. Heron, "The acoustic radiation efficiency of rectangular panels," Proc. R. Soc. London, Ser. A **382**, 245–271 (1982).
[6]S. F. Wu and L. Maestrello, "Responses of finite baffled plate to turbulent flow excitations," AIAA J. **33**, 13–19 (1995).
[7]E. H. Dowell, "Radiation from panels as a source of airframe noise," AIAA J. **13**, 1529–1530 (1975).
[8]M. S. Howe, "Diffraction radiation produced by turbulent boundary layer excitation of a panel," J. Sound Vib. **121**, 47–65 (1988).
[9]I. D. Abrahams, "Scattering of sound by a finite non-linear elastic plate bounding a nearly resonant cavity," J. Sound Vib. **130**, 387–404 (1989).
[10]F. G. Leppington, "Acoustic scattering by membranes and plates with line constraints," J. Sound Vib. **58**, 319–332 (1978).
[11]W. R. Graham, "The influence of curvature on the sound radiated by vibrating panels," J. Acoust. Soc. Am. **98**, 1581–1595 (1995).
[12]J. E. Ffowcs Williams and D. J. Lovely, "Sound radiation into uniformly flowing fluid by compact surface vibration," J. Fluid Mech. **71**, 689–700 (1975).
[13]H. G. Davies, "Sound from turbulent boundary layer excited panels," J. Acoust. Soc. Am. **49**, 878–889 (1971).
[14]L. L. Beranek, *Noise and Vibration Control Engineering, Principles and Applications* (Wiley, New York, 1992).
[15]M. J. Lighthill, "On sound generated aerodynamically I. General theory," Proc. R. Soc. London, Ser. A **211**, 564–587 (1952).
[16]N. Curle, "The influence of solid boundaries upon aerodynamic sound," Proc. R. Soc. London, Ser. A **231**, 505–514 (1955).
[17]M. S. Howe, *Theory of Vortex Sound* (Cambridge University Press, Cambridge, 2003).
[18]F. Obermeier, "On a new representation of aeroacoustic source distribution. II. Two-dimensional model flows," Acustica **42**, 62–71 (1979).
[19]R. C. K. Leung and R. M. C. So, "Noise generation of blade-vortex resonance," J. Sound Vib. **245**, 217–237 (2001).
[20]S. K. Tang and C. K. Lau, "Vortex sound in the presence of a wedge with inhomogeneous surface flow impedance," J. Sound Vib. **281**, 1077–1091 (2005).
[21]D. G. Crighton, "Basic principles of aerodynamic noise generation," Prog. Aerosp. Sci. **16**, 31–96 (1975).
[22]H. R. Vallentine, *Applied Hydrodynamics* (Butterworth, London, 1969).
[23]P. J. T. Filippi, O. Lagarrigue, and P.-O. Mattei, "Perturbation method for sound radiation by a vibrating plate in a light fluid: Comparison with the exact solution," J. Sound Vib. **177**, 259–275 (1994).
[24]J. D. A. Walker, C. N. Zhikharev, and T. J. Delph, "Induced oscillations of a finite plate," J. Guid. Control Dyn. **20**, 1172–1180 (1997).
[25]P. M. Morse and K. U. Ingard, *Theoretical Acoustics* (McGraw-Hill, New York, 1968).
[26]I. S. Gradshteyn, I. M. Ryzhik, and A. Jeffrey, *Tables of Integrals, Series and Products* (Academic, Boston, 1994).
[27]L. Huang, Y. S. Choy, R. M. C. So, and T. L. Chong, "Experimental study of sound propagation in a flexible duct," J. Acoust. Soc. Am. **108**, 624–631 (2000).
[28]A. Frendi, L. Maestrello, and A. Bayliss, "Coupling between plate vibration and acoustic radiation," J. Sound Vib. **177**, 207–226 (1994).
[29]S. K. Tang, "Effects of porous boundaries on the dynamics of an inviscid vortex filament," Q. J. Mech. Appl. Math. **54**, 65–84 (2001).
[30]S. K. Tang and N. W. M. Ko, "Sound generation by interaction of two inviscid two-dimensional vortices," J. Acoust. Soc. Am. **102**, 1463–1473 (1997).
[31]M. S. Howe, "Mechanism of sound generation by low Mach number flow over a wall cavity," J. Sound Vib. **273**, 103–123 (2004).
[32]L. E. Kinsler, A. R. Frey, A. B. Coppens, and J. V. Sanders, *Fundamentals of Acoustics*, 4th ed. (Wiley, New York, 2000).
[33]J. E. Ffowcs Williams and D. L. Hawkings, "Shallow water wave generation by unsteady flow," J. Fluid Mech. **31**, 779–788 (1968).

Acoustic analysis of a computer cooling fan

Lixi Huang[a] and Jian Wang
Department of Mechanical Engineering, The Hong Kong Polytechnic University, Kowloon, Hong Kong

(Received 29 September 2004; revised 3 July 2005; accepted 5 July 2005)

Noise radiated by a typical computer cooling fan is investigated experimentally and analyzed within the framework of rotor-stator interaction noise using point source formulation. The fan is 9 cm in rotor casing diameter and its design speed is 3000 rpm. The main noise sources are found and quantified; they are (a) the inlet flow distortion caused by the sharp edges of the incomplete bellmouth due to the square outer framework, (b) the interaction of rotor blades with the downstream struts which hold the motor, and (c) the extra size of one strut carrying electrical wiring. Methods are devised to extract the rotor-strut interaction noise, (b) and (c), radiated by the component forces of drag and thrust at the leading and higher order spinning pressure modes, as well as the leading edge noise generated by (a). By re-installing the original fan rotor in various casings, the noises radiated by the three features of the original fan are separated, and details of the directivity are interpreted. It is found that the inlet flow distortion and the unequal set of four struts make about the same amount of noise. Their corrections show a potential of around 10-dB sound power reduction. © *2005 Acoustical Society of America.* [DOI: 10.1121/1.2010367]

PACS number(s): 43.28.Ra, 43.50.Yw, 43.50.Gf [SFW] Pages: 2190–2200

I. INTRODUCTION

The problem of computer cooling fan noise is receiving increasing attention due to the continuous development of CPU power, and the trend of slim packaging. It may be said that, despite many unanswered questions, there is an abundance of general aeroacoustic knowledge regarding fan noise. However, to the best of the authors' knowledge, a detailed, systematic study on each component of the noise mechanism present in a specific type of cooling fan is yet to be reported. Using a typical computer cooling fan sample, the present experimental study aims to identify and quantify the exact source mechanisms in the fan assembly, and the directivity of the radiated sound. The emphasis is on the tonal noise but some preliminary results for the broadband noise are also reported. It is hoped that both qualitative and quantitative knowledge derived from such an experimental study would pave the way for further theoretical, computational modeling and, ultimately, design of a quiet computer cooling fan. In the remainder of this section, the relevant literature is briefly reviewed, followed by the description of the features of the sample fan.

In terms of general aeroacoustics research for rotating machines, Gutin (1936) was among the first to quantify the propeller noise caused by the rotation of steady loading, later called Gutin noise. Lighthill's (1952) acoustic analogy provided a formal platform of investigating aerodynamic sound, which was soon extended by Curle (1955) to include the effect of solid boundaries by replacing it with distributed dipoles while the explicit effect of acoustic scattering was neglected. It was not until Ffowcs Williams and Hawkings (1969) formally extended Lighthill's acoustic analogy by using the generalized functions to account for the effect of all solid boundaries in arbitrary motion. A comprehensive theoretical treatment of flow-induced noise was given by Blake (1986) and also by Howe (1998) in his recent monograph. The use of the so-called Ffowcs Williams and Hawkings' equation became a dominant feature from late 1970s in the field of acoustics for rotary machines. Generally speaking, there are three types of sources in a turbomachine or any machine with moving blades, monopole from the blade motion, dipole from fluctuating forces on blades, and quadrupole emanating from the core of turbulent jets. The sound power scales as the fourth, sixth, and eighth power of the representative flow speed for the three types of elementary sources, respectively. The tightly coupled monopoles on a rigid moving blade is effectively dipoles, and they are called thickness noise. For low speed applications, both thickness noise and the dipole related to the steady-flow loading, or Gutin noise, are unimportant when compared with the dipole arising from the unsteady flow features. Bulk turbulence noise is negligible, but its interaction with solid surface is not. As pointed out by Ffowcs Williams and Hall (1970), the scattering of convected boundary layer waves by a terminating edge of a half plane could generate powerful sound which scales as the fifth power of flow speed, and is known as the trailing edge noise. However, this reduction of the power exponent comes about as the solid surface provides a baffling effect. Such effect is absent and the power dependency goes back to the sixth when the blade is compact compared with the wavelength (Blake 1986). This is the case for the computer cooling fan being investigated here.

Focusing on the specific mechanisms at work in turbomachines and axial flow fans at subsonic speeds, it is found that the dominant noise source is often the unsteady pressure fluctuation arising from the interaction between rotating blades and stationary blades, or between rotating blades and steady but nonuniform incoming flow. Fitzgerald and Lauchle (1984) gave a comprehensive list of possible physi-

[a]Author to whom correspondence should be addressed; electronic mail: lixi.huang@polyu.edu.hk

cal mechanisms of noise radiation present in a subsonic fan. They have also made efforts to eradicate each one of these mechanisms and achieved success in noise reduction. Typical noise spectrum consists of a broadband superimposed by pure tones, mostly at the fundamental and the harmonics of the blade passing frequency (BPF). The dominant source for the pure tones is the interaction events. One of the most significant contributions was made by Tyler and Sofrin (1962), who revealed the important role played by the numbers of rotor and stator blades. The phenomenon of modal cut-off was discovered and shown to be consistent with duct acoustics. A contrast was made by Lowson (1970) between this cut-off behavior for the ducted fan and the acoustics of the unducted fan. He demonstrated that the radiation of the mismatched spinning modes cannot be cut off altogether but is rather reduced in acoustic efficiency. Kaji and Okazaki (1970), using the wake models of Kemp and Sears (1953, 1955), modeled the rotor-stator interaction with careful doublet arrays while preserving the blade effects on sound propagation in the duct and imposing Kutta conditions on trailing edges. Numerous studies on interaction noise were also conducted in the helicopter community. In most such studies, the focus has always been on the interaction between rotor and stator, and most noise is generated from the downstream part, namely the downstream stator or the rotor behind an inlet guidevane. The effect of a downstream stator on the upstream rotor is normally negligible in comparison. However, such effect seems to be the dominant noise source in the present study where the downstream stator are circular cylinders used to support a motor. The reason why the radiation from the downstream cylinders, or struts, is small compared with that from the upstream rotor blades is that the blades are so profiled to generate lifting forces while cylinders are not. The nature of the rotor-strut coupling in this case is mainly potential flow interaction, and the specific problem treated here represents a gap in literature.

In terms of the broadband noise, Sharland (1964) was one of the first to quantify it for axial-flow compressors. Three possible sources of broadband noise were described: the unsteady blade surface pressure arising from the turbulent boundary layer, lift fluctuation from the unsteady vorticity shed from the trailing edge, and random inlet flow fluctuations. The relationship between the first two mechanisms and the trailing edge noise described later by Ffowcs Williams and Hall (1970) was not clear at that point. Mugridge and Morfey (1972) also attempted to give an order of magnitude estimate for the broadband noise. A comprehensive review of earlier research was given by Morfey (1973). Longhouse (1976) categorized the tonal noise as rotational noise, and the broadband noise as nonrotational noise. His work demonstrated that design features good for reducing broadband noise could contradict those for discrete tones. Dominant nonrotational noise mechanisms are the vortex shedding from the blades and the tip clearance vortex interacting with the blade inner span or a neighboring blade. The former was studied in detail in Longhouse (1977) by using a rotor with very small tip clearance. It was shown that the vortex shedding can be suppressed by a leading edge serration which served as a vortex generator, and the resulting turbulent flow was less coherent and less efficient in radiating sound than the trailing edge scattering of instability waves in the laminar boundary layers in transition (Tollmien Schlichting, or TS, waves). It was proposed that Tollmien Schlichting waves are convected and magnified as they approach the trailing edge. The scattered sound initiates a disturbance back to the upstream TS waves forming a feedback loop. The noise radiated peaks at frequencies for which the distance between the transitional point and the trailing edge is an integer number of the TS wavelengths. The frequency of such discrete tone, as well as relative silence at other frequencies, has no bearing on the rotational speed of the fan, but a rigorous theory is yet to be formulated for such tones. Tip clearance noise is also regarded as the main mechanism of broadband noise by many researchers. Longhouse (1978) and Fukano *et al.* (1986) reported significant reductions of broadband noise when the clearance was minimized or a shroud was used. More recently, similar achievement was made by Quinlan and Bent (1998) albeit with some increase in low-frequency tonal noise. Apart from the two mechanisms described above, inlet flow turbulence is also regarded as a major contributor to the broadband noise although it serves as a tonal source at the same time when the turbulence scale is larger than the blade spacing. In most machines, the inlet flow passes through a contraction due to the bellmouth, and eddies present in the turbulent incoming flow get elongated as they squeeze through the tip clearance region of blades (Majumdar and Peake, 1998). Trunzo *et al.* (1981) investigated the sound radiated by the repeated chopping of such elongated eddies by the rotating blades. The tonal noise radiated was shown to be suppressed significantly when the eddies were broken up by an inlet grid at the expense of increased broadband noise. Majumdar and Peake (1998) treated the problem analytically in the context of quantifying the effect of ingested atmospheric turbulence during a ground based test of aeroengines.

Given such a variety of possible noise mechanisms, it would be of great practical interest to identify the dominant factor for a specific application. The current study focuses on the methodology of identifying such dominant noise source. For a computer cooling fan, much of the noise could be radiated by the interaction of the swirling exit flow and the cramped environment a cooling fan finds itself in. Nevertheless, the search for a quiet cooling fan has to start with a smooth flow condition when the fan operates in free space. A photograph of a typical cooling fan is shown in Fig. 1. As shown in the front view of Fig. 1(a), the fan has a rotor of seven well-profiled blades. The inner diameter of the casing is 9 cm, and the rotational speed is 3000 rpm when it is connected to a dc power supply of 12 V at a current of 0.4 A and operated at the free delivery condition. The inlet flow velocity is measured to be 5.1 m/s. The inlet has a bellmouth design with a straight slope of 5 mm in length, but the bellmouth is made incomplete by the square casing frame. The rotor is driven by a downstream motor attached to the casing via four struts, which are shown in the back view in Fig. 1(b). The lower left strut is larger than the rest in order to carry electric wiring. Figure 1(c) shows the top view (plane $x-y$) of the measurement plane with four symmetrical mi-

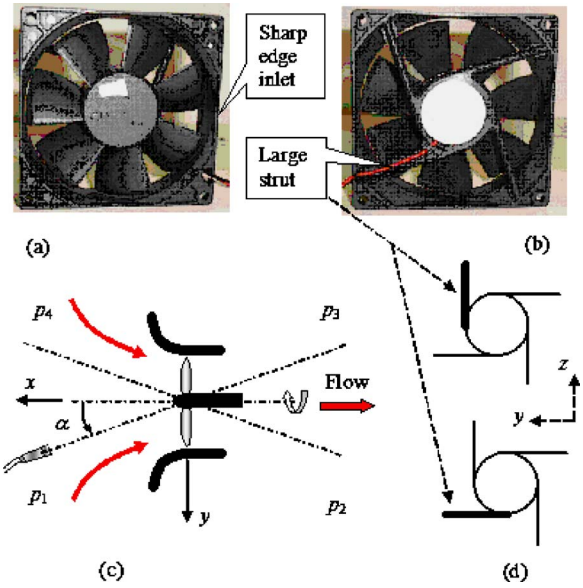

FIG. 1. (Color online) Experimental configuration. (a) and (b) The front and back views of the sample fan. (c) The top view of the horizontal measurement plane $(x-y)$ for the baseline rig. (d) The back view of two orientations of the large strut.

crophone positions, and the definition of α in the lower-left quadrant. The fan is always held in the upright position, perpendicular to the horizontal plane. It is shown in the following that the orientation of the large strut matters to the noise measured on the horizontal plane. Figure 1(b) shows the "natural" position of the large strut, while two more positions are illustrated in Fig. 1(d) in the back views of the fan (plane $y-z$). The upper drawing is for a vertical large strut and the lower one a horizontal large strut.

For such a cooling fan, Gutin noise is unlikely to be of any practical importance as the tip Mach number is of the order of 0.05. The main noise sources are the fluctuating pressures on rotor blades and struts caused by the unsteady flows. The mechanism for the broadband noise is left to future studies. For discrete tones, the following sources compete for dominance:

(1) The inlet flow distortion caused by the incomplete bellmouth frame.
(2) The tip leakage flow and the possible flow separation from both rotor blades and cylindrical struts.
(3) Scattering of unsteady boundary layer flow by the rotor trailing edges.
(4) The interaction between the rotor and downstream struts.

In terms of temporal characteristics, mechanisms 2 and 3 are not related to the fan rotation while mechanisms 1 and 4 are. If the fan rotation is accurately timed by an optical tachometer signal, the sound pressure measured by a microphone can be synchronously averaged to find the part of noise that is phase locked to the fan rotation. This part of noise is called rotary noise in the present study. The remaining sound is loosely defined as random noise although the source mechanism may have a periodical behavior. Having said that, there is a possibility of time-domain modulation by the fan rotation for mechanisms 2 and 3. For example, if the tip clearance is not uniform, fan rotation would be featured in the tip leakage flow. Due to such consideration, a baseline model is built to quantify mechanisms 2 and 3. The baseline model is illustrated in the central part of Fig. 1(c) and its construction is described as follows. First, the casing and struts of a sample fan are removed. The assembly of fan motor and rotor is mounted on a cylindrical rod extending downstream from the back of the motor. The rod has the same diameter as the motor base, and it does not cause any interference to the exit flow of the fan. A new casing with a proper bellmouth is fabricated and is held separately to form a uniform tip clearance for the rotor. Mechanisms 1 and 4 are thus excluded in the baseline model. It is shown that the baseline noise mainly features a broadband spectrum with few visible peaks. Following the same methodology, mechanisms 1 and 4 are also investigated separately by building models each being exclusive to one mechanism.

II. METHODOLOGY AND THE BASELINE CASE

In the following, the method of time-base-stretched synchronous averaging is described first, followed by the separation of the rotor-strut interaction event into drag and thrust forces by utilizing the acoustic directivity characteristics. The result of the baseline model is then analyzed together with the basic aerodynamic considerations.

A. Time-base-stretched synchronous averaging

The experiment is conducted in an anechoic chamber with a cut-off frequency of 80 Hz. The fundamental frequency of the fan noise is 350 Hz, so the laboratory environment simulates a free space. The instrumentation consists of the following components. A tachometer (B&K type M003) is used together with a stroboscope (B&K type 4913). The sample fan is installed vertically on a tripod, while a $\frac{1}{2}$ in. microphone (BSWA-MA201) is fixed at a distance of $r_0 = 0.5$ m from the fan center at a height level with the center. The tripod can be manually rotated around its vertical axis to map out the noise directivity, while the optical sensor is fixed relative to the mobile part of the tripod. The latitudinal angle α is defined in Fig. 1(c) as the angle between the rotational axis and the source-observer vector drawn from the fan center to the microphone. The microphone is calibrated by B&K's calibrator type 4231 before being used, and its signal is bandpass (200 Hz–10 kHz) filtered, and amplified by B&K's Nexus Conditioning Amplifier type 2693. The resultant signal is called the "raw" signal of sound before being further processed. The signals from the tachometer and the microphone are sampled by the National Instruments' 16-bit PCMCIA card (type SHC68-68-EP) at a rate of $F_s = 16$ kHz. Note that the required upper limit of the bandpass filter should be 8 kHz instead of 10 kHz for this choice of F_s. However, the filter design does not allow this. It is felt that this mismatch should not affect the results as trial measurement using a higher sampling rate did not show much fan noise beyond about 5 kHz. Typical traces of the two channels are shown in Fig. 2. The tachometer signal is shown in the upper part of Fig. 2(a), while the raw signal of sound is shown in the middle. The period of each rotational cycle is

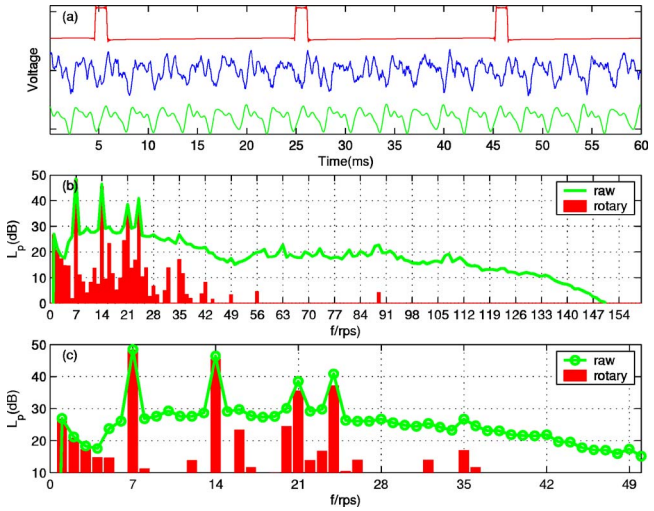

FIG. 2. (Color online) Time-base-stretched synchronous averaging. (a) The two channels of raw signals, together with the synchronously averaged wave form on the bottom part. (b) Comparison of the spectra for the raw signal with that of the averaged signal (bar chart). (c) Zoom-in view of (b).

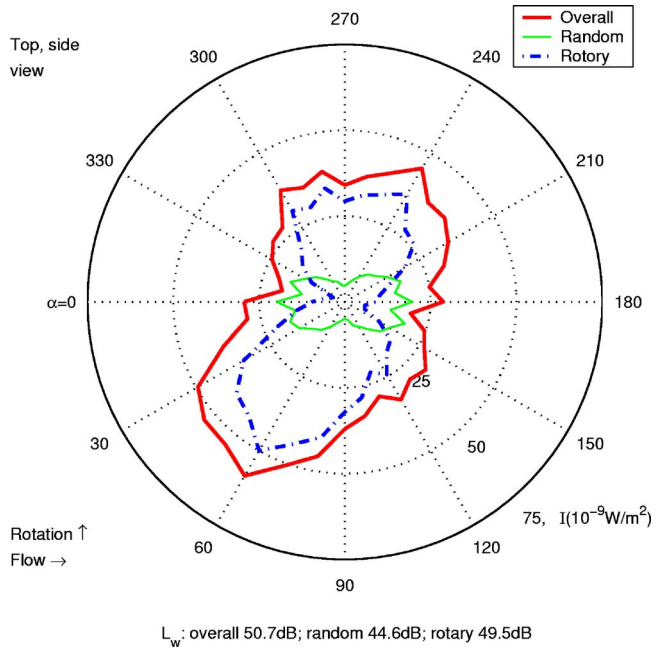

FIG. 3. (Color online) The directivity of sound intensity of all frequencies on the horizontal plane for the original fan when the large strut takes the natural position shown in Fig. 1(b).

found by the adjacent tachometer pulses. When the fan runs at a nominal speed of 3000 rpm, or 50 revolutions per second (rps), the standard deviation of instantaneous speed (rpm) is about 10–20, and the difference between two consecutive cycles is about 4 data points maximum in a total of N samples calculated as $N=\mathrm{Fs/rps}=16000/50=320$. The signals between the two rising edges of the pulses are treated as one complete rotational cycle and, during the post-data-acquisition analysis, the raw wave forms are digitally resampled to 320 points. The resampled cycles are overlapped for averaging. The result is a time-base-stretched synchronous average, and is called "rotary sound." A sample is shown in the lower part of Fig. 2(a). The duration for each data acquisition session at one measurement position is 10 s, which gives about 500 cycles for averaging. The spectrum of the raw signal is shown in Fig. 2(b) as a thick solid line, while that of the rotary sound is plotted as a bar chart. The data length for FFT is exactly one cycle, or 320, so the frequency resolution shown in the abscissa is the rotational speed (rps), and the frequency index of $B=7$ represents the BPF. Since signals below 200 Hz, or 4 rps, are contaminated by the microphone self-noise and are filtered out, the attention is focused on the noise at BPF and above. For the particular spectra shown in Fig. 2(b), the broadband noise ranges from a sound pressure level, L_p (re 20 μPa), of about 30 dB around the first BPF down to about 20 dB around the sixth BPF, while the background noise in the anechoic chamber is found to be below 10 dB based on the current spectral analysis setting. Three peaks at the frequencies of (1–3) BPF are found above the broadband level, and Fig. 2(c) provides a zoom-in view of Fig. 2(b). The difference between the raw noise power and the rotary sound power is defined as the random noise power although the underlying mechanisms might well be periodic in nature. This noise is also described as nonrotary noise in this paper. Note that the method of synchronous averaging is not new, e.g., Washburn and Lauchle (1988), but the use of the time-base stretching appears to be less common. If the results are re-processed without using the time-base stretching, random noise energy is found to be increased while the rotary noise is decreased due to the change of rotational speed for this particular fan. In other words, the energy of rotary noise "leaks" into that of random noise. For the original fan noise measured, shown later in Fig. 3, postprocessing using the time-base stretching gives an increase of 1.5 dB in rotary sound power compared with that without time-base stretching.

For a measurement point of spherical coordinates of (r_0, α, θ), where α is defined in Fig. 1(c) and θ is the rotational angle of the fan rotor, sound intensity is calculated as $I(\alpha,\theta)=p_{\mathrm{rms}}^2/\rho_0 c_0$ and the distribution of $I(\alpha)$ for a given θ is plotted as a two-dimensional directivity, $\theta=0$, π being located on the horizontal plane. The sound power is found by the integration of $I(\alpha,\theta)$ over the spherical surface of radius $r_0=0.5$ m, which is given in the following together with the definition of the sound power level, L_w,

$$W = r_0^2 \int_0^{2\pi} d\theta \int_0^{\pi} I \sin\alpha \, d\alpha,$$
$$L_w = 10 \log_{10}(W/W_{\mathrm{ref}}), \quad W_{\mathrm{ref}} = 10^{-12}\ \mathrm{W}. \tag{1}$$

Assuming that I does not change with θ, the sound power can be found by a measurement over the horizontal plane only. It is shown later that this assumption is invalid for sound generated by the interaction between the rotor and one downstream strut. In such case, more sound is generated on the horizontal plane than on other planes when the strut is placed upright, as shown in the upper drawing of Fig. 1(d). The actual sound power is between such overestimation and the underestimation produced by the horizontal plane integration when the strut is placed horizontally. Figure 3 shows the horizontal directivity of the original fan when the large strut is placed in its natural oblique position shown in Fig.

1(b). Comparisons are made later with measurements for the vertical and horizontal positions for the large strut. The solid line in Fig. 3 is the intensity of the raw noise, while the dot-dash line is the rotary sound. The difference is the so-called random noise, and is shown by a thin solid line. Note that all three sound intensity curves plotted are the result of summation over all frequencies. In this particular case, the rotary sound dominates, and the values of the sound power levels, L_w, are given in the lower horizontal label of the figure. The asymmetrical sound intensity pattern is a result of interference of sounds radiated by different unsteady force components. A brief account is given in the following for the point source formulation due to Lowson (1970) leading to the decomposition of sound pressure.

B. Point source formulation

As shown in our recent analysis (Huang, 2003), the physical size of the source can be compact, but whether the source can be described by a point source depends on the circumferential distribution of unsteady forces. Unsteady lift on airfoil, L, is decomposed into two components: thrust, T, in the direction of the rotational axis and drag, D, in the circumferential direction against the rotation. The amplitude of the far field acoustic pressure due to the rotor is found to be (Lowson, 1970)

$$C_{n=mB}^{(\text{rotor})} = \frac{im\omega B^2 S}{2\pi c_0 r_0} \sum_{k=-\infty}^{\infty} i^{-\nu} e^{-i\nu\Theta} \left(T_\lambda \cos\alpha - \frac{\nu}{nM} D_\lambda \right) \times J_\nu(nM \sin\alpha), \quad \nu = n - \lambda, \quad n = mB, \quad \lambda = kS, \tag{2}$$

where T_λ and D_λ are the λth Fourier series amplitudes of the thrust and drag forces, respectively, B and S are the rotor blade and strut numbers, respectively, $M=\omega r_s/c_0$ is the rotational Mach number of the point source at radius r_s, $n=mB$ is the frequency index and m is the index of BPF harmonics, $\lambda=kS$ is the index of the source frequency, k is an arbitrary integer, and Θ is the angular position of the first strut relative to the observer on the horizontal plane of $\theta=0$. The parameter of Θ is only useful when discussing the cross-modal coupling for the single-strut noise later on. The same formula holds for sound radiated by the strut except that the source frequency λ is replaced by n since the stationary source can only radiate sound at its own frequency. Parameter ν is the index of spinning pressure mode, and it very much controls the amount of sound power radiation. The argument of the Bessel function is small, $|nM \sin\alpha| \ll 1$, so the sound radiation is only efficient when the order of the function, ν, is very low, such as $\nu=n-\lambda=0, \pm 1, \pm 2$, for which the Bessel functions can be approximated as follows:

$$J_0(z) \approx 1 - \frac{z^2}{2}, \quad J_1(z) \approx \frac{z}{2}, \quad J_{|\nu|>1} \approx \frac{1}{\sqrt{2\pi\nu}} \left(\frac{ze}{2\nu} \right)^\nu. \tag{3}$$

The thrust force does not change direction, so it radiates noise most efficiently at the frequency of the source itself, for which $\nu=0$. For the drag force, $\nu=\pm 1$ is the most efficient mode since the force component changes its direction once per cycle even when its magnitude is constant. It is shown in (Huang, 2003) that the effect of angular noncompactness is small for the leading order modes of radiation, $\nu=0, \pm 1$. For these modes, the instantaneous pressure integration for lift L suffices for the purpose of acoustic calculation.

The sound power at frequency index n is essentially the spherical integration of $|c_n|^2$ where c_n given in Eq. (2) is the sum of all possible radiation modes. Apart from the quadratic terms from each mode/force, there are two types of coupling terms. It can be shown easily that the integration of the drag-thrust coupling, a cross-component coupling, vanishes, but the coupling between different modes of the same type of force component, a cross-modal coupling, does produce sound powers. Ignoring such cross-modal coupling for the moment and assuming the independence of sound intensity on θ, the sound power is found as

$$\begin{aligned} W_n &= \int_0^\pi \frac{|c_n|^2}{2\rho_0 c_0} 2\pi r_0^2 \sin\alpha \, d\alpha \\ &= \frac{(nBS\omega)^2}{4\pi\rho_0 c_0^3} \left[\left(\frac{2}{3} T_{\lambda,\nu=0}^2 + 0.336 D_{\lambda,\nu=\pm 1}^2 \right) \right. \\ &\quad \left. + (1.07 T_{\lambda,\nu=\pm 1}^2 + 1.16 D_{\lambda,\nu=\pm 2}^2) \left(\frac{nM}{4} \right)^2 \right. \end{aligned} \tag{4}$$

in which the leading order and higher order modes are separated into two groups inside the square brackets. For the leading orders, the source radius r_s does not matter as M is absent in the sound power expression. For the less efficient, higher order modes, a factor of M^2 appears. Notice that a factor of ω^2 is also present in front of the square bracket at the right-hand side of Eq. (4). If the force magnitudes scale with the kinetic energy of flow, $T_\lambda, D_\lambda \propto M^2$, the sound power radiated is proportional to M^6 for the leading orders of ν and M^8 for the next higher orders. For $M=O(0.05)$, the higher order modes are typically 20 dB below those of the leading order modes. Assuming that there is cross-modal coupling between $\nu=0$ and $\nu=\pm 1$ for the thrust noise, the result would be a sound power which depends on M^7. The same applies to the drag noise for $\nu=\pm 1$ and $\nu=\pm 2$. However, such coupling can only occur when there is only one strut, $S=1$, as S determines the gap between the possible modal indices ν. This topic is revisited in the following when $S=1$ is investigated experimentally.

The contribution from different force components can be separated by the horizontal directivity of the radiated sound. According to Eq. (2), the leading order thrust noise is for $\nu=0$, and the sound pressure is proportional to $\cos\alpha$. This is denoted as T0 noise. The leading order drag noise has $\nu=\pm 1$ and the sound pressure features $\sin\alpha$. This is denoted as D1. The immediate higher order thrust noise is from $\nu=\pm 1$, and its directivity features $\cos\alpha \sin\alpha$. This is denoted as T1. The drag noise of $\nu=\pm 2$ has a directivity of $\sin^2\alpha$, and is denoted by D2. The patterns of the four noise components are shown in the upper row of Fig. 4, while some possible combinations of different modes are shown in the lower row

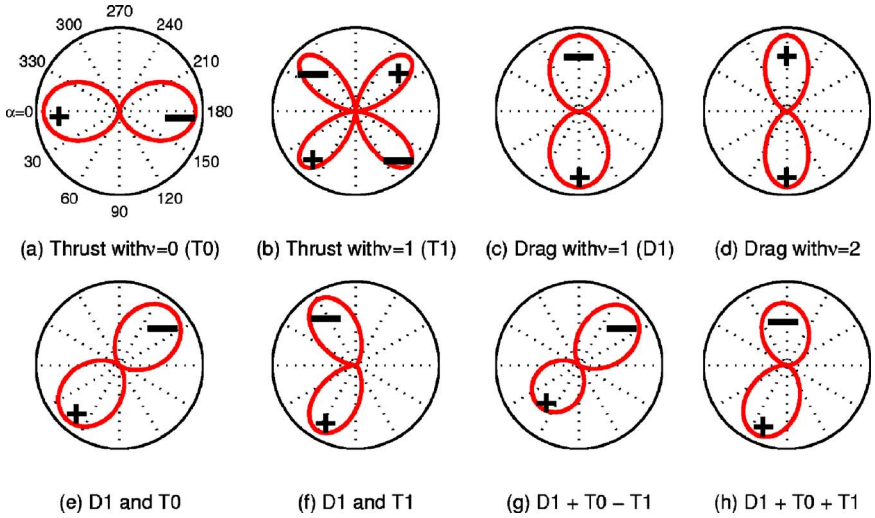

FIG. 4. (Color online) Sound intensity directivity for the most important modes (a)–(d), and a few interesting combinations. The sound pressure expressions are (a) $\cos\alpha$, (b) $\cos\alpha\sin\alpha$, (c) $\sin\alpha$, (d) $\sin^2\alpha$, (e) $\sin\alpha+\cos\alpha$, (f) $\sin\alpha+\cos\alpha\sin\alpha$, (g) $\sin\alpha+\cos\alpha-0.2\cos\alpha\sin\alpha$, (h) $\sin\alpha+0.2\cos\alpha+0.3\cos\alpha\sin\alpha$.

of Fig. 4. The labels in the main lobes denote phase angles, and the modal combinations are indicated in the coordinate labels.

Comparing phase distributions of thrust noise with drag noise, it is obvious that each has a unique feature of its own. Thrust noise changes sign across the rotational plane, while the drag noise does not. This difference, and the difference of sign between the first two quadrants of α and the other quadrants, allow the following separation of noise radiated by different force and modal components (indicated by the subscripts);

$$p_{T0}=\frac{p_1-p_2-p_3+p_4}{4},\quad p_{T1}=\frac{p_1-p_2+p_3-p_4}{4},$$
$$p_{D1}=\frac{p_1+p_2-p_3-p_4}{4},\quad p_{D2}=\frac{p_1+p_2+p_3+p_4}{4}, \tag{5}$$

where p_1,p_2,p_3,p_4 represent the synchronously averaged sound pressures measured at the four symmetrical positions in the four quadrants shown in Fig. 1(c). Note that the first quadrant is taken as the lower-left position where α ranges from 0° to 90° as shown in Fig. 1(c). This time domain separation requires a correct phase angle relation between measurements of sound at different times using the same microphone. This is achieved by fixing the tachometer relative to the fan.

The combination of different component noises can produce a huge variety of patterns, for which four are shown in the lower row of Fig. 4. Figure 4(e) shows the combination of the leading thrust noise, T0, with the leading drag noise, D0, which produces an oblique major axis of noise in the lower-left and upper-right quadrants. The directivity is nevertheless symmetrical with respect to this major axis. Figure 4(f) shows the combination of the leading mode drag noise (D1) with the higher order mode thrust noise (T1), and the result is a forward leaning directivity, which contrasts with the typical propeller noise, the latter being mainly beamed towards the rear. Figure 4(g) shows the combination of D1, D0, and T1, and the result is a pattern with a larger lobe in the upper-right quadrant than in the lower-left. Figure 4(h) shows another three-component noise with different phase angle relation, and the result is in fact the pattern found for the original fan when the large strut is in its natural position, cf. Figs. 1(b) and 3.

Shown in Fig. 5 are the experimental results for the four component noises, cf. Eq. (5), for which the overall directivity is shown in Fig. 3. In the plot of Fig. 5, the radius is the rms value of sound pressure and the scale is amplified for smaller noise components for visual clarity. The pattern shown in the lower-right quadrant is the leading mode drag noise, D1, for which the sound power level is $L_{wD1}=49.1$ dB. The lower-left quadrant shows the leading mode thrust noise, T0, which has $L_{wT0}=39.8$ dB, and the plot is magnified by five times, as indicated by the label of T0(×5). The upper-left quadrant is the higher order thrust noise with $L_{wT1}=30.2$ dB, while the upper-right quadrant is the radial noise for the mode of $\nu=0$ with $L_{wR0}=30.3$ dB. Radial noise is caused by the radial component of the unsteady forces on blades and struts, and it is excluded from

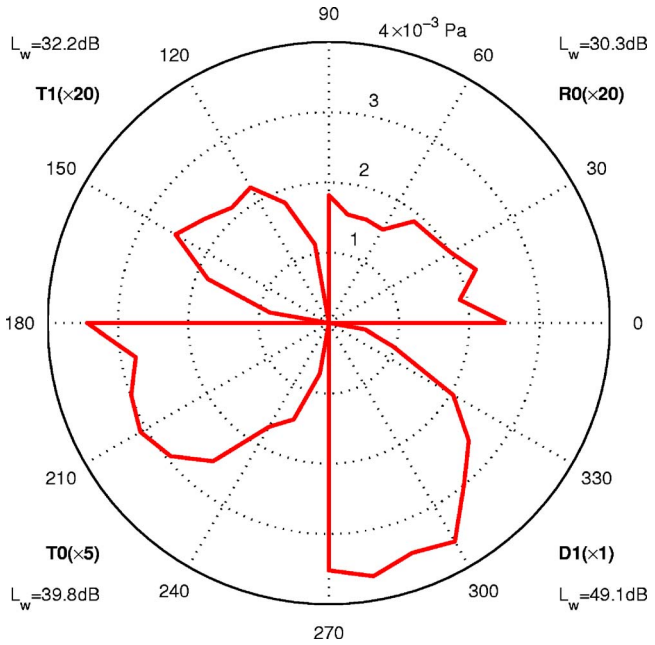

FIG. 5. (Color online) Source decomposition for the BPF noise measured for the original fan. The directivity is shown for the rms sound pressure.

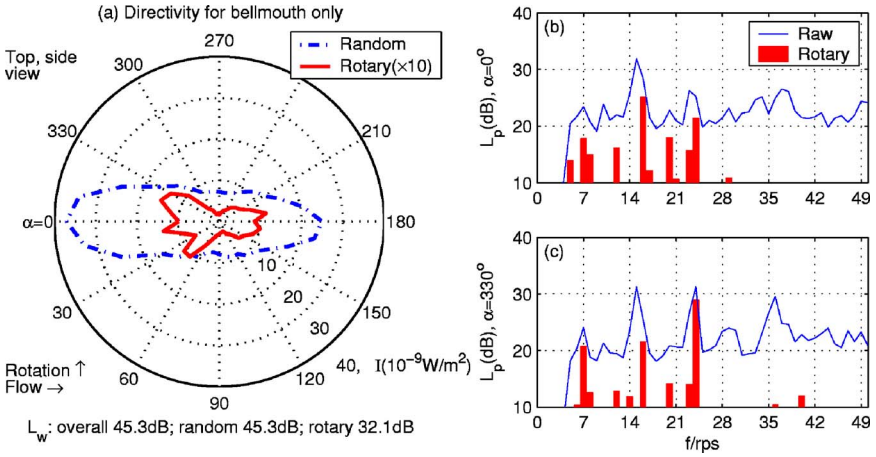

FIG. 6. (Color online) Noise from the baseline rig. (a) The directivity of random noise and rotary noise (amplified by 10 times). (b) and (c) The spectra at $\alpha=0$, 330°, respectively.

Eq. (2) as it is small for most cases considered in the current study. Radial noise could be important when the rotor or stator blades lean significantly. Details of the radial noise formulation can be found in (Huang, 2003).

C. The baseline noise

The noise made by the rotor blades alone can be investigated by a baseline case defined as the rotor blades operating in an all-clear condition with bellmouth inlet and no exit strut, the motor being supported by a solid cylinder extending downstream from the back of the motor, as illustrated in Fig. 1(c). The horizontal directivity and spectra at two latitudinal positions are shown in Fig. 6. Figure 6(a) shows that nonrotary sound (dash-dot line) dominates and the main noise axis is the rotational axis. The rotary part (solid line) is so small that it has to be amplified by ten times in terms of intensity to be seen clearly in the same plot. Noise spectra at the inlet position of $\alpha=0$ and another position of $\alpha=330°$ are shown in Figs. 6(b) and 6(c), respectively. The solid lines are for the raw noise, and the bar charts are for the synchronously averaged rotary noise. If an unsteady flow process, such as vortex shedding, is rotation-independent, it should feature in the raw noise spectrum but not much in the synchronously averaged. On the other hand, if the process is modulated by or synchronized with the rotation, the two spectra would coincide. The bar charts in Figs. 6(b) and 6(c) show that many peaks appear but most are below the broadband level of around 20 dB. Three clusters of peaks centered around 7, 16, and 24 rps are prominent. The noise at BPF =7 rps is likely to be caused by the presence of inevitable nonuniform inlet flow condition which produces regular lift fluctuations on the rotor blades. The frequencies of the peaks at 16, 24 rps, and indeed most lower peaks, are multiples of 4 rps, which may be caused by the motor vibration since there are four coils inside the brushless motor. This conjecture needs to be further validated by careful vibration measurement and analysis, which is not conducted in the present study as the peaks appearing on BPFs are dominant.

III. SINGLE- AND FOUR-STRUT RIGS

Noise radiated by the interaction between rotor blades and downstream struts can be better understood when struts are added to the baseline case in which a large inlet bellmouth is used. The following analyzes two cases, one with a single strut, denoted as S1, and another with four equal struts, denoted as S4. The case of a single strut is rather special, and its interpretation would go a long way to validating many aspects of the point source formulation presented in Sec. II. On the other hand, the case of four struts is very close to a fan of correct aeroacoustic design.

A. Single-strut interaction noise

The measured noise for S1 design is shown in Fig. 7. The strut is placed at the vertical position, as shown by the

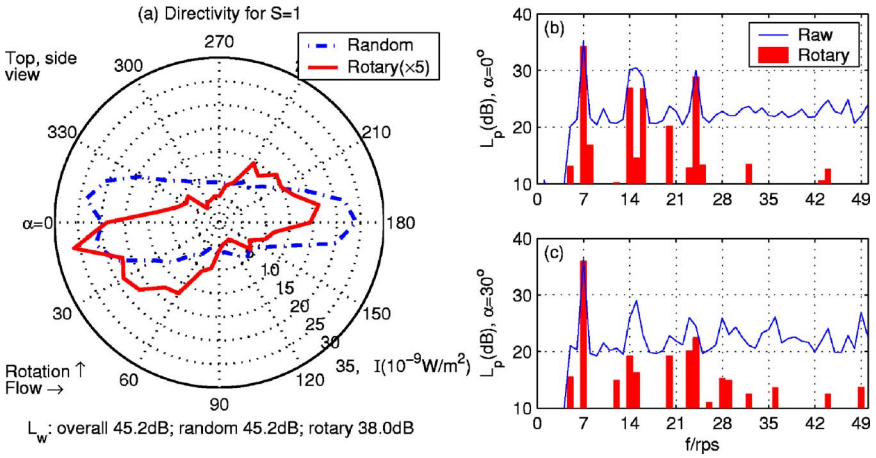

FIG. 7. (Color online) Noise radiated by a rotor interacting with a single downstream strut. (a) The directivity of rotary and non-rotary noise, (b) and (c) spectra at two important locations.

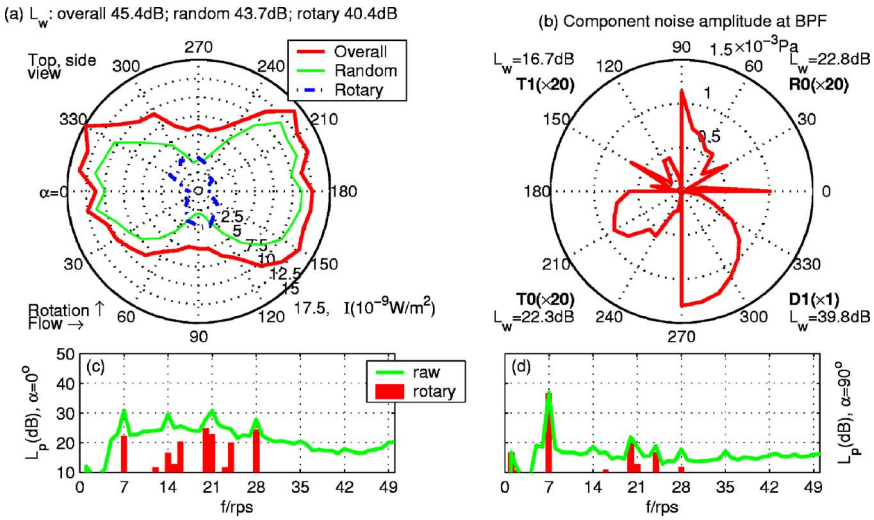

FIG. 8. (Color online) Noise radiated by a fan with four equal struts. (a) The directivity on the horizontal plane, (b) the decomposed modal directivity, (c) and (d) spectra at $\alpha=0$ and $\alpha=\pi/2$, respectively.

large strut in the upper drawing of Fig. 1(d), and the radiated noise is loudest on the horizontal plane. The rotary noise has a power of 38.0 dB, while the overall is 45.2 dB. In Fig. 7(a), the intensity for the rotary noise (solid line) is magnified by five times for visual clarity. A major rotary noise axis is found along the direction of $\alpha=30°$, and the pattern is clearly similar to Fig. 4(e) where the leading order drag noise (D1) interferes with the leading order thrust noise (T0). Figure 7(b) shows the spectrum at the inlet position of $\alpha=0$ with prominent peaks appearing at 16 and 24 rps. The highest peak is, however, at the BPF. The peak is highest for the major axis of $\alpha=30°$ in Fig. 7(c).

Recalling Eq. (2), the BPF noise radiated by the rotor with $S=1$ is found as a combination of the leading thrust mode of $\nu=0$, and the two leading modes of drag noise, $\nu=\pm1$. The combined leading order noise is

$$c_{n=B}^{(\text{rotor})}=\frac{i\omega B^2}{2\pi c_0 r_0}\left[T_7\cos\alpha+\frac{i}{2}\sin\alpha(D_6e^{-i\Theta}-D_8e^{i\Theta})\right]. \tag{6}$$

When the strut is placed on the horizontal plane, where the observer is, $\Theta=0$, and the drag noise is made by the drag magnitude of (D_6-D_8). When the strut is placed vertically, $\Theta=\pi/2$, and the source magnitude is (D_6+D_8). When considering the noise radiated by the pressure fluctuation on the strut, the source frequency has to be changed from $\lambda=kS$ to $n=B$, hence D_6 and D_8 are changed to D_7. Therefore the result for drag noise with a horizontal strut features $D_7-D_7=0$. Focusing again on the rotor noise, the major noise axis of 30° found from Fig. 7(a) means that the magnitude for thrust noise is higher than that of the drag noise. In other words, $|T_7|>|D_6+D_8|/2$. In fact, the decomposed thrust noise has $L_{wT0}=34.7$ dB, while the drag noise has $L_{w\text{D1}}=33.6$ dB.

B. Four-strut fan noise

The noise radiated by the interaction between the rotor blades and struts of equal size is investigated by using a large bellmouth at the inlet, which has been shown to be almost free from rotary noise at BPF and its harmonics. For four struts interacting with the rotor of seven blades, the theory of Eq. (2) predicts that the minimum order for the first BPF is $\nu=B-2S=-1$, implying that the drag force is the leading order noise source, while the thrust force is a higher order noise source. The measured noise radiation is shown in Fig. 8 for four struts skewed in the direction shown in Fig. 1(b) but with equal strut size. As shown by the dash-dot line of Fig. 8(a), the major rotary noise axis is along the direction of $\alpha=100°$. It is also found that most rotary noise concentrates on the BPF. The rotary noise is decomposed according to Eq. (5) and the component directivities for BPF are shown in Fig. 8(b). The leading order drag noise (D1) is shown in the lower-right quadrant and it has a power of $L_{w\text{D1}}=39.8$ dB, while the thrust noise of the first order (T1) is shown in the upper-left quadrant and it has $L_{w\text{T1}}=16.7$ dB. The comparison of these two components conforms to earlier analysis which predicts a 20 dB difference between the leading order noise and the higher order noise. However, Eq. (5) does not predict any thrust noise radiation by the mode of $\nu=0$. The actual thrust noise of this mode, shown in the lower-left quadrant of Fig. 8(b), is found to be 22.3 dB, and its combination with the drag noise determines the tilted pattern of the overall rotary intensity shown in Fig. 8(a). Such unpredicted thrust noise component could arise from the fact that not all rotor-strut interactions are wholly deterministic and identical aerodynamically, nor is the fan geometry free from any defect. Figures 8(c) and 8(d) show the spectra at the inlet and rotational plane positions. Self-noise at 16, 20, and 24 rps is also present, but the BPF noise dominates the spectrum on the rotational plane.

IV. NOISE FROM THE REAL FAN

As shown in Fig. 1, the real fan has three features which may be chiefly responsible for the noise generation: (a) the interaction between the rotor blades and the four downstream struts, which is represented above by the S4 rig, (b) incomplete bellmouth causing inlet flow distortion, and (c) the extra size of one strut which carries cables. Mechanisms (b) and (c) are now investigated separately. Mechanism (b) is represented by a configuration in which there is no strut and the motor is held by a cylindrical rod as in the baseline case,

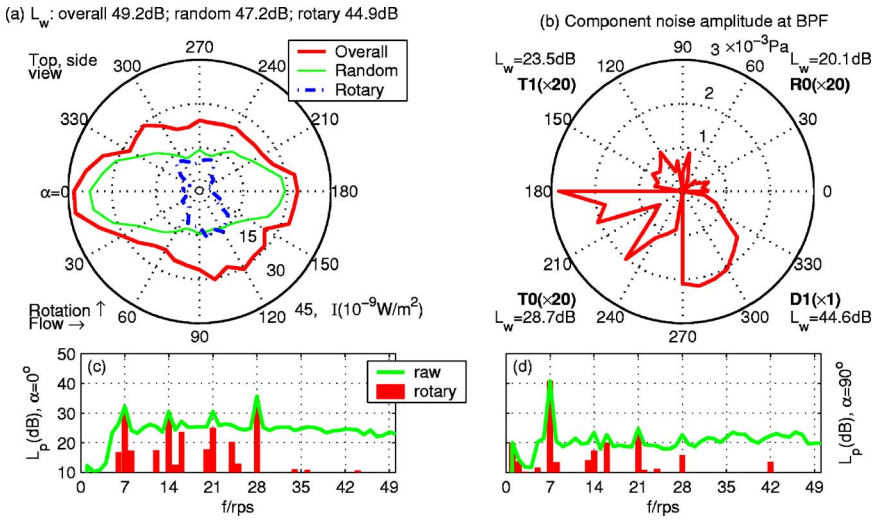

FIG. 9. (Color online) Noise radiated by the inlet flow distortion. (a) The directivity, (b) the decomposition of the radiated sound, (c) and (d) two typical spectra.

while mechanism (c) is simulated by adding an extra piece to one of the struts in the S4 rig, where a large bellmouth is installed.

A. Inlet frame noise

The presence of the four sharp edges in the incomplete inlet bellmouth is equivalent to having four upstream guide-vanes, and the formulation of Eq. (2) applies with $S=4$. The rig is denoted as IS4, and the measured noise is shown in Fig. 9, which is now compared with that from the four equal struts rig (S4) shown in Fig. 8. Figure 9(a) shows that the rotary noise of IS4 has a very similar pattern to that of S4. But the pattern of nonrotary noise is slightly different, so is the total noise. Both rotary and nonrotary noises are louder than that of S4, meaning that the inlet flow distortion is, in this case, more powerful in generating noise. This is perhaps due to the fact that the flow near the blade leading edge is more sensitive to perturbations than that near the trailing edge. The difference in the total rotary sound power is 4.5 dB while that in D1 noise power is 4.8 dB. In terms of component noise decomposition, the leading order drag noise (D1) is similar in pattern, which is shown in the lower-right quadrant of Fig. 9(b). The leading order thrust noise (T0), shown in the lower-left quadrant of Fig. 9(b), is not as regular as that in S4. Note that T0 noise derives from factors not apparent in the regular structure, and may be regarded as an indication of aerodynamic uncertainty. The difference of the T0 noise power is $28.7-22.3=6.4$ dB, which is higher than the difference in the D1 noise. This contrast also implies a more volatile aerodynamic feature for the inlet flow distortion.

B. Large strut size and orientation

Having measured the sound radiation from a single strut, cf. Fig. 7, the effect of extra strut size is investigated directly by making one of the struts in the S4 rig as large as the cable-carrying strut in the real fan sample, which is 6 mm wide in the circumferential direction and 4 mm thick in the axial direction. The large inlet bellmouth is still installed, and the large strut is held upright, as shown in the upper drawing of Fig. 1(d), while the directivity is measured on the horizontal plane. The rig is denoted as S13, implying one large strut with 3 regular struts. The measured noise is shown in Fig. 10. The nonrotary noise is shown as a thin solid line in Fig. 10(a). The power is 45.2 dB, and it has a tilted pattern very similar to the rotary noise shown as the dash-dot line. For the rotary noise, the difference between the S13 rig and the S4 rig represents the extra noise caused by the extra strut size. The extra noise consists of the extra drag noise, which is shown in the S1 study to be proportional to $|D_6+D_8|$, and the extra thrust noise proportional to T_7. As shown in the title of Fig. 10(b) for the BPF, the T0 noise is 39.7 dB, which is much higher than the 22.3 dB found in the S4 rig, the latter being unaccounted for from structural view point. Since the S4 noise is drag-dominated, this 39.7 dB should all be attributed to the so-called extra noise, and it is almost the same as the 39.8 dB drag noise found in the S4 rig. The leading mode drag noise, D1, for the present rig has 44.3 dB, which is much higher than the 39.8 dB from the S4 rig, but slightly lower than the 44.6 dB from the IS4 rig. A level-ground interference is expected for the D1 noise in the S4 rig and the extra drag noise.

The extra noise from the large strut is also responsible for the tilting of the major noise axis from around the rotational plane to about $\alpha=50°$. But the more striking feature of the rotary noise, shown as the dot-dash line in Fig. 10(a), is the difference between the lobes in the lower-left and upper-right quadrants, which is similar to that shown in Fig. 4(g). The best fit for the rotary BPF component is found by the following sound pressure expression:

$$p = \underbrace{4.628 \sin\alpha}_{D1} + \underbrace{3.858 \cos\alpha}_{T0} - \underbrace{0.965 \cos\alpha \sin\alpha}_{T1} (\times 10^{-3}\ \text{Pa}). \quad (7)$$

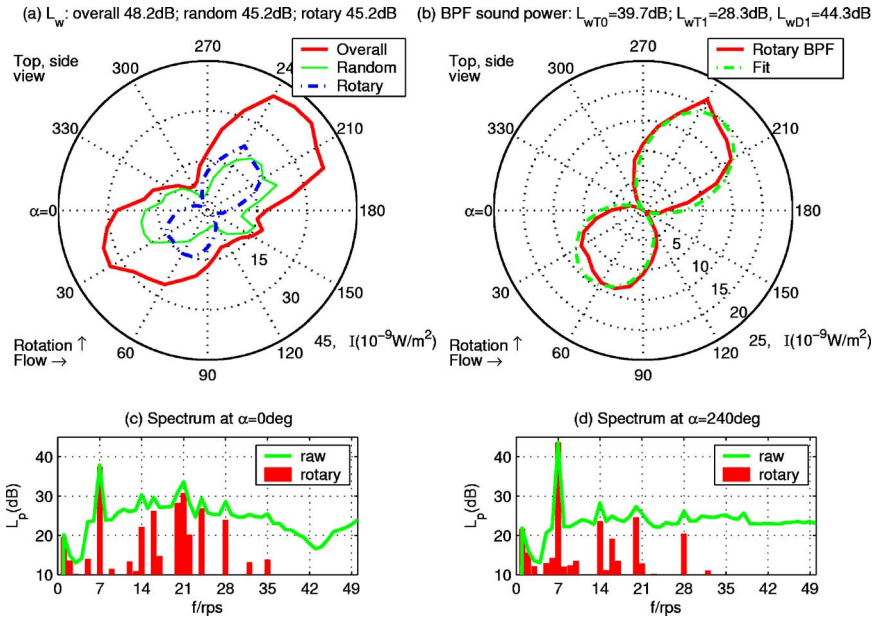

FIG. 10. (Color online) Noise radiated by the interaction of rotor blades with four struts in which one is larger than the others. (a) The overall directivity when the large strut is in the natural oblique position, (b) the effect of large strut orientation, (c) and (d) two typical spectra for (a).

The D1 noise is apparently derived from the drag noise from the interaction between the rotor and the four struts, the T0 noise is from the effect of the large strut, i.e., the extra noise, and the higher order thrust noise (T1) is derived from either the S4 noise or the extra noise. The sound power for T1 is 28.3 dB, which is much higher than the corresponding 16.7 dB from the S4 rig shown in Fig. 8(b). Again, the effect of the extra strut size is found to be dominant. The spectra on the major noise axis of α=0°, 240° are shown in Figs. 10(c) and 10(d), respectively, and both show a clear dominance of the BPF component.

The effect of the large strut orientation is investigated for the original fan by turning the direction of the large strut from the vertical to horizontal direction, cf. Fig. 1(d), while the directivity is measured on the fixed horizontal plane. The comparison of the rotary noise directivities is shown in Fig. 11. Recalling from Eq. (1) that the sound power integration should be carried out over the whole spherical surface, i.e., over both α and θ, it is pointed out that the current α-integration on the horizontal plane represents an approximation based on the assumption that the noise distribution on planes parallel to the rotational planes is uniform. The approximate sound power level obtained from the measurement when the large strut is in the vertical position, shown as the dash-dot line of Fig. 10(b), is certainly higher than that in the horizontal position, shown as the solid line, and the difference of rotary noise is 2.9 dB. In order to make a proper evaluation of the true sound power, measurement should be made over the whole sphere in this case instead of over the central horizontal plane. The approximate result obtained for the data taken at the oblique, or natural, position of the large strut, shown in Fig. 1(b), is probably closer to the true value than those from the two extreme orientations of the large strut shown in Fig. 1(d). The rotary noise for such natural position of the large strut is 49.5 dB. Comparing this rotary noise of 49.5 dB with the 40.1 dB from the rig with four equal struts (S4), one can see a potential of 9.4 dB noise reduction. The rotary sound powers made by the inlet flow distortion (IS4) and the unequal set of four struts (S13) are both around 45 dB. In order to eradicate both, the inlet bellmouth and the large strut size have to be corrected. Extra structural considerations are needed to achieve this. Although such corrections may mean extra manufacturing cost, the large noise reduction may well compensate for this.

V. CONCLUSIONS

Experimental analysis of a typical computer cooling fan noise has revealed many interesting features, and the understanding derived is expected to be helpful in devising quiet fans. For the sample fan used in the current study, a 9.4 dB noise abatement potential is identified. However, the focus of this study is on the directivity analysis of the radiated sound. The following conclusions are made.

(1) Time-base stretched synchronous averaging has been used to extract the part of noise which is phase locked to

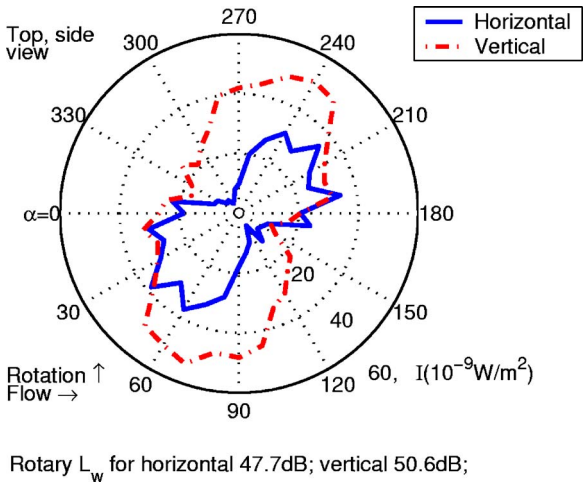

FIG. 11. (Color online) Effect of the large strut orientation for the original fan.

the fan rotation. The nonrotary part of the noise is found to be broadband in nature. However, within the rotary noise, there are peaks which do not coincide with the blade passing frequency and its harmonics. These peaks form a series of harmonics of 4 rps, which is probably caused by the vibration of the motor which has four coils. The contribution from such peaks to the total noise is small except in directions where the rotary sound is weak.

(2) The rotary noise radiated by the interaction between the rotor blades and the downstream struts or the upstream flow distortions can be understood within the framework of point source formulation of Lowson (1970). The effect of noncompactness is considered to be small. This is not purely because of the small size of the fan, but due to the fact that the leading radiation modes have an index of spinning pressure modes close to $\nu=0$. Noise from $|\nu|>1$ can be neglected, such as the Gutin noise.

(3) Based on the phase angle characteristics, the measured sound can be decomposed into four parts as a combination of two unsteady forces, drag and thrust, and two modes, $\nu=0$ and $|\nu|=1$. Results from such decomposition analysis have been interpreted within the framework of point source formulation.

(4) For the sample fan of seven rotor blades and four struts, the drag noise of $\nu=-1$ dominates. Structural decomposition shows that the noise radiated by the inlet flow distortion is equivalent to having four upstream guidevane and the noise radiated is found to be even higher than that from the interaction between the rotor blades and the four equal struts when a proper inlet bellmouth is installed.

(5) The large strut is found to cause a lot of extra noise. The extra noise has features similar to the noise radiated by the rotor interacting with one single strut, a configuration which is also studied. The extra noise is divided into extra thrust noise derived from the Bth Fourier component of the thrust fluctuation, T_B, and extra drag noise, which features a combination of two spectral components in different combinations, $D_{B-1}\pm D_{B+1}$, depending on the orientation of the strut. For the sample fan, the extra drag noise couples with the four-strut drag noise, and the result is a 5 dB increase. Trimming of the large strut size can reduce noise by 5 dB, so does the smoothing out of the inlet bellmouth.

(6) Combinations of component noise give a variety of total rotary noise patterns. All measured directivity can be interpreted as a sum of leading order drag and thrust noises, plus a higher order thrust noise which plays a subtle role in altering the outlook of the acoustic directivity.

ACKNOWLEDGMENTS

The project is funded by a Competitive Earmarked Research Grant from the Hong Kong SAR Government (Account B-Q439, RGC S/N: PolyU 5162/01E). J.W. also wishes to acknowledge the support of the PhD research studentship from the Hong Kong Polytechnic University.

Blake, W. K. (**1986**). *Mechanics of Flow-induced Sound and Vibration* (Academic, New York).

Curle, N. (**1955**). "The influences of solid boundaries upon aerodynamic sound," Proc. R. Soc. London, Ser. A **A231**, 505–514.

Ffowcs Williams, J. E., and Hall, L. H. (**1970**). "Aerodynamic sound generation by turbulent flow in the vicinity of a scattering half-plane," J. Fluid Mech. **40**, 657–670.

Ffowcs Williams, J. E., and Hawkings, D. L. (**1969**). "Sound generation by turbulence and by surfaces in arbitrary motion," Philos. Trans. R. Soc. London, Ser. A **A264**, 321–342.

Fitzgerald, J. M., and Lauchle, G. C. (**1984**). "Reduction of discrete frequency noise in small, subsonic axial-flow fans," J. Acoust. Soc. Am. **76**, 158–166.

Fukano, T., Takamatsu, Y., and Kodama, Y. (**1986**). "The effects of tip clearance on the noise of low pressure axial and mixed flow fans," J. Sound Vib. **105**, 291–308.

Gutin, L. (**1936**). "On the sound field of a rotating propeller," NACA TM 1195 (translated in 1948 from *Zhurnal tekhnicheskoĭ fiziki* **6**, 899–909).

Howe, M. S. (**1998**). "Trailing edge noise at low Mach numbers," J. Sound Vib. **225**, 211–238.

Huang, L. (**2003**). "Characterizing computer cooling fan noise," J. Acoust. Soc. Am. **114**, 3189–3200.

Kaji, S., and Okazaki, T. (**1970**). "Generation of sound by rotor-stator interaction," J. Sound Vib. **13**, 281–307.

Kemp, N. H., and Sears, W. R. (**1953**). "Aerodynamic interference between moving blade rows," J. Aeronaut. Sci. **20**, 583–598.

Kemp, N. H., and Sears, W. R. (**1955**). "Unsteady forces due to viscous wakes in turbomachines," J. Aeronaut. Sci. **22**, 478–483.

Lighthill, M. J. (**1952**). "On sound generated aerodynamically: I. General theory," Proc. R. Soc. London, Ser. A **A211**, 564–587.

Longhouse, R. E. (**1976**). "Noise mechanism separation and design considerations for low tip-speed, axial-flow fans," J. Sound Vib. **48**, 461–474.

Longhouse, R. E. (**1977**). "Vortex shedding noise of low tip speed, axial flow fans," J. Sound Vib. **53**, 25–46.

Longhouse, R. E. (**1978**). "Control of tip-vortex noise of axial flow fans by rotating shrouds," J. Sound Vib. **58**, 201–214.

Lowson, M. V. (**1970**). "Theoretical analysis of compressor noise," J. Acoust. Soc. Am. **47**, 371–385.

Majumdar, S. J., and Peake, N. (**1998**). "Noise generation by the interaction between ingested turbulence and a rotating fan," J. Fluid Mech. **359**, 181–216.

Morfey, C. L. (**1973**). "Rotating blades and aerodynamic sound," J. Sound Vib. **28**, 587–617.

Mugridge, B. D., and Morfey, C. L. (**1972**). "Sources of noise in axial flow fans," J. Acoust. Soc. Am. **51**, 1411–1426.

Quinlan, Q. A., and Bent, P. H. (**1998**). "High frequency noise generation in small axial flow fans," J. Sound Vib. **218**, 177–204.

Sharland, I. J. (**1964**). "Sources of noise in axial flow fans," J. Sound Vib. **1**, 302–322.

Trunzo, R., Lakshminarayana, B., and Thompson, D. E. (**1981**). "Nature of inlet turbulence and strut flow disturbances and their effect on turbomachinery rotor noise," J. Sound Vib. **76**, 233–259.

Tyler, J. M., and Sofrin, T. G. (**1962**). "Axial flow compressor noise studies," Soc. Autom. Eng. Trans. **70**, 309-332.

Washburn, K. B., and Lauchle, G. C. (**1988**). "Inlet flow conditions and tonal sound radiation from a subsonic fan," Noise Control Eng. J. **31**, 101–110.

Sonic-boom generated sound field under a wavy air–water interface: Analyses for incident *N* waves

H. K. Cheng
Department of Aerospace and Mechanical Engineering, University of Southern California, Los Angeles, California and HKC Research, Los Angeles, California 90089-1191

C. J. Lee
Applied Sciences Laboratories, Inc., Hacienda Height, California 91745

J. R. Edwards
Acquisition Civil Engineering, AF Space & Missile System Center, Los Angeles, California 90245

(Received 29 June 2004; revised 20 July 2005; accepted 21 July 2005)

Examples of the sonic-boom generated sound field under a wavy air–water interface based on the theory of Cheng and Lee [J. Fluid Mech. **514**, 281–312 (2004)] are studied to determine the surface-wave influence on sound-pressure level, frequency range, and waveform characteristics of disturbances generated by an aerial sonic-boom *N* wave over water. The study substantiates that, owing to their much lower attenuation rate, the time-dependent disturbances produced by the interaction with a surface-wave train can be comparable to, and overwhelm the flat-ocean (Sawyers) wave field at large as well as moderate depth levels, depending on Mach number, surface-wave length and-height, and the alignment angle of surface waves with respect to the flight track. Computed examples, assuming a 300 ft.(91 m) signature length and a 2 psf(96 Pa) peak sea-level overpressure, show that, under a mildly wavy ocean, sonic-boom disturbances at sound-pressure level of 100–126 dB (*re*: 1 μPa) can reach a depth of 750–1500 ft.(229–457 m), where the dominant waveform evolves into an infrasound wave packet of frequency 5–40 Hz. © *2005 Acoustical Society of America.* [DOI: 10.1121/1.2035590]

PACS number(s): 43.30.Nb, 43.30.Lz, 43.28.Mw, 43.30.Hw [AIT] Pages: 2201–2209

I. INTRODUCTION

Studies of sonic-boom impact on sea life and ocean environment have been concerned mostly with the sound level and frequency range that may cause physical harm to marine animals,[1,2] and do not address problems underlying the audibility issue which may affect undersea animals in the short and long term.[3,4]

A model used widely for predicting sonic-boom generated sound field underwater was proposed by Sawyers[5] for a flat ocean of infinite depth.[6,7] The more recent work of Ref. 8 revealed, however, that the interaction of surface waves with a sonic boom, even though a secondary effect near the water surface, can produce signals at depths that are distinctly different from, and more intense than, those given by the flat-ocean model. This paper will present a study of the wavy-surface influence based on the theory established in Refs. 8 and 9. To be presented are computational results in parameter domains of relevance to studies of the audibility issue; also explained are the analysis procedures and interpretations not adequately documented in published works. The investigation will focus on examples with incident *N* waves, for which analytical solution details are available[8,9] to aid assessing computation accuracy and understanding. A concurrent laboratory study has been carried out by Fincham and Maxworthy;[10] several major features that support the theoretical predictions were identified therein. Related studies on other sonic-boom wave forms, more general surface-wave trains, as well as problems of sediment-wave excitation, are documented in Refs. 11–13.

II. PRELIMINARY REMARKS

A. Assumptions and the interaction model

The theory adopts a model of two adjoining inviscid, compressible media; across the interface the pressure and normal velocity (in the absence of surface tension) are continuous. The water-to-air density ratio ρ_w/ρ_A is assumed to be much higher than unity; this high density ratio is expected to cause the water to behave very stiffly in response to incident sonic-boom waves. The water-to-air sound speed ratio is taken to be $a_W/a_A=4.53$ under standard conditions.

Of interest is the overpressure representing the change from the *local* equilibrium value $p+\rho gz$ which increases with depth z. The velocity U is assumed to be constant and much greater in magnitude than the surface-wave speed c. Following Ref. 8, all length and time scales are to be made dimensionless with the signature length L' and L'/U, respectively. As shown in Fig. 1, the surface-wave depression is denoted by $Z_w(x,y,t)$, which will be assumed to be a sinusoidal surface-wave train; the maximum of Z_w is given by the product $\delta\lambda$. The problem formulation and analyses were made in a Cartesian reference frame moving at a horizontal velocity U with respect to the media at rest. For underwater waveform studies in the time domain, the results will be transferred to the rest frame. The theory assumes a small

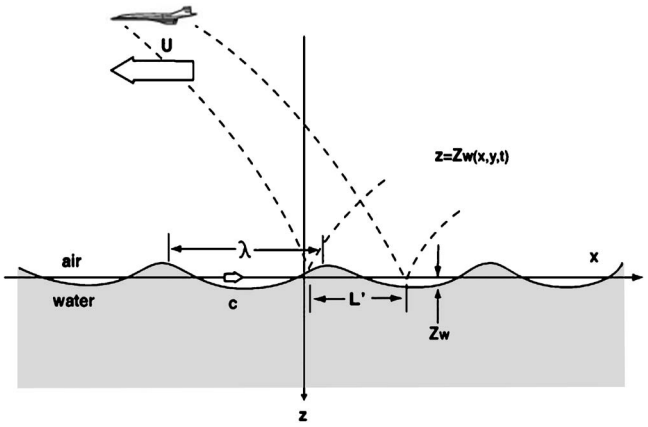

FIG. 1. Schematic representation of the interaction problem.

overpressure ratio $\varepsilon=(p-p_A)/p_A$ together with a small surface slope δ; thus, the interaction effect near the surface is of the order $\varepsilon\delta$ pertaining formally to a second-order influence.

As in Ref. 8, this paper addresses problems in which the underwater wave fields remain subsonic, corresponding to a requirement on the Mach number above the water $M_A \equiv U/a_A < 4.53$ under standard conditions. Another requirement is that the aspect ratio of the sonic-boom impact zone be very high, corresponding to L' being very small compared to the lateral extent of the impact zone (cf. Fig. 2). In the following and most other applications, the sea surface-wave speed c will be considered low and negligible in comparison with wave-field speed U; this amounts to treating the surface shape as being *frozen*.

B. Remarks on earlier laboratory and field measurements

Earlier theory and experiment on sound transmission from air to water by Medwin, Helbig, and Hagy[14] indicted that a rough water surface can augment the transmitted sound level; but, unlike the present work, the study dealt with the ray-acoustics domain for extremely short wavelength, inapplicable to the problem of interest here. Intrieri and Malcolm[15] conducted measurements in a still (nonwavy) water tank inside a ballistic range and found agreement with Sawyers' prediction, as expected. In Deshanais and Chapman's work,[16] underwater acoustic signals were recorded and identified to be disturbances generated by an overlying Concorde airliner at Mach 2.02. Reasonably good agreement with Sawyers' solution in waveform recording was found on the upper part of the array. Noticeable is a lee-wave-like, ringing feature that departs from Sawyers' prediction, which was attributed to results from excited sediment-interfacing waves. Similar ringing features may nevertheless be identified also among results from the wavy-surface interaction in Sec. IV below.

Undersea measurement of sonic-boom noise field was made by Sohn *et al.*[17] While the waveform data agreed reasonably well with Sawyers' prediction at depth down to 30–40 m, discrepancies among data appear in most records at depth greater than 50 m where no evidence of the wavy-surface influence could be found. A possible reason for the absence of the effect in question is believed to be the flight-Mach numbers (less than 1.26) being too low and beyond the principal domain of the wavy-surface influence, to be discussed more specifically in Sec. III B.

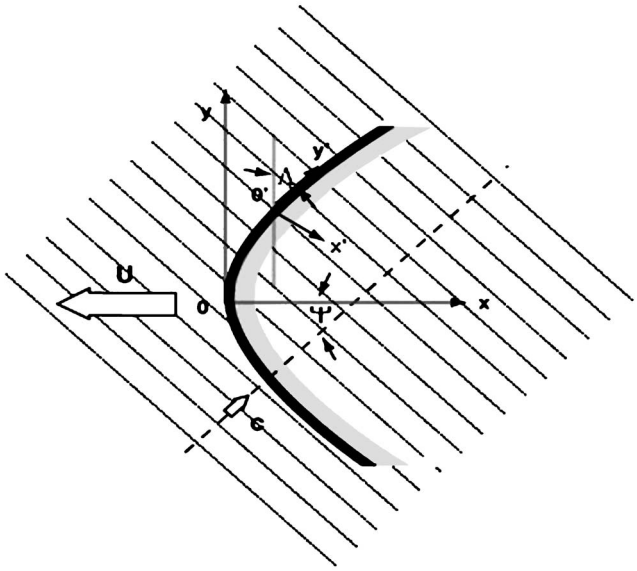

FIG. 2. Sketch of sonic-boom impact zone in the horizontal reference plane, with surface-wave crests represented by thin solid lines and two sets of coordinates (x,y) and (x',y').

III. FORMULATION, SOLUTION AND INTERPRETATION

A. Solving the direct and inverse problems, synchronous mode

The interaction effect of interest can be analyzed as a nonlinear, secondary correction to the linear, flat-ocean (Sawyers) theory. The problem is further simplified by the high water-to-air density ratio, which allows omission of surface-shape change in determining the interaction effect. The solution for the perturbation velocity potential above water may then be obtained in a manner similar to solving a *direct* problem in aerodynamics,[18] in which the (time-dependent) boundary conditions for the normal velocity on the interface can be taken as being known *a priori*. With the sea-level overpressure determined, the (subsonic) wave field underwater may then be solved as an *inverse* problem in aerodynamics[18] in that the boundary value of the overpressure is completely known. In formulating the perturbation problem, the boundary conditions at the air–water interface will be transferred analytically to the reference surface $z=0$.

In the moving frame, the acoustic wave field is composed of two parts, the time-independent primary part and a *time-dependent*, secondary part. The primary wave field is that of a steady, 2D supersonic flow ($M_A>1$) in the air (above water) and a steady 2D subsonic flow ($M_W<1$) under water (for $M_A>a_W/a_A=4.53$). With the assumption of a sinusoidal surface wave train, the interface equation in the moving frame may be expressed in terms of local Cartesians as

$$z = Z_w = \delta\Lambda \exp . i[k_1' x' + k_2' y' - \Omega t], \tag{3.1a}$$

with

$$k_1' = k\cos(\Lambda + \psi), \tag{3.1b}$$

$$k_2' = k\sin(\Lambda + \psi), \tag{3.1c}$$

$$\Omega = ck + Uk_1 = k(U\cos\Psi + c), \tag{3.1d}$$

where Λ is the local centerline swept angle of the surface-impact zone (cf. Fig. 2). As indicated in Fig. 2, ψ is the angle that the (horizontal) surface wave-number vector made with the flight track, and may be referred to as the "angle of nonalignment."

The contribution from the surface-wave speed c to the normalized frequency Ω is generally small in comparison with U and will be omitted in the present study. [The ocean surface may thus be regarded as being "frozen," as noted earlier] The assumptions of the sinusoidal surface-wave form (3.1a) and (3.1b), together with the high aspect ratio of the surface-impact zone, allow one to treat the secondary acoustic field in a form as *synchronous* with Z_w.The primary and the principal secondary components of the perturbation pressure p' may be expressed as

$$p' = p_1(x', \bar{z}; y') + \delta\hat{p}_2(x', \bar{z}) e^{ik_2' y'} e^{-i\Omega t}, \tag{3.2}$$

where $\bar{z} = |1 - M_n^2|^{1/2} z$, and the dependence of $\hat{p}$ on the parameter set $(M_A, \Lambda, k_1', k_2')$ or (M_A, k, Λ, ψ) is expected. A similar expression can be written for the perturbation velocity potential ϕ'.

B. Wave fields above and under water

1. Supersonic wave field above water

To the leading order, the perturbation velocity potential above water can be described by a form familiar from the Prandtl–Glauert theory in aerodynamics,[18] and satisfies the impermeability condition on the flat interface at $z=0$. As indicated, the secondary, time-dependent wave field above water may be analyzed as a direct problem with the known shape of a time-dependent "wavy wall," since the water behaves stiffly to sonic-boom disturbances. The synchronous part of the solution of (3.2) is governed by a hyperbolic partial differential equation (PDE) derived from the linear acoustics equation for a moving frame, together with the transferred boundary condition at $z=0$. The result, obtained by the method of Laplace transform, is reproduced in the Appendix of Ref. 8.

2. Subsonic wave field underwater: Two parametric domains

The leading approximation to the subsonic underwater field is simply the solution to the half-plane, Dirichlet problem for Sawyers' flat-ocean model. The PDE governing the underwater synchronous fields are formally the same as above water, except that the normal Mach number entering the normalized equation and its parameters is less than 1 owing to the requirement $M_A < 4.53$ mentioned earlier.

The $\hat{p}_2(x', \bar{z})$ of the time-dependent, 3D overpressure field of (3.2) is obtained after solving an *inversed, half-plane* problem in the Fourier domain (after transformation with respect to x').

The result satisfying the radiation condition at large z can be expressed in the form of a system of *plane*, *oblique waves* originated from the distributed source $\hat{A}(\xi)$

$$p_2' = \frac{\delta}{\sqrt{2\pi}} \int_{-\infty}^{\infty} \hat{A}(\xi) \exp i[-\xi x' + k_2' y' + \sqrt{\bar{K}(\xi)}\bar{z} - \Omega t] d\xi, \tag{3.3a}$$

with chosen branch cut for the square-root of $\bar{K}(\xi)$ according to the rule

$$\sqrt{\bar{K}(\xi)} = |\bar{K}(\xi)|^{1/2} \quad \text{if } \bar{K}(\xi) < 0, \tag{3.3b}$$

$$\sqrt{\bar{K}(\xi)} = i|\bar{K}(\xi)|^{1/2} \quad \text{if } \bar{K}(\xi) > 0, \tag{3.3c}$$

where, with $\beta_n^2 = 1 - M_n^2$,

$$\bar{K}(\xi) = [\beta_n^2 \xi^2 - P_w \xi - Q_w]/\beta_n^2. \tag{3.3d}$$

The constants P_n and Q_n in above can be simplified after dropping "c" from (3.1d) as

$$P_n = 2kM_n^2 \cos(\Lambda + \psi), \tag{3.3e}$$

$$Q_n = k^2[M_n^2 - (1 + M_n^2)\sin(\Lambda + \psi)]. \tag{3.3f}$$

The $\hat{A}(\xi)$ in (3.3a) is seen to be simply the Fourier transform of the boundary value for $\hat{p}_2$ at $z=0$; the latter is produced by the interaction as the incident sonic-boom waves sweep over the wavy surface.

As (3.3b) and (3.3c) indicate, the ξ range supports sinusoidal, downward, propagating waves where the function $\bar{K}(\xi)$ is negative, and furnishes components strongly attenuated in the z direction where $\bar{K}(\xi)$ is positive. The latter correspond to the horizontally propagating (plane) waves and contribute little to the deeper part of the wave field. The lower and upper limits of the ξ range where $\bar{K}(\xi) < 0$ can be analytically determined in terms of Λ, ψ, and M_A. The (M_A, ψ, Λ) domain where the (real) interval $[\xi_1, \xi_2]$ for $\bar{K} < 0$ exists will be called the *down-propagating wave domain*, while the domain in which this interval on the real ξ axis completely vanishes will be called the *evanescent or horizontally propagating wave domain*. The boundaries delimiting these two domains are reproduced in Fig. 3 from Ref. 8 for four flight Mach numbers based on the speed of sound above water: $M_A = 1.05$, 1.50, 2.00, and 3.00, determined by the requirements

$$M_w^2 \cos^2\Lambda - \sin^2(\Lambda + \psi) = 0, \tag{3.4a}$$

$$\Lambda = 90^\circ - \sin^{-1}\left(\frac{1}{M_A}\right), \tag{3.4b}$$

where the subscripts "w" and "A" refer to underwater and above water, respectively.

The down-propagating wave domain for each Mach number M_A is enclosed by the boundary defined above. The first condition corresponds to $\xi_2 = \xi_1$, where the interval

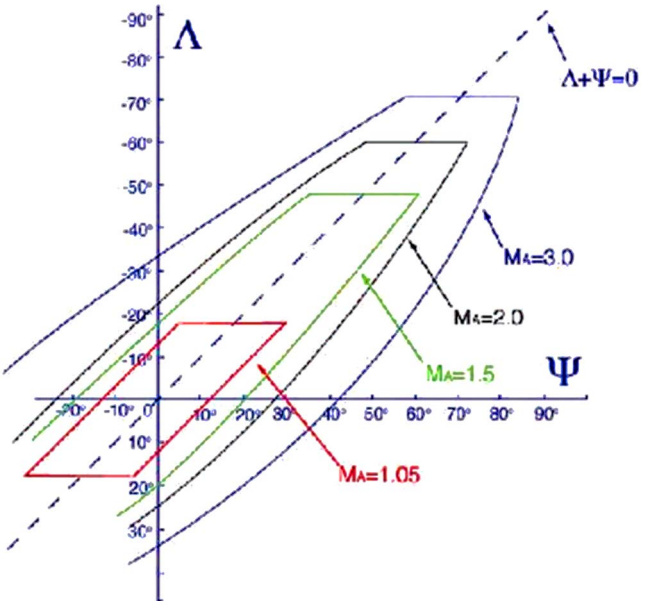

FIG. 3. (Color online) The boundaries in the $\Lambda-\psi$ realm enclosing the down-propagating wave domains illustrated for four surface Mach numbers $M_A=1.05$, 1.5, 2.0, and 3.0.

$[\xi_1, \xi_2]$ becomes imaginary, and the second condition corresponds to the limit set by the Mach cone angle. Figure 3 would suggest that, with the flight Mach numbers less than 1.26 in the field experiments of Sohn *et al.*,[17] measurements under the flight track should not find noticeable wavy-surface interaction effects, unless sea waves were propagating in a direction closely parallel to that of the flight ($|\psi| \ll 1$). Although the ambient-noise level was considered high during the test, the above observation is believed to give the primary reason for the absence of the signals of interest, as reported in Ref. 17.

C. Sonic-boom disturbances at large depth

In deep water where $\bar{z} \gg 1$, mainly those downward-propagating components can manifest; hence, deep water serves as a *band filter* to the down-propagating waves. More revealing results from (3.3a) can be obtained by the stationary-phase method, and alternatively by the saddle-point method.[19,20] The result of $\hat{p}_2(x', \bar{z})$ for large $\bar{z}$ is

$$\hat{p}_2(x', \bar{z}) = \sqrt{\frac{S_w}{2\beta_{nw}^2}} \frac{\hat{A}(\xi_*)}{(1+\eta^2)^{3/4}\sqrt{\bar{z}}} \times \exp . i\left[(2\beta_{nw}^2)^{-1}(S_w\sqrt{1+\eta^2} - P_w\eta)\bar{z} - \frac{\pi}{4} \right], \tag{3.5a}$$

$$\text{with } \eta = \frac{x'}{\bar{z}} = \frac{x'}{\beta_{nw} z}, \tag{3.5b}$$

$$\xi_* = \frac{\left[P_w - S_w \dfrac{\eta}{\sqrt{1+\eta^2}} \right]}{2\beta_{nw}^2}. \tag{3.5c}$$

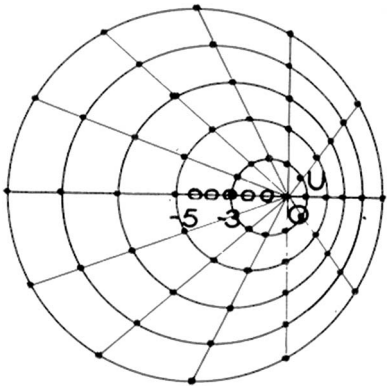

FIG. 4. Transient, dispersive wave-crest pattern of a monochromatic acoustic source, after von Kármán (Ref. 22), illustrated for a subsonic speed.

The asterisked wave number ξ_* corresponds to the stationary phase and is seen being identified with the ray of constant $\eta = x/\bar{z}$ (in the moving frame). Accordingly, not only the frequency Ω is constant along a ray of constant η but the two wave numbers k_1' and k_2' [cf. (3.1b) and (3.1c)], as well as the function $\hat{A}(\xi_*)$ can be seen to be also invariant by virtue of (3.5b) and (3.5c). The wave amplitude along the ray is proportional to $\hat{A}(\xi_*)$ but attenuates with increasing depth as the inverse square root of $\bar{z}$. Thus, the time-dependent part of p' found along each ray can be closely represented by the far field of a *monochromatic* source with a strength proportional to $\hat{A}(\xi_*)$. Since the wave number and strength of the equivalent wave field varies (slowly) among rays of different η, the signal waveform observed (at a fixed $\bar{z}$) must display a *packet* of nearly sinusoidal *wavelets*, owing to the oscillation made rapid by a large $\bar{z}$ (in either rest frame or moving frame), as η increases from $-\infty$ to ∞. The expression (3.5a) gives a monotone *frequency downshift* in the time domain, consistent with the expectation from Doppler's principle.[21]

These far-field features may be regarded as a consequence of wave dispersion found with an oscillating source in translational motion, qualitatively predictable in the manner depicted in Fig. 4 (reproduced from Ref. 22), which describes the instantaneous wave-crest pattern around the oscillating source moving at a subsonic speed. Note that the cylindrical-spreading feature is the result of a compact, oscillating source (moving at a subsonic speed) in a 2D acoustic field, irrespective of the presence of nonmonochromatic components. A more critical examination in the light of *dispersive-wave* theory[20,23] is made by comparing the wave-propagation velocity from (3.5a) with the *group velocity* of the medium in the moving frame. The two are indeed proved to be the same.[8]

IV. COMPUTATION PROCEDURES AND EXAMPLES

The central-difference algorithm and trapezoidal rule were used for the differentiation and integration in the computer program, except near singularities and at large x' and ξ, where calculations were implemented with known functional behaviors or asymptotic series. The study is presented in two parts, Subsections A and B. For the purpose of illustrating the solution procedures, numerical details obtained at succes-

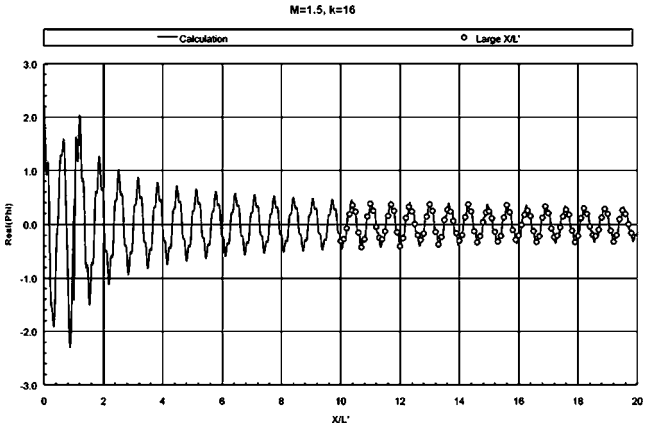

FIG. 5. Numerically integrated and asymptotic results of surface-velocity potential φ pertaining to the synchronous solution above water for an incident N wave at Mach number $M_A=1.5$ and surface-wave number $k=16$; only the real part is shown.

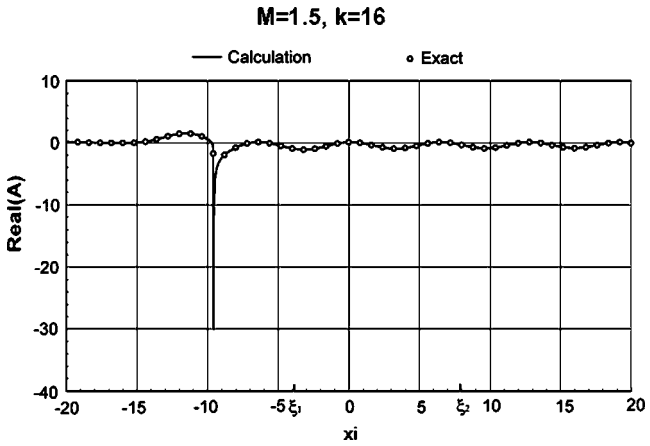

FIG. 6. Fourier transform of synchronous surface overpressure $\hat{p}_2(x',0)$ for N wave with $M_A=1.5$, $k=16$ and their comparison with the exact analytic results; only the real part is shown.

sive solution stages leading to $\hat{p}_2(x,\bar{z})$ are examined in Sec. IV A for the case of $k=16$, $M_A=1.5$, and $\Lambda=\psi=0$. Some results of a lower surface-wave number, $k=4$, for the same M_A, Λ, and ψ have been shown in Ref. 8. The important influence of Mach number on the underwater wave-field characteristics are investigated for $k=16$ in Sec. IV B. Note that, while $k=16$ may seem rather large, the corresponding surface wavelength $\lambda L'=2\pi L'/k=0.393L'$ is by no means too small compared to the signature length L'. Computer source code of the program can be found at the end of Ref. 12 and also in Refs. 24 and 25 with a user guide.

A. Example of solution procedure: $M_A=1.5$, $k=16$

1. Surface-velocity potential and $\hat{A}(\xi;k)$

The first stage of the calculation is to compute the normalized forms of surface velocity potential $\varphi(x',0)$ of the synchronous solution, using the convolution integral form obtained by the Laplace-transform method, [See (A1) in the Appendix]. The real part of the result is shown in Fig. 5 (the imaginary part is not shown to conserve space). Since the function $\hat{A}(\xi;k)$ will be sensitive to errors from φ at large x', a set of asymptotic expansions for large x' was developed to ascertain the solution accuracy and to reduce computation work (detailed in Ref. 11, Appendix III therein). The agreement between the large-x' expansion (in open circles) and the numerical integration is indeed good. With the x' derivative of $\varphi(x',0)$ and the analytic result for the boundary-value transfer term, the spatial-dependent part of the synchronous solution of the surface pressure, $\hat{p}_2(x',0)$, can be obtained. For this and other examples, the $\hat{A}(\xi)$ was computed from the Fourier transform of $\varphi(x',0)$ together with an explicit, analytic form of the boundary-transfer correction. The real part of $\hat{A}(\xi;k)$ computed for this example (from the source code) is shown along with the exact analytical results (in circles) in Fig. 6. (The corresponding imaginary part is not shown.)

2. Solution of $\hat{p}_2(x,\bar{z})$ by inversion, far-field formula

The solutions $\hat{p}_2(x',\bar{z})$ were obtained from the inverse Fourier transform of the product $\hat{A}(\xi)\sigma(\xi;\bar{z})$. Plots of these solutions are omitted for the sake of space, except for that in Fig. 7, where a comparison with the far-field expansion (3.5) at $\bar{z}=2.5$ is also shown. The far-field formula (light dashes) captures the wavelet amplitude and oscillatory features rather well at this and most depth levels, even at $\bar{z}=1.0$ (not shown).

3. Time-domain waveforms

To determine results for the complete overpressure field in the time domain, one can apply a Gallilean transformation to the foregoing results, for which specific values must also be assigned to the slope parameter δ, the signature length L', and the reference (peak) surface overpressure. For the present purpose, we take $\delta=0.01$, $L'=300$ ft.(91 m), and a maximum p_1' at $\bar{z}=0$ to be 2 psf(96 Pa). With $k=16$ and $L'=300$ ft.(91 m), the assumed surface slope parameter δ yields a surface wave height of 2.36 ft.(0.72 m). The time-domain overpressure waveforms (observed in the rest frame) predicted by the flat-ocean model p_1' (solid curve), by the time-dependent part of the wavy-ocean model p_2' (dashes), and by their sum p' (solid curve with dots) are presented in Figs. 8(a)–8(d) for the four depth levels $\bar{z}=0$, 0.5, 2.5, and 5, respectively. At the half-signature depth ($\bar{z}=0.5$), the wavy-

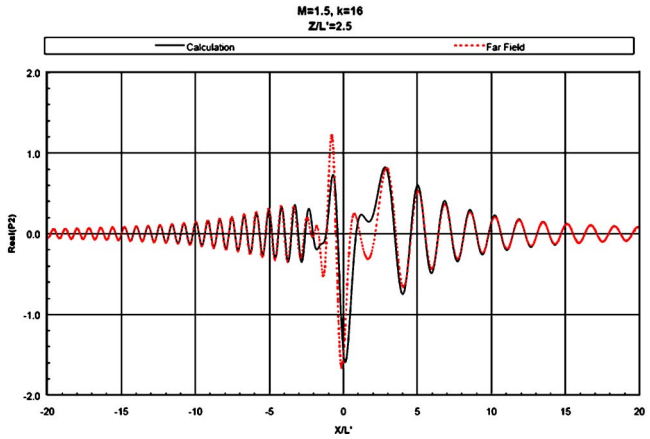

FIG. 7. (Color online) Synchronized surface pressure $\hat{p}_2(x',z)$ for N wave with $M_A=1.5$, $k=16$ at normalized depth level $\bar{z}=2.5$, and comparison with far-field prediction; only the real parts are shown.

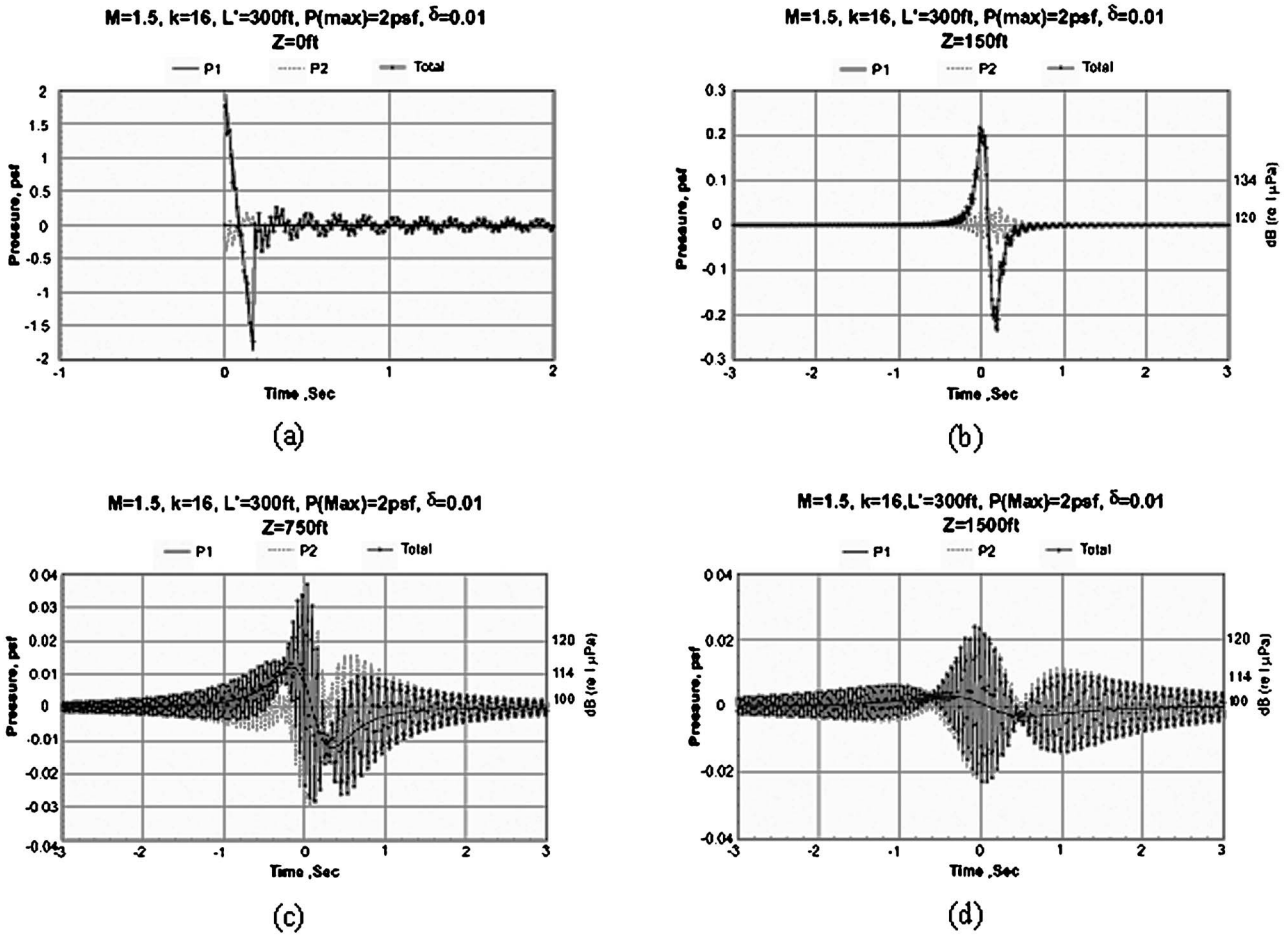

FIG. 8. Time-domain waveforms of overpressure produced by an incident N wave at $M_A=1.5$ and $k=16$, computed from the flat surface (in dashes), from the surface–wave interaction effect (dash-dot curve), and from the sum of the two (solid curve) at four depth levels: (a) $\bar{z}=0$; (b) $\bar{z}=0.5$; (c) $\bar{z}=2.5$; (d) $\bar{z}=5.0$. The maximum wave slope is $\delta=0.01$, sonic-boom signature length is $L'=300$ ft. (91 m), and maximum overpressure is 2 psf(96 Pa).

surface interaction effect (in dashes) begins to markedly alter the otherwise smoothly degenerated N-wave profile of the p_1'. At the 750-ft.(229-m) and 1500-ft.(457-m) depth levels (i.e., $\bar{z}=2.5$ and $\bar{z}=5.0$), the graphs confirm the expected dominance of the surface-wave interaction effect; here, the lee-wave-like, ringing feature found near the surface evolves itself into a *packet of wavelets* with frequency downshift, overwhelming the otherwise primary (Sawyers) wave field (solid curve).

B. Underwater waveform properties: M_A and k dependence

The solution changes from that for $(M_A,k)=(1.5,4)$ resulting from increasing M_A to 1.88 and to 2.38 at the same $k(=4)$ were found to be very similar to the comparisons made at $k=16$, and therefore will not be shown in the interest of conserving space. To study the change brought about by the Mach number M_A, comparison will be made among results of $(M_A,k)=(1.5,16)$, (1.88, 16), and (2.38, 16)—for the same $\delta=0.01$, max, $p_1=2$ psf(96 Pa), as in Sec. IV A.

1. Effects of higher k and M_A on $\hat{A}(\xi)$

The effect of increasing k on $\hat{A}(\xi)$ in question can be seen for $M_A=1.5$ by comparing available results of $k=4$ from Fig. 4 of Ref. 8 with those of $k=16$ shown in Figs. 6(a) and 6(b) above. The effects of increasing k on $\hat{A}(\xi)$ for $M_A=1.88$ and 2.38 have been similarly examined. The results will not be shown except to mention that $|\hat{A}(\xi)|$ can be scaled as $1/k$ for the larger M_A as the exact result (Ref. 8, (6.4)) has indicated.

2. Time-domain waveforms at depths

The overpressure wave forms in time domain, p_1', p_2' and their sum p' for $M_A=1.5$ and $k=4$ at depth levels $\bar{z}=0.5,5.0$ have been given in Ref. 8, Fig. 5 therein. The corresponding results for a higher surface-wave number $k=16$ (at the same Mach number, $M_A=1.5$) are shown here in Figs. 8(a)–8(d), by which the effect of a fourfold increase in k at a fixed M_A can be examined. The waveform changes from the last figure set, for the same k, to one at a higher $M_A(=1.88)$ and to another at a still higher $M_A(=2.38)$ are presented in Figs. 9(a)–9(d) and Figs. 10(a)–10(d). Apart from the distinctly different waveforms of flat and wavy surface models, these plots show unquestionable dominance of the surface-wave interaction effect over the sonic-boom signals from the flat-ocean model (solid curves) in the deeper parts of the water.

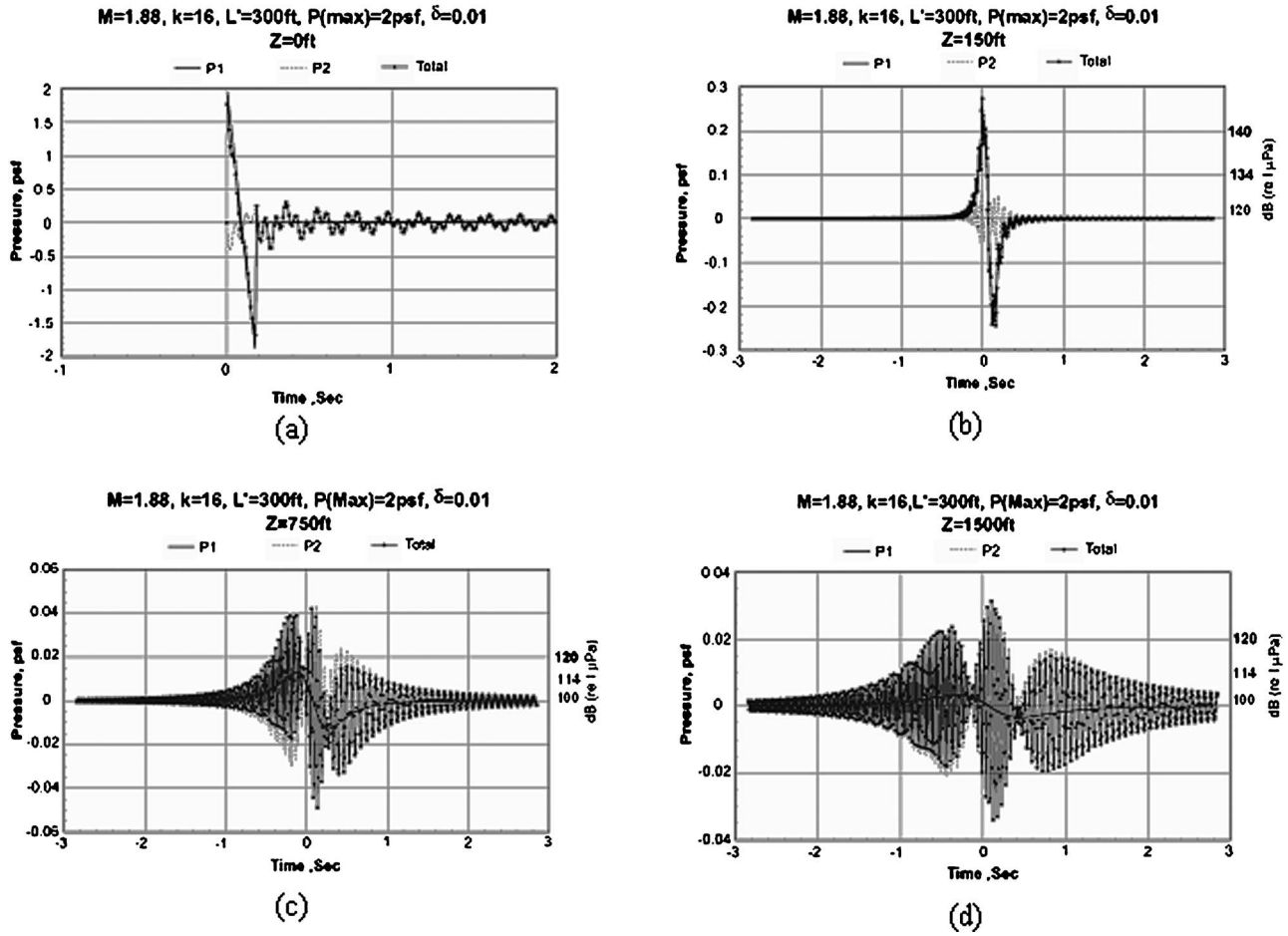

FIG. 9. Time-domain overpressure waveform with $M_A=1.88$, $k=16$, with conditions otherwise the same as in Fig. 8, at four normalized depth levels: (a) $\bar{z}=0$; (b) $\bar{z}=0.5$; (c) $\bar{z}=2.5$; (d) $\bar{z}=5.0$.

3. Effects of increasing surface wave number

The noticeable reductions in overpressure with increasing k found at the deeper levels ($\bar{z}=2.5,5.0$) are in accord with the $1/\sqrt{k\bar{z}}$ rule from the theory noted earlier for all M_A. On the other hand, at depths close to the surface ($\bar{z}=0,0.5$), the higher k is seen to increase, rather than to reduce, the time-dependent part of the overpressure. Increasing k is expected to make the wave packet more densely packed. The average wavelet frequency at $M_A=1.5$ is not far from the k value (with the exception of $k=16$ at $\bar{z}=0.5$). However, at the higher Mach numbers, the number of zero crossings, and hence the instantaneous frequency, in Figs. 9(c) and 9(d) and Figs. 10(c) and 10(d), are seen to increase much more rapidly than k.

4. Mach-number influence on overpressure peaks

The peak overpressure of the wavelets at the deepest level ($\bar{z}=5.0$) is seen to increase successively from 0.025 through 0.031 to 0.046 psf in a nonlinear fashion, as M_A increases from 1.5 through 1.88 to 2.35. Similarly, and with a greater magnitude, the overpressure at depth $\bar{z}=2.5$ is seen to increase nonlinearly with M_A.

5. Mach number influence on wavelet frequencies

The number of wavelets seen earlier in the waveforms at $M_A=1.5$ are now seen to give a more densely packed waveform at the higher Mach numbers, $M_A=1.88$ and 2.38 [cf. Figs. 9(b)–9(d) and 10(b)–10(d)]. Applying the separate counting for $t<0$ and for $t>0$ at depth level $\bar{z}=5.0$ yields two sets of frequency estimates below for $k=16$ and $L'=300$ ft.(91 m). These frequency estimates were based on the averages over the 1-s. intervals on the two sides of the peak near $t=0$; the differences confirm the expected *frequency downshift*. Added under the table below

M_A	1.5	1.88	2.38	
$t<0$	20 Hz	25 Hz	43 Hz	
$t>0$	13 Hz	16 Hz	21 Hz	
Duration	1.5 s	2 s	3 s	@$\|p'\|>0.01$ psf

are the *signal durations* detectable at $\bar{z}=5$ for the three Mach numbers in this case ($k=16$, $\delta=0.01$) under a sound-pressure threshold of 0.01 psf$\sim$114 dB(*re*: 1 μPa).

V. CLOSING REMARKS

Snell's law and ray acoustics cannot adequately describe sonic-boom penetration under water; the correct description

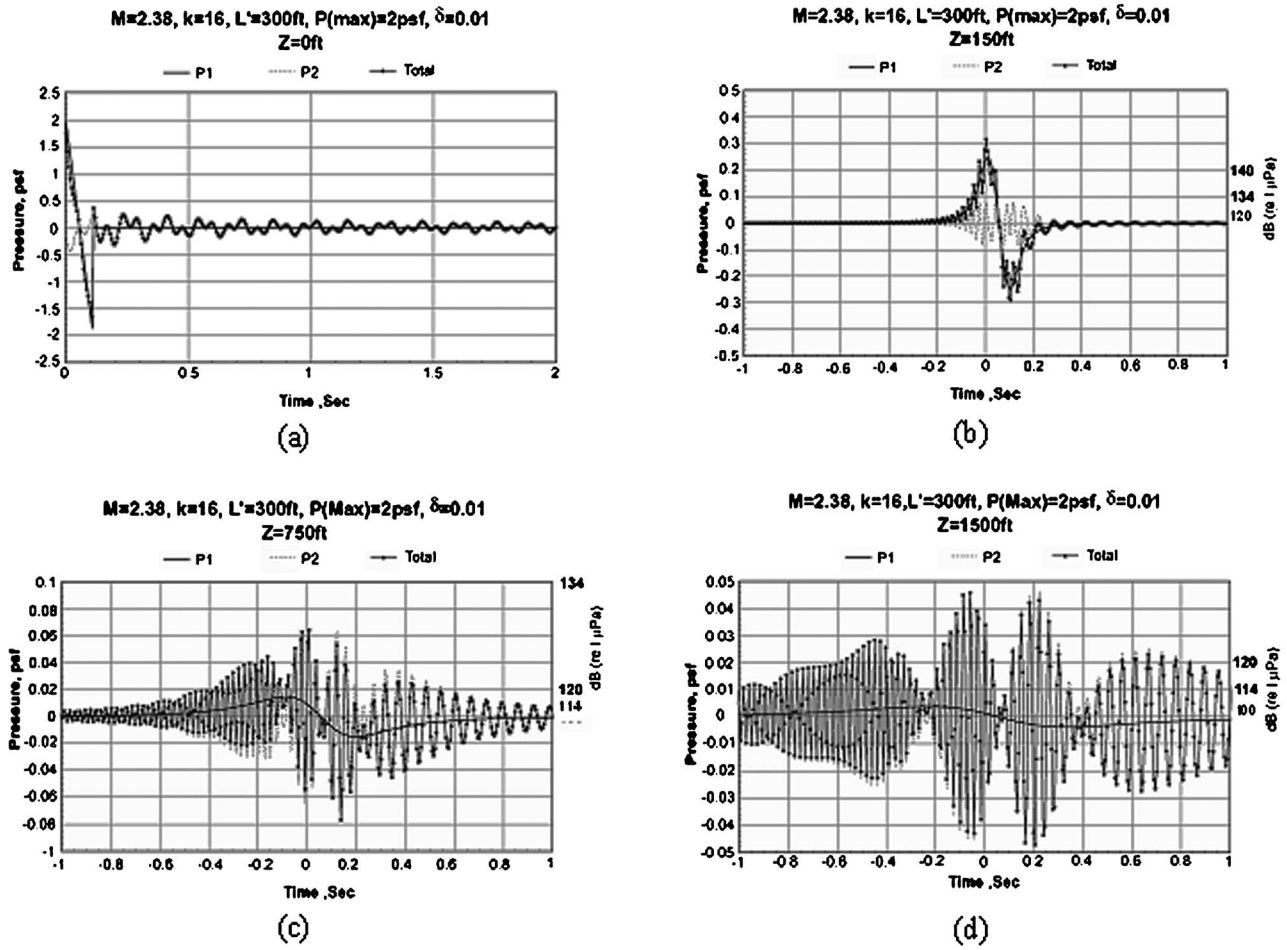

FIG. 10. Time-domain overpressure waveform with $M_A=2.38$, $k=16$, with conditions otherwise the same as in Figs. 8 and 9, at four depth levels: (a) $\bar{z}=0$; (b) $\bar{z}=0.5$; (c) $\bar{z}=2.5$; (d) $\bar{z}=5.0$.

was given by Sawyers for a flat-ocean model.[1] The analysis of Ref. 8 shows that the interaction with a wavy interface can produce additional disturbances which alter the tonal content of the sonic-boom signals underwater and dominate the sound field in the deep as well as not-so-deep parts of the water column. Unlike the wave fields of the flat-ocean model observed in the moving frame, the fields above and under the wavy interface have *time-dependent, oscillatory* parts resulting from the interaction—likened to the "synchronous noise" produced by a thimble striking the ridges of a washboard. These synchronous disturbances *disperse and spread* underwater according to elementary rules *of* acoustics for an oscillating source.

The numerical examples of incident N waves analyzed here for different surface wave numbers and Mach numbers illustrate, in more concrete terms, how disturbances generated by the interaction may change from a secondary effect near the surface to an effect of first-order importance in deep water, and to what extent the signal intensity and characteristics can be influenced by these and other wave-field parameters. The results confirm the $1/\sqrt{k\bar{z}}$ attenuation rule for a large enough combination of $\bar{z}$ and k, where the peak overpressure is seen to increase with M_A at more than a linear rate. Assuming a peak overpressure of 2 psf(96 Pa) and a mildly wavy sea in the calculation, the results show that sonic-boom noise at sound levels of 100–120 dB(re:1 μPa) can reach a depth of 750–1500 ft.(229–457 m) in the form of an infrasound wave packet, far louder than the normal ocean noise in the comparable frequency range.[26] Not included are examples with other sonic-boom waveforms, such as those found during a rocket space launch and in laboratory measurements[10,11] which are known to be affected to a large degree by the rocket plume or the projectile wake. The examples studied represent received sonic-boom signals in a *single* event; their overpressure levels are generally low in comparison with those recorded during SONAR operations and seismic air-gun surveys, which may also repeat over hours in duration. The foregoing analysis was made with the hope of shedding light on sound level and tonal characteristics received at depth, which may help assessing long-term effects of repeated sonic-boom occurrence on marine-mammal species.[1–4]

Although examples pertaining to the evanescent-wave domain have not been included for detailed study, the solution procedure and code are equally applicable to problems in this category. As Fig. 3 and the discussion in Sec. III B have indicated, the domain of evanescent waves can become very extensive if M_A is too close to unity, since the domain with down-propagating waves would diminish as M_A tends to 1. This is believed to be the primary cause for the lack of evidence supporting wavy-surface influence in Sohn *et al.*'s field measurements.[17] In passing, a computational study by

Rochat and Sparrow[27] on wavy water surface interacting with sonic boom may be noted; results therein were presented only at a depth very close to the surface, where the overpressure reveals mainly the minute, secondary effect as anticipated.

Implicit in Ref. 8 and the present study is the requirement $M_A < 4.53$ under standard conditions, beyond this speed limit the wave field under water would become supersonic and the flat-ocean model in its 2D version would allow uninhibited wave propagations until 3D effects take over. The seafloor influence, not considered above, could be an important issue for studying sonic-boom impact on the shallow coastal water. The underwater wave field interacting with the elastic seabed medium, with the potential for exciting seismic-sediment waves, represents a very outstanding issue, which was recognized and investigated by Desharnais and Chapman,[16] and also studied subsequently by Cheng *et al.* in Refs. 13 and 28. In addition to seafloor influence, the presence of coast line could also cause departure from the flat-ocean theory.[29]

ACKNOWLEDGMENTS

The authors acknowledge the helpful discussions and assistance of L. Aragon, B. Ariaei, A. Bowles, M. Buckingham, D.M.F. Chapman, C. S. Clay, F. Desharnais, O. Godin, A. Fincham, J. Garrelick, C.R. Greene, A. Hashad, T. Maxworthy, H. Medwin, D. Moody, K. Plotkin, V. Sparrow, R. Sohn, and J. Segurdson. Support by the Environmental Management Branch, AF Missile and Space System Center, Los Angeles, CA is much appreciated.

APPENDIX: VELOCITY POTENTIAL ABOVE WATER

The synchronous solution for the velocity potential above water is[8]

$$\hat{\phi}_2(x',z) = -2\frac{\delta\lambda}{B_n}\int_0^{x'+B_n z} e^{ik_1'(x'-x_1')} \cdot \left[ik_1'\frac{d}{dx'} - B_n^2\frac{d^2}{dx'^2}\right] f(x'-x_1') \times e^{i(P/2B_n^2)x_1'} \cdot J_0(\alpha\sqrt{(x_1')^2 - B_n^2 z^2})dx_1', \quad \text{(A1)}$$

where $f'(\xi)$ is a normalized incident wave form, d^2f/dx'^2 results from boundary-condition transfer, to be treated in the Stieltjes sense

$$\alpha = k\sqrt{M_n^2 - \sin^2(\Lambda+\psi)}/B_n, \quad \text{(A2)}$$

$$B_n \equiv |M_n^2 - 1|^{1/2}. \quad \text{(A3)}$$

The synchronous surface overpressure above water is computed from

$$p_2' = -\rho\frac{D'}{Dt}\phi_2 = -\rho U_n RP e^{ik_2' y'} e^{-i\Omega t}\left(\frac{d}{dx'} - ik_1'\right)\hat{\phi}_2(x',0). \quad \text{(A4)}$$

[1]A. E. Bowles, "Effects of Sonic Booms on Marine Mammals: Problem Review and Recommendation for Research," *NASA Conf. Pub* 3335 (1995).
[2]B. S. Stewart, R. W. Young, J. K. Francine, and M. Drawbridge, "Geological Effects of Launch-Specific Related Noise and Sonic Booms from Titan IV on 8 March 1991," *Huubs-Sea World Res. Inst. Report*, 96–264, 1–68 (1991).
[3]W. J. Richardson, C. R. Greene, Jr., C. I. Malme, and D. H. Thompson, *Marine Mammals and Noise* (Academic, New York, 1995), pp. 15–86, 525–552.
[4]Natural Resource Defense Council, "Sounding the Depth: Supertankers, Sonar, and the Rise of Undersea Noise," NRDC Report (1999).
[5]K. H. Sawyers, "Underwater Sound Pressure from Sonic Boom," J. Acoust. Soc. Am. **44**, No. 2, 523–524 (1968).
[6]V. W. Sparrow, "The Effect of Supersonic Aircraft Speed on the Penetration of Sonic Boom Noise into the Ocean," J. Acoust. Soc. Am. **97**, No. 1, 159–162 (1995).
[7]V. W. Sparrow and T. Ferguson, "Penetration of Sharp Sonic Boom Noise into a Flat Ocean," AIAA paper 97-0486 (1997).
[8]H. K. Cheng and C. J. Lee, "Sonic Boom Noise Penetration Under a Wavy Ocean: Theory," J. Fluid Mech. **514**, 281–312 (2004).
[9]H. K. Cheng and C. J. Lee, "Sonic Boom Noise Penetration Under Wavy Ocean: Part I. Theory," Univ. Southern Calif. Dept., Aerospace and Mechanical Engineering, USC AME Report 11-11-2000; documented on web site http://www-rcf.usc.edu/~hkcheng (2000).
[10]A. Fincham and T. Maxworthy, "An Experimental Study of Sonic Boom Penetration Under a Wavy Air-Water Interface," *USC AME Report* 9-11-2000; documented also at http://ax.losangeles.af.mil/axf/comments/comments.html (2001).
[11]H. K. Cheng, C. J. Lee, and J. R. Edwards, "Sonic Boom Penetration Under a Wavy Ocean: Part II. Example and Extensions," *USC AME Report* 4-4-2001, documented also at http://www-rcf.usc.edu/~hkcheng (2001).
[12]H. K. Cheng, "Final Report of Experimental and Theoretical Investigations on Ocean Sonic Boom Propagation," HKC Research, Los Angeles, CA, September 2001; documented at http://ax.losangeles.af.mil/axf/comments/comments.html (2001).
[13]H. K. Cheng, J. Kunc, and J. R. Edwards, "Sonic Boom Excited Sediment Waves: A Model Study," Can. Acoust. **31**, No. 4, 5–18 (2003).
[14]H. Medwin, R. A. Helbig, and J. D. Hagy, "Spectral Characteristics of Sound Transmission Through the Rough Sea Surface," J. Acoust. Soc. Am. **54**, No. 1, 99–109 (1973).
[15]P. F. Intrieri and G. N. Malcolm, "Ballistic Range Investigation of Sonic Boom Overpressure in Water," AIAA J. **11**, No. 4, 510–516 (1973).
[16]F. Desharnais and D. M. F. Chapman, "Underwater Measurement and Modeling of a Sonic Boom," J. Acoust. Soc. Am. **111**, Pt. 2, 540–553 (2002).
[17]R. A. Sohn, F. Vernon, J. A. Hildebrand, and S. C. Webb, "Field Measurement of Sonic Boom Penetration into the Ocean," J. Acoust. Soc. Am. **107**, No. 6, 3073–3082 (1999).
[18]H. Ashley and M. Landahl, *Aerodynamics of Wings and Bodies* (Addison-Wesley, Reading, MA, 1965).
[19]G. Carrier, M. Krook, and C. E. Pearson, *Functions of Complex Variables* (McGraw-Hill, New York, 1966), pp. 272–282, 301–332.
[20]M. J. Lighthill, *Waves in Fluid* (Cambridge University Press, Cambridge, 1978), pp. 249–250.
[21]L. D. Landau and E. M. Lifshitz, *Fluid Mechanics*, (Pergamon, New York, 1959), pp. 268–269.
[22]T. von Kármán, *Aerodynamics; Selected Topics in the Light of Their Developments* (Cornell University Press, Ithaca, NY, 1954).
[23]G. B. Whitham, *Linear and Nonlinear Waves* (Wiley, New York, 1974).
[24]C. J. Lee and H. K. Cheng, "Sonic Boom Generated Sound Field Under a Wavy Air–Water Interface: Computer Code and User Guide," USC AME Report 9-30-2005, available at http://www-rcf.usc.edu/~hkcheng (2005).
[25]D. M. Moody and C. P. Griffice, "Documentation of a Computer Code by HKC Research to Calculate the Transmission of a Sonic Boom through a Wavy Ocean Surface," Aerospace Corp. Report TR-2004 (8506) (2004).
[26]R. J. Urick, *Principles of Underwater Sound*, 3rd ed. (McGraw-Hill, New York, 1983).
[27]J. L. Rochat and V. W. Sparrow, "Two-Dimensional Focusing of Sonic Boom Noise Penetration and Air–Water Interface," AIAA J. **35**, No. 1, 35–39 (1997).
[28]H. K. Cheng, "Sonic Boom Generated Underwater Noise as Problem in Unsteady Aerodynamics," AIAA Paper 2005-4804 (2005).
[29]J. Garrelick, "The Effect of a Coastline on the Underwater Penetration of Sonic Booms," J. Acoust. Soc. Am. **101**, No. 1, Part 2, 610–613 (2002).

Tracking individual fish from a moving platform using a split-beam transducer

Nils Olav Handegard,[a] Ruben Patel, and Vidar Hjellvik
Institute of Marine Research, P.O. Box 1870 Nordnes, N-5817 Bergen, Norway

(Received 16 May 2003; revised 11 July 2005; accepted 11 July 2005)

Tracking of individual fish targets using a split-beam echosounder is a common method for investigating fish behavior. When mounted on a floating platform like a ship or a buoy, the transducer movement often complicates the process. This paper presents a framework for tracking single targets from such a platform. A filter based on the correlated fish movements between pings is developed to estimate the platform movement, and an extended Kalman filter is used to combine the split-beam measurements and the platform-position estimates. Different methods for gating and data association are implemented and tested with respect to data-association errors, using manually tracked data from a free-floating buoy as a reference. The data association was improved by utilizing the estimated velocity for each track to predict the location of the next observation. The data association was more robust when estimates of platform tilt/roll were used. Other techniques to estimate position and velocity, like linear regression and smoothing splines, were implemented and tested on a simulated data set. The platform-state estimation improved the estimates for methods like the Kalman filter and a smoothing spline with cross validation, but not for robust methods like linear regression and smoothing spline with a fixed degree of smoothing. © *2005 Acoustical Society of America.* [DOI: 10.1121/1.2011410]

PACS number(s): 43.30.Sf [KGF] Pages: 2210–2223

I. INTRODUCTION

The split-beam echosounder has become an important tool for investigating fish behavior. It provides four-dimensional observations (range, two angles, and time), making it possible to track objects over a period, thus obtaining information about fish movements in the acoustic beam.[1,2] The technique has several applications, including studies of migratory behavior, vessel-avoidance effects, and counting fish. Tracking objects with a split-beam echosounder is fairly easy for well-defined targets observed by a fixed transducer, but is more difficult if the targets are weak and/or the transducer platform is unstable.

The concept of the "single echo" often arises in fisheries acoustics. This is the echo formed by one fish in isolation. The split-beam echosounder measures the range and the angular direction to the target, and an algorithm for single-echo detection (SED) is used to detect these echoes, discarding any that have overlapping contributions from more than one fish. Different single-target algorithms have been tested, and it was found that algorithms based on the phase stability (measured by the standard deviation of the phase angle) rejected multiple targets most efficiently, and a method utilizing amplitude differences between the split-beam transducer elements performed well for strong targets.[3]

After the single targets are detected they must be combined into tracks. This can be achieved using an algorithm for multiple-target tracking (MTT). This is an automatic procedure that can handle several tracks simultaneously. MTT is used in several applications, and the literature is extensive.[4,5]

Any motion of the transducer complicates the tracking of fish. Data association is the process of combining the single echoes into useful tracks. Transducer motion makes this more difficult and causes error in the velocity estimates. In this paper, we investigate various methods of data association and velocity estimation under these conditions, leading to improved techniques for fish tracking.

II. MATERIALS

Observations made from a free-floating buoy[6] are used to test the performance of the tracker. The buoy contains a Simrad EK60 split-beam echosounder with an ES38-12 split-beam transducer of approximately 11.5° symmetrical beam width between the −3 dB directions. The transducer is mounted on a cable with floats and weights to stabilize it during operations.[7] The resulting depth of the transducer is 40 m. A compass is mounted on the transducer house to determine its alongship direction.

The test data set was recorded during a fish avoidance study in the Barents Sea in March 2001. The buoy was passed several times by a trawling vessel, and the purpose of the study was to investigate the behavior of the fish (mainly cod) in response to the vessel and gear.[7] Data from one such passing comprise the test set whose total duration is 10 min. The ping rate is 1 s^{-1} and the data include 5700 single-echo detections (see the echogram shown in Fig. 1).

The EK60 Mark 1 software (Ver. 1.3.0.54) was used to detect single targets within the echo beam. The settings for the SED algorithm are given in Table I.

[a]Electronic mail: nilsolav@imr.no

 0001-4966/2005/118(4)/2210/14/$22.50

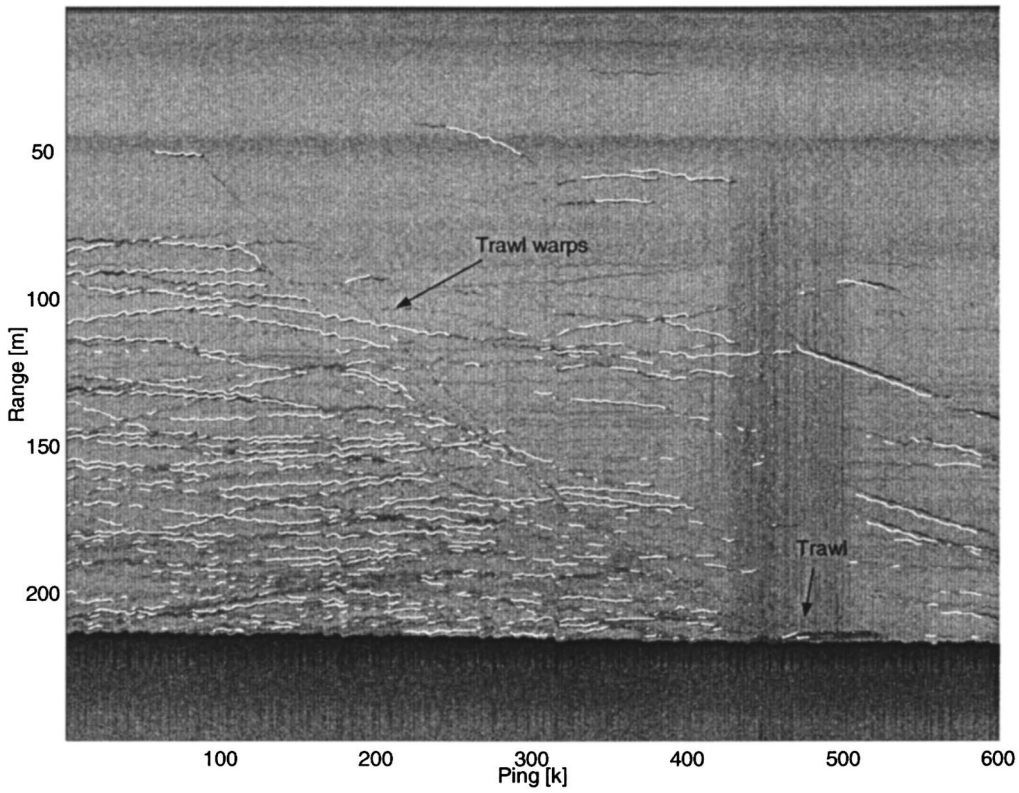

FIG. 1. Tracked buoy data. White lines indicate the tracks. The gray-scaled background is the volume backscattering values. In the middle of the echogram the trawl and the warps are seen. Vertical lines above the trawl are noise from the trawl, trawl sensors, and trawl doors.

III. METHODS

Our method of tracking single fish observed from a moving platform is divided into three subtasks: initial tracking, platform-state estimation, and final tracking. The initial tracking and the final tracking use the same MTT algorithm. The initial tracking gives a first association of measurements to tracks, from which we subsequently estimate the platform state (i.e., the position and direction of the acoustic axis). In the final tracking, the platform state is used to estimate the geo-relative position and velocity for each track at each time step. This set of positions and velocities is called the track state $\mathbf{x}_k$ which is obtained using several alternative methods. The extended Kalman filter (EKF) is only one method for estimating the track state, but since predictions of track state are easily obtained from the EKF, the EKF is presented together with the MTT in Sec. III A. The alternative track-state estimators require previously associated data points and are presented in Sec. III B. The technique for platform-state estimation is described in Sec. III C.

TABLE I. EK60 single echo detection (SED) settings according to the Simrad EK60 Scientific echosounder manual, p. 141. The echo lengths are given as a factor τ multiplying the pulse length (or pulse duration time).

Description	Value
Minimum Echo Length	0.8τ (m)
Maximum Echo Length	1.8τ (m)
Maximum Phase Deviation	8.0 (phase steps)
Maximum Gain Compensation	6.0 (dB)

Methods for measuring data-association errors based on manually associated data, and track-state-estimation errors based on simulated data, are presented. These are described in Secs. III D and III E, respectively. In addition, the sensitivities to the various tracking parameters are quantified for both measures.

A. Multiple target tracking (MTT) using extended Kalman filtering (EKF)

The MTT process associates measurements to tracks and estimates the track state based on the single-echo detections and the transducer platform state (measured or estimated). The MTT consists of several elements: track-state estimation, track-state prediction, gating, data association, and track support. The track-state estimation gives the location and velocity for each track indicated by the current and previous measurements. Based on this information, we predict where the next measurement is likely to be. The prediction is then used in the gating and in the data association. Gating is the process of removing unlikely track/observation pairs, and data association is the actual pairing of predictions and observations into tracks. The last element of the MTT is the track-support algorithms. These take care of initiating, terminating, and validating tracks.

1. The extended Kalman filter and track-state estimation and prediction

One method for estimating the track state is the extended Kalman filter (EKF). The advantage of the EKF is that the

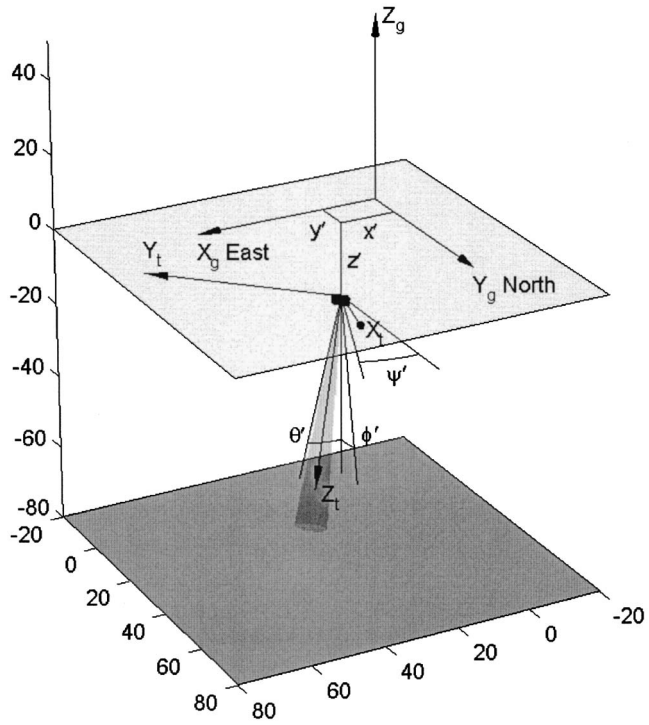

FIG. 2. The platform state shown in the geographical coordinate system, e_{gc}. The eastward, northward, and vertical directions are indicated with X_g, Y_g, and Z_g, respectively. The platform state $\mathbf{z}_k=\hat{\mathbf{z}}_k+\mathbf{v}_{y,k}=[x' \quad y' \quad z' \quad \theta' \quad \phi' \quad \psi']^T_{e_{gc}}$ is indicated in the figure. The alongship, athwartship, and vertical transducer axes are given by X_t, Y_t, and Z_t, respectively. The compass reading ψ' is the angle off Y_g for the projection of X_t onto the horizontal plane.

state is estimated by weighting the previous state with the new observation, thus it is unnecessary to recalculate the whole track. See Sec. III C for a description of alternative track-state estimators. The true position and velocity for target i at ping k and time t_k are given by the track-state vector

$$\mathbf{x}_k=[x_k \quad y_k \quad z_k \quad \dot{x}_k \quad \dot{y}_k \quad \dot{z}_k \quad \mathrm{TS}_k]^T_{e_{gc}},$$

where (x_k,y_k,z_k) is the position vector, $(\dot{x}_k,\dot{y}_k,\dot{z}_k)$ is the velocity vector, TS_k is the target strength, T denotes matrix transposition, and e_{gc} denotes the geo-referenced coordinate system (see Fig. 2). The corresponding estimate is denoted by $\hat{\mathbf{x}}$. In general there are several tracks i and measurements j for each ping k, but for easier readability we have here omitted i and j from the notation. Under a constant-velocity assumption, the track state at time $t_{k+1}=t_k+\Delta T_k$ is given by

$$\mathbf{x}_{k+1}=\Phi(\Delta T_k)\mathbf{x}_k+\mathbf{w}_\Phi, \tag{1}$$

where $\Phi(\Delta T_k)$ is the matrix of the track-state transition for the time interval ΔT_k and $\mathbf{w}_\Phi=\mathbf{w}(t_k)$ is an additive system error component (see Appendix A for details). The error is assumed to be normally distributed and the target-model-covariance matrix is defined as $\Sigma_\Phi=E(\mathbf{w}_\Phi\mathbf{w}_\Phi^T)$ (see Appendix A).

From the estimated track state at time step $k-1$, we can predict the state at step k. The predicted track state $\tilde{\mathbf{x}}$ is found by setting the model error $\mathbf{w}_\Phi=\mathbf{0}$ in Eq. (1),

$$\tilde{\mathbf{x}}_k=\Phi(\Delta T_k)\hat{\mathbf{x}}_{k-1}. \tag{2}$$

We have also implemented a "zero-velocity" prediction. This is achieved by setting $\Delta T_k=0$ in Eq. (2), which yields $\tilde{\mathbf{x}}_k=\hat{\mathbf{x}}_{k-1}$ since $\Phi(0)=I$. Note that this prediction is used in the data association algorithm only, and not in the Kalman-filter estimates (see below).

A split-beam echosounder with a SED algorithm calculates the alongship angle α_k, the athwart ship angle β_k, the range r_k, and the target strength TS_k, for each target at every time step k. These measurements are represented by

$$\mathbf{y}_k=[\alpha_k \quad \beta_k \quad r_k \quad \mathrm{TS}_k]^T_{e_{tp}}+\mathbf{v}_{y,k}.$$

Here, $\mathbf{v}_{y,k}$ is an additive error component that depends on the accuracy of the transducer, and e_{tp} denotes the transducer coordinate system.

The platform state $\mathbf{z}_k$ describes the acoustic axis of the transducer, which may move in space and point in any direction. It is given by

$$\mathbf{z}_k=\hat{\mathbf{z}}_k+\mathbf{v}_{z,k}=[\hat{x}'_k \quad \hat{y}'_k \quad \hat{z}'_k \quad \hat{\theta}'_k \quad \hat{\phi}'_k \quad \hat{\psi}'_k]^T+\mathbf{v}_{z,k}, \tag{3}$$

where $\hat{\mathbf{z}}_k$ is the estimated platform state, $(\hat{x}'_k,\hat{y}'_k,\hat{z}'_k)_{e_{gc}}$ is the transducer position at time t_k, $\hat{\psi}'_k$ is the corresponding transducer compass reading, $(\hat{\theta}'_k,\hat{\phi}'_k)$ are the tilt angles in east-west and north-south directions (see Fig. 2), and $\mathbf{v}_{z,k}$ is an additive error component. The errors are combined in $\mathbf{v}_{R,k}=\begin{bmatrix}\mathbf{v}_{z,k}\\ \mathbf{v}_{y,k}\end{bmatrix}$ and are assumed to be additive and normal with covariance $\Sigma_{R,k}=E(\mathbf{v}_{R,k}\mathbf{v}_{R,k}^T)$ (see Appendix B). In our case, all the off-diagonal elements of $\Sigma_{R,k}$ are assumed to be zero. The relationship between the track state $\mathbf{x}_k$, the platform state $\hat{\mathbf{z}}_k$, and the measurement $\mathbf{y}_k$ is defined by

$$\mathbf{y}_k=\mathbf{h}(\mathbf{x}_k,\hat{\mathbf{z}}_k,\mathbf{v}_{R,k}), \tag{4}$$

where $\mathbf{h}$ is a nonlinear function defined in Appendix B. Since the relationship between the track state and the measurement is nonlinear, an EKF must be used instead of an ordinary Kalman filter. The EKF uses a linear approximation of Eq. (4) about the predicted track state, $\tilde{\mathbf{x}}_k$, the estimated platform state, $\hat{\mathbf{z}}_k$, and the measurement-error vector set to zero, $\mathbf{v}_{R,k}=\mathbf{0}$. The linear relationship between the measurement and the track state is

$$\mathbf{y}_k\sim\mathbf{h}(\tilde{\mathbf{x}}_k,\hat{\mathbf{z}}_k,\mathbf{0})+H(\mathbf{x}_k-\tilde{\mathbf{x}}_k)+V\mathbf{v}_{R,k},$$

where

$$H_{[l,m,k]}=\frac{\partial h_{[l]}}{\partial x_{[m]}}(\tilde{\mathbf{x}}_k,\hat{\mathbf{z}}_k,\mathbf{0})$$

and

$$V_{[l,m,k]}=\frac{\partial h_{[l]}}{\partial v_{[m]}}(\tilde{\mathbf{x}}_k,\hat{\mathbf{z}}_k,\mathbf{0}).$$

The predicted measurement is found from the predicted track state by setting the measurement error $\mathbf{v}_{R,k}=\mathbf{0}$ in Eq. (4),

$$\tilde{\mathbf{y}}_k=\mathbf{h}(\tilde{\mathbf{x}}_k,\hat{\mathbf{z}}_k,\mathbf{0}). \tag{5}$$

The error covariance of the predicted estimate is given by

$$\tilde{\Sigma}_{\mathbf{x},k} = \Phi(\Delta T_k)\hat{\Sigma}_{\mathbf{x},k-1}\Phi(\Delta T_k)^T + \Sigma_\Phi,$$

where $\hat{\Sigma}_{\mathbf{x},k-1}$ is the estimated track-state-error covariance from the previous time step and Σ_Φ is the track-state-transition covariance. Initially $\hat{\Sigma}_{\mathbf{x},k-1} = \Sigma_{\mathbf{x},0}$ where

$$\Sigma_{\mathbf{x},0} = [P^2_{0\ xy}, P^2_{0\ xy}, P^2_{0\ z}, P^2_{0\ dxdy}, P^2_{0\ dxdy}, P^2_{0\ dz}, P^2_{0\ TS}]I. \quad (6)$$

The elements of $\Sigma_{\mathbf{x},0}$ are parameters. The estimated track state is found by weighting the predicted track state and the observation by the Kalman gain, K_k,

$$\hat{\mathbf{x}}_k = \tilde{\mathbf{x}}_k + K_k(\mathbf{y}_k - \mathbf{h}(\tilde{\mathbf{x}}_k, \hat{\mathbf{z}}_k, 0)),$$

where

$$K_k = \tilde{\Sigma}_{\mathbf{x},k} H_k^T (H_k \tilde{\Sigma}_{\mathbf{x},k} H_k^T + V_k \Sigma_{R,k} V_k^T)^{-1}.$$

The estimated track-state-error covariance is

$$\hat{\Sigma}_{\mathbf{x},k} = (I - K_k H_k)\tilde{\Sigma}_{\mathbf{x},k},$$

the linearized innovation, $\hat{\boldsymbol{\epsilon}}_k = \mathbf{y}_k - \tilde{\mathbf{y}}_k$, is

$$\hat{\boldsymbol{\epsilon}}_k = H(\mathbf{x}_k - \tilde{\mathbf{x}}_k) + V\mathbf{v}_{R,k},$$

and the linearized covariance of the innovation is

$$\Sigma_{\epsilon,k} = H_k \tilde{\Sigma}_k H_k^T + V_k \Sigma_{R,k} V_k^T.$$

2. Gating and data association

The next step in the MTT algorithm is to associate the observations with existing predictions. The challenge is to avoid associating a false prediction-observation pair, and to avoid *not* associating a true prediction-observation pair (track splitting). The innovation $\hat{\boldsymbol{\epsilon}}_{ijk}$ is the difference between the predicted measurement from track i and the observation j at ping k; it is used in the gating and data-association algorithms. Innovations based on both constant and "zero-velocity" predictions are implemented and tested. Gating is the initial step in the data association, where unlikely pairs of predictions and observations are removed. The distance indicated by the innovation is calculated, and any pair separated by more than a set amount is deemed to be outside the gate. The gate can be specified in several ways. We have implemented two types. Firstly, a static gate accepts pairs within a fixed ellipsoidal volume around the prediction:

$$d^2_{ijk} = \hat{\boldsymbol{\epsilon}}_{ijk} G \hat{\boldsymbol{\epsilon}}^T_{ijk} < 1, \quad (7)$$

where

$$G = \begin{bmatrix} \alpha_G^2 & 0 & 0 \\ 0 & \beta_G^2 & 0 \\ 0 & 0 & r_G^2 \end{bmatrix}^{-1}. \quad (8)$$

Here α_G, β_G, and r_G act as gates in angles and range, respectively. Note that different gate widths may be used in the initial and final tracking. These are indexed by numbers, i.e., r_{G1} and r_{G2}. If no measurement is associated with a given track at time step k, the algorithm continues the search at time step $k+1$. However, the volume likely to contain the next measurement of the track is now larger, and it will increase for each time step when no association is made. This suggests the use of a dynamic gate whose size increases with the prediction covariance. Such a gate requires *a priori* knowledge of the detection probabilities and measurement errors.[8] In order to test the concept of a dynamic gate, suppose the detection probabilities are constant, so that

$$d^2_{ijk} = \hat{\boldsymbol{\epsilon}}_{ijk}\, \Sigma^{-1}_{\boldsymbol{\epsilon},ijk}\, \hat{\boldsymbol{\epsilon}}^T_{ijk} \leqslant 2 \ln\left[\frac{c_G}{\sqrt{|\Sigma_{\boldsymbol{\epsilon},ijk}|}}\right] + \ln[|\Sigma_{\boldsymbol{\epsilon},ijk}|], \quad (9)$$

where c_G is a constant. The last term is a penalizing term to prevent tracks with high innovation covariance (many missing pings) being preferred over those with low innovation covariance.[8]

When gating is performed, a sparse matrix is obtained containing the d^2's for all combinations of predictions (i) and observations (j) for ping k that fall inside the gates. The association algorithm assigns observations to predictions based on the elements in this matrix. Several data-association methods are described in the literature.[8] One of the most common is the global nearest neighbor (GNN) method, which assigns observations to tracks by minimizing the total sum of distances. In this case an assignment with a higher d^2 may be chosen at a given time step if the total cost is lower. This assignment problem is solved by the Bertsekas auction algorithm.[9] We also implemented a simpler algorithm that first assigns the best pairing at each time step, then the next best, continuing until all observations inside the gates are assigned. In this case the total sum of distances may be higher than for the GNN method. We have compared the methods with respect to their data-association errors.

3. Track support

The last part of the MTT algorithm is track support. This starts, terminates, and validates the tracks. When an observation is not connected to an existing track, a new one is spawned. The new track state starts with the position indicated by the observation, the velocity set to zero, and $\Sigma_{\mathbf{x},0}$ as an assumed error covariance. A track is terminated at the last ping before the first sequence of MP consecutive missing pings. The track is rejected if it is less than ML (minimum track length), or if the number of missing pings divided by the track length is more than MN. The track length is simply the number of pings from start to finish, including any missing pings.

B. Other track-state estimators

In the previous section, the EKF was used both for prediction and estimation of the track state. Since the EKF estimates the new track state based on the new associated measurements and the present track prediction only, this technique is well suited to be integrated with the gating and data-association algorithms. However, after the measurements have been associated, other techniques can be used to estimate the position and velocity of the targets. The additional techniques we have tested are the Kalman-smoothing algorithm, linear regression, and a smoothing spline.

After estimating the tracks with the Kalman filter and computing the track-support functions, a Kalman smoothing algorithm may be applied. The advantage over the Kalman-

filter algorithm is that the influence of the initial values (zero velocity and $\Sigma_{\mathbf{x},0}$) is avoided. This is achieved by using the Kalman-filter predictions and estimates to compute the Kalman smoothed estimate

$$\hat{\hat{\mathbf{x}}}_k = \hat{\mathbf{x}}_k + J_k(\hat{\hat{\mathbf{x}}}_{k+1} - \Phi(\Delta T_k)\hat{\mathbf{x}}_k),$$

with covariance

$$\hat{\hat{\Sigma}}_{\mathbf{x},k} = \hat{\Sigma}_{\mathbf{x},k} - J_k(\hat{\hat{\Sigma}}_{\mathbf{x},k+1} - \tilde{\Sigma}_{\mathbf{x},k+1})J_k^T,$$

by moving backwards through the track. Here

$$J_k = \hat{\Sigma}_{\mathbf{x},k}\Phi(\Delta t_k)^T\hat{\Sigma}_{\mathbf{x},k}^{-1}.$$

Both the Kalman filter and the Kalman smoother estimate the position and velocity errors. However, the comparison with other methods is based on the position and velocity estimates only, not the errors. For the Kalman-filter estimate we define position and velocity vectors

$$\hat{\mathbf{s}}_k^{\mathrm{KF}} = \hat{\mathbf{x}}_{k[1\cdots3]}, \quad \hat{\mathbf{u}}_k^{\mathrm{KF}} = \hat{\mathbf{x}}_{k[4\cdots6]}$$

and for the Kalman smoothed estimate

$$\hat{\mathbf{s}}_k^{\mathrm{KS}} = \hat{\hat{\mathbf{x}}}_{k[1\cdots3]}, \quad \hat{\mathbf{u}}_k^{\mathrm{KS}} = \hat{\hat{\mathbf{x}}}_{k[4\cdots6]}.$$

The linear regression and the smoothing spline methods require us to map the measurements $\mathbf{y}_k$ to Cartesian coordinates (e_{gc}). This is achieved using the estimated platform state $\hat{\mathbf{z}}$,

$$\mathbf{s}_k = \mathbf{g}(\mathbf{y},\hat{\mathbf{z}}) = \begin{bmatrix} x \\ y \\ z \end{bmatrix}_{e_{gc}},$$

where $\mathbf{g}$ is found from $\mathbf{h}$ (see Appendix B). A constant-velocity track,

$$\mathbf{s}_k^L = \mathbf{s}_0^L + \mathbf{u}^L t_k, \tag{10}$$

is then fitted to $\mathbf{s}_k$ by minimizing $SS=\Sigma_{\mathbf{k}}\|\hat{\mathbf{s}}_k^L-\mathbf{s}_k\|_2^2$, and $\hat{\mathbf{s}}_0^L$ and $\hat{\mathbf{u}}^L$ are found. However, a straight regression line through the $\mathbf{s}_k$'s may be a rather crude approximation. Therefore, we also used a smoothing spline, which minimizes a compromise between the exact fit and the smoothness of the track. This is implemented in the R function[10] smooth.spline, where the degree of smoothness can be chosen automatically by cross validation, or by setting the parameter "spar" to a given value. We have used both the nonparametric (cross validation) and parametric (spar=0.7) methods, denoted by s_k^{SNP} and s_k^{SP}, respectively. For details see the documentation of smooth.spline in the R program,[10] and the standard-S literature.[11]

C. Platform-state estimation

When tracking targets from vessels and buoys, the position and the direction of the acoustic beam may change from ping to ping. Knowledge of the transducer position and orientation is required for accurate results. There are standard notation and sign conventions for the motion of a submerged body.[12] However, the angles defined in this section are relative to the east-west and north-south directions, not the vessel heading, i.e., the measurements of ship or buoy motion have to be mapped into $\mathbf{z}_k$ before evaluating Eq. (3). If direct measurements of transducer position and orientation were available, the initial tracking and platform-state estimation would be unnecessary.

However, this is often not the case. We have therefore developed a method to extract correlated fish movements relative to the acoustic beam, based on the association from the initial tracking. This common movement is attributed to movement of the transducer platform. In our test data, the transducer compass direction and the GPS positions are measured, while the tilt, roll, and heave are unknown. The unknown platform-state variables are set to zero before initial tracking. The measurements are mapped from e_{tp} coordinates to e_{gp} coordinates (see Appendix B for details), and the mean differences in angles and range between successive pings are used to estimate the transducer movement. For the east-west angle the mean difference is computed as

$$\delta_{\theta_k} = \frac{1}{N_k}\sum_{i=1}^{N_k}(\theta_{ki} - \theta_{k+1,i}), \tag{11}$$

where k is the ping number, i is the track number, N_k is the number of tracks with measurements in both ping k and $k+1$, and θ is the east-west angle to the target relative to the transducer position. Some tracks are short and are therefore rejected by the track-support functions. However, in this procedure these short tracks are retained since the platform movement may split tracks.

If fish are swimming in one direction through the beam, consecutive δ_{θ_k} will be positive. If the transducer is moving cyclically, consecutive δ_{θ_k} will vary from positive to negative within the cycle. To extract this cyclical movement, the differences are summed cumulatively to get $\theta'_{\mathrm{RAW},k}=\theta'_{\mathrm{RAW},k-1}+\delta_{\theta_k}$, starting with $\theta_0=0$. To compensate the effect of polarized swimming, a running-mean filter is used to remove the drift component (platform translation and fish migration) from $\{\theta'_{\mathrm{RAW},k}\}$,

$$\hat{\theta}_k = \theta'_{\mathrm{RAW},k} - \frac{1}{2M+1}\sum_{l=k-M}^{k+M}\theta'_{\mathrm{RAW},l},$$

where M is here the length of the running-mean filter. We set M equal to $1/f_0$ rounded up to the nearest integer, where f_0 is a constant defining the lowest tilt/roll frequency that the algorithm can detect. To estimate the north-south and range components of the transducer movement, the same process is applied to ϕ' and z'. Then the tracking is repeated utilizing the obtained estimates of transducer tilt, roll, and heave.

D. Testing data association

To test the performance of the data association algorithms, the buoy data set is first tracked manually (true tracks), and then compared with the tracks obtained from the various algorithms (auto tracks). The auto-track identifiers are compared with the true-track identifiers. If the auto-track identifier changes along a true track, a split error has oc-

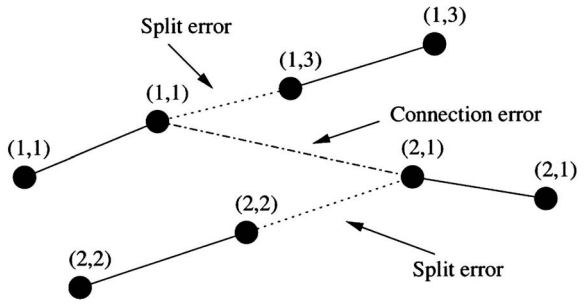

FIG. 3. The splits and false associations of a true track compared with an auto track. The pairs of numbers show (true-track number, auto-track number). The split error is found by counting the number of auto-track number changes along the true tracks (1+1) divided by possible number of changes (3+3). The connection error is the number of true-track changes along the auto tracks (1+0+0) divided by the possible number of changes (3+1+1).

curred. If the true-track identifier changes along an auto track, a connection error has occurred. The measure for track splitting is defined as

$$J_{\text{split}}(\mathbf{p}) = \frac{\Sigma_i C_i^s}{\Sigma_i (L_i - 1)}, \tag{12}$$

where $\mathbf{p}$ gives the parameter settings, C_i^s is the number of changes in the auto-track identifier along the true track i, and L_i is the length of the true track i. An example is given in Fig. 3. The measure for false associations is similarly defined as

$$J_{\text{connect}}(\mathbf{p}) = \frac{\Sigma_i C_i^c}{\Sigma_i (L_i - 1)}, \tag{13}$$

where C_i^c is the number of changes in the true-track identifier along auto track i and L_i is the length of auto track i. The two measures are combined into a single measure of the association error

$$J_{\text{alloc}} = \tfrac{1}{2}(J_{\text{split}} + J_{\text{connect}}). \tag{14}$$

To test the parameter sensitivity to the data association error, the tracker is run with one parameter perturbed by ±10% at each run. The sensitivity measure is defined as

$$S_{pa} = 0.5\left(\frac{|\Delta J_{+10\%}|}{J_{\text{alloc}}} + \frac{|\Delta J_{-10\%}|}{J_{\text{alloc}}}\right)\left(\frac{|\Delta p|}{p}\right)^{-1}, \tag{15}$$

where $\Delta J_{+10\%}$ and $\Delta J_{-10\%}$ are the changes in J_{alloc} when perturbing parameter $p \pm 10\%$, $\Delta p/p = 0.1$, except for MP, which is an integer. To test the sensitivity to MP, this parameter is increased or decreased by one. A relative measure is still used, i.e., $\Delta p/p = 1/\text{MP}_0$, where MP_0 is the unperturbed value.

E. Testing position and velocity estimates

A simulated data set is used to test the validity of the position and velocity estimates for each track. Different fish trajectories are simulated, including transducer tilt/roll effects. The track states estimated by the various techniques are then compared with the known positions and velocities from the simulations. The simulated data comprise four constant-speed tracks: two straight lines and two half circles (see Table II). Instead of simulating transducer tilt/roll/heave, we estimated the transducer platform state from the test data, $\hat{\mathbf{z}}_{k,\text{testdata}}$. These estimates are taken as the true platform state in the simulations, i.e., $\mathbf{z} = \hat{\mathbf{z}}_{k,\text{testdata}}$. This is applied only to the tilt/roll/heave; the transducer translation and compass heading are set to zero. The simulated tracks are mapped to measurement space and an error is added according to

$$\mathbf{y}_k = \mathbf{h}(\mathbf{x}_k, \mathbf{z}_k, \mathbf{0}) + \mathbf{v}_{k[7\cdots10]}. \tag{16}$$

To simulate missing pings, randomly selected data points are removed from the tracks. Short tracks are simulated by termination after the desired track length (L). Distributions of the track lengths and the ratio of missing pings to the track length are calculated from the test data. To make the test more realistic, we simulated 1230 data sets based on these distributions. An overview of the simulated data sets is given in Table III.

The mean along-track errors in position and velocity,

$$\text{ME}_s = \frac{1}{L}\sum_{k=1}^{L} \|\hat{\mathbf{s}}_k^E - \mathbf{x}_{k[1\cdots3]}\|_2 \tag{17}$$

and

$$\text{ME}_u = \frac{1}{L}\sum_{k=1}^{L} \|\hat{\mathbf{u}}_k^E - \mathbf{x}_{k[4\cdots6]}\|_2, \tag{18}$$

are evaluated as measures of the fit between the true and estimated position and velocity, respectively. Here L is the track length and E denotes the estimation technique (KS, KF, L, SNP, or SP). The means ME_s and ME_u are calculated for each of the four tracks in all the simulated data sets, using all the estimation techniques. Note that for the constant-velocity tracks, $\hat{\mathbf{u}}_k$ is the same for all k's.

The sensitivity of the estimated position and velocity to the tracking parameters is tested. The manually associated data set is the reference. Thus we can compare the impact of different parameter settings on the track estimates of the described algorithms. The sensitivity measure is

TABLE II. The simulated tracks.

Track	Curve	Speed (m/s)	Direction	Depth
1	Line	0.53	NE	200
2	Line	0.37	E	150
3	Semicircle	0.589	N to S	230
4	Semicircle	0.589	N to S	170

TABLE III. The number of simulated data sets for each track length (L) and each missing ping to track length ratio (MN). There are several duplicates for each setting due to the added normally distributed error.

		L						
		15	25	35	45	55	65	75
MN	0.1	90	120	60	60	30	30	30
	0.3	120	160	80	80	40	40	40
	0.5	60	80	40	40	10	10	10

$$S_{ps} = \frac{1}{\sum_{i=1}^{M} L_i} \sum_{i}^{M} \sum_{k}^{L_i} \|\hat{\mathbf{s}}_{ik}^{E} - \hat{\mathbf{s}}_{ik}^{E_p}\|_2 \tag{19}$$

for the position estimates and

$$S_{pv} = \frac{1}{\sum_{i=1}^{M} L_i} \sum_{i}^{M} \sum_{k}^{L_i} \|\hat{\mathbf{u}}_{ik}^{E} - \hat{\mathbf{u}}_{ik}^{E_p}\|_2 \tag{20}$$

for the velocity estimates. Here M is the number of tracks, L_i is the track length for track i, $\hat{\mathbf{s}}_{ik}^{E}$ and $\hat{\mathbf{u}}_{ik}^{E}$ are the position and velocity estimates for track i at time t_k using estimation technique E and the optimal parameter setting for the data association error, and $\hat{\mathbf{s}}_{ik}^{E_p}$ and $\hat{\mathbf{u}}_{ik}^{E_p}$ are the position and velocity estimate where parameter p is perturbed. The parameters are perturbed by ±10%, one at a time. The mean S_{ps} and S_{pv} are calculated for each parameter and each estimation technique.

IV. RESULTS

The various methods for data association and track estimation are examined by comparing the tracker results obtained, respectively, with simulated data and the test data. The questions are: how do the different data association algorithms perform, how accurate are the velocity and position estimates, and does the estimation of platform state improve the results?

TABLE IV. The test cases for the manually associated data.

Case	Description
1	Kalman prediction with a fixed Euclidean gate (static gate)
2	"Zero-velocity" prediction with a fixed Euclidean gate (static gate)
3	Kalman prediction with a maximum likelihood gate (dynamic gate)
4	As case 1, but with no correction for platform movement
5	As case 2, but with no correction for platform movement
6	As case 3, but with no correction for platform movement

A. Data association

We tested the performance of six different cases of data association on the manually associated data sets (see Table IV). The association measures defined in Eqs. (12)–(14) are used in the tests. All cases were tested with both GNN and BPF data-association methods.

TABLE V. List of parameters and the optimal parameter settings for the different cases. See Appendix A and Appendix B for details of the error model parameters. N/A indicates "not applicable." Note that all angles (θ, ϕ, ψ, α, and β) are given in degrees.

		Case 1	Case 2	Case 3	Case 4	Case 5	Case 6
Σ_{Φ}	Q_{xy}	0.100	0.100	0.100	0.100	0.100	0.100
	Q_z	0.050	0.050	0.050	0.050	0.050	0.050
	Q_{dxdy}	0.150	0.149	0.151	0.150	0.148	0.151
	Q_{dz}	0.100	0.100	0.100	0.100	0.100	0.099
$\Sigma_{\mathbf{x},0}$	$P_{0\ xy}$	0.200	0.200	0.200	0.200	0.200	0.200
	$P_{0\ z}$	0.100	0.100	0.100	0.100	0.100	0.100
	$P_{0\ dxdy}$	0.300	0.300	0.300	0.300	0.298	0.300
	$P_{0\ dz}$	0.200	0.200	0.200	0.200	0.200	0.200
Σ_R	$R_{x'}$	0.100	0.100	0.100	0.100	0.100	0.100
	$R_{y'}$	0.100	0.100	0.100	0.100	0.100	0.100
	$R_{z'}$	1.000	1.000	1.000	1.000	0.980	1.005
	$R_{\Theta'}$	1.000	1.000	0.995	1.000	1.005	0.995
	$R_{\phi'}$	1.000	1.000	1.000	1.000	1.005	0.995
	$R_{\psi'}$	0.500	0.500	0.500	0.500	0.500	0.500
	R_{α}	0.500	0.500	0.500	0.500	0.500	0.497
	R_{β}	0.500	0.500	0.500	0.500	0.502	0.500
	R_r	0.100	0.100	0.100	0.100	0.100	0.100
	R_{TS}	0.000	0.000	0.000	0.000	0.000	0.000
Track support	f_0	0.050	0.049	0.050	0.050	0.049	0.050
	MN	0.400	0.400	0.400	0.400	0.400	0.400
	MP	4.000	5.000	5.000	4.000	5.000	4.000
	ML	15.000	15.000	15.000	15.000	15.000	15.000
Initial gate	$\alpha_{G1}\beta_{G1}$	3.940	4.020	N/A	3.940	4.020	N/A
	r_{G1}	1.000	1.000	N/A	1.000	1.000	N/A
	c_{G1}	N/A	N/A	1.000	N/A	N/A	1.000
Final gate	$\alpha_{G2}\beta_{G2}$	6.862	4.018	N/A	6.724	4.996	N/A
	r_{G2}	1.082	1.000	N/A	1.082	1.040	N/A
	c_{G2}	N/A	N/A	1.000	N/A	N/A	1.000

TABLE VI. The data-association error for the six cases. The optimal parameter settings for each case are given in Table V.

	Case 1	Case 2	Case 3	Case 4	Case 5	Case 6
J_{alloc}	0.017	0.022	0.041	0.017	0.026	0.061
J_{split}	0.008	0.020	0.041	0.014	0.038	0.060
J_{connect}	0.025	0.024	0.041	0.021	0.014	0.062

To do a fair comparison of the methods, we use the parameters that give the lowest J_{alloc} for each case. These parameters are found initially by a searching over the parameter space, then a gradient method is used to minimize J_{alloc}. The resulting parameters are given in Table V. Note that MN and ML are not in the optimization since the association measure does not contain a penalizing term for excluding short tracks. If the longest track is correctly associated, the optimal ML will be equal to the length of the longest track. The parameter estimation procedure is performed using the BPF data-association algorithm.

The split error, the connect error, and the association error for the six cases are given in Table VI. The GNN and BPF methods showed no difference in the data association error, and BPF is used since it is computationally less demanding. The association error is lower for a static gate compared to a dynamic gate. Velocity prediction (cases 1 and 4) decreases the association error. Note that the optimal final horizontal gates (α_{G2} and β_{G2}) are larger when velocity prediction is included (see Table V). The platform-state estimation gives little improvement. When velocity prediction is used (cases 1 and 4), the connect error increases by 25%, while the split error is reduced by 50% by the platform estimation.

Another way to evaluate the effect of platform-state estimation is to look at the distribution of the innovations (i.e., the differences between predictions and observations). The innovation distributions for the initial and final tracking results for case 1 are shown in Fig. 4. To compare the distributions, the initial gate is set equal to the final gate. The innovation distribution is shifted left, indicating a better fit between prediction and measurement. Examples of data with and without correction for platform movements are given in Figs. 5 and 6.

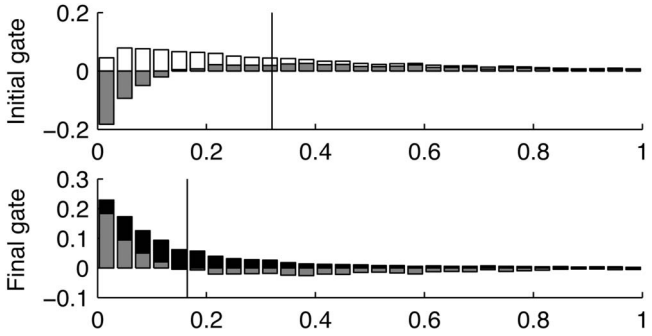

FIG. 4. The white bars (upper panel) and black bars (lower panel) show the gate distance (d^2) distribution for case 1 without and with platform-state estimation, respectively. The gray bars indicate the difference between the distributions. The vertical lines indicate the means for the distributions.

As indicated above, changes in the various parameters influence the association error. The sensitivity index defined in Eq. (15) is used to test this, and the results are shown in Fig. 7. The results are sensitive to MP and MN in all cases. When using static gates, the gate parameters are important. In particular, note the high sensitivity when platform-state estimation is omitted. This is seen for the vertical gates in cases 4 and 5, and especially for the horizontal gates in case 5. The sensitivity to horizontal gates is lower when velocity

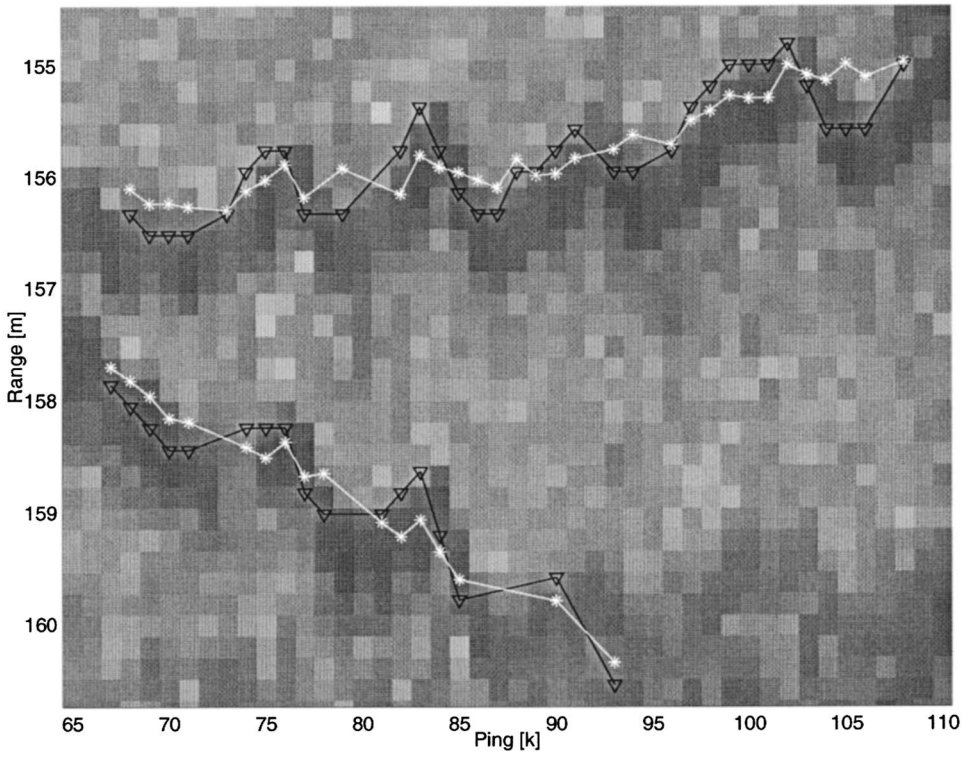

FIG. 5. Range as a function of ping number for two tracks. Asterisks (white) and triangles (black) show the tracks with and without buoy movement estimation, respectively.

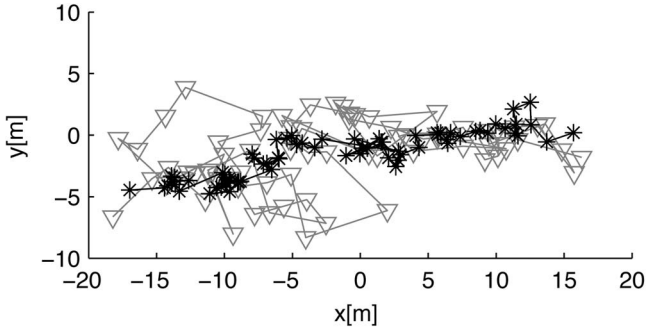

FIG. 6. Horizontal positions for a single track. Asterisks and triangles show the track with and without buoy movement estimation, respectively.

prediction is used. The sensitivity to the error model parameters (R) is higher when using dynamic gates. Note also that the detection probabilities, hidden in c_G, are less important compared to the error model parameters.

B. Track state estimation

We used the simulated data sets described in Sec. III E to investigate the accuracy of the various track-state estimators. The data sets are tracked, with and without platform-state estimation, and the position and velocity estimates are evaluated using the measures defined in Eqs. (17) and (18).

Tables VII and VIII show the mean position and velocity errors for the five estimation techniques and for three different scenarios. Firstly, the data are simulated with platform movement, and platform-state estimation is applied. Secondly, the platform movement is simulated but not estimated. The last simulation is the "control," where platform movement is neither simulated nor estimated. Comparing the results with and without platform movement estimation, the position estimate error is reduced for the Kalman methods KS and the KF when the platform movement is estimated, but for the L and SP methods it increases. For the velocity estimates, the errors of KS indicate divergence in all cases.

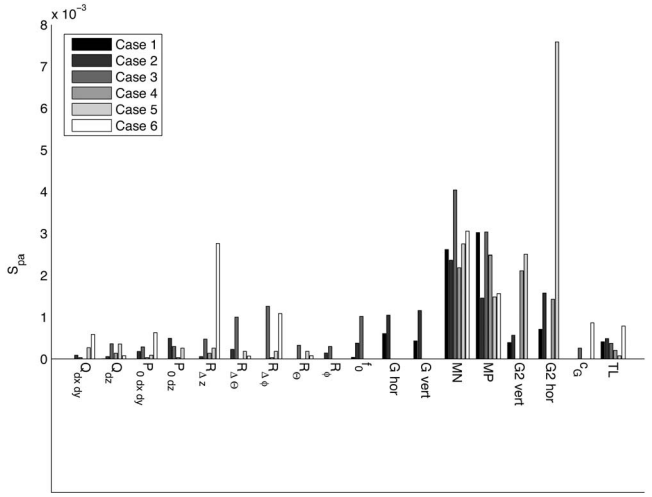

FIG. 7. Sensitivity indices for association error, S_{pa}. Nonsensitive parameters are not included.

TABLE VII. Mean absolute position errors for different track-state estimators.

	KS	KF	L	SNP	SP
PlatMove, PlatEst.	1.082	1.368	1.628	1.336	1.158
PlatMove, No PlatEst.	1.929	2.577	1.303	3.295	0.829
No PlatMove, No PlatEst.	0.627	1.138	1.029	0.417	0.346

For KF and the SNP the velocity error is reduced by estimating the platform state, whereas for L and SP the error levels are similar.

The sensitivity to the estimated velocity and position is tested by calculating the measures S_{ps} and S_{pv}, using the various track-state estimators on the test data set described in Sec. II. The position sensitivity measure, S_{ps}, is the mean difference in position. The position estimates deviate at the most 0.3 m when perturbing the parameters ±10% (Fig. 8), and they depend mainly on f_0. This parameter controls the platform estimation. All the techniques are equally sensitive, except that SP is also sensitive to the smoothing parameter spar.

As regards the velocity estimates, there are differences between the techniques, although all except SP are most sensitive to changes in f_0 (Fig. 9). The sensitivity to f_0 is extremely high for KS and SNP, while it is lower for KF and SP, with L being the most robust method. Note also the high sensitivity to *spar* for the SP method.

V. DISCUSSION

This paper presents a general framework for tracking fish with a split-beam echosounder when the transducer is moving. The performance of various methods of data association and track estimation is investigated.

A. The extended Kalman filter

The extended Kalman filter serves two purposes in the MTT. It links observations to predictions, taking into account errors due to the prediction, the echosounder, and the platform movement, and it is used to estimate positions and velocities. The extended version of the Kalman filter is required due to the nonlinear relationship between the measurement space and the state space. The main contribution here is a framework for tracking when the error models are known. The track-state-transition error may be seen as the deviation in swimming speed from a straight line (constant velocity) and has nothing to do with the measurement errors. This enables us to separate the observation error from that due to nonconstant fish velocity. Track state transition models based on the observed behavior, the coordinated turn model, for

TABLE VIII. Mean relative velocity errors for different track-state estimators.

	KS	KF	L	SNP	SP
PlatMove, PlatEst.	315%	52%	31%	68%	32%
PlatMove, No PlatEst.	721%	88%	28%	815%	35%
No PlatMove, No PlatEst.	428%	51%	23%	45%	16%

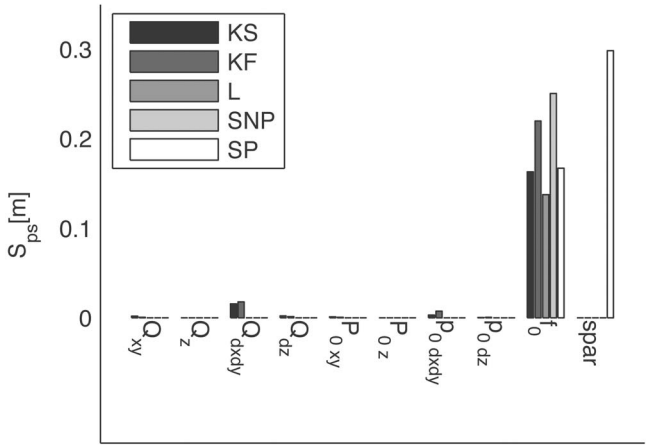

FIG. 8. Sensitivity indices for estimated position, S_{ps}. The P and Q parameters are the elements of the parametrized $\Sigma_{\mathbf{x},0}$ and Σ_Φ, respectively. See Eqs. (6) and (A1) for details. Nonsensitive parameters are not included.

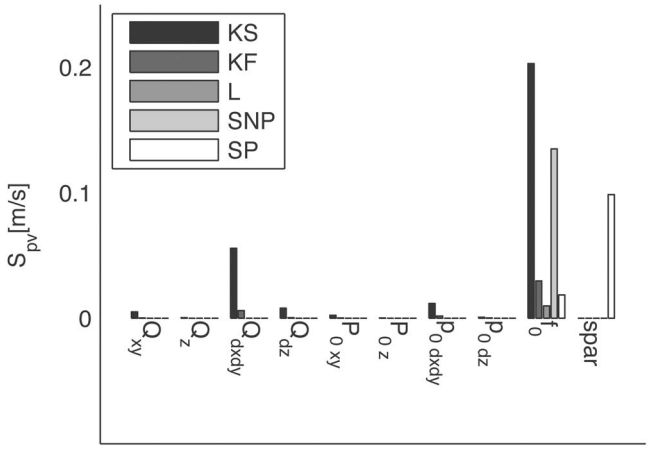

FIG. 9. Sensitivity indices for estimated velocity, S_{pv}. The P and Q parameters are the elements of the parametrized $\Sigma_{\mathbf{x},0}$ and Σ_Φ, respectively. See Eqs. (6) and (A1) for details. Nonsensitive parameters are not included.

example,[5] might improve the track-state transition (prediction). We decided against that approach because of the large errors in our observations. The convergence of the Kalman filter depends on the error model. This is discussed in Sec. IV D.

To take full advantage of the EKF, proper error models for the measurements and state transitions should be established. This would allow us to estimate the track state including both error models. This is not a feature of the alternative track-state estimators, except KS, and is the reason for the central role the EKF has in this work.

B. Platform-state estimation

Since we had no measurements of the platform tilt and roll, there was a need to estimate this movement somehow. We used a simple approach to solve this problem, but other techniques like fitting a model of wave-induced movement to the data could be considered. We tried using a bandpass filter to remove low and high frequencies, but the association error was more than that of our simple algorithm (which may be compared to a high-pass filter). We therefore chose not to proceed with more elaborate models. The reason why the simple filter works well in our example is probably due to the rigging of the transducer. The transducer hangs from a cable, and the dynamics of this arrangement are complicated. The motion of a transducer attached to a ship's hull is probably simpler to model, and more complex models may improve performance in that case. It is important to note that our method does not detect any constant tilt of the acoustic axis; only the periodic movement about the (unknown) mean is estimated. If measurements of the platform state are available, the platform estimation technique and the second tracking are unnecessary.

The algorithm seems to estimate the platform state quite well, but what are the consequences of utilizing these estimates? This is discussed below, both for data-association error and track-state estimation.

C. Data association

Correct data association is crucial for successful tracking. If the data-association algorithm fails, the platform state and the tracks will be poorly estimated. An important part of the data association is accurate prediction. We have tested two kinds of predictions, the constant-velocity prediction and the "zero-velocity" prediction. When comparing the constant-velocity and "zero-velocity" predictions, we see that the split error is smallest in the former prediction (cases 1 and 4). This indicates a better result from the constant-velocity prediction, which allows the data-association algorithm to handle more candidates within a gate, hence the larger optimal horizontal gates for cases 1 and 4. However, the larger horizontal gates cause more connection error, although the total association error is still improved. There is a trade-off between connect and split errors. If one desires to reduce the connect error, narrower horizontal gates may be applied. The total association error is then increased, but it is still lower than that of the "zero-velocity" prediction. We conclude that it is better to base predictions on the actual velocity estimates rather than the zero-velocity assumption.

The platform-state estimation has a similar effect: The split error is reduced, while the connect error is increased, but here the total association error remains the same. The benefit of platform-state estimation in the data-association process is not evident. However, if we decrease the horizontal gates from 6° to 4°, the platform-state estimation does improve the results. The J_{alloc} is then 0.07 and is reduced to 0.02 after platform-state estimation. For some parameter values the platform-state estimation is important, but not when using the optimal settings for our example. However, when considering the innovation distribution, it is seen that the platform-state estimation reduces the distance between the predictions and the observations. In addition, the sensitivity to the gate parameters is higher without platform-state estimation. Thus, the platform-state estimation makes the association algorithm more robust.

We tried to implement maximum-likelihood track-support functions.[5] This would avoid *ad hoc* parameters like missing pings, MN ratio, and predetermined gates. The idea

is to use the prediction covariance to define the gate, but it is necessary to estimate the detection probabilities. We tested whether we could improve the results by setting constant detection probabilities and then optimizing the parameters with respect to the data-association error. These probabilities are in fact not constant, and we were unable to come close to the performance of a fixed Euclidean static gate and *ad hoc* parameters. One reason for the failure could be the narrow acoustic beam. The transducer's pendulum movement causes the detection probabilities to change rapidly, thus the use of constant parameter values may be incorrect. Consequently, we cannot rule out the possibility that the maximum-likelihood track-support functions may work. However, with the accuracy of the detection probabilities and the error models in mind, we believe that the *ad hoc* approach is more robust.

A similar situation is found for the data-association algorithms. Although the GNN algorithm is quite simple, the even simpler method of picking the nearest target first works equally well. This indicates that the system has low vulnerability to the choice of the data-association algorithm. This may be explained by the nature of the SED which detects only one target at a given range, and rejects closely spaced targets. It is concluded that the choice of data-association algorithm is not crucial to the result. These conclusions are based on the data-association test. A crucial part in the test is the validity of the true tracks. These are obtained by first applying the tracker and then correcting the tracks manually. The manual data association is subjective to some extent, and only the target range, not the angles, is used in the manual process. Therefore some false track connections might occur. In addition, our results are based on only one data set, and the result is, strictly, only valid for this data set. The convergence of the optimization algorithm is also important. If the algorithm sticks on a local J_{alloc}, wrong conclusions may be drawn. Also, the relative weights of J_{split} and J_{connect} influence the results, as illustrated by the above-mentioned example of increased horizontal gates.

For our data, the constant-velocity prediction improves data association, while the platform-state estimation reduces the sensitivity to the gate parameters. In general, these effects are connected, and we argue that both methods improve the quality of the data association.

D. Track-state estimators

The validity of the estimated positions and velocities are central to the success of the tracker. Tracking fish from a free-floating and moving buoy with high noise in the positioning may require a different approach compared to the analysis of fine-scale behavior from a known or stable platform state.

The Kalman filter (KF) is an integral part of the MTT, and error models of the measurements and fish movement are taken into account. The KF works well for the position estimates. Each position includes an estimate of the error, assuming that the error models are correct. The velocity estimate is less good. One reason is that the initial velocity is set to zero, and it takes several pings for the velocity estimate to converge. This depends on the initial state estimate error and the measurement error model. An important feature of the KS estimate is that the tracker runs backwards through the tracks, thus eliminating the impact of the initial estimate covariance. The problem with KS is that accurate error models and platform-state estimates are usually necessary to prevent the results from diverging. In our case this was not so. KS is excellent for the position estimates, which are greatly improved when the platform estimation technique is applied.

A linear regression fit to the track loci may be a crude approximation. This is seen in the rather poor position estimates obtained from the regression method. However, the linear regression L is a robust method for estimating velocity. The velocity estimate from L is the same with or without platform-state estimation. This occurs because the periodic buoy movement is removed by the straight-line regression, provided the tracks are longer than half the period of the platform movement. Another advantage is the low sensitivity to the tracking parameters. The simple linear regression is a good choice when the noise level is high and a robust method is required, although the amount of detail in the results is limited.

The nonparametric spline works fairly well for the position estimates. Cross validation is used to set the parameters in the interpolation. This approach automatically determines the relative weights according to smoothness and fit and has the advantage that *ad hoc* parameters are avoided. However, the estimated positions are rather bad if the platform-state estimation is omitted. The cross-validation technique detects the periodic movement of the platform and tends to follow the observations and the buoy movement closely. This leads to bad position estimates. The velocity estimate of SNP is unsatisfactory. The derivative of the spline is used, and if the degree of smoothness is too low, the velocities will be grossly over estimated. On the other hand, SP seems to work well with spar=0.7. This velocity estimate is the best, but it is highly sensitive to spar. When a high degree of smoothing is applied, the spline smooths the buoy movement in a similar manner to the linear regression. In that case, there is no evidence that estimating the buoy movement is useful.

As discussed earlier, the various track-state estimators have different properties. However, these conclusions are based on the simulated data set, which is similar to our test data set. For our test data the robust linear regression seems to be the best choice. Other data sets may have different properties, like higher ping rates, fewer missing pings, etc. It might then be feasible to incorporate more detailed track-state estimators. A general statement of what is the best estimator is therefore difficult.

E. Other tracking issues

Although we have said little about the algorithm for single-echo detection (SED), the efficiency of this algorithm is an important factor in target tracking. Traditional SED methods are discussed in the literature.[3] For weak targets, systematic angle measurement errors may occur.[13] If the SED were improved, the maximum allowed number of missing pings could be reduced with consequent benefits for the

platform-state estimation, the data association, and the track estimation. There are promising developments in this field.[14]

The orientation of the transducer may change between the transmitted and the received pulses. The adverse effect on echo integration has been investigated.[15] The same problem may affect the SED efficiency, and also the target-angle measurements. This requires further investigation, as regards the effects on target detection algorithms and the performance of target trackers.

VI. CONCLUSIONS

We have shown that compensating for platform movement improves the quality of the data association, especially when that is combined with predictions. Consequently, the platform state should be taken into account whenever possible, and predictions should be based on the estimated velocity. The various data-association algorithms we tested performed very similar in our case, and we conclude that the tracker is not sensitive to the choice of data-association algorithm. On the other hand, the choice of gate had a large influence, and we found that the simple static gate worked best in our case. However, we cannot rule out the idea that dynamic gates might perform better, given better knowledge of detection probabilities and improved error models.

The choice of state estimation technique depends on the quality of the data and how they are used. For example, more detailed methods like SNP and KS require more accurate estimates of platform state in order to perform well. Coarse-scale estimators like linear regression are less vulnerable to incorrect platform-state estimates. Velocity is more difficult to estimate than position, and this should be taken into consideration when choosing the track-state estimator. For our data, the linear regression yielded a robust and relatively accurate estimate of the velocity.

The EKF approach differs from the other techniques for estimating the track state, since it takes account of errors both in the measurements and in the prediction model, and it models the two error types separately. To take full advantage of this approach, better error models must be developed. This work presents the framework for such an approach which, in our opinion, is the natural next step.

ACKNOWLEDGMENTS

We are grateful to Professor Egil Ona for useful comments on the manuscript and ideas and suggestions during the development of the method. The Norwegian Research Council has financially supported the work (Project 133426/120).

APPENDIX A: THE TRACK-STATE TRANSITION

Under the assumptions of constant velocity, the track state at time $t_{k+1}=t_k+\Delta T$ is given by

$$\mathbf{x}_{k+1}=\Phi(\Delta T)\mathbf{x}_k+\mathbf{w}_\Phi,$$

where $\Phi(\Delta T)$ is the track-state-transition matrix for the time interval ΔT and $\mathbf{w}_\Phi$ is an additive system error component. The track-state-transition matrix is given by

$$\Phi(\Delta T)=\begin{bmatrix} 1 & 0 & 0 & \Delta T & 0 & 0 & 0 \\ 0 & 1 & 0 & 0 & \Delta T & 0 & 0 \\ 0 & 0 & 1 & 0 & 0 & \Delta T & 0 \\ 0 & 0 & 0 & 1 & 0 & 0 & 0 \\ 0 & 0 & 0 & 0 & 1 & 0 & 0 \\ 0 & 0 & 0 & 0 & 0 & 1 & 0 \\ 0 & 0 & 0 & 0 & 0 & 0 & 1 \end{bmatrix},$$

and the target-model-covariance matrix is defined as $\Sigma_\Phi=E(\mathbf{w}_\Phi\mathbf{w}_\Phi^T)$. The error is assumed normal, independent, and constant for all track-state variables and

$$\Sigma_\Phi=[Q_{xy}^2 \quad Q_{xy}^2 \quad Q_z^2 \quad Q_{dxdy}^2 \quad Q_{dxdy}^2 \quad Q_{dz}^2 \quad Q_{TS}^2]I \tag{A1}$$

where the elements are parameters and I is the identity matrix.

APPENDIX B: THE MEASUREMENTS

A split-beam echosounder with an algorithm for single echo detection calculates the alongship angle α_k, the athwart ship angle β_k, the range r_k, and the target strength TS_k, for each target inside the sampled volume at every time step k. These measurements are represented by

$$\mathbf{y}_k=[\alpha_k \quad \beta_k \quad r_k \quad \mathrm{TS}_k]_{e_{tp}}^T+\mathbf{v}_{y,k}.$$

The measurement has an additive error component, $\mathbf{v}_{y,k}$, given by the accuracy of the transducer.

The transducer platform state is described by the position, $\hat{x}'$, $\hat{y}'$, and $\hat{z}'$ relative to geo-referenced coordinates (e_{gc}), the transducer yaw (transducer compass reading) ψ', and the tilt angles θ' and ϕ' relative to east-west and north-south directions, respectively (see Fig. 2). Note that this is not the same as the usual vessel tilt and roll angles,[12] which are relative to vessel heading. The translation, tilt, and twist of the transducer are given by

$$\mathbf{z}_k=\hat{\mathbf{z}}_k+\mathbf{v}_{y,k}=[\hat{x}' \quad \hat{y}' \quad \hat{z}' \quad \hat{\theta}' \quad \hat{\phi}' \quad \hat{\psi}']_{e_{gc}}^T+\mathbf{v}_{z,k},$$

where $\mathbf{v}_{z,k}$ is the additive error component. The error terms are combined into

$$\mathbf{v}_{R,k}=\begin{bmatrix}\mathbf{v}_{z,k}\\ \mathbf{v}_{y,k}\end{bmatrix}$$

and assumed additive and normal with covariances $\Sigma_{R,k}=E(\mathbf{v}_k\mathbf{v}_k^T)$. The covariances are given as

$$\Sigma_{R,k}=\begin{bmatrix}\Sigma_{z,k} & 0\\ 0 & \Sigma_{y,k}\end{bmatrix},$$

where

$$\Sigma_{z,k}=[R_{x'}^2 \quad R_{y'}^2 \quad R_{z'}^2 \quad R_{\Theta'}^2 \quad R_{\phi'}^2 \quad R_{\psi'}^2]I$$

and

$$\Sigma_{y,k}=[R_\alpha^2 \quad R_\beta^2 \quad R_r^2 \quad R_{TS_k}^2]I.$$

Here the elements are parameters and I is the identity matrix.

The mapping from state space to measurement space, $\mathbf{h}:(\hat{\mathbf{x}}_k,\hat{\mathbf{z}}_k,\mathbf{v}_k)\rightarrow\mathbf{y}_k$, is a central part in the EKF. The mapping involves Cartesian translation and rotation, and changing from Cartesian to transducer coordinates. Note that the positive component of the acoustic axis is pointing away from the transducer. The relationship between the transducer Cartesian coordinates (e_{tc}) and the transducer polar coordinates (e_{tp}) is given by

$$\mathbf{y}_{e_{tp}}=\begin{bmatrix}\arctan\dfrac{x}{z}\\ \arctan\dfrac{y}{z}\\ \sqrt{x^2+y^2+z^2}\\ \mathrm{TS}\end{bmatrix}_{e_{tp}}+\mathbf{v}_{y,k}, \tag{B1}$$

where x,y,z are the target position in e_{tc} coordinates and TS is the target strength. The target position in e_{tc} is given by the mapping between the geo-referenced track-state coordinates (e_{gc}) and transducer platform Cartesian coordinates (e_{tc}), defined by

$$\begin{bmatrix}x\\ y\\ z\\ \mathrm{TS}\\ 1\end{bmatrix}_{e_{tc}}=A_cA_t\begin{bmatrix}\mathbf{x}_{e_{gc}}\\ 1\end{bmatrix}, \tag{B2}$$

where A_t is the translation matrix and A_c is the rotation matrix, defined as

$$A_t(\mathbf{z}_{k[1\cdots3]})=\begin{bmatrix}1&0&0&0&0&0&0&-x'_k\\ 0&1&0&0&0&0&0&-y'_k\\ 0&0&1&0&0&0&0&-z'_k\\ 0&0&0&0&0&0&1&0\\ 0&0&0&0&0&0&0&1\end{bmatrix},$$

and

$$A_c(\mathbf{z}_{k[4\cdots6]})=\begin{bmatrix}&&&0&0\\ \{\mathbf{e}_x\}&\{\mathbf{e}_y\}&\{\mathbf{e}_z\}&0&0\\ &&&0&0\\ 0&0&0&1&0\\ 0&0&0&0&1\end{bmatrix}^{-1}$$

$$=\begin{bmatrix}\{\mathbf{e}_x^T\}&&0&0\\ \{\mathbf{e}_y^T\}&&0&0\\ \{\mathbf{e}_z^T\}&&0&0\\ 0&0&0&1&0\\ 0&0&0&0&1\end{bmatrix}.$$

The unity vectors are defined by

$$\mathbf{e}_x=k_2\begin{bmatrix}\sin\psi'\\ \cos\psi'\\ k_1\end{bmatrix}_{e_{gc}},$$

$$\mathbf{e}_y=k_2k_3\begin{bmatrix}k_1\tan\phi+\cos\psi\\ -\sin\psi-k_1\tan\theta\\ \tan\theta\cos\psi-\tan\phi\sin\psi\end{bmatrix}_{e_{gc}},$$

$$\mathbf{e}_z=k_3\begin{bmatrix}\tan\theta'\\ \tan\phi'\\ -1\end{bmatrix}_{e_{gc}},$$

where

$$k_1=\tan\theta'\sin\psi'+\tan\phi'\cos\psi',$$

$$k_2=(\sin^2\psi'+\cos^2\psi'+k_1^2)^{-1/2}, \tag{B3}$$

$$k_3=(\tan^2\theta'+\tan^2\phi'+1)^{-1/2}.$$

Note that the platform-state variables are the sum of the error and the estimate, i.e., $x'=\hat{x}'+v_{z,k[1]}$, thus giving the dependence of $\mathbf{v}_z$ in the mapping.

In order to spawn a new track and to facilitate the use of the alternative track-state estimators, the mapping from measurement $\mathbf{y}_k$ to position $\mathbf{s}_k$ is required, i.e., $\mathbf{g}:(\mathbf{y}_k,\hat{\mathbf{z}}_k)\rightarrow\mathbf{s}_k$. First the transducer coordinates (e_{tp}) are converted to transducer Cartesian coordinates,

$$z=r/\sqrt{\tan^2\alpha+\tan^2\beta+1},$$
$$x=z\tan\alpha,$$
$$y=z\tan\beta.$$

Rotation and translation are applied to arrive at the geographical Cartesian coordinates (e_{gc}),

$$\mathbf{s}_k=A_{ti}A_c^{-1}\begin{bmatrix}x\\ y\\ z\\ \mathrm{TS}\\ 1\end{bmatrix}, \tag{B4}$$

where A_c^{-1} is the inverse of A_c and

$$A_{ti}(\mathbf{z}_{k[1\cdots3]})=\begin{bmatrix}1&0&0&0&+x'_k\\ 0&1&0&0&+y'_k\\ 0&0&1&0&+z'_k\\ 0&0&0&1&0\\ 0&0&0&0&1\end{bmatrix}.$$

[1] R. Brede, F. H. Kristensen, H. Solli, and E. Ona, "Target tracking with a split-beam echo sounder," Rapp. P.-v. Réun. Cons. Int. Explor. Mer. **189**, 254–263 (1990).

[2] E. Ona, Chap. 10. Recent Developments of Acoustic Instrumentation in Connection with Fish Capture and Abundance Estimation, in *Marine Fish Behaviour*, edited by A. Fernö and S. Olsen (Fishing News Books, Oxford, England, 1994),

[3] M. Soule, I. Hampton, and M. Barange, "Potential improvements to current methods of recognizing single targets with a split-beam echosounder," ICES J. Mar. Sci. **53**, 237–243 (1996).

[4] S. S. Blackman, *Multiple Target Tracking with Radar Applications* (Artech House, Boston, MA, 1986).

[5] S. S. Blackman, *Design and Analysis of Modern Tracking Systems* (Artech House, Boston, MA, 1999).

[6] O. R. Godø, D. Somerton, and A. Totland, "Fish behaviour during sam-

pling as observed from free floating buoys - application for bottom trawl survey assessment," ICES CM 1999/J:10 (1999).
[7]N. O. Handegard, K. Michalsen, and D. Tjøstheim, "Avoidance behaviour in cod (*Gadus morhua*) to a bottom-trawling vessel Aquatic Living Resources **16**, 265-270 (2003).
[8]S. S. Blackman, in *Design and Analysis of Modern Tracking Systems* (Artech House, Boston, MA, 1999), Chap. 6.
[9]D. Bertsekas, "The auction algorithm for assignment and other network flow problems: A tutorial," Interfaces **20**, 133–149 (1990).
[10]R Development Core Team, *R: A language and environment for statistical computing*, R Foundation for Statistical Computing, Vienna, Austria, 2003.
[11]J. M. Chambers and T. J. Hastie, *Statistical Models in S* (Wadsworth/Brooks Cole, Pacific Grove, CA, 1992).
[12]SNAME, "Nomenclature for treating the motion of a submerged body through a fluid," Technical Report Bulletin 1-5. Society of Naval Architects and Marine Engineers, New York (1950).
[13]R. Kieser, T. Mulligan, and J. Ehrenberg, "Observation and explanation of systematic split-beam angle measurement errors," Aquatic Living Resources **13**, 275–281 (2000).
[14]H. Balk and T. Lindem, "Improved fish detection in data from split beam transducers," Aquatic Living Resources **13**(5), 297–303 (2000).
[15]T. Stanton, "Effects on transducer motion on echo-integration techniques," J. Acoust. Soc. Am. **72**, 947–949 (1982).

Depth-shifting of shallow water guide source observations

Lisa M. Zurk[a)]
Electrical and Computer Engineering, Portland State University, 1900 SW Fourth Avenue, FAB 160-17, Portland, Oregon 97207

Brian H. Tracey[b)]
NEUROMetrix, Inc., 62 Fourth Ave., Waltham, Massachusetts 02451

(Received 17 November 2004; revised 21 June 2005; accepted 4 July 2005)

In theory, matched field processing offers the significant benefit of higher signal gains and increased localization capability. However, this has not been robustly observed in practice because of inherent uncertainties about details of the shallow water propagation environments which limit the prediction of the channel response. The use of guide sources to directly measure the transfer function between source and receiver arrays has been proposed as a means for reducing mismatch. However, the guide source measurement only provides a measured transfer function at the guide source location. In this paper a method of depth-shifting guide source observations is proposed, making it possible to estimate transfer functions for points in the ocean other than the guide source location. The proposed depth-shifting process does not require knowledge of environmental parameters. The theoretical background for the technique is developed below and its range of applicability is examined © *2005 Acoustical Society of America.* [DOI: 10.1121/1.2010309]

PACS number(s): 43.30.Wi, 43.30.Bp [EJS] Pages: 2224–2233

I. INTRODUCTION

Passive sonar performance in shallow water can be degraded because these environments support complex multipath propagation and often include multiple loud surface interferers. Matched field processing (MFP), which incorporates a propagation model to determine the replicas used in beamforming, has been proposed as a way to recover the losses incurred due to multipath propagation and provide increased source localization.[1] Adaptive processing, in particular adaptive MFP (AMFP) can provide the ability to null surface interference. Receive arrays with significant vertical aperture can support discrimination between surface and submerged sources and, if accurate environmental inputs are available, can achieve significant adaptive rejection of surface sources. Under ideal situations, AMFP can provide improved performance in both localization and detection of sources.

In practice the performance gains possible from AMFP are difficult to achieve. High ambiguities typically exist in the MFP output, especially for arrays with limited vertical aperture, which limits interferer rejection. The motion of the targets and interferers can be a significant problem, introducing additional signal loss, smearing source peaks, and consuming adaptive degrees of freedom.[2] However, for arrays with significant vertical aperture the most important limitation on MFP performance is that precise information on the underwater channel is generally not available. The mismatch between the computed and actual array steering vectors can result in loss of array gain and, for adaptive processing, signficant target self-nulling.

A number of approaches have been proposed to deal with the problem of environmental mismatch in MFP. Algorithms can be designed that attempt to reduce sensitivity by directly building a model of the environmental uncertainty into the processing.[3–5] Alternatively, geoacoustic inversion methods can be used to estimate more accurate seabed parameters, which are typically the source of greatest environmental uncertainty. Inversions can be done using either transmissions of known wave forms from calibrated sources[6,7] or from sources of opportunity such as loud merchant ships.[7]

Other authors have suggested the use of *guide sources* for mitigating environmental uncertainty.[8,9] Guide sources may be calibrated sources deployed for an experiment or can be sources of opportunity such as surface ships, whose position might be obtained from an offboard sensor. In either case the guide source can be used to determine the acoustic response across the array, eliminating the need to predict the response using a propagation model. This response is immediately known for the source-receiver path of the guide source, but it is still unknown for sources at alternate locations.

The approach presented here attempts to determine the response of a source by translating the observed response from the guide source. In previous work,[10] translation of a response from one source range to another was demonstrated by utilizing multifrequency data. However, the guide source will generally be located at a different depth than the target of interest, meaning that a method of translating in *depth* is desired. This is particularly true when the guide source is a surface ship and the target of interest is a submerged source. In this paper a method of "depth shifting" the guide source response using a vertical line array (VLA) is presented. With knowledge of the guide source location, this vector can then be shifted in depth to provide a steering vector for beamforming to alternate depths. Thus, a replica vector is obtained

[a)]Electronic mail: zurkl@cecs.pdx.edu
[b)]Work was done when the author was with MIT Lincoln Laboratory, 244 Wood Street, Lexington, Massachusetts 02420.

without the need for environmental knowledge or the use of a propagation model.

The work presented here is similar in some respects to work done by Conti *et al.* for a time-reversal mirror application.[11] Conti *et al.* used image processing techniques to extract the curvature of the field received from an impulsive source across a fully spanning VLA. This curvature was related to an image source contribution. By adjusting the curvature before playing back the time-reversed signal, the location of the time-reversal focal point was shifted in depth and range. The approach in the following accomplishes a similar shifting but applies to cw sources, rather than the short-duration wave forms used in time-reversal operations.

The first section to follow outlines the theoretical background for depth shifting. The depth-shifted observation (or replica vector) is formed by applying an operator to the actual guide source observation. The choice of this operator is motived by the derivation of an approximate mode orthogonality condition. A calculation for estimating the location of the depth-shifted peak is shown and conditions for the depth-shifting operation to be accurate are discussed. Finally, simulation results are used to demonstrate the technique. The use of an alternate depth-shifting operation is also explored.

II. THEORETICAL BACKGROUND FOR DEPTH SHIFTING

The normal mode representation of the field at frequency ω and time t that is present on a sensor at depth z due to a unit normalized source at a range r_s and depth z_s can be written as

$$p(z_s,z,r_s;\omega,t)=\frac{i\rho(z_s)}{(8\pi)^{1/2}}\sum_{m=1}^{M}\Psi_m(z_s)\Psi_m(z)\frac{e^{i[k_m(\omega)-\alpha_m(\omega)]r_s(t)}}{\sqrt{k_m(\omega)r_s(t)}}, \tag{1}$$

where Ψ_m is the mode function, k_m is the horizontal wave number, α_m is the attenuation constant of the mth mode, and M is the total number of propagating modes. For simplicity, the explicit reference to frequency ω in Eq. (1) will be omitted in subsequent equations except when the frequency dependence is not clear.

One useful characteristic of the mode functions is their orthonormalacy relationship, which can be written as

$$\int_0^D \Psi_l(z)\Psi_m(z)=\delta(l-m), \tag{2}$$

where the integration is computed over the water column of depth D. In MFP, the above-noted relationship can be used to simplify the inner product of pressure fields sampled along a fully spanning VLA to a weighted summation over a single mode.[10] In this section, a similar relationship is pursued, but one that involves not only the mode functions but their spatial derivatives. The rationale is that there is a correspondence between mode number m and source depth, so that shifting in mode number produces an analogous effect to shifting in depth. This central idea will be motivated by the derivation in this section, followed by the expressions for the MFP output produced in the following section.

The derivation begins by noting that the depth dependence in Eq. (1) is contained entirely in the mode functions Ψ_m, which are a function of two parameters: the vertical mode wave number $k_{z,m}$ and source depth. An assumption is made that this dependence is on the *product of the two*, i.e., $\Psi_m(z)$ can be considered as a function of the form $f(k_{z,m}z)$. This is consistent with the Wentzel–Kramers–Brillion (WKB) approximation for mode shapes and eigenvalues.

Under this assumption, the partial derivatives with respect to depth and wave number, respectively, can be written as

$$\frac{\partial}{\partial z}\Psi_m(z)=g(k_{z,m}z)\left[k_{z,m}+\frac{\partial k_{z,m}}{\partial z}z\right]\approx g(k_{z,m}z)k_{z,m},$$
$$\frac{\partial}{\partial k_{z,m}}\Psi_m(z)=g(k_{z,m}z)z, \tag{3}$$

where the unknown function $g(k_{z,m}z)$ has been introduced as a common product of the two differentiations [for example, if $\Psi_m(z)=\sin k_{z,m}z$, then $g=\cos k_{z,m}z$]. In calculating the depth derivative, the depth dependence of the vertical wave number has been neglected. The unknown function g can be eliminated to give

$$\frac{\partial}{\partial k_{z,m}}\Psi_m(z)=\frac{\partial}{\partial z}\Psi_m(z)\frac{z}{k_{z,m}}, \tag{4}$$

which can be approximated using a centered finite difference:

$$\frac{\partial}{\partial k_{z,m}}\Psi_m(z)\approx\frac{\Psi_{m+1}(z)-\Psi_{m-1}(z)}{k_{z,m+1}-k_{z,m-1}}. \tag{5}$$

The results so far have introduced a parametrization of the mode functions and have shown how its derivatives are related. A new approximate orthogonality expression for the mode functions is now derived.

The standard mode orthogonality condition in Eq. (2) can be used to write the following difference expression:

$$\int_0^D[\Psi_{l+1}(z)-\Psi_{l-1}(z)]\Psi_m(z)dz=\delta(l+1-m)-\delta(l-1-m). \tag{6}$$

(This is obtained by applying the orthogonality condition twice, then subtracting the two results.) The resulting expression includes a term similar to the centered difference in Eq. (5), thus inserting and simplifying gives

$$\int_0^D z\frac{\partial}{\partial z}\Psi_l(z)\frac{k_{z,l+1}-k_{z,l-1}}{k_{z,l}}\Psi_m(z)dz=\delta(l+1-m)-\delta(l-1-m). \tag{7}$$

Now, the horizontal wave numbers are assumed to have a linear dependence on mode number:

$$k_{z,l}=q(z)l. \tag{8}$$

In general q will be a function of depth, but as noted earlier, this difference has been assumed to be weak. The difference between vertical wave numbers in Eq. (7) can then be sim-

plified, giving a new (but approximate) orthogonality expression for the mode functions:

$$\int_0^D z\frac{\partial}{\partial z}\Psi_l(z)\Psi_m(z)dz \approx \frac{l}{2}[\delta(l+1-m)-\delta(l-1-m)]. \tag{9}$$

The right-hand side above will be nonzero when either delta function is satisfied, i.e., when $m=l\pm1$. Thus the approximate orthogonality condition will hold between nearest-neighbor modes. The expression is approximate because of the first-order finite difference used to represent the vertical wave number derivative. If desired, higher-order approximations to the finite difference could be used to capture additional off-diagonal mode cross-talk terms.

From numerical experiments, it was observed that a similar approximate orthogonality can be obtained if the depth-shifted replica is taken to be simply the depth-derivative of the guide source data [without the factor of z on the left-hand side (LHS) of Eq. (9)]. This behavior can be explained in terms of the mode shapes expected for modes that are well above cutoff. In this case the mode shapes tend towards $\sqrt{(2/D)}\sin k_{z,l}z$, with vertical wave numbers given by $k_{z,l}=\pi l/D$. The integral of mode m with the depth derivative of mode l can be calculated to be

$$\int_0^D \frac{\partial}{\partial z}\Psi_l(z)\Psi_m(z)dz = \frac{l}{D}\left(\frac{1-\cos\pi(m-l)}{m-l}+\frac{1-\cos\pi(m+l)}{m+l}\right), \tag{10}$$

which will be identically zero for $l=m\pm2k$, where $k=[0,2,4,\ldots]$. The resulting zeros help to reduce cross-talk and sidelobe levels. Note that the factor of $1/D$ above results in lower cross-correlation values than were seen in Eq. (9). The different scaling between the two depth-shifting operations is removed when the depth-shifted replica is normalized.

III. MODIFIED BARTLETT PROCESSOR

The output from a Bartlett matched field processor evaluated at a position of (z,r) can be written as

$$P(z,r)=|\bar{w}^H(z,r)\cdot\bar{y}|^2, \tag{11}$$

where $\bar{w}(z,r)$ is the $Nx1$ weight vector and $\bar{y}$ is the received response across the N-element array. Since the intent of this paper is to describe an algorithm for the structured shifting of MFP output peaks, the case considered here is that of a single deterministic source (or target) at position (z_s,r_s), so that $\bar{y}=\bar{y}(z_s,r_s)$ and $P(z_s,r_s)$ is the matched field output at the target range and depth. [In general, for a signal in presence of noise, the beamformer output is a stochastic quantity that should be evaluated with an expectation operator. However, the goal of the present work is not to evaluate the signal to noise performance, but instead the ability to shift the beamformer focus direction by varying the steering vector applied to a deterministic signal. Thus, for the theoretical development we consider the case of deterministic MFP with the understanding that the usual signal and noise models apply (see, for example, Ref. 1). In the numerical simulations, background white noise at 60 dB is included.] For the standard Bartlett processor, $\bar{w}=\bar{w}_{\text{model}}$ and the weight is the normalized output of a propagation model (commonly referred to as the "replica" vector). Accurate detection and localization is heavily dependent on accurate knowledge of the ocean environment, which is typically not available in practice.

In this paper, a modified Bartlett processor is presented where the weight vectors are obtained not from model output, but from manipulation of a guide source response. Thus, the "matching" occurs between previously observed fields, and there is no loss due to model parameter mismatch. This modified Bartlett processor has the form given in Eq. (11) but with $\bar{w}=\bar{w}_{\text{guide}}$ computed from a guide source, and the exact form will now be presented. The weight vectors are obtained from observing the acoustic field from a guide source (the guide source SNR is assumed to be high enough so the effects of noise are negligible).

In the previous section, an approximate mode orthogonality relationship was presented which resulted from computing the derivative of the mode functions with respect to depth. To utilize this relationship in a modified Bartlett processor, the depth-shifted "replica" vectors are computed from

$$\bar{v}^H(z,r)=\bar{z}\odot\frac{\partial}{\partial z}\bar{x}(z_g,r_g), \tag{12}$$

where $\bar{x}(z_g,r_g)$ is the field received from the guide source, $\bar{z}$ is a vector of depths at each phone location, and $\odot$ indicates the Hadamard product, or element-wise multiplication. The depth-shifted weight is then calculated as

$$\bar{w}(z_s,r_s)=\frac{\bar{v}(z_s,r_s)}{|\bar{v}(z_s,r_s)|}. \tag{13}$$

The use of this weight vector can be evaluated by substituting Eqs. (12) and (13) into Eq. (11) to give

$$P(z,r)=|\bar{w}^H(z,r)\cdot\bar{y}(z,r)|^2=C\left|\bar{z}\odot\frac{\partial}{\partial z}\bar{x}(z_g,r_g)\cdot\bar{y}(z,r)\right|^2, \tag{14}$$

where C is a normalization constant. With sufficiently fine spacing, the depth derivative can be approximated by a finite difference equation, with the elements of the shifted replica given by

$$v_k(z_s,r_s)=z_k\frac{x_{k+1}(z_g,r_g)-x_{k-1}(z_g,r_g)}{2\Delta z}, \tag{15}$$

where k is the index to a particular hydrophone in the array and Δz is the depth spacing between hydrophones. [Effects of the discretization introduced in Eq. (15) will be discussed and examined in the numerical simulations.] Assuming that the acoustic field from the guide source and the target can be expressed in normal modes as given in Eq. (1) then gives

$$P(z,r) = C\left|\sum_{n}^{N} z_{rn}\frac{\partial}{\partial z}x_n(z_g,r_g)y_n(z_s,r_s)\right|^2 = C'\left|\sum_{l}^{L}\sum_{m}^{M}\left(\sum_{n}^{N} z_{rn}\frac{\partial}{\partial z}\Psi_l(z_g,r_g)\Psi_m(z_s,r_s)e^{i(k_l r_g - k_m r_s)}\right)\right|^2, \tag{16}$$

where the spatial summation in the inside brackets is evaluated at the $n=1,\ldots,N$ elements of the array, z_{rn} is the depth of the nth hydrophone, and C' is a new constant that contains the additional terms in Eq. (1). It can be seen that in Eq. (16) the summation is the discrete approximation of the LHS of Eq. (9); substituting in the delta function on the right-hand side of the equality then gives

$$P(z,r) = \left|\sum_{m}^{M}(m-1)\Psi_m(z)\Psi_{m-1}(z_g)e^{i(k_m r - k_{m-1}r_g)} - (m+1)\Psi_m(z)\Psi_{m+1}(z_g)e^{i(k_m r - k_{m+1}r_g)}\right|^2, \tag{17}$$

which is the modified Bartlett output evaluated at source position z, r and using the guide source response for depth shifting. This differs from the conventional MFP expression because the quantity is evaluated at mode indexes m and $m\pm1$ (the conventional expression contains only the index m for a fully spanning VLA). Thus, the maximum output does not occur when $z_g=z_s$ and $r_g=r_s$, but for some other "shifted" location.

In the simulation and analytic results to follow, the problem is restricted to that of obtaining depth-shifted replicas at the guide source range. Thus $r=r_s=r_g$ in Eq. (17). In this case the output power of the processor becomes

$$P(z,r) = \left|\sum_{m}^{M}(m-1)\Psi_m(z)\Psi_{m-1}(z_g)e^{i(k_m - k_{m-1})r} - (m+1)\Psi_m(z)\Psi_{m+1}(z_g)e^{i(k_m - k_{m+1})r}\right|^2. \tag{18}$$

Depth-shifted replicas at different ranges will be discussed in Sec. III B.

A. Location of shifted peak

Expressions for the location of the shifted peak can be derived using a WKB approach to describe the vertical wave numbers and mode shapes. The depth shifted peak will be calculated assuming that $r=r_s=r_g$, as described in Eq. (18). The power output will be maximized when terms match on a mode-by-mode basis. The shifted peak z_s should satisfy the following:

$$\Psi_m(z_s) = \Psi_{m-1}(z_g)e^{i(k_m - k_{m-1})r}, \qquad \Psi_m(z_s) = \Psi_{m+1}(z_g)e^{i(k_m - k_{m+1})r}. \tag{19}$$

An estimate of the shifted location is found using the following steps:

(1) the WKB approximation is used to express modes as a sum of up- and down-going waves.
(2) Equation (19) is rewritten as four equations, satisfying the up- and down-going portions of the wave field.
(3) Approximate values for the shifted location are found.

The steps involved are shown in the Appendix. As a final result, the shifted depth is given as

$$z_s \simeq z_g \pm \frac{q}{k_m}r. \tag{20}$$

Thus the depth-shifting process will cause two shifted peaks in depth to appear for every possible guide source depth. The Appendix shows that this is because the up- and down-going portions of the wave field are shifted differently. To first order, the mode wave numbers will be comparable to the medium wave number, so an approximate estimate for depth-shifting is given by

$$z_s \simeq z_g \pm \frac{q}{k_0}r. \tag{21}$$

As noted earlier, for modes well above their cut-off frequency, $q=\pi/D$. Using this value together with the frequency, guide source range, and guide source depth, the locations of the depth-shifted peaks can be estimated. Note that the depth shift is frequency-dependent, so that if multiple frequencies are available (i.e., the sources have some bandwidth or multiple tonals) these can be used to generate shifts at multiple target depths. Thus, Eq. (21) provides a means for generating a family of target depth values. Finally, it will be shown in Sec. III B, processing using the ambiguity introduced by the $\pm$ in Eq. (21) can be resolved by application of the invariance principle.

The analytic results can also be used to qualitatively explain several features that will be seen in simulation results. First, Eq. (20) shows that the exact location of the shifted peak is mode-dependent. Thus if the modes have very different phase speeds, a smearing of the peak location will result. Second, the derivations above assume that the variation in vertical wave number with depth can be neglected. To the extent that this is not true, i.e., significant sound speed gradients exist, an additional defocusing of the depth-shifted peak may be expected.

B. Range invariance shifting

The expression in Eq. (21) gives the relationship between the guide position z_g, r_g and a single target depth of z_s with $r_s=r_g=r$ at the single frequency ω. If the guide source is a broadband source, the concept of using the invariance principle to shift in range[10,12] can be utilized. As will be shown in this section, this provides the ability to consider $r_s \neq r_g$ and utilize multiple observations from the guide source when it moves in range.

The objective is to acquire a weight vector which allows one to beamform to a source at position z_s, r_s and at a target frequency of ω. Assume that observations have been acquired for a guide source traveling in range and radiating over some (broad) acoustic bandwidth. Then, consider the

Bartlett output using one of these weight vectors acquired when the guide source is at $z=z_g$, $r=r_g$ and the guide response at the frequency $\omega_g=\omega+\Delta\omega$ is used to give

$$P(z_s,r_s)=\left|\sum_m^M (m-1)\Psi_m(z)\Psi_{m-1}(z_g)e^{i(k_m(\omega)r_s-k_{m-1}(\omega+\Delta\omega)r_g)} - (m+1)\Psi_m(z)\Psi_{m+1}(z_g)e^{i(k_m(\omega)r_s-k_{m+1}(\omega+\Delta\omega)r_g)}\right|^2, \tag{22}$$

where the frequency dependence has been explicitly introduced for clarity and the assumption has been made the Ψ does not vary considerably between ω and $\omega+\Delta\omega$. (The frequency increment $\Delta\omega$ is considered small enough so that $\Delta\omega/\omega<0.1$.) To continue, follow the approach described in the Appendix of utilizing the WKB approximation and equating arguments of the exponentials to obtain the following expression for the processor peak:

$$z_s=\frac{1}{qm}[z_g q(m-1)+(k_m(\omega)(r_s)-k_{m-1}(\omega+\Delta\omega)r_s+\Delta r)], \tag{23}$$

where the substitution of $r_s=r_g+\Delta r$ has been used. Approximate the wave number k_m as

$$k_m(\omega+\Delta\omega)=\sqrt{(k_0+\Delta k)^2-q^2m^2}\approx k_0\left(1-\frac{q^2m^2}{2k_0^2}-\frac{\Delta k}{k_0}\right) \tag{24}$$

to give (see the Appendix for details)

$$k_m(\omega+\Delta\omega)-k_{m-1}(\omega)\approx -q^2\frac{m}{k_0}-\Delta k. \tag{25}$$

Retaining dominant terms then gives the following depth shift operation:

$$z_s\simeq z_g\pm\left[\frac{q}{k_0}r_g-\frac{1}{qm}(\Delta k r_g-k_0\Delta r_g)\right]. \tag{26}$$

The last term of Eq. (26) goes to zero when it satisfies the invariance relationship given by Brehovskih[12] as (for $\beta=1$)

$$\frac{\Delta\omega}{\omega}=\frac{\Delta r}{r}. \tag{27}$$

When Eq. (27) is satisfied, Eq. (26) reduces to the form of Eq. (21) except that the Bartlett processor peaks for guide range $r_g\neq r_s$, and each value of r_g provides a different depth shift as per Eq. (26). When responses from a number of guide positions are observed [e.g., the guide moves in range, r_g) this implies choosing the frequency $\omega=\omega_g-\Delta\omega$ to satisfy Eq. (27), resulting in the ability to shift to z_s as given in (26)]. For a guide source that has sufficient frequency extent, this fact can be used to resolve the ambiguity introduced by the ± in Eq. (21).

IV. DEPTH-SHIFTING ALGORITHM

To summarize the preceeding sections, the algorithm for depth shifting using a guide source is described in the following list.

(1) The acoustic pressure $\bar{x}(z_g,r_g)$ across the array due to a high SNR guide source is observed and retained, with the guide position (i.e., $z=z_g$ and $r=r_g$) known from other information. This acquisition potentially occurs for a number of guide source ranges as the guide transverses the region and over a substantial bandwidth.
(2) For each discrete frequency band and source range, the derivative of the pressure with respect to depth is computed. For a vertical array with sufficient depth sampling, this may be approximated by using a finite difference approximation as was utilized in the derivation in the previous section. Alternately, an acoustic vector sensor could be used to measure the particle velocity, from which the derivative of the pressure may be calculated.
(3) The resulting derivatives are then normalized to unit norm and stored as array weight vectors. Each weight vector is associated with an unique target range and depth (r_s,z_s) through the relationships given in Eqs. (21) and (26). Note that with sufficient range observations and signal bandwidth weight vectors can be obtained for all possible target locations.
(4) The output of the Bartlett processor in Eq. (11) is computed by applying the weight vectors from the previous step to pressure across the array to determine power in the direction of interest $(r=r_s,z=z_s)$. Note that if multiple steering vectors are available for a single source depth (due to multiple guide source ranges and broad signal bandwidth) these can be used to resolve the ambiguity arising from the ± sign in Eqs. (21) and (26).

The above-noted procedure is particularly interesting when a surface ship is considered as a potential guide source. In this case the algorithm is readily applied (with $z_g\equiv 2$ m) as surface interference typically has a high SNR and its position may be obtained from a surface radar or shipping lane information. Furthermore, the source is typically broadband and can be observed at multiple ranges as the ship moves—a fact which was exploited in Sec. III B.

V. SIMULATION RESULTS

Simulation results were generated using an environmental model based parameters gathered during the Santa Barbara Channel experiment (SBCX). Numerical results are shown for 148 and 235 Hz, which were tones used during the experiment, but no actual data results from SBCX are presented here. This is due to the fact that a data-driven evaluation of the depth shifting algorithm requires the presence (and position knowledge) of a guide source at multiple ranges, along with observations of a target source. It is hoped that constructing data collection opportunities for such an evaluation may occur in the future, but in absense of this data, the current work presents the theoretical background and only simulated results.

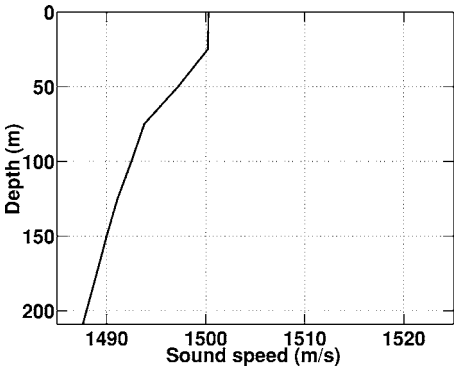

FIG. 1. Sound speed profile (SSP) for Santa Barbara Channel environment.

For all simulation results, a range-independent normal mode simulation based on KRAKEN output was used.[13] Figure 1 shows the sound speed profile used for the simulations, and Table I lists the assumed geoacoustic properties of the SBCX site. For comparison, results will also be shown for a 209-m-deep Pekeris waveguide with a constant sound speed of 1500 m/s in the water column overlying an acoustic half-space (parameters c_c=1800 m/s, ρ=2 g/cm^3, and α_c =0.04 dB/λ).

A. Mode orthogonality results

This section examines the approximate mode orthogonality condition derived in previous sections. Mode correlation matrices are calculated for a verticle line array (VLA) that fully spans the water column with 1 m vertical separation between phones. The array gives excellent sampling so the underlying orthogonality of the mode shapes is seen. While not plotted, evaluation of the "standard" mode orthogonality condition [i.e., Eq. (2)] gives cross-talk between modes (or off-diagonal elements of a mode correlation matrix) at very low values (less than −15 dB).

Figure 2 graphically shows the approximate orthogonality condition predicted by Eq. (9). For convenience, the figure is produced by weighting the right-hand side of Eq. (9) with a factor of $2/l$, so that perfect orthogonality would result in nonzero (first) off-diagonal terms with the value one, and zeros elsewhere. The depth-shifting operation $\boldsymbol{z}\odot\partial/\partial z$ is calculated using a centered finite difference on the mode shapes. As predicted, because of the depth-shifting operation, the correlation is highest between each mode and its two nearest neighbors but there is nonzero cross-talk between modes. This is believed to be a result of the approximations utilized in the derivation of the new mode orthogonality condition (such as the linear dependence of the vertical wave number on mode index) which are less applicable at the higher order modes that undergo increased bottom interaction, as discussed in the next section. This increased cross-talk may be expected to lead to higher sidelobe levels on the depth-shifted ambiguity surface.

TABLE I. Parameters for geoacoustic model used in SBCX data: z =depth from surface; c_c=compressional sound speed; ρ=density; α_c =compressional wave attenuation.

z(m)	c_c(m/s)	ρ(g/cm^3)	α_c(dB/λ)
209	1607	1.95	0.37
309	1702	1.95	0.37
309	1862	1.98	0.035
609	2374	1.98	0.035
609	2374	2.03	0.04

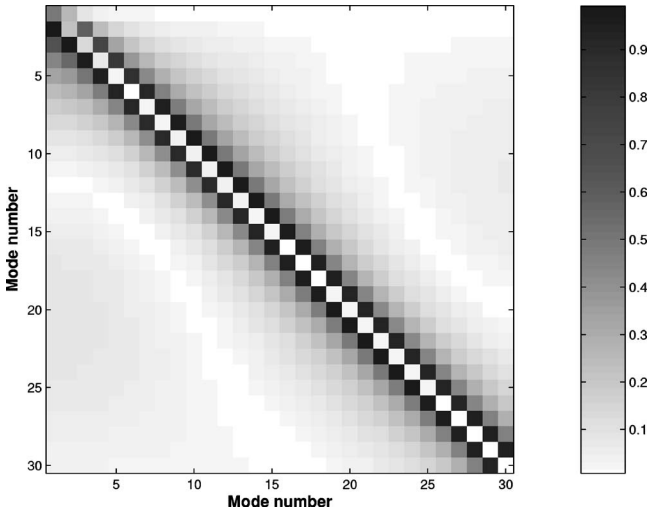

FIG. 2. Mode correlation matrix (outer product) between depth-shifted and original modes for fully spanning VLA in SBCX environment. Output is produced as specified in the left-hand side of Eq. (9) and the figure is plotted with a multiplicative factor of $1/2$ so that perfect agreement would result in a value of one on the off-diagonals, and zero elsewhere. Frequency is 235 Hz.

The accuracy of the discrete evaluation of both the standard orthogonality and the approximate differential orthogonality relationship depends on the spacing and extent of the discrete integral in Eqs. (2) and (9), respectively. Deviations from orthonormality occur for arrays that either do not span the entire water column or have insufficient array spacing. In Fig. 3, the mode correlation matrices for both orthogonality relations are shown for an array that is undersampled [Figs. 3(a) and 3(b)] or only partially spans the water column [Figs. 3(c) and 3(d)]. It can be seen from the figure that the accuracy of the discrete approximation deteriorates for both orthogonality relationships, and would result in decreased performance for a VLA without sufficient sampling.

This observed degradation is perhaps more pronounced for the new orthogonality relationship, and is particularly more noticeable at the higher mode numbers. It is believed that this is because those modes experience greater attenuation and loss due to bottom interaction. In the theoretical derivation, it was assumed that the vertical wave numbers increase approximately linearly with mode number, and will clearly not be the case for the higher modes. However, with sufficient energy at the lower modes (which is frequently the case for long range propagation scenarios) the losses due to deviations of the higher order modes may be negligible. Note also that other common sources of array degradation (such as error in element position) will apply to the mode correlation and hence also to the depth shifting.

Because the SBCX environment has a downward refracting sound speed profile (SSP), it does not exactly satisfy the assumptions made in deriving Eq. (9). As a check, depth-

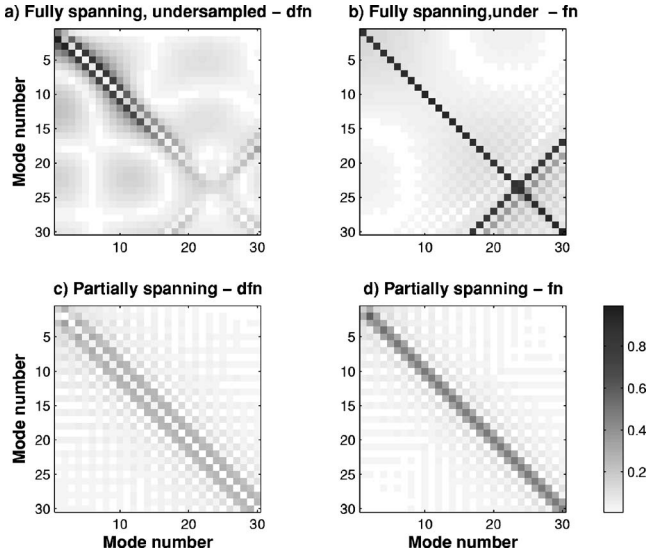

FIG. 3. Mode correlation matrix for SBCX environment using Eq. (9) (left-hand column) and Eq. (2) (right-hand column), plotted with a multiplicative factor of 1/2. Simulated VLA has inadequate spacing ($1.5*\lambda=9$ m) in (a) and (b), or covers the top half of the water column in (c) and (d). For both standard and new orthogonality relationships, degradation occurs as the array becomes less capable. Frequency is 235 Hz.

shifted correlation matrices for a variety of ocean environments were calculated. The mode correlation matrix for the cases considered were nearly identical to that calculated for the SBCX environment, indicating the specific ocean parameters do not have a critical effect on the results.

As discussed earlier, an alternate depth-shifting operation can be carried out by applying only the depth derivative to the guide source observation. The behavior of this alternate depth-shifted replica is seen from the mode correlation matrix in Fig. 4. This figure again shows high correlation between nearest-neighbor modes, but a "checkerboard" pattern is seen in the output. This pattern was predicted from

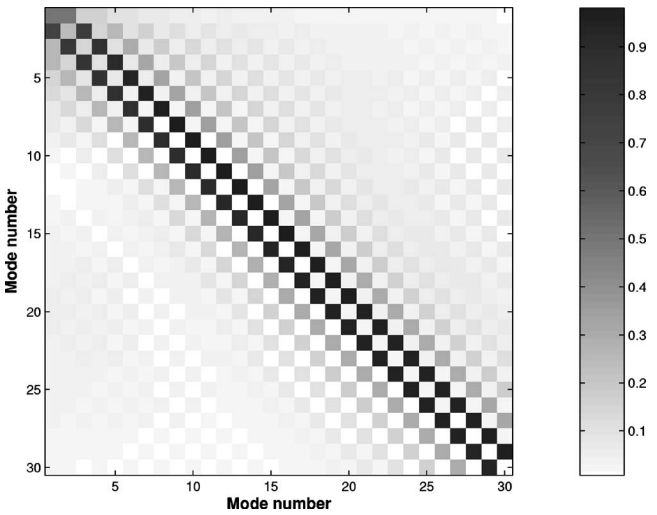

FIG. 4. Mode correlation matrix between depth-shifted and original modes for fully spanning VLA in SBCX environment, using the simple depth-derivative operation. The "checkerboard" pattern predicted by Eq. (10) is seen, giving reduced mode cross-talk as compared to Fig. 2.

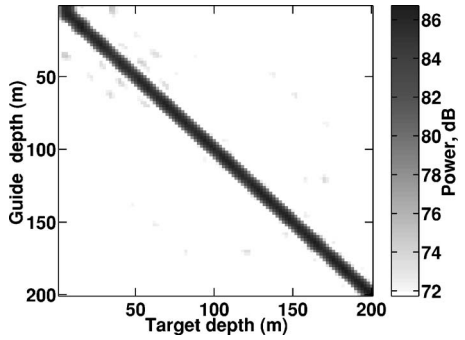

FIG. 5. Bartlett output for 2.5 km guide source at $f=235$ Hz in SBCX environment with no depth shifting.

Eq. (10). The different scalings between the two depth-shifting operations are removed when the depth-shifted replica is normalized.

B. Depth-shifted results

In this section the depth-shifting operation is applied to simulated guide source measurements to verify that shifting occurs and to understand how performance depends on the environment. The receive array used for simulation has a similar geometry to the VLAs used in SBCX, consisting of a bottom-mounted VLA with 30 hydrophones spaced at 5 m separation in the vertical, spanning roughly 80% of the water column. The uppermost phone in the array is at a depth of 5 m.

For reference, a simulation was run showing MFP output at 235 Hz using a guide source without applying the depth shifting algorithm developed in this paper. The result, shown in Fig. 5, is for the case $r_g=r_s=2.5$ km. The output is plotted as a function of the guide source depth and the target depth, z_g and z_s, respectively. As expected, the unshifted guide source can only be used to produce output at the depth of the guide source.

Figures 6 and 7 show the result of applying the depth-shifting algorithm to data collected from guide sources at ranges of 2.5 and 4 km, respectively, at a frequency of 235 Hz. The depth-shifted output is again produced at the same range as the guide source ($r_g=r_s$). In Fig. 8, the depth-shifted result is produced at $f=148$ Hz, with all other parameters remaining the same. In all three figures, as predicted by

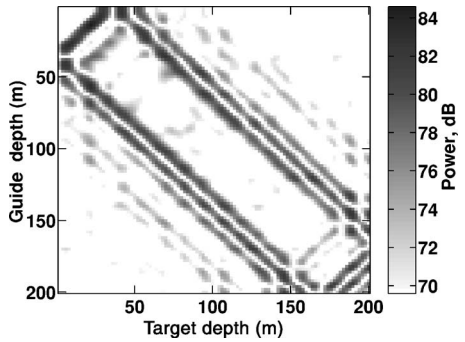

FIG. 6. Depth shifted output as given in Eq. (18) for 2.5 km guide source radiating at $f=235$ Hz in SBCX environment. Note that the peak is split in two as predicted, with predicted peaks at $z_s=z_g\pm40$ m.

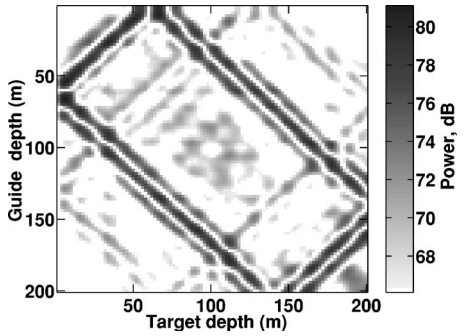

FIG. 7. Depth shifted output as given in Eq. (18) for 4.0 km guide source radiating at $f=235$ Hz in SBCX environment. Note that the peak is split in two as predicted, with predicted peaks at $z_s=z_g\pm64$ m.

theory, shifted peaks appear at two depths for every guide source depth. It can be seen from examination of the figures that diversity in source range and/or frequency produces multiple target depths or shift values (i.e., the ability to locate sources at multiple possible depths z_s).

Evaluating Eq. (21) with the values for the ocean depth, guide source range, and frequency used in the simulation example gives an estimate of the predicted shifted depths. For the $f=235$ Hz case, at 2.5 km in range a peak in output is expected for $z_s=z_g\pm40$ m, while for the 4 km range peaks are predicted at $z_s=z_g\pm64$ m. For $f=148$ Hz at 4 km range the peak is predicted at $z_s=z_g\pm101$ m. All these values are in good agreement with the simulation results, even though the environment is not an isospeed channel. This suggests that the relationship between the guide depth and the shifted depth may be only weakly sensitive to details of the environment.

As noted earlier good results can be obtained by using a simple depth derivative applied to the guide source data. Figure 9 and 10 shows the depth-shifted outputs for 2.5 and 4 km sources, respectively. The sidelobe levels obtained using this depth-shifting operation are lower than those seen in Figs. 6 and 7, due to the reduced cross-talk between modes seen in Fig. 4.

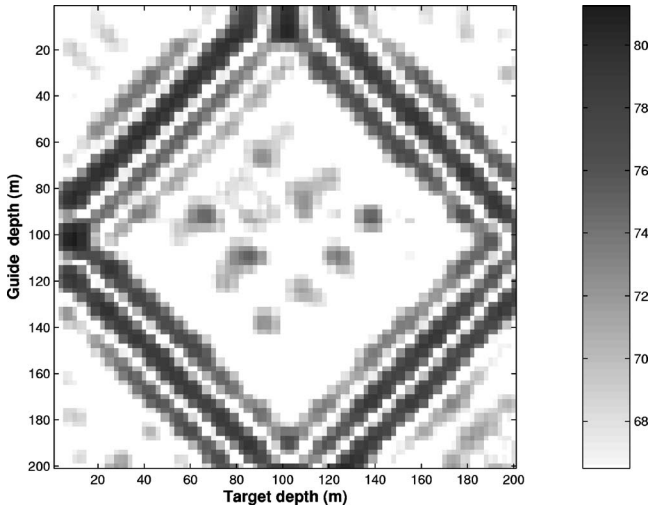

FIG. 8. Depth shifted output as given in Eq. (18) for 4.0 km guide source radiating at $f=148$ Hz in SBCX environment. Note that the peak is split in two as predicted, with predicted peaks at $z_s=z_g\pm101$ m.

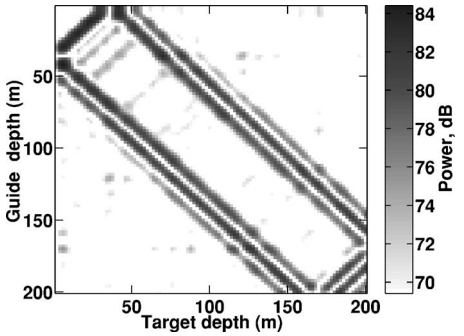

FIG. 9. Depth shifted output for 2.5 km guide source radiating at $f=235$ Hz, SBCX environment, obtained by applying a depth-derivative to the guide source data. Note that sidelobes are suppressed compared to Fig. 6.

The above-noted derivations assume that the vertical wave number for each mode is only weakly dependent on depth. When sound speed varies with depth, this is no longer strictly true and some defocusing can be expected. Additional simulations were run to better understand the sensitivity to sound speed profile. The simpler depth-derivative depth-shifting operation was used for these simulations. First, results were generated for a Pekeris waveguide, which has constant sound speed in the water column. Results were then generated for an environment with the extremely steep downward refracting sound speed profile shown in Fig. 11, having the same bottom properties as the SBCX site. Results for the Pekeris environment are shown in Fig. 12, while results for the steep SSP environment are seen in Fig. 13 (guide source range is 2.5 km in both cases). For the Pekeris waveguide, little evidence of mismatch loss and defocusing is seen. Increased mismatch is seen for the steep SSP environment. These results support the idea that the depth-shifted replicas will be most accurate when the change between the sound speed at the guide source depth and at the shifted peak depths are relatively small.

Comparing Figs. 9 and 12 to the standard MFP result (Fig. 5) shows a loss of signal energy in the depth-shifted results. This loss is believed to result from the increased weighting that depth-shifting places on high-order modes (shown in Fig. 2), which distorts the replicas. This signal loss will increase the SNR requirements for successful source lo-

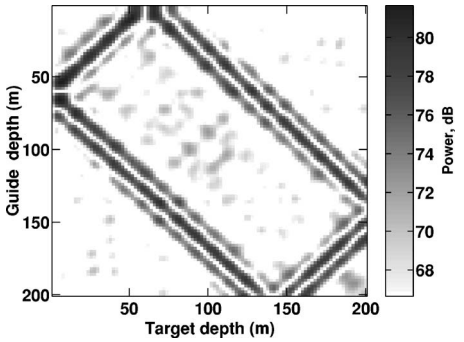

FIG. 10. Depth shifted output for 4 km guide source radiating at $f=235$ Hz, SBCX environment, obtained by applying a depth-derivative to the guide source data. Note that sidelobes are suppressed compared to Fig. 7.

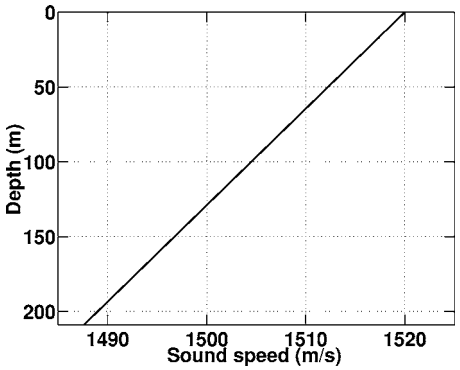

FIG. 11. Steep downward refracting sound speed profile designed to stress depth-shifting technique.

calization using depth-shifting. However, mismatch losses are also present in standard MFP due to environmental uncertainty. For the SBCX experiment, where good environmental calibration was available, mismatch losses for MFP were typically 1–2 dB.[2] For environments where ocean parameters are poorly known, the mismatch introduced by depth-shifting may be less than for standard MFP.

C. Invariance depth-shifted results

The theory of Sec. III B suggests that a response shifted in both range and depth can be produced by utilizing a guide with a broadband response as per Eq. (26). The results shown in Fig. 14 were produced by using the response from a guide source at range $r_g = r_s - \Delta r$ and frequency $\omega_g = \omega_s + \Delta\omega$ for a target range of 4 km and frequency at $f_s = 2\pi\omega_s = 148$ Hz. As previously seen in Fig. 8, the guide response produces a depth-shifted focus at $z_s = z_g \pm 101$ m when $\Delta r = 0$ (i.e., $r_g = r_s$) and $\Delta f = \Delta\omega/(2\pi) = 0$. When the modified Bartlett output in Eq. (18) is calculated using the guide response at $\Delta f = 10$ Hz, the peak occurs at the target depth z_s as given in Eq. (26) but for the guide range satisfying the invariance relationship in Eq. (27) : $\Delta r = \Delta f / f \times r_s$. In Fig. 14 the MFP output is plotted as a function of guide range and target depth with a peak occuring at 4.0 km range for $\Delta f = 0$ (left-hand plot) and at 4.3 km in range for $\Delta f = 0$ (right-hand plot); both of which which agree with the predicted values.

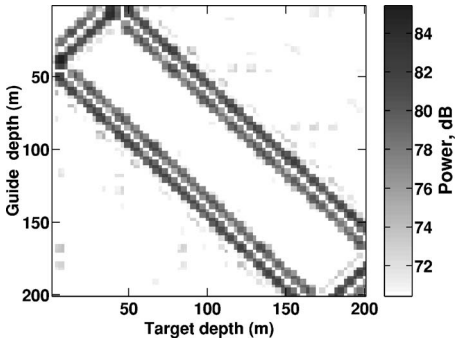

FIG. 12. Depth shifted output for 2.5 km guide source radiating at $f = 235$ Hz, Pekeris waveguide environment. Depth-shifting is done by applying a depth-derivative to the guide source data. Note that output is slightly cleaner than for the SBCX case.

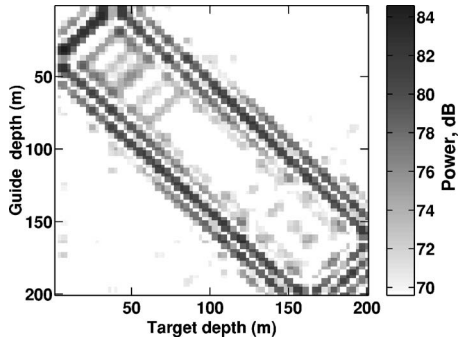

FIG. 13. Depth shifted output for 2.5 km guide source radiating at $f = 235$ Hz, for environment with steep sound speed profile. Depth-shifting is done by applying a depth-derivative to the guide source data. Note the increased sidelobe levels as compared to the environments which have smaller sound speed gradients.

VI. CONCLUSIONS

While matched field processing holds the promise of increased target gain and localization accuracy, MFP performance can be seriously degraded by uncertainties of the underwater environment. Guide sources at known positions in the ocean may be used to address this problem by directly measuring the source-to-receiver transfer functions for use in processing. In this work, a new algorithm for extending guide source observations for use in MFP has been introduced. This algorithm provides a method of observing the response (e.g., steering vector) from a guide source at one depth, and translating it to another depth. It relies on a new approximate orthogonality relationship which shifts the modes that contribute to the MFP output. The technique does not require environmental inputs, though performance will degrade for environments with steep sound speed profiles. The depth shifting operators examined here, which use a depth derivative to form the shifted replicas, introduce some signal losses that will increase SNR requirements for successful source localization. The development of other depth-shifting operations that aim to minimize this loss may be an interesting topic for further investigation.

ACKNOWLEDGMENTS

The authors would also like to thank William Kuperman, Hee Chun Song, and Philippe Roux for helpful feedback about depth-shifting concepts.

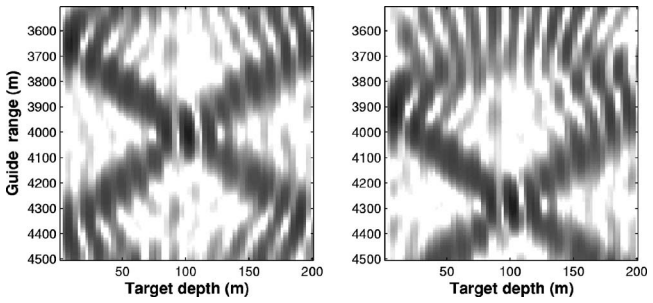

FIG. 14. Depth shifted MFP output for 4.0 km target at 235 Hz plotted as a function of target depth and guide range. The guide source is at 2 m depth and the response is at 148 Hz (left-hand plot) and 158 Hz (right-hand plot). The shifting of $\Delta f = 10$ Hz produces a shift in the range peak from 4.0 km to 4.3 km. Location of the target depth is given by Eq. (26).

APPENDIX: WKB CALCULATION FOR SHIFTED PEAK LOCATION

As in Eq. (8), the vertical wave numbers are assumed to be linearly related to mode number. The mode functions are approximated using the WKB approach, which models the mode as a sum of up- and down-going plane waves with angles that may vary in depth:

$$\psi_l(z) = Be^{i\int_0^z q(z)ldz} + Ce^{-i\int_0^z q(z)ldz}. \tag{A1}$$

The relative amplitudes B and C of the up- and down-going waves depend on boundary conditions of the problem.

The WKB approximation can be expected to be accurate for modes that are well above their cutoff frequencies. Another simplified ocean environment that yields modes which fit the above-mentioned model is the so-called ideal waveguide, which consists of an isospeed ocean with a pressure release surface and bottom. In this case the vertical wave number is given by $k_{z,l}=(\pi/D)l$, where D is the ocean depth, and mode shapes are given by $\sqrt{(2\rho/D)}\sin k_{z,l}z$. The ideal waveguide model can be a good approximation for modes that are well above their cut-off frequencies.

Using the WKB approximation for the mode shape, the two equations in Eq. (19) are split into four, by requiring the up-going and down-going parts of the modes to satisfy the equations separately. The first equation is

$$B_m e^{i\int_0^{z_s} qmdz} = B_{m-1} e^{i\int_0^{z_g} q(m-1)dz} e^{i(k_m - k_{m-1})r}, \tag{A2}$$

where the depth dependence of $q(z)$ is not shown explicitly.

A first step in completing this calculation is to find the horizontal wave number difference between adjacent modes. Given the above-mentioned assumptions, the horizontal wave number is given by

$$k_m = \sqrt{k_0^2 - q^2 m^2}, \tag{A3}$$

where k_0 is the medium wave number (ω/c). It is fairly easy to show that

$$k_{m-1} = k_m \sqrt{1 + \frac{q^2(2m-1)}{k_m^2}}. \tag{A4}$$

Approximating the square root operator and making the assumption that modes higher than the first few are important (so that $2m \gg 1$), an approximate horizontal wave number difference is found as

$$k_m - k_{m-1} \approxeq -q^2 \frac{m}{k_m}. \tag{A5}$$

Two simplifying assumptions are now made. First, the mode amplitude terms B_m and B_{m-1} are assumed to be are roughly equal and are divided out of Eq. (A2). The equality will then be satisfied if the arguments to the exponential terms are equal. Next the assumption is made, as above, that the vertical wave number term q is approximately constant with depth. In that case the depth integrals become trivial, and the depth of the shifted peak is given by

$$\begin{aligned} z_s &= \frac{m-1}{m} z_g - \frac{q}{k_m} r_s, \\ z_s &\approxeq z_g - \frac{q}{k_m} r_s, \end{aligned} \tag{A6}$$

where the approximation made on the second line will be valid beyond the first few modes. Carrying out a similar calculation with the down-going wave gives a second solution:

$$z_s \simeq z_g + \frac{q}{k_m} r_s. \tag{A7}$$

The same two solutions are found by equating the up- and down-going waves in the second line of Eq. (19). These results can be used to estimate the shifted locations of the depth peaks.

[1] A. Baggeroer, W. Kuperman, and P. Mikhalevsky, "An overview of matched field methods of ocean acoustics," IEEE J. Ocean. Eng. **18**, 401–424 (1993).

[2] L. Zurk, N. Lee, and J. Ward, "Source motion mitigation for adaptive matched field processing," J. Acoust. Soc. Am. **113**, 2719–2731 (2003).

[3] J. Krolik, "Matched-field minimum variance beamforming in a random ocean channel," J. Acoust. Soc. Am. **92**, 1408–1419 (1992).

[4] A. Richardson and L. Nolte, "*A posteriori* probability source localization in an uncertain sound speed, deep ocean environment," J. Acoust. Soc. Am. **89**, 2280–2284 (1991).

[5] P. Daly, "Stochastic matched field processing for localization and nulling of acoustic sources," Ph.D thesis, Massachusetts Institute of Technology, 2000.

[6] M. Siderius, M. Snellen, D. Simons, and R. Onken, "An environmental assessment in the Strait of Sicily: Measurement and analysis techniques for determining bottom and oceanographic properties," IEEE J. Ocean. Eng. **18**, 401–424 (1993).

[7] D. Knobles, R. Koch, L. Thompson, K. Focke, and P. Eisman, "Broadband sound propagation in shallow water and geoacoustic inversion," J. Acoust. Soc. Am. **113**, 205–222 (2003).

[8] M. Siderius, D. Jackson, D. Rouseff, and R. Porter, "Multipath compensation in shallow water environments using a virtual receiver," J. Acoust. Soc. Am. **102**, 3439–3449 (1997).

[9] L. Fialkowski, M. Collins, W. Kuperman, J. Perkins, L. Kelly, A. Larsson, J. Fawcett, and L. Hall, "Matched-field processing using measured replica fields," J. Acoust. Soc. Am. **107**, 739–746 (2000).

[10] A. Thode, "Source ranging with minimal environmental information using a virtual receiver and waveguide invariant theory," J. Acoust. Soc. Am. **108**, 1582–1594 (2000).

[11] S. Conti, P. Roux, and M. Fink, "Depth and range shifting of a focal spot using a time-reversal mirror in an acoustic waveguide," Appl. Phys. Lett. **80**, 3647–3649 (2002).

[12] L. M. Brekhovskiih and Y. Lysanov, *Fundamentals of Ocean Acoustics*, 2nd ed. (Springer, Berlin, 1991).

[13] M. Porter, "The KRAKEN normal mode program," SACLANT Undersea Research Centre Technical Report SM-245, 1991.

Propagation of Lamb waves in a plate with a periodic grating: Interpretation by phonon

Damien Leduc[a)]
Laboratoire d'Acoustique Ultrasonore et d'Electronique, UMR CNRS 6068, Université du Havre, Place Robert Schuman, BP 4006, 76610 Le Havre, France

Anne-Christine Hladky
Institut d'Electronique de Microélectronique et de Nanotechnologie, UMR CNRS 8520, 41 boulevard Vauban, 59046 Lille, France

Bruno Morvan, Jean-Louis Izbicki, and Pascal Pareige
Laboratoire d'Acoustique Ultrasonore et d'Electronique, UMR CNRS 6068, Université du Havre, Place Robert Schuman, BP 4006, 76610 Le Havre, France

(Received 11 February 2005; revised 20 June 2005; accepted 30 June 2005)

In this paper the propagation of Lamb waves in an aluminium plate with a periodic grating containing triangular grooves is studied. Numerical simulations (FEM) are performed. A single incident mode is excited on a flat area and the interaction with the periodic grating is studied. Reflected converted waves are observed when the incident Lamb wave passes through the grating. At the entrance of the periodic grating, a phonon relation is written between the incident signal, the converted mode, and the phonon related to the grating. An experimental verification of the phonon relation is carried out. © *2005 Acoustical Society of America.* [DOI: 10.1121/1.2005987]

PACS number(s): 43.35.Cg, 43.20.Mv [ANN] Pages: 2234–2239

I. INTRODUCTION

Ultrasonic waves are sensitive to surface roughness. Ultrasonic reflection and transmission at a rough fluid-solid interface have been widely dealt with in the past.[1,2] In particular, surface roughness characterization is a subject of great interest for bonded structures. Indeed, the bonding surface is often roughened before applying glue in order to improve the bonding quality. In this study in order to characterize the roughness of internal interfaces, we use guided Lamb-type waves which are well-suited to this purpose, contrary to surface waves (Rayleigh or Scholte).

Few studies concern the propagation and the scattering characteristics of guided waves in plates with rough surfaces. Lobkis *et al.*[3,4] have developed a model from the phase-screen approximation (PSA). Thanks to this model, the damping of Lamb waves by the interaction of partial waves (shear and compressional) with the rough surface can be explained. For rough surfaces, a usual characteristic parameter is the value of the root mean square roughness height R_q.[5] In Refs. 3 and 4, the Lamb wave damping is a function of R_q. Potel *et al.*[6,7] consider the problem with a perturbation approach; this approach also supposes restriction on the R_q value and it is assumed that the surface profile varies slowly. This model also provides for the Lamb wave the real and imaginary parts of the wave number. Whatever the model considered, the real part of the wave vector, and thus the wavelength λ, of the Lamb wave is not sensitive to the presence of roughness at least for the studied R_q values. The imaginary part of the wave vector (i.e., damping) in Ref. 6 is related both to the value of R_q and the spatial distribution of the roughnesses. From an experimental point of view, a power spectral density performed on a roughness profile shows dominant wavelengths Λ (spatial period). Indeed, a rough surface may be regarded as made up of a combination of several spatial periods with different wavelengths. For a given measured damping of one Lamb mode, it is possible to fit the result with one of the spatial periods present on the sample. The question is now how to choose the most influential spatial period Λ among them. In order to answer this question, it is important to find the condition between the wavelength λ of the Lamb mode and the different spatial periods Λ to obtain their interaction. To further comprehend this interaction, the study of a periodical grating made of identical groves is proposed. In the past, previous studies on periodical gratings have mainly concerned surface waves by means of the Rayleigh wave.[8–10] The main result is that the diffraction of the Rayleigh wave obeys a Bragg relation. The Scholte wave can also be diffracted by a grating.[8,11–13] In this paper, we present numerical and experimental results on Lamb waves propagating on a grooved surface, because the work is dedicated to the control of surface bonding. To the authors' knowledge, there is no recent work which deals with the propagation of Lamb waves on a plate with a surface grating. This paper shows that when a Lamb wave is incident on a periodical grating, reflected converted modes appear at particular frequencies. This result can be interpreted as a consequence of phonon interaction. Therefore, a relation between incident and converted mode wave numbers and the grating period Λ is established. This relation results from the law of conservation of phonon momentum.

First, after a brief description of the samples, numerical simulations are presented. Signal processing allows us to give an interpretation of the results in the dual space (wave-

[a)]Electronic mail: damien.leduc@univ-lehavre.fr

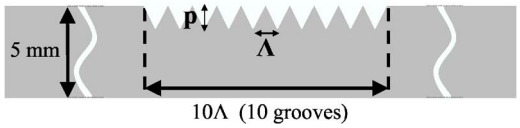

FIG. 1. Geometry of the studied samples.

number/frequency space). Several examples with various spatial periodicities are presented with a view to illustrating physical phenomenona, such as conversion modes, depth effect, and so on. Finally, an experimental study validating the numerical results is carried out.

II. NUMERICAL SIMULATIONS

A. Description of the studied samples

The studied samples are aluminium plates. Only a part of one side is treated with ten identical triangular grooves. This surface treatment can be found on only one side because the aim of this work will be to study the quality of a bonded structure with a rough interface. The other side of the plate is not treated and stands as a reference surface.

The grooves have a depth p and a spatial periodicity Λ (Fig. 1). The plates are 5 mm thick. The acoustics parameters, longitudinal and shear velocities, are respectively $c_L = 6320$ m/s and $c_T = 3115$ m/s. The density of the aluminium is equal to 2700 kg/m.

B. Numerical processing

The ATILA® finite element code was developed in the Acoustics Department of ISEN-France, for the modeling of sonar transducers.[14] It permits the static, modal, harmonic, and transient analysis of unloaded elastic, piezoelectric, or magnetostrictive structures, as well as the harmonic or transient analysis of radiating elastic or piezoelectric structures. It is able to analyze axisymmetrical, bi- or three-dimensional structures.

A transient analysis is performed to study the propagation of Lamb waves on a plate with a periodic grating. Because the plate is supposed to be infinite in one direction, a bi-dimensional mesh is used, using a plane strain condition. The plate is meshed and divided into elements connected by nodes. Isoparametric elements are used, with a quadratic interpolation along element sides. The elastic plate is submitted to analytical displacements on one edge of the plate with a view to exciting the S_0 Lamb mode. Then a Fourier transform clearly verifies that only the S_0 Lamb mode is excited. At a frequency of 800 kHz, a burst of five sinusoids is used. At this frequency, the wavelength of this Lamb mode is $\lambda = 3.75$ mm. The mesh must be long enough before and after the grating to avoid parasitic reflections on the edges. Transient analysis is then performed during 60 periods (75 μs), with a 0.05-μs time interval. Various meshes are considered: the spatial periodicity of the grooves varies from 2 to 3.9 mm. The grooves are supposed to all be identical with a depth of p. Computations provide the displacement at each node and at each time interval. In particular, the normal displacement before and after the grating are studied and time-space diagrams are drawn.

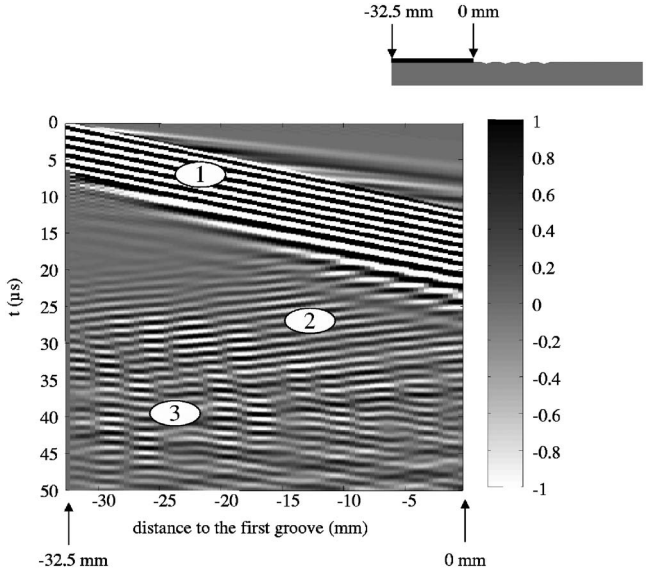

FIG. 2. Representation of the signal in the (x,t) space for a plate with a grating. The grating contains ten grooves. The spatial periodicity is $\Lambda = 2.4$ mm and the groove depth is equal to $p = 100$ μm. The origin of the spatial coordinate is the first groove. The levels of the incident signal are saturated in order to visualize the reflected signal.

C. Results

In Fig. 2, a time-space image of the normal surface displacements is given in the case of a grating with periodicity $\Lambda = 2.4$ mm. In the gray scale, the amplitude of the displacements of the surface located before the grating is represented. The zero of the spatial coordinate is fixed at the entrance of the grating. In this figure the gray scale is saturated in order to visualize the reflected signal whose amplitude is weaker than the incident signal. The depth of the grooves is $p = 100$ μm. Three parts of the signal are observed (Fig. 2): the incident signal (1), the reflection from the grating (2), and the reflection from the left edge of the plate (3). In this figure, it is shown that reflected waves appear on each groove. This explains the apparent temporal spreading of the reflected wave.

Reflected and incident waves are separated by applying a 2D FFT on the signals (Fig. 3). This calculation leads to a dual representation in the wave-number/frequency space (k,f). Positive components of wave number k correspond to the incident waves [Fig. 3(a)] whereas negative wavenumber values correspond to reflected waves [Fig. 3(b)]. Thus we can verify that the S_0 Lamb wave is properly excited on the plate. The theoretical S_0 dispersion curve is superimposed on the experimental signal. The signal excitation described in the previous paragraph explains why there is a spreading of the frequency bandwidth around a frequency of $f = 800$ kHz. According to Fig. 3(a), the main lobe of the frequency excitation extends from 660 to 920 kHz. This is not a problem because signal analysis is performed in dual space and each frequency component can be dealt with independently. Figure 3(b) shows a converted A_1 wave reflected from the grating. This wave is precisely located at frequency $f = 760$ kHz.

The FEM analysis is repeated for a grating with spatial periodicity Λ varying from 2 to 3.9 mm by 0.1 mm step.

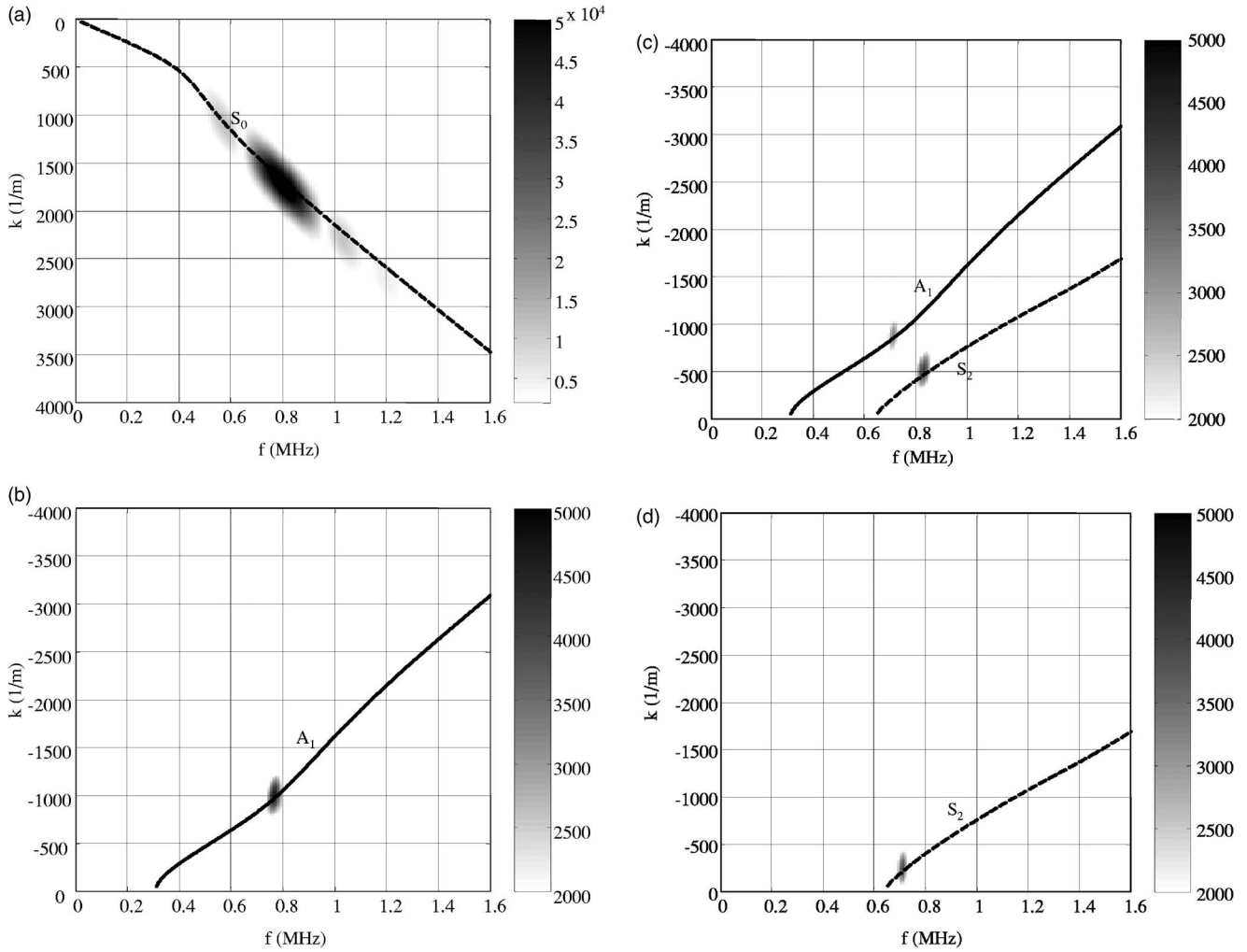

FIG. 3. Representation of the signal in dual space (k,f). The grating contains ten grooves. The grooves depth p is equal to 100 μm. (a) is the incident signal. The spatial periodicity is equal to (b) $\Lambda=2.4$ mm, (c) $\Lambda=2.7$ mm, and (d) $\Lambda=3.7$ mm. The lines correspond to the theoretical dispersion curves: solid line for A_1 mode and dotted lines for S_2 mode. Gray levels are fixed in order to compare the signals.

Two-dimensional fast Fourier transforms (2D FFTs) are carried out on the time-space signals for each value of Λ. Figures 3(b)–3(d) show that converted modes S_2 or/and A_1 can be seen at different frequencies. For instance, if $\Lambda=2.4$ mm [Fig. 3(b)], the conversion appears at $f=760$ kHz. At this frequency, the wave number for the A_1 converted mode is equal to 1010 m^{-1} and the wave number for the S_0 incident mode is equal to 1610 m^{-1}. The quantity $2\pi/\Lambda$ is homogeneous to a wave number and is a characteristic of the grating in dual space. For $\Lambda=2.4$ mm, $2\pi/\Lambda$ is equal to 2617 m^{-1}. One can notice that if we add the values of the incident and converted wave numbers ($k_{S0}=k_{S2}=2620$ m^{-1}), the obtained value is approximately $2\pi/\Lambda$ (relative error: 0.1%). This relation is verified for each grating periodicity and results are presented in Table I. This relation can be interpreted as a phonon relation and is described in detail in the next section.

III. INTERPRETATION: THE PHONON RELATION

The equality obtained in the previous section is in fact a relation between phonons. The S_0 incident mode is converted into S_2 or A_1 mode at the entrance of the grating. The scattering process occurring at the entrance can be described as a collision of phonons. The law of conservation of the phonon momentum can be written as

$$\mathbf{p}_{S0} = \mathbf{p}_{PH} + \mathbf{p}_{CM}, \tag{1}$$

where the converted mode (CM) propagates in the opposite direction to the S_0 incident mode. The phonon (PH) propagates under the grating in the direction of propagation of the incident wave. This implies a relation between the wave numbers:

$$k_{S0} = \frac{2\pi}{\Lambda} - k_{CM}. \tag{2}$$

Here we can recognize the relation which was verified in Table I with a maximum relative error of 3.4%. The incident and reflected waves verify a Bragg-type relation. Indeed, Eq. (2) can also be interpreted as a phase matching. The converted waves excited on two successive grooves must be in phase and the phase matching which corresponds to the smaller path implies

TABLE I. Comparison between the sum of the incident (k_{S0}) and converted wave numbers (k_{S2} or k_{A1}) and the phonon wave number related to the grating ($2\pi/\Lambda$). The column "frequency" corresponds to the frequency where the conversion is at a maximum.

Λ (mm)	$2\pi/\Lambda$ (m^{-1})	k_{S2} (m^{-1})	k_{S0} (m^{-1})	k_{A1} (m^{-1})	Frequency (kHz)	Σk (m^{-1})	Relative error
2	3140		1840	1260	850	3100	1.3%
2.1	2992		1770	1170	820	2940	1.7%
2.2	2856		1720	1115	805	2835	0.7%
2.3	2732		1670	1050	785	2720	0.4%
2.4	2618		1620	1000	765	2620	0.1%
2.5	2513		1570	955	745	2525	0.5%
2.6			1545	930	725	2475	2.4%
	2417	565	1845	845	2410	0.3%	
2.7			1490	885	710	2375	2.1%
	2327	520	1795	830	2315	0.5%	
2.8			1435	840	695	2275	1.4%
	2244	480	1745	815	2225	0.8%	
2.9	2167	460	1720		795	2180	0.6%
3	2094	420	1670		785	2090	0.2%
3.1	2027	400	1645		770	2045	0.9%
3.2	1963	380	1620		760	2000	1.9%
3.3	1904	355	1590		750	1945	2.2%
3.4	1848	330	1570		740	1900	2.8%
3.5	1795	310	1545		730	1855	3.3%
3.6	1745	290	1515		720	1805	3.4%
3.7	1698	260	1490		715	1750	3.1%
3.8	1653	240	1460		705	1700	2.8%
3.9	1611	220	1440		695	1660	3.0%

$$k_{S0} \cdot \Lambda + k_{CM} \cdot \Lambda = 2\pi. \quad (3)$$

Thus the physical problem of the interaction between the Lamb waves and the grating can be considered in dual space as a phonon process, and in direct space as an interference process involving a phase matching.

New curves can be plotted to predict the possible conversion. On the Lamb wave, k_{CM} values are superimposed on the theoretical Lamb waves dispersion curves for a free plate (Fig. 4). These curves are plotted for values of Λ varying from 2 to 3.9 mm. The intersections give the possible converted modes for a given grating. For instance, if the spatial periodicity of the grating is $\Lambda=3$ mm, intersections between the phonon relation curve and the dispersion curves give a predicted conversion into S_2 mode at $f=800$ kHz. This mode is effectively observed at $f=785$ kHz (Table I—relative error: 1.9%). S_1 mode is also a potential converted mode in the frequency bandwidth, at lower frequency, but the normal displacement of this mode is too weak on the surface and thus it is not possible to detect it.[10] There are other intersections but most of them are out of the frequency bandwidth of excitation.

At the exit of the grating we have verified that only the S_0 mode is propagating and consequently the phonon relation Eq. (1) is also valid.

The grating can also be characterized by the depth of the grooves. To see if this parameter influences the phonon relation, a parametric study of a grating with various depths is carried out.

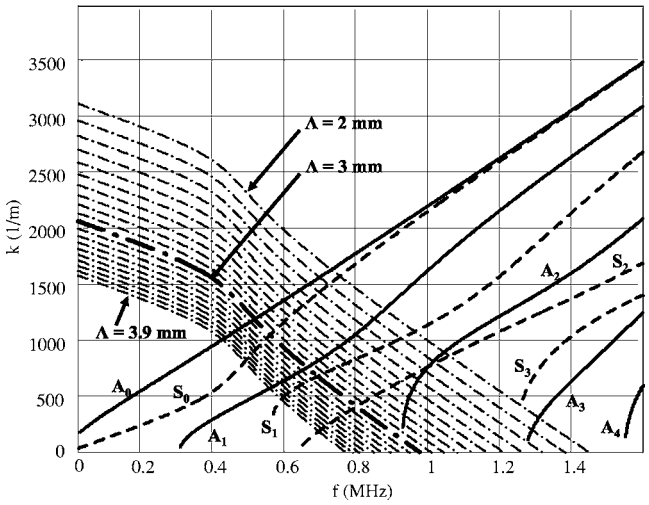

FIG. 4. Theoretical dispersion curves for the studied aluminium plates: solid lines for antisymmetric modes and dotted lines for symmetric modes. For each studied spatial periodicity, curves resulting from the phonon relation [Eq. (2)] are plotted in dashed-dotted lines.

A grating with ten grooves and a spatial periodicity of 3.7 mm is studied with depths varying from $p=50$ to 400 μm. Whatever the value of p, the wave number related to the converted mode always corresponds to the S_2 reflected mode (Fig. 5), where level one corresponds to the amplitude of the incident mode. We note that the amplitude of the S_2 mode increases with the value of p. If the depth is low compared to the Lamb wave wavelength and the plate thickness ($p<200$ μm), the amplitude of the S_2 mode is proportional to the depth of the grooves. The evolution for $p>200$ μm could be interpreted by a different distribution of the energy of the incident wave among more reflected waves (an S_0 converted-reflected mode is observed). In this case, the phonon relation involving only the S_2 reflected mode is not sufficient to describe the interaction of the Lamb waves with the periodical grating.

For a given depth, the amplitude of the reflected mode increases with the number of grooves.

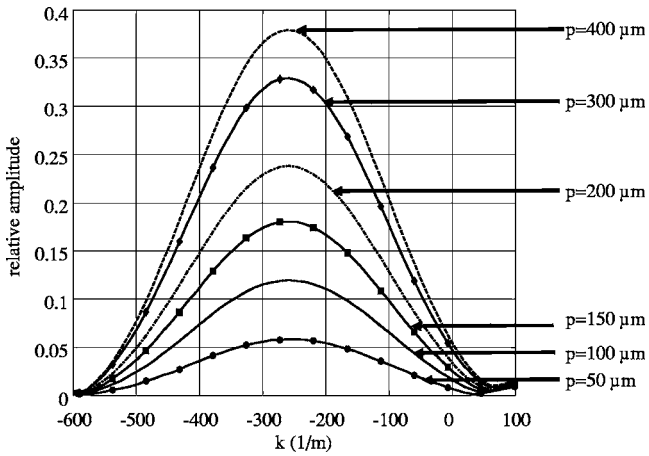

FIG. 5. Representation of the wave number related to the S_2 converted mode for various depths in dual space (k,f). The grating contains ten grooves. The spatial periodicity is equal to $\Lambda=3.7$ mm.

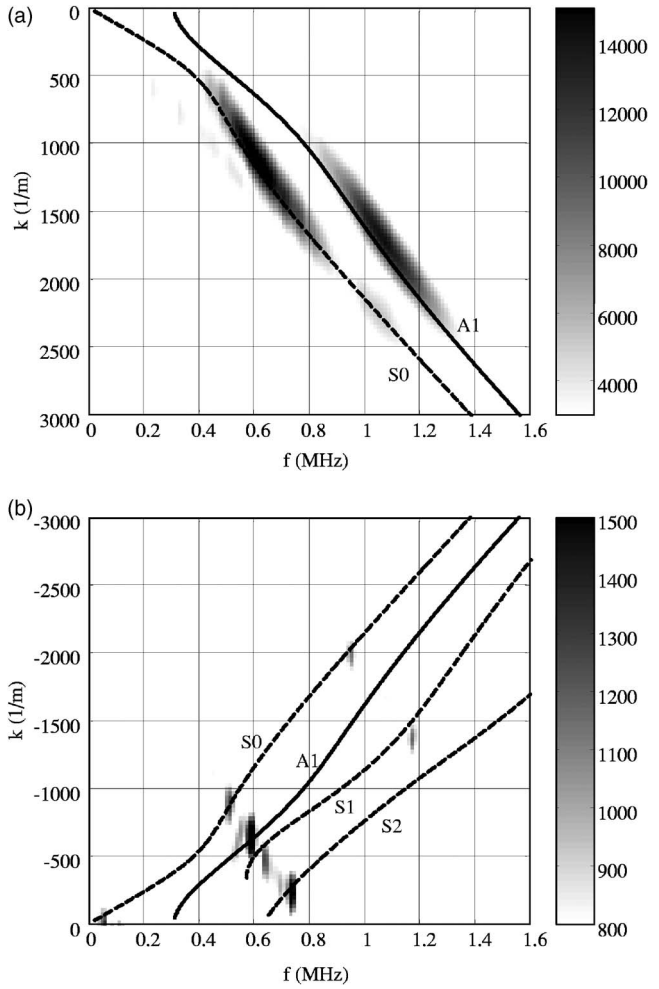

FIG. 6. (a) Representation of the experimental incident signal in dual space (k,f). (b) Representation of the experimental reflected signal in dual space (k,f).

IV. EXPERIMENTAL RESULTS

The experimental setup is the following. A pulse generator delivers a very short pulse voltage (about 300 V during a period of 300 ns) to a piezo-composite transducer. The central frequency of this emitting transducer is 1 MHz. Lamb waves are then generated by the wedge method with a wedge angle of 49° to excite the S_0 mode around a frequency equal to 800 kHz. The characteristics of the experimental grating are groove depth p equal to 100 μm and spatial periodicity of the grooves Λ equal to 3.7 mm. An optical profilometer is used to characterize the surface of the sample. The root mean square value (rms) R_q=29.2 μm is obtained.

The S_0 wave is generated on a flat area. Then the wave is propagated over 18 mm before reaching the grating. A noncontact detection is done using a laser vibrometer: it measures the normal surface displacement of the plate along the principal direction of propagation by 0.1 mm steps. For each spatial position, the amplitude is recorded and allows us to obtain an (x,t) image similar to Fig. 2 obtained in the FEM study. The evolution of the amplitude in the different modes is plotted as a function of the distance.

The S_0 wave is generated on the [430–850 kHz] frequency range [Fig. 6(a)]. Four reflected converted modes are obtained at different frequencies [Fig. 6(b)]: three reflected converted modes (A_1,S_1,S_2) and one nonconverted reflected mode (S_0). The corresponding wave-number values are reported in Table II. The phonon relation is verified with a maximum error of 2.5%. The S_2 converted mode is experimentally found at f=730 kHz. It was numerically found at f=710 kHz, using the FEM analysis (Table I). The small discrepancy is due to the acoustical parameters, which are slightly different in the experimental part and in the numerical study. For each conversion, the phonon relation is well verified.

TABLE II. Comparison between the sum of the incident (k_{S0}) and reflected-converted wave numbers (k_{A1},k_{S1},k_{S2}) and reflected (k_{S0}) and the phonon wave number related to the grating ($2\pi/\Lambda$). The column "frequency" corresponds to the frequency of the conversion.

	Incident	Reflected mode						
Frequency (kHz)	k_{S0} (1/m)	k_{S2} (1/m)	k_{S1} (1/m)	k_{A1} (1/m)	k_{S0} (1/m)	Σk (1/m)	$2\pi/\Lambda$ (1/m)	Relative error
730	1455	230				1685	1698	0.8%
635	1180		475			1655	1698	2.5%
585	1040			650		1690	1698	0.5%
515	815				875	1690	1698	0.5%

V. CONCLUSIONS

Incident Lamb waves propagating in a plate with a periodic grating are converted into reflected modes. A phonon relation is written between the incident signal, the converted mode and the phonon related to the grating.

The spatial periodicity of the grating determines the frequency of the converted modes, whereas the depth of the grooves only modifies the amplitude of the converted modes. Therefore, for the cases presented in this paper, the effects of the spatial periodicity of the grating and the groove depth are independent. Experiment and numerical results are in good agreement.

Future works will consist in studying surface profile with several spatial periodicities in order to have a more accurate representation of a rough surface.

ACKNOWLEDGMENTS

This work is supported by the research group on ultrasonics (GDR CNRS No. 2501, France). The authors would like to thank Philippe Saint-Martin (IUT, Le Havre, France) for machining experimental samples and Dawn Hallidy for proofreading the manuscript.

[1] J. A. Ogilvy, "Wave scattering from rough surfaces," Rep. Prog. Phys. **50**, 1553–1608 (1987).
[2] M. De Billy and G. Quentin, "Backscattering of acoustic waves by randomly rough surfaces of elastic solids immersed in water," J. Acoust. Soc. Am. **72**, 591–601 (1982).
[3] O. I. Lobkis and D. E. Chimenti, "Elastic guided waves in plates with surface roughness. I. Model calculation," J. Acoust. Soc. Am. **102**, 143–149 (1997).
[4] O. I. Lobkis and D. E. Chimenti, "Elastic guided waves in plates with surface roughness. II. Experiments," J. Acoust. Soc. Am. **102**, 150–159 (1997).
[5] D. Leduc, B. Morvan, P. Pareige, and J.-L. Izbicki, "Measurement of the

effects of rough surfaces on Lamb wave propagation," NDT & E Int. **37**, 207–211 (2004).
[6]C. Potel, D. Leduc, B. Morvan, P. Pareige, J. L. Izbicki, and C. Depollier, "Lamb wave propagation in isotropic media with rough interface: comparison between theoretical and experimental results," in *Proceedings of the World Congress on Ultrasonics* (ISBN 2-9515619-9-7, CD-ROM ISBN 2-9521105-0-6), Paris, France (2003), Vol. 2, pp. 609–612.
[7]C. Potel, D. Leduc, B. Morvan, P. Pareige, C. Depollier, and J.-L. Izbicki, "Propagation of Lamb waves in anisotropic rough plates: a perturbation method," in *Proceedings of the French Congress on Acoustic* (CFA/DAGA'04—ISBN 2-9521105-1-4, CD-ROM ISBN 2-9521105-3-0), Strasbourg, France (2004), Vol. 1, pp. 147–148.
[8]J. M. Clayes, O. Leroy, A. Jungman, and L. Adler, "Diffraction of ultrasonic waves from periodically rough liquid-solid surfaces," J. Appl. Phys. **54**(10), 5657–5662 (1983).
[9]K. Mampaert and O. Leroy, "Reflection and transmission of normally incident ultrasonic waves on periodic solid-liquid interfaces," J. Acoust. Soc. Am. **83**, 1390–1398 (1988).
[10]W. Lauriks, L. Kelders, and J. F. Allard, "Surface waves above gratings having a triangular profile," Ultrasonics **36**, 865–871 (1998).
[11]A. Jungman, L. Adler, J. D. Achenbach, and R. Roberts, "Reflection from a boundary with periodic roughness: theory and experiment," J. Acoust. Soc. Am. **74**, 1025–1032 (1983).
[12]J. R. Chamuel, "Transient Scholte wave transmission along rough liquid/solid interfaces," J. Acoust. Soc. Am. **83**, 1336–1344 (1988).
[13]H. Duflo, A. Tinel, and J. Duclos, "Scholte wave propagation and diffraction on a fluid/solid periodic rough surface," in *Proceedings of the I.E.E.E. International Ultrasonics Symposium* (ISBN 0-7803-2012-3), Cannes, France (1994), pp. 719–722.
[14]ATILA® Finite Element Code for Piezoelectric and Magnetostrictive Transducer Modeling, Version 5.2.1, User's Manual, ISEN, Acoustics Laboratory, Lille, France (2002).

Ultrasonic guided wave monitoring of composite wing skin-to-spar bonded joints in aerospace structures

Howard Matt, Ivan Bartoli, and Francesco Lanza di Scalea[a)]
NDE & Structural Health Monitoring Laboratory, Department of Structural Engineering, University of California–San Diego, 9500 Gilman Drive, M.C. 0085, La Jolla, California 92093-0085

(Received 21 April 2005; revised 20 July 2005; accepted 20 July 2005)

The monitoring of adhesively bonded joints by ultrasonic guided waves is the general topic of this paper. Specifically, composite-to-composite joints representative of the wing skin-to-spar bonds of unmanned aerial vehicles (UAVs) are examined. This research is the first step towards the development of an on-board structural health monitoring system for UAV wings based on integrated ultrasonic sensors. The study investigates two different lay-ups for the wing skin and two different types of bond defects, namely poorly cured adhesive and disbonded interfaces. The assessment of bond state is based on monitoring the strength of transmission through the joints of selected guided modes. The wave propagation problem is studied numerically by a semi-analytical finite element method that accounts for viscoelastic damping, and experimentally by ultrasonic testing that uses small PZT disks preferably exciting and detecting the single-plate s_0 mode. Both the models and the experiments confirm that the ultrasonic energy transmission through the joint is highly dependent on the bond conditions, with defected bonds resulting in increased transmission strength. Large sensitivity to the bond conditions is found at mode coupling points, as a result of the large interlayer energy transfer. [DOI: 10.1121/1.2033574]

PACS number(s): 43.35.Cg, 43.35.Mr, 43.20.Mv, 43.35.Zc [YHB] Pages: 2240–2252

I. INTRODUCTION

Fiber-reinforced polymer composites have being increasingly utilized in the aerospace industry due to their light weight and high strength. One example of a heavy use of composites is found in unmanned aerial vehicles (UAVs), which are employed for both military and civil purposes such as environmental monitoring. Adhesively bonded joints are found in the wing skin-to-spar assemblies of UAVs. These joints are critical structural components, necessitating effective tools for assessing their condition. A built-in structural health monitoring approach, rather than a traditional NDT-type maintenance approach, would be most desirable for this application.

Ultrasonic inspection of bonded joints has gone through decades of improvement and has proven to be a very powerful method. Early studies used normal-incidence ultrasonic testing to determine the modulus and thickness of the bond layer through spectroscopy principles, monitoring the through-thickness longitudinal resonances of the multilayered joint structure (Guyott and Cawley, 1988a, b). The reflection coefficients of bulk ultrasonic waves at oblique incidence have also been shown to be sensitive to bond conditions. A thorough theoretical analysis for this approach was presented by Rokhlin and Wang (1991), where reflection coefficients were predicted during the cure process of an epoxy resin layer between solid semispaces.

An alternative ultrasonic bond testing approach uses guided waves that exploit the natural waveguide geometry of most bonded aerospace components. The guided wave method can be an effective bond diagnostic tool due to its capability of long-range inspection as well as its flexibility in selecting sensitive mode-frequency combinations. Generally, sensitive combinations are those resulting in large strains/stresses at the bond layer. In addition, through the use of built-in actuators and sensors, the guided wave approach lends itself to the development of integrated systems for continuous bond diagnostics as opposed to regularly scheduled NDT maintenance. Such an integrated health monitoring system is needed in aerospace structures in order to implement a condition-based maintenance philosophy.

There are two approaches traditionally used for guided wave inspection of bonds. In the first approach, the waves are both generated and detected in the bonded region ("within the bond" testing configuration). In the second approach, the waves are generated in the adherend on one side of the bond and received across the bond ("across the bond" testing configuration). The main difference of the second approach is the occurrence of mode conversion when the wave enters and leaves the bond due to the transition from the single adherend geometry to the bonded assembly geometry, and vice versa. Several previous studies used the within the bond configuration to relate wave amplitude, velocity, and frequency to the elastic properties of the adhesive layer (Mal, 1988; Nagy and Adler, 1989; Mal *et al.*, 1990; Xu *et al.*, 1990; Pilarski and Rose, 1992; Lowe and Cawley, 1994; Kundu and Maslov, 1997; Chimenti, 1997; Kundu *et al.*, 1998; Rose *et al.*, 1998; Heller *et al.*, 2000; Cheng *et al.*, 2001; Seifried *et al.*, 2002). Recent applications of the within the bond configuration have also examined the possibility of inspecting the bond between a composite skin and a core in sandwich aerospace panels (Castaings and Hosten, 2003; Hay *et al.*, 2003). The across the bond configuration was also

a)Author to whom correspondence should be addressed. Electronic mail: flanza@ucsd.edu

used successfully for the inspection of lap-shear joints, tear strap-to-skin joints, and bonded patch repairs for damaged aircraft panels (Rohklin, 1991; Rose *et al.*, 1995; Chang and Mal, 1995; Mal *et al.*, 1996; Lowe *et al.*, 2000; Lanza di Scalea *et al.*, 2001; Sun *et al.*, 2002; Lanza di Scalea *et al.*, 2004).

These previous studies provided a great deal of knowledge on the behavior and defect sensitivity of various guided wave modes propagating in adhesively bonded joints. However, none of these works examined the case of composite-to-composite bonded joints, such as those found in wing skin-to-spar bonds of UAVs. In addition, the majority of previous works were not focused on built-in structural monitoring systems, an area that has gained increasing interest only recently (Light *et al.*, 2003). The use of arrays of built-in piezoceramic elements [Pb(Zr–Ti)O_3—PZT] for exciting and detecting ultrasonic guided waves goes back 10 years (Keilers and Chang, 1995). However, the preferred application has been the detection of impact damage in FRP aerospace panels, rather than the condition monitoring of bonds (Lakshmanan and Pipes, 1997; Wang and Chang, 1999; Ihn *et al.*, 2001; Lemistre and Balageas, 2001; Giurgiutiu and Zagrai, 2002; Sohn *et al.*, 2003; Giurgiutiu *et al.*, 2003; Staszewski *et al.*, 2004).

The present study investigates the propagation of ultrasonic guided waves in composite-to-composite bonded joints as a function of bond condition. The specific bond conditions considered are those of properly cured adhesive, poorly cured adhesive, and disbonds. The study is part of a broader effort aimed at developing a built-in structural monitoring system for the wing skin-to-spar joints of UAVs. The within the bond configuration and the across the bond configuration were examined numerically by a semi-analytical finite element method that provides modal solutions for the joints and accounts for the viscoelastic behavior of the composites. The cross-sectional power flows of the carrier modes in the bonded region (Poynting vectors), each weighted by an excitation factor based on displacement mode shapes, were used as the basis to predict changes in the ultrasonic strength of transmission through the different bond conditions. Experimental tests were conducted using PZT discs bonded on two simulated wing skin-to-spar joints that were constructed in the laboratory. The root mean square of the detected signals was used to quantify the strength of transmission across the varying bond conditions. Both the predictions and the experiments show that the degradation of the bond has a marked effect on the strength of the transmission of the guided wave modes.

II. PROBLEM STATEMENT

A partial cross section of a typical UAV wing assembly is shown in Fig. 1(a). The wing skin is generally made of a Nomex or aluminum honeycomb core sandwiched between two carbon fiber-reinforced plastic (CFRP) laminated composite plates. Each skin is bonded using high-strength epoxy adhesive to a tubular composite spar that runs down the length of the wing. The sandwiched skin tapers down in the bonded region, where only the CFRP laminates are bonded

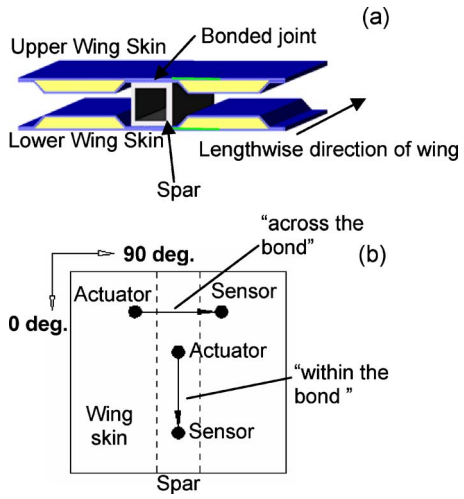

FIG. 1. (Color online) (a) Typical wing skin-to-spar assembly in unmanned aerial vehicles. (b) "Across the bond" and "within the bond" testing configurations.

to the spar. The theoretical and experimental tests that follow were performed on CFRP plates directly bonded to CFRP spars to represent the wing skin-to-spar joint.

The bond conditions that were examined included regions with poorly cured adhesive and disbonded regions, in addition to regions with properly cured adhesive. Details on the conditions of the bond defects considered are given in Sec. III A pertaining the model and in Sec. IV A pertaining to the experiment. In summary, the poorly cured region was obtained experimentally by improperly mixing a two-part epoxy adhesive; the resulting changes in cohesive stiffness and attenuation values were measured to determine the appropriate ultrasonic properties to use when modeling the bond layer. Any influence of the reduced cohesive properties on the adhesive properties between the bond layer and the substrates were not considered in the model. A severe case of interfacial degradation was considered for the simulated disbond defects. Analyses and experiments were performed in the two testing configurations of within the bond and across the bond, depicted in Fig. 1(b).

Two different plate lay-ups were studied, namely a quasi-isotropic $[0/\pm45/90]_S$ lay-up and a $[0/\pm45/0]_S$ lay-up, both consisting of eight plies and bonded to a woven $[0/90]$ tubular spar. The $[0/\pm45/0]_S$ lay-up is a better representation of most UAVs, where the 0° fibers provide flexural rigidity and the ±45° fibers provide torsional rigidity to the wing. The quasi-isotropic lay-up was examined as a simplified model of the UAV wing.

III. GUIDED WAVE MODELING

A. Modeling formulation and procedure

Modal solutions for the dispersive waves were obtained from a semi-analytical finite element (SAFE) approach. The SAFE technique requires only the discretization of the cross section of the waveguide, thus reducing a 3-D problem to a 2-D one. Harmonic behavior is then imposed in the wave propagation direction. Because of its computational efficiency, this method has been utilized to extract modal solu-

tions in waveguides of arbitrary cross sections (Gavric, 1995; Hayashi *et al.*, 2003; Finnveden, 2004), including FRP laminates (Mukdadi *et al.*, 2002; Mukdadi and Datta, 2003). The novelty of the SAFE method used in the present work is the introduction of viscoelastic material damping for both the CFRP adherends and the adhesive layer.

For the within the bond case, Fig. 2(a), the only model of interest was the bonded region with the wave propagating along the lengthwise direction of the spar. For the across the bond configuration, Fig. 2(b), the wing skin model was examined separately in addition to the bonded region with the wave propagating across the spar. In both cases the bond model assumed a uniform thickness for the spar, neglecting the localized increase in thickness at the bond edges found in the across the bond case due to the tubular geometry. This approximation was considered acceptable given that the frequency content of the waves examined was such that their penetration beyond the wall thickness of the spar was negligible. Also, mode conversion effects at the bond edges for the across the bond case were predicted based on the similarities between cross-sectional mode shapes of the excitation and the carrier modes found from the models, following the same philosophy adopted in previous works (Auld, 1990; Lowe *et al.*, 2000, Lanza di Scalea *et al.*, 2004).

The SAFE method was implemented in Matlab© using the PDE toolbox for creating the finite element mesh. The waveguide was modeled as a system of N homogeneous and generally viscoelastic anisotropic layers. As shown in Fig. 2(c), the dimensions were considered infinite in the width direction, y, perpendicular to the wave propagation direction, x. Thus the wave propagation problem could be studied by simply considering a longitudinal section in the x-z wave propagation plane. The section was discretized in the thickness direction, z, by a set of one-dimensional finite elements with quadratic shape functions and three nodes, with three degrees of freedom per node. Under the hypothesis of time-harmonic motion, the displacement vector $\mathbf{u}$ at any point within an element can be written as

$$\mathbf{u}(x,y,z,t)=\begin{bmatrix}u_x\\u_y\\u_z\end{bmatrix}=\begin{bmatrix}\sum_{i=1}^{3}N_i(z)U_{xi}\\\sum_{i=1}^{3}N_i(z)U_{yi}\\\sum_{i=1}^{3}N_i(z)U_{zi}\end{bmatrix}e^{j(kx-\omega t)}, \tag{1}$$

where t represents the time variable, j is the imaginary unit, N_i are the shape functions, k is the wave number, ω is the circular frequency, and U_{xi}, U_{yi}, and U_{zi} are the nodal displacements along directions x, y, and z, respectively.

Each ply of the CFRP wing skin was modeled as a transversely isotropic layer with the following standard constitutive laws in the global laminate directions (x,y,z):

$$\boldsymbol{\sigma}=\overline{\mathbf{C}^*}\boldsymbol{\varepsilon}=\mathbf{T}_1^{-1}\mathbf{C}^*\mathbf{T}_2\boldsymbol{\varepsilon}, \tag{2}$$

where $\overline{\mathbf{C}^*}$ is the complex stiffness matrix in the global directions of the laminate, $\mathbf{C}^*$ is the complex stiffness matrix in the principal material directions of the individual ply, $\mathbf{T}_1$ and $\mathbf{T}_2$ are the transformation matrices from the principal material directions to the global laminate directions as defined in Jones (1975), and the stress vector $\boldsymbol{\sigma}$ and strain vector $\boldsymbol{\varepsilon}$ are given by

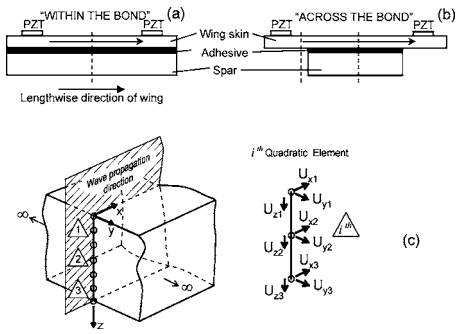

FIG. 2. Wave propagation models for (a) "within the bond" testing and (b) "across the bond" testing. (c) Finite element discretization.

$$\boldsymbol{\sigma}=[\sigma_{xx}\ \sigma_{yy}\ \sigma_{zz}\ \sigma_{yz}\ \sigma_{xz}\ \sigma_{xy}]^{\mathrm{T}}, \tag{3}$$

$$\boldsymbol{\varepsilon}=[\varepsilon_{xx}\ \varepsilon_{yy}\ \varepsilon_{zz}\ \gamma_{yz}\ \gamma_{xz}\ \gamma_{xy}]^{\mathrm{T}}. \tag{4}$$

The strain components in Eq. (4) can be evaluated by the usual linear strain-displacement relations.

The equations governing the wave propagation problem can be obtained by introducing the following expression of the principle of virtual works in the absence of external forces:

$$\int_V \delta\mathbf{u}^{\mathrm{T}}(\rho\ddot{\mathbf{u}})dV+\int_V \delta\boldsymbol{\varepsilon}^{\mathrm{T}}\boldsymbol{\sigma}\,dV=0, \tag{5}$$

where the dot indicates differentiation with respect to time, ρ is the density, and V is the volume of the waveguide. The components of the vectors $\delta\mathbf{u}$ and $\delta\boldsymbol{\varepsilon}$ represent the virtual displacements and the corresponding virtual strains. By substituting in Eq. (5) the constitutive laws of Eq. (2), the strain-displacement expressions, and introducing the interpolation of Eq. (1), the following eigenvalue problem is finally obtained for the entire structure after common finite element manipulations:

$$(\mathbf{A}-k\mathbf{B})\mathbf{Q}=\mathbf{0}. \tag{6}$$

This equation represents a standard linear (first-order) problem generated by expanding a general quadratic eigenvalue problem using standard procedures. Details on the calculation of the matrices $\mathbf{A}$ and $\mathbf{B}$ can be found in other works (Gavric, 1995; Hayashi *et al.*, 2003; Mukdadi and Datta, 2003). At each frequency ω, $2M$ eigenvalues k_m and, consequently, $2M$ eigenvectors are obtained where M is the number of total degrees of freedom in the system. The mth eigenvalue k_m represents the mth wave number, and $\mathbf{Q}_m$ is the corresponding eigenvector in which the first M components describe the mode shapes. Once the wave numbers are known as a function of frequency, the dispersion curves can be computed.

When considering viscoelastic material damping, the matrices $\mathbf{A}$ and $\mathbf{B}$ become both complex as a result of the complex stiffness matrix $\mathbf{C}^*$. Therefore all of the wave num-

TABLE I. Real and imaginary stiffness coefficients and geometric and physical properties for the bonded layers.

Layer	C'_{11} (GPa) C''_{11} (GPa)	C'_{12} (GPa) C''_{12} (GPa)	C'_{13} (GPa) C''_{13} (GPa)	C'_{22} (GPa) C''_{22} (GPa)	C'_{23} (GPa) C''_{23} (GPa)	C'_{33} (GPa) C''_{33} (GPa)	C'_{44} (GPa) C''_{44} (GPa)	C'_{55} (GPa) C''_{55} (GPa)	C'_{66} (GPa) C''_{66} (GPa)	Density (kg/m^3)	Thickness (mm)
CFRP Lamina	135 (8.23)[a]	5.70 (0.65)[a]	5.70 (0.60)[a]	14.2 (0.34)[a]	8.51 (0.25)[a]	14.2 (0.65)[a]	2.87 (0.24)[a]	4.55 (0.28)[a]	4.55 (0.25)[a]	1530	0.133
CFRP Spar	88.0 (4.28)	5.45 (0.65)	5.09 (0.425)	88.0 (4.28)	5.09 (0.425)	11.3 (0.65)	4.64 (0.26)	4.64 (0.26)	6.00 (0.25)	1530	5.235
Properly cured Bond	8.24 (0.39)	4.10 (0.028)	4.10 (0.028)	8.24 (0.39)	4.10 (0.028)	8.24 (0.39)	2.07 (0.18)	2.07 (0.18)	2.07 (0.18)	1421	0.203
Poorly cured Bond	6.89 (0.19)	4.58 (0.064)	4.58 (0.064)	6.89 (0.19)	4.58 (0.064)	6.89 (0.19)	1.16 (0.066)	1.16 (0.066)	1.16 (0.066)	1465	0.203
Disbond	0.0697 (0.0352)	0.0695 (0.0349)	0.0695 (0.0349)	0.0697 (0.0352)	0.0695 (0.0349)	0.0697 (0.0352)	0.000 118 (0.000 128)	0.000 118 (0.000 128)	0.000 118 (0.000 128)	1421	0.203

[a]From Neau *et al.* (2002).

bers and the eigenvectors are complex. The phase velocity can be evaluated by the expression $c_{ph}=\omega/k_{\text{real}}$ where k_{real} is the real part of the wave number. The imaginary part of the wave number corresponds to the attenuation, in Nepers per meter, of the mth mode at the frequency ω.

The energy velocity, rather than the group velocity, was used in this study as the only physically meaningful parameter for viscoelastic media (Bernard *et al.*, 2001). The expression for the energy velocity used in the present work is

$$V_e = \frac{(1/H)\int_H \mathbf{P}\cdot\hat{\mathbf{x}}\,dz}{(1/T)\int_T ((1/H)\int_H E\,dz)dt}, \tag{7}$$

where $\hat{\mathbf{x}}$ is the vector of unit length along the wave propagation direction, x, and $1/T\int_T(\cdots)dt$ denotes the average over the time period T. The integral $1/H\int_H(\cdots)dz$ evaluates the average power computed from the Poynting vector, $\mathbf{P}$ (real part only), and the average total energy density (kinetic and potential), E, over the entire waveguide thickness, H. The Poynting vector can be calculated from the known relation:

$$\mathbf{P} = -\frac{1}{2}\mathrm{Re}(\boldsymbol{\sigma}\dot{\mathbf{u}}^*) = \begin{pmatrix} P_x \\ P_y \\ P_z \end{pmatrix}, \tag{8}$$

where $\boldsymbol{\sigma}$ is the classical 3×3 stress tensor. The numerator of Eq. (7) is of particular interest for the results that follow. This term corresponds to the average power flow in the direction of wave propagation carried by a mode over a unit period of time, and it was used to predict the wave transmission strength across the different bond conditions.

The cross-sectional distribution of strains were normalized by the square root of the power flow through the entire thickness of a unit-width waveguide and averaged over a temporal period, $\sqrt{\int_H \mathbf{P}\cdot\hat{\mathbf{x}}\,dz}$. The cross-sectional distributions of power flows were normalized by the square of this factor, $\int_H \mathbf{P}\cdot\hat{\mathbf{x}}\,dz$. These normalizations were necessary to compare results between different modes and frequencies.

Complex constitutive matrices were used to model viscoelastic material damping in all components. The known hysteretic viscoelastic model was assumed where the imaginary part of the stiffness matrix is independent of frequency. Thus

$$C^*_{ij} = C'_{ij} - \mathrm{j}C''_{ij}. \tag{9}$$

The hysteretic model conveniently required to determine the stiffness matrix only once for the entire frequency range examined. This is in contrast to frequency-dependent models, such as the Kelvin-Voigt, where the stiffness values must be updated at each frequency step. The values of the real components, C'_{ij}, and of the imaginary components, C''_{ij}, of the stiffness matrix adopted in the models are shown in Table I. For the eight CFRP layers of the skin, the real components of the stiffness matrix were based upon manufacturing specifications and typical values for T300/5208 carbon epoxy. The imaginary components of the stiffness matrix were assumed equal to the values used by Neau *et al.* (2002).

The CFRP spar was modeled as one homogenous layer with anisotropic properties equivalent to the multilayer $[0/90]$ structure of T800/924. The real and imaginary components of the stiffness matrix, $\bar{\mathbf{C}}_{eq}$, for the equivalent spar layer were computed by averaging the coefficients of the stiffness matrices of two adjacent layers, $\bar{\mathbf{C}}_0$ and $\bar{\mathbf{C}}_{90}$, obtained from Eq. (2). These equivalent coefficients were consistent with those obtained from the independent approach of Karusena *et al.* (1991). The homogeneous equivalent coefficients are accurate when the number of layers is high and the wavelengths are large compared to the individual layer thickness, as it was the case for the test spar. The epoxy adhesive was modeled as a viscoelastic isotropic layer. In this case the viscoelastic matrix, $\mathbf{C}^*$, depends only on the two elastic constants, Young's modulus, E, and shear modulus, G, which were calculated from the bulk longitudinal and shear wave velocities, c^*_L and c^*_S. These complex velocities were calculated by the known expressions:

$$c^*_{L,S} = c_{L,S}\left(1 + j\frac{\alpha_{L,S}}{2\pi}\right)^{-1}, \tag{10}$$

where $\alpha_{L,S}$ are the longitudinal and shear attenuation in the material, expressed in Nepers per wavelength. The attenuation and elastic constants for the properly cured epoxy and for the poorly cured epoxy were obtained through normal-incidence ultrasonic tests on properly mixed and poorly

TABLE II. Ultrasonic bulk longitudinal and shear velocities and material attenuations for the adhesive layer.

Layer	C_L (m/s)	C_T (m/s)	α_L (Np/λ)	α_T (Np/λ)
Properly cured Bond	2410	1210	0.149	0.276
Poorly cured Bond	2170	890	0.089	0.178
Disbond	241	12.1	1.497	2.763

mixed bulk epoxy samples. The poorly cured epoxy resulted in a 42% degradation of the Young's modulus and a 44% degradation of the shear modulus compared to the properly cured epoxy. The disbond was simulated in the model by reducing the shear wave velocity (real part) of the properly cured adhesive by a factor of 100, reducing the longitudinal wave velocity by a factor of 10, and increasing the longitudinal and shear attenuation by a factor of 10. This simulation was considered representative of the Teflon release films used in the specimens to replicate disbonded conditions. The properties assumed for the various bond conditions are summarized in Table I in terms of stiffness coefficients, and in Table II in terms of bulk ultrasonic velocities and attenuations.

Convergence of the dispersion solutions was found satisfactory using one element for each ply in the wing skin, one element for the bond layer, and five elements for the spar. The number of elements was doubled to plot displacement, strain, and power flow cross-sectional shapes.

B. Dispersion results for different bond states

Phase velocity, energy velocity, and attenuation curves were obtained from the SAFE models for the three bond conditions examined (properly cured bond, poorly cured bond, and disbonded interface), each under the two testing configurations (within and across the bond) and the two wing skin lay-ups ($[0/\pm45/90]_S$ and $[0/\pm45/0]_S$).

For the ease of the reader, throughout this paper the conventional nomenclature of symmetric or antisymmetric character is used for all guided modes. However, the only true symmetric and antisymmetric modes exist when considering just the wing skin plate. The modes in the skin-to-spar bond are not truly symmetric nor antisymmetric because the cross section is not symmetric about its mid-plane. Modes propagating in the single skin plate will be indicated with a lower case, s_i, a_i, and sh_i for the symmetric, the antisymmetric, and the shear horizontal modes, respectively. Modes propagating in the bonded region will be indicated with an upper case, S_i, A_i, and SH_i. Due to the presence of the ±45° plies, the horizontally and vertically polarized partial waves are generally not decoupled, and thus the dispersion curves presented always include the shear horizontal modes. For the sake of space, dispersion results will be shown only for the $[0/\pm45/0]_S$ joint under the across the bond test configuration. The complete set of results for all test cases considered will be shown in terms of transmission strengths in Sec. III D.

The results for the $[0/\pm45/0]_S$ plate bonded to the spar with the properly cured adhesive are shown in Fig. 3 considering wave propagation in the across the bond test configuration. The frequency range shown is DC-300 kHz, which was the operating range of the experimental tests. The four modes of interest here are the zeroth-order symmetric, S_0, the zeroth- and first-order antisymmetric, A_0 and A_1, and the zeroth-order shear horizontal, SH_0. Figures 3(b) and 3(c) show that A_1 is propagative only above 135 kHz whereas the other three modes are propagative throughout the frequency range. Although other higher-order modes exist with cut-on frequencies above 135 kHz [Fig. 3(b)], they are not considered further due to their large attenuation [Fig. 3(c)].

The two modes with minimum attenuation losses are S_0 below 200 kHz and A_1 above 200 kHz [Fig. 3(c)]. Thus these two modes appear to be preferred candidates for a bond monitoring system within the frequency range examined.

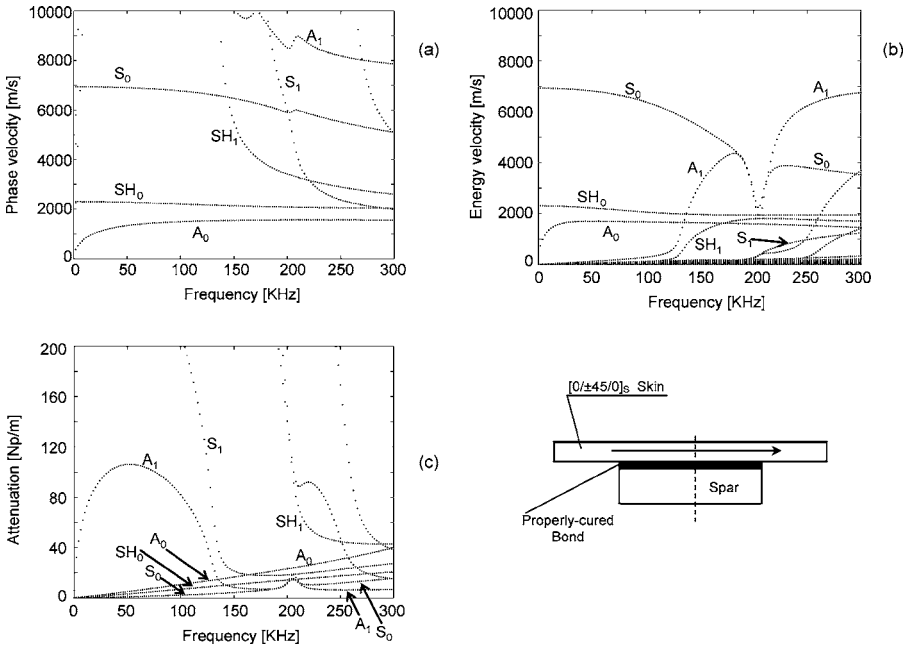

FIG. 3. (a) Phase velocity, (b) energy velocity, and (c) attenuation curves for the $[0/\pm45/0]_S$ skin bonded to the spar with properly cured adhesive ("across the bond" testing configuration).

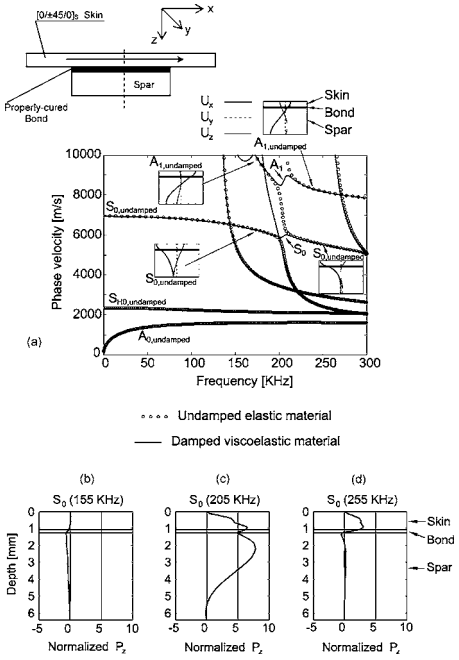

FIG. 4. (a) Phase velocity dispersion curves for the $[0/\pm45/0]_S$ skin-to-spar joint ("across the bond" testing configuration) with damping and without damping. Through-thickness Poynting vector for S_0 at (b) 155 kHz, (c) 205 kHz, and (d) 255 kHz.

Moreover, PZT disks used for built-in ultrasonic structural diagnostics are typically operated in the 3-1 electromechanical coupling mode, i.e., to generate and receive in-plane, rather than out-of-plane, displacements (Giurgiutiu *et al.*, 2003). The cross-sectional mode shapes presented in the next section indicate that both S_0 and A_1 have substantial in-plane displacements at the skin plate surface, and they are thus coupled very effectively to the built-in PZTs. The opposite is true for either A_0 (predominant out-of-plane displacement) or SH_0 (zero in-plane displacement along the wave propagation direction).

A closer look at Fig. 3 reveals a mode coupling effect occurring for both S_0 and A_1 at around 200 kHz. Mode coupling is a known phenomenon that can be caused by damping effects present in a single layer (Bernard *et al.*, 2001) or solely by geometrical effects in undamped multilayered structures (Castaings and Hosten, 2003). In this study mode coupling is due to both viscoelastic damping and multilayer geometrical effects, as seen in Fig. 4(a). In this figure the phase velocity results are obtained from the SAFE model of the bonded joint with and without damping losses. The examination of the displacement mode shapes of $S_{0,\text{undamped}}$ and $A_{1,\text{undamped}}$ reveals that apparently different branches on either side of the 200-kHz frequency value are indeed the same mode even in the undamped case. In other words, the branches are already coupled in the undamped case although they are not physically connected at 200 kHz. Once damping is included in the model, S_0 and A_1 essentially retrace the corresponding $S_{0,\text{undamped}}$ and $A_{1,\text{undamped}}$, and connect the branches at the mode coupling points around 200 kHz.

Mode coupling is generally associated to sharp changes in group or energy velocity, increased attenuation, and large transfer of energy across the thickness of the waveguide. The first two phenomena are clearly visible in Figs. 3(b) and 3(c) for both S_0 and A_1 at around 200 kHz. The third phenomenon is seen in the plots of Figs. 4(b)–4(d), comparing the normalized through-thickness power flow, P_z, of S_0 at the three frequencies of 155, 205, and 255 kHz, respectively. At the mode coupling frequency of 205 kHz [Fig. 4(c)], a large exchange of energy occurs between the top skin and the bottom spar. Contrarily, most of the energy flow occurs within the bottom spar at 155 kHz [Fig. 4(b)], and within the top skin at 255 kHz [Fig. 4(d)], with little interlayer flow. Similar Poynting vector results, not shown here, can be found for A_1. The large transfer of energy in the thickness direction is particularly relevant for a bond monitoring system as the one proposed here, that is based on relating bond defects to an increased strength of transmission through the joint. Exciting modes with large energy transfer between adherends, such as S_0 and A_1 at mode coupling frequencies, would clearly be beneficial in this case.

The dispersion curves for the case of the poorly cured bond, where only the material properties within the thin bond layer were altered according to Table I, did not show any notable change from those of the properly cured bond. This is because the thickness of the bond layer was very small compared to the thickness of the entire skin-to-spar assembly that dominates the dispersion. However, substantial changes in the wave power flow between the two cases were predicted, and this will be discussed in detail in the following sections.

As for the disbond case, shown in Figs. 5(a)–5(c), dramatic changes in the phase velocity, energy velocity, and attenuation curves are evident. The main observation in this case is the appearance of additional modes that did not exist for either of the two bond cases discussed previously. For most of the frequency range examined, the additional modes of the disbonded joint essentially coincide with the solutions of the single wing skin plate, represented in the plots by the open dots. Therefore, the introduction of a disbond allows for the propagation of two separate types of modes, namely those whose energy is mainly concentrated within the upper plate above the bondline (identified in Fig. 5 by $S_{0,\text{plate}}$, $A_{0,\text{plate}}$, $SH_{0,\text{plate}}$, etc.), and those whose energy is mainly concentrated within the spar below the bondline (identified by $S_{0,\text{spar}}$, $A_{0,\text{spar}}$, $SH_{0,\text{spar}}$, etc.). Mode $S_{0,\text{spar}}$ of the disbonded joint corresponds to mode S_0 of the properly cured joint. Similarly, $A_{1,\text{spar}}$ corresponds to A_1 of the properly cured joint. A comparison of Fig. 5 to Fig. 3 indicates that the behavior of S_0 does not change substantially between the two bond cases. However, the mode coupling for A_1 disappears when a disbond is present. Under the testing conditions used in this study, the predominant carrier of energy through the disbonded joint is $S_{0,\text{plate}}$; that should thus be considered the most relevant mode in Fig. 5. The dispersion curves of $S_{0,\text{plate}}$ in the disbonded joint are virtually coincident to those of the single-plate s_0 mode above 100 kHz. Below this frequency, the mode deviates from the single-plate behavior as more energy leaks through the spar.

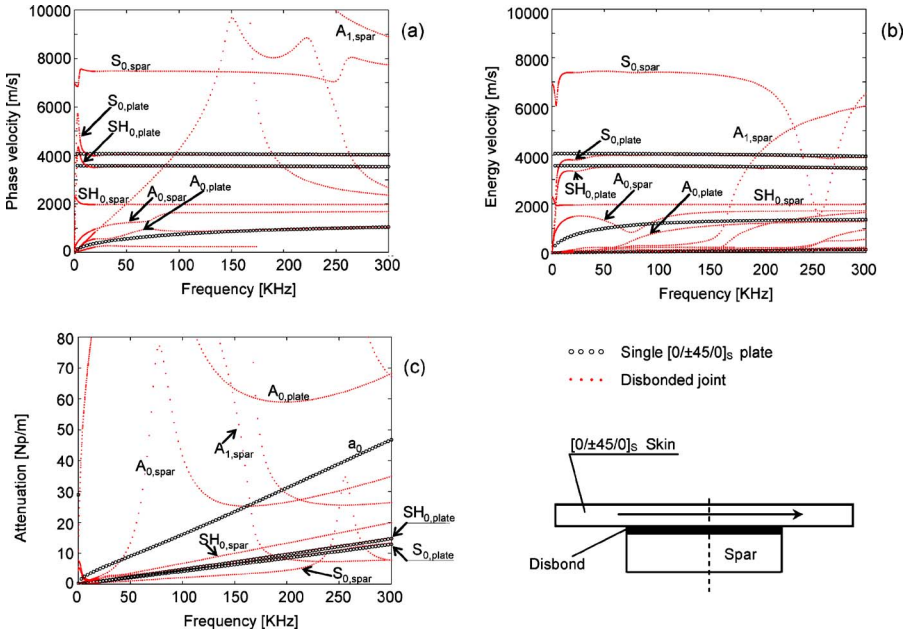

FIG. 5. (Color online) (a) Phase velocity, (b) energy velocity, and (c) attenuation curves for the $[0/\pm45/0]_S$ skin-to-spar joint with a disbonded interface and for the single $[0/\pm45/0]_S$ plate ("across the bond" testing configuration).

C. Identification of carrier modes

Mode conversion effects as the wave travels through the joints were evaluated on the basis of the similarity between the displacement mode shapes of an incoming mode and those of a carrier mode. Predictions of energy transmission across the bond in the across the bond test configuration were based upon initial excitation of the s_0 mode and subsequent mode conversion in the bonded region. Likewise, the predictions for the within the bond test configuration were based upon initial excitation of those overlap modes with similar modes shapes to those of the single-plate s_0 mode. These assumptions were consistent with the in-plane (3-1) electro-mechanical coupling characterizing the operation of the PZT disks employed in the experiments.

Figure 6(a) shows the displacement mode shapes for the $[0/\pm45/0]_S$ skin-to-spar bond tested in the across the bond configuration at the mode coupling frequency of 205 kHz. The left-hand plot in this figure shows the incoming s_0 mode in the wing skin. The plots to the right show the four possible carrier modes in the bond, namely S_0, A_0, A_1, and SH_0, considering the properly cured bond condition. The notation for the displacement components is consistent with the reference system in Fig. 2(c). The dominant displacement for s_0 is the in-plane component in the wave propagation direction, u_x, that thus also dominates the mode conversion process. The u_x displacement is also the dominant component for the S_0 and A_1 carrier modes, and its symmetry within the upper plate in both carrier modes is similar to that of the incoming mode. Conversely, u_x is not dominant for A_0 and it is altogether

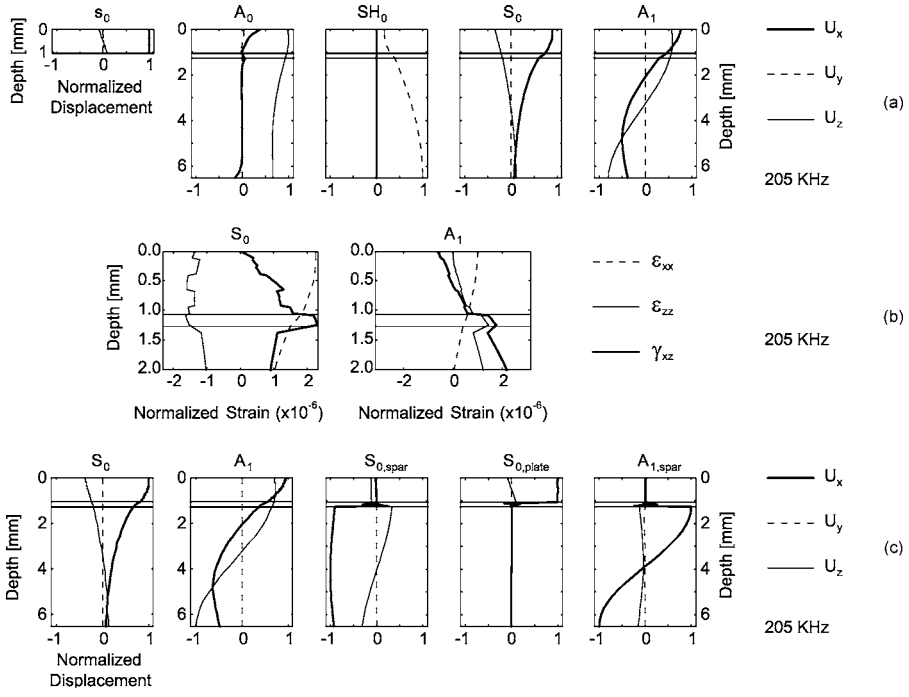

FIG. 6. The $[0/\pm45/0]_S$ skin-to-spar joint in the "across the bond" testing configuration: (a) displacement mode shapes at 205 kHz in the properly cured bond, (b) strain profiles for modes S_0 and A_1 at 205 kHz in the properly cured bond, and (c) displacement mode shapes at 205 kHz in the disbonded joint. Also shown are the corresponding mode shapes for the incoming s_0 mode in the single plate (a) and the S_0 and A_1 modes in the properly cured joint (c).

absent for the shear horizontal SH_0. It is therefore suggested that S_0 and A_1 will act as the primary energy carriers across the joint at this frequency.

Figure 6(b) shows the cross-sectional strain components in the plane of propagation of the wave for the two carrier modes S_0 and A_1 at 205 kHz. To emphasize the bonded region, only the upper portion of composite spar wall is shown. It can be seen that both modes show a concentration of both normal strain, ε_{zz}, and shear strain, γ_{xz}, within the adhesive layer. Thus both modes are suitable candidates for detecting changes in both longitudinal and shear stiffness of the adhesive layer. Between the two modes, it is S_0 that produces the larger concentration of strains at the bondline, suggesting a larger sensitivity to bond conditions. This result will be confirmed by power flow considerations in the next section.

Similar results were found when analyzing the mode shapes in the poorly cured joint. This is because the changes in the bond stiffness that were considered had little influence on the shapes of the modes, which are dominated by the skin and the spar adherends.

The next step is the case of wave propagation across a central disbonded portion of the skin-to-spar joint (again, $[0/\pm45/0]_S$ skin lay-up in the across the bond configuration). The s_0 mode is still assumed to be initially excited outside of the bond region. Mode conversion into the S_0 and A_1 modes occurs at the joint boundary. In turn, these two modes will mode convert once they reach the disbond. Figure 6(c) shows the S_0 and A_1 mode shapes for the properly cured region together with the $S_{0,\text{spar}}$, $S_{0,\text{plate}}$, and $A_{1,\text{spar}}$ mode shapes for the disbonded region at 205 kHz. For $S_{0,\text{spar}}$ and $A_{1,\text{spar}}$ the largest displacements occur below the bondline in the spar wall. Conversely, the largest displacements occur in the top plate for $S_{0,\text{plate}}$. Since the initial wave excitation is in the top plate, it is expected that the majority of the wave energy will remain confined to this component for short propagation distances. In the experimental setup adopted, the propagation distance to a centralized disbond was less than half of either S_0 or A_1 wavelengths at 205 kHz. Thus it can be assumed that $S_{0,\text{plate}}$ is the predominant carrier mode through the disbonded region.

D. Strength of transmission as a function of bond condition

The change in strength of transmission as a function of bond condition was predicted from the cross-sectional averaged power flow computed by the numerator of Eq. (7). This quantity was divided by the normalization factor $(\int_H \mathbf{P}\cdot\hat{\mathbf{x}}\, dz)$ to enable direct comparisons between the various bond conditions and carrier modes. Figure 7 shows the real P_x component profiles for the $[0/\pm45/0]_S$ skin-to-spar joint probed in the across the bond configuration for the different bond conditions. Notice that the discontinuities in the results for the skin layer reflect the different stiffnesses of the individual plies in the wave propagation direction. The properly cured bond and the poorly cured bond are compared in the top four plots for the two carrier modes S_0 and A_1. Figures 7(a) and 7(b) refer to S_0 propagating at 155 and 205 kHz, respectively. It can be seen that the S_0 strength of transmission is

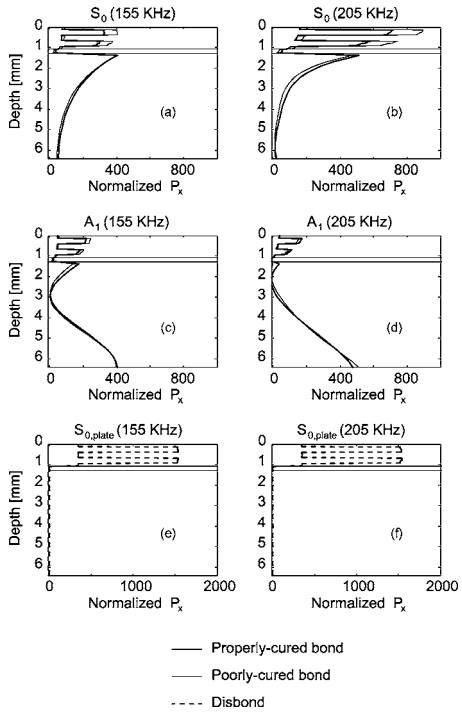

FIG. 7. P_x component of the Poynting vector in the properly cured bond and in the poorly cured bond for (a) S_0 at 155 kHz, (b) S_0 at 205 kHz, (c) A_1 at 155 kHz, and (d) A_1 at 205 kHz. Same quantity in the disbonded case for (e) $S_{0,\text{plate}}$ at 155 kHz and (f) $S_{0,\text{plate}}$ at 205 kHz.

larger in the poor bond as compared to the good bond. This phenomenon manifests itself mainly within the upper plate layer. The power flow profile justifies the commonly identified reduction in "energy leakage" that occurs when guided waves are transmitted across poor adhesive joints. It is also evident in Figs. 7(a) and 7(b) that the normalized power flow for a given bond condition is larger at 205 kHz than it is at 155 kHz, and the increase in transmission strength with degrading bond conditions is also larger at 205 kHz than it is at 155 kHz. The change in transmission strength between the two bond conditions in much less pronounced for the A_1 carrier mode shown in Figs. 7(c) and 7(d). In fact, a slight decrease in transmission strength within the upper plate occurs at 205 kHz as the bond is degraded. It can be further deduced that the S_0 mode would be primarily responsible for the sensitivity to bond stiffness based on transmission measurements. This conclusion is consistent with the cross-sectional strain profiles of Fig. 6(b) where S_0 is seen to produce larger strains than A_1 at the bond layer.

As for the disbonded case, shown in Figs. 7(e) and 7(f) for 155 and 205 kHz, respectively, the power flow results confirm that $S_{0,\text{plate}}$ is completely confined to the top plate. As a result, the strength of transmission should be expected much larger than what seen in either of the two carrier modes, S_0 or A_1, in the previous two bond conditions. Significant changes in the P_x component of the Poynting vector in the disbonded case were not observed over the frequency range of interest. In fact, the result at 155 kHz in Fig. 7(e) is indistinguishable from the one at 205 kHz in Fig. 7(f).

The cross-sectional power flow information was used to predict changes in transmission strength as a function of bond condition over the frequency range 100–300 kHz, for

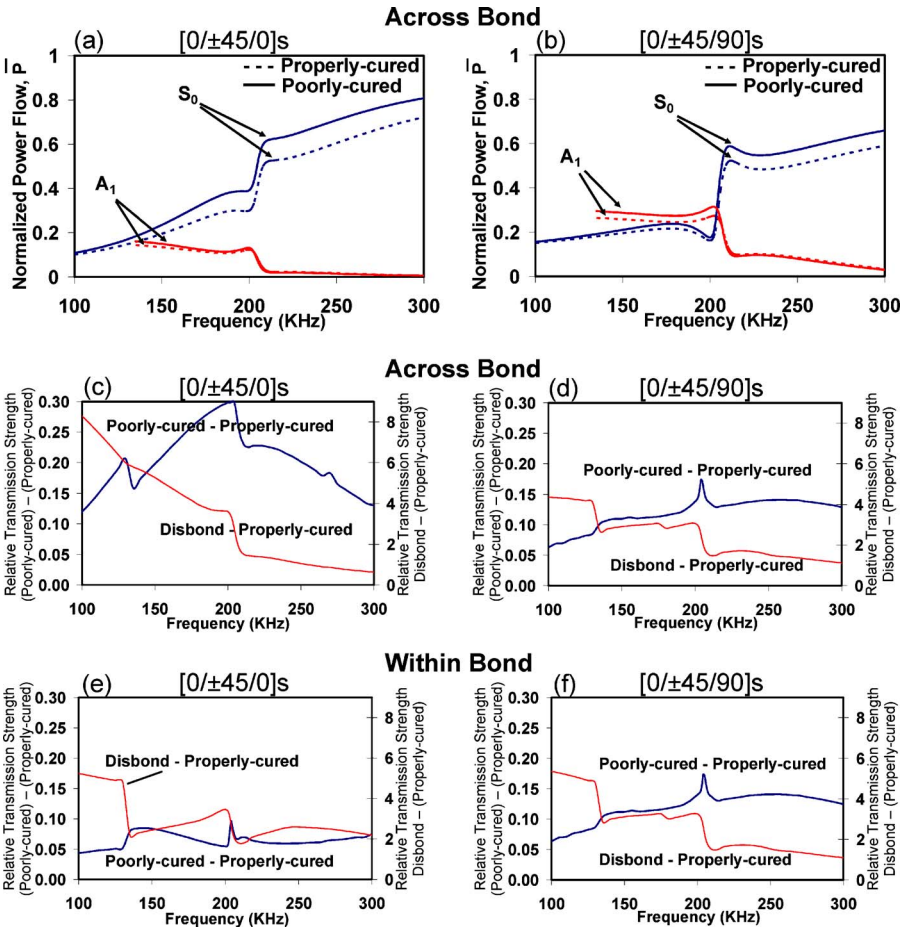

FIG. 8. (Color online) Above spar power flow of S_0 and A_1 for the properly cured and the poorly cured skin-to-spar bonds in the "across the bond" testing of (a) the $[0/\pm45/0]_S$ skin and (b) the $[0/\pm45/90]_S$ skin. Power flow differences in the "across the bond" testing of (c) the $[0/\pm45/0]_S$ skin, (d) the $[0/\pm45/90]_S$ skin, and for the "within the bond" testing of (e) the $[0/\pm45/0]_S$ skin and (f) the $[0/\pm45/90]_S$ skin.

both plate lay-ups ($[0/\pm45/0]_S$ and $[0/\pm45/90]_S$) and both testing configurations (within and across the bond).

Figures 8(a) and 8(b) plot the strength of transmission in terms of normalized power flow over the thickness of the upper plate and bond layer. This quantity was calculated by

$$\bar{P} = \frac{\int_h P_x dz}{\int_H \mathbf{P}\cdot\hat{\mathbf{x}}\, dz}, \tag{11}$$

where h is the combined thickness of the upper plate and the bond layer. Figure 8(a) compares A_1 and S_0 propagating across the properly cured and the poorly cured bonds, for the $[0/\pm45/0]_S$ lay-up. It can be seen that S_0 is the main energy carrier in most of the frequency range, with its transmission strength increasing with degrading adhesive properties. A_1 is seen to have a minor role in the energy transmission and it is also seen less sensitive to the change in bond condition. Also notice that the A_1 contribution is eliminated below the 135-kHz cut-on frequency. The same general behavior can be observed for the other plate lay-up, $[0/\pm45/90]_S$, shown in Fig. 8(b). The main difference in this case is the increased transmission strength of A_1 with degrading adhesive properties below 200 kHz.

The sensitivity to bond condition was compared directly by computing the relative differences in transmission strength between the degraded bonds and the properly cured bond. First, the relative excitability of the individual carrier modes needed to be taken into account considering the single incoming mode, s_0, for the across the bond configuration. An excitation factor for each potential carrier mode was evaluated based on the similarity between the displacement mode shapes of the incoming mode and those of the carrier mode. These displacements were normalized by the factor $\sqrt{\int_H \mathbf{P}\cdot\hat{\mathbf{x}}\, dz}$ in order to capture their relative magnitude at the various frequencies and for the various modes. The maximum of the cross-correlation function was used as the similarity index. The following excitation factor was defined for an ith carrier mode (CMi) under a single incoming mode (IM):

$$\text{excitation factor}_{\text{CMi}}(f) = \frac{\sum_{k=x,y,z} \text{Max}|u_{k,\text{IM}}(f) \otimes u_{k,\text{CMi}}(f)|}{\sum_{i=1}^{N}\sum_{k=x,y,z} \text{Max}|u_{k,\text{IM}}(f) \otimes u_{k,\text{CMi}}(f)|}, \tag{12}$$

where $\otimes$ is the cross-correlation operation between the kth cross-sectional displacement component of the incoming mode, $u_{k,\text{IM}}$, and that of the ith carrier mode, $u_{k,\text{CMi}}$, computed at the various frequencies and in the upper plate only. In Eq. (12) the excitation factor is normalized by the contribution of all possible N carrier modes existing at the incoming frequency. For the subject tests, the excitability remains dominated by the u_x displacement component outweighing the other components of the incoming s_0 mode.

The values of the excitation factor for the properly cured and the poorly cured bonds varied from 0.28 to 0.83 for S_0 and from 0 to 0.63 for A_1 in the 100–300 kHz range. The excitation factor for A_0 was significant only below 135 kHz with a maximum value of 0.26. In the disbonded case, the $S_{0,\text{plate}}$ mode was confirmed to be predominantly excited with an excitation factor ranging from 0.80 to 0.99 in the same frequency range.

Generally, the transmission strength will also be affected by attenuation losses. This effect was only factored explicitly into the contribution of the A_1 mode below 135 kHz where a zero excitation factor was assumed to reflect nonpropagative conditions (Fig. 3). Above 135 kHz, since the attenuation values for A_1 and S_0 were close, the relative weights of Eq. (12) were considered for the perfectly elastic case without loss of accuracy. The respective excitation factors computed in the across the bond configuration for S_0, A_0, A_1, and $S_{0,\text{plate}}$ were applied to the within the bond configuration.

Finally, the excitation-adjusted power flow differences, computed after weighing $\bar{P}$ of Eq. (11) with the respective excitation factors, are shown in the plots of Figs. 8(c)–8(f). These results were also normalized by the maximum power flow of the properly cured bond to provide a relative transmission change. There are three main observations that can be made from these plots. First, the transmission strength is always larger for the degraded bond cases relative to the properly cured bond for each plate lay-up and direction of propagation considered. Notice that the jump at 135 kHz in all plots is due to the zero weight assigned to A_1 below this frequency. Second, the difference in transmission strength for the disbonded joint is larger than that for the poorly cured bond in all cases (notice the different values in the left- and right-hand axes). This is a consequence of the unique character of the $S_{0,\text{plate}}$ mode that carries the incoming s_0 mode energy very efficiently. It should be reminded that the current simulation considers the limit case of a disbond extending for the entire joint width. Clearly, the effect will be much reduced for a localized disbond within a joint as is the case for the experimental tests that follow. Third, comparing the poorly cured to the properly cured bond, an abrupt increase in sensitivity is seen to occur around 200 kHz in all cases. The increase in sensitivity is due to the mode coupling phenomenon discussed earlier, affecting both S_0 and A_1 near this frequency value. The increased energy transfer through the thickness of the waveguide at the mode coupling frequencies is the physical basis for the abrupt increase in sensitivity.

IV. EXPERIMENTS ON SIMULATED WING SKIN-TO-SPAR JOINTS

A. Test specimens

Two specimens representative of UAV skin-to-spar joints were fabricated in the laboratory. The specimens matched closely the models analyzed numerically. One of the fabricated joints is shown in Fig. 9. Two composite plates were fabricated using T700/5208 carbon epoxy prepreg with the two lay-ups of $[0/\pm45/0]_S$ and $[0/\pm45/90]_S$. Each plate had a total thickness of 1.067 mm. The plate dimensions were cut to 330×330 mm^2. The composite piece used to replicate the wing spar was a woven T800/924 carbon epoxy square tube with measured outer dimensions of 50.8×50.8 mm^2 and a wall thickness of 5.23 mm. The composite tube was cut into two 330-mm-long sections to match the length of each plate. A two-part Hysol 9394 epoxy adhesive was used to bond the spar to the individual plates. Each of the two specimens was manufactured identically with the exception of the different plate lay-ups. Bonding of the plates was done such that the 0° fiber direction ran along the lengthwise direction of the spar.

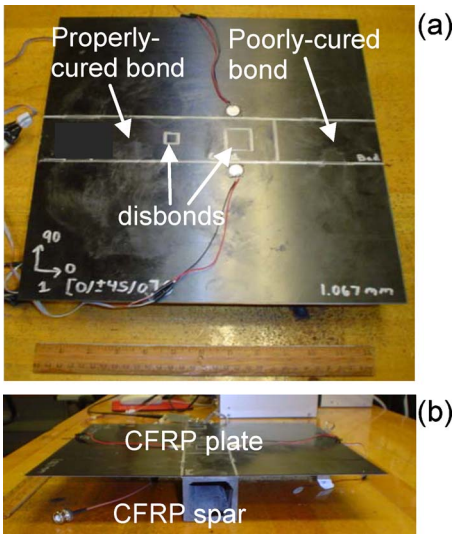

FIG. 9. (Color online) The $[0/\pm45/0]_S$ plate bonded to the tubular spar with two PZT disks in the "across the bond" testing configuration. (a) Top view and (b) side view.

The same type of bond conditions considered in the model were artificially created prior to assembling the joints (Fig. 9). The majority of the bond was comprised of a properly mixed epoxy, representing the well-bonded region. In order to form a region of degraded bond stiffness, an improperly mixed sample of epoxy was prepared resulting in an approximate 50% stiffness degradation compared to the properly cured case (the exact values from ultrasonic through-transmission testing of the mix were 42% degradation for the Young's modulus and 44% degradation for the shear modulus as reflected by the velocity values in Table II). Finally, two disbonded regions of different sizes were created by inserting Teflon release film with a thickness of 0.025 mm at the centerline of the bond. The release film was expected to severly degrade the shear stiffness of the bond while degrading its longitudinal stiffness to a smaller extent. The two simulated disbonds had dimensions of 12.7×12.7 mm^2 and 25.4×25.4 mm^2, respectively. The total bond thickess was measured to be 0.203 mm in both specimens.

B. Experimental setup and procedure

Guided wave testing was performed in the joints with the objective of relating changes in energy transmission strength to the presence and type of the simulated bond defects. PZT disks with a 12.7-mm diameter were used as wave actuators and sensors for the across the bond test configura-

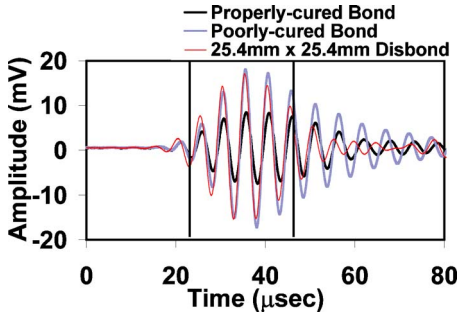

FIG. 10. (Color online) Typical waveforms from the "within the bond" test of the $[0/\pm45/0]_S$ skin-to-spar specimen at 205 kHz.

tion and the within the bond test configuration. Sensor spacings of 84 and 70 mm were used for the former configuration and for the latter configuration, respectively. Two PZTs are shown in the pictures of Fig. 9. The disks were bonded to the structure using a thermally activated film adhesive. To assist in the normalization of the testing procedure, the same pair of sensors was used throughout the tests. Tests run on a single composite plate confirmed that s_0 was the mode generated and detected by the PZTs with the greatest efficiency.

The signal generation and data acquisition system was a National Instruments PXI-1010 running under LabVIEW that was assembled and programmed in-house. The system used an arbitrary function generator to allow for swept frequency tests using Hanning windowed tonebursts sent to the actuating PZT. The frequency sweep was performed between 100 and 300 kHz, stepping in 1-kHz increments. At each frequency, the root mean square (rms) of the received time-domain signal (corresponding to the energy of the signal) was computed following the known relation:

$$\text{rms} = \sqrt{\frac{\sum_{i=1}^{N} x_i^2}{Z}}, \tag{13}$$

where x_i is a single measure within a collection of Z measurements.

Sample waveforms collected in the within the bond test of the $[0/\pm45/0]_S$ skin-to-spar joint are shown in Fig. 10 at 205 kHz corresponding to the properly cured bond, the poorly cured bond, and the large disbond. The time window where the rms of the signal was evaluated is identified on the plot by two vertical lines. Notice that the signal energy within this time gate is larger for the two degraded bonds relative to the properly cured bond. The time gates were maintained constant for each frequency sweep in a given test configuration.

The relative change in energy transmission was quantified by taking the rms spectra difference between each defected bond and the properly cured bond, and then normalizing the results by the rms spectrum of the properly cured bond. This procedure enabled a qualitative comparison with the power flow results from the model in Figs. 8(c)–8(f).

C. Experimental results

The relative rms changes as a function of bond state measured in each test are shown in Fig. 11. It can be seen that each of the spectra are positive, and thus the energy transmission is strengthened in the presence of any of the simulated bond defects. This general observation is consistent with the predictions from the models in Fig. 8. It can also be seen in the experimental results that the peak relative rms change occurs at around 200 kHz in all cases, and thus this frequency value is confirmed as the most sensitive to the bond defects considered in this study. This result was predicted by the model based on mode coupling occuring for S_0 and A_1 that are the primary energy carriers for the properly cured and for the poorly cured bonds.

Other identifiable trends can be observed in Fig. 11 when comparing the results amongst each defect case. First, in three of the four test sets, the strength of transmission for the poor bond is larger than that for the two disbonds across the entire frequency spectrum. The only exception is for the $[0/\pm45/90]_S$ in the across the bond test shown in Fig. 11(b).

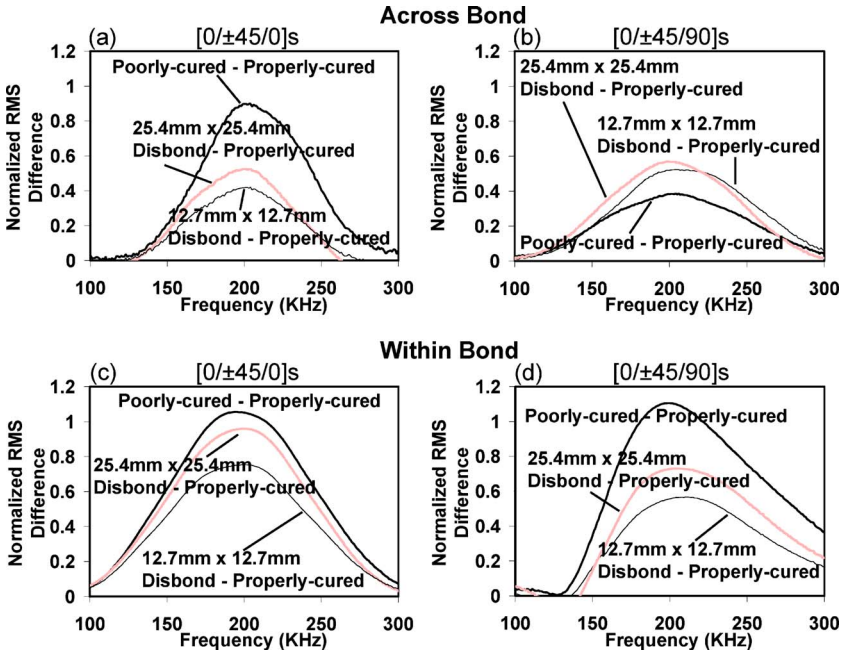

FIG. 11. (Color online) Normalized rms of each defected bond relative to the properly cured bond measured in the "across the bond" testing of (a) the $[0/\pm45/0]_S$ specimen, (b) the $[0/\pm45/90]_S$ specimen, and in the "within the bond" testing of (c) the $[0/\pm45/0]_S$ specimen, and (d) the $[0/\pm45/90]_S$ specimen.

Alternatively, the predictions from the model in Fig. 8 indicate that the power flow difference is larger for the disbond case compared to the poor bond case. However, issues regarding the defect size were not included in the model (that assumed a disbond extended for the entire width of the joint). Consequently it is expected that the strength of transmission will be somewhat reduced from the predicted values when the disbonds only extend for a portion of the joint.

Second, in every test set of Fig. 11 the relative rms difference associated with the large disbond is larger than that associated to the small disbond, with the exception of the usual $[0/\pm45/90]_S$ across the bond test above 220 kHz. The fact that the strength of transmission increases with increasing disbond size is due to the favorable P_x component of the Poynting vector of the $S_{0,\text{plate}}$ mode [Figs. 7(e) and 7(f)] that isolates the majority of the wave energy within the same upper plate where the PZT actuator and sensor are located.

Third, the relative rms difference for each defect is of the same order of magnitude in each test. The smallest rms differences are seen for the $[0/\pm45/90]_S$ across the bond test. Thus this test is the one with the smallest sensitivity to bond state. In terms of discriminating between the defect cases, the $[0/\pm45/90]_S$ across the bond test remains the least favorable since the three defects yield close results. The testing configuration providing maximum discrimination between the poorly cured bond and the disbond defects changes depending on the plate lay-up: the within the bond test is the most discriminating for the $[0/\pm45/90]_S$ lay-up [Fig. 11(d)], whereas the across the bond test is the most discriminating for the $[0/\pm45/0]_S$ lay-up [Fig. 11(a)].

V. SUMMARY AND CONCLUSIONS

The subject of this paper is the propagation of ultrasonic guided waves across composite adhesively bonded joints. The specific component investigated was representative of a skin-to-spar joint of UAVs. The research is part of a broader project aimed at developing a built-in diagnostics system for monitoring the structural integrity of UAVs. Two lay-ups for the composite skin were investigated, namely a quasi-isotropic $[0/\pm45/90]_S$ lay-up and a $[0/\pm45/0]_S$ lay-up. Two types of bond defects were considered, namely a poorly cured bond ($\sim$50% drop in Young's modulus and shear modulus) and a disbond where the shear stiffness was nominally lost.

The first portion of this study demonstrated the application of a semi-analytical finite element method that included viscoelastic material damping to predict modal solutions for the joints when probed across and within the bond. An excitation factor for the possible carrier modes in the joints was defined based on the similarity (cross correlation) between the displacement mode shapes of the incoming mode and those of the possible carrier modes. Given an incoming s_0 mode which was known to be generated most efficiently by the PZT actuators used for the experimental component of this study, it was found that S_0 and A_1 act as the primary carrier modes through the properly cured and the poorly cured bonds. Since both of these modes produce increased normal and shear strains at the bondline, they are suitable for monitoring changes in bond stiffness. The $S_{0,\text{plate}}$ mode will instead act as the primary carrier mode across disbonded regions, since its energy is confined within the top skin plate. The model indicated that frequency values around 200 kHz would produce mode coupling for S_0 and A_1. Mode coupling results in a large interlayer energy transfer, and it was thus expected to provide maximum sensitivity to the bond monitoring strategy adopted in this study. The strength of transmission across the defected joints was quantified based on the changes in the power flow (Poynting vector) along the wave propagation direction relative to the properly cured bond. For all the cases considered the power flow results predicted that the strength of transmission would be larger for the defected joints compared to the properly cured joint.

Experimental tests were conducted on two specimens constructed in the laboratory and consisting of $[0/\pm45/90]_S$ and $[0/\pm45/0]_S$ T700/5208 plates bonded to T800/924 woven tubular spars. The joints were manufactured by creating a region of poorly cured adhesive and two regions with isolated disbonds of two different sizes. The specimens were tested in the within the bond and the across the bond configurations using PZT disks. The strength of transmission was quantified by computing the rms of the detected signals in the 100–300 kHz range. The experimental results confirmed that the strength of transmission increases in the presence of the two types of bond defects compared to the properly cured bond. The best sensitivity to the defects was measured at around 200 kHz corresponding to the mode coupling point of the S_0 and A_1 carrier modes. In most of the cases, it was found that the poorly cured joint resulted in a larger transmission strength than the disbonded joints. This result was opposite to what was found by the SAFE power flow predictions, which, however, assumed an idealized disbond extending for the entire width of the joint. As expected, the measured strength of transmission generally increased with increasing disbond size. Among the cases examined, the across the bond configuration for the $[0/\pm45/90]_S$ joint was the least favorable one, resulting in the smallest rms changes and the smallest ability to discriminate among defect types and sizes. The most favorable testing configurations, providing maximum discrimination between the poor bond and the disbond defects, were found to be the within the bond test for the $[0/\pm45/90]_S$ lay-up, and the across the bond test for the $[0/\pm45/0]_S$ lay-up.

Clearly, the results presented are strictly applicable to the joints examined in this study. However, the general conclusions of an increased strength of transmission in the presence of bond defects and a large sensitivity at mode coupling points can be extended to other geometries or materials. Improvements can be made in the predictions of the power flow through the defected joints, particularly for the disbonded case. More accurate properties should be obtained for the bond created by a Teflon release film for a better simulation of this defect. A complete power flow analysis should also account for the finite size of the disbond and for the attenuation of each of the carrier modes involved in the energy transfer.

A factor that will play a substantial role in any field implementation of the bond monitoring system is the operat-

ing temperature. The nominal temperature range for UAVs is −40 °F to 165 °F (−40 °C to 74 °C) for high altitude flights and storage in closed hangers, respectively. Tests are being conducted to characterize the effects of temperature on the wave transmission strength.

ACKNOWLEDGMENTS

This project was funded by the Los Alamos/UCSD Education Collaboration Task 2 "Structural Integrity Monitoring of UAV Composite Wings" and by the UCSD/Los Alamos Cooperative Agreement on Research and Education (CARE). Professor John Kosmatka, Structural Engineering Department of UCSD, was responsible for fabricating the composite joints tested in this study. Thanks are also extended to Dr. Charles Farrar and Dr. Gyuhae Park of the Los Alamos National Laboratory, ESA Division, for the useful technical discussions throughout this study.

Auld, B. A. (**1990**). *Acoustic Fields and Waves in Solids* (Krieger, Malabar, FL).

Bernard, A., Lowe, M. J. S., and Deschamps, M. (**2001**). "Guided waves energy velocity in absorbing and non-absorbing plates," J. Acoust. Soc. Am. **110**, 186–196.

Castaings, M., and Hosten, B. (**2003**). "Guided waves propagating in sandwich structures made of anisotropic, viscoelastic, composite materials," J. Acoust. Soc. Am. **113**, 2622–2634.

Chang, Z., and Mal, A. K. (**1995**). "A global-local method for wave propagation across a lap joint," Numer. Methods Struct. Mech. **204**, 1–11.

Cheng, A., Murray, T. W., and Achenbach, J. D. (**2001**). "Simulation of laser-generated ultrasonic waves in layered plates," J. Acoust. Soc. Am. **110**, 848–855.

Chimenti, D. E. (**1997**). "Guided waves in plates and their use in materials characterization," Appl. Mech. Rev. **50**, 247–284.

Finnveden, S. (**2004**). "Evaluation of modal density and group velocity by a finite element method," J. Sound Vib. **273**, 51–75.

Gavrić, L. (**1995**). "Computation of propagating waves in free rail using a finite element technique," J. Sound Vib. **185**, 531–543.

Giurgiutiu, V., and Zagrai, A. (**2002**). "Embedded self-sensing piezoelectric active sensors for on-line structural identification," J. Vibr. Acoust. **124**, 116–125.

Giurgiutiu, V., Bao, J., and Zhao, W. (**2003**). "Piezoelectric wafer active sensor embedded ultrasonics in beams and plates," Exp. Mech. **43**, 428–44.

Guyott, C. C. H., and Cawley, P. (**1988a**). "The ultrasonic vibration characteristics of adhesive joints," J. Acoust. Soc. Am. **83**, 632–640.

Guyott, C. C. H., and Cawley, P. (**1988b**). "Evaluation of the cohesive properties of adhesive joints using ultrasonic spectroscopy," NDT & E Int. **21**, 233–240.

Hay, T. R., Wei, L., and Rose, J. L. (**2003**). "Rapid inspection of composite skin-honeycomb core structures with ultrasonic guided waves," Comput. Mater. Sci. **37**, 929–939.

Hayashi, T., Song, W. J., and Rose, J. L. (**2003**). "Guided wave dispersion curves for a bar with an arbitrary cross-section, a rod and rail example," Ultrasonics **41**, 175–183.

Heller, K., Jacobs, L. J., and Qu, J. (**2000**). "Characterization of adhesive bond properties using Lamb waves," NDT & E Int. **33**, 555–563.

Ihn, J., Chang, F. K., and Speckmann, H. (**2001**). "Built-in diagnostics for monitoring crack growth in aircraft structures," Proc. 4th Intl. Conf. on Damage Assessment on Structures, Cardiff, Vol. **204–205**, pp. 299–308.

Jones, R. M. (**1975**). *Mechanics of Composite Materials* (Scripta Book, Washington).

Karunasena, W., Shah, A. H., and Datta, S. K. (**1991**). "Wave propagation in a multilayered cross-ply composite plate," J. Appl. Mech. **58**, 1028–1032.

Keilers, C. H., and Chang, F. K. (**1995**). "Identifying delaminations in composite beams using built-in piezoelectrics: part 1—experiments and analysis; part 2—an identification method," J. Intell. Mater. Syst. Struct. **6**, 649–672.

Kundu, T., and Maslov, K. (**1997**). "Material interface inspection by Lamb waves," Int. J. Solids Struct. **34**, 3885–3901.

Kundu, T., Maji, A., Ghosh, T., and Maslov, K. (**1998**). "Detection of kissing disbonds by Lamb waves," Ultrasonics **35**, 573–580.

Lakshmanan, K. A., and Pipes, D. J. (**1997**). "Modeling damage in composite rotocraft flexbeams using wave mechanics," Smart Mater. Struct. **6**, 383–392.

Lanza di Scalea, F., Bonomo, M., and Tuzzeo, D. (**2001**). "Ultrasonic guided wave inspection of bonded lap joints: noncontact method and photoelastic visualization," Res. Nondestruct. Eval. **13**, 153–171.

Lanza di Scalea, F., Rizzo, P., and Marzani, A. (**2004**). "Propagation of ultrasonic guided waves in lap-shear adhesive joints: case of incident a0 Lamb wave," J. Acoust. Soc. Am. **115**, 146–156.

Lemistre, M. B., and Balageas, D. L. (**2001**). "Structural health monitoring system based on diffracted Lamb wave analysis by multiresolution processing," Smart Mater. Struct. **10**, 504–511.

Light, G. M., Kwun, H., Kim, S-Y., and Spinks, R. L. (**2003**). "Health monitoring for aircraft structures," Mater. Eval. **61**, 844–847.

Lowe, M. J. S., and Cawley, P. (**1994**). "Applicability of plate wave techniques for the inspection of adhesive and diffusion bonded joints," J. Nondestruct. Eval. **13**, 185–200.

Lowe, M. J. S., Challis, R. E., and Chan, C. W. (**2000**). "The transmission of Lamb waves across adhesively bonded lap joints," J. Acoust. Soc. Am. **107**, 1333–1345.

Mal, A. K. (**1988**). "Guided waves in layered solids with interface zones," Int. J. Eng. Sci. **26**, 873–881.

Mal, A. K., Chang, Z., and Guo, D. (**1996**). "Lap joint inspection using plate waves," Proc. SPIE **2945**, 128–137.

Mal, A. K., Xu, P., and Bar-Cohen, Y. (**1990**). "Leaky Lamb waves for the ultrasonic nondestructive evaluation of adhesive bonds," J. Eng. Mater. Technol. **112**, 255–259.

Mukdadi, O. M., and Datta, S. K. (**2003**). "Transient ultrasonic guided waves in layered plates with rectangular cross section," J. Appl. Phys. **93**, 9360–9370.

Mukdadi, O. M., Desai, Y. M., Datta, S. K., Shah, A. H., and Niklasson, J. (**2002**). "Elastic guided waves in a layered plate with rectangular cross section," J. Acoust. Soc. Am. **112**, 1766–1779.

Nagy, P. B., and Adler, L. (**1989**). "Nondestructive evaluation of adhesive joints by guided waves," J. Appl. Phys. **66**, 4658–4663.

Neau, G., Lowe, M. J. S., and Deschamps, M. (**2002**). "Propagation of lamb waves in anisotropic and absorbing plates: Theoretical derivation and experiments," Rev. Prog. Quant. Nondestr. Eval. **21**, 1062–1068.

Pilarski, A., and Rose, J. L. (**1992**). "Lamb wave mode selection concepts for interfacial weakness analysis," J. Nondestruct. Eval. **11**, 237–249.

Rokhlin, S. I. (**1991**). "Lamb wave interaction with lap-shear adhesive joints: theory and experiment," J. Acoust. Soc. Am. **89**, 2758–2765.

Rokhlin, S. I., and Wang, Y. J. (**1991**). "Analysis of boundary conditions for elastic wave interaction with an interface between two solids," J. Acoust. Soc. Am. **89**, 503–515.

Rose, J. L., Rajana, K. M., and Hansch, M. K. T. (**1995**). "Ultrasonic guided waves for NDE of adhesively bonded structures," J. Adhes. **50**, 71–82.

Rose, J. L., Zhu, W., and Zaidi, M. (**1998**). "Ultrasonic NDT of titanium diffusion bonding with guided waves," Mater. Eval. **56**, 535–539.

Seifried, R., Jacobs, L. J., and Qu, J. (**2002**). "Propagation of guided waves in adhesive bonded components," NDT & E Int. **35**, 317–328.

Sohn, H., Park, G., Wait, J., Limback, N., and Farrar, C. R. (**2003**). "Wavelet-based active sensing for delamination detection in composite structures," Smart Mater. Struct. **13**, 153–160.

Staszewski, W., Boller, C., and Tomlinson, G. (**2004**). *Health Monitoring of Aerospace Structures* (Wiley, New York).

Sun, Z., Rose, J. L., and Zaidi, M. (**2002**). "A phased array guided wave approach to adhesive bonding structural integrity analysis," Mater. Eval. **61**, 941–946.

Wang, C. S., and Chang, F. K. (**1999**). "Built-in diagnostics for impact damage identification in composite structures," Proc. 2nd Int. Workshop on Structural Health Monitoring, Stanford, pp. 612–621.

Xu, P. C., Mal, A. K., and Bar-Cohen, Y. (**1990**). "Inversion of leaky Lamb wave data to determine cohesive properties of bonds," Int. J. Eng. Sci. **28**, 331–346.

Lamb mode conversion in an absorptive bi-layer with a delamination

G. Shkerdin[a] and C. Glorieux[b]
Laboratorium voor Akoestiek en Thermische Fysica, Departement Natuurkunde, K. U. Leuven, Celestijnenlaan 200 D, B-3001 Leuven, Belgium

(Received 11 April 2005; revised 13 July 2005; accepted 13 July 2005)

A theoretical study of Lamb mode propagation through an absorptive composite plate consisting of two parallel layers with a finite-length delamination dividing these layers is presented. In the delamination boundary region, noncontact boundary conditions are assumed. The calculation is based on a modal decomposition method. In thin composite plates containing a few propagating Lamb modes, as a result of diffraction on a delamination, the incident Lamb mode can be efficiently converted into transmitted Lamb modes. Delaminations in absorptive composite plates result in a considerable change of transmitted acoustic energy if the plate is characterized by substantially different absorption coefficients in the layers of the plate. In particular, the delamination can considerably increase the transmission coefficient of the incident Lamb mode if the layer where the incident Lamb mode is mainly concentrated is much less absorptive than the other one. © *2005 Acoustical Society of America.* [DOI: 10.1121/1.2031970]

PACS number(s): 43.35.Ns, 43.35.Zc [YHB] Pages: 2253–2264

I. INTRODUCTION

Interaction of Lamb modes with different kinds of defects including delaminations was already extensively studied.[1–8] The interest to this problem is created by its importance for nondestructive testing and characterization of materials. In particular delaminationlike defects are likely to grow in mechanically strained structures, and finally lead to global failure or malperformance. The propagation of Lamb modes in plates turns out to be quite convenient to study the peculiarities of acoustic wave interaction with delaminations situated both in the depth and near the surface of a plate.

Auld and Tan[1,2] predicted the reflection of Lamb modes from vertical delaminations normal to the plate surfaces and this effect was later studied by many authors (see, for example, Refs. 6–8). Rokhlin studied Lamb modes diffraction on symmetrical horizontal delaminations situated exactly in the middle of the plate.[3–5] Reflection and transmission of an incident Gaussian acoustic beam through the plate with a horizontal delamination immersed in a liquid was analyzed and a considerable influence of a delamination on the nonspecular lobe in the reflected beam was found.[9] The effect of mode conversion on a horizontal delamination in a thick multimode plate was theoretically studied and it was shown that, depending on a delamination length, a considerable part of an incident Lamb mode (or Rayleigh wave) energy can be converted into several transmitted Lamb modes.[10]

It is necessary, however, to mention that all these papers were devoted to study Lamb modes interaction with a delamination located only in a simple homogeneous plate. However, delaminations are more likely to appear in composite layered plates where the existence of stresses leads to deterioration of the coupling between layers and to development of horizontal delaminations. Composite structures are frequently absorptive, therefore absorption in layers has to be taken into account as well. Studies along these lines have been performed by Lowe *et al.*,[11] Simonetti,[12] and Chan and Cawley.[13]

The present paper is concerned with two-dimensional propagation of Lamb modes through a composite plate consisting of two parallel isotropic layers with different material parameters including acoustic absorption. A finite delamination is contained at the interface between these layers. The calculation is based on a modal decomposition method. The first part of the paper is devoted to the fundamentals of the method in the absorptive composite plate. Lamb mode conversion at a delamination is studied in the second part of the paper. Numerical calculations are given for the case of a thin composite plate supporting only a few propagating Lamb modes.

II. MODAL DECOMPOSITION METHOD IN ABSORPTIVE COMPOSITE PLATE

The two-dimensional geometry under consideration is shown in Fig. 1. The incident acoustic wave is represented by Lamb modes propagating along the z direction in an isotropic composite plate of thickness d, consisting of two parallel layers with y coordinates: $0 \leqslant y \leqslant d_1$ and $d_1 \leqslant y \leqslant d$. The layers are supposed to be in perfect mechanical contact everywhere at the interface $y=d_1$, with the exception of the delamination region with coordinates $0 \leqslant z \leqslant L$ located at this interface. We assume that the plate surfaces $y=0$, $y=d$ and all surfaces of the delamination are stress-free, and that the delamination thickness is larger than the normal elastic displacements at its surfaces, such that the structure behaves linearly. On the other hand, the delamination thickness is

[a]Permanent address: Institute of Radio Engineering and Electronics of Russian Academy of Sciences, Vvedensky sq., 1, Fryazino, Moscow region, Russia.
[b]Also a Postdoctoral researcher with Fonds voor Wetenschappelijk Onderzoek-Vlaanderen. Electronic mail christ.glorieux@fys.kuleuven.be

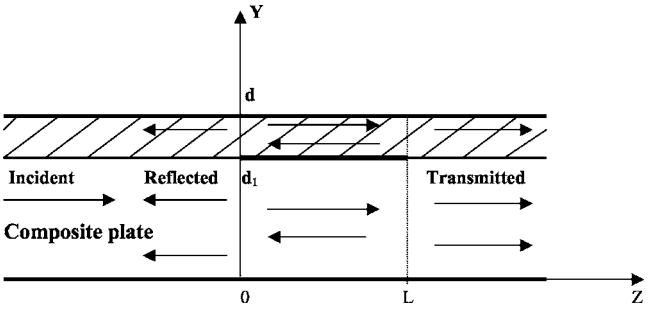

FIG. 1. Schematic view of the Lamb wave in a composite plate incident on a delamination region with length L.

taken much smaller than the acoustic wavelengths, such that the delamination can be treated as infinitesimally thin.

The method to calculate the transmitted and reflected acoustic field is based on an expansion of this field in the Lamb eigenmodes of the different parts of this composite plate, and on the use of boundary conditions at the vertical planes $z=0$ and $z=L$. This method is described in detail in Ref. 10, therefore only the expressions necessary for calculations are given here without the detailed derivation. Acoustic absorption was neglected in Ref. 10, but the whole procedure of calculation is valid for absorptive plates as well. The influence of absorption needs to be specified explicitly only for the calculation of the flow of acoustic energy.

The components of the stress tensor S_{ik}^n and the mechanical displacement vector U_i^n ($i=y,z$ and $k=y,z$) of the nth Lamb mode can be written down as follows:

$$(S_{ik}^n, U_i^n) = (\tilde{\sigma}_{ik}^n, \tilde{u}_i^n)\exp(-i\omega t) + (\tilde{\sigma}_{ik}^n, \tilde{u}_i^n)^* \exp(i\omega t). \quad (1)$$

Here $(\tilde{\sigma}_{ik}^n, \tilde{u}_i^n) = (\sigma_{ik}^n, u_i^n)\exp(iq_n z)$, q_n and ω are Lamb mode wave number and angular frequency, and the asterisk operation refers to complex conjugation. $S_{ik}^n, U_i^n, \sigma_{ik}^n, u_i^n$ are y dependent and satisfy the wave equation and the stress-strain relations, and satisfy as well the continuity conditions at the interface $y=d_1$ and stress-free conditions at $y=0$ and $y=d$. Displacements U_i^n and stresses S_{ik}^n are coupled by stress-strain relations. The quantities U_i^n and S_{ik}^n are for Lamb modes of the homogeneous parts of the composite plate: $0 \leqslant z \leqslant L$, $0 \leqslant y \leqslant d_1$ and $0 \leqslant z \leqslant L$, $d_1 \leqslant y \leqslant d$ are given by the usual expressions for symmetric and antisymmetric Lamb modes (see, for example, the Appendix in Ref. 10). The same values for the nonhomogeneous plate regions $z<0$ and $z>L$ are described by more complicated expressions for Lamb modes propagating in a composite plate (see the Appendix of this paper).

All Lamb modes satisfy orthogonality conditions. The most general orthogonality condition, applicable to both absorbing and nonabsorbing plates, is written down for the geometry of Fig. 1 (see Appendix of Ref. 10):

$$\int_0^d dy(\sigma_{yz}^n u_y^m + \sigma_{yz}^m u_y^n - \sigma_{zz}^n u_z^m - \sigma_{zz}^m u_z^n) = A(n)\delta_{n,m} \quad (2)$$

with $\delta_{n,m}$ the Kronecker delta symbol. For $n=m$, $A(n)$ is a normalization factor.

All different Lamb modes are orthogonal according to Eq. (2) and in general the $A(n)$ values are not equal to zero. Another orthogonality condition exists only for nonabsorbing plates. This condition can be written down as follows:

$$\int_0^d dy(\sigma_{yz}^n (u_y^m)^* + \sigma_{zz}^n (u_z^m)^* - u_z^u (\sigma_{zz}^m)^*) - u_z^n (\sigma_{zz}^m) = B(n)\delta_{n,m}. \quad (3)$$

Here, for $n=m$, $B(n)$ is proportional to the energy flow of the nth Lamb mode.

Orthogonality conditions Eqs. (2) and (3) are given for the plate regions with $z<0$ and $z>L$. Analogous conditions can be written down for the homogeneous parts of the plate with $0 \leqslant z \leqslant L$. Equation (2) gives a convenient test to check calculated wave numbers of Lamb modes in the composite plate.

The expansion of the mechanical displacement vector for the transmitted acoustic waves $\vec{u}^{tr}(z>L)$ is given by

$$\vec{U}^{tr} = \sum_n C_n^{tr} \vec{u}_{tr}^n \exp(i(q_n(z-L) - \omega t)) \quad (4)$$

with C_n^{tr} the expansion coefficients for transmitted acoustic waves, which are to be determined. An analogous expression can be given for the reflected acoustic waves ($z<0$) with the substitutions $C_n^{tr} \to C_n^{ref}$, $\vec{u}_{tr}^n \to \vec{u}_{ref}^n$, $L \to 0$, and $q_n \to -q_n$. There are two different kinds of expansions for the regions $0<z<L$, $0<y<d_1$ and $0<z<L$, $d_1<y<d$. The expansion of the mechanical displacement vector for transmitted acoustic waves $\vec{u}_{\pm}^{tr}$ is found by applying the following substitutions in Eq. (4): $C_n^{tr} \to C_{n,\pm}^{tr}$, $\vec{u}_{tr}^n \to \vec{u}_{tr}^{n,\pm}$, $L \to 0$, and $q_n \to q_{n,\pm}$. The $\pm$ signs mark, respectively, transmission in the upper ($d_1<y<d$) and lower ($0<y<d_1$) parts of the delamination region. Analogous expansions for the mechanical displacement of reflected acoustic waves $U_{\pm}^{ref}$ in the regions $0<z<L$, $d_1<y<d$, and $0<y<d_1$ are given by

$$\vec{U}_{\pm}^{ref} = \sum_n C_{n,\pm}^{ref} \vec{u}_{ref}^{n,\pm} \exp(-i(q_{n,\pm}(z-L) + \omega t)). \quad (5)$$

The expressions for the expansions of stress tensor components are completely analogous to Eqs. (4) and (5).

Applying boundary conditions at planes $z=0$, $z=L$ and using orthogonality condition Eq. (2), an infinite system of linear equations (6)–(9) in the unknown mode coefficients $C_n^{tr,ref}$ and $C_{m,\pm}^{tr,ref}$ can be derived:

$$A(n)C_n^{tr} = \sum_{m,\pm} (C_{m,\pm}^{tr} e^{iq_{m,\pm}L}(K_{n,m}^{\pm} + I_{n,m}^{\pm}) + C_{m,\pm}^{ref}(I_{n,m}^{\pm} - K_{n,m}^{\pm})), \quad (6)$$

$$A(n)C_n^{ref} = \sum_{m,\pm} (C_{m,\pm}^{ref} e^{iq_{m,\pm}L}(K_{n,m}^{\pm} + I_{n,m}^{\pm}) + C_{m,\pm}^{tr}(I_{n,m}^{\pm} - K_{n,m}^{\pm})), \quad (7)$$

$$A^{\pm}(m)C_{m,\pm}^{tr} = \sum_n (C_n^{in}(K_{n,m}^{\pm} + I_{n,m}^{\pm}) + C_n^{ref}(K_{n,m}^{\pm} - I_{n,m}^{\pm})), \quad (8)$$

$$A^{\pm}(m)C^{ref}_{m,\pm} = \sum_n (C^{tr}_n(K^{\pm}_{n,m} - I^{\pm}_{n,m})), \tag{9}$$

where $I^{\pm}_{n,m} = \int_{a_\pm}^{b_\pm} dy(\sigma^n_{yz,tr}u^{m,\pm}_{y,tr} - u^n_{z,tr}\sigma^{m,\pm}_{zz,tr})$, $K^{\pm}_{n,m} = \int_{a_\pm}^{b_\pm} dy(\sigma^{m,\pm}_{yz,tr}u^n_{y,tr} - u^{m,\pm}_{z,tr}\sigma^n_{zz,tr})$, $a_- = 0$, $a_+ = b_- = d_1$, and $b_+ = d$.

The general expression for the acoustic flow of energy P_z can be written down as follows:[14]

$$P_z = -\sum_{k=y,z} \int_0^d dy S_{kz} \frac{\partial U_k}{\partial t}. \tag{10}$$

Substituting the proper expansions [see Eq. (4)] in Eq. (10), the time-averaged expression P^{tr}_z for $z > L$ can be written down as follows (not important for calculations—coefficient 2ω was omitted in Ref. 10):

$$P^{tr}_z = 2\omega \int_0^d dy \, \mathrm{Im}\Bigg(\sum_n (C^{tr}_n \tilde{\sigma}^n_{zz,tr1}) \sum_m (C^{tr}_m \tilde{u}^m_{z,tr1})^* - \sum_n (C^{tr}_n \tilde{\sigma}^n_{yz,tr1})^* \sum_m (C^{tr}_m \tilde{u}^{\mathrm{m}}_{y,tr1}) \Bigg) \tag{11a}$$

with $(\tilde{\sigma}^n_{ik,tr1}, \tilde{u}^n_{i,tr1}) = (\sigma^n_{ik,tr}, u^n_{i,tr})\exp(iq_n(z-L))$.

An analogous expression for P^{in}_z in the region $z < 0$ is given by Eq. (12a):

$$P^{in}_z = 2\omega \int_0^d dy \, \mathrm{Im}\Bigg(\Bigg(\sum_n C^{in}_n \tilde{\sigma}^n_{zz,tr} + \sum_m C^{ref}_m \tilde{\sigma}^m_{zz,ref} \Bigg) \times \Bigg(\sum_n C^{in}_n \tilde{u}^n_{z,tr} + \sum_m C^{ref}_m \tilde{u}^m_{z,ref} \Bigg)^* - \Bigg(\sum_n C^{in}_n \tilde{\sigma}^n_{yz,tr} + \sum_m C^{ref}_m \tilde{\sigma}^m_{yz,ref} \Bigg)^* \Bigg(\sum_n C^{in}_n \tilde{u}^n_{y,tr} + \sum_m C^{tr}_m \tilde{u}^m_{y,ref} \Bigg) \Bigg) \tag{12a}$$

where $(\tilde{\sigma}^n_{ik,tr}, \tilde{u}^n_{i,tr}) = (\sigma^n_{ik,tr}, u^n_{i,tr})\exp(iq_n z)$, $(\tilde{\sigma}^n_{ik,ref}, \tilde{u}^n_{i,ref}) = (\sigma^n_{ik,ref}, u^n_{i,ref})\exp(-iq_n z)$, and C^{in}_n are expansion coefficients for the incident acoustic wave.

In the region $0 < z < L$ the expression for $P^{tr,1}_z$ can be written down as follows:

$$P^{tr,1}_z = 2\omega \sum_\pm \int_{a_\pm}^{b_\pm} dy \, \mathrm{Im}\Bigg(\Bigg(\sum_n C^{tr}_{n,\pm} \tilde{\sigma}^{n,\pm}_{zz,tr} + \sum_m C^{ref}_{m,\pm} \tilde{\sigma}^{m,\pm}_{zz,ref} \Bigg) \times \Bigg(\sum_n C^{tr}_{n,\pm} \tilde{u}^{n,\pm}_{z,tr} + \sum_m C^{ref}_{m,\pm} \tilde{u}^{m,\pm}_{z,ref} \Bigg)^* - \Bigg(\sum_n C^{tr}_{n,\pm} \tilde{\sigma}^{n,\pm}_{yz,tr} + \sum_m C^{ref}_{m,\pm} \tilde{\sigma}^{m,\pm}_{yz,ref} \Bigg)^* \Bigg(\sum_n C^{tr}_{n,\pm} \tilde{u}^{n,\pm}_{y,tr} + \sum_m C^{ref}_{m,\pm} \tilde{u}^{m,\pm}_{y,ref} \Bigg) \Bigg). \tag{13a}$$

Here $(\tilde{\sigma}^{n,\pm}_{ik,tr}, \tilde{u}^{n,\pm}_{i,tr}) = (\sigma^{n,\pm}_{ik,tr}, u^{n,\pm}_{i,tr})e^{iq_{n,\pm}z}$ and $(\tilde{\sigma}^{m,\pm}_{ik,ref}, \tilde{u}^{m,\pm}_{i,ref}) = (\sigma^{m,\pm}_{ik,ref}, u^{m,\pm}_{i,ref})e^{-iq_{m,\pm}(z-L)}$.

The use of orthogonality condition Eq. (3) results in considerable simplifications of Eqs. (11)–(13) in the absence of acoustic absorption. In this case the acoustic flow of energy for all nonpropagating Lamb modes is equal to zero and Eqs. (11a), (12a), and (13a) are reduced to Eqs. (11b), (12b), and (13b):

$$P^{tr}_z = 2\omega \sum_{n_p} |C^{tr}_{n_p}|^2 F_{n_p}, \tag{11b}$$

$$P^{in}_z = 2\omega \sum_{n_p} (|C^{in}_{n_p}|^2 - |C^{ref}_{n_p}|^2) F_{n_p}, \tag{12b}$$

$$P^{tr,1}_z = 2\omega \sum_{n_{p,\pm}} (|C^{tr}_{n_p,\pm}|^2 - |C^{ref}_{n_p,\pm}|^2) F_{n_p,\pm}, \tag{13b}$$

where $F_{n_p} = \mathrm{Im}(\int_0^d dy(\sigma^{n_p}_{zz,tr}(u^{n_p}_{z,tr})^* - (\sigma^{n_p}_{yz,tr})^* u^{n_p}_{y,tr}))$, $F_{n_{p,\pm}} = \mathrm{Im}(\int_{a_\pm}^{b_\pm} dy(\sigma^{n_p,\pm}_{zz,tr}(u^{n_p,\pm}_{z,tr})^* - (\sigma^{n_p,\pm}_{yz,tr})^* u^{n_p,\pm}_{y,tr}))$, and only propagating Lamb modes n_p are taken into account.

Taking into account the continuity of σ_{yz}, σ_{zz} and of the mechanical displacement vector components at $z = 0, L$ one obtains that P_z is continuous at $z = 0, L$. Therefore, in numerical approximative calculations, the levels of discontinuity of P_z at $z = 0, L$ can be used to estimate calculation errors. To quantify possible inaccuracies in calculated results, it is convenient to use dimensionless functions $\delta_{0,L}$ defined as follows:

$$\delta_0 = (P^{in}_z(z=0) - P^{tr,1}_z(z=0))/P_{in}, \tag{14a}$$

$$\delta_L = (P^{tr,1}_z(z=L) - P^{tr}_z(z=L))/P_{in}, \tag{15a}$$

where P_{in} is the incident acoustic flow of energy.

For a nonabsorptive plate Eqs. (14a) and (15a) are reduced to Eqs. (14b) and (15b):

$$\delta_0 = 1 - \frac{\sum_{n_p} |C^{ref}_{n_p}|^2 F_{n_p}}{\sum_{n_p} |C^{in}_{n_p}|^2 F_{n_p}} - \frac{\sum_{n_{p,\pm}} (|C^{tr,\pm}_{n_p}|^2 - |C^{ref,\pm}_{n_p}|^2) F_{n_p,\pm}}{\sum_{n_p} |C^{in}_{n_p}|^2 F_{n_p}}, \tag{14b}$$

$$\delta_L = \frac{\sum_{n_{p,\pm}} (|C^{tr,\pm}_{n_p}|^2 - |C^{ref,\pm}_{n_p}|^2) F_{n_p,\pm} - \sum_{n_{p,\pm}} |C^{tr}_{n_p}|^2 F_{n_p}}{\sum_{n_p} |C^{in}_{n_p}|^2 F_{n_p}}, \tag{15b}$$

$$\delta_0 + \delta_L = 1 - \frac{P_{ref} + P_{tr}}{P_{in}}, \tag{16}$$

where P_{tr} (P_{ref}) is the acoustic flow of energy transmitted at $z > L$ (reflected at $z < 0$). Equation (16) was used to estimate the inaccuracy of calculations in Ref. 10. For an absorptive plate the general expressions Eqs. (11a), (12a), (13a), (14a), and (15a) have to be used to estimate discontinuities of acoustic energy flow at $z = 0, L$. In this case the acoustic energy flow of all kinds of Lamb modes (propagating and nonpropagating) is not equal to zero, therefore all these modes have to be taken into account in Eqs. (11a), (12a), (13a), (14a), and (15a).

III. ACOUSTIC FIELD CALCULATIONS IN COMPOSITE PLATE WITH DELAMINATION

For the numerical implementation of the calculations of the acoustic field in a composite plate with a delamination we assume a composite plate consisting of a steel layer ($0 \leqslant y < d_1$) and a rubber layer $d_1 < y \leqslant d$. The material and geometrical parameters of these layers are taken as follows: density, shear, and longitudinal velocities of steel are equal to 7800 kg/m^3, 3160 m/s, and 5720 m/s, respectively; density,

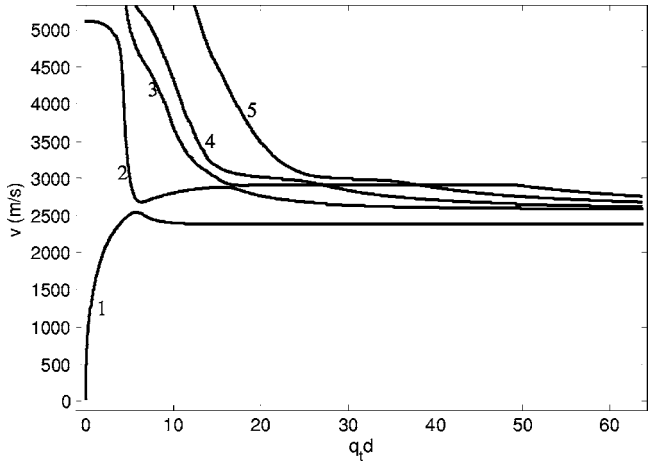

FIG. 2. Dependence of the lowest five Lamb mode phase velocities on dimensionless plate thickness $q_t d$.

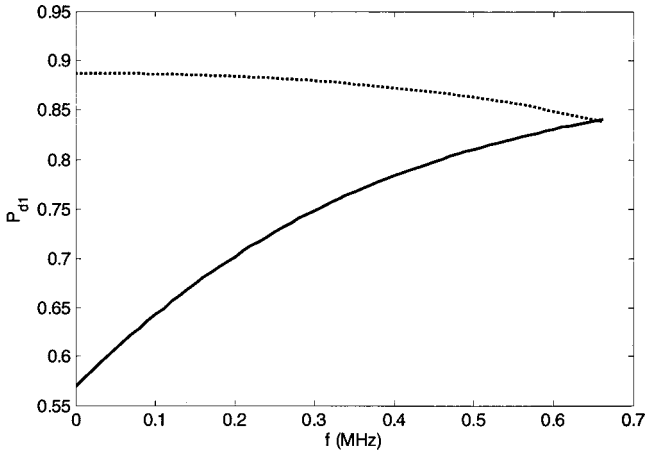

FIG. 3. Dependence of the energy flow relative part P_{d_1} concentrated in the steel layer of the composite plate for the first (full line) and second (dashed line) Lamb mode.

shear, and longitudinal velocities of rubber are equal to 1506 kg/m^3, 2580 m/s, and 4615 m/s, respectively. Further more, we take $d_1=d_2=1$ mm ($d_2=d-d_1$).

The interaction of Lamb modes with a delamination is easier to analyze for the case of a thin plate, when there are only a small number of propagating Lamb modes. In practice, it is difficult to excite a pure, single Lamb mode in a multimode plate. Taking into account that Lamb modes are dispersive, this leads to problems to make a correct interpretation of the signals. From this point of view a multimode regime is not attractive to experimentally study the effect of mode conversion on a delamination in a multimode plate. The phase velocities of the lowest five propagating Lamb modes in the composite nonabsorptive plate with aforesaid material and geometrical parameters are given in Fig. 2 as a function of the dimensionless parameter $q_t d$ (q_t is the wave number of shear wave in the steel layer). For high acoustic frequencies the phase velocity of the first Lamb mode tends to the velocity of Rayleigh wave propagating along the rubber/vacuum interface: $v_R^r \approx 2381.57$ m/s. The plateaus on the phase velocity dependencies of the third, fourth, and fifth Lamb modes near the velocity ~ 2920 m/s correspond to Rayleigh wave propagating along the steel/vacuum interface: $v_R^s \approx 2920.84$ m/s. These modes are localized in the steel layer and their field distributions are close to the field distribution of the steel/vacuum Rayleigh wave in the vicinity of the plateaus. The phase velocities of the higher Lamb modes evolve to the transverse bulk velocity of rubber for high acoustic frequencies.

In this composite plate there are only two propagating Lamb modes for $q_t d < 2.63$ (acoustic frequency $f < 0.661$ MHz). In the interval $4.59 < q_t d < 6.076$ (1.155 MHz $< f <$ 1.528 MHz) there are four propagating Lamb modes. Now we consider these two cases more in detail.

A. The case of two propagating Lamb modes

For $f < 0.661$ MHz, the composite plate with the abovementioned material and geometrical parameters supports only two propagating Lamb modes. We denote the first Lamb mode as Lm1 and the second one as Lm2. We define mode energy flow concentration coefficients for the Lm1 mode in the steel layer P_{d_1} as follows:

$$P_{d_1} = \int_0^{d_1} dy\, \mathrm{Im}(\sigma_{zz,tr}^{Lm1}(u_{z,tr}^{Lm1})^* - (\sigma_{yz,tr}^{Lm1})^* u_{y,tr}^{Lm1}) \Big/ \int_0^{d} dy\, \mathrm{Im}(\sigma_{zz,tr}^{Lm1}(u_{z,tr}^{Lm1})^* - (\sigma_{yz,tr}^{Lm1})^* u_{y,tr}^{Lm1}). \quad (17)$$

The coefficient P_{d_2} is defined analogously. The energy flow of the second Lamb mode is mainly concentrated in the steel layer for the whole frequency range $f < 0.661$ MHz. The concentration coefficient in the steel layer of the first Lamb mode is also large for higher acoustic frequencies but decreases with decreasing frequency. Their dependence on the acoustic frequency for a nonabsorptive composite plate is shown in Fig. 3.

The conversion coefficient of the incident mode Lm1 into the transmitted mode Lm2 (Q_{m2}), the conversion coefficient of the incident mode Lm2 into the transmitted mode Lm1 (Q_{m1}), the total reflection coefficients, and the largest relative errors of calculation described by the function δ_L are plotted versus delamination length L in Figs. 4(a) and 4(b) for nonabsorbing plate at acoustic frequency $f=0.6$ MHz. The conversion coefficients $Q_{m1,m2}$ are defined as follows:

$$Q_{m1} = F_{Lm1}|C_{Lm1}^{tr}|^2/(F_{Lm2}|C_{Lm2}^{in}|^2), \quad (18a)$$

$$Q_{m2} = F_{Lm2}|C_{Lm2}^{tr}|^2/(F_{Lm1}|C_{Lm1}^{in}|^2). \quad (18b)$$

The total reflection coefficients R_{m1} (R_{m2}) for the cases of incident modes Lm1 (Lm2) are defined by Eqs. (19a) and (19b):

$$R_{m1} = |C_{Lm1}^{ref}|^2/|C_{Lm1}^{in}|^2 + F_{Lm2}|C_{Lm2}^{ref}|^2/(F_{Lm1}|C_{Lm1}^{in}|^2), \quad (19a)$$

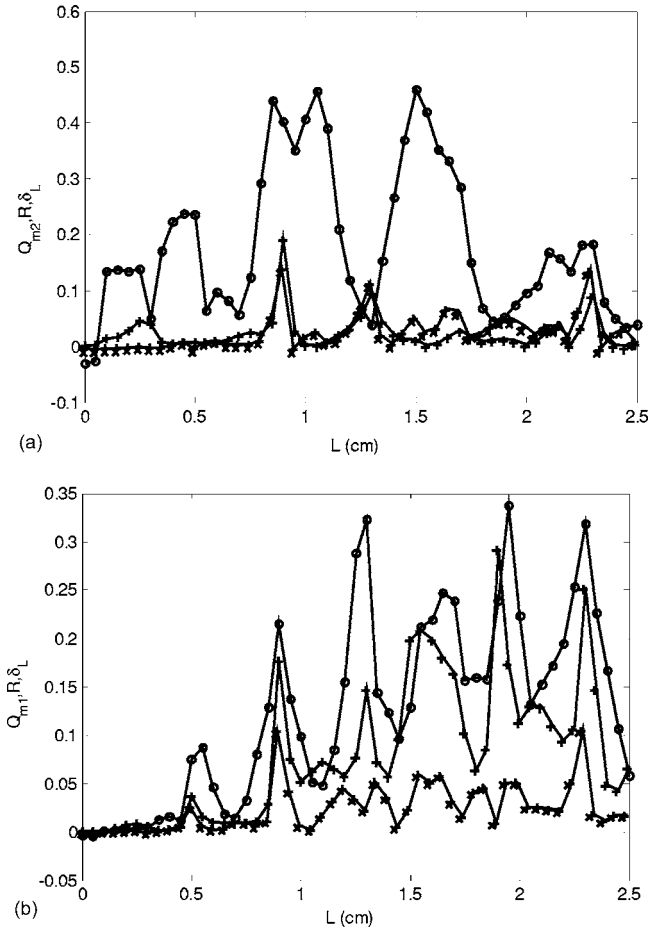

FIG. 4. (a) Dependence of conversion coefficients Q_{m2} (asterisk), reflection coefficient R (plus), and relative error δ_L (circle) on the delamination length L for an incident Lm1 mode at acoustic frequency $f=0.6$ MHz. (b) Dependence of conversion coefficient Q_{m1} (asterisk), reflection coefficient R (plus), and relative error δ_L (circle) on the delamination length L for an incident Lm2 mode at acoustic frequency $f=0.6$ MHz.

$$R_{m2} = |C^{ref}_{Lm2}|^2/|C^{in}_{Lm2}|^2 + F_{Lm1}|C^{ref}_{Lm1}|^2/(F_{Lm2}|C^{in}_{Lm2}|^2). \tag{19b}$$

The $F_{Lm1,Lm2}$ functions are given in Eqs. (11b), (12b), and (13b). The calculation is based on the solution of the system of linear equations (6)–(9). The wave numbers of propagating Lamb modes in the composite plate and the layers are as follows: composite plate: $q_{Lm1}\approx 17.89$, $q_{Lm2}\approx 7.46$; steel layer: $q_{A0}\approx 18.99$, $q_{S0}\approx 7.18$; rubber layer: $q_{A0}\approx 21.83$, $q_{S0}\approx 8.86$ (all wave numbers are given in 1/cm).

The conversion coefficients $Q_{m1,m2}$ are small and their values do not exceed the calculation error. The reflection coefficient R_{m1} is also below the calculation error, but for certain delamination lengths the reflection coefficient R_{m2} can be considerable, although the calculated R_{m2} values are not very reliable because these values are of the order of calculation error as well. To calculate the R_{m2} value more accurately, it is necessary to increase considerably the number of Lamb modes taken into consideration. The calculations presented in Figs. 4(a) and 4(b) have been performed taking into account 40 modes for the transmitted acoustic wave, 40 modes for the reflected acoustic wave, and 42 transmitted and 42 reflected modes in the region $0<z<L$

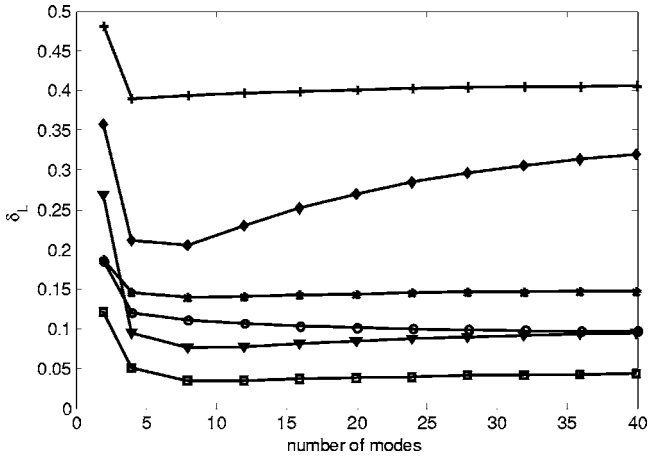

FIG. 5. Dependence of relative error δ_L on the number of modes taken into consideration for acoustic frequency $f=0.6$ MHz, different incident modes and different delamination lengths, for $L=1$ cm (plus), $L=1.75$ cm (asterisk), $L=0.6$ cm (circle), $L=1.3$ cm (diamond), $L=1$ cm (inverted triangle), $L=0.6$ cm (square) (the first three graphs are plotted for an incident Lm1 mode and the last three graphs for an incident Lm2 mode).

(21 transmitted and 21 reflected modes in the steel layer, 21 transmitted and 21 reflected modes in the rubber layer). These modes include fundamental propagating modes, nonpropagating modes, and the lowest inhomogeneous modes. The number of inhomogeneous modes was taken in such a way that the absolute values of the highest inhomogeneous mode wave numbers in all parts of the structure are close to each other.

As an example, the dependence of the relative error δ_L on the number of modes taken into account is shown in Fig. 5 for different delamination lengths. The order of additional modes taken into account was as follows. In the first step, only fundamental propagating modes were taken into account (two modes in every part of this plate—index 2 on the abscissa axis). In the second step, nonpropagating modes were added [two modes in the composite plate and 1 antisymmetric mode in every (steel and rubber) layer—index 4 on the abscissa axis]. In the third step, the four lowest inhomogeneous modes in the composite plate and the two lowest inhomogeneous modes (antisymmetric and symmetric) in every layer were additionaly taken into account—index 8 on the abscissa axis, and so on. Initially, increasing the number of modes leads usually to a better accuracy, but then this evolution saturates and fluctuates. The calculation error becomes especially large for cases of considerable reflection. Apparently, the discontinuity presented by the delamination renders it very difficult to satisfy the boundary conditions around it, using eigenmodes which have an inherently continuous character. Therefore, further increase of calculation accuracy can only be reached by taking into account a very large number of inhomogeneous modes. This is difficult to realize in practice because the sets of equations become extremely large and very computation (memory) intensive.

Now let us take into account acoustic absorption in the composite plate. It turns out that this feature can be used to detect the delamination with increased sensitivity, provided the absorption coefficients inside the layers of the composite plate are considerably different. An especially interesting

case takes place if the layer of major energy concentration of the incident wave is much less absorptive than the other one. Not surprisingly, in this case the existence of a long delamination with length $L > L_{abs}$ (L_{abs} is the absorption length of the incident wave in the composite plate without delamination) leads to considerable increase of transmitted acoustic wave energy in the region $z \approx L$.

To illustrate this, we consider a composite plate where only the rubber layer is absorptive. Absorption of shear and longitudinal waves in rubber is modelled to be considerable for propagation lengths ~ 1 cm at acoustic frequency ~ 1 MHz. To realize this in the simulation, imaginary parts $-0.05iv_s$ and $-0.05iv_l$ at acoustic frequency 0.6 MHz were added to the to shear v_s and longitudinal v_l velocities of rubber. These values for absorptive rubber were arbitrarily chosen only to show the influence of absorption on propagation of the acoustic wave through the delamination region of the composite plate. It is difficult to find values in the literature, partially because rubbers have strongly frequency- and temperature-dependent elastic moduli. Some values are given in Refs. 15–17. Usually an *ad hoc* model is used for the frequency dependence.[13] For our choice of values the wave numbers of Lm1 and Lm2 modes in the composite plate are about $17.89+0.16i$ and $7.46+0.06i$, respectively. The wave numbers of A0 and S0 modes in rubber layer are about $21.79+0.75i$ and $8.83+0.44i$, respectively (all wave numbers are given in 1/cm). Therefore, the absorption lengths of the Lm1 mode $[L_{abs,1}=0.5/\mathrm{Im}(q_{Lm1})]$, Lm2 mode $[L_{abs,2}=0.5/\mathrm{Im}(q_{Lm2})]$, the A0 mode in the rubber layer $[L_{abs,A0}=0.5/\mathrm{Im}(q_{A0})]$, and the S0 mode in the rubber layer $[L_{abs,S0}=0.5/\mathrm{Im}(q_{S0})]$ are about 3.09, 7.83, 0.67, and 1.12 cm, respectively, and a delamination with the length $L \sim 3$ cm can result in considerable increase of transmitted Lm1 mode.

The dependence of the transmission coefficients of Lm1 mode T_{m1}, the relative value of absorbed flow of energy in the delamination region W_{m1}, and the relative calculation errors δ_L on the delamination length L for incident Lm1 mode at acoustic frequency $f=0.6$ MHz are shown in Fig. 6. The transmission coefficient of Lm1 mode T_{m1} is defined as $T_{m1}=|C^{tr}_{Lm1}|^2/|C^{in}_{Lm1}|^2$. The relative value of absorbed flow of energy in the delamination region is equal to: $W_{m1}=(P^{tr,1}_z(z=0)-P^{tr,1}_z(z=L))/(F_{Lm1}|C^{in}_{Lm1}|^2)$ [the function $P^{tr,1}_z$ is given by Eq. (13)]. The conversion coefficient Q_{m2} and the reflection coefficient are small and below the level of calculation error. Therefore these values are not shown in this figure. The relative value of absorbed flow of energy in the delamination region W_{m1} increases with increasing delamination length L and reaches a value of about 0.13–0.16 for $L \geqslant 1.3$ cm. This is explained by the fact that the incident Lm1 mode is mainly located in the steel layer for acoustic frequency $f=0.6$ MHz (the concentration coefficient P_{d_1} in the steel layer of the Lm1 mode is about 0.83). This means that about 13%–17% of incoming acoustic energy penetrates inside the rubber layer at $z=0$ and almost all this energy is absorbed inside the rubber layer for a delamination length $L \geqslant 1.3$ cm. Therefore, the transmission coefficient of Lm1 mode T_{m1} can be larger than 0.8 for delamination length $L > 1.3$ cm (the T_{m1} values given in Fig. 6 for $L \geqslant 1.7$ cm are about 0.7–0.75 with calculation error about 0.1–0.15). As a result, a considerable part of incoming acoustic energy (about 80%) is transmitted through the delamination region with the absorptive rubber layer. A long delamination has a clearly larger transmission than a delamination free plate. This is illustrated in Fig. 6 where the dependence of the transmission coefficient of the Lm1 mode through the composite plate of length L without delamination $T_{m1,0}=\exp(-2\,\mathrm{Im}(q_{Lm1})L)$ is also given. The transmission coefficient of the Lm1 mode becomes starts to exceed the delamination free value when $L > 2$ cm.

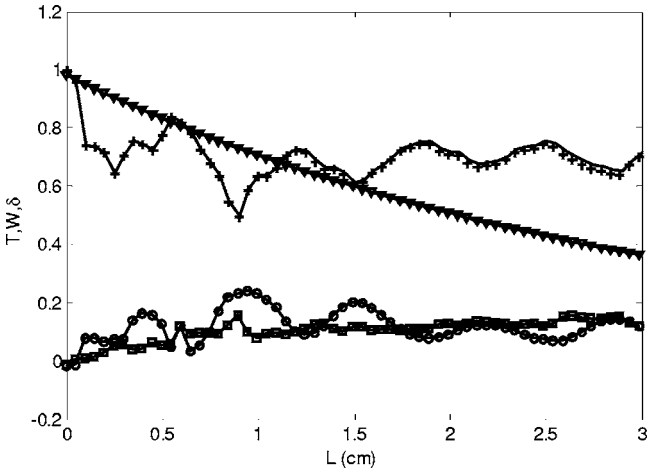

FIG. 6. Dependence of the transmission coefficient T_{m1} (plus), the transmission coefficient $T_{m1,0}$ (inverted triangle) without delamination, the relative value of absorbed flow of energy in the delamination region W_{m1} (square), and the relative error δ_L (circle) on the delamination length L for an incident Lm1 mode at acoustic frequency $f=0.6$ MHz.

B. The case of four propagating Lamb modes

The composite plate with aforesaid material and geometrical parameters is characterized by four propagating Lamb modes for 1.155 MHz $< f <$ 1.528 MHz. We denote the third Lamb mode as Lm3 and the fourth one as Lm4. The coefficients of energy concentration of the Lamb modes in the steel layer, P_{d_1}, P_{d_2}, P_{d_3}, and P_{d_4}, defined analogously to Eq. (17), are plotted in Fig. 7 for the frequency range 1.17 MHz $< f <$ 1.52 MHz. Lm3 and Lm4 modes are mainly concentrated in the rubber and steel layers, respectively, for the whole mentioned range of acoustic frequencies. The first modes Lm1 and Lm2 are mainly concentrated in the steel and rubber layers, respectively, for the lower end of the frequency interval, and these modes are more spread over the whole composite plate near the higher end. In order to investigate the effect of this difference, we consider acoustic wave propagation through the delamination region for two acoustic frequencies 1.2 and 1.5 MHz which are close to the extremes of this interval. To take into account the influence of absorption we again assume that only the rubber layer is absorptive, with consequently relative additions to the shear and longitudinal velocities of rubber of about $-0.01i$ at acoustic frequency 1.2 MHz.

For the acoustic frequency 1.2 MHz, the wave numbers of propagating modes in the composite plate and the steel and rubber layers are as follows: composite plate: q_{Lm1}

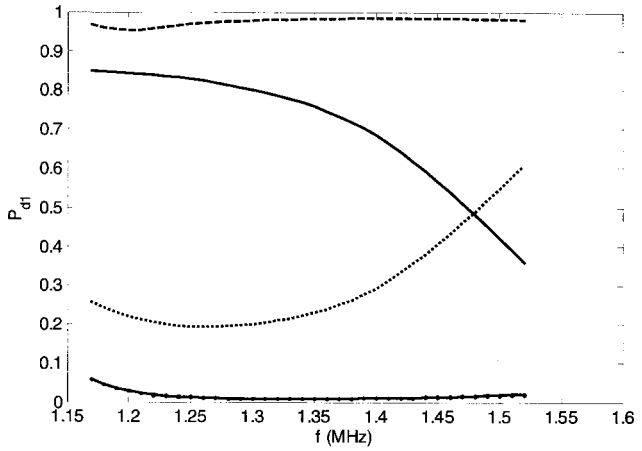

FIG. 7. Dependence of the energy flow relative part P_{d_1} concentrated in the steel layer of the composite plate, for the first (upper full line), second (dotted line), third (lower full line), and fourth Lamb modes (dashed line).

$\approx 30.31+0.054i$, $q_{Lm2}\approx 23.28+0.553i$, $q_{Lm3}\approx 14.52+0.22i$, and $q_{Lm4}\approx 12.54+0.25i$; steel layer: $q^s_{A0}\approx 31.1$, $q^s_{S0}\approx 14.55$; rubber layer: $q^r_{A0}\approx 36.51+0.29i$, and $q^r_{S0}\approx 18.11+0.2i$ (all values are given in cm^{-1}). The wave number of the first Lamb mode is close to the wave number of the A0 mode in the steel layer. Taking into account that the energy flow of the Lm1 mode is also mainly localized in the steel layer of the composite plate, we can assume that the calculation errors for the case of the incident Lm1 mode are comparatively small.

In Fig. 8, the dependences of the transmission coefficients of the Lm1 mode T_{m1} and the total transmission coefficient T through the region of delamination, the conversion coefficient of the Lm1 mode into the transmitted Lm2 mode Q_{m2}, the relative value of the absorbed flow of energy in the delamination region W_{m1}, and the relative calculation errors δ_L at acoustic frequency $f=1.2$ MHz are shown versus the delamination length, for the case of an incident Lm1 mode. The reflection and conversion coefficients of the Lm1 mode into another propagating mode are of the order of the calculation error and not shown in this figure. The total transmission coefficient T is defined by Eq. (11) at $z=L$ taking into account only propagating Lamb modes. The calculations presented in Fig. 8 have been performed taking into account 42 modes for the transmitted acoustic wave, and the same amount of modes for the reflected acoustic wave, and for the transmitted and reflected wave in the region $0<z<L$ (21 transmitted and reflected modes, respectively, in the steel and rubber layers). These modes include fundamental propagating modes, nonpropagating modes, and the lowest inhomogeneous modes. A number of inhomogeneous modes were taken using the same reason as for the case shown in Figs. 4(a) and 4(b). Calculation errors for this case are indeed quite small. The $|\delta_L|$ value is smaller than 0.06 for the whole range of calculations.

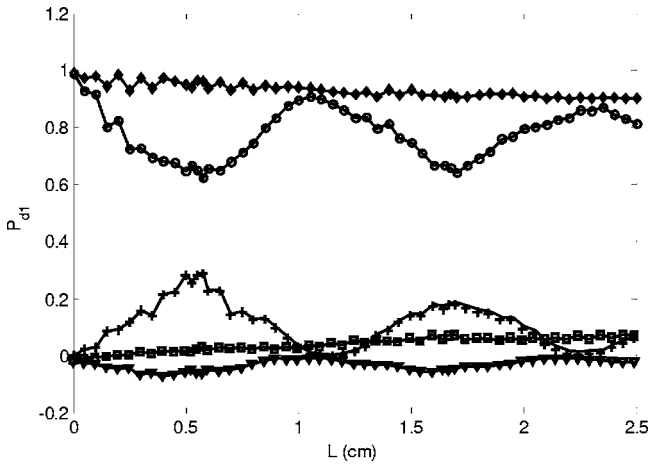

FIG. 8. Dependence of the transmission coefficient T_{m1} (circle), the total transmission coefficient T (diamond), the conversion coefficient Q_{m2} (plus), the relative value of absorbed flow of energy in the delamination region W_{m1} (square), and the relative error δ_L (inverted triangle) on the delamination length L for an incident Lm1 mode at acoustic frequency $f=1.2$ MHz.

There is a clear periodic behavior of the conversion coefficient Q_{m2} as a function of delamination length with a maximum at $L\approx 0.58$ cm and $L\approx 1.7$ cm, and a minimum at $L\approx 1.15$ cm. The maximum value $Q^{\max}_{m2}$ is about 0.3 at $L\approx 0.58$ cm and 0.19 at $L\approx 1.7$ cm. This means that a part of the incident Lm1 mode energy, equal to $Q^{\max}_{m2}$, is converted into the transmitted Lm2 mode at these delamination lengths. To explain such behavior of the conversion coefficient as a function of the delamination length, one notes that almost all incident Lm1 mode energy is converted into the A0 modes of steel and rubber plates at $z=0$ (between 88% and 90% is converted into the A0 mode of the steel layer and 8%–10% is converted into the A0 mode of the rubber layer). These A0 modes of the steel and rubber layers are converted into transmitted Lamb modes at $z=L$ and this conversion is the most effective if the delamination length lies around the beating length between A0 modes of steel and rubber layers $L_{b,A0,A0}=\pi/\mathrm{Re}(q^r_{A0}-q^s_{A0})\approx 0.58$ cm. In this case both A0 modes are out of phase at $z=L$, resulting in effective generation of transmitted Lm2 mode (see also Ref. 10). This effect almost disappears if $L\approx 2L_{b,A0,A0}$ when both A0 modes are again in phase at $z=L$ and the transmitted wave consists mainly of Lm1 mode. A new maximum of the conversion coefficient into the Lm2 mode appears again if $L\approx 3L_{b,A0,A0}$ and so on. But the absorption in the rubber layer (the absorption length of the A0 mode in the rubber layer is about 1.72 cm) results in the decrease of A0 mode amplitude in the rubber layer at $z=L$, leading to a decrease of the maximum values $Q^{\max}_{m2}$ of the conversion coefficient for larger delamination length. As a result the $Q^{\max}_{m2}$ value for $L=1.7$ cm is smaller than at $L=0.58$ cm. The delamination length $L=2.5$ cm is not large enough to realize the effect of a considerable increase of transmission induced by the delamination shown in Fig. 6. The total transmission coefficient T and the transmission coefficient of the Lm1 mode without delamination $T_{m1,0}$ for this delamination length are about 0.9 and 0.76, respectively. The effect of a considerable increase of transmission induced by the delamination can be realized in this case for longer delaminations with $L\sim L_{abs,1}=0.5/\mathrm{Im}(q_{Lm1})\approx 9.3$ cm.

Now we consider the case of an incident Lm2 mode. In Figs. 9(a) and 9(b), the dependence of the transmission coefficients of the Lm2 mode T_{m2} through the region of delamination, the transmission coefficient of the Lm2 mode $T_{m2,0}$

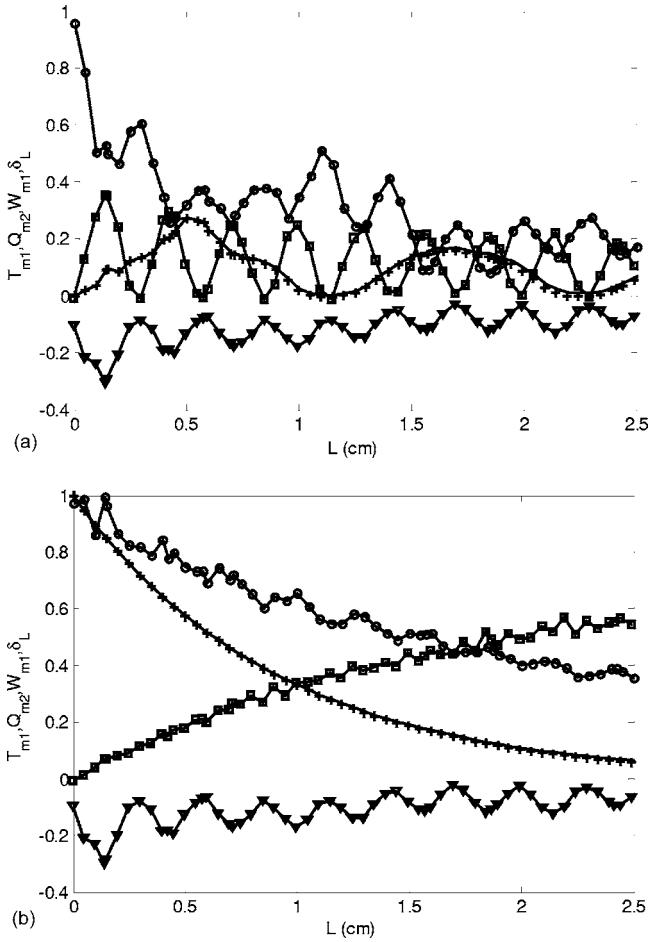

FIG. 9. (a) Dependence of the transmission coefficient T_{m2} (circle) through the delamination, the conversion coefficient of Lm2 mode into Lm1 mode Q_{m1} (plus), the conversion coefficient of the Lm2 mode into the Lm4 mode Q_{m4} (square), and the relative error δ_L (inverted triangle) on the delamination length L for an incident Lm2 mode at acoustic frequency $f=1.2$ MHz. (b) Dependence of the total transmission coefficients T (circle) through the delamination, the transmission coefficient $T_{m2,0}$ (plus) of Lm2 mode without delamination, the relative value of absorbed flow of energy in the delamination region W_{m2} (square), and the relative error δ_L (inverted triangle) on the delamination length L for an incident Lm2 mode at acoustic frequency $f=1.2$ MHz.

without delamination $[T_{m2,0}=\exp(-2\,\mathrm{Im}(q_{Lm2})L)]$, the overall transmission coefficient T, the conversion coefficients of the Lm2 mode into the transmitted Lm1 mode Q_{m1} and into the transmitted Lm4 mode Q_{m4}, the relative value of absorbed flow of energy in the delamination region W_{m2}, and the relative calculation errors δ_L are plotted versus delamination length for an acoustic frequency $f=1.2$ MHz. The reflection and conversion coefficient of the Lm2 mode into the Lm3 mode are below the calculation error and not shown in this figure. The total transmission coefficient is defined analogously to that shown in Fig. 8. The calculations presented in Figs. 9(a) and 9(b) have been performed in exactly the same way as the calculations of the graphs in Fig. 8. Calculation errors for this case are larger. This is connected with the fact that the wave number of the Lm2 mode is not close enough to wave numbers of A0 and S0 modes propagating in the layers.

There is a clear periodic dependence of conversion coefficients Q_{m1} and Q_{m4} on the delamination length. The maximum and minimum of Q_{m1} are realized at about the same lengths L as the maximum and minimum of Q_{m2} shown in Fig. 8. The maximum value $Q_{m1}^{\max}$ is about 0.27 at $L\approx0.5$ cm and 0.17 at $L\approx1.7$ cm. The maximum and minimum of the conversion coefficient Q_{m4} occur at the length $L=L_{m4}^{\max,\min}$. These lengths are now connected with the beating length between the A0 mode of the rubber layer and the S0 mode of the steel layer $L_{b,s0,A0}=\pi/\mathrm{Re}(q_{A0}^r-q_{S0}^s)\approx0.143$ cm. The maximum and minimum of Q_{m4} are reached for $L_{m4}^{\max}\approx(2n-1)L_{b,S0,A0}$ and $L_{m4}^{\min}\approx2nL_{b,S0,A0}$, respectively, and $n=1,2,3\ldots$. The maximum value $Q_{m1}^{\max}$ is about 0.37 at $L\approx0.143$ cm and decreases to 0.2 at $L\approx17L_{b,S0,A0}\approx2.43$ cm. The explanation of these conversions is exactly the same as the one already given for Q_{m2}. Now it should be taken into account that at $z=0$ the incident Lm2 mode is mainly converted into the A0 mode of the rubber layer and almost equally converted into the A0 and S0 modes of the steel layer (between 60% and 80% of Lm2 mode energy is converted into the A0 mode of the rubber layer and between 15% and 20% of Lm2 mode energy is converted into the A0 and S0 modes of the steel layer). This leads to comparable maximum values $Q_{m1}^{\max}$ and $Q_{m4}^{\max}$.

Figure 9(b) shows that the existence of a delamination leads to an enhancement of transmitted acoustic energy for $L>1$ cm. This is connected with the value of the absorption length of the Lm2 mode, $L_{abs,2}=0.5/\mathrm{Im}(q_{Lm2})\approx0.9$ cm, but the absorption of propagating Lamb modes inside the rubber layer is smaller. The absorption lengths of A0 and S0 modes in the absorptive rubber layer are about 1.72 and 2.56 cm, therefore the propagation of the acoustic wave through the delamination leads to a considerable decrease of the total absorbed energy for $L>1$ cm.

To make calculations for the acoustic frequency $f=1.5$ MHz we assume *ad hoc* (in particular rubbers have a complicated frequency dependence of absorption and dispersion properties) that the absorption coefficients for shear and longitudinal waves are proportional to f^2 (see, e.g., Ref. 18), so these values can be found from the appropriate absorption coefficients for $f=1.2$ MHz. In this case the wave numbers of the propagating modes in this composite plate and the steel and rubber layers are as follows: composite plate: $q_{Lm1}\approx36.96+0.33i$, $q_{Lm2}\approx35.02+0.34i$, $q_{Lm3}\approx19.95+0.31i$, and $q_{Lm4}\approx17.81+0.04i$; steel layer: $q_{A0}^s\approx37.04$, $q_{S0}^s\approx18.45$; rubber layer: $q_{A0}^r\approx43.79+0.46i$, $q_{S0}^r\approx23.34+0.36i$, and $q_{A1}^r\approx10.49+0.53i$ (all values are given in cm^{-1}).

In Figs. 10(a) and 10(b), the dependence of the transmission coefficients of the Lm1 mode T_{m1} through the delamination region, the transmission coefficient of the Lm1 mode $T_{m1,0}$ without delamination $[T_{m1,0}=\exp(-2\,\mathrm{Im}(q_{Lm1})L)]$, the total transmission coefficient T, the conversion coefficient of the Lm1 mode into transmitted Lm2 mode Q_{m2}, the relative value of absorbed flow of energy in the delamination region W_{m1}, and the relative calculation errors δ_0, δ_L at acoustic frequency $f=1.5$ MHz are shown versus the delamination length for the case of an incident Lm1 mode. In this case the δ_0, δ_L values are of the same order, therefore both functions are now shown. The reflection and conversion coefficients of the Lm1 mode into other propagating modes are below the

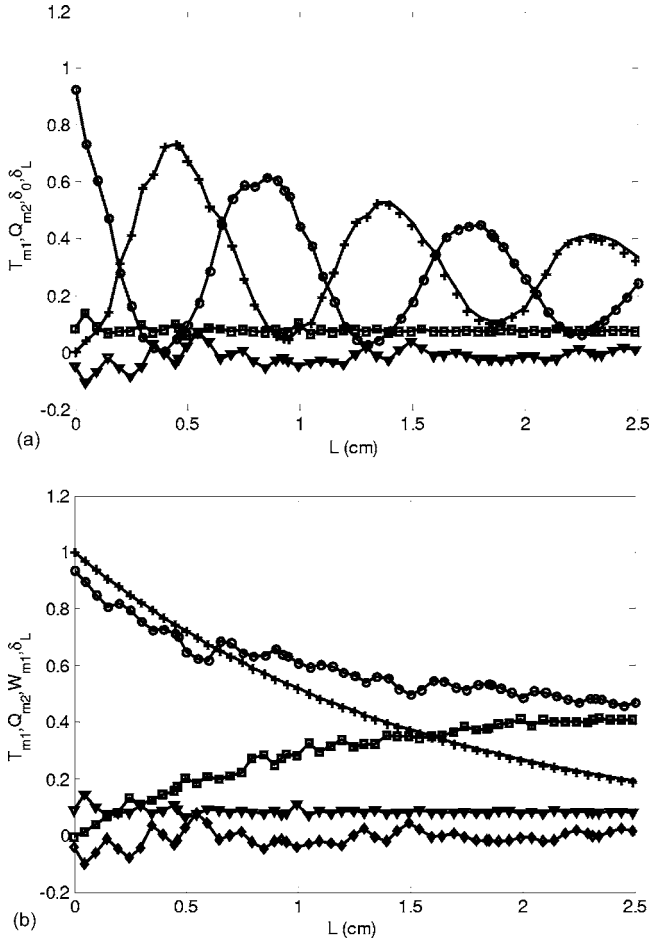

FIG. 10. (a) Dependence of transmission coefficients T_{m1} (circle) of Lm1 mode through the delamination, conversion coefficient of Lm1 mode into Lm2 mode Q_{m2} (plus) and relative errors δ_0 (square), δ_L (inverted triangle) versus delamination length L for an incident Lm1 mode at acoustic frequency $f=1.5$ MHz. (b) Dependence of the total transmission coefficient T (circle) through the delamination, transmission coefficient $T_{m1,0}$ (plus) of Lm1 mode without delamination, relative value of absorbed flow of energy in the delamination region W_{m1} (square), and relative error δ_0 (inverted triangle), δ_L (diamond) versus delamination length L for an incident Lm1 mode at acoustic frequency $f=1.5$ MHz.

level of calculation error and not shown in these figures. Calculations for this figure proceeded exactly in the same way as for Figs. 8, 9(a), and 9(b).

Again there is a clear periodic dependence of the conversion coefficients Q_{m2} on the delamination length. The maximum and minimum of Q_{m2} are realized at the delamination lengths connected with the beating length between the A0 modes of the rubber and steel layers $L_{b,A0,A0}=\pi/\mathrm{Re}(q^r_{A0}-q^s_{A0})\approx 0.46$ cm. A maximum and minimum of Q_{m1} are reached for $L^{\max}\approx(2n-1)L_{b,A0,A0}$ and $L^{\min}\approx 2nL_{b,A0,A0}$, respectively, and $n=1,2,3\ldots$. The maximum value $Q^{\max}_{m1}$ is about 0.73 at $L\approx 0.45$ cm and decreases down to 0.41 at $L\approx 5L_{b,A0,A0}\approx 2.3$ cm. The maximum values $Q^{\max}_{m1}$ are very large in this case. This is connected with an almost equal distribution of Lm1 mode energy flow among the steel and rubber layers in the composite plate (about 42% of Lm1 mode energy flow is concentrated in the steel layer at this frequency—see Fig. 7). The incident Lm1 mode is converted mainly into the A0 modes of the steel and rubber layers at $z=0$ (between 44% and 46% of Lm1 mode energy is converted into the A0 mode of the steel layer and between 40% and 43% of Lm1 mode energy is converted into the A0 mode of the rubber layer). Acoustic absorption existing in the rubber layer (absorption lengths of all propagating modes are about 1 cm) results in a continuous decrease of the maximum values $Q^{\max}_{m1}$ with increasing delamination length. One sees from Fig. 10(b) that the existence of a delamination increases the transmitted acoustic energy for $L>L_{abs,1}\approx 1.5$ cm. This is connected with the fact that a considerable part of the acoustic wave energy propagates through the steel layer without absorption.

Similar phenomena occur for the case of the incident Lm2 mode at $f=1.5$ MHz. Maximum and minimum Q_{m1} values occur near the same lengths L as for the case of the incident Lm1 mode and the influence of absorption is also close to the one shown in Fig. 10(b). This is explained by the similar distributions of the Lm1 and Lm2 modes inside the composite plate (about 55% of Lm2 mode energy flow is concentrated in the steel layer at $f=1.5$ MHz). As a result the incident Lm2 mode is converted mainly into the A0 modes of the steel and rubber layers at $z=0$ (about 50% of Lm2 mode energy is converted into the A0 mode of the steel layer and about 30% into the A0 mode of the rubber layer). The absorption lengths of the Lm2 and Lm1 modes in the composite plate are also close to each other ($L_{abs,2}\approx 1.5$ cm).

The dependence of transmitted relative energy flows in the steel and rubber layers $P^{s,r}_z$ on the z coordinate for $z>L$, taking into account only two major propagating Lm1 and Lm2 modes, are plotted in Fig. 11(a) for the case of an incident Lm1 mode at acoustic frequency $f=1.2$ MHz. The $P^{s,r}_z$ values are defined as follows:

$$P^{s,r}_z=\int_{a_\pm}^{b_\pm} dy\ \mathrm{Im}((C^{tr}_{Lm1}\tilde{\sigma}^{Lm1}_{zz,tr1}+C^{tr}_{Lm2}\tilde{\sigma}^{Lm2}_{zz,tr1})(C^{tr}_{Lm1}\tilde{u}^{Lm1}_{z,tr1}+C^{tr}_{Lm2}\tilde{u}^{Lm2}_{z,tr1})^*-(C^{tr}_{Lm1}\tilde{\sigma}^{Lm1}_{yz,tr1}+C^{tr}_{Lm2}\tilde{\sigma}^{Lm2}_{yz,tr1})^*(C^{tr}_{Lm1}\tilde{u}^{Lm1}_{y,tr1}+C^{tr}_{Lm2}\tilde{u}^{Lm2}_{y,tr1}))\Big/\int_0^d dy\ \mathrm{Im}\ (\sigma^{Lm1}_{zz,tr}(u^{Lm1}_{z,tr})^*-(\sigma^{Lm1}_{yz,tr})^*u^{Lm1}_{y,tr})), \tag{20}$$

where $a_-=0$, $a_+=b_-=d_1$, $b_+=d$; a_- and b_- are substituted for the steel layer, a_+ and b_+ are substituted for the rubber layer, $\tilde{\sigma}^n_{ik,tr1}$ and $\tilde{u}^n_{i,tr1}$ are defined in Eq. (11), and it is suggested that $C^{in}_{Lm1}=1$.

These graphs are plotted for three cases: without delamination ($L=0$) and delamination lengths $L=0.58$ cm and $L=1.16$ cm. The energy flows in the steel and rubber layers $P^{s,r}_z\sim\exp(-2z\ \mathrm{Im}(q_{Lm1}))$ in the absence of a delamination. Maximum conversion into the Lm2 mode is realized for a delamination length $L=0.58$ cm. This leads to the appearance of two transmitted propagating modes—Lm1 and Lm2 (amplitudes of other propagating modes are much smaller). Interference between these modes results in the beating of energy flows in the steel and rubber layers versus z coordinate with a beating length $\pi/\mathrm{Re}(q_{Lm1}-q_{Lm2})\approx 0.45$ cm. This is clearly seen in Fig. 11(a). Minimum conversion into the

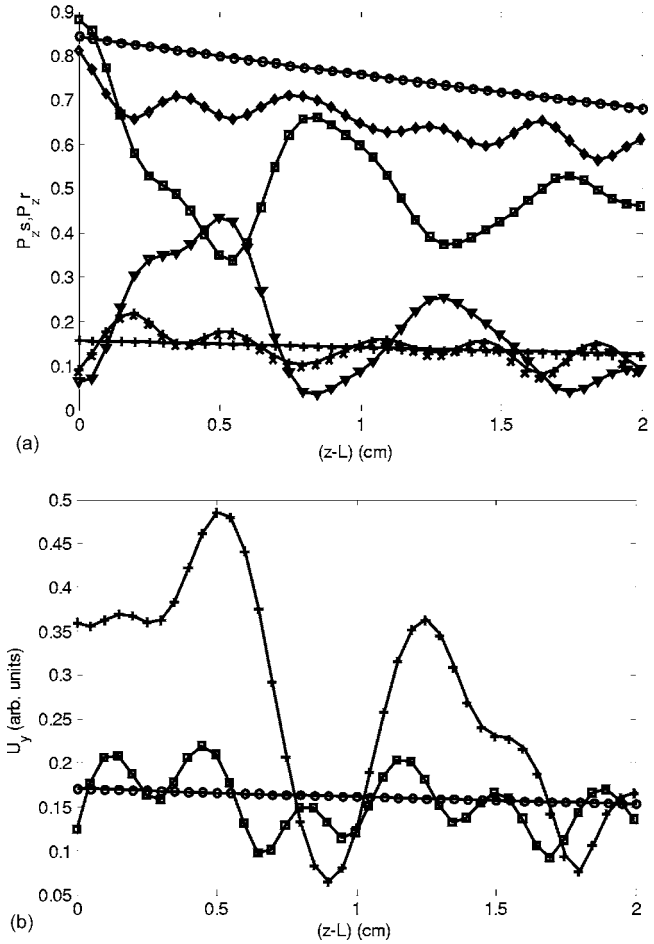

FIG. 11. (a) Dependence of relative acoustic energy flow in rubber and steel layers for acoustic frequency $f=1.2$ MHz and incident Lm1 mode versus z for $z \geqslant L$ at different delamination lengths. Acoustic energy flow P_z^s (circle) in the steel layer and P_z^r (plus) in the rubber layer in the absence of a delamination ($L=0$). P_z^s (square) and P_z^r (inverted triangle) for $L=0.58$ cm, P_z^s (diamond) for $L=1.16$ cm, and P_z^r (asterisk) for $L=1.16$ cm. (b) Dependence of the modulus of the mechanical displacement y component $|u_y(y=d)|$ for acoustic frequency $f=1.2$ MHz and incident Lm1 mode versus z for $z \geqslant L$ at different delamination lengths, in the absence of delamination, $L=0$ (circle), $L=0.58$ cm (plus), and $L=1.16$ cm (square).

Lm2 mode is realized for $L=1.16$ cm. In this case the transmitted wave consists mainly of the Lm1 mode; strong beating of energy flows in the steel and rubber layers is absent, i.e., there are relatively small fluctuations due to the presence of other propagating modes with relatively small amplitudes in the transmitted wave. The strong absorption of the Lm2 mode (absorption length is about 0.9 cm) leads to a decrease of energy flow beatings for $L>1$ cm. For the same cases ($L=0$, $L=0.58$ cm, and $L=1.16$ cm), the dependence of the modulus of the y component of the mechanical displacement at $y=d|u_y(y=d)|$ (arbitrary units) is plotted in Fig. 11(b). The $|u_y(y=d)|$ value for $z-L \sim 0.5$ cm is considerably larger for $L=0.58$ cm compared to the same values for $L=0$ or $L=1.16$ cm. This feature can be used to detect the presence of delaminations in the composite plate.

IV. CONCLUSIONS

The two-dimensional propagation of Lamb modes in an absorptive composite plate consisting of two parallel layers with a finite delamination dividing these layers was studied. The calculation was based on the modal decomposition method. To calculate transmission and reflection coefficients of Lamb modes induced by the delamination it is necessary to solve a system of linear equations for mode amplitudes taking into account all propagating modes and a number of inhomogeneous Lamb modes. The error due to the made approximations can be quantified using the discontinuities of the acoustic flow energy integrated over the vertical planes at the beginning and at the end of delamination.

As a result of diffraction on a delamination, an incident Lamb mode undergoes conversion into all possible transmitted and reflected Lamb modes. Specific numerical calculations were performed for the case of a composite plate consisting of steel and rubber layers of equal thickness. Only thin composite plates characterized by a few propagating Lamb modes were taken into consideration. It was found that the mode conversion effect in transmission for a thin plate characterized by only two propagating fundamental Lamb modes is usually quite weak. The effect of mode conversion becomes much stronger in the case of a composite plate characterized by four propagating Lamb modes, where, depending on acoustic frequency, it is possible to realize situations characterized by efficient mode conversion of the incident first (second) Lamb mode of the composite plate into a transmitted second (first) Lamb mode, where up to 70% of the incident mode energy can be transferred into the converted Lamb mode.

Delaminations in absorptive composite plates result in a considerable change of transmitted acoustic energy if the plate is characterized by substantially different absorption coefficients in the layers of the plate. In particular, the delamination can considerably increase the transmission coefficient of the incident Lamb mode if the layer where the incident Lamb mode is mainly concentrated is much less absorptive than the other one.

Numerical calculations show that the reflection of the incident Lamb modes from delamination is usually small (under the level of calculation errors). On the other hand, there are cases where this reflection can be considerable, e.g., the case of the incident second Lamb mode in a thin composite plate characterized by two propagating Lamb modes at specific delamination lengths, where the calculated reflection coefficient turns out to be more than 0.2. Calculation errors in these cases are also large and reliable results considerably above the level of calculation errors can only be obtained by taking into account a very large number of inhomogeneous Lamb modes.

The effect of mode conversion and influence of absorption on the transmission coefficient in absorptive composite plates with delaminations can be used to detect nondestructively the existence of delaminations.

ACKNOWLEDGMENT

The authors would like to thank the Research Council of the K. U. Leuven for the fellowship awarded to Professor G. N. Shkerdin, which enabled us to perform this research.

APPENDIX: CALCULATION OF DISPLACEMENT AND STRESS FIELDS FOR A TWO-LAYER COMPOSITE PLATE

The displacement fields for the forward propagating nth Lamb mode in the first ($0 \leqslant y \leqslant d_1$) and the second ($d_1 \leqslant y \leqslant d$) layers of the composite plate can be written as follows:

$$u^n_{y,1} = (-A^+_{1t} q_n e^{iq_{ty,1}y} - A^-_{1t} q_n e^{-iq_{ty,1}y} + A^+_{1l} q_{ly,1} e^{iq_{ly,1}y} - A^-_{1l} q_{ly,1} e^{-iq_{ly,1}y}) e^{i(q_n z - \omega t)}, \tag{A1}$$

$$u^n_{z,1} = (A^+_{1t} q_{ty,1} e^{iq_{ty,1}y} - A^-_{1t} q_{ty,1} e^{-iq_{ty,1}y} + A^+_{1l} q_n e^{iq_{ly,1}y} + A^-_{1l} q_n e^{-iq_{ly,1}y}) e^{i(q_n z - \omega t)}, \tag{A2}$$

$$u^n_{y,2} = (-A^+_{2t} q_n e^{iq_{ty,2}y} - A^-_{2t} q_n e^{-iq_{ty,2}y} + A^+_{2l} q_{ly,2} e^{iq_{ly,2}y} - A^-_{2l} q_{ly,2} e^{-iq_{ly,2}y}) e^{i(q_n z - \omega t)}, \tag{A3}$$

$$u^n_{z,2} = (A^+_{2t} q_{ty,2} e^{iq_{ty,2}y} - A^-_{2t} q_{ty,2} e^{-iq_{ty,2}y} + A^+_{2l} q_n e^{iq_{ly,2}y} + A^-_{2l} q_n e^{-iq_{ly,2}y}) e^{i(q_n z - \omega t)}, \tag{A4}$$

where $q^2_{ly,1} = q^2_{l,1} - q^2_n$, $q^2_{ty,1} = q^2_t - q^2_n$, $q^2_{ly,2} = q^2_{1,2} - q^2_n$, $q^2_{ty,2} = q^2_{t,2} - q^2_n$, $q_{l,1}$ and $q_{l,2}$ are the wave numbers of the longitudinal waves in the first and the second layers, $q_{t,2}$ is the wave number of shear wave in the second layer, q_n is the wave number of the Lamb mode, and $A^\pm_{1t,1l}$ and $A^\pm_{2t,2l}$ are the unknown coefficients to be found. Expressions for stress tensor components can be easily written down taking into account standard stress-strain relations.

Taking into account free boundary conditions at $y = 0, d$ and continuity of mechanical displacement vector components and stress tensor components σ_{yz} and σ_{yy} at $y = d_1$ the system of eight linear equations for eight unknown coefficients can be written down. The determinant of the system has to be equal to zero. This condition leads to the dispersion equation for Lamb mode wave numbers as follows:

$$\left(f^+_1 - \beta_1 \frac{m^+_2 - m^+_1 n^-_2/n^-_1}{n^+_2 + n^+_1 n^-_2/n^-_1}\right)\left(f^-_2 - \beta_2 \frac{m^-_2 + m^-_1 n^-_2/n^-_1}{n^+_2 + n^+_1 n^-_2/n^-_1}\right) + \left(f^+_2 + \beta_2 \frac{m^+_2 - m^+_1 n^-_2/n^-_1}{n^+_2 + n^+_1 n^-_2/n^-_1}\right)\left(f^-_1 - \beta_1 \frac{m^-_2 + m^-_1 n^-_2/n^-_1}{n^+_2 + n^+_1 n^-_2/n^-_1}\right) = 0, \tag{A5}$$

where $f^\pm_1 = m^\pm_3 \mp m^\pm_1 n^-_3/n^-_1$, $f^\pm_2 = m^\pm_4 - m^\pm_1 n^-_4/n^-_1$, $\beta_1 = n^+_3 + n^+_1 n^-_3/n^-_1$,

$$\beta_2 = n^+_4 - n^+_1 n^-_4/n^-_1, \quad n^+_1 = q_n b_2 \exp(i(q_{ty,2} - q_{ly,2})d_2) + q_n c_2 \exp(i(q_{ty,2} + q_{ly,2})d_2) + q_{ty,2},$$

$$n^-_1 = q_n c_2 \exp(-i(q_{ty,2} + q_{ly,2})d_2) + q_n b_2 \exp(i(q_{ly,2} - q_{ty,2})d_2) + q_{ty,2},$$

$$n^+_2 = -q_{ly,2} b_2 \exp(i(q_{ty,2} - q_{ly,2})d_2) + q_{ly,2} c_2 \exp(i(q_{ty,2} + q_{ly,2})d_2) + q_n,$$

$$n^-_2 = q_{ly,2} c_2 \exp(-i(q_{ty,2} + q_{ly,2})d_2) - q_{ly,2} b_2 \exp(i(q_{ly,2} - q_{ty,2})d_2) + q_n,$$

$$n^+_3 = -\alpha a_{2l} b_2 \exp(i(q_{ty,2} - q_{ly,2})d_2) + \alpha a_{2l} c_2 \exp(i(q_{ty,2} + q_{ly,2})d_2) - \alpha,$$

$$n^-_3 = \alpha a_{2l} c_2 \exp(-i(q_{ty,2} + q_{ly,2})d_2) - \alpha a_{2l} b_2 \exp(i(q_{ly,2} - q_{ty,2})d_2) - \alpha,$$

$$n^+_4 = \alpha b_2 \exp(i(q_{ty,2} - q_{ly,2})d_2) + \alpha c_2 \exp(i(q_{ty,2} + q_{ly,2})d_2) - \alpha a_{2t},$$

$$n^-_4 = \alpha c_2 \exp(-i(q_{ty,2} + q_{ly,2})d_2) + \alpha b_2 \exp(i(q_{ly,2} - q_{ty,2})d_2) - \alpha a_{2t},$$

$$m^+_1 = q_n b_1 \exp(iq_{ly,1}d_1) + q_n c_1 \exp(-iq_{ly,1}d_1) + q_{ty,1} \exp(iq_{ty,1}d_1),$$

$$m^-_1 = q_n c_1 \exp(iq_{ly,1}d_1) + q_n b_1 \exp(-iq_{ly,1}d_1) + q_{ty,1} \exp(-iq_{ty,1}d_1),$$

$$m^+_2 = q_{ly,1} b_1 \exp(iq_{ly,1}d_1) - q_{ly,1} c_1 \exp(-iq_{ly,1}d_1) - q_n \exp(iq_{ty,1}d_1),$$

$$m^-_2 = -q_{ly,1} c_1 \exp(iq_{ly,1}d_1) + q_{ly,1} b_1 \exp(-iq_{ly,1}d_1) - q_n \exp(-iq_{ty,1}d_1),$$

$$m^+_3 = a_{1l} b_1 \exp(iq_{ly,1}d_1) - a_{1l} c_1 \exp(-iq_{ly,1}d_1) + \exp(iq_{ty,1}d_1),$$

$$m^-_3 = -a_{1l} c_1 \exp(iq_{ly,1}d_1) + a_{1l} b_1 \exp(-iq_{ly,1}d_1) + \exp(-iq_{ty,1}d_1),$$

$$m^+_4 = b_1 \exp(iq_{ly,1}d_1) + c_1 \exp(-iq_{ly,1}d_1) - a_{1t} \exp(iq_{ty,1}d_1),$$

$$m^-_4 = c_1 \exp(iq_{ly,1}d_1) + b_1 \exp(-iq_{ly,1}d_1) - a_{1t} \exp(-iq_{ty,1}d_1), \quad b_1 = (a_{1t}a_{1l} - 1)/(2a_{1l}),$$

$$b_2 = (a_{2t}a_{2l} - 1)/(2a_{2l}), \quad c_1 = (a_{1t}a_{1l} + 1)/(2a_{1l}),$$

$$c_2 = (a_{2t}a_{2l} + 1)/(2a_{2l}),$$

$$\alpha = \mu_2(q^2_{t,2} - 2q^2_n)/(\mu_1(q^2_t - 2q^2_n)),$$

$$a_{1t} = 2q_n q_{ty,1}/(q^2_t - 2q^2_n),$$

$a_{2t} = 2q_n q_{ty,2}/(q^2_{t,2} - 2q^2_n)$, $a_{1l} = 2q_n q_{ly,1}/(q^2_t - 2q^2_n)$, $a_{2l} = 2q_n q_{ly,2}/(q^2_{t,2} - 2q^2_n)$, and μ_1 and μ_2 are Lame coefficients of the first and second layers, respectively.

All unknown coefficients can be connected to the coefficient A^+_{1t} by the following expressions:

$$A^-_{1t} = \chi A^+_{1t}, \tag{A6}$$

$$A^+_{1l} = (b_1 - c_1\chi)A^+_{1t}, \tag{A7}$$

$$A_{1l}^{-} = (c_1 - b_1\chi)A_{1t}^{+}, \tag{A8}$$

$$A_{2t}^{+} = \varphi A_{1t}^{+} \exp(-iq_{ty,2}d_1), \tag{A9}$$

$$A_{2t}^{-} = \xi A_{1t}^{+} \exp(iq_{ty,2}d_1), \tag{A10}$$

$$A_{2l}^{+} = \exp(-iq_{ly,2}d)(b_2\varphi \exp(iq_{ty,2}d_2) - c_2\xi \exp(-iq_{ty,2}d_2))A_{1t}^{+}, \tag{A11}$$

$$A_{2l}^{-} = \exp(iq_{ly,2}d)(c_2\varphi \exp(iq_{ty,2}d_2) - b_2\xi \exp(-iq_{ty,2}d_2))A_{1t}^{+}. \tag{A12}$$

Here $\xi = (n_1^{+}\varphi + m_1^{-}\chi - m_1^{+})/n_1^{-}$,

$$\chi = \frac{(f_2^{+}(n_2^{+} + n_1^{+}n_2^{-}/n_1^{-}) + \beta_2(m_2^{+} - m_1^{+}n_2^{-}/n_1^{-}))}{(f_2^{-}(n_2^{+} + n_1^{+}n_2^{-}/n_1^{-}) - \beta_2(m_2^{-} + m_1^{-}n_2^{-}/n_1^{-}))},$$

$$\varphi = \frac{m_1^{+}n_2^{-}/n_1^{-} - m_2^{+} - (m_2^{-} + m_1^{-}n_2^{-}/n_1^{-})\chi}{n_2^{+} + n_1^{+}n_2^{-}/n_1^{-}}.$$

Substituting (A6)–(A12) into (A1)–(A4), the displacement fields for Lamb modes in the composite plate are found.

[1] B. A. Auld and M. Tan, "Symmetrical Lamb wave scattering at a symmetrical pair of thin slots," Ultrasonic Symp. Proc. (1977), pp. 61–66.

[2] M. Tan and B. A. Auld, "Normal mode variational method for two and three dimensional acoustic scattering in an isotropic plate," Ultrasonic Symp. Proc. (1980), pp. 857–861.

[3] S. Rokhlin, "Interaction of Lamb waves with elongated delaminations in thin sheets," Int. Adv. Nondestr. Test. **6**, 263–285 (1979).

[4] S. Rokhlin, "Diffraction of Lamb waves by a finite crack in an elastic layer," J. Acoust. Soc. Am. **67**, 1157–1165 (1980).

[5] S. Rokhlin, "Resonant phenomena of Lamb waves scattering by a finite crack in a solid layer," J. Acoust. Soc. Am. **69**, 922–928 (1981).

[6] L. Wang and J. Shen, "Scattering of elastic waves by a crack in an isotropic plate," Ultrasonics **35**(6), 451–457 (1997).

[7] M. Castaings, E. Le Clezio, and B. Hosten, "Modal decomposition method for modeling the interaction of Lamb waves with cracks," J. Acoust. Soc. Am. **112**, 2567–2582 (2002).

[8] M. J. Love, P. Cawley, J.-Y. Kao, and O. Diligent, "The low frequency reflection characteristics of the fundamental antisymmetric Lamb wave a_0 from a rectangular notch in a plate," J. Acoust. Soc. Am. **112**, 2612–2622 (2002).

[9] J. Vandeputte, O. Leroy, R. Briers, and G. Shkerdin, "Influence of planar cracks on reflected and transmitted fields of gaussian acoustic beams," J. Acoust. Soc. Am. **114**, 634–643 (2003).

[10] G. Shkerdin and C. Glorieux, "Lamb mode conversion in a plate with a delamination," J. Acoust. Soc. Am. **116**, 2089–2100 (2004).

[11] M. J. S. Lowe, R. E. Challis, and C. W. Chan, "The transmission of Lamb waves across adhesively bonded lap joints," J. Acoust. Soc. Am. **107**, 1333–1345 (2000).

[12] F. Simonetti, "Lamb wave propagation in elastic plates coated with viscoelastic materials," J. Acoust. Soc. Am. **115**, 2041–2053 (2004).

[13] C. W. Chan and P. Cawley, "Lamb waves in highly attenuative plastic plates," J. Acoust. Soc. Am. **104**, 874–881 (1998).

[14] B. A. Auld, *Acoustic Fields and Waves in Solids* (Wiley, New York, 1973).

[15] W. Flüge, *Viscoelasticity*, 2nd ed. (Springer-Verlag, Berlin, 1975).

[16] J. D. Ferry, *Viscoelastic Properties of Polymers* (Wiley, New York, 1980).

[17] R. M. Christensen, *Theory of Viscoelasticity: An Introduction* (Academic, New York, 1971).

[18] B. A. Auld, *Acoustic Fields and Waves in Solids* (Krieger, Malabar, FL, 1990), Vol. 1.

Simulation of a traveling-wave thermoacoustic engine using computational fluid dynamics

J. A. Lycklama à Nijeholt
Nuclear Research & Consultancy Group, P.O. Box 1, 1755 ZG Petten, The Netherlands

M. E. H. Tijani
Energy Research Centre of the Netherlands, P.O. Box 1, 1755 ZG Petten, The Netherlands and Department of Applied Physics, Eindhoven University of Technology, P.O. Box 513, 5600 MB Eindhoven, The Netherlands

S. Spoelstra[a)]
Energy Research Centre of the Netherlands, P.O. Box 1, 1755 ZG Petten, The Netherlands

(Received 16 December 2004; revised 3 June 2005; accepted 21 July 2005)

A two-dimensional computational fluid dynamics (CFD) simulation study of a traveling-wave thermoacoustic engine is presented. The computations show an increase of the dynamic pressure when a linear temperature difference is applied across the regenerator. An amplification of the acoustic power through the engine is also illustrated. A satisfactory agreement between the calculated and expected gains of the traveling-wave thermoacoustic engine is obtained. The expected gain is defined as the ratio of the absolute temperatures at the ends of the regenerator. Nonlinear phenomena that cannot be captured by existing linear theory, like streaming mass flows and vortices formation, are also visualized. It is concluded that CFD codes could be used in the future to predict and optimize thermoacoustic systems. This is an important step towards the development of nonlinear simulation tools for the high-amplitude thermoacoustic systems that are needed for practical use. [DOI: 10.1121/1.2035567]

PACS number(s): 43.35.Ud [RR] Pages: 2265–2270

I. INTRODUCTION

During the past two decades significant progress has been made in the development of thermoacoustic systems. A number of thermoacoustic standing-wave engines and coolers have been built.[1–6] The thermal efficiency of these stack-based systems is limited to about 20%. This is due in part to the intrinsic irreversibility of the heat transfer in the stack. In contrast, a reversible Stirling cycle is executed in a traveling-wave system. However, traveling-wave systems have long suffered from high viscous losses in the regenerator.[7] The combination of a standing- and traveling wave by making use of a feedback inertance parallel to the regenerator opened the way to practical traveling-wave systems.[8,9] Researchers at Los Alamos National Laboratory have constructed a thermoacoustic traveling-wave engine with high efficiency.[9] This regenerator-based engine has shown a 50% efficiency improvement over the best standing-wave counterpart. This efficiency improvement has been obtained by suppressing a number of undesirable nonlinear effects. Further improvements would be possible if nonlinear effects could be better understood. Numerical simulations and visualizations of the unsteady flow field can help in understanding these phenomena; this could lead to a more rigorous design and optimization of thermoacoustic systems.

The aim of this paper is to present a computational fluid dynamics (CFD) study of a traveling-wave thermoacoustic engine. This study forms a first step towards the application of CFD as a full numerical nonlinear three-dimensional tool for the design and prediction of the behavior of thermoacoustic engines and heat pumps. Most of the numerical calculations done to date concern standing-wave systems and are based on the linear theory of thermoacoustics developed by Rott[10,11] and implemented into design tools such as DELTAE.[12] At low amplitude, the linear theory gives a good understanding of the physical phenomena involved and can be used to predict the behavior of thermoacoustic systems. However, thermoacoustic systems developed for practical use operate at high amplitude. At such conditions nonlinear effects, like turbulence, vortices, and streaming, will be present and the actual behavior will deviate from the linear theory. In this case the full nonlinear Navier–Stokes equations have to be considered. In the past some nonlinear models have been developed to simulate flows in the resonator, and around the stack, and to simulate nonlinear phenomena like streaming in stack-based systems.[13–15] To our knowledge, these are the first CFD results to be presented for a complete system containing an active, acoustic-power-producing, thermoacoustic element.

In the present work a commercially available CFD code[16] has been used. In this so-called structured CFD code, the engine is spatially discretized into a large number of hexahedral computational cells, and the governing unsteady Navier–Stokes equations and the equation for the total enthalpy are solved by the CFD code. The results of the computations show the onset of self-oscillations accompanied by an increase of the dynamic pressure. Amplification of the

[a)]Electronic mail: spoelstra@ecn.nl

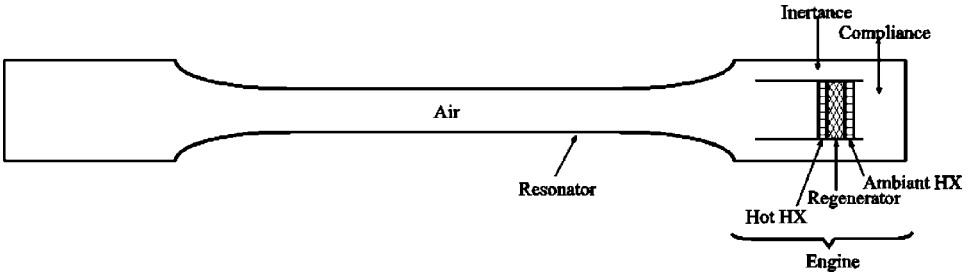

FIG. 1. Schematic view of the traveling-wave thermoacoustic engine.

acoustic power through the regenerator is also shown. Nonlinear phenomena like streaming mass flows and vortices formation are also visualized.

In Sec. II, the CFD model for the thermoacoustic traveling-wave engine is described. Special attention is given to the CFD submodel for the regenerator and heat exchangers. Section III presents the computational results. Finally, in Sec. IV some conclusions are drawn.

II. CFD MODEL

In this section the construction of the CFD model for the thermoacoustic engine is described. The geometry and boundary conditions used for the engine are also presented. ANSYS's computational fluid dynamics code CFX 4.4 is used to run all simulations. All computations are performed using a single CPU on a Linux cluster. Roughly 1 day on a single Pentium 4 processor is needed to run the simulation for the traveling-wave thermoacoustic engine.

Fixed time stepping with the Cranck–Nicolson central differencing scheme has been used for the time integration. An upwind differencing scheme has been used for the spatial discretization. Upwind differencing was needed to numerically stabilize the flow near the porous region of the regenerator. Test calculations have shown that the artificial acoustic losses associated with the application of the upwind scheme are rather small. Numerical tests revealed that, in particular, first-order time differencing caused large artificial acoustic losses. Using the second-order Cranck–Nicolson scheme diminishes these losses. The numerical tests showed that application of the first-order upwind differencing scheme resulted in a small increase in the acoustic losses compared to a second-order spatial differencing scheme. This increase was small compared to the difference between first- and second-order time differencing. The SIMPLEC algorithm has been used for updating pressure and correcting the velocity components for continuity.

A. Numerical model for the traveling-wave thermoacoustic engine

This subsection describes the modeled geometries for the three components, namely the resonator, the engine, and the regenerator and heat exchangers.

1. Resonator

Figure 1 shows a schematic illustration of the thermoacoustic system that has been modeled in the CFD computations. The system is composed of a traveling-wave thermoacoustic engine placed in a double-Helmholtz resonator. In order to simplify the modeling and to save computational time, a system without acoustic load has been considered. This results in very low damping of the acoustic wave. An axisymmetric grid has been applied for the modeling of the system. The resonator is filled with air at an average pressure of 1 bar and at 300 K initially. The 2D mesh is relatively small and consists of only 3462 computational cells for the total system in order to achieve a reasonable computational time.

2. Engine

Figure 2 shows the geometrical dimensions and the mesh of the engine part of the model. The engine consists of an ambient (300 K) and hot (500 K) heat exchanger (HX) with the regenerator placed in between. The engine is placed in a tube with a length of 204 mm and a diameter of 104 mm. This tube is placed concentrically in the resonator at the right side of the system (cf. Fig. 1). The annular gap between the tube and the resonator serves as a feedback inertance connected to the compliance at the right side of the engine. Porous metallic structures are used for both the heat exchangers and the regenerator.

3. Regenerator and heat exchangers

A CFD submodel for the regenerator and the heat exchangers has been developed. This submodel accounts for the flow resistance of the air in the porous metal structure and the thermal interaction between this structure and the air. The very detailed structure in the regenerator and in the heat exchangers is not geometrically modeled. Instead, a porous region is defined in which body forces account for the flow resistance of air in the porous metallic structure. Volume porosity is prescribed in this region to account for the reduction of the flow area in the heat exchangers and the regenerator; see Table I.

a. Flow resistance. The flow resistance is implemented as a function of the local air velocity in the heat exchangers and regenerator. This implementation is realized by means of body forces at the location of the regenerator and heat ex-

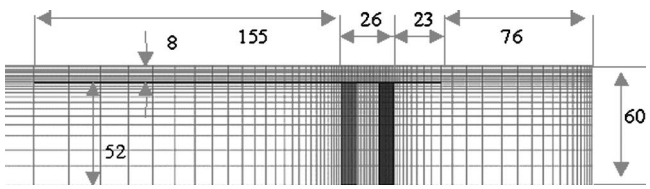

FIG. 2. Geometrical dimensions and computation mesh of the traveling-wave thermoacoustic engine. The dimensions are in millimeters.

TABLE I. Geometrical parameters of the heat exchangers and the regenerator.

	Porosity [%]	Hydraulic radius [μm]	Thickness [mm]
Heat exchangers	60	100	8
Regenerator	71	41	10

changers. The following one-dimensional equation is considered for the pressure gradient in the porous structure:[17]

$$\frac{dp}{dx} = \left(C_{fd} + \frac{C_{sf}}{\mathrm{Re}} \right) \frac{\rho u^2}{4 d_w}, \tag{1}$$

where C_{fd}=0.572, and C_{sf}=49.46. The Reynolds number Re is given by

$$\mathrm{Re} = \frac{\rho d_w \varepsilon u}{(1-\varepsilon)\mu}, \tag{2}$$

where ρ is the gas density, u is the gas velocity in the x direction, ε and d_w are the porosity and the wire diameter of the porous structure, respectively. The pressure drop from expression (1) is implemented in two dimensions by using the so-called body forces given by the following expressions:[16]

$$B_x = -\frac{dp}{dx} = -(R_C + R_F|\mathrm{v}|)u, \tag{3}$$

and

$$B_y = -\frac{dp}{dy} = -(R_C + R_F|\mathrm{v}|)\mathrm{v}, \tag{4}$$

where u and v are the gas velocities in the x- and y directions, respectively. $|v|$ is the magnitude of the velocity. The parameters R_c and R_F are given by the expressions[17]

$$R_c = \frac{C_{sf}\mu(1-\varepsilon)}{4 d_w^2 \varepsilon}, \tag{5}$$

and

$$R_F = \frac{\rho C_{fd}}{4 d_w}. \tag{6}$$

Expressions (5) and (6) apply in a Cartesian as well as in a cylindrical coordinate system.

b. Thermal model. The CFD model for the thermal interaction between the porous structure and the air is based on the following idealized assumptions:

(i) Perfect thermal contact between the porous metallic structure and the gas. The thermal penetration depth at the prevailing conditions at the ambient side of the regenerator and at the prevailing frequency amounts to about 350 μm. This distance is a factor of 8 more than the hydraulic radius of the regenerator (cf. Table I). The perfect thermal contact assumption (infinite heat transfer) therefore seems justified.
(ii) Very large heat capacity of the metallic structure. The heat capacity of any real regenerator will be much larger than air at 1 bar and the prevailing temperature conditions, so this assumption also seems justified.

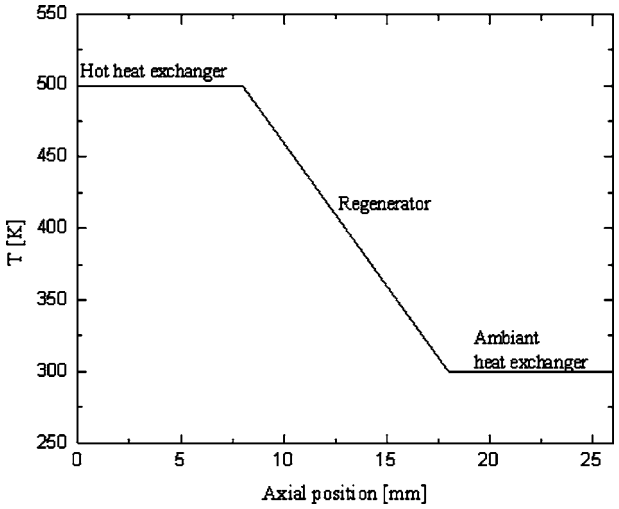

FIG. 3. Prescribed temperature profile in the regenerator and the heat exchangers.

(iii) A linear temperature profile is assumed in the regenerator by means of two heat exchangers as shown in Fig. 3.
(iv) No heat conduction through the metal structure of the regenerator. In reality, there will be a heat leakage through the regenerator from the hot to the ambient side. This heat does not participate in the thermoacoustic process. However, in a real regenerator this heat loss should be much less than 10% of the total heat. For the purpose of this study, it seems justified to neglect this heat loss.

A temperature profile T_s as shown in Fig. 3 is assumed for the heat exchangers, regenerator material, and the air inside these structures. The air inside the porous metallic structures is forced to adapt to this prescribed temperate profile. This is achieved by means of time-dependent heat sources in the enthalpy equation for air. The source is active in each grid cell located in the heat exchangers and regenerator regions. The heat source has the following form:

$$S_H = -\alpha(T_g - T_s), \tag{7}$$

where α is the heat transfer coefficient, T_g and T_s are the gas and solid matrix temperatures, respectively.

B. CFD model parameters

The following CFD modeling conditions are used for the computations:

(i) Time-dependent flow;
(ii) Axisymmetric flow;
(iii) Laminar compressible air flow;
(iv) Ideal-gas approximation;
(v) Constant material properties;
(vi) Nonbuoyant flow;
(vii) Air heat conduction and convection; and
(viii) Porous region for heat exchanger and regenerator.

The unsteady Navier–Stokes equations and the equation for total enthalpy are solved by the CFD code. The flow

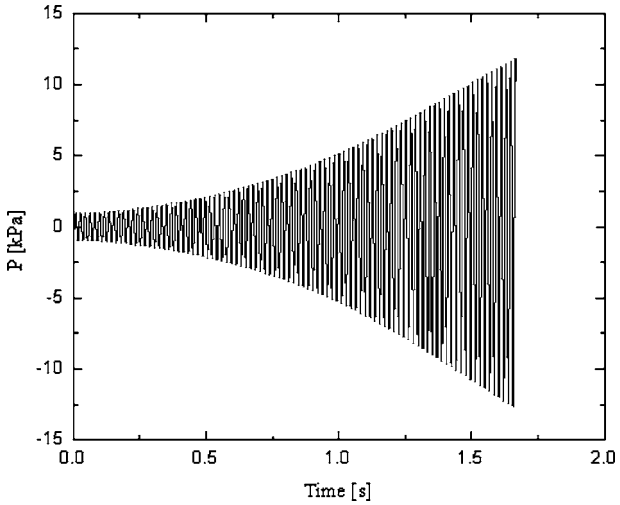

FIG. 4. Onset of oscillations for the traveling-wave thermoacoustic engine.

oscillations at a frequency of 56 Hz are solved with fixed time steps of $1.7 \cdot 10^{-4}$ s, resulting in 107 time integration points per oscillation period. Initially, at low-pressure amplitudes, the flow is laminar in the system. However, at high-pressure amplitudes the flow velocities at the pressure node in the resonator and in the feedback inertance will become turbulent, with Reynolds numbers exceeding 2300. In this first study, no attempt has been made to predict the very complicated transition from laminar to turbulent flow. Therefore, the flow has been approximated as being laminar during the whole transient.

C. Initial and boundary conditions

At $t=0$, a small pressure and temperature perturbation is present in the system. The initial perturbation is prescribed according to a standing wave with temporary zero velocity in the whole system and $\frac{1}{2}$-wavelength sine-shaped axial profiles for temperature and pressure.

The tube containing the regenerator is modeled as a cylindrical surface (tube with zero thickness) with no heat conduction. All other walls are also assumed to be adiabatic. Acoustic losses are minimized in the resonator by application of a slip-boundary condition for velocity. All other walls including the regenerator inner tube are treated as no-slip walls for velocity.

The calculation is stopped at the moment that the pressure amplitude exceeds 10 kPa. No attempt has been made to reach stationary conditions, since this would require too much computational time for the present model.

D. Postprocessing

The local acoustic power density P_{ac} is calculated from the CFD results for each computational cell according to the equation

$$P_{ac} = \frac{\sum_i p_i u_i}{N}. \tag{8}$$

In this equation the product of dynamic pressure p and axial velocity u is averaged over all time steps i during one cycle.

TABLE II. Time-averaged acoustic power in the axial direction at the ambient and hot side of the regenerator and their ratio (gain) at 10-kPa pressure amplitude.

Cross-section regenerator	Acoustic power (watt)	Gain
Ambient side	38.5	1.5
Hot side	57.7	

Positive values of the acoustic power correspond with transport of acoustic energy to the right side in Fig. 1.

The local time-averaged acoustic power P_{ac} according to Eq. (8) has been integrated at two cross sections to obtain the net acoustic power at these cross sections (P_{cross})

$$P_{cross} = \int_{A_{cross}} P_{ac}\, dA. \tag{9}$$

The same procedure as for the local acoustic power is applied to obtain time-averaged mass flux and time-averaged temperature distributions.

III. RESULTS AND DISCUSSION

The results of the calculations are discussed in two parts. The first part deals with the acoustic results like pressure amplitude, local acoustic power, and phase differences between gas velocity and dynamic pressure. The second part concerns nonlinear and multidimensional effects like flow fields, resulting vortices, and streaming.

A. Acoustic results

Figure 4 shows the development with time of the pressure at the antinode position as predicted by the CFD modeling. A strong increase of the pressure amplitude is predicted. The pressure increases up to 10 kPa (10% drive ratio) in only 1.5 s. Eventually, this increase in pressure amplitude will continue until the acoustic power generated by the engine is balanced by the dissipation within the resonator. Since there is very little damping in the system, this process will lead to very high pressure amplitudes.

The acoustic power is calculated at two cross sections and integrated with time over one period. One cross section is located at the right side of the ambient heat exchanger and the other cross section at the left side of the hot heat exchanger. The resulting acoustic power and gain can be found in Table II. The calculated gain of 1.5 is somewhat below the expected amplification factor of 1.67 due to acoustic losses in the regenerator. The expected amplification factor is defined as the ratio of the absolute temperatures at the ends of the regenerator.[7,9]

A detailed plot of the space distribution of acoustic power (time averaged for one period) in the engine is shown

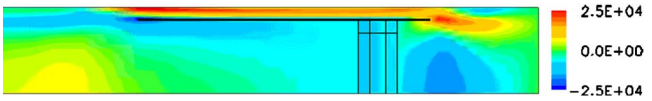

FIG. 5. (Color online) Time-averaged acoustic power density (W/m^2) in the axial direction at 10-kPa pressure amplitude.

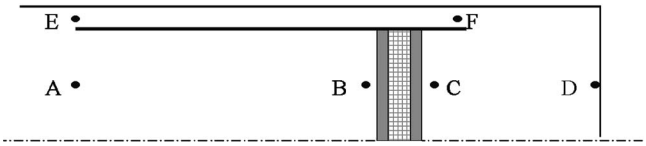

FIG. 6. Phase difference monitoring positions around the engine.

in Fig. 5. Positive values correspond with transport of acoustic energy to the right side. This figure shows that acoustic power is transported to the right side via the feedback inertance, and back to the left side through the heat exchangers and regenerator. Some of the phenomena observed in this figure can be understood by looking at the velocity fields, which are described in the next section.

Figure 6 defines six positions at which the phase difference between velocity and pressure is calculated from the CFD results. The calculated phase differences are given in Table III.

In an optimized traveling-wave thermoacoustic engine, conditions are established in the regenerator corresponding to a local phase shift of 0 or 180 deg (depending on the direction of the acoustic power). In the present system, a 180-deg phase difference between velocity and pressure would be optimal. A value between 146 and 160 deg across the regenerator is found from the present CFD results. This phase difference can be optimized by tuning the parameters of the acoustic network consisting of the feedback inertance, the compliance, and the flow resistance of the regenerator.

B. Multidimensional and nonlinear results

The calculated flow profile is shown in Fig. 7. The time period between each figure is $\frac{1}{4}$ of a full cycle and the figure at the top is taken at a maximum positive pressure at the engine side of the system. Note that not all grid points are used for the vector plots. The spatial resolution of the grid exceeds the spatial resolution of the vectors.

As can be seen from Fig. 7, the flow is strongly nonlinear. During the whole period a vortex can be observed in the compliance at the right side. This vortex shifts somewhat in position; also, the vortex's magnitude fluctuates during the period. In the first and third vector plots a vortex has also temporarily developed at the left side of the feedback inertance. These vortices are believed to be driven by the jet coming out of the feedback inertance, where velocities are rather high (on the order of 15 m/s). The vortex that is created in the thermal buffer tube leads to a strong two-dimensional temperature distribution of the air. The thermal buffer tube is the part of the tube containing the regenerator to the left of the hot heat exchanger in Fig. 1. Figure 8 shows the time-averaged gas temperature around the engine. Clearly visible is the convection of heat driven by the vortex.

TABLE III. Phase difference between velocity and pressure at the positions defined in Fig. 8.

Position	Phase difference (°)
A-End of thermal buffer Tube	121
B-Hot heat exchanger	146
C-Ambient heat exchanger	160
D-Compliance	118
E-Feedback inertance left side	94
F-Feedback inertance right side	96

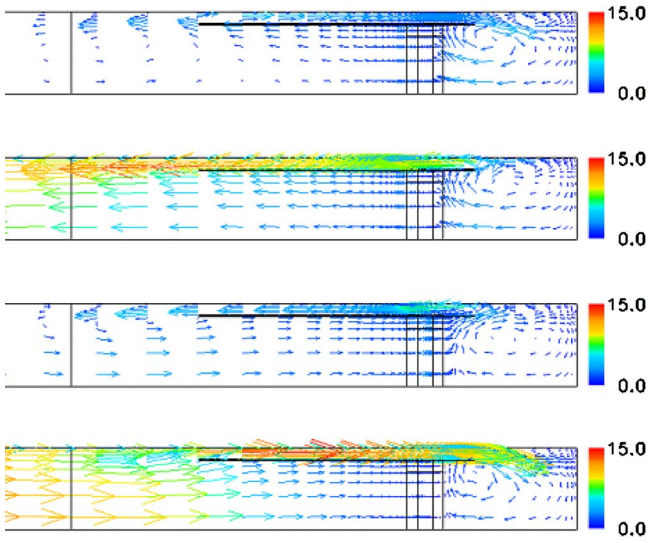

FIG. 7. (Color online) Velocity fields (m/s) in the engine at 10-kPa pressure amplitude.

One known nonlinear phenomenon in traveling-wave thermoacoustic systems is Gedeon or dc streaming.[18] This effect is due to a time-averaged pressure difference across the regenerator, resulting in a mass flow circulating from the hot side of the regenerator through the feedback inertance to the ambient side of the regenerator. In order to identify this phenomenon, the time-averaged air mass flow rate in the axial direction is calculated at 10-kPa pressure amplitude and presented in Fig. 9. This figure is somewhat hard to interpret, partly due to the fact that the system is not stationary. Also, the fact that the largest part of the area is located on the outer part of the cylinder makes it hard to get an impression of the total mass flow from the local mass fluxes. When the mass flow rate is integrated over the cross section, it turns out that there is a net negative flow (to the left side) within the thermal buffer tube and a net positive flow (to the right side) within the feedback inertance. Thus, dc streaming is indeed occurring.

IV. CONCLUSIONS

The main purpose of the study presented is to find out whether a commercially available CFD code is able to model a thermoacoustic system. Both the oscillatory flow behavior and the interaction between the sound wave and the porous structure are taken into account. This paper clearly shows that this can indeed be done by the code used. Although the model used is an idealization of the real situation, the phe-

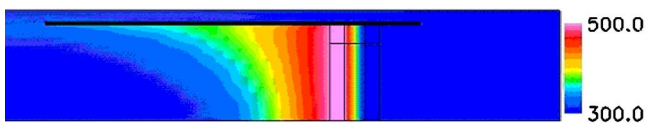

FIG. 8. (Color online) Time-averaged temperature distribution at 10-kPa pressure amplitude.

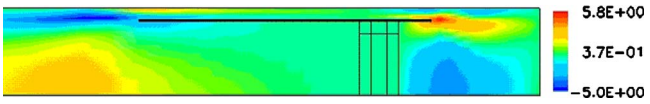

FIG. 9. (Color online) Time-averaged air mass flow rate ($kg/m^2\,s$) in the axial direction at 10-kPa pressure amplitude.

nomena observed correspond to a great extent to the expectations. The agreement between the calculated and expected gains of the traveling-wave thermoacoustic engine strengthens confidence in the computational results.

The CFD results clearly show strong nonlinear effects at high pressure amplitudes. Both dc streaming and jet-driven streaming are visualized. The jet-driven streaming results in vortices that lead to unwanted heat convection.

We think that CFD may prove to be a useful tool in the study of thermoacoustic phenomena that cannot be captured by today's one-dimensional linear codes. In the near future, the present CFD model will be extended to include temperature-dependent material properties, finite heat transfer in the regenerator and the heat exchangers, losses in the resonator, and the effect of gravity. In addition, higher average pressures and different working media will be used. And, last but not least, the CFD model should be validated against experimental data to obtain a design tool for a real thermoacoustic system.

[1]T. J. Hofler, "Thermoacoustic refrigerator design and performance," Ph.D. thesis, Physics Department, University of California, San Diego, 1986.
[2]S. L. Garrett, J. A. Adeff, and T. J. Hofler, "Thermoacoustic refrigerator for space applications," J. Thermophys. Heat Transfer **7**, 595–599 (1993).
[3]M. E. H. Tijani, "Loudspeaker-driven thermo-acoustic refrigeration," Ph.D. thesis, Department of Applied Physics, Eindhoven University of Technology, 2001.
[4]M. E. H. Tijani, J. C. H. Zeegers, and A. T. A. M. de Waele, "Design of thermoacoustic refrigerators," Cryogenics **42**, 49–57 (2002).
[5]M. E. H. Tijani, J. C. H. Zeegers, and A. T. A. M. de Waele, "Construction and performance of a thermoacoustic refrigerator," Cryogenics **42**, 59–66 (2002).
[6]W. Swift, "Analysis and performance of a large thermoacoustic engine," J. Acoust. Soc. Am. **92**, 1551–1563 (1992).
[7]P. H. Ceperley, "A pistonless Stirling engine—the traveling wave heat engine," J. Acoust. Soc. Am. **66**, 1508–1513 (1979).
[8]T. Yazaki, A. Iwata, T. Maekawa, and A. Tominaga, "Traveling wave thermoacoustic engine in a looped tube," Phys. Rev. Lett. **81**, 3128–3131 (1998).
[9]S. Backhaus and G. W. Swift, "A thermoacoustic-Stirling heat engine: Detailed study," J. Acoust. Soc. Am. **107**, 3148–3166 (2000).
[10]N. Rott, "Damped and thermally driver acoustic oscillations in wide and narrow tubes," Z. Angew. Math. Phys. **20**, 230–243 (1969).
[11]N. Rott, "Thermally driven acoustic oscillations. II. Stability limit for helium," Z. Angew. Math. Phys. **24**, 54–72 (1973); N. Rott, "Thermally driven acoustic oscillations. III. Second-order heat flux," *ibid.* **26**, 43–49 (1975).
[12]W. C. Ward and G. W. Swift, "Design environment for low amplitude thermoacoustic engines," J. Acoust. Soc. Am. **96**, 3671–3672 (1994).
[13]A. S. Worlikar and O. M. Knio, "Numerical study of oscillatory flow and heat transfer in a loaded thermoacoustic stack," Numer. Heat Transfer, Part A **35**, 49–65 (1999).
[14]M. F. Hamilton, Y. A. Ilinskii, and E. A. Zabolotskaya, "Nonlinear two-dimensional model for thermoacoustic engines," J. Acoust. Soc. Am. **111**, 2076–2086 (2002).
[15]P. Blanc-Benon, E. Besnoin, and O. M. Knio, "Experimental and computational visualization of the flow field in a thermoacoustic stack," C. R. Mec. **331**, 17–24 (2003).
[16]*CFX4.4 User Guide*, Computational Fluid Dynamics Services (AEA Technology, Harwell Laboratory, Oxfordshire OX11 0RA, United Kindom, 2001).
[17]B. Thomas and D. Pittman, in *Update on the evaluation of different correlations for the flow friction factor and heat transfer of Stirling engine regenerators*, Proceedings of the 35th Intersociety Energy Conversion Engineering Conference and Exhibit, Las Vegas, NV (AIAA, 2000).
[18]D. Gedeon, in *DC gas flows in Stirling and pulse tube cryocoolers*, Proceedings of the 9th International Cryocooler Conference, edited by R. G. Ross (Plenum, New York, 1997), pp. 385–392.

Characterizing heat transfer coefficients for heat exchangers in standing wave thermoacoustic coolers

Insu Paek, James E. Braun, and Luc Mongeau
Ray W. Herrick Laboratories, School of Mechanical Engineering, Purdue University, 140 S. Intramural Drive, West Lafayette, Indiana 47907

(Received 24 July 2003; revised 11 July 2005; accepted 11 July 2005)

The thermal performance of heat exchangers within a thermoacoustic cooler was investigated. Experimental procedures and calculation methods to evaluate the oscillating flow heat transfer coefficients were developed. Dimensionless heat transfer coefficients, or Colburn-*j* factors, were estimated based on the oscillating-flow variables and compared with results from steady-flow measurements. The results were also compared with heat transfer coefficients predicted from a boundary-layer conduction model, and methods that utilize steady-flow correlations with Reynolds numbers that characterize oscillating flow conditions. Although the boundary layer model is commonly employed for thermoacoustic calculations, it did not accurately predict heat transfer coefficients and the influence of Reynolds number on heat transfer performance. However, accurate predictions were obtained using a steady-flow correlation and a modified Reynolds number that accounts for the oscillating flow field, assuming a half-cycle Reynolds number correction value of 0.109. © *2005 Acoustical Society of America.* [DOI: 10.1121/1.2019425]

PACS number(s): 43.35.Ud, 43.35.Ty [RR] Pages: 2271–2280

I. INTRODUCTION

In standing-wave thermoacoustic coolers, heat transfer occurs between gas particles within high-amplitude acoustic standing waves and heat exchangers immersed into the working gas. Dynamic pressure, velocity, and temperature changes in the acoustic standing wave cause a net flow of heat up a mean temperature gradient along the direction of sound wave propagation.[1] Analytical or semiempirical models are needed to predict the gas-side net heat transfer in and out of the hot and cold heat exchangers, usually located at each end of the stack.

Most heat transfer models for oscillating flows assume steady-flow conditions in the primary (gas-side) working fluid. Garrett *et al.*[2] showed that an acoustic heat transfer coefficient derived from a conduction heat transfer model between gas particles and heat exchanger could be used for the preliminary design. They also suggested that the root-mean-square value of the heat transfer coefficient obtained from the conduction model could be indicative of the heat transfer in an oscillating acoustic flow.

Mozurkewich[3] measured heat transfer from heated wires located at a velocity antinode in a standing acoustic wave. The Nusselt number was accurately predicted using a steady-flow, forced-convection correlation based on an acoustic Reynolds number for high Reynolds numbers, in conjunction with a natural-convection model for low Reynolds numbers. More recently, Mozurkewich performed experiments within a quarter-wavelength modular thermoacoustic refrigerator using aluminum heat exchangers with simple geometries.[4] In this study, a correlation based on the Zukauskas[5] single-tube steady cross-flow correlation was developed based on the so-called time-averaged steady-flow equivalent (TASFE) approximation.[6] Methods based on the TASFE approximation involve averaging the steady-flow correlation over one cycle of the presumably sinusoidal particle displacement to evaluate the heat transfer in the oscillating flow. The TASFE approximation was reported to be accurate for simple-tube heat exchangers placed near the velocity node.

Poese and Garrett[7] assumed that the time-averaged value of the convective heat transfer coefficient was relevant to characterize heat transfer in oscillating flows, and proposed a modified laminar correlation. The modified correlation was obtained by averaging a laminar parallel-flow correlation for flow over a flat plate during one-half of the period. Swift[1] suggested that the substitution of a root-mean-square (rms) Reynolds number into published steady-flow correlations could be used to predict the heat transfer coefficient in oscillating flow.

There have been other noteworthy contributions to thermoacoustic heat transfer. Wetzel and Herman[8,9] visualized the time-dependent temperature profile around a single plate in oscillating flow using holographic interferometry and estimated a local heat transfer coefficient. Brewster *et al.*[10] studied the effects of heat transfer between the elements in a thermoacoustic system. They assumed a perfect thermal contact between the gas and the solid in the stack and also in the heat exchanger, and derived a heat transfer coefficient between the stack and the heat exchanger based on the longitudinal enthalpy flow.

Mozurkewich appears to be the only researcher to experimentally evaluate heat transfer coefficients for thermoacoustic applications and to evaluate the accuracy of the TASFE assumption. However, the geometries considered by Mozurkewich were not representative of heat exchangers that would be employed in actual applications (i.e., fin tube heat exchangers). Furthermore, the measurements were not performed within a thermoacoustic device and, as such, did not consider interactions between the heat exchangers and the stack material.

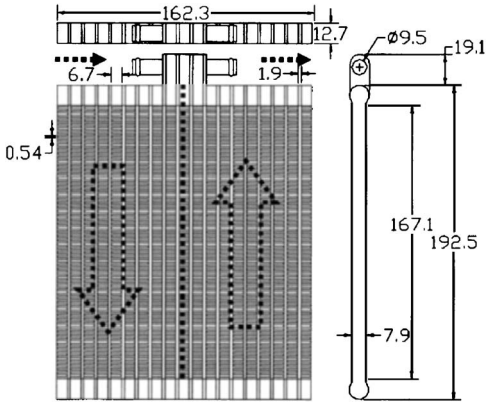

FIG. 1. Schematic of the heat exchanger (dimensions in millimeters).

Heat exchangers are widely considered to be a bottleneck to better performance within thermoacoustic coolers. As a result, it is important to have accurate models that can be used to investigate the impact of heat exchanger selection on overall thermoacoustic system performance. The goal of the study presented in this paper was to evaluate different approaches for estimating heat transfer coefficients for heat exchangers in thermoacoustic coolers, and to identify the most promising methods. In order to accomplish this goal, both steady- and oscillating-flow experiments were performed for one heat exchanger that was designed specifically for use in a thermoacoustic cooler. Procedures were established for estimating heat transfer coefficients in steady and oscillating flows from measured data, and for correlating heat transfer coefficients using dimensionless parameters. The oscillating flow heat transfer coefficients determined from the experiments were compared with predictions from different correlation models.

II. EXPERIMENTAL PROCEDURES

A heat exchanger made by the Modine manufacturing company with small primary (gas-side) fluid pore spacing and thin secondary (water-side) fluid tubing was used in this study. Figure 1 depicts the heat exchanger, and its inner liquid flow path. The heat exchanger had a standard commercial brazed aluminum construction with folded fins. Fin spacing of the heat exchanger was 0.54 mm and the tube width was 1.9 mm. The fin width was 7.9 mm, and the fins were flat and square in shape. The tubes had square leading edges. The water flow direction is shown in Fig. 1 using dotted arrows. The dotted line in the center of the heat exchanger shows the boundary between the two opposite vertical water flows. Several features distinguish this design from that of a conventional fin-tube design. First, the use of small rectangular flow channels for the secondary fluid reduces the obstruction to the flow of the primary thermoacoustic working fluid for a given tube surface area. Second, the use of the microchannel and two-pass secondary flow geometry enhances the secondary fluid heat transfer coefficients. Third, the microchannel design incorporates outer fins having a smaller depth, a tighter spacing, and a larger overall surface area.

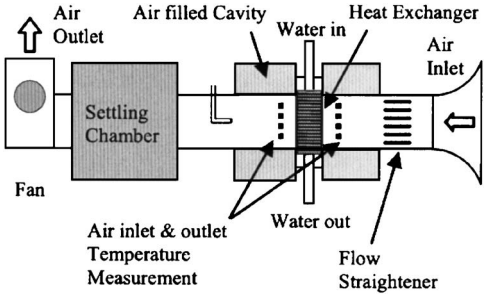

FIG. 2. Schematic of the wind tunnel used for the steady-flow measurements.

A. Steady-flow measurements in wind tunnel

A small wind tunnel was built and used to measure steady flow, steady-state, gas side heat transfer coefficients. The heat exchangers were operated with water flowing through the tubes. The wind tunnel, shown in Fig. 2, consisted of a centrifugal fan powered by an electric motor (Baldor, M3115), and a 150 mm diameter PVC pipe. A flow straightener was used to minimize inflow swirl and transverse flow motion. An inlet bell mouth and a plenum settling chamber downstream of the heat exchangers were utilized to improve the flow velocity profile uniformity across the duct. One heat exchanger with a polycarbonate housing was mounted between two sections of polyvinyl chloride pipe. The region near the heat exchanger was surrounded by air-filled cavities to reduce heat leak through the PVC pipe. A Pitot tube, in conjunction with a probe traversing mechanism and a differential capacitance manometer (MKS Instruments, Type 220), was used to measure the airflow velocity distribution across the pipe at one streamwise location. The velocity distribution was used to determine the air mass flow rate. The water flow rates through the heat exchanger were measured using an axial paddle-wheel turbine-type flow meter (JLC International, IR-Opflow Type 4) at the water outlet.

A differential temperature transducer (Delta-T Company, 75X) was used to measure the water temperature difference. At the inlet and the outlet of the wind tunnel, nine arrays of type T thermocouples were installed to measure air temperatures at the temperature measurement locations shown in Fig. 2. The rate of heat transfer was calculated from the measured flow rates and temperatures for both the air side and the water side of the heat exchanger.

B. Oscillating-flow measurements in thermoacoustic cooler

A thermoacoustic cooler prototype[11] was used for the heat transfer rate measurements in oscillating flow. A schematic of the thermoacoustic cooler is shown in Fig. 3. It is driven by a 300 W moving magnet linear actuator (CFIC, B-300) mounted on metal "leaf" springs to provide suspension stiffness. Type T thermocouples were used to perform detailed temperature measurements. It was found in a previous investigation[11] that the gas temperatures at both ends of the stack in the prototype vary in magnitude radially along the cross section of the stack. To estimate the average gas temperature at each end of the stack, four thermocouples

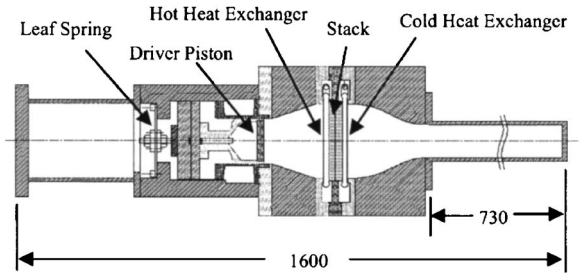

FIG. 3. Schematic of the standing wave thermoacoustic cooler (dimensions in millimeters).

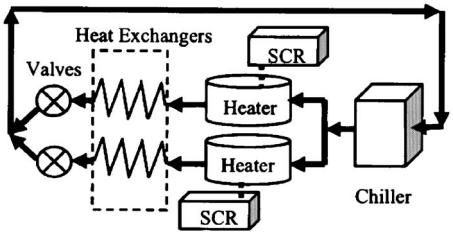

FIG. 4. Schematic of the temperature controlled closed water loop. The flow direction is indicated by the arrows.

equally spaced along the radial direction were used. The temperature values were weighted based on area. The sealed bodies of the thermocouples were carefully bonded to the heat exchangers, ensuring no contact between the sealed elements of the thermocouples and the heat exchangers. Foam tape was used to thermally insulate the heat exchangers from their housings and the surrounding environment.

An accelerometer (PCB, 353B15) was mounted on the driver piston to measure the axial wall acceleration. A dynamic pressure sensor (PCB, 102A07) was installed in a port near the piston. The dynamic pressure and velocity measured at the piston face allowed the estimation of the acoustic particle velocity within each heat exchanger using a linear acoustic model of the thermoacoustic cooler prototype. The commercially available software DELTAE was used.[12] Five target vectors were prescribed, including the spatially averaged gas temperatures at both heat exchangers, the amplitude of the oscillating pressure at the driver, the amplitude of the piston velocity, and the phase angle between the oscillating pressure at the driver and the piston velocity. The gas particle velocity at the cold-side heat exchanger was used to determine the acoustic Reynolds number, as discussed further in the next section.

The stack was made of a 76 μm thick polyester film, and a 254 μm thick nylon wire constructed by using the wire as a spacer and rolling the film into a cylinder. A differential temperature transducer (Delta-T Company, 75X) was used to measure the water temperature difference between at the inlet and at the exit of the heat exchangers. The hot-side heat exchanger was used to transfer heat outside the thermoacoustic cooler. Only the cold-side heat exchanger was used to estimate the gas-side heat transfer coefficient in oscillating flow. Water flow rates through the hot and the cold heat exchangers were about 40 and 11 ml/s, respectively. The water flow rates were chosen, based on consideration of the measurement accuracy. For the hot side, it is important to effectively transfer heat to the surrounding, and for the cold side, it is desirable to have a larger water temperature span across the heat exchanger to reduce the uncertainty of the measured heat transfer data. The water flow rates through the heat exchangers were measured using axial paddle wheel turbine-type flow meters (JLC International) at the water outlets.

To measure heat transfer rates through the heat exchangers, a closed path water loop was built. A schematic of the water loop is shown in Fig. 4. A water chiller equipped with a water pump was used to pump and cool water through the water loop. Downstream of the water chiller, the water loop was divided in two branches, each connected to an electrical water heater. The water loops from the water heaters were finally connected to the two heat exchangers. Two valves were installed downstream of the heat exchangers to control the water flow rate. Downstream of the valves, the two water loops were joined and connected to the chiller. The water loop was designed to control water flow rates and water temperatures of both the hot side and the cold side, more or less independently. The water temperature was controlled using two silicone controlled rectifier power controllers (Cristal Controls, CCPA-30-1-A-S3) by adjusting the current input to the heaters.

The heat transfer rate was estimated from an energy balance on the water stream using measured data. An Agilent C-size VXI mainframe (E8403A) with three 16-channel DSP boards (E1432A), and a 16-channel multimeter module (E1411A) with a multiplexer were used for data acquisition. The 8 acoustic and electric signals and 16 temperature signals were acquired simultaneously. The results were used to evaluate heat transfer coefficients on the gas side of the heat exchanger. One source channel was used to operate the moving magnet driver, and two other source channels were assigned to operate the SCR power controllers. "On-line" measurements of the calculated electrical power, acoustic power, heat transfer rates at the heat exchangers, driver efficiency, and coefficient of performance were available through the use of Agilent-Vee, in conjunction with MATLAB subroutines. These variables were displayed online in real time by using a data acquisition and display program.

III. ESTIMATION OF HEAT TRANSFER COEFFICIENTS

A. Steady flow

For heat transfer in steady flow, a local heat transfer coefficient is defined as the ratio of the heat transfer per unit area to the temperature difference between the surface and "bulk" fluid adjacent to the surface. However, in practice, a global heat transfer coefficient derived from a lumped analysis of the heat exchanger (UA-LMTD or effectiveness-NTU methods) is utilized.

The overall conductance (UA) of a heat exchanger operating in steady flow was estimated from experimental data using a log-mean temperature difference model. A cross-flow heat exchanger is considered in this study, with water flowing through the tubes and air flowing over the finned tubes. Therefore, the overall heat-exchanger conductance was estimated according to

$$\mathrm{UA} = \frac{\dot{Q}}{\mathrm{LMTD}_{CF}}, \tag{1}$$

where $\dot{Q}$ is the heat transfer rate determined from measurements, and LMTD_{CF} is the log-mean temperature difference, defined for a cross-flow heat exchanger as

$$\mathrm{LMTD}_{CF} = F \times \frac{(T_{h,i} - T_{c,o}) - (T_{h,o} - T_{c,i})}{\ln\left\{\dfrac{T_{h,i} - T_{c,o}}{T_{h,o} - T_{c,i}}\right\}}. \tag{2}$$

Here, $T_{h,i}$, $T_{c,i}$, $T_{h,o}$, and $T_{c,o}$ are the inlet (i) and outlet (o) temperatures of the hot (h) and cold (c) streams, and F is a correction factor for a conversion from a counterflow LMTD to a cross-flow LMTD. The correction factor, F, has been investigated for various heat exchangers.[13–15] A value of 0.98 was used as the correction factor for all the measured data presented in this paper.

The overall heat-exchanger conductance is related to local heat exchanger characteristics through a simplified model[13] as follows:

$$\mathrm{UA} = \frac{1}{\dfrac{1}{\eta_0 h_0 A_0} + R_{tw} + \dfrac{1}{h_i A_i}}, \tag{3}$$

where η is the overall fin efficiency, h is the global heat transfer coefficient, A is the surface area, and R_{tw} is the resistance of the tube wall. The subscripts o and i denote the outer (gas-side) and inner (water-side) surfaces of the microchannel heat exchanger, respectively.

The average water-side and the gas-side heat transfer coefficients, h_i, and h_0, were assumed to obey the following power laws:

$$h_i = h_{i\_a}\,\mathrm{Re}_i^{h_{i\_b}}, \tag{4}$$

and

$$h_0 = h_{o\_a}\,\mathrm{Re}^{h_{o\_b}}, \tag{5}$$

where Re_i is the water-side Reynolds number, Re is the gas-side Reynolds number, and h_{i_a}, h_{i_b}, h_{o_a}, and h_{o_b} are unknown variables. The four unknowns in Eqs. (4) and (5) were found by minimizing the sum of the square of the differences between values from Eq. (3), in conjunction with Eqs. (4) and (5) and Eq. (1).

In order to facilitate comparisons with theoretical calculations and extrapolations, the estimated gas-side heat transfer coefficients were expressed in nondimensional form as the Colburn-j factor,[14] defined as

$$j = \mathrm{St}\,\mathrm{Pr}^{2/3} = \frac{\mathrm{Nu}}{\mathrm{Re}\,\mathrm{Pr}^{1/3}}, \tag{6}$$

where St, Pr, Nu, and Re are the Stanton, Prandtl, Nusselt, and Reynolds numbers, respectively.

B. Oscillating flow

Heat transfer coefficients are typically defined for steady flow and are not strictly appropriate for oscillating flow. However, it is a very convenient representation for computing heat transfer rates and the concept can be employed by assuming that the heat transfer process occurs between the steady flow water stream and a source or sink that is at the time and spatially averaged gas temperature that is in contact with the end of the stack closest to the heat exchanger. With this assumption, the overall UA is estimated from oscillating flow measurements using

$$\mathrm{UA} = \frac{\dot{Q}}{\mathrm{LMTD}_{\mathrm{tac}}}, \tag{7}$$

where LMTD_{tac} is defined as

$$\mathrm{LMTD}_{tac} = \frac{(T_{w,o} - T_{w,i})}{\ln\left\{\dfrac{T_s - T_{w,i}}{T_s - T_{w,o}}\right\}}. \tag{8}$$

In Eq. (8), *tac* stands for thermoacoustic, $T_{w,o}$ and $T_{w,i}$ are the water outlet and inlet temperatures, and T_s is the time and spatially averaged stack-end gas temperature.

The gas-side heat transfer coefficient is estimated from the overall UA in a manner similar to that for steady flow given in Eq. (3). However, for oscillating flow the entire heat exchanger surface cannot participate in gas-side heat transfer when the peak-to-peak gas-particle displacement amplitude is smaller than the heat exchanger length in the gas flow direction. This causes an underestimation of the gas-side heat transfer coefficient, h_0, if the total heat exchanger surface area, A_0, is used when the peak-to-peak displacement is smaller than the heat exchanger length. Therefore, Eq. (3) was modified as

$$\mathrm{UA} = \frac{1}{\dfrac{1}{\eta_0 h_0 \min(A_0, A_p)} + R_{tw} + \dfrac{1}{h_i A_i}}, \tag{9}$$

where A_p is the effective gas-side heat exchanger surface area obtained by multiplying the perimeter of the heat exchanger by the peak-to-peak displacement amplitude of the particle.

For oscillating flow, the gas-side heat transfer coefficients determined from oscillating flow measurements are correlated with the acoustic Reynolds number obtained using the amplitude of the particle velocity u_1 or

$$\mathrm{Re}_1 = \frac{u_1 D_h}{\nu}, \tag{10}$$

where D_h is the hydraulic diameter, and υ is the kinematic viscosity.

Equations (7)–(9) were used to estimate the gas-side heat transfer coefficient from measured data. The heat transfer coefficient was cast into a Colburn-j factor using Eqs. (6) and (10) and then correlated in terms of the acoustic Reynolds number. It is important to note that the application of the resulting heat transfer correlation in modeling thermoacoustic heat exchangers needs to be consistent with the model used to determine the heat transfer coefficients from the data. In order words, the definition for LMTD_{tac} given in

Eq. (8) needs to be employed with the heat transfer coefficients determined using the correlation presented in this paper.

IV. EXPERIMENTAL ACCURACY

A. Steady flow

To verify the accuracy of the experimental data in steady flow, heat transfer rates were estimated using both the water-side and the air-side measured data, obtained from

$$\dot{Q}_w = \rho_w \dot{V} c_{p_w} \Delta T_w, \tag{11}$$

and

$$\dot{Q}_a = \rho_a \dot{V}_a c_{p_a} \Delta T_a, \tag{12}$$

where $\dot{Q}$ is the heat transfer rate, ρ is the density, $\dot{V}$ is the volume flow rate, c_p is the isobaric specific heat, and ΔT is the temperature difference between the inlet and outlet of the heat exchanger. The subscripts w and a denote the water-side and the air-side paths of the heat exchanger, respectively.

A thermodynamic first law imbalance ratio was then calculated using

$$\dot{Q}_{imb}(\%) = \frac{||\dot{Q}_w| - |\dot{Q}_a||}{|\dot{Q}_w|}, \tag{13}$$

and used as a figure of merit for the accuracy of the data. For all the measured data in steady flow, $\dot{Q}_{imb}$ was within 10%, and the mean value was 6.9%.

Relative uncertainties in Colburn-j factors were within 4%. Both the thermodynamic first law imbalances and the relative uncertainty values of the measured data indicated that the experiments performed in steady flow were reasonably accurate.

B. Oscillating flow

A similar thermodynamic first law imbalance ratio for oscillating flows was calculated using

$$\dot{Q}_{imb}(\%) = \frac{|\dot{W}_{ac} + |\dot{Q}| - |\dot{Q}_h||}{\dot{W}_{ac} + |\dot{Q}_c|}, \tag{14}$$

where $\dot{W}_{ac}$ is the measured acoustic power near the piston, $\dot{Q}_c$ is the heat transfer rate at the cold-side heat exchanger, and $\dot{Q}_h$ is the heat transfer rate at the hot-side heat exchanger. For all the data measured in oscillating flows, $\dot{Q}_{imb}$ was within 9%, and the mean value was 3.9%. This indicated that extraneous heat leaks were negligible compared to the heat exchanger heat fluxes of interest.

For all the measured data, the relative uncertainties in the Colburn-j factors were within 16%. Uncertainties associated with steady flow heat transfer correlations reported in basic heat transfer textbooks[13] are normally between 10% and 25%. Therefore, the uncertainty of 16% in this study was considered acceptable.

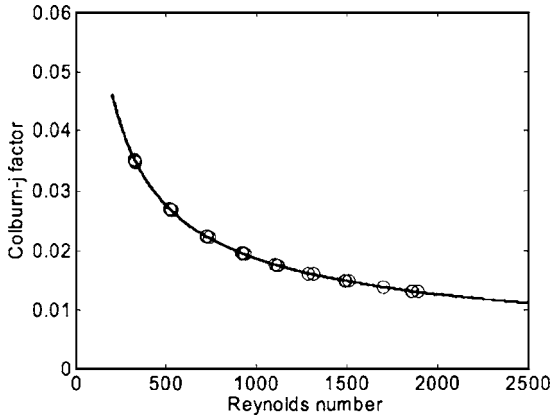

FIG. 5. Measured gas-side Colburn-j factor versus Reynolds number in steady flow. O: measured data,—: regression curve of measured data.

V. RESULTS

A. Steady flow

Here twenty eight datasets for four different water flow rates, between 11 and 25 ml/s, and 6 different air flow rates, between 0.1 and 0.2 m^3/s, were obtained. The gas-side Colburn-j factors were evaluated using Eqs. (1)–(6), and are plotted in terms of the steady-flow Reynolds number in Fig. 5. The regression model for the measured heat transfer coefficients data in steady flow was obtained numerically using a Nelder-Mead simplex method[16] and plotted in Fig. 5. The resulting semiempirical relation is

$$j_{steady} = 0.9384\ \mathrm{Re}^{-0.5673}. \tag{15}$$

The rms error of the residual in the regression was 3.2×10^{-5}.

B. Oscillating flow

For the measured oscillating flow data, the amplitudes of the peak-to-peak particle displacement range varied 2.5 to 5.3 mm and were smaller than the heat exchanger fin width, 7.9 mm. This means that gas particles having different particle displacements see different lengths of heat exchangers. Therefore, the effective heat exchanger surface area based on the amplitude of the peak-to-peak particle displacement was used to calculate the gas-side heat transfer coefficient h_0 using Eq. (9).

Figure 6 shows the gas-side Colburn-j factors determined from measurements in oscillating flow. To broaden the range of acoustic Reynolds numbers covered, three helium and argon mixtures (44% He, 33% He, 22% He) with three different mean pressures (2 MPa, 1.33 MPa and 0.67 MPa) were used. Various thermophysical properties of the measured data points are listed in Table I. For all the 22 data points, the thermoacoustic cooler was operated near the acoustic resonance frequency of the resonator. The phase angle between pressure and velocity at the driver was between −7° and +9°.

The solid line in Fig. 6 is the regression obtained for the measured data. The resulting correlation yields the expression

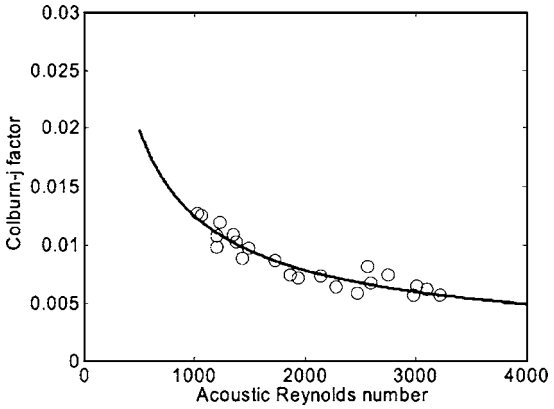

FIG. 6. Measured gas-side Colburn-j factor versus acoustic Reynolds number in oscillating flow. O: measured data,—: regression curve of measured data.

$$j_{oscillating} = 1.3030\,\mathrm{Re}_1^{-0.6729}. \tag{16}$$

The rms error of the residual in the regression was 7.1×10^{-4}.

C. Comparison with other models

Comparisons were made with predictions from a time-average steady-flow equivalent model (TASFE), a rms Reynolds number model,[17] and a boundary layer conduction model.[18] For consistency, the Colburn-j factors were based upon the acoustic Reynolds number using the definition in Eq. (10), even in cases where the rms Reynolds number was used in the correlation.

The TASFE model is based on the steady-flow regression model given in Eq. (15). A sinusoidal particle velocity was assumed with a zero mean value, and the oscillating velocity $u = u_1 \sin \omega t$ was substituted into Eq. (15). The Colburn-j factors were first used to evaluate the factor $\mathrm{Nu}\,\mathrm{Pr}^{-1/3}$, which was then numerically averaged over one-half period of one cycle using a recursive adaptive Simpson quadrature method[19] to yield the final Colburn-j factors. The TASFE model yielded the following expression:

$$j_{TASFE} = 0.7373\,\mathrm{Re}_1^{-0.5673}. \tag{17}$$

The rms Reynolds number model is obtained by substituting the rms acoustic Reynolds number for the Reynolds number in the steady-flow correlation. The rms acoustic Reynolds number is defined as

$$\mathrm{Re}_{rms} = \frac{u_{rms} D_h}{\nu}, \tag{18}$$

where u_{rms} is the rms velocity. The rms Reynolds number model in terms of the acoustic Reynolds number is given by

$$j_{rms} = 0.8077\,\mathrm{Re}_1^{-0.5673}. \tag{19}$$

In DELTAE, the heat transfer coefficient used to find the heat-exchanger metal temperature is calculated using a boundary layer conduction model described by

$$h = \frac{k}{\min(r_h, \delta_\kappa)}, \tag{20}$$

where k is the thermal conductivity of the working gas, r_h is the hydraulic radius of the fin spacing of the heat exchanger, and δ_κ is the thermal penetration depth that is defined by

TABLE I. Thermophysical properties of measured data in oscillating flow.

No.	Helium % in mixture	Mean pressure (Pa)	Frequency (Hz)	Peak-to-peak particle displacement (m)	Thermal conductivity (W/m K)	Thermal penetration depth (m)	Isobaric specific heat (J/kg K)	Density (kg/m^3)	Prandtl number
1	33%	6.89E+05	145.2	4.8E−03	0.0400	1.2E−04	740.0	8.0	0.43
2	33%	6.89E+05	145.2	5.1E−03	0.0400	1.2E−04	740.0	8.0	0.43
3	44%	2.00E+06	156.3	2.5E−03	0.0488	7.6E−05	861.3	20.0	0.42
4	44%	2.00E+06	156.3	3.1E−03	0.0488	7.6E−05	861.3	20.0	0.42
5	33%	2.00E+06	144.9	3.3E−03	0.0404	7.2E−05	740.0	23.3	0.44
6	33%	2.00E+06	144.9	3.7E−03	0.0404	7.2E−05	740.0	23.3	0.44
7	22%	2.00E+06	136.0	3.5E−03	0.0338	6.8E−05	648.7	26.5	0.46
8	22%	2.00E+06	136.2	3.8E−03	0.0338	6.8E−05	648.7	26.6	0.46
9	22%	2.00E+06	136.2	3.6E−03	0.0338	6.8E−05	648.7	26.5	0.46
10	22%	2.00E+06	136.2	3.2E−03	0.0338	6.8E−05	648.7	26.5	0.46
11	22%	2.00E+06	136.2	3.0E−03	0.0338	6.8E−05	648.7	26.5	0.46
12	44%	6.89E+05	155.6	4.1E−03	0.0486	1.3E−04	861.3	6.8	0.42
13	44%	6.89E+05	155.6	4.7E−03	0.0485	1.3E−04	861.3	6.9	0.42
14	44%	6.89E+05	155.4	4.7E−03	0.0485	1.3E−04	861.3	6.9	0.42
15	44%	6.89E+05	155.6	4.0E−03	0.0486	1.3E−04	861.3	6.8	0.42
16	33%	6.89E+05	145.8	4.9E−03	0.0401	1.2E−04	740.0	8.0	0.43
17	33%	6.89E+05	145.8	5.3E−03	0.0400	1.2E−04	740.0	8.0	0.43
18	33%	6.89E+05	145.8	4.4E−03	0.0401	1.2E−04	740.0	8.0	0.43
19	33%	1.38E+06	145.2	4.5E−03	0.0402	8.6E−05	740.0	16.1	0.44
20	33%	1.38E+06	145.1	3.9E−03	0.0403	8.6E−05	740.0	16.0	0.44
21	44%	1.38E+06	155.9	3.4E−03	0.0487	9.2E−05	861.3	13.8	0.42
22	44%	1.38E+06	155.9	3.8E−03	0.0486	9.2E−05	861.3	13.8	0.42

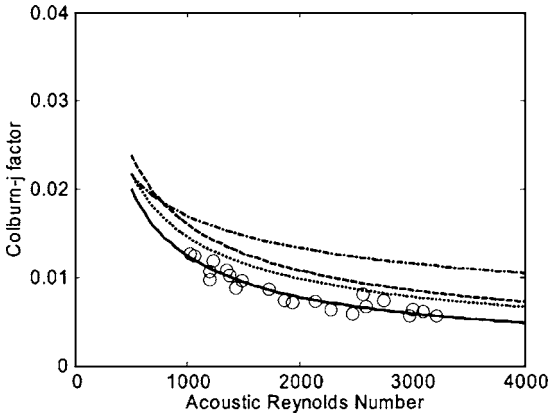

FIG. 7. Measured gas-side Colburn-j factor versus the acoustic Reynolds number comparison with other models. O: measured data, ---: rms Reynolds number model, ···: TASFE model,—: regression curve of measured data, --: boundary layer conduction model.

$$\delta_\kappa = \sqrt{\frac{2\alpha}{\omega}}, \tag{21}$$

where α is the thermal diffusivity of the fluid and ω is the angular frequency of the oscillations. The Colburn-j factor for the boundary layer conduction model can be calculated using Eq. (6), and it is given by

$$j_{DELTAE} = \frac{k}{\min(r_h, \delta_\kappa)} \frac{\mathrm{Pr}^{2/3}}{\rho c_p u_1}, \tag{22}$$

where ρ is the density and c_p is the isobaric specific heat.

The Colburn-j factors from the different prediction methods are presented as a function of the acoustic Reynolds number for oscillating flows in Fig. 7, alongside measured values. The TASFE model predictions were in good agreement with the measured Colburn-j factors, although they slightly overpredicted the measured heat transfer coefficients. Discrepancies of up to 36% were observed between the TASFE model predictions and the measured heat transfer coefficients.

The heat transfer model based on the rms acoustic Reynolds number overestimated the measured Colburn-j factors. This is because the rms acoustic Reynolds number is larger than the time-averaged acoustic Reynolds number in the TASFE model.

The Colburn-j factors obtained from the boundary layer conduction model used in DELTAE overestimated the heat transfer coefficients. Relative differences of up to 114% between the laminar conduction results and experimental data were found. This is consistent with the accuracy of this model stated in previous studies.[1]

The TASFE model, although it slightly overpredicted the heat transfer coefficients, was found to perform better than other models in this particular experiment.

VI. DISCUSSION AND MODEL IMPROVEMENTS

Existing heat transfer correlation models failed to accurately predict the measured heat transfer coefficients in oscillating flow. Therefore it is necessary to develop a more accurate model to predict the heat transfer in oscillating flow, especially for thermoacoustic coolers.

So far, most proposed correlation models[1–4,7] have investigated the influence of acoustic Reynolds number in oscillating flow, since the normalized heat transfer coefficients in steady flow are functions of the Reynolds numbers. The heat transfer coefficients in oscillating flow may be directly measured, and expressed in nondimensional form using the procedures described in Sec. III. To relate the heat transfer coefficients in oscillating flow to those in steady flow, a proper expression for the acoustic Reynolds number should be obtained in terms of the steady Reynolds number.

In the TASFE model, the Reynolds number is assumed to be sinusoidal, $\mathrm{Re}(t) = \mathrm{Re}_1 \sin \omega t$. To find the time-averaged heat transfer coefficient, this expression is substituted into the known steady-flow regression model, and the resulting expression is numerically averaged over one-half of the period. This procedure is based on the assumption that the convection heat transfer coefficient between the gas particles and the heat-exchanger surface is the same for the "forward flow" (the right direction in Fig. 3) and the "reverse flow" (the left direction in Fig. 3). In fact, these should be different, since the temperature history of the oscillating gas particles varies during each half-cycle.[1]

For the cold side of the stack and the cold heat exchanger, the stack temperature is always lower than the heat-exchanger metal temperature. Gas particles entrained from the stack into the heat-exchanger fin channels, before they reach their maximum displacement, convect heat with a reservoir at the gas temperature, T_1. After one-half period, when the gas particles move back into the stack, their temperature is higher than T_1 due to the heat transferred from the heat exchanger. Therefore the convective heat transferred during the reverse flow component of the cycle should be lower than that during the forward flow. For the hot side of the stack and the hot heat exchanger, the reverse flow should cause a greater convective heat transfer than the forward flow. This effect may be accounted for by reducing the acoustic Reynolds number during one-half of the cycle. If the reverse flow did not participate in the heat transfer process at all, the velocity history for the instantaneous Reynolds number could be represented by Fig. 8(b). The velocity history consistent with a reduced reverse flow is shown in Fig. 8(c) for an arbitrary reverse flow amplitude.

The time-dependent instantaneous Reynolds number was assumed to be

$$\mathrm{Re}(t) = \begin{cases} \mathrm{Re}_{11} \sin \omega t, & 2n\pi < t < 2n\pi + \pi/\omega, \\ & n = 0, 1, 2 \ldots, \\ -C\,\mathrm{Re}_1 \sin \omega t, & 2n\pi + \pi/\omega < t < 2n\pi + 2\pi/\omega, \\ & n = 0, 1, 2 \ldots, \end{cases} \tag{23}$$

where C, a correction factor assumed to vary between zero and unity, accounts for reduced heat transfer during one-half of the cycle (reverse flow for the cold heat exchanger and forward flow for the hot heat exchanger). The Reynolds

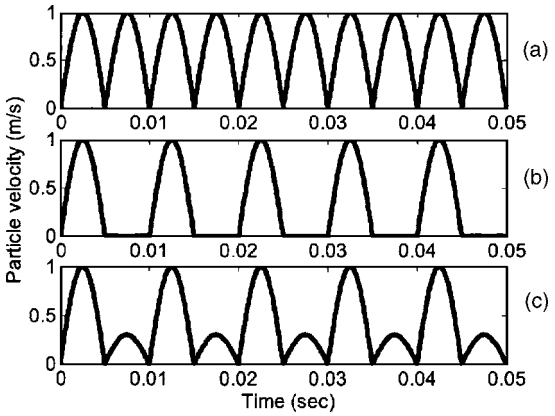

FIG. 8. Assumed velocity history for correlation models for a period of 10 ms. (a) TASFE model; (b) when the effect of the reverse flow is zero; (c) modified TASFE model imposing a lower heat transfer for the reverse flow than for the forward flow.

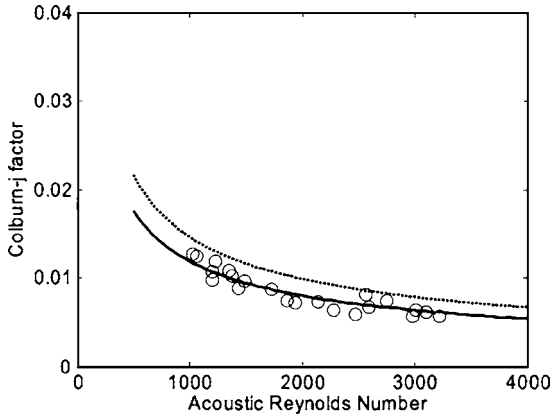

FIG. 9. Measured gas-side Colburn-j factor versus the acoustic Reynolds number with the modified and the original TASFE models. O: measured data, ⋯: TASFE model,—: modified TASFE model.

number was then obtained by averaging the instantaneous Reynolds numbers over one period.

After some algebra, a simple relation between the steady-flow Reynolds number and the acoustic Reynolds number was obtained in terms of the correction factor, C, in Eq. (24):

$$\mathrm{Re} = x\,\mathrm{Re}_1, \quad x = \frac{1+C}{\pi}, \tag{24}$$

where x is the conversion factor between the steady-flow Reynolds number and the acoustic Reynolds number. A modified TASFE is obtained by applying Eq. (24) to a known steady-flow correlation.

To determine the conversion factor, x, to convert the steady-flow correlation to the oscillating flow correlation, Eq. (24) was substituted into the steady-flow regression curve, Eq. (15), and it was numerically optimized for the calculated Colburn-j factors in oscillating flow using the Nelder-Mead simplex method. The overall Reynolds number conversion factor was found to be $x=0.353$, and the half-cycle Reynolds number flow correction factor, C, was about 0.109. As expected, the value for C is greater than zero and less than unity. This trend is consistent with the hypothesis that the heat transfer during this half of the period is substantially less than that for the other half.

In Fig. 9, the steady-flow Reynolds number conversion applied to the steady-flow heat transfer coefficient regression, Eq. (15), is compared with the measured oscillating flow heat transfer coefficient data, and the original TASFE model, Eq. (17). The modified TASFE model is more accurate than the original TASFE model. The rms errors of the original TASFE model and the modified TASFE model were 2.2×10^{-3} and 7.8×10^{-4}, respectively. However, more work is needed to determine whether the same correction factor works well for other heat-exchanger geometries.

The validity of the modified TASFE model for other geometries was briefly investigated. Mozurkewich's experimental results for heat exchangers made of an aluminum tube[4] with a simple geometry were compared with the Zukauskas' single tube cross-flow correlations. Figure 10 shows a comparison between the modified TASFE model and the original TASFE model for Mozurkewich's experimental results. The data was obtained with his heat-exchanger configuration A that is designed for the low Reynolds number measurement in Ref. 4. The modified TASFE model was obtained by substituting Eq. (24) with the conversion factor, $x=0.353$, into the Zukauskas low Reynolds number correlation, expressed as

$$\mathrm{Nu}\,\mathrm{Pr}^{-0.37} = 0.51\,\mathrm{Re}^{0.5}, \quad 40 < \mathrm{Re} < 1000. \tag{25}$$

The modified TASFE model predictions appear to be slightly better for Reynolds numbers less than 600, and slightly less accurate for Reynolds numbers over 600 compared with the original TASFE model. The rms errors of the TASFE model and the modified TASFE model were 1.1 and 1.6, respectively.

Zukauskas's steady-flow correlation for large Reynolds numbers was then used to evaluate the modified TASFE model for Mozurkewich's heat-exchanger configuration B, with bigger tube diameters than his heat-exchanger configuration A. The results, as shown in Fig. 11, are expressed using the relation

$$\mathrm{Nu}\,\mathrm{Pr}^{-0.37} = 0.26\,\mathrm{Re}^{0.6}, \quad 1000 < \mathrm{Re} < 20\,000. \tag{26}$$

The heat transfer coefficient in an oscillating flow predicted by the modified TASFE was significantly improved over that

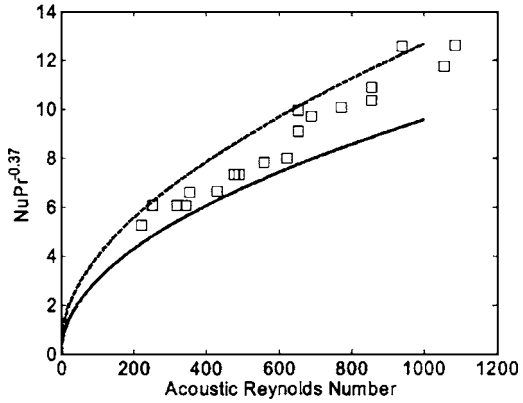

FIG. 10. Mozurkewich's measured gas-side heat transfer coefficient (Ref. 4) versus the acoustic Reynolds number for low acoustic Reynolds numbers. □: measured data, ---: TASFE model,—: modified TASFE model.

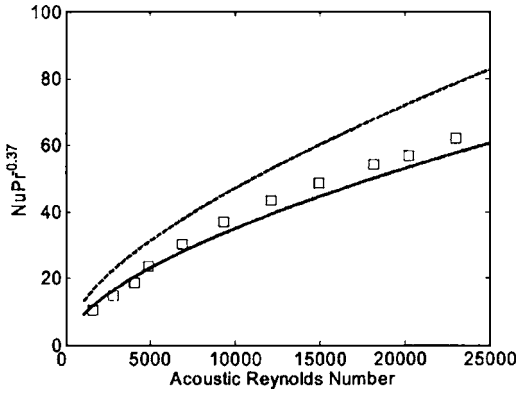

FIG. 11. Mozurkewich's measured gas-side heat transfer coefficient (Ref. 4) versus the acoustic Reynolds number for high acoustic Reynolds numbers. □: measured data, ---: TASFE model,—: modified TASFE model.

predicted by the TASFE model. The RMS errors of the TASFE model and the modified TASFE model were 10.7 and 3.2, respectively.

In Mozurkewich's calculation of heat transfer coefficients, however, the overall heat transfer coefficient between the water flow and the oscillating gas flow was used instead of the gas-side convection heat transfer coefficient. This approximation is only valid when the internal convection heat transfer coefficient for the water flow in the tubes is much larger than the overall gas-side heat transfer coefficient. Considering the effects of the internal convective heat transfer of the water flow, Mozurkewich's original data for configuration B is dramatically changed. The results, obtained by manipulating the data presented in Ref. 4 in conjunction with data from Ref. 20, are shown in Fig. 12.

For low Reynolds numbers, the water-side convection heat transfer coefficient, h_i, was about ten times larger than the global gas-side heat transfer coefficient, h_0. Thus, it was reasonable to ignore the thermal resistance of water flow in that regime, and to use U instead of h_0. For high Reynolds number, however, h_i was comparable to h_0, and as a result, h_0 was about twice U. Based on these results, no correlation model predicts the measured data well.

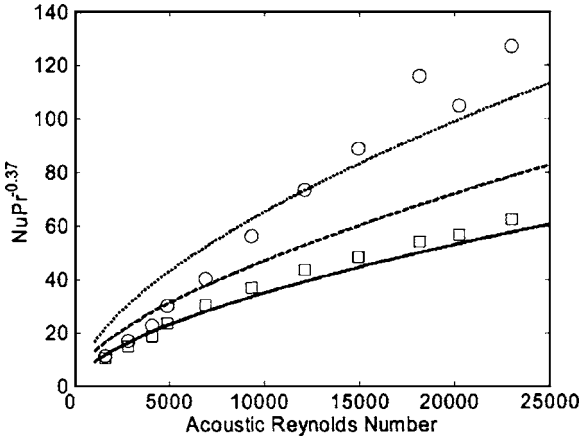

FIG. 12. Modified measured gas-side heat transfer coefficient from Mozurkewich (Ref. 4) versus the acoustic Reynolds number for high acoustic Reynolds numbers. □: original measured data; O: modified measured data; ---: TASFE model; ···: Zukauskas' steady flow correlation;—: modified TASFE model.

The heat transfer coefficients measured for high Reynolds numbers were much larger than those from both the TASFE and the modified TASFE models. They were even larger than the steady-flow heat transfer coefficients for the same Reynolds numbers. This cannot be explained by the TASFE model because TASFE should yield heat transfer coefficients smaller than or equal to the steady-flow heat transfer coefficients.

A few factors might have caused some uncertainties in Mozurkewich's measured data. First, the intercept, Q_0, was subtracted from the measured heat transfer rate, Q_H, based on the expectation that no heat should flow for a zero temperature difference. The heat transfer rate between the gas-side flow and the water-side flow, Q_H, is measured from the water flow in the heat exchanger. Thus, Q_H is the proper metric to calculate the heat transfer coefficients of the heat exchanger, and not $Q_H - Q_0$. Furthermore, it is possible that the difference between the stack end temperature and the mean water temperature in the heat exchanger, $T_H - T_{hhx}$, is not zero when the heat transfer rate, Q_H, is zero, because the thermal contact between the stack and the oscillating gas is imperfect and a temperature difference may exist between the gas and the stack.

Second, the heat transfer rate was divided by $T_H - T_{hhx}$. This procedure yields the global heat transfer coefficient between the water and the stack surface, and not between the water and the oscillating gas. This adds another unknown variable, namely the convection heat transfer coefficient between the stack and the oscillating gas, to Eq. (3), and, therefore, although the internal water temperature was considered in his calculation, the gas-side heat transfer coefficient between the gas and the heat exchanger could not be calculated.

Consequently, existing measured data can unfortunately not be used to verify the validity of the modified TASFE model for other heat-exchanger geometries, and it should be the subject of future work.

VII. CONCLUSIONS

The performance of a microchannel heat exchanger was measured in both steady and pulsating flows. A method to evaluate dimensionless heat transfer coefficients of microchannel heat exchangers in an oscillating flow was developed. The results suggest that the thermoacoustic heat transfer in microchannel heat exchangers could be predicted using a modified steady-flow correlation based on an acoustic Reynolds number. The previously proposed TASFE model also yielded reasonably good agreement, but it slightly overpredicted the heat transfer coefficients. Discrepancies of up to 36% were observed. Boundary layer conduction models overestimated the heat transfer coefficients. The maximum discrepancy was about 114% of the measured heat transfer coefficient. This implies that predicted temperature differences between the heat-exchanger metal and thermoacoustic fluid from DELTAE could be in error roughly by as much as a factor of 2. Substituting the Reynolds number with the acoustic Reynolds number multiplied by a conversion factor, $x=0.353$, in the steady-flow correlation models predicted the

heat transfer coefficients in oscillating flow better than any suggested correlation models by other authors. This simple conversion from the steady-flow correlation to the oscillating flow correlation can be applied to the steady-flow correlations in the design stage to predict the heat exchanger performance. More experiments are needed for validation of the proposed modified TASFE model with other heat-exchanger geometries.

ACKNOWLEDGMENTS

The authors express their thanks to Aaron Alexander, who initiated some of the initial analysis procedures. We deeply appreciate the assistance and data provided by Dr. Mozurkewich. The assistance of the Herrick Laboratories Technical Staff is also gratefully acknowledged. This work has been supported by the Office of Naval Research, the American Refrigeration Technology Institute (ARTI), and the Tecumseh Products Company. We also really appreciate the donation of heat exchanger equipment from Modine and the technical support of Steve Memory.

[1]G. W. Swift, *Thermoacoustics: A Unifying Perspective For Some Engines and Refrigerators* (Acoustical Society of America, New York, 2002).
[2]S. L. Garrett, D. K. Perkins, and A. Gopinath, "Thermoacoustic refrigerator heat exchangers: design, analysis and fabrication," in *Heat Transfer 1994*, Proceedings of the Tenth International Heat Transfer Conference, edited by G. F. Hewitt (Inst. of Chem. Engineers, London, 1994), Vol. **IV**, pp. 375–380.
[3]G. Mozurkewich, "Heat transfer from a cylinder in an acoustic standing wave," J. Acoust. Soc. Am. **98**, 2209–2216 (1995).
[4]G. Mozurkewich, "Heat transfer from transverse tubes adjacent to a thermoacoustic stack," J. Acoust. Soc. Am. **110**, 841–847 (2001).
[5]A. Zukauskas, "Heat transfer from tubes in crossflow," Adv. Heat Transfer **8**, 93 (1972), Eq. (33) on p. 131.
[6]P. D. Richardson, "Effects of sound and vibration on heat transfer," Appl. Mech. Rev. **20**, 201–217 (1967).
[7]M. E. Poese and S. L. Garrett, "Performance measurements on a thermoacoustic refrigerator driven at high amplitudes," J. Acoust. Soc. Am. **107**, 2480–2486 (2000).
[8]M. Wetzel and C. Herman, "Experimental study of thermoacoustic effects on a single plate Part II: Heat transfer," Heat Mass Transfer **35**, 433–441 (1999).
[9]M. Wetzel and C. Herman, "Experimental study of thermoacoustic effects on a single plate Part I: Temperature fields," Heat Mass Transfer **36**, 7–20 (2000).
[10]J. R. Brewster, R. Raspet, and H. E. Bass, "Temperature discontinuities between elements in thermoacoustic devices," J. Acoust. Soc. Am. **102**, 3355–3360 (1997).
[11]L. Mongeau, A. Alexander, B. L. Minner, I. Paek, and J. E. Braun, "Experimental investigations of an electro-dynamically driven thermoacoustic cooler," in *Proceedings of the 2001 International Mechanical Engineering Congress and Exposition* (American Society of Mechanical Engineers, New York, 2001), pp. 1–12.
[12]W. C. Ward and G. W. Swift, "Design environment for low amplitude thermoacoustic engines (DeltaE)," J. Acoust. Soc. Am. **95**, 3671–3672 (1994). Software and user's guide available either from the Los Alamos thermoacoustics website at www.lanl.gov/thermoacoustics/ or from the Energy Science and Technology Software Center, U.S. Department of Energy, Oak Ridge, Tennessee.
[13]F. Incropera and D. Dewitt, *Fundamentals of Heat and Mass Transfer* (Wiley, New York, 1996).
[14]R. A. Bowman, A. C. Mueller, and W. M. Nagle, "Mean temperature difference in design," Trans. ASME **62**, 283–294 (1940).
[15]M. Jakob, *Heat Transfer* (Wiley, New York, 1957), Vol. **2**.
[16]J. A. Nelder and R. Mead, "A simplex method for function minimization," Comput. J. **7**, 308–313 (1965).
[17]The correlation model obtained by substituting the rms acoustic Reynolds number for Reynolds number in the steady-flow correlation.
[18]W. C. Ward and G. W. Swift, DELTAE *Tutorial and User's Guide Version 5.1* (Los Alamos National Laboratory, City, NM, 2001).
[19]J. H. Mathews and K. D. Fink, *Numerical Methods using* MATLAB, 3rd ed. (Prentice–Hall, Englewood Cliffs, NJ, 1999).
[20]G. Mozurkewich (private communication).

Acoustic generation in piezoelectric materials by microwave excitation

A. R. Hadj Henni,[a] C. Bacon, and B. Hosten
Laboratoire de Mécanique Physique, Bordeaux 1 University, UMR CNRS 5469, 351 cours de la Libération, 33405 Talence Cedex, France

(Received 31 March 2005; revised 29 June 2005; accepted 29 June 2005)

As an application of ultrasound generation by microwave excitation, a study of piezoelectric material behavior is presented. Piezoelectric bars excited electrically or by microwave irradiation give different resonance frequencies. Piezoelectric materials are subject to a stiffening phenomenon (variation of the apparent Young's modulus) when the electrical boundary conditions change and, as a result, when the material is dynamically excited, a modification of the natural resonance frequencies occurs. A one-dimensional model, to predict the acoustic waves generated in piezoelectric materials by an unspecified excitation source, is presented and compared to experimental results. This model is used as a nondestructive evaluation method to characterize piezoelectric samples and to highlight the thermoelastic origin of the acoustic generation when the piezoelectric materials are excited by pulsed microwaves. © *2005 Acoustical Society of America.*
[DOI: 10.1121/1.2005968]

PACS number(s): 43.35.Zc, 43.35.Cg, 43.38.Fx [YHB] Pages: 2281–2288

I. INTRODUCTION

Piezoelectric materials are used in many technological fields (car industry, aircraft, electrical engineering, medical imagery, ultrasound generation,…). They play a major rule in the use of ultrasound in nondestructive testing of materials. A specific application could be the excitation at distance of embedded ultrasound generators to carry out structural health monitoring.

The piezoelectric materials behavior was extensively studied when they are excited by an electric field applied at the electrodes.[1–4]

The absorption of microwave energy by viscoelastic materials causes thermoelastic expansion that generates acoustic waves.[5–7] The use of pulsed microwaves for ultrasound generation in piezoelectric materials is here applied to excite piezoelectric bars without contact. The starting point of the present study has been the observation of a change in the resonance frequency of a piezoelectric bar when it is excited electrically and by pulsed microwave irradiation. In order to quantify this variation, a one-dimensional model for the displacement calculation of a piezoelectric bar excited by an unspecified volumic source is developed from the piezoelectricity equations and using a state vectors method. Then, the experimental study is presented to validate the theoretical model. It concerns cylindrical samples of piezoelectric ceramics (lead zirconate titanate, PZT) excited electrically and by pulsed microwaves in different configurations. The theoretical and experimental results are compared to explain the difference observed in the resonance frequencies. Finally, the experimental setup and the developed model are used to understand the origin of ultrasound generation by microwaves in piezoelectric materials.

[a]Author to whom correspondence should be addressed. Electronic mail: ar.hadjhenni@lmp.u-bordeaux1.fr

II. THEORY

A. General behavior equations for piezoelectric materials

The classical coupling equations[1,2] between the mechanical and the electrical properties are first reminded here. Let σ, ε, E, and D be the respective representations of the stress tensor, the strain tensor, the electrical field vector, and the electrical displacement vector. The three-dimensional equations of piezoelectricity are given by

$$\begin{aligned} \sigma_\alpha &= c^E_{\alpha\beta}\varepsilon_\beta - d_{i\beta}c^E_{\beta\alpha}E_i, \\ D_i &= e^\varepsilon_{ij}E_j + d_{i\beta}c^E_{\beta\alpha}\varepsilon_\alpha, \end{aligned} \quad i,j = 1,2,3,\ \alpha,\beta = 1,\ldots,6, \quad (1)$$

or in the following equivalent way

$$\begin{aligned} \varepsilon_\alpha &= s^E_{\alpha\beta}\sigma_\beta + d_{i\alpha}E_i, \\ D_i &= e^\sigma_{ij}E_j + d_{i\alpha}\sigma_\alpha, \end{aligned} \quad i,j = 1,2,3,\ \alpha,\beta = 1,\ldots,6 \quad (2)$$

with σ_α the stress tensor components in a vectorial form, ε_β the strain tensor components in a vectorial form, E_i the electrical field components, D_i the electrical displacement components, $c^E_{\alpha\beta}$ the stiffness tensor components at constant electrical field, e^ε_{ij} the permittivity tensor components at constant strain, e^σ_{ij} the permittivity tensor components at constant stress, $d_{i\beta}$ the piezoelectric charge tensor components, and $S^E_{\alpha\beta}$ the compliance tensor components at constant electrical field.

The superscripts E, σ, and ε mean that the characteristics are respectively given for constant electrical field, constant stress, and constant strain.

B. The one-dimensional model

A slender bar (of length L, along the direction z) is made of a piezoelectric material. In order to take into account the acoustic waves damping, a complex Young's modulus is adopted and the material is considered as viscoelastic. The

bar is excited by a volumic source of unspecified origin (electrical, thermal, mechanical impact, etc.,…) that produces stress and displacement fields inside it depending on the electrical and mechanical boundary conditions. To simplify the calculations, the equations given below are expressed in the frequency domain by applying a Fourier transform to the equations expressed in the time domain.

By calling ω the pulsation related to the frequency f by $\omega=2\pi f$, the equilibrium equation is given by

$$\frac{\partial \sigma_z}{\partial z} = -\rho\omega^2 U_z, \tag{3}$$

where σ_z and U_z are the normal stress and the theoretical displacement, respectively, according to the direction of propagation z, and ρ is the density of material.

Under the assumption of small displacements, the strain and the displacement are related by

$$\varepsilon_z = \frac{\partial U_z}{\partial z}. \tag{4}$$

The expression of the stress field induced by the generation phenomenon is represented by

$$\sigma_0(z,t) = \sigma_0(z) f(t), \tag{5}$$

where $\sigma_0(z)$ represents the space distribution and $f(t)$ the temporal evolution of $\sigma_0(z,t)$. In the particular case of a very short pulsed excitation, the source stress is a Dirac function and its Fourier transform depends only on the space distribution of the stress:

$$\sigma_0(z,t) = \sigma_0(z)\,\delta(t), \quad \sigma_0(z,\omega) = \sigma_0(z). \tag{6}$$

For the one-dimensional case and after a Fourier transform, the behavior equations (1) are simplified and become

$$\sigma_z = Y_{33}^E \varepsilon_z - d_{33} Y_{33}^E E_z + \sigma_0(z), \quad D_z = e_{33}^{\varepsilon} E_z + d_{33} Y_{33}^E \varepsilon_z, \tag{7}$$

where Y_{33}^E is the complex Young's modulus of the piezoelectric material in the z direction, at constant electrical field.

Two electrical boundary conditions are considered: The first one, when the electrodes at the ends of the bar are connected, is called "short circuit." The second one, when the electrodes are disconnected, is called "open circuit." The short circuit imposes the same electrical potentials at the ends of the bar and the electrical field is uniformly zero inside the bar. The open circuit induces a uniform electrical displacement:[8,9]

$$E_z = 0 \quad \text{at short circuit}, \quad \frac{\partial D_z}{\partial z} = 0 \quad \text{at open circuit}. \tag{8}$$

It is assumed that the propagation velocity of the electric waves is very large compared to the propagation velocity of the mechanical waves.

1. Short circuit

Since the electrical field is zero, there is no electromechanical coupling between the electrical field and the stress in the material. After calculations, the combination of Eqs. (3), (4), and (7) gives the differential equation of the movement expressed in terms of strain:

$$\frac{\partial^2 \varepsilon_z}{\partial z^2} + (S^E\omega)^2 \varepsilon_z = -\frac{1}{Y_{33}^E}\frac{\partial^2 \sigma_0}{\partial z^2}, \tag{9}$$

where $S^E=\sqrt{\rho/Y_{33}^E}$ is the acoustic wave slowness in the material at constant electrical field.

2. Open circuit

Under this boundary condition, the electrical displacement gradient is zero and Eqs. (3), (4), and (7) give

$$\frac{\partial^2 \varepsilon_z}{\partial z^2} + (S^D\omega)^2 \varepsilon_z = -\frac{1}{Y_{33}^D}\frac{\partial^2 \sigma_0}{\partial z^2}, \tag{10}$$

where $S^D=\sqrt{\rho/Y_{33}^D}$ is the acoustic waves slowness in the material at uniform electrical displacement. The stiffening of the piezoelectric material is expressed by a larger apparent Young's modulus[1] Y_{33}^D:

$$Y_{33}^D = Y_{33}^E + \frac{(d_{33}Y_{33}^E)^2}{e_{33}^{\varepsilon}}. \tag{11}$$

C. Solution of the differential equation

Equations (9) and (10) have similar forms and their resolution is identical. The scheme to compute the solution is based on the use of a state vector composed of stress and velocity.[7]

Let S^* and Y^* be the acoustic waves slowness in the material and the apparent Young's modulus, respectively, that depend on the electrical boundary conditions imposed to the piezoelectric bar. The differential equation of movement has the following general form:

$$\frac{\partial^2 \varepsilon_z}{\partial z^2} + (S^*\omega)^2 \varepsilon_z = -\frac{1}{Y_{33}^*}\frac{\partial^2 \sigma_0}{\partial z^2}. \tag{12}$$

The solution of equation (12) is

$$\varepsilon(z,\omega) = P(\omega)e^{-i\omega S^* z} + N(\omega)e^{+i\omega S^* z} + \varepsilon_0(z,\omega), \tag{13}$$

where $P(\omega)$ and $N(\omega)$ are two functions which depend on the mechanical boundary conditions at the ends of the bar. The function $\varepsilon_0(z,\omega)$ is the particular solution of the differential equation (12) and depends on the space distribution of the source stress $\sigma_0(z,\omega)$.

The state vector method links the stress and the velocity at interfaces $z=0$ and $z=L$ by means of transfer matrices.

The velocity and the stress can be formulated as functions of $P(\omega)$ and $N(\omega)$. According to the relations (3), (7), and (13) and independently of the electrical boundary conditions, the velocity expression is

$$V(z,\omega) = -\frac{S^*Y_{33}^*}{\rho}P(\omega)e^{-i\omega S^* z} + \frac{S^*Y_{33}^*}{\rho}N(\omega)e^{+i\omega S^* z} - \frac{iY_{33}^*}{\rho\omega}\frac{\partial \varepsilon_0}{\partial z} - \frac{i}{\rho\omega}\frac{\partial \sigma_0}{\partial z}. \tag{14}$$

For open circuit conditions, the electrical displacement is uniform ($\partial D_z/\partial z=0$) and the system (7) allows the calculation of the electrical field profile and the associated mechanical stress:

$$E(z,\omega) = -\frac{d_{33}Y_{33}^E}{e_{33}^{\varepsilon}}\varepsilon(z,\omega) + A(\omega), \tag{15}$$

$$\sigma(z,\omega) = Y_{33}^D\varepsilon(z,\omega) + \sigma_0(z,\omega) - d_{33}Y_{33}^E A(\omega), \tag{16}$$

where $A=A(\omega)$ is a function which depends on the electrical boundary conditions.

In the short circuit case $[E(z)=0]$, the stress expression is simplified and deduced from the first equation of (7):

$$\sigma(z,\omega) = Y_{33}^E\varepsilon(z,\omega) + \sigma_0(z,\omega). \tag{17}$$

Equations (16) and (17) are very similar. The stress expression in short circuit can be indeed obtained just by replacing Y_{33}^D by Y_{33}^E and by eliminating the term A in Eq. (16). According to the first equation of the system (7) and the strain deformation (13), the stress is expressed, in the general case, as

$$\sigma(z,\omega) = Y_{33}^*[P(\omega)e^{-i\omega S^* z} + N(\omega)e^{+i\omega S^* z} + \varepsilon_0(z,\omega)] + \sigma_0(z,\omega) - d_{33}Y_{33}^E A(\omega) \tag{18}$$

with $A=0$ in short circuit.

It is possible to express $P(\omega)$ and $N(\omega)$ as functions of the velocity and the stress at the interface $z=0$. By writing the velocity and the stress at $z=L$ and by replacing $P(\omega)$ and $N(\omega)$ by their expression, the state vector at $z=0$ is linked to the state vector at $z=L$ by the matrix relation[7]

$$\begin{bmatrix} \sigma(L,\omega) \\ V(L,\omega) \end{bmatrix} = P\begin{bmatrix} \sigma(0,\omega) \\ V(0,\omega) \end{bmatrix} + G. \tag{19}$$

The matrix P and the vector G are defined by

$$P = \begin{bmatrix} c & \frac{i\rho}{S^*}s \\ \frac{iS^*}{\rho}s & c \end{bmatrix}, \tag{20}$$

$$G = \begin{bmatrix} -\bar{\sigma}_0(0)c(L) - \frac{1}{\omega S^*}\left[\frac{\partial\bar{\sigma}_0}{\partial z}\right]_{z=0}s(L) + \bar{\sigma}_0(L) \\ -\frac{iS^*}{\rho}\bar{\sigma}_0(0)s(L) + \frac{i}{\rho\omega}\left[\frac{\partial\bar{\sigma}_0}{\partial z}\right]_{z=0}c(L) - \frac{i}{\rho\omega}\left[\frac{\partial\bar{\sigma}_0}{\partial z}\right]_{z=L} \end{bmatrix},$$

where $c(z)=\cos(\omega S^* z)$, $s(z)=\sin(\omega S^* z)$, and $\bar{\sigma}_0(z)$ indicates the following quantity:

$$\bar{\sigma}_0(z) = Y_{33}^*\varepsilon_0(z) + \sigma_0(z) - d_{33}Y_{33}^E A. \tag{21}$$

Note that the matrix P is related to the acoustic waves propagation because it only depends on the mechanical properties of the medium, whereas the vector G, which depends on the space profile of the imposed source stress $\sigma_0(z,\omega)$, is related to the generation phenomenon. The method can be generalized to a bar composed of n juxtaposed piezoelectric segments by taking into account, sequentially, the continuity of the stress and the velocity at the interfaces between two consecutive segments.[7] According to Eq. (19), one can find

$$\begin{bmatrix} \sigma(z_j,\omega) \\ V(z_j,\omega) \end{bmatrix} = S^{(j)}\begin{bmatrix} \sigma(z_1,\omega) \\ V(z_1,\omega) \end{bmatrix} + T^{(j)}, \quad j \geqslant 2, \tag{22}$$

where $z_1=0$.

The following recurrence relations define the matrix $S^{(j)}$ and the vector $T^{(j)}$:

$$\begin{aligned} &S^{(j)} = P^{(j-1)}S^{(j-1)}, \quad j>2, \quad S^{(2)} = P^{(1)}, \\ &T^{(j)} = P^{(j-1)}T^{(j-1)} + G^{(j-1)}, \quad j>2, \quad T^{(2)} = G^{(1)}. \end{aligned} \tag{23}$$

In order to obtain the displacement velocity spectrum at the interface $z=L$, the mechanical boundary conditions for a free bar are introduced:

$$\sigma(z=0) = \sigma(z=L) = 0, \tag{24}$$

and the velocity at the end of the bar is deduced from Eqs. (19) and (24):

$$V(L) = \frac{-P_{22}(L)G_1(L) + P_{12}(L)G_2(L)}{P_{12}(L)}. \tag{25}$$

For a pulsed excitation, which has a uniform space profile, the Fourier transform of the stress is given by Eq. (6) $[\sigma_0(z,\omega)=\sigma_0]$. The particular solution of the differential Eq. (12) is then equal to zero $[\varepsilon_0(z,\omega)=0]$, and the velocity at the end $z=L$ is written

$$V(L) = \frac{S^*\bar{\sigma}_0(1-\cos(\omega S^* L))}{i\rho\sin(\omega S^* L)}. \tag{26}$$

Depending on whether the assembly is an open circuit or a short circuit, Eq. (26) gives two different resonance frequencies:

$$f_r^D = \frac{1}{2L}\sqrt{\frac{Y_{33}^D}{\rho}} \quad \text{and} \quad f_r^E = \frac{1}{2L}\sqrt{\frac{Y_{33}^E}{\rho}}. \tag{27}$$

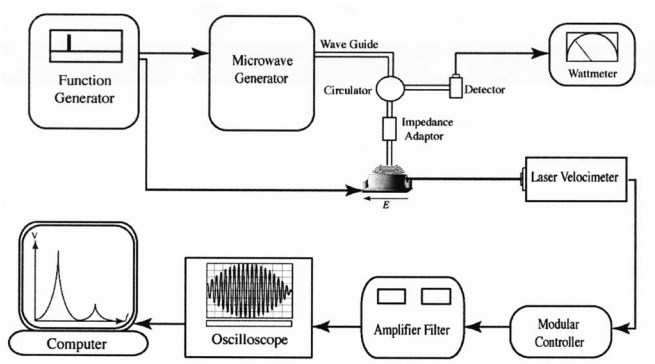

FIG. 1. Experimental setup for the electrical or microwaves excitation of a PZT bar.

III. EXPERIMENTAL SETUP

The experimental setup (Fig. 1) allows us to choose between two kinds of excitation: by microwave irradiation or by electrical excitation. The pulsed electromagnetic waves are produced by a magnetron at the frequency of 9.41 GHz

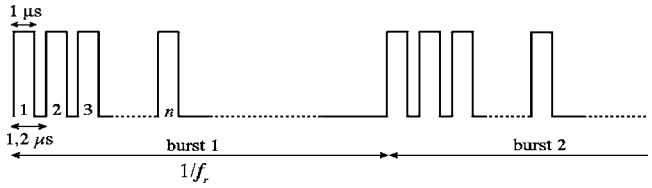

FIG. 2. Time shape of the excitation generated by the microwave generator.

with a peak power of 5.5 kW. This generator allows us to send bursts composed of 1-μs pulses. The number n of pulses and the repetition frequency f_{rep} (Fig. 2) are chosen with a function generator (Agilent 33120 A), which allows us to excite the sample by pulses or by bursts. The repetition frequency in a burst is 800 kHz (1.2 μs) and the repetition frequency of the bursts (controlled by the function generator) permits us to excite the bar at a given frequency f_r (in particular the resonance frequencies of the samples).

The generated microwaves are propagating inside a rectangular waveguide (WR 90), of internal size 23×10 mm^2, which only allows the propagation of the fundamental mode TE_{10} (the electrical field is then parallel to the small dimension of the waveguide). To obtain a maximum power in the sample, an impedance adaptor is adjusted in order to get the minimum reflected power measured with a wattmeter. It is made up of a hybrid tee associated to two sliding short circuits. The circulator permits us to direct the microwaves reflected by the sample to the detector and finally to the wattmeter.

The electrical excitation is produced by a function generator (Agilent 33120 A), which is connected to two electrodes (Fig. 1).

In both cases, it is possible to choose an excitation by pulses or by bursts and in open circuit or in short circuit. The electrical boundary conditions are realized by preventing or by ensuring the contact of the electrodes with the metallized ends of the piezoelectric bar.

The particulate velocity at the end of the sample is measured with a Laser velocimeter (Polytec OFV 353) related to a modular controller (Polytec OFV 3001) with a sensitivity of 5 mm/s/V if the bandwidth is limited to 250 kHz. The signal is acquired, through a filter amplifier (Electronic instrument 3627) and an oscilloscope (LeCroy 9450 A), in a computer.

IV. EXPERIMENTAL RESULTS AND MATERIAL CHARACTERIZATION

A. Effects of the nature of the excitation and of the boundary conditions

The following experimental results are obtained with piezoelectric ceramic bars (lead zirconate titanate, PZT). The study concerns two cylindrical bars with circular cross sections of lengths 10 and 15 mm (with a diameter equal to 10 mm) and two parallelepipedic bars of lengths 20 and 25 mm (with lateral dimensions equal to 10 mm).

The frequency spectra obtained by pulsed microwaves or electrical excitation in short circuit or in open circuit are presented and compared with the previously developed piezoelectric model. Table I presents the four tested configurations and the corresponding resonance frequencies. Configurations (1) and (2) (short circuit for electrical or microwaves excitation) give similar resonances. Configurations (3) and (4) (open circuit for electrical or microwaves excitation) give similar resonance frequencies as well. The small differences between the frequencies are only due to the variation of the experimental conditions (support of the bars, connectors, etc.) that slightly modify the mechanical boundaries conditions.

TABLE I. Experimental resonance frequencies (kHz) of piezoelectric bars excited by microwaves and electrically in short circuit and in open circuit (precision: ±0.4%).

Lengths	1)	2)	3)	4)
10 mm	122	124	163	163
15 mm	86	86	120	120
20 mm	67	67	89	89
25 mm	55	55	72	71

More details on the experimental spectra are given in Fig. 3. It is clear that the differences in resonances are only due to the electrical boundary conditions and the configurations (2) and (3) have been found to prove it. In fact, in short circuit the Young's modulus Y_{33}^E is smaller than the Young's modulus Y_{33}^D corresponding to the open circuit.[2,9] Finally, Fig. 3 does not show difference between electrical and microwaves excitations concerning resonance frequencies.

B. Piezoelectric materials characterization

The mechanical, electrical, and piezoelectric characteristics of the tested bars need to be evaluated to compare the experimental results and the model. To this end, the mechanical and piezoelectric characteristics are deduced from the resonance frequencies of a bar obtained in short circuit and open circuit, its dielectric permittivity at constant stress, and its density. This method, inspired of the classical methods of characterization,[10–12] is presented below.

In the first place, the characterization method is applied to samples that are parallelepipedic bars of PZ21 (FERROPERM Piezoceramics) polarized according to their axes. For those samples, the manufacturer characteristics are given[13] and can be compared with the results. Then, the validated method is applied to the circular cylinders samples with unknown properties.

From Eq. (27), one can find

$$Y_{33}^E = 4\rho L^2 (f_r^E)^2 \quad \text{and} \quad Y_{33}^D = 4\rho L^2 (f_r^D)^2. \tag{28}$$

The dielectric permittivity e_{ij}^{ε} is obtained at constant strain by rigidifying the connections or by exciting the material at high frequencies[9] (the strains are then very small because of the inertia of the sample). The permittivity e_{ij}^{σ}, measured for a free solid excited by a static electrical excitation or at low frequencies,[9] is usual and easier to determine than e_{ij}^{ε}.

In order to relate e_{ij}^{ε} and e_{ij}^{σ}, the stress expression in Eq. (1) is introduced in the electrical displacement expression of Eq. (2):

$$D_i = (e_{ij}^{\sigma} - d_{j\alpha} d_{j\beta} c_{\beta\alpha}^E) E_j + d_{i\alpha} c_{\alpha\beta}^E \varepsilon_{\beta}. \tag{29}$$

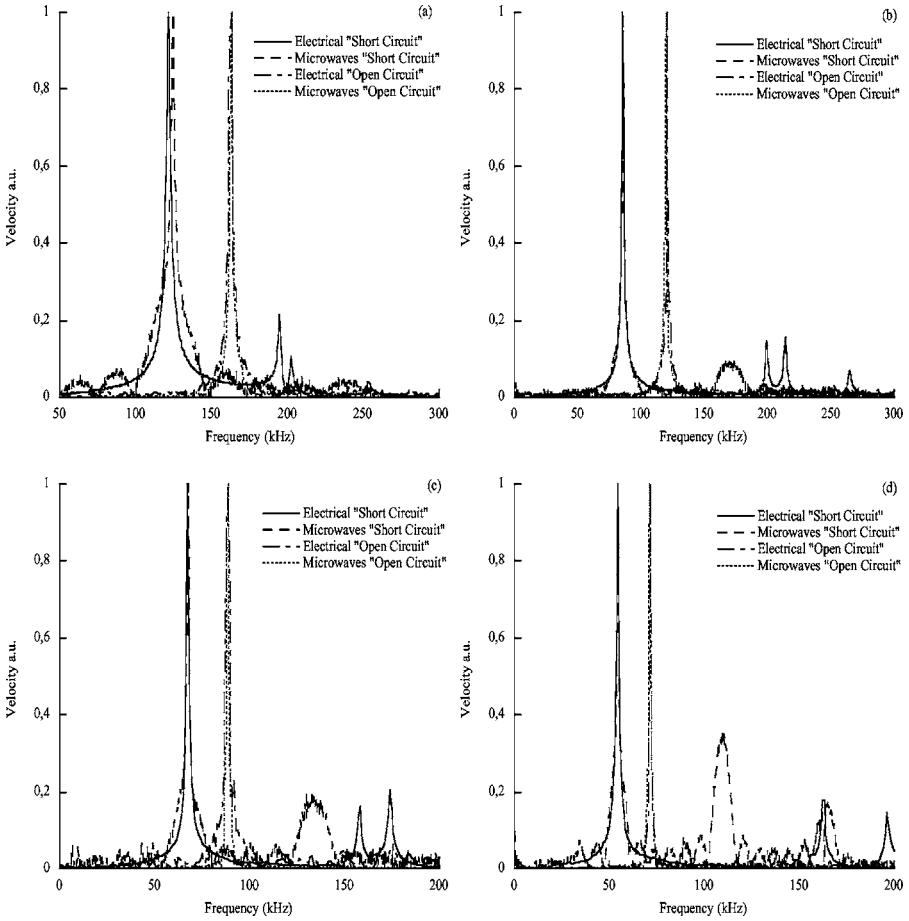

FIG. 3. Comparison of experimental velocity spectra for four bars excited electrically and by microwaves in short circuit and in open circuit: (a) 10 mm, (b) 15 mm, (c) 20 mm, and (d) 25 mm.

This relation is obtained by identification with the electrical displacement of Eq. (1):

$$e_{33}^{\varepsilon} = e_{33}^{\sigma} - d_{33}^2 Y_{33}^E. \tag{30}$$

Equation (30) gives the dielectric permittivity at constant strain from the knowledge of the piezoelectric charge constant d_{33} which is obtained from the combination of (30) and (11):

$$d_{33} = \left(\frac{Y_{33}^D - Y_{33}^E}{Y_{33}^E Y_{33}^D} e_{33}^{\sigma} \right)^{1/2}. \tag{31}$$

Moreover, the coupling factor k_{33}, which represents (for a piezoelectric material) the restitution rate of electrical energy into mechanical energy or vice versa, is given by

$$k_{33} = \left(\sqrt{1 - \frac{Y_{33}^E}{Y_{33}^D}} \right)^{-1}. \tag{32}$$

The measurements are taken on three slender bars (of lengths 35, 40, and 45 mm) in order to be able to use the equations given above. From the measurements of Young's moduli, the density (7800 kg/m^3) and the given manufacturer data of permittivity at constant stress ($e_{33}^{\sigma}=3980e_0$, with vacuum permittivity $e_0=8.85$ pF/m), the piezoelectric charge constant d_{33}, the dielectric permittivity e_{33}^{ε}, and the coupling factor k_{33} are computed and given in Table II. These calculated properties are very constant, whatever the samples, and are in adequacy with the manufacturer data, with nevertheless a small variation compared to the intervals of tolerance.

The method tested on samples with manufacturer known properties is now applied to the samples with unknown properties. The computed values of the cylindrical piezoelectric

TABLE II. Mechanical, electrical, and piezoelectric properties calculations for parallelepipedic piezoelectric Pz21 bars.

	Y_{33}^E (GPa)	Y_{33}^D (GPa)	d_{33} (pC/N)	e_{33}^{ε} (pF/m)	k_{33}
25 mm	58	99	500	2334 e_0	0.64
35 mm	58	98	493	2378 e_0	0.63
40 mm	58	100	501	2330 e_0	0.64
45 mm	58	99	502	2331 e_0	0.64
Average	58±0.5	99±0.8	499±19	(2343±398) e_0	0.64±0.02
Manufacturer	55.6±1.4	107.0±2.7	552±28	(1980±198) e_0	0.69±0.03

TABLE III. Mechanical, electrical, and piezoelectric properties calculations for cylindrical PZT bars.

	Y_{33}^{E} (GPa)	Y_{33}^{D} (GPa)	d_{33} (pC/N)	e_{33}^{ε} (pF/m)	k_{33}
25 mm	53	86	489	1800 e_0	0.61
30 mm	54	87	494	1850 e_0	0.61
Average	54±0.5	86.5±0.7	492±19	(1825±310) e_0	0.61±0.02

bars (given in Table III) are used to compute the frequency spectra based on the model. These spectra are compared to the measured spectra in Fig. 4.

Although the resonances are very sharp, the width of the peak indicates a small attenuation, due to the damping in the material and the effects of the surrounding supports. To take into account this attenuation, the imaginary parts of the Young's moduli are evaluated to 1% of the real parts.

The velocity spectra for an electrical excitation in short circuit and in open circuit, represented in Fig. 4, show that the theoretical model represents correctly the vibration phenomenon of piezoelectric slender bars. Indeed, when the length over diameter ratio is at least equal to 1.5, the bar can be considered as one-dimensional. The experimental and theoretical spectra of Fig. 4(a) are not superposed since the 10 -mm bar does not verify the slenderness condition to approach its behavior by the 1D model. Moreover, the three-dimensional effects that occur during the vibration of the bar are not taken into account. In the spectra of Figs. 3 and 4, other frequencies different from the harmonics of the fundamental mode appear. The 3D finite element modeling of the vibration of the samples shows that the frequencies obtained experimentally correspond to 3D eigenmodes (flexion, torsion, etc., …), which do not enter within the framework of this study and cannot be represented in the one-dimensional model.

V. NATURE OF ULTRASOUND GENERATION BY MICROWAVE EXCITATION

Expression (26) of the velocity spectrum leads to different resonance frequencies depending on the electrical boundary conditions and not on the generation mechanism. The model and the experimental results show that for the same electrical boundary conditions, the resonance frequencies obtained by a piezoelectric excitation and by microwaves are identical. Then, two-generation mechanisms can be assumed: a thermoelastic generation or a piezoelectric one due to the electric field included in the microwaves. The previous tests performed on single bars do not allow us to deduce this mechanism.

The configurations described in Fig. 5 permit us to study the theoretical and experimental response of a piezoelectric composed bar for which the results are strongly dependent on the generation nature. The samples are made with two bars glued together, named (1) and (2), of length L, excited either electrically or by microwaves in open circuit. Four configurations are tested by the combination of the excitation and the relative polarization orientations of the bars: either

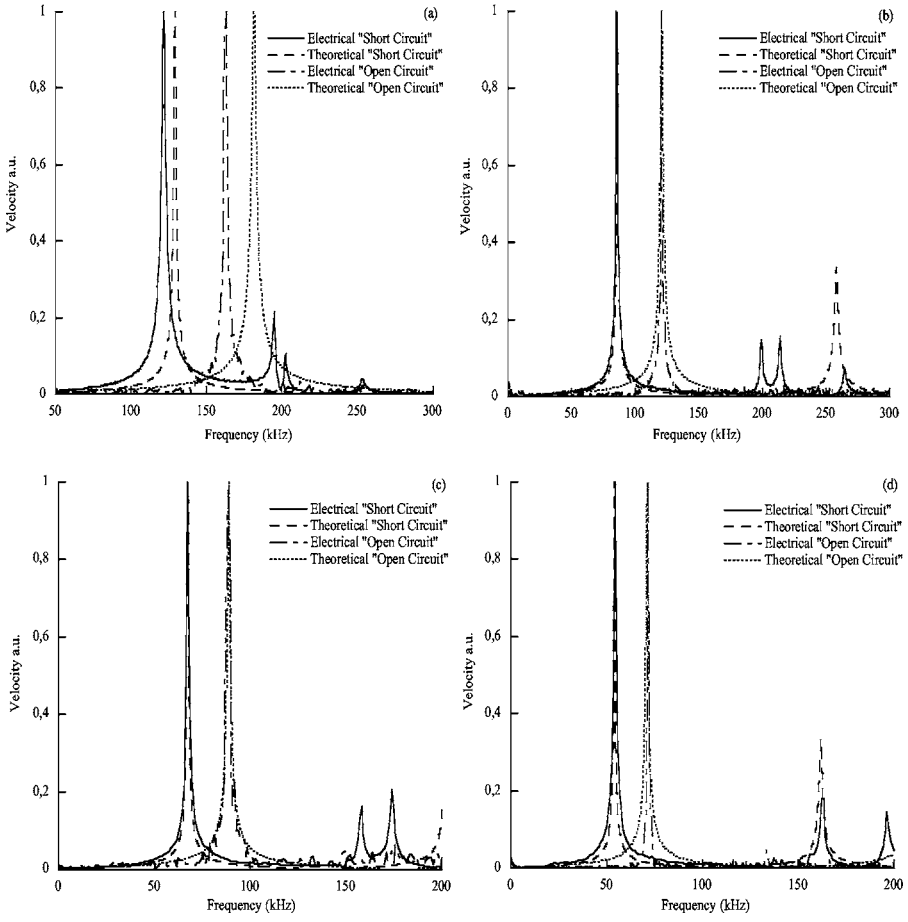

FIG. 4. Comparison of experimental and theoretical velocity spectra for four bars electrically excited in short circuit and in open circuit: (a) 10 mm, (b) 15 mm, (c) 20 mm, and (d) 25 mm.

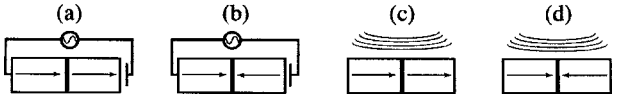

FIG. 5. Electrical and microwave excitation of a composed-bar in two experimental configurations: (a) and (c) same polarizations, (b) and (d)opposite polarizations.

polarization in the same direction (cases a and c) or polarization in opposite directions (case b and d) (see Fig. 5).

The intensity of the piezoelectric source stress $\sigma_0(z,\omega)$ is supposed to be uniform over the length of the bar. If the generation is piezoelectric, and for a given orientation of the electrical field excitation the pulsed source stress depends on the relative polarization orientations,

$$\sigma_0^{(1)} = \sigma_0^{(2)} = \sigma_0, \quad \text{same polarizations},$$
$$\sigma_0^{(1)} = -\sigma_0^{(2)} = \sigma_0, \quad \text{opposite polarizations}, \tag{33}$$

where $\sigma_0^{(1)}$ and $\sigma_0^{(2)}$ are the source stresses which act in the bars (1) and (2), respectively.

In both cases, the theoretical response of the composed bar is given by application of Eqs. (22) and (23) of the state vector method. If the generation is piezoelectric, the velocity spectra at the end of the composed bar are given by

$$V(2L) = \frac{-S^D[1+2c(2L)]\bar{\sigma}_0 s(L)}{i\rho c(L)}, \quad \text{same polarizations},$$
$$V(2L) = \frac{-S^D[1-c(L)]\bar{\sigma}_0}{i\rho s(L)}, \quad \text{opposite polarizations}. \tag{34}$$

The velocities given in (34) show that the resonance frequency of a composed bar excited by the microwave electric field depends on the relative orientations of the constitutive bars polarizations. Consequently, if the ultrasound generation by microwaves in the bars is induced by the microwave electric field, it must be sensitive to the polarizations orientation. On the contrary, if the generation is thermoelastic, the generation mechanism does not depend on the polarizations.

The experimental tests consist in exciting a bar (composed of two coupled identical PZT bars, of lengths 15 mm) electrically and by microwaves according to the configurations of Fig. 5. The obtained spectra are represented in Fig. 6, and Table IV summarizes the theoretical frequencies of each supposed generation mode and the experimental results for the studied composed bars.

TABLE IV. Experimental and guessed theoretical resonance frequencies of the composed bar excited electrically and by microwaves in two relative orientations of the polarizations.

	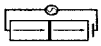			
Piezoelectric generation	f_r	$2f_r$	f_r	$2f_r$
Thermoelastic generation	----------		f_r	f_r
Resonance frequencies (kHz)	56	117	**56**	**58**

As guessed, if the composed bar is electrically excited, the resonance frequency is sensitive to the relative polarization orientations of the constitutive bars. When the two polarizations are identically oriented [Fig. 5(a)] the resonance frequency of the composed bar is 56 kHz, whereas for an opposed polarizations orientation [Fig. 5(b)], the resonance frequency is 117 kHz. The first frequency is that of a bar resonance of length 30 mm and corresponds, roughly, to the half of the 15 mm constitutive bar resonance frequency. As for the frequency obtained in opposed polarizations, it is only the resonance frequency of a bar of length 15 mm whose vibration is modified by the change of its mechanical boundary conditions.

The results obtained for the microwave excitation do not depend on the relative orientations of the polarizations. The resonance frequencies are almost the same when the two bars have identical [Fig. 5(c)] or opposite [Fig. 5(d)] polarizations. The generation by microwaves is thus independent of piezoelectric material polarization and has, in consequence, a thermoelastic origin. Physically, the microwaves excite dynamically the piezoelectric ceramic dipoles; their movements produce a temperature rise which finally results in the generation by thermal dilatation and the propagation of an elastic wave in the material.[5,6] In addition, the linearity of the microwaves excitation in the piezoelectric materials has been checked experimentally. Indeed, the ultrasonic amplitude in-

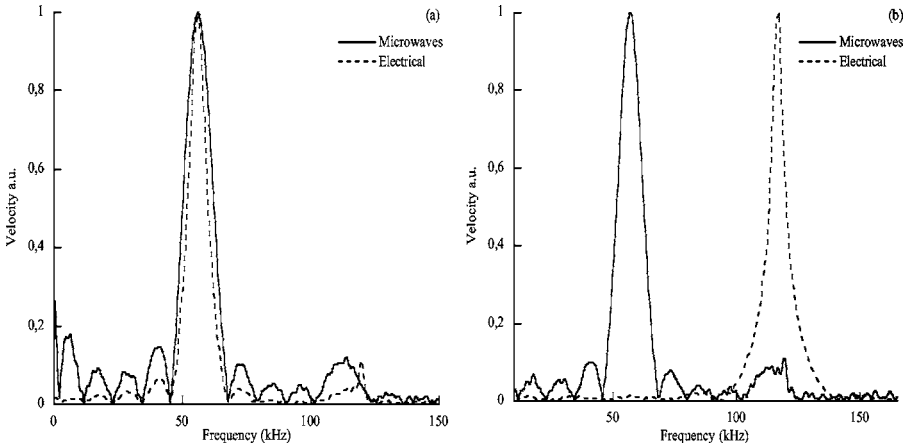

FIG. 6. Experimental spectrum of the composed bar excited electrically and by microwaves in the relative orientations of the polarizations: (a) same polarizations and (b) opposite polarizations.

creases linearly with respect to the microwave energy, which increases linearly the temperature in material (about 10^{-2} °C and 10^{-5} °C).

VI. CONCLUSIONS

The nature of the acoustic generation by microwaves in piezoelectric materials is thermoelastic. The sudden elevation of temperature is due to the excitation of the dipoles by the microwaves.

A one-dimensional model and some appropriated experiments were introduced to explain this mechanism and the various results that depend on the electrical boundary conditions. With these experiments and model, the various electrical and mechanical characteristics of the piezoelectric material were evaluated for the needs of calculations. The very good fitting between the theoretical and experimental frequency spectra obtained for various boundary conditions and excitations validates the physical explanations given about the thermoelastic generation mechanism.

Pulsed microwaves, producing acoustic waves in piezoelectric materials, could be used to excite buried piezoelectric elements, without contact, in structural health monitoring applications. The method can be extended to circular piezoelectric components, which can be uniformly excited by microwaves to produce radial dilatation in piezoelectric disks and, consequently, in the controlled structure.

[1]B. Jaffe, W. Cook, and H. Jaffe, *Piezoelectric Ceramics* (Academic, London, 1971).
[2]H. F. Tiersten, *Linear Piezoelectric Plate Vibrations* (Plenum, New York, 1969).
[3]B. A. Auld, *Acoustic Fields and Waves in Solids*, Volume 1 (2nd ed.) (Krieger, Malabar, FL, 1990).
[4]B. A. Auld, "Wave propagation and resonance in piezoelectric materials," J. Acoust. Soc. Am. **104**, 860–866 (1998).
[5]B. Hosten and P. Alain Bernard, "Ultrasonic wave generation by time-gated microwaves," J. Acoust. Soc. Am. **70**, 1577–1585 (1981).
[6]C. Bacon, E. Guilliorit, B. Hosten, and D. Chimenti, "Acoustic waves generated by pulsed microwaves in viscoelastic rods: Modeling and experimental verification," J. Acoust. Soc. Am. **110**, 1398–1407 (2001).
[7]C. Bacon, B. Hosten, and E. Guilliorit, "One dimensional prediction of the acoustic waves generated in a multilayer viscoelastic body by microwave irradiation," J. Sound Vib. **238**(5), 853–867 (2000).
[8]O. Guillon, "Caractérisation électromécanique et modélisation de céramiques ferroélectriques de type PZT," Ph.D. thesis, Université de Franche-Comté, 2003.
[9]D. Royer and E. Dieulesaint, *Ondes élastiques dans les solides* (Tome 1) (Masson, Paris, 1996).
[10]T. Fett and D. Munz, "Measurement of Young's moduli for lead zirconate titanate (PZT) ceramics," J. Test. Eval. **28**(1), 27–35 (2000).
[11]T. L. Jordan and Z. Ounaies, Piezoelectric Ceramics Characterization, NASA/ICASE Report, NASA/CR-2001-211225, ICASE Report No. 2001-28, 2001.
[12]IEEE Standard on Piezoelectricity, ANSI/IEEE Standard 176-1978.
[13]FERROPERM Piezoceramics—Piezoelectric material guide (website: ww.ferroperm-piezo.com).

Characterization of a small moving-magnet electrodynamic linear motor

Jin Liu and Steven Garrett
Graduate Program in Acoustics, The Pennsylvania State University, State College, Pennsylvania 16804

(Received 12 January 2005; revised 3 June 2005; accepted 11 July 2005)

The mechanical and electrodynamic parameters of a small, potentially inexpensive, moving-magnet electrodynamic linear motor are determined experimentally. Employing the formalism introduced by Wakeland, these parameters are used to predict the electromechanical efficiency of the motor. The transduction coefficient, *Bl*, was observed to be a function of position. But as shown in the paper, the variation in *Bl* with position has a smaller effect on the driver's output power because *Bl* is largest around the equilibrium position, where the piston velocity is also largest. By mechanical colinear joining of the armatures of two such motors, an electrodynamic load (dynamometer) is created to measure the efficiency as a function of energy dissipated in the dynamometer. The measured efficiencies are shown to be in good agreement with the predictions if a position-averaged effective transduction coefficient is introduced. Based on these results, this linear motor is judged to be an attractive power source in small electrically driven thermoacoustic refrigerator applications. © *2005 Acoustical Society of America.* [DOI: 10.1121/1.2011155]

PACS number(s): 43.38.Dv, 43.35.Ud [AJZ] Pages: 2289–2294

I. INTRODUCTION

The use of inert gases as the thermodynamic working fluid in thermoacoustic refrigerators[1] provides a potentially attractive alternative to the conventional vapor compression (Rankine Cycle) refrigeration technology that employs man-made chemicals.[2] Those chemicals have been shown to deplete the Earth's protective stratospheric ozone layer[3] and/or enhance the "greenhouse effect" that has led to worldwide concern over the effects of global warming.[4]

The environmental friendliness of the thermoacoustic alternative also requires that the thermoacoustic chillers be at least as energy efficient as the vapor compression units they replace, since greenhouse gases are emitted in the process of generating the energy consumed by electrically driven refrigerators. Recent advances in the efficiency of thermoacoustic heat transport processes[5–8] suggest that such an efficiency improvement is possible. For an electrically driven thermoacoustic refrigerator, high efficiency electroacoustic energy conversion is also required.

Advances have been made in the application of moving-magnet electrodynamic linear machines[9] to the production of high-amplitude sound fields in thermoacoustic refrigerators. To date, these advances have been focused on "loudspeakers" that generate acoustic output powers in excess of a kilowatt,[10] where the cost of these large linear motors[11] can be justified in the higher cooling capacity chillers. For the many lower power applications, such as domestic refrigerator/freezers and small food service refrigeration units, the cost and size of the mechanically resonant acoustic driver that would replace the rotary compressor in a conventional vapor compression unit presents a substantial barrier to the widespread adoption of thermoacoustic refrigeration.

The EnduraTEC™ Systems Group at Bose Corporation has developed a small moving magnet linear motor[12] (Model LM-1) that is currently used in medical instrumentation for the testing of biomedical materials.[13] The small size and weight of the LM-1, its 200 W power handling capacity, 12 mm stroke, and demonstrated reliability make it attractive for smaller-scale thermoacoustic refrigeration applications.[14] In this paper we report detailed measurements that were made on the LM-1 to determine its suitability.

II. THEORETICAL FRAMEWORK

Wakeland[15] has shown that the maximum electroacoustic efficiency of a linear electrodynamic motor (driver or loudspeaker) depends only upon the transduction coefficient (*Bl* product), the real (dissipative) part of the electrical impedance of the voice coil, $R_e \equiv \mathrm{Re}[Z_{\mathrm{el}}]$, where Z_{el} is the blocked complex electrical impedance of the voice coil, and the driver's open-circuit mechanical resistance R_m. From these driver properties, Wakeland defines two dimensionless parameters: $\beta \equiv (Bl)^2/R_e R_m$ and $\sigma \equiv (\beta+1)^{1/2}$. If the purely dissipative load, R_a, that is presented to the driver is optimized by making $R_a = \sigma R_m$, and the driver suspension is adjusted so that the driver is mechanically resonant at the intended frequency of operation, $f = \omega/2^*\pi = (1/2\pi)(k/m)^{1/2}$, where k is the driver's suspension stiffness and m is the driver's moving mass, then the maximum electroacoustic transduction efficiency, $\eta_{\max}$, is

$$\eta_{\max} = \frac{\sigma - 1}{\sigma + 1}. \tag{1}$$

These results can be derived for drivers with large β ($\geqslant 5$) by adjusting the load to equate the average power dissipated by Joule heating of the voice coil ($\Pi_{\mathrm{el}} = R_e i^2/2$) to the average power dissipated in the mechanical resistance of the driver ($\Pi_{\mathrm{mech}} = R_m v^2/2$).

Wakeland's analysis assumes that the *Bl* product is a constant that is independent of the driver's amplitude of motion, x. Although that is not true for the LM-1, nor for other

TABLE I. Summary of driver parameters measured for the two linear motors. The estimated uncertainties are based on the differences in the results obtained with the driver in two opposite vertical orientations. These uncertainties were consistent with the statistical uncertainties in the slopes of the least-squares fits to the measurements. The value for maximum efficiency, η_{max}, is calculated (Ref. 15) from the measured parameters in the table.

Motor Serial Number: Parameter	Symbol	Units	100181 Result	100181 Error	100070 Result	100070 Error
Suspension stiffness	k	N/m	7,760	±10(±0.1%)	6,470	±30(±0.5%)
Dynamic mass	m	Kg	0.1265	±0.001(±0.8%)	0.1071	±0.0008(±0.8%)
Natural frequency	f	Hz	39.4	±0.2(±0.4%)	39.1	±0.2(±0.4%)
Mechanical resistance	R_m	Kg/s	2.34	±0.04(±1.7%)	3.75	±0.06(±1.5%)
dc electrical resistance	R_{dc}	Ω	1.36	±0.035(±2.5%)	1.39	±0.03(±2.2%)
Inductance	L	mH	23.0	±0.07(±0.3%)	21.7	±0.3(±1.4%)
Bl product at x=0	c	N/A	18.36	±0.185(±1.0%)	18.12	±0.05(±0.2%)
Bl product (linear term)	b	N/A m	266	±137.5(±50%)	260	±36.9(±14.3%)
Bl product (quadratic term)	a	N/A m^2	−178,000	±4150(±2.3%)	−131,000	±5600(±4.26%)
Maximum efficiency	η_{max}		81.8%	±2.8%	77.4%	±2.7%

moving-magnet electrodynamic motors that have been studied at the Penn State Applied Research Laboratory,[16–18] it is shown in a subsequent section of this paper that the variation in (Bl) with piston position has a small effect on the driver's output power. This is because (Bl) is largest around the equilibrium position, where the piston velocity is also largest.

III. DRIVER MECHANICAL PARAMETER MEASUREMENTS

The suspension stiffness and dynamic mass of the driver can be determined nondestructively by measuring the mechanical resonance frequency as a function of the mass, m_i, added to the armature. The resonance frequencies, f_i, corresponding to m_i, are approximated by tracking the zero crossing of the phase of the input electrical impedance (using an HP4192A Impedance Analyzer) of the voice coil. Since the quality factor of the mechanical resonance is typically greater than ten, the neglect of the motor winding inductance ($L \simeq 21$ mH) that contributes a gradual linear variation in impedance through its inductive reactance ($X_L = \omega L$) is not significant for the determination of dynamic mass and suspension stiffness.

The armature of the LM-1 has a rectangular mounting plate that is approximately 38 mm long, 15.5 mm wide, and 1.8 mm thick. The plate has five tapped (4-40) mounting holes; one near each corner of the plate and one at the center. We attached a fixture with a $\frac{1}{4}$-20 threaded rod to that mounting plate to accommodate rigid attachment of standard slotted laboratory weights to the threaded rod. The mass of that fixture is 0.0241 kg, including the $\frac{1}{4}$-20 nut and washer used to constrain the added masses.

The resonance frequency, f_i, with a mass, m_i, added to the piston, can be plotted to produce a straight line.

$$\frac{1}{4\pi^2 f_i^2} = \frac{m}{k} + \frac{m_i}{k}. \tag{2}$$

The inverse of the slope of the line in Eq. (2) determines the suspension's stiffness and the ratio of the intercept to the slope determines the dynamic mass. These measurements were made on both LM-1 drivers (S/N: 100070 and S/N: 100181) using ten different weights with a maximum added mass of 0.30 kg. The correlation coefficients for the curve fits to Eq. (2) gave uncertainties in the slope[19] that were under ±1%. The measurements were repeated twice for each driver. The results reported in Table I include an uncertainty that is half of the difference of the results from the two measurements made with different orientations of the driver.

The mechanical resistance was measured with the same added mass fixture by recording the open-circuit voltage generated by the voice coil (recorded on a Nicolet 310 Digital Oscilloscope). A current applied at a frequency near the mechanical resonance excited oscillations of the driver. The current was abruptly removed and the digitized waveform was captured and curve fit[20] with a four parameter chi-squared algorithm to the form $V(t) = V_0 e^{-t/\tau} \sin(\omega t + \phi)$, to extract values for the exponential decay time, τ. The mechanical resistance can be expressed in terms of the dynamic mass and the decay time, $R_m = 2m/\tau$.[21] The decay time was plotted against the dynamic mass for eight different added masses up 0.15 kg. The mechanical resistance, R_m, is twice the reciprocal of the slope. Uncertainties in the individual slopes are typically ±2%, so the mechanical damping seems to be independent of frequency and armature orientation in the neighborhood of the resonance frequency.

IV. DRIVER *Bl*-PRODUCT VERSUS PISTON POSITION

The Bl product was measured in a static experiment using the apparatus shown in Fig. 1. A calibrated 100 lb stainless steel load cell (Omega LCCB-100, S/N: K736020N), energized by a precision 10.000 V_{dc} bias supply, was used to measure the force, $F(i_{dc})$ produced by a dc current, i_{dc}, flowing through the voice coil, as measured by a Yokogawa WT-110 Power Meter. The load cell was attached to one end of a turnbuckle that was connected by a short section of chain to the added mass fixture attached to the rectangular mounting plate of the armature. A machinist's dial indicator was placed in contact with the armature to determine its displacement from equilibrium caused by rotation of the turnbuckle. The Bl product was measured from equilibrium to 0.25 in. (6.35 mm) away from equilibrium in steps of 0.05 in. (1.27 mm). As shown in Fig. 2, the load cell output voltage was plotted against the current for 20 different currents ranging up to 5.0 A_{dc} at each position. The relative

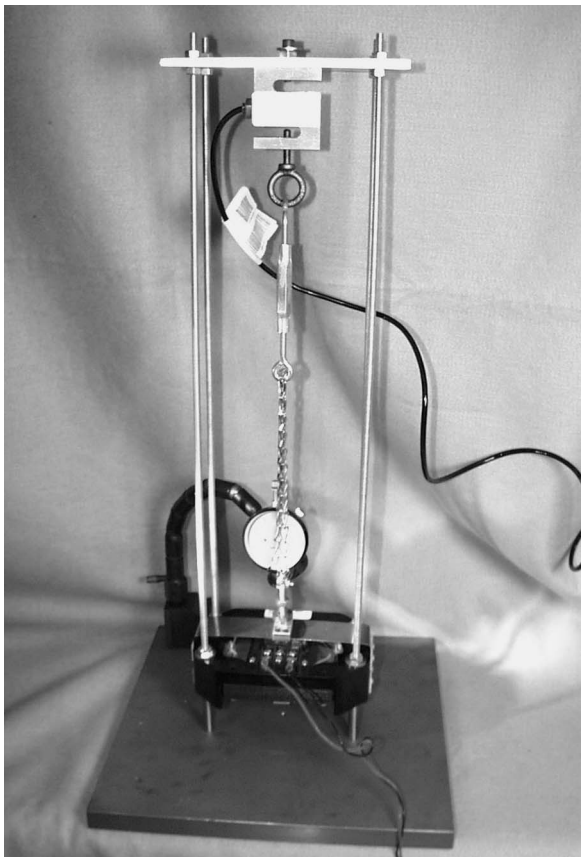

FIG. 1. Static test fixture for a measurement of the *Bl* product as a function of the armature's displacement from equilibrium. The S-shaped load cell at the top of the test stand is connected to the turnbuckle that is attached to the added mass fixture by a chain to avoid application of any torques to either the driver or the load cell. The dial indicator used to measure the piston position is visible behind the chain.

statistical uncertainties in the slopes are typically ±0.1%. This measurement was repeated on each driver for both directions of pull.

The *Bl* product as a function of position for S/N: 100181 is plotted in Fig. 3. The points are fit (least squares) with a second-degree polynomial of the form $Bl(x)=ax^2+bx+c$. It can be seen that (Bl) decreases by about 30% when the armature is pulled as far away from its equilibrium position as possible (6.35 mm). Although this decrease is substantial, its effect on the time-averaged acoustic power that the driver can deliver, $\langle \Pi_{ac} \rangle_t$,

$$\langle \Pi_{ac} \rangle_t = \frac{1}{T}\int_0^T \vec{F} \cdot \vec{v}\, dt = \frac{1}{T}\int_0^T Bl(x) i(t) v(t) dt, \tag{3}$$

is significantly smaller since the armature undergoes simple harmonic motion with the armature velocity being largest at the equilibrium position.

If the armature stroke is taken to be $2x_0$, substitution for $x(t)=x_0 \sin \omega t$, $v(t)=v_0 \cos \omega t=\omega x_0 \cos \omega t$, and $i(t)=i_0 \cos \omega t$, can create an effective *Bl* product, $(Bl)_{\text{eff}}$, based on the definition of average power in Eq. (3). The velocity and current (hence force) are assumed to be in phase since the linear motors are typically operated at their mechanical resonance frequency. Operation at resonance is frequently ensured by use of a feedback control system.[22,23] The resulting integral can be simplified if the time average is taken over only one quarter-cycle ($\pi/2$ radians), as shown in Eq. (4):

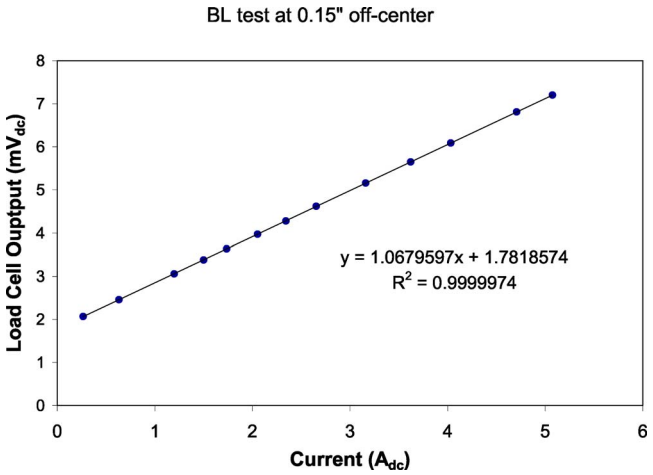

FIG. 2. Output of the load cell as a function of coil current for the driver's armature displaced by 3.81 mm (0.15 in.) from equilibrium. Using the calibrated sensitivity of the load cell, this plot corresponds to $Bl=17.21\pm0.008$ N/A.

$$\frac{(Bl)_{\text{eff}}}{Bl(x=0)} = \frac{\int_0^{T/4} (ax^2+bx+c)\cos^2 \omega t\, dt}{\int_0^{T/4} c \cos^2 \omega t\, dt}. \tag{4}$$

The substitution of $x(t)$ into Eq. (4) leads to simple integrals over products of trigonometric functions[24] that yield the stroke-dependent result for the normalized effective *Bl* product:

$$\frac{(Bl)_{\text{eff}}}{Bl(x=0)} = \frac{a}{4c}x_0^2 + \frac{4b}{3\pi c}x_0 + 1. \tag{5}$$

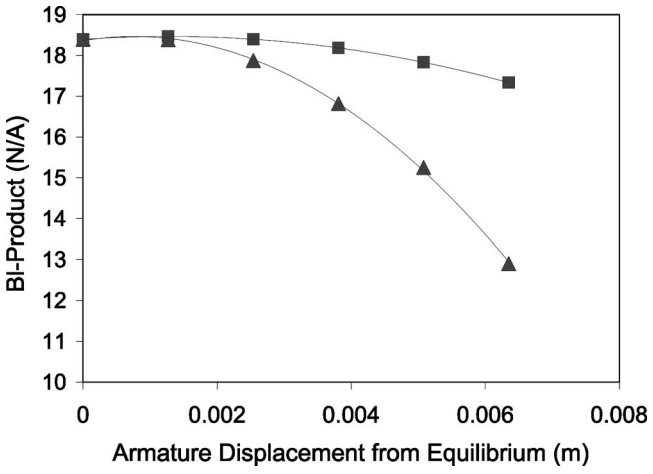

FIG. 3. The triangle-shaped points show the measured *Bl* product as a function of the displacement of the piston from its equilibrium position for LM-1, S/N: 100181. The line connecting the triangles is a second-order polynomial fit ($R^2=0.9995$). The effective *Bl* product, $(Bl)_{\text{eff}}$, (squares connected by a solid line) is based on those fit coefficients [($a=-176\,232$ N/A m^2; $b=266.3$ N/A m; $c=18.36$ N/A) and Eq. (5)].

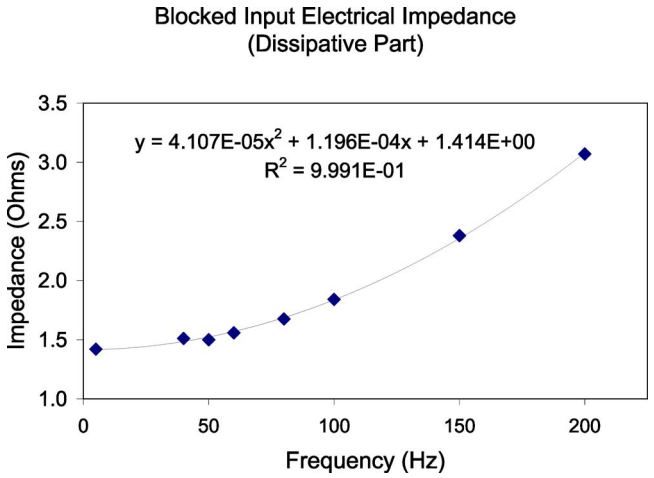

FIG. 4. Dissipative portion of the voice coil's blocked input electrical impedance of driver SN 100070, $R_e(f)=\mathrm{Re}[Z_{\mathrm{el}}]$, as a function of frequency. Extrapolation of the curve to zero frequency gives an intercept of $R_{\mathrm{dc}}=1.41\ \Omega$. That result is within experimental error for the corresponding value of $R_{\mathrm{dc}}=1.39\pm0.03\ \Omega$ in Table I.

The value of $(Bl)_{\mathrm{eff}}$ as a function of the armature displacement is plotted along with the static values of $Bl(\mathrm{x})$ in Fig. 3. It can be seen clearly that although Bl ($x=6.35$ mm) is only 70% of its equilibrium value, $(Bl)_{\mathrm{eff}}$ is still 94.3% of $Bl(\mathrm{x}=0)$ when averaged over a 12.7 mm stroke.

It should be noted that the variation of the Bl product with armature position also has the effect of introducing motion of the armature at frequencies that are harmonic multiples of the frequency of the electrical current. Because these linear motors have quality factors that are typically of order ten, the response of the armature at the harmonics of the drive are negligible.

V. VOICE COIL ELECTRICAL IMPEDANCE

The average power dissipated by the voice coil is caused by three effects.[16] For the LM-1 at the frequencies of interest (<100 Hz), Joule heating due to the current passing the electrical resistance of the coil, R_{dc}, is the largest contributor. Additional losses are created by the dissipation due to eddy currents generated in the laminations around which the coil is wound, as well as to magnetic hysteresis in the lamination material and the magnet carrier. The eddy current and hysteretic losses are frequency dependent.

R_{dc} was determined by a four-wire technique that measured the current and voltage over the current range of interest (typically $0.5-5.0\ A_{\mathrm{dc}}$). A straight line was fit to the data and the slope and uncertainty in the slope provided the dc resistance and its uncertainty reported in Table I. The complex input electrical impedance of the coil was measured with an impedance analyzer (HP 4192A). Care was taken to immobilize the driver's armature using a clamping fixture during these measurements. This minimizes the contribution of motional impedance during the measurement.

All of these three loss mechanisms can be represented by the frequency-dependent dissipative (real) component, $R_e(f)=\mathrm{Re}[Z_{\mathrm{el}}]$, of the voice coil's blocked electrical impedance. The real part of the frequency-dependent blocked electrical impedance of S/N:100070 is plotted in Fig. 4. The frequency-dependent inductive (imaginary) component of the blocked input electrical impedance of the coil, $X_e(f)=\mathrm{Im}[Z_{\mathrm{el}}]$, increased linearly with frequency corresponding to a voice coil inductance of 21.7 ± 0.3 mH.

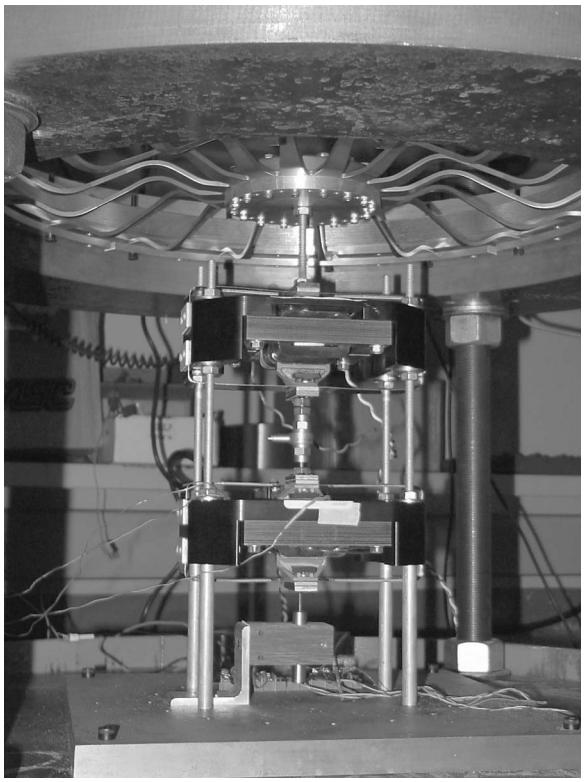

FIG. 5. Bottom view of the 104 Hz LM-1 dynamometer test apparatus. The higher frequency was achieved under atmospheric conditions by a 16-legged flexure spring (U.S. Patent No. 6,307,287, Oct. 23, 2001), developed for the CFIC C-2 motor alternator (Ref. 16). Under the spring, two LM-1's are visible. Their armatures are joined by an impedance head. The top LM-1 was operated as an alternator to provide an adjustable load on the lower LM-1 that was operated as a motor. The mass of the steel and aluminum structure, held together by four $1\frac{1}{4}$ in. diameter bolts, is approximately 140 kg. Since the total moving mass of the two armatures and spring is approximately 1 kg, motion of the structure was neglected.

VI. DRIVER DYNAMOMETER POWER MEASUREMENTS

A direct determination of the efficiency of one driver (S/N: 100181) was made by rigidly connecting its armature to the armature of the other driver (S/N: 100070) together with a spring[10] to increase the resonant frequency to 104 Hz. A photograph of the high-frequency dynamometer is shown in Fig. 5. Alternating current was applied to the driver being tested, while different electrical load resistances, R_{load}, and a load-matching 80 μF capacitor were connected in series with the terminals of the driver (used as an alternator) that was acting as the load for the driver under test.[25,26]

Electromechanical conversion efficiency was measured at a fixed stroke. The stroke was monitored by an accelerometer attached to the armature (PCB Model 353B65, S/N: 33055). One Yokogawa WT-110 electrical power meter measured the electrical power delivered to the driver under test and a second Yokogawa WT-110 electrical power meter measured the power dissipated in the load resistor, R_{load}. The

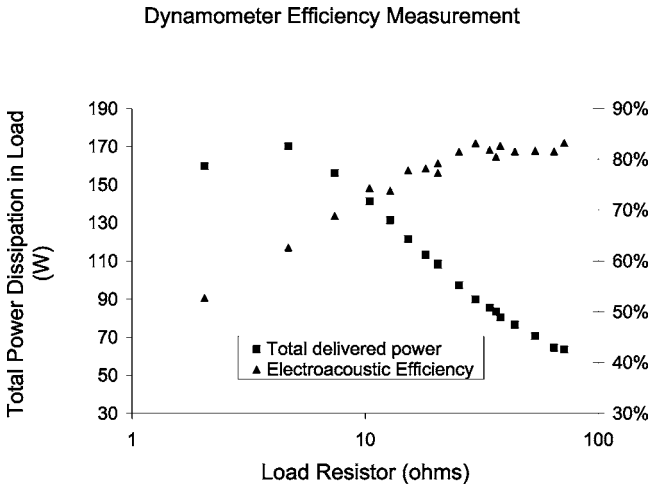

FIG. 6. Electroacoustic efficiency (triangles) and total electrical power dissipated (squares) versus dynamometer electrical load resistance. For this measurement, the driver stroke was maintained at a constant value of $2x_0 = 10.7$ mm and the operating frequency was 104 Hz. These results demonstrate that one can trade off power for efficiency by adjusting the load presented to the motor as required by a specific application.

total power dissipated by the load is the sum of the measured electrical power dissipated in R_{load}, the electrical power dissipated in R_{dc} by the coil, and the mechanical power dissipated by the measured mechanical resistance of the load, $R_{\text{m\&s}}$. The mechanical resistance of the load-side alternator (SN10070) with the spring was measured *via* the technique described in Sec. III. The mechanical resistance of the alternator, together with the spring, is $R_{\text{m\&s}}=6.6\pm1.34$ Kg/sec. The dissipation in the driver under test (SN 100181) is one contribution to its "inefficiency" that is being measured. Since both stroke and frequency were held constant as the electrical load resistance was varied, the mechanical power dissipated in the load was also constant. For the data shown in Fig. 6, the stroke was $2x_0=10.7$ mm and the frequency was 104 Hz, corresponding to a root-mean-squared piston velocity of $v_{\text{rms}}=2.47$ m/s, and an average mechanical power dissipation, $\Pi_{\text{mech}}=R_{\text{m\&s}}v_{\text{rms}}^2=40.3$ W. The maximum total dissipated power is 170 W at $R_{\text{load}}=4.7\ \Omega$

VII. CONCLUSIONS

The electrodynamic parameters of two Bose LM-1 moving-magnet linear motors were measured. The theoretical efficiencies for both motors were calculated. The metal structures that restrain the NdFeB magnet within the armature (i.e., magnet carriers) of the motors were different. S/N: 100181 has a titanium carrier and S/N: 100070 has a magnesium carrier. It appears that the titanium carrier experienced less mechanical damping and was therefore more efficient. The electrical resistivity of titanium (43 $\mu\Omega$ cm at 22 °C) is ten times higher than the resistivity of magnesium (4.3 $\mu\Omega$ cm at 22 °C), so it is likely that the difference in performance was due to eddy current losses[27] in the magnet carrier.

The efficiency of S/N: 100181 was measured as a function of load by connecting its armature to that of S/N: 100070 and varying the electrical resistance shunting the electrical terminals of S/N: 100070 while maintaining the stroke of both motors. The maximum measured efficiency as shown in Fig. 6 (approximately $81.8\pm2.8\%$) of the driven motor was found to agree with the Wakeland[15] formalism ($\eta_{\max}=82\pm2\%$) within experimental error.

ACKNOWLEDGMENTS

The authors are grateful to the Bose Corporation for the donation of the two LM-1 motors used in the research that was supported under a Research Agreement with Ben & Jerry's Homemade, Inc., of Burlington, VT. The authors thank Dr. M. E. Poese for his free-decay data acquisition and curve fitting programs and R. W. M. Smith for discussions regarding the derivation of $(Bl)_{\text{eff}}$. The Applied Research Laboratory supported Ms. Liu under their Exploratory and Foundation Program.

[1] G. W. Swift, *Thermoacoustics: A Unifying Perspective For Some Engines and Refrigerators* (Acoustical Society of America, New York, 2002).
[2] S. L. Garrett and S. Backhaus, "The power of sound," Am. Sci. **88**, 516–525 (2000).
[3] A. Makhijani and K. R. Gurney, *Mending the Ozone Hole: Science, Technology, and Policy* (MIT Press, Cambridge, MA, 1995).
[4] S. K. Fischer, J. J. Tomlinson, and P. J. Hughes, "Energy and global warming impacts of not-in-kind and next generation CFC and HCFC alternatives," U.S. Dept. Energy, 1994.
[5] G. W. Swift, S. N. Backhaus, and D. L. Gardner, "Traveling-wave device with mass flux suppression," U.S. Patent No. 6,032,464, Mar. 7, 2000.
[6] C. M. De Blok and N. A. H. J. Van Rijt, "Thermo-acoustic system," U.S. Patent No. 6,314,740, Nov. 13, 2001.
[7] R. W. M. Smith, M. E. Poese, S. L. Garrett, and R. S. Wakeland, "Thermoacoustic device," U.S. Patent No. 6,725,670, Apr. 27, 2004.
[8] M. E. Poese, R. W. M. Smith, R. S. Wakeland, and S. L. Garrett, "Bellows bounce thermoacoustic device," U.S. Patent No. 6,792,764, Sept. 21, 2004.
[9] I. Boldea and S. A. Nasar, "Linear electric actuators and generators," IEEE Trans. Energy Convers. **14**, 712–717 (1999); *Linear Electric Actuators and Generators* (Cambridge University Press, Cambridge, 1997).
[10] S. L. Garrett, R. M. Keolian, and R. W. M. Smith, "High-efficiency moving magnet loudspeaker," U.S. Patent No. 6,307,287, Oct. 23, 2001.
[11] G. A. Yarr and J. A. Corey, "Linear electrodynamic machine," U.S. Patent No. 5,389,844, Feb. 14, 1995; "HOTS to WATTS: The FPSE linear alternator system re-invented," in *Proceedings of the 27th Intersociety Energy Conversion Eng. Conf.* (Society of Automotive Engineers, Warrendale, PA, 1992).
[12] T. A. Froeschle and R. F. Carreras, "Permanent magnet transducing," U.S. Patent No. 5,216,723, June 1, 1993.
[13] EnduraTEC Systems Group, Bose Corp., 5610 Rowland Road, Suite 145, Minnetonka, MN 55343; http://www.enduratec.com/papers/revolutionary.html.
[14] Moving-magnet linear motors of similar power-handling capacity and efficiency (Models 1S102M/A and 1S132M/A) that we have used in the thermoacoustic refrigerator we built for Ben & Jerry's are offered for sale by Q-Drive™: www.qdrive.com. A general description of the Ben & Jerry's thermoacoustically chilled ice cream cabinet with a photograph of a Model 1S102M/A appears in an article by Karen Buscemi entitled "Sound power," in Appliance Design **53**, 42–45 (2005).
[15] R. S. Wakeland, "Use of electrodynamic drivers in thermoacoustic refrigerators," J. Acoust. Soc. Am. **107**, 827–832 (2000).
[16] R. W. M. Smith, "High efficiency two kilowatt acoustic source for a thermoacoustic refrigerator," Master's thesis in Engineering Mechanics, Penn State, Dec. 2000; Applied Research Laboratory Technical Report No. TR 01-001 (2001).
[17] R. W. M. Smith, S. L. Garrett, R. M. Keolian, and J. A. Corey, "High efficiency 2-kW thermoacoustic driver," from *Collected Papers, Proceedings of the 137th Meeting ASA*, and 2nd Convention European Acoustic Assn: Forum Acousticum, Techniche Universitaet Berlin, 14–19 March 1999 (Deutsche Gesellshaft für Akustik, ISBN 3-9804568-5-4).
[18] J. F. Heake, "Characterization of a 10-kilowatt linear motor/alternator for use in thermoacoustic refrigeration," Master's thesis in Acoustics, Penn State, Dec. 2001; Applied Research Laboratory Technical Report No. TR

02-003 (2002).
[19]J. Higbie,"Uncertainty in the linear regression slope," Am. J. Phys. **59**, 184–185 (1991).
[20]Igor Pro, Ver. 4.0 (WaveMetrics, Inc. 2000), www.wavemetrics.com.
[21]P. M. Morse, *Vibration and Sound*, 2nd ed. (Acoustical Society of America, New York, 1976), p. 25.
[22]S. L. Garrett, J. A. Adeff, and T. J. Hofler, "Thermoacoustic refrigerator for space applications," J. Thermophys. Heat Transfer **7**, 595–599 (1993).
[23]T. L. Shearer, H. F. Hofmann, R. W. M. Smith, and S. L. Garrett, "Sensorless control of a thermoacoustic refrigerator," J. Acoust. Soc. Am. **116**, 288–293 (2004).
[24]I. S. Gradshteyn and I. M. Ryzhik, *Table of Integrals, Series, and Products* (Academic, New York, 1980), Sec. 2.513, p. 133.
[25]S. E. Auyer and W. A. Miller, "Development of a high-power transducer DUMILOAD," J. Acoust. Soc. Am. **60**, 734–740 (1976).
[26]R. Redlich, R. Unger, and N. van der Walt, "Linear compressors: motor configuration, modulation and systems," *Proc., Int. Compressor Eng. Conf., Purdue University*, West Lafayette, IN, 23–26 July 1996; http://www.sunpower.com/tech_papers/pub68/purdue.html.
[27]P. Campbell, *Permanent Magnet Materials and their Application* (Cambridge University Press, Cambridge 1994); ISBN 0 521 56688 6.

An alternative numerical implementation of the Burnett family of acoustic infinite elements

T. K. Bhandakkar[a] and C. S. Jog
Facility for Research in Technical Acoustics (FRITA), Department of Mechanical Engineering, Indian Institute of Science, Bangalore 560012, India

(Received 11 November 2004; revised 5 July 2005; accepted 9 July 2005)

In a series of pioneering papers, Burnett and Holford presented the formulation and numerical implementation of three-dimensional acoustic infinite elements for modeling acoustic fields in exterior unbounded domains surrounding a structure. They are all based on a multipole expansion outside a closed coordinate surface that circumscribes the structure; the multipole expansion has a radial variable r, and two angular variables that describe the surfaces $r=$const. In the finite element representation, the pressure field is discretized using a product of radial and angular shape functions. The angular variables are discretized directly using nodal angular values. However, in some cases, and especially in problems involving symmetry, nodes are located in certain positions where one of the angular variables is undefined, thus leading to errors in the value of the angular variable in the interior of the elements connected to these nodes, and hence in the computed acoustic field. To overcome this problem, we propose an alternative numerical formulation in this work, which is based on the interpolation of the position vector expressed in the global Cartesian coordinate system (as in conventional finite elements) instead of the interpolation of angular variables. We present numerical solutions for a few benchmark problems using the proposed method. © *2005 Acoustical Society of America.* [DOI: 10.1121/1.2011151]

PACS number(s): 43.40.Rj, 43.20.Tb [LLT] Pages: 2295–2301

I. INTRODUCTION

Burnett and Holford[1–3] introduced new three-dimensional acoustic elements for modeling acoustic fields in exterior domains, which were shown to be computationally far more efficient compared to the boundary element method. These elements are based on a multipole expansion of the pressure field in terms of radial and angular variables outside a surface that circumscribes the structure. Our purpose in this article is to present an alternative numerical scheme that overcomes the problem of certain angular variables not being defined at certain nodal points (see later). We shall focus exclusively on the ellipsoidal element,[3] since the other "Burnett" elements are special cases of this particular element. For reasons of brevity, we shall not discuss the advantages and disadvantages of acoustic infinite elements, but instead refer the reader to the recent review articles by Gerdes[4] and Astley *et al.*,[5,6] where extensive discussions on the formulation and performance of various acoustic infinite elements have been presented.

The governing equation for the (complex-valued) pressure field p in the domain V due to a vibrating body is

$$\nabla^2 p + k^2 p = 0,$$

where $k=\omega/c_s$ is the wave number, ω is the angular frequency, and c_s is the sound speed. The boundary conditions at the surface S of the vibrating body and at the "outer" boundary at infinity are

$$(\boldsymbol{\nabla} p)\cdot\mathbf{n} = -i\omega\rho v_n, \quad \text{on } S,$$

$$\frac{\partial p}{\partial r} + ikp = o\left(\frac{1}{r}\right), \quad \text{as } r\to\infty,$$

where $\mathbf{v}$ is the velocity of a point on the surface, $v_n \equiv \mathbf{v}\cdot\mathbf{n}$ is the normal velocity, and r is the spherical polar radius. The latter boundary condition is known as the Sommerfeld radiation condition.

In the ellipsoidal element presented in Ref. 3, the finite element representation of the pressure is carried out using radial and angular shape functions. For example, the angular variables θ and ϕ are interpolated as [see Eq. (4.1) in Ref. 3]

$$\theta(\xi,\eta) = \sum_{\nu=1}^{n} \theta_\nu \chi_\nu(\xi,\eta); \quad \phi(\xi,\eta) = \sum_{\nu=1}^{n} \phi_\nu \chi_\nu(\xi,\eta), \qquad (1)$$

where n is the number of nodes in the quadrilateral or triangle, $\chi_\nu(\xi,\eta)$ are interpolation functions, and θ_ν and ϕ_ν are angular ellipsoidal coordinates of the νth node. The problem with the above interpolation is that θ (or ϕ) could be undefined at certain points. An an example, consider the spherically symmetric problem of a radially pulsating sphere; symmetry considerations allow us to use an octant of a sphere as a circumscribing surface (see Fig. 1), and this surface constitutes the base surface for the infinite elements. The relation between the Cartesian and spherical coordinates is given by $x=r\cos\theta\sin\phi$, $y=r\sin\theta\sin\phi$, and $z=r\cos\phi$. At node 1, although the Cartesian coordinates are well defined, the spherical coordinates are not, since the value of θ is undefined. If Eq. (1) is used, this ambiguity yields wrong values for θ in the interior of elements connected to node 1, so that, for example, one does not get the expected symmetric solution.

[a]Electronic mail: tanmay@mecheng.iisc.ernet.in

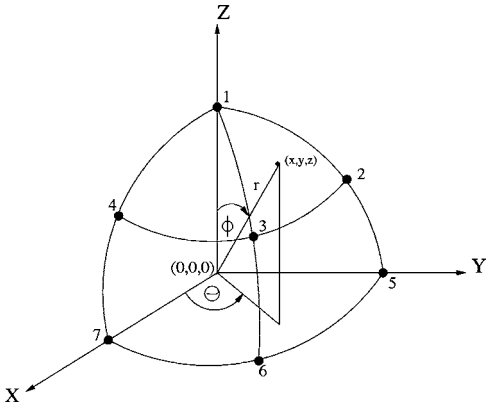

FIG. 1. For the case of a radially pulsating sphere, symmetry considerations allow us to model an octant of the sphere; the bounding surface that envelopes the structure can also be taken to be an octant of a larger sphere, and constitutes the base surface for the infinite elements as shown.

In this work, we propose an alternative numerical strategy, whereby, similar to conventional finite elements, the position vector in (global) Cartesian coordinates (which is well defined at all points) is interpolated. This proposed interpolation not only eliminates the ambiguity associated with a direct interpolation of angular variables, but also eliminates the problem of discontinuity of geometry between the finite-size and infinite elements that occurs at the bounding surface (see p. 62 of Ref. 3 for a discussion of this problem).

Keeping in view the fact that shell elements based on Cosserat models are also formulated using a local Cartesian coordinate system that is constructed on the curved shell surface, we shall often use the results from differential geometry that are used in such works, e.g., Ref. 7.

In Sec. II we discuss some preliminary material that is used in the numerical implementation strategy described in Sec. III. Examples based on the proposed strategy are presented in Sec. IV, and in Sec. V we conclude the paper.

II. ELLIPSOIDAL COORDINATES

The equation of the ellipsoid that circumscribes the structure is given by

$$\frac{x^2}{a^2}+\frac{y^2}{b^2}+\frac{z^2}{c^2}=1. \tag{2}$$

Assuming that $a \geqslant b \geqslant c$, the ellipsoidal coordinates (r,θ,ϕ) are defined as[3]

$$x = r(1-q\cos^2\theta)^{1/2}\cos\phi, \tag{3a}$$

$$y = (r^2-g^2)^{1/2}\sin\theta\sin\phi, \tag{3b}$$

$$z = (r^2-f^2)^{1/2}\cos\theta(1-p\cos^2\phi)^{1/2}, \tag{3c}$$

where $f^2=a^2-c^2$, $g^2=a^2-b^2$ and

$$p=\begin{cases}\dfrac{g^2}{f^2}, & \text{when } f\neq 0,\\ 0, & \text{when } f=0,\end{cases}$$

$$q=\begin{cases}\dfrac{b^2-c^2}{f^2}, & \text{when } f\neq 0,\\ 1, & \text{when } f=0,\end{cases}$$

while the ellipsoidal covariant base vectors $(\mathbf{a}_r,\mathbf{a}_\theta,\mathbf{a}_\phi)$ are given in terms of the Cartesian basis vectors $(\mathbf{i},\mathbf{j},\mathbf{k})$, by [see Eq. (4.21) in Ref. 3]

$$\begin{aligned}\mathbf{a}_r &= Q\cos\phi\mathbf{i}+G^{-1}\sin\theta\sin\phi\mathbf{j}+F^{-1}P\cos\theta\mathbf{k},\\ \mathbf{a}_\theta &= rqQ^{-1}\sin\theta\cos\theta\cos\phi\mathbf{i}+rG\cos\theta\sin\phi\mathbf{j}\\ &\quad -rFP\sin\theta\mathbf{k},\\ \mathbf{a}_\phi &= -rQ\sin\phi\mathbf{i}+rG\sin\theta\cos\phi\mathbf{j}\\ &\quad +rFpP^{-1}\cos\theta\sin\phi\cos\phi\mathbf{k},\end{aligned} \tag{4}$$

where $F=\sqrt{1-f^2/r^2}$, $G=\sqrt{1-g^2/r^2}$, $P=\sqrt{1-p\cos^2\phi}$, and $Q=\sqrt{1-q\cos^2\theta}$.

Given (r,θ,ϕ), it is straightforward to find (x,y,z) via Eq. (3); in the subsequent development, however, we will need to find r and the quantities $(\cos\theta,\sin\theta,\cos\phi,\sin\phi)$ that occur in Eq. (4), given a point (x,y,z) that lies on an ellipse confocal to the one defined by Eq. (2). The inversion is carried out as follows.

(1) Find the roots of the cubic equation [which is a rearrangement of Eq. (2.9) in Ref. 3],

$$\begin{aligned}&t^3+(a^2+b^2+c^2-x^2-y^2-z^2)t^2\\ &\quad+[a^2b^2+a^2c^2+b^2c^2-x^2(b^2+c^2)-y^2(a^2+c^2)\\ &\quad-z^2(a^2+b^2)]t+(a^2b^2c^2-x^2b^2c^2-y^2a^2c^2-z^2a^2b^2)=0,\end{aligned}$$

using, for example, the procedure presented in Ref. 8.

(2) Denoting the maximum root of the above equation by λ, the radius of the confocal ellipsoid is given by $r_c=\sqrt{a^2+\lambda}$.

(3) Substitute $r=r_c$ into Eq. (3) and eliminate ϕ to get the following quadratic equation in $\cos^2\theta$:

$$h_1\cos^4\theta+h_2\cos^2\theta+h_3=0,$$

where

$$h_1=r_c^2(r_c^2-f^2)q,$$

$$h_2=(r_c^2-f^2)px^2-(r_c^2-f^2)r_c^2-z^2r_c^2q,$$

$$h_3=z^2r_c^2.$$

Note that $h_2<0$.

(4) On solving the above quadratic equation, we get

$$\cos^2\theta=\frac{1}{2h_1}(-h_2-\sqrt{h_2^2-4h_1h_3}),\quad \text{if } h_1\neq 0,$$

$$=-\frac{h_3}{h_2},\quad \text{if } h_1=0,$$

$$\cos^2\phi = \frac{x^2}{r_c^2(1-q\cos^2\theta)}.$$

The sign of $\cos\phi$ and $\cos\theta$ is determined by noting, using Eqs. (3a) and (3c), that they have the same sign as x and z, respectively.

(5) To determine $\sin\theta$ and $\sin\phi$, note from Eq. (3b) that $\sin\theta\sin\phi$ has the same sign as y. If we choose $\sin\phi$ to be positive, then $\sin\theta$ has the same sign as y. The opposite choice can also be made (as long as the same choice is used for all elements), since it simply results in a reversal of directions of $\mathbf{a}_\theta$ and $\mathbf{a}_\phi$, but, nevertheless, maintains the orthogonality and right-handedness of the $(\mathbf{a}_r, \mathbf{a}_\theta, \mathbf{a}_\phi)$ coordinate system.

III. PROPOSED NUMERICAL STRATEGY

The matrix equations for the isoparametric elements of finite extent (that lie between the structure and the bounding ellipsoid) are formulated in the standard way, and are given by

$$(\mathbf{K}^f - \omega^2\mathbf{M}^f)\mathbf{P} = \mathbf{f}^f. \tag{5}$$

The above global matrices are obtained by assembling element level matrices given by

$$K^f_{ab} = \int_{V_e} \boldsymbol{\nabla}\chi_a \cdot \boldsymbol{\nabla}\chi_b \, dV_e,$$

$$M^f_{ab} = \int_{V_e} \frac{1}{c_s^2}\chi_a\chi_b \, dV_e,$$

$$f^f_a = -\int_{\Omega_e} i\rho\omega v_n \chi_a \, d\Omega_e,$$

where V_e and Ω_e denote the domain of the element and surface that is in contact with the vibrating body, respectively, χ_ν denote the three-dimensional Lagrange interpolation functions associated with node ν, and $i=\sqrt{-1}$.

The matrix equations for the infinite elements (that extend from the surface of the bounding ellipsoid to infinity) are

$$(\mathbf{K}^\infty - \omega^2\mathbf{M}^\infty)\mathbf{P} = \mathbf{0}, \tag{6}$$

where

$$K^\infty_{ij} = (A^{(1)}_{\nu'\nu}R^{(1)}_{\mu'\mu} + A^{(2)}_{\nu'\nu}R^{(2)}_{\mu'\mu} - A^{(3)}_{\nu'\nu}R^{(3)}_{\mu'\mu}),$$

$$M^\infty_{ij} = \frac{1}{c_s^2}(A^{(1)}_{\nu'\nu}R^{(4)}_{\mu'\mu} - A^{(4)}_{\nu'\nu}R^{(2)}_{\mu'\mu} + A^{(5)}_{\nu'\nu}R^{(3)}_{\mu'\mu}).$$

The matrices $A_{\nu'\nu}$ are constructed using angular shape functions ψ^a_ν, $\nu=1,\ldots,n$, and the matrices $R_{\mu'\mu}$ are constructed using radial shape functions ψ^r_μ, $\mu=1,\ldots,m$. The indices i and j are given by $i=n(\mu'-1)+\nu'$ and $j=n(\mu-1)+\nu$ (see Fig. 15 in Ref. 1 for a specific example). The stiffness matrix and load vector for the entire domain are obtained by assembling the stiffness matrices and load vectors in Eqs. (5) and (6). If r denotes the radial ellipsoidal coordinate, r_μ denotes the radial ellipsoidal coordinate of the layer μ (with $r_1=a$), and $\mathbf{h}$ is defined via Eq. (4.12) in Ref. 3 (constructing $\mathbf{h}$ requires the inversion of a Vandermonde matrix that is known to become rapidly ill conditioned as the radial order of the element grows; hence, to mitigate this problem, we use the inversion algorithm presented in Ref. 9), the radial integrals are given by

$$\begin{aligned}
R^{(1)}_{\mu'\mu} &= L_{\mu'\mu}\left(\frac{b_2}{2i}e^{-i2\zeta} + \sum_{\beta=0}^{2m} b_{\beta+2}I_\beta\right),\\
R^{(2)}_{\mu'\mu} &= L_{\mu'\mu}\sum_{\beta=2}^{2m} c_\beta J_\beta,\\
R^{(3)}_{\mu'\mu} &= L_{\mu'\mu}k^2\sum_{\beta=2}^{2m} c_\beta J_{\beta+2},\\
R^{(4)}_{\mu'\mu} &= L_{\mu'\mu}\frac{1}{k^2}\left(\frac{c_2}{2i}e^{-i2\zeta} + \sum_{\beta=0}^{2m-2} c_{\beta+2}J_\beta\right),
\end{aligned} \tag{7}$$

where, with μ ranging from 1 to m, α ranging from 1 to $m+1$, $h_{\mu 0}=0$, $h_{\mu\alpha}=0$ for $\alpha>m$, and $a_{\mu\alpha}=0$ for $\alpha>m+1$,

$$L_{\mu'\mu} = e^{ik(r_{\mu'}+r_\mu)}/k,$$

$$a_{\mu\alpha} = -ih_{\mu\alpha} - (\alpha-1)h_{\mu,\alpha-1},$$

$$b_\beta = \sum_{\gamma=1}^{\beta-1} a_{\mu'\gamma}a_{\mu,\beta-\gamma},$$

$$c_\beta = \sum_{\gamma=1}^{\beta-1} h_{\mu'\gamma}h_{\mu,\beta-\gamma},$$

$$\zeta = kr_1,$$

$$J_\beta = e^{-i2kr_1} \times \int_0^\infty \left(\frac{1}{(y+kr_1)^\beta\left(1-\frac{f^2k^2}{(y+kr_1)^2}\right)^{1/2}\left(1-\frac{g^2k^2}{y+kr_1}\right)^{1/2}} - \delta_{\beta 0}\right) \times e^{-i2y}\,dy, \quad 0\leqslant\beta\leqslant 2m+4,$$

$$I_\beta = J_\beta - (g^2+f^2)k^2J_{\beta+2} + f^2g^2k^4J_{\beta+4}, \quad 0\leqslant\beta\leqslant 2m.$$

As indicated, the base surface of the infinite elements is interpolated using Lagrange interpolation functions $\psi_\nu(\xi,\eta)$ as

$$\mathbf{x} = \sum_{\nu=1}^{n} \mathbf{x}_\nu\psi_\nu(\xi,\eta), \tag{8}$$

where $\mathbf{x}_\nu$ are the Cartesian coordinates of the nodes. The area element $dS=h_\theta h_\phi\,d\theta\,d\phi$ used in the formulation of the angular integrals[3] is now replaced by

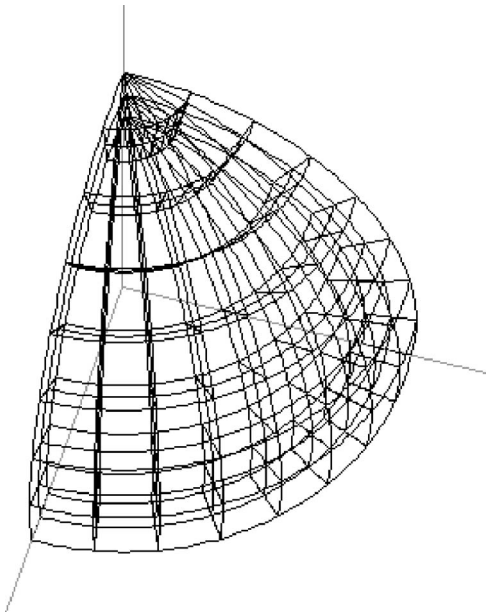

FIG. 2. An octant of the spherical envelope surrounding the radially pulsating sphere meshed using 8 W21 and 56 B27 elements; 8 IT7 and 56 IQ9 infinite elements (not shown in the figure) model the domain outside the envelope.

$$dS = \left\| \frac{\partial \mathbf{x}}{\partial \xi} \times \frac{\partial \mathbf{x}}{\partial \eta} \right\| d\xi \, d\eta. \tag{9}$$

We also need to compute the derivatives of the shape functions ψ_ν with respect to θ and ϕ. Using the chain rule and the definitions of $\mathbf{a}_\theta$ and $\mathbf{a}_\phi$, we have

$$\frac{\partial \mathbf{x}}{\partial \xi} = \frac{\partial \mathbf{x}}{\partial \theta}\frac{\partial \theta}{\partial \xi} + \frac{\partial \mathbf{x}}{\partial \phi}\frac{\partial \phi}{\partial \xi} = \mathbf{a}_\theta \frac{\partial \theta}{\partial \xi} + \mathbf{a}_\phi \frac{\partial \phi}{\partial \xi},$$

$$\frac{\partial \mathbf{x}}{\partial \eta} = \frac{\partial \mathbf{x}}{\partial \theta}\frac{\partial \theta}{\partial \eta} + \frac{\partial \mathbf{x}}{\partial \phi}\frac{\partial \phi}{\partial \eta} = \mathbf{a}_\theta \frac{\partial \theta}{\partial \eta} + \mathbf{a}_\phi \frac{\partial \phi}{\partial \eta}.$$

Taking the dot product of both the above equations with $\mathbf{a}_\theta$ and $\mathbf{a}_\phi$, using the facts $\mathbf{a}_\theta \cdot \mathbf{a}_\theta = h_\theta^2$, $\mathbf{a}_\phi \cdot \mathbf{a}_\phi = h_\phi^2$, $\mathbf{a}_\theta \cdot \mathbf{a}_\phi = 0$, $\mathbf{e}_\theta = \mathbf{a}_\theta / h_\theta$, and $\mathbf{e}_\phi = \mathbf{a}_\phi / h_\phi$, we get the expression for the "surface Jacobian" (note that a similar expression is used in Ref. 7) as

$$\mathbf{J} = \begin{bmatrix} \frac{\partial \theta}{\partial \xi} & \frac{\partial \phi}{\partial \xi} \\ \frac{\partial \theta}{\partial \eta} & \frac{\partial \phi}{\partial \eta} \end{bmatrix} = \begin{bmatrix} \frac{\mathbf{e}_\theta}{h_\theta} \cdot \frac{\partial \mathbf{x}}{\partial \xi} & \frac{\mathbf{e}_\phi}{h_\phi} \cdot \frac{\partial \mathbf{x}}{\partial \xi} \\ \frac{\mathbf{e}_\theta}{h_\theta} \cdot \frac{\partial \mathbf{x}}{\partial \eta} & \frac{\mathbf{e}_\phi}{h_\phi} \cdot \frac{\partial \mathbf{x}}{\partial \eta} \end{bmatrix}.$$

It now follows by using the chain rule that

$$\begin{Bmatrix} \frac{\partial \psi_\nu}{\partial \theta} \\ \frac{\partial \psi_\nu}{\partial \phi} \end{Bmatrix} = \mathbf{J}^{-1} \begin{Bmatrix} \frac{\partial \psi_\nu}{\partial \xi} \\ \frac{\partial \psi_\nu}{\partial \eta} \end{Bmatrix}.$$

We define

$$t_1 = (\mathbf{a}_\theta \cdot \mathbf{x}_{,\xi})(\mathbf{a}_\phi \cdot \mathbf{x}_{,\eta}) - (\mathbf{a}_\theta \cdot \mathbf{x}_{,\eta})(\mathbf{a}_\phi \cdot \mathbf{x}_{,\xi}),$$

$$(t_2)_\nu = (\mathbf{a}_\phi \cdot \mathbf{x}_{,\eta}) \frac{\partial \psi_\nu}{\partial \xi} - (\mathbf{a}_\phi \cdot \mathbf{x}_{,\xi}) \frac{\partial \psi_\nu}{\partial \eta},$$

$$(t_3)_\nu = -(\mathbf{a}_\theta \cdot \mathbf{x}_{,\eta}) \frac{\partial \psi_\nu}{\partial \xi} + (\mathbf{a}_\theta \cdot \mathbf{x}_{,\xi}) \frac{\partial \psi_\nu}{\partial \eta},$$

$$t_4 = \sqrt{r_1^2 - f^2 \sin^2 \theta - g^2 \cos^2 \theta},$$

$$t_5 = \sqrt{r_1^2 - g^2 \cos^2 \phi},$$

$$t_6 = f^2 \sin^2 \theta + g^2 \cos^2 \theta - g^2 \cos^2 \phi,$$

$$t_7 = f^2 \sin^2 \theta + g^2 \cos^2 \theta,$$

$$t_8 = f^2 - g^2 \cos^2 \phi,$$

$$t_9 = f^2 \sin^2 \theta + g^2 \cos^2 \theta + g^2 \cos^2 \phi,$$

$$t_{10} = g^2 \cos^2 \phi.$$

The angular integrals are now given by [with dS given by Eq. (9)]

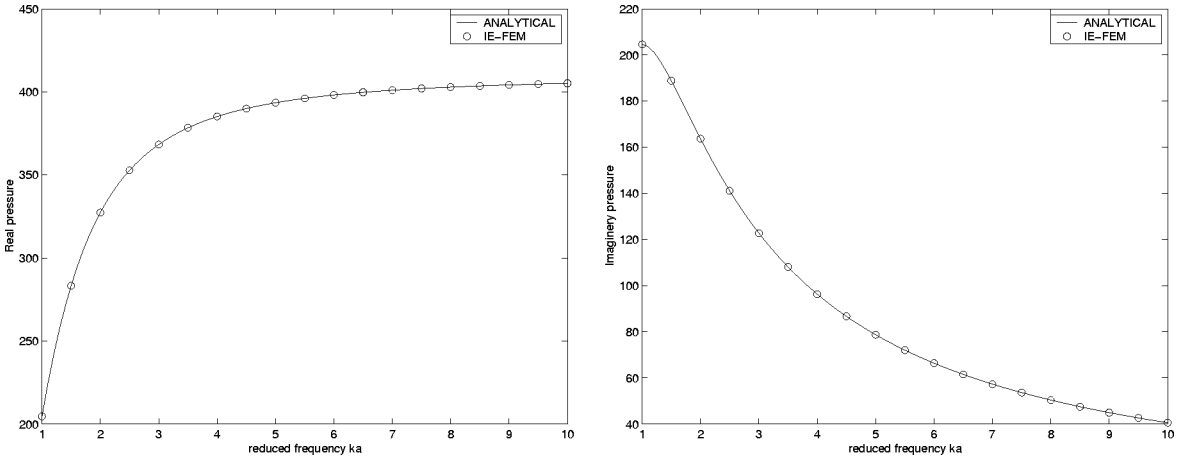

FIG. 3. A comparison of the numerically and analytically obtained real and imaginary parts of the surface pressure at (0,0,10) for $ka = 1, 2, \ldots, 10$ in the pulsating sphere problem.

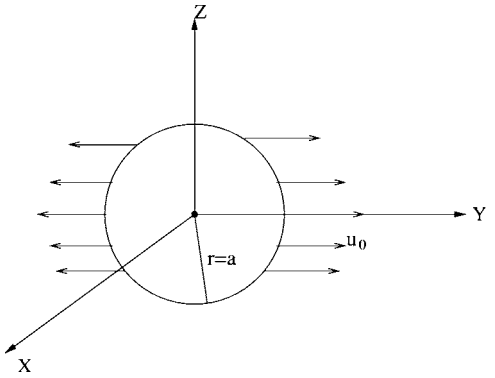

FIG. 4. Oscillating sphere problem geometry.

$$A^{(1)}_{\nu'\nu} = \int_{\sigma^{(e)}} \frac{1}{t_4 t_5} \psi_{\nu'} \psi_\nu \, dS,$$

$$A^{(2)}_{\nu'\nu} = \int_{\sigma^{(e)}} \frac{1}{t_1^2} \left[\frac{t_4^3 t_6}{t_5 t_7} (t_2)_{\nu'} (t_2)_\nu + \frac{t_5^3 t_6}{t_4 t_8} (t_3)_{\nu'} (t_3)_\nu \right] dS,$$

$$A^{(3)}_{\nu'\nu} = \int_{\sigma^{(e)}} \frac{1}{t_1^2} \left[\frac{t_4^3 t_6 t_{10}}{t_5 t_7} (t_2)_{\nu'} (t_2)_\nu + \frac{t_5^3 t_6 t_7}{t_4 t_8} (t_3)_{\nu'} (t_3)_\nu \right] dS,$$

$$A^{(4)}_{\nu'\nu} = \int_{\sigma^{(e)}} \frac{t_9}{t_4 t_5} \psi_{\nu'} \psi_\nu \, dS,$$

$$A^{(5)}_{\nu'\nu} = \int_{\sigma^{(e)}} \frac{t_7 t_{10}}{t_4 t_5} \psi_{\nu'} \psi_\nu \, dS,$$

where $\sigma^{(e)}$ is the base surface of an infinite element on the bounding ellipsoid.

Since the above integrals are evaluated by using standard Gaussian quadrature, we need to know the values of $(\cos\theta, \sin\theta, \cos\phi, \sin\phi)$ (these values are well defined since the Gauss points are located in the interior of the element), given the position vector $\mathbf{x}$ that has been found using Eq. (8). This is accomplished by using the procedure described in Sec. II. To reduce the computational cost, one can skip the first two steps of this procedure by approximating r_c by a.

IV. NUMERICAL EXAMPLES

We present a few numerical examples using the numerical strategy that has been presented in the preceding sections. We shall focus exclusively on radiation problems; more examples, including ones involving scattering can be found in Ref. 10. It is now well known (see, e.g., Ref. 6) that the unconjugated infinite element formulation, on which our numerical implementation is based, yields satisfactory results in the near field, but not in the farfield. Our numerical experiments bear this out, so that, knowing the pressure field on the surface of the radiating body, we use the Helmholtz integral equation given by

$$p(\mathbf{x}) = \int_S \frac{e^{-ik|\mathbf{x}-\mathbf{x}'|}}{4\pi|\mathbf{x}-\mathbf{x}'|^2} \left[p(\mathbf{x}')[(\mathbf{x}-\mathbf{x}')\cdot\mathbf{n}] \times \left(-ik - \frac{1}{|\mathbf{x}-\mathbf{x}'|} \right) + i\rho\omega v_n |\mathbf{x}-\mathbf{x}'| \right] dS,$$

to compute the farfield pressure.

The space between the radiating body and the bounding ellipsoid is discretized using a 21-node wedge (which are convenient for modeling regions near an axis) and 27-node isoparametric brick elements (henceforth referred to as W21 and B27 elements). The shape functions for the W21 element are generated using products of the seven-node in-plane shape functions given by the equations immediately following Eq. (38) in Ref. 7, and the standard one-dimensional quadratic Lagrange interpolation functions. The W21 elements are used to mesh the region adjacent to the axis while the B27 elements are used to model the remaining part; for example, see Fig. 2. The corresponding infinite elements of triangular and quadrilateral cross sections that mesh with these elements (starting from the bounding ellipsoid surface) are referred to as IT7 and IQ9 elements. We use a 7×3 Gaussian quadrature rule for the W21 element, a $3\times3\times3$ rule for the B27 element, and a radial order of $m=3$ (a higher

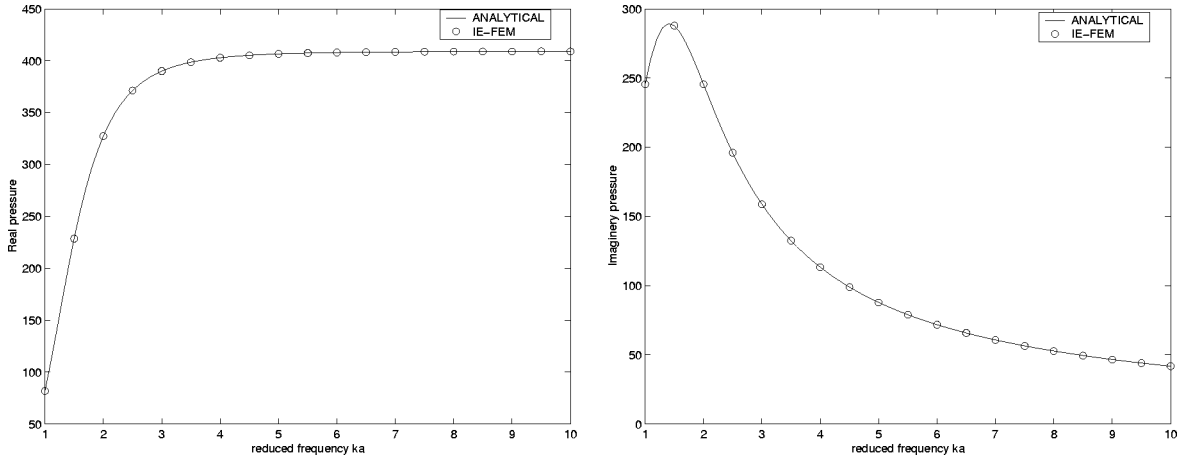

FIG. 5. A comparison of the numerically and analytically obtained real and imaginary parts of surface pressure at $(0, a, 0)$ for $ka=1,2,\ldots,10$ in the oscillating sphere problem.

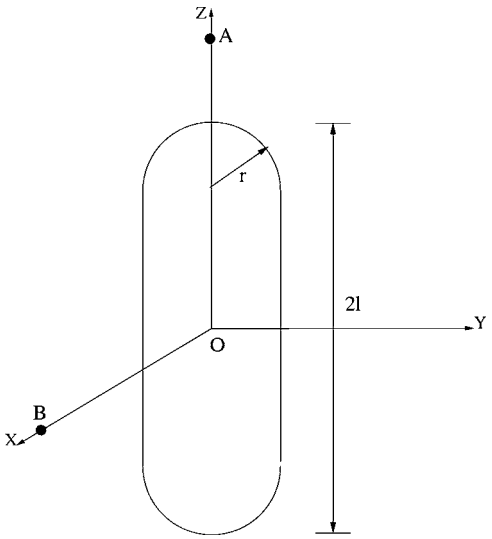

FIG. 6. Pulsating cylinder with hemispherical end caps.

order does not result in any significant increase in accuracy) for the infinite elements in all the examples that are presented below. Uniform meshes are used in all the examples.

A. Pulsating sphere problem

A sphere of radius $a=10$ vibrates with uniform radial velocity $v_n=1$. The analytical solution for the pressure as a function of the radial distance r is[11]

$$\frac{p(r)}{\rho c_s v_n} = \frac{a}{r}\frac{ika}{1+ika}e^{-ik(r-a)}.$$

Due to symmetry, we model only an octant of the sphere (see Fig. 2). The bounding surface is taken to be a sphere of radius $r_1=10.1$, and the radii of the other layers of nodes are taken to be $r_\mu=\mu r_1$, $\mu=2,3$. The solution obtained at (0, 0, 10) using one layer of elements of finite extent comprising of 8 W21 elements and 56 B27 elements (which mesh with 8 IT7 and 56 IQ9 infinite elements starting from the bounding surface), for $ka=1,2,\ldots,10$, is shown in Fig. 3. We also obtain the expected symmetry in the solution.

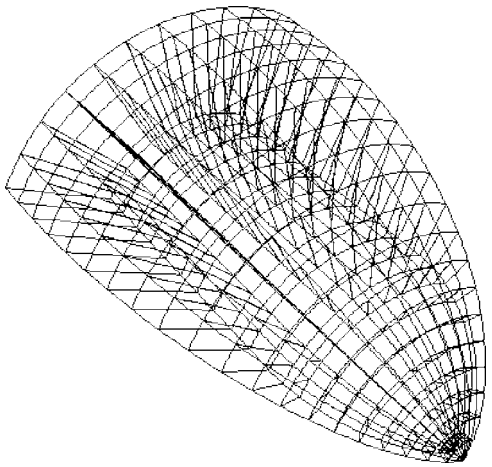

FIG. 7. An octant of the ellipsoidal envelope surrounding the radially pulsating cylinder with hemispherical endcaps meshed using 10 W21 and 190 B27 elements; 10 IT7 and 190 IQ9 infinite elements (not shown in the figure) model the domain outside the envelope.

TABLE I. A comparison of pressures at point A in the pulsating cylinder problem. $\|P_{\text{Liu}}\|$ denotes the norm of the pressure obtained by Yijun *et al.* in Ref. 13.

ω (rad/s)	P	$\|P\|$	$\|P_{\text{Liu}}\|$
62.83	24.457−4.917i	24.946	24.164
157.08	−36.391−14.809i	39.289	40
318.03	11.13+14.04i	17.916	17.222
475.66	−28.392−27.061i	39.222	40.294

B. Oscillating sphere problem

A rigid sphere of radius $a=10$ oscillates along the Y axis as shown in Fig. 4. The analytical solution for the pressure as a function of the radial distance r from the center of the sphere, and the angle α between the radius vector and the velocity vector is[12]

$$\frac{p(r,\alpha)}{\rho c_s u_o} = \left(\frac{a}{r}\right)^2 \cos\alpha \frac{ika(1+ikr)}{2(1+ika)-(ka)^2}e^{-ik(r-a)}.$$

Since the problem is symmetric about the X-Y and Y-Z planes, only one-fourth of the sphere is modeled using one layer of elements of finite extent comprising of 8 W21 and 56 B27 elements (the mesh is similar to the one shown in Fig. 2, but with half the mesh density). The radii of the various radial layers are taken to be the same as in the previous example. The solution obtained at $(0,a,0)$ for various frequencies of oscillation is shown in Fig. 5.

C. Pulsating sphere with hemispherical end caps

A cylinder with hemispherical end caps (see Fig. 6) pulsates with a uniform normal velocity of unit magnitude over the entire surface. The dimensions used are $l=3.5$ and $r=1$. Symmetry considerations allow us to model 1/8th part of the structure. As shown in Fig. 7, a single layer of elements of finite extent comprising of 10 W21 and 190 B27 elements are used between the structure and the bounding ellipsoid that has dimensions $a=2$, $b=2$, and $c=3.6$ (the condition $a \geq b \geq c$ in the formulation is enforced by relabeling the axes appropriately inside our code so that, for example, in this case, the X, Y, and Z axes are relabeled as Y, Z, and X axes). The solutions at points A and B with coordinates (0, 0, 10) and (10, 0, 0), respectively, are compared with the solutions obtained by Yijun and Shaohai[13] obtained using the boundary element method, and are presented in Tables I and II. We

TABLE II. A comparison of pressures at point B in the pulsating cylinder problem. $\|P_{\text{Liu}}\|$ denotes the norm of the pressure obtained by Yijun *et al.* in Ref. 13.

ω (rad/s)	P	$\|P\|$	$\|P_{\text{Liu}}\|$
66.06	24.157−8.035i	25.458	24.551
157.94	−55.622−6.110i	55.957	55.229
315.38	36.002−85.528i	92.796	94.063
472.26	79.592+80.361i	113.105	114.44

have presented both the actual value and the magnitude of the pressure for completeness.

V. CONCLUSIONS

An alternative numerical implementation for the Burnett series of acoustic infinite elements has been proposed, which overcomes certain problems associated with the numerical implementation that has been proposed earlier. The numerical examples presented with this strategy echo the conclusions that have been drawn in several review works, namely, the Burnett formulation yields accurate results in the near field, and when used in conjunction with the Helmholtz integral equation, yields accurate results both, in the near field and farfield, in a very economical manner.

[1]D. S. Burnett, "A three-dimensional acoustic infinite element based on a prolate spheroidal multipole expansion," J. Acoust. Soc. Am. **96**, 2798–2816 (1994).

[2]D. S. Burnett and R. L. Holford, "Prolate and oblate spheroidal acoustic infinite elements," Comput. Methods Appl. Mech. Eng. **158**, 117–142 (1998).

[3]D. S. Burnett and R. L. Holford, "An ellipsoidal acoustic infinite element," Comput. Methods Appl. Mech. Eng. **164**, 49–76 (1998).

[4]K. Gerdes, "A review of infinite element methods for exterior Helmholtz problems," J. Comput. Acoust. **8**, 43–62 (2000).

[5]R. J. Astley, "Infinite elements for wave problems: A review of current formulations and an assessment of accuracy," Int. J. Numer. Methods Eng. **49**, 951–976 (2000).

[6]R. J. Astley and J.-P. Coyette, "The performance of spheroidal infinite elements," Int. J. Numer. Methods Eng. **52**, 1379–1396 (2001).

[7]C. S. Jog, "Higher-order shell elements based on a Cosserat model, and their use in the topology design of structures," Comput. Methods Appl. Mech. Eng. **193**, 2191–2220 (2004).

[8]W. H. Press, S. A. Teukolsky, W. T. Vetterling, and B. P. Flannery, *Numerical Recipes in C* (Cambridge University Press, Cambridge, 2002), Chap. 5, pp. 184–185.

[9]C. S. Jog, "The accurate inversion of Vandermonde matrices," Comput. Math. Appl. **47**, 921–929 (2004).

[10]T. K. Bhandakkar, "Development of infinite elements for acoustic applications," Masters' thesis, Indian Institute of Science, 2004.

[11]L. E. Kinsler, A. R. Fray, A. B. Coppens, and J. V. Sanders, *Fundamentals of Acoustics* (Wiley, New York, 2000), pp. 127–129.

[12]I. Malecki, *Physical Foundations of Technical Acoustics* (Permagon, New York, 1969), pp. 175–177.

[13]L. Yijun and C. Shaohai, "A new form of the hypersingular boundary integral equation for 3-D acoustics and its implementation with C° boundary elements," Comput. Methods Appl. Mech. Eng. **173**, 375–386 (1999).

The influence of baffle fairings on the acoustic performance of rectangular splitter silencers

Ray Kirby
School of Engineering and Design, Mechanical Engineering, Brunel University, Uxbridge, Middlesex, UB8 3PH, United Kingdom

(Received 17 December 2004; revised 7 June 2005; accepted 1 July 2005)

A numerical model based on the finite element method is developed for a finite length, HVAC splitter silencer. The model includes an arbitrary number of bulk-reacting splitters separated from the airway by a thin perforated metal sheet and accommodates higher-order modes in the incident sound field. Each perforated sheet is joined to rigid, impervious, metallic fairing situated at either end of a splitter. The transmission loss for the silencer is quantified by application of the point collocation technique, and predictions are compared to experimental measurements reported in the literature. The splitter fairing is shown to significantly affect silencer performance, especially when higher-order incident modes are present. It is concluded that laboratory measurements, and theoretical predictions, that are based on a predominantly plane wave sound source are unlikely to reflect accurately the true performance of an HVAC silencer in a real ducting system. © *2005 Acoustical Society of America.* [DOI: 10.1121/1.2010267]

PACS number(s): 43.50.Gf, 43.20.Mv, 43.20.Bi [DKW] Pages: 2302–2312

I. INTRODUCTION

Dissipative silencers are commonly used in HVAC ducts to attenuate broadband noise emanating from an air-moving device such as a fan. HVAC ducts commonly have a rectangular cross section and a silencer made up of a number of parallel splitters. Each splitter normally consists of a bulk reacting porous material separated from the airway by a thin, perforated, metal sheet. Each perforated sheet is joined to metallic fairing at either end of the splitter (see Fig. 1). This helps to maintain the dimensional stability of a splitter, but also to channel airflow between each splitter, lowering the static air pressure loss across the silencer. Each section of fairing will, however, also affect the propagation of sound through the silencer by modifying the acoustic end correction at the inlet and outlet planes of the silencer. The influence of this fairing on the overall performance of a splitter silencer has largely been ignored in the literature, and so the aim of this paper is to investigate the effect of splitter fairing on HVAC silencer performance.

The effect on silencer performance of splitter fairing is normally assumed to be negligible. Moreover, the majority of theoretical studies on HVAC splitters are limited to computing modal attenuation in an infinite duct. For example, Cummings[1] quantified the attenuation of the first few least attenuated modes in a rectangular duct lined on opposite walls; Bies *et al.*[2] report general design curves for rectangular ducts lined on opposite walls, computed using the least attenuated mode; and Kakoty and Roy[3] examined infinite rectangular ducts lined on all four walls. The methods of Cummings and Sormaz,[4] and Astley and Cummings[5] are both capable of examining a large number of higher-order modes in a silencer that contains an arbitrary number of splitters, although both techniques are, again, restricted to infinite ducts.

Computing only modal attenuation suppresses the effects of acoustic scattering at either end of a silencer. To date, attempts to quantify end effects for bulk reacting HVAC silencers have been restricted to the specification of simplistic end correction factors. For example, Ramakrishnan and Watson[6] derive heuristic end correction factors by summing the decay rate of individual modes; Ramakrishnan and Stevens[7] use an expression developed by Beranek[8] for a plane wave expansion chamber; and Brandstätt *et al.*[9] generate transmission loss curves by comparing predicted modal attenuation with a large number of experimental measurements. Clearly, these methods do not fully characterize silencer end effects, nor are they likely to be applicable over a wide range of silencer parameters, including a silencer with a large number of splitters. In fact, end effects for bulk reacting splitter silencers have only recently been quantified by Kirby and Lawrie,[10] who demonstrated excellent agreement between numerical point collocation predictions and those found using an exact analytic approach. Kirby and Lawrie studied large HVAC silencers but the results were restricted to three splitters, and the effects of a perforate and splitter fairing were omitted. The addition of splitter fairing for a bulk reacting material has yet to be considered, although Mechel[11,12] did include fairings in a study of locally reacting splitters. The assumption of a locally reacting absorbent does, however, reduce the applicability of Mechel's technique, as it assumes either a relatively thin splitter, when compared to the overall duct dimensions, or a porous material of very high flow resistivity: neither case is likely to exist in most splitter silencer applications.

A numerical model aimed at quantifying the acoustic performance of a finite length splitter silencer is presented here. Included are the effects of a perforated sheet separating a bulk reacting material from the airway, an impervious fairing at either end of a splitter, and an arbitrary number of splitters making up the silencer. The silencer is assumed to

 0001-4966/2005/118(4)/2302/11/$22.50

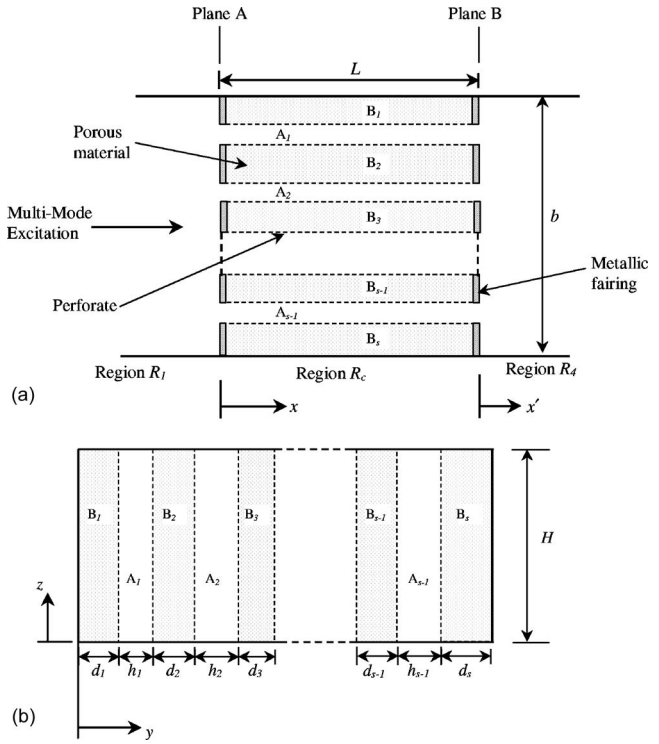

FIG. 1. (a) Plan view of silencer geometry (a splitter consists of a section of porous material that is bounded at either end by a metallic fairing and separated from the airway by a perforated sheet). (b) Geometry of silencer cross section.

have a uniform cross section and the effects of mean flow are neglected. To accommodate relatively large HVAC ducts, which are common in practice, a multi-modal sound field is chosen to excite the silencer. The effects of the splitter fairing are quantified by comparison with transmission loss predictions reported by Kirby and Lawrie[10] (who omit splitter end baffles), and with experimental results reported by Mechel.[12] The effects of varying both the porosity of the perforate, and the properties of the bulk reacting porous material, are also investigated.

II. THEORY

The analysis proceeds by assuming that the acoustic fields in the inlet/outlet ducts, and also the silencer section, may be expanded as an infinite sum over the duct/silencer eigenmodes. On finding the duct/silencer eigenfunctions and associated wave numbers, the modal amplitudes may be computed by application of the axial matching conditions, after suitable truncation of each modal sum. A numerical approach similar to the one described by Kirby,[13] and Kirby and Lawrie,[10] is adopted here and so, after introducing the duct geometry and governing wave equations, a finite element eigenvalue analysis is described; this is followed by a point collocation scheme that seeks to fulfill the axial continuity conditions.

A. Geometry and governing equations

An arbitrary number of bulk reacting splitters are shown in Fig. 1. A multi-mode sound source, propagating in the positive x direction in region R_1, is used to excite the silencer. The duct is terminated anechoically in region R_4. The duct walls in regions R_1 and R_4 are assumed to be rigid and impervious to sound. Each splitter has a length L and is terminated at $x=0$, and $x=L$, by a metallic fairing that is assumed to be rigid and impervious to sound propagation, and also of negligible thickness when compared to the overall silencer dimensions. Each splitter contains a bulk reacting porous material that is separated from the airway by a perforated sheet. A different porous material is assumed to be present in each splitter, although the material is assumed to be both homogeneous and isotropic. Furthermore, a different perforate sheet may be present on either side of a splitter, provided that the properties of the perforate remain uniform over $0 \leqslant x \leqslant L$, and $0 \leqslant z \leqslant H$. The duct walls (at $y=0$ and $y=b$ over $0 \leqslant z \leqslant H$; and $z=0$ and $z=H$ over $0 \leqslant y \leqslant b$) are assumed to be rigid and impervious to sound propagation for $0 \leqslant x \leqslant L$. A total of s splitters are depicted in Fig. 1: each splitter has a width d and is separated from the following splitter by an airway of width h. It is convenient to combine each section of airway and to denote region R_2 as

$$R_2 = A_1 + A_2 + A_3 + \cdots + A_{s-2} + A_{s-1}. \tag{1}$$

For each splitter,

$$R_3 = B_1 + B_2 + B_3 + \cdots + B_{s-1} + B_s. \tag{2}$$

In addition, region R_c consists of the airway, region R_2, added to the porous material, region R_3. The acoustic wave equation for the inlet duct region R_1, the outlet duct region R_4, and the airway region R_2 is given by

$$\frac{1}{c_0^2}\frac{D^2 p_q'}{Dt^2} - \nabla^2 p_q' = 0, \tag{3}$$

where c_0 is the isentropic speed of sound in air, p_q' is the acoustic pressure in region q (where $q=1$, 2, or 4), and t is time. For the porous material, the acoustic wave equation for any splitter k is given by

$$\frac{1}{c_k^2}\frac{D^2 p_k'}{Dt^2} - \nabla^2 p_k' = 0, \tag{4}$$

where c_k is the speed of sound in the porous material. The acoustic field in each region is expanded as an infinite sum over the duct eigenmodes to give

$$p_1'(x,y,z;t) = \sum_{j=0}^{\infty} F_j \Phi_j(y,z) e^{\mathrm{i}(\omega t - k_0 \gamma_j x)} + \sum_{j=0}^{\infty} A_j \Phi_j(y,z) e^{\mathrm{i}(\omega t + k_0 \gamma_j x)}, \tag{5}$$

$$p_c'(x,y,z;t) = \sum_{m=0}^{\infty} B_m \Psi_m(y,z) e^{\mathrm{i}(\omega t - k_0 \lambda_m x)} + \sum_{m=0}^{\infty} C_m \Psi_m(y,z) e^{\mathrm{i}(\omega t + k_0 \lambda_m x)}, \tag{6}$$

$$p_4'(x,y,z;t) = \sum_{n=0}^{\infty} D_n \Phi_n(y,z) e^{i(\omega t - k_0 \gamma_n x')}. \quad (7)$$

Here, A_j, B_m, C_m, D_n, and F_j are modal amplitudes, λ_m is the wave number in region R_c, and γ_j is the wave number in the inlet/outlet section. The quantities $\Phi_j(y,z)$ and $\Psi_m(y,z)$ are the transverse duct eigenfunctions in the inlet/outlet region and the silencer section, respectively. In addition, $i=\sqrt{-1}$, $k_0=\omega/c_0$, and ω is the radian frequency. Note that p_c' encompasses regions R_2 and R_3, so that λ is the (coupled) axial wave number for the silencer section.

B. Finite element eigenvalue analysis

A finite element eigenvalue analysis is carried out over the cross section of both the inlet/outlet ducts and the silencer section, although the analysis for an unlined rectangular duct is straightforward and so is not reported here. For the silencer section (region R_c) the assumed form for p_c' [Eq. (6)] is substituted into Eq. (3), and this yields, for mode m and airway section r,

$$\nabla_{yz}^2 \psi_r(y,z) + k_0^2[1-\lambda^2]\psi_r(y,z) = 0, \quad (8)$$

where $\psi_r(y,z)$ is the component of eigenfunction $\Psi(y,z)$ that lies in region A_r (see Fig. 1). Here, ∇_{yz} denotes a two-dimensional form of the Laplacian operator in the (y,z) plane. For mode m, the wave equation in splitter k yields

$$\nabla_{yz}^2 \varphi_k(y,z) + k_0^2[\Gamma_k^2 - \lambda^2]\varphi_k(y,z) = 0. \quad (9)$$

Here, $\varphi_k(y,z)$ is the component of the eigenfunction $\Psi(y,z)$ that lies in region B_k, and Γ_k is the (dimensionless) propagation constant of the porous material in splitter k. The eigenfunction in each region may be approximated by a trial solution of the form

$$\psi_r(y,z) = \sum_{j=1}^{n_r} N_{rj}(y,z)\psi_{rj} \quad (10)$$

and

$$\varphi_k(y,z) = \sum_{n=1}^{n_k} G_{kn}(y,z)\varphi_{kn}. \quad (11)$$

Here, $N_{rj}(y,z)$ and $G_{kn}(y,z)$ are the global trial (or shape) functions for the finite element mesh in airway r and splitter k, respectively; the number of nodes in airway r is n_r, and in splitter k is n_k. It is convenient to express these nodal values in vector form, and to number the nodes as follows: for airway r,

$$\psi_r(y,z) = [N_{r1}(y,z), N_{r2}(y,z), \ldots, N_{rn_r}(y,z)] \begin{bmatrix} \psi_{r1} \\ \psi_{r2} \\ \psi_{rn_r} \end{bmatrix} = \mathbf{N}_r \boldsymbol{\Psi}_{r2}, \quad (12)$$

and for splitter k,

$$\varphi_k(y,z) = [G_{k1}(y,z), G_{k2}(y,z), \ldots, G_{kn_k}(y,z)] \begin{bmatrix} \varphi_{k1} \\ \varphi_{k2} \\ \varphi_{kn_k} \end{bmatrix} = \mathbf{G}_k \boldsymbol{\Psi}_{k3}. \quad (13)$$

The nodal values for each airway and splitter are combined to give

$$\boldsymbol{\Psi}_2 = [\boldsymbol{\Psi}_{12} \quad \boldsymbol{\Psi}_{22} \quad \boldsymbol{\Psi}_{32} \quad \cdots \quad \boldsymbol{\Psi}_{(s-1)2}]^{\mathbf{T}}, \quad (14a)$$

$$\boldsymbol{\Psi}_3 = [\boldsymbol{\Psi}_{13} \quad \boldsymbol{\Psi}_{23} \quad \boldsymbol{\Psi}_{33} \quad \cdots \quad \boldsymbol{\Psi}_{s3}]^{\mathbf{T}}. \quad (14b)$$

The appropriate boundary conditions for regions R_2 and R_3 are zero normal acoustic particle velocity on the walls of the silencer, continuity of normal particle velocity over each perforate, and a pressure condition over each perforate. Accordingly, zero normal particle velocity for airway r gives

$$\frac{\partial \psi_r}{\partial z}(y,0) = 0 \quad \text{and} \quad \frac{\partial \psi_r}{\partial z}(y,H) = 0, \quad y \in R_2. \quad (15)$$

For splitter k,

$$\frac{\partial \varphi_k}{\partial z}(y,0) = 0 \quad \text{and} \quad \frac{\partial \varphi_k}{\partial z}(y,H) = 0, \quad y \in R_3. \quad (16)$$

For the side walls,

$$\frac{\partial \varphi_1}{\partial y}(b,z) = 0, \quad \text{and} \quad \frac{\partial \varphi_s}{\partial y}(0,z) = 0, \quad 0 \leqslant z \leqslant H. \quad (17)$$

Each splitter has a perforate located on both sides, except for those splitters located on the wall of the duct; thus for splitter $k(1 \leqslant k \leqslant s)$, continuity of normal particle velocity over a perforate yields

$$\frac{\partial \psi_{k-1}}{\partial y}(y_{2k-2}^-, z) = -\frac{\rho_0}{\rho_k(\omega)} \frac{\partial \varphi_k}{\partial y}(y_{2k-2}^+, z), \quad 0 \leqslant z \leqslant H; k \neq 1, \quad (18)$$

and

$$\frac{\partial \psi_k}{\partial y}(y_{2k-1}^-, z) = -\frac{\rho_0}{\rho_k(\omega)} \frac{\partial \varphi_k}{\partial y}(y_{2k-1}^+, z), \quad 0 \leqslant z \leqslant H; k \neq s. \quad (19)$$

Similarly, the pressure condition over each perforate yields

$$\psi_{k-1}(y_{2k-2}^-, z) - \varphi_k(y_{2k-2}^+, z) = \frac{i\zeta_{2k-2}}{k_0} \frac{\partial \psi_{k-1}}{\partial y}(y_{2k-2}^-, z), \quad 0 \leqslant z \leqslant H; k \neq 1, \quad (20)$$

and

$$\psi_k(y_{2k-1}^-, z) - \varphi_k(y_{2k-1}^+, z) = \frac{i\zeta_{2k-1}}{k_0} \frac{\partial \psi_k}{\partial y}(y_{2k-1}^-, z), \quad 0 \leqslant z \leqslant H; k \neq s. \quad (21)$$

Here, the (dimensionless) acoustic impedance of perforate e is denoted ζ_e, the mean fluid density in region R_2 is ρ_0, and $\rho_k(\omega)$ is the equivalent complex density of the porous material in splitter k. Equations (18)–(21) assume the thickness of the perforate is negligible. Each perforate is numbered ac-

cording to its location so that perforate 1 is located at y_1 and lies between splitter B_1 and airway A_1; perforate 2 is located at y_2 and lies between splitter B_2 and airway A_1; perforate 3 is located at y_3 and lies between splitter B_2 and airway A_2; and so on. Thus, the location of each perforate is given as

$$y_{2k-2} = \sum_{i=1}^{k-1} (d_i + h_i), \quad 1 < k \leqslant s, \tag{22}$$

and

$$y_{2k-1} = \sum_{i=1}^{k} d_i + \sum_{j=1}^{k-1} h_j, \quad 1 \leqslant k < s. \tag{23}$$

Here, d_k is the width of splitter k, and h_r is the width of airway r (see Fig. 1). Note that each perforate has been numbered individually to allow a different sheet to be placed on either side of a splitter. Furthermore, finite element discretization requires the specification of two nodes at a given location on a perforate: one node which belongs only to the mesh in the airway, and one only to the mesh in the absorbent. Here, a node at the perforate but lying in the airway is said to have location y^-; a node at the perforate but lying in the absorbent is said to have location y^+.

The boundary conditions specified in Eqs. (15)–(21) may be combined with Eqs. (8) and (9) to give a governing eigenequation for the silencer. The details of the weak Galerkin finite element formulation for this type of problem have been reported elsewhere,[5,13] and so only the final eigenequation is presented here:

$$[[\mathbf{A}] + \lambda^2[\mathbf{B}]]\{\boldsymbol{\Psi}\} = \{\mathbf{0}\}, \tag{24}$$

where $\boldsymbol{\Psi} = [\boldsymbol{\Psi}_2 \quad \boldsymbol{\Psi}_3]^{\mathbf{T}}$, and

$$[\mathbf{A}]\{\boldsymbol{\Psi}\} = [\mathbf{C}]\{\boldsymbol{\Psi}_2\} + [\mathbf{D}]\{\boldsymbol{\Psi}_3\}, \tag{25}$$

$$[\mathbf{B}]\{\boldsymbol{\Psi}\} = k_0^2[\mathbf{M}_2]\{\boldsymbol{\Psi}_2\} + k_0^2[\mathbf{M}_3]\{\boldsymbol{\Psi}_3\}. \tag{26}$$

Here,

$$[\mathbf{C}] = [\mathbf{K}_2] - k_0^2[\mathbf{M}_2] + \mathrm{i}k_0([\mathbf{M}_2^-] - [\mathbf{M}_3^+]) \tag{27}$$

and

$$[\mathbf{D}] = [\mathbf{K}_3] + k_0^2[\mathbf{M}_3] - \mathrm{i}k_0([\mathbf{M}_2^-] - [\mathbf{M}_3^+]). \tag{28}$$

For the airway,

$$[\mathbf{K}_2] = \begin{bmatrix} [\mathbf{K}_{12}] & \mathbf{0} & \mathbf{0} \\ \mathbf{0} & [\mathbf{K}_{22}] & \mathbf{0} \\ \mathbf{0} & \mathbf{0} & [\mathbf{K}_{(s-1)2}] \end{bmatrix} \tag{29}$$

and

$$[\mathbf{K}_{r2}] = \int_{A_r} \nabla_{yz} N_{ri}(y,z) \cdot \nabla_{yz} N_{rj}(y,z)\, dydz, \quad i = 1,\ldots,n_r; j = 1,\ldots,n_r. \tag{30}$$

In addition,

$$[\mathbf{M}_2] = \begin{bmatrix} [\mathbf{M}_{12}] & \mathbf{0} & \mathbf{0} \\ \mathbf{0} & [\mathbf{M}_{22}] & \mathbf{0} \\ \mathbf{0} & \mathbf{0} & [\mathbf{M}_{(s-1)2}] \end{bmatrix} \tag{31}$$

and

$$[\mathbf{M}_{r2}] = \int_{A_r} N_{ri}(y,z) \cdot N_{rj}(y,z)\, dydz; \quad i = 1,\ldots,n_r; j = 1,\ldots,n_r. \tag{32}$$

For the absorbent,

$$[\mathbf{K}_3] = \begin{bmatrix} [\mathbf{K}_{13}] & \mathbf{0} & \mathbf{0} \\ \mathbf{0} & [\mathbf{K}_{23}] & \mathbf{0} \\ \mathbf{0} & \mathbf{0} & [\mathbf{K}_{(s-1)3}] \end{bmatrix}, \tag{33}$$

where

$$[\mathbf{K}_{k3}] = \int_{B_k} \nabla_{yz} G_{ki}(y,z) \cdot \nabla_{yz} G_{kj}(y,z)\, dydz, \quad i = 1,\ldots,n_k; j = 1,\ldots,n_k. \tag{34}$$

In addition,

$$[\mathbf{M}_3] = \begin{bmatrix} [\mathbf{M}_{13}] & \mathbf{0} & \mathbf{0} \\ \mathbf{0} & [\mathbf{M}_{23}] & \mathbf{0} \\ \mathbf{0} & \mathbf{0} & [\mathbf{M}_{(s-1)3}] \end{bmatrix}, \tag{35}$$

where

$$[\mathbf{M}_{k3}] = \Gamma_k^2 \int_{B_k} G_{ki}(y,z) \cdot G_{kj}(y,z)\, dydz, \quad i = 1,\ldots,n_k; j = 1,\ldots,n_k. \tag{36}$$

For each node in the finite element mesh that lies on a perforate but belongs to the airway,

$$[\mathbf{M}_2^-] = \begin{bmatrix} [\mathbf{M}_{12}^-] & \mathbf{0} & \mathbf{0} \\ \mathbf{0} & [\mathbf{M}_{22}^-] & \mathbf{0} \\ \mathbf{0} & \mathbf{0} & [\mathbf{M}_{(s-1)2}^-] \end{bmatrix} \tag{37}$$

and

$$[\mathbf{M}_{r2}^-] = \begin{bmatrix} \mathbf{Q}_r^- & \mathbf{0} \\ \mathbf{0} & \mathbf{T}_r^- \end{bmatrix}. \tag{38}$$

Here,

$$[\mathbf{Q}_r^-] = \frac{1}{\zeta_{2r-1}} \int_0^H N_{ri}(y_{2r-1}^-, z) \cdot N_{rj}(y_{2r-1}^-, z)\, dz, \quad i = 1,\ldots,n_r; j = 1,\ldots,n_r. \tag{39}$$

and

$$[\mathbf{T}_r^-] = \frac{1}{\zeta_{2r}} \int_0^H N_{ri}(y_{2r}^-, z) \cdot N_{rj}(y_{2r}^-, z)\, dz, \quad i = 1,\ldots,n_r; j = 1,\ldots,n_r. \tag{40}$$

Similarly, for each node in the finite element mesh that lies on a perforate but belongs to the absorbent,

$$[\mathbf{M}_3^+] = \begin{bmatrix} [\mathbf{M}_{13}^+] & \mathbf{0} & \mathbf{0} \\ \mathbf{0} & [\mathbf{M}_{23}^+] & \mathbf{0} \\ \mathbf{0} & \mathbf{0} & [\mathbf{M}_{(s-1)3}^+] \end{bmatrix} \tag{41}$$

and

$$[\mathbf{M}_{k3}^+] = \begin{bmatrix} \mathbf{Q}_k^+ & \mathbf{0} \\ \mathbf{0} & \mathbf{T}_k^+ \end{bmatrix}. \tag{42}$$

Here,

$$[\mathbf{Q}_k^+] = \frac{\rho_k(\omega)}{\rho_0 \zeta_{2k-2}} \int_0^H N_{ki}(y_{2k-2}^+, z) \cdot N_{kj}(y_{2k-2}^+, z)\, dz,$$
$$i = 1,\ldots,n_k; j = 1,\ldots,n_k, \text{ for } 1 < k \leqslant s, \tag{43}$$

and

$$[\mathbf{T}_k^+] = \frac{\rho_k(\omega)}{\rho_0 \zeta_{2k-1}} \int_0^H N_{ki}(y_{2k-1}^+, z) \cdot N_{kj}(y_{2k-1}^+, z)\, dz,$$
$$i = 1,\ldots,n_k; j = 1,\ldots,n_k; \text{ for } 1 \leqslant k < s. \tag{44}$$

Here it is assumed that identical elements are chosen on either side of the perforate. The nonzero elements of matrices $[\mathbf{M}_2^-]$ and $[\mathbf{M}_3^+]$ that appear in Eq. (25) are limited to those nodes lying on a perforate, although for convenience Eqs. (39), (40), (43), and (44) are written in general form.

Finally, Eq. (24) may be rewritten as

$$[-[\mathbf{B}]^{-1}[\mathbf{A}]]\{\mathbf{\Psi}\} = \lambda^2\{\mathbf{\Psi}\} \tag{45}$$

and is solved for the axial wave number λ, which yields N_c eigenvalues and associated eigenvectors, where $N_c = N_2 + N_3$. Here, $N_2 = \Sigma_{r=1}^{s-1} n_r$, and $N_3 = \Sigma_{k=1}^{s} n_k$, so that N_2 is the number of nodes in the airway and N_3 the number of nodes in the absorbent.

C. Numerical matching of sound fields

On obtaining the eigenfunctions and wave numbers for regions R_1, R_c, and R_4, the axial matching conditions are enforced over planes A and B using point collocation. The appropriate matching conditions (at $x=0$ and $x=L$) are continuity of acoustic pressure and normal particle velocity over the airway, and zero normal acoustic velocity over each splitter fairing. The most convenient approach to enforcing these matching conditions, and the one adopted by Kirby and Lawrie,[10] is to choose an identical transverse finite element mesh in regions R_1, R_c, and R_4 and to match over every common node. However, the addition of a perforate complicates matters, as additional nodes in the transverse finite element mesh are required at each perforate location in the silencer section. For an automotive silencer, Kirby[13] addressed this problem by separately matching pressure and velocity at a node in the airway region (location y^-) and normal particle velocity at a node in the absorbent region (location y^+). For example, in Fig. 2(a) node b is said to have location y^- (position is exaggerated in the diagram, and for clarity only one dimension is shown), so that pressure and velocity conditions are enforced between nodes a and b. For node c (location y^+), matching conditions appropriate to the absorbent region only are enforced—in this case zero normal particle velocity. For the splitters in the current study, a further complication arises from the presence of the splitter fairings. For example, in Fig. 2(b) the location of nodes a and j (again, exaggerated in the diagram) is no longer certain as they could assume either a y^- or a y^+ location. A solution is to choose the location of y^- for nodes a and j and to apply matching conditions appropriate to the airway region between nodes a and b, and nodes j and l. Similarly, nodes c and k, in region R_c, are chosen to lie in a y^+ location, and zero normal particle velocity is applied at the fairing in the absorbent region. Thus, zero axial particle velocity is enforced over the fairing in region R_1 by using nodes d, f and h in Fig. 2(b). In general terms, therefore, a reduction in the number of matching locations takes place in region R_1, although this reduction serves to compensate exactly for the discrepancy between the number of nodes in region R_1 (or R_4) and region R_c. Note, this will not reduce the accuracy of the method, when compared to the method of Kirby and Lawrie,[10] since the mesh density in each region is not reduced: instead, nodes are added to account for the presence of a perforate.

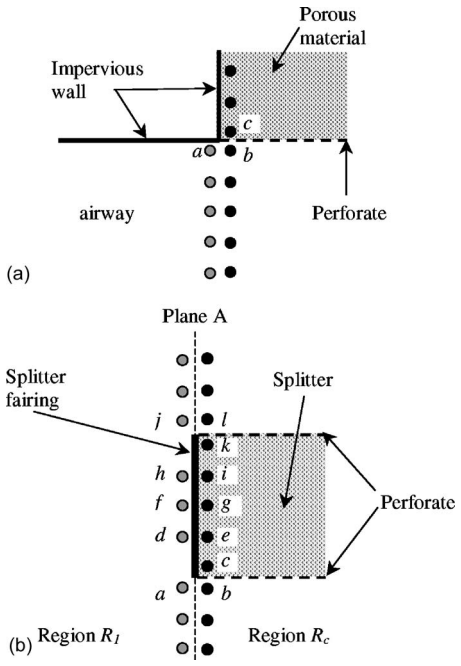

FIG. 2. (a) Example of nodal locations near a perforate for an automotive silencer.[13] (b) Example of nodal locations for a single splitter.

For the airway, continuity of pressure over plane A yields

$$\sum_{j=0}^{N_1} F_j \mathbf{\Phi}_{2j} + \sum_{j=0}^{N_1} A_j \mathbf{\Phi}_{2j} = \sum_{m=0}^{N_c} B_m \mathbf{\Psi}_{2m} + \sum_{m=0}^{N_c} C_m \mathbf{\Psi}_{2m}, \quad \text{on } R_2, \tag{46}$$

where N_1 is the number of nodes in region 1. Here, the vector $\mathbf{\Psi}_2$ holds those nodal values in the silencer section that lie in the airway (region R_2), including nodes with location y^- [for example, nodes b and l in Fig. 2(b)]. Similarly, vector $\mathbf{\Phi}_2$ holds those nodal values [for eigenfunction $\Phi(y,z)$] in the

inlet duct that lie on transverse locations identical to locations chosen for the nodes making up $\boldsymbol{\Psi}_2$. This assumes that each node lying adjacent to a perforate in the silencer section also lies in the airway [for example, nodes *a* and *j* in Fig. 2(b)]. Thus, vectors $\boldsymbol{\Phi}_2$ and $\boldsymbol{\Psi}_2$ both have a length N_2. Continuity of axial velocity over plane *A* yields

$$\sum_{j=0}^{N_1} F_j \gamma_j \boldsymbol{\Phi}_{2j} - \sum_{j=0}^{N_1} A_j \gamma_j \boldsymbol{\Phi}_{2j} = \sum_{m=0}^{N_c} B_m \lambda_m \boldsymbol{\Psi}_{2m} - \sum_{m=0}^{N_c} C_m \lambda_m \boldsymbol{\Psi}_{2m}, \quad \text{on } R_2. \tag{47}$$

For plane *B*, continuity of pressure yields

$$\sum_{m=0}^{N_c} B_m \boldsymbol{\Psi}_{2m} e^{-ik_0 \lambda_m L} + \sum_{m=0}^{N_c} C_m \boldsymbol{\Psi}_{2m} e^{ik_0 \lambda_m L} = \sum_{n=0}^{N_1} D_n \boldsymbol{\Phi}_{2n}, \quad \text{on } R_2, \tag{48}$$

and continuity of axial particle velocity

$$\sum_{m=0}^{N_c} B_m \lambda_m \boldsymbol{\Psi}_{2m} e^{-ik_0 \lambda_m L} - \sum_{m=0}^{N_c} C_m \lambda_m \boldsymbol{\Psi}_{2m} e^{ik_0 \lambda_m L} = \sum_{n=0}^{N_1} D_n \gamma_n \boldsymbol{\Phi}_{2n}, \quad \text{on } R_2. \tag{49}$$

For each splitter fairing, zero normal particle velocity over plane *A* yields

$$\sum_{m=0}^{N_c} B_m \lambda_m \boldsymbol{\Psi}_{3m} - \sum_{m=0}^{N_c} C_m \lambda_m \boldsymbol{\Psi}_{3m} = \mathbf{0}, \quad \text{on } R_3, \tag{50}$$

and, for plane *B*,

$$\sum_{m=0}^{N_c} B_m \lambda_m \boldsymbol{\Psi}_{3m} e^{-ik_0 \lambda_m L} - \sum_{m=0}^{N_c} C_m \lambda_m \boldsymbol{\Psi}_{3m} e^{ik_0 \lambda_m L} = \mathbf{0}, \quad \text{on } R_3. \tag{51}$$

Here, region R_3 encompasses all nodes that lie in the porous material, including nodes on a perforate with location y^+, so that vector $\boldsymbol{\Psi}_3$ has a length N_3. Finally, zero normal particle velocity over each splitter fairing is enforced for the inlet and outlet duct. Matching takes place over those nodes lying adjacent to region R_3, but does not include those nodes lying adjacent to a perforate. For example, in Fig. 2(b), conditions are enforced over nodes *h*, *f*, and *d*. Thus, for plane *A*,

$$\sum_{j=0}^{N_1} F_j \gamma_j \boldsymbol{\Phi}_{3j} - \sum_{j=0}^{N_1} A_j \gamma_j \boldsymbol{\Phi}_{3j} = \mathbf{0}, \quad \text{on } R_3, \tag{52}$$

and, for plane *B*,

$$\sum_{n=0}^{N_1} D_n \gamma_n \boldsymbol{\Phi}_{3n} = \mathbf{0}, \quad \text{on } R_3. \tag{53}$$

Here, vector $\boldsymbol{\Phi}_3$ contains all nodes adjacent to region R_3 except those lying on the perforate, so that vector $\boldsymbol{\Phi}_3$ has a length of $N_3 - N_p$, where N_p denotes the number of nodes positioned inside a splitter but adjacent to a perforate [nodes that have position y^+, for example nodes *c* and *k* in Fig. 2(b)]. Equations (46)–(53) form a complete set of $4(N_2+N_3)-2N_p$ equations (the collocation points) and $2(N_1+N_c)$ unknowns (the modal amplitudes), since $N_1=N_2+N_3-N_p$. It is convenient to rewrite Eqs. (46)–(53) and to introduce $C_m = \tilde{C}_m e^{-ik_0 \lambda_m L}$ to yield the final set of matching conditions:

$$\sum_{j=0}^{N_1} A_j \boldsymbol{\Phi}_{2j} - \sum_{m=0}^{N_c} B_m \boldsymbol{\Psi}_{2m} - \sum_{m=0}^{N_c} \tilde{C}_m \boldsymbol{\Psi}_{2m} e^{-ik_0 \lambda_m L} = -\sum_{j=0}^{N_1} F_j \boldsymbol{\Phi}_{2j}, \tag{54}$$

$$\sum_{j=0}^{N_1} A_j \gamma_j \boldsymbol{\Phi}_{2j} + \sum_{m=0}^{N_c} B_m \lambda_m \boldsymbol{\Psi}_{2m} - \sum_{m=0}^{N_c} \tilde{C}_m \lambda_m \boldsymbol{\Psi}_{2m} e^{-ik_0 \lambda_m L} = \sum_{j=0}^{N_1} F_j \gamma_j \boldsymbol{\Phi}_{2j}, \tag{55}$$

$$\sum_{m=0}^{N_c} B_m \lambda_m \boldsymbol{\Psi}_{3m} - \sum_{m=0}^{N_c} \tilde{C}_m \lambda_m \boldsymbol{\Psi}_{3m} e^{-ik_0 \lambda_m L} = \mathbf{0}, \tag{56}$$

$$\sum_{j=0}^{N_1} A_j \gamma_j \boldsymbol{\Phi}_{3j} = \sum_{j=0}^{N_1} F_j \gamma_j \boldsymbol{\Phi}_{3j}, \tag{57}$$

$$\sum_{m=0}^{N_c} B_m \boldsymbol{\Psi}_{2m} e^{-ik_0 \lambda_m L} + \sum_{m=0}^{N_c} \tilde{C}_m \boldsymbol{\Psi}_{2m} - \sum_{n=0}^{N_1} D_n \boldsymbol{\Phi}_{2n} = \mathbf{0}, \tag{58}$$

$$\sum_{m=0}^{N_c} B_m \lambda_m \boldsymbol{\Psi}_{2m} e^{-ik_0 \lambda_m L} - \sum_{m=0}^{N_c} \tilde{C}_m \lambda_m \boldsymbol{\Psi}_{2m} - \sum_{n=0}^{N_1} D_n \gamma_n \boldsymbol{\Phi}_{2n} = \mathbf{0}, \tag{59}$$

$$\sum_{m=0}^{N_c} B_m \lambda_m \boldsymbol{\Psi}_{3m} e^{-ik_0 \lambda_m L} - \sum_{m=0}^{N_c} \tilde{C}_m \lambda_m \boldsymbol{\Psi}_{3m} = \mathbf{0}, \tag{60}$$

$$\sum_{n=0}^{N_1} D_n \gamma_n \boldsymbol{\Phi}_{3n} = \mathbf{0}. \tag{61}$$

Equations (54)–(61) may be solved only after appropriate modal amplitudes F_j, which describe the incident sound field, have been specified. Source models are discussed in detail elsewhere (see, for example, work by Kirby and Lawrie,[10] Mechel,[11] and Joseph *et al.*[14]), although the most plausible representation of the noise emanating from a fan appears to be the assumption of equal modal energy density (EMED) for propagating modes. Accordingly, the inlet modal amplitudes, assuming EMED, are given as[11]

$$\left| \frac{F_j}{p_0} \right|^2 = I_0 \Big/ I_j \sum_{m=0}^{N_I} \gamma_m, \tag{62}$$

where p_0 is a reference pressure chosen here, arbitrarily, to be equal to unity; N_I is the number of modes propagating in the inlet duct (for modes that are "cut off," $F=0$), and

$$I_n = \int_{R_1} |\Phi_n(y,z)|^2 \, dydz. \tag{63}$$

Note that other source models, such as equal modal power, may readily be introduced here but are omitted in order to reduce the number of results presented later on. A finite element eigenvalue solution for the inlet duct yields an unordered list of eigenvalues, which are sorted and numbered so that $m=0$ has the smallest imaginary part, $m=1$ the second smallest imaginary part, and so on. Thus, Eq. (62) remains in general form, and the integral in Eq. (63) is computed numerically. After determining appropriate values for F_j, Eqs. (54)–(61) are solved simultaneously to find the $2(N_1+N_c)$ unknown modal amplitudes.

A common method for representing silencer performance is the silencer transmission loss (TL), which is defined as the ratio of transmitted to incident sound powers (note that for experimental measurements undertaken according to ISO standards,[15] the transmission loss of a silencer is equivalent to the insertion loss). The inlet sound power is equal to unity, hence, in decibels

$$\mathrm{TL} = -10 \log_{10} \sum_{n=0}^{N_I} \frac{\gamma_n I_n |D_n|^2}{I_0}. \tag{64}$$

III. RESULTS AND DISCUSSION

The addition of higher-order incident modes aims to replicate the incident sound pressure field typically present in a real HVAC ducting system. The measurement of silencer performance, when placed *in situ*, does, however, present many difficulties, not least in accurately measuring the sound pressure field emitted by a fan. To overcome these difficulties, laboratory measurements for splitter silencers are normally performed using plane wave excitation. For example, the measurements reported by Mechel[12] were performed according to standards (see also BS 7235[15]) that stipulate an incident sound field with "dominating plane wave mode." Accordingly, comparison between prediction and experiment is restricted here to transmission loss curves measured under plane wave excitation; the proposed model for multi-modal excitation is investigated theoretically and reported separately.

The absorbent material in each splitter is assumed to be fibrous and bulk reacting. Accordingly, the generalized results of Delany and Bazley[16] yield

$$\Gamma = 0.189\xi^{-0.595} + \mathrm{i}(1 + 0.098\xi^{-0.7}) \tag{65}$$

for the propagation constant and

$$\rho(\omega) = -\rho_0 \Gamma[0.087\xi^{-0.732} + \mathrm{i}(1 + 0.057\xi^{-0.754})] \tag{66}$$

for the complex density. Here, ξ is a nondimensional frequency parameter given by $\xi=\rho_0 f/\sigma$, where f is frequency and σ is the flow resistivity of the porous material. The formulas of Delany and Bazley are known to be invalid at low frequencies, and so the semi-empirical correction formulas of Kirby and Cummings[17] (see also Ref. 13) are adopted here to alleviate this inconsistency. Note that this method replicates, as far as possible, Delany and Bazley's regression formulas over the frequency range for which their data are known to be valid; outside of this frequency range, plausible limiting values are substituted. The theoretical analysis presented here is, however, sufficiently general so that alternative models for the porous material may be substituted (see, for example, alternative models suggested by Wilson[18] and Allard and Champoux[19]). The impedance of the perforate is given as[13]

$$\zeta = [\zeta' - 0.425\mathrm{i}k_0 d_p(\rho(\omega)/\rho_0 - 1)]/\Omega, \tag{67}$$

where

$$\zeta' = [1 + t/d_p]\sqrt{8k_0\nu/c_0} + \mathrm{i}k_0 d_p[0.25 + t/d_p]. \tag{68}$$

Here, t is the thickness of the perforate, d_p is the hole diameter, Ω is the perforate area porosity, and ν is the kinematic viscosity of air.

TABLE I. Data for silencers.

Silencer	$d1$ (m)	$h1$ (m)	$d2$ (m)	$h2$ (m)	$d3$ (m)	L (m)	H (m)	σ (Pa s/m2)
A	0.18	0.24	0.18	…	…	1.5	…	11 000
B	0.1	0.2	0.1	…	…	0.5	…	12 500
C	0.1	0.05	0.1	…	…	0.5	…	12 500
D	0.1	0.1	0.2	0.1	0.1	0.9	0.9	8000

A. Plane wave excitation

The experimental data reported by Mechel[12] are used here in order to compare prediction with experiment. The assumption of plane wave excitation greatly simplifies the analysis since silencer symmetry may be utilized in order to reduce the problem from three to two dimensions (x, y plane). Accordingly, the silencers tested by Mechel[12] may be simplified and a duct lined on opposite walls analyzed. Mechel examined five different silencer configurations, for which each splitter contained an end fairing, although no perforate was present. Only three of the five silencer configurations reported by Mechel are studied here, as this is deemed sufficient to evaluate the current analysis. The dimensions of each silencer, after accounting for lines of symmetry, are listed in Table I. A comparison between the measurements of Mechel[12] and predictions for silencer A is shown in Fig. 3. Predictions are shown with and without splitter fairings (see Ref. 10 for an equivalent model that omits splitter fairings) and for a high perforate porosity ($\Omega=0.95$) so that any effects of the perforate in the current analysis are negligible. Agreement between prediction and experiment in Fig. 3 is good, although in the medium frequency range some discrepancies are evident. Agreement is similar to that reported by Mechel,[12] who assumes a locally reacting liner, although for the medium frequency range the current method tends to over predict transmission loss, whereas Mechel underpredicts transmission loss. The good agreement between the two methods at low and high frequencies suggests that, at these frequency extremes, performance depends strongly on the silencer geometry. Moreover, the effect of adding splitter fairings is clearly evident, although only within the medium frequency range, which fur-

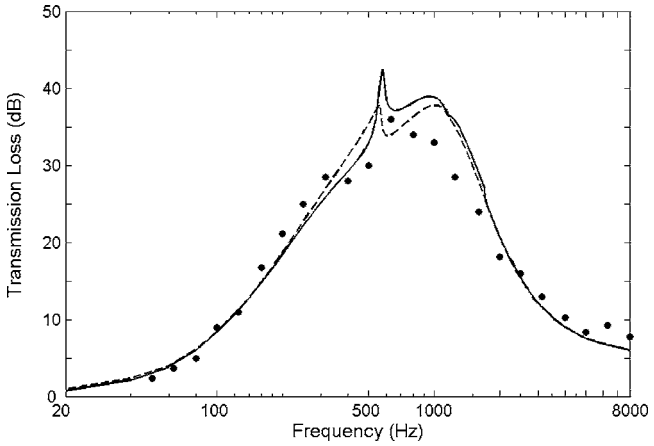

FIG. 3. Transmission loss for silencer A: •, experiment;[12] ———, prediction with fairings (N_1=41, N_c=43; – – –, prediction without fairings (N_1=N_c =41).

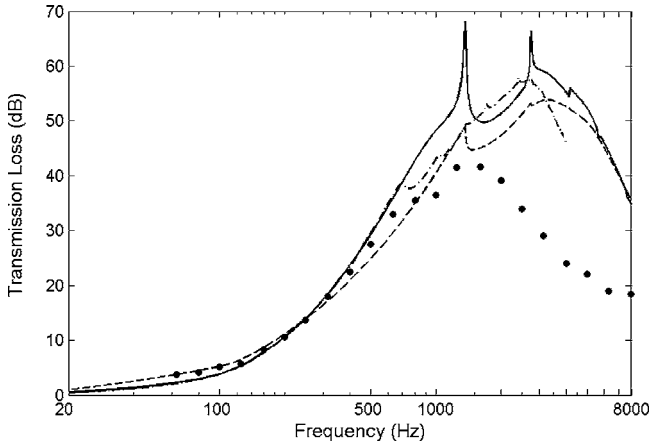

FIG. 5. Transmission loss for silencer C: •, experiment;[12] ———, prediction with fairings (N_1=21, N_c=23); – – –, prediction without fairings (N_1=N_c =21); ——–, three-dimensional model, EMED excitation, prediction with fairings (N_1=533, N_c=585).

ther supports this observation. The peak in transmission loss seen for silencer A (and also for silencers B and C to follow) is caused by the cut-on of the $(0,2)$ mode in regions R_1 and R_4. Such a peak in transmission loss is observed only in studies of finite length HVAC silencers (that include the inlet/outlet ductwork) and may be seen also in the predictions of Mechel.[12]

The material in silencer B has a higher flow resistivity than that in silencer A, and also a smaller cross-sectional area. Figure 4 reveals a maximum discrepancy of about 4 dB between prediction and experiment, although the current model again overpredicts silencer performance in the medium frequency range. Here, direct comparison between prediction and experiment is difficult as the experiment adopts a one-third-octave band analysis, whereas predictions are narrow band. Hence, experimental measurements are unlikely to exhibit the marked peaks seen in predicted transmission loss. Mechel[12] does, however, appear to obtain better agreement for this silencer at frequencies close to 1 kHz, although again the silencer transmission loss is under predicted.

For silencers A and B, consistent differences between the current model and that of Mechel[12] exist: the current model tends to overpredict transmission loss, whereas Mechel tends to underpredict transmission loss, especially in the medium frequency range. This difference is not surprising given that Mechel suppresses sound propagation in the material itself. However, neither method accurately reproduces experimental measurements over the whole frequency range, even though the current method properly represents the propagation of sound within the absorbing material. The accuracy of predictions do, however, compare well with those reported for dissipative automotive exhaust silencers, especially if one takes into account the relative complexity of the current silencer. It is possible that the differences observed between the current predictions and experimental measurements may partly be explained by inaccurate characterization of the absorbing material: the bulk acoustic properties are based here on the Delany and Bazley coefficients[16] averaged over a number of fibrous materials, and these may not accurately represent the performance of an individual real material. Note that the material data referred to by Mechel[12] were also obtained after averaging measurements over a number of fibrous materials and predictions are very similar to those found when using Delany and Bazley's coefficients. Furthermore, discrepancies at medium and high frequencies may be caused by neglecting the effects of structural flanking transmission, which may appear in the form of noise bypassing the silencer and traveling along the duct walls or, alternatively, breaking out of the test duct and breaking back in downstream of the silencer.

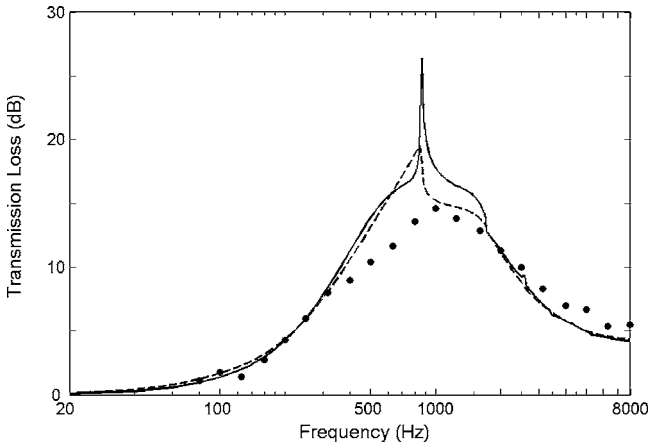

FIG. 4. Transmission loss for silencer B: •, experiment;[12] ———, prediction with fairings (N_1=33, N_c=35); – – –, prediction without fairings (N_1=N_c =33).

Silencer C has a more extreme geometry as the airway takes up only 20% of the overall cross-sectional area. Comparison between prediction and experiment in Fig. 5 shows discrepancies that are far more pronounced than for silencers A and B, especially above 1 kHz. Mechel[12] observed similar discrepancies, and both methods significantly overpredict silencer performance at higher frequencies. Mechel proposed that assuming a locally reacting material caused these discrepancies. The current analysis addresses this issue by treating the material as bulk reacting, although it is evident in Fig. 5 that agreement with measured data has not significantly been improved. Thus, at higher frequencies the model

used for the porous material cannot explain discrepancies; instead, it is highly likely that these differences are caused by structural flanking transmission. Cummings and Astley[20] investigated this effect for lined ducts and showed that flanking transmission places limits on silencer performance. They note also, "If the silencer presents a large attenuation (at a particular frequency) to the internal sound field, especially by virtue of its length, there is a possibility that flanking paths may exist, resulting in loss of acoustic performance." Furthermore, Brandstätt *et al.*[9] examine silencers similar to those studied here and use experimental techniques that are likely to be similar to those used by Mechel[12] (given the commonality in institutions between the lead authors). Brandstätt *et al.* acknowledge that flanking transmission may limit the attenuation values measured for their silencers, although they postulate that this effect is limited only to the medium frequency range (around 1 kHz). Brandstätt *et al.* further suggest that discrepancies between prediction and experiment at higher frequencies are caused by "reflection at the splitter, but also…higher-order modes in the air passage which are well attenuated." However, current results—that include all relevant duct modes—do not support the latter of these observations, as predictions lie above measured transmission loss values at higher frequencies. Instead, current results support the observations of Cummings and Astley[20] since a loss of silencer performance is observed at regions of high attenuation and this includes in the higher frequency range. Accordingly, the omission of structural flanking transmission limits the applicability of the current approach, at least for silencers that present a large attenuation at a particular frequency.

B. Multi-mode excitation

In HVAC ducts a multi-mode incident sound field, driven by the fan, is likely to be present above the cut-on frequency of the first higher order duct mode. It is normal to assume that these higher order modes share a common property, for example, equal modal energy density (EMED).[11,14] Modeling a multi-mode incident sound field does, however, require a fully three-dimensional approach, as lines of symmetry no longer exist.[11] Accordingly, a two-dimensional eigenvalue analysis (y, z plane) is necessary and this incurs a significant increase in computational expenditure when compared to the one-dimensional eigenvalue (y plane) approach suitable for plane wave excitation.

The effect of an EMED incident sound field on the acoustic performance of silencer C is shown in Fig. 5 (assuming a representative duct height of 0.4 m, as Mechel[12] did not publish values of H for his test silencers). For this silencer, transmission loss predictions are generally lower than for plane wave excitation. This behavior is likely to be caused by higher order modes propagating at angles that bypass the splitter fairings. This effect depends on silencer geometry and frequency, as well as the choice of absorbing material, although it is possible, under some circumstances, for the splitter fairings to preferentially reflect higher-order modes.

The multi-mode predictions for silencer C were generated using a transverse mesh refined according to excitation frequency. As frequency increases it's normal to increase the number of degrees of freedom in the finite element mesh: as a general guideline, between seven and ten finite element nodes should be adopted per wavelength.[21] Thus, for HVAC silencers a very large number of degrees of freedom are often necessary, even for relatively small silencers. For example, at 2 kHz, values of $N_1=533$ and $N_c=585$, were found to be necessary for silencer C; at 4 kHz double this number are required. It is clear that matrix dimensions can quickly become very large for multi-mode excitation, and transmission loss predictions for silencer C stop at 4 kHz in Fig. 5 because of computational limitations. Furthermore, at higher frequencies the number of propagating incident modes becomes very large: at 4 kHz, 96 modes are found to propagate. Many of these incident modes have very similar wave numbers and numerical problems arise if these modes are not accurately computed. In a real HVAC duct it is, however, unlikely that this number of incident modes will propagate at higher frequencies, and the usefulness of adopting EMED is probably limited at higher frequencies.

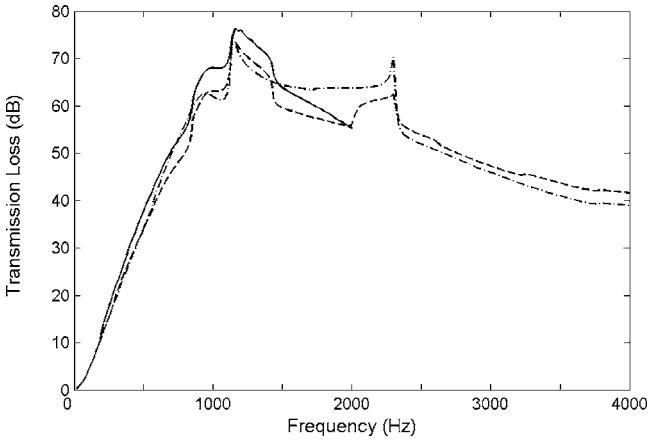

FIG. 6. Transmission loss predictions for silencer D with EMED excitation: ———, three-dimensional model; – – –, two-dimensional model for $0 \leqslant y \leqslant b$ ($N_1=25$, $N_c=29$); ——–, two-dimensional model for $0 \leqslant y \leqslant b/2$ ($N_1=13$, $N_c=15$).

The computational expenditure associated with modeling three-dimensional sound propagation encourages an investigation into the feasibility of approximating silencer performance using a two-dimensional approach. In Fig. 6 comparison between predictions generated with and without the assumption of cross-sectional symmetry are shown for a splitter silencer (silencer D, see Table I) that represents silencers typically found in HVAC systems. Silencer D contains both a perforate and splitter fairings: for the perforate, $t=1$ mm, $d_p=3.5$ mm, and $\Omega=0.3$. Transmission loss predictions shown in Fig. 6 were generated using a two-dimensional representation of the splitter (x, y axis), for $0 \leqslant y \leqslant b$, and $0 \leqslant y \leqslant b/2$, and these are compared against a three-dimensional solution. Silencer D is larger than silencer C and computational resources restrict predictions for the three-dimensional approach to a maximum frequency of 2 kHz (where $N_1=633$ and $N_c=765$). A comparison between two- and three-dimensional predictions shows reasonably good agreement and generally the predictions are within 10

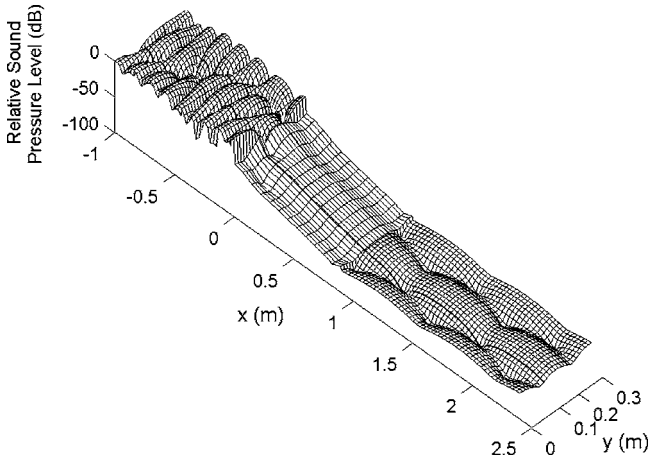

FIG. 7. Sound pressure distribution at 1500 Hz for silencer D with splitter fairings, $0 \leqslant y \leqslant b/2$.

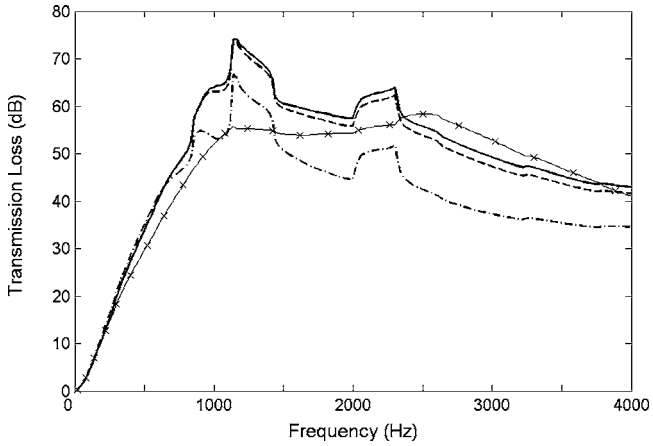

FIG. 9. Transmission loss predictions for silencer D with EMED excitation ($N_1=25$, $N_c=29$): ———, $\Omega=0.4$ with splitter fairing; – – –, $\Omega=0.3$ with splitter fairing; – – – –, $\Omega=0.1$ with splitter fairing; – × – × –, without perforate and fairing.

dB of one another. It is evident that the two-dimensional model, encompassing $0 \leqslant y \leqslant b$, produces better agreement with three-dimensional predictions, when compared to the model encompassing $0 \leqslant y \leqslant b/2$; this is to be expected, as a greater number of incident modes are included in the former model. Although the level of agreement between two- and three- dimensional formulations will depend on the particular silencer chosen, after analyzing a number of different splitter silencers (not shown here) the predictions shown in Fig. 6 appear to be representative of the general level of agreement to be expected. Therefore, it appears sensible, at least in the preliminary stages of an iterative design procedure, to adopt a two-dimensional model for a splitter silencer, even if the silencer is excited by higher order modes. Accordingly, all further results presented here were obtained using a two-dimensional representation (x, y plane) of the splitter silencer.

It is interesting to examine the effect of splitter fairings on the sound pressure distribution in the duct. For silencer D, the relative sound pressure level at a frequency of 1.5 kHz, calculated using a two-dimensional ($0 \leqslant y \leqslant b/2$) representation, is shown with splitter fairings in Fig. 7, and without fairings in Fig. 8. The influence of the fairings on sound pressure distribution is most obvious in the inlet duct, especially close to the inlet plane of the silencer. It is interesting also to note that the sound pressure fields, downstream of the silencer, are similar to one another in Figs. 7 and 8, especially well away from the silencer outlet plane. Moreover, the complex nature of this sound pressure field demonstrates the difficulty in measuring accurately silencer performance when higher order modes propagate downstream of the silencer.

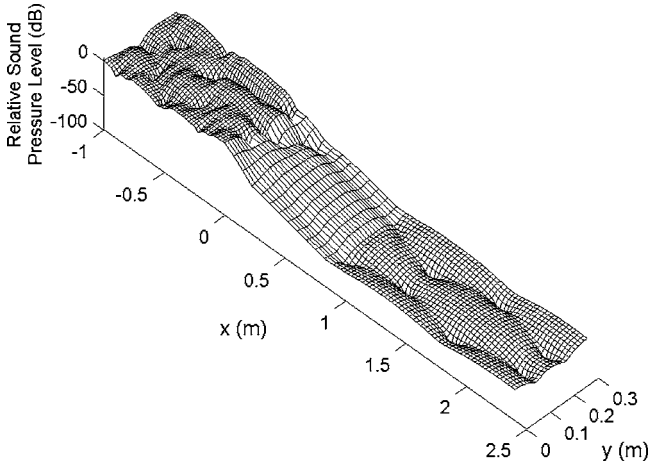

FIG. 8. Sound pressure distribution at 1500 Hz for silencer D without splitter fairings, $0 \leqslant y \leqslant b/2$.

The influence of perforate porosity on silencer transmission loss is shown, for silencer D, in Fig. 9. Here, the same perforate porosity is used for each baffle and it's evident that, as the perforate area porosity is reduced, the transmission loss increases slightly at low frequencies but reduces significantly at higher frequencies. This behavior is similar to that found by other authors[1,13] and indicates that, at least for larger HVAC silencers, it is preferable to use perforates with a high percentage open area. The model developed in Sec. II also allows for a different perforate porosity to be used for each splitter. By altering perforate porosity it is possible to manipulate the transmission loss curves shown in Fig. 9, although after conducting a number of numerical tests an improvement in transmission loss, over and above that found for a nominal limiting value of $\Omega=0.4$, was not forthcoming. Similarly, it is straightforward to alter the material properties for each splitter section, however after a number of parametric studies only relatively minor modifications in silencer performance were observed—predominantly in the medium frequency range. Moreover, such modifications in performance depend heavily on the silencer geometry chosen, which prevents the formulation of general guidelines regarding the optimum choice of material properties in splitters.

Transmission loss predictions obtained in the absence of splitter fairings and a perforate (see Ref. 10) are also shown in Fig. 9. It is clear that splitter fairings have a significant effect on silencer performance and, for the silencers studied here, the effect of splitter fairings is more noticeable when higher-order modes are present in the inlet duct.

IV. CONCLUSIONS

A two-dimensional analysis for a splitter silencer provides reasonable agreement with results obtained using a three-dimensional model. The largest discrepancy between the two methods is in the medium frequency range. The computational savings found when using the two-dimensional model are significant and it appears preferable to adopt a two-dimensional model, at least for a preliminary iterative design procedure.

Results indicate that, for splitter silencers, it is preferable to adopt as high a perforate porosity as possible and that no significant improvement in performance can be obtained by varying the porosity for different baffles. General guidelines do not, however, readily present themselves when it comes to the choice of absorbing material for each splitter. Moreover, at low and high frequencies silencer performance largely depends on silencer geometry rather than the type of material chosen.

Splitter fairings significantly affect HVAC silencer performance. This effect is most noticeable in the medium frequency range, and when the silencer is excited by higher order modes. Thus, laboratory measurements, or theoretical predictions, based on a predominantly plane wave sound source are unlikely to represent accurately the performance of a silencer in a real ducting system. Moreover, structural flanking effects may also limit both the accuracy of the current modeling approach, and also the applicability to real systems of silencer measurements taken under laboratory conditions (in which structural flanking has been suppressed).

[1]A. Cummings, "Sound attenuation in ducts lined on two opposite walls with porous material, with some application to splitters," J. Sound Vib. **49**, 9–35 (1976).

[2]D. A. Bies, C. H. Hansen, and G. E. Bridges, "Sound attenuation in rectangular and circular cross-section ducts with flow and bulk-reacting liner," J. Sound Vib. **146**, 47–80 (1991).

[3]S. K. Kakoty and V. K. Roy, "Bulk reaction modeling of ducts with and without mean flow," J. Acoust. Soc. Am. **112**, 75–112 (2002).

[4]A. Cummings and N. Sormaz, "Acoustic attenuation in dissipative splitter silencers containing mean fluid flow," J. Sound Vib. **168**, 209–227 (1993).

[5]R. J. Astley and A. Cummings, "A finite element scheme for attenuation in ducts lined with porous material: comparison with experiment," J. Sound Vib. **116**, 239–263 (1987).

[6]R. Ramakrishnan and W. R. Watson, "Design curves for rectangular splitter silencers," Appl. Acoust. **35**, 1–24 (1992).

[7]R. Ramakrishnan and R. Stevens, "Improving the accuracy of duct insertion loss predictions," J. Sound Vib. **169**, 423–427 (1994).

[8]L. L. Beranek, *Noise and Vibration Control* (McGraw-Hill, New York, 1971).

[9]P. Brandstätt, W. Frommhold, and M. J. Fisher, "Program for the computation of absorptive silencers in straight ducts," Appl. Acoust. **43**, 19–38 (1994).

[10]R. Kirby and J. B. Lawrie, "A point collocation approach to modeling large dissipative silencers," J. Sound Vib. **286**, 313–319 (2005).

[11]F. P. Mechel, "Theory of baffle-type silencers," Acustica **70**, 93–111 (1990).

[12]F. P. Mechel, "Numerical results to the theory of baffle-type silencers," Acustica **72**, 7–20 (1990).

[13]R. Kirby, "Transmission loss predictions for dissipative silencers of arbitrary cross section in the presence of mean flow," J. Acoust. Soc. Am. **114**, 200–209 (2003).

[14]P. Joseph, C. L. Morfey, and C. R. Lowis, "Multi-mode sound transmission in ducts with flow," J. Sound Vib. **264**, 523–544 (2003).

[15]European Standard EN ISO 7235, "Measurement procedures for ducted silencers—insertion loss, flow noise and total pressure loss" (2003).

[16]M. E. Delany and E. N. Bazley, "Acoustical properties of fibrous materials," Appl. Acoust. **3**, 105–116 (1970).

[17]R. Kirby and A. Cummings, "Prediction of the bulk acoustic properties of fibrous materials at low frequencies," Appl. Acoust. **56**, 101–125 (1999).

[18]D. K. Wison, "Simple, relaxational models for the acoustical properties of porous media," Appl. Acoust. **50**, 17–188 (1997).

[19]J.-F. Allard and Y. Champoux, "New empirical equations for sound propagation in rigid frame fibrous materials," J. Acoust. Soc. Am. **91**, 3346–3353 (1992).

[20]A. Cummings and R. J. Astley, "Effects of flanking transmission on sound attenuation in lined ducts," J. Sound Vib. **179**, 617–646 (1995).

[21]R. J. Astley, "Finite elements in acoustics," *Proceedings of Internoise 98*, Christchurch, New Zealand, 1998.

Vibroacoustics of three-dimensional drum silencer

Lixi Huang[a] and Y. S. Choy
Department of Mechanical Engineering, The Hong Kong Polytechnic University, Kowloon, Hong Kong, China

(Received 6 December 2004; revised 11 June 2005; accepted 5 July 2005)

When a segment of a rigid duct wall is replaced by a membrane and is backed by a cavity, incident noise induces membrane vibrations and causes noise reflection. The reflection is effective over a broad band in the low-frequency region when a certain high tension is applied on the membrane in the axial direction of the duct. The device is thus called a drumlike silencer. The existing vibroacoustic theory is based on a two-dimensional duct model and the membrane is reduced to a one-dimensional string. This study extends the theory to three dimensions for the duct and two dimensions for the membrane which has all four edges fixed. It is shown, analytically, that the lateral tension is always detrimental to the silencing performance. However, the optimal performance of the one-dimensional string is recovered exactly when the lateral tension on the two-dimensional membrane vanishes despite the very different boundary conditions. The conclusion is validated experimentally, paving the way for the application of the drum silencer in which the cavity is completely separated from the gas flow in the duct. © *2005 Acoustical Society of America.*
[DOI: 10.1121/1.2010353]

PACS number(s): 43.50.Gf, 43.20.Tb, 43.20.Ks [DKW] Pages: 2313–2320

I. INTRODUCTION

The problem of duct noise is found in many industrial and domestic applications, such as ventilation systems and exhaust chimneys. Existing noise abatement techniques can be broadly categorized by three approaches: sound absorption, sound reflection, and active noise control using destructive acoustic interference. Lining a duct with sound absorbing material, mostly porous, has been very common and often the most reliable engineering solution (Mechel and Vér, 1992; Ingard, 1994). If, for chemical or other reasons within the exhaust gas, the use of a porous material is not desirable, alternative sound absorbing structures are used. Most such structures utilize the principle of Helmholtz resonator (Fuchs, 2001), of which microperforation is one (Maa, 1975, 1998). Like duct lining of fibrous material, arrays of Helmholtz resonators can also provide effective noise absorption for a broad frequency band. However, one of the drawbacks of sound absorption is that, in general, it does not work well for very low frequencies, such as those below 200 Hz. The reason is that air is essentially incompressible at low frequencies. A cavity housing the sound absorption material would appear to be small relative to the wavelength, and the rigid walls of the cavity constrain the motion of air which then appears to be stiff. The problem of air stiffness also occurs in the use of a loudspeaker as a secondary source in active noise control. The loudspeaker becomes very ineffective at low frequencies when its back is enclosed by a cavity with rigid walls. Without such a rigid cavity, a device of active noise control would cause noise leaking instead of noise cancellation.

In some cases, the technique of sound reflection is more convenient to apply, or is at least highly complementary to the use of sound absorption technique, the most typical example being the vehicle exhaust muffler. The principle behind this technique is the use of discontinuity of acoustic impedance in a duct, such as an expansion chamber. For the same degree of impedance discontinuity, a sound wave reflector could be equally effective for low and intermediate frequencies. However, to achieve a very high rate of noise reduction in the receiving end of the duct, the expansion chamber has to be very large. This contrasts with the technique of duct lining for which the principal requirement concerns its length in the direction of the duct axis. The sudden expansion creates serious problems for any flow the duct may carry. Flow separation may occur and it results in more noise. Besides, passband exists in an expansion chamber. These drawbacks have prompted the present authors to introduce a tensioned membrane as a means of achieving broadband sound reflection in the region of low frequencies. As shown in Fig. 1, the prototype device is, broadly speaking, an expansion chamber with two side-branch cavities covered by light membranes under a fairly high tension, hence the name drumlike silencer, or simply drum silencer, in our previous publications.

The development of the drum silencer up to this point is briefly summarized here. The starting point was the exploration of acoustic impedance discontinuity inspired by the property of flexible tube in human respiratory system (Huang *et al.*, 1995; Huang, 1999). The propagation of sound waves coupled with the flexual waves of a membrane tends to be much slower than the free sound waves in air. Such low wave speed has also been measured experimentally (Huang *et al.*, 2000). The crucial advantage of such flexible tube is the preservation of a smooth flow passage. When utilized as a silencer, this feature carries two benefits. The first is the absence of any extra air pressure loss, such as that caused by flow separation in an expansion chamber, and the associated

[a]Electronic mail: mmlhuang@polyu.edu.hk

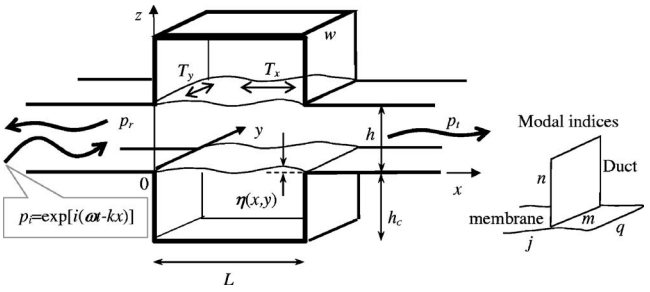

FIG. 1. Configuration of a drum silencer with two identical modules of cavity-backed membrane. Each cavity has a length of L, depth h_c, and width w.

extra noise from such turbulent flow. The second benefit is the complete separation of the gaseous flow in the duct from the cavity, which eliminates the chance of dust accumulation and other possible long-term environmental and maintenance problems. The complete separation of flow in the duct from the cavity also allows the use of a low impedance gas, such as helium, to fill the cavity to further enhance the silencer performance (Choy and Huang, 2003). Physically speaking, what happens in a drum silencer is as follows. When a sound wave is incident from the left-hand side of the device, it induces the membrane to vibrate and this vibration radiates sound in both left-hand and right-hand sides of the duct. The left-traveling waves form the reflected sound, while the right-traveling waves combine with the incident wave and form the transmitted sound. The principle of acoustic energy conservation guarantees that whatever amount of wave is reflected is accompanied by the same amount of reduction in the energy flux of the transmitted wave. In other words, the acoustic interference at the right-hand side is definitely destructive as the incident wave is the only energy flow source. Acoustically, the device behaves like a secondary source in the active noise control technique, the difference being the absence of sensors, actuators, and a control circuit. The important question of cavity air stiffness arises also, and the work has been carried out to optimize the design parameters such that the widest possible stopband is created with a given cavity volume (Huang, 2004). Both analytical (Huang, 2002) and experimental results (Choy and Huang, 2002) show that the performance of the drum silencer is very good.

It may be said that the use of membrane in noise abatement engineering is not entirely new. For example, panel absorbers were used in broadcasting studios and other architectural practices (Brown, 1964; Ford and McCormick, 1969; Sakagami *et al.*, 1996; Horoshenkov and Sakagami, 2001), membrane absorbers were also used as a splitter silencer in the form of arrays of Helmholtz resonators (Frommhold *et al.*, 1994). However, in all these applications, the membrane, or panel, is a component of resonator which works for a narrow frequency band, and the structural mass is a means to achieve a low resonance frequency. To the best of the authors' knowledge, the use of tensioned membrane to actively promote the vibroacoustic interaction for the purpose of wave reflection was new and unique (Huang, 1999).

The theoretical studies on the drumlike silencer have so far been confined to two dimensions for the duct, and one dimension for the membrane, which is essentially a string. However, the theoretical model was realistic enough to be simulated by an experimental rig to validate the theory (Choy and Huang, 2002). In such an experiment, the two edges of the membrane at $y=0$, w, where w is the membrane width, are free to move, and it in fact moves in step with the whole width of the membrane. With such a construction, the cavity is not air-tight, and it contradicts with the important potential environmental advantage of the device, namely the absolute separation between the duct and the cavity. To be air-tight, the four edges of the membrane have to be fixed on the duct walls so that the dusts from the gaseous flow are prevented from entering the cavity. Such boundary condition would inevitably make the membrane response highly two-dimensional, and the sound waves in the duct and cavity three-dimensional. The main motivation behind the current study is the concern of whether a membrane fixed on all edges would still yield the same silencing performance as the rather idealistic two-dimensional (2D) model. This concern arises since the constraints at all edges apparently reduce the response of the membrane to incident sound.

In what follows in Sec. II, complete formulation is given for the solution of the three-dimensional (3D) problem with all membrane edges fixed. The effect of the lateral tension, T_y, is studied in detail, and is found to be detrimental to the silencing performance. The special design of $T_y=0$ is studied in Sec. III. It is shown, analytically, that a 3D device with such property gives identical silencing performance as a drum silencer constructed on the basis of the 2D model despite the very different boundary conditions. This conclusion is encouraging and is validated experimentally.

II. THEORY

In the following, the formulation for calculating the response of the two-dimensional membranes in a three-dimensional duct is presented following the standard Galerkin procedure. The resulting set of linear equations is solved by general matrix inversion techniques. The effect of modal truncation is discussed first, followed by the study of the effect of the lateral tension, T_y.

A. The three-dimensional model

As shown in Fig. 1, a rectangular duct of height h and width w is equipped with two rigid-walled cavities of length L and depth h_c on two opposite sides. Each cavity is covered by a membrane of length L and width w, which forms part of the otherwise rigid duct wall. The membranes are fixed at the leading and trailing edges of $x=0$, L, as well as at the other two edges at $y=0$, w, which are henceforth called the lateral edges. A tensile force of T_x is applied on the membrane in the axial direction of the duct, and another tensile force of T_y is applied in the y direction. Plane incident wave p_i is introduced from the left-hand side with a unit amplitude. This wave induces membrane response of displacement $\eta(x,y,t)$ in the z direction with velocity $V=\partial\eta/\partial t$. The vibration radiates sound and imposes a radiation pressure on the membrane surface. The problems of acoustics and membrane vibration are fully coupled. As shown in the figure, the final reflected wave is denoted as p_r, and the transmitted wave p_t

assuming no further reflection in the far right-hand side. The transmission loss TL is defined as follows for harmonic incident wave p_i:

$$p_i(x,t) = \exp[i(\omega t - kx)],$$
$$\mathrm{TL} = 20\log_{10}|p_i/p_t| = -20\log_{10}|p_t|, \tag{1}$$

where $\omega = 2\pi f$ and $k = \omega/c_0$ are the angular frequency and the wave number, respectively, f is the frequency, and c_0 is the speed of sound in free space. The task now is to choose a set of properties for the membrane and cavity which would yield a TL higher than a certain criterion value over a widest possible continuous frequency band $f \in [f_1, f_2]$. The ratio f_2/f_1 can be seen as a logarithmic bandwidth, which is adopted as the quantity to be maximized in an optimization exercise for which more details are given in Huang (2004). Briefly, f_2/f_1 is maximized for a given cavity volume Lh_c and the main variables are the membrane tension and cavity shape. The motivation behind using such a bandwidth definition is the desire to put due emphasis on the low-frequency performance, which is a technical challenge in duct noise abatement.

The dynamics equation for the lower membrane with its nominal position at $z=0$ is

$$m_s\frac{\partial^2\eta}{\partial t^2} - T_x\frac{\partial^2\eta}{\partial x^2} - T_y\frac{\partial^2\eta}{\partial y^2} + (p_i + \Delta p) = 0, \tag{2}$$

where m_s is the mass per unit area of the membrane, $\Delta p = p_+ - p_-$ is the fluid loading acting on the upper (+) and lower (−) sides of the membrane induced by the membrane vibration itself. The solution for the problem with two identical membranes is simplified to a problem in which one membrane is installed in a duct of height $h/2$ and the symmetric plane of $z=h/2$ is replaced by a solid wall. With this simplification, the presence and the effect of the upper membrane at $z=h$ are ignored in the subsequent theoretical development. However, the duct height h is still used in the formulation as a length scale.

Notice that the effect of the bending stiffness, $B\partial^4\eta/\partial x^4$, has been left out of the dynamics equation (2). Here, $B = Es^3w/12$ is the flexual rigidity of the membrane of thickness s, width w, and E is the Young's modulus. The ratio of the neglected bending term, $B\partial^4\eta/\partial x^4$, to that of the tensile force, $T_x\partial^2\eta/\partial x^2$, is examined here for the second *in vacuo* vibration mode, $\eta = \sin(2\pi x/L)$, which is shown later to be the most important mode. The ratio is

$$\left|\frac{B\partial^4\eta/\partial x^4}{T_x\partial^2\eta/\partial x^2}\right| = \frac{Es^3w(2\pi)^2}{12T_xL^2}. \tag{3}$$

For the typical configuration used in the experiment of the current study, a stainless steel of thickness $s=0.025$ mm is used, $E=190$ GPa, $w=0.1$ m, $L=0.5$ m, and $T_x=750$ N. The ratio turns out to be $5.21\times10^{-6} \ll 1$, confirming that the structure is truly a membrane instead of a plate.

B. Solution to the model problem

The Galerkin procedure to solve the coupled problem is outlined as follows. First, the fluid loading Δp is divided into three parts:

$$\Delta p = p_{+\mathrm{rad}} - (p_{-\mathrm{rad}} + p_{-\mathrm{ref}}), \tag{4}$$

where $p_{+\mathrm{rad}}$ and $p_{-\mathrm{rad}}$ are the radiation sound pressures on the upper and lower membrane surfaces at $z=0+$ and $0-$, respectively, when the two vertical cavity walls at $x=0$ and L are temporarily ignored. $p_{-\mathrm{ref}}$ is the sound reflected by the two vertical cavity walls. One way to relate these pressures with the vibration velocity V is to express the coupled membrane response as a combination of *in vacuo* membrane vibration modes. For membranes fixed on all four edges, the *in vacuo* modes, denoted by φ, are simply sine functions, as shown in the following,

$$V(x,y,t) = \frac{\partial\eta}{\partial t} = e^{i\omega t}\sum_{j=1}^{\infty}\sum_{q=1}^{\infty} V_{jq}\varphi_{jq}(x,y),$$
$$V_{jq} = \frac{4}{Lw}\int_0^w\left[\int_0^L V\varphi_{jq}dx\right]dy, \tag{5}$$
$$\varphi_{jq}(x,y) = \sin(j\pi x/L)\sin(q\pi y/w),$$

where j and q are modal indices in x and y directions, respectively, and the double summations are abbreviated as Σ_{jq} henceforth. For convenience, modal indices for the duct acoustics and membrane vibration are indicated at the right-hand side of Fig. 1.

The crucial step now is to relate the modal amplitudes V_{jq} to the induced fluid loading Δp. To do so, sound radiation is first considered for a prescribed modal vibration of a unit amplitude, $V_{jq}=1$, and the resultant fluid loading, denoted as $e^{i\omega t}\Delta p^{(jq)}(x,y)$, is also expanded into *in vacuo* modes of indices $j'q'$,

$$Z_{jqj'q'} = \frac{4}{Lw}\int_0^w\left[\int_0^L \Delta p^{(jq)}\varphi_{j'q'}dx\right]dy,$$
$$\Delta p = e^{i\omega t}\sum_{j,q} V_{jq}\sum_{j',q'} Z_{jqj'q'}\varphi_{j'q'}. \tag{6}$$

Here, the matrix of $Z_{jqj'q'}$ can be called the modal impedance of the membrane. When Eq. (2) is multiplied by φ_{jq} and integrated over the membrane surface, it becomes a set of linear equations,

$$\mathcal{L}_{jq}V_{jq} + \sum_{j,q,j',q'} Z_{jqj'q'}V_{jq} + I_{jq} = 0,$$
$$j = 1,2,3,\ldots, \quad q = 1,2,3,\ldots, \tag{7}$$

where $\mathcal{L}_{jq}$ is the structural operator and I_{jq} is the modal amplitude of the incident wave p_i, as shown below:

$$\mathcal{L}_{jq} = m_s i\omega + \frac{T_x}{i\omega}\left(\frac{j\pi}{L}\right)^2 + \frac{T_y}{i\omega}\left(\frac{q\pi}{w}\right)^2,$$

$$I_{jq} = \underbrace{\frac{2}{w}\int_0^w \sin\left(\frac{q\pi y}{w}\right)dy}_{F_q} \times \underbrace{\frac{2}{L}\int_0^L p_i \sin\left(\frac{j\pi x}{L}\right)dx}_{I_j^{(2D)}},$$

$$F_q = 2\frac{1-\cos(q\pi)}{q\pi} = \begin{cases} \frac{4}{q\pi}, & \text{odd } q \\ 0, & \text{even } q \end{cases},$$

$$I_j^{(2D)} = 2j\pi e^{ikL/2}\left[\frac{1-e^{i(-kL+j\pi)}}{(j\pi)^2-(kL)^2}\right]. \tag{8}$$

The key to solving Eq. (7) is finding the modal impedance $Z_{jqj'q'}$. To do so, $p_{+\text{rad}}, p_{-\text{rad}}$, and $p_{-\text{ref}}$ are needed. Formulations for $p_{+\text{rad}}$ and $p_{-\text{rad}}$ are available in literature, such as Doak (1973), and $p_{-\text{ref}}$ is given in Huang (2002). Since all three pressure components have essentially the same functional relationships in the directions of y and z, only $p_{+\text{rad}}$ is shown below for essential discussions. Dropping the common time dependence factor e^{iwt} from this point onwards, the complex amplitude of the radiation pressure is written as

$$\begin{aligned} p_{+\text{rad}}(x,y,z) &= \frac{\rho_0}{2A}\sum_{m=0}^{\infty}\sum_{n=0}^{\infty} c_{mn}\psi_{mn}(y,z) \\ &\quad \times \int_0^w \left[\int_0^L \psi_{mn}(y',z')V(x',y')G_{mn}(x,x')dx'\right] \\ &\quad \times dy', \\ G_{mn}(x,x') &= H(x-x')e^{-ik_{mn}(x-x')} + H(x'-x)e^{+ik_{mn}(x-x')} \\ &= \cos[k_{mn}(x-x')] - i\,\sin[k_{mn}|x-x'|], \end{aligned} \tag{9}$$

where primes indicate the source coordinates on the membrane at $z'=0$, ρ_0 is the density of the undisturbed fluid, $G_{mn}(x,x')$ plays the role of a Green function, which contains Heaviside functions H, ψ_{mn} is the duct acoustics modal function, c_{mn} and k_{mn} are, respectively, the associated modal wave speed and wave number, which are defined in the following. The duct acoustics modes, denoted by ψ_{mn}, satisfying the rigid wall condition and the homogeneous wave equation in air,

$$\left(\frac{\partial^2}{c_0^2\,\partial t^2} - \nabla^2\right)p = 0, \quad \nabla p_{\text{wall}} = 0, \tag{10}$$

are

$$p = \psi_{mn}(y,z)\exp[i(\omega t \pm k_{mn}x)], \quad m,n = 0,1,2,3,\ldots,$$

$$k_{mn} = \frac{\omega}{c_{mn}}, \quad c_{mn} = \frac{ic_0}{\sqrt{(m\pi/kw)^2 + (n\pi/kh)^2 - 1}},$$

$$\psi_{mn} = \sqrt{(2-\delta_{0m})(2-\delta_{0n})}\cos\left(\frac{m\pi y}{w}\right)\cos\left(\frac{n\pi z}{h}\right),$$

$$\frac{1}{A}\int\int_A \psi_{mn}\psi^*_{m'n'}dA = \begin{cases} 0, & (m,n) \neq (m',n') \\ 1, & (m,n) = (m',n'), \end{cases} \tag{11}$$

where $A = h \times w$ is the cross section of the duct, and asterisk in the last expression indicates the complex conjugate. Note that the modal index for the common edge direction of y is q for the membrane vibration but m is used for the duct acoustics. The radiation loading on the membrane at $z=0$ caused by the membrane vibration of mode (j,q) with a unit amplitude is denoted as $p_{+\text{rad}}^{(jq)}$,

$$\begin{aligned} p_{+\text{rad}}^{(jq)} &= \frac{\rho_0}{2A}\sum_{m=0}^{\infty}\sum_{n=0}^{\infty} c_{mn}(2-\delta_{0m})(2-\delta_{0n})\cos\left(\frac{m\pi y}{w}\right) \\ &\quad \times \int_0^w \cos\left(\frac{m\pi y'}{w}\right)\sin\left(\frac{q\pi y'}{w}\right)dy' \\ &\quad \times \int_0^L \sin\left(\frac{j\pi x'}{L}\right)G_{mn}(x,x')dx', \end{aligned} \tag{12}$$

and the modal impedance from this term is denoted as $Z_{jqj'q'}^{(+\text{rad})}$,

$$Z_{jqj'q'}^{(+\text{rad})} = \frac{2\rho_0 L}{h}\mathcal{I}_{jj'}\sum_{m=0}^{\infty}\sum_{n=0}^{\infty}(2-\delta_{0m})(2-\delta_{0n})c_{mn}C_{mq}C_{mq'},$$

$$\begin{aligned} C_{mq} &= \int_0^1 \cos(m\pi\xi)\sin(q\pi\xi)d\xi \\ &= \begin{cases} \frac{2q/\pi}{q^2-m^2}, & m+q = \text{odd} \\ 0, & m+q = \text{even}, \end{cases} \end{aligned} \tag{13}$$

$$\begin{aligned} \mathcal{I}_{jj'} &= \frac{1}{L^2}\int_0^L \sin(j'\pi x/L) \\ &\quad \times \left[\int_0^L \sin(j\pi x'/L)G_{mn}(x,x')dx'\right]dx \\ &= \frac{jj'\pi(e^{ij\pi} - e^{-ik_mL})(e^{ij\pi} + e^{ij'\pi})}{[(k_mL)^2 - (j\pi)^2][(k_mL)^2 - (j'\pi)^2]} \\ &\quad - \frac{ik_mL\delta_{jj'}}{(k_mL)^2 - (j\pi)^2}. \end{aligned}$$

The double axial integration $\mathcal{I}_{jj'}$, is unlikely to vanish for any mode due to the different nature of the traveling acoustic waves and the standing waves on the structure. However, subtle modal coupling arises from $C_{mq}C_{mq'}$. For example, odd vibration mode of $q=1$ radiates sound which propagates as even duct acoustics modes of $m=0,2,4,\ldots$, and these acoustics modes in turn add loading on odd membrane modes of $q'=1,3,5,\ldots$. The conclusion is that odd membrane vibration modes put loading on odd modes and not on even modes, vice versa. Obviously, self loading for $q'=q$ is the strongest.

There is a complete decoupling between odd and even modes in the y direction. The set of linear equations in Eq. (7) can be separated into two sets and solved separately. The subset of equations for the even m modes are homogeneous since the incident wave p_i does not add load on even m

modes, as can be seen from the y-integration for F_q and I_{jq} in Eq. (8). This means that all even q modes, $q=2,4,6,\ldots$, should vanish if the determinant for the set of equations for the even modes does not vanish. When the determinant does vanish, the system experiences free vibration without excitation. As can be seen in the following, such a free vibration does not radiate sound into the far field, and the system therefore does not have fluid damping. A completely lossless system could have a real eigenfrequency for these even modes in the low-frequency range. In reality, there is always some damping present in the system. It is therefore argued that these even modes are not excited at all. Note that there is also a complete decoupling of modal impedance between odd and even modes in the axial direction, as shown earlier in Huang (2002). But the plane incident wave p_i has loading on both odd and even axial modes j. Therefore, both odd and even axial modes are excited.

Substituting the modal coefficient I_{jq} given in Eq. (8) and the modal impedance given in Eq. (13) into the linear equations of Eq. (7), the task of solution becomes essentially the inversion of matrix. Once the membrane response is found, the far field sound radiation can be calculated from Eq. (9) considering only the plane wave mode, $m=n=0$ for frequencies below the cut-on frequency of the duct, $\omega < \pi/h, \pi/w$. The combination of the downstream radiation wave with the incident wave forms the transmitted wave, while the upstream radiation becomes the reflection wave. The reflected wave is

$$p_r = p_{+\text{rad}x\to-\infty} = \frac{\rho_0 c_0}{2A} e^{ikx} \int_0^L V_w(x') e^{-ikx'} dx',$$

$$V_w(x) = \frac{1}{w}\int_0^w V(x,y)dy = \sum_{j=1}^{\infty} V_j \varphi_j(x), \tag{14}$$

$$V_j = \frac{2}{L}\int_0^L V_w(x)\varphi_j(x)dx, \quad \varphi_j(x) = \sin\left(\frac{j\pi x}{L}\right),$$

where the membrane vibration velocity V is simply averaged over the width w and denoted as V_w, and the modal index q is dropped when $V_w(x)$ is expanded in the axial direction. The integration for Eq. (14) is identical to that of the 2D silencer (Huang, 2002). In fact, it is shown in the next section that the reflected wave for a 3D silencer with $T_y=0$ is identical to that of a 2D silencer.

C. Modal truncation and 2D membrane response

In actual calculations, the number of modes has to be truncated for Eq. (7), and the solution should be scrutinized carefully before being accepted. Denote the axial number of modes as N_j and the lateral number of modes as N_q, the convergence of solution as these numbers increase is shown in Fig. 2(a). In this study, $N_q=2N$ is specified as it is found that more lateral modes are needed when the lateral tension T_y is low. The following set of geometry and membrane properties are chosen as the testing case, for which the 2D analytical results were obtained earlier (Huang, 2002):

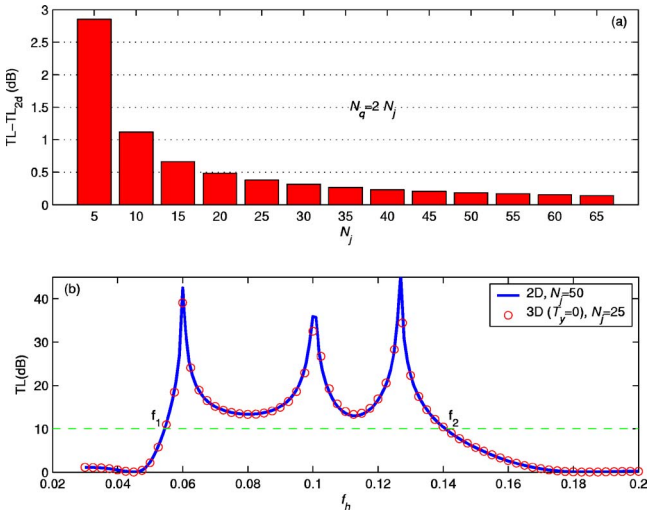

FIG. 2. (Color online) Convergence test for the modal truncation by comparison with the solution for the 2D silencer. (a) The error transmission loss for $f_h=0.11$ decreases with the mode number used, and (b) the close agreement between the transmission loss spectrum calculated by $N_j=25$.

$$L=5h, \quad h_c=w=h, \quad T_x=0.475(\rho_0 c_0^2 h^2),$$
$$T_y=0, \quad m_s/(\rho_0 h)=1 \tag{15}$$

For convenience, dimensionless frequency f_h and tensile forces, T_{xh}, T_{yh}, are defined as follows:

$$f_h=\frac{fh}{c_0}, \quad T_{xh}=\frac{T_x}{\rho_0 c_0^2 h^2}, \quad T_{yh}=\frac{T_y}{\rho_0 c_0^2 h^2}. \tag{16}$$

Tests are first conducted to see whether and how the results approach the 2D theory of Huang (2002) when N_j is gradually increased. When N_j is small, the main region of deviation between the 2D and 3D theories is found between the second and third peaks in the TL spectra. The dimensionless frequency of $f_h=0.11$ is therefore chosen as the test frequency to examine the effect of N_j on the results. At this frequency, TL=13.58 dB is predicted by the 2D theory with $N_j=50$, and the deviation by the 3D results is shown in Fig. 2(a). It is found that, beyond a certain moderate N_j, e.g., 25, the solution improvement becomes marginal. So, $N_j=25$ is chosen for the calculation of the 3D silencer for the whole frequency range. The result is compared with the 2D spectrum in Fig. 2(b) where the 3D result is shown in open circles and the 2D results in solid line. When a criterion value of 10 dB is used, the stopband in the figure is between $f_1=0.0545$ and $f_2=0.1406$, with a ratio of $f_2/f_1=2.58$.

Typical membrane responses for the frequency of $f_h=0.11$ are shown in Fig. 3. The top row is for $T_{yh}=0$, while the bottom row for $T_{yh}=0.02$, both with axial tension $T_{xh}=0.475$. The instantaneous vibration velocity distribution is shown in Figs. 3(a) and 3(c). As shown in Fig. 3(a), the membrane without lateral tension essentially behaves like a one-dimensional (1D) string in the sense that the membrane displacement rises very sharply from the fixed lateral edges, $y=0$, w, to the almost constant value over the central region.

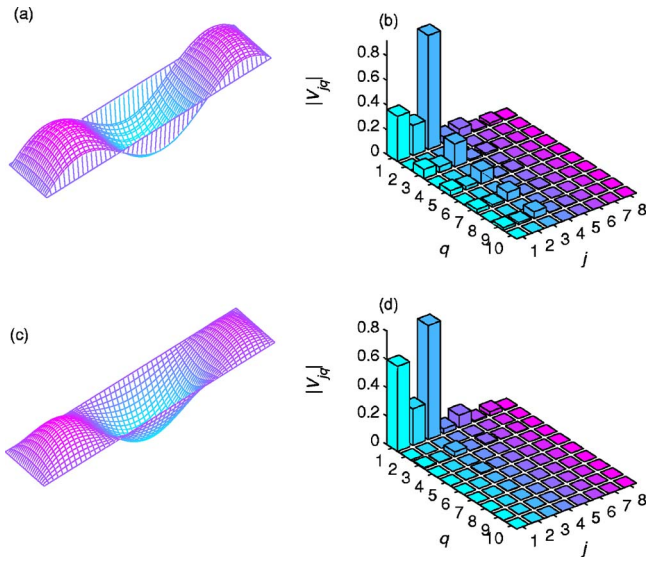

FIG. 3. (Color online) Comparison of membrane response for lateral tension $T_y=0$, for (a) and (b), and $T_y=0.02$, for (c) and (d). (a) and (c) The instantaneous membrane vibration velocity. (b) and (d) The distribution of the modal amplitudes.

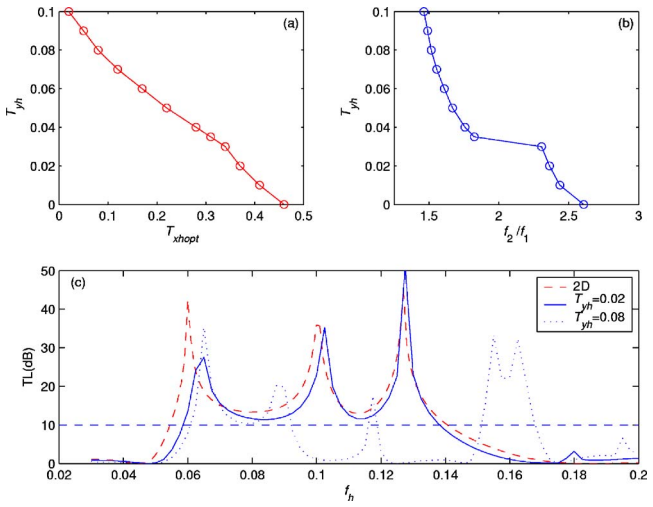

FIG. 4. (Color online) Variation with transverse tension T_{yh}. (a) The decrease of the optimal axial tension $T_{xh\text{opt}}$ as T_{yh} increases. (b) The reduction of the bandwidth of the optimal design using 10 dB as the criterion of stopband. (c) Comparison of the optimal transmission loss spectrum for the 2D configuration with the 3D configuration with $T_{yh}=0.02$, 0.08.

On the contrary, Fig. 3(c) shows that a rather smooth and fully two-dimensional distribution is found for the membrane with a small lateral tension.

The modulus of the membrane modal coefficient, $|V_{jq}|$, are shown in Figs. 3(b) and 3(d) as bar charts. Note that the modes with even q are absent since only odd q can be excited by a plane wave. For the odd modes, the decay with q is also reasonably fast. The largest responses in both cases are located near the first three axial modes. Comparing the two subfigures, it is found that a small T_{yh} can alter the membrane response drastically.

D. Effect of transverse tension

When a residual transverse tension T_{yh} is present, the system becomes truly three dimensional. It is found that the optimal design parameters are affected by T_{yh}. Following the procedure of Huang (2004) with a threshold transmission loss value of 10 dB, and using the parameters listed in Eq. (15), the optimal axial tensile forces $T_{xh\text{opt}}$ and the stopband parameters f_1, f_2 are found. The results are shown in Fig. 4 as a function of T_{yh}, the latter being shown as the vertical coordinate. Figure 4(a) shows that $T_{xh\text{opt}}$ diminishes rapidly as T_{yh} increases. A rather sudden change occurs near $T_{yh}=0.03$. This is partly due to the fact that the cavity is slender, so that any tension across the duct width causes a lot of stiffness effect. Figure 4(b) shows that, as T_{yh} increases, the stopband ratio f_2/f_1 also shrinks very rapidly. The optimal spectra under two typical $T_{yh}>0$ conditions are shown in Fig. 4(c). A small $T_{yh}=0.02$ is seen to make the stopband narrower with a higher starting frequency for the band, f_1, and a lower end frequency f_2. The frequency gap between the second and third peaks is also narrowed. Further increase in T_{yh} to 0.08 causes the merge of the second and third peaks, leading to a rather narrow, two-peak stopband. Similar peak movement can also be observed when the axial tensile force T_{xh} is increased beyond the optimal level when T_{yh} is absent. In conclusion, the effect of T_{yh} is generally considered to be counterproductive.

III. MEMBRANE WITHOUT LATERAL TENSION

In the following it is shown analytically that, when $T_y=0$, a two-dimensional membrane fixed on all edges performs exactly the same as a membrane with free edges behaving like a 1D string. Since this performance is also found to be the best in the last section, an experimental validation is given.

A. Plane wave solution

Equation (14) shows that the width-averaged membrane vibration velocity $V_w(x)$ alone determines the far field reflection, hence the silencing performance. In order to find V_w, Eq. (2) can be integrated over y. Assuming that the membrane surface density m_s and the axial tensile force T_x are not functions of y, the y integrations of the first two terms of Eq. (2) produce no functional changes except that the 2D displacement $\eta(x,y,t)$ is replaced by its 1D counterpart, say $\eta_w(x,t)=w^{-1}\int_0^w \eta(x,y,t)dy$. The same is true for the incident wave p_i which is also not a function of y. The question now is whether the same holds for the vibration induced fluid loading Δp, for which the upper surface term $p_{+\text{rad}}$ is given in Eq. (9).

When the modal function $\psi_{mn}(x,y)$ in Eq. (9), which contains $\cos(m\pi y/w)$, is integrated over y, the only contribution comes from the modes with $m=0$ while n can be any integer. These modes can be called two-dimensional duct acoustics modes with index m dropped,

$$\psi_n(z) \equiv \psi_{0n} = \sqrt{2-\delta_{0n}}\cos(n\pi z/h), \quad c_n \equiv c_{0n}. \tag{17}$$

Finally, the width-averaged loading from Eq. (9) becomes

$$\bar{p}_{+\mathrm{rad}}(x) = \frac{\rho_0}{2A}\sum_{n=0}^{\infty} c_n(2-\delta_{0n})\int_0^L G_{mn}(x,x')V_w(x')dx'. \tag{18}$$

It can be shown that similar results hold for the lower surface radiation pressure $p_{-\mathrm{rad}}$ and the cavity wall reflection pressure $p_{-\mathrm{ref}}$. The consequence of these results is that Eq. (2) can be formulated in a closed-form for the y-averaged membrane vibration velocity $V_w(x)$ using its expansion into the string vibration modes φ_j with modal coefficients V_j, as shown in the following:

$$\begin{aligned}
&\mathcal{L}_j V_j + \sum_{j,j'} Z_{jj'}V_j + I_j = T_y U_j, \quad j=1,2,3,\\
&\mathcal{L}_j = m_s i\omega + \frac{T_x}{i\omega}\left(\frac{j\pi}{L}\right)^2, \quad I_j = \frac{2}{L}\int_0^L p_i\varphi_j dx,\\
&U_j = \frac{2}{L}\int_0^L \left[\frac{\partial\eta}{\partial y}\right]_0^w \varphi_j(x)dx,\\
&Z_{jj'} = \frac{2}{L}\int_0^L \overline{\Delta p_j}(x)\sin(j'\pi x/L)dx,
\end{aligned} \tag{19}$$

where U_j is a stiffness term arising from the fixed lateral edges, and the width-averaged loading $\overline{\Delta p_j}$ depends only on V_w or V_j. When $T_y=0$, the term with the unknown U_j disappears, and the whole three-dimensional problem is reduced to two dimensions in which the membrane vibration is represented by the width-averaged velocity $V_w(x)$, and the modal impedance $Z_{jj'}$ is calculated purely on the basis of V_w with a total disregard for the boundary conditions at $y=0, w$. Since $Z_{jj'}$ does not contain any contribution from modes of $m>0$, and the excitation term I_j is identical to that in the 2D model, it follows that V_w is identical to the string displacement in the 2D model. The restriction of $\eta=0$ at the two edges of $y=0, w$ means that the induced vibration elsewhere is increased to compensate for the lateral edge constraints. In terms of the actual acoustic field around the membrane of finite width w, the structural boundary conditions at $y=0, w$ do influence the outcome. Higher order modes of $m>0$ exist but do not propagate. They become a purely reactive near-field oscillation which does not even influence the virtual mass on the width-averaged membrane response.

In fact, the above-presented analysis can be shown to hold when the membrane is not a rectangular piece of width w, but of any shape lined over a duct of any cross section, such as a circular duct with or without a solid clamp over the perimeter of the curved membrane. In the case of a circular duct, y in the above-presented analysis is replaced by the circumferential coordinate s and z is changed to radius r. Details of the modal functions ψ_{jq} and φ_{mn} would be quite different, but the method of plane wave solution using perimeter-integration stands. When $T_y>0$, or when m_s, T_x are functions of y, the full three-dimensional (3D) solution for the duct acoustics and the 2D solution for the membrane vibration have to be sought.

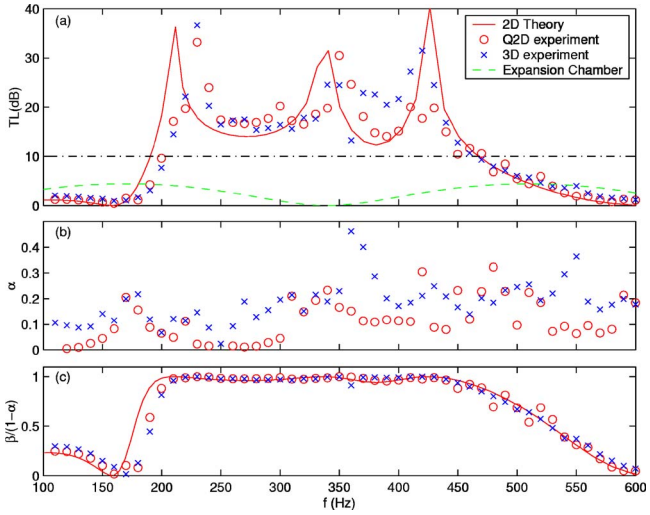

FIG. 5. (Color online) Comparison of the experimental data for the Q2D design (○) nd the 3D design (×) with the 2D theoretical prediction (solid line). (a) The transmission loss, (b) the sound energy absorption coefficient, and (c) the relative sound energy reflection coefficient.

B. Experimental validation

In order to validate the main conclusion that the membrane with all four edges fixed should perform the same way as one with two free lateral edges at $y=0, w$, experiments were conducted. The former configuration is called the 3D design, while the latter is called quasi-two-dimensional design denoted as Q2D. The procedure and methodology of the experiment are identical to that described in Choy and Huang (2002) where the Q2D design was used. Briefly, the standing wave pattern in the rectangular duct was resolved by the two-microphone method, while the transmission loss was deduced by the two-load method. The duct used had a dimension of $h=10$ cm by $w=10$ cm cross section, and the membrane had a length of $L=5h=0.5$ m and depth $h_c=h=10$ cm. The membrane was made of stainless steel, and the ratio of membrane to air mass calculated by $m_s/(\rho_0 h)$ was 1.4. The optimal tensile force predicted was close to $T_x=0.53(\rho_0 c_0^2 h^2)=750$ N. An optimal design here refers to the set of parameters with which the drum silencer attains the broadest continuous stopband of TL$\geqslant$10 dB. Note that the bandwidth is calculated as the ratio of the upper to lower frequency limits of the stopband (Huang, 2004). In Fig. 5, the experimental data from the Q2D design (○) and the 3D design (×) are plotted with the theoretical prediction (solid line) for the true 2D model (Huang, 2002). The dashed line is the 1D theory of the performance of an expansion chamber formed by the two cavities used in the drum silencer, and it is shown to be much lower in the stopband offered by the two drum silencers. Figure 5(a) compares TL, Fig. 5(b) shows the sound energy absorption coefficient, $\alpha=1-(|p_r|^2+|p_t|^2)$, measured in the experiment, Fig. 5(c) compares the relative sound energy reflection coefficient which is defined in the following. Several observations and discussions are given as follows.

(1) Figure 5(b) shows that a certain significant amount of sound energy absorption occurs in the experiment (between 10% and 20%), but the absorption is assumed to

be zero in theory. This discrepancy is not surprising. It is very hard to model energy dissipation mechanisms that occur in experiment with much theoretical certainty (Choy and Huang, 2002). Factors which may contribute to such energy dissipation include viscous friction between the air and the duct wall, possible duct wall vibration at low frequencies, sound leaking at some connection joints, material friction within the membrane and especially around membrane edges. Since the purpose of the drum silencer is for wave reflection, such additional damping is not pursued further theoretically. Besides, the damping may not be entirely beneficial in terms of TL as excessive damping has been shown to stifle the membrane vibration and wave reflection (Huang, 2004).

(2) As shown in Figs. 5(a) and 5(c), there is a frequency shift between the experimental data and the theoretical prediction around all three theoretical peaks of TL spectrum. This could be a result of measurement error for the tensile stress as it is difficult to fix the strain gauge on the thin and slippery membrane. The actual tensile force could be higher than 750 N. The disparity between theory and experiment, especially for the 3D design, is most significant between the second and third spectral peaks. There are two possibilities for this. First, the membrane had some residual tension in y direction when effort was made to flatten it. It is not uncommon that the membrane is a little crinkled during the experiment since the two clamps at $x=0$, L do not have very uniform gripping on the slippery membrane. In fact, the residual tension could be present in both Q2D and 3D experiments. In the case of the 3D experiment, a residual tension would lead to cross coupling between odd and even modes. If the membrane is crinkled, vibrations of complex modes would also lead to excessive damping of the system energy.

(3) Having considered the possible mechanisms of energy damping, a relative reflection coefficient, $\beta/(1-\alpha)$, where $\beta=|p_r|^2$, is introduced to examine to what extent the drum silencer reflects waves which are not absorbed, $1-\alpha$. The relative reflection is plotted in Fig. 5(c). Comparing Fig. 5(c) with Fig. 5(a), it is found that the collapse of experimental data on the theoretical prediction (solid line) for $\beta/(1-\alpha)$ is much better than that of TL or β (not shown).

(4) Notwithstanding all the differences between theory and experimental data, Figs. 5(a) and 5(c) show that there is a general agreement between the Q2D and the 3D experimental results throughout the whole stopband from about 200 to 450 Hz if 10 dB is used as a criterion value for the stopband. There is also a general agreement between the experimental data and the theoretical prediction.

IV. CONCLUSIONS

A theoretical study has been carried out to reveal the equivalence of the performance of a drum silencer with all membrane edges fixed and that simulating a two-dimensional model, the tension in the cross-sectional direction being zero. This result is brought out analytically and validated by experiment. The validation provides assurances that the cavity can be truly air-tight so that potential environmental advantages of the drum silencer can be realized. The reason why they are equivalent is that only the width-averaged membrane response is relevant to wave reflection into the far field, and the width-averaged response is decoupled from transverse modes. The latter only exists as a near field supplement to the problem of acoustic scattering by tensioned membranes. The conclusion actually holds for ducts with any cross sections.

The effect of transverse tension is found to be counterproductive as far as the performance of the drum silencer is concerned. In a real experiment, some residual transverse tension may always exist, but its negative impact would be small since the system does not behave singularly when the transverse tension changes.

ACKNOWLEDGMENT

The research carried out in this study was supported by grants from the Research Grants Committee of the Hong Kong SAR Government (PolyU 5169/02E, PolyU5298/03E).

Brown, S. (**1964**). "Acoustic design of broadcasting studios," J. Sound Vib. **1**, 239–257.

Choy, Y. S., and Huang, L. (**2002**). "Experimental studies of a drumlike silencer," J. Acoust. Soc. Am. **112**, 2026–2035.

Choy, Y. S., and Huang, L. (**2003**). "Drum silencer with shallow cavity filled with helium," J. Acoust. Soc. Am. **114**, 1477–1486.

Doak, P. E. (**1973**). "Excitation, transmission and radiation of sound from source distributions in hard-walled ducts of finite length. I. The effects of duct cross-section geometry and source distribution space-time pattern," J. Sound Vib. **31**, 1–72.

Ford, R. D., and McCormick, M. A. (**1969**). "Panel sound absorbers," J. Sound Vib. **10**, 411–423.

Frommhold, W., Fuchs, H. V., and Sheng, S. (**1994**). "Acoustic performance of membrane absorbers," J. Sound Vib. **170**, 621–636.

Fuchs, H. V. (**2001**). "From advanced acoustic research to novel silencing procedures and innovative sound treatments," Acta. Acust. Acust. **87**, 407–413.

Horoshenkov, K. V., and Sakagami, K. (**2001**). "A method to calculate the acoustic response of a thin, baffled, simply supported poroelastic plate," J. Acoust. Soc. Am. **110**, 904–917.

Huang, L., (**2002**). "Modal analysis of a drumlike silencer," J. Acoust. Soc. Am. **112**, 2014–2025.

Huang, L. (**2004**). "Parametric study of a drumlike silencer," J. Sound Vib. **269**, 467–488.

Huang, L. (**1999**). "A theoretical study of duct noise control by flexible panels," J. Acoust. Soc. Am. **106**, 1801–1809.

Huang, L., Choy, Y. S., So, R. M. C., and Chong, T. L. (**2000**). "Experimental studies on sound propagation in a flexible duct," J. Acoust. Soc. Am. **108**, 624–631.

Huang, L., Quinn, S. J., Ellis, P. D. M., and Ffowcs Williams, J. E. (**1995**). "Biomechanics of snoring," Endeavour **19**, 96–100.

Ingard, K. U. (**1994**). "Notes on the sound absorption technology," *Noise Control Foundation*, Poughkeepsie, N Y.

Maa, D.-Y. (**1975**). "Theory and design of microperforated panel sound absorbing constructions," Sci. Sin. **18**, 55–71.

Maa, D.-Y. (**1998**). "Potential of microperforated panel absorber," J. Acoust. Soc. Am. **104**, 2861–2866.

Mechel, F. P., and Vér, I. L. (**1992**). *Noise and Vibration Control Engineering: Principles and Applications*, edited by L. L. Beranek and I. L. Vér (Wiley, New York), Chap. 8.

Sakagami, K., Kiyama, M., Morimoto, M., and Takahashi, D. (**1996**). "Sound absorption of a cavity-backed membrane: A step towards design method for membrane-type absorber," Appl. Acoust. **49**, 237–247.

Beam-tracing model for predicting sound fields in rooms with multilayer bounding surfaces

Andrew Wareing[a] and Murray Hodgson[b]
School of Occupational and Environmental Hygiene and Department of Mechanical Engineering, University of British Columbia, 2206 East Mall, Vancouver, British Columbia, V6T 1Z3, Canada

(Received 28 February 2005; revised 5 July 2005; accepted 9 July 2005)

This paper presents the development of a wave-based room-prediction model for predicting steady-state sound fields in empty rooms with specularly reflecting, multilayer surfaces. A triangular beam-tracing model with phase, and a transfer-matrix approach to model the surfaces, were involved. Room surfaces were modeled as multilayers of fluid, solid, or porous materials. Biot theory was used in the transfer-matrix formulation of the porous layer. The new model consisted of the transfer-matrix model integrated into the beam-tracing algorithm. The transfer-matrix model was validated by comparing predictions with those by theory, and with experiment. The test surfaces were a glass plate, double drywall panels, double steel panels, a carpeted floor, and a suspended-acoustical ceiling. The beam-tracing model was validated in the cases of three idealized room configurations—a small office, a corridor, and a small industrial workroom—with simple boundary conditions. The number of beams, the reflection order, and the frequency resolution required to obtain accurate results were investigated. Beam-tracing predictions were compared with those by a method-of-images model with phase. The model will be used to study sound fields in rooms with local- or extended-reaction multilayer surfaces. © *2005 Acoustical Society of America.* [DOI: 10.1121/1.2011152]

PACS number(s): 43.55.Ka, 43.20.Dk, 43.20.Tb [NX] Pages: 2321–2331

I. INTRODUCTION

Room-prediction models are invaluable tools to assist designers in studying and optimizing room designs and sound fields. Room-acoustical prediction models fall into two categories—energy-based and wave-based. Recently models that are a combination of both categories have also been developed.

Energy-based models ignore phase, modeling propagating sound waves as rays or beams of energy, and describing sound/surface interactions using energy absorption and diffuse-reflection coefficients. They predict room echograms and steady-state levels in limited-frequency bands. Diffuse-field theory[1] is simple, but assumes a diffuse sound field and, in application, highly restrictive room characteristics.[2] The conventional method of images[3] accounts for arbitrary geometry and absorption distributions, but is limited to specular reflection; moreover, its generalization to nonrectangular geometry is computationally impracticable.[4] Radiosity[1,5,6] accounts for arbitrary geometry, but assumes diffuse surface reflection. Conventional ray tracing,[7] involving generating and tracing dimensionless rays to a receiver, models specular or diffuse reflection and arbitrary room geometry efficiently; however, a volume receiver must be used, resulting in temporal and spatial "smearing" of predicted room responses. Beam tracing[5,8,9] is similar to ray tracing, except that beams are traced rather than dimensionless rays, allowing a point receiver and requiring fewer beams than rays. However, problems occur when a beam intersects more than one surface, and when the beam-front becomes larger than a surface. These problems are resolved by adaptive ray/beam tracing.[10,11] Hybrid models combining these various methods also exist.[12,13]

Wave-based models are inherently more accurate, but can be computationally expensive. They include phase, and describe surfaces by their complex normal surface impedance. They predict room impulse responses and/or frequency responses, which are interrelated by the Fourier transform. Their application is generally limited to low frequencies and/or simple room shapes. The wave equation[1] can only be solved readily for rooms with simple geometries and boundary conditions. Finite- and boundary-element methods[14,15] can be used to solve the wave equation numerically, and work well for small rooms with arbitrary geometry at low frequencies. Methods have been developed to allow their application to large rooms.[16–18]. Phase has been introduced in an approximate manner into a ray-tracing model so that it could be applied to lower frequencies.[19] Bartsch[20] combined an energy-based ray-tracing model and a wave-based finite-element model to improve low-frequency prediction accuracy.

Recently, a number of models based on hybrid energy-based approaches, but extended to include phase for the calculation of binaural impulse responses, have been developed for the auralization of sound in virtual rooms. Naylor[21] developed the ODEON model based on a ray-tracing approach. In later versions extended for auralization, individual calculations are done for each octave band—phase is accounted for, in part by using pre-octave-band-filtered impulses as source signals. Dalenbäck[22] developed the CATT-Acoustic

[a]Current address: Bombardier Aerospace, 123 Garratt Blvd., Toronto, Ontario M3K 1Y5, Canada.
[b]Electronic mail: hodgson@mech.ubc.ca

model using the method of images and randomized tail-corrected ray/cone tracing. Ahnert's EASE/EARS model[23] and Vorländer's CAESAR model[24] are based on ray-tracing algorithms; phase is included by way of minimum-phase filters created using the Hilbert transform.

Wave effects resulting from a sound wave incident on a surface involve pressure magnitude and phase changes of the reflected sound waves. Complex pressure-reflection coefficients R, accounting for magnitude and phase changes at a boundary, are defined by $R=P_r/P_i$, where P_i and P_r are the incident and reflected complex pressures, respectively.

In wave-based models, it is common to specify the normal surface impedance as the boundary condition for a room surface. The normal surface impedance is defined, at a point immediately on the incident side of the boundary, as the ratio of pressure to the normal component of the particle velocity. A surface is assumed to be of either local or extended reaction; the choice has implications for the normal surface impedance of the boundary. Real room surfaces are generally of extended reaction; that is, the normal surface impedance varies with the angle of incidence at the boundary. However, for simplicity, many wave-based models assume local reaction, whereby the normal impedance does not vary with incident angle. The validity of this assumption and its effect on the accuracy of room sound-field predictions are not generally known. This was the main rationale for the present research.

Common to many of the above-discussed room-prediction models is the assumption of locally-reacting surfaces. This assumption is explicit in many wave-based models, as the boundary conditions are defined by a normal surface impedance that is independent of incident angle. The local-reaction assumption is implied in energy-based models, which define boundaries using an energy-absorption coefficient. This diffuse energy-absorption coefficient is obtained from the energy-absorption coefficient that is a function of incident angle. Angle-dependent absorption coefficients have been implemented into a ray-tracing model by Hodgson.[25] However, the angle-dependent absorption coefficients were determined from the normal surface impedance that was independent of incident angle. Presently, there is no known room-prediction model that accounts for extended-reaction surfaces.

How then has the extended-reaction behavior of surfaces been modeled? Sound propagation through single and multiple fluid layers of finite thickness and infinite extent is well known.[26] Wave propagation through a single elastic-solid layer, with finite thickness and infinite extent, has been described using a transfer-matrix approach.[27] Layers of elastic-porous materials, such as glass fibers and foams, are considered as a two-phase material with fluid and elastic-solid components. The well-known empirical relations of Delany and Bazley[28] calculate the characteristic impedance and wave number for a limited range of fibrous materials. A more rigorous model was developed by Attenborough[29] for rigid-frame porous materials. Further development of Attenborough's model was done by Johnson, Koplik, and Dashen.[30] Their physical description of the inertial and viscous interactions was used by Allard[31] for the effective density with a transposition of this description for the thermal exchanges. However, the Attenborough-Allard model does not include the elasticity effects of the frame, which involve wave-coupling effects that can significantly affect the surface impedance of the material. This can be accomplished using the theory of wave propagation through elastic-porous media, developed by Biot[32] and later adopted by acousticians to predict the acoustical properties of porous materials. Biot theory has been implemented into a FEM/BEM model by Panneton and Atalla,[33] and into a transfer-matrix method developed by Allard *et al.*[31,34] Panneton and Atalla modeled surfaces as locally reacting, while Allard's transfer-matrix model accounts inherently for extended-reaction surfaces.

Room surfaces rarely consist of a single layer-type; instead, they usually comprise multiple layers of different types of materials. The predictions of acoustical properties, such as normal surface impedance and reflection coefficient, for individual layers of fluid, elastic-solid, and elastic-porous materials have been combined in the form of a transfer-matrix model.[34] This involves calculating the acoustical properties of surfaces that consist of multiple layers of solids by assembling the transfer matrices for each layer, and interface matrices between layers, to yield one transfer matrix for the entire composite-layer surface. This transfer-matrix model applies to a system of layers that are finite in thickness, but infinite in lateral extent. Furthermore, it is applicable only to specular reflection and plane waves.

Few researchers have considered the relative accuracies of modeling surfaces as of local or extended reaction. The issue was discussed by Attenborough,[35] who pointed out that, although many have argued that the local-reaction assumption is valid for porous materials, experiment has shown otherwise. Experiments performed by, for example, Klein and Cops[36] and Tamura, Allard, and Lafarge[37] showed that the measured surface impedance of various porous materials varied significantly with the angle of incidence. However, the differences in the predicted steady-state sound field resulting from local- versus extended-reaction surfaces in typical rooms remain largely unknown.

This paper describes the development of a novel wave-based model for predicting sound fields in rooms with extended-reaction surfaces.[38] The model is based on combining a beam-tracing room-prediction model including phase, and a transfer-matrix model, involving Biot theory to describe the room surfaces. The component models were validated separately, by comparing predictions with other theory and with experimental measurements for selected test cases. In the interest of brevity, only key equations are presented here. Full model details, including all equations and transfer matrices, are presented in Ref. 38 and other references cited here.

II. MODELING SOUND PROPAGATION IN MULTILAYERED ROOM SURFACES

Consider the configuration illustrated in Fig. 1. A plane wave with angle of incidence θ is specularly reflected from the surface, on the outside of boundary A. The sound wave is transmitted through the layer. Another specular reflection of the transmitted wave occurs on the inside of boundary B, and a reflected wave propagates toward boundary A. In order to

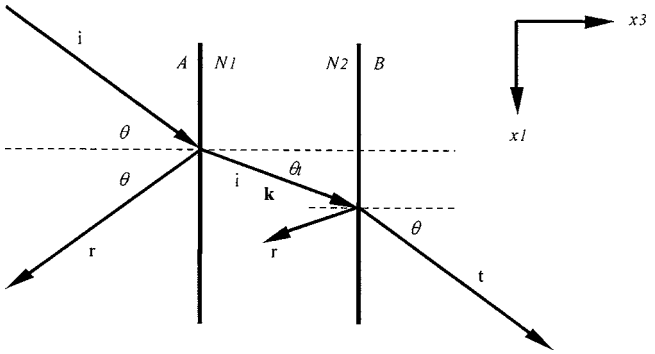

FIG. 1. Wave propagation through a single layer of material. The incident wave is denoted by *i*, the reflected wave by *r*, and the transmitted wave by *t*.

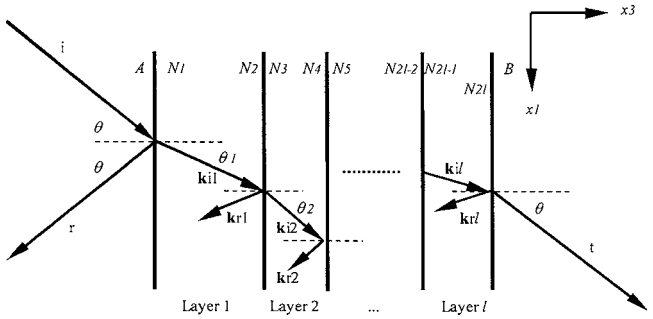

FIG. 2. Wave propagation through multiple layers of material. The incident wave is denoted by *i*, the reflected wave by *r*, and the transmitted wave by *t*.

calculate the normal surface impedance, $Z_A = p(A)/v_3(A)$, the normal component of velocity and stress are required at boundary A. They are determined from the properties inside the layer at boundaries N_1 and N_2. The properties at A are related to the properties at N_1 through boundary conditions that are such that continuity of displacement, and a force balance, exist. The situation is similar at the N_2-B boundary; however, the impedance at B is the characteristic impedance of air, with normal surface impedance $Z_B = Z_C/\cos(\theta)$. Therefore, the properties at N_2 are known from those at B, and the properties at A are determined from those at N_1. The properties at N_1 and N_2, expressed as a vector V containing the normal velocity and stress components, are related via a transfer matrix, $\mathbf{T}$:

$$V(\mathrm{N}_1) = \mathbf{T} \cdot V(\mathrm{N}_2). \tag{1a}$$

Calculation of the velocities and stresses at a boundary requires transfer matrices that have been developed for the appropriate types of media—fluid, elastic-solid, and porous-elastic materials. The theory of elasticity and wave propagation through elastic-solid media implemented here was reproduced from Allard,[31] in which full details can be found. The solid-layer transfer-matrix $\mathbf{T}_s$ was developed by Folds and Loggins,[27] but for a different time-dependence ($e^{-j\omega t}$) and different propagation directions (in the $-x_3$ direction). The solid transfer-matrix was re-worked, consistent with Allard's development for the porous transfer matrix (time dependence $e^{j\omega t}$ and incident wave traveling in the positive x_3 direction). Sound propagation through layers of porous-elastic material is described by Biot theory.[32] Porous materials consist of a solid (frame) component, and a fluid component. In room-acoustical applications, air-saturated porous materials only are considered; hence, the fluid component is air at standard temperature and pressure. The computation of the solid and porous transfer matrices, involving matrix inversion, required a pseudo-inverse function, as these matrices were nearly singular.

The transfer-matrix method for single layers can be extended to model multiple layers of fluid, elastic-solid, or porous-elastic materials.[34] This involves the transfer matrices for the above-discussed individual layer types, as well as interface matrices. The situation is illustrated in Fig. 2. Consider l layers, bounded by air on the incident side, with either air or a solid beyond layer l. For any two adjacent boundaries, at points i and $i+1$, a set of homogeneous equations describes the boundary conditions for that interface. At the boundary between two adjacent layers, there must be continuity of displacement, and force balance. Therefore, the set of homogeneous equations is expressed in terms of the velocity and stress components at the boundaries, and is related by two interface matrices, $\mathbf{I}$ and $\mathbf{J}$:

$$\mathbf{I}_{m,n} \cdot V(N_i) + \mathbf{J}_{m,n} \cdot V(N_{i+1}) = 0, \tag{1b}$$

where $m,n \in \{f,s,p\}$ and $i = 1,2,3,\ldots 2l$, and

$$\mathbf{I}_{m,n} \cdot V(N_i) + \mathbf{J}_{m,n} \cdot \mathbf{T}_n \cdot V(N_{i+2}) = 0,$$
$$i = A,2,4,6,\ldots 2l,B, \tag{1c}$$

where $V(N_{i+1}) = \mathbf{T}_n \cdot V(N_{i+2})$.

The elements of the interface matrices $\mathbf{I}$ and $\mathbf{J}$ for all combinations of adjacent layer types were published by Brouard, Lafarge, and Allard.[34] However, two errors in the published solid-porous interface matrix were corrected here. In Ref. 34, in the $\mathbf{J}_{s,p}$ matrix of Eq. (51), element $\mathbf{J}_{s,p}[4,6]$ should be 1 not 0, and $\mathbf{J}_{s,p}[5,6]$ should be 0 not 1.

The acoustical properties of a composite, multilayered structure with l layers are defined throughout the structure from points N_1 to N_{2l}. They can be found from the multilayer transfer matrix $\mathbf{T}$ such that $\mathbf{T} \cdot V(\mathrm{N}_i) = 0$ where $i = 2,4,6,\ldots,2l$ for l layers. The matrix $\mathbf{T}$ is an assembly of Eq. (1c) in separate rows for each layer, with the incident layer at the top. The matrices $\mathbf{I}_{m,n}$ and $\mathbf{J}_{m,n} \cdot \mathbf{T}_n$ are the nonzero elements of $\mathbf{T}$. The resulting multilayer transfer matrix is modified to include the media on the two sides of the multilayer. This yields the matrix that completely describes the sound field from points A to B. Next, the normal surface impedance Z_A is calculated. With knowledge of the normal surface impedance, the pressure reflection coefficient at point A is calculated, for angle of incidence θ, as follows:

$$R_A = \frac{Z_A - Z_c/\cos(\theta)}{Z_A + Z_c/\cos(\theta)}. \tag{2}$$

This is used as the input to the beam-tracing algorithm to model the reflection of sound waves from extended-reaction surfaces.

The transfer-matrix model can be used to model locally reacting materials by calculating the surface impedance at normal incidence and using this as the angle-independent

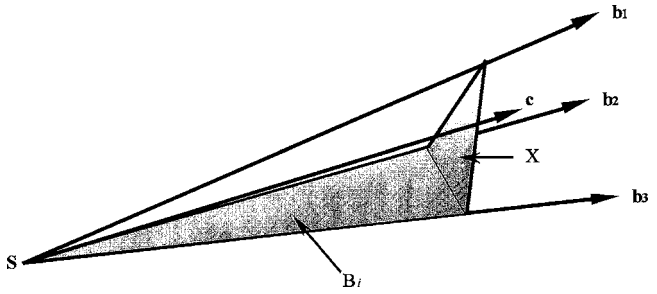

FIG. 3. Geometry of a triangularly faced beam.

surface impedance;[31] the reflection coefficient is still obtained from Eq. (2), and is angle-dependent, but the surface is of local reaction. Surfaces may also be defined by impedances that vary with frequency only (local reaction), or with an angularly constant reflection coefficient.

III. BEAM-TRACING MODEL

For the room-prediction component of the new model, the triangular-beam tracing approach described by Lewers,[5] but extended to include phase, was employed. The main components to the beam-tracing algorithm consisted of surface-geometry definition, source generation, a trajectory loop for a beam, receiver-point detection, and calculation of the steady-state sound-pressure level.

The fundamental component of the beam-tracing algorithm is the trajectory loop. Executed for each beam, it combines the process of determining the nearest plane, calculating the new image source, and calculating the new direction vectors and the angle of incidence of the reflected beam. Each beam originates at the defined source, and the trajectory loop is executed for each reflection number, until the maximum reflection order is reached. Upon completion of the trajectory loop, the beam number is incremented, and the next beam is traced, with direction vectors reset to the original source. After each execution of the trajectory loop, a test is made to determine if the receiver point is contained within the path of the beam from the previous source to the new image source. If the receiver point is contained within the beam's path, the pressure contribution of the current beam is calculated at the receiver point. Upon completion of tracing all the beams, the complex-pressure contributions of the beams are added and the results converted to decibels, to yield the steady-state sound-pressure level at the receiver position. All calculations are performed in the frequency domain.

This beam-tracing algorithm used beams with a triangular cross section, as illustrated in Fig. 3. Beams with triangular cross sections were used because a point source radiating spherical waves can be modeled with no overlapping beams, and with an even energy distribution across the beam face. A single beam is identified by three bounding rays (vectors $\mathbf{b}_1, \mathbf{b}_2$, and $\mathbf{b}_3$), center vector $\mathbf{c}$, three bounding planes $\mathbf{B}_1, \mathbf{B}_2$, and $\mathbf{B}_3$, and cross-section plane $\mathbf{X}$. The vertex or origin of the beam is the single point, $\mathbf{S}$. A beam's vertex is the real source in the room if it contains the direct source-receiver path. Otherwise, for a beam containing a source-receiver path due to reflections, the vertex is the image source that was last calculated.

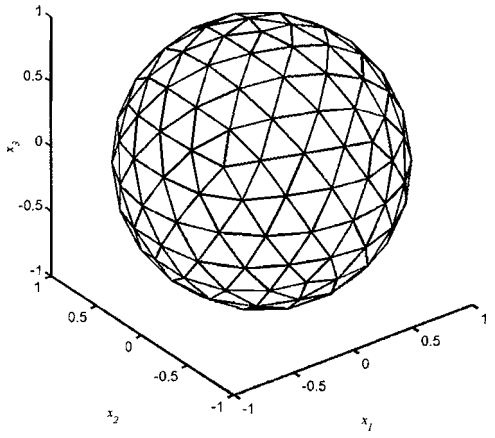

FIG. 4. Source with 320 beams (icosahedron frequency, f_i=4).

A. Defining surface geometry

The basic room is constructed with rectangular surfaces, each defined by the coordinates of its vertices. In order to perform the ray/beam-tracing calculations, the normal vectors and plane coefficients of each surface must be calculated. The surfaces Π_i are defined as a plane equation of the form $A_i x_1 + B_i x_2 + C_i x_3 = D_i$, where A_i, B_i, C_i, and D_i are the coefficients of plane i. The coefficients A_i, B_i, and C_i, are the components of the normal vector N_i of plane i, and D_i is the distance from plane i to the origin.

B. Modeling an omnidirectional source

The room-prediction model applies to a single source that is omnidirectional at all frequencies. A 20-face (or beam-front) icosahedron[39] was used as the basic model of a spherical source with center $\mathbf{S}$, with each face representing the triangular plane $\mathbf{X}$ of a beam. The icosahedron geometry was modified to allow more than the 20 faces of the basic icosahedron. To do this, each edge of each face of the basic icosahedron was divided into f_i equal lengths (f_i is referred to as the icosahedron frequency), resulting in a polygon with $20f_i^2$ faces or beam fronts. The face coordinates were further manipulated so that all vertices were points on the surface of a unit sphere centered at the origin. A further refinement was made by eliminating all duplicate vertices and forming a matrix that identified each face (along a row) with a set of three coordinate numbers (columns) corresponding to the elements of the vertex matrix that contained the vertices for that face. The coordinates were also scaled so that all vertices lie on a unit sphere. Together, the vertex matrix $\mathbf{V_S}$ and face matrix $\mathbf{F_S}$ for the source identified the starting coordinates for the vertices $\mathbf{b}_1, \mathbf{b}_2$, and $\mathbf{b}_3$ for all beams. A source constructed with 320 faces ($\mathbf{V_s}$ $[162\times3]$ with 162 unique vertices, and $\mathbf{F_s}$ $[320\times3]$) is shown in Fig. 4.

The center ray, $\mathbf{c}$, for each beam originating at the source was calculated as the unit vector that was the unit normal to the plane that contained the vertices $\mathbf{b}_1, \mathbf{b}_2$, and $\mathbf{b}_3$. This

plane was parallel to a plane tangential to the unit sphere, at the point that was intersected by the center ray for that beam.

The geometry of the source and beams is completely described by $\mathbf{V_S}, \mathbf{F_S}$, and $\mathbf{C_S}$ (a matrix that contains the center rays for each beam). With this geometric information, beams are traceable, but further acoustical information is required. The initial beam sound pressure $p(r,t)$ was calculated from the initial source sound power W, in a free field:

$$p(r,t) = \frac{A}{r} \cdot e^{j(\omega t - kr)}, \tag{3}$$

in which

$$A = \sqrt{\frac{\rho_0 \cdot c \cdot W}{4 \cdot \pi}}. \tag{4}$$

The initial phase angle was set to zero, completing the information required to begin the beam tracing. The beam-tracing procedure thus models a spherical wave propagating from a point source. The sound pressure of the spherical wave decays with distance L from the source as $1/L$, with phase angle $-kL$, where k is the wave number.

C. Finding a reflecting plane

Fundamental to the beam-tracing algorithm is the determination of the surface of reflection for a given beam with direction vectors and source point. Determining the surface of reflection involved two steps: first, the total number of room surfaces was reduced to include only the subset of permissible surfaces; then, the distance from **S** to the point of intersection with each of these surfaces, in the direction of **c** (the center vector), was calculated. The surface that corresponded to the minimum distance s is the surface intersected by the beam.

D. Finding an image source

When the beam originating from a source (or image source) reflects from a surface, the incident trajectory is replaced by an image source. The image source becomes the new start point for the reflected beam; the direct path from the image source to the beam front is equivalent to the reflected path from the previous source to the beam front.

E. Angle of incidence and direction vectors for the reflected beam

The angle of incidence of a beam that intersects a surface was calculated as the angle between the center ray and the surface normal. The angle of incidence and the frequency, together with the material properties for each layer in the surface, provide the input parameters to calculate the reflection coefficient by the transfer-matrix method. The complex reflection coefficient was multiplied by the complex pressure of the incident wave at the point of intersection, and the pressure magnitude and phase of the reflected wave thus determined. In addition to the angle of incidence, the direction vectors were calculated for the reflected beam. The reflected beam was the beam originating from the image source, with new direction vectors that represent the first-order-reflection vectors of the incident-direction vectors. The new reflected beam with the new direction vectors and image source are used to define a new incident beam.

F. Receiver detection

The possibility that the receiver point lies somewhere inside the volume of a beam that propagates from the start point **S** to the intersecting surface Π must be tested. Three tests are performed—one for each boundary plane of a beam—to determine on which side the point **R** is located. If the point **R** is located on the inside of all three planes, the receiver point is inside the beam. In this case, the complex-pressure amplitude is recorded for the path length L of the beam—from the point **S** to the point of intersection by the center vector **c**, and the plane **X** that contained the receiver point **R**.

G. Calculating the steady-state sound-pressure level

Following a positive receiver-point test, the complex-pressure amplitude for that beam is calculated. The pressure is calculated for the beam starting at **S**, to the point of intersection between the center ray **c** and the beam-front plane **X** that contained the receiver point **R**. The beam's contribution to the acoustical pressure at the receiver point **R** is calculated as follows:

$$p_r(L,\omega) = \left(\frac{A}{L}\right) \cdot R_{\text{eff}} \cdot e^{-jkL}, \tag{5}$$

where $R_{\text{eff}} = \prod_s R_s$ for all reflected surfaces s encountered by the beam from **S** to **R**.

The result is the complex pressure at the point **R** for a single frequency, and for a single beam, between reflections r and $r+1$. For the same beam, all pressures recorded at the receiver point are summed to yield the contribution to the steady-state pressure of that beam. The total steady-state acoustical pressure is calculated by summing the total pressures of all beams detected at **R**. The steady-state sound-pressure level is then calculated. Octave-band levels are calculated by energy summation of the levels of all predicted frequencies in the bands.

IV. MODEL VALIDATION

A. Transfer-matrix model

The validation of the transfer-matrix model involved comparing its predictions of the reflection coefficients or the surface impedances of various surfaces with predictions by another model, or with experiment. The following surface test cases were chosen:

(a) Single glass plate—transfer-matrix prediction of reflection coefficient compared to plate-theory prediction;[40]
(b) Double drywall plate structure with air-gap—transfer-matrix prediction of reflection coefficient compared to plate-theory prediction;[40]
(c) Glass-fiber porous material with rigid-backing—transfer-matrix prediction of normal surface impedance compared to measurements by Allard;[31]

TABLE I. Material properties for the drywall plates.

Material	Drywall (gypsum board)
Thickness (mm)	12.0
Density (kg/m^3)	1200.0
Young's modulus (GPa)	7.0
Poisson ratio	0.25

(d) Carpeted floor, modeled as a double porous-layer with rigid-backing—transfer-matrix prediction of normal surface impedance compared to measurements by Brouard, Lafarge, and Allard.[41]

Since the results for validation tests (a) and (b) were similar, results for only tests (b)–(d) are reported here. The material properties of the plates and porous materials are given in Tables I and II, respectively. The data for the cases involving plates were selected from data available for a broad range of elastic-solid materials. Data for the cases involving porous materials were given in the papers reporting the corresponding experimental results.[31,41] Validation predictions were done over the frequency range 50–4000 Hz, with a 10-Hz increment, and for incident angles between 0° and 90°. Only results for angles of 0°, 45°, and 75° are presented.

1. Double drywall plate

A common room surface for an interior wall consists of two drywall panels fixed to either side of 50 mm by 100 mm studs. Using transfer matrices, this surface was modeled as a solid layer, a fluid layer, and a second solid layer. Each solid layer represents identical drywall panels, with properties as in Table I. The fluid layer is 100 mm thick, but the studs are not taken into account in the modeling. Transfer-matrix predictions of the reflection coefficient were compared to plate-theory predictions;[40] the results are shown, for the three incident angles, in Figs. 5(a)–5(c). In general, the real part of the reflection coefficient approaches one, and the imaginary part is near to zero. This is expected for a hard surface, as most of the sound energy is reflected. The mass-air-mass resonance and coincidence phenomena are both evident in Figs. 5(a)–5(c). The mass-air-mass resonance is a low-

TABLE II. Material properties of the porous layers used in validation cases (c) and (d). Both layers had a rigid backing; the carpet consisted of two porous layers. Properties for the air-saturated pores of all porous materials were as follows: air density = 1.2 kg/m^3, sound speed = 344 m/s, standard air pressure=101.3 kPa, dynamic viscosity=18.2×10^{-6} N s/m^2, specific heat ratio=1.4, and Prandtl number=0.710.

Material property	Fiber-glass	Carpet	
	Layer 1	Layer 1	Layer 2
Thickness (mm)	56	3.5	3.5
Frame density (kg/m^3)	130	60	60
Frame shear modulus (MPa)	$(2200+j)\times10^{-3}$	$(10+j5)\times10^{-3}$	$(10+j5)\times10^{-3}$
Poisson ratio	0	0	0
Flow resistivity (Ns/m^4)	40 000	20 000	5000
Porosity	0.94	0.99	0.99
Tortuosity	1.06	1.00	1.00
Viscous dimension (m)	0.56×10^{-4}	1.5×10^{-4}	2.3×10^{-4}
Thermal dimension (m)	1.12×10^{-4}	2.2×10^{-4}	2.8×10^{-4}

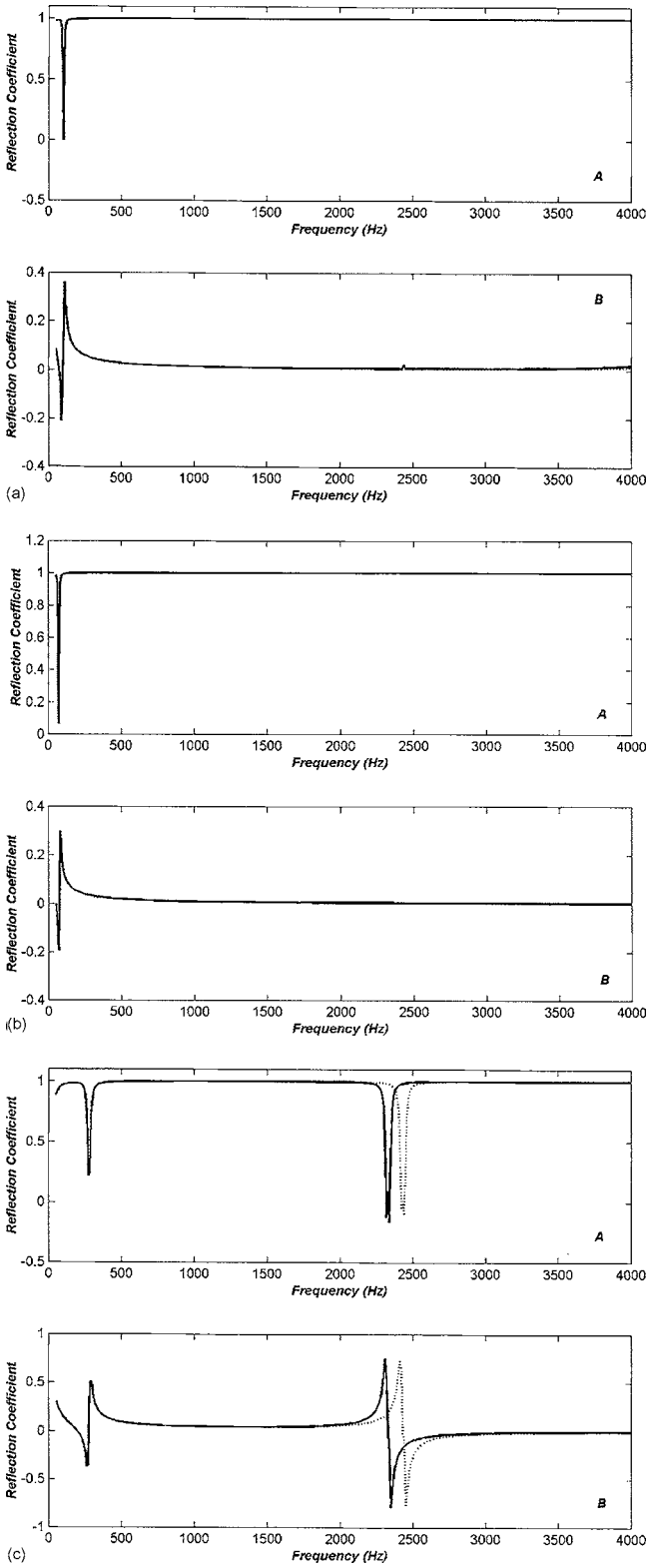

FIG. 5. (a) Prediction of the reflection coefficient of a double drywall plate with air gap, at normal incidence. Each drywall plate is 12 mm thick, and the air gap is 100 mm thick. Prediction with plate theory (—). Prediction with transfer-matrix model (---). Real part is shown in A, imaginary part in B. Note that the curves are superimposed. (b) Same as for (a), except at 45° angle of incidence. (c) Same as for (a), except at 75° angle of incidence.

frequency phenomenon, indicated by the first series of sharp peaks in both the real and imaginary parts. The real part decreases from one to almost zero, and the imaginary part fluctuates rapidly from 0 to −0.5 to 0.5 and back to 0. This indicates almost total sound transmission, with a 180° phase change, through a double panel at the mass-air-mass resonance frequency. Note, from Figs. 5(a)–5(c), that the mass-air-mass resonance frequency increases with increasing angle. Coincidence effects are noticeable in the double drywall panel, as with the single glass plate, at an angle of incidence of 75°. The coincidence frequency for smaller angles occurs at frequencies not visible in Figs. 5(a)–5(c).

Figure 5 shows an excellent agreement between transfer-matrix and plate-theory predictions. As can be seen in Fig. 5(c), however, a small difference occurred between the predictions by the two models at the coincidence frequency for an angle of 75°. A possible explanation for the difference is in the assumptions made in plate theory. Plate theory assumes a neutral stress plane at the center plane of the plate, and that displacements are in the surface-normal direction only. Furthermore, in plate theory the plate cross sections remain plane and undistorted. On the other hand, in the transfer-matrix formulation of an elastic-solid layer, displacements occur in both the surface-normal and surface-tangential directions, and plate cross sections can be distorted. Thus, the transfer-matrix results would be expected to be more accurate.

2. Porous materials

Two surface configurations involving single or double layers of porous materials were used as validation cases. Biot parameters and measurement data for the surface impedance at normal incidence were obtained from the literature. The first surface was a single layer of glass-fiber with a rigid-backing, studied by Allard.[31] The second surface was a carpeted floor, modeled as a double porous-layer with rigid-backing, studied by Brouard, Lafarge, and Allard.[41] For both surfaces, the validation was performed by comparing transfer-matrix prediction to the measurements of the surface impedance at normal incidence.

a. Glass-fiber layer with rigid backing. The normalized surface impedance at normal incidence for the glass-fiber case is shown in Fig. 6. The frequency range of 350–1400 Hz was used, to be consistent with the frequency range of Allard's measurements. The measurements and transfer-matrix prediction show reasonable agreement, particularly in predicting the dip at 800 Hz and the peak at 850 Hz in the real and imaginary parts, respectively. This local minimum and maximum of the surface impedance was identified by Allard as associated with resonance in the frame of the porous material. The frame resonance is possible from a partial coupling that occurs between air-borne and frame-borne waves that propagate through the fluid and solid parts, respectively, of the porous material. This effect was predicted using Biot theory for the porous material, as implemented in the transfer matrix for such a material, because the frame is considered elastic.

b. Carpet with rigid backing. The normalized surface impedance of the carpet with rigid backing at normal incidence is shown in Fig. 7. The impedance was predicted over the 50–4000-Hz range; however, measurement data were only available for 200 to 1300 Hz. The measurements are shown to agree well with prediction, for both the real and imaginary parts. At almost all frequencies, the transfer-matrix model predicted slightly lower impedances than were measured. Measurements were also performed at frequencies above 4 kHz, and agreed well with the transfer-matrix predictions; however, they are outside the frequency range of interest here, and are not shown.

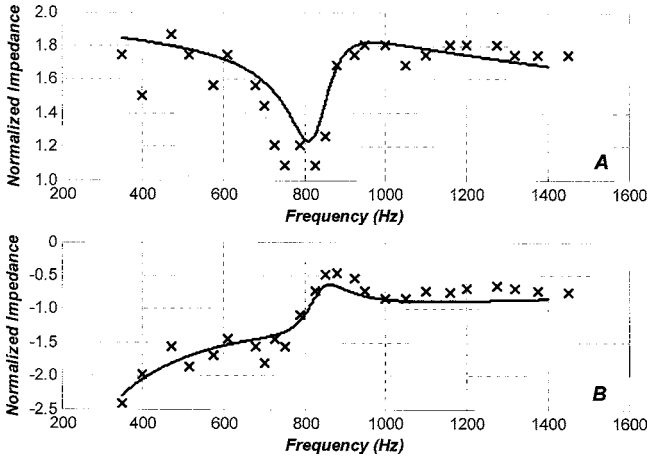

FIG. 6. Normalized surface impedance of a single layer of glass-fiber at normal incidence: (A) real part; (B) imaginary part. (—) Transfer-matrix prediction; (× × ×) measurements reproduced from Allard (Ref 25).

B. Beam-tracing model

The accuracy of the beam-tracing model was tested by comparing it to another available wave-based model—the method-of-images model that included phase (the "image-phase" model) developed by Guo and Hodgson.[42] The validation of the beam-tracing model was a two-step process. The first step involved determining the number of beams and the reflection order required to predict the steady-state

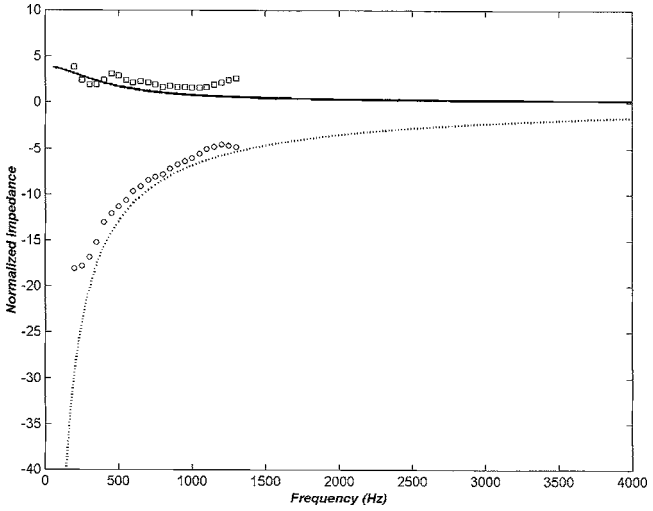

FIG. 7. Predicted and measured normalized surface impedances of a carpeted floor at normal incidence: (—) transfer-matrix prediction, real part; (□) measurement, real part; (---) transfer-matrix prediction, imaginary part; (○) measurement, imaginary part.

sound-pressure level with sufficient accuracy. The second step involved comparing the beam-tracing and image-phase models. Both steps were done for three rectangularly shaped rooms, with the same absorption on all surfaces. The dimensions of the three rooms were chosen to represent common rooms of different shapes: Room 1 was a $3\times3\times3$ m^3 small office; Room 2 was a $10\times3\times3$ m^3 corridor; Room 3 was a $10\times10\times3$ m^3 small industrial workroom.

The second step in the validation was performed for the three rooms, assuming that all surfaces had an average diffuse-field absorption coefficient of 0.1 at all frequencies. This was chosen to correspond to the typical ambient absorption of nonabsorptive surfaces in rooms. The energy absorption coefficient is related to the pressure-reflection coefficient as follows:

$$\alpha(\theta) = 1 - |R(\theta)|^2. \tag{6}$$

The pressure-reflection coefficient was obtained from the surface impedance, using Eq. (2). Now, the average diffuse-field absorption coefficient is related to the surface impedance by

$$\bar{\alpha} = \int_0^{\pi/2} \alpha(\theta)\cdot\sin(\theta)\cdot\cos(\theta)d\theta. \tag{7}$$

The surface impedance Z in Eq. (2), assumed real, was found from the diffuse-field absorption coefficient by solving Eqs. (6) and (7) symbolically using MATLAB™. For $\bar{\alpha}=0.1$, the corresponding surface impedance was 29 681 kg/m^{2}s. For all configurations, the source and receiver positions were chosen such that they remained at constant height, and were located at half the room width. The source/receiver distance varied with the length of the room. In all tests, and at each frequency, the sound power of the source was set arbitrarily at 80 dB ($re:10^{-12}$ W). Predictions were performed over the frequency range of 50–4000 Hz, with a constant 10-Hz interval.

1. Reflection order and number of beams

When performing beam-tracing predictions, the number of beams, the number of reflections, and the number of frequencies over which to calculate band results must be sufficiently high to ensure high accuracy. It was, therefore, important to study the variation of predicted levels with variations in these parameters. Predictions were made for the three rooms described earlier; results are shown for Room 1, which was typical. Predictions were made for all combinations of 320, 720, 1280, 5120, 20 480, or 42 320 beams, and 8, 12, 16, 24, 40, or 50 reflections. Constant frequency intervals of 1, 2, 5, and 10 Hz (resulting, for example, in the number of frequencies increasing from 5 to 44 in the 63-Hz band to 143 to 1416 in the 2000-Hz band, and equaling from 279 to 2787 for total levels). Predictions showed that all levels had converged to within about 0.1 dB of the apparent "target" answer in the case of 42 320 beams, 50 reflections and a constant frequency interval of 1 Hz.

Figures 8(a) and 8(b) show the variation of total and 63-Hz levels with the numbers of beams and reflections, for a constant 1-Hz frequency interval. Figures 9(a) and 9(b)

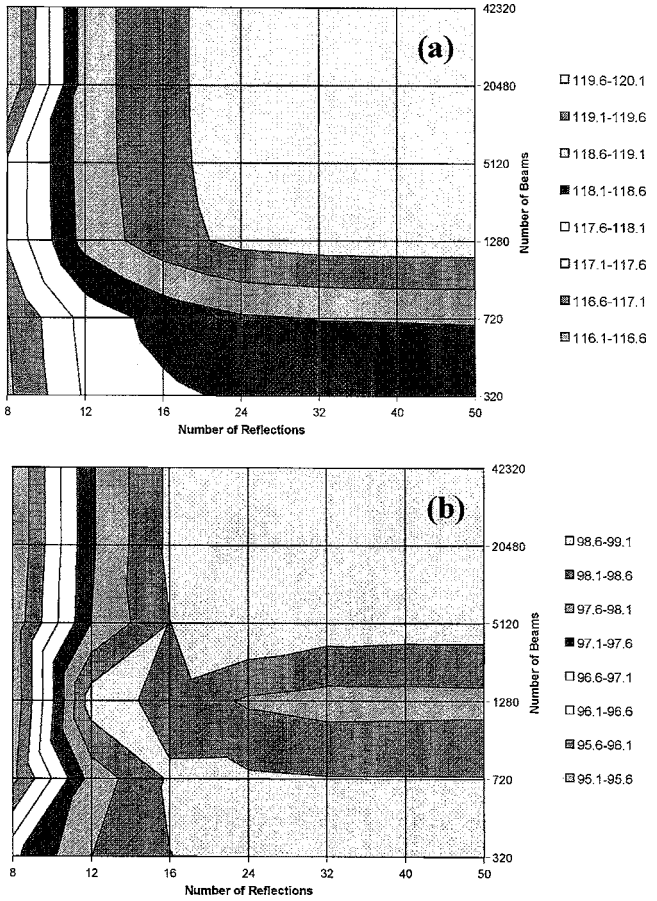

FIG. 8. Variation of (a) total and (b) 63-Hz octave-band levels in Room 1 with number of beams and reflections, for a constant 1-Hz frequency interval.

show how these levels varied with the frequency resolution using 42 320 beams and 50 reflections. Total levels and those in the 125- to 2000-Hz bands increased monotonically with the number of beams and reflections. This is as would be expected for an energy-based model, showing that phase had a minimal effect on these levels. However, at 63 Hz, levels fluctuated about the "target" answer, showing the significant effect of phase in this lower frequency band. Levels in all bands were within 0.5 dB of the "target" answer for 5120 beams traced for 24 reflections (1280 reflections at high frequencies and for total levels) and for a 10-Hz constant frequency resolution. Of course, the use of a geometric progression of frequencies would be expected to be more computationally efficient.

2. Comparison of the beam-tracing and image-phase models for selected rooms

The image-phase model was used to validate the beam-tracing model. This model also calculates the steady-state sound-pressure level at a receiver point in a rectangular room, containing one source. The complex pressure was calculated at the receiver point via an impedance transfer function between the source and receiver, and multiplied by the pressure amplitude constant, A, determined from Eq. (3), as follows:

$$p(r) = A\cdot Z_{pp}(r_1, r_0). \tag{8}$$

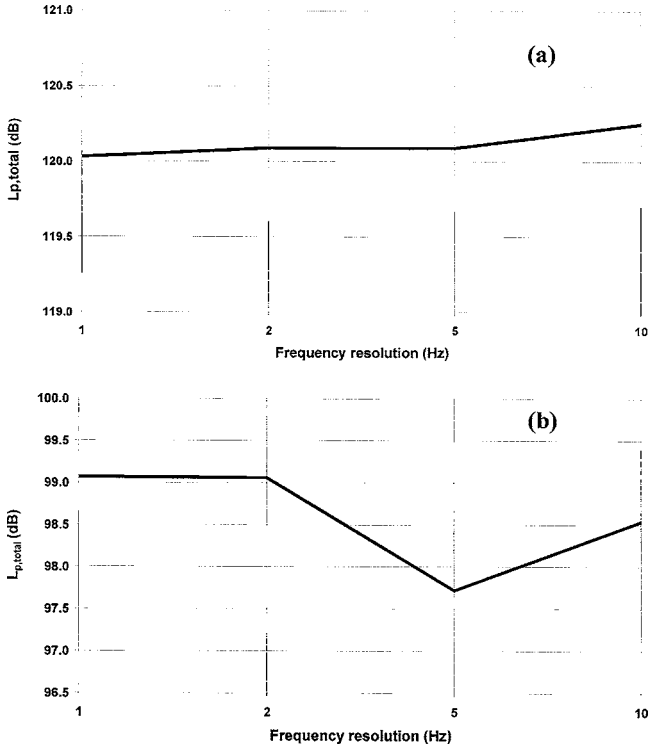

FIG. 9. Variation of (a) total ("target" answer=120.0 dB) and (b) 63-Hz levels ("target" answer=99.1 dB) in Room 1 with frequency resolution using 42 320 beams and 50 reflections.

Surfaces in this model are assigned a single, constant surface impedance that is independent of frequency and angle. To model a surface with no absorption, an infinite impedance is defined. A surface defined by an average diffuse-field absorption coefficient is implemented in the same way as in the beam-tracing model, using Eq. (7). Note that Guo and Hodgson[42] used a reflection order of 21 in the image-phase model for rooms similar in size to the rooms studied here.

The beam-tracing and image-phase models were applied to the three test rooms to compare predictions. Predictions used 2000 beams and a reflection order of 25. A comparison of steady-state sound pressure-level predictions by the two models is shown in Fig. 10 for the case of the corridor (Room 2).

Comparison of the predicted steady-state sound-pressure levels by the two models showed good overall agreement. Generally, all curves were very irregular in shape, with many local minima and maxima. Since these predictions were performed using wave-based models, it is expected that the peaks and dips in the curves represent excited modes in the room. The modal density of a room, however, is too dense to excite individual modes. These local minima and maxima are actually a close grouping of excited modes. The maxima correspond to a grouping of modes that are similar in phase, the minima are a grouping of modes that are nearly opposite in phase. There are noticeable differences in the predictions by the two models at some of these points for all rooms. The beam-tracing model appears to underestimate the sound energy predicted by the image-phase model at some of the peaks and dips, particularly at high frequency. Furthermore,

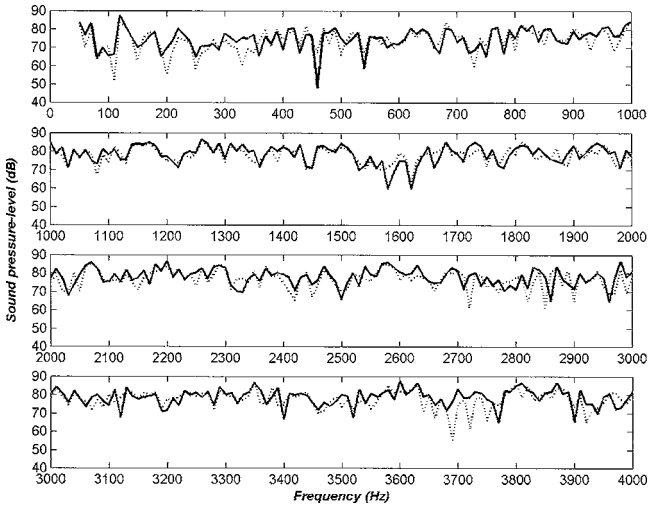

FIG. 10. Comparison of steady-state sound-pressure-level predictions by the image-phase and beam-tracing model, for Room 2. The beam-tracing model was used with 2000 beams. The reflection order for both models was 25: (—) image-phase model; (---) beam-tracing model.

there appear to be some minima predicted by the beam-tracing prediction that are not predicted by the image-phase model. Again, this appears to occur mostly at high frequency (above 2000 Hz), although for the corridor example (Room 2) it was noticeable at low frequency.

The slight underestimation of sound energy predicted by beam tracing compared to the image-phase model can be explained by the differences in calculating the path length. The source-receiver paths calculated by the image-phase model are exact. The source-receiver paths calculated by the beam-tracing model are, however, approximate. The source-receiver path calculated by the beam-tracing model is the path from the last image source to a point on a plane that contains the receiver point. Despite the differences in predictions by the two models, the majority of the peaks and dips were similar for the two models, and occurred at the same frequency. The beam-tracing-model predictions were excellent. Thus, the model which, unlike the image-phase method, can account for multilayer bounding surfaces, was applied with confidence to meet the ultimate research objectives.

V. CONCLUSION

The development of the triangular-beam-tracing model with phase for predicting sound fields in rooms with extended-reaction surfaces has been presented. This involved source and beam initialization, beam tracing, source-receiver-path estimation, and the calculation of the sound-pressure level at the receiver. A spherical wave was approximated by a point source surrounded by an icosahedron with subdivided triangular faces. A beam was defined by the point source as the vertex, and the three vertices of an icosahedron face. Each beam was propagated through the room by tracing its center ray up to a specified reflection order, in an attempt to find a valid source-receiver path. The beam-face represented a portion of the spherical sound wave front as a complex pressure. With each surface reflection, the associated complex pressure-reflection coefficient, calculated by a

transfer-matrix model for multilayer surfaces, was multiplied by the incident beam's complex pressure to find the pressure at the reflected beam-front. The sum of the complex pressures at the beam-face for each occurrence of a valid source-receiver path is that beam's contribution to the sound pressure at the receiver. The sum of the pressure contributions from all beams yields the steady-state sound-pressure level at the receiver point. The model works in the frequency domain; the time response can be obtained with an inverse fast Fourier transform.

The two component models were validated separately. The transfer-matrix model was tested in the case of surfaces that are commonly found in rooms: a single glass plate, double drywall panel, a carpeted floor (as a double porous layer with rigid backing), and a fiber-glass layer with rigid backing. Transfer-matrix predictions agreed well with relevant theory (plate surfaces) or experiment (a carpeted floor and fiber-glass surfaces).

The transfer-matrix and beam-tracing models were combined to form the new room-prediction model required for this research. The final model was tested in the cases of three room configurations: a small office, a corridor, and a small industrial workroom. Two numerical issues were involved in the validation of this model—the reflection order and the number of beams required to predict the steady-state sound-pressure level with sufficient accuracy had to be determined. It was found that 1280 beams (5120 at 63 Hz) and a reflection order of 24 resulted in sound-pressure levels predicted by the beam-tracing model to converge within 0.5 dB. As will be describe in a separate paper, the model was applied by comparing sound-field predictions for rooms with surfaces modeled as of either extended and of local reaction.

Runtimes for the beam-tracing algorithm are low, but those for the transfer-matrix algorithm can be long. For example, when run on a 3-GHz Pentium-4 personal computer, calculations of pressure spectra for a simple case with no multilayer surfaces take a few minutes. However, when one surface comprises multiple layers, extended-reaction calculations can take several tens of hours.

Improvements to the model are possible to increase its accuracy, computational efficiency, and functionality. They include using the exact source-receiver path (instead of that estimated as the path from the last image source to the point on a plane that contains the receiver point), implementation of an adaptive beam-tracing algorithm,[10,11] and precalculation of reflection coefficients of multilayered surfaces at appropriate frequencies and angles, and use an appropriate interpolation scheme to determine the values applicable for a given beam/surface interaction.

ACKNOWLEDGMENTS

The authors would like to thank Dr. Bruno Brouard, Université de Maine, for providing us with the pseudo-inverse function for matrix inversion, and Mark Bliss and Gary Chan for performing the validation predictions.

[1]H. Kuttruff, *Room Acoustics*, 4th ed. (Spon, London, 2000).
[2]M. R. Hodgson, "When is diffuse-field theory applicable," Appl. Acoust. **49**, 197–207 (1996).
[3]J. B. Allen and D. A. Berkley, "Image method for efficiently simulating small-room acoustics," J. Acoust. Soc. Am. **65**, 943–950 (1979).
[4]J. Borish, "Extension of the image model to arbitrary polyhedra," J. Acoust. Soc. Am. **75**, 1827–1836 (1984).
[5]T. Lewers, "A combined beam-tracing and radiant-exchange computer model of room acoustics," Appl. Acoust. **38**, 161–178 (1993).
[6]E.-M. Nosal, M. R. Hodgson, and I. Ashdown, "Improved algorithms and methods for room sound-field prediction by acoustic radiosity in arbitrary polyhedra," J. Acoust. Soc. Am. **116**, 970–980 (2004).
[7]A. Kulowski, "Algorithmic representation of the ray tracing technique," Appl. Acoust. **18**, 449–469 (1985).
[8]D. van Maercke and J. Martin, "The prediction of echograms and impulse responses within the Epidaure software," Appl. Acoust. **38**, 93–114 (1993).
[9]A. Farina, "RAMSETE-A new pyramid tracer for medium and large scale acoustic problems," *Proceedings of Euro-Noise'95*, pp. 55–60.
[10]I. A. Drumm and Y. W. Lam, "The adaptive beam-tracing algorithm," J. Acoust. Soc. Am. **107**, 1405–1412 (2000).
[11]T. Funkhouser, N. Tsingos, I Carlbom, G. Elko, M. Sondhi, J. E. West, G. Pingali, P. Min, and A. Ngan, "A beam tracing method for interactive architectural acoustics," J. Acoust. Soc. Am. **115**, 739–756 (2004).
[12]D. van Maercke, "Simulation of sound fields in time and frequency domain using a geometrical model," *Proceedings of the 12th ICA*, Toronto, 1986, E11-7.
[13]M. Vorländer, "Simulation of the transient and steady-state sound propagation in rooms using a new combined ray-tracing/image-source algorithm," J. Acoust. Soc. Am. **86**, 172–178 (1989).
[14]K. R. Fyfe, J. P. Coyette, and P. A. van Vooren, "Acoustical and elasto-acoustic analysis using finite element and boundary element methods," Sound Vib. 16–22 (December 1991).
[15]V. Easwaran and A. Craggs, "On further validation and use of the finite element method to room acoustics," J. Sound Vib. **187**, 195–212 (1995).
[16]M. Terao and H. Sekine, "A numerical analysis of sound field of a long space by a sub-region coupling approach," *Proceedings of Inter-Noise'96*, pp. 3007–3010.
[17]F. Ramiandrasoa, M. A. Hamdi, and M. Haddar, "A sub-domain decomposition method for large acoustic cavities," *Proceedings of Inter-Noise'96*, pp. 2975–2978.
[18]S. Sakamoto and H. Tachibana, "Calculation of impulse responses in 3-D sound field with absorptive boundary by the finite-difference method," *Proceedings of Inter-Noise '97*, p.1597.
[19]E. De Geest and H. Patzold, "Comparison between room transmission functions calculated with a boundary-element method and a ray-tracing method including phase," *Proceedings of Inter-Noise'96*, pp.3177–3180.
[20]G. Bartsch, "Simulation der tieffrequenten Schallausbreitung in Räumen, Zwischenbericht über das Forshungsverhaben, DFG VO 600/3-1," ITA, RWTH Aachen (1998).
[21]G. M. Naylor, "ODEON-Another hybrid room acoustical model," Appl. Acoust. **38**, 131–143 (1993).
[22]B. L. Dalenbäck, "Room acoustic prediction based on a unified treatment of diffuse and specular reflection," J. Acoust. Soc. Am. **100**, 899–909 (1996).
[23]http://www.renkus-heinz.com/ease/index.html
[24]http://www.akustik.rwth-aachen.de/Forschung/Forschungsgebiete/raum/caesar
[25]M. Hodgson, "On the prediction of sound fields in large empty rooms," J. Acoust. Soc. Am. **84**, 253–261 (1988).
[26]L. E. Kinsler, A. R. Frey, A. B. Coppens, and J. V. Sanders, *Fundamentals of Acoustics* (Wiley, New York, 1982).
[27]D. L. Folds and C. D. Loggins, "Transmission and reflection of ultrasonic waves in layered media," J. Acoust. Soc. Am. **62**, 1102–1109 (1977).
[28]M. E. Delany and E. N. Bazley, "Acoustical properties of fibrous materials," Appl. Acoust. **3**, 105–116 (1970).
[29]K. Attenborough, "Acoustical characteristics of rigid fibrous absorbents and granular media," J. Acoust. Soc. Am. **73**, 785–799 (1983).
[30]D. L. Johnson, J. Koplik, and E. R. Dashen, "Theory of dynamic permeability and tortuosity in fluid-saturated porous media," J. Fluid Mech. **176**, 379–402 (1987).
[31]J. F. Allard, *Propagation of Sound in Porous Media* (Elsevier Applied Science, London, 1993).
[32]M. A. Biot, "The theory of propagation of elastic waves in a fluid-saturated porous solid. I. Low frequency range. II. Higher frequency range," J. Acoust. Soc. Am. **28**, 168–191 (1956).
[33]R. Panneton and N. Atalla, "Numerical prediction of sound transmission

through finite multilayer systems with poroelastic materials," J. Acoust. Soc. Am. **100**, 346–354 (1996).
[34]B. Brouard, D. Lafarge, and J. F. Allard, "A general method of modeling sound propagation in layered media," J. Sound Vib. **183**, 129–142 (1995).
[35]K. Attenborough, "Acoustical characteristics of porous materials," Phys. Rep. **82**, 179–227 (1982).
[36]C. Klein and A. Cops, "Angle dependence of the impedance of a porous layer," Acustica **44**, 258–264 (1980).
[37]M. Tamura, J.-F. Allard, and D. Lafarge, "Spatial Fourier-transform method for measuring reflection coefficients at oblique incidence. II. Experimental results," J. Acoust. Soc. Am. **97**, 2255–2262 (1995).
[38]A. Wareing, "Acoustic modeling of rooms with extended-reaction surfaces," M.A.Sc. thesis, University of British Columbia, 2000.
[39]M. R. Hodgson, A. Wareing, and C. Campbell, "A combined beam-tracing and Biot-transfer-matrix model for predicting sound fields in enclosed spaces," *Proceedings of Euro-Noise '98*, pp. 1023–1028.
[40]F. Fahy, *Sound and Structural Vibration: Radiation, Transmission and Response* (Academic, London, 1985).
[41]B. Brouard, D. Lafarge, and J.-F. Allard, "Measuring and prediction of the surface impedance of a resonant sound absorbing structure," Acta Acustica **2**, 301–306 (1994).
[42]J. Guo and M. Hodgson, "Investigation of active noise control in non-diffuse sound fields," *Proceedings of Active'99*, Vol. 2, pp. 621–632.

Silencer design by using array resonators for low-frequency band noise reduction

Sang-Hyun Seo
Department of Structure & Materials, KSLV Technology Division, Korea Aerospace Research Institute (KARI), 45 Eoeun-Dong, Yuseong-Gu, Daejeon, 305-333, Korea

Yang-Hann Kim
Center for Noise and Vibration Control (NOVIC), Department of Mechanical Engineering, Korea Advanced Institute of Science and Technology (KAIST), Science Town, Daejeon, 305-701, Korea

(Received 1 December 2004; revised 26 July 2005; accepted 26 July 2005)

Helmholtz resonators are often used to reduce noise. They are particularly useful when noise has a narrow frequency band. In this study we aim to broaden its narrow band characteristics by combining many resonators. Serial and parallel arrangements of resonators have been tested to obtain broader impedance mismatch characteristics in the broader band. Theoretical and experimental results explain these characteristics in the absence of mean flow. The serial arrangement mainly increases the peak of TL at the resonance frequency. But the parallel arrangement logarithmically increases the peak of TL and expands the bandwidth. The change of acoustic characteristics is explained by introducing an "equivalent impedance analysis." This shows that the transmission loss has a maximum value when the distance between resonators is $\lambda/4$ of its wavelength. In this study we propose a novel design method that optimizes the arrangement of resonators while keeping the volume minimized. Various transmission loss characteristics are possible when we select different objective functions under constraints. © *2005 Acoustical Society of America.* [DOI: 10.1121/1.2036222]

PACS number(s): 43.55.Rg, 43.50.Gf [NX] Pages: 2332–2338

I. INTRODUCTION

The Helmholtz resonator is often used to reduce noise in a narrow frequency band. This type of resonator has a high transmission loss in a narrow band at its resonance frequency. It is easy to design this resonator to have a desired resonance frequency, because this is determined by the geometric ratio of the cavity and its neck.

There have been many studies about the disagreement between analytic and experimental results of the resonator due to the uncertainty of damping around the neck or end correction.[1–3] With regard to characteristics of the silencer using resonators, Anderson[4] studied the effect of flow when a single side branch Helmholtz resonator is attached to a circular duct. Chun[5] studied the acoustic characteristics of concentric pipe resonators to obtain a general solution for the acoustic field in the resonators by using the Green's function. Furthermore, many studies about the applications of a resonator are in progress in various fields.

In this paper, multiple array resonators are used to broaden the narrow band characteristics of a resonator in the low-frequency band. Kim[6] and Kuntz[7] studied the acoustic characteristics of the panel using multiple array resonators to obtain a high absorption coefficient at low frequency. These studies made use of impedance changes in the resonator configuration.

Also, in the case of a silencer using array resonators, in order to obtain broadband transmission loss characteristics, we can make use of an additional effect from many different impedance surfaces.

Therefore, we need to study the acoustic characteristics of array resonators for the design of an effective silencer model. Thus we intend to introduce the equivalent impedance that represents the total acoustic characteristics of the silencer and an optimization for determining resonance frequencies.

II. THEORY

A. Transmission loss of a branch resonator

Silencer using a resonator reduces noise by an impedance mismatch that causes reflection of the incident acoustic energy and attenuation in the resonator's neck. When a resonator is attached to a duct by a side branch, as depicted in Fig. 1, the basic assumption is that plane waves propagate in a duct and the reflected waves from downstream of a duct do not exist by using an anechoic termination in the absence of mean flow. Considering effects of grazing flow, if the mean flow's velocity is less than $M=0.1$ (M: Mach number), its effect is not serious.[4]

The sound pressure (P) and the volume velocity (U) can be expressed as follows:

$$P_1 = Ae^{-jkx} + Be^{jkx}, \quad P_2 = Ce^{-jkx}, \tag{1a}$$

$$U_1 = \frac{1}{Z}(Ae^{-jkx} - Be^{jkx}), \quad U_2 = \frac{1}{Z}(Ce^{-jkx}), \tag{1b}$$

where A, B, and C are the magnitude of the incident wave, reflected wave, and transmitted wave, respectively, and $Z=\rho c/S$ is the acoustic impedance of the duct. Here k

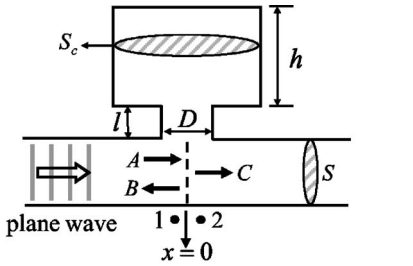

S_c : cross sectional area of cavity, h : height of cavity
l : length of neck, D : diameter of neck
S : cross sectional area of duct, A : incident wave
B : reflected wave, C : transmitted wave

FIG. 1. Helmholtz resonator with a duct.

$=2\pi f/c$ is the wave number, ρ is the density of air, and c is the sound speed.

The transfer matrix between point 1 and point 2 can be obtained as follows by using the continuity of the sound pressure and the volume velocity:

$$\begin{pmatrix} P_1 \\ U_1 \end{pmatrix} = \begin{bmatrix} 1 & 0 \\ \dfrac{1}{-jZ_c \cot kh + Z_h} & 1 \end{bmatrix} \begin{pmatrix} P_2 \\ U_2 \end{pmatrix} = \begin{bmatrix} T_{11} & T_{12} \\ T_{21} & T_{22} \end{bmatrix} \begin{pmatrix} P_2 \\ U_2 \end{pmatrix}, \tag{2}$$

where $Z_c=\rho c/S_c$ is the acoustic impedance of a resonator's cavity.

The impedance of resonator Z_r can be expressed as

$$Z_r = -jZ_c \cot kh + Z_h, \tag{3}$$

$$Z_h = \frac{\rho c}{S_h}[0.0072 + jk(l+0.75)], \tag{4}$$

where Z_h is the hole impedance of a resonator, as suggested by Sullivan.[8,9] Sullivan obtained the hole impedance of perforated elements in a concentric tube resonator by measurement. Here, the resistance of Z_h was modified in consideration of the experimental results of this study, and S_h is the cross-sectional area of the hole.

Transmission loss (TL) can be represented as follows by using the transfer matrix:

$$TL = 20 \log_{10} \left| \frac{A}{C} \right| = 20 \log_{10} \left| \frac{T_{11} + T_{12}/Z + T_{21} \cdot Z + T_{22}}{2} \right| \quad \text{(dB)}, \tag{5}$$

where A is acoustic pressure of the incident wave and C is the acoustic pressure of the transmitted wave.

Using Eqs. (2) and (5), the TL of a branch resonator in the duct can be obtained as

$$TL = 20 \log_{10} \left| \frac{2 + Z\left(\dfrac{1}{-jZ_c \cot kh + Z_h} \right)}{2} \right|. \tag{6}$$

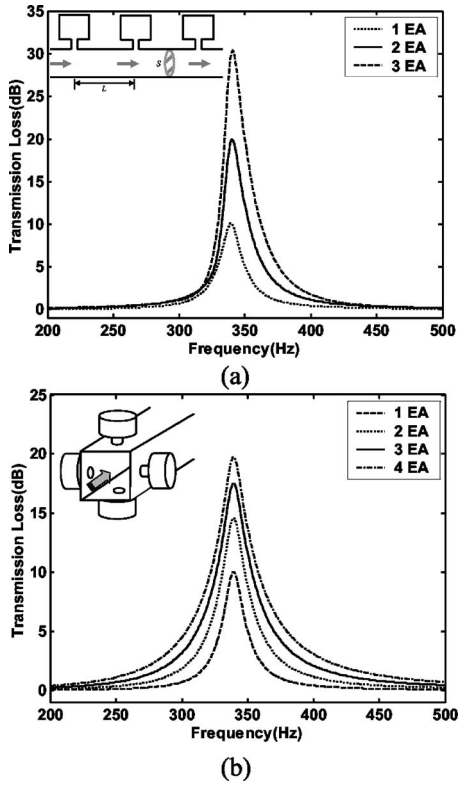

FIG. 2. The TL change varying the number of resonators. (a) The serial arrangement (S: cross-sectional area of duct, L: distance of resonators); (b) the parallel arrangement. (f_0=340 Hz, L:100 mm, l:25 mm, D:10 mm, S_c: $\pi(20)^2$ mm^2, h:48.5 mm, S:50*50 mm^2).

The TL of a branch resonator has a peak at its resonance frequency, as is well known. Thus, in order to obtain broadband characteristics, it is necessary to study the TL change for the serial and parallel array of resonators.

B. Serial and parallel array

Figure 2 illustrates the serial and parallel arrangement of identical resonators. Considering the TL change varying the resonator's number, the serial arrangement mainly increases the magnitude of TL at the resonance frequency. But the parallel arrangement logarithmically increases the magnitude of TL and the bandwidth.

These characteristics give the resonator array high TL in the broader band. In this sense, we can design the silencer by using multiple array resonators having different resonance frequencies, which are included in the objective frequency band.

Figure 3 illustrates a panel-type silencer using each of 8 resonators (i=1; 257 Hz, i=2; 297 Hz, i=3; 361 Hz, i=4; 413 Hz) in the parallel direction. Impedance of each resonator is expressed as follows, as given by Eq. (3):

$$Z_{r(i)} = -jZ_{c(i)} \cot kh_{(i)} + Z_{h(i)} \quad (i=1,2,3,4). \tag{7}$$

If the transfer matrix that represents a resonator having resonance frequency (f_i) is $T_{f_i\text{Hz}}$ and the direct tube between the resonators is T_{tube}, the total transfer matrix (T_{total}) of the panel-type silencer is obtained as follows:

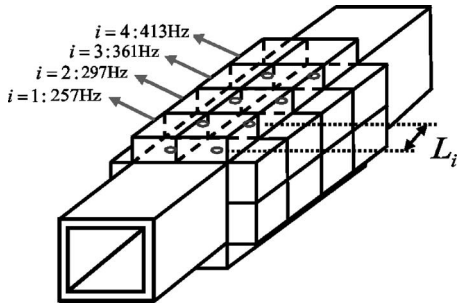

FIG. 3. Panel-type silencer using resonator array (L_i: distance of resonators).

$$T_{\text{tot}} = T_{257\ \text{Hz}} \cdot T_{\text{tube}} \cdot T_{297\ \text{Hz}} \cdot T_{\text{tube}} \cdot T_{361\ \text{Hz}} \cdot T_{\text{tube}} \cdot T_{413\ \text{Hz}} = \begin{bmatrix} 1 & 0 \\ \frac{N}{Z_{r1}} & 1 \end{bmatrix} \cdot T_{\text{tube}} \cdot \begin{bmatrix} 1 & 0 \\ \frac{N}{Z_{r2}} & 1 \end{bmatrix} \cdot T_{\text{tube}} \cdot \begin{bmatrix} 1 & 0 \\ \frac{N}{Z_{r3}} & 1 \end{bmatrix} \cdot T_{\text{tube}} \cdot \begin{bmatrix} 1 & 0 \\ \frac{N}{Z_{r4}} & 1 \end{bmatrix}, \tag{8}$$

where N denotes the number of resonators in the parallel direction.

Using Eqs. (5) and (8), the total TL of the panel-type silencer can be obtained. Figure 4 compares each resonator's TL with the total TL of the panel-type silencer. As depicted in Fig. 4, the total TL has each resonance frequency's peak and shows the additional effect.

Thus we confirmed that the panel-type silencer can obtain high TL characteristics in the broader band, as noted before. This theoretical result should then be verified experimentally.

III. EXPERIMENT

A. Experimental setup

Figure 5 shows the experimental setup for the TL measurement of the simplified panel-type silencer. The duct's cross-sectional area is $50 \times 50\text{mm}^2$ with a higher cutoff frequency of 3.43 kHz for plane wave propagation. An anechoic termination with a cutoff frequency of about 100 Hz is employed in this experiment to avoid the effects of the reflected waves.

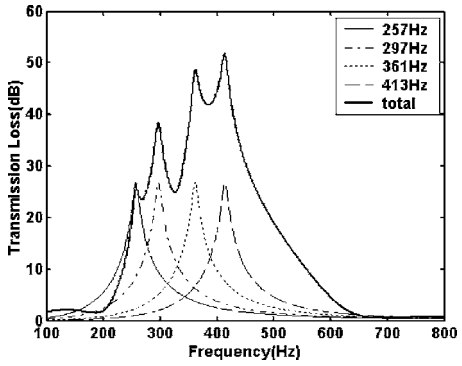

FIG. 4. Transmission loss of panel-type silencer. (N:8, l:25 mm, D:10 mm, S:50*50 mm^2, L:100 mm).

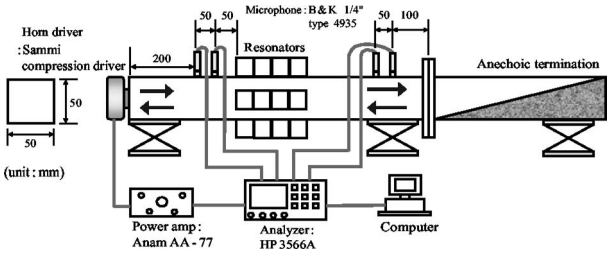

FIG. 5. The experiment setup for measurement of transmission loss.

In this study, TL was measured by a two-microphone method from the Seybert and Ross wave decomposition theory.[10]

B. Results

Figure 6 illustrates the panel-type silencer using each of four resonators (i=1; 257 Hz, i=2; 334 Hz, i=3; 387 Hz, i=4; 447 Hz) in the parallel direction. Figure 7 shows a comparison of the measured and predicted transmission loss.

IV. EQUIVALENT IMPEDANCE ANALYSIS

A. Parallel combination

The panel-type silencer has two important design parameters. Each resonator's resonance frequency and distance between the resonator's hole determine the TL of the panel-type silencer. This means that we have to study the acoustic characteristics of the array resonators to determine an effective resonator arrangement.

Using an equivalent impedance concept that represents the total acoustic characteristics of the silencer, we can explain the acoustic characteristics according to the resonator arrangement. Figure 8 illustrates the equivalent impedance of a silencer using array resonators.

The equivalent impedance (Z_{eq}) for a parallel arrangement is obtained as follows.

As depicted in Fig. 1, the pressure reflection coefficient and the pressure transmission coefficient at x=0 can be represented as follows:

$$R_{\text{coeff}} = \frac{B}{A}, \quad T_{\text{coeff}} = \frac{C}{A}. \tag{9}$$

Considering the number of resonators in the parallel direction (N), the transfer matrix between point 1 and point 2 can be written as

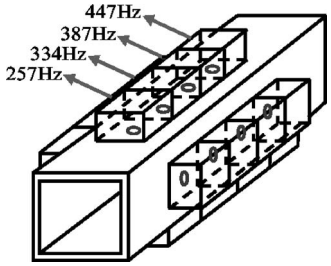

FIG. 6. Panel-type silencer using each of four resonators.

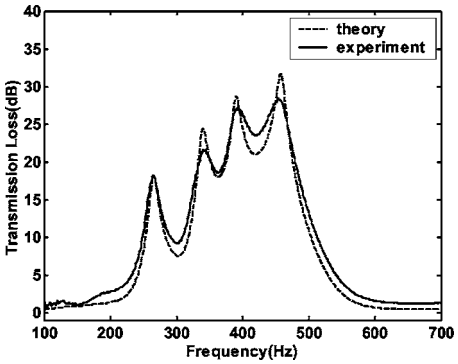

FIG. 7. A comparison between the experimental and theoretical result of the panel type using each of four resonators (L:100 mm, l:25 mm, D:10 mm, S:50*50 mm^2).

$$\begin{pmatrix} P_1 \\ U_1 \end{pmatrix} = \begin{bmatrix} 1 & 0 \\ \frac{N}{Z_r} & 1 \end{bmatrix} \begin{pmatrix} P_2 \\ U_2 \end{pmatrix}. \tag{10}$$

That is, Eq. (10) can be rearranged as

$$P_1 = P_2, \tag{11a}$$

$$U_1 = \frac{N \cdot P_2}{Z_r} + U_2. \tag{11b}$$

Using Eqs. (1), (9), and (11) at $x=0$, the pressure reflection coefficient (R_{coeff}) and the pressure transmission coefficient (T_{coeff}) at the impedance surface can be obtained in terms of the impedance of the resonator (Z_r) and the acoustic impedance (Z) of the duct:

$$R_{\text{coeff}} = \frac{-N \cdot Z}{N \cdot Z + 2 \cdot Z_r}, \tag{12}$$

$$T_{\text{coeff}} = \frac{2 \cdot Z_r}{N \cdot Z + 2 \cdot Z_r}. \tag{13}$$

Using Eq. (12), the equivalent impedance (Z_{eq}) for a parallel arrangement can be evaluated as

$$Z_{\text{eq}} = \frac{P_1}{U_1} = \frac{Z(A+B)}{A-B} = \frac{Z(1+R_{\text{coeff}})}{1-R_{\text{coeff}}} = \frac{Z \cdot Z_r}{N \cdot Z + Z_r}. \tag{14}$$

Figure 9 shows the change of equivalent impedance (Z_{eq}/Z), which is normalized by the acoustic impedance of the duct while varying the number of resonators in the parallel direction. As the number of resonators increases, the resistance (Re) of the impedance broadens. The reactance (Im) of the impedance has a value of zero at resonance frequency (200 Hz).

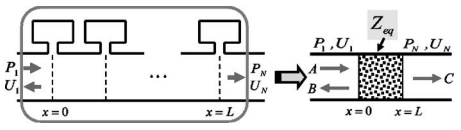

FIG. 8. Equivalent impedance of a silencer using array resonators (P: sound pressure, U: volume velocity, A: incident wave, B: reflected wave, C: transmitted wave).

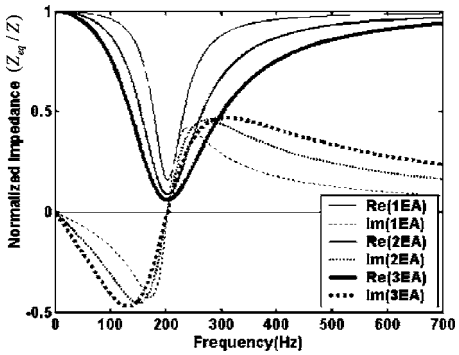

FIG. 9. Impedance change of the parallel arrangement varying the number of resonators (Re: resistance, Im: reactance).

B. Serial combination

As depicted in Fig. 8, the total transfer matrix can be expressed as follows for a serial array:

$$\begin{pmatrix} P_1 \\ U_1 \end{pmatrix} = T_1 \cdot T_2 \cdot T_3 \cdot \cdots \begin{pmatrix} P_N \\ U_N \end{pmatrix} = \begin{bmatrix} T_{11} & T_{12} \\ T_{21} & T_{22} \end{bmatrix} \begin{pmatrix} P_N \\ U_N \end{pmatrix}. \tag{15}$$

Equation (15) can be rewritten as

$$P_1 = T_{11} \cdot P_N + T_{12} \cdot U_N, \tag{16a}$$

$$U_1 = T_{21} \cdot P_N + T_{22} \cdot U_N. \tag{16b}$$

Using Eqs. (9) and (16), the pressure reflection coefficient (R_{coeff}) and the pressure transmission coefficient (T_{coeff}) can be obtained in terms of the element of total transfer matrix at $x=0 \sim L$:

$$T_{\text{coeff}} = \frac{2}{T_{11} + T_{12}/Z + T_{21} \cdot Z + T_{22}}, \tag{17a}$$

$$R_{\text{coeff}} = \frac{T_{11} + T_{12}/Z - T_{21} \cdot Z - T_{22}}{T_{11} + T_{12}/Z + T_{21} \cdot Z + T_{22}}. \tag{17b}$$

Figure 10 illustrates an electrical analogy[11] of a simple model using two resonators.

First, considering the second resonator and a direct tube between the first and the second resonator, the impedance at $x=L$ can be expressed as

$$Z_L = \frac{Z \cdot Z_2}{Z + Z_2}. \tag{18}$$

As depicted in Fig. 10, considering the wave propagation having magnitudes A and B in the direct tube, the sound pressure can be represented as

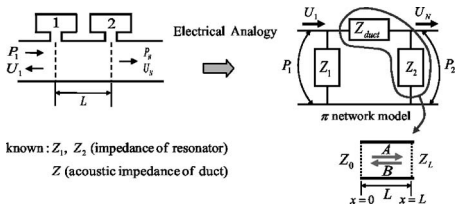

FIG. 10. Electrical analogy of the simple model using two resonators (P: sound pressure, U: volume velocity).

$$P(x) = Ae^{-jk(x-L)} + Be^{jk(x-L)}. \tag{19}$$

Using Eq. (19), the impedance at $x=0$, $x=L$ can be obtained as

$$Z_L = \frac{P(L)}{U(L)} = Z \cdot \frac{A+B}{A-B}, \tag{20}$$

$$Z_0 = \frac{P(0)}{U(0)} = Z \cdot \frac{Ae^{jkL} + Be^{-jkL}}{Ae^{jkL} - Be^{-jkL}}. \tag{21}$$

Using Eqs. (20) and (21), the impedance (Z_0) at $x=0$ can be evaluated as

$$Z_0 = Z \cdot \frac{(Z_L/Z) + j\tan(kL)}{1 + j(Z_L/Z)\tan(kL)}. \tag{22}$$

Finally, considering the first resonator, the equivalent impedance (Z_{eq}) of a serial array can be obtained as follows:

$$Z_{eq} = \left(\frac{1}{Z_1} + \frac{1}{Z_0}\right)^{-1}. \tag{23}$$

The change of acoustic characteristics is explained by using the equivalent impedance analysis. Thus, we can determine the effective resonator arrangement for obtaining the TL characteristics for low-frequency band noise reduction.

C. Characteristics change by the distance between resonators

As depicted in Fig. 10, in the case of using two resonators with 202 Hz (front) and 258 Hz (rear), the power transmission coefficient ($T_\Pi = |T_{coeff}|^2$) and the power reflection coefficient ($R_\Pi = |R_{coeff}|^2$), the absorption coefficient ($D_\Pi = 1 - R_\Pi - T_\Pi$) for varying the distance between resonators can be obtained as the contour graph in Fig. 11.

It has a periodic characteristic of $\lambda/2$ (λ: wavelength) as a whole and the TL between the first and second resonance frequency has a maximum value when the distance between resonators is $\lambda/4$ of its wavelength.

Figure 11 shows that the front resonator reflects sound power uniformly and the rear resonator attenuates sound power dominantly. When the arrangement is changed to 258 Hz (front) and 202 Hz (rear), the power reflection coefficient (R_Π) and the absorption coefficient (D_Π) have a symmetric shape of 202 Hz (front) and 258 Hz (rear). However, the TL is not changed in this case.

Thus, the change of distance between resonators is more important than the arrangement order of the resonators from the viewpoint of TL. These characteristics are identified by the equivalent impedance analysis, as noted earlier.

Figure 12 shows the resistance (Re) and reactance (Im) of equivalent impedance that is normalized by the acoustic impedance of the duct while varying the distance between resonators for the case of two resonators, 202 Hz (front) and 258 Hz (rear). The resistance of impedance is related to the energy dissipation and the reactance of impedance is related to the energy reflection. Figure 11 and Fig. 12 show that the absorption coefficient is high at the high resistance and the reflection coefficient is high at the zero-crossing point of the reactance.

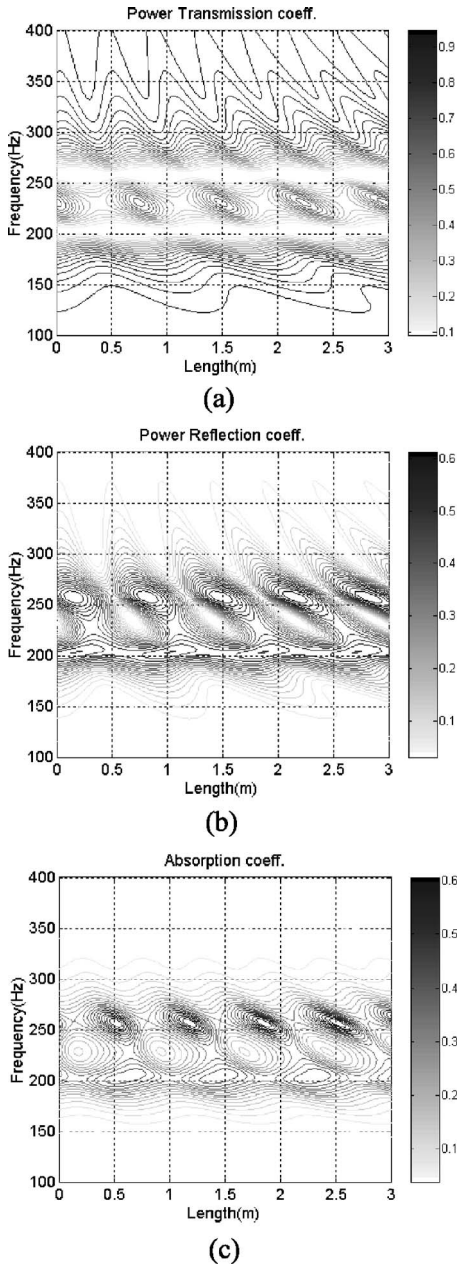

FIG. 11. Acoustic characteristics varying the distance between resonators with 202 Hz (front) and 258 Hz (rear). (a) Power transmission coefficient; (b) power reflection coefficient; (c) absorption coefficient.

D. Effective arrangement of resonators

According to the equivalent impedance analysis, we can determine the optimal distance between resonators to obtain a high TL in the objective frequency band.

In the model shown in Fig. 3 ($i=1$; 257 Hz, $i=2$; 297 Hz, $i=3$; 361 Hz, $i=4$; 413 Hz), the distance between resonator's hole can be determined as

$$L_i = \frac{\frac{\lambda_i}{4} + \frac{\lambda_{i+1}}{4}}{2} = \frac{c\left(\frac{1}{f_i} + \frac{1}{f_{i+1}}\right)}{8}. \tag{24}$$

Figure 13 shows a comparison of TL curves when the distances of the resonators are 100 mm and $\lambda/4$.

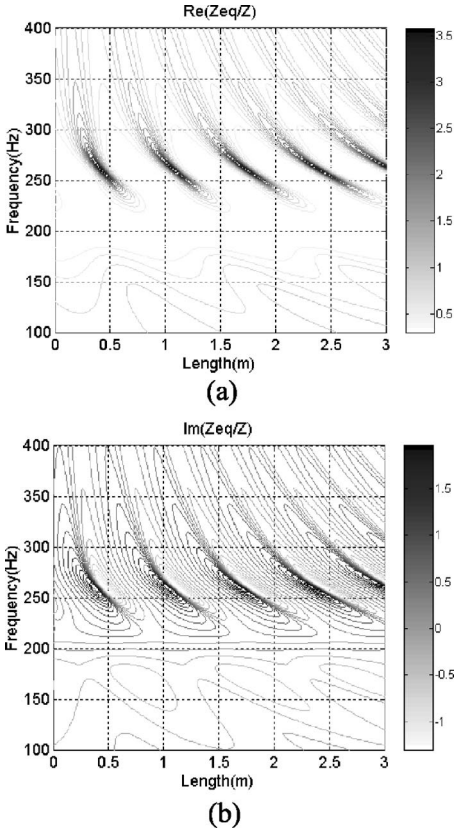

FIG. 12. Equivalent impedance varying the distance between resonators with 202 Hz (front) and 258 Hz (rear). (a) Resistance; (b) reactance.

When the distances between resonators are $\lambda/4$, the TL has a higher value in the objective frequency band. But the silencer must have a long length for in order to effectively control noise at low frequency because the wavelength is relatively long. Therefore we intend to propose a new design method that optimizes the arrangement of the resonators.

V. DESIGN PROBLEM

A. Problem definition

The silencer using array resonators has many design parameters (volume of cavity: $W \times H \times L_i$, neck length of resonator: l, hole diameter of resonator:D, distance between resonators: Δs_i). If all design parameters are considered, the silencer model becomes very complex. Therefore, it is necessary to minimize the design parameters. Figure 14 illustrates the silencer model that minimizes the design parameters. Here l, W, H, and D can be fixed by geometric shape.

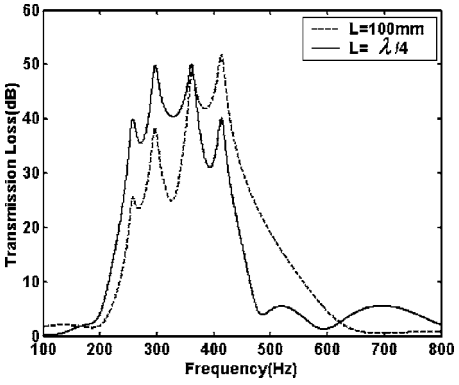

FIG. 13. Transmission loss of panel-type silencer when the distances between resonators are 100 mm and $\lambda/4$ (N:8, l:25 mm, D:10 mm, S:50*50 mm^2).

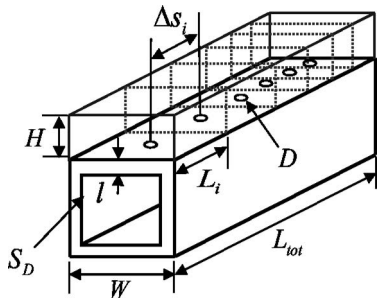

FIG. 14. The silencer model for the minimization of the design parameters ($W \times H \times L_i$: volume of cavity, l: neck length of resonator, D: hole diameter of resonator, Δs_i: distance between resonators, L_{tot}: total length of silencer).

The resonance frequency (f_i) can be expressed as

$$f_i = \frac{c}{2\pi}\sqrt{\frac{\pi D^2/4}{(l+0.75D)WHL_i}} \quad (i=1,2,\ldots,n), \tag{25}$$

where n is the number of resonators in the serial direction.

Thus the function of TL can be defined as

$$TL = \text{fun}(L_i, \Delta s_i). \tag{26}$$

From Eq. (25), L_i is expressed in terms of f_i as follows:

$$L_i = \frac{c^2 \cdot D^2}{16\pi(l+0.75D)W \cdot H \cdot f_i^2} = \frac{A}{f_i^2} \quad \left(A = \frac{c^2 \cdot D^2}{16\pi(l+0.75D)W \cdot H}\right), \tag{27}$$

where A is constant.

The distance between holes (Δs_i) also can be expressed in terms of f_i on the assumption that the resonator's hole is located at the center of the cavity:

$$\Delta s_i = \frac{L_i + L_{i+1}}{2} = \frac{A/f_i^2 + A/f_{i+1}^2}{2} = \frac{A(f_i^2 + f_{i+1}^2)}{2f_i^2 \cdot f_{i+1}^2}, \tag{28}$$

From Eqs. (26)–(28), the function of TL can be represented as

$$TL = \text{fun}(f_1, f_2, f_3, \ldots, f_n). \tag{29}$$

If the total volume of all resonators is given, the constraint of the silencer design can be expressed as

$$\sum_{i=1}^{n} L_i = L_{\text{tot}}. \tag{30}$$

Using Eq. (27), this constraint can be rewritten as

$$\sum_{i=1}^{n} \frac{A}{f_i^2} = L_{\text{tot}}. \tag{31}$$

Thus, we can obtain the multivariable optimization problem in terms of resonance frequency with a total volume constraint.

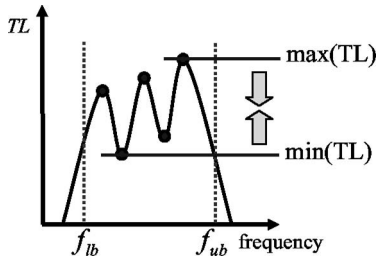

FIG. 15. The objective function for optimization (f_{lb}: low bound frequency, f_{ub}: upper bound frequency).

B. Optimization

For the desired TL, it is necessary to select a suitable objective function. The determination of the objective function for the design of TL shape is very important.

The optimization problem for TL shape having broadband characteristics at low frequency can be expressed as

$$\text{minimize } \max(TL) - \min(TL) \text{:objective function}$$

$$\text{subject to } \sum_{i=1}^{n} \frac{A}{f_i^2} = L_{\text{tot}} \text{:equality constraint}$$

$$f_{\text{lb}} \leqslant f_i \leqslant f_{\text{ub}} \text{:bound constraint.} \tag{32}$$

Figure 15 illustrates the objective function in Eq. (32).

When the bound constraint is 300 Hz$\leqslant f_i \leqslant$550 Hz and each parameter is S_D=50$\times$50 mm^2, W=70 mm, H=30 mm, D=10 mm, l=10 mm, L_{tot}=30 mm, the results of optimization are as presented in Fig. 16.

Figure 16 shows that each resonance frequency is 336, 342, 358, 385, 414, 448, and 481 Hz, and the difference between the maximum and minimum of total TL is less than 4.7 dB.

From these results, we can obtain various TL characteristics by selecting different objective functions under constraints. Finally, this optimization method shows that it is possible to design a transmission loss shape of a silencer using array resonators.

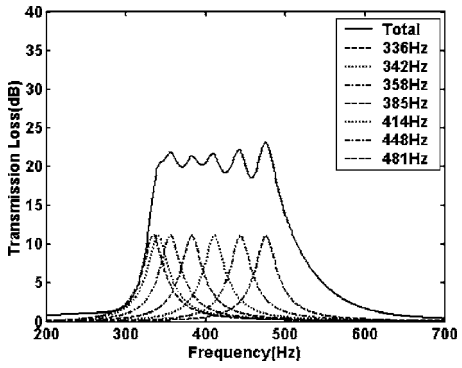

FIG. 16. The result of optimization for the broadband TL shape.

VI. CONCLUSION

Helmholtz resonators are used to reduce noise in the narrow frequency band. The transmission loss characteristics of a silencer through the use of many resonators are obtained by theoretical and experimental results. The results show that it is possible to design a silencer to have broadband characteristics through serial and parallel arrangements of resonators at low frequency.

The change of acoustic characteristics of the silencer model can be explained by using an equivalent impedance analysis. Considering the equivalent impedance analysis, the change of the distance between resonators is more significant than the arrangement order of resonators from the viewpoint of TL. As a result, it has a periodic characteristic of $\lambda/2$ as a whole and the transmission loss has a maximum value when the distance between resonators is $\lambda/4$ of its wavelength.

In this study we propose a new design method that optimizes the arrangement of resonators for a TL shape that has broadband characteristics in low frequency. Thus we can obtain various transmission loss shape by selecting a suitable objective function under given constraints.

ACKNOWLEDGMENTS

This study was partly supported by the NRL (National Research Laboratory) project of KISTEP (Korea Institute Of Science and Technology Evaluation and Planning) and the BK21 (Brain Korea 21) project initiated by Ministry of Education and Human Resources Development of Korea.

[1]K. Uno Ingard, "On the theory and design of acoustic resonators," J. Acoust. Soc. Am. **25**, 1037–1062 (1953).
[2]J.-G. Ih, "On the inertial end correction of resonators," Acustica **78**, 1–15 (1993).
[3]S.-T. Haa and Y.-H. Kim, "The limitation and applicability of Helmholtz resonator, regarding as equivalent single-degree of vibration system," Journal of the Korean Society for Noise and Vibration Engineering **4**, 209–219 (1994).
[4]J. S. Anderson, "The effect of an air flow on a single side branch Helmholtz resonator in a circular duct," J. Sound Vib. **52**, 423–431 (1977).
[5]Y.-D. Chun and Y.-H. Kim, "A study on the characteristics of concentric pipe resonators," Journal of the Korean Society for Noise and Vibration Engineering **8**, 49–56 (1998).
[6]S.-R. Kim, M.-S. Kim, Y.-H. Kim, and Y.-W. Kim, "Absorptive characteristics of resonator panel for low frequency noise control, and its applications," Inter-noise 2003, Seogwipo, Korea, N932, 2003.
[7]R. A. Prydz, L. S. Wirt, and H. L. Kuntz, "Transmission loss of a multilayer panel with internal tuned Helmholtz resonators," J. Acoust. Soc. Am. **87**, 1597–1602 (1990).
[8]J. W. Sullivan and M. J. Crocker, "Analysis of concentric-tube resonators having unpartitioned cavities," J. Acoust. Soc. Am. **64**, 207–215 (1978).
[9]J. W. Sullivan, "A method for modeling perforated tube muffler components," J. Acoust. Soc. Am. **66**, 772–788 (1979).
[10]A. F. Seybert and D. F. Ross, "Experimental determination of acoustic properties using a two-microphone random-excitation technique," J. Acoust. Soc. Am. **61**, 1362–1370 (1977).
[11]F. A. Firestone, "A new analogy between mechanical and electrical systems," J. Acoust. Soc. Am. **4**, 249–267 (1932).

Multichannel time-reversal processing for acoustic communications in a highly reverberant environment

James V. Candy,[a] Andrew J. Poggio, David H. Chambers, Brian L. Guidry, Christopher L. Robbins, and Claudia A. Kent
University of California, Lawrence Livermore National Laboratory, P.O. Box 808, Livermore, California 94551

(Received 11 January 2005; revised 8 July 2005; accepted 11 July 2005)

The development of time-reversal (T/R) communication systems is a recent signal processing research area dominated by applying T/R techniques to communicate in hostile environments. The fundamental concept is based on time-reversing the impulse response or Green's function characterizing the uncertain communications channel to mitigate deleterious dispersion and multipath effects. In this paper, we extend point-to-point to array-to-point communications by first establishing the basic theory to define and solve the underlying multichannel communications problem and then developing various realizations of the resulting T/R receivers. We show that not only do these receivers perform well in a hostile environment, but they also can be implemented with a "1 bit" analog-to-digital converter design structure. We validate these results by performing proof-of-principle acoustic communications experiments in air. It is shown that the resulting T/R receivers are capable of extracting the transmitted coded sequence from noisy microphone array measurements with zero-bit error. © *2005 Acoustical Society of America.* [DOI: 10.1121/1.2011167]

PACS number(s): 43.60.Dh, 43.28.We, 43.28.Tc [EJS] Pages: 2339–2354

I. INTRODUCTION

Communicating in a complex environment is a daunting problem. Such an environment can be a hostile urban setting populated with a multitude of buildings and vehicles, the simple complexity of a large number of sound sources that are common in the stock exchange, or military operations in an environment with topographic features, hills, valleys, mountains or even a maze of buried water pipes attempting to transmit information about any chemical anomalies in the water system servicing a city or town. These inherent obstructions cause transmitted signals to reflect, refract, and disperse in a multitude of directions distorting both their shape and arrival times at network receiver locations. Imagine troops attempting to communicate on missions in underground caves consisting of a maze of chambers causing multiple echoes with the platoon leader trying to issue timely commands to neutralize terrorists. This is the problem with transmitting information in a complex environment. Waves are susceptible to *multiple paths* and *distortions* created by a variety of possible obstructions, which may exist in the particular propagation medium. This is precisely the communications problem we solve using the physics of wave propagation to not only mitigate the noxious effects created by the hostile medium, but also to utilize it in a constructive manner enabling a huge benefit in communications. We employ *time-reversal* (T/R) communications to accomplish this task.

Time-reversal can be applied to "reconstruct" communication signals by *retracing* all of the multiple paths that originally distorted the transmitted signals, that is, if we transmit a signal into a hostile environment (medium), then the waves bounce, bend and spread, yet eventually make their distorted way to the desired receiver. Unfortunately, they arrive at the receiver at various times and signal levels creating a completely distorted message. In order to separate or decompose the individual components of the message, the T/R receiver must use its knowledge of the medium to not only separate each path, but also to superpose them together in some coherent manner to extract the message with little or no distortion while increasing their signal levels. The basic communications problem is to transmit coded information through the hostile environment or medium and receive it at desired receiver or client stations. These client stations can also broadcast through the medium characterized by unique Green's function paths to create a two-way communication link as depicted in Fig. 1.

Typical communications channels are subjected to a variety of noise and signal distortions corrupting the fidelity of the information being transmitted and reducing the effective capacity of the channel to reliably receive the information.[1,2] Contrary to intuitive notions, multipath propagation in a communications channel residing in a hostile environment can be considered a potential advantage by increasing the overall signal-to-noise ratio (SNR)—when utilized properly. T/R communications is based on taking advantage of the multipath arrivals and multiple scatterers to enhance SNR. Significant effort is continually directed toward developing new techniques for correcting or negating the effects of channel distortions. The ever-increasing demand for greater channel capacity continually necessitates better solutions for channel signal processing. This paper is based on utilizing T/R principles and theory[3,4] to communicate in a hostile environment contaminated by multipath arrivals and multiple (random) scatterers. Here we investigate the performance of

[a]Electronic mail: candy1@llnl.gov

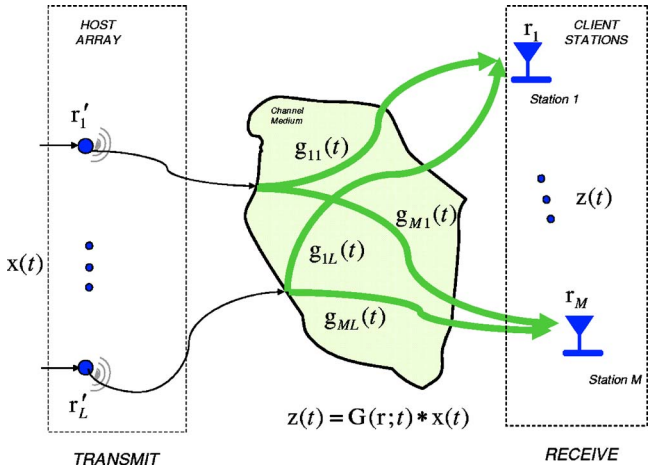

FIG. 1. (Color online) The basic communications problem: Host array transmission to client receiver stations through propagation channel (medium). The basic environment including the host transmitter/receiver, hostile medium along with the corresponding sets of Green's functions transmitter-receiver pairs from host array to client receiver stations in the communications network array.

time-reversal based communications systems employing sensor arrays using multichannel processors for client stations in a hostile multipath/multiple scatterer environment.

The basic idea in time-reversal signal processing for communications is to first estimate the set of Green's functions for transmitter-receiver pairs from pilot signal measurements. Many applications simply transmit a sharp, narrow pulse to approximate an impulse from the host thereby providing the Green's function response directly to the client receiver and then follow it with the coded information message.[1,2] This approach is fine as long as the transmitted pulse approximates an impulse sufficiently with enough time separation at the receiver elapsed *before* code arrival to capture all of the subsequent multipath returns. Another approach is to operate only within the information bandwidth (BW) specified, that is, only the BW to be utilized for communications is required. In this case, the set of Green's functions need only be estimated over the information BW which is equivalent to estimating the entire set of Green's functions and then performing bandpass filtering to extract the information bandwidth. Unfortunately, limiting the Green's functions to this restricted frequency band does not eliminate the effects of the multipath, since it is captured by the superposition of each return; however, noise reduction is achieved increasing the output SNR at the receiver. This approach is achieved by using a chirp (swept frequency) over the information bandwidth of the channel to extract the required set of Green's functions.[5] In any case, once the Green's functions are available to either host or client or both, then it is possible to realize a variety of T/R receivers. In this paper we will use the information BW approach to estimate the required set of Green's functions.

The communications problem, itself, can be decomposed into a suite of different scenarios to determine if the T/R approach is applicable and just how it may be applied. T/R communication receivers rely directly on their ability to utilize the underlying and unique propagation paths characterized by the set of Green's functions transmitter-receiver pairs from host-to-client or vice-versa (see Fig. 1). It is this knowledge that provides unique communication links even in hostile environments. In an *open* communications scenario, where every station is privy to all of the information to establish the link, then *both* host and clients know the pilot signals, Green's functions, synchronization times, carriers, etc. In a *secure* communications environment then some of the information is known, while in a *covert* operation only one or the other station need know the critical information. For instance, if the host array knows the set of Green's functions to a particular client station receiver, then it can transmit directly to it through its unique paths or it can broadcast directly into the medium and the client receiver can extract (on reception) the particular information from knowledge of its own set of Green's functions. The latter is an example of covert reception by the client.

The initial idea of T/R communications evolved from the seminal work of Parvulescu[6] where the underlying Green's function of the ocean was first estimated using a pilot signal or probe pulse, time reversed and retransmitted through the medium to focus and achieve a high SNR gain. The realization of this multichannel receiver is captured by that of *T/R Receiver I* structure described in Sec. II. Jackson[7] developed the formal theory of T/R (phase conjugation) in underwater acoustics, while the work of Dowling[8] was aimed at developing receivers capable of compressing coded acoustic pulses in a fading multipath channel. Here the receiver realization is equivalent to postprocessing the received data with the estimated Green's functions (*T/R Receiver III*). Hermand[9] and Brienzo[10] developed model-based methods by eliminating the pilot signal and using modeled Green's functions (*T/R Receiver III*). Subsequent experiments to demonstrate the performance of T/R in the ocean channel followed with the work of Kuperman[11] (*T/R Receiver I*), Hermand[12] (*T/R Receiver III*), Hodgkiss[13] and Edelmann[14] (*T/R Receiver I*). Rouseff[15] proposed a passive T/R approach in underwater acoustic communications using a realization equivalent to *T/R Receiver IV*. In a recent focusing study Yon[16] implemented the *T/R Receiver I* for acoustics in a room. Smith[17] and Heinemann[18] investigated incoherent communications in underwater acoustics using a T/R receiver realization (*T/R Receiver I*) demonstrating the effectiveness of T/R communications in a slowly (temporal) changing environment. Candy[5] demonstrated the effectiveness of a variety of T/R receiver designs in a highly reverberant environment for point-to-point communications. The work we present in this paper extends the point-to-point results of Ref. 5 to the array-to-point or array-to-multiple receivers, theoretically as well as experimentally, for both multibit resolution [24-bit analog-to-digital (A/D) conversion] and the new minimal resolution "1-bit" T/R receiver designs.[19] The realizations of various 1-bit T/R receivers are discussed and applied to noisy microphone array measurements in a hostile environment.

This paper is organized as follows. In Sec. II, the underlying T/R theory relative to the multichannel communication problem is discussed including the development of the T/R receivers and other essential components of an acoustics

communications system. We also develop the corresponding 1-bit (1-bit T/R) designs for comparison. The development of a multichannel experiment to assess the feasibility and performance of the T/R receivers is described in Sec. III along with the associated signal processing. The receiver performance on the raw measurement data to extract the information sequence is discussed in Sec. IV. Finally, we summarize these results and discuss future efforts.

II. T/R COMMUNICATIONS

In this section we develop a suite of "array-to-point" time-reversal receivers to recover a transmitted information sequence or code from a set of receiver measurements in a highly reverberant, temporally stationary environment. Here the emphasis is on the processing provided by the various realizations to extract the information signal and characterize their performance. It should also be noted that no attempt is made to optimize the receiver and configure it in a "real-time" operational mode. Rather, the subsequent experiment is performed to demonstrate the feasibility of using "time-reversal" to extract the information sequence.

A. Time-reversal background

The detection of a transmitted information sequence can be transformed to the problem of maximizing the output signal-to-noise ratio, $\mathrm{SNR}_{\mathrm{out}}$, at the receiver of a communications system. The underlying system model for the communications problem is given by

$$z(r;t) = s_{\mathrm{out}}(t) + n_{\mathrm{out}}(t) = g(r;t) * [s(t) + n(t)], \tag{1}$$

for $z(r;t)$, the noisy measurement at the rth-spatial location, $s_{\mathrm{out}}(t)$, the output signal consisting of the convolution of $s(t)$, the transmitted signal (information) and $g(r;t)$, the spatio-temporal channel response. The output noise, $n_{\mathrm{out}}(t)$, is also the convolution with the input noise, $n(t)$, an additive random (white) zero mean, noise of variance, σ_n^2. The matched-filter problem based on the model of Eq. (1) is *given* a "known" signal, $s(t)$, in additive white noise, *find* the filter response, $f(t)$, that maximizes the $\mathrm{SNR}_{\mathrm{out}}$. The solution to this problem is classical and reduces to applying the Schwartz inequality[1,2] yielding the optimal solution, $f(t)=s(T-t)$, the reversed, shifted signal or replicant. The matched-filtering operation, $mf(t)$, is then simply the cross-correlation function of the known signal, $s(t)$, and the measurement, $z(r;t)$, that is, $C_{sz}(T-t)$.

For time-reversal, the matched-filter problem is identical to that posed above with a "known" Green's function of the medium replacing the known replicant.[3,4,6,20] The Green's function, $g(r,r_o;t)$, is the result of a point-to-point communications link between a *client* station (source) at r_o to a *host* or master station (receiver) at r. In the T/R case, the matched-filter solution is again found by maximizing, $\mathrm{SNR}_{\mathrm{out}}$, leading to $f(t)=g(r,r_o;T-t)$. Thus, for T/R, the optimal matched-filter solution is the time-reversed Green's function from the host station-to-client station (source-to-receiver) or vice versa. Comparing these results with the usual matched-filter solution above, the Green's function of the channel is reversed rather than the transmitted replicant signal. Note that since T/R theory requires reciprocity,[3,4] this result is valid for *both* transmission and reception, that is, $g(r,r_o;T-t)\leftrightarrow g(r_o,r;T-t)$. Note also that if the array is included to sample the spatial field or transmit a wave, then a solution evolves with *sets* of Green's function transmitter-receiver pairs. These results include the focus at the client station (source) position, r_o, yielding the optimal, *spatio-temporal* matched-filter solution,[2,20] $g(\mathbf{r}_\ell,\mathbf{r}_o;T-t)$ at sensor position, $\mathbf{r}_\ell$. We will develop these solution in detail subsequently.

B. Multichannel T/R receivers

In this section, we develop the communications problem from the multichannel signal processing perspective[21] using vector-matrix relations to represent the environment and associated stations. With this in mind, we first define the notation and relations to characterize the basic problem under investigation and then develop the time-reversal approach to provide potential solutions.

We define the field received at the mth-station spatially located at $\mathbf{r}_m$ and at time t by the spatio-temporal signal, $z(\mathbf{r}_m;t)$, and the excitation signal transmitted from the ℓth array element spatially located at $\mathbf{r}'_\ell$ and t by $x(\mathbf{r}'_\ell;t)$. The transmitted signal propagates through the time invariant medium characterized by its impulse response or equivalently Green's function, $g(\mathbf{r}_m,\mathbf{r}'_\ell;t)$, representing the propagation medium from the excitation signal (source array sensor) to the receiver station. (In practice we do not know the Green's functions, so we estimate them from measured data. We use the caret notation, $\hat{\mathbf{g}}(\cdot)$, throughout with the caret annotating an estimate. See Sec. II C for more details.) Propagation is then governed by the convolution relation

$$z(\mathbf{r}_m;t) = g(\mathbf{r}_m,r'_\ell;t) * x(\mathbf{r}'_\ell;t). \tag{2}$$

Assuming that there are M-receiver stations and L elements in the transmit array, then Eq. (2) can be expanded as

$$\begin{bmatrix} z(\mathbf{r}_1;t) \\ \vdots \\ z(\mathbf{r}_M;t) \end{bmatrix} = \begin{bmatrix} g(\mathbf{r}_1,\mathbf{r}'_1;t) & \cdots & g(\mathbf{r}_1,\mathbf{r}'_L;t) \\ \vdots & \ddots & \vdots \\ g(\mathbf{r}_M,\mathbf{r}'_1;t) & \cdots & g(\mathbf{r}_M,\mathbf{r}'_L;t) \end{bmatrix} * \begin{bmatrix} x(\mathbf{r}'_1;t) \\ \vdots \\ x(\mathbf{r}'_L;t) \end{bmatrix}. \tag{3}$$

This *spatio-temporal propagation* relation can be written compactly as

$$\mathbf{z}(t) = \mathbf{G}(\mathbf{r};t) * \mathbf{x}(t), \tag{4}$$

where $\mathbf{z}\in\mathbf{C}^{M\times 1}$ is the received signal at all of the M stations, $\mathbf{x}\in\mathbf{C}^{L\times 1}$ is the information or message signal transmitted by the array into the medium represented by its transfer (impulse response) matrix, $\mathbf{G}\in\mathbf{C}^{M\times L}$ consisting of the channel impulse responses or equivalently Green's function, $g(\mathbf{r}_m,\mathbf{r}'_\ell;t)$, from the ℓth-transmit array sensor element to the mth-receiver station. More compactly, if we define

$$g_{m\ell}(t) \equiv g(\mathbf{r}_m,\mathbf{r}'_\ell;t), \tag{5}$$

then Eq. (3) can be rewritten in the standard vector-matrix format where the indices identify the spatial path vector locations, that is, $(\mathbf{r}_m,\mathbf{r}'_\ell)\rightarrow(m,\ell)$ as depicted in Fig. 1. Here

we define the *host* as the transmitting array and the *clients* as the receiving stations. The medium of Eq. (4) can now be expressed in terms of this notation as

$$G(r;t) = \begin{bmatrix} g_{11}(t) & \cdots & g_{1L}(t) \\ \vdots & & \vdots \\ g_{m1}(t) & \cdots & g_{mL}(t) \\ \vdots & & \vdots \\ g_{M1}(t) & \cdots & g_{ML}(t) \end{bmatrix} = \begin{bmatrix} \mathbf{g}_1^T(t) \\ \vdots \\ \mathbf{g}_m^T(t) \\ \vdots \\ \mathbf{g}_M^T(t) \end{bmatrix}, \tag{6}$$

where the set of row vectors, $\mathbf{g}_m^T(t)$, define the propagation path of the transmitted signals from the array to the mth-client station as depicted in Fig. 1. The spatio-temporal propagation of Eq. (4) can now be expressed in terms of these L-dimensional row vectors to give

$$\mathbf{z}(t) = \begin{bmatrix} \mathbf{g}_1^T(t) \\ \vdots \\ \mathbf{g}_M^T(t) \end{bmatrix} * \mathbf{x}(t) = \begin{bmatrix} \mathbf{g}_1^T(t) * \mathbf{x}(t) \\ \vdots \\ \mathbf{g}_M^T(t) * \mathbf{x}(t) \end{bmatrix}. \tag{7}$$

(Here vector-matrix operations hold with the convolution operator replacing the usual multiplication operator, that is,

$$\mathbf{x}^T(t) * \mathbf{y}(t) \equiv [x_1(t) \cdots x_N(t)] * \begin{bmatrix} y_1(t) \\ \vdots \\ y_N(t) \end{bmatrix}$$

$$= \sum_{i=1}^{N} x_i(t) * y_i(t) \quad [\text{inner convolution}].$$

Note also that the vector operations and commutivity take precedence over the convolution operator, that is, perform vector operations *first*, then the convolutions.) At the mth-client station the data received from the transmit array is therefore

$$z_m(t) = \mathbf{g}_m^T(t) * \mathbf{x}(t) = \sum_{\ell=1}^{L} g_{m\ell}(t) * x_\ell(t). \tag{8}$$

With this notation in hand, we can now develop a set of vector T/R receiver realizations.

1. T/R RECEIVER I: T/R receiver realization based on host array TRANSMISSION to the mth-client receiver station using estimated Green's functions ($\hat{\mathbf{g}}_m^T$)

This T/R receiver realization is depicted in Fig. 2 where the estimated Green's functions from the transmit array to the mth-client receiver station is time reversed and convolved on each sensor channel with the information signal on transmission. In this realization the transmitted code is given by

$$\mathbf{x}(t) = \hat{\mathbf{g}}_m(-t) \otimes i(t) = \begin{bmatrix} \hat{g}_{m1}(-t) * i(t) \\ \vdots \\ \hat{g}_{mL}(-t) * i(t) \end{bmatrix}, \tag{9}$$

where $\otimes$ is defined as the Kronecker convolution operator (element-by-element convolution) yielding an $L \times 1$ complex vector. Therefore from Eq. (4), we have that the wave propagated from the transmit array through the medium is

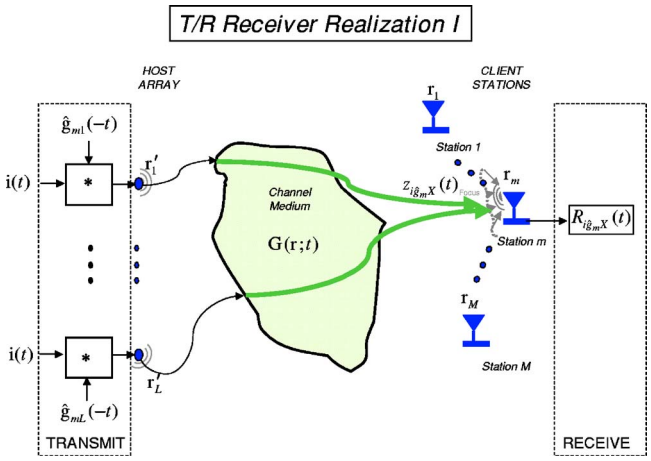

FIG. 2. (Color online) T/R Receiver I *transmission-based* realization.

$$\mathbf{z}_{i\hat{g}_m X}(t) = \mathbf{G}(\mathbf{r};t) * \mathbf{x}(t) = \mathbf{G}(\mathbf{r};t) * (\hat{\mathbf{g}}_m(-t) \otimes i(t)), \tag{10}$$

with the subscript representing the information signal (i) convolved with the estimated Green's functions ($\hat{\mathbf{g}}_m$) corresponding to the mth-client station on transmission (X). This expression can be written as

$$\mathbf{z}_{i\hat{g}_m X}(t) = \begin{bmatrix} \mathbf{g}_1^T(t) \\ \vdots \\ \mathbf{g}_M^T(t) \end{bmatrix} * (\hat{\mathbf{g}}_m(-t) \otimes i(t))$$

$$= \begin{bmatrix} \mathbf{g}_1^T(t) * \hat{\mathbf{g}}_m(-t) \otimes i(t) \\ \vdots \\ \mathbf{g}_M^T(t) * \hat{\mathbf{g}}_m(-t) \otimes i(t) \end{bmatrix}$$

$$= \begin{bmatrix} \sum_{\ell=1}^{L} g_{1\ell}(t) * \hat{g}_{m\ell}(-t) * i(t) \\ \vdots \\ \sum_{\ell=1}^{L} g_{M\ell}(t) * \hat{g}_{m\ell}(-t) * i(t) \end{bmatrix}. \tag{11}$$

Defining the cross-correlation function as

$$C_{g_k \hat{g}_m}(\ell;t) \equiv g_{k\ell}(t) * \hat{g}_{m\ell}(-t), \tag{12}$$

and therefore, from the distributive property of the convolution operator,[1,2] we obtain

$$\mathbf{z}_{i\hat{g}_m X}(t) = \begin{bmatrix} \sum_{\ell=1}^{L} C_{g_1 \hat{g}_m}(\ell;t) * i(t) \\ \vdots \\ \sum_{\ell=1}^{L} C_{g_M \hat{g}_m}(\ell;t) * i(t) \end{bmatrix} = \begin{bmatrix} \bar{C}_{g_1 \hat{g}_m}(t) \\ \vdots \\ \bar{C}_{g_M \hat{g}_m}(t) \end{bmatrix} \otimes i(t), \tag{13}$$

where

$$\bar{C}_{g_k\hat{g}_m}(t) \equiv \sum_{\ell=1}^{L} C_{g_k\hat{g}_m}(\ell;t) \quad \text{for } k=1,\ldots,M.$$

That is, the convolution of the sum is the sum of the convolutions.[1,2] It is interesting to note that at the kth-client receiver station, we have

$$z_k(t) \equiv z_{i\hat{g}_m X}(k;t) = \bar{C}_{g_k\hat{g}_m}(t) * i(t). \tag{14}$$

We obtain maximum coherence, when $k=m$, matching the set of Green's functions to the appropriate client receiver

$$z_k(t) = \begin{cases} \bar{C}_{g_m\hat{g}_m}(t) * i(t), & k=m \\ \bar{C}_{g_k\hat{g}_m}(t) * i(t), & k \neq m, \end{cases} \tag{15}$$

since the auto rather than cross correlation is achieved demonstrating that the transmitted wave field focuses at $k=m$ satisfying the time-reversal focusing principle.[3,4] The output of this realization, T/R Receiver I, at the receivers is simply

$$\mathbf{R}_{i\hat{g}_m X}(t) = \mathbf{z}_{i\hat{g}_m X}(t) \tag{16}$$

over the entire communications network (M receiver stations) or at the kth client as (as before)

$$R_{i\hat{g}_m X}(k;t) = z_{i\hat{g}_m X}(k;t) = z_k(t). \tag{17}$$

Clearly, if the correlation function at $k=m$ is impulsive, then $C_{g_k\hat{g}_m}(\ell;t) \to \delta(t)\,\forall\,\ell$, and we have

$$R_{i\hat{g}_m X}(m;t) = \bar{C}_{g_m\hat{g}_m}(t) * i(t) = \sum_{\ell=1}^{L} \delta(\ell;t) * i(t) = L \times i(t), \tag{18}$$

indicating a complete recovery of the transmitted information sequence with an array gain of L.

Before we consider the next T/R receiver realization, we assume that we have transmitted a *pilot signal* into the medium to give the following propagation:

$$\mathbf{z}_p(t) = \mathbf{G}(\mathbf{r};t) * \mathbf{p}(t), \tag{19}$$

where the pilot signal is simultaneously broadcast over each sensor channel and $\mathbf{z}_p \in \mathbf{C}^{M\times 1}$, $\mathbf{p} \in \mathbf{R}^{L\times 1}$. Note that we could also have the case where the pilot signals are different for each station, that is, $\mathbf{p}(t) \to \mathbf{p}_m(t)$. In that case we can consider transmitting orthogonal pilot signals to help discriminate between stations temporally as well. Therefore from Eq. (8) at the mth-receiver station, we have that the received pilot signal is

$$z_{p_m}(t) = \mathbf{g}_m^T(t) * \mathbf{p}(t) = \sum_{\ell=1}^{L} g_{m\ell}(t) * p_m(t). \tag{20}$$

Another scenario of importance is that in an *open* or cooperative communications environment (e.g., city) the client stations may simultaneously broadcast information to the host array, which from Eq. (4) implies that

$$\mathbf{x}(t) = \mathbf{G}^T(\mathbf{r};t) * \mathbf{z}(t). \tag{21}$$

However, a more likely scenario is that each client station individually sets up its communication link with the host by broadcasting a signal, that is, $\mathbf{z}(t) \to z_m(t)$ (a scalar); therefore, the signal received on the host array from the mth client would be

$$\mathbf{x}(t) = \mathbf{g}_m(t) * z_m(t) \quad \text{for } m=1,\ldots,M. \tag{22}$$

If, in fact, this is a known pilot signal from the mth station, then the host array receives the following signal:

$$\mathbf{x}_{p_m}(t) = \mathbf{g}_m(t) * p_m(t) \quad \text{for } m=1,\ldots,M \tag{23}$$

for $\mathbf{x}_{p_m}$, $\mathbf{g}_m(t) \in \mathbf{C}^{L\times 1}$ and p_m a scalar. Now with this information in mind we consider another T/R receiver realization based on these pilot signal measurements.

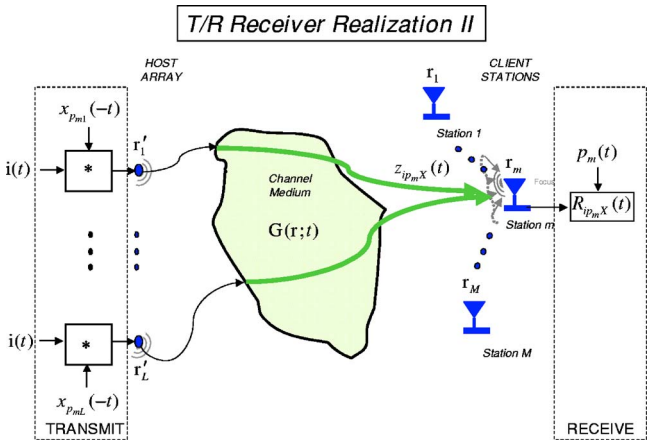

FIG. 3. (Color online) T/R Receiver II *transmission-based* realization.

*2. T/R RECEIVER II: T/R receiver realization based on host array TRANSMISSION to the m*th *receiver station using pilot signal vector* (**p**) *and measurement* ($\mathbf{x}_{p_m}$)

Following the same development of T/R Receiver I, we replace the reversed L-dimensional Green's functions estimate of Eq. (10) with the reversed, L-dimensional pilot signal measurement ($\mathbf{x}_{p_m}$) of Eq. (23) received from the mth-receiver station shown in Fig. 3. Here the measurement is convolved with the information signal and then broadcast into the medium to generate the wave field vector,

$$\mathbf{z}_{ipX}(t) = \mathbf{G}(\mathbf{r};t) * \mathbf{x}(t). \tag{24}$$

Performing the same operations as in Eq. (11), we have

$$\mathbf{z}_{ipX}(t) = \begin{bmatrix} \mathbf{g}_1^T(t) \\ \vdots \\ \mathbf{g}_M^T(t) \end{bmatrix} * \mathbf{x}(t) = \begin{bmatrix} \mathbf{g}_1^T(t) \\ \vdots \\ \mathbf{g}_M^T(t) \end{bmatrix} * (\mathbf{x}_{p_m}(-t) \otimes i(t))$$
$$= \begin{bmatrix} \mathbf{g}_1^T(t) * (\mathbf{g}_m(-t) * p_m(-t)) \otimes i(t) \\ \vdots \\ \mathbf{g}_M^T(t) * (\mathbf{g}_m(-t) * p_m(-t)) \otimes i(t) \end{bmatrix},$$

or expanding we obtain

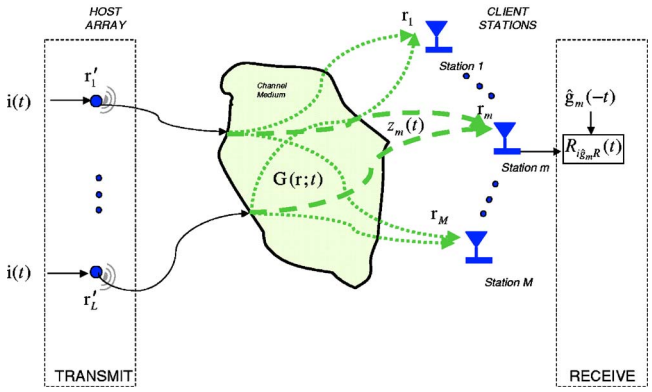

FIG. 4. (Color online) T/R Receiver III *reception-based* realization.

$$\mathbf{z}_{ipX}(t) = \begin{bmatrix} \sum_{\ell=1}^{L} g_{1\ell}(t) * g_{m\ell}(-t) * p_m(-t) * i(t) \\ \vdots \\ \sum_{\ell=1}^{L} g_{M\ell}(t) * g_{m\ell}(-t) * p_m(-t) * i(t) \end{bmatrix} = \begin{bmatrix} \sum_{\ell=1}^{L} C_{g_1 g_m}(\ell;t) * p_m(-t) * i(t) \\ \vdots \\ \sum_{\ell=1}^{L} C_{g_M g_m}(\ell;t) * p_m(-t) * i(t) \end{bmatrix}. \quad (25)$$

Again recognizing the correlation relation of Eq. (12), we obtain

$$\mathbf{z}_{ipX}(t) = \begin{bmatrix} \bar{C}_{g_1 g_m}(t) \\ \vdots \\ \bar{C}_{g_M g_m}(t) \end{bmatrix} \otimes (p_m(-t) * i(t)). \quad (26)$$

Thus, the receiver at the mth station is

$$R_{ip_mX}(t) = z_{ip_mX}(t) * p_m(t) = \bar{C}_{g_m g_m}(t) * C_{p_m p_m}(t) * i(t), \quad (27)$$

to recover the desired information. This completes the T/R Receiver II design, next we investigate the set of T/R receivers processing transmitted wavefield data.

3. T/R RECEIVER III: T/R receiver realization based on RECEPTION at the mth-station using the estimated Green's functions ($\hat{\mathbf{g}}_m^T$)

The realization for this receiver is similar to that of T/R Receiver I; however, the reversed client receiver station set of Green's functions is performed on *reception* rather than transmission as shown in Fig. 4. We start with the receiver input from the transmitted wave field of Eq. (8) as

$$z_m(t) = \mathbf{g}_m^T(t) * \mathbf{i}(t), \quad (28)$$

and convolve it with the estimated reversed Green's functions, that is,

$$\mathbf{R}_{i\hat{g}_m R}(t) = z_m(t) * \hat{\mathbf{g}}_m(-t) = (\mathbf{g}_m^T(t) * \mathbf{i}(t)) * \hat{\mathbf{g}}_m(-t) = (\mathbf{g}_m^T(t) * \hat{\mathbf{g}}_m(-t)) * \mathbf{i}(t), \quad (29)$$

where $\mathbf{R}_{i\hat{g}_m R}(t) \in \mathrm{R}^{L\times 1}$, $\mathbf{i}(t) = \mathbf{1}\cdot i(t)$ for $\mathbf{1} \in \mathrm{R}^{L\times 1}$, a vector of ones and we have interchanged the vectors using the associative property of the convolution operator.[1,2]

Intuitively, from the results of the scalar case[5] and T/R I, we expect that this vector signal should be summed over the sensor array to yield equivalent results, that is, T/R processing of this vector (array) data implies that each of the component vector outputs be summed, since they are aligned in phase from the basic nature of time-reversal. Therefore, this operation is equivalent to physically beam forming or focusing on receive.[21] Mathematically, to develop this intuition, let us re-arrange the receiver expression of Eq. (29) as

$$\mathbf{R}_{i\hat{g}_m R}(t) = \hat{\mathbf{g}}_m(-t) * z_m(t) = (\hat{\mathbf{g}}_m(-t) * \mathbf{g}_m^T(t)) * \mathbf{i}(t) = \mathbf{C}_\mathbf{m}(t) * \mathbf{i}(t), \quad (30)$$

for $\mathbf{C}_\mathbf{m}(t) \in \mathrm{R}^{L\times L}$ a *correlation matrix* defined by

$$\mathbf{C}_\mathbf{m}(t) \equiv \begin{bmatrix} \hat{g}_{m1}(-t) * g_{m1}(t) & \cdots & \hat{g}_{m1}(-t) * g_{mL}(t) \\ \vdots & & \vdots \\ \hat{g}_{mL}(-t) * g_{m1}(t) & \cdots & \hat{g}_{mL}(-t) * g_{mL}(t) \end{bmatrix} = \begin{bmatrix} C_{\hat{g}_1 g_1}(m;t) & \cdots & C_{\hat{g}_1 g_L}(m;t) \\ \vdots & & \vdots \\ C_{\hat{g}_L g_1}(m;t) & \cdots & C_{\hat{g}_L g_L}(m;t) \end{bmatrix},$$

with its $C_{\hat{g}_k g_\ell}(m;t) \equiv \hat{g}_{mk}(-t) * g_{m\ell}(t)$ for $k = 1,\ldots,L$; $\ell = 1,\ldots,L$; cross-correlation components. Note that these are senor-to-sensor correlations similar to those in Eq. (11). This matrix can be interpreted physically, since the diagonals are the autocorrelations of the individual sensor elements focused (on reception) at the mth-client receiver with the off-diagonals corresponding to the sensor cross correlations. Theoretically, T/R focusing conditions imply that the sensor cross-correlation terms should be null. This is also equivalent to the conditions that there is *no* mutual coupling between sensor elements, a reasonable array design constraint. Therefore,

$$\mathbf{C}_\mathbf{m}(t) \to \tilde{\mathbf{C}}_\mathbf{m}(t) \equiv \mathrm{diag}[\mathbf{C}_\mathbf{m}(t)]. \quad (31)$$

The information vector is simply, $\mathbf{i}(t) = \mathbf{1}\cdot i(t)$ for $\mathbf{1} \in \mathrm{R}^{L\times 1}$, a vector of ones (as before). Therefore, substituting into Eq. (30), we have that

$$\mathbf{R}_{i\hat{g}_m R}(t) = \mathbf{C}_{\mathbf{m}}(t) * \mathbf{1} \cdot i(t) = \begin{bmatrix} \sum_{\ell=1}^{L} C_{\hat{g}_1 g_\ell}(m;t) * i(t) \\ \vdots \\ \sum_{\ell=1}^{L} C_{\hat{g}_L g_\ell}(m;t) * i(t) \end{bmatrix}$$

$$= \begin{bmatrix} C_{\hat{g}_1 g_1}(m;t) + \sum_{\ell=1;\ell\neq 1}^{L} C_{\hat{g}_1 g_\ell}(m;t) \\ \vdots \\ C_{\hat{g}_L g_L}(m;t) + \sum_{\ell=1;\ell\neq L}^{L} C_{\hat{g}_1 g_\ell}(m;t) \end{bmatrix} \otimes i(t). \tag{32}$$

Assuming that there is *no* mutual coupling, then these cross-correlation terms vanish and

$$\mathbf{R}_{i\hat{g}_m R}(t) = \hat{\mathbf{C}}_{\mathbf{m}}(t) * \mathbf{i}(t) = \begin{bmatrix} C_{\hat{g}_1 g_1}(m;t) \\ \vdots \\ C_{\hat{g}_L g_L}(m;t) \end{bmatrix} \otimes i(t). \tag{33}$$

Summing at the receiver, the final output of this realization becomes

$$R_{i\hat{g}_m R}(t) = (\mathbf{1}^T \times \mathbf{R}_{i\hat{g}_m R}(t)) = \sum_{\ell=1}^{L} C_{\hat{g}_\ell g_\ell}(m;t) * i(t), \tag{34}$$

this is the scalar receiver output. Clearly, if $C_{\hat{g}_\ell g_\ell}(m;t)$ is a delta function, then we achieve (theoretically) the same performance (gain of L) as T/R I demonstrated in Eq. (18).

This completes the implementation of the T/R Receiver III. Note that in this receiver all of the client stations receive the transmitted wave field at their location; however, the transmitted energy has *not* been focused by the array as in the case of T/R Receivers I and II. Thus, the wave field is subject to more distortion and noise in this realization as well as even further degradation, if mutual coupling exists between sensors [see Eq. (32)]. Next we investigate the structure of the final T/R receiver design.

*4. T/R RECEIVER IV: T/R receiver realization on host array based on RECEPTION at the m*th *receiver station using pilot signal vector* (**p**) *measurement* ($\mathbf{x}_{p_m}$)

The realization of this receiver is similar to that of T/R Receiver II; however, the reversed pilot signal measurement is performed on *reception* rather than transmission as shown in Fig. 5. We start with the receiver input, $z_m(t)$, from the transmitted wave field of Eq. (28) and convolve it with the pilot signal (p_m) and reversed pilot signal measurement (z_{p_m}) on reception, that is, we have

$$z_{p_m}(t) = \mathbf{g}_m^T(t) * \mathbf{p}_m(t) = \mathbf{p}_m^T(t) * \mathbf{g}_m(t) \tag{35}$$

and therefore, at the receiver we obtain

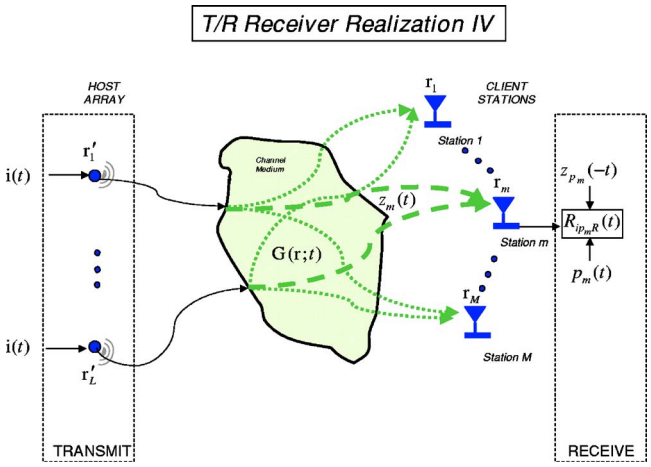

FIG. 5. (Color online) T/R Receiver IV *reception-based* realization.

$$R_{ip_m R}(t) = z_{p_m}(-t) * z_m(t) * p_m(t)$$
$$= (\mathbf{p}_m^T(-t) * \mathbf{g}_m(-t)) * (\mathbf{g}_m^T(t) * \mathbf{i}(t)) * p_m(t), \tag{36}$$

or

$$R_{ip_m R}(t) = \mathbf{p}_m^T(-t) * (\mathbf{C}_{\mathbf{m}}(t) * \mathbf{i}(t)) * p_m(t) \tag{37}$$

using the correlation matrix of Eq. (32). Using the commutative and associative properties of the convolution operator and again assuming *no* mutual coupling ($\mathbf{C}_{\mathbf{m}} \rightarrow \tilde{\mathbf{C}}_{\mathbf{m}}$) we obtain

$$R_{ip_m R}(t) = \sum_{\ell=1}^{L} C_{g_\ell g_\ell}(m;t) * i(t) * (p_m(t) * p_m(-t))$$
$$= \sum_{\ell=1}^{L} C_{g_\ell g_\ell}(m;t) * C_{p_m p_m}(t) * i(t). \tag{38}$$

This completes the development of the T/R receivers, next we investigate the results of applying these receivers to recover information in a noisy, reverberant environment. However, before we launch into that discussion let us discuss some of the basic theory underlying the development of the actual T/R receivers. We start with the estimation of the set of Green's functions using a pilot signal to characterize the transmitter-receiver pairs and then develop the basics of 1-bit T/R receiver implementations. Finally, we discuss the critical operations of code synchronization and quantization for receiver design.

C. Green's function estimation

As we discussed in Sec. II B, the Green's function is an integral part of the two T/R receiver realizations. It can be estimated from the pilot signal measurement of Eq. (19) and is similar to the operations used for equalization,[1,2] but is much better conditioned numerically for solution, since the forward, $g(r;t)$, rather than the inverse, $g^{-1}(r;t)$, is required for T/R. The estimated Green's function is used in the realizations to mitigate the distortion effects created by the medium and unknown transfer characteristics of the measure-

ment system. For the multichannel case, we assume that the Green's functions can be estimated in transmitter-receiver pairs by transmitting the pilot signal from host array sensor to the client receiver, individually. Therefore, we discuss the channel-by-channel approach using a scalar algorithm to estimate the propagation matrix of Eq. (19).

The estimate, $\hat{g}(r;t)$, can be obtained using the *optimal* Wiener[22] solution obtained from the pilot signal measurement by solving the minimum mean-squared error problem leading to the optimal estimate for the ℓth-Green's function given by

$$\hat{\mathbf{g}}_\ell = \mathbf{C}_{pp}^{-1}(\ell)\mathbf{c}_{zp}(\ell) \quad \text{for } \ell = 1, \ldots, L, \tag{39}$$

where $\mathbf{C}_{pp}$ is an $M \times M$ correlation matrix and $\mathbf{c}_{zp}$ is a $M \times 1$ cross correlation vector. Since the correlation matrix of Eq. (17) is Toeplitz,[22] the Levinson-Wiggins-Robinson recursion can efficiently perform the inversion (order M^2 operations).

The approach we employ for Green's functions estimation is to utilize the fact that the autocorrelation of a signal is the convolution with itself time reversed ($C_{xx}(t) = x(t) * x(-t)$). Therefore, if we convolve the pilot signal measurement, $z_p(t)$, with the reversed pilot signal for the ℓth-channel, that is,

$$\begin{aligned}\hat{g}_\ell(r;t) &= z_p(t) * p_\ell(-t) = [g_\ell(r;t) * p_\ell(t)] * p_\ell(-t) \\ &= g_\ell(r;t) * C_{pp}(\ell),\end{aligned} \tag{40}$$

then

$$\hat{g}(r;t) \approx g(r;t) \quad \text{for } C_{pp}(t) \to \delta(t).$$

This is the *reversed pilot signal* approach to Green's function estimation.[5] Note that one candidate pilot signal is a chirp that approximately satisfies the impulsive-like autocorrelation function property and samples the medium only within the information bandwidth.

D. 1-bit T/R receiver implementation

T/R receivers are based on the underlying T/R principle that rather than eliminating the multipath information, it can be exploited to significantly increase SNR, even in highly reverberant environments. To accomplish this enhancement the unique paths between host and clients are retraced throughout the medium using the spatial and temporal information obtained by employing the estimator of Sec. II C obtained in establishing the initial communications link. That is, the pilot signal is used to estimate the underlying set of Green's functions from transmitter array sensors to client receiver locations as illustrated in Fig. 1. The spatial information provided by the host array is not only used to establish the unique link between host sensor and client receiver, but also to increase SNR incorporating the inherent array gain (spatially) as well as the multipath arrivals (temporally). Both sets of spatial and temporal information enable the T/R receiver to perform as the optimal spatio-temporal matched filter.[20] Since the spatial information in the transmitted signal is essentially captured by the *phase* portion of the propagating wave ($g(\mathbf{r};t)$), the amplitude information is not as critical in utilizing the multipath; therefore, we developed a receiver

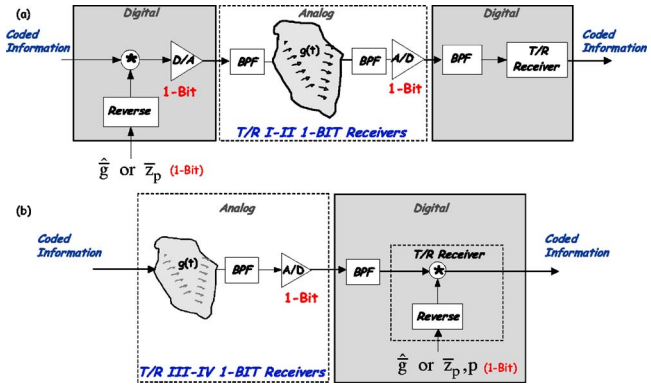

FIG. 6. (Color online) 1-bit T/R receiver realizations: (a) T/R I and II 1-bit designs on transmission. (b) T/R III and IV 1-bit designs on reception.

that ignores or quantizes the amplitude and merely exploits the "phase-only" time reversed signals. This is accomplished, quite simply, by recording the corresponding zero-crossings of the time-reversed signals quantized between ±1 amplitudes establishing what we define as the 1-bit T/R receiver realization.[19] This two-state system is commonly referred to as binary phase shift keying (BPSK) in the communications literature. The major advantage of such an implementation is that instead of requiring an expensive analog-to-digital (A/D) converter (e.g. 24 bits), a simple threshold switch can be used instead, since all that is required is to detect the zero-crossings. This is especially important in the electromagnetic case or for that matter any high frequency applications where digitization is expensive and prohibitive to consider (e.g., terahertz[23] regime). The disadvantage of this approach is increased quantization error and noise. That is, the noise will also be quantized to the ±1 amplitudes and its inherent high frequency zero-crossings as well. However, the high frequency noise is removed quite naturally by the usual bandpass filtering within the information bandwidth.

Although the 1-bit receiver design is simple in concept, it does introduce uncertainty into the processed data. First, 1-bit quantization is a *nonlinear* process identical to a switch or relay in a physical system. The crudeness of 1-bit sampling introduces large quantization errors relative to the amplitude sampling. In fact the lower bound on quantization error indicates that the 1-bit design introduces eight orders of magnitude larger deviations (errors) than the 24-bit design.[1] This error translates into an equivalent measurement noise decreasing the "in-band" (signal frequency bandwidth) SNR. The 1-bit quantization also acts as a strong amplifier of low amplitude data (usually noise) thereby reducing the overall processing gain. However from the time-reversal perspective, it offers a cheap solution to phase sampling high frequency signals (EM, ultrasound) providing a mechanism to use T/R processing thereby increasing the overall spatial gain and coherence available at the receiver.

We illustrate the two generic realizations, reversal-on-transmit or reversal-on-receive, for the 1-bit design in Fig. 6. For T/R I and II (reverse-on-transmit), the realization is shown in *a* separating the analog and digital implementations required along with T/R III and IV (reverse-on-receive) in *b*.

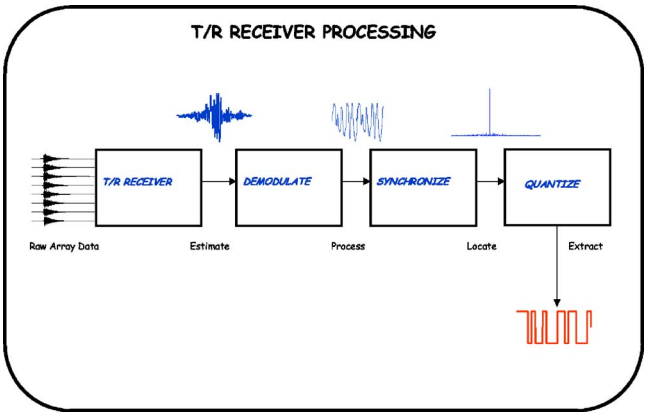

FIG. 7. (Color online) Signal processing of experimental data: T/R reception (estimate code), demodulation (process), synchronization (locate code), quantization (extract code).

Here we annotate the 1-bit quantized functions by the overbar, $(^{-})$. For instance, if we were to quantize the estimated Green's function using a 1-bit A/D, we would obtain

$$\hat{\bar{g}}(\mathbf{r};t) = \begin{cases} 1, & \hat{g}(\mathbf{r};t) \geqslant T \\ -1, & \hat{g}(\mathbf{r};t) < T \end{cases} \tag{41}$$

with T the selected quantization threshold. The underlying mathematics was actually developed using the quantized notation, but little insight was gained, since the quantization process is nonlinear and the operations could not be decomposed. Suffice it to say that we simply describe the operation of the 1-bit designs in Fig. 6.

In Fig. 6(a) we illustrate the design of a 1-bit T/R receiver for transmission. In both T/R I and II, the quantized signals are reversed and convolved (in software) with the information sequence, converted for transmission using a digital-to-analog (D/A) converter, bandpass filtered (BPF) and transmitted by the array into the medium. Even though these signals have been quantized as signified by the overbar notation, once a digital convolution operation occurs, new amplitude information other than a ±1 is superposed. On reception, two BPF are utilized prior to A/D conversion. Out of band interference as well as anti-alias filtering is provided by the first analog BPF, while the second digital BPF (after A/D) smoothes the quantized measurement reducing quantization error and eliminates the high frequency noise created by the 1-bit quantization process. This processed data are then input to the usual demodulation, synchronization, and information extraction operations (see Fig. 7).

The 1-bit T/R designs for reception are shown in Fig. 6(b). Here coded information is transmitted into the medium, analog BPF and digitized using the 1-bit A/D as before, while the second digital BPF performs the same basic role of filtering, smoothing and noise rejection. The processed measurement is then convolved (in software) with the reversed signals to extract the coded information using the T/R III and IV algorithms. Although not quite as good as the 24-bit designs, the results of the 1-bit T/R implementations are quite reasonable, while simultaneously providing a huge cost savings for high frequency communications in a reverberant medium.

This completes the development of the 1-bit T/R receiver designs, next we consider the synchronization problem.

E. Code synchronization

After the processed T/R signal is demodulated using a phase-locked method to align the carrier,[1,2] synchronization is then performed. Synchronization is the process of aligning and locally generating the extracted code between receiver and transmitter and in many cases proves to be most complex and critical.[1,2] BPSK codes using the double side band suppressed carrier amplitude modulation technique.[1,2] are simultaneously transmitted from each array element to the client network. We *detect* the transmitted information, using a matched-filter receiver such that the cross correlation of $i(t)$ and its estimate at the output of a T/R receiver $\hat{i}(t)$ achieve a maximum at some lag T, that is,

$$\hat{T} = \max C_{i\hat{i}}(k-T)\big|_{k=T} = C_{i\hat{i}}(0). \tag{42}$$

Note that $\hat{i}(t)$ can be from any of the T/R receiver realizations. Therefore, in essence, all that is necessary is to "detect" that the transmitted information code has been recovered. This detection is accomplished by performing the matched-filter calculation above and locating the well-defined peak at $\hat{T}$. The known pilot signal can be used to estimate $\hat{T}$. It should also be noted that extracting the actual information sequence, as in the case of voice communications, requires the solution of the problem of estimating, $\hat{i}(t)$, from the noisy, reverberant transmission through the medium, which is desired output of the T/R receiver. The estimated information is next quantized to compare with the actual transmitted code.

F. Quantization

For any of these receivers, the final processing step is to *quantize* the estimated and detected BPSK coded information sequence. The quantizer simply limits the estimated coded signal to A, above or below a specified threshold, that is,

$$i(t) = \begin{cases} +A, & \hat{i}(t) > T \\ -A, & \hat{i}(t) \leqslant T \end{cases}, \tag{43}$$

where A is the quantization level or amplitude and T is the preset threshold. It is interesting to note that just as in classical detection theory,[24] the value of the threshold is also selected for the receivers based on some performance criterion. We use a *symbol error criterion* to evaluate the performance of each of the receiver realizations in this paper. *Symbol error* is defined as the percentage of symbols missed over the total transmitted. In our application, since a symbol is represented by one bit, symbol error is synonymous to bit error.

We summarize the operations performed on the received data to extract the desired coded information sequence from the noisy, reverberant data in Fig. 7. All of the T/R receiver realizations incorporate the common functions of demodula-

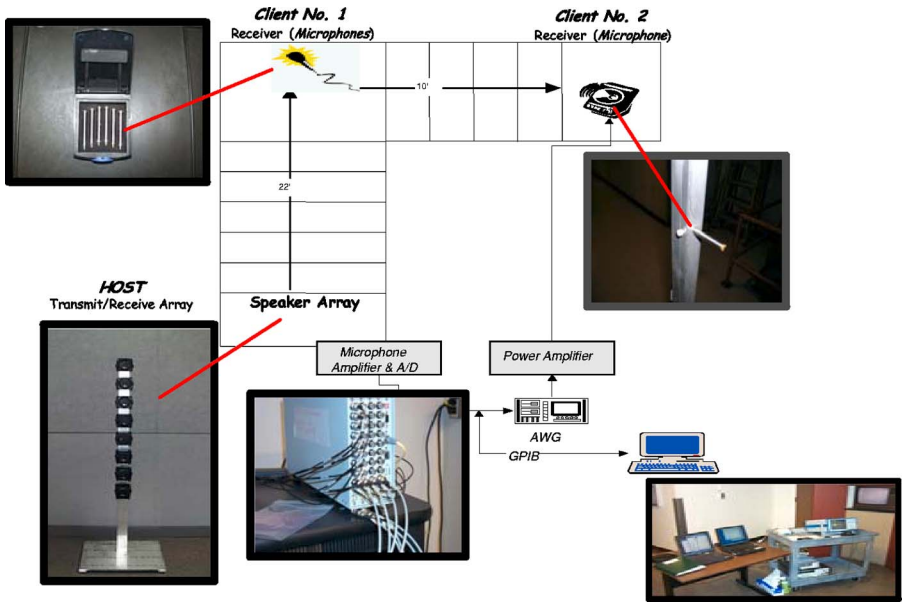

FIG. 8. (Color online) Experimental environment and setup for T/R communications testing: stairway layout with three landings and high corrugated steel ceilings (10–12 ft) along with the equipment setup for array-to-point communications. Note that client receiver No. 1 has a direct path from host array, while client receiver No. 2 does not.

tion, synchronization, and quantization to extract the transmitted codes from the host station. In the figure, we see that the *raw* signal is received by the T/R receiver and processed to produce the *estimated* code sequence. The data are then *demodulated* to remove the carrier providing the processed data for synchronization. Note that this step usually incorporates a phase-locked loop[1,2] to align the carrier phase of the receiver with the transmitted carrier, perform the demodulation (multiplication) and low-pass filtering. We found the loop an elegant solution to the problem but quite difficult to implement. Thus, we chose to search for the initial phase yielding the best performance by minimizing the symbol error. A standard matched filter is then used to synchronize the processed data and temporally locate the onset of the code which is then quantized, extracted, and compared to the transmitted for performance analysis. This completes this section, next we describe the multichannel experiment established to evaluate both multi and 1-bit T/R receiver designs.

III. T/R COMMUNICATIONS EXPERIMENT

With theory in hand, we discuss the experimental environment and processing to gather the T/R receiver data. We describe the steps required to extract the coded information sequence using the various T/R receiver realizations. As before,[5] the experiments are performed in a stairway located between two floors consisting of three landings, high ceilings of corrugated steel, pipes, handrails and other nonsound absorbing protrusions as well as ambient building noise. The geometry of this stairway is shown in Fig. 8, clearly indicating the potential for a highly reverberant, hostile environment.

The array-to-point (host array-to-client) experiments are performed using Meyer Sound, MM-4, 4-in. single element speakers configured in an 8-element vertical array with a 6-in. pitch powered by a Crown Audio CTS 8200, 8-channel, 150 W amplifier and a Data Physics, DP-703 arbitrary wave form generator/digitizer for transmitting both the pilot signal chirp pulse swept from 0.1 to 2 kHz and the BPSK modulated code of 0.1-kHz bandwidth at a carrier frequency of 1.207 kHz. On reception, B&K 4935, $\frac{1}{4}$ in. microphones are used in an 8-element receiver array along with the 24-bit Data Physics digitizer sampling at 12.8 kHz. The experiment is controlled using a laptop computer. The transmitted code received on a single microphone with the corresponding spectrum is shown in Fig. 9. The response is dominated by a long reverberation response and noise.

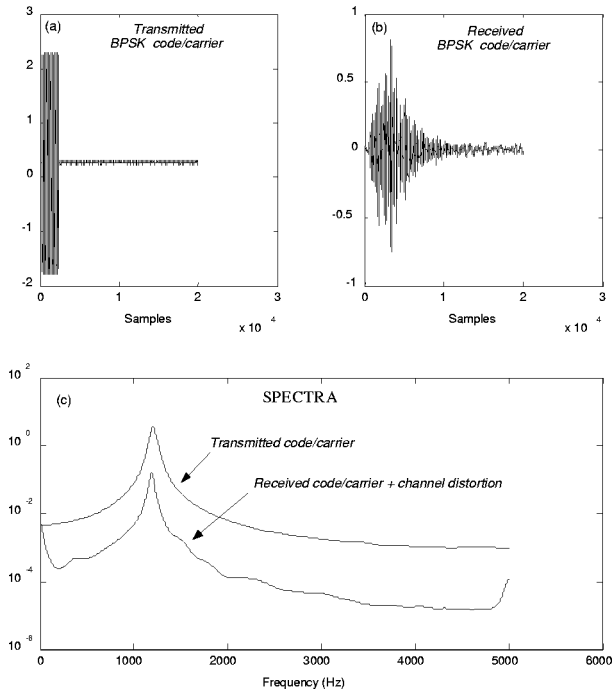

FIG. 9. Transmitted and received code sequence in a stairwell: (a) transmitted BPSK coded sequence with carrier. (b) Received BPSK coded sequence with carrier including all stairwell effects. (c) Transmitted and received spectra.

The basic experimental approach is summarized as:

(1) *transmit* the pilot signal, that is, excite the medium with a chirp pilot signal sequence to estimate the set of Green's functions transmitter-receiver pairs;
(2) *transmit* the modulated information signal from the source (speaker) along with the required Green's functions, measured pilot signal, etc., through the reverberant medium (stairway) to the microphone receiver;
(3) *receive* (microphone) the noisy, reverberant signal and digitize;
(4) *process* the raw data with the T/R receiver (software);
(5) *demodulate* the processed data to estimate the information;
(6) *locate* the temporal onset of the code extracting it from the demodulated data; and
(7) *quantize* the results for further performance analysis.

We note in passing that client receiver No. 1 has a direct path from the host array, while client receiver No. 2 does not. This implies a better SNR at client No. 1 compared to that of client receiver No. 2. This completes the description of the experimental setup, equipment, and processing. Next we discuss the results.

IV. RESULTS

In this section we discuss the results of proof-of-principle experiments demonstrating the performance of multichannel T/R communications systems for both the multibit and 1-bit designs developed in Sec. II. As mentioned previously, we estimate the set of Green's functions of the stairwell for each transmitter-receiver pair. The BPSK code is designed to occupy an information bandwidth of 0.1 kHz centered at 1.207 kHz as shown in Fig. 9. Using these Green's functions, we developed an experimental computer simulation for design and implementation of the various receivers for processing. We investigated a number of cases that can be extrapolated to a variety of real world scenarios corresponding to open, secure and covert communications.

We use two, 8-element, linearly-spaced (6-in. pitch), vertical arrays to construct the host array: one for transmission consisting of the eight speakers and one for reception consisting of the eight microphone receivers. Individual speakers and microphones are positioned at each client station in the reverberative stairwell. Client receiver No. 1 is located at the middle landing, while client receiver No. 2 is at the top landing as shown in Fig. 8. As noted previously, client No. 1 has a higher SNR than that at client No. 2 due to the direct path. After obtaining the set of Green's functions for each client receiver, we investigate the following cases: (1) focused transmission to each client receiver, *individually* and checked the other (nonfocused) client receiver station for leakage of the cross-correlation functions; (2) focused on *both* client receiver stations, simultaneously, by superposing the reversed channel transmissions; and (3) repeated the tests for 1-bit realizations. For each of the T/R I and II receivers (focus on transmit), we focused on the individual client receiver stations and evaluated their performance, while receivers (focus on receive), T/R III and IV were evaluated as well.

It should be noted that since we chose to use the reversed pilot signal approach to estimate the Green's functions, then T/R III and T/R IV realizations provide identical results (convolution is commutative); therefore, we did not implement T/R IV for this experiment. However, we did validate its performance using the 1000 symbol codes and different realizations for each. These results are included in the figures.

For our receiver performance analysis, we use a symbol (bit) error criterion. We determine the symbol error by varying the threshold at the processed receiver output and determine the number of symbols missed at that threshold. The performance function (% symbol error versus threshold) is "U-shaped" with the base of the "U" residing in the *zero-symbol error* region (see, e.g., Fig. 11 for T/R I). Of particular interest is the percentage of the threshold interval corresponding to the zero-symbol error region *relative* to the *total* threshold interval (−1 to +1) evaluated. We use this threshold interval percentage to provide a metric for evaluating the robustness of the particular receiver design. The *higher* the percentage, the larger the threshold interval corresponding to zero-symbol error is and therefore the more robust the design. We compared all of the receiver designs and a bar chart with these percentages listed is illustrated in Figs. 16 and 17. We also calculated the percentage threshold intervals for each realization using both 24-bit and 1-bit designs. As a final performance evaluation, we transmitted a 1000 symbol code and calculated the symbol error criterion for overall performance evaluation.

A. T/R I receiver performance

The realization of this T/R I receiver (see Fig. 2) uses the estimated set of Green's functions from the array sensors convolved with the code *transmitted* into the stairwell [Fig. 9(a)]. This is a common realization that has been applied in the literature.[6,7,11,13,14,16–18] After demodulation and synchronization, we see the corresponding information code estimates produced from the output of the T/R I receiver in Fig. 10. For each client receiver the 24-bit (upper row) and 1-bit designs (lower row) are illustrated using solid lines. This code estimate is then downsampled to the symbol rate and then quantized based on a selected threshold. Each estimated symbol (∗) is then compared to the true transmitted symbol (○). We overlay the "true" code in the figure for illustrative purposes. For T/R I, it is clear that raw coded information pulses are clearly discerned in the receiver output data (solid line). For the given threshold, the downsampled (to symbol rate) quantized output perfectly captures the transmitted BPSK sequence. These results are verified by the "overlayed" true symbols (○) and estimated symbols (∗). Since all of the symbols estimated by T/R I quantizer perfectly match those transmitted, the BPSK information code is captured with zero-symbol error for the selected threshold. Note also the high SNR achieved through T/R focusing and inherent array gain compared to point-to-point experiments reported on previously.[5] It is also interesting to note that the

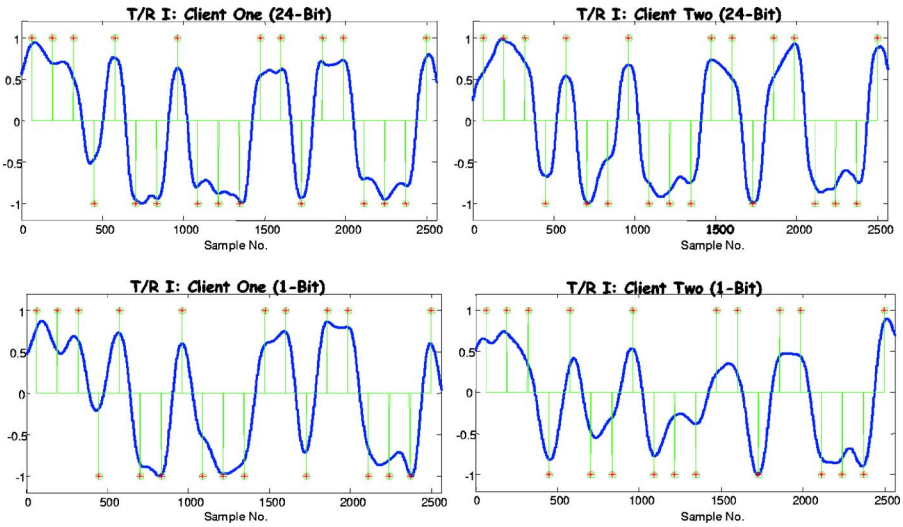

FIG. 10. (Color online) Multichannel T/R I (normalized) receiver output coded estimates (solid line) along with true BPSK code sequence for 24-bit (upper row) and 1-bit (lower row) designs at each client receiver for true symbols (○) and estimated symbols (∗) yielding a zero-bit error performance for the selected threshold.

1-bit designs at each client have deteriorated somewhat compared to the 24-bit design. This performance is expected due to increased quantization noise and will be explained in more detail subsequently.

By varying the threshold over the entire T/R receiver estimate, the performance U curve (% symbol error versus threshold) is generated as shown in Fig. 11. This curve plays a role similar to the operating characteristic curve[24] in classical detection theory—thresholds can be selected to minimize symbol error. As mentioned previously, the length or range of the threshold interval yielding zero-symbol error compared to the total range gives an indication of the performance capability of the receiver. Each receiver is compared in the bar charts of Figs. 16 and 17. The interesting property is that it is possible to find a threshold interval yielding zero-symbol error indicating the robustness of the receiver, that is, the larger the interval, the more threshold values can be selected to yield zero-symbol error. The performance on these data are as expected, some robustness is sacrificed as the cost of simplicity using the 1-bit designs. Examining the U curves for each client, we see that both are able to achieve approximately 49% and 45% threshold intervals using the 24-bit design, while the intervals decrease to 36% and 16%, respectively, using the 1-bit designs. A possible explanation for this deterioration in performance is based on larger errors in 1-bit quantization and its inherent in-band noise amplification decreasing SNR. The 1-bit designs capture the spatial information by using the zero-crossings of *both* signal and noise, they essentially "throw away the amplitude information." When noise only is quantized, it has an amplitude level of ±1. Clearly when there are gaps between signal arrivals even the low frequency in-band noise only is quantized to the same levels. Filtering removes the high noise frequencies, but the in-band signal and noise have now also been quantized to the *same* level thereby causing the performance degradation. In terms of the higher performance degradation at client receiver No. 2 compared to that on No. 1, it relates back to the fact that the SNR at No. 1 is inherently higher due to the direct path from the host array.

B. T/R II receiver performance

The realization of this T/R receiver uses the set of pilot signal measurements from the array convolved with the code *transmitting* into the stairwell and then convolves the *received* output with the known pilot signal to recover the code (Fig. 3). After receiving the raw data, it is demodulated and

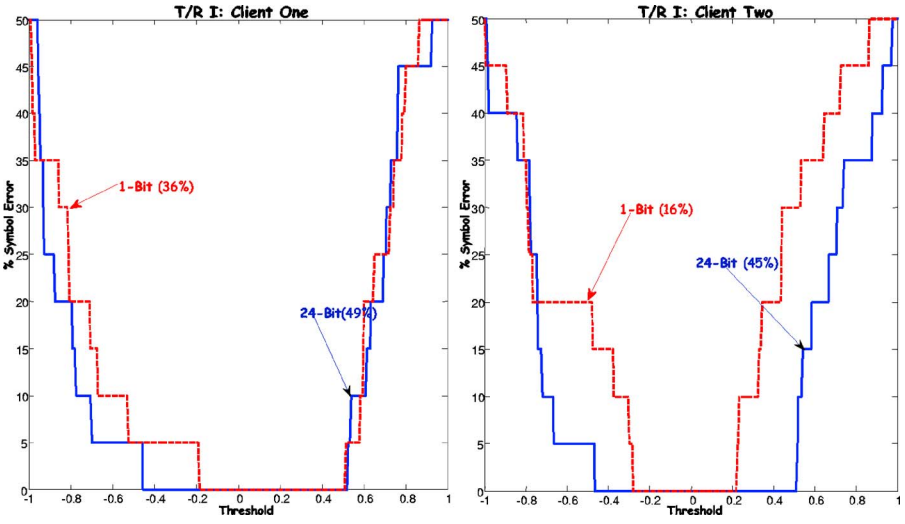

FIG. 11. (Color online) T/R I receiver design performance U curves for focusing at clients 1 and 2 using 24- and 1-bit designs. The degradation of the 1-bit design is from 49% to 36% threshold interval for the first client receiver and from 45% to 16% for the second client receiver.

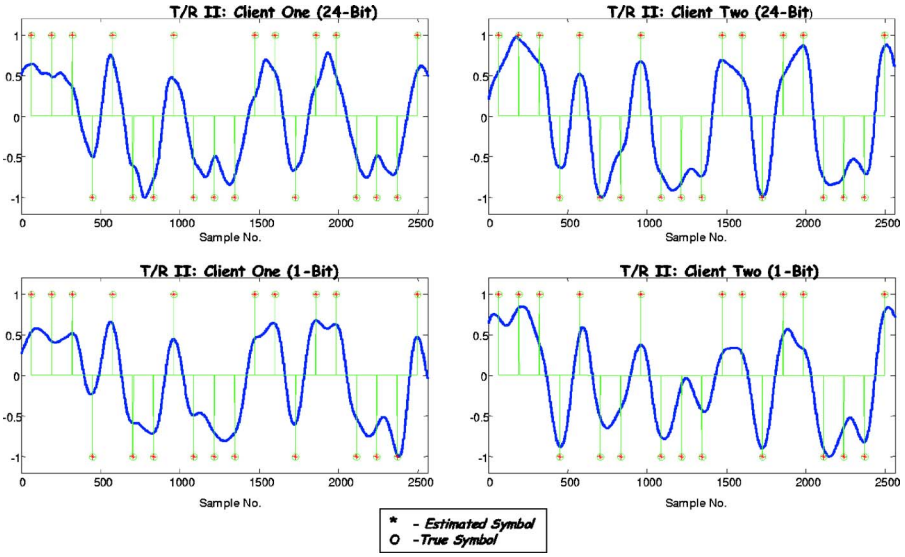

FIG. 12. (Color online) Multichannel T/R II (normalized) receiver output coded estimates (solid line) along with true BPSK code sequence for 24-bit (upper row) and 1-bit (lower row) designs at each client receiver for true symbols (○) and estimated symbols (∗) yielding a zero-bit error performance for the selected threshold.

synchronized to extract the transmitted code as shown in Fig. 12 (solid line). The comparison with the transmitted BPSK coded sequence is also shown. After downsampling and quantization, the transmitted code can be recovered with zero-symbol error depending on the choice of threshold. As before, these results are verified by the true symbols (○) "overlayed" onto the estimated symbols (∗). Since all of the symbols match perfectly with those transmitted, the BPSK information code is captured with zero-symbol error for the selected threshold. The performance of the T/R III receiver is again captured by its "U" curves shown in Fig. 13. Here we see that the 24-bit receivers again perform much better than the previous point-to-point designs of Ref. 5. Using the 1-bit rather than 24-bit design the overall performance degrades from 36% zero-symbol error to 33% (not much) at client receiver No. 1 and from 45% to 20% at client No. 2. It is also interesting to note that this 1-bit performance is still superior to the point-to-point designs ($\sim 15\% - 18\%$).[5] In this case T/R II performs better at client No. 2 for the 24-bit design implying the possibility of strong coherent multipath enabling the time-reversal to increase the temporal processing gain, that is, the coherent addition of multiple aligned arrivals. The overall performance is shown in Fig. 13 and compared to the other realizations in Fig. 16.

C. T/R III receiver performance

This T/R receiver uses the estimated set of Green's functions convolved with the raw received code data (Fig. 4) on *reception*. The results of the performance of this realization are shown by the plots in Fig. 14. After the usual processing, the experimental and simulated results track each other. For the selected threshold, zero-symbol error is achieved with perfect code recovery. In the figure we observe the excellent performance of both the 24-bit (upper row) and 1-bit (lower row) designs at each client station. The overall performance is shown at each client station in Fig. 15 where we observe the U-shaped symbol error curves. The performance of this receiver is quite good; however, we again note some performance degradation in the 1-bit design.

Here we observe the outstanding capability of this design which achieves the best zero-symbol error performance at both clients: 58% and 70%, respectively. Performance degradation due to the 1-bit quantization is also quite good

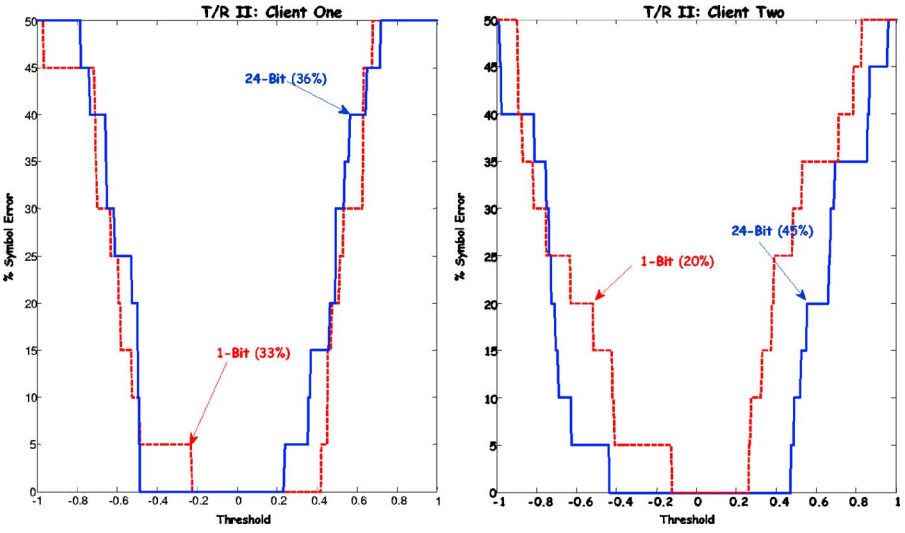

FIG. 13. (Color online) T/R II receiver design performance U curves for focusing at client receivers 1 and 2 using 24- and 1-bit designs. The degradation of the 1-bit design is from 36% to 33% threshold interval for the first client receiver and from 45% to 20% for the second client receiver.

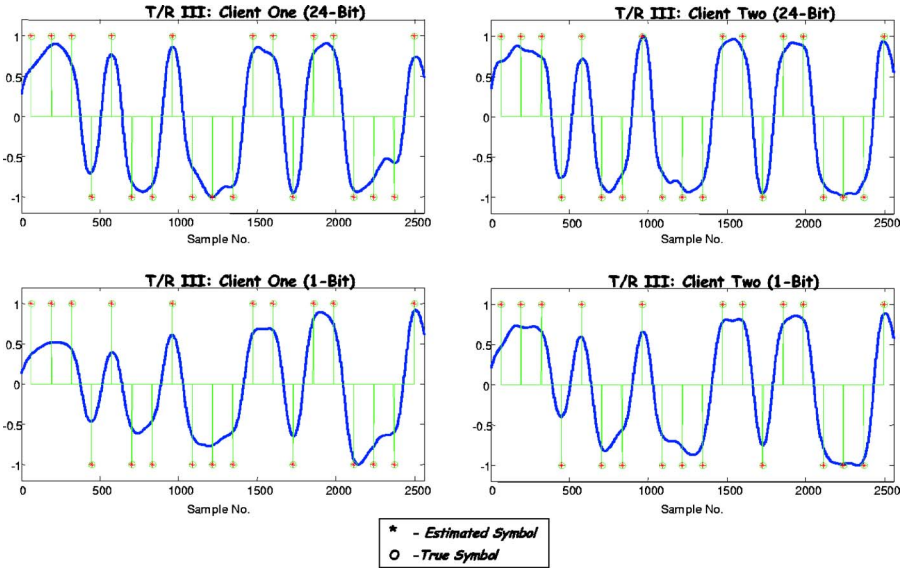

FIG. 14. (Color online) Multichannel T/R III (normalized) receiver output coded estimates (solid line) along with true BPSK code sequence for 24-bit (upper row) and 1-bit (lower row) designs at each client receiver for true symbols (○) and estimated symbols (∗) yielding a zero-bit error performance for the selected threshold.

going from 58% to 40% at client No. 1 and 70% to 43% at client No. 2. Note that both the 24- and 1-bit designs are far superior to the previous point-to-point designs of Ref. 5.

D. T/R IV receiver performance

The final T/R receiver realization uses both the measured pilot signal medium response and known pilot signal convolved with the transmitted code measurement on *reception* for recovery. The results are identical to those of T/R III because of the implementation, therefore see Figs. 14 and 15.

E. Overall performance comparison

Next we compare the overall robustness performance of each design at the individual client stations for both 24- and 1-bit designs shown in Figs. 16 and 17. We illustrate the performance by bar charts with the height of the bar determined by the % threshold range occupied by zero-symbol error of the corresponding U curve. In Fig. 16 the 24-bit design chart shows a significant performance improvement over previous point designs[5] with the average range over 40% of the total threshold interval for zero-symbol error compared to approximately 15%–20% performance of the point-to-point design. This significant increase is due to the improved SNR at the receiver afforded by the array (spatial gain) and improved focusing capability. By simultaneously superposing the two foci associated with the sets of corresponding reversed Green's functions, the receiver performance at both client stations improved. Channel isolation, that is, focus at one client receiver and checking for no focus at the other appears quite reasonable for T/R receivers I and II.

Observing the performance of the 1-bit T/R receivers in Fig. 17, we see that the performance is somewhat degraded, especially when superposing the foci, as the 24-bit design (as expected), but still much better than the previous point-to-point designs reported on earlier.[5] However, for some applications, where cost is a major consideration, the 1-bit designs are satisfactory.

From the zero-symbol error and the % threshold range interval bar charts, it is clear that the T/R receivers can achieve zero-symbol errors over a reasonable range of the available thresholds for robust operations. The implementation advantages and simplicity of the T/R receivers offer an

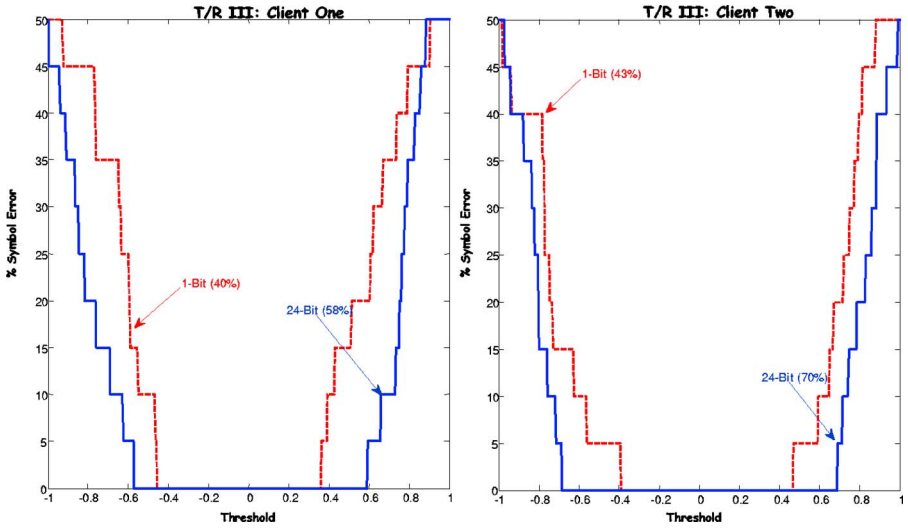

FIG. 15. (Color online) T/R III receiver design performance U curves at client receivers 1 and 2 using 24- and 1-bit designs. The degradation of the 1-bit design is from 58% to 40% threshold interval for the first client receiver and from 70% to 43% for the second client receiver.

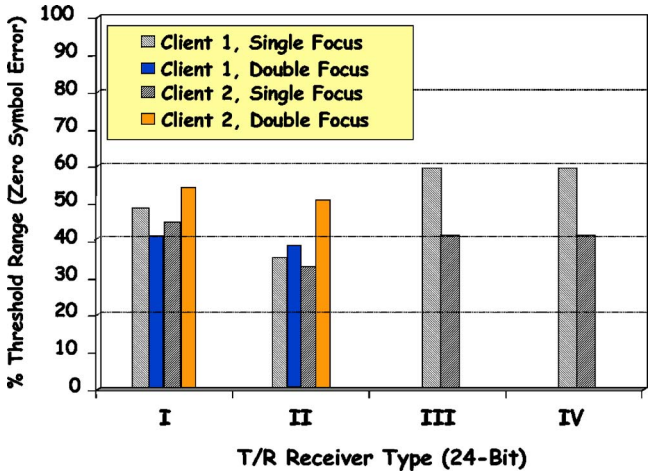

FIG. 16. (Color online) T/R receiver performance based on the threshold range (% of total) for zero-symbol error performance at both client stations for 24-bit designs.

attractive alternative to the optimal. However, for a slowly time-varying channel, the T/R receivers may require more pilot signal transmissions to maintain the validity of the underlying set of Green's functions which is the key to T/R receiver design in a highly reverberant environment. In fact, our experience is to periodically transmit a pilot signal prior to the information codes to update the Green's functions using the reverse pilot signal approach. This scheme eliminates and changes in the environment or location changes of the clients and host array. Before we conclude our analysis, we performed one more test to evaluate the T/R receivers—long symbol length code transmissions.

F. Long symbol length performance

We choose to construct and transmit our BPSK information sequence in a code consisting of 1000 symbols and estimate the corresponding bit error U curves for each receiver. This test enables us to determine how the T/R receivers will perform in a more realistic environment. We performed this

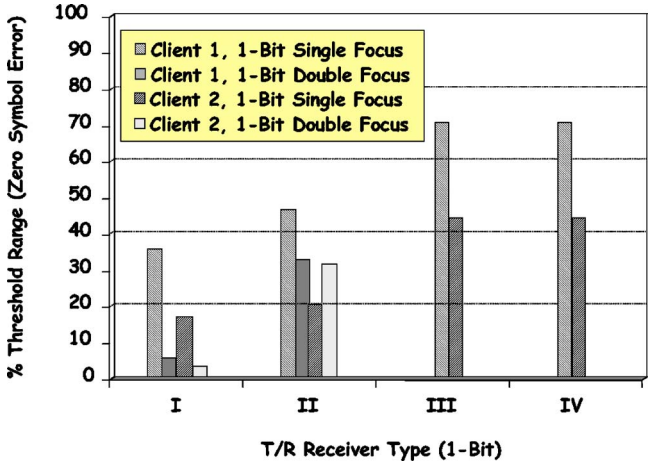

FIG. 17. (Color online) T/R receiver performance based on the threshold range (% of total) for zero-symbol error performance at both client stations for 1-bit designs.

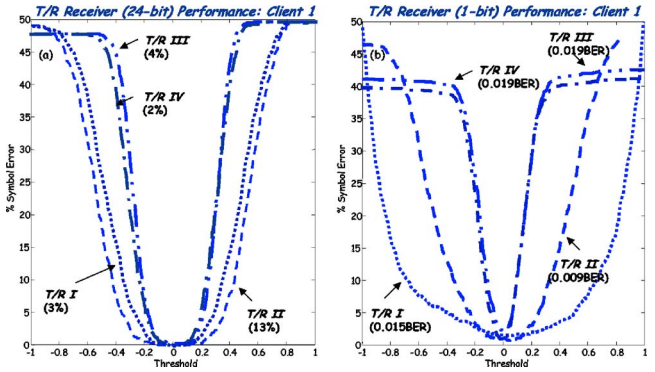

FIG. 18. (Color online) 1000 symbol code test on 24- and 1-bit realizations of T/R receivers for focusing at client station No. 1. (a) 24-bit realizations (% zero-bit error). (b) 1-bit realizations (bit error rate).

analysis through simulation, since our sets of Green's functions accurately capture and predict the received data. The results are shown in Figs. 18 and 19 where we observe each of the receivers' performance for this test.

It is clear from the figures [see Figs. 18(a) and 19(a)] that the 24-bit T/R receivers I and II outperform III and IV (client 2/client 1): T/R I (20%/30%), T/R II (22%/13%), T/R III (4%/4%), and T/R IV (2%/2%), which is somewhat expected, since focusing on transmit tends to eliminate extraneous noise due to the spatial filtering effect of the array. The results are quite different for the 1-bit designs as shown in Figs. 18(b) and 19(b). The 1-bit designs are *not* able to achieve 0-bit error as the 24-bit designs, since their performance is degraded due to the quantization errors and noise. We list the actual bit error rate performance (client 2/client 1): T/R I (0.015/0.001), T/R II 0.009/0.005, T/R III (0.019/0.003), and T/R IV (0.019/0.003). Although not as good as the 24-bit designs, the 1-bit receiver performance is satisfactory for such a highly reverberant environment. In any case the receivers perform quite reasonably in this hostile (simulated) environment. This completes the description of receiver performance, next we conclude our results and discuss our future work.

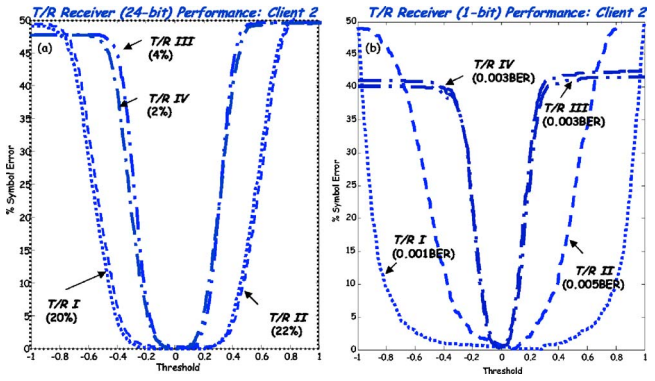

FIG. 19. (Color online) 1000 symbol code test on 24- and 1-bit realizations of T/R receivers for focusing at client station No. 2. (a) 24-bit realizations (% zero-bit error). (b) 1-bit realizations (bit error rate).

V. CONCLUSIONS

The feasibility of time-reversal (T/R) receiver designs for an acoustic array-to-point to array-to-multiple receiver's communication experiment in air is investigated in this paper. It is shown that the array enhances the transmitted information codes by providing spatial gain (diversity) at the receiver thereby increasing the overall SNR. Focusing using the host array also eliminates much of the extraneous spatial interference as well. The overall capability of the T/R communication system clearly outperformed the point-to-point designs reported on previously.[5]

Coupling the array to a 1-bit realization of the T/R receivers' results in some performance degradation, but the designs still performed quite reasonably in such a highly reverberant environment. The 1-bit T/R receiver design can have a large impact on cost-constrained applications especially at high frequencies (e.g., electromagnetic or ultrasonic cases).

Research continues to proceed in this area of high interest and new ideas, comparisons, performance evaluations for specific acoustic technical areas (e.g., underwater sound, room acoustics, etc.) are starting to evolve.[25–34] Even the more classical approaches to communications are beginning to appreciate the spatial diversity offered by multichannel communications systems where T/R will find its place when the environment becomes overly hostile. We plan to investigate wide bandwidth designs for future applications concentrating on tunnels and cave-like structures.[35,36]

ACKNOWLEDGMENTS

Dr. Farid Dowla of LLNL has provided timely advice and direction during the course of this research. This work was performed under the auspices of the U.S. Department of Energy contract by the Lawrence Livermore National Laboratory under Contract No. W-7405-Eng-48.

[1]J. G. Proakis, *Digital Communications* (McGraw-Hill, New York, 1995).
[2]S. Haykin, *Communication Systems* (Wiley, New York, 2001).
[3]M. Fink and C. Prada, "Acoustic time reversal mirrors," Inverse Probl. **17**, R1–R38 (2001).
[4]M. Fink, "Time reversal in acoustics," Contemp. Phys. **37**, 95–109 (1996).
[5]J. V. Candy, A. W. Meyer, A. J. Poggio, and B. L. Guidry, "Time-reversal processing for an acoustic communications experiment in a highly reverberant environment," J. Acoust. Soc. Am. **115**, 1621–1631 (2004).
[6]A. Parvulescu, "Matched-signal (MESS) processing by the ocean," J. Acoust. Soc. Am. **98**, 943–960 (1995).
[7]D. R. Jackson and D. R. Dowling, "Phase conjugation in underwater acoustics," J. Acoust. Soc. Am. **89**, 171–181 (1991).
[8]D. R. Dowling, "Acoustic pulse compression using passive phase-conjugate processing," J. Acoust. Soc. Am. **95**, 1450–1458 (1994).
[9]J.-P. Hermand and W. Roderick, "Acoustic model-based matched filter processing for fading time-dispersive ocean channels: Theory and experiment," IEEE J. Ocean. Eng. **18**, 447–465 (1993).
[10]R. K. Brienzo and W. S. Hodgkiss, "Broadband matched-field processing," J. Acoust. Soc. Am. **94**, 2821–2831 (1993).
[11]W. A. Kuperman, W. S. Hodgkiss, and H. C. Song, "Phase conjugation in the ocean: Experimental demonstration of an acoustic time-reversal mirror," J. Acoust. Soc. Am. **103**, 25–40 (1998).
[12]J.-P. Hermand, "Broad-band geoacoustic inversion in shallow water from waveguide impulse response measurements on a single hydrophone: Theory and experimental results," IEEE J. Ocean. Eng. **24**, 41–66 (1999).
[13]W. S. Hodgkiss, H. C. Song, W. A. Kuperman, T. Akal, C. Ferla, and D. R. Jackson, "A long range and variable focus phase-conjugation experiment in shallow water," J. Acoust. Soc. Am. **105**, 1597–1604 (1999).
[14]G. Edelmann, T. Akal, W. S. Hodgkiss, S. Kim, W. A. Kuperman, and H. C. Song, "An initial demonstration of underwater acoustic communication using time reversal," IEEE J. Ocean. Eng. **27**, 602–609 (2002).
[15]D. Rouseff, D. R. Jackson, W. L. Fox, C. D. Jones, J. A. Ritcey, and D. R. Dowling, "Underwater acoustic communication by passive-phase conjugation: Theory and experiment," IEEE J. Ocean. Eng. **26**, 821–831 (2001).
[16]S. Yon, M. Tanter, and M. Fink, "Sound focusing in rooms: The time-reversal approach," J. Acoust. Soc. Am. **113**, 1533–1543 (2003).
[17]K. B. Smith, A. M. Abrantes, and A. Larraza, "Examination of time-reversal acoustics in shallow water and applications to noncoherent underwater communications," J. Acoust. Soc. Am. **113**, 3095–3110 (2003).
[18]M. Heinemann, A. Larraza, and K. B. Smith, "Experimental studies of applications of time-reversal acoustics to noncoherent underwater communications," J. Acoust. Soc. Am. **113**, 3111–3116 (2003).
[19]A. Derode, A. Tourin, and M. Fink, "Ultrasonic pulse compression with one-bit time reversal through multiple scattering," J. Appl. Phys. **85**, 6343–6352 (1999).
[20]D. H. Chambers, J. V. Candy, S. K. Lehman, J. S. Kallman, A. J. Poggio, and A. W. Meyer, "Time-reversal and the spatio-temporal matched-filter," J. Acoust. Soc. Am. **116**, 1348–1350 (2004).
[21]D. H. Johnson and D. E. Dudgeon, *Array Signal Processing: Concepts and Techniques* (Prentice-Hall, Englewood Cliffs, NJ, 1993).
[22]J. V. Candy, *Model-Based Signal Processing* (Wiley/IEEE Press, Hoboken, NJ, 2005).
[23]P. H. Siegel, "Terahertz technology," IEEE Trans. Microwave Theory Tech. **50**(3), 910–928 (2002).
[24]H. L. Van Trees, *Detection, Estimation, and Modulation Theory* (Wiley, New York, 1968).
[25]T. C. Yang, "Performance comparisons between passive-phase conjugation and decision-feedback equalizer for underwater acoustic communications," J. Acoust. Soc. Am. **115**, 2505 (2004).
[26]T. Folégot, J. de Rosny, C. Prada, and M. Fink, "Adaptive instant record signals applied to shallow water detection," J. Acoust. Soc. Am. **115**, 2468 (2004).
[27]T. Folegot, P. Roux, W. A. Kuperman, W. S. Hodgkiss, H. C. Song, T. Akal, and M. Stevenson, "Using acoustic orthogonal signals in shallow water time-reversal applications," J. Acoust. Soc. Am. **115**, 2468 (2004).
[28]H. Song, W. S. Hodgkiss, W. A. Kuperman, P. Roux, T. Akal, and M. Stevenson, "Simultaneously multiple-depth coherent communications using time reversal," J. Acoust. Soc. Am. **115**, 2467 (2004).
[29]G. Papanicolaou, "Remote sensing and communications in random media," J. Acoust. Soc. Am. **113**, 2212 (2003).
[30]G. F. Edelmann, S. Kim, W. S. Hodgkiss, W. A. Kuperman, H. C. Song, and T. Akal, "Combining and comparing time reversal processing and adaptive channel equalization for communication sequences," J. Acoust. Soc. Am. **112**, 2447 (2002).
[31]J. A. Root and P. H. Rogers, "Performance of an underwater acoustic volume array using time-reversal focusing," J. Acoust. Soc. Am. **112**, 1869 (2002).
[32]M. Tanter, J.-L. Thomas, and M. Fink, "Time-reversal and the inverse filter," J. Acoust. Soc. Am. **108**, 223–234 (2000).
[33]P. Blomgren and G. Papanicolaou, "Super-resolution in time-reversal acoustics," J. Acoust. Soc. Am. **111**, 230–248 (2002).
[34]A. Derode, A. Tourin, J. de Rosny, M. Tanter, S. Yon, and M. Fink, "Taking advantage of multiple scattering to communicate with time-reversal antenna," Phys. Rev. Lett. **90**, 014301-1–014301-4 (2003).
[35]A. F. Naguib, N. Seshadri, and A. R. Calderbank, "Space-time coding and signal processing for high data rate wireless communications," IEEE Signal Process. Mag. **17**, 76–92 (2000).
[36]A. J. Paulraj and C. B. Papadias, "Space-time processing for wireless communications," IEEE Signal Process. Mag. **14**, 49–83 (1997).

Source visualization by using statistically optimized near-field acoustical holography in cylindrical coordinates

Yong Thung Cho[a] and J. Stuart Bolton
Ray W. Herrick Laboratories, School of Mechanical Engineering, Purdue University, 140 South Intramural Drive, West Lafayette, Indiana 47907-2031

Jørgen Hald
Brüel & Kjær Sound & Vibration Measurement A/S, Skodsborgvej 307, DK-2850 Nærum, Denmark

(Received 2 November 2004; revised 7 July 2005; accepted 26 July 2005)

Nearfield acoustical holography (NAH) is a useful tool for visualizing noise sources. However, to avoid spatial Fourier transform-related truncation effects, the measurement, or hologram, surface must extend beyond the source to a region where the sound pressure drops to a level significantly lower than the peak level within the measurement aperture. Statistically optimized nearfield acoustical holography (SONAH), first derived by Steiner and Hald in planar geometry, is based on a formulation similar to that of NAH. However, in SONAH, surface-to-surface projection of the sound field is performed by using a transfer matrix defined in such a way that all propagating waves and a weighted set of evanescent waves are projected with optimal average accuracy: i.e., no spatial Fourier transforms are performed. Thus the requirement that the measurement surface be extended is eliminated without compromising the accuracy of the procedure. In the present work, SONAH was re-formulated in cylindrical coordinates and was applied to the measurement of the sound field radiated by a refrigeration compressor. It was found that it is possible to visualize source regions accurately by using SONAH while using fewer measurement positions than would be required to achieve a similar level of accuracy when using conventional NAH procedures. © *2005 Acoustical Society of America.* [DOI: 10.1121/1.2036252]

PACS number(s): 43.60.Sx [EGW] Pages: 2355–2364

I. INTRODUCTION

Near-field acoustical holography (NAH) is a useful tool for visualizing noise sources and their associated sound fields since it allows sound fields that are measured on a two-dimensional surface to be projected throughout a three-dimensional space. However, to avoid spatial Fourier transform-related truncation effects, the measurement aperture (i.e., the hologram surface) must typically extend well beyond the source to a region where the sound pressure level drops to a level significantly lower than the peak level within the measurement aperture. If it is not possible to extend the measurement surface into the region where the sound pressure drops to sufficiently low levels, owing to physical obstructions, for example, it is impossible to perform accurate backprojections by using NAH.

Statistically optimized near-field acoustical holography (SONAH), derived in a planar formulation by Steiner and Hald,[1] and subsequently, following a simpler approach by Hald,[2] was developed to accommodate situations in which the measurement aperture size was limited either by physical necessity or as a way of reducing the measurement cost. In the SONAH procedure, the surface-to-surface projection of the sound field is performed by using a transfer or mapping matrix, defined in such a way that all propagating waves and a weighted set of evanescent waves are projected with optimal average accuracy. No spatial Fourier transforms are performed. In this way, the requirement that the measurement surface extend well beyond the source region can be eliminated without necessarily compromising the accuracy of the procedure. The SONAH process may therefore be viewed as an alternative to the sound field extrapolation procedure suggested by Saijyou and Yoshikawa[3,4] and further elaborated by Williams.[5,6]

The present procedure is superficially similar to the Helmholtz equation least squares (HELS) method for reconstructing acoustic pressure fields, as proposed by Wang and Wu,[7,8] in that both procedures make use of orthogonal expansions that satisfy the wave equation: in the present case, the expansions are in terms of cylindrical wave functions while spherical wave function expansions are used in HELS. However, the two procedures are significantly different in philosophy and practice. In HELS, the measured pressure on the hologram surface is expressed as a linear combination of spherical waves that are particular solutions of the Helmholtz equation.[9] In that sense, HELS is similar to the spherical holography procedure suggested by Weinreich and Arnold[10] and Maynard *et al.*,[11] except that the spherical harmonic coefficients are found by using a least square solution instead of exploiting the orthogonality of the spherical harmonics over a spherical hologram surface. As a result, in HELS, the hologram surface need not be spherical, and thus can accommodate arbitrarily shaped sources. In HELS, the sound field projection is then performed by evaluating the spherical harmonic expansion at different locations. Note, in particular, that the number of terms included in the spherical harmonic

[a]Corresponding author. Electronic mail: choy@purdue.edu

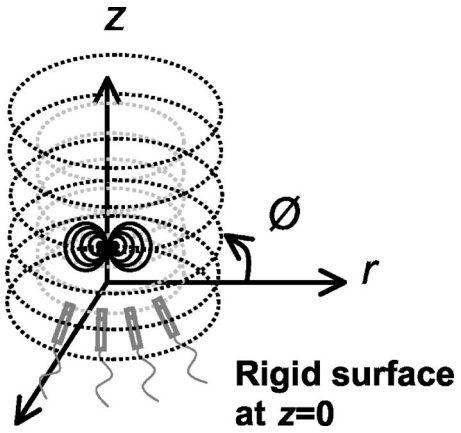

FIG. 1. Cylindrical geometry definition.

expansion must be less than or equal to the number of pressure measurements on the hologram surface. SONAH differs from HELS in that the sound field projection is performed by using a transfer matrix that is optimized for an assumed source characteristic, and that is thus not data dependent. The advantage of the latter approach is that the transfer matrix may be evaluated to an arbitrary degree of precision since the number of terms that can be used in the wave function expansion is not limited by the number of measured data points. Thus, the main difference between HELS and SONAH is that HELS provides an optimal representation of the pressure on the hologram surface (as a function of assumed origin location and number of terms in the spherical harmonic expansion), but not necessarily anywhere else. In contrast, SONAH is based on performing a non-data-dependent projection that is optimal for a particular type of source.

In the present work, the procedure used by Hald[2] to formulate SONAH in planar coordinates was repeated in cylindrical coordinates. The new formulation was then applied to both simulated and measured data (in particular, the sound field radiated by a cylindrical refrigeration compressor). A comparison with results obtained by using conventional NAH in cylindrical coordinates suggests that the new procedure is accurate and, owing to mathematical features of the cylindrical application, relatively fast.

II. SONAH PROCEDURES IN CYLINDRICAL COORDINATES

In this section, a reformulation of SONAH in cylindrical coordinates is presented. The procedures outlined here follow Hald's derivation[2] closely, except for the change in the coordinate system. To begin with, the sound pressure on a cylindrical surface of radius r can be expressed as

$$p(r,\phi,z) = \sum_{m=-\infty}^{m=\infty} \frac{1}{2\pi} \int_{-\infty}^{\infty} P_m(r,k_z) e^{im\phi} e^{ik_z z} dk_z, \tag{1}$$

where $P_m(r,k_z)$ is the cylindrical wave number spectrum of $p_m(r,\phi,z)$, the mth circumferential component of the sound field (see Fig. 1 for the definition of the problem geometry)[12,13] and k_z is the axial component of the wave number. The wave number spectrum at radius r can also be expressed in terms of the wave number spectrum of the sound field on a cylindrical source surface of radius r_s that encloses the source by using a propagator expressed in terms of Hankel functions, i.e.,

$$P_m(r,k_z) = \frac{H_m^{(1)}(k_r r)}{H_m^{(1)}(k_r r_s)} P_m(r_s,k_z), \tag{2}$$

where $H_m^{(1)}$ is the mth-order Hankel function and the radial wave number is

$$k_r = \begin{cases} \sqrt{k^2 - k_z^2}, & \text{for } |k| \geqslant |k_z|, \\ i\sqrt{k_z^2 - k^2}, & \text{for } |k| < |k_z|, \end{cases} \tag{3}$$

with $k=\omega/c$, ω being the angular frequency and c the ambient sound speed. The spatial distribution of the sound pressure at radius r can then be found by inverse transforming the projected wave number spectrum at r, i.e.,

$$p(r,\phi,z) = \sum_{m=-\infty}^{m=\infty} \frac{1}{2\pi} \int_{-\infty}^{\infty} \frac{H_m^{(1)}(k_r r)}{H_m^{(1)}(k_r r_s)} P_m(r_s,k_z) e^{im\phi} e^{ik_z z} dk_z. \tag{4}$$

Now define a three-dimensional cylindrical wave function, $\Phi_{k_z,m}(r,\phi,z)$, as

$$\Phi_{k_z,m}(\mathbf{r}) = \Phi_{k_z,m}(r,\phi,z) \equiv \frac{H_m^{(1)}(k_r r)}{H_m^{(1)}(k_r r_s)} e^{im\phi} e^{ik_z z}, \quad r \geqslant r_s. \tag{5}$$

Note that the wave function amplitudes are equal to unity at all locations on the source surface, $r=r_s$, since in that case the Hankel functions in the numerator and denominator are equal. The wave function, $\Phi_{k_z,m}(r,\phi,z)$, decays approximately as $1/\sqrt{r}$ for $k_z<k$, $k_r r>m$, but much faster otherwise, and consequently the higher-order functions (i.e., those with larger values of m or larger values of k_z) become progressively less significant as r increases. To illustrate the latter point, the ratio of the wave functions, $\Phi_{k_z,m}(r,\phi,z)/\Phi_{k_z,m}(r_s,\phi,z)$ at 1000 Hz, is plotted in terms of m and k_z in Fig. 2, where the assumed source radius is $r_s=5.7$ cm, and the radius, r, is either 9 or 14.15 cm (note that these parameters are relevant to the measurements discussed in Sec. III B). In Fig. 2, a sharp transition from propagating to nonpropagating waves is visible at approximately $k_z=18.3\ \mathrm{m}^{-1}$, as is the continuous decrease with increasing m. Finally, note that the rate of decrease with both k_z and m increases when r is increased from 9 to 14.15 cm.

The sound pressure at radius r can then be expressed in an alternative form, i.e., in terms of the wave number spectrum, $P_m(r_s,k_z)$, on the cylindrical source surface, and the wave functions, $\Phi_{k_z,m}(r,\phi,z)$, the result being identical to Eq. (4) except for notation: i.e.,

$$p(\mathbf{r}) = \frac{1}{2\pi} \sum_{m=-\infty}^{m=\infty} \int_{-\infty}^{\infty} P_m(r_s,k_z) \Phi_{k_z,m}(\mathrm{r}) dk_z. \tag{6}$$

When $\mathbf{r}_h$ is used to represent positions on the measurement (or hologram) surface at $r=r_h>r_s$, an expression is obtained for the pressure on the hologram surface, i.e.,

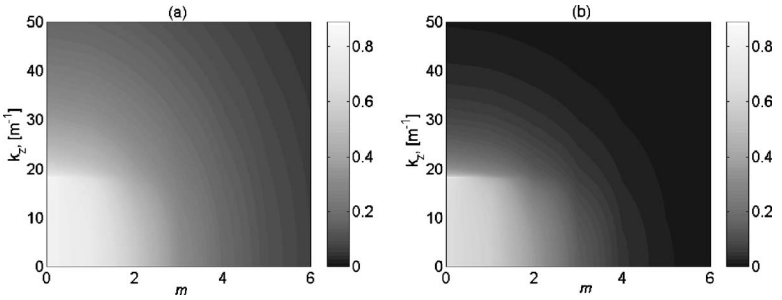

FIG. 2. Ratio of wave functions, $\Phi_{k_z,m}(\mathbf{r})/\Phi_{k_z,m}(\mathbf{r}_s)$, at 1000 Hz: (a) $r=9$ cm, $r_s=5.7$ cm (b) $r=14.15$ cm, $r_s=5.7$ cm.

$$p(\mathbf{r}_h)=\frac{1}{2\pi}\sum_{m=-\infty}^{m=\infty}\int_{-\infty}^{\infty}P_m(r_s,k_z)\Phi_{k_z,m}(\mathbf{r}_h)dk_z. \tag{7}$$

Assume now that the complex sound pressure $p(\mathbf{r}_{h,j})$ has been measured at J positions, $\mathbf{r}_{h,j}\equiv(r_h,\phi_j,z_j)$, on the hologram surface. It is then desired to estimate the pressure $p(\mathbf{r})$ at an arbitrary position $\mathbf{r}\equiv(r,\phi,z)$ in the source-free, region $r>r_s$, as a linear combination of the measured sound pressure data, $p(\mathbf{r}_{h,j})$, i.e.,

$$p(\mathbf{r})\approx\sum_{j=1}^{J}c_j(\mathbf{r})\cdot p(\mathbf{r}_{h,j}). \tag{8}$$

It is required here that the coefficients, $c_j(\mathbf{r})$, that appear in the latter linear prediction formula be independent of the particular sound field, but they are allowed to depend on the reconstruction position $\mathbf{r}$. Note that conventional cylindrical NAH can, if desired, also be posed as a linear prediction problem in the same form as Eq. (8), since a projection is created by performing a series of linear operations on the measured data. Since Eq. (8) holds for all sound fields, it must also hold for the cylindrical wave functions, $\Phi_{k_z,m}(\mathbf{r})$, themselves, i.e.,

$$\Phi_{k_z,m}(\mathbf{r})\approx\sum_{j=1}^{J}c_j(\mathbf{r})\Phi_{k_z,m}(\mathbf{r}_{h,j}). \tag{9}$$

Alternatively, it can be said that if Eq. (9) holds for all the cylindrical wave functions $\Phi_{k_z,m}(\mathbf{r})$, then it holds for any sound pressure field $p(\mathbf{r})$ created by sources within the source cylinder with radius r_s and wave number spectrum, $P_m(r_s,k_z)$, on the cylindrical source surface, i.e.,

$$\begin{aligned}p(\mathbf{r})&=\frac{1}{2\pi}\sum_{m=-\infty}^{m=\infty}\int_{-\infty}^{\infty}P_m(r_s,k_z)\Phi_{k_z,m}(\mathbf{r})dk_z\\&\approx\frac{1}{2\pi}\sum_{m=-\infty}^{m=\infty}\int_{-\infty}^{\infty}P_m(r_s,k_z)\sum_{j=1}^{J}c_j(\mathbf{r})\Phi_{k_z,m}(\mathbf{r}_{h,j})dk_z\\&=\sum_{j=1}^{J}c_j(\mathbf{r})\frac{1}{2\pi}\sum_{m=-\infty}^{m=\infty}\int_{-\infty}^{\infty}P_m(r_s,k_z)\Phi_{k_z,m}(\mathbf{r}_{h,j})dk_z\\&=\sum_{j=1}^{J}c_j(\mathbf{r})p(\mathbf{r}_{h,j}).\end{aligned} \tag{10}$$

Here, use has been made of Eqs. (6), (7), and (9).

Thus, in order to determine the coefficients c_j, we first require Eq. (9) to provide a good estimate for a finite subset of the cylindrical wave functions $\Phi_{k_z,m}(\mathbf{r})$, i.e.,

$$\Phi_{k_{zq},m}(\mathbf{r})\approx\sum_{j=1}^{J}c_j(\mathbf{r})\Phi_{k_{zq},m}(\mathbf{r}_{h,j}),\quad m=1\ldots M,\quad q=1\ldots N. \tag{11}$$

The solution of the latter set of MN linear equations for the J coefficients in a least squares sense means that we obtain an estimator [i.e., Eq. (8)] that is optimal for sound fields containing only the above subset of cylindrical wave functions, with approximately equal weight given to each of the functions. Since all of the functions have amplitudes equal to unity on the cylindrical source surface, the estimator is optimized for wave number spectra, $P_m(r_s,k_z)$, that are "white" on the source cylinder $r=r_s$. Since the amplitudes of high axial wave number and high circumferential order components are then attenuated on the hologram surface with respect to their value on the source surface, the equations corresponding to these components will be given a smaller weight in a (regularized) least squares solution of Eq. (11) for the coefficients c_j. The values of one of the evanescent cylindrical wave functions across the measurement positions will constitute a row in the matrix equation to be solved. If the values in that row are very small, and if the least squares solution is performed, for example, by using a singular value decomposition of the matrix, then the filtering of the singular values (performed for the purpose of regularization) will suppress the influence of the small-amplitude evanescent wave functions on the coefficients c_j. A more severe regularization will suppress the influence of a correspondingly larger subset of the evanescent wave components.

Before proceeding, it is convenient to rewrite the various quantities involved in the latter calculation in the form of matrices and vectors. Here we define

$$\mathbf{A}\equiv[\Phi_{k_{zq},m}(\mathbf{r}_{h,j})], \tag{12a}$$

$$\boldsymbol{\alpha}(\mathbf{r})\equiv[\Phi_{k_{zq},m}(\mathbf{r})], \tag{12b}$$

$$\mathbf{c}(\mathbf{r})\equiv[c_j(\mathbf{r})]. \tag{12c}$$

Equation (11) can then be rewritten in compact form as

$$\boldsymbol{\alpha}(\mathbf{r})\approx\mathbf{A}\,\mathbf{c}(\mathbf{r}). \tag{13}$$

The optimal (i.e., the regularized least squares) solution for the weight vector, $\mathbf{c}(\mathbf{r})$, is then

$$\mathbf{c}(\mathbf{r})=(\mathbf{A}^{\mathrm{H}}\mathbf{A}+\theta^2\mathbf{I})^{-1}\mathbf{A}^{\mathrm{H}}\boldsymbol{\alpha}(\mathbf{r}), \tag{14}$$

where the superscript $^{\mathrm{H}}$ denotes the Hermitian or conjugate transpose, $\mathbf{I}$ is the identity matrix, and the regularization

parameter, θ, is, in accordance with Ref. 2, chosen to be

$$\theta^2 = [\mathbf{A}^{\mathrm{H}}\mathbf{A}]_{ii} 10^{-\mathrm{SNR}/10}, \tag{15}$$

where SNR, the signal-to-noise ratio, has been expressed in decibel form. The subscript *ii* is used here to denote the diagonal elements of a matrix, which are all equal in this case.

The regularization expressed by Eq. (15) is necessary since the matrix $\mathbf{A}^{\mathrm{H}}\mathbf{A}$ will, particularly at low frequencies, be badly conditioned since, typically, the number of measurement points exceeds (and often far exceeds) the number of significant cylindrical wave functions that are linearly independent across the measurement positions. At low frequencies only wave functions $\Phi_{k_z,m}(\mathbf{r})$ of low-order m and with small axial wave number k_z would normally have a significant amplitude on the hologram surface, $r=r_h$.

The reconstructed pressure, $p(\mathbf{r})$, can finally be expressed as

$$p(\mathbf{r}) \approx \sum_{j=1}^{J} c_j(\mathbf{r}) p(\mathbf{r}_{h,j}) = \mathbf{p}^{\mathrm{T}}(\mathbf{r}_h)\mathbf{c}(\mathbf{r}) = \mathbf{p}^{\mathrm{T}}(\mathbf{r}_h)(\mathbf{A}^{\mathrm{H}}\mathbf{A} + \theta^2\mathbf{I})^{-1}\mathbf{A}^{\mathrm{H}}\boldsymbol{\alpha}(\mathbf{r}), \tag{16}$$

where $\mathbf{p}(\mathbf{r}_h)$ is the vector of measured pressures, and the terms following $\mathbf{p}^{\mathrm{T}}(\mathbf{r}_h)$ transfer, or map, the measured hologram pressure to the reconstruction surface.

The radial particle velocity on the reconstruction surface, $u_r(\mathbf{r})$, can be found by using Euler's equation, i.e.,

$$u_r(\mathbf{r}) = \frac{1}{i\rho_0\omega}\frac{\partial p(\mathbf{r})}{\partial r}. \tag{17}$$

By substituting the estimated spatial distribution of the sound pressure from Eq. (16) into Eq. (17), the radial particle velocity, $u_r(\mathbf{r})$, is obtained as

$$u_r(\mathbf{r}) \approx \frac{1}{i\rho_0\omega}\frac{\partial}{\partial r}[\mathbf{p}^{\mathrm{T}}(\mathbf{r}_h)(\mathbf{A}^{\mathrm{H}}\mathbf{A} + \theta^2\mathbf{I})^{-1}\mathbf{A}^{\mathrm{H}}\boldsymbol{\alpha}(\mathbf{r})] = \mathbf{p}^{\mathrm{T}}(\mathbf{r}_h) \times (\mathbf{A}^{\mathrm{H}}\mathbf{A} + \theta^2\mathbf{I})^{-1}\mathbf{A}^{\mathrm{H}}\boldsymbol{\beta}(\mathbf{r}) \tag{18}$$

where the vector $\boldsymbol{\beta}(\mathbf{r})$ is defined as

$$\boldsymbol{\beta}(\mathbf{r}) \equiv \frac{1}{i\rho_0\omega}\frac{\partial \boldsymbol{\alpha}(\mathbf{r})}{\partial r} = \left[\frac{1}{i\rho_0\omega}\frac{\partial}{\partial r}\Phi_{k_{zq},m}(\mathbf{r})\right]. \tag{19}$$

The elements of $\boldsymbol{\beta}(\mathbf{r})$ are modified cylindrical wave functions, which, by use of Eq. (5), can be expressed as

$$\Phi^{u}_{k_{zq},m}(r,\phi,z) \equiv \frac{-ik_r}{\rho_0\omega}\frac{H_m^{(1)\prime}(k_r r)}{H_m^{(1)}(k_r r_s)} e^{im\phi} e^{ik_{zq}z}, \tag{20}$$

where the superscript prime denotes differentiation with respect to the function's argument and ρ_0 is the ambient density. The vector $\boldsymbol{\beta}(\mathbf{r})$ can then be written simply as

$$\boldsymbol{\beta}(\mathbf{r}) \equiv [\Phi^{u}_{k_{zq},m}(\mathbf{r})]. \tag{21}$$

To obtain the pressure, $p(\mathbf{r})$, and the particle velocity, $u_r(\mathbf{r})$, the matrix $\mathbf{A}^{\mathrm{H}}\mathbf{A}$ and the vectors $\mathbf{A}^{\mathrm{H}}\boldsymbol{\alpha}$ and $\mathbf{A}^{\mathrm{H}}\boldsymbol{\beta}$ must all be estimated. They can be written in expanded form as

$$[\mathbf{A}^{\mathrm{H}}\mathbf{A}]_{ji} = \sum_{m=-\infty}^{\infty}\sum_{q=-\infty}^{\infty} \Phi^{*}_{k_{zq},m}(\mathbf{r}_{h,j})\Phi_{k_{zq},m}(\mathbf{r}_{h,i}) = \sum_{m=-\infty}^{\infty}\sum_{q=-\infty}^{\infty} \left|\frac{H_m^{(1)}(k_r r_h)}{H_m^{(1)}(k_r r_s)}\right|^2 e^{i(m(\phi_{h,i}-\phi_{h,j})+k_{zq}(z_{h,i}-z_{h,j}))}, \tag{22}$$

$$[\mathbf{A}^{\mathrm{H}}\boldsymbol{\alpha}]_j = \sum_{m=-\infty}^{\infty}\sum_{q=-\infty}^{\infty} \Phi^{*}_{k_{zq},m}(\mathbf{r}_{h,j})\Phi_{k_{zq},m}(\mathbf{r}) = \sum_{m=-\infty}^{\infty}\sum_{q=-\infty}^{\infty} \frac{H_m^{(1)^*}(k_r r_h)H_m^{(1)}(k_r r)}{|H_m^{(1)}(k_r r_s)|^2} e^{i(m(\phi-\phi_{h,j})+k_{zq}(z-z_{h,j}))}, \tag{23}$$

$$[\mathbf{A}^{\mathrm{H}}\boldsymbol{\beta}]_j = \sum_{m=-\infty}^{\infty}\sum_{q=-\infty}^{\infty} \Phi^{*}_{k_{zq},m}(\mathbf{r}_{h,j})\Phi^{u}_{k_{zq},m}(\mathbf{r}) = \sum_{m=-\infty}^{\infty}\sum_{q=-\infty}^{\infty} \frac{-ik_r}{\rho_o\omega}\frac{H_m^{(1)^*}(k_r r_h)H_m^{(1)\prime}(k_r r)}{|H_m^{(1)}(k_r r_s)|^2} \times e^{i(m(\phi-\phi_{h,j})+k_{zq}(z-z_{h,j}))}. \tag{24}$$

In Eqs. (22)–(24), * denotes the complex conjugate, and the radial wave number, k_r, is given by Eq. (3) with the axial wave number, k_z, being equal to k_{zq}, defined as

$$k_{zq} = q \cdot \Delta k_z. \tag{25}$$

In a computer implementation, the infinite summations in Eqs. (22)–(24) must, of course, be truncated. For large values of $|m|$ and for large values of $|q|$, the corresponding terms in the summations decay in such a way that the degree of truncation does not have a critical impact on the accuracy of the procedure, but is required simply to minimize the computational effort. If desired, the maximum values of m and k_{zq}, i.e., m_{max} and $k_{zq,max}$, to be included in the various summations can be estimated by assuming that the measured pressure is a superposition of a signal linearly related to the source radiation and random noise (in practice, spatial noise resulting, for example, from slight mispositioning of the field microphones during a measurement or from slight source level variations from scan to scan[14]). The effect of the noise component is to create a "noise floor" in the wave number domain that extends into the high wave number region associated with evanescent field components. At sufficiently high wave numbers and orders, the level of the noise floor will exceed the amplitude of the signal linearly related to the source, since the latter high wave number components decay very rapidly while propagating from the source to the hologram surface. The summations can be truncated at the point where the noise floor begins to dominate, since there is no benefit in attempting to reconstruct higher wave numbers and orders. By truncating the summations, the linear prediction coefficients, c_j, are not required to reconstruct the higher wave number components. If those terms *are* included, the latter requirement is added, but with a very small weighting, since the wave functions have a very small amplitude on the hologram surface: see Eqs. (22)–(24). Because of the small

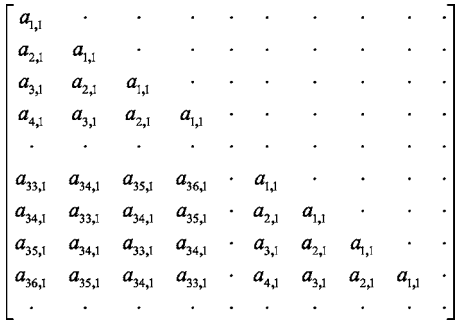

FIG. 3. Square matrices in Eqs. (22)–(24) are symmetric and only the first column is unique.

weight, the higher wave number components will correspond to small-amplitude singular values of the matrix $\mathbf{A}^{\mathrm{H}}\mathbf{A}$, and therefore they will be suppressed by an appropriate choice of the regularization parameter, θ, that appears in Eqs. (14) and (15).

So far, only the estimation of the pressure and the radial particle velocity at a single position, $\mathbf{r}$, has been considered: in that case the matrices $\boldsymbol{\alpha}(\mathbf{r})$ and $\boldsymbol{\beta}(\mathbf{r})$ (and therefore $\mathbf{A}^{\mathrm{H}}\boldsymbol{\alpha}$ and $\mathbf{A}^{\mathrm{H}}\boldsymbol{\beta}$) consist of a single column. In a typical measurement, however, measurement and reconstruction points cover the same regular grid in the (ϕ,z) domain, only at different radii, r_h and r, respectively. In that case a column is added for each calculation position, implying that $\mathbf{A}^{\mathrm{H}}\mathbf{A}, \mathbf{A}^{\mathrm{H}}\boldsymbol{\alpha}$, and $\mathbf{A}^{\mathrm{H}}\boldsymbol{\beta}$ all become $N_\Phi N_z$ by $N_\Phi N_z$ square matrices, where N_Φ and N_z are the number of measurements in the circumferential and axial directions, respectively. The number of matrix elements, and the time required to form these matrices, increases rapidly as the number of measurements increases. However, owing to the properties of the cylindrical functions, very few elements of those matrices are unique: the structure of the matrices is illustrated in Fig. 3. They have a symmetric square structure, with only a single unique column, that consists of submatrices having the form of nonsymmetric Toeplitz matrices. By avoiding repeated calculation, those matrices can be created by the calculation of approximately $N_\Phi N_z$ elements instead of $(N_\Phi N_z)^2$ elements: this feature results in a dramatic reduction of calculation time when the number of measurements is large.

If the signal-to-noise ratio of the measured pressure is known, the regularization parameter, θ, can be calculated using Eq. (15), and Eq. (16) then allows a calculation of the coefficient matrix relating the measured and projected pressures. Alternatively, regularization can be performed by using improved Tikhonov regularization in combination with Generalized Cross Validation (GCV) or the Morozov Discrepancy Principle (MDP) to identify optimal regularization parameters.[15,16] From Eq. (18), the particle velocity on the source surface, for example, can be expressed in terms of the measured pressure on the hologram as

$$\mathbf{u}_r^{\mathrm{T}}(\mathbf{r}_s) = \mathbf{p}^{\mathrm{T}}(\mathbf{r}_h)\mathbf{R}_{\mathbf{A}^{\mathrm{H}}\mathbf{A}}\mathbf{A}^{\mathrm{H}}\boldsymbol{\beta}(\mathbf{r}_s), \tag{26}$$

where $\mathbf{R}_{\mathbf{A}^{\mathrm{H}}\mathbf{A}}$ is the regularized inverse of $\mathbf{A}^{\mathrm{H}}\mathbf{A}$. Because the matrices $\mathbf{A}^{\mathrm{H}}\mathbf{A}$ and $\mathbf{A}^{\mathrm{H}}\boldsymbol{\beta}$ are both symmetric, the vector Eq. (26) can be transposed to obtain

$$\mathbf{u}_r(\mathbf{r}_s) = (\mathbf{A}^{\mathrm{H}}\boldsymbol{\beta}(\mathbf{r}_s))\mathbf{R}_{\mathbf{A}^{\mathrm{H}}\mathbf{A}}\mathbf{p}(\mathbf{r}_h), \tag{27}$$

which is a more standard column matrix/vector representation of the quantities involved. Equation (27) can be expressed in alternative form by using the auxiliary variable vector, $\mathbf{q}$, and the regularized solution of the system

$$\mathbf{p}(\mathbf{r}_h) = (\mathbf{A}^{\mathrm{H}}\mathbf{A})\mathbf{q}, \tag{28}$$

$$\mathbf{u}_r(\mathbf{r}_s) = (\mathbf{A}^{\mathrm{H}}\boldsymbol{\beta}(\mathbf{r}_s))\mathbf{q}. \tag{29}$$

By comparing Eqs. (16) and (18), the pressure on the source surface is

$$\mathbf{p}(\mathbf{r}_s) = (\mathbf{A}^{\mathrm{H}}\boldsymbol{\alpha}(\mathbf{r}_s))\mathbf{q}. \tag{30}$$

The regularization of Eq. (28) can be implemented directly, following the formulation in Ref. 16, by making use of the fact that the system matrix, $\mathbf{A}^{\mathrm{H}}\mathbf{A}$, is Hermitian (conjugate symmetric). Even though the matrix multiplication in Eqs. (29) and (30) might remove some noise components that were amplified in Eq. (28) because of under-regularization, nothing is gained by allowing such under-regularization. After performing a symmetric singular value decomposition of the conjugate symmetric matrix $\mathbf{A}^{\mathrm{H}}\mathbf{A}$, i.e.,

$$\mathbf{A}^{\mathrm{H}}\mathbf{A} \equiv \mathbf{V}\mathbf{G}\mathbf{V}^{\mathrm{H}}, \tag{31}$$

the regularized inverse of $\mathbf{A}^{\mathrm{H}}\mathbf{A}$ is found to be[16]

$$\mathbf{R}_{\mathbf{A}^{\mathrm{H}}\mathbf{A}} = \mathbf{V}(\alpha(\mathbf{F}_1^\alpha)^2 + \mathbf{G}^{\mathrm{H}}\mathbf{G})^{-1}\mathbf{G}^{\mathrm{H}}\mathbf{V}^{\mathrm{H}}, \tag{32}$$

where the high pass filter (operating on the singular values) $\mathbf{F}_1^\alpha$ is

$$\mathbf{F}_1^\alpha = \mathrm{diag}\left\{\cdots, \alpha \Big/ \left[\alpha + |\lambda_i|^2\left(\frac{\alpha + |\lambda_i|^2}{\alpha}\right)^2\right], \cdots\right\}, \tag{33}$$

and where the λ_i's are the diagonal elements of $\mathbf{G}$. The regularization parameter, α, can be found, for example, by using GCV, which minimizes the function $J(\alpha)$,

$$J(\alpha) \equiv \frac{\|\mathbf{F}_1^\alpha\mathbf{V}^{\mathrm{H}}\mathbf{p}(\mathbf{r}_h)\|^2}{[\mathrm{trace}(\mathbf{F}_1^\alpha)]^2}. \tag{34}$$

Alternatively, the MDP can be used to determine the regularization parameter α so that the energy removed by the high pass filtering (found by multiplying the matrix $\mathbf{F}_1^\alpha\mathbf{V}^{\mathrm{H}}$ by the vector of measured pressure) is equal to the noise energy in the measured pressure signals, i.e.,

$$\|\mathbf{F}_1^\alpha\mathbf{V}^{\mathrm{H}}\mathbf{p}(\mathbf{r}_h)\|^2 = \varepsilon\|\mathbf{V}^{\mathrm{H}}\mathbf{p}(\mathbf{r}_h)\|^2 = \varepsilon\|\mathbf{p}(\mathbf{r}_h)\|^2, \tag{35}$$

where ε is the ratio of the noise energy to the entire energy of the measured pressure on the hologram.

III. IMPLEMENTATION OF SONAH PROCEDURES

A. Double dipole simulation

To test the accuracy of the SONAH procedure, a double-dipole simulation was performed, and the backprojections of the sound pressure and particle velocity calculated by using SONAH were compared with both direct "measurements" (i.e., the simulated data) and conventional NAH results. The simulated sound pressure field was created by superposing the fields of two coherent dipoles of equal strength, whose

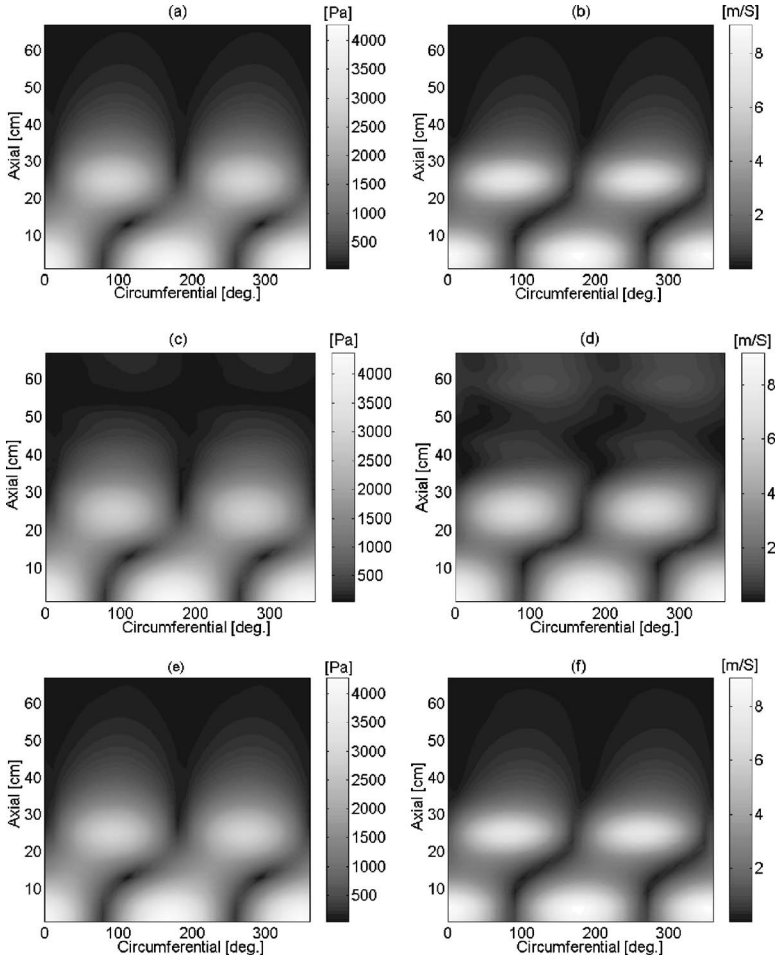

FIG. 4. Backprojected pressure and particle velocity for the double-dipole at $r=0.09$ m, 1000 Hz, $N_z=34$: (a) directly measured p; (b) directly measured u_r; (c) backprojected p(NAH); (d) backprojected u_r(NAH); (e) backprojected p(SONAH); (f) backprojected u_r(SONAH).

axes were aligned in the x and y directions. The simulation was performed at a frequency of 1000 Hz. The dipoles were located 5 and 25 cm above the coordinate origin in the z direction; a rigid boundary surface was placed at $z=0$ (see Fig. 1). Images of the sources were used to represent the effect of the rigid boundary: that is, the effective size of the hologram in the axial direction was doubled. The details of the simulation were as follows: radius of hologram, $r_h=14.15$ cm, reconstruction radius, $r=9$ cm, assumed source radius $r_s=5.7$ cm, number of measurements in the circumferential direction, $N_\Phi=32$, number of measurements in axial direction, $N_z=34$ or 17, microphone spacing in the axial direction, 2 cm. Note that the NAH calculations were performed as they would have been in an experimental situation: a spatial window (a Tukey, three- or five-point window, for the $N_z=17$ and $N_z=34$ cases, respectively) was applied to the data to smooth the transition at the upper edge of the aperture and the spatial data was zero padded to 256 points in the z direction. In addition, conventional wave number filtering procedures were applied.[11]

The backprojected pressures and particle velocities for the double-dipole calculated using both NAH and SONAH are shown in Fig. 4, as are the directly "measured" results for the $N_z=34$ case. The corresponding results for the $N_z=17$ case are shown in Fig. 5. The regularization procedure expressed in Eqs. (14) and (15) was used to obtain the SONAH results shown in Figs. 4 and 5.

Note that both the SONAH and NAH backprojections that are shown in Figs. 4 and 5, were optimized (by the choice of θ and k_c, the cutoff wave number,[12] respectively) so that the pressure reconstruction errors were as small as possible (a procedure that was possible since the exact result was known). Thus, the results presented here are the "best possible" NAH and SONAH results. The optimized values for k_c were 20 and 29 rad/m for the $N_z=17$ and 34 cases, respectively, and the optimal values of θ were 90 and 80 dB for the $N_z=17$ and 34 cases, respectively.

In the $N_z=34$ case, the level of the sound pressure is small at the upper edge of the aperture, thus minimizing truncation effects. As a result, the NAH and SONAH backprojections appear nearly identical to the directly measured results for both pressure and particle velocity, although some distortion in the NAH results is visible near the upper edge of the measurement aperture, particularly in the particle velocity [spurious peaks are visible near $z=60$ cm in Fig. 4(d)]. When $N_z=17$, i.e., when the measurement aperture is cut in half, the sound pressure is still relatively large at the aperture edge. Thus, while the SONAH backprojections are essentially identical to the directly measured results, the NAH results are clearly distorted by the effects of windowing and truncation. In particular, the NAH results suggest that the upper dipole is located several centimeters below its actual location at $z=25$ cm.

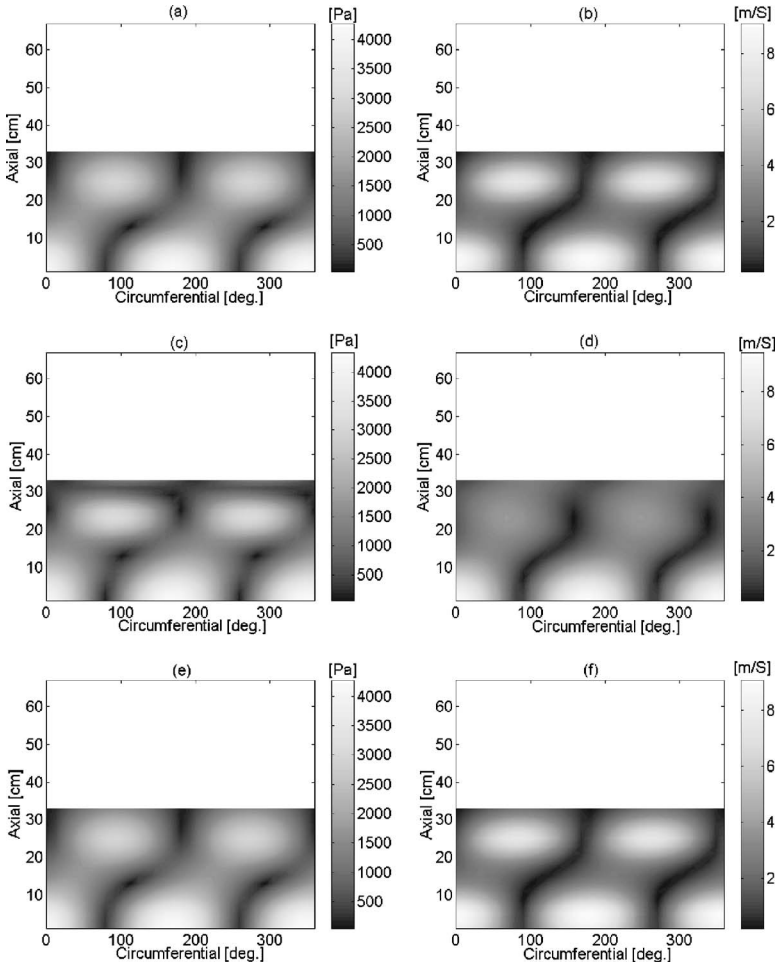

FIG. 5. Backprojected pressure and particle velocity for the double dipole at $r=0.09$ m, 1000 Hz, $N_z=17$: (a) directly measured p; (b) directly measured u_r; (c) backprojected p(NAH); (d) backprojected u_r(NAH); (e) backprojected p(SONAH); (f) backprojected u_r(SONAH).

The mean square reconstruction error was also calculated in order to quantify the relative accuracy of the SONAH and NAH procedure. The percentage error was defined as

$$\mathrm{MSE} = \sqrt{\frac{\sum_i |p_{t,i} - p_{s,i}|^2}{\sum_j |p_{t,j}|^2}} (\times 100), \tag{36}$$

where p_t is the directly "measured" pressure on the reconstruction surface, and p_s is the estimated pressure on the reconstruction surface. A similar calculation was performed to quantify the accuracy of the radial particle velocity, u_r, on the reconstruction surface. As summarized in Table I, the mean square error resulting from the backprojection performed using SONAH was less than 1% for both the pressure and the particle velocity for both the $N_z=34$ and $N_z=17$ cases. When using NAH, the mean square errors were 7.9% and 14.7% for the pressure and particle velocity, respectively, in the $N_z=34$ case. When the number of measurements in the axial direction was reduced to $N_z=17$, the NAH mean square projection error increased to 24.6% and 31.6% for the pressure and particle velocity, respectively. For the same case, the SONAH mean square projection errors increased by approximately a factor of three in magnitude but were still less than 1%.

Additionally, the percentage mean square errors between the "directly measured" and backprojected properties for the double-dipole simulation at 1000 Hz when calculated using improved Tikhonov regularization in conjunction with the MDP are shown in Table II. Results are shown for both SONAH and NAH. In the SONAH calculations, the value of the energy ratio, ε, was set to 10^{-8} (corresponding to an 80 dB signal-to-noise ratio), since a further decrease of ε did not

TABLE I. Percentage mean square error between "directly measured" and backprojected properties for double-dipole simulation at 1000 Hz evaluated using optimal values of θ and k_c.

	SONAH		NAH	
	p	u_r	p	u_r
$N_z=34$	0.15	0.26	7.9	14.7
$N_z=17$	0.42	0.76	24.6	31.6

TABLE II. Percentage mean square error between "directly measured" and backprojected properties for double-dipole simulation at 1000 Hz using improved Tikhonov regularization and MDP.

	SONAH		NAH	
	p	u_r	p	u_r
$N_z=34$	0.22	0.86	7.8	14.2
$N_z=17$	0.48	1.44	25.7	32.8

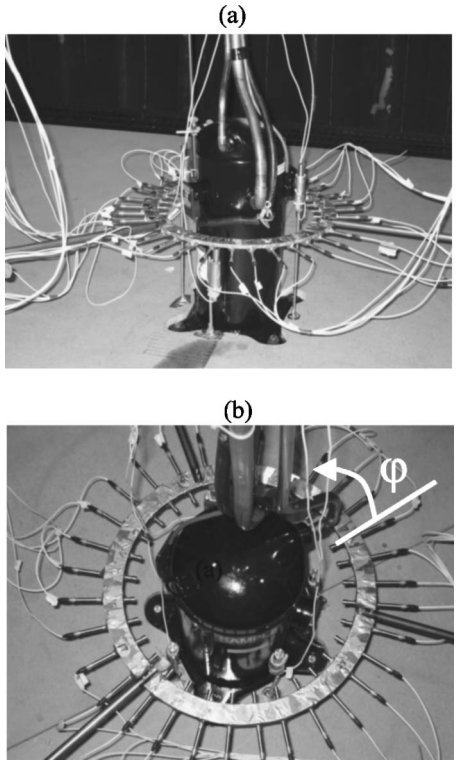

FIG. 6. Refrigeration compressor and measurement apparatus.

result in any changes in the regularization parameter α, which was found to be 0.10. If the value of α was reduced to smaller values manually, the mean square error was further reduced, but those results are not shown in Table II. In NAH, the same cutoff wave number was used as in Table I, which also proved to be optimal for the improved Tikhonov regularization with MDP.

Taken together, the results presented in this sub-section suggest that the SONAH procedure can yield more accurate results than the conventional NAH procedure when based on the same number of measurement points, especially when the sound field is truncated.

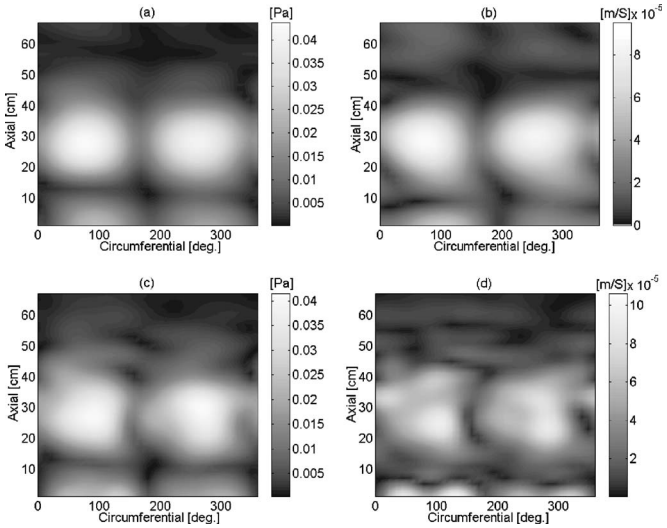

FIG. 7. Backprojected pressure and particle velocity for the compressor at $r=0.09$ m, 882 Hz, $N_z=34$: (a) backprojected p(NAH); (b) backprojected u_r(NAH); (c) backprojected p(SONAH); (d) backprojected u_r(SONAH).

B. Measurement of the sound field radiated by a refrigeration compressor

Both NAH and SONAH were applied to the measurement of the sound field radiated by a cylindrical refrigeration compressor in operation, under load (see Fig. 6). The height and diameter of the compressor shell were 40 and 18 cm, respectively. The details of the compressor measurement were the same as those of the double-dipole simulation, except that the number of measurements in the axial direction, N_z, was either 34 or 25, and the frequency of interest was 882 Hz. The rigid reflecting surface was accounted for by creating a mirror image of the measured dataset in the region $z<0$, i.e., the effective hologram size was doubled in the axial direction. The backprojected pressures and particle velocities on the surface of the compressor ($r=9$ cm) made by using NAH and SONAH are shown in Fig. 7 for the $N_z=34$ case. The corresponding results for the $N_z=25$ case are

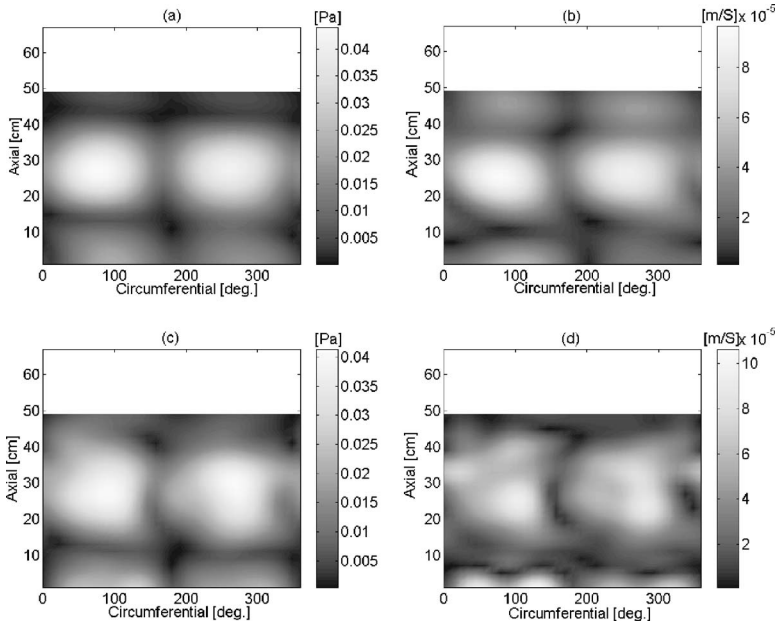

FIG. 8. Backprojected pressure and particle velocity for the compressor at $r=0.09$ m, 882 Hz, $N_z=25$: (a) backprojected p(NAH); (b) backprojected u_r(NAH); (c) backprojected p(SONAH); (d) backprojected u_r(SONAH).

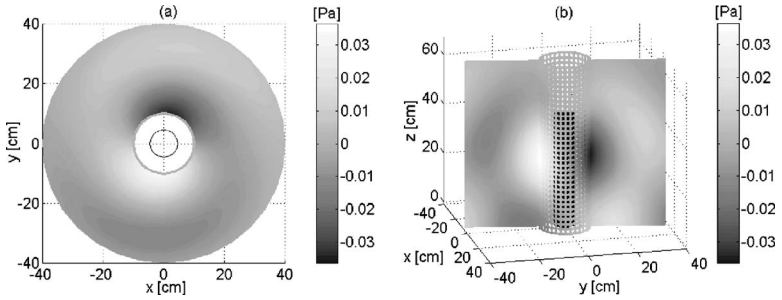

FIG. 9. Visualization of the real component of the sound pressure field of the compressor at $t=0$, 882 Hz, $N_z=34$: (a) horizontal view ($z=0.27$ m); (b) vertical view ($\phi=79$ deg).

shown in Fig. 8. The regularization parameter in the SONAH calculations and the cutoff wave number in the NAH projections were chosen to include the major wave components and to remove high wave number component noise as much as possible based on an inspection of both the wave number components and the reconstruction of the acoustical properties. For the SONAH calculations, θ was set to 10 dB and for the NAH calculations, k_c was set to 22 rad/m. When the improved Tikhonov regularization with MDP was implemented in the SONAH calculation, the results (not shown here) were similar to those shown in Figs. 7 and 8. A visualization of the sound field radiated by the compressor is shown in Fig. 9 (performed by using NAH), both in horizontal and vertical views. The latter results suggest that the radiation from the compressor is largely dipole-like at this frequency, resulting from a solid-body, oscillatory motion of the compressor shell.

The backprojected pressures obtained by using NAH and SONAH were similar in both cases (although there is slightly more detail visible in the SONAH results). However, the particle velocity results appear to be distorted when calculated using NAH, particularly in the $N_z=25$ case. In contrast, the SONAH particle velocity results for the $N_z=25$ and $N_z=34$ cases were practically identical. In addition, the SONAH results are better resolved, i.e., three peaks can be observed in the particle velocity in the region between 15 to 45 cm and 0° to 160° instead of just one large peak, as in the NAH result. It is also interesting to note that the four small peaks in the SONAH particle velocity results that are visible just above $z=0$ correspond to the locations of the compressor's feet. In the NAH $N_z=25$ case, the peak particle velocity location is lower than in the corresponding $N_z=34$ results (as was found in the dipole simulation). In addition, spurious peaks appear in the NAH particle velocity results at $z=45$ cm. Based on the fact that the results of NAH with $N_z=25$ were significantly different from those obtained in the $N_z=34$ case, while the SONAH results were consistent in both cases, it was judged that the SONAH results were more accurate than the NAH results in the $N_z=25$ case.

IV. CONCLUSIONS

The results of both the double-dipole simulation and the compressor measurements indicate that it is not possible to perform accurate backprojections by using NAH when the measurement aperture does not extend into the region where the sound pressure drops to negligible levels. However, consistent backprojections of both simulated and the measured data could be obtained by using SONAH, even when the sound pressure level was still reasonably large at the upper aperture edge. The mean square backprojection error in the double-dipole simulation case remained small for SONAH when the aperture size was decreased, but increased significantly in the NAH case, and more detailed information about the source could be obtained by using SONAH rather than NAH. In addition, more consistent backprojection results were obtained in the compressor case when using SONAH rather than NAH, particularly when the number of measurements in the axial direction was reduced. Finally, by avoiding a repeated calculation, the calculation of the SONAH matrices can be performed efficiently, which makes it practical to use SONAH when visualizing a sound source for which it is not possible to make measurements in the region where the sound pressure drops to negligible levels.

[1]R. Steiner and J. Hald, "Near-field acoustical holography without the errors and limitations caused by the use of spatial DFT," *Proceedings of ICSV6, 1999*, pp. 843–850.
[2]J. Hald, "Patch near-field acoustical holography using a new statistically optimal method," *Proc. INTER-NOISE 2003*, 2003, pp. 2203–2210.
[3]K. Saijyou and S. Yoshikawa, "Reduction methods of the reconstruction error for large-scale implementation of near-field acoustical holography," J. Acoust. Soc. Am., **110**, 2007–2023 (2001).
[4]K. Saijyou and H. Uchida, "Data extrapolation method for boundary element method-based near-field acoustical holography," J. Acoust. Soc. Am., **115**, 785–796 (2004).
[5]E. G. Williams, "Continuation of acoustic near-fields," J. Acoust. Soc. Am., **113**, 1273–1281 (2003).
[6]E. G. Williams and B. H. Houston, "Fast Fourier transform and singular value decomposition formulations for patch nearfield acoustical holography," J. Acoust. Soc. Am., **114**, 1322–1333 (2003).
[7]Z. Wang, "Helmholtz equation-least-squares (HELS) method for inverse acoustic radiation problem," Ph.D. dissertation, Wayne State University, Detroit (1995).
[8]Z. Wang and S. F. Wu, "Helmholtz equation-least-squares method for reconstructing the acoustic pressure field," J. Acoust. Soc. Am., **102**, 2020–2032 (1997).
[9]P. M. Morse and K. U. Ingard, *Theoretical Acoustics* (Princeton University Press, Princeton, NJ, 1968).
[10]G. Weinreich and E. B. Arnold, "Method for measuring acoustic radiation fields," J. Acoust. Soc. Am., **68**, 404–411 (1980).
[11]J. D. Maynard, E. G. Williams, and Y. Lee, "Nearfield acoustic holography: I. Theory of generalized holography and the development of NAH," J. Acoust. Soc. Am. **78**, 1395–1413 (1985).
[12]E. G. Williams, H. D. Dardy, and K. B. Washburn, "Generalized nearfield acoustic holography for cylindrical geometry: Theory and experiment," J. Acoust. Soc. Am., **81**(2), 389-407 (1987).
[13]E. G. Williams, *Fourier Acoustics: Sound Radiation and Nearfield Acoustical Holography* (Academic Press, London, UK, 1999).

[14]H. S. Kwon, Y. J. Kim, and J. S. Bolton, "Compensation for source nonstationarity in multi-reference, scan-based nearfield acoustical holography," J. Acoust. Soc. Am., **113**, 360–368 (2003).
[15]S. H. Yoon and P. A. Nelson, "Estimation of acoustic source strength by inverse methods: Part II, experimental investigation of methods for choosing regularization parameters," J. Sound Vib., **233**, 669–705 (2000).
[16]E. G. Williams, "Regularization methods for near-field acoustical holography," J. Acoust. Soc. Am., **110**, 1976–1988 (2001).

Synthetic aperture time-reversal communications in shallow water: Experimental demonstration at sea

W. J. Higley,[a] Philippe Roux, W. A. Kuperman, W. S. Hodgkiss, H. C. Song, and T. Akal
Marine Physical Laboratory, Scripps Institution of Oceanography, University of California, San Diego, La Jolla, California 92093-0238

Mark Stevenson
NATO Undersea Research Centre, La Spezia, Italy

(Received 15 April 2004; revised 6 July 2005; accepted 7 July 2005)

Time reversal has been shown as an effective way to focus in both time and space. The temporal focusing properties have been used extensively in underwater acoustics communications. Typical time-reversal communication experiments use vertical transducer arrays both to increase the signal-to-noise ratio and decrease the temporal sidelobes created in the time reversal process. Comparable temporal focusing is achieved using a horizontal array. In this paper, synthetic aperture time-reversal communications are accomplished, requiring only two transducers (one transmitter and one receiver). Deriving results from an at-sea experiment, this work confirms the viability of synthetic aperture time-reversal communications. © *2005 Acoustical Society of America.* [DOI: 10.1121/1.2011147]

PACS number(s): 43.60.Tj, 43.60.Dh [DRD] Pages: 2365–2372

I. INTRODUCTION

Time reversal has been shown to be an effective way to combat the temporal spreading classically observed in a waveguide.[1] Indeed, after pulse transmission from a point source, if the wave forms recorded at a set of receivers are time-reversed and retransmitted simultaneously into the medium, the result is spatial focusing and temporal compression. Spatial focusing means that the time-reversed field is strong at the location of the original source and relatively weaker elsewhere in the medium. Specifically, spatial focusing implies that the ratio of the intensities between any point not at the focus and that of the focus is low. Temporal compression means that the time-reversed signal at the source has the same pulse width to the signal previously emitted by the source. Because time reversal refocuses the desired signal in time, it has been applied to underwater communications.[2–4]

Recent time-reversal communications experiments[1–3] have used a vertical array of transducers moored to the ocean bottom or hung over the side of a ship. Indeed, a vertical array provides spatial diversity that is turned into an advantage when time reversal is performed.[5] Proposed in this work is a communication system using a synthetic aperture[6] time-reversal array that would require only two transducers, a transmitter and a receiver, of which at least one is moving. The advantage of a synthetic aperture array is that it provides spatial diversity with the use of only one source. However, the drawback of a synthetic aperture array is that the wave forms are received at different times, as the transducer is only at one place at any given time. This makes synchronization an issue. Steps must be taken to coherently sum the wave forms received on a synthetic aperture array. The motion of the transducer also induces a Doppler shift which may be different for each wave form, or even time varying. This must also be corrected before the received wave forms can be summed coherently.

Our proposed synthetic aperture communication system is based on the idea that a horizontal time-reversal array focuses well in the temporal domain.[7] Time reversal, as a simple and computationally inexpensive form of pulse compression, allows for a faster bit rate than systems without such pulse compression because intersymbol interference is mitigated. To affirm the feasibility of the proposed communication system to an oceanic environment, an experiment has been performed off the coast of Italy. The goal is to study, experimentally, the acoustical physics of a one-channel time-reversal communication system in a multipath environment. At this stage, no encoder/decoder (like turbo codes,[8] for example) or equalization[9] to potentially further reduce the error rate at the output of the communication system has been employed.

During the at-sea experiment, passive time reversal[4] rather than active time reversal is used. As long as the communications sequence sent from each synthetic aperture element is not too long, the Green's function used in passive time reversal can be viewed as time-invariant. This is in contrast to the concept that as the transducer moves from synthetic aperture element to element, the Green's functions vary.

The purpose of the experiment is to demonstrate the low bit error rates achievable at sea using a two-element system and passive synthetic aperture time reversal. Section II describes the experiment performed at sea and Sec. III details the processing done on the acquired data to extract the bit error rates. In Sec. IV, the possibility of using a few verti-

[a]Author to whom correspondence should be addressed; electronic mail: bhigley@mpl.ucsd.edu

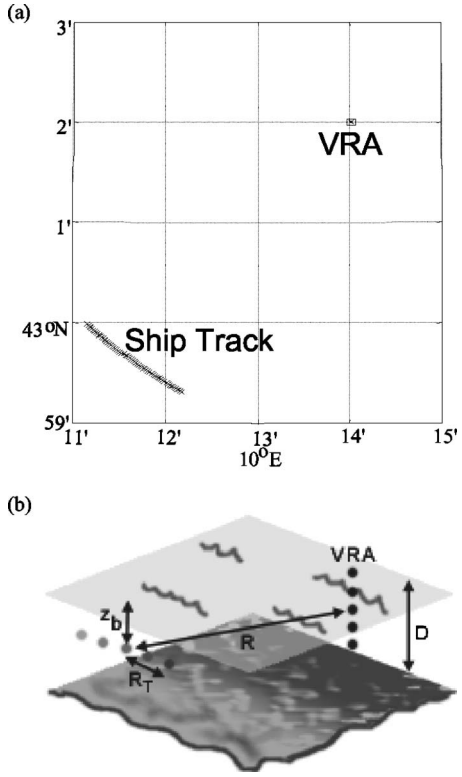

FIG. 1. (a) A vertical receiver array (VRA) moored off the coast of Italy received signals from a transducer towed by a moving vessel following the path shown. Each × represents a position in the almost 2-km-long synthetic aperture array. It is of note that the synthetic aperture array is oriented in such a manner that the VRA is approximately broadside to the track. The average distance between the moving source and the VRA is 5.5 km. (b) The same setup from another angle, showing the depth of the water, D, the range of the synthetic aperture array, R, the depth of the array, z_b, and the distance along the track of a single element, R_T.

cally oriented hydrophones, which spans only a small portion of the water column, to further lower the bit error rates of the system is examined.

II. EXPERIMENTAL DETAILS

A vertical receiver array (VRA) was moored off the coast of Italy, approximately 30 km north of the Island of Elba, where the mean depth, D, was approximately 120 m. In this environment, the sound speed was relatively constant, ranging from 1506 to 1508 m/s. From various geoacoustic experiments in the same area, the bottom properties were obtained through inversion yielding a sound speed of 1600 m/s and an attenuation of 0.3 dB/λ. This vertical array consisted of 32 elements each separated by 2 m, spanning from 30 to 92 m in the water column. A transducer was towed (at a 35-m depth) by a moving vessel at a speed of 2 knots on a track shown in Fig. 1. It is noticeable that the track is oriented such that the VRA is broadside to the synthetic aperture array (as viewed from above), as opposed to endfire. In a range-independent environment, the Green's function should not *a priori* vary over such a track path, thus limiting the gain in spatial diversity. However, at the frequency of 3 kHz, the wavelength (0.5 m) is very small compared to the propagation range ($R \sim 5.5$ km) so that a minimal bathymetry change leads to a noticeable modification of the Green's function. Also, the path is such that the VRA is not perfectly broadside to the track, and the small amount of range difference between elements may be enough to induce changes in the Green's function. A measure of the Green's functions change is discussed quantitatively in the following. The moving transducer transmitted a 1-ms pulse at 3 kHz, followed by a 10-s communication sequence coded using binary Amplitude Shift Keying (ASK), also at 3 kHz, consisting of 9800 bits with a bit length of 1 ms. The initial choice of an incoherent communication scheme [versus a coherent scheme like Binary Phase Shift Keying (BPSK)] was driven by its robustness to Doppler or synchronization issues.[10] The pulse and the communication sequence were separated by 200 ms so that they do not overlap after propagation through the dispersive channel. The purpose of the pulse is to probe the medium and to provide the Green's function that will be used to deconvolve the communication sequence.[4] The incident field was then received by all 32 channels on the vertical array, producing a matrix of Green's functions. In Sec. III, passive time-reversal is performed on one element of the vertical array only, whereas a 4-m vertical aperture made of three contiguous elements is used in Sec. IV. The pulse and communication sequence were transmitted every 30 s, each time producing a new Green's function matrix. During a 33-min-long track, 65 such matrices of Green's functions were acquired separated by a mean distance of 30 m. The synthetic aperture array thus consisted of up to 65 elements (though, typically no more than four at a time are examined in this paper) spanning just less than 2 km. The signal-to-noise ratio of the communication sequence varied between 25 and 30 dB over the ship track (see Fig. 5).

III. DATA PROCESSING

A. Decorrelation along the track

As can be seen in Fig. 1, the track of the moving transducer creates a synthetic aperture array, such that the VRA (as viewed from above) is oriented broadside to this array. Considering, for now, only one channel on the VRA (depth ~38 m), the source depth, receiver depth, and range between the source and the receiver can all be considered approximately constant. To distinguish between different transmissions of the moving transducer, the variable, R_T, which is the distance along the track at the time of transmission, is introduced. Thus, the Green's function between a point on the track and the VRA can be written as $G(t,R_T)$. The fact that the synthetic aperture is oriented broadside to the VRA rather than endfire does not present a problem for the time-reversal process since the Green's function changes azimuthally, thereby providing the required spatial diversity. The change in Green's function is calculated as follows: The Green's functions are normalized to have unit power and autocorrelated. Each autocorrelated Green's function corresponds to the point-to-point time reversal between one VRA element and the moving source [see Eq. (1)]. Spatial diversity will be used efficiently if the time-reversal sidelobes cancel each other along the source track, i.e., the temporal sidelobes of the autocorrelated Green's function decorrelates as the source moves. The point-to-point time-reversal sidelobes[1]

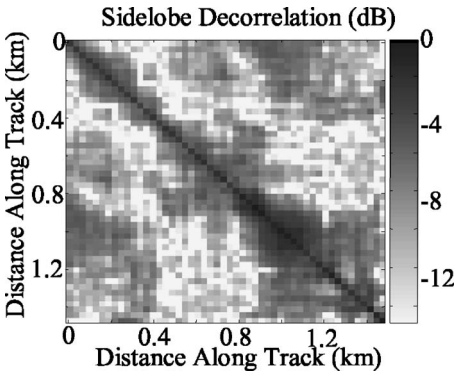

FIG. 2. Point-to-point time-reversal sidelobe decorrelation. These results are obtained by first normalizing the Green's functions at the distances along the track indicated on the axis, autocorrelating each of them, and then cross-correlating the resulting sidelobes. The results are a measure of how much the Green's function changes as a function of the distance along the track. The distance between Green's functions that results in a total decorrelation of the point-to-point time reversal sidelobes varies between 100 and 300 m.

decorrelation is shown in Fig. 2. It can be noticed that the Green's function changes enough to affect the sidelobes of the autocorrelation over a distance that varies between 100 and 300 m along the track.

The change in Green's functions along the track can be attributed to either the 30-m azimuthal or the 3-m radial distance (with respect to the VRA) between each source position. In the extreme case, where 300 m along the track is necessary to decorrelate the autocorrelation sidelobes, this corresponds to less than 300-m azimuthal distance and 30 -m radial distance. There is an ambiguity as to which of these distances causes the decorrelation. However, this radial distance corresponds to 60 wavelengths, which is enough to cause a decorrelation of the field in the waveguide. In the other extreme case, where only 100 m is necessary to decorrelate the autocorrelation sidelobes, it is likely that a combination of azimuthal and radial distance changes is responsible for the decorrelation.

B. Extracting bit error rates

After propagation through the channel, the received signals are not matched in frequency due to time-dependent Doppler shift. The Doppler shift may be either due to relative motion between the two transducers, or a mismatch between

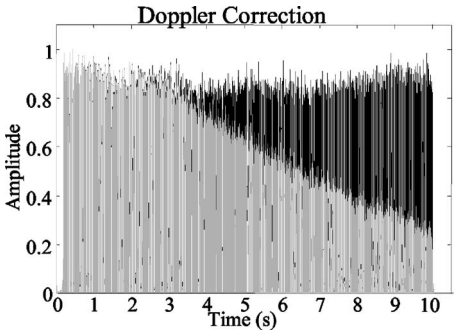

FIG. 3. The results of summing coherently the 65 received wave forms before Doppler correction (in gray) and after Doppler correction (in black). As time progresses, it is shown that the amplitude of the noncorrected sum decreases as the noncorrected signals do not add coherently at later times.

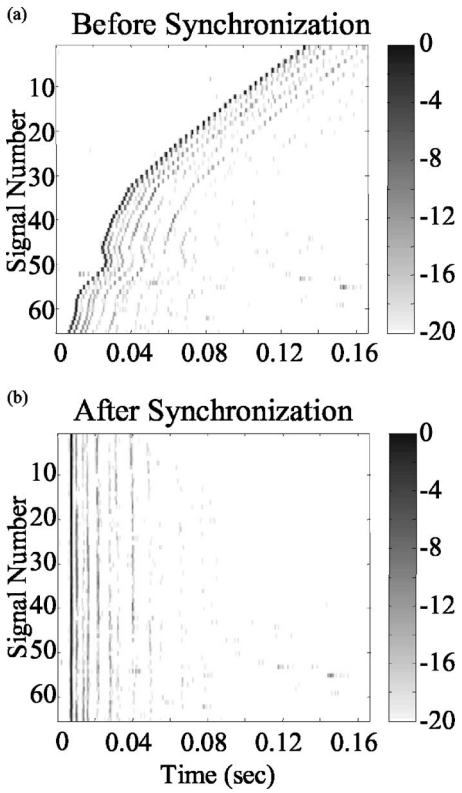

FIG. 4. The received wave forms before and after synchronization. Synchronization is an issue as time-reversal cannot be performed simultaneously from the synthetic aperture array. The signals must be accurately synchronized before time-reversal so they may be summed coherently. Shown are the received wave forms in dB, normalized to the maximum.

the sampling frequencies of the transducers. Also, as the signals are not received simultaneously, they are not synchronized in time. Both of these effects must be compensated before the signals can be added coherently.

To correct for the Doppler shift, a Fast Fourier Transform (FFT) is taken of the zero-padded communications sequence. As the Green's functions of this data set have a strong ballistic path and the communications are encoded with ASK, in the absence of Doppler shift, one would expect a strong peak at 3 kHz, the carrier frequency. Due to Doppler effects, this peak is shifted a small amount, ranging from 0.4 to 0.9 Hz. If the motion of the transducer were endfire, one would expect the Doppler shift to be greater. The signal is then dilated or compressed in time so that the value of the peak is shifted back to 3 kHz. Figure 3 shows the coherent sum over the synthetic aperture of all received time-domain signals (after synchronization and time reversal described in the following) with no Doppler correction in gray, and with Doppler correction in black. It is seen that the two sums are similar in amplitude at the beginning, but that as time progresses, the amplitude of the noncorrected sum decreases. This is due to the fact that the noncorrected signals do not add coherently at later times.

Once the signal has been Doppler corrected, the next step is to synchronize the signals in time. In order to do that, the signals with the highest signal-to-noise ratio is used as a reference. As mentioned earlier, the received signal consists of two parts, the dispersed pulse, which has become the

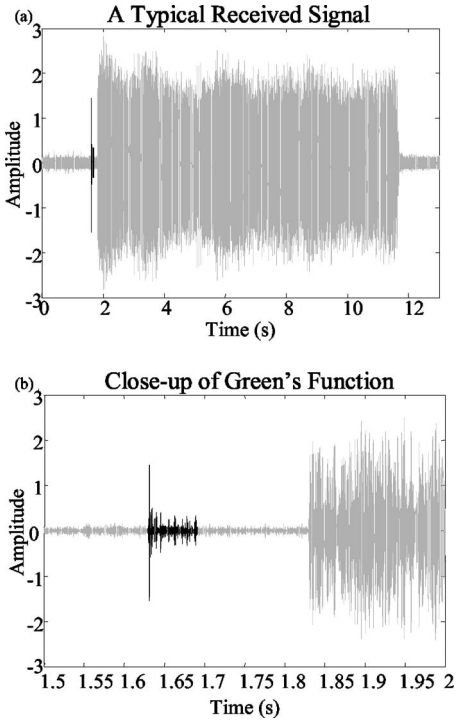

FIG. 5. (a) A typical received signal consisting of an initial pulse and a 10-s communication sequence, after both have propagated through the medium. The selected Green's function is shown in black. (b) The same signal, zoomed in to show the detail of the Green's function, which has spread from an original 1-ms pulse, to a 70-ms-long dispersed signal. Signal-to-noise ratio is about 25 dB.

Green's function, and the dispersed communication sequence. In order to synchronize the wave forms, one may focus on the Green's function. Knowing the time between the beginning of the Green's function and the communication sequence (200 ms), the synchronization of the Green's functions along the track yields the synchronization of all the communication sequences. Figure 4 shows the 65 Green's functions received before and after synchronization. For each of the 65 received wave forms the following steps are taken. The Green's functions are time-gated to select the first arrival of the impulse response. The first arrivals are then synchronized along the aperture using cross correlation. After synchronization of the first arrival a larger time window, approximately 70 ms, is taken and designated the Green's function. Figure 5 shows a typical signal received on the VRA, with the selected Green's function darkened. In the case of a set of Green's functions lacking a dominant first arrival, the method of synchronization would have to be modified.[6] For example, a particularly strong and stable path of the Green's function could be chosen in place of the first arrival. In the case of low signal-to-noise ratios, one could consider that the only thing in common between any two received wave forms is the communication sequence, $m(t)$ [see Eq. (1)]. Cross correlation between received wave forms will exhibit a peak when the embedded sequence in each wave form overlaps. The time at which these peaks occur correspond to the relative delay in each received signal. By removing this delay, the signals are synchronized.

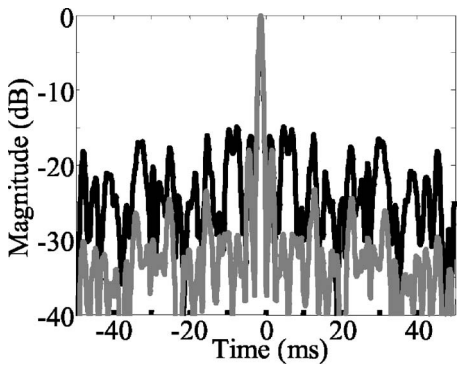

FIG. 6. The Q-function (Ref. 10) resulting from a single element is shown in black, and from the coherent summation of five widely spaced elements is shown in gray. It can be seen that the summation results in lower sidelobe levels, which produce lower bit error rates.

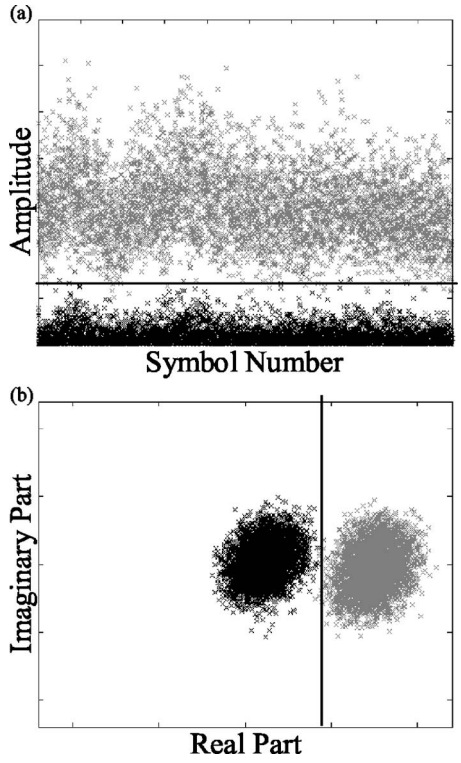

FIG. 7. (a) The results of incoherently decoding a signal composed of the sum of three widely spaced synthetic aperture elements, that is synthetic aperture elements that have decorrelated Q-function sidelobes. Binary 0s are shown in black, binary 1s are shown in gray, and a threshold is indicated by a dark line. The number of errors in the case shown was 31, giving a bit error rate of 0.32%. (b) The results of decoding the same signal coherently. Again, binary 0s are shown in black, binary 1s are shown in gray, and a threshold is indicated by a dark line. The number of errors in this case, decoded coherently was 7, giving a bit error rate of 0.071%.

After synchronization, each Green's function is extracted, time reversed, and convolved with the communication sequence to cancel the multipath propagation as classically done in passive time-reversal. The result of these convolutions is 65 wave forms that can be summed coherently to produce the message estimate, written as

$$\hat{m}(t) = m(t) * \sum_j [G(-t,R_{Tj}) * G(t,R_{Tj})], \quad (1)$$

where $m(t)$ is the coded communication sequence. The summation part of the equation has been referred to as the

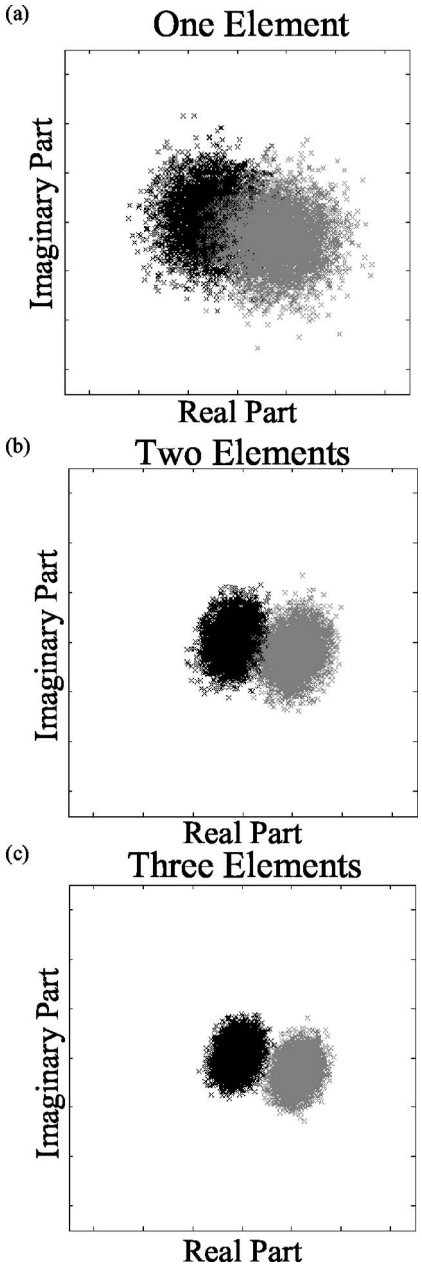

FIG. 8. The evolution of the in-phase/quadrature plot as more synthetic elements are summed together before decoding. The elements added are widely spaced. Binary 0s are in black and binary 1s are in gray.

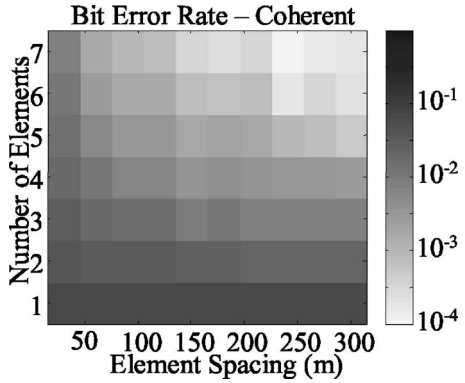

FIG. 9. Bit error rate found from 9800 bits, each with a bit length of 1 ms, as a function of the number of transducer positions (or synthetic array elements) for various values of element spacing, δR_T.

Q-function.[10] A typical Q-function for one element (which is the point-to-point time-reversal described in Sec. III A) and for five elements is shown in Fig. 6. As expected, the time-reversal sidelobes are reduced as more elements are added coherently, suggesting that better communication can be achieved with a time reversal synthetic aperture.

Although the modulation used (ASK) is an incoherent modulation, it can be demodulated either incoherently or coherently. In either case, the message estimate is base-banded by multiplication with a sinusoid at the carrier frequency and filtered. The resulting wave form is then resampled at the symbol rate producing N complex numbers, where N is the number of symbols. To demodulate incoherently, the absolute value of each of these numbers is compared to a threshold to determine whether the bit is a binary 1 or a binary 0. The threshold is chosen as half the mean of the N positive numbers. Figure 7(a) shows the resulting values from incoherent modulation before the hard decision is made. The figure was made using only three widely spaced synthetic aperture elements with decorrelated Q-function sidelobes. In Fig. 7(a), binary 0s are shown in black and binary 1s are shown in gray. The threshold is shown by a dark line. To demodulate coherently, the real part of each of the N complex numbers is compared to a threshold to determine whether the bit is a binary 1 or a binary 0. The threshold is chosen as the mean of the real part of the N complex numbers. Figure 7(b) shows the resulting values from the coherent modulation before the hard decision is made. This figure was made using the same three widely spaced synthetic ap-

TABLE I. Selected values of the bit error rate found from 9800 bits, each with a bit length of 1 ms, as a function of the number of transducer positions (or synthetic array elements) for various values of element spacing, δR_T.

	Data rate in bits per second (number of elements in the synthetic aperture)						
δR_T (m)	1000 (1)	500 (2)	333 (3)	250 (4)	200 (5)	167 (6)	143 (7)
30	6.9$E-2$	4.2$E-2$	2.8$E-2$	2.0$E-2$	1.5$E-2$	1.0$E-2$	7.5$E-3$
60	⋯	3.6$E-2$	2.0$E-2$	1.1$E-2$	6.1$E-3$	3.1$E-3$	1.6$E-3$
150	⋯	2.6$E-2$	9.5$E-3$	4.1$E-3$	1.9$E-3$	8.5$E-4$	3.2$E-4$
300	⋯	2.1$E-2$	7.6$E-3$	2.9$E-3$	5.3$E-4$	2.3$E-4$	2.0$E-4$

(a) XXXXOOOO++++

(b) X X X X O O O O + + + +

(c) XO+XO+XO+XO+

FIG. 10. Schematic of a synthetic aperture time reversal communication system. For the sake of simplicity, the communication sequences are represented by the symbols ×, ○, and +. (a) Multiple sequences transmitted as quickly as allowed by the equipment. (b) The same sequences, with the spacing between transmissions increased in order to increase the length of the synthetic aperture endfire aperture. This creates a better focus and decreases the bit error rate. (c) By interleaving sequences, one may achieve the same bit error rate as in step b, but maintains the same data rate as in step a.

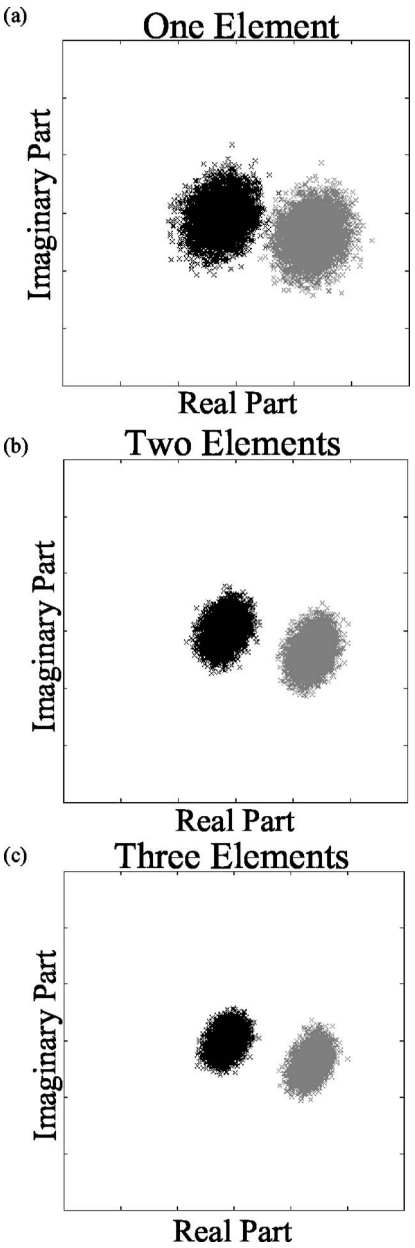

FIG. 11. The evolution of the in-phase/quadrature plot as more vertical elements are summed together before decoding. Before summation over the vertical elements, a horizontal synthetic aperture of three widely spaced elements is used.

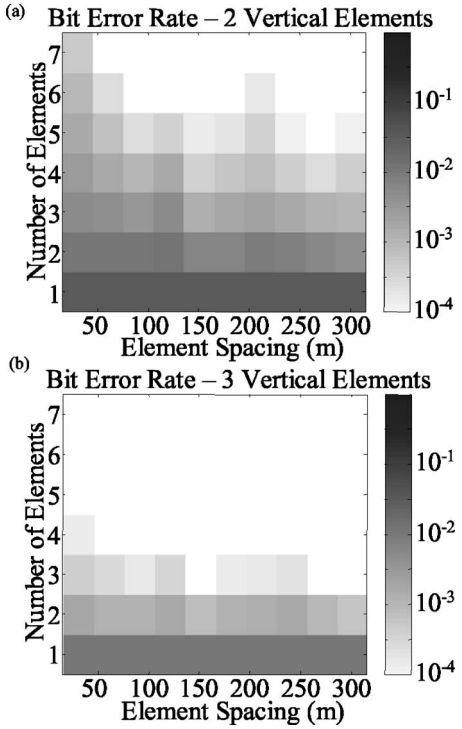

FIG. 12. Bit error rate found from 9800 bits, each with a bit length of 1 ms, as a function of the number of synthetic array elements, element spacing, δR_T, and number of vertical array elements. The bit error rates using only one vertical element can be found in Fig. 9.

erture elements. Again, binary 0s are shown in black, binary 1s are shown in gray, and threshold is shown by a dark line. The comparison between the estimate sequence and the sequence sent produces a bit error rate. From Fig. 7, it can be deduced that coherent demodulation is not only possible, but gives lower bit error rates than the incoherent demodulation. From this, one may anticipate that it is possible to use synthetic aperture time reversal with more complicated, coherent modulation techniques such as BPSK or Quaternary Phase Shift Keying (QPSK). As coherent demodulation gives lower bit error rates, the rest of the paper presents results for coherent modulation. Lower bit error rates are expected as more synthetic aperture elements are added together, which is seen in Fig. 8. This figure shows the evolution of the in-phase/quadrature plot as synthetic aperture elements are summed. As seen in Fig. 8, the result of using more synthetic aperture elements are tighter clouds of points and ultimately, lower bit error rates.

C. Results

We present the bit error rates as a function of two parameters of the synthetic aperture array: the number of elements used in summation and the element spacing. Despite the orientation of the track, such that the VRA is broadside to it, it is shown that the Q-function sidelobes decorrelate as the distance along the track increases, thus element spacing plays an important role in determining bit error rates. Results are shown as a grayscale plot in Fig. 9. The bit error rate decreases as the number of elements is increased and also decreases as the element spacing is increased. However, by increasing the number of elements used, as this is a synthetic

TABLE II. Selected values of the bit error rate found from 9800 bits, each with a bit length of 1 ms, summed over three vertical elements, as a function of the number of transducer positions (or synthetic array elements) for various values of element spacing, δR_T.

	Data rate in bits per second (number of elements in the synthetic aperture)						
δR_T (m)	1000 (1)	500 (2)	333 (3)	250 (4)	200 (5)	167 (6)	143 (7)
30	1.0$E-2$	1.9$E-3$	4.4$E-4$	1.4$E-4$	7.3$E-5$	2.5$E-5$	1.4$E-5$
60	⋯	1.3$E-3$	2.8$E-4$	5.3$E-5$	1.8$E-5$	3.7$E-6$	0
150	⋯	7.6$E-4$	7.1$E-5$	4.1$E-6$	2.2$E-6$	0	0
300	⋯	6.1$E-4$	7.7$E-5$	2.3$E-5$	4.1$E-6$	0	0

aperture, the effective data rate is diminished. Using only one element in the system, corresponding to a data rate of 1000 bps, yields a bit error rate of 7%. By using two elements spaced 300 m apart, corresponding to a data rate of 500 bps, the bit error rate is dramatically lowered to 2.1%. An increase to three elements with a mean spacing of 300 m, corresponding to a data rate of 333 bps, yields a bit error rate below 1%.

D. Interleaving communication sequences

If one were to transmit as quickly as allowed by the equipment, the element spacing, δR_T, would be small, requiring a large number of transducer positions to achieve a low bit error rate. For instance, in Table I, it is shown that it takes seven elements to achieve a bit error rate of 0.75% when the element spacing is only 30 m, but when the element spacing is 300 m, the same bit error rate is achieved with only three elements. The spacing of 300 m is chosen from the decorrelation of the Q-function sidelobes shown in Fig. 2. If one were to simply increase the aperture by increasing the element spacing, δR_T, there would be times when the transducers were unused since it is necessary to wait for one of the transducers to move and the aperture to further increase. In this spare time between transmissions of the first communication sequence, other sequences can be sent. By interleaving communication sequences, the data rate is the same as the fastest allowed by the equipment, but the bit error rate will be significantly lower. Figure 10 demonstrates this concept graphically.

IV. VERTICAL SUMMATION

The experiment at sea was done using a vertical array consisting of 32 elements, only one of which has been used so far in decoding the data. By using up to three contiguous elements, one may examine the decrease in bit error rate that would occur if one were to use a 4-m-long vertical array (centered at 38 m) that spanned only a small portion of the 120-m-deep water column. Such an array would still be relatively cheap, one of the primary advantages of the proposed system. The in-phase/quadrature plots resulting from the summation over a small number of vertically oriented elements are shown in Fig. 11. The summation is done vertically after the horizontal summation had been done over three widely spaced synthetic aperture elements. The bit error rates using a small number of vertically oriented elements are presented in Fig. 12. The addition of a few vertical elements dramatically lowers the bit error rates of the system. For example, with a synthetic aperture of four elements, a vertical line array of three elements yields 12 wave forms that can be coherently summed. The results demonstrate that with a vertical line array of three elements, at three locations forming a synthetic horizontal line array, bit error rates lower than 10^{-5} can be achieved with a 1-ms bit length (Table II).

V. CONCLUSION

This paper serves to confirm the feasibility of an inexpensive communication system using a synthetic aperture time reversal array at sea. The main benefit of this system is that it requires only two transducers (one transmitter and one receiver), significantly decreasing the technological cost compared to typical time reversal communication schemes. The disadvantage of this system is that the repeated transmission of the communication sequence tends to lower to data rate. As in many communication systems, a tradeoff must be made between the data rate and the desired bit error rate. It is also shown that the addition of a few transducers oriented vertically in addition to the horizontal aperture significantly decreases the bit error rate without a significant increase in cost or complexity of the system. Finally, it is reiterated that this study is limited to how synthetic aperture time reversal can utilize shallow water propagation complexity; additional communication algorithms can always be appended to increase performance.

[1]W. A. Kuperman, W. S. Hodgkiss, H. C. Song, T. Akal, C. Ferla, and D. Jackson, "Phase conjugation in the ocean: Experimental demonstration of an acoustic time-reversal mirror," J. Acoust. Soc. Am. **98**, 25–40 (1998).

[2]G. F. Edelmann, T. Akal, W. S. Hodgkiss, S. Kim, W. A. Kuperman, and H. C. Song, "An initial demonstration of underwater acoustic communication using time reversal," IEEE J. Ocean. Eng. **27**, 602–609 (2002).

[3]K. B. Smith, A. A. M. Abrantes, and A. Larraza, "Examination of time-reversal acoustics in shallow water and applications to noncoherent underwater acoustic communications," J. Acoust. Soc. Am. **113**, 3095–3110 (2003).

[4]D. Rouseff, D. R. Jackson, W. L. J. Fox, C. D. Joes, J. A. Ritcey, and D. R. Dowling, "Underwater acoustic communication by passive phase conjugation: Theory and experimental results," IEEE J. Ocean. Eng. **26**, 821–831 (2001).

[5]P. Roux and M. Fink, "Time reversal in a waveguide: Study of the temporal and spatial focusing," J. Acoust. Soc. Am. **107**, 2418–2429 (2000).

[6]S. Stergiopolous, "Implementation of adaptive and synthetic-aperture processing schemes in integrated active-passive sonar systems," Proc. IEEE **86**, 358–398 (1998).

[7]M. R. Dungan and D. R. Dowling, "Orientation effects on linear time

reversing array retrofocusing in shallow water," J. Acoust. Soc. Am. **112**, 1842–1852 (2002).
[8]C. Berrou and A. Glavieux, "Near optimum error correcting coding and decoding: turbo-codes," IEEE Trans. Commun. **44**, 1261–1271 (1996).
[9]G. F. Edelmann, S. Kim, W. S. Hodgkiss, W. A. Kuperman, H. C. Song, and T. Akal, "Combining and comparing time reversal processing and adaptive channel equalization for communications sequences," J. Acoust. Soc. Am. **112**, 2447 (2002).
[10]T. C. Yang, "Temporal resolution of time-reversal and passive-phase conjugation for underwater acoustic communications," IEEE J. Ocean. Eng. **28**, 229–245 (2003).

Transmission properties of bone conducted sound: Measurements in cadaver heads

Stefan Stenfelt[a] and Richard L. Goode
Department of Otolaryngology—Head and Neck Surgery, Stanford University Medical Center, Stanford, California 92305-5328
and Palo Alto Veterans Affairs Health Care System, Palo Alto, California 94304

(Received 20 January 2005; revised 24 June 2005; accepted 28 June 2005)

In the past, only a few investigations have measured vibration at the cochlea with bone conduction stimulation: dry skulls were used in those investigations. In this paper, the transmission properties of bone conducted sound in human head are presented, measured as the three-dimensional vibration at the cochlear promontory in six intact cadaver heads. The stimulation was provided at 27 positions on the skull surface and two close to the cochlea; mechanical point impedance was measured at all positions. Cochlear promontory vibration levels in the three perpendicular directions were normally within 5 dB. With the stimulation applied on the ipsilateral side, the response decreased, and the accumulated phase increased, with distance between the cochlea and the excitation position. No significant changes were obtained when the excitations were on the contralateral side. In terms of vibration level, the best stimulation position is on the mastoid close to the cochlea; the worst is at the midline of the skull. The transcranial transmission was close to 0 dB for frequencies up to 700 Hz; above it decreased at 12 dB/decade. Wave transmission at the skull-base was found to be nondispersive at frequencies above 2 kHz whereas it altered with frequency at the cranial vault. [DOI: 10.1121/1.2005847]

PACS number(s): 43.64.Bt [BLM] Pages: 2373–2391

I. INTRODUCTION

The mechanical properties of the human skull in relation to bone conduction (BC) stimulation have been well described in the literature. Many of these reports have focused on vibrations of the relatively thin bones of the skull, while only a few have focused on vibration transmission in the skull-base where the cochleae are situated. In order to obtain a better understanding of BC transmission in the human skull, the vibration transmission in both the cranial vault and the skull-base should be measured.

Several different aspects of skull response produced by BC excitation have been studied. von Békésy (1932) analyzed the vibration mode of the human skull and approximated it as a vibrating thin-shell sphere. The mechanical point impedance, at the mastoid portion and the forehead, with and without skin, has been investigated (Corliss and Coidan, 1955; Smith and Suggs, 1976; Flottorp and Solberg, 1976; Khalil *et al.*, 1979). The most comprehensive study of the mechanical point impedance of the human skull was made by Håkansson *et al.* (1986) on live human subjects with osseointegrated skin-penetrating titanium implants in the parietal bone for attaching bone-anchored hearing aids. In another investigation, Håkansson *et al.* (1996) investigated the linearity of vibration transmission in the skull and found it linear for normal levels and frequencies used for hearing by BC.

Khalil *et al.* (1979) used modal analysis to extract resonance frequencies from two dry skulls. Håkansson *et al.* (1994) used similar techniques to extract resonance frequencies from living human skulls. Also, the vibration of a large part of the human cranial vault has been visualized with holographic interferometry (Ogura *et al.*, 1979; Hoyer and Dörheide, 1983; Dorheide and Hoyer, 1984). Other investigations have aimed at estimating the propagation velocity and type of wave transmission in the human skull (von Békésy, 1948; Zwislocki, 1953; Franke, 1956; Tonndorf and Jahn, 1981).

Theoretical approaches to estimate the skull response during vibration stimulation have also been used. For this, thin-shell theories of spheres with fluid loading were used to achieve analytical results, or finite element analysis was used to obtain the vibration pattern (Advani and Lee, 1970; Hickling and Wenner, 1973; Khalil and Hubbard, 1977; Charalambopoulos *et al.*, 1998; Young, 2002, 2003). These analyses were intended primarily for head injury protection and not for the transmission and hearing of BC sound.

Most of these studies focused on the mechanical properties and vibration transmission characteristics of the human cranial vault. One study by Stenfelt *et al.* (2000) measured skull vibration in three perpendicular directions close to the cochlea with stimulation at the ipsilateral and contralateral mastoid as well as at the forehead. The drawback with that study was that only one dry human skull was used. The current study presents measurements of the cochlear promontory vibration in three perpendicular directions, using stimulation at numerous positions on the skull in intact hu-

[a]Present address: Department of Signals and Systems, Chalmers University of Technology, SE-412 96 Göteborg, Sweden. Electronic mail: stenfelt@chalmers.se

TABLE I. Data of the six human cadaver heads used for the measurements. The circumference was measured as a line going from the center of the forehead passing just above the ear canal openings, over the occiput and back to the mid-forehead.

No.	Sex	Age (years)	Circumference (cm)	Ear-ear via vertex (cm)	Mass (kg)
1	M	60–70	53	31	3.25
2	M	60–70	54	33	3.31
3	M	60–70	56	31	3.43
4	M	60–70	57	34	3.59
5	M	60–70	58	35	3.71
6	M	60–70	58	36	3.78

TABLE II. Typical stimulation vectors at the test positions. The figure given in the table for a particular position and direction should be multiplied by the input force to give the stimulation in that direction at that position.

Position	Forehead			Vertex			Occiput		
	x	*y*	*z*	*x*	*y*	*z*	*x*	*y*	*z*
0	0	0.34	−0.94	0	1	0	0	0.09	1
1	0.24	0.34	−0.91	0.45	0.89	0	0.34	0.09	0.94
2	0.58	0.42	−0.69	0.71	0.71	0	0.87	0	0.50
3	0.85	0.17	−0.49	0.98	0.17	0	0.98	−0.14	−0.17
4	0.97	0	−0.26	0.98	−0.17	0	0.98	−0.17	0.03

man heads. Furthermore, the mechanical point impedances at the stimulation positions have been analyzed to reveal the mechanical properties of the human head.

II. MATERIAL AND METHODS

A. The cadaver heads

For the experiments, six male human cadaver heads were used. The heads were severed between the third and fourth vertebra and frozen at the time of autopsy. Apart from being severed, no drilling or cutting of the heads was done during the autopsy; the soft tissues and brain were left intact. No history of the heads was known except that they were male and between 60 and 70 years old; the sizes and weights of the heads are presented in Table I. All heads were defrosted 24 h prior to the measurements. A thin probe thermometer was positioned through the foramen magnum into the center of the brain to verify that the heads were properly defrosted. This thermometer was thereafter removed.

Three imaginary arcs were identified on the skull. The occiput arc connects the two ear canal openings over the most posterior part of the occiput (Fig. 1). On this arc, nine positions were identified. Position 4, the position closest to the ear canal opening, was placed about 20 mm posterior to the entrance to the ear canal, while position 3 was 20 mm posterior to position 4. The others were placed at equal distances, with a distance of 30 mm for the smallest head and 36 mm for the largest head. One position, position 0, was at the midline between the ears.

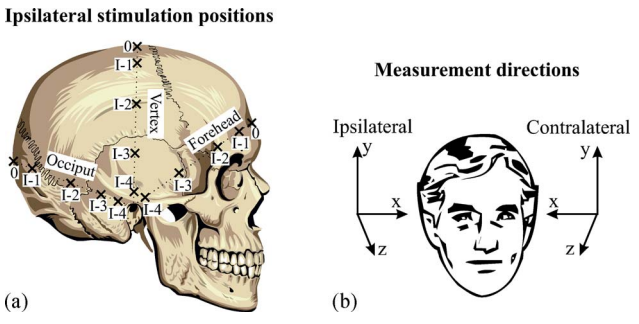

FIG. 1. (Color online) (a) Three stimulation arcs were identified on the heads: forehead, vertex, and occiput. Nine stimulation positions with an approximate spacing of 30 mm were equally spread on each line: the figure shows the positions on the ipsilateral side. (b) The measurement directions of the ipsilateral and contralateral cochleae: *x* direction—towards the middle of the head, *y* direction—towards the top of the head, and the *z* direction—towards the front of the head. The ipsilateral and contralateral *x* direction points towards each other (180° out of phase) while the two other directions are the same for the ipsilateral and contralateral sides.

At each position a small hole was drilled and tapped (diameter 3 mm). A connector comprising a screw with 3-mm metric threads (M3) was placed in this tapped hole. To further ensure a rigid bond between the connector and the skull, a drop of cyanoacrylate glue (Garf Reef glue™, Garf, Boise, ID, USA) was put into the threaded hole prior to placement of the connector. The connector had also a threaded part to attach a mini-transducer for the vibration excitation; the connector enabled rigid attachment between the transducer and the skull.

The vertex arc is between the ear canal openings passing over the vertex and the forehead arc connects the ear canal openings passing over the center of the forehead. Positions 4 for these two arcs are 30 mm from the ear canal openings, and the rest of the positions are between 31 and 38 mm apart, depending on head size. For each arc, four positions were at each side of the skull with one position at the midline. The heads were excited at 27 positions in total. A 1-cm^2 piece of skin and soft tissue was removed around each stimulation position to enable placement of the connector with attached stimulation transducer.

Three perpendicular directions were defined for the skull vibration measurements. The three directions are shown in Fig. 1 (right): *x* direction medially (towards the midline of the skull), *y* direction cranially (towards the top of the skull), and *z* direction anteriorly (towards the front). It should be noted that the *x* directions at the two sides of the skull are directed towards each other, while the *y* and *z* directions are the same on both sides. The stimulation was applied to the skull bone surface in a direction approximately perpendicular to the skull bone surface. This means that the direction of the vibration stimulation is different at each stimulation position. Table II presents, for one head, the vector components of the stimulation direction according to the coordinate system given in Fig. 1. Although not exactly equal, the stimulation directions at the positions were similar for all heads.

The stimulation direction influences the response direction. For example, if the skull moves as a whole and translational vibration is the dominating mode, the response direction is expected to be similar to the stimulation direction. However, if the dominating mode of vibration is rotational or some type of wave propagation, vibration responses in all spatial directions can be expected.

One phenomenon that can contribute to the perception of BC sound is the relative motion between the middle ear ossicles and the surrounding bone. This occurs due to the inertial movement of the ossicles. Although the middle ear ossicles move regardless of the vibration direction, the greatest relative motion is obtained when the vibration is along the low-frequency in-and-out motion direction of the stapes (Stenfelt *et al.*, 2002). According to the coordinate system given in Fig. 1, the low-frequency in-and-out motion of the stapes is in the *x*-*z* plane, 30° from the *x* axis and 60° from the *z* axis.

B. Mechanical impedance measurements

Measurements of the mechanical point impedance[1] were conducted at each stimulation position. The force and acceleration at the attachment point was obtained by a B&K type 8001 impedance head (Brüel and Kjær, Nærum, Denmark). The impedance head was rigidly attached to the connector at the stimulation positions. The cadaver heads were oriented so the impedance head was aligned vertically for each measurement. This was done to avoid excessive shear and bending forces on the force gauge in the impedance head, and also to ensure translational stimulation of the impedance head and connector. The cadaver heads were, for the impedance measurements as well as all other measurements, placed on a pillow to vibrationally decouple the heads from the measurement table.

The outputs from the acceleration and force gauges were supplied to two charge amplifiers (B&K type 2635) and then to the inputs of the measurement system. The PC based software SYSid 6.5 (www.sysid-labs.com), together with a DSP-16+ signal processing card, formed a two-input-channel measurement system that also provided the stimulation signal. The stimulation signal was fed through a power amplifier (D-75, Crown, Elkhart, IN, USA) to a miniaturized bone-transducer, termed the mini-transducer. This transducer has a screw attachment that could connect to either the impedance head or to the screw connectors in the skull. The SYSid measurement system, together with the power amplifier and mini-transducer, was used for all measurements conducted in this investigation.

C. Accelerometer measurements

The vibratory response during excitation was measured as the acceleration of the cochlear promontory in three perpendicular directions. In order to measure the vibration responses in these three directions, a triaxial accelerometer was used (Endevco model 7253C-10, Endevco, San Juan Capistrano, CA, USA). This accelerometer has a size of $15 \times 15 \times 7$ mm^3 and weighs 3.6 g. The triaxial accelerometer was attached to the cochlear promontory by cyanoacrylate glue (Garf Reef glue™, Garf, Boise, ID, USA). To enable positioning of the accelerometer on the cochlear promontory, the auricle was removed and the bony ear canal widened using a drill. To verify that the widening of the ear canal did not affect the vibratory response of the skull, the vibration of the cochlear promontory was measured by a laser Doppler vibrometer before and after the drilling. For these measurements, the vibration transducer was attached to position I-4 on the occiput arc. The two measurements were within the test-retest results found for the vibration measurements when all equipment was removed between the measurements.

D. Laser Doppler vibrometer measurements

The triaxial accelerometer was glued to one cochlear promontory in each of the six heads; on the right side in three and on the left side in three. On the cochlear promontory opposite to the side where the accelerometer was attached, the vibratory response was measured by a laser Doppler vibrometer (LDV)(HLV-1000, Polytec, Waldbronn, Germany). The auricle was removed on this side as well; no drilling of the ear canal was required and the ear canal was left intact. The ear drum was removed together with the malleus and incus. This enabled the laser-beam to reach the cochlear promontory. A good reflection of the laser beam was achieved by a glass bead approximately 5 μm in diameter positioned on the cochlear promontory. Such LDV measurements of BC vibrations have previously been demonstrated reliable (Stenfelt *et al.*, 2002).

The laser head was mounted on an operating microscope with a joystick to control the laser beam. During the measurement, the laser beam was oriented to align with the *x* direction. Since the stimulation positions were symmetrically spread over the skull, the ipsilateral stimulation positions for the accelerometer measurements served as contralateral positions for the LDV measurements and vice versa. Consequently, the accelerometer and LDV measurements are only expected to be similar, not exactly equal. Also, the LDV measures in one direction (*x* direction), whereas three perpendicular directions were obtained with the triaxial accelerometer.

E. Stimulation close to the cochlea

After the previously mentioned measurements were finished, the mastoid portion of the temporal bone was drilled open down to the semicircular canals. A connector screw was attached at the point where the three semicircular canals come close together. This was done bilaterally, and then the same measurements repeated with the mini-transducer attached close to the cochlea. The reasons for the measurement with the stimulation close to the cochlea are twofold. First, the stimulation and response are both in the petrous part of the temporal bone that encapsulates the cochlea. Some of the transmission properties in this bone are normally masked by the skull structure response when the stimulation is applied at the skull surface. Such transmission properties can be revealed using this approach. Second, any improvement in the cochlear promontory vibration level with a source close to the cochlea can be quantified.

F. Calibration

The mini-transducer used was similar to the transducers used in the bone-anchored hearing aid (BAHA®, Tjellström *et al.*, 2001). It was the same transducer as the one used in the study of vibration transmission in a dry human cadaver skull (Stenfelt *et al.*, 2000). The calibration of the mini-

transducer was done on a Skull-Simulator TU-1000 (Håkansson and Carlsson, 1989). This calibration produces the dynamic output force from the transducer for a specific input voltage. The B&K impedance head used for the mechanical impedance measurements was calibrated by two measurements. First, a mass of 50.00 g was attached to the impedance head and the sensitivity of the impedance head was determined (force/acceleration). Then, a measurement was made with the connector unit attached to the impedance head. This measurement was later used for cancellation of the mass below the force gauge and connector unit in the impedance data. During the calibration measurements, the impedance head was driven by a B&K type 4810 mini-shaker.

The low-pass and high-pass filters incorporated in the LDV were used; the low-pass filter cutoff frequency was set at 15 kHz and the high-pass filter was set at 100 Hz. The response of the LDV with these settings was calibrated using an accelerometer (B&K type 4371). According to the manufacturer, this accelerometer has a maximum level deviation of 0.2 dB and a maximum phase deviation of 5°. The accelerometer was mounted on the B&K 4810 mini-shaker and the laser beam aimed perpendicular to the accelerometer surface. With this setup, the amplitude and phase of the LDV were calibrated for the frequencies 0.1 to 10 kHz.

The Endevco model 7253C-10 triaxial accelerometer was calibrated using the LDV. The triaxial accelerometer was mounted with beeswax on a circular adapter attached to the B&K 4810 mini-shaker with the laser beam aimed perpendicular to the accelerometer surface. With this setup, the accelerometer response in the three directions was compared with the calibrated LDV response for frequencies between 0.1 and 10 kHz. Within this frequency range, the maximum level and phase deviation between any direction of the accelerometer and the LDV were 0.2 dB and 3°, respectively. Since this was within the uncertainty limits for the LDV calibration, the sensitivity data given by the manufacturer were used for the triaxial accelerometer.

The rigidity of the glue bond between the cochlear promontory and the triaxial accelerometer was also verified. The laser beam was aimed at the cochlear promontory close to the accelerometer and the vibration response in the x direction measured with both the LDV and accelerometer when the mini-transducer was attached to position occiput arc I-4. With this setup and for frequencies between 0.1 and 10 kHz, the maximum level and phase deviation in any of the six cadaver heads between the LDV and accelerometer measurements were 2.1 dB and 17°, respectively. However, these maximum deviations occurred when the skull showed resonances or antiresonances and were of narrow frequency bandwidth. Discounting these larger deviations of narrow bandwidth, the differences in level and phase between the LDV and accelerometer were bounded by 0.6 dB and 7°, respectively.

G. Distortion

In an investigation by Håkansson *et al.* (1996), the linearity of bone-conducted sound was investigated in live humans for levels corresponding to 77 dB HL. They reported, for those levels, the BC sound transmission to be predominantly linear. In this investigation, the linearity of BC vibration transmission in the skull was not analyzed *per se*. However, the second and third harmonics were studied at each measurement to verify that all equipment functioned properly. The levels of these harmonics were similar to those generated when calibrating the mini-transducer on the skull simulator. Hence, the harmonics in the measurements in this study were chiefly caused by the stimulus generating electronics and the mini-transducer, and not by the vibration transmission through the skull bone. Consequently, any distortion that might be generated in the skull bone was minimal during these tests where the BC stimulation corresponded to levels of 80 to 100 dB HL.

III. RESULTS

A. The mechanical point impedance

The mechanical point impedance was measured at 27 positions on each of the six heads. We considered the heads to be symmetric about the sagittal plane and pooled measurements from the right and left side of the skulls. This pooling produced 12 separate measurements (from the two sides of the six heads) to describe the response at each of four positions (1–4) along the three stimulation arcs (forehead, vertex, and occiput). However, at each of the 0 positions (which are on the sagittal plane), there was only one measurement made in each skull (for a total of six).

The results, as magnitude and phase, of the individual measurements as well as the mean for all positions, are presented in Fig. 2. Similar trends in the impedance data are seen for the individual data at all positions. At the lowest frequencies, below 150–400 Hz, the impedance increases with frequency indicating a mass-controlled system. This is also indicated by a positive phase. At these low frequencies, the head moves as a whole which is reflected in the impedance data.

Depending on position, the maximum magnitude of the mechanical impedance is between 150 and 400 Hz. At the maximum magnitude frequency, the corresponding phase is close to 0° and this frequency is defined as the resonance frequency for the mechanical impedance. Above the resonance frequency, the magnitude of the mechanical point impedance falls with frequency and the accompanying phase drops to approximately −80°, suggesting a stiffness controlled system. At higher frequencies, the phase increases slightly and the average phase of the impedances is between −60° and −20° at 10 kHz. At around 3 kHz, the impedance becomes influenced by the losses in the system. This is seen in the phase as well as in the magnitude data that starts to flatten out above that frequency.

Two general trends can be seen when comparing the impedance data between the positions. First, slightly greater levels of the mechanical point impedances are found at the positions on the occiput arc compared with the other two stimulation arcs. Second, greater impedance magnitudes and higher resonance frequencies are found when moving from the ear canal (position 4) to the mid-sagittal plane (position

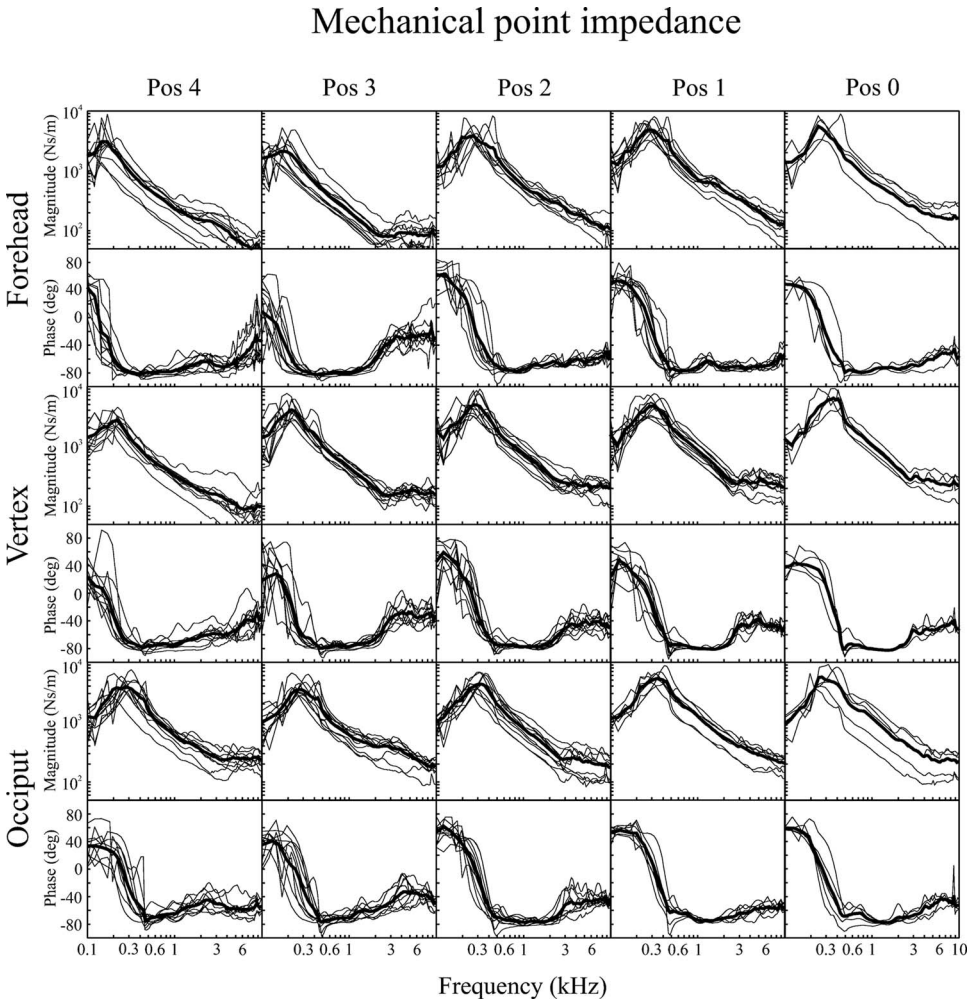

FIG. 2. The mechanical point impedance as magnitude and phase for the positions 0–4 at the three stimulation arcs, forehead, vertex, and occiput. Since the measurement positions are symmetrically spread, the impedance results are pooled to the positions 0–4 regardless of head-side (12 measurements at position 1–4 and 6 measurements at position 0). The individual results are displayed as thin lines and the average as a thick line.

0). We would like to present two possible explanations for the observed results based on (1) geometrical differences and (2) bone thickness and density differences.

The measured point impedance reflects the motion perpendicular to the skull surface at that specific position. However, this motion is a combination of whole head translational and rotational motions as well as local deformation motion of the skull bone. With this in mind, the explanation for the first observation can be that the occiput arc is closer to the skull-base and has a smaller curvature radius than the vertex and forehead arcs. This would give slightly greater stiffness of the bone and corresponding greater impedance magnitude and higher resonance frequency. Another explanation for the first observation can be that the skull bone is thicker along the occiput arc than at the other two arcs. A thicker skull bone would result in a higher stiffness and corresponding higher impedance magnitude and resonance frequency.

The second observation can be explained similarly. The skull is not symmetrical as a sphere but more like an ellipsoid with flat sides. Such geometry produces greater stiffness at positions with a smaller curvature radius and smaller flat sections (as at the sagittal plane) than at positions in the middle of a larger flat section. The sides of the head, where the ears are situated, form a relatively large flat section including the temporal part of the parietal bone. Consequently, the bone close to the ear (positions 3 and 4) is more flexible than the bone close to the sagittal plane (positions 0 and 1), so the impedance and resonance frequency should be elevated closer to the sagittal plane than close to the ear, as shown in Fig. 2. However, the thickness of the skull bone is not constant. In general, slightly thicker skull bone is found around the sagittal plane of the head than at the sides. Such thickness distribution would also produce the result seen in Fig. 2. Since these two phenomena produce similar results, it is difficult to conclude if one is dominating.

B. Accelerance of the cochlea in a single head

With the triaxial accelerometer on the cochlear promontory, the response acceleration was measured in three perpendicular directions (x, y, and z direction) for 27 stimulation positions. The acclerances (acceleration divided by force) from these measurements in one head, as level and phase, are presented in Fig. 3. The results are grouped for each stimulation position; the responses in the x direction are shown with a solid line, in the y direction with a dashed line, and in the z direction with a dotted line. The panels labeled I-1 to I-4 are the results obtained with the stimulation applied at positions 1–4 at the ipsilateral side. Panels labeled C-1 to C-4 are the vibration responses at the cochlear promontory with the stimulation at the positions 1–4 on the contralateral

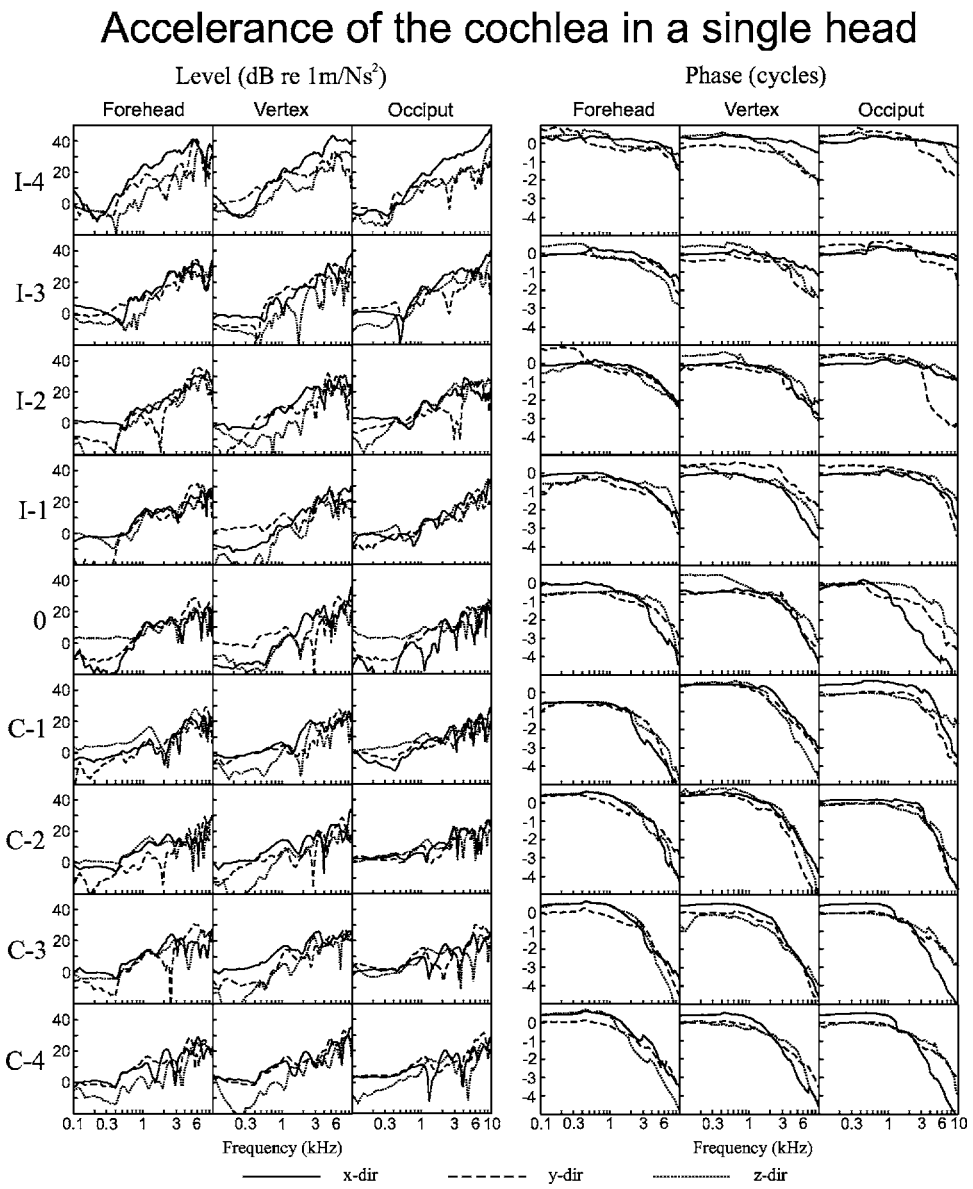

FIG. 3. The accelerance (acceleration/force) as level (*re*: 1 m/Ns^2) and phase (cycles) measured on the cochlear promontory for all three measurement directions (x,y,z) and all stimulation positions (27) in one individual head. The stimulation was applied by a mini-transducer rigidly attached to the skull-bone surface. With the stimulation applied on the ipsilateral side, the results are displayed as I-1 to I-4, with the stimulation at the mid-sagittal plane as 0, and with the stimulation positions on the contralateral side as C-1 to C-4. The results are divided into the stimulation arcs, forehead, vertex, and occiput, and the directions are separated by the patterns: *x* direction—solid line, *y* direction—dashed line, and *z* direction—dotted line.

side; the panels labeled 0 are the results with the stimulation applied on the mid-sagittal plane of the skull.

The level responses should be interpreted as the acceleration level in m/s^2 in the three directions, when the excitation is a vibration of 1 N at the stimulation position. The accumulation of phase is indicative of the time delay, due to vibratory wave transmission in the skull bone between the stimulation position and the cochlear promontory. At low frequencies, approximately below 500 Hz, the responses are similar for all stimulation positions: around 0 dB *re*: 1 m/Ns^2 and a flat phase close to 0 or ±0.5 cycles. At theses low frequencies, the skull moves as a whole (rigid body motion) and the responses are determined by translational and rotational inertia. Since the application of the vibration transducer is approximately perpendicular to the skull surface, the stimulation direction differs between the positions (cf. Table II). The low-frequency response is a function of the relative excitation in the three stimulation vectors and the six degrees of freedom rotational and translational responses.

Above the frequency area of rigid body motion of the skull, the accelerance increases with frequency. The differences between the response directions depend on stimulation position. With the stimulation at positions I-4, the response vibration at the cochlear promontory is greatest in the *x* direction. Also, the overall accelerance is greatest at positions I-4. In general, for stimulation on the ipsilateral side, the response level decreases and accumulated phase increases with distance between the stimulation position and the cochlear promontory. When the stimulation is applied on the contralateral side, no systematic differences between the positions C-1 and C-4 can be identified; the responses are similar in both level and phase. Except for the stimulation positions closest to the cochlea (I-4), no overall dominating response direction is seen; the response is in all three directions whether the stimulation is applied at the ipsilateral or contralateral side.

The number of antiresonances[2] in the accelerance functions in Fig. 3 increases with distance from the cochlea. Most antiresonances are found when stimulation is on the contralateral side close to the sagittal plane (positions 0 to C-2). A general observation is that these antiresonances do not

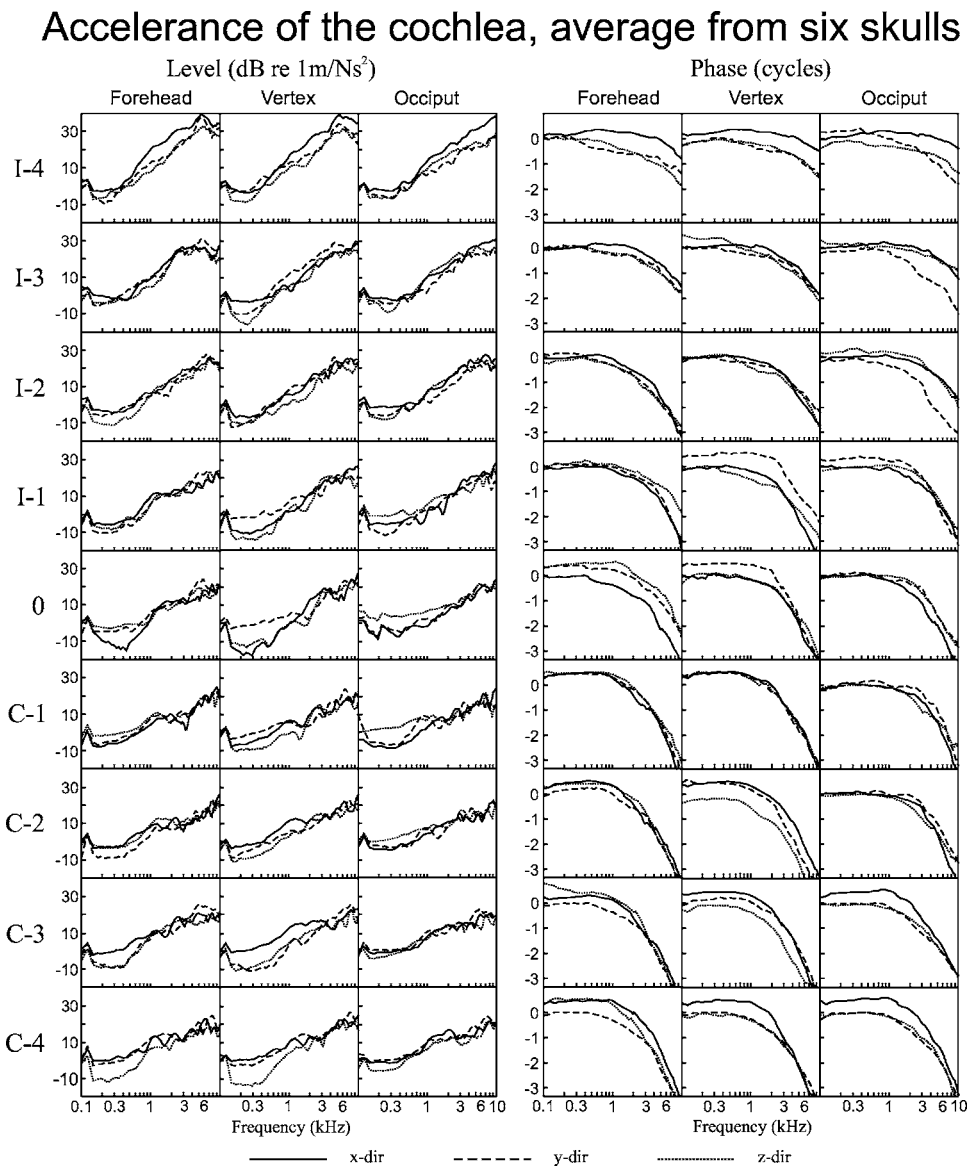

FIG. 4. The average of the accelerance as level and phase from the six heads. The results are averaged for each direction (x, y, and z) and each stimulation position (27). The data have been divided into the stimulation arcs, forehead, vertex, and occiput. The results in the x direction are displayed with a solid line, in the y direction with a dashed line, and in the z direction with a dotted line.

occur in all three directions at the same frequency. The antiresonances can be easily seen in the level response whereas the resonances are difficult to identify by examining the level and phase data in Fig. 3; this indicates that they are highly damped and do not significantly influence the measured response levels.

A phenomenon that may contribute to the vibration response is intracranial standing waves. With a wave speed of approximately 1500 m/s, such intracranial standing waves would produce an antiresonance near 4 kHz and a resonance near 8 kHz that would appear in the contralateral responses. Since it is almost impossible to distinguish between resonances and antiresonances caused by intracranial standing waves and wave transmission in the cranial vault, the results obtained can neither verify nor refute the existence of intracranial standing waves.

C. Average accelerance of the cochlea from six heads

Figure 4 presents the results of the accelerance measurements from the 27 stimulation positions in three directions similar to Fig. 3: the difference is that Fig. 4 presents the average results from all six heads used in this investigation. When the stimulation is applied in the x direction close to the cochlea, that direction produces the greatest responses. When the stimulation is further away from the cochlea, no dominating response direction is found; the response levels are similar in all three directions. At the low frequencies, below approximately 500 Hz, the accelerance level is close to 0 dB *re*: 1 m/Ns^2 and the phase is flat, indicating rigid body motion. At higher frequencies, the accelerance level increases and more phase is accumulated. Also, more phase is accumulated with distance between the stimulation position and the cochlear promontory, indicating longer time delay for the wave transmission in the skull bone. With the stimulation at the ipsilateral side, the accelerance level at frequencies above 500 Hz decreases with distance between stimulation position and the cochlear promontory. When the stimulation is at the contralateral side, no significant difference in the accelerance levels is found.

One way to compare the vibration at the cochlear promontory for different stimulation positions is to calculate a

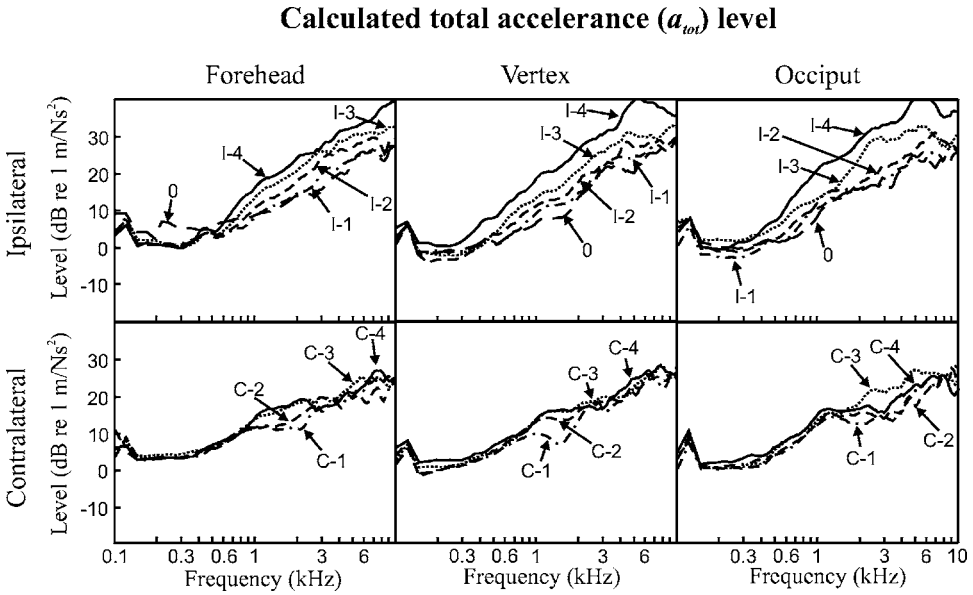

FIG. 5. The average of the total accelerance (a_{tot}) level calculated as the quadratic summation of the accelerances in the three directions from each stimulation position. The results are displayed for the stimulation arcs (forehead, vertex, and occiput) and for the stimulation side of the skull (ipsilateral and contralateral). The accelerance levels with stimulation at the ipsilateral side are displayed as position I-4—solid line, position I-3—dotted line, position I-2–dashed line, position I-1—dashed-dotted line, and position 0 (mid-sagittal plane)—long dashed line. Similarly, the results with contralateral stimulation are position C-4—solid line, position C-3—dotted line, position C-2—dashed line, and position C-1—dashed-dotted line.

single vibration response for each frequency. The total accelerance can be computed as a sum of the three orthogonal accelerance components (quadratic summation). This can be seen as a measure of the vibratory energy. The summation is

$$a_{\text{tot}}^2 = a_x a_x^* + a_y a_y^* + a_z a_z^*, \tag{1}$$

where a_{tot} is the calculated accelerance and a_x, a_y, and a_z are the accelerances in the x, y, and z directions, respectively. The $*$ in Eq. (1) indicates the complex conjugate. The total accelerance a_{tot} according to Eq. (1) is presented in Fig. 5. The acclerances with ipsilateral stimulation are presented in one panel for each stimulation arc, and the results with contralateral stimulation in one panel for each stimulation arc (forehead, vertex, and occiput). The results in Fig. 5 are the averages from all six heads investigated; they include the results already found in the single and averaged accelerances (Figs. 3 and 4). At low frequencies, approximately below 500 Hz, no significant difference in accelerance is found between stimulation at the different positions, whether ipsilateral or contralateral. Above 500 Hz and with ipsilateral stimulation, the accelerance level is greatest when the stimulation is closest (position I-4) and worse when it is at the mid-sagittal plane (position 0), gradually decreasing from position 4 to position 0. With the stimulation at the contralateral side, the accelerances are similar. No significant difference can be seen between the three measurement arcs, forehead, vertex, and occiput.

D. Laser Doppler measurements

Accelerances measured with the LDV are presented in Fig. 6 as level and phase averaged from the six heads. The LDV only measures the vibration in one direction, here the x direction, and the results in Fig. 6 are compared with the results in the x direction in Fig. 4. However, the stimulation positions used for the ipsilateral results with the LDV are the same stimulation position used for the contralateral results with the triaxial accelerometer and vice versa. The results using the two measurement techniques are therefore not expected to be exactly equal, only similar. The level correspondence of the accelerance measurement with the LDV and the accelerometer is in general better than 2 dB; however, some exceptions with up to 5-dB differences at limited frequency areas exist. The phase difference of the accelerance between the two measurement methods increases with frequency and are, for most measurements, between 0.1 and 0.5 cycles at 10 kHz. The exception is for stimulation at position C-4 in the vertex arc where the phases differ by more than 1.5 cycles at the highest frequencies. Although the phases differ greatly at some positions, the results obtained with the LDV correspond fairly well with the x direction results obtained with the accelerometer. Unless otherwise stated, the vibration results of the cochlear promontory presented hereafter are from data obtained with the accelerometer.

E. Relative sensitivity, ipsilateral stimulation

From Figs. 3–6 it is clear that the greatest vibration of the cochlear promontory is obtained when the stimulation is closest to the cochlea, i.e., when the stimulation is at positions I-4. To compare the efficiency of vibration transmission, in terms of vibration level, from the ipsilateral positions to the cochlear promontory, the relative accelerance was computed (Fig. 7). All measurements presented in Fig. 7 are compared with position occiput arc I-4 (reference position). The comparisons are conducted for vibration measurements in the x direction and the total vibration response (a_{tot}) according to Eq. (1). In the x direction, relative levels and phases are presented, whereas only the relative levels are presented for total accelerance (a_{tot}).

The general finding of the comparison is that the closer to the cochlea the stimulation position is, the greater the stimulation level and the less phase accumulates (less time delay). The relative total accelerance levels are similar, and the x direction phase differences are close to 0 cycles at frequencies below 500 Hz. This is where the heads move as a whole and the relative a_{tot} results are expected to be similar. However, some differences can occur due to imperfect alignment of the stimulation axis and the heads center of gravity;

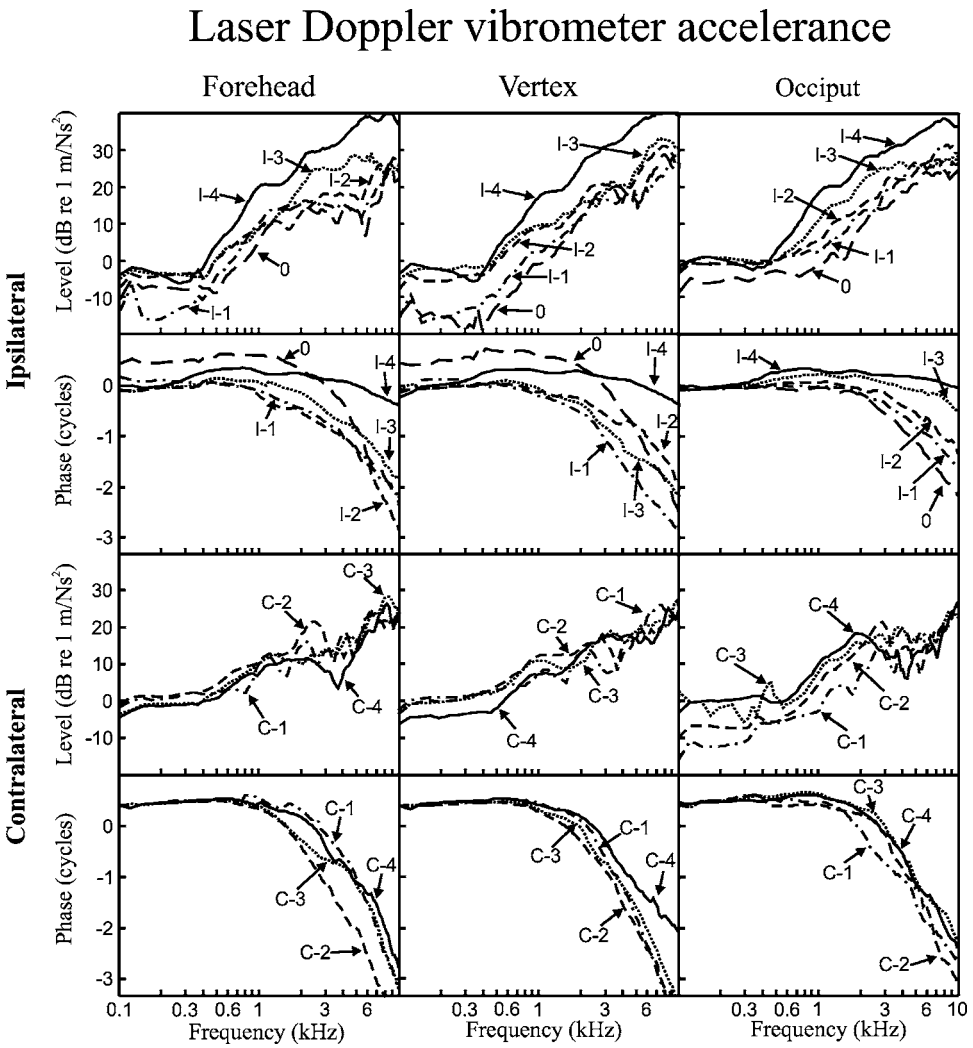

FIG. 6. The accelerance in the x direction as level and phase measured with the laser Doppler vibrometer aimed at the cochlear promontory. The accelerances displayed are the average of the result from the six heads. The results with ipsilateral stimulation are displayed as position I-4—solid line, position I-3—dotted line, position I-2—dashed line, position I-1—dashed-dotted line, and position 0 (mid-sagittal plane)—long dashed line. Similarly, the results with contralateral stimulation are position C-4—solid line, position C-3—dotted line, position C-2—dashed line, and position C-1—dashed-dotted line.

this could give slightly different translational and rotational skull motions. The relative levels of the x direction differ considerably with stimulation position at low frequencies. This is caused by the stimulation direction: at positions close to the cochlea (positions 3 and 4) the stimulation direction is almost solely in the x direction while, at positions further from the cochlea (positions 0–2), it gradually aligns in the y-z plane (cf. Table II).

According to the a_{tot} panels in Fig. 7, the transmission loss increases by approximately 1 to 3 dB for each position further away from the cochlea at frequencies above 1.0 kHz. Positions I-4 at the vertex and forehead stimulation arcs show greater cochlear vibration response compared with position I-4 at the occiput arc: position I-4 at the vertex arc produces 3 to 7 dB greater vibration response for frequencies between 0.5 and 7.0 kHz, and position I-4 at the forehead arc produces 5 to 10 dB greater response between 0.7 and 7.0 kHz. The results measured in the x direction are similar to the total accelerance results for all three stimulation arcs with stimulation at positions 3 and 4. At these positions, vibration in the x direction dominates the vibration response and, consequently, the total x direction accelerance responses are similar. For the other positions, stimulation in the x direction shows generally worse transmission relative to position occiput arc I-4 than when the response is analyzed according to the total transmission (a_{tot}). In terms of transmission efficiency, the worst position to place a BC transducer is on the mid-sagittal plane. For frequencies above 1 kHz, the difference in vibration transmission between positions I-4 and the position 0 is 10 to 20 dB for the total accelerance transmission and 15 to 25 dB when the measurements are in the x direction.

F. Transcranial transmission

The term transcranial attenuation is often used as a measure for the difference in vibration level between the ipsilateral and the contralateral side of a human head. Here, we use the term transcranial transmission defined as the vibration at the contralateral cochlear promontory relative to the vibration at the ipsilateral cochlear promontory for a specific stimulation position. With this definition, the transcranial transmission is theoretically 1 for any stimulation applied on the sagittal plane (same vibration response at both cochleae). The transcranial transmissions for stimulation positions 1–4 at all three stimulation arcs are presented in Fig. 8. Similar to the presentation in Fig. 7, the analysis is conducted for measurements in the x direction (level and phase) and for the total vibration response (a_{tot}) according to Eq. (1).

Several general trends are found in the data displayed in

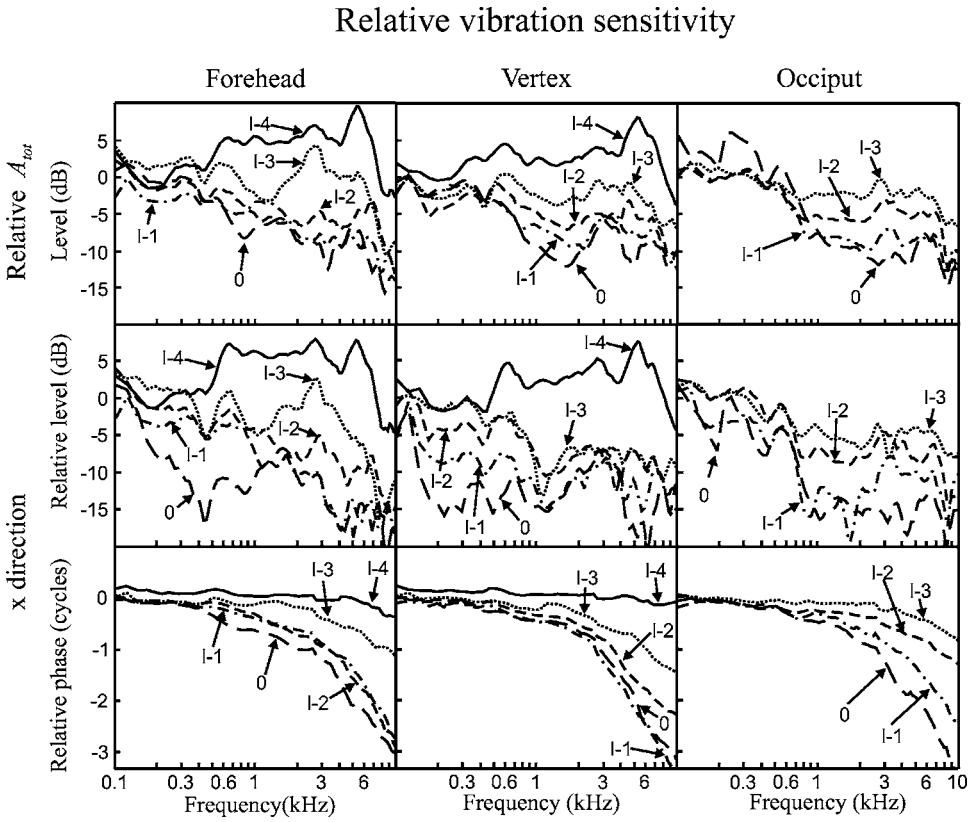

FIG. 7. The relative vibration of the cochlear promontory presented for the x direction as level and phase, and as the level for the total accelerance analysis (all directions quadratically summed, a_{tot}). The stimulation is at the ipsilateral side. All results are relative to the result from occiput arc I-4 and averaged for the six heads. The relative cochlear promontory vibration is displayed as position I-4—solid line, position I-3—dotted line, position I-2—dashed line, position I-1—dashed-dotted line, and position 0 (mid-sagittal plane)—long dashed line.

Fig. 9. At the low frequencies, below 500 Hz, where the skulls move primarily as a whole, 2 to 3 dB greater a_{tot} responses are found at the contralateral cochlear promontory compared with the ipsilateral cochlear promontory. For the x direction response, the transcranial transmission is close to 0 dB at the occiput and forehead stimulation arcs; at the vertex arc the transcranial transmission is approximately 5 dB at these low frequencies. For frequencies above 1 kHz, the transcranial transmission for positions 1–3 show similar level responses (both a_{tot} and x direction results): the levels

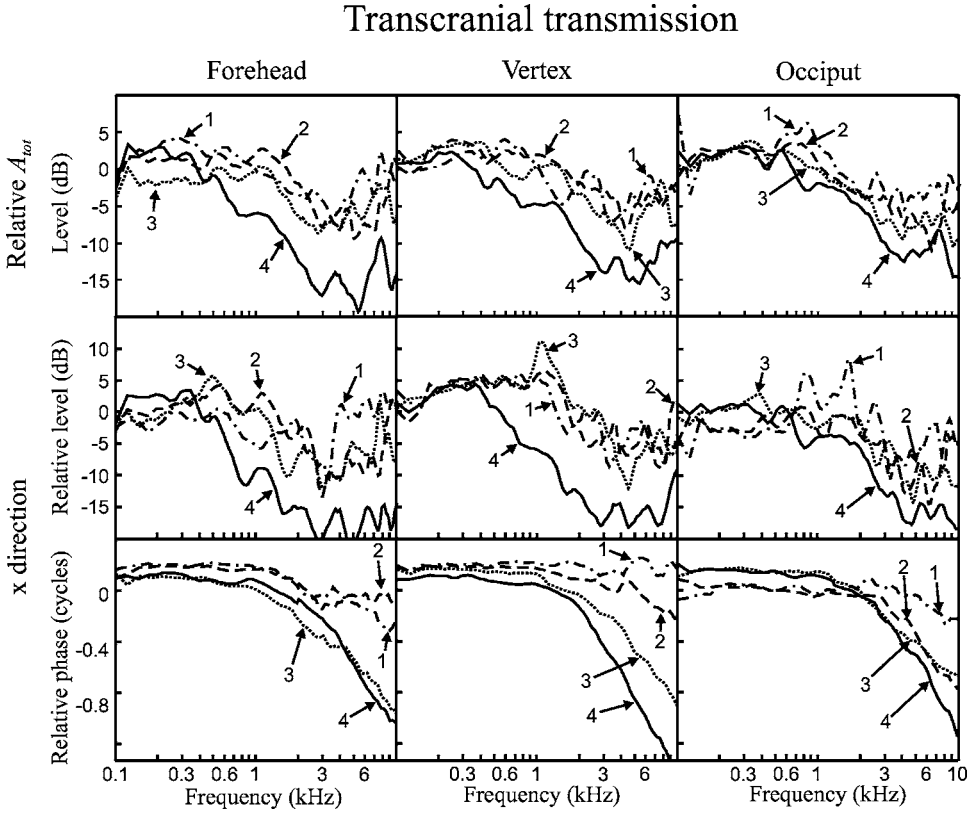

FIG. 8. The transcranial transmission is calculated as the acceleration response at the contralateral cochlear promontory divided by the acceleration response at the ipsilateral cochlear promontory for the same stimulation and position. The results are presented as the total accelerance level (quadratic summation of all three directions), and level and phase for the x direction. The presented transcranial transmission is averaged over the six heads. The results are displayed for the positions at each stimulation arc: position 4—solid line, position 3—dotted line, position 2—dashed line, and position 1—dashed dotted line.

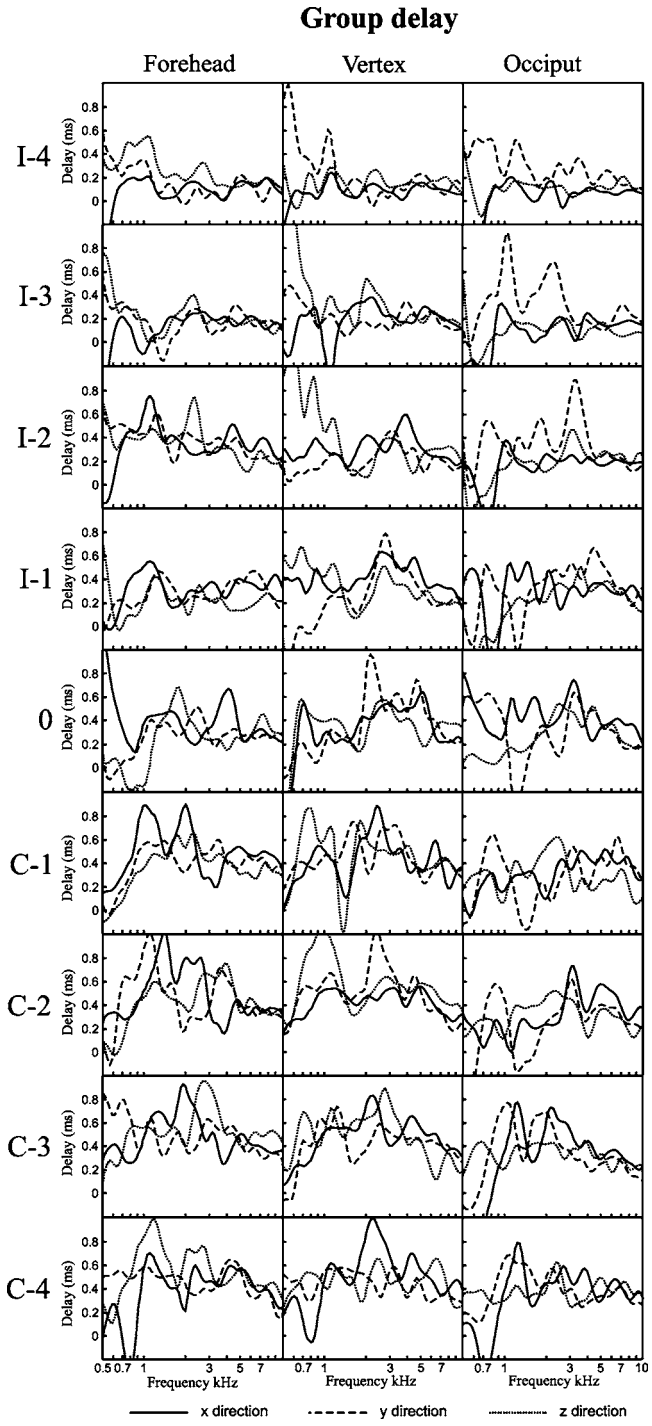

FIG. 9. The group delay calculated from the acceleration on the skull surface to the acceleration on the cochlear promontory. The delays are the average of the result from the six heads. The results are displayed for all positions at each stimulation arc and in the three measurement directions: x direction—solid line, y direction—dashed line, and z direction—dotted line.

decrease and become −5 to −10 dB around 5 kHz. At the highest frequencies investigated, above 6 kHz, the transcranial transmission increases slightly and generally becomes 0 to −5 dB.

When the stimulation is closer to the cochlea, at position 4, greater interaural differences are obtained. At frequencies above 500 Hz, the transcranial transmission decreases with frequency up to around 3 kHz, where the changes with frequency are irregular. The transcranial transmission at all positions 4 at frequencies above 3 kHz stays between −10 and −20 dB, with slightly greater interaural differences for the x direction measurements than for the a_{tot} analysis.

In the x direction, the relative phases in Fig. 8 show similar results at all three measurement arcs. At frequencies below 1 kHz, the relative phases for all stimulation positions are flat and, above 1 kHz, the relative phases fall off. The relative phase difference between the cochlear promontories is greatest when the stimulation is close to the ipsilateral cochlea. In Fig. 4, the accelerance phases with contralateral stimulation show similar results regardless of stimulation position, whereas the phases differ between the responses of the ipsilateral stimulation positions. As a result, the relative phase differences at high frequencies in the x direction transcranial transmission presented in Fig. 8 are mainly due to the accumulated phase in the ipsilateral transmission path. This can also be observed when comparing the relative phases presented in Figs. 7 and 8; although not exactly equal, the relative phases show similar results. It should be noted that the positions are switched; position 1 in Fig. 7 should be compared with position 4 in Fig. 8, position 2 in Fig. 7 with position 3 in Fig. 8, etc.

G. Wave velocity and time delay

The time delay from stimulation at the skull surface to a vibration of the cochlear promontory can be calculated from the phase of the frequency response function. For that analysis, the acceleration at the skull surface to the acceleration of the cochlear promontory (acceleration transfer function) was calculated. This was achieved by using the accelerance function together with the mechanical impedance function measured at the stimulation positions. Using the acceleration transfer function, the group time delay τ_{gd} was calculated from the phase according to

$$\tau_{gd} = -\frac{1}{2\pi}\frac{d\phi(f)}{df}, \tag{2}$$

where $\phi(f)$ is the phase of the acceleration transfer function in radians per second and f is the frequency in Hz. The results from the group delay calculation at each stimulation position are averaged for the six heads and presented in Fig. 9 for the frequencies 0.5 to 10 kHz. In this frequency range, the group delay varies with frequency. For some of the measurements, and at some frequencies, predominately the lower, the delay is negative. A negative time delay indicates a noncausal system which is unphysical. However, a negative group delay does not necessarily indicate a noncausal system; numerous causal systems with negative group delays exist (Mitchell and Chiao, 1998). It is only if the frequency response function has a relatively constant group delay over a frequency region that a signal with a bandwidth corresponding to that frequency range is delayed according to the group delay. If this prerequisite is not fulfilled, the delay of a signal is not easily related to the group delay. The group delays in Fig. 9 vary with frequency, and no simple time delay for the acceleration transmission in the skulls can be extracted. However, if

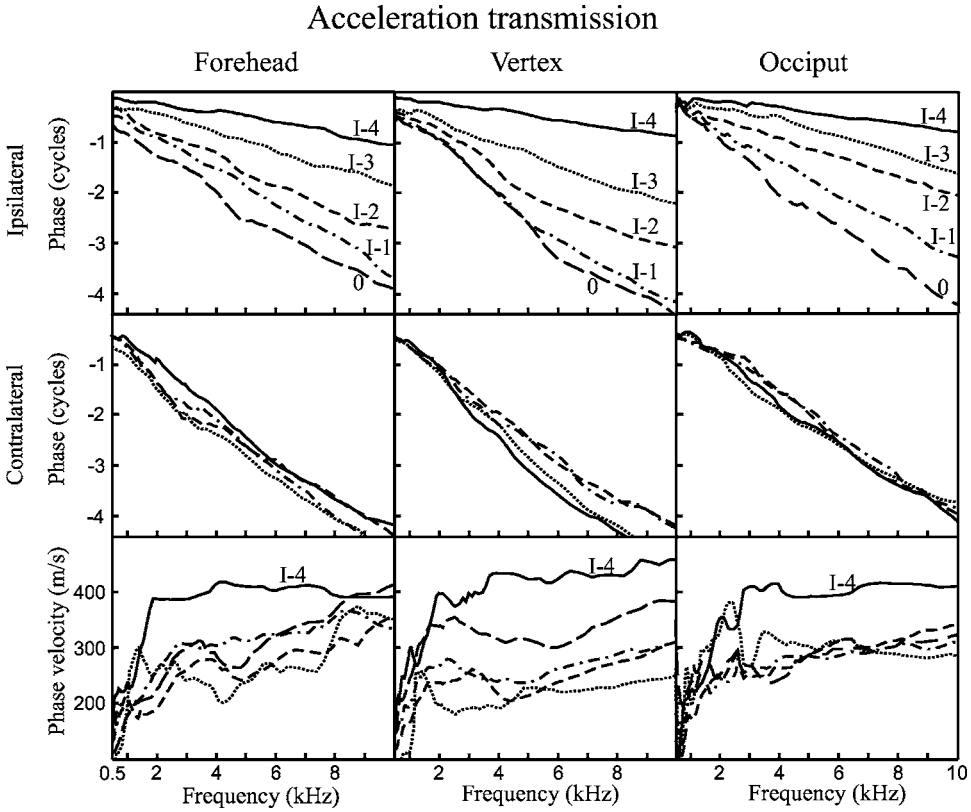

FIG. 10. The phases of acceleration at the skull bone surface to the acceleration at the ipsilateral and contralateral cochlear promontories are displayed with a linear frequency scale (0.5–10 kHz). The calculated phase velocities for the ipsilateral stimulation positions are also displayed. All data are from measurements in the *x* direction and averaged for all six heads. The phase velocity for position I-4 is calculated using the phase difference between the acceleration at the cochlear promontory and position I-4, whereas the phase velocities at positions I-3 to 0 are calculated using the phase differences between the accelerances at position I-4 and position I-3 to 0, respectively. Consequently, the phase velocity of position I-4 is an estimate of the wave speed in the skull-base whereas the others are estimates of the wave speed in the cranial bone.

the analysis is limited to frequencies between 1 and 10 kHz, some general trends can be found.

The overall result in Fig. 9 shows that on the ipsilateral side, the group delay increases with distance from the stimulation position to the cochlea. Close to the cochlea (position I-4), the group delay is approximately between 0 and 0.2 ms while it is closer to 0.4 ms when the stimulation is at the sagittal plane (typically between 0.2 and 0.6 ms). When the stimulation is on the contralateral side, the group delay stays primarily between 0.2 and 0.6 ms. Since the time delay is not constant but varies irregularly with frequency, dispersion of BC sound can be expected.

Another analysis of wave transmission and wave velocity of BC sound in the human head is presented in Fig. 10. Here, the average of phases and phase velocities of the acceleration transmission are presented for the stimulation positions. The data are displayed using a linear frequency scale between 0.5 and 10 kHz. The panels are divided into ipsilateral phase, contralateral phase, and ipsilateral phase velocity. When examining the phase data, the ipsilateral phases seem to decrease fairly linearly with frequency indicating a constant phase velocity. The phases from the four contralateral stimulation positions show similar phases. This means that the time delays from the contralateral positions are similar.

The phase velocities for the ipsilateral stimulation positions are calculated and presented in the panels at the bottom of Fig. 10. The phase velocity with stimulation at position I-4 is calculated according to

$$V_p = \frac{2\pi f d}{\phi_d(f)}, \tag{3}$$

where $\phi_d(f)$ is the phase difference of the acceleration between position I-4 and the cochlear promontory, f is the frequency, and d is the distance between position I-4 and the cochlear promontory. Position I-4 is on, or very close to, the petrous part of the temporal bone in the skull-base; the velocity estimate for position I-4 is for the wave propagation in that bone. The other positions are on the cranial bone surface where the bone thickness is thinner. Therefore, if the phase velocity is calculated similar to what was done for position I-4, the phase velocity is a mixture of the phase velocities in the thin cranial bone and the dense petrous bone. In order to separate between the phase velocity in the cranial bone and the petrous bone, position I-4 represents the phase velocity in the petrous bone and the positions 0 to I-3 are computed to produce an estimate of the phase velocity of the wave propagation in the cranial bone. This is achieved by calculating the phase difference of the accelerance function between position 0 to I-3 and position I-4. This phase difference (in radians) and the distance between the position and position I-4 forms the $\phi_d(f)$ and d used in Eq. (3) to calculate the phase velocity. Accordingly, the phase velocities in Fig. 10 are estimated for sound transmission in the petrous bone (position I-4) that represents the thicker skull-base and the thinner cranial bone (position 0 to I-3), separately. No estimate of the phase velocity is done for stimulation on the contralateral side. This is primarily due to the problem of estimating the correct wave transmission distance between the contralateral positions and the ipsilateral cochlear promontory.

The rapid increase in phase velocity at frequencies between 0.5 and 2 kHz seen in Fig. 10 is caused by the transition from the low-frequency mass-spring system of the skull to wave transmission motion of the skull at the higher frequencies. At the low frequencies, where the skull motion is dominated by the distributed mass and compliance, phase velocity and wave velocity have no meaning. The phase ve-

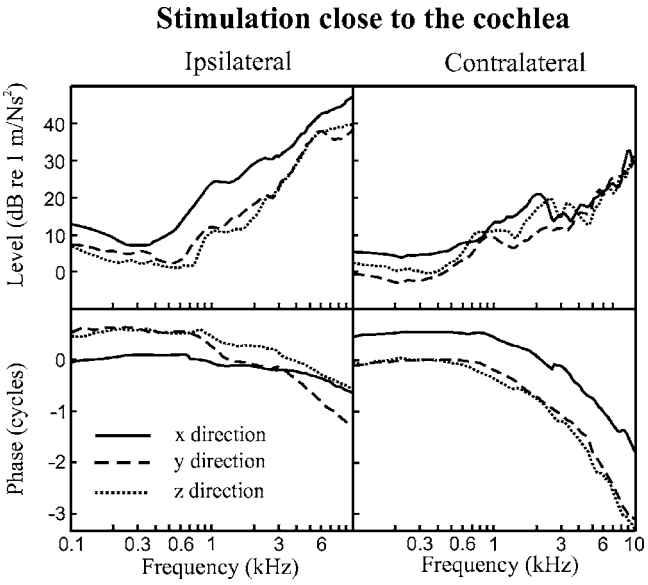

FIG. 11. Accelerances as level and phase measured in the three directions at the cochlear promontory when the stimulation is at the solid angle (intersection of the three semi-circular canals) close to the cochlea. The accelerances are displayed separately for ipsilateral and contralateral stimulation; the results are the average from the six heads. Results in the x direction are shown with a solid line, in the y direction with a dashed line, and in the z direction with a dotted line.

locity in Fig. 10 at these low frequencies is a result of the stationary phase difference of the motion between two positions on the skull; it does not represent the wave speed of the skull vibrations. At higher frequencies, above 2 kHz, the phase velocity gives an indication of the wave transmission mode and its velocity.

The phase velocity at frequencies above 2 kHz in the petrous bone (position 4) shows velocities close to 400 m/s, except on the vertex arc where the velocity increases slightly with frequency. The wave transmission at position 4 is almost solely in the petrous bone in the skull base, and the wave motion is believed to be predominantly longitudinal. At the other ipsilateral positions, the phase velocity was calculated between the stimulation positions and position I-4. In this way, and for frequencies above 2 kHz, the phase velocity in the cranial bone is estimated to increase from around 250 m/s at 2 kHz to 300 m/s at 10 kHz. Such an increase indicates a mixture of wave modes; these may include bending as well as longitudinal wave motion.

H. Stimulation close to the cochlea

After all the previously described measurements were finished, a bilateral mastoidectomy was conducted on the heads enabling stimulation directly on the otic capsule. The mean accelerance from the six heads with stimulation at the ipsilateral and contralateral cochlea is shown in Fig. 11. The stimulation axis is predominantly in the x direction; this can be seen in the 5 to 10 dB greater level in that direction with ipsilateral stimulation compared with the vibration in the perpendicular plane. Compared with stimulation on the skull surface at positions I-4, the ipsilateral vibration level is approximately 10 dB greater with stimulation close to the cochlea. Also the response with contralateral cochlear stimulation is greater compared with stimulation at the skull surface at positions C-4; at frequencies above 1 kHz, stimulation close to the cochlea gives about 5 dB greater levels.

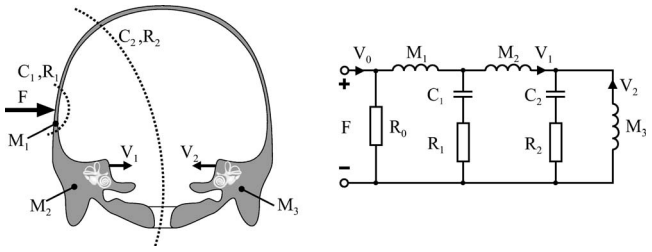

FIG. 12. A cross sectional view of the skull (left) and a corresponding lumped parameter impedance model of the vibration (right). The model is appropriate for the dynamic behavior of the skull at frequencies below the first skull resonance (approximately 1 kHz). The input force at the stimulation position is F, while V_1 and V_2 are the velocities at the ipsilateral and contralateral cochlea, respectively. The elements used in the model are masses (M), compliances (C), and dissipative elements (R).

I. Model of skull motion

In order to better conceptually grasp skull motion and the transition from low-frequency whole body motion to high-frequency wave transmission, a simplified one-dimensional mass-spring model of the skull was devised. This model, a lumped element impedance model, is in principle the same model proposed for low-frequency skull motion in a dry skull (Stenfelt *et al.*, 2000); the difference is an additional damping element (resistance R_0) in the present model, and the element values differ. A cross-sectional view of the skull bone going through the petrous bone is depicted in Fig. 12 (left) together with the lumped element impedance model (right). The velocities at the two cochleae when the stimulation is a force at the mastoid skull surface are shown in both the cross section and the impedance model. Although the model estimates the low-frequency velocity at the cochleae in one direction, the model does not provide the full motion of the cochlea.

The greatest limitation of the model is that the results are in one direction; from this study it is clear that the vibration at the cochlear promontory is in all three dimensions when the mastoid bone is excited. However, at low frequencies and with the stimulation at the mastoid in primarily the x direction, the response is greater in that direction. Another limitation is that, though the model topography is general, the values of the model elements depend on the position of the stimulation. For example, the element values in the model are different for vibration estimation with excitation at position I-4 and position I-3.

Although with limitations, the model can highlight some of the low-frequency phenomena seen in the vibration results. According to the model, the skull can be divided into three parts: (1) the area around the stimulation position that moves in phase (M_1), (2) part of the ipsilateral side comprising the ipsilateral petrous bone (M_2), and (3) the contralateral side including the contralateral petrous bone (M_3). These three areas are coupled with compliances (the inverse of a spring) including losses (C_1, R_1, and C_2, R_2). The three areas are not constant but change with frequency. Therefore, the

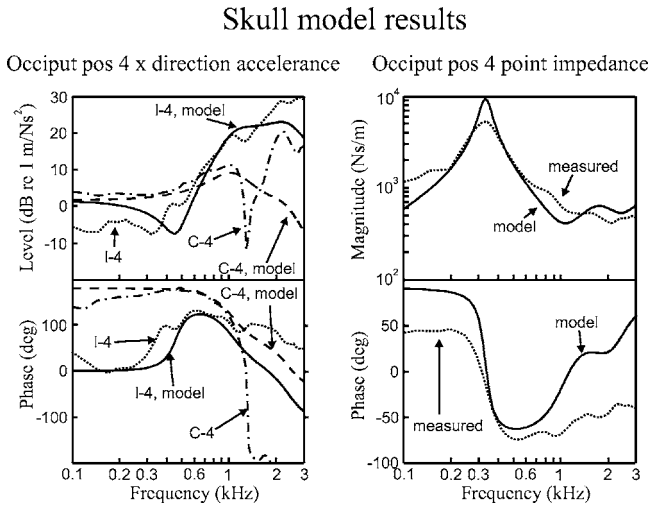

FIG. 13. Comparison of model and measured data. The x direction ipsilateral and contralateral accelerances with the stimulation at position occiput arc 4 are shown as level and phase (left). The impedance data for position occiput arc 4 are shown as level and phase (right). In the accelerance data, ipsilateral model results are shown with a solid line, contralateral model results with a dashed line, ipsilateral measured data with a dotted line, and contralateral measured data with a dash-dotted line. In the impedance data, the model data are shown with a solid line while the measured data are shown with a dotted line. The measured data are the same as the single head data presented in Fig. 3.

element values are a function of frequency. For example, the mass around the stimulation position (M_1) decreases with frequency since a smaller part of this mass vibrates in phase as the frequency increases. However, since the greatest effect of the individual elements are found when they interact with each other (producing resonances or antiresonances), we use constant values in the present model to represent the elements at the frequencies around these resonances and antiresonances.

The model was supplied with element values to fit the results from occiput arc I-4 in Fig. 3. More details about the element values and fitting procedure can be found in the Appendix. Since some characteristics of the vibration response are lost when the data are averaged, the model results were compared with data from a single head. The results can be seen in Fig. 13. With a slight adjustment of the element values, similar comparisons can be conducted with any stimulation position in any of the heads. The model results are compared with the level and phase data of the x-direction accelerance and mechanical impedance from position occiput arc I-4. The measured data presented in Fig. 13 are the same as presented in Fig. 3.

In the accelerance level panel, an indication of a skull resonance is found at 1050 Hz. The model is therefore only valid at frequencies below this frequency. At the lowest frequencies, the response is a true rigid body motion where the ipsilateral and contralateral accelerances are of the same level with opposite phases. At higher frequencies, an antiresonance can be seen in the ipsilateral accelerance function with a resonance frequency near 450 Hz. The level of the contralateral accelerance is greater than the ipsilateral around this antiresonance frequency, and this is the reason for the low-frequency gain in the transcranial transmission (Fig. 8). The accelerance level with ipsilateral stimulation becomes greater than the contralateral at 700 Hz. The low-frequency mass behavior of the skull can be seen in the impedance panels as well. However, the measured impedance phase at the lowest frequencies indicates a large influence of damping, producing a phase of 45°. Although a loss element was included at the stimulation position in the model, such phase behavior of the model impedance was not achieved. It is the mechanical impedance phase that shows the greatest discrepancy between model and measured data. The impedance resonance appears at 310 Hz; above this frequency the impedance data are primarily compliance dominated except the phase data at the higher frequencies.

The resonance seen in the impedance data is in principle the same as the antiresonance found in the ipsilateral accelerance data. If the stimulation is applied directly on the petrous bone (e.g., Fig. 10), the ipsilateral accelerance is the inverse of the integrated mechanical impedance, and, consequently, the antiresonance in the accelerance function appears as a resonance in the impedance function. Since the impedance and ipsilateral accelerance are measured at two spatially different positions in Fig. 13, the vibration is measured at the stimulation position to calculate the impedance and on the ipsilateral cochlear promontory (M_2) for the accelerance, the resonance frequency differs. The general finding is that the frequency of this antiresonance increased with distance between the stimulation position and the ipsilateral cochlea.

For the phase response of the ipsilateral transmission in Fig. 12, the model was extended with a high-frequency part. At frequencies below 1 kHz, the phase response from the model in Fig. 12 was used, and at frequencies above 2 kHz a phase response derived with a constant time delay was used. The model changes gradually from the low-frequency model to the high-frequency model at frequencies between 1 and 2 kHz. The details of this phase model and transition between low- and high-frequency parts in the model are described in the Appendix. Using this model, with a time delay corresponding to a phase velocity of 450 m/s and a distance between stimulation position (occiput arc I-4) and cochlear promontory of 3.5 cm, Fig. 14 displays the results and a comparison with the skull measurements as phase, phase velocity, and group delay, similar to that presented in Figs. 9 and 10. As in Fig. 13, the model data are compared with occiput arc I-4 data from the skull shown in Fig. 3.

The results in Fig. 14 show that the model data were similar to the measured responses. The model phase increases at the lowest frequencies (500 Hz) and falls off at frequencies above 1 kHz. The measured phase shows a similar trend: increases at the lowest frequencies and decreases at frequencies above 1.2 kHz. However, the measured phase has a local minimum at 1 kHz and decreases at a slower rate for frequencies above 6 kHz. The model and measured phase velocities are also similar. The model phase velocity increases from around 100 m/s at 500 Hz to around 450 m/s at frequencies above 1 kHz (according to the model, the phase velocity is set to 450 m/s at frequencies above 2 kHz). Once again, the measured data have a local minimum at 1 kHz and stays between 400 and 550 m/s at frequencies above 1.2 kHz. Compared with the model data, the measured

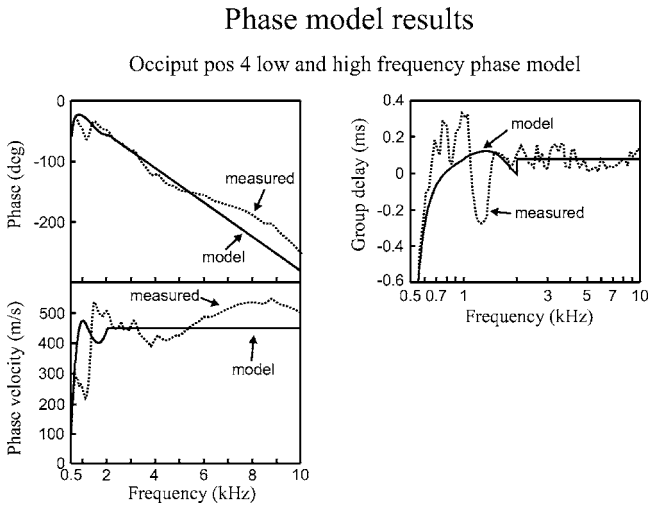

FIG. 14. Comparison of model and measured phase data. The phase and phase velocity is plotted at the left with a linear frequency scale (0.5–10 kHz), while the group delay is plotted at the right with a logarithmic frequency scale (0.5–10 kHz). The model data are shown with a solid line and the measured data are shown with a dotted line. The measured data are the same as the single head data presented in Fig. 3 using position occiput arc I-4.

data have a somewhat lower velocity around 4 kHz and a higher velocity at frequencies above 6 kHz. The measured data indicate dispersion at both low and high frequencies.

The panel displaying the group delay indicates similarities between measured and model data. At the lowest frequencies, the delays are negative; this is seen at several positions in Fig. 9. The model data have a constant group delay of 0.078 ms at frequencies above 2 kHz (given by the model). The measured group delay is spread around this delay with a tendency of greater delays at around 3 to 4 kHz and lower delays at 5 to 8 kHz. The transition from the mixture of two phase models to the constant velocity model at 2 kHz is clearly visible in the group delay data. This is due to the computation of the group delay as the derivative of the phase versus frequency [Eq. (2)]. At both transitions between models, at 1 kHz where the model goes from a low-frequency model to a mixed model, and at 2 kHz where it goes from a mixed to a constant delay model, the derivative of the phase is noncontinuous. This noncontinuity gives rise to the abrupt rise in the group delay data of the model at 2 kHz.

IV. DISCUSSION

Nearly a thousand measurements were made of the cochlear promontory vibration using accelerometers and a LDV with stimulation at 29 positions in six intact human cadaver heads for the frequency range 0.1 to 10 kHz. Furthermore, the mechanical impedance was measured at the stimulation positions at the skull surface. This thorough investigation has given some insight to the mechanics of the skull, and the motion of the cochlear promontory when the stimulation is a vibration at the skull bone surface. Although there are several published studies of human skull mechanics, those studies are limited to the point impedance, vibration of the cranial vault, vibration response in one direction, and/or investigations in dry skulls.

Most measurements in this study are on the vibration of the cochlear promontory when the excitation is at the skull bone surface. For this to be interesting for BC hearing, the cochlear vibration should be related to a sensation level for BC sound. It is at present not absolutely clear which phenomena contribute, and to what extent they contribute, to a BC perception. It is generally assumed that a BC sensation is primarily caused by sound radiation into the external ear canal, inertial motion of the middle ear ossicles, inertial effects of the cochlear fluid, and alteration of the cochlear space (Tonndorf, 1966). Of these, the external ear canal component is not significant when the ear canal is open (Stenfelt *et al.*, 2003). All others are related to the vibration level of the cochlear promontory. Although it is not possible to translate a vibration level of the cochlear promontory to a hearing sensation level due to several unknown factors, such as the directional sensitivity and vibration modes of the cochlea, the vibration level of the cochlear promontory can be used as a rough approximation of the BC sensation level.

A. Mechanical point impedance of the skull

Several investigations of the skull point impedance have been reported in the literature, both with and without the skin covering the skull bone, using living and cadaver heads as well as severed dry skulls (Corliss and Coidan, 1955; Franke, 1956; Stalnaker and Folge, 1971; Gurdjian *et al.*, 1970; Flottorp and Solberg, 1976; Smith and Suggs, 1976; Håkansson *et al.*, 1986). Of these, the most thorough investigation is Håkansson *et al.* (1986), where the mechanical point impedance at an osseointegrated titanium implant, as well as at the skin in the parietal bone (about 55 mm behind the ear canal entrance), was investigated in seven living humans. Moreover, the mechanical impedance of a 175 mm^2 circular area of the average human skin covered mastoid was standardized in 1971 (IEC 373, 1971) for the calibration of BC transducers used in audiometry. However, it was difficult to design mechanical couplers that met this impedance, and the standard of the mechanical impedance for calibrating BC transducers was revised in 1990 to the mechanical impedance of the Brüel and Kjær type 4930 artificial mastoid (IEC 373, 1990).

The mechanical point impedance was measured at 27 positions at the skull surface in each of the six cadaver heads according to Fig. 1. The results from these measurements were pooled and averaged in Fig. 2. The impedance measurements obtained, although at several additional positions, are similar to the measurements of Håkansson *et al.* (1986) where the impedance was measured at a screw connection directly in the skull bone. When comparing the mean results from the study of Håkansson *et al.* with our occiput arc position 3 data, which is the closest position to that used in the Håkansson *et al.* study, similar results are found for both magnitude and phase. The greatest difference between the two investigations is found at the very high frequencies (8 to 10 kHz). At those frequencies, the impedance magni-

tude in the Håkansson *et al.* study is 3 to 6 dB lower and the phase is up to 40° lower than in this study. This difference may be due to the rigid connection used in the present study; Håkansson *et al.* used a metal connection at the implant that produces a local compliance that could affect their high-frequency data.

Although most previous mechanical impedance studies have been made with the skin interposed between the skull and the impedance measurement device, it was here measured directly to the skull bone. The skin acts chiefly as a spring at the frequencies used; this spring is the first element in the impedance chain and it dominates the impedance response. Therefore, the skin may mask mechanical characteristics that could have been seen in the impedance measurements. Three general areas can be identified in the magnitude and phase curves presented in Fig. 2. At the lowest frequencies, below 150 to 400 Hz, the skull acts as a pure mass. This is where the skull moves truly as a rigid body and the skull motion is determined by translational and rotational whole body motions. Above this frequency range, the cranial bone starts flexing around the stimulation position, giving a stiffness-controlled impedance (cf. Sec III A). At frequencies of 3 kHz and above, losses start to influence the impedance; however, the impedance is still dominated by the stiffness of the bone around the stimulation position.

Except for the low-frequency impedance resonance, no resonances and antiresonances of the skull structure are identifiable from the impedance measurements. The reason is that the resonances of the skull structure are well damped, as has been noted in previous reports on the mechanical impedance. Accordingly, the structural responses of the skulls are hidden behind the local mass and stiffness behavior at and around the attachment position.

B. Vibration of the cochlea

In the literature on BC vibration of the skull, different measurement techniques, such as impulse hammers, accelerometers, holographic interferometry, and LDV, have been used to reveal the mode of vibration of the cranial vault when a BC sound is applied (von Békésy, 1932; Bárány, 1938; Kirikae, 1959; Khalil *et al.*, 1979; Ogura *et al.*, 1979; Kobayashi *et al.*, 1983; Dorheide and Hoyer, 1984; Håkansson *et al.*, 1994). These investigations have used live humans, cadavers, and dry skulls. The present study has focused on the vibration at the cochlear promontories when the stimulation is a vibration at the skull bone surface. Previous investigations of cochlear vibration during BC stimulation are limited to two studies. In the first, an accelerometer was attached to the petrous part of the mastoid bone in a sectioned dry skull when the stimulation was applied to the mastoid (Buchman *et al.*, 1991). In the other study, three perpendicular accelerometers were mounted at the petrous part of both mastoid bones in an intact dry skull that was internally coated with damping material. In that study, the excitation was applied at four positions on the mastoid and parietal bone, and one position on the forehead (Stenfelt *et al.*, 2000).

The present study is similar to the study by Stenfelt *et al.* (2000) in that the cochlear promontory vibration in three directions was measured while vibrating the skull surface. The difference is that a dry skull and five stimulation positions were used by Stenfelt *et al.* while intact cadaver heads and a large number of stimulation positions distributed over a substantial area of the skull bone were used in this investigation. One potential concern is that the cadaver heads used had been removed from the bodies. According to Stalnaker and Folge (1971), the head-neck junction is insignificant for frequencies above 0.4 kHz. It is therefore assumed that the effect of severing the heads in this study is negligible.

Two different methods to measure the vibration at the cochlear promontory were used: a triaxial accelerometer was glued to the cochlear promontory that measured the acceleration in three perpendicular directions, and the laser beam of a LDV was aimed at the cochlear promontory that measured the velocity in the direction of the laser beam. The measurement direction of the LDV was the same as the x direction of the accelerometer measurement. Similar vibration results were obtained with the triaxial accelerometer in the x direction as with the LDV. The average result from the six heads with the two measurement methods differed no more than 5 dB at any position or frequency; the difference was generally less than 2 dB. This indicates further that the slight drilling of the ear canal that was done in order to fit the triaxial accelerometer to the cochlear promontory did not greatly affect the vibration transmission, and the glue bond attaching the accelerometer to the cochlear promontory could be considered rigid.

The results from the individual heads show that there were several resonances and antiresonances present. They did not appear at the same frequencies in all three directions. Furthermore, they differed in frequency between the heads and their influence disappeared when the results from the six heads were averaged. The resonances were greatly damped and have therefore only a minor influence on BC sound. The antiresonances have greater impact and produced attenuation of up to 20 dB. However, since they were of narrow bandwidth and did not appear in the three directions at the same frequency, their influence on BC transmission is dependent on the directional sensitivity of the cochlea. This directional sensitivity of the cochlea is at present unknown. Most antiresonances were found when the stimulation was applied close to the midline of the skull, or when it was on the contralateral side (predominantly C-1 and C-2). This is believed to be an effect of wave transmission through the cranial vault when the stimulation is close to the sagittal plane (producing more antiresonances). When the stimulation was closer to the cochlea, the skull-base transmitted more of the energy with less influence from the structural response of the cranial vault.

From both the analysis of the cochlear promontory vibration in the individual heads and the averaged responses, it was clear that, as long as the stimulation was on the ipsilateral side, the closer the excitation position was to the cochlea, the greater the response level and the less phase accumulated (shorter time delays). However, when the excitation was applied on the contralateral side, no significant difference between the response from the stimulation positions

were found, either in level or in phase. In general, the worst place to apply a BC stimulation, in terms of vibration level at the cochlear promontory, was on the mid-sagittal plane. The greatest vibration level at the cochlear promontory was obtained when the stimulation was applied directly at the cochlea; almost 10 dB greater levels were achieved compared with the occiput arc I-4 position.

At lower frequencies, the direction of stimulation dominated the response direction. At higher frequencies, no dominant direction was seen except when the stimulation position was close to the response position (stimulation at positions I-4 and otic capsule). The averaged responses in the three directions were normally within 5 to 10 dB of each other. The response pattern was similar whether the stimulation was applied at the forehead, vertex, or occiput part of the skull; it depended primarily on the distance between the stimulation and response positions. This finding was similar to that reported by Stenfelt *et al.* (2000), where the vibrations were found similar for the three perpendicular directions, except when the stimulation was close to the cochlea; then, the vibration in the stimulation direction dominated the vibration response.

When the quadratic summation of the accelerance results in the three perpendicular directions was performed [Eq. (1)], a result termed total accelerance response was obtained. It is an approximation of the vibration power transmitted to the cochlear promontory. This is a useful measure since it converts the vibration response in the three directions to a single number facilitating comparisons between results from different stimulation positions. Using this analysis, the transmission loss at the ipsilateral skull surface was 0.5 to 1.5 dB/cm for frequencies above 1 kHz (Fig. 7). Positions I-4 at the forehead and vertex arcs resulted in approximately 5 dB greater vibration level at the cochlear promontory for frequencies above 1 kHz, compared with position I-4 at the occiput arc. At this time, we have no explanation for this result.

In the international standard for calibration of BC transducers (ISO 389-3, 1994), an interim standard is proposed for the sensitivity difference between forehead and mastoid stimulation. This standard states that, for BC, stimulation at the forehead produces 8 to 14 dB worse thresholds than stimulation at the mastoid. This sensitivity difference corresponds well with the x direction results for frequencies below 3 kHz when the relative sensitivity between stimulation positions was analyzed (Fig. 8). Above 3 kHz, the measured x direction difference in vibration levels was greater than that stated in the standard and the a_{tot} results correspond better. This is another indication that cochlear promontory vibration data can be used to estimate the perception of BC sound, though the relationship between acceleration and perception is probably a function of the amplitude and phase of all directions of motion.

C. Transcranial transmission

The transcranial transmission measured in these skulls is an objective measure; it is the vibration measured at the contralateral cochlea divided by that at the ipsilateral cochlea. The inverse of this is referred to as the transcranial attenuation and is often used when BC transmission through the skull is estimated by psychoacoustic measurements. Nolan and Lyon (1981) reported the mean subjective transcranial attenuation to be approximately 10 dB for the frequencies 0.25 to 4 kHz in live humans; the range was from −10 to 40 dB. Hurley and Berger (1970) found the transcranial attenuation to be around 5 dB between 0.5 and 2 kHz, whereas Kirikae (1959) reported it to be 5 dB between 0.25 and 1 kHz and 10 to 15 dB at 2 kHz. In the transcranial vibration transmission that is presented in Fig. 8, the vibration at the contralateral side is generally 0 to 5 dB greater than at the ipsilateral side for frequencies below 1 kHz. This is not normally reported when the transcranial transmission is estimated by psychoacoustic measurements. At higher frequencies, the transcranial transmission is worse resulting in an attenuation of 10 to 20 dB at 10 kHz, depending on measurement direction and position.

In the study by Stenfelt *et al.* (2000), where the vibration was measured close to the cochlea in a dry skull, less attenuation was obtained: around 0 dB below 1 kHz that became 5 to 10 dB at 10 kHz. Since a dry skull was used in that study, less attenuation was expected. However, the transcranial transmission level differs between this study and the several studies that used a psychoacoustic approach. At low frequencies, where the skull moves primarily as a rigid body, the sensation level at both cochleae should be similar. There may, however, be other factors such as the directional sensitivity of the cochlea that influences the results when psychoacoustic measurements are used; e.g., if the cochlea is sensitive primarily in the y direction, other transcranial transmission functions than those presented in Fig. 8 would be appropriate. The vibration sensitivity of the cochlea (vibration of the cochlea to a perceived sensation) is probably a function of the vibration amplitude and phase in all three directions, as well as the vibration mode; it is therefore meaningless to try to find a single sensitivity direction.

D. Wave motion of bone conducted sound

Tonndorf (1966) initially proposed that the waves along the bones of the cranial vault propagate as flexural waves (bending waves). Later, this was revised, since no frequency dependence of the wave motion was found in their own study (Tonndorf and Jahn, 1981) or in others (Zwislocki, 1953; Franke, 1956). They suggested that the wave propagation of the cranial vault occurs as plate waves, which constitutes both longitudinal and transverse components. Although the special case of plate waves that was proposed by Tonndorf and Jahn (1981) does not have frequency-dependent propagation velocity, plate waves are dispersive in general; the phase (and group) velocity changes with frequency. The phase velocity for BC stimulation in this study showed dispersion (velocity changed with frequency) (Fig. 10), especially for the estimation of the propagation velocity in the cranial bone. When the wave transmission was primarily through the skull-base (position I-4), less dispersion was found at the higher frequencies. There was also a variation of

the group delays for almost the whole frequency range, indicating dispersive wave transmission (Fig. 10).

The skull bone has a complicated structure; at the cranial vault it consists of two parallel thin structures of dense bone (lamina externa and lamina interna) with a scaffoldlike bone structure termed diploë in between. Fluid is present within this diploë, and the cranial bone is loaded on the outside by the skin and soft tissues, and on the inside by the brain and cerebrospinal fluid. All these factors influence the wave transmission of the vibration in the skull, and it can be assumed that several modes of wave transmission in the skull bone are present at the frequencies used here. By separating the analysis for the stimulation at position I-4 with the other positions, some indication of the nature of the wave transmission was found. At the skull-base, a higher phase velocity (around 400 m/s) was obtained than that obtained at the cranial vault (250 to 300 m/s). The velocity at the skull base appeared to be almost constant at the higher frequencies, whereas frequency dependence of the phase velocity at the cranial vault was found. This was likely a result of different wave propagations in the different areas of the skull: at the skull base in thicker bone, longitudinal wave transmission dominated whereas a mixture of modes, including bending wave motion, might exist in the cranial bones. Position occiput arc I-4 was at the skull-base, forehead arc I-4 was just outside the skull-base, whereas vertex arc I-4 was positioned in the cranial bone, about 30 mm above the ear canal opening. The slight frequency dependence seen in the phase velocity at vertex arc I-4 was believed to be caused by the transmission in the cranial bone at this position.

At the lowest frequency presented in Fig. 10, the phase velocity estimated was below 100 m/s. This result was due to the phase of the local compliance around the stimulation position. This stiffness behavior at the attachment position caused a phase alteration that appeared as a low phase velocity at those relatively low frequencies. The phase and group velocity of BC sound have been reported to be between 260 and 540 m/s (von Békésy, 1948; Zwislocki, 1953; Franke, 1956; Tonndorf and Jahn, 1981). Except for von Békésy, who did not investigate the low-frequency wave speed, low phase velocities at the lower frequencies were reported, similar to our findings. By devising a mass-spring model of the skull for the low frequencies and a wave propagation model with constant phase velocity at higher frequencies, the alteration from low phase velocities at low frequencies to higher velocities at frequencies above 2 kHz could be explained. Also, the finding of negative group delays at the low frequencies could be explained by this model. However, it should be noted that, due to the low-frequency characteristics of phase response, neither the phase velocities nor the group delays presented were easily converted to a time delay for BC transmission in the head.

The current study was based on mechanical point impedance measurements of the skull and cochlear vibration measurement when the excitation was at the skull surface. Although slightly different levels were found, the mechanical impedance showed similar behavior for all measurements. When a vibration excited the skull, even if in a single direction, the vibration at the cochlear promontory was in all space dimensions. It was only at the lower frequencies, below 0.5 to 1 kHz, and when the stimulation position was close to the cochlea, that the stimulation direction dominated the response direction. Otherwise, the cochlea vibrated in all space dimensions without any dominating direction. In terms of vibration level of the cochlear promontory, the best stimulation position was close to the cochlea and the worst stimulation position was on the sagittal plane. Also, the greatest difference, in both level and phase, between the cochleae was when the stimulation was close to the cochlea. Both the group and phase velocity of the skull bone wave propagation depended on the frequency: at low frequencies the skull acted as a mass-spring system with a low phase velocity. At higher frequencies, the speed of the wave propagation depended on the location on the skull: the skull-base showed a close to constant wave speed of around 400 m/s whereas the cranial bone produced phase velocities around 250 m/s at 2 kHz that became close to 300 m/s at 10 kHz.

ACKNOWLEDGMENT

This work was supported in part by a V. A. Merit Review Grant (GDE0010ARG), the Swedish Institute, and Swedish Research Council for Engineering Sciences (Grant No. TFR 299-2000-576). We gratefully acknowledge the help of Timothy Wild and Nahito Hato, who assisted with the preparations of the heads.

APPENDIX: SKULL MODEL DATA

The element values of the one-dimensional mass-spring model of the skull depicted in Fig. 12 were fitted to the results of stimulation at position 4 at the occiput arc in the skull data presented in Fig. 3. It was decided to fit the results to some key properties in the results. At low frequencies, the model result should be mass dominated with the total mass ($M_1+M_2+M_3$) close to that obtained in the impedance data. The sum of the two compliances (C_1 and C_2) together with the large mass (M_3) forms the resonance seen in the impedance data. The damping of this resonance is formed by the three resistive elements (R_0, R_1, and R_2). The antiresonance of the I-4 data is caused by the interaction of the masses M_2 and M_3 together with the compliance C_1. Finally, the first skull resonance (around 1.1 kHz) is primarily formed by the compliance C_2 together with the mass M_3. From this, the values were adjusted manually to visually fit the measured data. Accordingly, the values used for the model in Fig. 13 were $M_1=0.05$ kg, $M_2=0.1$ kg, $M_3=0.7$ kg, $C_1=140$ nm/N, $C_2=170$ nm/N, $R_0=30$ kNs/m, $R_1=200$ Ns/m, and $R_2=600$ Ns/m.

It can be observed that the total mass of the skull model ($M_1+M_2+M_3$) is 0.85 kg, which is considerably less than the 3 kg for the head reported in Table I. This can be explained by the decoupling of the brain and soft tissues for the frequencies used here. The dry skull itself weighs slightly less than 1 kg. The decoupling of the brain and soft tissues can be one explanation for the deviation in magnitude and phase of the impedance at the lowest frequencies (below 200 Hz) in Fig. 12. At these frequencies, parts of the soft tissues and/or brain vibrate with the skull bone, thus increas-

ing the effective mass. According to the impedance data at 100 Hz, the effective mass is 1.6 kg, which is about twice the mass seen at 200 Hz.

For the results presented in Fig. 14, a model of the phase between the velocities at the cochlear promontory and the stimulation position was devised. This model was divided into three frequency areas. At frequencies below 1 kHz, the low-frequency part of the phase was defined as the phase difference between V_1 and V_0 in the mass-spring model in Fig. 12, i.e., $\phi_{LF}=\angle V_1/V_0$. At the high frequencies, above 2 kHz, the phase was described by a constant time delay, i.e., $\phi_{HF}=\angle e^{-j\omega t_d}$. For the mid-frequencies, between 1 and 2 kHz, the phase was a function of the low- and high-frequency phase functions, i.e., $\phi_{MF}=\phi_{LF}+a(f)(\phi_{HF}-\phi_{LF})$. Here, the function $a(f)$ increased linearly from 0 at 1 kHz to 1 at 2 kHz. The delay t_d used to compute ϕ_{HF} in Fig. 14 was 0.078 ms. This was derived by assigning the phase velocity to be 450 m/s, and the distance between the stimulation position and the cochlear promontory for occiput arc I-4 in that skull was 3.5 cm.

[1]The mechanical point impedance is defined as the force divided by the velocity at the stimulation position.

[2]Antiresonance is here defined as a significantly low level response of narrow bandwidth in the frequency response function.

Advani, S. H., and Lee, Y.-C. (**1970**). "Free vibrations of fluid-filled spherical shells," J. Sound Vib. **12**, 453–462.

Bárány, E. (**1938**). "A contribution to the physiology of bone conduction," Acta Oto-Laryngol., Suppl., (Stockh.) **26**, 1–223.

Buchman, E., Rosenhouse, G., Shupak, A., and Shimoni, U. (**1991**). "On the transmission of sound generated by an electromagnetic device from the mastoid process to the petrous bone," J. Acoust. Soc. Am. **90**, 895–903.

Charalambopoulos, A., Fotiadis, D. I., and Massalas, C. V. (**1998**). "Free vibrations of the viscoelastic human skull," Int. J. Eng. Sci. **36**, 565–576.

Corliss, E. L. R., and Coidan, W. (**1955**). "Mechanical impedance of the forehead and mastoid," J. Acoust. Soc. Am. **27**, 1164–1172.

Dörheide, J., and Hoyer, H.-E. (**1984**). "Holographic investigation of the impact response of human heads," J. Neurosurg. **60**, 718–723.

Flottorp, G., and Solberg, S. (**1976**). "Mechanical impedance of human headbones (forehead and mastoid portion of temporal bone) measured under ISO/IEC conditions," J. Acoust. Soc. Am. **59**, 899–906.

Franke, E. (**1956**). "Response of the human skull to mechanical vibrations," J. Acoust. Soc. Am. **28**, 1277–1284.

Gurdjian, E., Hodgson, V., and Thomas, L. (**1970**). "Studies on mechanical impedance of the human skull: Preliminary report," J. Biomech. **3**, 239–247.

Håkansson, B., and Carlsson, P. (**1989**). "Skull simulator for direct bone conduction hearing devices," Scand. Audiol. **18**, 91–98.

Håkansson, B., Carlsson, P., and Tjellström, A. (**1986**). "The mechanical point impedance of the human head, with and without skin penetration," J. Acoust. Soc. Am. **80**, 1065–1075.

Håkansson, B., Brandt, A., Carlsson, P., and Tjellström, A. (**1994**). "Resonance frequency of the human skull *in vivo*," J. Acoust. Soc. Am. **95**, 1474–1481.

Håkansson, B., Carlsson, P., Brandt, A., and Stenfelt, S. (**1996**). "Linearity of sound transmission through the human skull*in vivo*," J. Acoust. Soc. Am. **99**, 2239–2243.

Hickling, R., and Wenner, M. (**1973**). "Mathematical model of a head subjected to an axisymmetric impact," J. Biomech. **6**, 115–132.

Hoyer, H.-E., and Dörheide, J. (**1983**). "A study of human head vibrations using time-averaged holography," J. Neurosurg. **58**, 729–733.

Hurley, R. M., and Berger, K. W. (**1970**). "The relationship between vibrator placement and bone conduction measurements with monaurally deaf subjects," J. Aud Res. **10**, 147–150.

IEC 373 (**1971**). "Mechanical coupler for measurements on bone vibrators."

IEC 373 (**1990**). "Mechanical coupler for measurements on bone vibrators (2nd ed.)."

ISO 389-3 (**1994**). "Reference zero for the calibration of audiometric equipment. Part 3: Reference equivalent threshold force levels for pure tones and bone vibrators."

Khalil, T. B., and Hubbard, R. P. (**1977**). "Parametric study of head response by finite element modeling," J. Biomech. **10**, 119–132.

Khalil, T. B., Viano, D. C., and Smith, D. L. (**1979**). "Experimental analysis of the vibrational characteristics of the human skull," J. Sound Vib. **63**, 351–376.

Kirikae, I. (**1959**). "An experimental study on the fundamental mechanism of bone conduction," Acta Oto-Laryngol., Suppl.(Stockh.) **145**, 1–111.

Kobayashi, F., Miyao, M., Sakakibara, H., Nakagawa, T., Kito, K., Shimosato, K., Koide, Y., Sugiyama, S., Hongo, T., and Oka, T. (**1983**). "Research note. Vibration modes of a human skull at low frequencies. Measurement with holographic interferometry," J. Low Freq. Noise Vib. **2**, 51–59.

Mitchell, M., and Chiao, R. (**1998**). "Causality and negative group delays in a simple bandpass amplifier." Am. J. Phys. **66**, 14–19.

Nolan, M., and Lyon, D. J. (**1981**). "Transcranial attenuation in bone conduction audiometry," J. Laryngol. Otol. **95**, 597–608.

Ogura, Y., Masuda, Y., Miki, M., Takeda, T., Watanabe, S., Ogawara, T., Shibata, S., Uyemura, T., and Yamamoto, Y. (**1979**). "Vibration analysis of the human skull and auditory ossicles by holographic interferometry," in *Holography in Medicine and Biology*, edited by G. von Bally (Springer-Verlag, Berlin), pp. 218–222.

Smith, J. B., and Suggs, C. W. (**1976**). "Dynamic properties of the human head," J. Sound Vib. **48**, 35–43.

Stalnaker, R., and Fogle, J. (**1971**). "Driving point impedance characteristics of the head," J. Biomech. **4**, 127–139.

Stenfelt, S., Håkansson, B., and Tjellström, A. (**2000**). "Vibration characteristics of bone conducted sound *in vitro*," J. Acoust. Soc. Am. **107**, 422–431.

Stenfelt, S., Hato, N., and Goode, R. L. (**2002**). "Factors contributing to bone conduction: The middle ear," J. Acoust. Soc. Am. **111**, 947–959.

Stenfelt, S., Wild, T., Hato, N., and Goode, R. L. (**2003**). "Factors contributing to bone conduction: The outer ear," J. Acoust. Soc. Am. **113**, 902–912.

Tjellström, A., Håkansson, B., and Granström, G. (**2001**). "Bone-anchored hearing aids: Current status in adults and children," Otolaryngol. Clin. North Am. **34**, 337–364.

Tonndorf, J. (**1966**). "Bone conduction. Studies in experimental animals," Acta Oto-Laryngol., Suppl. (Stockh) **213**, 1–132.

Tonndorf, J., and Jahn, A. F. (**1981**). "Velocity of propagation of bone-conducted sound in a human head," J. Acoust. Soc. Am. **70**, 1294–1297.

von Békésy, G. (**1932**). "Zur theorie des hörens bei der schallaufnahme durch knochenleitung," Ann. Phys. **13**, 111–136.

von Békésy, G. (**1948**). "Vibration of the head in a sound field, and its role in hearing by bone conduction," J. Acoust. Soc. Am. **20**, 727–748.

Young, P. G. (**2002**). "A parametric study on the axisymmetric modes of vibration of multi-layered spherical shells with liquid cores of relevance to head impact modeling," J. Sound Vib. **256**, 665–680.

Young, P. G. (**2003**). "An analytical model to predict the response of fluid-filled shells to impact—a model for blunt head impacts," J. Sound Vib. **267**, 1107–1126.

Zwislocki, J. (**1953**). "Acoustic attenuation between the ears," J. Acoust. Soc. Am. **25**, 752–759.

Reducing individual differences in the external-ear transfer functions of the Mongolian gerbil

Katuhiro Maki[a] and Shigeto Furukawa
Human and Information Science Laboratory, NTT Communication Science Laboratories, NTT Corporation, 3-1, Morinosato-Wakamiya, Atsugi, Kanagawa, 243-0198 Japan

(Received 12 May 2005; revised 6 July 2005; accepted 20 July 2005)

This study examines individual differences in the directional transfer functions (DTFs), the directional components of head-related transfer functions of gerbils, and seeks a method for reducing these differences. The difference between the DTFs of a given animal pair was quantified by the *intersubject spectral difference* (ISSD), which is the variance in the difference spectra of DTFs for frequencies between 5 and 45 kHz and for 361 source directions. An attempt was made to reduce the ISSD by scaling the DTFs of one animal in frequency and/or rotating the DTFs along the source coordinate sphere. The ISSD was reduced by a median of 12% after optimal frequency scaling alone, by a median of 19% after optimal spatial rotation alone, and by a median of 36% after simultaneous frequency scaling and spatial rotation. The optimal scaling factor (OSF) and the optimal coordinate rotation (OCR) correlated strongly with differences in head width and pinna angles (i.e., pinna inclination around the vertical and front–back axes), respectively. Thus, linear equations were derived to estimate the OSF and OCR from these anatomical measurements. The ISSD could be reduced by a median of 22% based on the estimated OSF and OCR. © *2005 Acoustical Society of America.* [DOI: 10.1121/1.2033571]

PACS number(s): 43.64.Ha, 43.66.Qp, 43.66.Pn [WPS] Pages: 2392–2404

I. INTRODUCTION

The head-related transfer functions (HRTFs) of an animal and their directional components, *directional transfer functions* (DTFs) (Middlebrooks and Green, 1990), can be used to present virtual acoustic space (VAS) stimuli to the animal through earphones in physiological (e.g., Brugge *et al.*, 1996, 1998; Delgutte *et al.*, 1999; Schnupp *et al.*, 2001; Euston and Takahashi, 2002; Mrsic-Flogel *et al.*, 2001, 2003; Sterbing *et al.*, 2003, Behrend *et al.*, 2004) and psychophysical (e.g., Wenzel *et al.*, 1993; Middlebrooks, 1999b; Poganiatz *et al.*, 2001) experiments. VAS sound presentation has several advantages when compared with free-field stimulation. The VAS technique allows us to manipulate individual cues for sound localization, such as interaural time- and level differences (ITD and ILD, respectively), and spectral information, and thereby enables us to examine the roles of these cues in the sound localization mechanisms. Furthermore, the VAS stimuli are free from the stimulus distortion that results from sound obstructions and reflections caused by physiological apparatus such as head holders and electrode manipulators placed around the subject's head.

There are generally individual differences between the DTFs of animals because of the variability in the size and shape of the head and external ears (humans: Middlebrooks, 1999a; ferrets: Schnupp *et al.*, 2003; cats: Xu and Middlebrooks, 2000). VAS stimuli synthesized using another individual's DTFs lead to localization errors in humans (Middlebrooks, 1999b; Wenzel *et al.*, 1993) and alter the virtual-spatial sensitivities of neurons in the central nervous system (Mrsic-Flogel *et al.*, 2001; Schnupp *et al.*, 2001; Sterbing *et al.*, 2003). Thus, it is ideal to use the target subject's own DTFs, which are measured prior to an experiment. However, DTF measurement is usually time-consuming and requires special facilities such as an anechoic room and a movable speaker system. This often makes such measurements impractical within the limited time allowed for experiments.

A practical method of synthesizing reasonable VAS stimuli for a given subject is to use a set of DTFs that is close or identical to the subject's own DTFs. Previous studies have indicated that the human sound-localization performance (Middlebrooks, 1999b) and the auditory neuron's spatial sensitivity (Mrsic-Flogel *et al.*, 2001) for VAS stimuli synthesized with another individual's DTFs became progressively closer to those for VAS stimuli based on the subject's own DTFs as the difference between the two DTF sets decreased ; . Middlebrooks (1999a) proposed that spectral differences between the DTFs of two subjects could be reduced by scaling the DTFs in frequency. Subsequently, the effectiveness of frequency scaling was confirmed in other animal species (ferrets: Schnupp *et al.*, 2003; cats: Xu and Middlebrooks, 2000).

The goal of the present study was to establish a method for estimating DTFs that are reasonably close to the target subject's own DTFs with a view to presenting VAS stimuli in physiological experiments using the Mongolian gerbil (*Meriones unguiculatus*), by advancing Middlebrooks' (1999a) idea of frequency scaling. The Mongolian gerbil is an animal species widely used for physiological and behavioral studies on sound localization (e.g., Kelly and Potas, 1986; Heffner and Heffner, 1988; Sanes, 1990, 2002; Brückner and Rübsamen, 1995; Spitzer and Semple, 1995; Behrend *et al.*, 2002). In this study, we first examined the individual differences in DTFs. Second, we tested whether these

[a]Electronic mail: maki@avg.brl.ntt.co.jp

individual differences could be reduced by scaling one animal's DTFs in frequency, as demonstrated in previous studies. Additionally, we showed that the DTF differences could also be reduced by rotating one animal's DTF along the source coordinate sphere. Third, we attempted to find anatomical measurements that would accurately predict the amounts of frequency scaling and coordinate rotation required to minimize DTF differences between individual animals. We then estimated the DTFs of a target animal based on these anatomical measurements. In addition, we examined the ITD as regards its individual differences and investigated a method for its estimation.

II. MATERIALS AND METHODS

A. Animal preparation

The experiments were performed on 19 Mongolian gerbils (*Meriones unguiculatus*) of both sexes, weighing 32–102 g and aged 4–36 weeks (also see Table I). The animals were supplied by CLEA Japan, Inc. Initially, the animal was deeply anesthetized with pentobarbital sodium (25 mg/kg, i.p.). A small incision was made in the skin near the ventro-posterior fringe of the pinna, and a small hole was made in the wall of the bony meatus, through which a silicone tube (Etymotic Research, ER7-14C, 2.5 cm long, 0.95-mm outer diameter, 0.5-mm inner diameter) was inserted. The tube was fixed to the bone with cyanoacrylate adhesive so that the tip of the tube in the ear canal was usually located 0.3–0.7 mm from the canal entrance. After fixing the tube in the ear canal, the head and pinnae of the animal were adjusted so that they appeared as in a natural state. Then, the animal was euthanized with a lethal dose of pentobarbital sodium. Neither the use of anesthesia nor the placing of the probe tube had any apparent effect on the pinna position. The head and body were secured by fixing the lower incisors, waist, and chest on a custom-made wire frame so that the animal appeared to adopt a natural standing posture. That is, the animal's body inclined forward by about 30° relative to the vertical axis, and the lower jaw was angled at about 110° relative to the chest.

B. Stimulus presentation

Experiments were conducted in a double-walled, soundproof, anechoic room ($4.8 \times 5.4 \times 4.7$ m). A movable speaker system was used for manipulating the sound direction [Fig. 1(e); Maki and Furukawa, 2005]. The system consisted of a semicircular arm (3/4 circular arc, 1.2-m radius), along which a speaker mount could move when driven by a stepping motor controlled by a personal computer (PC). The speaker mount had an extendable radial arm to which a loudspeaker was attached. The system allowed us to vary the sound source location on an imaginary sphere with various radii. The center of the interaural axis of the animal's head was carefully positioned at the center of the imaginary sphere, and this was confirmed by using a laser pointer attached at the speaker position in the absence of the speaker. The distance from the sound source to the center of the interaural axis was fixed at 79 cm.

The stimulus used for estimating the transfer functions was a time-stretched pulse (TSP), which was a kind of frequency sweep with a flat and broadband power spectrum (Suzuki *et al.*, 1995) that covered the gerbil's audible frequency range (up to 45–50 kHz; Ryan, 1976). The TSP was synthesized digitally by the PC at a sampling rate of 97 656.25 Hz with a resolution of 24 bits. The TSP signal consisted of a total of 65 536(2^{16}) sample points. The TSP signal was generated through a digital-to-analog converter (Tucker-Davis Technology, RP 2.1), amplified (Nittobo Acoust. Eng., HA-94C), and emitted from a 2.5-cm-diameter tweeter (Sony, SS-TW100ED) on the movable speaker system.

C. Coordinate system

The source-direction coordinate system was formed so that the median sagittal plane (or the median plane) of the animal corresponded to 0° azimuth and the horizontal plane (i.e., the plane formed by the ear canal entrances and the eyes) corresponded to 0° elevation. The azimuth is the angle from the median plane to the right or left. A *positive* azimuth indicates a source direction in the hemisphere *contralateral* to the recorded ear. The elevation is the angle above (positive elevation) and below (negative elevation) the horizontal plane. Thus, a source direction of 0° elevation and 0° azimuth indicates a source directly in front of the animal.

In some analyses, the orientation of the whole coordinate sphere was rotated around the origin (described in later sections). The rotation was made in three dimensions, namely yaw, roll, and pitch. Yaw and roll are the angles around the vertical and the front–back axes, respectively. A *positive* yaw and roll indicate the animal's face and top, respectively, turning around the axes from the midline to the side *contralateral* to the ear of interest. Pitch is the angle around the interaural axis. A *positive* pitch indicates an angle *above* the horizontal plane.

D. Measurement system

The end of the silicone tube (opposite to that inserted in the ear canal) was connected to a probe microphone (Brüel & Kjær, type 4182). The output of the microphone was amplified (Brüel & Kjær, type 2636) and stored on the hard disk of a PC through an analog-to-digital converter (Tucker-Davis Technology, RP 2.1) at a sampling rate of 97 656.25 Hz with a resolution of 24 bits. Recorded signals of 15 repetitions for each sound direction were averaged in the time domain to increase the signal-to-noise ratio. We measured microphone signals from both the left and the right ears for a total of 937 sound directions ranging from −40° to 90° in 5° steps in elevation and from −180° to 180° in 10° azimuth steps. In the present study, the sampled directions were decimated as needed for individual analyses. We also recorded the TSP signal in the absence of the animal, using a microphone with a silicone tube (2.5 cm in length) located at the center of the source-location coordinate system. This was undertaken to estimate the frequency response of the speaker–microphone system.

E. Data analysis

1. DTF and ITD calculations

We calculated the impulse response from a recorded TSP signal based on the time-stretched pulse theory (Suzuki *et al.*, 1995). Each impulse response was then truncated to 512 points by a Hamming window. The center of the window was always set at the 230th point of the impulse response, so that the maximum point of the impulse responses lay around the window's center. We calculated the frequency response from the impulse response using a 512-point fast Fourier transform. We derived the HRTF amplitude spectrum by dividing the amplitude spectrum of the frequency response derived from the animal's ear by that of the speaker–microphone system. The DTFs were calculated by dividing the HRTF amplitude spectrum for each direction by the geometric average of the HRTF amplitude spectrum across all measurement directions (Middlebrooks and Green, 1990).

The ITD was derived by cross correlating the recorded time-domain TSP signals between the left and right ears. Each TSP signal was first oversampled 7–15 times by linear interpolation, bandpass filtered (passband from 0.5 to 3.5–5.0 kHz), and then the cross correlation between the ears was computed for each matching source direction. In the present study, a *positive* ITD indicates that the *right-ear* signal was in advance of the left-ear signal.

2. Quantification of individual differences in DTFs

The obtained raw DTFs passed through a bank of rectangular bandpass filters whose bandwidths were the same as the critical bandwidths of gerbils (1/3–1/4 octaves above 1 kHz; Kittel *et al.*, 2002). This was done to eliminate the contributions of spectral details in the DTFs that would be unresolved in the gerbil auditory periphery. The filter bank consisted of 305 filters, and their center frequencies were spaced at equal intervals of 1/80 (0.0125) octave from 3.5 Hz to 49 kHz. For a given center frequency, f, the critical bandwidth, Δf_{CB}, was given by Δf_{CB} (Hz) $= d_{\mathrm{CB}} \cdot a \cdot \log_{\mathrm{e}}(10.0) \cdot (f + A)$, where the parameters of d_{CB}, a, and A were 0.037, 2.2, 398, respectively (Kittel *et al.*, 2002). Hereafter, the processed DTFs are referred to simply as DTFs.

The difference between the DTFs of a given pair of animals was quantified by the *intersubject spectral difference* (ISSD), which was calculated as follows. (1) For each source direction, the dB amplitudes of the DTF for one animal were subtracted frequency-by-frequency from those for the other animal. (2) The variance of the differences was calculated over frequencies between 5 and 45 kHz. We chose this frequency range because DTFs generally have adequate spectral features for frequencies above 5 kHz (Maki and Furukawa, 2005) and because the higher audible frequency limit of the gerbil is roughly 45 kHz (Ryan, 1976). The variance, expressed in dB^2, indicates the difference between the DTFs for that sound direction. Thus, we refer to the variance as the *direction-specific ISSD*. A greater value for the direction-specific ISSD indicates a larger difference between the DTFs. (3) The direction-specific ISSDs were averaged over 361 directions for elevations ranging from −10° to +90° and for azimuths ranging from −180° to +180° in 10° steps. In the present paper, "ISSD" indicates this averaged ISSD.

3. Correction of alignment error

We tried hard to position the animal's head at the origin of the source coordinate system, and to align the head orientation as accurately as possible. Nonetheless, it was still possible for the head orientation to include some degree of alignment error. Such errors could have a detrimental effect on the interpretation of the results.

We reduced the influence of any alignment error by using ITD information. Preliminary measurements indicated that the ITD is determined mainly by the head width and the source direction, and is robust to detailed differences in the shape and orientation of the pinna; see also the last part of Sec. III. We then chose one animal as a reference, whose ITD spatial distribution between the left and the right hemispheres appeared the most symmetrical among our sample animals. The symmetry of the distribution indicates that the animal's actual median plane closely matched our intended median plane for the source-direction coordinate system. To estimate the alignment error for a given animal (referred to as the test animal), we rotated the whole coordinate system of the animal in yaw, roll, and pitch dimensions, and searched for the rotation after which the ITD distribution for the test animal best matched that of the reference animal. Specifically, the rotation value of the coordinate system for the test animal was varied from −10° to +10° in 0.5° steps independently for the yaw, roll, and pitch dimensions. The ITD values for unmeasured directions were estimated by a linear interpolation based on four neighboring points that had been measured. To account for the difference in ITD resulting from the difference in the head size, we also scaled the ITDs, independently of the coordinate system rotation, from 0.7 to 1.4 times in steps of 0.001 times. For each rotation and ITD scaling, we computed the differences between the ITDs of the reference and test animals for the 361 directions, with elevations ranging from −10° to +90° and azimuths ranging from −180° to +180° in 10° steps. The alignment error was defined as the rotation (in yaw, roll, or pitch) that minimized the average of the absolute ITD differences across the 361 directions. The absolute values of alignment errors in yaw, roll, and pitch had mean values of 2.2°, 1.7°, and 6.6°, respectively, and the standard deviations were 2.3°, 1.0°, and 2.9°, respectively, across 18 animals.

All the subsequent analyses were conducted on the DTF for the coordinate sphere after rotation had been used to correct the alignment error. DTFs for unmeasured source directions after the rotation were estimated by linear interpolation.

4. Optimal frequency scaling and coordinate rotation

We attempted to reduce the ISSD by scaling the DTFs in frequency. The *optimal scale factor* (OSF) is defined as the frequency scaling factor (common across all the source directions) for the DTFs of one ear that minimizes the ISSD for a given ear pair (Middlebrooks, 1999a). The OSF was expressed in octave units. To compute the OSF for a given

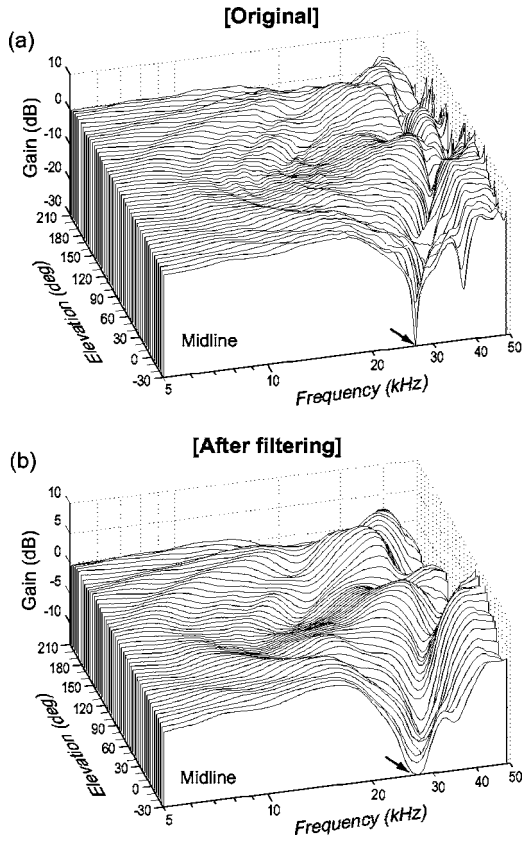

FIG. 1. Directional transfer functions (DTFs) for various sound source elevations on the midline. Panels (a) and (b), respectively, show DTFs before and after the cochlea filtering, in which the raw DTFs passed through a bank of rectangular bandpass filters whose bandwidth was to the same as the critical bandwidth of gerbils (see Sec. II).

ear pair, the DTFs of one ear were shifted up and down along the logarithmic frequency axis by up to 40 steps of 1/80 octave. The shift number (i.e., the scaling factor) that gave the lowest ISSD was taken as the OSF.

Another attempt was made to reduce the ISSD by rotating the coordinate sphere for the DTF. The *optimal coordinate rotation* (OCR) for a given ear pair is defined as the amount of rotation (in yaw, roll, or pitch) of the source coordinate sphere for one of the ears required to minimize the ISSD. The amount of rotation tested varied between −30° and +30° in 0.5° steps independently for the yaw, roll, and pitch dimensions. The DTFs (after a rotation) for unmeasured directions were estimated by linear interpolation.

We also combined frequency scaling and coordinate rotation to reduce the ISSD. There, we sought the minimum ISSD by simultaneously varying the scaling factor and the coordinate rotation to determine the OSF and the OCR.

The OSFs and the OCRs were computed for pairs of ears on the same side (i.e., two right or two left ears) and on the opposite side (i.e., a left and right ear). Thus, for a pair of animals, we computed a set of four OSFs or OCRs.

III. RESULTS

A. Directional transfer functions

Figure 1(a) shows the original DTFs (i.e., before cochlear filtering; see Sec. II) of a representative animal [No. 521M(right)] for source elevations from −30° to 210° along the midline. Deep spectral notches were evident for frequencies above 25 kHz (arrow). The center frequencies of the spectral notches varied with sound-source elevation, increasing monotonically with increasing elevation. The spectral features were more evident for sources on the frontal midline (i.e., elevations from −30° to 90°) than for upper or rear elevations. Figure 1(b) shows DTFs after they had passed through a bandpass filter bank that simulated cochlea filtering. The figure indicates that filtered DTFs in Fig. 1(b) maintained the major trend of notch frequency with varying source direction. We used these filtered DTFs in the following analyses.

B. Individual differences between DTFs

We calculated the direction-specific ISSDs for 684 pairs of ears and for 361 source directions. The direction-specific ISSD for a given direction is the across-frequency variance of the spectral difference between the DTFs of two ears for that direction (see Sec. II for details). A greater ISSD indicates that the DTFs of the two animals differ by a greater amount.

Figures 2(a) and 2(b) show examples of the spatial distributions of the direction-specific ISSDs for two pairs of ears [Nos. 517F(left)–1020F(left) and Nos. 521M(right)–701F(right), respectively]. The overall difference between the DTFs (i.e., not specific to the source direction) is represented as the geometric average of direction-specific ISSDs across 361 directions, which we refer to as the average ISSD or simply as the ISSD, hereafter. The ISSDs for the ear pairs shown in Figs. 2(a) and 2(b) are indicated in the upper right corners of the figures, and ranked 6th and 669th of the total 684 pairs, respectively. Figure 2(c) shows the direction-specific ISSDs averaged over all pairs of ears. Before averaging, the direction-specific ISSDs for each animal pair were normalized by representing them as fractions of the maximal value across the source directions. As seen in the figure, it was consistent among ear pairs that, in general, the direction-specific ISSDs were relatively large for front-contralateral and low-elevation directions. An appreciable amount of the direction-specific ISSD was also seen, although to a lesser extent, for ipsilateral azimuths and for a relatively broad range of elevations.

We expected the distribution of the direction-specific ISSDs to reflect the spatial distribution of the complexity or the "richness" of the spectral features. That is, for directions in which direction-sensitive spectral features (e.g., notches) are evident, a slight difference between the DTF spectra of two animals would result in a large direction-specific ISSD. We quantified the complexity of the DTF spectral features (such as notches) by the variance of the DTF frequency components across frequencies between 5 and 45 kHz. We refer to this variance as the complexity index. A lower complexity index indicates that the DTF had a flatter spectrum, i.e., poorer spectral features. Figure 2(d) shows the spatial distribution of the complexity index averaged across all the 38 ears. Before averaging, the complexity index for each ear was normalized by representing it as a fraction of the maxi-

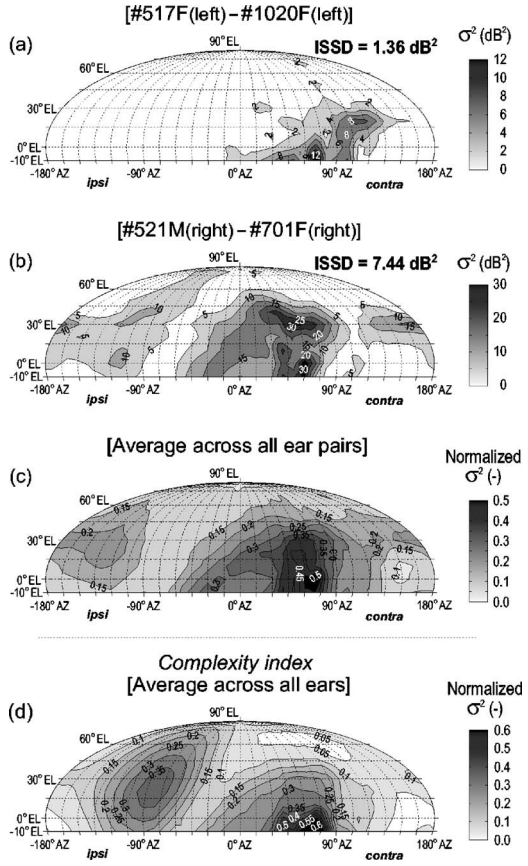

FIG. 2. Spatial distributions of the direction-specific ISSD and the spectral complexity of DTFs. The distributions are represented on a Mollweide projection. Panels (a) and (b) show the direction-specific ISSD for ear pairs Nos. 517F(left)–1020F(left) and Nos. 521M(right)–701F(right), respectively. The ISSD shown by the number in the upper right corner of panel (a) and (b) is the geometric average of the direction-specific ISSDs across 361 directions. Panel (c) shows the direction-specific ISSD averaged over all pairs of ears ($n=684$). Before the averaging, the direction-specific ISSDs for each pair of animals were normalized as representing the fraction relative to the maximum value across all directions. Panel (d) represents the complexity index averaged across all ears ($n=38$). The spectral complexity of a DTF is defined as the variance of the DTF across frequencies, indicating the "richness" of the spectral features in the DTF (see the text for details).

mal value across all directions. The spatial distributions of the direction-specific ISSD [Figs. 3(a)–3(c)] and of the complexity index [Fig. 3(d)] resembled each other. That is, there was a peak around the contralateral and low-elevation direction, and there was a distribution in the ipsilateral hemisphere for a broad range of elevations. This is consistent with our expectation with respect to the association between the ISSD and the richness of the spectral features.

C. Reducing ISSDs

1. Example of ISSD reduction

Figure 3(a) shows the DTFs of a pair of ears [Nos. 521M(left) and 703M(left)] for elevations of 0°, 30°, and 60° and for azimuths of −60°, 0°, and 60°. Figure 3(b) shows the spatial distributions of the direction-specific ISSD for the pair of ears. Consistent with the results shown in Figs. 2(a)–2(c), the direction-specific ISSDs were most evident for front-contralateral and low-elevation directions, and were above 2 dB^2 for a broad range of sound-source directions [Fig. 3(b)]. A close inspection of the plots in Fig. 3(a) reveals that this DTF difference could be largely characterized in terms of two not entirely independent features. One was the difference in the center frequency of the deep spectral notch around 30 kHz (single-headed arrows). The other was the difference in DTF gains above 15 kHz (double-headed arrows).

We first attempted to reduce these spectral differences by scaling one ear's DTF in frequency to account for the DTF differences arising due to differences between the animal's head and pinna sizes. The amount of frequency scaling that minimized the ISSD is referred to as the optimal scaling factor (OSF) (see Sec. II). The solid lines in Fig. 3(c) show the DTFs of ear No. 521M(left) after scaling the frequency upward with the OSF (0.24 octaves). The notch center frequencies of the two animals almost coincided with each other for all the sound-source directions. However, marked differences in the DTF gain remained even after the optimal frequency scaling. The maximum direction-specific ISSD reached as much as 22 dB^2 [around 40° azimuth and 0° elevation; Fig. 3(d)].

Our next attempt to reduce the ISSD involved rotating one animal's DTF along the source coordinate sphere to account for the DTF difference possibly arising due to differences in the pinna angle. We referred to the amount of rotation that minimized the ISSD as the optimal coordinate rotation (OCR) (see Sec. II). The solid lines in Fig. 3(e) show the DTFs after coordinate rotation by the OCR (yaw, roll, and pitch rotations of 11.5°, 5.0°, and −20.0°, respectively). After the rotation, the direction-specific ISSDs decreased to $\leqslant 12$ dB^2 [Fig. 3(f)]. However, the coordinate rotation alone failed to remove the difference in the notch frequency of the DTFs [e.g., 60° azimuth and 0° elevation; Fig. 3(e)].

Finally, we performed frequency scaling and coordinate rotation simultaneously to find the OSF and OCR (see Sec. II). The solid lines in Fig. 3(g) show the DTFs of ear No. 521M(left) after simultaneous optimal frequency scaling and coordinate rotation (OSF:0.15 octaves; OCR: yaw, roll, and pitch rotations of 7.5°, 2.5°, and −17.5°, respectively). The figure indicates that the DTFs of the two ears are now closely matched as regards both notch frequency and DTF gain, and the direction-specific ISSDs fell well below 2 dB^2 for most sound directions [Fig. 3(h)].

The OSF and the OCR could be determined uniquely for a given ear pair. Panels (a)–(d) in Fig. 4 plot the ISSDs as a function of the frequency-scaling factor, and the coordinate rotations in the yaw, roll, and pitch dimensions, respectively. For graphical convenience, all the parameters other than that of interest are fixed at their optimal values. To draw panel (a), for instance, we first find the OSF and the OCRs for the three rotation dimensions, and then vary the frequency scaling factor while the coordinate rotations were fixed at the OCR values. The filled circles in the panels indicate the OSF and the OCR. All the plots show single valleys, indicating that all the parameter values could be determined uniquely. Similarly, we were able to determine the optimal parameters for our sample in almost all cases.

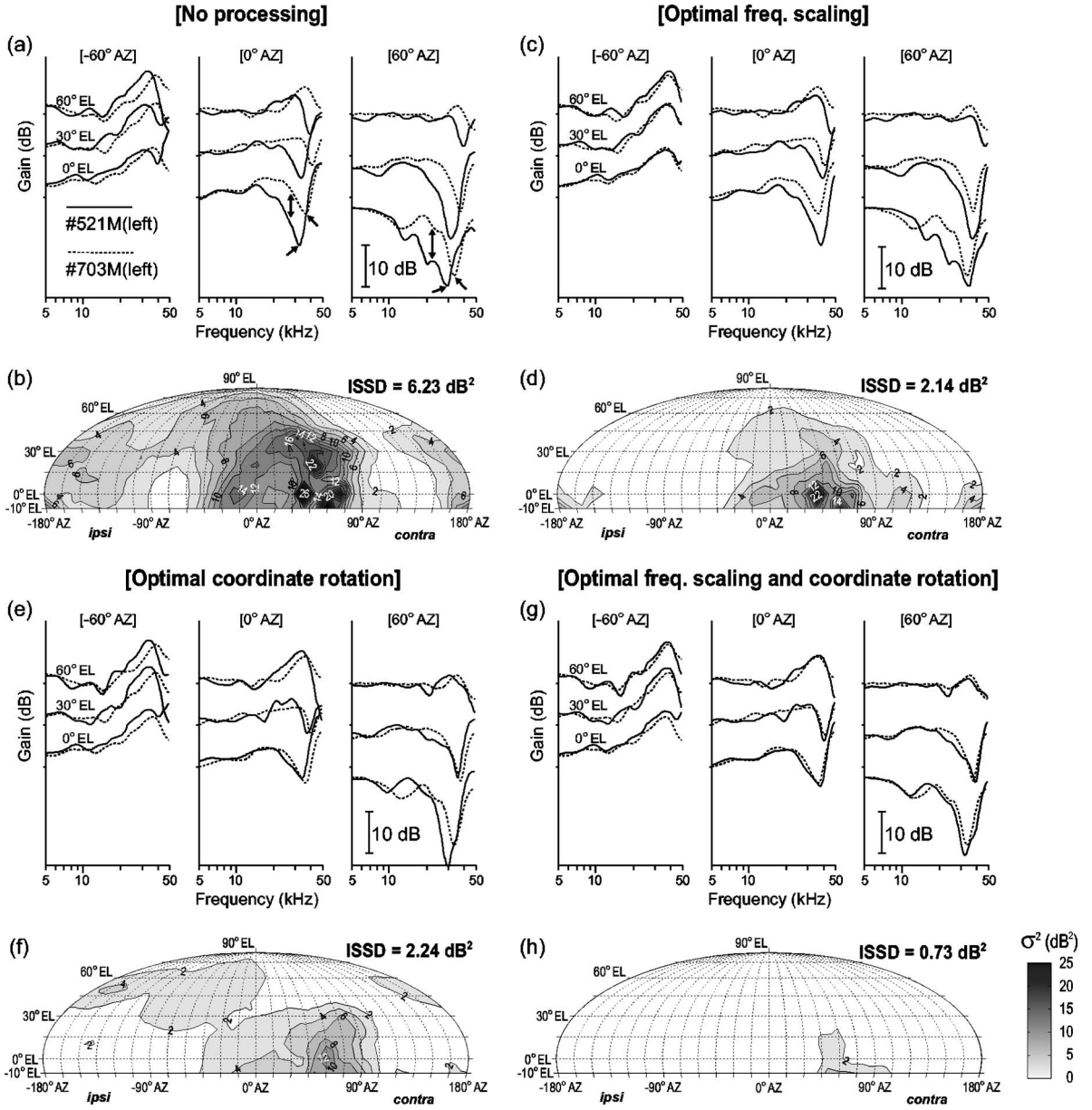

FIG. 3. DTFs and the direction-specific ISSDs for an ear pair with and without optimal frequency scaling and/or optimal coordinate rotation. Panels (a), (c), (e), and (g) show DTFs of the two ears for elevations of 0°, 30°, and 60° and for azimuths of −60°, 0°, and 60°. The DTF gain is shown on an arbitrary scale; the vertical bar beside the ordinate indicates a 10-dB gain. The solid and dotted lines indicate DTFs of ears Nos. 521M(left) and 703M(left), respectively. The data for ear No. 703M(left) (dotted line) are identical in all the panels. The data for ear No. 521M(left) (solid lines) indicate DTFs (a) before optimization; (c) after optimal frequency scaling; (e) after optimal coordinate rotation; and (g) after simultaneous optimal frequency scaling and coordinate rotation. Panels (b), (d), (f), and (h) show the spatial distributions of the direction-specific ISSDs for the ear pair before/after the optimization process. The average ISSDs are indicated in the upper right corners of the panels. The spatial distributions are represented on a Mollweide projection.

2. Population results

We examined the ISSDs for 684 pairs of ears, and conducted frequency scaling and coordinate rotation as described in the previous section.

The ISSD distribution before the optimization processes is shown in Fig. 5(a). The median of the ISSD was 3.72 dB^2. When the DTFs were scaled in frequency by the OSF [Fig. 5(b)], the median ISSD was reduced to 2.65 dB^2. This median value was close to that obtained when the coordinate system for the DTFs was rotated by the OCR [2.82 dB^2; Fig. 5(c)]. The reduction rates of the ISSDs relative to their nonprocessed condition, however, exhibited markedly different distributions for frequency scaling [Fig. 5(e); median 12.2%] and for coordinate rotation [Fig. 5(f); median 19.3%]. This difference reflected the fact that the factors leading to the ISSD reduction by optimal coordinate rotation were different from those for optimal frequency scaling.

When optimal frequency scaling and optimal coordinate rotation were employed simultaneously [Fig. 5(d)], the ISSDs were reduced further to a median of 1.98 dB^2. The reduction rate had a median of 35.8% [Fig. 5(g)]. The ISSD reduction was >50% for 28% of the pairs.

The OSF and the OCR were relatively insensitive to whether the frequency scaling and coordinate rotation were used simultaneously or separately. The correlation coefficient of the OSFs for the simultaneous and the separate estima-

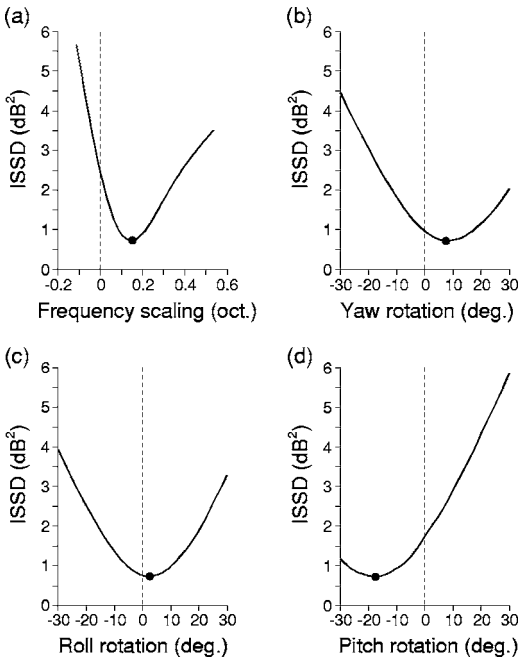

FIG. 4. ISSD dependence on the individual optimization parameters, namely the frequency-scaling factor and the coordinate rotations in the yaw, roll, and pitch dimensions. As in Fig. 3, the data for the ear pair of Nos. 521M(left) and 703M(left) are shown. Each panel shows the ISSD as a function of a single optimization parameter, while other parameters are fixed at their optimal values. The filled circle in each panel indicates the point where the parameter value was optimal, i.e., the ISSD was lowest.

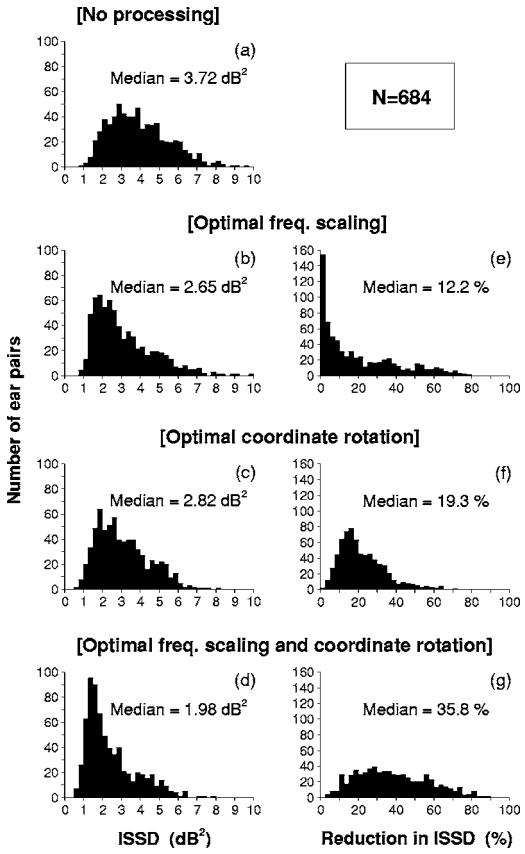

FIG. 5. Population results for frequency scaling and coordinate rotation. The rows of panels indicate the results when we applied (a) no scaling or rotation; (b), (e) optimal frequency scaling; (c), (f) optimal coordinate rotation; and (d), (g) optimal frequency scaling and coordinate rotation simultaneously. The left and right columns of the panels are histograms of the ISSDs, and of percentage reduction in the ISSD after each optimization, respectively. Each panel represents a total of 684 ear pairs.

tions was 0.80 ($p<0.001$). Similarly, the coefficients of the OCRs (yaw, roll, and pitch) for the two estimation methods were 0.75 to 0.95 ($p<0.001$). Figure 6 shows the OSF and OCR distributions as regards yaw, roll, and pitch, obtained when the frequency scaling and coordinate rotation were applied simultaneously [cf. Figs. 5(d) and 5(g)].

There was no apparent relationship between the OSF and OCR values. The correlation coefficient between the absolute OSF and the OCR (the sum of the absolute optimal rotations in yaw, roll, and pitch) was as small as 0.11.

We expected that the OSF should reflect the overall spectral disparity between DTFs (i.e., the ISSD). We tested this expectation by plotting the ISSD as function of the OSF [Fig. 7(a)], as undertaken by Middlebrooks (1999a; Fig. 8) and Schnupp *et al.* [2003; Fig. 3(B)]. As expected, there was a weak but positive correlation between the ISSD before scaling and the OSF ($r=0.35$; open circles). This correlation was eliminated by the optimal frequency scaling ($r=-0.18$; filled triangles). The result suggests that frequency scaling can remove a component that contributes to the ISSD.

Similarly, we found a correlation between the ISSD and the OCR [Fig. 7(b)]. However, the elimination of this correlation by optimal spatial rotation was not as evident as with the frequency scaling ($r=0.46$ before rotation versus $r=0.33$ after the rotation). Nonetheless, the slope of a linear fit of the data decreased in a way that was statistically significant with coordinate rotation ($p<0.0005$, parallelism test by covariance analysis).

3. Influence of alignment error

One might suspect that the OCR would not indicate individual differences in ear orientation, but merely reflect a systematic bias owing to errors that occurred when aligning the animal's head orientation for the measurements. Although we attempted to correct any alignment errors before computing the OCRs (see Sec. II), it is possible that residual errors confounded our estimates of the "true" OCRs. However, the following analysis leads us to dismiss such a possibility.

In the analysis, we assumed that the orientations of the

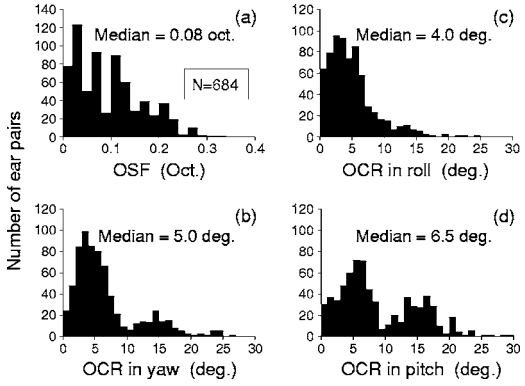

FIG. 6. Histograms of the OSF (a) and the OCRs for the three rotation dimensions; (b) yaw; (c) roll; and (d) pitch. Each panel represents a total of 684 ear pairs.

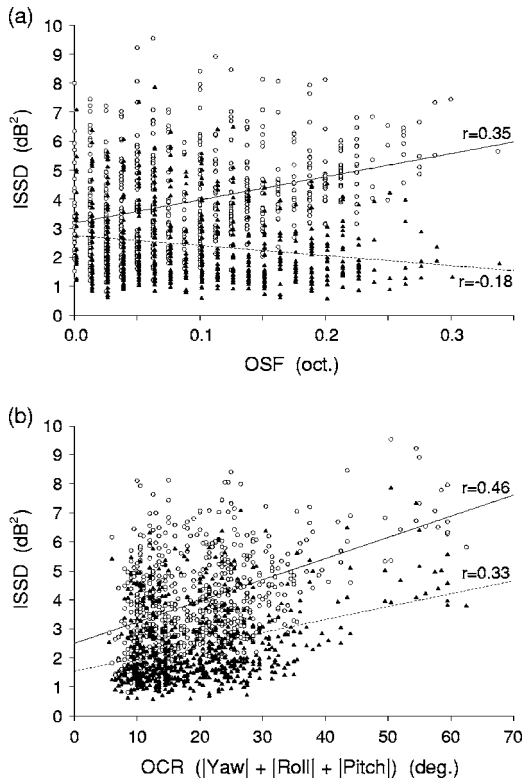

FIG. 7. The ISSD plotted as a function of OSF (a) and OCR (b). The OCR represented by the abscissa is the sum of the absolute OCR values for the yaw, roll, and pitch dimensions. Each symbol indicates one pair of ears. The open circles and the filled triangles indicate the ISSD before and after the optimization was performed, respectively. The straight and dotted lines indicate linear fits to the data before and after the optimization, respectively.

left and the right ears were, as a first approximation, symmetric about the midline. This assumption was confirmed to be acceptable when we plotted the yaw angle of the left pinna versus that of the right pinna (the pinna angles will be defined fully in the next section as shown in Fig. 9) for our sample of 19 animals [Fig. 8(g)]. The dots in the figure cluster around the diagonal line, indicating that the left and right ears were roughly symmetrical about the midline.

Now, let us consider two hypothetical cases. In case 1, a pair of hypothetical animals, the reference and the target, had pinna angles of α and β, respectively [Figs 8(a) and 8(b)]. the suffixes, L and R, indicate the angles of the left and right ears, respectively ($\alpha_L = \alpha_R$ and $\beta_L = \beta_R$, on the assumption of left–right symmetry). The target animal shown in Fig. 8(b) has ears that face backward relative to the ears of the reference animal (i.e., $\alpha_L < \beta_L$; $\alpha_R < \beta_R$). Note that in the convention of the present section, a positive yaw direction indicates a direction away from the midline. Thus, if the OCR in the yaw direction reflects the difference in the yaw pinna angles, we expect that the direction of the OCR will correspond to the direction of the pinna rotation needed for the reference's pinna angle to match the target's [$+\Delta_{LL}$ and $+\Delta_{RR}$ in Fig. 8(c)]. Because of the assumption of symmetry, the signs of the rotations should be the same (namely positive in this example) for the left and right ears.

In case 2, the target animal is assumed to have pinnae with the same angles as those of the reference animal, but its head was misoriented (hence, the alignment error) by a certain angle [indicated by γ in Fig. 8(e)]. In this case, the signs of the pinna rotation directions needed for the reference and

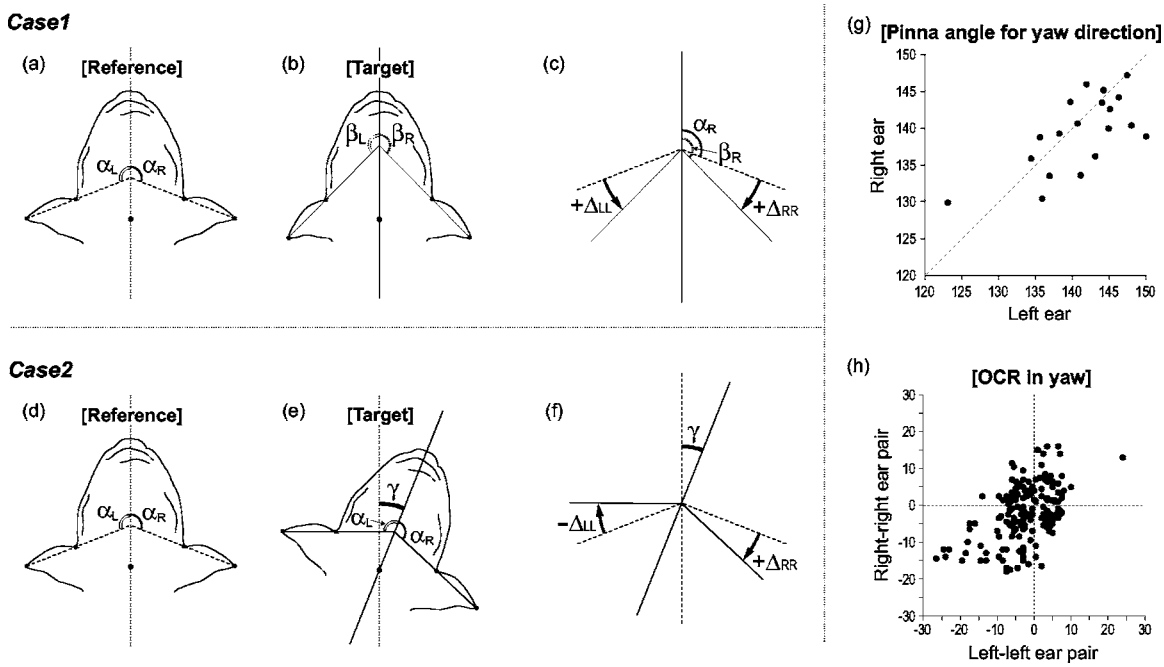

FIG. 8. Tests on the impacts of the alignment error on the OCR estimates. Panels (a)–(c) illustration of hypothetical case 1: The reference and target animals had pinnae that were symmetric between the midline, but differed from each other in yaw angle (indicated as α and β, respectively). This difference could be accounted for by rotating the reference's left and right pinnae towards the same yaw direction (i.e., away from the midline) [indicated as the signs of the Δ's in panel (c)]. Panels (d)–(f) illustration of hypothetical case 2. The reference and the target are assumed to have pinnae with the same yaw angle (α), but the target's head was misaligned in the experiment (indicated by γ). Then, the reference's left and right ears have to be rotated towards the opposite yaw directions to account for the difference in the pinnae angle between the animals [indicated by signs of the Δ's in panel (f)]. Panel (g) the yaw angle of the right pinna plotted versus that of the left pinna. The figure represents 19 animals. Panel (h) the plot of the OCRs in the yaw dimension for the pairs of the right ears of the reference and target versus the OCRs for the pairs of the left ears. Each filled circle represents one animal pair, and the figure represents 171 animal pairs.

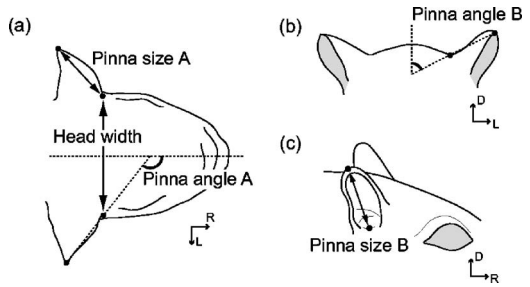

FIG. 9. Anatomical measurements examined in this study. Physical landmarks are indicated by dots. Head width and pinna sizes (*A* and *B*) were measured directly with a micrometer caliper. Pinna angles (*A* and *B*) were derived from photographs that were taken directly overhead and directly in front of the animals as illustrated in (a) and (b).

target pinna angles to match should be opposite for the left and right ears [$-\Delta_{LL}$ and $+\Delta_{RR}$ in Fig. 8(f)]. Thus, we expect the signs of the OCR to be different for the left and right ears.

In Fig. 8(h), the OCRs for pairs consisting of the right ears of the reference and target (right–right pairs) are plotted versus those for pairs consisting of their left ears (left–left pairs). The figure represents a total of 171 animal pairs indicated by the filled circles. It can be seen that a large number of points fell in the first and third quadrants, indicating that the signs of the OCRs for the right–right and left–left pairs were generally the same. This is consistent with our expectation based on case 1 [Figs 8(a) and (b)]. Of the 171 animal pairs, 106 pairs showed the same OCR signs.

We observed similar results for the OCR in the roll dimension. Thus, we conclude that the major factor determining the OCR was not the head orientation alignment error in the experiments, but the differences between animals as regards pinna orientation.

D. Predicting individual DTFs by using anatomical measurements

We expected the optimal frequency scaling and coordinate rotation to correlate with differences in anatomical measurements, such as the animal size and the pinna angles of two animals. In this section, we evaluate this expectation by comparing the OSF and OCR with several anatomical measurements. Then, we attempt to establish a method for estimating the OSF and OCR based on these anatomical measurements.

1. Anatomical measurements

Figure 9 illustrates the anatomical measurements that we examined in the present study. Dots in the figure indicate physical landmarks. Head width and pinna size *A* and *B* were measured by directly applying a micrometer caliper to the animal. Pinna angles *A* and *B* were derived from photographs that were taken from directly overhead [Fig. 9(a)] and from straight in front of the animal [Fig. 9(b)]. We regarded the pinna angles *A* and *B* as measurements of the pinna orientation in the yaw and roll dimensions, respectively. We were not able to define confidently a measurement that would correspond to the orientation in the pitch dimension.

TABLE I. Summary of anatomical measurements in the data set consisting of 19 animals and 38 ears. Mean, standard deviation (S.D.), minimum, and maximum are shown. Each value shown in the far right column is a correlation coefficient between age (days after birth) on a logarithmic scale and the anatomical measurement. Physical landmarks for measuring head width, pinna sizes (*A* and *B*), and pinna angles (*A* and *B*) are shown in Fig. 9.

	Mean	S.D.	Min.	Max.	r to age
Age (days)	90.1	53.5	34	247	
Weight (g)	62.8	17.5	32.6	102.5	0.95
Head width (mm)	17.0	1.1	14.7	18.5	0.86
Pinna size *A* (mm)	12.1	0.7	10.6	13.4	0.81
Pinna size *B* (mm)	10.8	0.8	9.3	12.6	0.84
Pinna angle *A* (deg.)	140.3	5.6	123.1	150.0	−0.03
Pinna angle *B* (deg.)	64.2	5.0	56.5	80.9	−0.09

Table I summarizes the anatomical measurements, as well as the body weight, for all the animals used in this study. Physical sizes, namely the body weight, head width, and pinna sizes (*A* and *B*), correlated strongly with the age (day after birth; on a logarithmic scale) [$r=0.81-0.95$, $p<0.001$]. The pinna angles were independent of age [$|r|\leqslant 0.09$, $p>0.05$]. No differences between sexes were evident in any of the measurements.

2. Correlation between optimization and anatomical measurements

We examined the correlations between the optimization parameters (i.e., the OSF and the OCR) and the difference or the ratio of anatomical measurements for animal pairs. For weight, head width, and pinna sizes (*A* and *B*), we computed the logarithms of the ratios (the log ratios) between two animals (i.e., the target and the reference). Note that the log ratio has the same dimension as the OSF, and could be expressed in octave units. For pinna angles, we simply computed the linear differences between animals.

Table II summarizes the results of the correlation coefficients between the measurements. Not surprisingly, the measurements related to animal size, namely body weight, head width, and pinna size (*A* and *B*), correlated strongly with each other ($r=0.83-0.88$). The log ratios of these size measurements exhibited negligible correlation with the difference in pinna angle (*A* and *B*) ($|r|\leqslant 0.14$).

The OSF correlated closely with the log ratios of the head width and pinna size ($r=0.74-0.79$), and moderately with the log ratio of the weight ($r=0.62$). The OCRs in the yaw and the roll dimensions correlated closely with the difference in pinna angle *A*($r=0.78$) and pinna angle *B*($r=0.68$), respectively. The OCR in the pitch dimension, however, correlated only moderately with the ratio of pinna angle *A* or *B* ($r=-0.52$ and 0.54, respectively). These results are reasonable because, as stated in the previous section, the rotations in the yaw and roll dimensions are associated with pinna angles *A* and *B*, respectively, but there was no anatomical measurement directly associated with the rotation in the pitch dimension.

TABLE II. Correlation coefficients between log ratios/differences of anatomical measurements for ear pairs, OSF, and OCRs. We used log ratios for the weight, head width, and pinna sizes (*A* and *B*), and used differences for pinna angles (*A* and *B*). The OSF is expressed in octaves, and the OCR (yaw, roll, and pitch) are expressed in degrees. The asterisk indicates statistical significance at the $p<0.001$ level. The "*n*" in parenthesis indicates the number of samples.

	Head width log ratio (n=171)	Pinna size A log ratio (n=684)	Pinna size B log ratio (n=684)	Pinna angle A difference (n=684)	Pinna angle B difference (n=684)	OSF (n=684)	OCR in yaw (n=684)	OCR in roll (n=684)	OCR in pitch (n=684)
Weight log ratio	0.88*	0.85*	0.83*	−0.11	−0.05	0.62*	0.09	−0.22*	0.19*
Head width log ratio		0.87*	0.85*	−0.12	0.12	**0.79***	0.02	−0.03	0.22*
Pinna size *A* log ratio			0.88*	0.06	−0.04	0.77*	0.13*	−0.11	0.13*
Pinna size *B* log ratio				0.14*	−0.14*	0.74*	0.22*	−0.17*	0.03
Pinna angle *A* difference					−0.59*	−0.04	**0.78***	−0.27*	**−0.52***
Pinna angle *B* difference						0.13*	−0.50*	**0.68***	**0.54***

3. Estimating OSF and OCRs based on anatomical measurements

We performed linear regression analyses as regards the relationship between each optimal parameter value and one or two anatomical measurements. For the OSF and the OCRs in the yaw and roll dimensions, the regression analyses were performed for single anatomical measurements that exhibited the largest correlation coefficients, namely, the head width, pinna angle *A*, and *B*, respectively. The regression lines are represented by the following equations:

$$\text{OSF(oct.)} = 0.73 \cdot \log_2(\text{head width}/\text{head width}_{\text{Ref}}), \quad (1)$$

$$\text{OCR in yaw(deg.)} = 0.79(\text{pinna angle } A - \text{pinna angle } A_{\text{Ref}}), \quad (2)$$

$$\text{OCR in roll(deg.)} = 0.58(\text{pinna angle } B - \text{pinna angle } B_{\text{Ref}}). \quad (3)$$

Here, the suffix "Ref" indicates the measurement of an arbitrary reference animal. It should be noted that a regression line was forced to pass the origin in order to make the OSF or OCR zero when there was no difference between the anatomical measurements of the ear pair. The correlation coefficients for the actual values and the predictions from Eqs. (1)–(3) were 0.79, 0.78, and 0.68, respectively. Thus, the squared values of those correlation coefficients, namely the coefficients of determination, were 0.63, 0.62, and 0.46, indicating the fractions of the variance of the optimal parameters accounted for by the regression.

For the OCR in the pitch dimension, we performed a multiple regression, using the pinna angles *A* and *B* as independent variables. This was because those measurements correlated equally, although not closely, with the OCR in the pitch dimension. The result is given by the following equation:

$$\text{OCR in pitch(deg.)} = -0.41(\text{pinna angle } A - \text{pinna angle } A_{\text{Ref}}) + 0.53(\text{pinna angle } B - \text{pinna angle } B_{\text{Ref}}). \quad (4)$$

Note again that the regression was performed under the constraint that the OCR would be zero when there was no difference between the animals' pinna angles. The correlation coefficient for the predicted and actual OCRs was 0.68, and thus the coefficient of determination for the regression was 0.46.

4. Reduction of ISSD using anatomical measurements

We evaluated the extent to which we could reduce the ISSD by using the OSF and the OCRs estimated from the anatomical measurements. Figure 10(a) shows the distribution of the ISSDs after frequency scaling and coordinate rotation by the estimated OSF and OCRs values obtained using Eqs. (1)–(4). The ISSDs were appreciably reduced by the processing, compared with those before the processing [Fig. 5(a)]; a median ISSD of 2.58 dB^2 versus 3.72 dB^2. The reduction rate [Fig. 10(b)] had a median of 22.4%. The ISSD reduction was >50% for 12.0% of pairs. A small percentage of ear pairs (7.5%) showed an *increase* in the ISSD after the processing [as indicated by the negative percentage in Fig. 10(b)]. This was because the ISSDs for those ear pairs were

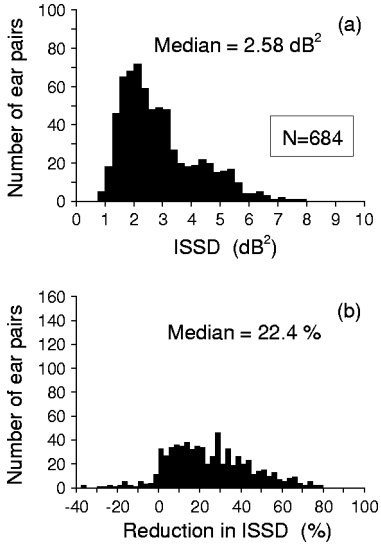

FIG. 10. (a) Histogram of the ISSD after frequency scaling and coordinate rotation were performed on DTFs based on the OFS and the OCRs predicted by Eqs. (1)–(4). (b) Histogram of the ISSD reduction rate by the frequency scaling and the coordinate rotation. The data represent 684 ear pairs.

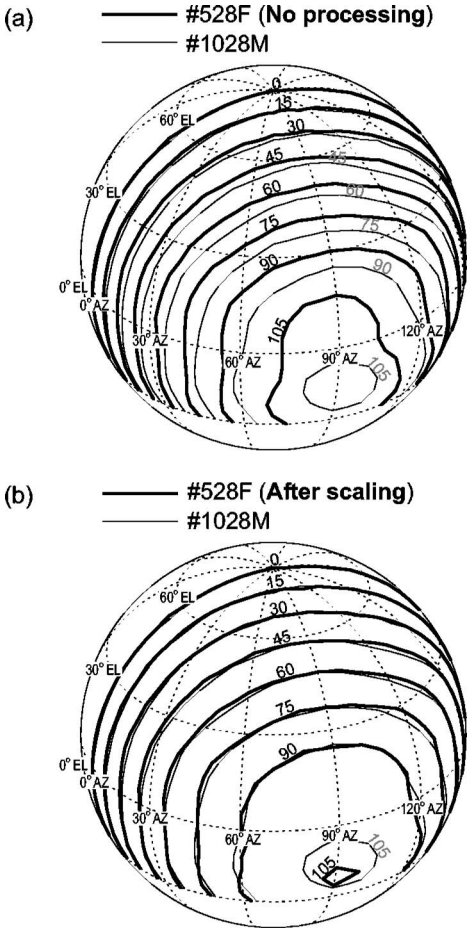

FIG. 11. The iso-ITD contours for a pair of animals. The contour lines are drawn on the coordinate sphere viewed laterally to the animal. The iso-ITD contour lines are drawn at 15-μs intervals; corresponding ITD values are indicated by numbers beside the lines. The thick and thin lines indicate animals Nos. 528F and 1028M, respectively. The data for animal No. 1028M are identical in the two panels. For animal No. 528F, the original ITD and the ITD scaled by the head-width ratio (0.93) are shown in panel (a) and (b), respectively. Only positive azimuth data are shown.

relatively small even before the processing, and thus a small error in estimating the OSF or the OCR increased the ISSD.

E. Individual differences in ITDs

In this section, we examine the individual differences in the ITDs, and explore a method of reducing them based on an anatomical measurement. Figure 11(a) represents animals Nos. 528F and 1020M, and displays the iso-ITD contours on the coordinate sphere viewed laterally to the animals. The contour lines differed markedly between the two animals, but they were all concentric. We found that this difference in the spatial distribution of the ITDs could be accounted for well by scaling the ITD distribution functions according to the ratio of the maximum ITDs between animals. We considered that the difference in the maximum ITD was due to the differences between the animals' head sizes. The head width of animal No. 528F (17.37 mm) was larger than that of animal No. 1020M (16.20 mm). When the ITDs of animal No. 528F were scaled by the ratio of the head width for the two animals [0.93 times; thick lines in Fig. 11(b)], the iso-ITD contours overlapped considerably.

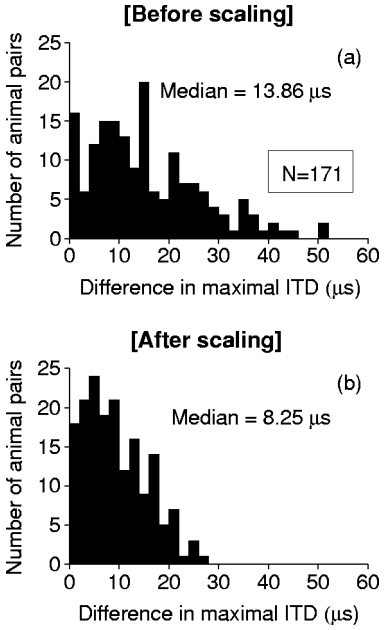

FIG. 12. Histograms of the differences in the maximal ITDs between animal pairs. Panels (a) and (b) represent the differences before and after the ITD scaling, respectively. The data represent a total of 171 animal pairs.

We found it reasonable to assume that, for a population of animal pairs, the ratio of the maximal ITDs for the animals (the ITD ratio) is equal to the ratio of the head widths (the head-width ratio). This was because, for our sample population of 19 animals, the maximal ITD was generally proportional to the head width (r=0.85). Here, the maximal ITD for a given animal was defined as the mean between the left and the right hemifields of the maximal absolute values of ITDs among the directions in the hemifields. When the ratio of the maximal ITD was plotted versus the ratio of the head width for 171 pairs of animals (data not shown), the slope of the linear fit (passing the origin) was 1.01, that is, very close to unity (r=0.85).

Figures 12(a) and 12(b), respectively, show the distributions of the differences between animals in the maximal ITD before and after the ITD scaling based on the head-width ratios. The difference between animals was markedly reduced by the ITD scaling; namely there was a median difference of 8.25 μs compared with 13.68 μs. The median reduction rate was 39%.

IV. DISCUSSION

This study demonstrated that the intersubject differences in DTF (indicated as the ISSD) could be reduced appreciably by frequency scaling the DTFs. A unique finding of the present study was that the ISSD could also be reduced by rotating the coordinate sphere that would account for individual differences in pinna angles. By combining coordinate rotation with frequency scaling, we were able to reduce the ISSD further than with frequency scaling. We consider that the contribution of the coordinate rotation was not an artifact of the errors made during DTF recording. This is because the direction of the OCR was not as predicted based on the alignment error of the animal's head in the experiments (Sec.

III C 3), and because the OCR exhibited a high correlation with the pinna angle, which was measured independently of the DTF measurement. Regression analyses of the relationship between the OSF and the OCR and certain anatomical measurements revealed that the OSF and the OCR could be estimated with some degree of accuracy from the head width and pinna angles, respectively.

A. Comparison with previous studies

The ISSDs for gerbils measured in the present study (average 3.93 dB^2) were generally smaller than those for humans (average 8.29 dB^2; Middlebrooks, 1999a), cats (average 17.02 dB^2; Xu and Middlebrooks, 2000), and ferrets (average >11 dB^2; Schnupp *et al.*, 2003). However, we consider the differences between the absolute ISSDs among species to be trivial. One reason for this was that we adopted relatively wide bandwidths for the bandpass filter bank used in the preprocessing of the raw DTF data (see Sec. II). A wider bandwidth should result in greater smoothing of the DTF spectrum, which should reduce the contributions of the detailed spectral difference between ears. Another reason is that the number of spectral notches within the audible frequency range for gerbils was generally fewer than that for humans, cats and ferrets (humans: Middlebrooks, 1999a; Møller *et al.*, 1995; cats: Musicant *et al.*, 1990; Rice *et al.*, 1992; Xu and Middlebrooks, 2000; ferrets: Carlile, 1990; Schnupp *et al.*, 2003). Since the ISSD was well associated with the complexity of the DTF (Fig. 2), fewer spectral notches (i.e., less spectral complexity) should lead to a smaller ISSD. We note that the reduction rate of the ISSD, rather than the absolute ISSD, obtained for the gerbil by optimal frequency scaling [median 12.2%; Fig. 5(e)] was similar to that for other species, despite marked variations among species in the range of weight and physical size across individuals; e.g., the gerbils in the present study varied in weight by a factor of 3.12, whereas the human range was smaller. The reduction rate was 15.5% for humans (Middlebrooks, 1999a), 11.5% for cats (Xu and Middlebrooks, 2000), 11.8% for ferrets (Schnupp *et al.*, 2003).

Our results were consistent with previous findings in that the OSF could be relatively well predicted by the ratio of the physical sizes, namely the head width and/or the pinna size of the animal pair (Middlebrooks, 1999a, Schnupp *et al.*, 2003). Previous studies have proposed regression equations that could be used to predict the OSF from the pinna size (ferret: Schnupp *et al.*, 2003) or from a combination of the pinna size and the head width (human: Middlebrooks, 1999a). The correlation coefficients for the predicted and actual OSFs were 0.84 (in absolute value, Schnupp *et al.*, 2003) and 0.82 (Middlebrooks, 1999a). These numbers are comparable to our $r=0.79$ obtained with Eq. (1). Similarly, the predictability of the maximum ITD from the head width has been demonstrated consistently in the present study and in a previous study of humans (Middlebrooks, 1999a).

When coordinate rotation was applied in combination with frequency scaling, the ISSD reduction rate was as much as a median of 35.8% [Fig. 5(g)]. This rate was markedly greater than the reduction rate when frequency scaling alone was applied not only for gerbils [present study, Fig. 5(e)], but also for humans (Middlebrooks, 1999a), cats (Xu and Middlebrooks, 2000), and ferrets (Schnupp *et al.*, 2003). It should also be noted that a relatively large ISSD reduction rate could be achieved [median 22.4%, Fig. 10(b)] even when the frequency scaling and coordinate rotation were performed based on the OSF and the OCR predicted from anatomical measurements with Eqs. (1)–(4).

B. Significance in psychophysical and physiological studies

The present study demonstrated that the ISSD could be reduced substantially by frequency scaling and by coordinate rotation by amounts estimated from anatomical measurements [Fig. 10(b)]. This indicates that we can estimate the DTFs of a given animal with some accuracy by measuring a few anatomical features of the animal, given the DTFs and anatomical measurements of a reference animal. It is arguable as to the extent to which the VAS stimuli based on our quasi-individualized DTFs would be adequate to simulate the free-field stimuli for the purpose of psychophysical or physiological experiments. This remains unclear until behavioral sound localization performance or physiological responses are compared for conditions in which simulated and actual free-field stimuli are used (Behrend *et al.*, 2004; Middlebrooks, 1999b; Mrsic-Flogel *et al.*, 2001; Schnupp *et al.*, 2001). Nonetheless, we expect our proposed method to be useful for psychophysical or physiological experiments, by permitting us to present relatively faithful VAS stimuli to a target animal without the need for the time-consuming process of measuring actual DTFs.

ACKNOWLEDGMENTS

We thank Dr. Tatsuhiko Harada at Tokai University for providing us with experimental facilities, and the Interdepartmental Laboratories of Tokai University for assistance in conducting the experiments.

Behrend, O., Brand, A., Kapfer, C., and Grothe, B. (**2002**). "Auditory response properties in the superior paraolivary nucleus of the gerbil," J. Neurophysiol. **87**, 2915–2928.

Behrend, O., Dickson, B., Clarke, E., Jin, C., and Carlile, S. (**2004**). "Neural responses to free field and virtual acoustic stimulation in the inferior colliculus of the guinea pig," J. Neurophysiol. **92**, 3014–3029.

Brückner, S., and Rübsamen, R. (**1995**). "Binaural response characteristics in isofrequency sheets of the gerbil inferior colliculus," Hear. Res. **86**, 1–14.

Brugge, J. F., Reale, R. A., and Hind, J. E. (**1996**). "The structure of spatial receptive fields of single neurons in primary auditory cortex of the cat," J. Neurosci. **16**, 4420–4437.

Brugge, J. F., Reale, R. A., and Hind, J. E. (**1998**). "Spatial receptive fields of primary auditory cortical neurons in quiet and in the presence of continuous background noise," J. Neurophysiol. **80**, 2417–2432.

Carlile, S. (**1990**). "The auditory periphery of the ferret. I. Directional response properties and the pattern of interaural level differences," J. Acoust. Soc. Am. **88**, 2180–2195.

Delgutte, B., Joris, P. X., Litovsky, R. Y., and Yin, T. C. (**1999**). "Receptive fields and binaural interactions for virtual-space stimuli in the cat inferior colliculus," J. Neurophysiol. **81**, 2833–2851.

Euston, D. R., and Takahashi, T. T. (**2002**). "From spectrum to space: The contribution of level difference cues to spatial receptive fields in the barn owl inferior colliculus," J. Neurosci. **22**, 284–293.

Heffner, R. S., and Heffner, H. E. (**1988**). "Sound localization and use of

binaural cues by the gerbil (*Meriones unguiculatus*)," Behav. Neurosci. **102**, 422–428.
Kelly, J. B., and Potas, M. (**1986**). "Directional responses to sounds in young gerbils (*Meriones unguiculatus*)," J. Comp. Psychol. **100**, 37–45.
Kittel, M., Wagner, E., and Klump, G. M. (**2002**). "An estimate of the auditory-filter bandwidth in the Mongolian gerbil," Hear. Res. **164**, 69–76.
Maki, K., and Furukawa, S. (**2005**). "Acoustical cues for sound localization by the Mongolian gerbil, *Meriones unguiculatus*," J. Acoust. Soc. Am. **118**, 872–886.
Middlebrooks, J. C. (**1999a**). "Individual differences in external-ear transfer functions reduced by scaling in frequency," J. Acoust. Soc. Am. **106**, 1480–1492.
Middlebrooks, J. C. (**1999b**). "Virtual localization improved by scaling nonindividualized external-ear transfer functions in frequency," J. Acoust. Soc. Am. **106**, 1493–1510.
Middlebrooks, J. C., and Green, D. M. (**1990**). "Directional dependence of interaural envelope delays," J. Acoust. Soc. Am. **87**, 2149–2162.
Møller, H., Sørensen, M. F., Hammershøi, D., and Jensen, C. B. (**1995**). "Head-related transfer functions of human subjects," J. Audio Eng. Soc. **43**, 300–320.
Mrsic-Flogel, T. D., King, A. J., Jenison, R. L., and Schnupp, J. W. (**2001**). "Listening through different ears alters spatial response fields in ferret primary auditory cortex," J. Neurophysiol. **86**, 1043–1046.
Mrsic-Flogel, T. D., Schnupp, J. W., and King, A. J. (**2003**). "Acoustic factor govern developmental sharpening of spatial tuning in the auditory cortex," Nat. Neurosci. **6**, 981–988.
Musicant, A. D., Chan, J. C., and Hind, J. E. (**1990**). "Direction-dependent spectral properties of cat external ear: New data and cross-species comparisons," J. Acoust. Soc. Am. **87**, 757–781.
Poganiatz, I., Nelken, I., and Wagner, H. (**2001**). "Sound-localization experiments with barn owls in virtual space: Influence of interaural time difference on head-turning behavior," J. Assoc. Res. Otolaryngol. **2**, 1–21.
Rice, J. J., May, B. J., Spirou, G. A., and Young, E. D. (**1992**). "Pinna-based spectral cues for sound localization in cat," Hear. Res. **58**, 132–152.
Ryan, A. (**1976**). "Hearing sensitivity of the mongolian gerbil, *Meriones unguiculatus*," J. Acoust. Soc. Am. **59**, 1222–1226.
Sanes, D. H. (**1990**). "An *in vitro* analysis of sound localization mechanisms in the gerbil lateral superior olive," J. Neurosci. **110**, 3494–3506.
Sanes, D. H. (**2002**). "Right place and at the right time," Nat. Neurosci. **5**, 187–188.
Schnupp, J. W., Booth, J., and King, A. J. (**2003**). "Modeling individual differences in ferret external ear transfer functions," J. Acoust. Soc. Am. **113**, 2021–2030.
Schnupp, J. W., Mrsic-Flogel, T. D., and King, A. J. (**2001**). "Linear processing of spatial cues in primary auditory cortex," Nature (London) **414**, 200–204.
Spitzer, M. W., and Semple, M. N. (**1995**). "Neurons sensitive to interaural phase disparity in gerbil superior olive: Diverse monaural and temporal response properties," J. Neurophysiol. **73**, 1668–1690.
Sterbing, S. J., Hartung, K., and Hoffmann, K. P. (**2003**). "Spatial tuning to virtual sounds in the inferior colliculus of the guinea pig," J. Neurophysiol. **90**, 2648–2659.
Suzuki, Y., Asano, F., Kim, H.-Y., and Sone, T. (**1995**). "An optimum computer-generated pulse signal suitable for the measurement of very long impulse responses," J. Acoust. Soc. Am. **97**, 1119–1123.
Wenzel, E. M., Arruda, M., Kistler, D. J., and Wightman, F. L. (**1993**). "Localization using nonindividualized head-related transfer functions," J. Acoust. Soc. Am. **94**, 111–123.
Xu, L., and Middlebrooks, J. C. (**2000**). "Individual differences in external-ear transfer functions of cats," J. Acoust. Soc. Am. **107**, 1451–1459.

Comparison of an analytic horn equation approach and a boundary element method for the calculation of sound fields in the human ear canal

Michael R. Stinson[a] and Gilles A. Daigle
Institute for Microstructural Sciences, National Research Council, Ottawa, Ontario K1A 0R6, Canada

(Received 15 February 2005; revised 29 June 2005; accepted 29 June 2005)

The sound field inside a model human ear canal has been computed, to show both longitudinal variations along the canal length and transverse variations through cross-sectional slices. Two methods of computation were used. A modified horn equation approach parametrizes the sound field with a single coordinate, the position along a curved center axis—this approach can accommodate the curvature and varying cross-sectional area of the ear canal but cannot compute transverse variations of the sound field. A boundary element method (BEM) was also implemented to compute the full three-dimensional sound field. Over 2000 triangular mesh elements were used to represent the ear canal geometry. For a plane piston source at the entrance plane, the pressure along the curved center axis predicted by the two methods is in good agreement, for frequencies up to 15 kHz, for four different ear canals. The BEM approach, though, reveals spatial variations of sound pressure within each canal cross section. These variations are small below 4 kHz, but increase with frequency, reaching 1.5 dB at 8 kHz and 4.5 dB at 15 kHz. For source configurations that are more realistic than a simple piston, large transverse variations in sound pressure are anticipated in the vicinity of the source. [DOI: 10.1121/1.2005947]

PACS number(s): 43.64.Ha, 43.20.Mv [BLM] Pages: 2405–2411

I. INTRODUCTION

An understanding of the acoustical behavior of the ear canal is important for the design of audiometric and hearing aid devices. At relatively low frequencies, below 3 kHz, the ear canal can be approximated as a straight, cylindrical tube. At higher frequencies, the ear canal is long enough that one or more minima in the standing wave patterns will arise, and an account must be made of both the varying cross-sectional area of the canal along its length and the curvature of the canal.

The horn equation originally developed by Webster (1919) has been applied usefully to a variety of problems of acoustical propagation in waveguides of varying cross-sectional area. It is usually assumed that the transverse dimensions are small so that ingoing and outgoing waves are planar and that propagation is one dimensional. With an average diameter of about 7.5 mm, the human ear canal diameter is small compared to a wavelength and the first requirement is approximately satisfied up to 15 kHz. This approach cannot be immediately applied to ear canals, however, because of their significant curvature. An extension to Webster's approach that can accommodate curved waveguides was presented by Khanna and Stinson (1985). This modified horn equation has been shown to give accurate predictions of the ear canal sound field for cat ear canals (Khanna and Stinson, 1985; Stinson and Khanna, 1994) and for scaled replicas of human ear canals (Stinson, 1985). It can accommodate the distributed load presented by the eardrum (Stinson and Khanna, 1989) and can be used to compute particle velocity and energy flow (Stinson and Khanna, 1994).

The modified horn equation, though, predicts only the longitudinal sound pressure along a curved axis that follows the center of the ear canal. Transverse variations cannot be calculated. However, there will be applications for which the prediction of such variations is important. A prime example can be drawn from the Burkhard and Sachs (1977) study of sound pressure distributions in earphone couplers. Probe tube measurements were made within a 2 cm^3 cavity, commonly used for earphone calibrations. Spectra obtained in the center of the cavity, in front of the earphone sound tube leading into the cavity, were compared to spectra obtained 3 mm transverse, toward the side of the cavity. Large differences, over 20 dB at 3 kHz, were noted. These differences can be understood in terms of transverse modes of oscillation in the cavity (for long cavities, as for an ear canal, these modes would be evanescent and would decay rapidly with depth into the canal). Thus, significant localized effects can be expected to arise at the entrance end of the ear canal where the sound source (such as a hearing aid) is located.

The approach of Farmer-Fedor and Rabbitt (2002) may provide a better approximation for the sound field in the ear canal, by introducing a curvilinear coordinate system and parametrizing the sound field in terms of curved coordinate surfaces rather than planes normal to a center axis. However, this approach still assumes that pressure and velocity are constant over a coordinate surface, inconsistent with our intended applications for which significant transverse variations in sound pressure are anticipated. Slender waveguide theory (Rabbitt and Holmes, 1988) can accommodate the three-dimensional character of the ear canal sound field by

[a]Electronic mail: mike.stinson@nrc-cnrc.gc.ca

accounting for cross-sectional acoustic modes. Asymptotic expansions, valid for a small aspect ratio of canal radius to length, are used.

A computational approach that can generate three-dimensional sound fields is the boundary element method (BEM). The calculation makes use of mesh elements representing the bounding surface of the structure under study. Since the method is a numerical solution of the full three-dimensional (3-D) wave equation, there are no geometrical restrictions and no assumptions of constant pressure over coordinate surfaces. The BEM approach has been used to compute head-related transfer functions (Kahana, 2000; Nelson and Kahana, 2001) for localization studies and open-loop transfer functions (Stinson and Daigle, 2004) for hearing aid feedback. Use of the BEM to determine sound fields in ear canals was explored by Ciskowski and Royster (1991). More recently, Walsh *et al.* (2004) has applied the BEM approach to the human auditory system, including a realistic meshing of the head, pinna, and ear canal. At frequencies of 2 and 2.9 kHz, standing waves in the ear canal are evident. We have performed subsidiary calculations using the boundary element method (SYSNOISE) to confirm its accuracy in several test cases for which analytical solutions are available: these include the prediction of sound fields in uniform cylinders, radiation of a plane piston in a flat baffle, and diffraction of sound by a sphere.

In this paper, the utility of the boundary element method to calculate sound fields within the human ear canal is examined more closely. Realistic and detailed ear canal geometries are assumed for these calculations, in conjunction with simple eardrum impedance conditions (Stinson, 1985). The boundary element method and the modified horn equation are used to compute the longitudinal sound pressure distribution, along the center axis of the ear canal, and shown to give consistent results for frequencies up to 15 kHz. Then, the boundary element method is used to predict the transverse variations of sound pressure through an ear canal cross section.

II. CALCULATION OF EAR CANAL SOUND FIELD

The sound field in an ear canal will be calculated using two approaches: the first, a solution of the analytic Webster's horn equation, and the second, a numerical boundary element technique. The same ear canal geometries will be used for both approaches.

We make use of geometrical data obtained by Stinson and Lawton (1989) for several ear canals (their canals #1, #3, #7, and #13). The geometry for canal #1 was fairly representative and it will be the focus of our comparisons. A mechanical probe system was used to generate coordinate points over the surface of silicone rubber molds of human cadaver ear canals. The 1144 coordinate points obtained for canal #1, shown in panel (a) of Fig. 1, are spaced approximately 1 mm apart and capture qualitatively the geometrical detail for this ear canal.

The nominal length of this ear canal (along a curved central axis) was reported as 32 mm in the original study.

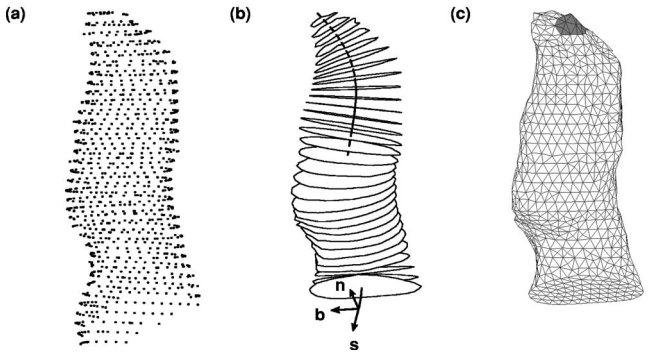

FIG. 1. Representations of the ear canal geometry used for the calculations. Panel (a) shows the point cloud data for ear canal #1 that is used as a starting point. Each point is a coordinate position on the surface of a human ear canal. From this coordinate data, a curved center axis (the s axis) and cross-sectional slices normal to the axis (normal $\hat{n}$ and binormal $\hat{b}$ unit vectors) are derived as in (b) that can be used as input for a modified Webster's horn equation calculation of sound pressure. The coordinate data can also be used to form a boundary element mesh of the ear canal surface, as shown in panel (c) that can be used for a calculation of the internal sound pressure using the boundary element method. The shaded region indicates the elements used to represent the eardrum.

For both computational approaches, a sound speed of 353 m/s and an air density ρ of 1.14 kg/m^3 have been assumed.

A. Webster horn equation

We consider a curved coordinate axis s that follows the curvature of the ear canal and a unit vector $\hat{s}$ tangential to this curve. The origin, $s=0$, is located at the innermost end of the canal. Normal $\hat{n}$ and binormal $\hat{b}$ unit vectors are introduced through the Serret-Frenet equations (e.g., Widder, 1965),

$$\frac{d\hat{s}}{ds} = \kappa\hat{n}, \quad \frac{d\hat{n}}{ds} = -\kappa\hat{s} + T\hat{b}, \quad \frac{d\hat{b}}{ds} = -T\hat{n}, \tag{1}$$

where the local radius of curvature and the torsion are κ and T, respectively. If the s axis is arranged to follow the centroid of each ear canal cross section, i.e.,

$$\int_{A(s)} \vec{r}\, dA, \tag{2}$$

where $\vec{r}$ is a vector within the cross-sectional slice $A(s)$, at each s, then we obtain the modified horn equation (Khanna and Stinson, 1985),

$$\frac{d}{ds}\left(A(s)\frac{dp(s)}{ds}\right) + k^2 A(s)p(s) = 0, \tag{3}$$

with k being the wave number.

Equation (3) is solved for the sound pressure $p(s)$ using MATLAB. The area function $A(s)$ must be supplied as input. We have used the area function shown in Fig. 10 of the paper by Stinson and Lawton (1989) for their ear canal #1. This function was derived from the coordinate data, as described in that paper, to obtain both a parametrized curved center

axis and cross-sectional slices normal to this center axis at 1 mm steps. These cross sections are shown in panel (b) of Fig. 1.

To accommodate the absorption of acoustic energy at the eardrum, an impedance Z_d is located at $s_d=3$ mm. This gives a discontinuity in the volume velocity (and pressure gradient) at this position, leading to the condition (Stinson, 1985)

$$\frac{dp}{ds}(s_d^+) = \frac{dp}{ds}(s_d^-) + \frac{i\rho\omega}{A_d Z_d} p(s_d), \tag{4}$$

where A_d is the cross-sectional area at this position, ω is the angular frequency, the superscripts (+) and (−) denote the approach to s_d from outer and inner sides of the canal, respectively, and an $\exp(+i\omega t)$ time dependence has been assumed. At the inner end of the ear canal, we set boundary conditions. The pressure gradient along the s axis (dp/ds) is zero here. For the pressure, it proved convenient to set $p(0)=1$, initially. Because the boundary value problem is linear, the pressure distribution can be scaled by a constant factor later to match the actual pressure at $s=0$. Subsequently, we will be obtaining a pressure distribution from the BEM procedure. We then scale the horn equation pressure distribution $p(s)$ so that it has the same value of pressure at the innermost position.

The output of the computation is the sound pressure along the curved center axis. The calculation cannot predict sound pressure variations in the transverse directions, i.e., within the n-b plane.

B. Boundary element approach

The boundary element calculation was performed using the SYSNOISE computational bundle (with options Direct, Interior, Element). A collocation solution scheme is used to solve for the pressure and normal velocity at each mesh element. From these, the pressure and particle velocity at any interior field point can be computed in a post-processing stage. Mesh elements representing the surface of the ear canal are first required. The original coordinate data, shown in Fig. 1(a), were used as the starting point. A MATLAB program was written to automate the assignment of triads of points to elements. The resulting mesh had some irregularities and unphysical assignments, particularly in the vicinity of the eardrum and the canal entrance. Altair HyperMesh was used to visualize the mesh and interactively correct the irregular mesh elements. The ear canal mesh was truncated near the canal entrance, using a plane normal to the center axis at a position of $s=31.5$ mm. A mesh coarsening and edge-collapse procedure (Stinson and Daigle, 2004; Kahana, 2000) was then used to optimize the mesh elements, producing triangular elements of approximately 1 mm length on each edge. Finally, HyperMesh was used to create mesh elements over the entrance plane. The final boundary element mesh for ear canal #1 is shown in panel (c) of Fig. 1. The rule of thumb for BEM calculations that element dimensions should be less than 1/8 the wavelength is satisfied up to the maximum frequency considered (20 kHz).

Some model mesh elements have been arbitrarily selected to introduce absorption by the eardrum. These have been highlighted with shading in Fig. 1(c). The surface area of these elements is $S_d=12.44$ mm^2, representing about 20% of the actual area of a human eardrum, and they are centered about a position 3 mm from the innermost end of the canal (consistent with the $s=3$ mm position of eardrum impedance for the horn equation calculation). In SYSNOISE, these elements are assigned a specific impedance Z_{sp} that is matched to the impedance Z_d used in the corresponding horn equation calculations through $Z_d=Z_{sp}/S_d$. At the entrance plane, the elements forming the entrance plane were all assigned a velocity amplitude of 1 m/s.

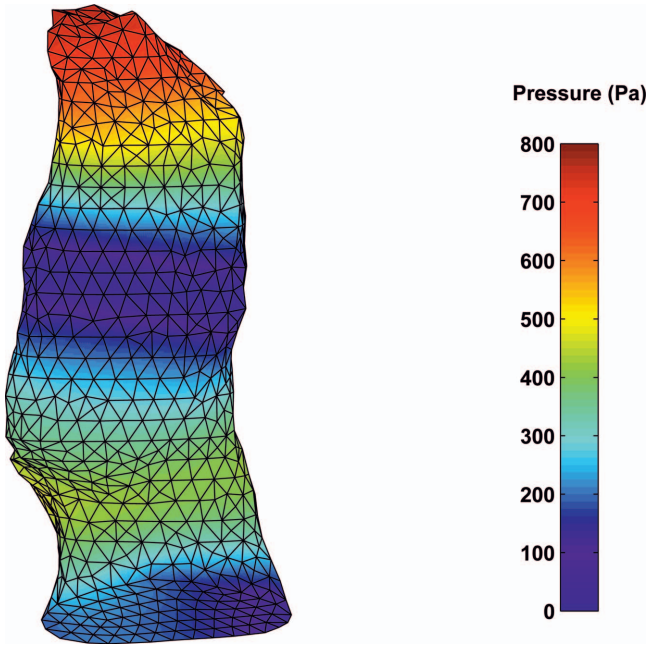

FIG. 2. Color representation of the sound pressure at the surface of the ear canal #1. The boundary element method was used, with a plane piston source at the entrance and an assumed rigid eardrum, at a frequency of 9 kHz. The sound field is, to a first approximation, governed by the longitudinal position along the curved ear canal, as given by the arclength coordinate s.

The BEM calculation gives the sound pressure at the elements of the ear canal model mesh. As well, interior field point meshes can be defined and the sound pressures at these points derived. One set of results generated was the pressure along the curved center axis—these results will be compared directly to the modified Webster horn equation calculation. The sound pressure was also determined within planes normal to the s axis—variations within this plane cannot be determined with the horn equation approach.

III. LONGITUDINAL PRESSURE VARIATION IN THE EAR CANAL

Figure 2 shows a color plot representation of the sound pressure at the ear canal walls at 9 kHz, as obtained using the BEM approach. The eardrum has been assumed to be rigid, so $Z_d=\infty$. The variation of the sound field is controlled mainly by the longitudinal position along the canal. To a first approximation, the sound pressure is a function of the coordinate s, as assumed by the modified horn equation. The

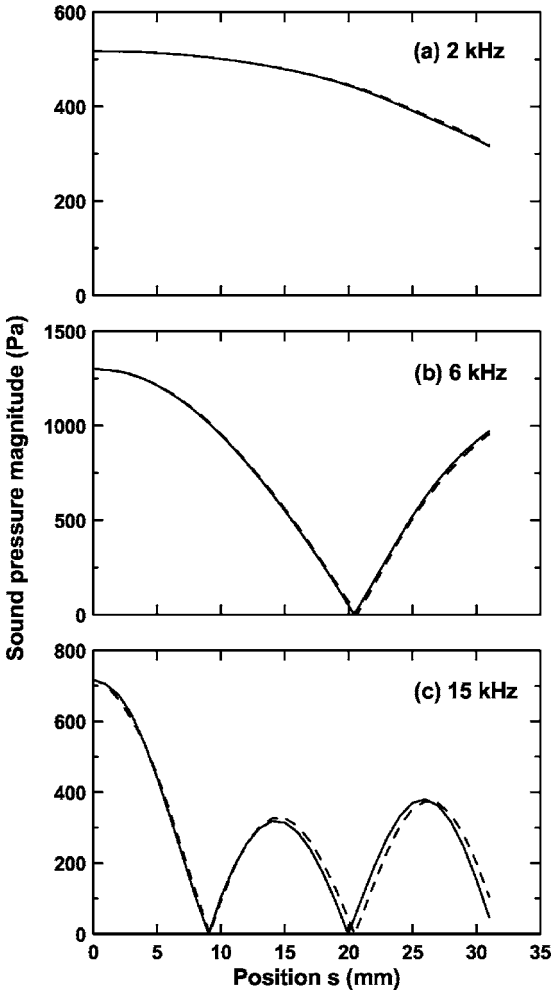

FIG. 3. Longitudinal variation of sound pressure in the human ear canal #1, at frequencies of 2, 6, and 15 kHz, for the rigid eardrum case. Results obtained using the boundary element method are shown as solid lines; those obtained using the modified horn equation are shown as dashed lines.

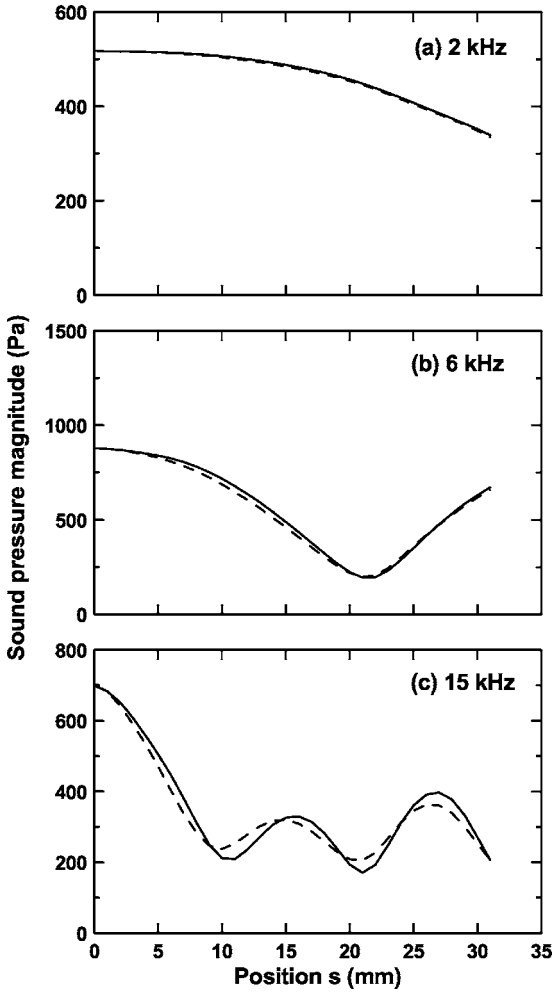

FIG. 4. Longitudinal variation of sound pressure in the human ear canal #1, at frequencies of 2, 6, and 15 kHz, for an eardrum specific impedance of $Z_{sp}=402$ Pa m^{-1} s. Results obtained using the boundary element method are shown as solid lines; those obtained using the modified horn equation are shown as dashed lines.

standing wave pattern shows a sequence of maxima and minima. When the calculation is repeated with a nonrigid eardrum, the pattern looks very similar, except that the sound pressure minima are not so deep.

The sound pressure along the curved center axis of canal #1 is shown in Fig. 3, for three frequencies, assuming a rigid eardrum. The solid curves correspond to BEM calculations and the dashed curves correspond to the modified horn equation calculations. The standing wave patterns become increasingly complex as frequency increases; by 15 kHz, two minima are apparent and the height of the maxima are quite different. Overall, the agreement between the two approaches is good. There is some mismatch in the prediction of the location of minima, about 0.5 mm at 15 kHz. At frequencies greater than 16 kHz, the pseudo-one-dimensional nature of the canal sound field disappears, large transverse modes are apparent in the BEM results, and agreement between the two computational approaches is lost.

A similar comparison is shown in Fig. 4 for an absorptive eardrum. An eardrum impedance $Z_{sp}=\rho c=402$ Pa m^{-1} s was used, somewhat arbitrarily, for the calculations. This value was chosen to give sound pressure distributions whose standing wave ratios approximately match previous measurements (Lawton and Stinson, 1986) in the 4–6 kHz range; at higher frequencies, this choice represents too much absorption by the eardrum but does provide a useful extreme for comparison. For this impedance case, the minima of the standing wave patterns do not reach zero as for the rigid eardrum case. The agreement between modified horn equation and BEM approaches is again good for this ear canal #1. It is noted that the computed pressure distributions are sensitive to the choice of eardrum impedance: a different (more realistic) treatment of the eardrum impedance could result in greater discrepancies between the two methods of calculation.

To corroborate the results above, three other ear canals have been considered, namely canals #3, #7, and #13 from Stinson and Lawton (1989). These have been chosen as representing extremes within the collection of 15 ear canals in this study. The original point cloud data for these canals has been processed, as for canal #1, to obtain both boundary

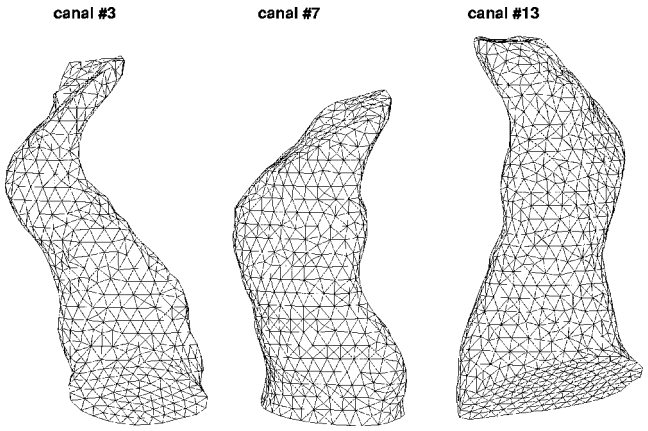

FIG. 5. Boundary element meshes of three other ear canals used for a comparison of the longitudinal variation of sound pressure along the canal.

element meshes and cross-sectional area functions $A(s)$. The boundary element meshes are shown in Fig. 5 and the differences in geometry are evident. Ear canal #3 is quite narrow and exhibits a sharp bend near the eardrum. Canal #7 is shorter and quite wide over most of its length. Canal #13 is one of the larger canals considered in this earlier study.

The longitudinal sound pressure computed for these ear canal geometries is shown in Fig. 6 as panels (a), (b), and (c) for canals #3, #7, and #13, respectively. All three sets correspond to a sound frequency of 10 kHz and the rigid eardrum condition. The boundary element method (solid curves) and the modified horn equation calculations (dashed curves) show good agreement along the length of the ear canals. The agreement for canal #3 actually holds for frequencies as high as 20 kHz. For canal #7, the agreement between BEM and horn equation breaks down above 13 kHz. For canal #13, agreement is good up to 15 kHz.

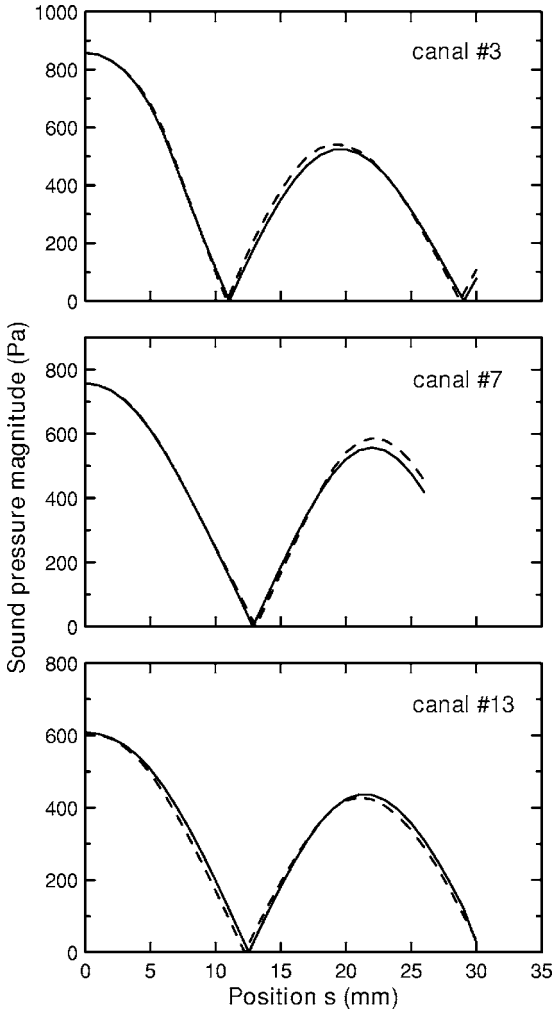

FIG. 6. Longitudinal variation of sound pressure in the three different ear canals, canals #3, #7, and #13, for a frequency of 10 kHz and assuming a rigid eardrum. Results obtained using the boundary element method are shown as solid lines; those obtained using the modified horn equation are shown as dashed lines.

IV. TRANSVERSE PRESSURE VARIATION IN THE EAR CANAL

The variation in sound pressure through a cross-sectional slice normal to the ear canal axis can be computed with the BEM approach. Results were obtained within cross sections at $s=5$ mm, 10 mm, etc. It needs to be noted that the evaluation of pressure at field points that are very close to the model mesh elements can introduce numerical errors. Therefore, only interior field points more than 1 mm away from the canal walls were used. The sound field in between the valid internal points and the model mesh nodes was found to change fairly slowly with position and so sound pressures near the walls could be obtained by interpolation.

In Fig. 5, color plot representations of the sound field variation through the cross section of ear canal #1 at $s=15$ mm are shown, for frequencies of 2, 6, and 15 kHz and for an eardrum specific impedance of 402 Pa m^{-1} s. The polygon defining the canal cross section is the intersection of the boundary element mesh with the plane normal to the s axis. The normal and binormal unit vectors give the coordinate axes, n and b, respectively. The difference in sound pressure level between various points within the cross section and that at the nominal center of the cross section ($n=b=0$) are shown, in decibels. At 2 kHz, there is very little variation of sound pressure through the cross section. At 6 kHz, approximately 1 dB variation is noted from one side of the canal to the other. By 15 kHz, the total variation is nearly 4.5 dB. This degree of variation and its dependence with frequency is similarly observed at other cross-sectional positions and for different eardrum impedance conditions. The assumption that the sound pressure is constant through an ear canal cross section is only valid, strictly, at low frequencies. It should be noted that the Webster's horn equation is unable to predict these variations—it simply gives the constant average values of sound pressure through the cross section at these longitudinal locations.

There is another source of sound pressure variation within a cross-sectional slice. The orientation of the selected slice may be somewhat tilted relative to the pseudo-one-dimensional bands found in the sound field (e.g., as shown in Fig. 2). Sound pressures vary rapidly near a minimum of the

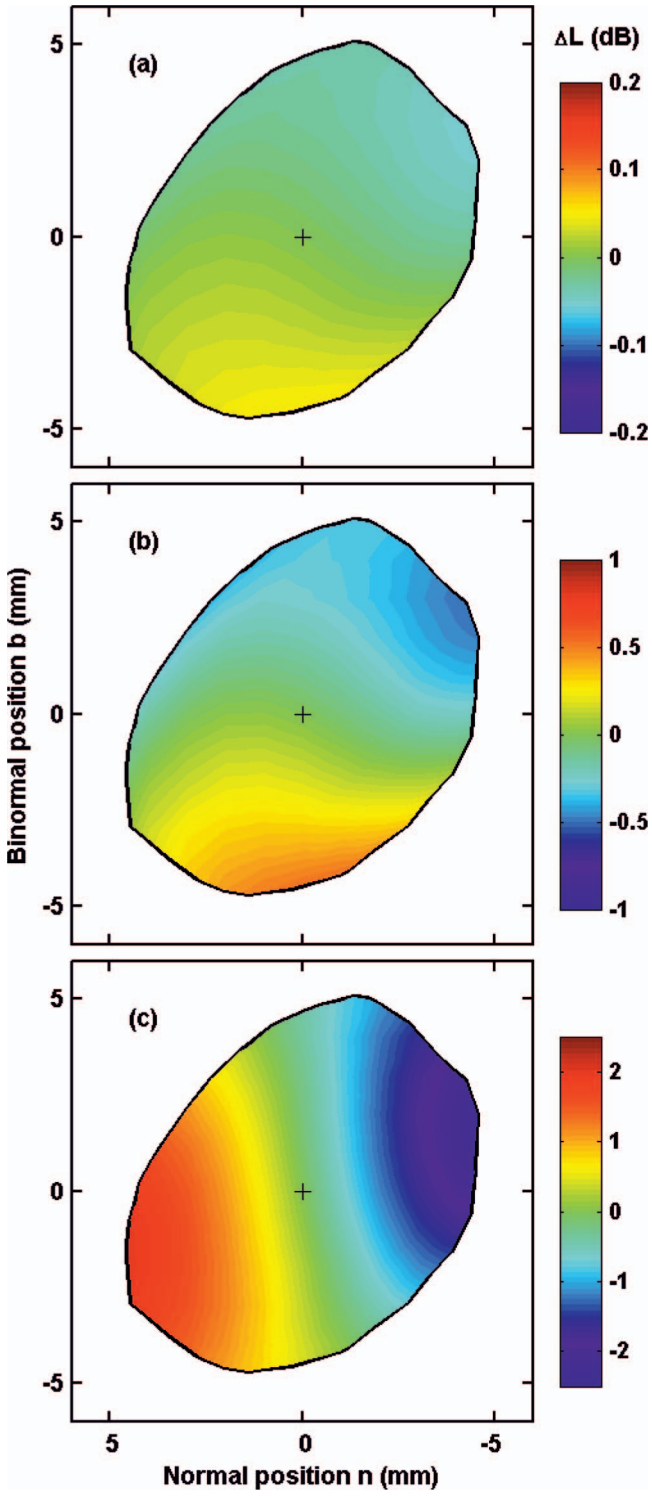

FIG. 7. Transverse variations of sound pressure through a cross-sectional slice of ear canal #1 at longitudinal position $s=15$ mm, for frequencies of (a) 2 kHz, (b) 6 kHz, and (c) 15 kHz. A difference of nearly 5 dB, from one side of the slice to the other, is noted at 15 kHz.

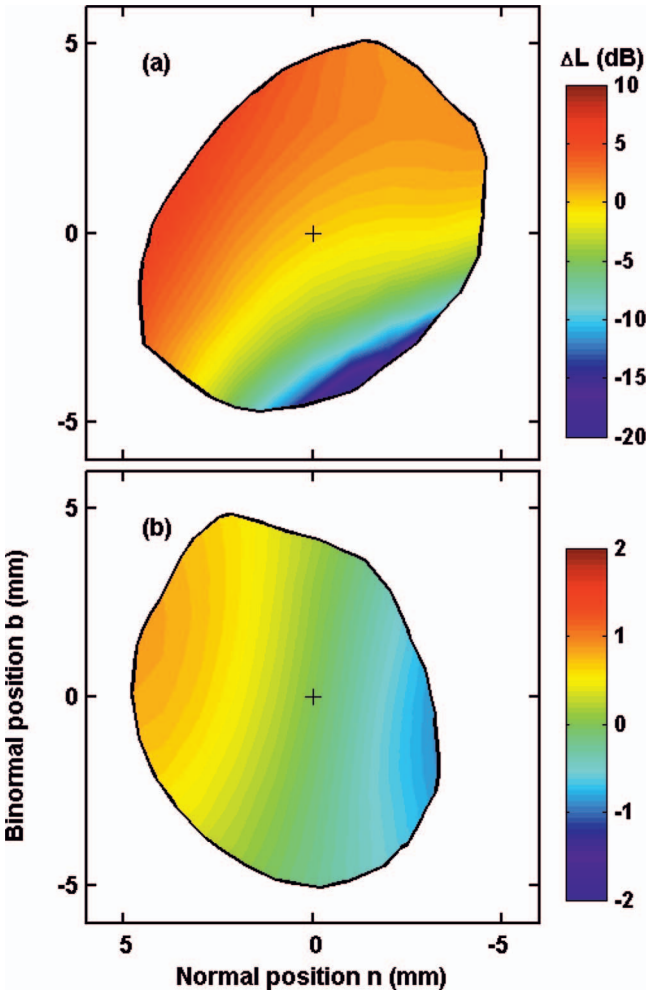

FIG. 8. Transverse variations of sound pressure through two cross-sectional slices of ear canal #1, at a frequency of 9 kHz. In panel (a), the longitudinal position is $s=15$ mm. Huge variations of SPL with position, over 25 dB, are evident. In panel (b), for $s=25$ mm, variations are much less.

standing wave pattern, so if the slice is near such a minimum, large variations of sound pressure through the slice could arise. An example of this is shown in Fig. 6. The variation in sound pressure level at 9 kHz for the rigid eardrum condition, at longitudinal positions $s=15$ mm and $s=25$ mm, in panels (a) and (b), respectively. There is a minimum in the standing wave pattern close to the 15 mm position. As a result, variations of over 25 dB are evident through this cross section. (See Figs. 7 and 8.)

V. CONCLUDING REMARKS

The sound field arising in a model human ear canal has been calculated using two approaches: one is a modified Webster horn equation (one dimensional) that accounts for the curvature of the ear canal and the varying cross-sectional area along its length; the other is a three-dimensional boundary element method. A detailed and realistic geometrical representation of a human ear canal was used. The calculations were performed assuming a simple plane piston source at the entrance position and simple eardrum impedance conditions. Examining the sound pressure variation along the curved central ear canal axis, excellent agreement between the computational methods was found for frequencies as high as 15 kHz.

The relative simplicity of the horn equation argues in favor of its use rather than the BEM approach. Previous measurements in cat ear canals and in replicas of human ear canals have shown that the horn equation does a good job of predicting the sound pressure along the center of the ear canal. However, there are situations for which it will not be appropriate. First, at higher frequencies, the assumption that the sound pressure is constant through a cross-sectional slice is not accurate. The variations through a cross section observed here are 1 dB or less for frequencies below 6 kHz; but the variations increase to 1.5 dB by 8 kHz, 3 dB by 8 kHz, and 5 dB by 16 kHz. These are typical of the variations observed, but actual numbers will vary with different ear canal geometries and different choice of cross section. (For a straight, circular tube with uniform velocity excitation at the entrance, there are no variations.) Applications requiring an accurate representation of the sound field through a cross section, not just along the ear canal length, will require a three-dimensional calculation like the BEM. Second, the sound field near the canal entrance will generally be much more complicated than the one-dimensional horn equation assumes. Burkhard and Sachs (1977) examined the pressure distributions in earphone couplers using a probe tube technique. They found that very large variations in sound pressure can arise in the region where an earphone sound tube opens into the canal cavity, with as much as 20 dB variation over a 3 mm transverse distance, at 3 kHz. The coupling of sound generating equipment (e.g., hearing aids or audiometric test heads) to the ear canal is more complex than the plane piston assumed in the present work. To model accurately the coupling of actual transducers to the ear canal, the modified horn equation will not be sufficient. A three-dimensional sound field calculation, such as that provided by the BEM technique, will be necessary.

Burkhard, M. D., and Sachs, R. M. (**1977**). "Sound pressure in insert earphone couplers and real ears," J. Speech Hear. Res. **20**, 799–807.

Ciskowski, R. D., and Royster, L. H. (**1991**). "Applications in bioacoustics," in *Boundary Element Methods in Acoustics*, edited by R. D. Ciskowski and C. A. Brebbia (Computational Mechanics Publications, Southampton, Boston with Elsevier Applied Science, London) Chap. 8, pp. 147–175.

Farmer-Fedor, B. L., and Rabbitt, R. D. (**2002**). "Acoustic intensity, impedance and reflection coefficient in the human ear canal," J. Acoust. Soc. Am. **112**, 600–620.

Kahana, Y. (**2000**). "Numerical modelling of the head-related transfer function," Ph.D. thesis, University of Southampton, Faculty of Engineering and Applied Science, Institute of Sound and Vibration Research.

Khanna, S. M., and Stinson, M. R. (**1985**). "Specification of the acoustical input to the ear at high frequencies," J. Acoust. Soc. Am. **77**, 577–589.

Lawton, B. W., and Stinson, M. R. (**1986**). "Standing wave patterns in the human ear canal used for estimation of acoustic energy reflectance at the eardrum," J. Acoust. Soc. Am. **79**, 1003–1009.

Nelson, P. A., and Kahana, Y. (**2001**). "Spherical harmonics, singular-value decomposition and the head-related transfer function," J. Sound Vib. **239**, 607–637.

Rabbitt, R. D., and Holmes, M. H. (**1988**). "Three-dimensional acoustic waves in the ear canal and their interaction with the tympanic membrane," J. Acoust. Soc. Am. **83**, 1064–1080.

Stinson, M. R. (**1985**). "The spatial distribution of sound pressure within scaled replicas of the human ear canal," J. Acoust. Soc. Am. **78**, 1596–1602.

Stinson, M. R., and Daigle, G. A. (**2004**). "Effect of handset proximity on hearing aid feedback," J. Acoust. Soc. Am. **115**, 1147–1156.

Stinson, M. R., and Khanna, S. M. (**1989**). "Sound propagation in the ear canal and coupling to the eardrum, with measurements on model systems," J. Acoust. Soc. Am. **85**, 2481–2491.

Stinson, M. R., and Khanna, S. M. (**1994**). "Spatial distribution of sound pressure and energy flow in the ear canals of cats," J. Acoust. Soc. Am. **96**, 2170–2180.

Stinson, M. R., and Lawton, B. W. (**1989**). "Specification of the geometry of the human ear canal for the prediction of sound-pressure level distribution," J. Acoust. Soc. Am. **85**, 2492–2503.

Walsh, T., Demkowicz, L., and Charles, R. (**2004**). "Boundary element modeling of the external human auditory system," J. Acoust. Soc. Am. **115**, 1033–1043.

Webster, A. G. (**1919**). "Acoustical impedance, and the theory of horns and of the phonograph," Proc. Natl. Acad. Sci. U.S.A. **5**, 275–282.

Widder, D. V. (**1965**). *Advanced Calculus*, 2nd ed. (Prentice–Hall, Englewood Cliffs, NJ), Chap. 3.

Contribution of frequency modulation to speech recognition in noise[a)]

Ginger S. Stickney,[b)] Kaibao Nie, and Fan-Gang Zeng[c)]
Department of Otolaryngology - Head and Neck Surgery, University of California, Irvine, 364 Medical Surgery II, Irvine, California 92697-1275

(Received 28 February 2005; revised 5 July 2005; accepted 13 July 2005)

Cochlear implants allow most patients with profound deafness to successfully communicate under optimal listening conditions. However, the amplitude modulation (AM) information provided by most implants is not sufficient for speech recognition in realistic settings where noise is typically present. This study added slowly varying frequency modulation (FM) to the existing algorithm of an implant simulation and used competing sentences to evaluate FM contributions to speech recognition in noise. Potential FM advantage was evaluated as a function of the number of spectral bands, FM depth, FM rate, and FM band distribution. Barring floor and ceiling effects, significant improvement was observed for all bands from 1 to 32 with the additional FM cue both in quiet and noise. Performance also improved with greater FM depth and rate, which might reflect resolved sidebands under the FM condition. Having FM present in low-frequency bands was more beneficial than in high-frequency bands, and only half of the bands required the presence of FM, regardless of position, to achieve performance similar to when all bands had the FM cue. These results provide insight into the relative contributions of AM and FM to speech communication and the potential advantage of incorporating FM for cochlear implant signal processing. [DOI: 10.1121/1.2031967]

PACS number(s): 43.64.Me, 43.66.Ts, 43.71.Ky [BLM] Pages: 2412–2420

I. INTRODUCTION

Current signal processing for cochlear implants allows adequate speech perception in quiet environments for most users. However, their speech recognition performance in more realistic settings, where interfering noise is common, is severely limited. The current multichannel cochlear implant utilizes 12–22 electrodes distributed along the scala tympani to transmit frequency information based on place coding. Typically, each electrode receives an amplitude-modulated pulse train representing the narrow-band temporal envelope of a sound from a particular frequency band. Amplitude modulations from low frequencies are delivered to apical electrodes and amplitude modulations from high frequencies are delivered to basal electrodes. Shannon *et al.* (1995) demonstrated that amplitude modulations from as few as three frequency bands are sufficient to support sentence recognition in quiet. This observation highlighted the importance of amplitude modulation in speech perception. However, more recent studies have shown that amplitude modulation is not sufficient to support speech recognition in noise (Dorman *et al.*, 1998; Friesen *et al.*, 2001; Nelson *et al.*, 2003), and the greatest perceptual difficulties arise when the noise is also speech (Qin and Oxenham, 2003; Stickney *et al.*, 2004).

One means of improving performance for speech in noisy backgrounds is for the listener to perceptually identify, group, and track acoustic segments belonging to the target speech. Although it is not known for certain what role formant transitions play in segregating speech sounds, it has been suggested that gradual changes in the pattern of formant peaks of either the target or masker (or both) might provide cues for grouping and subsequently tracking sounds belonging to one of the two talkers (Assmann, 1995; Bregman, 1990). An alternative suggestion is that one or more of the masker's formants could move into a different frequency range unoccupied by the frequency components of the target, offering a temporal window in which portions of the target speech might be glimpsed (Assmann, 1995). It has also been suggested that the pitch of the voice, specifically the f0 contour, might allow listeners to improve their performance by attending to the f0 of one voice while ignoring a competing voice (Darwin and Hukin, 2000).

The pitch of the voice can be conveyed by the temporal envelope, however this cue provides a relatively weak representation of pitch (Burns and Viemeister, 1976). Green *et al.* (2004) addressed this issue using a traditional cochlear implant simulation, which transmitted amplitude modulations from several frequency bands which modulate a white noise carrier (Shannon *et al.*, 1995). They examined the separate contributions of spectral and temporal cues to pitch by varying the number of bands (single band or four-band) and envelope cutoff frequencies (rates of 32 or 400 Hz), respectively. Subjects were asked to label a single glide (sawtooth or dipthong) as "rising" or "falling" in pitch for f0's of 146, 208, and 292 Hz. They noted that the simulation's spectral cues contributed very little to pitch perception and that the weaker temporal envelope cues were useful only at lower

[a)]Portions of this work were presented at the Pan-American/Iberian Meeting on Acoustics (2002) and the Conference on Auditory Implants and Prostheses (2003).

[b)]Electronic mail: stickney@uci.edu
[c)]Electronic mail: fzeng@uci.edu

pitches. This indicates that pitch information is not effectively coded either by the envelope modulation or by a spectrally based distribution of temporal envelopes, and the greatest detriment occurs at higher pitches approximating the f0 of a female voice.

More recently, Green *et al.* (2004) modified the carrier of the implant simulation to include the periodicity of the input vowel. Compared to the traditional simulation, which used a noise carrier, the carrier containing periodicity information significantly improved pitch labeling. Lan *et al.* (2004) conducted a similar study in which they modified a traditional implant simulation to extract and include f0 for voiced segments in addition to amplitude modulations to represent the temporal envelope. They found that normal-hearing listeners presented with the novel algorithm could more accurately identify the pitch patterns of four Chinese tones than with the traditional simulation; performance also improved for phrases and sentences. These results are encouraging and indicate that modulation of the carrier frequency in addition to the temporal envelope could improve speech recognition in cochlear implant users, and perhaps also in noise.

In a study by Nie *et al.* (2005), a traditional cochlear implant simulation, containing amplitude modulations (AM) of a sinusoidal carrier, was combined with an additional frequency modulation cue (FM) to represent a slowed down version of the original sound's temporal fine structure. The instantaneous frequency was slowed so that it may be more applicable to cochlear implants. With electric stimulation, increases in temporal pitch can be perceived with increases in stimulation rate only up to 500–1000 Hz. Beyond this upper limit, there is no perceived change in pitch (Chen and Zeng, 2004). Therefore, the instantaneous frequency information, coded by the FM rate, was restricted by passing it through a low-pass filter with a cutoff frequency of 500 Hz. Nie *et al.* demonstrated that the combined AM and FM cues provided better representations of not only pitch information, but also formant transitions. They also state that because of this, higher levels of performance could be attained in tasks that involve melody recognition, speaker identification, and speech recognition with other competing talkers. In their study, sentences were processed into a 2-, 4-, or 8-band AM or AM+FM implant simulation and presented to normal-hearing listeners at five target-to-masker levels (TMR), with the masker being a competing sentence. They showed that, overall, the additional FM cue improved performance relative to AM only, and by as much as 71% for the 8-band condition at a 5 dB TMR. They state that the additional FM cue helps the listener better segregate the envelope of the target separate from the masker (Nie *et al.*, 2005; Zeng *et al.*, 2005).

The following study extends the work of Nie *et al.* by (1) further examining the benefits provided by the additional FM cue and (2) investigating FM processing parameters most critical for sentence recognition with a competing talker. The first experiment directly compared the FM advantage for sentences presented in quiet or with a competing talker as a function of the number of bands from 1 to 32. Aside from demonstrating a significant benefit provided by the additional FM cue, it was hypothesized that the greatest differences between AM and AM+FM processing would occur when the number of spectral bands was small and that maximum performance would be observed for AM+FM processing with far fewer bands than with AM-only processing. Additionally, AM+FM processing, because it provides more information for speech tracking (e.g., cues to pitch and formant transitions), was hypothesized to show a greater FM advantage in noise than in quiet. The influence of FM processing parameters on speech recognition with a competing talker was examined in experiments 2–4. Experiment 2 examined sentence recognition as a function of FM depth for bandwidths of 50 or 500 Hz at a fixed FM rate of 400 Hz. Since formants can sweep over a wide range of frequencies, much more than a range of 50 Hz, it was hypothesized that performance would improve as the FM depth was increased from 50 to 500 Hz since wider bandwidths would best capture the full formant transition. Experiment 3 examined the effect of FM rate on sentence recognition performance by comparing two rates (50 and 400 Hz) at a fixed FM depth of 500 Hz. Both normal-hearing and cochlear implant listeners can perceive changes in frequency for rates of 300–500 Hz and this frequency range is sufficient for coding the pitch of both male and female voices (adults and children). It was hypothesized that FM rate could influence performance so long as it captured the pitch of the voices used in the experiment. In other words, performance would improve by increasing the FM rate from 50 to 400 Hz. Last, in experiment 4, speech recognition performance was measured using hybrid AM and FM conditions in which the FM cue was systematically added to a subset of bands from low to high frequency and vice versa. The parameters of interest were (1) the number of AM+FM bands needed to reach a performance plateau and (2) the frequency bands (high vs. low) where AM+FM showed the greatest benefit. It was hypothesized that FM information would provide the greatest benefit when added to low-frequency bands since the range of frequencies for these bands is more likely to be associated with the low FM rate, which was limited to only 400 Hz in this study. Furthermore, the most salient formant transitions can be conveyed by only a subset of FM bands, therefore performance should improve gradually as the number of FM bands is increased, eventually reaching a plateau when the formant pattern is adequately represented.

II. SIGNAL PROCESSING

Frequency modulation (FM) was used to code the instantaneous frequency, or temporal fine structure of the speech waveform, independently from its instantaneous amplitude. A diagram of this algorithm is shown in Fig. 1. The sound is filtered into n narrow bands. Each of the narrow bands is then subjected to an AM-extraction pathway and an FM-extraction pathway. The AM pathway obtains the slowly varying envelope, using full-wave rectification followed by a low-pass cutoff filter which controls the amplitude modulation rate. The FM pathway extracts the slowly varying frequency modulation. This is obtained by first removing each narrow band's center frequency through phase-orthogonal

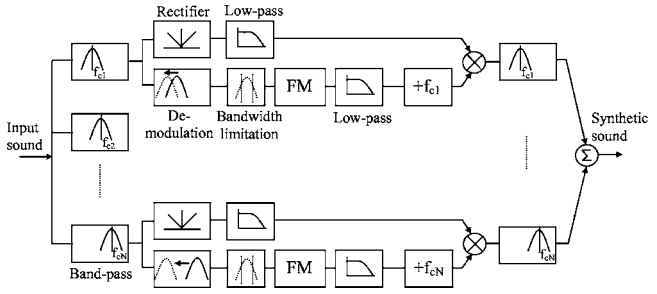

FIG. 1. Diagram of the speech processing strategy which combines AM and FM information. This speech processing strategy was used for the simulations.

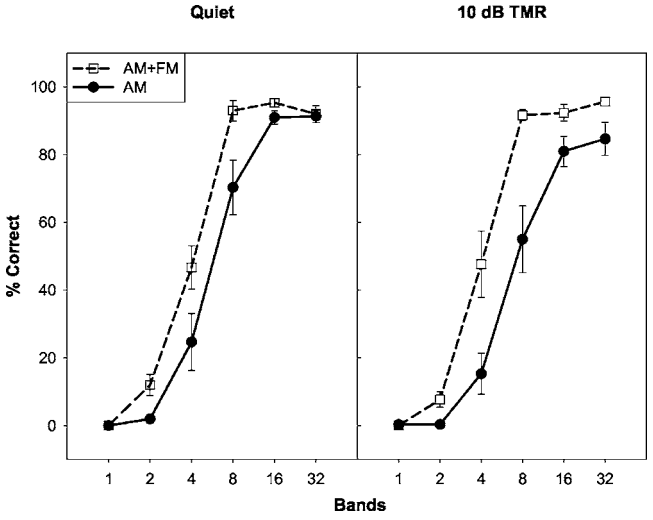

FIG. 2. Comparison of AM (filled circle, solid line) and AM+FM (unfilled squares, dashed lines) speech recognition performance in quiet (left panel) or with a competing talker at +10 dB TMR (right panel). Speech recognition performance in percent correct (y axis) is shown as a function of the number of bands (x axis). The error bars represent the standard error of the mean.

demodulators as used in implementing phase vocoders (Flanagan and Golden, 1966). This is followed by low-pass filtering to limit the FM depth and rate to relatively slowly varying FM components that can be potentially perceived by cochlear-implant users (Chen and Zeng, 2004). The delay between the two pathways is adjusted before combining the AM and FM components into a subband signal. The subband signal is then further bandpass filtered to remove frequency components that are introduced by AM and FM but fall outside the original analysis filter's bandwidth. Finally, the band-passed signals are summed to form the synthesized signal that contains only slowly varying AM and FM components around each analysis filter's center frequency.

In this study, the sentence stimuli were first preemphasized with a high-pass, first-order Butterworth filter with a cutoff frequency of 1.2 kHz. The sentences were then filtered into narrow bands using fourth-order elliptic bandpass. The AM and FM extraction was accomplished with fourth-order Bessel filters. The overall processing bandwidth was 80–8800 Hz. The AM cutoff filter was set to 500 Hz, while the FM rate and depth were manipulated in accordance with the aims of the specific experiment.

III. EXPERIMENT 1: SPEECH RECOGNITION WITH A SINGLE COMPETING TALKER

A. Methods

1. Listeners

A total of 24 normal-hearing listeners participated in this experiment. There were six subjects in each of four conditions. All subjects were native English speakers with no reported hearing loss. Subjects were recruited from the University of California, Irvine Social Science subject pool and received course extra credit for their participation.

2. Test materials

Sixty IEEE sentences (Rothauser *et al.*, 1969) were presented to the listeners, producing a total of ten sentences for each of the six conditions. The sentences consisted of five keywords, for a total of 50 stimuli per condition. Every subject received a different ordering of sentences for each condition according to a digram-balanced design. The sentences were spoken by a male talker (mean f0=108 Hz) either in quiet or in the presence of a competing sentence, which was spoken by a different talker of the same gender (mean f0 =136 Hz). The f0 values were estimated with the TEMPO program (Kawahara *et al.*, 1999). The competing sentence was "Port is a strong wine with a smoky taste." The target and masker sentences had the same onset, but the masking sentence was always longer in duration. No sentences were repeated.

3. Signal processing

The sentences were filtered into 1 to 32 narrow bands. In this experiment, the AM cutoff filter was set to 500 Hz. The FM rate was set to 400 Hz and the FM depth was set to 500 Hz or the critical bandwidth, whichever was narrower.

4. Procedure

The stimuli were presented in a sound-attenuated chamber monaurally through the right headphone. The target sentence was presented at an average rms level of 65 dB SPL. Prior to testing, subjects were asked to complete two practice sessions. The first presented natural sentences in quiet. A score of 85% or higher was required to continue with testing. The second practice session was used to familiarize the listener with the testing condition to which they were assigned. One group of 12 listeners heard the sentences in quiet and the second group heard the sentences masked by the competing talker at a 10 dB TMR. For each of these two groups of 12 listeners, six heard AM-processed stimuli and the other six heard the combined AM+FM stimuli. All subjects heard each of the six band conditions: 1, 2, 4, 8, 16, or 32 bands. Listeners were asked to type in the words of the target sentence into the computer and to guess if unsure. Each keyword was scored automatically with a MATLAB program.

B. Results

Figure 2 shows the results for AM and AM+FM speech recognition in quiet (left panel) and at a 10 dB TMR (right panel) as a function of the number of bands.[1] A mixed design

ANOVA was performed, with the type of processing and presence or absence of masking as between subject factors and the number of bands as the repeated factor. The results showed a main effect for the number of bands [$F(2,50)=441.20, p<0.001$], and Bonferroni-adjusted planned comparisons showed significant differences between all but the 16- and 32-band conditions. There was a strong effect for the type of processing [$F(1,20)=22.73, p<0.001$], with AM+FM processing producing sentence recognition scores that were on average 13% higher than AM-only scores. A significant interaction was also found between the type of processing and the number of bands [$F(5,16)=5.03, p<0.01$]. An analysis with each band condition showed that higher performance for AM+FM processing occurred in the 2-, 4-, 8-, and 16-band conditions but not in the 1- or 32-band conditions. To investigate the improvement plateau with more bands for each type of processing, separate ANOVAs were conducted for AM and for AM+FM conditions followed by Bonferroni-adjusted planned comparisons. The results showed that performance with AM processing improved from 2 to 16 bands, whereas AM+FM processing showed improved performance from 1 to 8 bands. Because of ceiling and floor effects in many of the band conditions, there were no significant main effects or interactions for the type of masking (i.e., target sentence presented in quiet or masked). However, an inspection of Fig. 2 for the mid-band conditions (e.g., 8 and 16 bands) shows that there was a greater drop in performance with the addition of noise with AM compared to AM+FM processing. With 8 bands, performance dropped by 18% with the addition of noise for AM processing, but there was no difference in performance for AM+FM processing. Similarly, with 16 bands, performance with AM processing dropped by 10% with the addition of noise, whereas AM+FM processing showed relatively little change in performance.

IV. EXPERIMENT 2: EFFECT OF FM DEPTH

A. Methods

1. Listeners

A second group of 24 listeners were recruited from the Social Science subject pool for experiment 2. All subjects reported normal hearing and were native English speakers.

2. Test materials

The same target and masking sentences from experiment 1 were used. The target sentence was presented in quiet or combined with the masking sentence at several target-to-masker ratios: 20, 15, 10, 5, and 0 dB.

3. Signal processing

In this experiment, the stimuli were processed into 4 or 8 bands. The FM depth (i.e., bandwidth) was set to 50 or 500 Hz, or the critical bandwidth, whichever was narrower. The FM rate (i.e., cutoff frequency) was fixed at 400 Hz.

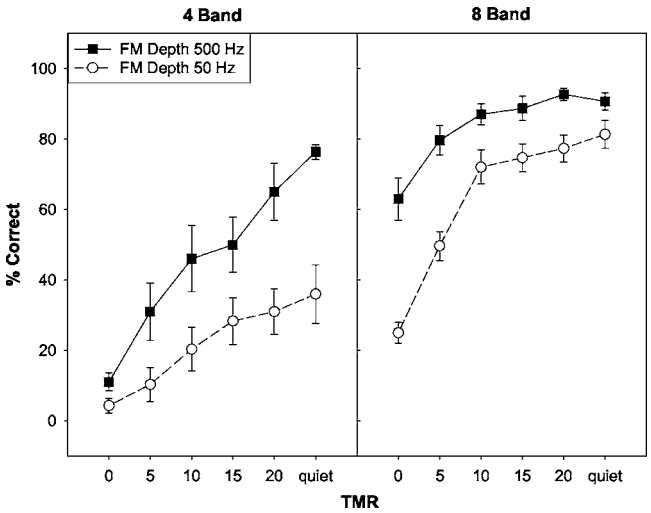

FIG. 3. The effects of FM depth on speech recognition performance (y axis) as a function of the TMR condition (x axis). Comparisons are made between a 500-Hz (filled squares, solid line) and a 50-Hz depth (unfilled circles, dashed line). In experiment 2, the FM rate was fixed at 400 Hz. Separate plots show the results for the 4- (left panel) and 8-band conditions (right panel).

4. Procedure

Four groups (2 band conditions $\times$ 2 FM depths) of six listeners each participated in the practice and test sessions. Each group heard speech processed into 4 or 8 bands with an FM depth of 50 or 500 Hz. All subjects heard the AM+FM sentences in quiet and at five TMRs. All other procedures were the same as experiment 1.

B. Results

Figure 3 shows speech recognition performance with a competing talker as a function of FM depth and TMR for sentences processed into 4 (left panel) or 8 bands (right panel). A mixed design ANOVA was performed with the number of bands and FM depth as between-subjects factors and the TMR condition as a within-subjects factor. There was a main effect of the number of bands [$F(1,20)=96.07, p<0.001$], TMR [$F(5,16)=75.86, p<0.001$], and FM depth [$F(1,20)=31.59, p<0.001$], and a significant interaction between these three factors [$F(5,16)=8.00, p<0.01$]. As expected, the 8-band condition produced higher scores than the 4-band condition, and scores improved with increasing TMRs. Of greater interest was the higher levels of performance attained with the 500-Hz depth (65.1%) than with the 50-Hz depth (42.5%). The three-factor interaction can be explained by greater differences between the two depths at high TMRs with 4 bands and at low TMRs with 8 bands, an outcome due to floor and ceiling effects, respectively.

V. EXPERIMENT 3: EFFECT OF FM RATE

A. Methods

1. Listeners

Twenty-four additional subjects participated in experiment 3. All criteria and recruiting procedures were the same as the previous experiments.

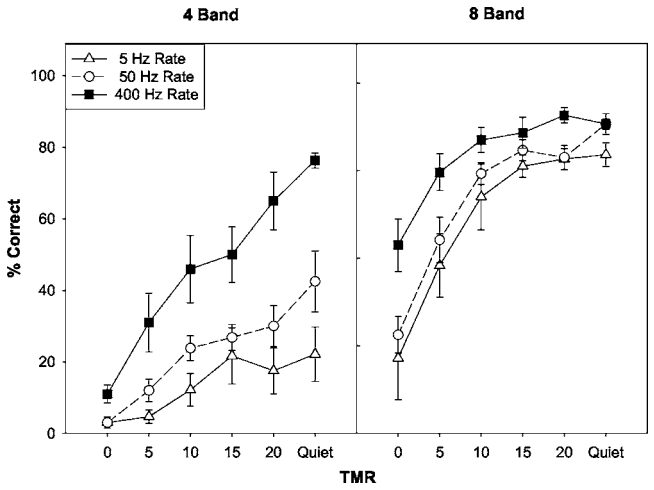

FIG. 4. The effects of FM rate on speech recognition performance (y axis) as a function of the TMR condition (x axis). Results are shown for the three rate conditions: 400 Hz (filled squares, solid line), 50 Hz (unfilled circles, dashed line), and 5 Hz (unfilled triangles, solid line). The FM depth was fixed at 500 Hz. Note that the data for the 400 Hz condition were replotted from experiment 2 (Fig. 2). Separate plots show the results for the 4- (left panel) and 8-band conditions (right panel).

2. Test materials

Experiment 3 included the same sentence stimuli and TMR conditions as experiment 2.

3. Signal processing

The only modification in experiment 3 from the previous experiment was that the FM rate was set to 5 or 50 Hz, and the FM depth was fixed at 500 Hz.

4. Procedure

Four groups (2 band conditions $\times$ 2 FM rates) of six listeners each participated in the practice and test sessions. All other procedures and conditions were the same as experiment 2.

B. Results

For comparison, the data from the 500-Hz depth, 400-Hz rate (from experiment 2) was included in the analysis. The results are shown in Fig. 4. A mixed design ANOVA was performed with FM rate and number of bands as between-subjects factors and TMR as the within-subjects factor. There was a main effect of TMR $[F(5,26)=45.91, p<0.001]$, number of bands $[F(1,30)=275.52, p<0.001]$, and FM rate $[F(2,30)=22.94, p<0.001]$. There was also a significant interaction among these three factors $[F(10,52)=2.08, p<0.05]$ and a significant interaction between the number of bands and FM rate $[F(2,30)=3.76, p<0.05]$. A simple effects analysis of each band condition showed that, with 4 bands, the 400-Hz rate produced higher performance than either the 50- or 5-Hz rates (Scheffé *posthoc*: $p<0.01$). In contrast, the 50-Hz and 400-Hz rate conditions produced equivalent performance in the 8-band condition, and both produced significantly higher performance than the 5-Hz rate (Scheffé *posthoc*: $p<0.05$).

VI. EXPERIMENT 4: EFFECTS OF THE LOCATION AND NUMBER OF FM BANDS

A. Methods

1. Listeners

Twenty-two additional subjects were recruited from the UCI Social Science subject pool.

2. Test materials

The target sentences were taken from the same corpus of IEEE sentences and the same masking sentence and talker were used from the previous experiments. Because of the large number of conditions, a new group of sentences were processed in addition to those used in the previous experiments. To reduce the number of conditions and avoid ceiling and floor effects, the masker sentence was combined with the target sentence at a 10 dB TMR for the 8-band group and at a 20 dB TMR for the 4-band group. Based on the results from experiment 1 and a pilot study, these TMRs avoid ceiling and floor effects for the 8- and 4-band conditions, respectively.

3. Procedure and signal processing

Two groups of twenty-two listeners (7 for the 4-band group and 15 for the 8-band group) participated in a practice and test session. The number of subjects varied in the two band groups because of the use of a digram-balanced Latin square design which uses the same number of subjects as conditions so that all conditions are received in a different order for each subject.

For the 4-band group, there were five conditions where FM information was added to a subset of the total number of bands: (1) AM+FM was on band 4 only; (2) bands 4, 3, and 2, hereafter referred to as 4–2; (3) band 1 only; (4) bands 1 and 2, hereafter referred to as 1–2; or (5) all 4 bands, hereafter referred to as 1–4. Remaining bands, if any, contained only AM. The higher the band number, the higher the frequencies coded within that band. The FM rate and depth were 400 and 500 Hz, respectively. In two additional conditions, performance was compared for all-AM-bands using either a noise carrier or sinusoidal carrier. This resulted in seven conditions total for the 4-band group.

For the 8-band group, AM+FM was on band 8 only, 8–7, 8–6, 8–5, 8–4, 8–2, 1 only, 1–2, 1–3, 1–4, 1–5, 1–6, or 1–8, with remaining bands consisting of AM information only. An all-AM-band comparison was also included using a noise or sinusoidal carrier, producing a total of 15 conditions for the 8-band group. All other procedures were the same as the previous experiments.

B. Results

Results for the 4-band data are shown in Fig. 5, with filled bars representing the all-AM condition (which used a sinusoidal or noise carrier), unfilled bars representing conditions where the FM information ranged from low- to high-frequency bands, and hatched bars representing conditions

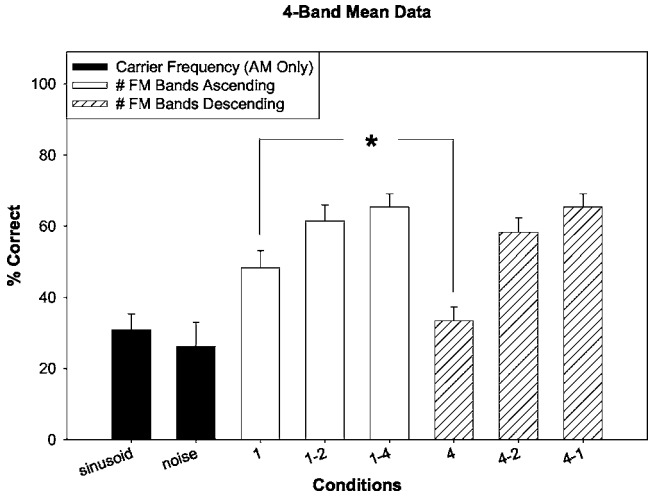

FIG. 5. Results from a 4-band hybrid AM and FM simulation. The *y* axis shows the conditions, with numbers representing the frequency band(s) containing FM information. Unfilled bars represent conditions with FM information added from low to high frequency bands. Hatched bars represent conditions with FM information added from high- to low-frequency bands. The left-most, dark vertical bars show results for the all-AM band condition comparing noise and sinusoidal carriers. Asterisks identify significant differences between conditions.

where the FM information ranged from high- to low-frequency bands. Similar labeling was used for the 8-band data shown in Fig. 6.

The first analysis examined whether a subset of AM+FM bands could reach levels of performance attained with AM+FM information on all bands. This question was addressed for AM+FM information on the lower frequency bands ("FM low") and also for AM+FM information on the higher frequency bands ("FM high"). Separate repeated measures ANOVAs were performed for the 4- and 8-band conditions and these were divided into separate ANOVAs for the

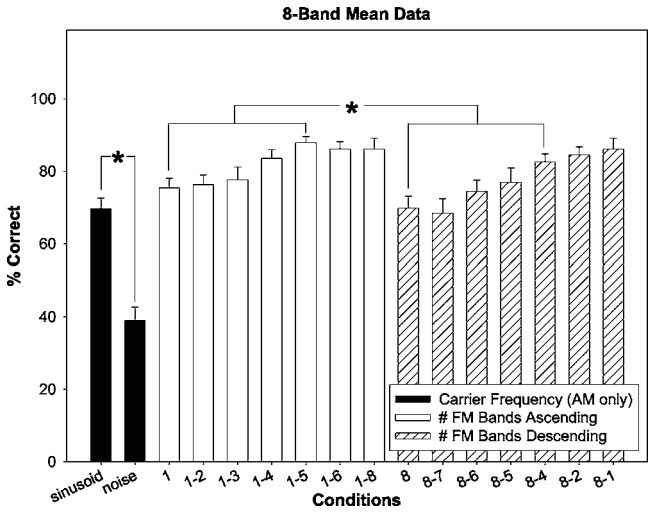

FIG. 6. Results from an 8-band hybrid AM and FM simulation. The *y* axis shows the conditions, with numbers representing the frequency band(s) containing FM information. Unfilled bars represent conditions with FM information added from low- to high-frequency bands. Hatched bars represent conditions with FM information added from high- to low-frequency bands. The left-most, dark vertical bars show results for the all-AM band condition comparing noise and sinusoidal carriers. Asterisks identify significant differences between conditions.

"FM low" and "FM high" conditions, resulting in four ANOVAs total. The results did indeed demonstrate that only a subset of AM+FM bands was needed to obtain similar performance to the all-band AM+FM condition. For the 4-band "FM high" analysis, Bonferroni adjusted planned comparisons showed that although there was a significant improvement from AM+FM on band 4 only to AM+FM on all bands $[F(1,6)=68.92, p<0.001]$, AM+FM on bands 4–2 was not significantly different from having AM+FM on all 4 bands ($p=0.29$). In other words, AM+FM information on the 3 upper bands produced similar levels of performance as the AM+FM all-band condition. Likewise, for the 4-band "FM low" analysis, planned comparisons resulted in significant differences between the all-band compared to the band-1-only AM+FM condition $[F(1,6)=11.88, p<0.02]$, but not with the band 1-2 condition ($p=0.36$). In this case, AM+FM information on only the lowest 2 bands was needed for performance to reach levels found for the all-band condition.

A similar analysis was performed for the 8-band group. For the 8-band "FM high" analysis, Bonferroni-adjusted planned comparisons showed that AM+FM information on at least 5 of the upper frequency bands produced similar performance as having all 8 AM+FM bands ($p>0.008$). For the 8-band "FM low" analysis, AM+FM information on only the lowest 3 AM+FM bands was sufficient to produce performance levels that were similar to the all-band condition ($p>0.008$).

The results discussed above indicate that fewer AM+FM bands were required to reach a plateau in performance when FM information was added to low- than to high-frequency bands. To examine this in more detail, direct comparisons were made between FM on high vs. low bands for conditions sharing the same number of bands. In the 4-band condition, performance with FM information only in the lowest band produced significantly higher scores (48.3% compared to 33.4%) compared to FM information only in the highest band (paired *t* test: $p<0.01$). In the 8-band condition, similar single condition comparisons (i.e., bands 1–2 vs. 8–7) failed to reach significance. However, a comparison of the five "FM high" vs. "FM low" conditions with the same number of bands (repeated measures ANOVA with FM region and band combination as factors) demonstrated higher scores (80.2%) with low-frequency FM bands compared to high-frequency FM bands (74.5%) $[F(1,14)=12.95, p<0.01]$.

In the final analysis, performance levels were compared for AM stimuli using sinusoidal or noise carriers. Significant differences were found between sinusoidal and noise carriers with 8 AM-only bands (paired *t* test: $p<0.001$), but not with 4 bands. In the 8-band condition, performance with sinusoidal carriers was significantly higher (by 30%) than with a noise carrier. The lower performance with the noise carrier can be attributed to the introduction of frequency modulation artifacts brought about by filtering the signal into narrow bands. The 4-band condition was more resistant to potential artifacts because of its broader bandwidth. This outcome is described in more detail in Sec. VII.

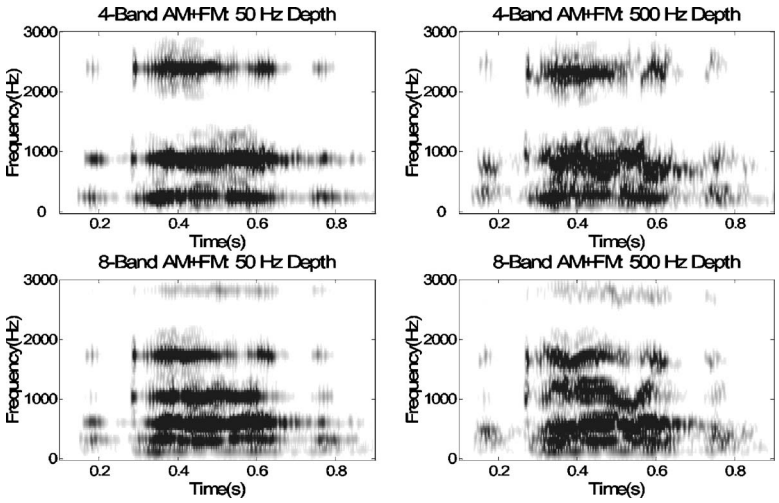

FIG. 7. Spectrogram of the phrase ("The girl at") for the 4-band (top panels) and 8-band conditions (bottom panels) with an FM depth (i.e., bandwidth) of 50 (left) and 500 Hz (right). The FM rate was 400 Hz. The spectrum is shown from 0 to 3 kHz, however the original bandwidth was 8.8 kHz.

VII. DISCUSSION

A. Roles of AM and FM in speech recognition

To compensate for the reduced spectral resolution in cochlear implants, an alternative and complementary code for transmitting frequency information was proposed, namely, frequency modulation. The AM+FM processing significantly improved performance relative to AM processing in all but the two most extreme band conditions: with 1 band, speech recognition performance with either type of processing was not intelligible, and with 32 bands, speech recognition performance was producing scores that were close or equal to 100%. Because cochlear implant users receive at most eight effective information bands (Friesen *et al.*, 2001), the additional information provided by AM+FM processing would be of great benefit when listening to speech in realistic listening environments. A consistent finding in each of the experiments was the improvement in speech recognition scores with more spectral bands. This was true regardless of the type of processing (e.g., AM vs. AM+FM, rate, depth), acknowledging that although alternative processing techniques may improve the performance of cochlear implant users when listening to speech in the presence of a competing talker, further benefit can be achieved by increasing the number of effective spectral bands. From experiment 1, the results showed that performance improved up to 16 bands with AM processing. Performance also improved by adding more bands with AM+FM processing, however performance with AM+FM processing reached maximum performance levels with fewer bands (8 bands) compared to AM processing.

B. Effects of FM depth and rate

A further examination of the effects of AM+FM processing on speech recognition performance revealed sensitivity to the FM depth (experiment 2) and FM rate (experiment 3). Specifically, when the depth was increased from 50 to 500 Hz, higher scores were observed in both the 4- and 8-band conditions. The spectral cues available with FM depths of 50 and 500 Hz are demonstrated in Fig. 7. In this figure, 4- and 8-band spectra of the phrase "The girl at" are shown. A comparison of the 50-Hz depth (left panels) and 500-Hz depth conditions (right panels) demonstrates that formant movement is most accurately represented with the greater FM depth (i.e., larger bandwidth). For the phrase shown in the figure, this is particularly noticeable between approximately 0.4 and 0.6 s. With increasing depth, there is a greater range of frequencies per band to capture the formant transition, potentially allowing the listener to better track the target sentence.

In experiment 3, a comparison of FM rates showed higher performance with higher rates. However, unlike FM depth, the rate that provided the most benefit varied depending on the number of bands. The 8-band condition resulted in similarly high levels of performance with an FM rate of 400 and 50 Hz. In contrast, with 4 bands, the 50-Hz rate produced significantly poorer performance than with 400 Hz. These results indicate that there is a tradeoff between FM rate and the number of bands. To clarify these results, Fig. 8 shows the f0 contour of natural and processed speech for the vowel /u/ at each of the two FM rates. As can be seen in the figure, the f0 contour is more adequately represented with the higher rate. The figure also demonstrates that if the number of bands is large enough to provide the spectral detail, then increasing the FM rate above 50 Hz will contribute little, if at all. On the other hand, more spectral smearing occurs as the number of bands is decreased and, consequently, higher FM rates can provide the listener with f0 information not readily available from the 4-band envelopes. In such cases, the listener could take advantage of the FM rate to follow the f0 contour of one or both talkers, and since the f0 of most talkers is at least 100 Hz, the higher rate would allow for better performance.

The FM rates and depths used in the present study can be perceived by users of cochlear implants. In a study by Chen and Zeng (2004), three adults with the Nucleus-22 cochlear implant and three normal-hearing listeners were presented with three types of frequency modulation: an upward sweep, a downward sweep, and a sinusoidal frequency modulation. They demonstrated that although the frequency difference limen increased with increases in the standard frequency in cochlear implant subjects, their difference limens were comparable to the normal-hearing listeners at low standard frequencies ($<$1000 Hz) and low sinusoid modulation

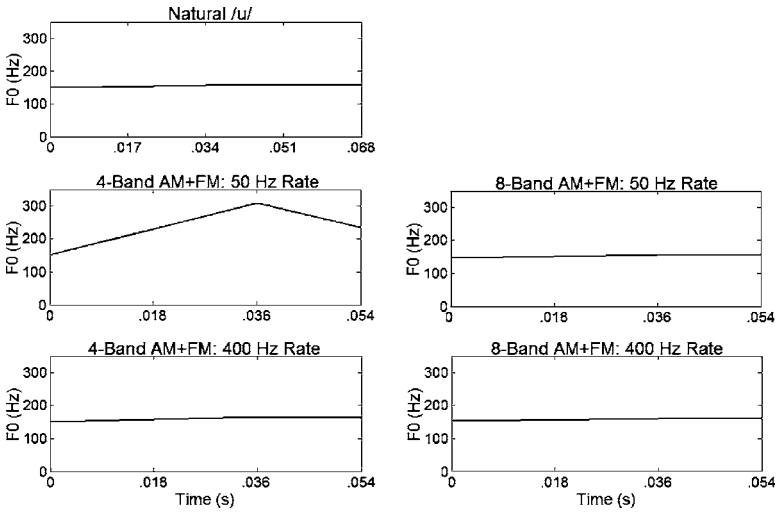

FIG. 8. The F0 contours of the vowel /u/ for the natural, unprocessed condition (top, left panel). Separate F0 contours are shown for the 4-band (left panels) and 8-band conditions (right panels) with FM rates of 50 (middle panels) and 400 Hz (bottom panels).

rates (<320 Hz). Beyond this, discrimination performance decreased monotonically. Their results suggest that cochlear implant users could have access to the FM information offered in the present study, i.e., 400 Hz FM rate and 500 Hz FM depth.

C. Effects of the number and distribution of FM bands

Experiment 4 demonstrated that only half of the bands required AM+FM information to reach similar levels of performance as the all-band AM+FM condition. This would correspond to a cutoff frequency of 1318 Hz for both the 4- and 8-band conditions. Providing FM information in this frequency range would allow for a better representation of key formants F1 and F2 known to be crucial for the identification of most speech sounds.

Experiment 4 also demonstrated that FM information provides greater benefit in low- than high-frequency bands. The low-frequency FM likely provided pitch information that could be used to segregate the two competing voices. This finding is not surprising since temporal fine structure, which is coded by FM, is critical for pitch perception (Smith *et al.*, 2002; Zeng *et al.*, 2004). In support of this, there are several recent studies showing that cochlear implant users benefit greatly from low-frequency, residual acoustic hearing when listening to speech in the presence of other speech sounds. This has been demonstrated both in cochlear implant listeners who combine an implant with a hearing aid on the non-implanted ear (Kong *et al.*, 2005) as well as cochlear implant users who have received a short electrode cochlear implant (Turner *et al.*, 2004). In sum, the results from experiment 4 are consistent with those from the bandwidth and rate experiments, and highlight the acoustic features coded by the additional FM cue and their potential role in improving speech perception with a competing talker.

D. Effects of the AM carrier

The comparison of carrier frequencies for the all-AM conditions revealed higher performance for sinusoidal than noise carriers, but only when the number of bands was increased from 4 to 8. The better performance with sinusoidal than noise carriers was likely due to additional envelope fluctuations present in the narrow-band noise carriers. To demonstrate this point, Fig. 9 compares the highest- and lowest-band waveforms of the sentence "The girl at the booth sold fifty bonds" possessing either a sinusoidal or noise carrier, or left unprocessed. As can be seen in the "Lowest Band" panels of the figure, the unprocessed waveform (top panel) is more accurately replicated with the sinusoidal carrier (bottom panels of each band condition) than with the noise carrier (middle panels of each band condi-

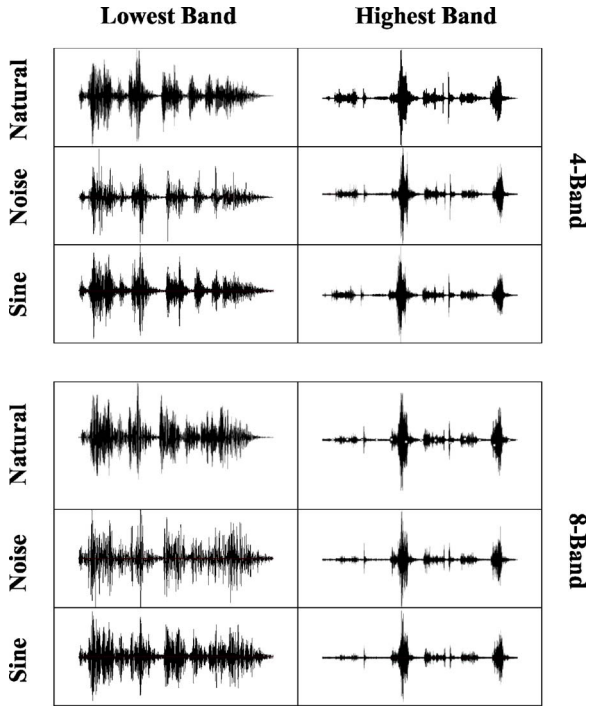

FIG. 9. Waveforms of a single-frequency band from the sentence "The girl at the booth sold fifty bonds" for the natural, unprocessed condition or the AM-only processed speech having either a sinusoidal or noise carrier. The upper three rows show waveforms from a single band in the 4-band condition (natural condition shown in the top panels and AM-processed in the middle and lower panels). Likewise, the lower three rows show waveforms for a single band in the 8-band condition (natural condition shown in the top panels and AM-processed in the middle and lower panels). The lowest band waveforms (band 1) are shown in the left column and the highest band waveforms (band 4 or 8) are shown in the right column.

tion). The noise carrier introduces additional spikes to the waveform (amplitude modulations). Thus, the reason that sinusoidal carriers outperformed noise carriers with 8 bands, but not with 4, can be explained by the greater amplitude modulation associated with narrower bandwidths when the number of bands was increased. Sinusoidal and noise carriers will therefore produce different levels of performance for stimuli processed into the midrange (e.g., approximately 8–16 bands), but not at the extremes. For this reason, previous studies using a noise carrier for an 8–16-band simulation might have underestimated performance due to modulations introduced during stimulus processing.

VIII. CONCLUSIONS

(i) These results underscore the importance of FM in speech recognition under realistic listening situations, particularly when the competing sound is speech. However, FM may have its greatest role when speech is severely impoverished, as it is with cochlear implants.

(ii) Formant transitions and voice pitch can be useful for segregating competing speech sounds. However, these cues are not adequately coded in current cochlear implant speech processing algorithms. The addition of FM could potentially provide these cues.

(iii) Low-frequency FM information contributes more to speech perception with a competing talker than high-frequency FM. This finding suggests that listeners may rely more on low-frequency temporal fine structure cues to segregate the target from the masking voice.

(iv) The slowly varying FM cue can be readily extracted from the temporal fine structure and may enhance cochlear implant performance.

ACKNOWLEDGMENTS

The authors thank Jivesh Sabnani and Neil Biswas for their help in data collection. The IEEE sentences were created by Dr. Lou Braida and recorded by Dr. Monica Hawley and Dr. Ruth Litovsky. This work was supported by grants from the National Institutes of Health (F32 DC05900 to GSS and 2R01 DC02267 to FGZ).

[1]Results with a 5 dB TMR have been presented in Zeng *et al.* (2005).

Assmann, P. F. (**1995**). "The role of formant transitions in the perception of concurrent vowels," J. Acoust. Soc. Am. **97**, 575–584.

Bregman, A.. (1990). "Auditory scene analysis." Cambridge, MA, MIT Press.

Burns, E. M., and Viemeister, N. F. (**1976**). "Nonspectral pitch," J. Acoust. Soc. Am. **60**, 863–869.

Chen, H., and Zeng, F-G. (**2004**). "Frequency modulation detection in cochlear implant subjects," J. Acoust. Soc. Am. **116**, 2269–2277.

Darwin, C. J., and Hukin, R. W. (**2000**). "Effectiveness of spatial cues, prosody, and talker characteristics in selective attention," J. Acoust. Soc. Am. **107**, 970–977.

Dorman, M., Loizou, P., and Tu, Z. (**1998**). "The recognition of sentences in noise by normal-hearing listeners using simulations of cochlear-implant signal processor with 6–20 channels," J. Acoust. Soc. Am. **104**, 3583–3585.

Flanagan, J. L., and Golden, R. M. (**1966**). "Phase vocoder," Bell Syst. Tech. J. **45**, 1493–1509.

Friesen, L., Shannon, R., Baskent, D., and Wang, X. (**2001**). "Speech recognition in noise as a function of the number of spectral channels: Comparison of acoustic hearing and cochlear implants," J. Acoust. Soc. Am. **110**, 1150–1163.

Green, T., Faulkner, A., and Rosen, S. (**2004**). "Enhancing temporal cues to voice pitch in continuous interleaved sampling cochlear implants," J. Acoust. Soc. Am. **116**, 2298–2310.

Kawahara, K., Masuda-Katsuse, I., and de Cheveigne, A. (**1999**). "Restructuring speech representations using a pitch-adaptive time-frequency smoothing and an instantaneous-frequency-based F0 extraction: Possible role of a repetitive structure in sounds," Speech Commun. **27**, 187–207.

Kong, Y-Y., Stickney, G., and Zeng, F-G. (**2005**). "Contribution of acoustic low-frequency information in speech and melody recognition in cochlear implants," J. Acoust. Soc. Am. **117**, 1351–1361.

Lan, N., Nie, K., Gao, S. K., and Zeng, F-G. (**2004**). "A novel speech processing strategy incorporating tonal information for cochlear implants," IEEE Trans. Biomed. Eng. **51**(5), 752–760.

Nelson, P., Jin, S.-H., Carney, A., and Nelson, D. (**2003**). "Understanding speech in modulated interference: Cochlear implant users and normal-hearing listeners," J. Acoust. Soc. Am. **113**, 961–968.

Nie, K., Stickney, G. S., and Zeng, F-G (**2005**). "Encoding frequency modulation to improve cochlear implant performance in noise," IEEE Trans. Biomed. Eng. **52**(1), 64–73.

Qin, M. K., and Oxenham, A. J. (**2003**). "Effects of simulated cochlear-implant processing on speech reception in fluctuating maskers," J. Acoust. Soc. Am. **114**, 446–454.

Rothauser, E. H., Chapman, W. D., Guttman, N., Nordby, K. S., Silbiger, H. R., Urbanek, G. E., and Weinstock, M. (**1969**). "I.E.E.E. recommended practice for speech quality measurements," IEEE Trans. Audio Electroacoust. **17**, 227–246.

Shannon, R., Zeng, F.-G., Wygonski, J., Kamath, V., and Ekelid, M. (**1995**). "Speech recognition with primarily temporal cues," Science **270**, 303–304.

Smith, Z., Delgutte, B., and Oxenham, A. J. (**2002**). "Chimeric sounds reveal dichotomies in auditory perception," Nature (London) **416**, 87–90.

Stickney, G. S., Zeng, F.-G., Litovsky, R., and Assmann, P. F. (**2004**). "Cochlear implant speech recognition with speech maskers," J. Acoust. Soc. Am. **116**, 1081–1091.

Turner, C. W., Gantz, B. J., Vidal, C., Behrens, A., and Henry, B. A. (**2004**). "Speech recognition in noise for cochlear implant listeners: Benefits of residual acoustic hearing," J. Acoust. Soc. Am. **115**, 1729–1735.

Zeng, F-G., Nie, K-B., Liu, S., Stickney, G., Del Rio, E., Kong, Y-Y., and Chen, H. (**2004**). "On the dichotomy in auditory perception between temporal envelope and fine structure cues," J. Acoust. Soc. Am. **116**, 1351–1354.

Zeng, F-G., Nie, K-B., Stickney, G., Kong, Y-Y., Vongphoe, M., Wei., C, and Cao, K. (**2005**). "Speech recognition with slowly-varying amplitude and frequency modulation cues," Proc. Natl. Acad. Sci. U.S.A. **102**(7), 2293–2298.

Medial-olivocochlear-efferent inhibition of the first peak of auditory-nerve responses: Evidence for a new motion within the cochlea

John J. Guinan, Jr.[a)]
Eaton-Peabody Laboratory of Auditory Physiology, Department of Otolaryngology, Massachusetts Eye and Ear Infirmary, 243 Charles St., Boston, Massachusetts 02114-3002, Department of Otology and Laryngology, Harvard Medical School, Boston, Massachusetts 02115, and Speech and Hearing Biosciences and Technology Program, Harvard–MIT Division of Health Sciences and Technology, Massachusetts Institute of Technology, Cambridge, Massachusetts 02139

Tai Lin[b)]
Eaton-Peabody Laboratory of Auditory Physiology, Department of Otolaryngology, Massachusetts Eye and Ear Infirmary, 243 Charles St., Boston, Massachusetts 02114-3002

Holden Cheng
Eaton-Peabody Laboratory of Auditory Physiology, Department of Otolaryngology, Massachusetts Eye and Ear Infirmary, 243 Charles St., Boston, Massachusetts 02114-3002, and Speech and Hearing Biosciences and Technology Program, Harvard–MIT Division of Health Sciences and Technology, Massachusetts Institute of Technology, Cambridge, Massachusetts 02139

(Received 8 April 2005; revised 30 June 2005; accepted 13 July 2005)

Despite the insights obtained from click responses, the effects of medial-olivocochlear (MOC) efferents on click responses from single-auditory-nerve (AN) fibers have not been reported. We recorded responses of cat single AN fibers to randomized click level series with and without electrical stimulation of MOC efferents. MOC stimulation inhibited (1) the whole response at low sound levels, (2) the decaying part of the response at all sound levels, and (3) the first peak of the response at moderate to high sound levels. The first two effects were expected from previous reports using tones and are consistent with a MOC-induced reduction of cochlear amplification. The inhibition of the AN first peak, which was strongest in the apex and middle of the cochlea, was unexpected because the first peak of the classic basilar-membrane (BM) traveling wave receives little or no amplification. In the cochlear base, the click data were ambiguous, but tone data showed particularly short group delays in the tail-frequency region that is strongly inhibited by MOC efferents. Overall, the data support the hypothesis that there is a motion that bends inner-hair-cell stereocilia and can be inhibited by MOC efferents, a motion that is present through most, or all, of the cochlea and for which there is no counterpart in the classic BM traveling wave. © *2005 Acoustical Society of America.* [DOI: 10.1121/1.2017899]

PACS number(s): 43.64.Kc, 43.64.Pg, 43.64.Nf [BLM] Pages: 2421–2433

I. INTRODUCTION

For many decades, excitation of auditory-nerve (AN) fibers in the mammalian cochlea has been thought to be due solely to motion produced by the basilar membrane (BM) traveling wave (Békésy, 1960). In the classic view, the traveling wave drives the motion throughout the organ of Corti, including bending inner hair cell (IHC) stereocilia, thereby exciting AN fibers (Patuzzi, 1996). The traveling wave is thought to be amplified by outer hair cells (OHCs), mechanoreceptor cells endowed with sound-frequency somatic motility produced by the motor protein prestin (Brownell *et al.*, 1985; Zheng *et al.*, 2002; Liberman *et al.*, 2002), and/or with stereocilia motility, as suggested by stereocilia negative stiffness (Kennedy *et al.*, 2005).

Conceptions of the classic traveling wave are based primarily on BM measurements from the basal turn of the cochlea but are typically assumed to hold throughout the cochlea, or at least in regions where AN click-response "glides" go upward [characteristic frequencies (CFs) $>$ 1 kHz]. The classic BM traveling wave is frequency dispersive such that at each place, low-frequency energy arrives before high-frequency energy (Shera, 2001). Consistent with this, in BM responses to clicks in the basal turn of the cochlea, the frequency content starts below the local CF and increases to CF, i.e., it shows an upward "glide" (de Boer and Nuttall, 1997; Shera 2001). In contrast, in the apex, glides go in the opposite, nonclassic direction (Carney *et al.*, 1999; Lin and Guinan 2000; 2004). In the classic traveling wave, an important consequence of the low-frequency energy arriving first is that the click-response first peak is from energy that is below

[a)]Author to whom correspondence should be addressed at Eaton-Peabody Laboratory, Massachusetts Eye and Ear Infirmary, 243 Charles St. Boston, Massachusetts 02114. Electronic mail: jjg@epl.meei.harvard.edu
[b)]Present address: Hearing Emulations LLC, 8825 Page Ave., St. Louis, Missouri 63114-6105.

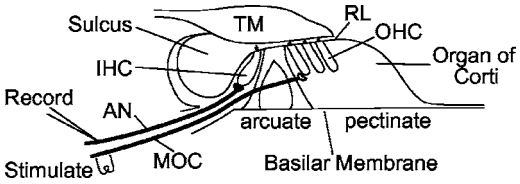

FIG. 1. A diagram of the experimental setup. AN: auditory nerve; IHC: inner hair cell; MOC: medial olivocochlear efferent nerve; OHC: outer hair cell; RL: reticular lamina; TM: tectorial membrane.

the local CF and receives little or no amplification. This aspect of the classic traveling wave is consistent with basal-turn BM motion, which shows a click-response first peak that has almost linear growth and that changes little after death (Robles *et al.*, 1976; Ruggero *et al.*, 1992; Recio *et al.*, 1998; Recio and Rhode, 2000).

BM motion is modulated by medial olivocochlear (MOC) efferents, nerve fibers that originate in the brainstem and synapse on OHCs (Guinan, 1996). Activation of MOC fibers decreases BM motion in response to low-level tones, presumably by decreasing the gain of the cochlear amplifier (Murugasu and Russell 1996; Russell and Murugasu 1997; Dolan *et al.*, 1997; Cooper and Guinan, 2003). The role of MOC efferents in hearing is not fully understood, but it is thought that MOC efferents reduce damage due to intense sounds and reduce the masking of transient sounds by background sounds, among other things (Guinan, 1996).

Since MOC efferents synapse directly on OHCs, they provide a way to reversibly change OHC properties without opening or damaging the cochlea. Extending previous work on AN responses to clicks (Lin and Guinan, 2000, 2004), we studied the effects of MOC efferents on click responses of single AN fibers. We report here the unexpected finding that MOC efferents inhibit the click-response first peak of AN fibers throughout much of the cochlea. This first-peak inhibition cannot be explained with the common view that motion throughout the cochlea is produced solely by a traveling wave that mimics BM motion in the cochlear base, because the first peak of BM motion receives little or no amplification and is little changed by MOC stimulation (Guinan and Cooper, 2005). Thus, MOC inhibition of the AN first peak indicates that this peak is due to motion separate from the classic traveling wave, and that this motion is strongly influenced, perhaps produced, by OHCs.

Our analysis of MOC effects on the first peak of the AN click response did not produce a clear result for fibers with CFs >10 kHz so we pursued this issue in a second set of experiments using low-frequency tones. The rational for these additional experiments is developed in a second Introduction (Sec. IV), and the results are presented in (Sec. V). Methods for both experiments are presented in Sec. II (Methods).

II. METHODS

We stimulated MOC efferents electrically in the brainstems of anesthetized cats, and monitored cochlear output by recording spikes from single AN fibers, as schematized in Fig. 1. Treatment of experimental animals was in accordance with protocols approved by the Committee on Animal Care at the Massachusetts Eye and Ear Infirmary.

A. Animal preparation and MOC stimulation

The surgical preparation, methods for single-fiber recording and the paradigms for MOC stimulation and click presentation were based on previously published methods (Guinan and Stankovic, 1996; Lin and Guinan, 2000). Adult cats were anesthetized with diallyl barbiturate in urethane. The floor of the fourth ventricle and the AN were exposed dorsally. AN fibers were monitored with pipette electrodes and only recordings with an accurate spike timing were used. AN compound action potentials (CAPs) were monitored with an electrode near the round window, and an automated tone-pip audiogram determined the sound levels for CAP thresholds (10 μV) at frequencies 1–32 kHz. Data were used only when CAP thresholds were in the normal range.

MOC fibers were stimulated with a bipolar electrode along the midline of the floor of the fourth ventricle using trains of shocks lasting 0.6–1.1 s, with 200 shocks/s at levels that evoked little or no visible animal movement. Shock pulses were monophasic or diphasic ($\sim$300 μs per phase) and were shaped to reduce high frequencies that could produce electrical artifacts on the microelectrode. Such shocks excite medial but not lateral efferent (LOC) fibers (Gifford and Guinan, 1987; Stankovic and Guinan, 1999). In some cats middle-ear-muscle (MEM) tendons were cut to prevent the shocks from affecting middle-ear transmission. In other cats, we avoided exciting MEMs by adjusting electrode configuration, placement, and shock level. We determined when there were MEM contractions from measurements of ear-canal sound pressure using a low-frequency probe tone (typically 500 Hz, 50 dB SPL). This test was made selective for middle-ear impedance changes by suppressing the stimulus-frequency otoacoustic emission (SFOAE) from the probe tone with a second tone that was $\sim$100 Hz lower in frequency and 20 dB more intense.

B. Clicks

Clicks were generated by rectangular electrical pulses to a condenser earphone (Bruel & Kjaer 4145) in a closed acoustic assembly (Lin and Guinan, 2000). Although condenser earphones are nonlinear, they have the important advantage of producing less ringing than most earphone types. To compensate for the nonlinear, square-law characteristic of the earphone, the electrical output was adjusted in amplitude so that rarefaction and condensation clicks were equivalent in peak acoustic level and had almost identical spectra (they were within 1 dB at all frequencies of interest). For fibers with CFs <7 kHz and some fibers with higher CFs, we used 90 or 100 μs pulses. These relatively long-duration click pulses were chosen to provide as much low-frequency energy as possible without causing acoustic trauma (Lin and Guinan, 2000) but have the disadvantage of nulls in their acoustic spectra at multiples of 11.1 or 10 kHz. For animals in which high-CF fibers were targeted, spectral nulls near fiber CF were avoided by using 50 μs clicks for CFs 7–15 kHz, 24 μs clicks for CFs 15–30 kHz, and 14 μs clicks for

CFs > 30 kHz. Trains of clicks were presented with the interval between clicks typically 15–30 ms for CFs < 7 kHz, 8 ms for CFs 7–15 kHz, and 5 ms for CFs > 15 kHz. These rates were chosen to be as high as possible while providing enough time for each response to finish before the next click. The use of high-rate clicks produced strong adaptation, which was necessary to lower the overall probability of spikes. Without adaptation, high-level clicks evoke spikes with near unity probability early in each click response, which makes it impossible to calculate recovered probability histograms (Lin and Guinan, 2000). In early experiments, each click level series had a constant polarity (condensation or rarefaction) and a run with one polarity was followed by a run with the other polarity. In later experiments alternating polarity clicks were used in each run. Similar results were found with both methods. The click level is expressed as peak-equivalent sound pressure (pSPL) computed as in Lin and Guinan (2000) from calibrations done on each animal and each click duration. A click level series had 6–18 levels (typically 11) ranging downward from the highest level the acoustic system produced (typically 110 dB for 50–100 μs clicks; less for shorter clicks). In each level series, the level steps were normally 6 dB at high levels where click responses often changed rapidly with level, and 10–12 dB at lower sound levels.

C. Stimulus paradigm

On each AN fiber, we obtained a tuning curve (from which CF was determined) and one or more click-level-series runs with and without MOC stimulation. A click-level-series run consisted of a series of same-duration trials that were long enough (3–4 s) for a fixed burst of MOC shocks to produce an MOC effect, and for the MOC effect to recover before the next trial. On each trial, clicks were presented at a fixed sound level and fixed repetition rate, but the sound level was randomized across trials. Two basic paradigms were used. In the first [Fig. 2(a)], both the click level and the presence/absence of shocks were randomized across levels, and "with MOC stimulation," versus "without MOC stimulation," comparisons were done using data from the same time period in each trial. In the second paradigm [Fig. 2(b)], MOC stimulation was presented on every trial, and "with MOC stimulation" versus "without MOC stimulation" comparisons were done using data from a time window during the shocks versus a time window more than 1 s after any shocks. No differences were noted between results from these two methods.

On a fiber that was contacted sufficiently long, multiple runs were obtained, each with a different randomization of click levels, and (when applicable) shock presence. The results from runs with identical parameters were combined.

D. Data analysis

From the spike and click times at each level, we calculated peristimulus-time (PST) histograms, recovered-probability PST (rpPST) histograms, and compound rpPST histograms. A rpPST histogram shows the probability that a spike will occur in a time bin at a given latency, using only

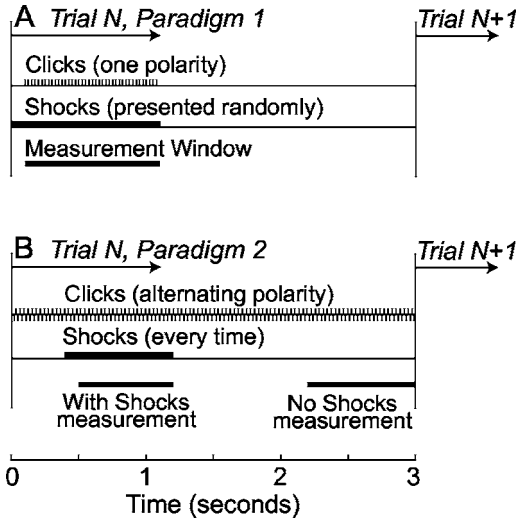

FIG. 2. The timing of clicks, shocks, and response windows for a single trial of paradigms 1 and 2. A: Across the trials of a paradigm 1 run, both click level and the presence/absence of the shock train were randomized; the response was always measured in the same time window which was either "with shocks" or "without shocks" depending on the shock randomization of the trial. B, across the trials of a paradigm 2 run, click level was randomized and shocks were always present; "with shocks" and "no shocks" measurements were obtained each trial from separate windows, as indicated. In both paradigms, response histograms for a trial were formed from all of the same-polarity click responses within the measurement window. With paradigm 1, a run with one click polarity was always followed by a run with the other click polarity, whereas paradigm 2 used alternating polarity clicks so one run provided responses from clicks of both polarities.

time bins (and spikes) at least P seconds after a previous spike. This computation reduces the distortion of the PSTs caused by fiber refractoriness and fast adaptation (Gray, 1967). We used a P of 3 ms that appeared to maximize the number of spikes while preserving the rpPST shapes shown by recovered histograms with longer P's. For Fig. 3, we formed compound rpPST histograms from the rpPSTs by combining rarefaction-click rpPSTs plotted upward with condensation-click rpPSTs plotted downward. Since individual rpPSTs resemble rectified versions of stereocilia motion and IHC receptor potentials, compound rpPST histograms, which combine data from both odd and even half cycles of the response, provide a better estimate of the overall waveform of these variables (Pfeiffer and Kim, 1972; Lin and Guinan, 2000).

To quantify MOC effects, we segmented the click responses into first and second peaks. For each fiber, boundaries were chosen by hand with rarefaction and condensation click responses done separately, and each boundary applying to responses at all levels. For fibers of all CFs, a boundary was chosen just before the onset of the first peak (at any level). For fibers in which separate peaks could be distinguished (CFs < 4 kHz, sometimes up to 6 kHz), boundaries were chosen at the valleys between peaks 1–3. Normally the boundary line at one click polarity was at the response peak of the other click polarity. For CFs > 4–6 kHz, where separate peaks at 1/CF intervals could not be distinguished, we tried two methods for setting boundaries. In high-CF fibers, a distinguishable initial peak can often be seen that corresponds to the "offset-peaks" response (Lin and Guinan,

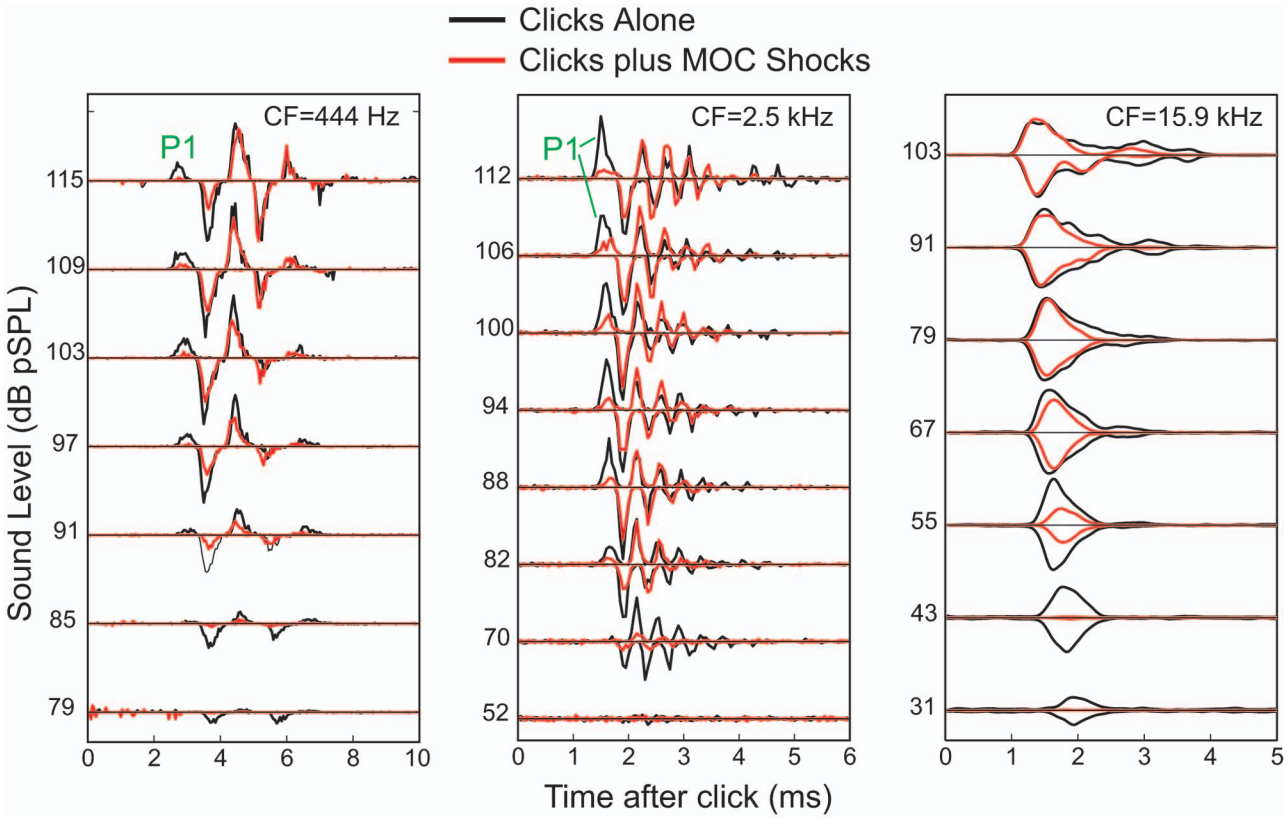

FIG. 3. Examples of the effects of MOC stimulation on AN responses to clicks from fibers with low, medium, and high CFs. Compound rpPST histograms from three AN fibers showing responses to clicks at selected sound levels, with (red) and without (black) MOC stimulation. "P1" indicates the first peak.

2000) in which high-level clicks elicit early peaks with different latencies for rarefaction and condensation clicks. The first method attempted to use this peak, with the second peak assumed to be equal in duration to the first. However, this first peak could be clearly distinguished only on a minority of fibers, and we saw no consistent pattern of MOC effects using this method. The second method, which was used in making Fig. 6, placed the boundaries that marked the supposed end of the first and second "peaks" so that each peak lasted a fixed time and there was no gap between the peaks. The fixed time (which was the same for all fibers) was varied from 0.1–1 ms in trial analyses of the data. After determining the peak boundaries, the amplitude of each peak was taken to be the average spike rate within its time window. Finally, data were used only from fibers for which the recovered-probability firing rate exceeded 1.5 spikes/ms at least at one click level. This criterion mainly removed fibers with low spontaneous rates and some with medium spontaneous rates, and was done because these fibers showed few, if any, short-latency spikes so that the time of the first peak was uncertain.

E. Group delays

Group delays at frequencies in the low-frequency "tail" of high-CF tuning curves were obtained from measurements of tone-response phase versus frequency functions on AN fibers in two cats. These measurements used tone bursts that were swept in frequency at a fixed level (80–85 dB SPL) with tone-burst parameters and phase measuring techniques as in Stankovic and Guinan (2000). Briefly, the phase was determined from period histograms of the spikes relative to the zero crossings of the tone waveform, and data were only used if the standard error of the phase, Φ_{SE}, was $|\Phi_{SE}| <= 30°$. Group delays were calculated from the phase gradient across two to four points (two to three at the edges and four in the center of the frequency functions).

III. RESULTS A: MOC EFFECTS ON CLICK RESPONSES

The stimulation of MOC efferents produced effects on auditory-nerve responses to clicks that depended on the click level and time after the start of the response. Typical MOC effects for AN fibers with low, medium, and high CFs are shown in Fig. 3. This figure shows compound rpPST histograms of responses with and without MOC stimulation from selected levels of the click-level series. The pattern of MOC effects can be seen in Fig. 3 but requires detailed comparisons across peaks and sound levels, so we developed an easier way to visualize such data, as illustrated in Fig. 4. This figure shows rpPST histograms of all of the click responses that were obtained as a function of level without and with MOC stimulation (columns A and B), and the difference, the MOC-induced change in the response, in column C. Data from rarefaction clicks (top) and condensation clicks (bottom) are shown separately in Figs. 4(a)–4(c). The MOC-induced changes, with rarefaction and condensation changes added together, are shown in D, in rpPST format at left, and as a color-coded plot of the same data at right. The color plot provides a presentation of the MOC-induced changes that is

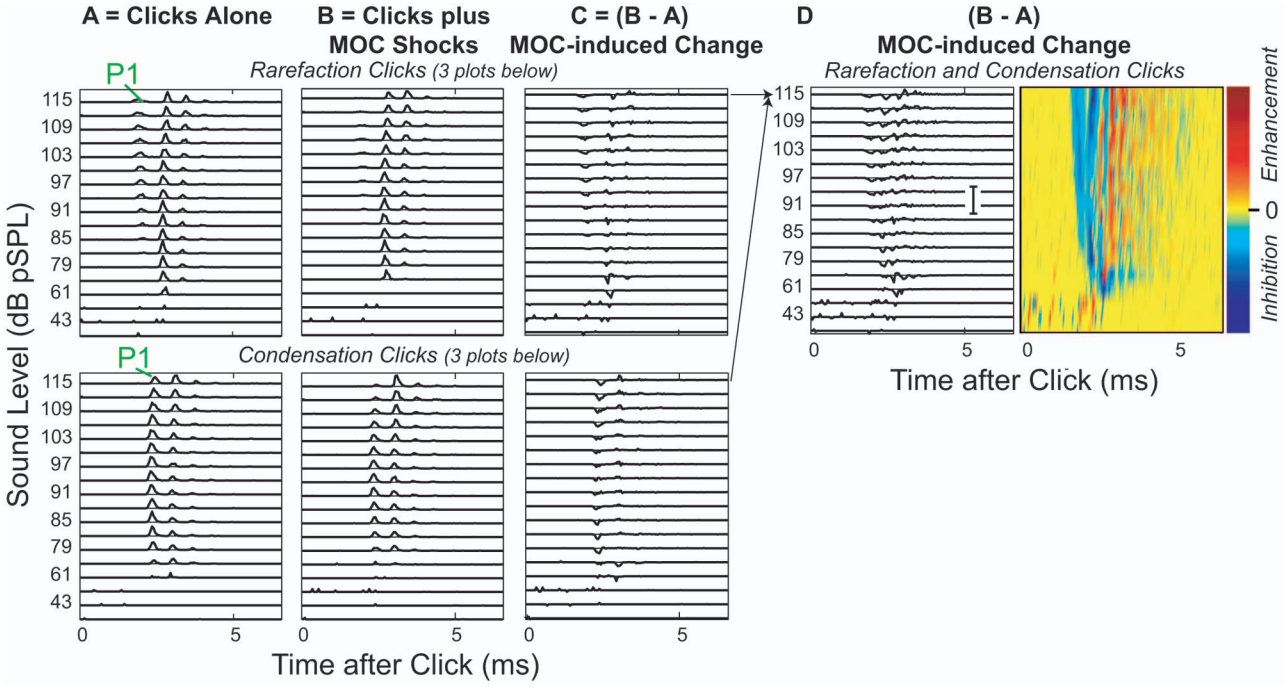

FIG. 4. MOC effects on click responses from a single AN fiber showing the formation of color-coded response plots. A,B: rpPST histograms from 18 levels of rarefaction clicks (top) and condensation clicks (bottom), with (B) and without (A) MOC shocks. "P1" indicates the first peak. C: the MOC-induced change, which is B-A. D: MOC-induced changes from rarefaction and condensation responses added together at each level, in rpPST format (D—left, scale bar =10 spikes/ms also applies to A–C) and as a color-coded plot of the same data (D—right). Fiber #39-12, CF=1.52 kHz.

both easy to see and much more compact. Color plots from 9 fibers with CFs from 0.44 to 19.6 kHz are shown in Fig. 5, which illustrates the patterns of MOC effects found across a wide range of CFs.

Figures 3–5 show that in the responses of auditory-nerve fibers to clicks, activation of MOC efferents produced (1) the inhibition of all peaks at low sound levels, (2) the inhibition in the decaying part of the response at all sound levels, and (3) the inhibition of the first peak of the response at moderate to high sound levels. MOC inhibition of AN click responses at low levels and at the end of the ringing is what is expected from previous reports that MOC stimulation inhibits tone responses at low sound levels and broadens most tuning curves (Guinan and Gifford, 1988; reviewed by Guinan, 1996). Broadening of tuning curves corresponds, in click responses, to a reduction in the duration of ringing, which is seen in Figs. 3–5 as an inhibition in the decaying parts of the responses.

A. First-peak inhibition

The new finding is that the first peaks of AN click responses were strongly inhibited by MOC stimulation, at least for fibers with CFs <4 kHz. For fibers with CFs <4 kHz, individual peaks can be readily discerned in the rpPST histograms. Presumably, these peaks are due to the click-response half-cycles that are excitatory at IHC stereocilia. Inhibition of the first peak can be seen in Figs. 3, 4(a)–4(b) (the peak labeled P1) and in the color plots of Figs. 4(d) and 5 (the initial blue/purple at moderate to high sound levels). Note that by "first peak" we mean the peak with the shortest latency across all sound levels; the earliest peak that can be seen at low sound levels is *not* the "first peak." This definition of the "first peak" was chosen so that the AN first peak would be as comparable as possible to the first peak of BM click responses (also defined as the first peak seen at any sound level). Presumably the "first peak" is not seen in AN responses at low sound levels because the corresponding mechanical motion is below threshold for evoking an AN response. Above 100 dB pSPL, some responses showed a reversal of the polarity that produced the first peak (Lin and Guinan, 2000). In these cases, there was inhibition of the first peak at levels below the reversal, but little MOC effect at levels above the reversal.[1]

We quantified the inhibition of the AN first peak by counting spikes in the click-response peaks with and without MOC stimulation for sound levels 75–100 dB pSPL. Quantification was straightforward for fibers with CFs <4 kHz, where individual peaks could be discerned easily. The results (Fig. 6, left half of each panel) show that for CFs <4 kHz, the rarefaction first peak is consistently inhibited and the condensation first peak is often inhibited, whereas the second peaks from both condensation and rarefaction, on average, show little change from MOC stimulation. The MOC-induced change for the rarefaction first peak was significantly stronger than the MOC-induced change for the rarefaction second peak (T test, $P<0.0001$). In almost all AN fibers, the rarefaction first peak preceded the condensation first peak, which indicates that the rarefaction-click first peak corresponds to the first half-cycle of the mechanical response that drives IHC stereocilia and the condensation-click first peak corresponds to the second half-cycle of the mechanical drive. Thus, Fig. 6 shows that, for CFs <4 kHz, the strength of the inhibition is related to the sequence in which the peaks

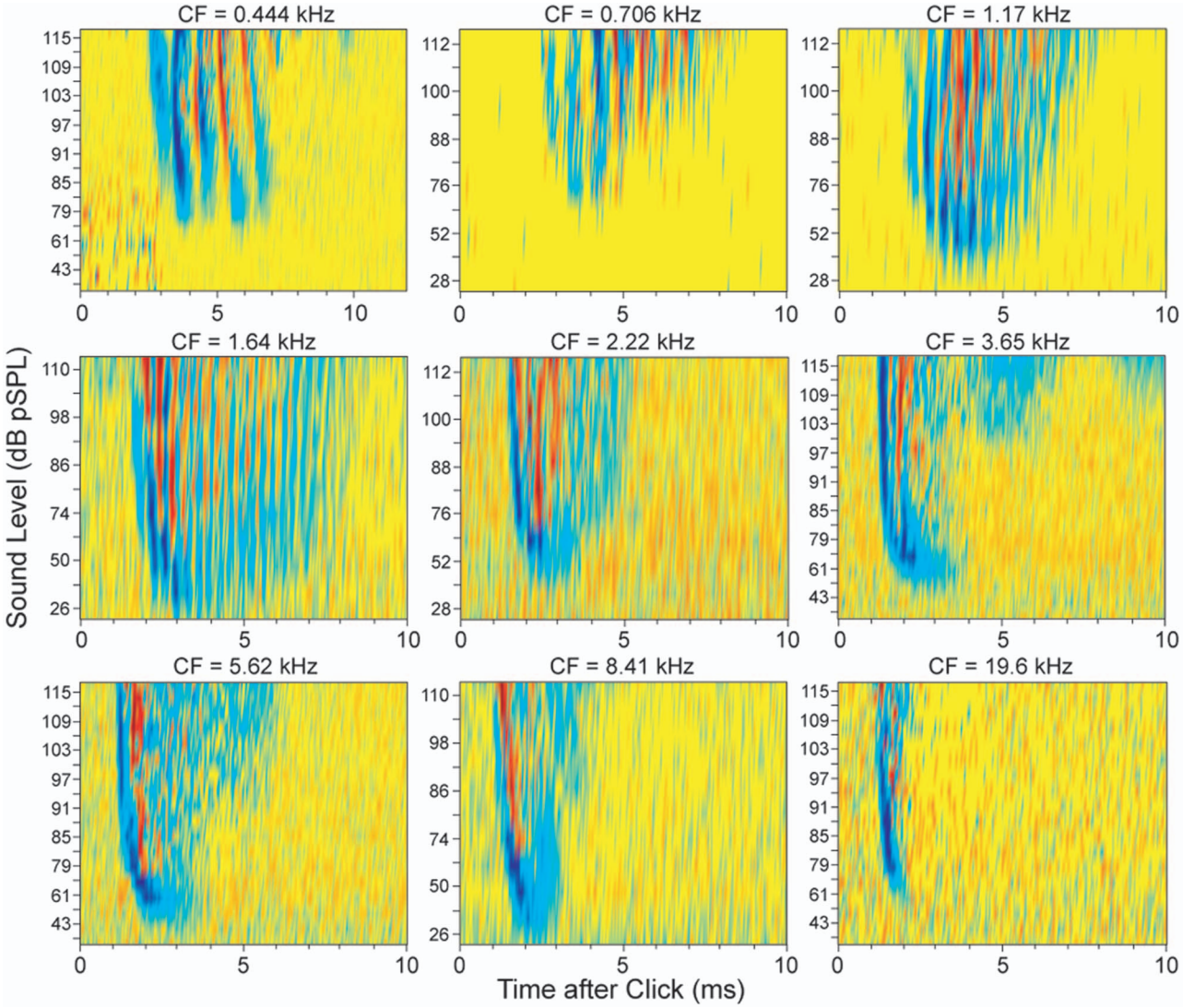

FIG. 5. MOC effects on click responses from nine AN fibers spanning a wide range of CFs. Color-coded response plots as in Fig. 4 with purple-blue showing inhibition and red-orange showing enhancement.

appear, i.e., inhibition is strongest on the first half-cycle, moderate on the second half-cycle, and negligible on the next cycle.

For fibers with CFs 4–6 kHz, individual peaks separated by 1/CF are no longer separate. However, for many fibers, clear, although overlapping, peaks could still be seen and similar counts were made on the first and second peaks. These showed trends similar to fibers with CFs <4 kHz.

For fibers with CFs >4–6 kHz, where individual peaks were no longer visible, the determination of whether there was MOC inhibition of the first peak could not be done in the way used for low-CF fibers. Instead, we compared responses with and without MOC stimulation in two sequential, equal-duration windows, starting at the onset of the click response. MOC-induced changes measured with a window duration of 0.2 ms are shown in Fig. 6 (the right half of each panel). Loess-fit (Cleveland, 1993) trend lines for the data are shown in Figs. 6(a)–6(d), and are superimposed in Fig. 6(e). Window durations from 0.1 to 1 ms were tried. When a short window of 0.1 ms was used, the rarefaction-peak-1 trend line was lower than the others at almost all CFs, but the scatter in the points increased greatly. As the window was made longer than 0.2 ms, the scatter changed little, but all four trend lines became similar at CFs greater than ~8 kHz.

The data in Fig. 6 show that for fibers with CFs below about 10 kHz, MOC stimulation inhibited rarefaction peak 1 more than rarefaction or condensation peak 2. For fibers 4–10 kHz, taken together, the MOC-induced change for the rarefaction first peak was significantly stronger than the MOC-induced change for the rarefaction second peak (t test, $P<0.01$). For fibers with CFs above 10 kHz, the difference between rarefaction first and second peaks was small and not statistically significant. Condensation peak 1 was inhibited about the same, on average, at all CFs. Overall, the data in Fig. 6 show that at moderate-to-high sound levels and for CFs <4 kHz, there is strong first peak inhibition and little second peak inhibition, and that as CF increases, the difference between these peaks decreases, at least with the methods used to detect these peaks. Considering the dependence of the trend lines on the window duration for CFs >8–10 kHz, the data in this CF range are consistent with there being first peak inhibition, but are not at all conclusive.

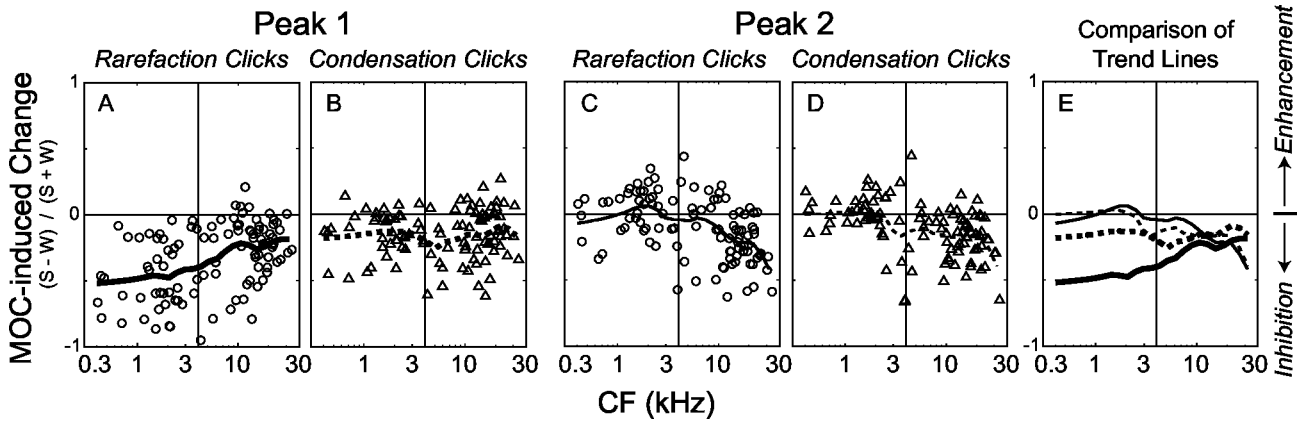

FIG. 6. MOC-induced changes in the first and second click-response peaks. Panels A–D: Each symbol shows the change from an individual fiber; panel E: Comparison of MOC-induced changes on different peaks using the Loess-fit curves from A–D. "MOC-induced change" is the rpPST peak amplitude with MOC shocks, S, minus the rpPST peak amplitude without shocks, W, normalized by their sum, S+W. For each fiber, rarefaction and condensation responses were considered separately, the response was segmented into peaks, responses from levels 75–100 dB pSPL were averaged, the average number of spikes in each peak was computed, and the MOC-induced change was calculated from these averages. Points from 104 fibers from 10 cats. The lines are Loess-fit (Cleveland, 1993) curves to the data that show trends across frequency. The vertical lines mark 4 kHz, below which individual peaks were readily discernable.

IV. INTRODUCTION B: RATIONALE FOR STUDYING TAIL-FREQUENCY INHIBITION

As an alternate method for gaining insight into possible first-peak inhibition in high-CF fibers, we looked at AN responses to tones at frequencies far below CF ("tail" frequencies). There are several reasons for thinking that tail-frequency tone responses correspond to the earliest peak of click responses. First, in the classic traveling wave the low-frequency energy arrives first so the low-frequency tail response would be expected to have the shortest latency (Shera, 2001). Second, click- and tone-evoked AN responses from normal guinea pigs are fit well by a model with two drives that mimic tuning-curve tips and tails, and this model shows that the excitation drive that produces tuning-curve tails also produces short-latency peaks in click responses, whereas the drive that produces tuning-curve tips also produces long-latency peaks in click responses (Schoonhoven *et al.* 1994). Furthermore, the patterns of both click and tone responses in noise-damaged guinea pigs fit this model (Versnel *et al.*, 1997). Thus, all of these data are consistent with the hypothesis that tail-frequency responses correspond to the first peak of click responses, at least for high-CF fibers.

In previous work, we found that MOC stimulation inhibited AN responses to tones at frequencies in the tuning-curve tails of fibers with high-CFs (CFs > 10 kHz) (Stankovic and Guinan, 1999). The inhibition was weak (a few dB) at low frequencies (0.5–1.3 kHz) and strong (up to 10 dB) in a narrow frequency range of approximately 2–4 kHz [Fig. 7(b)]. It has long been known that MOC stimulation produces a small decrease in endocochlear potential (EP) (Fex, 1967; Gifford and Guinan, 1987). This decrease in EP reduces the voltage drive to IHC mechanoelectric transduction and thereby reduces responses at all frequencies by a few dB (Sewell, 1984) and can account for the MOC inhibition of high-CF-fiber responses to 0.5–1.3 kHz tones (Stankovic and Guinan, 1999). The "strong tail inhibition" in the 2–4 kHz range is too large to be accounted for by the decrease in EP and was attributed by Stankovic and Guinan (1999; 2000) to MOC-induced changes in cochlear micromechanics. We hypothesize that, in high-CF fibers, the tone "strong tail inhibition" corresponds to a click "first peak inhibition" similar to the first peak inhibition seen in low-CF fibers. If true, the frequency region with "strong tail inhibition" should have the shortest latency. As a test of this, we measured group delays at different tail frequencies.

V. RESULTS B: LATENCIES AT FREQUENCIES WITH TAIL-FREQUENCY INHIBITION

Group delays determined from the slopes of tone-response phase-versus-frequency plots from AN fibers with CFs > 5 kHz revealed a tail-frequency region with particularly short group delays [Fig. 7(a)]. The frequencies with short group delays correspond to the frequencies with "strong tail inhibition" found by Stankovic and Guinan (1999) [Fig. 7(b)]. Furthermore, group delays at "strong tail inhibition" frequencies were similar to the average first-peak click latency of 1.2 ms for AN fibers with CFs > 5 kHz [from Fig 6(a) of Lin and Guinan, 2000].

VI. DISCUSSION

It is well known that MOC stimulation reduces the amplitude of AN compound action potential responses to clicks (Galambos, 1956; Wiederhold and Peake, 1966; Gifford and Guinan, 1987), but no previous study has reported MOC effects on click responses in single AN fibers. As already noted, the MOC inhibition of click responses at low levels and in the decaying part of the response was expected based on MOC effects on AN responses to tones. The surprising new finding is the MOC inhibition of the first peak of the single-fiber AN click response, a finding that is clear for fibers with CFs < ~6 kHz. This inhibition is strongest on the first half-cycle of the response, is less on the second half cycle, and is negligible on the next cycle (Fig. 6).

A factor to consider when using shocks to evoke MOC activity is whether LOC efferents are also activated and whether they might account for the effects seen. With the midline electrical stimulation of the olivocochlear bundle

used in these experiments, the efferent effects are almost certainly due to MOC efferents that terminate on OHCs, rather than LOC efferents that terminate on the dendrites of AN fibers, because (1) we use high-rate shocks (>=200/s). LOC fibers are thin and unmyelinated (Guinan *et al.*, 1983), and such unmyelinated fibers do not give sustained responses to shock rates greater than 20–50/s (Hallin and Torebjork, 1973; Fitzgerald and Woolf, 1981). (2) There are few LOC fibers that cross the midline (Guinan *et al.*, 1984). (3) In experiments in which LOC efferents were activated, the responses attributable to LOC efferents had time courses on the scale of minutes, much slower than the durations of the effects studied here (Groff and Liberman, 2003). Finally, (4) it is difficult to imagine how any LOC effect on the dendrites of AN fibers could selectively inhibit the first peak of the response (which is present at moderate-to-high click levels in only a fraction of the responses) without also inhibiting the other peaks.

Another issue in interpreting AN responses is that neural adaptation limits the extent to which AN responses show the mechanical drive to IHCs, but not so much that adaptation invalidates the comparison of MOC inhibition of the first versus the second click-response peaks. In order to get valid rpPST histograms, which show the overall shape of the AN response while minimizing the effects of refractoriness and ms-time-scale adaptation, we used high-rate clicks, rates that can cause substantial long-term adaptation from high-level clicks. Thus, the overall firing rates in the AN click responses are partially determined by AN adaptation so that inhibition of the first peak and/or the decaying part of the response can have the effect of slightly increasing the spike probability in the rest of the response. We think that this effect is responsible for the apparent increase in the firing rate during MOC shocks in the middle of the click response (e.g., the red/orange areas in Fig. 5). However, this effect cannot account for the inhibition of the first peak being more than the inhibition of the second peak (Figs. 3–6) because in all the cases considered here, the second peak was within 3 ms (the recovered-probability exclusion time) of the first peak, so that the probability of the second peak was always determined from responses in which there was no first-peak response, and any long-term adaptation would have affected the two peaks equally.

In summary, we conclude that the observed pattern of MOC inhibition, in particular the strong inhibition of the first response peak relative to the second response peak, cannot be explained by experimental artifacts and represents the actual pattern of MOC inhibition of AN-fiber click responses. This pattern of MOC inhibition contrasts sharply with the MOC inhibition of BM motion in response to clicks that is zero or very small in the first half-cycle of the response and grows over many cycles (Guinan and Cooper, 2005).

A. First peak inhibition in high-CF fibers

Since current conceptions of mammalian cochlear mechanics are based largely on measurements of BM motion from the high-CF basal turn (Robles and Ruggero, 2001), it is important to determine the extent to which our results

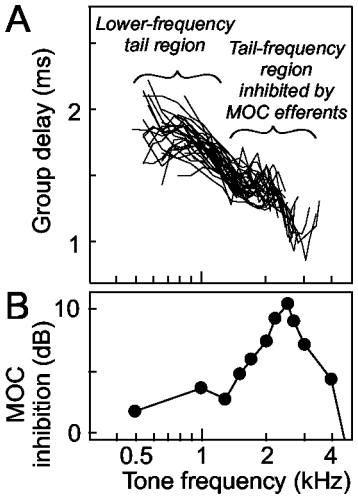

FIG. 7. Group delays from the slopes of tone-response phase-versus-frequency plots from 32 AN fibers (CFs>5 kHz) from 2 cats (A), and MOC inhibition at tail frequencies (data from Fig. 8(b) of Stankovic and Guinan, 1999) (B). To obtain the "MOC inhibition" shown in B, normalized level shifts from single AN fibers were averaged at each measurement frequency. The level shift is the amount (in dB) that the sound level must be increased with MOC stimulation to produce the same firing rate that is produced without efferent stimulation. For each unit at each stimulus frequency, all level shifts at sound levels <=85 dB SPL were averaged, and to make measurements across animals comparable, they were normalized by the level shift of the AN compound action potential in that animal. For further details see Stankovic and Guinan (1999).

apply to high-CF fibers. Our attempts to use click data to determine whether the first peak of AN click responses is inhibited in high-CF fibers were not conclusive. The most telling data on this issue are our tone-response results that the frequencies with strong tail inhibition have particularly short group delays (Fig. 7). A similar pattern of group delays, i.e., that the shortest below-CF delay was not at the lowest frequency, has been reported previously for fibers with CFs >1 kHz (Geisler *et al.*, 1974; Gummer and Johnstone, 1982; Allen, 1983; van der Heijden and Joris, 2003). The presence of a region of particularly short group delays just below the tip of the tuning curve is interesting because it is not expected from excitation by the classic traveling wave. In the classic traveling wave, for frequencies below CF, lower-frequency energy arrives before higher-frequency energy, and the lowest-frequency would be expected to excite fibers with the earliest latency (Shera, 2001).

Group delays must be interpreted with caution. The short group delays at ~1.5–4 kHz (Fig. 7) do not necessarily mean that a click response from energy in this frequency region would start before a click response from the lower-frequency region because a group delay includes both a wave-front latency and a filter buildup time. However, the "strong tail inhibition" component appears to be narrower in bandwidth than the rest of the tail (Fig. 7; also see Stankovic and Guinan, 1999), which would indicate that it has a longer buildup time. Thus, to account for its shorter overall group delay, the "strong tail inhibition" component would have to have a very short wave-front latency which suggests that in a click response, this component would correspond to the first peak. Finally, group delays at "strong tail inhibition" frequencies [Fig. 7(a)] were similar to the average first-peak

click latency of 1.2 ms for AN fibers with CFs > 5 kHz (Lin and Guinan, 2000), which also supports the correspondence of tone "strong tail inhibition" responses and click first-peak responses.

In summary, the data show that the tone-frequency region with short group delays [Fig. 7(a)] corresponds to the tone "strong tail inhibition" region of Stankovic and Guinan (1999) [Fig. 7(b)], which, in turn, provides strong support for the hypothesis that this tone inhibition corresponds, in click responses, to an inhibition of the first peak similar to that seen in low-CF fibers. Thus, the data in Fig. 7 are consistent with the hypothesis that for fibers with CFs > 5 kHz, there is MOC inhibition of the first peak of the click response.

Since Fig. 7 provides evidence of MOC inhibition at short latencies in high-CF fibers, one might ask "Why is similar inhibition not seen more clearly in the click-response data of Fig. 6?" In high-CF fibers, the "strong tail inhibition" frequency range appears to be quite narrow (~1.5–4 kHz) so that possibly our clicks did not go to high enough levels to provide the energy necessary to excite this region. Another possibility is that an inhibited first-peak response is present in the data of Fig. 6 for CFs > 10 kHz, but is so merged with other response peaks that it cannot be separated. Whatever the reasons for not seeing clear first peak inhibition for CFs > 10 kHz, the tone data provide evidence that MOC efferents inhibit an aspect of the cochlear response that starts very early, with a latency comparable to the first click-response peak. Finally, judging from the latencies in Fig. 7, the response inhibited by MOC efferents has a shorter latency than the earliest response produced by low-frequency energy in the tail, which is presumably the earliest energy to arrive from the classic traveling wave.

B. Relationship of first peak inhibition to the classic traveling wave

The MOC inhibition of the first peak of AN responses to clicks does not fit with current conceptions of mammalian cochlear mechanics. The usual view (e.g., Patuzzi, 1996; Geisler, 1998) is that all motion of the organ of Corti is produced by the BM traveling wave that mimics BM motion in the basal turn and extends throughout the cochlea [although it is recognized that the classic traveling wave does not explain many phenomena in the apical turn, e.g. downward glides (Carney *et al.*, 1999; Shera, 2001; Lin and Guinan, 2004)]. However, MOC inhibition of the AN click-response first peak cannot be explained by inhibition of the classic traveling wave first peak because, as shown by basal BM responses, the first peak of the classic traveling wave receives little or no cochlear amplification, and is little changed by MOC stimulation or by death (Robles *et al.*, 1976; Ruggero *et al.*, 1992; Recio, *et al.*, 1998; Recio and Rhode, 2000; Robles and Ruggero, 2001; Guinan and Cooper, 2005). Thus, the strong MOC inhibition of the AN first peak must be due to inhibition of something other than the classic traveling wave.

We hypothesize that MOC inhibition of the AN first peak is due to an OHC-dependent motion of structures or fluid that bends IHC stereocilia and is separate from motion of the classic traveling wave. Electrical coupling from OHCs to IHCs via local extracellular fields is unlikely to account for the AN first peak inhibition because MOC efferents increase OHC extracellular current, the opposite direction to the effect seen, and any electrical effect in the first peak should be bigger on later peaks. To account for strong AN first-peak inhibition, there must normally be an OHC-dependent motion of structures and/or fluid that bends IHC stereocilia and produces the AN initial peak (ANIP), and this ANIP motion must be reduced by MOC activation. The ANIP motion could come from OHC somatic motility or the hypothesized OHC stereocilia motility as long as MOC efferents can inhibit the motion. Presumably, the ANIP motion is the first part of a vibrational response mode that continues past the first peak. However, the lack of MOC inhibition of the second cycle of the AN click-response (Fig. 6) suggests that the ANIP motion decays quickly so that by the second cycle it is less than the little-inhibited motion that evokes the second AN peak, presumably motion due to the classic traveling wave.

A variety of previous data provide evidence for cochlear motion that is separate from, or in addition to, the motion of the classic traveling wave. First, in the apex, two group delays in AN responses and cochlear motion have been reported many times (Pfeiffer and Molnar, 1970; Kiang and Moxon, 1972; Geisler *et al.*, 1974; Kiang, 1984; Gummer *et al.*, 1996; Cooper and Rhode, 1997; Khanna and Hao, 1999; Zinn *et al.*, 2000; van der Heijden and Joris, 2003, 2005). Although an artifactual "fast wave" from opening the cochlea can contaminate apical mechanical measurements (Cooper and Rhode, 1996), Zinn and co-workers (2000) found that computationally removing the fast wave still left response dips and multiple group delays. Furthermore, in intact cochleae, AN responses show tuning curves with multilobed shapes (Liberman and Kiang 1978) and different group delays in each lobe (Kiang *et al.*, 1977; Kiang, 1984). These data provide evidence from intact cochleae that two interacting drives with different group delays excite apical AN fibers. Second, the previously anomalous phenomenon of downward glides in the apex may be explained by the interaction of two motions: a first-arriving, above-CF wave and a later-arriving CF wave (Lin and Guinan, 2004). Finally, interference of two motions may explain many observations of apparent cancellations and phase reversals in AN and BM responses (reviewed by Ruggero *et al.*, 2000). Although all of the phenomena just cited indicate the presence of two cochlear motions, it cannot be said whether the two motions in each example correspond to the ANIP motion and the motion produced by the classic traveling wave. However, all of these examples indicate that motion of the classic traveling wave does not provide the only excitation of AN fibers.

The ANIP motion appears to extend through most the cochlea. MOC inhibition of the ANIP motion is evident, for CFs up to ~8 kHz, as inhibition of the AN click-response first peak (Figs. 3–6); and for fibers with CFs > 5 kHz, perhaps by the inhibition of short-latency, tail-frequency tone responses (Fig. 7). The dividing line between the supposed basal and apical patterns of BM motion is often thought to be ~1 kHz, the region where click-response glides change from

upward to downward (Carney *et al.*, 1999; Lin and Guinan, 2004) and tuning-curve "tails" change from below CF to above CF (Kiang *et al.*, 1977; Kiang 1984). There are, however, almost no motion measurements in living cochleae with good thresholds between the basal turn and the apex on which to base a judgment of the dividing line. It seems plausible that the classic traveling wave and the ANIP motion are both present throughout the cochlea, perhaps with their relative strengths changing from base to apex. In this view, the classic traveling wave is dominant in the base and the ANIP motion gains in prominence going toward the apex.

C. What is the origin of the ANIP motion?

Since the ANIP motion appears to be separate from the classic traveling wave and is inhibited by MOC efferents that synapse on OHCs, it appears to be due to OHCs, or at least is strongly influenced by OHCs. It seems possible that the ANIP motion is due to an active, energy-consuming process and may be, in some sense, an amplified motion. Even though we have quantified the AN first-peak inhibition only at moderate to high sound levels, it may be present at low sound levels, especially in the apex. Which mechanisms in OHCs produce and/or modify the ANIP motion are unknown.

Nonetheless, it is useful to elaborate on some hypothetical mechanisms by which the ANIP motion might be produced and to consider the consequences of these hypotheses. To fit all of the data, the mechanism should excite AN fibers early enough to produce the first peak of the click response in the middle and apex of the cochlea and to produce the short-group-delay tone response in the base, and should be inhibited by MOC efferents without changing the first peak of the BM response in the base.

1. Possible ANIP source: OHC fluid pumping

One hypothesis for the origin of the ANIP motion is OHC "fluid pumping." Sound-frequency electrical stimulation in an excised gerbil cochlea produces OHC contractions and expansions that squeeze and extend the cochlear partition producing sound-frequency fluid motion along the tunnel of Corti, i.e., OHCs act as fluid pumps (Karavitaki and Mountain, 2003). OHC squeezing and extension of the organ of Corti has also been reported in guinea pigs[2] (Mammano and Ashmore, 1993) and may be the origin of the phase differences between BM motion in the arcuate and pectinate zones (Xue *et al.*, 1993; Nilsen and Russell, 1999; Nuttall *et al.*, 1999; Cooper 1999). With this hypothesis, pressure differences across the cochlear partition produce the classic traveling wave that is a transverse motion of the basilar membrane, and pressure differences inside to outside the organ of Corti produce the ANIP motion which, presumably, is an encircling wave in which the walls of the organ of Corti expand and contract. Presumably, the pressure difference inside to outside the organ of Corti produces a large ANIP motion at the reticular lamina, but not at the BM, because the first peak is primarily from below-CF energy (where stiffness dominates) and the effective stiffness of the reticular lamina is much less than that of the BM (Mammano and Ashmore, 1993; Scherer and Gummer, 2004). Thus, the ANIP motion should be much greater at the reticular lamina (and presumably, at IHC stereocilia and in AN firing) than at the BM. Finally, the ANIP motion might have a shorter delay than the classic traveling wave because tunnel fluid motion extends ahead of OHC contractions (Karavitaki and Mountain, 2003).

2. Possible ANIP source: Stereocilia motility

Another possible source of the ANIP motion is calcium-mediated stereocilia motility, a motility suggested to be present in the mammalian cochlea by recent experiments (Kennedy *et al.*, 2003, 2005; Chan and Hudspeth, 2005). One appeal of this mechanism is that an OHC stereocilia twitch could be readily coupled from OHC stereocilia to IHC stereocilia by the tectorial membrane without requiring intervening BM motion. In this hypothesis, the ANIP motion is the motion of the tectorial membrane and/or the fluid in the space between the reticular lamina and the tectorial membrane that bends IHC stereocilia. A drawback of this hypothesis is the lack of a clear mechanism by which MOC synapses would affect this motion. Although stereocilia motility is influenced by membrane voltage, MOC synapses hyperpolarize OHCs, which would be expected to increase the OHC stereocilia motility, not inhibit it.

3. Possible ANIP source: Direct acoustic coupling to OHCs

Yet another mechanism that might produce the ANIP motion is direct acoustic coupling from the forward cochlear pressure wave. Ren (2004) and Ruggero (2004) have provided data that suggests that mammalian OAEs may be generated by organ-of-Corti motion that is coupled back to stapes motion by fast fluid-pressure waves. Any cochlear process that couples organ-of-Corti motion to fluid pressure waves is likely to be reciprocal, which would imply that normal (forward) cochlear pressure waves may directly produce motion of the organ of Corti. To account for the ANIP motion, such motion, or the amplification of this motion, must be affected by OHCs. This mechanism has the advantage that it readily explains how the ANIP motion can produce a response peak that starts before the lowest-frequency part of the traveling wave. However, it is difficult to account for the long delays of the ANIP motion in the apex of the cochlea if the classic traveling wave is bypassed completely.

As can be noted from the above, a question related to the origin of the ANIP motion is how the ANIP motion travels along the cochlea. Is the ANIP motion a second wave along the cochlea, a separate vibrational mode excited by the classic traveling wave, or a vibrational mode excited directly by the fast cochlear pressure wave (e.g., due to OHC pressure sensitivity)? An important constraint is that the latency of the click-response first peak changes over ~2.5 ms from the base to the apex (Lin and Guinan, 2000), but this does not separate the hypotheses. Since the ANIP response is clearly first in the apex (Figs. 3–6) and appears to arise before the lowest-frequency tone response (which we earlier argued is due to the classic traveling wave) in the base (Fig. 7), it

seems unlikely that the ANIP response is a separate vibrational mode excited by the classic traveling wave. However, definitive data are needed to settle this issue.

In the context of considering mechanisms that might account for the AN first peak inhibition, it might be thought that the OHC hyperpolarization produced by MOC synapses would cause a lengthening of OHCs, and thereby change the coupling of BM motion to IHC stereocilia. Whether this is true, or not, it cannot explain how MOC excitation inhibits the first peak of the click response without producing a similar change in the second and later peaks.

As the above hypotheses point out, there are many possible ways by which the ANIP motion may be produced and determining which one, or if more than one, is correct requires additional data. Whatever mechanisms are involved, the presence of the OHC-generated ANIP motion early in the response puts it at a time that could influence, shape, or be a first step in cochlear amplification.

D. Effects of the ANIP motion on signal coding and hearing function

Excitation of AN fibers by the ANIP motion seems likely to have a different frequency filter than the classic traveling wave, but does not appear to sharpen the response and produce an old-style "second filter" (Evans and Wilson, 1975). Our click results suggest that the ANIP motion has an important influence on neural responses at moderate-to-high sound levels (Figs. 3–5). For tones, a component of the AN response due to ANIP motion was not evident at the threshold at the base of the cochlea (Narayan *et al.*, 1998), but an ANIP response may be evident at higher sound levels in the base, and perhaps at low sound levels in the apex.

Since the first peak is part of the neural response to clicks at moderate to high sound levels (Figs. 3–5), neural inhibition of the first peak can be expected to have behavioral consequences. Medial efferents improve the detection of transient sounds in background noise (May and McQuone, 1995; Micheyl and Collet, 1996; Zeng *et al.*, 2000) and MOC inhibition of the ANIP response may be partly responsible for this. MOC fibers are also functionally significant in providing protection from sound trauma (Rajan, 1988; Maison *et al.*, 2002). Again, MOC inhibition of the ANIP response may be involved. In short, any MOC effect at moderate to high sound levels may have a component, or be entirely, due to MOC inhibition of the ANIP response.

VII. CONCLUSIONS

(1) In click responses of single AN fibers with CFs $<$ $\sim$8 kHz, stimulation of MOC efferents unexpectedly inhibits the first peak of the response, in addition to inhibiting at low sound levels and in the decaying part of the response, as expected from tone data.
(2) For AN fibers with CFs $>$ 5 kHz, tones at tail frequencies produce responses with the shortest group delays at frequencies with "strong tail inhibition," which shows that there is short-latency MOC inhibition in the cochlear base.
(3) The MOC inhibition of the first peak of the AN click response cannot be attributed to a corresponding inhibition of the first peak of the click response in the classic traveling wave. This implies that there is a motion, the ANIP motion, which bends IHC stereocilia, is produced (or strongly influenced) by OHCs, and is separate from (and perhaps comes before) the first peak of the classic traveling wave.
(4) Although the origin of the ANIP motion is unknown, its presence highlights the need for a new conceptual paradigm for cochlear mechanics in which the classic BM traveling wave is not the only motion that excites AN fibers.

ACKNOWLEDGMENTS

We thank Dr. M. C. Brown, Dr. M. C. Liberman, and Dr. C. A. Shera for comments on a previous version of the manuscript. This study was supported by NIDCD Grant No. RO1-DC-00235.

[1]Lin and Guinan (2000) interpreted the first-peak reversal to the entry at high click levels of an excitation drive (presumably a motion that bends IHC stereocilia) that is opposite in direction, and more than cancels the low-level drive. If true, the lack of inhibition above a first-peak reversal implies that this high-level drive is *not* inhibited by MOC efferents.

[2]Using electrical stimulation across an isolated guinea-pig organ-of-Corti, Nowotny *et al.* (2004) found a squeezing and extension of the subtectorial space. This implies a radial fluid motion in the subtectorial space that could drive IHC stereocilia. The motion seen by Nowotny *et al.* (2004) was presumably produced by OHC motility, and might be inhibited by MOC efferents. How OHCs produce the squeezing and extension of the subtectorial space is not clear, but it is possible that in the intact cochlea, this motion might be produced without a corresponding motion of the basilar membrane, at least in the basal turn. If so, such a motion is a candidate for the ANIP motion.

Allen, J. B. (**1983**). "Magnitude and phase-frequency response to single tones in the auditory nerve." J. Acoust. Soc. Am. **73**, 2071–2092.

Békésy, G. v. (**1960**). *Experiments in Hearing* (McGraw Hill, New York).

Brownell, W. E., Bader, C. R., Bertrand, D., and de Ribaupierre, Y. (**1985**). "Evoked mechanical response of isolated cochlear outer hair cells." Science **277**, 194–196.

Carney, L. H., McDuffy, M. J., and Shekhter, I. (**1999**). "Frequency glides in the impulse responses of auditory-nerve fibers." J. Acoust. Soc. Am. **105**, 2384–2391.

Chan, D. K., and Hudspeth, A. J. (**2005**). "Ca(2+) current-driven nonlinear amplification by the mammalian cochlea in vitro." Nat. Neurosci. **8**, 149–155.

Cleveland, W. S. (**1993**). *Visualizing Data* (AT&T Bell Laboratories, Murray Hill, NJ).

Cooper, N. P. (**1999**). "Radial variation in the vibrations of the cochlear partition," in edited by H. Wada *et al.*, *Recent Developments in Auditory Mechanics*, (World Scientific, Singapore).

Cooper, N. P., and Guinan, J. J., Jr. (**2003**). "Separate mechanical processes underlie fast and slow effects of medial olivocochlear efferent activity." J. Appl. Physiol. **548**, 307–312.

Cooper, N. P., and Rhode, W. S. (**1996**). "Fast travelling waves, slow travelling waves and their interactions in experimental studies of apical cochlear mechanics." Aud. Neurosci. **2**, 289–299.

Cooper, N. P., and Rhode, W. S. (**1997**). "Apical cochlear mechanics: A review of recent observations," in *Phychophysical and Physiological Advances in Hearing, Proceedings of the 11th International Symposium on Hearing*, edited by A. R. Palmer *et al.* (Whurr, London), pp. 11–17.

de Boer, E., and Nuttall, A. L. (**1997**). "The mechanical waveform of the basilar membrane. I. Frequency modulations ("glides") in impulse responses and cross-corelation functions." J. Acoust. Soc. Am. **101**, 3583–3592.

Dolan, D. F., Guo, M. H., and Nuttall, A. L. (**1997**). "Frequency-dependent enhancement of basilar membrane velocity during olivocochlear bundle stimulation." J. Acoust. Soc. Am. **102**, 3587–3596.
Evans, E. F., and Wilson, J. P. (**1975**). "Cochlear tuning properties: concurrent basilar membrane and single nerve fiber measurements." Science. **190**, 1218–1221.
Fex, J. (**1967**). "Efferent inhibition in the cochlea related to hair-cell dc activity: Study of postsynaptic activity of the crossed olivo-cochlear fibers in the cat." J. Acoust. Soc. Am. **41**, 666–675.
Fitzgerald, M., and Woolf, C. J. (**1981**). "Effects of cutaneous nerve and intraspinal conditioning on C-fibre efferent terminal excitability in decerebrate spinal rats." J. Physiol. (London). **318**, 25–39.
Galambos, R. (**1956**). "Suppression of auditory activity by stimulation of efferent fibers to the cochlea." J. Neurophysiol. **19**, 424–437.
Geisler, C. D. (**1998**). *From Sound to Synapse. Physiology of the Mammalian Ear* (Oxford University Press, New York).
Geisler, C. D., Rhode, W. S., and Kennedy, D. T. (**1974**). "Responses to tonal stimuli of single auditory nerve fibers and their relationship to basilar membrane motion in the squirrel monkey." J. Neurophysiol. **37**, 1156–1172.
Gifford, M. L., and Guinan, J. J., Jr. (**1987**). "Effects of electrical stimulation of medial olivocochlear neurons on ipsilateral and contralateral cochlear responses." Hear. Res. **29**, 179–194.
Gray, P. R. (**1967**). "Conditional probability analyses of the spike activity of single neurons." Biophys. J. **7**, 759–777.
Groff, J. A., and Liberman, M. C. (**2003**). "Modulation of cochlear afferent response by the lateral olivocochlear system: activation via electrical stimulation of the inferior colliculus." J. Neurophysiol. **90**, 3178–3200.
Guinan, J. J., Jr. (**1996**). "The physiology of olivocochlear efferents", in *The Cochlea*, edited by P. J. Dallos (Springer-Verlag, New York), pp. 435–502.
Guinan, J. J., Jr., and Cooper, N. P., (**2005**). "Medial olivocochlear efferent inhibition of basilar-membrane click responses." Assoc. Res. Otolaryngol. Abstr. **28**, #340.
Guinan, J. J., Jr., and Gifford, M. L. (**1988**). "Effects of electrical stimulation of efferent olivocochlear neurons on cat auditory-nerve fibers. III. Tuning curves and thresholds at CF." Hear. Res. **37**, 29–46.
Guinan, J. J., Jr., and Stankovic, K. M. (**1996**). "Medial efferent inhibition produces the largest equivalent attenuations at moderate to high sound levels in cat auditory-nerve fibers." J. Acoust. Soc. Am. **100**, 1680–1690.
Guinan, J. J., Jr., Warr, W. B., and Norris, B. E. (**1983**). "Differential olivocochlear projections from lateral vs. medial zones of the superior olivary complex." J. Comp. Neurol.. **221**, 358–370.
Guinan, J. J., Jr., Warr, W. B., and Norris, B. E., (**1984**). "Topographic organization of the olivocochlear projections from the lateral and medial zones of the superior olivary complex." J. Comp. Neurol.. **226**, 21–27.
Gummer A. W., and Johnstone, B. M. (**1982**). "Group delay measurements from spiral ganglion cells in the guinea pig cochlea." Arch. Oto-Rhino-Laryngol. **234** 189–190.
Gummer, A. W., Hemmert, W., and Zenner, H. P. (**1996**). "Resonant tectorial membrane motion in the inner ear: its crucial role in frequency tuning." Proc. Natl. Acad. Sci. U.S.A.. **93**, 8727–8732.
Hallin, R. G., and Torebjork, H. E. (**1973**). "Electrically induced A and C fibre responses in intact human skin nerves." Exp. Brain Res. **16**, 309–320.
Karavitaki, K. D., and Mountain, D. C. (**2003**)."Is the cochlear amplifier a fluid pump?," in *The Biophysics of the Cochlea: Molecules to Models*, edited by A. W. Gummer, *et al.* (World Scientific, Singapore), pp. 310–311.
Kennedy, H. J., Evans, M. G., Crawford, A. C., and Fettiplace, R. (**2003**). "Fast adaptation of mechanoelectrical transducer channels in mammalian cochlear hair cells." Nat. Neurosci. **6**, 832–836.
Kennedy, H. J., Crawford, A. C. and Fettiplace, R. (**2005**). "Force generation by mammalian hair bundles supports a role in cochlear amplification." Nature. **433**, 880–883.
Khanna, S. M., and Hao, L. F. (**1999**). "Reticular lamina vibrations in the apical turn of a living guinea pig cochlea." Hear. Res. **132**, 15–33.
Kiang, N. Y. S. (**1984**). "Peripheral neural processing of auditory information." *Handbook of Physiology, Section 1: The Nervous System, Vol. 3 (Sensory Processes)*. (Am. Physiological Soc., Bethesda, MD), pp. 639–674.
Kiang, N. Y. S., Liberman, M. C., and Baer, T. (**1977**). "Tuning curves of auditory-nerve fibers." J. Acoust. Soc. Am. **61**, S27 (A).
Kiang, N. Y. S., and Moxon, E. C. (**1972**). "Physiological considerations in artificial stimulation of the inner ear." Ann. Otol. Rhinol. Laryngol. **81**, 714–731.
Liberman, M. C., Gao, J., He, D. Z., Wu, X., Jai, S., and Zuo, J. (**2002**). "Prestin is required for electromotility of the outer hair cell and for the cochlear amplifier." Nature. **419**, 300–304.
Liberman, M. C., and Kiang, N. Y. S. (**1978**). "Acoustic trauma in cats. Cochlear pathology and auditory-nerve activity." Acta Oto-Laryngol., Suppl. **Supplement 358**, 1–63.
Lin, T., and Guinan, J. J., Jr. (**2000**). "Auditory-nerve-fiber responses to high-level clicks: interference patterns indicate that excitation is due to the combination of multiple drives." J. Acoust. Soc. Am. **107**, 2615–2630.
Lin, T., and Guinan, J. J., Jr. (**2004**). "Time-frequency analysis of auditory-nerve-fiber and basilar-membrane click responses reveal glide irregularities and non-characteristic-frequency skirts." J. Acoust. Soc. Am. **116**, 405–416.
Maison, S. F., Luebke, A. E., Liberman, M. C., and Zuo, J. (**2002**). "Efferent protection from acoustic injury is mediated via alpha9 nicotinic acetylcholine receptors on outer hair cells." J. Neurosci. **22**, 10838–10846.
Mammano, F. and Ashmore, J. F. (**1993**). "Reverse transduction measured in the isolated cochlea by laser Michelson interferometry." Nature. **365**, 838–841.
May, B. J. and McQuone, S. J. (**1995**). "Effects of bilateral olivocochlear lesions on pure-tone discrimination in cats." Aud. Neurosci.. **1**, 385–400.
Micheyl, C., and Collet, L. (**1996**). "Involvement of the olivocochlear bundle in the detection of tones in noise." J. Acoust. Soc. Am.. **99**, 1064–1610.
Murugasu, E., and Russell, I. J. (**1996**). "The effect of efferent stimulation on basilar membrane displacement in the basal turn of the guinea pig cochlea." J. Neurosci. **16**, 325–332.
Narayan, S. S., Temchin, A. N., Recio, A., and Ruggero, M. A. (**1998**). "Frequency tuning of basilar membrane and auditory nerve fibers in the same cochleae." Science. **282**, 1882–1884.
Nilsen, K. E., and Russell, I. J. (**1999**). "Timing of cochlear feedback: spatial and temporal representation of a tone across the basilar membrane [published erratum appears in Nat Neurosci 1999 Sep;2(9):848]." Nat. Neurosci. **2**, 642–648; **2**, 848 (**1999**).
Nowotny, M., Zenner, H. P., and Gummer, A. W. (**2004**). "Impact of outer hair cell electromotility on organ of Corti vibration - Results from an *In-Situ* preparation." Assoc. Res. Otolaryngol. Abstr. **27**, Abs. 1002.
Nuttall, A. L., Guo, M. and Ren, T. (**1999**). "The radial pattern of basilar membrane motion evoked by electric stimulation of the cochlea." Hear. Res. **131**, 39–46.
Patuzzi, R. (**1996**). "Cochlear micomechanics and macromechanics." in *The Cochlea*, edited by P. J. Dallos *et al.* (Springer-Verlag, New York), pp. 186–257.
Pfeiffer, R. R., and Kim, D. O. (**1972**). "Response patterns of single cochlear nerve fibers to click stimuli: descriptions for cat." J. Acoust. Soc. Am. **52**, 1669–1677.
Pfeiffer, R. R., and Molnar, C. E. (**1970**). "Cochlear nerve fiber discharge patterns: Relationship to the cochlear microphonic." Science **167**, 1614–1616.
Rajan, R. (**1988**). "Effect of electrical stimulation of the crossed olivocochlear bundle on temporary threshold shifts in auditory sensitivity. I. Dependence on electrical stimulation parameters." J. Neurophysiol. **60**, 549–568.
Recio, A., and Rhode, W. S. (**2000**). "Basilar membrane responses to broadband stimuli." J. Acoust. Soc. Am. **108**, 2281–2298.
Recio, A., Rich, N. C., Narayan, S. S., and Ruggero, M. A. (**1998**). "Basilar-membrane responses to clicks at the base of the chinchilla cochlea." J. Acoust. Soc. Am. **103**, 1972–1989.
Ren, T. (**2004**). "Reverse propagation of sound in the gerbil cochlea." Nat. Neurosci. **7**, 333–334.
Robles, L., and Ruggero, M. A. (**2001**). "Mechanics of the mammalian cochlea". Physiol. Rev.. **81**, 1305–1352.
Robles, L., Rhode, W. S., and Geisler, C. D. (**1976**). "Transient response of the basilar membrane measured in squirrel monkeys using the Mössbauer effect." J. Acoust. Soc. Am. **59**, 926–939.
Ruggero, M. (**2004**). "Comparison of group delays of 2f1-f2 distortion product otoacoustic emissions and cochlear travel times." ARLO. **5**, 143–147.
Ruggero, M. A., Rich, N. C., and Recio, A. (**1992**). "Basilar membrane responses to clicks." in *Cazals, Auditory Physiology and Perception*, edited by Y. Cazals *et al.* (Pergamon, Oxford), pp. 85–91.
Ruggero, M. A., Narayan, S. S., Temchin, A. N., and Recio, A. (**2000**). "Mechanical bases of frequency tuning and neural excitation at the base of the cochlea: comparison of basilar-membrane vibrations and auditory-

nerve-fiber responses in chinchilla." Proc. Natl. Acad. Sci. U.S.A.. **97**, 11 744–11 750.
Russell, I. J., and Murugasu, E. (**1997**). "Medial efferent inhibition suppresses basilar membrane responses to near characteristic frequency tones of moderate to high intensities." J. Acoust. Soc. Am. **102**, 1734–1738.
Scherer, M. P., and Gummer, A. W. (**2004**). "Impedance analysis of the organ of Corti with magnetically actuated probes." Biophys. J. **87**, 1378–1391.
Schoonhoven, R., Keijzer, J., Versnel, H., and Prijs, V. F. (**1994**). "A dual filter model describing single-fiber responses to clicks in the normal and noise-damaged cochlea." J. Acoust. Soc. Am. **95**, 2104–2121.
Sewell, W. F. (**1984**). "The effects of furosemide on the endocochlear potential and auditory-nerve fiber tuning curves in cats." Hear. Res. **14**, 305–314.
Shera, C. A. (**2001**). "Frequency glides in click responses of the basilar membrane and auditory nerve: Their scaling behavior and origin in traveling-wave dispersion." J. Acoust. Soc. Am. **109**, 2023–2034.
Stankovic, K. M., and Guinan, J. J., Jr. (**1999**). "Medial efferent effects on auditory-nerve responses to tail-frequency tones I: Rate reduction." J. Acoust. Soc. Am. **106**, 857–869.
Stankovic, K. M., and Guinan, J. J., Jr. (**2000**). "Medial efferent effects on auditory-nerve responses to tail-frequency tones II: Alteration of Phase." J. Acoust. Soc. Am. **108**, 664–678.
van der Heijden, M., and Joris, P. X. (**2003**). "Cochlear phase and amplitude retrieved from the auditory nerve at arbitrary frequencies." J. Neurosci. **23**, 9194–9198.
van der Heijden, M., and Joris, P. X. (**2005**). "Group delays in the auditory nerve of the cat." Assoc. Res. Otolaryngol. Abstr. **28**, #349.
Versnel, H., Prijs, V. F., and Schoonhoven, R. (**1997**). "Auditory-nerve fiber responses to clicks in guinea pigs with a damaged cochlea." J. Acoust. Soc. Am. **101**, 993–1009.
Wiederhold, M. L., and Peake, W. T. (**1966**). "Efferent inhibition of auditory nerve responses: dependence on acoustic stimulus parameters." J. Acoust. Soc. Am. **40**, 1427–1430.
Xue, S., Mountain, D. C., and Hubbard, A. E. (**1993**). "Direct measurement of electrically-evoked basilar membrane motion." in edited by H. Duifhuis *et al.* (Eds.), *Biophysics of Hair Cell Sensory Systems*, (World Scientific, Singapore), pp. 361–368.
Zeng, F., Martino, K. M., Linthicum, F. H., and Soli, S. D. (**2000**). "Auditory perception in vestibular neurectomy subjects." Hear. Res. **142**, 102–112.
Zheng, J., Madison, L. D., Oliver, D., Fakler, B., and Dallos, P. (**2002**). "Prestin, the motor protein of outer hair cells." Audiol. Neuro-Otol. **7**, 9–12.
Zinn, C., Maier, H., Zenner, H., and Gummer, A. W. (**2000**). "Evidence for active, nonlinear, negative feedback in the vibration response of the apical region of the in-vivo guinea-pig cochlea." Hear. Res. **142**, 159–183.

Delays of stimulus-frequency otoacoustic emissions and cochlear vibrations contradict the theory of coherent reflection filtering

Jonathan H. Siegel and Amanda J. Cerka
The Hugh Knowles Center, Department of Communication Sciences and Disorders, and Institute for Neuroscience, Northwestern University, 2240 Campus Drive, Evanston, Illinois 60208

Alberto Recio-Spinoso
Department of Physiology, University of Wisconsin, Madison, Wisconsin 53706

Andrei N. Temchin
The Hugh Knowles Center, Department of Communication Sciences and Disorders, and Institute for Neuroscience, Northwestern University, 2240 Campus Drive, Evanston, Illinois 60208

Pim van Dijk
Department of Otorhinolaryngology, University Medical Centre Groningen, P.O. Box 30.001, 9700 RB Groningen, The Netherlands

Mario A. Ruggero[a)]
The Hugh Knowles Center, Department of Communication Sciences and Disorders, and Institute for Neuroscience, Northwestern University, 2240 Campus Drive, Evanston, Illinois 60208

(Received 29 March 2005; revised 26 June 2005; accepted 28 June 2005)

When stimulated by tones, the ear appears to emit tones of its own, stimulus-frequency otoacoustic emissions (SFOAEs). SFOAEs were measured in 17 chinchillas and their group delays were compared with a place map of basilar-membrane vibration group delays measured at the characteristic frequency. The map is based on Wiener-kernel analysis of responses to noise of auditory-nerve fibers corroborated by measurements of vibrations at several basilar-membrane sites. SFOAE group delays were similar to, or shorter than, basilar-membrane group delays for frequencies >4 kHz and <4 kHz, respectively. Such short delays contradict the generally accepted "theory of coherent reflection filtering" [Zweig and Shera, J. Acoust. Soc. Am. **98**, 2018–2047 (1995)], which predicts that the group delays of SFOAEs evoked by low-level tones approximately equal twice the basilar-membrane group delays. The results for frequencies higher than 4 kHz are compatible with hypotheses of SFOAE propagation to the stapes via acoustic waves or fluid coupling, or via reverse basilar membrane traveling waves with speeds corresponding to the signal-front delays, rather than the group delays, of the forward waves. The results for frequencies lower than 4 kHz cannot be explained by hypotheses based on waves propagating to and from their characteristic places in the cochlea. © *2005 Acoustical Society of America.*
[DOI: 10.1121/1.2005867]

PACS number(s): 43.64.Jb, 43.64.Kc, 43.64.Bt, 43.64.Pg [BLM] Pages: 2434–2443

I. INTRODUCTION

When stimulated by sound, the ear absorbs some of its energy, signals it to the brain, and also broadcasts "echoes" or otoacoustic emissions (OAEs). These OAEs, generated in the cochlea and transmitted to the environment via the middle-ear ossicles, were discovered more than a quarter-century ago in humans (Kemp, 1978) and have since been demonstrated and intensively studied in many mammals, as well as birds, reptiles, and amphibians (Manley, 2001). OAEs appear to be manifestations of cochlear amplification, the active feedback process whereby hair cells enhance, by the injection of biological energy, the sensitivity and frequency selectivity of vibrations in the hearing organs of tetrapod vertebrates (Dallos, 1992; Hudspeth, 1997; Manley, 2001; Robles and Ruggero, 2001; Ruggero and Rich, 1991). Appropriately, OAEs are routinely used in audiology clinics as diagnostic tools (Robinette and Glattke, 2002). Yet, in spite of their practical and theoretical importance, OAEs are poorly understood and it is not even known with certainty how they propagate from their sites of origin in the cochlea to the middle ear. Here we present evidence that casts doubt on the dominant view of the origin and propagation of stimulus-frequency OAEs (SFOAEs), single-frequency OAEs stimulated by same-frequency tones (Kemp and Chum, 1980; Shera and Guinan, 2003).

[a)]Author to whom correspondence should be addressed. Electronic mail: mruggero@northwestern.edu

The dominant view of the origin and propagation of SFOAEs (Goodman *et al.*, 2003; 2004; Guinan *et al.*, 2003; Konrad-Martin and Keefe, 2003; Lineton and Lutman, 2003; Mauermann *et al.*, 1999; Shera *et al.*, 2002; Shera and Guinan, 1999; Talmadge *et al.*, 1998; Zweig and Shera, 1995) is embodied in the "theory of coherent reflection filtering" (henceforth, "CRF theory") proposed by (Shera and Zweig 1993; Zweig and Shera, 1995). According to the CRF theory, at low and moderate levels SFOAEs are generated by "coherent scattering of cochlear traveling waves off small, random perturbations in the mechanical properties of the cochlea" (Shera *et al.*, 2002). A "key prediction (of the CRF theory) is that reflection-source-emission group delay is determined by the group delay of the basilar-membrane (BM) transfer function at its peak" (Shera and Guinan, 2003). More precisely, the CRF theory predicts that, for low stimulus levels, "the SFOAE group delay, τ_{SFOAE}…, is approximately equal to twice the group delay of the BM mechanical transfer function, evaluated at the cochlear location with CF equal to the stimulus frequency" (Shera and Guinan, 2003; see also Shera *et al.*, 2002; Shera and Guinan, 1999; Zweig and Shera, 1995). [CF (characteristic frequency) is the frequency at which a normal and fully mature auditory structure is most sensitive in response to low-level stimulation.] Minority views of OAE propagation [(Nobili *et al.*, 2003; Ren, 2004; Ruggero, 2004; Wilson, 1980); see also p. 2397 of Robles *et al.* (1997) and pp. 583–585 of Gummer *et al.* (2003)] predict shorter delays.

Two studies tested the validity of the CRF theory by comparing SFOAE and BM group delays (Cooper and Shera, 2004; Shera and Guinan, 2003). One study found evidence favoring the CRF theory for frequencies of 17 kHz in guinea pig and 32 kHz in cat but also found contradictory evidence for 300–400 Hz in guinea pig (Shera and Guinan, 2003) (see their Fig. 5). Another study reported data fully consistent with the CRF theory for frequencies of 20–30 kHz in guinea pig (Cooper and Shera, 2004). We test the delay predictions of the CRF theory far more extensively than in previous attempts by comparing, in chinchilla, newly measured τ_{SFOAE}'s with a unique new map of BM delays as a function of cochlear distance (Temchin *et al.*, 2005) derived by second-order Wiener-kernel analysis of responses to noise of auditory-nerve fibers (ANFs) (Recio-Spinoso *et al.*, 2005). [A preliminary report of the present findings was presented at the 2005 Mid-Winter Meeting of the Association for Research in Otolaryngology (Siegel *et al.*, 2005).]

II. MATERIALS AND METHODS

A. Animal preparation

Recordings of SFOAEs were carried out in chinchillas deeply anesthetized with Dial in urethane. Core temperature was kept near 38 °C with a servo-controlled heating pad. Chinchillas were tracheotomized and intubated to ensure a clear airway. The cartilaginous part of the ear canal and pinna were resected and part of the bony external ear canal was chipped away to permit visualization of the umbo of the tympanic membrane and the close placement of the emission-probe assembly, which was sealed to the ear canal using silicone earmold impression material. The middle ear cavity was opened to allow placement of an electrode on the round window to monitor compound action potential thresholds. The tendons of both middle ear muscles were severed from their bony anchors. In most respects, the animal preparations for recording SFOAEs were identical to those recently used to derive BM cochlear delays from Wiener kernels of chinchilla ANF responses to noise (Recio-Spinoso *et al.*, 2005; Temchin *et al.*, 2005).

B. Stimulation and recording of SFOAEs

The amplitudes and phases of SFOAEs were measured by first Fourier transforming the averaged responses to the probe tone alone and in the presence of a suppressor tone and then subtracting the vectors (Dreisbach *et al.*, 1998). This method is identical to that used by Shera and Guinan (Shera and Guinan, 1999) and mathematically equivalent to the method used by Brass and Kemp, who first subtracted time-domain responses with and without suppressors and then extracted the SFOAE amplitude and phases by Fourier transformation (Brass and Kemp, 1993). The probe and suppressor tones were presented, via separate transducers, at 30 and 55 dB SPL, respectively. The frequency of the suppressor tone was always 43 Hz below the frequency of the probe tone. The probe tones were presented with a frequency spacing of 21.53 Hz from 300 Hz to 2 kHz and a spacing of 43.06 Hz for higher frequencies. This insured that the response phases could be unwrapped unambiguously over the entire frequency range. No smoothing of the data was used due to the large signal-to-noise ratio (see Figs. 3–5). The phase of the probe-tone stimulus was measured as a function of frequency in the presence of the suppressor to minimize contamination by the SFOAEs. Those phases were subsequently subtracted from the phases of the SFOAEs to compensate the stimulus delay. The SFOAE magnitude and phase were expressed as the equivalent magnitude and phase of a tone that would have produced the measured change in probe response (Guinan, 1990). Finally, the SFOAE group delay for each individual chinchilla ear was calculated as the negative of the slope of the phase versus frequency function.

The earphone assembly included an *Etymōtic ER-10B+* otoacoustic emission probe. The probe assembly was heated, using electric current passed through a network of resistors, to raise its temperature above that of the animal's core temperature. Heating the probe helped to maintain cochlear temperature by compensating for the effects of deep anesthesia and the widely opened bulla (Brown *et al.*, 1983; Shore and Nuttall, 1985). Acoustic stimuli were delivered via tubes connected to transducers (modified *Radio Shack RS-1377 Super Tweeters*) housed in separate steel boxes. Stimulus delivery and response measurement were controlled by *Emav* software (Neely and Liu, 1993), using a 24-bit sound card (*Card Deluxe—Digital Audio Labs*). The differential outputs of both D/A channels were routed through balanced 600-Ω attenuators to separate differential power amplifiers (*Symetrix 420*) configured in bridge mode. The sound source transducers received their input from the amplifiers via balanced and shielded microphone cable. Likewise, the signal from

the *ER-10B+* preamplifier was connected pseudo-differentially to a differential-input equalizer (*Symetrix 202*) and subsequently routed from the equalizer's differential output to one of the differential inputs of the sound card. The equalizer was used to flatten the frequency response of the *ER-10B+* probe microphone (±1 dB from 500 Hz to 20 kHz) using a *Bruel and Kjaer 4138* $\frac{1}{8}$-in. reference microphone following the calibration procedure described previously (Siegel, 2002).

The acoustic system could deliver tonal stimuli in excess of 100 dB SPL as well as high-quality low-level tones. For stimulus levels of 70 dB SPL or lower, measurements in a test cavity (50 frequencies between 300 Hz and 11 kHz) revealed no harmonic distortion exceeding the noise floor of approximately −25 dB SPL with the sampling parameters typically used (sample rate: 44.1 kHz; FFT size: 2048 points, total sample time: 4 s). Acoustic and electrical crosstalks were insignificant. This performance allowed emission signals to be measured accurately over the entire 100+ dB dynamic range of the system.

III. RESULTS

A. Measures of cochlear delay: Near-CF group, signal-front, and filter delays

According to the CRF theory (Shera and Guinan, 2003), $\tau_{\mathrm{SFOAE}} \approx 2\tau_{\mathrm{BMgroup}}$, where τ_{BMgroup} is the BM group delay (Ruggero, 1980) at the CF. The upper and middle panels of Fig. 1, respectively, depict BM responses to clicks at apical (Cooper and Rhode, 1996) and basal (Recio *et al.*, 1998) sites of the chinchilla cochlea. Near-CF group delay, signal-front delay, and filter delay are illustrated in the upper panel of Fig. 1, which indicates that τ_{BMgroup}, the BM group delay at the CF [more precisely: the "weighted-average group delay" for responses to low-level stimuli (Goldstein *et al.*, 1971; Ruggero, 1994)], is identical to the latency of the "center of gravity" of the impulse response. τ_{BMgroup} is the sum of a signal-front delay, τ_{BMfront} [also referred to as absolute latency, travel time, "dead time," or "Sommerfeld forerunner" (Brillouin, 1960; Goldstein *et al.*, 1971; Papoulis, 1962; Recio *et al.*, 1998; Ruggero, 1980)], which in apical regions of the chinchilla cochlea corresponds to the onset of nonlinear (compressive) responses, and a filter delay, τ_{BMfilter} [also referred to as "resonance build-up time" (de Boer and Nuttall, 1996)].

B. Signal-front and group delays of directly measured BM vibrations in chinchilla

Due to anatomical and technical constraints, direct measurements of BM delays in active cochleae (i.e., exhibiting high sensitivity and pronounced nonlinearity) are available for only a few sites in a few species (Robles and Ruggero, 2001). The most complete measurements in healthy cochleae have been obtained in chinchilla. Such measurements include recordings in the apical region of the cochlea, probably the most representative of fully normal apical responses available for any species (Cooper, 1997; Cooper and Rhode, 1996), as well as recordings at many different sites spanning the most basal 5 mm of the BM (Narayan and Ruggero,

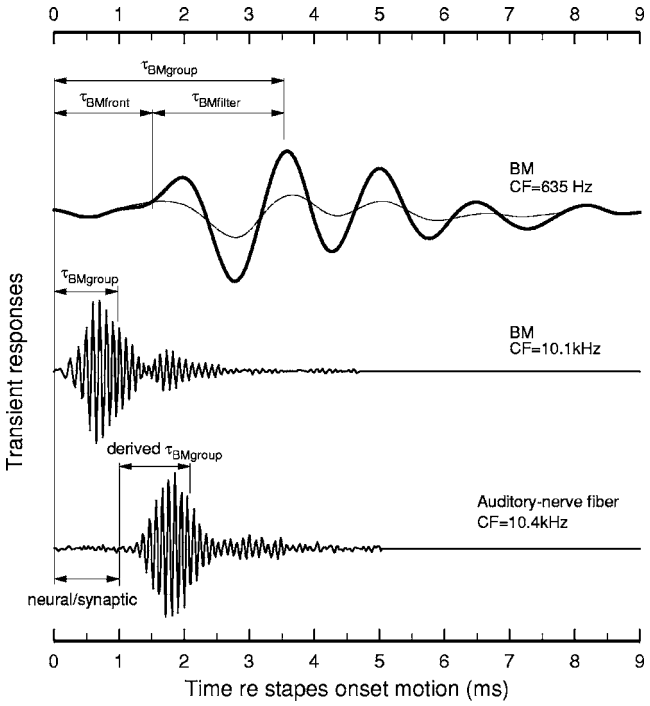

FIG. 1. Time-domain measures of cochlear delay for BM vibrations and ANF responses. Time is expressed relative to the onset of malleus motion. Top traces: gains (i.e., amplitudes normalized to stimulus level) of tectorial membrane responses to clicks at a cochlear site with CF=635 Hz. Responses are shown for clicks with peak pressures of 45 and 95 dB SPL (thick and thin traces, respectively). In these recordings in chinchilla, the initial response deflection is an artifact which grows linearly with stimulus level and is absent from hydraulically sealed cochleae (Cooper and Rhode, 1996). [Similar finding have been presented for apical sites in the guinea pig cochlea (Zinn *et al.*, 2000).] The onset of the "real" response (τ_{BMfront}), which occurs 1.51 ms after the onset of malleus motion, is identifiable as the transition between linear and nonlinear vibrations. τ_{BMgroup}, τ_{BMfront}, and τ_{BMfilter} are indicated for the responses at the 635-Hz site. Middle trace: velocity response to clicks of a BM site with CF=10.1 kHz. At this site, τ_{BMfront} is nearly insignificant (30 μs; not indicated). Bottom trace: the first singular vector of a second-order Wiener kernel computed from responses to noise of a chinchilla ANF with CF=10.4 kHz. The ANF response closely resembles the click response of the BM site with similar CF but is retarded by about 1 ms (due to intervening synaptic processes and neural conduction time). Top panel data: from Fig. 5 of Cooper and Rhode (1996). Middle panel data: from Fig. 2 of Recio *et al.* (1998). Bottom panel: unpublished data of Recio-Spinoso *et al.* (2005).

2000; Recio *et al.* 1997, 1998; Recio and Rhode, 2000; Rhode and Recio, 2000; Ruggero *et al.*, 1997, 2000). Such delays (τ_{BMgroup}'s and τ_{BMfront}'s) are shown in Fig. 2 (open and closed symbols, respectively). The delays were derived from published BM responses to clicks, tones, or noise [which yield equivalent frequency-tuning and timing information (Recio *et al.*, 1997, 1998)]. To permit meaningful comparison with the delay predictions of the CRF theory, which are strictly valid only for linear responses, i.e., evoked by low-level stimuli (Shera and Guinan, 2003), Fig. 2 indicates the range of variation of τ_{BMgroup} as a function of stimulus level (brackets), with the highest τ_{BMgroup}'s usually corresponding to the lowest stimulus levels. Figure 2 makes it evident that whereas basal regions of the chinchilla cochlea have been sampled with substantial density [note distance scale (Greenwood, 1990) at top], BM data exist only for a single apical region, and that no data at all exist for either more apical regions (13–18 mm from the base) or for the

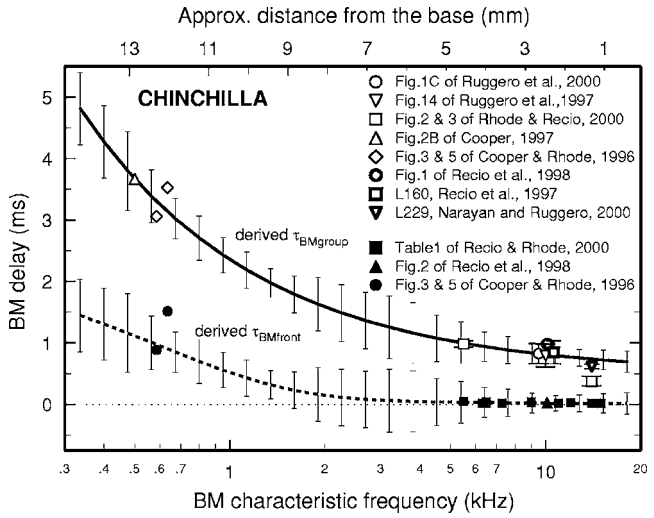

FIG. 2. BM near-CF group delays and signal-front delays. Open symbols: $\tau_{BMgroup}$'s, i.e., near-CF group delays, measured directly with laser interferometers in the cochleae of chinchillas. The brackets indicate the range of $\tau_{BMgroup}$'s, with the upper and lower brackets typically coinciding with the lowest- and highest-level stimuli, respectively. Filled symbols: signal-front delay, $\tau_{BMfront}$'s, of responses to clicks measured directly with laser interferometers in the cochleae of chinchillas. Continuous line: trend line for BM near-CF group delays, $\tau_{BMgroup}$ (ms), derived from second-order Wiener kernels computed from responses to noise of ANFs (Recio-Spinoso *et al.*, 2005; Temchin *et al.*, 2005). BM $\tau_{BMgroup}(\text{ms}) = 0.496 + 1.863\text{CF}^{-0.771}$. Dashed line: BM $\tau_{BMfront}$ derived from responses of ANFs to intense rarefaction clicks [adapted by Temchin *et al.*, (2005) from measurements of Ruggero and Rich (1987)]. BM $\tau_{BMfront}(\text{ms}) = 0.018 + 2.4e^{-1.70\text{CF}} + 0.083e^{-0.27\text{CF}}$. Means plus-minus standard deviations of $\tau_{BMgroup}$'s and $\tau_{BMfront}$'s derived from ANFs are indicated by the envelopes of the vertical lines. Top abscissa scale: approximate distance from the basal end of the cochlea [according to the map for the chinchilla cochlea of Greenwood (1990)].

mid-cochlear region (5–12 mm from the base). [Among other mammals, apical vibration data in relatively normal cochleae exist only for guinea pig, a species in which BM recordings have been recorded at only two basal sites [see Fig. 7(a)]. In cat, BM vibration data in normal cochleae are solely available for one basal site [see Fig. 7(b)].

C. BM group delays derived from second-order Wiener-kernel analysis of ANF responses to noise

In principle, the dearth of BM data can be compensated by deriving $\tau_{BMgroup}$'s from the responses of ANFs, which in many respects faithfully reflect the frequency tuning and timing of the underlying BM vibrations (Narayan *et al.*, 1998b; Ruggero *et al.*, 2000). Until recently, however, such estimates were not available for chinchilla ANFs with CF >4 kHz because of the nearly complete absence of phase locking at high frequencies. Recently, Recio-Spinoso and Temchin *et al.* circumvented that problem by taking advantage of second-order Wiener-kernel analysis, a technique that extracts high-frequency timing information from nonlinearities encoded in the (low-frequency) response envelopes (Recio-Spinoso *et al.*, 2005; Temchin *et al.*, 2005). The bottom trace of Fig. 1 shows the highest-rank singular vector computed from the second-order Wiener kernel of responses to noise of an ANF with CF of 10.4 kHz. That trace is very similar to the response to clicks of a BM site with similar CF (middle trace of Fig. 1). The main difference between the traces is the extra delay (amounting to 1 ms) exhibited by the ANF response, due to neural and synaptic processes (Temchin *et al.*, 2005).

Figure 2 shows trend lines [reproduced from Fig. 13 of Temchin *et al.* (2005)] for $\tau_{BMgroup}$'s (continuous line) and $\tau_{BMfront}$'s (dashed line) derived from responses of ANFs innervating inner hair cells throughout most of the length of the chinchilla cochlea. $\tau_{BMgroup}$'s were derived by Wiener-kernel analysis from ANF responses to noise presented at near-threshold levels, i.e., appropriate for comparison with the delay predictions of the CRF theory. $\tau_{BMfront}$'s were derived from responses to intense rarefaction clicks (Ruggero and Rich, 1987). Figure 2 shows that the $\tau_{BMgroup}$'s (open symbols) directly measured at basal (Recio *et al.*, 1998; Recio and Rhode, 2000; Rhode and Recio, 2000; Ruggero *et al.*, 1997, 2000) and apical (Cooper, 1997; Cooper and Rhode, 1996) BM sites in chinchilla cochleae are well matched by the $\tau_{BMgroup}$ estimates derived from neural responses (continuous line) except for the site with CF ≈ 14 kHz, near the extreme basal end of the cochlea. Similarly, the estimates of $\tau_{BMfront}$ (dashed line) based on ANF responses closely match the $\tau_{BMfront}$'s directly measured at both apical (Cooper and Rhode, 1996) and basal (Recio *et al.*, 1998; Recio and Rhode, 2000) BM sites (filled symbols). Note that the excellent matches between directly measured BM delays and the trend lines support the appropriateness of the 1-ms correction used in the derivation of BM delays from neural data (Temchin *et al.*, 2005).

D. Basic features of SFOAEs in individual chinchillas

SFOAEs were originally measured in 21 chinchillas but the ears of 4 chinchillas were deemed abnormal because they had elevated compound action potential thresholds and/or unusually small SFOAE amplitudes. Therefore, SFOAE data from only 17 chinchilla ears are presented here.

Figure 3 illustrates the magnitudes and phases of SFOAEs recorded in a representative chinchilla. SFOAEs were evoked by single tones presented at 30 dB SPL. Figure 3(a), which presents the amplitudes of the SFOAEs (thick line and symbols) and the noise floor (thin line) as functions of frequency, demonstrates that the SFOAEs were recorded with a high signal-to-noise ratio, amounting to 20–40 dB over most of the range of measurements, 300 Hz to 12 kHz. Figure 3(a) also shows that the measurements of SFOAE magnitudes were highly repeatable. SFOAEs were first measured in this chinchilla at relatively widely spaced frequencies (open circles) and then measured again with finer frequency resolution (thick line) over an interval of about 1 h. The two sets of SFOAE magnitudes were very similar. Finally, Fig. 3(a) exemplifies the universal finding that amplitude notches were interspersed between frequency regions with more uniform magnitudes. The frequencies of the prominent notches are marked by the arrowheads.

Figure 3(b) presents the SFOAE phases corresponding to the magnitudes of Fig. 3(a) (solid line and open symbols). As was the case for the SFOAE amplitudes [Fig. 3(a)], the SFOAE phases were also quite stable. To a first approximation, phase varied with frequency more or less linearly, sug-

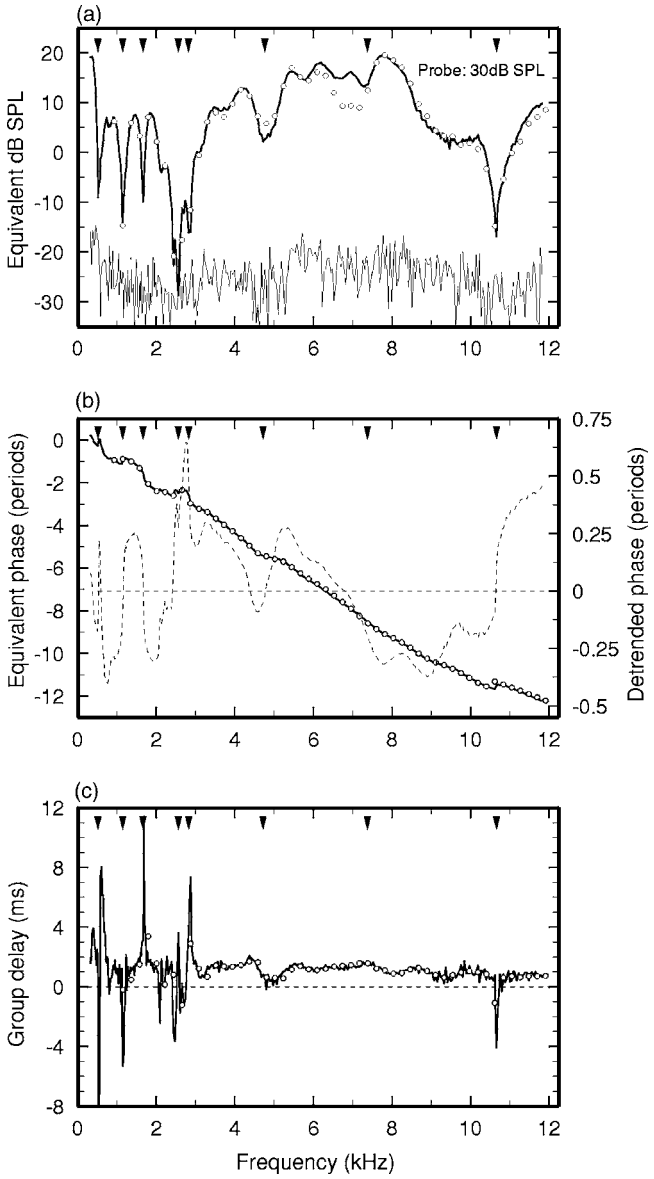

FIG. 3. High signal-to-noise ratio and repeatability of SFOAE measurements in a typical chinchilla ear. (a) Amplitudes of SFOAEs, evoked by tones presented at 30 dB SPL, plotted against frequency. The open circles indicate the initial measurements. The thick line indicates a second set of measurements in the same chinchilla, obtained between 14 and 66 min after the initial measurements. The thin line indicates the magnitudes of the baseline noise. (b) Phase versus frequency functions for the same measurements illustrated in panel (a). Initial (open circles) and repeat (solid line) phase measurements, with scale at left. Dashed line: detrended phase versus frequency curve, with scale at right. (c) Group delay as a function of frequency. The group delay at each frequency is the negative of the slope (i.e., first derivative) of phase with respect to frequency. The arrow heads indicate that amplitudes notches (a), π phase shifts (b), and maxima or minima in the group delay function (c) occur at the same frequencies.

gesting that SFOAEs are generated with delays that are nearly frequency independent. However, when the phase versus frequency measurements are detrended (dotted line) the phases are seen to undergo sharp shifts, amounting to about 180°, at the same frequencies [arrowheads in Fig. 3(b)] at which amplitude notches occur [arrowheads in Fig. 3(a)]. This is as expected for complete cancellation of equal-amplitude components. Sharp but smaller (<180°) phase shifts were also seen, corresponding to relatively shallow magnitude notches and probably indicating incomplete cancellation of two or more components with unequal amplitudes.

Figure 3(c) shows the group delays corresponding to the phase versus frequency curves of Fig. 3(b). The group delays (the negative slope of the phase versus frequency curve) were computed from phases of adjacent samples (intervals of 21.53 and 43.06 Hz for frequencies lower and higher than 2 kHz, respectively). Over much of the frequency range of measurements, group delays are fairly constant and amount to 1–2 ms. However, upward and downward spikes occur at the frequencies (arrowheads) of the sharp phase shifts seen in Fig. 3(b).

E. Variation of SFOAEs across animals

Figure 4(a) shows amplitude versus frequency curves for SFOAEs measured in 17 chinchillas using probe tones presented at 30 dB SPL. This relatively low stimulus level was chosen to match the stimulus level used for τ_{BMgroup} measurements and to approximate the levels for which CRF-theory predictions are most accurate (Shera and Guinan, 2003). [Previous comparisons of τ_{SFOAE}'s and τ_{BMgroup}'s, in guinea pig and cat, stimulated SFOAEs with probe tones presented at a higher level, 40 dB SPL (Shera and Guinan, 2003).] Figure 4(a) reveals that the prominent notches and other stable features of individual amplitude versus frequency curves [Fig. 3(a)] occurred at different frequencies in different subjects, causing substantial variability of SFOAE amplitudes at any given frequency across the subject population.

Figure 4(b) shows phase versus frequency curves for the same SFOAEs represented in Fig. 4(a). The phase versus frequency curves were roughly linear but counterparts of the phase jumps evident in detrended individual curves [e.g., Fig. 3(b)] can be detected in many curves.

The SFOAE group delays (τ_{SFOAE}'s) corresponding to the phase versus frequency curves of Fig. 4(b) are shown in Fig. 4(c) as a function of probe frequency (dots). At most frequencies, τ_{SFOAE}'s were largely confined within a band between 0.7 and 2 ms but there were also many outliers, caused mainly by the phase jumps corresponding to amplitude notches. As illustrated in Fig. 3, most of the between-animal variability in the group delays was the result of differences in the phase slopes that were repeatable within a particular animal and not due to random noise.

Figure 5 shows the mean of the SFOAE amplitude versus frequency curves, averaged across all 17 chinchillas (thick black line), plus/minus one standard deviation. The SFOAE amplitude curve was relatively flat above 4 kHz and exhibited a notch at around 3 kHz. Figure 5 also shows the mean plus/minus one standard deviation for the noise-floor curves of the individual subjects (gray line), demonstrating the wide separation between SFOAE amplitudes and the noise floors (20–30 dB) at all frequencies except those exhibiting deep notches [see Fig. 4(a)].

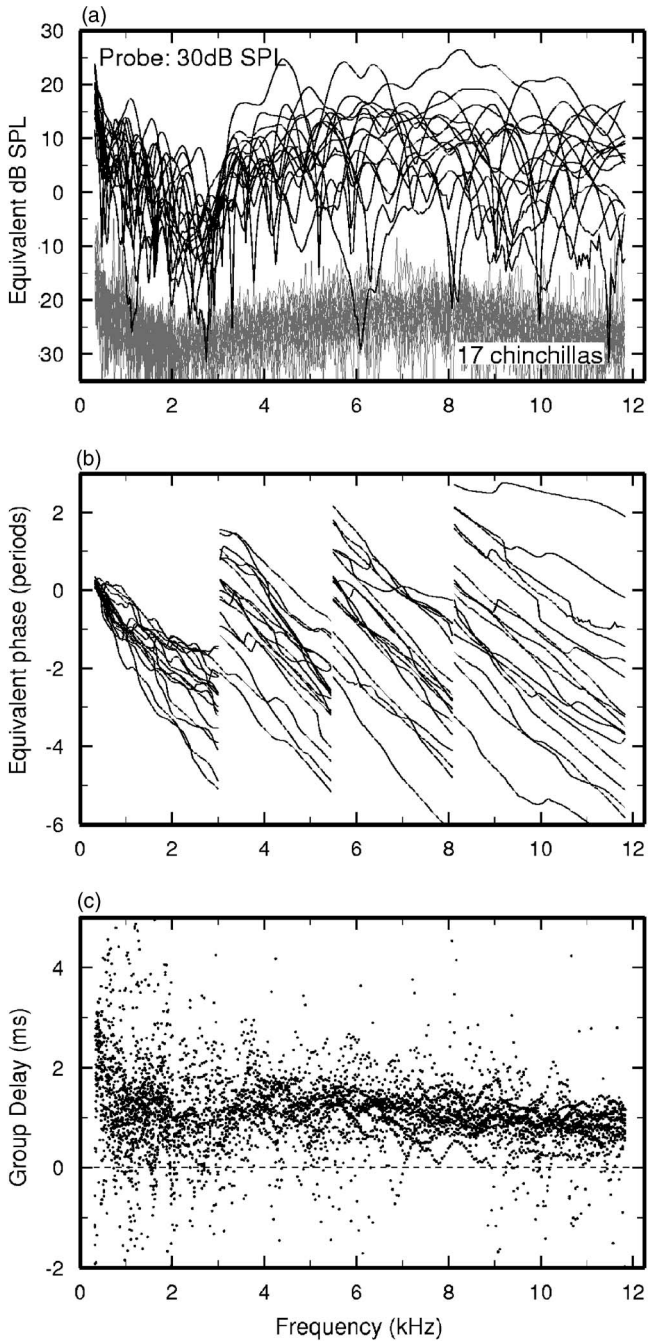

FIG. 4. Frequency dependence of the amplitudes and phases of SFOAEs in 17 chinchillas. (a) Amplitudes of SFOAEs evoked by tones presented at 30 dB SPL (thick traces). Magnitudes of baseline noise (thin traces). (b) Phase versus frequency functions for the same measurements. (c) Group delays for the same measurements. Some data points with extreme group-delay values are not shown.

F. Comparison of SFOAE and BM delays for the chinchilla cochlea

Figure 6 shows frequency-by-frequency averages (thick solid line) of the τ_{SFOAE}'s shown in Fig. 4(c), plotted against frequency. Figure 6 also includes a trend line for $\tau_{BMgroup}$'s in chinchilla (thin solid line), replotted from Fig. 2. At all frequencies, $\tau_{SFOAE} < 2\tau_{BMgroup}$, contradicting the delay prediction of the CRF theory. (According to the CRF theory, $\tau_{SFOAE} \approx 2\tau_{BMgroup}$.) Also contradicting the delay prediction of the CRF theory, τ_{SFOAE}'s and $\tau_{BMgroup}$'s differed substantially in their dependence on frequency: τ_{SFOAE}'s decreased only slightly and somewhat irregularly as a function of frequency whereas $\tau_{BMgroup}$'s decreased smoothly and monotonically from about 4.5 ms at 400 Hz to 0.7 ms at 18 kHz. Thus, $\tau_{SFOAE} \approx \tau_{BMgroup}$ at frequencies >3.5 kHz and $\tau_{SFOAE} < \tau_{BMgroup}$ at lower frequencies, with the difference between τ_{SFOAE} and $\tau_{BMgroup}$ growing larger as a function of decreasing frequency.

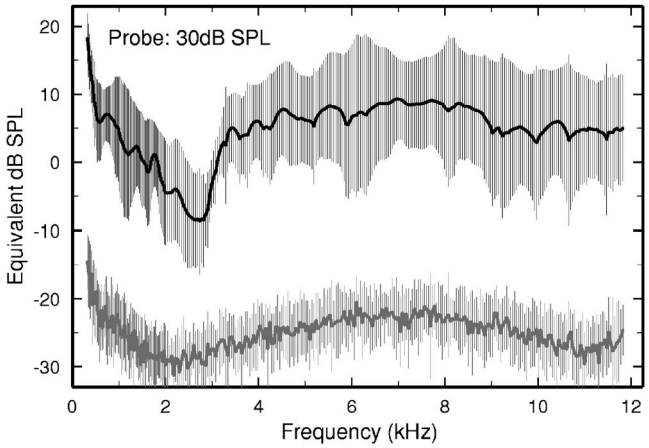

FIG. 5. Frequency dependence of the amplitudes of SFOAEs averaged across 17 chinchillas. Mean amplitudes of SFOAEs evoked by tones presented at 30 dB SPL (thick trace), computed from the 17 sets of SFOAE amplitudes illustrated in Fig. 4(a). Mean magnitudes of baseline noise (thin trace). The upper and lower envelopes of the vertical lines indicate, respectively, mean plus and mean minus one standard deviation.

Although Fig. 6 contradicts the delay prediction of the CRF theory, it does not rule out that SFOAEs propagate via retrograde BM waves that propagate at faster rates than those predicted by the CRF theory. Ruggero (2004) proposed an alternative hypothesis of OAE propagation via retrograde BM traveling waves founded on the view that forward BM travel time equals $\tau_{BMfront}$ (Ruggero, 1980) rather than

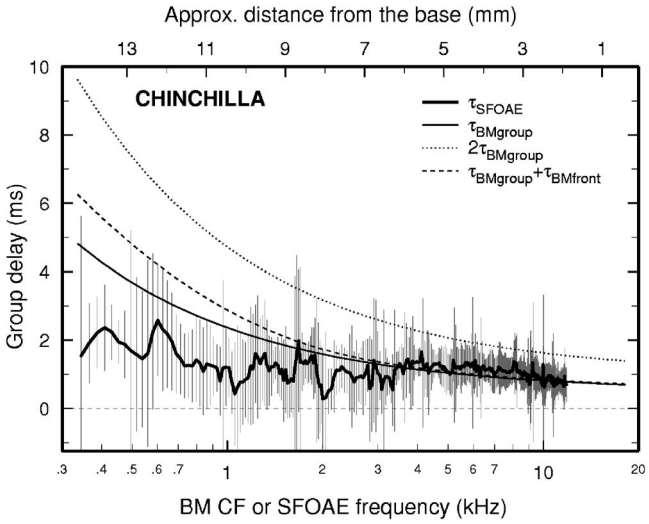

FIG. 6. Group delays of SFOAEs and cochlear vibrations in chinchilla. Comparison of measured τ_{SFOAE}'s (thick continuous line) with τ_{SFOAE}'s predicted by the CRF theory (dotted line; $\tau_{SFOAE} \approx 2\tau_{BMgroup}$), the signal-front hypothesis (dashed line; $\tau_{SFOAE} = \tau_{BMgroup} + \tau_{BMfront}$), and the acoustic-wave hypothesis (thin continuous line; $\tau_{SFOAE} \approx \tau_{BMgroup}$). The upper and lower envelopes of the vertical lines indicate, respectively, mean τ_{SFOAE} plus and minus one standard deviation.

$\tau_{BMgroup}$. On the assumption that forward travel time (from the stapes to the SFOAE generation site) and reverse travel time (from the SFOAE generation site to the stapes) are equal, the "signal-front hypothesis" ["hypothesis IA" of Ruggero (2004)] states that $\tau_{SFOAE}=2\tau_{BMfront}+\tau_{BMfilter}=2\tau_{BMfront}+(\tau_{BMgroup}-\tau_{BMfront})=\tau_{BMfront}+\tau_{BMgroup}$. Yet a third possibility is that SFOAEs do not propagate at all via "slow" BM displacement waves [and associated "slow" pressure waves (Olson, 1998; Robles and Ruggero, 2001)] but rather via "fast" acoustic waves in the cochlear fluids (Ren, 2004; Ruggero, 2004) or "instantaneous … fluid coupling between BM and stapes" (Nobili *et al.*, 2003). According to this "acoustic wave hypothesis" ["hypothesis III" of Ruggero (2004)], $\tau_{SFOAE}\approx\tau_{BMgroup}$. (This near-equality reflects the fact that sound propagates in the cochlear fluids faster, by orders of magnitude, than BM waves.)

The τ_{SFOAE}'s predicted by the signal-front hypothesis and the acoustic-wave hypothesis are illustrated in Fig. 6 (dashed and thin solid lines, respectively). For frequencies >4 kHz, τ_{SFOAE} is consistent with both the signal-front hypothesis ($\tau_{SFOAE}=\tau_{BMgroup}+\tau_{BMfront}$) and the acoustic-wave hypothesis ($\tau_{SFOAE}\approx\tau_{BMgroup}$). Below 4 kHz, however, $\tau_{SFOAE}<\tau_{BMgroup}$, a result inconsistent with the signal-front hypothesis, the acoustic-wave hypothesis, the CRF theory, and, in fact, any other hypothesis or theory postulating the origin of SFOAEs at a single cochlear place, i.e., the characteristic place for the SFOAE probe frequency.

IV. DISCUSSION

A. SFOAEs in chinchilla compared with those in cat, guinea pig, and humans

The present findings for SFOAEs in chinchilla are generally consistent with measurements of SFOAEs in guinea pig and cat (Shera and Guinan, 2003). In particular, the magnitudes of SFOAEs (Figs. 3–5) are roughly comparable, in relation to stimulus levels, in all three species (not shown). However, published studies from guinea pig or cat do not address the prevalence of the deep notches that are routinely found in chinchilla SFOAE magnitude versus frequency functions [Fig. 3(a)]. Such notches are predicted by the CRF theory as a consequence of mutual cancellation among wavelets reflected from mechanical irregularities in the region of the peak of the traveling wave (Zweig and Shera, 1995). However, the spacing of multiple notches in individual chinchillas appears to be quasi-periodic [Figs. 3(c) and 4(c)], a result presumably not predicted by the CRF theory. Nevertheless, a scatter plot illustrating τ_{SFOAE}'s from two guinea pigs [Fig. 1 of Shera and Guinan (2000)] exhibits quasi-periodic fluctuations in group delay and outliers reminiscent of those in chinchilla. Those fluctuations might indicate the presence of quasi-periodic amplitude notches in SFOAE amplitude versus frequency curves for guinea pig.

τ_{SFOAE}'s in guinea pig and cat are shown in Fig. 7 as functions of frequency (thick solid lines). Again, τ_{SFOAE}'s are similar in the three species, especially for high frequencies corresponding to the basal third of the cochlea. For lower frequencies, τ_{SFOAE}'s in cat [Fig. 7(b)] and guinea pig [Fig. 7(a)] are, respectively, slightly larger and smaller than in chinchilla (Fig. 6).

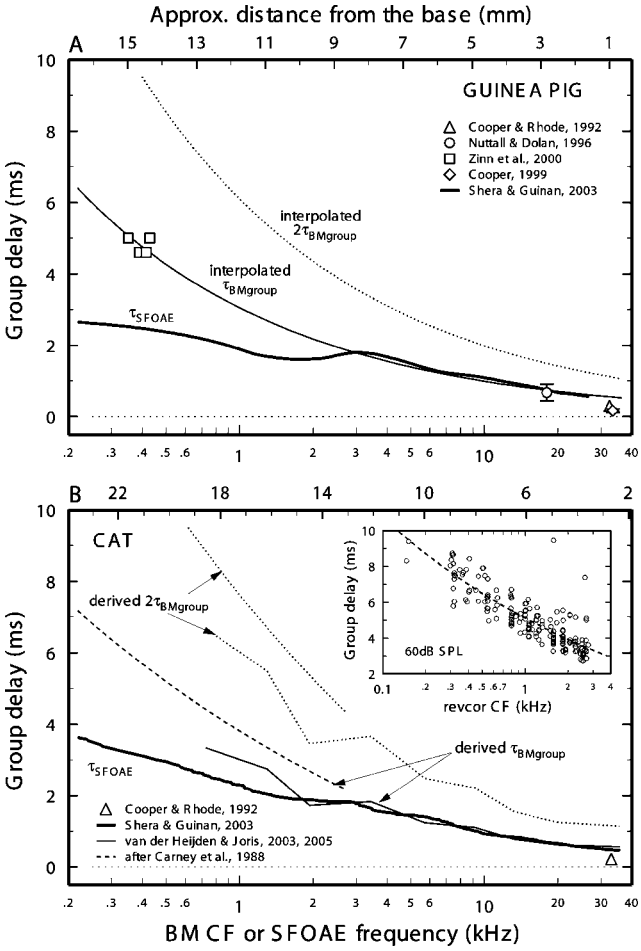

FIG. 7. Comparison of BM and SFOAE group delays for guinea pig and cat. (a) Guinea pig. Thick solid line: τ_{SFOAE}'s from Fig. 1 of Shera and Guinan (2003). Symbols: directly-measured $\tau_{BMgroup}$'s (Cooper, 1999; Cooper and Rhode, 1992; Nuttall and Dolan, 1996; Zinn *et al.*, 2000). Dashed line: $2\tau_{BMgroup}$. Thin solid line: a trend line illustrating an equation [$\tau_{BMgroup}(ms)=3.05^{*}CF_{(kHz)}^{-0.486}$] of the same form as the one summarizing $\tau_{BMgroup}$ for chinchilla in Fig. 6, fitted to the directly measured guinea pig $\tau_{BMgroup}$ (excepting measurements for CFs > 30 kHz). (b) Cat. Inset. Symbols and dashed line: group delays of revcors of ANF responses to noise. Revcors, measured by (Carney and Yin, 1988), were downloaded from Boston University's Earlab (http://earlab.bu.edu/). The revcor group delays for cat were computed with the same procedures used by (Temchin *et al.*, 2005) for chinchilla revcors and were time advanced by 0.3 ms to compensate for equipment and acoustic delays (Laurel Carney, personal communication). Main panel. Thick solid line: τ_{SFOAEs} from Fig. 1 of (Shera and Guinan, 2003). Thin dashed line: BM $\tau_{BMgroup}$'s obtained by subtracting 1 ms (i.e., neural/synaptic delays) from the trend line for revcor group delays (inset). Thin solid line: BM $\tau_{BMgroup}$'s derived from ANF responses to tonal complexes (van der Heijden and Joris, 2003; van der Heijden and Joris, 2005). Near-CF group delays were computed as grand averages for the 8 phase-vs.-frequency curves of Fig. 4C of (van der Heijden and Joris, 2003) and the mean group delays of Fig. 4B of (van der Heijden and Joris, 2005). Dotted lines: $2\tau_{BMgroup}$. Triangle: directly-measured $\tau_{BMgroup}$ (Cooper and Rhode, 1992).

τ_{SFOAE}'s in chinchilla, cat and guinea pig are much smaller than in humans (Shera and Guinan, 2003) or monkeys (Martin *et al.*, 1988). It is partly this difference that Shera and Guinan (2003) cited as the basis for their contention that the sharpness of cochlear frequency filtering is much greater in humans or monkeys than in other mammalian species. The present results dispute that conclusion to the extent that it depends on the assumption that $2\tau_{BMgroup}=\tau_{SFOAE}$ (Shera and Guinan, 2003).

B. The relationship between SFOAE and BM group delays for cat and guinea pig

The present comparison between τ_{SFOAE}'s and $\tau_{BMgroup}$'s for chinchilla are consistent with similar, but less complete, comparisons for guinea pig and cat (Fig. 7). Figure 7 was drafted using SFOAE and BM data culled from the literature. Figure 7(a) demonstrates that for SFOAEs of 300–400 Hz and 18 kHz in guinea pig, τ_{SFOAE}'s are much smaller than the $2\tau_{BMgroup}$'s estimated from direct BM or tectorial membrane measurements, thus contradicting the delay prediction of the CRF theory. The thin solid line in Fig. 7(a) illustrates an equation, of the same form as that used in Fig. 6 to indicate $\tau_{BMgroup}$ for chinchilla, interpolated between the directly measured $\tau_{BMgroup}$'s for guinea pig. For frequencies higher than 3 kHz, there is an excellent match between the fitted curve and the τ_{SFOAE}'s.

Figure 7(b) compares τ_{SFOAE}'s and $\tau_{BMgroup}$'s for cat. In addition to the $\tau_{BMgroup}$'s of directly measured BM vibrations (Cooper and Rhode, 1992), Fig. 7(b) shows $\tau_{BMgroup}$'s derived from the near-CF group delays of ANFs measured with two different methods. One set of data consists of revcors [first-order Wiener kernels (Recio-Spinoso *et al.*, 2005)] measured by (Carney and Yin, 1988). The revcor group delays for responses to noise presented at 60 dB SPL are plotted against CF in the inset of Fig. 7(b). The trend line in the inset, a least-squares fit, is reproduced in the main section of Fig. 7(b) after subtraction of 1 ms, the synaptic/neural delay (dashed line). The other set of cat data consists of $\tau_{BMgroup}$s (thin solid line) obtained with an ingenious technique which, like second-order Wiener-kernel analysis, takes advantage of nonlinearities to extract high-frequency timing information from the low-frequency envelopes of responses to high-frequency stimuli, in this case tonal complexes (van der Heijden and Joris, 2003, 2005). Over the entire range of comparison for the cat cochlea, 250 Hz to 30 kHz, the estimates of $\tau_{BMgroup}$ derived from responses of ANFs (van der Heijden and Joris, 2003, 2005) are similar to or larger than τ_{SFOAE}, contradicting the delay prediction of the CRF theory.

To summarize: in all three species in which comparisons are feasible (chinchilla, cat, and guinea pig), $\tau_{SFOAE} \leqslant \tau_{BMgroup}$ over most of the length of the cochlea (Figs. 3(b) and 4), contradicting the CRF theory, which predicts that $\tau_{SFOAE} \approx 2\tau_{BMgroup}$. In other words, the CRF theory errs considerably, by a factor $\geqslant 2$. A factor of 2 difference in τ is equivalent to 5.5 mm or more than 30% of the length of the chinchilla cochlea (measured as a horizontal distance in Fig. 6; see upper scale in Figs. 2 and 6).

C. BM and SFOAE group delays from the extreme base of the cochlea

At the extreme basal end of the cochlea (CFs >30 kHz in guinea pig [Fig. 7(a)] and cat [Fig. 7(b)], and >14 kHz in chinchilla (Fig. 2)), directly measured $\tau_{BMgroup}$'s are exceptionally short and, also exceptionally, consistent with the CRF-theory delay predictions. Taking into account that recordings of BM vibrations, in contrast with recordings of SFOAEs or from ANFs, require surgical invasion of the cochlea, often with traumatic effects, and that loss of cochlear sensitivity is typically accompanied by shortened $\tau_{BMgroup}$ [see review on p. 1336 of Robles and Ruggero (2001)], it is possible that the exceptionally short $\tau_{BMgroup}$'s of high-CF BM responses are artifacts of surgically induced trauma.

D. BM and SFOAE group delays from apical regions of the cochlea

For SFOAEs stimulated by tones with frequency <4 kHz, the errors of the CRF-theory prediction are even greater than the errors for frequencies >4 kHz. This relationship between low-frequency BM and SFOAE delays ($\tau_{SFOAE} < \tau_{BMgroup}$) is paradoxical, implying that SFOAEs emerge from the cochlea *before* they are generated at the sites "with CF equal to the stimulus frequency" (Shera and Guinan, 2003). Similar paradoxical relationships between SFOAE and BM delays were previously noted for apical regions of the guinea pig and cat cochleae (Shera and Guinan, 2003). Thus, the present results for low-frequency SFOAEs in chinchilla, as well as their counterparts in guinea pig and cat (Shera and Guinan, 2003), appear to contradict one of the fundamental premises of the CRF, namely that SFOAEs originate at the sites where the BM traveling waves reach their peaks (Shera and Zweig, 1993; Zweig and Shera, 1995). Shera and Guinan attributed the "apparent breakdown (of the CRF theory) in the apex of the cochlea" to a breakage of "scaling symmetry," the property whereby "transfer functions … measured at nearby locations overlie one another when plotted as a function of normalized frequency f/f_{CF}, where f_{CF} is the characteristic frequency" [pp. 2767–2768 of Shera and Guinan (2003)]. However, Shera and Guinan did not address the theoretical implications of the breakage of scaling symmetry.

E. Alternatives to the CRF theory

Although the present results contradict one of the major predictions of the CRF theory (i.e., that $\tau_{SFOAE} \approx 2\tau_{BMgroup}$), they do not address directly the reflection mechanism of the CRF theory *per se*. Thus, it is possible that the CRF theory can be modified to take into account the present findings while retaining the reflection mechanism (Shera *et al.*, 2005).

The present findings for basal regions (where $\tau_{SFOAE} \approx \tau_{BMgroup}$) are consistent with hypotheses positing very fast backward propagation of SFOAEs and distortion-product OAEs (DPOAEs) in the cochlea [(Nobili *et al.*, 2003; Ren, 2004; Ruggero, 2004; Wilson, 1980), but see also Shera *et al.* (2004)]. The first such hypothesis was put forth by Pat Wilson to explain his finding that relatively low-frequency SFOAEs and their correlates in the cochlear microphonics occurred essentially simultaneously, making it unlikely that SFOAEs reach the middle ear via a backward (but otherwise conventional) BM traveling wave (Wilson, 1980) (see also Rutten, 1980). Later it was noted [see p. 2397 of Robles *et al.*, (1997) and pp. 583–585 of Gummer *et al.* (2003)] that acoustic propagation of DPOAEs is likely in frog ears, which produce such emissions (van Dijk and Manley, 2001) but lack BMs (Geisler *et al.*, 1964) and in gerbil and chinchilla, in which the delays of DPOAEs and BM vibration at the f_2 site are identical in individual ears (Narayan *et al.*, 1998a;

Ren, 2004; Ruggero, 2004; Gong *et al.*, 2005). The present conclusions, questioning the existence of backward "slow" traveling waves on the basis of SFOAE measurements, are more strongly founded than previous similar conclusions based on DPOAEs (Gong *et al.*, 2005; Ren, 2004; Ruggero, 2004): criteria for testing hypotheses of DPOAE propagation do not exist (Knight and Kemp, 2001; Shera *et al.*, 2000; Shera and Guinan, 1999; Tubis *et al.*, 2000), whereas the CRF theory spells out a specific and crucial prediction (i.e., $\tau_{\mathrm{SFOAE}} \approx 2\tau_{\mathrm{BMgroup}}$) which we have shown to be incorrect. The present results are also more definitive than those of previous tests of the mode of propagation of DPOAEs which were based on BM motion at a single cochlear site (Narayan *et al.*, 1998a; Ren, 2004). In contrast, the present comparisons of SFOAEs and BM delays span the entire length of the chinchilla cochlea (Fig. 6) as well as several regions of the guinea pig and cat cochleae (Fig. 7).

Although our results at the base of the cochlea might be consistent with a modified version of the CRF theory incorporating a faster version of the reflection mechanism, results for the apical region of the cochlea may demand a different mechanism altogether. We propose that SFOAEs can be explained with a single mechanism if the emissions originate from sources (or generators) that are widely distributed along the length of the cochlea near and basal to the peak of the traveling wave. These sources should undergo spatial summation in basal (long-wavelength) cochlear regions, and strong cancellation near the peak or apical (short-wavelength) region of the forward BM traveling wave, thus deemphasizing long-latency contributions and emphasizing short latency contributions. The general trend in the emission phase would be established either by sources in the short-wave or long-wave region, depending on the relative magnitudes of the net contribution to the total SFOAE from the two regions. The consistently observed reduction of τ_{SFOAE} below τ_{BMgroup} at frequencies below 3–4 kHz would presumably reflect relatively larger contributions from the short-wave region. For higher frequencies, sources closer to the peak are presumably relatively larger. Combining emission-generator vectors with a phase profile that changes progressively more rapidly with distance from the long-wave region into the short wave region could lead to amplitude notches paired with corresponding phase shifts, such as we have found [Figs. 3(a) and 3(b)]. Properties of cochlear mechanics would be required to change sufficiently with distance to produce a large enough deviations from scaling symmetry to account for the observed SFOAE phase and corresponding group delays (Shera and Guinan, 2003).

ACKNOWLEDGMENTS

Special thanks to Steve Neely for providing the *EMAV* software. This work was also aided by comments on previous versions of the paper by Mary Ann Cheatham, Nigel Cooper, Peter Dallos, Sumitrajit Dhar, Luis Robles, and Chris Shera, support from an NIH grant to MAR, and from the Netherlands Organization for Scientific Research (NWO) and the Heinsius Houbolt Foundation to PVD.

Brass, D., and Kemp, D. T. (**1993**). "Suppression of stimulus frequency otoacoustic emissions," J. Acoust. Soc. Am. **93**, 920–939.

Brillouin, L. (**1960**). *Wave Propagation and Group Velocity* (Academic, New York).

Brown, M. C., Smith, D. I., and Nuttall, A. L. (**1983**). "Anesthesia and surgical trauma: their influence on the guinea pig compound action potential," Hear. Res. **10**, 345–358.

Carney, L. H., and Yin, T. C. (**1988**). "Temporal coding of resonances by low-frequency auditory nerve fibers: single-fiber responses and a population model," J. Neurophysiol. **60**, 1653–1677.

Cooper, N. P. (**1997**). "Mid-band sensitivity notches in apical cochlear mechanics," in *Diversity in Auditory Mechanics*, edited by E. R. Lewis, G. R. Long, R. F. Lyon, P. M. Narins, C. R. Steele, and E. Hecht-Poinar (World Scientific, Singapore), pp. 298–304.

Cooper, N. P. (**1999**). "Vibration of beads placed on the basilar membrane in the basal turn of the cochlea," J. Acoust. Soc. Am. **106**, L59–L64.

Cooper, N. P., and Rhode, W. S. (**1992**). "Basilar membrane mechanics in the hook region of cat and guinea-pig cochleae: sharp tuning and nonlinearity in the absence of baseline position shifts," Hear. Res. **63**, 163–190.

Cooper, N. P., and Rhode, W. S. (**1996**). "Fast traveling waves, slow travelling waves and their interactions in experimental studies of apical cochlear mechanics," Aud. Neurosci. **2**, 289–299.

Cooper, N. P., and Shera, C. A. (**2004**). "Backward traveling waves in the cochlea?" Assoc. Res. Otolaryngol. Mid-Winter Meet. Abst. **27**, 342.

Dallos, P. (**1992**). "The active cochlea," J. Neurosci. **12**, 4575–4585.

de Boer, E., and Nuttall, A. L. (**1996**). "Cochlear travel time and minimum phase," Assoc. Res. Otolaryngol. Mid-Winter Meet. Abst. **19**, 57.

Dreisbach, L. E., Siegel, J. H., and Chen, W. (**1998**). "Vector decomposition of distortion product otoacoustic emission sources in humans," Assoc. Res. Otolaryngol. Mid-Winter Meet. Abst. **21**, 87.

Geisler, C. D., van Bergeik, W. A., and Frishkopf, L. S. (**1964**). "The inner ear of the bullfrog," J. Morphol. **114**, 43–57.

Goldstein, J. L., Baer, T., and Kiang, N. Y. S. (**1971**). "A theoretical treatment of latency, group delay and tuning. Characteristics for auditory nerve responses to clicks and tones," in *The Physiology of the Auditory System*, edited by M. B. Sachs (National Educational Consultants, Baltimore), pp. 133–141.

Gong, Q., Temchin, A. N., Siegel, J. H., and Ruggero, M. A. (**2005**). "Similarity of group delays of basilar-membrane vibrations and distortion-product otoacoustic emissions in chinchilla," Assoc. Res. Otolaryngol. Mid-Winter Meet. Abst. **28**, 113.

Goodman, S. S., Withnell, R. H., and Shera, C. A. (**2003**). "The origin of SFOAE microstructure in the guinea pig," Hear. Res. **183**, 7–17.

Goodman, S. S., Withnell, R. H., de Boer, E., Lilly, D. J., and Nuttall, A. L. (**2004**). "Cochlear delays measured with amplitude-modulated tone-burst-evoked OAEs," Hear. Res. **188**, 57–69.

Greenwood, D. D. (**1990**). "A cochlear frequency-position function for several species—29 years later," J. Acoust. Soc. Am. **87**, 2592–2605.

Guinan, J. J., Jr. (**1990**). "Changes in stimulus frequency otoacoustic emissions produced by two-tone suppression and efferent stimulation in cats," in *Mechanics and Biophysics of Hearing*, edited by P. Dallos, C. D. Geisler, J. W. Matthews, M. A. Ruggero, and C. R. Steele (Springer-Verlag, Berlin), pp. 170–177.

Guinan, J. J., Jr., Backus, B. F., Lilaonitkul, W., and Aharonson, V. (**2003**). "Medial olivocochlear efferent reflex in humans: otoacoustic emission (OAE) measurement issues and the advantages of stimulus frequency OAEs," J. Assoc. Res. Otolaryngol. **4**, 521–540.

Gummer, A. W., Dalhoff, E., Nowotny, M., and Scherer, M. P. (**2003**). *Biophysics of the Cochlea: From Molecules to Models* (World Scientific Publishing, Singapore).

Hudspeth, A. J. (**1997**). "Mechanical amplification of stimuli by hair cells," Curr. Opin. Neurobiol. **7**, 480–486.

Kemp, D. T. (**1978**). "Stimulated acoustic emissions from within the human auditory system," J. Acoust. Soc. Am. **64**, 1386–1391.

Kemp, D. T., and Chum, R. A. (**1980**). "Observations on the generator mechanism of stimulus frequency acoustic emissions—Two tone suppression," in *Psychophysical, Physiological and Behavioral Studies in Hearing*, edited by G. van den Brink and F. A. Bilsen (Delft University Press, Delft), pp. 34–42.

Knight, R. D., and Kemp, D. T. (**2001**). "Wave and place fixed DPOAE maps of the human ear," J. Acoust. Soc. Am. **109**, 1513–1525.

Konrad-Martin, D., and Keefe, D. H. (**2003**). "Time-frequency analyses of transient-evoked stimulus-frequency and distortion-product otoacoustic emissions: testing cochlear model predictions," J. Acoust. Soc. Am. **114**,

2021–2043.
Lineton, B., and Lutman, M. E. (**2003**). "The effect of suppression on the periodicity of stimulus frequency otoacoustic emissions: experimental data," J. Acoust. Soc. Am. **114**, 871–882.
Manley, G. A. (**2001**). "Evidence for an active process and a cochlear amplifier in nonmammals," J. Neurophysiol. **86**, 541–549.
Martin, G. K., Lonsbury-Martin, B. L., Probst, R., and Coats, A. C. (**1988**). "Spontaneous otoacoustic emissions in a nonhuman primate. I. Basic features and relations to other emissions," Hear. Res. **33**, 49–68.
Mauermann, M., Uppenkamp, S., van Hengel, P. W., and Kollmeier, B. (**1999**). "Evidence for the distortion product frequency place as a source of distortion product otoacoustic emission (DPOAE) fine structure in humans. II. Fine structure for different shapes of cochlear hearing loss," J. Acoust. Soc. Am. **106**, 3484–3491.
Narayan, S. S., and Ruggero, M. A. (**2000**). "Basilar-membrane mechanics at the hook region of the chinchilla cochlea," in *Recent Developments in Auditory Mechanics*, edited by H. Wada, T. Takasaka, K. Ikeda, K. Ohyama, and T. Koike (World Scientific, Singapore), pp. 95–101.
Narayan, S. S., Recio, A., and Ruggero, M. A. (**1998a**). "Cubic distortion products at the basilar membrane and in the ear canal of chinchillas," Assoc. Res. Otolaryngol. Mid-Winter Meet. Abst. **21**, 181.
Narayan, S. S., Temchin, A. N., Recio, A., and Ruggero, M. A. (**1998b**). "Frequency tuning of basilar membrane and auditory nerve fibers in the same cochleae," Science **282**, 1882–1884.
Neely, S. T., and Liu, Z. (**1993**). "EMAV: Otoacoustic emission averager," Technical Memo, Boys Town National Research Hospital, Omaha, NE.
Nobili, R., Vetesnik, A., Turicchia, L., and Mammano, F. (**2003**). "Otoacoustic emissions from residual oscillations of the cochlear basilar membrane in a human ear model," J. Assoc. Res. Otolaryngol. **4**, 478–494.
Nuttall, A. L., and Dolan, D. F. (**1996**). "Steady-state sinusoidal velocity responses of the basilar membrane in guinea pig," J. Acoust. Soc. Am. **99**, 1556–1565.
Olson, E. S. (**1998**). "Observing middle and inner ear mechanics with novel intracochlear pressure sensors," J. Acoust. Soc. Am. **103**, 3445–3463.
Papoulis, A. (**1962**). *The Fourier Integral and its Applications* (McGraw-Hill, New York).
Recio, A., and Rhode, W. S. (**2000**). "Basilar membrane responses to broadband stimuli," J. Acoust. Soc. Am. **108**, 2281–2298.
Recio, A., Narayan, S. S., and Ruggero, M. A. (**1997**). "Wiener-kernel analysis of basilar-membrane responses to white noise," in *Diversity in Auditory Mechanics*, edited by E. R. Lewis, G. R. Long, R. F. Lyon, P. M. Narins, C. R. Steele, and E. Hecht-Poinar (World Scientific, Singapore), pp. 325–331.
Recio, A., Rich, N. C., Narayan, S. S., and Ruggero, M. A. (**1998**). "Basilar-membrane responses to clicks at the base of the chinchilla cochlea," J. Acoust. Soc. Am. **103**, 1972–1989.
Recio-Spinoso, A., Temchin, A. N., van Dijk, P., Fan, Y.-H., and Ruggero, M. A. (**2005**). "Wiener-kernel analysis of responses to noise of chinchilla auditory-nerve fibers," J. Neurophysiol. **93**, 3615–3634.
Ren, T. (**2004**). "Reverse propagation of sound in the gerbil cochlea," Nat. Neurosci. **7**, 333–334.
Rhode, W. S., and Recio, A. (**2000**). "Study of mechanical motions in the basal region of the chinchilla cochlea," J. Acoust. Soc. Am. **107**, 3317–3332.
Robinette, M. S., and Glattke, T. J. (**2002**). *Otoacoustic Emissions: Clinical Applications* (Thieme, New York).
Robles, L., and Ruggero, M. A. (**2001**). "Mechanics of the mammalian cochlea," Physiol. Rev. **81**, 1305–1352.
Robles, L., Ruggero, M. A., and Rich, N. C. (**1997**). "Two-tone distortion on the basilar membrane of the chinchilla cochlea," J. Neurophysiol. **77**, 2385–2399.
Ruggero, M. A. (**1980**). "Systematic errors in indirect estimates of basilar membrane travel times," J. Acoust. Soc. Am. **67**, 707–710.
Ruggero, M. A. (**1994**). "Cochlear delays and traveling waves: comments on 'Experimental look at cochlear mechanics'," Audiology **33**, 131–142.
Ruggero, M. A. (**2004**). "Comparison of group delays of 2f1-f2 distortion product otoacoustic emissions and cochlear travel times," ARLO **5**, 143–147.
Ruggero, M. A., and Rich, N. C. (**1987**). "Timing of spike initiation in cochlear afferents: dependence on site of innervation," J. Neurophysiol. **58**, 379–403.
Ruggero, M. A., and Rich, N. C. (**1991**). "Furosemide alters organ of corti mechanics: evidence for feedback of outer hair cells upon the basilar membrane," J. Neurosci. **11**, 1057–1067.
Ruggero, M. A., Narayan, S. S., Temchin, A. N., and Recio, A. (**2000**). "Mechanical bases of frequency tuning and neural excitation at the base of the cochlea: comparison of basilar-membrane vibrations and auditory-nerve-fiber responses in chinchilla," Proc. Natl. Acad. Sci. U.S.A. **97**, 11744–11750.
Ruggero, M. A., Rich, N. C., Recio, A., Narayan, S. S., and Robles, L. (**1997**). "Basilar-membrane responses to tones at the base of the chinchilla cochlea," J. Acoust. Soc. Am. **101**, 2151–2163.
Rutten, W. L. C. (**1980**). "Latencies of stimulated acoustic emissions in normal human ears," in *Psychophysical, Physiological and Behavioural Studies in Hearing*, edited by G. van den Brink and F. A. Bilsen (Delft U.P., Delft, The Netherlands), pp. 68–71.
Shera, C. A., and Guinan, J. J., Jr. (**1999**). "Evoked otoacoustic emissions arise by two fundamentally different mechanisms: a taxonomy for mammalian OAEs," J. Acoust. Soc. Am. **105**, 782–798.
Shera, C. A., and Guinan, J. J., Jr. (**2000**). "Frequency dependence of stimulus-frequency-emission phase: implications for cochlear mechanics," in *Recent Developments in Auditory Mechanics*, edited by H. Wada, T. Takasaka, K. Ikeda, K. Ohyama, and T. Koike (World Scientific, Singapore), pp. 381–387.
Shera, C. A., and Guinan, J. J. (**2003**). "Stimulus-frequency-emission group delay: A test of coherent reflection filtering and a window on cochlear tuning," J. Acoust. Soc. Am. **113**, 2762–2772.
Shera, C. A., and Zweig, G. (**1993**). "Order from chaos: resolving the paradox of periodicity in evoked otoacoustic emissions," in *Biophysics of Hair Cell Sensory Systems*, edited by H. Duifhuis, J. W. Horst, P. van Dijk, and S. M. van Netten (World Scientific, Singapore), pp. 54–60.
Shera, C. A., Guinan, J. J., and Oxenham, A. J. (**2002**). "Revised estimates of human cochlear tuning from otoacoustic and behavioral measurements," Proc. Natl. Acad. Sci. U.S.A. **99**, 3318–3323.
Shera, C. A., Talmadge, C. L., and Tubis, A. (**2000**). "Interrelations among distortion-product phase-gradient delays: their connection to scaling symmetry and its breaking," J. Acoust. Soc. Am. **108**, 2933–2948.
Shera, C. A., Tubis, A., and Talmadge, C. L. (**2004**). "Do forward- and backward-traveling waves occur within the cochlea? Countering the critique of Nobili *et al.*," J. Assoc. Res. Otolaryngol. **5**, 349–359.
Shera, C. A., Tubis, A., and Talmadge, C. L. (**2005**). "Coherent-reflection models of reflection-source OAEs with and without slow transverse retrograde waves," Assoc. Res. Otolaryngol. Mid-Winter Meet. Abst. **28**, 231.
Shore, S. E., and Nuttall, A. L. (**1985**). "The effects of cochlear hypothermia on compound action potential tuning," J. Acoust. Soc. Am. **77**, 590–598.
Siegel, J. H. (**2002**). "Calibration of Otoacoustic Emission Probes," in *Otoacoustic Emissions: Clinical Applications*, edited by M. S. Robinette and T. J. Glattke (Thieme, New York), pp. 416–441.
Siegel, J. H., Cerka, A. J., Recio-Spinoso, A., Temchin, A. N., van Dijk, P., and Ruggero, M. A. (**2005**). "Map of basilar-membrane delays reveals fast exit of stimulus-frequency otoacoustic emissions from the chinchilla cochlea," Assoc. Res. Otolaryngol. Mid-Winter Meet. Abst. **28**, 232.
Talmadge, C. L., Tubis, A., Long, G. R., and Piskorski, P. (**1998**). "Modeling otoacoustic emission and hearing threshold fine structures," J. Acoust. Soc. Am. **104**, 1517–1543.
Temchin, A. N., Recio-Spinoso, A., van Dijk, P., and Ruggero, M. A. (**2005**). "Wiener kernels of chinchilla auditory-nerve fibers: verification using responses to tones, clicks and frozen noise and comparison to basilar-membrane vibrations," J. Neurophysiol. **93**, 3635–3648.
Tubis, A., Talmadge, C. L., and Tong, C. (**2000**). "Modeling the temporal behavior of distortion product otoacoustic emissions," J. Acoust. Soc. Am. **107**, 2112–2127.
van der Heijden, M., and Joris, P. X. (**2003**). "Cochlear phase and amplitude retrieved from the auditory nerve at arbitrary frequencies," J. Neurosci. **23**, 9194–9198.
van der Heijden, M., and Joris, P. X. (**2005**). "The speed of auditory low-side suppression," J. Neurophysiol. **93**, 201–209.
van Dijk, P., and Manley, G. A. (**2001**). "Distortion product otoacoustic emissions in the tree frog Hyla cinerea," Hear. Res. **153**, 14–22.
Wilson, J. P. (**1980**). "Model for cochlear echoes and tinnitus based on an observed electrical correlate," Hear. Res. **2**, 527–532.
Zinn, C., Maier, H., Zenner, H., and Gummer, A. W. (**2000**). "Evidence for active, nonlinear, negative feedback in the vibration response of the apical region of the *in vivo* guinea-pig cochlea," Hear. Res. **142**, 159–183.
Zweig, G., and Shera, C. A. (**1995**). "The origin of periodicity in the spectrum of evoked otoacoustic emissions," J. Acoust. Soc. Am. **98**, 2018–2047.

An analysis of the impact of auditory-nerve adaptation on behavioral measures of temporal integration in cochlear implant recipients[a)]

Marcia J. Hay-McCutcheon[b)]
Department of Speech Pathology and Audiology, University of Iowa, Iowa City, Iowa 52242

Carolyn J. Brown and Paul J. Abbas
Department of Speech Pathology and Audiology, and Department of Otolaryngology—Head and Neck Surgery, University of Iowa, Iowa City, Iowa 52242

(Received 3 April 2005; revised 19 July 2005; accepted 21 July 2005)

The objective of this study was to determine the impact that auditory-nerve adaptation has on behavioral measures of temporal integration in Nucleus 24 cochlear implant recipients. It was expected that, because the auditory nerve serves as the input to central temporal integrator, a large degree of auditory-nerve adaptation would reduce the amount of temporal integration. Neural adaptation was measured by tracking amplitude changes of the electrically evoked compound action potential (ECAP) in response to 1000-pps biphasic pulse trains of varying durations. Temporal integration was measured at both suprathreshold and threshold levels by an adaptive procedure. Although varying degrees of neural adaptation and temporal integration were observed across individuals, results of this investigation revealed no correlation between the degree of neural adaptation and psychophysical measures of temporal integration. © *2005 Acoustical Society of America.* [DOI: 10.1121/1.2035593]

PACS number(s): 43.64.Me, 43.64.Pg, 43.66.Lj [BLM] Pages: 2444–2457

I. INTRODUCTION

It has been stated that one of the most significant and puzzling problems facing the field of neuroscience today is determining the link between neuronal activity and sensory perception (Parker and Newsome, 1998). This problem has been addressed recently in studies that have examined the impact that high-rate electrical stimulation has upon both neuronal activity and the perception of those stimuli. Specifically, several investigators have reported evidence of adaptation in both single unit and whole-nerve auditory fibers when using high-rate electrical stimuli (Abbas *et al.*, 2001; Killian *et al.*, 1994; Litvak *et al.*, 2001; van den Honert and Stypulkowski, 1987; Wilson *et al.*, 1997b). Additionally, it has been shown that cochlear implant recipients experience decay in the loudness of high-rate pulse trains (i.e., 5000 pps) within minutes of onset of stimulation (Hong and Rubinstein, 2003; Hong *et al.*, 2003). The rate of change in loudness of these stimuli has been shown to have a time course that is similar to the time course of adaptation observed for single neurons and whole-nerve activity (Abbas *et al.*, 2001; Hong and Rubinstein, 2003; Litvak *et al.*, 2001; Wilson *et al.*, 1997b).

The exact mechanisms responsible for the decreased loudness of a high-rate pulse train that is experienced by cochlear implant recipients is not known, but it has been hypothesized that decreased auditory-nerve activity associated with high-rate stimuli may be partially responsible (Hong and Rubinstein, 2003). When rapid rates of stimulation are used, auditory-nerve adaptation might have an impact upon the perceived loudness of that signal, thereby suggesting a link between peripheral neural activity and perception. The decrease in auditory-nerve activity associated with high-rate stimuli could affect higher order processes such as temporal integration. A degraded auditory-nerve output could impact the processing of duration information at the central level, which could subsequently lead to poorer temporal integration.

Previous research has suggested that the processing of temporal information occurs primarily in the central, as opposed to the peripheral, auditory system (Relkin and Turner, 1988; Shannon, 1989, 1990, 1993; Shannon and Otto, 1990; Turner *et al.*, 1994). In a series of experiments by Shannon (1989; 1990; 1993) and Shannon and Otto (1990), it was revealed that the time course of forward masking, temporal integration functions, and gap-detection thresholds were similar for normal-hearing individuals, cochlear implant recipients, and auditory brainstem implant recipients after loudness was normalized across these different groups of listeners. It was concluded, therefore, that the mechanisms responsible for these phenomena are situated primarily in the central auditory pathway. Additionally, Relkin and Turner (1988) and Turner, Relkin, and Doucet (1994) presented data suggesting that the degree of forward masking at the level of the auditory nerve in chinchillas was minor in comparison to the degree of forward masking measured behaviorally in normal-hearing individuals. Direct comparison of physi-

[a)]Portions of this article were presented at the 2004 VIII International Cochlear Implant Conference in Indianapolis, IN.
[b)]Current address: Indiana University Medical Center, Department of Otolaryngology—HNS, Indianapolis, IN.

ological measures of forward masking and psychophysical measures of temporal processing in humans, however, is not available.

A number of published studies have shown that the largest decrease of auditory-nerve activity in response to rapid rate stimuli occurs within the first few milliseconds after stimulus onset for cochlear implant recipients (Abbas *et al.*, 2001; Wilson *et al.*, 1997a; 1997b). Wilson *et al.* (1997b) demonstrated that, when using a 1016-pps stimulus, the amplitude of the electrical compound action potential (ECAP) rapidly declined within the first few milliseconds of stimulus presentation, and this decrease was subsequently followed by a more gradual decline of neural activity occurring up to 30 ms. This decrease in amplitude also showed an alternating pattern largely thought to result from the effects of refractoriness (Abbas *et al.*, 2001; Finley *et al.*, 1997; Matsuoka *et al.*, 2000; Wilson *et al.*, 1997a). Specifically, when the period of time between pulse presentations was less than approximately 3 or 4 ms (i.e., the time period for total neural recovery from the response to a single pulse), the probability that some of the neurons in the auditory nerve would be in a refractory state, and therefore unable to fire to each pulse in the train, was increased (Finley *et al.*, 1997; Matsuoka *et al.*, 2000). As a result, the amplitude of the ECAP to the first pulse in a train would be large but the amplitude to the second pulse would be reduced. Generally, neurons that were refractory for one pulse presentation would recover and be excitable for the following pulse in a pulse train, resulting in a pattern of ECAP amplitude alternation between small and large amplitudes across pulse presentations (Wilson *et al.*, 1997a; 1997b). Wilson, *et al.* (1997a) observed that the degree of alternation and the alternation pattern were variable across individual cochlear implant recipients.

Because the response of the auditory nerve is the input to the central auditory system, the goal of this study was to examine auditory-nerve adaptation in cochlear implant recipients and to determine its impact upon behavioral measures of temporal integration. Temporal integration may be defined as a reduction in behavioral threshold that occurs with increasing signal duration. It is thought to occur either because the auditory system acts as a long-term integrator of energy and/or of neural events over a 20-to 200-ms time window (Plomp and Bouman, 1959; Zwislocki, 1960), and/or the result of a number of or multiple "looks" at the signal over a short time period (i.e., approximately 3 ms) (Viemeister and Wakefield, 1991). Each "look" is stored in short-term memory to be used by the listener in the decision-making process of signal detection. A greater number of looks would imply that the signal would be detected with greater ease. For purposes of this study, it was assumed that decreased behavioral thresholds resulted from the long-term integration of energy.

The decrease in behavioral threshold with increasing stimulus duration has been shown to be almost a linear relationship for normal-hearing listeners (Green *et al.*, 1957; Plomp and Bouman, 1959; Zwislocki, 1960) and a nonlinear relationship for cochlear implant recipients (Donaldson *et al.*, 1997; Shannon, 1983). That is, for normal-hearing listeners the slope of the temporal integration function is approximately −3-dB/doubling of signal duration for signals that range in duration from approximately 20 to 200 ms. Much shallower temporal integration functions have been observed for cochlear implant recipients (Donaldson *et al.*, 1997; Shannon, 1983). Donaldson *et al.* (1997) reported that some cochlear implant recipients showed very little temporal integration as a 100-pps biphasic monopolar pulse train was increased in duration. Other participants in their study showed large amounts of temporal integration for this same stimulus. The mean slope of the temporal integration function across 21 electrodes in eight study participants was −0.42-dB/doubling of signal duration with a range from −0.06-dB/doubling to −1.94-dB/doubling. The data from Shannon (1983) showed temporal integration function slopes of approximately −2-dB/doubling across seven electrodes for two subjects using a 1000-Hz tone-burst stimulus. In this same study, the effects of temporal integration were also observed when suprathreshold, rather than threshold level stimuli, were used. Specifically, for two cochlear implant recipients, the subjective loudness ratings of a 1000-Hz tone burst with constant amplitude increased as the duration of the tone burst increased. The differences in temporal integration functions between normal-hearing listeners and cochlear implant recipients has been thought to be the result of the loss of peripheral compressive nonlinearity and spontaneous neural activity associated with hearing impairment and electrical stimulation (Carlyon *et al.*, 1990; Moore, 2003).

In light of the recent findings revealing that the perception of high-rate stimuli decays over time in cochlear implant recipients, and also that auditory-nerve adaptation occurs in response to stimuli presented at rates faster than approximately 300 pps (Wilson *et al.*, 1997a; 1997b), assessing the impact that peripheral activity has upon behavioral responses seems warranted. The overall objective of this study, therefore, was to assess the impact that peripheral auditory-nerve adaptation has on behavioral measures of temporal integration in cochlear implant recipients. Zeng and Shannon (1994) have suggested that the growth of loudness occurs exponentially for sinusoidal stimuli or for pulses presented above 300 Hz or 300 pps, and logarithmically for frequencies less than 300 Hz or 300 pps. In their model, the output from the auditory nerve impacts the output from higher order processing stages to the final behavioral response generated centrally. It would seem possible, therefore, that an adapted input to the central integrator would generate temporal integration functions that would be quite different from temporal integration functions generated from an auditory nerve that was minimally adapted. If auditory-nerve adaptation affects temporal integration, then poor temporal integration would be associated with large degrees of auditory-nerve adaptation.

II. METHODS

A. Experiment 1: Recording ECAP waveforms using pulse trains

1. Subjects

Eleven postlingually deafened adults who received either Cochlear Corporation's Nucleus CI24M (seven indi-

viduals) or CI24R (four individuals) cochlear implant at the University of Iowa Hospitals and Clinics participated in this experiment and in experiments 2 and 3. The participants ranged in age from 38 to 63 years old (mean 51 years), the length of cochlear implant use ranged from 1 to 6 years (mean 3.6 years), and the duration of deafness prior to implantation ranged from 0.2 to 35 years (mean 7.4 years). All participants experienced an uneventful surgery and all had a fully inserted electrode array. Impedance telemetry levels for each electrode were within normal limits (i.e., <20 kilo -ohms) as determined using Cochlear Corporation's WINDPS software version R116.02.

2. Recording ECAP waveforms to single pulses and pulse trains

Cochlear Corporation's NEURAL RESPONSE TELEMETRY (NRT) software version 3.0 was used to obtain individual ECAP waveforms. In order to record single-pulse ECAP waveforms that are not contaminated by large amounts of stimulus artifact, an online subtraction procedure is performed that takes advantage of the refractory properties of the auditory nerve. This procedure uses the data collected from four different recording conditions: a probe-alone condition (A), a masker-plus-probe condition (B), a masker-alone condition (C), and a control condition (D), and is described in detail elsewhere (Abbas *et al.*, 1999; Brown *et al.*, 2000).

The objective of this study, however, was to measure ECAP responses to individual pulses along a pulse train. The NRT software does not allow for this type of measurement. Rather, it is only possible to measure the ECAP response to the last pulse in a pulse train. Therefore, in order to assess the degree of adaptation it was necessary to measure the response to a probe that was preceded by a varying number of a series of masker pulses. This version of the subtraction method is illustrated in Fig. 1. Two separate ECAP recordings were obtained, one using the traditional two-pulse recording procedure and the other using a train of masker pulses, rather than the single-masker pulse. The traditional recording was used to provide a stimulus artifact template that was then used to subtract out the artifact from the pulse-train recording. The response obtained to a single pulse also was used to normalize ECAP amplitudes obtained using trains of pulses. By varying the number of maskers in the train, the amplitude of the response evoked by individual pulses within the train could be assessed, thereby providing an indication of the degree of short-term auditory-nerve adaptation.

In order to obtain an ECAP response using trains of masker pulses, software constraints dictated that all four recording conditions be performed. These included the probe-alone condition (A'), the masker pulse train-plus-probe condition (B'), the masker pulse train-alone condition (C'), and the control condition (D'). These recording conditions are illustrated schematically in Fig. 1. While all four recordings were made using the NRT software, an off-line analysis procedure only used the recordings from conditions B' (masker pulse train plus-probe) and C' (masker pulse train-alone). In addition, the recording made in the masker-plus-probe (C)

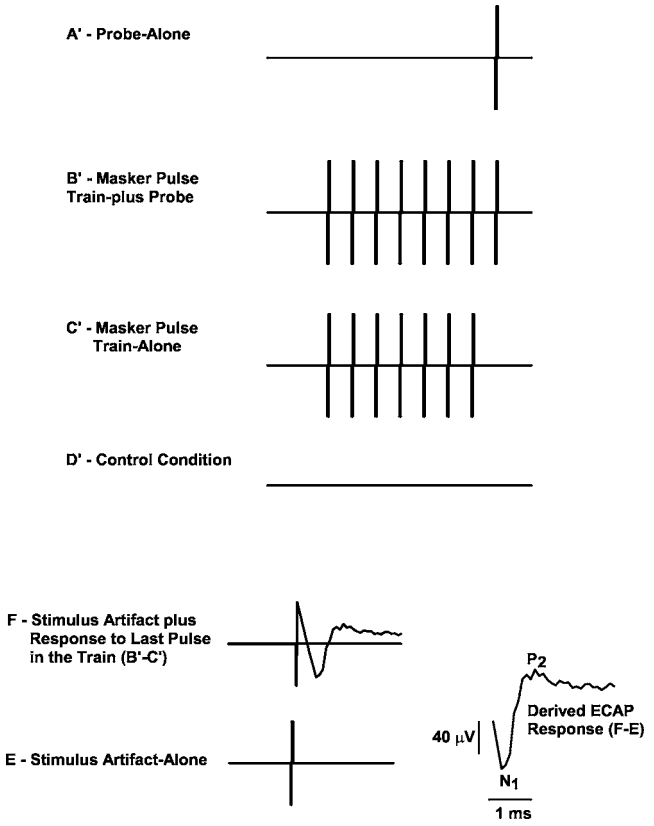

FIG. 1. Recording conditions used to obtain an ECAP response to a pulse train. Four recordings are obtained: A', probe-alone; B'; masker pulse train-plus probe; C', masker pulse train-alone; and D', control. The recording from B' is subtracted from C', which yields an ECAP response to the last pulse in the train along with the stimulus artifact (F). An artifact template (E), obtained from the traditional two-pulse ECAP recording procedure, is used to remove the artifact and reveal the ECAP response.

was subtracted from recording obtained using a masker alone (B) from the traditional two-pulse recording to produce a template of the stimulus artifact (condition E in Fig. 1). The two responses obtained using the masker pulse train also were subtracted from each other (B'-C'), which provided an ECAP response to the last pulse in the pulse train, along with a recording of the stimulus artifact (condition F in Fig. 1). The required ECAP response, therefore, was obtained through the subtraction of the derived responses, E and F. This subtraction revealed the ECAP response to the last pulse in the train of maskers without the associated stimulus artifact.

Time constraints prohibited the recording of an ECAP response to each of the pulses in the masker pulse trains. Therefore, 15 different masker pulse-train lengths were chosen to assess the degree of auditory-nerve adaptation. The 1000-pps masker pulse trains ranged from those containing 2 to 6 pulses, 23 to 26 pulses, 48 to 51 pulses, and 99 to 100 pulses. The range of these pulse-train lengths gave an indication of the degree of ECAP amplitude change over varying intervals of the masker pulse train (see Fig. 4). In addition, because the overall degree of adaptation was highly dependent on the amplitude of the response to the first pulse in the train, an ECAP waveform was obtained for five single-

masker conditions (presented at a rate of 5 frames per second) in order to ensure that this amplitude measure was accurate and reliable.

3. Recording procedures

Prior to collecting the electrophysical data, the dynamic range of hearing for the stimuli used to evoke the ECAP was measured for each of the test electrodes. Dynamic range measures were obtained by presenting both the probe and the masker pulse train at the same intensity levels. The stimulation level used to evoke the ECAP was determined on an individual basis, but typically fell within 70% to 95% of the subject's dynamic range of hearing. For all study participants, the highest intensity level within the dynamic range that provided an undistorted ECAP waveform was used for evoked potential testing. Additionally, these intensity levels were balanced for loudness to ensure that each ECAP was recorded at the same comfortably loud listening level across cochlear place. These same intensity levels were used to begin each psychophysical task described in experiments 2 and 3.

In order to record an ECAP response, the NRT software requires that two different stimulation rates be specified. One stimulation rate specifies the rate of pulses within the train of pulses that serves as the masker. The other slower rate determines the overall presentation rate of the four stimulation conditions or frames (A', B', C', and D' in Fig. 1). In this study, the stimulus frames were presented at 5 per s. The individual pulses within the masker train were presented at 1000 pps. This stimulation rate was the fastest rate that could be chosen for the presentation of 100 masker pulses. Pilot data showed that using 5 frames/s as the frame stimulation rate with a 2-min rest period provided between recordings did not lead to longer term adaptation of the ECAP. These findings, therefore, indicated that using a masker pulse train rate of 1000 pps and a frame presentation rate of 5 frames/s were sufficient for recording purposes.

Adaptation of the ECAP response was recorded using a monopolar configuration; up to six different intracochlear electrodes, 3, 6, 9, 11, 15, and 19, were measured for each study participant. For all study participants, the masker probe interval was set at 500 μs and an amplifier gain of 60 dB was used. It was necessary, however, to vary the recording electrode and sampling delays for individual participants in order to obtain an ECAP that was relatively free of amplifier saturation effects. Typically, the recording electrode was located two to three electrodes away from the stimulating electrode for the CI24M cochlear implant recipients, and four to eight electrodes away for the CI24R recipients. Research has shown that the recording electrode can vary without significantly affecting the ECAP amplitude (Abbas *et al.*, 1999). Additionally, the sampling delay, or the time interval between the offset of the probe pulse and the initiation of sampling, varied between 35 and 60 μs across individual electrodes.

Upon completion of the ECAP data collection, each recorded waveform was analyzed using a specially designed MATLAB software program. This program performed the waveform pulse-train subtraction technique as previously described and, in addition, it selected the negative N_1 and positive P_2 peaks. The amplitude of the ECAP, in μV, was measured between the negative peak, N_1, to the positive peak, P_2. The amplitude of the noise floor also was obtained through the off-line analysis. The noise measurement was taken from the peak-to-peak recorded data that followed the P_2 peak of the ECAP waveform.

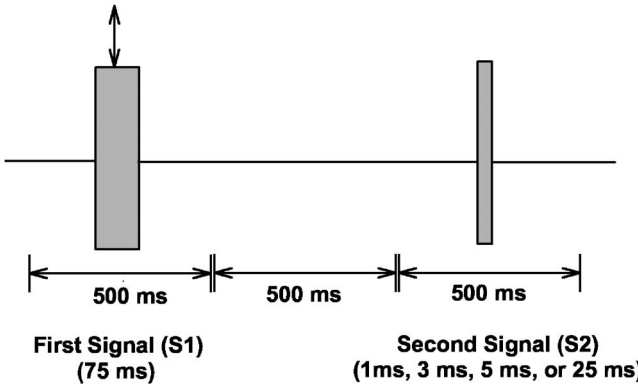

FIG. 2. Stimuli used for the suprathreshold loudness balancing procedure. The signals were 1000-pps biphasic pulses each with 25 μs per phase. The first signal (S1) presented in the 500-ms window was 75 ms in duration. The second signal (S2) also was presented in a 500-ms window and had duration of 1, 3, 5, or 25 ms. The two signals were separated by a 500-ms time period. The listener's task was to adjust the intensity level of S1 until it matched the loudness of S2. The level of S2 was fixed at the intensity level used for ECAP recording.

B. Experiment 2: Assessment of temporal integration at suprathreshold levels

1. Stimuli

Figure 2 is a schematic that shows the stimuli that were used for the experiment 2 procedure. The signals were generated using Cochlear Corporation's NUCLEUS IMPLANT COMMUNICATOR (NIC) software. They consisted of 1000-pps biphasic pulse trains, each pulse having a duration of 25 μs/phase and an interphase gap of 8 μs. For experiments 2 and 3, a monopolar stimulation mode was used with MP1, the extracochlear ball electrode, chosen as the reference. The selected electrodes were the same as those used for the electrophysiological testing in experiment 1 (i.e., a maximum of six electrodes, 3, 6, 9, 11, 15, 19). The listener first heard the 75-ms pulse train which was initially presented at the same intensity level that was used for the ECAP recordings. The second pulse train presented to the listener was 1, 3, 5, or 25 ms in duration, and it was presented at a fixed stimulus level equal to the level used for electrophysiological testing. Both the first signal (S1) and the second signal (S2) were separated by a 500-ms interstimulus interval and presented on the same electrode.

2. Procedure

In this experiment the participants listened to a pair of pulse trains. The listener's task was to judge whether the first signal was softer or louder than the second signal. As illustrated in Fig. 2, the second signal was always shorter in duration (i.e., 1, 3, 5, or 25 ms) than the first signal. This procedure was used in order to assess how the loudness of a

signal increases as it is increased in duration, and to allow for a more direct comparison of electrophysiological and psychophysical data. An adaptive procedure was used to find the point of equal loudness for the two presented signals. Fourteen reversals were obtained using a step size of 5 clinical level (cl) units (i.e., from Cochlear Corporation software) for the first four reversals, and the subsequent ten reversals used 2 clinical level units as a step size. Clinical level units were converted to μA using the formula provided by Cochlear Corporation (i.e., $\mu A = 10 \times 175^{(cl/255)}$) (Nucleus Technical Reference Manual, 1999). The mean of the last eight reversals was computed and used as the intensity level where the first signal, the longer duration signal, was judged to be equal in loudness to the second short-duration signal. This procedure was performed twice on each test electrode. Prior to testing, each study participant was given a practice session to familiarize them with the task. No feedback was given throughout the test trials. Study participants were provided necessary breaks in testing to avoid fatigue.

C. Experiment 3: Assessment of temporal integration at threshold levels

1. Stimuli

Biphasic pulses presented at 1000 pps (each pulse 25 μs/phase and separated by an interphase gap of 8 μs) were used in this experiment. Psychophysical thresholds were established for stimuli with durations of 1, 3, 5, and 25 ms.

2. Procedure

A three-interval, forced-choice (3IFC) adaptive procedure was used to determine threshold for each pulse train. Three listening intervals were visually cued on a computer screen and the stimulus was presented randomly in one interval. The study participant was required to select the interval that contained the signal. Each listening interval was 500 ms in duration, and was separated by a 500-ms interstimulus interval. Testing began at the intensity level used for ECAP testing, and the level was systematically decreased until it was no longer audible. As in experiment 2, 14 reversals were obtained using the same step sizes as were used for that experiment. The mean of the last eight reversals was used as an estimate of threshold. This procedure was performed twice on up to six of the test electrodes (i.e., 3, 6, 9, 11, 15, or 19). A practice trial was provided prior to the actual testing. No feedback was provided throughout the testing period.

III. RESULTS

Preliminary data analyses were conducted using the slope values derived from the auditory-nerve adaptation functions. However, due to the very rapid decline in ECAP amplitudes that was observed during the first few milliseconds of stimulus presentation (as shown in Fig. 4), the slopes generated from these neural adaptation functions were very steep in nature and very narrow in range, across electrodes and study participants. As a result, the slope measures were not very informative. Alternate measures that assessed the overall degree of neural adaptation were therefore used for data analyses and are presented below.

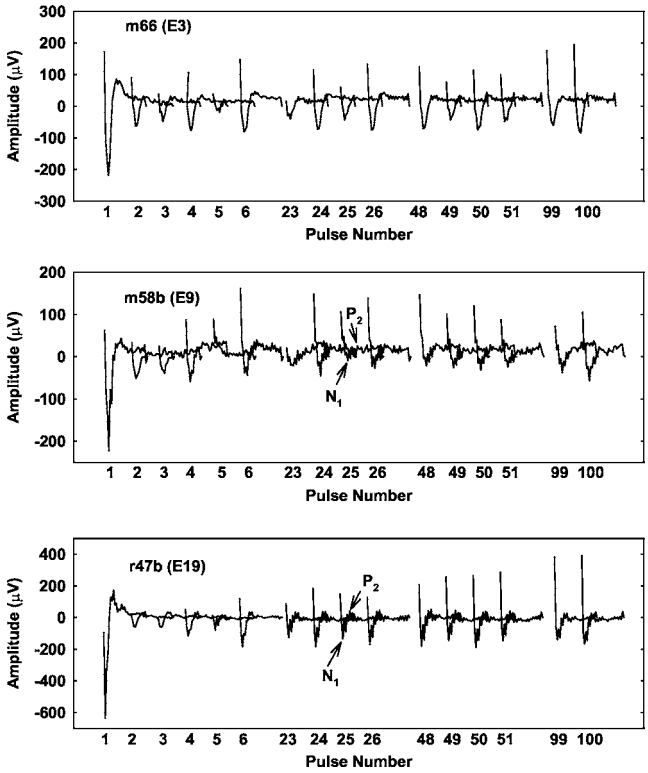

FIG. 3. ECAP waveforms for three different subjects and three different stimulating electrodes. The N1 and P2 peaks for two sample waveforms that were slightly obscured by artifact are indicated.

A. Measures of auditory-nerve adaptation

Figure 3 shows ECAP waveforms recorded for three different study participants and three different stimulating electrodes. The ECAP waveforms are shown as a function of the pulse number in the 100-ms pulse train. The waveforms presented in this figure are representative of those obtained within and across individuals. Specifically, some waveforms were robust and relatively free of stimulus artifact, as shown with m66 (E3), and others were quite small in amplitude and rather noisy, as in the case of m58b (E9). In each case, the response to the first pulse in the train had the largest amplitude. Pilot data indicated that ECAP amplitude adaptation was not present for a single pulse (collected using a frame presentation rate of 5 frames/s). The first pulse amplitude, therefore, represented a nonadapted ECAP amplitude. The effects of adaptation and refractoriness are shown in the varying amplitudes of the subsequent responses.

The data in Fig. 4 show the mean group normalized ECAP amplitudes across all study participants for each electrode. The ordinate in this figure shows the normalized ECAP amplitude, and the abscissa displays the pulse number in the train. The open and closed symbols represent the data for individual study participants and the gray hexagon in each panel shows the mean amplitude. The number of individuals (N) for whom data were obtained is indicated in the upper-right-hand corner of each panel. As can be seen in this

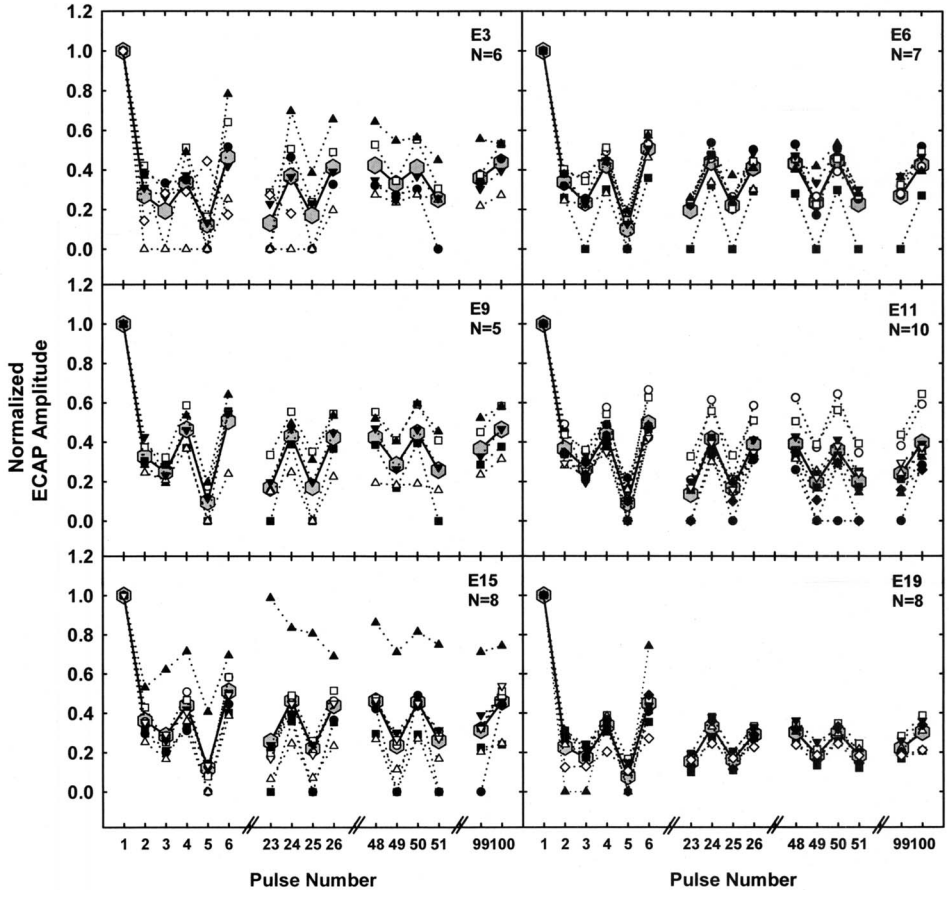

FIG. 4. Normalized ECAP amplitudes for all electrodes and study participants. The amplitude is displayed as a function of the pulse number in the 1000-pps train. The closed and open symbols are the data points for individual participants and the gray hexagon is the mean data. The number of data points included for each electrode is displayed in the top right hand corner of each panel.

figure, the largest ECAP amplitude occurs in response to the first pulse in the train, there was a rapid decline in the amplitude for subsequent pulses, and the alternation pattern was evident for each electrode, with the even-numbered pulses resulting in significantly larger ECAP amplitudes than the odd-numbered pulses. One-way ANOVA analyses indicated that the differences in amplitude obtained from the odd and even pulses were significantly different for each electrode [i.e., E3: $F(1,81)=20.0$, $p<0.001$; E6: $F(1,95)=101.19$, $p<0.001$; E9: $F(1,74)=44.51$, $p<0.001$; E11: $F(1,139)=125.98$, $p<0.001$; E15: $F(1,119)=39.16$, $p<0.001$; E19: $F(1,98)=79.13$, $p<0.001$]. Additionally, the smallest mean ECAP amplitude for each electrode was typically obtained for the fifth pulse in the train. This finding was revealed for 35 out of a total of 42 tested electrodes, and is contrary to the data presented in Wilson *et al.* (1997b), suggesting that the lowest amplitude occurs in response to the second pulse in a pulse train.

Figure 5 displays an example ECAP amplitude as a function of the pulse number in the train along with an outline of the measure of auditory-nerve adaptation that is described below. To quantify the overall degree of auditory-nerve adaptation, two separate calculations were performed. The first measure, A_{asym}, provided an indication of the ECAP amplitude (i.e., A) during the stable or asymptotic portion of the amplitude function, subsequent to the rapid amplitude decline that occurred within the first few milliseconds of stimulus presentation. This measure was determined using the formula below.

$$A_{\text{asym}} = \left(\sum_{23}^{26} A + \sum_{48}^{51} A + \sum_{99}^{100} A \right) /10 \tag{1}$$

In this equation, the A_{asym} is the amplitude of the average of the last ten ECAP waveforms that were recorded, and it was used to calculate a measure of the overall degree of auditory-nerve adaptation in the following formula:

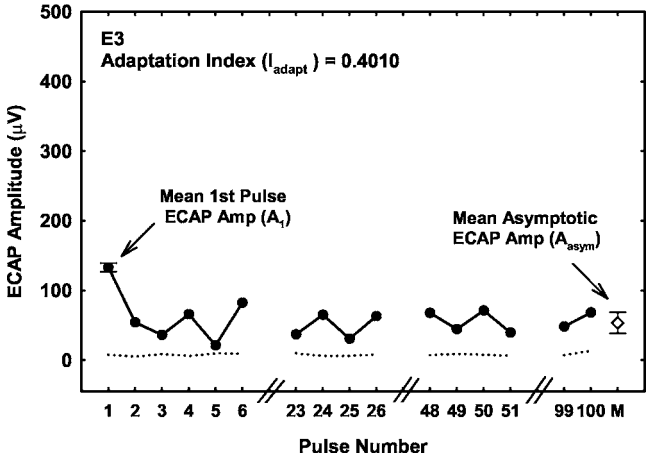

FIG. 5. ECAP amplitude for one individual electrode as a function of the pulse number in the 1000-pps pulse train. The hash marks on the abscissa indicate that the axis is not continuous. The dotted line represents the amplitude of the noise floor in the recording system. The mean first pulse ECAP amplitude (A_1) and the mean asymptotic ECAP amplitude (A_{asym}) are shown with ±1 standard deviation bars. The adaptation index (I_{adapt}) value is displayed in the top left hand corner.

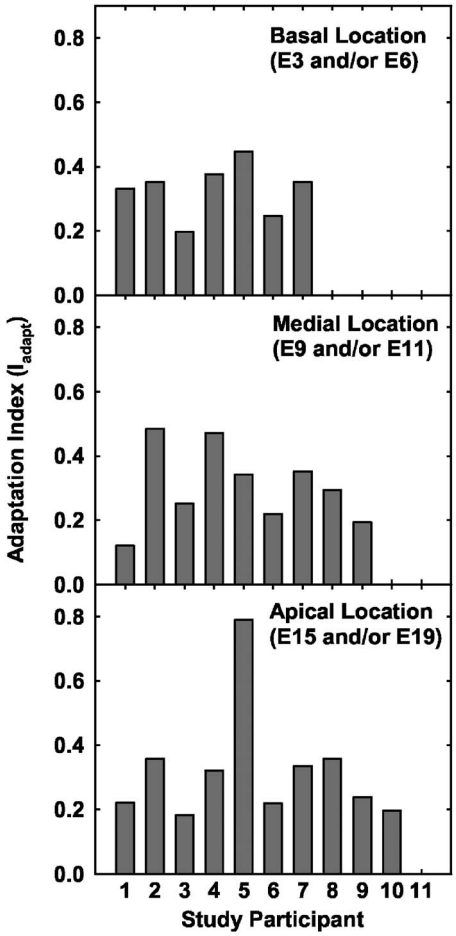

FIG. 6. Bar graphs showing the adaptation index (I_{adapt}) for all study participants. The data are grouped according to place of stimulation. The data for the basal electrodes (3 and/or 6) are shown in the top panels, the data for the medial electrodes (9 and/or 11) are shown in the middle panels, and the data for the apical electrodes (15 and/or 19) are shown in the bottom panels. Missing bars indicate that data were not collected for a study participant.

$$I_{\text{adapt}} = A_{\text{asym}}/A_1. \tag{2}$$

In this equation, the A_{asym} is divided by the ECAP amplitude to the first pulse (A_1) to provide an overall degree of auditory-nerve adaptation (i.e., adaptation index-I_{adapt}).

Figure 6 displays the adaptation index for all study participants in a series of bar graphs. The data presented in this figure were grouped according to place of stimulation along the length of the cochlea. That is, electrodes 3 and 6 were classified as basal electrodes, electrodes 9 and 11 were classified as medial electrodes, and electrodes 15 and 19 were classified as apical electrodes. The electrodes were grouped according to place in order to assess the effects that place of stimulation might have on ECAP adaptation. The basal location observations are presented in the top panels, the medial location observations are presented in the middle panels, and the apical location observations are presented in the bottom panels. For study participants who had data available at all of the electrodes, the mean value of the two electrodes corresponding to basal, medial, or apical were averaged. For study participants who had only one observation per cochlear location, that value alone is presented. Missing bars in the figure indicate that no data were obtained for that electrode location for that individual. These graphs show that ECAP adaptation is variable across study participants. For example, the adaptation index for study participant 5 at each electrode location is larger than the respective adaptation index for study participant 6. With the exception of the adaptation index at the apical location for study participant 5, these values are relatively similar across cochlear place. That is, there is not a convincing trend for auditory-nerve adaptation to be more pronounced at either end of the cochlea.

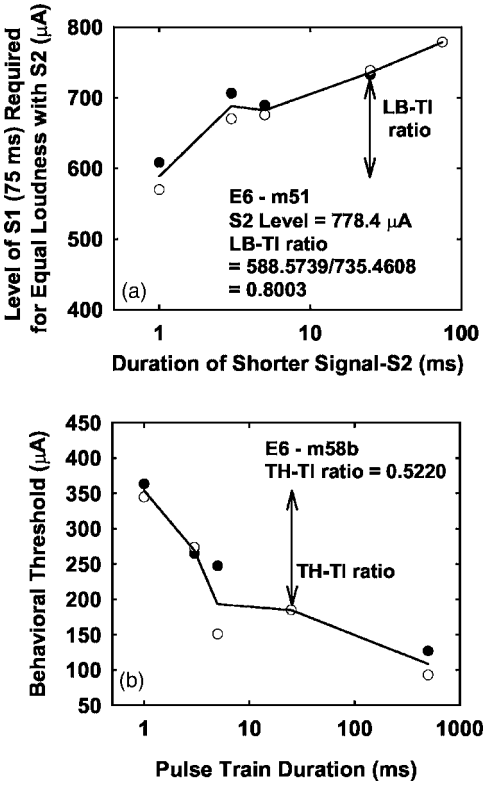

FIG. 7. Individual suprathreshold and threshold temporal integration data. Panel (a) shows the level of S1 as a function of the duration of S2, and panel (b) shows the behavioral threshold as a function of the pulse-train duration. In panel (a) the intensity level used for each S2 is shown. In both panels (a) and (b) the temporal integration ratio is provided. The open symbols represent the data from the two trials and the solid line represents the mean data. Note the use of a log scale on the abscissa.

B. Measures of temporal integration

A loudness balance temporal integration (LB-TI) ratio was calculated using the suprathreshold data for each individual electrode. Specifically, the intensity level of S1 required for a judgment of equal loudness between a 75-ms-duration signal and a 1-ms-duration signal was used, and the stimulus level of S1 required for equal loudness between the 75-ms-duration signal and the 25-ms-duration signal also was used. The 75-ms–1-ms signal comparison typically generated an intensity level that was lower than the 75-ms–25-ms signal comparison. The lower level (i.e., the level generated from the 75-ms–1-ms comparison) was divided by the higher level (i.e., the level generated from the 75-ms–25-ms comparison) to obtain the LB-TI ratio. An example LB-TI ratio and the intensity levels used for this calculation are displayed in Fig. 7, panel (A). Additionally, a

behavioral threshold temporal integration (TH-TI) ratio was calculated using the two threshold levels obtained for the 1-ms signal and the 25-ms signal for each electrode tested. Specifically, the TH-TI ratio was calculated by dividing the threshold level for the 25-ms signal by the threshold level obtained for the 1-ms signal. An example TH-TI ratio is displayed in Fig. 7, panel (B).

The suprathreshold and threshold temporal integration data obtained from two different cochlear implant recipients for electrode 6 are displayed in Fig. 7. Panel (A) shows the data for the suprathreshold task and panel (B) shows the data for the threshold task. In both panels, the data for the two testing trials are indicated by the filled and open circles, and the straight line represents the average of the trials. In panel (A), the level of S1 (i.e., 75 ms) needed in order to match the loudness of S2 is displayed as a function of the duration of S2 (i.e., 1, 3, 5, or 25 ms). For this participant and electrode, the expected rising function was obtained. That is, the level of S1 required for equal loudness with S2 increased as the duration of the second signal increased form 1 to 25 ms. The arrowed straight line shows the amount of temporal integration that was used to obtain the LB-TI ratio. As was the case for this temporal integration calculation and the TH-TI ratio calculation, a small ratio suggested that a greater degree of temporal integration was occurring, and conversely, a large value suggested that very little temporal integration was taking place. Panel (B) shows an individual behavioral threshold temporal integration function. The behavioral threshold, in μA, is displayed as a function of the pulse-train duration presented in a log scale. The degree of temporal integration (i.e., TH-TI ratio) calculated from the data for this task is shown using the arrowed straight line. For this individual, the expected declining temporal integration function was observed. That is, shorter signal durations required a greater intensity level to reach threshold than longer duration signals. For all individual electrodes examined using the suprathreshold and threshold temporal integration behavioral tasks, a test–retest standard deviation analysis was conducted. For all study participants, the standard deviation for all of the test–retest trials was less than 100 μA, with the majority of test–retest differences less than 40 μA.

Figure 8 shows the data obtained from the suprathreshold loudness balance task for all study participants. To compare these data across individuals, the normalized level of the 75-ms signal (S1) required for equal loudness with a shorter duration signal (S2) is displayed as a function of the duration of the shorter signal in this figure. Each curve, and the respective symbol, represents the data for one study participant. The individual loudness balance functions indicate that for some there is very little difference between the intensity levels chosen for equal loudness percepts between the 75-ms signal and the shorter comparison signals, while for others there is a larger difference between the intensity levels required for equal loudness. Generally, as shown with the rising exponential functions, the intensity level chosen for S1 to be equal in loudness to S2 is less than the set level of the shorter comparison signal. Additionally, the standard deviation of the mean S1 levels (when S2 was 1 ms) was larger for E3, E11, and E19 (i.e., a standard deviation of 0.1777, 0.1823, and 0.1952 for E3, E11, and E19, respectively) than it was for E6, E9, and E15 (i.e., standard deviation of 0.1088, 0.1252, and 0.1360, respectively). However, a one-way analysis of variance indicated that these mean normalized S1 levels were not significantly different across electrodes [$F(5,45)=0.517$, $p=0.762$]. Finally, the mean LB-TI ratios obtained for each electrode also were not significantly different across cochlear place as assessed using a one-way analysis of variance [$F(5,43)=0.342$, $p=0.884$].

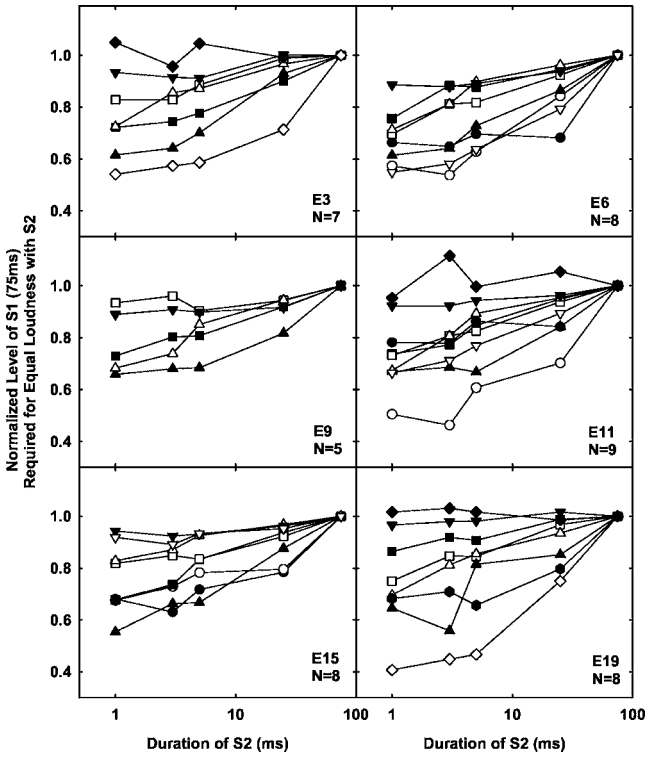

FIG. 8. The normalized level of S1 required for equal loudness with S2 shown as a function of the duration of S2. Note the use of a log scale on the abscissa. Each curve and the respective symbol represents the data for one individual electrode (the same individual symbols are used as those in Fig. 4). The number of participants evaluated for the six different electrodes is shown in the lower right hand corner in each panel.

Figure 9 shows the normalized behavioral threshold data as a function of pulse-train duration for all study participants at each electrode. As with Fig. 8, each curve and the respective symbol represents the threshold temporal integration function for one study participant. Also presented in each panel of this figure is the ideal energy integration model shown using the dash-dot line. In order to generate this ideal model of energy integration, it was assumed that no auditory-nerve adaptation was present, and that the energy in the signal (ECAP amplitude squared) in response to one pulse presentation was equal to the sum of the squares of the amplitude generated from multiple pulse presentations. In addition, the response amplitude was assumed to grow linearly with stimulus current level.

Generally, as observed in Fig. 9, detection thresholds decreased as the duration of the pulse train was increased. It also can be observed that the degree of threshold decrease is variable across study participants, as some of the temporal integration functions follow the ideal energy integration model, and for others very little threshold decrease is noted

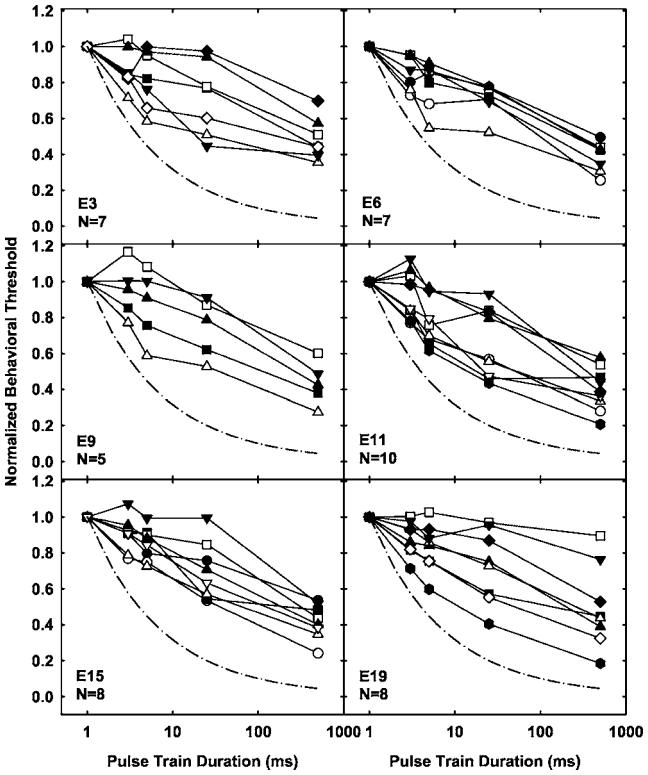

FIG. 9. Normalized behavioral threshold as a function of pulse-train duration at each electrode for all study participants. Note the use of a log scale on the abscissa. Each curve and the respective symbol represents the data for one individual (the same symbols as used in Figs. 4 and 8 are used in this figure). The dash-dot line represents the ideal integration of energy model (see the text for explanation). The number of participants evaluated at each electrode is shown in the lower left hand corner.

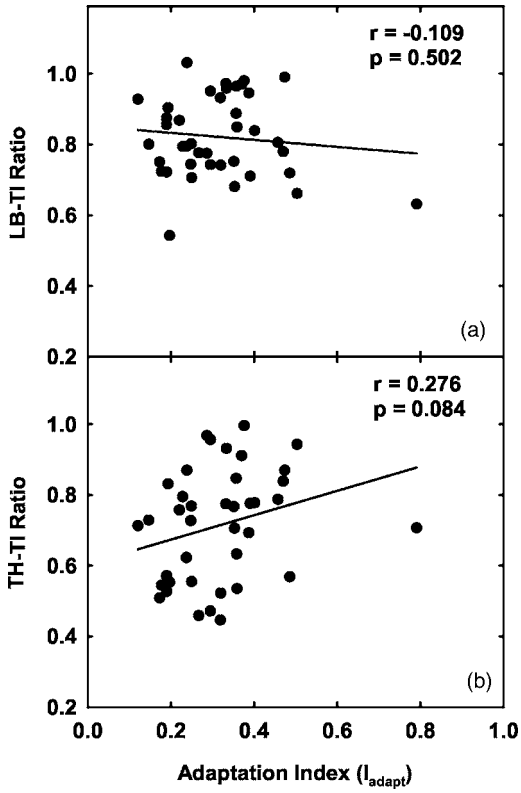

FIG. 10. The correlation between the suprathreshold (LB-TI ratio) and threshold (TH-TI ratio) temporal integration measures and the adaptation index (I_{adapt}). Each symbol represents the data for an individual electrode. In both panels (a) and (b), a larger amount of either neural adaptation or temporal integration is indicated by a smaller ratio value. As indicated by the Pearson correlation coefficients, both of the correlations are not significant.

with increasing stimulus duration. Examination of the overall degree of threshold change at 500 ms revealed that the variability of threshold decrease for the apically placed electrode, E19, was larger (i.e., standard deviation of 0.2320) than the other electrodes (i.e., standard deviation of 0.1171, 0.0847, 0.1217, 0.1265, and 0.0975 for electrodes E3, E6, E9, E11, and E15, respectively). The mean behavioral thresholds at 500 ms for each electrode, however, were not found to be significantly different across location as assessed using a one-way analysis of variance [$F(5,44)=0.719$, $p=0.613$]. Additionally, a one-way analysis of variance revealed that the mean TH-TI ratios for each electrode were not significantly different across electrode location [$F(5,43)=0.241$, $p=0.942$].

C. Combined electrophysiological and behavioral results

To ensure that both measures of temporal integration (i.e., LB-TI and TH-TI ratios) were each measuring the same phenomenon, these measures were correlated with each other. The Pearson coefficient indicated that the correlation was statistically significant ($r=0.381$, $p=0.01$). An increase in the suprathreshold temporal integration measure concomitantly corresponded to an increase in the threshold temporal integration measure.

Figure 10 displays the correlated results from the behavioral and electrophysiological ratio values, calculated from the data obtained in each of the three experiments. The correlation between the adaptation index (I_{adapt}) and the two measures of temporal integration are displayed in panels (A) and (B). For each panel, the temporal integration indices are shown as a function of the neural adaptation index. A larger amount of either neural adaptation or temporal integration is indicated by a smaller ratio value, and likewise, a lesser degree of neural adaptation or temporal integration is indicated by a large ratio. If a large degree of temporal integration, therefore, was significantly correlated with a lesser amount of neural adaptation, a negatively sloping linear regression line would be obtained. A Pearson's correlation coefficient was computed based on the data shown in both panels. These two coefficients do not indicate a significant correlation between the electrophysiological and psychophysical indices. Additionally, as shown in the figure, the range of ratios, or the degree of temporal integration, obtained from the suprathreshold task (LB-TI ratio range=0.5424–1.0308, mean=0.8163) was slightly narrower than the range of ratios obtained from the threshold temporal integration tasks (TH-TI ratio range=0.4036–0.9960, mean=0.6982).

The behavioral threshold temporal integration data for two individuals also were compared to both an ideal integration of energy model and a model of integration based on the individual degree of neural adaptation (i.e., the adaptation index). These data are presented in Fig. 11. Panel (A) shows two individual ECAP functions for E15, one representative

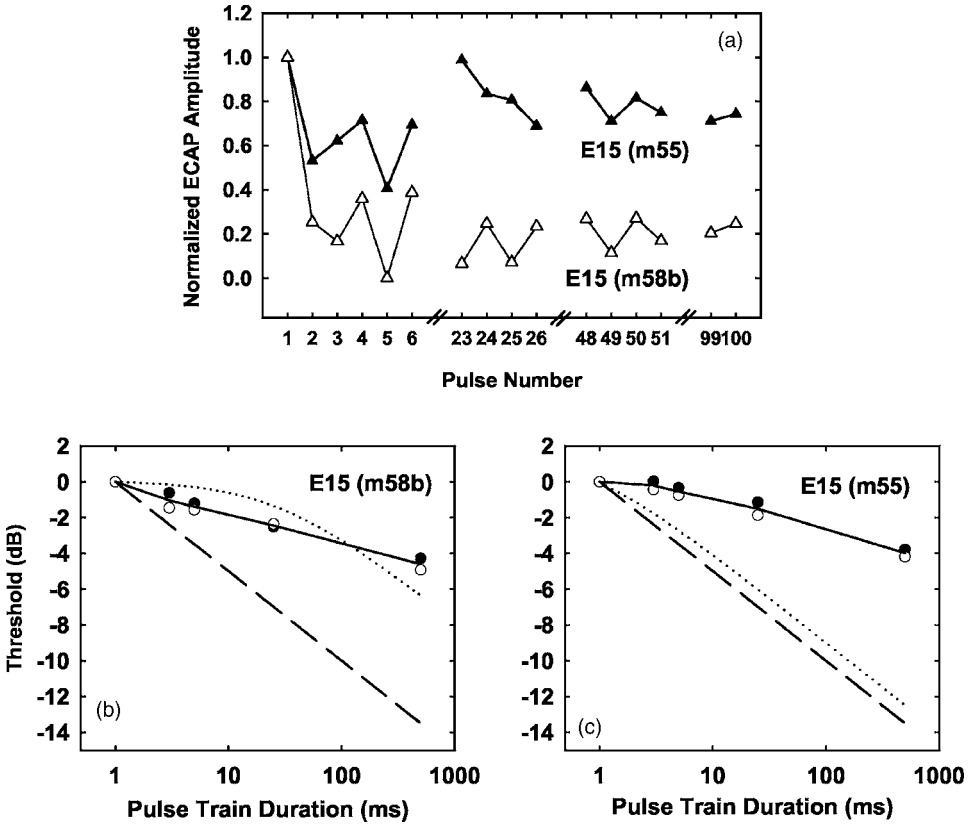

FIG. 11. Comparison of the behavioral threshold temporal integration functions to two models of energy integration. Panel (a) shows two individual ECAP functions (i.e., m55 and m58b) for E15. Panels (b) and (c) show the behavioral temporal integration data for m55 and m58b, along with two models of energy integration. The open and closed symbols are the behavioral thresholds obtained from two trials, and the solid line is the mean of these trials. The dashed line represents the threshold values that would result based on the ideal integration of energy. The dotted line in panels (b) and (c) represents the threshold values that were predicted based on individual degrees of adaptation (i.e., adaptation index) and obtained using Eqs. (3) and (4) (see the text for explanation).

of a large degree of neural adaptation (i.e., m58b) and one representative of little neural adaptation (i.e., m55). In panels (B) and (C) the individual behavioral threshold temporal integration data for these individuals are displayed along with the two models of energy integration. The open and closed symbols and the respective solid line are the behavioral data. The dashed line represents the threshold values that would result based on the ideal integration of energy (shown in Fig. 9). The dotted line in panels (B) and (C) represents the threshold values that were predicted based on individual degrees of adaptation (i.e., the adaptation index). These functions were determined using the following equations:

$$A_1^2 = (bT_1)^2, \tag{3}$$

$$A_1^2 = (bT_n)^2 + n - 1(bT_n I_{\text{adapt}})^2. \tag{4}$$

Equation (3) provides the predicted current level required to reach threshold (T_1) using the individual ECAP amplitude (μV) for the single pulse in the train (A_1) and an assumed slope of 1 for the amplitude growth function (b). The predicted threshold current levels for the subsequent pulses in the train (T_n) were derived using Eq. (4). To generate this model, it was assumed that the energy output for the first pulse (A_1) was equivalent to the energy output for each subsequent pulse ($n-1$), and the adaptation observed was characterized by the individual adaptation index (I_{adapt}). It also was assumed that the ECAP amplitude was growing linearly with each pulse presentation, or alternatively that the slope of the growth function (b) was linear. Finally, the generated T_n values were normalized to the current threshold value to the first pulse in the train (T_1). The normalized threshold values based on the actual and predicted data are presented in dB with the normalized value of 1 used as the reference.

The data from study participant m58b, who demonstrated a large degree of auditory-nerve adaptation, are presented in panel (B) of Fig. 11. The predicted threshold values based on the adaptation index (i.e., the dotted line) did not follow the ideal energy integration model (i.e., dashed line) due to the degree of adaptation observed for this electrode and study participant. Conversely, the predicted model of energy integration based on very little adaptation, as shown in panel (C), very closely matched the ideal energy integration model. However, for both of these study participants, who were representative of the upper and lower range of neural adaptation observed in this study, the degree of adaptation appeared to have no impact on their respective behavioral temporal integration. Specifically, the observed behavioral temporal integration data for these two individuals did not dramatically differ. The slopes of the functions were −1.08-dB/doubling for m55 and −1.18-dB/doubling for m58b. The TH-TI ratios for these individuals were 0.5706 for m58b and 0.7073 for m55.

IV. DISCUSSION

The results of this study suggest that greater amounts of auditory-nerve adaptation do not have a significant impact upon temporal integration. It was revealed that adaptation at the level of the auditory nerve did not correlate with the LB-TI ratios or the TH-TI ratios, as shown in Fig. 10. It was expected that the output of both the auditory nerve and the cochlear nucleus would impact loudness perception, and that a degraded input to the central auditory system, resulting

from a large degree of auditory-nerve adaptation, would decrease temporal integration. Although the modeling data presented in panel (B) of Fig. 11 suggested that for a large degree of neural adaptation the behavioral temporal integration function was much shallower than the ideal integration of energy function, the opposite case (i.e., a lesser amount of adaptation resulting in a temporal integration function that closely matched the ideal energy integration model) was not observed [panel (C)]. Given the range of the neural adaptation that was presented in Fig. 11, it was expected that the two temporal integration functions would have been significantly different.

It is possible that the observed findings can be attributed to sampling effects that may occur with a relatively small study participant pool. Perhaps the variability of auditory-nerve adaptation was quite small compared to the total energy derived from the signal as it was processed throughout the auditory pathway. The variability in the behavioral tasks, therefore, could have been much greater than the differences observed in integrated energy due to adaptation, which might have limited the observed correlation between electrophysiological and behavioral measures. It also is possible that the amount of auditory-nerve adaptation observed across study participants in this study was minor in degree and therefore incapable of being reflected in the temporal integration measures. If the output from the auditory nerve was not significantly degraded, then the integration of neural activity along the auditory pathway would be minimally affected. This result would suggest that other processes are involved in the variable temporal integration observed across cochlear implant recipients. Further study is warranted to confirm or negate the findings of this study.

A. The ECAP and auditory-nerve adaptation

For all study participants, an adapted ECAP response was observed with successive pulses in a 100-ms pulse train presented at a rate of 1000 pps. As demonstrated in Figs. 3 and 4, the ECAP amplitudes rapidly decreased within the first few milliseconds of pulse-train presentation, and then settled into a relatively steady pattern of amplitude alternation. These adapted ECAP responses were similar to those presented in previously published human studies using high-rate pulse-train stimulation (Abbas *et al.*, 2000; Wilson *et al.*, 1997a; 1997b). In these studies, a 1016-pps pulse train generated large ECAP amplitudes in response to the first pulse and much smaller amplitudes in response to successive pulses in the train. In all cases there was a rapid decrease of the ECAP amplitude after the first pulse presentation.

When considering the degree of auditory-nerve adaptation along the length of the electrode array, the results from this study have suggested that neural adaptation does not systematically change with cochlear place. While there was some across-electrode variation in the degree of auditory-nerve adaptation for some individuals, for others the adaptation did not increase or decrease with cochlear place. These findings are generally consistent with the limited previously published results also suggesting that neural adaptation does not systematically vary with cochlear place. Schmidt Clay (2003) examined auditory-nerve adaptation at one basal and one apical location in Nucleus 24 cochlear implant recipients using the traditional two-pulse ECAP recording paradigm. In that study, ECAP adaptation was assessed over a 5-min period for each of three rates of stimulation, 15, 80, and 300 pps. The results revealed no consistent differences in the degree of adaptation for the two cochlear locations that were examined.

B. The ECAP and amplitude alternation

Along with adaptation of the ECAP amplitude, all study participants showed some degree of alternation in ECAP amplitude with increasing pulse number, as shown in Figs. 3 and 4. After the first few pulse presentations, ECAP amplitudes alternated from larger responses for even-numbered pulses and smaller amplitudes for odd-numbered pulses. The alternation pattern demonstrated by study participants in this study varied slightly from those obtained by Wilson *et al.* (1997a) and by Wilson *et al.* (1997b) using Ineraid cochlear implant recipients. The smallest ECAP amplitude typically occurred in response to the second pulse in the train in those studies, but was observed to generally occur for the fifth pulse in the present study. Additionally, it was noted that in Wilson *et al.* (1997a) and Wilson *et al.* (1997b) the amplitudes for even-numbered pulses were smaller than they were for odd-numbered pulses, but the opposite finding was revealed in this study. One factor having an impact upon the differences obtained between the current study and those previously published is the differences in study participants themselves. Three individuals were used in the Wilson *et al.* (1997a) and Wilson *et al.* (1997b) studies, while the total number of individuals who participated in this study was 11. It is possible that differences between these studies were simply related to sampling issues.

Additionally, as indicated above, all individuals in the Wilson *et al.* (1997a) and the Wilson *et al.* (1997b) studies used the Ineraid cochlear implant device. The cochlear implant candidacy criteria have significantly changed since these Ineraid devices were implanted, and it is possible that the individuals participating in the current study had better neural survival than those individuals who participated in the Wilson *et al.* (1997a) and the Wilson *et al.* (1997b) studies. The degree of neural survival and neural integrity could potentially affect the ECAP responses that were obtained. Specifically, it is possible that the number of neurons contributing to an evoked potential response, the ability of neural membranes to integrate pulses, and the refractory and stochastic properties of the neurons could be different between the groups of individuals. All of these factors would have an impact upon the responsiveness of the auditory nerve when stimulated with a pulse train (Wilson *et al.*, 1994; Wilson *et al.*, 1997b).

Although evidence from both human and animal studies has suggested that varying stimulus parameters, such as stimulation rate and intensity level, can have an impact upon the degree of neural adaptation and ECAP amplitude alternation (Abkes *et al.*, 2003; Haenggeli *et al.*, 1998; Matsuoka *et al.*, 2000; Wilson *et al.*, 1997a, 1997b), it is unlikely that

differing stimulus parameters between the present study and those previously published resulted in the different findings across studies. In this study, pulse trains of 1000 pps consisting of 25-μs/phase biphasic pulses presented for 100-ms duration were used. Additionally, a monopolar mode of stimulation was used. The comparison stimuli used in Wilson *et al.* (1997a) and Wilson *et al.* (1997b) also were presented using a monopolar mode of stimulation and were 33-μs/phase biphasic pulses presented in trains at a rate of 1016 pps for 200 ms. The intensity levels used in all the studies corresponded to comfortably loud levels for the study participants. Therefore, differing stimulus parameters between the studies were likely not responsible for the different alternation patterns observed.

C. Suprathreshold and threshold temporal integration

For this study, it was assumed that the decrease of behavioral thresholds or the increase in loudness with increasing stimulus duration was occurring due to the integration of energy over a window of approximately 200 ms. Additionally, it was hypothesized that the neural adaptation observed over a 100-ms time window would impact the integration of energy with increasing signal duration. The multiple-looks theory suggests that decreased behavioral thresholds result from a number of short "looks" at the signal over a few milliseconds, and, although the intention of this study was not to assess the validity of these two theories, it could be reasoned that a number of looks at a severely degraded or adapted signal also would impact behavioral temporal integration.

Regardless of the mechanism responsible for temporal integration, this phenomenon was observed to some degree for all study participants. The data from the suprathreshold task presented in Fig. 8 suggested that, when S1 was compared to the shortest 1-ms signal, generally less intensity was required to obtain equal loudness than when this signal was compared to the 25-ms signal. Additionally, the threshold data presented in this study demonstrated that, with increasing signal duration, decreased behavioral thresholds were obtained (see Fig. 9). As was observed from both Figs. 8 and 9, a large degree of variable temporal integration was observed across study participants.

Both Donaldson *et al.* (1997) and Shannon (1983) demonstrated that cochlear implant recipients perceive stimuli to be increased in loudness when they are increased in duration. When using either threshold or suprathreshold stimuli presented at a rate of 100 pps and for durations of 1 to 64 pulses, Donaldson *et al.* (1997) demonstrated that, within and across a group of eight Nucleus 22 cochlear implant recipients, the degree of temporal integration varied from less than 1 dB up to 6 dB. Similarly, Shannon (1983) revealed that, in a group of three individuals implanted with an early version of the Advanced Bionics cochlear implant, thresholds decreased by as much as 10 dB as a 1000-Hz stimulus burst was increased in duration from 5 to 300 ms. In this same study, Shannon (1983) measured increases in loudness using a subjective loudness estimate scale ranging from 0 to 100, with 100 representing the maximum loudness level. For some individuals, an increase in the loudness estimate of 40 units was observed as a 1000-pps pulse train increased from 0 to 100 ms, and for others a 70-unit increase in loudness was observed over the same time frame.

Generally, as shown in Fig. 10, the overall degree of temporal integration generated from the suprathreshold measure was smaller than the degree observed for the threshold temporal integration measures. This finding is commonly observed in the normal-hearing and hearing impaired population (Florentine *et al.*, 1996; 1998; Pedersen and Poulsen, 1973), and also has been observed in cochlear implant recipients when using stimuli of increasing rate (Skinner *et al.*, 2002; 2000; Vandali *et al.*, 2000). Data from Donaldson *et al.* (1997), however, which examined threshold and maximum acceptable loudness estimates as the 100-pps pulse train was increased in duration, revealed that the greater degrees of temporal integration for threshold measures compared with suprathreshold measures were not consistently observed. Although greater degrees of temporal integration for threshold measures than for suprathreshold measures were generally observed in the present study, individual variation suggests that this trend was not universal (see the individual data in Figs. 8 and 9), and therefore consistent with the findings of Donaldson *et al.* (1997). Unfortunately, the overall results from this study do not provide further insight into the possible mechanisms behind the observed individual variability. Although it is probable that the loss of peripheral compressive nonlinearity and spontaneous neural activity has a role to play in the temporal integration functions observed in the cochlear implant population, the exact causes behind the observed variability in individual temporal integration remain unknown.

D. Study limitations

For purposes of this study, it was assumed that the central integrator was uniform across cochlear implant recipients. This assumption was based upon work conducted by Shannon (1983) using cochlear implant recipients, and Shannon and Otto (1990) using auditory brainstem implant recipients. As previously mentioned, the Shannon (1983) study demonstrated that threshold for three cochlear implant recipients improved by up to 10 dB as a 1000-pps stimulus was increased in duration from 5 to 300 ms. A somewhat smaller range of threshold improvement (i.e., approximately 1 to 2 dB) was noted for auditory brainstem implant recipients in Shannon and Otto (1990) using 300-ms burst duration stimuli presented once per second. Because these threshold temporal integration functions were similar in shape across individuals in the Shannon (1983) and Shannon and Otto (1990) studies, and because these normalized temporal integration functions were similar to those obtained for normal-hearing individuals, it was suggested that the central integrator was uniform across individuals. However, it cannot be ruled out that hearing loss and the subsequent use of a cochlear implant may have affected the integrity of the central auditory system. Neural plasticity data, for example, have suggested that hearing loss can alter the physiological responses from the central auditory pathway (Shepherd *et al.*,

1999; Shepherd and Hardie, 2001). Shepherd *et al.* (1999) reported that inferior colliculus neurons in neonatally deafened cats displayed increases in response latencies and temporal jitter compared to those obtained from acutely deafened control animals. However, data from Synder *et al.* (1990) demonstrated that the spatial tuning curves of neurons within the inferior colliculus of neonatally deafened cats were not significantly different in threshold or width compared to those obtained from normal-hearing cats. This finding suggested that the inferior colliculus neurons were maintained despite the atrophic changes in the peripheral auditory nerve. The findings of the present study must be interpreted in light of the possibility that the hearing loss could have impacted the auditory system at both the central and peripheral level.

V. CONCLUSIONS

The results from this study suggest that larger degrees of auditory-nerve adaptation do not have a significant negative impact upon the degree of temporal integration observed in cochlear implant recipients. Future studies might evaluate a more diverse population of adults and examine the effects of auditory-nerve adaptation upon temporal integration using faster stimulation rates and/or using lower intensity levels. It is possible that a null relationship was observed in this study due to the relatively small degree of variability observed for both the electrophysiological and psychophysical responses. Had a larger and more diverse population been evaluated (i.e., normal-hearing and hearing-impaired individuals), or had it been possible to use faster stimulation rates or lower intensity levels, which would have allowed for the examination of auditory-nerve adaptation on a more restricted subset of auditory-nerve fibers, the results from this study might have been stated more definitively.

ACKNOWLEDGMENTS

We would like to thank Charles A. Miller, J. Bruce Tomblin, Christopher W. Turner, and Daniel F. Eberl for their helpful contributions to this paper. We also thank Arik Wald for providing computer programming support. The comments of Fan Gang-Zeng and an anonymous reviewer on a previous version of this paper also are very much appreciated. Funding was provided by the NIH NRSA predoctoral grant program (F31 DC006532) and NIH/NIDCD P50 Grant DC00242.

Abbas, P. J., Miller, C. A., Rubinstein, J. T., Robinson, B. K., and Hu, N. (**2001**). "The neurophysiology effects of simulated auditory prosthesis stimulation," Eighth Quarterly Progress Report N01-DC-9-2107, University of Iowa, Iowa City, IA.

Abbas, P. J., Brown, C. J., Hughes, M. L., Gantz, B. J., Wolaver, A. A., Gervais, J. P., and Hong, S. H. (**2000**). "Electrically evoked compound action potentials recorded from subjects who use the Nucleus CI24M device," Ann. Otol. Rhinol. Laryngol. **185**, 6–9.

Abbas, P. J., Brown, C. J., Shallop, J. K., Firszt, J. B., Hughes, M. L., Hong, S. H., and Staller, S. J. (**1999**). "Summary of results using the Nucleus CI24M implant to record the electrically evoked compound action potential," Ear Hear. **20**, 45–59.

Abkes, B. A., Miller, C. A., Hu, N., and Abbas, P. J. (**2003**). "Adaptation in the auditory nerve in response to a continuous electric pulse train," Twenty-Sixth Annual MidWinter Research Meeting of the Association for Research in Otolaryngology, Daytona Beach, FL.

Brown, C. J., Hughes, M. L., Luk, B., Abbas, P. J., Wolaver, A., and Gervais, J. (**2000**). "The relationship between EAP and EABR thresholds and levels used to program the Nucleus 24 speech processor: Data from adults," Ear Hear. **21**, 151–163.

Carlyon, R. P., Buus, S., and Florentine, M. (**1990**). "Temporal integration of trains of tone pulses by normal and by cochlearly impaired listeners," J. Acoust. Soc. Am. **87**, 260–268.

Donaldson, G. S., Viemeister, N. F., and Nelson, D. A. (**1997**). "Psychometric functions and temporal integration in electric hearing," J. Acoust. Soc. Am. **101**, 3706–3721.

Finley, C. C., Wilson, B. S., van den Honert, C., and Lawson, D. T. (**1997**). "Speech processors for auditory prostheses," Sixth Quarterly Progress Report N01-DC-5-2103, Research Triangle Institute, Research Triangle Park, NC.

Florentine, M., Buus, S., and Poulsen, T. (**1996**). "Temporal integration of loudness as a function of level," J. Acoust. Soc. Am. **99**, 1633–1644.

Florentine, M., Buus, S., and Robinson, M. (**1998**). "Temporal integration of loudness under partial masking," J. Acoust. Soc. Am. **104**, 999–1007.

Green, D. M., Birdsall, T. G., and Tanner, W. P. (**1957**). "Signal detection as a function of signal intensity and duration," J. Acoust. Soc. Am. **29**, 523–531.

Haenggeli, A., Zhang, J., Vischer, M., Pelizzone, M., and Rouiller, E. M. (**1998**). "Electrically evoked compound action potential (ECAP) of the cochlear nerve in response to pulsatile electrical stimulation of the cochlea in the rat: Effects of stimulation at high rates," Audiology **37**, 353–371.

Hong, S. H., and Rubinstein, J. T. (**2003**). "High-rate conditioning pulse trains in cochlear implants: Dynamic range measures with sinusoidal stimuli," J. Acoust. Soc. Am. **114**, 3327–3342.

Hong, S. H., Rubinstein, J. T., Wehner, D., and Horn, D. (**2003**). "Dynamic range enhancement for cochlear implants," Otol Neurotol. **24**, 590–595.

Killian, M. J. P., Klis, S. F. L., and Smoorenburg, G. F. (**1994**). "Adaptation in the compound action potential response of the guinea pig VIIIth nerve to electric stimulation," Hear. Res. **81**, 66–82.

Litvak, L., Delgutte, B., and Eddington, D. (**2001**). "Auditory nerve fiber responses to electric stimulation: Modulated and unmodulated pulse trains," J. Acoust. Soc. Am. **110**, 368–379.

Matsuoka, A. J., Abbas, P. J., Rubinstein, J. T., and Miller, C. A. (**2000**). "The neuronal response to electrical constant-amplitude pulse train stimulation: Evoked compound action potential recordings," Hear. Res. **149**, 115–128.

SMoore, B. C. J. (**2003**). "Coding of sounds in the auditory system and its relevance to signal processing and coding in cochlear implants," Otol Neurotol. **24**, 243–254.

Nucleus Technical Reference Manual (**1999**). (Cochlear Corporation, Lane Cove, Australia).

Parker, A. J., and Newsome, W. T. (**1998**). "Sense and the single neuron," Annu. Rev. Neurosci. **21**, 227–277.

Pedersen, C. B., and Poulsen, T. (**1973**). "Loudness of brief tones in hearing-impaired ears," Acta Oto-Laryngol. **76**, 402–409.

Plomp, R., and Bouman, M. A. (**1959**). "Relation between hearing threshold and duration for tone pulses," J. Acoust. Soc. Am. **31**, 749–758.

Relkin, E. M., and Turner, C. W. (**1988**). "A reexamination of forward masking in the auditory nerve," J. Acoust. Soc. Am. **84**, 584–591.

Schmidt Clay, K. M. (**2003**). "Variations in neural adaptation across Nucleus 24 cochlear implant users and the relationship to behavioral dynamic range and word recognition performance," Ph.D. dissertation, University of Iowa, Iowa City.

Shannon, R. V. (**1983**). "Multichannel electrical stimulation of the auditory nerve in man. I. Basic psychophysics," Hear. Res. **11**, 157–189.

Shannon, R. V. (**1989**). "Detection of gaps in sinusoids and pulse trains by patients with cochlear implants," J. Acoust. Soc. Am. **85**, 2587–2592.

Shannon, R. V. (**1990**). "Forward masking in patients with cochlear implants," J. Acoust. Soc. Am. **88**, 741–744.

Shannon, R. V. (**1993**). Quantitative comparison of electrically and acoustically evoked auditory perception: Implications for the location of perceptual mechanisms, in *Progress in Brain Research*, edited by J. H. J. Allum, D. J. Allum-Mcklenburg, F. P. Harris, and R. Probst (Elsevier Science, Amsterdam), Vol. **97**, pp. 261–269.

Shannon, R. V., and Otto, S. R. (**1990**). "Psychophysical measures from electrical stimulation of the human cochlear nucleus," Hear. Res. **47**, 159–168.

Shepherd, R. K., and Hardie, N. A. (**2001**). "Deafness-induced changes in

the auditory pathway: Implications for cochlear implants," Audiol. Neuro-Otol. **6**, 305–318.
Shepherd, R. K., Baxi, J. H., and Hardie, N. A. (**1999**). "Response of inferior colliculus neurons to electrical stimulation of the auditory nerve in neonatally deafened cats," J. Neurophysiol. **82**, 1363–1380.
Skinner, M. W., Arndt, P. L., and Staller, S. J. (**2002**). "Nucleus 24 advanced encoder conversion study: Performance versus preference," Ear Hear. **23**, 2S–17S.
Skinner, M. W., Holden, L. K., Holden, T. A., and Demorest, M. E. (**2000**). "Effect of stimulation rate on cochlear implant recipients' thresholds and maximum acceptable loudness levels," J. Am. Acad. Audiol **11**, 203–213.
Synder, R. L., Rebscher, S. J., Cao, K., Leake, P. A., and Kelly, K. (**1990**). "Chronic intracochlear electrical stimulation in the neonatally deafened cat. I. Expansion of central representation," Hear. Res. **50**, 7–34.
Turner, C. W., Relkin, E. M., and Doucet, J. R. (**1994**). "Psychophysical and physiological forward masking studies: Probe duration and rise-time effects," J. Acoust. Soc. Am. **96**, 795–800.
van den Honert, C., and Stypulkowski, P. H. (**1987**). "Temporal response patterns of single auditory nerve fibers elicited by periodic electrical stimuli," Hear. Res. **29**, 207–222.
Vandali, A. E., Whitford, L. A., Plant, K., and Clark, G. M. (**2000**). "Speech perception as a function of electrical stimulation rate: Using the Nucleus 24 cochlear implant system," Ear Hear. **21**, 608–624.
Viemeister, N. F., and Wakefield, G. H. (**1991**). "Temporal integration and multiple looks," J. Acoust. Soc. Am. **90**, 858–865.
Wilson, B. S., Finley, C. C., Lawson, D. T., and Zerbi, M. (**1997a**). "Temporal representations with cochlear implants," Am. J. Otol. **18** (suppl), S30–S34.
Wilson, B. S., Finley, C. C., Zerbi, M., and Lawson, D. T. (**1994**). "Speech processors for auditory prostheses," Seventh Quarterly Progress Report N01-DC-2-2401, Research Triangle Institute, Research Triangle Park, NC.
Wilson, B. S., Finley, C. C., Zerbi, M., Lawson, D. T., and van den Honert, C. (**1997b**). "Speech processors for auditory prostheses," Seventh Quarterly Progress Report N01-DC-5-2103, Research Triangle Institute, Research Triangle Park, NC.
Zeng, F. G., and Shannon, R. V. (**1994**). "Loudness-coding mechanisms inferred from electric stimulation of the human auditory system," Science **264**, 564–566.
Zwislocki, J. J. (**1960**). "Theory of temporal auditory summation," J. Acoust. Soc. Am. **32**, 1046–1060.

Detection of high-frequency spectral notches as a function of level[a)]

Ana Alves-Pinto and Enrique A. Lopez-Poveda[b)]
Unidad de Computación Auditiva y Psicoacústica: Instituto de Neurociencias de Castilla y León, Universidad de Salamanca, Avenida Alfonso X "El Sabio" s/n, 37007 Salamanca, Spain

(Received 17 November 2004; revised 14 July 2005; accepted 18 July 2005)

High-frequency spectral notches are important cues for sound localization. Our ability to detect them must depend on their representation as auditory nerve (AN) rate profiles. Because of the low threshold and the narrow dynamic range of most AN fibers, these rate profiles deteriorate at high levels. The system may compensate by using onset rate profiles whose dynamic range is wider, or by using low-spontaneous-rate fibers, whose threshold is higher. To test these hypotheses, the threshold notch depth necessary to discriminate between a flat spectrum broadband noise and a similar noise with a spectral notch centered at 8 kHz was measured at levels from 32 to 100 dB SPL. The importance of the onset rate-profile representation of the notch was estimated by varying the stimulus duration and its rise time. For a large proportion of listeners, threshold notch depth varied *nonmonotonically* with level, increasing for levels up to 70–80 dB SPL and decreasing thereafter. The nonmonotonic aspect of the function was independent of notch bandwidth and stimulus duration. Thresholds were independent of stimulus rise time but increased for the shorter noise bursts. Results are discussed in terms of the ability of the AN to convey spectral notch information at different levels. © *2005 Acoustical Society of America.* [DOI: 10.1121/1.2032067]

PACS number(s): 43.66.Ba, 43.66.Fe, 43.66.Qp [GDK] Pages: 2458–2469

I. INTRODUCTION

High-frequency spectral notches generated by the filtering action of the pinna (Lopez-Poveda and Meddis, 1996; Shaw, 1974; Shaw and Teranishi, 1968) are important cues for sound localization (Butler and Belendiuk, 1977; Butler and Humanski, 1992; Hebrank and Wright, 1974). Particularly important is the notch whose center frequency increases gradually from around 6500 to 10000 Hz as the vertical location of the sound source moves from −40° to +60° relative to the horizontal plane (for a review see Lopez-Poveda, 1996). The bandwidth of this notch at its 5-dB-down points ranges from 1000 Hz at −40° elevation to 4000 Hz at +10° elevation (c f. Shaw and Teranishi, 1968; Chap. 4 in Lopez-Poveda, 1996).

The auditory nerve (AN) is the only transmission path of acoustic information to the central auditory system. Therefore, the ability to detect and employ high-frequency spectral notches for sound localization requires that they be adequately represented in the AN response. In the AN, spectral features can be represented in the temporal pattern of AN fiber response across characteristic frequencies (CFs) or as rate profiles; that is, in terms of the fibers' discharge rate as a function of their CF (Sachs and Young, 1979). However, spectral features with frequencies above the cutoff of phase locking [>4000 Hz; Johnson (1980); Palmer and Russell (1986)] are most likely to be represented in terms of AN discharge rate alone (Rice *et al.*, 1995).

AN fibers have been classified in either two (Evans and Palmer, 1980; Kiang *et al.*, 1965) or three (Liberman, 1978; Winter *et al.*, 1990) types on the basis of their spontaneous rate. Fibers with high spontaneous rates (HSR) (>15 spikes/s) amount to approximately 61% of the population. These have low thresholds (<10 dB SPL) and dynamic ranges of approximately 30–40 dB (Sachs and Abbas, 1974; Evans and Palmer, 1980). The remaining 40% of the fibers are of a medium- (MSR) or low-spontaneous rate (LSR) type. These have higher thresholds (>15 dB SPL) and wider dynamic ranges (~50–60 dB; Evans and Palmer, 1980; Sachs and Abbas, 1974).

The existence of at least two fiber types with distinct thresholds and dynamic ranges have led several investigators (Delgutte and Kiang, 1984a; Rice *et al.*, 1995; Sachs and Young, 1979) to suggest that the *high-frequency* spectral characteristics of a stimulus could be conveyed to the central auditory system in the rate profile of HSR and LSR fibers at low and high levels, respectively. However, the apparent quality[1] of rate profiles degrades as the stimulus level is increased even when the rate profile of LSR fibers is considered separately from that of HSR fibers (Delgutte and Kiang, 1984a, b; Rice *et al.*, 1995; Sachs and Young, 1979). Among the factors that may contribute to the deterioration of the quality of the rate profiles at high levels are the broadening of the fibers frequency response with level (Rose *et al.*, 1971), the saturation of their discharge rate[2] (Sachs and Young, 1979), and the fiber-to-fiber variation in rate (Rice *et al.*, 1995).

Therefore, if the perception of high-frequency spectral features is based on analyzing the shape of AN rate profiles, the detection of high-frequency spectral notches should be-

[a)]Portions of this work were presented at the 27th Midwinter Meeting of the Association of Research in Otolaryngology, Daytona Beach, FL, February 2004.

[b)]Author to whom correspondence should be addressed; electronic mail: ealopezpoveda@usal.es

come increasingly more difficult as the sound level increases. The aim of this study is to test this hypothesis. In the main experiment, the threshold notch depth necessary to discriminate between a flat spectrum broadband noise and a similar noise with a spectral notch centered at 8 kHz was measured at levels from 32 to 100 dB SPL (Fig. 1). It will be shown that, contrary to the above-noted hypothesis, the threshold notch depth for discrimination is a *nonmonotonic* function of stimulation level.

In addition to the role of LSR fibers, other mechanisms have been proposed to explain how high-frequency spectral features are encoded in the AN response at high levels. For instance, Delgutte and Kiang (1984a, b) suggested that at high levels, when the adapted (steady-state) response of many of the fibers is saturated, the stimulus spectrum may still be represented reasonably well in the *onset* rate profiles. Their suggestion is based on the fact that AN fibers have a wider dynamic range over the first few (5–20) milliseconds of their response (Smith and Brachman, 1980).

Direct evidence is lacking (to the present authors' knowledge) that the dynamic range of AN fibers gets wider the shorter the stimulus rise time. However, this is likely to be the case as the maximum onset rate of AN fibers depends on the stimulus rise time [see Fig. 3 in Delgutte (1980)] and models of AN adaptation suggest that the level at which the maximum onset rate occurs gets higher the shorter the rise time [e.g., Fig. 2 in Meddis (1988)]. Therefore, following Delgutte and Kiang's suggestion (1984a, b), it is reasonable to hypothesize that the AN rate-profile representation of the stimulus spectrum should be clearer for sounds with abrupt onsets, particularly at high stimulus levels. Moreover, if at high levels an important proportion of the spectral information were indeed conveyed in the onset AN rate profile, spectral shape discrimination should hardly depend on the stimulus duration.

These hypotheses were tested by repeating the above-presented experiment but using different noise burst durations (20 vs 220 ms) and rise/fall times (2, 10, and 30 ms). It will be shown that contrary to the hypotheses, threshold notch depth is hardly affected by the stimulus rise time and depends strongly on stimulus duration, even at high levels.

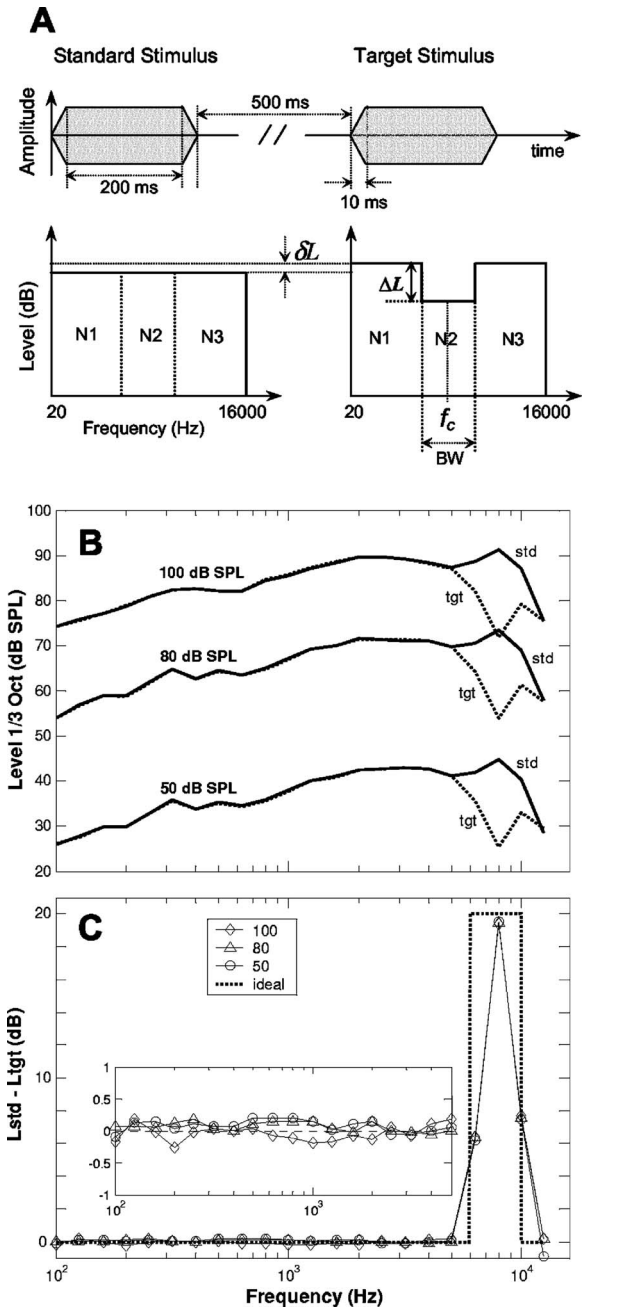

FIG. 1. (a) Wave forms and spectra of the standard and target noises. (b) Actual SPLs for the flat-spectrum (continuous lines) and the notched (dotted lines) noises delivered by the Etymotic ER2 transducer (see footnote 4).[4] The notched noise contained a 4000-Hz-wide, 20-dB-deep spectral notch. The reference spectrum level was the same for the flat-spectrum and the notched noises, and such that the overall SPL for the flat-spectrum noise was equal to 50, 80, and 100 dB SPL (indicated by the number next to each line). (c) SPL differences between the flat-spectrum and the notched noises for stimuli with overall levels of 50, 80, 100 dB SPL. The inset provides greater detail on the differences. The thick dotted line illustrates an ideal difference spectrum. Note that the actual difference profiles are almost identical at the three overall levels tested. This demonstrates that the cues available for the discrimination are identical at overall levels of 50, 80, and 100 dB SPL, at least for frequencies up to 12500 Hz.

II. METHODS

A. Procedure

Notch depths at threshold were measured using a three-interval, three-alternative forced-choice paradigm. In two of the intervals (standard intervals), the stimulus consisted of a noise burst with a flat spectrum from 20 to 16000 Hz. In the other (target) interval, the stimulus consisted of a burst of noise with a notch in its spectrum (Fig. 1). The three intervals were presented in random order to the listener who was instructed to detect the odd one out. The silence period between interval presentations was 500 ms.

The initial notch depth (ΔL in Fig. 1) was always fixed at 20 dB below the reference spectrum level of the noise. An adaptive procedure was employed to estimate the 70.7% correct point in the psychometric function (Levitt, 1971). During the adaptive procedure, notch depth decreased after two consecutive correct responses and increased after an incorrect response. Notch depth increased or decreased by 6 dB for the first four turn points and by 1 dB thereafter. Sixteen turn points were recorded for each measurement and the threshold estimate was taken as the mean of the notch depths

for the last 12 turn points. When the corresponding standard deviation (SD) exceeded 6 dB, the measurement was discarded (invalid threshold) and a new threshold was obtained. The thresholds reported in this study correspond to the *geometric* mean of at least three valid measurements (see Sec. III A for more details). Sometimes detecting the notch was impossible (the adaptive procedure did not converge). Whenever this happened and to prevent endless sessions, the automatic adaptive paradigm was set to stop after 80 stimulus presentations.

Notch depths at threshold were measured as a function of the overall level of the stimulus. Overall levels ranged from 32 to 100 dB SPL (these correspond to spectrum levels of −10 to 58 dB SPL for the flat-spectrum noise). 10-dB steps were used for levels from 32 to 92 dB SPL. Sessions were organized in blocks of eight runs; each run for a single overall level. Within each block, levels were ordered quasirandomly, although the stimuli with the higher-levels (>70 dB SPL) were presented at the end of the block. This aimed at minimizing any effect that temporary threshold shifts may have on spectral discrimination of low-level sounds.

Listeners were tested individually in a double-wall sound-attenuating chamber. Interaction was provided by means of a response box. Lights were used to mark the presentation of the stimuli and to give listeners trial-by-trial feedback on their responses. Stimuli were delivered monaurally to the listener via Etymotic Research ER2 insert earphones. This earphone is designed to have a flat frequency response at the eardrum up to approximately 16000 Hz. The sound pressure levels (SPLs) reported in the following are calibrated values [for a flat-spectrum broadband noise (20 to 16000 Hz), the calibrated SPL output at a microphone coupled to a Zwislocki occluded ear simulator was 100 dB SPL for 2.3 V_{rms}].

B. Stimuli

The center frequency (f_c) of the spectral notch was fixed at 8000 Hz. The reference condition was with a notch bandwidth (BW) of 2000 Hz, and a stimulus duration of 220 ms, including 10-ms cosine-squared rise/fall ramps. The effect of notch bandwidth was investigated by testing notch BWs of 1000, 2000, and 4000 Hz. The effect of the stimulus duration was investigated by testing stimulus durations of 20 and 220 ms, both including 10-ms rise/fall times. The effect of the stimulus rise time was investigated by setting the stimulus duration at 220 ms and using rise/fall times of 2, 10, and 30 ms.

1. Noise generation

The standard and the target noise bursts were made by adding three separately generated noises with different narrowband flat spectra (N1, N2, and N3 in Fig. 1): N1 with frequency components from 20 to $f_c-0.5$ BW Hz; N2 with a spectrum centered at $f_c=8000$ Hz and a bandwidth equal to the notch bandwidth; and N3 with components ranging from $f_c+0.5$ BW to 16000 Hz.

Each of the three noises, N1, N2, and N3, were generated digitally in the time domain (sampling frequency =48 828 Hz) by adding sinusoids of equal amplitude but random phases uniformly distributed between 0 and 2π rad. The frequencies of the sinusoids spanned the spectral bandwidth of each of the noises in steps of 1 Hz. The wave forms of N1, N2, and N3 were then added together on a sample-by-sample basis in a TDT™ System 3 psychoacoustics workstation. The noise burst corresponding to a standard interval was generated by adding N1, N2, and N3, all with identical spectrum levels. The notched-noise burst (target interval), however, was generated by attenuating N2 by ΔL dB (the notch depth) as required (Fig. 1), and adding the resulting wave form to those of N1 and N3. Notch depths (ΔL in Fig. 1) are, therefore, expressed in dB relative to the spectrum level of N1 or N3.

Before delivering the stimuli, the overall level of the combined noise (N1+N2+N3) was set digitally by attenuating the signal as required. Signal clipping at high levels was avoided by ensuring that no sample of the combined digital noise reached the maximum output voltage of the TDT system (±10 V). This is an important point because the distortion associated with clipping could smear the spectrum of the notched noise in the target interval, hence making notch detection and the interpretation of the results more difficult. Furthermore, transducer distortion did not affect the results at high levels, as shown in Figs. 1(b) and 1(c), because the voltage required (2.3 V_{rms}) to produce the maximum level considered in this study (100 dB SPL) was within the nominal operational limits (2.5 V_{rms}) of the Etymotic ER2 transducer.

2. Strategies for making level differences unreliable discrimination cues

The presence of the notch in the target stimulus makes its overall level lower than that of the standard stimuli. For example, a level difference of 1.23 dB occurs for the broadest (4000-Hz-wide) notch considered and with the maximum notch depth measured (18.4 dB as shown in Fig. 2). Such a level difference could be used as a cue in a task aimed at measuring the listeners' ability to discriminate between spectral shapes. Hence, it could complicate the interpretation of the results.

Two different strategies were employed to reduce this unwanted effect. The first strategy consisted of presenting the standard and the target stimuli with *equal* overall levels. This was achieved by reducing the spectrum level of the standard noise as necessary (δL in Fig. 1) to make its overall level identical to that of the notched-noise (target) stimulus. It can be shown that the necessary reduction (in dB) is equal to

$$\delta L(\mathrm{dB}) = 10 \cdot \log_{10}\left[1 + \frac{\mathrm{BW}_{\mathrm{N2}}}{\mathrm{BW}_T}\left(10^{-\Delta L/10} - 1\right)\right], \qquad (1)$$

where $\mathrm{BW}_{\mathrm{N2}}$ is the bandwidth of noise N2 (Hz); BW_T is the total bandwidth (Hz) of the noise (15980 Hz); and ΔL is the notch depth (dB). To get an idea of the necessary reduction in spectrum level, δL equals −0.58 dB for a 2000-Hz-wide, 27-dB-deep notch. Notice that δL [Eq. (1)]

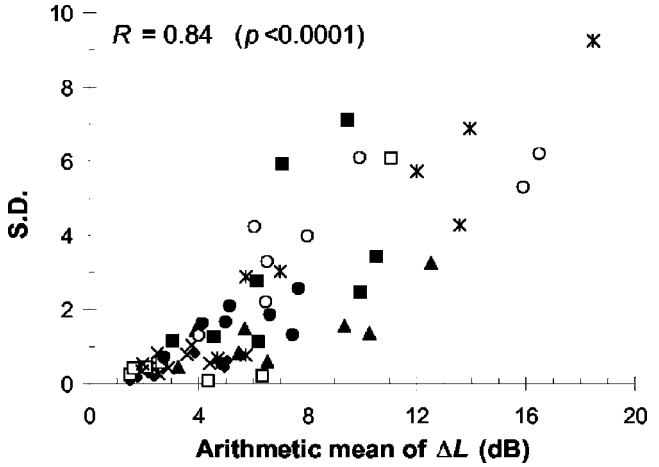

FIG. 2. Standard deviation of threshold notch depths (SDs) as a function of their associated arithmetic means. Data are pooled from Fig. 4 and thus are for eight listeners and the whole range of levels. Different symbols illustrate data for different listeners. The strong significant correlation (Pearson's $R = 0.84$, $p < 0.0001$) between the arithmetic mean and SD suggests that threshold notch depth does *not* conform to an "equal-variance" distribution.

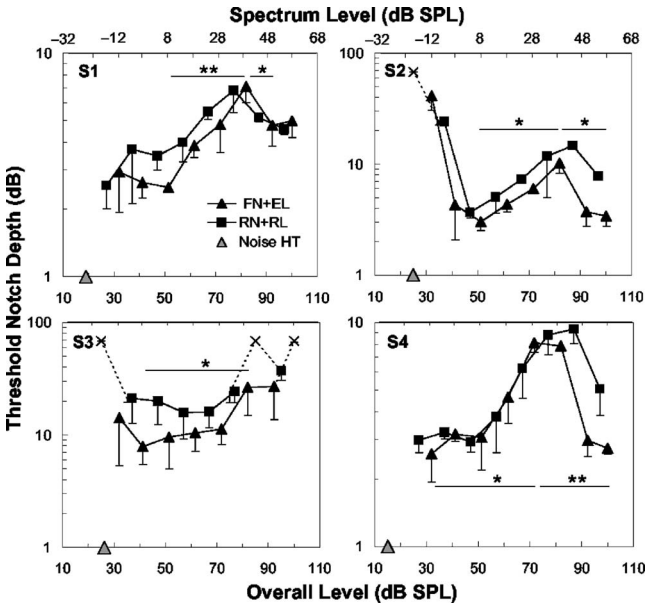

FIG. 3. Threshold notch depths for discriminating between a flat-spectrum noise and a notched noise plotted as a function of the stimulus overall level (the corresponding spectrum level scale is also shown at the top of the upper panels). The notches were centered at 8000 Hz and had a bandwidth of 2000 Hz. Each panel illustrates data for a single listener as indicated in the upper-left corner of each panel (note the different scales on the y axis of each panel). Each data point corresponds to the geometric mean of at least three measurements. Error bars illustrate the 68% confidence interval (see the text for details). Crosses indicate conditions for which no discrimination between the target and the standard stimuli was possible. Shaded triangles on the abscissa indicate the listener's absolute hearing threshold (HT) for the standard noise. Thresholds were measured in two experimental conditions: in the frozen noise/equalized level (FN-EL) condition and in the random noise/roving level (RN-RL) condition. Horizontal bars and asterisks apply to the FN-EL condition only, and denote statistically significant differences between the maximum threshold notch depth that occurs around 70–80 dB SPL and the lowest values that occur on each side of the maximum (single-tailed paired Student's t-test; one and two asterisk denote $p < 0.1$ and $p < 0.01$, respectively). The main result is the *nonmonotonic* variation of threshold notch depth with stimulus level observed for S1, S2, and S4 in the two conditions tested.

is also equal to the overall level difference between the standard, flat-spectrum noise of bandwidth BW_T and the target noise with a spectral notch of bandwidth BW_{N2} and depth ΔL.

Whenever this equalized-level strategy was employed, the same noise tokens N1, N2, and N3 were used for the standard and the target intervals and for every block of every condition. This condition will be hereafter referred to as *frozen-noised/equalized-level* (FN-EL).

The second strategy to prevent the use of level differences as discrimination cues consisted of presenting each of the intervals in a given trial at a different overall level (level roving). The idea is to make differences in overall level *and also* level differences within any given frequency band unreliable cues for detecting the spectral notch, forcing stimulus discrimination to be based solely on differences in overall spectral shape. This method of level randomization has been used in other notch detection experiments (Moore *et al.*, 1989) and is a common practice in spectral-shape discrimination tasks [for a review see Green (1988)]. Here, for any given trial, the overall level of the stimuli was randomly attenuated by an amount between 0 and 10 dB with respect to the corresponding reference level (uniform distribution, 0.25-dB steps). As a result of this, for any given reference spectrum level, the actual spectrum level for this condition was on average 5 dB lower. This will be taken into account when illustrating the results.

Even with a roving level, a notch that is deep enough could in principle be detected on the basis of comparing the overall level across intervals (cf., Green, 1988). According to Eq. (1), the overall level difference between the target and the standard stimuli increases asymptotically with increasing notch depth (ΔL in dB). Such a difference approaches 1.25 dB for the broadest (4000-Hz-wide) notch considered in the present study. Given that level was roved between 0 and 10 dB with a uniform distribution, this implies that spectral discrimination based on overall level comparisons can still occur despite the level roving, but only in 12.5% of the occasions and in the least favorable case; that is, for the broadest and deepest notch. In summary, the present level roving strategy guarantees that the listeners' responses be based on spectral shape discrimination in more than 87.5% of the occasions.

Whenever this level-roving strategy was employed, different (*random*) N1, N2, and N3 noise tokens were employed for different intervals and for different conditions. This was intended to investigate to what extent the use of stimuli with different temporal structures makes notch detection more difficult relative to the FN-EL condition. This condition will be hereafter referred to as *random-noise/roving-level* (RN-RL).

No significant differences were observed in the results obtained with either strategy (see Fig. 3 and Sec. III B). For this reason and for convenience, the frozen-noise/equalized-level strategy was more generally used in the experiments reported in the following.

C. Listeners

Data were collected for eight listeners with ages ranging from 20 to 40 years, although some of the listeners were not

tested in all conditions. Their absolute thresholds were within 20 dB re. ANSI 3.6-1996 (Specifications for Audiometers) at the audiometric frequencies (250–8000 Hz). All listeners were given at least one training session in the task. Only S1 (author A.A.P.) had previous experience in psychoacoustic tasks.

III. RESULTS

A. The statistical distribution of notch depth

Figure 2 illustrates that there is a strong correlation ($R=0.84, p<0.0001$) between the *arithmetic* mean and the corresponding SD of threshold notch depth. Furthermore, threshold notch depths are limited to values $\geqslant 0$ dB. These properties demonstrate that threshold notch depth does *not* conform to an "equal-variance" distribution (cf., Bland and Altman, 1996a). Indeed, the data in Fig. 2 conform to a *lognormal* distribution with a probability of $p=0.94$ (two-tailed Kolmogorov-Smirnoff test). For this reason, the results are hereafter illustrated as the *geometric* mean plotted on a *logarithmic* scale (Bland and Altman, 1996a, b, c). Furthermore, the variability of the results is illustrated as the 68% confidence interval of the geometric mean (equivalent to the more conventional arithmetic mean plus and minus one SD) (Bland and Altman 1996b, c, d).

This procedure is similar to and inspired by a previous level-discrimination study (Buus and Florentine, 1991) where it is suggested that level-discrimination thresholds are appropriately represented by plotting the difference limen for a change in sound level on a logarithmic scale. In that case, the argument in favor of this procedure was that this type of representation "provides a straightforward relation between measurements of discrimination thresholds and the sensitivity of the auditory system" as estimated in terms of *d*-prime (Buus and Florentine, 1991, p. 1379 and their Fig. 7).

B. Discrimination is based on detecting differences in overall spectral shape

Figure 3 illustrates threshold notch depth versus level functions for four representative listeners (S1–S4) for a notch bandwidth of 2000 Hz. Each panel illustrates data for a different listener (as indicated in the upper left corner of the panels). Shaded triangles on the abscissa illustrate the listener's absolute threshold for the flat-spectrum (standard) noise. Crosses indicate conditions for which the notch was undetected consistently in three or more trials. Note that the *y*-axis scale differs across panels.

Threshold notch depth values for the random-noise/roving-level condition (squares; RN-RL) are comparable or slightly larger than those for the frozen noise/equalized-level condition (triangles, FN-EL). Except for listener S3, the poorest performer, the main differences between the results for the two conditions occur at the highest overall levels. For the most part, these differences may be attributed to roving the level rather than to using random noise. If the use of frozen noise facilitated notch detection as a result of the listeners memorizing its temporal pattern, depths would be considerably lower at *all* levels for the FN-EL condition (triangles in Fig. 3) and this is not the case. Furthermore, all participants reported that level randomization was an important distracter, particularly at high levels. This agrees with the observations of Moore *et al.* (1989), who showed a deterioration in the detection of notches centered at 8000 Hz with level randomization. Moore *et al.* attributed this deterioration to a reduction of the listener's attention towards the fainter spectral features when more prominent perceptual changes are introduced.

Given that the observed differences are small and that randomizing the level for each stimulus presentation makes energy within or outside the notch band an unreliable cue for stimulus discrimination, it can be reasonably concluded that even in the frozen-noise/equalized-level condition listeners discriminate between the target and the standard stimuli by detecting a notch in a flat reference spectrum rather than by monitoring the level over certain frequency regions (i.e., in the notch band or elsewhere).

C. Notch depth increases *nonmonotonically* with level

Figure 3 illustrates that for three of the four listeners (S1, S2, and S4), threshold notch depth increases *nonmonotonically* with level. Consider, for example, the frozen-noise/equalized-level condition (triangles). Depth values increase from approximately 3 dB at 40 dB SPL to approximately 9 dB at 70–80 dB SPL and then decrease again to 3 dB (S2 and S4) or 5 dB (S1). For these three listeners, the differences between the largest and the smallest threshold notch depth values are statistically significant, as indicated by the horizontal bars and their associated asterisks in Fig. 3 [single-tailed paired Student's *t*-test on the ln-transformed data (Bland and Altman, 1996d); one asterisk: $p<0.1$; two asterisks: $p<0.01$]. The other listener (S3) was the "poorest" performer and reported that the task was very difficult. Her threshold depth values are larger across levels than those for the other three listeners. They increase from 8 dB at 42 dB SPL to 10 dB at 72 dB SPL, and then increase more rapidly with level until the notch becomes undetectable at 100 dB SPL (indicated by a cross). Also, the variability of her results is overall larger than those for the other three listeners. This may occur as a result of her having worse frequency resolution and/or her finding it more difficult to follow an appropriate spectral discrimination cue.

It is noteworthy that for listeners S2 and S3, threshold notch depth values are larger at the lowest overall level (32 dB SPL) and decrease rapidly for the next level tested (42 dB SPL). It is likely that this result reflects simply that 32 dB SPL is only 4 and 5 dB above the noise absolute threshold of listeners S2 and S3, while it is 11 and 15 dB above the absolute threshold of listeners S1 and S4, respectively.

To confirm that nonmonotonic threshold notch depth versus level functions are the norm, the experiment was carried out for eight listeners (S1–S8) for the frozen-noise/equalized-level condition. This time, however, the notch bandwidth was set to 4000 Hz because it is an easier condition. The results are illustrated in Fig. 4. Although the actual values vary considerably across listeners, notch depth increases nonmonotonically with level for *all* of them except S3, at least qualitatively. Quantitatively, however, the differ-

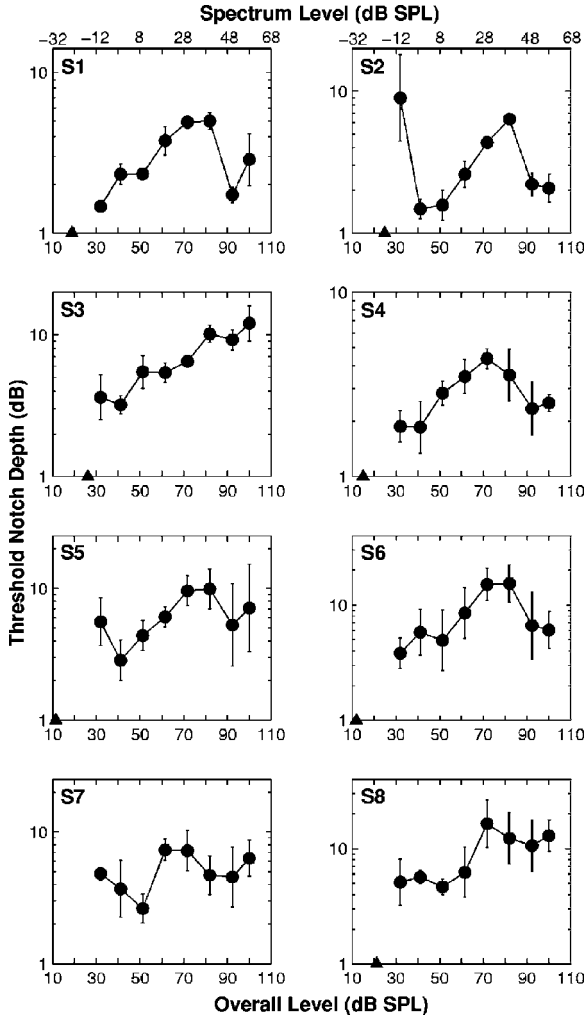

FIG. 4. Threshold notch depth vs. level functions for a spectral notch centered at 8000 Hz and a bandwidth of 4000 Hz. Except for the notch bandwidth, the experimental conditions were the same as for the FN-EL condition of Fig. 3. Each panel illustrates data for a single listener as indicated in the upper-left corner of each panel (note the different scales on the *y* axis of each panel). Error bars illustrate the 68% confidence interval of the geometric mean. Horizontal bars and asterisks denote statistically significant differences between the maximum threshold notch depth that occurs around 70–80 dB SPL and the lowest values that occur on each side of the maximum (single-tailed paired Student's *t*-test; one and two asterisk denote $p < 0.1$ and $p < 0.01$, respectively). Shaded triangles illustrate the hearing thresholds for the standard noise. For four of the eight listeners (S1, S2, S4, and S6), threshold notch depth is a clear nonmonotonic function of level. For three other listeners (S5, S7, and S8), the function is qualitatively nonmonotonic but the result is statistically not significant. S3 is the only listener for whom threshold notch depth increases monotonically with increasing level.

ence between the largest threshold notch depth value and the lowest one that occurs at a higher level is statistically significant for four (S1, S2, S4, and S6) out of the eight listeners only (single-tailed paired Student's *t*-test on the ln-transformed data; one asterisk: $p < 0.1$; two asterisks: $p < 0.01$). A maximum in the nonmonotonic functions occurs at approximately the same level (70–80 dB SPL) for *all* listeners except S3.

D. Notch depths are comparable at overall levels of 42 and 100 dB SPL

The quality of the rate-profile representation of the spectral notch is expected to deteriorate at high levels as a result of the broadening of the fibers' frequency response with level (Rose *et al.*, 1971), the saturation of their discharge rate (Sachs and Young, 1979), and/or the fiber-to-fiber variation in rate (Rice *et al.*, 1995). However, the nonmonotonic character of the threshold notch depth versus level functions suggests that the spectral notch is equally well represented in the AN response at 42 and 100 dB SPL. To investigate whether this is actually the case, threshold notch depths at 100 dB SPL were statistically compared with those at 42 dB SPL for each listener (single-tailed, paired Student's *t*-test on the ln-transformed data). Results are illustrated in Fig. 5 for the two notch bandwidths tested (2000 and 4000 Hz) and for the frozen-noise/equalized-level condition. Threshold notch depth values are larger at 100 dB SPL for approximately 50% of the listeners. However, statistically significant ($p < 0.05$) differences are rare (denoted by asterisks in Fig. 5). The significance of this result is discussed later (Sec. IV A)

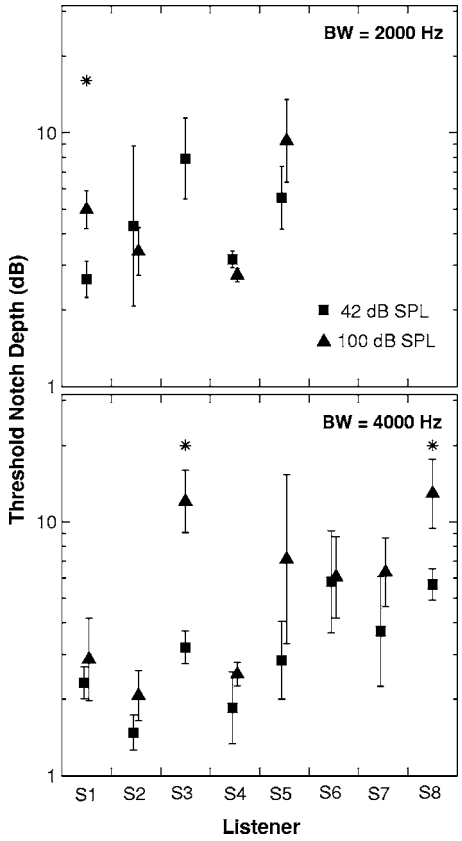

FIG. 5. Comparison of individual threshold notch depths at overall levels of 42 and 100 dB SPL, for notch bandwidths of 2000 (top panel) and 4000 Hz (bottom panel). To facilitate the comparison between the results at the two sound levels, data points for any given listener appear slightly displaced horizontally as necessary. Error bars indicate the 68% confidence interval of the geometric mean. Asterisks indicate significant differences between the thresholds at 42 and 100 dB SPL (single-tailed, paired Student's *t*-test; $p < 0.05$). Although notch depths are generally larger at 100 dB SPL, statistically significant differences are rare.

E. The effect of notch bandwidth

Figure 6 illustrates threshold notch depth versus level functions for the frozen-noise/equalized-level condition for three notch bandwidths: 1000, 2000, and 4000 Hz. Crosses illustrate conditions for which notch detection became erratic and three valid measurements could not be obtained.

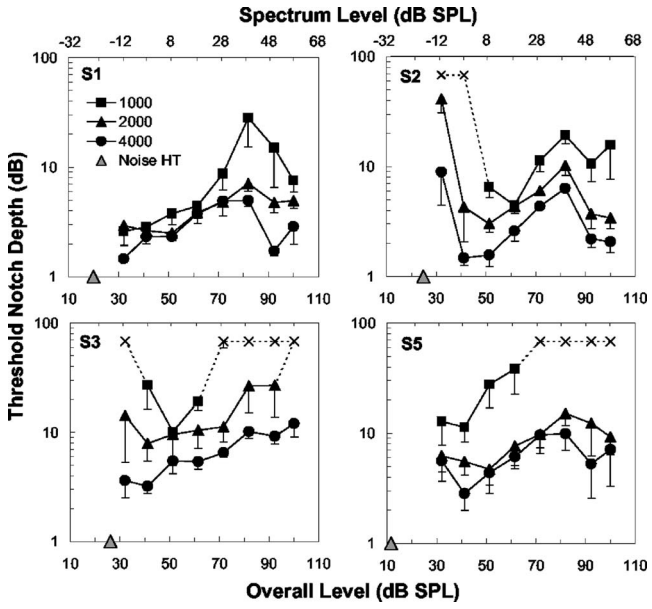

FIG. 6. Threshold notch depth vs. level functions for notch bandwidths of 1000, 2000, and 4000 Hz (as indicated by the inset in the top left panel). Error bars indicate the 68% confidence interval of the geometric mean. Data were obtained using the FN-EL strategy. Stimuli had a total duration of 220 ms, including rise/fall ramps of 10 ms. Each panel illustrates the results for a single listener. Shaded triangles on the abscissa illustrate the HTs for the standard noise.

Results vary widely across listeners. Generally, however, threshold notch depth increases as the notch bandwidth decreases. Interestingly, a significant increase in threshold notch depth occurs for the narrowest, 1000-Hz-wide notch. This is true particularly for listeners S3 and S5 and for overall levels higher than 70 dB SPL. For these listeners and conditions, obtaining a threshold notch depth was impossible.

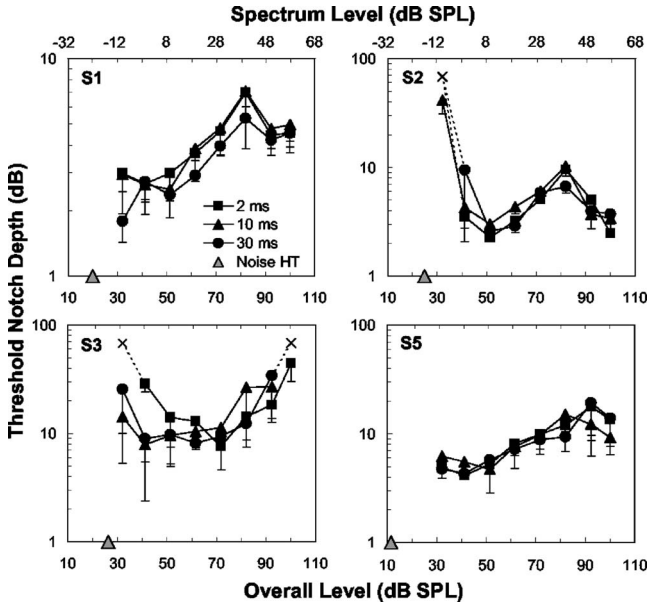

FIG. 7. Threshold notch depth vs. level functions for stimuli with different rise times (as indicated by the inset in the top left panel). Error bars indicate the 68% confidence interval of the geometric mean. In all conditions, the notch had a bandwidth of 2000 Hz and stimuli had a total duration of 220 ms including the rise/fall times. Data were obtained using the FN-EL strategy. Each panel illustrates the results for a single listener. Shaded triangles on the abscissa illustrate the hearing thresholds (HTs) for the standard noise.

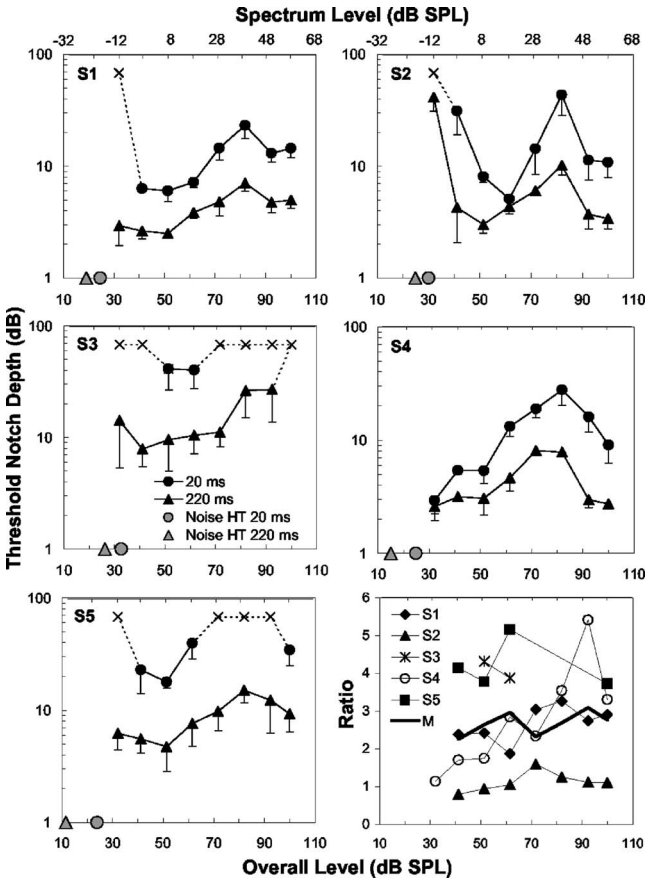

FIG. 8. Threshold notch-depth vs. level functions for stimuli with different durations (as indicated by the inset in the mid left panel). Error bars indicate the 68% confidence interval of the geometric mean. Stimuli rise/fall times were equal to 10 ms in both conditions. Notches had a bandwidth of 2000 Hz. Data were obtained using the FN-EL strategy (see the text for details). Shaded triangles and circles on the abscissa indicate the listener's absolute HTs for the standard noises of 220 and 20 ms of duration, respectively. Each panel illustrates the results for a single listener. The bottom right panel illustrates the ratio of threshold notch depths for the short and long (short/long) stimuli. Each symbol corresponds to a different listener. Note that on average (thick continuous line) the ratio is independent of stimulus level.

Similar results have been described elsewhere. Moore *et al.* (1989) reported that none of their listeners could detect 1000-Hz-wide notches centered at 8000 Hz while they had no problem detecting wider notches. Heinz and Formby (1999) also reported that detecting energy decrements in the spectrogram of a random-level noise was possible only if the spectral bandwidth of the decrement was $\geqslant$500 Hz.

It should also be noted in Fig. 6 that the nonmonotonic effect, when present, is comparable for different notch bandwidths.

F. The effect of stimulus rise time and stimulus duration

Figures 7 and 8 illustrate the effects of stimulus rise time (in four listeners) and of stimulus duration (in five listeners), respectively. The data are for a notch bandwidth of 2000 Hz and for the frozen-noise/equalized-level condition. Clearly,

the stimulus rise time has no significant or systematic effect on notch depth at any of the levels tested (Fig. 7). On the other hand, stimulus duration has a clear effect (Fig. 8). Threshold notch depth values are significantly larger for the short (20-ms) than for the long (220-ms) noise bursts at *all* levels with very few exceptions. The bottom right panel of Fig. 8 illustrates the *ratios*[3] of threshold notch depths for the long and the short stimuli for every listener. Although the ratio varies widely across listeners, its average value equals 2.5 and is approximately independent of level. This shows that the effect of level is comparable for the long and the short stimuli.

IV. DISCUSSION

The aim of the study was to investigate how the detection of spectral notches with center frequencies well above the cutoff of phase locking depends on stimulus level. The effects of other factors such as the notch bandwidth, the stimulus duration and the stimulus rise time have also been investigated. Two hypotheses were tested. First, since the AN rate-profile representation of the stimulus spectrum deteriorates at high levels, threshold notch depths for discrimination should increase monotonically with increasing stimulus level. Second, if at high levels the stimulus spectrum were encoded mostly in the onset rate-profile, threshold notch depths should be smaller for stimuli with abrupt onsets (short rise times) and comparable for long and short stimuli.

Results show that none of these hypotheses hold. For notches 2000- and 4000-Hz wide, although the actual values vary widely across listeners, threshold notch depth is a *nonmonotonic* function of level (Figs. 3 and 4). A clear maximum in the function occurs for overall levels around 70–80 dB SPL for most listeners. Furthermore, threshold notch depths are hardly affected by the stimulus rise time (Fig. 7) and are clearly larger for noise bursts of 20 ms of duration than for bursts 220-ms in duration (Fig. 8).

A. Physiological interpretation

1. The nonmonotonic character of the threshold notch depth versus level functions

Nonmonotonic threshold notch depth versus level functions have been observed for both the equalized and roving level conditions (Fig. 3). For the reasons explained earlier (Sec. II B 2), this suggests that discriminating between the flat-spectrum and the notched noise bursts is based on detecting differences in overall spectral shape, rather than on detecting energy differences in the frequency region of the notch or elsewhere. The notches tested span a region of frequencies higher than the cutoff of phase locking (Johnson, 1980). Hence, they are unlikely to be encoded in the temporal aspects of the AN response. Instead, they must be encoded in the rate of the response, possibly as a rate profile. Therefore, the nonmonotonic character of the threshold notch depth versus level functions suggest that the quality of the AN rate profile representation of the stimulus spectrum must be a nonmonotonic function of level. In other words, the stimulus spectrum must be reasonably well encoded in the AN rate profile at low and high levels, but more poorly represented at 70–80 dB SPL.

Considering the classification of AN fibers suggested by Winter *et al.* (1990), this result may be interpreted as an indication that humans have HSR and LSR fibers but *no* MSR fibers, at least in the 8000-Hz region. In that case, it is possible that the notch be encoded in the rate profile of HSR fibers at low levels and in that of LSR fibers at high levels. The maximum that occurs for overall levels around 70–80 dB SPL (spectrum levels of 28–38 dB SPL) would reflect the transition between the dynamic ranges of the two. That is, it would occur at levels for which HSR fibers are almost saturated and LSR fibers are just below threshold. MSR fibers have thresholds that are intermediate between those of HSR and LSR fibers (Winter *et al.*, 1990, p. 199). Furthermore, over the range of levels (100 dB) used by Winter *et al.*, their dynamic range appears to be wider than that of HSR and LSR fibers as a result of their showing sloping saturation (cf. Fig. 2 of Winter *et al.*, 1990). Therefore, if MSR fibers were present in the human AN, they could probably encode for the spectral notch at moderate-to-high levels. As a result, the threshold notch depth versus level functions would be unlikely to show a maximum and instead threshold notch depth would probably appear independent of level.

The exact way that the two fiber populations translate into nonmonotonic threshold notch depth versus level functions is unclear. However, the above-given interpretation imposes the restriction that the saturation threshold of HSR fibers *and* the rate threshold of LSR fibers should both occur around the level for which the maximum threshold notch depth occurs. That is, both thresholds would be around an overall level of 70–80 dB SPL or its equivalent spectrum level of 28–38 dB SPL (Figs. 3 and 4). For this range of spectrum levels, the effective SPL seen by an AN fiber with a CF=8000 Hz and an effective bandwidth of 1000 Hz would be approximately equal to 38–48 dB SPL. These values agree well with those estimated from pure-tone AN rate-level functions for other mammalian species (e.g., Fig. 1 of Winter and Palmer, 1991).

The above-noted interpretation also agrees with the conclusions of Zeng *et al.* (1991). They studied the effects of prior stimulation upon intensity discrimination and found unusually large just-noticeable differences for midlevel sounds. Zeng *et al.* (1991) argued that their result is consistent with humans having only two types of auditory nerve fibers, HSR and LSR, each with a different time of recovery from adaptation and a different threshold [see Zeng *et al.* (1991) for a full discussion].

It has been shown (Fig. 5) that threshold notch depths are, with some exceptions, comparable for stimulation levels of 42 and 100 dB SPL so long as the notches are wide enough ($\geqslant$2000 Hz). This is somewhat surprising considering that the frequency response of AN fibers broadens with increasing sound level (Rose *et al.*, 1971), hence the spectral notch should be less clearly represented in the AN rate profile at the highest level tested. One possible explanation for the result is that peripheral suppression may enhance the spectral notch (as represented in the AN rate profile) at high

levels but less so (or nothing at all) at low levels, somehow compensating for the broadening of the fibers' frequency response at high levels. This is a likely explanation because, as discussed by Poon and Brugge (1993), suppression would be expected to cause a decrease in the discharge rate of AN fibers with CFs in the notch region, hence "…enhancing the contrast between the energy level at the spectral notch frequency and that at the surrounding frequencies," and the amount of suppression is more prominent at high levels (e.g., Schalk and Sachs, 1980).

Other explanations exist for the nonmonotonic character of threshold notch depth versus level functions. For example, discrimination based on AN rate responses is likely to be directly proportional to the rate difference between the two stimuli but inversely proportional to their corresponding rate variances (e.g., Young and Barta, 1986; Winter and Palmer, 1991). Consequently, small rate variances may lead to discriminable percepts even when the associated-rate difference is small. The variance-to-mean ratio of AN rate responses decreases with increasing mean rate, that is, with increasing stimulus level (e.g., Winter and Palmer, 1991; Young and Barta, 1986). Therefore, it is possible that the improvement in spectral discrimination observed at high levels results from a reduction in the fibers' variance-to-mean ratio in combination with (or perhaps instead of) the above-mentioned spectral-enhancing effects of suppression.

Basilar membrane (BM) compression may also contribute to the nonmonotonic character of the threshold notch depth versus level functions. Some studies (though not all; see Robles and Ruggero, 2001, pp. 1308–1309) suggest that the basal region of the BM responds linearly at low ($<$40 dB SPL) and high ($<$90 dB SPL) levels, but compressively at intermediate levels. If this were the case, the spectral notch would be more clearly represented in the BM excitation pattern at low and high levels, where linear responses occur, than at moderate levels, for which the notch would appear shallower in the BM excitation pattern as a result of compression. Additionally, cochlear distortion may negatively affect the BM representation of the spectral notch as a result of distortion-product energy traveling from remote BM sites, where they are generated, to those with CFs within the notch band (cf. Robles *et al.*, 1997). This effect is likely to be maximal at moderate levels for which compression is greatest. On the other hand, the effects of BM compression are unlikely to explain by themselves the nonmonotonic character of the function. BM compression is approximately constant over a wide range of input levels ($\sim$40-90 dB SPL, e.g., Ruggero *et al.*, 1997); hence, should the previous explanation be correct, it would lead to a plateau-shaped nonmonotonic function rather than to the peak-shaped curve that is more common in the present results.

It must be acknowledged that all the above-noted interpretations implicitly assume that listeners use the same cues at all levels and that the internal representation of the spectral notch degrades at levels around 70–80 dB SPL. However, an *alternative* explanation could be that the cues used for spectral discrimination are different at low and high levels. It could well happen that the cues that are salient at low levels degrade as the level increases and that new cues improve with increasing level to become most salient at high levels. The nature of these cues is uncertain at this time. It is unlikely that spectral discrimination at high levels be facilitated by distortion in the stimuli because, as shown in Fig. 1(c), the actual difference spectrum between the target and the standard noises are comparable for overall levels of 50, 80, and 100 dB SPL.

It should be noted that the above-discussed explanations are not mutually exclusive. They can all contribute simultaneously to explain the data. On the other hand, it is not the purpose of this report to provide a convincing explanation of the nonmonotonic effect. Physiological and modeling work is currently under way to clarify this issue (Alves-Pinto *et al.*, 2005a, b).

2. The effect of notch bandwidth and its interaction with level

Detection of spectral notches with bandwidths equal or greater than 2000 Hz was generally possible at all levels. On the other hand, detection of notches 1000-Hz wide was clearly much more difficult, particularly at high levels.

Notch detection must be based on spectral discrimination. Given the nature of the stimuli, the most salient information for spectral discrimination is likely to be provided by AN fibers with CFs within and near the notch band (cf. Poon and Brugge, 1993). Those fibers will be driven with less energy by the target, notched stimulus than by the reference, flat-spectrum one. The effective bandwidth of those fibers is around 1000 Hz at low SPLs (e.g. Fig. 10 of Evans, 1975) and increases as the SPL increases (Rose *et al.*, 1971). Therefore, at high levels, the fibers in question will also respond to energy in frequency regions adjacent to the 1000-Hz-wide notch (see Chap. 8 in Lopez-Poveda, 1996). Hence, their response to the notched stimulus will be only slightly smaller than that to the flat-spectrum stimulus, making discrimination between the two more difficult even when the notch is very deep. In psychophysical terms, this relates to the fact that the critical band at 8000 Hz is comparable to the bandwidth of the 1000-Hz-wide notch (Glasberg and Moore, 1990) and increases with level (e.g. Baker *et al.*, 1998). Furthermore, the interlistener variability observed in the present results, particularly for the narrowest notch (Fig. 6), is likely to relate to the wide interlistener variability in auditory filter bandwidth (Patterson and Moore, 1986). As noted earlier (Sec. III B), this may account for the poorer performance of listener S3.

Spectral discrimination is also likely to be affected, though to a lesser extent, by the number of fibers with CFs within the notch band. This number increases as the notch bandwidth increases and this might explain, at least in part, that threshold notch depths be lowest for stimuli with the widest notch. In any case, the shape of the threshold notch depth versus level function is comparable for different notch bandwidths (see Fig. 6), which suggests that the nonmonotonic effect is independent of the number of fibers signaling for the notch.

3. The effect of stimulus duration

AN fibers show a wider dynamic range at the onset of the stimulus (Smith and Brachman, 1980). For this reason, Delgutte and Kiang (1984a, b) suggested that at high levels, when the rate response of the majority of AN fibers is saturated, the stimulus spectrum may still be conveyed in the onset rate profile. Earlier, it has been shown that maximizing the effects of the stimulus onset by reducing the stimulus rise time hardly affected threshold notch depths (Fig. 6). It has also been shown that threshold notch depths were considerably lower for a stimulus duration of 220 ms than for a duration of 20 ms, even at the highest levels tested (Fig. 7). If at high levels notch detection were based *solely* on the onset representation of the stimulus spectrum, no differences would be observed between the long and the short stimuli. Therefore, although the present results do *not* rule out a possible contribution of the onset rate profile to the encoding of the stimulus spectrum, they suggest that the contribution in question is less important than previously suggested (Delgutte and Kiang, 1984a, b; Lopez-Poveda, 1996).

Since both the stimulus and the nature of the AN response are stochastic, the rate-profile representation of the stimulus spectrum surely varies over time. The fact that threshold notch depths are smaller for the longer stimuli across *all* levels tested (Fig. 8) suggests that the longer stimulus provides a clearer representation of the stimulus spectrum. It is possible that the brain integrates (or averages) the rate profile over time with a relatively long time window (Green, 1960). Alternatively, it is possible that the decision be based on taking multiple "looks" at rate profiles computed over a much shorter time window, as suggested by Viemeister and Wakefield (1991). Either of the two mechanisms serves to explain (at least qualitatively) the smaller values of notch depth for the longer stimulus.

Furthermore, it is noteworthy that the effect of level is comparable for the short and the long stimuli when threshold notch depths are plotted on a logarithmic scale. This indicates that the nonmonotonic character of the threshold notch depth versus level function is independent of stimulus duration and, consequently, that it is not determined by temporal integration or multiple looks.

B. Relation with level discrimination results

The dynamic-range problem has been widely investigated by previous psychophysical studies of level discrimination. Indeed, the present results resemble those of level discrimination experiments in a number of respects. First, here it has been shown (Figs. 3 and 4) that threshold notch depth varies nonmonotonically as a function of level. Similarly, the threshold for detecting a level change in a high-frequency stimulus is a nonmonotonic function of level, both for tones (e.g. Carlyon and Moore, 1984; Florentine, 1986; Florentine *et al.*, 1987) and noise (e.g., Buus, 1990; Nizami *et al.*, 2001). Second, the nonmonotonic aspect of the threshold notch depth versus level function appears more obvious for the short (20 ms) than for the long (220 ms) stimuli when the ordinate is on a linear scale, rather than on the logarithmic scale used in Fig. 8. The same is true for the level-change versus level function (e.g., Carlyon and Moore, 1984; Nizami *et al.*, 2001). Finally, here it has been shown that dynamic responses to the signal onset play little role in spectral discrimination (Fig. 7) and this seems to be the case also for level discrimination (Carlyon and Moore, 1984).

The results of level-discrimination experiments led Carlyon and Moore (1984) to suggest a bimodal distribution of thresholds in human primary auditory neurons. Such a suggestion is in line with the "two types of fibers" interpretation proposed earlier for the nonmonotonic aspect of the threshold notch depth versus level function. Of course, detecting a level change is not the same as detecting a spectral notch. Furthermore, as discussed earlier, the detection of the spectral notch is unlikely to be based on comparing the levels of the standard and the target noises (neither the overall level or the level within or outside the notch band). Instead, it is likely to depend on the quality with which the spectral notch is represented in the overall auditory nerve rate profile. Nevertheless, the operation range of auditory nerve fibers will determine, in a similar way, the level-dependence of the quality of the internal representation of the notch (i.e., its depth in the rate profile) and the fibers' difference response to a change in the stimulus level.

C. Relation with sound localization results

Sound localization relies partly on accurately detecting the spectral content of the head-related transfer function (HRTF). Specifically, it has been reported that spectral notches with sound source elevation-dependent center frequencies constitute prominent cues for judging the vertical location of sound sources (e.g., Butler and Belendiuk, 1977; Butler and Humanski, 1992). On the other hand, the bandwidth and the depth of HRTF notches vary widely across listeners [see, for instance, Fig. 3 in Shaw (1982) or Chap. 3 in Lopez-Poveda (1996)], possibly reflecting differences in the shapes and sizes of the listeners' ears (Lopez-Poveda and Meddis, 1996). The present study shows that the ability to detect high-frequency spectral notches varies widely across listeners (Fig. 4), and depends on the notch bandwidth (Fig. 6) as well as on the stimulus level and duration (Figs. 3 and 8). As a result, the ability of listeners to actually use the notches in their individual HRTFs as cues for sound localization must depend on a complex combination of their level of performance in notch detection tasks, the shape of their ears, and the characteristics of the stimulus (duration and level). In any case, since vertical localization relies on detecting HRTF notches, the present results suggest that, in general, localization judgments should be more precise for long stimuli than for short ones and for levels below 60–70 dB SPL than for levels around 70–80 dB SPL and this is indeed the case (Hartmann and Rakerd, 1993; Macpherson and Middlebrooks, 2000; Vliegen and Van Opstal, 2004). Furthermore, in light of the present results an improvement in localization accuracy should occur for levels higher than 80 dB SPL, although this remains to be tested.

Despite the emphasis given here to spectral notches, it must be acknowledged that other authors (e.g., Blauert, 1969/70; Humanski and Butler, 1988) have suggested that

spectral peaks may be as important for sound localization as spectral notches, if not more. The auditory nerve rate-profile representation of spectral peaks at high levels would be also negatively influenced by the limited dynamic range of most nerve fibers. On the other hand, the broadening of the fiber's frequency response with increasing level would not deteriorate the rate-profile representation of peaks. If anything it would enhance it by spreading the energy of the peak to fibers with a wider range of CFs. Consequently, comparing the present results with those of experiments aimed at discriminating between flat-spectrum and peaked noise bursts may help elucidating the relative contribution of both mechanisms (i.e., limited dynamic range and filter broadening) to the auditory nerve representation of spectral features.

V. CONCLUSIONS

The extent that the detection of high-frequency spectral notches is affected by stimulus level was investigated by measuring the threshold notch depth necessary to discriminate between a flat-spectrum wideband noise and a similar noise with a rectangular spectral notch centered at 8000 Hz. The main conclusions are:

(1) High-frequency spectral notches are detected by detecting differences in the overall spectral shape of the stimulus rather than by detecting level differences over certain frequency regions.
(2) For a large proportion of listeners, threshold notch depth is clearly a *nonmonotonic* function of stimulation level. It increases for levels up to 70–80 dB SPL and decreases for higher levels; thus a maximum in the function occurs at levels around 70–80 dB SPL. Interpretations of this result have been discussed based on the physiological response properties of the mammalian auditory nerve.
(3) The nonmonotonic character of the threshold notch depth versus level function is independent of notch bandwidth and stimulus duration.
(4) Threshold notch depths are hardly affected by the stimulus rise time and depend strongly on the stimulus duration. Notch depth values are larger for shorter stimuli. These results suggest that the onset rate-profile contributes less than previously thought to encoding for the stimulus spectrum at high levels. It is also consistent with the idea that the detection of the stimulus spectrum involves either integrating the AN rate profile over a relatively long time window or multiple looks at the rate profiles computed over relatively narrow time windows.

ACKNOWLEDGMENTS

The authors thank David A. Eddins for useful suggestions on a poster version of this work, and Ray Meddis and Alan R. Palmer for their comments on a draft of this paper. The authors are indebted to two anonymous reviewers for their very helpful comments, particularly for suggesting that we use the geometric mean instead of the arithmetic mean and to plot the results on a logarithmic scale. Work supported by the Spanish Fondo de Investigaciones Sanitarias (Grant Nos. PI02/0343 and G03/203) and by European Regional Development Funds.

[1]In this context, the word "quality" must be understood to refer to the degree of similarity between the stimulus spectrum and the AN rate-profile representation.
[2]Some studies report *nonsaturating* LSR fibers (e.g., Winter *et al.*, 1990). The existence of this type of fiber seems to be species and frequency specific but the issue is still controversial.
[3]Since threshold notch depth conforms to a log-normal distribution (Sec. III A), the *ratio* is more appropriate than the *difference* to quantify the effect of duration or of any other stimulus parameter.

Alves-Pinto, A., Lopez-Poveda, E. A., and Palmer, A. R. (**2005a**). "Auditory nerve encoding of high-frequency spectral information," in *Mechanisms, Symbols, and Models Underlying Cognition*, edited by J. Mira and J. R. Álvarez, Lecture Notes in Computer Science **3561**, 223–232.
Alves-Pinto, A., Lopez-Poveda, E. A., and Palmer, A. R. (**2005b**). "Auditory nerve response to broadband noise with high-frequency spectral notches," Abstract 4pPP16, *149th Meeting of the Acoustical Society of America*, Vancouver, Canada, 16–20 May; J. Acoust. Soc. Am. **117**, 2654.
Baker, R. J., Rosen, S., and Darling, A. M. (**1998**). "An efficient characterization of human auditory filtering across level and frequency that is also physiologically reasonable," in *Psychophysical and Physiological Advances in Hearing*, edited by A. R. Palmer, A. Rees, Q. Summerfield, and R. Meddis (Whurr, London), pp. 81–88.
Bland, J. M., and Altman, D. G. (**1996a**). "Measurement error and correlation coefficients," Br. Med. J. **313**, 106.
Bland, J. M., and Altman, D. G. (**1996b**). "Transformations, means and confidence intervals," Br. Med. J. **312**, 1079.
Bland, J. M., and Altman, D. G. (**1996c**). "Transforming data," Br. Med. J. **312**, 770.
Bland, J. M., and Altman, D. G. (**1996d**). "The use of transformation when comparing two means," Br. Med. J. **312**, 1153.
Blauert, J. (**1969/70**). "Sound localization in the median plane," Acustica **22**, 205–213.
Butler, R. A., and Belendiuk, K. (**1977**). "Spectral cues utilized in the localization of sound in the median sagittal plane," J. Acoust. Soc. Am. **61**, 1264–1269.
Butler, R. A., and Humanski, R. A. (**1992**). "Localization of sound in the vertical plane with and without high-frequency spectral cues," Percept. Psychophys. **51**, 182–186.
Buus, S. (**1990**). "Level discrimination of frozen and random noise," J. Acoust. Soc. Am. **87**, 2643–2654.
Buus, S., and Florentine, M. (**1991**). "Psychometric functions for level discrimination," J. Acoust. Soc. Am. **90**, 1371–1380.
Carlyon, R. P., and Moore, B. C. J. (**1984**). "Intensity discrimination: A severe departure from Weber's law," J. Acoust. Soc. Am. **76**, 1369–1376.
Delgutte, B. (**1980**). "Representation of speech-like sounds in the discharge patterns of auditory-nerve fibers," J. Acoust. Soc. Am. **68**, 843–857.
Delgutte, B., and Kiang, N. Y. S. (**1984a**). "Speech coding in the auditory nerve. III. Voiceless fricative consonants," J. Acoust. Soc. Am. **75**, 887–896.
Delgutte, B., and Kiang, N. Y. S. (**1984b**). "Speech coding in the auditory nerve. IV. Sounds with consonant-like dynamic characteristics," J. Acoust. Soc. Am. **75**, 897–907.
Evans, E. F. (**1975**). "Cochlear nerve and cochlear nucleus," in *Handbook of Sensory Physiology*, edited by W. D. Keidel and W. D. Neff (Springer, Berlin), Vol. **5/2**, pp. 1–108.
Evans, E. F., and Palmer, A. R. (**1980**). "Relationship between the dynamic range of cochlear nerve fibers and their spontaneous activity," Exp. Brain Res. **40**, 115–118.
Florentine, M. (**1986**). "Level discrimination of tones as a function of duration," J. Acoust. Soc. Am. **79**, 792–798.
Florentine, M., Buus, S., and Mason, C. R. (**1987**). "Level discrimination as a function of level for tones from 0.25 to 16 kHz," J. Acoust. Soc. Am. **81**, 1528–1541.
Glasberg, B. R., and Moore, B. C. J. (**1990**). "Derivation of auditory filter shapes from notched noise data," Hear. Res. **47**, 103–138.
Green, D. M. (**1960**). "Auditory detection of a noise signal," J. Acoust. Soc. Am. **32**, 121–131.
Green, D. M. (**1988**). *Profile Analysis* (Oxford University Press, New York).
Hartmann, W. M., and Rakerd, B. (**1993**). "Auditory spectral discrimination and the localization of clicks in the sagittal plane," J. Acoust. Soc. Am. **94**, 2083–2092.
Hebrank, J., and Wright, D. (**1974**). "Spectral cues used in the localization

of sound sources on the median plane," J. Acoust. Soc. Am. **56**, 1829–1834.
Heinz, M. G., and Formby, C. (**1999**). "Detection of time- and band-limited increments and decrements in a random-level noise," J. Acoust. Soc. Am. **106**, 313–326.
Humanski, R. A., and Butler, R. A. (**1988**). "The contribution of the near and far ear toward localization of sound in the sagittal plane," J. Acoust. Soc. Am. **83**, 2300–2310.
Johnson, D. H. (**1980**). "The relationship between spike rate and synchrony in responses of auditory-nerve fibers to single tones," J. Acoust. Soc. Am. **68**, 1115–1122.
Kiang, N. Y. S., Watanabe, T., Thomas, E. C., and Clark, L. F. (**1965**). *Discharge Patterns of Single Fibers in the Cat's Auditory Nerve* (MIT, Cambridge).
Levitt, H. (**1971**). "Transformed up down methods in psychoacoustics," J. Acoust. Soc. Am. **49**, 467–477.
Liberman, M. C. (**1978**). "Auditory-nerve response from cats raised in a low-noise chamber," J. Acoust. Soc. Am. **63**, 442–455.
Lopez-Poveda, E. A. (1996). "The physical origin and physiological coding of pinna-based spectral cues," Ph.D. thesis. Loughborough University, Loughborough, UK.
Lopez-Poveda, E. A., and Meddis, R. (**1996**). "A physical model of sound diffraction and reflections in the human concha," J. Acoust. Soc. Am. **100**, 3248–3259.
Macpherson E. A., and Middlebrooks, J. C. (**2000**). "Localization of brief sounds: Effects of level and background noise," J. Acoust. Soc. Am. **108**, 1834–1848.
Meddis, R. (**1988**). "Simulation of auditory-neural transduction: Further studies," J. Acoust. Soc. Am. **83**, 1056–1063.
Moore, B. C. J., Oldfield, S. R., and Dooley, G. J. (**1989**). "Detection and discrimination of spectral peaks and notches at 1 and 8 kHz," J. Acoust. Soc. Am. **85**, 820–836.
Nizami, L., Reimer, J. F., and Jesteadt, W. (**2001**). "The intensity-difference limen for Gaussian-enveloped stimuli as a function of level: Tones and broadband noise," J. Acoust. Soc. Am. **110**, 2505–2515.
Palmer, A. R., and Russell, I. J. (**1986**). "Phase-locking in the cochlear nerve of the guinea-pig and its relation to the receptor potential of inner hair-cells," Hear. Res. **24**, 1–15.
Patterson, R. D., and Moore, B. C. J. (**1986**). "Auditory filters and excitation patterns as representations of frequency resolution," in *Frequency Selectivity in Hearing*, edited by B. C. J. Moore (Academic, London), pp. 123–177.
Poon, P. W. F., and Brugge, J. F. (**1993**). "Sensitivity of auditory nerve fibers to spectral notches," J. Neurophysiol. **70**, 655–666.
Rice, J. J., Young, E. D., and Spirou, G. A. (**1995**). "Auditory-nerve encoding of pinna-based spectral cues: Rate representation of high-frequency stimuli," J. Acoust. Soc. Am. **97**, 1764–1776.
Robles, L., and Ruggero, M. A. (**2001**). "Mechanics of the mammalian cochlea," Physiol. Rev. **81**, 1305–1352.
Robles, L., Ruggero, M. A., and Rich, N. C. (**1997**). "Two-tone distortion on the basilar membrane of the chinchilla cochlea," J. Neurophysiol. **77**, 2385–2399.
Rose, J. E., Hind J. E., Anderson, D. J., and Brugge, J. F. (**1971**). "Some effects of stimulus intensity on response of auditory-nerve fibers in the squirrel monkey," J. Neurophysiol. **34**, 685–699.
Ruggero, M. A., Rich, N. C., Recio, A., Narayan, S. S., and Robles, L. (**1997**). "Basilar-membrane responses to tones at the base of the chinchilla cochlea," J. Acoust. Soc. Am. **101**, 2151–2163.
Sachs, M. B., and Abbas, P. J. (**1974**). "Rate versus level functions for auditory-nerve fibers in cats: Tone-burst stimuli," J. Acoust. Soc. Am. **56**, 1835–1847.
Sachs, M. B., and Young, E. D. (**1979**). "Encoding of steady-state vowels in the auditory nerve: Representation in terms of discharge rate," J. Acoust. Soc. Am. **66**, 470–479.
Schalk T. B., and Sachs, M. B. (**1980**). "Nonlinearities in auditory-nerve fiber responses to bandlimited noise," J. Acoust. Soc. Am. **67**, 903–913.
Shaw, E. A. G. (**1974**). "Transformation of sound pressure level from the free field to the eardrum in the horizontal plane," J. Acoust. Soc. Am. **56**, 1848–1861.
Shaw, E. A. G., and Teranishi, R. (**1968**). "Sound pressure generated in an external-ear replica and real human ears by a nearby point source," J. Acoust. Soc. Am. **44**, 240–249.
Shaw, E. A. G. (**1982**). "External ear response and sound localization," in *Localization of Sound: Theory and Applications*, edited by R. W. Gatehouse (Amphora Press, Groton), pp. 30–41.
Smith, R. L., and Brachman, M. L. (**1980**). "Operating range and maximum response of single auditory nerve fibers," Brain Res. **184**, 499–505.
Viemeister, N. F., and Wakefield, G. H. (**1991**). "Temporal integration and multiple looks," J. Acoust. Soc. Am. **90**, 858–865.
Vliegen, J., and Van Opstal, A. J. (**2004**). "The influence of duration and level on human sound localization," J. Acoust. Soc. Am. **115**, 1705–1713.
Winter, I. M., and Palmer, A. R. (**1991**). "Intensity coding in low-frequency auditory-nerve fibers of the guinea pig," J. Acoust. Soc. Am. **90**, 1958–1967.
Winter, I. M., Robertson, D., and Yates, G. K. (**1990**). "Diversity of characteristic frequency rate-intensity functions in guinea pig auditory nerve fibres," Hear. Res. **45**, 191–202.
Young, E. D., and Barta, P. E. (**1986**). "Rate responses of auditory nerve fibers to tones in noise near masked threshold," J. Acoust. Soc. Am. **79**, 426–442.
Zeng, F.-G., Turner, C. W., and Relkin, E. M. (**1991**). "Recovery from prior stimulation. II. Effects upon intensity discrimination," Hear. Res. **55**, 223–230.

[4]The SPLs were measured with a Brüel & Kjaer sound level meter (model 2238A) coupled to a Zwislocki occluded ear simulator over a frequency range from 100 to 12500 Hz in 1/3 octave bands.

Perceptual interaction between carrier periodicity and amplitude modulation in broadband stimuli: A comparison of the autocorrelation and modulation-filterbank model

Alexandra Stein
Department Biologie II, Universität München, Großhadernerstrasse 2, 82152 Planegg-Martinsried, Germany

Stephan D. Ewert
Centre for Applied Hearing Research, Acoustic Technology, Ørsted DTU, Technical University of Denmark, DK-2800 Kgs. Lyngby, Denmark

Lutz Wiegrebe[a)]
Department Biologie II, Universität München, Großhadernerstrasse 2, 82152 Planegg-Martinsried, Germany

(Received 24 July 2003; revised 22 June 2005; accepted 24 June 2005)

Recent temporal models of pitch and amplitude modulation perception converge on a relatively realistic implementation of cochlear processing followed by a temporal analysis of periodicity. However, for modulation perception, a modulation filterbank is applied whereas for pitch perception, autocorrelation is applied. Considering the large overlap in pitch and modulation perception, this is not parsimonious. Two experiments are presented to investigate the interaction between carrier periodicity, which produces strong pitch sensations, and envelope periodicity using broadband stimuli. Results show that in the presence of carrier periodicity, detection of amplitude modulation is impaired throughout the tested range (8–1000 Hz). On the contrary, detection of carrier periodicity in the presence of an additional amplitude modulation is impaired only for very low frequencies below the pitch range (<33 Hz). Predictions of a generic implementation of a modulation-filterbank model and an autocorrelation model are compared to the data. Both models were too insensitive to high-frequency envelope or carrier periodicity and to infra-pitch carrier periodicity. Additionally, both models simulated modulation detection quite well but underestimated the detrimental effect of carrier periodicity on modulation detection. It is suggested that a hybrid model consisting of bandpass envelope filters with a ripple in their passband may provide a functionally successful and physiologically plausible basis for a unified model of auditory periodicity extraction.
 [DOI: 10.1121/1.2011427]

PACS number(s): 43.66.Ba, 43.66.Hg, 43.66.Mk [NFV] Pages: 2470–2481

I. INTRODUCTION

Within the last decades, many psychoacoustical models have converged to share relatively detailed implementations of auditory peripheral processing. Moreover, these models have been very successful in explaining a large variety of psychoacoustical phenomena, among them periodicity pitch and amplitude-modulation detection.

Even though it is unquestioned that envelope periodicity (such as sinusoidal amplitude modulation) imposed on broadband carriers is extracted in the time domain, the exact neural basis for the perception of harmonic complex sounds which elicit strong pitch sensations is still under debate. One line of research favors frequency domain models which evaluate the degree of neural excitation at harmonically spaced places along the auditory tonotopic axis (Cohen *et al.*, 1995; Goldstein, 1973; Terhardt, 1974). Time-domain models, in contrast, extract the pitch of harmonic sounds through an analysis of the temporal firing characteristics of the auditory nerve.

One of these time-domain models was introduced by Meddis and Hewitt (1991a, b). This model is based on Licklider's (1951) suggestion that the auditory system performs a process similar to autocorrelation in order to extract the periodicity of sounds. In addition, Meddis and Hewitt (1991a) suggested that the result of this autocorrelation is aggregated along the tonotopic frequency axis to produce a purely temporal representation of periodicity. This model accounts for various pitch perception phenomena, e.g., the pitch of the missing fundamental, the existence region, and the dominance region of pitch. Recent tests have also included the pitches of harmonic complexes with alternating phases and sensitivity to mistuned harmonics (Meddis and O'Mard,

[a)]Author to whom correspondence should be addressed; electronic mail: lutzw@lmu.de

1997). With some exceptions, (Carlyon, 1998), this model has been quite successful in predicting the results of many experiments on pitch perception.

A different model, designed to simulate the perception of amplitude modulation, was introduced by Dau *et al.* (1997a, b). It is based on the hypothesis that the envelope wave form undergoes a spectral decomposition similar to the decomposition of the wave form in the inner ear (Houtgast, 1989). This hypothesis is based on the demonstration of frequency selectivity in the envelope domain. Dau *et al.* (1997a) designed a modulation filterbank as a functional implementation of envelope-frequency selectivity. As in the above-mentioned pitch model, the modulation filterbank is preceded by a relatively detailed simulation of peripheral preprocessing stages. The modulation-filterbank model has been quite successful in simulating many aspects of amplitude-modulation perception, e.g., modulation detection for narrow-band noise carriers and envelope-frequency selectivity.

Even though both models aim to simulate different types of experiments, their basic design is very similar. The models share a gammatone filterbank and a functional simulation of mechano-neural transduction in inner hair cells. In both models, these stages are followed by a module which performs a temporal periodicity extraction which in Dau *et al.* (1997a, b) is implemented as a modulation filterbank and in Meddis and Hewitt (1991a, b) and Meddis and O'Mard (1997) is implemented as an autocorrelator. Even though the existence region of pitch and amplitude-modulation detection differs (Krumbholz *et al.*, 2000; Viemeister, 1979), there is still considerable overlap in the periodicity range between about 30 and 1000 Hz.

Most pronounced pitches are generated by stimuli with a periodic carrier which results in a harmonic power spectrum. Supposing that both carrier periodicity (CP) and amplitude modulation (AM) is extracted in the time domain, it is not parsimonious to assume two independent neural mechanisms of periodicity extraction. Moreover, there is already some evidence that carrier periodicity and modulation perception for broadband carrier are not independent. Burns and Viemeister (1976; 1981) demonstrated that sinusoidally amplitude modulated (SAM) noise can also produce a tonal sensation and convey melodic information. In SAM noise, the carrier is Gaussian noise (GN), which is aperiodic. Therefore, the pitch information can only be conveyed by the envelope.

This paper is concerned with the perceptual interaction between envelope and carrier periodicity in broadband stimuli. A typical stimulus with envelope periodicity is SAM noise. In contrast, iterated rippled noise (IRN) is a stimulus with pronounced carrier periodicity. Although this carrier periodicity is reflected, to some extent, in the IRN envelope, a series of psychoacoustical experiments have demonstrated that the perception of IRN is dominated by the carrier periodicity, not by the envelope periodicity (Wiegrebe and Patterson, 1999; Yost *et al.*, 1998). IRN is derived from GN. To generate this stimulus, a sample of GN is subjected to a delay-and-add process, which is iterated several times (Yost, 1996). This process results in a quasiperiodic stimulus. The magnitude spectrum of an IRN stimulus shows a ripple with peaks at the reciprocal of the delay and integer frequency multiples. As a consequence, the fundamental frequency (f0) of IRN corresponds to the reciprocal of the delay.

Thus, there are two broadband stimuli at hand, where the perception is dominated either by the envelope or by the carrier. Moreover, both stimuli allow for a continuous variation of the degree of periodicity. In SAM noise, this is done by varying the modulation depth of the modulator whereas in IRN, the degree of periodicity can be varied by changing the gain factor in the delay-and-add loop. When the gain factor is set to unity, the delay-and-add loop produces the maximum periodicity, determined by the number of iterations. A gain factor of zero results in an unchanged GN wave form at the output of the loop. In the current study the nomenclature IRN(d,g,n) is used to specify the delay, d, in ms; the linear gain, g, and the number of iterations, n, respectively. To provide an easier comparison of carrier and envelope periodicity, the term fundamental frequency (f0) is used instead of delay for IRN.

An exemplary illustration of the recruited stimuli is shown in Fig. 1: The stimuli are SAM noise with a modulation frequency of 125 Hz and 0 dB (100%) modulation index, an IRN(8,1,16) with a delay corresponding to 125 Hz, and a SAM IRN where the sinusoidal amplitude modulation was imposed on an IRN carrier instead of a Gaussian-noise carrier. Note that in this stimulus, the modulation frequency always equals f0. The illustration shows the time and frequency domain representations of exemplary versions of the stimulus wave forms (first and second rows) and their Hilbert envelopes (third and fourth rows). Both the audio- and the envelope spectrum of the stimuli with a carrier periodicity (IRN or SAM IRN) are harmonically structured. While the AM does not change the audio spectrum, it adds a distinct peak at the modulation frequency (indicated by the arrows) in the envelope spectrum. The highest component in the envelope spectrum is the dc component equivalent to the mean of the envelope wave form. It was fixed at 100 dB. Comparing the SAM peak height in the envelope spectrum with the magnitude of the spectral ripple of the IRN envelope spectrum, the overall envelope magnitude is much smaller for the IRN stimulus than for the stimuli with the SAM. As shown in the following, this feature is critical for the encoding of the IRN envelope spectrum with modulation filters having an appreciable dc sensitivity.

In the following, two psychoacoustic experiments are presented. The first experiment investigated to which extent AM detection was impaired by the presence of CP. The second experiment investigated to which extent CP detection was impaired by the presence of AM. In the second part of the paper, the predictions of an autocorrelation model and of a modulation-filterbank model are compared to the experimental data. Both models were tested on each set of obtained data. Finally, the basic differences between modulation filters and autocorrelation are highlighted and possible improvements of the models are discussed.

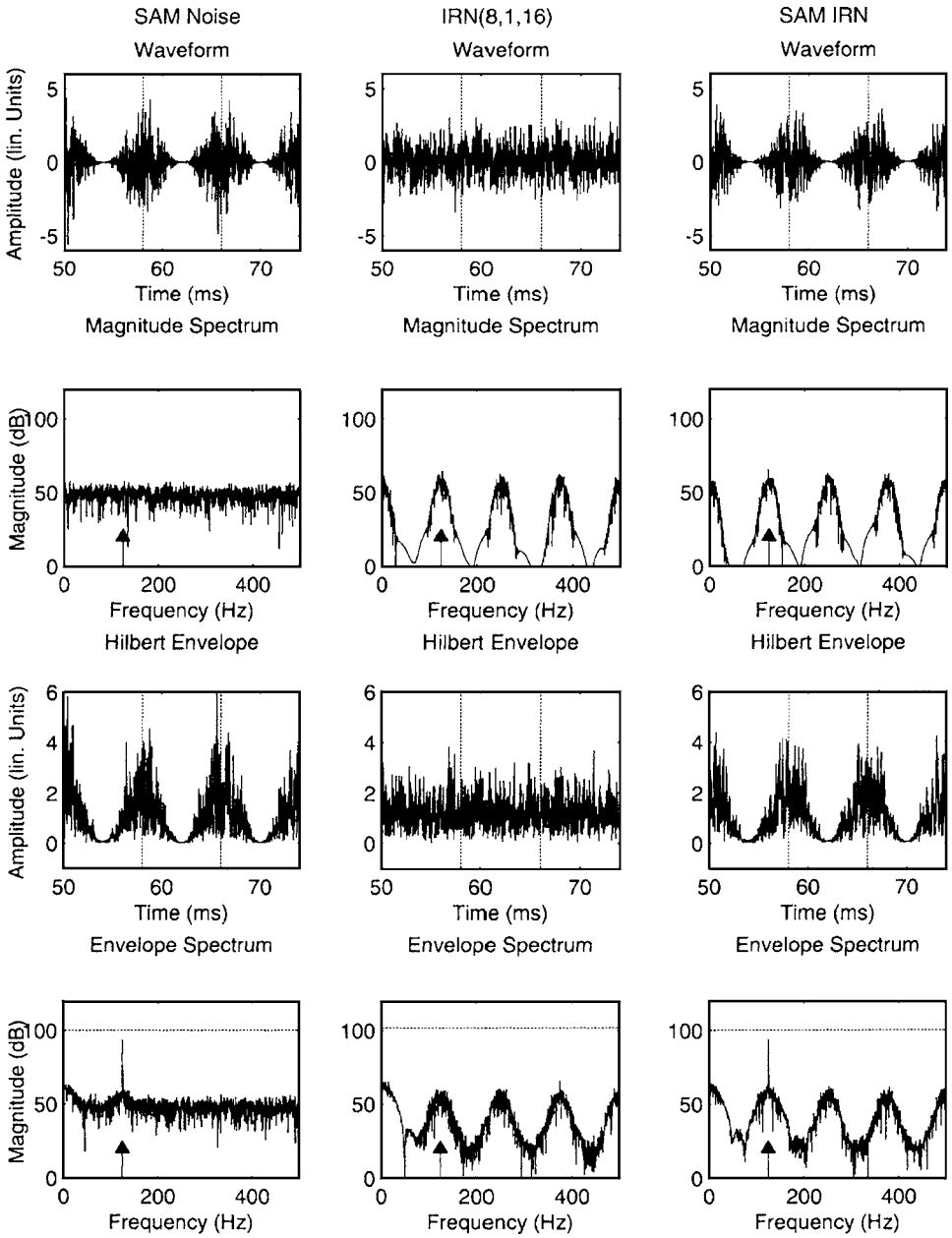

FIG. 1. Examples of the stimuli used in the present study: Stimuli are either sinusoidally amplitude modulated noise (first column), iterated rippled noise (second column), or iterated rippled noise with an additional sinusoidal amplitude modulation superimposed (third column). The modulation frequency and the IRN f0 are 125 Hz (indicated by the arrows). The four rows show the stimulus wave form, the wave form magnitude spectrum, the Hilbert envelope, and the magnitude spectrum of the Hilbert envelope, respectively. Note that both the wave form and the envelope spectrum of IRN stimuli have a harmonic structure. The amplitude modulation does not change the wave form spectrum but it generates a distinct peak at the modulation frequency in the envelope spectrum. Due to the stochastic nature of the stimuli, the plots represent only sample realizations of the stimuli.

II. EXPERIMENTS

A. Experiment I: The effect of CP on AM detection

1. Rationale

This experiment examined the influence of CP on the detection of AM. Listeners were asked to detect a sinusoidal AM imposed on a broadband carrier. The carrier was either aperiodic (GN) or quasiperiodic (IRN). When an IRN carrier was used, the IRN f0 always matched the modulation frequency. Since the magnitude spectrum of IRN shows harmonic peaks at integer multiples of f0, the modulation sidebands fall on the peaks of the spectral ripples. This minimized the spectral cues available to the listeners.

2. Method

a. Stimuli and apparatus. The stimulus carrier was either GN or IRN. In the signal interval, a sinusoidal amplitude modulation was applied. Modulation frequencies ranged from 7.8125 to 1000 Hz in one-octave steps. The IRN carrier was generated in the add-same configuration (Yost, 1996). This add-same configuration was used for all IRN stimuli in this paper. The IRN gain was set to unity and 16 iterations were used. The duration of all stimuli was 500 ms including 20 ms, raised-cosine ramps. The stimuli were digitally generated on an IBM compatible PC at a sampling rate of 44.1 kHz and subsequently downloaded onto a TDT AP2 array processor. They were then converted to analog signals by a TDT DA 3-2 D/A converter. All stimuli were amplified by a Yamaha M35 2/4 Channel Power Amplifier followed by a passive end attenuation of 40 dB. The stimuli were presented diotically via AKG K240DF headphones. The average presentation level was 60 dB SPL. In order to compensate for level changes due to the IRN generation and the amplitude modulation, all digital stimuli where equalized to have the same rms level. The presentation level was then randomized by ±6 dB using a TDT PA4 programmable attenuator, in

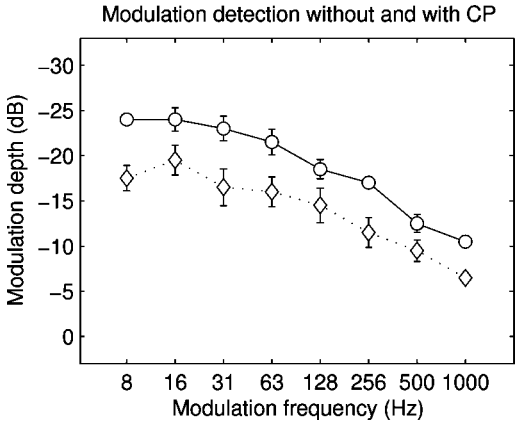

FIG. 2. The effect of carrier periodicity on amplitude-modulation detection: Circles and the solid line show modulation-detection thresholds with a Gaussian-noise carrier as a function of the modulation frequency. Diamonds and the dotted line show modulation-detection thresholds with an IRN(d,1,16) carrier where the IRN delay, d, was equal to the reciprocal of the modulation frequency. Throughout the range of the tested modulation frequencies, the IRN carrier resulted in an impairment of modulation detection by about 5 dB.

order to eliminate residual level cues. The listeners were seated individually in a sound attenuating booth.

b. Procedure. Modulation detection thresholds were obtained using an adaptive two-interval, two-alternative, forced-choice procedure. The listeners' task was to detect the amplitude modulation of one randomly selected interval. Visual feedback was provided after every decision. The adaptive parameter was the modulation index, m, which was varied in terms of dB ($20 \log m$). Its value was changed following a three-down, one-up rule. At the beginning of a run, the modulation index was changed in steps of 5 dB. After the third reversal, the step size was reduced to 2 dB, and after the fifth reversal, it was set to 1 dB. The mean over the following six reversals was taken as the threshold value for that run. This procedure estimates the 79.4% correct point of the psychometric function (Levitt, 1971). For each threshold run, one modulation frequency was randomly selected out of the whole range. Subjects were trained on the stimuli until they reached stable performance, i.e., until the standard error for the performance of three consecutive runs per signal configuration was no more than 2 dB. The mean of these last three runs per signal configuration was taken as the final threshold estimate.

c. Listeners. Four listeners (two female, two male) ranging in age from 25 to 35 years took part in Experiment I. One of them was the last author (LW). All subjects participated voluntarily and had clinically normal hearing.

3. Results

Figure 2 shows the threshold modulation depth as a function of the modulation frequency. The plot represents the average performance of all four listeners. The error bars indicate the standard error of the mean across listeners. The circles indicate data for the GN carrier, i.e., detection thresholds for AM in the absence of CP. The diamonds indicate data for the IRN carrier, i.e., detection thresholds for AM in the presence of CP.

For the GN carrier the subjects' ability to detect amplitude modulation decreases continuously as the modulation frequency increases. This finding is in line with the results obtained in previous studies (Eddins, 1993; Eddins, 1999; Ewert and Dau, 2000; Viemeister, 1979). For the IRN carrier condition, the overall shape of the threshold curve is the same, but it is shifted downwards by, on average, 5 dB. These results indicate that the sensitivity to AM is impaired by the presence of CP independent of the modulation frequency.

B. Experiment II: The effect of AM on CP detection

1. Rationale

Experiment II serves as a counter experiment to Experiment I. Listeners were asked to detect CP in a broadband noise carrier. Since the IRN gain factor allows changing the degree of CP continuously, this feature enables quantitative measurements of perceptual CP thresholds. To investigate the effect of AM on CP detection, the experiment was performed in the absence and in the presence of a sinusoidal AM imposed in both presentation intervals of a trial.

2. Method

a. Stimuli. The task was to discriminate an IRN stimulus from a GN stimulus. The IRN stimuli were generated with f0's between 7.8125 and 1000 Hz (equivalent to IRN delays between 128 and 1 ms) in octave steps. In order to change the degree of CP, the IRN gain was changed adaptively. The number of IRN iterations was fixed at 16. The imposed AM had the same frequency as the carrier f0 and a modulation index of 0 dB (100%). The presentation level and apparatus were the same as in Experiment I.

b. Procedure. The experimental procedure was equivalent to Experiment I, only differences are reported here. The adaptive parameter was the gain factor of the IRN. The step sizes were 10 dB for the first two reversals, 5 dB for reversals three to five, and 2 dB after the fifth reversal. For each threshold run, one f0 was randomly selected out of the whole range.

c. Listeners. Four listeners (two female, two male) ranging in age from 28 to 35 years participated in Experiment II. Except for listener LW, the listeners were different from those in Experiment I and included the first author (AS). All listeners had clinically normal hearing and participated voluntarily in this study.

3. Results

Figure 3 shows the threshold IRN gain required to detect carrier periodicity as a function of the IRN f0. The plot represents the average performance of all four listeners and the error bars indicate the standard error across listeners. The circles and solid line represent CP detection in the absence of AM; the diamonds and dotted line represent CP detection in the presence of AM.

In the absence of AM, the ability to detect CP improves with increasing f0 and reaches a plateau for an f0 of 125 Hz and above. In the presence of AM, sensitivity for carrier periodicity appears not to be affected by the AM for an f0 of

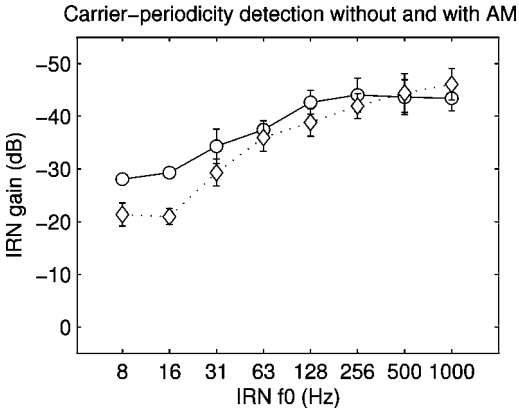

FIG. 3. The effect of amplitude modulation on carrier-periodicity detection: Circles and the solid line show carrier-periodicity detection thresholds without additional amplitude modulation as a function of the IRN f0. Diamonds and the dotted line show carrier-periodicity detection thresholds with a 0 dB SAM imposed on both the signal and standard stimuli. Additional amplitude modulation impaired sensitivity to carrier periodicity only for f0's below the pitch range (7.8125 and 15.625 Hz).

31.25 Hz and above. Only for the lowest f0's of 15.625 and 7.8125 Hz, the sensitivity to CP is impaired by the presence of AM.

III. DISCUSSION

The experimental results show that sensitivity to AM is significantly impaired by the presence of CP. However, sensitivity to CP is not impaired by the presence of AM as long as the carrier f0 is 31.25 Hz or above. As pointed out in Sec. I, CP as well as AM can evoke a pitch perception and it is conceivable that pitch and pitch strength are important perceptual cues used in these experiments. However, pitch is only perceived when the f0 is higher than about 30 Hz (Krumbholz *et al.*, 2000; Pressnitzer *et al.*, 2001).

In the following, the experimental results are discussed with respect to the possible role of pitch perception. The discussion is focused on two regions, the infra-pitch region, represented by the stimulus f0 of 7.8125 and 15.625 Hz, and the pitch region, represented by f0's of 31.25 Hz and above.

The lower limit of pitch coincides with the deviation of the performances for CP detection in Experiment II. This means that in the range of f0's eliciting a pitch sensation, sensitivity to CP is not impaired by additional AM. In the infra-pitch region, the thresholds for CP detection are significantly reduced. Experiment II shows that the IRN carrier periodicity remains well detectable for f0's of 7.8125 and 15.625 Hz (IRN delays of 128 and 64 ms). These low f0's result in the perception of a repeating feature rather than pitch. It appears that the listeners were confused whether this repeating feature arose from CP or AM. This assumption would result in impaired CP detection in the presence of AM as it was observed in Experiment II.

A confusion of CP and AM may also underlie the impaired AM detection in the presence of CP for the low f0's of 7.8125 and 15.625 Hz in Experiment I. However, in Experiment I this impairment is also found throughout the whole pitch range, i.e., also for all f0's of 31.25 Hz and above. A possible explanation for the impairment of AM detection in the pitch region may lie in the differences of pitch strength elicited by the carrier and modulator. Experiments on rate discrimination with IRN (Krumbholz *et al.*, 2000) and SAM noise (Formby, 1985) indicate that with 16 iterations, the pitch strength of IRN is much larger than the pitch strength of SAM noise. Assuming that listeners partly relied on pitch cues for AM detection in Experiment I, the detection of the weak SAM noise pitch was supposedly impaired in the presence of the relatively strong pitch of the IRN carrier. In contrast, the weak SAM noise pitch was unable to impair the detection of the relatively strong IRN pitch in Experiment II for f0's of 31.25 Hz and above.

IV. MODEL SIMULATIONS

In the following, model simulations of the data in previous experiments are presented. The focus lies on the comparison of different implementations of periodicity extraction. Two model approaches are compared that share a common preprocessing and decision stage. The first model is a modulation filterbank (MFB) based on the model of effective signal processing by Dau *et al.* (1997a, b). The second, an autocorrelation (AC) model, is based on a model suggested by Meddis and O'Mard (1997). The most important difference between both model structures lies in the functional implementation of the way the auditory system extracts the periodicity (see Sec. I). Except for the different forms of periodicity extraction, both models have slight differences as the adaptation loops in the MFB model and outer- and middle-ear filtering as well as a detailed inner hair cell stage in case of the AC model. For the current study, the existing models were rearranged in a way that allows for a direct comparison between the two different forms of periodicity extraction.

A. Model structure

1. Peripheral processing

To account for effects of auditory filtering, the signals were subjected to a 20-channel gammatone filterbank with center frequencies equally spaced on a logarithmic axis between 100 and 6000 Hz. Effects of outer- and middle-ear filtering were not considered. After passing the gammatone filterbank, the internal representation of the stimuli was half-wave rectified, compressed with an exponent of 0.4 and subsequently low-pass filtered with a 1000 Hz, second-order Butterworth filter. These stages simulated the mechano-neural transduction of the inner hair cells. At this level, where the model's internal representation can be interpreted as representing the spike probability functions in the auditory nerve, either a modulation filterbank or an autocorrelator was applied.

2. Periodicity extraction

In one case, a modulation filterbank was included for each auditory frequency channel. The modulation filters were first-order resonant filters with a Q value of 2 as described in Dau *et al.* (1997a, b). Modulation filters were equally spaced on a logarithmic envelope-frequency axis, overlapping at their −3 dB points. They ranged from 10 Hz to a quarter of

the auditory-filter center frequency. The upper restriction of the center frequency is necessary, since the modulation spectrum which results from the process of half-wave rectification, compression and low-pass filtering, still contains information about the audio-frequency spectrum. The restriction ensures that only envelope information at the output of the respective auditory filters is extracted from the stimulus. For auditory filter center frequencies greater than 4000 Hz, the maximum modulation-filter center frequency was restricted to 1000 Hz. For modulation frequencies below 10 Hz, an additional second-order Butterworth modulation low-pass filter with a cut-off frequency of 7.5 Hz was applied. Modulation filtering was implemented in the modulation frequency domain by multiplying the envelope magnitude spectrum of a specific (audio-) frequency channel with the magnitude transfer function of the desired modulation filter. Only the rms value of the filter's envelope was considered. Thus, the time dimension of the model is lost and the model output is two-dimensional along the dimensions of audio frequency and modulation frequency. To restrict the model sensitivity to the amount of AM in the stimulus, by factoring out sensitivity to overall sound-level changes (see Sec. IV B 5), each bandpass modulation filter output was normalized to the corresponding low-pass modulation filter output which is equivalent to the average degree of excitation (level) in the respective auditory channel. Subsequently, the outputs of the modulation low-pass filters, which represent a spectral excitation pattern across audio-frequency channels, were discarded.

The AC model was implemented as a long-term autocorrelation. This is justified since the stimuli were time invariant and the time constant of a running autocorrelation is only a critical parameter for time variant stimuli (Wiegrebe, 2001). Thus the simulation output is two dimensional as in the MFB model, in this case along the dimensions of audio frequency and correlation lag. The AC model makes use of level differences in the spectral excitation pattern. To allow for the simulation with a roving-level paradigm, the model had to be made level independent (see Sec. IV B 5). Therefore the autocorrelation in each auditory channel was normalized, i.e., correlation coefficients were calculated. The resulting autocorrelation function was multiplied with a linear weighting function as suggested by Pressnitzer *et al.* (2001). The maximum correlation lag was 33 ms. In summary, the AC model used in the present study deviates from the model by Meddis and O'Mard (1997) in the following aspects: (a) The Meddis hair cell is replaced by a module which contains half-wave rectification, compression, and low-pass filtering, (b) the autocorrelation is normalized, and (c) the autocorrelation is not calculated in a short time window at the stimulus end. Instead a long-term autocorrelation over the whole stimulus duration is used.

3. A spectral model

Purely spectral models operate on the evaluation of the degree of excitation in each auditory frequency channel. Effectively, the rms at the output of the modulation low-pass filter from the MFB model is the average power in each auditory channel. By using only the modulation low-pass filter, the output of the model corresponds to an auditory spectral excitation pattern. Therefore this model representation is comparable to purely spectral "pattern matching" pitch models like, e.g., Cohen *et al.* (1995), Goldstein (1973), and Terhardt (1974).

4. The decision device

The decision device was implemented as an optimal detector (Dau *et al.*, 1996). Model decisions were based on the cross correlation between a template derived from 20 suprathreshold signal presentations of the two presentation intervals. The overall sensitivity can be adjusted by the variance of internal noise [see Dau *et al.* (1996) for details]. For the simulation using the AC model, the variance of internal noise was adjusted to achieve a predicted gain threshold of −45 dB for carrier periodicity detection of IRN with an f0 of 250 Hz. The internal noise variance was kept constant for all simulations using the autocorrelation stage. For simulations using the modulation filterbank, the variance of internal noise was set to a value for which the model predicted a threshold modulation depth of −16 dB for a modulation frequency of 15.625 Hz applied to a GN carrier. Within the MFB model, the AM detection in the region of −16 dB is limited by the external statistics of the broadband Gaussian noise carrier. The internal noise was set to a small value, with negligible influence on AM thresholds. Again, this value was the same for all simulations using the modulation filterbank. Model predictions were obtained using the same adaptive two-alternative, forced-choice procedure as in the experiments.

B. Simulation results and discussion

The simulation results of the modulation-filterbank model and the AC model are shown together with the experimental data in the top and bottom row of Fig. 4, respectively. The bold lines indicate the empirical data. The basis for the model performances is discussed with respect to the templates generated by the decision device. Some of these templates are shown in Figs. 5 and 6.

1. CP detection in the MFB model

The MFB model provides reasonable predictions of CP detection for intermediate f0's around 125 Hz [open circles in panel (a) of Fig. 4]. The templates for these f0's [e.g., Fig. 5(a)] indicate that the MFB model relies mostly on the detection of a modulation magnitude peak (dark areas) equal to f0 and an area of reduced modulation magnitude (dip, indicated by the brighter areas) for modulation filters tuned below the f0 of the stimulus [see the arrow in Fig. 5(a)]. The rippled structure of the IRN envelope spectrum is only partially resolved below the first harmonic by the modulation filterbank. The MFB model cannot correctly predict CP detection for the lowest f0 of 8 Hz. This deficit results from the dc sensitivity of the modulation filters. The dc response of the filters essentially swamps the dip-peak structure in the envelope magnitude spectrum up to f0. When additional AM was applied to the IRN carrier [open diamonds in panel (a) of Fig. 4], the MFB model performance is unaffected by the addition of the AM to the IRN for all f0's greater than 16 Hz.

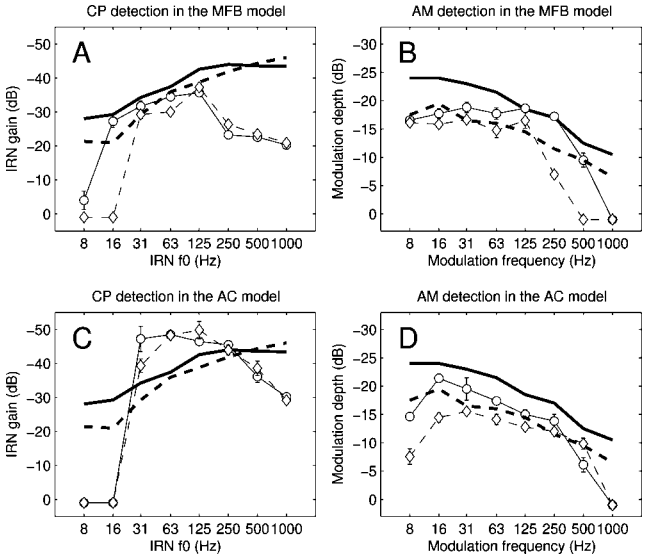

FIG. 4. Simulation of CP and AM detection in the modulation-filterbank (MFB) model (upper row) and in the autocorrelation (AC) model (lower row). The experimental data are replotted from Figs. 2 and 3 with bold lines. The solid lines represent data for CP and AM detection without interfering AM or CP. The dashed lines represent data for CP and AM detection with interfering AM or CP. The symbols connected by the fine lines show the simulation results. Open circles represent simulated data for CP detection without AM or AM detection without CP. Open diamonds represent simulated data for CP detection in the presence of AM or AM detection in the presence of CP. The error bars represent standard errors across three simulations.

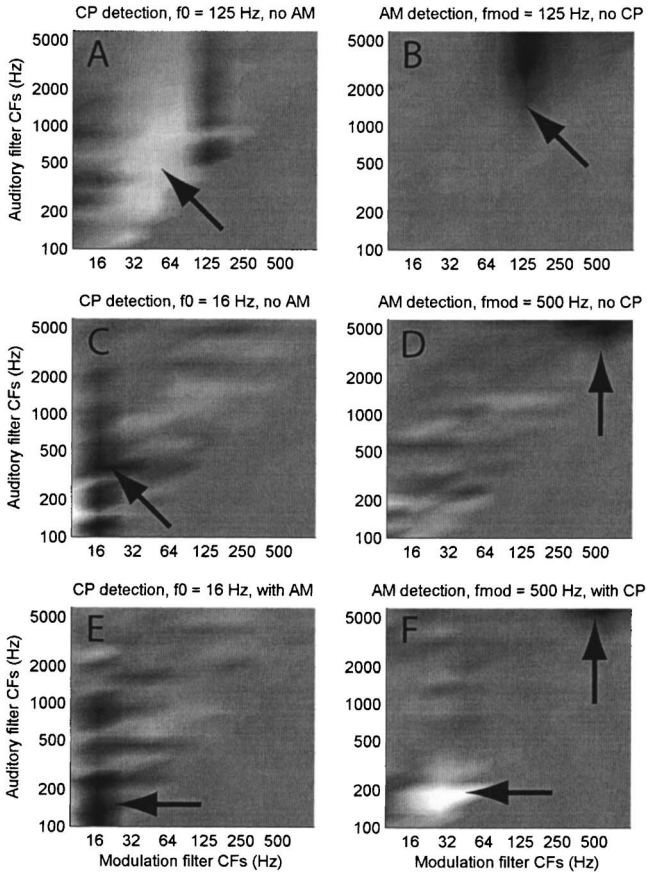

FIG. 5. Templates generated by the optimal detector connected to the output of the MFB model. Templates generated for CP detection (left column) and AM detection (right column) with various fundamental or modulation frequencies are shown. The arrows indicate prominent features in the templates that were used by the optimal detector to perform the CP or AM detection. See the text for further details.

For 8 and 16 Hz the performance breaks down completely. The templates for these two conditions are shown in Figs. 5(c) and (e). Note that the dip region in the modulation magnitude pattern [white area in Fig. 5(c)] is absent with additional AM, as seen in Fig. 5(e). This confirms the idea that the MFB model relies on the detection of the first dip in the envelope spectrum for CP detection.

The MFB model considerably underestimates CP detection performance for high f0's above 125 Hz. In this case, the templates (not shown) reveal only spurious information on the reason for this lack in sensitivity. None of the activations in the templates correspond to either spectrally resolved harmonics or resolved peaks in the modulation spectrum. Note, in the present implementation, the MFB model cannot use audio-spectral information, since only the output of the modulation filters normalized by the overall power in the respective audio-frequency channel was considered. The output of the modulation low-pass was omitted.

2. AM detection in the MFB model

The MFB model predicts AM sensitivity quite well for the broadband noise carrier [open circles in Fig. 4(b)]. The template for the AM detection for a modulation frequency of 125 Hz [Fig. 5(b)] shows a clear vertical ridge of activation in the modulation filter tuned to 125 Hz. This ridge is more prominent for higher auditory filter CFs because only these filters are broad enough to pass the modulation. While for low and intermediate modulation frequencies almost no effect of additional CP is predicted [open diamonds in Fig. 4(b)], a strong deterioration in AM detection is observed at a modulation frequency of 500 Hz when the GN carrier is replaced by an IRN carrier. The corresponding templates are shown in Figs. 5(d) and (f). Figure 5(d) shows a small peak of excitation in the modulation filter tuned to 500 Hz which is only observed for the highest auditory-filter CFs. With an IRN carrier [Fig. 5(f)], the template reveals a pronounced dip in the modulation excitation pattern well below the modulation frequency and only for low auditory-filter CFs. This feature is highly reproducible and it appears to impair AM detection for these high modulation frequencies. For both carrier types no sensitivity to an AM of 1000 Hz is predicted. This is probably caused by the relatively narrow auditory filters at the highest center frequency of 6000 Hz as used in the model. They essentially do not pass AM for modulation frequencies above about 660 Hz. It is conceivable that the nonlinear human cochlear filters transmit more of these high-frequency modulations since they might be considerably broader at sound-pressure levels as used in the present study when compared to the linear gammatone filters used here.

3. CP detection in the AC model

Panel (c) of Fig. 4 shows thresholds for CP detection as predicted by the AC model, in absence and presence of additional AM (open circles and diamonds, respectively). Since

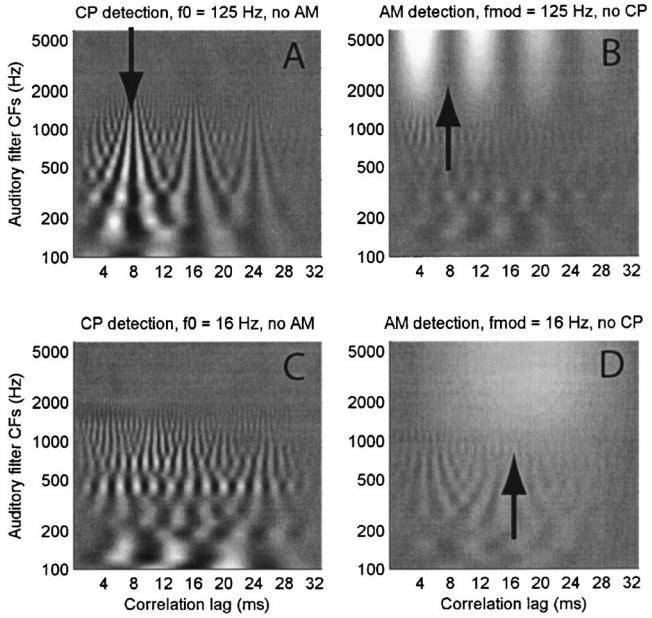

FIG. 6. Templates generated by the optimal detector connected to the output of the AC model. Comparable to Fig. 5, templates generated for CP detection (left column) and AM detection (right column) with various fundamental or modulation frequencies are shown. The arrows indicate prominent features in the templates that were used by the optimal detector to perform the CP or AM detection. See the text for further details.

the maximum autocorrelation lag was set to 33 ms, the AC model is unable to detect the CP of f0's lower than 30 Hz. When the f0 of the CP is 125 Hz [Fig. 6(a)], the CP causes a vertical ridge in the template at a correlation lag of 8 ms equal to the stimulus period [Fig. 6(a), arrow]. When the f0 is 16 Hz [Fig. 6(c)], this ridge falls outside the template, and the model is unable to detect the CP.

While the model shows better detection performance for intermediate carrier periodicities than observed in the data, the AC model is too insensitive for high f0's. Again, note that the AC model could not rely on spectral information since the autocorrelation was normalized in order to make the model level insensitive. In the correlation-lag dimension, the half-wave rectification and low-pass filtering impairs the encoding of the periodicity of the relatively high absolute frequencies of even the low harmonics.

The AC model correctly predicts virtually no influence of AM on CP detection.

4. AM detection in the AC model

Panel (d) of Fig. 4 shows good agreement between the predicted AM detection thresholds for the AC model and the empirical data. The good performance of the AC model in AM detection of low AM frequencies appears surprising since the maximum autocorrelation lag was limited. However, the autocorrelation of the model's internal representation of a sinusoidally amplitude modulated stimulus is also sinusoidal. The internal representation is similar to the envelope of the stimulus simulated by half-wave rectification and low-pass filtering in the inner hair cell stage. This is shown in the template of the AC model for the detection of an AM of 125 Hz [Fig. 6(b), arrow]. Thus AM detection is possible even when only a portion of the modulator period (e.g., the first dip) fits into the autocorrelation function [Fig. 6(d)]. The current simulations show that this residual information in case of low AM frequencies provides a reliable cue for AM detection in the AC model.

A slight deterioration of AM sensitivity is observed in the presence of CP [open diamonds in Fig. 4(d)].

As in the MFB model, the degree of this deterioration appears to be too small when compared to the empirical data.

5. CP and AM detection in a spectral model

At first sight, it appears pointless to simulate AM detection on broadband carriers in a purely spectral model since the AM does not produce any changes in the long-term spectrum of a broadband stimulus. However, a spectral model provides very useful insights on the detection strategies of more complex auditory models as they are investigated here.

Simulation results for CP and AM detection in the spectral (modulation low-pass) model are shown in Fig. 7. As in the previous plots, the solid lines with open circles represent empirical data for CP and AM detection without interfering AM or CP. The dashed lines with open diamonds represent empirical data for CP and AM detection with interfering AM or CP. The top row shows the simulation results obtained with a roving level paradigm (±6 dB SPL), the bottom row shows the results for the same experiment without roving level. The simulation results in the top row show that CP detection is possible for higher IRN f0's where the audiospectral peaks of the IRN become partially resolved [panel (a) of Fig. 7], as expected. For f0's of 125 Hz and below, this spectral ripple profile, as it is preserved after peripheral processing, appears not to be sufficient for detecting CP when a roving level paradigm is used. Without level roving [panel (c)] CP detection is well predicted for all f0's above 31 Hz.

Panel (b) of Fig. 7 shows that AM detection cannot be predicted at all when a level rove is applied to the signal. The simulation results in panel (d) of Fig. 7 reveal the importance of level roving. Without roving level, the spectral model becomes capable of AM detection. It is a well-described phenomenon that nonlinear peripheral auditory processing influences the degree of central auditory excitation (Gockel *et al.*, 2003; Kohlrausch and Sander, 1995). This problem also applies to the detection of AM in a spectral model: The AM sensitivity of the spectral model is based on the fact that the amplitude-modulated stimulus produces less auditory excitation than the unmodulated stimulus. The compressive nonlinearity has a stronger effect on the modulated stimulus than on the unmodulated stimulus. Note that the loss of excitation is a result of both the half-wave rectification and the power-law compression. The loss of excitation occurs although the rms value at the model input is the same for the modulated and for the unmodulated stimulus as in the present study. The effect of the compressive nonlinearity applies differently in auditory frequency channels with different center frequencies dependent on the amount of modulation that is passed by the filters. When the modulation frequency is very low (below about 64 Hz) all auditory filters are broad enough to pass the modulation and the activity is strongly reduced in all filters as a consequence of the compressive nonlinearity. For intermediate modulation frequencies, the strong effect of auditory

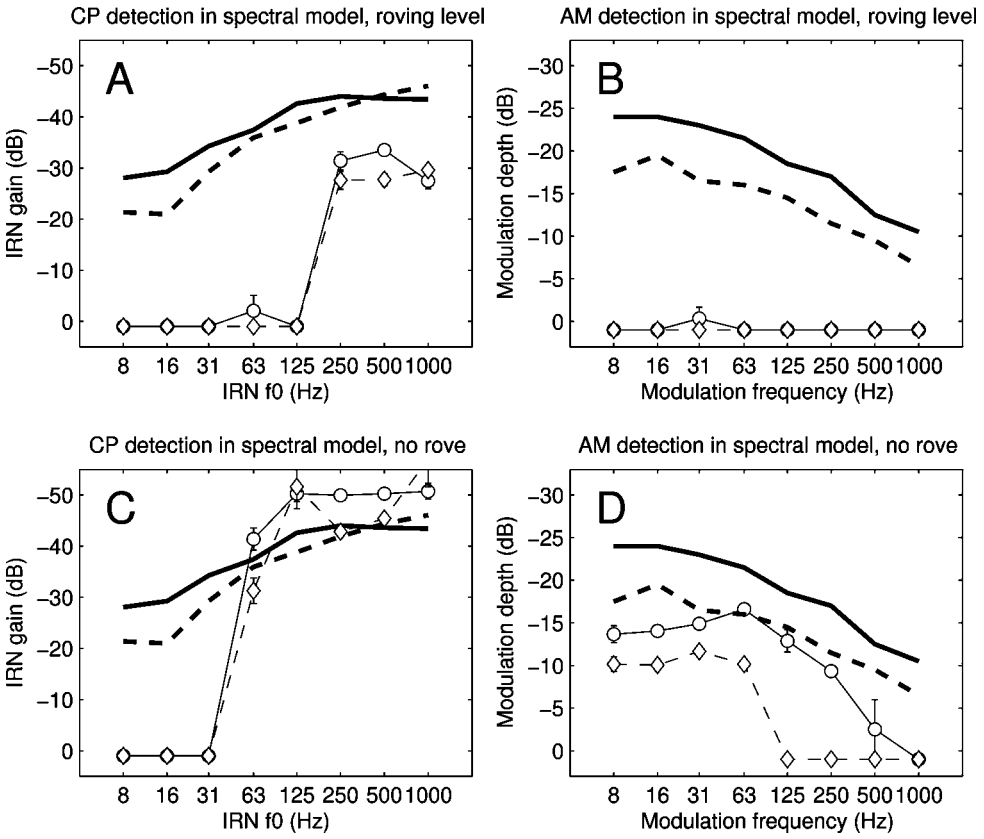

FIG. 7. CP detection (left column) and AM detection (right column) in a spectral model. The same line types and symbols as in Fig. 4 are used. In the upper row, simulation results were obtained with a roving-level paradigm, in the lower row, no level roving was used. The roving level had a dramatic effect on the model predictions. Without roving level, the spectral model was able predict AM sensitivity quite well although the long-term magnitude spectrum of the stimulus was not affected by the AM.

nonlinearity only applies to those filters with a center frequency higher than about eight times the modulation frequency. Very high modulation frequencies (1000 Hz) are transmitted by none of the auditory filters used for the current simulations. Thus, the broadband AM noise generates a characteristic auditory excitation pattern with reduced activity in channels that pass the modulation. This pattern serves as a spectral detection cue for the decision stage in AM detection experiments with broadband noise carriers. While the psychophysical relevance of these modeling results has not been formally investigated, it appears highly unlikely that listeners exploit such auditory cues, related to spectral profile analysis, to detect AM.

In order to study the effect of level roving with the MFB and the AC model, the internal representation of the models had to be level independent. Otherwise, the level roving would have completely deteriorated the models' performance as it would have acted as a strong source of "external" noise. Such an effect is clearly not observed in the empirical data. Effectively, the requirement of level independence removed the availability of purely spectral excitation cues in the MFB and AC model.

V. THEORETICAL RELATIONSHIP BETWEEN MODULATION FILTERS AND AUTOCORRELATION

The current paper assesses the relationship between a modulation filterbank analysis and an autocorrelation based analysis of the internal representation of auditory models at a stage comparable to the auditory nerve. Up to this point, modulation filterbank analysis and autocorrelation have been compared and treated as two independent modeling approaches to extract periodicity from the internal representation of the stimuli within the models. This section gives some insight into the mathematical relationship between the two processing schemes.

A modulation filter is described in the time domain by the convolution of the filter's impulse response and the internal representation, which is generally referred to as wave form in the following. A hypothetical impulse response (IR) of a modulation filter with a modulation center frequency of 62.5 Hz is given in the upper left panel of Fig. 8.

The autocorrelation function (ACF) of a wave form for a given time lag is mathematically described by summing the product of the wave form and a delayed version of it along the time axis. The ACF for a specific lag is often associated with a corresponding comb-filter type analysis of the stimulus spectrum, which, in this case, resembles a comb-filter type modulation filter. The impulse response of the respective comb filter is unipolar having two peaks separated by the lag ("U-shape," see upper right panel of Fig. 8). However, the convolution with such an impulse response is mathematically described by a summation of the stimulus and the time delayed version of it, clearly differing from the ACF, where the stimulus and its delayed version are first multiplied and then summed over time. A similarity between the two processes is introduced when the power or the variance of the comb-filter output is obtained and compared to the ACF for the respective lag. The computation of either quantity includes squaring of the filter output and successive summation. The squaring introduces a multiplicative cross-term to the filtering process which makes it comparable to the ACF. Figure 9 compares autocorrelation and convolution of

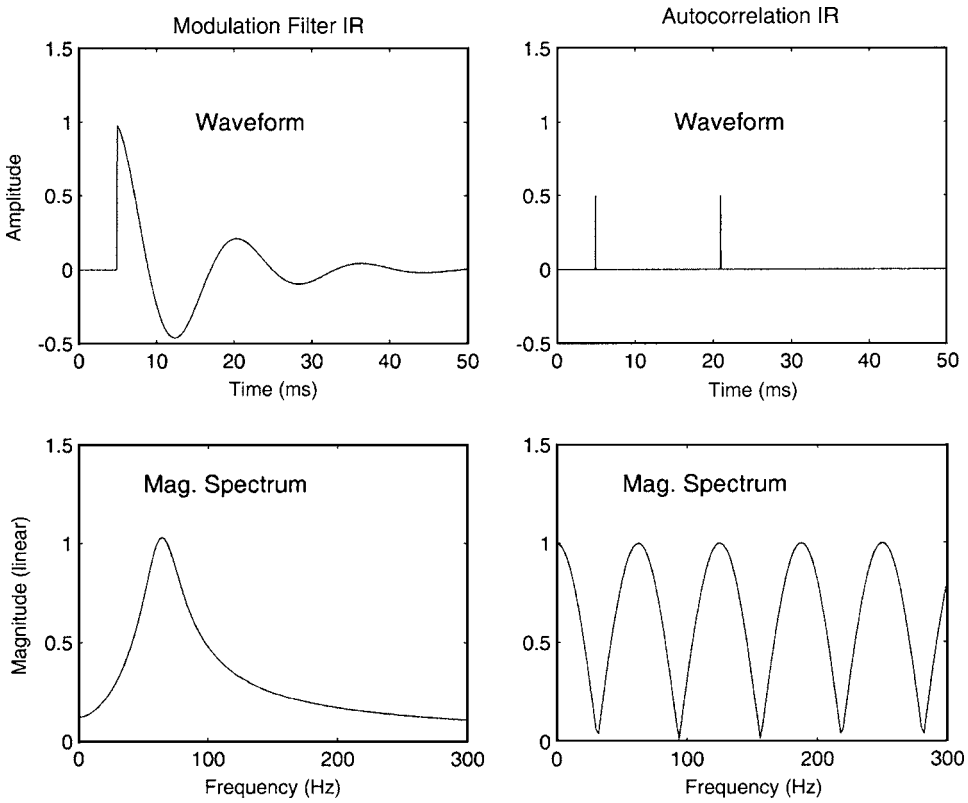

FIG. 8. Comparison of the impulse response of a modulation filter (left column) and the impulse response which produces results most similar to an autocorrelator (see Fig. 9). The respective transfer functions of the filters are shown in the lower row. While the modulation filter has a bandpass characteristic, the autocorrelation can be approximated with a "U-shaped" impulse response having a comb-filter transmission characteristic.

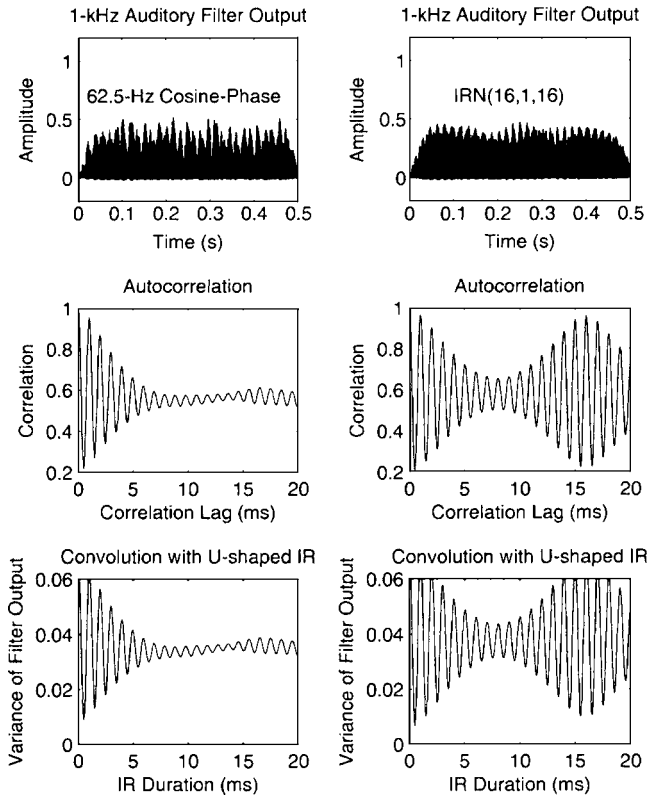

FIG. 9. Comparison of autocorrelation with the output of a filterbank of "U-shaped modulation filters." The input to the periodicity analysis consists of the wave form at the output of the 1 kHz auditory filter stage generated by either a 62.5 Hz SAM noise (left column) or by an IRN(16,1,16) with the same f0 (right column). The variance of the filterbank output (bottom row) leads to results that are very similar to the autocorrelation function (middle row).

the output wave form from a 1 kHz auditory frequency channel in response to either a 62.5 Hz SAM noise (left column) or in response to IRN(16,1,16). The auditory-filter, output wave forms (after half-wave rectification, compression, and low-pass filtering) are plotted in the upper row and the ACFs of these wave forms are shown in the middle row. The lower row shows the variance of a filterbank output produced with U-shape IRs having a duration equal to the correlation lag in the middle row. In fact, the variance of the U-shape modulation-filter outputs and the ACF are qualitatively similar. Thus, the difference between autocorrelation and a modulation-filterbank analysis can be reduced to three critical points.

First, with the observation of equally spaced correlation lags, the spacing of the fundamental frequencies of the comb filters is equal on a *linear* periodicity axis for an autocorrelator. For the modulation filterbank, the spacing is assumed to be equal on a *logarithmic* envelope-frequency axis.

Second, the IR representing the autocorrelation for a specific lag differs from that of a modulation filter as used in the present study. This difference is shown in Fig. 8. The magnitude spectra in the lower row reveal that unlike the bandpass modulation filter of the modulation filterbank (left), the autocorrelation IR has a rippled (comb-filter) spectrum (right). In the context of the purely temporal pitch extraction, this rippled spectrum is essential to capture the contribution of higher-order harmonics to the overall pitch. The modulation-filter magnitude-spectrum shows only a single peak.

Third, in the current implementation of the modulation filterbank, the highest modulation-filter center frequency was limited to a quarter of the center frequency of the preceding auditory filter. This was done to ensure that residual carrier

information is effectively removed from the internal representation of the envelope. In the templates shown in Fig. 5, this area where no modulation filters were applied can be seen as the uniformly grey triangle in the lower right of each template. With this restriction, the modulation filterbank model would be unable to extract the pitch of a sinusoid or the pitch of low harmonics in the time domain. In the autocorrelation approach, this restriction was ignored: The autocorrelation is calculated for a correlation lag of 10 ms for the output of an auditory filter centered at 100 Hz. Thus, it appears that the autocorrelation makes extensive use of information which has been deliberately excluded in the modulation-filter approach.

When modulation filters with center frequencies similar to the auditory-filter center frequencies were included in an additional test, the simulation results as shown in Fig. 4(a) improved for CP detection with high f0's of 250, 500, and 1000 Hz (not shown). AM detection was not affected because the AM is not transmitted by auditory filters tuned to relatively low frequencies. This approach, however, would add information to the MFB output which is not contained in the (Hilbert) envelope of the stimulus. Note that a 100 Hz pure tone sounds quite different from any percept generated by a high-frequency tone amplitude modulated at 100 Hz (apart from the quadratic distortion product). If there was a 100 Hz modulation filter analyzing the output of a 100 Hz auditory filter, this modulation filter would be strongly excited since the internal representation of the envelope in the model, unlike the Hilbert envelope, would contain pronounced carrier periodicity information. In the MFB model, this carrier periodicity could then not be separated from envelope periodicity.

VI. TOWARDS A UNIFIED MODEL OF MODULATION- AND PITCH PERCEPTION

It appears that the AC model and the modulation filter model share many properties that are essential for a successful extraction of carrier- and envelope periodicity. The remaining question is what the ingredients for a unified model should be. From the current study some manipulations to the MFB model which could turn it into a successful pitch model are suggested.

First, it appears that the dc sensitivity of the modulation filters as used in Dau *et al.* (1997a, b) should be omitted. This dc sensitivity can swamp the sensitivity to relatively smaller features in the envelope-frequency domain. The modulation filters suggested in Ewert and Dau (2000) and Ewert *et al.* (2002) show no dc sensitivity.

Second, modulation filters should be included with a modulation center frequency equal to the audio center frequency. These filters should have a harmonic ripple in their transfer function. This is mandatory to catch, in the envelope-frequency domain, the strong influence of higher-order spectrally resolved harmonics on pitch (e.g., the pitch equal to f0 caused by the third, fourth, and fifth harmonic). This rippled transfer function may only be necessary for modulation filters with modulation center frequencies above the lower limit of pitch. The transfer function of modulation filters as inferred from modulation masking experiments does not contradict such a ripple fine structure, in particular if it is assumed that the ripples might be less pronounced than the first (center-frequency) peak of the modulation filter.

Regarding useful changes to the AC model, the linear periodicity axis as produced by the autocorrelation should be replaced by a logarithmic periodicity axis. Both perceptual evidence and physiological properties of the auditory brainstem render a linear periodicity axis highly unlikely.

It remains to be investigated how the modulation filterbank deals with inharmonically shifted stimuli: Related to the stimuli used in the current study, inharmonic stimuli can be generated by using a negative gain factor in the IRN delay-and-add loop. The pitch of IRN with negative gain differs substantially from the pitch produced with positive gain (Yost, 1997). This is the case although the envelope spectra of IRN with positive and negative gain are identical. Wiegrebe and Winter (2001a) have shown that, as a consequence, the spectrally unresolved harmonics of IRN are encoded in the same way independent of the sign of the IRN gain. As the current implementation of the modulation-filterbank model does not evaluate the spectral excitation pattern since the modulation low-pass was omitted, it would not be sensitive to the differences in the audio spectrum produced by the resolved harmonics of IRN with positive and negative gain. Thus, while a quantitative simulation of these effects is beyond the scope of this paper, it appears unlikely that the modulation-filterbank model in its present form can account for the perception of inharmonically shifted stimuli. However, the above-suggested improvements, especially the use of spectrally rippled modulation filters, may enable an improved model performance in this domain. Presumably, these rippled modulation filters will allow one to analyze the mismatch between carrier and envelope period which is typical for inharmonically shifted stimuli.

VII. SUMMARY AND CONCLUSIONS

The current experiments investigated interactions between AM perception and CP perception in broadband stimuli. The results showed that sensitivity to AM decreased significantly when the GN carrier was replaced by an IRN carrier whose f0 was equivalent to the modulation frequency. This was the case for all modulation frequencies tested.

In contrast, sensitivity to CP did not decrease when the stimuli were amplitude modulated with a modulation frequency equal to the f0, as long as the f0 was above the lower limit of pitch [about 30 Hz, Krumbholz *et al.*, (2000); Pressnitzer *et al.*, (2001)]. Below the lower limit of pitch, the presence of AM decreased sensitivity to CP. In this region, the interference might be related to a confusion effect of the repeating envelope pattern.

The simulation of the experimental results in a generic implementation of either the modulation filterbank or the autocorrelation model of periodicity extraction indicates that while both models capture the general trends of the data, none of the two provides a satisfactory explanation for AM and CP interaction. The direct comparison of the autocorrelation and the modulation-filter approach combined with a power or variance based decision variable reveals that the

basic difference lies in the transfer function of the modulation filter and the transfer function of the autocorrelator: Modulation filters have a bandpass transfer function while the filters which produce an output akin to autocorrelation have a comb-filter transfer function. The simulation of the experimental results with a spectral model shows that AM of broadband stimuli can produce changes in the spectral excitation pattern which, however, are very unlikely to underlie AM sensitivity.

From these simulations it appears promising to construct a hybrid temporal model with properties of both a modulation filter and an autocorrelator. It is intriguing that the temporal filtering properties of Chop-S units described in the ventral cochlear nucleus of many mammals can be regarded as such a hybrid of a modulation filter and an autocorrelator (Wiegrebe and Winter, 2001b; Winter *et al.*, 2001). Thus, the parallel pursuit of both physiological and functional models of periodicity encoding (like the present ones) may lead to a unified understanding of the auditory extraction of periodicity and the perception of pitch.

ACKNOWLEDGMENTS

We would like to thank Neal Viemeister and two anonymous reviewers for their very detailed and helpful comments on earlier versions of the manuscript. This work was supported by a grant from the Deutsche Forschungsgemeinschaft Wi1518/6 to the last author.

Burns, E. M., and Viemeister, N. F. (**1976**). "Nonspectral pitch," J. Acoust. Soc. Am. **60**, 863–868.

Burns, E. M., and Viemeister, N. F. (**1981**). "Played-again Sam: Further observation on the pitch of amplitude- modulated noise," J. Acoust. Soc. Am. **70**, 1655–1660.

Carlyon, R. P. (**1998**). "Comments on 'A unitary model of pitch perception' [J. Acoust. Soc. Am. **102**, 1811–1820 (**1997**)]," J. Acoust. Soc. Am. **104**, 1118–1121.

Cohen, M. A., Grossberg, S., and Wyse, L. L. (**1995**). "A spectral network model of pitch perception," J. Acoust. Soc. Am. **98**, 862–879.

Dau, T., Kollmeier, B., and Kohlrausch, A. (**1997a**). "Modeling auditory processing of amplitude modulation. I. Detection and masking with narrow-band carriers," J. Acoust. Soc. Am. **102**, 2892–2905.

Dau, T., Kollmeier, B., and Kohlrausch, A. (**1997b**). "Modeling auditory processing of amplitude modulation. II. Spectral and temporal integration," J. Acoust. Soc. Am. **102**, 2906–2919.

Dau, T., Puschel, D., and Kohlrausch, A. (**1996**). "A quantitative model of the 'effective' signal processing in the auditory system. I. Model structure," J. Acoust. Soc. Am. **99**, 3615–3622.

Eddins, D. A. (**1993**). "Amplitude modulation detection of narrow-band noise: Effects of absolute bandwidth and frequency region," J. Acoust. Soc. Am. **93**, 470–479.

Eddins, D. A. (**1999**). "Amplitude-modulation detection at low- and high-audio frequencies," J. Acoust. Soc. Am. **105**, 829–837.

Ewert, S. D., and Dau, T. (**2000**). "Characterizing frequency selectivity for envelope fluctuations," J. Acoust. Soc. Am. **108**, 1181–1196.

Ewert, S. D., Verhey, J. L., and Dau, T. (**2002**). "Spectro-temporal processing in the envelope-frequency domain," J. Acoust. Soc. Am. **112**, 2921–2931.

Formby, C. (**1985**). "Differential sensitivity to tonal frequency and to the rate of amplitude modulation of broadband noise by normally hearing listeners," J. Acoust. Soc. Am. **78**, 70–77.

Gockel, H., Moore, B. C., and Patterson, R. D. (**2003**). "Asymmetry of masking between complex tones and noise: Partial loudness," J. Acoust. Soc. Am. **114**, 349–360.

Goldstein, J. L. (**1973**). "An optimum processor theory for the central formation of the pitch of complex tones," J. Acoust. Soc. Am. **54**, 1496–1516.

Houtgast, T. (**1989**). "Frequency selectivity in amplitude-modulation detection," J. Acoust. Soc. Am. **85**, 1676–1680.

Kohlrausch, A., and Sander, A. (**1995**). "Phase effects in masking related to dispersion in the inner ear. II. Masking period patterns of short targets," J. Acoust. Soc. Am. **97**, 1817–1829.

Krumbholz, K., Patterson, R. D., and Pressnitzer, D. (**2000**). "The lower limit of pitch as determined by rate discrimination," J. Acoust. Soc. Am. **108**, 1170–1180.

Levitt, H. (**1971**). "Transformed up-down methods in psychoacoustics," J. Acoust. Soc. Am. **49**, 467–477.

Licklider, J. C. R. (**1951**). "A duplex theory of pitch perception," Experientia **7**, 128–133.

Meddis, R., and Hewitt, M. J. (**1991a**). "Virtual pitch and phase sensitivity of a computer model of the auditory periphery. I. Pitch identification," J. Acoust. Soc. Am. **89**, 2866–2882.

Meddis, R., and Hewitt, M. J. (**1991b**). "Virtual pitch and phase sensitivity of a computer model of the auditory periphery.II. Phase sensitivity," J. Acoust. Soc. Am. **89**, 2883–2894.

Meddis, R., and O'Mard, L. (**1997**). "A unitary model of pitch perception," J. Acoust. Soc. Am. **102**, 1811–1820.

Pressnitzer, D., Patterson, R. D., and Krumbholz, K. (**2001**). "The lower limit of melodic pitch," J. Acoust. Soc. Am. **109**, 2074–2084.

Terhardt, E. (**1974**). "Pitch, consonance, and harmony," J. Acoust. Soc. Am. **55**, 1061–1069.

Viemeister, N. F. (**1979**). "Temporal modulation transfer functions based upon modulation thresholds," J. Acoust. Soc. Am. **66**, 1364–1380.

Wiegrebe, L. (**2001**). "Searching for the time constant of neural pitch extraction," J. Acoust. Soc. Am. **109**, 1082–1091.

Wiegrebe, L., and Patterson, R. D. (**1999**). "The role of envelope modulation in spectrally unresolved iterated rippled noise," Hear. Res. **132**, 94–108.

Wiegrebe, L., and Winter, I. M. (**2001a**). "Psychophysics and physiology of regular-interval noise: Critical experiments for current pitch models and evidence for a 1st-order, temporal pitch code," in *Physiological and Psychophysical Bases of Auditory Function*, edited by J. Breebaart, A. J. M. Houtsma, A. Kohlrausch, V. F. Prijs, and R. Schoonhoven (Shaker, Maastricht).

Wiegrebe, L., and Winter, I. M. (**2001b**). "Temporal representation of iterated rippled noise as a function of delay and sound level in the ventral cochlear nucleus," J. Neurophysiol. **85**, 1206–1219.

Winter, I. M., Wiegrebe, L., and Patterson, R. D. (**2001**). "The temporal representation of the delay of iterated rippled noise in the ventral cochlear nucleus of the guinea-pig," J. Physiol. (London) **537**, 553–566.

Yost, W. A. (**1996**). "Pitch of iterated rippled noise," J. Acoust. Soc. Am. **100**, 511–518.

Yost, W. A. (**1997**). "Pitch strength of iterated rippled noise when the pitch is ambiguous," J. Acoust. Soc. Am. **101**, 1644–1648.

Yost, W. A., Patterson, R., and Sheft, S. (**1998**). "The role of the envelope in processing iterated rippled noise," J. Acoust. Soc. Am. **104**, 2349–2361.

Informational masking for simultaneous nonspeech stimuli: Psychometric functions for fixed and randomly mixed maskers

Nathaniel I. Durlach,[a] Christine R. Mason, Frederick J. Gallun, Barbara Shinn-Cunningham, H. Steven Colburn, and Gerald Kidd, Jr.
Hearing Research Center, Boston University, 635 Commonwealth Avenue, Boston, Massachusetts 02215

(Received 18 October 2004; revised 19 July 2005; accepted 20 July 2005)

Sensitivity d' and response bias β were measured as a function of target level for the detection of a 1000-Hz tone in multitone maskers using a one interval, two-alternative forced-choice (1I-2AFC) paradigm. Ten such maskers, each with eight randomly selected components in the region 200–5000 Hz, with 800–1250 Hz excluded to form a protected zone, were presented under two conditions: the fixed condition, in which the same eight-component masker is used throughout an experimental run, and the random condition, in which an eight-component masker is chosen randomly trial-to-trial from the given set of ten such maskers. Differences between the results obtained with these two conditions help characterize the listener's susceptibility to informational masking (IM). The d' results show great intersubject variability, but can be reasonably well fit by simple energy-detector models in which internal noise and filter bandwidth are used as fitting parameters. In contrast, the β results are not well fit by these models. In addition to presentation of new data and its relation to energy-detector models, this paper provides comments on a variety of issues, problems, and research needs in the IM area. [DOI: 10.1121/1.2032748]

PACS number(s): 43.66.Dc, 43.66.Lj, 43.66.Ba [RAL] Pages: 2482–2497

I. INTRODUCTION AND GENERAL BACKGROUND

Although there is still no consensus on how best to define informational masking (IM), it is generally agreed that it is central in origin; related to uncertainty, confusion, distraction, and/or misdirected attention; and clearly distinguished from masking that results from direct interaction between target and masker in the auditory periphery ("energetic" masking). Recent comments on definitional issues are available in Durlach *et al.* (2003a) and Watson (2005).

Substantial work has been done on both sequential IM and simultaneous IM. Background on the former is available in publications by Watson and his colleagues (e.g., Watson, 1987; Watson and Kelly, 1981; and Watson, 2005). Within the domain of simultaneous IM, work has been done on both speech and simplified nonspeech signals. Background on the work using speech signals (and on transformed versions of speech signals) is available in a number of publications (e.g., Freyman *et al.*, 1999, 2001; Brungart *et al.*, 2001; Arbogast *et al.*, 2002; and Kidd *et al.*, 2005).

This article is focused on the effects of randomizing the spectrum of the masker in situations where a tonal target is being masked by a simultaneously presented multitone complex (e.g., Neff and Green, 1987; Neff and Dethlefs, 1995; Oh and Lutfi, 1998; Wright and Saberi, 1999; Richards *et al.*, 2002).[1] Previous research in this area has shown that large amounts of masking occur (e.g., 40 dB) even when the masker is constrained to have no components in the vicinity of the target (e.g., Neff and Green, 1987; Neff *et al.*, 1993; Kidd *et al.*, 1994); that the slopes of the psychometric functions (in the few cases measured) are relatively shallow (e.g., Neff and Callaghan, 1987; Lutfi *et al.*, 2003a; Kidd *et al.*, 2003); and that the amount of masking depends strongly on the listener tested (e.g., Neff and Dethlefs, 1995; Durlach *et al.*, 2003b; Lutfi *et al.*, 2003b). In addition, it has been shown that the amount of masking varies nonmonotonically as a function of the density of the tonal maskers on the frequency axis (e.g., Neff and Green, 1987; Oh and Lutfi, 1998); and that when two-interval paradigms are used, the effect of randomizing the spectrum of the masker is greater when the changes occur between intervals rather than only between trials (e.g., Neff and Callaghan, 1988; Neff and Dethlefs, 1995; Wright and Saberi, 1999; Tang and Richards, 2003; Richards and Neff, 2004). Finally, it has been shown that a substantial decrease in IM can be achieved by decreasing the similarity between target and masker (e.g., Kidd *et al.*, 1994, 2002; Neff, 1995; Durlach *et al.*, 2003b) or by employing trial-by-trial masker cuing (e.g., Richards and Neff, 2004; Richards *et al.*, 2004).

Among the ideas that have been put forward in connection with the empirical findings on IM are the following. First, making use of the standard decision-theory framework, Lutfi and his associates have made detection-performance predictions under the assumption that the decision variable X consists of a weighted sum of the power outputs of various independent nonoverlapping auditory filters (e.g., Lutfi, 1993; Oh and Lutfi, 1998). In particular, they have predicted with considerable accuracy the nonmonotonic dependence of threshold level on the number of frequency components used in the maskers. Apart from choosing the filter shapes appropriately, a major challenge within this structure is to develop appropriate rules for determining the weighting functions

[a]Electronic mail: durlach@mit.edu

and how these functions depend on the psychoacoustic task, the stimulus, and the listener (see also Richards *et al.*, 2002). Among other things, these weighting functions provide a means for capturing certain aspects of attentional phenomena. For example, a weighting function that includes substantial weights for a wide range of auditory filter outputs corresponds to the listener attending to a wide range of frequencies in the stimulus, i.e., employing a wide "attentional band" (e.g., Green, 1961; Oh and Lutfi, 1998).

Some ideas that have been put forward by Allen and Wightman (1994, 1995) and Lutfi *et al.* (2003a) concern the shape and interpretation of psychometric functions. For example, focusing on percent correct (PC) (as opposed to d'), these authors have stressed the importance of recognizing and taking account of the difference λ between ideal asymptotic performance (PC=100) as target-to-masker ratio becomes very large and observed asymptotic performance. The basic notion here is that the value of λ (referred to as the "lapse" parameter) is generally greater than zero, and that this parameter is important with respect both to the fitting of psychometric-function data and to the development of adequate theory.[2] Also of interest in this general domain is consideration of how the shape of the psychometric function is influenced by the density of the maskers (Lutfi *et al.*, 2003a).

Finally, an additional set of ideas relevant to interpretation of the empirical findings concerns the analysis of a given amount of masking into informational and energetic components (or, alternately, how the informational and energetic masking effects of a given masker should be combined). Material relevant to this issue is available in Lutfi (1990) and Neff and Jesteadt (1996), as well as in Kidd *et al.* (2005).

The research discussed in this paper is concerned with the detection of a tonal target in simultaneous multitone maskers with spectra that have relatively little energy in the vicinity of the target (i.e., in the "protected zone"). In particular, these experiments have been designed to study the effects of randomizing the masker spectrum (over a specified finite set of maskers) on how detection performance varies with target energy level. Among the characteristics of this research that distinguish it from most previous research on simultaneous IM for nonspeech stimuli are the following. First, it is concerned with psychometric functions, not only thresholds. Second, it compares psychometric functions obtained with a random masker to the psychometric functions obtained with the fixed constituents of this random masker (as well as to derived psychometric functions obtained by sorting the results obtained with the random masker and by pooling the results obtained with the fixed maskers). Third, apart from the uncertainty associated with the presence or absence of the target, this research restricts the stimulus uncertainty to the spectrum of the masker. It does not confound the effects of this uncertainty with uncertainty in the masker level (the masker level is held fixed rather than roved) or uncertainty in the target level (rather than use adaptive procedures or the method of constant stimuli, the target level is held fixed throughout each experimental run). Fourth, this research makes use of a one-interval paradigm which, aside from maximizing the number of trials per unit time that can be collected, enables one to examine the dependence of listener response bias on masker spectrum. Fifth, the empirical results are analyzed in terms of simple energy-detector models in which performance is characterized by the sensitivity index d' and the response bias β, and the decision variable is identified with the energy at the output of a linear filter centered on the target frequency. Sixth, rather than testing a large group of listeners and examining the performance statistics for this group, our study examines a few listeners in depth (using the "case-study" approach). Clearly, both approaches are needed to gain full understanding of IM and the large individual differences associated with IM.

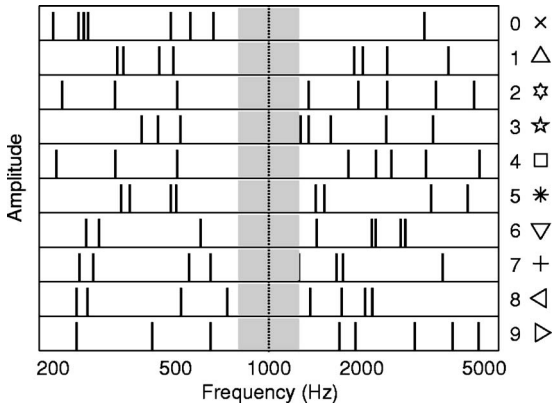

FIG. 1. Line spectra of the ten maskers F_i, $0 \leq i \leq 9$, together with identifying symbols. The shaded region shows the protected zone.

II. DETAILS OF THE EXPERIMENTAL DESIGN

Performance was measured for the detection of a 1000-Hz tone in multitone maskers consisting of eight tonal components. The level of each masker component was 60 dB SPL and the level of the overall masker was 69 dB SPL. The duration of the target and masker, which were gated on and off together, was 300 ms (with 20-ms cosine-squared ramps).

The experiment made use of ten different eight-tone maskers, $F_i, 0 \leq i \leq 9$, each of which was constructed by randomly selecting eight frequencies (with a random phase for each frequency) from the range 200–5000 Hz (on a logarithmic scale) with the subregion 800–1250 Hz around the 1000-Hz target omitted (to form a protected zone). In addition, the components were required to be at least 3.3 Hz (i.e., 1/300 ms) apart. The eight frequencies that comprised each of the ten maskers F_i are shown in Fig. 1. These same ten "frozen" masker samples were then fixed throughout the experiment. All stimuli were digitally generated in the time domain (addition of sine waves) with a sampling frequency of 20 000 Hz. The target and masker were played (using Tucker-Davis Technologies hardware) from separate D/A channels, low-pass filtered at 7500 Hz, attenuated, then summed and passed through a headphone buffer, the output of which was connected through the booth to the headphones. The desired levels were achieved by attenuating targets and maskers appropriately (and separately before sum-

ming) utilizing the reference levels obtained by measuring the sound-pressure levels for a known voltage in the TDH 50 headphones.

The experiment employed a one-interval, two-alternative, forced-choice (yes–no) procedure with a 0.5 *a priori* probability of target present and trial-by-trial correct-answer feedback. On each trial, the 300-ms observation interval was followed by a response period of at least 500 ms (additional time beyond 500 ms being available if the listener failed to enter a response during the 500-ms interval). The stimuli were presented monaurally over earphones (to the right ear) in a sound-treated (double-walled IAC) room, and responses were entered using a keyboard.

In the fixed condition, one of the ten eight-tone maskers F_i was held fixed from trial-to-trial. In the random condition, denoted R, the eight-tone masker was varied randomly from trial-to-trial (with uniform probability) over the set of ten maskers F_i specified in Fig. 1. In all cases, detection performance was measured at a variety of signal levels and, for each level, specified in terms of the sensitivity index d' and response bias β. Different sets of signal levels were chosen for the different F_i cases (as well as for the R case) in order to focus on the portions of the d'-vs-level curves that showed significant changes in d' with level.[3] Overall, we obtained 22 empirical functions of level (ten F_i functions and one R function for each of d' and β) for each listener.

The five listeners (three males, two females) tested in these experiments (L1–L5), all of whom were college students with normal hearing (thresholds of 15-dB HL or better at octave frequencies from 250 to 8000 Hz in both ears), had participated in previous IM experiments in this laboratory. For any given condition, data were gathered in 50-trial runs with signal level varied only between runs (decreasing in successive runs). The various F_i cases were tested in random order (different for each listener) and blocks of F_i runs were alternated with blocks of R runs. Also, after the whole sequence of tests was completed, it was repeated to increase the reliability of the results. Each point on the data graphs for the ten F_i functions (for each listener) is based on 100 trials, and each data point for the single R function (for each listener) is based on 1000 trials. Because of the way in which the various test blocks were ordered (as well as the relevant previous experience of all the listeners in IM), we believe that the differences among the various F_i functions and between these functions and the R functions were not influenced strongly by learning or fatigue factors.

In addition to the empirically determined F_i and R functions, the data were processed to obtain derived functions R_p and $F_{s,i}$, $0 \leqslant i \leqslant 9$ (for both d' and β). The derived function R_p was obtained by *pooling* the 2×2 stimulus–response matrices obtained in the F_i runs over all these runs, and the derived functions $F_{s,i}$, $0 \leqslant i \leqslant 9$ were obtained by *sorting* the matrices obtained in the R runs according to which F_i was presented, where each of the pooling and sorting processes was conducted once for each target level (so that the derived functions, like the empirical ones, are functions of target level). By definition, the pooling and sorting processes are inversely related. In other words, sorting the results obtained for R_p leads back to the results for F_i, $0 \leqslant i \leqslant 9$, from which R_p was derived, and pooling the results obtained for $F_{s,i}$, $0 \leqslant i \leqslant 9$, leads back to the results for R from which $F_{s,i}$, $0 \leqslant i \leqslant 9$ was derived.

In terms of these four types of functions of target level, the primary issues of interest, i.e., the IM issues, concern the way in which the function R differs from the function R_p and the function vector $(F_0, \ldots, F_9)$ differs from the function vector $(F_{s,0}, \ldots, F_{s,9})$. The two equalities

$$R_p = R, \qquad F_{s,i} = F_i, \quad 0 \leqslant i \leqslant 9, \tag{1}$$

hold if and only if the listener's detection behavior for the target in the presence of the masker F_i is independent of whether that behavior occurs in an F_i run with that masker or on trials of an R run in which that masker occurs. In other words, these two equalities hold if and only if there is no IM.[4]

For all of the functions $R, R_p, F_i, F_{s,i}$, $0 \leqslant i \leqslant 9$, the quantities d' and β were obtained from the appropriate 2×2 matrix by using the entries to estimate the probabilities of detection (P_D) and false alarm (P_{FA}), converting to normal deviates $z(P_D)$ and $z(P_{\mathrm{FA}})$, and then computing $d' = z(P_D) - z(P_{\mathrm{FA}})$ and $\beta = -[z(P_D) + z(P_{\mathrm{FA}})]/2$. Whereas for the F_i case the target levels at which d' and β were measured depended on i, for the $F_{s,i}$ case these levels were independent of i (because all the d' and β results for the $F_{s,i}$ case were obtained by sorting the R data and thus made use of the same levels as those used in the R tests).

III. EXPERIMENTAL RESULTS ON SENSITIVITY d'

The dependence of d' on target level for both the empirical functions F_i and R and the derived functions $F_{s,i}$ (obtained by sorting the R data) and R_p (obtained by pooling the F_i data) is shown in Fig. 2. We note the following features of these psychometric functions:

(1) For each listener, the F_i cases have d' functions (within the measured range) that are roughly linear in the given coordinates, share a roughly common slope, and cover a lateral range (e.g., at the $d' = 2$ level) of approximately 15–30 dB. Although not evident in the figure, all these functions must converge to $d' = 0$ as the target level goes to zero (i.e., to $-\infty$ in dB SPL) and must plateau at some high level of d' as a consequence of occasional errors having nothing to do with hearing, e.g., caused by lapses in attention.[2] (In our computation of the R_p curves shown in Fig. 2, the d' plateau was set at $d' = 4.7$.)

(2) Compared to the d' functions for the F_i cases, the d' functions for the R case tend to have a shallower slope and to be laterally displaced to the right. The tendency of these d' functions to converge with those for the F_i cases at the lower signal levels occurs of necessity because of the existence of the $d' = 0$ (chance) asymptote for all the functions.

(3) The R_p curve tends to deviate from the R curve by being steeper and displaced to the left. Correspondingly, the $F_{s,i}$ curves tend to deviate from the F_i curves by being shallower and displaced to the right. The extent to which

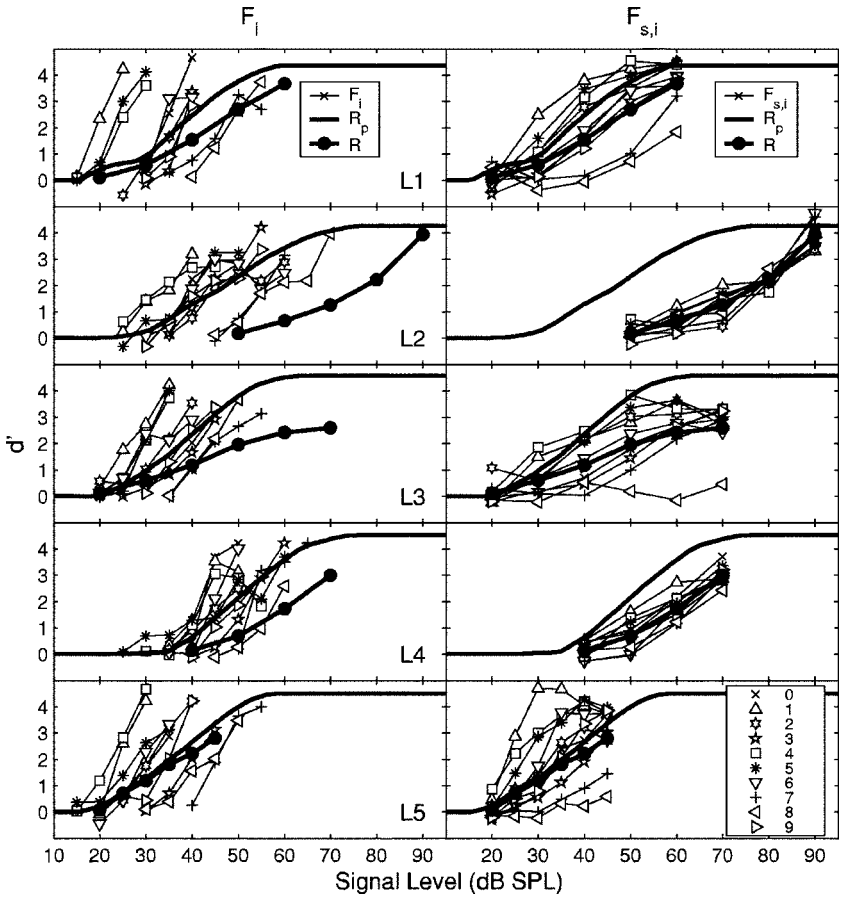

FIG. 2. Results on sensitivity d' as a function of target level for each of the cases F_i, R, $F_{s,i}$, and R_p. The left column gives the empirical functions for the individual maskers ($F_i, 0 \leqslant i \leqslant 9$). The right column gives the derived functions for the individual maskers ($F_{s,i}, 0 \leqslant i \leqslant 9$, obtained by sorting the R data). The empirical R function is shown in both the left and right columns. Also shown in both columns is the derived function R_p (obtained by pooling the F_i data). The correspondence between masker symbol and masker for $i=0$ to 9 is shown in the lower right corner. For details concerning the choice of target levels tested, see the text and footnotes 3 and 5.

these deviations are greater than zero is a measure of IM. That the slope of the R_p curve is shallower than the mean slope of the F_i curves (referred to as the "reduced-slope artifact") is a consequence of the pooling process used to construct the R_p curve combined with the decrease in slope of the F_i curves at small and large values of d'.

(4) The results differ substantially among subjects. For example, L5 exhibits F_i curves and $F_{s,i}$ curves that are relatively steep, quite far to the left, and strongly overlapping, as well as an R curve and R_p curve that are relatively steep, far to the left, and roughly coincident. In contrast, L2 is distinguished by a very large lateral shift to the right of the R curve and the $F_{s,i}$ curves, a very large (almost 30 dB) difference between the R curve and the R_p curve, and relatively shallow slopes for the F_i curves. Listener L1 appears somewhat similar to L5 except that the divergence between the R and R_p curves [and between the F_i and $F_{s,i}$ curves] is greater for L1. These divergences are even greater for L3 and L4 (although not as great as for L2). Note also the differences between L2 and L4 on the one hand and L1, L3, and L5 on the other hand with respect to the relatively tight bunching of the $F_{s,i}$ curves for L2 and L4 (relative both to the F_i curves of L2 and L4 and to the $F_{s,i}$ curves of L1, L3, and L5).

(5) The $F_{s,i}$ results for L3 show a monstrous outlier—a psychometric function that remains close to $d' \approx 0$ over the whole range tested! The psychometric function for this same masker (masker #8) is also the slowest rising function of all those measured in the $F_{s,i}$ data for L1 and L5. As shown in Fig. 1, masker #8 is distinguished by containing frequency components relatively close to the target frequency both above and below it. However, this factor by itself does not explain the strange results for masker #8 in the $F_{s,i}$ case for L3. For this listener, we do not understand why the function is so flat, why the difference in flatness for the F_i case and the $F_{s,i}$ case is so much larger for masker #8 than for all the other maskers, and why the results for masker #8 are so different than the results for masker #7, which also has components close to the target on both sides. (It should be noted, however, that this similarity between maskers #7 and #8 is reflected in the results for listeners L1 and L5.) Finally, it should be noted that based on L2's $F_{s,i}$ data for masker #2 (and, to a lesser extent, for a few other maskers as well), which are basically flat in the range 50–70 dB SPL and only begin to rise at 70 dB SPL, one might expect masker #8 to begin its rise for L3 just at the level at which the data terminate (i.e., 70 dB SPL).

(6) The tendency for the results on the functions F_i and $F_{s,i}$ to deviate from linearity and to evidence reduced slopes at both high and low values of d' (a tendency that must occur for sufficiently extreme values of d') varies considerably with the choice of masker and listener. These deviations are greater for the $F_{s,i}$ results than the F_i results and increase with the lateral spread of the $F_{s,i}$ results.[5]

In general, it is clear from the results in Fig. 2 that the amount of IM varies strongly among the five listeners.

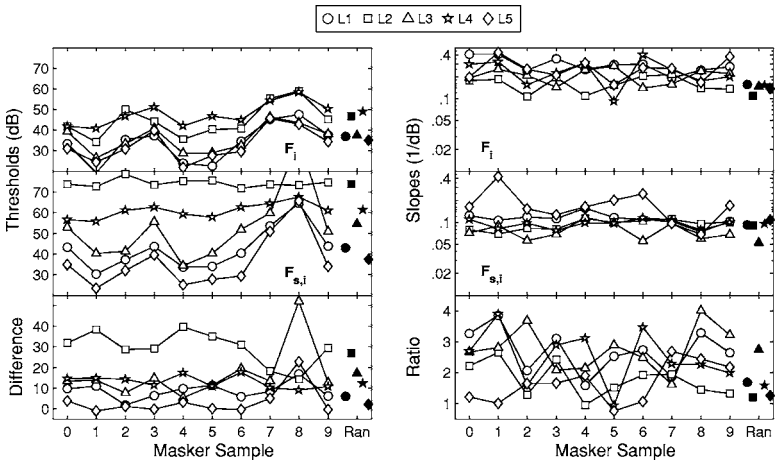

FIG. 3. Thresholds and slopes from straight-line fits to all psychometric functions for all listeners. The top two panels show the thresholds and slopes for the F_i case and the middle two panels for the $F_{s,i}$ case. The bottom two panels show the relation of the F_i results to the $F_{s,i}$ results (differences for thresholds and ratios for slopes). The corresponding results for the R and R_p cases are shown at the right edge of each panel (above abscissa label "Ran") using filled symbols (the R_p results in the top two panels, the R results in the middle panels, and the relation of the two in the bottom panels). The points in all panels are joined by straight-line segments to aid in following the results for individual listeners. For further details, see the text and footnotes 6 and 7.

Whereas L2 exhibits very large IM, listener L5 exhibits hardly any IM. Listeners L1, L3, and L4 appear to fall between these two extremes, with L1 showing the least IM (not much more than that for L5) and L3 and L4 somewhat more (although not as much as L2). Obviously, any satisfactory theory of IM will have to be capable of handling a wide range of listener susceptibilities to IM. The reduced-slope artifact is evidenced in the results for all listeners by the shallowness of the R_p function relative to the F_i functions.

To facilitate quantitative analysis, straight lines were fit to all the psychometric functions for each masker and each listener.[6] The threshold (defined as the level for which $d'=2$) and the slope were chosen individually for each line to minimize the rms deviation in d' of the points from this line. The thresholds and slopes obtained with these straight-line fits are shown in Fig. 3 for each masker, each condition, and each listener (open symbols for the F_i and $F_{s,i}$ results and filled symbols for the R and R_p results). The extreme behavior associated with masker #8 in the $F_{s,i}$ case is clearly evident in the threshold data but not the slope data (because in the fitting process asymptotic values were ignored and the emphasis was on the points at which d' showed an orderly change with target level[6]). Also shown in this figure are the relationships of the F_i results to the $F_{s,i}$ results and the relationships of the R results to the R_p results (differences for thresholds and ratios for slopes). The strength of the IM in this experiment, i.e., the extent to which the thresholds and slopes of the psychometric functions for the various maskers depend on the context in which the masker was presented (alone in the fixed case or mixed together with the other maskers in the random case) is clearly evident in these relationships. If there were no IM, all the data in the bottom left panel of Fig. 3 would be at 0 dB and all the data in the bottom right panel would be at unity. For each of the five listeners, the means and standard deviations (across maskers) for each of the cases F_i and $F_{s,i}$, as well as the results for the R case, are shown in Table I. An indication of the overall quality of the straight-line fits used to obtain the results shown in Fig. 3 and Table I is given by the rms deviations of the points from the straight lines along the y axis, Y_{dev} (d'), and along the x axis, X_{dev} (target level in dB). These rms deviations are shown in Table II. According to these results, the worst fits occur for L1 and L2 in the $F_{s,i}$ case and L2 in the R case.

TABLE I. Thresholds and slopes derived from straight-line fits to the data. For the F_i and $F_{s,i}$ columns, the means and standard deviations are given across the ten masker samples for each listener. The R and R_p columns give the thresholds and slopes for the one relevant function per listener. The last two rows give the average and standard deviation of the means across listeners. Mean slopes are geometric means and standard deviations for slopes are given in percent. In keeping with our treatment of the outlier (masker #8 for the $F_{s,i}$ case), both its threshold and slope were excluded from the mean and standard deviation over maskers for L1, L3, and L5.

		Thresholds (dB SPL)				Slopes (1/dB)			
		F_i	$F_{s,i}$	R	R_p	F_i	$F_{s,i}$	R	R_p
L1	Mean	33.7	40.1	43.0	37.0	0.29	0.12	0.09	0.16
	sd	9.3	7.1			27	14		
L2	Mean	44.7	74.3	73.8	46.8	0.16	0.09	0.09	0.11
	sd	8.0	2.0			29	18		
L3	Mean	35.9	47.5	54.7	37.5	0.20	0.08	0.05	0.15
	sd	6.8	8.6			28	29		
L4	Mean	47.8	61.0	61.3	49.0	0.22	0.10	0.10	0.15
	sd	5.8	3.7			53	15		
L5	Mean	32.9	33.0	37.4	35.2	0.25	0.18	0.11	0.14
	sd	7.9	8.4			39	52		
Average		39.0	51.2	54.0	41.1	0.22	0.11	0.09	0.14
sd		6.8	16.6	14.5	6.3	26	37	32	15

TABLE II. Rms deviations between straight-line fits to the data and the data themselves in both y-(Y_{dev}) and x (X_{dev}) directions. The mean and standard deviation for each listener is across the masker samples for the F_i and $F_{s,i}$ columns (masker #8 was excluded in the $F_{s,i}$ case for L1, L3, and L5). The last two rows gives the average and standard deviation of the means across listeners.

		F_i		$F_{s,i}$		R	
		Y_{dev} (d')	X_{dev} (dB)	Y_{dev} (d')	X_{dev} (dB)	Y_{dev} (d')	X_{dev} (dB)
L1	Mean	0.29	1.0	0.37	3.2	0.17	1.8
	sd	0.22	0.7	0.16	1.6		
L2	Mean	0.27	1.8	0.34	3.6	0.35	3.9
	sd	0.11	0.9	0.19	1.7		
L3	Mean	0.21	1.1	0.25	3.5	0.14	2.7
	sd	0.13	0.8	0.11	2.2		
L4	Mean	0.30	1.5	0.26	2.7	0.19	2.0
	sd	0.23	1.3	0.08	0.8		
L5	Mean	0.20	0.9	0.22	1.2	0.05	0.5
	sd	0.09	0.5	0.11	0.6		
Average		0.25	1.2	0.29	2.9	0.18	2.2
sd		0.04	0.4	0.06	1.0	0.11	1.3

As part of our effort to compare thresholds for the F_i case to thresholds for the $F_{s,i}$ case, scattergrams and correlation coefficients r were examined for $F_{s,i}$ vs F_i across the ten maskers (separately for each listener). With the exception of L2, the results of this analysis (excluding masker #8 for L1, L3, and L5) showed scattergrams with slopes between 0.6 and 1.2 and values of r in the range 0.89 to 0.97. In other words, for subjects L1, L3, L4, and L5, the variation of threshold with masker was roughly the same for F_i and $F_{s,i}$. For L2, as a consequence of the tiny variation in threshold for the $F_{s,i}$ case, the value of r was found to be close to zero ($r=0.13$). Furthermore, correlations of thresholds between listeners over the set of maskers were generally high for all pairs of listeners in the F_i case (0.78 to 0.94, including all ten masker samples) and all pairs of listeners in the $F_{s,i}$ case (excluding masker #8) in which L2 did not appear (0.60 to 0.95). If the pair included L2, the correlation in the $F_{s,i}$ case for the pair was close to zero or negative (−0.47 to 0.20). In other words, the dependence of threshold on masker was similar across all listeners in the F_i case and across listeners L1, L3, L4, and L5 in the $F_{s,i}$ case (with masker #8 excluded). The main slope result to be noted is the general tendency for the $F_{s,i}$ slopes to be smaller than the F_i slopes (particularly for L1, L3, and L4).

To examine the statistical significance of these results, two separate two-factor repeated-measures analyses of variance (ANOVA) were done, one for threshold data and one for slope data. The two factors in each ANOVA were the uncertainty condition (F_i vs $F_{s,i}$) and the masker sample (always excluding masker #8). In the case of thresholds, the uncertainty condition (F_i vs $F_{s,i}$) alone did not quite reach significance [$F(1,4)=7.1$, $p=0.056$], the masker condition (nine samples) was significant [$F(8,32)=15.1$, $p<0.001$], and the interaction of those two factors was not significant [$F(8,32)=1.07$, $p=0.41$]. Clearly, the variance across masker samples and listeners obscured the difference between the F_i and $F_{s,i}$ thresholds in this ANOVA. When five separate paired-comparisons t-tests were done (one for each listener) on the set of F_i and $F_{s,i}$ thresholds, the result was highly significant for all listeners except L5. The results were $t=-7.7$, df=8, $p<0.001$; $t=-11.7$, df=9, $p<0.001$; $t=-9.3$, df=8, $p<0.001$; $t=-13.7$, df=8, $p<0.001$, and $t=-1.8$, df=8, $p=0.12$ for L1 to L5, respectively. The results of the ANOVA on log-slope values revealed a significant effect of uncertainty condition [$F(1,4)=41.7$, $p=0.003$], but no significant effect of masker sample [$F(8,32)=0.86$, $p=0.56$]. This supports the result that the slopes get shallower in going from F_i to $F_{s,i}$, but that the slope does not depend on masker sample.

IV. ANALYSIS OF THE d' DATA IN TERMS OF SIMPLE ENERGY-DETECTOR MODELS

A. Description of the models

The basic framework used in our analysis of the data shown in Fig. 2 is that of a simple energy-detector model. It is assumed that (1) the decision variable X is stimulus energy or power (measured in dB) at the output of a linear filter with transfer function $H(f)$ centered on the target frequency; (2) the probability density functions of X for the masker-alone case (M) and the target-plus-masker case ($T+M$) are Gaussian with means $\mathcal{M}_M=10\log E_M$ and $\mathcal{M}_{T+M}=10\log E_{T+M}\approx 10\log(E_T+E_M)$ and common variance σ^2, where E_T and E_M are the target and masker energies at the output of the filter; and (3) the listener responds "target present" if and only if $X>C$, where C is the listener's decision criterion. As usual, the sensitivity d' is given by

$$d'=\frac{\mathcal{M}_{T+M}-\mathcal{M}_M}{\sigma}. \tag{2}$$

For the given $\mathcal{M}_{T+M}$ and $\mathcal{M}_M$, one has

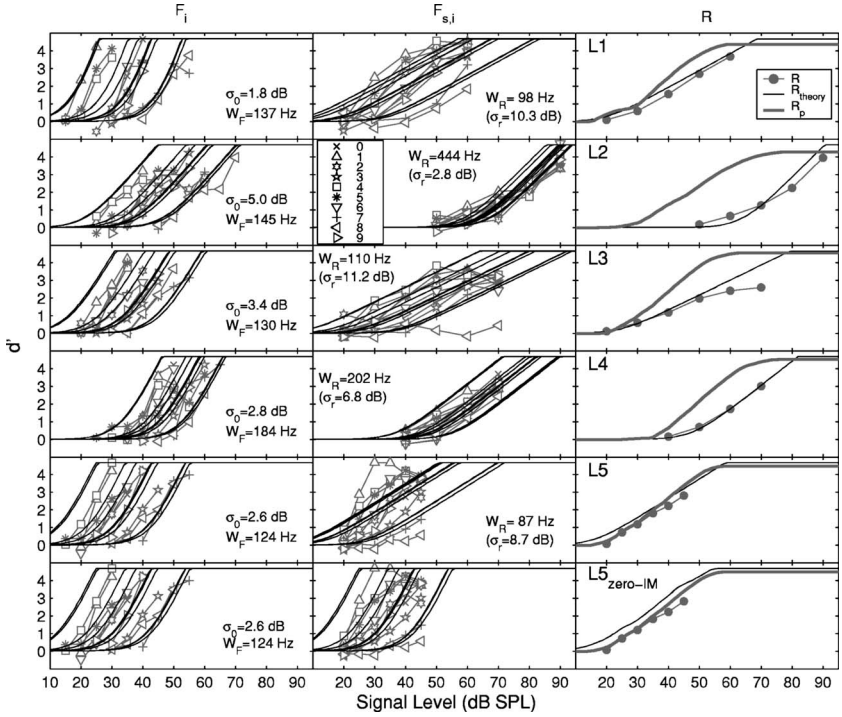

FIG. 4. The results of fitting theory to data. Column 1 is for the F_i case, column 2 for the $F_{s,i}$ case, and column 3 for the R and R_p cases. The F_i data, the R data, and the derived $F_{s,i}$ and R_p results (obtained by sorting the R data and pooling the F_i data, respectively) are identical to those shown in Fig. 2. The upper five rows show the results of applying the simple energy-detector model to each of the five listeners L1–L5. The thin, continuous curves in the upper five rows are determined from Eq. (3) using the parameter values specified in the figure. In the F_i case, both σ_0 and W_F were used as fitting parameters. In the $F_{s,i}$ case, it was required that the value of σ_0 be identical to that used for the F_i case, and thus only W_R was used as a fitting parameter (the value of σ_r being determined by the value of W_R). In the R case, no new fitting was performed (the values of σ_0 and W_R being identical to those obtained from the fitting of the F_i and $F_{s,i}$ results). For further details concerning the fitting of this model to listeners L1–L5, see the text and footnote 7. The bottom row in this figure shows the results of applying the zero-IM model to listener L5. In this model, the predictions for the $F_{s,i}$ case are identical to those for the F_i case and there are only two fitting parameters, σ_0 and W_F. Also, the value of W_R is the same as that of W_F and there is no σ_r term (see the text for details).

$$d' = \frac{10\log(1 + E_T/E_M)}{\sigma}, \tag{3}$$

a formulation that is consistent with Weber's law for intensity discrimination.

It will be assumed that $H(f)$ is chosen to increase the T/M ratio by focusing on T rather than by nulling out M; that $H(f)$ represents the integrated frequency-selectivity behavior of the whole auditory system (including attentional phenomena), not only that associated with the periphery (i.e., the "critical band"); and that $H(f)$ is independent of the identity of the masker, but may depend on the listener and/or the experimental condition to which the listener is exposed (specifically, whether the test is an F_i test or an R test). It will further be assumed that in the R tests the listener has zero knowledge of which masker is presented on a given trial and thus sets the decision criterion C in a manner that is independent of the masker and designed to distinguish between the broad probability densities on the decision axis that characterize the energy at the output of the filter $H(f)$ over all of the maskers F_i (one density for the case of target absent and one for the case of target present). Although such a simple model (namely, one in which detection is assumed to depend only on energy and, furthermore, only on energy at the output of a single filter) is clearly inadequate to explain all results on IM, we believe it is instructive to examine how it relates to the data reported in this study.

The variance σ^2 will be assumed to consist of two components

$$\sigma^2 = \sigma_0^2 + \sigma_r^2, \tag{4}$$

where σ_0 represents internal noise (arising centrally as well as peripherally) and σ_r represents the increase in the variance associated with randomization of the masker. The term σ_0 will be allowed to vary with the listener, but will be held fixed otherwise. This term appears in all the F_i cases and the R case, and is the only variance term in the F_i cases. The quantity σ_r will be computed as the rms deviation in energy level (in dB) at the output of the filter $H(f)$ resulting from the masker-spectrum randomization (and will be referred to as the "roving-level" component of the variance). Note that the σ_r is completely determined by the filter $H(f)$ and the masker spectra, and thus is not a free parameter. Note also that as the filter $H(f)$ becomes increasingly broad in the R case, both the numerator and denominator of the equation for d' [Eq. (3)] decrease. The numerator decreases because the masker energy that gets through the filter (E_M) increases, and the denominator decreases because the roving-level variance (σ_r^2) decreases. For very broad filters, σ_r approaches zero because all the maskers F_i were constructed to have the same total energy.

B. Application of the model to the data

In applying this model to the data, the filter $H(f)$ was assumed to be a symmetric roex(p,r) filter (Patterson and Moore, 1986) centered at 1000 Hz with equivalent rectangular bandwidth (ERB) W, and in those cases in which σ_r was relevant, σ_r was computed as the rms deviation of the masker energy about its mean at the output of this filter (where the energy was measured in dB). Although no rigorous study was made, based on a few informal probes it is believed that modest modifications of the assumed filter shape would lead to only modest changes in the results presented in this section. The results of fitting this model to the data are shown in the upper five rows of Fig. 4 (the bottom row is considered below).

Consider first the fitting of the F_i functions. Because the masker was fixed in this case, one has $\sigma_r = 0$ and the predictions are given by Eq. (3) with $\sigma = \sigma_0$ (the internal noise) and

TABLE III. rms deviations between model and data for threshold (T_{dev}) and slope (S_{dev}). The bottom row gives the results for the "zero-IM" model. Masker #8 was excluded in the $F_{s,i}$ case for L1, L3, and L5.

	F_i		$F_{s,i}$		R	
	T_{dev} (dB)	S_{dev} (%)	T_{dev} (dB)	S_{dev} (%)	T_{dev} (dB)	S_{dev} (%)
L1	4.1	21	4.8	23	2.3	2
L2	5.0	24	3.5	71	1.0	75
L3	4.8	22	5.4	26	6.7	59
L4	4.3	38	4.7	36	0.8	36
L5	4.1	29	2.9	71	3.4	0
Average	4.5	27	4.2	44	2.9	31
sd	0.4	5	1.0	17	2.4	29
$L5_{zero\text{-}IM}$	4.1	29	4.7	61	6.0	12

with E_T and E_M given by the target and masker energies at the output of the roex filter. The fitting in this case was achieved by choosing (for each subject) σ_0 and W_F to match the theoretical F_i thresholds and slopes to the empirical F_i thresholds and slopes.[7] The results of this fitting and the values of σ_0 and W_F used to achieve these fits are shown in the left column of Fig. 4. Whereas the theoretical slopes are determined by σ_0, the theoretical thresholds are determined by W_F as well as σ_0. Further computations showed that the mean of the correlation coefficient r between theoretical and empirical thresholds across maskers (over the five listeners) was 0.89 (range 0.81–0.95). The relatively high value of this correlation, combined with the assumptions of the model, necessarily implies that the correlation between the empirical thresholds and the amounts of energy through the assumed filter is relatively high.

Consider next the $F_{s,i}$ case. The fitting here was performed in exactly the same manner as the F_i case except that (1) the parameter σ_0, rather than being treated as a fitting parameter, was chosen to be the same as in the F_i case and (2) the variance term σ^2 now included a σ_r^2 term as well as the σ_0^2 term. The fits in the $F_{s,i}$ case, shown in the middle column of Fig. 4, were then achieved by choosing W_R to best fit the empirical $F_{s,i}$ thresholds and slopes (the slopes in this case are determined by the fixed σ_0 term and by W_R which determines σ_r).[7] Excluding L2, the correlation results (between theoretical and empirical thresholds) showed a mean of 0.85 and a range of 0.72 to 0.94. For L2, whose thresholds (both empirical and theoretical) were roughly independent of the masker, r was essentially zero ($r=-0.16$).

Consider, finally, the results for the random-masker case and the two theoretical curves shown in the right column of Fig. 4. One of the these curves, namely, the curve for R_p, is the same curve as that shown in Fig. 2. The second curve is obtained from Eq. (3) using the same values of σ_0, σ_r, and W_R that were used to generate the theoretical curves for the $F_{s,i}$ functions. In other words, no further fitting was done to match the theoretical R curves to the empirical R curves.

The quality of the fits of the theoretical results to the empirical results can be judged not only by visual inspection of Fig. 4, but also by examining the deviations in thresholds and slopes derived from the straight-line representations of the theory and of the data (denoted T_{dev} and S_{dev}). These deviations are shown in Table III. As one might expect from an examination of Fig. 4, the largest deviations occur with the $F_{s,i}$ slopes for L2 and L5, the R slopes for L2 and L3, and the R threshold for L3.

Beyond the issue of consistency between theoretical and empirical results, of course, is the issue of plausibility for the values of the constants obtained in the fitting process, i.e., the values of σ_0, W_F, and W_R shown in Fig. 4. Overall, these values appear quite reasonable. The values of σ_0 vary over the range 1.8–5 dB, corresponding to a range of 0.5–2.2 for the value of the ratio T/M at which d' is unity; and the values of W_F vary from 124 to 184 Hz, values roughly consistent with those encountered in various independent studies of the auditory filter bandwidth (e.g., Neff *et al.*, 1993). The values of W_R, which also determine in this case the values of σ_r, show relatively modest changes from W_F with the notable exception of L2, who is modeled best by assuming a dramatically wider bandwidth (roughly a factor of 3) for W_R. More surprising, perhaps, are the decreases in W for L1, L3, and L5 in going from W_F to W_R.[8]

For certain listeners, such as L5, there is relatively little vulnerability to IM and the above model may be inappropriate. Thus, we briefly examined an alternate model in which no IM is predicted (the "zero-IM" model). In this model, it is assumed that the listener not only uses the same decision variable in the R tests as in the F_i tests [the energy at the output of the same $H(f)$ filter], but also the same decision criteria. In other words, it is assumed that the listener can identify the masker F_i presented on each trial in an R run (by listening to the stimulus at frequencies away from the target frequency) and set the criterion on that trial in the same manner that it would be set in an F_i run with that masker. With this zero-IM model, not only is $H(f)$ the same for the F_i runs and the R run, thus reducing the number of free parameters in the model, but one has $\sigma=\sigma_0$ (there is no σ_r term), $F_{s,i}=F_i$, and $R_p=R$. Because in our experiment the total energy in the masker is independent of the masker, and only the spectrum of the masker is randomized, potential cues for identifying the masker by examining the stimulus at frequencies away from the target include masker energy as well as spectral shape at these frequencies. It should also be noted that in this zero-IM model the trial-to-trial identification of the masker in an R run is required only to the extent that it facilitates the choice of criterion for that trial, i.e., provides knowledge of E_M on that trial.

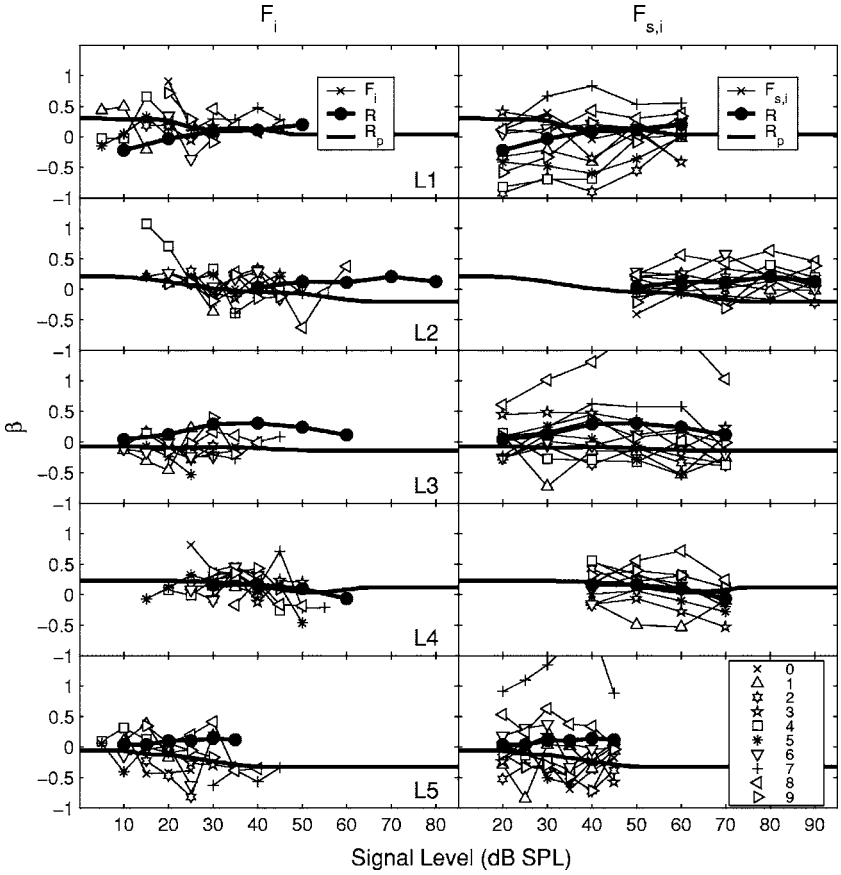

FIG. 5. Data on response bias β corresponding to data on d' shown in Fig. 2.

The results of comparing this zero-IM model to the data for L5 (using the same values of σ_0 and W_F as previously used for the F_i cases) are shown in the bottom row of Fig. 4 along with the fits obtained using the previous model. The theoretical curves for this model are the same as those derived for the previous model for F_i and R_p, but not for $F_{s,i}$ or R (with this zero-IM model, the curves for $F_{s,i}$ are identical to those for F_i). The values of T_{dev} and S_{dev} obtained with this model are included in Table III along with the values obtained with the previous model. According to these results, the change in model causes little change in S_{dev} but increases T_{dev} for both $F_{s,i}$ and R.

Finally, in concluding this section, three points should be noted. First, the results would not have been substantially altered if in the fitting process the data themselves rather than the thresholds and slopes determined from the straight-line fits to the data had been used. Second, the two models considered above reflect behavior extremes. Models of intermediate behaviors (which are likely to be appropriate to a substantial number of listeners) can be constructed by appropriate blending of these two models (e.g., by assuming some, but not perfect, knowledge of E_M on each trial). Third, the discrepancies between the simple energy detector model and the d' data are relatively small compared to the variations in the data across subjects, but relatively large compared to the variations in the data associated with the use of a finite number of trials in the experiments. If one determines the deviations T_{dev} and S_{dev} that arise when the results for one listener are used as a model for another listener, one obtains the following mean results (across all subject pairs): T_{dev}=9.3, 21.4, and 18.2 dB and S_{dev}=53%, 50%, and 34% for F_i, $F_{s,i}$, and R, respectively. A comparison of either of these sets of numbers with the corresponding numbers in Table III (T_{dev} =4.5, 4.2, and 2.9 dB and S_{dev}=27%, 44%, and 31%) provides support for the first of the above-mentioned statements, namely, that differences between theory and data are relatively small compared to differences among subjects. The validity of the second of these statements is proved by simulations we have done using 100 trials per data point (roughly equivalent to the number of trials per data point used in our tests). According to the results of these simulations, if the only source of deviation were the finite number of trials per data point, then T_{dev} should lie in the range 1–3 dB for the F_i and R cases and 2–6 dB for the $F_{s,i}$ case, and S_{dev} should lie in the range 11%–36% for all cases. All of these comparisons reflect the emphasis on thresholds relative to slopes in the process used to fit the model to the data.[7]

V. RESULTS ON RESPONSE BIAS

The results on response bias β (obtained according to the procedures outlined at the end of Sec. II) are shown in Fig. 5 in a manner similar to that used to display the d' results in Fig. 2. As with d', the β results for $F_{s,i}$ are obtained from the R results using the sorting process, and the β results for R_p are obtained from the F_i results using the pooling process. In general, a positive value of β corresponds to a bias to respond "no signal" too frequently, i.e., an overly conservative criterion.

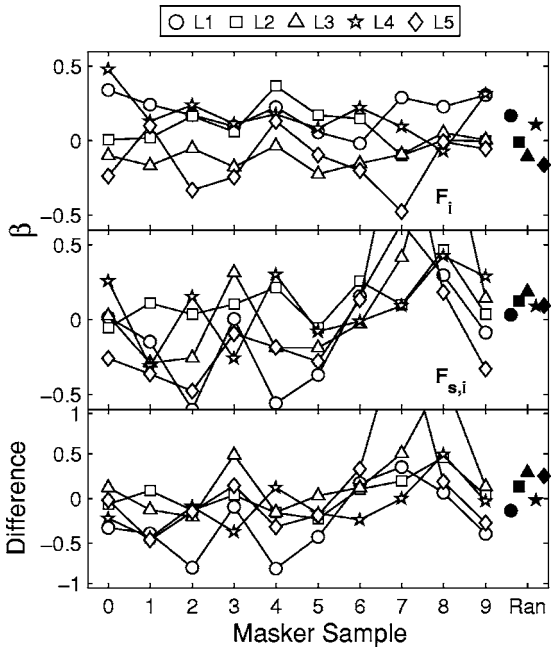

FIG. 6. Mean values of β over level as a function of masker, test condition, and listener. The top panel gives the results for the F_i case, the middle panel for the $F_{s,i}$ case, and the bottom panel for the difference. The filled symbols on the right (abscissa label "Ran") show the corresponding results for the R_p (top panel) and R (middle panel) cases. As in Fig. 3, the points are joined by straight-line segments to aid in following the results for individual listeners.

Visual inspection of the results shown in Fig. 5 indicate (1) the existence of two "outliers" in the $F_{s,i}$ case (generated by masker #8 for L3 and masker #7 for L5); (2) very weak (if any) dependence of β on signal level; and (3) excluding the two outliers, a general tendency for the values of β to cluster around $\beta=0$. In addition, it appears that (4) there is a slight tendency for β to decrease with level (become less conservative as signal level increases) in the R_p case (for all listeners but L3) and to be lower in the R_p case than in the R case (at least for listeners L2, L3, and L5).

As will be seen below, the most important result obtained from measurement and examination of the β data concerns the correlation between the value of β and the value of the threshold (over the set of maskers) for the $F_{s,i}$ case. With the goal of examining this correlation in mind, and the knowledge that β is at least roughly independent of level (as seen in Fig. 5), our initial processing of the β data consisted of eliminating the level parameter by averaging over it, i.e., of representing the β-vs-level data shown in Fig. 5 by best-fit horizontal straight lines. The results of this processing are shown in Fig. 6 and Table IV. Whereas Fig. 6 shows how β, averaged over level, depends on all maskers, all cases, and all listeners, Table IV provides information on the horizontal-straight-line fits. Even excluding the two outliers in the $F_{s,i}$ case, the results in Fig. 6 show a somewhat greater variation with masker in the $F_{s,i}$ case than in the F_i case. Examination of β scattergrams and correlation coefficients r for F_i vs $F_{s,i}$ (over the maskers) showed no relationship between the β values for these two cases; for all listeners, the value of r was close to zero ($0.06 \leqslant r \leqslant 0.18$).

As expected, the β results for the R_p case (solid symbols in top panel of Fig. 6) for each listener tend to be near zero

TABLE IV. Results of horizontal-straight-line fits to β-vs-level data. For each of the F_i and $F_{s,i}$ cases, the entries give the means and standard deviations over the set of maskers of the rms deviation (Y_{dev}) of the data points from the horizontal lines. For the R case, the entries give the single rms deviation of the data points from the single horizontal line. The row on the bottom gives the means and standard deviations of the results in the rest of the table across listeners. (In computing the entries in this table, the two outliers seen in Fig. 5 were omitted.)

		F_i	$F_{s,I}$	R
L1	Mean	0.22	0.24	0.15
	sd	0.12	0.10	
L2	Mean	0.21	0.16	0.06
	sd	0.12	0.06	
L3	Mean	0.14	0.22	0.10
	sd	0.08	0.07	
L4	Mean	0.18	0.17	0.09
	sd	0.10	0.04	
L5	Mean	0.21	0.22	0.04
	sd	0.10	0.07	
Average		0.19	0.20	0.09
sd		0.03	0.04	0.04

and look much like an average of the β values shown for each masker sample in the F_i case in the same panel. The range of values across listeners is −0.16 to 0.17. The β values shown for the R case (solid symbols in the middle panel of Fig. 6) appear more similar across listeners, all having slightly positive β values in the range 0.03 to 0.19. This is due in part to the inclusion of all data in the R case (including the outliers that are seen in the $F_{s,i}$ case). The differences between the β values for the R_p case and for the R case [and also for F_i vs $F_{s,i}$] are shown in the bottom panel. As can be seen more readily in Fig. 5, listeners L2, L3, and L5 all have more positive β values in the R case than in the R_p case, whereas L1 shows a slight negative difference and L4 shows virtually no difference. A two-way repeated-measures ANOVA on the β values with uncertainty (F_i vs $F_{s,i}$) and masker sample (excluding maskers #7 and #8) as the factors showed that neither main effect is significant [$(F(1,4)=3.24$, $p=0.15$ for F_i vs $F_{s,i}$; $F(7,28)=1.46$, $p=0.22$ for masker sample)].

Consider finally (and most importantly) the relationship of response bias β for a particular masker to the target threshold for that masker. Scattergrams and correlation coefficients r for β vs threshold over the set of maskers for each of the five listeners are shown in Fig. 7. The results for the F_i case (column 1) show no pronounced structure, with the values of r varying over the range −0.60 to 0.41, depending on the listener. In contrast, the results for the $F_{s,i}$ case (column 2) show a tendency to produce correlations that are positive. Not only do L1 and L3 show the relatively high correlations of 0.80 and 0.90 for the $F_{s,i}$ case, but for all listeners the value of r for the $F_{s,i}$ case is more positive than for the F_i case. Specifically, the values of $r(F_{s,i})-r(F_i)$ are given by 0.60, 0.15, 0.49, 0.97, and 0.71 for L1–L5, respectively. Note, moreover, the relationship for the outliers: both maskers #8 and #7 tend to combine a very high threshold with a very high value of β (see the results for both of these maskers in Figs. 3 and 6). Overall, with the exception of

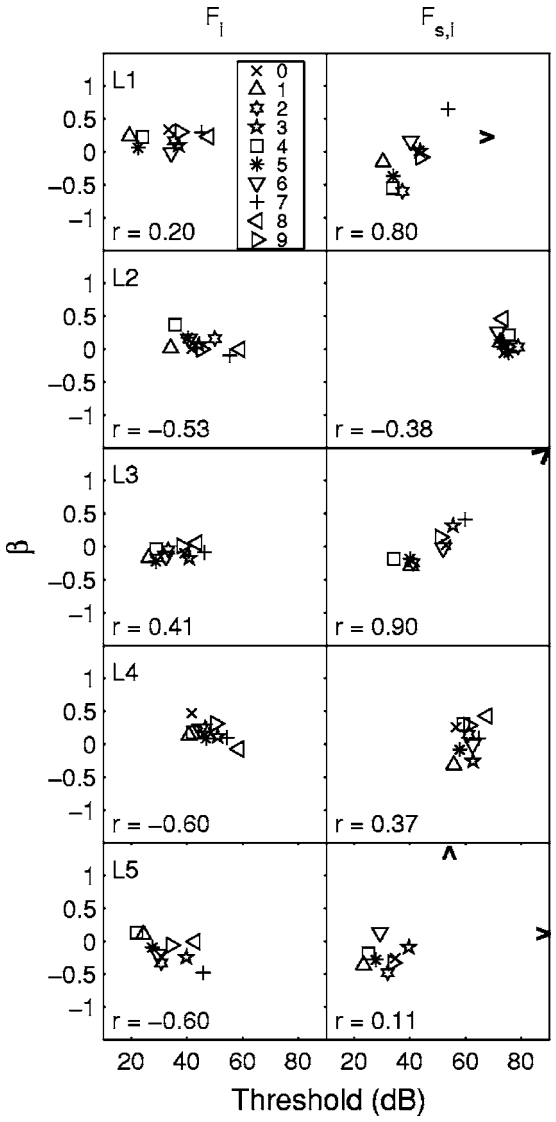

FIG. 7. Scattergrams and correlation coefficients r for response bias β vs threshold (across maskers). The first column gives results for the F_i case and the second column for the $F_{s,i}$ case. Arrowheads indicate the existence of outliers (not included in the computations of r).

listeners L2 and L5, whose d' results have already been shown to be relatively special, it appears that in the $F_{s,i}$ case, β and threshold tend to be positively correlated (with this positive correlation being smaller for the intermediate listener L4 than for L1 and L3).

Turning attention now to theoretical interpretations, we note the following. First, in the F_i case, where the same masker is presented trial after trial, there is no reason to anticipate large systematic deviations of β from zero and strong correlations (either positive or negative) with threshold because of the opportunity provided to each listener (via the trial-by-trial correct-answer feedback) to eliminate any initial bias the listener might have had based on the particular characteristics of the masker. Second, in the $F_{s,i}$ case, we would expect the β results to depend on the type of listener (as discussed previously in connection with the d' results). For the "normal" case, in which the listener (a) maintains a relatively narrow filter and (b) cannot identify the masker on individual trials of an R run, we would expect the listener to choose a single response criterion more or less in the middle of the whole range of energies coming out of the filter, and thereby produce results that would show a significant dependence of β on the energy of the masker coming through the filter and hence on the threshold of the target for the specific masker in question. In contrast, no such dependence would be expected if the listener either (a) opens up the filter to the extent that essentially all maskers produce roughly the same energy at the output of the filter (so that a fixed response criterion will not lead to a substantial dependence of β on the threshold) or (b) identifies the masker on each trial and locates the criterion in a manner that is appropriate for that masker. With these comments and the previous discussion of the data on d' for listeners L1–L5 in mind, the results showing the relation of β to the threshold shown in Fig. 7 look quite reasonable: whereas L1 and L3 show a clear dependence of β on threshold, L2 and L5 do not (with L4 lying somewhere in the middle of these two groups). Note also the extent to which the $F_{s,i}$ results shown in Fig. 7 for L5 support the zero-IM model rather than the original model for this listener.

There is, however, a big problem associated with these β results: according to our initial model, the predicted correlation between β and threshold that is seen in the results for L1 and L3 should be negative, not positive. For this model, the value of β is given by

$$\beta = \frac{C - \left(\frac{\mathcal{M}_{T+M} + \mathcal{M}_M}{2} \right)}{\sigma}, \tag{5}$$

where $\mathcal{M}_{T+M}$, $\mathcal{M}_M$, and σ are the same as considered previously in the analysis of the d' data, and the listener's decision criterion C is placed in the middle of the energy distribution as mentioned above. *This implies, however, that as the threshold increases the value of β should decrease* (corresponding to an increased tendency to respond signal present), *not increase* (corresponding to an increased tendency to respond signal absent). More specifically, if this model were correct, a masker that produced a high target threshold (i.e., a masker that produced a high level of energy at the output of the filter) would be associated with a high value of the quantity in parentheses in Eq. (5), which in turn would lead to a negative value of β. Further evidence of this model's inadequacy can be found in the range of values observed for β. If the response criterion were really the same for all maskers in the R case, the range of β would be much greater (because of the large range of masker energies at the output of the filter).

VI. SUMMARY AND DISCUSSION

A. Comparison with previous results

Previous work on psychometric functions in IM has been performed by AW (Allen and Wightman, 1994, 1995), WS (Wright and Saberi, 1999), and LKCW (Lutfi, Kistler, Callahan, and Wightman, 2003a). In principle, it should be useful to compare our results to theirs. In practice, however, meaningful comparisons are exceedingly difficult to make because of the major differences in stimuli, experimental procedures, methods of analysis, and groups of listeners. One

such difference is that all the previous studies used a 2I-2AFC paradigm. Also, rather than using fixed constituents of the random masker for the "minimum uncertainty" case, AW and LKCW used broadband Gaussian noise for this case. Furthermore, AW did not use a notch in this noise to create a protected zone, and LKCW provided a target cue on each trial prior to the 2I-2AFC presentation. In addition, with the exception of one portion of the WS study, none of the previous studies held the target level constant during an experimental run. Finally, in the AW study, the analog to our *R* case was achieved by adding a single random-frequency tonal masker (referred to as a "distractor") to the Gaussian noise masker, and in the WS study the analog involved pairing each masker with only one other masker in the 2I-2AFC paradigm.

Based on our attempts to process the data presented in all the studies in a manner that permitted comparisons among all the results, we found that the mean slope for the minimum uncertainty condition in the WS study was outstandingly low, that the mean threshold for all cases considered by AW were outstandingly high (presumably due to the lack of a protected zone in their noise masker), and that the ranges of thresholds and slopes found in the LKCW study were outstandingly large (presumably due to their large and age-varied listener pool). Most surprising was the high degree of consistency between the mean thresholds and mean slopes obtained in the LKCW study and in our own study. Apparently, to a large extent, the effects of the main differences in how the two studies were conducted were surprisingly small or canceled each other out.

Comparisons of our data on response bias β with results of previous studies are even more problematic, in part because most of the previous IM studies did not report on response bias. In the one IM study that was concerned with bias, the WS study, the methodology for exploring bias was so radically different that comparisons are difficult to perform. Nevertheless, to the best of our understanding, the results in WS imply *a negative* correlation between threshold and bias, consistent with our model but inconsistent with our data. To add to the puzzle, examination of the correlation between response bias β and d' at one signal level (inversely related to threshold) in "frozen noise" tone-in-noise detection experiments (Siegel and Colburn, 1989; Gilkey *et al.*, 1985; Isabelle and Colburn, 1991; Evilsizer *et al.*, 2002; and Davidson and Carney, 2003) leads to the conclusion, like our own experimental work but not our model, that the correlation between bias and threshold is positive. Further information concerning these comparisons of response-bias results, as well as the comparisons of psychometric-function results, can be obtained directly from the authors.

In addition to examining how our data compare to previous data, we have explored the extent to which our data are consistent with and/or can be usefully interpreted with the help of the theoretical model in the LKCW study (related to the CoRE model, as discussed, for example, in Oh and Lutfi, 1998). This model is similar to the simple energy-detector model considered in the present paper in that it assumes that decisions are based on the values of energy variables, but it differs in a variety of other respects. Making use of the two equations in the LKCW paper concerned with the dependence of threshold and slope of a psychometric function on their model parameter n (see page 3280 in that article), we found, as did they when examining their own data, that the value of n needed to match the threshold data could differ dramatically from the value of n needed to match the slope data. In our data, this problem was most pronounced (by a large margin) for listener L2, the listener who was most susceptible (by a large margin) to IM.

B. Summary of our results

Even with a subject pool of only five listeners, a wide variety of listener behaviors in response to randomization of the masker was revealed. As shown in Fig. 2, the changes in both threshold and slope of the psychometric functions caused by randomization of the masker (as well as the thresholds and slopes of the psychometric functions for the fixed cases) varied considerably over the set of listeners.

Despite these variations, to at least a rough approximation all the psychometric functions for all cases and all listeners obtained using the given psychophysical procedures (one-interval paradigm, masker energy held constant, target energy held constant within each run, etc.) can be described by a simple energy-detector model in which the listener's detection decision is assumed to be based solely on the energy at the output of the filter centered on the target signal. The free parameters in the model, whose values were selected individually for each listener to fit that individual's d'-vs-level data (see Fig. 4), are the internal noise variance σ_0^2 (assumed to be independent of the stimulus), the bandwidth W_F (assumed to be applicable for fixed maskers), and the bandwidth W_R (assumed to be applicable for the random masker). Also found for all listeners, the relative effectiveness of the various maskers is roughly independent of whether one examines the F_i results or the $F_{s,i}$ results.

By far the largest differences across listeners in the d' results are those associated with listener L2. Whereas the values of σ_0, W_F, and W_R required to fit the energy-detector model to the d' data for L1, L3, L4, and L5 are all roughly what one would expect on the basis of previous work on energetic masking (taking account of both the reduced-slope artifact and past estimates of internal noise and critical bandwidth), the values of these parameters required to fit the d' data for L2 are quite different. Not only is the value of the internal noise term σ_0 for L2 unusually large, but the value of W_R for L2 is three times larger than the value of W_F for L2 (corresponding to the notion that L2, unlike the other listeners, responds to randomization of the masker spectrum by widening the effective acceptance filter).

Perhaps the most notable results of our study concern the data on response bias β (which were found to be essentially independent of target level). Of most importance is the correlation of response bias β with target threshold (over the maskers) for the $F_{s,i}$ case (see Fig. 7). For listeners L2 and L5, this correlation is relatively small, as would be expected on the basis of our interpretation of their d' data. In contrast, for L1 and L3 (and to a lesser extent L4), a positive correlation exists. Inasmuch as one would expect a negative cor-

relation using the simple energy-detector model and the most obvious criterion-placement behavior by these listeners, i.e., placing a single decision criterion more or less in the middle of the roving-energy-level range at the output of the filter, it was concluded that the simple energy-detector model outlined in this paper was seriously inadequate for these listeners even for the simple detection tasks considered in this paper.

Finally, it is important to note with respect to listeners L1 and L3 (and to a lesser extent L4) that if it were not for the above-mentioned discrepancy between theory and data with respect to the correlation between detection threshold and response bias for these listeners, one could legitimately have concluded that the results of these experiments for these listeners are interpretable entirely within the context of energetic masking (even with the large "protected zone" employed). In other words, the detection data by themselves (i.e., ignoring the bias data) are totally consistent with a model in which the masked thresholds are determined solely by the "leakage" of masker energy into the target critical band (via the skirts of the masker spectra and the critical band). Thus, aside from the large value of W_R (and perhaps σ_0) observed for listener L2 in the d' data, the main results reported in this paper that appear to require ideas beyond those classically associated with energetic masking are those associated with response bias.

C. Comments on future research

In the remainder of this section, we comment briefly on some studies related to our results that we believe are important to pursue in the future.

First, focusing on intersubject differences, we note that even with only five listeners in the subject pool, our empirical results evidence a wide variety of behaviors, ranging from strong IM (L2) to essentially no IM (L5). Extension to a larger group of listeners would not only provide better estimates of the distribution of the observed behavior types, but also possibly lead to the discovery of still further types. For example, we would not be surprised to discover listeners who exhibit weak (or covert) IM in the sense of producing data that satisfy the equation $R=R_p$ but not $F_{s,i}=F_i$ $(0\leqslant i \leqslant 9)$. Inasmuch as different sets of functions for the F_i case can result in the same function for the R_p case, there is no reason to believe that $R=R_p$ necessarily implies $F_{s,i}=F_i$ $(0 \leqslant i\leqslant 9)$. In fact, the extent to which L5 in our study should be viewed as exhibiting no IM rather than a small amount of covert IM depends on how seriously one regards the deviations between $F_{s,i}$ and F_i relative to the deviations between R and R_p.

Second, even within the given restricted listener domain of this study, the observed differences in performance and the associated differences in assumed strategies lead to differential predictions to be tested by further experiments with the same (or similar) subjects. For example, for a subject like L2, who appears to have addressed the R task by simply opening up the filter and sensing the overall loudness of the stimulus, one might expect d' to be relatively insensitive to the number of maskers but to increase substantially with training and/or the introduction of target or masker cuing (due to an alteration in strategy). In contrast, for a subject like L5 whose performance (in both d' and β) is roughly consistent with the notion of identifying the masker on each trial and establishing a criterion matched to that masker, one might expect performance to show only limited improvement as a consequence of cuing or training and to deteriorate as the number of maskers increased.

Third, it seems likely that our characterization and understanding of IM could be significantly improved by further analyzing existing data to (a) explore the extent to which previous studies have failed to take appropriate account of the reduced-slope artifact in assessing the existence and magnitude of IM and (b) examine trial-to-trial sequential effects (e.g., the dependence of filter and criterion settings on a given trial on the stimulus, response, and feedback associated with previous trials). Inasmuch as the phenomenon of IM is based on trial-to-trial changes in the stimulus, it seems very likely that considerable further insight into IM can be gained by detailed study of trial-to-trial sequential effects.

Fourth, there is a variety of additional theoretical studies that could play an important role in addressing the failure of the simple energy-detector model considered in this paper to explain the empirical findings on the sign of the correlation between response bias β and threshold (for subjects L1 and L3, to a lesser extent for L4, and for the results on frozen noise mentioned above). A revised energy-detector model that might be able to solve this bias-threshold correlation problem could be constructed by assuming that the listener estimates the identity of the masker on each trial and sets the criterion C according to that estimate, but, unlike listener L5, does this rather poorly. According to this model, not only is the ability to identify the masker somewhat degraded, but the setting of the criterion C suffers from both a tendency to overshoot its optimum value on the decision axis and a random jitter on this axis (criterion noise) that is proportional to the range of masker energy levels at the output of the filter (consistent with the context-coding model of intensity perception (e.g., Durlach and Braida, 1969; Braida *et al.*, 1984). An alternative, more attractive, model addressed to this problem would be one in which the masker energy outside the filter (in the "spectral fringe") plays a role in the formation of the decision variable as well as in the placement of the criterion C. Although such "background" can always play a useful role as a reference and reduce memory load, it could be of special significance in this case because of the constraint in masker construction that the sum of the masker energy in the filter plus the masker energy in the fringe is a constant independent of the choice of masker (plus the fact that, unlike the energy in the filter, which may or may not include target energy, the energy in the fringe could always be assigned unambiguously to the masker).

Fifth, there is a variety of further experiments to conduct that are likely to have important theoretical implications not only with respect to the β-threshold correlation problem, but also with respect to the assumption that variation in masker spectrum influences the listener solely via variation in energy

level, and within the domain of energy-level models, the assumption that only the energy level at the output of a single filter containing the target is important.

In one set of such experiments, the basic stimuli would remain the same (a fixed-frequency target tone in multitone-complex maskers with a protected zone around the target), but the masker level variable would be treated differently. Among the experiments envisioned in this class are a "squeeze" experiment and two "roving-level" experiments. In the squeeze experiment, the levels of the various fixed maskers are adjusted prior to the R tests so that all the F_i psychometric functions are not only roughly parallel but also produce the same threshold. In one roving-level experiment, the level of the masker, as well as its spectrum, is randomly varied from trial-to-trial in an R run; in another, only the level of the masker is varied (the spectrum is held fixed, as in an F_i run). The results of such experiments should help separate out the effects of spectrum randomization into those effects that can be ascribed to the associated level randomization and those effects that cannot be so ascribed.[9]

In a second set of experiments, the basic stimuli would be altered and attention would focus not on determining the extent to which level is the key variable, but on results obtainable with this variable. In these experiments, both the target and the masker would consist of Gaussian noise. In the first of these experiments, the target would consist of narrowband noise; the masker would consist of broadband noise; the central portion of the masker (i.e., that portion that overlaps the target spectrum's) would be roved in level; and the fringe portion of the spectrum would be roved in level in a complementary fashion (so that the total energy in the masker remains constant). In the second experiment, the fringe in the masker would be eliminated (so that the experiment degenerates into an intensity discrimination experiment with a roving reference level). Of particular interest in these experiments would be the β results obtained. Although it is relatively obvious that the correlation between β and threshold for the second experiment would be negative (consistent with our model but not with the results for L1 and L3), it is not obvious how this correlation would come out for the first of these experiments.

Sixth, and finally, we believe that the understanding of IM would benefit greatly from in-depth empirical studies of how performance in various tasks (both inside and outside the IM domain) is correlated, and how performance in these tasks is altered by various types of training. Although some previous work has been conducted along these lines (e.g., Watson *et al.*, 1976; Leek and Watson, 1984, 1988; Neff and Dethlefs, 1995), knowledge in this area remains extremely limited. Unfortunately, these types of studies are very difficult to perform because of the large amounts of data required. Nevertheless, deep understanding of IM cannot be gained without such studies.

ACKNOWLEDGMENTS

We are deeply indebted to our listeners for providing us with such interesting data, to Christine Carter and Sally Tressler for helping us collect this data, and to Dr. Tanya Arbogast, Dr. Laurel Carney, Dr. Robert Gilkey, Dr. G. Bruce Henning, Dr. Scott Isabelle, Dr. Robert Lutfi, Dr. Donna Neff, Dr. Virginia Richards, and Dr. Beverly Wright, as well as Sean Davidson and Yan (Felicia) Gai, for very useful communications during the preparation of this paper. We also wish to thank the associate editor and the reviewers for their substantial contributions to this effort. This work was supported by Grants NIH R01 DC04545 and DC00100, NIH F32 DC006526, and ONR N00014-04-1-0131.

[1]The exact counterpart to this situation in which a multitone masker is held fixed and the frequency of a tonal target is randomized has never been tested; however, the results obtained with approximate counterparts show relatively small randomization effects. Aside from noting that such results are consistent with a detection strategy that focuses on nulling out the masker rather than enhancing the target so that randomizing the masker disturbs detection performance more than randomizing the target (see the discussion of listener min vs listener max in Durlach *et al.*, 2003a), this issue is ignored throughout the rest of this paper. The focus in this article is exclusively on randomization of the masker.

[2]Apart from some subtle statistical issues associated with the definition and identification of performance asymptotes below perfect performance, serious study of the lapse parameter must take account of the differences between such asymptotes that reflect hearing phenomena (which are not likely to persist as asymptotes as the loudness of the target becomes much greater than that of the masker) and asymptotes that reflect nonauditory phenomena such as loss of general attentiveness and/or imperfect motor control in responding to the stimulus. Whereas in the limit, the auditory portion of the lapse parameter must go to zero (i.e., any apparent flattening in the psychometric function below perfect performance must be expected to disappear as the target becomes very loud), there is no reason to believe that the nonauditory portion goes to zero (i.e., that the listener is capable of performing perfectly over an infinite number of trials no matter how loud the target).

[3]Our detailed choice of the target levels to be tested was guided by knowledge about detection thresholds acquired in previous IM experiments for the same listeners. Based on this knowledge, tests were conducted that ensured coverage of the range 60% to 90% correct (the range in which the d'-vs-level function tends to be roughly linear) in 5-dB increments for the F_i tests and 10-dB increments for the R tests, the only exception being the R test for L5, where a 5-dB increment was used in response to what appeared to be an exceptionally steep slope for the R case.

[4]This definition of IM is obviously a very restrictive one. Although useful in the context of this paper, it is not intended to be applicable to all cases of interest. It should also be noted that, whereas the first of these two equations implies the second, the second does not imply the first. Unless explicitly stated otherwise, the term "IM" refers to the case in which neither equality holds. In Sec. VI, we briefly consider the case in which the second equation holds but not the first (which we refer to as "covert IM").

[5]This follows from the fact (discussed in footnote 3) that for the F_i curves the target test levels were chosen for each value of i to focus on the linear portion of F_i, whereas for the $F_{s,i}$ curves the relevant levels are those chosen to focus on the linear portion of R (and are thus independent of i). Had we measured d' in the R case over a much wider range of levels (so that we had a substantial number of data points at levels where $d' \approx 0$ and $d' > 3.0$ for the R case), the $F_{s,i}$ functions would have appeared more like horizontal translations of each other.

[6]In fitting these straight lines to the data, we ignored those points that were strongly influenced by the zero-slope asymptotic behavior of the data at very low or very high values of d'. More specifically, we ignored points outside the interval $0.25 \leqslant d' \leqslant 3.0$ that resulted in nonmonotonic behavior of the d'-vs-level function. The number of data points ignored constituted roughly 8% of the total number of data points obtained. As one would expect (see footnote 5), most of the data points ignored came from the $F_{s,i}$ case (the number of points ignored for each case constituted 5% of the F_i points, 12% of the $F_{s,i}$ points, and 0% of the R points).

[7]The fitting procedure we have used involved computing model psychometric functions for various values of the parameters σ_0, W_F, and W_R (about 500 000 such psychometric functions were computed) and determining thresholds and slopes for the linear portion of these functions (in the same manner as for the empirical psychometric functions). Root-mean-square

(rms) deviations were then calculated and denoted T_{dev} and S_{dev} (T_{dev} is the rms deviation between the set of theoretical and empirical thresholds, whereas S_{dev} is the rms deviation for the ratios of theoretical and empirical slopes). Determination of the values to be assigned to the parameters σ_0, W_F, and W_R was then carried out in two steps. First, in fitting the F_i results, the value of σ_0 was chosen to minimize S_{dev} (which depends almost exclusively on σ_0) and, given that value of σ_0, the value of the bandwidth W_F was chosen to minimize T_{dev} (the value of T_{dev} thus obtained being within 1 dB of the minimum T_{dev} obtainable over all σ_0). Second, with the same value of σ_0 being maintained, the value of W_R was chosen to fit the $F_{s,i}$ results by choosing this value to minimize T_{dev} (because T_{dev} depended much more strongly on W_R than S_{dev} depended on W_R). Although we cannot claim that the fits we have obtained using the given values of σ_0, W_F, and W_R are the best fits that can be obtained according to some explicit fitting criterion X, we can claim that all such optimum fits would be better than or equal to the relatively good fit demonstrated in Fig. 4 and Table III with respect to that criterion. Furthermore, based on the values of T_{dev} and S_{dev} shown in Table III for the values of σ_0, W_F, and W_R chosen (together with some further computations), we have shown that our results (in terms of the values of σ_0, W_F, W_R, T_{dev}, and S_{dev} obtained) are roughly comparable to the results that would be obtained using any linear fitting criterion in which the weights assigned to T_{dev} and S_{dev} result in a trading ratio such that 1 dB in T_{dev} corresponds to roughly 6%–12% in S_{dev}.

[8]Note, however, that this result is surprising only to the extent that one believes that the main effect of the trial-to-trial variation in masker spectrum in regions away from the target frequency is to cause the listener to attend to these nontarget spectral regions (i.e., to distract the listener from the task at hand). One might equally well believe that the difficulty associated with these trial-to-trial variations stimulates highly motivated listeners to focus more intensely on the target region.

[9]It is amusing to note that to the extent the increased masking caused by uncertainty in the masker spectrum can be explained in terms of uncertainty in the energy level at the output of a peripheral filter with critical-band-like filter characteristics, it may not be appropriate to use the term "IM" to refer to this increased masking. Although the increased masking would still be the result of stimulus uncertainty, it would not necessarily be the result of imperfections in central processing. In other words, it is possible that in certain cases the detection performance would be consistent with a model in which the central processing is ideal and the only defect in the processing results from the peripheral limitation on frequency resolution associated with the critical band (and therefore that the masking should be thought of as energetic rather than informational). For a discussion of definitional issues, see Durlach *et al.*, 2003b and Watson, 2005.

Allen, P., and Wightman, F. (**1994**). "Psychometric functions for children's detection of tones in noise," J. Speech Hear. Res. **37**, 205–215.

Allen, P., and Wightman, F. (**1995**). "Effects of signal and masker uncertainty on children's detection," J. Speech Hear. Res. **38**, 503–511.

Arbogast, T. L., Mason, C. R., and Kidd, G., Jr. (**2002**). "The effect of spatial separation on informational and energetic masking of speech," J. Acoust. Soc. Am. **112**, 2086–2098.

Braida, L. D., Lim, J. S., Berliner, J. E., Durlach, N. I., Rabinowitz, W. M., and Purks, S. R. (**1984**). "Intensity perception. XIII. Perceptual anchor model of context-coding," J. Acoust. Soc. Am. **76**, 722–731.

Brungart, D. S., Simpson, B. D., Ericson, M. A., and Scott, K. R. (**2001**). "Informational and energetic masking effects in the perception of multiple simultaneous talkers," J. Acoust. Soc. Am. **110**, 2527–2538.

Davidson, S. A., and Carney, L. H. (**2003**). "Monaural and diotic detection of tones in narrow-band and wideband reproducible noise maskers," J. Acoust. Soc. Am. **113**(4), 2197.

Durlach, N. I., and Braida, L. D. (**1969**). "Intensity perception. I. Preliminary theory of intensity resolution," J. Acoust. Soc. Am. **46**, 372–383.

Durlach, N. I., Mason, C. R., Kidd, G., Jr., Arbogast, T. L., Colburn, H. S., and Shinn-Cunningham, B. G. (**2003a**). "Note on informational masking," J. Acoust. Soc. Am. **113**, 2984–2987.

Durlach, N. I., Mason, C. R., Shinn-Cunningham, B. G., Arbogast, T. L., Colburn, H. S., and Kidd, G., Jr. (**2003b**). "Informational masking: Counteracting the effects of stimulus uncertainty by decreasing target-masker similarity," J. Acoust. Soc. Am. **114**, 368–379.

Evilsizer, M. E., Gilkey, R. H., Mason, C. R., Colburn, H. S., and Carney, L. H. (**2002**). "Binaural detection with narrow-band and wideband reproducible noise maskers. I. Results for human," J. Acoust. Soc. Am. **111**, 336–345.

Freyman, R. L., Balakrishnan, U., and Helfer, K. S. (**2001**). "Spatial release from informational masking in speech recognition," J. Acoust. Soc. Am. **109**, 2112–2122.

Freyman, R. L., Helfer, K. S., McCall, D. D., and Clifton, R. K. (**1999**). "The role of perceived spatial separation in the unmasking of speech," J. Acoust. Soc. Am. **106**, 3578–3588.

Gilkey, R. H., Robinson, D. E., and Hanna, T. E. (**1985**). "Effects of masker waveform and signal-to-masker phase relation on diotic and dichotic masking by reproducible noise," J. Acoust. Soc. Am. **78**, 1207–1219.

Green, D. M. (**1961**). "Detection of auditory sinusoids of uncertain frequency," J. Acoust. Soc. Am. **33**, 897–903.

Isabelle, S. K., and Colburn, H. S. (**1991**). "Detection of tones in reproducible narrow-band noise," J. Acoust. Soc. Am. **89**, 352–359.

Kidd, G., Jr., Mason, C. R., and Arbogast, T. L. (**2002**). "Similarity, uncertainty and masking in the identification of nonspeech auditory patterns," J. Acoust. Soc. Am. **111**, 1367–1376.

Kidd, G., Jr., Mason, C. R., and Gallun, F. J. (**2005**). "Combining energetic and informational masking for speech identification," J. Acoust. Soc. Am. **118**, 982–992.

Kidd, G., Jr., Mason, C. R., and Richards, V. M. (**2003**). "Multiple bursts, multiple looks and stream coherence in the release from informational masking," J. Acoust. Soc. Am. **114**, 2835–2845.

Kidd, G., Jr., Mason, C. R., Deliwala, P. S., Woods, W. S., and Colburn, H. S. (**1994**). "Reducing informational masking by sound segregation," J. Acoust. Soc. Am. **95**, 3475–3480.

Leek, M. R., and Watson, C. S. (**1984**). "Learning to detect auditory pattern components," J. Acoust. Soc. Am. **76**, 1037–1044.

Leek, M. R., and Watson, C. S. (**1988**). "Auditory perceptual learning of tonal patterns," Percept. Psychophys. **43**, 389–394.

Lutfi, R. A. (**1990**). "How much masking is informational masking?" J. Acoust. Soc. Am. **80**, 2607–2610.

Lutfi, R. A. (**1993**). "A model of auditory pattern analysis based on component-relative-entropy," J. Acoust. Soc. Am. **94**, 748–758.

Lutfi, R. A., Kistler, D. J., Callahan, M. R., and Wightman, F. L. (**2003a**). "Psychometric functions for informational masking," J. Acoust. Soc. Am. **114**, 3273–3282.

Lutfi, R. A., Kistler, D. J., Oh, E. L., Wightman, F. L., and Callahan, M. R. (**2003b**). "One factor underlies individual differences in auditory informational masking within and across age groups," Percept. Psychophys. **65**, 396–406.

Neff, D. L. (**1995**). "Signal properties that reduce masking by simultaneous, random-frequency maskers," J. Acoust. Soc. Am. **98**, 1909–1920.

Neff, D. L., and Callaghan, B. P. (**1987**). "Psychometric functions for multicomponent maskers with spectral uncertainty," J. Acoust. Soc. Am. **81**(S1), 53.

Neff, D. L., and Callaghan, B. P. (**1988**). "Effective properties of multicomponent simultaneous maskers under conditions of uncertainty," J. Acoust. Soc. Am. **83**, 1833–1838.

Neff, D. L., and Dethlefs, T. M. (**1995**). "Individual differences in simultaneous masking with random-frequency, multicomponent maskers," J. Acoust. Soc. Am. **98**, 125–134.

Neff, D. L., and Green, D. M. (**1987**). "Masking produced by spectral uncertainty with multicomponent maskers," Percept. Psychophys. **41**, 409–415.

Neff, D. L., and Jesteadt, W. (**1996**). "Intensity discrimination in the presence of random-frequency, multicomponent maskers and broadband noise," J. Acoust. Soc. Am. **100**, 2289–2298.

Neff, D. L., Dethlefs, T. M., and Jesteadt, W. (**1993**). "Informational masking for multicomponent maskers with spectral gaps," J. Acoust. Soc. Am. **94**, 3112–3126.

Oh, E. L., and Lutfi, R. A. (**1998**). "Nonmonotonicity of informational masking," J. Acoust. Soc. Am. **104**, 3489–3499.

Patterson, R. D., and Moore, B. C. J. (**1986**). "Auditory filters and excitation patterns as representations of frequency resolution," in *Frequency Selectivity in Hearing*, edited by B. C. J. Moore (Academic, London).

Richards, V. M., and Neff, D. L. (**2004**). "Cuing effects for informational masking," J. Acoust. Soc. Am. **115**, 289–300.

Richards, V. M., Huang, R., and Kidd, G., Jr. (**2004**). "Masker-first advantage for cues in informational masking," J. Acoust. Soc. Am. **116**, 2278.

Richards, V. M., Tang, Z., and Kidd, G., Jr. (**2002**). "Informational masking with small set sizes," J. Acoust. Soc. Am. **111**, 1359–1366.

Siegel, R. A., and Colburn, H. S. (**1989**). "Binaural processing of noisy stimuli: Internal/external noise ratios for diotic and dichotic stimuli," J. Acoust. Soc. Am. **86**, 2122–2128.

Tang, Z., and Richards, V. M. (**2003**). "Examination of a linear model in an

informational masking study," J. Acoust. Soc. Am. **114**, 361–367.
Watson, C. S. (**1987**). "Uncertainty, informational masking and the capacity of immediate auditory memory," in *Auditory Processing of Complex Sounds*, edited by W. A. Yost and C. S. Watson (Erlbaum, Hillsdale, NJ), pp. 267–277.
Watson, C. S. (**2005**). "Some comments on informational masking," Acta. Acust. Acust. **91**, 502–512.
Watson, C. S., and Kelly, W. J. (**1981**). "The role of stimulus uncertainty in the discriminability of auditory patterns," in *Auditory and Visual Pattern Recognition*, edited by D. J. Getty and J. H. Howard, Jr. (Erlbaum, Hillsdale, NJ), pp. 37–59.
Watson, C. S., Kelly, W. J., and Wroton, H. W., (**1976**). "Factors in the discrimination of tonal patterns. II. Selective attention and learning under various levels of stimulus uncertainty," J. Acoust. Soc. Am. **60**, 1176–1186.
Wright, B. A., and Saberi, K., (**1999**). "Strategies used to detect auditory signals in small sets of random maskers," J. Acoust. Soc. Am. **105**, 1765–1775.

Psychophysical tuning curves at very high frequencies

Ifat Yasin[a] and Christopher J. Plack
Department of Psychology, University of Essex, Wivenhoe Park, Colchester, CO4 3SQ, England

(Received 28 January 2005; revised 21 July 2005; accepted 21 July 2005)

For most normal-hearing listeners, absolute thresholds increase rapidly above about 16 kHz. One hypothesis is that the high-frequency limit of the hearing-threshold curve is imposed by the transmission characteristics of the middle ear, which attenuates the sound input [Masterton *et al.*, J. Acoust. Soc. Am. **45**, 966–985 (1969)]. An alternative hypothesis is that the high-frequency limit of hearing is imposed by the tonotopicity of the cochlea [Ruggero and Temchin, Proc. Nat. Acad. Sci. U.S.A. **99**, 13206–13210 (2002)]. The aim of this study was to test these hypotheses. Forward-masked psychophysical tuning curves (PTCs) were derived for signal frequencies of 12–17.5 kHz. For the highest signal frequencies, the high-frequency slopes of some PTCs were steeper than the slope of the hearing-threshold curve. The results also show that the human auditory system displays frequency selectivity for characteristic frequencies (CFs) as high as 17 kHz, above the frequency at which absolute thresholds begin to increase rapidly. The findings suggest that, for CFs up to 17 kHz, the high-frequency limitation in humans is imposed in part by the middle-ear attenuation, and not by the tonotopicity of the cochlea.
[DOI: 10.1121/1.2035594]

PACS number(s): 43.66.Dc, 43.66.Mk, 43.66.Ba [AJO] Pages: 2498–2506

I. INTRODUCTION

Hearing thresholds increase rapidly above about 16 kHz for normal-hearing listeners (e.g., Zhou and Green, 1995). It has been proposed that this high-frequency limit of the human auditory system is set by the transmission characteristics of the middle ear (Masterton *et al.*, 1969). The human middle ear acts as a resonant system tuned to between 0.7 and 1.2 kHz, with a falloff in transmission on either side of this frequency range. The middle ear passes a band of frequencies from about 20 Hz to 20 kHz to the cochlea fluids (Aibara *et al.*, 2001). If the high-frequency limit of hearing is set by the middle-ear attenuation, then for a very high-frequency signal the high-frequency slope of psychophysical tuning curves (PTCs) should be steeper than the slope of the hearing-threshold curve. A steeper PTC slope is predicted since the masker level required for the signal to be masked has to be elevated to overcome *both* the frequency selectivity of the filter centered at the signal frequency and the middle-ear attenuation (Buus *et al.*, 1986). However, recent human *in vivo* investigations of stapes vibration (Huber *et al.*, 2001) suggest that the range of frequencies transmitted by the middle ear may be wider than originally thought. If this is the case, then the transmission characteristics of the middle ear may not pose the main limitation on the high-frequency range of hearing.

An alternative hypothesis is that the high-frequency limit of hearing is related to the tonotopicity of the cochlea (Ruggero and Temchin, 2002). This hypothesis suggests that the high-frequency limit of hearing corresponds to the high-frequency slopes of neural tuning curves with the highest characteristic frequencies (CFs). The high-frequency limit of the hearing-threshold curve is then related to the CF of the filter at the most basal end of the cochlea. Buus *et al.* (1986) put forward a similar idea to explain the shape of high-frequency PTCs. This hypothesis was called the "end of the cochlea" hypothesis. Each point of the hearing-threshold curve represents the lowest detectable level of a signal for a given signal frequency (f_s), and the frequency at which hearing detectability starts to rapidly decrease is the breakpoint frequency (f_{bp}) of the hearing-threshold curve. The end of the cochlea theory proposes that, for an f_s that lies above f_{bp}, the high-frequency slope of the PTC for f_s should be similar to that of the hearing-threshold curve, with the tip of the PTC at a frequency close to f_{bp}. The results of Buus *et al.*'s study showed that the high-frequency slopes of some of the PTCs for the highest signal frequencies paralleled the slope of the hearing-threshold curve and the tips of the PTCs did correspond to f_{bp}. However, Buus *et al.* used simultaneous masking to derive PTCs for high signal frequencies. Estimates of frequency selectivity as suggested by simultaneous masking are often less than those suggested by forward masking (Moore and Glasberg, 1981). The reason for this is that in simultaneous masking the masker may suppress the basilar-membrane (BM) response to the signal (Ruggero *et al.*, 1992), leading to broader estimates of filter tuning. In the case of a PTC, this means that masker levels for masker frequencies removed from f_s would be decreased relative to masker frequencies close to f_s (the tip of the PTC) (Yasin and Plack, 2003). A simultaneous-masking paradigm may provide a shallower estimate of the filter slopes than is actually the case (Moore and Glasberg, 1981). Indeed, a recent psychophysical study by Shera *et al.* (2002), using forward masking, found sharper filter tuning at high frequencies than

[a]Present address: Department of Experimental Psychology, University of Oxford, South Parks Road, Oxford, OX1 3UD, England. Electronic mail: ifat.yasin@psy.ox.ac.uk

predicted by the simultaneous masking data. These results were confirmed by filter estimates derived from otoacoustic emissions recorded in the same study.

The present study was undertaken to investigate the characteristics of very high-frequency PTCs using a forward-masking task, and thereby to test the two explanations for the slope of the hearing-threshold curve at high frequencies. Forward-masked PTCs were obtained for signal frequencies of 12–17.5 kHz and masker frequencies ranging from 8–19 kHz. If the high-frequency limit of hearing is set by the middle-ear attenuation, then for a f_s well above f_{bp}, the high-frequency slope of the PTC should be steeper than the slope of the hearing-threshold curve, with the PTC tip typically above f_{bp}, and close to f_s. [Although if the rate of increase of the middle-ear attenuation is steeper than the rate of decrease of the low-frequency side of the PTC, across frequency, then the PTC tip may be located at a frequency below f_s (Buus *et al.*, 1986).] If, however, the slopes of the high-frequency PTCs are similar to the slope of the hearing-threshold curve (masker levels are elevated solely to overcome the frequency selectivity of the filter centered at f_s), with the tips of the PTCs close to f_{bp} for $f_s > f_{bp}$, then this would suggest that the highest cochlear CF available to the auditory system imposes the upper-frequency limit of the hearing-threshold curve. It is assumed in this case, that there is no level dependence of the high-frequency slope of the PTC tuned to f_{bp} between threshold level and the signal levels used to measure the PTC.

II. METHOD

A. Conditions

The level of a sinusoidal forward masker required to mask a sinusoidal signal was obtained for a range of masker frequencies higher, and lower, in frequency than f_s. There were eight signal frequencies (12, 13, 14, 15, 16, 16.5, 17, and 17.5 kHz). For a given f_s, a range of masker frequencies (f_m) above and below f_s (a PTC set), was used to define the shape of the PTC. The range of f_m was from 8–19 kHz, although for some subjects the complete set of masker frequencies could not be tested as the masker levels at these frequencies surpassed the output limit of the equipment (102 dB SPL). In other cases, extra masker frequencies were tested in order to obtain a more accurate estimate of the filter shape. All f_m for a given PTC set were randomized.

B. Stimuli

The signal had a 5-ms steady-state portion, and 5-ms raised-cosine onset and offset ramps. The masker had a 100-ms steady-state portion and 2-ms raised-cosine onset and offset ramps. Thresholds were obtained in the presence of a broadband noise which was gated with the masker and had a spectrum level of 0 dB (*re*: 20 μPa). The noise acted as a cue to the offset of the masker, to prevent any confusion effects (Neff, 1986). The time interval between the masker and the signal was 0 ms, specified as the silent time interval between the zero-voltage points of the envelopes at the end of the masker and at the beginning of the signal. All stimuli were digitally generated by a personal computer (PC) situated outside the sound booth, using a sampling rate of 48 kHz. Stimuli were output via a soundcard with 24-bit resolution. Antialiasing was provided by built-in filters. The stimuli were presented to the right channel of a set of Sennheiser HD 580 headphones. The headphone input came directly from the output of the soundcard DAC.

C. Procedure

Subjects were tested individually while seated in an IAC double-walled sound-attenuating booth. A 2I-2AFC adaptive procedure was used to determine the masker level at which the subject would achieve 70.7% correct on the psychometric function (Levitt, 1971). A block of trials began with the presentation of a light on a computer-simulated response box. Subjects started a block of trials by pressing a start key. A light on the response box in one of two rectangles indicated the length of each observation interval. The interstimulus interval was 500 ms. On each trial, the masker was presented in both intervals. The signal was presented at random in one of the intervals. The task within each trial was to select the signal interval. Subjects responded by pressing the appropriate response key. After a response, visual feedback was provided by the presentation of a colored light. Initially, the masker was decreased by 8 dB after an incorrect response and increased by 8 dB after every two consecutive correct responses. A reversal was counted every time the masker level changed direction. The masker level was varied in steps of 8 dB for the first four reversals. For the following 12 reversals the step size was reduced to 2 dB. The levels for the last 12 reversals were averaged to obtain the threshold value. In this way, an estimate of threshold was obtained from each block of trials. Five estimates of threshold were obtained for each condition. The most deviant threshold was discarded and the mean was calculated from the remaining four estimates of threshold. The maximum masker level that could be produced by the system was 102 dB SPL. The system peak clipped at this level, producing distortion at the headphone output. If a masker level of 102 dB SPL was reached within a block of trials, the estimate of threshold from that block was discarded.

One of the main concerns in deriving psychophysical estimates of auditory filter shapes at high frequencies is that of variability. The variability arises when the quarter wavelength of the high-frequency sound is close to the ear canal length (Stinson, 1990). Standing waves are set up between the incident and reflected sound wave, producing regions of minimum and maximum sound amplitudes and hence large variations in sound pressure across the length of the canal. Even slight changes in the position of earphones can have a large effect on the locations of these sound-pressure differences. In order to control for the high variability of thresholds at high frequencies, the following procedure was used. Absolute thresholds were first obtained for a randomized set of all f_s from 12–19 kHz on six separate test occasions. The total of six estimates of threshold for each f_s was averaged to obtain a value for the mean signal threshold. This mean signal threshold was then used to estimate the presentation levels of the signal in dB SL in the experiment. The signal for

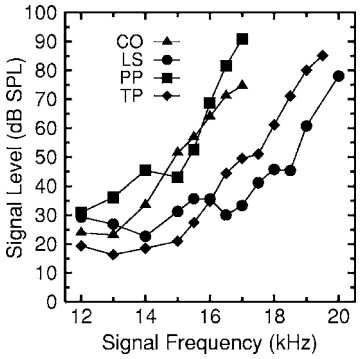

FIG. 1. Absolute thresholds for the four subjects as a function of frequency.

each PTC set was presented at 15 dB SL for subjects CO, PP, and TP, and at 25 dB SL for subject LS. On each test session a complete PTC was estimated for a given f_s. Per subject, only one value of f_s was tested in any given experimental session, with f_s values randomized across sessions. On each session the subject was instructed to ensure that the headphone position remained constant. Preceding data collection for a given PTC, two estimates of absolute threshold for the signal were obtained. If the mean of these two thresholds deviated by more than 6 dB from the original estimate of threshold for this f_s, then the data for that PTC set were not collected.

D. Subjects

Four normal-hearing subjects were tested: CO, LS, PP, and TP. They were aged 29, 26, 36, and 20 years, respectively. All were paid for their services. Absolute thresholds were obtained for signal frequencies of 0.25, 0.5, 1, 2, and 8 kHz, using an adaptive track in which the signal level was varied in a 2-down, 1-up procedure. All subjects had absolute thresholds better than 20 dB HL (ANSI, 1996).

III. RESULTS

A. Absolute threshold variation with frequency

Absolute thresholds for the high-frequency signals for all subjects are shown in Fig. 1. Signal threshold generally increases with increasing f_s; for all subjects the increase is gradual for a relatively low f_s, followed by a steeper increase in threshold for a higher f_s. For each subject, f_{bp} was estimated by finding the value of f_s for which each of two linear regression lines fitted to the shallow and steep portions of the hearing-threshold curve accounted for at least 70% of the variance ($R^2 > 0.7$). Linear regression analysis of the shallow and steep portions of individual hearing-threshold curves resulted in slope estimates for the shallow portion of the hearing-threshold curve of between −3.32 and 4.55 dB/kHz (mean slope of 0.3 dB/kHz; mean $R^2 = 0.87$). Slope estimates for the steep portion of the hearing-threshold curve are between 8.32 and 24.95 dB/kHz (mean slope of 15.39 dB/kHz; mean $R^2 = 0.94$). The values of the estimated f_{bp} for CO, LS, PP, and TP are 13, 14, 15, and 15 kHz, respectively.

For all subjects, absolute thresholds begin to rapidly increase above f_{bp}. For CO and PP thresholds begin to increase rapidly above an f_{bp} of 13 and 15 kHz, respectively. For TP and LS, absolute thresholds are still relatively low at frequencies between about 13–15 kHz. Mean signal thresholds and standard deviations (s.d.'s) for all subjects are shown in Table I. The average s.d. across subjects and frequencies is 3.13 dB.

B. Filter shapes

Individual PTCs[1] for each of the subjects are shown in the left columns of Fig. 2 (f_s of 12–14 kHz) and Fig. 3 (f_s of 15–17.5 kHz). Each panel presents a set of PTCs. Each PTC represents the level of a masker of a given frequency required to mask a signal for a fixed f_s. For comparison, the hearing-threshold curve is also shown by dashed lines. In some cases, particularly for higher f_s, the complete high-frequency slope of the PTC could not be obtained as the masker level reached the output limit of the equipment. Although there are individual differences in the shapes of the PTCs, the form of the PTCs is generally similar across subjects. With increasing f_s, the PTCs tend to broaden. For f_s above f_{bp}, for most subjects the PTC tips are close to f_s, although for f_s above 16 kHz the PTC tip shifts to a frequency less than f_s. For example, for CO (Fig. 3), the PTC tip for an f_s of 16 kHz (filled circles) shifts to a frequency of about 15 kHz, and for TP the PTC tip for an f_s of 16.5 kHz (filled squares) shifts to a frequency close to about 16 kHz. For all subjects, the low-frequency PTC slopes are generally shallower than the high-frequency slopes. As f_s increases, the low-frequency slopes of the PTCs tend to flatten. In some

TABLE I. Mean absolute signal thresholds (dB SPL) and standard deviations (s.d.) for the four subjects.

		f_s (kHz)												
Subject		12	13	14	15	15.5	16	16.5	17	17.5	18	18.5	19	19.5
CO	Mean	23.94	23.22	33.58	51.50	56.84	64.00	71.23	74.69	⋯	⋯	⋯	⋯	⋯
	s.d.	1.15	3.28	5.22	3.32	1.87	2.54	3.44	2.24	⋯	⋯	⋯	⋯	⋯
LS	Mean	29.36	26.95	22.72	31.31	35.72	35.61	30.05	33.34	41.22	45.75	45.34	60.75	78.11
	s.d.	13.05	6.14	4.38	1.83	0.71	1.48	1.80	1.77	6.05	5.54	4.21	2.78	3.38
PP	Mean	30.95	36.19	45.41	43.06	52.61	68.72	81.61	90.94	⋯	⋯	⋯	⋯	⋯
	s.d.	2.78	3.51	2.41	2.80	2.39	3.16	4.49	3.31	⋯	⋯	⋯	⋯	⋯
TP	Mean	19.38	16.33	18.61	20.97	27.44	34.81	44.39	49.50	50.99	61.17	71.11	80.11	85.16
	s.d.	1.52	1.82	2.47	1.98	4.18	2.28	2.44	2.82	1.20	2.54	3.98	3.31	1.57

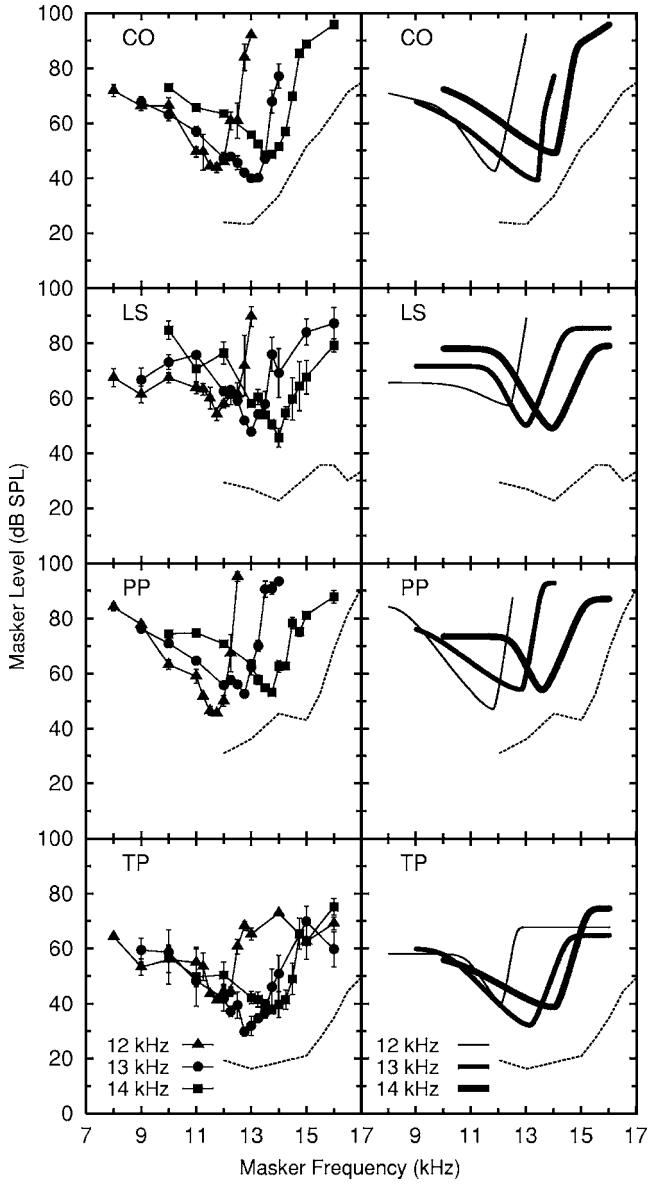

FIG. 2. The left column presents PTCs for the four subjects. Each PTC shows the masker level at threshold for a signal at f_s as a function of masker frequency. Filled triangles, circles, and squares represent PTCs for 12, 13, and 14 kHz, respectively. The right column presents the roex (p,w) or (p,w,t) filter-shape fits to the PTC data. Each panel presents PTCs for 12, 13, and 14 kHz, represented by lines of increasing thickness. Dashed lines represent the hearing-threshold curve.

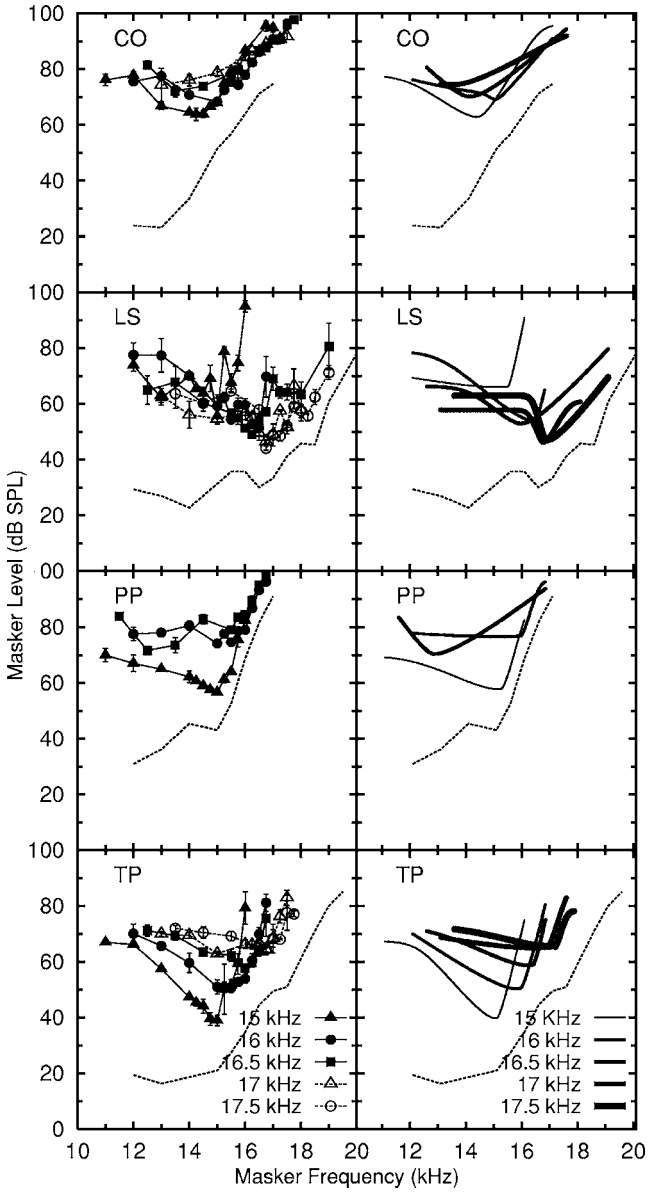

FIG. 3. As Fig. 2 except showing the PTCs for the higher signal frequencies. Filled triangles, circles, and squares represent PTCs for 15, 16, and 16.5 kHz, respectively. Unfilled triangles and squares represent PTCs for 17 and 17.5 kHz, respectively. The right column presents the roex (p,w) or (p,w,t) filter-shape fits to the PTC data. Each panel presents PTCs for 15, 16, 16.5, 17, and 17.5 kHz represented by lines of increasing thickness. Dashed lines represent the hearing-threshold curve.

cases the high-frequency PTC slopes are similar in slope to the hearing-threshold curve, for instance the 16-kHz PTC for CO and the 15- and 16-kHz PTCs for PP. In a few cases the high-frequency slope of the PTC flattens for higher masker levels. This is particularly noticeable for the PTCs for an f_s between 12–14 kHz (Fig. 2). For instance, the PTCs for an f_s of 14 kHz (filled squares), for both PP and CO, start to flatten at around 80 dB SPL. For TP, for the 13-kHz PTC, masker levels were so low that it is possible that the 0-dB spectrum level noise [approximately 31.5 dB at the output of the 13-kHz auditory filter according to the equation of Glasberg and Moore (1990)] may have contributed to the forward masking of the signal. However, the PTC shape should not have been greatly affected by this, since the PTC describes the masker level as a function of frequency needed to produce a constant excitation at the signal place, whatever excitation contribution is required to mask the signal.

The PTC data of the individual subjects were fitted with a rounded exponential (roex) function with two free parameters for each slope (p,w) (Patterson *et al.*, 1982). The roex (p,w) filter shape is defined by

$$W(g) = (1-w)(1+pg)\exp(-pg) + w, \quad (1)$$

where $W(g)$ is the filter shape. The exponential slope parameter p defines the passband of the filter. Here, w determines the filter weight outside of the passband and operates to flatten the filter at frequencies well away from the center frequency, thereby limiting the dynamic range of the filter; and

TABLE II. Roex (p,w) and (p,w,t) filter shape predicted values for BF, p_u, p_l, w_u, w_l, t_u, t_l, and bandwidth estimates of ERB_{PTC} and $Q_{ERB_{PTC}}$, for PTCs of f_s in the range 12–17.5 kHz.

Subject	f_s (kHz)	L_{BF} (dB)	BF (kHz)	p_l	p_u	w_l	w_u	t_l	t_u	ERB_{PTC}	$Q_{ERB_{PTC}}$
CO	12	42.63	11.80	50.60	145.39	2.13E−03	7.94E−07			631.02	18.77
	13	40.53	13.20	33.71	200.00	1.90E−03	8.21E−05			917.97	14.42
	14	49.42	14.00	30.87	200.00	3.85E−03	4.00E−05			1048.40	13.37
	15	62.97	14.40	32.10	65.71	3.17E−02	4.80E−04			1331.50	10.78
	16	69.14	15.00	12.18	100.00	4.59E−01	6.05E−01	100.00	48.37	2757.10	5.43
	16.5	70.25	14.10	37.15	31.90	2.83E−05	2.32E−04	12.56	32.01	3001.60	4.69
	17	74.58	13.50	0.04	21.64	6.39E−04	5.16E−03			⋯	⋯
LS	12	57.27	12.40	28.61	200.00	1.47E−01	6.73E−14			990.81	12.51
	13	50.12	13.00	75.20	101.65	7.04E−03	2.92E−04			601.21	21.61
	14	49.09	13.90	66.78	90.18	1.30E−03	9.94E−04			726.79	19.18
	15	66.10	15.40	9.00	200.00	1.46E−05	3.34E−09			⋯	⋯
	16	54.17	16.40	38.86	200.00	3.49E−03	3.78E−12			1007.20	16.27
	16.5	53.01	15.90	44.57	43.52	4.64E−02	1.49E−10			1447.40	11.01
	17	46.36	16.70	164.50	101.88	7.17E−02	3.32E−02			530.45	31.46
	17.5	47.00	16.80	200.00	55.93	2.55E−02	2.11E−15			769.05	21.85
PP	12	47.04	11.80	40.76	200.00	1.69E−04	1.43E−14			697.19	16.93
	13	54.15	12.83	27.63	200.00	3.83E−03	1.38E−04			1056.82	12.14
	14	53.97	13.58	85.69	90.47	1.13E−02	4.96E−04			617.20	22.00
	15	57.85	15.17	24.19	151.13	6.14E−02	1.06E−03			1454.98	10.43
	16	76.81	15.85	5.02	156.69	4.83E−02	1.02E−02			⋯	⋯
	16.5	70.40	12.78	48.99	24.13	2.41E−03	3.69E−09			1581.02	8.08
TP	12	40.38	12.10	60.53	200.00	1.70E−02	1.84E−03			520.69	23.23
	13	32.12	13.13	38.12	99.21	1.61E−03	5.40E−04			953.82	13.77
	14	38.77	14.03	25.21	129.58	1.32E−02	2.64E−04			1329.38	10.55
	15	39.83	15.01	47.20	159.24	1.76E−03	3.09E−10			824.48	18.20
	16	50.45	15.85	28.29	163.13	7.14E−04	1.20E−09			1315.03	12.05
	16.5	58.86	16.29	25.49	200.00	3.85E−02	2.23E−11			1441.40	11.30
	17	65.19	16.80	9.86	159.07	2.36E−03	6.47E−03			⋯	⋯
	17.5	65.72	17.08	20.76	200.00	1.77E−01	5.44E−02			1817.03	9.40

g is the deviation of the evaluation frequency (f) from the best frequency (BF), normalized by the BF of the filter

$$g = |f - \mathrm{BF}|/\mathrm{BF}. \tag{2}$$

Since the filter was assumed to be asymmetric, p and w were allowed to have different values for the low-frequency (p_l, w_l) and high-frequency (p_u, w_u) slopes of the filter. These different functions were used for frequencies below and above BF, respectively. A high value of the exponential parameter p indicates sharp filter tuning, whereas a low value of p indicates broad filter tuning. A least-squares minimization routine was implemented to fit the roex (p,w) filter shape to the PTC data. The roex filter shape was converted to dB attenuation and inverted. To find the best fit, the filter was shifted in frequency (i.e., BF was varied) and in level (i.e., L_{BF}, the level of the fitted PTC at BF, was varied). Values of parameters p_l, w_l, p_u, w_u, BF, and L_{BF} were found that minimized the rms deviation between the experimental and predicted data values.

For cases where there were discrepancies between the data and the derived filter shape, particularly for some of the higher-frequency PTCs, the roex (p,w,t) filter shape was fitted to the data. The roex (p,w,t) filter shape comprises two rounded exponentials; the first characterizes the passband of the filter and the second the tail of the passband. This rounded exponential (roex) function has three free parameters; p, w, and t for each side (Patterson *et al.*, 1982)

$$W(g) = (1-w)(1+pg)\exp(-pg) + w(1+tg)\exp(-tg), \tag{3}$$

where t determines the slope of the tail of the filter (the rate of fall of the second exponential term) and w in this case determines when the second exponential takes over from the first. As before, the parameters p, w, and t were allowed to have different values for the low-frequency (p_l, w_l, t_l) and high-frequency (p_u, w_u, t_u) slopes of the filter. The best fit to the PTC data was again found by implementing a least-squares minimization routine as described for the roex (p,w) filter shape. The use of two rounded exponentials on each skirt of the filter may generate a more accurate fit to the data in cases in which the PTCs have low- and high-frequency tails. The PTC data for f_s of 16 and 16.5 kHz, for subject CO, were refitted with the (p,w,t) filter shape.

The roex (p,w) and (p,w,t) filter-shape fits to the experimental data are shown in the right columns of Fig. 2 (f_s of 12–14 kHz) and Fig. 3 (f_s of 15–17.5 kHz). The values for L_{BF}, BF, $p_l, p_u, w_l, w_u, t_l, t_u$, for all subjects are presented

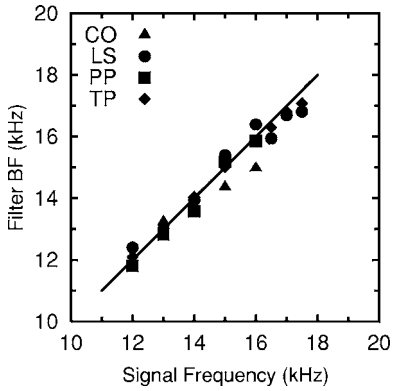

FIG. 4. Values of BF derived from the roex (p,w) or (p,w,t) filter-shape fits to the PTC data, as a function of f_s, for all subjects. Filter BF equal to the signal frequency is illustrated by the straight line (gradient of 1.0). Three values of PTC tuning are omitted; the PTCs were too broad to yield a meaningful estimate of tuning.

in Table II. The filter shapes generally provide good fits to the data with rms errors for subjects CO, LS, PP, and TP, averaging 1.43, 3.47, 2.36, and 2.02 dB, respectively. The filter shapes reflect the main features of the PTC data including the broadening of the PTCs, and a convergence of the high-frequency slopes of the PTCs, with increasing f_s. Figure 4 shows how the estimates of filter BF for each subject vary as a function of f_s. Three BF values are omitted (CO; 16.5 and 17 kHz, and PP; 16.5 kHz) since the PTCs were too broad to yield a meaningful estimate of BF. A reference function with a gradient of 1.0 is also shown for comparison. There appears to be a close-to-linear relationship between f_s and BF. This relationship holds with the exception of some BF estimates for an f_s greater than 16 kHz. For subjects LS and TP, the data points lie below the reference function and the estimated BF is slightly lower than f_s. In the cases of PP and CO, for an f_s greater than 16 kHz, the BF is much lower than the f_s. This shift of the tip of the PTC, to a frequency lower than f_s can also be seen most clearly in the PTCs for both PP and CO in Fig. 3, as described earlier. However, the slopes of the PTCs were quite shallow in these cases, and it is difficult to be precise about the value of BF. As f_s increases, the low-frequency slope of the PTC as defined by p_l generally decreases for CO, PP, and TP, with more varied results for LS.

For each subject, the slope of the high-frequency skirt, of PTCs with BF$>f_{bp}$, was compared to the slope of the hearing-threshold curve, across the same frequency range. High-frequency PTC slope estimates were obtained for PTCs of f_s 13, 14, 15, and 16 kHz (CO); 15, 16, 16.5, 17, and 17.5 kHz (LS); 15 and 16 kHz (PP); 15, 16, 16.5, 17, and 17.5 kHz (TP). Two PTCs was excluded from the analysis (CO; 16.5 and 17 kHz) as the PTCs were too broad to yield a meaningful estimate of BF. The slope of the high-frequency skirt of the filter-shape fit of each PTC was estimated by fitting a linear regression function to the data points for frequencies above BF (mean $R^2=0.98$). Estimates of the slope of the hearing-threshold curve were also obtained (mean $R^2=0.96$) for data points over the same frequency range. A paired-samples t-test showed that the slopes of the high-frequency skirt of PTCs with BF$>f_{bp}$, were significantly greater (steeper) than the slope of the hearing-threshold curve. [Mean high-frequency PTC slope $=30.85$ dB/kHz(s.d.$=14.22$), mean hearing-threshold curve slope$=9.68$ dB/kHz(s.d.$=8.27$), $t(13)=4.367$, p(2-tailed) $=0.001$.]

The value of the highest BF is greater than f_{bp} for all subjects, with the smallest difference for PP. For each of the other three subjects, f_{bp} is outside (less than) the 95% confidence limit for the mean of the BF values for $f_s>f_{bp}$; f_{bp} does not seem to correspond to the highest CF available to the auditory system.

C. Estimates of frequency selectivity

An estimate of the sharpness of tuning is provided by the equivalent rectangular bandwidth (ERB) of a filter. The ERB of a filter is defined as the width of a rectangular filter whose height equals the peak gain of the filter and which passes the same total power as the filter given a flat spectrum input such as white noise or an impulse (Moore, 1997). The $\mathrm{ERB}_{\mathrm{PTC}}$ of the auditory filter, as defined by the PTC, for a given f_s, can be calculated as follows [Moore, 1995, Eq. (4)]:

$$\mathrm{ERB}_{\mathrm{PTC}} = 2(\mathrm{BF})/p_l + 2(\mathrm{BF})/p_u. \quad (4)$$

(Note that this equation ignores the contribution of the flat tails, defined by w_l and w_u. When these values are relatively high the ERBs are likely to be underestimated.) The predicted values of $\mathrm{ERB}_{\mathrm{PTC}}$ are presented in Table II. Some broader PTC data did not yield meaningful estimates of $\mathrm{ERB}_{\mathrm{PTC}}$, reaching infinite values for the bandwidth; these values have been omitted.

The range of $\mathrm{ERB}_{\mathrm{PTC}}$ estimates at a given f_s was defined as the difference between the lowest and highest $\mathrm{ERB}_{\mathrm{PTC}}$ estimates, across subjects, for a given f_s. The range of $\mathrm{ERB}_{\mathrm{PTC}}$ estimates, across subjects for PTCs of f_s 12, 13, and 14 kHz is 486.51, 455.61, and 712.18, respectively. For PTCs of f_s 15, 16, 16.5, and 17.5 kHz, the range of $\mathrm{ERB}_{\mathrm{PTC}}$ estimates is 630.5 (CO, PP, TP), 1749.9 (CO, LS, TP) 1560.2 (all subjects), and 1047.98 (LS, TP), respectively. In general, across subjects, the variability of the $\mathrm{ERB}_{\mathrm{PTC}}$ estimates tends to increase with increasing f_s. For instance, the range of $\mathrm{ERB}_{\mathrm{PTC}}$ estimates for a PTC of $f_s=16.5$ kHz is about 68% greater than the range of $\mathrm{ERB}_{\mathrm{PTC}}$ estimates for a PTC of $f_s=12$ kHz, across subjects.

An normalized estimate of frequency selectivity can be obtained by deriving values of Q_{ERB} (Shera *et al.*, 2002). The Q_{ERB} is defined as the BF divided by the $\mathrm{ERB}_{\mathrm{PTC}}$ of the filter, where both BF and $\mathrm{ERB}_{\mathrm{PTC}}$ are in Hz

$$Q_{\mathrm{ERB}_{\mathrm{PTC}}} = \mathrm{BF}/\mathrm{ERB}_{\mathrm{PTC}}. \quad (5)$$

The values of $Q_{\mathrm{ERB}_{\mathrm{PTC}}}$ for the present data are presented in Table II. $Q_{\mathrm{ERB}_{\mathrm{PTC}}}$ values as a function of the BF of the PTCs are shown in Fig. 5, with individual data plotted as a scatter plot. The solid line shows the linear regression fit to the data. For comparison, the filter bandwidth was also estimated using an equation described by Glasberg and Moore (1990) which describes how the filter bandwidth varies as a function of f_s

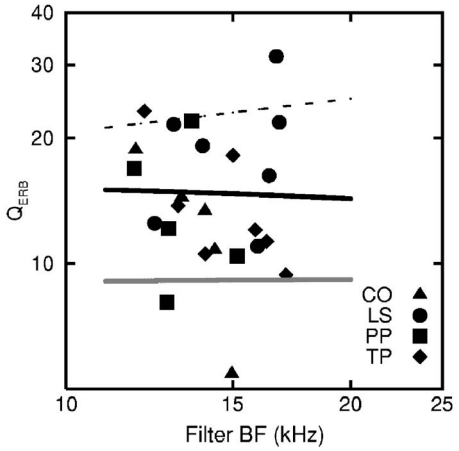

FIG. 5. Estimates of Q_{ERB} from Eq. (6) as a function of filter BF. The solid line represents a regression fit to the data. The dashed line represents the power-law fit of Oxenham and Shera (2003) for filter BFs up to 20 kHz. The gray line represents values of Q_{ERB} for estimates of ERB_{GM}.

$$ERB_{GM} = 24.7(4.37BF + 1), \quad (6)$$

where ERB_{GM} is the bandwidth estimate in Hz, and BF is the center frequency of the auditory filter in kHz. This equation for ERB_{GM} provides a good description of simultaneous-masking data for f_s ranging from 0.1 to 10 kHz. Values of Q_{ERB} were calculated for estimates of ERB_{GM} ($Q_{ERB_{GM}}$) and are shown by the gray line in Fig. 5. Finally, a power-law expression describing the relationship between Q_{ERB} and filter BF, used by Oxenham and Shera (2003) to fit human tuning data, was extrapolated from 8 kHz to the higher frequencies used in this study; the function $Q_{ERB}=11.1\ BF^{0.27}$ was used to estimate tuning for BFs above 12 kHz. The dashed line in Fig. 5 represents this power-law fit for filter BFs up to 20 kHz.

The values of $Q_{ERB_{PTC}}$ for all subjects are in the range of 4.69–31.46. Individual values of $Q_{ERB_{PTC}}$ tend to decrease with increasing f_s for CO, and in general for TP. This is also the case for LS (except for f_s between 12–15 kHz) and PP (except for 15 kHz). The value of $Q_{ERB_{PTC}}$ averaged across subjects and f_s (from 12–17.5 kHz) is about 15. Overall, estimates of $Q_{ERB_{GM}}$ are on average 36% smaller than the estimates of $Q_{ERB_{PTC}}$ from the forward-masked PTC data. For instance, for an f_s of 14 kHz, the average value of $Q_{ERB_{PTC}}$ from the present study is 16.28 and the average predicted value of $Q_{ERB_{GM}}$ from simultaneous masking is 9.11. The estimate of filter tuning is sharper (bandwidth reduced by 44%) at an f_s of 14 kHz when using forward- rather than simultaneous-masking data. The values of Q_{ERB} derived from the power-law fit of Oxenham and Shera (2003) (shown by the dashed line) ranged from 21.71 (for a filter BF of 12 kHz) to 23.85 (for a filter BF of 17 kHz), and are on average 35% greater (more sharply tuned) than the estimates of $Q_{ERB_{PTC}}$ from the present study for filter BFs between 12–17 kHz.

IV. DISCUSSION

A. Absolute threshold variability at high frequencies

Some studies have shown the variability of high-frequency thresholds to increase with increasing f_s (Stelmachowicz *et al.*, 1989; Green *et al.*, 1987), while others have shown decreased variability with increasing f_s (Schechter *et al.*, 1986). However the variability of the threshold data from this study does not appear to follow a trend. Values of s.d. across all subjects and frequencies average 3.13 dB, which is lower than the s.d.'s from other studies, typically ranging between 5–10 dB for f_s of 8–20 kHz (Beiter *et al.*, 1976; Frank and Dreisbach, 1991). One possible reason for the smaller s.d.'s found in this study may be that the subjects were instructed not to move the headphones during the testing session.

B. Estimates of filter shapes from forward masking

Overall, the form of the PTCs is in agreement with earlier psychophysical data, which show high-frequency slopes to be steeper than low-frequency slopes (Nelson and Freyman, 1984; Jesteadt and Norton, 1985; Nelson, 1991; Zhou, 1995). Some PTCs for f_s between 12 and 14 kHz show a flattening of the high-frequency slope for masker levels around 80 dB SPL and above. Similar high-frequency plateaus have been identified for some BM iso-velocity tuning curves (e.g., Robles *et al.*, 1986), although it is not clear to what extent these plateaus result from recording artifacts (Cooper and Rhode, 1996). The BFs of the PTCs increase with increasing f_s, although at higher f_s the BF shifts slightly to lower frequencies. For two subjects in this study (PP and CO) the difference between BF and f_s was quite large for PTCs derived with an f_s above 16 kHz. Zhou (1995) found a similar shift of the BF to lower frequencies with increasing f_s. The smaller shifts of the filter BF to a lower frequency with increasing f_s could be explained by the detection of the higher-frequency signal being mediated by the most basal filter tuned to a lower BF. However, the larger shifts of BF observed for subjects CO and PP are probably best explained by a poorer estimate of BF for the broader PTCs at these higher f_s (especially for PP for the 16.5-kHz PTC), since the PTC slopes were shallow in these cases.

The estimate of bandwidth (ERB_{PTC}) generally increases with f_s, consistent with a broadening of the auditory filter with increasing f_s (Shailer *et al.*, 1990; Zhou, 1995). However, the variability of ERB_{PTC} estimates at a given f_s also tends to increase with f_s. The findings of some previous studies also suggest variability in estimates of filter bandwidth with increasing f_s (1–4 kHz: Patterson *et al.*, 1982; 8–10 kHz: Shailer *et al.*, 1990). For instance, Shailer *et al.* (1990) showed that the variability in ERB estimates (across three subjects) increased by about 67% for an increase in f_s of 8–12 kHz.

Values of Q_{ERB} average about 15 for f_s from 12–17.5 kHz. These estimates of tuning ($Q_{ERB_{PTC}}$) based on forward-masking data are generally higher than the predictions based on simultaneous-masking data ($Q_{ERB_{GM}}$) by an average of 36% for f_s from 12–17.5 kHz. Previous PTC

studies have also shown greater frequency selectivity in forward masking (Wightman *et al.*, 1977; Moore, 1978). It has been suggested that, in a simultaneous-masking situation, the masker may act to suppress (reduce) the BM response to the signal over a wide range of frequencies (Heinz *et al.*, 2002; Nelson and Schroder, 1997; Ruggero *et al.*, 1992). Hence, remote masker frequencies contribute more to masking than they would if the masking depended solely on excitation at the signal place. Forward masking may provide a more accurate estimate of the shape of the auditory filter. The values of Q_{ERB} derived from an extrapolated power-law fit to lower-frequency data (Oxenham and Shera, 2003) were on average 35% higher than the estimates of $Q_{\mathrm{ERB}_{\mathrm{PTC}}}$ for filter BFs between 12–17 kHz. Although the present data were very variable, the results suggest that the equation of Oxenham and Shera may not apply to these very high frequencies.

C. What determines the high-frequency limit of human hearing?

As described in the Introduction, it has been suggested that the high-frequency limit of the human auditory system is set by the transmission characteristics of the middle ear (Masterton *et al.*, 1969), which is assumed to decline at high frequencies. Alternatively, it has been suggested that the high-frequency slope of the hearing-threshold curve corresponds to the high-frequency slope of the highest-frequency auditory filter (Buus *et al.*, 1986; Ruggero and Temchin, 2003): the "end of the cochlea" hypothesis. The present results show that in most cases the slopes of the highest-frequency PTCs are steeper than the slope of the hearing-threshold curve over the same frequency range. Crucially, the highest BF measured for an individual is above the breakpoint in that individual's hearing-threshold curve; this is the case for all subjects. These findings are inconsistent with the end of the cochlea hypothesis, but consistent with the middle-ear hypothesis.

Ruggero and Temchin (2003) suggested that the estimation of the middle-ear response differs greatly depending on whether the data are obtained *in vivo* or *postmortem*; the middle-ear response obtained *postmortem* may not reflect the actual middle-ear transmission characteristics. Very little human *in vivo* data are yet available. Huber *et al.* (2001) made *in vivo* measurements of stapes vibrational velocity in humans. The middle-ear stapes vibrational velocity was found not to fall off with frequency as rapidly as the hearing threshold. The physiology of the ear of the chinchilla is often used to infer what we want to know about the human middle-ear response. Chinchilla data, and data from other species such as the guinea pig, seem to suggest that the bandwidth of middle-ear vibrations exceeds that of the hearing-threshold curve (Ruggero and Temchin, 2002). It is still not clear if the rate of decrease of the middle-ear stapes velocity with frequency is less than or greater than the rate of decrease of absolute sensitivity with frequency, across a similar frequency range. In addition, chinchilla estimates of auditory filter shape can also differ from human estimates, so it may not be valid to compare across species in these cases (Halpern and Dallos, 1986). However, it seems possible that an additional component may be necessary to explain the steep high-frequency slope of the hearing-threshold curve. For example, there could be a CF-dependent reduction in the efficiency of mechanical to electrical transduction by the inner hair cells, although this remains speculative at present. Finally, it must be acknowledged that at extremely high frequencies (above 17.5 kHz) it is still quite possible that the hearing-threshold slope is determined by the high-frequency slope of the final auditory filter.

V. CONCLUSIONS

(i) PTCs measured using forward masking at very high frequencies show narrower bandwidths (by about 36%) than predictions based on simultaneous masking data.

(ii) For the highest frequencies used in this study (f_s of 15.0–17.5 kHz), the high-frequency slope of the PTC is in most cases steeper than the slope of the hearing-threshold curve. The PTC data also show that some subjects display frequency selectivity for CFs as high as 17 kHz, well above the breakpoint in the hearing-threshold curve.

(iii) The findings suggest that the human high-frequency threshold limitation for f_s up to 17.5 kHz is imposed in part by the middle-ear attenuation, and not by the tonotopicity of the cochlea.

ACKNOWLEDGMENTS

We thank the editor and two anonymous reviewers for helpful comments on an earlier version of the manuscript. The research was supported by EPSRC Grant GR/N07219. The first author was supported by a studentship from the ESRC.

[1]In order to investigate the effect of a frequency-dependent middle-ear transform on the shape of the PTCs, a middle-ear correction was applied to a sample of the PTC data. Puria *et al.* (1997) estimated the middle-ear pressure gain of human cadaver ears by measuring the ratio of the vestibule pressure to the ear-canal pressure. The data of Puria *et al.* [1997, Fig. 11 (B)] for the middle-ear transmission in humans were extrapolated above 12 kHz to the higher frequencies used in this study. A linear function ($y = -0.0015x + 22.768$) was fitted to the frequencies above 12 kHz. The masker-level values for a sample of PTCs from this study were readjusted with this correction and the PTCs replotted. PTCs with a middle-ear correction showed only a slight shift of the low-frequency slope of the PTC to lower masker levels, but the tip of the PTC (the BF) and the higher-frequency slopes were relatively unaffected. The BF of the PTC is defined as the frequency of the masker most effective at masking the signal. Based on these findings, the middle-ear correction was not applied to the data set used in subsequent analyses, since inclusion of the correction would have only a negligible effect on the high-frequency PTC slopes estimated in this study. A similar finding was reported by Zhou (1995), who used a middle-ear correction for high-frequency PTCs; there was a negligible effect on PTC slope for a high-frequency f_s.

Aibara, R., Welsh, J. T., Puria, S., and Goode, R. L. (**2001**). "Human middle-ear sound transfer function and cochlear input impedance," Hear. Res. **152**, 100–109.

ANSI (**1996**). ANSI S3.6–1996. *Specification for Audiometers* (American National Standards Institute, New York).

Beiter, R. C., and Talley, J. N. (**1976**). "High-frequency audiometry above 8000 Hz," Audiology **15**, 207–214.

Buus, S., Florentine, M., and Mason, C. R. (**1986**). "Tuning curves at high

frequencies and their relation to the absolute threshold curve," in *Auditory Frequency Selectivity*, edited by B. C. J. Moore and R. D. Patterson (Plenum, New York), pp. 341–350.
Cooper, N. P., and Rhode, W. S. (**1996**). "Two-tone distortion suppression in apical cochlear mechanics," Aud. Neurosci. **3**, 123–134.
Frank, R., and Dreisbach, L. E. (**1991**). "Repeatability of high-frequency thresholds," Ear Hear. **12**, 294–295.
Glasberg, B. R., and Moore, B. C. J. (**1990**). "Derivation of auditory filter shapes from notched-noise data," Hear. Res. **47**, 103–138.
Green, D. M., Kidd, G., and Stevens, K. N. (**1987**). "High-frequency audiometric assessment of a young adult population," J. Acoust. Soc. Am. **81**, 485–494.
Halpern, D. L., and Dallos, P. (**1986**). "Auditory filter shapes in the chinchilla," J. Acoust. Soc. Am. **80**, 765–775.
Heinz, M. G., Colburn, H. S., and Carney, L. H. (**2002**). "Quantifying the implications of nonlinear cochlear tuning for auditory-filter estimates," J. Acoust. Soc. Am. **111**, 996–1011.
Huber, A., Linder, T., Ferrazzi, M., Schmid, S., Dillier, N., Stoeckli, S., and Fisch, U. (**2001**). "Intraoperative assessment of stapes movement," Ann. Otol. Rhinol. Laryngol. **110**, 31–35.
Jesteadt, W., and Norton, S. (**1985**). "The role of suppression in psychophysical measures of frequency selectivity," J. Acoust. Soc. Am. **78**, 365–374.
Levitt, H. (**1971**). "Transformed up–down methods in psychoacoustics," J. Acoust. Soc. Am. **49**, 467–477.
Masterton, B., Heffner, H., and Ravissa, R. (**1969**). "The evolution of human hearing," J. Acoust. Soc. Am. **45**, 966–985.
Moore, B. (**1978**). "Psychophysical tuning curves measured in simultaneous and forward masking," J. Acoust. Soc. Am. **63**, 524–532.
Moore, B. C. J. (**1995**). "Frequency analysis and masking," in *Hearing*, edited by B. C. J. Moore (Academic, London), pp. 161–205.
Moore, B. C. J. (**1997**). *An Introduction to the Psychology of Hearing* (Academic, London).
Moore, B. C. J., and Glasberg, B. (**1981**). "Auditory filter shapes derived in simultaneous and forward masking," J. Acoust. Soc. Am. **70**, 1003–1014.
Neff, D. L. (**1986**). "Confusion effects with sinusoidal and narrow-band forward maskers," J. Acoust. Soc. Am. **79**, 1519–1529.
Nelson, D. (**1991**). "High-level psychophysical tuning curves: Forward masking in normal-hearing and hearing-impaired listeners," J. Speech Hear. Res. **34**, 1233–1249.
Nelson, D. E., and Freyman, R. (**1984**). "Broadened forward-masked tuning curves from intense masking tones: Delay-time and probe-level manipulations," J. Acoust. Soc. Am. **75**, 1570–1577.
Nelson, D. A., and Schroder, A. C. (**1997**). "Linearized response growth inferred from growth of masking slopes in ears with cochlear hearing loss," J. Acoust. Soc. Am. **101**, 2186–201.
Oxenham, A. J., and Shera, C. (**2003**). "Estimates of human cochlear tuning at low levels using forward and simultaneous masking," J. Assoc. Res. Otolaryngol. **4**, 541–554.
Patterson, R., Nimmo-Smith, I., Weber, D., and Milroy, R. (**1982**). "The deterioration of hearing with age: Frequency selectivity, the critical ratio, the audiogram, and speech threshold," J. Acoust. Soc. Am. **72**, 1788–1803.
Puria, S., Peake, W. T., and Rosowski, J. J. (**1997**). "Sound-pressure measurements in the cochlear vestibule of human-cadaver ears," J. Acoust. Soc. Am. **101**, 2754–2769.
Robles, L., Ruggero, M., and Rich, N. (**1986**). "Basilar membrane mechanics at the base of the chinchilla cochlea. I. Input–output functions," J. Acoust. Soc. Am. **80**, 1364–1374.
Ruggero, M. A., and Temchin, A. N. (**2002**). "The roles of the external, middle, and inner ears in determining the bandwidth of hearing," Proc. Natl. Acad. Sci. U.S.A. **99**, 13206–13210.
Ruggero, M. A., Robles, L., and Rich, N. (**1992**). "Two-tone suppression in the basilar membrane of the cochlea: Mechanical basis of auditory-nerve rate suppression," J. Neurophysiol. **68**, 1087–1099.
Schechter, M. A., Fausti, S. A., Rappaport, B. Z., and Frey, R. H. (**1986**). "Age categorization of high-frequency auditory threshold data," J. Acoust. Soc. Am. **79**, 767–771.
Shailer, M. J., Moore, B. C. J., Glasberg, B. R., and Watson, N. (**1990**). "Auditory filter shapes at 8 and 10 kHz," J. Acoust. Soc. Am. **88**, 141–148.
Shera, C. A., Guinan, J. J., and Oxenham, A. J. (**2002**). "Revised estimates of human cochlear tuning from otoacoustic and behavioral measurements," Proc. Natl. Acad. Sci. U.S.A. **99**, 3318–3323.
Stelmachowicz, P. G., Beauchaine, K. A., Kalberer, A., Kelly, W. J., and Jesteadt, W. (**1989**). "High-frequency audiometry: Test reliability and procedural considerations," J. Acoust. Soc. Am. **85**, 879–887.
Stinson, M. R. (**1990**). "Revision of estimates of acoustic energy reflectance at the human eardrum," J. Acoust. Soc. Am. **88**, 1773–1778.
Wightman, F., McGee, T., and Kramer, M. (**1977**). "Factors influencing frequency selectivity in normal and hearing-impaired listeners," in *Psychophysics and Physiology of Hearing*, edited by E. F. Evans and J. P. Wilson (Academic, London), pp. 341–350.
Yasin, I., and Plack, C. J. (**2003**). "The effects of a high-frequency suppressor on tuning curves and derived basilar membrane response functions," J. Acoust. Soc. Am. **114**, 322–332.
Zhou, B. (**1995**). "Auditory filter shapes at high frequencies," J. Acoust. Soc. Am. **98**, 1935–1942.
Zhou, B., and Green, D. M. (**1995**). "Reliability of pure-tone thresholds at high frequencies," J. Acoust. Soc. Am. **98**, 828–836.

Monaural and interaural temporal modulation transfer functions measured with 5-kHz carriers

Mark A. Stellmack,[a] Neal F. Viemeister, and Andrew J. Byrne
Department of Psychology, University of Minnesota, Minneapolis, Minnesota 55455

(Received 28 September 2004; revised 22 June 2005; accepted 18 July 2005)

Temporal modulation transfer functions (TMTFs) were measured for detection of monaural sinusoidal amplitude modulation and dynamically varying interaural level differences for a single set of listeners. For the interaural TMTFs, thresholds are the modulation depths at which listeners can just discriminate interaural envelope-phase differences of 0 and 180°. A 5-kHz pure tone and narrowband noises, 30- and 300-Hz wide centered at 5 kHz, were used as carriers. In the interaural conditions, the noise carriers were either diotic or interaurally uncorrelated. The interaural TMTFs with tonal and diotic noise carriers exhibited a low-pass characteristic but the cutoff frequencies changed nonmonotonically with increasing bandwidth. The interaural TMTFs for the tonal carrier began rolling off approximately a half-octave lower than the tonal monaural TMTF (~80 Hz vs ~120 Hz). Monaural TMTFs obtained with noise carriers showed effects attributable to masking of the signal modulation by intrinsic fluctuations of the carrier. In the interaural task with dichotic noise carriers, similar masking due to the interaural carrier fluctuations was observed. Although the mechanisms responsible for differences between the monaural and interaural TMTFs are unknown, the lower binaural TMTF cutoff frequency suggests that binaural processing exhibits greater temporal limitation than monaural processing. © *2005 Acoustical Society of America.* [DOI: 10.1121/1.2032057]

PACS number(s): 43.66.Pn, 43.66.Mk [AK] Pages: 2507–2518

I. INTRODUCTION

Comparisons of intensity across the ears and comparisons of intensity over time within one ear are performed physiologically by different mechanisms. Neural circuits in the lateral superior olive are configured such that they effectively compare intensity information arriving simultaneously at the two ears (Yin, 2002). The result is neurons that are "tuned" to interaural level differences (ILDs). Perceptually, for stimuli presented to the two ears over headphones that differ only in interaural level, an intracranial image is typically perceived at some lateral position determined by the ILD. Thus, binaural comparisons of intensity result in a spatial component to the internal representation of the stimulus. In contrast, monaural comparisons of intensity over time would seem to depend upon the intensity of each stimulus being encoded in some way (perhaps in terms of loudness) and retention of those representations in memory for subsequent comparison. Stellmack *et al.* (2004) presented data indicating that, despite these physiological and perceptual differences, the auditory system is nearly equally sensitive to differences in intensity for a 4-kHz pure tone and broadband noise when those differences are presented over time to one ear or simultaneously to both ears. In addition, both monaural and binaural comparisons of intensity were shown to exhibit Weber's law for broadband noise and the near miss for a 4-kHz pure tone, likely reflecting the effects of common stages of processing preceding monaural and binaural comparison.

The above-described conditions involved monaural and binaural comparisons of intensities that remained constant for the duration of the individual stimuli. The present paper examines monaural and binaural processing of dynamically varying stimulus intensity. It has been shown that the auditory system exhibits a decreasing ability to resolve the fluctuations associated with sinusoidal amplitude modulation (SAM) with increasing modulation frequency and that this limitation is not due to the reduction of effective modulation depth as a result of critical-band filtering of the stimulus (e.g., Viemeister, 1979; Kohlrausch *et al.*, 2000). It also has been shown that binaural processing exhibits a limitation in temporal resolution that is not attributable to critical-band filtering (Bernstein and Trahiotis, 1994; 2005).

Temporal limitations in monaural and binaural processing are often modeled as integration of the relevant parameter of the stimulus (e.g., intensity in the monaural case and interaural parameters in the binaural case) within a temporal window that is limited by some minimum integration time. Because of the minimum integration time, rapid fluctuations in the parameter of interest are effectively "smoothed over" or low-pass filtered by the system, producing a limitation on the temporal resolution of the system. This limitation in temporal resolution is often characterized in terms of the cutoff frequency or time constant of a low-pass filter or in terms of the minimum integration time of a temporal window that produces an equivalent limitation on temporal resolution.

A number of studies have estimated cutoff frequencies and time constants or minimum integration times for monaural and binaural processing of dynamically varying stimulus parameters. Generally, these studies have shown that binaural processing exhibits lower temporal resolution than mon-

[a]Electronic-mail: stell006@umn.edu

aural processing (e.g., Grantham and Wightman, 1979; Kollmeier and Gilkey, 1990; Culling and Summerfield, 1998). For example, Kollmeier and Gilkey (1990) measured binaural temporal resolution through binaural forward- and backward-masking tasks in which listeners detected an interaurally out-of-phase signal (S_π) in the presence of a concurrent interaurally in-phase noise masker (N_0), where the in-phase masker was preceded or followed by interaurally phase-inverted noise (N_π). Thresholds were measured as a function of the time between the signal presentation and the change in the masker configuration. Time constants of a two-sided exponential window that produced best fits to the data ranged from 16.1 to 42.7 ms (across all listeners and conditions). In contrast, estimated time constants of a temporal window that predicted data in comparable monaural forward- and backward-masking tasks ranged from 5.9 to 14.7 ms, indicating better monaural temporal resolution. In an extension of the Kollmeier and Gilkey (1990) task, Culling and Summerfield (1998) measured thresholds for an S_π signal in the presence of N_0 noise that was both preceded and followed by N_π noise. In considering a number of different temporal windows, Culling and Summerfield (1998) found that an asymmetrical Gaussian window fit their data best. Best-fitting time constants for the forward lobe ranged from 11.7 to 28.7 ms for the forward lobe and from 33.3 to 61.1 ms for the rearward lobe, reflecting more masking of the S_π signal by the leading N_π fringe than the trailing N_π fringe. Grantham and Wightman (1979), in a task in which listeners detected an S_π signal in the presence of a masker whose interaural configuration varied sinusoidally between N_0 and N_π, estimated binaural time constants that ranged from 44 to 243 ms across listeners and conditions. In the present experiments, the ability to detect periodically time-varying ILDs is compared to monaural detection of SAM in order to compare limitations on temporal resolution in the two situations. A single set of listeners was run in analogous monaural and binaural tasks that allow for a direct comparison between monaural and binaural performance.

A. Monaural TMTF

In a typical monaural modulation detection task, the listener attempts to detect sinusoidal fluctuations in amplitude that are present in the signal interval but not in the nonsignal interval. In this case, the limits of monaural temporal resolution can be described by the temporal modulation transfer function (TMTF), which plots threshold modulation depth as a function of modulation frequency (Viemeister, 1979). For broadband noise carriers, thresholds are relatively constant across a range of low modulation frequencies, while above some cutoff modulation frequency thresholds increase with increasing modulation frequency, in effect describing a low-pass characteristic for modulation processing. The form of the TMTF generally is interpreted as indicating that the fluctuations of the stimulus envelope are encoded by the auditory system with less precision as modulation frequency increases. That is, the representation of the envelope within the auditory system becomes "smoothed over" at higher modulation frequencies, such that an increase in modulation depth is required in order for the modulation to be detected. The cutoff modulation frequency and rate of increase of thresholds (representing a decrease in sensitivity) with increasing modulation frequency sometimes are used to describe the auditory system's low-pass characteristic for modulation. The form of the TMTF measured with puretone carriers differs from that for broadband noise carriers in that the puretone TMTF typically has a higher cutoff modulation frequency (Dau *et al.*, 1999; Kohlrausch *et al.*, 2000). For example, in the TMTFs measured with a high-frequency pure-tone carrier by Kohlrausch *et al.* (2000), thresholds are relatively constant for modulation frequencies below about 130 Hz. As modulation frequency increases above 130 Hz, thresholds first increase as temporal resolution diminishes and then decrease as the modulation sidebands become resolved at the auditory periphery (see the following). Because the TMTFs measured with noise and tonal carriers exhibit different cutoff frequencies, one must consider the potential advantages and disadvantages of using each type of carrier to measure the monaural TMTF.

When a pure tone is sinusoidally amplitude modulated, two spectral sidebands are introduced, one above and one below the carrier frequency, with frequency spacings equal to the modulation frequency. When the modulation frequency is low, the sidebands are unresolved at the auditory periphery and the listener performs the modulation-detection task by detecting the fluctuating stimulus envelope. When the modulation frequency becomes sufficiently high, the sidebands become increasingly resolved and the listener simply detects the sidebands rather than the modulation per se (e.g., Kohlrausch *et al.*, 2000). This leads to sharply decreasing thresholds at high modulation frequencies and can make it difficult to obtain an accurate assessment of the temporal resolution of the auditory system.

In contrast, the long-term spectrum of a broadband noise carrier remains unchanged when it is sinusoidally amplitude modulated, so this provides a potential means for studying auditory temporal resolution at high modulation frequencies. However, the envelope of a broadband noise itself fluctuates in amplitude. These intrinsic envelope fluctuations, in turn, produce envelope fluctuations at the outputs of peripheral auditory filters as a result of their bandpass filtering of the broadband noise. It has been suggested that these intrinsic fluctuations in the noise carrier mask the sinusoidal modulation to be detected (Dau *et al.*, 1999). In order for this type of explanation to account for the data, one must assume some type of frequency selectivity in the modulation domain, for example, processing of the peripherally filtered signal by modulation frequency-selective channels, a so-called modulation filterbank (Dau *et al.*, 1997). In this scheme, when both the signal modulation and intrinsic fluctuations of the carrier are passed by a common modulation filter, the signal modulation is less detectable resulting in higher thresholds. Consistent with that notion, the monaural TMTF for a broadband noise carrier starts to increase at lower modulation rates and with a different slope than the TMTF for a pure-tone carrier (Kohlrausch *et al.*, 2000). Also consistent with the concept of processing by a modulation filterbank, TMTFs for narrowband noise exhibit a bandpass or high-pass character-

istic depending upon the bandwidth of the carrier, which approximately determines the frequency range of the intrinsic carrier fluctuations (Dau *et al.*, 1999). If the fact that thresholds in the TMTF for broadband noise increase at a lower frequency is in part a result of masking of the signal modulation by the intrinsic fluctuations of the carrier, this produces a deceptively low estimate of the temporal resolution of the auditory system. Therefore, it seems that the best stimulus for use in assessing monaural temporal resolution is a pure-tone carrier (to avoid intrinsic carrier fluctuations) that is very high in frequency (to minimize resolution of the sidebands with increasing modulation frequency).

B. Interaural TMTF

What is the appropriate stimulus for assessing the temporal resolution of the binaural system? Consider a dichotic stimulus in which a sinusoidally amplitude-modulated pure tone is presented to each ear, with the envelopes at the two ears 180° out-of-phase with one another. The resulting stimulus is, in effect, a pure tone for which the ILD oscillates about zero at a rate equal to the monaural modulation frequency in each ear, as shown in the right column at the top of Fig. 1, in which the instantaneous ILD functions were defined as

$$\mathrm{ILD}(t) = 20\ \log_{10}\left(\frac{E_L(t)}{E_R(t)}\right), \tag{1}$$

where $E_L(t)$ and $E_R(t)$ are the envelopes of the left- and right-ear signals, respectively. [The function ILD(t) is nearly sinusoidal for the threshold modulation depths measured in this paper, while the form of the function approaches that of a triangle wave for larger monaural modulation depths. See Fig. 2.] At low modulation frequencies, this stimulus typically produces the percept of a tone that moves slowly from side to side within the listener's head. The extent of the perceived lateral movement is determined by the peak interaural level difference that is attained by the stimulus, which increases with increasing monaural modulation depth. At higher modulation frequencies, the stimulus is no longer perceived as a discrete, moving image but instead as a diffuse or broadened image (when the envelopes at the two ears are 180° out-of-phase with one another), with the degree of diffuseness directly related to the monaural modulation depth. Variation of the stimulus ILD over time will be called "interaural modulation" in this paper.

In his study of interaural modulation detection, Grantham (1984) sought to eliminate "diffuseness" as a cue by using an interaurally uncorrelated noise as the carrier. When the carrier is interaurally uncorrelated, the instantaneous interaural level difference of the noise carrier fluctuates randomly about zero (Fig. 1, lower panels) which itself produces a perception of diffuseness. [In Fig. 1, the instantaneous ILD functions in the right-hand panels were computed from the Hilbert envelopes of the corresponding noise wave forms using Eq. (1).] In this case, the listener must detect sinusoidal interaural modulation in the presence of random interaural fluctuations intrinsic to the interaurally uncorrelated noise carrier. Note that this is analogous to the

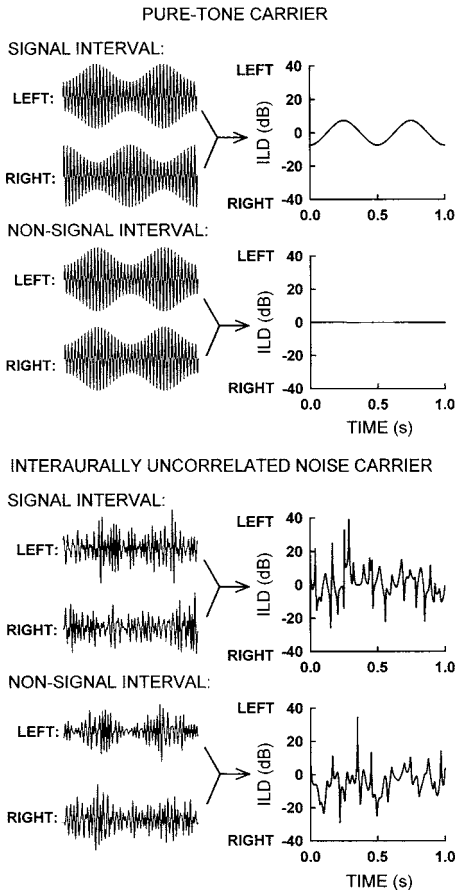

FIG. 1. The pressure wave forms presented to the left and right ears (left column) and instantaneous interaural level difference (ILD, right column) of stimulus envelopes in signal and nonsignal intervals of an interaural modulation detection task. In the upper set of panels, the carrier is a pure tone while in the lower panels the carrier is a 30-Hz-wide interaurally uncorrelated band of noise. The depth of the sinusoidal amplitude modulation of each stimulus is the same in the upper and lower panels (m=0.4). The instantaneous ILD functions in the lower panels were computed from the Hilbert envelopes of the noise wave forms using Eq. (1).

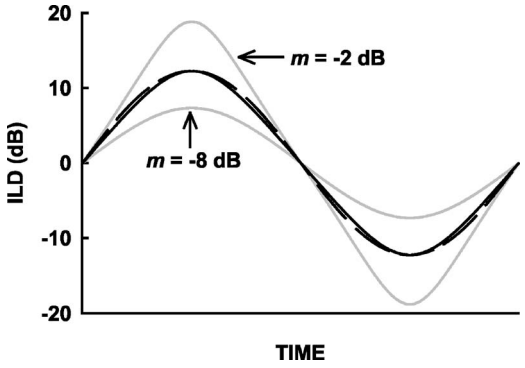

FIG. 2. One cycle of ILD(t) (as in Fig. 1) computed using Eq. (1) for several SAM pure tones with various monaural modulation depths. The solid black line is ILD(t) for a stimulus with m=−4.33 dB, the largest threshold measured in this experiment. The dashed black line is a sinusoid with the same peak amplitude as the solid black line. The largest instantaneous difference between the solid and dashed black lines is 0.71 dB. The gray lines represent ILD(t) for the values of m indicated in the figure. It can be seen that ILD(t) is nearly sinusoidal for the range of threshold m measured in this experiment.

situation in the monaural modulation detection task with a broadband noise carrier in which the listener must detect sinusoidal amplitude modulation in the presence of random fluctuations of amplitude. It is possible that the intrinsic interaural fluctuations of the interaurally uncorrelated carrier might interfere with detection of the sinusoidal interaural modulation. Therefore, it seems that the best stimulus for measuring an interaural TMTF that is analogous to the monaural TMTF is a diotic carrier, for which there are no intrinsic interaural fluctuations that might interfere with detection of the signal interaural modulation.

In the present experiment, monaural and interaural modulation detection is compared for narrowband noise carriers (30- and 300-Hz wide centered at 5 kHz) for which intrinsic fluctuations of the carrier might be expected to interfere with detection of the target sinusoidal modulation. In separate conditions, interaural modulation detection thresholds are measured for diotic and dichotic (interaurally uncorrelated) noise carriers. In the diotic case, there are no intrinsic interaural fluctuations in the carrier that might interfere with the interaural modulation to be detected. The dichotic conditions are included to assess the effects on the interaural TMTF of degrading the "image-width" cue. Monaural and interaural modulation detection also is measured for a 5-kHz pure-tone carrier for which there likewise are no intrinsic fluctuations in the monaural or interaural modulation functions. Furthermore, given the 5-kHz carrier, the sidebands of the modulated stimulus are high enough in frequency so that interaural delays of the resolved sidebands cannot serve as a cue for detection in the binaural condition (Klumpp and Eady, 1956). Such a cue can complicate the interpretation of interaural TMTFs measured with low-frequency carriers. For the narrowband noise carriers, when the sinusoidal modulators are interaurally 180° out of phase, the phases of the fine structures of the modulation sidebands are inverted relative to one another but the envelopes of the modulation sidebands are identical at the two ears. Thus, even if the modulation sidebands of the narrowband noise carrier are resolved, they carry no interaural envelope cues to the detection of the interaural modulation in the signal interval.

The primary focus of the present paper is a comparison of monaural and binaural temporal resolution as reflected by the monaural and interaural TMTFs. An additional issue that will be addressed is the influence of intrinsic fluctuations in monaural intensity or interaural intensity differences on the forms of the monaural and interaural TMTFs.

II. METHODS

A. Stimuli and procedure

In all (monaural and interaural) conditions, a three-interval, three-alternative forced-choice task consisting of one signal and two nonsignal intervals was used. In the monaural conditions, the nonsignal intervals consisted of unmodulated carriers and the signal interval contained a sinusoidally amplitude-modulated carrier, with signals and nonsignals presented only to the left ear. The starting phase of the envelope in the signal interval was chosen randomly from trial to trial.

In the interaural modulation-detection task, stimuli were presented to both ears and were sinusoidally amplitude-modulated in all three intervals of every trial. In the signal interval, the interaural phase difference of the sinusoidal modulator was 180° while the interaural phase difference of the sinusoidal modulator was 0° in the nonsignal intervals. The absolute starting phase of the modulator was randomized between intervals (while maintaining the appropriate interaural phase difference) to eliminate possible monaural cues associated with changing the phase of one channel in the signal interval.

The monaural and interaural tasks were performed with a number of different carriers. For the monaural tasks, the carriers were a 5-kHz pure tone and 30- and 300-Hz-wide bands of noise centered at 5 kHz. These bandwidths were chosen to permit comparison to the data of Dau *et al.* (1997). In the interaural tasks, the carriers were a 5-kHz pure tone, 30- and 300-Hz-wide diotic bands of noise, and 30- and 300-Hz-wide interaurally uncorrelated bands of noise, with all noise bands centered at 5 kHz. The pure-tone carrier was interaurally in-phase in the interaural condition. Independent samples of narrowband noise were generated for the left- and right-ear stimuli of the interaurally uncorrelated carriers. For all of the noise carrier conditions, different samples of noise were generated for each interval of each trial (that is, the carriers were not "frozen" across intervals).

The monaural and interaural conditions were run in the presence of continuous, low-pass noise with a cutoff frequency of 1.3 kHz designed to mask potential distortion products at the modulation frequency (e.g., Nuetzel and Hafter, 1976; Wiegrebe and Patterson, 1999). In addition, the monaural TMTF was measured without the low-pass masker in order to facilitate comparison to the data of Kohlrausch *et al.* (2000), who also measured thresholds without a low-pass masker.

In all conditions, modulation depth was varied adaptively using a two-down, one-up adaptive tracking rule that estimated the 70.7% correct point on the psychometric function (Levitt, 1971). Modulation depth was varied in the signal and nonsignal intervals in the interaural modulation detection task. (Recall that varying the monaural modulation depth in the interaural modulation condition has the effect of varying the peak interaural level difference attained by the dichotic stimulus.) The initial step size was set to 2 dB (in units of 20 log m, where m is the modulation index) and was reduced to 1 dB after four reversals. A block of trials was terminated after a total of 12 reversals, and the modulation depths at which the final eight reversals occurred (in dB) were averaged to produce a threshold estimate. If the adaptive procedure attempted to track above a modulation depth of 0 dB ($m=1$), the block of trials was terminated immediately. If the adaptive track was terminated prematurely in two consecutive runs, the threshold was considered to be unmeasurable. When possible to do so, the initial modulation depth was set approximately 8 dB above the expected threshold modulation depth based on prior experience and the performance of the listeners. The highest initial modulation depth used was −5 dB to allow listeners to make at least two incorrect responses without prematurely terminating the adap-

tive run because of overmodulation. Four blocks of trials were run in each condition and the four threshold estimates (in dB) were averaged to obtain the final threshold estimate for that condition.

The 5-kHz pure-tone carrier was presented at a level of 75 dB SPL at each ear. The 30- and 300-Hz-wide bands of noise were presented at spectrum levels of 50 and 40 dB, respectively, measured at 1-kHz for unfiltered stimuli. The temporal characteristics of the stimuli were based upon those used by Kohlrausch *et al.* (2000) although there were minor differences in the specific parameters. Each interval was 1 s in duration (the intervals of Kohlrausch *et al.* were 800 ms in duration), including 150-ms raised-cosine on-off ramps. The intervals were temporally contiguous with no silence between them, the on-off ramps serving to demarcate the intervals. Thresholds were measured for modulation frequencies (f_m) ranging from 4 to 650 Hz with all but the lowest f_m identical to those used by Kohlrausch *et al.* (2000).

Listeners were given a list of computer files associated with each experimental condition and were allowed to initiate adaptive runs themselves. They were given instructions to complete two adaptive runs for each f_m in an order of their choosing and then two additional runs in a different order, again of their choosing, and the experimenters confirmed that these instructions were followed. The instructions to complete the adaptive runs in various orders was intended to control for potential order effects on thresholds measured across f_m's. As a result, listeners in many cases performed adaptive runs for the f_m's within an experimental condition in different orders, for example, listeners may have run the f_m's from low to high for the first two runs then high to low for the second two, or a listener might have chosen to proceed through the f_m's in a less systematic way. All f_m's for a particular condition were run before a different condition was run. Listeners ran the main conditions of the experiment in the following order: monaural tonal without masker, monaural tonal with masker, interaural tonal, monaural noise (both bandwidths), interaural with correlated noise (both bandwidths), and interaural with uncorrelated noise (both bandwidths). With regard to the conditions with noise carriers, listeners ran the 30- and 300-Hz bandwidth conditions in different orders.

To compensate for the increase in intensity resulting from amplitude modulation and to limit the usefulness of changes in overall intensity as a cue (a potential problem in the monaural modulation detection tasks), all modulated wave forms in all conditions were scaled by a factor of $(1+m^2/2)^{-0.5}$. Although intensity changes associated with modulation did not provide a cue in the binaural listening tasks because all intervals were modulated, the modulated wave forms in all three intervals of the binaural conditions also were rescaled by the above-noted factor for consistency.

Each block of trials was initiated by the listener. On each trial, a "ready" light flashed on the computer screen for 250 ms followed by a 300-ms pause after which a trial was presented. A separate marker on the screen was illuminated during each stimulus interval. Listeners entered their responses on the computer keyboard at which time the correct answer was indicated by once again illuminating the appropriate interval marker on the screen. Listeners were run in 2-h sessions, during which approximately 12–14 blocks of trials were run, until all stimulus conditions were completed.

B. Apparatus

Signals and nonsignals were generated and presented via MATLAB (Math Works) on a PC equipped with a high-quality, 24-bit sound card (Echo Audio Gina) at a sampling rate of 44.1 kHz. Each noise carrier was generated digitally in the frequency domain with maximally steep roll-offs at the cutoff frequencies and was converted to the time domain via a 44 100-point inverse fast Fourier transform (FFT) that yielded a 1-s sample of noise. The low-pass masker used in the interaural conditions was dichotic Gaussian noise produced continuously at each ear by separate noise generators (General Radio 1381). The noise at each ear was low-pass filtered by a programmable filter (Kemo VBF/25) with a cutoff of 1.3 kHz (135-dB/octave rolloff). The noise had a spectrum level of 40 dB SPL measured at 1 kHz after filtering. When the continuous noise masker was presented in the monaural conditions, it was presented to only the left ear. Stimuli were mixed with the noise maskers and presented over Sony MDR-V6 stereo headphones to listeners seated in an IAC sound-attenuating chamber.

C. Subjects

The three listeners consisted of the first and third authors (S1 and S2, respectively) and one female undergraduate student from the University of Minnesota (S3) who was paid to participate in the study. All listeners had pure-tone thresholds of 15 dB HL or better at octave frequencies from 250 to 8000 Hz. S1 and S2 had extensive experience in similar listening tasks and received no training prior to performing the present tasks. S3 was allowed to practice in a variety of the monaural and binaural conditions over the course of 2 weeks (approximately 12 h of practice) after which time she appeared to have reached asymptotic performance.

III. RESULTS

The pattern of results was very similar in all but one condition for the three listeners, so only the mean data are shown in Fig. 3. (The exception, the interaural TMTFs measured with a diotic 300-Hz-wide noise carrier, will be discussed in Sec. IV A.) In the left column of Fig. 3, the data are shown in the top panel for the tonal carrier, the middle panel for the 30-Hz-wide noise, and in the bottom panel for the 300-Hz-wide noise. In the right column of Fig. 3, the data from the left column are replotted such that the monaural data are in the top panel and the interaural data are in the bottom panel, with the same symbols representing the same conditions across the two columns. In each panel, threshold modulation depth is plotted as a function of f_m, with the ordinate inverted such that larger modulation depths are toward the bottom of the panel. Dashed portions of the interaural functions indicate that thresholds could not be measured above a particular modulation frequency. Some general

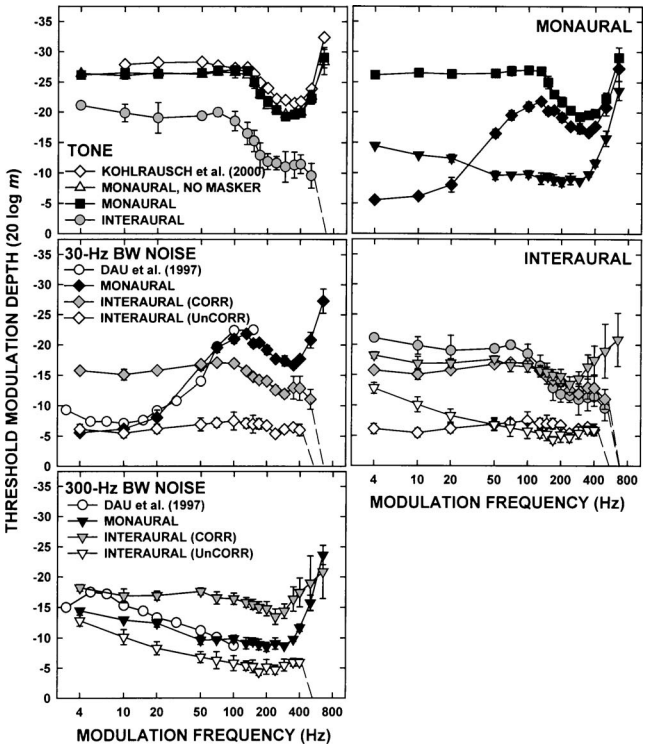

FIG. 3. Monaural and interaural TMTFs showing threshold modulation depth (in dB) as a function of modulation frequency averaged across three listeners. In the left column, TMTFs for different carriers are represented in each panel: top panel, 5-kHz pure-tone carrier; middle panel, 30-Hz-wide band of noise; bottom panel, 300-Hz-wide band of noise. The two bands of noise were centered at 5 kHz. The different symbol types represent monaural and interaural TMTFs, as indicated in the legend. Error bars represent standard errors of the mean computed across three listeners and are in many cases smaller than the symbols. In the top panel, the monaural, no-masker TMTF is almost completely obscured by the monaural TMTF (with masker). The open diamonds in the top panel represent the monaural TMTF for a 5-kHz pure-tone carrier reported by Kohlrausch *et al.* (2000). The open circles in the middle and bottom panels represent monaural TMTFs for 31- and 314-Hz-wide bands of noise, both centered at 5 kHz, reported by Dau *et al.* (1997). In the right column, in separate panels, the monaural and interaural TMTFs are replotted from the left column. The same symbol type represents the same data in each column.

features of the TMTFs will be described in this section, while specific parameter estimates are described in Sec. IV A.

Referring to the top left panel of Fig. 3, the monaural data gathered in the presence of a low-pass masker (filled squares) fall almost directly on top of the monaural data gathered without a masker (open triangles), indicating that the continuous low-pass masker had no effect on the monaural pure-tone TMTFs. (Note that all remaining monaural and binaural thresholds were measured in the presence of the low-pass masker.) Rickert and Viemeister (1998) measured TMTFs for a 2-kHz pure tone carrier with and without a broadband noise masker designed to mask distortion products and reduce off-frequency listening. (Figures showing those TMTFs were published by Viemeister *et al.*, 2002.) Rickert and Viemeister found that thresholds were elevated in the presence of noise, but the TMTF measured with noise was similar in form to that measured without noise. They concluded that the form of the TMTF is not dependent upon the detection of distortion products.

The form of the tonal monaural TMTF measured here is very similar to that reported by Kohlrausch *et al.* (2000) for a 5-kHz tone (open diamonds) despite some procedural differences (e.g., Kohlrausch *et al.* used 800-ms stimuli and roved the carrier frequency and level). Monaural thresholds are nearly constant up to about f_m=130 Hz, above which thresholds begin to increase. Thresholds decrease as f_m increases above 290 Hz, presumably reflecting detection of the increasingly resolved modulation sidebands.

In the middle and lower panels in the left column of Fig. 3, the monaural TMTFs for narrowband noise carriers (filled symbols) were similar in form to those reported by Dau *et al.* (1997) for f_m up to about 100–150 Hz (open circles). These similarities exist despite the fact that Dau *et al.* used slightly different bandwidths (31 and 314 Hz), shorter-duration stimuli (300 ms), and they bandpass filtered their wider-bandwidth stimuli back down to 314 Hz after modulation to limit spectral cues to the presence of modulation. Bandpass filtering after modulation reduces the effective modulation depth by an amount dependent upon modulation frequency (for example, for the 314-Hz-wide stimuli, by just over 3 dB for f_m=100 Hz and by about 1.5 dB for f_m=50 Hz).

The effects of intrinsic fluctuations in the narrowband noise carriers on the form of the TMTF can by examined by comparing the monaural TMTFs for the tone and noises (top right panel of Fig. 3). For the 30-Hz-wide carrier, thresholds are drastically elevated at low f_m's relative to the pure-tone TMTF. As described in Sec. I, this reflects the fact that the power in the envelope spectrum of the unmodulated carrier is concentrated below the frequency corresponding to its bandwidth and that these intrinsic low-frequency fluctuations in the carrier interfere with detection of low rates of sinusoidal modulation (assuming a modulation frequency-selective mechanism with limited spectral resolution such as a modulation filterbank; Dau *et al.*, 1999). Relative to the tonal TMTF, thresholds for the 300-Hz-wide carrier are elevated across the entire range of f_m used here, reflecting the fact that energy in the envelope of the unmodulated 300-Hz-wide carrier extends over much of that range of envelope frequency.

Referring to the interaural TMTFs for the diotic carriers (the pure tone and two interaurally correlated carriers; see the shaded symbols in the lower right panel of Fig. 3), the roll-off rates seem to decrease with increasing carrier bandwidth but it appears that all show a low-pass characteristic with roll-offs beginning at modulation frequencies above about 50–100 Hz. The pure-tone and 30-Hz TMTFs roll off to a plateau from around f_m=200-400 Hz, above which thresholds increase abruptly to the extent that thresholds were unmeasurable above f_m=500 Hz. Mean thresholds for the 300-Hz-wide, correlated noise carrier (shaded triangles) decrease substantially above f_m=240 Hz. This decrease in thresholds is due primarily to the data of one listener and will be discussed in Sec. IV A.

The TMTFs for the interaurally uncorrelated noise carriers (open symbols in the lower right panel of Fig. 3) are more irregular in form with a less obvious low-pass characteristic than those for the diotic carriers. Overall thresholds with uncorrelated carriers are higher than those for the diotic carriers. For the uncorrelated-carrier interaural TMTFs,

TABLE I. For each set of data listed in the first column, the 3-dB-down cutoff frequency (f_c) is shown for the best-fitting, low-pass Butterworth filter of first order (second column) and second order (third column). Fits were performed on all data of each TMTF up to the modulation frequency at which the slope changed from positive to negative. Parameters of the best-fitting functions consisting of two line segments are shown in the remaining columns. Fit 1 was performed on all data of each TMTF up to the modulation frequency at which the slope changed from positive to negative. Fit 2 was performed on one less data point than Fit 1 (the data point for the highest modulation frequency was excluded). The breakpoint for each fit is the frequency at the point of intersection of the two line segments, the 3-dB cutoff is the frequency at which the function is 3 dB down from its maximum, and the roll-off is the slope of the line above the breakpoint. The percentage in parentheses beneath each f_c and breakpoint is the percentage of variance accounted for by each fitted function [computed as shown in Eq. (2)].

			2 line segments—Fit 1			2 line segments—Fit 2		
	First-order Butterworth f_c (3 dB down)	Second-order Butterworth f_c (3 dB down)	Breakpoint (Hz)	3-dB cutoff (Hz)	roll-off (dB/oct)	Breakpoint (Hz)	3-dB cutoff (Hz)	roll-off (dB/oct)
Kohlrausch *et al.* (2000)	160 Hz (95%)	229 Hz (81%)	104 (97%)	177	3.91	114 (97%)	178	4.65
Monaural tone	144 Hz (84%)	184 Hz (92%)	116 (99%)	166	5.79	121 (98%)	167	6.60
Interaural tone	93 Hz (89%)	126 Hz (96%)	79 (96%)	117	5.21	85 (96%)	120	6.02
Interaural noise (30 Hz)	225 Hz (78%)	241 Hz (80%)	118 (90%)	224	3.24	113 (86%)	222	2.59
Interaural noise (300 Hz)	203 Hz (91%)	217 Hz (80%)	59 (89%)	210	1.63	48 (87%)	258	1.25

thresholds for f_m=50-400 Hz are within a few dB of one another. Below f_m=50 Hz, thresholds for the 30-Hz-wide uncorrelated noise are higher than those for the 300-Hz-wide uncorrelated noise, as is the case for the monaural TMTFs. This indicates that intrinsic interaural fluctuations in the uncorrelated noise may affect the interaural TMTF in a way that is similar to the effect of intrinsic monaural fluctuations on the monaural TMTF. This will be discussed further in Sec. IV B.

IV. DISCUSSION

A. Monaural versus interaural TMTF

This section will focus on a comparison of monaural and interaural TMTFs measured with carriers that introduce no intrinsic fluctuations in the monaural or binaural domain of the signal modulation, that is, the monaural tonal TMTF and the interaural TMTFs measured with tonal or diotic noise carriers. In Fig. 3, it appears that the monaural tonal TMTF and the interaural TMTFs measured with diotic carriers show a low-pass characteristic. Thresholds are nearly constant over a broad range of low f_m's and increase (reflecting attenuation of the modulation by the auditory system) above some cutoff frequency. As f_m increases further, thresholds eventually begin to decrease, changing the slope of the TMTF from positive to negative. In order to quantify the cutoff frequencies of the TMTFs, a process of fitting various functions to the data was undertaken. In the fits described in the following, unless noted otherwise, functions were fit only to the portion of the TMTFs up to the modulation frequency where the change from positive to negative slope occurred (i.e., only to the low-pass portion of the TMTFs).[1]

As a first attempt to quantify their cutoff frequencies, each TMTF was fit with the inverted frequency response of a low-pass Butterworth filter. (Recall that the TMTFs are plotted here on inverted ordinates.) The MATLAB Optimization Toolbox function "lsqnonlin" was used to estimate the cutoff frequency, order, and gain of the filter such that the mean-squared error between the inverted frequency response of the filter and the data was minimized. For each fit, predicted threshold values were computed and the percentage of variance in the actual data that was accounted for by the best-fitting filter was calculated as follows:

$$100 \times \left(1 - \frac{\sum (O_i - P_i)^2}{\sum (O_i - \bar{O})^2}\right), \tag{2}$$

where O_i and P_i are the observed and predicted threshold values, respectively, and $\bar{O}$ is the mean of the observed threshold values. It was found that the best-fitting filters had orders of either 1 or 2, that is, neither order yielded best-fitting filters to all the data. This was due to the different apparent roll-offs of the TMTFs. In Table I, the cutoff frequency and percent of variance accounted for by filters of order 1 and 2 for each TMTF are shown.

In order to describe more precisely the differences between roll-off rates of the TMTFs, it was decided that the TMTFs would be fit with two straight lines, one with slope zero and a second with a positive slope. It was found that the greatest percentage of variance in the observed data could be accounted for in most cases by the straight-line fits, therefore the remainder of the discussion will refer only to the results of those fits. The fits were determined via least-squares linear regression for various groupings of the data within each TMTF to find the two lines that produced the maximum percentage of variance accounted for as computed in Eq. (2). The breakpoint (point of intersection of the two best-fitting straight lines), roll-off rate (positive slope), and percentage of variance accounted for by each fit are shown in the fourth

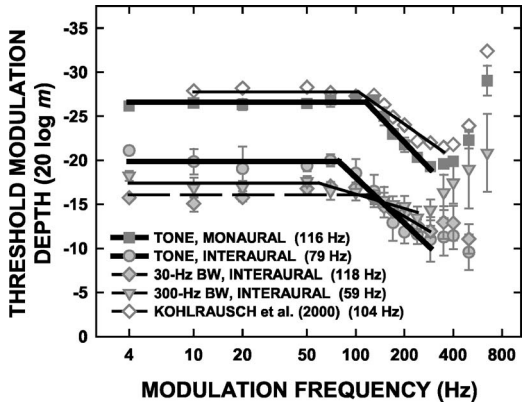

FIG. 4. The monaural tonal TMTF and the interaural TMTFs measured with a pure tone and diotic noise carriers fitted with functions consisting of two straight lines. The data are replotted from Fig. 3. The data points have been grayed out to improve the clarity of the fitted functions. The fitted functions correspond to the parameters shown for Fit 1 in Table I and are plotted over only those data points that were included in the fitting procedure. The breakpoint of each fitted function (point of intersection of the two straight lines) is shown in parentheses after each entry in the figure legend.

and sixth columns of Table I (Fit 1). (The 3-dB-down cutoff for each straight-line fit is shown in the fifth column, but the usefulness of this quantity is limited when comparing across functions with different roll-off rates.) The best-fitting pairs of straight lines corresponding to these parameters are plotted among the data in Fig. 4. The plotted lines extend over only the data points that were included in the fitting procedure.

Recognizing that the estimated breakpoints and roll-offs will be influenced by the number of data points included in the fitting procedure, the straight-line fits were repeated with one less data point included for each TMTF (excluding the data point for the highest modulation frequency included in Fit 1). The breakpoints, 3-dB-down cutoffs, roll-offs, and percentages of variance accounted for are shown in the last three columns of Table I (Fit 2). Fits 1 and 2 provide a range of breakpoints for each TMTF and a more conservative basis for assessing differences across TMTFs than would a single estimate of the breakpoint.

As shown in Table I, the ranges of breakpoints across Fits 1 and 2 for the two monaural TMTFs are quite comparable, failing to overlap by only a few hertz. Table I shows that the roll-offs estimated for the monaural TMTF measured here are slightly steeper than those estimated for the TMTF of Kohlrausch *et al.* (2000). The shallower slope of the Kohlrausch *et al.* (2000) TMTF appears to be driven by the two points of the TMTF for the highest modulation frequencies included in the fitting procedure (see Fig. 4).

Comparison of the monaural and binaural TMTFs is complicated by the fact that there appears to be an effect of carrier bandwidth on the form of the interaural TMTF. As shown in Table I, the three interaural TMTFs span ranges of breakpoints across Fits 1 and 2 that differ greatly. For example, the midpoints of the breakpoint ranges for the narrowband noises differ by more than an octave. Furthermore, the roll-offs of the interaural TMTFs decrease with increasing carrier bandwidth. There is presently no obvious explanation for the effect of bandwidth on the interaural TMTF.

The interaural TMTFs for stimuli of different bandwidth are sufficiently different that it is probably inappropriate to average across them. Therefore, it seems that the most reasonable comparison that can be made between the monaural and interaural TMTFs is for those measured with a tonal carrier. As noted by Grantham (1984), the vertical separation between TMTFs reflects differences in overall sensitivity in the monaural and interaural tasks while differences in cutoff frequency represent differences in temporal resolution. In the present work, the ranges of breakpoints for the monaural and interaural tonal TMTFs were 116–121 and 79–85 Hz, respectively, indicating lower temporal resolution for the binaural system. (The breakpoints estimated here are compared to cutoff frequencies derived from previously published data in Sec. IV B.) This outcome is qualitatively consistent with the physiological observation that cells in the lateral superior olive that encode interaural level differences have a temporal limitation with a lower cutoff frequency than observed monaurally in their afferent fibers (Joris, 1996). Although these physiological cutoff frequencies are higher than those measured psychophysically, it seems plausible that this relative difference between monaural and binaural temporal resolution is maintained at higher neural levels of the auditory system where physiological measures of temporal resolution more closely match psychophysical performance.

While the monaural tonal TMTF rolls off continuously up to the f_m at which sideband detection provides a strong cue, the interaural tonal TMTF (shaded symbols, upper left panel of Fig. 3) rolls off between f_m=70 and 200 Hz then becomes relatively flat for f_m=200–400 Hz, above which thresholds increase to the point of being unmeasurable. (Note that in the interaural conditions, in contrast to the monaural conditions, the mere presence of the modulation sidebands cannot serve as a cue for solving the listening task because the sidebands are present in all listening intervals.) The interaural TMTFs for diotic noise carriers (shaded symbols, middle and bottom left panels of Fig. 3) also do not roll-off monotonically above the estimated breakpoint. In fact, thresholds in the average interaural TMTF for the 300-Hz diotic noise carrier (shaded symbols, bottom left panel of Fig. 3) decrease dramatically above f_m=200 Hz. As indicated earlier, this is due primarily to the data of one listener. All three listeners' interaural TMTFs for the 300-Hz diotic noise are shown in Fig. 5. While the TMTFs for S1 and S2 show relatively little systematic variation across f_m, each varying over a range of less than 10 dB, the TMTF for S3 shows steeply improving (decreasing) thresholds at higher f_m's.

One explanation that was considered in attempting to account for S3's performance at high frequencies is related to off-frequency listening. Perhaps S3 made use of the output of a critical-band filter that effectively equalized the levels of the carrier band and modulation sideband such that the modulation depth at the output of that filter would be greater than the nominal modulation depth of the stimulus (Goldstein, 1967). In order to pursue this possibility, S3 performed the binaural modulation detection task again for the 300-Hz diotic carrier at f_m=650 Hz, except with either the upper or lower modulation sideband filtered out of the stimulus.

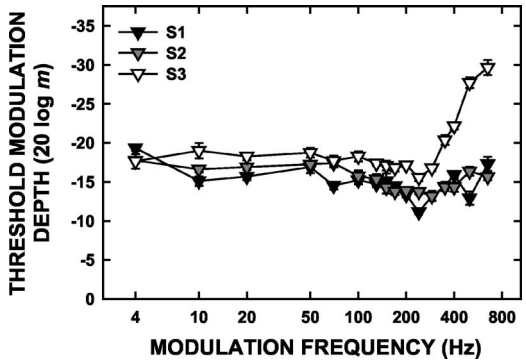

FIG. 5. The interaural TMTFs measured for the individual listeners for a diotic 300-Hz-wide band noise carrier. Error bars represent standard errors of the mean computed across four threshold estimates for each listener.

Thresholds were immeasurably large in these conditions. Whatever cue S3 made use of at high f_m with the 300-Hz diotic carrier apparently depended on the presence of both the upper and lower modulation sidebands.

Previous estimates of monaural time constants and binaural time constants (described in Sec. I) also indicate lower temporal resolution for binaural processing relative to monaural but the respective time constants correspond to cutoff frequencies that are much lower than the cutoff frequencies (breakpoints) estimated here. To facilitate comparison to the present results, the time constants (τ) estimated by Grantham and Wightman (1979), Kollmeier and Gilkey (1990), and Culling and Summerfield (1998) were converted to 3-dB-down cutoff frequencies (f_c) assuming a first-order, lowpass filter so that $f_c=1/(2\pi\tau)$. Grantham and Wightman (1979) estimated τ between 44 and 243 ms, corresponding to values of f_c between 0.66 and 3.62 Hz. For the results of Kollmeier and Gilkey (1990), the corresponding range of binaural f_c is 3.73–9.88 Hz, and the range of monaural f_c is 10.83–26.98 Hz. A simple conversion of the time constants reported by Culling and Summerfield (1998) for the two sides of an asymmetric temporal window yields a range of f_c from 2.6 to 13.6 Hz. It is possible that the large discrepancy between cutoff frequencies estimated for the data from the present study and from the previous studies indicates that the previous studies measured a fundamentally different aspect of binaural temporal resolution than the present experiment. If one considers an interaurally uncorrelated noise to have a time-varying instantaneous ILD (as depicted in Fig. 1), then variation in the value of interaural correlation is effectively modulation of the interaural modulator, or second-order interaural modulation. Lorenzi *et al.* (2001) compared first-order and second-order monaural TMTFs. When detecting first-order monaural modulation, listeners discriminate between an unmodulated carrier and one that is sinusoidally amplitude-modulated. Detection of second-order modulation involves discrimination between a stimulus that is sinusoidally amplitude-modulated at a fixed modulation depth and a stimulus for which the modulation depth varies over time. Lorenzi *et al.* (2001) showed that cutoff frequencies implied by the low-pass segments of second-order TMTFs were lower than those for first-order TMTFs. Perhaps in a similar way the binaural system exhibits better temporal resolution for detection of static interaural modulation (measured here) than for time-varying interaural modulation (as measured in the studies cited above).

A difference in overall sensitivity in the monaural and interaural modulation-detection tasks was observed in the present experiment (as indicated by the vertical separation between the TMTFs of Fig. 4). In contrast, Stellmack *et al.* (2004) reported that thresholds for binaural discrimination of static intensity in a single-interval task were nearly equal to monaural intensity-discrimination thresholds measured in a two-interval task. This further supports the idea that the monaural and interaural TMTFs represent the temporal characteristics of two different processes.

Although the sources of all the differences between the monaural and interaural TMTFs are not apparent, a clear result is that the temporal resolution characteristics of the binaural system for detection of fluctuating interaural intensity cannot be extrapolated directly from the pure-tone monaural TMTF. For the TMTFs for which direct comparison seems most appropriate, the breakpoint of the interaural tonal TMTF is substantially lower than the monaural tonal TMTF. In addition, there are differences between the interaural TMTFs across carrier bandwidths that cannot be explained at this time.

B. Influence of intrinsic fluctuations on the form of the TMTFs

As noted earlier, the monaural TMTFs measured with noise carriers differed from the tonal TMTF (see the upper right panel of Fig. 3) in ways that can be explained on the basis of intrinsic fluctuations in the carrier masking or interfering with the signal modulation. Plotted in the top panel of Fig. 6 are the differences between monaural thresholds measured with the tonal carrier and those measured with the 30-Hz-wide noise (diamonds) and 300-Hz-wide noise (triangles), that is, the amount of masking in each case. In the top panel of Fig. 7, average monaural envelope power spectra for 1000 independent samples of narrowband Gaussian noise (each 1 s in duration and windowed with 150-ms raised-cosine on-off ramps) are shown for bandwidths of 30 and 300 Hz, with the total power equal at the two bandwidths. It can be seen that energy in the envelope spectrum is concentrated below the frequency corresponding to the bandwidth of the noise (which also can be demonstrated analytically, e.g., Lawson and Uhlenbeck, 1950). (The specific shape of the spectra in the top panel of Fig. 7 below about 5 Hz depends upon the form and duration of the onset-offset ramps of the stimuli.) The crossover of the two functions in the top panel of Fig. 6 occurs at approximately the modulation frequency at which the envelope power spectra cross in the top panel of Fig. 7. The intrinsic fluctuations in the noise envelope presumably interfere with or mask the signal modulation to the largest extent when the signal f_m is less than the bandwidth of the carrier (Dau *et al.*, 1999). As described in Sec. I, an additional assumption of some type of limited modulation-frequency selectivity must be made in order to account for the form of the TMTFs on the basis of masking by the intrinsic fluctuations of the noise carrier, re-

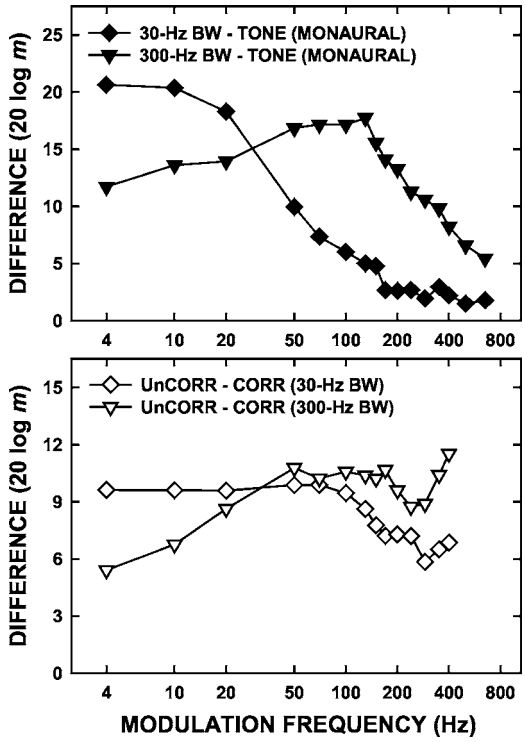

FIG. 6. Top panel: Difference between monaural modulation-detection thresholds measured with a narrowband-noise carrier (diamonds, 30-Hz wide; triangles, 300-Hz wide) and those measured with a tonal carrier. Bottom panel: Difference between interaural modulation-detection thresholds measured with interaurally uncorrelated noise carriers and interaurally correlated noise carriers (diamonds, 30-Hz wide; triangles 300-Hz wide). All differences were computed on the mean data shown in Fig. 3.

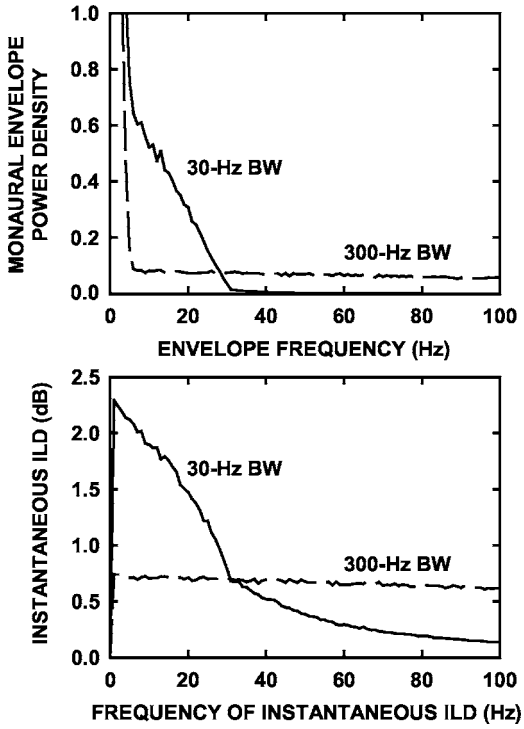

FIG. 7. Top panel: Monaural envelope power spectra averaged over 1000 random noise samples for 30-Hz-wide noise (solid line) and 300-Hz-wide noise (dashed line), where the total power was equal at the two bandwidths. Bottom panel: Spectra of instantaneous ILD functions averaged over 1000 samples of interaurally uncorrelated noise with bandwidths of 30 Hz (solid line) and 300 Hz (dashed line). Instantaneous ILD functions were computed from the Hilbert envelopes of the left- and right-ear wave forms using Eq. (1). In all cases, the stimuli were 1 s in duration and were windowed with 150-ms raised-cosine on-off ramps. Spectra were obtained by computing FFTs on digital waveforms sampled at 44.1 kHz.

sulting in more masking when masker energy is present in the modulation spectrum near the modulation frequency of the signal.

In order to assess the effects of intrinsic interaural fluctuations of the carrier on the interaural TMTF for uncorrelated noise carriers, the differences between thresholds measured with correlated and uncorrelated 30- and 300-Hz-wide noise carriers were computed and plotted in the bottom panel of Fig. 6. The amount of masking was larger at frequencies below f_m=50 Hz for the 30-Hz-wide noise than for the 300-Hz-wide noise, as was the case for the monaural TMTFs (see the top panel of Fig. 6), although the overall amount of masking in the interaural conditions was less than in the monaural conditions. The curves in the bottom panel of Fig. 7 represent the average spectra of the instantaneous ILD functions for carrier bandwidths of 30 and 300 Hz. The spectra were computed by generating two independent narrowband Gaussian noise samples (each 1 s in duration, windowed with 150-ms raised-cosine on-off ramps), representing uncorrelated left- and right-ear noise carriers. The instantaneous ILD function was computed from the Hilbert envelopes of the left- and right-ear carriers as described by Eq. (1) and the spectrum of that function then was computed via FFT. Spectra were computed in this way and averaged for 1000 randomly generated pairs of noise yielding the mean spectra plotted in the bottom panel of Fig. 7. The bottom panel of Fig. 7 shows that, as was the case for intrinsic fluctuations in monaural intensity, energy in the spectra of the intrinsic interaural fluctuations is concentrated at frequencies below the bandwidth of the carrier. For both the monaural and interaural TMTFs, the amount of masking as a function of f_m (Fig. 6) appears to be related to the corresponding spectrum of the intrinsic carrier fluctuations (Fig. 7).

Comparison of the tonal and diotic noise interaural TMTFs (shaded symbols, lower right panel of Fig. 3) seems to reveal little effect of intrinsic monaural fluctuations in and of themselves on the interaural TMTF for f_m up to about 200 Hz. Thresholds are slightly elevated for the lower f_m's for the diotic noise carriers relative to those for the tonal carrier, but this small difference does not appear to depend on the frequency range of the intrinsic monaural fluctuations in the carrier, as shown in the top panel of Fig. 7. For example, with the 30-Hz-wide correlated carrier, the effect of intrinsic monaural fluctuations on interaural thresholds at low f_m where substantial energy exists in the spectrum of the carrier envelope (shaded diamonds versus shaded circles in the lower right panel of Fig. 3) is much smaller than that in the corresponding monaural TMTF (diamonds versus squares in the upper right panel of Fig. 3).

These results suggest that intrinsic monaural or binaural fluctuations due to a noise carrier exhibit the most masking when those fluctuations occur in the same domain (monaural or binaural) as the sinusoidal signal modulation. For the

monaural TMTFs (top right panel of Fig. 3), thresholds increase by the largest amount for the noise carriers (relative to those for the tonal carrier) over the range of f_m in which there are substantial intrinsic fluctuations in the carrier. For the interaural TMTFs measured with uncorrelated noise carriers (open symbols, bottom right panel of Fig. 3), the largest change in thresholds (relative to those for the diotic carriers), or the most masking, occurs over the range of f_m in which there are intrinsic fluctuations in interaural level, although the degree of "tuning" (represented by the variation in the amount of masking with changes in f_m) is much smaller than for the monaural TMTFs. In particular, for the interaural TMTF for the 30-Hz-wide noise, the amount of masking remains nearly constant for modulation frequencies up to about 70 Hz. The differences between the amounts of masking in the monaural and binaural conditions may be due in part to the fact that for the 30-Hz bandwidth, the spectrum of the instantaneous ILD function (bottom panel of Fig. 7) rolls off more gradually than the monaural envelope power spectrum (top panel of Fig. 7) and nonzero ILDs are present at frequencies well above the nominal bandwidth of the carrier. In addition, the fact that the amount of masking remains high well above the f_m corresponding to the carrier bandwidth may indicate that any frequency-selective mechanism in the binaural domain may be more broadly tuned than that for monaural modulation.

Grantham and Bacon (1991) performed a study of "Binaural modulation masking" which is somewhat related to the present experiment, but it does not address the issue of masking produced by intrinsic interaural fluctuations in the same manner as the present experiment. They first measured thresholds for detection of monaural signal modulation in the presence of a monaural masker modulator, both modulating a common broadband noise carrier. The masker f_m was fixed at 16 Hz and the signal f_m ranged from 2 to 512 Hz. They then measured thresholds for detection of interaurally out-of-phase modulation (relative to no signal modulator) in the presence of a diotic masker modulator for an interaurally uncorrelated broadband noise carrier. These monaural and binaural conditions would correspond to the binaural masking-level difference conditions N_mS_m and N_0S_π, respectively, in the modulation domain. Both sets of thresholds showed tuning in that the greatest amount of masking occurred when the signal and masker modulation frequencies were equal. In addition, a binaural MLD was observed in that the mean N_0S_π thresholds were consistently lower than the N_mS_m thresholds. While the data of Grantham and Bacon (1991) show that thresholds for detection of dichotic modulation depend upon the relative modulation frequencies of the signal and masker modulation, it is difficult to relate their N_0S_π thresholds to any of the conditions run in the present experiment. The N_0S_π thresholds of Grantham and Bacon (1991) involved detection of a dichotic modulator while the binaural conditions of the present experiment involved discrimination of interaural phase of the modulator. In other words, in the present binaural conditions, there were no potential monaural cues available which is not true in the Grantham and Bacon (1991) experiment.

C. Role of center frequency in the measurement of the interaural TMTF

Grantham (1984) measured TMTFs primarily with uncorrelated noise carriers for low- and high-frequency carriers of varying bandwidths. However, Grantham (1984, footnote 2) did describe pilot data comparing thresholds gathered with correlated and uncorrelated noise carriers centered at 1 kHz. The forms of the interaural TMTFs measured here for the diotic and uncorrelated noise carriers seem to differ from those described by Grantham. Grantham states that the TMTF for a diotic noise carrier centered at 1 kHz showed a sharp upturn (decrease in thresholds) for $f_m > 50$ Hz. He concluded that this was due to detection of the modulation on the basis of interaural decorrelation of the stimulus for high f_m. In contrast, the interaural TMTFs measured with diotic carriers centered at 5 kHz in the present experiment (shaded symbols of Fig. 3) were nearly flat (within a few decibels) for f_m up to about 70 Hz, above which thresholds tended to increase. Grantham (1984) also stated that there were little or no differences between the TMTFs for diotic and uncorrelated noise carriers centered at 1 kHz for $f_m < 50$ Hz, while in the present experiment the TMTFs for diotic and uncorrelated noise carriers centered at 5 kHz differed by more than 10 dB over the same range of f_m.

The different center frequencies used by Grantham (1984) to gather the data described above (from Grantham's footnote 2) and in the present experiment for a diotic noise carrier may be important. Grantham's diotic carrier centered at 1 kHz was over 250 Hz wide (at its 3-dB bandwidth). Given that the equivalent rectangular bandwidth of the auditory filter is about 130 Hz at 1 kHz (Glasberg and Moore, 1990), this means that Grantham's modulated stimuli spanned several critical bands and, perhaps more important, the modulation sidebands fell in a frequency region in which listeners are sensitive to interaural phase differences in the fine structure. For the results described by Grantham for a diotic carrier, regardless of the modulation frequency, listeners may have responded to interaural phase differences in the fine structure of the modulation sidebands that are produced when the phase of the signal modulator was interaurally changed. Such cues were not available in the high-frequency stimuli of the present experiment. This may account for the sharply decreasing thresholds for $f_m > 50$ Hz reported by Grantham, while in most cases in the present data thresholds increased with increasing modulation frequency. However, Grantham (1984) also reported almost no difference between thresholds measured with correlated and uncorrelated carriers for $f_m < 50$ Hz, while in the present experiment thresholds were up to 10 dB lower for the correlated carriers relative to the uncorrelated carriers. The explanation put forth above regarding sensitivity to interaural phase differences in the fine structure of the sidebands would seem to predict the opposite result: better diotic thresholds for the low-frequency carriers of Grantham and no difference between diotic and dichotic thresholds for the high-frequency carriers of this experiment. Thus, although it is true that fine-structure cues exist in the modulated low-frequency carriers but not the

high-frequency carriers, this fact does not appear to account for all differences between the data gathered with low- and high-frequency carriers.

V. CONCLUSIONS

(1) Temporal resolution for fluctuating interaural intensity differences was poorer than monaural temporal resolution for intensity fluctuations. For the present data, the breakpoint of the interaural TMTF appeared to be about a half-octave lower than the breakpoint of the monaural TMTF for a 5-kHz pure-tone carrier. Breakpoints were estimated for two subsets of the interaural and monaural data and ranged from 79 to 85 Hz for the interaural TMTF and from 116–121 Hz for the monaural TMTF. Roll-off rates of the fitted functions were approximately equal for the interaural and monaural TMTFs.

(2) The breakpoints and roll-off rates of the interaural TMTFs measured with interaurally correlated narrow-band noise carriers differed from those for the interaural TMTF measured with a tonal carrier. The source of these differences is not clear.

(3) Consistent with the results of previous research, the monaural TMTFs measured with a noise carrier exhibited higher thresholds (relative to monaural TMTFs measured with a pure-tone carrier) at modulation frequencies at which there are intrinsic fluctuations in the envelope of the carrier. In a similar way, the interaural TMTFs measured with uncorrelated noise carriers showed effects consistent with interference produced by intrinsic interaural fluctuations in the noise carrier. Specifically, thresholds were slightly elevated for f_m's at which there are larger intrinsic fluctuations in the interaural intensity differences of the carrier. The masking functions (amount of masking produced by intrinsic fluctuations as a function of signal modulation frequency) for the monaural and interaural TMTFs differed in form. Intrinsic monaural fluctuations generally produced more masking than binaural fluctuations at lower signal modulation frequencies.

ACKNOWLEDGMENTS

The authors would like to thank Dr. Armin Kohlrausch, Dr. Wesley Grantham, and an anonymous reviewer for their helpful comments. This work was supported by Research Grant No. R03 DC 05343-01 and Research Grant No. R01 DC 00683, both from the National Institute on Deafness and Communication Disorders, National Institutes of Health.

[1]The choice of which points of each TMTF would be included in each fit was arbitrary to some extent. The stated criterion for data points to be included was to include those points up to the f_m at which the slope of the TMTF changes from positive to negative. Strictly speaking, the slope of the monaural and interaural TMTFs for the tone changed from positive to negative at f_m=20 Hz, while the slopes of the two correlated noise interaural TMTFs changed sign at f_m=10 Hz. In practice, the slope-change criterion was applied to each TMTF above the f_m at which each function appeared to show a systematic rolloff or clear lowpass characteristic, determined by eye. The fitted functions are plotted through only those points used to obtain the fits in Fig. 4.

Bernstein, L. R., and Trahiotis, C. (**1994**). "Detection of interaural delay in high-frequency sinusoidally amplitude-modulated tones, two-tone complexes, and bands of noise," J. Acoust. Soc. Am. **95**, 3561–3567.

Bernstein, L. R., and Trahiotis, C. (**2005**). "Processing of interaural temporal disparities with both 'transposed' and conventional stimuli," in *Auditory Signal Processing: Physiology, Psychoacoustics, and Models* edited by D. Pressnitzer, A. de Cheveigne, S. McAdams, and L. Collet (Springer, New York, in press).

Culling, J. F., and Summerfield, Q. (**1998**). "Measurements of the binaural temporal window using a detection task," J. Acoust. Soc. Am. **103**, 3540–3553.

Dau, T., Kollmeier, B., and Kohlrausch, A. (**1997**). "Modeling auditory processing of amplitude modulation. I. Detection and masking with narrow-band carriers," J. Acoust. Soc. Am. **102**, 2892–2905.

Dau, T., Verhey, J., and Kohlrausch, A. (**1999**). "Intrinsic envelope fluctuations and modulation-detection thresholds for narrow-band noise carriers," J. Acoust. Soc. Am. **106**, 2752–2760.

Glasberg, B. R., and Moore, B. C. J. (**1990**). "Derivation of auditory filter shapes from notched-noise data," Hear. Res. **47**, 103–138.

Goldstein, J. L. (**1967**). "Auditory spectral filtering and monaural phase perception," J. Acoust. Soc. Am. **41**, 458–479.

Grantham, D. W. (**1984**). "Discrimination of dynamic interaural intensity differences," J. Acoust. Soc. Am. **76**, 71–76.

Grantham, D. W., and Bacon, S. P. (**1991**). "Binaural modulation masking," J. Acoust. Soc. Am. **89**, 1340–1349.

Grantham, D. W., and Wightman, F. L. (**1979**). "Detectability of a pulsed tone in the presence of a masker with time-varying interaural correlation," J. Acoust. Soc. Am. **65**, 1509–1517.

Joris, P. X. (**1996**). "Envelope coding in the lateral superior olive. II. Characteristic delays and comparison with responses in the medial superior olive," J. Neurophysiol. **76**, 2137–2156.

Klumpp, R. G., and Eady, H. R. (**1956**). "Some measurements of interaural time difference thresholds," J. Acoust. Soc. Am. **28**, 859–860.

Kohlrausch, A., Fassel, R., and Dau, T. (**2000**). "The influence of carrier level and frequency on modulation and beat-detection thresholds for sinusoidal carriers," J. Acoust. Soc. Am. **108**, 723–734.

Kollmeier, B., and Gilkey, R. H. (**1990**). "Binaural forward and backward masking: Evidence for sluggishness in binaural detection," J. Acoust. Soc. Am. **87**, 1709–1719.

Lawson, J. L., and Uhlenbeck, G. E. (**1950**). *Threshold Signals*, Radiation Laboratory Series, Vol. 24 (McGraw-Hill, New York).

Levitt, H. (**1971**). "Transformed up-down methods in psychophysics," J. Acoust. Soc. Am. **49**, 467–477.

Lorenzi, C., Soares, C., and Vonner, T. (**2001**). "Second-order temporal modulation transfer functions," J. Acoust. Soc. Am. **110**, 1030–1038.

Nuetzel, J. M., and Hafter, E. R. (**1976**). "Lateralization of complex waveforms: Effects of fine structure, amplitude, and duration," J. Acoust. Soc. Am. **60**, 1339–1346.

Rickert, M. E., and Viemeister, N. F. (**1998**). "Temporal versus spectral cues in AM detection," J. Acoust. Soc. Am. **103**, 2842.

Stellmack, M. A., Viemeister, N. F., and Byrne, A. J. (**2004**). "Monaural and interaural intensity discrimination: Level effects and the 'binaural advantage'," J. Acoust. Soc. Am. **116**, 1149–1159.

Viemeister, N. F. (**1979**). "Temporal modulation transfer functions based upon modulation thresholds," J. Acoust. Soc. Am. **66**, 1364–1380.

Viemeister, N. F., Rickert, M., Law, M., and Stellmack, M. (**2002**). "Psychophysical and physiological aspects of auditory temporal processing," in *Genetics and the Function of the Auditory System*, Proceedings of the 19th Danavox Symposium, edited by L. Tranebjaerg, J. Christensen-Dalsgaard, T. Andersen, and T. Poulsen (Holmens Trykkeri, Denmark), pp. 273–291.

Wiegrebe, L., and Patterson, R. D. (**1999**). "Quantifying the distortion products generated by amplitude-modulated noise," J. Acoust. Soc. Am. **106**, 2709–2718.

Yin, T. C. T. (**2002**). "Neural mechanisms of encoding binaural localization cues in the auditory brainstem," in *Integrative Functions in the Mammalian Auditory Pathway*, edited by D. Oertel, R. R. Fay, and A. N. Popper (Springer, New York), pp. 99–159.

Consequences of cochlear damage for the detection of interaural phase differences

Stéphane Lacher-Fougère[a] and Laurent Demany[b]
Laboratoire de Neurophysiologie, UMR CNRS 5543, BP 63, Université Victor Segalen, 146 rue Leo Saignat, F-33076 Bordeaux, France

(Received 2 February 2005; revised 19 July 2005; accepted 20 July 2005)

Thresholds for detecting interaural phase differences (IPDs) in sinusoidally amplitude-modulated pure tones were measured in seven normal-hearing listeners and nine listeners with bilaterally symmetric hearing losses of cochlear origin. The IPDs were imposed either on the carrier signal alone—not the amplitude modulation—or *vice versa*. The carrier frequency was 250, 500, or 1000 Hz, the modulation frequency 20 or 50 Hz, and the sound pressure level was fixed at 75 dB. A three-interval two-alternative forced choice paradigm was used. For each type of IPD (carrier or modulation), thresholds were on average higher for the hearing-impaired than for the normal listeners. However, the impaired listeners' detection deficit was markedly larger for carrier IPDs than for modulation IPDs. This was not predictable from the effect of hearing loss on the sensation level of the stimuli since, for normal listeners, large reductions of sensation level appeared to be more deleterious to the detection of modulation IPDs than to the detection of carrier IPDs. The results support the idea that one consequence of cochlear damage is a deterioration in the perceptual sensitivity to the temporal fine structure of sounds.
 [DOI: 10.1121/1.2032747]

PACS number(s): 43.66.Sr, 43.66.Mk, 43.66.Pn [AK] Pages: 2519–2526

I. INTRODUCTION

The response of an auditory nerve (AN) fiber to a pure tone is normally phase-locked to the stimulus, as long as its frequency does not exceed a few kilohertz (Rose *et al.*, 1967). Owing to this phase-locking mechanism, information on the temporal fine-structure of sounds is conveyed to higher levels of the auditory system. Listeners with normal hearing do process that information. This is most clearly demonstrated by their ability to detect small interaural phase differences in binaurally presented pure tones, even in the absence of onset or offset cues (Hafter *et al.*, 1979). It is believed that, in addition to its important role in the localization of sounds, the peripheral encoding of temporal fine-structure also plays a role in the perception of pitch (e.g., Moore, 1973) and the identification of spectral profiles such as those of vowels (Young and Sachs, 1979).

A few physiological studies have been devoted to the consequences of cochlear damage for the phase-locking capacity of AN fibers. Woolf *et al.* (1981) produced substantial destruction of outer hair cells in the cochleas of chinchillas, and found that this reduced significantly the precision of phase-locking in individual AN fibers. However, the results of Woolf *et al.* are at odds with those reported by Harrison and Evans (1979) and Miller *et al.* (1997), who found no loss in the quality of phase-locking following severe hair cell lesions due to the injection of kanamycin in guinea pigs (Harrison and Evans) or an acoustic trauma in cats (Miller *et al.*). From the physiological literature, therefore, it is far from clear that human listeners with damaged cochleas should have a subnormal perceptual sensitivity to the temporal fine structure of sound waveforms. Yet, several psychophysical studies have suggested that this is the case.

Part of the psychophysical evidence comes from experiments on the detection of slow frequency modulation (Zurek and Formby, 1981; Moore and Glasberg, 1986; Lacher-Fougère and Demany, 1998; Moore and Skrodzka, 2002; Buss *et al.*, 2004). For normal listeners, the perceptual detection of slow frequency modulation imposed on low-frequency sinusoidal carriers seems to rest, at the AN level, on temporal cues rather than on tonotopic cues [see Moore and Sek (1996) or Lacher-Fougère and Demany (1998) for a review of the psychophysical arguments supporting that view]. In cases of cochlear damage, the detection thresholds of such modulations are generally elevated, and this elevation is very pronounced if the damage is severe. Recently, Moore and Moore (2003) have also argued that cochlear damage has a deleterious effect on the ability to discriminate the fundamental frequency of harmonic complex tones on the basis of cues related to the temporal fine structure of the waveform.

More direct evidence has been provided by two studies on the detection of interaural time delays (ITDs) in binaural stimuli (Hawkins and Wightman, 1980; Buus *et al.*, 1984). In listeners with severe, wide-band, and bilaterally symmetric hearing losses of cochlear origin, the detectability of an ITD in a narrow-band noise centered at 500 Hz (Hawkins and Wightman, 1980) or in a 500- or 1000-Hz tone burst (Buus *et al.*, 1984) is strongly impaired. For the same listeners, in contrast, the detectability of an interaural intensity difference can be normal, according to Hawkins and Wightman. More-

[a]Present address: Institut Georges Portmann, Clinique St Augustin, 114 avenue d'Arès, F-33074 Bordeaux, France.
[b]Author to whom correspondence should be addressed; electronic mail: laurent.demany@psyac.u-bordeaux2.fr

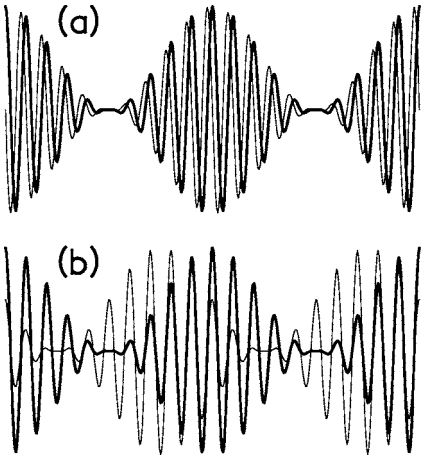

FIG. 1. Sinusoidally amplitude-modulated sinusoids. Two pairs of such functions are shown. In the top part (a), the two modulations are in phase but there is a 90° phase difference between the two carriers. In the bottom part (b), the two carriers are in phase but there is a 90° phase difference between the two modulations.

over, according to Buus *et al.*, the detectability of an ITD in a 4000-Hz tone burst presented at a high SPL (100 dB) is in general nearly normal. In agreement with the latter finding, Smoski and Trahiotis (1986) reported that an ITD in a narrow-band sound centered at 4000 Hz is generally not harder to detect by impaired listeners than by normal ones when the stimulus is presented at a constant sensation level of 25 dB. In the case of a 500- or 1000-Hz tone burst, normal listeners are sensitive to the ongoing interaural phase difference produced by an ITD; but this is no longer true at 4000 Hz, in which case an ITD is detectable only by virtue of the delay in the amplitude envelope. Thus, the frequency-selective detection deficit observed by Buus *et al.* (1984) in listeners with cochlear damage suggests that such listeners have a subnormal sensitivity to temporal fine structure *per se*.

This suggestion is still not logically compelling, however. Besides, it should be noted that Hawkins and Wightman (1980) did not find a stronger deficit of ITD detection at 500 Hz than at 4000 Hz in their hearing-impaired subjects, although the audiometric deficit of some of these subjects was larger at 500 than at 4000 Hz. We reasoned that a more convincing demonstration might be provided by dissociating, within a given set of binaural stimuli, the interaural relations between the fine structures and the envelopes. In the present study, binaural stimuli consisting of sinusoidally amplitude-modulated pure tones were used and listeners had to detect interaural phase differences (IPDs) imposed either on the carrier signal alone—not the amplitude modulation—or *vice versa* (see Fig. 1). The carrier frequency was varied but kept within the range for which the binaural system is normally sensitive to fine-structure IPDs. The modulation frequency was always low enough to preclude cochlear resolution of the sounds' three spectral components. In our main experiment (experiment 1), the performance of normal listeners in the two tasks (carrier versus modulation, i.e., fine structure versus envelope) was compared to that of sensorineurally impaired listeners. Two additional experiments were conducted to determine if the impaired listeners' detection deficits in experiment 1 could simply originate from the fact that, for these listeners, the sensation level of the stimuli was abnormally low.

II. EXPERIMENT 1

A. Listeners

Sixteen listeners were tested. Seven of them (forming the normal group; age range: 24–45 yr) had, for each ear, absolute thresholds that did not exceed 20 dB HL (ISO 389 standard) from 250 to 8000 Hz. The other nine listeners (forming the impaired group; age range: 42–68 yr) had purely cochlear hearing losses which were similar for the two ears. The cochlear origin of their auditory deficits was established following a clinical examination including otoscopy, tonal and speech audiometry with air/bone gap measures, immitance audiometry, and BER recording (or MRI in one case). Their audiograms are presented in Table I. Listeners 1 and 5 were presbycusic. The hearing loss of Listeners 4 and 6 was congenital. The hearing loss of Listener 8 had been of the "sudden" type. For the remaining four impaired listeners, the origin of hearing loss was unknown.

B. Stimuli

We used 500-ms stimuli which were gated on and off with interaurally synchronous linear amplitude ramps of 50 ms. At each ear, before gating, the stimulus was an amplitude-modulated sinusoid defined by

TABLE I. Audiograms of the hearing-impaired listeners. In columns 2–7, the two numbers in each cell are the absolute thresholds for the left and right ears, in dB HL.

Listener (age)	250 Hz	500 Hz	1000 Hz	2000 Hz	4000 Hz	8000 Hz
1 (59)	5/10	10/15	20/20	15/25	45/65	65/90
2 (55)	15/20	20/20	20/20	30/25	45/35	50/30
3 (68)	25/20	30/20	35/30	45/30	55/50	55/40
4 (42)	30/20	30/30	40/40	50/55	60/65	70/60
5 (61)	20/20	25/35	45/50	70/60	65/55	75/65
6 (57)	30/25	50/35	65/55	65/70	70/95	80/100
7 (64)	25/35	35/35	40/40	35/35	35/25	35/20
8 (47)	45/40	50/40	40/45	45/45	50/60	50/60
9 (67)	40/45	55/50	55/60	50/45	25/15	35/20

$$s(t) = \sin(2\pi \,.\, F_{car} \,.\, t + \varphi_{car}) \cdot [1 + \sin(2\pi \,.\, F_{mod} \,.\, t + \varphi_{mod})], \quad (1)$$

in which F_{car} represents the carrier frequency–250, 500, or 1000 Hz–, F_{mod} the modulation frequency–20 or 50 Hz–, and t is time. The phases φ_{car} and φ_{mod} had a fixed value of 0° at the right ear. One of these two phases could be different from 0° at the left ear. In this case, it was always positive (without exceeding 180°). During the measurement of just-detectable IPDs, the sound pressure level was 75 dB at each ear. For the impaired listeners, this was always sufficient to make the stimuli clearly detectable at both ears (as confirmed by the listeners' verbal reports). The stimuli were generated via 16-bit digital-to-analog converters (Oros AU22), at a sampling rate of 19 kHz, and presented by means of TDH-39P earphones, in a double-walled soundproof booth.

C. Procedure

Each listener took part in four experimental sessions of about 1 h, on different days. At the beginning of every session, before the measurement of just-detectable IPDs, the listener was required to perform a series of (typically six) across-ear intensity-matching trials. This test had two goals. The first was to check that, when the stimulus was diotic, the spatial position of the perceived sound was approximately central (rather than lateralized on the left or right due to an asymmetry of loudness). The second goal was to obtain information on the listener's sensitivity to interaural intensity differences. In each intensity-matching trial, the listener was repeatedly presented with a stimulus for which φ_{car} and φ_{mod} were 0° at both ears, F_{mod} was 20 Hz, and F_{car} was either 250, 500, or 1000 Hz. Consecutive stimulus presentations were separated by a 500-ms silent interval. The SPL was fixed at 75 dB at one ear (the left ear on about 50% of trials) and was variable at the other ear. Initially, the variable SPL differed from 75 dB by a random amount, within a range of ±10 dB. The listener's task was to center the sound image, as accurately as possible, by adjusting the variable SPL. This could be done by steps of ±1 or 4 dB, using four labeled buttons. The listener had an unlimited amount of time to perform his or her adjustment, and pressed a fifth button to record it when satisfied.

Detection thresholds for IPDs were then measured with an adaptive forced-choice method, the SPL being 75 dB at each ear. In a given block of trials, F_{car} and F_{mod} were fixed. On each trial, three successive stimuli separated by 500-ms silent pauses were presented. There was an IPD in only one of them: either the second or the third stimulus, at random and equiprobably. The listener's task was to identify the position of this stimulus by pressing one of two buttons. Visual feedback was provided by means of light-emitting diodes. Initially, the IPD was large. It was divided by the cube root of 1.5 following every correct response. Following a wrong response, it was multiplied by 1.5, or set to 180° if a multiplication by 1.5 produced an IPD exceeding 180°. Each block of trials ended after 14 reversals in the IPD variation. The geometric mean of the last 10 reversal points was taken as an estimate of the just-detectable IPD. In the absence of ceiling effects in the IPD variation, this threshold estimate corresponded to the 75% correct point of the psychometric function (Kaernbach, 1991). Overall, 24% of the threshold measurements forming the impaired listeners' raw data were biased by ceiling effects. Such effects occurred more frequently when the IPD was imposed on φ_{car} (30.5% of threshold measurements) than when the IPD was imposed on φ_{mod} (17.0%).

Thresholds were mainly measured for three combinations of F_{car} and F_{mod}: 500/20 Hz (in which case data were obtained from each listener), 1000/20 Hz (data obtained from four normal listeners and the entire impaired group), and 500/50 Hz (five impaired listeners and the entire normal group). Two normal and two impaired listeners were also tested using the 250/20-Hz combination. For a given F_{car}/F_{mod} combination and a given type of IPD (φ_{car} or φ_{mod}), the total number of threshold estimations per subject was typically equal to 7; however, it was sometimes smaller; its mean value was 6.3. As a rule, when more than four estimates had been obtained, only the last four were considered in the data analysis; their geometric mean was taken as the listener's threshold. For one impaired listener, however, only the last two estimates were averaged owing to the existence of a very strong practice effect (improvement of thresholds) in all conditions.

D. Results

The data collected during the intensity-matching trials are summarized in Fig. 2. For a given listener and F_{car}, we computed: (i) the absolute value of the mean of the adjusted interaural intensity differences—an index called "absolute shift" (from 0, i.e., no ear asymmetry); (ii) the standard deviation of the adjusted interaural intensity differences—an index called "random error." The top panel of Fig. 2 displays the mean value of the absolute shifts measured in the normal group (open circles) and the impaired group (closed circles), as a function of F_{car}. What must be noted here is the absence of a definite difference between the two groups. A two-way analysis of variance (ANOVA) with listeners as the random factor confirmed that the "group" factor had no significant main effect [$F(1,42) < 1$] and did not interact significantly with the "frequency" factor [$F(2,42) < 1$]. This outcome implies that, as we wished, the detection of IPDs by the hearing-impaired listeners was not liable to be significantly disrupted by abnormal asymmetries in loudness. The apparent absence of such asymmetries is not very surprising since, up to 2000 Hz, the two monaural audiograms of the impaired listeners were closely matched: the average interaural difference between the absolute thresholds at a given frequency was only 5 dB (cf. Table I).

In the bottom panel of Fig. 2, it can be seen that there was also no pronounced difference between the two groups with respect to the within-subject variability of the adjustments. An ANOVA performed on these data showed that the main effect of group was only marginally significant [$F(1,42) = 2.92$; $P = 0.095$]. This result is consistent with

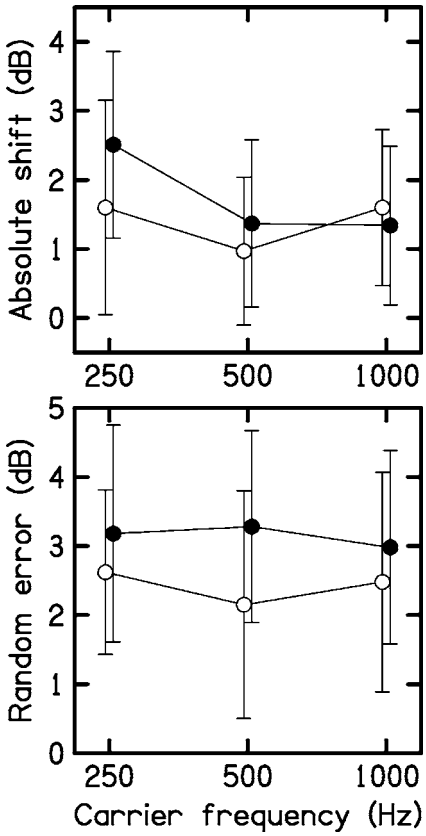

FIG. 2. Results of the intensity-matching test. Open and closed circles, respectively, represent normal and hearing-impaired listeners. Top panel: mean absolute shifts. Bottom panel: mean random errors. The error bars represent standard deviations.

Hawkins and Wightman's (1980) finding of normal interaural intensity difference thresholds in listeners with sensorineural hearing loss.

In Fig. 3, we have plotted the mean IPD thresholds measured in the normal group. For the fine-structure task (detection of interaural differences in φ_{car}), the mean thresholds increased very slightly from 250 to 500 Hz, and to a larger extent from 500 to 1000 Hz; at 500 Hz, no effect of F_{mod} was found. As shown in Fig. 3, our results are similar to those reported by Durlach and Colburn (1978) for unmodulated pure tones at 50 dB SL. For the envelope task (detection of interaural differences in φ_{mod}), the effect of F_{car} on thresholds was different: thresholds were highest at 250 Hz and almost the same at 500 and 1000 Hz; but at 500 Hz, again, no marked effect of F_{mod} was found. At 1000 Hz, essentially identical mean thresholds were obtained for the two tasks.

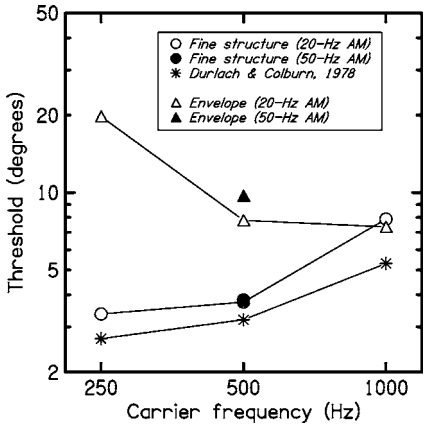

FIG. 3. IPD thresholds measured for normal listeners in experiment 1. For comparison, the fine-structure IPD thresholds displayed by Durlach and Colburn (1978, p. 417) are also plotted; these thresholds represent a synthesis of data published by Klumpp and Eady (1956) and Zwislocki and Feldman (1956). A logarithmic scale is used on both axes.

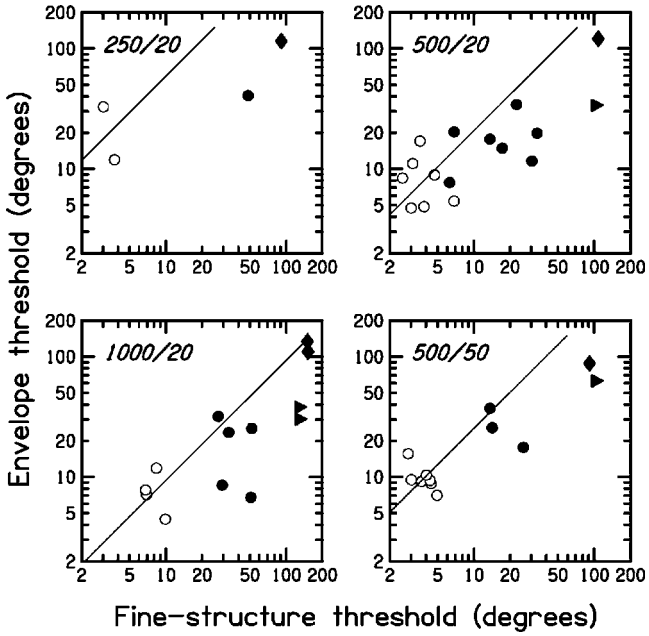

FIG. 4. IPD thresholds measured in experiment 1 for each member of the two groups of listeners. The four panels correspond to the four combinations of F_{car} and F_{mod}. Open and closed symbols, respectively, represent normal and impaired listeners. Diamonds symbolize pairs of thresholds which are both underestimated due to ceiling effects. When only the fine-structure threshold is underestimated, the symbol used is a triangle pointing to the right. The oblique line displayed in each panel has a slope of 1 and goes through the centroid of the normal listeners' data.

Figure 4 shows the IPD thresholds measured for each member of the two groups of listeners. The four panels correspond to the four combinations of F_{car} and F_{mod}. Open and closed symbols, respectively, represent normal and impaired listeners. Diamonds symbolize pairs of thresholds (fine-structure and envelope) which are both underestimated due to ceiling effects (cf. Sec. II C). When only the fine-structure threshold is underestimated, the symbol used is a triangle pointing to the right. Globally, thresholds were poorer in the impaired group than in the normal group for both tasks, but the impaired listeners' deficit was larger for the fine-structure task. This was true for every F_{car}/F_{mod} combination. In each panel is drawn an oblique line which has a slope of 1 and goes through the centroid of the normal listeners' data. If the impaired listeners had been equally deficient in the fine-structure task and the envelope task, then their data points would have fallen equally often above and below the oblique lines. It can be seen that this was not the case. Overall, out of the 25 relevant data points, only three fall above the line. This asymmetry is statistically significant ($P<0.001$, binomial test). Moreover, 7 times out of 25, an impaired listener's fine-structure performance was strongly subnormal while his or her envelope performance was normal. The converse was

TABLE II. Geometric means of the individual thresholds measured (in degrees) for the two groups of listeners, and ratios of the two means (impaired/normal) obtained for each condition.

	Fine-structure thresholds				Envelope thresholds			
F_{car}/F_{mod}	250/20	500/20	500/50	1000/20	250/20	500/20	500/50	1000/20
Normal-hearing group	3.37	3.75	3.82	7.89	19.79	7.80	9.72	7.36
Impaired-hearing group	66.28	24.50	34.35	67.30	68.54	22.25	39.29	29.85
Ratio	19.7	6.5	9.0	8.5	3.5	2.9	4.0	4.1

never observed. For each task and F_{car}/F_{mod} combination, we indicate in Table II the geometric mean of the thresholds measured in each group, as well as the ratio of the two means (impaired/normal). The ratios have a geometric mean of 9.9 for the fine-structure task, and 3.6 for the envelope task.

For the three main F_{car}/F_{mod} combinations (500/20, 500/50, and 1000/20 Hz), the impaired listeners' IPD thresholds are replotted in Fig. 5 as a function of the absolute threshold (for the ear with greater loss in case of inequality) at F_{car}. Here, digits identify the listeners. In the upper left panel, it can be seen that the fine-structure IPD threshold measured in a given listener for the 500/50-Hz combination (small digits) was generally similar to his or her fine-structure threshold for the 500/20-Hz combination (large digits). There was also a within-subject similarity of the envelope thresholds measured for these two F_{car}/F_{mod} combinations (lower left panel). However, the fine-structure thresholds were not significantly correlated with the absolute thresholds at 500 Hz ($r=0.09$ for $F_{mod}=20$ Hz; $r=0.26$ for $F_{mod}=50$ Hz). This result conflicts with the rather high (approximately 0.7) correlations between ITD thresholds and absolute thresholds observed by Hall *et al.* (1984) for 500-Hz tone bursts at 70 dB SPL and by Hawkins and Wightman (1980) for 85-dB narrow-band noises in the same spectral region. On the other hand, our data confirm previous evidence (Hawkins and Wightman, 1980; Smoski and Trahiotis, 1986) that, in listeners with bilateral cochlear hearing losses at high frequencies but normal absolute thresholds at low frequencies, the ITD threshold at low frequencies may be abnormally large: at 500 Hz, Listener 1 had abnormal fine-structure IPD thresholds, but normal absolute thresholds and normal envelope IPD thresholds. At 1000 Hz, however, we found a higher and significant correlation ($r=0.68$, $P=0.04$) between fine-structure IPD thresholds and absolute thresholds. Similar correlations were found, at 500 and 1000 Hz, between the envelope IPD thresholds and the absolute thresholds (average r:0.62). Note finally that there was no significant correlation between the impaired listeners' ages and their fine-structure thresholds (average r: 0.35) or envelope thresholds (average r:0.32).

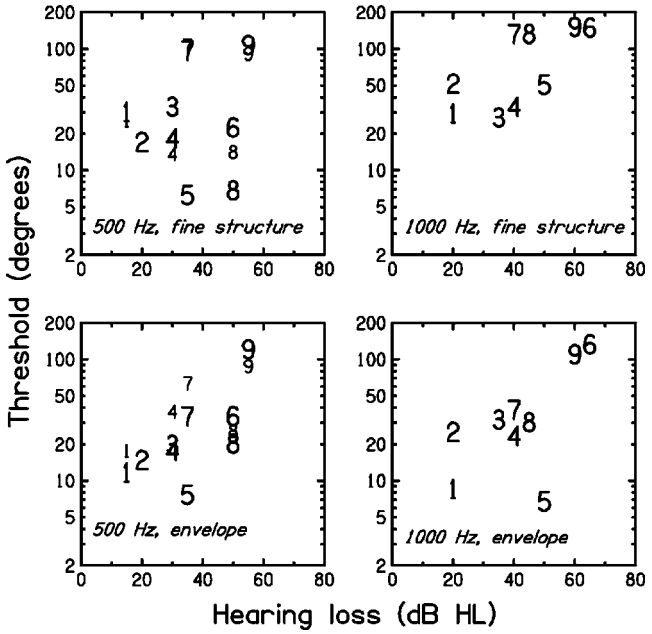

FIG. 5. IPD thresholds of the impaired listeners as a function of their absolute threshold (for the ear with greater loss in case of inequality) at F_{car}. Each listener is identified by a digit consistent with Table I. Large digits are used for $F_{mod}=20$ Hz, smaller digits for $F_{mod}=50$ Hz.

III. EXPERIMENTS 2 AND 3

A. Rationale and method

In experiment 1, the hearing-impaired listeners showed a larger deficit for the fine-structure task than for the envelope task. Could this be due to the fact that the sensation level of the stimuli (which had a fixed SPL, 75 dB) was generally lower for the impaired listeners than for the normal ones? To answer that question, we performed two experiments assessing, in normal listeners, the effect of a reduction in sensation level on the detectability of fine-structure and envelope IPDs.

The stimuli used in experiment 2 were identical to those used in the 500/20-Hz condition of experiment 1. They thus had a fixed SPL of 75 dB. They were presented either alone or together with a masker which reduced their sensation level. The masker was a diotic and continuous white noise low-pass filtered at 1250 Hz. It was produced by an analog generator (Brüel & Kjaer, WB 1314) and presented at an SPL of 69.5 dB. In the presence of this masker, for the authors, the sensation level of the stimuli was about 22 dB. Three listeners were tested. Two of them—the authors—had previously served as subjects in experiment 1. The third listener—a student with normal hearing—was trained during four 1-h sessions before data collection began.

In experiment 3, one of the two conditions of testing was again identical to the 500/20-Hz condition of experiment 1. In the other condition, the sensation level of the stimuli was reduced not by the addition of noise but simply by a 40-dB decrease of intensity: the stimuli were presented at 35 dB SPL. The three listeners who served as subjects included author L.D. and two audiometrically normal students, who were initially trained for 3–4 h.

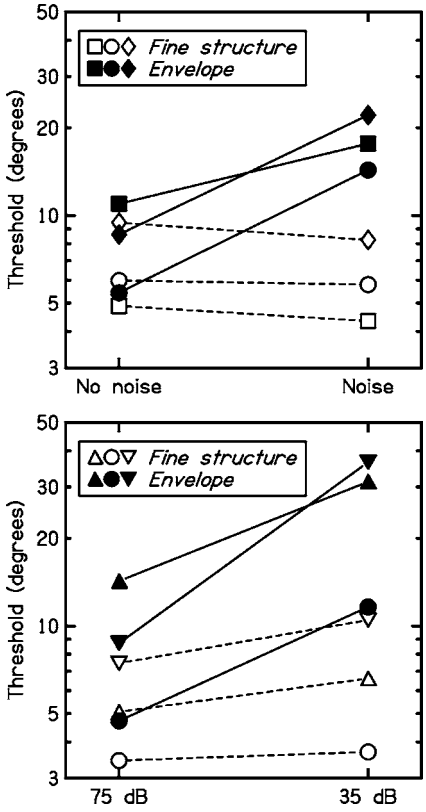

FIG. 6. IPD thresholds measured in experiment 2 (upper panel) and experiment 3 (lower panel). The five listeners are represented by different symbol shapes.

B. Results

The data collected in experiment 2 consisted of five threshold estimates in each cell of the design [3 subjects $\times 2$ IPD types (fine structure versus envelope)$\times 2$ contexts (no noise versus noise)]. The geometric means of these estimates are displayed in the top panel of Fig. 6. Adding noise to the stimuli had similar consequences for the three listeners. This produced a degradation of thresholds for the envelope task, but had no effect for the fine-structure task. A three-way ANOVA performed on the logarithms of the threshold estimates confirmed the existence of a significant interaction between the "IPD type" and "context" factors [$F(1,48)=36.3$, $P<0.001$].

In experiment 3, ten threshold estimates were obtained for each cell of the design [3 subjects$\times 2$ IPD types (fine structure versus envelope) $\times 2$ intensities]. The results, displayed in the bottom panel of Fig. 6, were similar to those of experiment 2: reducing the sensation level of the stimuli did not markedly affect performance for the fine-structure task, but was definitely deleterious for the envelope task. An ANOVA confirmed the existence of a significant interaction between the "IPD type" and "intensity" factors [$F(1,108)=56.2$, $P<0.001$].

C. Discussion

In a previous study by Smoski and Trahiotis (1986), the ability of normal listeners to detect ITDs has been assessed using narrow-band sounds spectrally centered at 500 or 4000 Hz and presented either at 80 dB SPL—i.e., about 60 dB SL—or at 25 dB SL. At both frequencies, it was found that detection thresholds were poorer for the lower SL. However, the SL effect appeared to be markedly larger at 4000 than at 500 Hz. The latter finding is qualitatively consistent with our own results insofar as ITDs at 4000 and 500 Hz are, respectively, detected on the basis of envelope and fine-structure cues.

From the present results, two conclusions can be drawn with regard to the source of the hearing-impaired listeners' deficits observed in experiment 1. First, their deficit in the detection of envelope IPDs is probably due, at least in part, to the fact that the stimuli had, for them, a lower SL than for the normal group. Second, their larger deficit in the detection of fine-structure IPDs must originate, at least in part, from factors other than the elevation of their absolute thresholds.

IV. GENERAL DISCUSSION

The aim of this study was to test the hypothesis that one consequence of cochlear damage is a deficit in the sensitivity to the temporal fine structure of sounds. This hypothesis was tested by comparing the effects of cochlear damage on the detection of fine-structure IPDs and envelope IPDs. By making such comparisons in common spectral regions, using identical standard stimuli, we ensured that the two detection tasks would recruit the same cochlear cells for a given listener. In addition, it is reasonable to conjecture that the *central* mechanisms involved were also the same for both tasks. In support, two points should be made. First, at least for normal listeners and near threshold, the subjective cue permitting identification of the target stimulus presented on a given trial was spatial position for both tasks—a lateralization of the target on the left. Second, Colburn and Esquissaud (1976) and Bernstein and Trahiotis (2002) have explicitly suggested that ITDs in the fine structure of sound wave forms and in their envelopes are processed by one and the same binaural mechanism. Bernstein and Trahiotis (2002) argued that the detection of both types of ITDs can be accounted for by a model based on normalized interaural correlations computed subsequent to known stages of peripheral auditory processing (augmented by a realistic low-pass filtering of envelopes). It should be pointed out, however, that Stellmack *et al.* (2005) recently questioned the validity of this model for the detection of envelope IPDs.

In our group of hearing-impaired listeners, we found a large variability of performance, in line with previous studies of binaural processing by similar populations (e.g., Hawkins and Wightman, 1980; Gabriel *et al.*, 1992). We also found a global deficit in the detection of envelope IPDs, which could be ascribed in part to the elevation of these listeners' absolute thresholds. However, a markedly larger deficit was observed for the detection of fine-structure IPDs, and this was not expected on the basis of the elevation in absolute threshold. Therefore, it does seem warranted to conclude from the present research that cochlear damage produces, independently of its deleterious effect on absolute thresholds, a deterioration in the monaural encoding of temporal fine-structure. A similar suggestion had been made before, on the

basis of different data and more speculatively (Hall *et al.*, 1984; Buus *et al.*, 1984; Lacher-Fougère and Demany, 1998; Moore and Skrodzka, 2002; Buss *et al.*, 2004).

In our experiments, the IPD-type factor (fine structure versus envelope) was combined with a periodicity factor: the fine-structure cycles (1–4 ms) were always shorter than the envelope cycles (20–50 ms). This was essentially unavoidable. Should one interpret the main finding as an effect of periodicity rather than as an effect of IPD type? Against such a view, the deficits observed in the impaired listeners for the detection of fine-structure IPDs were not stronger at 1000 Hz than at 500 or 250 Hz (see Fig. 4 and Table II). This suggests that the crucial factor was IPD type *per se*. In cases of cochlear damage, presumably, pure tones tend to have an abnormal temporal representation at the AN level.

How could this happen? A straightforward idea is that, in consequence of cochlear damage, the precision of phase-locking in individual AN fibers is reduced. However, as pointed out in Sec. I, the results of two physiological studies (Harrison and Evans, 1979; Miller *et al.*, 1997) do not support this notion. Thus, another possible scenario should be looked for. In this regard, Buss *et al.* (2004) suggested that cochlear damage is rather often associated with a reduction in the number of inner hair cells that are responsive to sound, and that reductions in performance are due to the fact that there are fewer channels providing information. A decrease in the number of responsive AN fibers could indeed lead to a poorer sensitivity to temporal fine structure because the responses of distinct AN fibers to a tone are statistically independent point processes (Johnson and Kiang, 1976): if, for instance, one fiber does not respond to a given cycle of the tone, a neighboring fiber may not miss this cycle. The inputs to the binaural neurons do not come from AN fibers but from the anteroventral cochlear nuclei. At this level, remarkably, Joris *et al.* (1994) have found that phase-locking is typically *more* accurate than in AN fibers. This improvement presumably requires a convergence of AN inputs, which might be reduced in case of damage to the inner hair cells.

In addition, as pointed out by Moore and Skrodzka (2002), an optimum combination of the fine-structure temporal information conveyed by separate AN fibers may require a specific traveling wave pattern on the basilar membrane, and cochlear damage is liable to modify significantly the normal pattern. The second part of this hypothesis is consistent with the results of recent studies concerning the consequences of cochlear damage for the masking of pure tones by harmonic complexes with low fundamental frequencies (Summers and Leek, 1998; Oxenham and Dau, 2004). In normal listeners, the magnitude of masking is strongly dependent on the relative phases of the masker's components, and the phase relationships producing maximum and minimum masking apparently correspond to uniform phase curvatures of the masker. In cochlear hearing-impaired subjects, on the other hand, the effect of masker phase curvature on the magnitude of masking is much weaker. This might simply originate from a reduction of cochlear compression in case of cochlear damage. However, Oxenham and Dau (2004) proposed an interesting alternative interpretation. They argue that, in hearing-impaired listeners, the phase response of the cochlea itself could be markedly nonuniform. If this were true, large variations in masking would not be expected from maskers with variable but always uniform phase curvatures.

The validity of the above-mentioned hypotheses is uncertain. Further research is obviously needed to determine precisely why cochlear lesions affect the perceptual sensitivity to the temporal fine structure of sounds.

ACKNOWLEDGMENTS

We thank René Dauman and the ENT department of Pellegrin hospital (head: Jean-Pierre Bébéar) for their help in the recruitment of patients. We are also grateful to Emily Buss, Joseph W. Hall, and William M. Hartmann for useful discussions, and to Armin Kohlrausch, Marjorie Leek, Brian C.J. Moore, and an anonymous reviewer for their judicious comments on a previous version of this article.

Bernstein, L. R., and Trahiotis, C. (**2002**). "Enhancing sensitivity to interaural delays at high frequencies by using 'transposed' stimuli," J. Acoust. Soc. Am. **112**, 1026–1036.

Buss, E., Hall, J. W., and Grose, J. H. (**2004**). "Temporal fine-structure cues to speech and pure tone modulation in observers with sensorineural hearing loss," Ear Hear. **25**, 242–250.

Buus, S., Scharf, B., and Florentine, M. (**1984**). "Lateralization and frequency selectivity in normal and impaired hearing," J. Acoust. Soc. Am. **76**, 77–86.

Colburn, H. S., and Esquissaud, P. (**1976**). "An auditory-nerve model for interaural time discrimination of high-frequency complex stimuli," J. Acoust. Soc. Am. **59**, S23.

Durlach, N. I., and Colburn, H. S. (**1978**). "Binaural phenomena," in *Handbook of Perception*, edited by E. C. Carterette and M. P. Friedman (Academic, New York), vol. IV, pp. 365–466.

Gabriel, K. J., Koehnke, J., and Colburn, H. S. (**1992**). "Frequency dependence of binaural performance in listeners with impaired binaural hearing," J. Acoust. Soc. Am. **91**, 336–347.

Hafter, E. R., Dye, R. H., and Gilkey, R. H. (**1979**). "Lateralization of tonal signals which have neither onsets nor offsets," J. Acoust. Soc. Am. **65**, 471–477.

Hall, J. W., Tyler, R. S., and Fernandes, M. A. (**1984**). "Factors influencing the masking level difference in cochlear hearing-impaired and normal-hearing listeners," J. Speech Hear. Res. **27**, 145–154.

Harrison, R. V., and Evans, E. F. (**1979**). "Some aspects of temporal coding by single cochlear fibres from regions of cochlear hair cell degeneration in the guinea pig," Arch. Oto-Rhino-Laryngol. **224**, 71–78.

Hawkins, D. B., and Wightman, F. L. (**1980**). "Interaural time discrimination ability of listeners with sensorineural hearing loss," Audiology **19**, 495–507.

Johnson, D. H., and Kiang, N. Y. (**1976**). "Analysis of discharges recorded simultaneously from pairs of auditory nerve fibers," Biophys. J. **16**, 719–734.

Joris, P. X., Carney, L. H., Smith, P. H., and Yin, T. C. (**1994**). "Enhancement of neural synchronization in the anteroventral cochlear nucleus. I. Responses to tones at the characteristic frequency," J. Neurophysiol. **71**, 1022–1036.

Kaernbach, C. (**1991**). "Simple adaptive testing with the weighted up-down method," Percept. Psychophys. **49**, 227–229.

Klumpp, R. G., and Eady, H. R. (**1956**). "Some measurements of interaural time difference thresholds," J. Acoust. Soc. Am. **28**, 859–860.

Lacher-Fougère, S., and Demany, L. (**1998**). "Modulation detection by normal and hearing-impaired listeners," Audiology **37**, 109–121.

Miller, R. L., Schilling, J. R., Franck, K. R., and Young, E. D. (**1997**). "Effects of acoustic trauma on the representation of the vowel /ɛ/ in cat auditory nerve fibers," J. Acoust. Soc. Am. **101**, 3602–3616.

Moore, B. C. J. (**1973**). "Frequency difference limens for short-duration tones," J. Acoust. Soc. Am. **54**, 610–619.

Moore, B. C. J., and Glasberg, B. R. (**1986**). "The relationship between frequency selectivity and frequency discrimination for subjects with unilateral and bilateral cochlear impairments," in *Auditory Frequency Selec-*

tivity, edited by B. C. J. Moore and R. D. Patterson (Plenum, New York).
Moore, B. C. J., and Moore, G. A. (**2003**). "Discrimination of the fundamental frequency of complex tones with fixed and shifting spectral envelopes by normally hearing and hearing-impaired subjects," Hear. Res. **182**, 153–163.
Moore, B. C. J., and Sek, A. (**1996**). "Detection of frequency modulation at low modulation rates: Evidence for a mechanism based on phase-locking," J. Acoust. Soc. Am. **100**, 2320–2331.
Moore, B. C. J., and Skrodzka, E. (**2002**). "Detection of frequency modulation by hearing-impaired listeners: Effects of carrier frequency, modulation rate, and added amplitude modulation," J. Acoust. Soc. Am. **111**, 327–335.
Oxenham, A. J., and Dau, T. (**2004**). "Masker phase effects in normal-hearing and hearing-impaired listeners: Evidence for peripheral compression at low signal frequencies," J. Acoust. Soc. Am. **116**, 2248–2257.
Rose, J. E., Brugge, J. F., Anderson, D. J., and Hind, J. E. (**1967**). "Phase-locked response to low-frequency tones in single auditory nerve fibers of the squirrel monkey," J. Neurophysiol. **30**, 769–793.
Smoski, W. J., and Trahiotis, C. (**1986**). "Discrimination of interaural temporal disparities by normal-hearing listeners and listeners with high-frequency sensorineural hearing loss," J. Acoust. Soc. Am.," **79**, 1541–1547.
Stellmack, M. A., Viemeister, N. F., and Byrne, A. J. (**2005**). "Discrimination of interaural phase differences in the envelopes of sinusoidally amplitude-modulated 4-kHz tones as a function of modulation depth," J. Acoust. Soc. Am. **118**, 346–352.
Summers, V., and Leek, M. R. (**1998**). "Masking of tones and speech by Schroeder-phase harmonic complexes in normally hearing and hearing-impaired listeners," Hear. Res. **118**, 139–150.
Woolf, N. K., Ryan, A. F., and Bone, R. C. (**1981**). "Neural phase-locking properties in the absence of cochlear outer hair cells," Hear. Res. **4**, 335–346.
Young, E. D., and Sachs, M. B. (**1979**). "Representation of steady-state vowels in the temporal aspects of the discharge patterns of populations of auditory-nerve fibers," J. Acoust. Soc. Am. **66**, 1381–1403.
Zurek, P. M., and Formby, C. (**1981**). "Frequency discrimination ability of hearing-impaired listeners," J. Speech Hear. Res. **24**, 108–112.
Zwislocki, J., and Feldman, R. S. (**1956**). "Just noticeable differences in dichotic phase," J. Acoust. Soc. Am. **28**, 860–864.

Tactile information transfer: A comparison of two stimulation sites

Ian R. Summers[a] and Jon J. Whybrow
Biomedical Physics Group, School of Physics, University of Exeter, Exeter EX4 4QL, United Kingdom

Denise A. Gratton, Peter Milnes, Brian H. Brown, and John C. Stevens
Department of Medical Physics and Clinical Engineering, University of Sheffield, Royal Hallamshire Hospital, Sheffield S10 2JF, United Kingdom

(Received 17 September 2004; revised 14 July 2005; accepted 15 July 2005)

Two experiments on the discrimination of time-varying tactile stimuli were performed, with comparison of stimulus delivery to the distal pad of the right index finger and to the right wrist (palmar surface). Subjects were required to perceive differences in short sequences of computer-generated stimulus elements (experiment 1) or differences in short tactile stimuli derived from a speech signal (experiment 2). The pulse-train stimuli were distinguished by differences in frequency (i.e., pulse repetition rate) and amplitude, and by the presence/absence of gaps (~100-ms duration). Stimulation levels were 10 dB higher at the wrist than at the fingertip, to compensate for the lower vibration sensitivity at the wrist. Results indicate similar gap detection at wrist and fingertip and similar perception of frequency differences. However, perception of amplitude differences was found to be better at the wrist than at the fingertip. Maximum information transfer rates for the stimuli in experiment 1 were estimated at 7 bits s^{-1} at the wrist and 5 bits s^{-1} at the fingertip. © *2005 Acoustical Society of America.* [DOI: 10.1121/1.2031979]

PACS number(s): 43.66.Wv, 43.71.Ma [RAL] Pages: 2527–2534

I. INTRODUCTION

In recent years there has been increased interest in tactile perception in the context of information transfer in touch-based human-machine interaction (Tan *et al.*, 2000; van Erp and van Veen, 2001; Bach-y-Rita and Kercel, 2003; Cholewiak and Collins, 2003; Murray *et al.*, 2003; Jansen *et al.*, 2004; van Erp and Verschoor, 2004). Earlier studies on tactile information transfer were often related to sensory substitution devices for the hearing or visually impaired, with many of these devices involving spatially distributed stimulation (Pickett and Pickett, 1963; Bliss, 1970; Clements *et al.*, 1982; Kirman, 1974; Snyder *et al.*, 1982; Bach-y-Rita, 1983; Boothroyd, 1985; Brooks *et al.*, 1985). As might be expected, the literature for basic studies of tactile perception is dominated by studies on the hand, particularly the fingertip. This part of the skin is particularly sensitive in terms of detection threshold. However, in applications such as tactile communication with drivers or pilots (Raj *et al.*, 1998; Tan *et al.*, 2000; van Erp and van Veen, 2001), it may be advantageous to use stimulation sites other than the hand: for example, the forearm or torso. Similarly, of the vibrotactile devices which have been designed to provide sensory substitution for the hearing impaired, some of the most successful have been designed for the wrist (Thornton and Phillips, 1992). There is some anecdotal evidence to suggest these alternative, less sensitive, sites are less effective for tactile information transmission. (For example, users of wrist-worn tactile devices have been observed using the fingers of their "free" hand to rest on the output vibrator, in an attempt to gain more information.) It has generally been assumed that, even if the lower sensitivity at these alternative sites is compensated by the use of stronger stimuli, other aspects of tactile perceptual acuity are reduced in comparison to the more sensitive sites, but there is no direct evidence for this from previous studies. The present investigation addresses this issue with measurements on vibrotactile stimuli presented equivalently at the fingertip and at the wrist.

Only a small proportion of the substantial literature on vibrotactile perception is related to the perception of time variations in vibrotactile stimuli (e.g., Rothenberg *et al.*, 1977; Weisenberger, 1986; Formby *et al.*, 1992). Similarly, the literature contains few studies which compare acuity of vibrotactile perception between body sites. Verrillo, in separate investigations (Verrillo, 1963, 1966, 1971), measured detection thresholds as a function of frequency for sinusoidal stimulation at the thenar eminence, the volar forearm, and the middle fingertip. His results show the fingertip to be the most sensitive of these sites and the forearm to be the least sensitive. Perception of changes in stimulation amplitude across different sites has been investigated by Verrillo and Chamberlain (1972), who found that subjective intensity magnitude grows more rapidly with vibration amplitude at less sensitive sites such as the forearm, as compared to more sensitive sites such as the fingertip. Similarly, Cholewiak (1979) reported a rapid growth of sensation magnitude for stimulation on the thigh, which is a less sensitive site. [Gescheider (1990) measured the just-noticeable-difference (jnd) for stimulus intensity at the thenar eminence and found that subjects could detect increments of 0.7 dB, superimposed on a continuous background "pedestal" of vibration, although larger jnd's were observed under less favorable ex-

[a]Electronic mail: i.r.summers@exeter.ac.uk

perimental conditions.] Perception of changes in stimulation frequency at the forearm was investigated by Rothenberg *et al.* (1977), for sinusoidal and pulse stimuli over the frequency range 20 to 300 Hz, with a comparison to results from earlier measurements at the fingertip. Perception at the two sites was found to be broadly similar, with jnd's in frequency corresponding to a Weber fraction ($\Delta f/f$) of around 0.2. Similar results for frequency discrimination at the fingertip have been reported by Goff (1967). [Sherrick (1985) reported that perceived frequency grows much less rapidly with actual frequency in the frequency range above 100 Hz, as compared to below 100 Hz.]

In the present study, two experiments on the perception of time-varying tactile stimuli were performed, the first using closely controlled computer-generated stimuli and the second using stimuli with inherent variability, derived from a speech input. The methodology is broadly the same as that described in a previous paper (Summers *et al.*, 1997) on perception at the fingertip only.

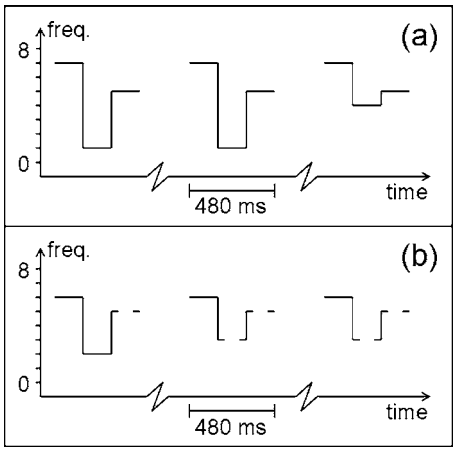

FIG. 1. Schematic diagrams of the variation of stimulus frequency over the time course of typical test items: (a) stimuli without gaps and (b) stimuli with gaps. The nine possible stimulus frequencies are indicated on the vertical axes. In (b), gaps are indicated by breaks in the lines representing the stimulus elements. In the "half-AM" and "full-AM" conditions the stimulus amplitude is covaried redundantly with frequency (see main text for details).

II. EXPERIMENT 1

A. Stimuli

As in the previous experiment (Summers *et al.*, 1997), the computer-generated stimuli were short sequences of quasi-steady elements, overall duration 480 ms, intended as a simplified representation of the longer sequences of stimulus elements that might be used in a practical tactile-communication device. Stimuli were presented as a frequency-modulated signal (monophasic pulses) with a dynamic range for frequency (i.e., pulse repetition rate) of 25–400 Hz. Each stimulus comprised three 160-ms elements, with each element selected from nine possible frequencies (at steps of 0.5 oct across the 25–400 Hz range). In an "odd-one out" task, each test item comprised three 480-ms stimuli, separated by pauses of 1520 ms, including one stimulus which differed in terms of the second of its three elements. A typical test item might be

7 **1** 5 7 **1** 5 7 **4** 5

[see Fig. 1(a)] where the nine possible frequencies from 25 to 400 Hz are labeled by integers from 0 to 8. (In this example the contrast between the stimuli is 1.5 oct, between 35 and 100 Hz.) The rationale for selecting frequencies for the "context" elements (first and third elements within the stimuli) and the "target" elements (second elements within the stimuli), in order to give a representative variety of test discriminations, is the same as has been described previously (Summers *et al.*, 1997).

A redundant combination of frequency modulation and amplitude modulation has previously been demonstrated to provide an effective strategy for tactile information transmission (Summers *et al.*, 1994, 1997). For a tactile signal with pulse waveform (but not for one with sinusoidal waveform) the subjective intensity at constant pulse amplitude is relatively independent of pulse frequency, for frequencies below approximately 500 Hz (Rothenberg *et al.*, 1977; Bernstein *et al.*, 1986). The addition of amplitude modulation to a frequency-modulated signal is therefore likely to give additional cues to discrimination of signal contrasts. However, there is a suggestion from the previous investigation (Summers *et al.*, 1997) that high levels of amplitude modulation within a sequence of stimulus elements may result in the masking of weaker stimulus elements by preceding or following stronger elements, and so may not produce the intended enhancement of information transfer. In order to investigate such an effect, the present study includes stimulus sets at three degrees of amplitude modulation (in combination with the frequency modulation outlined above): in the "no-AM" condition, the stimulus amplitude was held constant at 24 dB sensation level (SL); in the "half-AM" condition the stimulus amplitude was covaried redundantly with frequency, in the same sense, with a dynamic range of 19–29 dB SL (2.5 dB amplitude change for each 1 oct change of frequency); in the "full-AM" condition the stimulus amplitude was covaried redundantly with frequency, in the same sense, with a dynamic range of 14–34 dB SL (5 dB amplitude change for each 1 oct change of frequency).

In addition to frequency and amplitude modulation of suprathreshold signals, information can be transmitted simply in terms of the presence/absence of the tactile signal. This aspect of information transfer [not covered in the previous investigation (Summers *et al.*, 1997)] was incorporated into the experiment by including short gaps within the stimuli. The gaps were implemented by eliminating a sequence of consecutive pulses from the stimulus waveform. With stimulus elements at frequencies labeled 0–8, as described above, gaps were included within elements at frequencies 1, 3, 5, 7 but not within elements at frequencies 0, 2, 4, 6, 8 [see Fig. 1(b)]. The intention was to enhance the discrimination of the 0.5-oct contrasts between "nearest neighbors" within the frequency set—these contrasts are very difficult to discriminate on the basis of frequency/amplitude information alone. (Note that this strategy incidentally also provides a "gap/no-gap" cue for the other "half-integer" contrasts of 1.5, 2.5, and 3.5 oct. There is no such cue for the "integer" contrasts of 1.0, 2.0, 3.0, and 4.0

oct—in fact the stimulus gaps that may occur in these cases are expected to hinder discrimination by reducing the duration of frequency and amplitude cues).

A typical test item with gaps might be

$$6\ \mathbf{2}\ 5^{*} \quad 6\ \mathbf{3}^{*}\ 5^{*} \quad 6\ \mathbf{3}^{*}\ 5^{*}$$

where the asterisks indicate elements with gaps. Gaps were positioned at the midpoint of the 160-ms element. Four different gap durations were used: 0 (i.e., no gap), 40, 80, and 120 ms. There are thus 24 test conditions in all: three levels of amplitude modulation and four levels of gap duration at two stimulation sites.

The stimulus delivery system, based around a Bruel & Kjaer type 4810 vibrator which drives a 2-cm^2 circular contactor with no surround, has been described previously (Summers *et al.*, 1997). Stimuli were presented at the fingertip and at the wrist—more precisely, to the distal pad of the right index finger and to the palmar surface of the right distal forearm. Subjects were instructed to rest the finger or wrist lightly on the contactor, whose surface was horizontal. (The static contact force was not controlled. In principle, consequent variation of subjective intensity might lead to weak stimulus elements being lost in some cases. However, this is not expected to be a problem in the present study since all stimulus elements are well above the nominal detection threshold.) Noise masking via headphones was used to eliminate acoustic cues from the vibrator. The stimulus waveform was trains of Gaussian-like pulses, obtained by passing 1-ms rectangular pulses through a fourth-order low-pass Bessel filter at 500 Hz. Sensation levels were calculated from the baseline-to-peak pulse amplitude, with respect to nominal thresholds of 0.5 μm for the fingertip and 1.6 μm for the wrist. The latter figure is higher because of lower sensitivity to vibration at the wrist. The figure of 0.5 μm for the fingertip was taken from the previous investigation (Summers *et al.*, 1997), where the nominal threshold was set slightly above the estimated threshold of 0.3 μm, obtained from preliminary measurements. In informal preliminary experiments for the present study it was established that absolute levels around 10 dB higher at the wrist than at the fingertip are required to produce equal subjective intensity for suprathreshold stimuli at the two sites. Hence the choice of 1.6 μm as the nominal threshold for the wrist, so that stimuli at the wrist and at the fingertip with this 10-dB difference in absolute level are calculated to have the same sensation level.

B. Subjects

These were 12 normally hearing adults (age range 20 to 57 years), 5 male and 7 female, including authors DAG, PM, and BHB. They were not paid for their participation in the experiment. All but two had previous experience with tactile tests. One subject became unavailable at the midpoint of testing. A similar replacement subject was used to complete the data. In both this experiment and experiment 2, described below, the age range of subjects was such that some variation in performance might be expected due to age-related changes in tactile acuity (Van Doren *et al.*, 1990). In practice it was not possible to separate any such age-related effects from the intersubject variability typically observed in experiments of this type.

C. Procedure

Subjects were presented with test items, each containing three stimuli, and required to identify the "odd one out." Response (forced choice) was by keyboard entry. Each test sequence (24 in all: one for each test condition) included 25 such discriminations, the last 20 of which were scored. There was no specific training for the test, as the test protocol was designed to avoid the necessity for this. However, at the start of the experiment there was a short explanation and demonstration session lasting approximately five minutes. Subjects with no previous experience of tactile experiments were given additional time for demonstrations and familiarization before their first test session. Each subject attended for 12 test sessions, with two test sequences (i.e., two test conditions) in each session. The order of test conditions was permutated across the subject group to balance any learning effects, except that testing with 0- and 40-ms gaps was performed some weeks before testing with 80- and 160-ms gaps. [The original (balanced) experimental design involved only 0- and 40-ms gaps, but longer gaps were added in the light of results obtained with the shorter gaps. Fortunately, observed learning effects were small, with equivalent test items in the first and second rounds of tests producing scores around two percentage points higher in the latter case].

D. Results

Figure 2 shows mean scores for each of the 24 test conditions. The "no AM" scores, for stimuli with frequency modulation only, are generally well above the chance score of 33% and are similar for the two stimulation sites. The addition of amplitude modulation ("half AM" and "full AM" data) results in increased mean scores, with greater enhancement at the wrist than at the fingertip, and hence corresponding mean scores for stimuli with both frequency and amplitude modulation are generally higher for the wrist than for the fingertip.

Analysis of variance (ANOVA) indicates a significant effect of site ($p=0.019$), a significant effect of amplitude modulation ($p=0.001$), and a significant interaction between site and amplitude modulation ($p=0.011$). There is also a significant effect of gap duration ($p=0.001$), corresponding to the general rising trend observed for all six lines in Fig. 2. This rising trend appears to be maintained across the full range of gap durations, i.e., the enhancement due to gaps outweighs the fact that gaps degrade other aspects of the stimulus, even for the longer gaps.

As a consequence of the experimental design (see above) the presence of gaps is expected to enhance discrimination of half-integer stimulus contrasts only. Gaps offer no additional cue in the case of integer contrasts and are expected to hinder discrimination by reducing the duration of frequency and amplitude cues. This is confirmed by the experimental data: When the effect of gap duration is considered separately for half-integer contrasts and for integer con-

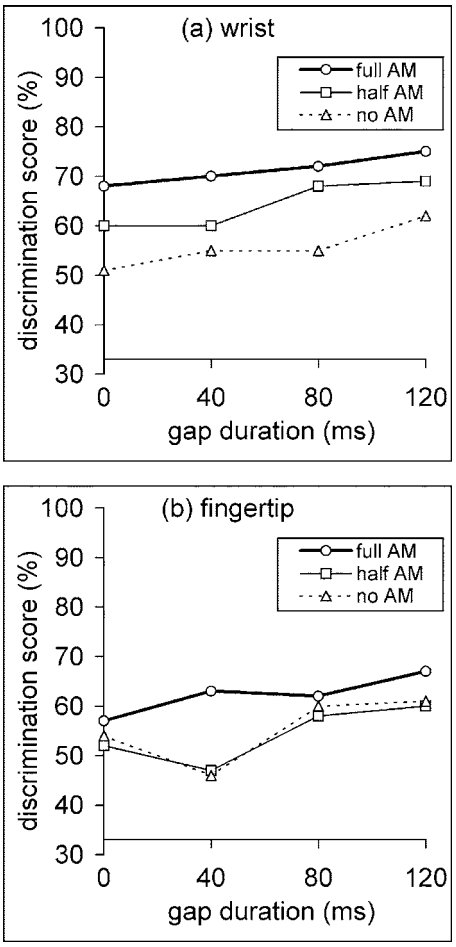

FIG. 2. Mean scores from experiment 1 plotted as a function of gap duration for the three AM conditions: (a) stimulation at the wrist and (b) stimulation at the fingertip. The standard error in each score is typically 3 or 4 percentage points. The horizontal axis is positioned at the chance score of 33%.

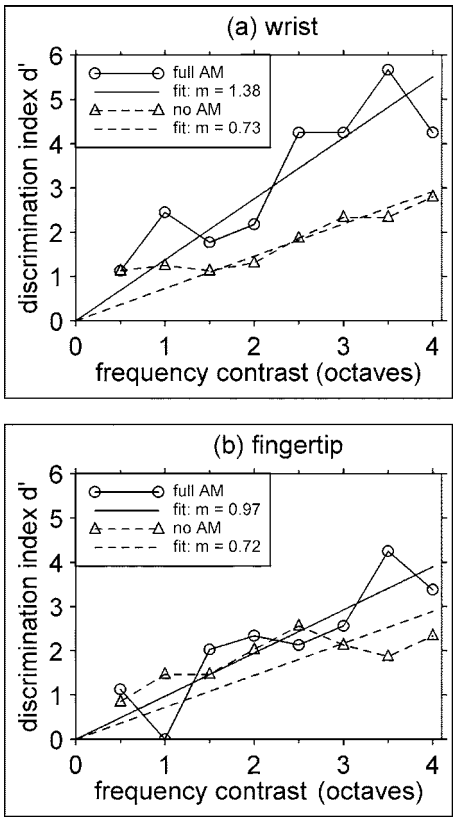

FIG. 3. Discrimination index d' for the stimuli in experiment 1, plotted as a function of the contrast in frequency between the stimuli: (a) stimulation at the wrist and (b) stimulation at the fingertip. In the "full AM" condition the stimuli are distinguished by a contrast in amplitude as well as a contrast in frequency (5 dB amplitude change per octave of frequency change); in the "no AM" condition the stimuli are distinguished by a contrast in frequency only. Straight-line fits to the data are also shown.

trasts, the overall rising trend observed in Fig. 2 (around 9 percentage points across the range at each stimulation site, for data pooled over the various AM conditions) is seen to be a combination of two effects: There is a larger rising trend (around 20 percentage points across the range) for the half-integer contrasts, and a smaller falling trend (around 2 percentage points across the range) for the integer contrasts, approximately half of which include gaps of no utility.

A closer examination of the experimental data shows that the gap-related enhancement of discrimination (i.e., the difference between scores in the absence of gaps and in the presence of the longest, 120-ms, gaps) varies across the set of half-integer contrasts (0.5, 1.5, 2.5, and 3.5 oct). The enhancement is greatest for the 0.5-oct contrasts and is progressively reduced for contrasts of 1.5, 2.5, and 3.5 oct—to the extent that there is typically no enhancement for the 3.5-oct contrasts. This may be explained in terms of the gaps providing a direct positive effect (via the gap/no-gap cue) but an indirect negative effect (because frequency and amplitude cues are reduced by the 120-ms gaps within the 160-ms stimulus elements). For the larger frequency contrasts there is expected to be a greater negative effect (because the disrupted frequency and amplitude cues are greater) and a smaller positive effect (because discrimination of the gap/no-gap cue is presumably more difficult between stimulus elements which differ significantly in frequency, or in both amplitude and frequency).

A more detailed picture of the information provided by frequency and amplitude modulation is obtained from error patterns in the "no-gap" data (i.e., gap duration of 0 ms). Figure 3 shows values of discrimination index d', derived from mean scores using the conversion table given by Craven (1992), plotted as a function of the frequency contrast between the stimuli. Data are shown for stimuli with frequency modulation only ("no AM") and for stimuli with both frequency modulation and maximum amplitude modulation ("full AM"), at both stimulation sites. (Results for the "half AM" conditions follow the same general pattern but, for the sake of clarity, are not shown here.) The best-fit line to each set of data is also shown, from whose gradient may be calculated the discrimination index d' across the full range of stimulus contrast (4 oct, or 4 oct and 20 dB). As noted above, discrimination of frequency modulation is similar at the two sites, and this is seen in full-range d' values for the no-AM case of 2.9 ± 0.6 at the wrist and 2.9 ± 0.7 at the fingertip. Similarly, the ANOVA results (see above) indicate that amplitude modulation is more effective at the wrist than at the fingertip, and this is seen in full-range d' values for the full-AM case of 5.5 ± 0.6 (wrist) and 3.9 ± 0.7 (fingertip). These data compare well with data from the previous inves-

tigation (Summers *et al.*, 1997) in which full-range d' at the fingertip for the full-AM case was found to be around 4.5. As a further comparison, the maximum gap-related enhancement to discrimination is for 120-ms gaps with 0.5-oct contrasts (see above), and may be calculated as equivalent to an increase of d' by 1.8 on average, from around 0.8 to around 2.6.

There is some evidence (Summers *et al.*, 1997) that the stimulus dimensions of frequency and amplitude are perceived as orthogonal in this context and hence their corresponding d' values combine vectorially, in which case it is possible to estimate full-range d' values relating to amplitude modulation alone (full AM) of 4.7 (wrist) and 2.6 (fingertip). These may be compared to the values for frequency modulation alone (2.9 in each case) indicating that amplitude and frequency cues are roughly equal on the fingertip, for the dynamic ranges of 20 dB and 4 oct used here, but amplitude cues dominate at the wrist.

[Note that the conversion table given by Craven (1992) assumes a model of the task in which the subject holds a "mental image" of all three stimuli for simultaneous comparison. In practice, each subject applies his/her own strategy to the task, and this may not correspond to Craven's model. The computed d' values in Fig. 3 are subject to some uncertainty because of this.]

III. EXPERIMENT 2

A. Rationale

In situations where it is required to tactually transmit information derived from human or environmental sources the tactile signal will be less closely specified than a computer-generated signal, with more inherent variability. This may lead to difficulties in interpretation. This problem has been encountered, for example, in the context of tactile transmission of speech to the hearing impaired [Summers *et al.*, 1996; Galvin *et al.*, 2000; see also Summers (1992), for a general review of this topic]. Discrimination of this type of signal is investigated in experiment 2, which involves the same wrist/fingertip comparison as experiment 1 but uses stimuli which are derived from a speech signal. (These stimuli are chosen as an example of the broad class of stimuli which might be directly derived from human or environmental sources. The intention is not to focus particularly on an application to speech transmission).

B. Stimuli

Stimuli were derived from vowel-consonant-vowel nonsense syllables (e.g., *ama*, *asa*, *ata*—always the same vowels but various consonants) recorded from a female speaker. The tactile signal, with the same pulse waveform as in experiment 1, was frequency and amplitude modulated according to the zero-crossing frequency of the speech signal. A PIC microprocessor was programmed to map the nominal range of zero-crossing frequency, 800–6400 Hz, onto the same dynamic ranges in the tactile signal that were used in experiment 1: frequency range 25–400 Hz; amplitude fixed at 24 dB SL ("no AM"), amplitude range 19–29 dB SL ("half AM"), or amplitude range 14–34 dB SL ("full AM"). Silences in the speech signal, including small silences within some syllables, were mirrored by gaps in the tactile signal. In an "odd-one out" task, each test item comprised three stimuli, separated by pauses of around 1.5 s, including one stimulus which differed in terms of the choice of consonant. A typical test item might be

aka ana aka

In the tactile signal, the target is indicated by frequency/amplitude features relating to differences in zero-crossing frequency and by short gaps (~100-ms duration) relating to silences which precede some consonants (e.g., in *ada*, *aka*). It can be seen that there is a close correspondence between the test items in experiment 1 and in experiment 2—in each case a test item comprises three stimuli, each with three elements, with the target stimulus distinguished by a contrast in the second element. The contrast is indicated by differences in stimulus frequency, differences in amplitude, and/or the presence of gaps. Stimuli were derived from speech recordings used in a previous investigation of tactile speech transmission to the hearing impaired. A more detailed discussion of the speech material, the contrasts within the test items, and the procedure for extracting zero-crossing frequency is available in relation to that study (Summers *et al.*, 1996). There were multiple recordings of each syllable and the two "same" syllables in each set of three were different utterances. Thus the experimental task was, as intended, affected by the inherent variability of the stimuli (at least in principle).

There are six test conditions in experiment 2: three degrees of amplitude modulation at two stimulation sites. Stimulus delivery was identical to experiment 1, with absolute levels of stimulation 10 dB higher on the wrist in order to compensate for reduced sensitivity compared to the fingertip.

C. Subjects

These were 12 normal-hearing adults (age range 20 to 57 years), 5 male and 7 female, including authors BHB, DAG, PM, and JCS. They were not paid for their participation in the experiment. All had previous experience of tactile tests.

D. Procedure

Subjects were presented with test items, each containing three stimuli, and required to identify the "odd one out." Response (forced choice) was oral, recorded on a response sheet by the experimenter. Each test sequence included 15 such discriminations, the last 12 of which were scored (covering 12 consonant contrasts: *b*/*m*, *b*/*p*, *d*/*k*, *d*/*n*, *f*/*v*, *g*/*k*, *k*/*n*, *l*/*n*, *r*/*w*, *s*/*sh*, *s*/*t*, and *s*/*z*). [For the purposes of the previous investigation of tactile speech transmission (Summers *et al.*, 1996), the consonant pairs chosen for discrimination were selected from viseme groups (i.e., groups within which the member consonants are difficult to discriminate by speechreading) on the basis of frequency of occurrence in standard English.] The six test conditions were tested separately in six test sessions, each including two test sequences

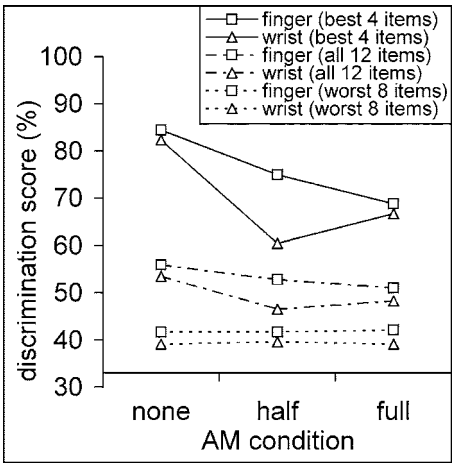

FIG. 4. Variation of mean discrimination scores across the three AM conditions in experiment 2. Data are shown for each of the two stimulation sites and pooled over all 12 test items, over the best 4 test items *s*/*t k*/*n d*/*n* and *b*/*m*, and over the remaining 8 test items. Typical standard errors are around 3 percentage points for the 12-item data, around 4 percentage points for the 8-item data, and around 5 percentage points for the 4-item data. The horizontal axis is positioned at the chance score of 33%.

(i.e., 24 scored test items). The order of test conditions was permutated across the subject group to balance any learning effects. Other details are similar to experiment 1.

E. Results

Overall discrimination scores in the six test conditions are relatively modest: around 50% in each case, with standard errors typically 3%, against a chance score of 33%. However, a detailed inspection of the data suggests that the 12 consonant contrasts fall into two groups: 4 "best" contrasts (*b*/*m*, *d*/*n*, *k*/*n*, and *s*/*t*) which produce scores averaging around 70%, and 8 "worst" contrasts which produce scores averaging around 40% (see Fig. 4). Examination of stimulus waveforms shows that the four higher-scoring contrasts are those which are reliably indicated by a gap/no-gap cue. It thus appears that, in this experiment, subjects rely almost entirely on gap cues and are able to make little use of the zero-crossing information which is presented as frequency and amplitude modulation. With hindsight, it is clear that the experiment would be improved by the inclusion of consonant contrasts with more accessible frequency/amplitude cues. (For example, *asa* and *ama* have consonants of relatively long duration, distinguished by zero-crossing frequencies which fall towards the high and low extremes of the range, respectively. Although these syllables are present in the speech material used for experiment 2, the *asa*/*ama* contrast was not included in the test material.) It seems likely that performance differences between stimulation sites would be observed with such test items, similar to those seen in experiment 1, i.e., an advantage for the wrist.

The data in Fig. 4 show that the addition of amplitude modulation results in a reduction of scores for the four "best" items—i.e., any enhancement to perception of the (less important) zero-crossing information is outweighed by interference to perception of the (more important) gap cues by varying the amplitude of the tactile signal.

Analysis of variance (ANOVA) on the complete data set indicates the effect of site is not significant ($p=0.128$) and the effect of amplitude modulation is also not significant ($p=0.510$). Analysis of variance on the data for only the best four consonant contrasts indicates the effect of site is not significant ($p=0.082$) but there is a significant effect of amplitude modulation ($p=0.001$) relating to the higher scores in the "no-AM" condition.

IV. DISCUSSION

Results from both experiments are consistent with (a) similar gap detection at wrist and fingertip, (b) similar perception of frequency modulation at each site, and (c) better perception of amplitude modulation at the wrist than at the fingertip. In experiment 1, cues of all three types contribute to subjects' performance and hence there is an overall advantage for perception at the wrist. Experiment 2 is dominated by cues from gaps in the stimuli, with subjects apparently making little use of cues from amplitude modulation or frequency modulation; hence performance is similar for the two stimulation sites. The negative effect of amplitude modulation in experiment 2 may be explained in terms of gap detection being easier within a signal of constant amplitude—as discussed above, a similar effect is seen in experiment 1, where gap-related information is seen to be less effective in the context of the larger contrasts of frequency or frequency and amplitude. However, amplitude modulation is seen to have a generally positive effect in experiment 1: there is no evidence for the masking effect proposed above, i.e., the masking of weaker stimulus elements by preceding or following stronger elements.

Compared to quasi-steady stimuli, the stimuli used in the present study are more difficult to perceive because of sensory constraints (e.g., larger jnd's for shorter stimuli, masking between successive stimulus elements), and presumably also because of cognitive constraints (e.g., problems in interpreting the structures of stimuli and holding these for comparison in short-term memory). However, within a given experiment it seems likely that cognitive constraints are similar between test conditions, and so differences in subjects' performance between test conditions are largely attributable to sensory constraints.

The apparently enhanced perception of amplitude modulation at the wrist is an unexpected finding: initial predictions (see above) were that the more sensitive fingertip would offer better transmission of information. This advantage for the wrist can be interpreted in terms of the just noticeable difference (jnd) for amplitude being larger at the fingertip than at the wrist. [There is arguably a correspondence here with the finding of Verrillo and Chamberlain (1972) that subjective intensity magnitude grows more rapidly with vibration amplitude at less sensitive sites such as the forearm, as compared to the fingertip.] The estimated values from experiment 1 for full-range d' relating to amplitude modulation alone (20-dB range) are 4.7 at the wrist and 2.6 on the fingertip. These may be interpreted as jnd's for amplitude (defined by $d'=1$) of 4.3 dB at the wrist and 7.7 dB at the fingertip, i.e., around 1.8 times larger at the fingertip. Some additional evi-

dence for a difference in jnd's for amplitude between the two stimulation sites comes from informal measurements on five subjects at a stimulation frequency of 100 Hz, taken during a previous investigation (Summers *et al.*, 1994). These gave jnd values of 1.4 dB at the wrist and 1.9 dB at the fingertip, i.e., around 1.4 times larger at the fingertip. However, these previous data are for quasi-steady stimuli and hence do not correspond well to the case in experiment 1, where stimulus elements have a duration of only 160 ms and the perception task is also hindered by the presence of other elements with different amplitude within the same stimulus.

The available information transfer (IT) for the stimulus elements used in experiment 1 may be estimated from the values of full-range d' (for the "no-gap" cases, as in Fig. 3), using the technique of Braida and Durlach (1972). This gives IT values at the wrist of 0.6 and 1.05 bits, respectively, for frequency modulation alone ("no AM") and frequency modulation plus amplitude modulation ("full AM"). Corresponding IT values at the fingertip are 0.6 and 0.8 bits, respectively. Since these figures represent the IT for a 160-ms stimulus element, the corresponding available information transfer rates may be estimated. For example, for the "full AM" conditions the estimated IT rate is around 7 bits s^{-1} at the wrist and 5 bits s^{-1} at the fingertip. Tan *et al.* (1999) have measured an information transfer rate of 12 bits s^{-1} for three-channel tactile and kinesthetic stimulation on the thumb and two fingers, corresponding to a rate per channel in the range 7–9 bits s^{-1} (Tan, 1997). The estimates from the present study compare well with this, bearing in mind that the present experiment involves tactile stimulation only. Blamey and Clark (1987) and Blamey *et al.* (1990), using electrotactile stimulation of the digital nerve, measured an IT of around 1.5 bits with variation of stimulus intensity, and around 1 bit with variation of stimulus repetition rate. Rabinowitz *et al.* (1987), using vibrotactile stimuli on the middle fingertip which differed in terms of frequency, intensity, and/or contactor area, measured an information transfer of 1–2 bits for each dimension and 4–5 bits for all three dimensions. These values are somewhat larger than those obtained in the present study, presumably because the stimuli in the two previous studies were simpler than the time-varying sequences used in the present study.

The presence/absence of gaps in the stimuli provides binary information which might be expected to contribute an additional IT of 1 bit. However, reliable transmission of binary information requires a d' of at least 5.0 for discrimination of the binary alternatives (Braida and Durlach, 1972). In experiment 1, for 0.5-oct contrasts where the effect of gap-related information is seen most clearly, scores for test items cued by 120-ms gaps convert to d' values of around 2.6 only. In experiment 2, where results appear to be dominated by cues from gaps in the stimuli of ~100-ms duration, the highest discrimination scores (over 80% for the four best test items in the absence of amplitude modulation; see Fig. 4) convert to a d' of around 3.4 only. Thus reliable transmission of the gap/no-gap distinction is not observed in either experiment, although better results would presumably be obtained if the information were presented via gaps of greater duration. Discrimination of gap-related information does not appear to be more difficult in experiment 2, suggesting that the inherent variability of the speech-derived stimuli has no adverse effects on this aspect of subjects' performance. (As mentioned above, the choice of test material for experiment 2 did not, in the event, allow a full investigation of the effect of stimulus variability on discrimination of frequency and amplitude modulation.)

In the strategy adopted for stimulus design, amplitude modulation has been used to provide a possible enhancement of the perceived stimulus variations due to frequency modulation, i.e., amplitude is covaried redundantly with frequency. In principle, amplitude modulation might be used in a different way—to provide a second, independent channel for information transfer, running alongside the information transfer from frequency modulation. However, the full-range d' values obtained in experiment 1 indicate that tactile frequency and amplitude are not very effective means for information transfer and (bearing in mind also the cognitive problems of dealing with two independent "messages" delivered via a single site) it seems unlikely that a system based on independent frequency and amplitude modulation would be workable in practice.

V. CONCLUSION

It may be concluded that, provided correction is made for reduced sensitivity, perception at the underside of the wrist is not inherently worse than at the fingertip. Indeed, there is evidence that perception of certain stimuli can be better at the wrist than at the fingertip. These findings suggest that data in the literature relating to the hand or finger do not necessarily represent an overestimate of perceptual capabilities at less-sensitive sites such as the forearm or torso. For some types of tactile communication devices the wrist may be a good choice of stimulation site, since it offers advantages of convenience and cosmetic acceptability.

However, it is clear that single-channel transmission of information of the type described here has severe limitations. In particular, tactile frequency and intensity—individually or in combination—offer very limited information transfer of around 1 bit at a single site (or, equivalently, around two reliably discriminable categories only). It is probable that greater information capacity may be obtained by using multiple stimulation sites so as to involve the spatial aspects of tactile perception (Szaniszlo *et al.*, 1998; Taylor *et al.*, 1998; Vega-Bermudez and Johnson, 1999; Summers and Chanter, 2002; see also earlier studies involving spatially distributed stimulation which are cited in the Introduction). As a *coda* to the present study, a brief experiment (Whybrow, 2002) was carried out to explore the possibilities of spatial coding. A 100-contactor stimulator array covering 1 cm^2 on the fingertip (Summers and Chanter, 2002) allowed a speech-derived signal (in this case, the voice-pitch contour) to be presented as a spatial variation of 320-Hz vibrotactile stimulation. A "moving-bar" display (1-cm line of stimulation traversing the fingertip with a dynamic range of 0.9 cm) proved no more effective for information transfer than single-channel delivery of the same signal (equivalent to the "full-AM" presentation used in the main part of this study). However, a

"variable area" display (square zone of stimulation with a dynamic range from 0.01 to 1 cm^2) produced significantly better results [mean score of 91±3% in a two-alternative identification task, chance score 50%, compared to 74±5% for the single-channel system], suggesting that stimulator arrays may have some utility in this context.

ACKNOWLEDGMENTS

This research was supported by the UK Engineering and Physical Sciences Research Council. Two anonymous reviewers are thanked for their helpful suggestions.

Bach-y-Rita, P. (**1983**). "Tactile vision substitution—past and future," Int. J. Neurosci. **19**, 29–36.

Bach-y-Rita, P., and Kercel, S. W. (**2003**). "Sensory substitution and the human-machine interface," Trends in Cognitive Science **7**, 541–546.

Bernstein, L. E., Schechter, M. B., and Goldstein, M. H. (**1986**). "Child and adult vibrotactile thresholds for sinusoidal and pulsatile stimuli," J. Acoust. Soc. Am. **80**, 118–123.

Blamey, P. J., and Clark, G. M. (**1987**). "Psychophysical studies relevant to the design of a digital electrotactile speech processor," J. Acoust. Soc. Am. **82**, 116–125.

Blamey, P. J., Alcantara, J. I., Cowan, R. S. C., Galvin, K. L., Sarant, J. Z., and Clark, G. M. (**1990**). "Perception of amplitude variations of pulsatile electrotactile stimuli," J. Acoust. Soc. Am. **88**, 1765–1772.

Bliss, J. C., Katcher, M. H., Rogers, C. H., and Shepard, R. P. (**1970**). "Optical-to-Tactile Image Conversion for the Blind," IEEE Trans. Man-Machine Syst. **11**, 58–65.

Boothroyd, A. (**1985**). "A wearable tactile intonation display for the deaf," IEEE Trans. Acoust., Speech, Signal Process. **33**, 111–117.

Braida, L. D., and Durlach, N. I. (**1972**). "Intensity perception. II. Resolution in one-interval paradigms," J. Acoust. Soc. Am. **51**, 483–502.

Brooks, P. L., Frost, B. J., Mason, J. L., and Chung, K. (**1985**). "Acquisition of a 250-word vocabulary through a tactile vocoder," J. Acoust. Soc. Am. **77**, 1576–1579.

Cholewiak, R. W. (**1979**). "Spatial factors in the perceived intensity of vibrotactile patterns," Sens Processes **3**, 141–156.

Cholewiak, R. W., and Collins, A. A. (**2003**). "Vibrotactile localization on the arm: Effects of place, space, and age," Percept. Psychophys. **65**, 1058–1077.

Clements, M. A., Braida, L. D., and Durlach, N. I. (**1982**). "Tactile communication of speech: II. Comparison of two spectral displays in a vowel discrimination task," J. Acoust. Soc. Am. **74**, 1131–1135.

Craven, B. J. (**1992**). "A table of d' for M-alternative odd-man-out forced-choice procedures," Percept. Psychophys. **51**, 379–385.

Formby, C., Morgan, L. N., Forrest, T. G., and Raney, J. J. (**1992**). "The role of frequency selectivity in measures of auditory and vibrotactile temporal resolution," J. Acoust. Soc. Am. **91**, 293–305.

Galvin, K. L., Blamey, P. J., Cowan, R. S. C., Oerlemans, M., and Clark, G. M. (**2000**). "Generalization of tactile perceptual skills to new context following tactile-alone word recognition training with the Tickle Talker," J. Acoust. Soc. Am. **108**, 2969–2979.

Gescheider, G. A., Bolanowski, S. J., Verrillo, R. T., Arpajian, D. J., and Ryan, T. F. (**1990**). "Vibrotactile intensity discrimination by three methods," J. Acoust. Soc. Am. **87**, 330–338.

Goff, G. D. (**1967**). "Differential discrimination of frequency of cutaneous mechanical vibration," J. Exp. Psychol. **74**, 294–299.

Jansen, C., Oving, A., and van Veen, H.-J. (**2004**). "Vibrotactile movement initiation," *Proc. Eurohaptics 2004*, Munich, Germany, pp. 110–112.

Kirman, J. H. (**1974**). "Tactile perception of computer-derived formant patterns from voiced speech," J. Acoust. Soc. Am. **55**, 163–169.

Murray, A. M., Klatzky, R. L., and Khosla, P. K. (**2003**). "Psychophysical characterization and testbed validation of a wearable vibrotactile glove for telemanipulation," Presence-Teleop. Virt. **12**, 156–182.

Pickett, J. M., and Pickett, P. H. (**1963**). "Communication of speech sounds by a tactual vocoder," J. Speech Hear. Res. **6**, 207–222.

Rabinowitz, W. M., Houtsma, A. J. M., Durlach, N. I., and Delhorne, L. A. (**1987**). "Multidimensional tactile displays: Identification of vibratory intensity, frequency and contactor area," J. Acoust. Soc. Am. **82**, 1243–1252.

Raj, A. K., McGrath, B. J., Rochlis, J., Newman, D. J., and Rupert, A. H. (**1998**). "The application of tactile cues to enhance situation displays," in *Proc. 3rd Annual Symposium on Situational Awareness in the Tactical Environment*, Patuxent River, MD, pp. 77–84.

Rothenberg, M., Verrillo, R. T., Zahorian, S. A., Brachman, M. L., and Bolanowski, S. J., Jr., (**1977**). "Vibrotactile frequency for encoding a speech parameter," J. Acoust. Soc. Am. **62**, 1003–1012.

Sherrick, C. E. (**1985**). "A scale rate for tactual vibration," J. Acoust. Soc. Am. **78**, 78–83.

Snyder, J. C., Clements, M. A., Reed, C. M., Durlach, N. I., and Braida, L. D. (**1982**). "Tactile communication of speech: I. Comparison of Tadoma and a frequency-amplitude spectral display in a consonant discrimination task," J. Acoust. Soc. Am. **71**, 1249–1254.

Summers, I. R., ed. (**1992**). *Tactile Aids for the Hearing Impaired* (Whurr, London).

Summers, I. R., and Chanter, C. M. (**2002**). "A broadband tactile array on the fingertip," J. Acoust. Soc. Am. **112**, 2118–2126.

Summers, I. R., Milnes, P., Stevens, J. C., and Cooper, P. G. (**1996**). "Coding of acoustic features for a single-channel tactile aid," Br. J. Audiol. **30**, 238–248.

Summers, I. R., Cooper, P. G., Wright, P., Gratton, D. A., Milnes, P., and Brown, B. H. (**1997**). "Information from time-varying vibrotactile stimuli," J. Acoust. Soc. Am. **102**, 3686–3696.

Summers, I. R., Dixon, P. R., Cooper, P. G., Gratton, D. A., Brown, B. H., and Stevens, J. C. (**1994**). "Vibrotactile and electrotactile perception of time-varying pulse trains," J. Acoust. Soc. Am. **95**, 1548–1558.

Szaniszlo, J. A., Essick, G. K., Kelly, D. G., Joseph, A. K., and Bredehoeft, K. R. (**1998**). "Evocation and characterization of percepts of apparent motion on the face," Percept. Psychophys. **60**, 785–804.

Tan, H., Lim, A., and Traylor, R. (**2000**). "A psychophysical study of sensory saltation with an open response paradigm," Proc. ASME DSC **69-2**, 1109–1115.

Tan, H. Z. (**1997**). Personal communication.

Tan, H. Z., Durlach, N. I., Reed, C. M., and Rabinowitz, W. M. (**1999**). "Information transmission with a multifinger tactual display," Percept. Psychophys. **61**, 993–1008.

Taylor, P. M., Moser, A., and Creed, A. (**1998**). "A sixty-four element tactile display using shape memory alloy wires," Displays **18**, 163–168.

Thornton, A. R. D., and Phillips, A. J. (**1992**). "A comparative trial of four vibrotactile aids," in *Tactile Aids for the Hearing Impaired*, edited by I. R. Summers (Whurr, London), pp. 231–251.

Van Doren, C. L., Gescheider, G. A., and Verrillo, R. T. (**1990**). "Vibrotactile temporal gap detection as a function of age," J. Acoust. Soc. Am. **87**, 2201–2205.

van Erp, J. B. F., and van Veen, A. H. C. (**2001**). "Vibro-tactile information presentation in automobiles," *Proc. Eurohaptics 2001*, Birmingham, UK, pp. 99–104.

van Erp, J. B. F., and Verschoor, M. H. (**2004**). "Cross-modal visual and vibrotactile tracking," Appl. Ergon **35**, 105–112.

Vega-Bermudez, F., and Johnson, K. O. (**1999**). "SA1 and RA receptive fields, response variability, and population responses mapped with a probe array," J. Neurophysiol. **81**, 2701–2710.

Verrillo, R. T. (**1963**). "Effect of contactor area on the vibrotactile threshold," J. Acoust. Soc. Am. **35**, 1962–1966.

Verrillo, R. T. (**1966**). "Vibrotactile thresholds for hairy skin," J. Exp. Psychol. **72**, 47–50.

Verrillo, R. T. (**1971**). "Vibrotactile thresholds measured at the finger," Percept. Psychophys. **9**, 329–330.

Verrillo, R. T., and Chamberlain, S. C. (**1972**). "The effect of neural density and contactor surround on vibrotactile sensation magnitude," Percept. Psychophys. **11**, 117–120.

Weisenberger, J. M. (**1986**). "Sensitivity to amplitude-modulated vibrotactile signals," J. Acoust. Soc. Am. **80**, 1705–1715.

Whybrow, J. J. (**2002**). "Experiments relating to the tactile perception of speech," unpublished Ph.D. thesis, University of Exeter, UK.

Multidimensional analyses of voicing offsets and onsets in female speakers[a)]

Laura L. Koenig[b)]
Haskins Laboratories, New Haven, Connecticut 06511, and Long Island University, Brooklyn, New York

W. Einar Mencl[c)]
Haskins Laboratories, New Haven, Connecticut 06511

Jorge C. Lucero[d)]
Department of Mathematics, University of Brasilia, Brazil

(Received 24 August 2004; revised 20 July 2005; accepted 20 July 2005)

This study investigates cross-speaker differences in the factors that predict voicing thresholds during abduction–adduction gestures in six normal women. Measures of baseline airflow, pulse amplitude, subglottal pressure, and fundamental frequency were made at voicing offset and onset during intervocalic /h/, produced in varying vowel environments and at different loudness levels, and subjected to relational analyses to determine which factors were most strongly related to the timing of voicing cessation or initiation. The data indicate that (a) all speakers showed differences between voicing offsets and onsets, but the degree of this effect varied across speakers; (b) loudness and vowel environment have speaker-specific effects on the likelihood of devoicing during /h/; and (c) baseline flow measures significantly predicted times of voicing offset and onset in all participants, but other variables contributing to voice timing differed across speakers. Overall, the results suggest that individual speakers have unique methods of achieving phonatory goals during running speech. These data contribute to the literature on individual differences in laryngeal function, and serve as a means of evaluating how well laryngeal models can reproduce the range of voicing behavior used by speakers during running speech tasks. © *2005 Acoustical Society of America.*
[DOI: 10.1121/1.2033572]

PACS number(s): 43.70.Aj, 43.70.Gr [ARB] Pages: 2535–2550

I. INTRODUCTION

The goal of this work is to investigate cross-speaker variation in the conditions under which sustained vocal-fold vibration (voicing) ceases and begins again during abduction–adduction gestures in running speech. Our measurements, made on noninvasively obtained aerodynamic signals from six women, sample across the range of factors that are known to affect voicing thresholds. Our analyses are designed to determine the factors most responsible for sustaining and/or achieving voicing in individual speakers.

Since van den Berg (1958), researchers have recognized that voicing depends upon achieving a balance among vocal-fold parameters and aerodynamic forces. Vocal-fold parameters include thickness, degree of adduction, glottal shape, and tissue characteristics (longitudinal tension, damping); aerodynamic forces include the transglottal pressure and the Bernoulli effect. In recent decades, theoretical and modeling studies have formalized the requirements for voicing in laryngeal models of varying complexity, capturing many features of human vocal behavior and providing estimates of the quantities involved in achieving and sustaining phonation (e.g., Ishizaka and Flanagan, 1972; Stevens, 1977; Titze, 1988, 1989, 1992).

Yet, relatively few data exist on the aerodynamic and laryngeal conditions at voicing offset and onset in living humans performing connected speech tasks involving abduction as well as adduction. Empirical investigations of phonation have frequently relied on measurements made from nonhuman (typically, canine) larynges (e.g., Alipour *et al.*, 1997; Alipour-Haghighi and Titze, 1991; Berke *et al.*, 1989; Finkelhor *et al.*, 1987; Saito *et al.*, 1983; Titze *et al.*, 1993; Yumoto *et al.*, 1993) or from excised human larynges (e.g., Baer, 1975; Matsushita, 1975; van den Berg and Tan, 1959). Such experiments elucidate general principles of vocal-fold vibration, but there are also limitations: Laryngeal geometry and histology differ across species (Cox *et al.*, 1999; Jiang *et al.*, 2001; Kim *et al.*, 2004), and excised larynges lack natural patterns of muscle contraction. The position of the human larynx is such that direct measurement of phonation during running speech requires using patients who have had surgical alterations such as tracheostomy or hemilaryngectomy (e.g., Hirano *et al.*, 1991, Jiang and Titze, 1993) or performing invasive techniques including tracheal puncture and/or inserting cameras and light sources into the pharynx (e.g., Baer *et al.*, 1983; Hertegård and Gauffin, 1995; Hertegård *et al.*, 1995; Plant *et al.*, 2004; Timcke *et al.*, 1958). Investigations using such methods typically record data from few speakers

[a)]Portions of this work were presented at the 3rd and 4th International Conferences on Voice Physiology and Biomechanics (Denver, September, 2002, and Marseille, August, 2004).
[b)]Author to whom correspondence should be addressed. Electronic mail: koenig@haskins.yale.edu
[c)]Electronic mail: einar@haskins.yale.edu
[d)]Electronic mail: lucero@mat.unb.br

(often, only one), making it difficult to ascertain the degree of cross-speaker variation. Less invasive observation of laryngeal function via the oral cavity (e.g., Kitzing and Sonneson, 1974) permits recording a larger number of speakers, but imposes strict limitations on the speech task (usually to sustained low vowels). To complement this work, many researchers have relied on indirect measurements made on acoustic, electroglottographic, or oral airflow signals (e.g., Behrman and Baken, 1997; Childers and Lee, 1991; Dromey *et al.*, 1992, Hanson, 1997; Higgins and Saxman, 1993; Holmberg *et al.*, 1988, 1989, 1994; Löfqvist *et al.*, 1995; Ní Chasaide and Gobl, 1993; Price, 1989; Rothenberg, 1973). These methods facilitate measurement of multiple speakers, and also allow for recording protected populations such as children. These studies have provided much information on phonatory behavior in steady-state (adducted) conditions, again contributing to our general understanding of vocal-fold vibration. With a few exceptions (Löfqvist *et al.*, 1995; Löfqvist and McGowan, 1992; Ní Chasaide and Gobl, 1993), however, this literature has typically considered sustained vowels or the vocalic portions of repetitive CV syllable productions. In naturalistic, running speech, the larynx alternates between adducted and abducted postures. Thus, to understand fully how speakers control phonation during speech, we also need to consider voicing characteristics in the vicinity of an abduction gesture.

Past work on phonation threshold pressures (P_{th}; Ishizaka and Flanagan, 1972; Titze, 1992) provides insight into the factors that speakers can manipulate to achieve phonation offsets and onsets. Variations in P_{th} reflect changes in the conditions that make phonation more or less likely. For the body-cover model of the vocal folds (Titze, 1988), P_{th} is defined as follows:

$$P_{th} = \frac{cBx_0k_t}{T}, \tag{1}$$

where c=the mucosal wave velocity in the vocal-fold cover; B=tissue damping; x_0=glottal half-width; k_t is a translaryngeal pressure coefficient; and T is the thickness of the vocal folds. From this equation, we infer that the likelihood of phonation will vary with changes in translaryngeal pressure, abduction degree, longitudinal tension of the vocal folds (which affects the tissue compliance and, consequently, the mucosal wave velocity; cf. Titze, 1992), tissue damping, and vocal-fold thickness. Both tissue damping and vocal-fold thickness may vary with laryngeal setting.

Since the parameters that affect phonation thresholds are relatively independent of each other, it follows that speakers can satisfy the physical requirements for phonation offset and onset in a variety of ways. One question raised in past work is whether speakers actively increase longitudinal tension of the vocal folds to suppress voicing during speech. Halle and Stevens (1971) proposed that voiceless consonants such as [p, p^h, h] are characterized by stiff vocal folds, whereas voiced consonants such as [b, ɦ] have slack vocal folds. Authors investigating laryngeal muscle activity in the vicinity of voiced and voiceless consonants (e.g., Dixit and MacNeilage, 1980; Kagaya and Hirose, 1975; Löfqvist *et al.*, 1989) have obtained conflicting findings. One possible explanation for the disagreement across studies is that individuals vary in whether or not they supplement abduction with increased vocal-fold tension. Cross-speaker variation in voicing and devoicing strategies would be consistent with the larger literature on speech production, where researchers have observed that different speakers may produce the same consonant or vowel with different muscle activation patterns (Raphael and Bell-Berti, 1975) and/or articulatory postures (Borden and Gay, 1979; Johnson *et al.*, 1993). Although some studies of glottal function have described speaker differences (e.g., Hanson, 1997; Löfqvist *et al.*, 1995), these have not explicitly considered cross-speaker variability in the presence or absence of phonation, or in the methods speakers use to control voicing offsets and onsets.

The focus of our analysis is specifically on the factors that relate to the *timing* of phonation offset and onset. This emphasis is based on the extensive literature indicating that voice timing differentiates phonologically voiced and voiceless consonants across diverse languages (e.g., Abramson and Lisker, 1970, 1985; Lisker and Abramson, 1964, 1970). Whereas most of the work on contrastive voicing has investigated obstruent consonants, our work investigates phonation offsets and onsets in the context of /h/. Since /h/ involves abduction in the context of a relatively open vocal tract, it provides a convenient method of assessing phonatory behavior via easily obtained oral airflow signals. It is true that supraglottal conditions differ between /h/ and oral obstruents; in particular, supraglottal pressure does not vary much during the production of /h/, whereas obstruents involve a pressure buildup in the supraglottal vocal tract, which affects the transglottal pressure differential and, possibly, aspects of glottal geometry (Bickley and Stevens, 1986). Despite these differences, there is evidence that analysis of /h/ can provide insight into phonatory behavior for other voiceless consonants. First, most speakers systematically produce /h/ with a vocal-fold abduction gesture (e.g., Koenig, 2000; Klatt *et al.*, 1968; Löfqvist *et al.*, 1995), and measures of voice source features surrounding /h/ are often qualitatively similar to those features measured before and after other voiceless consonants (Löfqvist *et al.*, 1995). Further, within speakers, the voicing characteristics of /h/ and those of contrastively voiceless stops show significant correlations (Koenig, 2000). Thus, laryngeal behavior in /h/ can serve as a foundation for understanding voicing control in consonants for which voicing is contrastive. For comparison with the results of modeling, /h/ data are also useful in that we can consider phonatory behavior free of the complicating effects of upper vocal-tract constrictions.

As part of characterizing phonation offset and onsets, we consider how the two conditions differ. Several past studies have indicated that the requirements for initiating phonation are more stringent than those for sustaining it (e.g., Baer, 1975; Berry *et al.*, 1995, Chan *et al.*, 1997, Hirose and Niimi, 1987; Lindqvist, 1972; Lisker *et al.*, 1970; Munhall *et al.*, 1994, Titze *et al.*, 1995). The physical principles underlying this hysteresis phenomenon have been described in some detail for simple laryngeal models (e.g., Lucero, 1995, 1999). By quantifying the differences between voicing off-

TABLE I. Speaker information.

Speaker	Age (years)	Grew up where?	Devoiced /h/ (%)
F1	32	ME	52.3
F2	22	IA	37.1
F3	22	CT	28.1
F4	26	NY	56.3
F5	34	NY	54.8
F6	28	NY	85.9

sets and onsets in our data, we hope to inform future studies of hysteresis using more complex laryngeal models.

In general, then, we seek to provide detailed data on phonatory behavior in multiple speakers, to elucidate the range of strategies that individuals use to achieve phonatory goals, and to serve as a reference for evaluating how accurately laryngeal models reproduce the voicing patterns of normal speakers performing connected speech tasks. The data presented here are drawn from a larger study comparing voicing behavior for /h/ in several male and female speakers. Theoretical considerations and our past work (Koenig, 2000; Lucero and Koenig, 2005) suggest that women are more likely to devoice during an abduction gesture than men are. In this paper, we focus on female speakers who devoice at least 25% of their /h/ productions. In future manuscripts, we will undertake comparisons between men and women, and between speakers who produce mostly voiced /h/ vs those who produce a mixture of voiced and voiceless /h/.

II. METHODS

A. Speakers

Data were obtained from six adult females, who provided informed consent to take part in the experiment. All spoke American English as their native language; none had a strong regional accent. Participants were nonsmoking, in good health at the time of recording, reported no history of speech-, language-, or hearing disorders, and had vocal qualities within normal limits as judged informally by the first author. To restrict variation in vocal parameters as a function of aging, speakers were required to be between 20 and 40 years of age. Studies of laryngeal changes across the life span (Hirano *et al.*, 1983; Kahane, 1987, 1988) show little change in either the vocal folds or the laryngeal cartilages over this age range. Since the present analysis sought to quantify the conditions around voicing offset and onset, a final selection criterion was that speakers show a voicing break in 25% or more of their /h/ productions, to ensure that at least 50 tokens were available for statistical comparison of voicing offsets vs onsets. Table I shows speaker information and the percentage of devoiced /h/ produced by each speaker.

B. Speech materials

Speakers were recorded producing the following utterances, in three blocks of normal, loud, and soft speech:

A Papa Hopper [ə,pʰɑpəˈhɑpɚ],

A Papa Hippie [ə,pʰɑpəˈhɪpi],

A Papa Hooper [ə,pʰɑpəˈhupɚ].

The focus of analysis was the intervocalic /h/ initiating the fourth, primary stressed syllable. The target /h/ was placed at the beginning of a stressed syllable to decrease the likelihood that it would be lenited or deleted (Pierrehumbert and Talkin, 1992). The differing vowel contexts were intended to induce variation in supraglottal resistance. Small variation in $f0$ might also occur due to intrinsic $f0$ effects (e.g., Whalen and Levitt, 1995). The loudness conditions were intended to yield a range of subglottal pressures for each speaker.

Participants were asked to use their typical conversational speech rate throughout the experiment. During recording, the investigator or an assistant presented each utterance orally, and the speaker then repeated it five times. Each utterance appeared five times per loudness block, with utterances randomized within block. Thus, for each speaker, approximately 225 tokens of /h/ were collected: Five repetitions per 45 input trials (3 utterances $\times$ 3 loudness conditions $\times$ 5 presentations per loudness block). The first block of utterances was produced at normal loudness, described as "What you would use for normal conversation." The second block was produced in loud voice, described as "What you would use for a person in the next room." To encourage louder speech, the investigator or assistant stood several feet away from the speaker throughout this condition and provided the utterances in a loud voice. The soft condition was recorded last. Here, speakers were asked to talk in a voice that they would use with "a person sitting with his/her ear very close to your mouth." Subjects were explicitly asked not to whisper in this condition. To elicit soft speech, the investigator/assistant sat close to the subject and presented the utterances in a soft voice.

For one participant (F1), a fourth block was recorded, consisting of a longer carrier phrase ("Mama Papa Hopper/Hippie/Hooper") produced at normal loudness. The purpose of this manipulation was to determine whether /h/ voicing varied as a function of position in utterance. Although this speaker demonstrated lower subglottal pressures in this block than in her first block at normal loudness, there were no significant differences in the voice timing measures, so the two blocks were combined for the analyses reported here.

C. Equipment and recording

Three signals were recorded for each utterance. An acoustic signal was recorded using a directional microphone (Sennheiser MKH816T) positioned approximately 2 feet from the speaker. The acoustic signals were low-pass filtered at 9.5 kHz and sampled at 20 kHz. Two aerodynamic signals were collected, filtered at 4.8 kHz, and sampled at 10 kHz. Oral airflow was collected using a Rothenberg mask and Glottal Enterprises hardware (MSIF-2). Speakers were reminded throughout recording to keep the mask pressed firmly to the face to prevent leaks, and the investigator or assistant visually assessed mask fit throughout recording. An

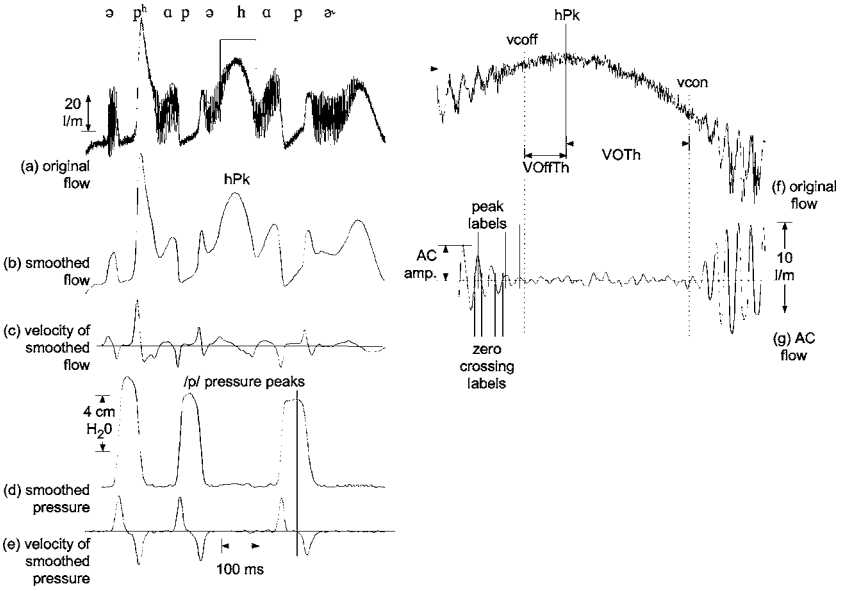

FIG. 1. One token from speaker F1, showing events used in measurement. The token shown here has a voicing break of approximately 70 ms. Panel (a) Original flow signal (lightly smoothed to remove noise). Panel (b) Smoothed or DC flow signal. Panel (c) First derivative (velocity) of the smoothed flow. Panel (d) Smoothed pressure signal. Panel (e) First derivative (velocity) of smoothed pressure. Panel (f) A short segment of the original flow signal expanded to show voicing offset and onset. Panel (g) The AC flow signal for the same time frame shown in panel (f).

intraoral pressure signal was obtained using a catheter-tip pressure transducer (Gaeltek CT/S) positioned within a piece of medical tubing fed through one of the holes in the mask's front. A plastic clamp was screwed tightly to the distal end of the tube, securing the transducer inside the tube and ensuring an airtight seal. Tube length and angle were adjusted at the beginning of the experiment so that the tube was positioned just inside the oral cavity, past the teeth, but not so far as to interfere with articulation. Occasionally, a speaker noted that, even after adjustment, she could still feel the tube during production of the high vowels, especially /ɪ/. In these cases, tube position was considered acceptable when (a) the speaker was not uncomfortable; (b) she felt that the tube did not alter her speech patterns; and (c) the pressure signal showed expected shape variations during oral closures.

Calibration signals were obtained immediately after each input session using a rotameter for the flow and a standing-water manometer for the pressure. Straight-line fits were obtained from these signals and the slope coefficient was applied to the raw signals as the first step in data processing. To correct for low-level drift in the signals over the course of the recording session, a unique baseline (intercept) was obtained for each pressure and flow signal (five repetitions in response to one utterance presentation). The /p/ closures (during which there is no airflow) were used to set the zero flow level for each signal, whereas the stressed vowels (when the vocal tract is most open) were used to set the zero-pressure level.

D. Signal processing

Signals were transferred to a VAX computer for analysis. The acoustic signal was used only for auditory assessment of the productions; all measurements were performed on the airflow, air pressure, or signals derived from them. Processing involved the following steps:

(a) The calibrated flow signals were lightly smoothed with a 5-point triangular window (0.5 ms) to remove low-amplitude, high-frequency noise in the signals. Henceforth, we will refer to these lightly smoothed signals as the "original flow signals."

(b) Smoothed versions of the flow and pressure were obtained by smoothing the signals twice with a 133-point triangular window. This process obliterated all or most evidence of glottal pulses. The smoothed flow signal shows low-frequency variation over the course of the utterance, reflecting articulatory movements, including vocal-fold abduction. For ease of reference, we will also refer to this smoothed, slowly varying signal as the DC flow, to contrast it with the rapidly varying AC flow signal that reflects vocal-fold vibration.

(c) AC flow signals were generated by subtracting the smoothed flow signal from the original (lightly smoothed) flow signal, and smoothing the result with a 25-point triangular window.

(d) First time derivatives (velocity signals) were estimated from the smoothed flow and pressure signals using a 3-point difference algorithm, and smoothed iteratively (typically twice) with a 133-point triangular window until zero crossings for major aerodynamic events could be easily obtained.

E. Measurements

The following measures were made for each token (see Fig. 1):

(a) Peak airflow during abduction for /h/ (hPk) was defined by the zero crossing in the first derivative of the smoothed flow signal [Fig. 1, panels (b) and (c)]. In the simple case of nonrotational flows through an open vocal tract, the baseline or DC flow signal at the mouth provides a good approximation to the low-frequency flow at glottal exit, which is in turn proportional to glottal area when other factors (chiefly, air density and subglottal pressure) are held constant (Titze, 1988). Thus, the baseline flow variation during /h/ reflects changes in glottal cross-sectional area, and the hPk measure pro-

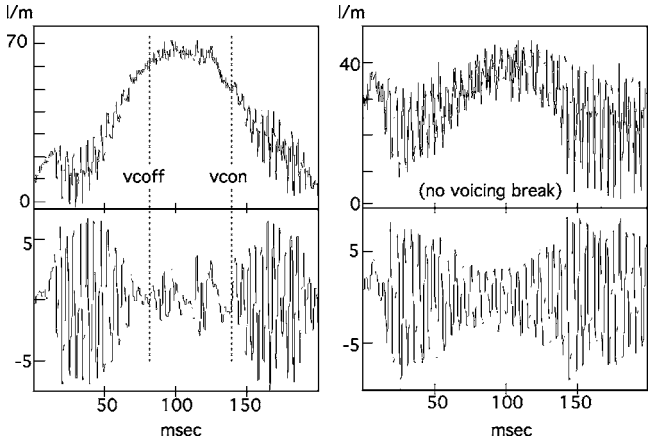

FIG. 2. Two signals from speaker F2, showing the original flow signals (above) and the AC flow signals (below). The token at left shows irregular flow variations around the /h/ flow peak. The voicing offset (vcoff) and onset (vcon) labels mark the region considered devoiced in this token. The token at right shows an /h/ with regular voicing continuing throughout.

vides an estimate of maximum glottal abduction. We discuss factors that affect the accuracy of this estimate below in Sec. II F.

(b) Peak pressures were measured during the second and third /p/ closures (i.e., those preceding and following the /h/). As with hPk, these were obtained via zero crossings in the first derivative of the smoothed pressure signal [see Fig. 1, panels (d) and (e)]. The two values were averaged to provide an estimate of subglottal pressure, or P_{sub} (cf. Löfqvist *et al.*, 1982; Smitheran and Hixon, 1981).

(c) Times of voicing offset and onset were determined by visual inspection of the AC flow signals, with reference to the original flow signals [Fig. 1, panels (f) and (g)]. Voicing was defined as periodic oscillation in the AC flow signal. Some tokens in some speakers showed AC flow variations around the /h/ flow peak that were highly irregular in frequency and amplitude. These were considered to represent unstable, chaotic movements of the vocal folds rather than the sustainable, regular vibration characteristic of voicing. An example of such chaotic oscillation is shown in Fig. 2, along with a fully voiced /h/ from the same speaker.

Two duration measures were calculated from the voicing offset and onset times: Voicing offset to hPk (VOffTh) and hPk to voicing onset (VOTh). VOTh is analogous to the voice onset time (VOT; Lisker and Abramson, 1964) in an aspirated stop consonant, in which the peak abduction occurs at approximately the time of oral release (cf. Löfqvist, 1992 for some qualifications). For tokens of /h/ with a voicing break, VOTh and/or VOffTh were positive. For cases of fully voiced /h/, both VOTh and VOffTh were approximately 0; specifically, the voicing offset and onset labels were placed within one glottal pulse of the hPk, as described below.

Presence or absence of a voicing break was also determined based on the times of voicing offset and onset. The automatic measurement routines for $f0$ and pulse (AC) amplitude required a whole number of glottal pulses before and after voicing offset/onset, or, in cases of fully voiced /h/, the time of peak abduction (hPk). Glottal pulses whose open phase coincided with the hPk label were thus not measured. Such tokens had a measured "voicing break" duration of about a pulse period. To prevent counting these tokens as instances of devoiced /h/, a two-pulse-period criterion was defined for each subject, based on the session average of her $f0$ values at voicing offset and onset (an average of three pulses, as described below). Tokens with a voicing break two periods or longer were labeled as "devoiced."

(d) Flow amplitudes in the smoothed (DC) signal were measured at the times of voicing offset and onset (DCOff, DCOn). These are the amplitude values that correspond to the voicing offset and onset times indicated in Fig. 1, panel (f).

(e) Fundamental frequency ($f0$) at the times of voicing offset and onset ($f0$Off, $f0$On) was obtained from zero crossings in the phonated regions of the AC flow signal [Fig. 1, panel (g)]. Two measures of $f0$ were obtained at both offset and onset: The $f0$ of the last/first pulse, and an average of the last/first three pulses. As discussed below, the average measures proved to be more reliable, and were therefore used for the final statistical analyses.

(f) Glottal pulse (AC flow) amplitudes immediately before/after voicing offset/onset (ACOff, ACOn) were obtained by performing peak picking in the AC flow signal [Fig. 1, panel (g)]. As with $f0$, two measures were obtained at offset and onset: The amplitude of the last/first pulse, and an average of the last/first three pulses; the statistical analyses ultimately included only the average measures.

In summary, the measures provide information on (a) the degree of abduction during /h/ (hPk); (b) the subglottal pressure level during the utterance (P_{sub}); (c) voice timing (VOffTh, VOTh); (d) the degree of abduction at which voicing stopped and started (DCOff, DCOn); (e) changes in passive and actively induced longitudinal tension within the folds, as reflected by $f0$ measures ($f0$Off, $f0$On); and (f) the vibratory amplitude of the vocal folds (ACOff, ACOn).

F. Accuracy of estimated measures

As noted in the previous section, we use the hPk measure as an estimate of the extent of glottal abduction during /h/, and the average of the intraoral pressure peaks for the two /p/'s flanking the VhV sequence as an estimate of subglottal pressure (P_{sub}). Two factors limit the precision of these estimates.

In the case of hPk, the qualification involves the extent to which P_{sub} remains constant during abduction. When P_{sub} is stable, airflow varies in proportion to the extent of glottal opening, and variations in hPk directly reflect changes in glottal opening. In fact, P_{sub} may decrease somewhat when the glottis opens and the vocal tract is open (Löfqvist, 1975; Ohala, 1990); as a result, the airflow changes may underestimate glottal area change. Few direct measurements exist to quantify the extent of such a decrease across speakers, but in our recent modeling work (Lucero and Koenig, 2005) we

used P_{sub} as a control parameter for reproducing voicing patterns in intervocalic /ɑhɑ/ produced by eight speakers (including some of the women analyzed here). The results of those simulations showed an average P_{sub} decrease across speakers of about 2 cm H_20 during the /h/ compared to the neighboring vowel. The corresponding value obtained by Löfqvist (1975) was about 1.2 cm H_20.

In the case of P_{sub}, it should be noted that the /h/ in our utterances introduced a stressed syllable, whereas the pressure peaks were measured during /p/ closures initiating unstressed syllables. One effect of stress is to increase subglottal pressure momentarily. Past studies on subglottal pressure variation as a function of stress suggest that stressed syllables are typically produced at pressures 1–2 cm H_20 higher than unstressed syllables (Brown and McGlone, 1974; Dixit and Brown, 1978; Dixit and Shipp, 1985; McGlone and Shipp, 1972).

Decreases of P_{sub} as a function of abduction and increases as a function of stress are thus similar in magnitude. In combination, therefore, the two factors should roughly balance out in our data. We note two additional points about these measures. In the case of hPk, the effect of a subglottal pressure decrease during abduction should become more extreme as abduction extent becomes larger. The implication is that the hPk measure should be considered a conservative measure of abduction degree; in other words, the hPk variation in our data is probably more limited than the actual variation in abduction degree. As for P_{sub}, our intent was to capture major variations in pressure as a function of loudness condition, and the statistical analyses generally show the expected pressure variation across loudness conditions.

G. Statistics

Paired *t*-tests were used to test for offset–onset differences. To explore the effects of vowel and loudness condition on measured variables, analyses of variance (ANOVAs) and χ^2 analyses were performed. Finally, simple correlations, multiple regression, and principal components analyses were performed for each subject in order to clarify the relationships among correlated variables. For these relational analyses, the loudness condition was recoded into a quasicontinuous variable with loud=1, normal=0, soft=−1; the vowel variable was recoded into two variables, one with /ɑ/=1, /u/=/ɪ/=0 ("/ɑ/-ness") and one with /ɪ/=1, /ɑ/=/u/=0 ("/ɪ/-ness"). An alpha level of 0.01 was set as the significance criterion for all analyses.

H. Measurement reliability

A subset of the data was remeasured by the same investigator (the first author) several weeks after the original measurements were completed (for some subjects, a duration of several months). Specifically, voicing offsets and onsets, which were determined visually, were remeasured for the third repetition (out of five) in the even-numbered input trials (22 of 45) for each speaker. The set of remeasured data comprised 128 tokens, or approximately 9% of the data. All measures associated with voicing offsets and onsets (DC and AC flow, *f*0) were also derived again. Pressure peaks during /p/ and flow peaks during /h/ were not remeasured because they were defined automatically rather than visually. The original and remeasured values were compared by performing a correlation on the two sets of data, and by calculating means and standard deviations of the differences between each pair of measurements.

TABLE II. Results of reliability analyses: *r*- and *p* values from the correlation analysis, and the average and standard deviation (SD) of the differences between the original and remeasured data sets. Durational measures (VOffTh, VOTh) are in ms; flow values (DCOff/On, ACOff/On) are in l/m; *f*0 values are in Hz. VOffTh=time of voicing offset, relative to the peak flow in /h/; VOTh=time of voicing onset relative to the peak flow in /h/; DCOff and DCOn refer to the baseline, or DC, flow values at voicing offset and onset; ACOff and ACOn refer to the pulse amplitudes at offset and onset; *f*0Off and *f*0On refer to the *f*0 values at offset and onset.

Variable	*r*	*p*	Mean diff.	SD of diff.
VOffTh	0.95	<0.001	−0.56	4.61
VOTh	0.95	<0.001	0.12	6.30
DCOff	1.00	<0.001	0.03	2.37
DCOn	0.99	<0.001	<0.01	3.22
ACOff	0.91	<0.001	0.10	0.85
ACOn	0.92	<0.001	0.08	1.01
*f*0Off	0.91	<0.001	−0.42	11.05
*f*0On	0.82	<0.001	−0.51	19.37

The correlations between the original and the remeasured data were highly significant, with $p<0.001$ for all measures, but some differences were observed between the single and the three-pulse averaged measures performed for AC flow and *f*0. In the case of AC flow, the two measurement sets were similar, with all *r* values between 0.8 and 0.92. However, the *r* values for the single-pulse *f*0 measures were considerably lower than those for the three-pulse averaged measures: Single-pulse *r* values were 0.56 for offsets and 0.69 for onsets, but 0.91 for offsets and 0.82 for onsets in the averaged measures. In order to maintain high reliability across measures, we opted to use the averaged measures in all subsequent analyses. The reliability results for the final set of measures are given in Table II.

Because laryngeal conditions change rapidly in the vicinity of an abduction gesture, the three-pulse average measures do represent some loss of information on conditions around voicing thresholds. To determine how closely the averaged measures captured the patterns of the single-pulse measures, we also computed correlations between the single-pulse and averaged measures for the entire dataset (all productions, all speakers). All correlations were significant at $p<0.001$; *r* values ranged from 0.8–0.87. When the correlations were run within single speakers, the *r* values varied from 0.53–0.92, but all were again highly significant at $p<0.001$.

III. RESULTS

A. Offset–onset differences

Past work has indicated that vocal-fold vibration is subject to a hysteresis effect, whereby voicing offsets and onsets occur under different conditions. To investigate offset–onset differences in the current data, paired *t*-tests were performed

TABLE III. Offset–onset differences in tokens with voicing breaks for all speakers F1–F6: Means, SDs, and results of two-tailed *t*-tests. Temporal measures (VOffTh, VOTh) are in ms; amplitude (DC, AC) measures are in 1/m; *f*0 is in Hz.

	F1	F2	F3	F4	F5	F6
VOffTh means (SD)	9.3 (14.3)	6.5 (13.3)	8.7 (13.0)	4.0 (7.2)	15.2 (14.4)	22.0 (13.9)
VOTh means (SD)	45.9 (18.8)	33.1 (18.1)	27.5 (16.7)	24.5 (10.0)	39.9 (18.8)	47.0 (19.2)
t	−18.64	−9.83	−5.59	−21.04	−11.03	−12.62
p	<0.001	<0.001	<0.001	<0.001	<0.001	<0.001
DCOff means (SD)	60.4 (12.9)	51.6 (19.0)	15.5 (5.2)	35.0 (16.8)	17.5 (7.5)	37.3 (13.6)
DCOn means (SD)	43.2 (13.4)	42.3 (20.3)	13.6 (5.7)	23.5 (16.1)	11.6 (7.9)	27.6 (11.9)
t	20.85	8.48	4.04	15.30	14.15	13.40
p	<0.001	<0.001	<0.001	<0.001	<0.001	<0.001
*f*0Off means (SD)	175.2 (12.0)	195.7 (17.1)	184.0 (15.9)	209.4 (14.4)	135.8 (19.4)	208.3 (16.4)
*f*0On means (SD)	204.3 (14.5)	216.0 (15.7)	205.1 (15.1)	243.5 (16.6)	179.5 (25.7)	257.8 (32.1)
t	−20.82	−10.25	−9.02	−20.18	−18.61	−18.44
p	<0.001	<0.001	<0.001	<0.001	<0.001	<0.001
ACOff means (SD)	1.8 (0.9)	3.4 (2.0)	0.9 (0.6)	3.2 (1.9)	2.6 (1.1)	1.3 (1.1)
ACOn means (SD)	2.9 (1.6)	3.6 (1.9)	1.1 (0.7)	4.3 (2.8)	2.3 (1.1)	1.8 (1.6)
t	−8.33	−0.93	−2.56	−5.6	2.08	−5.63
p	<0.001	0.357	0.013	<0.001	0.040	<0.001

on the following sets of measures in tokens with voicing breaks: VOffTh vs VOTh; DCOff vs DCOn; *f*0Off vs *f*0On; and ACOff vs ACOn. Results, given in Table III, indicate that, for all speakers (a) voicing offsets occurred significantly closer in time relative to the flow peak than voicing onsets (VOffTh < VOTh); (b) voicing offsets occurred at significantly higher DC flow amplitudes than voicing onsets (DCOff > DCOn); and (c) voicing began at significantly higher levels of *f*0 than it ceased (*f*0Off < *f*0Off). Qualitatively, five of the six speakers had lower AC flows at voicing offset than onset, but the difference was only significant in three speakers. It may be that the use of the three-pulse average measure masked short-term changes in pulse amplitude near voicing offset and onsets. The results for voice timing and DC flow amplitudes at voicing offset and onset are consistent with our expectations of a hysteresis effect. In these data, the higher *f*0 following /h/ most likely reflects the stress pattern of the utterance, namely the fact the target /h/ initiated a stressed syllable.

A final observation from Table III is that standard deviations (SDs) tended to be higher overall for voicing onsets than for offsets. The *t*-tests on the 6 SDs for each measurement pair showed that the difference was significant for VOffTh vs VOTh [$t(5)=11.795$, $p<0.0001$; mean difference=4.25]. Given the small number of data points for each comparison, however, the results of these analyses must be considered preliminary.

B. Categorical effects of loudness and vowel on devoicing

Figure 3 shows the percentage of devoiced /h/ for each speaker as a combined function of vowel and loudness. The statistical tests for loudness- and vowel-related changes are summarized in Table IV. Full results of the ANOVAs, with means and standard deviations for the measures, are given in the Appendixes. In the following section, we present an overview of the results; individual patterns are considered in more detail below.

Figure 3 and Table IV indicate that the vowel and loud-

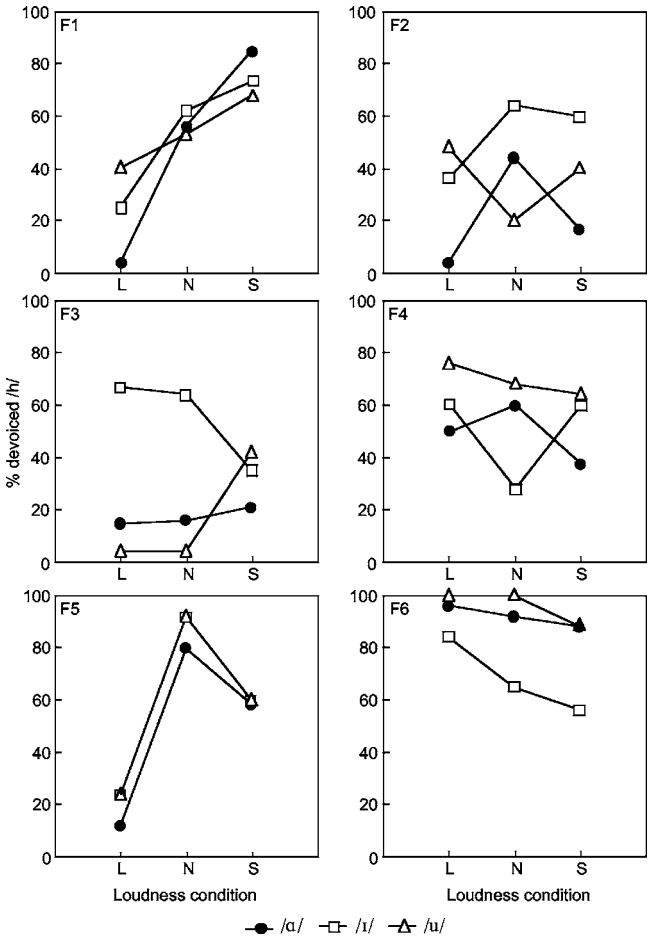

FIG. 3. Percentage of voiceless /h/ as a function of loudness condition and vowel for each speaker. *L*=loud; *N*=normal; *S*=soft.

TABLE IV. Summary of vowel and loudness effects. Percentage of devoicing across conditions was assessed using χ^2 analyses; effects of loudness and vowel on P_{sub} and hPk measures were assessed using ANOVAs. Asterisks indicate significance at $p<0.01$. The results of the post-hoc tests are summarized in cases of significant p-values. For example, speaker F1 had significant P_{sub} differences among all 3 of her loudness conditions; for F2, loud and normal were not significantly different from each other, but both were significantly different from the soft condition.

Speaker	% devoicing as a function of loudness	% devoicing as a function of vowel	P_{sub} as a function of loudness condition	hPk as a function of loudness condition	P_{sub} as a function of vowel	P_{sub} vowel-by-loudness interaction
F1	*		*			
			$L>N>S$			
F2		*	*	*	*	
			$L,N>S$	$L>N,S$	/ɑ,u/>/ɪ/	
F3		*	*		*	($p=0.012$)
			$L>N,S$		/u/>/ɑ,ɪ/	Average pressure pattern /u/>/ɑ,ɪ/ true of loud and normal; in the soft condition, /u/ had the lowest pressure, and /ɪ/ had the highest.
F4		($p=0.02$)	*	*		*
			$L>N>S$	$S>N,L$		Steeper pressure decrease for /ɪ/ from loud to normal than for /ɑ, u/
F5	*		*	*	*	*
			$L,S>N$	$L>N,S$	/ɪ,u/>/ɑ/	$L>S>N$ differences smaller for /u/
F6	($p=0.02$)	*	*	*		*
			$L,N>S$	$L>N>S$		$L>N>S$ for /ɪ/ and /u/; for /ɑ/, ($L=N>S$).

ness conditions had different effects on devoicing across speakers. To understand these effects, we must consider how the vowel and loudness manipulations affected underlying production parameters. The loudness manipulation was chiefly intended to yield variation in subglottal pressure (P_{sub}). To determine whether this was achieved, ANOVAs were run on P_{sub} as a function of loudness level (L=loud, N=normal, S=soft). The results (summarized in Table IV) showed that P_{sub} varied significantly ($p<0.001$) across loudness condition for all speakers. Five of the six speakers presented the expected pattern of $L>N>S$, although not all pairwise tests were significant. In one speaker (F5), average P_{sub}'s were higher in both the loud and soft conditions than in normal loudness ($L,S>N$). This pattern is discussed further in Sec. III D below.

Dromey and Ramig (1998) have demonstrated that speakers may change articulatory patterns as well as subglottal pressure in varying loudness conditions. To investigate whether the speakers recorded here varied their degree of abduction as loudness changed, ANOVAs were run on hPk measures as a function of loudness condition. The results (see Table IV) indicated that loudness had significant effects on hPk for four speakers, but the direction of the effect was inconsistent: One speaker (F6) showed decreasing hPk flows as loudness decreased; two (F2, F5) showed higher hPk flows for the loud condition only; and one (F4) had the highest hPk values in the soft condition.

To determine whether speakers altered P_{sub} in response to changing vocal-tract (vowel) postures, ANOVAs were run on P_{sub} as a function of vowel. The results (see Table IV) were significant for three speakers (F2, F3, F5), but the direction of the effect varied across speakers. Further, P_{sub} showed significant interactions between loudness and vowel for three speakers (F4, F5, F6; results are again summarized in Table IV). We will return to these data below, and integrate them with the results of the relational analyses.

C. Predicting VOffTh and VOTh from measured variables

1. Correlations

As indicated above, interrelationships among many variables were expected. For example, loudness condition was expected to affect P_{sub}, but might also affect $f0$, via changes in P_{sub} and/or laryngeal setting. To quantify the relationships among the experimental variables, and to determine which variables were most strongly correlated with the voice timing variables (VOffTh, VOTh), simple regression analyses were performed. The occurrence of both voiced and voiceless /h/ meant that there were two populations of data points for both VOTh and VOffTh (zero vs a range of positive values); thus, two separate analyses were performed: One including the full data set, and another including the voiceless tokens only. Comparison of the results with and without fully voiced /h/ suggested that the pattern of results was similar across the two analyses. To formally quantify the relationship between the two datasets, we performed an r-to-z transform, correcting for non-normality of r-value distributions, and ran a correlation on the data from the full and the voiceless-only analyses. Results indicated high correlations for all data analyzed together ($r=0.900$, $p<0.0001$) and for offsets and onsets analyzed separately (offsets, $r=0.918$, $p<0.0001$; onsets, $r=0.879$, $p<0.0001$). These high correlations indicate that the variables associated with voicing vs devoicing also tend to predict the duration of devoicing when it occurs.

Table V presents the correlation matrices for the full data set (including both voiced and voiceless /h/). These data reveal some consistencies across speakers, and provide fur-

TABLE V. Correlation matrices for all tokens (voiced and voiceless) in all subjects. For the sake of compactness, the left column serves both offset and onset matrices; the offset variables (VOffTh, DCOff, *f*0Off, ACOff) refer to the left matrix, and the onset variables refer to the right matrix. Ellipses indicate correlations that were not significant at $p < 0.01$.

	Voicing offset									Voicing onset								
	VOffTh	/ɑ/	/ɪ/	Ld	DCOff	hPk	Pres	*f*0Off	ACOff	VOTh	/ɑ/	/ɪ/	Ld	DCOn	hPk	Pres	*f*0On	ACOn
									F1									
VOffTh/VOTh	1.00	⋯	⋯	⋯	0.15	0.26	⋯	⋯	⋯	1.00	⋯	⋯	−0.43	−0.52	0.21	−0.16	0.72	0.27
/ɑ/-ness		1.00	−0.49	⋯	−0.31	−0.31	⋯	⋯	⋯		1.00	−0.49	⋯	−0.22	−0.31	⋯	⋯	−0.15
/ɪ/-ness			1.00	⋯	0.26	0.27	⋯	⋯	⋯			1.00	⋯	⋯	0.27	⋯	⋯	0.27
Loudness				1.00	⋯	⋯	0.59	⋯	0.19				1.00	0.23	⋯	0.59	−0.28	⋯
DCOff/On					1.00	0.99	⋯	⋯	⋯					1.00	0.63	⋯	−0.33	−0.16
hPk						1.00	⋯	⋯	⋯						1.00	⋯	0.30	0.15
Pres							1.00	−0.18	⋯							1.00	⋯	⋯
f_0Off/On								1.00	⋯								1.00	0.30
ACOff/On									1.00									1.00
									F2									
VOffTh/VOTh	1.00	⋯	0.25	⋯	0.24	0.32	⋯	⋯	⋯	1.00	−0.24	⋯	⋯	−0.28	⋯	⋯	0.39	⋯
/ɑ/-ness		1.00	−0.50	⋯	⋯	⋯	⋯	⋯	−0.25		1.00	−0.5	⋯	⋯	⋯	⋯	−0.20	⋯
/ɪ/-ness			1.00	⋯	0.42	0.42	−0.21	⋯	⋯			1.00	⋯	0.34	0.42	−0.21	⋯	0.20
Loudness				1.00	0.52	0.50	0.22	0.32	0.42				1.00	0.56	0.50	0.22	0.25	0.40
DCOff/On					1.00	0.98	⋯	0.19	0.39					1.00	0.89	⋯	⋯	0.38
hPk						1.00	⋯	0.19	0.37						1.00	⋯	0.22	0.37
Pres							1.00	⋯	0.23							1.00	⋯	0.21
f_0Off/On								1.00	0.25								1.00	0.20
ACOff/On									1.00									1.00
									F3									
VOffTh/VOTh	1.00	⋯	0.45	⋯	⋯	0.27	⋯	⋯	⋯	1.00	⋯	0.19	⋯	⋯	0.20	⋯	0.28	⋯
/ɑ/-ness		1.00	−0.47	⋯	−0.60	−0.61	⋯	−0.27	−0.37		1.00	−0.47	⋯	−0.58	−0.61	⋯	−0.29	−0.25
/ɪ/-ness			1.00	⋯	0.44	0.53	⋯	⋯	0.41			1.00	⋯	0.46	0.53	⋯	0.28	0.54
Loudness				1.00	⋯	⋯	0.75	0.48	⋯				1.00	⋯	⋯	0.75	0.49	⋯
DCOff/On					1.00	0.95	⋯	0.24	0.60					1.00	0.91	⋯	⋯	0.48
hPk						1.00	⋯	0.23	0.61						1.00	⋯	0.27	0.54
Pres							1.00	0.67	⋯							1.00	0.57	⋯
f_0Off/On								1.00	0.29								1.00	0.32
ACOff/On									1.00									1.00
									F4									
VOffTh/VOTh	1.00	⋯	⋯	⋯	⋯	⋯	⋯	⋯	⋯	1.00	⋯	⋯	⋯	−0.48	⋯	⋯	0.68	0.26
/ɑ/-ness		1.00	−0.49	⋯	⋯	⋯	⋯	0.21	−0.16		1.00	−0.49	⋯	⋯	⋯	⋯	⋯	⋯
/ɪ/-ness			1.00	⋯	⋯	⋯	⋯	⋯	0.10			1.00	⋯	⋯	⋯	⋯	⋯	⋯
Loudness				1.00	−0.70	−0.70	0.93	⋯	0.28				1.00	−0.61	−0.70	0.93	0.34	0.25
DCOff/On					1.00	0.99	−0.61	⋯	−0.30					1.00	0.85	−0.53	−0.43	−0.44
hPk						1.00	−0.60	⋯	−0.31						1.00	−0.60	⋯	−0.31
Pres							1.00	0.22	0.23							1.00	0.41	0.22
f_0Off/On								1.00	−0.36								1.00	⋯
ACOff/On									1.00									1.00
									F5									
VOffTh/VOTh	1.00	⋯	⋯	⋯	−0.27	⋯	−0.22	⋯	⋯	1.00	⋯	⋯	−0.27	−0.64	⋯	−0.25	0.31	−0.21
/ɑ/-ness		1.00	−0.49	⋯	−0.47	−0.49	−0.29	⋯	−0.35		1.00	−0.49	⋯	−0.30	−0.49	−0.29	⋯	−0.30
/ɪ/-ness			1.00	⋯	0.43	0.50	⋯	0.19	0.32			1.00	⋯	0.36	0.50	⋯	⋯	0.23
Loudness				1.00	0.30	0.27	⋯	0.72	0.40				1.00	0.39	0.27	⋯	0.58	0.55
DCOff/On					1.00	0.95	0.30	0.26	0.45					1.00	0.76	0.35	⋯	0.41
hPk						1.00	0.22	0.23	0.44						1.00	0.22	0.25	0.42
Pres							1.00	0.19	0.25							1.00	⋯	0.27
f_0Off/On								1.00	0.70								1.00	0.58
ACOff/On									1.00									1.00

TABLE V. (*Continued.*)

	Voicing offset									Voicing onset								
	VOffTh	/ɑ/	/ɪ/	Ld	DCOff	hPk	Pres	*f*0Off	ACOff	VOTh	/ɑ/	/ɪ/	Ld	DCOn	hPk	Pres	*f*0On	ACOn
									F6									
VOffTh/VOTh	1.00	0.35	⋯	0.20	⋯	0.19	0.21	⋯	⋯	1.00	⋯	−0.47	⋯	−0.48	⋯	⋯	⋯	⋯
/ɑ/-ness		1.00	−0.49	⋯	−0.42	−0.29	⋯	⋯	⋯		1.00	−0.49	⋯	−0.21	−0.29	⋯	⋯	⋯
/ɪ/-ness			1.00	⋯	0.37	0.36	⋯	⋯	⋯			1.00	⋯	0.65	0.36	⋯	⋯	⋯
Loudness				1.00	0.51	0.59	0.51	−0.24	⋯				1.00	0.42	0.59	0.51	⋯	⋯
DCOff/On					1.00	0.93	0.44	−0.30	⋯					1.00	0.74	0.36	0.18	⋯
hPk						1.00	0.48	−0.28	⋯						1.00	0.48	⋯	⋯
Pres							1.00	−0.18	0.23							1.00	0.38	0.33
f_0Off/On								1.00	⋯								1.00	0.44
ACOff/On									1.00									1.00

ther evidence for offset–onset differences. First, in five of six speakers (all but F3), VOTh had a significant negative correlation with DCOn. This reflects the fact that a longer VOTh corresponds to voicing occurring later in the adduction gesture, and at lower flow rates. Correlations between VOffTh and DCOff were weaker and significant for only three of six speakers. However, DCOff and hPk were highly, significantly correlated for all speakers: For both the full and the voiceless-only analysis, all *r* values were above 0.89. (Recall that in tokens with no voicing break the times of voicing "offset" and "onset" were set within a pulse of the /h/ flow peak, so that offset, onset, and peak values were virtually identical; for this analysis, therefore, the voiceless-only dataset is more valid.) These high correlations were also expected given that voicing offset typically occurred very close in time to the peak abduction in /h/. The comparable onset correlations (DCOn–hPk) were significant for all speakers, but the *r* values were lower than for offsets (0.63–0.89 in the voiceless-only analysis).

Apart from these consistencies, the variables correlated with VOffTh and VOTh to different degrees across speakers. For example, VOTh in speaker F4 correlated with DCOn, *f*0On, and, to a lesser degree, ACOn. For F5, VOTh correlated with loudness, DCOn, pressure, *f*0On, and ACOn; note that the direction of the AC effect is the opposite of that for F4. Speaker F6 showed no effect of loudness, pressure, *f*0On, or ACOn; instead, VOTh values correlated with the /ɪ/ context along with DCOn.

2. Multiple regression

To determine how strongly each of the experimental variables predicted voice timing in each speaker, within-subject multiple regression (MR) analyses were performed, with dependent variables of VOffTh and VOTh. Table VI shows the results for the full data set (voiced and voiceless tokens). As with the correlational analyses, results were similar for the full dataset as compared to the voiceless-only analysis, although the *F* values were lower for the smaller (voiceless only) data set. These analyses supplement the principal components analysis (discussed below), which is not inferential and does not provide statistical significance levels.

Table VI indicates that the measured variables significantly predicted the times of voicing offset and onset in all speakers, but the *r* values and *F* values were in all cases higher for voicing onset than voicing offset. The *t*-tests on the log-transformed *r* values indicated that these offset–onset

TABLE VI. Results of multiple regression analyses for the full data set (voiced and voiceless tokens together), with VOffTh and VOTh as dependent variables. Double asterisks (⋆⋆) indicate cases of $p<0.001$; single asterisks (⋆) indicate $p<0.01$; tildes (∼) indicate $p<0.05$.

	F1		F2		F3		F4		F5		F6	
	Off	On	Off	On	Off	On	Off	On	Off	On	Off	On
Overall *r*	0.66	0.89	0.58	0.9	0.74	0.91	0.67	0.94	0.69	0.9	0.74	0.86
Overall *F*	28.49	144.57	13.36	110.48	29.83	110.37	21.49	194.59	24.02	111.86	31.23	72.14
p value	<0.001	<0.001	<0.001	<0.001	<0.001	<0.001	<0.001	<0.001	<0.001	<0.001	<0.001	<0.001
Intercept								⋆⋆				⋆⋆
/ɑ/-ness			⋆⋆	∼	∼	∼	⋆	∼				⋆⋆
/ɪ/-ness		⋆⋆	⋆⋆	⋆⋆	⋆⋆	⋆⋆					⋆	∼
Loud		⋆⋆						⋆⋆				
DCOff/On	⋆⋆	⋆⋆	⋆⋆	⋆⋆	⋆⋆	⋆⋆	⋆⋆	⋆⋆	⋆⋆	⋆⋆	⋆⋆	⋆⋆
hPk	⋆⋆	⋆⋆	⋆⋆	⋆⋆	⋆⋆	⋆⋆	⋆⋆	⋆⋆	⋆⋆	⋆⋆	⋆⋆	⋆⋆
Pres							⋆⋆					
f_0Off/On	∼	⋆⋆		∼				⋆⋆		⋆⋆		
AC3Off/On					∼					⋆⋆		

differences were significant [$t(5)=6.836$, $p=0.001$; mean difference=0.283]. Again, given the small number of data points for these tests, the conclusions must be considered tentative. The multiple regression also shows that the contributions of DCOff/DCOn and hPk were significant in all cases. The universal significance of DCOff and DCOn as predictors of VOffTh and VOTh (respectively) implies that, as one would expect, the degree of abduction is a major factor in determining voice timing. Otherwise, the results are mixed, suggesting that other variables contribute to voicing control to differing degrees across subjects.

3. Principal components analysis (PCA)

The general goal of principal components analysis is to determine the underlying dimensionality among a large number of correlated variables. Loadings on a single factor represent variables that are intercorrelated; conversely, correlations are minimized across factors (Dunteman, 1989). Thus, the PCA results provide greater insight into how variables associated with voicing control are interrelated within a speaker.

Table VII presents the orthogonal solutions yielded by principal components analysis, showing the results for all data (voiced and voiceless tokens). The factors were rotated using the Varimax procedure. The number of factors retained for each analysis was determined using a composite procedure, in order to minimize dependence upon a single method and criterion. Specifically, factors were retained depending on the larger of two values as determined by (a) the change point on a scree plot (Cattell, 1966) and (b) a 75% total variance criterion (cf. Dunteman, 1989; Jackson, 1991).

The factor solutions effectively characterized the data sets for all subjects (all χ^2 significant at $p<0.001$). This was true when the analysis was run on the entire data set and when voiced tokens were removed, though the χ^2's were lower in the latter case. In both the full and voiceless-only analyses, four factors were extracted for all subjects except F3, for whom three factors characterized her dataset. Table VII indicates that certain factors group together across subjects: In particular, all subjects have at least one factor with moderate to heavy loadings of hPk and DCOff/On, for both voicing offsets and onsets. Other variables loading on these factors differ across speakers. For example, speaker F1 (factor 1, voicing offsets) has DCOff and hPk combined with AC flow only, whereas in F4 (factor 1, voicing offsets) this factor includes loudness and pressure. Cross-speaker differences are also observed in the variables that load together with the voice timing variables (VOffTh, VOTh), in the number of factors the voice timing variables are loaded on, and in the factor groupings for voicing offsets vs onsets. For speaker F2, for example VOffTh loads with vowel quality (/ɪ/-ness), DCOff, and hPk, whereas for speaker F3, the factor that includes VOffTh loads only on vowel quality (/ɪ/-ness), with no other contributing factors.

Overall, the results of the relational analyses reveal a few consistencies across speakers in the variables associated with voice timing; specifically, voice timing was found to be related to the DC flow variables in all speakers, and the DC flow variables were highly correlated with each other (i.e., they loaded on common factors in the PCA). At the same time, the data indicate considerable interspeaker variability in the other factors expected to affect voicing thresholds. We explore this variability in more detail in the next section.

D. Individual speaker patterns

In this section, we bring together all the data and attempt a detailed explanation of voicing behavior in three of the six speakers (F1, F3, F5). These speakers, chosen arbitrarily from among the six, illustrate some of the ways in which speakers can differ in phonatory function.

Speaker F1 had a significant effect of loudness on devoicing, with more devoicing as loudness and P_{sub} decreased (see Fig. 3 and Table IV). The MR analysis showed vowel quality, loudness, and $f0$ to contribute to voicing onset along with DCOn and hPk. The PCA showed that loudness and pressure loaded on a single factor, with no other contributing variables. The vowel variables loaded together with AC flow, and the factors that included VOffTh and VOTh also included $f0$. Taken together, these results suggest that the loudness manipulation had the simple effect of increasing subglottal pressures in this speaker; that the vowel manipulation affected the amplitude of vocal-fold vibration; and that $f0$ made an independent contribution to voice timing.

Speaker F3 showed significant vowel effects on devoicing, and P_{sub} varied with vowel as well as loudness condition. In the loud and normal conditions, she had the least devoicing in the /u/ context (see Fig. 3), whereas in the soft condition this vowel showed the most devoicing. The devoicing pattern follows the P_{sub} data for this speaker; although her loudness-by-vowel interaction did not reach significance ($p=0.012$; cf. Table IV), qualitatively /u/ had the lowest P_{sub}'s in the soft condition, whereas it had the highest P_{sub}'s in the normal and loud conditions. Vowel effects are also evident in the MR results, where voice timing was predicted by vowel quality along with the usual hPk and DC flow. In the PCA (a) loudness, P_{sub}, and $f0$ loaded on a single factor; (b) the vowel variables loaded with AC flow as well as hPk and DC flows; and (c) the voice timing variables load with vowel (offsets) and $f0$ (onsets). The PCA loadings suggest that, for this speaker, varying vowel quality affected laryngeal abduction for /h/ (measured by DC flow) as well as on vocal-fold vibratory amplitudes (AC flow), which together yielded the significant vowel effects on phonation. The factor loadings also suggest that the loudness manipulation may have affected voicing partly via effects on $f0$.

Speaker F5 was distinguished by an unusual pattern of pressure variation in which the loud and soft conditions had higher pressures than normal loudness (Fig. 3, Table IV). Her higher amount of devoicing in the normal condition follows from the lower pressures. In the PCA, loudness is grouped together with $f0$ and AC flow, and the MR analysis shows that $f0$ and AC flow variables predicted voicing onsets along with DC flow and hPk. For this speaker, the loudness manipulation appears to have had complex effects on glottal function, affecting $f0$ and vibratory amplitudes along with simple driving pressures. In the soft condition, this speaker may have increased P_{sub} in response to greater glottal leak-

TABLE VII. Results of principal components analysis, including all tokens (voiced and voiceless) in the analysis. For clarity, only loadings of 0.4 or greater are shown.

	Voicing offset				Voicing onset			
	Factor 1	Factor 2	Factor 3	Factor 4	Factor 1	Factor 2	Factor 3	Factor 4
				F1				
VOffTh/VOTh				0.76	0.91			
/ɑ/-ness			−0.74					−0.75
/ɪ/-ness			0.79					0.86
Loudness		0.89					0.86	
DCOff/On	0.93				−0.45	0.85		
hPk	0.94					0.90		
Pres		0.88					0.90	
f_0Off/On				−0.67	0.89			
ACOff/On	−0.40		0.52		0.41			0.54
				F2				
VOffTh/VOTh			0.74				0.78	
/ɑ/-ness		−0.90				−0.83		
/ɪ/-ness		0.75	0.47			0.83		
Loudness	0.82				0.72			
DCOff/On	0.64		0.67		0.95			
hPk	0.62		0.71		0.89			
Pres	0.44			−0.70				0.83
f_0Off/On	0.46			0.74			0.86	
ACOff/On	0.73				0.41			0.62
				F3				
VOffTh/VOTh			0.94				0.92	
/ɑ/-ness	−0.76				−0.73			
/ɪ/-ness	0.55		0.64		0.73			
Loudness		0.88				0.90		
DCOff/On	0.93				0.90			
hPk	0.91				0.93			
Pres		0.93				0.92		
f_0Off/On		0.78				0.73	0.45	
ACOff/On	0.72				0.66			
				F4				
VOffTh/VOTh				0.99		0.92		
/ɑ/-ness		−0.86					−0.87	
/ɪ/-ness		0.83					0.84	
Loudness	0.93				0.96			
DCOff/On	−0.89				−0.66			0.56
hPk	−0.89				−0.79			0.43
Pres	0.88				0.94			
f_0Off/On			0.87			0.87		
ACOff/On			−0.73					−0.88
				F5				
VOffTh/VOTh			0.86				−0.93	
/ɑ/-ness	−0.68			−0.47	−0.75			−0.43
/ɪ/-ness	0.79				0.86			
Loudness		0.86				0.85		
DCOff/On	0.82				0.51		0.77	
hPk	0.87				0.78			
Pres				0.91				0.93
f_0Off/On		0.94				0.89		
ACOff/On	0.40	0.70				0.76		

TABLE VII. (*Continued.*)

	Voicing offset				Voicing onset			
	Factor 1	Factor 2	Factor 3	Factor 4	Factor 1	Factor 2	Factor 3	Factor 4
				F6				
VOffTh/VOTh	0.41	0.62				−0.93		
/ɑ/-ness		0.83						−0.95
/ɪ/-ness		−0.74				0.69		0.61
Loudness	0.78				0.87			
DCOff/On	0.77	−0.47			0.62	0.70		
hPk	0.88				0.85			
Pres	0.74				0.66		0.47	
f_0Off/On				0.94			0.81	
ACOff/On			0.95				0.84	

age; visual inspection of averaged DC flow signals over the entire VCV sequence for her three loudness conditions showed higher flows during the unstressed vowel preceding the /h/ in the soft condition than for the normal or loud conditions. The soft condition also tended to have low-amplitude, sinusoidal pulse shapes, suggestive of incomplete glottal closure.

IV. DISCUSSION

A. Differences between voicing offset and onset

As expected, voicing offsets occurred closer in time to the peak abduction, and at greater degrees of abduction (higher DC flows) than voicing onsets in all speakers. This finding is consistent with a hysteresis effect, in which the requirements for initiating phonation are more stringent than those for sustaining it (e.g., Lucero, 1999; Lucero and Koenig, 2005). However, speakers varied in the extent of this effect. Across the six speakers, offset–onset differences in voice timing relative to peak abduction showed a range of 19–37 ms, with VOTh durations two to six times longer than VOffTh durations. Offset–onset differences in DC flow levels varied from 2–18 l/m; DCOff values were 1.15–1.51 times greater than DCOn values. Plant *et al.* (2004), using tracheal puncture to assess subglottal pressures at phonation offset and onset, have also reported variability in the degree of hysteresis across speakers; in their study, some subjects did not demonstrate hysteresis at all.

Several factors may contribute to this variation. One possibility is that speakers differ in anatomical parameters such as tissue damping or vocal-fold thickness. Other contributors may be the degree to which the speakers vary their subglottal pressure and/or longitudinal vocal-fold tension for the stressed syllable. The speech context used here was necessarily asymmetrical; the /h/ followed an unstressed syllable and initiated a stressed one, to ensure that the /h/ would not be lenited or deleted (Pierrehumbert and Talkin, 1992). Increased P_{sub} as a function of syllable stress should lead to a shorter VOTh (earlier phonation onset), yielding a smaller hysteresis effect. On the other hand, greater longitudinal tension to achieve elevated *f*0 in a stressed syllable should have the effect of postponing voicing. As noted in the Introduction, past studies have found inconsistent results on whether speakers use longitudinal tension as one means of suppressing voicing. For four of the six speakers presented here (F1, F2, F3, F4), the PCA results showed *f*0 loading on the factor(s) that included VOffTh and/or VOTh, suggesting that longitudinal tension of the vocal folds correlated with voice timing in these speakers. The relationship between *f*0 and offset–onset differences is not entirely straightforward, however, a *post hoc* review of each speaker's *f*0 data for stressed and unstressed syllables indicated that neither the absolute *f*0 difference nor the relative *f*0 increase (as a percentage of the unstressed vowel *f*0) showed a clear relationship with the degree of offset–onset differences. A final explanation for the variability in offset–onset differences across speakers might be found in the work of Ní Chasaide and Gobl (1993). In a cross-language study of voice source characteristics around intervocalic consonants, these authors argued that voice offsets are by nature gradual, but that speakers have some leeway in whether they initiate phonation rapidly or more slowly, and further that there may be variation across languages in the manner of voicing onset (rapid vs slow). Interestingly, the five (British) English speakers in their study had greater interspeaker variability in their voice source onset patterns than the speakers of Swedish, German, Italian, and French. Hanson (1997) has also noted considerable cross-speaker variability in voice source characteristics among 22 female speakers, and suggested that women may demonstrate greater interspeaker differences than men with respect to glottal settings. It is a question for further research to what extent the variations in onset–offset differences here reflect language effects, context effects, speaker-specific variations, and/or gender differences. Combining these data with modeling work (cf. Lucero and Koenig, 2005) may help clarify this issue.

Three other general differences between voicing offsets and onsets were observed. First, there was a greater spread of values (higher within-subject SDs) for measures taken at voicing onset than voicing offset. Second, higher *r*- and *F* values for voicing onsets in the multiple regressions indicated that the independent measures were more successful in

predicting voicing onsets than offsets. Finally, VOffTh and VOTh did not always group with the same variables in the principal components analysis. For example, in speaker F3, VOffTh and vowel quality (/ɪ/-ness) loaded together, whereas the factor that included VOTh had contributions from *f*0 but not from vowel quality. This suggests that, for this speaker, measures of voicing offsets were highly correlated with vowel quality, whereas variation in voicing onsets was more closely related to changes in *f*0. In other words, voicing offsets and onsets may be subject to somewhat different patterns of control within an individual speaker.

B. Cross-speaker similarities

Along with the offset–onset differences described above, some patterns were consistent across speakers. Most notably, hPk and DCOff/On loaded together on at least one factor in the PCA solutions for all speakers. These variables also significantly predicted VOffTh and VOTh in the multiple regression analysis. The consistency of the MR results across speakers implies that, as one might have suspected, all speakers used abduction degree as one way of achieving devoicing.

C. Cross-speaker differences

Apart from the DC flow variables (DCOff, DCOn, hPk), the variables that significantly predicted voice timing in the multiple regressions differed across speakers. Further, the factors that were grouped with VOffTh and VOTh in the principal components analyses differed across speakers. They frequently included *f*0 and the vowel factors, but the direction of vowel effects differed across speakers. This kind of variability is precisely what we would expect in a situation where phonatory timing is determined by a balance among several factors, and where speakers have a variety of options for achieving or sustaining voicing.

The loudness condition also yielded differing effects on the degree of devoicing across speakers. These results are consistent with those of Holmberg and colleagues (1988), who argued that speakers produce changes in loudness via a combination of respiratory and laryngeal adjustments. Vowel and loudness variations also interacted significantly for some speakers in their effects on the frequency of devoicing, suggesting that individual speakers make unique laryngeal and/or respiratory adjustments (or, possibly, show unique patterns of source–tract interaction) in response to changes in supraglottal postures. These contextual changes may affect not only aspects of phonation such as fundamental frequency or voice quality, but the likelihood of phonation itself.

All in all, the results reported here indicate that, while abduction degree (as measured by DCOff/On and hPk) is a major contributing factor to phonation offset and onset, the contributions of other factors vary across speakers. Thus, to some degree, individual speakers appear to develop unique means of achieving voicing and devoicing in running speech. Given the relatively small number of subjects in the current study, we cannot make conclusions about which of the observed patterns may be more common, but the data do give some indication of the possible range of variation among a group of normal female speakers. This variation has implications for understanding the nature of speech production as well as for modeling work that aims to reproduce natural speech behavior and formalize the underlying physical principles of voice production. Since individual speakers satisfy the requirements for voicing in different ways, verifying that a laryngeal model can reproduce the range of normal human vocal behavior requires comparison data from numerous speakers.

As indicated earlier, the current analyses are intended, in part, to provide input to modeling work in which we explore both individual and gender differences in voicing behavior in connected speech. Recently (Lucero and Koenig, 2005), we attempted to reproduce a range of data from male and female speakers using a two-mass model of the vocal folds coupled to a two-tube representation of /ɑ/. The simulation results generally yielded good fits to the data for this vowel context, suggesting that the model does capture a variety of phonatory patterns. The data presented here will permit modeling of phonatory behavior under different supraglottal (vowel) conditions. In future work, we will expand our measured database to include male and female speakers who show little or no devoicing in typical productions of /h/. An additional feature we plan to include in future analyses is voice source measures. These may provide additional information on individual patterns of voicing control, especially in those cases where the current factor analysis did not combine any other variables with the voice timing measures.

ACKNOWLEDGMENTS

This work was supported by NIH Grants DC-00865 and HD-01994 to Haskins Laboratories and by CNPq, Brazil. We are grateful to Anders Löfqvist, Anne Bradlow, and three anonymous reviewers for comments on earlier versions of this manuscript, and we thank the speakers for their participation.

Appendix A

Effect of loudness condition on subglottal pressure (P_{sub}) measures: Means and standard deviations (cm H_20); ANOVA results; and *p*-values of post-hoc Scheffé tests. *L*=Loud; *N*=Normal; *S*=Soft.

	Means (SD) (cm H_20)			ANOVA results		Post-hoc *p*-values		
Speaker	*L*	*N*	*S*	F (df=2)	*p*	*L* vs *N*	*L* vs *S*	*N* vs *S*
F1	6.2 (0.5)	5.4 (1.1)	4.4 (0.3)	81.67	<0.001	<0.001	<0.001	<0.001
F2	7.0 (1.5)	6.9 (1.3)	6.2 (1.7)	6.77	0.001	0.876	0.003	0.015
F3	7.9 (0.8)	6.2 (0.5)	5.9 (0.5)	199.31	<0.001	<0.001	<0.001	0.011
F4	10.6 (0.8)	7.5 (1.3)	4.9 (0.3)	745.46	<0.001	<0.001	<0.001	<0.001
F5	8.3 (2.0)	6.5 (2.3)	7.7 (1.7)	23.95	<0.001	<0.001	0.054	<0.001
F6	9.7 (1.6)	9.0 (2.0)	7.1 (1.8)	43.88	<0.001	0.088	<0.001	<0.001

Appendix B

Effect of loudness condition on hPk values: Means and standard deviations (l/m); ANOVA results; and p-values of post-hoc Scheffé tests. L=Loud; N=Normal; S=Soft. Post-hoc results of n/a indicate cases where the post-hoc analyses were not run because the F-test was not significant.

	Means (SD) (l/m)			ANOVA results		Post-hoc p-values		
Speaker	L	N	S	F (df=2)	p	L vs N	L vs S	N vs S
F1	57.9 (14.0)	57.6 (16.4)	61.6 (12.3)	1.97	0.140	n/a	n/a	n/a
F2	64.2 (18.4)	41.9 (15.3)	40.5 (14.5)	50.80	<0.001	<0.001	<0.0001	0.863
F3	14.2 (5.7)	15.7 (6.9)	13.7 (4.7)	2.33	0.100	n/a	n/a	n/a
F4	27.8 (9.5)	27.9 (12.5)	55.3 (8.5)	174.20	<0.001	0.998	<0.001	<0.001
F5	23.0 (7.3)	18.0 (7.5)	17.9 (7.6)	11.03	<0.001	<0.001	<0.001	0.998
F6	52.3 (12.7)	43.8 (16.1)	30.4 (7.0)	59.40	<0.001	<0.001	<0.001	<0.001

Appendix C

Effect of vowel on subglottal pressure (P_{sub}) measures: Means and standard deviations (cm H_20); ANOVA results; and p-values of post-hoc Scheffé tests.

	Means (SD) (cm H_20)			ANOVA results		Post-hoc p-values		
Speaker	/ɑ/	/ɪ/	/u/	F (df=2)	p	/ɑ/ vs /ɪ/	/ɑ/ vs /u/	/ɪ/ vs /u/
FD1	5.1 (0.9)	5.3 (1.0)	5.4 (1.1)	3.10	0.047	0.283	0.034	0.594
FD2	7.0 (1.2)	6.2 (2.1)	6.8 (1.1)	5.79	0.004	0.005	0.659	0.057
FD3	6.4 (0.9)	6.5 (0.9)	6.9 (1.2)	6.81	0.001	0.721	<0.001	0.002
FD4	7.5 (2.5)	7.6 (2.6)	7.7 (2.4)	0.48	0.621	0.903	0.374	0.622
FD5	6.7 (2.0)	7.4 (2.3)	8.4 (1.4)	20.51	<0.001	0.045	<0.001	0.001
FD6	8.4 (2.2)	8.9 (2.2)	8.4 (1.9)	1.82	0.164	0.315	1.000	0.329

Abramson, A. S., and Lisker, L. (**1970**). "Discriminability along the voicing continuum: Cross-language tests," in *Proceedings of the 6th International Congress of Phonetic Sciences, Prague 1967*, edited by B. Hála, M. Romportl, and P. Janota (Academia, Czechoslovak Academy of Sciences, Prague), pp. 569–573.

Abramson, A. S., and Lisker, L. (**1985**). "Relative power of cues: *F*0 shift versus voice timing," in *Linguistic Phonetics: Essays in Honor of Peter Ladefoged*, edited by V. Fromkin (Academic, New York), pp. 25–33.

Alipour-Haghighi, F., and Titze, I. R. (**1991**). "Elastic models of vocal fold tissues," J. Acoust. Soc. Am. **90**, 1326–1331.

Alipour, F., Scherer, R. C., and Finnegan, E. (**1997**). "Pressure-flow relationships during phonation as a function of adduction," J. Voice **11**, 187–194.

Baer, T. (**1975**). "Investigation of phonation using excised larynges," unpublished Ph.D. dissertation, MIT, Cambridge, MA.

Baer, T., Löfqvist, A., and McGarr, N. S. (**1983**). "Laryngeal vibrations: A comparison between high-speed filming and glottographic techniques," J. Acoust. Soc. Am. **73**, 1304–1308.

Behrman, A., and Baken, R. J. (**1997**). "Correlation dimension of electroglottographic data from healthy and pathologic subjects," J. Acoust. Soc. Am. **102**, 2371–2379.

Berke, G. S., Moore, D. M., Monkewitz, P. A., Hanson, D. G., and Gerratt, B. R. (**1989**). "A preliminary study of particle velocity during phonation in an *in vivo* canine model," J. Voice **3**, 306–313.

Berry, D., Herzel, H., Titze, I. R., and Story, B. (**1995**). "Bifurcations in excised larynx experiments," NCVS Status and Progress Report 8, 15–24.

Bickley, C. A., and Stevens, K. N. (**1986**). "Effects of a vocal-tract constriction on the glottal source: Experimental and modelling studies," J. Phonetics **14**, 373–382.

Borden, G. J., and Gay, T. (**1979**). "Temporal aspects of articulatory movements for /s/-stop clusters," Phonetica **36**, 21–31.

Brown, W. S., Jr., and McGlone, R. E. (**1974**). "An aerodynamic and acoustic study of stress in sentence productions," J. Acoust. Soc. Am. **56**, 971–980.

Cattell, R. B. (**1966**). "The scree test for the number of factors," Mult. Behav. Res. **1**, 245–276.

Chan, R. W., Titze, I. R., and Titze, M. R. (**1997**). "Further studies of phonation threshold pressure in a physical model of the vocal fold mucosa," J. Acoust. Soc. Am. **101**, 3722–3727.

Childers, D. G., and Lee, C. K. (**1991**). "Vocal quality factors: Analysis, synthesis, and perception," J. Acoust. Soc. Am. **90**, 2394–2410.

Cox, K. A., Alipour, F., and Titze, I. R. (**1999**). "Geometric structure of the human and canine cricothyroid and thyroarytenoid muscles for biomechanical applications," Ann. Otol. Rhinol. Laryngol. **108**, 1151–1158.

Dixit, P., and Brown, W. S., Jr. (**1978**). "Peak magnitudes of supraglottal air pressure associated with affricated and nonaffricated stop consonant productions in Hindi," J. Phonetics **6**, 353–365.

Dixit, R. P., and MacNeilage, P. F. (**1980**). "Cricothyroid activity and control of voicing in Hindi stops and affricates," Phonetica **37**, 397–406.

Dixit, R. P., and Shipp, T. (**1985**). "Study of subglottal air pressure during Hindi stop consonants," Phonetica **42**, 53–77.

Dromey, C., and Ramig, L. O. (**1998**). "Intentional changes in sound-pressure level and rate: Their impact on measures of respiration, phonation, and articulation," J. Speech Lang. Hear. Res. **41**, 1003–1018.

Dromey, C., Stathopoulos, E. T., and Sapienza, C. M. (**1992**). "Glottal airflow and electroglottographic measures of vocal function at multiple intensities," J. Voice **6**, 44–54.

Dunteman, G. H. (**1989**). *Principal Components Analysis* (Sage, Beverly Hills).

Finkelhor, B. K., Titze, I. R., and Durham, P. L. (**1987**). "The effect of viscosity changes in the vocal folds on the range of oscillation," J. Voice **1**, 320–325.

Halle, M., and Stevens, K. N. (**1971**). "A note on laryngeal features," MIT Quart. Prog. Rep. **101**, 198–213.

Hanson, H. M. (**1997**). "Glottal characteristics of female speakers: Acoustic correlates," J. Acoust. Soc. Am. **101**, 466–481.

Hertegård, S., and Gauffin, J. (**1995**). "Glottal area and vibratory patterns studied with simultaneous stroboscopy, flow glottography, and electroglottography," J. Speech Hear. Res. **38**, 85–100.

Hertegård, S., Gauffin, J., and Lindestad, P. Å. (**1995**). "A comparison of subglottal and intraglottal pressure measurements during phonation," J. Voice **9**, 149–155.

Higgins, M. B., and Saxman, J. H. (**1993**). "Inverse filtered air flow and EGG measures for sustained vowels and syllables," J. Voice **7**, 47–53.

Hirano, M., Kurita, S., and Nakashima, T. (**1983**). "Growth, development, and aging of human vocal folds," in *Vocal Fold Physiology: Contemporary Research and Clinical Issues*, edited by D. M. Bless and J. H. Abbs (College Hill, San Diego), pp. 22–43.

Hirano, M., Yoshida, T., and Tanaka, S. (**1991**). "Vibratory behavior of human vocal folds viewed from below," in *Vocal Fold Physiology: Acoustic, Perceptual, and Physiological Aspects of Voice Mechanisms*, edited by J. Gauffin and B. Hammarberg (Singular, San Diego), pp. 1–6.

Hirose, H., and Niimi, S. (**1987**). "The relationship between glottal opening and the transglottal pressure differences during consonant production," in *Laryngeal Function in Phonation and Respiration*, edited by T. Baer, C. Sasaki, and K. S. Harris (College Hill, Boston), pp. 381–390.

Holmberg, E. B., Hillman, R. E., and Perkell, J. S. (**1988**). "Glottal airflow and transglottal air pressure measurements for male and female speakers in soft, normal, and loud voice," J. Acoust. Soc. Am. **84**, 511–529.

Holmberg, E. B., Hillman, R. E., and Perkell, J. S. (**1989**). "Glottal airflow and transglottal air pressure measurements for male and female speakers in low, normal, and high pitch," J. Voice **3**, 294–305.

Holmberg, E. B., Hillman, R. E., Perkell, J. J., and Gress, C. (**1994**). "Relationships between intra-speaker variation in aerodynamic measures of voice production and variation in SPL across repeated recordings," J.

Speech Hear. Res. **37**, 484–495.
Ishizaka, K., and Flanagan, J. L. (**1972**). "Synthesis of voiced sounds from a two-mass model of the vocal cords," Bell Syst. Tech. J. **51**, 1233–1268.
Jackson, J. E. (**1991**). *A User's Guide to Principal Components* (Wiley, New York).
Jiang, J. J., and Titze, I. R. (**1993**). "A methodological study of hemilaryngeal phonation," Laryngoscope **103**, 872–882.
Jiang, J., Raviv, J. R., and Hanson, D. G. (**2001**). "Comparison of the phonation-related structures among pig, dog, white-tailed deer, and human larynges," Ann. Otol. Rhinol. Laryngol. **110**, 1120–1125.
Johnson, K., Ladefoged, P., and Lindau, M. (**1993**). "Individual differences in vowel production," J. Acoust. Soc. Am. **94**, 701–714.
Kagaya, R., and Hirose, H. (**1975**). "Fiberoptic electromyographic and acoustic analyses of Hindi stop consonants," Ann. Bulletin, Res. Inst. Logop. and Phoniat. Univ. Tokyo **9**, 27–46.
Kahane, J. C. (**1987**). "Connective tissue changes in the larynx and their effects on voice," J. Voice **1**, 27–30.
Kahane, J. C. (**1988**). "Age related changes in the human cricoarytenoid joint," in *Vocal Physiology: Voice Production, Mechanisms and Functions*, edited by O. Fujimura (Raven, New York), Vol. **2**, pp. 145–157.
Kim, M. J., Hunter, E. J., and Titze, I. R. (**2004**). "Comparison of human, canine, and ovine laryngeal dimensions," Ann. Otol. Rhinol. Laryngol. **113**, 60–68.
Kitzing, P., and Sonesson, B. (**1974**). "A photoglottographic study of the female vocal folds during phonation," Folia Phoniatr. **26**, 138–149.
Klatt, D. H., Stevens, K. N., and Mead, J. (**1968**). "Studies of articulatory activity and airflow during speech," in *Sound Production in Man*, edited by A. Bouhuys (New York Academy of Sciences, New York), pp. 42–55.
Koenig, L. L. (**2000**). "Laryngeal factors in voiceless consonant production in men, women, and 5-year-olds," J. Speech Lang. Hear. Res. **43**, 1211–1228.
Lindqvist, J. (**1972**). "Laryngeal articulation studied on Swedish subjects," Quart. Status & Prog. Rep. (Spch. Transm. Lab., Royal Inst. of Tech., Stockholm) **2–3**, 10–27.
Lisker, L., and Abramson, A. S. (**1964**). "A cross-language study of voicing in initial stops: Acoustical measurements," Word **20**, 384–422.
Lisker, L., and Abramson, A. S. (**1970**). "The voicing dimension: Some experiments in comparative phonetics," in *Proceedings of the 6th International Congress of Phonetic Sciences, Prague 1967*, edited by B. Hála, M. Romportl, and P. Janota (Academia, Czechoslovak Academy of Sciences, Prague), pp. 563–567.
Lisker, L., Sawashima, M., Abramson, A. S., and Cooper, F. S. (1970). "Cinegraphic observations of the larynx during voiced and voiceless stops," Haskins Labs. Status Repts. on Speech Res. **21/22**, 201–210.
Löfqvist, A. (**1975**). "A study of subglottal pressure during the production of Swedish stops," J. Phonetics **3**, 175–189.
Löfqvist, A. (**1992**). "Acoustic and aerodynamic effects of interarticulator timing in voiceless consonants," Lang Speech **35**, 15–28.
Löfqvist, A., Baer, T., McGarr, N. S., and Story, R. S. (**1989**). "The cricothyroid muscle in voicing control," J. Acoust. Soc. Am. **85**, 1314–1321.
Löfqvist, A., Carlborg, B., and Kitzing, P. (**1982**). "Initial validation of an indirect measure of subglottal pressure during vowels," J. Acoust. Soc. Am. **72**, 633–635.
Löfqvist, A., Koenig, L. L., and McGowan, R. S. (**1995**). "Vocal tract aerodynamics in /aCa/ utterances: Measurements," Speech Commun. **16**, 49–66.
Löfqvist, A., and McGowan, R. S. (**1992**). "Influence of consonantal environment on voice source aerodynamics," J. Phonetics **20**, 93–110.
Lucero, J. C. (**1995**). "The minimum lung pressure to sustain vocal fold oscillation," J. Acoust. Soc. Am. **98**, 779–784.
Lucero, J. C. (**1999**). "A theoretical study of the hysteresis phenomenon at vocal fold oscillation onset–offset," J. Acoust. Soc. Am. **105**, 423–431.
Lucero, J. C., and Koenig, L. L. (**2005**). "Simulations of temporal patterns of oral airflow in men and women using a two-mass model of the vocal folds under dynamic control," J. Acoust. Soc. Am. **117**, 1362–1372.
Matsushita, H. (**1975**). "The vibratory mode of the vocal folds in the excised larynx," Folia Phoniatr. **26**, 7–18.
McGlone, R. E., and Shipp, T. (**1972**). "Comparison of subglottal air pressures associated with /p/ and /b/," J. Acoust. Soc. Am. **51**, 664–665.
Munhall, K. G., Löfqvist, A., and Kelso, J. A. S. (**1994**). "Lip–larynx coordination in speech: Effects of mechanical perturbations to the lower lip," J. Acoust. Soc. Am. **95**, 3605–3616.
Ní Chasaide, A., and Gobl, C. (**1993**). "Contextual variation of the vowel voice source as a function of adjacent consonants," Lang Speech **36**, 303–330.
Ohala, J. J. (**1990**). "Respiratory activity in speech," in *Speech Production and Speech Modelling*, edited by W. J. Hardcastle and A. Marchal (Kluwer Academic, Dordrecht), pp. 23–54.
Pierrehumbert, J., and Talkin, D. (**1992**). "Lenition of /h/ and glottal stop," in *Papers in Laboratory Phonology II: Segment, Gesture, Tone*, edited by G. Docherty and D. R. Ladd (Cambridge University Press, Cambridge), pp. 90–117.
Plant, R. L., Freed, G. L., and Plant, R. E. (**2004**). "Direct measurement of onset and offset phonation threshold pressure in normal subjects," J. Acoust. Soc. Am. **116**, 3640–3646.
Price, P. J. (**1989**). "Male and female voice source characteristics: Inverse filtering results," Speech Commun. **8**, 261–277.
Raphael, L. J., and Bell-Berti, F. (**1975**). "Tongue musculature and the feature of tension in English vowels," Phonetica **32**, 61–73.
Rothenberg, M. (**1973**). "A new inverse-filtering technique for deriving the glottal air flow waveform during voicing," J. Acoust. Soc. Am. **53**, 1632–1645.
Saito, S., Fukuda, H., Kitahara, S., Isogai, Y., Tsuzuki, T., Muta, H., Takayama, E., Fujioka, T., Kokawa, N., and Makino, K. (**1983**). "Pellet tracking in the vocal fold while phonating—experimental study using canine larynges with muscle activity," in *Vocal Fold Physiology: Biomechanics, Acoustics and Phonatory Control*, edited by I. R. Titze and R. C. Scherer (Denver Center for the Performing Arts, Denver), pp. 169–182.
Smitheran, J. R., and Hixon, T. J. (**1981**). "A clinical method for estimating laryngeal airway resistance during vowel production," J. Speech Hear Disord. **46**, 138–146.
Stevens, K. N. (**1977**). "Physics of laryngeal behavior and larynx modes," Phonetica **34**, 264–279.
Timcke, R., von Leden, H., and Moore, P. (**1958**). "Laryngeal vibrations: Measurement of the glottic wave. I. The normal vibratory cycle," AMA Arch. Otolaryngol. **68**, 1–19.
Titze, I. R. (**1988**). "The physics of small-amplitude oscillation of the vocal folds," J. Acoust. Soc. Am. **83**, 1536–1552.
Titze, I. R. (**1989**). "Physiologic and acoustic differences between male and female voices," J. Acoust. Soc. Am. **85**, 1699–1707.
Titze, I. R. (**1992**). "Phonation threshold pressure: A missing link in glottal aerodynamics," J. Acoust. Soc. Am. **91**, 2926–2935.
Titze, I. R., Jiang, J. J., and Hsiao, T.-Y. (**1993**). "Measurement of mucosal wave propagation and vertical phase difference in vocal fold vibration," Ann. Otol. Rhinol. Laryngol. **102**, 58–62.
Titze, I. R., Schmidt, S. S., and Titze, M. R. (**1995**). "Phonation threshold pressure in a physical model of the vocal fold mucosa," J. Acoust. Soc. Am. **97**, 3080–3084.
van den Berg, J. (**1958**). "Myoelastic-aerodynamic theory of voice production," J. Speech Hear. Res. **1**, 227–244.
van den Berg, J., and Tan, T. S. (**1959**). "Results of experiments with human larynxes," Pract. Otorhinolaryngol. (Basel) **21**, 425–450.
Whalen, D. H., and Levitt, A. G. (**1995**). "The universality of intrinsic *f*0 of vowels," J. Phonetics **23**, 349–366.
Yumoto, E., Kadota, Y., and Kurokawa, H. (**1993**). "Infraglottic aspect of canine vocal fold vibration: Effect of increase of mean airflow rate and lengthening of vocal fold," J. Voice **7**, 311–318.

Comparison of nonlinear dynamic methods and perturbation methods for voice analysis

Yu Zhang,[a] Jack J. Jiang,[b] and Stephanie M. Wallace
Department of Surgery, Division of Otolaryngology Head and Neck Surgery, University of Wisconsin Medical School, Madison, Wisconsin 53792-7375

Liang Zhou
Eye, Ear, Nose and Throat Hospital, Fudan University Medical School, 83 Fen Yang Road, Shanghai 200031, P. R. China

(Received 13 September 2004; revised 28 June 2005; accepted 29 June 2005)

Nonlinear dynamic methods and perturbation methods are compared in terms of the effects of signal length, sampling rate, and noise. Results of theoretical and experimental studies quantitatively show that measurements representing frequency and amplitude perturbations are not applicable to chaotic signals because of difficulties in pitch tracking and sensitivity to initial state differences. Perturbation analyses are only reliable when applied to nearly periodic voice samples of sufficiently long signal lengths that were obtained at high sampling rates and low noise levels. In contrast, nonlinear dynamic methods, such as correlation dimension, allow the quantification of chaotic time series. Additionally, the correlation dimension method presents a more stable analysis of nearly periodic voice samples for shorter signal lengths, lower sampling rates, and higher noise levels. The correlation dimension method avoids some of the methodological issues associated with perturbation methods, and may potentially improve the ability for real time analysis as well as reduce costs in experimental designs for objectively assessing voice disorders. © *2005 Acoustical Society of America.* [DOI: 10.1121/1.2005907]

PACS number(s): 43.70.Bk, 43.70.Dn, 05.45.Tp, 05.45.Pq [AL] Pages: 2551–2560

I. INTRODUCTION

Acoustic perturbation measures such as jitter and shimmer describe the frequency and amplitude perturbation characteristics of voices. They have been applied to noninvasively and objectively assess laryngeal function and voice quality since the 1960s.[1,2] Recently, methodological issues regarding these perturbation measures have received considerable attention. It has been suggested that systems employed to calculate perturbation measures are only reliable for nearly periodic voice signals and cannot reliably analyze strongly aperiodic signals.[3–6] Furthermore, jitter and shimmer have been found to be sensitive to variations in microphone type and placement,[7] recorder and tape types,[8,9] sampling size or signal length,[10] noise,[11] extraction algorithm,[12] and analysis systems.[13,14] The errors introduced by factors such as signal length, sampling rate, and environmental as well as measurement noise affect the perturbation values.

Nonlinear dynamic methods such as the correlation dimension and Lyapunov exponents are quantitative measures that can be applied to aperiodic and chaotic behaviors generated by deterministic systems.[15] The application of nonlinear dynamic methods to laryngeal systems has received recent interest. Nonlinear dynamic methods have shown potential value for describing disordered voices from laryngeal pathologies,[16–19] diagnosing laryngeal pathologies,[20,21] and assessing the effects of clinical treatments.[22] However, until now there have not been quantitative voice studies to investigate how signal length, sampling rate, and noise affect nonlinear dynamic measures of voices, although a qualitative study by Behrman and Baken[18] showed that nonstationarity, noise, and finite signal length might affect the correlation dimension estimate of electroglottographic data. In addition, there has been no quantitative comparison of traditional perturbation methods and nonlinear dynamics methods in terms of the effects of signal length, sampling rate, and noise.

The purpose of this study is to compare nonlinear dynamic analysis and perturbation analysis of voices in terms of the effects of signal length, sampling rate, and noise. In the theoretical analysis section, the Lorenz model is used to demonstrate the difficulties in tracking the pitch of aperiodic or chaotic signals. Furthermore, test signals from the asymmetric two-mass model of Steinecke and Herzel[23] are analyzed to investigate the variances of nonlinear dynamic measures and perturbation measures in response to different initial conditions, and to show the effects of signal length, sampling rate, and noise amplitude. In the experimental study section, sustained vowels from normal subjects and patients with laryngeal pathologies are analyzed using correlation dimension, jitter, and shimmer. For a nearly periodic voice and an aperiodic voice, the time variances of correlation dimension, jitter, and shimmer are compared. The effects of signal length, sampling rate, and noise amplitude are investigated to evaluate the usefulness of the correlation dimension for practical voice analysis.

[a]Electronic mail: zhang@surgery.wisc.edu
[b]Author to whom correspondence should be addressed; electronic mail: Jiang@surgery.wis.cedu

II. METHODS

Theoretically, the dynamics of a vibratory system such as the vocal folds can be described by the equation

$$\frac{d\mathbf{x}}{dt} = \mathbf{v},$$

$$\frac{d\mathbf{v}}{dt} = \mathbf{F}(\mathbf{x}, \mathbf{v}, \boldsymbol{\mu}), \tag{1}$$

where $\mathbf{x}$ and $\mathbf{v}$ are the displacement and velocity vectors, respectively, $\mathbf{F}$ denotes the force vector applied to the system, and $\boldsymbol{\mu}$ is the system parameter vector. In lump parameter models of the vocal folds,[23–25] $\boldsymbol{\mu}$ includes the mass $\mathbf{M}$, damping $\mathbf{D}$, and stiffness $\mathbf{K}$ parameter vectors. The time evolution of the equation solution produces a continuous time series $x(t)$. Nonlinear dynamic methods, including phase space, Poincaré map, generalized dimensions (Hausdorff dimension, information dimension, correlation dimension, etc.), generalized entropies (Kolmogrov entropy, etc.), and Lyapunov exponents, can describe irregular or chaotic activities.[15] In a vibratory system, such as the vocal folds, phase space is a space defined by multiple dynamic variables composed of positions and velocities. With time evolution, vocal fold vibration can be shown as a trajectory in a phase space. After an initial transient, a trajectory in phase space asymptotically approaches an invariant set, termed an attractor.

In practical application, nonlinear time series analysis of voices also has received recent interest.[6,16–22] The time delay technique has been applied to reconstruct the dynamics from measured experimental data. For a time series $x(t_i) \in \mathbf{R}$, $t_i = t_0 + i\Delta t$ $(i = 1, 2, \ldots, N)$, sampled at the time interval $\Delta t = 1/f_s$ (f_s is the sampling rate), a phase space can be reconstructed with a time delay vector, $\mathbf{X}(t) = \{x(t), x(t-\tau), \ldots, x(t-(m-1)\tau)\}$ where τ is the time delay and m is the embedding dimension.[26] It is important to choose an appropriate time delay τ when reconstructing a phase space. If τ is too small, the lagged coordinates will be too strongly correlated, such that the reconstructed attractor will be stretched around a diagonal line. If τ is too large, the reconstructed attractor will produce self-intersection. An appropriate τ can be estimated by using the mutual information method proposed by Fraser and Swinney.[27] The first minimum value of the mutual information function provides an effective criterion for choosing the time delay τ. Takens[28] has demonstrated that when $m > 2D+1$, where D is the dimension of the attractor, the reconstructed phase space with the lagged coordinates is topologically equivalent to the original phase space with physical coordinates. Thus, the dynamics of a voice signal can be studied in its reconstructed phase space; a closed periodic trajectory in a phase space is closed in its reconstructed phase space, whereas a chaotic trajectory in phase space is noiselike in its reconstructed phase space.

The correlation dimension proposed by Grassberger and Procaccia[29] quantitatively measures the complexity of a dynamic system. A system with a higher dimension may need more degrees of freedom to describe the system's dynamics. Detailed descriptions of the nonlinear dynamic methods are widely found.[6,15–22,29–32] In this study, our calculations were based on the numerical algorithms that we previously applied to analyze human voices[19,21,22] and excised larynx phonations.[6] Briefly, the correlation dimension can be calculated as[29]

$$D_2 = \lim_{r \to 0} \frac{\log C(r)}{\log r}, \tag{2}$$

where r is the radius around $\mathbf{X}_i$. The correlation integral $C(r)$ of the time series with length N can be obtained using the formula by Theiler:[30]

$$C(W, N, r) = \frac{2}{(N+1-W)(N-W)} \sum_{n=W}^{N-1} \sum_{i=0}^{N-1-n} \theta(r - \|\mathbf{X}_i - \mathbf{X}_{i+n}\|), \tag{3}$$

where $\theta(x)$ is the Heaviside step function defined by

$$\theta(x) = \begin{cases} 1, & x > 0, \\ 0, & x \leqslant 0. \end{cases}$$

This formula eliminates all sets of vectors that lie within W of each other, and, in this study, W was set to be the proper time delay τ. In the curve of $\log C(W, N, r)$ vs. $\log r$, if the radius r were too small, random noise would be dominant so that the estimate of D_2 would continue to increase with m. On the other hand, if r were too large (about the overall size of the attractor), all dot pairs in the reconstructed phase space would be smaller than r so that the estimate of D_2 would approach zero. There is a finite region between these two regions, termed the scaling region,[29] in which the slopes of $\log C(W, N, r)$ vs. $\log r$ curves increases at first but eventually converge with the increase of m. The dimension estimate and its standard deviation were derived using a linear curve fit to the curve of $\log_2 C(r)$ vs. $\log_2 r$ in this scaling region. For the substantially large embedding dimension m, a small standard error of the slope within the scaling region leads to a reliable dimension estimation of a chaotic time series.

Jitter and shimmer are measures of the frequency and amplitude perturbations of a voice. Jitter is a cycle-to-cycle frequency perturbation measure and shimmer is a cycle-to-cycle amplitude perturbation measure. Traditionally, jitter and shimmer have been used to objectively evaluate patients with laryngeal pathologies as well as to track improvements after treatment. Abnormal jitter and shimmer values may be associated with laryngeal pathologies. There are quite a few algorithms, including Multi-Dimensional Voice Program (MDVP)[3] and Cspeech 4.0,[33,34] to measure jitter and shimmer. All these methods require that the voice period be accurately extracted. Thus, although MDVP and Cspeech were applied in our study to show the limitation of pitch extraction, the principle and results can be generalized to other algorithms for calculating jitter and shimmer. In addition, MDVP and Cspeech as commercial products have been widely applied in clinical practice and research labs. The results based on these two analysis systems might be comparable with previous study.[3–14] In this study, Jit_MDVP,

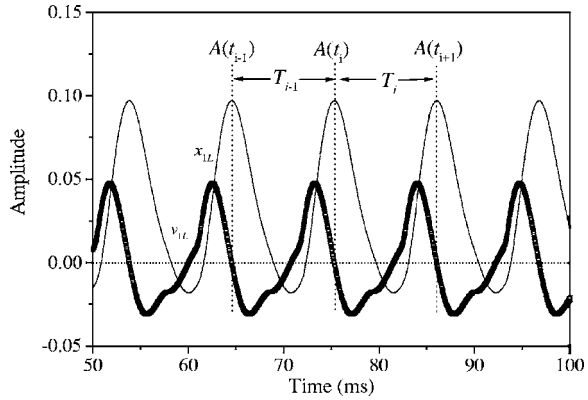

FIG. 1. The maximal amplitude $A(t_i)$ and the period T_i of a periodic signal, where $x_{1L}(t)$ and $v_{1L}(t)$ represent the displacement and velocity of the left-lower mass in the asymmetric two-mass vocal fold model, respectively.

Shim_MDVP, Jit_Cspeech, and Shim_Cspeech correspond to the jitter estimated with MDVP, shimmer estimated with MDVP, jitter estimated with Cspeech, and shimmer estimated with Cspeech, respectively.

III. THEORETICAL ANALYSIS

For a nearly periodic scalar time series $x(t)$ obtained from theoretical models or experimental measurements, the maximal amplitude $A(t_i)$ and the corresponding period $T_i = t_i - t_{i-1}$ can be determined using waveform matching, peak-picking, and zero-crossing methods.[12] The waveform matching method applies a least squared error criterion to determine the minimal value of the adjacent waveforms, the peak-picking method applies peak-picking to a signal, and the zero-crossing method is used on a signal having two zero crossings each cycle, where positive zero-crossing is located between consecutive markers. Theoretically, the peak-picking method and the zero-crossing method are equivalent. The maximal amplitude $A(t_i)$ and the period T_i of the displacement signal $x(t)$ determined in the peak-picking procedure correspond to its zero velocity $v(t_i)=0$ and $\dot{v}(t_i)<0$ determined in the zero-crossing procedure according to the second derivative test for local extreme value (see Fig. 1). $x_{1L}(t)$ and $v_{1L}(t)$ represent the displacement and velocity of the left-lower mass in the asymmetric two-mass vocal fold model of Steinecke and Herzel,[23] which was proposed to simulate the vibrations of vocal folds with superior nerve paralysis. The subglottal pressure is 0.0145, the tension imbalance parameter is $Q=0.6$, and the other model parameters are the default values.[23,24] The waveform matching method requires a signal to be decomposed into periodic and aperiodic components.[33] The aperiodic component is assumed to be mean square stationary and mean zero, and the consecutive aperiodic components are uncorrelated. From a nonlinear dynamic point of view, these methods provide three ways of arriving at the Poincaré map, in which a continuous time series $x(t)$ is projected onto a series of points of amplitude $A(t_i)$ and period T_i. For example, a two-dimensional next-period-map or next-maximal-map composed of the maximal amplitude $A(t_i)$ versus its previous maximal $A(t_{i-1})$ can be derived from the amplitude or fundamental frequency contour of a signal.[16,17,23] A topologically equivalent method[25] based on inverse interpolation has also been applied in vocal fold models to exactly determine the Poincaré map at a zero velocity plane.

Based on the amplitude $A(t_i)$ and time interval T_i series of a voice signal, jitter and shimmer have been used to describe the short-term variations from cycle to cycle in amplitude and frequency, respectively. In MDVP, jitter and shimmer are typically defined as

$$\frac{[1/(K-1)]\sum_{i=1}^{K-1}|T_i - T_{i+1}|}{(1/K)\sum_{i=1}^{K} T_i}$$

and

$$\frac{[1/(K-1)]\sum_{i=1}^{K-1}|A(t_i) - A(t_{i+1})|}{(1/K)\sum_{i=1}^{K} A(t_i)}, \quad (3)$$

respectively, where $i=1,2,\ldots,K$ and K equals the number of pitch periods. For a nearly periodic signal, small variations in amplitude and pitch period can be measured by using these two perturbation measures since $|T_i - T_{i+1}|/T_i \ll 1$ and $|A(t_i) - A(t_{i+1})|/A(t_i) \ll 1$. However, if a signal is chaotic or aperiodic, it is difficult to produce reliable estimates of jitter and shimmer using MDVP. One important reason is that the signal period T_i is difficult to track using waveform matching, peak-picking, and zero-crossing methods because period markers may not be appropriately placed for an aperiodic signal. The fundamental assumption of the waveform matching method is also difficult to satisfy because a chaotic system does not possess the property of superposition and a chaotic time series cannot be independently decomposed into a periodic component and an aperiodic component. Other algorithms designed to calculate these perturbation measures are also fundamentally limited since they depend on accurate extraction of fundamental frequency and amplitude.[8,12,14] Nonlinear dynamic methods, including correlation dimension and Lyapunov exponents, do not require the determination of pitch period and are not restricted by this limitation of the perturbation methods. Figure 2 presents a typical example revealing how pitch tracking can complicate perturbation analysis. The chaotic waveform with length 2 s and sample frequency $f_s=44.1$ kHz is from the Lorenz chaotic system[35] whose dynamics satisfy $\dot{x}=10(y-x)$, $\dot{y}=x(28-z)-y$, and $\dot{z}=xy-8z/3$. Figures 2(a) and 2(b) show the chaotic time series and the corresponding frequency spectrum. There is not a stable fundamental period or a strong frequency component that can be found in this signal with a continuous spectrum. The waveform matching, peak-picking, and zero-crossing methods cannot stably estimate the signal period, and thus jitter and shimmer cannot reliably analyze this aperiodic signal. In contrast to this, correlation dimensions and Lyapunov exponents are both capable of describing this chaotic time series. The correlation dimension D_2 converges to 2.05 ± 0.01 in the scaling region when the embedding dimension m is sufficiently large, as shown in the graph of the estimated D_2 vs. $\log_2(r)$ of Fig. 2(c). With the increase of time, the Lyapunov exponents of the Lorenz system converge to

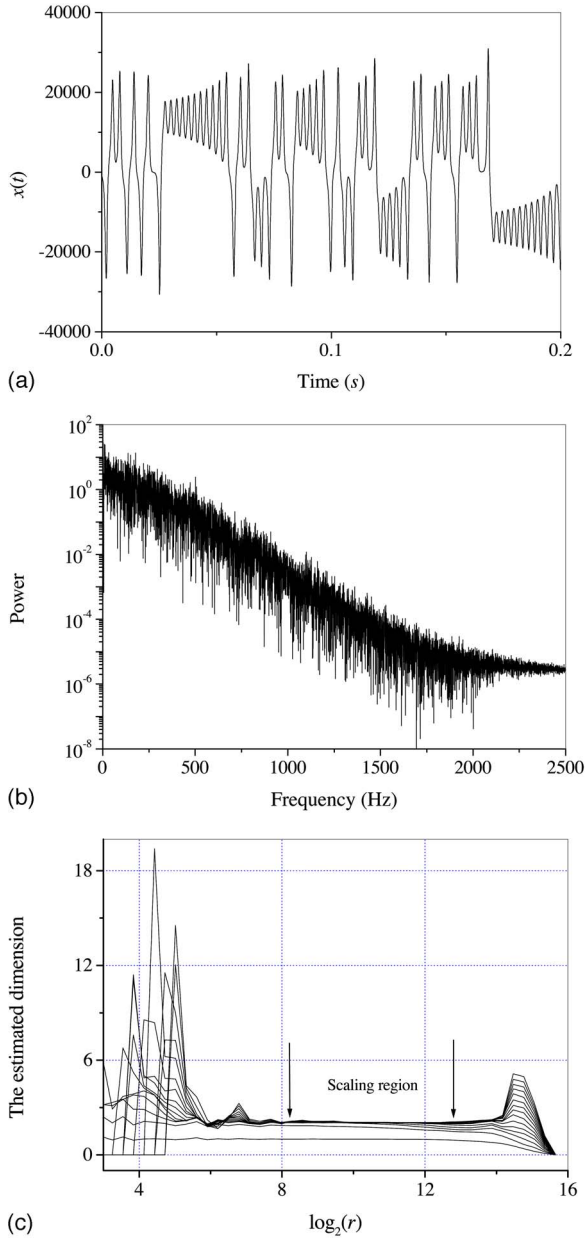

FIG. 2. (a) The time series $x(t)$ of the Lorenz chaotic time series. (b) Frequency spectrum. (c) The estimated correlation dimension versus $\log_2(r)$, in which the curves correspond to the embedding dimension $m=1,2,\ldots,15$, respectively.

$\lambda_1 \approx 0.91$, $\lambda_2 \approx 0$, and $\lambda_3 \approx -14.58$ [see Fig. 2(d)]. Both these nonlinear dynamic methods give effective descriptions of the chaotic system.

Furthermore, even if the maximal amplitude $A(t_i)$ and time interval T_i of a chaotic signal can be determined using a Poincaré map, the large variances of $|T_i - T_{i+1}|/T_i$ and $|A(t_i) - A(t_{i+1})|/A(t_i)$ prevent stable estimates of jitter and shimmer. Such large variances attribute to the extreme sensitivity to initial conditions and local instabilities of chaotic systems, which are characterized by at least one positive Lyapunov exponent. The extreme sensitivity causes any slight error in the estimation of the state or pitch to be exponentially amplified so that a totally different estimate of the perturbation measures will be obtained. The local instability causes $|T_i - T_{i+1}|/T_i$ and $|A(t_i) - A(t_{i+1})|/A(t_i)$ to change rapidly and unpredictably, resulting in unstable estimates of jitter and shimmer. To demonstrate this, we compare the Jit_MDVP, Shim_MDVP, and D_2 analysis results for 20 time series of the left-lower mass amplitude $x_{1L}(t)$ from the asymmetric two-mass vocal fold model,[23] where each time series was sampled at 44.1 kHz and has a length of 2 s. The initial amplitude $x_{1L}(0)$ of each time series was randomly chosen within $[-0.1, 0.1]$ and 1-s transient processes of x_{1L} are skipped. When the tension imbalance parameter $Q=0.6$, a periodic vibration $x_{1L}(t)$ with Lyapunov exponents $\lambda_1 \approx 0$, $\lambda_2 \approx -0.049$, $\lambda_3 \approx -0.138$, $\lambda_4 \approx -0.148$, $\lambda_5 \approx -0.201$, $\lambda_6 \approx -0.201$, $\lambda_7 \approx -0.399$, and $\lambda_8 \approx -0.400$ and Kaplan-Yorke dimension[25] $D_L \approx 1$ is observed in the vocal fold model. Figure 3(a) shows the distributions of Jit_MDVP, Shim_MDVP, and D_2 of 20 periodic signals with randomized initial conditions. Jitter (0.031), shimmer (0.002), and D_2 (1.000) all display small variances and give stable analyses for the periodic signals. However, when the tension imbalance parameter $Q=0.529$, a chaotic vibration with Lyapunov exponents $\lambda_1 \approx 0.012$, $\lambda_2 \approx 0$, $\lambda_3 \approx -0.123$, $\lambda_4 \approx -0.139$, $\lambda_5 \approx -0.154$, $\lambda_6 \approx -0.269$, $\lambda_7 \approx -0.341$, and $\lambda_8 \approx -0.454$ and Kaplan-Yorke dimension $D_L \approx 2.1$ occurs. For 20 chaotic $x_{1L}(t)$ signals with randomized initial condition $x_{1L}(0)$, jitter (18.6 ± 6.3) and shimmer (19.9 ± 8.0) in Fig. 3(b) both show large variances, indicating their extreme sensitivities to changes in initial conditions. In Fig. 3, the line inside the box marks the median, whiskers show 10th and 90th percentiles, and the dots are the outlying points. Also, the large variances in the jitter and shimmer measurement dynamically changes because of the unstable pitch extraction. Such unstable variances prevent quantitatively reliable measurements of jitter and shimmer for aperiodic voices. In contrast to this, correlation dimension D_2 (2.06 ± 0.02) gives comparatively stable estimates, demonstrating that it is less sensitive to initial condition differences and better suited to provide an effective measure of such an ergodic system. Similar results also can be found in Fig. 3(c) where we added Gaussian noise with a mean value of 0 and a standard deviation of $\sigma=0.08$ to the normalized periodic signal from Fig. 3(a) within $(-0.5, 0.5)$. For the randomized initial conditions $x_{1L}(0)$, jitter (3.71 ± 0.31) and shimmer (5.24 ± 0.44) show a lack of consistency; however, the correlation dimension D_2 gives a more consistent estimate (1.55 ± 0.01). The increased D_2 value is associated with noise.[36,37] Thus, these results suggest that if a signal is periodic or nearly periodic, perturbation methods and nonlinear dynamic methods are both capable of voice analysis. However, if the analyzed signal is chaotic or aperiodic, jitter and shimmer may not be capable of presenting a stable analysis, while nonlinear dynamic methods may represent more reliable analysis methods.

Signal length, sampling frequency or rate, and noise may affect the measurements of jitter and shimmer for periodic signals. Sinusoidal waves, triangular waves, and synthetic vowels have been previously applied as test signals.[12] In this study, the vibratory signal produced by a vocal fold model is applied as a test signal. For the sample in Fig. 1, which has a length of 1 s and was sampled at 44.1 kHz, when the embedding dimension m is increased from 1 to 10, the correlation dimension approaches 1.0 within the scaling

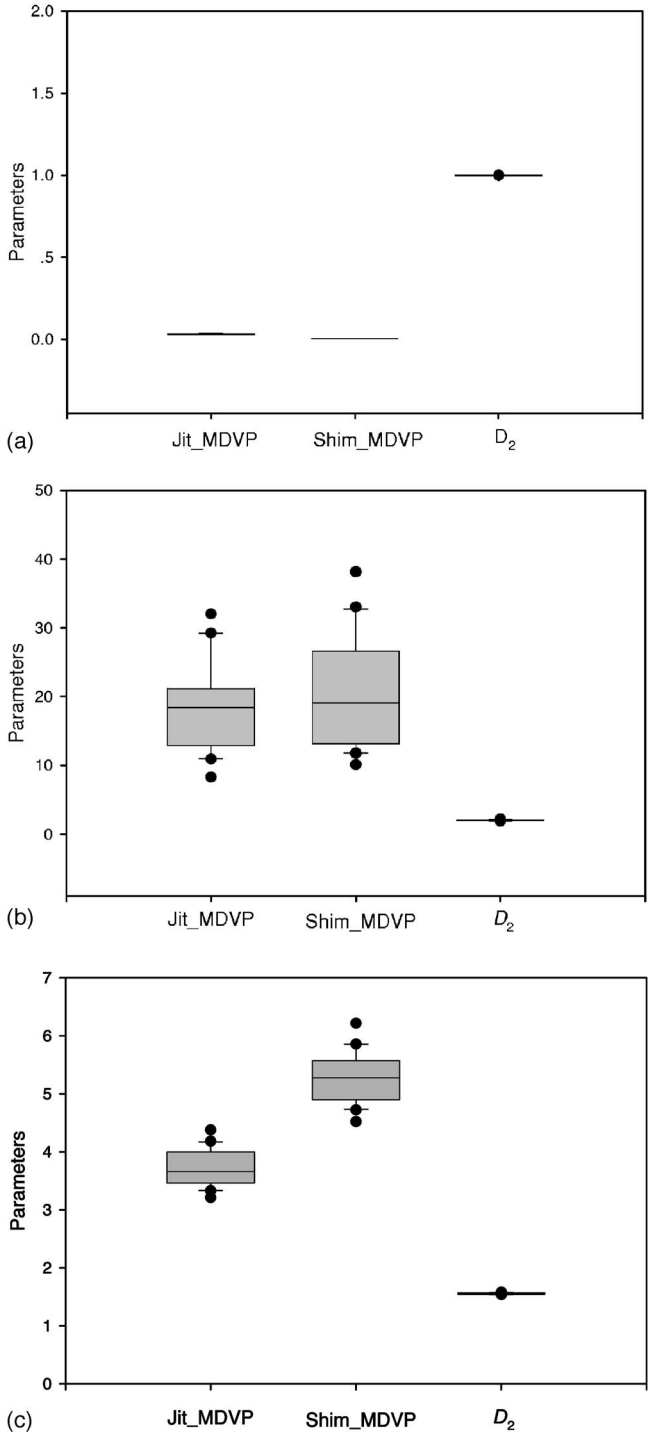

FIG. 3. The distributions of Jit_MDVP, Shim_MDVP, and D_2 of the vibratory signals from the vocal fold model under 20 randomized different initial states, where the line inside the box marks the median, whiskers show 10th and 90th percentiles, and the dots are the outlying points. (a) Periodic signal. (b) Chaotic signal. (c) Periodic signal with additive noise, where a Gaussian noise with mean value 0 and standard deviation $\sigma=0.08$ is added to the normalized periodic signal.

region ($2^6<r<2^{14}$), as shown in Fig. 4(a). For this voice sample, jitter and shimmer were both estimated at 0.0 using Cspeech, and 0.051 and 0.002, respectively, using MDVP. For the 50-ms signal in Fig. 4(b), which was sampled at 44.1 kHz, Jit_Cspeech (0.0) and Shim_Cspeech (0.0) gave the expected estimates; however, when sampling frequency is decreased to 2 kHz and signal length is 1 s in Fig. 4(c), Jit_Cspeech (57.8) and Shim_Cspeech (27.8) are abnormally high. Jit_MDVP and Shim_MDVP cannot analyze voice signals with a length less than 200 ms or sampling rate smaller than 25 kHz, and thus these measures were not calculated for Figs. 4(b) and 4(c). For the signal with a noise amplitude of 0.02, which has a signal length of 1 s and was sampled at 44.1 kHz, Jit_MDVP (3.17), Shim_MDVP (1.87), Jit_Cspeech (0.25), and Shim_Cspeech (0.39) all show significant distortions. For correlation dimension analysis of the test signal, short signal length, low sampling rate, and large noise amplitude smear out the scaling property at small r, causing the scaling region to shrink. The scaling regions in Figs. 4(b), 4(c), and 4(d) are reduced to ($2^{10}<r<2^{14}$), ($2^{10}<r<2^{14}$), and ($2^{12}<r<2^{13.8}$), respectively. Despite this, the scaling law characteristics are still revealed in these scaling regions. Although jitter and shimmer sufficiently change when the sampling rate is decreased and noise amplitude is increased, the correlation dimension continues to yield stable estimates.

For continuous increases in signal length, sampling frequency, and noise, Figs. 5(a), 5(b), and 5(c) show the results of Jit_MDVP, Shim_MDVP, Jit_Cspeech, Shim_Cspeech, and D_2 analyses. In Fig. 5(a), the signal length is increased from 20 to 2000 ms. The minimal signal lengths N of MDVP and Cspeech are 200 and 50 ms, respectively, which correspond to 18.6 and 4.7 cycles for the test signal with a fundamental frequency $f_0=93$ Hz. When the length of the periodic signal decreases, the estimates of Jit_MDVP and Shim_MDVP increase, while the estimates of Jit_Cspeech and Shim_Cspeech remain consistent until the signal length exceeds 50 ms. Using correlation dimension analysis, the minimal signal length of this periodic signal is reduced to 20 ms (1.9 cycles). For a signal of 20 ms, the scaling law characteristic is still clearly revealed in its scaling region. Eckmann and Ruelle[38] have given a low bound for the signal length N for a D-dimensional attractor as: $N>\tau(1/\rho)^{D/2}$. τ is the sampling time and should not be very small in order to avoid the correlation of temporally close points in a reconstructed phase space. We set τ as the proper time delay estimated using the mutual information method.[27] For the periodic test signal, τ is estimated as $112/f_s$. ρ is the ratio between the scaling at which the dimension is estimated and the diameter of the attractor. Using the formula of Eckmann and Ruelle,[38] for $\rho=5\%$ and $D\approx 1$, the minimal signal length of the periodic test signal is about 11 ms (one cycle). This length estimate is reasonable since one cycle length is long enough for a periodic signal to form a closed trajectory in the reconstructed phase space, while more cycles repeatedly reconstruct the same periodic attractor. The correlation dimension method allowed a shorter signal length for the analysis of a nearly periodic signal as compared to jitter and shimmer calculated using MDVP and Cspeech.

To investigate the effects of sampling frequency, the signal with 44.1 kHz was downsampled from 44.1 to 2 kHz. The minimal sampling rate required by MDVP is 25 kHz for perturbation analysis. Cspeech analyzed the voices sampled at frequencies ranging from 44.1 to 2 kHz. However, at some low sampling frequencies (2 and 6 kHz), Jit_Cspeech

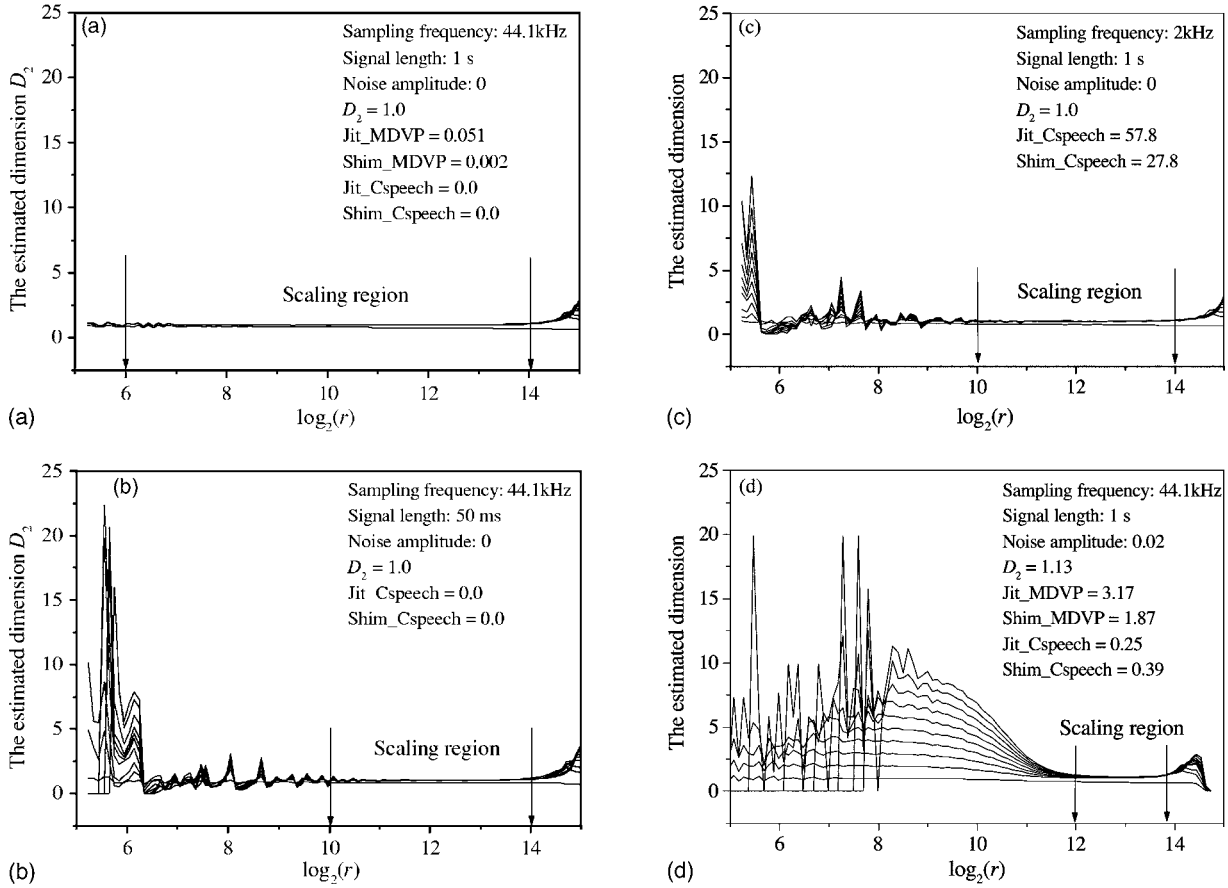

FIG. 4. The estimated correlation dimension versus $\log_2 r$ of the periodic vibratory signal from the two mass model, in which the curves correspond to the embedding dimension $m=1,2,\ldots,10$, respectively. (a) 1-s signal length, 44.1-kHz sample rate, and 0 noise amplitude. (b) 50-ms signal length, 44.1-kHz sample rate, and 0 noise amplitude. (c) 1-s signal length, 2-kHz sampling rate, and 0 noise amplitude. (d) 1-s signal length, 44.1-kHz sample rate, and 0.02 noise amplitude.

and Shim_Cspeech show abnormally high values. Sampling noise from low sampling frequencies may disrupt pitch tracking. Figure 5(b) shows that in order to obtain dependable estimates of jitter and shimmer, the sampling frequency must be sufficiently high. Unlike the perturbation measures, correlation dimension yields a very consistent estimate for the periodic test signal when the sampling rate is decreased from 44.1 to 2 kHz.

Because of random influences and measurement inaccuracies, noise inevitably exists in any measure system. To simulate the effects of noise, we normalized $x_{1L}(t)$ with length 2 s within $(-0.5,0.5)$ and then added Gaussian noise with amplitude σ to the test signal. The curves from the top to bottom in Fig. 5(c) correspond to Jit_MDVP, Shim_MDVP, Jit_Cspeech, Shim_Cspeech, and D_2. Noise directly affects pitch tracking and the estimates of amplitude and fundamental frequency of a signal. When noise amplitude is increased from 10^{-5} to 10^{-1}, Jit_MDVP, Shim_MDVP, Shim_Cspeech, and Jit_Cspeech all show rapid increases, indicating their sensitivity to noise. Although the correlation dimension also increases with the Gaussian noise amplitude σ, it demonstrates greater robustness to external noise. An attractor is robust to weak noise perturbation because low levels of noise cannot drive the trajectory out of the vicinity of the attractor. Unlike jitter and shimmer, which were developed for time domain and frequency domain analysis, correlation dimension measures the geometric scaling properties of an attractor. Noise and sampling errors may break down the self-similarity of a chaotic attractor and smear out the scaling properties at the lower scales of the order of magnitude of the noise amplitude. However, the power law rule can still be observed in the scaling region, which is higher than the region affected by noise on the graph of the estimated dimension vs. $\log_2 r$. This may be a reason why correlation dimension analysis is more resistant to noise than perturbation analysis. Correlation dimension analysis continues to yield stable estimates when the noise level is increased to 8% and the sampling frequency is decreased to 2 kHz for the periodic test signal. When noise amplitude is excessively large, the scaling behaviors at all length scales of the signal are destroyed, and the correlation dimension cannot be estimated. Recent studies in reducing the noise bias in estimates of correlation dimension show that applying the Gaussian-kernel-based method to the correlation dimension can further increase the noise level to 20%.[39,40]

IV. EXPERIMENTAL STUDY

To further verify the above theoretical analysis, in this section we apply perturbation and nonlinear dynamic methods to analyze the sustained vowels from two normal subjects and 11 patients with laryngeal pathologies, including

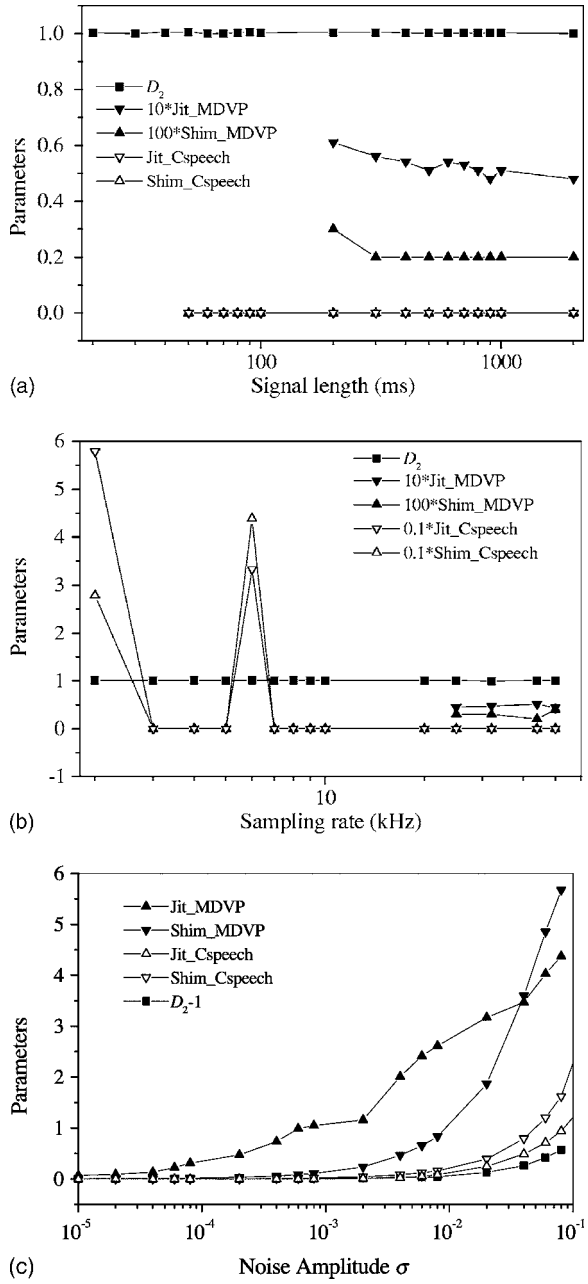

FIG. 5. The effects of signal length, sampling rate, and noise on perturbation and nonlinear dynamic measures for the periodic vibratory signal of the vocal fold model. (a) Signal length. (b) Sampling rate. (c) Noise perturbation.

vocal polyps, nodules, cysts, and Parkinson's disease. The ages of the subjects were 34–69 years. Table I shows the subject information. Voice recordings were made in a double-walled, sound-attenuated room at a sampling rate of 44.1 kHz. Subjects were asked to sustain the vowel /a/ at a comfortable pitch and intensity, as steadily and as long as possible. The middle, stationary-appearing segments of the voices were chosen for analysis.

Figures 6(a) and 6(b) shows two typical waveforms of a nearly periodic signal from a normal subject and an aperiodic signal from a patient with a vocal polyp, respectively. To show the time variances of jitter, shimmer, and correlation dimension for the analysis of these two signals, 11 consecutive voice segments, each of length 400 ms, were selected,

TABLE I. Information of subjects.

Case no.	Sex	Age (years)	Diagnosis
1	Female	36	Normal
2	Male	67	Normal
3	Male	44	Polyp
4	Male	52	Polyp
5	Female	34	Polyp
6	Male	50	Polyp
7	Male	48	Nodules
8	Female	37	Nodules
9	Female	37	Cyst
10	Female	46	Cyst
11	Female	39	Cyst
12	Male	69	Parkinson's disease
13	Male	66	Parkinson's disease

with the time shift between two consecutive voice segments equal to 20 ms. Figures 7(a) and 7(b) give the distributions of Jit_Cspeech, Shim_Cspeech, Jit_MDVP, Shim_MDVP, and D_2 of the nearly periodic and aperiodic signals, respectively. Titze[4] has qualitatively classified voice signals into nearly periodic type 1 signals, type 2 signals containing strong modulations or subharmonics, and irregular or aperiodic type 3 signals. Recent studies[4–6] of the human voice and excised larynx phonations have suggested that jitter and shimmer are reliable for periodic and nearly periodic type 1 signals but not for aperiodic or chaotic type 3 signals. In Fig. 7(a), both the perturbation methods and the correlation dimension

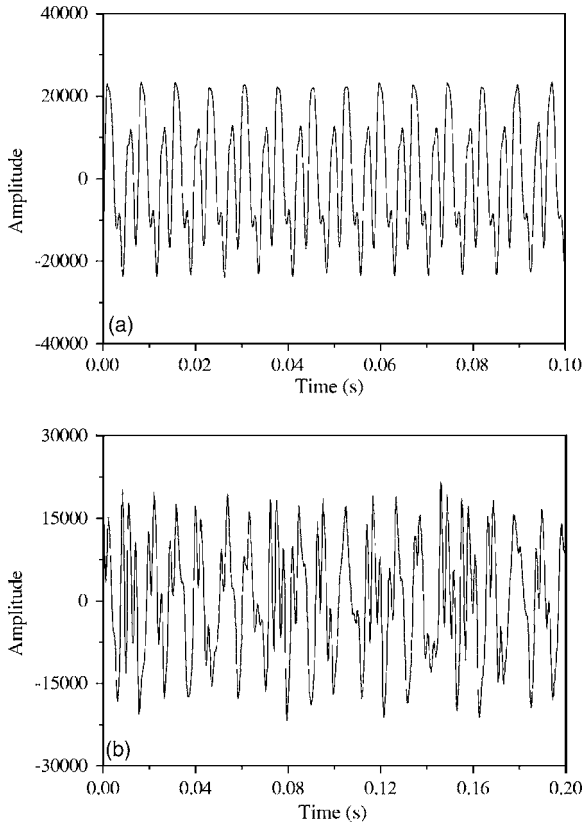

FIG. 6. Waveforms of a nearly periodic signal from a normal subject and an aperiodic signal from a patient with vocal polyp. (a) Nearly periodic voice signal. (b) Aperiodic voice signal.

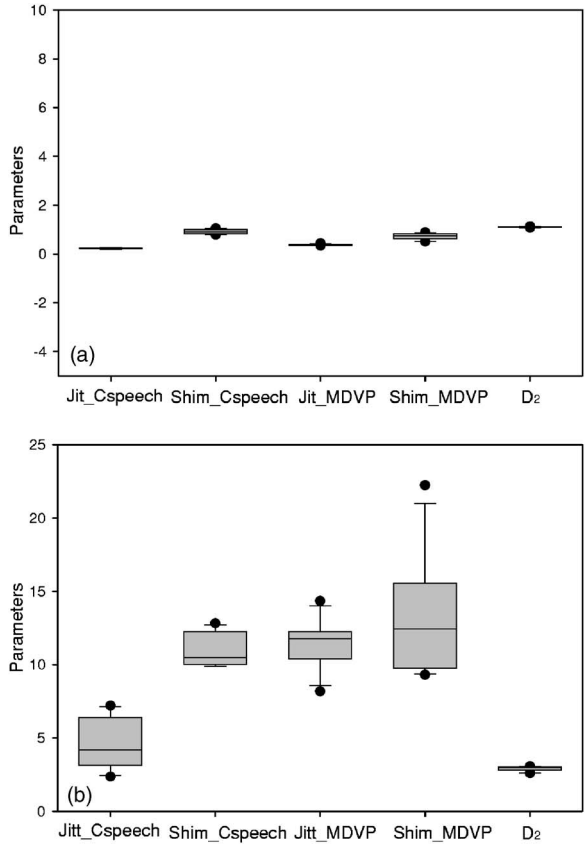

FIG. 7. The distributions of Jit_Cspeech, Shim_Cspeech, Jit_MDVP, Shim_MDVP, and D_2 of the nearly periodic and aperiodic signals, where 11 consecutive voice segments, each of length 400 ms, were selected from the nearly periodic and aperiodic signals, with the time shift between two consecutive voice segments equal to 20 ms. The line inside the box marks the median, whiskers show 10th and 90th percentiles, and the dots are the outlying points. (a) Nearly periodic voice signal. (b) Aperiodic voice signal.

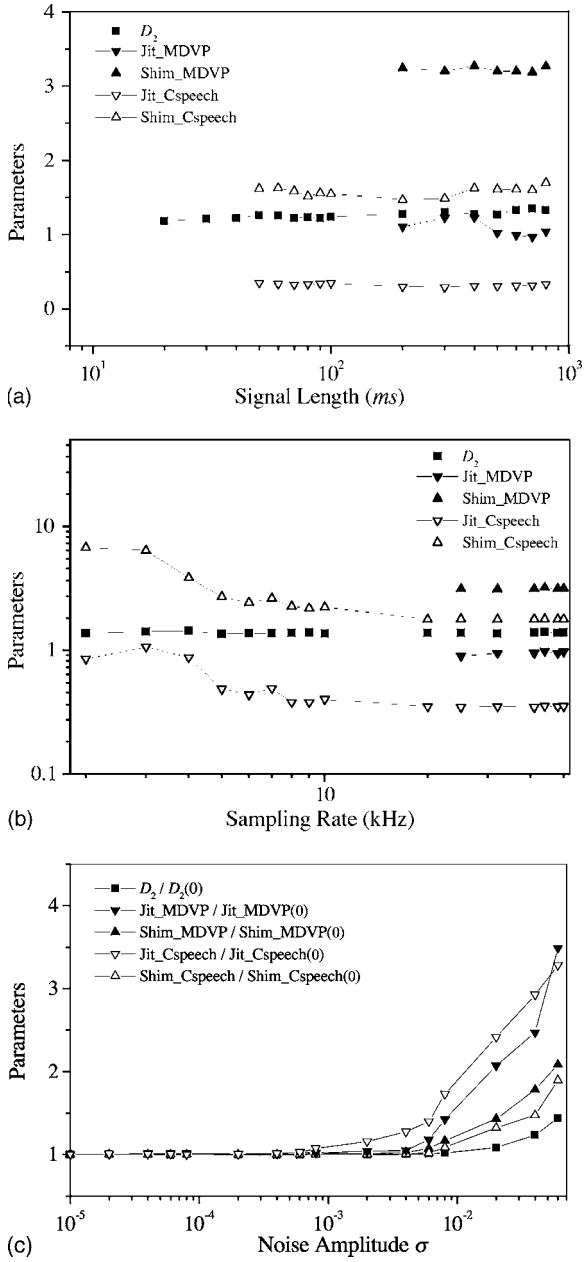

FIG. 8. The effects of signal length, sampling rate, and noise on perturbation and nonlinear dynamic measures for the voices from 14 human subjects. (a) Signal length. (b) Sampling rate. (c) Noise perturbation.

method give stable estimates for 11 consecutive voice segments of the nearly periodic type 1 signal from Fig. 6(a). However, for the aperiodic type 3 signal from Fig. 6(b), jitter and shimmer measures in Cspeech and MDVP show large time variances and poor reliability as seen in Fig. 7(b), whereas the estimate of the correlation dimension is much more stable, demonstrating its reliability and applicability for analyzing disordered or aperiodic voices. In addition, between Cspeech and MDVP, large discrepancies can be found in the measurements of jitter and shimmer in Fig. 7(b) for the aperiodic voice. Such a disagreement among different perturbation analysis systems also has been shown in the study by Bielamowicz *et al.*,[14] where they questioned the applicability of perturbation measurement to quantify mildly and severely disordered voices. The results of the perturbation analysis in Fig. 7(b) show agreement with these previous studies. The correlation dimension method, on the other hand, shows itself to be of potential value in the analysis of aperiodic voices. These results further verify the analysis in Fig. 3.

For all the nearly periodic voices, Fig. 8(a) shows the effects of signal length on the mean values of D_2, Jit_MDVP, Shim_MDVP, Jit_Cspeech, and Shim_Cspeech. Although the length of time and number of cycles are both given for the nearly periodic signals in Fig. 8, we suggest using length of time instead of number of cycles because the number of cycles of aperiodic voice signals may not be easily determined, as discussed in the above section. In Fig. 8(a), for the shimmer measurements, Shim_Cspeech and Shim_MDVP give stable results when the signal lengths are higher than 50 ms (12.2 cycles) and 200 ms (48.6 cycles), respectively. For the jitter measurements, Jit_Cspeech and Jit_MDVP give stable results when the signal lengths are higher than 50 ms (about 12.2 cycles) and 500 ms (about 122 cycles), respectively. Titze *et al.*[8] analyzed normal human voice samples and suggested that a meaningful perturbation measurement can be obtained for nearly periodic signals that include at least 20 cycles. By analyzing pathological voices from patients with laryngeal dysfunction, Karnell[10] found that 130 cycles were needed for a steady measure of shimmer and 190 cycles for jitter. In comparison with these results,

correlation dimension analysis allows a much smaller signal length of 20 ms (about 4.8 cycles), as shown in Fig. 8(a). The correlation dimension does not greatly change when the signal length decreases from 800 to 20 ms.

In this study, the middle stationary-appearing segments of sustained vowels were used for perturbation and nonlinear dynamic analyses. However, for a whole vowel or running speech, time-varying or nonstationary characteristics are also important. Behrman and Baken[18] suggested that nonconstant dimension estimates might be associated with nonstationary electroglottographic data. We suggest that for a stationary voice signal, substantial scaling regions and stable dimension estimates can be obtained, as shown in Figs. 4 and 7 and in many previous studies.[6,17,19,21,22,37,41] However, for a nonstationary voice signal, a fixed parameter value may not describe the signal's time-varying process.[42–44] A more reasonable procedure would be to apply a short-time correlation dimension analysis to such a signal, similar to a short-time Fourier analysis.[44] This would entail that a nonstationary signal be divided into a series of quasi-steady segments using a moving window since vocal configuration parameters change much more slowly compared to voices during phonation. Then the short-time formula of perturbation and nonlinear dynamic measures would allow us to describe the time-varying or nonstationary characteristics of a voice signal. Real time analysis requires that an analysis method give a stable result for as short a signal as possible. In Fig. 8(a), the correlation dimension allows a shorter signal length than perturbation methods, suggesting that the correlation dimension may present a more valuable method for the real time analysis of vowels and running speech. Further study is needed in this potentially important subject.

In Fig. 8(b), when the sampling rate is above 20 kHz in Cspeech and above 25 kHz in MDVP, jitter and shimmer measures are both stable. When the sampling rate is less than 20 kHz, jitter and shimmer estimated with Cspeech continuously increase. In contrast with this, correlation dimension values are stable when the sampling rate decreases from 44.1 to 2 kHz. Sampling errors resulting from low sampling frequencies did not significantly affect the correlation dimension estimates.

Figure 8(c) illustrates that the mean values of D_2, Jit_MDVP, Shim_MDVP, Jit_Cspeech, and Shim_Cspeech increase with the Gaussian noise amplitude σ, where the voice signals are normalized within $(-0.5, 0.5)$, and the relative values $D_2/D_2(0)$, Jit_MDVP/Jit_MDVP(0), Shim_MDVP/Shim_MDVP(0), Jit_Cspeech/Jit_Cspeech(0), and Shim_Cspeech/Shim_Cspeech(0) are given. $D_2(0)=1.3$, Jit_MDVP$(0)=1.02$, Shim_MDVP$(0)=3.3$, Jit_Cspeech$(0)=0.37$, and Shim_Cspeech$(0)=1.72$ represent the results without any noise. Jitter and shimmer are not resistant to noise. When noise amplitude is increased about 0.6% (38 dB), the relative values of all perturbation parameters increase above 5%. Titze and Liang[12] obtained similar results in their high-precision perturbation measurements of jitter and shimmer. In both sutides, white noise with a broadband spectrum was added to the signal. A computer-generated fan noise with center frequency 235 Hz was applied in the study of Carson *et al.*,[11] where jitter and shimmer values also increased with additive noise. When noise amplitude is increased above 2% (28 dB), the relative value $D_2/D_2(0)$ of the correlation dimension increases above 5%. In comparison to jitter and shimmer, the correlation dimension increases more slowly with increased white noise amplitude, demonstrating that it is more resistant to noise.

Environmental noise, as well as measurement noise from recording, sampling, and analysis systems, inevitably produces perturbations in the time and frequency domain, affecting pitch tracking and estimation of jitter and shimmer. However, laryngeal pathologies also contribute to variations in jitter and shimmer. The sensitivity of jitter and shimmer to variations in recording systems, analysis systems, and extraction algorithms makes high-quality and high-cost computing equipment necessary. If these are unavailable, it may be unclear whether variations in jitter and shimmer result from system noise or from laryngeal pathologies. A more feasible analysis method would depend less on external environmental factors and equipment and more on the laryngeal pathologies. The correlation dimension represents a geometric measure of a system. The preservation of the scaling properties of a dynamic system permits reliable and stable correlation dimension analysis for larger external noise perturbations and much lower sampling frequencies than for perturbation methods. Correlation dimension may help decrease the cost of recording and analysis systems for clinical voice analysis.

V. CONCLUSION

In this paper, we compared the applicability of nonlinear dynamic methods and perturbation methods for voice analysis. The effects of signal length, sampling rate, and noise were quantitatively investigated. Results of our theoretical and experimental studies demonstrated that large variances in perturbation measurements caused them to be inapplicable for chaotic or aperiodic signals. For nearly periodic voices from healthy subjects and patients with laryngeal pathologies, perturbation analysis required voice recordings of sufficiently long signal length, high sampling frequency, and low noise levels. In contrast, nonlinear dynamic methods can quantify chaotic signals. Furthermore, the correlation dimension presented a more reliable analysis measure for nearly periodic voices of shorter signal length, lower sampling rate, and larger noise levels. Thus, the correlation dimension method might be helpful in avoiding some methodological issues associated with perturbation methods, and it may offer the advantages of real time analysis as well as the possibility of lower costs in experimental designs. The appropriate application of perturbation analysis and nonlinear dynamic analysis can provide different but complementary information and may potentially improve our ability to objectively assess voice disorders and evaluate the effects of treatment of laryngeal pathologies.

ACKNOWLEDGMENTS

This study was supported by NIH Grant No. 1-RO1DC006019 from the National Institute of Deafness and other Communication Disorders and NSFC Grand No. 30328029.

[1]P. Lieberman, "Perturbations in vocal pitch," J. Acoust. Soc. Am. **33**, 597–603 (1961).
[2]P. Lieberman, "Some acoustic measures of the fundamental periodicity of normal and pathologic larynges," J. Acoust. Soc. Am. **35**, 344–353 (1963).
[3]Kay Elemetrics Corp, Multi-Dimensional Voice Program: Software Instruction Manual, Pine Brook, NJ (1993).
[4]I. R. Titze, "Workshop on acoustic voice analysis; Summary statement," National Center for Voice and Speech, Denver, CO (1995), p. 36.
[5]M. P. Karnell, A. Chang, A. Smith, and H. Hoffman, "Impact of signal type of validity of voice perturbation measures," NCVS Status Prog. Rep. **11**, 91–94 (1997).
[6]J. J. Jiang, Y. Zhang, and C. N. Ford, "Nonlinear dynamic of phonations in excised larynx experiments," J. Acoust. Soc. Am. **114**, 2198–2205 (2003).
[7]I. R. Titze and W. S. Winholtz, "Effect of microphone type and placement on voice perturbation measurements," J. Speech Hear. Res. **36**, 1177–1190 (1993).
[8]I. R. Titze, Y. Horii, and R. C. Scherer, "Some technical considerations in voice perturbation measurements," J. Speech Hear. Res. **30**, 252–260 (1987).
[9]J. J. Jiang, E. Lin, and D. G. Hanson, "Effect of tape recording on perturbation measures," J. Speech Lang. Hear. Res. **41**, 1031–1041 (1998).
[10]M. P. Karnell, "Laryngeal perturbation analysis: minimum length of analysis window," J. Speech Hear. Res. **34**, 544–548 (1991).
[11]C. P. Carson, D. R. S. Ingrisano, and K. D. Eggleston, "The effect of noise on computer-aided measures of voice: A comparison of CSpeechSP and the multi-dimensional voice program software using the CSL 4300B module and multi-speech for windows," J. Voice **17**, 12–20 (2003).
[12]I. R. Titze and H. Liang, "Comparison of F0 extraction method for high-precision voice perturbation measurements," J. Speech Hear. Res. **36**, 1120–1133 (1993).
[13]M. P. Karnell, R. S. Scherer, and L. B. Fischer, "Comparison of acoustic voice perturbation measures among three independent voice laboratories," J. Speech Hear. Res. **34**, 781–790 (1991).
[14]S. Bielamowicz, J. Kreiman, B. R. Gerratt, M. S. Dauer, and G. S. Berke, "Comparison of voice analysis systems for perturbation measurements," J. Speech Hear. Res. **39**, 126–134 (1996).
[15]E. Ott, T. Sauer, and J. A. Yorke, *Coping with Chaos: Analysis of Chaotic Data and the Exploitation of Chaotic Systems* (Wiley, New York, 1994).
[16]H. Herzel, D. Berry, I. R. Titze, and M. Saleh, "Analysis of vocal disorders with methods from nonlinear dynamics," J. Speech Hear. Res. **37**, 1008–1019 (1994).
[17]I. R. Titze, R. Baken, and H. Herzel, "Evidence of chaos in vocal fold vibration," in *Vocal Fold Physiology: New Frontier in Basic Science*, edited by I. R. Titze (Singular, San Diego, 1993), pp. 143–188.
[18]A. Behrman and R. J. Baken, "Correlation dimension of electroglottographic data from healthy and pathologic subjects," J. Acoust. Soc. Am. **102**, 2371–2379 (1997).
[19]Y. Zhang and J. J. Jiang, "Nonlinear dynamic analysis of signal typing of pathological human voices," Electron. Lett. **39**, 1021–1023 (2003).
[20]A. Giovanni, M. Ouaknine, and J.-M. Triglia, "Determination of largest Lyapunov exponents of vocal signal: application to unilateral laryngeal paralysis," J. Voice **13**, 341 (1998).
[21]J. J. Jiang and Y. Zhang, "Nonlinear dynamic analysis of speech from pathologic subjects," Electron. Lett. **38**, 294–295 (2002).
[22]Y. Zhang, C. McGilligan, L. Zhou, M. Vig, and J. J. Jiang, "Nonlinear dynamic analysis of voices before and after surgical excision of vocal polyps," J. Acoust. Soc. Am. **115**, 2270–2277 (2004).
[23]I. Steinecke and H. Herzel, "Bifurcations in an asymmetric vocal-fold model," J. Acoust. Soc. Am. **97**, 1874–1884 (1995).
[24]K. Ishizaka and J. L. Flanagan, "Synthesis of voiced sounds from a two-mass model of the vocal cords," Bell Syst. Tech. J. **51**, 1233–1268 (1972).
[25]J. J. Jiang, Y. Zhang, and J. Stern, "Modeling of chaotic vibrations in symmetric vocal folds," J. Acoust. Soc. Am. **110**, 2120–2128 (2001).
[26]N. H. Packard, J. P. Crutchfield, J. D. Farmer, and R. S. Shaw, "Geometry from a time series," Phys. Rev. Lett. **45**, 712 (1980).
[27]A. M. Fraser and H. L. Swinney, "Independent coordinates for strange attractors from mutual information," Phys. Rev. A **33**, 1134–1140 (1986).
[28]F. Takens, "Detecting strange attractors in turbulence," in *Lecture Notes in Mathematics*, edited by D. A. Rand and B. S. Young (Springer-Verlag, Berlin, 1981), Vol. **898**, pp. 366–381.
[29]P. Grassberger and I. Procaccia, "Measuring the strangeness of strange attractors," Physica D **9**, 189–208 (1983).
[30]J. Theiler, "Spurious dimension from correlation algorithms applied to limited time series data," Phys. Rev. A **34**, 2427–2432 (1986).
[31]A. Wolf, J. B. Swift, H. L. Swinney, and J. A. Vastano, "Determining Lyapunov exponents from a time series," Physica D **16**, 285–317 (1985).
[32]J. Holzfuss and W. Lauterborn, "Lyapunov exponents from a time series of acoustic chaos," Phys. Rev. A **39**, 2146–2152 (1989).
[33]P. Milenkovic, "Least mean square measures of voice perturbation," J. Speech Hear. Res. **30**, 529–538 (1987).
[34]P. Milenkovic and C. Read, *Cspeech version 4 user's manual*, Madison, WI (1992).
[35]K. M. Cuomo, A. V. Oppenheim, and S. H. Strogatz, IEEE Trans. Circuits Syst. II **40**, 626–633 (1993).
[36]M. Moller, W. Lance, F. Mitschke, N. B. Abraham, and U. Hubner, "Errors from digitizing and noise in estimating attractor dimension," Phys. Lett. A **138**, 176 (1989).
[37]A. Kumar and S. K. Mullick, "Nonlinear dynamical analysis of speech," J. Acoust. Soc. Am. **100**, 615–629 (1996).
[38]J. P. Eckmann and D. Ruelle, "Fundamental limitations for estimating dimensions and Lyapunov exponents in dynamical systems," Physica D **56**, 185–187 (1992).
[39]C. Diks, "Estimating invariants of noisy attractors," Phys. Rev. E **53**, R4263–R4266 (1996).
[40]G. Nolte, A. Ziehe, and K.-R. Muller, "Noisy robust estimates of correlation dimension and K2 entropy," Phys. Rev. E **64**, 016112 (2001).
[41]S. S. Narayanan and A. A. Alwan, "A nonlinear dynamical systems analysis of fricative consonants," J. Acoust. Soc. Am. **97**, 2511 (1995).
[42]S. Blanco, H. Garcia, R. Q. Quiroga, L. Romanelli, and O. A. Rosso, "Stationarity of the EEG series," IEEE Eng. Med. Biol. Mag. **14**, 395–399 (1995).
[43]J. W. Havstad and C. L. Ehlers, "Attractor dimension of nonstationary dynamical systems from small data sets," Phys. Rev. A **39**, 845–853 (1989).
[44]L. R. Rabiner and R. W. Schafer, *Digital Processing of Speech Signals* (Prentice-Hall, Englewood Cliffs, NJ, 1978).

Lexical frequency and acoustic reduction in spoken Dutch

Mark Pluymaekers
Radboud University Nijmegen, Wundtlaan 1, 6525 XD Nijmegen, The Netherlands

Mirjam Ernestus
Max Planck Institute for Psycholinguistics and Radboud University Nijmegen, Wundtlaan 1, 6525 XD Nijmegen, The Netherlands

R. Harald Baayen
Radboud University Nijmegen and Max Planck Institute for Psycholinguistics, Wundtlaan 1, 6525 XD Nijmegen, The Netherlands

(Received 2 December 2004; revised 1 July 2005; accepted 9 July 2005)

This study investigates the effects of lexical frequency on the durational reduction of morphologically complex words in spoken Dutch. The hypothesis that high-frequency words are more reduced than low-frequency words was tested by comparing the durations of affixes occurring in different carrier words. Four Dutch affixes were investigated, each occurring in a large number of words with different frequencies. The materials came from a large database of face-to-face conversations. For each word containing a target affix, one token was randomly selected for acoustic analysis. Measurements were made of the duration of the affix as a whole and the durations of the individual segments in the affix. For three of the four affixes, a higher frequency of the carrier word led to shorter realizations of the affix as a whole, individual segments in the affix, or both. Other relevant factors were the sex and age of the speaker, segmental context, and speech rate. To accommodate for these findings, models of speech production should allow word frequency to affect the acoustic realizations of lower-level units, such as individual speech sounds occurring in affixes. © *2005 Acoustical Society of America.* [DOI: 10.1121/1.2011150]

PACS number(s): 43.70.Bk, 43.70.Fq [AL] Pages: 2561–2569

I. INTRODUCTION

In everyday speech, words are often pronounced shorter than their citation forms would suggest. This is not a marginal phenomenon: In Johnson's (2004) study on conversational American English, 25% of the words had one or more segments deleted. Deletion of complete syllables occurred in 6% of the words. Similar observations were made by Ernestus (2000) for Dutch. For example, the word *natuurlijk* ("of course") was sometimes reduced to [tyk]. Despite the frequent nature of these reductions, their presence has not yet been accommodated in any of the main psycholinguistic theories (e.g., Garrett, 1975; Dell, 1986; Levelt, 1989; Bock, 1995).

Reductions have often been linked to word frequency (e.g., Jespersen, 1922; Zipf, 1929), the hypothesis being that high-frequency words are more reduced than low-frequency words. Several explanations have been offered for this relationship, such as the compression of motor routines as a result of practice (Bybee, 2001), or the fact that high-frequency words are more predictable for the listener (e.g., Jurafsky *et al.* 2001). Many studies have confirmed the pivotal role of word frequency in predicting diachronic phonetic abbreviations (Zipf, 1929; Bybee, 2001). It has proven more difficult, however, to demonstrate synchronic effects of frequency on acoustic realizations.

The main problem lies in the lack of suitable reference material. Since words generally differ not only in frequency, but also in at least one of their speech sounds, they are bound to differ in duration as well. Therefore, most authors have restricted themselves to comparing instances of the same phoneme occurring in different words. Umeda (1977) found that in American English, word-initial [s]-es were shorter if the frequency of their carrier word was high. Likewise, Cooper and Paccia-Cooper (1980) showed that palatalization of [d] before [j] was more likely in high-frequency than in low-frequency words. Van Coile (1987) used word frequency as a criterion to distinguish between function words and content words in Dutch, and found that vowels occurring in function words were shorter than the same vowels occurring in content words. Finally, Jurafsky *et al.* (2001) compared tokens of word-final [d] and [t] occurring in English words with different frequencies. In words with a high frequency, the plosive had a greater chance of being deleted, and if it was present in the signal, its duration was significantly shorter.

Over the years, attempts have been made to demonstrate frequency effects on units larger than the phoneme as well. Wright (1979) used pairs of rare and common words matched on length in letters, but, as most speech researchers will agree, this type of matching does not offer enough experimental control for comparing durations. Gregory *et al.* (1999) measured the durations of a large number of words ending in *–t* or *–d*, and found an effect of word frequency on these durations. However, their target words probably differed on other dimensions as well, such as the number of phonemes and their complexity (Landauer and Streeter, 1973). Therefore, the evidence for effects of word frequency on the durations of larger linguistic units remains inconclusive.

To overcome the difficulties sketched above, we decided to focus on morphemes that can occur in a large number of words with different frequencies: affixes. This approach is similar to that of Aylett and Turk (2004), who compared syllables occurring in different words. The main difference lies in the fact that affixes by definition carry meaning, while for syllables this is not necessarily the case. An additional advantage of affixes is that most of them never bear stress, providing us with valuable control over factors like word stress and sentence accent.

Most studies on word frequency and reduction used English materials. Recently, a new database of spoken Dutch has become available, containing a large section of spontaneous, face-to-face conversations. This provided us with an excellent opportunity to investigate the effects of frequency on acoustic reduction in a language other than English.

In summary, this study investigates the effects of word frequency on the durations of Dutch affixes. Durational shortening is of course not the only acoustic correlate of reduction, but the nature of the materials (spontaneous, overlapping speech) precluded us from studying variables such as mean amplitude (e.g., Shields and Balota, 1991) or center of gravity (e.g., Van Son and Pols, 2003). Section II describes our materials and method of measurement. Section III is concerned with the control variables we incorporated. Sections IV–VII contain the results for the different affixes. Section VIII, finally, discusses the results and their implications for future research.

II. METHODOLOGY

A. Materials

All materials were drawn from the Corpus of Spoken Dutch (Oostdijk, 2000). This corpus contains approximately 800 hours of speech recordings, of which only the 225 hours of spontaneous, face-to-face conversations were considered for the present study. Orthographic transcriptions are available for the entire corpus. We restricted ourselves to Dutch speakers, since they have been shown to use reduced forms more than speakers from Flanders [Keune *et al.*, 2005; see Adank *et al.*, (2004), for other acoustic differences between the two varieties of Dutch].

The affixes under investigation were the prefixes *ge-*, *ver-*, and *ont-*, and the suffix *-lijk*. *Ge-* is used mainly to create the perfect participle in Dutch, although it can also function as a nominal or verbal prefix. In this study, we restricted ourselves to the participial use of *ge-*. *Ver-* and *ont-* are verbalizing prefixes expressing states of change (*ver-*) and reversal or inchoation (*ont-*). For example, *ver-* + *plaats* "place" gives *verplaatsen* "to move," and *ont-* + *eigen* "own" gives *onteigenen* "to disown." The suffix *-lijk* can be found in adverbs and adjectives [e.g., *natuurlijk*, "natural(ly)," and *eigenlijk*, "actual(ly)."] The citation forms of these four affixes are [xə], [vər], [ɔnt], and [lək].

For each of the affixes, a randomized list was made of all occurrences in the corpus. For each word type containing a target affix, the first token on the list was selected for further analysis. If the quality of the recording was too poor for acoustic analysis, it was replaced with the next token on the list. We considered as word types not only words belonging to different lemmas, but also different word forms of the same lemma. Thus, the sample for *ont-* included both *ontwikkelt* ("develops") and *ontwikkelde* ("developed").

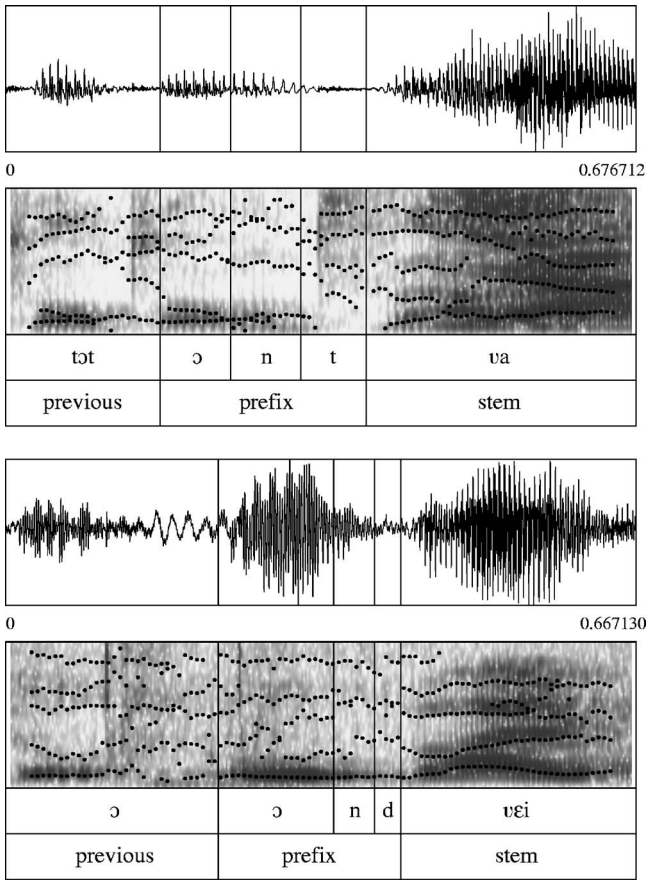

FIG. 1. Manual segmentations for the tokens *ontwaken* (top) and *ontwijken* (bottom). *Ontwaken* was a more or less ideal case, in which there was no background noise or overlapping speech. For *ontwijken*, the amount of background noise was much greater. In both cases, we placed boundaries where we could see both visible changes in the waveform pattern supported by abrupt format transitions in the spectrogram.

B. Measurements

Acoustic measurements of the target words were made using the software package PRAAT (Boersma, 2001). For all words, we measured the duration of the affix and the durations of the individual segments in the affix (both in milliseconds). Since the amount of background noise differed considerably between tokens, it was hard to establish a general segmentation strategy (see also Vorstermans *et al.*, 1996). Figure 1 shows the manual segmentations for the prefix *ont-* in the tokens *ontwaken* "to wake" (top), and *ontwijken* "to avoid" (bottom), including the previous word and the first syllable of the stem. *Ontwaken* was relatively easy to segment, since there was hardly any background noise and no overlapping speech around the prefix. The sample for *ontwijken* contained more background noise, resulting in a waveform in which the different segments could not be easily distinguished. In all cases, we placed the segment boundaries where we found clear formant transitions in the spectrogram supported by visible changes in the waveform pattern.

III. CONTROL VARIABLES

A. Probabilistic measures

Besides frequency, other measures of word probability are known to affect acoustic realizations as well. Fowler and Housum (1987) found that the second realization of a word in a monologue was shorter than the first one. Bard *et al.* (2000) replicated this effect for dialogues, showing that it was present irrespective of whether the speaker or the listener uttered the first token of the word. To check whether our target words might be subject to repetition effects, we counted how often the target word (or a word from the same inflectional paradigm) had been used in the conversation prior to the occurrence of the selected token. Since most tokens turned out to be first occurrences, this factor was not included in the final analyses. In addition, we counted how often the affix under investigation had already occurred. This variable, which varied in value between 0 and 72, turned out to have no effect.

The probability of occurrence of a word also depends on neighboring words. In recent years, numerous studies have addressed the relationship between predictability from neighboring words and acoustic reduction (e.g., Hunnicutt, 1985; Fosler-Lussier and Morgan, 1999; Gregory *et al.*, 1999; Bush, 2001; Jurafsky *et al.*, 2001; Bell *et al.*, 2003). To determine the predictability of their target words, most authors have used measures like *conditional probability* or *mutual information*, which are computed using frequency estimates from large speech corpora. Both measures capture the likelihood of a certain word occurring given one or more of its neighboring words. Mutual Information is arguably the more elegant of the two, as it combines conditional probability with the frequency of the word itself. The corresponding equation is as follows (X and Y denote either the previous word and the target word or the target word and the following word):

$$MI(X;Y) = \log \frac{(\text{Frequency}(XY))}{(\text{Frequency}(X)) * (\text{Frequency}(Y))}.$$

From this equation, it is easy to see why mutual information could also be relevant for our purposes. Since word frequency is incorporated in the denominator, any effect observed for frequency might in fact be an effect of mutual information in disguise. Our sampling method prevented us from computing mutual information values for all of our target words, as some of them were at the beginning or end of utterances. For those words for which mutual information could be computed, we checked whether it was a better predictor of duration than word frequency alone. This was never the case.

As we are dealing with morphologically complex words, probabilistic variables affecting morphological processing should also be taken into account. Hay (2003) found that derived words that are more frequent than their stems are judged less morphologically complex by language users. This suggests that speakers may only consider an affix a separate morpheme if the stem is at least as frequent as the combination of stem and affix. If, on the other hand, the affix-stem combination is more frequent, the word is more likely to be accessed as a whole, implying less psychological reality for the affix. Since Hay showed that this perceived morphological complexity can also affect acoustic realizations, we included the ratio between the frequency of the target word and that of its stem (word-stem ratio) in the analyses.

All frequency estimates, including the ones used to compute mutual information and word-stem ratio, were taken from the Corpus of Spoken Dutch and logarithmically transformed.

B. Other control factors

This section discusses the nonprobabilistic variables that were incorporated in this study. When rate of speech is high, words have a higher probability of deviating from the standard (Fosler-Lussier and Morgan, 1999). We estimated speech rate by computing the number of syllables per second in the longest stretch of speech containing the target word that did not contain an audible pause. For all words in the utterance except the target word, the number of syllables was determined on the basis of the orthographic transcription. For the target word, we used the information from the manual transcription instead.

Sociolinguistic variables such as sex, age, and regional origin of the speaker also have a considerable impact on pronunciation (e.g., Byrd, 1994; Keune *et al.*, 2005). Information about these three factors was gathered for all speakers. Age was operationalized by subtracting 1900 from the year of birth of the speaker.

Words that are positioned at the beginning of an utterance are often acoustically strengthened, while words at the end of an intonational phrase can show durational lengthening (e.g., Fougeron and Keating, 1997; Cambier-Langeveld, 2000; Bell *et al.*, 2003). This was controlled for by coding all target words for position in their carrier utterance (beginning, end, or middle).

Fox Tree and Clark (1997) and Bell *et al.* (2003) showed that words that occur near disfluencies are lengthened compared to words occurring in fluent contexts. Therefore, the presence of a false start or filled pause directly before or after the target word was also coded.

Not all phonetic environments are equally suitable for reduction. Zsiga (1994) found that word-final consonants are more likely to be reduced if they are followed by another consonant. We determined for each token whether the segment following the affix was a consonant or a vowel. For the prefixed words, we also counted the number of consonants in the onset of the stem (henceforth referred to as onset complexity).

Finally, the absence of certain segments in the affix was sometimes included as an extra factor in the analyses. If, for example, the final segment in the affix is absent, this may have implications for the durations of the other segments, as well as for the duration of the affix as a whole. Segments were considered as absent if they could not be isolated in the acoustic signal.

To evaluate the effects of word frequency on duration while controlling for all other possibly relevant factors, we

used least squares regression. The application of this method on speech data is described in detail by Bell *et al.* (2003). The signs of the reported beta coefficients indicate whether there was a positive or a negative correlation between two variables. Since we do not want to report effects that depend crucially on a single data point, we excluded observations that were outliers with regard to leverage or Cook's distance values (Chatterjee *et al.*, 2000).

IV. RESULTS FOR GE-

A. Duration of the prefix as a whole

For *ge-*, the sample consisted of 428 words uttered by 132 different speakers. No speaker contributed more than 12 tokens to the sample. Broad phonetic transcriptions of the encountered realizations are [xə], [x], [χə], and [χ].

We fitted a stepwise multiple regression model to the data with the duration of *ge-* as the response variable. There were four outliers, which were removed. We found main effects of frequency [$\hat{\beta}=-4.1$, $t(420)=-3.05$, $p<0.005$], speech rate [$\hat{\beta}=-8.6$, $t(420)=-5.62$, $p<0.0001$], and onset complexity [$\hat{\beta}=-7.3$, $t(420)=-2.03$, $p<0.05$]. Words with a higher frequency had shorter realizations of *ge-*. When speech rate was high, the prefix was also shorter, as was the case if it was followed by a large number of consonants. The amount of variance explained by this model (also referred to as R^2) was 10%.

B. Durations of the individual segments

To gain more insight into the articulatory dynamics underlying the above-mentioned effects, separate models were fitted for the two segments in *ge-*.

For the fricative, a model was fitted to the entire data set, including the data points that were outliers in the model for the entire prefix. After the removal of three new outliers, there were main effects of frequency [$\hat{\beta}=-3.6$, $t(421)=-3.71$, $p<0.0005$], speech rate [$\hat{\beta}=-3.5$, $t(421)=-3.79$, $p<0.0005$], and word-stem ratio [$\hat{\beta}=34.7$, $t(421)=2.46$, $p<0.05$]. This model explained 7% of the variance.

The vowel was present in 414 tokens (97%). Four outliers were removed. Vowel duration was predicted by frequency [$\hat{\beta}=-2.1$, $t(406)=-2.31$, $p<0.05$], speech rate [$\hat{\beta}=-3.0$, $t(406)=-2.93$, $p<0.005$], and initial position [$\hat{\beta}=14.5$, $t(406)=2.45$, $p<0.05$]. The vowel was longer in words that were in initial position. The R^2 of this model was 6%.

C. Discussion of the results for ge-

The results for *ge-* are summarized in Table I. The observed effects of frequency, speech rate, initial position, and onset complexity all went in the expected direction. The frequency effect was present for both the fricative and the vowel, as was the effect of speech rate.

It might seem counter-intuitive that a higher ratio between the frequency of the word and the frequency of its stem should lead to longer fricatives. After all, a higher value of this ratio is supposed to be associated with less morphological complexity and, hence, less psychological reality for the prefix. We return to this issue in our general discussion in Sec. VIII.

TABLE I. Beta coefficients and significance values of the effects for *ge-*. The beta coefficients indicate the magnitude of the effect in milliseconds. "–" means there was no significant effect. The bottom row shows the amount of variance explained (R^2) by each model.

Predictor	Prefix	Fricative	Vowel
Frequency	−4.1[a]	−3.6[b]	−2.1[c]
Initial position	–	–	14.5
Onset complexity	−7.3[c]	–	–
Speech rate	−8.6[d]	−3.5[b]	−3.0[a]
Word-stem ratio	–	34.7[c]	–
Explained variance (R^2)	0.10	0.07	0.06

[a] $p<0.05$.
[b] $p<0.01$.
[c] $p<0.001$.
[d] $p<0.0001$.

V. RESULTS FOR ONT-

A. Duration of the prefix as a whole

There were 102 word types starting with *ont-* in the corpus. The tokens in the sample were uttered by 63 different speakers, who contributed no more than four tokens each to the data set. The realizations we encountered ranged from canonical [ɔnt] to highly reduced [ət].

A model was fitted to the data with duration of *ont-* as the response variable. Three outliers were removed. Prefix duration was predicted by year of birth [$\hat{\beta}=-1.4$, $t(95)=-4.81$, $p<0.0001$]. Younger speakers produced shorter prefixes. Frequency was not significant as a main effect, but it was in interaction with speech rate [$\hat{\beta}=-2.9$, $t(95)=-3.31$, $p<0.005$] and year of birth [$\hat{\beta}=0.2$, $t(95)=2.84$, $p<0.01$]. The interaction between frequency and speech rate is shown in Fig. 2. Frequency had either a lengthening or no effect when speech rate was low (the bottom left and middle panels), a shortening effect when speech rate was neither low nor high, and no effect when speech rate was extremely high (the top right panel). In Fig. 3, the interaction between frequency and year of birth is illustrated. For the youngest speakers (the top middle and right panels) the effect of frequency was absent, whereas for the other age groups a higher frequency correlated with shorter realizations. All in all, this model accounted for 24% of the variance.

B. Durations of the individual segments

Since the vowel was present in all 102 tokens, we fitted a model for vowel duration to the entire data set. Three observations were identified as outliers and removed. Younger speakers produced shorter vowels [$\hat{\beta}=-0.3$, $t(96)=-2.19$, $p<0.05$], while women's vowels were longer [$\hat{\beta}=8.7$, $t(96)=2.33$, $p<0.05$]. The R^2 of this model was 10%.

The nasal was produced in 97 tokens, three of which were outliers. The duration of the nasal was affected by the presence of the plosive [$\hat{\beta}=-34.2$, $t(89)=-5.58$, $p<0.0001$]

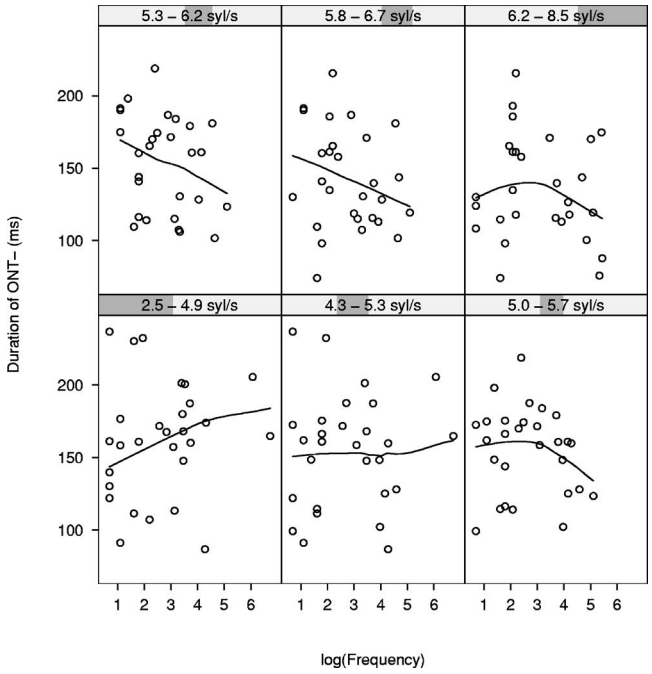

FIG. 2. Interaction between frequency and speech rate as observed for the duration of *ont-*. The panels should be read from left to right and from bottom to top: speech rate is lowest in the bottom left panel and highest in the top right panel. There is no frequency effect when speech rate is low (the bottom left and middle panels) or extremely high (the top right panel).

and year of birth [$\hat{\beta}=-0.2$, $t(89)=-2.74$, $p<0.01$]. Younger speakers produced shorter nasals, and if the plosive was absent the nasal was longer. We also found a significant interaction between the presence of the plosive and frequency

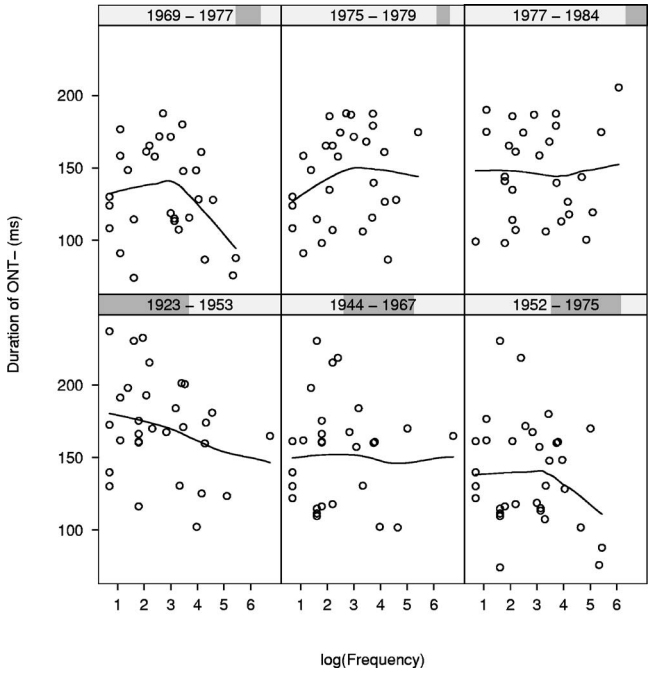

FIG. 3. Interaction between frequency and year of birth as observed for the duration of *ont-*. The panels should be read from left to right and from bottom to top: the oldest speakers are in the bottom left panel and the youngest speakers in the top right panel. There is no effect of frequency for the youngest age groups (top middle and right panels).

TABLE II. Beta coefficients and significance values of the effects for *ont-*. The beta coefficients indicate the magnitude of the effect in milliseconds. "–" means there was no significant effect. The bottom row shows the amount of variance explained. (R^2) by each model.

Predictor	Prefix	Vowel	Nasal	Plosive
Frequency	–	–	–	-17.8^{a}
Frequency * Speech rate	-2.9^{b}	–	–	–
Frequency * Year of birth	0.2^{b}	–	–	0.3^{b}
Frequency * Plosive present	–	–	5.9^{a}	–
Plosive present	–	–	-34.2^{c}	–
Sex	–	8.7^{d}	–	–
Speech rate	–	–	–	-3.6^{d}
Year of birth	-1.4^{c}	-0.3^{d}	-0.2^{b}	-1.0^{b}
Explained variance (R^2)	0.24	0.10	0.48	0.28

[a] $p<0.05$.
[b] $p<0.01$.
[c] $p<0.001$.
[d] $p<0.0001$.

[$\hat{\beta}=5.9$, $t(89)=3.67$, $p<0.0005$]. Frequency was only significant if there was no plosive. Together, these three predictors explained 48% of the variance.

Finally, we fitted a model for the duration of the plosive. Three outliers were removed. There were main effects of frequency [$\hat{\beta}=-17.8$, $t(66)=-3.50$, $p<0.001$], year of birth [$\hat{\beta}=-1.0$, $t(66)=-3.87$, $p<0.0005$], and speech rate [$\hat{\beta}=-3.6$, $t(66)=-2.39$, $p<0.05$]. All effects went in the expected direction. Furthermore, there was an interaction between frequency and year of birth [$\hat{\beta}=0.3$, $t(66)=3.30$, $p<0.005$], which was similar to the one observed for the entire prefix (see Fig. 3). In total, 28% of the variance in the duration of the plosive was explained by this model.

C. Discussion of the results for ont-

Table II provides an outline of the results for *ont-*. There were frequency effects in the expected direction for the duration of the plosive if it was present and for the duration of the nasal if the plosive was not present. This did not lead to a main effect of frequency for the prefix as a whole, but there were two significant interactions.

The interaction with speech rate suggested that the effect of frequency was limited to situations in which speech rate was not extremely low or high. The absence of a frequency effect when speech rate is high can be explained by assuming that speakers try to avoid complete deletion of the prefix, since this may hamper communication. This is confirmed by the fact that no tokens were encountered in which *ont-* was completely absent. When speech rate is low, on the other hand, there is less need to reduce articulatory effort, which also diminishes the probability of finding a frequency effect.

The interaction with year of birth showed that the frequency effect was not present for the youngest speakers. This can be accounted for by the finding that younger speakers already produced shorter realizations (as evidenced by the negative main effects of year of birth observed in all models fitted for *ont-*).

TABLE III. Beta coefficients and significance values of the effects for *ver-*. The beta coefficients indicate the magnitude of the effect in milliseconds. "–" means there was no significant effect. The bottom row shows the amount of variance explained. (R^2) by each model.

Predictor	Prefix	Fricative	Rime
Onset complexity	−14.7[a]	−7.4[b]	−12.8[c]
Sex	–	−12.1[c]	–
Year of birth	−0.5[b]	–	−0.3[b]
Explained variance (R^2)	0.09	0.12	0.17

[a] $p<0.05$.
[b] $p<0.01$.
[c] $p<0.001$.

VI. RESULTS FOR VER-

A. Duration of the prefix as a whole

The prefix *ver-* occurred in 140 different word types produced by 82 different speakers. The maximum number of tokens uttered by a single speaker was eight. Observed pronunciations included [vər], [və], and [f].

We fitted a model to predict the duration of *ver-*. After removing three outliers, there were significant main effects of year of birth [$\hat{\beta}=-0.5$, $t(134)=-2.58$, $p<0.05$] and onset complexity [$\hat{\beta}=-14.7$, $t(134)=-2.64$, $p<0.01$]. Younger speakers produced shorter prefixes. If the number of consonants in the onset of the stem was high, the prefix was shorter as well. The R^2 of this model was 11%.

B. Durations of the individual segments

We fitted separate models only for the fricative and the rime (i.e., the combination of the vowel and [r]), since the vowel and [r] (if present) could not be reliably distinguished.

The fricative was present in all cases. Four outliers were removed. We found main effects of onset complexity [$\hat{\beta}=-7.4$, $t(133)=-2.37$, $p<0.05$] and sex of the speaker [$\hat{\beta}=-12.1$, $t(133)=-3.43$, $p<0.001$]. Women produced shorter fricatives. These variables explained 12% of the variance.

For the rime, a model was fitted to the 117 data points for which it was present. Three outliers were removed. There were main effects of onset complexity [$\hat{\beta}=-12.8, t(111)=-3.49, p<0.001$] and year of birth [$\hat{\beta}=-0.3, t(111)=-2.52, p<0.05$], together explaining 17% of the variance.

C. Discussion of the results for ver-

Beta coefficients and significance values of the effects for *ver-* are given in Table III. For this prefix, there were no effects of frequency. The effect of onset complexity (the higher the number of consonants in the onset of the stem, the shorter the prefix) can be traced back to both the fricative and the rime. As was the case for the other prefixes, younger speakers produced shorter realizations of *ver-*. This effect was mainly due to durational shortening of the rime.

VII. RESULTS FOR -LIJK

A. Duration of the suffix as a whole

The data set for the suffix *-lijk* consisted of 158 tokens, uttered by 88 different speakers. No speaker contributed more than six tokens to the data set. The realizations we observed ranged from the citation form [lək] to [ə] or [k]. Because of the semantic opacity of many of the words containing *-lijk*, the word-stem ratio we discussed in Sec. III was not included in the analyses.

Again, we first fitted a model to predict the duration of the affix as a whole. Visual inspection of the fitted model revealed that the variance in the residuals was much larger for words in final position than for words in nonfinal position [$F(42,114)=4.33, p<0.0001$]. Therefore, separate models were fitted for words in final and in nonfinal position. For words in final position (43 observations), four outliers were removed. The data set for nonfinal words contained 115 tokens, four of which were outliers.

For words in nonfinal position, there were main effects of frequency [$\hat{\beta}=-7.7, t(108)=-3.73, p<0.0005$] and year of birth [$\hat{\beta}=-0.7, t(108)=-3.12, p<0.005$], explaining 18% of the variance.

If the word was in final position, the duration of *-lijk* was affected by speech rate [$\hat{\beta}=-36.4, t(36)=-4.24, p<0.0005$] and the presence of the plosive [$\hat{\beta}=147.5, t(36)=3.23, p<0.005$]. If the plosive was absent, the suffix was shorter. The R^2 of this model was 47%.

B. Durations of the individual segments

The [l] was produced in 140 tokens. This time, a split on the basis of position was not necessary, as visual inspection of the residuals did not reveal any abnormalities. We removed four outliers and found main effects of frequency [$\hat{\beta}=-2.1, t(130)=-2.95, p<0.005$], speech rate [$\hat{\beta}=-4.2, t(130)=-4.14, p<0.0001$], year of birth [$\hat{\beta}=-0.2, t(130)=-2.96, p<0.005$], and final position [$\hat{\beta}=10.0, t(130)=3.66, p<0.0005$]. All effects went in the expected direction. Together, they accounted for 32% of the variance.

The vowel was realized in all but eight tokens. Three outliers were removed. Vowel duration was affected by speech rate [$\hat{\beta}=-4.2, t(143)=-2.77, p<0.01$], final position [$\hat{\beta}=12.2, t(143)=3.03, p<0.005$], and the presence of the plosive [$\hat{\beta}=-30.6, t(143)=-4.77, p<0.0001$]. If the plosive was absent, the vowel was longer. The R^2 of this model was 23%.

For the plosive, the situation was similar to that of the entire suffix. The variances of the residuals of the initially fitted model differed significantly between tokens that were in final and nonfinal position [$F(38,105)=7.27, p<0.0001$]. Therefore, we fitted separate models for the 39 final and 106 nonfinal plosives.

For the nonfinal plosives, three outliers were removed. The only significant effect we found was one of following disfluency: if there was no disfluency following the target word, the plosive was shorter [$\beta=-66.2, t(101)=-5.73, p<0.0001$]. By itself, this factor accounted for 25% of the

TABLE IV. Beta coefficients and significance values of the effects for *-lijk*. The beta coefficients indicate the magnitude of the effect in milliseconds. "–" means there was no significant effect. The bottom row shows the amount of variance explained. (R^2) by each model.

Predictors	Suffix (Nonfinal)	Suffix (Final)	[l]	Vowel	Plosive (Nonfinal)	Plosive (Final)
Frequency	-7.7^{a}	–	-2.1^{b}	–	–	–
Final position	–	–	10.0^{a}	12.2^{b}	–	–
Following disfluency	–	–	–	–	-66.2^{c}	–
Plosive present	–	147.5^{b}	–	-30.6^{c}	–	–
Speech rate	–	-36.4^{c}	-4.3^{c}	-4.2^{b}	–	-22.9^{b}
Year of birth	-0.7^{b}	–	-0.2^{b}	–	–	–
Explained variance (R^2)	0.18	0.47	0.32	0.23	0.25	0.24

[a] $p<0.01$.
[b] $p<0.001$.
[c] $p<0.0001$.

variance. For the final plosives, we removed three outliers and found an effect of speech rate $[\hat{\beta}=-22.9, t(34)=-3.28, p<0.005]$ in the expected direction, explaining 24% of the variance.

C. Discussion of the results for -lijk

An outline of the results for *-lijk* is given in Table IV. The duration of *-lijk* was most strongly affected by whether the word was in final position or not. For the suffix as a whole and the plosive, this effect was so pervasive that separate models had to be fitted to the final and the nonfinal data points. For the other two segments, such drastic measures were not necessary, although final position remained a significant predictor. The effect always went in the same direction: Final words had longer realizations of *-lijk*. This could be explained by referring to the well-documented phonetic effect of phrase-final lengthening (e.g., Fougeron and Keating, 1997), but we feel that such an explanation would be too restricted. The majority (70%) of the words in final position were predicates in an utterance of the type "that is [adjective]." When saying something like *dat is belachelijk* "that is ridiculous," it would make no sense to reduce articulatory effort on the word *belachelijk*, as it is the only information carrier in the utterance. This might also be reflected in the presence of sentence accent, leading to durational lengthening (e.g., Nooteboom, 1972).

Despite the dominance of final position as a predictor, we still found effects of frequency, although these were restricted to the nonfinal suffixes and realizations of [l]. Speech rate was significant for all durations except that of the nonfinal plosive. The effect of following disfluency we found was in line with the earlier findings of Fox Tree and Clark (1997) and Bell *et al.* (2003).

Interestingly, the two significant effects for presence of the plosive went in opposite directions. If the plosive was absent, final suffixes were shorter, but vowels were longer. It might be the case that speakers more or less compensate for the absence of the plosive by lengthening the vowel. For the subset of final suffixes, this effect might not have surfaced since the entire suffix was lengthened.

VIII. GENERAL DISCUSSION

This study provides strong evidence for the relationship between lexical frequency and acoustic reduction. For the Dutch affixes *ge-*, *ont-*, and *-lijk*, we found effects of frequency on the durations of individual segments, the affix as a whole, or both. Apparently, the effect of word frequency in speech production is not restricted to the speed of lexical retrieval; it manifests itself in the subtle acoustic details of the word as well. This lends further support to the probabilistic framework developed by Bybee (2001), Pierrehumbert (2003), and others. They view probabilistic information as an integral part of our linguistic knowledge, exerting its influence at every level of language processing, including articulation.

How can these findings be incorporated in models of speech production? Most current theories are based on either speech errors or reaction time data, and have not been concerned with fine-grained differences in articulation. Nevertheless, models like the one proposed by Levelt *et al.* (1999) can be modified in such a way that they can account for the results of the current study. One possible modification is the inclusion of reduced word forms in the lexicon, which are selected if the conceptual structure of the message specifies a word as redundant. Although this might work for obviously reduced forms such as [tyk] for *natuurlijk* "of course," it seems less appropriate to include all possible durational variants of words in the lexicon. A more efficient solution is to pass information about redundancy on to the articulator, where it could influence the amount of effort put into articulation.

Another possibility is that effects of frequency arise during phonological processing. All words in a speaker's mental lexicon are believed to have a certain resting activation level. When this activation level is high (as is the case for highly frequent words), activation may spread to the constituent speech sounds more quickly that when it is low, resulting in quicker preparations of the speech sounds and, thus, shorter articulatory durations (e.g., Balota *et al.*, 1989). Our current data do not allow us to distinguish between these two hypotheses, as the words under investigation were produced after both conceptual and articulatory preparation had taken

place. If, however, frequency effects were to be found in situations where no conceptual preparation was required (e.g., in shadowing or speeded naming tasks), this would suggest that at least part of the effect of frequency on durations arises during the later stages of the speech production process.

One assumption made by many theories of speech production remains problematic, however. They regard the syllable as the principal unit of articulation, as well as the primary locus of frequency effects below the word form level (e.g., Levelt *et al.*, 1999; Sevald *et al.*, 1995). Given the results of the present study, this view appears to be too restricted. First of all, we find evidence for word-specific frequency effects that operate below the level of the syllable. More importantly, the different segments in a syllable were shown to be subject to different, sometimes even contradictory, forces. This suggests that the motor program that is executed during articulation is very likely not the syllable, since one would expect similar processes to apply to all subcomponents of such a program.

Related to this issue is the question why some segments were affected by frequency while others were not. Although it is very difficult to abstract a general pattern from the data, it is at least clear that durational reduction is not restricted to vowels. Furthermore, we find some evidence that speakers sometimes compensate for the absence of one segment by lengthening another. This presents interesting challenges for frameworks such as articulatory phonology (Browman and Goldstein, 1992), since it suggests that reduction of articulatory effort does not necessarily involve either increased overlap or reduced magnitude of speech gestures.

Of course, the morphological status of affixes is relevant as well. Hay (2003) showed that the psychological reality of affixes depends on the ratio between the frequency of the morphologically complex word and the frequency of its stem. Moreover, she found that *t*'s preceding the English suffix *-ly* were more likely to be deleted if this ratio was high. We included the ratio in our analyses and found that a higher value led to longer fricatives in the prefix *ge-*. Apparently, less psychological reality for the affix does not necessarily imply shorter realizations. A possible explanation for this finding is that in most Dutch monomorphemic words, the first syllable receives stress (Booij, 1995). If speakers no longer regard the prefix as a separate morpheme, it will eventually become a "normal" word-initial syllable and therefore more likely to receive stress. The longer duration we observed for the fricative in *ge-* might be the precursor of such a change.

One of the four affixes we investigated, *ver-*, failed to show an effect of frequency. This could be related to the fact that the initial fricative can be devoiced, leading to more variation in the sample. In addition, verbal prefixes like *ver-* and *ont-* contribute much more to the meaning of their carrier words than *ge-* and *-lijk*, which merely signal grammatical function. Since the main objective of speakers is to get the meaning of their utterances across, it is not inconceivable that relatively meaningful units are less affected by frequency than more or less meaningless ones. Redundancy has many different dimensions, and the role of semantics in defining it should not be underestimated. This is confirmed by other studies, which also report differences between words in their sensitivity to reduction (e.g., Jurafsky *et al.*, 2001; Bell *et al.*, 2003).

A useful step in combining different dimensions of redundancy was taken by Gregory *et al.* (1999), who incorporated latent semantic analysis in their study. Latent semantic analysis (Landauer and Dumais, 1997) is a method to compute semantic relatedness scores from large-scale cooccurrence statistics. Since relatedness scores can be computed between a word and the whole discourse preceding it, this measure effectively combines word repetition, predictability from neighboring words, and semantic association with other words used in the conversation. Importantly, Gregory *et al.*'s (1999) results also show that other predictors remain relevant as well. For example, they report effects of mutual information and repetition over and above semantic relatedness. This suggests that this particular measure of semantic relatedness is not the only variable that should be taken into account.

One might ask whether our methodology could also be used to investigate acoustic reduction in stems. Indeed, it would be possible to compare the durations of identical stems that are combined with different affixes. However, in most languages the number of stems that lend themselves to such an approach will be rather restricted, as stems are generally less productive than affixes.

If the aim is to compare reduction in stems to reduction in affixes, word frequency is probably not the best variable to focus on. In nonagglutinative languages, the number of words containing an identical combination of stem and affix will be too small to make a comparison of words with different frequencies possible. For example, the English stem-affix combination *disable* only occurs in *disable, disables, disabled, disabling*, and *disablement*. Therefore, it might be a better idea to study measures like conditional probability or mutual information, and see whether they affect stems and affixes differently (Pluymaekers *et al.*).

With regard to future research, several issues need to be addressed. First of all, we need to know more about the way the different measures of probability interact. This requires large databases of carefully segmented speech, so that multiple tokens of the same word can be examined in their respective contexts. Second, more attention needs to be paid to semantic variables. Taken together, these lines of research could result in a model in which probabilistic and semantic relationships are exploited to the fullest and play a role at the finest level of acoustic detail.

ACKNOWLEDGMENTS

This research was supported by Netherlands Organization for Scientific Research (NWO) Grant No. 360-70-130 to the third author. We thank Sarah Hawkins, Willem Levelt, Anders Löfqvist, and an anonymous reviewer for their helpful comments on earlier versions of this paper.

Adank, P., Van Hout, R., and Smits, R. (**2004**). "An acoustic description of the vowels of Northern and Southern Standard Dutch," J. Acoust. Soc. Am. **116**, 1729–1738.

Aylett, M., and Turk, A. (**2004**). "The smooth signal redundancy hypothesis: a functional explanation for relationships between redundancy, prosodic prominence, and duration in spontaneous speech," Lang Speech **47**, 31–56.
Balota, D., Boland, J., and Shields, L. (**1989**). "Priming in pronunciation: beyond pattern recognition and onset latency," J. Mem. Lang. **28**, 14–36.
Bard, E., Anderson, A., Sotillo, C., Aylett, M., Doherty-Sneddon, G., and Newlands, A. (**2000**). "Controlling the intelligibility of referring expressions in dialogue," J. Mem. Lang. **42**, 1–22.
Bell, A., Jurafsky, D., Fosler-Lussier, E., Girand, C., Gregory, M., and Gildea, D. (**2003**). "Effects of disfluencies, predictability, and utterance position on word form variation in English conversation," J. Acoust. Soc. Am. **113**, 1001–1024.
Bock, J. (**1995**). "Sentence production: From mind to mouth," in *Handbook of Perception and Cognition, Vol. 11: Speech, language, and communication*, edited by J. Miller and P. Eimas (Academic, New York), pp. 181–216.
Boersma, P. (**2001**). "Praat, a system for doing phonetics by computer," Glot Int. **5**, 341–355.
Booij, G. E. (**1995**). *The Phonology of Dutch* (Clarendon, Oxford).
Browman, C., and Goldstein, L. (**1992**). "Articulatory phonology: An overview," Phonetica **49**, 155–180.
Bush, N. (**2001**). "Frequency effects and word-boundary palatalization in English," in *Frequency and the Emergence of Linguistic Structure*, edited by J. Bybee and P. Hopper (Benjamins, Amsterdam), pp. 255–280.
Bybee, J. L. (**2001**). *Phonology and Language Use* (Cambridge U.P., Cambridge).
Byrd, D. (**1994**). "Relations of sex and dialect to reduction," Speech Commun. **15**, 39–54.
Cambier-Langeveld, T. (**2000**). *Temporal Marking of Accents and Boundaries* (LOT, Utrecht).
Chatterjee, S., Hadi, A., and Price, B. (**2000**). *Regression Analysis by Example* (Wiley, New York).
Cooper, W., and Paccia-Cooper, J. (**1980**). *Syntax & Speech* (Harvard U.P., Cambridge, MA).
Dell, G. (**1986**). "A spreading-activation theory of retrieval in sentence production," Psychol. Rev. **93**, 283–321.
Ernestus, M. (**2000**). *Voice Assimilation and Segment Reduction in Casual Dutch, a Corpus-based Study of the Phonology-Phonetics Interface* (LOT, Utrecht).
Fosler-Lussier, E., and Morgan, N. (**1999**). "Effects of speaking rate and word frequency on pronunciations in conversational speech," Speech Commun. **29**, 137–158.
Fougeron, C., and Keating, P. (**1997**). "Articulatory strengthening at the edges of prosodic domains," J. Acoust. Soc. Am. **101**, 3728–3740.
Fowler, C., and Housum, J. (**1987**). "Talkers' Signalling of New and Old Words in Speech and Listeners' Perception and Use of the Distinction," J. Mem. Lang. **26**, 489–504.
Fox Tree, J., and Clark, H. (**1997**). "Pronouncing 'the' as 'thee' to signal problems in speaking," Cognition **62**, 151–167.
Garrett, M. (**1975**). "The analysis of sentence production," in *The psychology of learning and motivation*, edited by G. Bower (Academic, New York), pp. 133–178.
Gregory, M., Raymond, W., Bell, A., Fosler-Lussier, E., and Jurafsky, D. (**1999**). "The effects of collocational strength and contextual predictability in lexical production," Chicago Ling. Soc. **35**, 151–166.
Hay, J. (**2003**). *Causes and Consequences of Word Structure* (Routledge, New York).
Hunnicutt, S. (**1985**). "Intelligibility versus redundancy—conditions of dependency," Lang Speech **28**, 47–56.
Jespersen, O. (**1922**). *Language: its nature, development and origin* (George Allen & Unwin, London).
Johnson, K. (**2004**). "Massive reduction in conversational American English," in *Spontaneous speech: data and analysis. Proceedings of the 1st session of the 10th international symposium* (The National International Institute for Japanese Language, Tokyo, Japan), pp. 29–54.
Jurafsky, D., Bell, A., Gregory, M., and Raymond, W. (**2001**). "Probabilistic relations between words: Evidence from reduction in lexical production," in *Frequency and the emergence of linguistic structure*, edited by J. Bybee and P. Hopper (Benjamins, Amsterdam), pp. 229–254.
Keune, K., Ernestus, M., Van Hout, R., and Baayen, R. H., (2005). "Social, geographical, and register variation in Dutch: From written 'mogelijk' to spoken 'mok,'," Corpus Linguist. Linguist. Theor. **2**.
Landauer, T. K., and Dumais, S. (**1997**). "A solution to Plato's problem: The Latent Semantic Analysis theory of acquisition, induction, and representation of knowledge," Psychol. Rev. **104**, 211–240.
Landauer, T. K., and Streeter, L. A. (**1973**). "Structural differences between common and rare words: Failure of equivalence assumptions for theories of word recognition," J. Verbal Learn. Verbal Behav. **12**, 119–131.
Levelt, W. J. M. (**1989**). *Speaking. From Intention to Articulation* (MIT, Cambridge, MA).
Levelt, W. J. M., Roelofs, A., and Meyer, A. S. (**1999**). "A theory of lexical access in speech production," Behav. Brain Sci. **22**, 1–38.
Nooteboom, S. G. (**1972**). *Production and Perception of Vowel Duration: A Study of the Durational Properties of Vowels in Dutch* (University of Utrecht, Utrecht).
Oostdijk, N. (**2000**). "The Spoken Dutch Corpus project," ELRA Newsletter **5**, 4–8.
Pierrehumbert, J. B. (**2003**). "Probabilistic phonology: Discrimination and robustness," in *Probability Theory in Linguistics*, edited by R. Bod, J. Hay, and S. Jannedy, (MIT, Cambridge, MA), pp. 177–228.
Pluymaekers, M., Ernestus, M., and Baayen, R. H. "Articulatory planning is continuous and sensitive to informational redundancy," Phonetica (submitted).
Sevald, C., Dell, G., and Cole, J. (**1995**). "Syllable structure in speech production: Are syllables chunks or schemas?," J. Mem. Lang. **34**, 807–820.
Shields, L., and Balota, D. (**1991**). "Repetition and associative context effects in speech production," Lang Speech **34**, 47–55.
Umeda, N. (**1977**). "Consonant duration in American English," J. Acoust. Soc. Am. **61**, 846–858.
Van Coile, B. (**1987**). "A model of phoneme durations based on the analysis of a read Dutch text," in *Proc. Europ. Conf. Speech Techn., vol. 2*, edited by J. Laver and M. Jack Edinburgh, United Kingdom, pp. 233–236.
Van Son, R., and Pols, L. (**2003**). "Information structure and efficiency in speech production," *Proc. Eurospeech-2003*, Geneva, Switzerland.
Vorstermans, A., Martens, J., and Van Coile, B. (**1996**). "Automatic segmentation and labelling of multi-lingual speech data," Speech Commun. **19**, 271–293.
Wright, C. (**1979**). "Duration differences between rare and common words and their implications for the interpretation of word frequency effects," Mem. Cognit. **7**(6), 411–419.
Zipf, G. (**1929**). "Relative frequency as a determinant of phonetic change," Harv. Studies Classi Philol. **15**, 1–95.
Zsiga, E. (**1994**). "Acoustic evidence for gestural overlap in consonant sequences," J. Phonetics **22**, 121–140.

Acoustic and spectral characteristics of young children's fricative productions: A developmental perspective[a)]

Shawn L. Nissen[b)]
Department of Audiology and Speech-Language Pathology (138 TLRB), Brigham Young University, Provo, Utah 84602

Robert Allen Fox
Department of Speech and Hearing Science, The Ohio State University, Columbus, Ohio 43210

(Received 14 October 2004; revised 5 July 2005; accepted 6 July 2005)

Scientists have made great strides toward understanding the mechanisms of speech production and perception. However, the complex relationships between the acoustic structures of speech and the resulting psychological percepts have yet to be fully and adequately explained, especially in speech produced by younger children. Thus, this study examined the acoustic structure of voiceless fricatives (/f, θ, s, ʃ/) produced by adults and typically developing children from 3 to 6 years of age in terms of multiple acoustic parameters (durations, normalized amplitude, spectral slope, and spectral moments). It was found that the acoustic parameters of spectral slope and variance (commonly excluded from previous studies of child speech) were important acoustic parameters in the differentiation and classification of the voiceless fricatives, with spectral variance being the only measure to separate all four places of articulation. It was further shown that the sibilant contrast between /s/ and /ʃ/ was less distinguished in children than adults, characterized by a dramatic change in several spectral parameters at approximately five years of age. Discriminant analysis revealed evidence that classification models based on adult data were sensitive to these spectral differences in the five-year-old age group. © *2005 Acoustical Society of America.* [DOI: 10.1121/1.2010407]

PACS number(s): 43.70.Ep, 43.70.Fq [AL] Pages: 2570–2578

I. INTRODUCTION

A considerable amount of research has attempted to explain how the human perceptual system so accurately and efficiently perceives speech. Although many of these endeavors have made great strides toward understanding speech communication, the complex relationships between the acoustic structures of speech and the resulting psychological percepts have yet to be fully and adequately explained. Fortunately, advances in computer technology have allowed scientists to utilize more specific types of analysis on a variety of different acoustic parameters.

Previous investigations into the acoustic nature of speech have been aided by "spectral moments analysis" (e.g., Forrest *et al.*, 1988; Jongman *et al.*, 2000; Nittrouer, 1995). This type of analysis examines the spectral characteristics of discrete time segments of the speech signal in terms of multiple statistical moments (i.e., mean, variance, skewness, and kurtosis). By combining these various "statistical snapshots" of perceptually relevant segments of the physical waveform, researchers have attempted to identify unique and discrete patterns of acoustic energy within the speech signal.

Historically, speech research utilizing spectral moments has generally followed two lines of investigation. One line of research has examined whether spectral moment data could provide a high rate of obstruent classification through discriminant function analysis. In particular, this research has aimed to identify acoustic parameters that might serve to differentiate or discriminate adult productions of stop and fricative consonants in terms of place of articulation. Utilizing spectral moments data as well as more traditional types of acoustic measures, several studies have found that the acoustic signal of adult obstruent productions can be characterized by distinct spectral patterns of acoustic energy (e.g., Forrest *et al.*, 1988; Jongman *et al.*, 2000; Tomiak, 1990). A second associated area of research has utilized spectral moments analysis to examine how the acoustic properties of stop bursts and/or fricatives change as a function of normal speech development and aging (e.g., Forrest *et al.*, 1990, 1994; Miccio, 1996; Nittrouer, 1995; Nittrouer *et al.*, 1989).

One of the earliest studies to utilize spectral moments data in discriminant classification of obstruents was conducted by Forrest *et al.* (1988). The authors reported that adult productions of voiceless stops and fricatives could be discriminated by an analysis of the first (mean), third (skewness), and fourth (kurtosis) spectral moments. Using discriminant functions based on linear data from a single window of analysis, stops were classified with an overall average of 79.9% and fricatives slightly lower at 74.5%. However, the authors concluded that the second spectral moment of variance did not make a significant contribution to the discrimination of different voiceless obstruents. Interestingly, subsequent spectral moments studies of child productions

[a)]Portions of this work are contained in the unpublished doctoral dissertation, "An acoustic study of voiceless obstruents produced by adults and typically developing children," The Ohio State University, 2003.

[b)]Previously affiliated with the Department of Speech and Hearing Sciences, The Ohio State University, Columbus, Ohio; electronic mail: shawn_nissen@byu.edu

 0001-4966/2005/118(4)/2570/9/$22.50

(e.g., Forrest *et al.*, 1990; Nittrouer, 1995) have not included the measure of spectral variance in their analyses. Some researchers (Jongman *et al.*, 2000) have suggested that the disregard for the second spectral moment in recent literature may be due in part to this original finding by Forrest *et al.*

A more recent investigation of adult fricative productions (Jongman *et al.*, 2000) found that all four spectral moments (mean, variance, skewness, and kurtosis) could be used to distinguish among the fricatives in terms of place of articulation. Unlike previous spectral research on fricatives (e.g., Forrest *et al.*, 1988), Jongman *et al.* reported that spectral variance does differ significantly as a function of place of fricative articulation (labiodental, dental, alveolar, and palato-alveolar) and likewise contributes to the spectral classification of fricatives in adults. The authors reported that, in terms of place of articulation, the differences between four voiceless fricative productions (/f, θ, s, ʃ/) remained robust even when comparing across differing window locations. Discriminant analysis based on spectral peak location and spectral moments at four locations for each fricative demonstrated a classification accuracy of 77%.

A second associated line of research has employed spectral moments analysis (i.e., mean, skewness, and kurtosis) to investigate the acquisition and development of speech in children. Several studies (Forrest *et al.*, 1994, 1990, 1988; Miccio, 1996; Nittrouer *et al.*, 1989) have documented age-related differences in the development of children's obstruent productions. Of particular interest has been the development of the voiceless /t/ vs /k/ stop contrast, as well as the fricative contrast of /s/ vs /ʃ/.

An influential spectral moments study on the developmental order of obstruent acquisition was conducted by Nittrouer in 1995. Following the methodology outlined in Forrest *et al.* (1988), Nittrouer examined the acoustic patterns of several obstruents (/t, k, s, ʃ/) as revealed by the first, third, and fourth spectral moments. Findings indicated that some of the obstruent articulatory gestures of children are not as precisely specified as those of adult speakers. From a developmental perspective, these results provide support for the theory that acoustic differences between the obstruent productions of young children and adults may be related to articulatory changes that occur with maturation. Interestingly, Nittrouer found that some developmental differences vary as a function of the place and type of obstruent contrast. For example, Nittrouer found that the difference in spectral mean values between /s/ and /ʃ/ was larger for adult speakers than for children ages 3 through 7, yet the differences between /t/ and /k/ were relatively similar. The author interpreted this finding as support for the conclusion that in terms of the first spectral moment the child speakers were continuing to "fine tune" sibilant fricative articulations toward an adult-like contrast.

Researchers have established a foundation for the effectiveness of spectral moments analysis as a means of evaluating the acoustic nature of obstruent productions. However, despite the above-mentioned findings, there is still a limited amount of knowledge on the acoustic structure and developmental nature of young children's fricative productions. Many findings reported with adult speakers (e.g., Jongman *et al.*, 2000) have yet to be fully addressed with younger speakers, especially children younger than 6 years of age. Thus, the specific aims of this study are threefold:

(1) Describe the acoustic structure of voiceless fricative productions of adults and typically developing children in terms of multiple acoustic parameters, including several measures (i.e., spectral slope and variance) and fricative types (i.e., /f/ and /θ/) not commonly included in spectral studies involving children.
(2) Examine to what extent the individual acoustic characteristics of voiceless fricative productions change as a function of age, gender, place of articulation, and vowel context.
(3) Utilize discriminant analysis to determine how well combinations of acoustic parameters based on specific groups of speakers successfully categorize fricative productions in terms of place of articulation.

II. METHODOLOGY

A. Subjects

Three groups of children between the ages of 3 and 6 years ($N=30$) and one comparison group of adults were recruited to participate in the present study ($N=10$). All subjects were monolingual speakers of American English and had minimal exposure to a second language. No children had a diagnosed history of speech, language, or hearing problems. At the time of their participation in the study all subjects had visible front incisors and were required to pass a hearing screening and an oral/motor exam. Prior to recording, the phonemic inventory of each child was informally evaluated by a certified SLP using the "Sounds-in-Words" subtest of the Goldman-Fristoe Test of Articulation (GFTA: Goldman and Fristoe, 1986). All children who participated in the study exhibited target appropriate fricatives, as measured by the GFTA. Since many of the targeted phonemes are typically acquired between the ages of 3 and 6, no subject was excluded from the study based on their inability to produce the target phonemes in a medial or final word position.

B. Stimuli

The corpus of elicited productions consisted of monosyllabic words with an initial syllable CV(C)(C) containing a combination of four different voiceless obstruents (/f, θ, s, ʃ/) in initial position followed by three different monophthongal vowels (/i, ɑ, u/). Specifically, the corpus included the following words: *field, fox, food, thief, thought, "Thoot," seal, sock, soup, sheep, shark*, and *shoe*. Each stimulus item was repeated five times; thus, the entire corpus of elicited productions yielded a total of 60 tokens per subject. To elicit relatively similar vocal emphasis across different productions, the targeted CV(C) syllable combinations were always in the initial and stressed position of each elicited word. Stimulus words in this set were produced in the carrier phrase "This is a ____." In one instance, an age-appropriate word did not exist that exemplifies the targeted syllable. For example, American English does not contain an age-appropriate word beginning with a /θu/ consonant-vowel combination. To ad-

dress this lexical "gap," an invented proper name that follows the phonotactic rules of Standard English was substituted for the missing word. In this case, subjects were instructed to produce the proper name "Thoot" in reference to a fictional character.

C. Acoustic analysis

Speech samples were recorded online to computer in a quiet room environment. More specifically, a low impedance dynamic microphone (Shure SM10A-CN) and a preamplifier (Samson Mixpad-4) were used to facilitate the recording of subject productions. The microphone was affixed to a headset and placed approximately 4 cm from the speaker's lips during recording. The speech tokens were sampled at a rate of 44.1 kHz with a quantization of 16 bits and low-pass filtered at 22.05 kHz.

The productions were elicited from all subjects through picture identification. Pictures representing the target words were presented in a randomized order (between presentations and across subjects) on a 15 in. computer screen. All pictures utilized in the study were selected to be age-appropriate for preschool aged children. The subjects were familiarized with the names of the pictures and the elicitation procedure prior to the recording session. If a subject incorrectly identified a picture as a different lexical item during the recording session, the correct target word was modeled by the experimenter and the child was instructed to repeat the identification of that particular item.

Segmentation of the onset and offset of the fricative target was conducted using waveform display assisted by spectrographic inspection (Adobe Systems Incorporated, 2003). The fricative onset was characterized by a rapid increase in zero-crossings and/or spectrographic identification of high frequency energy, whereas the offset was the intensity minimum prior to the onset of vowel periodicity and/or absence of high frequency energy (Jongman *et al.*, 2000). Segmentation values were then recorded into a text file [in milliseconds (ms)] and later checked and corrected (and then rechecked) using a MATLAB program that displayed the segmentation marks superimposed over a display of the token's waveform. In addition, to test for segmentation accuracy and reliability, 240 randomly chosen tokens (one subject from each age group) were independently analyzed by a second individual. The fricative boundary measurements were subsequently correlated ($r=0.99, p<0.001$) to the original segmentation values extracted for these same tokens and were found to differ by an average of approximately 3 ms.

Acoustic and statistic analysis followed procedures outlined in previous research examining the acoustic properties of voiceless fricatives (i.e., Forrest *et al.*, 1988; Jongman *et al.*, 2000; Nittrouer, 1995). Fricative durations were reported in ms increments from raw time points extracted during segmentation. A measure of normalized amplitude was computed for each fricative segment. This measure was the rms amplitude in decibels of the entire segment of friction minus the rms amplitude of the strongest component within the initial 40 ms of the following vowel (Behrens and Blumstein, 1988a, b; Jongman *et al.*, 2000). This type of amplitude measure served to normalize for differences in speaker intensity.

A series of three 40 ms Hamming windows, located at the beginning, middle, and end of each target, was used to analyze the acoustic structure of the fricative productions. Moments were only calculated for fricative tokens that were at least 80 ms in duration (following this rule one token was eliminated from the analysis). Each window interval was then pre-emphasized by first-differencing. Though the need for pre-emphasis is minimalized when analyzing voiceless sounds, it was determined that such a procedure was necessary to more effectively compare subsequent results to previously published findings (e.g., Forrest *et al.*, 1988; Jongman *et al.*, 2000; Nittrouer, 1995). Using a 2048-point FFT with zero-padding, the spectral amplitudes of a series of frequency points were derived from the complex acoustic signal within each 40 ms window. The resulting power spectra were considered random distribution probabilities, from which the spectral moments were computed. The third and fourth spectral values were subsequently normalized by variance. These normalization procedures, as well as the other algorithms utilized in this study are specifically described in previous spectral moments studies (e.g., Forrest *et al.*, 1988; Nittrouer, 1995). Measures of spectral slope were derived from the power spectra (1 to 15 kHz) generated during the spectral moments analysis. The slope was derived from a linear regression line fit to the relative amplitudes extracted from each analysis window, specifically describing the amplitude slope of the FFT power spectra.

All elicitation, recording, and analysis of stimuli were facilitated by custom designed computer programs (MATLAB) created by the authors. A corpus of test tokens comprised of known acoustic components was utilized to evaluate the accuracy and reliability of these computer programs. For example, a test token composed of several sinusoidal frequencies (1, 3, and 5 kHz) of equal amplitude was analyzed by the computer programs and found to have the appropriate values for the various acoustic measures.

D. Statistical analysis

Prior to statistical analysis all data were collapsed across repetitions of a given stimulus item. Spectral mean values were then transformed to a perceptually normalized scale, specifically, the Equivalent Rectangular Bandwidth (ERB) scale (Glasberg and Moore, 1990; Moore, 1997). The ERB auditory scale is a recently developed psychophysical metric, which employs a "notched-noise" method rather than traditional masking procedures to measure the auditory filter bandwidth of the human auditory system. The ERB metric is somewhat similar to the previously developed Bark scale (Zwicker, 1975; Zwicker and Terhardt, 1980), except that for lower frequencies, the slope of the ERB function decreases with decreasing center-frequency, while the Bark scale remains nearly linear.

Repeated measures analyses of variance (ANOVA) were then used to determine significant acoustic variation in the fricative productions as a function of place of articulation,

vowel context, gender, and age group. Results of significant *F*-tests include a measure of effect size, partial eta squared, or η^2 (the value of η^2 can range from 0.0 to 1.0, and can be considered a measure of the proportion of variance explained by a dependent variable when controlling for other factors). Greenhouse-Geisser adjustments were utilized to adjust *F*-tests with regard to degrees of freedom when significant deviations from sphericity were found. Furthermore, pairwise comparisons for significant within-subject factors were done using General Linear Model repeated-measures contrasts, comparison significance was determined using the appropriate *F*-tests (see SPSS, 1997). *T*-test statistics were reported for all significant between-subject post hoc results.

To allow comparison to the study by Jongman *et al.* (2000), a series of liner discriminant analyses were completed determining how well a set of acoustic measures obtained categorized fricatives from each group. Discriminant analysis is an application which derives a set of linear equations (discriminant functions) that classify individual cases (fricatives) into one of several mutually exclusive groups (place of articulation) based on their values for a set of predictor variables (acoustic measures). The analysis method utilized here selects predictor variables used in the discriminant functions on a stepwise basis (in terms of which of the available acoustic variables will significantly minimize Wilkes Λ). When all such variables have been selected, the stepwise procedure stops, leaving out of the discriminant functions all variables that do not significantly contribute (at the 0.01 level as determined by an *F*-test) to the categorization of the fricatives. A second use of Wilkes Λ is in an overall chi-square test of significance of the analysis; all the discriminant results to be discussed were significant at 0.01 or better.

Discriminant analysis allows us to examine how well a categorization model based on a set of acoustic parameters could classify individual fricative tokens by place of articulation. The accuracy of the classification was considered as the percentage of cases that were correctly classified into groups based on a particular discriminant function. These functions differed in terms of the acoustic parameters originally entered into the stepwise linear analysis and the particular individual or group of individuals upon which the function was developed. The discriminant functions were developed using both the cross-validation ("jack-knife") procedure and an approach that selects a subset of the data to train the classification model which is then used to classify the fricatives from the remaining data (the "specific group" approach).

In the cross-validation approach, data from one subject was excluded and the remaining data used to estimate a discriminant function for that particular subject, thus each case is classified on the basis of the discriminant functions derived from all cases other than itself. This process is repeated until each set of individual subject data has been successfully or unsuccessfully classified. When the number of individual cases is relatively small, this type of discriminant procedure provides a more accurate classification (Forrest *et al.*, 1990).

In the specific group approach, the overall data set is split into two subsets. The first subset is employed to develop or "train" a discriminant function and the other subset is then used to validate the resulting function. In our use of this procedure, discriminant functions were trained on only the adult data, the adult male data, and the adult female data. The resulting discriminant functions were then applied to specific speaker groups in the remaining data set. Predictor variables in both types of analysis included the duration measures, normalized amplitude, spectral slope, and spectral moments (mean, variance, skewness, and kurtosis).

III. RESULTS

Table I gives the acoustic measures (durations, normalized amplitude, spectral slope, spectral moments) from the four classes of voiceless English fricatives. Spectral moment values were taken from the analysis window centered over the temporal midpoint of the fricative. The data are tabularized according to speaker age, fricative place of articulation, and vowel context.

A. Fricative duration

For the measure of fricative duration, a main effect of place of articulation $[F(3,96)=14.16, p<0.001, \eta^2=0.31]$ was found to be significant. Subsequent pairwise comparisons indicated that the basis for this effect was derived from the significantly decreased ($p<0.001$) duration of labiodental fricatives /f/. Collapsed across speaker and vowel context, the mean fricative durations for /f, θ s, ʃ/ were found to be 182, 205, 205, and 199 ms, respectively. There was also a significant place by age interaction effect $[F(9,96)=3.14, p<0.003, \eta^2=0.23]$. Adult speakers were found to have relatively shorter fricative durations than the groups of child speakers when the primary constriction of the consonant was more anterior in the oral cavity (/f/ and /θ/). However, this trend changed for alveolar and palato-alveolar fricatives (/s/ and /ʃ/), with the 5-yr-old speakers exhibiting the shortest durations.

In addition, the ANOVA also revealed a significant difference in fricative duration as a function of vowel context $[F(2,64)=35.30, p<0.001, \eta^2=0.52]$. Pairwise comparisons indicated that the significant differences ($p<0.001$) between contexts were characterized by a decrease in the fricative duration when followed by an /ɑ/ vowel. A significant difference ($p=0.05$) between the /i/ and /u/ vowel contexts was also found. The mean fricative durations for the /i/, /ɑ/, and /u/ vowel contexts were 200, 186, and 208 ms, respectively.

B. Normalized amplitude

A main effect of place $[F(3,96)=157.69, p<0.001, \eta^2=0.83]$ was obtained for normalized amplitude. As expected, Bonferroni-adjusted comparisons indicated that this effect was derived primarily from significant differences ($p<0.001$) between the nonsibilant and sibilant fricatives. The normalized amplitude of the nonsibilant fricatives (−13.7 dB for /f/, −11.9 dB for /θ/) was significantly less than that of the sibilant fricatives (−3.6 dB for /s/, −3.0 dB for /ʃ/).

Significant differences in the normalized amplitude of the fricative also depended on the articulation of the following vowel $[F(2,64)=16.08, p<0.001, \eta^2=0.33]$. Overall,

TABLE I. Acoustic measures from four classes of voiceless English fricatives, grouped as a function of speaker age, fricative place of articulation, and vowel context. Average durations in milliseconds (Dur), normalized amplitude in dB (NAmp), spectral slope (Slope), and the first four spectral moments (mean in ERB, M1; variance in MHz, M2; skewness, M3; and kurtosis, M4).

	Labiodental—/f/			(Inter)dental—/θ/			Alveolar—/s/			Palato-alveolar—/ʃ/		
	/i/	/ɑ/	/u/	/i/	/ɑ/	/u/	/i/	/ɑ/	/u/	/i/	/ɑ/	/u/
3 yr old												
Dur	203	198	201	233	216	260	215	211	240	204	210	224
NAmp	−15.88	−17.99	−13.72	−15.27	−16.69	−13.90	−5.66	−7.90	−4.72	−3.97	−3.61	−3.33
Slope	2.58	3.24	2.95	2.72	2.96	2.30	3.96	4.81	4.60	8.08	8.84	8.36
M1	27.94	28.20	28.80	28.94	29.29	28.94	29.06	30.67	30.74	31.29	30.78	31.21
M2	7.09	6.33	6.00	6.20	6.09	6.17	3.02	2.95	2.74	3.26	3.83	3.83
M3	−2.37	−2.32	−2.26	−2.19	−2.21	−2.02	−2.32	−2.08	−2.25	−0.92	−0.69	−0.92
M4	4.40	4.07	4.41	3.43	4.15	3.83	4.60	3.20	4.71	1.46	0.09	0.26
4 yr old												
Dur	187	180	207	214	202	217	215	206	208	197	168	218
NAmp	−11.84	−15.56	−11.29	−10.66	−11.40	−7.29	−2.57	−3.93	−2.79	−2.43	−2.81	−3.00
Slope	3.23	3.14	3.33	3.87	3.82	3.72	4.59	5.35	5.45	8.97	8.70	8.11
M1	28.85	28.63	27.26	29.11	30.60	29.88	30.88	30.93	30.70	31.77	31.13	31.19
M2	6.61	6.12	6.34	5.43	3.81	4.79	2.39	2.44	2.68	3.46	3.75	3.42
M3	−2.20	−2.32	−2.46	−2.36	−2.35	−2.30	−2.20	−2.02	−2.17	−0.45	−0.34	−0.49
M4	3.03	4.08	4.69	4.51	4.75	4.15	4.48	3.58	4.34	−0.09	−0.18	0.53
5 yr old												
Dur	195	158	174	206	188	210	201	180	189	187	173	214
NAmp	−11.63	−15.97	−11.55	−11.86	−12.26	−9.76	−2.64	−2.72	−2.49	−3.41	−3.74	−2.84
Slope	4.03	3.32	3.51	3.19	3.74	2.99	5.32	5.99	6.36	10.06	9.73	10.26
M1	28.48	28.17	27.92	29.78	30.22	29.51	31.27	31.93	31.67	30.82	30.14	30.10
M2	6.02	6.71	6.52	5.91	4.50	4.39	1.73	1.86	2.40	3.98	3.87	3.55
M3	−2.25	−2.27	−2.40	−2.22	−2.25	−2.35	−1.80	−1.79	−1.82	−0.02	0.29	0.27
M4	3.34	3.54	4.27	4.26	4.01	4.51	2.92	2.91	2.93	−0.58	−0.33	−0.29
Adult												
Dur	173	153	162	173	161	188	200	185	209	203	181	212
NAmp	−10.26	−15.76	−12.68	−10.67	−13.29	−10.90	−2.56	−2.81	−2.99	−1.91	−2.16	−2.78
Slope	4.24	3.57	3.89	4.30	3.69	3.55	6.02	6.26	6.88	9.71	8.85	9.39
M1	30.47	30.49	30.42	30.40	29.92	30.08	32.90	32.84	32.52	27.65	27.34	27.38
M2	5.84	6.13	5.44	5.22	6.29	5.81	1.85	1.91	2.81	2.31	2.28	2.17
M3	−1.91	−1.88	−2.21	−2.00	−1.83	−2.11	−1.59	−1.44	−1.20	1.80	2.14	1.92
M4	2.91	2.25	4.38	2.84	1.78	3.02	3.87	3.13	1.89	4.54	7.18	4.93

the normalized amplitude measures for the fricatives were significantly ($p<0.001$) decreased when followed by an /ɑ/ vowel. The normalized values for the fricatives in the /i, ɑ, and u/ vowel context were −7.7, −9.3, and −7.2 dB, respectively. A place by vowel interaction was also found to be significant $[F(6,192)=42.86, p<0.001, \eta^2=0.18]$. The decreased normalized amplitude found in the /ɑ/ vowel context was significant ($p<0.01$) for /f, θ, and s/, but was actually slightly increased for /ʃ/.

C. Spectral measures

To better compare these results with previous findings concerning the spectral properties of young children's speech (i.e., Nittrouer, 1995), this study will present detailed findings from only the analysis window centered at the midpoint of the fricative segment. It is hoped that since the characteristics of the fricative are of primary interest in this study, utilizing the middle analysis window will limit the effects of stimulus onset variations and the formant transitions of the subsequent vowel. However, it is important to report that the patterns of spectral differences across window locations were similar to those that have been previously found with adult speakers (Behrens and Blumstein, 1988a; Jongman *et al.*, 2000). For example, window locations at the beginning and end of the fricative were generally found to have higher spectral peak and mean values than measures extracted from the middle portion of the fricative.

1. Spectral slope

A significant main effect of place of articulation $[F(3,96)=266.16, p<0.001, \eta^2=0.89]$ was obtained for spectral slope. Subsequent pairwise comparisons ($p<0.001$) demonstrated that three of the four places of fricative articulation were statistically different in terms of mean spectral slope, with no significant difference noted between nonsibilant fricatives (/f/ and /θ/). The mean spectral slope values for the different fricative types (/f, θ, s, ʃ/) were 3.42, 3.40, 5.46, and 9.08, respectively. In addition, the statistical

analysis indicated that when collapsed across age group and vowel context, the mean spectral slope of the four fricative types varied significantly [$F(3,96)=10.31, p<0.001, \eta^2=0.24$] as a function of speaker gender. Female speakers exhibited higher slope values for all places of fricative articulation, except for the alveolar fricatives (/s/).

Interestingly, a main effect was obtained for age group [$F(3,32)=4.84, p<0.01, \eta^2=0.31$], as well as a significant gender by age group interaction [$F(3,32)=3.08, p<0.05, \eta^2=0.22$]. Spectral slope values rise as the age of speaker increases (the mean slope values for 3-, 4-, 5-yr-old, and adult speakers were 4.61, 5.18, 5.70, and 5.86, respectively). Significant differences were found between the two youngest groups and the adult speakers [3 yr old, $t(9)=-3.42$, $p=0.008$; 4 yr old, $t(9)=-3.43$, $p=0.007$]. However, the extent of these differences between age groups varies widely as a function of gender. For males, the spectral slope increased with the age of the speaker. However, for female speakers, the 4-year-old age group exhibited the lowest slope values and the 5-yr-old group the highest.

2. Spectral mean

As expected, the spectral mean differed significantly across the place of fricative articulation [$F(3,96)=25.47, p<0.001, \eta^2=0.44$]. Pairwise comparisons indicated variation ($p<0.001$) between three of the four places of fricative articulation, with no statistical difference in spectral mean between nonsibilant /θ/ and /ʃ/ fricative tokens. There was also a significant place by gender interaction effect [$F(3,96)=4.46, p=0.008, \eta^2=0.12$]. This interaction is characterized by higher spectral means for male speakers on the three more anteriorly produced fricatives (/f, θ, s/) and a lower spectral mean for the more posterior /ʃ/ fricative. It is somewhat surprising to find that the male speakers exhibited elevated spectral means in the majority of fricative types. However, this result is somewhat explained by the finding that the elevated means for male speakers were only found in the child speakers. Since anatomical differences in vocal tract size are likely insignificant for child speakers of this age (Fitch and Giedd, 1999), gender differences may be a product of learned behavioral factors. However, data from future studies must be obtained before such a claim can be fully justified.

Similar to previous research (Nittrouer, 1995), a significant place by age group [$F(9,96)=10.90, p<0.001, \eta^2=0.51$] interaction was noted for the dependent measure of spectral mean. As can be seen in Fig. 1, a contrast between /s/ and /ʃ/ was exhibited by the 5-year-old speakers and further differentiated by the adults, with the spectral mean of /ʃ/ being significantly lower than /s/. Interestingly, this within-sibilant contrast is not evident in the younger groups of speakers (3 and 4 yr old).

3. Spectral variance

A significant main effect of place [$F(3,96)=50.48, p<0.001$], characterized by a relatively large effect size ($\eta^2=0.61$), was obtained for spectral variance. Subsequent pairwise comparisons indicated that all four fricative types (/f, θ, s, ʃ/) were significantly ($p<0.001$) different in terms of variance, with means of 6.26, 5.38, 2.39, and 3.30 MHz, respectively. When collapsed into two groups according to sibilance, the measure of spectral variance was found to significantly ($p<0.001$) differentiate between sibilant and nonsibilant fricatives.

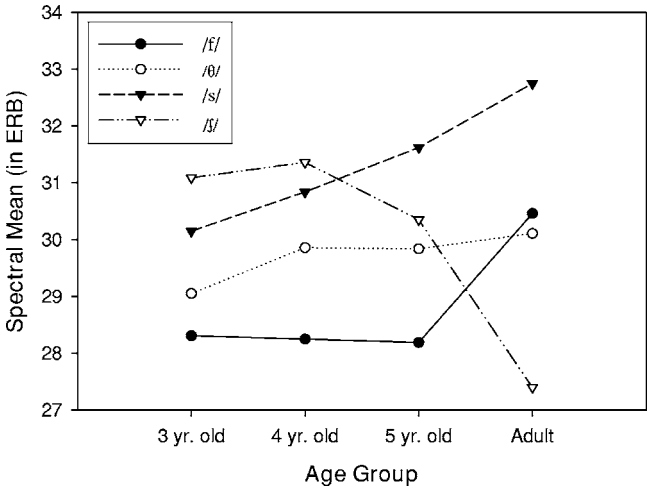

FIG. 1. Spectral mean as a function of place of fricative articulation and speaker age. Linear measures in hertz were converted to an ERB scale (Glasberg and Moore, 1990; Moore, 1997) prior to analysis.

4. Spectral skewness

As with many of the other spectral measures, statistical analyses of the data also indicated a significant main effect of place [$F(3,96)=242.97, p<0.001, \eta^2=0.88$] for spectral skewness. Subsequent pairwise comparisons indicated that the main effect of place was due to the significantly ($p<0.001$) elevated skewness of palato-velar fricatives. Skewness values for the four fricatives types (/f, θ, s, ʃ/) were found to be −2.23, −2.18, −1.88, and 0.21, respectively.

In addition, a significant main effect of age group [$F(3,32)=24.96, p<0.001, \eta^2=0.70$] and a significant place by age group [$F(9,96)=12.37, p<0.001, \eta^2=0.54$] interaction effect was noted. As seen in Fig. 2, post hoc tests indicated significant differences between each of the groups of

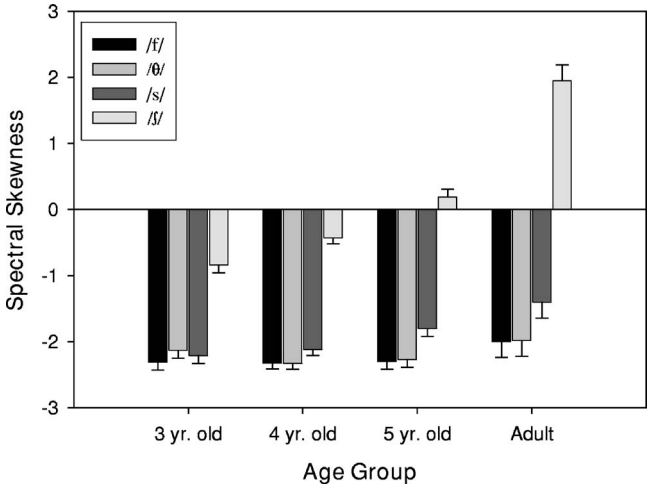

FIG. 2. Spectral skewness as a function of speaker age group and place of fricative articulation.

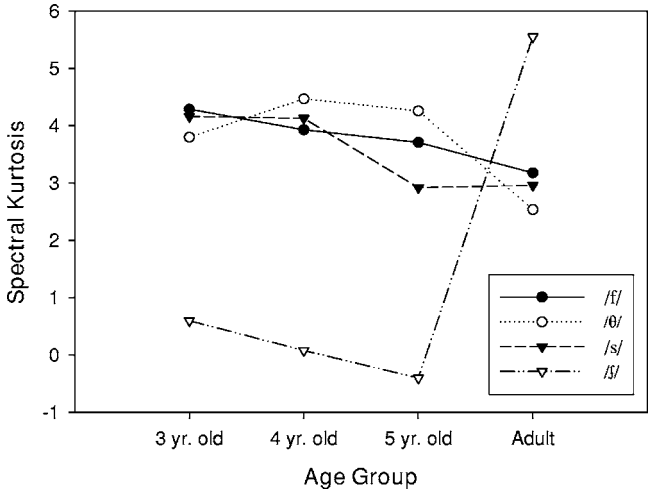

FIG. 3. Spectral kurtosis as a function of speaker age and place of fricative articulation.

children and the adults [3 yr old, $t(9)=5.51$, $p<0.001$; 4 yr old, $t(9)=7.18$, $p<0.001$; 5 yr old, $t(9)=3.94$, $p=0.003$], with no differences between the child groups found to be significant. Overall differences in age group are further explained by examining the place by age group interaction. Similar to findings reported by Nittrouer (1995), the contrast in spectral skewness between /ʃ/ and the other fricative types widened as the age of the speaker increased, with adult speakers exhibiting more positively skewed spectra for /ʃ/.

5. Spectral kurtosis

The main effect of place of articulation was statistically significant for spectral kurtosis [$F(3,96)=266.16, p<0.001, \eta^2=0.89$]. Pairwise comparisons demonstrated that only two of the four places of fricative articulation were statistically different ($p<0.001$) from each other in terms of mean spectral kurtosis. These differences were due mainly to the decreased kurtic value of palato-velar fricatives, with the mean kurtic values for the four fricative types (/f, θ, s, ʃ/) found to be 3.78, 3.77, 3.54, and 1.46, respectively. In addition, a significant place by gender interaction [$F(3,96)=10.31, p<0.001, \eta^2=0.24$] and subsequent pairwise comparisons indicated that for alveolar fricatives (/s/) the values of spectral kurtosis for male speakers were significantly lower ($t(19)=-3.92, p<0.001$) than female speakers (2.21 vs 4.90). Significant differences in gender were not found for the other fricative types.

As shown in Fig. 3, the ANOVA also yielded a significant place by age group interaction [$F(9,96)=4.64, p<0.001, \eta^2=0.30$]. Although an overall main effect of age group was not found to be significant, the interaction reveals significant age difference for each child age group when compared to the adult speakers [3 yr old, $t(9)=2.85$, $p=0.019$; 4 yr old, $t(9)=2.92$, $p=0.017$; 5 yr old, $t(9)=3.55$, $p=0.006$] for palato-velar fricatives (/ʃ/). This finding may indicate that with regard to kurtosis, the child speakers have not yet acquired an adult-like palato-velar fricative. Similar age differences concerning the measure of spectral kurtosis have not been reported in previous research (i.e., Nittrouer, 1995).

TABLE II. Results of discriminant classification using both cross-validation and "specific group" procedures. All values represent % correct classification.

	Classification model training set			
Data set evaluated	Cross validation	All adults	Male adults	Female adults
Original training set	···	76.7	85	83.3
3-yr-old speakers	70	34.2	28.3	42.5
4-yr-old speakers	70	38.3	40	48.3
5-yr-old speakers	77.5	54.2	55.8	57.5
Adult speakers	65	···	···	···
Male only	75.0	···	···	60.0
Female only	78.3	···	61.7	···
Entire data set	69.2	42.2	44.3	51.0

D. Discriminant analysis

As shown in Table II, when classification results are based on a cross-validation (jack-knife) procedure, 69.2% of the entire data set were classified correctly in terms of place of articulation. The adult speakers had a classification rating of 65.0%, while the 3-, 4-, and 5-yr-old speakers exhibited a rating of 70.0%, 70.0%, and 77.5%, respectively. Overall, differences between male (67.5%) and female (68.8%) speakers were minimal.

Utilizing the specific group approach, the discriminant analysis trained on the adult fricative productions resulted in two significant discriminant functions [$(\Lambda=0.03, \chi^2(15, N=120)=416.81, p<0.001)$ and $(\Lambda=0.32, \chi^2(8, N=120)=129.98, p<0.001)$, respectively]. The two canonical functions were found to cumulatively accounting for 99.9% of the variance between productions. The first discriminant function had an eigenvalue of 11.24 and a canonical correlation of 0.96, thereby accounting for 84.4% of the variance. The second function accounted for 15.5% of variance, with an eigenvalue of 2.07 and an associated correlation of 0.82.

Of the seven input variables utilized in the analysis, five acoustic parameters (spectral mean, variance, skewness, kurtosis, and slope) were found to have a substantial contribution to the overall classification of the adult fricative tokens. Thomas (1992) found that the partial contribution of each of the selected variables to a particular discriminant function can be characterized by discriminant ratio coefficients (DRCs). The DRCs are calculated as the product of the absolute values of the structure coefficients and the corresponding standardized discriminant function coefficients. Thus, the larger the DRC, the greater the unique contribution of that respective variable to the discrimination between fricative types in terms of place of articulation. As shown in Table III, the acoustic variables of spectral skewness, variance, and slope were found to have the greatest relative contribution to the first discriminant function, whereas spectral mean, variance, and slope were found to be the top three contributors to the second discriminant function.

Classification models developed on adult-only productions resulted in an overall classification rate of 76.7% for data in the training set. High classification rates were found for the sibilant fricatives (95%), while the nonsibilant frica-

TABLE III. Discriminant variable coefficients for adult fricative data. Input variables are ordered according to their relative contribution to the discriminant function as measured by the DRCs (Thomas, 1992).

First discriminant function				Second discriminant function			
Input variable	SDFCs[a]	SCs[b]	DRCs[c]	Input variable	SDFCs[a]	SCs[b]	DRCs[c]
Spectral skewness	−0.550	−0.666	0.366	Spectral mean	0.194	0.146	0.028
Spectral variance	0.915	0.258	0.236	Spectral variance	−0.375	−0.536	0.201
Spectral slope	−0.458	−0.506	0.232	Spectral slope	0.130	0.284	0.037
Spectral mean	0.598	0.312	0.187	Spectral skewness	0.845	0.920	0.777
Spectral kurtosis	0.274	0.073	0.020	Spectral kurtosis	−0.378	−0.034	0.013

[a]Standardized discriminant function coefficients.
[b]Structure coefficients.
[c]Discriminant ratio coefficients (DRC=SDFC×SC).

tives were correctly identified at a lower rate (70%). Errors in classification were usually the result of confusions within "neighboring" fricatives (e.g., /f/ vs /θ/) and rarely crossed the sibilant/nonsibilant distinction. When applied to data produced by child speakers, the classification model categorized fricatives with an overall accuracy of only 42.2%. Interestingly, the rate of successful classification improved as the age of the child speakers increased, with the mean classification rates for the 3-, 4-, and 5-yr-old age groups found to be 34.2%, 38.3%, and 54.2%, respectively. The higher classification rates for productions from the 5-year and adult speakers are primarily due to the increased categorization of the sibilant fricatives. For the two youngest groups of speakers, the discriminant model accurately identified /s/ and /ʃ/ productions only slightly above chance (26.6%), whereas, the categorization for 5-yr-old and adult speakers was dramatically higher (65% and 95%, respectively).

IV. DISCUSSION

Statistical analysis (ANOVA) indicated that the dependent measures of fricative duration, normalized amplitude, spectral slope, and all four spectral moments varied significantly as a function of place of articulation. However, only spectral variance was found to significantly distinguish all four places of fricative articulation. Interestingly, with the exception of Jongman *et al.* (2000) and Tomiak (1990), the measure of spectral variance has often not been analyzed or reported in the previous literature (e.g., Forrest *et al.*, 1988; Miccio, 1996; Nittrouer, 1995). In general, these results are in agreement with the research of Jongman *et al.*, where it was found that spectral variance could be used to acoustically distinguish four places of fricative articulation in adult productions.

Although spectral variance was the only measure to distinguish all four fricative types, many of the derived acoustic parameters were found to successfully distinguish three out of four places of fricative articulation. The measures of spectral slope, mean, and skewness were able to separate nonsibilant from sibilant fricatives, as well as between the two sibilant fricatives (/s/ and /ʃ/). However, contrary to research findings on the acoustic characteristics of fricatives in adults (Jongman *et al.*, 2000), results of this study indicated that the majority of spectral parameters (with the exception of variance) did not differ significantly between nonsibilant fricatives (/f/ and /θ/). It is important to note that the spectral measure of slope was found to be an important cue in the distinction and classification of fricative productions.

Of particular interest, significant place by age interaction effects were noted for the measures of spectral mean, skewness, and kurtosis. In each of these measures, the interaction effect was due primarily to a widening in the acoustic distinction between /s/ and /ʃ/ as the age of speaker increased. In terms of spectral mean, a significant difference between /s/ and /ʃ/ was exhibited by the 5-yr-old speakers and further differentiated by the adults. For spectral skewness, an adult-like contrast appears to begin developing in the 4-yr-old speakers and widened as the speakers increased in age. These findings suggest that for several acoustic parameters the development of the sibilant contrast continues to be fine-tuned throughout young childhood toward an adult-like stage of articulation. This same general trend across age groups was reported by Nittrouer (1995), who also found age-related acoustic differences. Nittrouer concluded that these differences were the product of continuing articulatory development, even for children 7 years of age. The lack of acoustic difference between the sibilants in the youngest groups of speakers may also be partially due to the relatively smaller size of the vocal tract. In adults, the difference between an alveolar and palatal place of fricative articulation is likely to result in comparatively large acoustic variations, which may not be the case for young children.

In terms of place of articulation, a discriminant analysis based on the extracted acoustic measures was able to correctly classify the fricative data at a rate well above chance. Interestingly, the spectral measures of variance and slope were found to be important coefficients in the classification of the fricative productions. It is important to note that based on a cross-validation procedure the overall classification accuracy for the fricative productions (69%) was similar to the classification results obtained by Forrest *et al.* (1988). As expected, discriminant functions based on the adult tokens were less accurate in classifying the segments produced by the younger speakers. For adults, the majority of classification errors occurred with nonsibilant fricatives, with few categorization confusions crossing the sibilant/nonsibilant distinction. Conversely, the discriminant function classified the nonsibilant productions from the youngest child speakers at a rate higher than that of the sibilant fricatives. However, it is

interesting to note that the overall classification rate improved systematically as the age of the child speakers increased, with a marked improvement occurring at 5 years of age. Analysis of the classification of specific fricative types indicated that this improvement was primarily the result of the increased categorization of sibilant fricatives. Thus, these data once again support the theory that young children's sibilant fricative articulations are not differentiated in an adult-like manner, but are continuing to be "fine-tuned" as the child matures (Nittrouer, 1995). Of further interest is that unlike preliminary research conducted on the fricatives of older children (Fox and Nissen, 2003), discriminant functions trained on only male adult and only female adult data did not reveal systematic gender differences in the productions of the child speakers.

Future spectral research involving children's speech elicited in more naturalistic settings and across less predictable contexts would likely extend our understanding of the acoustic nature of speech in young children. Since acoustic studies provide only a "post-production" view of articulation, more studies are also needed that combine both kinematic and acoustic analysis techniques in a more dynamic investigation into the nature of fricative production. Finally, our use of discriminant analysis was designed to allow a comparison between the different age and gender groups in terms of the acoustic characteristics of the fricatives and, in particular, in terms of how well these acoustic measures could be used to categorize these fricatives. However, there are two limitations to our approach. First, as in previous studies such as Jongman *et al.* (2000), all the acoustic measures utilized here represented only static acoustic cues. Clearly, any future study should also examine the utility of dynamic cues (e.g., the change in the spectral mean over the fricative's duration) in the discriminant functions. Second, one should determine whether listeners make use of the same acoustic cues (and whether they rely on them to the same degree) as those used in the discriminant analyses discussed. Despite these limitations, this study contributes valuable results concerning the spectral nature of a broad set of voiceless fricative productions from a substantial number of speakers; findings which serve to establish a more comprehensive knowledge of how fricative consonants develop in younger speakers.

ACKNOWLEDGMENTS

This research was supported by a Graduate Student Alumni Research Association grant from The Ohio State University and a McKay School of Education Grant from Brigham Young University.

Adobe Systems Incorporated. (**2003**). Adobe Audition (Version 1.3) [Computer software], San Jose, CA, Adobe Systems Incorporated.

Behrens, S., and Blumstein, S. E. (**1988a**). "Acoustic characteristics of English voiceless fricatives: A descriptive analysis," J. Phonetics **16**, 295–298.

Behrens, S., and Blumstein, S. E. (**1988b**). "On the role of the amplitude of the fricative noise in the perception of place of articulation in voiceless fricative consonants," J. Acoust. Soc. Am. **84**, 861–867.

Fitch, W. T., and Giedd, J. (**1999**). "Morphology and development of the human vocal tract: A study using magnetic resonance imaging," J. Acoust. Soc. Am. **106**, 1511–1522.

Forrest, K., Weismer, G., Elbert, M., and Dinnsen, D. A. (**1994**). "Spectral analysis of target-appropriate /t/ and /k/ produced by phonologically disordered and normally articulating children," Clin. Linguist. Phon. **8**, 267–281.

Forrest, K., Weismer, G., Hodge, M., and Dinnsen, D. A. (**1990**). "Statistical analysis of word-initial /k/ and /t/ produced by normal and phonologically disordered children," Clin. Linguist. Phon. **4**, 327–340.

Forrest, K., Weismer, G., Milenkovic, P., and Dougall, R. N. (**1988**). "Statistical analysis of word-initial voiceless obstruents: Preliminary data," J. Acoust. Soc. Am. **84**, 115–123.

Fox, R. A., and Nissen, S. L. (**2003**). "Age-related acoustic changes in voiceless English fricatives," Proceedings from the Meikai Linguistics and Phonetics Conference, Meikai University, Japan.

Glasberg, B. R., and Moore, B. C. J. (**1990**). "Derivation of auditory filter shapes from notched-noise data," Hear. Res. **47**, 103–138.

Goldman, R., and Fristoe, M. (**1986**). *Goldman-Fristoe Test of Articulation* (American Guidance Service, Circle Pines, MN).

Jongman, A., Wayland, R., and Wong, S. (**2000**). "Acoustic characteristics of English fricatives," J. Acoust. Soc. Am. **108**, 1252–1263.

Miccio, A. W. (**1996**). "A spectral moments analysis of the acquisition of word-initial voiceless fricatives in children with normal and disordered phonologies," Doctoral dissertation, Indiana University.

Moore, B. C. J. (**1997**). *An Introduction to the Psychology of Hearing* (Academic, New York).

Nittrouer, S. (**1995**). "Children learn separate aspects of speech production at different rates: Evidence from spectral moments," J. Acoust. Soc. Am. **97**, 520–530.

Nittrouer, S., Studdert-Kennedy, M., and McGowan, R. S. (**1989**). "The emergence of phonetic segments: Evidence from the spectral structure of fricative-vowel syllables spoken by children and adults," J. Speech Hear. Res. **32**, 120–132.

SPSS, Inc. (**1997**). *SPSS Advanced Statistics* 7.5 [Computer Software Manual] (SPSS Incorporated, Chicago).

Thomas, D. (**1992**). "Interpreting discriminant functions: A data analytic approach," Multivar. Behav. Res. **27**, 335–362.

Tomiak, G. R. (**1990**). "An acoustic and perceptual analysis of the spectral moments invariant with voiceless fricative obstruents," Doctoral dissertation, SUNY Buffalo.

Zwicker, E. (**1975**). "Scaling," in *Handbook of Sensory Physiology*, Auditory System Vol. 3, edited by D. Keidel and W. Neff (Springer, Berlin), pp. 401–408.

Zwicker, E., and Terhardt, E. (**1980**). "Analytical expressions for critical band rate and critical bandwidth as a function of frequency," J. Acoust. Soc. Am. **68**, 1523–1525.

Finding intonational boundaries using acoustic cues related to the voice source

Jeung-Yoon Choi
Department of Electrical and Computer Engineering, 2005 Beckman Institute, 405 North Mathews Avenue, University of Illinois at Urbana–Champaign, Urbana, Illinois 61801

Mark Hasegawa-Johnson
Department of Electrical and Computer Engineering, 155 Everitt Laboratory, 1406 West Green Street, University of Illinois at Urbana–Champaign, Urbana, Illinois 61801

Jennifer Cole
Department of Linguistics, 4088 Foreign Languages Building, 707 South Mathews Avenue, University of Illinois at Urbana–Champaign, Urbana, Illinois 61801

(Received 1 July 2004; revised 7 February 2005; accepted 2 July 2005)

Acoustic cues related to the voice source, including harmonic structure and spectral tilt, were examined for relevance to prosodic boundary detection. The measurements considered here comprise five categories: duration, pitch, harmonic structure, spectral tilt, and amplitude. Distributions of the measurements and statistical analysis show that the measurements may be used to differentiate between prosodic categories. Detection experiments on the Boston University Radio Speech Corpus show equal error detection rates around 70% for accent and boundary detection, using only the acoustic measurements described, without any lexical or syntactic information. Further investigation of the detection results shows that duration and amplitude measurements, and, to a lesser degree, pitch measurements, are useful for detecting accents, while all voice source measurements except pitch measurements are useful for boundary detection. [DOI: 10.1121/1.2010288]

PACS number(s): 43.70.Fq, 43.70.Gr, 43.72.Ne [AL] Pages: 2579–2587

I. INTRODUCTION

Speech prosody comprises many forms of nonsegmental and nonlexical information. Prosody is related to emotion,[1] and selective emphasis,[2] and helps to resolve syntactically ambiguous utterances.[3] However, there is much debate as to the structure of prosody, as well as the acoustic manifestations of those structures.[4]

One widely used system, TOBI,[5] has been formulated based on phonological study of prosodic units. The system assigns tones to each prominence and boundary, and a break index to each boundary. Briefly, tones are classified as low (L), high (H), or downstepped-high (!H). Prominences are marked with stars (*), and intermediate boundaries with dashes (-). Full intonational boundaries are marked with both a dash (-) and a percent (%). Tones may be combined to form composite tones, such as L^*+H and L-H%. It is assumed that these entities have corresponding acoustic (and presumably articulatory) correlates that may be observed directly.

If so, in order to determine where the acoustic cues for prosody may be found, it is useful to consider which part of the speech signal contains the most information related to prosody. In previous works, sentential prosody imposed on nonsense syllables was found to facilitate short-term memory for the stimuli. Also, based on prosody, listeners were able to choose the correct interpretation when ambiguous sentences were in reiterant form as well as they did when the sentences were spoken normally.[6]

A few observations may be made from these results. One is that listeners are able to perceive acoustic indicators for prosody independently of syntactic or lexical information. Also, the acoustic indicators should be contained within the temporal, spectral, and amplitudinal dimensions of the signal. Another observation is that, when normal speech is transformed into reiterant speech or nonsense syllables, acoustic features of the vocalic segments appear to be rich channels for the transmission of prosodic information. Although a large number of syllables in natural speech contain vocalic segments in the onset and/or the coda, it is also the case that these segments are often absent, while all syllables include a vocalic nucleus. Therefore, in this study, the focus will be on finding the correspondence between characteristics of vocalic segments in the nucleus with prosodic events.

Vocalic sound can be modeled as the glottal voice source filtered by the vocal tract. The identity of the vocalic segment being produced is mostly determined by the formant structure, which corresponds to the filtering by the vocal tract. Hence, it is reasonable to expect that study of acoustic cues that characterize the glottal voice source for correlates of prosodic events will yield useful results.

The glottal voice source can be modeled as a series of glottal pulses, whose spectrum can be broadly characterized by the spacing and relative amplitudes of the component harmonics. The spacing of the harmonics is determined by the fundamental frequency, or pitch, of the glottal pulse train. The relative amplitudes of the harmonics are affected by the shape of the glottal pulse itself. For example, a larger portion of the fundamental period where there is nonzero airflow (open quotient) leads to a more dominant first harmonic am-

plitude. The faster the glottal pulse returns to zero after the peak, the smaller the amplitude of the first harmonic.[7] These characteristics are results of manipulation of the laryngeal structures that are employed in phonation during vocalic segments.

In a study by Klatt and Klatt,[8] the authors present evidence that declarative sentences may be terminated such that the arytenoid cartilages begin to separate in preparation for breathing, leading to a breathy-voiced offset to the final syllable. This early abduction gesture may be implemented as a general "relaxed" separation of the arytenoids, or a "laryngealized" mode where the abduction is accompanied by a rotational motion of the arytenoids so that medial compression is applied.

For both cases, the spectral noise increases due to the presence of the posterior interarytenoid separation. In the first case ("breathy"), the glottal waveform exhibits a larger open quotient, so that the first-harmonic amplitude ($h1$) is increased and the harmonic spectrum tilts down. The converse is true for the laryngealized case, i.e., $h1$ and spectral tilt both decrease. In the paper by Klatt and Klatt,[8] cues to breathiness increased for unstressed syllables, for final syllables, and at the margins of voiceless consonants. In stressed vowels with a relatively high fundamental frequency, the spectrum showed little evidence of breathiness. On the other hand, many utterances appeared to end in a "breathy-laryngealized" type of vibration, along with diplophonic irregularities in the timing of glottal periods. This observation agrees with findings where aperiodicity associated with creaky voice was more frequent at L-L% than L-boundaries.[9]

An underlying mechanism for such irregular phonation may be due to changes in subglottal pressure. In previous studies, including a study by Slifka,[10] utterance endings were found to be correlated with a drop in subglottal pressure, and irregular phonation with partially spread vocal folds was frequently observed. Additionally, the first stressed syllable in an utterance was found to be correlated with the initial subglottal pressure peak.

Also, in a work by Pierrehumbert and Talkin,[11] harmonic structure (and amplitude) measurements for /h/ and glottal stop were found to become more vocalic (i.e., less aspiration, more phonation) at accents, and more consonantal (i.e., more aspiration, less phonation) at boundaries. The observations above suggest that acoustic measurements related to the glottal voice source will be useful in finding the various types of prosodic events.

In addition to the spectral characteristics of the voice source, temporal and amplitudinal characteristics may be observed, such as length and amplitude of the vocalic segment, and the length of surrounding speech/nonspeech units. Previous studies show that durational cues, such as segmental durations, were found to be correlated with the presence of prosodic boundaries.[12–14]

In light of the discussion above, an attempt has been made to find acoustic cues associated with accents and boundaries by examining measurements related to the glottal source for vocalic segments. The glottal characteristics can be found by examining durational, spectral, and amplitudinal measurements. This study will focus on finding these acoustic cues independent of other knowledge, such as syntactic structure, part of speech of constituent words, or the identity of the words or segments.

II. EXPERIMENTS

A. Prosodic units

The prosodic units that are considered in this study are based on the TOBI system and can be described as two types—boundaries and accents. The first type includes markers for discourse, turn, intonational boundaries, intermediate boundaries, and words. The second type includes markers for phrase-level stress or prominence, and are localized to accented syllables. In this study, boundary will be limited to intermediate (ip) and intonational (IP) boundaries.

Each syllable in a section of speech can be assigned to one of six categories: (1) not accented and not at a boundary (0), (2) accented but not at a boundary (A), (3) not accented and at an ip boundary (ip), (4) accented and at an ip boundary (Aip), (5) not accented, at IP boundary (IP), and (6) accented, at IP boundary (AIP). The type of accent and/or boundary may be used to further specify the syllable environment. In the Boston University Radio Speech Corpus,[15] intermediate boundaries with low, downstepped high, and high tones are indicated by L-, !H-, and H-, respectively, and intonational boundaries, comprising one intermediate and one final tone, are indicated by L-L%, L-H%, !H-L%, H-L%, and H-H%. (The !H-H% IP boundary was not observed in this corpus.) Simple accents are indicated by L^*, $!H^*$, and H^*. Complex accents are indicated as combinations of two accent tones such as L^*+H, etc. In this study, prosodic events marked with a question mark (?) in the corpus were ignored, i.e., syllables associated with those incompletely marked events were considered to be prosodically unmarked. Based on counts of these events, about 9% of the syllables marked as neutral (0) are estimated to belong to this category. An exhaustive tally of the different types of prosodic markers in the corpus includes 90 markers that can be assigned to a syllable (1 neutral, 8 accents, 3 intermediate +6 intonational boundaries, and 24+48 accented at intermediate/intonational boundaries). However, the focus on this study will be on examining the six broad classes described above.

B. Acoustic measurements

The acoustic cues related to the voice source examined in this paper to identify the presence of prosodic events can be divided into five categories: duration, pitch, harmonic structure, spectral tilt, and amplitude.

Durational measurements include length of following pause (if any) and speech rate. A pause is defined to be an interval of speech where the probability of voicing is below 0.5, and rms energy is below 150, for longer than 30 ms, as extracted automatically using the *formant* command in the *xwaves* package.[16] If no such interval exists after a syllable, the pause length was assigned as zero. It is expected that pause length will be longer after boundaries.[12] Speech rate, calculated as the reciprocal of the length of the vocalic seg-

ment, is expected to be slower at boundaries (final lengthening effect).[13,14] Here, a vocalic segment is defined as all vowels (including diphthongs), syllabic liquids (e.g., phones labeled as /er/, /el/), and syllabic nasals (e.g., phones labeled as /em/, /en/, /eng/). The start and end times of the vocalic segments were identified using the phone labels in the *.lbl* or *.lba* files (see Sec. II C). Speech rate was not normalized, either for speaker or phone identity.

Pitch measurements include fundamental frequency (f0) measured at the end of a vocalic segment, and the slope and the convexity of the fundamental frequency over the vocalic segment. The fundamental frequency was measured at the last frame of a vocalic segment where the probability of voicing was above 0.95. Pitch contours for boundary tones have been described as occuring from the nuclear pitch to the end of the utterance, so that the ending fundamental frequency value of the last syllable of an intermediate or intonational phrase would be more similar for utterances with similar boundary tones, but with different numbers of syllables from the nuclear pitch to the end of the utterance. The convexity was calculated as the sum of the difference between each signal point and the linear interpolation between the start and end values of the segment. That is,

$$\frac{\sum_{t=t_1}^{t_2} s(t) - h(t)}{t_2 - t_1},$$

where t_1 and t_2 are respectively the start and end times of the vocalic segment, $s(t)$ is the value of the measurement at time t, and $h(t)$ is the linear interpolated function,

$$h(t) = \frac{s(t_2) - s(t_1)}{t_2 - t_1}(t - t_1), \quad \text{for } t_1 \leqslant t \leqslant t_2, \quad t_1 < t_2.$$

The normalized pitch (nf0) at the end of the vocalic segment, and the slope and convexity of the normalized pitch over the segment are also included in the pitch measurements. Normalized pitch was obtained by training a three-mixture Gaussian distribution over all fundamental frequency measurements of an utterance (sentence), where the means were constrained to be 0.5μ, μ, and 2μ, to separate pitch-halved and pitch-doubled measurements. The outlying values are eliminated, and the resulting fundamental frequency values are smoothed. Normalized pitch values are then computed to be between 0 and 2, with 1 corresponding to the mean fundamental frequency of the utterance.[17,18] This measure normalizes with respect to the speaker over the utterance.

Pitch measurements are expected to be lower for L- and L-L% boundaries, and higher for H- and H-H% boundaries. Pitch is also thought to be affected by low or high accent, but this effect was not examined in this study. However, since the majority of the accents in the corpus were of the H^* type (see Sec. II C), it may be assumed that, mostly, pitch will be *increased* by the presence of accent. Pitch slope is expected to fall for L- or L-L% boundaries, remain mostly level for H-L% boundaries, and rise for H-, H-H%, or L-H% boundaries. Pitch convexity is expected to be flat for L-, L-L%, H-, or H-H% boundaries and to be upward (more positive) for a H-L% boundary and downward (more negative) for a L-H% boundary.

Harmonic structure measurements included end value, slope, and convexity of $h1-h2$, where $h1$ and $h2$ are the amplitudes of the first and second harmonics, respectively. The values for the amplitudes of the first harmonic $h1$ were measured as the amplitude of the spectral component closest to the fundamental frequency, using the spectral analysis procedures in *xwaves*. The amplitude of the second harmonic $h2$ was measured as the amplitude of the spectral component closest to twice the fundamental frequency. In this study, the harmonic measurements were made uniformly for all vocalic segments—the influence of the first formant or presence of liquids and nasals were not factored into the analysis. A more detailed procedure could be used to compensate for these effects, but that approach was not explored in this study.

The $h1-h2$ measurement is greater for a larger open quotient, corresponding to a breathy voice; conversely, it is lesser for a smaller open quotient in a laryngealized voice. It is expected to be lower for accented syllables, which were described as being less breathy. At boundaries, a more breathy offset is expected to correspond to a larger $h1-h2$ measurement, while a more laryngealized offset should produce a smaller measurement.

Spectral tilt measurements included end value, slope, and convexity of $h1-a1$, $h1-a3$, and $a1-a3$, where $a1$ and $a3$ are the amplitudes of the first and third formants, respectively. For both breathy and laryngealized phonation, higher noise and harmonic components relative to the lower frequency amplitudes are observed. Consequently, spectral tilt measurements are expected to exhibit smaller differences at breathy/laryngealized L- or L-L% boundaries and larger differences for more modal H- or H-H% boundaries.

Finally, amplitude measurements included the end value, slope, and convexity of the rms, and these are expected to be lesser at boundaries and greater at accents.

The pitch, harmonic, formant, and rms values were found automatically using the *formant*, and *sgram* commands in *xwaves*. The voice source measurements described above were made over each single vocalic interval, found using the phone labels in the *.lbl* or *.lba* files.

C. Database

The acoustic cues characterizing the voice source were obtained for each vocalic segment in analysis, training, and test subsets of the Boston University Radio Speech Corpus.[15] The corpus contains radio news stories from seven speakers and is divided into two sections, *labnews* and *radio*. Prosodic labels are available for five speakers, f1a, f2b, f3a, m1b, and m2b. In this study, an analysis set was picked to include all files in the *labnews* section with both TOBI labels (i.e., *.ton* files) and hand-corrected (automatically generated) phone labels (i.e., *.lbl* files). The analysis set includes 22 stories from speaker f1a and 41 stories from speaker f2b, both of whom are female. The training set includes 36 stories each from one male speaker (m1b) and one female speaker (f2b) from the *radio* section. The test set includes 24 stories each from one male speaker (m2b) and 1 female speaker (f3a) from the

TABLE I. Number of tokens for each prosodic category for the analysis, training, and test subsets of the Boston University Radio Speech Corpus. The counts for ip boundaries and IP boundaries are further divided into subcategories. (The !H-H% IP boundary was not observed in this corpus.)

	Analysis		Training		Test	
	unacc	acc	unacc	acc	unacc	acc
nonbnd	4944	2193	4849	2133	3994	1958
ip bnd	356	130	213	127	178	121
L-	203	32	110	47	56	16
!H-	74	29	42	35	79	49
H-	79	69	61	45	43	56
IP bnd	732	340	583	236	357	121
L-L%	373	188	335	144	214	68
L-H%	329	116	246	81	126	31
!H-L%	6	9	0	3	0	0
H-L%	21	24	2	8	17	20
H-H%	3	3	0	0	0	2

labnews section. The analysis, training, and test subset utterances are all disjoint. The speakers in the test subset are not included in the analysis or training subsets. For the analysis and training subsets, utterances from speaker f2b appear in both subsets, but only utterances from the *labnews* section are included in the analysis set, and utterances from the *radio* section are included in the training set. Only automatically generated phone labels (i.e., *.lba* files), which are not as accurate as the hand-corrected labels, were available for the training and test data. The measurements were made using the start and end times of vocalic segments included in the *.lbl* files (analysis set) or the *.lba* files (training and test sets).

Each syllable in the three data sets was assigned to one of six prosodic categories described in Sec. II A using the TOBI labels in the *.ton* files, the word transcription in the *.wrd* files, and the phone labels in the *.lbl* or *.lba* files. First, accent markers in the TOBI label files were matched with each vocalic segment in the phone label files, to find accented syllables. Next, the final vocalic segment of a word was found using the word transcriptions and the phone labels. These word-final vocalic segments were then matched with intermediate and intonation boundary markers in the TOBI label files, to find vocalic segments at boundaries. Finally, all vocalic segments were assigned to one of the six prosodic categories, by combining the list of vocalic segments in the accented and boundary categories. If a vocalic segment appeared in neither list, it was assigned to the unaccented, nonboundary (0) category.

The number of syllables at each prosodic category for the three data sets are shown in Table I. There are more full intonational boundaries (IP) than intermediate boundaries (ip) for all data sets. Of the intermediate boundaries, a greater number of L- boundaries occur for the analysis and training sets; more !H- boundaries are observed for the test set. Of the intonational boundaries, the largest number are L-L% boundaries, followed by L-H% boundaries. For all data sets, there were few or no occurrences of the !H-L%, !H-H%, H-L%, and H-H% boundaries. The training set did not include any H-H% boundaries, and the test set did not include any !H-L% boundaries. The ratio of nonboundary syllables to ip+IP boundary syllables is about 5.96 for the three data sets, implying an average phrase length of about six syllables.

Accents were mostly of the H^* type (i.e., H^*, $L+H^*$) accents, followed by comparable numbers of the $!H^*$ type (i.e., $!H^*$, $H+!H^*$, $L+!H^*$) and L^* type (i.e., L^*, L^*+H, $L^*+!H$) accents. For example, in the analysis set, there were 1885 H^* type accents, 447 $!H^*$ type accents, and 167 L^* type accents. More detailed counts for each type of accent are not presented in this paper.

The distribution of tones found in this corpus may be a characteristic of the prosody of broadcast news—a dialogue may include more questions, leading to a greater number of high boundary tones.

III. RESULTS

A. Distributions

Figure 1 shows the distributions of six representative measurements for different prosodic categories from the analysis set, i.e., neutral, the three ip boundaries, L-, !H-, and H-, and the two frequently occurring IP boundaries, L-L% and L-H%. Overall, the presence of an accent tends to lengthen pauses, decrease speech rate, and increase f0, $h1$-$h2$, $h1$-$a1$, and rms. Pause length remains similar for syllables not at boundaries and at ip boundaries, but increases for IP boundaries. Speech rate becomes slower as boundary level increases. The f0, $h1$-$h2$, and $h1$-$a1$ spectral measurements show slight decrease as the boundary level increases, but the effect is not as pronounced as for durational measurements. Amplitude of the syllable decreases as the boundary level increases.

There is little difference in pause length of the different types of ip boundaries, but f0, $h1$-$h2$, $h1$-$a1$, and rms all show slight increases in the order of L-, !H-, and H-ip boundaries. Pause length is longer for the L-L% IP boundaries, compared to the L-H% IP boundaries. However, speech rate seems to show less distinction between the two groups. The f0 measurements show that the presence of a high boundary tone H% leads to an increase. For the $h1$-$h2$

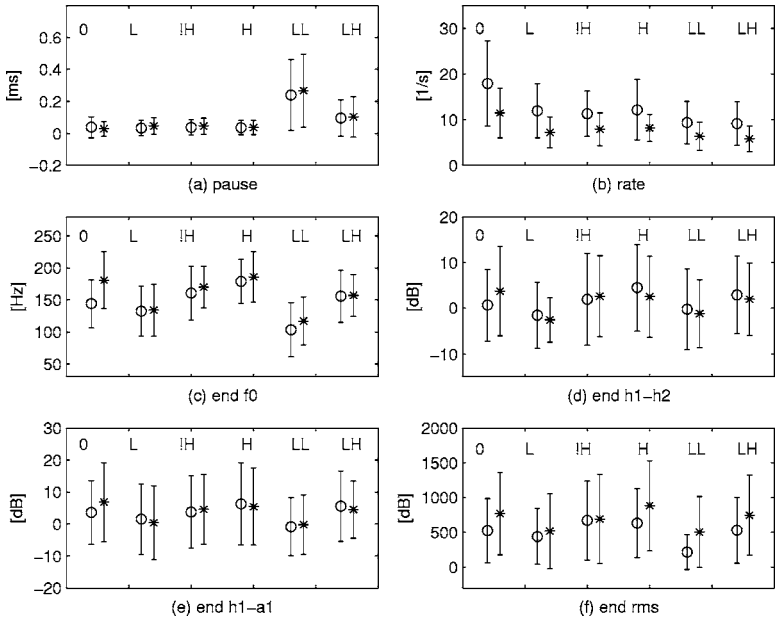

FIG. 1. Distributions of representative measurements for six prosodic categories. The circles/stars are the means, and the bars denote the standard deviations. Each pair of distributions represent unaccented (o) and accented (∗) tokens. The pairs show, in order, non-boundary (0), the L-, !H-, and H-intermediate boundaries (ip), and the L-L% and L-H% intonational boundary (IP) distributions.

and $h1$-$a1$ measurements, accented syllables at boundaries show slightly lower values than unaccented syllables. However, it appears that accented syllables which are not at boundaries show higher values, contrary to expectations, implying that the presence or absence of a boundary affects the production of accented syllables. For example, for this analysis set, the difference in f0 values between accented and unaccented syllables that are not at boundaries seem to be greater than the difference for syllables at boundaries.

Finally, amplitude measurements also show a distinction between the two IP boundaries, with syllables at L-L% IP boundaries showing a lesser amplitude. It must be noted that the standard deviations of the plots are great, with much overlap between the different groups.

B. Statistical analysis

The measurements obtained for all syllables in the training subset of the Radio News Corpus were examined using an analysis of variance (ANOVA). First, a two-way analysis was performed for each of the 23 voice source measurements, with the first factor being boundary level (nonboundary, ip boundary, IP boundary) and the second factor being presence of accent (unaccented, accented). Next, a one-way analysis was carried out, with syllables at all IP boundaries as one group, and the rest as the other group. The F and partial η^2 results are listed in Table II. The critical value for probabilities to be considered significant is $P<0.05$ divided by 46 (23 measurements $\times$ 2 analyses), corresponding to a critical value of $P<0.001$. The degree of freedom between groups is 2 for the first factor (boundary), 1 for the second factor (accent), and 2 for the interaction (boundary $\times$ accent), and 8135 within groups for the two-way analysis. The degree of freedom between groups is 1, and within groups is 8139 for the one-way analysis.

Table II shows that overall, except for the spectral tilt measures related to $h1$-$a3$, the measurements showed significant differences for the two analyses.

TABLE II. ANOVA results (F and partial η^2 values) for 23 voice source measurements for the training data set. Two-way analysis with factor 1: boundary level $\{0,\text{ip},\text{IP}\}\times$ factor 2: accent level $\{0,^*\}$ is shown in columns 2–4. One-way analysis with group 1: IP boundary and group 2: non-IP boundary is shown in the last column. Entries with probabilities greater than ($P>0.001$) (critical value with study correction) are not significant and marked with a dash (-). The degree of freedom between groups for the two-way analysis is 2 for the first factor, 1 for the second factor, and 2 for the interaction; the degree of freedom within groups is 8135, for all measurements. For the one-way analysis, the degree of freedom between groups is 1, and within groups is 8139, for all measurements. Partial η^2 values are shown in parentheses.

Measurements	acc	bnd	acc × bnd	IP vs. not
pause	-	805.6(0.165)	15.4(0.004)	1725.7(0.175)
rate	216.8(0.026)	237.3(0.055)	-	410.9(0.048)
f0 end	90.9(0.011)	92.2(0.022)	33.3(0.008)	122.7(0.015)
f0 slp	-	10.6(0.003)	30.1(0.007)	-
f0 cnv	93.7(0.011)	36.7(0.009)	-	98.3(0.012)
nf0 end	144.3(0.017)	336.7(0.076)	33.9(0.008)	547.1(0.063)
nf0 slp	12.3(0.002)	27.5(0.007)	30.7(0.007)	-
nf0 cnv	103.2(0.013)	37.2(0.009)	-	107.6(0.013)
h1-h2 end	-	11.9(0.003)	-	12.7(0.002)
h1-h2 slp	-	-	-	-
h1-h2 cnv	-	13.3(0.003)	-	35.0(0.004)
h1-a1 end	-	24.8(0.006)	-	41.7(0.005)
h1-a1 slp	-	-	-	-
h1-a1 cnv	-	13.5(0.003)	-	38.0(0.005)
h1-a3 end	-	-	-	-
h1-a3 slp	-	-	-	-
h1-a3 cnv	-	-	-	-
a1-a3 end	-	9.0(0.002)	-	11.5(0.001)
a1-a3 slp	-	-	-	-
a1-a3 cnv	14.0(0.002)	-	-	-
rms end	71.2(0.009)	49.5(0.012)	-	106.6(0.013)
rms slp	-	-	-	-
rms cnv	91.9(0.011)	39.9(0.010)	-	43.9(0.005)

For the two-way analysis, pause length was different for the three boundary levels, but not between unaccented/accented groups. Speech rate was different for all six groups. Except for f0 slope, all pitch measurements showed significant differences across boundary levels and accent levels. The harmonic and spectral tilt measurements show less significant differences, but end measurements for $h1$-$h2$ and $h1$-$a1$, and to a lesser degree, $a1$-$a3$, were significant indicators for boundaries. Only $a1$-$a3$ convexity was significant for accent, however. For amplitude measurements, end rms and rms convexity were significant. Overall, compared to the duration, pitch, and amplitude measurements, harmonic and spectral tilt measurements show small, though significant results.

The interaction between boundary and accent factors are listed in column 4. There is no significant interaction for spectral tilt measurements and amplitude measurements, implying that these measurements show additive effects for boundary and accent. This can be observed in the plots for rms amplitude in Fig. 1(f), from the analysis data.

In the one-way analysis, measurements that were significant indicators for boundary level remained mostly significant for IP versus non-IP discrimination, but pitch slope measurements were not significant.

Partial η^2 values show that effect size is greatest for pause, rate, and rms values, followed by fundamental frequency measurements. The harmonic and spectral tilt measurements show smaller effect sizes, with values less than 0.01, or 1% of the error. (Partial η^2 values are found as $SS_{\text{effect}}/(SS_{\text{effect}}+SS_{\text{error}})$, where SS_{effect} is the type III sum of squares of the measurement, and SS_{error} is the type III sum of squares of the error, respectively.)

C. Boundary detection

The 23 voice source acoustic cues were next used to detect accent and boundary for the training and test sets from the Boston University Radio Speech Corpus. Two boundary detectors were trained and tested: one was trained to detect any IP or ip boundary, the other was trained to detect only IP boundaries, and ignore ip boundaries. The training data set was used to find means and covariance matrices for 23-dimensional Gaussian distributions for nonaccented versus accented tokens (accent detection), for nonboundary versus ip and IP boundary tokens (IP+ip boundary detection), and for non IP versus IP boundary tokens (IP boundary detection). The trained parameters were then used to assign each token in the test set to one group for each task using a simple maximum likelihood measure.

The detection rate versus insertion rate (i.e., receiver operating curve) for accent detection on the training and test data are shown in Fig. 2. Equal error detection rates are about 74.4% for the training set and 70.4% for the test set using all the measurements. The detection rate using only pause, rate, and amplitude (dur+rms) is 71.1%. This curve is included as a baseline to compare the results of including the pitch, harmonic, and spectral tilt measurements. For the case

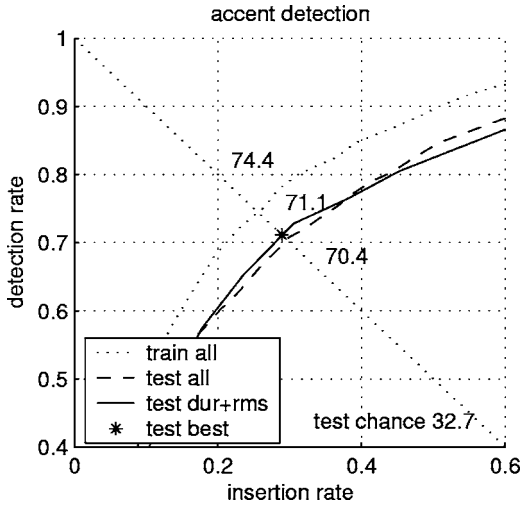

FIG. 2. Detection rate versus insertion rate for accent detection. The diagonal dotted line indicates equal error. Using 23 voice source measurements, equal error detection rates are about 74.4% and 70.4% for the training and test sets, respectively. A best detection rate of 71.1% is obtained using a selected subset of the measurements, and chance is 32.7%, for the test set. A baseline detection rate of 71.1% is obtained using only pause, rate, and amplitude measurements. For accent detection, the baseline and best detection rates are the same.

of accent detection, the baseline performance using dur+rms was better than the results using additional measurements.

The results for detecting both IP and ip boundaries on the training and test data are shown in Fig. 3. Equal error detection rates are about 75.3% and 69.0% for the training and test sets, respectively. The dur+rms detection rate is 69.4%. Finally, as shown in Fig. 4(c), for IP boundary detection, equal error detection rates are about 79.8% and 74.2% for the training and test sets, respectively, with a dur+rms detection rate of 73.7%. For the IP+ip and IP boundary de-

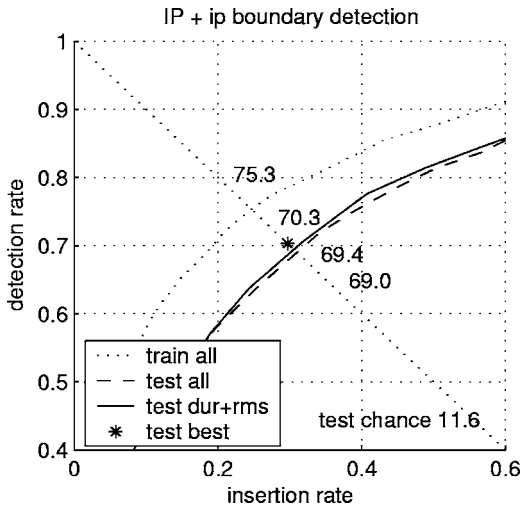

FIG. 3. Detection rate versus insertion rate for IP+ip boundary detection. The diagonal dotted line indicates equal error. Using 23 voice source measurements, equal error detection rates are about 75.3% and 69.0% for the training and test sets, respectively. A best detection rate of 70.3% is obtained using a selected subset of the measurements, and chance is 11.6%, for the test set. A baseline detection rate of 69.4% is obtained using only pause, rate, and amplitude measurements.

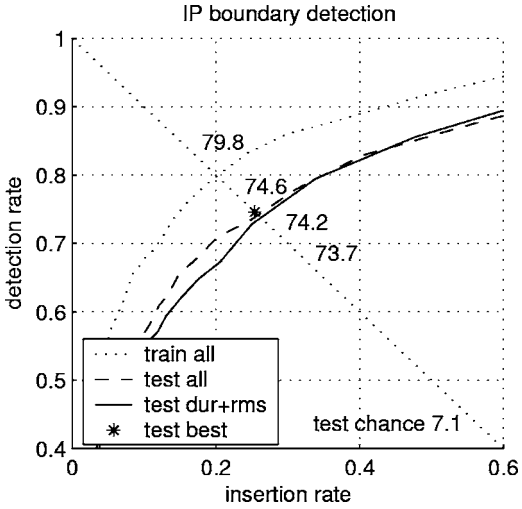

FIG. 4. Detection rate versus insertion rate for IP boundary detection. The diagonal dotted line indicates equal error. Using 23 voice source measurements, equal error detection rates are about 79.8% and 74.2% for the training and test sets, respectively. A best detection rate of 74.6% is obtained using a selected subset of the measurements, and chance is 7.1%, for the test set. A baseline detection rate of 73.7% is obtained using only pause, rate, and amplitude measurements.

tection experiments, using additional measurements results in improved detection rates, compared to the dur+rms detection rates.

To further explore the contributions from various components, detection experiments were carried out using subsets of the 23 voice source measurements. Equal error detection rates for the various subsets are shown in Table III for detection of accent, IP+ip boundary detection, and IP boundary detection. The dur subset (1) includes pause length and speech rate; the rms subset (2) includes end rms, rms slope, and rms convexity; and the pitch subset (3) includes end f0, f0 slope, f0 convexity, end nf0, nf0 slope, and nf0 convexity. The harms subset (4) includes end $h1$-$h2$, $h1$-$h2$ slope, and $h1$-$h2$ convexity, while the tilt subset (5) includes end value, slope and convexity of h1-a1, h1-a3, and a1-a3 measurements. These subsets (i.e., dur, rms, pitch, harms, tilt) were considered the basic component subsets. The harms and tilt subsets were further combined into the glottal subset (6).

From the table, minimum detection rates using the basic component subsets occurred for the tilt, pitch, and harms subsets for accent, IP+ip, and IP detection, respectively. Maximum detection rates were found for the dur subset for all tasks, showing that using pause length and speech rate gives detection rates that approach detection rates using all measurements. For IP+ip and IP boundary detection, pitch and harms measurements are the least useful, while tilt information seems to be somewhat useful. Combining harms and tilt measurements into the glottal subset leads to improvement in detection rates for all three tasks.

Adding glottal measurements to the dur, rms, and pitch subsets (subsets 7–9) increases detection rates for accent detection. However, adding pitch measurements to the glottal measurements decreases performance. Combining basic component subsets (10–12) again results in better detection rates for accent detection, and worse detection rates for IP +ip and IP boundary detection when pitch measurements are

TABLE III. Equal error detection rates using subsets of the 23 voice source measurements for accent, IP+ip, and IP boundary detection. The numbers in parentheses next to the subset names indicate the number of measurements included. Minimum detection rates for each task are shown in boldface; maximum detection rates are shown in underlined boldface. The numbers in parentheses next to the detection rates show minimum detection rate changes from component subsets. A negative number indicates a worse detection rate than a component subset.

Subset	acc	IP+ip	IP
1 **d**ur (2)	66.6	68.6	71.7
2 **r**ms (3)	65.5	62.2	68.0
3 **p**itch (6)	63.2	**51.7**	**55.9**
4 harms (3)	61.8	57.2	**55.8**
5 tilt (9)	**61.0**	61.2	60.2
6 **g**lottal (12)	64.0(2.2)	62.6(1.4)	62.3(2.1)
7 **d+g** (14)	67.4(0.8)	69.7(1.1)	72.9(1.2)
8 **r+g** (15)	69.3(3.8)	65.6(3.0)	67.6(−0.4)
9 **p+g** (18)	67.3(3.3)	56.7(−5.9)	58.8(−3.5)
10 **d+r** (5)	**71.1**(4.5)	69.4(0.8)	73.7(2.0)
11 **d+p** (8)	69.0(2.4)	65.6(−3.0)	72.3(0.6)
12 **r+p** (9)	67.2(1.7)	55.4(−6.8)	58.8(−9.2)
13 **d+r+g** (17)	70.3(−0.8)	**70.3**(0.6)	**74.6**(0.9)
14 **d+p+g** (20)	69.4(0.4)	68.4(−1.3)	73.3(0.4)
15 **r+p+g** (21)	68.6(−0.7)	59.1(−6.5)	60.4(−7.6)
16 **d+r+p** (11)	70.7(−0.4)	67.4(−2.0)	73.8(0.1)
17 all (23)	70.4(−0.7)	69.0(−1.3)	74.2(−0.4)

added. The best detection rate for accent detection is obtained using dur and rms measurements only, as shown above in Fig. 2. Further addition of glottal measurements (13–15) show slight decrease in performance for accent detection, but produce the best results for IP+ip and IP boundary detection, using dur, rms, and glottal measurements. Finally, combining dur, rms, and pitch information results in better performance for only IP boundary detection, and using all 23 measurements provides somewhat suboptimal results compared to using only a selected subset of measurements.

The results of the table seem to indicate that duration and rms measurements (and to a lesser degree, pitch measurements) are most useful for accent detection, while IP +ip and IP boundary detection benefit from all measurements except pitch measurements.

Next, the errors for each detection task were further examined for each of the six broad prosodic categories, and the results are listed in Table IV. In accent detection, the highest

TABLE IV. Error analysis of six prosodic categories for three types of detection tasks. Each column lists detection error rates for neutral (0), accented (A), intermediate boundary (ip), accented intermediate boundary (Aip), intonational boundary (IP), and accented intonational boundary (AIP) tokens, respectively. The tasks are detection of accent, boundary (IP+ip), and IP boundaries.

Task	0	A	ip	Aip	IP	AIP
acc	27.5	31.2	44.4	18.2	49.3	9.9
IP+ip	26.0	36.5	56.2	34.7	27.2	10.7
IP	13.2	12.2	20.2	33.1	40.9	26.5

error rates are found for ip and IP syllables, and the lowest for AIP syllables. These results show that unaccented syllables at boundaries have a slight tendency to be mislabeled as accented. For IP+ip boundary detection, the highest error rates are for ip, A, and Aip syllables, i.e., intermediate boundary syllables and accented nonboundary syllables are more difficult to classify correctly as occurring at a boundary. The least error rate is found for accented intonational boundary syllables. For IP boundary detection, the largest error rate occurs for IP and Aip syllables—unaccented intonational boundary and accented intermediate boundary syllables were the most difficult to recognize correctly.

IV. SUMMARY AND DISCUSSION

In this paper, acoustic cues related to the voice source, including harmonic structure and spectral tilt, were examined in detecting prosodic events, in particular, intonational boundaries. The measurements comprise five categories: duration, pitch, harmonic structure, spectral tilt, and amplitude.

Distributions and statistical analysis of the measurements from the analysis data show that the following pause length increases at intonational boundaries, and speech rate decreases in the presence of both accents and boundaries. Pitch tends to fall for L- and L-L% boundaries and rise for H- and H-H% boundaries. These results are in agreement with previous studies on the relationship between durational and pitch measurements on prosody.[12–14] Pitch also tends to rise for accents, probably due to the dominant number of H^* type accents in this corpus. Further investigation for different types of accents will be needed to accurately correlate the effect of accent on pitch, since f0 cues for different types of boundary tones differ, and thus should be better modeled with a mixture, rather than a single distribution. Although the absolute and normalized f0 measures of this study both seem to be useful for finding accents, more detailed normalization techniques that take into account phone identity or average local f0 values may provide better results.

Two harmonic structure measurements, end $h1$-$h2$ and $h1$-$h2$ convexity, were useful for finding boundaries. Spectral tilt measurements end $h1$-$a1$, $h1$-$a1$ convexity, and end $a1$-$a3$ were also good indicators for boundaries. However, no harmonic structure measurement was significant in discriminating accented from nonaccented syllables, and of the spectral tilt measurements, only $a1$-$a3$ convexity was useful. In the analysis set for this study, the accented syllables at boundaries showed smaller values of $h1$-$h2$ and spectral measurements, which indicated more laryngealized or creaky voicing, than unaccented syllables. Pitch measurements were similar for accented and unaccented syllables at boundaries. However, compared to nonboundary unaccented syllables, nonboundary accented syllables showed greater $h1$-$h2$ and spectral tilt measurements (less creaky) but with much higher pitch values. This result seems to indicate that, in general, syllables at boundaries are more creaky than syllables that are not at boundaries, and the presence of an accent reinforces creakiness at boundaries, but the higher pitch associated with an accent for nonboundary syllables results in less creaky accented syllables, compared with unaccented nonboundary syllables. Finally, amplitude measurements were larger for accented syllables, and smaller for boundary syllables. Compared to duration, pitch, and amplitude measurements, harmonic and spectral tilt measurements exhibited small but significant effects.

Using the 23 acoustic measurements related to the voice source, detection experiments showed equal error rates around 70% detection for accent recognition. Finding both intermediate and intonational boundaries resulted in around 69% detection, and finding intonational boundaries yielded around 74% detection. Using subsets of the 23 voice source measurements shows that duration and amplitude measurements, and to a lesser degree, pitch measurements, are most useful for accent detection, while all measurements except pitch measurements are useful for finding intermediate and intonational boundaries. Analysis of the errors indicates that syllables at boundaries are more easily misclassified as accented. Also, compared to intonational boundary syllables, intermediate boundary syllables are more susceptible to being misclassified as nonboundary syllables.

In this paper, measurements for voice source characteristics were made over single syllables. Further studies will focus on extending the window of analysis to include two and three syllables, to examine the effect of longer-term changes in the source acoustic cues. Experiments with the Switchboard Telephone Speech Corpus[19] of spontaneous speech are also planned, to examine whether the results of this study will generalize to a more natural style of speech.

ACKNOWLEDGMENTS

The authors would like to thank Ken Chen for providing the pitch normalization algorithm, Taejin Yoon for help with statistical analysis, and Janet Slifka for valuable discussions. This work was supported by a grant from the University of Illinois Critical Research Initiative.

[1]V. Auberge, N. Audibert, and A. Rilliard, "Acoustic morphology of expressive speech: What about contours?" *Proceedings of Speech Prosody 2004*, Nara, Japan (2004), pp. 201–204; http://www.isca-speech.org/archive/sp2004/index.html

[2]Y. Xu, C. Xu, and X. Sun, "On the temporal domain of focus," *Proceedings of Speech Prosody 2004*, Nara, Japan (2004), pp. 81–84; http://www.isca-speech.org/archive/sp2004/index.html

[3]P. J. Price, M. Ostendorf, S. Shattuck-Hufnagel, and C. Fong, "The use of prosody in syntactic disambiguation," J. Acoust. Soc. Am. **90**, 2956–2970 (1991).

[4]D. Hirst, "The phonology and phonetics of speech prosody: Between acoustics and interpretation," *Proceedings of Speech Prosody 2004*, Nara, Japan (2004), 163–169; http://www.isca-speech.org/archive/sp2004/index.html

[5]M. Beckman and G. Ayers, "Guidelines for TOBI labeling (version 3.0)," The Ohio State University (1997).

[6]L. Larkey, "Reiterant speech: An acoustic and perceptual validation," J. Acoust. Soc. Am. **73**, 1337–1345 (1983).

[7]K. N. Stevens, *Acoustic Phonetics* (Massachusetts Institute of Technology, Cambridge, MA, 1998).

[8]D. H. Klatt and L. C. Klatt, "Analysis, synthesis, and perception of voice quality variations among female and male talkers," J. Acoust. Soc. Am. **87**, 820–857 (1990).

[9]S. Chavarria, T. Yoon, J. Cole, and M. Hasegawa-Johnson, "Acoustic differentiation of ip and IP boundary levels: Comparison of L- and L-L% in the Switchboard corpus," *Proceedings of Speech Prosody 2004*, Nara, Japan (2004), pp. 333–336; http://www.isca-speech.org/archive/sp2004/index.html

[10]J. Slifka, "Respiratory constraints on speech production at prosodic boundaries," Ph.D. dissertation, Massachusetts Institute of Technology, Cambridge, MA, 2000.
[11]J. Pierrehumbert and D. Talkin, "Lenition of /h/ and glottal stop," in *Papers in Laboratory Phonology II: Gesture, Segment, Prosody*, edited by G. Doherty and D. R. Ladd (Cambridge University Press, Cambridge, UK, 1992), pp. 90–119.
[12]C. Wightman, S. Shattuck-Hufnagel, M. Ostendorf, and P. Price. "Segmental durations in the vicinity of prosodic phrase boundaries," J. Acoust. Soc. Am. **91**, 1707–1717 (1992).
[13]A. E. Turk, and L. White, "Structural influences on accentual lengthening in English," J. Phonetics **27**, 171–206 (1990).
[14]J. Edwards, M. Beckman, and J. Fletcher, "The articulatory kinematics of final lengthening," J. Acoust. Soc. Am. **89**, 369–382 (1991).
[15]M. Ostendorf, P. J. Price, and S. Shattuck-Hufnagel, "The Boston University Radio Speech Corpus," Linguistic Data Consortium (1995); http://www.ldc.upenn.edu/Catalog/LDC96S36.html
[16]Entropic Research Laboratory, Inc., *xwaves+manual* (1996).
[17]K. Chen, M. Hasegawa-Johnson, A. Cohen, and J. Cole, "A maximum likelihood prosody recognizer," *Proceedings of Speech Prosody 2004*, Nara, Japan (2004), pp. 509–512; http://www.isca-speech.org/archive/sp2004/index.html
[18]K. Sonmez, E. Shriberg, L. Heck, and M. Weintraub, "Modeling dynamic prosodic variation for speaker verification," *Proceedings of Int. Conf. on Spoken Lang. Proc. 1998*, Sydney, Australia (1998), pp. 3189–3192.
[19]J. J. Godfrey and E. Holliman. "The Switchboard-1 Telephone Speech Corpus Release 2," Linguistic Data Consortium (1997); http://www.ldc.upenn.edu/Catalog/LDC97S62.html

Effects of cochlear hearing loss on perceptual grouping cues in competing-vowel perception

Jessica A. Rossi-Katz and Kathryn Hoberg Arehart
Department of Speech, Language and Hearing Sciences, University of Colorado at Boulder, Boulder, Colorado 80309-0409

(Received 15 December 2004; revised 10 July 2005; accepted 14 July 2005)

This study compared how normal-hearing listeners (NH) and listeners with moderate to moderately severe cochlear hearing loss (HI) use and combine information within and across frequency regions in the perceptual separation of competing vowels with fundamental frequency differences (ΔF_0) ranging from 0 to 9 semitones. Following the procedure of Culling and Darwin [J. Acoust. Soc. Am. **93**, 3454–3467 (1993)], eight NH listeners and eight HI listeners identified competing vowels with either a consistent or inconsistent harmonic structure. Vowels were amplified to assure audibility for HI listeners. The contribution of frequency region depended on the value of ΔF_0 between the competing vowels. When ΔF_0 was small, both groups of listeners effectively utilized ΔF_0 cues in the low-frequency region. In contrast, HI listeners derived significantly less benefit than NH listeners from ΔF_0 cues conveyed by the high-frequency region at small ΔF_0's. At larger ΔF_0's, both groups combined ΔF_0 cues from the low and high formant-frequency regions. Cochlear impairment appears to negatively impact the ability to use F_0 cues for within-formant grouping in the high-frequency region. However, cochlear loss does not appear to disrupt the ability to use within-formant F_0 cues in the low-frequency region or to group F_0 cues across formant regions.
 [DOI: 10.1121/1.2031975]

PACS number(s): 43.71.Es, 43.71.Ky [PFA] Pages: 2588–2598

I. INTRODUCTION

Listeners with cochlear hearing loss have considerable difficulty understanding speech in the presence of background noise, especially when the background noise is competing speech (e.g., Festen and Plomp, 1990). This difficulty has been linked to reductions in audibility and to spectro-temporal processing deficits associated with cochlear hearing loss (for a detailed review, see Moore, 1995). Although these deficits are associated with listeners' degraded performance on competing speech tasks (e.g., Dreschler and Plomp, 1980, 1985; Glasberg and Moore, 1989), it is not completely understood how these deficits impact the usefulness of cues in perceptual organization (e.g., Bregman, 1990; Darwin and Carlyon, 1995). The present study considers how cochlear hearing loss influences the use of fundamental frequency cues in the perceptual separation of two simultaneously presented vowels (i.e., double vowels).

In listeners with normal hearing, differences in fundamental frequency (ΔF_0) facilitate the perceptual separation of competing voices. Brokx and Nootebom (1982) reported that recognition of monotone competing sentences was 40% when ΔF_0 was 0 semitones (ST) and increased to 60% when ΔF_0 was 3 ST. Others have shown that listeners' identification of competing sentences continues to improve for even larger ΔF_0's (Bird and Darwin, 1998; Summers and Leek, 1998). In contrast to competing-sentence identification, improvements in double-vowel identification are constrained to a narrow range of ΔF_0's. Specifically, normal-hearing listeners show the greatest ΔF_0 benefit for values of ΔF_0 below 2 ST, above which identification levels off (e.g., Assmann and Summerfield, 1990; Culling and Darwin, 1993; Scheffers, 1983). The different patterns of benefit may reflect differences in how ΔF_0 cues are used in the perceptual separation of vowels and sentences. The patterns of benefit may also be affected by differences in experimental design (e.g., restricting listeners' responses to a set number of alternatives as well as the complexity and predictability of the speech materials).

Past studies have measured how listeners with hearing loss use ΔF_0 cues in the perceptual separation of competing sentences and vowels (Arehart, 1998; Arehart *et al.*, 1997, 2005; Stubbs and Summerfield, 1988; Summers and Leek, 1998). In competing-sentence perception, Summers and Leek (1998) demonstrated that ΔF_0 benefit was similar in listeners with and without hearing loss for smaller but not for larger values of ΔF_0. Average identification of competing sentences for the hearing-impaired listeners improved as ΔF_0 increased from 0 to 2 ST; however, beyond 2 ST performance did not improve. In contrast, normal-hearing listeners showed comparable improvements (~10 percentage points) in sentence identification between 0 and 2 ST and between 2 and 4 ST.

Identification of competing vowels is typically worse in listeners with hearing loss, due in part to increased susceptibility to masking (Arehart *et al.*, 2005). Despite degraded identification, listeners with hearing loss show improved double-vowel perception as ΔF_0 increases. The amount of ΔF_0 benefit varies among studies and experimental procedures. In some studies, listeners with hearing loss show ΔF_0 benefit that is comparable to that in listeners with normal hearing (Arehart *et al.*, 1997, 2005). In other studies (Summers and Leek, 1998) and in other experimental paradigms (Arehart *et al.*, 1997—masked vowel task), listeners with

 0001-4966/2005/118(4)/2588/11/$22.50

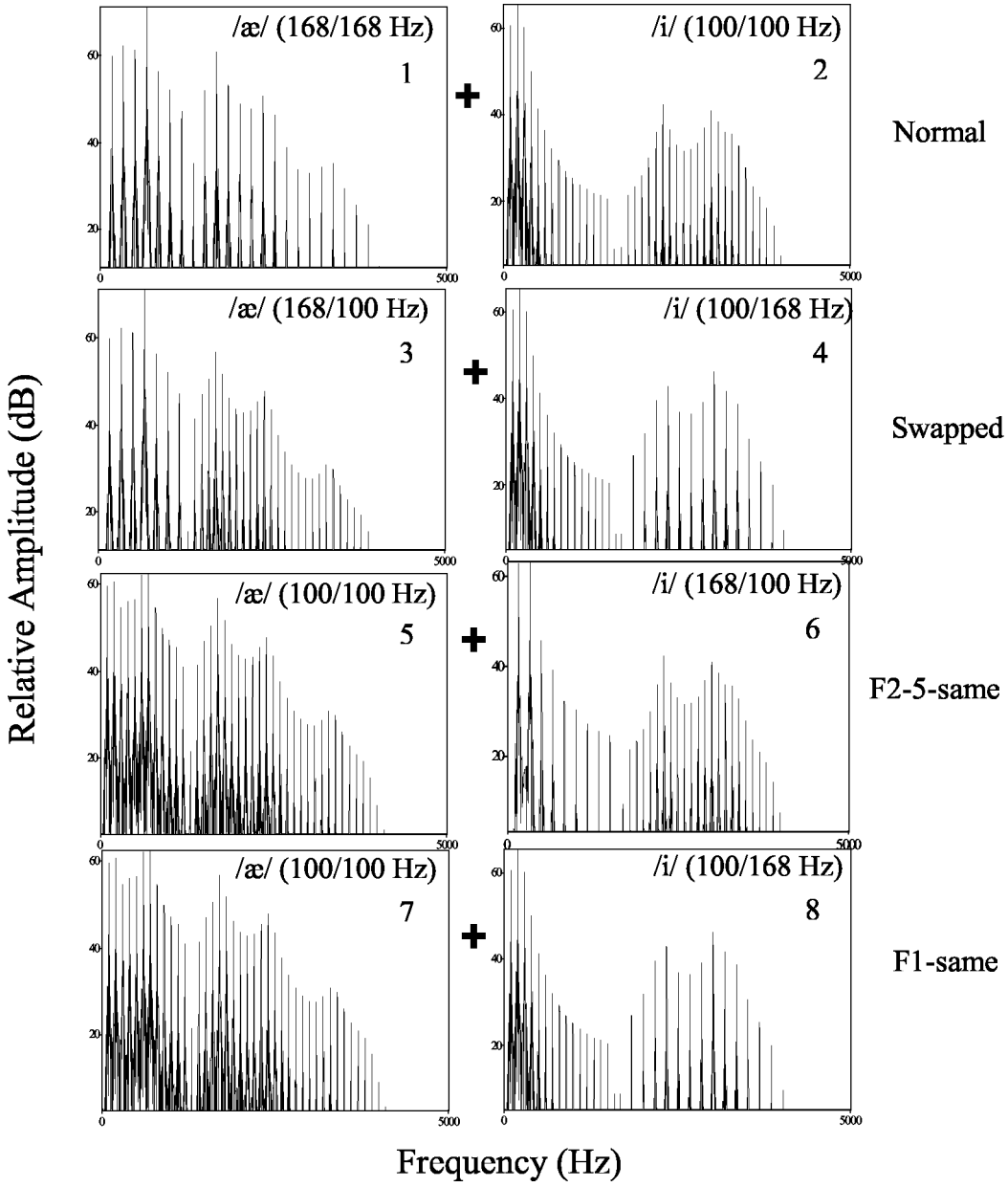

FIG. 1. Amplitude spectra of two competing vowels (left column: æ and right column: /i/) for each of the four experimental conditions (first row: normal condition; second row: swapped condition; third row: F2-5-same condition; fourth row: F1-same condition). In each panel (1–8), the values in parentheses correspond to the F_0's of the first formant-frequency region and the higher formant-frequency region, respectively.

hearing loss show reduced ΔF_0 benefit. To gain further insight into how hearing loss impacts the usefulness of ΔF_0 cues, this study investigates how restricting ΔF_0 cues to the low- and/or high-frequency regions may impact double-vowel perception in listeners with hearing loss.

Culling and Darwin (1993) explored the role of frequency region in ΔF_0 benefit in normal-hearing listeners. Using a clever twist on the standard double-vowel paradigm, they investigated how listeners use and combine ΔF_0 cues within and across formant-frequency regions. Culling and Darwin used "misleading" double vowels: in some stimuli, the F_0 was consistent across the constituent vowels' formants (Fig. 1: panels 1, 2, 5, 7); in others, the F_0 was inconsistent across the constituent vowels' formants (Fig. 1: panels 3, 4, 6, 8). Although introducing F_0 inconsistencies across the constituent vowels' formants would likely disrupt processes that rely on combining F_0 information from the low and high formant-frequency regions, ΔF_0 cues may still be preserved within a formant-frequency region (i.e., the first formant-frequency region and/or the higher formant-frequency region). Table I presents how three variations on the F_0-inconsistent condition either preserve or eliminate ΔF_0 cues in the low- and high-frequency regions, respectively. On the basis of listeners' pattern of ΔF_0 benefit for the F_0-consistent and the F_0-inconsistent conditions, Culling and Darwin inferred the relative contributions of the low- and high-frequency regions to improvements in double-vowel identification with increasing ΔF_0. A key finding was that the contribution of frequency region depended on the value of ΔF_0 between the competing vowels.

When ΔF_0 is small (up to 2 ST), the primary cues in the perceptual separation of competing vowels are within the

TABLE I. Following Culling and Darwin (1993), the availability of ΔF_0 cues in the low and high formant-frequency regions, respectively, associated with an experimental condition. The presumed effect of condition on across-formant grouping is also presented. Note: The experimental labels are from the current study. The corresponding conditions in Culling and Darwin (1993) are labeled: normal; F_0-swapped; same F_0 for F2-5; and same F_0 for F1, respectively.

Experimental condition	Potential cues
F_0 consistent[a]	
Normal	ΔF_0 cues preserved in both low and high formant-frequency regions. Permits across-formant grouping.
F_0 inconsistent[b]	
Swapped	ΔF_0 cues preserved in both low and high formant-frequency regions. Across-formant grouping presumed to be disrupted.
F2-5-same	ΔF_0 cues limited to the low formant-frequency region. Across-formant grouping presumed to be disrupted.
F1-same	ΔF_0 cues limited to the high formant-frequency region. Across-formant grouping presumed to be disrupted.

[a]In both of the constituent vowels, the F_0 of the first formant-frequency region was consistent with the F_0 of the higher formant-frequency region.
[b]In either both or one of the constituent vowels, the F_0 of the first formant-frequency region was inconsistent with the F_0 of the higher formant-frequency region.

low-frequency region (Culling and Darwin, 1993). Two different processes may potentially explain how normal-hearing listeners exploit these low-frequency cues. First, listeners may rely on a process of F_0-guided segregation whereby F_0 is estimated from spectral and temporal information within the low-frequency channels (e.g., Assmann and Summerfield, 1990; Meddis and Hewitt, 1992). de Cheveigné (1999) provided evidence that an F_0-guided segregation mechanism can explain performance at small ΔF_0's, although it would operate less effectively than at larger ΔF_0's. In F_0-guided segregation, a vowel would be separated from its competitor by grouping together the components that share a common F_0. Culling and Darwin (1993) suggested that this process may help parse a composite formant peak (e.g., first formant) in the combined spectral envelope into the formant peaks of the constituent vowels.

An alternative explanation is that for small values of ΔF_0, grouping low-frequency components based on harmonicity may not be necessary. Waveform interactions or beating between adjacent low-frequency components may mediate double-vowel identification for ΔF_0's less than 1 ST (Assmann and Summerfield, 1994; Culling and Darwin, 1994). The fluctuations caused by beating may result in evidence of each vowel being more readily discerned during various points in the stimulus waveform. In addition, the beating would be most perceptible from the outputs of the low-frequency auditory filters because of constraints imposed by the frequency spacing of harmonics relative to the auditory filter bandwidths (Assmann and Summerfield, 1994; de Cheveigné, 1999).

At larger ΔF_0's, normal-hearing listeners combine ΔF_0 cues from the low- and high-frequency regions in the perceptual separation of competing vowels (Culling and Darwin, 1993). That is, formants from different frequency regions are grouped based on a common F_0. This process of "across-formant grouping" (cf. Broadbent and Ladefoged, 1957) assumes an F_0-guided segregation mechanism in which F_0 is estimated within and across low- and high-frequency channels (e.g., Assmann and Summerfield, 1990; Meddis and Hewitt, 1992).

To the extent that listeners employ an F_0-guided segregation strategy in the separation of competing vowels, it is expected that ΔF_0 benefit would be associated with other measures that are mediated by F_0 estimation. Support for this assumption comes from the finding that the ability to discriminate F_0 differences among sequential vowel stimuli is positively correlated with ΔF_0 benefit in double-vowel identification in both normal-hearing and hearing-impaired listeners (Summers and Leek, 1998).

Similarly, difference limens for complex-tone F_0 discrimination (F_0DLs) are consistent with the contribution of frequency region to ΔF_0 benefit at small and large ΔF_0's. In normal-hearing listeners, F_0DLs are substantially smaller for stimuli containing lower-order resolved harmonics compared to stimuli containing higher-order unresolved harmonics (e.g., Houtsma and Smurzynski, 1990).[1] These results, together with those of Culling and Darwin (1993) described above, indicate that F_0 estimation is facilitated best by cues from low frequencies for both complex-tone discrimination and for double-vowel identification. Furthermore, listeners combine cues from low- and high-frequency regions for both complex-tone discrimination (Carlyon *et al.*, 1992) and for double-vowel identification (Culling and Darwin, 1993), presumably because of the greater ΔF_0's required for F_0 estimation for unresolved higher-frequency harmonics.

To the extent that F_0DLs reflect limitations on the ability to derive estimates of F_0, we hypothesize that the contribution of the low- and high-frequency regions to ΔF_0 benefit will differ in hearing-impaired listeners. In comparison to F_0DLs in listeners with normal hearing, listeners with hearing loss generally show elevated F_0DLs in both the low and high frequencies (Arehart, 1994; Moore and Peters, 1992). In Arehart (1994), the average F_0DLs in listeners with hearing loss exceeded 10 Hz for both lower- and higher-order harmonic stimuli (in contrast, the average F_0DLs of the normal-hearing listeners were 1 Hz for low-order harmonics and 5.8 Hz for higher-order harmonics). When the ΔF_0 between competing vowels is small, ΔF_0 cues might not be discernible in the low- or high-frequency regions (e.g., at ΔF_0 equal to 1 ST, the difference in F_0 corresponds to 6 Hz *re*: 100 Hz F_0).

The purpose of the present study was to compare how normal-hearing and hearing-impaired listeners use and combine information within and across frequency regions in double-vowel identification for small and large values of ΔF_0. To investigate the effects of frequency region on ΔF_0

TABLE II. Audiometric thresholds (in dB HL) for listeners with hearing loss. Note: Asterisks indicate test ear; NR indicates no response.

			Frequency					
Listener	Age	Ear	250 Hz	500 Hz	1 KHz	2 KHz	4 KHz	6 KHz
HI1	23	R	25	30	50	65	65	60
		L*	30	35	50	65	60	55
HI2	48	R*	15	25	25	30	50	55
		L	15	25	25	30	50	60
HI3	50	R	15	10	10	30	30	25
		L*	20	10	10	35	35	25
HI4	46	R*	30	20	35	55	105	NR
		L	20	35	50	70	105	NR
HI5	81	R	40	20	15	75	70	65
		L*	30	20	25	60	65	65
HI6	42	R*	20	30	55	60	75	65
		L	25	30	60	80	70	60
HI7	23	R	35	35	45	60	55	45
		L*	30	30	35	55	50	50
H18	26	R*	15	10	10	35	40	55
		L	5	5	15	30	40	50

benefit, a paradigm similar to Culling and Darwin (1993) was used in which F_0 inconsistencies were introduced among the constituents of the double vowel. We predicted that the greatest difference in the contribution of frequency region between the listener groups will be observed at small values of ΔF_0.

II. METHOD

A. Listeners

Participants in this study included eight listeners with normal hearing (mean age=31 years old; age range =22–47 years) and eight listeners with hearing loss of presumed cochlear origin (mean age=42 years old; age range =23–81 years). Normal hearing is defined here as thresholds of 15 dB HL (ANSI, 1989) or better at octave frequencies from 250 to 8000 Hz, inclusive. Listeners underwent an audiometric evaluation during their initial visit. All of the listeners with hearing loss demonstrated test results that were consistent with cochlear impairment: normal tympanometry, absence of excessive reflex decay, absence of air-bone gap exceeding 10 dB at any frequency, and absence of otoacoustic emissions in regions of threshold loss. Table II provides a summary of the audiometric thresholds of the listeners with hearing loss. All participants were recruited from the Boulder/Denver metro area and were native speakers of American English.

All listeners were tested monaurally and individually in a double-walled sound-treated booth. In listeners with hearing loss, the test ear was selected so that thresholds approximated a moderate degree of hearing loss. Listeners were compensated $10/hour for their participation.

B. Stimuli

Double-vowel stimuli used in this experiment were created by adding together two single vowels. The single vowels included five vowels of American English: /u/ as in who'd, /i/ as in heed, /ɝ/ as in herd, /æ/ as in had, and /ɛ/ as in head. Single vowels were synthesized using Sensimetrics cascade formant software (Klatt, 1980) with a sampling rate of 20 Hz and a 16-bit quantization. Table III shows the formant frequencies of the single vowels; the first three formants were based on averages for adult males as published by Peterson and Barney (1952). Single vowels were generated with an F_0 of 100 Hz+ΔF_0, where ΔF_0 ranged from 0 to 9 ST. Seven values of ΔF_0 were included in this study (Table IV). The single vowels were 500 ms in duration, which in-

TABLE III. Formant frequencies (in Hz) for vowels. Note: Values in parentheses represent formant bandwidths (in Hz).

	/u/	/i/	/ɝ/	/æ/	/ɛ/
F1 (90)	250	270	730	660	530
F2 (110)	850	2290	1090	1720	1840
F3 (170)	2250	3010	2440	2410	2480
F4 (250)	3350	3350	3350	3350	3350
F5 (300)	3850	3850	3850	3850	3850

TABLE IV. Differences in fundamental frequency between the two constituent vowels.

ΔF_0 (in semitones) *re*: 100 Hz	F_0 (in Hz)
0	100.0
$\frac{1}{2}$	102.9
1	106.0
2	112.3
4	126.0
6	141.4
9	168.2

cluded a 20-ms rise-fall time. A single vowel had either a consistent harmonic structure across its formants or an inconsistent harmonic structure between the first formant-frequency region and the higher formant-frequency region (i.e. second through fifth formants). Following Culling and Darwin (1993), the following procedure was employed to create single vowels with either a consistent or inconsistent harmonic structure.

Each vowel was digitally filtered with 256-point linear-phase finite impulse response (FIR) filters to create two half vowels. That is, an original vowel was low-pass filtered to include the harmonics in the first formant-frequency region and high-pass filtered to include the harmonics in the higher formant-frequency region. The cutoff frequencies for the five original vowels were selected to coincide with a dip in the vowel's spectrum between the first and second formant. The five cutoff frequencies were /u/=600 Hz, /i/=1650 Hz, /ɜ˞/=1000 Hz, /æ/=1300 Hz, and /ɛ/=1350 Hz. The original vowels were filtered with a high-pass filter that was 50 Hz greater than the selected cutoff frequency and a low-pass filter that was 50 Hz less than the selected cutoff frequency. This 100-Hz region around the cutoff frequency was employed to ensure that there were not spectral modulations when the half vowels were added together (see Culling and Darwin, 1993).

Half vowels were combined into processed single vowels. Processed single vowels were created by digitally adding the vowel's first formant-frequency region with its higher formant-frequency region. The harmonic structure of the processed vowel was either consistent or inconsistent across its formant frequencies. For example, in the consistent condition, if the vowel /i/ had an underlying harmonic spacing of 100 Hz in the first formant-frequency region, the harmonic spacing of the higher formant-frequency region would be 100 Hz. In the inconsistent condition, if the vowel /i/ had an underlying harmonic spacing of 100 Hz in the first formant-frequency region, the harmonic spacing of the higher formant-frequency region would be $100+\Delta F_0$ (where ΔF_0 ranges from 0.5 to 9 ST). Figure 1 shows the amplitude spectrum of single vowels with either a consistent harmonic structure (row 1) or an inconsistent harmonic structure (rows 2–4). For a given vowel, there were 14 possible single-vowel combinations ($7\ \Delta F_0$'s $\times 2$ formant-frequency regions). All processed single vowels were equated for root-mean-square (rms) amplitude.

Two processed single vowels (i.e., constituents), which differed in their phonetic identity, were combined for the double-vowel task. Four conditions were included in this study: normal, swapped, F2-5-same, and F1-same. Figure 1 shows sample amplitude spectra for each condition. The normal condition served as the control condition with a consistent harmonic structure across the constituent vowels' formants. In the swapped condition, the first formant-frequency region of a given constituent had the same F_0 as its competitor's higher formant-frequency region (and vice versa). In the F2-5-same condition, the ΔF_0 between the constituents was restricted to the first formant-frequency region. In the F1-same condition, the ΔF_0 between the constituents was restricted to the higher formant-frequency region. There were 140 unique stimuli for the normal and swapped conditions (10 different double vowels $\times 7\ \Delta F_0$'s $\times 2\ F_0$ combinations). There were 280 unique stimuli (10 different double vowels $\times 7\ \Delta F_0$'s $\times 4\ F_0$ combinations) for the F1-same and F2-5-same conditions.

Double vowels were presented at a level of 65 dB SPL to listeners with normal hearing. The 65-dB-SPL stimuli were amplified for each listener with hearing loss using a prescriptive formula based on individual thresholds (Byrne and Dillon, 1986). By way of example, a listener with a flat 50 dB HL hearing loss would receive approximately 22 dB of gain at 2000 Hz. The amplification was implemented through digital filtering (via a 128-point linear-phase FIR filter) prior to the experiment. Stimuli were customized for each individual listener and were stored on a personal computer prior to being played out over earphones.

C. Procedure

Double vowels were played out in the following way: two processed single vowels were routed separately through programmable attenuators (TDT PA5) and then combined in a mixer (TDT SM5). The stimuli were delivered to the listener's ear with a Telephonics TDH-49 earphone.

Listeners participated in four listening sessions. A session typically took one hour to complete. All conditions were evaluated within a session. For each block of trials, the stimulus condition (e.g., normal, swapped, F1-same, and F2-5-same) was fixed and all values of ΔF_0 were included. Within a block, the trials were presented in random order.

For each trial, listeners selected the two vowels they heard from a closed set of potential responses. A computer monitor displayed response buttons which were labeled with each vowel and an example word for that vowel (e.g., "ae as in 'had'"). Listeners had to make two unique selections (that is, a vowel could not be selected twice). No feedback was provided. Results were scored in terms of the percentage of trials in which both vowels were correctly identified. After training on the task, each listener participated in 80 experimental trials in each condition at each value of ΔF_0. Listeners received four repetitions of the normal and swapped conditions (4 repetitions $\times$ 140 trials) and two repetitions of the F1-same and F2-5-same conditions (2 repetitions $\times$ 280 trials).

Listeners had to identify single vowels with at least 90% accuracy. Listeners were assessed on this criterion prior to beginning data collection and at the start of each experimental session. Both F_0-consistent and F_0-inconsistent vowels were included in the single-vowel training to ensure that identification of single vowels was not influenced by (a) dips in the amplitude spectrum (corresponding to the regions at which the original vowels were split) and (b) inconsistencies in the single vowel's underlying harmonic structure. Feedback was provided after each single-vowel trial. Only one listener who was recruited to participate could not achieve the 90% single-vowel criterion and was not enrolled in the study. It appears that the spectral dips and the inconsistencies in harmonic structure did not influence phonetic identifica-

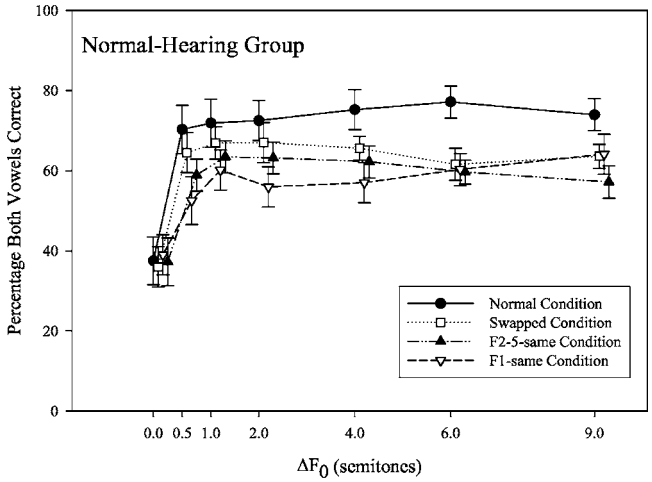

FIG. 2. Percentage of trials in which both vowels were correct is shown as a function of ΔF_0 for each of the experimental conditions in the NH group. Error bars represent ± one standard error of the mean.

tion of processed single vowels. Listeners also received at least one hour of training on the double-vowel task prior to data collection.

III. RESULTS

Average results for the group of listeners with normal hearing (NH group) and the group of listeners with cochlear hearing loss (HI group) are shown in Figs. 2 and 3, respectively. Percentage of trials in which both vowels were correctly identified is shown as a function of ΔF_0 in semitones for each of the four conditions. As summarized in Table V, a repeated-measures analysis of variance [using an arc-sine transform of the percent-correct scores (Studebaker, 1985)] showed significant within-subject main effects of ΔF_0 and condition. The between-subject main effect of group approached but did not reach statistical significance.

The significant within-subject main effect of condition indicates that double-vowel identification significantly differs among the F_0-consistent and F_0-inconsistent conditions. However, the group × condition interaction, which approached but did not reach statistical significance, suggests that the performance of the NH and HI groups may have differed for some but not all of the experimental conditions. To clarify the nature of these effects, separate repeated-measures ANOVAs were performed for each of the four conditions. This analysis investigated (a) whether double-vowel identification differed between the listener groups on conditions that either preserved or eliminated ΔF_0 cues in the low- and high-frequency regions, respectively (cf. Table I) and (b) if, on these conditions, listeners showed different patterns of ΔF_0 benefit (reflected in the $\Delta F_0 \times$ group interaction). The results of this analysis are described below and summarized in Table VI.

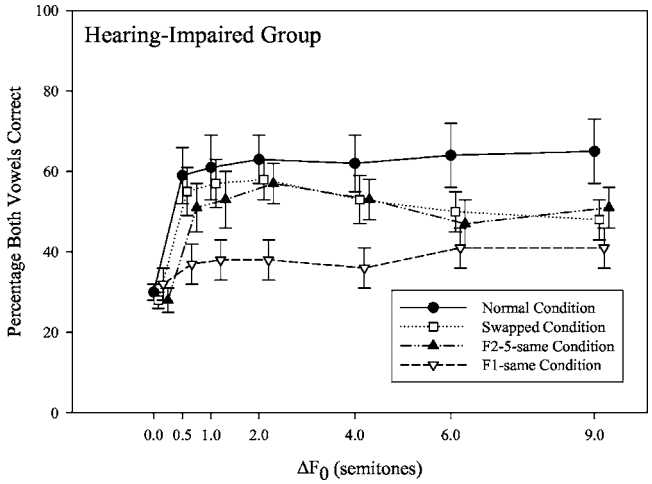

FIG. 3. Percentage of trials in which both vowels were correct is shown as a function of ΔF_0 for each of the experimental conditions in the HI group. Error bars represent ± one standard error of the mean.

TABLE V. Summary of repeated-measures ANOVA for arc-sine transformed percent-correct scores. Shown are the main effects.

Effect	df	*F*	Significance
Group	1,14	3.593	0.079
ΔF_0	6,84	70.886	<0.001
Condition	3,42	34.703	<0.001
Group × ΔF_0	6,84	1.066	0.389
Group × Condition	3,42	2.670	0.060
ΔF_0 × Condition	18,252	10.786	<0.001
Group × ΔF_0 × Condition	18,252	1.56	0.299

A. Normal condition

The NH and HI groups did not significantly differ in their identification of double vowels when the harmonic structure of the two constituent vowels was consistent. This finding was supported by the nonsignificant main effect of group in the normal condition (Table VI). A significant main effect of ΔF_0 was observed in both groups. The largest improvement in double-vowel identification (ΔF_0 benefit) was observed for small values of ΔF_0. Both groups showed poorest performance when ΔF_0 was 0 ST (mean-identification accuracy was 37% in the NH group and 30% in the HI group). As ΔF_0 increased from 0 to 0.5 ST, double-vowel identification improved by 33 percentage points in the NH group (37% to 70%) and by 29 percentage points in the HI group (30% to 59%). In both groups, ΔF_0 benefit began to

TABLE VI. Summary of repeated-measures ANOVA for arc-sine transformed percent-correct scores. Shown are the within- and between-subject effects for each of the four conditions.

Condition	Effect	df	*F*	Significance
Normal	Group	1,14	1.633	0.222
	ΔF_0	6,84	54.110	<0.001
	Group × ΔF_0	6,84	0.459	0.837
Swapped	Group	1,14	3.317	0.090
	ΔF_0	6,84	45.318	0.001
	Group × ΔF_0	6,84	0.626	0.709
F2-5-same	Group	1,14	2.260	0.155
	ΔF_0	6,84	31.485	0.001
	Group × ΔF_0	6,84	0.498	0.809
F1-same	Group	1,14	8.188	0.013
	ΔF_0	6,84	19.044	0.001
	Group × ΔF_0	6,84	4.220	0.001

asymptote when ΔF_0 was greater than 0.5 ST. The NH group achieved their maximum average score of 78% when ΔF_0 was 6 ST. The HI group achieved their maximum average score of 65% when ΔF_0 was 9 ST.

B. Swapped condition

The NH and HI groups did not significantly differ in their identification of double vowels when the harmonic structure across the constituent vowels was inconsistent. This finding was supported by the nonsignificant main effect of group in the swapped condition (Table VI). Both groups showed the largest improvements in identification accuracy for small values of ΔF_0. As ΔF_0 increased from 0 to 0.5 ST, double-vowel identification improved by 29 percentage points in the NH group (36% to 65%) and by 27 percentage points in the HI group (28% to 55%).

At larger values of ΔF_0, both the NH and HI groups showed a trend towards *decreasing* double-vowel identification when the harmonic structure of the constituent vowels was inconsistent. Therefore, above 2 ST, ΔF_0 cues were not advantageous. As shown in Fig. 2 (NH group) and in Fig. 3 (HI group), as ΔF_0 exceeded 2 ST, the discrepancy in identification scores between the normal (control) condition and the swapped condition increased. For example, scores between the normal and swapped conditions for the NH group differed by 6 percentage points (73% to 67%) when ΔF_0 equaled 2 ST. This difference increased to 15 percentage points when ΔF_0 equaled 6 ST (77% to 62%). In the HI group, when ΔF_0 equaled 2 ST, scores between the normal and swapped conditions differed by 5 percentage points (63% to 58%). This difference increased to 14 percentage points when ΔF_0 equaled 6 ST (64% to 50%).

C. F2-5-same condition

The NH and HI groups did not significantly differ in their identification of double vowels when ΔF_0 cues were restricted to the low-frequency region. This finding was supported by the nonsignificant main effect of group in the F2-5-same condition (Table VI). Both groups showed the largest improvements in identification accuracy for small values of ΔF_0. As ΔF_0 increased from 0 to 0.5 ST, identification accuracy improved by 22 percentage points in the NH group (37% to 59%) and by 23 percentage points in the HI group (28% to 51%).

When ΔF_0 cues were restricted to the low-frequency region, identification did not asymptote for the largest values of ΔF_0 included in this study (i.e., up to 9 ST). Both the NH and HI groups showed a trend towards *decreasing* performance such that further increases in ΔF_0 beyond 2 ST were detrimental to double-vowel identification. The extent to which identification differed between the normal (control) conditions and the F2-5-same condition was similar between the NH and HI groups. In the NH group, when ΔF_0 equaled 2 ST, scores between the normal and F2-5-same conditions differed by 10 percentage points (73% to 63%). This difference increased to 17 percentage points when ΔF_0 equaled 6 ST (77% to 60%). In the HI group, when ΔF_0 equaled 2 ST, the normal and F2-5-same conditions differed by 6 percentage points (63% to 57%). This difference increased to 17 percentage points when ΔF_0 equaled 6 ST (64% to 47%).

D. F1-same condition

The NH and HI groups significantly differed in their overall identification of double vowels when ΔF_0 cues were restricted to the higher-frequency region (i.e., second through fifth formants). This finding was supported by the significant main effect of group for the F1-same condition (Table VI). Both groups showed similar double-vowel identification when ΔF_0 was 0 ST: 39% in the NH group and 32% in the HI group. Double-vowel identification improved in the NH group by 19 percentage-points as ΔF_0 increased (collapsing across values of ΔF_0 larger than 0 ST). However, in the HI group, identification improved by only 7 percentage points with increased ΔF_0.

Consistent with the significant group $\times \Delta F_0$ interaction, the effect of ΔF_0 on double-vowel identification differed between the two groups. At increasing values of ΔF_0, double-vowel identification improved in the NH group. However, in the HI group, double-vowel identification remained flat across all ΔF_0's.

E. Across-condition comparisons

The results above suggest that at larger values of ΔF_0, the discrepancy in identification scores between the normal (control) condition and the swapped and F2-5-same conditions increased for both the NH and HI groups. To verify that the pattern of ΔF_0 benefit (improvement in identification accuracy as a function of ΔF_0) significantly differed between the F_0-consistent and F_0-inconsistent conditions, the effect of ΔF_0 on specific pairings of experimental conditions was examined. These focused analyses considered if the pattern of ΔF_0 benefit associated with a particular F_0-inconsistent condition significantly differed from that in the F_0-consistent condition [$\Delta F_0 \times$(paired) condition interaction]. These analyses investigated the extent to which introducing F_0 inconsistencies across a formant-frequency region influenced a listener's ability to use and combine ΔF_0 cues within and across frequency regions as a function of ΔF_0.

In both the NH and HI groups, the patterns of ΔF_0 benefit associated with the normal condition significantly differed from those associated with the swapped and F2-5-same conditions. This finding was supported by a repeated-measures ANOVA that showed a significant interaction between ΔF_0 and the normal versus swapped conditions (NH: $F_{6,42}=3.597$, $p=0.006$ and HI: $F_{6,42}=4.819$, $p=0.001$) and a significant interaction between ΔF_0 and the normal versus F2-5-same conditions (NH: $F_{6,42}=5.606$, $p<0.001$ and HI: $F_{6,42}=14.127$, $p=0.005$). For the normal, swapped and F2-5-same conditions, ΔF_0 benefit was greatest when ΔF_0 increased from 0 to 0.5 ST. However, further increases in ΔF_0 resulted in different patterns of ΔF_0 benefit between the conditions. In the normal condition, both listener groups showed stable performance with increased values of ΔF_0. Conversely, both listener groups showed a decline in double-vowel identification when ΔF_0 exceeded 2 ST in the swapped and F2-5-same conditions.

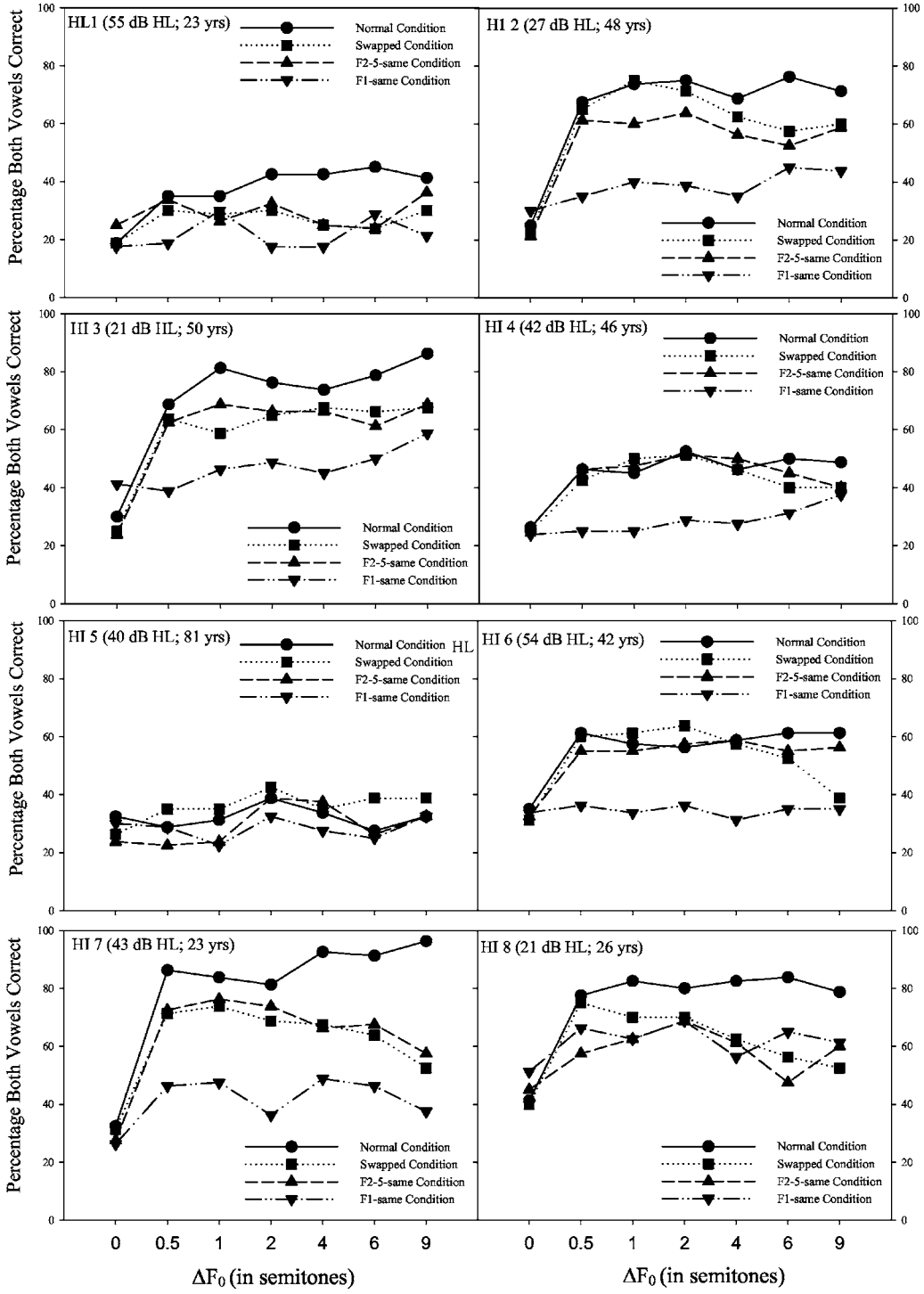

FIG. 4. Percentage of trials in which both vowels were correct is shown as a function of ΔF_0 for each of the experimental conditions in individual listeners with hearing loss. In each panel the values in parentheses correspond to the listener's average thresholds at 500, 1000, and 2000 Hz and the age of the listener, respectively.

The patterns of ΔF_0 benefit associated with the normal and F1-same conditions also differed in both listener groups. This finding was supported by a repeated-measures ANOVA that showed a significant interaction between ΔF_0 and the normal versus F1-same conditions in the NH group ($F_{6,42}=6.876$, $p<0.001$) and the HI group ($F_{6,42}=13.4$, $p<0.001$). However, it is likely that the factors mediating this interaction differed between the two listener groups. In the NH group, identification improved more gradually as a function of ΔF_0 in the F1-same condition relative to the normal condition. In the HI group, there was slight to no improvement in double-vowel identification with increased ΔF_0's in the F1-same condition. Consequently, the pattern of performance for the HI group was flat as a function of ΔF_0.

F. Individual differences

Figure 4 shows the results of the individual listeners

with hearing loss in each of the four conditions. Among the individual listeners, absolute performance varied across conditions and values of ΔF_0. However, with the exception of listener HI 5, listeners with hearing loss generally showed patterns of ΔF_0 benefit that were consistent with the group trends for the normal, swapped, and F2-5-same condition. For the F1-same condition, although the group data showed a relatively flat pattern of ΔF_0 benefit, the performance of individual listeners in the HI group fell broadly into two categories. Several of the listeners showed a relatively flat pattern of ΔF_0 benefit, consistent with the group trends (e.g., HI 1, HI 4, HI 5, and HI 6). The remaining listeners (e.g., HI 2, HI 3, HI 7, and HI 8) showed some improvement in vowel identification as a function of ΔF_0. Possible explanations for this finding are discussed below.

IV. DISCUSSION

A. Comparison to previous literature

The primary goal of this study was to compare how normal-hearing and hearing-impaired listeners use and combine ΔF_0 cues within and across formant-frequency regions in the perceptual separation of competing vowels. To investigate the effects of frequency region on ΔF_0 benefit, a paradigm similar to Culling and Darwin (1993) was used in which F_0 inconsistencies were introduced among the constituents of the double vowel. The results from our normal-hearing group generally replicate the results of Culling and Darwin. The listeners with hearing loss show patterns of ΔF_0 benefit that are comparable to those of listeners with normal hearing for some but not all of the conditions listed in Table I.

As the control condition, the F_0-consistent (normal) condition allows comparison to previous research. In this condition, ΔF_0 benefit was similar between the two listener groups. This finding is consistent with some studies of double-vowel identification in listeners with hearing loss (Arehart *et al.*, 1997, 2005) but not others (e.g., Summers and Leek, 1998). Whereas past studies reported significantly worse overall double-vowel identification in hearing-impaired listeners, this difference was not observed in this study. Although Arehart (1998) showed that the poorer performance of listeners with hearing loss persisted even when correcting for reductions in audibility by generic amplification, the present study used amplification customized for each individual listener. This customization may have contributed to the improved overall scores among the listeners with hearing loss. Given the small number of participants and variability among individual listeners, the statistical power of the present experiment may also have been too low to reveal a group difference in overall performance in the normal condition.

B. Effects of frequency region

The ability of hearing-impaired listeners to use and combine F_0-information from low and high frequencies can be inferred by comparing the patterns of ΔF_0 benefit across the consistent and inconsistent conditions listed in Table I. We predicted that the greatest difference in the contribution of frequency region to the pattern of ΔF_0 benefit between the listener groups would be observed at small ΔF_0's. The current results support this prediction for high-frequency ΔF_0 cues, but are counter to this prediction for low-frequency ΔF_0 cues.

1. Small ΔF_0

At small ΔF_0's, listeners with hearing loss attain as much benefit from low-frequency cues as do listeners with normal hearing. This low-frequency benefit is evident even when the harmonic structure across formant frequencies is inconsistent. Our original expectation was that ΔF_0 cues might not be as discernible in the low-frequency region due to previous studies that showed hearing-impaired listeners often have abnormally large F_0DLs for complex tones containing lower-order harmonics. It is possible that the majority of hearing-impaired listeners in this study had good F_0 estimation in the low-frequency region, such that both F_0DLs for lower-order harmonics and ΔF_0 cues in the low-frequency region would be similar to those reported for normal-hearing listeners. In Arehart's study (1994), two out of eight listeners showed normal F_0DLs for lower-order harmonics. Therefore it is possible, although not probable, that the majority of listeners in the current study had F_0DLs similar to a small subgroup of Arehart's listeners.

Another plausible explanation is that waveform interactions or beating between adjacent (concurrent) low-frequency harmonics may contribute to double-vowel identification at small values of ΔF_0 (Assmann and Summerfield, 1994; Culling and Darwin, 1994). These peripheral interactions would not occur in sequential presentation of stimuli. If, at small values of ΔF_0, listeners rely on beating between the double-vowel components, a strong relationship between F_0DLs and ΔF_0 benefit might not be expected.

Several of the hearing-impaired listeners showed no benefit from ΔF_0 cues in the high-frequency region when the value of ΔF_0 was small, as reflected by their flat pattern of ΔF_0 benefit. The inaccessibility of high-frequency ΔF_0 cues for small ΔF_0's is consistent with the idea that deriving F_0 information from higher-order harmonics is worse in some hearing-impaired listeners (Arehart, 1994; Moore and Peters, 1992). For these listeners, the impaired frequency resolution resulting from cochlear hearing loss may have greater impact on the higher-numbered harmonics because the ratio of harmonic spacing to filter width would be less advantageous for the higher harmonics. Other hearing-impaired listeners showed some improvement in vowel identification as a function of ΔF_0, although the amount of improvement was less than that in the normal-hearing listeners. These particular listeners may have estimated F_0 information from the high-frequency region due to partial resolution of harmonics in the second formant-frequency region (cf. Culling and Darwin, 1993) or from periodicity cues that resulted from the interaction of higher-order unresolved harmonics (Arehart, 1994). Interestingly, the listeners who demonstrated no benefit from high-frequency ΔF_0 cues seemed to have poorer audiometric thresholds; as such, the ability to use high-frequency ΔF_0 cues may be associated with degree of hearing loss. This trend is supported by a significant correlation between pure-

tone average and amount of ΔF_0 benefit in the F1-same condition (between 0 and 2 ST) such that increased degree of hearing loss is associated with decreased ΔF_0 benefit for high-frequency ΔF_0 cues [$r=-0.79$, $N=8$, $p<0.05$]. Although we employed a customized amplification scheme for each hearing-impaired listener (Byrne and Dillon, 1986), the increased audibility provided by the scheme may not have been as effective for listeners with worse high-frequency thresholds. On the other hand, the association between degree of hearing loss and performance in the F1-same condition may not reflect audibility *per se*, but may reflect an underlying association between spectro-temporal processing deficits and degree of hearing loss (see Moore, 1995). If this is the case, suprathreshold processing deficits may impact the salience of cues in the high-frequency region even when sufficient audibility has been restored.

2. Large ΔF_0

Both groups of listeners appear to combine ΔF_0 cues from the low and high formant-frequency regions in the perceptual separation of competing vowels at larger ΔF_0's. This is supported by the worse identification in the F_0-inconsistent condition (relative to the normal condition) when ΔF_0 is greater than 2 ST. It follows that listeners with and without hearing loss group "distant" formant-frequency regions on the basis of a common F_0 at increased values of ΔF_0 (Culling and Darwin, 1993).

Bird and Darwin (1998) provided evidence that a similar across-formant grouping process mediates improvements in competing-sentence identification with increasing ΔF_0's. Listeners with hearing loss may rely on a similar strategy when identifying competing sentences. However, recent evidence may suggest otherwise. Summers and Leek (1998) showed that for a group of listeners with hearing loss, sentence identification did not improve as ΔF_0 increased from 2 to 4 ST. Although across-formant grouping was not explicitly evaluated by Summers and Leek, it is likely that, to some extent, this strategy would contribute to performance when ΔF_0 is 4 ST. As such, the usefulness of an across-formant grouping strategy may vary between competing-vowel and competing-sentence tasks in listeners with hearing loss. Future studies will investigate this possibility by evaluating the ability of listeners with hearing loss to identify competing sentences in conditions that both preserve and restrict across-formant grouping. To the extent that across-formant grouping is preserved and used by listeners with hearing loss in perceptually separating competing sentences, it is predicted that sentence identification will continue to improve for increased values of ΔF_0.

V. SUMMARY

The listeners with hearing loss show patterns of ΔF_0 benefit that are comparable to those of listeners with normal hearing for some but not all of the conditions.

(1) At small ΔF_0's, listeners with hearing loss attain as much benefit from low-frequency cues as do listeners with normal hearing. This interpretation is supported by both groups' improvements in double-vowel identification for small ΔF_0's in the swapped and F2-5-same conditions.
(2) At small ΔF_0's, listeners with hearing loss were not able to rely on ΔF_0 cues carried exclusively by the high-frequency region. This is supported by the NH and HI groups' different patterns of performance in the F1-same condition.
(3) At larger ΔF_0's, both groups of listeners combine ΔF_0 cues from the low and high formant-frequency regions in the perceptual separation of competing vowels. This result is supported by increasing difference in percent correct identification between the normal and swapped conditions.
(4) Cochlear hearing loss appears to negatively impact the ability to use within-formant F_0 cues in the high-frequency region in the perceptual separation of competing vowels. In contrast, cochlear hearing loss does not appear to disrupt the ability to use within-formant F_0 cues in the low-frequency region or the ability to group F_0 cues across formant regions.

ACKNOWLEDGMENTS

This research was supported by a grant from the Whitaker Foundation. In addition, the preparation of this article was partially supported by Centers for Disease Control and Prevention (CDC) Grant/Cooperative Agreement UR3/CCU824219. The contents are solely the responsibility of the authors and do not necessarily represent the official views of CDC. The authors extend thanks to Shonan Noronha for technical and programming assistance and Rosalinda Baca for assistance in data collection. The valuable suggestions of Peter Assmann and two anonymous reviewers on an earlier version of this manuscript are also gratefully acknowledged.

[1]In a normal-functioning cochlea, the internal representation of a complex sound can be viewed as an excitation pattern which reflects the output of a set of bandpass filters. Because the bandwidth of the filters increases with center frequency, lower-order harmonics pass through separate filters and are effectively resolved, whereas neighboring high-order harmonics pass through a single filter and so are not individually resolved.

ANSI (1989). ANSI S3.6-1989, "Specifications for audiometers," (ANSI, New York).

Arehart, K. H. (**1994**). "Effects of harmonic content on complex-tone fundamental-frequency discrimination in hearing-impaired listeners," J. Acoust. Soc. Am. **95**, 3574–3585.

Arehart, K. H. (**1998**). "Effects of high-frequency amplification on double-vowel identification in listeners with hearing loss," J. Acoust. Soc. Am. **104**, 1733–1736.

Arehart, K. H., King, C. A., and McLean-Mudgett, K. S. (**1997**). "Role of fundamental frequency differences in the perceptual separation of completing vowel sounds by listeners with normal hearing and listeners with hearing loss," J. Speech Lang. Hear. Res. **40**, 1434–1444.

Arehart, K. H., Rossi-Katz, J. A., and Swensson-Prutsman, J. (**2005**). "Double-vowel perception in listeners with cochlear hearing loss: Differences in fundamental frequency, ear of presentation and relative amplitude," J. Speech Lang. Hear. Res. **48**, 236–252.

Assmann, P. F., and Summerfield, Q. (**1990**). "Modeling the perception of concurrent vowels: Vowels with different fundamental frequencies," J. Acoust. Soc. Am. **88**, 680–697.

Assmann, P. F., and Summerfield, Q. (**1994**). "The contribution of waveform interactions to the perception of concurrent vowels," J. Acoust. Soc. Am. **95**, 471–484.

Bird, J., and Darwin, C. J. (**1998**). "Effects of a difference in fundamental

frequency in separating two sentences," in *Psychophysical and Physiological Advances in Hearing*, edited by A. R. Palmer, A. Rees, A.Q. Summerfield, and R. Meddis (Whurr, London, UK), pp. 263–269.
Bregman, A. S. (**1990**). *Auditory Scene Analysis: The Perceptual Organization of Sound* (Brandford Books, MIT, Cambridge, MA).
Broadbent, D. E., and Ladefoged, P. (**1957**). "On the fusion of sounds reaching different sense organs," J. Acoust. Soc. Am. **29**, 708–710.
Brokx, J. P. L., and Nootebom, S. G. (**1982**). "Intonation and the perceptual separation of simultaneous voices," J. Phonetics **10**, 23–36.
Byrne, D., and Dillon, H. (**1986**). "The National Acoustic Laboratories' (NAL) new procedure for selecting the gain and frequency response of a hearing aid," Ear Hear. **7**, 257–265.
Carlyon, R. P., Demany, L., and Semal, C. (**1992**). "Detection of across-frequency differences in fundamental frequency," J. Acoust. Soc. Am. **91**, 279–292.
Culling, J. F., and Darwin, C. J. (**1993**). "Perceptual separation of simultaneous vowels: Within and across-formant grouping by F0," J. Acoust. Soc. Am. **93**, 3454–3467.
Culling, J. F., and Darwin, C. J. (**1994**). "Perceptual and computational separation of simultaneous vowels: Cues arising from low-frequency beating," J. Acoust. Soc. Am. **95**, 1559–1569.
Darwin, C. J., and Carlyon, R. P. (**1995**). "Auditory Grouping," in *Hearing: Handbook of Perception and Cognition*, 2nd ed., edited by B. C. J. Moore (Academic, London), pp. 387–424.
de Cheveigné, A. (**1999**). "Waveform interactions and the segregation of concurrent vowels," J. Acoust. Soc. Am. **106**, 2959–2972.
Dreschler, W. A., and Plomp, R. (**1980**). "Relations between psychophysical data and speech perception for hearing-impaired subjects. I.," J. Acoust. Soc. Am. **68**, 1608–1615.
Dreschler, W. A., and Plomp, R. (**1985**). "Relations between psychophysical data and speech perception for hearing-impaired subjects. II.," J. Acoust. Soc. Am. **78**, 1261–1270.
Festen, J. M., and Plomp, R. (**1990**). "Effects of fluctuating noise and interfering speech on the speech-reception threshold for impaired and normal hearing," J. Acoust. Soc. Am. **88**, 1725–1736.
Glasberg, B. R., and Moore, B. C. J. (**1989**). "Psychoacoustic abilities of subjects with unilateral and bilateral cochlear impairments and their relationship to the ability to understand speech," Scand. Audiol. Suppl. **32**, 1–25.
Houtsma, A. J. M., and Smurzynski, J. (**1990**). "Pitch identification and discrimination for complex tones with many harmonics," J. Acoust. Soc. Am. **87**, 304–310.
Klatt, D. H. (**1980**). "Software for a cascade/parallel formant synthesizer," J. Acoust. Soc. Am. **67**, 971–995.
Meddis, R., and Hewitt, M. J. (**1992**). "Modeling the identification of concurrent vowels with different fundamental frequencies," J. Acoust. Soc. Am. **91**, 233–245.
Moore, B. C. J. (**1995**). *Perceptual Consequences of Cochlear Hearing Loss* (Oxford U.P., Oxford).
Moore, B. C. J., and Peters, R. W. (**1992**). "Pitch discrimination and phase sensitivity in young and elderly subjects and its relationship to frequency selectivity," J. Acoust. Soc. Am. **91**, 2881–2893.
Peterson, G. E., and Barney, H. L. (**1952**). "Control methods used in a study of the vowels," J. Acoust. Soc. Am. **24**, 175–184.
Scheffers, M. T. M. (1983). "Sifting vowels: Auditory pitch analysis and sound segregation," Ph.D. thesis, Groningen.
Stubbs, R. J., and Summerfield, Q. (**1988**). "Evaluation of two voice-separation algorithms using normal-hearing and hearing-impaired listeners," J. Acoust. Soc. Am. **89**, 1236–1249.
Studebaker, G. A. (**1985**). "A 'rationalized' arcsin transform," J. Speech Hear. Res. **28**, 455–462.
Summers, V., and Leek, M. R. (**1998**). "F0 processing and the separation of competing speech signals by listeners with normal hearing and with hearing loss," J. Speech Lang. Hear. Res. **41**, 1294–1306.

Pattern Playback revisited: Unvoiced stop consonant perception[a)]

Michael Kiefte[b)]
School of Human Communication Disorders, Dalhousie University, Halifax, Nova Scotia B3H 1R2, Canada

Keith R. Kluender
Department of Psychology, University of Wisconsin, Madison, Wisconsin 53706-1696

(Received 7 February 2005; revised 23 July 2005; accepted 25 July 2005)

Among the most influential publications in speech perception is Liberman, Delattre, and Cooper's [Am. J. Phys. **65**, 497–516 (1952)] report on the identification of synthetic, voiceless stops generated by the *Pattern Playback*. Their map of stop consonant identification shows a highly complex relationship between acoustics and perception. This complex mapping poses a challenge to many classes of relatively simple pattern recognition models which are unable to capture the original finding of Liberman *et al.* that identification of /k/ was bimodal for bursts preceding front vowels but otherwise unimodal. A replication of this experiment was conducted in an attempt to reproduce these identification patterns using a simulation of the *Pattern Playback* device. Examination of spectrographic data from stimuli generated by the *Pattern Playback* revealed additional spectral peaks that are consistent with harmonic distortion characteristic of tube amplifiers of that era. Only when harmonic distortion was introduced did bimodal /k/ responses in front-vowel context emerge. The acoustic consequence of this distortion is to add, e.g., a high-frequency peak to midfrequency bursts or a midfrequency peak to a low-frequency burst. This likely resulted in additional /k/ responses when the second peak approximated the second formant of front vowels. Although these results do not challenge the main observations made by Liberman *et al.* that perception of stop bursts is context dependent, they do show that the mapping from acoustics to perception is much less complex without these additional distortion products. © *2005 Acoustical Society of America.* [DOI: 10.1121/1.2040047]

PACS number(s): 43.71.Es, 43.71.−k [RLD] Pages: 2599–2606

I. INTRODUCTION

Among the most influential publications in speech perception research is Liberman, Delattre, and Cooper's (1952) report on the identification of synthetic, voiceless stops in CV syllables. These syllables were generated by the *Pattern Playback*, which was capable of converting spectrograms—either photographic copies or hand-painted patterns—into sound (Cooper, 1950; Cooper, Liberman, and Borst, 1951). This was the first study to examine perceptual effects of initial stop bursts by parametrically manipulating their spectral properties.

Reproduced as Fig. 1, the classic map of Liberman *et al.* of identification as a function of vowel quality and burst center frequency is easily recognized by psychologists, linguists, and speech researchers. This figure has often been shown as a demonstration of the complex relation between acoustics and perception of the speech signal. From these data, the authors concluded that, not only does place perception depend on the center frequency of the burst, but also on the vowel context in which the burst occurs. Specifically, the same burst was heard as different consonants before different vowels. For example, a burst centered at 1440 Hz was perceived as /k/ before /ɑ/ but as /p/ before /i/ and /u/.

This apparent context sensitivity encouraged models of speech perception that proposed "decoding" of the speech signal via mediation by speech production mechanisms (Liberman *et al.*, 1967). This followed the presumption that articulatory gestures are less complex than their acoustic consequences. However, other models of speech perception are able to capture some complex context dependency as well. For example, Nearey's Normal A Posteriori Probability (NAPP) model is able to capture context dependence in responses to vowel-consonant and fricative-vowel stimuli (Nearey, 1990). In addition, it is not difficult to generate a model that would predict differential responses to the same burst before different vowels (see the following). However, the data reported by Liberman *et al.* are yet more complex. For example, the NAPP model is unable to capture the original finding by Liberman *et al.* (p. 506) that identification data for /k/ was bimodal for bursts preceding high-front vowels but unimodal preceding back vowels. For example, bursts set at either 720 and 2500 Hz were heard as /k/ before /e/, but as /p/ when the burst frequency was between these two frequencies. Liberman *et al.* speculated that the burst needed to be just above or at the frequency of any of the formants that were essential for the perception of the vowel. Because it

[a)]Portions of this work were presented in "Pattern Playback revisited: Unvoiced stop consonant perception," Proceedings of the XVth International Congress of Phonetic Sciences, Barcelona, Spain, August, 2003.

[b)]Electronic mail: mkiefte@dal.ca

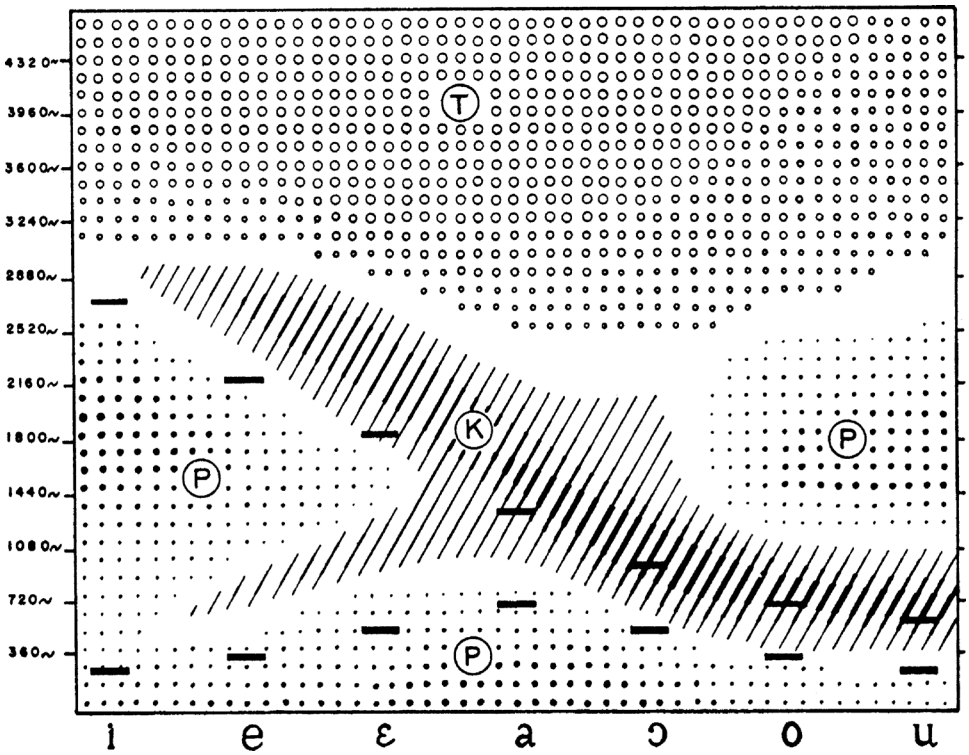

FIG. 1. Modal decision regions based on responses to synthetic burst stimuli found in seven vowel contexts (Liberman *et al.*, 1952). From *American Journal of Psychology*. Copyright 1952 by the Board of Trustees of the University of Illinois. Used with permission of the University of Illinois Press.

was believed that F_1 was not essential for the perception of the back vowels (Delattre *et al.*, 1952), it was thought that this rule may only apply to the front vowels.

Section III reports an attempt to replicate this classic experiment on the perception of voiceless stops. A number of important aspects of the patterns of perception found earlier, including bimodal patterns for /k/ for high-front vowels, could not be replicated. Efforts then proceeded to more faithfully reproduce the acoustic output of the analogue *Pattern Playback* device. Examination of spectrographic data from stimuli generated by the *Pattern Playback* revealed additional spectral peaks that are consistent with second-harmonic distortion. Section IV shows that when second-harmonic distortion characteristic of tube diode amplifiers was introduced, bimodal patterns of /k/ responses in low-front-vowel context were obtained.

II. NAPP MODEL OF SPEECH PERCEPTION

In the hand-painted spectrograms designed by Liberman *et al.* which were converted to sound via the *Pattern Playback*, vowels were represented by two horizontal bars while release bursts of syllable-initial stops were modeled as narrow vertical "teardrop" shapes centered at one of twelve frequencies ranging from 360 to 4320 Hz in 360-Hz steps. Each painted burst was prepended to each of seven pairs of horizontal bars corresponding to the first two formants of the vowels /i,ɛ,æ,ɑ,ɔ,o,u/ in a fully crossed design. Because the experimenters were only interested in the perception of the release burst, consonant-vowel formant transitions were not varied and remained flat in all stimuli. Thirty subjects listened to each stimulus twice and were asked to respond with one of the labels "p," "t," or "k" following each stimulus presentation for a total of 60 responses to each syllable.

Figure 1 indicates the consonants for which a plurality of responses was recorded or *modal response regions* as a function of vowel second formant (F_2) and burst center frequency. Although it is the best known figure from this work, it presents a fairly gross generalization of the original data. Liberman *et al.* (1952) also provided frequency polygons that appear to be more accurate and detailed and are reproduced here as Fig. 2. It is this depiction that is used here to estimate the original aggregate subject responses. Figure 2 was digitally scanned and the number of "p," "t," and "k" responses for each stimulus was estimated using a graphical editor, i.e., the approximate number of responses for each consonant was estimated by lining up each point on each frequency polygon with the corresponding number of responses on the x axis. The range of the sum of responses estimated from Fig. 2 was 60 ± 5 indicating that estimates were reasonably accurate.

Figure 3 shows modal response regions as a function of burst center frequency and vowel F_2 based on this secondary analysis. Black rectangles illustrate first and second formant frequency and bandwidth of each vowel. Figure 3 differs from the better known version of Liberman *et al.* in two main respects. Unlike Fig. 1, vowel F_2 in Fig. 3 is linear along the x axis, and boundaries are determined by linear interpolation of the *a posteriori* probabilities estimated from frequency polygons, whereas the boundaries in Fig. 1 appear to be highly schematized representations of the data.

Both versions (Figs. 1 and 3) show a highly complex relationship between subject responses and stimulus properties. Liberman and Mattingly (1985) interpreted this complex relationship as evidence in support of the *Motor Theory of Speech Perception* which posits that speech perception is necessarily mediated by articulation, and that talkers' intended gestures are somehow encoded in the acoustic signal to maximize efficiency of transmission. The apparent com-

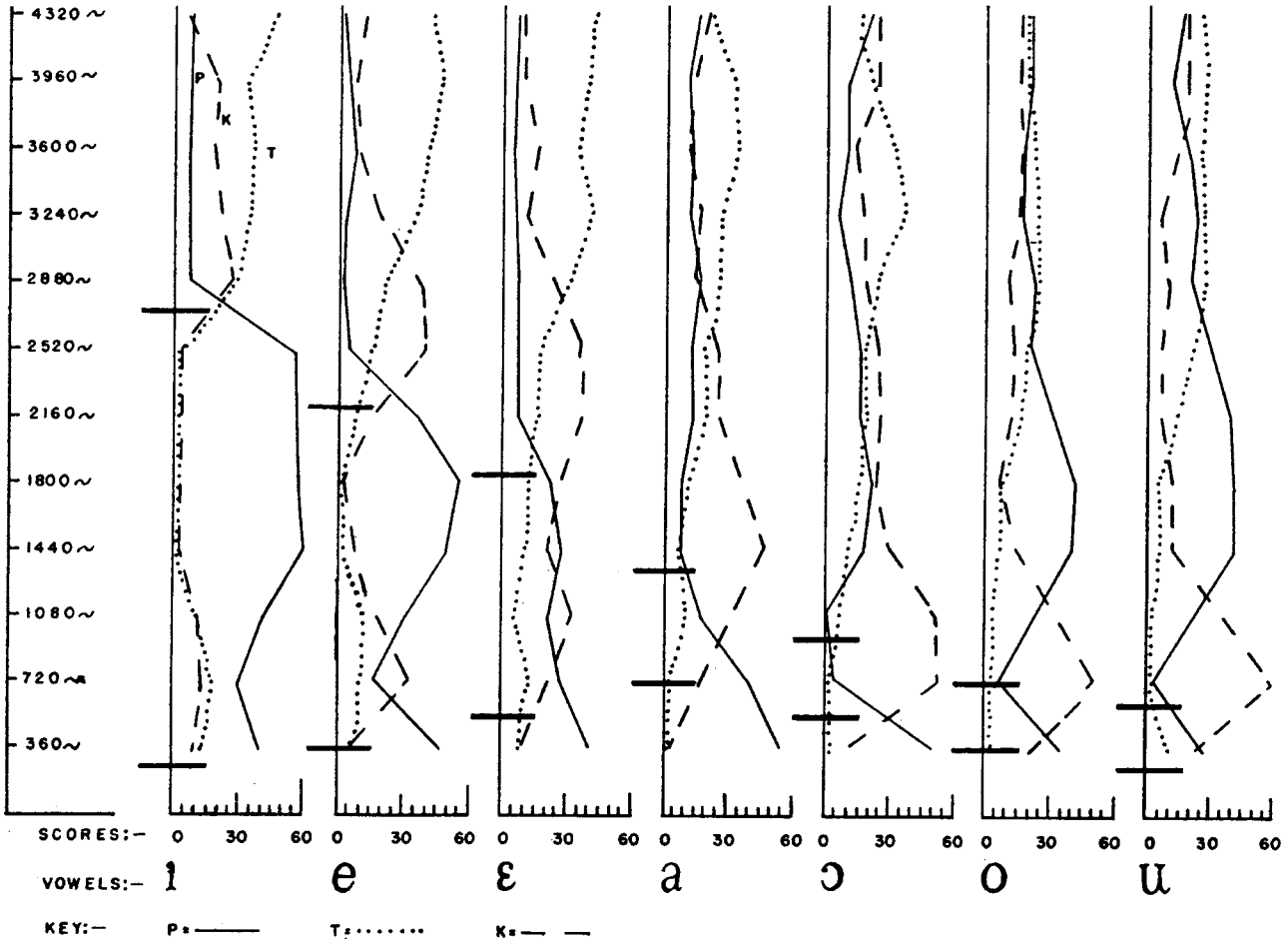

FIG. 2. Frequency polygons based on responses to synthetic burst stimuli found in seven vowel contexts (Liberman *et al.*, 1952). From *American Journal of Psychology*. Copyright 1952 by the Board of Trustees of the University of Illinois. Used with permission of the University of Illinois Press.

plexity of the relationship between phoneme and acoustics was seen as a consequence of this elaborate encoding.

One of the challenges for purely acoustic theories of speech perception is to solve the problem of this complex mapping from acoustics to perception. Nearey (1990) has demonstrated that a number of other apparently complex relationships between acoustics and perception can, in fact, be easily modeled based on acoustic properties alone. For example, many well-known trading relations between acoustic properties in adjacent phonemes, such as consonant-vowel syllables, are easily predicted if one assumes that stimulus attributes are drawn from a multivariate normal distribution with a simple covariance structure. In Nearey's NAPP model, it is assumed that perception is tuned to these covariances and that the likelihood $p_c(\mathbf{x})$ of a listener identifying a given stimulus $\mathbf{x}$ as a particular category c can be determined by the probability density functions of the underlying distributions $d_i(\mathbf{x})$,

$$p_c(x) = \frac{d_c(x)}{\sum_{i-1}^{K} d_i(x)}. \tag{1}$$

This model is potentially very powerful. For example, if different categories do not share a common covariance structure, then bimodal *a posteriori* probabilities are possible. For example, Fig. 4 shows hypothetical covariance ellipsoids representing the distribution of the three stop places of articulation as a function of vowel F_2 and burst center frequency. Because covariances for the categories /k/ and /p/ are different, as represented by the shape and orientation of the

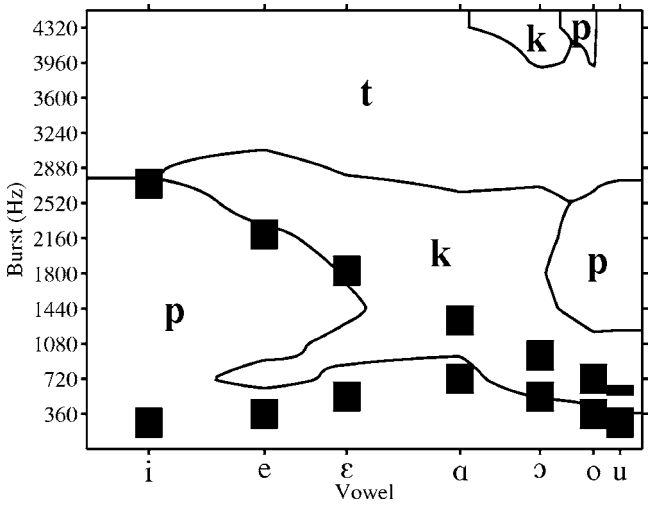

FIG. 3. Modal decision regions estimated from Fig. 2 as a function of burst center frequency and vowel second formant. Vertical position of black rectangles indicate frequencies of F_1 and F_2 for each vowel. The x axis is linear in nominal F_2 frequency. Because synthetic-vowel F_2 frequency is unevenly spaced, vowels are also unevenly spaced along the x axis.

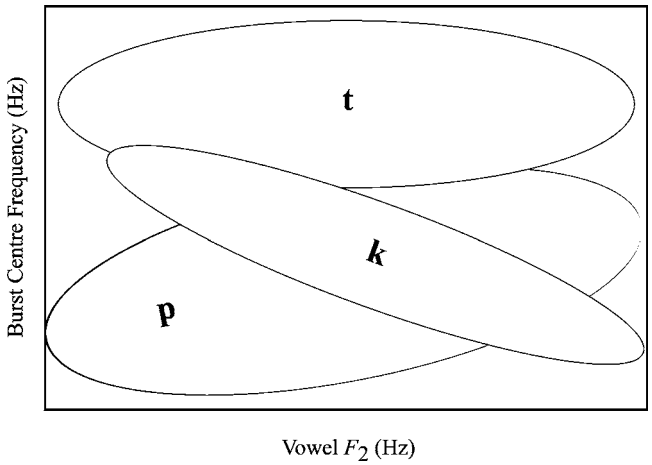

FIG. 4. Hypothetical covariance between burst center frequency and vowel F_2 frequency for each of the three voiceless stop consonant categories. Ellipses illustrate means (ellipsoid centers), variances (ellipsoid width parallel to x and y axes), and covariances (elipsoid orientation) for the two parameters.

ellipsoids, bimodal responses to /p/ are both possible and optimal in this case. A simple perceptual model based on acoustic properties alone could exploit the natural covariation in this hypothetical example. However, there are some empirical data that cannot be modeled in this way.

Figure 5 shows fitted modal response regions from a NAPP model estimated from the data of Liberman *et al.* The model assumes different underlying covariance structures for the three consonant categories and was estimated via quadratic logistic regression (McCullagh and Nelder, 1989) with two variates: vowel F_2 and burst center frequency. Although this model captures the bimodal nature of /p/ responses, fitted response regions oversimplify the complex relationship between /k/ responses and vowel formants, i.e., in the original data, responses to /k/ are clearly bimodal for mid front vowels /e/ and /ɛ/ in Figs. 1 and 2.

The data of Liberman *et al.* represent a challenge for Nearey's NAPP model and for any other simple model that predicts listener's responses based on covariance among

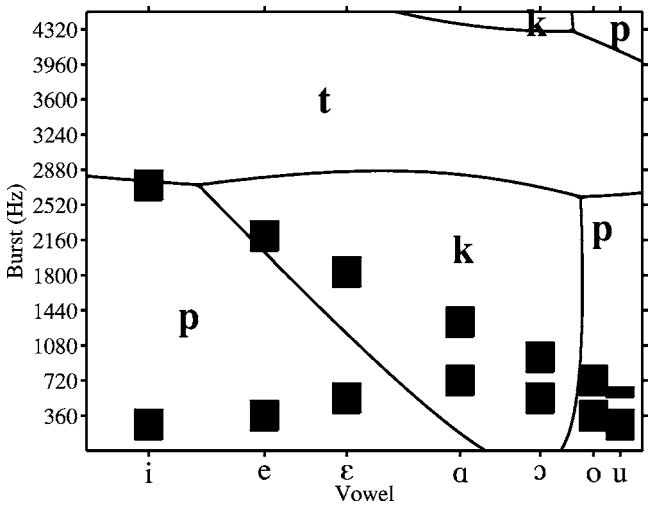

FIG. 5. Estimated model response regions from quadratic logistic regression fit of the 1952 data of Liberman *et al.*

simple acoustic properties. While it would be desirable if relatively straightforward and tractable statistical models can faithfully capture listener behavior, such models are of limited value if data such as those for place of articulation defy such efforts. This issue, in addition to historical considerations, motivate replication of the half-century-old study.

III. EXPERIMENT 1

An attempt was made to simulate the *Pattern Playback* in software to produce synthetic stimuli that were similar to the original set used by Liberman *et al.* (1952). Although it is possible to generate stimuli using modern speech synthesis techniques, replication requires mimicking the original study as closely as possible to learn if response regions similar in shape to those illustrated in Fig. 3 can be generated. Further, one ought not expect that more natural-sounding stimuli would produce these response patterns because the original stimuli are so highly impoverished with respect to acoustic properties known to be used by listeners. For example, formant transitions are normally present in naturally produced consonant-vowel syllables and are known to be very important for identifying stop place (e.g., Cooper, *et al.*, 1952; Liberman *et al.*, 1954; Fruchter and Sussman, 1997). The original stimuli of Liberman *et al.* had no formant transitions. It has been suggested that release bursts are less effective than formant transitions for stimuli in which these two acoustic attributes are mismatched (Dorman, Studdert-Kennedy, and Raphael, 1977). Although this latter claim has been challenged (e.g., Repp and Lin, 1989), the absence of formant transitions likely had a strong effect on identification of stop place from these stimuli.

A. Stimuli

Stimuli were generated by summing harmonics of a 120-Hz fundamental. Stimuli were sampled at 10 kHz. Similar to the *Pattern Playback*, each harmonic was assigned to a 120-Hz wide channel. Harmonic amplitudes were controlled by two-dimensional patterns on a spectrogram. Amplification of each harmonic was proportional to the fraction of the corresponding channel that was covered by the pattern. For example, if only one quarter of the channel was covered by the pattern at a given moment, the instantaneous intensity of that harmonic was attenuated to 25% (e.g., a horizontal bar with a width of 30 Hz entirely within one 120-Hz channel). Stop bursts were generated using a diamond shape 15 ms long and 360 Hz wide. Harmonics were additionally attenuated by 9 dB/octave above 1500 Hz, similar to that described for the Pattern Playback (Delattre *et al.*, 1952).[1]

Bursts were followed by 20 ms of silence followed by one of the seven vowel stimuli/i,e,ɛ,ɑ,ɔ,o,u/ which were generated in a similar fashion. Vowels were 300 ms long. All formants had 300-Hz bandwidth with the exception of F_2 for /u/ which had a 100-Hz bandwidth (Delattre *et al.*, 1952). Formant center frequencies are given in Liberman *et al.* (1952). All formants had a 20-ms triangular onset and offset (as viewed from a spectrogram). All twelve stop bursts were fully crossed with all seven vowels for a total of 84 stimuli. Figure 6 gives a schematic illustration of one such stimulus.

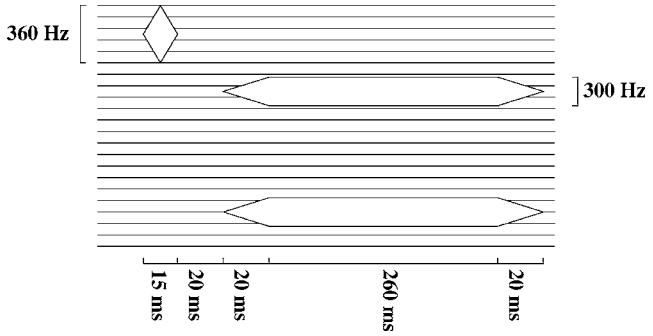

FIG. 6. Schematic illustration of stimulus parameters. Bursts and formants were "painted" on virtual spectrograms and processed by the *Pattern Playback* simulation. Sinusoid amplitudes were proportional to coverage within each 120-Hz channel illustrated by horizontal bands.

Thus it was intended that this simulation of the Pattern Playback processes these images in approximately the same manner as the original device.

Stimuli were rms-normalized and stored on a computer at 16 bits per sample and 10-kHz sampling rate for stimulus presentation.

B. Subjects

42 native speakers of American English were recruited from the Department of Psychology at the University of Wisconsin—Madison. None reported any hearing impairment. All listeners were undergraduate Psychology students and received course credit for their participation.

C. Procedure

Listeners heard stimuli via headphones in a sound attenuated booth. Stimulus presentation and response collection were under the control of an 80486-25 microcomputer. Following D/A conversion (Ariel DSP-16), stimuli were low-pass filtered (4.8-kHz cutoff frequency, Frequency Devices, #677), amplified (Stewart HDA4), and presented via headphones (Beyer DT-100) at a level of 75 dB SPL. In keeping with the original study by Liberman *et al.* (1952), stimuli were presented twice on each trial with a 200-ms interstimulus interval. Listeners then identified each consonant by pressing one of three buttons labeled "p," "t," or "k." Each of the 84 stimuli were presented in four trials in each of two 15-min sessions for a total of 672 responses from each subject.

D. Results

Modal response regions from data collected in this experiment are shown in Fig. 7. Unlike Fig. 3, none of the response categories are clearly bimodal, nor is the shape of the response region for "k" in this figure similar to the original.

However, from the point of view of the NAPP model, the response regions are relatively easy to model. Figure 8 shows fitted modal response regions based on a quadratic logistic model similar to the one described in Sec. I.

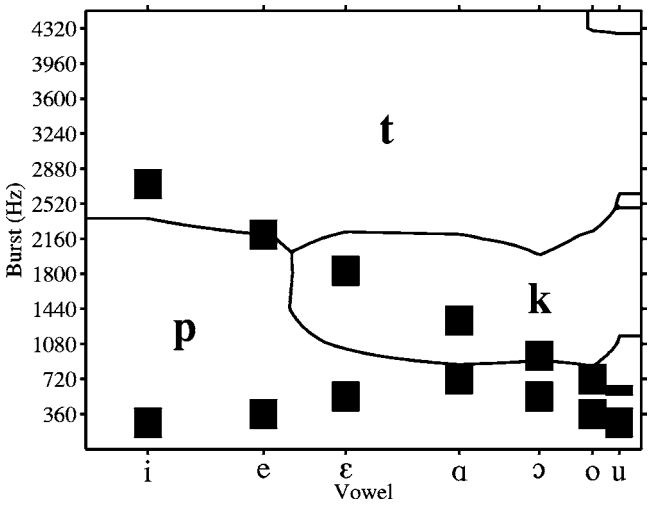

FIG. 7. Modal response regions from Experiment 1.

IV. EXPERIMENT 2

Because the results of Liberman *et al.* (1952) could not be replicated using stimuli that were intended to be equivalent, similar stimuli that were generated by the *Pattern Playback* device were acquired and examined more closely for possible confounds. Figure 9 shows a spectrogram of /pikɑpu/ produced by the *Pattern Playback*.[2] Whereas stimuli presented to subjects in Experiment 1 were clean and undistorted, the spectrogram in Fig. 9 reveals multiple formants above F_2. In addition, the burst which is centered at 1440 Hz has additional higher-frequency peaks. This visually apparent pattern is consistent with harmonic distortion produced by tube amplifiers as used in the *Pattern Playback*. The same pattern of distortion is found in another set of recordings of the /ba-da-ga/series (Liberman *et al.*, 1957) available from Haskins Laboratories:[3] although Liberman *et al.* state that only two formants were synthesized for the vowels, spectrographic analysis of these stimuli reveal multiple regularly spaced formants above the second.

Although these signals were generated by the same device, they are not the original stimuli used by Liberman *et al.*

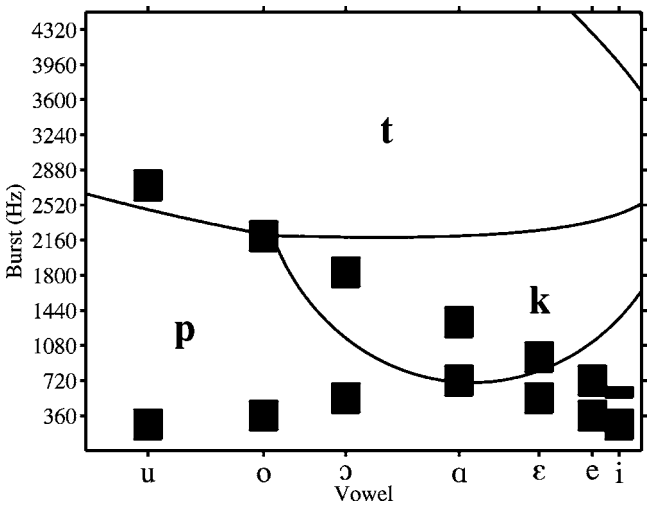

FIG. 8. Estimated modal response regions for responses from Experiment 1 based on a quadratic logistic model similar to the one used for Fig. 4.

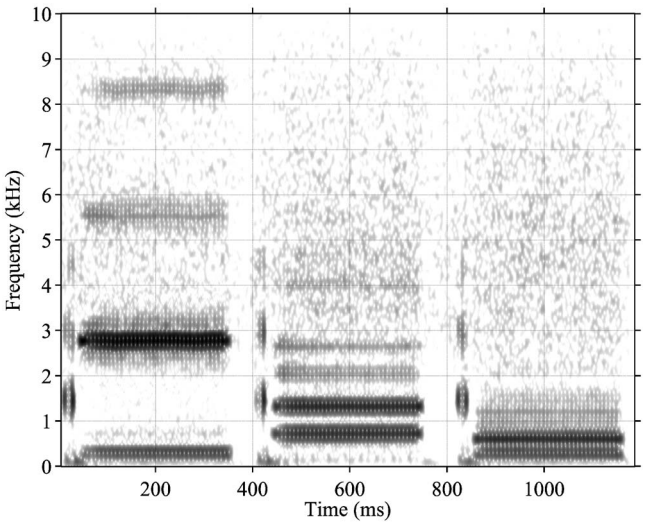

FIG. 9. Spectrogram of /pikɑpu/ produced by the *Pattern Playback* device. Although they were produced by the same device as was those in Liberman *et al.* (1952) they are not the original stimuli themselves. See footnote 2.

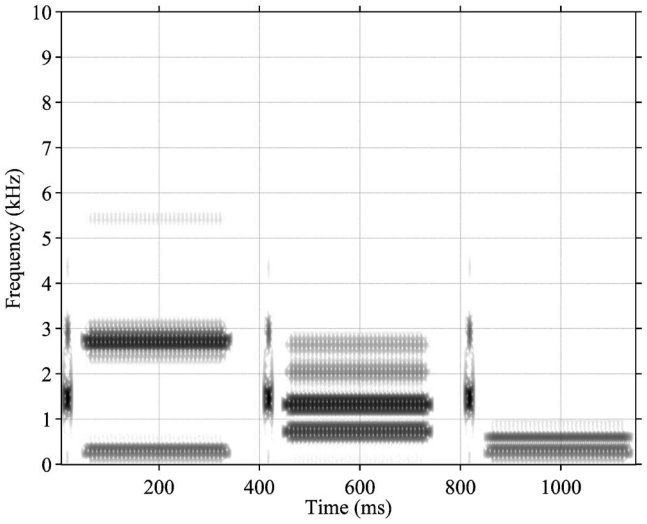

FIG. 10. Spectrogram of /pikɑpu/ from the simulated Pattern Playback from Experiment 2 with 3% harmonic distortion. Because the center frequency of the burst is relatively low, there is very little spectral energy above 5 kHz that is due to harmonic distortion.

(1952). In addition, the recording conditions under which the sample represented by the figure was taken are not known, and it is possible that much of the distortion could be due to the recording conditions instead of the Pattern Playback itself.

It is impossible to know how the sound quality of these samples compares to the stimuli that were presented to subjects in the 1950s because playback and recording equipment of that era suffered multiple shortcomings relative to contemporary devices. However, Liberman *et al.* do state that harmonic distortion (THD) for individual tones was no more than 3% (p. 503, 1952) and these levels of harmonic distortion are entirely consistent with the distortion patterns evident in Fig. 9. Whether or not distortion was restricted to these relatively low levels, one factor may cause this distortion to be perceptually relevant. Because the *Pattern Playback* ideally produces no energy in channels that are not painted, harmonic distortion can result in additional peaks in channels that would otherwise contain no energy. By contrast, naturally produced voiced speech consists of harmonics at both peaks and valleys. Harmonic distortion in natural speech would therefore produce shallower spectral valleys and flatter peaks instead of producing additional peaks. The next experiment examines the effect of harmonic distortion on perception of simulated *Pattern Playback* stimuli.

A. Stimuli

Stimuli were designed in the same manner as in Experiment 1. However, once initial stimuli were generated, they were processed by a simulated tube amplifier with 3% THD. The amplifier modeled is a simple Class A power amplifier whose current I is described by Child's law:

$$I = CV^{3/2}, \tag{2}$$

where V is the potential difference in volts and C is an arbitrary constant (Anderson and Beeman, 1973). Input voltages are half-wave rectified. Therefore a dc voltage must be added to the input signal. This operating point, or bias voltage Q, can be manipulated to produce different levels THD. Q was selected so that 3% THD was produced for a single sinusoid. Equation (2) was applied to the stimuli and overall dc level was then subtracted.

Figure 10 shows spectrograms of the resulting stimuli which show additional peaks characteristic of harmonic distortion. With the additional distortion, the prevocalic bursts show the same pattern of additional peaks as illustrated in Fig. 9. However, the vowels in Fig. 9 show a spectral pattern suggestive of even greater distortion. Nevertheless, we have restricted the simulated distortion to 3% THD as suggested by Liberman *et al.* (1952).

B. Subjects

30 native speakers of American English were recruited from the Department of Psychology at the University of Wisconsin—Madison. None reported any hearing impairment. Subjects received course credit for their participation. No student participated in both experiments.

C. Procedure

The procedure is the same as for Experiment 1 with the exception that stimuli were saved at a 20-kHz sampling rate and were low-pass filtered with a 9.6-kHz cutoff frequency in order to preserve harmonics above 5 kHz that resulted from distortion.

D. Results

Responses to stimuli were biased towards /p/ (40% overall) while only 27% responses were obtained for /k/. Out of 84 stimuli, only three stimuli received a majority of /k/ responses. In the original data presented by Liberman *et al.* 24 out of 84 stimuli were estimated to give rise to a majority of /k/ responses. Because responses to /k/ did not reach majority for a large number of stimuli, Fig. 11 instead shows a contour plot of the percent /k/ responses to the stimuli that

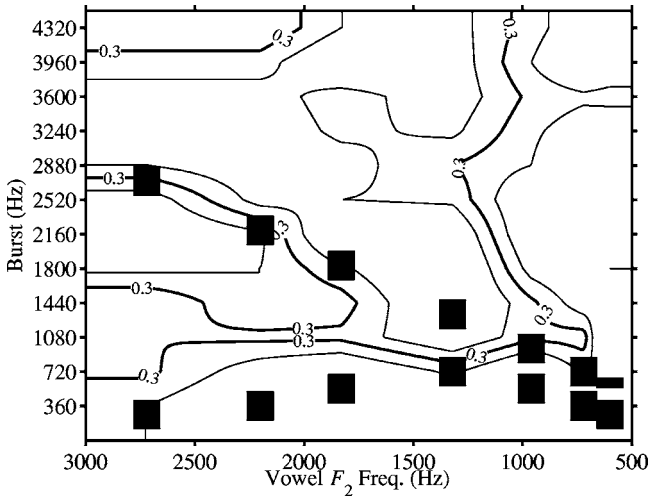

FIG. 11. Contour plot of the proportion of "k" responses in Experiment 2. Contours represent 25%, 30%, and 35% cutoffs for "k" responses with the thick line representing 30%.

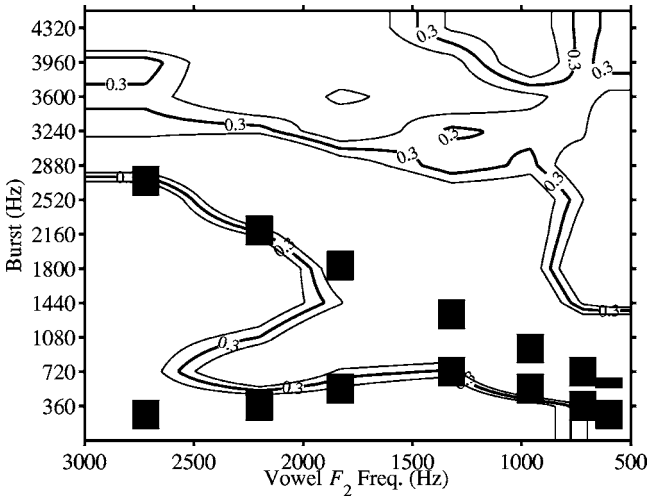

FIG. 13. Contour plot of the proportion of "k" responses from the original data of Liberman *et al.* (1952) as estimated visually from the original frequency polygons. Contours represent 25%, 30%, and 35% cutoffs for "k" responses with the thick line representing 30%.

include harmonic distortion. It is not known why responses were biased against /k/. It is possible that intensity of the burst was attenuated relative to the vocalic portion because of differential effects of harmonic distortion, resulting in fewer /k/ responses. Nevertheless, the figure shows an emerging bimodal distribution for /k/ for front vowels similar to that seen in Fig. 3. For comparison, Fig. 12 gives the contours for the same response region from Experiment 1 in which no harmonic distortion was introduced, while Fig. 13 gives the contours as estimated from the frequency polygons given by Liberman *et al.* (1952).

V. DISCUSSION

We have attempted to replicate the original findings of Liberman *et al.* (1952) by simulating the effects of tube amplification on *Pattern Playback*-like stimuli with the goal of reproducing bimodal /k/ responses before /i/ and /e/. However, it should be noted that Liberman *et al.* did not focus on this single aspect of their responses. Their most significant finding was that the perception of stop-vowel syllables is context dependent, i.e., the fact that the same burst is heard as /p/ before /i/ and /u/ and as /k/ before /ɑ/. Nothing in this paper contradicts this important observation. However, while many models of speech perception, including the NAPP model, are able to predict this pattern of performance, the observation that /k/ responses are bimodal before some vowels represented a more challenging problem.

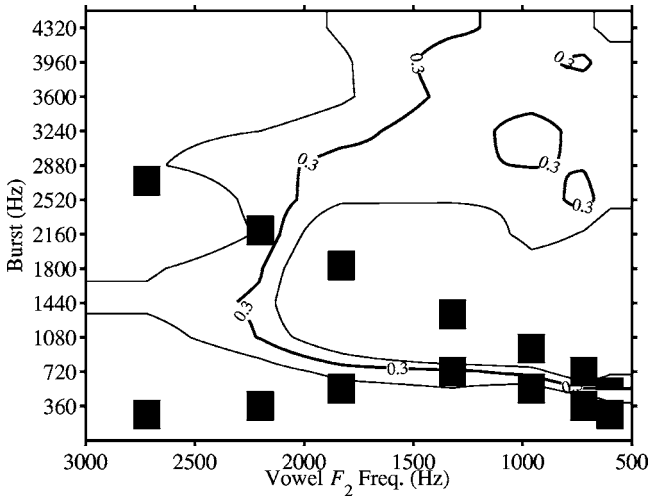

FIG. 12. Contour plot of the proportion of "k" responses from Experiment 1. Contours represent 25%, 30%, and 35% cutoffs for "k" responses with the thick line representing 30%.

The acoustic consequence of harmonic distortion is to add additional burst peaks at integer multiple frequencies of the original. The bimodal structure of the response area for /i/ begins to emerge only when harmonic distortion, typical of tube amplifiers in the 1950s, was incorporated into these replicas of the original Liberman *et al.* (1952) stimuli.

However, this paper likely does not present a faithful replication of the results reported by Liberman *et al.* and cannot hope to do so. Although we have introduced a very simple form of nonlinear distortion, other types of distortion, such as clipping (insufficient bias voltage or heat dissipation), loudspeaker characteristics, and signal-to-noise ratio could have been simulated as well. However, it would be impossible to reproduce the stimuli used in the original experiments. The few recent *Pattern Playback* stimuli that are available likely differ substantially from those used by Liberman *et al.* For example, the *Pattern Playback* is now more than 50 years old and its functioning is likely to have changed in that time. In addition, the equipment and software used to digitize and encode the examples that are available may have introduced additional nonlinear distortion. With iterative and *post hoc* manipulations of these stimuli, it is likely that the original patterns of responses could be derived. However, pursuing some or all of these potential confounds, while interesting, would be in the service of historical curiosity rather than understanding the true nature of perception of stop consonants.

It bears note that secondary peaks in naturally produced velar stops have been reported (Fischer-Jørgensen, 1954; Zue, 1976); however, it is not known if these are perceptu-

ally relevant. When present, secondary peaks for velar stops should be roughly three times the frequency of the first (based on an acoustic approximation of the vocal tract anterior to the point of velar constriction, Stevens, 2000)—not at integer multiples as they are when caused by harmonic distortion typical of tube amplifiers.

Although it may be impossible to faithfully replicate the results of Liberman *et al.*, we have shown that harmonic distortion can have a profound effect on the pattern of listeners' responses to relatively simple synthetic speech stimuli, and that the complex pattern of responses obtained by Liberman *et al.* are likely confounded by factors other than desired stimulus parameters. With regard to the undistorted stimuli used in the present study, the main conclusion is that the pattern of responses for noise bursts preceding steady-state vowel sounds is, in fact, relatively simple and amenable to modeling with simple pattern classification models.

ACKNOWLEDGMENTS

This work was supported by Grant No. R01 DC04072 to K.R.K. from the National Institutes of Health. The authors would like to thank James Hillenbrand and one anonymous reviewer for comments on previous drafts of this article.

[1]Conflicting reports regarding the rolloff have been given. For example, Liberman *et al.* (1952) describe the rolloff as −6 dB/octave, while Delattre *et al.* (1952) state that the rolloff was −9 dB/octave. However, analysis of the Pattern Playback stimuli illustrated by the spectrogram in Fig. 8 suggest that the rolloff described by Delattre *et al.* (1952) is more accurate. Nevertheless, the difference between these two settings is small (e.g., 3 dB at 3 kHz; 6 dB at 6000 Hz). Given that the highest F_2 frequency is less than 3 kHz and the highest burst center frequency is 4320 Hz, the differences between these two rolloffs are not expected to have a large influence on results.

[2]Stimuli were downloaded from http://connection.lww.com/products/borden/audio6-7.asp on 7 February 2005.

[3]Stimuli available from http://www.haskins.yale.edu/haskins/MISC/PP/bdg/bdg.html on 26 April 2005.

Anderson, L. W., and Beeman, W. W. (**1973**). *Electric Circuits and Modern Electronics* (Holt, Rinehart, & Winston, New York).

Cooper, F. S. (**1950**). "Spectrum analysis," J. Acoust. Soc. Am. **22**, 761–762.

Cooper, F. S., Delattre, P. C., Liberman, A. M., Borst, J. M., and Gerstman, L. J. (**1952**). "Some experiments on the perception of synthetic speech sounds," J. Acoust. Soc. Am. **24**, 597–606.

Cooper, F. S., Liberman, A. M., and Borst, J. M. (**1951**). "The interconversion of audible and visible patterns as a basis for research in the perception of speech," Proc. Natl. Acad. Sci. U.S.A. **37**, 318–325.

Delattre, P., Liberman, A. M., Cooper, F. S., and Gerstman, L. J. (**1952**). "An experimental study of the acoustic determinants of vowel color; Observations on one- and two-formant vowels synthesized from spectrographic patterns," Word **8**, 195–210.

Dorman, M. F., Studdert-Kennedy, M., and Raphael, L. J. (**1977**). "Stop consonant recognition: Release bursts and formant transitions as functionally equivalent, context-dependent cues," Percept. Psychophys. **22**, 109–122.

Fischer-Jørgensen, E. (**1954**). "Acoustic analysis of stop consonants," Miscellanea Phonetica **2**, 42–59.

Fruchter, D., and Sussman, H. M. (**1997**). "The perceptual relevance of locus equations," J. Acoust. Soc. Am. **102**, 2997–3008.

Liberman, A. M., Cooper, F. S., Shankweiler, D. P., and Studdert-Kennedy, M. (**1967**). "Perception of the speech code," Psychol. Rev. **74**, 431–461.

Liberman, A. M., Delattre, P. C., and Cooper, F. S. (**1952**). "The role of selected stimulus-variables in the perception of the unvoiced stop consonants," Am. J. Phys. **65**, 497–516.

Liberman, A. M., Delattre, P. C., Cooper, F. S., and Gerstman, L. J. (**1954**). "The role of consonant-vowel transitions in the perception of the stop and nasal consonants," Psychol. Monogr. **68**, 1–13.

Liberman, A. M., Harris, K. S., Hoffman, H. S., and Griffith, B. C. (**1957**). "The discrimination of speech sounds within and across phoneme boundaries," J. Exp. Psychol. **54**, 358–368.

Liberman, A. M., and Mattingly, I. G. (**1985**). "The motor theory of speech perception revised," Cognition **21**, 1–36.

McCullagh, P., and Nelder, J. A. (**1989**). *Generalized Linear Models* (Chapman & Hall, London), 2nd. ed.

Nearey, T. M. (**1990**). "The segment as a unit of speech perception," J. Phonetics **18**, 347–373.

Repp, B. H., and Lin, H.-B. (**1989**). "Acoustic properties and perception of stop consonant release transients," J. Acoust. Soc. Am. **85**, 379–396.

Stevens, K. N. (**2000**). *Acoustic Phonetics* (MIT, Cambridge, MA).

Zue, V. W. (1976). "Acoustic characteristics of stop consonants: A controlled study," Doctoral thesis, Massachusetts Institute of Technology.

Phonetic identification in quiet and in noise by listeners with cochlear implants

Benjamin Munson[a] and Peggy B. Nelson
Department of Speech-Language-Hearing Sciences, University of Minnesota, Twin Cities, Minneapolis, Minnesota 55455

(Received 28 July 2004; revised 27 June 2005; accepted 28 June 2005)

This study examined the effect of noise on the identification of four synthetic speech continua (/rɑ/-/lɑ/, /wɑ/-/jɑ/, /i/-/u/, and *say-stay*) by adults with cochlea implants (CIs) and adults with normal-hearing (NH) sensitivity in quiet and noise. Significant group-by-SNR interactions were found for endpoint identification accuracy for all continua except /i/-/u/. The CI listeners showed the least NH-like identification functions for the /rɑ/-/lɑ/ and /wɑ/-/jɑ/ continua. In a second experiment, NH adults identified four- and eight-band cochlear implant stimulations of the four continua, to examine whether group differences in frequency selectivity could account for the group differences in the first experiment. Number of bands and SNR interacted significantly for /rɑ/-/lɑ/, /wɑ/-/jɑ/, and *say-stay* endpoint identification; strongest effects were found for the /rɑ/-/lɑ/ and *say-stay* continua. Results suggest that the speech features that are most vulnerable to misperception in noise by listeners with CIs are those whose acoustic cues are rapidly changing spectral patterns, like the formant transitions in the /wɑ/-/jɑ/ and /rɑ/-/lɑ/ continua. However, the group differences in the first experiment cannot be wholly attributable to frequency selectivity differences, as the number of bands in the second experiment affected performance differently than suggested by group differences in the first experiment.
[DOI: 10.1121/1.2005887]

PACS number(s): 43.71.Ky, 43.71.Es [PFA] Pages: 2607–2617

I. INTRODUCTION

A great deal of research has shown that cochlear implants (CIs) are remarkably successful at facilitating speech perception in some listeners with severe to profound hearing loss. [See Shannon (2002) and Dorman *et al.* (2002) for reviews.] Despite the success of CIs in conveying acoustic information about speech, numerous researchers have demonstrated that there is great variability in speech perception within the population of listeners with CIs (e.g., Munson *et al.*, 2003). Some of this variability arises because the speech perception of listeners with CIs is disproportionately affected by the presence of background noise relative to people with normal-hearing (henceforth NH) sensitivity (e.g., Fu *et al.*, 1998; Nelson *et al.*, 2003; Nelson and Jin, 2004). Nelson *et al.* (2003) demonstrated that CI listeners show significant decrements in sentence recognition at relatively favorable signal-to-noise ratios (SNRs), such as +16 dB. Garnham *et al.* (2002) demonstrated that CI listeners' understanding of monosyllabic words dropped from approximately 60% correct to approximately 30% correct when they were presented in pink noise at +10 dB SNR.

It is not fully understood why CI listeners experience such a dramatic decrement in speech perception in noise. A variety of explanations for this decrement have been proposed. Some investigators have proposed that the reduced frequency selectivity of CI listeners (i.e., reduced ability to respond selectively to different-frequency stimuli) explains their poor speech perception in noise. This conjecture is supported by studies examining the speech perception in noise of CI listeners with varying frequency selectivity, and by examining the influence in changes in the number of activated electrodes in the CI device (which effectively changes frequency selectivity) in listeners with CIs (e.g., Nelson *et al.*, 2003; Fu *et al.*, 1998; Loizou *et al.*, 2000; Qin and Oxenham, 2003; Nelson and Jin, 2004). In general, these investigations find that CI listeners with better frequency selectivity are better in perceiving speech in noise than listeners with poorer frequency selectivity, and that increasing the number of activated electrodes improves speech perception in noise. This notion is also supported by studies that examine the influence of the number of simulation bands on the perception of acoustic simulations of CI speech perception in quiet and in noise. Varying the number of bands in acoustic stimulations allows for the simulation of speech perception by listeners with CIs with varying frequency selectivity. The finding that speech perception in noise improves in simulations with more bands supports the notion that differences in frequency selectivity underlie some of the variance in speech perception in noise among listeners with CIs.

In addition to there being a relatively poor understanding of why listeners with CIs as a group perceive speech poorly in noise, relatively little is known about individual differences in CI listeners' ability to understand speech in noise. Nelson and Jin (2004) observed a modest, statistically significant correlation ($r=0.50$) between listeners' overall speech recognition ability and their ability to perceive speech in noise, suggesting that CI listeners with better overall speech recognition may also be better at segregating speech from noise. A continuing challenge in research on speech

[a]Electronic mail: munso005@umn.edu

perception in listeners with CIs is to determine why some listeners with CIs are better able to perceive speech in noise than others.

One of the challenges in understanding speech perception in quiet and in noise by listeners with CIs—both as a group and in individual listeners—has been to identify the specific acoustic parameters that are most vulnerable to misperception in noise. One methodology that addresses this problem is the use of synthetic speech stimuli in perception experiments. The careful stimulus control that is possible with synthetic speech allows investigators to determine the specific acoustic information that is utilized by listeners to identify speech stimuli. Indeed, there is precedent for using synthetic speech to study speech perception in noise, and to examine individual variability in speech perception. Hazan and Rosen (1991) used synthetic stimuli to study individual variability for understanding full-cue and reduced-cue initial stop consonants. They found that some listeners showed a large decrement in identification performance on synthetic *bait-date* and *date-gate* continua when cues were reduced, while others did not. Nabelek *et al.* (1996) used synthetic diphthongs to study the specific effects of noise and reverberation on formant transition cues used by NH listeners and listeners with hearing impairment. They found that the perception of diphthongs was dependent on the relative intensity of the transition and steady-state portions of the vowel, and that the influence of relative intensity interacted with reverberation.

Despite its frequent use in speech-perception studies, relatively few studies have examined listeners with CIs' performance on synthetic continua. One exception is Hedrick and Carney (1997), who studied four CI listeners' use of spectral and amplitude information for the identification of synthetic /s/-/ʃ/ and /p/-/t/ continua. They found that normal-hearing listeners relied on both consonant amplitude (relative to that of the following vowel) and formant transition information when identifying /s/-/ʃ/ and /p/-/t/ continua. In contrast, the CI listeners' performance was greatly influenced by relative amplitude, and considerably less influenced by format transitions. This suggested that a primary cue for identification of fricative and stop consonants for some CI listeners is the amplitude envelope of the consonants. However, these listeners utilized the older MPEAK speech-processing strategy, and Hedrick and Carney's findings may not be applicable to current clinical populations.

More recently, Iverson (2003) investigated relationships between open-set word recognition and the identification and discrimination of a synthetic /t/-/d/ continuum by 25 listeners with CIs and 12 NH listeners. Iverson observed extensive between-subject variability on the word recognition task, as might be expected for a group of CI listeners. In addition, he found that CI listeners had sensitivity peaks and identification boundaries at longer VOT durations than NH listeners. Their identification boundaries were more variable and less sharp than those of NH listeners, and the discrimination sensitivity peaks were less well defined. He observed a nonmonotonic relationship between sensitivity peak location on the synthetic discrimination task and percent correct phoneme identification on an open-set word recognition task. There was no significant relationship between word recognition accuracy and discrimination sensitivity for the VOT continuum.

Much remains to be learned about synthetic speech perception by listeners with CIs. Hedrick and Carney (1997) examined only a small number of listeners using a speech-processing strategy that is no longer in wide use. The other study to examine synthetic speech perception in listeners with CI, Iverson (2003), examined only one continuum and did not examine perception in noise. The present study expands on this earlier work by examining the ability of listeners with CIs and NH listeners to perceive multiple synthetic continua varying a number of different acoustic cues, both in quiet and in noise. The continua were designed to contrast static spectral cues (/i/ versus /u/, in which the frequencies of the first three formants vary), temporal cues (*say* versus *stay*, in which the duration of the silence between the /s/ and /eɪ/ portion varies), and dynamic spectral cues (/rɑ/ versus /lɑ/ and /wɑ/ versus /jɑ/, which vary in the onset frequency of the first, second, and/or third formant transitions). Studying continua that differ in the type of cues that vary allows us to make definitive statements about relative vulnerability of different types of cues to misperception in noise. Moreover, individual differences in CI listeners' performance in quiet and in noise on these continua is examined to determine whether there was uniformity across listeners in the types of cues that are most vulnerable to misperception in noise.

This investigation has two hypotheses. First, we propose that the greatest differences between CI and NH listeners will be in the two continua that vary dynamic spectral cues, /rɑ/-/lɑ/ and /wɑ/-/jɑ/. This hypothesis arises from the observation that the speech-processing strategies employed by CI do not preserve all of the frequency information in the original acoustic signal. These algorithms extract the amplitude envelope of energy bands from acoustic signals, which are coded as pulse trains that are sent to an array of electrodes that stimulate the auditory nerve. Rapidly changing spectral information, such as the formant transitions that serve as cues to consonant place of articulation in /rɑ/-/lɑ/ and /wɑ/-/jɑ/, might fall within an acoustic band; consequently, the frequency changes would not be coded directly in the resulting pulse train. Perception of these continua would be more strongly affected by spectral reduction than continua varying steady-state formant frequencies, such as an /i/-/u/ continuum, or temporal cues, such as the *say-stay* continuum. Given that the /rɑ/-/lɑ/ and /wɑ/-/jɑ/ continua are hypothesized to be the most challenging continua for CI listeners to perceive in quiet, we further hypothesize that perception of these continua will be most vulnerable to decrements in noise. This hypothesis is examined in experiment 1, which compares synthetic speech perception in CI and NH listeners. The second hypothesis is that the CI listeners' poorer perception of the /rɑ/-/lɑ/ and /wɑ/-/jɑ/ continua is due to their poor frequency selectivity. This is tested in experiment 2, in which we examine NH listeners' identification of four- and eight-band cochlear implant simulations of the four continua from experiment 1 in quiet and in noise. We predict that perception of the /rɑ/-/lɑ/ and /wɑ/-/jɑ/ continua

TABLE I. Demographic characteristics of listeners with CIs. Listeners used a variety of Nucleus (N22 and N24) and Clarion (CI and CII) electrode configurations, including standard spiral (SPRL), HiFocus (HF), and HiFocus with electrode positioning (HF+EFS) system.

Subject ID	Age	Device	Strategy	NU-6 percentage correct words/phonemes
301	59;06	N22	SPEAK	8.0/27.3
302	64;08	N24	ACE	12.0/39.3
303	73;01	C-II HF+EPS	CIS	10.0/40.0
304	53;10	C-II HFII	HiRes	36.0/60.7
305	54;10	C-I SPRL	CIS	68.0/82.6
306	57;10	N22	SPEAK	16.0/42.0
307	72;07	C-II HF	HiRes	14.0/39.3
308	36;03	N22	SPEAK	30.0/55.0
310	48;06	C-I SPRL	CIS	50.0/66.0
311	50;03	C-II HF	PPS	70.0/85.3
312	64;07	N22	SPEAK	16.0/41.3
313	53;10	C-II HF+EPS	HiRes	52.0/77.3
Average	57;01			31.8/55.6
(Standard deviation)	(10;08)			(22.9/19.5)

will be more affected by noise and by number of bands in the simulation than perception of /i/-/u/ and *say-stay*.

II. EXPERIMENT 1: SYNTHETIC SPEECH PERCEPTION BY CI AND NH LISTENERS

A. Methods

1. Participants

Twelve listeners with CIs and 13 NH listeners participated in the experiment. The 12 listeners with CIs were recruited from a larger cohort of people who had been implanted at the University of Minnesota Otolaryngology Clinic. This was a quasi-random sample of the larger group; the only requirement for participation was that the participants were native, monolingual speakers of English. Demographic information for the listeners with CIs can be found in Table I. Many etiologies, device types, and speech-processing strategies were represented. Four CI participants used Nucleus N-22 with a spectral peak extraction (SPEAK) strategy; one used the Nucleus N-24 with the advanced combination encoder (ACE) strategy; two used a Clarion C-I with the continuous interleaved sampling (CIS) strategy; one used a Clarion C-II with the paired pulsatile stimulation (PPS) strategy; one used a Clarion C-II with CIS; and three used a Clarion C-II with the high-resolution broadband sampling (HiRes) strategy. Listeners with NH were recruited from the University of Minnesota community. Their average age was 25;04 (years;months). All testing was completed in a single session lasting approximately $1\frac{1}{2}$ hours. Subjects were paid $10/hour for their participation.

2. Stimuli

Synthetic stimuli consisted of four speech continua. These continua were created using the cascade formant synthesizer described by Klatt and Klatt (1990). All of the stimuli were sampled at 22050 Hz and low-pass filtered at 11 025 Hz to prevent aliasing. Two of the continua contained seven steps, one contained eight steps, and one contained ten steps. The number of steps was determined by the authors in preexperiment testing. Originally, seven-step continua were developed using endpoint values taken from Klatt (1980). In cases where an endpoint was not reliably perceived by both authors to be a good example of the intended syllable, additional stimuli were created until both authors agreed that both endpoints were unambiguous tokens of their intended syllables. This happened in two cases, the /lɑ/ endpoint of the /rɑ/-/lɑ/ continuum and the *stay* endpoint of the *say-stay* continuum.

The first was a seven-step /i/-/u/ continuum. All stimuli in this continuum were 500 ms long. All of the stimuli had an f0 that began at 125 Hz, rose to 145 Hz over a 75 ms span, remained steady at 145 Hz for 75 ms, then fell linearly to 100 Hz over the remaining 350 ms. The stimulus intensity was manipulated such that each stimulus had a linear ramping of the intensity from 0 to 100 ms, then a damping from 100 ms to the end of the stimulus. The /i/ endpoint had an F1 frequency/bandwidth of 342 Hz/45 Hz, F2 of 2322 Hz/200 Hz, and F3 of 3000 Hz/400 Hz. The /u/ endpoint had an F1 frequency/bandwidth of 427 Hz/60 Hz, F2 of 2034 Hz/90 Hz, and F3 of 2684 Hz/90 Hz. Intermediate stimuli were created containing values of these parameters in equal linear steps between those of the endpoint stimuli.

The second continuum was a seven-step /wɑ/-/jɑ/ continuum. All of these stimuli were 500 ms long. The formant transitions were 150 ms long; the steady-state portion was 350 ms long. The f0 and intensity contours of these stimuli were identical to those for the /i/-/u/ continuum. The steady-state /ɑ/ portion of the stimulus had an F1 center frequency/bandwidth of 768 Hz/130 Hz, F2 of 1333 Hz/70 Hz, and F3 of 2522 Hz/60 Hz. The F1 onset frequency/bandwidth for the /wɑ/ endpoint was 290 Hz/60 Hz, the F2 was 610 Hz/80 Hz, and the F3 from 2150 Hz/60 Hz. For the /jɑ/ endpoint, the F1 onset frequency was 260 Hz/40 Hz, the F2 of 2070 Hz/250 Hz, and F3 was 3020 Hz/500 Hz. During the transition period of the stimulus, the formant frequencies and bandwidths were interpolated from the onset values to the steady-state values. Intermediate stimuli were created with onset F1, F2, and F3 frequencies with values in equal linear steps between those of the endpoint stimuli.

The third continuum was an eight-step /rɑ/-/lɑ/ continuum. All of these stimuli were 500 ms long. The formant transitions were 150 ms long; the steady-state portion was 350 ms long. The f0 and intensity contours of these stimuli were identical to those for the /i/-/u/ continuum. The steady-state /ɑ/ portion of the stimulus was identical to that for the /wɑ/-/jɑ/ continuum. The F1 onset frequency/bandwidth was 310 Hz/47 Hz and the F2 onset was 1060 Hz/100 Hz. The F3 onset frequency/bandwidth varied from 2150 Hz/60 Hz for the /rɑ/ endpoint to 3020 Hz/500 Hz for the /lɑ/ endpoint in equal linear steps. During the transition period of the stimulus, the formant frequencies and bandwidths were interpolated from the onset values to the steady-state values.

The fourth continuum was a 10-step *say-stay* continuum. This continuum was created by concatenating a 140 ms synthetic /s/ with a 500 ms synthetic /deɪ/. The /s/ portion had a

center frequency of 5000 Hz. The F1 of the /eɪ/ portion had a starting frequency of 390 Hz and a steady-state frequency of 550 Hz; the F2 had a starting frequency of 1500 Hz and rose to 1850 Hz. The transitions were 50 ms long. The gap between the /s/ and the /deɪ/ varied from 0 to 90 ms in 10-ms steps. The total stimulus duration varied from 640 to 730 ms.

Stimuli were normalized for rms amplitude prior to being presented. Each stimulus was presented both in quiet and at a +10-dB signal-to-noise ratio. For each continuum, noise was constructed to match the long-term spectrum of the continuum with which it was mixed. Stimuli were mixed with noise prior to presentation. To reduce the possibility that a particular sample of noise would have an idiosyncratic masking effect on a particular stimulus, three samples of noise were generated and mixed to each stimulus (i.e., there were three separate tokens of the stimuli in noise). The noise was gated on concurrent with the stimulus onset.

3. Procedure

The experiment took place in a double-walled sound-attenuated booth in a university laboratory. Stimuli were output from a personal computer through a powered speaker (Roland DS-90A) located 0° azimuth at a level of 65 dB A, as calibrated prior to the experiment using a sound-level meter located at the approximate location of the listeners' heads during the experiment. The session was blocked by continuum and by SNR. The order of the eight experiments (4 continua $\times$ 2 SNR) was randomized across participants. Each experiment began with a block in which listeners heard the endpoint stimuli concurrent with a video display of the stimulus' identity in standard orthography (e.g., *EE*$\sim$*OO* for the /i/-/u/ continuum). This was followed by a block in which listeners identified endpoint stimuli, with feedback on their accuracy. This was followed by the experimental block. During the experimental block, listeners heard nine tokens of each stimulus. For the quiet stimuli, these were nine presentations of the same stimulus. In the +10 dB SNR condition, there were three presentations of each of the different noise-plus-stimulus combinations described in Sec. II A 2. Presentation was controlled by the *E-Prime* experiment-management software and was fully randomized. During all phases of the experiment, participants responded on a button-box on which the endpoint stimuli were labeled using standard orthographic transcriptions (i.e., *EE*$\sim$*OO*, *Ra*$\sim$*La*, *Wa*$\sim$*Ya*, *Say*$\sim$*Stay*). Responses were logged automatically.

4. Analysis

Three dependent measures were analyzed. These dependent measures were chosen because they represent measures of listeners' ability to perceive the acoustic characteristics of the individual endpoint stimuli (*within-category* measures) and to perceive the differences between the endpoint stimuli (*between-category* measures). The first of these was *endpoint accuracy*. For this analysis, we measured the accuracy with which subjects identified the endpoint stimuli only. This was measured separately in quiet and in noise. This variable indicates the relative ease with which listeners identified the synthesized tokens that were intended to be most prototypical. Endpoint accuracy can be thought of as a within-category measure, as it shows how well the listeners could identify the stimuli that were, within the constraints of the synthesis algorithm, closest to the prototypes for the endpoint categories.

The second dependent measure was *total responses*. This is calculated by integrating the observed identification functions. This measure indicates whether there is a systematic bias to respond to one of the endpoint stimuli.[1] The third measure we examined was *slope*, derived from a probit analysis. The maximum likelihood procedure described by Bock and Jones (1968) was used to fit a probit function to identification functions. The slope of this function is calculated as probit units per stimulus step. This measure is presumed to reflect the extent to which the endpoint stimuli are differentiated in the identification task. Strongly sigmoidal functions have steep slopes; these are presumed to indicate that the two endpoint stimuli are perceived to be categorically different. In contrast, more linear functions have shallower slopes; these are presumed to indicate that the two endpoint stimuli are perceived to be continuously different. This dependent measure is frequently used in the analysis of data on the identification of synthetic continua (e.g., Hazan and Barret, 2000). Total responses and slope can be thought of as between-category measures, as they reflect participants' knowledge of the differences between the endpoint stimuli.

B. Results

1. Endpoint accuracy

For each of the four continua, arcsine-transformed percent accuracy in identifying the endpoint stimuli was calculated separately for the two groups in quiet and in noise. Each of the four continua was submitted to a separate three-factor mixed-model ANOVA, with SNR (quiet vs. +10 dB) and endpoint (i.e., /i/ vs. /u/ for the /i/-/u/ continuum, /rɑ/ vs. /lɑ/ for the /rɑ/-/lɑ/ continuum, etc.) as the within-subjects factors, and group (CI vs. NH) as the between-subjects factor.

When performance on the /i/-/u/ continuum was examined, no significant effects of SNR, endpoint, or group were found. In addition, none of the interactions were significant. This can be seen in Fig. 1, which shows similar performance on endpoint identification in quiet and in noise by listeners with CIs and listeners with NH.

When performance on the /wɑ/-/jɑ/ continuum was examined, no significant main effects were found. However, a significant interaction between SNR and group was found, $F[1,23]=5.2$, $p<0.05$. As Fig. 2 shows, the two groups performed similarly in quiet. The listeners with CIs were less accurate in endpoint identification than the listeners with NH in noise. This appears to be limited to their performance on the /wɑ/ endpoint; however, the three-way interaction among group, SNR, and endpoint did not achieve statistical significance. None of the other interactions achieved significance.

Performance on the /rɑ/-/lɑ/ continuum is shown in Fig. 3. ANOVAs revealed significant main effects of SNR ($F[1,23]=9.2, p<0.05$) and group ($F[1,23]=9.6, p<0.05$).

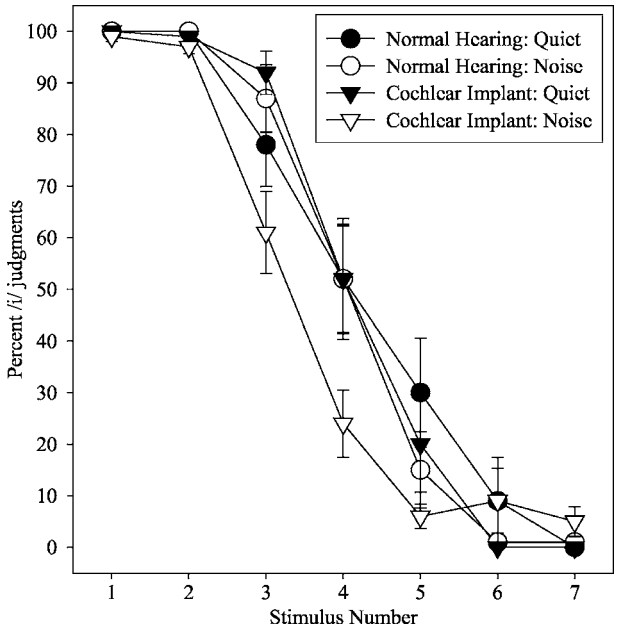

FIG. 1. Average performance for listeners with CIs and listeners with NH on the continuum /i/-/u/ in quiet and in noise. Error bars represent one standard error of measurement.

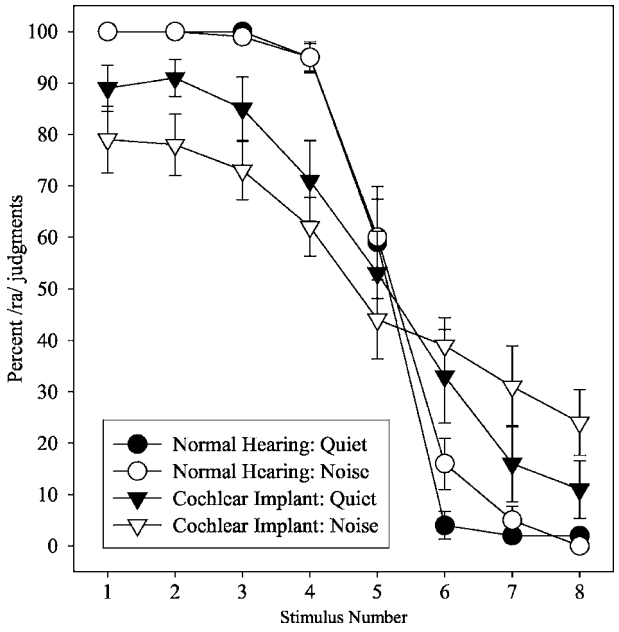

FIG. 3. Average performance for listeners with CIs and listeners with NH on the /rɑ/-/lɑ/ continuum in quiet and in noise. Error bars represent one standard error of measurement.

No significant main effect of endpoint was found. A significant interaction between SNR and group was found, $F[1,23]=11.5$, $p<0.05$. As Fig. 3 shows, listeners with CIs identified endpoints less accurately than listeners with NH both in quiet and in noise; however, the difference was larger in noise. None of the other interactions achieved statistical significance.

When performance on the *say-stay* continuum was examined, a significant main effect of SNR was found, $F[1,23]=6.3$, $p<0.05$. No significant main effect was found for endpoint. The effect of group approached significance, $F[1,23]=3.5$, $p=0.07$. Two significant interactions were found: group by SNR ($F[1,23]=4.3, p<0.05$) and group by endpoint ($F[1,23]=4, p=0.05$). The interactions can be observed in Fig. 4. The interaction between group and SNR arose because the performance of the listeners with CIs was more affected by noise than the performance of listeners with NH. The interaction between group and endpoint arose because there were greater group differences in performance on the *say* end of the continuum than on the *stay* end. None of the other interactions achieved statistical significance.

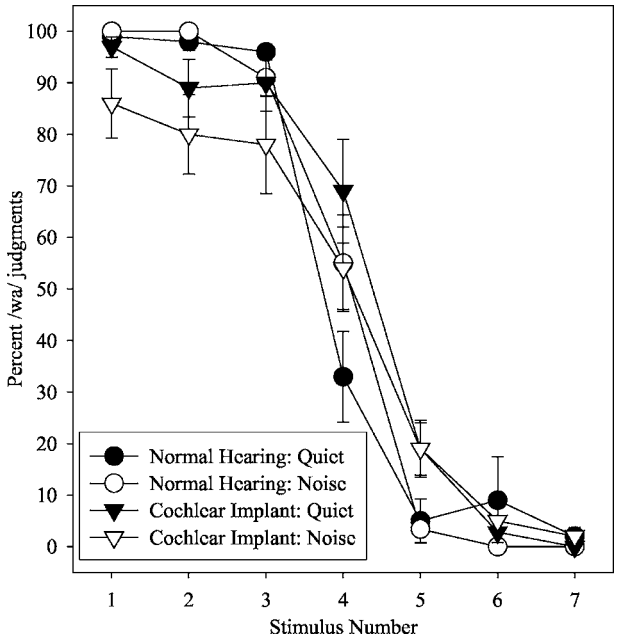

FIG. 2. Average performance for listeners with CIs and listeners with NH on the /wɑ/-/jɑ/ continuum in quiet and in noise. Error bars represent one standard error of measurement.

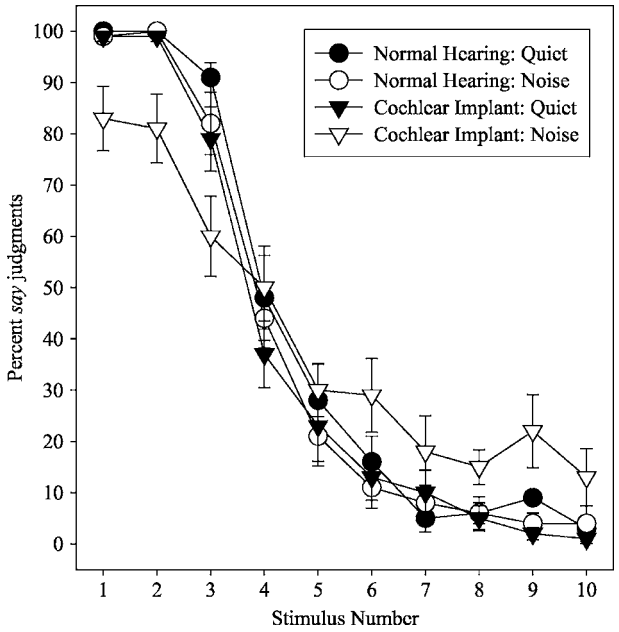

FIG. 4. Average performance for listeners with CIs and listeners with NH on the *say-stay* continuum in quiet and in noise. Error bars represent one standard error of measurement.

2. Total responses

The second set of ANOVAs examined the total responses to one of the endpoint stimuli. As explained in Sec. II A 4, this measure reveals whether there were systematic biases to respond to one of the endpoint stimuli. The four continua were examined separately. For each continuum, total endpoint responses were calculated separately for the two groups' performance in the two SNR conditions. These measures were submitted to a two-factor, mixed-model ANOVA, with SNR (quiet vs. +10 dB) as the within-subjects factor, and group (CI vs. NH) as the between-subjects factor.

When performance on the /i/-/u/ continuum was examined, no effect of group was found. A significant main effect of SNR was found, $F[1,23]=7.3$, $p<0.05$. More /u/ responses were noted in the +10 dB SNR condition than in quiet. The interaction between these two factors approached significance, $F[1,23]=3.5$, $p=0.07$. This interaction can be seen in Fig. 1. As this figure shows, the effect of SNR was significant only for listeners with CIs, who perceived fewer /i/ tokens in noise than in quiet: on average, listeners perceived 49% of all responses in noise as /i/ (SD=10%), and 59% as /i/ in quiet (SD=8%). Responses by the listeners with NH in the two conditions were comparable.

When performance on the /wɑ/-/jɑ/ continuum was examined, no significant main effects were found for group or SNR. The interaction between these factors achieved statistical significance, $F[1,23]=7.4$, $p<0.01$. This interaction is shown in Fig. 2. As Fig. 2 shows, the listeners with CIs perceived more /wɑ/ tokens in quiet than noise: on average, 52% of all responses in quiet were /wɑ/, while 46% of responses in noise were /wɑ/. The pattern was opposite for the listeners with NH, who perceived more /wɑ/ tokens in noise (50%) than in quiet (47%).

When the /rɑ/-/lɑ/ continuum was examined, no effects were found of group or SNR. Moreover, these factors did not interact significantly. The same pattern was found for the *say-stay* continuum. There was no significant effect of SNR or group, and these factors did not interact significantly.

3. Slope

The final set of ANOVAs examined the influence of group and SNR on the slopes of individual listeners' identification functions. These were calculated separately in quiet and in noise for each of the continua. When the /i/-/u/ continuum was examined, no significant effect was found for group. The effect of SNR approached significance, $F[1,23]=3.6$, $p=0.07$. As Fig. 1 shows, the slopes of the identification functions were shallower in noise than in quiet. These factors did not interact significantly. A similar pattern was found for the *say-stay* continuum: no significant main effects were found for either SNR or group, nor did these factors interact significantly.

When the /wɑ/-/jɑ/ continuum was examined, no significant main effect of SNR was found. A significant effect of group was found, $F[1,23]=15.5$, $p<0.05$. Across the two SNRs, the listeners with CIs demonstrated shallower identification functions than listeners with NH. Group and SNR did not interact significantly. A similar pattern was found for the /rɑ/-/lɑ/ continuum. No significant main effect was found for SNR. Again, a significant effect of group was found, $F[1,23]=10.6$, $p<0.05$. Across the two SNR conditions, the listeners with CIs showed shallower identification functions than the listeners with NH. Again, these factors did not interact significantly.

C. Summary of ANOVAs

There were significant main effects of group for 3 of the 12 ANOVAs, with one additional condition showing a group difference that approached statistical significance. For the /rɑ/-/lɑ/ continuum, the listeners with CIs were less accurate in identifying endpoint stimuli than NH listeners, and showed shallower identification functions. For the /wɑ/-/jɑ/ continuum, the listeners with CIs showed less accurate endpoint identification in noise, and shallower identification functions overall. For the *say-stay* continuum, listeners with CIs were less accurate than NH listeners in identifying endpoints in noise. Listeners with CIs and NH listeners differed in within- and between-category measures. That is, listeners with CIs appear to show an overall reduced ability to perceive the acoustic cues of the endpoint stimuli and in perceiving the differences between endpoint stimuli, rather than an isolated difference in perceiving one of the endpoint stimuli, or a shallow identification function in the absence of inaccurate endpoint identification.

Based on the results of the ANOVAs, we can conclude that perception of the /i/-/u/ continuum is least affected by noise. The only robust, statistically significant group differences were in total responses in one of the SNR conditions. In addition, performance on the *say-stay* continuum was relatively stable across groups and SNR conditions. The only significant effect was on endpoint accuracy by the listeners with CIs in the +10 dB SNR condition. In contrast, performance on the /rɑ/-/lɑ/ and /wɑ/-/jɑ/ continua was far more vulnerable to manipulations in SNR and demonstrated the largest group differences. Endpoint accuracy and slope measures differed significantly between groups. Endpoint accuracy was also affected by SNR, and this interacted with group. These differences can be seen most clearly in Fig. 3, which plots performance on the /rɑ/-/lɑ/ continuum: endpoints were identified less accurately by listeners with CIs, particularly in the unfavorable SNR condition. Moreover, the identification functions of the listeners with CIs are clearly shallower than those of the listeners with NH.[2]

D. Analysis of individual differences

1. Method

One of the goals of this investigation was to examine individual variability among listeners with CIs systematically. Performance of individual CI listeners varied greatly, as is illustrated by the large error bars in Figs. 1–4. This finding was not unexpected: listeners with CIs are a heterogeneous group and high levels of within-group variability can be found in almost any study of listeners with CIs (e.g., Munson *et al.*, 2003). The purpose of our individual-subjects analysis was to determine whether there was a hierarchy of difficulty among the four continua we examined. That is, we

TABLE II. Performance for the individual listeners with CIs on experiment 1, measured as mean squared difference from the average performance of the NH listeners. See text for details.

	Continuum								
	/rɑ/-/lɑ/		*say-stay*	/wɑ/-/jɑ/		/i/-/u/		*say-stay*	
Subject	Noise	Quiet	Noise	Noise	Quiet	Noise	Quiet	Quiet	Average
307	17.3	26.8	2.9	31.4	12.1	12.5	4.5	2.8	13.8
306	19.4	4.6	8.0	10.2	9.0	5.5	11.1	3.2	8.9
313	15.2	11.2	6.2	12.5	4.5	4.8	3.1	6.8	8.0
304	13.8	16.4	15.1	1.1	2.4	4.1	2.1	4.0	7.4
305	14.0	5.2	15.1	2.3	4.5	2.5	4.4	1.3	6.2
308	1.1	1.5	16.0	0.8	6.4	14.3	5.4	1.9	5.9
312	11.5	10.8	8.4	2.7	5.5	1.7	3.5	0.9	5.6
302	9.6	7.8	1.2	5.3	8.6	0.6	2.4	0.3	4.5
311	6.5	0.7	4.1	5.6	9.2	1.1	3.4	3.6	4.3
303	11.7	1.9	0.5	1.1	3.3	1.6	4.1	1.5	3.2
301	2.4	5.4	4.2	0.3	0.4	5.6	3.0	0.5	2.7
310	3.1	0.9	0.6	0.5	0.4	0.3	6.0	0.9	1.6
Average	10.5	7.8	6.9	6.1	5.5	4.5	4.4	2.3	
Standard deviation	6.0	7.7	5.8	8.9	3.7	4.5	2.4	1.8	

wanted to determine whether performance that was very unlike that of the NH listeners on one continuum (e.g., /rɑ/-/lɑ/) implied performance that was unlike the NH listeners' performance on another continuum (e.g., /i/-/u/), or whether listeners with CIs varied randomly in the continua on which they deviated from the performance of the NH listeners. To do this, we needed to develop a measure through which we could quantify the difference between the individual listeners with CIs and the average performance of the listeners with NH. To accomplish this, we quantitatively compared the identification functions of each listener with a CI to the average identification functions of the entire group of listeners with NH. Specifically, we calculated the difference between each CI listener and the average performance of the NH listeners for each step on the continuum. We then squared this, and calculated the mean-squared difference (MSD) across the entire continuum. These MSD measures were calculated separately for the four continua in the two SNRs, for a total of eight data-points per participant with a CI. Higher MSD values indicate a larger deviation from the listeners with NH (i.e., poorer performance) than lower MSD values.

2. Results

MSD values are shown in Table II, which is organized from the least-NH-like participant at the top, to the most-NH-like participant at the bottom. For this analysis, *least-NH-like* and *most-NH-like* were determined by ranking the average MSD across the eight continua for each listener with a CI. The columns are organized from the condition in which the listeners with CIs differed most from NH listeners overall at the left, to the condition in which the listeners with CIs performed most like the listeners with NH listeners overall at the right, as determined by the average MSD across the 12 listeners with CIs. As Table II shows, the variability within conditions was greatest for the four continua on which the listeners with CIs demonstrated the least-NH-like performance.

Table II shows that there was not perfect consistency among the 12 listeners in which continua were the least NH-like. For example, simple correlations (Pearson's r) showed that performance on the *say-stay* condition in noise did not correlate significantly with performance on any of the other conditions ($r<0.2, p>0.05$ for all comparisons). In contrast, correlations between the /rɑ/-/lɑ/ and /wɑ/-/jɑ/ continua were significant, both in quiet and in noise ($r>0.60, p<0.01$ for both correlations). This suggests that differences at the group level potentially arise from different mechanisms, with most listeners showing greatest decrements in the two continua in which dynamic spectral cues varied (/rɑ/-/lɑ/ and /wɑ/-/jɑ/), and a smaller subset of listeners showing greater decrements in the temporal-cue only *say-stay* continuum.

E. Discussion

The results of this experiment confirm that the acoustic cues that are most vulnerable to noise-related decrements are rapidly changing spectral cues, such as the formant transitions in the /rɑ/-/lɑ/ and /wɑ/-/jɑ/ continua. One reasonable hypothesis that follows from this finding is that these group differences are related to listeners' frequency selectivity. As described above, there is a well-established relationship between CI listeners' frequency selectivity and their speech perception in noise (Friesen *et al.*, 2001; Fu *et al.*, 1998; Qin and Oxenham, 2003). Listeners who gain greater benefit from increases in the number of spectral channels show better speech perception in noise than those who can perceive fewer spectral channels. It is possible that the listeners with CIs in this investigation showed poorer perception of /rɑ/-/lɑ/ and /wɑ/-/jɑ/ continua in noise because of their poorer frequency selectivity than the NH listeners. To further evaluate this hypothesis, we conducted a second experiment

in which we presented NH listeners with four- and eight-band cochlear implant simulations of the four synthetic continua. If frequency selectivity is implicated in the group differences we observed, then manipulating the number of simulation bands in experiment 2 should influence synthetic speech perception in a manner similar to how group influenced performance in experiment 1.

III. EXPERIMENT 2: COCHLEAR IMPLANT SIMULATIONS IN NORMAL-HEARING LISTENERS

A. Methods

1. Participants

Eleven college-age adults participated in experiment 2. All of the adults were native speakers of English, with no reported history of speech, language, or hearing disorders. None participated in the first experiment. Testing took place in a single session, which lasted approximately 3 h. Participants received $30.00 for their participation.

2. Stimuli

Stimuli for experiment 2 were four- and eight-band simulations of the four continua from experiment 1. The choice to use both four- and eight-band simulations was motivated by Friesen *et al.*'s (2001) finding that poorer-performing listeners with CIs do not improve beyond four spectral channels, while better-performing listeners improve up to seven spectral channels. The algorithm used to generate the stimuli was identical to that used by Nelson and Jin (2004). Briefly, the algorithm of Shannon *et al.* (1995) was used, in which stimuli were filtered into bands; the amplitude envelopes were extracted from each band using the amplitude-extraction algorithm in the Cool Edit Pro software (Syntrillium, Inc., 1996); appropriate narrow-band noise-sources with the same bandwidth were fit to the amplitude envelope of each band; and the bands were mixed together preserving the original relative amplitudes. The filter cutoffs for the four- and eight-band stimuli are shown in Table III. Stimuli were normalized for rms amplitude prior to being presented.

TABLE III. Filter cutoffs for four- and eight-band simulations used in the CI simulations.

Four-band simulations		
Band	Low-pass cutoff (Hz)	High-pass cutoff (Hz)
1	327	648
2	677	1341
3	1400	2773
4	2898	5739
Eight-band simulations		
Band	Low-pass cutoff (Hz)	High-pass cutoff (Hz)
1	283	546
2	546	870
3	870	1300
4	1300	1810
5	1810	2460
6	2460	3265
7	3265	4280
8	4280	5540

3. Procedure

The procedures were the same as in experiment 1, with the exception that experiment 2 was blocked by number of bands in addition to being blocked by continuum and SNR. Experimental blocks were randomized, and each subject participated in a unique order. As in experiment 1, each experimental block was preceded by a block in which participants heard the endpoint stimuli with a concurrent visual display providing its identity, with no response required. This was followed by a block in which they identified the endpoints, with feedback on their accuracy. In the experimental block, nine presentations of each stimulus were given.

B. Results

1. Endpoint accuracy

Four three-factor within-subjects ANOVAs were used to examine the influence of SNR (quiet vs. +10 dB), and number of bands (4 vs. 8) on accuracy of identification of the two endpoints. In the ANOVA examining performance on the /i/-/u/ continuum, none of the main effects were significant. There was, however, a significant two-way interaction between endpoint and number of bands ($F[1,10]=7.2$, $p<0.05$) as well as a three-way interaction among endpoint, number of bands, and SNR ($F[1,10]=6.2, p<0.05$). Inspection of Fig. 5 suggests that this three-way interaction resulted from the effect of SNR being restricted to the /i/ endpoint in the four-band condition.

When performance on the seven-step /wɑ/-/jɑ/ con-

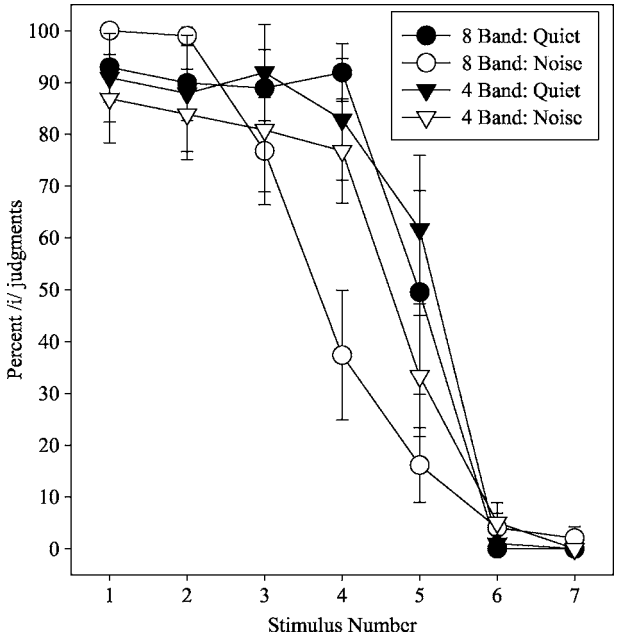

FIG. 5. Average performance for NH listeners on the four- and eight-band simulations of the continuum /i/-/u/ in quiet and in noise. Error bars represent one standard error of measurement.

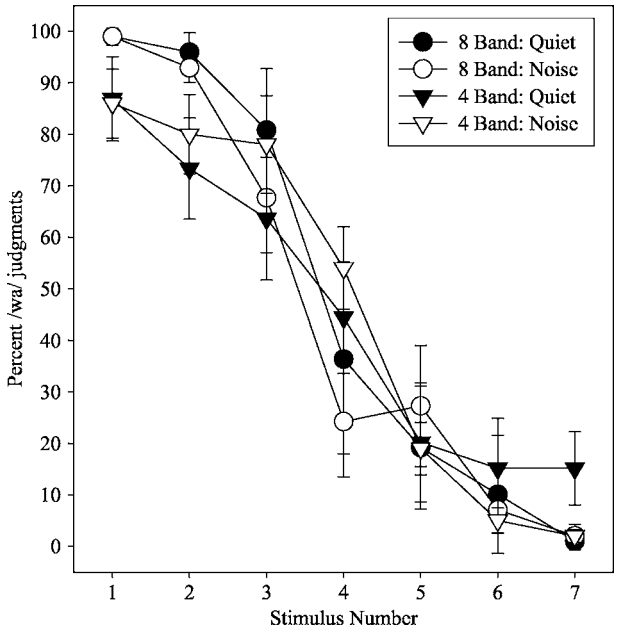

FIG. 6. Average performance for NH listeners on the four- and eight-band simulations of the /wɑ/-/jɑ/ continuum in quiet and in noise. Error bars represent one standard error of measurement.

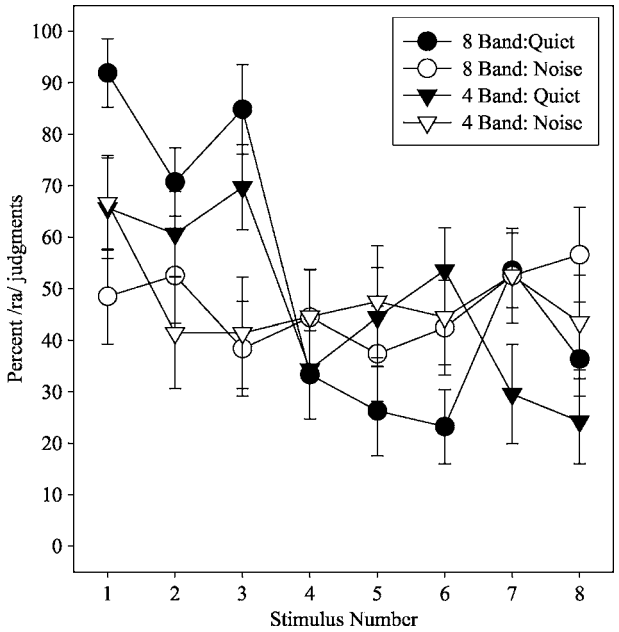

FIG. 7. Average performance for NH listeners on the four- and eight-band simulations of the /rɑ/-/lɑ/ continuum in quiet and in noise. Error bars represent one standard error of measurement.

tinuum was examined, a main effect of SNR was found ($F[1,10]=15.3, p<0.01$). Endpoints were identified less accurately in noise than in quiet. There was also a significant main effect of number of bands, $F[1,10]=6.7$, $p<0.05$. Identification was lower overall for the four-band stimuli than for the eight-band stimuli. Finally, there was an interaction between number of bands and SNR, $F[1,10]=9.0$, $p<0.05$. This interaction can be seen by comparing the identification functions in Fig. 6. As this figure shows, the influence of noise on endpoint accuracy was greater for the four-band simulations than for the eight-band simulations.

When performance on the /rɑ/-/lɑ/ continuum was examined, a significant main effect of SNR was found, $F[1,10]=14.1$, $p<0.01$. There were no significant main effects of number of bands or of endpoint; however, there was a significant three-way interaction among SNR, number of bands, and endpoint, $F[1,10]=7.7$, $p<0.05$. Inspection of Fig. 7 suggests that this interaction arose because SNR did not influence endpoint identification for the /rɑ/ endpoints in the four-band simulation, but it did affect /lɑ/ endpoints in the four-band condition.

Finally, when the *say-stay* continuum was examined, a significant main effect of endpoint was found, $F[1,10]=6.3$, $p<0.05$. Across the two SNRs and the two band conditions, the *stay* endpoint was identified less accurately than the *say* endpoint. There was also a significant effect of number of bands, $F[1,10]=11.4$, $p<0.01$. Across the two endpoints and the two SNRs, stimuli were identified less accurately in the four-band condition than in the eight-band condition. There were no interactions. The identification data for *say-stay* are shown in Fig. 8.

2. Total responses

Four two-factor within-subjects ANOVAs examined the influence of SNR and number of bands on total endpoint responses. When the /i/-/u/ continuum was examined, a significant main effect of SNR was found, $F[1,10=18.8$, $p<0.01]$. Fewer /i/ tokens were heard in noise than in quiet. In contrast, no significant effect of SNR or number of bands was found for the other three continua.

3. Slope

The final set of four ANOVAs examined the influence of SNR and number of bands on the slopes of individual listeners' identification functions. A two-factor within-subjects de-

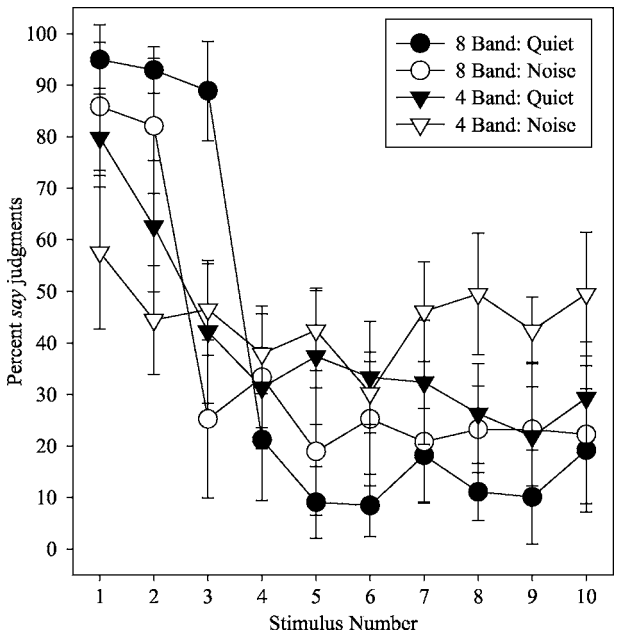

FIG. 8. Average performance for NH listeners on the four- and eight-band simulations of the *say-stay* continuum in quiet and in noise. Error bars represent one standard error of measurement.

sign was used for each ANOVA. When /i/-/u/ performance was examined, a significant main effect of SNR was found, $F[1,10]=5.0, p=0.05$. This occurred because the identification functions were shallower in the +10 dB SNR condition than in the quiet condition. There was no significant main effect of number of bands, and the interaction was not significant. A similar pattern was found for slopes for the /wɑ/-/jɑ/ continuum. A significant main effect of SNR was found, $F[1,10]=9.0, p<0.05$. Again, slopes in the +10 dB SNR condition were shallower than in the quiet condition. There was no effect of number of bands, nor an interaction between the two factors. The same pattern was found for performance on the /rɑ/-/lɑ/ continuum. There was a significant main effect of SNR, $F[1,10]=12.5, p<0.05$. Again, slopes were shallower in the +10 dB SNR condition than in quiet. There was no effect of number of bands, nor an interaction between the two factors. Finally, when performance on the *say-stay* continuum was examined, no significant effects of number of bands or SNR were found.

C. Discussion

The results of this experiment suggest that perception of the /rɑ/-/lɑ/ and *say-stay* continua is most vulnerable to reductions in the number of spectral bands in the CI simulation and to unfavorable signal-to-noise ratios. These continua included one that varied a dynamic spectral cue (/rɑ/-/lɑ/) and one that varied a temporal-only cue (*say-stay*). In contrast, perception of the /wɑ/-/jɑ/ and /i/-/u/ continua were relatively less affected by spectral reductions and the introduction of noise. These findings stand in contrast to those of experiment 1, in which the two continua for which spectral cues were varied showed greater group differences and larger decrements in noise than the temporal-only *say-stay* continuum, which showed larger group differences and decrements in noise than the /i/-/u/ continuum. However, two general findings were common to the two experiments: perception of /rɑ/-/lɑ/ was most vulnerable to experimental manipulations, while /i/-/u/ was least vulnerable. This suggests that the group differences between listeners with CIs and NH listeners in experiment 1 cannot be attributed solely to spectral distinctiveness alone. If this conjecture were true, then number of bands would have affected NH simulation listeners in experiment 2 in a manner similar to the effect of group in experiment 1.

This conclusion is qualified by two observations. First, the average identification functions for the two most affected continua, /rɑ/-/lɑ/ and *say-stay*, are highly nonmonotonic in some conditions, and this was true for many individual subjects. This makes probit analyses less appropriate than for the other continua, /i/-/u/ and /wɑ/-/jɑ/. Second, the listeners in this experiment were not provided with extensive preexperiment training on perceiving CI simulations. It is well established that some of the variability in speech perception by listeners with CIs can be attributed to the experience that they have using a CI device (Gantz *et al.*, 1993). More-experienced listeners are more successful in perceiving speech than less-experienced listeners. The listeners in experiment 2 did not have extensive practice and training listening to spectrally degraded signals. While familiarization with the stimuli was provided, this cannot be considered comparable to the experience that real-world CI listeners have in perceiving degraded signals.

IV. GENERAL DISCUSSION

Overall, the identification performance of most listeners with CIs in experiment 1 was quite similar to that of NH listeners for stimuli presented in quiet, especially when endpoint accuracy and total responses were examined. Listeners with CIs were more adversely affected by the noise, however, for the continua that varied dynamic spectral cues, /wɑ/-/jɑ/ and /rɑ/-/lɑ/. Some of the individual CI listeners performed very similarly to the NH listeners; other CI listeners performed considerably more poorly. The cause of these differences in performance is unclear. The results of experiment 2, which examined NH listeners perception of cochlear implant simulations of the four continua in quiet and in noise, suggest that the group differences in experiment 1 are not wholly attributable to differences in frequency selectivity. As in the earlier experiment, perception of /rɑ/-/lɑ/ was most vulnerable to manipulations in number of bands—which models differences in frequency selectivity—and SNR. However, perception of *say-stay* was also strongly influenced by these variables, and perception of /wɑ/-/jɑ/ was not. This suggests that the differences between CI and NH listeners are not due solely to frequency selectivity. If that were true, then we would expect that /rɑ/-/lɑ/ *and* /wɑ/-/jɑ/ would have been more affected by noise and reductions in the number of bands in experiment 2 than /i/-/u/ and *say-stay*.

These findings complement those of previous studies that have demonstrated significant sentence-perception deficits in noise by CI and NH simulation listeners (e.g., Nelson *et al.*, 2003; Qin and Oxenham, 2003; Nelson and Jin, 2004). In each of those previous studies, CI and NH simulation listeners experienced significant decrements in sentence perception in the presence of background noise at SNRs similar to those of the current study. In Nelson *et al.* (2003) and Nelson and Jin (2004), CI and NH simulation listeners' performance dropped by 20% to 50% (as measured by key words correctly repeated) between the quiet and steady noise conditions at +8 dB SNR.

The results of this study demonstrate that the influence of noise on speech perception by adults with CIs is not the same for all phonetic features. This study demonstrates that using synthetic speech can help better understand which aspects of speech sounds are most vulnerable to misperception in noise. Specifically, the results show that sounds that are most vulnerable to misperception in noise are those whose critical acoustic cues are rapidly changing spectral patterns, such as the /rɑ/-/lɑ/ and /wɑ/-/jɑ/ continua used in this study. Future studies should examine this using more continua that vary rapidly changing spectral cues. Future research should also examine systematically why listeners with CIs are more susceptible than listeners with NH to misperceiving those cues in noise.

ACKNOWLEDGMENTS

This research was supported by NIH Grant No. P01 DC00110 to David A. Nelson, by the Lions 3M Hearing Foundation, and by the Bryn Bryngelson fund in the Department of Speech-Language-Hearing Sciences. We generously thank Ankita Patel, Patrick J. Van Groll, and Heather Kreft for assistance in participant recruitment, data collection, and data analysis for experiment 1. We thank Edward Carney for assistance in writing software to conduct a pilot version of experiment 1, and for conducting probit analyses. We generously acknowledge Jill Muecke for creating stimuli and testing subjects for experiment 2. This work was presented at the Fall 2003 and Spring 2004 meetings of the Acoustical Society of America. We thank those audiences for their helpful comments. We also thank Su-Hyun Jin and Gail Donaldson for their valuable comments on this work as it was in progress.

[1]This measure is used herein instead of the more-commonly used 50% crossover point derived from a probit analysis (e.g., Bock and Jones, 1968). The stability of parameter estimates from probit analyses is dependent on the observed identification functions showing a monotonic relationship between stimulus changes and response changes. With the exception of the slope measure, we made every attempt to avoid probit-based measures in this investigation, in case any of the listeners with CIs, particularly the poorer-performing listeners, showed nonmonotonic identification functions.

[2]One cautionary note in interpreting these data concerns the age differences between the listeners with CIs and the NH listeners. These differences are not unprecedented in studies of CI speech perception [e.g., Nelson and Jin (2004) and Wojtczak *et al.* (2003), both of whom examined some of the same listeners with CI as participated in the current investigation]. The use of younger listeners may inflate the group differences between CI listeners and NH listeners, given that older adults, even those with normal hearing, perceive speech differently from younger adults [e.g., they require more acoustic information to perceive words in a gated-word recognition task than younger adults (Fox *et al.*, 1992)].

Bock, K., and Jones, L. (**1968**). *The Measurement and Prediction of Judgment and Choice* (Holden-Day, San Francisco).

Dorman, M. F., Loizou, P. C., Spahr, A. J., and Maloff, E. (**2002**). "Factors that allow a high level of speech understanding by patients fit with cochlear implants," Am. J. Audiol. **11**, 119–123.

Fox, R. A., Wall, L., and Gokcen, J. (**1992**). "Age-related differences in processing dynamic information to identify vowel quality," J. Speech Hear. Res. **35**, 892–902.

Friesen, L. M., Shannon, R. V., Baskent, D., and Wang, X. (**2001**). "Speech recognition in noise as a function of the number of spectral channels: Comparison of acoustic hearing and cochlear implants," J. Acoust. Soc. Am. **110**, 1150–1163.

Fu, Q. J., Shannon, R. V., and Wang, X. (**1998**). "Effects of noise and spectral resolution on vowel and consonant recognition: acoustic and electric hearing," J. Acoust. Soc. Am. **104**, 3586–3596.

Gantz, B. J., Woodworth, G. G., Abbas, P. J., Knutson, J. F., and Tyler, R. S. (**1993**). "Multivariate predictors of audiological success with multichannel cochlear implants," Ann. Otol. Rhinol. Laryngol. **102**, 909–916.

Garnham, C., O'Driscoll, M., Ramsden, R., and Saeed, S. (**2002**). "Speech understanding in noise with a Med-E1 COMBI 40+ cochlear implant using reduced channel sets," Ear Hear. **23**, 540–552.

Hazan, V., and Barret, S. (**2000**). "The development of phonemic categorization in children aged 6–12," J. Phonetics **28**, 377–396.

Hazan, V., and Rosen, S. (**1991**). "Individual variability in the perception of cues to place contrasts in initial stops," Percept. Psychophys. **49**, 187–2000.

Hedrick, M. S., and Carney, A. E. (**1997**). "Effect of relative amplitude and formant transitions on perception of place of articulation by adult listeners with cochlear implants," J. Speech Lang. Hear. Res. **40**, 1445–1457.

Iverson, P. (**2003**). "Evaluating the function of phonetic perceptual phenomena within speech recognition: An examination of the perception of /d/-/t/ by adult cochlear implant users," J. Acoust. Soc. Am. **113**, 1056–1064.

Klatt, D. H. (**1980**). "Software for a cascade/parallel formant synthesizer," J. Acoust. Soc. Am. **67**, 971–995.

Klatt, D. H., and Klatt, L. C. (**1990**). "Analysis, synthesis, and perception of voice quality variations among female and male talkers," J. Acoust. Soc. Am. **87**, 820–857.

Loizou, P. C., Dorman, M. F., Tu, Z., and Fitzke, J. (**2000**). "Recognition of sentences in noise by normal-hearing listeners using simulations of SPEAK-type cochlear implant signal processors," Ann. Otol. Rhinol. Laryngol. Suppl. **185**, 67–68.

Munson, B., Donaldson, G., Allen, S., Collison, E., and Nelson, D. (**2003**). "Patterns of phoneme misperceptions by listeners with cochlear implants varying in overall speech perception ability," J. Acoust. Soc. Am. **113**, 925–935.

Nabelek, A. K., Ovchinnikov, A., Czyzewski, Z., and Crowley, H. J. (**1996**). "Cues for perception of synthetic and natural diphthongs in either noise or reverberation," J. Acoust. Soc. Am. **99**, 1742–1753.

Nelson, P. B., and Jin, S.-H. (**2004**). "Factors affecting speech understanding in gated interference: Cochlear implant users and normal-hearing listeners," J. Acoust. Soc. Am. **115**, 2286–2294.

Nelson, P. B., Jin, S.-H., Carney, A. E., and Nelson, D. A. (**2003**). "Understanding speech in modulated interference: Cochlear implant users and normal-hearing listeners," J. Acoust. Soc. Am. **113**, 961–968.

Qin, M. K., and Oxenham, A. J. (**2003**). "Effects of simulated cochlear-implant processing on speech reception in fluctuating maskers," J. Acoust. Soc. Am. **114**, 446–454.

Shannon, R. V. (**2002**). "The relative importance of amplitude, temporal and spectral cues for cochlear implant design," Am. J. Audiol. **11**, 124–127.

Shannon, R. V., Zeng, F.-G., Kamath, V., Wygonski, J., and Ekelid, M. (**1995**). "Speech perception without spectral cues," Science **270**, 303–304.

Syntrillium, Inc. (**1996**). *Cool Edit (Version 96) [Computer Program]*, Phoenix, AZ.

Wojtczak, M., Donaldson, G. S., and Viemiester, N. (**2003**). "Intensity discrimination and increment detection in cochlear implant users," J. Acoust. Soc. Am. **114**, 396–407.

Incidental categorization of spectrally complex non-invariant auditory stimuli in a computer game task

Travis Wade[a] and Lori L. Holt
Department of Psychology and the Center for the Neural Basis of Cognition, Carnegie Mellon University, Pittsburgh, Pennsylvania 15213

(Received 23 November 2004; revised 14 June 2005; accepted 11 July 2005)

This study examined perceptual learning of spectrally complex nonspeech auditory categories in an interactive multi-modal training paradigm. Participants played a computer game in which they navigated through a three-dimensional space while responding to animated characters encountered along the way. Characters' appearances in the game correlated with distinctive sound category distributions, exemplars of which repeated each time the characters were encountered. As the game progressed, the speed and difficulty of required tasks increased and characters became harder to identify visually, so quick identification of approaching characters by sound patterns was, although never required or encouraged, of gradually increasing benefit. After 30 min of play, participants performed a categorization task, matching sounds to characters. Despite not being informed of audio-visual correlations, participants exhibited reliable learning of these patterns at posttest. Categorization accuracy was related to several measures of game performance and category learning was sensitive to category distribution differences modeling acoustic structures of speech categories. Category knowledge resulting from the game was qualitatively different from that gained from an explicit unsupervised categorization task involving the same stimuli. Results are discussed with respect to information sources and mechanisms involved in acquiring complex, context-dependent auditory categories, including phonetic categories, and to multi-modal statistical learning. © *2005 Acoustical Society of America.* [DOI: 10.1121/1.2011156]

PACS number(s): 43.71.−k, 43.71.An, 43.66.Ba, 43.66.Lj [ALF] Pages: 2618–2633

I. INTRODUCTION

Experience plays an essential role in shaping auditory perception in general, and speech perception in particular. However, there is a major complicating factor in characterizing this role experimentally; listeners come to the laboratory already shaped by considerable experience, the history of which may not be known to the experimenter. Since language experience cannot be controlled ethically, this is particularly troubling for speech perception. As a result, there are often limits on the certainty with which underlying learning or perceptual mechanisms can be inferred from patterns in adult (or even infant) perception. As a result, many long-standing questions concerning phonetic categories remain and current theories vary even in their most basic assumptions, including the very nature of perceptual objects (Diehl *et al.*, 2004; Fowler, 1986; Liberman and Mattingly, 1985; Lotto and Kluender, 1998; Nearey, 1997). In cases like this where ecological validity and experimental control are at odds, it can be useful to take a converging methods approach, for example examining adult and infant speech perception where control over experience is less realizable and, in addition, investigating experimental paradigms where strict control over the history of experience is possible. Along with studies of nonhuman animal perception and learning of speech sounds (e.g., Hauser *et al.*, 1998, 2000; Holt *et al.*, 1997, 2001; Kluender *et al.*, 1987, 1998; Sinnott *et al.*, 1976; Sinnott and Brown, 1997), human nonspeech auditory categorization designs provide an important controlled testing ground of the latter type. With properly selected nonspeech sounds, listeners' exposure to category instances can be carefully monitored. Observing the effects of this exposure during and after acquisition, then, aids in understanding the auditory and cognitive constraints upon sound category acquisition, and knowledge of these constraints in turn informs the examination of phonetic perception. Analogous lines of research have proven valuable in other domains; expert visual perception of non face objects, for example, has provided a new understanding of the cognitive and neural mechanisms involved in face perception (Gauthier and Tarr, 1997; Gauthier *et al.*, 1998; 1999a, b; Rossion *et al.*, 2002).

Observation of nonspeech category learning has already revealed some interesting and potentially informative parallels to speech categorization. However, interpretation of these results with respect to their link to phonetic categorization is challenged by the limited ecological validity of both the category stimulus distributions and the training methods used in studies thus far. Sounds and sound inventories for which learning has been observed are simpler by orders of magnitude than those involved in speech communication. Relatedly, the methods used to drive this learning have been limited to explicit training tasks demonstrably unlike anything encountered during speech category acquisition and considerably simpler than those used to affect non-face expertise in visual training studies (e.g., Gauthier *et al.*, 1998). The purpose of the present study is twofold: we describe a

[a]Address for correspondence: Posit Science, 114 Sansome Street, 5th floor, San Francisco, CA 94104. Electronic mail: Travis.Wade@positscience.com

method of exposing participants to novel nonspeech auditory categories that better resembles the natural category acquisition process and we explore the success of this method by investigating listeners' development of categories that, to varying degrees, involve some of the same challenges associated with the acquisition of naturally occurring speech categories. We first review a few relevant previous findings from nonspeech categorization studies.

A. Nonspeech auditory categorization

Several important parallels between speech and nonspeech categories have been observed. First, there is evidence that as a result of training human adults do, in fact, learn auditory categories that, like speech sounds, have nonlinear acoustic distributions. Lotto (2000), for example, taught listeners to categorize novel sounds as members of categories. Sounds varied continuously along one temporal and two spectral dimensions and categories overlapped thoroughly in all three acoustic dimensions. Category membership was determined by a complex rule and could depend on the acoustic characteristics of a given sound along any two of the three dimensions. Despite this complexity, however, listeners' categorization reliably improved over the course of training; they correctly labeled more sounds on the tenth day of training than on the first.

Also in line with phonetic acquisition, not all nonspeech acoustic distributions are learned with equal ease or in the same manner. Holt *et al.* (2004), for example, showed that general auditory perceptual discontinuities may interact with sound categorization. Listeners in this study learned sound categories defined along a single temporal dimension, tone onset time (TOT), a measure of the difference in onset time between two coterminous tones that has been previously used to model voice onset time (VOT) in speech (Pisoni, 1977). Nonspeech TOT categories were easiest to learn when the stimulus distributions defining the categories were positioned along the TOT dimension such that their boundary coincided with a temporal region (~20 ms) associated with increased discriminability in humans (Pisoni, 1977) and nonhumans (Kuhl and Miller, 1975) and known to underly a disproportionate number of phonetic distinctions in the world's languages (Keating, 1984; Lisker and Abramson, 1964). When the category distributions were shifted such that the natural peak in discriminability no longer coincided with the boundary between the category stimulus distributions, categories were more difficult to learn. Relatedly, Mirman *et al.* (2004) found qualitatively different learning patterns for categories as a function of the type of acoustic cue that differentiated category exemplars. Listeners who learned complex nonspeech sounds differing along a rapidly changing temporal dimension (amplitude rise time) were better at categorizing, but worse at discriminating, category exemplars than listeners who learned categories differing along a steady-state spectral dimension. This difference was observed even when pretraining sensitivity to the spectral and temporal cues was equalized across the two acoustic dimensions. This pattern of perception parallels differences observed in perception of steady-state (vowels and fricatives) and rapidly changing (consonants) speech sounds (e.g., Eimas, 1963).

In addition to the acoustic characteristics and distributional properties of sound categories, the category training procedure used also seems to have important consequences in auditory categorization. It is well known that, particularly for complex categories, the learner's task during training may affect resulting knowledge (e.g., Allen and Brooks, 1991; Ashby *et al.*, 1999, 2002). In nonspeech categorization, categorization-with-feedback designs have thus far been assumed to provide a reasonable approximation of the natural acquisition process. One notable finding in this respect was reported by Guenther *et al.* (1999) who examined listeners' ability to discriminate very similar within-category sounds as a function of different types of training. When training emphasized discrimination, listeners improved in detecting small acoustic differences among stimuli. However, when training emphasized categorization, they instead demonstrated "acquired similarity," becoming less sensitive to within-category acoustic differences. These findings may be informative regarding the structure of information encountered during acquisition, since perceptual warping of the acoustic space seems to accompany the categorization of speech sounds (Kuhl, 1991; Kuhl, 1992; cf. Lotto *et al.*, 1998).

The import of observations of nonspeech categorization is generally taken to be their qualitative similarity to patterns known to exist in speech perception. To the extent that effects in nonspeech acquisition and perception can be conclusively linked to similar effects in speech, nonspeech designs offer an important ground for investigating the limits and possible mechanisms governing categorization. However, also noteworthy are the differences between perception of speech and the nonspeech categories for which learning has been thus far observed. One striking difference involves the degree of competence typically reached in nonspeech training studies. Lotto (2000), for example, observed only 70% accuracy in participants' learning of two categories after ten hour-long sessions of intensive training; language users obviously must maintain many more categories much more accurately to achieve communication proficiency. Certainly, performance might continue to improve with more experience; language-acquiring infants receive thousands of hours of language exposure. However, with the impossibility of imposing this level of exposure in nonspeech training experiments comes the risk that the learning observed is fundamentally different from that involved in language acquisition (see Reber, 1989).

Another important (and potentially more manageable) difference involves the training method used in the studies. The categorization-with-feedback training commonly used in studies of nonspeech categorization is demonstrably quite unlike the processes by which humans are exposed to natural language sounds, and perhaps so fundamentally different as to preclude informative comparison. In the typical categorization training study participants sometimes undergo a short period of passive familiarization with the sounds to be learned and then hear a large number of exemplars from two

or (rarely) more categories. After each sound presentation, listeners press a button corresponding to a category label; following this response, some sort of visual feedback indicates whether the previously-heard sound corresponds to the same category as the button pressed.

Phonetic acquisition does not seem to involve explicit category labels, explicit response trials, or explicit feedback (e.g., Bruner, 1983; Jusczyk, 1997b). To the extent that category information accompanies category instances during (first) language acquisition, it involves complex correlations among acoustic event sequences and various visual, auditory, olfactory, tactile, and other events occurring in the environment. While it is far from clear how infants make use of this barrage of co-occurrences, it is known that human infants and adults are sensitive to statistical regularities at multiple levels (Jusczyk, 1997b; Kuhl *et al.*, 1992; Maye *et al.*, 2002; Saffran *et al.*, 1996; 1997, 1999). Moreover, there seem to be differences in the learning resulting from explicit training and that resulting from more incidental, implicit exposure. At least for patterns that are not particularly salient or easy to describe with simple rules, implicit exposure leads to faster, more accurate learning of the patterns than does explicit instruction (Reber, 1976; Reber *et al.*, 1980; Reber, 1989 for review). It has been suggested (e.g., Lacerda, 2003; Lacerda and Sundberg, 2004) that sensitivity to statistical regularities given rich, multimodal input from the environment results in the recognition of systematic patterns, including an awareness of phonetic categories that eventually interacts with other levels of linguistic processing.

With the aim of addressing this issue from multiple, converging methods, the purpose of this study was to develop and test a method of exposing learners to auditory categories that better resembles the natural acquisition process in these respects. In the next section a training method is described that captures several essential aspects of phonetic acquisition. In this method, subjects play a computer game in which they must navigate through a three-dimensional space, performing actions specific to animated characters they encounter along the way. Each of these characters is associated with both a distinctive movement pattern and predetermined sound category; an exemplar of this category is presented repeatedly each time the character is encountered in the game. Participants are not informed of the nature of these sound categories, nor of their significance in the game task, and other sound effects including a repetitive, synthetic background music score are also present throughout the game. However, as the game progresses, the speed and difficulty of the required tasks increase so that quick identification of approaching characters by means of their characteristic sounds is, while never required or explicitly encouraged, of gradually increasing benefit to the player. Following one or more sessions of this type of exposure, listeners complete a categorization task involving explicit matching of sounds to characters encountered during the game. This training method was used to examine listeners' categorization of a somewhat larger (four category) inventory of sound categories composed of sound exemplars that incorporate somewhat more of the nonlinear, context-dependent nature of speech sounds than have exemplars employed in previous auditory categorization studies. Categorization patterns were compared across differences in category structure (experiment 1) and to categorization patterns resulting from an explicit, unsupervised categorization task that did not involve the interactive game (experiment 2).

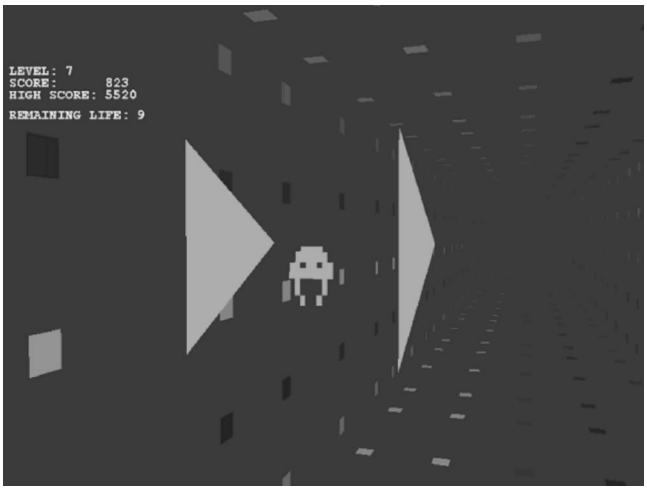

FIG. 1. Screenshot of typical game. The two-eyed figure in the center is an approaching irf-bat character; the orientation of the targeting graphic (two triangles) and background scene indicate that the player has adjusted the line of sight to the left to target the character.

B. Outline of the game

The design of the training task is conceptually, audiovisually, and ergonomically similar to that of typical commercial first-person shooting games. A screenshot of a typical game scene is shown in Fig. 1. For the duration of a game, the player moves forward at a constant perceived speed through a pseudo-three-dimensional tunnellike space. As the player progresses, he or she is periodically approached by animated *irf-bat* (interactive robot figure-based auditory training) characters, generally from the forward direction. The game involves four irf-bat characters that are easily distinguished from each other by shape, motion, and color patterns.

The player's tasks are to shoot and to capture these characters. Two of the four characters are *enemy irf-bats,* designated for shooting, and the remaining two are *friend irf-bats,* to be captured. These tasks are accomplished as follows, in a manner typical of similar games. Although the player moves uniformly forward throughout the game, it is possible to adjust the visual line of sight, to look or aim in any direction. This is accomplished using the LEFT, RIGHT, UP, and DOWN arrow keys with the right hand. Shooting and capturing require a combination of this movement and a multistep aiming process using the left hand. Specifically, when the Q key is pressed and held, a targeting graphic (the two triangles in Fig. 1) is illuminated in the center of the screen. This graphic is used to aim at enemy irf-bat characters in preparation for shooting. The player adjusts the sight line using the arrow keys, until a color change in the targeting graphic indicates that the irf-bat is currently on target for shooting. Finally, pressing the SPACE bar activates a shooting function. Capturing involves a similar process. When the

R key is pressed and held, a targeting graphic appears on the screen that aids the player in aiming at an irf-bat character using the arrow keys. Instead of pressing the SPACE bar, the subject must continually adjust the target using the arrow keys to keep the character in line as it approaches. As this is happening, the irf-bat character moves continuously forward, closer to the player's vantage point. Once the character reaches the player, with the capturing graphic displayed and on target, a capturing function is activated. If any irf-bat reaches the player's location without having been successfully shot or captured, it is said to have *escaped* and disappears from the player's line of sight.

Three variables figure prominently in the game's structure: *score, level*, and *life*. The player's primary objective is to acquire and maintain a high score. This is accomplished by shooting; each time the player successfully shoots an enemy irf-bat, the score increases, by an amount determined by (1) the current level and (2) the proximity of the character to the player at the time of shooting. More points are awarded for faster shooting and at higher levels of game play. The player advances one level each time a predetermined number of enemy characters (three in the present experiments) are successfully shot. Life is a measure of how many characters have recently escaped without being successfully shot or captured. At the beginning of a game, life is set at 10; it decreases by 2 each time a character escapes. This variable's value has no effect on the workings of the game, but the game terminates when it reaches zero. Its value increases by 1 each time a friend irf-bat is successfully captured and each time a level is completed. If the player shoots, instead of captures, a friend character, life is not increased and the score is decremented by a constant value. The values of each of these parameters in a given experiment is under the control of the experimenter.

C. Auditory category presentation in the game

In the present experiments, the game just described was used to present auditory categories that, like many speech sounds, are spectrally complex stimuli of a few hundred milliseconds duration. The game involves four sound categories, each of which possesses multiple exemplars and is associated with a single irf-bat character. The manner in which participants are exposed to these categories was designed to mirror several key aspects of natural phonetic acquisition.

Sound categories always co-occur with their associated characters. Each time a character appears visually in the context of the game, an exemplar of its corresponding sound category is presented auditorily. The sound is repeated continuously (with brief silences between repetitions) the entire time the character is active, i.e., from the time it is introduced until it is caught or captured or escapes. As a result, the auditory category (defined by multiple exemplars) tends to co-occur over the course of a game with both the visual image of the character and the distinctive motor/tactile patterns involved in shooting or capturing it. Whereas this combination is certainly simplistic compared to the rich set of visual, olfactory, auditory, kinesthetic, and other cues that may be correlated with speech sounds as they occur in the world, it represents much richer contextual support in category presentation than that typically present in explicit learning paradigms, where categories simply co-occur with their labels and feedback assignments. Additionally, repetition of a sound throughout a character's appearance is consistent with an apparently significant aspect of human language learners' early speech input; infant-directed speech appears to be repetitive (Fernald and Simon, 1984; Lacerda and Sundberg, 2004; Papousek *et al.*, 1985).

At the beginning of a game, exposure to these patterns of co-variance is expected to be fairly implicit, since knowledge of or attention to the acoustic exemplars is of no apparent consequence to game performance and no mention of their importance is made; participants are instructed only that they will be playing a video game. Characters appear near the center of the screen and approach the player slowly. Their accompanying sounds are merely part of a stylistically and texturally coherent game score, accompanied by background music and separate sound effects when the player shoots or captures a character or a character escapes. However, with each new level, the game becomes progressively more difficult in two ways. First, all motion in the game, including the approach of the characters and the targeting mechanism's responsiveness to the player's key presses, speeds up gradually. In addition, the characters begin approaching from locations that are gradually further displaced from the center of the screen. Each irf-bat character is associated with a single direction of origin (up, down, left, or right) from the center of the screen; on average (there is always an additional element of random noise), characters begin their approaches further in these directions as a game progresses.

These trends can be seen in the Fig. 2(a), which shows the starting locations of characters encountered over the course of a typical game. In this figure, the x and y dimensions represent the absolute distance in screen coordinates from the center of an approaching irf-bat character to the point at the center of the screen when the player is facing forward, a measure proportional to the apparent angular displacement of the character from the forward direction. Enemy characters approach the player in a straight line, and friend characters approach in a straight line infused with random jitter, so these locations remain nearly constant as long as a character is active. Each time a character is caught or captured or escapes, the player's line of sight is returned to the forward direction.

As shown in Fig. 2(a), as the game progresses, characters appear in more and more distal locations, requiring faster movement and hand-eye coordination on the part of the player. In the figure, the visible area of the game screen is represented by the range $(1,-1)$ in each dimension, so that the player's viewing frustum always extends only one unit in each direction from the current line of sight. Importantly, since this line is adjusted so that the player faces forward each time a character becomes inactive, only characters falling within the range $[(1, 1), (-1,-1)]$ are initially visible to the player; this range is represented by the shaded box. As shown in Fig. 2(a), at some point during a game (approximately level 8) the mean starting points of approaching characters move beyond this visible area. Since in this case an

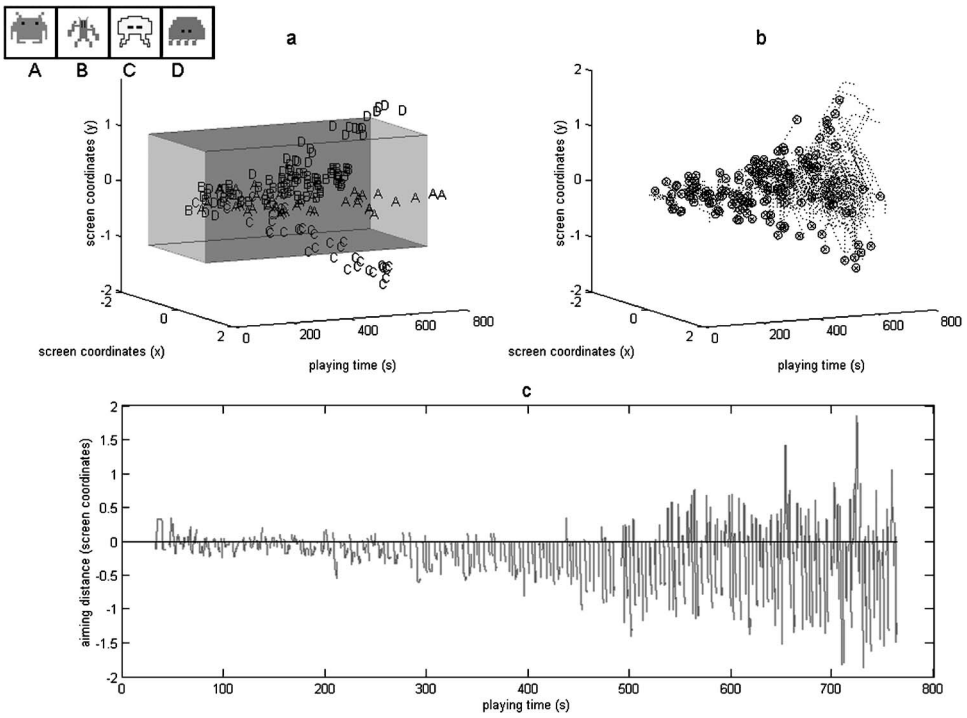

FIG. 2. Sample game. (a) Initial positions of irf-bat characters occurring during the game (inset shows individual characters), overlayed with the player's initial viewing frustum at each character's appearance. (b) Traces of player movements in response to the same characters. (c) Degree of player orientation toward characters over the course of the game, defined $((x_i^{\text{player}}-x_i^{\text{character}})^2+(y_i^{\text{player}}-y_i^{\text{character}})^2)^{1/2}-((x_0^{\text{player}}-x_0^{\text{character}})^2+(y_0^{\text{player}}-y_0^{\text{character}})^2)^{1/2}$.

irf-bat's sound is the only cue to its identity and location available to the player when it appears, the correlation between irf-bats, their sound patterns, and their typical starting locations is of increasing benefit to quick, accurate targeting. As starting points become still more distal, targeting becomes nearly impossible without quick categorization of sound patterns. Good performance at higher levels, then, requires a repeated, instantaneous, functionally oriented identification of sound categories that is generally not demanded of participants in explicit auditory category training studies.

Figure 2(b) shows a typical player's responses to the set of irf-bat character stimuli. The dashed line shows the player's current aim trajectory (also in screen coordinates), and $\otimes$ symbols denote successful hits and captures. Despite a lack of previous exposure to the game or to the sound categories, this relatively successful player was able to maintain game play for several minutes after characters began originating from outside the viewing area, apparently using acquired knowledge of sound-character-location correlations to successfully target many characters.

D. Measurement of category acquisition

There are several means of measuring and characterizing participants' acquisition of sound categories with the game (henceforth, Irfbats) task. One ecologically attractive method is to observe participants' ability to translate acquired knowledge to successful game performance. Rough measures such as the absolute or average high score or level reached in a training session have proven to be effective and are discussed in the next section. More detailed information can be obtained by examining players' aiming responses to individual audiovisual stimuli encountered over the course of the game. Figure 2(c) is derived from the same player movements depicted in Fig. 2(b), portraying the direction of movement with respect to target characters. The y axis represents, over the course of the game, the Euclidean distance in screen coordinates between the current (at each moment during game play) line of sight and the character's location, compared to this same distance at the time the character first appeared:

$$((x_i^{\text{player}}-x_i^{\text{character}})^2+(y_i^{\text{player}}-y_i^{\text{character}})^2)^{1/2}-((x_0^{\text{player}}-x_0^{\text{character}})^2+(y_0^{\text{player}}-y_0^{\text{character}})^2)^{1/2}.$$

Negative values, therefore, indicate the player is adjusting the targeting device toward the character. As shown by the sequences of positive values in Fig. 2(c), the player makes periodic mistakes, adjusting the target in the direction opposite the character, particularly later in the game when characters are initially invisible, occasionally allowing characters to escape. However, even very late in the game, the majority of movement is toward the (often out-of-range) character. This measure was compared across games and participants in the experiments described below.

A more direct means of investigating acquired category knowledge is performance on an explicit postgame categorization task, in which players match sounds with pictures of characters encountered during game play. Such a test was also implemented in the present experiments. In the test, participants view a screen in which all characters are displayed with numbers while a sound is presented, and responses are made by pressing number keys (1–4) on the same keyboard used during game play.

II. EXPERIMENT 1

The purpose of experiment 1 was to measure and characterize the effectiveness of the Irfbats training paradigm in learning complex nonspeech auditory categories. Employing this method, participants were exposed to an inventory of sound categories intended to present categorization chal-

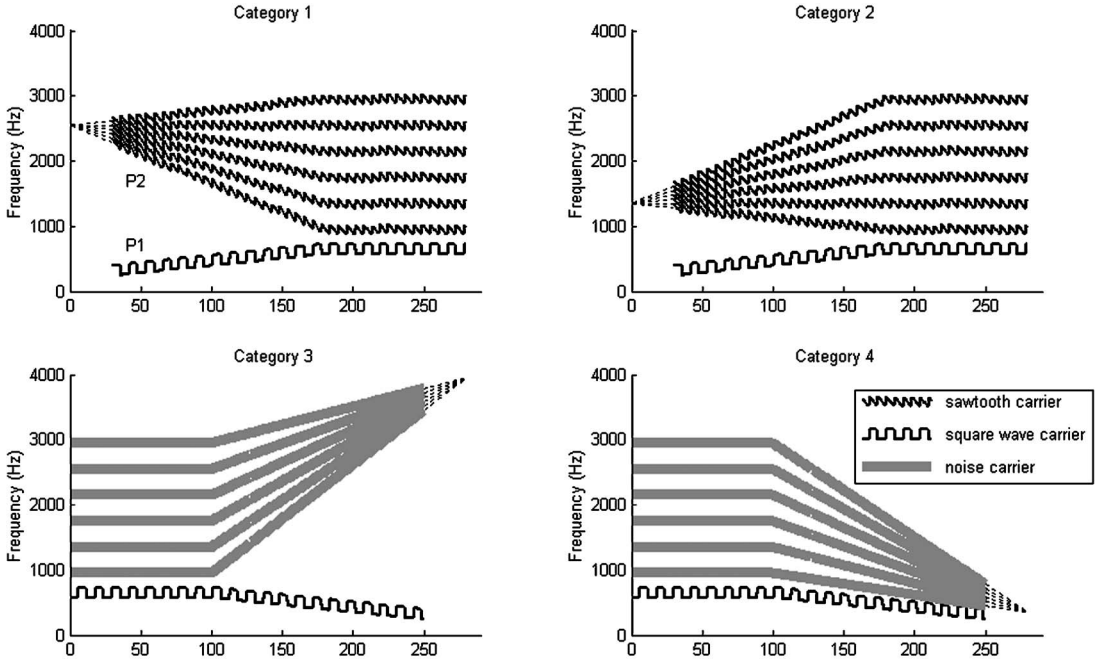

FIG. 3. Schematic representations category exemplars encountered during game play (each exemplar is comprised of the invariant P1 resonance and one P2 pattern.) Thin dashed lines show interpolation to P2 category loci for clarity.

lenges involving both spectral complexity and context-dependent category structure similar to those encountered in acquisition of phonetic categories.

A. Method

1. Stimuli

An inventory of four nonspeech categories, each composed of six stimulus exemplars, was used in training. Each stimulus was 250 ms in duration and had spectral peaks in two locations, *P*1 and *P*2. Category stimulus exemplars were differentiated by dynamic spectrotemporal patterns in P2, as shown in Fig. 3. For two of the categories, P2 onset frequency increased or decreased linearly over the initial 150 ms and then remained at a steady-state frequency for the following 100 ms. We refer to these stimuli as "onset" stimuli. The remaining two categories were "offset" stimuli with a symmetrical pattern; P2 frequency was constant for the first 100 ms and increased or decreased linearly to a final offset value across 150 ms. P1 frequency had a similar onset or offset pattern and was constant across stimuli within a category.

These stimuli modeled some of the spectrotemporal characteristics of speech signals in that P1 and P2 can be thought of as analogous to formant resonances of the vocal tract. Critically, however, the stimuli were perceptually very dissimilar to speech sounds and unlikely to have been perceived in a "speechlike" manner (Pisoni, 1987). No category involved a set of dynamic P2 patterns (category exemplars are described in detail below) that corresponded in absolute terms to observed formant patterns of any known set of phonologically equivalent speech sounds. Moreover, stimuli all possessed a complex fine temporal structure completely unlike that of speech. For all stimuli, the two spectral peaks were created by filtering two separate sources and combining the resulting waveforms additively. P1 was always derived from a square wave of periodicity 143 Hz. For onset stimuli, P2 was derived from a sawtooth wave of periodicity 150 Hz, and for offset stimuli it was derived from uniform random noise. (This last difference also helped to maximize the perceived difference between onset and offset categories).

To help ensure that stimuli were not perceived as speechlike, several naive observers, including some experiment 1 participants, were interviewed informally regarding the sounds. When asked for general impressions, observers invariably commented that they resembled "video-game sounds" or something similar; none mentioned speech sounds. When pressed to identify individual stimuli as speech sounds, responses were inconsistent across observers and did not reflect any relevant properties of the CV and VC sequences discussed above. Samples of the sounds are available online.[1]

Figure 3 shows schematized versions of P1 and P2 patterns of the six exemplars of each category encountered during the game task. The range of P2 patterns within categories was designed to reflect—to varying degrees—the same types of variability with which consonants are cued by formant transitions in the context of simple CV and VC sequences. Steady-state portions, roughly analogous to vowel place of articulation, varied in center frequency from 950 to 2950 Hz in 400-Hz steps within and across categories, thus carrying no first-order information to category membership. P2 transition trajectories were determined by a combination of (1) this steady-state frequency and (2) category-specific loci, toward or away from which P2 varied in frequency across time. As shown in Fig. 3, the beginning (offset stimuli) or end (onset stimuli) of P2 transitions always corresponded to the steady-state location; the transition itself spanned a linear trajectory of approximately[2] 83% of the distance from the

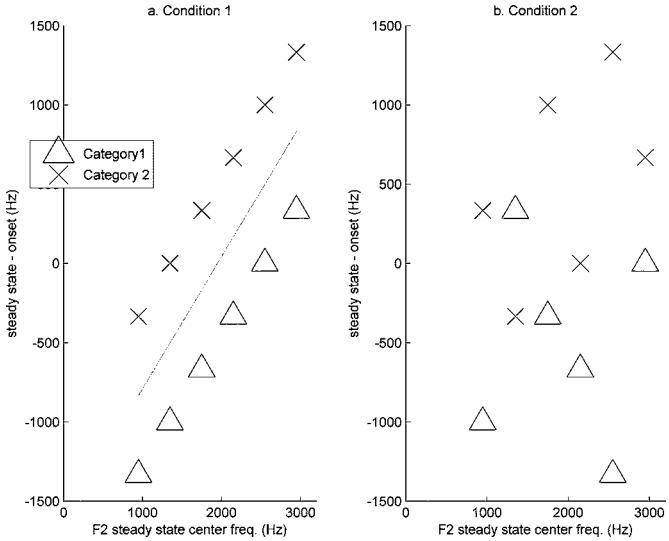

FIG. 4. Onset category stimuli shown in P2 steady state—onset trajectory space.

steady-state frequency to a constant target locus frequency for each category. This was intended to represent the way production (Delattre *et al.*, 1955, 1964) and perhaps perception (Sussman *et al.*, 1993, 1998) of consonant formant transitions varies depending on adjacent vowel context. For offset stimuli (categories 3 and 4), P2 loci were placed such that the categories would be easily distinguished based on only transition information. Since offset loci were either substantially higher (3950 Hz) or substantially lower (350 Hz) in frequency than the range of steady-state frequencies, the P2 trajectories of offset stimuli, while varying somewhat in slope and offset frequency, either always decreased in frequency or always increased in frequency within a category. For onset stimuli (categories 1 and 2), however, P2 loci were *within* the possible steady-state frequency range at 1350 and 2550 Hz and, as a result, no single invariant acoustic characteristic of onset transitions defined category membership. Category 1 onsets, for example, varied from steeply decreasing in frequency, to flat, to slightly increasing in frequency depending on the following steady-state frequency. As a result, the category 1 trajectories corresponding to the three highest P2 steady-state frequencies overlap completely in terms of slope with the category 2 trajectories preceding the lowest three steady-state frequencies.

Members of these categories, in particular the onset categories, thus lacked constant necessary and sufficient cues to category identity. This was intended to reflect the notoriously non-invariant nature of acoustic cues to many speech categories. However, also in line with phonetic categories (e.g., Lindblom *et al.*, 1992; Lindblom, 1996) and with many categories shown to be learnable in the visual domain (Ashby and Gott, 1988; Ashby and Maddox, 1990), onset stimulus categories were in fact linearly separable in a slightly higher dimensional space. Figure 4(a) shows P2 transition slope, a cue known to be useful in consonant discrimination (e.g., Liberman *et al.*, 1954), plotted against steady-state frequency for the onset categories (categories 1 and 2). As indicated by the dotted line, perfect discrimination between the two classes may be achieved by simple integration of information from these two sources. Thus, although there is no first-order acoustic information upon which to reliably base categorization decisions, there is higher-order structure that may be of use to learners. As a first step in evaluating the importance of this higher-dimensional relationship in category learning, a control condition (condition 2) was devised in which this relationship was absent. Stimuli for this condition are represented in Fig. 4(b); whereas categories 1 and 2 possess precisely the same P2 steady-state and trajectory ranges—and the same degree of cross-category overlap in these two dimensions—as the set just described (condition 1), the correlation between the two cues, rather than being determined by a category-specific locus, is pseudo-random. To the extent that information integration takes place as a result of category learning in game play, it was predicted that participants in condition 1 would outperform condition 2 participants during the game and/or in posttest category identification.

All sounds were created using Matlab (Mathworks, Inc.). Source signals were first generated at a sampling frequency of 22.05 kHz and filtered with an eighth-order elliptical bandpass filter with 2-dB peak-to-peak ripple, 50-dB minimum attenuation, and 500-Hz bandwidth. After filtering, all spectral peaks (P1 and P2 within and across categories) were equalized for rms amplitude, and 25-ms linear on-off ramps were applied. Finally, waveforms for each pair of formants were added together. Following synthesis, stimuli were inspected using spectrogram and waveform representations and found to closely match the intended parameters depicted in Fig. 3. A constant 50-ms silent interval separated repetitions of individual stimuli during game play.

2. Procedure

The game procedure used in training was identical to that described in the introduction; each of the four categories just described was associated with one of the four characters pictured in Fig. 2 and one direction of approach. Specifically, the two friend characters [A and B in Fig. 2(a)] progressively appeared from the right and left of the screen, respectively, and enemy characters [C and D in Fig. 2(a)] came from the bottom and top. Friend and enemy classes each included one onset and one offset category, such that P2 transition patterns (and not simply the onset-offset difference) took on the function of denoting character type. Friend characters A and B involved the two falling P2 patterns (high onset category 1 and low offset category 4, respectively) and characters C and D were matched with rising P2 patterns (categories 2 and 3).

Subjects were first familiarized with the game with a short tutorial program in which they were allowed to practice capturing and destroying stationary characters as the experimenter verbally explained the concepts of the game. No sounds were present during this familiarization session, and no mention was made of sound categories or their importance in the game task. Once subjects demonstrated to the experimenter's satisfaction that they understood the game procedure (familiarization typically took about 5 min), they were given a pair of headphones and informed that they

would play the game for 30 min, during which time their objective would be to achieve as high a score as possible. A *pause* screen (toggled by pressing the P key) was available to remind players of the details of the task, including summary instructions for shooting and capturing and descriptions of visual characters as friend or enemy. Participants were encouraged not to pause the game unless it was necessary. The participant was instructed to press the F1 key to begin a new game each time the life variable reached zero and a game terminated. Individual games ranged in length from tens of seconds to several minutes, and the number of games completed during the 30-min session ranged from 2 to 14.

Following the game session, subjects completed a categorization test in which they matched visual images of the irf-bat characters with exemplars of the four sound categories. Sound-category exemplars in the test were the 24 stimuli depicted in Fig. 3 and presented during game play and five novel sounds created to match the characteristic locus of each category. Novel stimulus P2 trajectories were determined by the same locus relationship depicted in Fig. 3, but had steady-state frequencies intermediate those of each pair of adjacent values used in training (1150–2750 Hz in five 400-Hz steps). Each stimulus was presented four times in the test, for a total of 176 trials, in random order. To provide maximal continuity with the game task, the same auditory and visual backgrounds were present during the test. A trial began with the simultaneous presentation of a sound stimulus and appearance of all four character images on the screen, arranged horizontally in an arbitrary constant order and accompanied by a number 1–4. As in the game, the sound repeated, with 30-ms silent gaps between repetitions, for 1.5 s or until the subject pressed a number 1–4 on a standard keyboard to register a response.

Game and test sessions took place in sound-attenuated booth using a laptop computer. All sounds were presented diotically over linear headphones (Beyer DT-150) at approximately 70 dB SPL.

3. Participants and design

Forty-two college students from the Carnegie Mellon University community reporting normal hearing participated in the experiment. Participants received undergraduate psychology credit for their participation.

To test whether any observed effects were due to the arbitrary mappings of categories to screen directions, visual characters, source signals, and stimulus types (onset versus offset) described above, two additional control subconditions were introduced in condition 1. Although the number of possible manipulations introduced by the richness of the game environment precluded fully factorial counterbalancing of game elements, we expected that these conditions would capture the effects of any major confounds. Condition 1b addressed the possibility that preference for a particular visual character or direction of origin might affect learning for some categories. In condition 1b the character correspondences described in Sec. II A 2 were reversed, with categories 1,2,3, and 4 occurring with characters C, A, B, and D, respectively. Since this manipulation involved a change in character assignment, location, and task (*shoot* or *capture*) for each sound category, it was predicted that any major bias patterns would be revealed in differences in performance between condition 1a (the originally described mappings) and condition 1b. Condition 1c was designed to test whether the difference in source signals between onset and offset categories would contribute to differences in learning. In this condition, the source-category type correspondences from condition 1a were reversed, so that onset category P2 resonances were derived from noise and offset P2s from the sawtooth source.

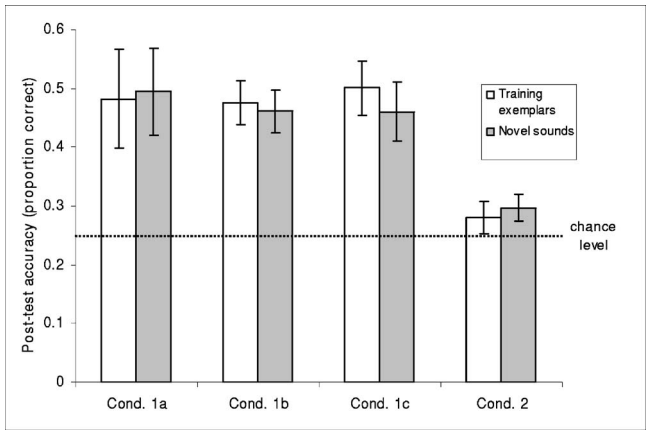

FIG. 5. Posttest accuracy across experiment 1 conditions (error bars show standard error of the mean).

Ten participants each were arbitrarily assigned to conditions 1a, 1b, and 1c. The remaining 12 participants were assigned to condition 2. (Condition 2 character-source-category correspondences were constant, identical to those of condition 1a).

B. Results

Participants gave a variety of reactions when faced with the posttest task of matching sounds to visual characters. The continuum of responses ranged from total surprise to relative confidence, although self-reported category knowledge did not always correspond with test performance.

1. Overall learning effects

Figure 5 summarizes overall categorization posttest performance across experiment 1 conditions. It was assumed that, if participants learned patterns of covariance between characters and sounds as a result of the game task, they would be able to match characters to sounds in a subsequent explicit identification task. When game characters cooccurred with onset categories defined by the structured variability patterns shown in Fig. 4(a), this learning indeed occurred. Subjects in conditions 1a, 1b, and 1c all performed reliably above chance level (25%) at posttest, for both previously heard [condition 1a: $t(9)=2.76$, $p=0.022$; condition 1b: $t(9)=5.92$, $p<0.001$; condition 1c: $t(9)=4.28$, $p=0.002$] and novel [condition 1a: $t(9)=3.3$, $p=0.009$; condition 1b: $t(9)=5.91$, $p<0.001$; condition 1c: $t(9)=5.29$, $p<0.001$] category exemplars. No overall differences in accuracy were observed between familiar and novel stimuli or between condition 1a, 1b, and 1c participants, indicating that

the learning effect was reproducible and robust over (at least) modest changes in the game procedure and the acoustics of sound category exemplars. Critically, condition 1 participants in both subgroups performed better than chance both for offset category stimuli, which were linearly separable by P2 trajectory [condition 1a: $t(9)=2.92$, $p=0.017$; condition 1b: $t(9)=7.65$, $p<0.001$; condition 1c: $t(9)=5.48$, $p<0.001$] and for onset category stimuli, which were not invariant in this manner [condition 1a: $t(9)=3.17$, $p=0.022$; condition 1b: $t(9)=4.31$, $p=0.002$; condition 1c: $t(9)=3.48$, $p=0.007$].

Condition 2 participants heard onset categories that were not structured reliably in the higher-dimensional acoustic space defined by P2 trajectory and steady-state frequency dimensions [Fig. 4(b)], and did not demonstrate learning. These participants did not differ reliably from chance in posttest identification of either novel [$t(11)=2.1$; $p=0.06$] or previously encountered [$t(11)=1.08$; $p=0.302$] stimuli. A one-way between-subjects ANOVA revealed that condition 1 participants reliably outperformed condition 2 participants in accurately categorizing both novel [$F(1,40)=11.69$; $p=0.001$] and previously encountered [$F(1,40)=13.5$; $p=0.001$] stimuli. Moreover, the difference observed was rather large; the difference in overall *p(c)* between conditions 1 and 2 was 19%, corresponding to an effect size $d=1.12$ (conservatively using the larger of the two observed standard deviations, from condition 1). This effect size corresponds to a power of approximately 0.8 with the smaller condition 2 sample size $n=12$, so it seems the moderate subject numbers were sufficient.

Since only condition 1a participants' sound-character pairing perfectly matched that of condition 2 participants (condition 1b differed in sound-character and condition 1c in source-category correspondences), this comparison was repeated including only condition 1a and condition 2 participants. The results were similarly reliable [novel stimuli: $F(1,20)=7.63$, $p=0.012$; familiar stimuli: $F(1,20)=6.003$, $p=0.024$].

2. Category comparisons

The top two rows of Fig. 7 show responses to each exemplar of each of the four categories at posttest across steady-state frequencies. Here several important trends in categorization are apparent. First, while condition 1 participants tended to recognize stimuli from all four categories reliably, condition 2 participants performed uniformly at chance level. Interestingly, this was true even for offset categories 3 and 4, for which exemplars were identical to those heard by condition 1 listeners. It would seem that the lack of structure in the onset categories discouraged condition 2 participants from making use of any audio-visual correspondences in the game.

To test for effects of the complexity of category distinctions on their learning for condition 1 subjects, a 3(training condition; 1a, b, c) $\times$ 2 (category type; onset versus offset) mixed model ANOVA compared subjects' sensitivity (%hits − %false alarms) to categories of each type. A main effect of category type was observed [$F(1,27)=24.25$; $p<0.001$], indicating that the unidimensionally defined offset categories were recognized slightly more accurately than the onset categories. This was not at all surprising given the more difficult nature of the two-dimensional onset distinction. Additionally, while no training condition main effect was observed ($F<1$), the training condition $\times$ category type interaction reached significance [$F(2,17)=4.6$; $p=0.019$]. *Posthoc* comparisons indicated that this effect was due to a slightly greater category type difference in condition 1c, where noise replaced a sawtooth wave as the source for the onset P2 resonance. Whereas learning occurred for both groups, the harmonic source thus seems to have been a slightly better carrier of P2 information than the noise source.

Finally, inspection of category 1 and 2 identification by condition 1 subjects suggests that, while the structured variability in the onset stimulus cues helped the listeners to establish the two categories, the high-level distinction was not learned perfectly. Specifically, category 1 accuracy tends to decline at higher P2 steady-state frequencies (i.e., where P2 is falling), while category 2 accuracy is worst for the lowest steady states (where P2 is rising). This suggests that (some) listeners may have been relying too heavily on the slope of the P2 transition and not compensating maximally for the steady-state part of the locus rule. Still, however, the fact that condition 1 subjects outperformed condition 2 subjects indicates that the higher-order structure played a role in learning, even in the brief (30-min) training period employed.

3. Game performance effects

In characterizing the effect of the Irfbats task on listeners' categorization, it was informative to examine performance during the game as well as at posttest. Due to errors in test administration, game performance data from two participants (one in condition 1a, one from condition 1b) were not recorded for comparison with posttest scores. Figure 6 shows posttest accuracy plotted against three measures of success at the game task for the remaining 40 listeners: mean high score achieved, mean high level attained, and the mean aiming distance measure pictured in Fig. 2(c).

Figure 6 illustrates a few important patterns in game performance across participants and groups. First, condition 1 participants (games with structured onset category variability) outperformed condition 2 participants (random onset variability) not only at posttest but also during the game itself. On average, condition 1 participants achieved higher scores [$F(1,38)=8.7$, $p=0.005$; means (s.d.) for conditions 1, 2: 40 230 (14 763), 26 998 (7012)], reached higher levels of the game [$F(1,38)=8.5$, $p=0.006$; means: 11.5 (2.7), 9.01 (1.7)], and navigated more accurately toward characters throughout the game [$F(1,38)=4.3$, $p=0.045$; means: −33.02(12.1), −24.9(9.05)] than did condition 2 participants. Moreover, game performance and category learning accuracy appear to be related. For condition 1 participants, all three performance measures correlate reliably with post test accuracy; players who demonstrated success (higher score and level values) and accuracy (lower aiming difference values) during the game also exhibited better category learning at posttest. It is not surprising that these correspondences did not hold for condition 2 subjects, who did not

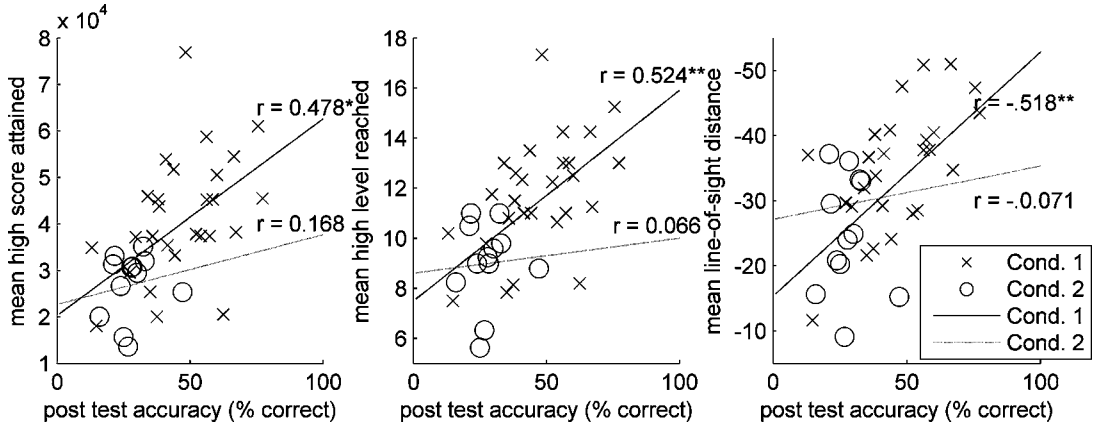

FIG. 6. Experiment 1 posttest accuracy plotted against game performance measures. Regression lines indicate correlation patterns between measures for each participant group * indicates correlation $p<0.05$, ** indicates $p<0.01$.

demonstrate learning overall, although this might also be due to the smaller total number of subjects in condition 2.

Thus, the higher-order structure imposed on condition 1 stimuli affected category learnability and learning in the Irfbats exposure task was sensitive to differences in this structure. At posttest, condition 1 participants (1) demonstrated learning for both simple and more complex category exemplar distributions and (2) reliably outperformed condition 2 participants, who did not learn overall. Furthermore, it seems likely that the interactive, incidental nature of the game was important in achieving this result, since success at the Irfbats task was related to posttest performance both within and between participant groups. This indicates that the game task was not merely a superficial addition to an unrelated incidental learning task. Game performance was also affected by category learning and sensitive to differences in category structure.

III. EXPERIMENT 2

Experiment 1 demonstrated that simple audio-visual correlation patterns in a game task enabled listeners to learn complex sound categories, whether the category distinctions involved unidimensionally invariant acoustic cues (categories 3 and 4) or required integration of two or more cues (categories 1 and 2). In beginning to characterize the type of learning that took place in familiar terms, it is important that both of these distinction types were tested. Previous studies have shown that training conditions affect learning differentially depending on the complexity of category distinctions. Ashby *et al.* (1999), for example, observed visual categorization under unsupervised conditions, where observers grouped visual patterns into a given number of categories. Optimal categorization occurred only when stimuli were unidimensionally separable, and not when distinctions involved more than one dimension. Similarly, Ashby *et al.* (2002) found an interaction between category structure and the way category information was presented during training. "Observational training," in which category labels were presented to participants simultaneously with training stimuli, and "feedback training," in which corrective feedback was provided after stimuli (and sometimes after a subject response), led to similar learning for simple, unidimensional category distinctions. However, for categories whose recognition required integration of information along two separate visual dimensions (length and orientation), feedback training provided a substantial advantage. These differences were tentatively taken as evidence of the learning systems involved, namely whether a simple explicit system was complemented by more complex, implicit learning over the course of training (Ashby *et al.*, 1998).

The game used here combines elements of all of these methods of category exposure, as (perhaps) does natural language acquisition. At various points in the game, the relative order of occurrence of auditory stimuli, visual characters, and participant responses reflect elements of unsupervised, observational, feedback, and other types of training. As a first step in comparing learning in the game task to that previously observed in more controlled designs, and in general to further characterize the effects of the game on learning, an additional experiment measured learning of the same sound categories used in experiment 1, in more explicit circumstances and absent the game task. Specifically, an unsupervised training design was used, in which listeners were told the number of sound categories and exposed repeatedly to category exemplars but given no category label information or other feedback. Essentially, this was expected to reveal which aspects of category structure were critically presented by the structure of the game environment and those that were more self-evident given minimal instruction and explicit, deliberate comparison of salient acoustic properties of the stimuli.

A. Method

1. Stimuli

Stimuli were identical to those used in experiment 1. Only the six exemplars of each category presented during experiment 1 game play and depicted in Fig. 3 were used in exposure and testing.

2. Procedure

The categorization task consisted of five familiarization blocks alternated with five transfer blocks in a single session. Each block consisted of three repetitions of each of the six

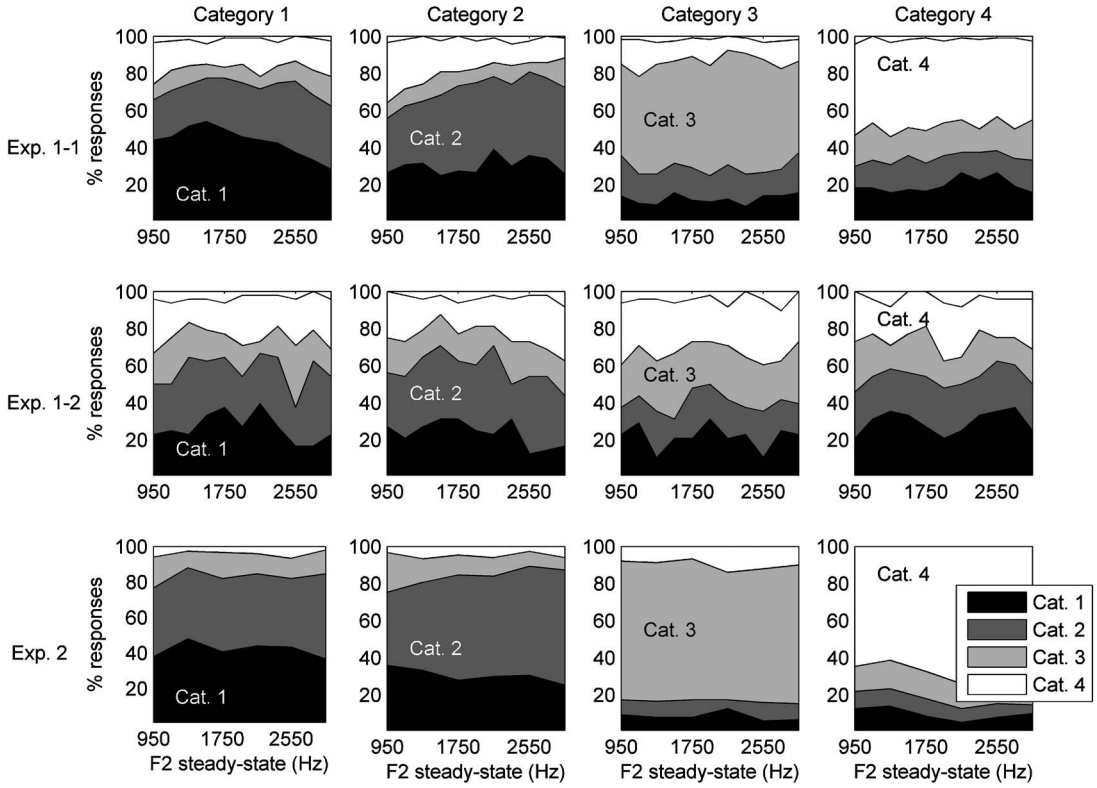

FIG. 7. Response patterns across test stimuli for experiment 1, condition 1 (a and b collapsed; top), condition 2 (middle), and experiment 2 participants. Labeled areas correspond to intended category responses; total area less than 100% indicates missed (timed-out) responses.

exemplars of each category, for a total of 720 stimuli (360 familiarization, 360 transfer). This was in keeping as closely as possible with session length and stimulus exposure experienced in experiment 1 (experiment 1 participants, on average, encountered 367.3 characters during their 30 min of game play). Participants heard isolated sound stimuli in sound-attenuated booths over headphones at approximately 70 dB SPL. Stimuli were presented in random order within blocks, using *ALVIN*, a software system recently developed by Hillenbrand and Gayvert (2005). In familiarization blocks, participants were instructed to listen to each stimulus carefully and learn as much as possible about the sounds in order to reliably divide them into four categories, pressing a button labeled "continue" after each trial. In transfer blocks, they were instructed to press one of four numbered buttons, depending on which of the four arbitrarily labeled categories they chose to assign to the sound's category. Participants were urged to be as consistent as possible and were informed that perfect performance was possible, following Ashby *et al.* (1999).

3. Participants

Ten college students from the Carnegie Mellon University community reporting normal hearing participated in the experiment. Participants received undergraduate psychology credit for their participation.

B. Results

Each participant's response patterns were first translated into a set of category labels by choosing the set of response-to-stimulus category mappings that maximized overall accuracy (% correct). Resulting overall accuracy scores averaged 59.9%, well above chance (25%) performance $[t(9)=6.003;\ p<0.001]$ and in fact somewhat higher than overall experiment 1, condition 1 (a,b; condition 1c involved a different set of sounds) game participants' scores $[F(1,28)=3.41;\ p=0.076]$. This last result was not especially surprising or indicative of fundamental differences in learning. Experiment 2 involved an explicit auditory categorization task, while exposure to sounds in experiment 1 was purely incidental (participants did not even know they were learning sounds), so direct comparison of overall accuracy after a single session is not particularly informative. More critical was the interaction of training type and whether category distinction cues were unidimensional (offset stimuli) or integrative (onset stimuli) in nature.

The bottom row of Fig. 7 shows responses to each exemplar of each of the four categories averaged across the five transfer blocks. A qualitatively different categorization pattern seemed to result from explicit unsupervised training. Experiment 2 participants performed quite well on the linearly separable offset categories, but confused the two cue-integrating onset categories (1 and 2) with each other at near-chance level. To illustrate this pattern more clearly, Fig. 8 shows the difference between correct responses and locus-differing competitor responses for onset and offset categories across testing conditions (zero indicates chance-level performance). This comparison demonstrates that, while experiment 2 participants labeled offset categories fairly accurately, they responded to onset categories with almost no tendency to discriminate between competitors. A

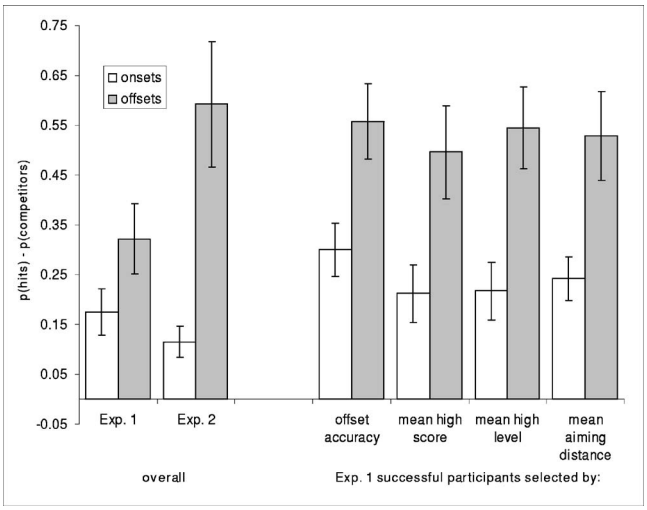

FIG. 8. Onset and offset distinction accuracy (correct responses minus locus-varying competitor responses) across training conditions (left) and for experiment 1 subsets (right) defined by removal of ten worst-performing participants on four measures of game training success (error bars show standard error of the mean).

2(training condition) $\times$ 2(category distinction type) mixed model ANOVA with training condition as a between-subjects factor revealed that onset categories were most difficult overall [$F(1,28)=26.4$; $p<0.001$]. The training condition effect did not reach significance; critically, however, a training $\times$ category type interaction was observed [$F(1,28)=7.5$; $p=0.011$]. Relative to overall performance, unsupervised categorization participants had considerably more difficulty with onset stimuli compared to offset stimuli.

One interpretation of this difference is that game participants, like observers trained with feedback in previous experiments (e.g., Ashby *et al.*, 1999, 2002), were relatively better able to learn the higher-dimensional onset distinction than listeners explicitly comparing the sounds in the unsupervised categorization task. However, the training $\times$ category interaction cannot be conclusively attributed to an advantage on complex distinctions for game participants, since absolute performance levels precluded direct comparison of responses across groups. The unsupervised training might instead have given experiment 2 listeners a special advantage in categorizing the offset categories, although it is unclear what the source of this advantage might have been. As a first step in addressing this issue, it was observed that the Irfbats task introduced at least two sources of variability to the category identification task that were not introduced by experiment 2's simple, constant procedure. Absolute average performance in experiment 1 posttest was probably deflated by subsets of participants who either (1) due to initial difficulty with the game task failed to advance sufficiently during 30 min of play for much learning to occur or (2) were surprised or confused by the posttest task and did not optimally display their acquired knowledge. Although study involving longer-term game play will be required to solve these problems completely, for the present data it was useful to equate performance across the tasks by considering subsets of experiment 1 participants who were successful at the game task and able to demonstrate acquired category knowledge in the explicit posttest. The right portion of Fig. 8 shows onset and offset identification patterns for Irfbats participants selected based on several possible criteria. Offset category identification accuracy was selected as a measure of success at the posttest task, since considering experiment 2 results it should have been fairly easy for successful participants and since it did not directly involve the more critical onset performance. For game success, the mean high score, level, and aiming speed measures presented above were considered. The performance of successful players was similar across criteria; they performed similarly to experiment 2 participants for offset categories and tended to *outperform* experiment 2 participants for onset categories. (The onset difference reached significance only when the offset score or mean distance criterion was used.) Thus, it does seem that, at least for the more successful participants, Irfbats-style feedback provided an advantage for learning the complex onset category distinction.

IV. GENERAL DISCUSSION

This study introduced Irfbats, an interactive video game developed for use in investigating the acquisition of auditory categories. While playing Irfbats, participants were incidentally exposed to sound category exemplars in the presence of other richly correlated multimodal cues. Observations of postgame sound categorization and patterns in game performance allowed for measurement of the types of auditory distributions that are learnable in the absence of explicit feedback.

A. Posttest categorization

Postgame sound categorization patterns demonstrated that even without explicit feedback Irfbats players can learn spectrally complex non-invariant auditory categories within a rather short period (30 mins) of incidental exposure when higher-dimensional acoustic cue relationships are present. In experiment 1, the inventory of sounds presented during the game included both categories possessing distinctive, invariant spectral cues (rising versus falling offset patterns in categories 3 and 4, as shown in Fig. 3), and categories that were not unidimensionally separable (onset categories 1 and 2). Much has been made of the significance of non-invariant category cues with respect to speech perception (Delattre *et al.*, 1955; Kluender *et al.*, 1987; Stevens and Blumstein, 1981). Like the speech categories they modeled, the non-invariant category distributions were linearly separable in a higher-dimensional space when two separate acoustic cues (onset trajectory and steady-state frequency) were integrated. Experiment 1 demonstrated that participants exposed to such categories exhibited robust learning over the course of a single 30-min game session. In a posttest they were able to match visual characters from the game reliably to sound category exemplars encountered during game play, as well as to novel sound exemplars drawn from the same category distributions. Another group of participants heard categories that possessed the same distributions of onset trajectories and steady states but lacked structured second-order cues to cat-

egory membership. These listeners did not differ from chance in their posttest categorization responses.

This finding is of potential significance concerning the types of knowledge required for context-dependent speech perception. Though, like many phonetic categories of the world's languages, onset categories 1 and 2 could not be differentiated by any single invariant acoustic cue, listeners (experiment 1, condition 1) learned the sounds, even without feedback or instructions to learn the categories. Together with the fact that nonhuman animals can learn similarly non-invariant speech categories (Kluender *et al.*, 1987), this finding is consistent with an account of speech perception that exploits general learning mechanisms for phonetic acquisition (Diehl, *et al.*, 2004) rather than specialized processes (e.g., Liberman and Mattingly, 1985; 1989; Trout, 2001).

Learning in the game was also compared with that resulting from an explicit unsupervised categorization task in experiment 2. An interaction involving category type was observed, such that game participants showed relatively more learning for the non-invariant onset categories requiring cue integration. This is informative in beginning to characterize the type of learning that resulted from the game. With respect to category exemplar distribution effects, the categorization responses of game participants were more like learners trained with explicit feedback in previous studies; exposure through game play seems to provide a similar advantage to feedback in learning complex, information-integrating category structures (Ashby *et al.* 1999, 2002), whereas observation and unsupervised training are helpful only for simpler, invariant categories. Additional study will be required to fully characterize the effects of the interactive game task on the types and extent of learning. In particular, comparison of category knowledge resulting from extended, explicit feedback training with that of expert game players will be necessary.

B. Interactive task effects

The structure of the Irfbats game was designed to model some of the interactions and multimodal correlations through which listeners may come to recognize the acoustic regularities underlying the sound distributions of a native language. Repeated presentations of category exemplars co-occurred with distinct visual events and motor tasks inherent to the game. Although sound categorization was not explicitly mentioned to or required of the players, it was of increasing benefit to achieve high levels of game performance as play progressed.

Indeed, it does not appear that the game task provided only a superfluous precursor to the more standard categorization posttest; rather, several characteristics of players' game performance proved to be good predictors of posttest categorization accuracy. Participants' ability to achieve higher scores, reach higher levels, and navigate successfully in the game environment was related to their knowledge of sound categories, and also was sensitive to differences in the non-invariant category distributions. As participants acquired knowledge of the sound categories relevant to the game task, skill at the task increased. Likewise, as increased skill enabled players to reach more difficult stages of the game, continued success demanded increasingly efficient, accessible knowledge of sound categories. This pattern is consistent with the interactive processes known to be important in category learning in other species (e.g., Baptista and Petrinovich, 1986; Eales, 1989) and thought to underly the phonetic and phonological acquisition processes (Bruner, 1983; Kuhl *et al.*, 2003; Lacerda, 2003; Lacerda and Sundberg, 2004).

Developing a precise mechanistic account of how experience shapes the acquisition of phonetic categories is challenging because it is impossible to attain full control over the histories of listeners' experience with speech. Even very young infants possess significant experience with, and demonstrate sensitivity to, the sound structure of the native language (e.g., Jusczyk, 1997a; Kuhl *et al.*, 1992). In domains like this where control over the input is elusive, a converging methods approach can be useful in balancing the competing demands of experimental control and ecological validity. One perspective on this issue is that understanding how human listeners extract information from the auditory environment can be informative about the constraints and mechanisms the system brings to phonetic (speech) categorization. Presently, there exists a limited literature describing general auditory (nonspeech) categorization (e.g., Guenther *et al.*, 1999; Holt *et al.*, 2004; Lotto, 2000; Mirman *et al.*, 2004), so there is still much that can be learned about how listeners categorize acoustic stimuli using these more traditional methods. Nevertheless, we believe that the present paradigm has value in providing an intermediate step along the continuum from experimental control to naturalistic observation. To be sure, this video game environment is a considerable step removed from the rich structure present in learning speech categories. Even so, Irfbats appears to capture some of the characteristics of correlation among multiple cues, function-based categorization, and exploration of an environment that likely accompany phonetic category acquisition. Just 30 min of incidental exposure to the multimodal statistical regularities present in the game was sufficient to promote category learning for a set of stimulus exemplars that model one of the central challenges in speech categorization, the lack of invariance.

Recent studies support the utility of examining nonspeech learning to understand potential mechanisms available to speech perception. Adults, infants, and nonhuman primates exhibit sensitivity to the statistical regularities present in sequences of speech syllables (Hauser *et al.*, 2000; Saffran *et al.*, 1996, 1997) and statistical learning of this sort appears to be deployed for both speech and nonlinguistic sounds (Saffran *et al.*, 1999). Thus, there is evidence that general (statistical) learning mechanisms may be operative across linguistic and nonlinguistic sound classes. The Irfbats paradigm relates to this literature in that it likewise requires sensitivity to statistical regularity for learning to be observed. However, the present work differs in a couple of important ways from previous approaches.

For the most part, investigation of statistical learning has been limited to single modalities. Statistical learning appears to be operative for both auditory (e.g., Saffran *et al.*, 1997)

and visual (Fiser and Aslin, 2002; Kirkham *et al.*, 2002) stimuli, but there thus far has been little investigation of how multimodal regularities are learned. It is, of course, presumed that learners take advantage of informative regularity where it exists, even if it occurs cross-modally (e.g., Massaro, 1987). The present paradigm provides a means of addressing this assumption explicitly and gaining an understanding of potential constraints upon the types of multimodal regularities that are learnable. Here, we have demonstrated that listeners acquire sound categories for spectrally complex, non-invariant acoustic exemplars through incidental exposure in a video game environment provided that they possess second-order acoustic regularity and they covary with multimodal perceptual/motor cues introduced in the game.

The Irfbats game is also differentiated from previous studies of statistical learning by how it assesses learning. Investigations of statistical learning have primarily relied upon measures of familiarity to assess whether participants learned statistical regularities presented in an experiment; adult participants, for example, are above chance at judging whether stimuli are consistent (familiar) or inconsistent (unfamiliar) with the regularities they encountered incidentally in previous exposure (Saffran *et al.*, 1997), and extensions of this same paradigm are used with human infant and nonhuman primate listeners (Hauser *et al.*, 2000; Saffran *et al.*, 1996). The results of the present studies move a step beyond familiarity. Participants were able to apply what they learned in the course of the game to the task of categorization.

C. Conclusions

The present results provide evidence that adult listeners can solve what has been thought to be a rather difficult auditory categorization challenge, acquiring categories for spectrally non-invariant acoustic exemplars, in a task in which categorization is largely incidental. Observation of learning was contingent upon the existence of a higher-dimensional acoustic relationship between the non-invariant cues and the presence of rich statistical regularity with other perceptual/motor cues provided in game play. Moreover, the categorization behavior of participants who played the game was demonstrably different from that of participants who merely classified the stimuli in an unsupervised categorization task. We interpret these results as evidence of human adults' general capacity to make use of informative statistical regularities in the input in interactive, functionally oriented situations and suggest that understanding more about the manner by which listeners discover sound structure in the environment can instruct us about the general learning mechanisms that may be brought to bear on phonetic categorization.

Some caution might be warranted in making strong claims regarding phonetic categorization or multimodal learning based on the present results, however. First, there is the possibility that the onset categories 1 and 2 in experiment 1, condition 1 did in fact possess invariant acoustic cues. As shown in Fig. 3, the initial energy distributions of category 1 exemplars did involve a P2 center frequency region (roughly 2.06–2.67 kHz over the first 25 ms) that was uniformly higher than that of category 2 exemplars during the same time frame (1.23–1.84 kHz). Listeners, then, could conceivably have identified categories based on the spectral properties of this distinctive region alone, disregarding the remainder of the onset patterns. Indeed, it has been similarly proposed in speech that the overall spectral shape of voiced consonants' initial bursts, rather than the non-invariant following formant transitions, are responsible for their context-independent recognition (Blumstein and Stevens, 1980). Dynamic formant patterns, though, have long been considered a salient acoustic property of voiced stops (e.g., Cooper *et al.*, 1952; Delattre *et al.*, 1955; Liberman *et al.*, 1954). In fact, language users have a persistent tendency to label consonants primarily based on formant transitions even after extensive training emphasizing instead the role of burst spectra (Francis *et al.*, 2000). It is especially unlikely that listeners in the present experiment classified category exemplars based only on their initial spectra, since unlike consonants they did not begin with acoustically prominent burst patterns but instead with brief onset ramps. It seems reasonable, therefore, to characterize categories 1 and 2 as having a "lack of invariance" of the same type that phonetic categories exhibit. Nonetheless, additional study in which the initial locations of similar dynamic spectral peaks are further removed from category-specific loci would help to clarify this issue. It would also be informative to examine the effects of differing types and degrees of "unstructured" variability like that employed in experiment 1, condition 2. Onset-trajectory–steady-state correspondences for the present study were a single pseudo-random distribution; further manipulation of these correspondences—perhaps involving their variation independent of absolute initial P2 ranges—could help to uncover more precisely the dependence of categorization on higher-order acoustic structure.

Another cause for caution in interpreting the results of experiment 1 is the overall level of categorization accuracy observed at posttest. As shown in Fig. 6, some individual participants performed quite well; overall, however, like the Japanese Quail in Kluender *et al.*'s (1987) phonetic category learning study and the human listeners in Lotto's (2000) complex nonspeech learning study, even condition 1 participants demonstrated far-from-perfect recognition. Judging by the results of the present study, this deficit seems more likely a methodological issue than a fundamental learning constraint. That is, it is expected that achieving expert-level performance may require more than a single 30-min learning session. In experiment 1, none of the participants approached the level of performance (score, level, etc.) that the experimenter reached after several hours of game play. This room for improvement indicates first of all that the game is well suited for longer-term studies. Furthermore, the correlation between game performance and posttest accuracy illustrated in Fig. 6 suggests that as skill level at the game continues to increase, so too will category knowledge. Pilot data suggest that listeners may begin to recognize categories like those described above at near 100% accuracy after as little as an hour of game play. Further study, perhaps involving hours of

game play over multiple sessions, will help in further characterizing the learnability of non-invariant sound classes like those explored here.

Finally, care must be taken in interpreting the correlation between game performance and learning as evidence that it was precisely the interactive nature of the task that helped drive learning. While learning sound classes had clear consequences for game performance, further study will be necessary to determine how truly interactive the process was. Training conditions, probably also over longer training periods, in which various potentially informative aspects of the Irfbats design (e.g., character-response, character-direction, and category-character contingencies) are altered or withheld will have to be compared to address this issue and to evaluate the relative importance of each type of information.

In sum, the Irfbats game paradigm appears to capture characteristics of auditory category learning that may be essential to learning natural sound categories, including phonetic categories. Moreover, it provides a learning environment in which to empirically manipulate experience to mechanistically address the bases of complex auditory categorization.

ACKNOWLEDGMENTS

This work was supported by a James S. McDonnell Foundation award for Bridging Mind, Brain, and Behavior to LLH, NIH Grant No. 5 RO1 DC04674-02 to LLH, a grant from the Bank of Sweden Tercentenary Foundation, and by a fellowship from the NIH Postdoctoral Training Grant on "Individual Differences in Cognition." The authors thank Christi Adams, Sara Kapner, Kelly Bunch, and Brian Mathias for help in conducting the experiments.

[1]http://www.psy.cmu.edu/~lholt/php/gallery_irfbats.php

[2]The 25-ms onset-offset amplitude ramps may have caused endpoint percepts to be somewhat further from the locus than illustrated in Fig. 3.

Allen, S. W. and Brooks, L. R. (**1991**). "Specializing the operation of an explicit rule," J. Exp. Psychol. Gen. **120**, 3–19.

Ashby, F. G., Alfonso-Reese, L. A., Turken, A. U., and Waldron, E. M. (**1998**). "A neuropsychological theory of multiple systems in category learning," Psychol. Rev. **105**, 442–481.

Ashby, F. G., Queller, S., and Berretty, P. M. (**1999**). "On the dominance of unidimensional rules in unsupervised categorization," Percept. Psychophys. **61**, 1178–1199.

Ashby, F. G., Maddox, W. T., and Bohl, C. J. (**2002**). "Observational versus feedback training in rule-based and information-integration category learning," Mem. Cognit. **30**, 666–677.

Ashby, F. G., and Gott, R. E. (**1988**). "Decision rules in the perception and categorization of multidimensional stimuli," J. Exp. Psychol. Learn. Mem. Cogn. **14**, 33–53.

Ashby, F. G., and Maddox, W. T. (**1990**). "Integrating information from separable psychological dimensions," J. Exp. Psychol. Hum. Percept. Perform. **16**, 598–612.

Baptista, L. F., and Petrinovich, L. (**1986**). "Song development in the white-crowned sparrow: social factors and sex differences," Anim. Behav. **34**, 1359–1371.

Blumstein, S. E., and Stevens, K. N. (**1980**). "Perceptual invariance and onset spectra for stop consonants in different vowel environments," J. Acoust. Soc. Am. **67**, 648–662.

Bruner, J. (**1983**). *Child's Talk; Learning to Use Language* (Norton, New York).

Cooper, F. S., Delattre, P. C., Liberman, A. M., Borst, J. M., and Gerstman, L. J. (**1952**). "Some experiments on the perception of synthetic speech sounds," J. Acoust. Soc. Am. **24**, 597–606.

Delattre, P. C., Liberman, A. M., and Cooper, F. S. (**1955**). "Acoustic loci and transitional cues for consonants," J. Acoust. Soc. Am. **27**, 769–773.

Delattre, P. C., Liberman, A. M., and Cooper, F. S. (**1964**). "Formant transitions and loci as acoustic correlates of place of articulation in American fricatives," Studia Lingusti. **18**, 104–121.

Diehl, R., Lotto, A., and Holt, L. L. (**2004**). "Speech perception," Annu. Rev. Psychol. **55**, 149–179.

Eales, L. A. (**1989**). "The influences of visual and vocal interaction on song learning in zebra finches," Anim. Behav. **37**, 507–508.

Eimas, P. D. (**1963**). "The relation between identification and discrimination along speech and nonspeech continua," Lang Speech **6**, 206–217.

Fernald, A., and Simon, T. (**1984**). "Expanded intonation contours in mothers' speech to newborns," Dev. Psychol. **20**, 104–113.

Fiser, J., and Aslin, R. N. (**2002**). "Statistical learning of higher-order temporal structure from visual shape sequences," J. Exp. Psychol. Learn. Mem. Cogn. **28**, 458–467.

Fowler, C. A. (**1986**). "An event approach to the study of speech perception from a direct-realist perspective," J. Phonetics **14**, 3–28.

Francis, A. L., Baldwin, K., and Nusbaum, H. C. (**2000**). "Effects of training on attention to acoustic cues," Percept. Psychophys. **62**, 1668–1680.

Gauthier, I., and Tarr, M. J. (**1997**). "Becoming a 'Greeble' expert: exploring mechanisms for face recognition," Vision Res. **37**, 1673–1682.

Gauthier, I., Behrmann, M., and Tarr, M. J. (**1999a**). "Can face recognition really be dissociated from object recognition?" J. Cogn Neurosci. **11**, 349–370.

Gauthier, I., Williams, P., Tarr, M. J., and Tanaka, J. (**1998**). "Training 'Greeble' experts: A framework for studying expert object recognition processes," Vision Res. **38**, 2401–2428.

Gauthier, I., Tarr, M., Anderson, A., Skudlarski, P., and Gore, J. (**1999b**). "Activation of the middle fusiform face area increases with expertise in recognizing novel objects," Nat. Neurosci. **2**, 568–573.

Guenther, F. H., Husain, F. T., Cohen, M. A., and Shinn-Cunningham, B. G. (**1999**). "Effects of categorization and discrimination training on auditory perceptual space," J. Acoust. Soc. Am. **106**, 2900–2912.

Hauser, M. D., Agnetta, B., and Perez, C. (**1998**). "Orienting asymmetries in rhesus monkeys: The effect of time-domain changes on acoustic perception," Anim. Behav. **56**, 41–47.

Hauser, M. D., Newport, E. L., and Aslin, R. N. (**2000**). "Segmentation of the speech stream in a non-human primate: Statistical learning in cotton-top tamarins," Cognition **75**, 1–12.

Hillenbrand, J. M., and Gayvert, R. T. (**2005**). "Open source software for experiment design and control," J. Speech Lang. Hear. Res. **48**, 45–50.

Holt, L. L., Kluender, K. R., and Lotto, A. J. (**1997**). "Discrimination of single-formant stimuli by chinchillas (*Chinchilla villidera*)," J. Acoust. Soc. Am. **102**, 3188.

Holt, L. L., Lotto, A. J., and Kluender, K. R. (**2001**). "Influence of fundamental frequency on stop-consonant voicing perception: A case of learned covariation or auditory enhancement?" J. Acoust. Soc. Am. **109**, 764–774.

Holt, L. L., Lotto, A., and Diehl, R. (**2004**). "Auditory discontinuities interact with categorization: implications for speech perception," J. Acoust. Soc. Am. **116**, 1763–1773.

Jusczyk, P. W. (**1997a**). "Finding and remembering words: Some beginnings by English-learning infants," Curr. Dir. Psychol. Sci. **6**, 170–174.

Jusczyk, P. W. (**1997b**). *The Discovery of Spoken Language* (MIT, Cambridge, MA).

Keating, P. A. (**1984**). "Phonetic and phonological representation of stop consonant voicing," Language **60**, 286–319.

Kirkham, N. Z., Slemmer, J. A., and Johnson, S. P. (**2002**). "Visual statistical learning in infancy: Evidence for a domain general learning mechanism," Cognition **83**, B35–B42.

Kluender, K. R., Diehl, R. L., and Killeen, P. R. (**1987**). "Japanese quail can learn phonetic categories," Science **237**, 1195–1197.

Kluender, K. R., Lotto, A. J., Holt, L. L., and Bloedel, S. L. (**1998**). "Role of experience for language-specific functional mappings of vowel sounds," J. Acoust. Soc. Am. **104**, 3568–3582.

Kuhl, P. K. (**1991**). "Human adults and human infants show a 'perceptual magnet effect' for the prototypes of speech categories, monkeys do not," Percept. Psychophys. **50**, 93–107.

Kuhl, P. K. (**1992**). "Psychoacoustics and speech perception: Internal standards, perceptual anchors, and prototypes," in *Developmental Psychoacoustics*, edited by L. A. Werner and E. W. Rubel (American Psychological Association, Washington, DC), pp. 293–332.

Kuhl, P. K., and Miller, J. D. (**1975**). "Speech perception by the chinchilla:

Voiced-voiceless distinction in alveolar plosive consonants," Science **190**, 69–72.
Kuhl, P. K., Tsao, F.-M., and Liu, H., -M. (**2003**). "Foreign-language experience in infancy: Effects of short-term exposure and social interaction on phonetic learning," Proc. Natl. Acad. Sci. U.S.A. **100**, 9096–9101.
Kuhl, P. K., Williams, K. A., Lacerda, F., Stevens, K. N., and Lindblom, B. (**1992**). "Linguistic experience alters phonetic perception in infants by six-months of age," Science **255**, 606–608.
Lacerda, F. (**2003**). "Phonology: An emergent consequence of memory constraints and sensory input," Read. and Writ.: An Interdiscip. J. **16**, 41–59.
Lacerda, F., and Sundberg, U. (**2004**). "An ecological theory of language learning," J. Acoust. Soc. Am. **116**, 2523.
Liberman, A., Delattre, P. C., Cooper, F. S., and Gerstman, L. J. (**1954**). "The role of consonant-vowel transitions in the stop and nasal consonants," Psychol. Monogr. **68**, 1–13.
Liberman, A. M., and Mattingly, I. G. (**1985**). "The motor theory of speech perception revised," Cognition **21**, 1–36.
Liberman, A. M., and Mattingly, I. G. (**1989**). "A specialization for speech perception," Science **243**, 489–494.
Lindblom, B. (**1996**). "Role of articulation in speech perception: Clues from production," J. Acoust. Soc. Am. **99**, 1683–1692.
Lindblom, B., Brownlee, B. D., and Moon, S.-J. (**1992**). "Speech transforms," Speech Commun. **11**, 357–368.
Lisker, L., and Abramson, A. S. (**1964**). "A cross-linguistic study of voicing in initial stops: Acoustical measurements," Word **20**, 384–422.
Lotto, A. J. (**2000**). "Language acquisition as complex category formation," Phonetica **57**, 189–196.
Lotto, A. J., and Kluender, K. R. (**1998**). "General contrast effects of speech perception: Effect of preceding liquid on stop consonant identification," Percept. Psychophys. **60**, 602–619.
Lotto, A. J., Kluender, K. R., and Holt, L. L. (**1998**). "Depolarizing the perceptual magnet effect," J. Acoust. Soc. Am. **103**, 3648–3655.
Massaro, D. W. (**1987**). *Speech Perception by Ear and Eye: A Paradigm for Psychological Inquiry* (Erlbaum, Hillsdale, NJ).
Maye, J., Werker, J. F., and Gerken, L. (**2002**). "Infant sensitivity to distributional information can affect phonetic discrimination," Cognition **82**, B101–B111.
Mirman, D., Holt, L. L., and McClelland, J. L. (**2004**). "Categorization and discrimination of nonspeech sounds: Differences between steady-state and rapidly-changing acoustic cues," J. Acoust. Soc. Am. **116**, 1198–1207.
Nearey, T. M. (**1997**). "Speech perception as pattern recognition," J. Acoust. Soc. Am. **101**, 3241–3254.
Papousek, M., Papousek, H., and Bornstein, M. H. (**1985**). "The naturalistic vocal environment of young infants: On the significance of homogeneity and variability in parental speech," in *Social Perception in Infants*, edited by T. M. Field and N, Fox (Ablex, Norwood, NJ), pp. 269–295.
Pisoni, D. B. (**1977**). "Identification and discrimination of the relative onset time of two component tones: Implications for voicing perception in stops," J. Acoust. Soc. Am. **61**, 1352–1361.
Pisoni, D. B. (**1987**). "Auditory perception of complex sounds: Some comparisons of speech vs nonspeech signals," in *Auditory Processing of Complex Sounds*, edited by W. A. Yost and C. S. Watson (Erlbaum, Hillsdale, NJ), pp. 247–256.
Reber, A. S. (**1976**). "Implicit learning of synthetic languages: The role of instructional set," J. Exp. Psychol. [Hum Learn] **2**, 88–94.
Reber, A. S. (**1989**). "Implicit learning and tacit knowledge," J. Exp. Psychol. **118**, 219–235.
Reber, A. S., Kassin, S. M., Lewis, S., and Cantor, G. W. (**1980**). "On the relationship between implicit and explicit modes in the learning of a complex rule structure," J. Exp. Psychol. [Hum Learn] **6**, 492–502.
Rossion, B., Gauthier, I., Goffaux, V., Tarr, M., and Crommelinck, M. (**2002**). "Expertise training with novel objects leads to left-lateralized face-like electrophysiological responses," Psychol. Sci. **13**, 250–257.
Saffran, J. R., Aslin, R. N., and Newport, E. L. (**1996**). "Statistical learning by 8-month-old infants," Science **274**, 1926–1928.
Saffran, J. R., Johnson, E. K., Aslin, R. N., and Newport, E. L. (**1999**). "Statistical learning of tone sequences by human infants and adults," Cognition **70**, 27–52.
Saffran, J. R., Newport, E. L., Aslin, R. N., Tunick, R. A., and Barrueco, S. (**1997**). "Incidental language learning: Listening (and Learning) out of the corner of your ear," Psychol. Sci. **8**, 101–105.
Sinnott, J. M., and Brown, C. H. (**1997**). "Perception of the American English liquid /ra-la/ contrast by humans and monkeys," J. Acoust. Soc. Am. **102**, 588-602.
Sinnott, J. M., Beecher, M. D., Moody, D. B., and Stebbins, W. C. (**1976**). "Speech sound discrimination by monkeys and humans," J. Acoust. Soc. Am. **60**, 687-695.
Stevens, K. N. and Blumstein, S. E. (**1981**). "The search for invariant acoustic correlates of phonetic features," in *Perspectives on the Study of Speech*, edited by P. D. E. J. L. Miller (Erlbaum Hillsdale, NJ), pp. 1–38.
Sussman, H. M., Hoemeke, K. A., and Ahmed, F. S. (**1993**). "A cross-linguistic investigation of locus equations as a phonetic descriptor for place of articulation," J. Acoust. Soc. Am. **94**, 1256–1268.
Sussman, H. M., Fruchter, D., Hilbert, J., and Sirosh, J. (**1998**). "Linear correlates in the speech signal: The orderly output constraint," Behav. Brain Sci. **21**, 241–299.
Trout, J. D. (**2001**). "The biological basis of speech: What to infer from talking to the animals," Psychol. Rev. **108**, 523–549.

Robust acoustic object detection

Yali Amit,[a] Alexey Koloydenko,[b] and Partha Niyogi[c]
Departments of Computer Science and Statistics, The University of Chicago, Hyde Park, Chicago, Illinois 60637

(Received 14 March 2002; revised 19 July 2004; accepted 24 May 2005)

We consider a novel approach to the problem of detecting phonological objects like phonemes, syllables, or words, directly from the speech signal. We begin by defining *local* features in the time-frequency plane with built in robustness to intensity variations and time warping. Global templates of phonological objects correspond to the coincidence in time and frequency of patterns of the local features. These global templates are constructed by using the statistics of the local features in a principled way. The templates have clear phonetic interpretability, are easily adaptable, have built in invariances, and display considerable robustness in the face of additive noise and clutter from competing speakers. We provide a detailed evaluation of the performance of some diphone detectors and a word detector based on this approach. We also perform some phonetic classification experiments based on the edge-based features suggested here. © *2005 Acoustical Society of America.* [DOI: 10.1121/1.2011411]

PACS number(s): 43.72.Ne, 43.72.Ar [DDO] Pages: 2634–2648

I. INTRODUCTION

We consider the problem of detecting phonological objects from the speech signal. Humans are able to accomplish this task reliably and robustly. In spite of significant progress in automatic speech recognition over the years, robustness still appears to be a stumbling block. Current commercial products are quite sensitive to changes in recording device, to acoustic clutter in the form of additional speech signals, and so on. The goal of replicating human performance in a machine remains far from sight.

By detection we are referring to the identification of time points at which a specific predefined object or class of objects is found. Detection is essentially a two class classification problem—object versus background or nonobject. In this sense it is a simpler problem than multiclass classification which requires more complex boundaries in the representation space. In detection the two classes are not treated symmetrically as in classification. Typically one aims for *low* false negative rates (missed detections of the selected class), at the expense of a higher false alarm rate (the rate at which background is labeled as object). Detection may serve a limited purpose such as word spotting. However it can also be viewed as a building block in a speech recognition algorithm. In the context of speech, trying to faithfully classify every time segment as one particular phoneme is recognized as a very difficult problem. Instead each phoneme detector separately flags time points where that phoneme may be present. Some time instants may be labeled with multiple phonemes, and clearly many of the labelings will be wrong. This results in a transformation of the data into a labeled point process which would serve as input to higher level algorithms. The advantage of such an approach is that training detectors, based on very simple and parsimonious statistical models, require much smaller data sets and are much less sensitive to noise not encountered during training. The final disambiguation would be left for the higher level algorithms that employ context, knowledge of vocabulary, and syntax. Assuming the false negative rates are low, the efficiency and accuracy of the next level depends on the false positive rate. The main purpose of this paper is to demonstrate that it is possible to produce detectors that are robust to a variety of degradation, are easily trained, and efficient to compute at the price of a relatively low false positive rate.

Since the pioneering work of Harvey Fletcher [(1995); see a recent interpretation by Allen (1994)] speech perception experiments have suggested that the acoustic correlates of linguistic categories are locally distributed in the time-frequency plane and irrelevant parts may be perturbed leaving recognition intact. Some speech recognition models try to exploit this fact. For example, subband based models of recognition (Tibrewala and Hermansky, 1997; Bourlard and Dupont, 1997; Saul *et al.*, 2001) attempt to construct separate detectors/recognizers in each of several frequency subbands that are then combined to yield a global recognizer. Since the individual recognizers in the ensemble are based on only local frequency subband information, they are naturally poorer and the consequences of having an ensemble of several poor recognizers need to be better understood.

Our approach gives a different computational expression to some of the ideas presented in Fletcher (1995) and Allen (1994) where global templates are made from the coincidence of binary features that are local both in time and frequency. These features are computed through adaptive thresholding of simple difference linear filters with very small local support in the time-frequency plane. Borrowing from vision terminology, we employ local oriented edges in the time frequency plane.

There are several important advantages to constructing models based on simple binary local features. First we obtain

[a]Electronic mail: amit@galton.uchicago.edu
[b]Electronic mail: koloyden@cs.uchicago.edu
[c]Electronic mail: niyogi@cs.uchicago.edu

invariance to local amplitude modulations as well as a simple mechanism to filter out moderate levels of acoustic clutter and noise. Second by "spreading" the detected binary features either along the time axis or the frequency axis, we easily introduce invariance to a considerable range of linear and nonlinear variations in the duration of components of the acoustic object, as well as variations in the basic formant frequencies across individuals. The use of global templates composed of large numbers of these "spread" features introduces robustness to occlusion or degradation of part of the signal. Thus, one of the primary advantages of this approach is having the robustness hardwired in the detection algorithm. Furthermore, since the only quantities estimated in training are the frequency of occurrence of each of the local features, templates produced with very small training sets generalize well. Finally since the actual detection involves a sequence of simple binary template matches it can be computed very efficiently and lends itself easily to parallel implementations with neural network type architectures.

An additional motivation for employing such models has been the success of similar approaches in visual detection tasks, see for example Grimson (1990), Ullman (1996), Amit (2000), Fleuret and Geman (2001), Viola and Jones (2002). Object detectors in gray level images are constructed from templates based on "spread" oriented edges or conjunctions of oriented edges, yielding very efficient detection algorithms, all produced with very small training sets. The idea of importing methods from computer vision to the speech domain can also be found in some earlier work, e.g., Leung and Zue (1986) or Riley (1989), where computer vision techniques are used to detect complex time-frequency features though the details are quite different.

The use of edge based representations in vision has been fueled in part by the seminal work of Hubel and Wiesel (1968) and subsequent neurophysiological investigations. Recent work on the auditory cortex of animal species suggests the existence of neurons that fire selectively when oriented "acoustic edges" in the time-frequency plane are presented (Kowalski *et al.*, 1996; Theunissen and Doupe, 1998; Sen *et al.*, 2001). While it is still unclear what role such edge detectors play in speech perception, it is certainly worthwhile to understand more fully the statistics of speech sounds in representational spaces constructed from these edge maps. There have been very few detailed studies in this direction although Schwartz and Simoncelli (2001) present preliminary steps. Most studies of speech have tended to use vector quantization on the continuous valued vectors of spectral or cepstral coefficients, and it is in these representational spaces that acoustic phonetic insights have primarily been developed.

It is worthwhile to note that formants correspond to local maxima in the time-frequency plane and in this sense constitute a form of local feature that has received considerable attention in speech production and perception studies. As we shall see, the edge based representations considered in this paper are strongly related with the formant structure in the speech signal. For example, the template corresponding to a stop consonant may be interpreted as a series of sharp changes in each of several frequencies simultaneously. The templates corresponding to phonetic categories with strong formant structure (for example, in most sonorant regions of the signal) ultimately "learn" to represent such structure. In Fig. 4, we show how the emergent templates resemble the formant patterns. Indeed the templates derived for the various acoustic objects are strikingly similar to the classical templates shown in phonetics texts. We see this acoustic-phonetic interpretability as a significant strength of our approach. We note that regions of great spectral change seem to have a certain kind of perceptual saliency and play an important role in landmark based approaches to speech recognition (Stevens, 1991; Liu, 1996) as well as the approach to stop detection pursued in Niyogi and Sondhi (2002).

The approach described here is clearly statistical in nature. However it marks a departure from the usual statistics based models of recognition at several levels. For one, an unusually large number of highly local acoustic properties are measured. Second, the global templates that are constructed may be interpreted as a rather sparse representation of the time-frequency plane that are correlated with phonetic content. This sparse nature of the modeling suggests that one does not need to account for the *entire* signal but only informationally significant portions of it. We note that similar types of sparse representations were used in Amit and Murua (2001) for robust recognition of isolated spoken digits using relational decision trees.

The work in Hopfield *et al.* (1998) bears some similarity with our approach to acoustic detection. There the binary local features are defined as local maxima in time of the spectrogram at different frequencies, and invariance to multiplicative time stretching is obtained by taking logarithms of the time coordinates. In the context of syllable detection in bird songs the work in Chi and Margoliash (2001) also makes use of local maxima and invariance is achieved by "spreading." It therefore seems that there is much promise in using predesigned binary local features, both in achieving robustness to noise and clutter and in providing a straightforward way to incorporate invariance to nonlinear warping in time and frequency.

We should emphasize that detection per-se is not a solution to the continuous speech problem. One will ultimately need to recognize words. One approach to this might be to make word detectors—a possibility we briefly describe later in the paper. However, even if we could produce very accurate word detectors it is not computationally feasible to detect each word from even a moderately sized vocabulary in order to parse the entire speech signal. In Sec. VII we outline several possible ways in which detection may be integrated into a continuous speech algorithm including as a higher level entry into an HMM.

The rest of the paper is organized as follows. In Sec. II, we describe the binary features, and formulate a statistical model for the features on object and on background, yielding a classifier for object versus background. In Sec. III we describe an efficient two stage detection algorithm for implementing the classifier at every time instant. The training procedure is presented in Sec. IV. The experimental results on a number of acoustic objects—a phoneme, some diphones, and a word—are presented in Sec. V. Here we study different

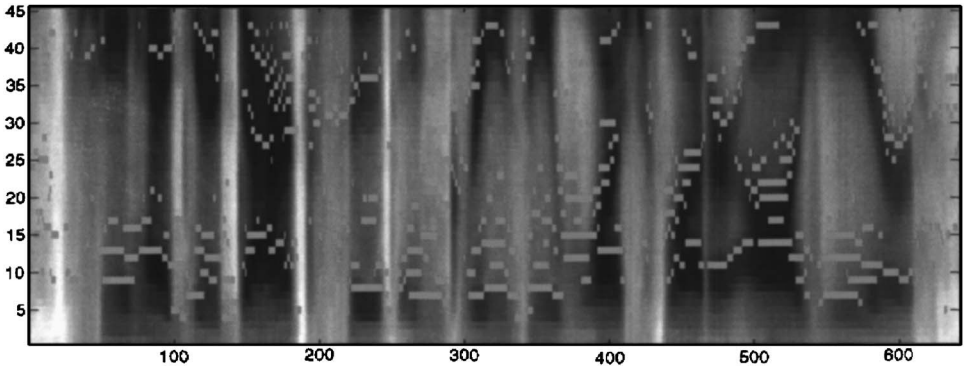

FIG. 1. Edge maps. Locations of edges $Y_{(0,-1)}$ on a spectrogram, detecting transitions from high to low energy in the frequency dimension.

aspects of the detectors constructed. We examine their accuracy in terms of ROC curves as well as where in the duration of each phonological segment the detector peak is usually obtained. We examine the robustness of the detector by considering the effect of various kinds of noise and clutter. We analyze the confusion caused by some of the diphone detectors and try to understand if there are any phonetic regularities in such confusion. We also compare the proposed detector to an idealized, nearest neighbor baseline classifier. We show that our detector is less sensitive to training set sizes and noise than the baseline. The experiments are conducted on TIMIT—an acoustic phonetic database of 630 different speakers. In Sec. VI we perform some preliminary phonetic classification experiments to give the reader a sense of what one might expect when these edge-based features are used for such a task. Finally, in Sec. VII we discuss further directions of investigation within the proposed framework.

II. MODELS FOR ACOUSTIC OBJECTS

A. Robust local binary features

Let $W(t,f)$ denote the windowed Fourier transform of the acoustic signal, at time t and frequency f. In our experiments we use a 20 ms window moved every 5 ms. These values were empirically chosen to provide an appropriate trade-off between fine spectral detail and smoothing on which the local edge detection process worked reliably. Preprocessing consists of taking the log of $|W(t,f)|$, and smoothing the result both in time and in frequency. The smoothing kernel K_G is a 7-pixel-long discrete Gaussian with standard deviation of 1 pixel. (One pixel corresponds to 31.25 Hz in the frequency dimension and 5 ms in the temporal dimension.) The result is subsampled at every other frequency unit, followed by a 3 kHz frequency cutoff since most of the formant activity resides in this region. Thus, we define the *spectrogram* as $S(t,f)=2((\log(|W|))*K_G)(t,2f)$, $f=1,\ldots,F$. A fragment of $S(t,f)$ ($F=45\approx 2.8$ kHz) is shown in the left image of Fig. 2 and corresponds to the diphone "aa-r."

The detection algorithm is not based on the continuous valued spectrogram, but rather on local binary features extracted from the spectrogram, that capture transitions, and are analogous to oriented edge detectors used in computer vision. As shown in the following, such features offer a straightforward framework for incorporating invariance or robustness to amplitude variations and time warping. We also note that neurons in the primary auditory cortex are known to respond to transitions in the energy in the time-frequency plane (Kowalski *et al.*, 1996; Sen *et al.*, 2001; Theunissen and Doupe, 1998).

Eight orientations $v=(\delta t,\delta f)$ where

$$(\delta t,\delta f)\in\{(1,0),(1,1),(0,1),(-1,1),(-1,0),(-1,-1),\times(0,-1),(1,-1)\}$$

are defined, corresponding to each multiple of 45°. An edge of orientation v at point $x=(t,f)$ is a local maximum of the derivative of the spectrogram in the direction of v,

$$S(x+v)-S(x)\geqslant \max\{S(x)-S(x-v),S(x+2v)-S(x+v),\tau_\alpha\},\quad(1)$$

where τ_α is an adaptable local threshold, used to eliminate very small transitions. Specifically, all local differences $S(x+v)-S(x)$ in a region are computed and the αth percentile τ_α of the positive subsample is determined. (If no positive difference is found then $\tau_\alpha=+\infty$. In our experiments $\alpha=70\%$.) We write $Y_v(x)=Y_v(t,f)=1$ if condition (1) is satisfied, otherwise $Y_v(x)=0$. In Fig. 1 we show the locations of all edges in the frequency direction $v=(0,-1)$. Note how the features pick up part of the formant structure.

B. Invariance

By definition, since the inequalities are preserved, these local features are invariant to affine transformations of S and are robust to a wide range of smooth monotone transformations.

Robustness to time warping and frequency variations is obtained by "spreading" each detected feature to a neighborhood of the original location. For example, an edge of type v with $v=(\pm 1,0)$, corresponding to a local maximum of the time derivative, will be assigned to all locations (s,f) in the strip $(t-\Delta,t+\Delta)$. Other edges are spread the same way in the direction of v. Thus we define

$$\tilde{Y}_v(x)=\max_{-\Delta\leqslant j\leqslant\Delta} Y_v(x+jv).\quad(2)$$

The right panel in Fig. 2 is a spread version of the edge map shown in the middle panel, corresponding to transitions from high to low amplitude along the frequency axis. Note how the raw edge map before the spreading operation (middle panel) captures local structure such as pitch. This is smoothed out and the edge map in the right panel captures the overall spectral resonance profile (formant profile). In

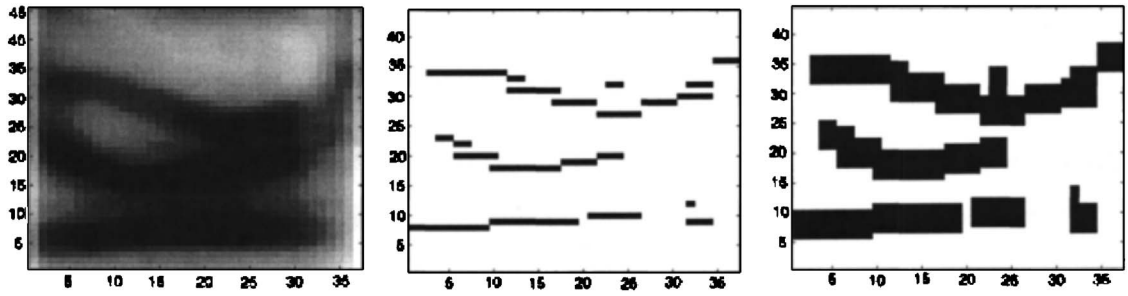

FIG. 2. The spreading operation. Left panel: the spectrogram $S(t,f)$. Middle panel: the extracted edges $Y_{(0,-1)}$ (same orientation as in Fig. 1). Right panel: the result of spreading $\tilde{Y}_{(0,-1)}, \Delta=2$. The x axis corresponds to time (in milliseconds) and the y axis to frequency (0–3 kHz quantized into 45 bins).

general, for all speech signals with clear formant structure, the edge maps capture the formant patterns in a similar way.

Spreading can be motivated as follows. Assume a certain transition in time (an edge of type $Y_{(1,0)}$) is characteristic of the object population at approximately t time units from the beginning of the signal, and at frequency f. The probability of finding this transition at precisely (t,f) may be quite small, but with high probability the transition will be found at frequency f somewhere in a small time interval $(t-\Delta, t+\Delta)$. This is equivalent to saying that the spread feature $\tilde{Y}_{(1,0)}(t,f)=1$ with high probability. Depending on the degree of variability of the object population larger degrees of spreading can be used. However larger spreading increases the background frequency of the features possibly reducing their discriminatory power. In our experiments we use $\Delta=2$.

Since the variables are all binary, spreading, which is defined through a local maximization, becomes a simple OR-ing operation. This has proved to be a crucial element in constructing efficient invariant detectors and classifiers in the visual domain [see Amit and Geman (1999), Amit (2002)]. The original continuous valued spectrogram is now reduced to a set of binary maps indexed by frequency and time, one map for each binary feature. Alternatively one can view this as one eight dimensional vector map in time and frequency, where the vector at each point (t,f) is binary valued and indicates which features are present at that point. We note that one of the main attractions of using local features is the ability to *adapt* their parameters online as discussed in Sec. VII A.

C. The statistical model

Let T denote the average duration of the acoustic object we seek to detect and let F denote the highest frequency in the (preprocessed) spectrogram. For a given time t, let $\mathbf{Y}(\mathbf{t})$ denote the vector of binary variables $\tilde{Y}_v(t+s,f), 0 \leq s < T, 1 \leq f \leq F$ (s corresponds to time and f to frequency) for all eight directions v. Conditional on the object being present at time t (its starting time is t) we assume these variables are independent, and with marginal probability

$$p_{s,f,v,o} = P(\tilde{Y}_v(t+s,f)=1 | \textit{object at } t),$$

yielding a joint distribution

$$P(\mathbf{Y}(\mathbf{t})|\textit{object at } t) = \prod_{s,f,v} p_{s,f,v,o}^{\tilde{Y}_v(t+s,f)} \cdot (1-p_{s,f,v,o})^{(1-\tilde{Y}_v(t+s,f))}. \tag{3}$$

Conditional on the object *not* being present at time (i.e., background) t the features are again assumed independent with a *different* marginal probability

$$p_{f,v,b} = P(\tilde{Y}_v(t+s,f)=1 | \textit{background at } t),$$

that does not depend on s, assuming stationarity of the background population. This yields a background joint distribution

$$P(\mathbf{Y}(\mathbf{t})|\textit{background at } t) = \prod_{s,f,v} p_{f,v,b}^{\tilde{Y}_v(t+s,f)} \cdot (1-p_{f,v,b})^{(1-\tilde{Y}_v(t+s,f))}. \tag{4}$$

This is a very simplistic model. Clearly the features are dependent due to the spreading operation both on object and on background, and on object there are strong correlations due to variability in the time duration of the object. We ignore these aspects in the current model.

The log-likelihood ratio of object to background at time t is then

$$\begin{aligned} J(t) &= \log \frac{P(\mathbf{Y}(\mathbf{t})|\textit{object at } t)}{P(\mathbf{Y}(\mathbf{t})|\textit{background at } t)} \\ &= \sum_{s,f,v} \tilde{Y}_v(t+s,f) \log \frac{p_{s,f,v,o}(1-p_{f,v,b})}{(1-p_{s,f,v,o})p_{f,v,b}} + C \\ &= \sum_{s,v,f} \tilde{Y}_v(t+s,f) \cdot w_{s,f,v} + C, \end{aligned} \tag{5}$$

where C is a constant that does not depend on the data.

Detection proceeds by evaluating the log-likelihood ratio $J(t)$, and identifying those locations where $J(t)>\rho$ for some predetermined threshold $\rho>0$. *No time warping is performed.* This test is useful only if there are many locations s for which $p_{s,f,v,o}/p_{f,v,b}$ is either much larger or much smaller than 1. Only the location t of the object is specified in the model, whereas the length of the object can vary. Since the probabilities are attached to a specific location $t+s$, as explained earlier, they will tend to be close to the background probabilities, unless spreading is performed.

Assume for example that given the object starts at time t, for each of the five points in the interval $[t+s-2, t+s+2]$,

one-fifth of the population has an edge of type $E_{(1,0)}$ at that point. It seems reasonable however that these edges all correspond to the same "event" on the object. The *entire* population would have an edge $\tilde{Y}_{(0,1)}$ at $t+s$ if spreading with $\Delta=2$ is performed. Thus the spreading operation is a mechanism for increasing on-object probabilities. Although background probabilities increase as well, there is a range of spreading that provides significant gains in the ratio, for those cases where it is greater than 1. Moreover those locations where the ratio remains significantly less than 1, are now much more reliable.

The threshold ρ can be determined in several ways. If the conditional independence assumption were indeed appropriate, under the null hypothesis of an object at t, $J(t)$ in Eq. (5) can be approximated as a normal random variable with mean $\mu=\Sigma_{s,f,v}^{N} p_{s,f,v,o} w_{s,f,v}+C$ and variance $\sigma^2=\Sigma_{s,f,v} p_{s,f,v,o}(1-p_{s,f,v,o}) w_{s,f,v}^2$. If our goal is to minimize *false negatives*, i.e., the proportion of object missed by the detector, we could keep all instances of time for which

$$J(t) > \mu - k\sigma \equiv \rho,$$

for some choice of k. Clearly conditional independence is not a valid assumption; nearby edges are highly correlated. However as the distance between two features increases it is safe to assume that conditionally they are weakly dependent. Thus $J(t)$ still may be approximated as a normal variable but the variance would have to include a term involving covariances of pairs of variables. Finally it is possible to choose ρ from the training set, for a particular predetermined false negative rate.

Note that the detector can be viewed as a simple linear classifier (perceptron) between object and background. The weights are obtained from the probability estimates of the individual features. Directly training a perceptron for object against background data could produce more powerful weights, however there is always the danger of overfitting and we recall that one of our goals is to use small training sets. This is even more so if nonlinear classifiers are used. However under the same conditional independence assumptions as noted earlier the Fisher linear discriminant analysis yields an alternative linear classifier of the form

$$w_{s,f,v} = \frac{p_{s,f,v,o} - p_{f,v,b}}{p_{s,f,v,o}(1-p_{s,f,v,o}) + p_{f,v,b}(1-p_{f,v,b})}. \tag{6}$$

In our experiments we find that the outcome of these two classifiers is essentially the same.

It is also possible to construct more complex features, in terms of the elementary ones in such a way that p_b decreases much faster than p_o and independence becomes a more credible assumption, this has been implemented in the context of visual detection [see Amit (2000)].

III. DETECTION

Computing $J(t)$ for all t amounts to nothing more than a convolution of a filter composed of the chosen weights $w_{s,f,v}$ with the binary output $\mathbf{Y}$ obtained from computing the local features [see Eq. (5)]. However this is quite a large filter given that T can be on the order of several tens of time units and F several tens of frequency units. The computation can be quite intensive. Our solution is to perform the computation in a two stage manner.

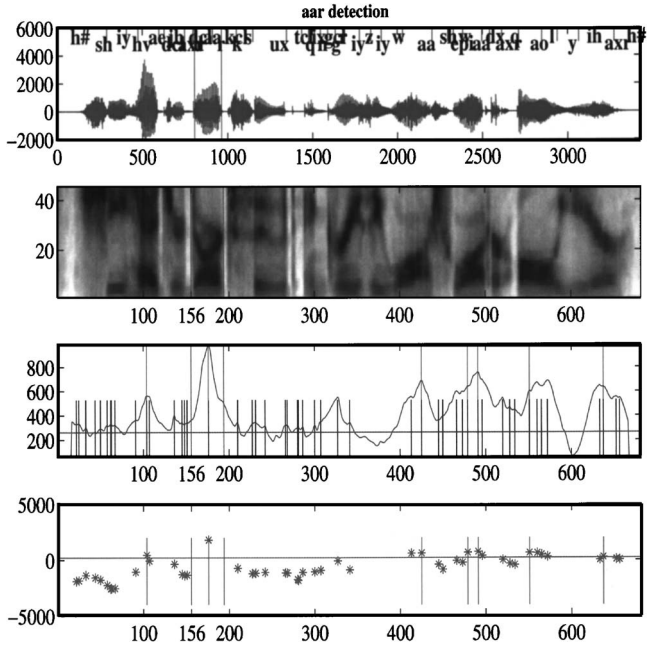

FIG. 3. Detection of **aar**. The target segment is marked with green stems. Top panel: Original wave form. Second panel: preprocessed spectrogram. Third panel: continuous J_0 response (blue curve), J_0 peaks with $J_0 \geqslant \rho_0$ (black stems). Fourth panel: J responses (blue stars), cluster centers (red stems), and empirical 0.99 threshold ρ (blue).

A. A two stage detector

First a simpler model is defined in which the weights $w_{s,f,v}$ are nonzero only on a feature set I for which $p_{s,f,v,o} \geqslant \lambda$, where λ is chosen to be higher than all the background probabilities, so that $p_{s,f,v,o} \gg p_{f,v,b}$. Furthermore we use equal weights for all the features in I yielding a sum

$$J_0(t) = \sum_{(s,f,v)\in I} \tilde{Y}_v(t+s,f), \tag{7}$$

which again will be compared to a predetermined threshold ρ_0. This sum is over a much smaller set I and only involves counts, with no multiplications, and is hence much faster to compute. Only at times t for which $J_0(t) > \rho_0$ do we compute the full model $J(t)$. Thus, our overall detection rule is $J_0(t) \geqslant \rho_0$ *and* $J(t) \geqslant \rho$ (we denote this conjunction by $J \circ J_0$) combined with a *clustering* procedure described in the following section.

In Fig. 3 we show the original wave form, the preprocessed spectrogram, and the detections obtained by $J_0(t)$ and $J(t)$.

B. Clustering

The statistics J_0 and J are essentially convolutions and therefore are inherently smooth in t. Consequently, a match between the template and a realization of the object will result in a cluster of time points $\{t_0 < t_1 < \ldots < t_L\}$ at which the detection statistic will stay above the prespecified threshold. It is then necessary to choose a small number of discrete

times to represent the cluster. We do this in two steps, treating the J_0 and J responses separately. At the J_0 stage, we simply declare $J_0(t)$ a detection if and only if $J_0(t) \geq \rho_0$ *and* $J_0(t)$ is a local maximum: $J_0(t-1) \leq J_0(t) \geq J_0(t+1)$. Examples of such detections are represented by the black stems in Fig. 3, the third panel from top. Note that instead of computing J at all 700 time points it is computed at only about 50 points.

Next, $J(t)$ is evaluated at all the points selected in the previous step, and we keep only those points where $J(t) \geq \rho$. These we cluster as follows.[1] Initially, the set of the detection points is partitioned into chains $\{t_0 < t_1 < \ldots < t_L\}$ with links $t_l - t_{l-1} < C_0$. As these resulting clusters may still extend across several object lengths, we split them further, successively cutting their longest links (i.e., t_{k-1} and t_k move apart to different clusters if $t_k - t_{k-1} \geq t_l - t_{l-1} l = 1, \ldots, L$) until all resulting clusters satisfy $t_L - t_0 \leq C_1$, for some prescribed constant C_1. This gives us clusters no longer than C_1 time units. Finally, one response $[t_k, J(t_k)]$ is reported for the kth cluster, corresponding to the maximum of J within that cluster. The two bottom images of Fig. 3 mark the clustered $J \circ J_0$ responses by red vertical lines. Presently, our constants $C_0 \approx T$ and $C_1 \approx 1.5T$ are determined empirically and thus depend on the average duration of the object (i.e., the length of the template). We also note that simple coarsening of the time scale might prove to be a sufficiently effective alternative to our clustering.

Thus after applying $J \circ J_0$ and clustering, the algorithm postulates a set of times at which the target object is thought to occur. Our experiments are conducted on a labeled data set (TIMIT) for which a phonetic segmentation is available. A detection time t_i is deemed a *correct detection* if it lies anywhere within the segmentation provided by the TIMIT labeling, otherwise it is deemed a *false alarm*. If the object class was present over a time interval and no detection occurred within that interval, then this event was deemed a *false negative*. Thus the number of false negatives and false alarms are calculated for any detection scheme. In this paper, we compare our approach with a baseline nearest neighbor classifier using the same criterion for scoring false alarms and false negatives.

C. Time invariance

Although we are performing a rigid template match, invariance to time warping of the acoustic signal is incorporated both through the spreading of the features in the data, as described earlier, and through the use of conservative thresholds. For short objects such as phonemes or diphones of average duration 80–100 ms, the variance is on the order of 10–15 ms. The spreading in time of each feature is on the order of ±8 ms (for those features corresponding to a time discontinuity in the spectrogram).

IV. TRAINING

The TIMIT set is a phonetically balanced labeled data set consisting of 6300 sentences spoken by 630 speakers, representing various US dialects. The set is partitioned into eight directories, DR1 through DR8, corresponding to the distinct dialects. The entire database is divided into a training and a test portion. Each dialect region (DR1 through DR8) is thus correspondingly split into a training and a test subset. This is the standard split of the TIMIT database and we have used this to separate training and test data for all our experiments.

A training subset of 1460 sentences is used for estimating probabilities and determining thresholds, and a test set (disjoint from the training one) has 4840 sentences on which the performance of the algorithm is evaluated. We use the diphone "aar" (as in the word "dark") to illustrate the training procedure.

All (1046) instances of "aar" are segmented from the training data, using the phonetic transcriptions provided with the TIMIT data set. The binary local feature maps are computed on each training example. A fixed interval time T_{ref} is chosen for the template reference grid, given by the average duration of the training examples. For a training example of duration T' each local feature at a location (t,f) is *registered* (aligned) to location $(tT_{\text{ref}}/T', f)$ on the reference grid. This creates a uniform time of the binary features of the different training examples. At each location on the reference grid we then count the number of local features found in the training set at that location after *registration*. The images in the left panel of Fig. 4 show these counts as brightness maps on the reference grid with highest values given in dark. There are eight images corresponding to the eight orientations of the elementary features.

For the first stage of the detection (computing J_0), a set of feature/location pairs (v_i, s_i, f_i), $i = 1, \ldots, N_I$ is chosen by picking only those with frequency (on the training set) above the threshold $\lambda = 0.5$. This produces the set of features I of Eq. (7), and is shown in the right panel of Fig. 4 as black regions. In the templates shown here there are 3729 of feature location pairs (<20% of a total of all feature location pairs.)

For the second stage the counts at each location are stored and become preliminary estimates $\tilde{p}_{s,f,v,o}$, of the (on object) probabilities $p_{s,f,v,o}$. The background probabilities are estimated similarly but assuming translation invariance. Thus, only one probability is computed for each frequency and each orientation. The background probabilities are computed only once and then used in any new detector. The final estimates $\hat{p}_{f,v,b}$ are found to be in the range 0.1–0.5. In order to keep the weight values $w_{s,f,v}$ bounded, it is important to bound the on-object estimates away from 0 and 1. We thus constrain the final estimators $(\hat{p}_{t,f,v,o})$ to be less than 0.995 and greater than 1% of the background probability of the same frequency and orientation. Specifically

$$\hat{p}_{s,f,v,o} = \min(0.995, \max(\tilde{p}_{s,f,v,o}, \epsilon \cdot \hat{p}_{f,v,b})),$$

where $\epsilon = 0.01$. The upper value of 0.995 and the lower value of $0.01 \cdot \hat{p}_{f,v,b}$ were chosen empirically and have no particular theoretical justification.

Note that learning reduces to local estimation of frequencies of features as opposed to the estimation of complex and high dimensional parameters. Thus training is very fast and requires only small data sets. We view this as a crucial property of our approach which is a major departure from the

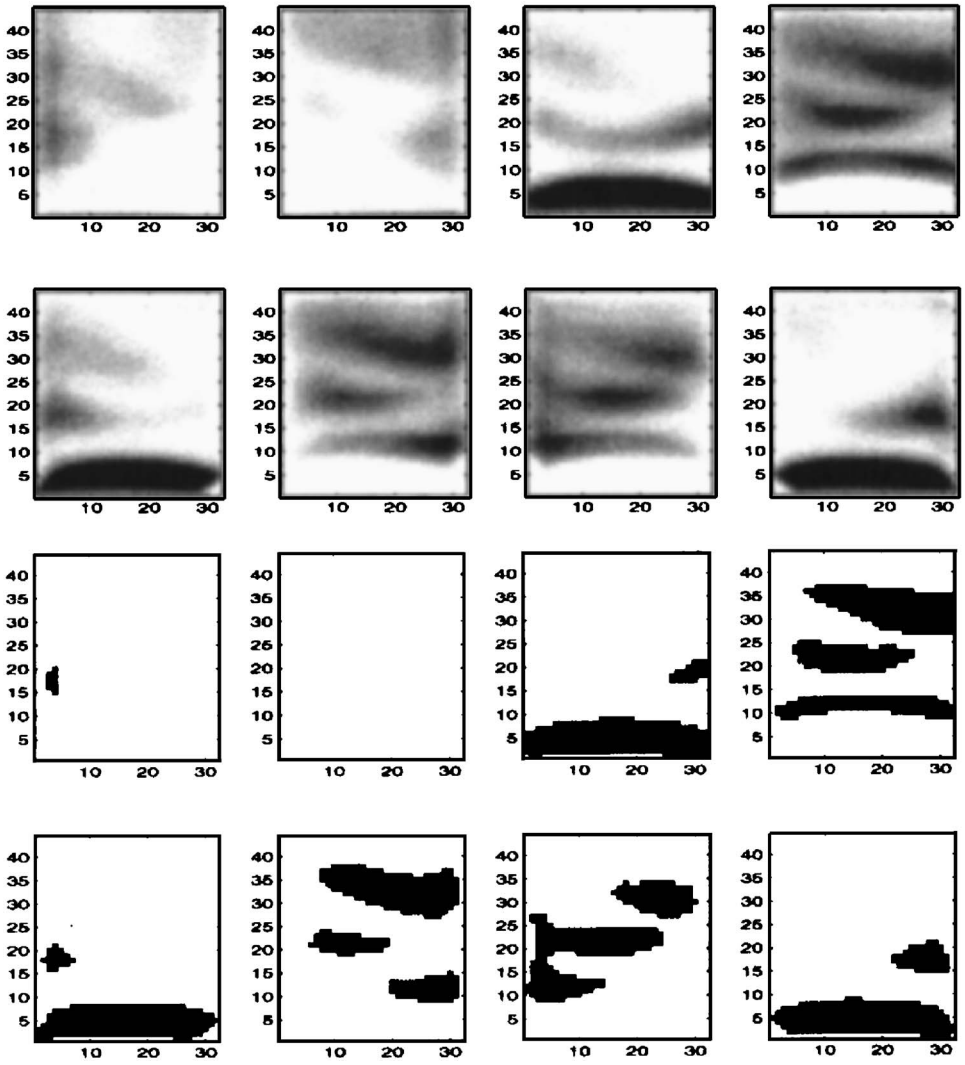

FIG. 4. Templates. Top panel: Probability templates for J—frequencies of local features of eight orientations. Bottom panel: Binary templates after thresholding by $\lambda=0.5$.

existing HMM paradigm. Note also that if templates for all objects which need to be detected are defined in terms of the same local features, the feature extraction step is carried out only once.

Thresholds. The values for the thresholds ρ_0 and ρ (for J_0 and J, respectively) are estimated using the full training sentences; the maximal on-object values of J_0 and J are recorded within the boundaries of the instance of the object in the full sentence, as given by the phonetic transcription. No registration is performed in this step. This yields a histogram of values for the two statistics. For ρ_0 we take $\hat{\mu}_0-4\hat{\sigma}_0$ where $\hat{\mu}_0$ and $\hat{\sigma}_0$ are the mean and standard deviation of J_0 on the training set. The threshold ρ is obtained using a predetermined false negative rate, which in Sec. V B is taken to be 1% on the training set.

V. EXPERIMENTS

We test our algorithm, henceforth called the edge-based detector (EBD), on phonemes, diphones, and words in clean speech and under several degradation conditions, and compare it to an idealized baseline nearest neighbor classifier (see the following), henceforth called the baseline detector (BLD). Our sources of degradation are:

(1) Additive white noise with SNR=5, 10 dB.
(2) Addition of auditory clutter in the form of a second speaker chosen at random with SNR=5, 10 dB.
(3) Addition of Babble noise (ten background speakers chosen at random) at SNR=5, 10 dB.

In all cases, SNR is calculated by using rms ratios. Thus, if $y=x+\eta$ is the corrupted speech where x is the clean speech and η is the added noise, then SNR is computed as

$$\mathrm{SNR}=10\log_{10}\frac{\langle x^2\rangle}{\langle \eta^2\rangle}=20\log_{10}\frac{\sqrt{\langle x^2\rangle}}{\sqrt{\langle \eta^2\rangle}},$$

where $\langle x^2\rangle=(1/T)\Sigma_t x(t)^2$ denotes the average value of the signal energy and $\langle \eta^2\rangle=(1/T)\Sigma_t \eta(t)^2$ denotes the average value of the noise. Table I summarizes the specifications of all the parameters involved in our experiments.

A. A baseline classifier

The baseline detector is a relatively accurate but highly inefficient and idealized nearest neighbor classifier between object and background, using the spectrogram data. Each training example of the object is segmented, using the phonetic transcription provided with the TIMIT data set, and the

TABLE I. Specifications of the model settings and parameters.

Stage	Specifications
Global	Time unit=5 ms, frequency unit=31.25 Hz
Preprocessing	Smoothing: 7×7 Gaussian, $\sigma=1$
	Frequency subsampling: step=2
Feature extraction	Adaptive threshold: $\alpha=70\%$
	Spread: $\Delta=2$ pixels
	Template dimensions: $T\times F\times8$, $F=45\approx2.8$ kHz
Detection Statistics	Estimation: $\hat{p}_{t,f,v,o}=\min(0.995,0.01\hat{p}_{f,v,b})$
	Feature selection for J_0: $I=\{(t,f,v):\hat{p}_{t,f,v,o}\geqslant\lambda=0.5\}$
	J_0-thresholding: $\rho_0=\hat{\mu}_0(J_0\|obj)-4\cdot\hat{\sigma}_0(J_0\|obj)$,
	$J\circ J_0$-clustering: C_0, minimal intercluster distance, $\approx T$
	C_1, maximal cluster length $\approx1.5T$
Sentence parsing	Partition block length $\approx T$
Robustness	White noise: SNR=5, 10; Babble noise: SNR=5, 10
	Clutter: Random speaker SNR=5, 10

spectrogram data (frequencies higher than 3 kHz being always cut off) is scaled in time to $T_{\text{ref}}\times F$, a reference grid of the same dimensions as in the EBD template construction (Sec. II A). A random sample of T_{ref}-long background data segments is obtained, scaled to exactly the same dimensions $T_{\text{ref}}\times F$.

For testing, each instance of the *object* in the test set is *segmented* and the spectrogram on that time segment is rescaled to $T_{\text{ref}}\times F$. This is then compared in sum of squares norm to the training samples of both object and background. Let d_o be the sum of the distances to the three nearest object examples, and d_b the sum of the distances to the three nearest background examples. Classification is given by

$$\frac{d_o}{d_o+d_b}\leqslant\rho_{\text{nn}},$$

in which case the instance is assigned to the "object" class. In order to produce ROC curves for this classifier, we vary $\rho_{\text{nn}}\in(0,1)$. For false alarm rates we apply the same criterion to a sample of full sentences that do not contain the object, at each time instant. Thus, at each time t a segment of duration T_{ref} is extracted, rescaled to $T_{\text{ref}}\times F$ and the above ratio is computed. A clustering mechanism similar to that used for the EBD is then applied to the output.

We reiterate that in addition to the advantage of using nearest neighbors which is known to be a very accurate, albeit inefficient, classifier this baseline also uses a manually determined segmentation and a rescaling for the object samples. This was done to ensure that the performance of the baseline detector was measured in the most favorable circumstances. *The EBD requires no segmentation or rescaling*.

B. Diphone detection

We performed experiments on a number of diphone, phoneme, and word detection tasks. These are too numerous to report so in this paper we will illustrate our general findings by considering the example of a very small number of them. These will provide the reader a sense of the various issues that arise in using this technology for detection tasks.

A detailed analysis is provided for the diphone **aar**

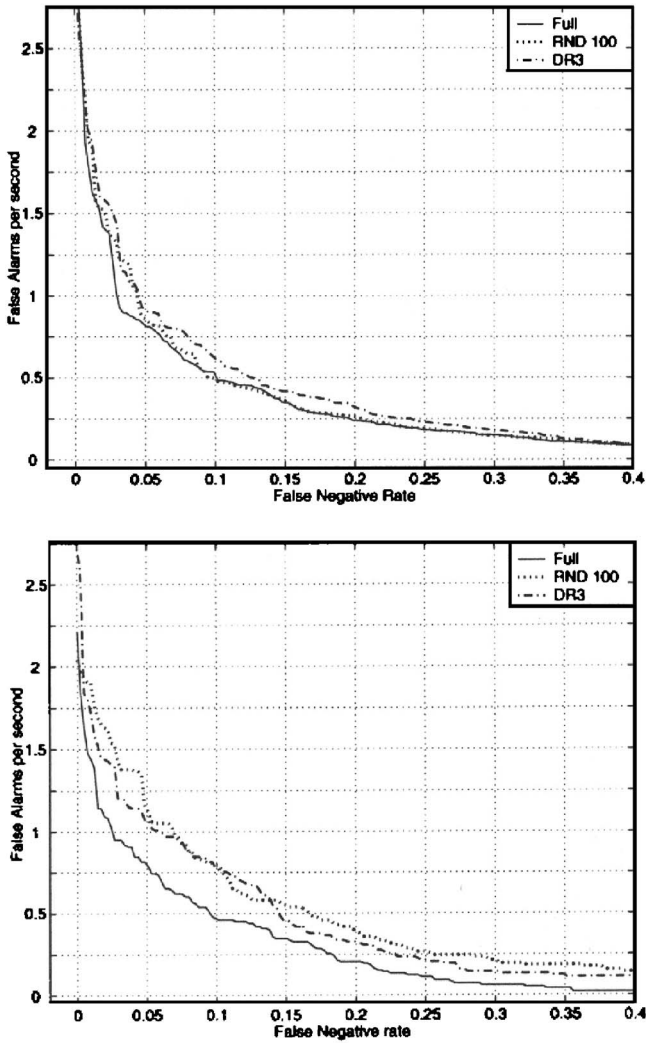

FIG. 5. Performance of **aa-r** detectors as a function of training set size: Top—EBD, Bottom—BLD.

where we show comparisons to the baseline nearest neighbors detector described earlier, and present the full ROC curves. We show that our detector is less sensitive to training set sizes and more robust than the baseline. We also study the confusions made by these detectors in general and try to see if there are any phonetic regularities in these confusions. It is worth noting that ultimately a detector for a particular phonological class does not return a segment but rather returns only a point in time around which it thinks the segment is present. We study where this point in time is located with respect to the actual boundaries of the phonological segment.

1. Dependence on training set size

In Fig. 5, left panel, we show the performance of the EBD as a function of the size of the training set for three choices: all 1046 samples from the training data, 100 random samples from the positive training data, and all 178 samples from the North Midland dialect (DR3). The background probabilities were estimated once and for all from a small sample of sentences and were found to be stable. The horizontal axis measures the false negative rate (proportion of target class phonemes not detected) and the vertical axis

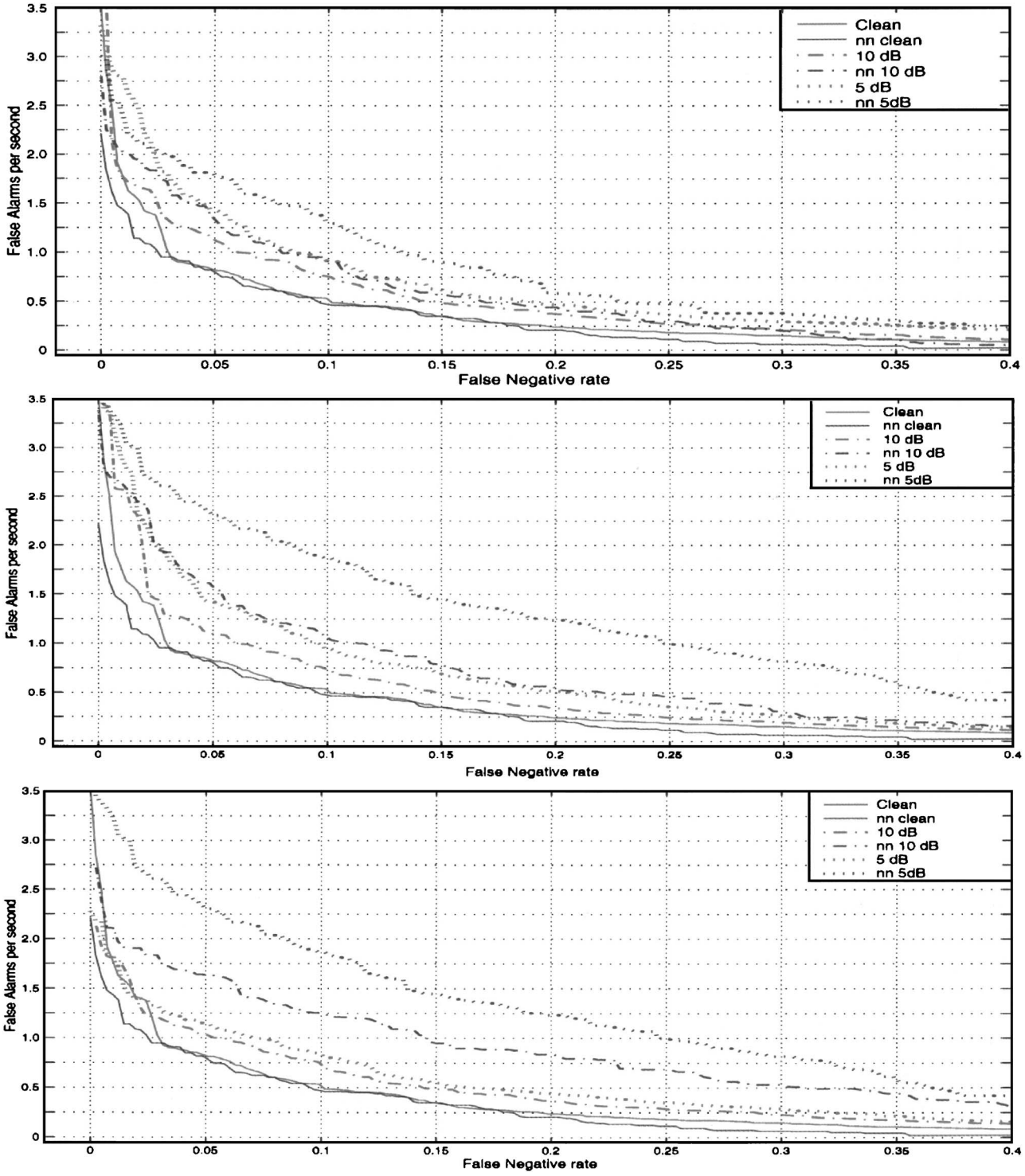

FIG. 6. Sensitivity of **aar** detector to degradation. Top: clean speech and one random background speaker at 10 and 5 dB, red—EBD, blue—BLD. Middle: clean speech and background babble noise at 10 and 5 dB, red—EBD, blue—BLD. Bottom: clean speech and additive white noise at 10 and 5 dB, red—EBD, blue—BLD.

measures the number of *false alarms* (i.e., detections not on the object) *per second*. It is not surprising that the algorithm performs essentially the same with the different training sets, since training only involves the estimation of the probabilities of binary variables, and the algorithm as a whole is not very sensitive to the accuracy of these estimates. For comparison in Fig. 5, right panel, we show the same data for the BLD. There is evidence of some degradation for the smaller training sets.

2. Sensitivity to degradation

The three panels of Fig. 6 show the ROC curves of the algorithm under various degradations. The ROC curve for clean data is shown for comparison. We observe that the performance of the EBD and that of the BLD, with the full training set and on clean data, is essentially the same. We emphasize that without the idealized setting in the baseline algorithm, where the objects are segmented and rescaled, the

TABLE II. Detection results: False negative probabilities and false alarms per second. Threshold ρ is set to first $J \circ J_0$ percentile (i.e., **0.01** false negative probability) on the training set. Each row indicates a different condition. The training set was always clean. N_{train} and N_{test} refer to the total number of instances of each object in the training and test sets, respectively (second row). The first column (for each object) shows the false negative probability and the second column shows the false alarm rate per second.

Object	**aar**		**shiy**		**sux**	
N_{tr} N_{test}	1046	413	812	299	532	191
Clean train set	**0.01**	1.717	**0.01**	1.359	**0.009**	1.451
Clean test set	0.01	1.788	0.03	1.317	0.016	1.373
White N 10 dB	0.024	1.27	0.137	0.714	0.037	1.094
White N 5 dB	0.063	1.064	0.331	0.433	0.084	0.851
Clutter 10 dB	0.005	2.169	0.124	0.902	0.115	1.135
Clutter 5 dB	0.019	2.232	0.224	0.839	0.147	1.093
Babble 10 dB	0.015	2.563	0.428	0.259	0.178	0.601
Babble 5 dB	0.012	2.795	0.659	0.129	0.44	0.373
Object	**oy**		**rae**		**dark**	
N_{tr} N_{test}	684	263	672	243	452	166
Clean train set	**0.01**	1.46	**0.01**	1.394	**0.011**	1.694
Clean test set	0.008	1.548	0.008	1.423	0.012	1.663
White N 10 dB	0.015	1.178	0.012	0.865	0.03	0.455
White N 5 dB	0.038	1.004	0.045	0.667	0.114	0.19
Clutter 10 dB	0.015	1.969	0.004	1.785	0.006	1.461
Clutter 5 dB	0.023	2.045	0.004	1.834	0.018	1.452
Babble 10 dB	0.008	2.294	0.008	1.959	0.036	0.707
Babble 5 dB	0.023	2.432	0.0	2.035	0.048	0.5

baseline algorithm would perform much worse. In all cases: additive noise, clutter and babble noise, the BLD shows significantly greater deterioration. The ROC curve of the BLD at 10 dB is comparable or worse than that of the EBD at 5 dB. This is most pronounced in the case of babble noise. It is clear that the EBD is more robust in the experiments we have performed so far.

Table II summarizes our experiments on all the objects under the various degradations. Here the threshold ρ was predetermined on the training data at a very conservative rate of 1% false negatives. Several conclusions can be drawn from the data presented in Table. II First, at low false negative rates the threshold obtained from training is quite robust and generalizes well to the clean data set as well as to the noisy ones. The main problems are with the diphones starting with a fricative. We feel that the current approach is particularly good when the underlying sounds have a well-developed formant structure that maintains itself robustly against additive noise. Since the fricative regions are noisy and lack such formant structure, the spectrograms in these regions are particularly degraded by noise and clutter. This leads to poorer performance in noisy conditions as can be seen in the examples of **shiy** and **sux**. Interestingly, we find that for sononant sounds, the false negatives go up slightly but the false alarms go up significantly. On the other hand, for fricated sounds, the false negatives go up significantly while the false alarms actually decrease.

On the whole false alarm rates are of the order of two *per second* but less in many cases. Note that the performance of **rae** appears to be particularly good: the false negative rates are always close to the prescribed 1%, while the false alarm rates stay below 2 per second. The detection of **aar**, while also exhibiting well-behaved false negatives, shows, on the other hand, false alarm rates that are consistently higher than the ones of **rae**. However, it is important to realize that the test data have more instances that are confusible with **aar** than those with **rae**.

3. Analysis of confusions

The ROC curves document overall performance for each of the detectors. Additional insight may be obtained by an analysis of the most common confusions. Indeed, the false alarms flagged by the detector are not random but rather appear to have similar phonetic structure to the target object. This is summarized in Table III, where for each of the six detectors we show ten false alarms with the highest probability of detection (skipping the ones that occur less than ten times in the test set). Note that there are between 1500 and 1800 diphone pairs and it is virtually impossible to display the entire confusion matrix but a partial view of it provided in Table III is most instructive.

From examining the confusions made by the diphone detectors (**aa-r, sh-iy, s-ux, r-ae**) we conclude that the most common false alarms are those for which the underlying diphone shares similar broad class features as the target diphone. For example, consider the **aa-r** detector. Most of the false alarms seem to be of the form **low/back-vowel-semi-vowel**. Thus the consonantal part of the diphone is one of **w,l,r,n**. Note that **w,l,r** are all semi-vowels while **n** shares with **r** the property of having an alveolar closure. Perceptually these sounds are also similar. Sometimes, the consonant is not completely released but affects the vowel so some of the false alarms consist of two vowels with a consonantal

TABLE III. Analysis of false alarms: Most frequent confusions. The numbers indicate the proportion of each class detected by a specific detector. Thus the (first row, second column) entry under **aa-r** indicates that the **aa-r** detector fired for 72% of the cases when the underlying object was an **er-ao** transition. Standard TIMIT transcription labels are used.

aa-r		**sh-iy**		**s-ux**		**oy**		**r-ae**		**dcl-d-aa-r-kcl-k**	
er-ao	0.72	sh-ey	0.66	s-ey	0.53	ao	0.81	axr-aa	0.57	l-ay-kcl-k	0.25
aw-axr	0.7	sh-ux	0.62	th-iy	0.5	aa	0.78	er-ao	0.56	dh-ae-tcl-t	0.25
ay-axr	0.69	pau-y	0.6	pau-ih	0.5	ay	0.75	aa-axr	0.55	dcl-d-ey-z	0.24
ao-w	0.67	pau-ih	0.59	f-ey	0.5	aw	0.63	axr-ay	0.54	r-ae-gcl-g	0.23
ay-l	0.66	ch-iy	0.58	sh-er	0.5	ow	0.61	ae-r	0.54	d-ow-n-tcl-t	0.22
axr-ao	0.65	s-iy	0.57	ch-iy	0.5	ah	0.42	axr-ey	0.53	l-iy-r	0.22
ae-l	0.63	s-ux	0.56	f-y	0.48	el	0.41	ay-ae	0.53	dh-ax-s	0.21
axr-ay	0.62	sh-ih	0.56	z-y	0.46	ae	0.4	f-ae	0.52	y-ih-er	0.19
nx-ao	0.6	iy-sh	0.56	sh-ux	0.46	l	0.35	r-aw	0.5	dx-axr-q	0.18
r-aw	0.59	f-iy	0.55	kcl-m	0.45	er	0.32	r-ay	0.53	dx-er-q	0.17

coloring in one of them. Thus **axr**, which is a retroflexed vowel, occurs often in the false alarm list.

Similarly, one may consider the false alarms made by the **sh-iy** detector. These seem to have the structure of **fricative-high/front vowel**. The fricatives **sh,s,f** and the affricate **ch** all share the property of frication. The two cases of **pau-y** and **pau-ih** are unreasonable errors. **pau** refers to a pause in the signal where the energy is very low but has a spectrum resembling background noise and therefore more like the fricatives superficially. This is actually one case where our amplitude invariance may have hurt us since **pau** is discriminated most by total energy rather than spectral detail.

4. Location of detector peak

Recall that the detector for a phonological class is obtained by picking a peak in the output of $J \circ J_0$. Therefore the detector provides a mapping from the speech stream to a labeled point process. Consider a detector for a phonological class X. If there is an instantiation of X in the utterance between times $t=t_1$ and $t=t_2$ (i.e., t_1 and t_2 mark the segmental boundaries of X in the acoustic realization), then the detector is deemed to fire correctly if it fires anywhere in the interval (t_1,t_2). If the detector fires correctly at $t_d \in (t_1,t_2)$, then it may be of interest to have some information about the statistics of t_d with respect to the segment (t_1,t_2).

Before we examine these statistics, it is useful to keep in mind some aspects of our detection framework. First, note that the framework is designed to detect the phonological class and not necessarily the boundaries of that class. A correct firing of the detector would lead to *one* firing somewhere within the segment (time t_d). There is no reason to expect this firing to be an estimate of either t_1 or t_2 (the segmental boundaries). Second, note that we have explicitly incorporated *spreading* of the binary features. This has been done to provide some temporal invariance to variations in speaking rate and other durational properties over the course of the utterance. While this spreading indeed provides such invariance, a consequence of this is also a resulting variability in the precise location of the detector peak. We shall see this variability in the plots that follow.

Shown in Fig. 7 are histograms of $(t_d-t_1)/(t_2-t_1)$ for a number of detectors. The quantity $(t_d-t_1)/(t_2-t_1)$ represents the distance to the left boundary of the segment normalized by the total duration of the segment. Such a normalized measure allows for more direct comparison across different

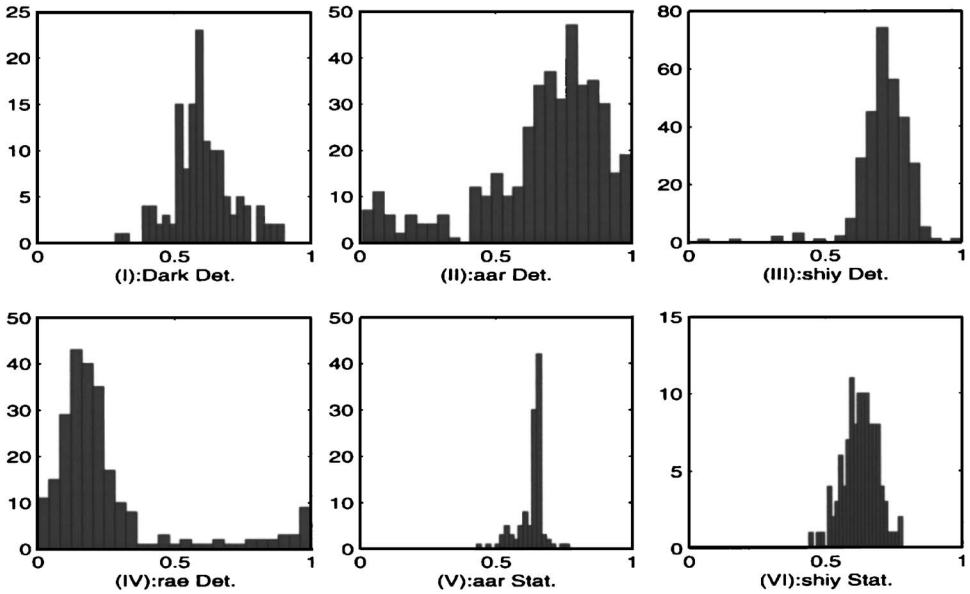

FIG. 7. Histograms indicating the statistics of detector peak locations ($(t_d-t_1)/(t_2-t_1)$-normalized distance to left segmental boundary; see the text) for a variety of detectors (panels I through IV). Panels V and VI are statistics for phonetic boundaries between **aa** and **r** (for the diphone **aar**) and **sh** and **iy** (for the diphone **shiy**), respectively.

acoustic realizations of the same segment. All detectors were operated with a 1% false alarm rate and the statistics are computed for all the correct detections obtained for each detector on the test set. Panel I shows the statistics of the detector output for the detector of the word "Dark." For this case, t_1 represents the beginnng of the **d**-closure and t_2 represents the end of the **k** burst obtained from the phonetic segmentation provided. Notice that the detector is seen to fire at a time that is mostly between 40% and 90% of the duration of the whole segment. Panels II through IV show similar detector statistics for the detectors of the diphones **aa-r, sh-iy**, and **r-ae**, respectively.

Some natural variation is observed. Thus, for example, the detector for **sh-iy** seems to fire mostly at a time around 70% of the duration of the **sh-iy** realization. The spread around this is indicated by the histogram in panel III. The detector for **r-ae** seems to fire mostly at a time around 15% into the duration of the **r-ae** segment. Both the **r-ae** and **sh-iy** detectors have similar variability. On the other hand, the detector for **aa-r** has much more variability as to where in the segment it fires (see panel II).

As we have mentioned before, it is not clear whether t_d ought to be aligned with any phonetic boundary. However, for the case of diphones, it is natural to wonder whether the detector fires usually at the boundary between the first phoneme and the second. Our analysis suggests that this need not be the case. For illustrative purposes, we show in panels V and VI, the statistics for the durations for **aa-r** and **sh-iy**, respectively. If $X=AB$ represents a diphone (phoneme A followed by phoneme B) then one can compute the statistics of duration of$A$/duration of$X$. Shown in panels V and VI are these statistics for **aa-r** and **sh-iy**, respectively. As we can see, the durational statistics for **sh - iy** is tightly clustered around 0.65 suggesting the duration of the fricative **sh** is about 65% of the duration of the whole diphone. This correlates well with the statistics of the corresponding detector output shown in panel III. On the other hand, we see that although there is considerable variation in the statistics of the detector output for the **aa-r** detector (panel II), there is much less variation in the duration of **aa** (normalized by the duration of **aar**) as shown in panel V.

In conclusion, we see that there is some variation as to where in the duration of the segment X, the detector for X will actually fire. It is not obvious whether the statistics of the detector firing will correlate with any natural phonological boundaries if X is made up of multiple phonemes. Thus our detectors should be viewed as detectors for the segment as a whole rather than any boundaries.

As a result of all the above-mentioned experiments, it might be fair to conclude that the detectors are unable to make fine phonetic distinctions but are able to work *robustly* for broad class transitions.

C. Words

In general, the approach presented in this paper can be used to detect phonological objects of arbitrary sizes like syllables, morphemes, or words. Consider for a moment the problem of making a word detector based on these ideas.

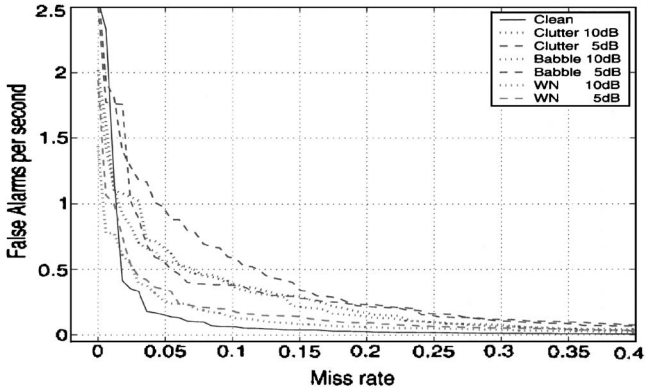

FIG. 8. Sensitivity of **dark** detector to degradation.

There are two basic approaches. One could make the word detector out of several component phoneme (or diphone) detectors and a sequential firing of each of these component detectors in the correct order would trigger the word detection. Alternatively, one could make a whole word template in much the same manner in which the diphone templates were constructed in the earlier section. A fuller investigation of the pros and cons of each of these two approaches is beyond the scope of the current paper and will be the subject of future work. However, to provide the reader with some sense of the performance of word detectors in general, we describe here the behavior of a detector for the word dark based on the whole word template approach.

The six ROC curves for degraded signals are shown in Fig. 8 against the similar curve computed for the clean signal. A detection was deemed correct if it occurred anywhere within the boundary of the word as determined from the transcription labels. If a detection occurred outside the boundary, it was deemed a false alarm. Due to the small amount of data in the test set the ROC curves are not very reliable at the very low false negative rate of under 1%–2%. We do observe that at the range of 5%–10% false negatives, the false alarm rate is several times smaller than that observed for phonemes. For example on the clean data at 5% false negative the false alarm rate for the word is approximately 0.12 per second compared to 0.75 per second for the **arr** detector. At 10% false alarm rate the corresponding values are 0.05 and 0.5 per second. The additional structure contained in the word dark eliminates many of the false alarms detected by the **aar** detector.

VI. EDGE BASED PHONETIC CLASSIFICATION

Thus far we have investigated the issue of efficient detection of phonological objects using the spread edges as the input features. Of interest is the ability to use the spread edges proposed in this paper for more standard classification problems. Do these features capture the necessary information to discriminate between phonetic objects with reasonable accuracy? We do not explore this issue in depth but report some results on the classification of segmented phonemes. Since phonetic classification is a more traditional task (than detection) in the speech community, these experiments

TABLE IV. Confusion matrix of eight broad classes.

	1	2	3	4	5	6	7	8
1	0.82	0.032	0.0039	0.076	0.044	0.0073	0.013	0.003 2
2	0.1	0.69	0	0.028	0.047	0.066	0.066	0.006 3
3	0.36	0.0034	0.43	0.19	0.0067	0.0051	0.0051	0
4	0.12	0.02	0.0018	0.79	0.04	0.012	0.014	0.002 2
5	0.018	0.036	0	0.018	0.82	0.04	0.066	0.001 1
6	0.0042	0.013	0	0.0086	0.028	0.82	0.12	0.000 6
7	0.0021	0.0027	0	0.0049	0.0084	0.068	0.91	0.000 15
8	0.11	0.1	0	0.14	0.074	0.07	0.065	0.44

will provide a sense to the reader as to how this technology might be expected to perform on this more standard task.

We applied a tree based classification procedure we have used in vision problems [see Amit (2002)]. Edges are computed on the continuous signal and the segments are extracted using the attached phonetic transcription. Each edge data segment of size $T\times F$ is placed in a fixed sized grid $T_{\max}\times F$ where $T_{\max}$ is the largest time extent of the segmented data, in our case $T_{\max}=40$ time units corresponding to 200 ms. (A small number of segments may be longer and is simply truncated at $T_{\max}$). We assume the data have all zeros on the remaining subgrid segment $[T,T_{\max}]\times F$. This implicitly conveys information on the length of the segment although this is not explicitly used in the classification procedure. Robustness to local time warping and frequency modulations is obtained by the spreading operation described earlier.

Classification is achieved by training multiple decision trees, with randomization (Amit and Murua, 2001), at each node only a small subsample of all $T_{\max}\times F\times 8$ binary edge features is inspected to find the most important split. We also implement boosting (Schapire *et al.*, 1998) whereby after each tree the data are reweighted, increasing the weight on misclassified examples. We grow M trees per class that are trained to classify that class against all others (as one negative class), for a total of $M\cdot C$ trees. At each terminal node of a tree grown for class c there is a weight between 0 and 1 corresponding to the proportion of training points of class c that reached that node in training. For testing we drop a data point X down all $M\cdot C$ trees. Let $\mu_{c,m}(X)$ be the weight assigned to c at the terminal node reached by X on the mth tree of that class. We choose the class that accumulates the highest weight:

$$\hat{c}=\text{argmax}_{c=1,\ldots,C}\frac{1}{M}\sum_{m}\mu_{c,m}(X).$$

We use 100 000 training segments from the TIMIT training data set, and 50 000 testing segments. 200 trees are grown for each class. With the full 52 phonetic classes of TIMIT, we achieve a classification rate of 58.5%. It is common to consider performance on a reduced set of 39 phonemic classes for which we achieve 61.37%. On a set of broad classes (8 in all) we achieve 83.8%. Shown in Table IV is the confusion matrix for the eight broad classes. These correspond to *stops, flaps, affricates, fricatives, nasals, semivowels, vowels*, and *aspiration* (corresponding to **h** in TIMIT), respectively (numbered 1 through 8 in that order in the confusion table). Performance for vowels is best at 91% correct class identification. Performance for all other classes is reasonable except for affricates (43%) and the phoneme **h** (aspiration) (44%), respectively. For affricates, we see that there is significant confusion with stops (36%) and fricatives (19%), respectively. The confusion, though high, is not entirely unreasonable. For the phoneme **h** (class 8), we see that the confusion is a little more random though even here, stops (11%), flaps (10%), and fricatives (14%) dominate. These last three categories often contain a degree of aspiration in their phonetic realizations and we conjecture that this probably leads to the confusion.

VII. DISCUSSION

From the experiments reported here it appears that the statistics of the local features on object and background are sufficiently different to allow for a simple weighted sum to successfully discriminate between object and background. More complex local features may yield even higher power. For example in Amit and Geman (1999) local edge conjunctions are used. Furthermore the simplicity of the models allows for some simple mechanisms of online adaptation which we briefly discuss in the next section, after which we discuss the issue of how such detections may be incorporated into a more comprehensive continuous speech recognition system.

A. Template adaptability

When the acoustic characteristics of the speaker changes, or the acoustic channel changes (from free space to a telephone channel or changes in microphone), when there is reverberation, or noise of various sorts, or auditory clutter, a human displays varying degrees of perceptual constancy that current machines are unable to achieve. It is unreasonable to assume that the stored and learned representation of the acoustic objects are relearned for each new environment. Instead, two aspects come into play. One consists of invariances hardwired in the representation which make them insensitive to certain changes. An example could be limiting the representation for sonorant regions to frequencies under 3000 Hz, so that irrelevant perturbations in higher frequency regions do not affect recognition. Another example is the amplitude invariance in the definition of the local features. However by far more important is the ability to *adapt* pa-

rameters of the representations *on line* as the signal is being processed.

1. Online adaptation of template weights

The templates are defined in terms of binary variables which are functions of local time-frequency information. Detection involves thresholding a weighted sum, where the weights derive from fixed estimates of object and background probabilities. It is possible to have a continuously updated estimate of the background probabilities $p_{b,i}$, performed *online*, over time intervals of larger duration. If there is significant background activity at a particular range of frequencies $[f,f']$, the probability estimates $p_{b,i}$ for the corresponding features would increase, reducing the weight on that feature in the sum in Eq. (5). The threshold ρ would have to be adjusted accordingly. This mechanism for adapting the template to the statistics of the background is simple and transparent in large part due to the simplicity of the original template.

2. Adapting to the individual speaker

Templates of the form shown in Fig. 4 are quite coarse. During training some local features are spread in the frequency direction to accommodate variations in the basic formant frequencies among speakers. However, if the three basic formant frequencies of a particular speaker are known, it is possible to adjust the templates around these frequencies and narrow down their spread. This does not require retraining, rather a simple modification of the list of feature location pairs, based on the estimated baseline formant frequencies. This would enhance the detection rate, especially in terms of false alarm rates.

B. From detection to continuous speech recognition

This paper focuses on the detection of acoustic objects, and demonstrates that robust detection is possible with small training sets. In all experiments described here we experience a certain percentage of false negatives, as well as a certain false alarm rate measured for example as false detections per second. Note, however, that with a relatively small library of detectors, either for all phonemes or perhaps all diphones, one can transform the original spectrogram into a sequence of labeled phonetic features. Since false alarms occur in detection for each feature, it is important to note that the same time point may sometimes be labeled with two different features. These ambiguities are to be resolved at higher processing levels. Thus the approach provides us with a parse of the time-frequency plane in terms of a vocabulary of phonetic feature detectors.

One possible use of these features is to construct word templates. Larger degrees of time invariance can be introduced by more extensive spreading. These are very powerful features in that they are detected with very high probability on the object (word) and very low probability (the false alarm rate) on background. The templates constructed from these features would then provide robust and invariant word detectors. Note that in Sec. V we experimented with a word detector derived directly from the original edge features. This works well for short words but would not provide for sufficient time invariance for longer words.

Another possible use of the new feature map would be as input into an HMM directly trained on the outputs of the phoneme or diphone detectors. Thus higher level knowledge of vocabularies and syntax is incorporated directly at this more symbolic level. We do not advocate resolving all the linguistic content based solely on the new feature map. At some places there will be ambiguities between competing interpretations which may need a more intensive analysis of the original spectral data. However, it is hoped that these will be relatively few, and the high level analysis will provide only a small number of candidate interpretations which require such intensive analysis.

[1]In order to compute ROC curves efficiently (Sec. V), we have to perform the clustering prior to the thresholding. Strictly speaking, this alters the overall detector, but the extent of this effect appears to be insignificant.

Allen, J. (**1994**). "How do humans process and recognize speech," IEEE Trans. Speech Audio Process. **2**, 567–577.

Amit, Y. (**2000**). "A neural network architecture for visual selection," Neural Comput. **12**, 1059–1082.

Amit, Y. (**2002**). *2d Object Detection and Recognition: Models, Algorithms and Networks*, (MIT, Cambridge, MA, in press).

Amit, Y., and Geman, D. (**1999**). "A computational model for visual selection," Neural Comput. **11**, 1691–1715.

Amit, Y., and Murua, A. (**2001**). "Speech recognition using randomized relational decision trees," IEEE Trans. Speech Audio Process. **9**, 333–342.

Bourlard, H., and Dupont, S. (**1997**). "Subband based speech recognition," in *Proceedings of the International Conference on Acoustics, Speech, and Signal Processing*, Germany, pp. 1251–1254.

Chi, Z., and Margoliash, D. (**2001**). "Feature representation, pattern filtering, and temporal alignment for birdsong detection," Technical report, Department of Statistics, University of Chicago.

Fletcher, H. (**1995**). *Speech and Hearing in Communication* (Acoustical Society of America, New York).

Fleuret, F., and Geman, D. (**2001**). "Coarse-to-fine face detection," Int. J. Comput. Vis. **41**, 85–107.

Grimson, W. E. L. (**1990**). *Object Recognition by Computer: The Role of Geometric Constraints* (MIT, Cambridge, MA).

Hopfield, J., Brody, C., and Roweis, S. (**1998**). "Computing with action potentials," in *Advances in Neural Information Processing Systems*, Vol. **10**.

Hubel, D. H., and Wiesel, T. N. (**1968**). "Receptive fields and functional architecture of monkey striate cortex," J. Physiol. (London) **195**, 215–243.

Kowalski, N., Depireux, D. A., and Shamma, S. A. (**1996**). "Analysis of dynamic spectra in ferret primary auditory cortex: I. Characteristics of single unit responses to moving ripple spectra," J. Neurophysiol. **76**, 3503–3523.

Leung, H., and Zue, V. (**1986**). "Visual characterization of speech signals," in *Proceedings of ICASSP'86*, Tokyo, Japan, pp. 2751–2754.

Liu, S. (**1996**). "Landmark detection for distinctive feature based speech recognition," J. Acoust. Soc. Am. **100**, 3417–3430.

Niyogi, P., and Sondhi, M. M. (**2002**). "Detecting stop consonants in continuous speech," J. Acoust. Soc. Am. **111**, 1063–1076.

Riley, M. (**1989**). *Speech Time Frequency Representations*, (Kluwer Academic, Dordrecht).

Saul, L., Rahim, M., and Allen, J. (**2001**). "A statistical model for robust integration of narrowband cues in speech," Comput. Speech Lang. **15**, 175–194.

Schapire, R. E., Freund, Y., Bartlett, P., and Lee, W. S. (**1998**). "Bossting the margins: A new explanation for the effectiveness of voting methods," Ann. Stat. **26**, 1651–1686.

Schwartz, O., and Simoncelli, E. (**2001**). "Natural sound statistics and divisive normalization in the auditory system," in *Advances in Neural Information Processing Systems*, Vol. **13**.

Sen, K., Theunissen, F. E., and Doupe, A. J. (**2001**). "Feature analysis of natural sounds in the songbird auditory forebrain," J. Neurophysiol. **86**, 1445–1458.

Stevens, K. N. (**1991**). "Speech perception based on acoustic landmarks: Implications for speech production," in *Perilus XIV: Proceedings of the Symposium on Current Phonetic Research Paradigms: Implications for Speech Motor Control*, Institute of Linguistics, University of Stockholm.

Theunissen, F. E., and Doupe, A. J. (**1998**). "Temporal and spectral sensitivity of complex auditory neurons in the nucleus hvc of male zebra finches," J. Neurosci. **18**, 3786–3802.

Tibrewala, S., and Hermansky, H. (**1997**). "Multiband and adaptation aproaches to robust speech recognition," in *Proceedings of Eurospeech'97*, Rhodes, Germany.

Ullman, S. (**1996**). *High-Level Vision* (MIT, Cambridge, MA).

Viola, P., and Jones, M. J. (2002). "Robust real time object detection," Int. J. Comput. Vis.

Vibrato of saxophones

J. Gilbert, L. Simon,[a] and J. Terroir
Laboratoire d'Acoustique de l'Université du Maine, UMR-CNRS 6613, Université du Maine, Avenue Olivier Messiaen 72085 Le Mans Cedex 09, France

(Received 18 January 2005; revised 18 July 2005; accepted 22 July 2005)

Several alto saxophone players' vibratos have been recorded. The signals are analyzed using time-frequency methods in order to estimate the frequency modulation (vibrato rate) and the amplitude modulation (vibrato extent) of each vibrato sample. Some parameters are derived from the results in order to separate the two ways of vibrato playing: vibrato "à la machoire" and vibrato "sur l'air." Moreover, time domain simulations of single-reed instrument vibratos are created. The model is controlled by two parameters: the mouth overpressure and a parameter characterizing the reed-mouthpiece system. Preliminary comments and comparisons between the simulated vibratos and recorded vibratos results are made. © *2005 Acoustical Society of America.*
[DOI: 10.1121/1.2036027]

PACS number(s): 43.75.Bc, 43.75.Pq [NHF] Pages: 2649–2655

I. INTRODUCTION

Vibrato is one of the common ornaments in occidental classical music, particularly in singing, but in wind and bowed instruments too. When the instruments are played using vibrato ornaments, deliberate fluctuations in the period and the amplitude of the acoustic pressure signals are applied.

Most of the studies dedicated to vibrato have been concerned with lyric singers,[1–5] trying to measure the properties like the vibrato rate (frequency modulation) or the vibrato extent (amplitude modulation), and then to analyze these properties as functions of time, or to study their pitch perception. Some other studies have been dedicated to musical instruments like bowed instruments or flutes.[6,7] Our study is devoted to the single reed wind instruments and particularly to the alto saxophone. According to Christophe Bois (a french professional saxophone player, Professor at the CNSM of Paris), there are many kinds of vibratos that can be separated in two sets according to the way they are produced: (1) the vibratos "à la machoire" (the vibrato effect comes from a slight mechanical vibration of the jaw), (2) the vibratos "sur l'air" (the vibrato effect comes from a slight modulation of the mouth cavity air pressure controlled by the tongue). The study is based on the analysis of different stable vibratos, by extracting their amplitude modulation parameters. Our aim in the study is to estimate characteristics of the saxophone vibrato oscillations. One question is as follows: are saxophone vibratos mainly linked to frequency modulation like vibratos of singers? Another question is at the end, is it possible to separate the two kinds of vibratos by analyzing the corresponding generated sounds? By using physical modeling of reed instruments, simulations of the sound regeneration allow mimiking of some aspects of the musical performance. A last question may then be are simplified models able to simulate vibratos and to exhibit the same kind of characteristics?

[a]Corresponding author. Electronic mail: laurent.simon@univ-lemans.fr

The present paper is divided into four sections. After this brief Introduction, the methods to extract the parameters of the amplitude modulation and of the frequency modulation are presented in Sec. II. Then the methods are checked on known test signals in order to estimate accuracies, then applied to alto saxophone players' vibratos and applied to simulated vibratos in Sec. III. Finally, the preliminary conclusions and the perspectives of this work are discussed in the conclusion, Sec. IV.

II. SIGNAL PROCESSING METHODS

Vibrato in the permanent regime may be modeled as both an amplitude modulation and a frequency modulation of a signal. Estimating both modulations allows the extraction of parameters of modeling. For amplitude modulation, we show that estimations based on methods such as envelope detection are accurate enough. For frequency modulation, time–frequency analysis is required. Several time–frequency methods (spectrogram,[1,2] modal distribution[8]) were used in other vibrato studies. In the paper, we use the spectrogram, and the instantaneous frequency is estimated as the local frequency of the spectrogram.[9]

A. Modeling of test signal

For most musical signals, the multicomponent AM-FM signal $s(t)$ is modeled as a discrete sum of partials,[8] i.e.,

$$s(t) = \sum_{n=1}^{N_h} a_n(t)\cos(\phi_n(t)), \tag{1}$$

where $a_n(t)$ is the amplitude modulation and $\phi_n(t)$ is the instantaneous phase of the nth partial, respectively, and where N_h is the number of harmonics of the playing frequency. It is furthermore supposed that $a_n(t)\cos(\phi_n(t))$ is the canonical representation of the signal, for all n, or equivalently[9] that the low-frequency content of the nth partial is in the amplitude, $a_n(t)$, and that the high-frequency content of the nth partial is in the term $\cos(\phi_n(t))$.

1. Amplitude modulation modeling

Only the permanent regime is studied in this paper. Consequently, the expression of the amplitude modulation $a_n(t)$ we consider in this paper is such that

$$a_n(t) = \gamma_n\left(1 + \sum_{k=1}^{N_{v,a}} \alpha_k \cos(2\pi k F_m t + \psi_k)\right), \tag{2}$$

for $n \in [1, N_h]$, where γ_n is the positive weight in amplitude modulation of the nth partial, where $N_{v,a}$ is the number of harmonics of the vibrato frequency F_m, and where the parameters α_k and ψ_k of the Fourier series have to be estimated. Note that α_k is the amplitude modulation rate of vibrato harmonic k, $\forall k \in [1, N_{v,a}]$.

2. Frequency modulation modeling

On the other hand, we suppose that the instantaneous phase of the permanent regime is expressed as

$$\phi_n(t) = 2\pi n F_s t + \sum_{l=1}^{N_{v,\phi}} \frac{n\beta_l F_s}{l F_m} \cos\left(2\pi l F_m t + \chi_l\right), \tag{3}$$

where F_s is the playing frequency, β_l and χ_l are, respectively, the vibrato rate and the phase of vibrato harmonic l, and $N_{v,\phi}$ is the number of harmonics of the vibrato frequency F_m. An instantaneous frequency is associated with the nth partial, defined as[9]

$$f_i^{(n)}(t) = \frac{1}{2\pi}\frac{d\phi_n(t)}{dt}. \tag{4}$$

If instantaneous frequency is an intuitive concept, its mathematical description [Eq. (4)] does sometimes satisfy our perception regarding instantaneous frequency, and sometimes does not.[9]

Inserting (4) into (3) yields

$$f_i^{(n)}(t) = nF_s\left(1 - \sum_{l=1}^{N_{v,\phi}} \beta_l \sin(2\pi l F_m t + \chi_l)\right). \tag{5}$$

Note that for both modulations, the modulation frequency in Eqs. (2) and (5) is the same.

3. Assumptions and parameters to be estimated

In the paper, only the permanent regime is studied. For the amplitude modulation [Eq. (2)], it is furthermore supposed that $a_n(t) > 0$, $\forall t$ and $\forall n \in [1, N_{v,a}]$, or, equivalently, that

$$\sum_{k=1}^{N_{v,a}} |\alpha_k| < 1. \tag{6}$$

For the frequency modulation [Eq. (5)], it is also supposed that there is no overlap of instantaneous frequency from partial n to partial $n+1$. This means that the maximum value of instantaneous frequency of the nth partial is considerably less than the minimum value of instantaneous frequency of the $(n+1)$th partial. First, the maximum of instantaneous frequency of the nth partial is bounded (upper limit) by

$$\mathrm{Max}(f_i^{(n)}(t)) = nF_s\left(1 + \sum_{l=1}^{N_{v,\phi}} |\beta_l|\right), \tag{7}$$

and second, the minimum of instantaneous frequency of the $(n+1)$th partial is bounded (lower limit) by

$$\mathrm{Min}(f_i^{(n+1)}(t)) = (n+1)F_s\left(1 - \sum_{l=1}^{N_{v,\phi}} |\beta_l|\right). \tag{8}$$

As a consequence, there is no overlap of instantaneous frequency from partial n to partial $n+1$ if

$$(2N_h + 1)\sum_{l=1}^{N_{v,\phi}} |\beta_l| \ll 1. \tag{9}$$

In the case of simulation, the controlled parameters are the numbers of vibrato harmonics $N_{v,a}$ (for the amplitude modulation) and $N_{v,\phi}$ (for the frequency modulation), the number of playing frequency vibrato harmonics N_h, and the sampling frequency f_e. The parameters to be estimated are the vibrato frequency F_m, the playing frequency F_s, the amplitude modulation parameters α_k (vibrato extent), ψ_k, the frequency modulation parameters β_l (vibrato rate), γ_n and χ_l, for $n \in [1, N_h]$, for $k \in [1, N_{v,a}]$ and for $l \in [1, N_{v,\phi}]$. In this study, we focus on the estimation of F_m, F_s, α_k, and β_l, for $k \in [1, N_{v,a}]$ and for $l \in [1, N_{v,\phi}]$.

B. Amplitude modulation and instantaneous frequency estimations

Instantaneous amplitude and frequency concepts were originally developed in the theory of modulation in communications. These time-varying parameters are important features to estimate for many applications such as radar, sonar, or seismology. Their estimations allow, in particular, location of the time-varying frequency content of the signal. Many algorithms were developed to estimate these features and a tutorial review[10,11] was published in 1992. In the present paper, we use the envelope detection algorithm for estimating the amplitude modulation $a_n(t)$ [Eq. (2)] and time–frequency distributions to estimate the instantaneous frequency $f_i^{(n)}(t)$ [Eq. (5)].

1. Amplitude modulation estimation

In order to estimate the amplitude modulation, we first demodulate the signal $s(t)$ by means of a quadratic envelope detector. The principle of this detector is as follows: the signal is squared, before being low-pass filtered. Then, by taking the square root of the low-pass filtered signal, we can obtain an estimation of the amplitude modulation.[12] The filter used is a Finite Impulse Response (FIR) digital filter, and its impulse response is calculated thanks to the Parks-McClellan algorithm.[13] Second, a synchronous detection is processed, in order to estimate F_m, α_k, and ψ_k, for $k \in [1, N_{v,a}]$.

TABLE I. (a) First set of parameters of a test signal. (b) Second set of parameters of a test signal. (c) Third set of parameters of a test signal. Simulated values and associated errors.

(a)		
Parameter	Simulated value	Associated error (%)
$[F_s, F_m]$ (Hz)	[392, 4.5]	[<0.1, 1.3]
$[\alpha_1, \alpha_2, \alpha_2]$ [Eq. (2)]	[0.441, 0.176, 0.029]	[0.45, 0.56, 0.45]
$[\beta_1, \beta_2, \beta_3]$ [Eq. (5)]	[0.006, 0.003, 0.002]	[1.7, 10, 25]
$[HD_\alpha, HD_\beta]$ [Eqs. (12) and (13)]	[0.375, 0.515]	[0.53, 12.23]
$[SGC_\alpha, SGC_\beta]$ [Eqs. (14) and (15)]	[1.362, 1.636]	[0.6, 5.07]

(b)		
Parameter	Simulated value	Associated error (%)
$[F_s, F_m]$ (Hz)	[392, 5]	[<0.1, 1]
$[\alpha_1, \alpha_2, \alpha_3]$ [Eq. (2)]	[0.75, 0.25, 0.125]	[0.67, 2.4, 15.2]
$[\beta_1, \beta_2, \beta_3]$ [Eq. (5)]	[0.01, 0.004, 0.004]	[2, 5, 32.5]
$[HD_\alpha, HD_\beta]$ [Eqs. (12) and (13)]	[0.349, 0.492]	[3.7, 15.45]
$[SGC_\alpha, SGC_\beta]$ [Eqs. (14) and (15)]	[1.362, 1.636]	[0.6, 5.07]

(c)		
Parameter	Simulated value	Associated error (%)
$[F_s, F_m]$ (Hz)	[1590, 4.75]	[<0.1, 1.9]
$[\alpha_1, \alpha_2, \alpha_3]$ [Eq. (2)]	[0.7, 0.3, 0.067]	[0.57, 1.33, 11.94]
$[\beta_1, \beta_2, \beta_3]$ [Eq. (5)]	[0.002, 0.0015, 0.002]	[5, 2, 25]
$[HD_\alpha, HD_\beta]$ [Eqs. (12) and (13)]	[0.402, 0.781]	[1, 8.6]
$[SGC_\alpha, SGC_\beta]$ [Eqs. (14) and (15)]	[1.407, 2]	[0.92, 5]

2. Instantaneous frequency estimation

Paraphrasing Cohen,[9] "instantaneous frequency is one of the most intuitive concepts, since we are surrounded [$\cdots$] by many phenomena whose periodicity changes." While instantaneous frequency seems to be a natural concept for describing our environment, its mathematical description is still an open question.[9,10]

Furthermore, it has been shown[9,10] that instantaneous frequency may be related to time-frequency distributions (TFD). Indeed, such distributions allow a representation of the frequency content of a signal as a joint function of time and frequency, and the instantaneous frequency may be then viewed as the average frequency at a given time.

Some distributions verify this property of the local average (such as the Wigner-Ville distribution), while other TFD only approximate it (such as the spectrogram).[9,10] Moreover, work has been done to construct a TFD that gives a perfect location of the instantaneous frequency.[14] In this paper, we use the spectrogram as an estimator of the instantaneous frequency. Once the instantaneous frequency is estimated, a synchronous detection is processed, in order to estimate F_m, β_l, and χ_l, for $l \in [1, N_{v,\phi}]$.

If the concept of instantaneous frequency is meaningful for a monocomponent signal, i.e., a signal where there is only one frequency varying with time for all time, a preliminary breakdown of the signal has to be done for a multicomponent signal. In the present case, we suppose that the instantaneous frequencies of partials n and $(n+1)$ do not overlap (which is clearly the case for real-world vibrato signals). As a consequence, instantaneous frequency may be estimated for all the partials $n \in [1, N_h]$.

Following Cohen,[9] we note $P_{SP}(t,f)$, the spectrogram of $s(t)$, according to

$$P_{SP}(t,f) = \left| \int s(\tau) h(\tau - t) e^{-j2\pi f \tau} d\tau \right|^2, \tag{10}$$

where $h(t)$ is a window function. In the following, we furthermore use the spectrogram to estimate the instantaneous frequency related to the nth partial as above,

$$\hat{f}_i^{(n)}(t) = \frac{\int_{B_n} f P_{SP}(t,f) df}{\int_{B_n} P_{SP}(t,f) df}, \tag{11}$$

where the partial n is related to the bandwidth B_n around the frequency nF_s. Even if $\hat{f}_i^{(n)}(t)$ is not a good estimator of the instantaneous frequency (due to an entanglement of the signal and window[9]), narrowing the window $h(t)$ (or equivalently broadening the bandwidths B_n) allows a correct estimation of the instantaneous frequency,[9] as shown in the next section.

III. RESULTS AND DISCUSSION

A. Instantaneous amplitude and frequency estimators for test signals

Three test signals are simulated in this section, according to Eqs. (1)–(5), for $N_h=1$ and for three harmonics of the vibrato frequency ($N_{v,a}=N_{v,\phi}=3$). The values of the parameters f_s, f_m, α_k, and β_l are given in Table I (for k and $l \in [1,3]$), corresponding to realistic values of real-world vibrators. For each of the three signals, a Gaussian white noise is added with different signal-to-noise ratios (from 0 to 50 dB).

We note in the following the levels of the vibrato strength from 1 (no vibrato) to 5 (exaggerated vibrato). In Table I(a), the level of the vibrato strength is 2, with a low modulation rate in both amplitude and frequency. In Table I(b), the level of the vibrato strength is 4, with a high modulation rate in both amplitude and frequency. Finally, the level of the vibrato strength in Table I(c) is 4, with a low modulation rate in frequency and a high modulation rate in amplitude. Furthermore, the rate of harmonic distortion (HD) for the amplitude modulation is expressed as

$$\mathrm{HD}_{\alpha} = \sqrt{\frac{\sum_{k=2}^{N_{v,a}} \alpha_k^2}{\sum_{k=1}^{N_{v,a}} \alpha_k^2}}. \tag{12}$$

For the frequency modulation, the rate of harmonic distortion will be

$$\mathrm{HD}_{\beta} = \sqrt{\frac{\sum_{l=2}^{N_{v,\phi}} \beta_l^2}{\sum_{l=1}^{N_{v,\phi}} \beta_l^2}}. \tag{13}$$

We also estimate the spectral gravity center (SGC) according to

$$\mathrm{SGC}_{\alpha} = \frac{\sum_{k=1}^{N_{v,a}} k\alpha_k}{\sum_{k=1}^{N_{v,a}} \alpha_k}, \tag{14}$$

for the amplitude modulation, and

$$\mathrm{SGC}_{\beta} = \frac{\sum_{l=1}^{N_{v,\phi}} l\beta_l}{\sum_{l=1}^{N_{v,\phi}} \beta_l}, \tag{15}$$

for the frequency modulation.

The values of the associated errors given in Table I show good agreement between the simulations and the estimations. The associated errors for the estimation of α_1 are less than 1%, while the associated errors for the estimation of β_1 are less than 5%. Furthermore, the playing frequency F_s and the vibrato frequency F_m are, respectively, estimated with errors less than 0.1% and 2%. Although the values of β_3 and α_3 are worse estimated, due to the very weak values of the simulated parameters, we maintain that the signal processing methods described in Sec. II are well suited for the analysis of vibratos. Last, the harmonic distortion rate is better estimated for the amplitude modulation than for the frequency modulation.

B. Real-world signals, estimation of parameters, and discussion

In order to apply the signal processing methods to real sounds, the saxophone player Christophe Bois has recorded self-sustained notes, from which one second of the permanent regime is selected and analyzed. The database contains 21 samples that are summarized in Table II. The database has been filled by playing the note E3, at two dynamic levels, piano and forte, at five vibrato strength levels, from soft (1) to high (5), using the two kinds of vibrato, "a la machoire" and "sur l'air." A class of records has been set from 2 to 11. A given class of record corresponds to the same note, the same dynamic, and the same vibrato strength level, the way of playing being "a la machoire" or "sur l'air." Most of the possibilities have been explored, giving the 21 samples. The samples have been analyzed using the signal processing methods described in Sec. II in order to extract the parameters α_k representative of the amplitude modulation, and β_l representative of the frequency modulation. The first coefficients β_1 as a function of α_1 are displayed in Fig. 1. Having a look at Fig. 1, no obvious conclusion can be drawn; the two kinds of vibratos cannot be separated by their (α_1, β_1) values, even though two samples having a close pair value (α_1, β_1) in Fig. 1 can be easily distinguished by an informal listening test. A first result is that the kind of vibrato is not directly linked with a kind of signal modulation. Another coefficient has then to be found. As explained previously in Sec. III A, harmonic distortion rates can be computed from the higher coefficients α_k and β_l (for $k,l>1$) of the real signals. The rate of harmonic distortion for the amplitude

TABLE II. Database of real signals. Record number, vibrato strength (from 1: no vibrato, to 5: exaggerated vibrato), dynamic, kind of vibrato and class of record.

Record number	Vibrato strength [1–5]	Dynamic	Kind of Vibrato	Class of record
2	1	piano	a la machoire	**2**
3	2	piano	a la machoire	**3**
4	3	piano	a la machoire	**4**
5	4	piano	a la machoire	**5**
6	5	piano	a la machoire	**6**
7	1	forte	a la machoire	**7**
8	2	forte	a la machoire	**8**
9	3	forte	a la machoire	**9**
10	4	forte	a la machoire	**10**
11	5	forte	a la machoire	**11**
12	1	piano	sur l'air	**2**
13	2	piano	sur l'air	**3**
15	3	piano	sur l'air	**4**
16	4	piano	sur l'air	**5**
17	5	piano	sur l'air	**6**
18	1	forte	sur l'air	**7**
19	2	forte	sur l'air	**8**
20	3	forte	sur l'air	**9**
21	4	forte	sur l'air	**10**

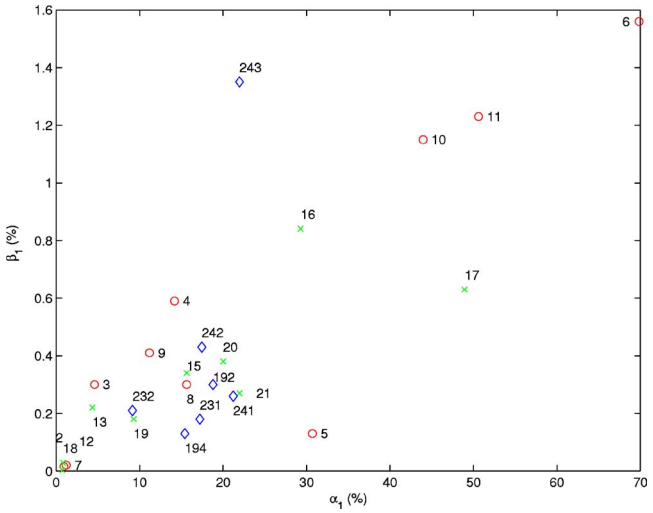

FIG. 1. β_1 as a function of α_1. The associated record numbers are in Tables II and III. Circles: Vibrato "a la machoire." Crosses: Vibrato "sur l'air." Diamonds: Vibrato coming from playing performance.

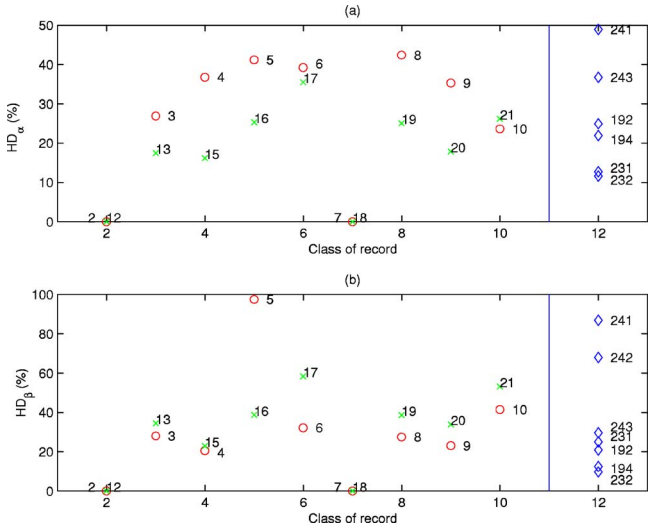

FIG. 2. (a) Harmonic distortion coefficient HD_α as a function of the class of record. An estimation from the amplitude modulation. (b) Harmonic distortion coefficient HD_β as a function of the class of record. An estimation from the frequency modulation. The associated record numbers and the classes of records are in Tables II and III. Circles: Vibrato "a la machoire." Crosses: Vibrato "sur l'air." Diamonds: Vibrato coming from playing performance arbitrarily associated to class 12.

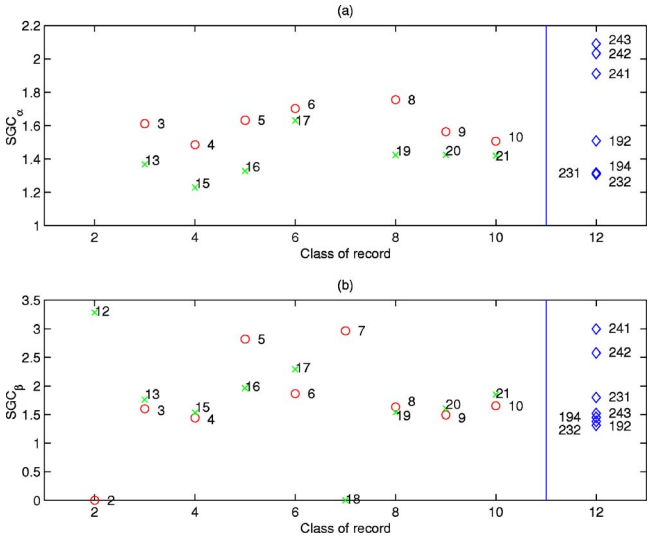

FIG. 3. (a) Spectral gravity center SGC_α as a function of the class of record. An estimation from the amplitude modulation. (b) Spectral gravity center SGC_β as a function of the class of record. An estimation from the frequency modulation. The associated record numbers and the classes of records are in Tables II and III. Circles: Vibrato "a la machoire." Crosses: Vibrato "sur l'air." Diamonds: Vibrato coming from playing performance arbitrarily associated to class 12.

modulation [Fig. 2(a)] and for the frequency modulation [Fig. 2(b)] are estimated successively from the real signals as a function of the class of record. Note that the two ways of playing vibrato are quite well separated: the vibratos "a la machoire" exhibit higher values of the amplitude modulation distortion than the vibratos "sur l'air" [Fig. 2(a)]. At the opposite, the vibratos "a la machoire" exhibit lower values of the frequency modulation distortion than the vibratos "sur l'air" [Fig. 2(b)]. Nevertheless, the separation is not exclusive. For each of the two distortion rates, there is a counterexample corresponding to a high pronounced vibrato at forte dynamic [record numbers 10 and 21 in Fig. 2(a)], and to a high pronounced vibrato at piano dynamic (record numbers 5 and 16 in Fig. 2(b)). As an alternative to the distortion rate, a spectral gravity center of the vibrato modulation can be defined. The corresponding results associated with amplitude and frequency modulations are, respectively, displayed in Figs. 3(a) and 3(b). For the amplitude modulation, the conclusions are the same as the ones drawn from the distortion rate [Fig. 2(a)], but there is no counterexample anymore, and the two ways of vibrato playing are well separated then. Note that several samples corresponding to other notes than E3, E4, for example, have been recorded and analyzed. The results obtained are compatible with the conclusions drawn from the E3 note's extensive study.

The algorithm of both amplitude and frequency modulation estimations is also applied to signals coming from playing performance. The database is made up of extracts of several recordings, where only the vibrato of the saxophonist is present. The selected musical tunes are presented in Table III. In Fig. 1, the estimations of α_1 and β_1 are compared with the estimations of the vibratos of self-sustained notes. Moreover, we compare the estimations of HD_α [Fig. 2(a)], HD_β [Fig. 2(b)], SGC_α [Fig. 3(a)] and SGC_β [Fig. 3(b)], for these signals coming from playing performance, with the cases of self-sustained note vibratos. We call class 12 the class associated with the signals coming from playing performance.

Figures 1–3 show how the estimated parameters of the signals coming from playing performance (class number 12) are coherent with the values of the database of real-world signals. For the record number 242 (Table III), note that the harmonic distortion rate HD_α [Fig. 2(a)] is about 70%. Parameter values of α_1, β_1, HD_α, HD_β, SGC_α, and SGC_β are clearly in the same area of the corresponding parameters for self-sustained notes.

C. Simulated signals

1. Physical modeling

The nature of the sound production of single reed instruments is now well understood.[15] Using an elementary model

TABLE III. Database of signals coming from playing performance. Record number, title of musical tune, vibrato strength (from 1: no vibrato, to 5: exaggerated vibrato). The class associated to these signals is class 12.

Record number	Title of musical tune	Vibrato strength
192	*Syrinx* of C.Debussy, played by F.Chouraki	3–4
194	*Syrinx* of C.Debussy, played by F.Chouraki	1–2
231	*Quatuor* of Olav Berg, played by H.Bergersens	2–3
232	*Quatuor* of Olav Berg, played by H.Bergersens	2–3
241	*An der schönen blauen Donau* of J.Strauss, by Spike Jones	4–5
242	*An der schönen blauen Donau* of J.Strauss, by Spike Jones	4–5
243	*An der schönen blauen Donau* of J.Strauss, by Spike Jones	5

for the reed and the mouthpiece, coupled with an idealized instrument, here an alto saxophone, a large range of the musical behavior of the single reed instruments is described. The elementary model is based on two equations: one for the nonlinear excitation mechanism, the reed-mouthpiece system [Eq. (16)], and the one for the resonator, regarded as a linear system [Eq. (17)]. The two equations make the coupling between the two following variables: $u(t)$, the volume flow entering into the instrument, and $p(t)$, the acoustical pressure in the mouthpiece,

$$u(t) = wH_O\left(1 - \frac{p_m - p(t)}{P_M}\right)\text{sign}[p_m - p(t)] \times \sqrt{\frac{2|p_m - p(t)|}{\rho}}, \quad \text{if} \quad p_m - p(t) \leqslant P_M,$$

$$u(t) = 0, \quad \text{if } p_m - p(t) \geqslant P_M, \tag{16}$$

$$p(t) = \rho c u(t) + r(t) * [p(t) + \rho c u(t)], \tag{17}$$

where w is the effective width of the reed channel, H_0 the reed opening at rest, p_m the mouth pressure, ρ the air density, and c the speed of sound in free space. The limit value P_M for which the reed closes the opening is given by $P_M = kH_0$, where k is the reed stiffness. P_M is the minimum value of the mouth pressure above which the static solution corresponding to the reed blocked against the lay is stable. The reflection function $r(t)$ of the pipe is obtained by an inverse Fourier transform of the reflection coefficient $R(j\omega)$ defined as a function of the dimensionless input impedance $Z(j\omega)$,

$$R(j\omega) = \frac{Z(j\omega) - 1}{Z(j\omega) + 1}. \tag{18}$$

The saxophone bore is mainly conical. An approximation of the truncated cone by using a system of two cylinders can be used. Their lengths L_b and L_a, respectively, are equal to the lengths of the truncated cone and of the truncature, respectively. Typically the ratio L_a/L_b has been chosen to be equal to 5. The dimensionless input impedance $Z(j\omega)$ is defined as follows:[16]

$$\frac{1}{Z(j\omega)} = \frac{1}{\tanh(\Gamma L_a)} + \frac{1}{\tanh(\Gamma L_b)}, \tag{19}$$

where Γ is the propagation constant, taking into account the viscothermal effects (losses and dispersion).

In order to get oscillations, a simulation technique in a discrete time domain is used.[17,18] Assuming the control parameters (P_m, H_0, k) to be constant, periodic oscillations are obtained in permanent regimes after a short transient. A way to reproduce vibratos by simulations is to use control parameters slowly varying slowly in time. Typically, simulations have been done using control parameters varying harmonically at 5 Hz.

2. Estimation of parameters and discussion

A set of simulations corresponding to each one of the two control parameters, P_m and H_0, have been done. The modulation rate of each parameter is equal to 5 Hz. The modulation extent of P_m and H_0 is varying from 5% to 30%, and from 10% to 40%, respectively, of their mean value. Three sets of simulations have been calculated: one set corresponding to a variation of H_0, another one to a variation of P_m, the third one corresponding to a modulation of both the control parameters. Then, the simulated signals have been analyzed in the same way as the real sounds by using the signal processing methods described in Sec. II, in order to evaluate the values of α_1 and β_1. The results are shown in Fig. 4 and Fig. 5 using the same kind of display as those of real sounds given in Sec. III B.

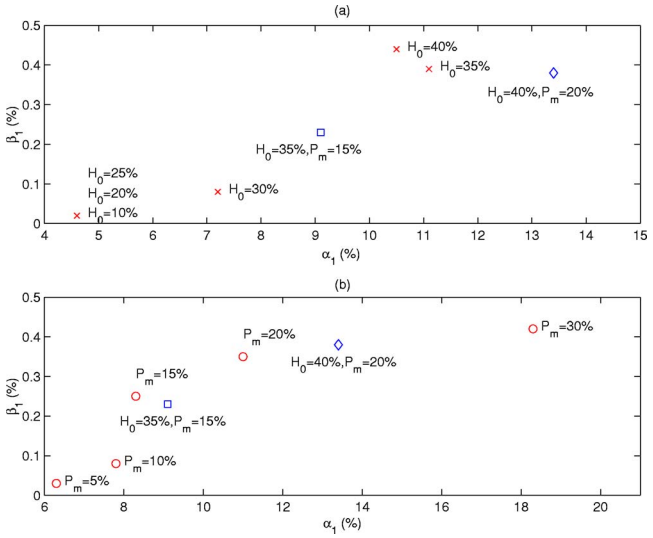

FIG. 4. β_1 as a function of α_1 (simulated signals), (a) for different values of H_0 and (b) for different values of P_m. Two special cases are to be considered: H_0=40%, P_m=20% (diamond) and H_0=35%, P_m=15% (square).

The preliminary results of Fig. 4 show that the mouth pressure P_m mainly controls the amplitude modulation, and

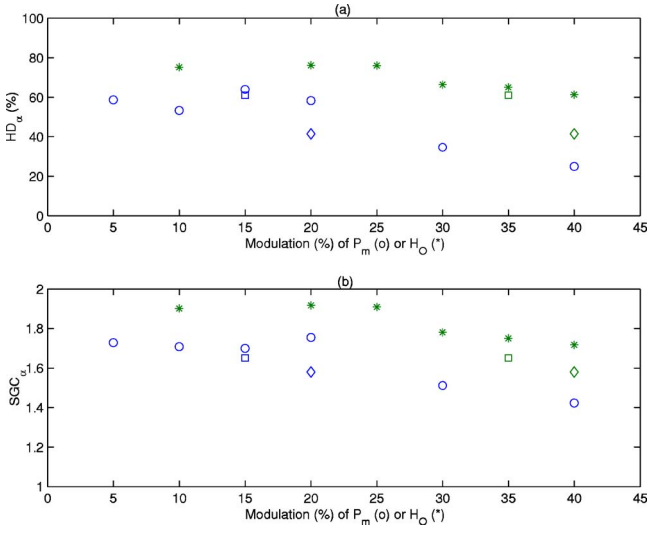

FIG. 5. (a) Harmonic distortion coefficient HD_α as a function of the modulation rate H_0 (*) or P_m (○). An estimation from the amplitude modulation of simulated signals. (b) Spectral gravity center SGC_α as a function of the modulation rate H_0 (*) or P_m (○). An estimation from the amplitude modulation of simulated signals. Two special cases are to be considered: H_0=40%, P_m=20% (diamond), and H_0=35%, P_m=15% (square).

the reed opening H_0 mainly controls the frequency modulation. But each control parameter does influence both the amplitude and frequency modulations significantly. The results displayed in Fig. 4 do not show any separation between each of the three sets of simulations. At the opposite, both the rate of harmonic distortion and the SGC results applied to amplitude modulation (Fig. 5) seem to be able to separate the set of simulations of H_0 variations, and the set of simulations of P_m variations. According to our hypotheses, assuming that the vibrato "a la machoire" is linked with a H_0 variation, and the vibrato "sur l'air" with a P_m variation, then the two kinds of vibratos are separated quite successfully.

IV. CONCLUDING REMARKS

In this paper, some vibratos on alto saxophone instruments have been studied. Suitable signal processing methods have been developed in order to estimate parameters of amplitude and frequency modulations. First the methods have been validated for test signals, and then they have been applied to the real saxophone vibrato sounds, and to simulated vibrato sounds coming from physical modeling of saxophone-like instruments. The methods are able to estimate the characteristics of the vibrato oscillations by extracting the first harmonics of the periodic vibrato oscillation, the vibrato extent, and the vibrato rate, with errors of less than 5%.

From the extraction of the amplitude and frequency modulations harmonic components of the real vibrato sounds, a first conclusion is drawn: although vibratos of singing voices are mainly linked to frequency modulation, significant amplitude modulations have been estimated from saxophone vibratos. Otherwise, no straightforward difference between the two techniques of playing vibratos, "a la machoire" and "sur l'air," have been shown directly from these components. But, by using a coefficient representing the vibrato amplitude distortion, like a spectral gravity center, some trends in the ability to separate the two techniques have been shown. At the end, more sophisticated coefficients will have to be defined in order to improve the separation.

In parallel, by using physical modeling of reed instruments, simulations of vibratos have been carried out. The simplified models are based on a few parameters characterizing the saxophone (the input impedance) and the player (the reed parameters and the mouth pressure). After having an extensive discussion with professional saxophone players, their two vibrato playing techniques have been simulated as follows: the vibrato "a la machoire" and the vibrato "sur l'air," are taken into account in the model by a slow variation in time of the parameter, H_0, and of the parameter, P_m, respectively. At the end, the simulated sounds have been studied by the same processing methods than the one used to study the real sounds. The same kind of trends in the ability to separate the two vibrato simulated techniques has been shown.

Further studies might be done on other wind instrument vibratos. An important work has to be produced on players in order to extract direct information on the slowly varying control parameters. If it seems easy to extract the mouth pressure modulation, to get the opening reed-lay modulation during the performance technique seems to be a hard task.

ACKNOWLEDGMENTS

The authors would like to express gratitude to the professional saxophone players Christophe Bois and Gregory Letombe for helpful discussions and for providing vibrato database. The authors would also like to thank Murray Campbell and Bertrand David for their scientific suggestions. The help of Pierre Couratier at the beginning of the project is acknowledged too.

[1]E. Prame, "Measurements of the vibrato rate of ten singers," J. Acoust. Soc. Am. **96**, 1979–1984 (1994).
[2]E. Prame, "Vibrato extent and intonation in professional western lyric singing," J. Acoust. Soc. Am. **102**, 616–621 (1997).
[3]I. Arroabarren, M. Zivanovic, J. Bretos, A. Ezcura, and A. Carlosena, "Measurements of vibrato in lyric singers," IEEE Trans. Instrum. Meas. **51**, 660–665 (2002).
[4]J. C. Brown, "Frequency ratios of spectral components of musical sounds," J. Acoust. Soc. Am. **99**, 1210–1218 (1995).
[5]C. D'Allesandro and M. Castellengo, "The pitch of short-duration vibrato tones," J. Acoust. Soc. Am. **95**, 1617–1630 (1993).
[6]J. Meyer, "Zur klanglichen wirklung des streicher-vibratos," Acustica **76**, 283–291 (1992) (text in German).
[7]N. H. Fletcher, "Acoustical correlates of flute performance techniques," J. Acoust. Soc. Am. **57**, 233–237 (1975).
[8]M. Mellody and G. H. Wakefield, "The time-frequency characteristics of violin vibrato: Modal distribution analysis and synthesis," J. Acoust. Soc. Am. **107**, 598–611 (2000).
[9]L. Cohen, *Time Frequency Analysis* (Prentice–Hall, Englewood Cliffs, NJ, 1995).
[10]B. Boashash, "Estimating and interpreting the instantaneous frequency of a signal. Part 1: Fundamentals," Proc. IEEE **80**, 520–538 (1992).
[11]B. Boashash, "Estimating and interpreting the instantaneous frequency of a signal. Part 2: Algorithms and applications," Proc. IEEE **80**, 540–568 (1992).
[12]B. P. Lathi, *Modern Digital and Analog Communications Systems* (Oxford University Press, Oxford, 1998).
[13]A. V. Oppenheim and R. W. Schafer, *Discrete-Time Signal Processing*, 2nd ed. (Prentice–Hall, Englewood Cliffs, NJ, 1999).
[14]C. Mellet, J.-C. Valière, and V. Valeau, "Use of frequency trackers in Laser Doppler Velocimetry for sound field measurement: comparative study of two estimators," Mech. Syst. Signal Process. **17**, 329–344 (2003).
[15]J. Kergomard, "Elementary considerations on reed instrument oscillations," in *Mechanics of Musical Instruments*, edited by Hirschberg *et al.* (Springer-Verlag, Berlin, 1995), pp. 229–290.
[16]S. Ollivier, J.-P. Dalmont, and J. Kergomard, "Idealized models of reed instruments. Part I: analogy with the bowed string," Acust. Acta Acust. 90, 1192-1203 (2004).
[17]M. Atig, J.-P. Dalmont, and J. Gilbert, "Saturation mechanism in clarinet-like instruments, the effect of the localized non-linear losses," Appl. Acoust. **65**, 1133-1154 (2004).
[18]B. Gazengel, J. Gilbert, and N. Amir, "Time domain simulations of single reed wind instrument. From the measured input impedance to the synthesis signal. Where are the traps?," Acta Acust. **3**, 445–472 (1995).

Study of the brightness of trumpet tones

Emilie Poirson[a] and Jean-François Petiot
Institut de Recherche en Communications et en Cybernétique de Nantes, UMR CNRS, 6597 Ecole Centrale de Nantes, Nantes, France

Joël Gilbert
Laboratoire d'Acoustique de l'Université du Maine, UMR CNRS, 6613 Université du Maine, Le Mans, France

(Received 21 March 2005; revised 29 June 2005; accepted 30 June 2005)

This study focuses on a particular attribute of trumpet tones, the brightness, and on the physical characteristics of the instrument thought to govern its magnitude. On the one hand, an objective study was carried out with input impedance measurements, and, on the other hand, a subjective study with hearing tests and a panel of subjects. To create a set of different trumpets a variable depth mouthpiece was developed whose depth can be easily and continuously adjusted from "deep" to "shallow." Using this mouthpiece and the same trumpet, several instruments were generated which may be played in three ways: (*i*) by a musician, (*ii*) by an artificial mouth, and (*iii*) using physical modeling simulations. The influence of the depth of the mouthpiece on the perception of the trumpet's tones was investigated, and the ability of a musician, the artificial mouth, or physical modeling simulations to demonstrate perceptively noticeable differences was assessed. Physical characteristics extracted from the impedance curves are finally proposed to explain the brightness of trumpet tones. As a result, the physical modeling simulations now seem to be mature enough to exhibit coherent and subtle perceptual differences between tones. This opens the door to virtual acoustics for instrument makers. [DOI: 10.1121/1.2006007]

PACS number(s): 43.75.Fg [NHF] Pages: 2656–2666

I. INTRODUCTION

Studying the quality of musical instruments is particularly interesting to help their development and to improve quality assessment procedures.

In the existing literature, two kinds of studies tackle the quality assessment of musical instruments. On the one hand, there are subjective studies which aim at characterizing the subjective response given by a musician or a listener. The main difficulties with these approaches are that the subjective answers of a "subject" are generally nonreproducible, semantically ambiguous, and depend on cultural and training aspects of the subject. Several studies using user-tests and sensory analysis techniques are proposed (Pratt and Bowsher, 1979). On the other hand, there are objective studies which aim at ascertaining which physical measurements seem to govern the subjective quality of the instrument (Pratt and Bowsher, 1978).

In parallel, in recent years, physical modeling simulations (Adachi and Sato, 1995) have provided interesting results to understand the functioning of brass instruments which could be used by instrument makers in the development process of new instruments. Assessing certain attributes of the quality of an instrument on a virtual prototype and using simulated tones have been proposed by Farina and Tronchin (2000).

Concerning the brass instruments, the main physical measurement is the input impedance of the bore. In order to propose a model for predicting certain qualities of brass instruments, the approach consists in discovering correlations for a set of instruments between the subjective response (given by the subject) and measurements (extracted from the impedance curve). These experiments are difficult to carry out, because one must finely control which parameters vary between the set of instruments, in order to be sure that the differences observed in the subjective assessment are effectively due to these variations. Plitnik and Lawson (1999) test several assumptions for the correlations between subjective attributes of horns and information extracted from the impedance curve. The conclusion is that searching for a one-to-one correspondence between a subjective attribute and an acoustic variable (coming from the input impedance) is counterproductive if not futile. These conclusions are the starting point of our study. Other studies have already been carried out to establishing the influence of the mouthpiece on the sound perceived. The influence of the mouthpiece cup volume and the impedance peaks no longer need to be proved (Benade, 1976). Wright and Campbell (1998) attempt to relate timbral changes perceived by the human ear-brain system to specific features of mouthpiece design. Psychoacoustical listening tests have also been carried out (Caral and Campbell, 2002), to evaluate the perceived difference in timbre related to a change of mouthpiece and to find a threshold of distinguishability. They show that a small change (less than 5%) influences the signals sufficiently to be then perceived by a subject.

Let us underline that in these studies, a lot of parameters vary from one mouthpiece to the next, and one cannot identify which parameter is the most influential on the subjective

[a]Author to whom correspondence should be addressed; electronic mail: emilie.poirson@irccyn.ec-nantes.fr

evaluation. In order to isolate and finely control the influencing variables of the timbre quality of brass instruments, we developed a trumpet mouthpiece with a depth that can be easily and continuously adjusted from "deep" to "shallow." Using this device and the same trumpet, we generated a set of instruments with notably different acoustical behavior, varying only the internal geometry of the mouthpiece. This set of instruments has been evaluated in two ways: (1) a particular attribute of tones (played by a musician and an artificial mouth, or numerically simulated), the "brightness," has been assessed via hearing tests (Petiot *et al.* 2003), and (2) the input impedance of the instruments has been measured. The objectives of this paper are as follows:

(i) To show how a change in the depth of the mouthpiece influences the impedance curve and the perception of the brightness of tones.
(ii) To study to what extent tones generated by a musician, an artificial mouth, or by physical modeling simulations are similarly perceived. The question here is to know if the perception of numerically simulated tones is in accordance with the perception of tones played by a musician or an artificial mouth, and if simulations are mature enough to exhibit subtle perceptual differences between sounds.
(iii) To find indicators extracted from the impedance curve correlated with the assessment of brightness, in order to predict this subjective assessment by objective measurements, and finally help the design of instruments.

Section II presents the experimental devices and the procedures used for the study. The input impedance setup is briefly described and the procedures used to generate the trumpet tones are explained. We put particular emphasis on the method used for physical modeling simulations. The hearing tests which have been carried out are explained.

Section III describes the results concerning the subjective study (hearing tests) and the objective measurements (input impedance). The subjective data are analyzed by sensory analysis techniques.

Section IV focuses on the interpretation of the results and on the correlations between subjective evaluations and objective measurements which can be found. Conclusions and perspectives are proposed in Sec. V.

II. EXPERIMENTAL DEVICES AND PROCEDURES

A. Brass instrument

1. The variable depth mouthpiece

The mouthpiece of the trumpet, and more generally of all brass wind instruments, plays a paramount role both for the overall "comfort" of the musician and the sound produced. It is, however, difficult to investigate the correlations between the geometry and the sound produced. If one tries to explain the perceived differences, many parameters vary at the same time (the shape of the cup, thickness of the rim, width of the throat, the back bore,…) (Plitnik and Lawson, 1999). For this reason, we developed a special mouthpiece for which a single geometric parameter, the depth of the mouthpiece cup, can be controlled. The system is made of a micrometer screw which increases the mouthpiece cup depth by 0.5 mm each turn (Fig. 1). The mouthpiece can evolve easily and continuously from position T0 "shallow" (0 turn, 0 mm) to position T10 "deep" (10 turns, 5 mm) The mouthpiece is designed in such a way that the variation between position Ti and T$(i+1)$ is equivalent to the addition to the bore of a 0.5-mm-thick cylinder. Eleven positions of the mouthpiece, from T0 (shallow) to T10 (deep), have been retained for the study (beyond ten turns, the instrument becomes greatly denatured to remain playable). Using this mouthpiece, and the same trumpet (Yamaha model 1335), we generate a family of 11 different instruments, named Ti (i =0 to 10, number of turns).

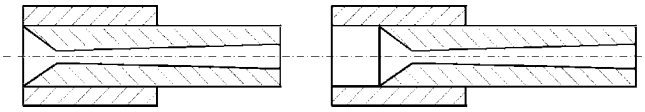

FIG. 1. Cross section of the mouthpiece with two positions of the depth: shallow (T0, left) and deep (T10, right).

This family of instruments is the reference set for the subjective tests and the objective measurements presented in the next paragraphs.

2. Input impedance setup

Brass wind instruments and more generally wind instruments can be characterized by their input impedance. Input impedances of the trumpet described above have been measured using the impedance sensor described in Dalmont and Bruneau (1991). Impedance sensors are linear sensors with two entries whose signals are influenced by both the pressure and volume velocity on the reference plane (input of the mouthpiece in our study). Pressure is generally measured with a microphone, therefore impedance sensors are classified according to the way the volume velocity is determined or controlled. Initially, most of the impedance sensors used a source of constant velocity and a microphone giving a pressure signal approximatively proportional to the impedance measured (impedance sensor with capillary tube, for example). Other systems based only on pressure measurements have become widespread [for an overview of impedance sensors see Dalmont (2001), for example]. The sensor used in this study is based on one pressure and one volume velocity transducer, the source signal being a swept sine [see details in Dalmont and Bruneau (1991)]. Figure 2 presents examples of input impedance curves (magnitude and phase) of the trumpet with no valve depressed according to two cup depths, "shallow" (T0 configuration) and "deep" (T10 configuration) as described in the previous section.

Two kinds of measurements have been made. The first, called "narrow-band measurements," corresponds to measurements made step by step from 50 to 150 Hz, using a step equal to 1 Hz (Fig. 2). The second, called "broadband measurement," corresponds to measurements made from 4 Hz step by step to 4096 Hz using a step equal to 4 Hz. The narrow-band measurements are used in order to extract the resonance frequencies and their associated parameters as the quality factor and the impedance magnitude value (Sec.

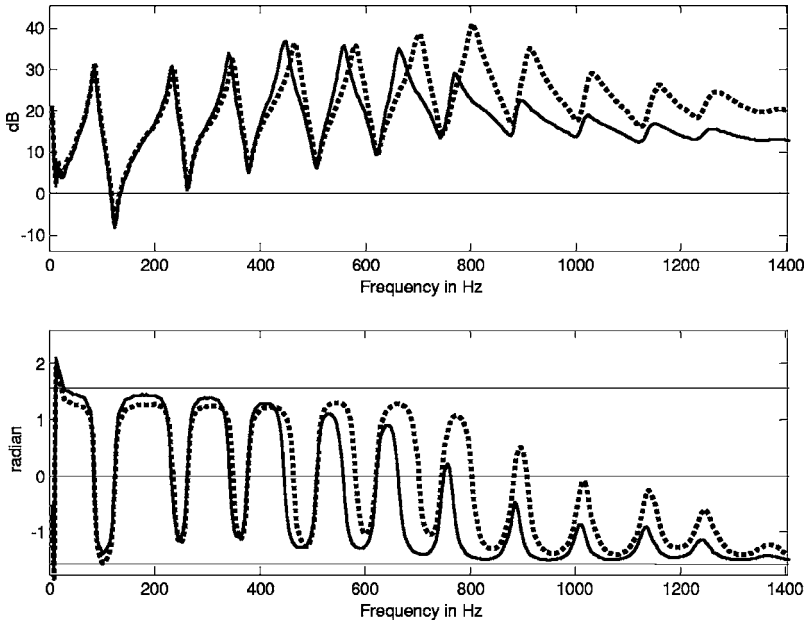

FIG. 2. Measured dimensionless input impedance (magnitude in dB and phase) of the trumpet with the "shallow" mouthpiece T0 (dotted) and with the "deep" mouthpiece T10 (continuous).

III A 1). The broadband measurements are used as an input parameter of the simulated tones (Sec. II B 2).

A set of the input impedances corresponding to all the configurations of the mouthpiece cup is needed. Each input impedance is calculated from the measured impedance $Z_0(j\omega)$ of the "shallow" configuration T0. The calculation is based on the electro-acoustical line theory by adding to the bore a cylindrical element of the same diameter as the input diameter of the mouthpiece. The calculated dimensionless impedance $Zc_i(j\omega)$ is given from $Z_0(j\omega)$ by the following formula [Eq. (1)]:

$$Zc_i(j\omega) = \frac{Z_o(j\omega) + j\tan(kL_i)}{1 + j\tan(kL_i)Z_o(j\omega)}, \quad (1)$$

where L_i is the length of the added cylindrical tube, ω is the angular frequency, and k is the wave number. For the present study, L_i is equal to 0.5 mm (case $i=1$), 1.0 mm (case $i=2$), ..., 5.0 mm (case $i=10$). Then a set of ten calculated impedances is available from the measured one. Notice that the calculated impedance Zc_{10} has been compared to a measurement corresponding to the "deep" configuration in order to check that the calculation method is sufficiently accurate.

B. Generation of tones

1. The artificial mouth and the trumpet player

Several authors have worked on artificial mouths because they are essential devices to produce reproducible measurements (Gilbert *et al.*, 1998). It is possible to finely control the embouchure and this makes it possible to take extensive measurements during stable playing conditions. It has been proved (Petiot *et al.*, 2003) that the artificial mouth is able to exhibit differences between similar instruments via objective measurements and, in this way, may be used as a test bench for instrument makers. The "artificial mouth" for brass winds primarily consists of "artificial lips" (latex tube filled with water) whose vibration characteristics are mainly controlled by the pressure of water and the mechanical pressure exerted by an "artificial jaw." The air overpressure in the oral cavity is another essential parameter for the control of the system.

For our study, several categories of tones, produced either by the artificial mouth or by a musician, were recorded. All the recordings (sampling frequency 44 100 Hz, 16 bits) were made in the same room (same place, same temperature) with a Sennheiser e604 microphone. The microphone was placed in the axis of the bell (distance=10 cm) and connected to the preamplifier and the Digigram Vx Pocket V2 sound card. The dynamic of the sound was measured with a sound level meter placed at the output of the bell.

For the 11 positions of the mouthpiece (T0–T10), two notes, ♭3 and C4, were recorded. Three categories of notes were considered:

AM: played by the artificial mouth, with a dynamic *forte* (115 dB),

MF: played by the musician, dynamic *mezzo forte* (100 dB),

MP: played by the musician, dynamic *piano* (80 dB).

A 600-ms window of the signal, stable in pitch and amplitude, was selected from the recordings. Each tone, a steady-state segment, was normalized in duration (600 ms), in intensity and in frequency (frequency corresponding to the note of the well-tempered scale) with a signal processing software. A linear attack and decay of 50 ms were added to the tones.

In order to limit as much as possible the variability inherent to the musician, he was asked to play the note in the easiest and most natural way (without trying to adjust the height or the timbre of the tones).

2. Simulated tones

Besides musical tones played by musicians or an artificial mouth, simulated tones can be obtained by finding approached solutions of acoustic models of the trumpet under playing conditions. Many authors have dealt with modeling

wind instruments in order to construct a computer simulation for synthesis (called physical modeling synthesis) or to understand the physical behavior of these instruments. The first wind instrument time-domain simulation to appear in the literature has been the clarinet model by Schumacher (1981). This method was adapted in order to study real instruments by using measured impedance as an input parameter of the simulation [see, for example, Gazenge *et al.* (1995)]. An alternative to the time-domain approach is a simulation characterizing the periodic steady-state oscillation using a calculation of their spectrum. This asymptotic method based on the harmonic balance technique was first used by Schumacher (1978) and by Gilbert *et al.* (1989). Because the harmonic balance technique can easily show the evolution of the solutions versus a parameter of the physical model, this technique is used to study the evolution of the spectrum of the simulated tones versus the cup's depth parameter of the trumpet mouthpiece.

Basically the harmonic balance technique is a numerical method computing converging periodic solutions $p(t)$ of a system while taking a given finite number N of harmonics into account in a truncated Fourier series [Eq. (2)]:

$$\begin{aligned} p(t) &= \sum_{n=-N}^{N} C_n e^{2\pi jnF_o t} \\ &= C_o + \sum_{n=1}^{N} \{2\,\mathrm{Re}(C_n)\cos(2\pi jnF_o t) \\ &\quad - 2\,\mathrm{Im}(C_n)\sin(2\pi jnF_o t)\} \\ &= C_o + \sum_{n=1}^{N} A_n \cos(2\pi jnF_o t + \varphi_n). \end{aligned} \tag{2}$$

The unknowns of the system are the harmonic amplitudes (C_o, the real part and the imaginary part of the N complex values of C_n; the alternative real unknowns A_n and φ_n can be used, too) and the operating frequency F_o [details of the technique in Gilbert *et al.* (1989)].

The system of equations comes from an acoustic model of a brass instrument adapted from Elliot and Bowsher (1982) and detailed in Cullen *et al.* (2000), $p(t)$ the input mouthpiece pressure being an approached periodic solution. The acoustic model can be summarized as a system of three equations, a function of three periodic variables; the opening height $H(t)$ between the two lips of the player, the volume flow $v(t)$ at the entrance to the mouthpiece, and $p(t)$. The lips act as a valve controlling the air flow $v(t)$ from the mouth (at pressure P_m) to the instrument mouthpiece [at pressure $p(t)$]; this flow depends primarily on the pressure drop $\Delta p = P_m - p(t)$, and secondly on the opening height $H(t)$. The behavior of the valve can be represented by a nonlinear equation [Eq. (3)] of the form

$$v(t) = bH(t)\sqrt{\frac{2(P_m - p(t))}{\rho}}, \tag{3}$$

where b is an effective width of the lip's opening area and ρ is the density of air. Notice that the opening height $H(t)$ varies around a rest value H_o which is characteristic of the trumpet player embouchure. The simplest model which represents the lip motion is based on a one degree of freedom mechanical system represented by the following equation [Eq. (4)]:

$$\frac{d_2}{dt_2}H(t) + \frac{\omega_L d}{Q_L dt}H(t) + \omega_L^2 H(t) = \frac{P_m - p(t)}{\mu_L}, \tag{4}$$

where ω_L and Q_L are the resonance (angular) frequency and the quality factor of a mechanical resonance of the lips. The parameter μ_L is an effective mass per area of the lips. The two previous equations [Eqs. (3) and (4)] represent the nonlinear aeroelastic valve which is coupled with the air column. The sign of the parameter μ_L in Eq. (4) determines the "outward" ($\mu_L < 0$) or "inward" striking ($\mu_L > 0$) behavior of the lip-reed model. Notice that there is no unambiguous answer about the question of "inward" or "outward" behavior of the lip reed. In other words, most of the time, the two behavior can be observed on the same brass instrument under playing conditions [for an exhaustive review of this question, see for example Cullen *et al.* (2000)]. Then following Elliot and Bowsher (1982), we have chosen by default the "outward" analogy by choosing a negative value of μ_L (Table I). An effective way to model the acoustic behavior of the air column is to write an impedance relationship in the frequency domain [Eq. (5)]:

$$P(j\omega) = \frac{\rho c}{S} Z_{ci}(j\omega) V(j\omega), \tag{5}$$

where $Z_{ci}(j\omega)$ is the dimensionless input impedance of the brass instrument [as defined in Eq. (1)], c is the speed of sound, and S is the input section area, $P(j\omega)$ and $V(j\omega)$ being the mouthpiece pressure and the volume flow written in the frequency domain.

The elementary model based on Eqs. (3)–(5) is adapted to find numerical solution of steady self-sustained oscillations of the trumpets using the harmonic balance technique. In order to do the simulations, values of the parameters used in the model are needed. If the trumpet is well described by its input impedance which is known (see Sec. II A 2), providing lip parameters needed in Eqs. (3) and (4) is not an easy task. The lip parameters values used in the harmonic balance technique to simulate the trumpet player embouchure are listed in Table I. The values have been adapted from the study of Cullen *et al.* (2000) and particularly from their Table III in order to get realistic and sensible simulations.

This leads to a very fine spectral analysis and is very convenient for showing the modifications of the playing frequency and the spectrum produced by the variation of the

TABLE I. Lip parameters used in the harmonic balance technique to simulate the trumpet player embouchure.

b (mm)	10
H_o (mm)	0.05
$\omega_L/2\pi$ (Hz)	410
Q_L	5
$1/\mu_L$ ($\mathrm{m^2\,kg^{-1}}$)	−0.5

trumpet mouthpiece cup geometry (e.g., a change of the input impedance associated to each mouthpiece geometry), the lip parameters being constant during all the simulations. Eleven simulated acoustic pressures associated to the 11 input impedances T0–T10 are calculated.

The approached solutions $p(t)$ coming from the elementary model correspond to the instrument mouthpiece acoustic pressure. Now external acoustic pressures are needed in order to be comparable with the recorded trumpet tones described in the previous section. Then the concept of "spectrum transformation function" was used. According to Benade's theory (1976), the general trend of the spectrum transform function $T(j\omega)$ relating the external pressure amplitudes of the various harmonics to the internal pressure amplitudes being a linear relationship varying from 0 to 1 as a function of frequency from 0 Hz to a cutoff frequency f_c, we have chosen f_c equal to 1400 Hz. Then above f_c, $T(j\omega)$ is assumed to be equal to 1, the spectrum transform function representing an ideally high-pass filter.

At the end, the solutions of the harmonic balance simulation are given by a set of external pressure amplitudes of the harmonics. To be used during the perceptive tests, the 11 solutions defined in the frequency domain have to be recalculated in the time domain by adding all the harmonics, Fourier theorem and are windowed and normalized by using the method applied to the recorded tones (see Sec. II B 1). The normalization frequency was equal to 466 Hz. The minimum and the maximum frequency of the simulated tones were equal to 469 Hz (position T10) and 479 Hz (position T0), respectively. We assume that this normalization of the frequency, extremely weak (max=46 cents), does not influence the brightness perception of the subjective tests.

The method was then used to generate simulated tones (**Simu**) corresponding to our set of instruments (T0–T10) by using as input parameter of the simulation the measured impedance.

C. Subjective tests

The subjective tests consisted in psychoacoustical hearing tests and have involved several subjects and stimuli. A detailed presentation of the various hearing tests we have carried out with the variable depth mouthpiece is presented by Petiot *et al.* (2004). We will describe in this section how the stimuli were designed and the tests we have focused on.

1. Stimuli of the tests

The stimuli of the tests are made of tones belonging to the following categories:

AM: played by the artificial mouth, with a dynamic *forte* (115 dB),

MF: played by the musician, dynamic *mezzo forte* (100 dB),

MP: played by the musician, dynamic *piano* (80 dB),

Simu: numerically simulated tones.

The subjects listened to the stimuli via a headphone *Audio-Technica ATH-M40*.

TABLE II. The 11 pairs of sounds proposed for the subjective evaluations.

Instrument for sound 1	Instrument for sound 2				
	T0	T2	T5	T6	T10
T0		×	×	×	×
T2			×		
T5			×		
T6		×	×		×
T10		×	×		

2. Test 1: Threshold of distinguishability

The variations of the bore of the instruments (T0–T10) being very weak, the aim of this first test was to estimate if differences of timbre corresponding to different instruments can be perceived. The assessment of the difference was done by pairwise comparison. The objectives of this test were firstly to evaluate, for each category of tones, the threshold of distinguishability of the sounds differentiation, and secondly to show if the value of this threshold depends on the category.

In order to limit the duration of the tests, only five sounds (corresponding to positions T0, T2, T5, T6, T10) were selected, for each category. All the ten possible pairs among the five sounds were considered. A typical stimulus of test 1 (e.g., ♭3, AM T0–T6) consists of a pair of sounds of the same category (e.g., AM, MF, MP, or Simu) and corresponding to the same note, separated by 600 ms of silence. In order to check the coherency of the subject, one pair of identical sounds (T5–T5) was added to the stimuli. A total of 11 pairs of sounds, for each category (AM, MF, MP, or Simu), constituted the stimuli of the tests. The pairs proposed for the evaluation are marked with an "X" in the following matrix (Table II).

The pairs were presented three times to the subject in a random order, so as to check the consistency of the subjects.

The subjects were asked to indicate whether or not the two tones of a pair were different. They could listen to the pair as many times as they wished, and gave their answers by clicking on boxes via an interface programmed in *VisualBasic6* (Fig. 3).

Due to time constraints, test 1 was performed in two parts.

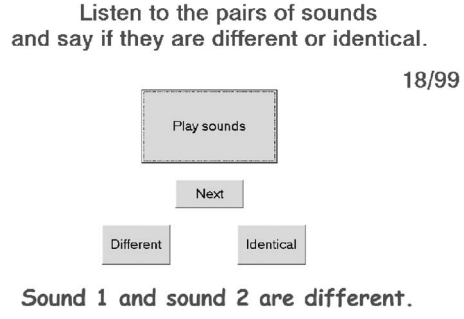

FIG. 3. Interface for test 1.

TABLE III. Percentage of correct answers in the paired comparisons for test 1.

AM		Instrument for sound 2 T0	T2	T5	T6	T10
Instrument for sound 1	T0		**43**	88	96	100
	T2			61		
	T5					
	T6		80	**53**		96
	T10		100	98		

MF		Instrument for sound 2 T0	T2	T5	T6	T10
Instrument for sound 1	T0		57	86	98	94
	T2			76		
	T5					
	T6		69	**41**		**55**
	T10		96	59		

MP		Instrument for sound 2 T0	T2	T5	T6	T10
Instrument for sound 1	T0		**53**	76	61	80
	T2			**6**		
	T5					
	T6		**14**	**4**		59
	T10		84	**41**		

Simu		Instrument for sound 2 T0	T2	T5	T6	T10
Instrument for sound 1	T0		**46**	69	80	94
	T2			**50**		
	T5					
	T6		**48**	**15**		56
	T10		91	**48**		

In a first session, subjects assessed all the pairs of the AM, MF, and MP categories, for the note ♭3.[1] There were 99 pairs (11pairs × 3categories × 3replications) proposed in this session.

In a second session, subjects assessed all the pairs of the Simu category, for the same note ♭3 (total of 33 pairs in this session: 11 pairs × 1 categories × 3 replications). A total of 20 subjects (including 12 musicians), performed test 1. In addition to these evaluations, subjects were asked to indicate at the end of the assessments the more relevant terms to describe the differences between tones.

3. Test 2: Ranking on a gradual axe of brightness

After a study of the differences between tones (test 1), we examined the nature of these differences (test 2).

For test 2 we focused on a particular attribute of the timbre: the *brightness* of the sound (Krimphoff, 1993; Grey, 1977). Psychoacoustic studies have shown that this dimension is one of the main perceptual dimensions of the timbre in steady-state regime. The tones having been previously balanced in pitch and intensity; the differences are based on the timbre only. Furthermore, to the question asked at the end of test 1 "which word qualifies for you these differences," brightness was one of the most recurrent terms.

For the categories of tones MF, AM, and Simu, with the 11 tones T0–T10 as input, the subjects were asked to rank them on a graduate scale from "dull" to "bright," with a "click and drag" interface programmed in *VisualBasic6*.

The objective of test 2 is first to know if differences of brightness can be significantly detected, to check the existence of a correlation between the subjective assessment of brightness and the depth of the mouthpiece, and finally to see if the correlation depends on the category of tones.

The experimental data and results are presented in the following section.

III. EXPERIMENTAL DATA AND RESULTS

A. Subjective study

1. Test 1: Threshold of distinguishability

First, three subjects, suspected to be noncoherent because they assessed at least once the pair of identical tones as "different," were excluded from the final results.

Next, for the remaining 17 subjects and for each pair of tones, we assigned a "1" for a correct answer and "0" for incorrect. Subjects' answers are cumulated and expressed in percentages: thus, 100% means that all the subjects found that, each time they heard it, the pair of tones was "different," 0% means that the pair has always been evaluated as similar by all the subjects. The results for each category of sounds are shown in Table III.

The results show the same tendency for all categories of tones: the larger the difference in the mouthpiece depth, the higher the percentage of correct answers, i.e., more the tones are perceived as different. The greater the difference of mouthpiece depth, the better the differentiation of timbre. The results indicate in particular that the importance of the perceived differences between the simulated tones varies in the same way for the tones played by a musician as by the artificial mouth. Simulation is able to reproduce differences between sounds which are similar to those played by the musician or the artificial mouth. This result, not obvious at all in the beginning of the study, is a first important conclusion.

In order to evaluate the threshold of distinguishability for each category of tones, two criteria are next calculated.

The first one is based on a statistical test. Given that our test is based on a forced choice question (two possible answers, "identical" or "different"), we have to check the risk of obtaining such results by chance. The statistical law adapted in this case is the binomial law,[2] which gives in our case that up to 55% of correct answers, the risk of obtaining this score at random is less than 5%. The pairs for which the

TABLE IV. Criteria proposed to rank the category of sounds according to the threshold of distinguishability

Category	No. of pairs removed by the statistical test	Average percentage of correct answers
AM	2	81.5%
MF	2	73.1%
Simu	5	59.7%
MP	5	47.8%

risk is greater than 5% are shaded in Table III; the number of pairs concerned is indicated in Table IV, column 2.

The second criterion is the average percentage of correct answers for all the tested pairs.

These two criteria are given for each category of tones in Table IV.

Given that the higher the average percentage of correct answers and the lower the number of removed pairs, the higher the threshold of distinguishability, we can conclude that the ranking of the categories according to this threshold is

$$\mathbf{thres_{AM} < thres_{MF} < thres_{Simu} < thres_{MP}}.$$

The threshold of differentiation is the lowest with the AM. Thus, the artificial mouth seems to be a good device to exhibit subtle differences between instruments.

Perceived differences for MP (musician, dynamic *p*) are less marked than for the other categories. The musician seems to "smooth" the differences between the instruments, and, furthermore, the dynamic "*piano*" is not favorable to reveal differences of timbre (the dynamic *piano* does not allow the generation of high-order harmonics).

This first test shows finally that subjects perceived differences between sounds even for small variations of the bore of the instrument. For the case of MP, differences were so small (the threshold is high) that we decided to exclude this category for test 2.

2. Test 2: Ranking on an axe of brightness

Each subject provided a ranking of the tones on an axe of brightness. Before aggregating the assessments of the subjects in an average answer, we first have to check whether or not the group of subjects is homogeneous and to select a panel of subjects who agree enough in their evaluation. The intersubject Spearman coefficient r_{ab} between two subjects is a measurement of the agreement between their rankings:

$$r_{ab} = 1 - \frac{6\sum_{i=1}^{n} (C_a(T_i) - C_b(T_i))^2}{n(n^2-1)}, \tag{6}$$

with n the number of tones (here 11) and C_a and C_b rankings proposed by subject a and subject b.

This coefficient is equal to 1 if the rankings are exactly the same, −1 if they are exactly opposite. A cluster analysis (hierarchical ascendant classification) on the distance matrix between all the subjects (distance$=1-r_{ab}$) has been done for each category of tones. It reveals that the group of subjects was not necessarily homogeneous.

For the category AM, three subjects were discordant (atypical) and proposed roughly reverse rankings relative to the rest of the group.[3] The rest of the group agreed in the assessment and constituted an homogeneous panel.

For the category Simu, all the subjects agreed in their assessments.

For the category MF, the answers were very disparate: after an analysis of the dendrogram, we selected a panel of seven subjects but the agreement between them is rather poor, so the average value will be suspected as unreliable.

In order to exhibit a specific tendency of the panel of subjects in the assessment of brightness, we removed the data of the atypical subjects and we considered only the data of the panel to get an average answer. Table V presents for each instrument and each category of tones the average rank of brightness (brightness score).

For AM and Simu, the brightness score is highly correlated with the mouthpiece depth. For MF, this correlation is less marked. This could be explained by the fact that the musician compensates for the difference of mouthpiece and adapts his embouchure to the instrument in order to produce the sound he has in mind.

The Friedman statistic test on the average ranks shows that, for all categories of sounds (AM, MF, and Simu, there is globally a significant difference between the sounds according to their brightness with a p value $<1\%$.

Next, for each pair of sounds, the Friedman test shows that some pairs are significantly perceived as different with a p value $<5\%$. These pairs are shaded in Table VI. For the other pairs (e.g., T0–T2), the difference of brightness is too small to be statistically significant.

For the AM and Simu categories, the results show that the greater the difference of mouthpiece depth, the more the

TABLE V. Brightness score resulting of test 2.

	Position										
	T0	T1	T2	T3	T4	T5	T6	T7	T8	T9	T10
Brightness for AM	10.93	10.07	9.00	6.60	5.87	7.67	4.47	3.07	3.20	3.33	1.60
Brightness for Simu	10.76	9.76	9.18	7.65	6.59	6.06	4.82	4.00	3.12	2.29	1.76
Brightness for MF	8.72	5.89	10.17	6.28	8.06	5.33	4.67	2.56	2.17	6.28	5.78

TABLE VI. Pairs for which the difference of brightness is significantly perceived as different (Friedman test with p value indicated in the corresponding cell).

AM		Instrument for sound 2 T0	T2	T5	T6	T10	MF		Instrument for sound 2 T0	T2	T5	T6	T10	SIMU		Instrument for sound 2 T0	T2	T5	T6	T10
Instrument for sound 1	T0				**1%**	**1%**	Instrument for sound 1	T0			**3%**	**1%**		Instrument for sound 1	T0			**1%**	**1%**	**1%**
	T2				**2%**	**1%**		T2			**1%**	**1%**	**1%**		T2				**1%**	**1%**
	T5					**1%**		T5	**3%**	**1%**					T5	**1%**				**2%**
	T6	**1%**	**2%**					T6	**1%**	**1%**					T6	**1%**	**1%**			
	T10	**1%**	**1%**	**1%**				T10		**1%**					T10	**1%**	**1%**	**2%**		

difference of brightness is significantly perceived. It has to be noticed that the perceived brightness of the simulated tones is coherent with the perceived brightness of real tones (AM). This is a strong point for the validation of simulations.

For the MF category, the previous tendency for the perceived difference of brightness is less obvious. The variability created by the musician is of the same order as the subtleties that we want to explain. For this reason, in order to interpret the difference of brightness with objective variables, we will focus for the rest of our work on sounds produced by the artificial mouth.

B. Objective study

1. From the instrument

The resonance frequencies: Given that we focused our subjective study on a particular tone of the trumpet (partial #4), additional variables of the impedance curve related to the fourth and eighth resonance peaks have been extracted.

In the playing situation, the musician produces a note whose frequency—the playing frequency—is close to the resonance frequency of the vibration mode that controls the self-sustained excitation process. The resonance frequencies can be defined as the frequencies corresponding to the maximum—peak amplitude—of the input impedance magnitude of the air column of the instrument with its input section closed. Then the resonance parameters are directly extracted from the "narrow-band measurement" (see Sec. II A 2); the frequency accuracy being equal to the frequency sampling, it means 1 Hz. Another way of defining the resonance and to extract the resonance parameters (resonance frequency, quality factor, and magnitude) from the measured impedance $Z(j\omega)$ is to fit locally around the resonance number n the experimental result with a model of resonance like the Lorentz model as follows [Eq. (7)]:

$$Z(j\omega) = G0_n + G1_n \frac{j(\omega/2\pi \mathrm{fres}_n)Q_n^{-1}}{-(\omega/2\pi \mathrm{fres}_n)^2 + j(\omega/2\pi \mathrm{fres}_n)Q_n^{-1} + 1}, \tag{7}$$

where fres_n and Q_n are the resonance frequency and the quality factor of the nth resonance, the complex number $G0_n$ and the real positive value $G1_n$ being useful to get the magnitude of the input impedance at the frequency fres_n. More precisely, the individual peak number n is selected and the complex input impedance is locally fitted with a circle in the Nyquist complex plane using a least-squares minimization—for a review of the curve-fitting methods, see for example, Ewins (1984). Even if the frequency accuracy is not easy to determine, by circle-fitting based on four experimental data we assume that it is less than 0.1 Hz.

The resonance frequencies were extracted from the impedance curves.

Because the subjective study (see Sec. III) is focused on a particular tone of the trumpet—the partial number 4—the frequencies, the Q values, and the magnitudes associated to the fourth and eight resonance peaks are especially needed and listed in Table VII—notice that the inharmonicity $f_{\mathrm{res8}}/2f_{\mathrm{res4}}$ is given, too. The resonance parameters of the 11 following input impedances—T0, T1, T2,…, T10—are extracted.

2. From the tones

Spectral centroid: The *spectral centroid* is commonly associated with the measure of the brightness of a sound (Grey and Gordon, 1978). This measurement is obtained by evaluating the "center of gravity" using the Fourier transform's frequency and magnitude information, where A_n represents the amplitude of harmonic n of the spectrum and N the number of harmonics considered (in our case, $N=6$):

TABLE VII. Resonance frequencies, Q values, and magnitude of the resonance peaks (0 dB is corresponding to $\rho c/S$) obtained by circle-fitting. The resonance parameters and inharmonicity corresponding to peak 4 and peak 8 of the 11 following input impedances—T0, T1, T2,…, and T10—are given.

	Fourth resonance			Eight resonance			
	f_{res4}(Hz)	Q_4	$\lvert Z_4\rvert$	f_{res8}(Hz)	Q_8	$\lvert Z_8\rvert$	Inharmonicity $f_{\mathrm{res8}}/2f_{\mathrm{res4}}$
T0	465.2	41.7	36.9	912.9	46.3	35.2	0.9812
T1	463.5	40	37.2	909.2	46.2	33.5	0.9808
T2	461.7	39.9	37.4	906.4	47.8	31.9	0.9816
T3	459.9	39.5	37.7	904	46.2	30.4	0.9828
T4	458	39	37.8	902.1	45.5	29	0.9848
T5	456	37.6	38	900.6	46.9	27.7	0.9875
T6	454.1	38.8	38.1	899.3	47.8	26.6	0.9902
T7	452.1	37.2	38.2	898.2	47.2	25.5	0.9934
T8	450	36.7	38.3	897.2	45.1	24.5	0.9969
T9	448	36.9	38.3	896.3	45.4	23.6	1.0003
T10	446	35.9	38.2	895.6	46.5	22.8	1.0040

TABLE VIII. Spectral centroid for AM, Simu, and MF for each instrument.

	Instruments										
Sc	T0	T1	T2	T3	T4	T5	T6	T7	T8	T9	T10
AM	2.72	2.74	2.65	2.37	2.46	2.32	2.38	2.14	2.18	2.16	2.16
Simu	2.62	2.57	2.54	2.51	2.48	2.45	2.42	2.39	2.36	2.34	2.32
MF	2.53	2.50	2.71	2.55	2.54	2.52	2.66	2.61	2.65	2.77	2.82

$$Sc = \frac{\sum_{i=1}^{n} nA_n}{\sum_{i=1}^{n} A_n}. \quad (8)$$

Table VIII shows for each position of the mouthpiece the *Sc* of the tones, for three categories of tones (AM, MF, and Simu).

For the categories AM and Simu, we notice that the deeper the mouthpiece, the lower the *Sc*. This behavior is not true for the category MF. This can be explained by the fact that the musician is not reproducible enough (his embouchure varies according to the instrument played). The musician produces variations of the timbre of the same order as those which are created while varying the mouthpiece, and this phenomenon certainly disrupts and masks the effect of the mouthpiece on the spectral content of the tones.

C. Interpretation of the results

1. Correlation between the brightness and the spectral centroid

The correlation between the brightness scores of the tones (Table V) and the spectral centroid (Table VIII) has been studied. For each category of tones, the linear correlation coefficient (Pearson) is given Table IX.

For AM and Simu, the results are in agreement with a well-known result in psychoacoustics: the brightness of the sounds is correlated with their spectral centroid (Krimphoff *et al.*, 1994). This result gives credit to our procedure of brightness assessment. For MF, there is surprisingly no correlation ($R=-0.04$). In fact, the agreement between the subjects of the panel in their brightness assessment is probably too weak, so the average scores of brightness are not reliable and representative of a tendency.

2. Correlation between the brightness and the resonance parameters of the instrument

The study of sound production in brass instruments shows that there is a coupling between the lips of the musician and the resonator. The intonation of the instrument is not only controlled by the closest resonance frequency of the input impedance but possibly conditioned by upper resonance frequencies of the resonator.

TABLE IX. Correlation coefficient between the brightness score and the spectral centroid.

	AM	Simu	MF
R_{Pearson}	0.93	0.99	−0.04

The relation between the brightness and the amplitude of the high-frequency components of the spectrum is clearly demonstrated. So, in order to study the brightness of the note ♭3, we propose to study the influence of resonance parameters of the instrument on the spectral centroid.

Secondly, we limit our analysis to the influence of the magnitude of the second harmonic of the note on the spectral centroid (the higher this magnitude, the higher the spectral centroid). Finally, we propose to explain the influence of the impedance curve on the magnitude of this harmonic.

We make the assumption that the spectrum and then the spectral centroid of the note in the permanent regime are mainly governed by the characteristics of the impedance curve corresponding to partials 4 and 8 of the impedance curve (the resonance frequency 8 corresponds roughly to the second harmonic of the note ♭3). Our objective is to find which characteristics of the impedance curve are the more influencing on the magnitude of the spectral centroid *Sc* of the tones, and then on their brightness.

We considered the following variables of the impedance curve: $f_{\text{res8}}/2f_{\text{res4}}$, $|Z_8|/|Z_4|$, and Q_8/Q_4.

Figure 4 shows a superimposed representation of the characteristics of the impedance curve around the resonances 4 and 8, and of the fundamental f and second harmonic $2f$ of the note ♭3. The solid line represents the impedance curve around resonances 4 and 8. These resonances are characterized by f_{res4}, f_{res8}, $|Z_4|$, $|Z_8|$, Q_4, and Q_8. The dashed line represents a modified impedance curve around resonance 8 when Q_8 increases. The dash-dot line represents a modified impedance curve around resonance 8 when $|Z_8|$ increases. We suppose that the playing frequency of the note (f) is close to the resonance frequency f_{res4}, and we limit our study to the case where the inharmonicity $f_{\text{res8}}/2f_{\text{res4}}$ is lower than 1 (Fig. 4).

We assume for this analysis that the playing frequency f is greater than f_{res4} and that the second harmonic is greater

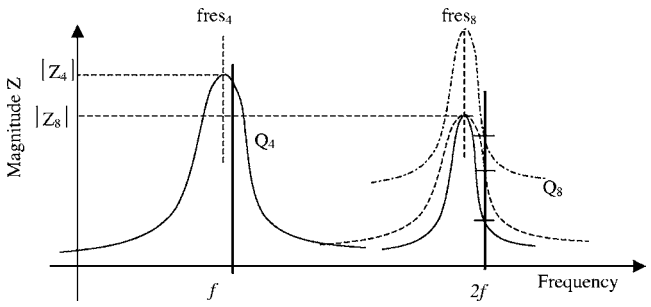

FIG. 4. Representation of the impedance curve around resonances 4 and 8 and of the playing frequency f and its second harmonic $2f$ (arbitrary units).

TABLE X. Correlation coefficients between the brightness score and the variables $|Z_8|/|Z_4|$, Q_8/Q_4, and $f_{res8}/2f_{res4}$

	AM	Simu	MF
$R_{Pearson}\|Z_8\|/\|Z_4\|$	0.96	0.99	0.63
$R_{Pearson}Q_8/Q_4$	−0.81	−0.85	−0.57
$R_{Pearson}f_{res8}/2.f_{res4}$	−0.90	−0.95	−0.54

than f_{res8} (case of Fig. 4). A simplified analysis of the physics of the coupled system lips-resonator, based on the input impedance curve given in Fig. 4, indicates the following sensible conclusions:

(i) The amplitude of the second harmonic of ♭3 (frequency=$2f$) is favored if the inharmonicity $f_{res8}/2f_{res4}$ increases to 1, all other parameters of the impedance curve being constant. So, the *Sc* of a tone is favored if $f_{res8}/2f_{res4}$ increases until 1.

(ii) The amplitude of the second harmonic of ♭3 is favored if the magnitude of Z_8 increases, all other parameters of the impedance curve being constant. So, the *Sc* of a tone is favored if $|Z_8|/|Z_4|$ increases.

(iii) The amplitude of the second harmonic of ♭3 is favored if the quality factor Q_8 decreases, all other parameters of the impedance curve being constant. So, the *Sc* of a tone is favored if Q_8/Q_4 decreases.

These conclusions remain valid if the playing frequency f is lower than f_{res4} and the second harmonic $2f$ is greater than f_{res8}. If the playing frequency f is lower than f_{res4} and the frequency $2f$ is lower than f_{res8}, one can easily verify that the conclusions are similar except that the inharmonicity must decrease.

Of course, things are not so simple when we want to interpret the values of the brightness of the tones using characteristics of the impedance of our set of instruments: all the characteristics vary at the same time and their influence is combined. For example, the linear correlation coefficient (given Table X) between the brightness scores of the tones and $|Z_8|/|Z_4|$ on the one hand and $|Q_8|/|Q_4|$ on the other hand confirm the suggested conclusion above ($R_{Pearson}(|Z_8|/|Z_4|) > 0$ and $R_{Pearson}(|Q_8|/|Q_4| < 0)$. The correlation between the brightness and inharmonicity $f_{res8}/2f_{res4}$ is in our case negative and remains in accordance with the conclusions of the previous physical study.

In order to reveal the underlying variables among the three variables ($f_{res8}/2f_{res4}$, $|Z_8|/|Z_4|$, and $|Q_8|/|Q_4|$) we performed a principal component analysis on the standardized data (correlation matrix) concerning 11 individuals and the three variables (from Table VII). The first factor accounts for 92% of variance, the second factor for 7%. So a representation on a plane accounts for 99% of variance. Figure 5 represents the position of the individuals (T0–T10) in the factorial plane, and the directions of the initial variables ($f_{res8}/2f_{res4}$, $|Z_8|/|Z_4|$, and $|Q_8|/|Q_4|$). The evolution of the variables is actually complex and when $f_{res8}/2f_{res4}$ increases, $|Q_8|/|Q_4|$ increases and $|Z_8|/|Z_4|$ decreases.

In order to interpret the brightness scores, we performed a multiple linear regression of the brightness scores b_i (the dependent variable) on the factorial coordinates ($F1_i$ $F2_i$) (independent variables). This classical technique in sensory analysis leads to the determination of the coefficients (α, β) of the regression, given by

$$b_i = \alpha F1_i + \beta F2_i + \gamma. \quad (9)$$

The determination coefficient R^2 of the regressions are given in Table XI.

A very good adjustment is observed for AM and Simu (significant with p value $<1\%$). For MF, only 37% of the variance is taken into account by the regression. This is because the average score of brightness is, in the case of MF, certainly not reliable.

For the AM and Simu categories, a graphic interpretation of the regression can be given by plotting in the factorial plane the vector model of the attribute "brightness," B.AM and B.Simu (Fig. 5). The origin of the vector is arbitrarily located in the origin of the frame, the values of the regression coefficients (α, β) give the position of the arrow, and the arrowhead points in the direction of increasing brightness. This vector is parallel to the steepest slope line of the plane [Eq. (9)] and the perpendiculars to the vector are the "iso-brightness lines."

The results of the regression are entirely in agreement (vectors B.AM and B.Simu are almost merged): the brightness of simulated tones is similarly interpreted as the brightness of sounds played by the artificial mouth. This is again a strong point for the validation of simulations.

Concerning the relations between the brightness and characteristics of the impedance curve, we noticed that the higher $|Z_8|/|Z_4|$, and the lower Q_8/Q_4, the brighter the sound. This result conforms to the physicist's intuition presented above. But we noticed too that the lower $f_{res8}/2f_{res4}$, the

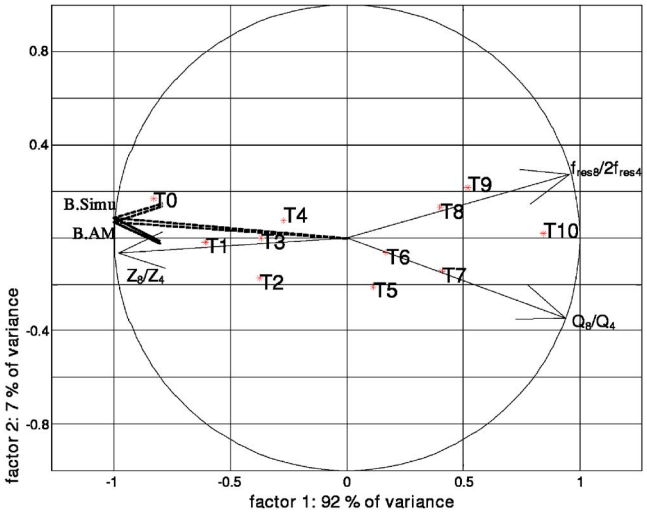

FIG. 5. Factorial plane $|Z_8|/|Z_4|$-Q_8/Q_4-$f_{res8}/2f_{res4}$.

TABLE XI. Determination coefficient of the multiple linear regressions between the brightness scores and the factorial scores.

	AM	Simu	MF
R^2	0.89	0.98	0.37

brighter the sound. This result could appear to be counterintuitive, but we must keep in mind that the influence of this variable can be masked by the influence of the others.

IV. CONCLUSIONS

In this paper, we studied the brightness of trumpet tones, the tones being generated in three ways: by a musician, by an artificial mouth, and by physical modeling simulations. Two studies were conducted on a set of instruments using a variable-depth mouthpiece: a subjective study with hearing tests for the assessment of the threshold of distinguishability between pairs of sounds and for the evaluation of the brightness and an objective study with the extraction of objective variables from the impedance curve.

We showed that the artificial mouth and the simulations give results coherent with those of the musician concerning the perception of differences of timbre. We verified that the threshold of distinguishability between sounds is of the same order for the artificial mouth, the simulated tones, and the musician. We demonstrated that the artificial mouth and the simulations give similar results concerning the brightness of trumpet tones. We emphasized the fact that the musician is not reproducible enough and creates difference of timbre of the same order as the difference produced by the depth-change in the mouthpiece. We conclude that the artificial mouth is an essential device for the study of the quality of wind instruments, for the conception of new instruments, and for the validation of realistic simulated tools.

Concerning the interpretation of brightness of sound, we have proposed a method based on principal component analysis and multiple regression for the research of the underlying and more influencing characteristics of the impedance curve on the brightness of sounds. We found that the magnitude of the impedance peak corresponding to the second harmonic of a tone is highly correlated with its brightness and seems to be the cause. But we must keep in mind that correlation is not equivalent to causality. The simulation will be a useful tool to study experimentally the influence of variables of the impedance curve on attributes of the sounds. By making it possible to test a wide range of different virtual instruments, statistical studies will be possible to test assumptions concerning the causal links between objective characteristics of instruments and sound attributes. These causal links will be finally used for the design of new instruments.

Concerning the simulations, we have proved that sounds simulated by the harmonic balance technique are able to reproduce differences of timbre which are similarly perceived to those played by a musician or the artificial mouth. This is a first step for the use of virtual acoustics techniques in the conception of new instruments.

ACKNOWLEDGMENTS

The authors are indebted to J.L. Le Carrou for his participation in experiments and to V. Fitzpatrick for her editorial support.

[1]The test has been done with the note C4, too. The results were quite similar and are not presented here.

[2]The probability to have k successes in a fixed number n of independent random trials, all of which have the same probability p (here $p=0.5$), is given by ${}_nC_k p^k(1-p)^{n-k}$, with ${}_nC_k = n!/(k!(n-k)!)$.

[3]We cannot say if these three subjects had actually understood the instruction, had a defective hearing, or have really judged that in a different way.

Adachi, S., and Sato, M. A. (**1995**). "Time-domain simulation of sound production in the brass instrument," J. Acoust. Soc. Am. **97**, 3850–3861.

Benade, A. H. (**1976**). *Fundamentals of Musical Acoustics* (Oxford U.P., New York).

Caral, S., and Campbell, M. (**2002**). "The influence of the mouthpiece throat diameter on the perception of timbre of brass instrument," Proceedings of the International Symposia on Musical Acoustics, Mexico, 2002, pp. 233–245.

Cullen, J. S., Gilbert, J., and Campbell, D. M. (**2000**). "Brass instruments: linear stability analysis and experiments with an artificial mouth," Acust. Acta Acust. 86, 704–724.

Dalmont, J. P. (**2001**). "Acoustic impedance measurement. Pt. 1: A review," J. Sound Vib. **243**, 427–439.

Dalmont, J. P., and Bruneau, A. M. (**1991**). "Acoustic impedance measurement: Plane-wave mode and first helical-mode contributions," J. Acoust. Soc. Am. **91**, 3026–3033.

Elliot, S. J., and Bowsher, J. M. (**1982**). "Regeneration in brass wind instruments," J. Sound Vib. **83**, 181–217.

Ewins, D. J. (**1984**). *Modal Testing: Theory and Practice* (John Wiley and Sons, New York, 1984).

Farina, A., and Tronchin, L. (**2000**). "On the 'virtual' reconstruction of sound quality of trumpets," Acust. Acta Acust. 86, 737–745.

Gazengel, B., Gilbert, J., and Amir, N. (**1995**). "Time domain simulation of a single reed wind instrument. From the measured input impedance to the synthesis signal. Where are the tramps?" Acustica **3**, 445–472.

Gilbert, J., Kergomard, J., and Ngoya, E. (**1989**). "Calculation of the steady state oscillations of a clarinet using the harmonic balance technique," J. Acoust. Soc. Am. **86**, 35–41.

Gilbert, J., Ponthus, S., and Petiot, J. F. (**1998**). "Artificial buzzing lips and brass instruments: Experimental results," J. Acoust. Soc. Am. **104**, 1627–1632.

Grey, J. M. (**1977**). "Multidimensional perceptual scaling of musical timbre," J. Acoust. Soc. Am. **61**, 1270–1277.

Grey, J., and Gordon, G. (**1978**) "Perceptual effects of spectral modifications on musical timbres," J. Acoust. Soc. Am. **63**(5), 1493–1500.

Krimphoff, J. (**1993**). "Analyse acoustique et perception du timbre," DEA d'acoustique appliquée, IRCAM.

Krimphoff, J., McAdams, S., and Winsberg, S. (**1994**). "Caractérisation du timbre des sons complexes. Analyses acoustiques et quantification psychophysique," J. Phys. IV **4**, 625–628.

Petiot, J.-F., Poirson, E., and Gilbert, J. (**2004**). "Study of the brightness of trumpets' sounds by analyzing the impedance curves," Proceedings of the CFA/DAGA04, 22–25 March **2004**, Strasbourg, France.

Petiot, J. F., Tessier, F., Gilbert, J., and Campbell, M. (**2003**). "Comparative Analysis of Brass Wind Instruments With an Artificial Mouth: First Results," Acta Acust. (Beijing) **89**(6), 974–979.

Plitnik, G. R., and Lawson, B. A. (**1999**). "An investigation of correlations between geometry, acoustic variables, and psychoacoustic parameters for French horn mouthpieces," J. Acoust. Soc. Am. **106**, 1111–1125.

Pratt, R. L., and Bowsher, J. M. (**1978**). "The subjective assessment of trombone quality," J. Sound Vib. **57**, 425–435.

Pratt, R. L., and Bowsher, J. M. (**1979**). "The objective assessment of trombone quality," J. Sound Vib. **65**, 521–547.

Schumacher, R. T. (**1978**). "Self sustained oscillations of the clarinet: an integral equation approach," Acustica **40**, 298–309.

Schumacher, R. T. (**1981**). "*Ab initio* calculations of the oscillations of a clarinet," Acustica **48**, 73–84.

Wright, H. A. K., and Campbell, D. M. (**1998**). "The influence of the mouthpiece on the timbre of cup-mouthpiece wind instruments," ISMA 98, Leavenworth, Washington.

Modeling elastic wave propagation in kidney stones with application to shock wave lithotripsy

Robin O. Cleveland[a)]
Department of Aerospace and Mechanical Engineering, Boston University, 110 Cummington Street, Boston, Massachusetts 02215

Oleg A. Sapozhnikov
Department of Acoustics, Faculty of Physics, Moscow State University, Leninskie Gory, Moscow 119992, Russia

(Received 16 March 2005; revised 14 July 2005; accepted 17 July 2005)

A time-domain finite-difference solution to the equations of linear elasticity was used to model the propagation of lithotripsy waves in kidney stones. The model was used to determine the loading on the stone (principal stresses and strains and maximum shear stresses and strains) due to the impact of lithotripsy shock waves. The simulations show that the peak loading induced in kidney stones is generated by constructive interference from shear waves launched from the outer edge of the stone with other waves in the stone. Notably the shear wave induced loads were significantly larger than the loads generated by the classic Hopkinson or spall effect. For simulations where the diameter of the focal spot of the lithotripter was smaller than that of the stone the loading decreased by more than 50%. The constructive interference was also sensitive to shock rise time and it was found that the peak tensile stress reduced by 30% as rise time increased from 25 to 150 ns. These results demonstrate that shear waves likely play a critical role in stone comminution and that lithotripters with large focal widths and short rise times should be effective at generating high stresses inside kidney stones. © *2005 Acoustical Society of America.* [DOI: 10.1121/1.2032187]

PACS number(s): 43.80.Gx, 87.54.Hk, 43.20.Gp [FD] Pages: 2667–2676

I. INTRODUCTION

Lithotripsy is the clinical procedure whereby extracorporeally generated shock waves are focused onto kidney stones to fragment them into small enough pieces that they can be passed naturally. Lithotripsy was first introduced in 1980 (Ref. 1) and in the United States about 70% of kidney stones are treated with shock waves.[2] Despite the wide acceptance of shock wave lithotripsy the mechanisms by which the shock waves comminute stones are not agreed upon. In addition it is now recognized that lithotripsy is not a benign procedure but results in tissue damage to most if not all kidneys which can lead to both acute and chronic complications.[3–6] Until the mechanisms of kidney stone fragmentation and kidney tissue damage are identified, improvements to lithotripsy are principally found empirically.

Identification of the mechanisms of kidney stone fragmentation requires that one first determine the state of loading on the stone and after which a fracture mechanics model needs to be applied to determine the material failure. A few models to determine the loading within kidney stones have been published. Dahake and Gracewski[7,8] used a finite-difference time-domain (FDTD) simulation for elastic waves but their study was motivated by intracorporeal shock wave lithotripsy and they treated the case of point sources on the surface of spherical stones. Xi and Zhong[9] have used ray tracing of compression and shear waves to determine locations of interactions but the ray tracing model cannot predict stress amplitudes and does not account for diffractive effects. Cleveland and Tello[10] described a FDTD model for calculating pressure waves in kidney stones subject to lithotripsy shock waves but the model treated the stone as a fluid and neglected the presence of shear waves. Mihradi *et al.*[11] employed a finite-element model (FEM) to predict the stress loadings on kidney stones in lithotripsy. The incident waveform was modeled as a half-sinusoid of purely positive pressure and simulations were carried out for pulses of different durations (0.5 to 5 μs) in a two-dimensional Cartesian coordinate system. It was concluded that fracture occurs due to spall, that is, reflection of the positive pressure from the distal surface of the stone.

Once the state of loading is determined the criteria for failure has to be identified. Most measurements on stone strength have reported either compressive strength or fracture toughness in experiments that were carried out at low strain rates.[12–14] This data shows enormous variation and because the strain rate in lithotripsy is 10^5 s^{-1} it is not clear whether measurements at low strain rates provide data relevant to lithotripsy.[15] Also, it is likely that the fracture is a fatigue process and requires further data, such as dynamic fracture toughness.[16]

This paper aims to address the issue of determining the stresses and strains in kidney stones during lithotripsy. We employ a finite-difference scheme, which is widely used in the geophysics community, to model the propagation of shock waves in kidney stones. This allows us to compute the stress and strain inside stones accounting for pressure waves in the surrounding fluid and elastic waves in the solid includ-

a)Electronic mail: robinc@bu.edu

ing all surface interactions. Using the simulations we are able to quantify a key role of shear waves that has only been alluded to in previous work.

II. MODEL

In this work kidney stones were assumed to behave as a linear, isotropic, elastic medium (the validity of this assumption is addressed in the discussion), in which case the underlying equations are Newton's second law and Hooke's law:

$$\frac{\partial v_i}{\partial t} = \frac{1}{\rho_0}\frac{\partial \tau_{ij}}{\partial x_j}, \tag{1}$$

$$\frac{\partial \tau_{ij}}{\partial t} = \lambda \delta_{ij}\frac{\partial v_k}{\partial x_k} + \mu\left(\frac{\partial v_i}{\partial x_j} + \frac{\partial v_j}{\partial x_i}\right). \tag{2}$$

The equations are written in index notation where v_i represent the velocity at each location, τ_{ij} the stress tensor, δ_{ij} the Kronecker delta function, a repeated index implies summation, ρ_0 is the material density, and λ and μ are the Lame coefficients of the material.

We further assumed that the problem was axisymmetric and cast the equations in cylindrical coordinates (r,θ,z). The z axis was the axis of propagation of the shock wave and the stones were modeled as volumes of rotation around the z axis (in this paper either spheres or cylinders). For cylindrical coordinates $v_\theta = 0$ and all derivatives with respect to θ vanish (see, for example, Ref. 17, pp. 26–27; Ref. 18, p. 77; or Ref. 19, Chap. 12) in which case Eq. (1) becomes

$$\frac{\partial v_r}{\partial t} = \frac{1}{\rho_0}\left(\frac{\partial \tau_{rr}}{\partial r} + \frac{\partial \tau_{rz}}{\partial z} + \frac{\tau_{rr}-\tau_{\theta\theta}}{r}\right),$$

$$\frac{\partial v_z}{\partial t} = \frac{1}{\rho_0}\left(\frac{\partial \tau_{zz}}{\partial z} + \frac{\partial \tau_{rz}}{\partial r} + \frac{\tau_{rz}}{r}\right), \tag{3}$$

and the nonzero stresses in Eq. (2) are given by

$$\frac{\partial \tau_{rr}}{\partial t} = \lambda \nabla\cdot\mathbf{v} + 2\mu\frac{\partial v_r}{\partial r}, \quad \frac{\partial \tau_{zz}}{\partial t} = \lambda \nabla\cdot\mathbf{v} + 2\mu\frac{\partial v_z}{\partial z},$$

$$\frac{\partial \tau_{\theta\theta}}{\partial t} = \lambda \nabla\cdot\mathbf{v} + 2\mu\frac{v_r}{r}, \quad \frac{\partial \tau_{rz}}{\partial t} = \mu\left(\frac{\partial v_r}{\partial z} + \frac{\partial v_z}{\partial r}\right), \tag{4}$$

where the dilatation rate is

$$\nabla\cdot\mathbf{v} = \frac{\partial v_r}{\partial r} + \frac{v_r}{r} + \frac{\partial v_z}{\partial z}. \tag{5}$$

Equations (3)–(5) were solved using a finite-difference grid that was staggered in both time and space, referred to as the Vireux scheme in geophysics[20–22] or the Yee cell in electromagnetics (Ref. 23 and Ref. 24, pp. 107–144). In this formulation it is assumed that the velocities are known at time $t-\Delta t/2$ and the stresses known at time t. To march forward one step first the velocities are advanced from $t-\Delta t/2$ to $t+\Delta t/2$ using Eqs. (3) and in the second the stresses are advanced from t to $t+\Delta t$ using Eqs. (4) and (5). Due to the nature of the staggered grids the v_r/r term is never evaluated at $r=0$ and therefore does not need special attention within the algorithm. The material properties were allowed to vary arbitrarily in space and were assumed to be defined at the same spatial location as the normal stresses. Linear interpolation was used to determine material properties at staggered grid points.

The edges of the numerical grid produce reflections that can be avoided by either solving on a large enough domain that the reflections are delayed enough in time that they can be gated out of the analysis or by use of boundary layers that absorb incident waves in particular the perfectly matched layer (PML).[25,26] In these 2D simulations (where computer memory limitations are not a significant issue) the grid was chosen to be very large (at least 8 mm away from any interface) to ensure that reflections did not enter the domain of interest (the stone) during the time of interest. For these simulations the boundary condition applied along each boundary was that the shear stress and normal component of the velocity were zero which ensured that along the $r=0$ axis the axis-symmetric assumption in cylindrical coordinates was satisfied.

From a material failure point of view, the principal stresses and strains and maximum shear stress and strain are important indicators of fracture. Two of the principal stresses lie in the r-z plane and are given by

$$\sigma_{1,2} = (\tau_{rr}+\tau_{zz})/2 \pm \sqrt{\tau_{rz}^2 + (\tau_{rr}-\tau_{zz})^2/4} \tag{6}$$

with the angle of σ_1 with respect to the r axis given by

$$\tan 2\theta_{p1} = 2\tau_{rz}/(\tau_{rr}-\tau_{zz}). \tag{7}$$

Due to the absence of the other two shear stresses the third principle stress is $\sigma_3 = \tau_{\theta\theta}$. We define the maximum tensile stress as $\sigma_T = \max(\sigma_1,\sigma_3)$ and the peak compressive stress $\sigma_C = -\min(\sigma_2,\sigma_3)$ (large compression is associated with a large negative number). The maximum shear stress is given by

$$\tau_{\max} = (\max(\sigma_i) - \min(\sigma_i))/2. \tag{8}$$

The principal strains u_i are related to the corresponding principal stresses σ_i by $u_i = (1/2\mu)\sigma_i + A$, where $A = p/(2\mu + 4\mu^2/3\lambda)$ is a scalar value proportional to the effective pressure in the stone $p = -(\tau_{zz}+\tau_{rr}+\tau_{\theta\theta})/3$.[27] This means that the maximum and minimum strains are oriented in the same directions as the corresponding maximum and minimum stresses. Note that maximum strain associated with shear waves does not depend on p, that is, it is proportional to maximum shear stress.

To aid interpretation of the results we will employ the fact that the divergence of the particle velocity [Eq. (5)] can be used to identify the disturbances that travel at the longitudinal sound speed. Similarly the curl of the particle velocity $\nabla\times\mathbf{v}$ can be used to identify disturbances that travel at the shear (transverse) wave speed. In our case only the θ component ω is nonzero:

$$\omega = \frac{\partial v_r}{\partial z} - \frac{\partial v_z}{\partial r}. \tag{9}$$

Tracking the divergence and curl allows the propagation of different types of waves within kidney stones to be followed.

For one set of simulations we were interested in solving the elastic equations in Cartesian coordinates. We used Eqs.

TABLE I. Physical properties of media used in the simulations. The properties ρ, λ, and μ were the three independent properties that were input to the code.

	ρ (kg/m^3)	c_L (m/s)	c_S (m/s)	λ (GPa)	μ (GPa)	v
Water	1000	1500	⋯	2.25	0	0.500
PSM-9	1150	2493	1108	4.32	1.41	0.377
Solid E30	1700	3000	1500	7.65	3.83	0.333
Fluid F30	1700	3000	⋯	15.30	0	0.500

(3)–(5) with the substitution $(r,\theta,z)\rightarrow(x,y,z)$ and all terms with $1/r$ drop from the equations. We assumed a state of plane strain in which case the stress in the out-of-plane axis (y) is given by $\tau_{yy}=-\tau_{xx}+\tau_{zz}/v$ where $v=\lambda/[2(\lambda+\mu)]$ is Poisson's ratio. All the other field variables can be calculated using the same formulas given above.

A. Material properties

The model requires three material properties for each medium—the density and the two Lame coefficients. The most common measurements made on natural and artificial kidney stones are the density, longitudinal sound speed, and shear wave speed which are related to the Lame coefficients through

$$c_L=\sqrt{\frac{\lambda+2\mu}{\rho_0}},\quad c_S=\sqrt{\frac{\mu}{\rho_0}}. \tag{10}$$

In Table I we show the material properties used in the simulations here.

In the simulations presented here we considered stones surrounded by water, which is a reasonable approximation of both *in vitro* and *in vivo* environments in which stones are destroyed. The material properties over the entire grid were therefore first initialized to that of water. In this work we considered stones of either cylindrical or spherical shape with homogeneous internal structure. Once the location and geometry of the stone were specified the indices on the grid that fell within the stone volume were identified and then ρ, λ, and μ for those indices set to the properties of the stone.

B. Source condition

The source condition was taken to be a classic lithotripsy pulse[28] modified with a hyperbolic tangent function to provide a smooth shock front:

$$p_s(t)=0.5(1+\tanh(t/t_{RT}))\exp(-t/t_L)\cos(2\pi f_L t+\pi/3), \tag{11}$$

where $t_L=1.1$ μs and $f_L=83.3$ kHz control the pulse shape and t_{RT} controls the rise time which was varied from 50 to 200 ns. The source was input in one of two ways. (1) The source was modeled as a boundary condition in a plane placed in the fluid at a distance of 5 mm from the stone. The source pressure was coupled into the simulations by setting the normal stresses in the source plane to $\tau_{rr}=\tau_{zz}=\tau_{\theta\theta}=-p_S$, where the negative sign accounts for the fact that in solid mechanics a compressed material has negative stress where as in fluid mechanics a compressed material is under positive pressure. The shear stress in the fluid was zero. (2) The source was modeled as an initial condition with the pressure distributed in space, obtained by replacing t in Eq. (11) by $-z/c_0$, and the particle velocity was determined based on the plane wave relationship $v=p/(\rho c_0)$. The results were insensitive to the manner in which the source was included.

Most of the simulations considered the incident pulse as a homogeneous plane wave (that is, the amplitude of the pulse did not vary with r). In addition a finite-sized focal zone was modeled by applying a Gaussian shading as a function of radial distance to the amplitude of the pulse:

$$p_s(r,z,t)=\exp(-(r/r_G)^2)p_s(0,z,t), \tag{12}$$

where the effective diameter (half pressure) of the focal spot is $1.66r_G$. No phase correction was applied as in the focal region of a lithotripter the wavefronts are close to planar.

III. RESULTS

In what follows the code is first used to identify the role that shear waves play in determining the peak stresses and strains in a finite length cylindrical stone and a spherical stone. The code is then compared against published experimental data. Finally, the code is used to determine how the peak stress inside a stone is affected by (1) the size of the shock wave focal spot, (2) the size of the stone, and (3) the shock wave rise time.

A cylindrical stone was chosen to match artificial stones reported in the literature[29] (diameter 6.5 mm, length 7.5 mm, and material properties identified by E30 in Table I). Figure 1 includes snapshots of the divergence and the curl, which show disturbances propagating at the longitudinal wave and shear wave speed, respectively. Also shown are the maximum tensile stress and the maximum shear stresses. The top row (2.8 μs) corresponds to when the leading compressive phase of the incident wave has almost reached the distal surface of the stone. It is seen that there are almost no longitudinal perturbations after the shock wave passage (see divergence images). However, at the edges of the stone a shear wave is produced (see curl images) and in addition an inverted diffracted compression wave is produced—analogous to the edge wave from finite amplitude aperture. Because of the higher sound speed in the stone the compression wave inside the stone runs ahead of the wave in the fluid and so to ensure the boundary conditions with the fluid a shear wave is generated in the stone at the boundary. Because the speed of the longitudinal wave is higher than that of the shear wave the effective source of shear waves at the stone boundary is "supersonic" and results in a conical wavefront (similar to a sonic boom). The longitudinal wave in the stone also launches an acoustic wave in the fluid which also has a conical wavefront. The incident wave propagating in the fluid outside of the stone induces a stress in the stone that also produces a shear wave in the solid but because the speed in the fluid is the same as the shear wave speed the wavefront is curved. Finally the passage of the pressure wave in the fluid over the outer surface of the stone generates a surface wave in the stone at the stone-water interface—this is a coupling

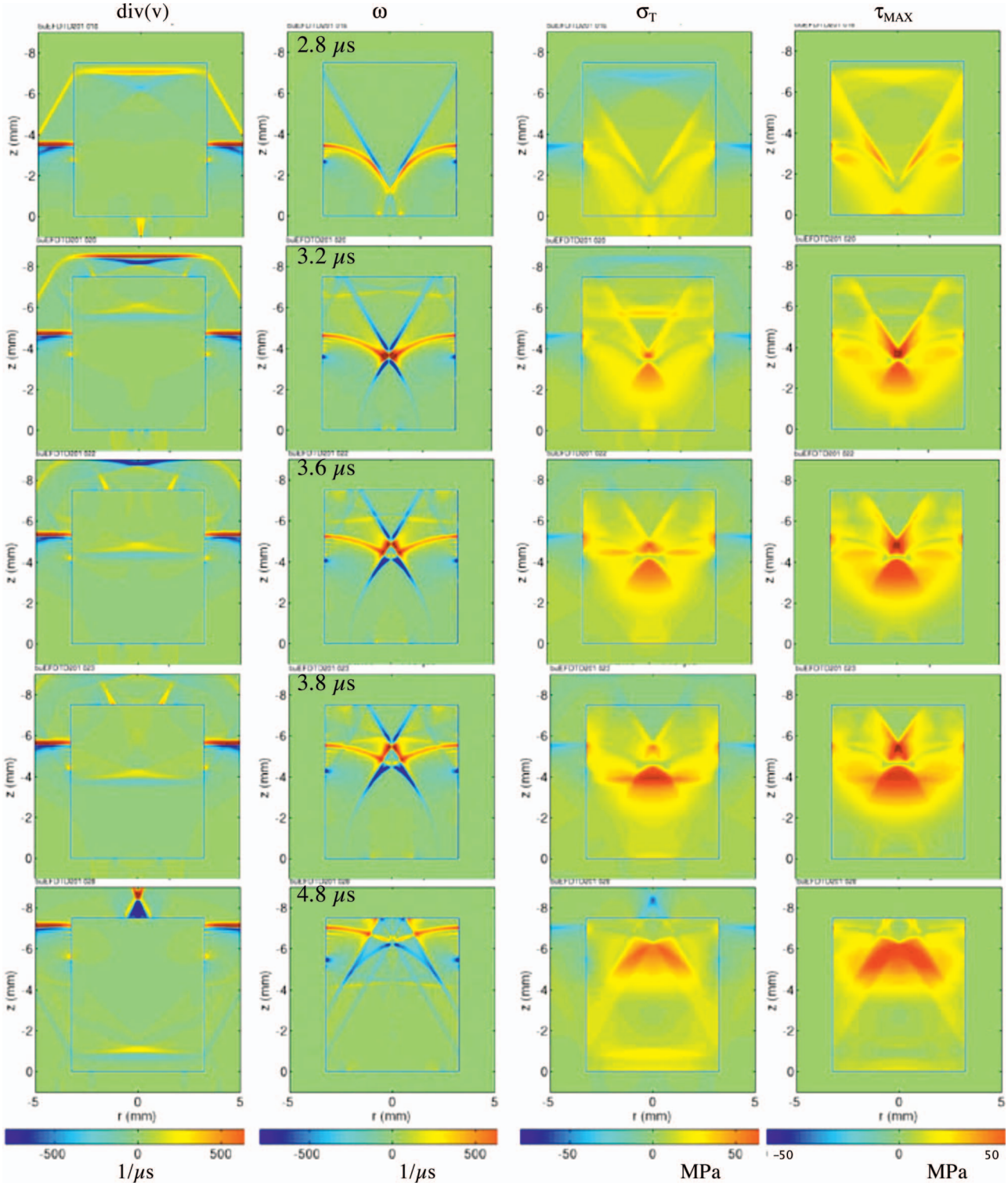

FIG. 1. (Color) Snapshots of the divergence, curl, max tensile stress, and maximum shear stress inside a cylindrical stone at 2.6, 3.2, 3.6, 3.8, and 4.8 μs after the SW is incident on the stone. The shock wave is incident from beneath the stone.

of shear and longitudinal waves and can be seen in both the divergence and curl images. This wave is restricted to a small region ($<$0.5 mm) near the interface.

When the wavefronts reflect at the distal surface (3.2 μs) a rich interaction between compressional and shear waves occurs. The compression wavefront is not planar when it is incident on the distal surface, as the presence of the fluid has "slowed down" and attenuated the outer portions of the wavefront. Therefore it reflects primarily as a compression wave but also partially as a shear wave. The next wave incident on the rear surface is the conical shear wave which is close to a plane wavefront and so when it interacts with the distal surface it does reflect as shear wave. However, the second shear wavefront does have curvature and so although it reflects primarily as a shear wave it also mode converts into a compression wave. The surface wave

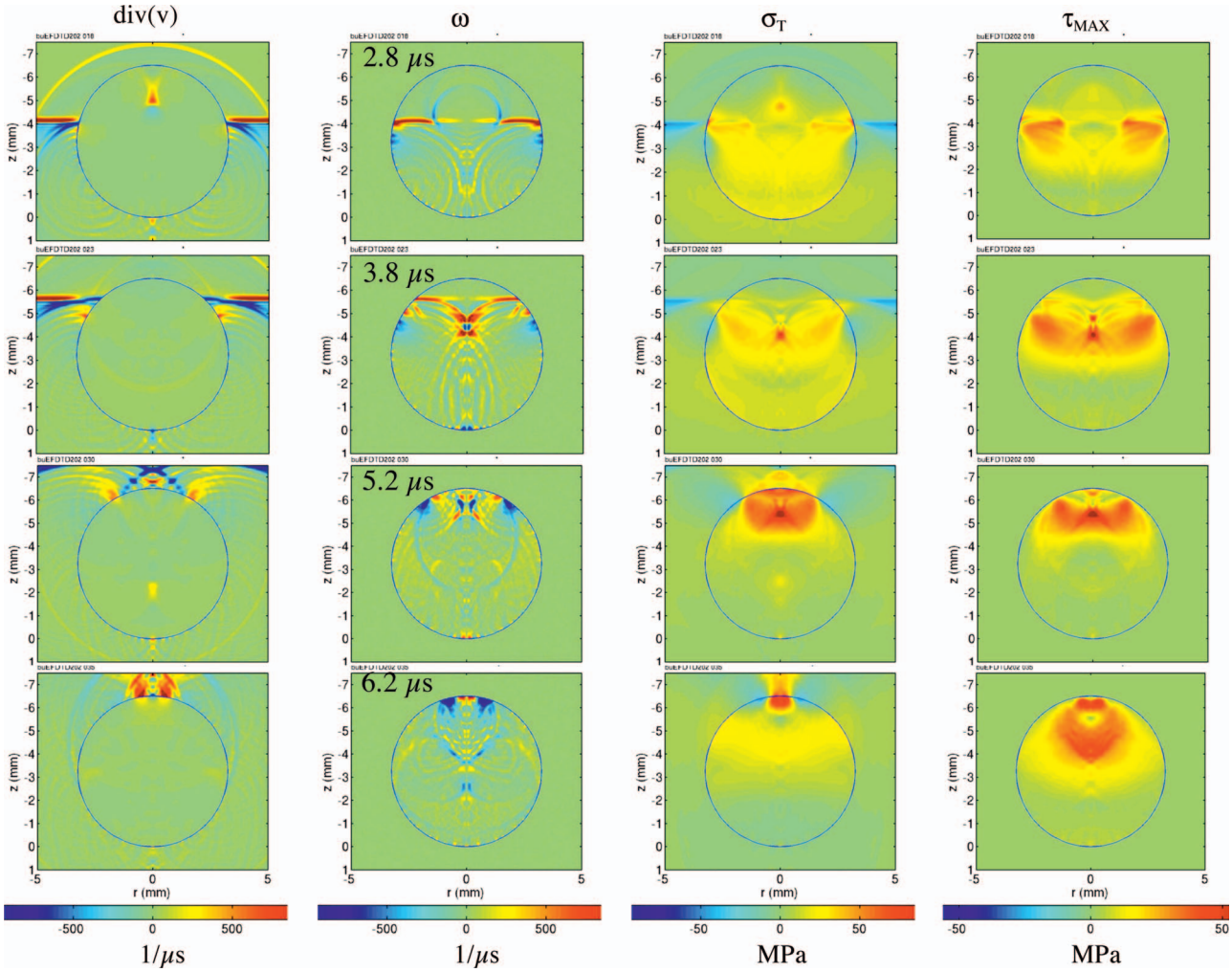

FIG. 2. (Color) Snap shots of the divergence, curl, max tensile stress, and maximum shear stress inside a spherical stone at 2.8, 3.8, 5.2, and 6.2 μs.

reflects too; it generates a diffracted shear wave at the corner and also launches a shear wave along the distal surface.

We now consider what happens to the maximum principal stresses (tensile stress) and maximum shear stress in the material. The numerical results indicate that the maximum tensile stress does not occur due to the interaction of the reflected compressive wave with the incoming tensile phase (3.2 μs). Rather the peak tensile stress occurs due to an interaction of the reflected longitudinal wave with a shear wave generated from the outer surface of the stone (3.8 μs). This shear wave is generated due to the interaction of the shock wave in the water passing the outside of the stone. This interaction also results in the highest shear stress. We also find that a large tensile stress is developed in a region localized near the lateral surfaces of the stone (3.6 μs) due to an interaction of a shear wave reflected from the rear surface of the stone and the wave traveling in the fluid outside the stone.

Figure 2 shows analogous snapshots for a spherical stone made of the same material. At 2.8 μs the longitudinal wave has passed the stone with a part of it having reflected off the distal surface and focused about 1.5 mm from the rear surface. At 3.8 μs the shear wave generated by the internal compression wave **traveling inside** the stone (where it interacts with the surface) focuses to a point about 2 mm from the distal surface. At 5.2 μs the shear wave generated by the wave **traveling outside** the stone arrives at the distal end and results in the largest tensile stress. At 6.2 μs the surface waves reach the distal point (aphelion) of the stone and generates both a large tensile stress and shear stress at the distal surface.

Figure 3 shows snapshots of the peak tensile strain in the cylindrical and spherical stones at the time 3.8 μs—this time was when the highest strain occurred in the simulations. By comparing these images to the snapshots in Figs. 1 and 2 at the same time it can be seen that the spatial distribution of the peak tensile strain is almost identical to that of the peak tensile stress. That is, the same phenomenon that produces the highest tensile stress also resulted in the highest tensile strain in the stone. We found that evolution and distribution of the peak compressive strain and the peak shear strain were also equivalent to the peak compressive stress and peak shear stress, respectively.

Therefore, for both the spherical and cylindrical geometry, it is the arrival of shear waves generated by the passage of pressure waves in the fluid outside of the stone that results in the highest stresses and strains in the stone. In what fol-

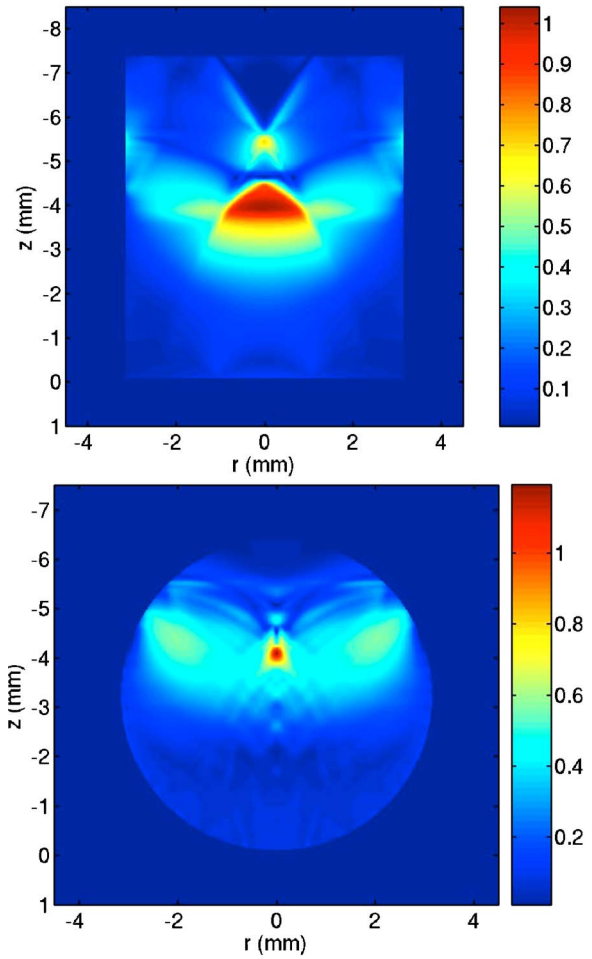

FIG. 3. Snapshot of the peak tensile strain (%) at 3.8 μs for the cylindrical stone (upper) and spherical stone (lower). The distribution of the tensile strain corresponds closely to the equivalent tensile stress shown in Figs. 1 and 2, respectively.

lows data are only presented for the principal stresses but the results equally well apply to the principal strains.

The results from the simulations were compared to measurements of the stress induced by a lithotripsy shock wave in a photoelastic material (PSM-9).[9] In the photoelastic images the number of fringes is proportional to the difference in the principal stresses in the material (which is equivalent to the maximum shear stress). In the water the presence of the pressure waves leads to a shadowgraph effect. We simulated the experimental setup solving the stress equations on a two-dimensional Cartesian grid assuming plain strain as discussed in Sec. II using the nominal material properties reported in Ref. 9 (reproduced in Table I). In Fig. 4 we compare the images of the measured fringes with the prediction of the peak shear stress from the model described here (rotated and scaled to match the published photoelastic images) and it can be seen that the features depicted in the photoelastic measurements are captured by the elastic wave model. For example, at 10 μs (experiment time 186 μs) the head wave in the fluid, the high stresses near the equator of the stone, and the circular distribution of stress near the distal wall of the stone are in good agreement. The simulations do appear to properly capture the stress field of this experiment.

The observation that the interaction of the shock wave with the outer surface of the stone leads to high tensile stress implies that for lithotripters with small focal zones (less than the diameter of a stone) there will not be strong generation of shear waves and so the constructive interference of large stresses may not occur. We considered the effect of the diameter of the focal zone by introducing Gaussian shading to the incident shock profile and keeping the pressure amplitude on axis ($r=0$) the same. In Fig. 5 we show the dependence of the peak principal stresses as a function of the diameter of the focal zone of the shock wave. The peak stress was determined by detecting the maximum stress for each point in the grid over the course of the simulation and then taking the largest of the maximum stresses within the volume of the stone.

All of the peak stresses decreased dramatically as the focal zone diameter decreased. For the spherical stone, as the focal diameter decreased from 11 to 4 mm all of the peak stresses were reduced by at least 50%. For the cylindrical stone the peak stresses had halved once the focal diameter was 5 mm. The result was consistent for stones of properties covering the range reported for natural stones: c_L between 2500 and 4000 m/s and υ between 0.33 and 0.37 (data not shown).

We found that the generation of high stresses in the stone was not strongly dependent on the stone size. Figure 6 shows the peak stresses as a function of the diameter of a spherical stone for the case of an incident plane wave. There was little change in the peak stress as a function of diameter. We note that this is in disagreement with the results of the pressure simulations (where the stone modeled as an effective liquid) which predicted that the peak negative pressure (equivalent to tensile stress) in the stone should decrease dramatically for stones less than 4 mm in diameter.[30] The explanation for this discrepancy is that the pressure code does not capture shear waves in the stone, which play a dominant role in determining the peak stress. In Fig. 7 the spatial distribution of the peak tensile stress is shown for spherical stone treated as either a fluid or an elastic solid. There are both quantitative and qualitative differences in the spatial distribution and the amplitude of the stress in the stone. This is further evidence of the importance of shear waves in determining the state of stress in the stone.

We finally considered the effect of shock rise time on the stresses induced in the stone. The rise time was controlled using the $\tanh(t/t_{RT})$ term in Eq. (11) and the waveform was scaled to ensure the same peak pressure. The calculated peak stresses in the cylindrical stone are shown in Fig. 8. We see that as shock rise time increased all of the peak stresses (tensile, compressive, and shear) in the stone decreased. This occurs due to two effects: (1) The leading compressional wave in the stone suffers more from diffraction due to the longer rise time and so the peak pressure of the tensile wave reflected off the back of the stone ("spall wave") is about 31 MPa for a 50-ns rise time but only 12.9 MPa for a 200-ns rise time. (2) The spatial extent of the shear waves generated by the passage of the wave outside the stone is

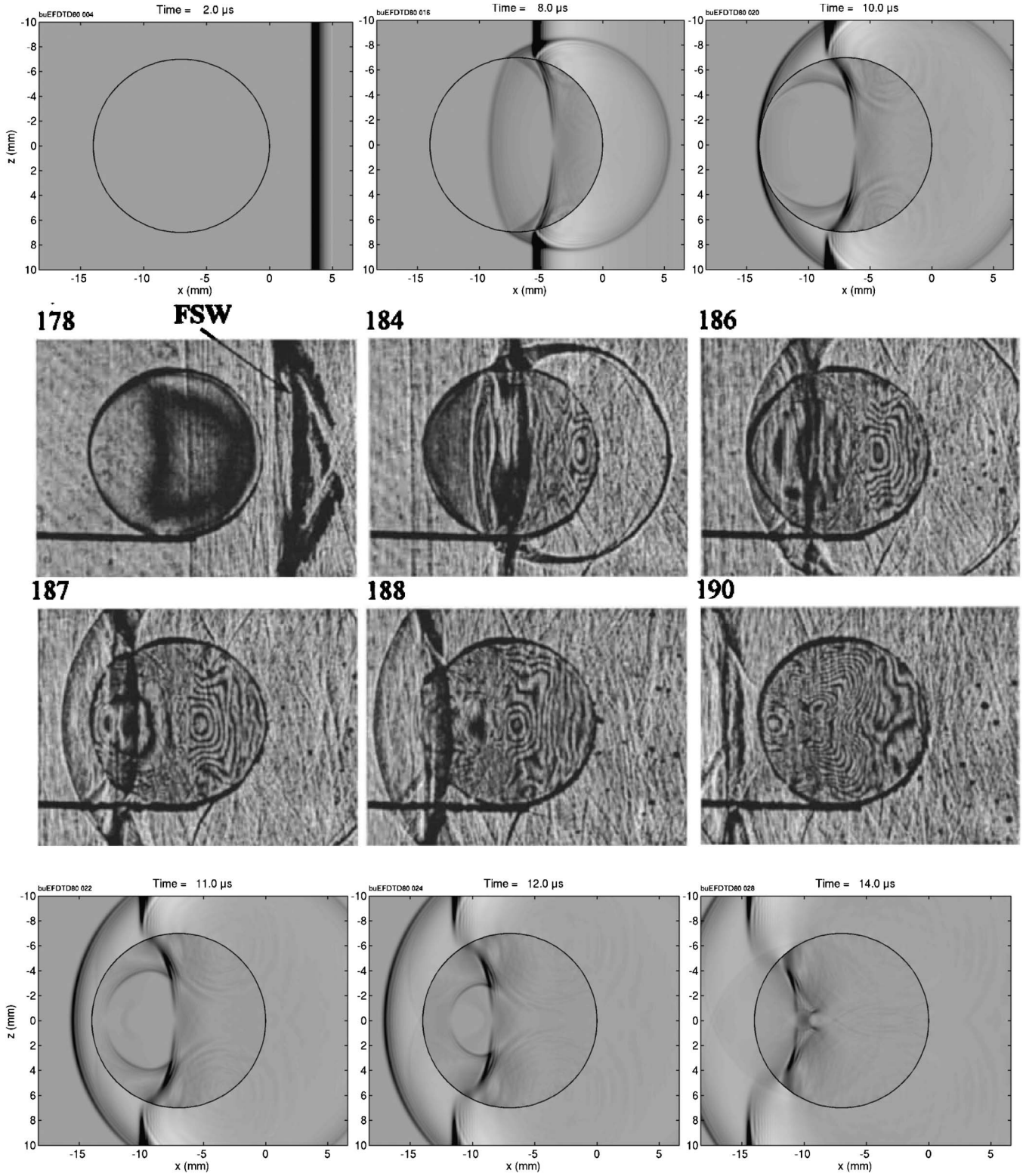

FIG. 4. Comparison of the photoelastic images from PSM-9 (Fig. 9 from Ref. 9) with predictions of the maximum shear stress in the stone and the pressure in the surrounding fluid. Experimental data are shown in the middle two rows. The top row shows snapshots from the simulation corresponding to the upper row of experimental data. The bottom row shows snapshots from the simulation corresponding to the lower row of experimental data.

related to the spatial extent of the shock front. For a shock front with a 50-ns rise time the resulting shear wave had a length of 0.36 mm and for a 200-ns rise time the length was 0.66 mm. These lengths were determined from measurements of the shear stress predicted by the FDTD simulations. In the latter case the shear wave was so extended in space that near the surface it was difficult to isolate it from the surface wave. The shorter length shear wave (associated with short rise time) is focused more efficiently along the axis of the stone and so results in stronger focusing and higher stresses than the longer length shear wave (associated with longer rise time). Therefore a shorter rise time shock wave

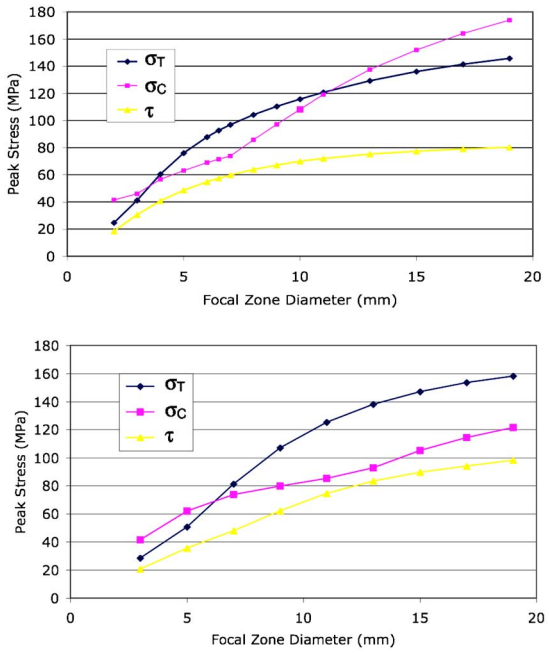

FIG. 5. Peak stresses (tensile, compression, and shear) as a function of diameter of the focal zone. Top: spherical stone 6.5 mm in diameter. Bottom: cylindrical stone 6.5 mm in diameter and 7.5 mm long.

yields larger stresses because the shear waves generated at the lateral side of the stone focus more strongly and the "spall wave" is higher in amplitude.

IV. DISCUSSION AND CONCLUSIONS

We used a finite-difference time-domain solution of the linear elasticity equations to determine the evolution of the state of stress and strain inside kidney stones subject to a lithotripter shock wave. The model accounted for all wave interactions at fluid-elastic boundaries and the interaction of the various types of waves that the solid structure can support. From the model it was possible to determine the peak stresses and strains (compressive, tensile, and shear) in the stone, which are often important indicators of material failure.

The key conclusion from the simulations is that the peak stresses and strains in a kidney stone are critically dependent on the presence of shear waves. In particular for the studies here we found that the passage of the shock wave in the fluid surrounding the stone generated shear waves or surface waves at the "equatorial" surface of the stone which propagated into the stone and interfered constructively with other waves to generate the peak stresses. This conflicts with the conclusions of Mihradi *et al.*[11] that the classical spall or Hopkinson effect is responsible for the peak tensile stresses in the stone. The probable explanation for this is that the waveform they used did not have a short shock front and as we show in Fig. 8 the peak tensile stress is reduced dramatically as the rise time increases.

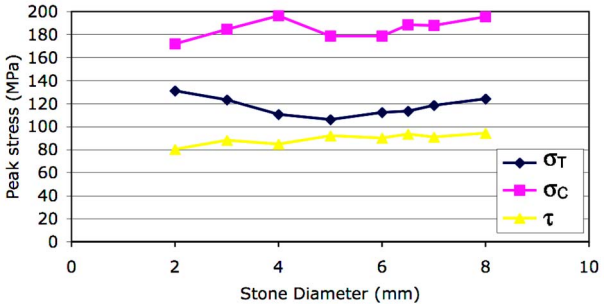

FIG. 6. Peak stresses (tension, compression, and shear) inside a spherical stone as a function of stone diameter. The peak stresses are relatively insensitive to stone diameter.

Therefore, to obtain efficient generation of high stress inside a kidney stone it is desirable to have a high-amplitude pressure wave passing on the outside of the stone. This conclusion is identical to that of squeezing that has been postulated by Eisenmenger,[31] however the rationale for our conclusion is different. In squeezing it is postulated that the pressure wave in the surrounding fluid acts as a compressive hoop stress which, based on a static model for stress, generates splitting of the material. In our model the shock wave in the fluid launches shear waves and surface waves which constructively interfere to generate high stresses. The role of shear waves generated at the outer surface of the stone has also been identified using ray tracing,[9] but, although ray tracing can identify possible wave-wave interactions, it cannot predict the amplitude of the stresses induced by the waves. In this work we were able to show quantitatively that the role of the shear wave generated by the external shock wave is dramatic. In particular, as the diameter of the focal spot of the shock wave reduced from 11 to 4 mm, the peak stresses reduced by at least a factor of 2. This result was robust to stones of different size and material properties. We note that the stone geometries simulated here had cylindrical symmetry which should maximize the constructive interference on axis. This effect may be less pronounced for natural stones with more complex geometries but we still anticipate that shear wave effects will play an important role.

In addition, we found that peak stresses increased as the rise time of the shock wave decreased. As rise time increased from 50 to 200 ns the peak stresses decreased by approximately 30%. This was attributed to two processes: (1) the spatial extent of the shear wave increased and so the shear wave could not focus as efficiently on axis and (2) the compressive wave in the stone was affected by diffraction and the amplitude of the tensile wave reflected from the distal surface was less. We speculate that this finding may explain clinical reports that stones trapped in the ureter are difficult to break.[32] When the shock wave passes through the tissue the absorption of the tissue will lengthen the shock rise time to around 100 ns.[33] For stones in the collecting system of the kidney there is a volume of urine surrounding the stone and as the shock wave propagates through the urine it can "heal," recover a very short rise time, due to nonlinear distortion. The "healing" distance can be calculated as the shock formation distance[34] and for a lithotripter shock wave in water is less than 5 mm. Therefore, even a small amount of fluid around the stone will allow the shock rise time to recover. For stones in the ureter there is little or no urine surrounding the stone and therefore the shockwave cannot heal and will impact the stone with a relatively long rise time. We ac-

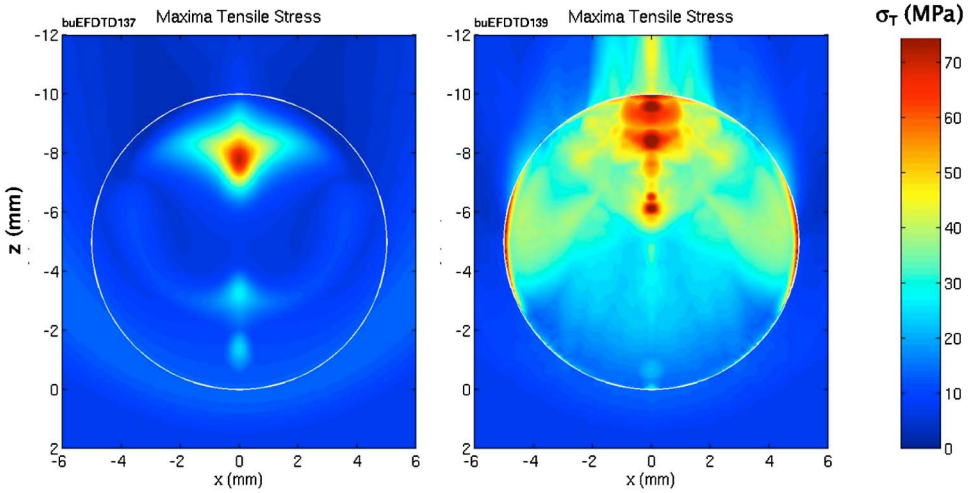

FIG. 7. Comparison of the spatial distribution of the peak tensile stress in spherical stone. Left stone modeled as a fluid with sound speed 3000 m/s (F30 from Table I). Right: stone modeled as an elastic solid with longitudinal wave speed 3000 m/s (E30 from Table I).

knowledge that the difficulty in breaking stones in the ureter can also be explained by invoking cavitation.

We note that there are limitations of the model employed here including the use of cylindrical symmetry, homogenous stones, and linear elasticity. The use of cylindrical symmetry can be relaxed at the cost of higher computational burden and the use of an absorbing boundary condition, such as the Beringer PML, will likely be required. Extension to inhomogeneous stones is relatively straightforward as it simply requires altering the material properties of the stone but this was beyond the scope of this study. The linear approximation is justified within the stone as the propagation distances are quite short. Nonlinear distortion is cumulative and is important over the range of propagation through the tissue to the stones (greater than 100 mm) but less important in the stone (propagation distances less than 10 mm). Further, incorporation of nonlinear elasticity is confounded by a paucity of data for the higher order elastic constants of kidney stones. Most information on the properties of kidney stones results from ultrasonic measurements which invoke linear elasticity theory or axial loading which cannot determine all the higher order constants. However, it is not unreasonable to assume that most kidney stones are brittle in nature and therefore can be reasonably approximated using linear elasticity up to the point of failure. Also alternative failure criteria could be employed, such as von Mises and Tresca conditions or fracture toughness, rather than the maxiumum stresses and strains calculated in this work. Finally, we note that viscoeleasticity can be incorporated into the model—which could be of particular importance to the binder phase of kidney stones.[15]

In conclusion the results indicate that lithotripters with large focal widths and short rise times will result in high peak stresses inside the stone. If direct stress is responsible for stone comminution, then a large-focal-zone short-rise-time lithotripter should result in the best comminution of the stone. We note that the gold standard in clinical lithotripsy is the Dornier HM3 which has these characteristics. However, the trend among current clinical lithotripters is towards small focal zone lithotripters (diameters less than 5 mm) with high pressure amplitudes but not necessarily short rise times. The results from our simulations indicate that these characteristics may not be advantageous.

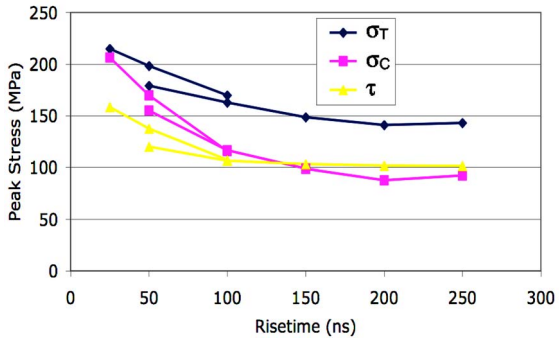

FIG. 8. Variation of peak stress inside a cylindrical stone as a function of the shock rise time. All the peak stresses decreased as the rise time increased. The second set of curves show calculations carried out on a 10-μm grid which show approximately a 10% increase in peak stresses for a rise time of 50 ns.

ACKNOWLEDGMENTS

We would like to acknowledge helpful discussions with Dr. Michael Bailey and other members of the Consortium for Shock Waves in Medicine. This work was supported by the Whitaker Foundation (RC), the National Institutes of Health (RC, OS), ONRIFO (OS), Fogarty (OS), and RFBR (OS).

[1]C. Chaussy, W. Brendel, and E. Schmiedt, "Extracorporeally induced destruction of kidney stones by shock waves," Lancet **2**(8207), 1265–1268 (1980).
[2]K. Kerbl, J. Rehman, J. Landman, D. Lee, C. Sundaram, and R. V. Clayman, "Current management of urolithisasis: Progress or regress?" J. Endourol **16**(5), 281–288 (2002).
[3]K. U. Kohrmann, J. J. Rassweiler, M. Manning, G. Mohr, T. O. Henkel, K. P. Junemann, and P. Alken, "The Clinical Introduction of a 3rd Generation Lithotriptor—Modulith Sl-20," J. Urol. (Baltimore) **153**(5), 1379–1383 (1995).
[4]J. E. Lingeman and J. Newmark, "Adverse bioeffects of shock-wave lithotripsy," in *Kidney Stones: Medical and Surgical Management*, edited by F. L. Coe *et al.* (Lippincott-Raven, Philadelphia, 1996), pp. 605–614.
[5]G. Janetschek, F. Frauscher, R. Knapp, G. Höfle, R. Peschel, and G. Bartsch, "New onset hypertension after extracorporeal shock wave lithotripsy: age related incidence and prediction by intrarenal resistive index," J. Urol. (Baltimore) **158**(2), 346–351 (1997). (See comments).
[6]A. P. Evan, L. R. Willis, J. E. Lingeman, and J. A. McAteer, "Renal trauma and the risk of long-term complications in shock wave lithotripsy," Nephron **78**, 1–8 (1998).
[7]G. Dahake and S. M. Gracewski, "Finite difference predictions of P-SV

wave propagation inside submerged solids. II. Effect of geometry," J. Acoust. Soc. Am. **102**, 2138–2145 (1997).
[8]G. Dahake and S. M. Gracewski, "Finite difference predictions of P-SV wave propagation inside submerged solids. I. Liquid-solid interface conditions," J. Acoust. Soc. Am. **102**, 2125–2137 (1997).
[9]X. Xi and P. Zhong, "Dynamic photoelastic study of the transient stress field in solids during shock wave lithotripsy," J. Acoust. Soc. Am. **109**, 1226–1239 (2001).
[10]R. O. Cleveland, R. Anglade, and R. K. Babayan, "Effect of stone motion on *in vitro* comminution efficiency of a Storx Modulith SLX," J. Endourol **18**, 629–633 (2004).
[11]S. Mihardi, H. Homma, and Y. Kanto, "Numerical Analysis of Kidney Stone Fragmentation by Short Pulse Impingemen," JSME Int. J., Ser. A **47**(4), 581–590 (2004).
[12]J. R. Burns, B. E. Shoemaker, J. F. Gauthier, and B. Finlayson, "Hardness testing of urinary calculi," in *Urolithiasis and Related Clinical Research*, edited by P. O. Schwille and E. T. C. Others (Plenum, New York, 1985), pp. 703–706.
[13]N. P. Cohen and H. N. Whitfield, "Mechanical testing of urinary calculi," J. Urol. (Baltimore) **11**(1), 13–18 (1993).
[14]P. Zhong, C. J. Chuong, and G. M. Preminger, "Characterization of fracture toughness of renal calculi using a microindentation technique. (Extracorporeal shock wave lithotripsy)," J. Mater. Sci. Lett. **12**(18), 1460–1462 (1993).
[15]E. T. Sylven, S. Agarwal, R. O. Cleveland, and C. L. Briant, "High Strain Rate Testing of Kidney Stones," J. Mater. Sci.: Mater. Med. **15**, 613–617 (2004).
[16]M. Lokhandwalla and B. Sturtevant, "Fracture mechanics model of stone comminution in ESWL and implications for tissue damage," Phys. Med. Biol. **45**(7), 1923–1940 (2000).
[17]B. L. N. Kennett, *Seismic Wave Propagation in Stratified Media*, Cambridge Monographs on Mechanics and Applied Mathematics, edited by G. K. Batchelor and J. W. Miles (Cambridge, U.P., Cambridge, 1983).
[18]H. Ford, *Advanced Mechanics of Materials*, 2nd ed. (Wiley, New York, 1977).
[19]S. P. Timoshenko and J. N. Goodier, *Theory of Elasticity* (McGraw-Hill, New York, 1982).
[20]J. Vireux, "P-SV wave propagation in heterogenous media: Velocity stress finite-difference method," Geophysics **51**, 889–901 (1986).
[21]Q. H. Liu, E. Schoen, F. Daube, C. Randall, H. L. Liu, and P. Lee, "A three-dimensional finite difference simulation of sonic logging," J. Acoust. Soc. Am. **100**, 72–79 (1996).
[22]R. W. Graves, "Simulating seismic wave propagation in 3D elastic media using staggered-grid finite differences," Bull. Seismol. Soc. Am. **86**, 1091–1106 (1996).
[23]K. Yee, "Numerical solutions of initial boundary value problems involving Maxwell's equations in isotropic media," IEEE Trans. Antennas Propag. **AP-14**, 302–307 (1966).
[24]A. Taflove, *Computational Electrodyamics: The Finite-Difference Time-Domain Method* (Artech House, Norwood, MA, 1995).
[25]J. P. Berenger, "A perfectly matched layer for the absorption of electromagnetic waves," J. Comp. Physiol. **114**, 185–200 (1994).
[26]W. C. Chew and Q. H. Liu, "Perfectly matched layers for elastodynamics: A new absorbing boundary condition," J. Comput. Acoust. **4**, 341–359 (1996).
[27]L. D. Landau and E. M. Lifshitz, *Theory of Elasticity*, 3rd ed. (Pergamon, New York, 1986).
[28]C. Church, "A theoretical study of cavitation generated by an extracorporeal shock wave lithotripter," J. Acoust. Soc. Am. **86**, 215–227 (1989).
[29]J. A. McAteer, J. C. Williams, Jr., R. O. Cleveland, J. van Cauwelaert, M. R. Bailey, D. A. Lifshitz, and A. P. Evan, "Ultracal-30 Gypsum Artificial Stones for Lithotripsy Research," Urol. Res., in press (2005).
[30]R. O. Cleveland and J. S. Tello, "Effect of the diameter and the sound speed of a kidney stone on the acoustic field induced by shock waves," ARLO **5**, 37–43 (2004).
[31]W. Eisenmenger, "The mechanisms of stone fragmentation in ESWL," Ultrasound Med. Biol. **27**(5), 683–693 (2001).
[32]K. T. Pace, M. J. Weir, N. Tariq, and R. J. D. Honey, "Low Success Rate Of Repeat Shock Wave Lithotripsy For Ureteral Stones After Failed Initial Treatment," J. Urol. (Baltimore) **164**, 1905–1907 (2000).
[33]R. O. Cleveland, D. A. Lifshitz, B. A. Connors, A. P. Evan, L. R. Willis, and L. A. Crum, "*In vivo* pressure measurements of lithotripsy shock waves in pigs," Ultrasound Med. Biol. **24**, 293–306 (1998).
[34]M. F. Hamilton and D. T. Blackstock, eds. *Nonlinear Acoustics* (Academic, New York, 1998).

Male sperm whale acoustic behavior observed from multipaths at a single hydrophone

Christophe Laplanche,[a] Olivier Adam, Maciej Lopatka, and Jean-François Motsch
Laboratoire Images, Signaux et Systèmes Intelligents Groupe Ingénierie des Signaux Neuro-Sensoriels, Université Paris XII, France

(Received 5 November 2004; revised 11 June 2005; accepted 20 July 2005)

Sperm whales generate transient sounds (*clicks*) when foraging. These clicks have been described as echolocation sounds, a result of having measured the source level and the directionality of these signals and having extrapolated results from biosonar tests made on some small odontocetes. The authors propose a passive acoustic technique requiring only one hydrophone to investigate the acoustic behavior of free-ranging sperm whales. They estimate whale pitch angles from the multipath distribution of click energy. They emphasize the close bond between the sperm whale's physical and acoustic activity, leading to the hypothesis that sperm whales might, like some small odontocetes, control click level and rhythm. An echolocation model estimating the range of the sperm whale's targets from the interclick interval is computed and tested during different stages of the whale's dive. Such a hypothesis on the echolocation process would indicate that sperm whales echolocate their prey layer when initiating their dives and follow a methodic technique when foraging. © *2005 Acoustical Society of America.* [DOI: 10.1121/1.2033567]

PACS number(s): 43.80.Ka, 43.66.Qp, 43.30.Sf [WWA] Pages: 2677–2687

I. INTRODUCTION

The scientific community is compelled to research sperm whales (*Physeter macrocephalus*) for a variety of reasons; some researchers may strive to assess the risks associated with anthropogenic noise (Gisiner, 1998), while others conduct experiments to protect the whales from excessive boat traffic (Delory *et al.*, 2002). Another motivation is the quest for new knowledge regarding the foraging behavior of sperm whales, since this aspect of their behavior is still the most puzzling (Fristrup and Harbison, 2002; Jaquet, 1996). Underwater visual observations of free-ranging, foraging sperm whales have never been carried through convincingly (Mccarey and Rubin, 1998), and the information available on the sperm whale diet is limited to stomach or fecal samplings. This is due to the fact that sperm whales mostly feed on mid sea and deep sea squid and fish, and at such depths research is difficult to conduct (Santos *et al.*, 2001; Smith and Whitehead, 2000). However, many experiments have been conducted to address the whales' foraging behavior, using tagging techniques, visual observations, and passive acoustics.

Tagging sperm whales with depth-meters has led to an understanding of their diving behavior. Sperm whales undertake series of 30–90-min four-stage foraging cycles, composed of a breathing break at the sea surface, a vertical descent to the hunting depth, the hunt itself, and a vertical resurfacing (Watkins *et al.*, 1993). Visual observations of sperm whales breathing at the sea surface provide some understanding of their social behavior. For instance, the males tend to travel solitarily, whereas the females and their calves travel in groups (Arnbom and Whitehead, 1989).

The use of passive acoustics enables scientists to better understand the sperm whale acoustic activity. Sperm whales emit a multitude of transient sounds (*clicks*) when diving. The function of the clicks may be to communicate (Watkins and Schevill, 1977; Weilgart, 1990) or echolocate (Jaquet *et al.*, 2001; Mohl *et al.*, 2000). The directionality and source level of the clicks are measured to determine their use in communication or echolocation (Madsen *et al.*, 2002b). Echolocating sperm whales emit *usual click* sequences ($0.2 < \mathrm{ICI} < 2$ s, interclick intervals), interrupted by faster click trains (*creaks*, $\mathrm{ICI} < 0.2$ s) and then silences (Mullins *et al.*, 1988). Sperm whales emit echolocation clicks mostly during the descent and while hunting within the prey layer (Madsen *et al.*, 2002b). Sperm whales within social groups also send stereotyped ICI structure click sequences, called *codas* (Weilgart, 1990). Male sperm whales may make some other rare vocalizations, called *slow clicks* (Jaquet *et al.*, 2001; Madsen *et al.*, 2002b). The use of passive acoustics is not only limited to the study of the click rythmics, but it also leads to an understanding of the click production mechanism (Mohl *et al.*, 2003; Thode *et al.*, 2002) and to the reconstruction of sperm whale diving trajectories (Wahlberg, 2002).

New tagging techniques, using depth-meters, hydrophones, accelerometers, and magnetometers, have enabled scientists to gain knowledge of sperm whale behavior. These tags enable scientists to record sperm whale movements together with their acoustic activity (Johnson and Tyack, 2003; Zimmer *et al.*, 2003). Fluking has been measured while sperm whales swim down and resurface (Miller *et al.*, 2004a). Sperm whales maneuvering is measured during the hunting process (Miller *et al.*, 2004b). Such tagging techniques, like passive acoustics, have also lead to the description of the click production mechanism and to the reconstruction of diving trajectories, but with increased levels of precision (Zimmer *et al.*, 2005).

[a]Electronic mail: laplanche@univ-paris12.fr

While the aforementioned tagging techniques provide insight into sperm whale behavior, the technique itself can disrupt or alter the natural tendencies of the tagged mammals. Also the tagging procedure is time consuming and difficult to implement (Madsen *et al.*, 2002a). Because of this, the authors bring forward a passive acoustic technique that will uncover new behavioral information without such shortcomings. Passive acoustics may give results close to those attained using depth-meter/hydrophone tags (Madsen *et al.*, 2002b). The depth (and range) of sound sources can be estimated by using a single hydrophone. This method has been successfully carried out on sperm whales (Thode *et al.*, 2002) and dolphins (Aubauer *et al.*, 2000). Nevertheless, the accuracy on the depth and range measurements is not enough for estimating subtle foraging sperm whale movements.

The authors estimate subtle sperm whale movements by measuring pitch angle variations using a single towed hydrophone. The comparison of these variations to the acoustic activity then leads to a hypothesis on the sperm whale echolocation system: sperm whales, like some other toothed whale species, would control click level and ICI when echolocating on targets at different ranges. The authors then compute an echolocation model estimating sperm whale target ranges from the ICI. They apply this echolocation model during the sperm whale descent and hunt, and assess its consistency. They estimate the water mass geometry analyzed by the whale's sonar during both stages, leading to the hypothesis of a dive-scale sperm whale foraging strategy.

II. MATERIAL AND METHODS

A. Single hydrophone localization

The authors need to assess the vertical distribution of click level to estimate sperm whale pitch angle. To this end, they compare the click levels emitted along different rays of multipath propagating sperm whale clicks. The authors estimate the depth and range of phonating sperm whales, before reconstructing the multipath ray geometry, to measure the attenuation of the click signals when transmitting along these rays.

The sea surface and the seafloor reflect and diffuse propagating acoustic waves (Clay and Medwin, 1977). The hydrophones collect multiple delayed, dephased, and attenuated versions of the signals emitted by sound sources (Fig. 1). The use of a single hydrophone, and the detection of n surface/seafloor echoes, serves as a substitute of a large virtual vertical $(n+1)$-hydrophone array (one real, n virtual) (Aubauer *et al.*, 2000). A sound source can be localized in depth and range from this array, by measuring the time of arrival differences of the source signal between the virtual hydrophones, then by measuring the time of arrival differences between the echoes (Fig. 2). One needs to detect two echoes of a click to estimate the depth and range of a phonating sperm whale. The detection of an additional echo leads to an estimation of the depth of the recording hydrophone (Thode *et al.*, 2002).

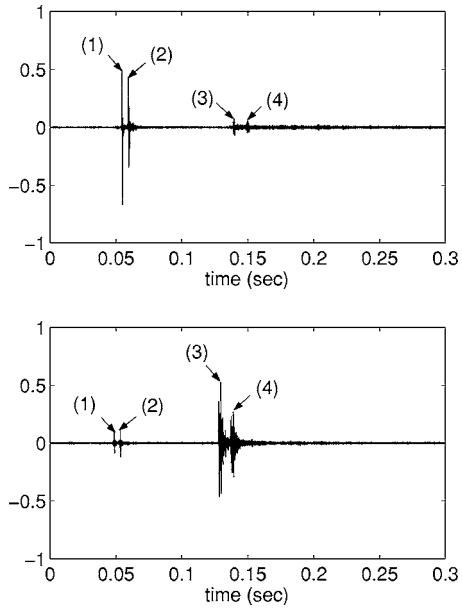

FIG. 1. Signals received from a single emitted sperm whale click. Here, assuming $z_h < z_s < z_b - z_h$ (Fig. 2), the direct path click signal (1) comes first, followed by the surface echo (2), the seafloor echo (3), and the-twice reflected seafloor/surface echo (4). Click signals reflected by the seafloor are more attenuated when propagating (by reflecting and by transmitting on a longer distance) than click signals transmitted via direct path. The amplitude of the former may anyway be greater than the amplitude of the latter, suggesting click directionality.

B. Accuracy

The depth, range, and propagation loss are estimated using a spherical propagation model, by assuming that the speed of sound is constant along the water column. The validity of this convenient hypothesis is assessed by comparing this model with a ray-tracing model. The vertical variations of the speed of sound are estimated from temperature and salinity values given by the MERCATOR oceanic model (MERCATOR, 2004). The authors have compared the propagation times of sperm whale clicks by ray tracing, in a me-

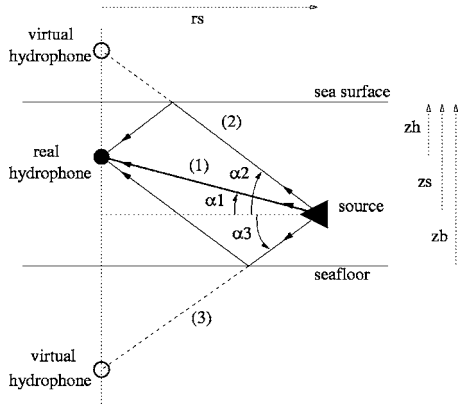

FIG. 2. Multipath ray geometry. The depths of the sperm whale, the hydrophone, and the seafloor are respectively z_s, z_h, and z_b. The sperm whale is at the range r_s from the hydrophone. The direct path ray, surface reflected ray, and seafloor reflected ray form the algebraic angles $\alpha_1(\alpha_1 > 0 \Leftrightarrow z_s > z_h)$, $\alpha_2(\alpha_2 > 0)$, and $\alpha_3(\alpha_3 < 0)$ to the horizontal. The detection of two surface/seafloor echoes serves as a substitute of a large virtual vertical hydrophone array of length $2z_b$. The whale depth and range define the geometry of the multipath rays (length and inclination).

dium of a varying speed of sound, and in a medium of a constant speed of sound. The curvature of the rays has negligible effects on the propagation times (Laplanche *et al.*, 2004). An adjustment of the single hydrophone localization technique (Thode *et al.*, 2002), taking into account speed of sound variations (Laplanche *et al.*, 2004), would indicate that in the context of the author's experiments, the assumption of a spherical propagation model would be enough. This assumption would be valid in some sensible settings, with a hydrophone and a source not too close to the sea surface, and a source at close enough range, so as to limit the interference and refraction phenomena.

The accuracy of the localization process when using the spherical propagation model is evaluated using a random variable error estimator (Laplanche *et al.*, 2004) modeling with Gaussian random variables the nonlinear error estimation method presented in Wahlberg (2004). The source depth and range are calculated from the seafloor depth, the hydrophone depth, the surface/seafloor echo delays, and the mean speed of sound (Thode *et al.*, 2002). A large number of samples (100 000) of these parameters are drawn around a mean (the measured value) with a standard deviation (half the accuracy of the measurement). The accuracies (twice the standard deviations) of the source depth and range are estimated from the depth and range samples calculated from the parameter samples. The linearity of the localization process is evaluated by estimating the kurtosis excess of the depth and range samples.

C. Click level

Acoustic waves are attenuated when propagating in the sea water and when reflecting on the sea water interfaces. Still using the spherical propagation model, the attenuation of an acoustic wave when traveling through a distance r of sea water is close to $20\log_{10}(r)+ar$ (Aubauer *et al.*, 2000). The absorption coefficient a depends on the frequency of the transmitting wave and on chemical properties of the sea water (such as pH, salinity, and temperature). In this particular case, it is close to $a=10^{-3}$ dB/m using the Thorp model. The authors consider sperm whale click central frequency at 9 kHz, given the limited band of the recording system, as compared to the 15-kHz sperm whale click central frequency (Madsen *et al.*, 2002a).

The attenuation of an acoustic wave when reflecting to the seafloor is estimated using the Hall-Watson model. It is contingent upon the incidence angle of the wave on the seafloor, the frequency of the wave, and the porosity ($0<p<1$) of the seafloor.

Using the sonar equation, the measurement of the input levels, and the estimation of the propagation attenuation of direct path transmitted sperm whale click signals and seafloor reflected click signals will then lead to an evaluation of the apparent source levels of the clicks in these ray directions (in dB *re*: 1 V/μPa). The comparison of the apparent source levels in these ray directions will then lead to an estimation of the vertical distribution of the click beam energy.

D. Sperm whale pitch angle variations

Let us consider a sperm whale at a depth z_s and a range r_s from a hydrophone, itself at a depth z_h, in a basin of depth z_b (Fig. 2). The direct path ray (1), the surface echo ray (2), and the seafloor echo ray (3) form the algebraic angles to the horizontal $\alpha_1=\text{atan}[(z_s-z_h)/r_s]$, $\alpha_2=\text{atan}[(z_s+z_h)/r_s]$, and $\alpha_3=\text{atan}[(z_s+z_h-2z_b)/r_s]$. Let p_1, p_2, and p_3 be sperm whale click level sent in these three directions. The ratios $(p_i/p_j)_{\text{dB}}=20\log_{10}(p_i/p_j)$ would lead to an estimation of the vertical click level distribution.

Sperm whales may alter the click level while diving, as discussed below. There would be no consequences of click level variations on the values of the ratios $(p_i/p_j)_{\text{dB}}$, if the sperm whale click frequency content were constant. But sperm whales, like smaller odontocetes, alter jointly click frequency and level (Madsen *et al.*, 2002a). Such a frequency emphasis would lead, after transmission, to an alteration of the measurement of the ratios $(p_i/p_j)_{\text{dB}}$, and a resulting bias in the estimation of the sperm whale pitch angle. The authors, given the limited band of their recording system, assume these effects to be negligible. Directionality variations, as directly induced by a modification of the shape of the click beam, would also alter the whale pitch angle estimation. However, such variations do not take place, as discussed below. The variations of the ratio $(p_i/p_j)_{\text{dB}}$ would then be representative of a change in the direction the sperm whale click beam.

The surface ray is directed upwards ($\alpha_2>0$), and the seafloor ray is directed downwards ($\alpha_3<0$). The upwards/downwards direction of the direct ray (Fig. 2) depends on the depth of the source ($\alpha_1>0\Leftrightarrow z_s>z_h$). For short cable surface hydrophones ($z_h\ll z_b$), the direct ray would be directed upwards, as sperm whales usually start clicking a few minutes after beginning a dive, stop clicking a few minutes before surfacing, and are usually silent at the sea surface level (Whitehead and Weilgart, 1990). For short cable hydrophones mounted on the seafloor ($z_b-z_h\ll z_b$), the direct ray would be directed downwards. For long cable hydrophones, a preliminary source localization is necessary to conclude the direction of the ray. One can demonstrate that the aperture angles defined by the direct/surface rays and the seafloor ray are greater than $\pi/4$ for a usual source range/depth setting, $\alpha_1-\alpha_3\geqslant\pi/4$ for $r_s\leqslant 2(z_b-z_h)$ and $z_s>z_h$, $\alpha_2-\alpha_3\geqslant\pi/4$ for $r_s\leqslant 2z_b$ and $z_s>z_h$.

The ratio $(p_2/p_3)_{\text{dB}}$ [or $(p_1/p_3)_{\text{dB}}$, assuming a short cable surface hydrophone] would then assess the trend in the vertical direction of the click energy. Assuming a vertical symmetry of the sperm whale click acoustic beam (Zimmer *et al.*, 2005), then $p_2/p_3=0$ dB for clicks emitted in the direction $(\alpha_2+\alpha_3)/2$, $p_2/p_3>0$ dB for clicks emitted in directions $\alpha>(\alpha_2+\alpha_3)/2$, and $p_2/p_3<0$ dB for clicks emitted in directions $\alpha<(\alpha_2+\alpha_3)/2$. For $|\alpha_2|\simeq|\alpha_3|$, the sign of $(p_2/p_3)_{\text{dB}}$ gives the vertical direction of the click beam. Assuming that sperm whales need to move their head to change the direction of the click beam, the variations of $(p_2/p_3)_{\text{dB}}$ would then indicate changes in sperm whale vertical movement. The authors define the whale pitch angle β as the angle formed by the whale's dorso-rostral axis and the horizontal.

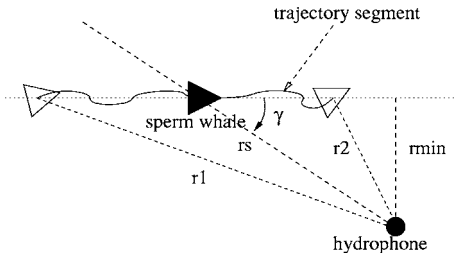

FIG. 3. Sperm whale trajectory. The sperm whale trajectory is deconstructed into segments (here a single segment, projected into the horizontal plane), the whale moving straight at constant speed in each segment. In this example, the whale moves along the segment from the range r_1 at t_1 to the range r_2 at t_2. The range of the whale while crossing the segment is $r_s = \sqrt{r_{\min}^2 + v_r^2 (t - t_{\min})^2}$, and its heading is defined by the angle γ. The range $r_{\min}$ is the horizontal distance of the segment to the hydrophone. $t_{\min}$ is the time the whale passes (or would pass) at the range $r_{\min}$.

E. Sperm whale pitch angle

The use of a sperm whale click beam pattern (Zimmer *et al.*, 2005) theoretically leads to a quantification of the values of sperm whale pitch angles. Using a whale heading to the direction γ (defined as the projection of the off-axis angle on the horizontal plane, Fig. 3) with the pitch angle β, a trigonometry calculation leads to the value of the off-axis angle δ of the hydrophone to the whale click beam:

$$\cos \delta = \cos \alpha_1 \cos \beta \cos \gamma + \sin \alpha_1 \sin \beta. \tag{1}$$

And by defining $\zeta \in]-\pi/2, \pi/2[$ such that $\tan \zeta = \cos \gamma / \tan \alpha_1$, the whale pitch angle can be calculated from the off-axis angle, by selecting $\beta \in [-\pi/2, \pi/2]$ from

$$\beta = \operatorname{asin}\left(\frac{\cos \delta \cos \zeta}{\sin \alpha_1} \right) - \zeta \quad \text{or}$$
$$\beta = \pi - \operatorname{asin}\left(\frac{\cos \delta \cos \zeta}{\sin \alpha_1} \right) - \zeta. \tag{2}$$

Using the sperm whale click beam pattern and the estimation of the click gain, the estimation of the click beam level emitted towards the hydrophone leads to the estimation of the ray off-axis angle δ, which then leads to an estimation of the whale pitch angle β. The sperm whale heading γ is estimated from the three-dimensional whale trajectory, as described below.

F. Sperm whale trajectory reconstruction

The authors estimate small scale sperm whale pitch movements from the vertical distribution of click level. Large scale movements can be estimated from the sperm whale depth and range estimations, which are found by measuring click echo delays. Large scale movements will give an estimation of the sperm whale heading γ, as required in the sperm whale pitch angle quantification process. Large scale movement will also lead to the rough three-dimensional reconstruction of sperm whale trajectories.

The authors deconstruct the sperm whale trajectory into segments, while assuming a uniform sperm whale movement (straight and at constant speed) on each segment. Let us consider a whale at depth z_1, range r_1, and time t_1 heading straight to reach the depth z_2, range r_2, and time t_2 at the constant speed v_{12} (Fig. 3). The sperm whale depth and range at a time $t_1 \leqslant t \leqslant t_2$ are

$$z_s = z_1 + v_z (t - t_1),$$
$$r_s^2 = r_{\min}^2 + v_r^2 (t - t_{\min})^2, \tag{3}$$

while the vertical and horizontal speeds of the whale are

$$v_z = (z_2 - z_1)/(t_2 - t_1),$$
$$v_r = \sqrt{r_1^2 - r_{\min}^2}/(t_1 - t_{\min}), \tag{4}$$

where $r_{\min}$ is the horizontal distance of the hydrophone to the line containing the trajectory segment, and $t_{\min}$ is the time when the whale would reach the range $r_{\min}$ (Fig. 3). Interpolating the whale depth variations during $[t_1, t_2]$ with a straight line leads to an estimation of depths z_1, z_2 and vertical speed v_z. Interpolating the squared whale range variations r_s^2 with a parabola leads to an estimation of the ranges r_1, r_2, $r_{\min}$ and the horizontal speed v_r. Such interpolations lead to an estimation of the three-dimensional geometry of the trajectory segment (a symmetry and a rotation around the hydrophone vertical axis apart), the whale speed $v_{12} = \sqrt{v_z^2 + v_r^2}$, and the whale heading γ when crossing this segment (Fig. 3).

G. Recording system

The data were recorded during two missions in the Mediterranean Sea, in the Main Channel of the Strait of Gibralter in March 2003, and in the abyssal plain offshore Toulon in August 2004, using preamplified, omnidirectional, ceramic Vinci-Technologies HC2000 hydrophones, with an output sensitivity of, −155 dB *re*: 1 V/μPa, and a frequency response flat in the frequency window [80 Hz, 13 kHz]. The signals were sampled at 44.1 kHz, PCM coded with 16 bits using a laptop with a Digigram VXpocket 440 soundcard, and recorded using the multitrack software Sek'd Samplitude. In this experiment, the signals have been highpassed at 3 kHz with a digital filter, so as to enhance the S/N ratio in the click detection process, given the relative frequency bands of sperm whale clicks and background noise. Solitary male sperm whales were recorded, from the CIRCé ship *Elsa* (10 m) during the 2003 mission, and from three Breach sail boats *Brin d'alu* (10 m), *Saoufe* (12 m), and *Zino* (14 m) during the 2004 mission.

Hydrophones were at 30-m depth in 2003 and 70 m in 2004. The sea bottom was at 900 m in 2003 and 2000 m in 2004. The depth of the seafloor was measured using marine charts and is defined as the depth below the hydrophones. The depth of the hydrophones z_h was estimated using the method presented in Thode *et al.* (2002). The seafloor is assumed to be flat at a known depth and of known porosity. The assumption of a flat seafloor is applicable in the author's examples but not in all other cases. When sperm whales are recorded in front of the continental slope, clicks reflect on the cliff into many echoes, making difficult their identification. The clear detection of seafloor echoes is a good test for substantiating the flatness of the seafloor. In both recording locations cited above, the seafloor was flat enough to identify

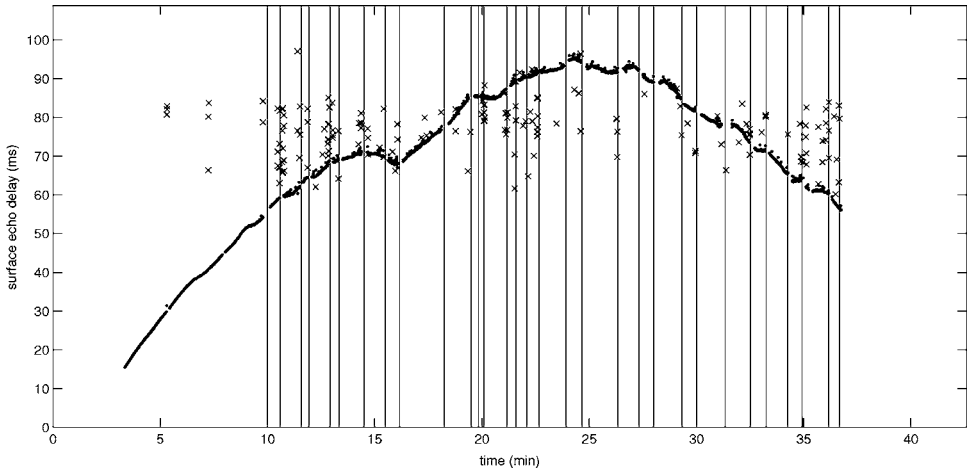

FIG. 4. Surface echo delay variations during a complete dive. A whale (2004 data set) emitted 2380 usual clicks and 31 creaks (vertical lines) during a 45-min dive. Two thousand clicks are detected using a threshold/cross-correlation algorithm, leading to 2000 measurements of the surface echo delay (dots). The algorithm wild points are also plotted (200, crosses). The whale emitted the first creak at $t=10$ min, at the depth $z_b=400$ m, with a 57-ms surface echo delay. The whale repeats 31 search/terminal phases, in this example ending with creaks.

the detected echoes. Short-scale relief variations scatter seafloor echoes and decrease the accuracy of the measurement of their delays. The consequence of this lack of accuracy is estimated using the random variable error estimation method described above.

H. Delay/level measurements

The data is recorded from isolated male sperm whales. The authors study the acoustic behavior of isolated male sperm whale individuals and do not deal with group strategies. The methods (click detection) and results would apply within this framework. Nevertheless, hypotheses on the acoustic behavior of isolated sperm whales could also help in understanding the behavior of each individual within a group.

Surface echoes are always detected jointly with direct path click signals. Twice reflected seafloor/surface echoes are also always detected with once-reflected seafloor echoes (Fig. 1). Seafloor echoes are well detected during the first 10 min of dives, when sperm whales vertically swim down and echolocate towards the seafloor (Thode *et al.*, 2002). The seafloor echo detection during the hunting stage depends on the seafloor properties (depth and relief) and the whale range. The seafloor echoes were more easily detected during the 2003 mission, by recording sperm whales from a longer range in a more shallow bassin. Surface and seafloor echo delays are measured by cross-correlating the echoes with the direct path signal. The localization and click level measurement processes have been automated by estimating the *a priori* probability density functions of the surface/seafloor delays as described in Laplanche *et al.* (2005).

III. RESULTS

A. Acoustic behavior

The variations of the surface echo delay during a complete dive of a single sperm whale (recorded during the 2004 mission) are plotted in Fig. 4. The whale emitted 2380 usual clicks and 31 creaks. The additional detection of seafloor echoes at the beginning of the dive leads to the plotting of the sperm whale depth and range variations which indicate a vertical dive, as illustrated by Madsen *et al.* (2002a) and Thode *et al.* (2002). The ICI variations during the descent are plotted in Fig. 5.

After vertically diving to 400 m, the whale repeats an acoustic pattern lasting between 30 and 180 s, composed of a block of usual clicks, hereafter referred to as *search phase*, ending with a creak or a pause, hereafter referred to as *terminal phase*. Such a notation, used by different authors regarding Blainville's beaked whales (Madsen *et al.*, 2005), is discussed below. Some of these search/terminal phases are plotted in Fig. 6. Usual click sequences during search phases (as described below) are not always such stereotypes, but similar patterns were found in 2003 and 2004. Creaks are not always emitted during the terminal phases (Madsen *et al.*, 2002b). If no creaks were detected in 2003, every search phase ended with a creak in 2004. And silences are also sometimes skipped during the terminal phases (Mullins *et al.*, 1988).

B. Click directionality and level

The estimated direct path and seafloor reflected click levels (p_1 and p_3, respectively) and ICI variations during search/terminal phases are plotted in Fig. 6. Here, the whale is located at a depth $z_s=600\pm30$ m (kurtosis excess 3×10^{-3}), and a range $r_s=3700\pm250$ m (kurtosis excess 2×10^{-3}), from a hydrophone at a depth $z_h=32\pm2$ m, in a basin of depth $z_b=880\pm30$ m and mean speed of sound $c_0=1512\pm10$ m/s, measuring surface echo delays ±0.1 ms and seafloor echo delays ±0.5 ms. The direct ray, the surface ray, and the seafloor ray then create respectively $\alpha_1=8.5\pm0.6$, $\alpha_2=9.5\pm0.6$, and $\alpha_3=-17\pm1.3$ (kurtosis excess 5×10^{-2}) degree angles with the horizontal (Fig. 2). The 0 dB value of the level ratio $(p_1/p_3)_{\mathrm{dB}}$ would then correspond to a click emitted slightly downwards, forming a $\alpha=(\alpha_1+\alpha_3)/2=-4.2°\pm0.6°$ angle with the horizontal.

The sperm whale click beam pattern is extremely narrow $[(p_1/p_3)_{\mathrm{dB}}=-30$ at $t=780$ s, Fig. 6]. Sperm whale clicks are also very powerful (Fig. 7), reaching 210 dB *re*: 1 μPa (pp) (limiting to the band [3 kHz, 13 kHz]). These two results are consistent with previous findings, i.e., the sperm whale click generator can also serve as an echolocation system (Mohl *et al.*, 2003).

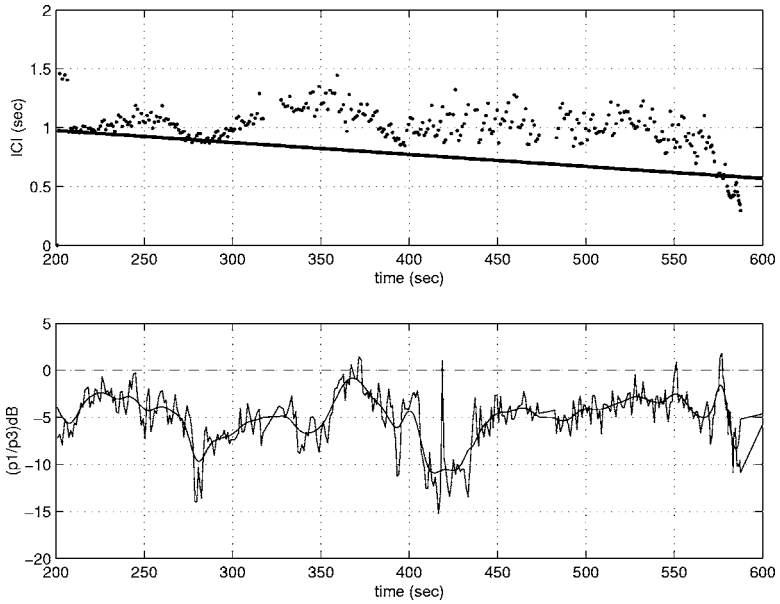

FIG. 5. ICI and pitch angle variations during the descent. ICI during the first 10 min of a dive (dots, at the top). Using the echolocation model, the estimated ICI during the descent, when using targets vertically below the whale inside the prey layer, is also plotted (solid line). The pitch angle variations are plotted [ratio $(p_1/p_3)_{\mathrm{dB}}$, raw values and moving average, at the bottom]. The bissecting angle [for which $(p_1/p_3)_{\mathrm{dB}}=0$] between the direct ray and the bottom ray varies from $-39° \rightarrow -27°$ to the horizontal for $t=200 \rightarrow 600$ s. The whale pitch angle is then greater than 30° during the descent [as $(p_1/p_3)_{\mathrm{dB}}<0$]. The ICI variations are correlated to the pitch angle variations. Pitch angle variations suggest a three-phase pitch movement ($(t=200 \rightarrow 250 \rightarrow 280$ s, $t=280 \rightarrow 350 \rightarrow 400$ s, $t=400 \rightarrow 480 \rightarrow 570$ s). The ICI plotting ends ([580,600] s) with the first search phase inside the prey layer.

C. Sperm whale movements

In this study, only relative (and not absolute) values of sperm whale pitch angles are estimated, by using the ratio $(p_1/p_3)_{\mathrm{dB}}$. The complexity of the sperm whale click beam pattern as formed by various components of different levels and frequency contents (Zimmer *et al.* 2005), the lack of knowledge in the variations amongst sperm whale individuals of this click beam pattern, the lack of knowledge in the click level variations, and the use by the authors of a limited bandwith recording system kept the authors from conducting a reliable pitch angle quantification process [using Eq. (2)].

Sperm whale pitch angle variations are plotted during a descent (Fig. 5) and during two successive search/terminal phases (Fig. 6). The respective acoustic activity is also plotted. The sperm whale pitch movements go together with the rhythmic variations while descending (Fig. 5). The sperm whale pitch movements while hunting are periodic and in sync with the rhythmic variations (Fig. 6). In the next section, the authors propose a hypothesis on the sperm whale biosonar, so as to clarify this correlation between the sperm whale acoustical and physical activity.

IV. DISCUSSION

A. Echolocation model

The recorded sperm whales emitted bursts of usual clicks each lasting 5–15 s during the search phases, followed by clicks at a higher rate (creaks) and/or silence periods during the terminal phases (Fig. 6). As shown in Fig. 7, during the search phase, clicks from a burst are first emitted every $\mathrm{ICI}_{\mathrm{max}}$ second. The interclick interval then progressively decreases to $\mathrm{ICI}_{\mathrm{min}}$, before gradually increasing to a new maximum $\mathrm{ICI}'_{\mathrm{max}}$. These variations of the interclick interval are correlated to those of the levels p_1 and p_3 of the direct path/seafloor reflected click signals. During the search phases, 20-dB level peaks are simultaneously detected in both direct path and seafloor path directions. Such peaks were only detected when recording from directions close to the whale axis, as discussed below. Click level maximums p_{max} emitted towards these paths are detected when the interclick interval of a 5–15-s burst reaches its maximum $\mathrm{ICI}_{\mathrm{max}}$. And click level minimums p_{min} are detected when the interclick interval reaches its minimum $\mathrm{ICI}_{\mathrm{min}}$ (Fig. 7).

Four hypotheses could explain such apparent click level

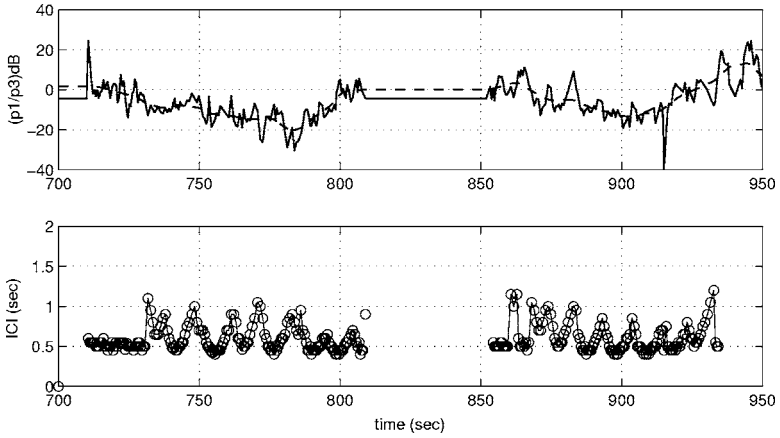

FIG. 6. Sperm whale pitch angle and ICI during two successive search/terminal phases. Relative sperm whale pitch angle $(p_1/p_3)_{\mathrm{dB}}=20\log_{10}(p_1/p_3)$ (solid line) and moving average (dashed line, at the top). It is positive for clicks emitted upwards, and negative for click emitted downwards. ICI (at the bottom).

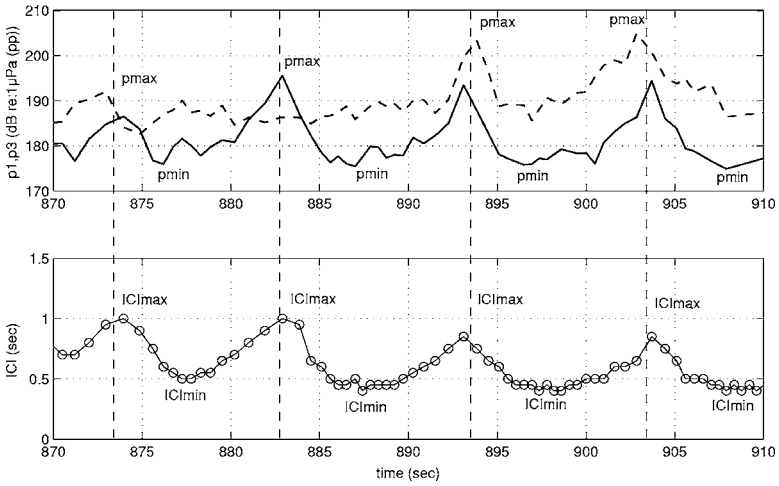

FIG. 7. Sperm whale click level and ICI during a search phase. (Top) Click source level p_1 emitted (upwards) towards the direct path (solid line), and click source level p_3 emitted (downwards) towards the seafloor reflected path (dashed line). (Bottom) ICI. Peaks of source level in p_1 and p_3 are detected when the sperm whale clicks at the lowest rate (ICI=$\mathrm{ICI}_{\max}$), and minimum values of level are detected when the sperm whale clicks at the highest rate (ICI=$\mathrm{ICI}_{\min}$). The difference of click level within a click burst may reach 20 dB.

variations: vertical movement of the sperm whale head (pitch), horizontal movement (yaw), click directionality control, and click level control. The first hypothesis is rejected given the pitch angle variations plotted in Fig. 6. The second hypothesis is rejected, as maximums/minimums of click levels are always in sync with maximums/minimums of ICI (this also applies to the first hypothesis). The whale would have to systematically direct its click beam towards the hydrophone when clicking at a slow rate, and turn its head when clicking faster, which is highly unlikely. The third hypothesis would suggest that sperm whales would emit highly directional clicks when clicking fast, and widen the click beam when clicking slower. The fourth hypothesis would suggest that sperm whales would send less powerful clicks when clicking fast, and increase the click level when clicking slower. Homogenous off-axis angle variations of a measured sperm whale click beam pattern (Zimmer *et al.* 2005) would suggest that sperm whales would not change the click directionality when diving. The variations in click level given in Fig. 7 would rather suggest click level control.

These click level variations are in sync with the ICI variations, suggesting click level and ICI adjustment to the target range, as found on some smaller odontocetes, as discussed below. Yet some sperm whale tag recordings show no correlation between click level and ICI variations (Madsen *et al.*, 2002a). Click level variations as plotted in Fig. 7 were not detected when making off-axis recordings (especially in 2004, when recording from a shorter range). The authors then suggest that these level variations would only appear, using Mohl *et al.* (2003) notation, on the forward echolocation pulse (P_1). The initial backward pulse (P_0) level would not be altered by this process. Off-axis recordings, from a distant towed hydrophone or a tag attached to the whale's back, would then not detect the click level variations as plotted in Fig. 7. Still, what would explain P_0 20-dB level variations detected from the tags (Madsen *et al.*, 2002a)? Would click level adjustment to target range take place while transmitting within the nasal complex, and a different click level adjustment (to target kind?) take place when emitting the initial pulse at the phonic lips? Understanding click level variations may be a key point in learning the workings of the sperm whale's biosonar. The hypothesis on click level (and ICI) control to target range would lead to sensible results, as discussed below, and provide some clues regarding the understanding of the sperm whale's biosonar.

Results from biosonar tests carried out on some smaller odontocetes suggest click level control (Au and Herzing, 2003; Au and Wursig, 2004; Rasmussen and Miller, 2002) with target range. Dolphins would adjust the click level by 6 dB for every halved or doubled target range. ICI control has also been observed on bottlenose dolphins (Au, 1993). Such an acoustic behavior does not seem to be characteristic of all ondontocete species (Madsen *et al.*, 2005). The sperm whale's and dolphin's biosonar share many similarities (Madsen *et al.*, 2002a), and, given measurements illustrated in Fig. 7, it would be interesting to assess the consistency of the hypothesis of click level and ICI control to target range on sperm whales.

The author's echolocation model speculates that sperm whales control click level and ICI to target range as bottlenose dolphins do. The click level variations presented in Fig. 7 would then result in adjustments by 6 dB for every halved or doubled target range. The ICI would directly depend on the whale's target range r, $\mathrm{ICI}=2r/c_0+t_{\mathrm{proc}}$ (Au, 1993). The constant processing delay t_{proc} would be the delay between the reception of the echo of a click and the production of the next click.

B. Processing delay

Sperm whales would adjust the level of clicks to compensate for the one-way transmission loss between the whale and its target. If a click emitted with a 0-dB gain aims at a target at a range r, a click emitted with a gain G (dB) would then aim at a target at a range $10^{G/20}r$, assuming only spherical spreading loss. Then, by labeling $r_{\max}$ and $r_{\min}$ the range of the targets aimed using clicks at the rates $1/\mathrm{ICI}_{\max}$ and $1/\mathrm{ICI}_{\min}$, one arrives at $r_{\max}=10^{G/20}r_{\min}$ with $G=20$ dB, leading to

$$r_{\max} \simeq \alpha r_{\min} \quad \text{with } \alpha = 10. \tag{5}$$

Assuming a processing time t_{proc} of the click echoes independent of the range of the target, then

$$\mathrm{ICI}_{\min} = \frac{2r_{\min}}{c_0} + t_{\mathrm{proc}} \quad \text{and} \quad \mathrm{ICI}_{\max} = \frac{2r_{\max}}{c_0} + t_{\mathrm{proc}}, \qquad (6)$$

leading to

$$t_{\mathrm{proc}} = \frac{\alpha \mathrm{ICI}_{\min} - \mathrm{ICI}_{\max}}{\alpha - 1}. \qquad (7)$$

From the ICI values given for the first plotted 5–15-s click burst ($\mathrm{ICI}_{\max}=1$ s and $\mathrm{ICI}_{\min}=0.5$ s) (Fig. 7), one can find the processing delay $t_{\mathrm{proc}}=0.45$ s. This value would be equal to the minimum ICI corresponding to the shortest target echolocation range ($r=0$). This value ICI=0.45 s would set the limit of validity of the sperm whale echolocation model described above. The same 0.45-s value has been found in a statistical analysis, setting the limit between usual clicks and creaks (Zimmer *et al.*, 2005). Sperm whale acoustic activity then splits into two distinct modes, usual clicking ($\mathrm{ICI} \geqslant 0.45$ s) and creaking ($\mathrm{ICI} < 0.45$ s), in view of the temporal pattern of the click sequences (search phase/terminal phase), the click rate production (Zimmer *et al.*, 2005), and the echolocation model limit. The delay t_{proc} has been defined as the delay between the reception of the echo of a click and the production of the next click. It may be interpreted as the sum of the processing delay of the first click target echo, and the delay required to produce the next click. The distinction between usual clicks and creaks mentioned above would then suggest that sperm whales would either process usual click and creak echoes differently, or produce usual clicks and creak clicks differently.

The echolocation model is now calibrated by estimating $t_{\mathrm{proc}}=0.45$ s. Its consistency is then evaluated during sperm whale descent and hunting.

C. Scan during the descent

Sperm whales emit echolocation clicks during most of the descent. What do they echolocate? Some authors have suggested that sperm whales echolocate to the sea floor. ICI variations are indeed correlated to the whale depth variations and consistent with a vertical scan of the sea bottom (Thode *et al.*, 2002). The authors have in this case used the echolocation model $\mathrm{ICI}=2r/c_0$, close to the one presented here but with a null processing delay. The seafloor scanning hypothesis, however, would not seem to be correct. Different authors have shown that the ICI of click sequences emitted during the descent may sometimes be much shorter than the two-way travel time to the sea bottom (Zimmer *et al.*, 2005). These authors have suggested that sperm whales rather scan their prey layer while descending. ICI variations during the descent are indeed correlated to whale pitch angle variations (Zimmer *et al.*, 2003).

The authors apply the echolocation model $\mathrm{ICI}=2r/c_0 + 0.45$ s to the descent. Pitch variations correlated to ICI variations are also noticed using the method presented by the authors (Fig. 5). The authors assess the consistency of the aforementioned hypothesis of prey layer scanning while descending. In the example of Fig. 4, the prey layer is at 400 m, which is equal to the depth of the sperm whale when emitting the first creak. Using the echolocation model, the estimated ICI during the descent, when using targets vertically below the whale inside the prey layer, is plotted in Fig. 5. Measured and estimated ICIs are equal at $t=200$, 280, 400, and 570 s. The measured ICI is greater than the estimation between these instants; it increases for $t=200\rightarrow250$ s, $t=280\rightarrow350$ s, and $t=400\rightarrow480$ s; and decreases for $t=250\rightarrow280$ s, $t=350\rightarrow400$ s, and $t=480\rightarrow570$ s. These variations are correlated to those of the estimated pitch angle (Fig. 5). This would suggest, as mentioned in Zimmer *et al.* (2003), that the sperm whale indeed echolocated vertically at the prey layer (at $t=200,280,400$ s), and echolocated at a horizontal prey layer strip by a vertical movement of its body while descending. The sperm whale pitch angle and the prey layer strip geometry can be quantified using the echolocation model. The sperm whale would start echolocating vertically, and make three scans of the prey layer, with pitch angles varying to $90°\rightarrow60°\rightarrow90°$ for $t=200\rightarrow250\rightarrow280$ s, $90°\rightarrow30°\rightarrow50°$ for $t=280\rightarrow350\rightarrow400$ s, and $50°\rightarrow20°$ for $t=400\rightarrow570$ s, before entering the prey layer and hunting. Such pitch estimations are consistent with those found using digital tags (Zimmer *et al.*, 2003). The prey strip is estimated as 600 m long (from the whale pitch angle and distance to the prey layer) and 80 m deep (from the whale pitch angle and its ICI standard deviation). The results presented in this section would suggest that sperm whales would indeed echolocate at their prey layer while descending, and follow an acoustic behavior which would be close to the aforementioned echolocation model.

D. Whale heading

The authors then estimate the whale trajectory from the interpolation of the whale range variations between $t_1=16$ min and $t_2=37$ min (Fig. 8). Such variations of the whale range could be explained assuming a straight trajectory at a constant speed, as described above. Based on this hypothesis, the whale would move, in the example of Fig. 8, in a straight line at $v_r=0.8$ m/s from the range $r_1=480$ m to the range $r_2=650$ m, passing at $t_{\min}=25$ min at the minimum range $r_{\min}=200$ m. The whale would then swim at a constant heading within the prey layer. Such behavior is consistent with surface visual observations, describing a general constant heading movement of male sperm whales based on the location of the surface breathing points (Watkins *et al.*, 1999). The authors' measurements would support the hypothesis of a sperm whale broken-line trajectory, whereas trajectory reconstructions using tagged accelerometers would support more chaotic underwater behavior (Zimmer *et al.*, 2005). The straightforward movement pointed out by the authors is a large scale movement and does not prevent short scale chaotic movements when closing on prey (Miller *et al.*, 2004a).

E. Scan during the hunt

Sperm whales would move straightforward while hunting within the prey layer. The whale's physical activity while crossing the prey layer is estimated from the pitch angle variations, as described below. Its acoustic activity and the

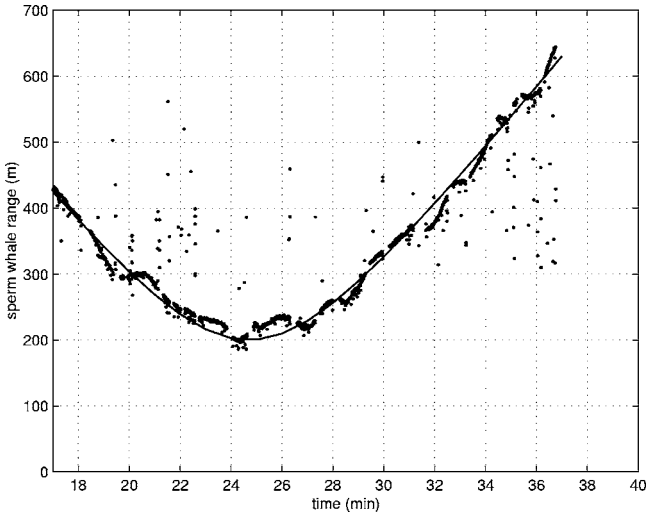

FIG. 8. Sperm whale trajectory reconstruction. Sperm whale range variations (dots) and parabola interpolation (solid line) between $t_1=16$ min and $t_2=37$ min. The whale would move in a straight line at $v_r=0.8$ m/s from the range $r_1=480$ m to the range $r_2=650$ m, passing at $t_{\min}=25$ min at the minimum range $r_{\min}=200$ m.

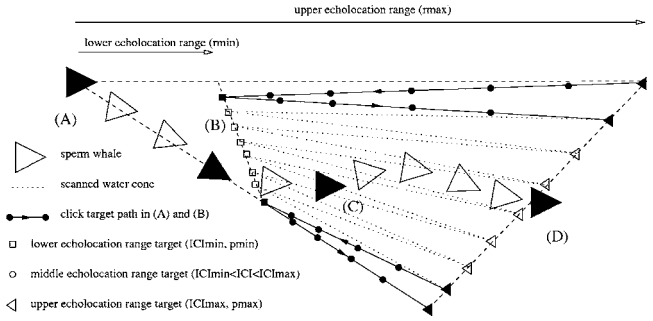

FIG. 9. Sperm whale scan during a search phase. The sperm whale would start scanning the top of a cone of water [from (A), beginning of the search phase], carry on the scan by gradually pointing downwards [to (B)], gradually (but faster) point back upwards [to (C)], before entering the scanned zone and feeding [to (D), end of the terminal phase, beginning of the next search phase]. Click target ranges are plotted here only during the beginning of the first part of a search phase, from (A) to (B).

range of the whale's targets are estimated from the ICI using the echolocation model. The conjunction of all these bits of information would lead to the authors' hypothesis asserting that sperm whales would methodically scan a cone-shaped water mass searching for prey with usual clicking at depth. Sperm whales would then attack while silencing or creaking. This methodic scan is a hypothesis, and a consequence of the assessed assumption that sperm whales control ICI when searching for their prey.

The sperm whale's physical activity is estimated from the pitch angle variations (Fig. 6). In this example, the sperm whale would start usual clicking aiming horizontally ($p_1/p_3=0$ dB). It would then progressively point downwards ($p_1/p_3<0$ dB, decreasing), before gradually (but more quickly) coming back to a horizontal line ($p_1/p_3<0$ dB, increasing). During the terminal phase, the sperm whale would start with a horizontal click beam and move upwards, increasing its click rate or silencing, before aiming back horizontally so as to start a new search/terminal phase. The low S/N ratio during the terminal phases makes difficult the assessment of the acoustical/physical activity of the whale. Nevertheless, the fast click activity and silence would suggest feeding (Miller *et al.*, 2004a).

From the value of the delay t_{proc}, the authors estimate the ranges $r_{\min}$ and $r_{\max}$ during the search phases. At the beginning of the plotted search phases ($\text{ICI}_{\max}=1$ s and $\text{ICI}_{\min}=0.5$ s), the sperm whale would aim at targets located at $r_{\min}\simeq 42$ m and $r_{\max}\simeq 420$ m. At the end of the search phase ($\text{ICI}_{\max}=0.8$ s and $\text{ICI}_{\min}=0.45$ s), it would aim at targets located at $r_{\min}\simeq 30$ m and $r_{\max}\simeq 300$ m.

Given the echolocation and the progressive variations of the ICI during a single 5–15-s click burst, decreasing from $\text{ICI}_{\max}$ to $\text{ICI}_{\min}$ before reincreasing to a maximum $\text{ICI}'_{\max}$ (Fig. 7), the authors suggest that the whole would echolocate between the ranges $r_{\max}$ and $r_{\min}$ (ICI decreasing from $\text{ICI}_{\max}$ to $\text{ICI}_{\min}$) and then back to a maximum range $r'_{\max}$ (ICI increasing from $\text{ICI}_{\min}$ to $\text{ICI}'_{\max}$) every 5–15-s burst of clicks.

The authors suggest that during the search phase sperm whales would methodically scan a cone-shaped mass of water searching for prey (Fig. 9). Each scan would last 5–15 s and would analyze the water twice between the upper ranges $r_{\max}$, the lower range $r_{\min}=r_{\max}/\alpha$, and the upper range $r'_{\max}$. This scan would suggest that each sperm whale click is generated to aim in a specific direction at a specific range. Sperm whales would move physically to change the click beam direction, and control level and ICI to change the click target range. Similar results have been found during the sperm whale descent studied above.

There are some variations in the geometric features of the scanned water mass: variations within a dive, between dives, and from one sperm whale to another. These geometric features would depend on the number of scans, the ICI minimum and maximum values, the duration of the search phase, and the whale pitch angle variations. For instance, the cones scanned by the whale tracked in 2004 would be shorter (lower ICI) and thinner (only three to four 5–15-s click bursts) than the cone scanned by the whale tracked in 2003, whose ICI sequence is plotted in Fig. 7. This result suggests that sperm whales would, if methodically scanning the prey layer when hunting, adapt their scanning depending on existing prey.

V. CONCLUSIONS

The authors have estimated sperm whale pitch angle relative (not absolute) values by studying multipaths at a single hydrophone. Such an estimation enables the authors to analyze sperm whale physical activity during different dive stages: descent and hunt. In both cases, the whale's physical activity correlates to the whale's acoustic activity.

The authors then point out a correlation between click level variations and ICI. The hypothesis explaining such a correlation would be click level control: sperm whales would click slowly at a high source level and faster at a lower source level. Inspired by results found for small odontocete species, the authors propose an echolocation model, *click focusing*. This echolocation model specifies that sperm whales would aim at closer targets while emitting clicks with lower source level at higher rhythmic rate, and aim at farther

targets emitting clicks with higher source level and slower rhythmic rate. Based on this hypothesis, the authors compute an echolocation model estimating the sperm whale target range from the ICI.

The authors find a click processing delay of 0.45 s, setting the limit of validity of the sperm whale echolocation model. This value is equal to what has been found by different sources to be the limit between usual clicks and creaks. The authors apply this echolocation model during the descent. The coherency of the model would suggest that sperm whales would indeed, as suggested by different authors, echolocate at the prey layer while vertically descending. Estimated sperm whale pitch angle variations based on this hypothesis are consistent with those found when using tags.

The authors then apply the echolocation model during the hunt at the prey depth. Periodic sperm whale target range variations and pitch movements suggest that sperm whales would scan the water before attacking when foraging. The authors estimate the scanned water mass dimension from the echolocation model.

Finally, the animal range interpolation suggests that sperm whales move at constant heading and speed while hunting. The synthesis of all the results leads the authors to suggest that sperm whales would follow a dive-scale strategy when foraging. Sperm whales would preanalyze their prey layer while descending, and cross this layer by repeating a methodic scanning/catching technique, before resurfacing.

ACKNOWLEDGMENTS

Thanks to Christophe Guinet of the CEBC-CNRS (Centre d'Etude Biologique de Chizé, France) for initiating this project. Recordings during the 2003 mission could not have been made without the help of Renaud De Stephanis from CIRCé (Conservation Information and Research on Cetaceans, Spain) and Xavier Demoulin from MAREE (Lorient, France). Thanks to the Association Breach (http://www.breach-asso.org, France) for providing boats, skillful skippers, and ecovolunteers during the 2004 mission, and to the Association KetoΣ (France) for undertaking the airborne survey. The MERCATOR Project (France) helped in providing the oceanographic data required for this project. This study was sponsored by the Association Dirac (France). Many thanks to the two anonymous reviewers for their contribution in improving the clarity and the rigorousness of this paper. Also thanks to L. Adam, M. Adam, and M. Campbell for refining the English. Many thanks to F. Rondepierre, L. Mortier (LODYC, Laboratoire d'Océanographie Dynamique et de Climatologie, France), N. Pérez Gimeno (Laboratorio de Acústica y Vibraciones de la Universidad de Cádiz, Spain), V. Toumazou (MERCATOR), and G. Vinay (MERCATOR).

Arnbom, T., and Whitehead, H. (**1989**). "Observations on the composition and behavior of groups of female sperm whales near the Galapagos Islands," Can. J. Zool. **67**, 1–7.

Au, W. (**1993**). *The Sonar of Dolphins* (Springer-Verlag, New York).

Au, W., and Herzing, D. (**2003**). "Echolocation signals of wild Atlantic spotted dolphins (*stenella frontalis*)," J. Acoust. Soc. Am. **113**, 598–604.

Au, W., and Wursig, B. (**2004**). "Echolocation signals of dusky dolphins (*lagenorhynchus obscurus*) in Kaikoura, New Zealand," J. Acoust. Soc. Am. **115**, 2307–2313.

Aubauer, R., Lammers, M., and Au., W. (**2000**). "One-hydrophone method of estimating distance and depth of phonating dolphins in shallow water," J. Acoust. Soc. Am. **107**, 2744–2749.

Clay, C. S., and Medwin, H. (**1977**). *Acoustical Oceanography: Principles and Applications* (Wiley-Interscience, New York).

Delory, E., Andr, M., and Potter, J. (**2002**). "An ambient noise imaging sonar to detect nonvocalizing sperm whales," *Proceedings of the European Cetacean Society Meeting*.

Fristrup, K., and Harbison, G. (**2002**). "How do sperm whales catch squids?" Marine Mammal Sci. **18**(1), 42–54.

Gisiner, R. (**1998**). Workshop on the effects of anthropogenic noise in the marine environment, pp. 75–96.

Jaquet, N. (**1996**). "How spatial and temporal scales influence understanding of sperm whale distribution: A review," Mammal Rev. **26**, 51–65.

Jaquet, N., Dawson, S., and Douglas, L. (**2001**). "Vocal behavior of male sperm whales: Why do they click?" J. Acoust. Soc. Am. **109**, 2254–2259.

Johnson, M., and Tyack, P. (**2003**). "A digital recording tag for measuring the response of wild marine mammals to sound," IEEE J. Ocean. Eng. **28**(1), 3–12.

Laplanche, C., Adam, O., and Motsch, J. (**2004**). "Accuracy in the localization of sperm whales resident in the Strait of Gibraltar using one hydrophone," Can. Acoust. **32**, 161–166.

Laplanche, C., Adam, O., Lopatka, M., and Motsch, J. (**2005**). "Real time sperm whale depth estimation using passive acoustics," *IEEE Oceans'05 Europe Conf.*

Madsen, P., Payne, R., and Kristiansen, N. (**2002a**). "Sperm whale sound production studied with ultrasound time/depth-recording tags," J. Exp. Biol. **205**, 1899–1906.

Madsen, P., Wahlberg, M., and Mohl, B. (**2002b**). "Male sperm whale (*physeter macrocephalus*) acoustics in a high-latitude habitat: implications for echolocation and communication," Behav. Ecol. Sociobiol. **53**, 31–41.

Madsen, P., Johnson, M., Aguilar de Soto, N., Zimmer, W., and Tyack, P. (**2005**). "Biosonar performance of foraging beaked whales (*mesoplodon densirostris*)," J. Exp. Biol. **208**, 181–194.

Mccarey, K., and Rubin, J. (**1998**). "Sea monsters: Search for the giant squid," produced by National Geographic Television.

MERCATOR (**2004**). "Mercator working for operational oceanography, oceanic analyses and forecasts," http://www.mercator-ocean.fr/en/.

Miller, P., Johnson, M., and Tyack, P. (**2004a**). "Sperm whale behavior indicates the use of echolocation click buzzes 'creaks' in prey capture," Proc. R. Soc. London, Ser. B **271**, (1554), 2239–2247.

Miller, P., Johnson, M., Tyack, P., and Terray, E. (**2004b**). "Swimming gaits, passive drag and buoyancy of diving sperm whales *physeter macrocephalus*," J. Exp. Biol. **207**, 1953–1967.

Mohl, B., Wahlberg, M., and Madsen, P. (**2000**). "Sperm whale clicks: Directionality and source level revisited," J. Acoust. Soc. Am. **107**, 638–648.

Mohl, B., Wahlberg, M., and Madsen, P. (**2003**). "The monopulsed nature of sperm whale clicks," J. Acoust. Soc. Am. **114**, 1143–1154.

Mullins, J., Whitehead, H., and Weilgart, L. (**1988**). "Behaviour and vocalizations of two single sperm whales, *physeter macrocephalus*, off Nova Scotia," Can. J. Fish. Aquat. Sci. **45**, 1736–1743.

Rasmussen, M., and Miller, L. (**2002**). "Source levels of clicks from free-ranging white-beaked dolphins (*lagenorhynchus albirostris* gray 1846) recorded in Icelandic waters," J. Acoust. Soc. Am. **111**, 1122–1125.

Santos, M., Clarke, M., and Pierce, G. (**2001**). "Assessing the importance of cephalopods in the diets of marine mammals and other top predator: Problems and solutions," Fisheries Res. **52**, 121–139.

Smith, S., and Whitehead, H. (**2000**). "The diet of Galapagos sperm whales (*physeter macrocephalus*) as indicated by fecal sample analysis," Marine Mammal Sci. **16**(2), 315–325.

Thode, A., Mellinger, D., and Stienessen, S. (**2002**). "Depth-dependant acoustic features of diving sperm whales (*physeter macrocephalus*) in the Gulf of Mexico," J. Acoust. Soc. Am. **112**, 308–321.

Wahlberg, M. (**2002**). "The acoustic behavior of diving sperm whales observed with a hydrophone array," J. Exp. Mar. Biol. Ecol. **281**, 53–62.

Wahlberg, M. (**2004**). "Comparing a linear with a non-linear method for acoustic localization," Can. Acoust. **32**, 125–131.

Watkins, W., and Schevill, W. (**1977**). "Sperm whale codas," J. Acoust. Soc. Am. **62**, 1485–1490.

Watkins, W., Daher, M., and DiMarzio, N. (**1999**). "Sperm whale surface activity from tracking by radio and satellite tags," Marine Mammal Sci. **15**(4), 1158–1180.

Watkins, W., Daher, M., and Fristrup, K. (**1993**). "Sperm whales tagged with transponders and tracked underwater by sonar," Marine Mammal Sci. **9**(1), 55–67.
Weilgart, L. (1990). "Vocalizations of the sperm whale, *physeter macrocephalus*, off the Galapagos Islands as related to behavioral and circumstantial variables," Ph.d. thesis, Dalhousie University, Halifax.
Whitehead, H., and Weilgart, L. (**1990**). "Click rates from sperm whales," J. Acoust. Soc. Am. **87**, 1798–1806.
Zimmer, W., Johnson, M., D'Amico, A., and Tyack, P. (**2003**). "Combining data from a multisensor tag and passive sonar to determine the diving behavior of a sperm whale (*physeter macrocephalus*)," IEEE J. Ocean. Eng. **28**(1), 13–28.
Zimmer, W., Tyack, P., Johnson, M., and Madsen, P. (**2005**). "Three-dimensional beam pattern of regular sperm whale clicks confirms bent-horn hypothesis," J. Acoust. Soc. Am. **117**, 1473–1485.

Behavioral and auditory evoked potential audiograms of a false killer whale (*Pseudorca crassidens*)

Michelle M. L. Yuen,[a] Paul E. Nachtigall, and Marlee Breese
Marine Mammal Research Program, Hawaii Institute of Marine Biology, University of Hawaii, Kailua, Hawaii 96744-1106

Alexander Ya. Supin
Institute of Ecology and Evolution, Russian Academy of Sciences, 33 Leninsky Prospekt, 119071 Moscow, Russia

(Received 21 December 2004; revised 13 June 2005; accepted 5 July 2005)

Behavioral and auditory evoked potential (AEP) audiograms of a false killer whale were measured using the same subject and experimental conditions. The objective was to compare and assess the correspondence of auditory thresholds collected by behavioral and electrophysiological techniques. Behavioral audiograms used 3-s pure-tone stimuli from 4 to 45 kHz, and were conducted with a go/no-go modified staircase procedure. AEP audiograms used 20-ms sinusoidally amplitude-modulated tone bursts from 4 to 45 kHz, and the electrophysiological responses were received through gold disc electrodes in rubber suction cups. The behavioral data were reliable and repeatable, with the region of best sensitivity between 16 and 24 kHz and peak sensitivity at 20 kHz. The AEP audiograms produced thresholds that were also consistent over time, with range of best sensitivity from 16 to 22.5 kHz and peak sensitivity at 22.5 kHz. Behavioral thresholds were always lower than AEP thresholds. However, AEP audiograms were completed in a shorter amount of time with minimum participation from the animal. These data indicated that behavioral and AEP techniques can be used successfully and interchangeably to measure cetacean hearing sensitivity. [DOI: 10.1121/1.2010350]

PACS number(s): 43.80.Lb [JAS] Pages: 2688–2695

I. INTRODUCTION

In 1966, Johnson measured the first complete audiogram of an individual Atlantic bottlenose dolphin, *Tursiops truncatus* (Johnson, 1966). The results indicated that the animal's range of sensitivity to pure tones was from 75 Hz to 150 kHz, an exceptionally wide range covering more than 100 kHz and 11 octaves. The significant data collected were considered to be an innovative breakthrough in marine mammal science, where a single animal can be used to demonstrate the capability that may exist within a species. The use of behavioral, psychometric techniques became the standard to investigate hearing thresholds of captive odontocetes. Since this experiment, behavioral audiograms measuring the auditory sensitivity have been collected for the harbor porpoise, *Phocoena phocoena* (Andersen, 1970; Kastelein *et al.*, 2002), killer whale, *Orcinus orca* (Hall and Johnson, 1972), Amazon River dolphin, *Inia geoffrensis* (Jacobs and Hall, 1972), beluga whale, *Delphinapterus leucas* (White *et al.*, 1978), Eastern Pacific bottlenose dolphin, *Tursiops spp.* (Ljungblad *et al.*, 1982), false killer whale, *P. crassidens* (Thomas *et al.*, 1988), Chinese River dolphin, *Lipotes vexillifer* (Wang *et al.*, 1992), Risso's dolphin, *Grampus griseus* (Nachtigall *et al.*, 1995), tucuxi, *Sotalia fluviatilis guianensis* (Sauerland and Dehnhardt, 1998), and the striped dolphin, *Stenella coeruleoalba* (Kastelein *et al.*, 2003).

For more than 30 years, psychometric research with marine mammals developed based on the success using a single or few research subjects. Considerable hearing threshold differences between individual animals of different ages and sexes have been demonstrated in previous behavioral hearing research (Ridgway and Carder, 1997), differences that may not be evident when only a single animal subject is used. Such psychometric analysis was constrained by the significant investment to train the subjects for the behavioral paradigm and to maintain the animals in captive environments to conduct thorough research.

An alternative to the psychometric methods of measuring behavioral audiograms was the collection of auditory evoked potentials (AEP). When an acoustic stimulus is presented, the cells within the auditory pathway are excited. When this occurs, AEPs are the far-field electrophysiological recording of the resulting small voltages generated by the brain's neural activity. Measuring the evoked responses to stimuli became a valuable and advantageous method to collect auditory data, requiring minimal training and reduced time. The characteristics of AEPs were first described using invasive, intracranial electrodes in the dolphin brainstem (Bullock *et al.*, 1968) and in the cerebral cortex (Popov *et al.*, 1986), and using noninvasive extracranial electrodes (Ridgway *et al.*, 1981). In more recent times, noninvasive techniques have been employed to investigate auditory brainstem responses (ABR), a type of AEP involving a series of five to seven "waves" evoked by clicks or short tone bursts of acoustic stimuli. ABRs to tone pips were successfully

[a]Electronic mail: myuen@hawaii.edu

 0001-4966/2005/118(4)/2688/8/$22.50

used to measure hearing thresholds and collect audiograms in dolphins (Popov and Supin, 1990a, 1990c).

Measuring hearing thresholds was more precise when using envelope-following responses (EFR), the occurrence in which ABRs follow the envelope of a sinusoidally amplitude-modulated (SAM) tone burst (Dolphin *et al.*, 1995; Supin and Popov, 1995). The advantages of using SAM stimuli instead of brief tone pips were: (1) the intensity of a long tone burst was characterized by its rms sound pressure, which could provide a basis for correct comparison of behavioral and AEP data, and (2) EFRs contained many evoked potential cycles instead of one, increasing the precision of the response detection, in particular, by the use of Fourier analysis.

ABR- and EFR-based audiograms were collected in a number of odontocetes, including the beluga whale, *D. leucas* (Popov and Supin, 1987), bottlenose dolphin, *T. truncatus* (Popov and Supin, 1990a), Amazon River dolphin, *I. geoffrensis* (Popov and Supin, 1990b), false killer whale, *P. crassidens* (Dolphin *et al.*, 1995), common dolphin, *Delphinus delphis* (Popov and Klishin, 1998), and killer whale, *O. orca* (Szymanski *et al.*, 1999).

Although measuring AEPs has proven to be a reliable technique for investigating the hearing sensitivity of odontocetes, it remained unresolved how the electrophysiological thresholds compared with the thresholds collected by behavioral techniques. Some analyses attempted to compare data gathered using the two different methods (Szymanski *et al.*, 1999). In that study, two killer whales were used to measure both ABR and behavioral audiograms. The stimuli used for the electrophysiological measurements were cosine-gated tone bursts, and ABR thresholds were determined by calculating the minimum amount of stimulus power needed to generate an adequate ABR response. EFRs were not used in that experiment, and the frequency ambiguity of ABR thresholds was described. The behavioral methods varied slightly to maintain the motivation of the animal subjects, and the final thresholds were the average of four reversals.

In the current study, the hearing capability of a false killer whale was measured using both behavioral and AEP techniques, using the same animal subject as well as the same experimental and acoustical conditions. The objective of this project was to investigate and compare auditory thresholds collected by psychometric and AEP techniques, more specifically, EFR procedures. Based on the paradigm differences and the conservative nature of the animal subject, it was expected that the behavioral methods would produce thresholds lower than the ABR thresholds.

II. METHODS

A. Animal subject

Both the behavioral and AEP data were collected from a single animal subject named Kina, an approximately 30 year old, female false killer whale (*Pseudorca crassidens*). Kina was about 3.7 m in length and weighed 487 kg. The animal was housed in floating pens at the HI Institute of Marine Biology on Oahu, HI, and had been the subject of previous hearing and echolocation research, including a masked hearing study (Thomas *et al.*, 1990), the measurement of echolocation transmission beam patterns (Au *et al.*, 1995) and experiments collecting ABRs during echolocation (Supin *et al.*, 2003; Supin *et al.*, 2004).

B. Electronic equipment

The pure-tone stimuli used during the behavioral measurements were created with a Wavetek FG3B Sweep Function Generator. The frequencies tested were 4, 5, 7, 8, 10, 14, 16, 19, 20, 22.5, 27, 32, 38, and 45 kHz. The input voltage of the stimulus was 3 V peak-to-peak. The stimulus was sent to a custom-built signal shaping box that could attenuate the tone in 1-dB decrements, control the trial sequence and trial condition, and turn the signal on and off with a 20-ms rise and fall time. The signal was then projected through an ITC 1042 60 mm spherical piezoceramic transducer. A Techtronix TDS 1002 Oscilloscope was used to monitor the signal sent from the signal-shaping box to the transducer. A Biomon 8235 hydrophone that had a flat frequency response (±3 dB) up to 200 kHz was used to calibrate the frequency levels of the signal as it was received in the center of the hoop where the animal would be positioned during the stimulus presentation. The calibrations were conducted before the data were collected and not during the trials.

In AEP experiments, SAM tone bursts were digitally synthesized with a customized LABVIEW 6I data acquisition program from a desktop computer implemented with a National Instruments PCI-MIO-16E-1 DAQ card, using an update rate of 200 kHz. The SAM tone bursts were 20 ms long, with a modulation rate of 875 Hz, a modulation depth of 100%, and a variable carrier frequency. The stimulus was sent from the DAQ card to the same amplification, attenuation, monitoring, and projection equipment as in the behavioral experiments.

The AEPs were received through 10-mm gold disc electrodes that were mounted in rubber suction cups and placed on the animal's skin along the dorsal midline, with the active electrode about 5 cm behind the blowhole and the reference electrode on the animal's back, anterior to the dorsal fin. These responses were amplified by $\times 10\,000$ with an IsoDam Isolated Biological Amplifier, bandpass filtered (for anti-aliasing protection) with a Krohn-Hite Model 3103 filter (bandpass of 200–3000 Hz), and transferred to an analog input of the PCI-MIO-16E-1 DAQ card. To extract the recorded AEP from noise, the signal was digitized at a rate of 16 kHz, and 1000 samples were averaged to stimuli presented at a rate of 20/s, thereby extending the entire trial to about 1 min.

C. Experimental setup

The experimental conditions were nearly the same for both the behavioral and the AEP experiments. Both kinds of experiments were conducted within the same test pen, a 6 $\times$ 9 m floating pen in Kaneohe Bay, off the island of Oahu, HI (Fig. 1). This wire-fence enclosed pen was supported by floating buoys under the pen's wooden frame. The transmitting hydrophone was suspended 1 m below the water surface and secured at one corner of the pen deck. An acoustic baffle

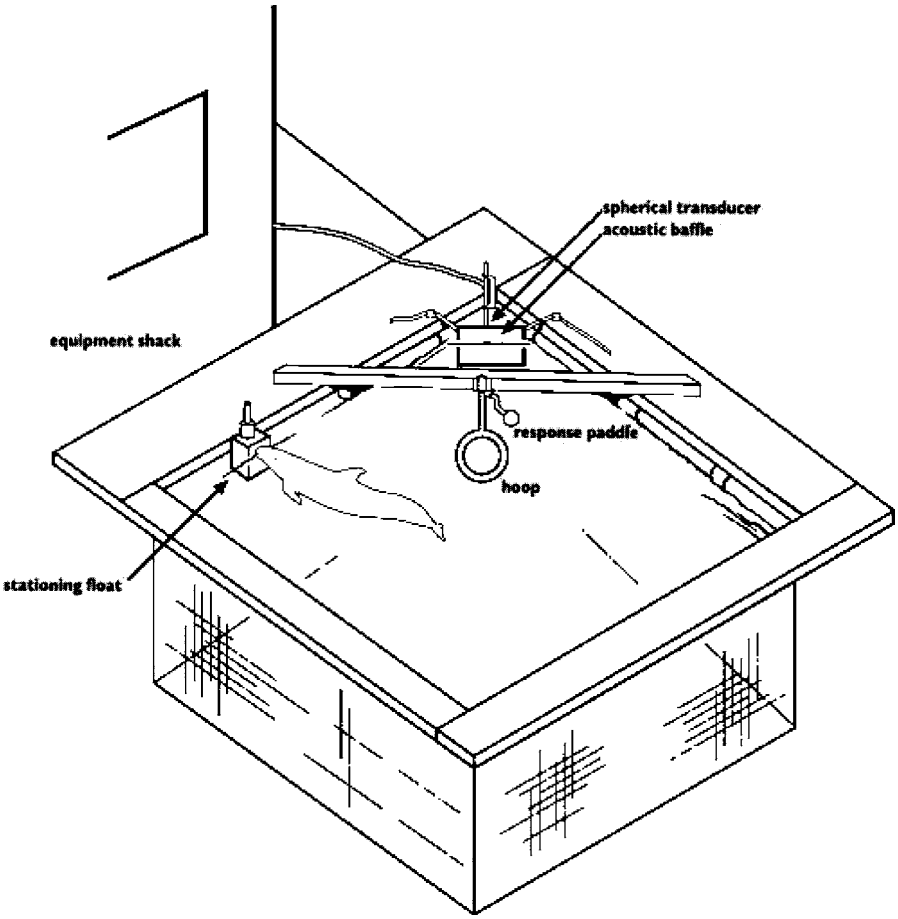

FIG. 1. Experimental configuration for the audiogram measurements of a false killer whale.

was made of a 0.6×0.9 m aluminum sheet that was covered with neoprene on the side facing the transducer, and was hung at the surface of the water at the half-distance between the transducer and the animal (Fig. 2). The water's surface will reflect additional sound underwater, and the baffle was used to reduce and block some of this surface reflection that could have reached the animal. The hoop was placed 2 m from the sound source and fixed firmly from a wooden beam that stretched across the pen deck. A Styrofoam ball response paddle was attached to the wooden beam directly above the hoop and the surface of the water. During the intertrial intervals, the animal was trained to station on a Styrofoam float at the water surface about 3 m away from the transducer, and about 5 m away from the hoop. A small transmitting hydrophone was placed in the water near this float and projected only a 7-kHz tone. This tone was used as a signal to send the animal to the hoop at the beginning of each trial.

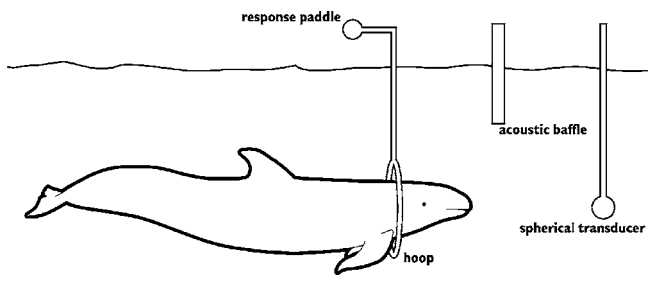

FIG. 2. Underwater profile of the experimental configuration with the false killer whale in the hoop 1 m below the surface, 1 m away from the acoustic baffle, and 2 m away from the spherical transducer.

D. Behavioral audiogram measurements

The behavioral audiogram of the false killer whale was measured by using a go/no-go modified staircase procedure (Schusterman, 1980) in 2001 and 2004. The 7-kHz tone was played to send the whale to an underwater hoop. When the whale was positioned correctly with her pec fins touching the hoop, a 3-s, pure-tone test stimulus was transmitted underwater from the spherical transducer. If the whale heard this sound, she exited the hoop and touched a response paddle that was located directly above the hoop and the surface of the water. This correct "go" response was followed by the trainer's whistle and fish reinforcement. For a correct rejection or a "no-go" response, no sound was projected, and the whale was required to remain in the hoop for the full 10-s trial, after which the trainer whistled to signal to the whale that she had performed the correct response. The whale was again rewarded with fish. For an incorrect detection or a "false alarm," the whale would indicate that she heard a sound and touch the paddle. However, no sound was played and therefore, no reward or whistle was given. The whale returned to her stationing float, and the next trial proceeded. When an incorrect rejection, or "miss" occurred, the whale remained in the hoop and did not respond to the sound that was played. The trainer would call the animal back to her stationing float with no reward at the end of the 10-s trial.

Ten warm-up trials were presented before each session to gauge the whale's response behavior with five of the trials with a sound transmitted and five without. The sounds played in the warm-up trials were at intensity levels that were at least 20 dB above the presumed threshold based on published audiograms, loud enough for the whale to detect without difficulties. The session only proceeded if 80% of the warm-up trials were correct. The trials following warm-ups were conducted in blocks of ten, with 50% of each block containing a signal present and the other 50% with a signal absent. The sequence of the trials was randomized based on a modified Gellermann series (Gellermann, 1933), with no more than three consecutive trials of the signal present or absent to avoid any bias of the whale to respond the same way to every trial.

Every correct go-response was followed by a stimulus intensity reduction of 2 dB, until the animal made a miss response, after which the intensity was increased by 2 dB. This change in direction of intensity level was defined as a reversal. The intensity continued to be increased until there was another correct go-response, which was followed by an intensity decrease, another change of direction or reversal.

For each session, one frequency threshold was tested, and the value of that threshold was the average intensity level of five reversals. It was determined from a preliminary study that there was no significant difference between a threshold calculated from five reversals versus a threshold calculated from ten reversals. Thresholds were equivalent and completed within a shorter amount of time if only five reversals were used. The final threshold for each frequency was calculated when two consecutive sessions contained reversal thresholds within 3 dB. Finally, this entire staircase procedure was repeated to determine the thresholds at 4, 5, 7, 8, 10, 14, 15, 16, 19, 20, 21, 22.5, 24, 27, 32, 38, and 45 kHz. The animal's hearing sensitivity was tested at 64 kHz, and demonstrated that she was not able to hear this high frequency when it was played at the highest intensity level possible for the equipment available, which was 132 dB. As a result, no further testing was conducted at frequencies above 45 kHz.

E. AEP audiogram measurements

There were three main differences in the experimental procedure between the AEP and behavioral audiograms. One was that gold disc electrodes in rubber suction cups were placed on the animal. The second difference was that no behavioral reporting response was required from the animal. The animal remained in the hoop for a trial length of about 1 min while the stimulus was projected underwater and the AEP was recorded. The final difference was the stimulus type that was presented, in this case being a 20-ms SAM tone-burst repeated 1000 times, as opposed to the 3-s pure-tones generated for the behavioral audiogram.

Following the application of the suction cups, the animal was sent to the underwater hoop from a stationing float by a 7-kHz tone. When the animal was positioned correctly with her pectoral fins touching the hoop, the SAM tone bursts were projected through the transducer. After about 1 min, the trainer whistled to indicate the end of the trial, and the animal was rewarded with fish. The amplitude of the signal was reduced in 5-dB steps, until the EFR response recorded on the computer could no longer be distinguished from the background noise. An average of five stimulus intensities were presented at each frequency, and an average of three frequencies was tested in 1-h sessions. Sessions were conducted twice a day. The frequencies tested were in quarter-octave steps: 4, 4.7, 5.6, 6.7, 8, 9.5, 11.2, 13.5, 16, 19, 22.5, 27, 32, 38, and 45 kHz. A total of three AEP audiograms were measured, one in May 2001, a second in August 2001, and a third in April 2004. An average of two weeks of consecutive days was needed to complete each of these audiograms.

No additional training was required for the whale when the task was switched from behavioral to AEP experiments. The very rapid transfer between paradigms was most likely due to the differences in the experimental setup, the most obvious of which included the suction cups attached to the animal and the SAM tone-bursts. It is possible that these distinct features allowed for the whale to easily discriminate between the two experimental tasks.

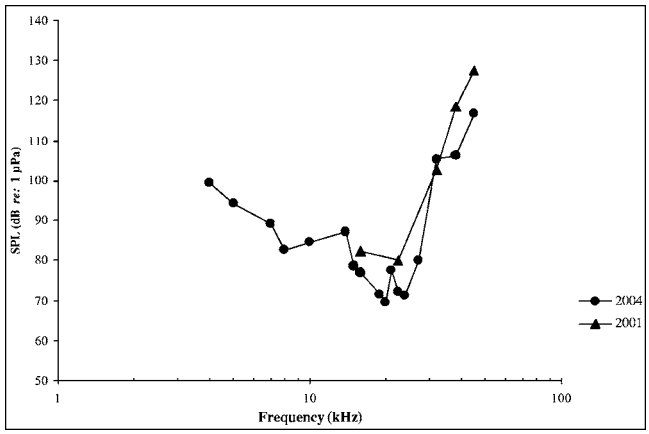

FIG. 3. Behavioral audiograms of a false killer whale collected in 2001 and 2004.

III. RESULTS

A. Behavioral audiograms

The first behavioral audiogram from 2001 was a preliminary study that included only a partial audiogram with thresholds for only five frequencies. The behavioral audiogram from 2004 was much more complete, with 16 frequencies covering at least 4 octaves (Fig 3). The complete audiogram from 2004 had the U-shape curve characteristic of mammalian hearing. The thresholds were very similar over the 3-yr gap, with some values differing by as little at 2.6 dB at 32 kHz, and as great as 12.1 dB at 38 kHz (Table I). However, the shapes of the two curves were very consistent, with comparable regions of best sensitivity and steep high frequency range. The region of best sensitivity was from 16 to 24 kHz, with the lowest threshold of 69 dB at 20 kHz. Above 24 kHz, the thresholds increased significantly at a rate of about 28 dB per octave, with a high frequency cutoff

TABLE I. Auditory threshold values from two behavioral audiograms of a false killer whale. Each threshold is an average of the reversal values of two consecutive sessions that were within 3 dB.

Freq (kHz)	Threshold 2001 (dB *re*: 1 μPa)	Threshold 2004 (dB *re*: 1 μPa)	Difference (dB *re*: 1 μPa)	Average (dB *re*: 1 μPa)
4	⋯	99.5	⋯	⋯
5	⋯	94.4	⋯	⋯
7	⋯	89.3	⋯	⋯
8	⋯	82.7	⋯	⋯
10	⋯	84.5	⋯	⋯
14	⋯	87.3	⋯	⋯
15	⋯	78.6	⋯	⋯
16	82.4	77	5.4	79.7
19	⋯	71.6	⋯	⋯
20	⋯	69.5	⋯	⋯
22.5	80.1	72.2	7.9	76.1
24	⋯	71.3	⋯	⋯
27	⋯	80.2	⋯	⋯
32	102.9	105.5	2.6	104.2
38	118.4	106.3	12.1	112.3
45	127.6	116.7	10.9	122.1

at 45 kHz. The low frequency thresholds decreased as the frequencies increased, at a rate of about 5–17 dB per octave.

A total of 16 frequencies were tested for the 2004 audiogram, 11 of which required only two consecutive sessions that resulted with reversal averages within 3 dB. Three frequencies needed three sessions to meet this requirement, one frequency (21 kHz) needed four sessions, and one frequency (8 kHz) needed five sessions. There was a very low false alarm rate throughout the experiment. Over 76% of the sessions consisted of zero false alarms, and of the remaining sessions (24%) with false alarms, the rate was about 5%.

B. AEP audiograms

The electrophysiological responses from the AEP collection is presented in Fig. 4 and depicts how EFRs recorded at different stimulus intensities decreased from 125 to 90 dB by 5-dB steps. As the intensity decreased, the EFR amplitude synchronously decreased until the response disappeared in noise. For a better evaluation of the response amplitude, these wave forms were Fourier transformed to obtain their frequency spectra [Fig. 4(b)]. The spectra contained a definite peak at the stimulus-modulation frequency of 875 Hz. The magnitude of this peak was taken as a measure of the response magnitude. It was plotted as a function of stimulus intensity (Fig. 5) and approximated by a regression line. The crossing point of this line with the zero-magnitude level was calculated as the threshold estimate for that frequency.

The three AEP audiograms were consistent over time (Fig. 6). All three had a range of best hearing sensitivity from 16 to 22.5 kHz with the lowest threshold of 80.9 dB at 22.5 kHz (Table II). The thresholds at lower frequencies all had a slope that declined gradually as frequency increased, about 8–18 dB per octave. The thresholds at higher frequencies sharply increased, about 32 dB per octave, and quickly reached higher intensity at 45 kHz. All three AEP audiograms had relatively consistent threshold values at the lower

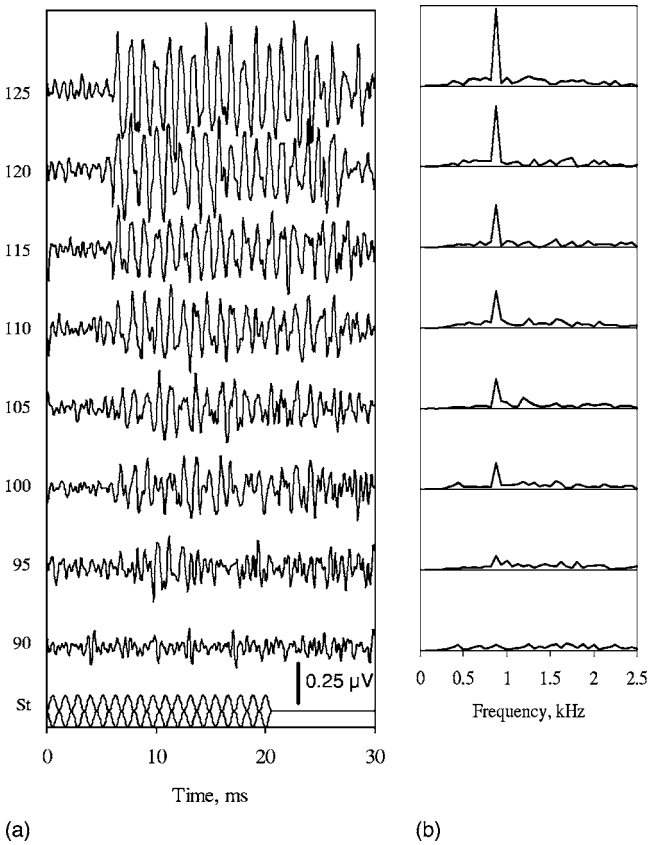

FIG. 4. Examples of (a) EFR wave forms and (b) their frequency spectra for a threshold determination at 27 kHz.

frequencies, some with differences less than 1 dB. The May 2001 and April 2004 thresholds for the higher frequencies were closer, with some thresholds fluctuating by as little as 0.2 dB. However, the August 2001 AEP audiogram had the highest thresholds for the higher frequencies that were noticeably different, despite the consistency of the lower frequencies with the other two AEP audiograms.

IV. DISCUSSION

A. Comparison of behavioral and AEP audiograms

The results of the behavioral audiograms demonstrated that the data accumulated from psychometric methods were

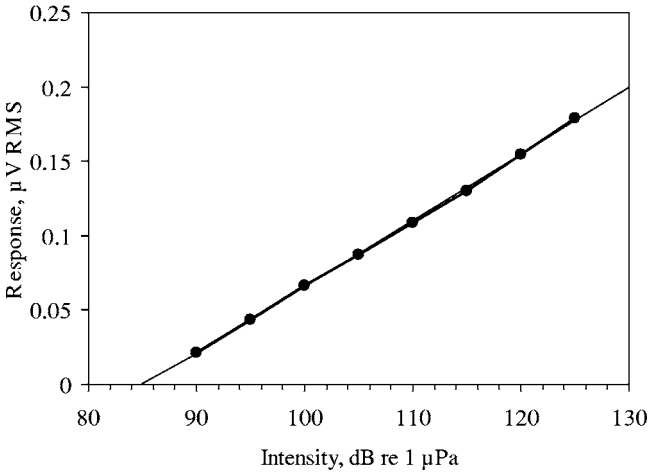

FIG. 5. EFR magnitude dependence on stimulus intensity (by the records presented in Fig. 2).

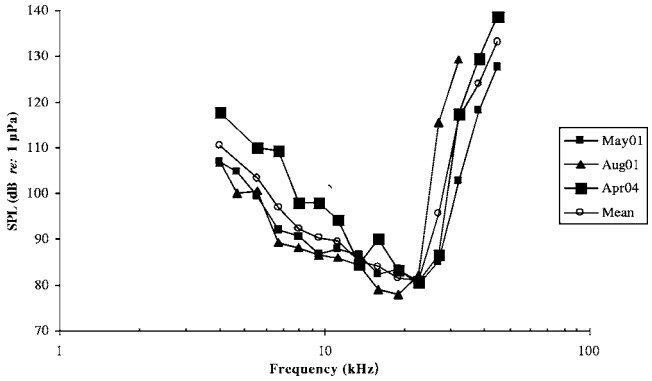

FIG. 6. Three AEP false killer whale audiograms measured over three years. Also included is a curve of the average value of all three audiograms.

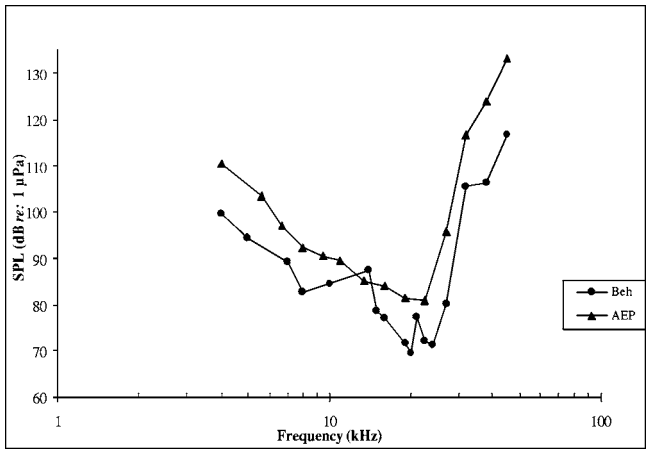

FIG. 7. Comparison of both the behavioral and AEP audiograms of a false killer whale. The threshold values are averaged over all audiograms collected for each method in this study.

reliable and repeatable. It was not necessary to retrain the animal. She was able to repeat an experiment that was conducted over 3 years prior, with precise and accurate responses and no behavioral difficulties.

For the AEP audiograms, the low frequency thresholds were also quite reliable and constant. From 4 through 22.5 kHz, the threshold values varied only slightly, indicating that this technique provided consistent results for estimating auditory sensitivity values. When compared with the low frequency thresholds of the behavioral audiograms, the data collected from the behavioral methods were always lower than those using AEPs, with differences as small as 4.8 dB at 22.5 kHz, and as large as 11 dB at 4 kHz (Fig. 7).

In the high frequency regions, both the behavioral and AEP audiograms shared the common feature of steep increases in threshold values as frequency also increased. However, the thresholds measured with AEPs were less sensitive by 11 to 15.5 dB from those collected behaviorally. With such discrepancies, it was evident that behavioral results consistently indicated more sensitive auditory threshold levels for the subject.

TABLE II. Auditory thresholds and average value of three AEP audiograms of a false killer whale. Also included are the averaged values of all three auditory thresholds for each frequency. Units are in dB *re*: 1 μPa.

Freq (kHz)	Threshold May 01 (dB *re*: 1 μPa)	Threshold August 01 (dB *re*: 1 μPa)	Threshold April 04 (dB *re*: 1 μPa)	Average (dB *re*: 1 μPa)
4	106.9	107.0	117.7	110.5
4.7	104.6	100.0	⋯	102.3
5.6	99.5	100.7	109.9	103.4
6.7	92.0	89.3	109.4	96.9
8	90.8	88.1	98.1	92.3
9.5	86.8	86.6	98.2	90.5
11.2	88.0	86.1	94.4	89.5
13.5	86.7	84.2	84.6	85.2
16	82.4	79.2	90.2	83.9
19	83.5	77.9	83.1	81.5
22.5	80.1	82.0	80.7	80.9
27	85.0	115.5	86.6	95.7
32	102.9	129.2	117.5	116.5
38	118.4	⋯	129.6	124.0
45	127.6	⋯	138.7	133.1

A similar gap between AEP and behavioral threshold estimates was found in two killer whales *O. orca* (Szymanski *et al.*, 1999), with an average of 12 dB more sensitive behavioral thresholds. However, there were some technical differences between that and the present study. The tone burst stimuli used were not SAM tone bursts, and ABRs not EFRs were measured. As mentioned earlier, the advantages of using SAM stimuli instead of brief tone pips were that the intensity of the longer tone burst could be characterized by its rms sound pressure, thereby providing a basis for correct comparison of behavioral and AEP data, and that the many evoked potential cycles contained within an EFR increased the response detection precision and analysis. Despite these discrepancies, the final conclusions in the 1999 study were somewhat similar to those of the present study, that both the behavioral and ABR audiograms had consistent shapes with higher ABR threshold levels.

The significant feature of the different stimulus types clearly distinguished each technique and possibly contributed to the data differences. SAM tone bursts of 875-Hz modulation rate and 20 ms long were necessary to collect AEPs. Contrary to this, behavioral methods involved pure-tone signals with a duration of about 3 s. The longer pure-tone may have been more detectable and unambiguous, and consequently allowed for a clearer response by the subject. For EFR responses, temporal summation was limited by SAM cycle duration which can be as short as 1.14 ms. As shown by Johnson (1968), hearing thresholds decreased as stimulus duration increased from a fraction of milliseconds to hundreds of milliseconds. Thus, the threshold difference between behavioral measurements and AEP measurements reflected the real temporal summation processes in the auditory system rather than an imprecision of one or another method.

It is important to remember that any estimate of a threshold, AEP or behavioral, was arbitrary, and that the results depended on the used threshold criterion. However, the good correspondence of behavioral and AEP thresholds, with different summation times taken into account and with the

use of the above-described criteria, indicated that both methods provided good estimates of the real sensitivity of the auditory system.

One of the practical differences between the psychophysical and AEP techniques was the shorter amount of time required to complete the AEP audiogram. For the behavioral audiogram, each session lasted approximately 30 min, and a total of 42 sessions were needed to test all of the frequencies. The time invested for data collection in this portion was about 2 months with a well trained and experienced animal subject. This amount of time does not include the years of behavioral training that was initially dedicated and required for this subject.

One session for an AEP audiogram lasted about 45 min, during which three frequencies could be tested. Therefore, one AEP session tested three frequencies in about the same amount of time that one behavioral session tested one frequency. When these sessions were conducted twice a day, the total time dedicated to this phase was an average of two weeks, remarkably more condensed and still with results comparably robust to the behavioral paradigm. With such a reduced time and training requirement, and the minimum participation required by the animal subject, the AEP technique for measuring auditory thresholds appeared more suitable and convenient to a wider number of research opportunities that include untrained or stranded animals.

ABR audiograms served as a resource for evaluating the sensitivity and functionality of auditory systems for many vertebrate species, including birds (Brittan-Powell *et al.*, 2002), bats (Wenstrup, 1984), fish (Kenyon *et al.*, 1998), and humans (van der Drift *et al.*, 1987; Mitchell *et al.*, 1989; Watson, 1996). When the data from the AEP audiograms were compared to behavioral audiograms, most AEP thresholds were higher than behavioral thresholds, although the differences were usually not significant. There was a common conclusion that the advantages of the electrophysiological technique included the rapid evaluations and reliability of data, allowing for good predictions of basic audiogram shape.

B. Manifestation of hearing loss

When the results from our study were compared with the behavioral audiogram of another false killer whale (Thomas *et al.*, 1988), the thresholds diverged considerably, with two distinguishing features. The first was that the animal subject from the 1988 study heard frequencies as high as 115 kHz reasonably well, and at about the same SPL that Kina heard 45 kHz. The high frequency cutoff for the current audiogram was about 70 kHz lower than the previous audiogram. The second feature was the different frequency region of best sensitivity and the corresponding sensitivity thresholds. In this 2004 study, the region was between 16 and 24 kHz with the lowest threshold at 69 dB at 20 kHz. However, in the 1988 study, the region of best sensitivity was between 32 and 64 kHz, and with thresholds as low as 39 dB at 64 kHz. Therefore, the current audiogram had a lower high frequency cutoff, in addition to the region of best sensitivity shifted to lower frequencies and heard only at higher threshold levels, clearly indicating that the whale hearing sensitivity lessened when compared to the subject of the previous study. Not only could the whale not hear higher frequencies, but also her best hearing was at lower frequencies and higher amplitudes.

Both audiograms were made using standard psychometric techniques and pure-tone stimuli. Despite similar paradigms, such discrepancies could have resulted from the different locations of each experiment, where the earlier subject lived in a concrete and virtually quiet tank, and the current subject resided in the open waters of Kaneohe Bay where the ambient noise level has been documented, in particular the noise produced snapping shrimp (Au and Banks, 1998). This noise has an extremely broad frequency spectrum with energy beyond 200 kHz with a peak frequency at about 2 kHz. It does not follow from those data that the ambient noise in Kaneohe Bay may specifically mask sounds above 45 kHz.

In 1990, the same false killer whale as the present study was also the experimental subject for a masked hearing study also situated in Kaneohe Bay, HI (Thomas *et al.*, 1990). That experiment was conducted 14 years prior to the current study, and at that time, the whale's masked hearing audiogram depicted exceptional hearing capabilities, indicating good hearing sensitivity. Therefore, it has been hypothesized that this animal probably suffered some hearing loss associated with age or presbycusis, an occurrence demonstrated among older bottlenose dolphins (Ridgway and Carder, 1997; Ketten *et al.*, 2001) and a beluga whale (Finneran *et al.*, 2003).

C. Perspectives for future studies

Auditory threshold information exists for only about 12% of odontocete species, creating a significant deficiency of scientific evidence for the potential hearing damage and behavioral impacts of anthropogenic noise on marine mammals. There is a serious need for additional research on more cetacean species, especially since the accessibility of marine mammals for behavioral research is rare. Research opportunities are limited because there are very few laboratory facilities in the world where marine mammals are available for scientific research. The behavioral and electrophysiological techniques to investigate hearing are conducted very differently, one with considerable time and effort involved in training psychometric methods, versus the other with very limited subject participation required to collect AEPs, an advantage that may strengthen the need for AEP techniques by broadening its applicability to untrained animal subjects. There are differences with signal type used in the behavioral and AEP techniques that may influence the research outcomes. However, with these differences taken correctly into account, both techniques give comparable results.

ACKNOWLEDGMENTS

The authors are grateful to Whitlow Au for his invaluable expertise, Jeff Pawloski for his work and dedication, Dera Look, Aran Mooney, Stuart Ibsen, Kristen Taylor, Vincent De Paolo, Marc Lammers, Christopher Kam for his graphic designs, and the generosity from everyone at the

Marine Mammal Research Program at the Hawaii Institute of Marine Biology of the University of Hawaii. This study was supported by the Office of Naval Research Grant No. N00014-98-1-0687, for which the authors thank Mardi Hastings and Bob Gisiner, and by the Russian Ministry of Science and Technology, Award No. NSh.2152.2003.4 (Russia). Work was conducted under U.S. Marine Mammal Permit No. 978-1567 issued to Paul E. Nachtigall by the U.S. National Marine Fisheries Service Office of Protected Resources. This is Hawaii Institute of Marine Biology Contribution No. 1203.

Andersen, S. (**1970**). "Auditory sensitivity of the harbor porpoise, *Phocoena phocoena*," in *Investigations on Cetacea*, edited by G. Pilleri (Berne-Bumpliz, Switzerland), pp. 255–259.

Au, W. W. L., and Banks, K. (**1998**). "The acoustics of the snapping shrimp, *Synalpheus parneomeris* in Kaneohe Bay," J. Acoust. Soc. Am. **103**, 41–47.

Au, W. W. L., Pawloski, J., Nachtigall, P. E., and Gisiner, R. C. (**1995**). "Echolocation signals and transmission beam pattern of a false killer whale (*Pseudorca crassidens*)," J. Acoust. Soc. Am. **98**, 51–59.

Brittan-Powell, E. F., Dooling, R. J., and Gleich, O. (**2002**). "Auditory brainstem response in adult budgerigars (*Melopsittacus undulatus*)," J. Acoust. Soc. Am. **112**, 999–1008.

Bullock, T. H., Grinnell, A. D., Ikezono, F., Kameda, K., Katsuki, Y., Nomoto, M., Sato, O., Suga, N., and Yanagisava, K. (**1968**). "Electrophysiological studies of the central auditory mechanisms in cetaceans," Z. Vergl. Physiol **59**, 117–156.

Dolphin, W. F., Au, W. W. L., and Nachtigall, P. E. (**1995**). "Modulation transfer function to low-frequency carriers in three species of cetaceans," J. Comp. Physiol. **177**, 235–245.

Finneran, J. J., Carder, D., Dear, R., Belting, T., and Ridgway, S. H. (**2003**). "Pure-tone audiograms and hearing loss in the white whale (*Delphinapterus leucas*)," J. Acoust. Soc. Am. **114**, 2434.

Gellermann, L. W. (**1933**). "Chance orders of alternating stimuli In visual discrimination experiments," J. Genet. Psychol. **42**, 206–208.

Hall, J. D., and Johnson, C. S. (**1972**). "Auditory thresholds of a killer whale, *Orcinus orca*," J. Acoust. Soc. Am. **51**, 515–517.

Jacobs, D. W., and Hall, J. D. (**1972**). "Auditory thresholds of a freshwater dolphin *Inia geoffrensis*," J. Acoust. Soc. Am. **51**, 530–533.

Johnson, C. S. (1966). "Auditory thresholds of the bottlenosed porpoise (*Tursiops truncatus*)," U. S. Naval Ordanance Test Station (NOTS) TP 4178.

Johnson, C. S. (**1968**). "Relation between absolute threshold and duration-of-tone pulses in the bottlenosed porpoise," J. Acoust. Soc. Am. **43**, 757–763.

Kastelein, R., Bunskoek, P., Hagedoorn, M., Au, W. W. L., and de-Haan, D. (**2002**). "Audiogram of a harbor porpoise (*Phocoena phocoena*) measured with narrow-band frequency-modulated signals," J. Acoust. Soc. Am. **112**, 334–344.

Kastelein, R. A., Hagedoorn, M., Au, W. W. L., and Haan, D. d. (**2003**). "Audiogram of a striped dolphin," J. Acoust. Soc. Am. **113**, 1130–1137.

Kenyon, T. N., Ladich, F., and Yan, H. Y. (**1998**). "A comparative study of hearing ability in fishes: The auditory brainstem response approach," J. Comp. Physiol. **182**, 307–318.

Ketten, D. R., O'Malley, J., Moore, P. W. B., Ridgway, S. H., and Merigo, C. (**2001**). "Aging, injury, disease, and noise in marine mammal ears," J. Acoust. Soc. Am. **110**, 2721.

Ljungblad, D. K., Scoggins, P. D., and Gilmartin, W. G. (**1982**). "Auditory thresholds of a captive Eastern Pacific bottle-nosed dolphin, *Tursiops spp*," J. Acoust. Soc. Am. **72**, 1726–1729.

Mitchell, C., Phillips, D. S., and Trune, D. R. (**1989**). "Variables affecting the auditory brainstem response: Audiogram, age, gender, and head size," Hear. Res. **40**, 75–86.

Nachtigall, P. E., Au, W. W. L., Pawloski, J., and Moore, P. W. B. (**1995**). "Risso's dolphin (Grampus griseus) hearing thresholds in Kaneohe Bay, Hawaii," in *Sensory Systems of Aquatic Mammals*, edited by R. A. Kastelein, J. A. Thomas, and P. E. Nachtigall (DeSpil, Woerden, The Netherlands), pp. 49–53.

Popov, V. V., and Klishin, V. O. (**1998**). "EEG study of hearing in the common dolphin *Delphinus delphis*," Aquat Mamm **24**, 13–21.

Popov, V. V., Ladygina, T. F., and Supin, A. Y. (**1986**). "Evoked potentials in the auditory cortex of the porpoise, *Phocoena phocoena*," J. Comp. Physiol. **158**, 705–711.

Popov, V. V., and Supin, A. Y. (**1987**). "Characteristics of hearing in the beluga *Delphinapterus leucas*," Dokl. Biol. Sci. **294**, 370–372.

Popov, V. V., and Supin, A. Y. (**1990a**). "Auditory brain stem responses in characterization of dolphin hearing," J. Comp. Physiol. **166**, 385–393.

Popov, V. V., and Supin, A. Y. (**1990b**). "Electrophysiological investigation of hearing of the fresh-water dolphin *Inia geoffrensis*," Dokl. Biol. Sci. **313**, 488–491.

Popov, V. V., and Supin, A. Y. (**1990c**). "Electrophysiological studies of hearing in some cetaceans and a manatee," in *Sensory Abilities of Cetaceans: Laboratory and Field Evidence*, edited by J. Thomas and R. Kastelein (Plenum, New York), pp. 405–415.

Ridgway, S. H., and Carder, D. (**1997**). "Hearing deficits measured in some *Tursiops truncatus*, and discovery of a deaf/mute dolphin," J. Acoust. Soc. Am. **101**, 590–594.

Ridgway, S. H., Bullock, T. H., Carder, D. A., Seeley, R. L., Woods, D., and Galambos, R. (**1981**). "Auditory brainstem response in dolphins," Proc. Natl. Acad. Sci. U.S.A. **78**, 1943–1947.

Sauerland, M., and Dehnhardt, G. (**1998**). "Underwater audiogram of a tucuxi (*Sotalia fluviatilis guianensis*)," J. Acoust. Soc. Am. **103**, 1199–1204.

Schusterman, R. J. (**1980**). "Behavioral methodology in echolocation by marine mammals," in *Animal Sonar Systems*, edited by R. G. Busnel and J. F. Fish (Plenum, New York), pp. 11–41.

Supin, A. Y., Nachtigall, P. E., Au, W. W. L., and Breese, M. (**2004**). "The interaction of outgoing echolocation pulses and echoes in the false killer whale's auditory system: Evoked-potential study," J. Acoust. Soc. Am. **115**, 3218–3225.

Supin, A. Y., Nachtigall, P. E., Pawloski, J., and Au, W. W. L. (**2003**). "Evoked potential recording during echolocation in a false killer whale *Pseudorca crassidens*," J. Acoust. Soc. Am. **113**, 2408–2411.

Supin, A. Y., and Popov, V. V. (**1995**). "Envelope-following response and modulation transfer function in the dolphin's auditory system," Hear. Res. **92**, 38–46.

Szymanski, M. D., Bain, D. E., Kiehl, K., Pennington, S., Wong, S., and Henry, K. R. (**1999**). "Killer Whale (*Orcinus orca*) hearing: Auditory brainstem response and behavioral audiograms," J. Acoust. Soc. Am. **106**, 1134–1141.

Thomas, J., Chun, N., Au, W. W. L., and Pugh, K. (**1988**). "Underwater audiogram of a false killer whale (*Pseudorca crassidens*)," J. Acoust. Soc. Am. **84**, 936–940.

Thomas, J., Pawloski, J., and Au, W. W. L. (**1990**). "Masked hearing abilities of a false killer whale (*Pseudorca crassidens*)," in *Sensory Abilities of Cetaceans*, edited by J. Thomas and R. Kastelein (Plenum, New York), pp. 395–404.

van der Drift, J. C., Brocaar, M. P., and Zanten, GAv. (**1987**). "The relation between the pure-tone audiogram and the click auditory brainstem response threshold in cochlear hearing loss," Audiology **26**, 1–10.

Wang, D., Wang, K., Ziao, Y., and Sheng, G. (**1992**). "Auditory sensitivity of a Chinese river dolphin (*Lipotes vexillifer*)," in *Marine Mammal Sensory Systems*, edited by J. A. Thomas, R. Kastelein, and A. Y. Supin (Plenum, New York), pp. 213–221.

Watson, D. R. (**1996**). "The effects of cochlear hearing loss, age, and sex on the auditory brainstem response," Audiology **35**, 246–258.

Wenstrup, J. J. (**1984**). "Auditory sensitivity in the fish-catching bat, *Noctilio leporinus*," J. Comp. Physiol. **155**, 91–101.

White, J. M. J., Norris, J., Ljungblad, D., Baron, K., and Sciara, Gd. (1978). "Auditory thresholds of two beluga whales (*Delphinapterus leucas*)," Hubbs Marine Research Institute, San Diego, CA.

Temporary threshold shift in bottlenose dolphins (Tursiops truncatus) exposed to mid-frequency tones[a)]

James J. Finneran[b)] and Donald A. Carder
U.S. Navy Marine Mammal Program, Space and Naval Warfare Systems Center, San Diego, Code 2351, 53560 Hull Street, San Diego, California 92152

Carolyn E. Schlundt
EDO Professional Services, 3276 Rosecrans Street, San Diego, California 92110

Sam H. Ridgway
U.C. Veterinary Medical Center–San Diego, Department of Pathology, School of Medicine, University of California, La Jolla, California 92093-0612

(Received 17 February 2005; revised 18 July 2005; accepted 18 July 2005)

A behavioral response paradigm was used to measure hearing thresholds in bottlenose dolphins before and after exposure to 3 kHz tones with sound exposure levels (SELs) from 100 to 203 dB re 1 μPa^2 s. Experiments were conducted in a relatively quiet pool with ambient noise levels below 55 dB re 1 $\mu Pa^2/Hz$ at frequencies above 1 kHz. Experiments 1 and 2 featured 1-s exposures with hearing tested at 4.5 and 3 kHz, respectively. Experiment 3 featured 2-, 4-, and 8-s exposures with hearing tested at 4.5 kHz. For experiment 2, there were no significant differences between control and exposure sessions. For experiments 1 and 3, exposures with SEL=197 dB re 1 μPa^2 s and SEL$\geqslant$195 dB re 1 μPa^2 s, respectively, resulted in significantly higher TTS_4 than control sessions. For experiment 3 at SEL=195 dB re 1 μPa^2 s, the mean TTS_4 was 2.8 dB. These data are consistent with prior studies of TTS in dolphins exposed to pure tones and octave band noise and suggest that a SEL of 195 dB re 1 μPa^2 s is a reasonable threshold for the onset of TTS in dolphins and white whales exposed to midfrequency tones.
[DOI: 10.1121/1.2032087]

PACS number(s): 43.80.Nd, 43.80.Lb [WWA] Pages: 2696–2705

I. INTRODUCTION

Certain anthropogenic underwater sounds, such as those produced by underwater explosions, seismic surveys, and military and oceanographic research sonars, have the potential to adversely affect marine animals (rev. Green *et al.*, 1994). Exposure to high intensity sound for a sufficient duration may result in physical injury to nonauditory structures such as the lungs and other gas-containing structures (Yelverton *et al.*, 1973; Dalecki *et al.*, 1999) and/or auditory effects such as a noise-induced threshold shift (NITS)—an increase in the auditory threshold after exposure to noise. A NITS may be permanent, called a permanent threshold shift (PTS), or temporary, called a temporary threshold shift (TTS).

Increased public concern and the application of the U.S. Marine Mammal Protection Act and Endangered Species Act to activities involving anthropogenic sound have resulted in a pressing need for specific information regarding safe limits for marine mammals exposed to underwater sound. Mass strandings of whales spatially and temporally coincident with the use of military midfrequency (generally from 1 to 10 kHz) tactical sonar (U.S. Department of Commerce and U.S. Department of the Navy, 2001; Jepson *et al.*, 2003) have further increased concern about the potential effects of intense sound on marine mammals and possible mitigation strategies. Since many marine mammals have sensitive hearing and rely upon underwater sound for communicating, foraging, and navigating, auditory effects such as a TTS or PTS are of particular concern.

Although there have been no efforts to directly measure PTS in marine mammals, a number of investigators have measured TTS. Schlundt *et al.* (2000) reported the results of TTS experiments conducted with five bottlenose dolphins (*Tursiops truncatus*) and two white whales (belugas, *Delphinapterus leucas*) exposed to 1-s tones at frequencies of 0.4, 3, 10, 20, and 75 kHz. At frequencies of 3, 10, and 20 kHz, sound pressure levels (SPLs) necessary to induce measurable amounts (6 dB or more) of TTS were between 192 and 201 dB re 1 μPa (mean of 195 dB re 1 μPa). Finneran *et al.* (2000; 2002b) conducted TTS experiments with dolphins and white whales exposed to impulsive sounds similar to those produced by distant underwater explosions and seismic waterguns. These studies showed that, for very short duration impulsive sounds, higher sound pressures were required to induce TTS than for longer duration tones. Nachtigall *et al.* (2003; 2004) measured TTS in a bottlenose dolphin exposed to octave-band noise centered at 7.5 kHz. Exposures with

[a)]Portions of these data were presented at the 142nd Meeting of the Acoustical Society of America [Finneran, *et al.* (2001). "Temporary threshold shift (TTS) in bottlenose dolphins (Tursiops truncatus) exposed to tonal signals," J. Acoust. Soc. Am.**110**, 2749(A)] and 15th Biennial Conference on the Biology of Marine Mammals [Finneran, *et al.* (2003). "Auditory effects of mid-frequency tones on cetaceans"].

[b)]Electronic mail: james.finneran@navy.mil

SPLs of 160 dB re 1 μPa and durations of 30–50 minutes induced 5–8 dB of TTS measured 5 min after exposure. Kastak *et al.* (1996) reported TTS in a harbor seal (*Phoca vitulina*) exposed to airborne noise from nearby construction. Kastak *et al.* (1999) reported TTS in a California sea lion (*Zalophus californianus*), harbor seal, and Northern elephant seal (*Mirounga angustirostris*) exposed to underwater octave band noise. Finneran *et al.* (2003) exposed California sea lions to single underwater impulses produced from an arc-gap transducer, but found no measurable TTS at SPLs up to 178–183 dB re 1 μPa.

Because Schlundt *et al.* (2000) used tones similar to sonar pings, these data are the most directly applicable to military tactical sonars. However, by necessity this study was conducted in San Diego Bay, where ambient noise levels are relatively high and quite variable. For this reason, Schlundt *et al.* employed broadband masking noise to provide a "floor effect" and keep thresholds consistent from session to session despite variations in ambient noise levels. Specific tests to determine the effects, if any, of the masking noise were inconclusive (Schlundt *et al.*, 2000); however, terrestrial mammal data suggest that the presence of masking noise would result in smaller observed TTS (Parker *et al.*, 1976; Humes, 1980).

This paper presents the results of three TTS experiments with bottlenose dolphins exposed to 3-kHz tones. This particular frequency was selected because it falls within the range used by the U.S. Navy's AN/SQS-53 mid-frequency tactical sonar (U.S. Department of Commerce and U.S. Department of the Navy, 2001). The first two experiments were designed to address lingering questions regarding the potential effects of masking noise used by Schlundt *et al.* (2000) by conducting tests in a pool with low ambient noise level and no masking noise. The third experiment was designed to investigate the effects of tone duration and the growth of TTS with increasing exposure.

II. METHODS

A. Subjects

Subjects were two male bottlenose dolphins: BEN (estimated age 38–40 yr during the study, approximately 250 kg) and NAY (18–20 yr, approximately 255 kg). Both subjects had substantial prior experience in cooperative psychophysical testing, including hearing tests. Subjects were housed in floating netted enclosures 9×9 to 12×24 m located in San Diego Bay, CA. The study followed a protocol approved by the Institutional Animal Care and Use Committee at The Space and Naval Warfare Systems Center, San Diego. Both BEN and NAY were tested during experiments 1 and 2; only BEN was tested during experiment 3.

B. Hearing test apparatus

Figure 1 shows the experimental configuration. Tests were conducted in an above-ground, 6.1-m-diam, 1.5-m-deep circular, vinyl-walled pool. Figure 2 compares ambient noise levels in the test pool and San Diego Bay measured with a low-noise hydrophone (Reson TC 4032). The San Diego Bay data are mean noise levels over a one-month period. The pool data are mean levels from a single measurement (100 averages, 195-Hz frequency resolution) and are representative of typical mean ambient noise levels in the pool. At frequencies above approximately 1 kHz, mean ambient noise pressure spectral density levels were below 55 dB re 1 μPa^2/Hz.

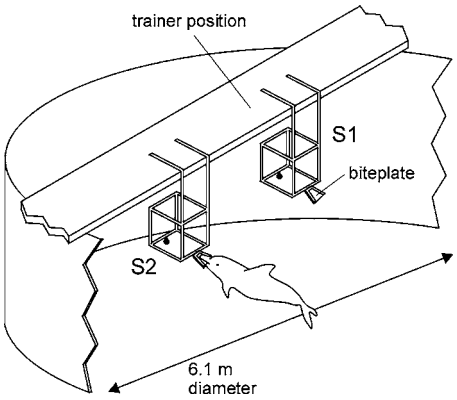

FIG. 1. Experimental setup for hearing tests and sound exposures.

A wooden deck located above the pool supported two "listening stations," designated as the "S1 station" and the "S2 station." The S1 station was the site for the presentation of the fatiguing sound exposure and a "start" signal to begin the hearing test. Hearing tests were conducted at the S2 station. Two stations were used to physically separate the site of the fatiguing sound exposure from the hearing test location. Each station consisted of a PVC frame with a plastic "biteplate" upon which the subjects were trained to position. The S1 and S2 biteplates were located at mid-depth. Each station contained an underwater video camera; a third video camera was located in-air with a view of both stations.

The S1 station contained an underwater sound projector (ITC 1042 or ITC 1032) used to produce a 1-s sinusoidal amplitude modulated tone as a signal for the subject to begin hearing tests. These start tones, or "S1 tones," had a carrier frequency of 12 kHz, modulation frequency and depth of 700 Hz and 100%, respectively, and a SPL of approximately 100 dB re 1 μPa. S1 tones were generated using a PC containing a multifunction data acquisition board (National Instruments

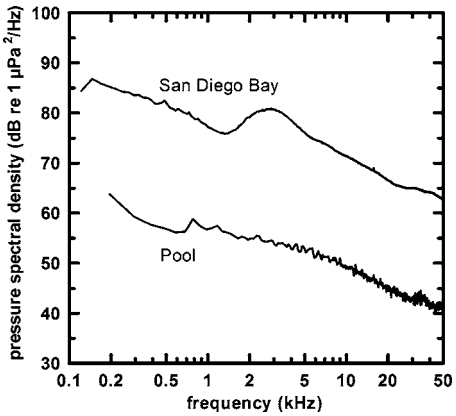

FIG. 2. Ambient noise levels measured in test pool and San Diego Bay.

TABLE I. Exposure and hearing test parameters for experiments 1–3.

Experiment	Exposure frequency (kHz)	Exposure SPL (dB re 1 μPa)	Exposure duration (s)	Hearing test frequency (kHz)
1	3	100–200	1	4.5
2	3	180–200	1	3
3	3	144–195	2–8	4.5

PCI-MIO-16E-1), filtered (Ithaco 4302), and amplified (HP 467A or BGW PS 4) before being input to the S1 sound projector.

The S2 station contained an underwater sound projector (ITC 1001 or ITC 1032) used to generate hearing test tones, or "S2 tones." The S2 tones had frequencies of 4.5 kHz (experiments 1 and 3) and 3 kHz (experiment 2) and durations of 500 ms, including 50-ms rise and fall times. S2 tones were digitally generated (PCI-MIO-16E-1), attenuated (Tucker-Davis PA4, PA5), filtered (Ithaco 4302), and amplified (BGW PS2 or PS4) before being input to the sound projector. The sound pressure during each S2 tone presentation was measured using a hydrophone (B&K 8105 or Reson TC4033) located near the S2 biteplate. The hydrophone signal was filtered and amplified (B&K 2692), digitized (PCI-MIO-16E-1), and stored on the PC. The time each S1 and S2 tone was presented was recorded and stored on the PC. Custom software (Finneran, 2003) was used to generate, record, and calibrate hearing test tones and to record the subjects' responses during hearing tests.

The small volume of the test pool resulted in large spatial variations in sound pressure. To mitigate this effect, S2 tone SPLs were calibrated before each session using two hydrophones (B&K 8105) positioned at the approximate locations of the subjects' ears (without the subject present). The hydrophone signals were filtered and amplified (B&K 2692) before being digitized (PCI-MIO-16E-1). Hearing test tone levels were estimated using the (incoherent) mean SPL from the two hydrophones. This gave an estimate of the spatial average of the SPL on a scale comparable with the subject's head.

C. Fatiguing stimuli

Fatiguing stimuli were generated using a piezoelectric cylinder (ITC 2015) positioned approximately 1 m in front of the S1 biteplate. Fatiguing stimuli were digitally generated (PCI-MIO-16E-1), attenuated (Tucker-Davis PA4 or PA5), filtered (Ithaco 4302), amplified (BGW PS4 or Crown Macro-Tech 2400), and input to the sound projector. Fatiguing stimuli were 3-kHz tones with rise and fall times of 100 ms, total durations (including the rise and fall) from 1 to 8 s, and SPLs from 100 to 200 dB re 1 μPa (depending on the particular experiment). Table I lists the fatiguing stimulus parameters and S2 frequencies for the three experiments. Exposure levels began at low levels and gradually increased during experiment 1; during experiments 2 and 3 exposure levels (and durations) were tested in quasirandom sequences.

Fatiguing sound levels for experiments 1 and 2 were estimated from calibration measurements conducted without the subject present. Instantaneous sound pressures were measured using two hydrophones (B&K 8105) positioned at the approximate locations of the subjects' ears when on the S1 biteplate. The hydrophone signals were filtered and amplified (B&K 2635 and Krohn-Hite 3C series modules), and digitized (PCI-MIO-16E-1). Since each subject normally left the S1 station before cessation of the fatiguing stimulus, and sound pressures spatially varied in the pool, calibration levels for experiments 1 and 2 must be considered as only estimates of the actual exposure. During experiment 3, the instantaneous sound pressure during the actual fatiguing exposure was measured from two suction cup-mounted hydrophones (B&K 8105) worn by the subject. The hydrophones were located near the left and right external auditory meatus. This allowed a more meaningful estimate of the actual received sound level during the exposure.

For all experiments, custom software was used to calculate the SPL and (unweighted) sound exposure level (SEL) from the digitized pressure waveforms. SEL was calculated using

$$\mathrm{SEL} = 10 \log_{10}\left(\frac{\int_0^T p^2(t)dt}{P_0^2 T_0}\right), \quad (1)$$

where $p(t)$ is the instantaneous sound pressure, $P_0 = 1$ μPa, and $T_0 = 1$ s [American National Standards Institute (ANSI), 1994]. Numeric values and units for SEL are equivalent to those of the energy flux density (EFD) level metrics used by previous authors (e.g., Finneran *et al.*, 2000; 2002b; Finneran *et al.*, 2003), where EFD level was expressed in decibels relative to the EFD of a plane wave with rms pressure P_0 and duration T_0, in the same environment (Marshall, 1996). Exposure levels were defined using the mean values of the SPL and SEL measurements from the two hydrophones. It was common during experiment 3 for the SPL/SEL measured during the exposure to differ from the desired values by 1–3 dB. For analysis purposes, exposures were placed into discrete SPL and SEL groups. Most analyses were based on the SEL of the exposure (regardless of the SPL/duration that produced that SEL).

D. Procedure

1. Overview

A single "exposure session," featuring an exposure to a fatiguing stimulus, or "control session," where the fatiguing sound exposure was simulated but no intense sound was actually produced, was conducted each test day. The control sessions were randomly interspersed with the exposure sessions; exposure sessions never occurred on consecutive days. A hearing test was performed before the exposure (or mock exposure) to provide the subject's pre-exposure hearing threshold. Another hearing test was conducted after the exposure (or mock exposure) to provide the post-exposure hearing threshold. The amount of TTS was determined by subtracting the pre-exposure threshold from the post-exposure threshold. Total session time was approximately 45 min.

2. Pre-exposure hearing tests

The hearing test procedure was based on the Method of Free Response, or MFR (Egan *et al.*, 1961) and was similar to that used by Schlundt *et al.* (2000) and Finneran *et al.* (2000; 2002b; 2003). Each hearing test consisted of a number of relatively long observation periods, or "dives," during which the subject was presented with a number of hearing test tones. Each dive began with the trainer directing the animal (with a hand signal) to the S1 station. The subject was trained to remain on the S1 station until presented with the S1 start signal, which signaled the subject to proceed to the S2 station. Once the subject was positioned at the S2 station, a block of hearing test trials was presented. The trial block was ended when the trainer sounded an underwater buzzer to signal the subject to return to the surface and receive fish reward. The process was then repeated as necessary.

Each trial block contained a variable number of 2-s duration trials. The time interval between trials, defined from the start of one trial to the start of the next trial, was fixed at 4 s. Fifty-percent of the trials contained an S2 tone beginning 50 ms before the trial start. The remaining 50% of the trials were no-tone or "catch" trials. Since the subject was not notified at the start of each trial, the catch trial periods functioned as "equipment catch trials" and were primarily used to confirm that the sound system was not producing artifacts coinciding with the stimulus. Subjects were trained to whistle if they heard a tone and to remain quiet otherwise. The first S2 tone was presented approximately 10 dB above the baseline threshold. The amplitudes of the S2 tones were decreased 2 dB following each hit and increased 2 dB following each miss (e.g., Cornsweet, 1962).

The false alarm rate R_{FA} was defined as

$$R_{FA} = \frac{N_{FA}}{T - N_{S2}T_1}T_1, \tag{2}$$

where N_{FA} is the number of false alarms (whistles occurring during no-tone trials or between trials), T is the total amount of time the subject spent on the S2 station, N_{S2} is the number of S2 tone trials presented, and T_1 is the trial duration. The denominator of Eq. (2) is the total amount of time during which the subject was on the S2 station without a tone trial present, therefore R_{FA} is a way of normalizing the number of false alarms with respect to the amount of time that the subject had an opportunity to commit a false alarm (see Finneran *et al.*, 2002a; 2002b). This study employed a modified version of the MFR, so the R_{FA} values calculated here are not identical to those obtained with the MFR or a single interval experiment; however, they do enable one to assess a subject's response bias from session to session.

A randomized schedule was used to determine the point at which reinforcement was delivered (i.e., the number of trials per dive). Dives were concluded following a number of correct responses (i.e., either hits or correct rejections) randomly chosen from a predefined schedule. The number of required correct responses varied from 4 to 8. Dive times were normally kept to less than 2 min. The amount of reward was scaled to the performance of the subject during the dive (e.g., more reinforcement was given for more correct responses) by assigning individual scores for hits, misses, correct rejections, and false alarms and summing the scores for each dive. The dive score was multiplied by a subject-specific scale factor to obtain a number representing the amount of fish to be given. To maintain each subject's performance, periodic (about once/week) training sessions were conducted where responses to low-level tones (i.e., at a lower level than any previously responded to) were preferentially reinforced. Training sessions did not feature fatiguing stimulus exposures and were not used to estimate audiograms.

After reinforcement, the next dive was begun and the procedure repeated until the hearing test was complete. Pre-exposure hearing thresholds were based on the last 10 hit/miss and miss/hit "reversal" points from the staircase. The pre-exposure threshold could usually be estimated after 2–5 dives or 25–30 trials. Pre-exposure thresholds were required to be within ±5 dB of established baseline values for fatiguing sound exposures to occur. Baseline threshold standard deviations were 2–3 dB at 3 and 4.5 kHz; less than 10% of sessions were excluded for failure for pre-exposure thresholds to occur within ±5 dB of baseline values.

3. Post-exposure hearing tests

The post-exposure hearing test procedure was identical to the pre-exposure procedure with two exceptions: (1) During exposure sessions, the fatiguing stimulus was presented instead of the first S1 start tone of the post-exposure hearing test. (2) The post-exposure hearing tests were conducted for at least 10 minutes to enable any NITS to be tracked over time.

The post-exposure hearing test resulted in a record of the subject's performance (hit or miss) for each tone trial. These data were then converted to a series of reversals. The time and amplitude of each reversal were defined as the mean time and mean SPL, respectively, of the hit/miss pair. The hearing threshold as a function of the time post-exposure was estimated by applying a 10-point moving average to the set of reversals. Each output of the moving average consisted of the mean SPL over the 10 reversals and the mean time over which the 10 reversals occurred. Thresholds at specific times post-exposure were obtained by interpolating within the collection of thresholds from the moving average. The amount of TTS 4 min (TTS_4) and 10 min (TTS_{10}) after exposure were used to compare the results of the different exposure conditions. For this study, 4 min was about the shortest time in which a threshold could reliably be obtained after exposure. Four minutes is commonly used as an early TTS measurement time; measurements before 2 min may be susceptible to the "bounce" phenomenon observed in terrestrial mammals and result in less observed TTS than at later times (Hirsh and Ward, 1952; Hirsh and Bilger, 1955). For the specific reinforcement schedules and available food per session, TTS_{10} was found to be a practical upper limit for the maximum time for TTS measurement after exposure. TTS_4 was obtained in all but one of the exposure and control sessions: for subject NAY exposed to a 200 dB re 1 μPa tone during experiment 1, the first post-exposure threshold was not obtained until 7.2 min after the exposure.

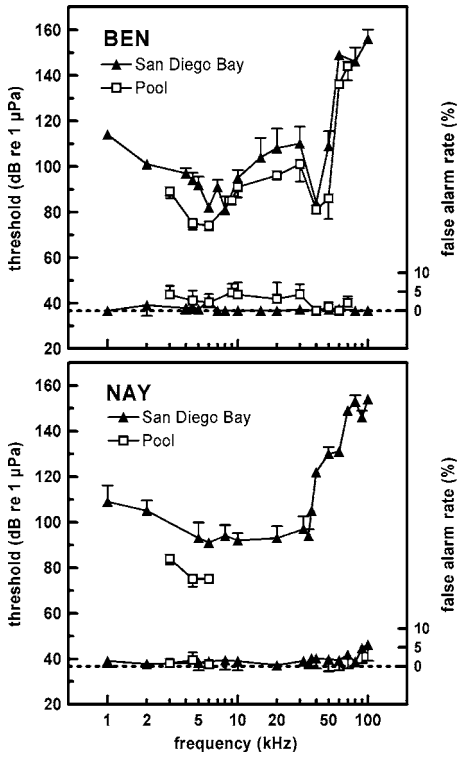

FIG. 3. Behavioral hearing thresholds and false alarm rates for subjects BEN (upper panel) and NAY (lower panel) measured in test pool and San Diego Bay. Symbols represent mean values and error bars indicate one standard deviation.

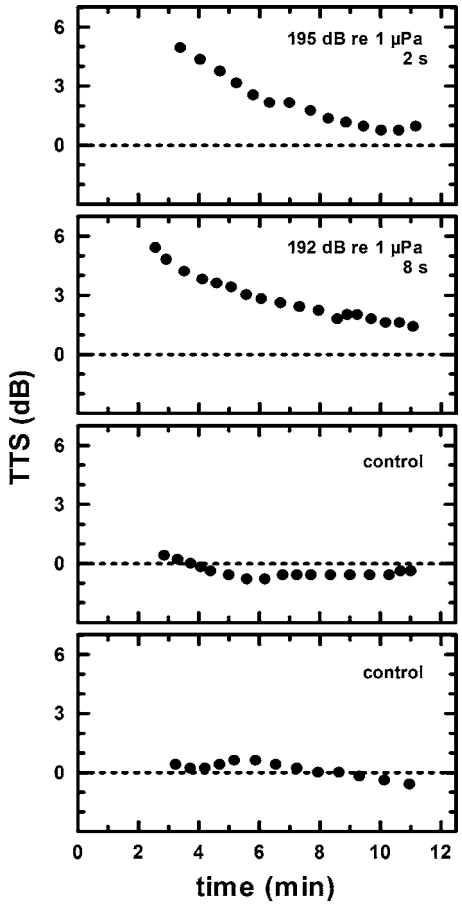

FIG. 4. Examples of TTS measured as a function of time post-exposure for exposure and control sessions.

Previous studies of TTS in marine mammals have reported, in addition to auditory effects of noise exposure, effects on the behavior of the subjects. Specific behavioral effects most often reported can be broadly described as attempts by the subjects to leave the area of a continuing exposure (e.g., Kastak *et al.*, 1999) or to avoid the site of previous exposures (Finneran *et al.*, 2000; Schlundt *et al.*, 2000; Finneran *et al.*, 2002b). Behavioral reactions observed during experiments 1 and 2 have been previously reported (Finneran and Schlundt, 2004). Behavioral reactions of BEN during experiment 3 were analyzed using the same approach used in Finneran and Schlundt (2004). Observations of the subject's behavior during training, control, and exposure sessions were used to subjectively grade each exposure session as "normal behavior" or "altered behavior." The most common example of altered behavior was a reluctance to return to the S1 station on the dive immediately following the fatiguing sound exposure. For each exposure SEL, the percentage of sessions with altered behavior was calculated.

III. RESULTS

A. Baseline hearing thresholds and ambient noise levels

Figure 3 shows hearing thresholds and false alarm rates measured for BEN (upper panel) and NAY (lower panel) in San Diego Bay and in the test pool. Thresholds were measured in the pool before experiments 1–3; the data were pooled to create Fig. 3. NAY was only tested in the pool at frequencies near the fatiguing stimulus and hearing test tone frequencies. The number of replications at each frequency varied: for tests in San Diego Bay, between 2 and 9; in the test pool, between 1 and 28, depending on frequency (most tests were conducted at 3, 4.5, and 6 kHz). Although both subjects had poor sensitivity above 40–50 kHz, within the range of 3–4.5 kHz sensitivity was comparable to that measured for bottlenose dolphins by Johnson (1967) and suggests "normal" hearing at these frequencies. Both subjects were relatively conservative and did not commit large numbers of false alarms, especially when tested in San Diego Bay.

B. TTS Growth and recovery

Figure 4 shows four examples of the measured TTS as a function of time post-exposure. The upper two panels show the results of exposure sessions with SPLs and durations of 195 dB re 1 μPa, 2 s and 192 dB re 1 μPa, 8 s, respectively. The lower two data sets are from control sessions. The patterns seen in the upper two panels were common—an initial shift that decreased with increasing time post-exposure. In most cases (88% of exposure sessions) TTS_{10} was less than 3 dB. Most exceptions occurred at the higher exposure conditions. For example, at exposure SELs of 201 and 203 dB re 1 μPa^2 s, two-thirds of the exposures resulted in TTS_{10} >3 dB; the mean values for TTS_{10} at these exposure levels were 3.8 and 4.3 dB, respectively. Variation of 2–4 dB was common in the control sessions and was consistent with the

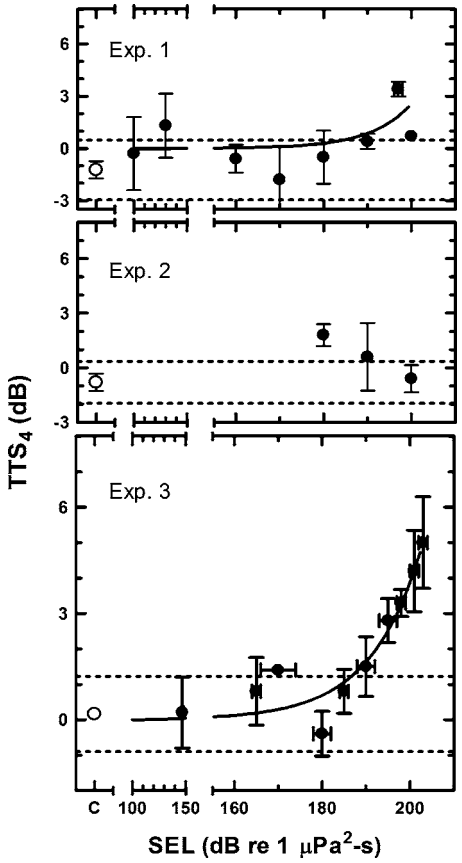

FIG. 5. Growth of TTS_4 as a function of exposure SEL for experiments 1 (upper), 2 (middle), and 3 (lower). The symbols and vertical error bars represent the mean and the standard error of the mean, respectively. The horizontal error bars indicate the range of exposure SELs grouped together for analysis. The open circles indicate the mean TTS_4 measured during control sessions. The dashed lines represent the control mean ± one standard deviation. The solid lines in the top and bottom panels were generated by performing a nonlinear regression with an exponential growth equation and are intended to be a visual aid only.

normal variation seen in thresholds measured using behavioral response paradigms [e.g., Johnson, 1967; National Institute for Occupational Safety and Health (NIOSH), 1998)]. There were no permanent shifts in either subjects' hearing thresholds.

Figure 5 summarizes the measured TTS_4 as a function of SEL for experiments 1 (upper), 2 (middle), and 3 (lower), respectively. Results were pooled from both subjects in experiments 1 and 2. A one-way ANOVA with Dunnett's post-test (GraphPad Software, 2003) was performed to test for significant differences between the mean values of TTS_4 measured during control and exposure sessions within each experiment. For experiment 1, significant differences existed between the control data and exposures with SEL = 197 dB re 1 μPa^2 s ($p < 0.01$). The ANOVA did not include the point at SEL = 200 dB re 1 μPa^2 s, since only one value of TTS_4 was obtained (TTS_4 may have been larger than the TTS measured 7.2 min post-exposure in the second exposure at this SEL). For experiment 2, there were no significant differences between control and exposure results ($p > 0.05$). For experiment 3, significant differences existed for all exposures with SEL $\geq$ 195 dB re 1 μPa^2 s ($p < 0.01$). For experiment 3 at SEL = 195 dB re 1 μPa^2 s, the mean TTS_4 was 2.8 dB. Exposure SPLs resulting in statistically significant differences ($p < 0.01$) between control and exposure sessions were 197 dB re 1 μPa (1 s), 190 and 195 dB re 1 μPa (2 s), 184, 190, and 195 dB re 1 μPa (4 s), and 190, 192, 195 dB re 1 μPa (8-s exposure).

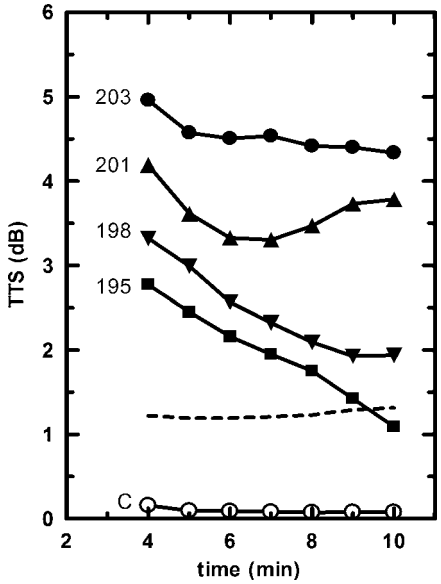

FIG. 6. Recovery of TTS for exposures producing statistically significant TTS_4. The numbers by each series indicate the exposure SEL in dB re 1 μPa^2 s. The open circles show the mean values of TTS for the control sessions; the dashed line is the control mean plus one standard deviation. Standard deviations for the exposure TTSs were generally 1–2 dB and, to preserve visual clarity, are not shown.

Figure 6 shows the mean values of TTS measured between 4 and 10 min post-exposure for exposure SELs of 195 to 203 dB re 1 μPa^2 s (the exposure SELs producing statistically significant amounts of TTS_4). The measured TTS generally decreased with increasing time post-exposure. For SELs < 200 dB re 1 μPa^2 s, TTS_{10} was less than approximately 2 dB and was not significantly different than the control session mean TTS_{10}. Exposures with higher SELs produced larger amounts of TTS_4 and subsequently required longer times for recovery. For SELs of 201 and 203 dB re 1 μPa^2 s, recovery was not complete by 10 min. In all cases, recovery to within the normal range of pre-exposure thresholds was complete by the next testing day (generally the next calendar day).

C. Behavioral results

Figure 7 shows the percentage of sessions with "altered behavior." The same trends reported by Finneran and Schlundt (2004) exist: little or no changes in behavior at low exposure levels and an increasing frequency of behavioral changes as the exposure level increased. The sparse data prevented fitting a sigmoidal dose-response curve.

D. Relationship to previous studies

The results of the present study were combined with the 3-, 10-, and 20-kHz TTS data from Schlundt *et al.* (2000) to create a dose-response curve for the occurrence of TTS in dolphins and white whales exposed to mid-frequency tones.

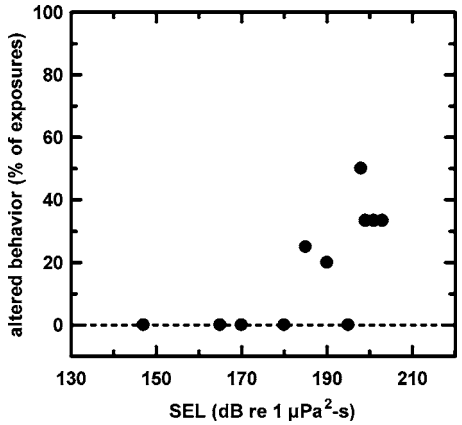

FIG. 7. Percentage of fatiguing sound exposure sessions with altered behavior as a function of exposure SEL for experiment 3.

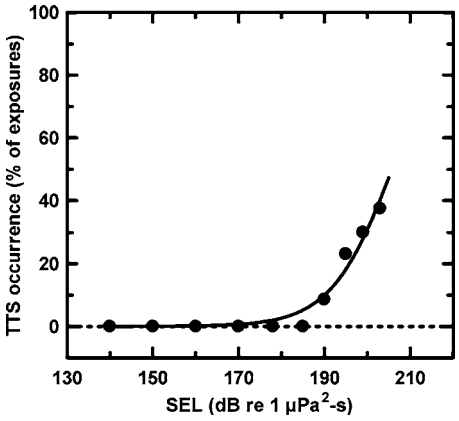

FIG. 8. Pooled data from Schlundt *et al.* (2000) and the present study showing the percentage of exposures resulting in detectable TTS (Schlundt *et al.*, 6 dB or more; present study, 2.8 dB or more) as a function of exposure SEL.

This required the result of each sound exposure, normally described by the amount of TTS, to be converted to a binary result indicating "TTS" or "no TTS." Since Schlundt *et al.* (2000) used a 6-dB criterion for the occurrence of TTS, sound exposures from Schlundt *et al.* producing 6 dB or more TTS were classified as TTS and those producing less than 6 dB TTS were categorized as no TTS. For the present study, data from experiment 3 revealed that exposures with SEL $\geqslant$ 195 dB re 1 μPa^2 s produced statistically significant amounts of TTS. The mean amount of TTS at SEL = 195 dB re 1 μPa^2 s was 2.8 dB, therefore, for the present study, 2.8 dB of TTS was selected as the criterion: Individual exposures resulting in 2.8 dB or more TTS were classified as causing TTS; those producing less than 2.8 dB of TTS were considered to result in no TTS. The data were pooled by exposure SEL. Exposures with SELs (in dB re 1 μPa^2 s) within the following ranges were assigned the nominal SEL listed in parentheses: 100 (100), 125–134 (130), 135–144 (140), 145–154 (150), 155–164 (160), 165–174 (170), 175–182 (178), 183–187 (185), 188–192 (190), 193–197 (195), 198–202 (200), and 203–204 (203). For each exposure SEL group having more than two members (all but the 100 and 130 dB re 1 μPa^2 s groups), the percentage of exposures resulting in TTS was calculated. Figure 8 shows the resulting occurrence of TTS (percentage of exposure sessions resulting in TTS) as a function of exposure SEL. A nonlinear regression was used to fit a four-parameter logistic model to the data (GraphPad Software, 2003) in order to generate a smooth dose-response curve.

Figure 9 compares exposure levels necessary to cause measurable amounts of TTS from the present study to those previously published for cetaceans (Finneran *et al.*, 2000; 2002b; Schlundt *et al.*, 2000; Nachtigall *et al.*, 2004). The solid line in the middle panel of Fig. 9 has a slope of -3 dB per doubling of time and passes through the point where SPL is 195 dB re 1 μPa [the mean SPL required for measurable TTS from Schlundt *et al.*, (2000)] and the exposure duration is 1 s. This type of line is sometimes referred to as an "equal energy line," because all points on the line have the same sound exposure, which for a plane progressive wave is proportional to sound energy flux density. This line appears in the lower panel as a horizontal line at 195 dB re 1 μPa^2 s.

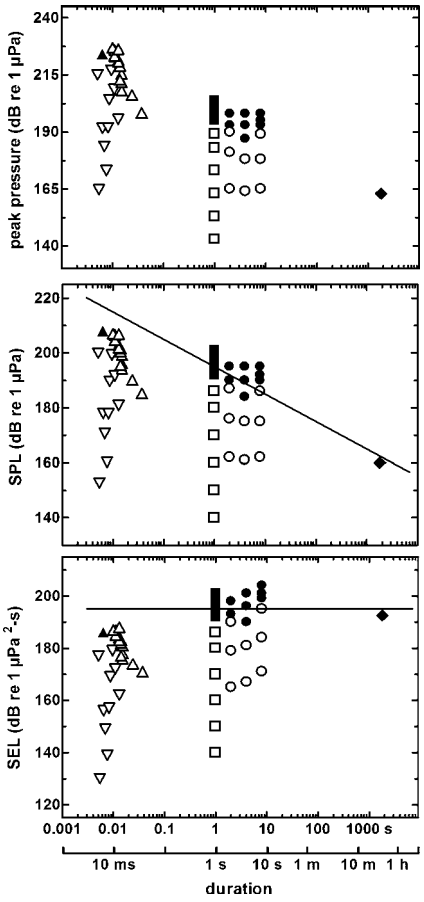

FIG. 9. Summary of bottlenose dolphin and white whale TTS experimental data. Individual exposures are shown in terms of peak pressure (upper panel), SPL (middle panel), and SEL (lower panel) vs exposure duration. Closed symbols indicate exposures where measurable TTS was observed; open symbols represent exposure conditions that did not produce TTS. The circles indicate the results of the present study. The triangles represent impulsive test results from Finneran *et al.* (2000; 2002b). The squares show the 3-, 10-, and 20-kHz data from Schlundt *et al.* (2000). The diamond represents data from Nachtigall *et al.* (2003; 2004). Peak pressures from Nachtigall *et al.* (2003; 2004) were approximated as the (rms) SPL+3 dB. The solid lines represent an "equal-energy" condition.

IV. DISCUSSION

A. Testing environment and baseline hearing thresholds

One of the main motivations for this study was to determine the effects, if any, of the masking noise employed by Schlundt *et al.* (2000) while measuring TTS in San Diego Bay. To accomplish this, tests were conducted in an aboveground pool with low, relatively constant ambient noise levels, therefore no intentional masking noise was introduced. Because of the small volume of the pool, large spatial variations in sound pressure were observed, making calibration of hearing test tones difficult. To overcome this, two hydrophones were used to provide an average sound pressure over a spatial scale comparable to the size of the subjects' heads. This lessened the chance of sound pressure peaks or nulls giving a false impression of the SPL actually received by the subject and allowed consistent hearing threshold measurements from day-to-day.

The spatial variations in sound pressure also affected estimates of the received levels during the fatiguing sound exposure. During experiments 1 and 2, fatiguing levels were estimated from two (stationary) sound pressure measurements made without the subject present. Because the subjects moved away from the exposure site toward the hearing test location shortly after the exposure start, exposure levels for experiments 1 and 2 must be considered as only approximate. The actual exposures may have been higher or lower (perhaps up to 4–5 dB), depending on the subject's path and the spatial variation in the sound field. For experiment 3, a better representation of the received sound level was obtained by having the subject wear hydrophones mounted on suction cups. The hydrophones were positioned to place the receiving element near each external auditory meatus, in order to provide an estimate of the sound pressure near the ear during the actual exposure—a sort of "acoustic dosimeter." As a result, the instantaneous sound pressure received by the subject was estimated and the desired quantities (SPL and SEL) calculated. In many cases the measured SPL and SEL differed from the intended exposures by 1–3 dB and replications could not be obtained with exactly the same exposure levels, forcing data to be consolidated into groups of similar exposure level for analysis.

Because of time constraints, detailed audiograms were not obtained for both subjects in the pool, and the audiograms in Fig. 3 are primarily intended to show the hearing sensitivity of each subject near the exposure and hearing test frequencies. Both subjects had relatively poor high-frequency hearing (above 40–50 kHz), which may be relatively common for adult male dolphins (Ridgway and Carder, 1997; Moore *et al.*, 2004). Sensitivity of both subjects within the range of 3 to 4.5 kHz was comparable to values commonly reported for bottlenose dolphins (e.g., Johnson, 1967) and suggests "normal" hearing at the exposure and hearing test frequencies. There are no data to indicate that the amount of TTS resulting from a narrow-band exposure is affected by hearing loss at frequencies outside the range where TTS would is expected to occur. Therefore, even though both subjects had pre-existing high-frequency hearing loss (above 40–50 kHz), this should not have affected the amount of TTS produced by exposures at much lower frequencies (3 kHz) where their hearing sensitivities appeared normal.

B. Growth of TTS

Figure 5 summarizes the growth of TTS with increasing SEL observed during experiments 1–3. The most important results were obtained in experiment 3, where the exposure SELs and relatively large number of exposure sessions enable more definitive conclusions. Over the range of exposures tested, the amount of TTS was correlated with and increased monotonically with increasing SEL. Statistically significant amounts of TTS were observed for exposure SELs $\geqslant$ 195 dB re 1 μPa^2 s. This is identical to the mean SEL for causing "onset-TTS," defined as 6 dB or more of TTS by Schlundt *et al.* (2000) for 3-, 10-, and 20-kHz exposures. It is also very close to the SELs of 193-194 dB re 1 μPa^2 s reported by Nachtigall *et al.* (2004) for a bottlenose dolphin exposed to long duration octave band noise. The data from the present study also suggest that the masking noise employed by Schlundt *et al.* (2000) did not have a substantial effect on the onset-TTS levels observed.

An important application of marine mammal TTS data is to estimate exposure levels that may cause PTS. This requires an estimate for the rate of TTS growth with exposure—how much additional TTS is produced by increases in exposure level. At the highest SEL tested in this study (203 dB re 1 μPa^2 s), the slope of the curve in the lower panel of Fig. 5 is approximately 0.4 dB/dB, indicating that each additional dB of SEL would produce an additional 0.4 dB of TTS_4. This is much lower than related quantities reported in humans ($\sim$1.6 dB TTS_2/dB SEL, Ward *et al.*, 1958; 1959) after exposures of 12–102 min causing TTS_2 up to 30–40 dB. Because the slopes of the exponential curves in Fig. 5 increase with increasing SEL, the relatively low slope estimates may be a result of the very small amounts of TTS observed. It is likely that the observed growth rate would increase if larger SELs (and thus larger amounts of TTS) were employed. Experiments producing larger amounts of TTS are necessary to estimate the growth rate of TTS beyond the range of the TTS amounts experimentally observed.

C. Recovery from TTS

Figure 6 summarizes the recovery from statistically significant amounts of TTS_4 observed during experiment 3. For TTS_4 of about 3–4 dB (exposure SELs of 195-199 dB re 1 μPa^2 s), recovery is nearly complete (i.e., TTS was no longer measurable) by 10 min post-exposure. For exposure SELs of 201 and 203 dB re 1 μPa^2 s, TTS_4 was larger (4–5 dB) and recovery was not complete by 10 min. The recovery curves decreased monotonically with increasing time, except for the 201 dB re 1 μPa^2 s curve; however, since the standard deviations associated with each TTS data point were 1–2 dB, this pattern should be treated with some caution. The recovery times are related to the initial TS and exposure SEL: higher SELs produced larger initial shifts which required longer recovery times. Studies of TTS in people ex-

posed to noise also revealed that the exposure duration is important in recovery; that given identical initial shifts, longer duration exposures required longer recover times (e.g., Mills, 1983). Nachtigall *et al.* (2004) reported recovery times for slightly higher amounts of TTS (TTS_5 about 7 dB) to be much longer (up to 105 min), suggesting that this relationship may occur in dolphins as well. As with the TTS growth data, the interpretation of the recovery curves is hampered by the very small amounts of TTS relative to the variability of the measurements. Larger amount of initial NITS and longer recovery times are necessary for proper analysis. Because of the difficulties involved in generating underwater SPLs in excess of 190–195 dB re 1 μPa in a normal laboratory setting, a larger initial NITS will most likely only be accomplished by increasing exposure duration.

D. Behavioral reactions

Behavioral reactions of the subjects of experiments 1 and 2 of the present study were reported by Finneran and Schlundt (2004), who summarized behavioral reactions of dolphins and white whales exposed to 1-s tones during TTS experiments [experiments 1 and 2 of the present study and the experiments described by Schlundt *et al.* (2000)]. Observed behavioral reactions in the present study were relatively minor. The most common example of altered behavior was a reluctance or refusal to return to the S1 station on the dive immediately following the fatiguing sound exposure. On two occasions during experiments 1 and 2, NAY ignored the trainer following the exposure, preventing TTS_4 from being obtained in one instance. In general, BEN was very tolerant of the exposures and exhibited only minor changes in behavior. For experiment 3, the percentage of sessions with behavioral reactions as a function of exposure SEL is shown in Fig. 7. The small number of exposures at each SEL contributed to large variability within the dose-response data of Fig. 7 (e.g., with only two data points, all percentages will be 0, 50%, or 100%). Coupled with the lack of observed percentages greater than 50%, this prevented a true dose-response curve from being created.

E. TTS Dose-response curve

Predictions for the effects of sound on marine mammals often rely upon some numeric "threshold for effect," where sound exposures less than the threshold are assumed to cause no effect and those above the threshold are assumed to cause the effect. Ideally, a specific numeric threshold value is derived from a dose-response curve relating the sound exposure to the percentage of individuals experiencing a particular effect. A suitable value is then chosen for the percentage of individuals affected, often the 50% point, and the exposure threshold value interpolated from the dose-response curve. Similar approaches are common in pharmacological studies to determine the efficacy of drugs, studies of animal mortality in response to underwater blasts (e.g., Yelverton *et al.*, 1973), and have been used to summarize behavioral responses to noise (e.g., Finneran and Schlundt, 2004).

Figure 8 was created by combining the results of the present study with the 3-, 10-, and 20-kHz TTS data from Schlundt *et al.* (2000) to show the percentage of exposures that resulted in TTS as a function of exposure SEL. The percentage of exposures resulting in TTS is small at relatively low SELs and increases with increasing SEL, as expected. The curve resulted in a 50% affected point of approximately 206 dB re 1 μPa^2 s; however, this value should be interpreted with caution since the data are limited and the 50% point lies beyond the range of measured values. Also, because of the limited number of subjects (8), the data used to create the dose-response curve are based on the percentage of *exposures* in which TTS was observed, not the percentage of individuals experiencing TTS, and therefore much of the data come from only a few subjects. It is important to note that not all exposures above a certain TTS threshold will necessarily cause TTS; at a SEL of 195 dB re 1 μPa^2 s, the level required for significant TTS_4 in this study, the percentage of exposures which actually resulted in measurable TTS is only about 18%.

F. Summary of existing cetacean TTS data

Figure 9 summarizes the existing onset-TTS data for cetaceans. These data emphasize that the effects of the different sound exposures do not depend on the sound pressure alone, but also depend on the duration. As the exposure duration decreases, higher SPLs are required to cause TTS. In contrast, SELs required for TTS do not show the same type of variation with exposure duration, since the duration is included in the SEL calculation. The equal energy line at 195 dB re 1 μPa^2 s fits the tonal and noise data (the nonimpulsive data) well, despite differences in exposure duration, SPL, experimental techniques, and subjects. Together, these data indicate that a SEL of 195 dB re 1 μPa^2 s is a reasonable threshold to use for onset-TTS in dolphins and white whales exposed to mid-frequency sounds.

V. CONCLUSIONS

Amounts of TTS_4 measured in bottlenose dolphins after exposure to 3-kHz tones with SELs $\geq$ 195 dB re 1 μPa^2 s were significantly higher than amounts of TTS_4 measured after control sessions with simulated exposures. These data agree with prior TTS data from Schlundt *et al.*, 2000) and Nachtigall *et al.*, 2004). Together, these data point to a SEL of 195 dB re 1 μPa^2 s as a threshold for onset-TTS in dolphins and white whales exposed to midfrequency sounds. The data from the present study also suggest that the masking noise employed by Schlundt *et al.* (2000) did not have a substantial effect on the onset-TTS levels observed.

Because of the small amounts of TTS_4, estimates of the rate of growth of TTS with increasing exposure may be under-estimates. Experiments producing larger amounts of TTS will be necessary to estimate the growth rate of TTS beyond the range of the TTS amounts experimentally observed. Similarly, larger amounts of initial NITS will be required for proper measurements of recovery time.

ACKNOWLEDGMENTS

Animal training and/or experimental data collection were performed by J. Jeffress, T. Kamolnick, F. Shafer, J.

Alder, T. Aguayo, A. Sheridan, E. Ferguson, and K. St. John. Financial support was provided by the U.S. Office of Naval Research Marine Mammal Science and Technology Program, Navy CNO(N45), and NOAA Fisheries Office of Protected Resources Acoustics Program. We also thank Dr. Roger Gentry, Dr. Robert Gisiner, and Dr. Mardi Hastings for support and encouragement.

American National Standards Institute (ANSI) (**1994**). "Acoustical terminology," ANSI S1.1-1994.

Cornsweet, T. N. (**1962**). "The staircase method in psychophysics," Am. J. Psychol. **75**, 485–491.

Dalecki, D., Raeman, C. H., Child, S. Z., McAleavey, S. A. and Carstensen, E. L. (**1999**). "Lung response to low-frequency underwater sound," J. Acoust. Soc. Am. **106**, 2165(A).

Egan, J. P., Greenberg, G. Z., and Schulman, A. I. (**1961**). "Operating characteristics, signal detectability, and the method of free response," J. Acoust. Soc. Am. **33**, 993–1007.

Finneran, J. J. (**2003**). "An integrated computer-controlled system for marine mammal auditory testing," TD 3159, SSC San Diego, San Diego, CA.

Finneran, J. J., Dear, R., Carder, D. A., and Ridgway, S. H. (**2003**). "Auditory and behavioral responses of California sea lions (Zalophus californianus) to underwater impulses from an arc-gap transducer," J. Acoust. Soc. Am. **114**, 1667–1677.

Finneran, J. J., and Schlundt, C. E. (**2004**). "Effects of intense pure tones on the behavior of trained odontocetes," TR 1913, SSC San Diego, San Diego, CA.

Finneran, J. J., Schlundt, C. E., Carder, D. A., Clark, J. A., Young, J. A., Gaspin, J. B., and Ridgway, S. H. (**2000**). "Auditory and behavioral responses of bottlenose dolphins (*Tursiops truncatus*) and a beluga whale (*Delphinapterus leucas*) to impulsive sounds resembling distant signatures of underwater explosions," J. Acoust. Soc. Am. **108**, 417–431.

Finneran, J. J., Schlundt, C. E., Carder, D. A., and Ridgway, S. H. (**2002a**). "Auditory filter shapes for the bottlenose dolphin (*Tursiops truncatus*) and the white whale (*Delphinapterus leucas*) derived with notched-noise," J. Acoust. Soc. Am. **112**, 322–328.

Finneran, J. J., Schlundt, C. E., Dear, R., Carder, D. A., and Ridgway, S. H. (**2002b**). "Temporary shift in masked hearing thresholds (MTTS) in odontocetes after exposure to single underwater impulses from a seismic watergun," J. Acoust. Soc. Am. **111**, 2929–2940.

GraphPad prism 4.0.2, GraphPad Software, San Diego, CA.

Green, D. M., DeFerrari, H. A., McFadden, D., Pearse, J. S., Popper, A. N., Richardson, W. J., Ridgway, S. H., and Tyack, P. L. (**1994**). *Low Frequency Sound and Marine Mammals: Current Knowledge and Research Needs* (National Academy Press, Washington, DC).

Hirsh, I. J., and Bilger, R. C. (**1955**). "Auditory-threshold recovery after exposure to pure tones," J. Acoust. Soc. Am. **27**, 1186–1194.

Hirsh, I. J., and Ward, W. D. (**1952**). "Recovery of the auditory threshold after strong acoustic stimulation," J. Acoust. Soc. Am. **24**, 131–141.

Humes, L. E. (**1980**). "Temporary threshold shift for masked pure tones," Audiology **19**, 335–345.

Jepson, P. D., Arbelo, M., Deaville, R., Patterson, I. A. R., Castro, P., Baker, J. R., Degollada, E., Ross, H. M., Herráez, P., Pocknell, A. M., Rodriguez, E., Howie, F. E., Espinosa, A., Reid, R. J., Jaber, J. R., Martin, V., Cunningham, A. A., and Fernandez, A. (**2003**). "Gas-bubble lesions in stranded cetaceans," Nature (London) **425**, 575–576.

Johnson, C. S. (**1967**). "Sound detection thresholds in marine mammals," in *Marine Bioacoustics*, edited by W. N. Tavolga (Pergamon, Oxford), pp. 247–260.

Kastak, D., and Schusterman, R. J. (**1996**). "Temporary threshold shift in a harbor seal (*Phoca vitulina*)," J. Acoust. Soc. Am. **100**, 1905–1908.

Kastak, D., Schusterman, R. J., Southall, B. L., and Reichmuth, C. J. (**1999**). "Underwater temporary threshold shift induced by octave-band noise in three species of pinniped," J. Acoust. Soc. Am. **106**, 1142–1148.

Marshall, W. J. (**1996**). "Descriptors of impulse signal levels commonly used in underwater acoustics," IEEE J. Ocean. Eng. **21**, 108–110.

Mills, J. H., Osgithorpe, J. D., Burdick, C. K., Patterson, J. H., and Mozo, B. (**1983**). "Temporary threshold shifts produced by exposure to low-frequency noises," J. Acoust. Soc. Am. **73**, 918–923.

Moore, P. W. B., Finneran, J. J., and Houser, D. S. (**2004**). "Hearing loss and echolocation signal change in dolphins," J. Acoust. Soc. Am. **116**, 2503(A).

Nachtigall, P. E., Pawloski, J., and Au, W. W. L. (**2003**). "Temporary threshold shifts and recovery following noise exposure in the Atlantic bottlenosed dolphin (Tursiops truncatus)," J. Acoust. Soc. Am. **113**(6), 3425–3429.

Nachtigall, P. E., Supin, A., Pawloski, J., and Au, W. W. L. (**2004**). "Temporary threshold shifts after noise exposure in the bottlenose dolphin (Tursiops truncatus) measured using evoked auditory potentials," Marine Mammal Sci. **20**, 673–687.

National Institute for Occupational Safety and Health (NIOSH) (**1998**). "Criteria for a recommended standard: Occupational noise exposure, revised criteria 1998," Publication No. 98-126, Cincinnati, OH.

Parker, D. E., Tubbs, R. L., Johnston, P. A., and Johnston, L. S. (**1976**). "Influence of auditory fatigue on masked pure-tone thresholds," J. Acoust. Soc. Am. **60**, 881–885.

Ridgway, S. H., and Carder, D. A. (**1997**). "Hearing deficits measured in some *Tursiops truncatus*, and discovery of a deaf/mute dolphin," J. Acoust. Soc. Am. **101**, 590–594.

Schlundt, C. E., Finneran, J. J., Carder, D. A., and Ridgway, S. H. (**2000**). "Temporary shift in masked hearing thresholds of bottlenose dolphins, *Tursiops truncatus*, and white whales, *Delphinapterus leucas*, after exposure to intense tones," J. Acoust. Soc. Am. **107**, 3496–3508.

U.S. Department of Commerce and U.S. Department of the Navy (**2001**). "Joint interim report Bahamas marine mammal stranding event of 14-16 March 2000," Department of Commerce, Washington, DC.

Ward, W. D., Glorig, A., and Sklar, D. L. (**1958**). "Dependency of temporary threshold shift at 4 kc on intensity and time," J. Acoust. Soc. Am. **30**, 944–954.

Ward, W. D., Glorig, A., and Sklar, D. L. (**1959**). "Temporary threshold shift from octave-band noise: applications to damage-risk criteria," J. Acoust. Soc. Am. **31**, 522–528.

Yelverton, J. T., Richmond, D. R., Fletcher, E. R., and Jones, R. K. (**1973**). "Safe distances from underwater explosions for mammals and birds," DNA 3114T, Lovelace Foundation for Medical Education and Research, Albuquerque, New Mexico.

Alarm signals of the great gerbil: Acoustic variation by predator context, sex, age, individual, and family group

Jan A. Randall
Department of Biology, San Francisco State University, San Francisco, California 94132

Brenda McCowan
Department of Population Health and Reproduction and Veterinary Medicine Teaching and Research Center, School of Veterinary Medicine, University of California at Davis, 18830 Road 112, Tulare, California 93274

Kellie C. Collins
Department of Biology, San Francisco State University, San Francisco, California 94132

Stacie L. Hooper
Department of Population Health and Reproduction and Veterinary Medicine Teaching and Research Center, School of Veterinary Medicine, University of California at Davis, 18830 Road 112, Tulare, California 93274

Konstantin Rogovin
Severtzov Institute of Ecology and Evolution, Leninskii Prospect 33, Moscow, Russia

(Received 21 December 2004; revised 18 May 2005; accepted 14 July 2005)

The great gerbil, *Rhombomys opinus*, is a highly social rodent that usually lives in family groups consisting of related females, their offspring, and an adult male. The gerbils emit alarm vocalizations in the presence of diverse predators with different hunting tactics. Alarm calls were recorded in response to three predators, a monitor lizard, hunting dog, and human, to determine whether the most common call type, the rhythmic call, is functionally referential with regard to type of predator. Results show variation in the alarm calls of both adults and subadults with the type of predator. Discriminant function analysis classified an average of 70% of calls to predator type. Call variation, however, was not limited to the predator context, because signal structure also differed by sex, age, individual callers, and family groups. These variations illustrate the flexibility of the rhythmic alarm call of the great gerbil and how it might have multiple functions and communicate in multiple contexts. Three alarm calls, variation in the rhythmic call, and vibrational signals generated from foot-drumming provide the gerbils with a varied and multi-channel acoustic repertoire. © *2005 Acoustical Society of America.* [DOI: 10.1121/1.2031973]

PACS number(s): 43.80.−n, 43.80.Ka, 43.80.Lb, 43.80.Jz [JAS] Pages: 2706–2714

I. INTRODUCTION

Alarm vocalizations can contain multiple messages. Ground-dwelling rodents and primates call to warn group members of danger (Sherman, 1977; Seyfarth *et al.*, 1980; Hoogland, 1996; Blumstein and Armitage, 1997). The alarm signals convey referential information about the specific type or category of predator (Seyfarth *et al.*, 1980; Zuberbühler, 2000, 2001), degree of risk as often determined by distance from the predator (Owings and Hennessy, 1984; Burke da Silva *et al.*, 1994; Blumstein, 1995; Randall and Rogovin, 2002), size and shape of the predator (Evans *et al.*, 1993; Ackers and Slobodchikoff, 1999), and amount of arousal (Hammerschmidt and Fischer, 1998) or emotional state (Evans, 1997). Alarm signals also act in the self-interests of the caller by reducing its vulnerability. The calls assemble conspecifics to attack the predator as a group (Seyfarth *et al.*, 1980) or cause conspecifics to scatter and confuse the predator (Sherman, 1985). The target of an alarm may also be the predator in which the alarm communicates detection and alertness to deter pursuit (Caro, 1995; Randall and Matocq, 1997). The signals are not mutually exclusive, however, and multiple messages can be transmitted in alarm calls (Zuberbühler *et al.*, 1997), including information about the identity of the caller (Cheney and Seyfarth, 1988; Hare, 1998; Hare and Atkins, 2001; McCowan and Hooper, 2002; Blumstein and Munos, 2005).

The great gerbil, *Rhombomys opimus*, is unique among murid rodents in the subfamily Gerbillinae because it is the only species known to give alarm vocalizations in conjunction with footdrumming in the presence of predators (Randall *et al.*, 2000). Great gerbils live in family groups consisting of a male with one to six females and their offspring (Kutcheruk *et al.*, 1972; Naumov and Lobachev, 1975; Randall *et al.*, 2000). Females are philopatric and highly related; males disperse into family groups and are usually unrelated to the females (Randall *et al.*, 2006). All family members footdrum and give vocal and visual displays in the presence of diverse predators: monitor lizards, snakes, dogs, foxes, weasels, polecats, and humans (Nikolsky, 1970, 1984; Randall *et al.*, 2000; Randall and Rogovin, 2002). As a predator or threat approaches, the gerbils stand in a bipedal posture

 0001-4966/2005/118(4)/2706/9/$22.50

and give a rhythmic call consisting of repetitive chevron-shaped notes at intervals of 0.2–0.5 s. If the threat continues, the gerbils emit a call (intense) with notes as couplets and an internote interval averaging 0.07 s. Gerbils also give a short whistle and immediately run into the burrow when startled by the sudden arrival or the fast movement of a terrestrial predator and in response to aerial predators. [See Randall and Rogovin (2002) for spectographs of all three alarm calls.] In general, about 70%–80% of alarm calls are rhythmic, 10%–20% intense, and 10%–20% whistles. Playback tests revealed that great gerbils can distinguish the three calls and respond differently to them (Randall and Rogovin, 2002). Although the gerbils stopped feeding and stood in an alert posture to all three calls, they were more vigilant in response to the intense call and the whistle than to the rhythmic call. The calls apparently function to communication degree of risk or "response urgency" (Blumstein and Armitage, 1997).

The question of whether gerbils might classify alarm vocalizations by their meaning and use them to identify the category of predator in "functionally referential" calls was not addressed by Randall and Rogovin (2002). The strongest evidence for semantic alarm systems in mammals comes from studies of primates (Cheney and Seyfarth, 1988; Pereira and Macedonia, 1991; Fischer, 1998; Zuberbühler, 2000, 2001), whereas studies of rodents show that their alarm calls usually function to communicate risk or "response urgency" (Leger *et al.*, 1979; Blumstein, 1995; Blumstein and Armitage, 1997). However, predator-specific alarm calls have been documented in rodents as well (Greene and Meagher, 1998). We wondered, therefore, whether great gerbils produce sufficient variation in their alarm calls to communicate more than the degree of risk (Hare, 1998; Hare and Atkins, 2001; Blumstein and Munos, 2005; Blumstein *et al.*, 2004). With this question in mind we conducted a detailed analysis of the most common alarm call of the gerbils, the rhythmic call, for differences in call structure that could function to provide potential information about the caller as well as about the type and hunting style of the various predators. We tested whether (1) signals differ according to the type of predator in subadults and adults and predicted more variation in subadults (Randall, 1995; Blumstein and Daniel, 2004); (2) males and females emit structurally different calls; (3) calls vary by age category; (4) members of family groups emit calls unique to the group; and (5) calls of individual gerbils are distinctive.

II. METHODS

A. Subjects, study site, and observation

We studied the great gerbil on the Ecocentre Dzeiran, a reserve for endangered Asian gazelles, in the Kyzylkum desert of Uzbekistan about 30 km south of Bukhara (39°35′–39°40′N 64°36′–64°43′E). We recorded alarm calls in 1999 and 2000. The 1999 population had a very high density (94% of burrow systems were occupied with a mean group size of 13.0±1.8 animals, $n=41$ groups) because of favorable conditions for reproduction in 1998 and spring 1999. Very dry conditions beginning in late spring of 1999 caused high mortality so that population density in 2000 was much lower (40% of burrow systems were occupied with group size equal to 7.6±1.3 individuals) and there was a significant turnover in the population. This fluctuation in density reflects patterns typical for desert environments.

We identified and numbered family groups and captured and marked individuals in the spring and fall. We distinguished different-aged gerbils by weight and stage of reproduction in each family group. Adults were fully grown, reproducing animals (130–200 g); subadults were young gerbils born in that year that almost approached adult size (about 90–120 g). Pups were small animals, recently emerged from the burrow, that weighed 30–90 g.

We captured individual gerbils with $30\times15\times15$ cm wire-mesh live-traps baited with a mixture of rolled oats, sunflower seeds, carrots, greens, and peanut butter. We marked each animal with numbered ear tags (Monel #1) and clipped brown guard hairs on the backs and sides of adults to expose unique patterns in the underhairs for individual identification at a distance. All pups from the same litter had the same mark. We monitored females for signs of pregnancy and lactation so we could predict the emergence of pups. Pregnancy was determined by weight gain and lactation by the appearance of swollen, pink nipples. We observed gerbils with binoculars at a distance of 20–40 m and recorded behavior by speaking quietly into a hand-held tape recorder. The gerbils habituated to a human sitting quietly on the ground behind low vegetation.

B. Vocal recording

1. Human approaches

We recorded alarm calls in the field from 23 March to 12 June 1999, with a Sennheiser (Md 421 U4) microphone through a 25-dB preamplifier into a Marantz stereo cassette recorder (PMD 201). We also recorded vocalizations from 5 April to 22 May and 23 October to 6 November 2000 with the same microphone arrangement but with a DAT Sony 8 recorder (TCD-D8).

Calls were recorded in response to human approaches by walking slowly toward a family group until gerbils began to give alarm calls or escaped into the burrow. The human continued walking toward the calling gerbil or center of the group if gerbils were in the burrow. At approximately 10–15 m the human stood and recorded calls of the calling gerbil or waited for gerbils to emerge and give alarm calls. When a gerbil emerged and stood in bipedal posture the microphone was pointed toward it. If no call was given, the human moved a few steps toward the gerbil, which caused the gerbil either to call or run into a burrow.

We recorded calling bouts (a continuous series of calls) from individually identified adults and pups and subadults, which were not individually marked but had a group-specific mark. In spring 1999 we recorded 95 calling bouts from gerbils in 21 different family groups. In spring 2000, we recorded 39 calling bouts of animals in 8 family groups. In the fall, we recorded 65 calling bouts in 19 family groups to yield a data set of 9712 calls for the 2 years. After elimination of unidentified animals and whistles and intense calls we had a data set of 6309 rhythmic calls of adults, subadults,

TABLE I. Summary acoustic variables used in analyses.

Acoustic variable	Description
Minimum frequency	Lowest frequency attained by call in Hz
Maximum frequency	Highest frequency attained by call in Hz
Mean frequency	Average frequency across call in Hz
Frequency range	Peak frequency minus minimum frequency in Hz
Maximum frequency/mean frequency	Peak frequency divided by mean frequency
Mean frequency/minimum frequency	Mean frequency divided by minimum frequency
Frequency peak amplitude	Frequency at which peak amplitude occurs in Hz
Minimum frequency location	Location minimum frequency in call as % duration
Maximum frequency location	Location peak frequency in call as % of duration
Duration	Length of call measured in ms
Start slope	Slope of initial third of call contour in Hz/ms
Middle slope	Slope of middle third of call contour in Hz/ms
Final slope	Slope of final third of call contour in Hz/ms

and pups of which 3630 were from adults (2000 calls from females and 1630 males) with the remainder from subadults and pups.

2. Different predator contexts

To answer the question of whether great gerbil alarm calls have productional specificity, we recorded alarm calls of adults and subadults in the presence of three different predators with different hunting tactics. We recoded alarm calls to a known predator, the gray monitor lizard, *Varanus griseus* (Cellarius *et al.*, 1991; Rogovin *et al.*, 2004), and a representative of a live mammalian predator, a wolfhound hunting dog, *Canis familiaris*. The lizard hunts by entering larger burrows and digging into smaller ones whereas a canid would run and pounce and not be able to enter the burrow. A human (K. Collins) represented the third predator category.

We tethered a large monitor lizard (1.4-m snout-vent length) in the center of the active area of 16 family groups. The tether was made of a braided cotton rope that was tied like a belt just anterior to the lizard's hind legs. A 2-m length of nylon robe, tied to the belt, was attached to a stake inserted into the ground. The lizard could move and dig within a 2-m radius. The dog was also tethered in the center of family groups ($n=17$) with a 2-m cotton rope tied to a stake inserted in the ground. The dog could also move on the tether. The activity of tethering the predator caused the gerbils to run into the burrow. While the gerbils were in their burrows, the person recording the alarm calls hid from view behind vegetation about 20 m away and recorded calls with the Sennheiser microphone through a 25-dB preamplifier into the Marantz stereo cassette recorder as gerbils emerged and began to emit alarm vocalizations. Identification of the caller and the time called was recorded separately into a hand-held Sony M530 micro-cassette recorder. Because we recorded free-ranging animals, we could not control the distance between the predator and caller and estimate that the distance ranged from about 5 to 20 m.

All calls to humans used in the analysis were recorded at an approximate distance of 5 to 20 m from the gerbil during spring 1999 in the same family groups in which the lizard and dog were tethered. Although we recorded calls in the same family groups, we only used a calling bout from an individual once in the same data set. Because of high densities and the large number of gerbils in family groups we sometimes were unable to identify the caller. After elimination of recordings of unknown callers and pups we had 1415 alarm calls of 17 individually marked adults and 628 calls from 13 subadults from 13 different families.

C. Acoustic analysis

Vocal recordings were digitized onto a Micron Pentium Computer using a SoundBlaster soundcard (sampling rate up to 44.1 kHz) and Cool Edit Pro Signal Analysis software (sampling rate of 44.1 kHz and using 512-point FFT with a Hamming filter for generating spectrograms). Acoustic files were filtered for background noise using standard parametric filtering in Cool Edit Pro on the PC computer, and each call was cued for subsequent digital analysis.

D. Statistics

We measured acoustic variables in 3630 rhythmic alarm calls recorded from 46 individual adults using a modified version of the technique described in McCowan (1995) and McCowan and Reiss (2001). [See Randall and Rogovin (2002) for spectogram of call.] The computer measured 60 points of frequency, amplitude, and time across the duration of each call using a 1024-point FFT with a Hamming filter from the spectrum taken at each time point. After call digitization and measurement were completed, we conducted subsequent calculations to obtain summary acoustic variables that defined spectral, temporal, amplitude, and contour variables of the calls. (See Table I for a list of analyzed variables.)

The outcomes and covariates of the statistical tests were either categorical or continuous in structure. Thus, mixed effects linear models (Pinheiro and Bates, 2000) (with individual as the grouped random effect for repeated measure) and discriminant function analysis (DFA) were the statistical methods of choice. Continuous variables were tested for and confirmed for normality. Covariates included individual, sex, age, and context (lizard, human, or dog induced).

All statistical tests were conducted using programmable S-Plus statistical software. The linear mixed effects model

TABLE II. Results of analysis of 13 acoustic variables for the gerbil rhythmic alarm call by sex (df=1,3440), age (df=2,6199) and predator context for subadults (df=2,697) and adults (df=2,1394) using the F-statistic from the linear mixed effects model (LME) in S-Plus with ID as the grouped random effect variable (Pinheiro and Bates, 2000). Pairwise tests denoted by superscripts for significant variables with more than two categories are also presented [age: P=pup, S=subadult, A=adult; predator context for subadults and adults: D=dog, H=human, L=lizard; includes differences between adults (listed first) and subadults when they occurred].

			Context		
Acoustic variables	Sex	Age	Subadults	Adults	Pairwise tests
Minimum frequency	348.1^{****}	333.12^{****}	102.38^{****}	229.26^{****}	P^a, S^a, A^b; D^a, H^b, L^c
Maximum frequency	1.86	9.08^{***}	212.61^{****}	36.13^{****}	P^b, S^a, A^b; D^a, H^b, L^c
Mean frequency	3332.05^{****}	386.11^{****}	162.62^{****}	116.22^{****}	P^a, S^b, A^c; D^a, H^b, L^c
Frequency range	3.21	19.62^{****}	135.39^{****}	48.58^{****}	P^a, S^a, A^b; D^a, H^b, L^c
Maximum frequency/ mean frequency	4.74^{*}	35.61^{****}	97.16^{****}	19.25^{****}	P^a, S^a, A^b; D^a, H^b, L^c
Mean frequency/ minimum frequency	0.49	1.17	2.46	1.51	
Frequency at peak amplitude	321.83^{****}	321.74^{****}	159.13^{****}	64.45^{****}	P^a, S^b, A^c; D^a, H^b, L^c; D^a, H^a, L^b
Minimum frequency location	143.92^{****}	52.85^{****}	15.84^{****}	2.60	P^{ab}, S^a, A^b; D^a, H^b, L^b
Maximum frequency location	99.05^{****}	37.71^{****}	8.67^{***}	2.37	P^a, S^a, A^b; D^a, H^a, L^b
Duration	2.38	0.79	164.16^{****}	0.52	L^a, H^b, D^b
Start slope	32.86^{****}	18.03^{****}	15.17^{****}	14.21^{****}	P^a, S^a, A^b; D^a, H^b, L^a; D^a, H^a, L^b
Middle slope	15.29^{***}	36.24^{****}	61.58^{****}	8.34^{***}	P^a, S^a, A^b; D^a, H^b, L^c; D^a, H^{ab}, L^b
Finish slope	26.57^{****}	30.86^{****}	41.10^{****}	0.57	P^a, S^a, A^b; D^a, H^b, L^c

$^{*}p<0.05$.
$^{**}p<0.01$.
$^{***}p<0.001$.
$^{****}p<0.0001$.
Letter superscripts indicate significance if different and no significance if the same.

included individual as a grouped random effect variable. Therefore all p values were appropriately adjusted to variance imposed by this repeated measure, which also corrected for pseudoreplication. We checked for variance problems by plotting residuals versus fitted values and used a within-group variance structure, usually the "exponential" function, to correct variance problems (S-Plus outputs confidence intervals for variance structure and random effects.). We also tested for problems using within group correlation with S-Plus, but did not find any. We used S-Plus to conduct Bonferroni corrected, pairwise tests on each model generated using the following command: anova(<model name, L=c (<factor name1=1, <factor name 2=−1) .

All 13 summary variables as described in Table I were entered into the DFA. Cross validation in the DFA was done with the "leave-one-out" method. We conducted two sets of DFA. In one set we used all samples of rhythmic calls available for each classification by age, sex, context, individual identity, and family group. We then conducted a second series of DFA with much smaller, but balanced, sample sizes (randomly selected from the original data set) to verify that our unbalanced data were not biased. Because of questions about the use of unbalanced designs in DFA we report both sets of data.

The calls of adults and subadults in response to the three predator stimuli were analyzed separately after we determined that the calls varied by age. We were unable to separate by sex because of small sample sizes and unknown sexes of subadults. We also used mixed-sex groups for comparisons in the age category of adults, subadults, and pups. We selected to analyze for individual differences in animals from 1999 and 2000. The animals recorded in 1999 had been on the study site for at least a year in stable family groups. In 2000 there was a large turnover in animals and dispersal in the fall so that the family groups were not considered as stable. We were therefore interested to see whether calls were less consistent in 2000 compared with 1999. All calls analyzed for differences by age, sex, individual, and family group were responses only to humans.

III. RESULTS

A. Differences in predator-induced calls

Gerbils showed significant acoustic differences in rhythmic call structure in the predator context. Eight of 13 acoustic variables for adults and 12 of 13 variables for subadults differed significantly (Table II). Paired tests demonstrated further that acoustic variables differed in the three predator contexts. For adults, we found significant differences between calls to the dog and human in 10 of 13 variables and to the lizard-human and lizard-dog calls in 11 of 13 variables. For subadults, the comparison between dog and human was significant in only 7 of 13 variables, but the dog and lizard comparison differed by 12 of 13 acoustic variables and the human-lizard comparison in 10 of 13 acoustic variables (Tables II and III).

Cross-validation DFA using pooled data from individuals on the 13 acoustic variables revealed a high classification

TABLE III. Mean±SE of 13 acoustic variables measured in three different predator contexts for adults. See Table II for results from paired comparisons.

	Dog		Human		Lizard	
Acoustic variable	Adult	Subadult	Adult	Subadult	Adult	Subadult
Minimum frequency	1764.6±32.0	2005.3±20.4	1707.4±10.1	2233.7±16.7	1239.1±18.9	1829±16.3
Maximum frequency	2413.9±25.4	2585.0±17.0	2077.2±13.5	2386±14.3	2278.6±12.9	2171.1±11.5
Mean frequency	2207.3±21.9	2380.6±13.0	1970±11.68	2341.2±14.8	1945.3±11.6	2085.5±11.1
Frequency range	649.2±36.6	579.7±22.10	369.8±11.7	153.2±7.5	1039.4±16.0	341.7±14.6
Maximum frequency/ mean frequency	1.098±0.01	1.087±0.0045	1.052±0.002	1.099±0.001	1.18±0.009	1.042±0.002
Mean frequency/ minimum frequency	2.46±0.59	2.156±0.56	1.052±0.002	1.050±0.004	1.661±0.026	1.202±0.054
Frequency at peak amplitude	2312.96±36.6	2475.14±14.5	2052.00±12.9	2365.40±14.7	2119.6±16.3	2155.35±10.6
Minimum frequency location	0.635±0.033	0.379±0.028	0.29±0.14	0.175±0.028	0.36±0.027	0.216±0.025
Maximum frequency location	0.54±0.017	0.59±0.013	0.60±0.005	0.62±0.013	0.62±0.012	0.54±0.01
Duration	54.17±2.36	50.90±0.656	55.93±4.93	35.21±0.63	61.19±4.77	53.44±0.77
Start slope	1.72±0.217	1.20±0.13	1.44±0.05	0.80±0.068	3.73±0.154	1.60±0.09
Middle slope	0.35±0.24	0.46±0.028	0.24±0.014	0.30±0.019	0.423±0.073	0.11±0.015
Finish slope	−2.16±0.298	−1.76±0.028	−1.21±0.47	−0.39±0.05	−3.21±0.144	−1.14±0.07

by type of predator for adults (65%–73%) and subadults (64%–96%) and general agreement in classifications in the balanced and unbalanced designs (Table IV).

B. Differences by sex

We found a significant difference in the acoustic structure of adult males and females in 8 of 13 acoustic variables (Tables II and V). Females had a greater minimum and mean frequency and a lower frequency range than males. Variables of minimum and maximum frequency location and start, middle, and final slope also differed significantly (Table V). DFA using pooled data from individuals on these variables revealed that 65% (balanced design) to 70% (unbalanced design) of calls were correctly classified to the appropriate sex class (Table IV).

C. Differences by age

Eleven of 13 acoustic variables differed by age category (Tables II and V). Although sex might account for some of the variation in our analysis, we found clear differences between the calls of adults and younger gerbils. Adults differed significantly from subadults on 11 of 13 variables and from pups on 9 of 13 variables (Table II). Pups and subadults only differed significantly on 3 of 13 acoustic variables: minimum frequency, mean frequency, and frequency at peak amplitude. In almost every comparison the calls of pups and subadults had higher frequencies than adults (Tables III and V).

DFA using pooled data classified 45% (balanced design) to 50.4% (unbalanced design) of the calls correctly by age group (Table IV). Of these, subadults and pup calls were the most varied and showed a lower classification than adults.

D. Individual differences

We found evidence for individual differences in the rhythmic alarm call. Cross-validation DFA revealed that individuals could be distinguished based upon the acoustic structure of their rhythmic calls (Table IV). Average percent correct classification across 8 individuals in 1999 was 75.4% (range for individuals, 37%–100%) and 40% for 16 individuals in 2000 (range=13%–74.6%). When we reanalyzed the data using a balanced design we found even higher rates of classification. Average percent classification across 6 individuals in 1999 was 82% (range=71%–97%) and across 18 individuals in 2000 was 65% (range=20%–100%). Because percent correct classification (PCC) by chance alone was only 6%, this average percent correct classification represents significant discrimination for individual calls.

E. Family group differences

DFA using pooled data from individuals on the 13 acoustic variables revealed that 60%–89% of calls were correctly classified to the appropriate family group in the spring and 38%–70% in the fall of 2000 in the balanced design (Table IV). Classification in the unbalanced design was similar to the balanced design for the fall (39%–71%) and somewhat lower for the spring (50%–76%).

IV. DISCUSSION

Could the alarm calls of the great gerbil contain specific information about type and hunting tactics of predators as well as general information about predation risk? Alarm calls that communicate both risk and referential information about predators do occur (Zuberbühler, 2000; Manser, 2001; Fichtel and Kappeler, 2002). Our analysis revealed that gerbils varied the rhythmic alarm call with the type of predator. It seems possible, therefore, that the level of response urgency is reflected in changes in acoustic structure of the call as well as in call rate and duration when gerbils switch from the rhythmic alarm to the intense alarm or the whistle (Manser, 2001). Since the rhythmic call is usually given when a predator is some distance away and the situation is not life-threatening, gerbils have time to communicate information

TABLE IV. Results from cross validation tables of discriminant function analyses showing percentage of calls correctly classified by sex, age, predator context, individual, and family group in both balanced (Bal) and unbalanced (Unbal) designs. Included are the number of calls analyzed, number of animals giving the calls, and sex ratio in groups.

	Percent Classified		No. of calls		No. of animals		Group composition	
Category	Bal	Unbal	Bal	Unbal	Bal	Unbal	Bal	Unbal
Sex								
Male	67	72	1127	1630	14	14	All adult	All adult
Female	63	69	1127	2000	32	32	All adult	All adult
Age								
Pup	36	54	1331	1348	14	14	Unknown sex	Unknown sex
Subadult	40	36	1331	1331	14	19	Unknown sex	Unknown sex
Adult	58	61	1331	3576	14	45	10F, 4M	31F, 14M
Predator context								
Adult								
Dog	73	72	60	196	4	4	3F, 1M	3F, 1M
Human	70	73	60	950	4	12	4F	9F, 3M
Lizard	68	65	60	269	4	4	2F, 2 sex unknown	2F, 2 sex unknown
Subadult								
Dog	76	64	45	208	3	5	All unknown sex	
Human	96	92	45	175	3	5	All unknown sex	
Lizard	80	91	45	245	3	3	All unknown sex	
Individuals (all adults)								
1999	82	75	210	862	6	8	4F, 2M	5F, 3M
2000	64	40	450	2082	18	16	13F, 5M	13F, 3M
Family Groups (all adults)								
Spring 2000								
A	89	76	45	270	3	3	2F, 1M	2F, 1M
B	89	79	45	162	3	4	3F	3F, 1M
C	60	50	30	66	2	2	1F, 1M	1F, 1M
Fall 2000								
A	38	39	60	463	2	5	2F	4F, 1M
B	57	58	60	116	2	2	1F, 1M	1F, 1M
C	70	71	60	300	2	2	2F	2F
D	57	50	60	89	2	2	2F	2F

about predator type in the rhythmic call before communicating response urgency in the intense call or whistle when the situation becomes more threatening.

Functionally referential alarm calls must show a strong association between a specific event or object and a particular call and elicit a unique behavioral response (Evans, 1997). They are most likely to evolve when animals are hunted by predators with different hunting strategies which require different modes of escape (Macedonia and Evans, 1993). The great gerbil is preyed on by a variety of terrestrial and aerial predators that employ different hunting tactics. Major terrestrial predators that enter burrows include the marbled polecat (*Vormela perigusna*) (Bekenov, 1982), a fast moving predator especially adapted for hunting rodents in burrows, the monitor lizard, and various snake species. Mammalian predators unable to enter the burrow that depend on stealth include steppe cats (*Felis libicus*) and foxes (*Vulpes vulpes, Vulpes corsac*). Survival depends on different escape responses to these varied predators. For instance, instead of running into the burrow, gerbils exit the burrow when a predator goes inside. An entire family group may move into a new burrow system in response to the arrival of a polecat in the colony ($n=11$, unpublished observations).

Variation in the rhythmic alarm call was not limited to predator context in the gerbils, and the calls differed among individual callers and family groups as well as by sex and age. Because great gerbils have no long-distance vocalizations other than alarm signals, evolution of a secondary function in the calls to convey information in the social group would be adaptive. Individual differences in alarm calls have already been documented in other social rodents (Owings and Leger, 1980; McCowan and Hooper, 2002; Blumstein and Munos, 2005), and animal signals often have more than one function and occur in different contexts (Smith, 1991; Tamura, 1995; Reby *et al.*, 1999). It, therefore, seems reasonable that alarm signals could also be signals of identity in highly social mammals.

Why would individual identity be conveyed in alarm calls? One hypothesis is that individually distinctive alarm calls evolve so that the receiver can evaluate reliability of the caller (Krebs and Dawkins, 1984; Hare, 1998; Blumstein *et al.*, 2004). Response to unreliable or false alarms may cause

TABLE V. Mean±SE of 13 acoustic variables measured for differences by sex and age. See Table II for paired comparisons by age.

	Sex		Age		
Acoustic variable	Male	Female	Adult	Subadult	Pup
Minimum frequency	1631.65±6.84	1987.70±7.32[a]	1729.5±5.2	1853.88±7.9	1985.26±9.85
Maximum frequency	2574.02±49.1	2680.51±35.39	2673.14±30.33	2515.36±9.69	2753.61±31.19
Mean frequency	2034.87±8.18	2222.89±7.01[a]	2142.90±5.59	2285.66±7.61	2419.28±10.07
Frequency range	942.37±50.02	872.80±35.59[a]	943.64±30.23	661.48±10.87	768.35±30.23
Maximum frequency/ mean frequency	1.22±0.02	1.18±0.01	1.22±0.010	1.10±0.003	1.12±0.007
Mean frequency/ minimum frequency	1.51±0.17	1.40±0.07	1.41±0.08	1.32±0.05	1.23±0.005
Frequency at peak amplitude	2080.77±8.94	2279.26±7.31	2192.0±5.92	2335.31±7.60	2462.61±10.80
Minimum frequency location	0.28±0.01	0.45±0.01[a]	0.36±0.007	0.51±0.01	0.43±0.012
Maximum frequency location	0.60±0.005	0.53±0.005[a]	0.56±0.003	0.52±0.006	0.50±0.006
Duration	371.2±203.2	98.78±76.0	223.65±92.2	89.59±0.76	89.71±0.71
Start slope	1.18±0.03	0.80±0.06[a]	0.91±0.3	1.195±0.03	1.17±0.05
Middle slope	0.013±0.006	0.059±0.02[a]	0.086±0.01	−0.089±0.01	−0.13±0.045
Finish slope	−0.098±0.14	−0.79±0.14[a]	−0.37±0.08	−1.26±0.04	−0.94±0.07

[a]All $P < 0.01$.

an animal to waste time and energy (Cheney and Seyfarth, 1985, 1988; Bachman, 1993), lose resources (Munn, 1986; Møller, 1988), and mating opportunities (Møller, 1990). Recent studies of Richardson ground squirrels (Hare, 1998; Hare and Atkins, 2001) and yellow-bellied marmots (Blumstein *et al.*, 2004) demonstrated that individual distinctiveness in alarm calls is related to estimates of reliable signals by the receiver. Whether great gerbils have the same ability should be tested in future experiments.

The discovery that alarm calls are distinctive to family groups is an interesting result. In general, group-distinctive calls have been demonstrated in few mammals (Boughman, 1997), although birds use calls to recognize group membership (Hopp *et al.*, 2001). Family groups in the spring had a somewhat higher correct classification of alarm calls than family groups in the fall when dispersal was occurring. Because great gerbils are very territorial, recognition of neighbor calls may be an important spacing mechanism (Frommolt *et al.*, 2003).

Age differences occur in the structural characteristics of rodent alarm calls (Nesterova, 1996; Blumstein and Daniel, 2004; Blumstein and Munos, 2005). We found that the rhythmic alarm call of adult gerbils differed from the calls of subadults and pups on 85% and 69% of acoustic variables, respectively, compared with the calls of pups and subadults differing on only 23% of the acoustic variables. Subadult and pups had lower classification in the DFA than adults. These results suggest that some learning and refining of call structure may occur in the younger animals. In contrast, although we predicted that subadults might demonstrate less consistency in their calls than adults because of less experience, we found that the rhythmic call of subadults had an even higher classification by predator type than adults. If there is a learning period for production of predator-specific calls, it must occur before gerbils are reproductive adults.

The variations in the rhythmic alarm call of the great gerbil illustrate the flexibility of alarm signals and how they might have multiple functions and communicate in multiple contexts (Partan and Marler, 1999). Calls that serve different functions can be acoustically quite similar, and listeners can learn to discriminate between the different call types (Fischer *et al.* 2001, 2002). The variation in the rhythmic alarm call, the two other call types (intense and whistle), and vibrational signals generated from footdrumming provide great gerbils with a varied and multi-channel acoustic repertoire (Randall *et al.*, 2000; Randall and Rogovin, 2002). How much of this acoustic variation is meaningful and can be discriminated by the great gerbil to make adaptive responses must be investigated in future studies to understand fully their communication system and how it compares with other social mammals.

ACKNOWLEDGMENTS

We are grateful to the Uzbekistan government and to the director of the Ecocentre Dzeiran for allowing us to conduct our research there. We thank Natalia Soldatove, Aziz Kasimov, Dr. Yuri Chikin, Oksana Chikina, and Colin Smith for their help and kindness and the National Science Foundation (Grant No. IBN-9723033) for grant support. Dan Blumstein and James Hare provided many helpful comments. All research was conducted with approval of the University Animal Care and Use Committee under permit 98-412.

Ackers, S. H., and Slobodchikoff, C. N. (**1999**). "Communication of stimulus size and shape in alarm calls of Gunnison's prairie dogs, *Cynomys gunnisoni*," Ethology **105**, 149–162.

Bachman, G. C. (**1993**). "The effect of body condition on the trade-off between vigilance and foraging in Belding's ground squirrels," Anim. Behav. **46**, 233–244.

Bekenov, I. A. (**1982**). "The marbled polecat, *Vormela peregusna*, Guldenstaedt 1770," in *Mammals of Kazakhstan*, edited by E. V. Gvozdev and E. I. Strautman (NAUKA, Alma-Alta) (in Russian).

Blumstein, D. T. (**1995**). "Golden-marmot alarm calls. I. The production of situationally specific vocalizations," Ethology **100**, 113–125.

Blumstein, D. T., and Armitage, K. B. (**1997**). "Alarm calling in yellow-bellied marmots: I. The meaning of situationally variable alarm calls," Anim. Behav. **53**, 143–171.

Blumstein, D. T., and Daniel, J. C. (**2004**). "Yellow-bellied marmots discriminate between the alarm calls of individuals and are more responsive to calls from juveniles," Anim. Behav. **68**, 1257–1265.
Blumstein, D. T., and Munos, O. (**2005**). "Individual, age and sex-specific information is contained in yellow-bellied marmot alarm calls," Anim. Behav. **69**, 353–361.
Blumstein, D. T., Verneyre, L., and Daniel, J. C. (**2004**). "Reliability and the adaptive utility of discrimination among alarm callers," Proc. R. Soc. London, Ser. B **271**, 1851–1857.
Boughman, J. W. (**1997**). "Greater spear-nosed bats give group-distinctive calls," Behav. Ecol. Sociobiol. **40**, 61–70.
Burke da Silva K., Kramer, D. L., and Weary, D. M. (**1994**). "Context-specific calls of the eastern chipmunk, *Tamias striatus*," Can. J. Zool. **72**, 1087–1092.
Caro, T. M. (**1995**). "Pursuit-deterrence revisited," Trends Ecol. Evol. **10**, 500–503.
Cellarius, A. Yu., Cherlin, V. A., and Menshikov, Yu. G. (**1991**). "Preliminary report about the study of biology of *Varanus griseus* (Reptilia, Varanidae) in Middle Asia," in *Herpetological Research*, edited by V. A. Cherlin and A. Yu. Cellarius (V.1, Publ. "LISS," Leningrad), pp. 61–103 (in Russian).
Cheney, D. L., and Seyfarth, R. M. (**1985**). "Vervet monkey alarm calls: manipulation through shared information?" Behaviour **94**, 150–166.
Cheney, D. L., and Seyfarth, R. M. (**1988**). "Assessment of meaning and the detection of unreliable signals by vervet monkeys," Anim. Behav. **36**, 477–486.
Evans, C. S. (**1997**). "Referential signals," Perspect Ethol. **12**, 99–143.
Evans, C. S., Evans, L., and Marler, P. (**1993**). "On the meaning of alarm calls: functional reference in an avian vocal system," Anim. Behav. **46**, 23–38.
Fichtel, C., and Kappeler, P. M. (**2002**). "Anti-predator behavior of group-living Malagasy primates: mixed evidence for a referential alarm call system," Behav. Ecol. Sociobiol. **51**, 262–275.
Fischer, J. (**1998**). "Barbary macaques categorize shrill barks into two call types," Anim. Behav. **55**, 799–807.
Fischer, J., Hammerschmidt, K., Cheney, D. L., and Seyfarth, R. M. (**2002**). "Acoustic features of male baboon loud calls: Influences of context, age, and individuality," J. Acoust. Soc. Am. **111**, 1465–1474.
Fischer, J., Metz, M., Cheney, D. L., and Seyfarth, R. M. (**2001**). "Baboon responses to graded bark variants," Anim. Behav. **61**, 925–931.
Frommolt, K.-H., Goltsman, M. E., and Macdonald, D. W. (**2003**). "Barking foxes, *Alopex lagopus*: field experiments in individual recognition in a territorial mammal," Anim. Behav. **65**, 509–518.
Greene, E., and Meagher, T. (**1998**). "Red squirrels, *Tamiasciurus hudsonicus*, produce predator-class specific alarm calls," Anim. Behav. **55**, 511–518.
Hammerschmidt, K., and Fischer, J. (**1998**). "The vocal repertoire of Barbary macaques: a quantative analysis of a graded signal system," Ethology **104**, 203–216.
Hare, J. F. (**1998**). "Juvenile Richardson's ground squirrels, *Spermophilus richardsonii*, discriminate among individual alarm callers," Anim. Behav. **55**, 451–460.
Hare, J. F., and Atkins, B. A. (**2001**). "The squirrel that cried wolf: reliability detection by juvenile Richardson's ground squirrels (*Spermophilus richardsonii*)," Behav. Ecol. Sociobiol. **51**, 108–112.
Hoogland, J. L. (**1996**). "Why do Gunnison's prairie dogs give anti-predator calls?" Anim. Behav. **51**, 871–880.
Hopp, S. L., Jablonski, P., and Brown, J. L. (**2001**). "Recognition of group membership by voice in Mexican jays, *Aphelocoma ultramarina*," Anim. Behav. **62**, 297–303.
Krebs, J. R., and Dawkins, R. (**1984**). "Animal signals: mind-reading and manipulation," in *Behavioral Ecology. An Evolutionary Approach*, edited by J. R. Krebs and N. B. Davies (Sinauer, Sunderland, MA), pp. 380–402.
Kutcheruk, V. V., Kulik, I. L., and Dubrovsky, Yu. A. (**1972**). "Great gerbil as a life form of a desert," in *Fauna and Ecology of Rodents*, edited by V. V. Kutcheruk (Moscow U. P., Moscow), pp. 5–70 (in Russian).
Leger, D. W., Owings, D. H., and Boal, L. M. (**1979**). "Contextual information and differential responses to alarm calls in California ground squirrels," Z. Tierpsychol **49**, 142–155.
Macedonia, J. M., and Evans, C. S. (**1993**). "Variation among mammalian alarm call systems and the problem of meaning in alarm signals," Ethology **93**, 177–197.
Manser, M. B. (**2001**). "The acoustic structure of suricates' alarm calls varies with predator type and the level of response urgency," Proc. R. Soc. London, Ser. B **268**, 2315–2324.
McCowan, B. (**1995**). "A new quantitative technique for categorizing whistles using simulated signals and whistles from captive bottlenose dolphins, *Delphindae tursiops truncates*," Ethology **100**, 177–193.
McCowan, B., and Hooper, S. L. (**2002**). "Individual acoustic variation in Belding's ground squirrel alarm chirps in the High Sierra Nevada," J. Acoust. Soc. Am. **111**, 1157–1160.
McCowan, B., and Reiss, D. (**2001**). "The fallacy of 'signatures whistles' in bottlenose dolphins: a comparative perspective of 'signature information' in animal vocalizations," Anim. Behav. **62**, 1151–1162.
Møller, A. P. (**1988**). "False alarm calls as a means of resource usurpation in the great tit *Parus major*," Ethology **79**, 25–30.
Møller, A. P. (**1990**). "Deceptive use of alarm calls by male swallows, *Hirundo rustica*: a new paternity guard," Behav. Ecol. **1**, 1–6.
Munn, C. A. (**1986**). "Birds that 'cry wolf'," Nature (London) **319**, 143–145.
Naumov, N. P., and Lobachev, V. S. (**1975**). "Ecology of desert rodents of the USSR (jerboas and gerbils)" in *Rodents in Desert Environments*, edited by I. Prakash and P. K. Ghosh (Junk, The Hague), pp. 465–598.
Nesterova, N. L. (**1996**). "Age-dependent alarm behaviour and response to alarm call in bobac marmots (*Marmota bobac Mull.*)," in *Biodiversity in Marmots*, edited by M. Le Berre, R. Rmousse, and L. Le Guelte (International Network on Marmots, Moscow), pp. 181–186.
Nikolsky, A. A. (**1970**). "On acoustic behavior of diurnal rodents inhabiting open territories," Vestnik MGU., Biologiya-Pochvovedenie **5**, 16–19 (in Russian).
Nikolsky, A. A. (**1984**). *Vocal Signals of Mammals in Evolutionary Process* (Nauka, Moscow) (in Russian).
Owings, D. H., and Hennessy, D. F. (**1984**). "The importance of variation in sciurid visual and vocal communication," in *The Biology of Ground Dwelling Squirrels: Annual Cycles, Behavioral Ecology, and Sociality*, edited by J. O. Murie and G. R. Michener (Univ. Nebraska, Lincoln), pp. 169–200.
Owings, D. H., and Leger, D. W. (**1980**). "Chatter vocalizations of California ground squirrels: predator and social role specificity," Z. Tropenmed Parasitol. **54**, 163–184.
Partan, S., and Marler, P. (**1999**). "Communication goes multimodal," Science **283**, 1272–1273.
Pereira, M. E., and Macedonia, J. M. (**1991**). "Ringtailed lemur anti-predator calls denote predator class, not response urgency," Anim. Behav. **41**, 543–544.
Pinheiro, J. C., and Bates, D. M. (**2000**). *Mixed-effects Models in S and S-Plus* (Springer, New York).
Randall, J. A. (**1995**). "Modification of footdrumming signatures by kangaroo rats: changing territories and gaining new neighbours," Anim. Behav. **49**, 1227–1237.
Randall, J. A., and Matocq, M. D. (**1997**). "Why do kangaroo rats (*Dipodomys spectabilis*) footdrum at snakes?" Behav. Ecol. **8**, 404–413.
Randall, J. A., and Rogovin, K. A. (**2002**). "Variation in and meaning of alarm calls in a social desert rodent, *Rhombomys opimus*," Ethology **108**, 513–527.
Randall, J. A., Rogovin, K. A., and Shier, D. M. (**2000**). "Antipredator behavior of a social desert rodent: footdrumming and alarm calling in the great gerbil, *Rhombomys opimus*," Behav. Ecol. Sociobiol. **48**, 110–118.
Randall, J. A., Rogovin, K. A., Parker, P. G., and Eimes, J. A. (**2006**). "Flexible social structure of a desert rodent, *Rhombomys opimus*: Philopatry, kinship and ecological constraints," Behav. Ecol. (in press).
Reby, D., Cargnelutti, B., and Hewison, A. J. M. (**1999**). "Contexts and possible functions of barking in roe deer," Anim. Behav. **57**, 1121–1128.
Rogovin, K., Randall, J. A., Kolosova, I., and Moshkin, M. (**2004**). "Predation on a social desert rodent, *Rhombomys opimus*: effect of group size, composition, and location," J. Mammal. **85**, 723–730.
Seyfarth, R. M., Cheney, D. L., and Marler, P. (**1980**). "Vervet monkey alarm calls: semantic communication in a free-ranging primate," Anim. Behav. **28**, 1070–1094.
Sherman, P. W. (**1977**). "Nepotism and the evolution of alarm calls," Science **197**, 1246–1253.
Sherman, P. W. (**1985**). "Alarm calls of Belding's ground squirrels to aerial predators: Nepotism or self-preservation?" Behav. Ecol. Sociobiol. **17**, 313–323.
Smith, W. J. (**1991**). "Animal communication and the study of cognition," in *Cognitive Ethology: The Minds of other Animals*, edited by C. A. Ristau (Erlbaum, Hillsdale, NJ), pp. 209–230.
Tamura, N. (**1995**). "Postcopulatory mate guarding by vocalization in the

Formosan squirrel," Behav. Ecol. Sociobiol. **36**, 377–386.
Zuberbühler, K. (**2000**). "Referential labelling in Diana monkeys," Anim. Behav. **59**, 917–927.
Zuberbühler, K. (**2001**). "Predator-specific alarm calls in Campbell's monkeys, *Cercopithecus campbelli*," Behav. Ecol. Sociobiol. **50**, 414–422.
Zuberbühler, K., Noë, R., and Seyfarth, R. M. (**1997**). "Diana monkey long-distance calls: messages for conspecifics and predators," Anim. Behav. **53**, 589–604.

Bulk ablation of soft tissue with intense ultrasound: Modeling and experiments

T. Douglas Mast,[a] Inder Raj S. Makin,[b] Waseem Faidi, and Megan M. Runk
Ethicon Endo-Surgery, 4545 Creek Rd., Cincinnati, Ohio 45242

Peter G. Barthe and Michael H. Slayton
Guided Therapy Systems, 33 S. Sycamore St., Mesa, Arizona 85202

(Received 22 December 2004; revised 1 July 2005; accepted 11 July 2005)

Methods for the bulk ablation of soft tissue using intense ultrasound, with potential applications in the thermal treatment of focal tumors, are presented. An approximate analytic model for bulk ablation predicts the progress of ablation based on tissue properties, spatially averaged ultrasonic heat deposition, and perfusion. The approximate model allows the prediction of threshold acoustic powers required for ablation *in vivo* as well as the comparison of cases with different starting temperatures and perfusion characteristics, such as typical *in vivo* and *ex vivo* experiments. In a full three-dimensional numerical model, heat deposition from array transducers is computed using the Fresnel approximation and heat transfer in tissue is computed by finite differences, accounting for heating changes caused by boiling and thermal dose-dependent absorption. Similar ablation trends due to perfusion effects are predicted by both the simple analytic model and the full numerical model. Comparisons with experimental results show the efficacy of both models in predicting tissue ablation effects. Phenomena illustrated by the simulations and experiments include power thresholds for *in vivo* ablation, differences between *in vivo* and *ex vivo* lesioning for comparable source conditions, the effect of tissue boiling and absorption changes on ablation depth, and the performance of a continuous rotational scanning method suitable for interstitial bulk ablation of soft tissue. © *2005 Acoustical Society of America.* [DOI: 10.1121/1.2011157]

PACS number(s): 43.80.Sh, 43.80.Gx, 43.35.Wa [FD] Pages: 2715–2724

I. INTRODUCTION

Thermal ablation using intense ultrasound is a therapy with potential utility for treatment of pathological soft tissues.[1] For many applications, such as the treatment of primary and metastatic liver tumors, a goal of thermal ablation treatments is to reliably cause thermal necrosis in a relatively large tissue volume (e.g., greater than 5 cm diameter, including a safety margin).[2] In current practice, the thermal destruction of large tissue volumes is most commonly performed using radiofrequency (RF) ablation (electromagnetic radiation in the 400–700 kHz range).[3,4]

Intense ultrasound treatment, first proposed in the 1950s,[5,6] has the potential advantages of selectivity, integrated image guidance, and a noninvasive or minimally invasive approach. To date, most effort in this area has concentrated on extracorporeal[7,8] or intracavitary[9,10] high-intensity focused ultrasound (HIFU). A number of analytic[11–14] and numerical[15–20] studies have provided insight into the dynamics of lesion formation in HIFU treatments, including the effects of blood flow cooling,[15,16] acoustic nonlinearity,[16,18–20] cavitation,[17] and thermoacoustic lensing effects.[19,20]

An alternative approach to HIFU, which can allow the faster ablation of large tissue volumes at the expense of minimal invasiveness, is thermal coagulation by intense ultrasound (IUS) using interstitial probes based on ultrasound transducers in cylindrically omnidirectional,[21] planar,[22] and weakly focused[23] configurations. Clinical applications of interstitial intense ultrasound probes have included intraductal treatment of cholangiocarcinoma and papillary carcinoma.[24]

The modeling of interstitial ablation has also been performed using numerical solutions of the bioheat-transfer equation[25] with various methods for simulation of the ultrasound-induced heat deposition.[26–28] Effects considered in these simulations have included the loss of tissue perfusion due to thermal coagulation.[26,28] The effects of coagulation on ultrasound absorption, as measured experimentally,[29,30] have been modeled using both step[26] and piecewise-linear[28] dependence on the ultrasound-induced thermal dose.

Recent developments in transducer technology[31,32] have allowed the construction of miniaturized linear arrays capable of both IUS treatment and B-scan imaging. Although miniaturized array transducers are not capable of the sharp focusing achievable with large HIFU transducers, these arrays can effectively ablate tissue in bulk,[32] similar to RF ablation devices but with greater selectivity. Treatment planning and monitoring also benefit from the imaging capability of such arrays.

[a]Current address: Department of Biomedical Engineering, University of Cincinnati, Cincinnati, Ohio 45267-0586. Electronic mail: doug.mast@uc.edu
[b]Current address: Guided Therapy Systems, 33 S. Sycamore St., Mesa, Arizona 85202.

In this paper, approaches to the ablation of large tissue volumes using minimally invasive ultrasound probes are presented. A simple analytic model for bulk tissue ablation is presented and compared with experimental results for *ex vivo* and *in vivo* bulk ablation of mammalian liver tissue. Compared to full numerical models of bulk ablation such as those in Refs. 26–28 and the second model presented here, this simple analytic model provides a more convenient means to predict power requirements for thermal ablation under given source and tissue conditions. The analytic model can also be employed to predict differences between *in vivo* and *ex vivo* ablation results for comparable source conditions.

Methods for the detailed simulation of ultrasonic heat deposition and tissue ablation are presented. Intense ultrasound beams, simulated using a Fresnel approximation, induce tissue heating that is modeled using a three-dimensional finite-difference simulation. The heat deposition pattern is adaptively modified based on changes in tissue temperature and thermal dose. Unlike previous numerical models of bulk ablation using ultrasound,[26–28] these methods account for the effect of tissue vaporization on the ultrasound heat deposition. This effect is shown to be important for the realistic prediction of bulk ultrasound ablation. Comparisons of simulated and experimental results show that these simulation methods can effectively predict the depth, rate, and volume of ultrasonic ablation, and thus are a useful tool for the design of therapeutic approaches.

The effect of tissue boiling and absorption changes on ablation depth is illustrated by a matching experiment and simulation. An example bulk ablation method designed to minimize these effects, based on continuous rotational (interstitial) transducer scanning is presented. This method is shown in simulation and experiments to allow the ablation of significant volumes of soft tissue.

II. THEORY

This paper addresses the bulk ablation of soft tissue using intense ultrasound. As a starting point, basic requirements for bulk ablation can be considered. Most previous analytic modeling for ultrasonic tissue ablation has concentrated on highly focused situations,[11–14] for which perfusion effects are limited and beam geometries are very different from unfocused or weakly focused cases. Below, a simple analysis is given that illustrates power requirements for bulk tissue ablation and differences between *in vivo* and *in vitro* ablation experiments.

The bio-heat transfer equation,[25] which is a heat diffusion equation with an added term for perfusion losses, can be written as

$$\rho C\frac{\partial T'}{\partial t} = Q + \kappa\nabla^2 T' - wC_b T', \tag{1}$$

where T' is the tissue temperature rise over its equilibrium temperature T_∞, Q is the power deposited per unit volume, ρ is the tissue mass density, C is the tissue-volume specific heat, w is the blood mass flow rate per unit tissue volume, C_b is the blood-volume specific heat, and κ is the tissue thermal conductivity. For bulk tissue ablation employing broad ultrasound beams, the induced temperature rise will be slowly varying in space, and the thermal conduction term can be neglected to a first approximation. An approximate bioheat equation suitable for simple analytic study can then be written as

$$\frac{\partial T'}{\partial t} \approx \frac{Q}{\rho C} - \frac{1}{\tau}T', \tag{2}$$

where the characteristic perfusion time τ is defined as

$$\tau = \rho C/(wC_b). \tag{3}$$

To obtain an approximate solution for thermal lesioning using Eq. (2), one can assume that all tissue properties are spatially uniform, constant in time, and unchanged by the thermal treatment. For an infinite medium, Eq. (2) then has the solution

$$T' = \frac{Qt}{\rho C}\frac{1-e^{-t/\tau}}{t/\tau}. \tag{4}$$

The quotient $(1-e^{-t/\tau})/(t/\tau)$ reduces to unity for $t/\tau \to 0$ (short treatment times or negligible perfusion) and to τ/t for $t/\tau \to \infty$ (long treatment times).

Equation (4) can be used to illustrate requirements for bulk tissue ablation using intense ultrasound therapy. For heating caused in soft tissue by an arbitrary ultrasound field, the power deposited per unit volume is approximated by $\alpha\langle|p(z)|^2\rangle/(\rho c)$, where α is the acoustic absorption in Nepers per unit length, $\langle\cdot\rangle$ denotes temporal averaging, and c is the speed of sound. This model for heat deposition assumes that acoustic absorption in tissue is due to thermal relaxation.[33]

In order to obtain a simple estimate of requirements for bulk ablation, spatially averaged ultrasound heat deposition may be considered as the heat source in Eq. (4). Since the model results should not depend strongly on the geometry of the ultrasound beam, a general, slowly varying ultrasound field can be approximated for the present purposes as an exponentially attenuated plane wave. The acoustic pressure magnitude $|p(z)|$ is equal to $p_0 e^{-\alpha z}$, where z is the depth of penetration into the tissue and p_0 is the pressure amplitude at the tissue surface. A nominal value for the average heat deposition can be obtained by spatially averaging the acoustic heat deposition over the region where $|p|^2 > \epsilon|p_0|^2$, where ϵ is a parameter less than unity. In the present work, the parameter ϵ was taken to be 0.05, so that for an exponentially attenuated plane wave this region corresponds to the depth range $0 < z < 3/(2\alpha)$. The temporally and spatially averaged heat deposition is then given by

$$Q \sim \frac{\alpha}{\rho c}\left[\langle|p_0|^2\rangle\frac{2\alpha}{3}\int_0^{3/2\alpha} e^{-2\alpha z}\,dz\right] = 0.634\alpha\langle I_0\rangle, \tag{5}$$

where the bracketed term is the spatial average of $|p|^2$ over the depth considered and I_0 is the plane-wave intensity $p_0^2/(2\rho c)$.

For simplicity, it may be assumed that tissue ablation occurs at a threshold temperature T_{thresh}. The minimum acoustic amplitude needed for bulk ablation can then be estimated as the amplitude needed to raise the tissue temperature to its ablation threshold within its characteristic perfu-

sion time $t=\tau$. Inserting the heat deposition from Eq. (5) into Eq. (4) with $t\rightarrow\tau$ yields the threshold amplitude

$$\langle I_0\rangle_{\text{thresh}} \sim \frac{(T_{\text{thresh}}-T_\infty)\rho C}{0.4\alpha\tau}. \tag{6}$$

Representative parameters for human liver tissue *in vivo* are $T_{\text{thresh}}=60\ ^\circ\text{C}$, $T_\infty=37\ ^\circ\text{C}$, $\alpha=5.76\ \text{Np/m/MHz}^{1.2}$, $\rho=1060\ \text{kg/m}^3$, $C=3600\ \text{J/kg/}^\circ\text{C}$, $C_b=3720\ \text{J/kg/}^\circ\text{C}$, $w=18.7\ \text{kg/m}^3\text{/s}$, and $\kappa=0.524\ \text{W/m/}^\circ\text{C}$.[34,35] The resulting characteristic perfusion time is $\tau=55$ s.

For a frequency of 3 MHz and a transducer duty cycle of 75%, the pulsed source intensity required for ablation is thus about $25\ \text{W/cm}^2$. Analogous thresholds for nonplanar ultrasound fields can be obtained from the spatial and temporal average of the acoustic intensity within the region of significant heat deposition, taken here to be the region where the acoustic intensity magnitude is greater than 5% of the spatial peak value.

The simple analysis employed here can also be used to illustrate differences between *in vivo* and *in vitro* ablation experiments. The primary differences affecting ablation performance are differences in perfusion and starting temperature. For example, the formation of a particular ablative lesion *in vitro* may require an exposure of duration t_{vitro}. If the same ultrasonic transducer configuration and power are used for *in vitro* and *in vivo* exposures, the time required to achieve the same ablation *in vivo* can be estimated from Eq. (4) with $\tau\rightarrow\infty$ (no perfusion) for the *in vitro* case. The result is

$$t_{\text{vivo}} = -\tau\log\left(1-\frac{T_{\text{thresh}}-T_{\text{vivo}}}{T_{\text{thresh}}-T_{\text{vitro}}}\frac{t_{\text{vitro}}}{\tau}\right), \tag{7}$$

where T_{vivo} and T_{vitro} are the starting tissue temperatures for the *in vivo* and *in vitro* cases. The relation defined by Eq. (7) is plotted as the solid line in Fig. 1. For example, taking $T_{\text{thresh}}=60\ ^\circ\text{C}$, $T_{\text{vivo}}=37\ ^\circ\text{C}$, $T_{\text{vitro}}=25\ ^\circ\text{C}$, and the tissue parameters defined previously, Eq. (7) predicts that source conditions producing ablation in about 50 s *in vitro* will produce the same ablation *in vivo*, while a power level that requires more than about 83 s to ablate *in vitro* will produce no ablation *in vivo*.

Similarly, one may estimate the *in situ* source intensity required for ablation *in vivo* within the same exposure time t required *in vitro* as

$$I_{\text{vivo}} = I_{\text{vitro}}\frac{T_{\text{thresh}}-T_{\text{vivo}}}{T_{\text{thresh}}-T_{\text{vitro}}}\frac{t/\tau}{1-e^{-t/\tau}}. \tag{8}$$

The ratio of the source intensity required *in vivo* to that *in vitro* is plotted as the solid line in Fig. 1(b). Because of the higher assumed starting temperature, ablative lesions achievable in very short times (e.g., due to high source intensity) will require less power delivery *in vivo*, while lesions achievable by 3 min exposures *in vitro* will be achievable in the same time *in vivo* only if the delivered power is more than doubled. However, if *in vitro* experiments are performed with a starting temperature $T_{\text{vitro}}=T_{\text{vivo}}$, the achievement of a given ablation condition in the same time will always require greater power *in vivo*.

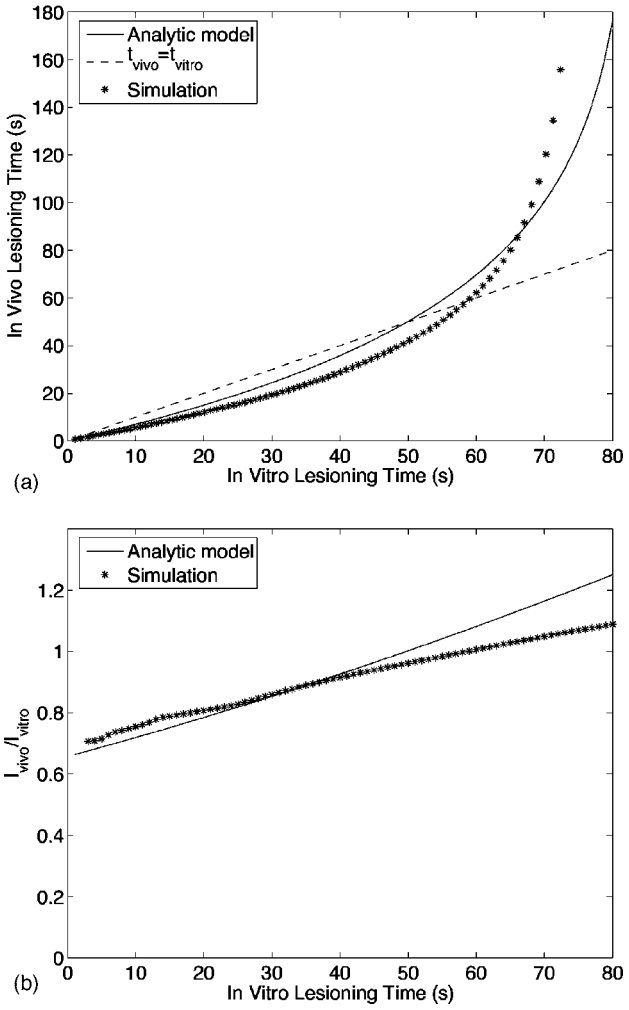

FIG. 1. A comparison of theoretical requirements for *in vitro* and *in vivo* ablation, taking into account blood perfusion and differences in the starting temperature. (a) Time required for *in vivo* and *in vitro* ablation given constant source conditions, estimated from an analytic model and from numerical simulations, shown with the equal-time line (dashed). (b) The ratio between required *in vivo* and *in vitro* source intensities for equal exposure times *in vivo* and *in vitro*, estimated using the analytic model and numerical simulations, and plotted versus exposure time.

These methods can also be used to model bulk ablation using other beam configurations, such as omnidirectional or weakly focused beams, in addition to the nominally planar sources used for most of the results reported here. Whatever the beam configuration, the condition for validity of this analysis is that local heating effects dominate heat conduction effects to a first approximation. Although the above analysis uses a plane wave field as a primary example, Eq. (11) can be used to estimate the appropriate average heat deposition for other transducer configurations, as was done in the analysis reported below in Sec. IV.

III. NUMERICAL METHODS

Heat deposition caused by planar ultrasound transducer arrays was modeled here using the Fresnel approximation for the field of rectangular sources.[36] For simplicity, the medium was assumed to be spatially homogeneous except for a spatially varying absorption coefficient. The total acoustic field was approximated as

$$p(\mathbf{r}) = p_0 \sum_n e^{i\phi n(\mathbf{r_F})} p_n(\mathbf{r}) \int_0^z e^{-\alpha(x,y,\zeta)}\, d\zeta, \tag{9}$$

where $\mathbf{r}$ represents the field point (x,y,z), p_0 is the pressure amplitude at the transducer face, $\alpha(\mathbf{r})$ is the medium attenuation coefficient in Nepers per unit length, $\phi_n(\mathbf{r}_F)$ is the phase shift associated with electronic focusing for the focal point $\mathbf{r}_F$, and $\phi_n(\mathbf{r}_f) = -k|\mathbf{r}_F - \mathbf{r}_n|$, where k is the acoustic wave number. Focusing phase shifts were additionally discretized to multiples of $\pi/8$, in accordance with the phasing capabilities of the electronics employed in the experiments. The field of an individual element centered at position (x_n, y_n) is given under the Fresnel approximation by

$$p_n(\mathbf{r}) = -\frac{ik}{2\pi z \beta^2} e^{ikz} (\mathbf{F}[\beta(x - x_n + a)] - \mathbf{F}[\beta(x - x_n - a)]) \times (\mathbf{F}[\beta(y - y_n + b)] - \mathbf{F}[\beta(y - y_n - b)]), \tag{10}$$

where a is the element half-width in the x (elevation) direction, b is the element half-width in the y (array) direction, $\beta = \sqrt{k/\pi z}$, and the complex Fresnel integral is denoted by $\mathbf{F}[\xi] = \int_0^\xi e^{i\pi\zeta^2/2}\, d\zeta$. The Fresnel integral was evaluated using a fast rational approximation.[37]

Ablation thresholds were computed for array transducers using Eq. (6), with an additional normalization factor accounting for the nonplanar nature of the acoustic fields. The computed acoustic heat deposition was averaged within the volume where the squared pressure was greater than 5% of its maximum value. For consistency with the threshold expressions derived above for plane waves, an effective plane-wave intensity is defined by analogy with Eq. (5) as

$$\langle I_0 \rangle_{\text{eff}} = \frac{1}{0.634 \rho c V_0} \int |p(\mathbf{r})|^2\, dV_0, \tag{11}$$

where the integration volume V_0 covers all points where $|p(\mathbf{r})|^2 > 0.05 \max[|p|^2]$. The factor 0.634 derives from the mean-square amplitude of an exponentially attenuated unit-amplitude plane wave, as in Eq. (5).

To obtain more detailed comparisons between theory and experiment, the bioheat transfer equation (1) was solved in three dimensions using second-order accurate centered differences in space and first-order accurate forward differences in time. The time step for this method was chosen in each case to satisfy the stability condition

$$\Delta t > \frac{\rho C}{2\kappa \left(\frac{1}{(\Delta x)^2} + \frac{1}{(\Delta y)^2} + \frac{1}{(\Delta z)^2} \right) + w C_b}. \tag{12}$$

The heat deposition term was taken to be $Q(\mathbf{r}) = \alpha(\mathbf{r}) |p(\mathbf{r})|^2 / (\rho c)$.[33] The tissue thermal dose[38] was cumulatively calculated in units of equivalent minutes at 43 °C, as

$$\text{EM}_{43}(\mathbf{r}) = \sum R^{T(\mathbf{r}) - 43\,^\circ\text{C}} \Delta t / 60, \tag{13}$$

where Δt is the time step in seconds, $R = 2$ for $T >= 43$ °C, and $R = 4$ for $T < 43$ °C.

Convection boundary conditions were employed at tissue boundaries. Available empirical relations[39] were used to calculate temperature-gradient-dependent convective heat transfer coefficients for water and air media and for vertical and horizontal orientations of the tissue boundaries. The average heat transfer coefficient $\bar{h}$ was assumed to take the form[39]

$$\bar{h} = H \left(\frac{T - T_\infty}{L} \right)^{1/4}, \tag{14}$$

where L is a characteristic length scale, T is the tissue boundary temperature, T_∞ is the free-stream temperature in the surrounding fluid, and H is a constant that depends on the material properties and surface orientation, with dimensions W $\text{m}^{7/4}$ $^\circ\text{C}^{5/4}$. Values of the constant H employed for water bath, *ex vivo* conditions were 194.5 for vertical surfaces, 178.0 for upward-facing horizontal surfaces with $T \geqslant T_\infty$, and 89.0 for upward-facing horizontal surfaces with $T < T_\infty$. For downward-facing horizontal surfaces, conditions for the two values of H are reversed. For air boundaries, the corresponding values of H are 1.4 for vertical surfaces, 1.32 for upward-facing horizontal surfaces with $T \geqslant T_\infty$, and 0.59 for upward-facing horizontal surfaces with $T < T_\infty$.

For the case of rotational scanning, the flow of cooling water in the coupling balloon was accounted for using a constant-temperature boundary condition $T = 15$ °C at the interface of the coupling balloon and the tissue. This boundary condition corresponds to the assumption that the cooling system is sufficient to remove all heat conducted into the cooling fluid from the ultrasound applicator and the surrounding tissue.

Changes in tissue absorption associated with ablation were incorporated in a manner similar to that of Ref. 28, using an empirical formula consistent with available experimental data on the thermal-dose dependence of ultrasonic absorption in mammalian liver tissue:[29]

$$\alpha = \begin{cases} \alpha_0, & \text{EM}_{43} < \text{EM}_0, \\ \alpha_0 \left(1 + \dfrac{\text{EM}_{43} - \text{EM}_0}{\text{EM}_1 - \text{EM}_0} \right), & \text{EM}_0 \leqslant \text{EM}_{43} \leqslant \text{EM}_1, \\ 2\alpha_0, & \text{EM}_{43} > \text{EM}_1, \end{cases} \tag{15}$$

so that the absorption rises linearly to twice its original value between two thermal dose thresholds, taken here to be $\text{EM}_0 = 200$ equivalent minutes and $\text{EM}_1 = 10^7$ equivalent minutes. The form of Eq. (9) allowed this absorption correction to be performed at each time step of the bioheat simulation, without recalculation of the full acoustic field.

Tissue boiling is known to cause substantial changes in acoustic heat deposition, including the shifting of heat deposition toward the ultrasonic source and limiting depth of ablation.[40,41] To account for these effects, a simple model for acoustic shadowing and the redistribution of thermal energy was employed. In Ref. 18, these effects were modeled for single HIFU lesions by assuming that, after any grid point (usually near the acoustic focus) reached a temperature of 100 °C, all of the thermal energy originally deposited in the half-space $z > z_0$ was redistributed in a 0.5 cm spherical region centered around the initial location of tissue boiling. The model employed here extends this idea to more general

heat distributions. Here, when the temperature at any grid point (x_i, y_i, z_i) exceeded 100 °C, the thermal energy deposited along the line $(x=x_i, y=y_i, z>z_i)$ was deposited in a cubic region with 2 mm sides, centered at the point (x_i, y_i, z_i). This operation was performed at each time step for all points exceeding 100 °C at that time, and the redistributed thermal energy sources associated with each location of tissue boiling were superposed. In one implementation of tissue boiling modeling, the temperature at each boiling point can be held constant at 100 °C until the energy deposited after boiling exceeds the latent heat of vaporization of water. However, since use of the latent heat model did not significantly change the numerical results, and since the boiling of a pure liquid may not fully model the boiling of tissue, the latent heat model was not used in the simulations reported here.

To model scanned exposures, the bioheat equation was first solved for the initial ultrasonic exposure. The acoustic heat deposition field was then spatially rotated or translated to the next position, and the bioheat simulation was further iterated using the previous temperature distribution as an initial condition. Corrections for absorption changes and tissue boiling were performed in the same manner at each time step.

IV. RESULTS

Ablation experiments were performed using the methods described in Ref. 32. These included *in vivo* exposures performed on porcine liver as well as *ex vivo* exposures performed on porcine and bovine liver. A variety of miniaturized ultrasound probes were employed, including the image-treat arrays described in Ref. 32 as well as other arrays and single-element, therapy-only transducers. All transducers were driven using tone-burst excitation with acoustic power between 8–60 W and duty cycles between 60%–100%. Single-element transducers were driven by a signal generator and radiofrequency amplifier, while array transducers were driven by a custom electronics system capable of both imaging and therapy.[32] *Ex vivo* experiments were performed in room-temperature water bath conditions, while *in vivo* experiments were performed in open surgical procedures. For the *in vivo* experiments, ultrasound arrays were inserted into actively water-cooled applicators that were applied directly to the liver tissue, either superficially or interstitially. After each experiment, thermal lesions were sliced, photographed, and quantitatively evaluated for ablation depth, volume, and rate.[32]

Intensity thresholds computed using Eqs. (6) and (11) were retrospectively compared with 54 *in vivo* ablation experiments performed in porcine liver with various single-element and array probes operating at frequencies between 2.8 and 7.6 MHz. These probes included various miniaturized arrays and single-element probes designed for interstitial or laparoscopic deployment, with packaging similar to the array applicator described in Ref. 32. Active dimensions for these transducers ranged between 1.5–5 mm in elevation and 16–48 mm in azimuth, with 1–64 independent elements. Also employed was a 3.95 MHz, spherically focused transducer with rectangular active dimensions of 22×40 mm^2.

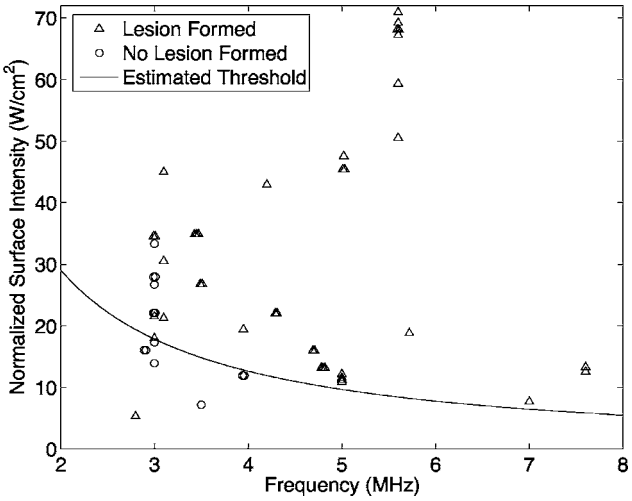

FIG. 2. Theoretical threshold source conditions compared with ablation results from 54 *in vivo* experiments on porcine liver. The smooth curve shows the theoretical time average, equivalent-plane-wave source intensity threshold as a function of frequency. Frequency and normalized source intensity for each experiment are shown using plus symbols where observable lesioning occurred, and open circle symbols where no lesioning occurred.

The theoretical threshold time-average intensity, from Eq. (6) is plotted in Fig. 2 as a function of frequency. Because of increased tissue absorption, intensity requirements for ablation are considerably smaller at higher frequencies. On the same graph, scatter plots show the frequency and normalized (equivalent plane wave) intensity for each of the experiments. Normalized intensity values were obtained using Eq. (11) based on theoretical beam profiles for each source configuration, scaled by surface intensities determined from radiation-force acoustic power measurements.

Those experiments resulting in observable thermal lesioning are plotted in Fig. 2 with plus symbols, while those resulting in no lesioning are plotted with open circles. Observable lesioning was defined here as gross lightening of tissue color due to thermal coagulative denaturation, seen after tissue slicing. For experiments with source conditions below the theoretical lesioning threshold, 7 of 8 produced no lesion. For experiments with source conditions above the theoretical threshold, 39 of 46 produced observable lesions. Thus, in these experiments, the theoretical lesioning threshold corrected the presence or absence of ablation in a majority of cases. However, the range of ablation experimental results available for this retrospective study is not sufficient to rigorously test the ablation threshold model. In general, positive predictions of lesioning may be more challenging than negative predictions, because several experimental unknowns, including tissue motion and probe performance irregularities, can reduce the probability of successful treatment.

To illustrate the differences between *in vitro* and *in vivo* exposures with greater detail, as well as to assess the validity of assumptions made in the analytic ablation modeling described above, numerical simulations were carried out for representative *in vitro* and *in vivo* exposures. The simulated configuration employed a single-element source of frequency 3.0 MHz, active surface dimensions 1.5×25.4 mm^2, and liver tissue with the physical parameters described above,

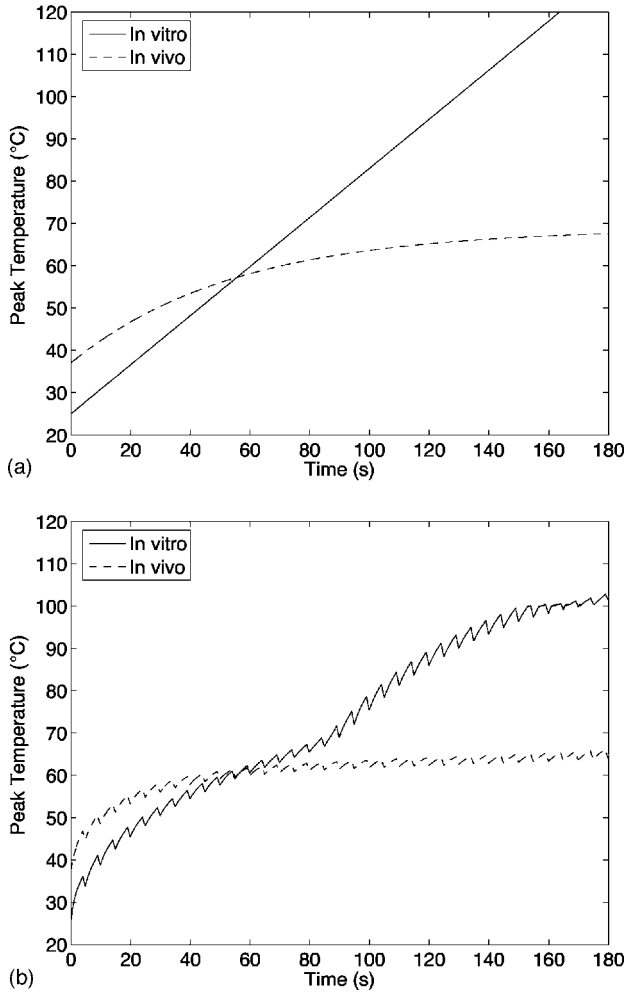

FIG. 3. Peak computed temperature versus time for comparable *ex vivo* (solid lines) and *in vivo* (dashed lines) ablation cases. (a) Approximate analytic model. (b) Finite-difference simulation.

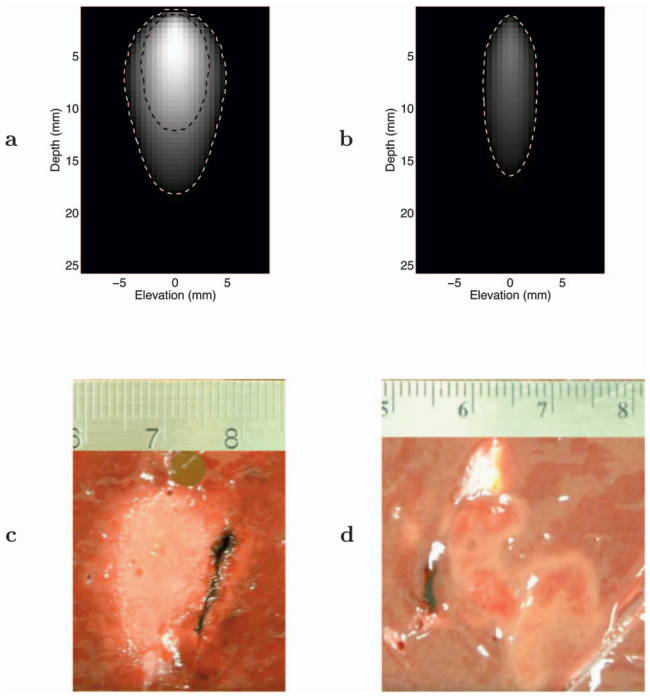

FIG. 4. Ablation *ex vivo* and *in vivo* under comparable exposure conditions. (a) Simulated thermal dose after a 3 min interstitial *ex vivo* exposure, shown on a logarithmic gray scale with superimposed contours at $EM_{43}=200$ and 10^7 equivalent minutes. (b) Simulated temperature after a 3 min *in vivo* exposure. (c) Lesion from a *ex vivo* interstitial exposures at two adjacent angles. The circular overlay indicates the approximate probe position. (d) Lesion from *in vivo* interstitial exposures at seven adjacent locations. The precise probe location is unknown in this case.

and 3 min exposures with an 80% duty cycle (4 s on, 1 s off). The only differences between the *in vitro* and *in vivo* simulations were the starting temperature (25 °C and 37 °C, respectively) and perfusion (zero and 18.7 $kg/m^3/s$, respectively). To ensure that differences between the results depended only on starting temperature and perfusion, identical boundary conditions (convection with coefficients for water at 25 °C, as described previously) were employed in the two cases. For comparison with the analytic model, simulations were performed for surface power densities between 23 and 250 W/cm^2. The time for the onset of ablation, based on a threshold peak temperature of 60°, was determined for each simulation, allowing the comparison of source conditions and ablation times required for *in vitro* and *in vivo* exposures. The results are plotted as individual points in Figs. 1(a) and 1(b). The general agreement with the analytic model confirms the ability of the simpler model to predict ablation trends. The two models differ mainly for long ablation times, greater than about one minute, for which heat conduction plays a more significant role.

More detailed simulation results are shown for this source configuration with a surface power density of 38 W/cm^2, which corresponds most closely to the available experimental data. Simulated time-dependent spatial peak temperatures for the *in vitro* and *in vivo* cases, shown in Fig. 3, show comparable trends for the full numerical approach and the simple analytic model, confirming the validity of the simple analytic model. Both simulations predict that the *in vitro* exposure will cause significant thermal lesioning for the given source conditions, while the comparable *in vivo* exposure will cause little or no lesioning.

Although experimental results exactly analogous to these simulated results are not available, the simulated conditions were similar to those from previous *in vivo* and *in vitro* experiments performed with the same transducer configuration and comparable acoustic power. The *in vitro* experiment used here for comparison employed 2 min exposures at two adjacent angular locations separated by 15° with a power density of about 38 W/cm^2, while the *in vivo* experiment employed seven 3 min exposures at locations separated by 20° with a power density of about 53 W/cm^2. Lesions from the two experiments, shown in Fig. 4 together with the simulated thermal dose for the finite difference simulations, follow the predicted trends. The *ex vivo* lesion is severe, consistent with a temperature rise to ~100 °C and the plotted thermal dose contour at $EM_{43}=10^7$ equivalent minutes, while the *in vivo* lesion shows only regions of coagulation, consistent with a temperature rise to ~60 °C and the plotted thermal dose contour at 200 equivalent minutes. Although these ablation results qualitatively follow the predicted trends, the precise lesion shapes should not be directly

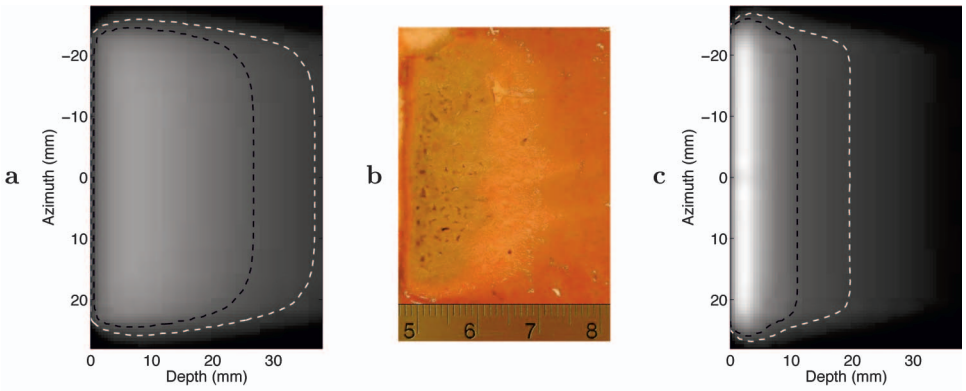

FIG. 5. The effect of boiling and thermal-dose-dependent attenuation. (a) Simulation without boiling and dose-dependent attenuation modeling. The simulated thermal dose is shown on a logarithmic gray scale with superimposed contours at $EM_{43}=200$ and 10^7 equivalent minutes. (b) *Ex vivo* lesion. (c) Simulated thermal dose with boiling and dose-dependent attenuation modeling.

compared with the above simulations because of the different scanning configurations and exposure times employed.

To demonstrate the effect of the present boiling and adaptive attenuation models, simulations were carried out under conditions matching those for an available *ex vivo* experiment, with and without the consideration of boiling and thermal dose-dependent attenuation. The source employed was a 32-element array with dimensions 2.3×49 mm and a frequency of 3.1 MHz, placed 6 mm from the tissue surface. All elements were fired in phase with a surface power density of 39 W/cm^2 for 3 min with an 80% duty cycle (8 s on, 2 s off).

The experimental and simulated results for these ablation conditions, shown in Fig. 5, indicate that the present boiling and adaptive attenuation models effectively characterize the screening effects associated with tissue ablation. The experimental results showed an ablation depth of 10–15 mm for severe ablation (brown and cracked tissue) and 20–25 mm for any ablation (discolored tissue), while the measured ablation rate was 1.92 ml/min. The simulation results with unmodified heat deposition significantly overpredict the depth of ablation (37 mm based on an $EM_{43}=200$ threshold for ablation or 27 mm based on an $EM_{43}=10^7$ threshold for severe ablation) as well as the ablation rate (4.0 ml/min). Results from the simulations including the boiling and adaptive attenuation models show much better agreement with experiment for both the depth of ablation (20 mm based on an $EM_{43}=200$ threshold for ablation or 11 mm based on an $EM_{43}=10^7$ threshold for severe ablation) as well as the ablation rate (2.1 ml/min).

Bulk ablation experiments employing interstitially scanned configurations were also performed. The example illustrated here was performed using a continuous angular scanning configuration that was found to reduce premature proximal tissue ablation, so that the depth-limiting effects illustrated in Fig. 5 were minimized. A 3 mm image-treat array, having 32 elements with an active aperture of 2.3×49 mm and a frequency of 3.1 MHz, was inserted interstitially into an excised lobe of bovine liver. All array elements were simultaneously fired in phase with an acoustic power of 74.3 W and an 80% duty cycle (0.8 s on, 0.2 s off) while the array was rotated by a stepping motor at a rate of 22 s per revolution, the maximum rate available for the motor employed. The active exposure time for these source conditions was 19 min. Since continuous unidirectional rotation is not feasible due to cabling, the probe was alternately rotated clockwise for one revolution and counterclockwise for the next, with each revolution beginning at the same turning point.

To simulate this experiment, a sequence of individual exposures was performed with numerical rotation of the ultrasonic heat deposition field before each exposure. To minimize the computation time while maintaining a smooth rotation of the heating pattern, the angular steps were separated by 10°, so that the exposure time at each step was 0.61 s and a total of 52 rotations were performed to model an exposure time of 19 min. The duty cycle, source intensity, and back-and-forth rotation pattern matched those employed in the experiment. Thus, exposures were alternately performed for the sequence of angular positions 0°, 10°,…,350° and the se-

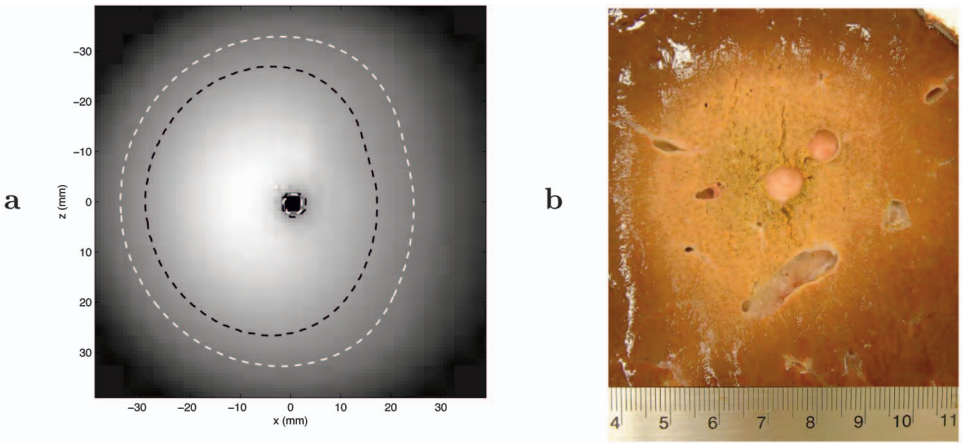

FIG. 6. Thermal lesioning from an *in vitro* continuous-sweep rotational scan. (a) Simulated thermal dose, plotted on a logarithic gray scale, with contours shown for $EM_{43}=200$ and 10^7 equivalent minutes. (b) Cross section of *ex vivo* lesion.

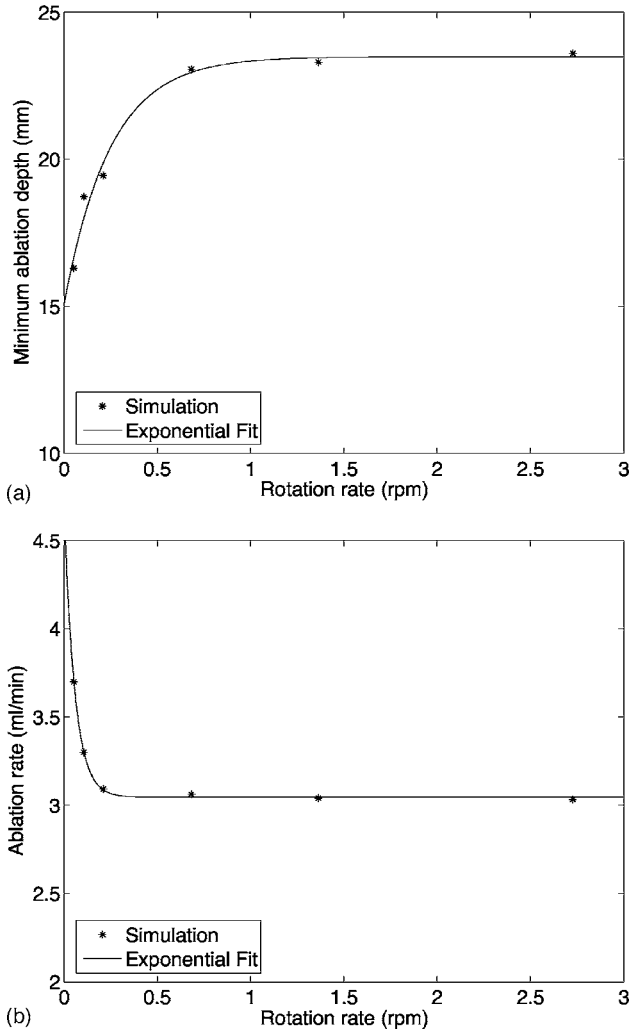

FIG. 7. Simulated effect of rotational scanning rate on interstitial bulk ablation, based on simulations using the configuration of Fig. 6. In both plots, simulated data are shown with exponential fits of the form $y=Ae^{-\Omega\tau}+B$. (a) Minimum ablation depth, measured radially from the transducer axis. (b) Ablation rate.

quence 0°, 350°,…,10°. A cross section of the resulting bulk ablation at the array midpoint is shown in Fig. 6, together with the simulated thermal dose map in the same plane and contours at $EM_{43}=200$ and 10^7 min. The lesion shape and depth are seen to agree fairly well, including the lesser depth ablated near the rotational turning point. An examination of simulated temperature fields suggests that this asymmetry occurs because larger temperature rises initially occur opposite the turning point, resulting in increased tissue absorption [Eq. (15)] and thus greater heat deposition. The simulated volume of ablation, based on an $EM_{43}=200$ min threshold, is 57.8 ml, while the experimentally measured ablation volume was 63.9 ml.

The example illustrated by Fig. 6 employed rapid rotational scanning, with the purpose of maximizing the ablation depth. The effect of the rotation rate on the ablation depth and rate is illustrated further by analogous simulations for a range of rotational speeds. Several simulations were performed for the same configuration as the previous example (Fig. 6), but with reduced rotational speeds corresponding to 1, 2, 4, 13, and 26 rotations within the 19 min treatment duration. The resulting simulated ablation depths and rates are plotted in Fig. 7. The minimum ablation depth, which occurred near the rotational turning point in all cases, was determined by an interpolation of a contour corresponding to a thermal dose $EM_{43}=200$ min, while the ablation rate was determined based on the same thermal dose threshold. As illustrated in Fig. 7, the slowest rotational rates result in larger ablation rates but smaller minimum ablation depths. Both simulated datasets are fit well by curves of the form $y=Ae^{-\Omega\tau}+B$, where Ω, measured in revolutions per minute (rpm), is the rotational scanning rate. Parameters determined by a least-squares fit are $A=-8.41$ mm, $\tau=4.04$ min, $B=23.5$ mm for minimum depth ($r=0.990$), and $A=1.63$ ml/min, $\tau=17.5$ min, $B=3.05$ ml/min for the ablation rate ($r=0.999$). The increased ablation rate for slow scanning rates is due to more rapid local heating, which reduces losses due to heat conduction. The decreased depth for slow scanning rates is due to the boiling and thermal dose-dependent absorption effects illustrated by Fig. 5.

V. DISCUSSION

This work describes methods using intense ultrasound energy to achieve bulk ablation for soft tissue. The simple analytic approach described here allows an estimation of the source and timing conditions required for ablation, while the full numerical approach provides greater detail. The capabilities, limitations, and applications of each of these approaches are discussed below.

The simple analytic approach to bulk ablation modeling presented here effectively assumes a uniform temperature distribution within the region of interest. This model is clearly limited by the neglect of heat conduction, spatial variations in heat deposition, and changes in tissue state due to the thermal treatment. However, comparisons between the analytic model, experimental results, and full numerical simulations suggest that the simple analytic method is useful in defining the source requirements necessary for ablation. The analytic method predicts the differences between *in vivo* and *ex vivo* source conditions needed for ablation, as seen by the comparison with full numerical simulations in Figs. 1 and 3. This method also predicts intensity thresholds for *in vivo* ablation under a variety of probe configurations, as illustrated by Fig. 2.

The prediction success of this analytic approach is possible because, for bulk ultrasonic ablation, perfusion effects are the dominant limiting factor for *in vivo* ablation. While it has previously been established that perfusion can significantly change ablation characteristics for HIFU,[42] perfusion losses play a larger role when less intense (unfocused, planar, or weakly focused) acoustic fields are used to achieve bulk ablation. Although the analytic model breaks down for long-duration exposures in the absence of perfusion, it effectively predicts the trends of temperature time history in perfused tissue.

Full numerical simulations provide a more complete prediction of ablation *ex vivo* and *in vivo*, including the spatial characteristics of ablation. The simulation methods reported here extend previous approaches by incorporating a more

detailed model for heat redistribution due to tissue boiling. Neglected effects include acoustic nonlinearity, temperature-dependent changes in tissue properties other than ultrasonic absorption, and the structural inhomogeneity of tissue. Of these effects, the inhomogeneous structure of tissue is likely to be among the most important. For example, if source conditions are close to the ablation threshold illustrated in Fig. 2, small variations in heat deposition due to refraction and scattering as well as inhomogeneous perfusion losses may cause some areas of tissue to be undertreated while others are overtreated.

In addition, losses of tissue perfusion due to thermal coagulation, which were neglected here, could cause increased heating after initial tissue ablation. These effects could be straightforwardly incorporated into the numerical methods described above by defining a perfusion function specified to be zero at all locations where the thermal dose has exceeded a threshold value, such as the 10^7 equivalent minutes used above as a criterion for severe ablation. Notably, the inclusion of this effect would not change the *in vivo* simulation results presented here (Fig. 4), because the thermal dose did not reach this threshold in that simulation.

The comparisons with experiment reported here indicate that both of the present modeling approaches can be used to predict bulk ablation of soft tissue. An estimation of threshold source amplitudes obtained using the analytic model predicted trends of ablation for *in vivo* ablation experiments under a wide range of source conditions. Ablation results predicted using the full numerical model agreed well with experimentally measured ablation depths, volumes, and rates. To obtain close correspondence between simulated and actual ablation, consideration of temperature- and thermal-dose-dependent changes in heat deposition are important.

Both of the modeling approaches presented here have potential use in guiding further development of devices and methods for the ultrasonic ablation of soft tissue. The analytic approach can be employed to estimate the source conditions required for reliable ablation *in vivo*. This approach also allows the extrapolation of *ex vivo* experimental results, which can be obtained under controlled conditions, to predict ablation effects in living, perfused tissue. The second approach presented here, which includes detailed modeling of acoustic heat deposition and transfer, is suitable for more detailed design of bulk ablation devices, methods, and experiments.

In the present work, use of these models has facilitated the design of source conditions for the improved bulk ablation of liver tissue. Design goals based on ablation as currently performed using RF devices include rapid ablation ($\sim$1.5–2.0 ml/min) and a large depth of ablation ($\sim$30 mm). Scanning schemes such as the continuous rotational scan shown in Fig. 6 and the sweeping linear scan illustrated in Ref. 32 were designed to minimize shadowing effects associated with the ablation of tissue near the acoustic source. As illustrated by Fig. 7, the simulation of a range of scanning configurations can allow the minimization of these shadowing effects, resulting in more uniform ablation of clinically relevant tissue volumes.

VI. CONCLUSIONS

Two approaches to modeling bulk ablation using intense ultrasound have been presented. These approaches include a simple analytic method for a definition of treatment requirements and a more complete simulation method for modeling of the details of ablation. A comparison between the two models confirms that the analytic method predicts trends of source requirements for bulk ablation, with the greatest accuracy for fairly short treatment times (e.g., the achievement of initial ablation within one minute). Comparisons with experiments indicate that the simple analytic model can predict ablation thresholds and approximate heating characteristics of tissue, while the full numerical methods can predict the shape, volume, depth, and rate of ablation effectively. A combination of these techniques is promising for the design of future approaches for bulk ablation of soft tissue.

[1] J. E. Kennedy, G. R. ter Haar, and D. Cranston, "High intensity focused ultrasound: Surgery of the future?" Br. J. Radiol. **76**, 590–599 (2003).
[2] S. N. Goldberg, G. S. Gazelle, and P. R. Mueller, "Thermal ablation therapy for focal malignancy: A unified approach to underlying principles, techniques, and diagnostic imaging guidance," AJR, Am. J. Roentgenol. **174**, 323–331 (2000).
[3] S. A. Curley, "Radiofrequency ablation of malignant liver tumors," Ann. Surg. Oncol. **10**, 338–347 (2003).
[4] R. J. Zagoria, "Percutaneous image-guided radiofrequency ablation of renal malignancies," Radiol. Clin. North Am. **41**, 1067–1075 (2003).
[5] W. J. Fry, "Biological and medical acoustics," J. Acoust. Soc. Am. **30**, 387–393 (1958).
[6] P. P. Lele, "Production of deep focal lesions by focused ultrasound—Currrent status," Ultrasonics **5**, 105–112 (1967).
[7] G. R. ter Haar, D. Sinnett, and I. Rivens, "High-intensity-focused ultrasound: a surgical technique for the treatment of discrete liver tumors," Phys. Med. Biol. **34**, 1743–1750 (1989).
[8] F. Wu, W.-Z. Chen, J. Bai, J.-Z. Zou, Z.-L. Wang, H. Zhu, and Z.-B. Wang, "Pathological changes in human malignant carcinoma treated with high-intensity focused ultrasound," Ultrasound Med. Biol. **27**, 1099–1106 (2001).
[9] A. Gelet, J. Y. Chapelon, R. Bouvier, O. Rouviere, Y. Lasne, D. Lyonnet, and J. M. Dubemard, "Transrectal high-intensity focused ultrasound: minimally invasive therapy of localized prostate cancer," J. Endourol **14**, 519–528 (2000).
[10] T. Uchida, N. T. Sanghvi, T. A. Gardner, M. O. Koch, D. Ishii, S. Minei, T. Satoh, T. Hyodo, A. Irie, and S. Baba, "Transrectal high-intensity focused ultrasound for treatment of patients with stage T1b-2n0m0 localized prostate cancer: a preliminary report," Urology **59**, 394–398 (2002).
[11] J. B. Pond, "The role of heat in the production of ultrasonic focal lesions," J. Acoust. Soc. Am. **47**, 1607–1611 (1970).
[12] T. C. Robinson and P. P. Lele, "An analysis of lesion development in the brain and in plastics by high-intensity focused ultrasound at low-megahertz frequencies," J. Acoust. Soc. Am. **47**, 1607–1611 (1970).
[13] F. L. Lizzi and M. Ostromogilski, "Analytical modelling of ultrasonically induced tissue heating," Ultrasound Med. Biol. **10**, 289–298 (1984).
[14] C. R. Hill, I. Rivens, M. G. Vaughan, and G. R. ter Haar, "Lesion development in focused ultrasound surgery: a general model," Ultrasound Med. Biol. **20**, 259–269 (1994).
[15] M. C. Kolios, M. D. Sherar, and J. W. Hunt, "Blood flow cooling and ultrasonic lesion formation," Med. Phys. **23**, 1287–1298 (1996).
[16] F. P. Curra, P. D. Mourad, V. A. Khoklova, R. O. Cleveland, and L. A. Crum, "Numerical simulations of heating patterns and tissue temperature response due to high-intensity focused ultrasound," IEEE Trans. Ultrason. Ferroelectr. Freq. Control **47**, 1077–1089 (1999).
[17] F. Chavrier, J. Y. Chapelon, A. Gelet, and D. Cathignol, "Modeling of high-intensity focused ultrasound-induced lesions in the presence of cavitation bubbles," J. Acoust. Soc. Am. **108**, 432–440 (2000).
[18] P. M. Meaney, M. D. Cahill, and G. R. ter Haar, "The intensity dependence of lesion position shift during focused ultrasound surgery," Ultrasound Med. Biol. **26**, 441–450 (2000).
[19] I. M. Hallaj and R. O. Cleveland, "Simulations of the thermo-acoustic lens

effect during focused ultrasound surgery," J. Acoust. Soc. Am. **109**, 2245–2253 (2001).
[20]C. W. Connor and K. Hynynen, "Bio-acoustic thermal lensing and nonlinear propagation in focused ultrasound surgery using large focal spots: a parametric study," Phys. Med. Biol. **47**, 1911–1928 (2002).
[21]C. J. Diederich, W. H. Nau, and P. R. Stauffer, "Ultrasound applicators for interstitial thermal coagulation," IEEE Trans. Ultrason. Ferroelectr. Freq. Control **46**, 1218–1228 (1999).
[22]R. Chopra, C. Luginbuhl, A. J. Weymouth, F. S. Foster, and M. J. Bronskill, "Interstitial ultrasound heating applicator for MR-guided thermal therapy," Phys. Med. Biol. **46**, 3133–3145 (2001).
[23]C. Lafon, D. M. de Lima, Y. Theillière, F. Prat, J.-Y. Chapelon, and D. Cathignol, "Optimizing the shape of ultrasound transducers for interstitial thermal ablation," Med. Phys. **29**, 290–297 (2002).
[24]F. Prat, C. Lafon, D. M. de Lima, Y. Theilliere, J. Fritsch, G. Pelletier, C. Buffet, and D. Cathignol, "Endoscopic treatment of cholangiocarcinoma and carcinoma of the duodenal papilla by intraductal high-intensity US: Results of a pilot study," Gastrointest Endosc **56**, 909–915 (2002).
[25]H. H. Pennes, "Analysis of tissue and arterial blood temperatures in the resting human forearm," J. Appl. Physiol. **1**, 93–122 (1948).
[26]C. Lafon, F. Prat, J. Y. Chapelon, F. Gorry, J. Margonari, Y. Theillere, and D. Cathignol, "Cylindrical thermal coagulation necrosis using an interstitial applicator with a plane ultrasonic transducer: *in vitro* and *in vivo* experiments versus computer simulations," Int. J. Hyperthermia **16**, 508–522 (2000).
[27]R. Chopra, M. J. Bronskill, and F. S. Foster, "Feasibility of linear arrays for interstitial ultrasound thermal therapy," Med. Phys. **27**, 1281–1286 (2000).
[28]P. D. Tyreus and C. J. Diederich, "Theoretical model of internally cooled interstitial ultrasound applicators for thermal therapy," Phys. Med. Biol. **47**, 1073–1089 (2002).
[29]C. A. Damianou, N. T. Sanghvi, F. J. Fry, and R. Maass-Moreno, "Dependence of ultrasonic attenuation and absorption in dog soft tissues on temperature and thermal dose," J. Acoust. Soc. Am. **102**, 628–634 (1997).
[30]A. E. Worthington and M. D. Sherar, "Changes in ultrasound properties of porcine kidney tissue during heating," Ultrasound Med. Biol. **27**, 673–682 (2001).
[31]P. G. Barthe and M. H. Slayton, "Efficient wideband linear arrays for imaging and therapy," *1999 IEEE Ultrasonics Symposium Proceedings*, Vol. **2**, pp. 1249–1252.
[32]I. R. S. Makin, T. D. Mast, W. Faidi, M. M. Runk, P. G. Barthe, and M. H. Slayton, "Miniaturized ultrasound arrays for interstitial ablation and imaging," Ultrasound Med. Biol. (in press).
[33]W. L. Nyborg, "Heat generation by ultrasound in a relaxing medium," J. Acoust. Soc. Am. **70**, 310–312 (1981).
[34]International Commission on Radiation Units and Measurements, *ICRU Report 61: Tissue Substitutes, Phantoms and Computational Modeling in Medical Ultrasound* (ICRU Publications, Bethesda, MP, 1998).
[35]F. A. Duck, *Physical Properties of Tissue: a Comprehensive Reference Book* (Academic Press, London, 1990).
[36]A. Freedman, "Sound field of a rectangular piston," J. Acoust. Soc. Am. **32**, 197–209 (1960).
[37]M. Abramowitz and I. A. Stegun, *Handbook of Mathematical Functions* (National Bureau of Standards, Washington DC, 1972), Chap. 7.
[38]S. A. Sapareto and W. C. Dewey, "Thermal dose determination in cancer therapy," Int. J. Radiat. Oncol., Biol., Phys. **10**, 787–800 (1984).
[39]J. P. Holman, *Heat Transfer*, 7th ed. (McGraw-Hill, New York, 1990), Chap. 7.
[40]N. A. Watkin, G. R. ter Haar, and I. Rivens, "The intensity dependence of the site of maximal energy deposition in focused ultrasound surgery," Ultrasound Med. Biol. **22**, 483–491 (1996).
[41]W.-S. Chen, C. Lafon, T. J. Matula, S. Vaezy, and L. A. Crum, "Mechanisms of lesion formation in high intensity focused ultrasound therapy," ARLO **4**, 41–46 (2003).
[42]A. Arafiev, F. Prat, J. Y. Chapelon, J. Tavakkoli, and D. Cathignol, "Ultrasound-induced tissue ablation: studies on isolated, perfused porcine liver," Ultrasound Med. Biol. **24**, 1033–1043 (1998).

Whistles of small groups of *Sotalia fluviatilis* during foraging behavior in southeastern Brazil

Daniela Pivari[a)]
Laboratório de Ecologia Marinha (Labmar), Departamento de Ecologia, Instituto de Biociências, Universidade de São Paulo. Rua do Matão 321, Cidade Universitária, São Paulo, 05508-900, São Paulo, Brazil, and Projeto Atlantis, Instituto de Biologia da Conservação, Barão Geraldo, Campinas, São Paulo, Brazil

Sergio Rosso
Laboratório de Ecologia Marinha (Labmar), Departamento de Ecologia, Instituto de Biociências, Universidade de São Paulo. Rua do Matão 321, Cidade Universitária, São Paulo, 05508-900, São Paulo, Brazil

(Received 3 March 2005; revised 29 June 2005; accepted 20 July 2005)

Whistle emissions were recorded from small groups of marine tucuxi dolphins (*Sotalia fluviatilis*) in two beaches located in an important biological reserve in the Cananéia estuary (25°03′S, 47°58′W), southeastern Brazil. A total of 17 h of acoustic data was collected when dolphins were engaged in a specific feeding foraging activity. The amount of 3235 whistles was recorded and 40% ($n=1294$) were analyzed. Seven acoustic whistle parameters were determined: duration (ms), number of inflection points, start and end frequency (kHz), minimum and maximum frequency (kHz), and frequency range (kHz). Whistles with up to four inflection points were found. Whistles with no inflection points and rising frequency corresponded to 85% ($n=1104$) of all analyzed whistles. Whistle duration varied from 38 to 627 ms (mean=229.6±109.9 ms), with the start frequency varying between 1 and 16 kHz (mean=8.16±3.0 kHz) and the end frequency between 2 and 18 kHz (mean=14.35±3.0 kHz). The importance of this study requires an accurate measurement of the whistles' emissions in an unusual foraging feeding behavior situation on two beaches where several tucuxis, mostly mother–calf pairs, are frequently present. These two beaches are located in a federal and state environment Environmental Protected Area threatened by the progressive increase of tourism. [DOI: 10.1121/1.2033569]

PACS number(s): 43.80.−n, 43.80.Ka [WWA] Pages: 2725–2731

I. INTRODUCTION

Dolphins usually rely on acoustic signals to negotiate their physical and social environment (Smolker *et al.*, 1993). Many delphinid species are known to produce narrow-band, frequency-modulated whistles as part of a larger repertoire of sound used for social communication (Herman and Tavolga, 1980; Popper, 1980). Bioacoustics research provides insights into animal behavior that can aid conservations efforts, helping in studies focusing on taxonomy and systematics, communication, vocal ontogeny, behavioral genetics, and behavioral ecology (Baptista and Gaunt, 1997). An important point in the methodology used in bioacoustics research is the fact that researchers do not necessarily need to capture individuals to record their vocal behavior. This is very important in conservation efforts because capture–release methods can frequently stress the animals with the possible consequence of obtaining unreliable data. Many studies conducted with animals in captivity (e.g., Caldwell *et al.*, 1990) or with animals enclosed in large nets in natural environment (Sayigh *et al.*, 1990; 1995) are questionable because this potentially changes the animal's behavior. The highly developed acoustic sense in dolphins allows researchers to use the recording and analysis of vocalizations (Herman and Tavolga, 1980; Popper, 1980; Herzing, 1996) as a means to better understand their population dynamics. Dolphins seem to produce and share a large number of whistles contours that comprise the whistle repertoire of a given species (Mc Cowan and Reiss, 1995). Whistle repertoire studies are important in comparison between different populations from different geographical areas along the distribution of the species. This kind of information seems to reflect the social structure and document important relationships within the ecology of populations (Wang *et al.*, 1995).

Little is known about the acoustic behavior of tucuxi, *S. fluviatilis*. This dolphin is listed as "insufficiently known" by the International Union for Nature Conservation (Reeves *et al.*, 2003). There are two known ecotypes for this species, the marine and the freshwater tucuxi. The marine tucuxi occurs exclusively along the Western Atlantic coastal waters from Santa Catarina (27°S) (Brazil) to Honduras (14°N) (da Silva and Best, 1996). Group sizes ranging between one and 80 individuals were reported for marine tucuxis in Brazilian waters (Flores, 1999; 2003; Santos, 2004; and Azevedo *et al.*, 2005). The freshwater tucuxi is endemic to the Amazon and Orinoco basins (da Silva and Best, 1996). Monteiro-Filho *et al.* (2002) suggested the existence of two *Sotalia* species: the freshwater ecotype, *S. fluviatilis* and the marine ecotype, *S. guianensis*. Genetics studies have been conducted to solve

[a)]Electronic mail: danipivari@yahoo.com.br

this question (Caballero *et al.*, 2003). This study increases the understanding of this species and will enable future bioacoustics research that, as an alternative tool, could help to separate, or not, the two ecotypes, marine and freshwater, into two species. Isolated populations have distinct adaptations to environmental conditions and have differences in taxonomy which could affect whistle characteristics (Steiner, 1981; Wang *et al.*, 1995). It is unknown if these two ecotypes are genetically isolated. Photoidentification, bioacoustics, and genetics studies at the junction of the Amazon River with the Atlantic Ocean are necessary to address this question. Currently, we use the *Sotalia fluviatilis* terminology for the marine tucuxi dolphin.

Most bioacoustics studies on tucuxi have focused on the freshwater ecotype (Caldwell and Caldwell, 1970; Norris *et al.*, 1972; Nakasai and Takemura, 1975; Wiersmsa, 1982; Alcuri and Busnel, 1989; Kamminga *et al.*, 1993; Terry, 1983; Sauerland and Dehnhardt, 1998; Wang *et al.*, 2001; Podos *et al.*, 2002). The acoustic repertoire of the marine tucuxi has been recently described (Figueiredo, 1997; Pereira, 1997; Monteiro-Filho and Monteiro, 2001; Azevedo and Simão, 2002; Erber and Simão, 2004). Azevedo and Van Sluys (2005) reported a quantitative and comparative analysis of the acoustic whistle parameters of marine tucuxi along part of its distribution in Brazilian waters. The magnitude of the whistle parameters' variation was comparatively smaller between adjacent areas than between nonadjacent ones.

In this study we described whistles of marine tucuxi produced while foraging and feeding on two beaches (Ponta da Trincheira and Praia do Itacuruçá) of an important calving area located in an Environmental Protected Area in the Cananéia estuary, São Paulo State, southeastern Brazil. Approximately ten photo-identified dolphins frequent these two beaches to raise calves, capture prey in shallow waters close to the sand beach (Santos, 2004), and to teach their calves to catch food (Santos *et al.*, 2000). According to Santos (2004), land-based observations developed in Ponta da Trincheira, Praia da Barra, and Praia do Itacuruçá showed small groups of tucuxis (3.7±2.6 individuals) approaching and using these areas. Foraging and feeding behavior were characterized by visual activity, such as fish (mullets, *Mugil sp.*) jumping near the tucuxis. One specific capture prey strategy is also employed in both areas: tucuxis surround fish in shallow waters (about 50 cm) using the sand beach as a barrier to trap them. Sometimes, dolphins stop in front of the beach. It is easy to see the dorsal fin out of the water; suddenly, they swim fast along the shoreline and take the fish close to the sand. This situation has only been described in these two areas in the Cananéia estuary and adjacent to an island in north of Paraná state, Ilha das Peças, also in Brazil. These days tourist problems affect these areas. In 1998 a bridge linking the Cananéia island to the mainland was built and the number of tourists in Cananéia region increased. Many tourists, either in private or "dolphin watch" vessels navigate through the estuary and chase groups of dolphins. The regular occurrence of dolphins near these two beaches increases the number visiting those areas, and it is common to see people in the water swimming with them. The increasing tourist population has resulted in greater destruction and degradation of the environment. Large mangrove areas have been destroyed to make way for residences and commercial buildings. Garbage, sewerage, and organochlorines contamination coming from insecticides used in plantations next to the region have leaked into the estuarine waters and have directly affected the top predator of the local food chain, the tucuxi population (Santos, 2004).

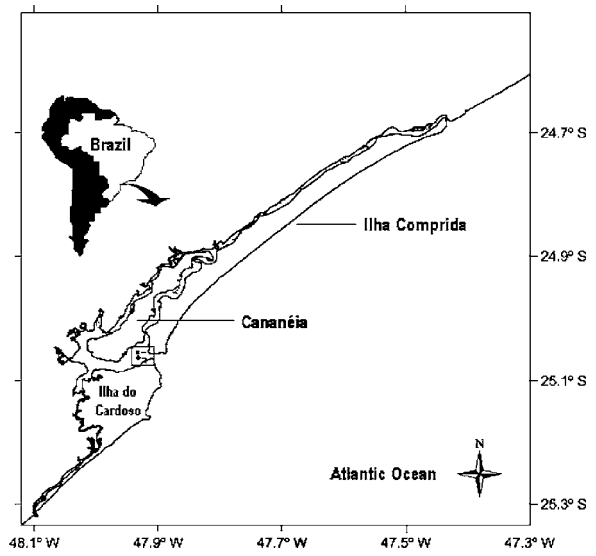

FIG. 1. Map showing the estuarine complex of Cananéia, southeastern Brazil and the two beaches where data were collected during foraging and feeding behavior displayed by marine tucuxi dolphins (*Sotalia fluviatilis*) (■=Ponta da Trincheira, Ilha Comprida and ●=Praia do Itacuruçá, Ilha do Cardoso, an Environmental Protected Area).

The importance of this study requires an accurate measurement of the whistle emissions while in an unusual foraging feeding behavior situation: near two beaches located in an important biological reserve threatened by the progressive increase of the tourism, where several tucuxis, mostly mother–calf pairs, are frequently present.

II. METHODOLOGY

A. Records and surveyed area

Recordings were made over 8 days in August 2002, 2 days in December 2002, and 4 days in March 2003. A HTI SSQ 94 hydrophone was deployed at 1-m depth and connected to a SONY TCM 5000 eV analog audio tape recorder. The system's frequency response was 40 Hz to 18 kHz (±1 dB), but tucuxis whistles with fundamental frequency components beyond 24 kHz were recorded by Azevedo and Van Sluys (2005). The data collection occurred in the Cananéia estuary (25°03′S, 47°58′W), São Paulo state, southeastern Brazil (Fig. 1), close to two beaches 1.2 km apart, Ponta da Trincheira, located in Ilha Comprida and Praia do Itacuruçá, located in Ilha do Cardoso. These two beaches are located in an important biological reserve, which gathers federal and state environment Environmental Protected Areas (SMA, 1996). This estuary is located inside a 160-km area with relatively turbid waters surrounded by a large mangrove area (Schaeffer-Novelli *et al.*, 1990). Only *Sotalia fluviatilis* odontocete species occurs in the Cananéia estuary. This estuary is a calving area where calves are com-

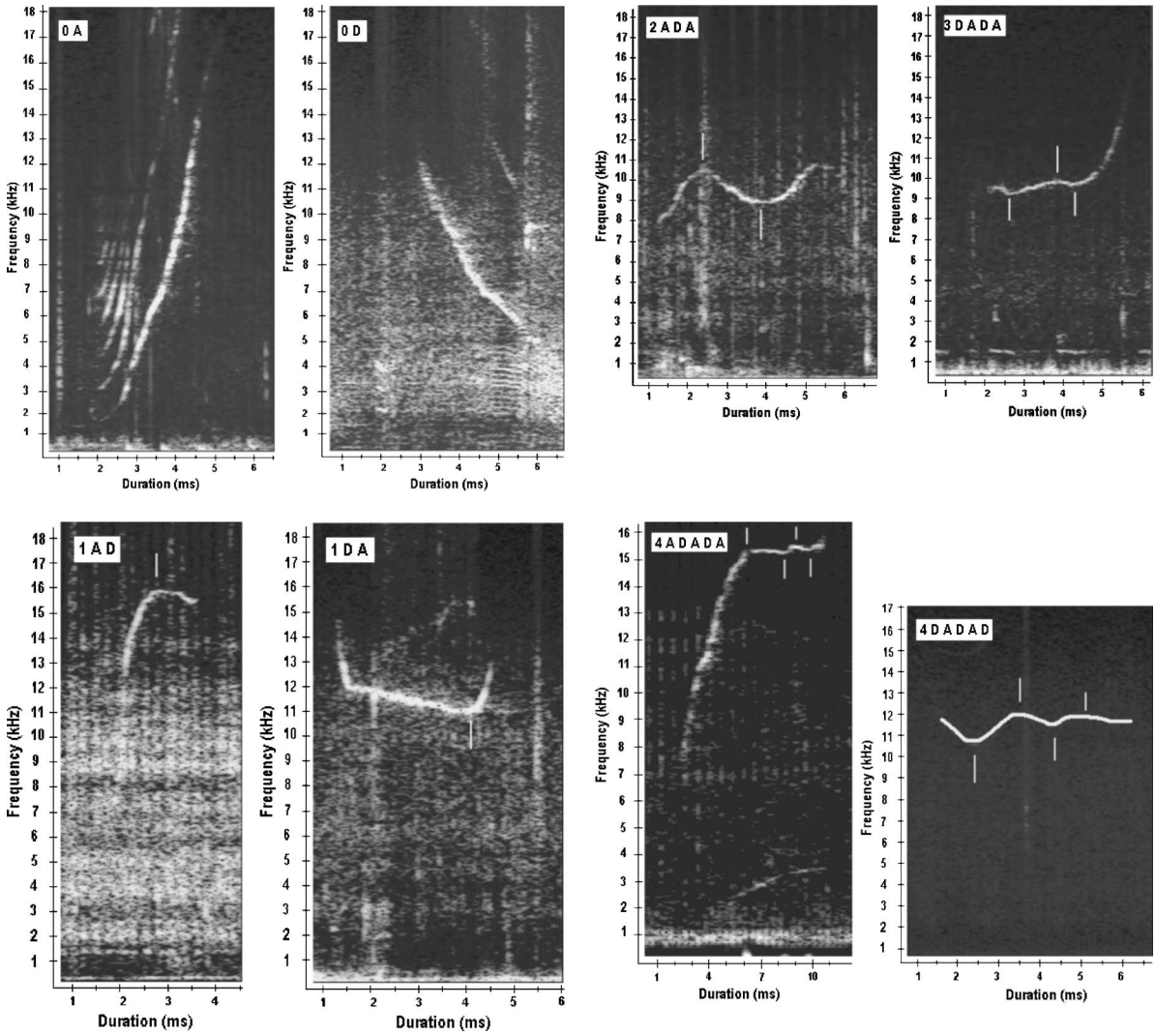

FIG. 2. Spectrogram representation of the five whistle contour types (0, 1, 2, 3, and 4) and their variants (A, D, AD, DA, ADA, DADA, ADADA, DADAD) emitted by marine tucuxi dolphins (*Sotalia fluviatilis*) from Cananéia estuary, São Paulo, Brazil. (0=no inflection point: A=ascendant; D=descendant); (1 =one inflection point: AD=ascendant–descendant; DA=descendant–ascendant); (2=two inflection points: ADA=ascendant–descendant–ascendant; DADA =descendant–ascendant–descendant–ascendant); (3=three inflection points: ADADA=ascendant–descendant–ascendant–descendant–ascendant); and (4 =four inflection points: DADAD=descendant–ascendant–descendant–ascendant–descendant).

monly observed throughout the entire year (Santos *et al.*, 2000; 2001). Thus, only tucuxi whistles were analyzed. Recordings were made from an aluminum boat with the engine off and during good weather conditions (Beaufort scale $\leqslant$2).

B. Acoustic analyses

The acoustic recordings were digitized and spectrograms were generated using COOL EDIT PRO 1.2© software (*Syntrillium Software Corporation*; sampling at 44.1 kHz, 16 bits, FFT size: 512, triangular window). Over 3000 whistles were recorded (n=3235). Whistles were separated into two different quality categories based upon their spectrogram quality: good and poor. The poor quality category represented 43% of the total recorded whistles. The upper range of our measurements was 18 kHz, based on the frequency response of the recorder. Then, whistles exhibiting frequencies above 18 kHz (17%) were excluded because the acoustic parameters could be distorted. Only 1294 (40%) good quality whistles below 18 kHz, with all whistle parameters of a spectral contour measurable, were analyzed. Seven acoustic whistle parameters were measured from the selected whistles: duration (in milliseconds, ms), number of inflection points, start and end frequency (in kHz), minimum and maximum frequency (in kHz), and frequency range (in kHz). These whistle parameters were chosen to be consistent with previous studies conducted of other odontocetes (e.g., Rendell *et al.*, 1999) and were examined in most tucuxis bioacoustic studies (e.g., Azevedo and Simão, 2002; Podos *et al.*, 2002; Erbe and Simão, 2004, Azevedo and Van Sluys, 2005). An inflection point was defined as a change in the slope of the whistle contour from negative to positive, or vice versa (e.g., an ascendant whistle does not have an inflection point but an ascendant–descendant whistle does). The descriptive statistics for all measured parameters listed above included minimum and maximum values, mean, standard deviation, and coefficient of variation. We examined the distribution of the duration, start, end, minimum, and maximum frequencies, frequency range and duration in histograms. The depen-

TABLE I. Number of inflection points of the marine tucuxi dolphin's whistles in the Cananéia estuary ($n=1294$).

Whistle contour types	n	%
No inflection point—rising frequency	1104	85.30
No inflection point—falling frequency	24	1.80
One inflection point	119	9.20
Two inflection points	39	3
Three inflection points	3	0.20
Four inflection points	5	0.30

dent paired sample t-test (STATISTICA software, 1984–2000) was applied to verify if the end frequency of all analyzed whistles was significantly different from the start frequency. This was important to show the ascendant or descendant frequency tendency of the whistles in a specific context.

III. RESULTS

Seventeen hours of acoustic recordings were obtained while marine tucuxi engaged in foraging behavior. The recording included sounds from solitary adults, juveniles, and calves. Group sizes varied from two to ten individuals (mean=3.5±2.3). Whistles with up to four inflection points were found (Fig. 2). Whistles with no inflection points and ascendant modulation frequency corresponded to 85% ($n=1104$) of the analyzed whistles ($n=1294$) (Table I). The descriptive statistics of the measured whistle parameters is presented in Table II. The mean of the end frequency was significantly greater than the mean start frequency ($P<0.001$). The distribution of the duration values is given in Fig. 3(A). Most whistles ranged between 101 and 300 ms (70%). Values of the start frequency varied between 4 and 13.99 kHz [89%, Fig. 3(B)].

Distribution of the end frequency values showed that 84% of whistles ended with frequencies between 12 and 17.99 kHz [Fig. 3(C)]. The values of the minimum frequency were between 4 and 9.99 kHz [67%, Fig. 3(D)]. Eighty-five percent of the maximum frequency values were distributed between 12 and 17.99 kHz [Fig. 3(E)]. Approximately 80% of the frequency range values varied from 2 to 9.99 kHz [Fig. 3(F)].

IV. DISCUSSION

Our research focused on the whistles emitted by small groups of tucuxis, during an unusual foraging feeding behavior situation on two beaches where several tucuxis, mostly mother–calf pairs, are frequently present. These two beaches are located in an important biological reserve, gathering federal and state environment Environmental Protected Areas threatened by the progressive increase of tourism. In this area, about ten photo-identified dolphins usually approach these two beaches to surround fish in shallow waters using the sand beach as a barrier to trap them (Santos, 2004). Acoustics play an important role in feeding behavior of cetaceans. Acevedo-Gutiérrez and Stienessen (2004) reported that dolphins increase their rate of whistles during feeding

TABLE II. Descriptive statistics for acoustic whistles parameters of marine tucuxi dolphins in the Cananéia estuary ($n=1294$). The duration is measured in ms and frequency variables were measured in kHz. Range=maximum minus minimum value.

Acoustics parameters	Range	Mean	Standard deviation	Coefficient of variation
Inflections	0–4	0.17	0.51	294.70
Duration	38–627	229	109.91	47.87
Start frequency	1.0–16.00	8.15	3	36.77
End frequency	2.0–17.90	14.35	3.04	21.20
Minimum frequency	1.0–15.80	7.97	2.89	36.20
Maximum frequency	2.2–17.90	14.46	2.88	19.91
Frequency range	0–16.30	6.48	3.13	48.29

events to recruit new individuals. In the surveyed beaches in the Cananéia estuary, the high number of whistles recorded in feeding behavior was probably related to communication between mothers and calves, in an estuarine system with muddy bottom and relatively turbid waters with high concentrations of nutrients (Schaeffer-Novelli *et al.*, 1990). Delphinids produce different sounds in different behavioral contexts (Herzing, 1996; McCowan and Reiss, 1995). It is unknown if these small groups of tucuxis that usually approach Ponta da Trincheira and Praia do Itacuruçá produce specific feeding whistles. Recordings and comparisons between whistles among all behavior categories and between other tucuxis groups feeding in different areas of the estuary are necessary.

About 17% of all recorded whistles ($n=3235$) were excluded from the analysis because they were above the upper frequency limit of the recording system. Tucuxis can probably reach frequencies higher than 24 kHz. Azevedo and Van Sluys (2005) recorded frequencies up to 24 kHz for the marine ecotype. For the freshwater ones the maximum fundamental frequency was 23.86 kHz (Wang *et al.*, 2001). A broader band system may be useful in future tucuxi whistle studies.

Marine tucuxis in the Cananéia estuary emitted highly varied whistles, mainly in the number of inflection points and duration parameters (Table II), showing a high variability in these whistle acoustic parameters, as reported by Azevedo and Simão (2002) for the marine tucuxi in Guanabara Bay, and by Wang *et al.* (2001) and Podos *et al.* (2002) for the freshwater ecotype in the Amazon basin. This study reported more whistles with no inflection points and thus ascendant frequencies (Table I), like some authors reported for the marine ecotype (Azevedo and Simão, 2002 in Guanabara Bay, Erber and Simão, 2004 in Sepetiba Bay, and Azevedo and Van Sluys, 2005 along the tucuxi distribution in Brazil) and for the freshwater tucuxi in the Amazon basin (Norris *et al.*, 1972; Wang *et al.*, 2001; and Podos *et al.*, 2002). Monteiro-Filho and Monteiro (2001) reported more variable frequency whistles (57%) than ascendant frequency whistles (43%) for the marine ecotype in Cananéia estuary. This frequency pattern may be related to the short duration of the whistles analyzed (<1 second) (Azevedo and Simão, 2002).

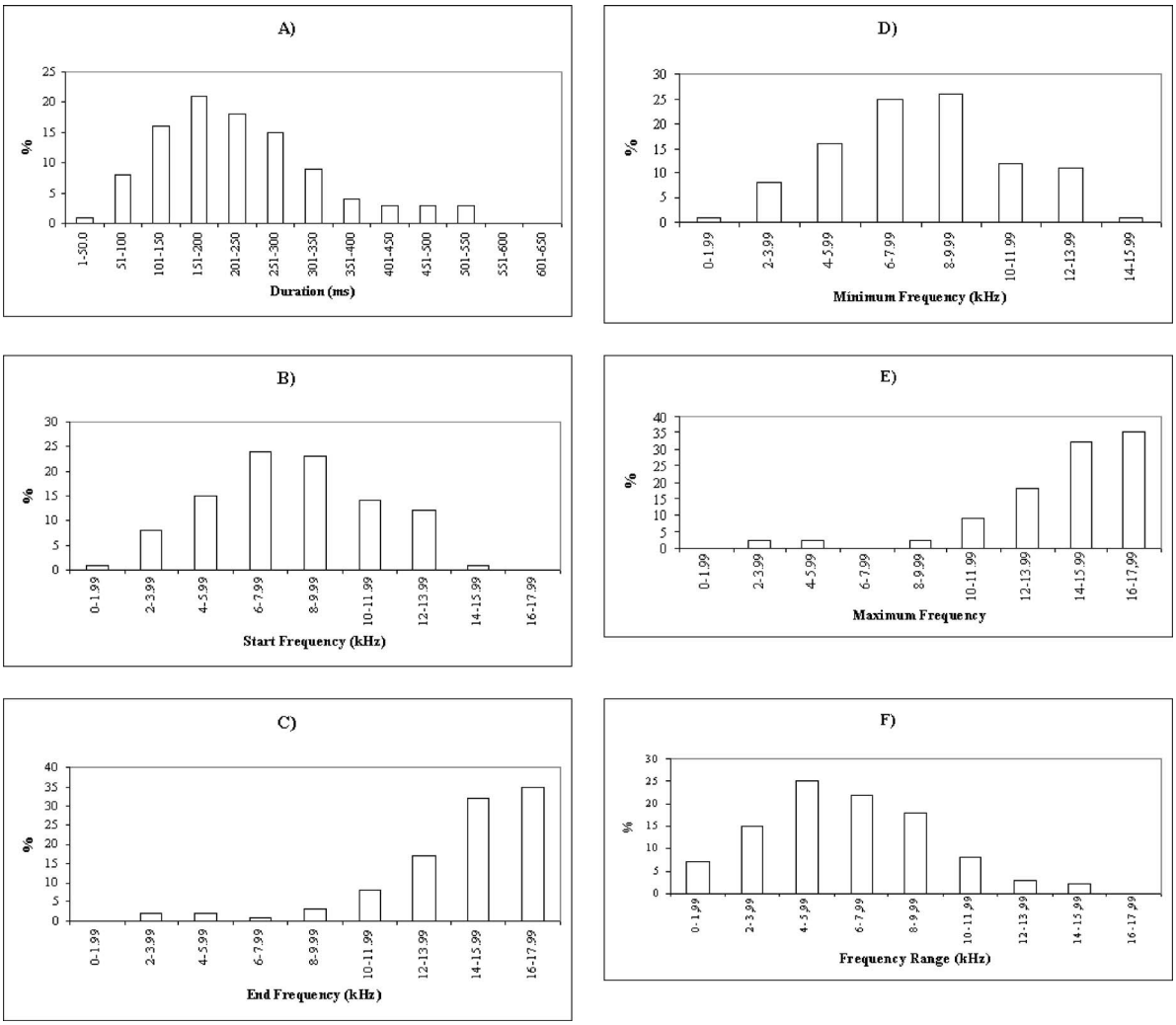

FIG. 3. Histograms of five acoustic parameters measured from marine tucuxi dolphin whistles ($n=1294$) from Cananéia estuary. (A) duration; (B) start frequency; (C) end frequency; (D) minimum frequency; (E) maximum frequency; and (F) frequency range.

Spinner dolphins, *Stenella longirostris* (Steiner, 1981; Norris *et al.*, 1994; Bazúa-Durán and Au, 2002; Bazúa-Durán, 2004) also reported high rates of whistles with no inflection points. Bazúa-Durán and Au (2002) suggested, based on the relationship between start and end frequencies, that *S. fluviatilis, Delphinus delphis, Stenella attenuata, Stenella clymene, S. longirostris*, and *Lagenorhynchus albirostris* share some characteristics of their whistles.

Analysis of acoustic whistle variables of the 1294 whistles recorded from marine tucuxis in the Cananéia estuary (Table II) showed a mean duration similar to that reported for the same ecotype in the same area by Monteiro-Filho and Monteiro (2001), with mean duration whistles about 210 ms ($n=94$). In a study from eight locations along the *S. fluviatilis* distribution in Brazil, Azevedo and Van Sluys (2005) described values of mean duration comparative higher, 308 ms. Erber and Simão (2004) found highest duration mean values in Sepetiba Bay (789 ms; $n=5086$). For the riverine ecotype, Norris *et al.* (1972) reported a similar mean duration (200 ms) (n was not provided) in the Amazon basin. Wang *et al.* (2001) reported a mean duration of 114 ms for 76 whistles with low frequencies and 410 ms mean duration for 155 whistles with high frequencies. Podos *et al.* (2002) found 630-ms mean duration ($n=50$). Differences in the recording and analysis of whistles can result in significant differences in the described repertoire of the two ecotypes. Differences in habitat, ecology, and contextual behavior of the two ecotypes may also influence the whistle parameters. Populations of dolphins in isolated areas may be isolated geographically from the influence of other acoustic characteristics (Wang *et al.*, 1995). Steiner (1981) reported that there are some characteristics that are unique for each population. Species like Irrawaddy dolphins, *Orcaella brevirostris* (van Parijs *et al.*, 2000) and Pacific humpback dolphins, *Sousa chinensis* (van Parijs and Corkeron, 2001) showed similar whistle mean duration as found in this study.

Whistle frequency parameters exhibited lower values coefficients of variation. The variation of whistle frequencies observed in our research was similar to the variation reported by Azevedo and Simão (2002) (0.5–18 kHz) in Guanabara Bay for the marine ecotype, but very different to the frequency values between 2.8 and 6 kHz that Monteiro-Filho and Monteiro (2001) reported. Azevedo and Van Sluys (2005) reported whistles with a frequency range that varied between 0.21 and 22.20 kHz. For riverine tucuxi whistles from the Amazon basin, whistle frequencies ranged from

10 to 15 kHz (Norris *et al.*, 1972), from 6 to 16 kHz (Nakasai and Takemura, 1975), from 0.22 to 23.86 (Wang *et al.*, 2001) and from 9.18 to 15.65 kHz (Podos *et al.*, 2002). Low (Monteiro-Filho and Monteiro, 2001) and high (Azevedo and Van Sluys, 2005) values of whistle frequency range may be explained by different recording systems' frequency response. Thus, it can be inferred that *Sotalia* can emit whistles with frequencies upper than 24 kHz, as Azevedo and Van Sluys (2005) described.

Frequency and duration measurements are useful for describing dolphin whistles and comparing across different dolphin populations (Bazúa-Durán and Au, 2002). Azevedo and Van Sluys (2005) concluded significant differences in whistle acoustic parameters were found in different tucuxi population from northern and southern Brazil but not between adjacent regions within each major area. Each population is likely affected by different evolutionary and environmental influences (Conner, 1982).

V. CONCLUSIONS

Small groups of marine tucuxis in two beaches in the Cananéia estuary during feeding behavior produce high rates of whistles. Inflection points and duration parameters showed the highest variation, and frequency parameters exhibited the lowest variation across whistles. Whistles with no inflection point and ascendant frequencies were the most frequently produced.

ACKNOWLEDGMENTS

We thank the anonymous referees for providing constructive comments on this manuscript. Renata Souza-Lima, Denise Herzing, Alexandre Azevedo, Sofie van Parijs, Brenda McCowan, and Marcos César de Oliveira Santos made useful comments on this paper in earlier drafts. Tom Burstow provided an excellent review of the English version. Financial support was provided by the Reitoria de Pós-Graduação of Universidade de São Paulo, Cetacean Society International (CSI) and Rayovac. Daniela Pivari has been supported by Conselho Nacional de Desenvolvimento Científico e Tecnológico (CNPq).

Acevedo-Gutiérrez, A., and Stienessen, S. C. (**2004**). "Bottlenose dolphins (*Tursiops truncatus*) increase number of whistles when feeding," Aquat. Mamm. **30**, 357–362.

Alcuri, G., and Busnell, R. G. (**1989**). "Unicité functionelle des clics sonar et des sifflement dans les emissions acoustiques d'un Dauphin Amazonien *S. fluviatilis* Gervais et Deville," C. R. Acad. Sci. Paris. **308**, 379–384.

Azevedo, F. A., and Simão, S. M. (**2002**). "Whistles produced by marine tucuxi dolphins (*Sotalia fluviatilis*) in Guanabara Bay, southeastern Brazil," Aquat. Mamm. **28**, 261–266.

Azevedo, A. F., and Van Sluys, M. (**2005**). "Whistles of tucuxi dolphins (*Sotalia fluviatilis*) in Brazil: Comparisons among populations," J. Acoust. Soc. Am. **117**, 1456–1464.

Azevedo, A. F., Viana, S. C., Oliveira, A. M., and Van Sluys, M. (**2005**). "Group characteristics of marine tucuxis (*Sotalia fluviatilis*) (Cetacea: Delphinidae) in Guanabara Bay, south-eastern Brazil," J. Mar. Biol. Assoc. U.K. **85**, 209–212.

Baptista, L. F., and Gaunt, S. L. L. (**1997**). "Bioacoustics as a tool in conservation studies," in *Behavioral Approaches to Conservation in the Wild*, edited by J. R. Clemmons and R. Buchholtz (Cambridge University Press, Cambridge), pp. 212–242.

Bazuá-Durán, C. (**2004**). "Differences in the whistle characteristics and repertoire of bottlenose and spinner dolphins," An. Acad. Bras. Cienc. **76**, 386–392.

Bazuá-Durán, C., and Au, W. W. L. (**2002**). "The whistles of Hawaiian spinner dolphins," J. Acoust. Soc. Am. **112**, 3064–3072.

Caballero, S., Barrios, H., Beltran, S., Montiel, M. G., Trujillo, F., and Baker, C. S. (**2003**). "We are a family… Still? Mitochondrial DNA diversity and differentiation among South American river and coastal dolphins *Sotalia sp.*," in Abstracts of the 15th Biennial Conference of the Biology of Marine Mammals, 13–19 December, 2003, Greensboro, North Carolina, p. 27.

Caldwell, M. C., and Caldwell, D. K. (**1970**). "Echolocation-types signals by two dolphins, Genus *Sotalia*," Quart. J. Florida Acad. Sci. **33**, 124–131.

Caldwell, M. C., Caldwell, D. K., and Tyack, P. L. (**1990**). "Review of the signature-whistle hypothesis for the Atlantic bottlenose dolphin," in *Bottlenose Dolphin*, edited by S. Leatherwood and R. R. Reeves (Academic, San Diego), pp. 199–234.

Conner, D. A. (**1982**). "Dialects versus geographic variation in mammalian vocalizations," Anim. Behav. **30**, 297–298.

da Silva, V. M. F., and Best, R. C. (**1996**). "*Sotalia fluviatilis*," Mamm. Species **527**, 1–7.

Erber, C., and Simão, S. M. (**2004**). "Analysis of whistles produced by the tucuxi dolphin *Sotalia fluviatilis* from Sepetiba Bay, Brazil," An. Acad. Bras. Cienc. **76**, 381–385.

Figueiredo, L. D. (**1997**). "Análise quantitativa e qualitativa dos assobios de freqüência ascendente do boto, *Sotalia fluviatilis* Gervais, 1853 (Cetacea, Delphinidae) na Baía de Sepetiba, RJ," unpublished B.S. thesis, Universidade Federal Rural do Rio de Janeiro, Brazil.

Flores, P. A. C. (**1999**). "Preliminary results of a photoidentification study of the marine tucuxi *Sotalia fluviatilis* in southern Brazil," Marine Mammal Sci. **15**, 840–847.

Flores, P. A. C. (**2003**). "Ecology of the marine tucuxi (*Sotalia fluviatilis*) in southern Brazil," unpublished Ph.D. thesis, Pontifícia Universidade Católica do Rio Grande do Sul, Porto Alegre, Brazil.

Herman, L. M., and Tavolga, W. N. (**1980**). "The communication systems of cetacean," in *Cetacean Behavior: Mechanisms and Functions*, edited by L. M. Herman (Wiley Interscience, New York), pp. 149–209.

Herzing, D. L. (**1996**). "Vocalizations and associated underwater behavior of free-ranging Atlantic spotted dolphins, *Stenella frontalis* and bottlenose dolphins, *Tursiops truncatus*," Aquat. Mamm. **22**, 61–79.

Kamminga, C., van Hove, M. T., Engelsma, F. J., and Terry, R. P. (**1993**). "Investigation on cetacean sonar x: A comparative analysis of underwater echolocation clicks of *Innia sp.* and *Sotalia sp.*," Aquat. Mamm. **19**, 31–43.

McCowan, B. A., and Reiss, D. (**1995**). "Quantitative comparison of whistle repertoires from captive adult bottlenose dolphin (Delphinidae, *Tursiops truncatus*): A re-evaluation of the signature whistles hypothesis," Ethnology **100**, 194–209.

Monteiro-Filho, E. L. A., and Monteiro, K. D. K. A. (**2001**). "Low-frequency sounds emitted by *Sotalia fluviatilis guianensis* (Cetacea, Delphinidae) in an estuarine region in southeastern Brazil," Can. J. Zool. **79**, 59–66.

Monteiro-Filho, E. L. A., Monteiro, L. R., and dos Reis, S. F. (**2002**). "Skull shape and size divergence in dolphins of the genus *Sotalia*: A tridimensional morphometric analysis," J. Morphol. **83**, 125–134.

Nakasai, K., and Takemura, A. (**1975**). "Studies on the underwater sound. VI. On the underwater calls of fresh dolphins in South America," Bull. Fac. Fish. Nagasaki Univ. **40**, 7–13.

Norris, K. S., Harvey, G. W., Burzell, L. A., and Kartha, T. D. K. (**1972**). "Sound production in the freshwater porpoises *Sotalia fluviatilis* and *Inia geoffrensis*, in the Rio Negro, Brazil," Invest. Cetacea **4**, 251–260.

Norris, K. S., Wursig, B., Wells, R. S., and Wursig, M. (**1994**). *The Hawaiian Spinner Dolphin* (University of California Press, Berkeley, CA).

Pereira, T. C. C. L. (**1997**). "Análise quantitativa e qualitativa dos assobios de freqüência descendente, de freqüência up-down e de freqüência down-up do boto *Sotalia fluviatilis* Gervais, 1853 (Cetacea, Delphinidae) na Baía de Sepetiba, R. J.," unpublished B.S. thesis, Universidade Federal Rural do Rio de Janeiro, Brazil.

Podos, J., da Silva, V. M. F., and Rossi-Santos, M. R. (**2002**). "Vocalizations of Amazon River dolphins, *Inia geoffrensis*: Insights into the evolutionary origins of delphinid whistles," Ethnology **108**, 601–612.

Popper, A. N. (**1980**). "Sound emission and detection by delphinids," in *Cetacean Behavior: Mechanisms and Functions*, edited by L. M. Herman (Wiley Interscience, New York), pp. 1–52.

Reeves, R. R., Smith, B. D., Crespo, E. A., and di Sciara, G. N. (**2003**).

"Dolphins, whales and porpoises: 2001–2010 Conservation action plan for the world's cetaceans," in IUCN/SSC. Cetacean Specialist Group. IUCN (Gland, Switzerland and Cambridge, UK).
Rendell, L. E., Matthews, J. N., Gill, A., Gordon, J. C. D., and MacDonald, D. W., (**1999**). "Quantitative analysis of tonal calls from five odontocete species, examining interspecific and intraspecific variation," Acta Med. Austriaca Suppl. **249**, 403–410.
Santos, M. C. O. (**2004**). "Uso de área e organização social do boto-tucuxi marinho, *Sotalia fluviatilis* (Cetácea, Delphinidae), no estuário de Cananéia, SP," unpublished Ph.D. thesis, Univeridade de São Paulo, São Paulo, Brazil.
Santos, M. C. de O., Acuña, L. B., and Rosso, S. (**2001**). "Insights on site fidelity and calving intervals of the marine tucuxi dolphin (*Sotalia fluviatilis*) in south-eastern Brazil," J. Mar. Biol. Assoc. U.K. **81**, 1–4.
Santos, M. C. de O., Rosso, S., Siciliano, S., Zerbini, A., Zampirolli, E., Vicente, A., and Alvarenga, F. (**2000**). "Behavioral observations of the marine tucuxi dolphin (*Sotalia fluviatilis*) in São Paulo estuarine waters, Southeastern Brazil," Aquat. Mamm. **26**, 260–267.
Sauerland, M., and Dehnhardt, G. (**1998**). "Underwater audiogram of a tucuxi (*Sotalia fluviatilis guianensis*)," J. Acoust. Soc. Am. **103**, 1199–1204.
Sayigh, L. S., Tyack, P. T., Wells, R. S., and Scott, M. D. (**1990**). "Signature whistles of free-ranging bottlenose dolphins *Tursiops truncatus*: Stability and mother–offspring comparisons," Behav. Ecol. Sociobiol. **26**, 247–260.
Sayigh, L. S., Tyack, P. T., Wells, R. S., and Scott, M. D. (**1995**). "Sex difference in signature whistle production of free-ranging bottlenose dolphins *Tursiops truncatus*," Behav. Ecol. Sociobiol. **36**, 171–177.
Schaeffer-Novelli, Y., Mesquita, H. S. L., and Cintrón-Molero, G. (**1990**). "The Cananéia lagoon estuary system, São Paulo, Brazil," Estuaries **13**, 193–203.
SMA (**1996**). "Regulamentação da APA de Cananéia—Iguape—Peruíbe: Plano de gestão," Secretaria de do Meio Ambiente do Estado de São Paulo & Instituto Brasileiro do Meio Ambiente e dos Recursos Naturais Renováveis, São Paulo, Brazil.
Smolker, R. A., Mann, J., and Smuts, B. B. (**1993**). "Use of signature whistles during separations and reunions by wild bottlenose dolphins mothers and infants," Behav. Ecol. Sociobiol. **33**, 393–402.
Steiner, W. (**1981**). "Species-specific differences in pure tonal whistle vocalizations of five western north Atlantic dolphin species," Behav. Ecol. Sociobiol. **9**, 241–246.
Terry, P. H. (**1983**). "Observations on the captive behavior of *Sotalia fluviatilis guianensis*," Aquat. Mamm. **10**, 95–105.
van Parijs, S. M., and Corkeron, P. J. (**2001**). "Vocalizations and behavior of Pacific humpback dolphins, *Sousa chinensis*," Ethnology **107**, 701–716.
van Parijs, S. M., Parra, G. J., and Corkeron, P. J. (**2000**). "Sounds emitted by Australian Irrawaddy dolphins, *Orcaella brevirostris*," J. Acoust. Soc. Am. **108**, 1938–1940.
Wang, D., Würsig, B., and Evans, W. E. (**1995**). "Whistles of bottlenose dolphins: Comparisons among populations," Aquat. Mamm. **21**, 65–77.
Wang, D., Würsig, B., and Leatherwood, S. (**2001**). "Whistles of boto, *Inia geoffrensis*, and tucuxi, *Sotalia fluviatilis*," J. Acoust. Soc. Am. **109**, 407–411.
Wiersmsa, H. (**1982**). "Investigations on sonar. IV. A comparison of wave shapes of odontocete sonar signals," Aquat. Mamm. **9**, 57–66.

Erratum: "Numerical simulation of shock wave focusing at fold caustics, with application to sonic boom" [J. Acoust. Soc. Am. 114(4), Pt. 1, 1758–1771 (2003)]

Régis Marchiano and François Coulouvrat
Laboratoire de Modélisation en Mécanique, UMR CNRS 7607, Université Pierre et Marie Curie, 8 rue du Capitaine Scott, 75015 Paris, France

Richard Grenon
Département d'Aérodynamique Appliquée, DAAP/ACI, ONERA, 29 avenue de la division Leclerc, BP 72, 92322 Châtillon Cedex, France

(Received 5 July 2005; accepted 10 July 2005)

[DOI: 10.1121/1.2011153]

PACS number(s): 43.25.Cb, 43.25.Jh, 43.10.Vx [MFH]

The acknowledgments section of this article states: "No part of this manuscript may be used, reproduced and/or disclosed in any form or by any means without the prior written permission of Université Pierre et Marie Curie and the SOBER project partners. 16/11/2001 All rights reserved." This statement was included in error and should be removed. The copyright of this article belongs to the Acoustical Society of America.

 0001-4966/2005/118(4)/2732/1/$22.50

Erratum: "Nonlinear focusing of acoustic shock waves at a caustic cusp" [J. Acoust. Soc. Am. 117(2), 566–577 (2005)]

Régis Marchiano and François Coulouvrat
Laboratoire de Modélisation en Mécanique,Université Pierre et Marie Curie and CNRS (UMR 7607), 4 place Jussieu, 75252 Paris cedex 05, France

Jean-Louis Thomas
Laboratoire des Milieux Désordonnés et Hétérogènes, Université Pierre et Marie Curie and CNRS (UMR 7603), 4 place Jussieu, 75252 Paris cedex 05, France

(Received 5 July 2005; accepted 10 July 2005)

[DOI: 10.1121/1.2011154]

PACS number(s): 43.25.Cb, 43.25.Hg, 43.28.Mw, 43.10.Vx [MFH]

The acknowledgments section of this article states: "No part of this manuscript may be used, reproduced and/or disclosed in any form or by any means without the prior written permission of Université Pierre et Marie Curie and the SOBER project partners. 16/11/2001 All rights reserved." This statement was included in error and should be removed. The copyright of this article belongs to the Acoustical Society of America.